# Formation of Manganese(II) Ion in the Discharge of the Manganese Dioxide Electrode

## II. Effect of Volume and pH of Electrolyte

**W. C. Vosburgh, Mary Jo Pribble, Akiya Kozawa, and Ahmad Sam**

*Department of Chemistry, Duke University, Durham, North Carolina*

ABSTRACT

Discharge of the $MnO_2$ electrode at pH 5 to 8 is known to give $Mn^{++}$ in solution as well as a lower oxide. When the volume of electrolyte is varied the amount of $Mn^{++}$ formed in constant time and at constant current density is practically independent of volume. It decreases as the pH increases, becoming small at pH 8. The reaction of lower Mn oxides with electrolytes shows a similar relation to volume and pH. In the early part of a discharge the electrode surface resembles MnOOH in its reaction with the electrolyte. Later, at high pH, the surface seems to be at a lower state of oxidation than $Mn_3O_4$.

Under certain conditions $Mn^{++}$ in the electrolyte is a product of the discharge of the $MnO_2$ electrode (1,2). In a sufficiently acid electrolyte of relatively large volume it is the only product (3), but at pH 5 and pH 7.5 a lower oxide is left on the electrode in addition to $Mn^{++}$ in solution.

In all of these experiments the ratio of electrolyte volume to the amount of $MnO_2$ was large and much different from that in the Leclanche dry cell. One object of the present investigation was to find the relation of the amount of $Mn^{++}$ formed in a discharge to the volume of the electrolyte. A second object was a further investigation of the relation to pH. The results have added to the understanding of the electrode mechanism.

### Experimental

*Procedure*

Electrodes were prepared by electrodeposition of $MnO_2$ on graphite rods from an electrolyte of 50 g/l of $MnSO_4$ and 65 g/l of $H_2SO_4$ at 90°C (except as otherwise noted) with a current of 25 ma for 30 min, the electrode area being 8 $cm^2$. The total Mn was about 0.2 mmole/electrode. They were discharged with a current of 2 ma in electrolytes of varying volume and composition, the apparatus and procedure being essentially as described previously (4). With $(NH_4)_2SO_4$ electrolytes a well cleaned lead anode was used. With $NH_4Cl$ electrolytes the anode was either a silver electrode well covered with AgCl (5) or several graphite rods placed around the central $MnO_2$ electrode.

Most of the discharges were terminated after either 100 or 150 min. Some were carried to completion for the study of the last part of the discharge.

At the termination of a discharge the cathode was removed from the cell either immediately or after 35 min on open circuit and the $Mn^{++}$ concentration of the solution determined colorimetrically. When graphite anodes were used the solution contained little $Mn^{++}$, but most of what had been dissolved from the cathode during the discharge was found in oxidized form on the anode rods. This was dissolved by $H_2SO_4$ and $H_2O_2$ and determined colorimetrically.

*Relation of $Mn^{++}$ in the electrolyte to the volume.* —Table I shows the results of a number of experiments with electrolytes of 1M $(NH_4)_2SO_4$ buffered at pH 5.2 by 0.2M pyridine and 0.07M $H_2SO_4$. Discharges were terminated after 150 min, during which no appreciable change in pH took place. Electrolyte volumes of 33-825 ml were used and a number of discharges made in each. The variation among experiments under the same conditions was large, as shown by the standard deviations. It is nevertheless clear that the total amount of Mn(II) ion produced is independent of the volume, within the limits of these experiments, whereas the concentration clearly varies with the volume.

Table I. Mn(II) ion in the electrolyte after discharge for 150 min at 2 ma in electrolytes of different volumes; pH 5.2

| Vol, ml | No. discharges | $Mn^{++}$ in electrolyte: Conc, M x $10^4$ | $Mn^{++}$ in electrolyte: Total, mmoles x $10^2$ |
|---|---|---|---|
| 33 | 3 | 24 ± 1.2 | 7.9 ± 0.37 |
| 110 | 5 | 5.7 ± 1.0 | 6.3 ± 1.3 |
| 190 | 7 | 3.0 ± 0.7 | 5.6 ± 1.7 |
| 240 | 6 | 1.9 ± 0.5 | 4.5 ± 1.2 |
| 825 | 4 | 0.8 ± 0.08 | 6.2 ± 0.8 |

Table II. Mn(II) ion in the electrolyte after discharge for 150 min at 2 ma in electrolytes of different volumes; pH 7.5

| Vol, ml | No. discharges | Charge of pH | Total $Mn^{++}$ mmoles x $10^2$ |
|---|---|---|---|
| 33 | 1 | 7.5-8.1 | 2.0 |
| 110 | 1 | 7.5-7.7 | 1.6 |
| 240 | 2 | 7.5-7.9 | 1.7 |
| 825 | 2 | 7.5-7.6 | 2.6 |

Table II shows that the same relationship holds at pH 7.5. The experiments were the same as before except that the 1M $(NH_4)_2SO_4$ electrolyte was buffered with $NH_3$. A small increase in pH took place during the discharge, as shown in Table II. At pH 5.2 the average total $Mn^{++}$ was 0.061 mmole, with a standard deviation of 0.011, while at pH 7.5 the average total $Mn^{++}$ was 0.020 mmole, with a standard deviation of 0.005. A decrease with increasing pH is expected since it has been shown previously that very little $Mn^{++}$ is formed in the first 100 ma-min of discharge at pH 7 while its formation starts at or near the beginning at pH 5 (2).

A few additional experiments at pH 5.2 were made with electrodes prepared at 80°C instead of 90°C and volumes of 110 and 240 ml. The results were not significantly different from those of Table II. The temperature of plating the electrodes has an effect on the overpotential (4), but too little to detect on the formation of $Mn^{++}$.

*Relation to pH.*—The results of experiments undertaken to find in more detail the relation between $Mn^{++}$ dissolved and pH are shown in Fig. 1. The circles represent discharges in about 240 ml of solution of 2M $NH_4Cl$ and $NH_3$ with graphite anodes. Discharges lasted 100 min at 2 ma and the cathode remained in the electrolyte after discharge for 35 min on open circuit during which time a small further increase in the $Mn^{++}$ content of the solution took place. The values given are the sums of the Mn in the solution and that dissolved from the anodes. The line shows the general trend of these experiments, but has no theoretical significance.

The squares in Fig. 1 represent discharges in 240 ml of 2M $NH_4Cl$ and either $NH_3$ or pyridine with Ag anodes. An atmosphere of nitrogen was maintained. The greater scattering of the points was probably the result of making the electrodes at different times rather than as a group. The electrodes for the more concordant experiments represented by the circles were all made on the same day and washed and stored in the same way and for about the same time before use. The nature of the $MnO_2$ is probably the uncontrolled variable leading to the scattering. However, it is clear that the $Mn^{++}$ dissolved decreases with increase in pH and becomes very small above pH 8; two experiments above this pH with negligible dissolved $Mn^{++}$ are not shown.

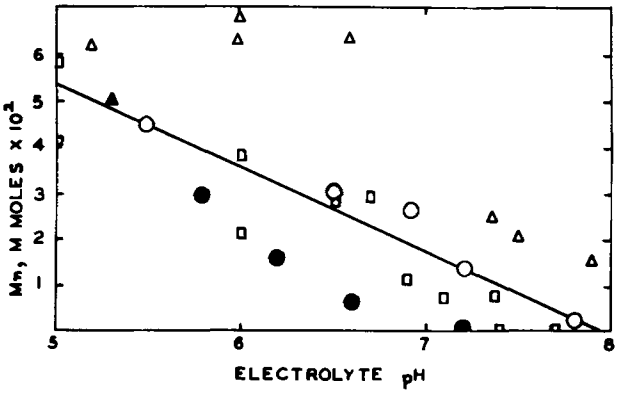


Fig. 1. The relation of the total $Mn^{++}$ dissolved from a discharging electrode to the pH of the electrolyte. Open circle and solid circle represent discharges in 2M $NH_4Cl$ and $NH_3$ without and with 0.1M $ZnSO_4$, respectively (by A. Kozawa). Open square represents discharges in 2M $NH_4Cl$ and $NH_3$ or pyridine, and open triangle and solid triangle represent discharges in 1M $(NH_4)_2SO_4$ and $NH_3$ or pyridine for 300 instead of 200 ma-min, without and with 0.1M $ZnSO_4$ (by M. J. Pribble).

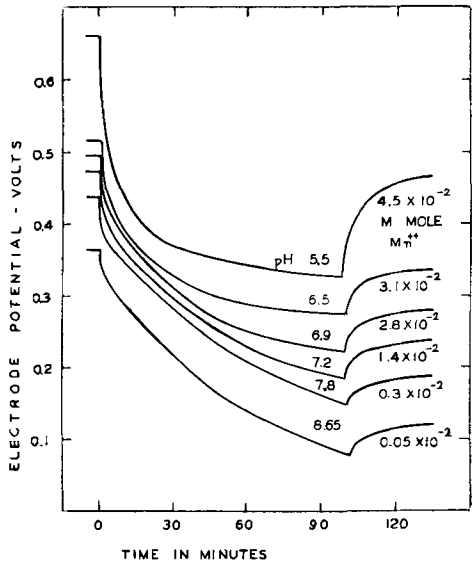


Fig. 2. Discharge curves in 2M $NH_4Cl$ with different pH values and with different amounts of $Mn^{++}$ produced.

The triangles in Fig. 1 represent similar experiments in 1M $(NH_4)_2SO_4$ electrolyte and an atmosphere of nitrogen, with discharges lasting 150 min. In the longer time somewhat more $Mn^{++}$ was dissolved. The solid circles represent experiments like those of the open circles, but with 0.1M $ZnSO_4$ in the electrolyte. The single solid triangle likewise stands for the conditions of the open triangles, but with 0.1M $ZnSO_4$. Two experiments with $ZnSO_4$ like the latter but at pH 7.2 gave no measurable $Mn^{++}$, in good agreement with the solid circle shown at that pH. The presence of $Zn^{++}$ reduces the amount of $Mn^{++}$ formed.

The larger amounts of $Mn^{++}$ are considerable fractions of the total Mn on the electrode. In some of the discharges over a third of the Mn reduced was found in solution. If all of the reduced Mn after initial drop in potential should go into solution and not change the $Mn^{++}$ concentration appreciably, a flat portion of the discharge curve would be expected, as in acid discharges (3). When all of the reduced Mn remains on the electrode, the closed-circuit potential should decrease throughout the discharge. Figure 2 shows that discharge curves at different pH values vary in shape in the expected manner. These discharges are the ones from which the data for the open circles of Fig. 1 were obtained.

*$Mn^{++}$ near the end of the discharge.*— In explaining why $Mn^{++}$ is not formed appreciably in the early part of a discharge at pH 7, it was pointed out previously (2) that MnOOH is not dissolved appreciably in a short time by 2M $NH_4Cl$ and $NH_3$ at pH 7 while $Mn_3O_4$ is dissolved. As a discharge proceeds the closed-circuit electrode potential decreases continuously (Fig. 2) indicating a lower and lower state of oxidation of the electrode surface (2,6). At pH 8 little $Mn^{++}$ is formed in the first 200 ma-min, and it was of interest to see whether more would

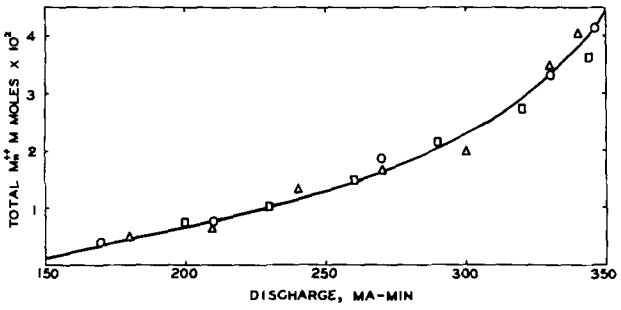


Fig. 3. $Mn^{++}$ formed in the latter part of a discharge in 1M $(NH_4)_2SO_4$ at pH 8. The 3 symbols represent 3 different electrodes.

be formed in the later portion of the discharge, at lower potentials.

Three electrodes plated at 80°C were discharged at 2 ma to a cut-off of zero against the saturated calomel electrode in a cell containing 240 ml of 1M $(NH_4)_2SO_4$ and about 0.07M $NH_3$ with *p*H 8. Samples of the electrolyte were taken periodically after 90 min of discharge for determination of $Mn^{++}$. The results are shown in Fig. 3, in which the total $Mn^{++}$ is plotted against the amount of discharge in ma-min. It is shown that $Mn^{++}$ is formed at an increasing rate between 180 ma-min and the end of the discharge. The total $Mn^{++}$ at the end of the discharge at *p*H 8 is about equal to that after 200 ma-min at *p*H 7.5 (Table II) and is about 10% of the total Mn on the electrode.

*Reaction of* Mn *oxides with electrolytes.*—If the surface of a discharging electrode is considered to resemble a lower oxide, it is of interest to know in more detail how some of the Mn oxides react with an ammonium salt solution.

Five different oxides were prepared by oxidation of 0.1M $MnSO_4$ in a solution of 1M $NH_4Cl$ and $NH_3$ with $K_2S_2O_8$ at 70°C. The composition of the product depended primarily on the *p*H, but the amount of oxidant and the time allowed were of some importance. The reaction was slow and the rate of addition of the oxidant was unimportant. In all cases the reaction was allowed to proceed until its rate became very small. The amount of oxidant was usually about 10% less than theoretical for the formation of MnOOH. It was added slowly in 0.1M solution. Since acid is formed in the reaction, it was necessary to add $NH_3$ frequently to hold the *p*H approximately constant.

In one preparation no attempt was made to control the *p*H, which was 8 at the beginning and fell to 1.5 at the end. Analysis showed the product to be $MnO_{1.88}$. The *p*H is much more important in determining the product than the proportions of the reactants. When the *p*H was kept at 8 throughout the oxidation, the product was $Mn_3O_4$ and when kept at either 6 or 7 the product was $MnO_{1.5}$, or MnOOH. When the *p*H was kept at 8 and a 20% excess of persulfate was used (calculated for MnOOH), the composition of the product in two trials was $MnO_{1.4}$. When the theoretical amount of persulfate was used at *p*H 7 instead of a deficiency the product was $MnO_{1.6}$. Each preparation was washed repeatedly with a very dilute slightly alkaline $(NH_4)_2SO_4$ solution until the wash solution gave no test for $Mn^{++}$.

These oxides react slowly in slightly acid solutions. For example, 50-mg portions of an oxide of the composition $MnO_{1.78}$ were stirred at 25°C with 50-ml portions of $(NH_4)_2SO_4$ solution of *p*H 4.7 (buffered with pyridine and pyridinium sulfate) for different periods of time. Samples were filtered and the $Mn^{++}$ determined colorimetrically. After 3, 5, and 15 hr and 2, 3, and 7 days the $Mn^{++}$ found was 25, 28, 31, 40, 50, and 55 mg/liter. Equilibrium evidently would require considerably more than a week by this procedure.

However, in a discharge only a limited time is available for the reaction of any lower oxide on the electrode surface with the solution. Therefore, for comparison with discharge data the oxide reacting in a limited time is of more interest than equilibrium data. A 3-hr reaction period was chosen as being of the order of magnitude of the duration of the discharge experiments and long enough for a considerable amount of reaction.

Table III shows the reaction in 3 hr of the above described oxides with 8 different solutions. The solutions were 2M $(NH_4)_2SO_4$ and 0.01M $H_2SO_4$ to which was added enough pyridine to give the desired pH. For each measurement 50 mg of the oxide was stirred with 50 ml of solution for 3 hr and 25° and the $Mn^{++}$ concentration in the solution determined.

At lower *p*H values a considerable fraction of the total Mn of each of the oxides goes into solution, the maximum being about 13% of the sample by weight. At *p*H 7 the 2 highest oxides gave too little $Mn^{++}$ to measure, and the others about 0.2% of the sample. It may be concluded that the surface of a discharging electrode is something like these oxides in the early part of the discharge, since very little $Mn^{++}$ is dissolved up to 100 ma-min by an electrolyte of *p*H 7.5. Since $Mn^{++}$ is dissolved in larger quantity in the latter part of a discharge, even at *p*H 8, the electrode surface must eventually be reduced to something considerably more reactive than $Mn_3O_4$, which reacts only to a small extent at *p*H 7.

If the logarithm of the $Mn^{++}$ concentration is plotted against the *p*H for any one oxide, the points fall fairly well along a straight line. This may be compared with Fig. 1 in which the line expresses a rough relation between the *p*H and the $Mn^{++}$ concentration rather than the logarithm of the latter. This apparent disagreement is probably not real because the relationship in Fig. 1 is a more complicated one than the reaction of a definite solid

**Table III. $Mn^{++}$ dissolved in 3 hr by 2M $(NH_4)_2SO_4$ buffered with 0.01M $H_2SO_4$ and pyridine at different *p*H values from different oxides at 25°C**

| Oxide | $Mn^{++}$ dissolved, M x $10^4$ | | | | | | | |
|---|---|---|---|---|---|---|---|---|
| | pH 4.7 | 5.0 | 5.3 | 5.6 | 5.9 | 6.2 | 6.5 | 7.0 |
| $MnO_{1.83}$ | 24 | 13 | 7.6 | 5.1 | 2.2 | 1.8 | 1.2 | 0.4 |
| $MnO_{1.41}$ | 18 | 8.3 | 5.5 | 4.0 | 1.8 | 1.1 | 0.7 | 0.4 |
| $MnO_{1.50}$ | 12 | 6.3 | 4.4 | 3.1 | 1.6 | 1.3 | 0.6 | 0.3 |
| $MnO_{1.59}$ | 7.3 | 4.3 | 3.0 | 2.7 | 1.3 | 1.2 | 0.4 | — |
| $MnO_{1.88}$ | 3.8 | 2.1 | 1.1 | 0.8 | 0.6 | 0.3 | — | — |

Table IV. Effect of volume of solution on amount of MnOOH dissolved in 3 hr by buffered 2M $(NH_4)_2SO_4$, 25°C

| Volume, ml | pH | $Mn^{++}$ conc, M x $10^4$ | $Mn^{++}$ total mmoles x $10^2$ |
|---|---|---|---|
| 50 | 4.7 | 12 | 6.0 |
| 150 | 4.7 | 4.4 | 6.6 |
| 250 | 4.7 | 3.0 | 7.5 |
| 50 | 5.3 | 5.8 | 2.9 |
| 150 | 5.3 | 2.1 | 3.1 |
| 250 | 5.3 | 1.4 | 3.4 |

with electrolytes of varying pH. In a discharge the composition of the surface of the electrode changes as the discharge proceeds and the formation of appreciable $Mn^{++}$ seems to start at different stages of the discharge in different electrolytes.

The reactivity of a lower oxide resembles the reactivity of the surface of a discharging electrode in the effect of volume. Table IV shows the results of experiments on the reactivity of 50 mg portions of MnOOH with 3 different volumes of solution at pH 4.7 and 5.3, the experimental details being as described above. The total amount dissolved in 3 hr varies considerably less with volume than the concentration.

## Conclusions

The above results are in agreement with the theory of the electrode reaction that has been developed in previous papers (3,4).The decrease in closed circuit potential on discharge has been ascribed to the accumulation of lower oxide on the surface of the $MnO_2$. This is removed by reaction with the electrolyte to give $Mn^{++}$ or by diffusion into the $MnO_2$ or in both ways. The rate of removal by reaction with the electrolyte is a function of pH and of the oxygen content of the surface oxide. When the pH is too high for the surface oxide to react with the solution as fast as it is produced, its oxygen content decreases as the discharge proceeds. At the higher pH values (>6.5) the lower oxide produced in the early part of the discharge does not react appreciably with the solution. Eventually, the surface becomes reduced to such an extent that $Mn^{++}$ passes into solution. The surface then resembles in its reaction an oxide reduced considerably below MnOOH or $Mn_3O_4$. For the study of the electrode reaction leading only to lower oxide, electrodes of the type described above can be used at pH 8 with no $Mn^{++}$ formation during the larger part of the discharge.

It will be shown in a later paper that these observations do not apply to all types of $MnO_2$. They are valid for $MnO_2$ electrodeposited from an acid $MnSO_4$ bath with negligible impurities. Such $MnO_2$ can be expected to be $\gamma$-$MnO_2$ (7,8).

## Acknowledgment

This work was supported in part by the Office of Naval Research. Grateful acknowledgment is also made of a grant by the Research Council of Duke University.

Manuscript received July 15, 1957. This paper was prepared for delivery before the Buffalo Meeting, October 6-10, 1957.

Any discussion of this paper will appear in a Discussion Section to be published in the December 1958 JOURNAL.

REFERENCES

1. N. C. Cahoon, *This Journal*, **99**, 343 (1952).
2. A. M. Chreitzberg, Jr., D. R. Allenson, and W. C. Vosburgh, *ibid.*, **102**, 557 (1955).
3. S. Yoshizawa and W. C. Vosburgh, *ibid.*, **104**, 399 (1957).
4. A. M. Chreitzberg, Jr., and W. C. Vosburgh, *ibid.*, **104**, 1 (1957).
5. W. C. Vosburgh, D. R. Allenson, and Stanley Hills, *ibid.*, **103**, 91 (1956).
6. A. Kozawa and K. Sasaki, *J. Electrochem. Soc. Japan*, **22**, 569 (1954).
7. H. F. McMurdie, *Trans. Electrochem. Soc.*, **86**, 313 (1944).
8. W. F. Cole, A. D. Wadsley, and A. Walkley, *ibid.*, **92**, 133 (1947).

# Oxidation of Niobium between 375°C and 700°C

**Earl A. Gulbransen and Kenneth F. Andrew**

*Westinghouse Research Laboratories, Pittsburgh, Pennsylvania*

ABSTRACT

Niobium has been found to oxidize in a complex manner. At 400°C and lower a slow rate of reaction is observed with the kinetics following the parabolic rate law. At a weight gain of 55-70 $\mu g/cm^2$ a transition in the kinetics occurs to a nearly linear rate law. Between 550° and 625°C the oxidation rate is nearly constant as a function of temperature, while above 625°C the oxidation rate again increases with the temperature. The adherence of the oxide is poor above the transition point.

Owing to its high melting point of 2415°C, its relatively low neutron cross section, and its workability at room temperature, Nb has many potential uses as a metallurgical material. The metal is very inert at room temperature to gas and liquid phase corrosion. However, its reactivity with oxygen, hydrogen, and nitrogen at elevated temperatures is a major difficulty associated with its use as a high temperature material.

Gulbransen and Andrew (1) studied the reaction of Nb in 0.1 atmospheres of oxygen over the temperature range of 250°-375°C. For this temperature

range the parabolic rate law was found to fit the data. No evidence was found for a transition in the rate of oxidation.

Inouye (2) studied the scaling of Nb in dry and in wet air over the temperature range of 400°-1200°C. At 400°C in dry air the oxide film was initially protective. After 21 hr a sharp transition occurred in the rate of oxidation. A linear rate law was found after transition. Water vapor was found to accelerate the reaction at 400°C but not at higher temperatures.

Bridges and Fassell (3) studied the oxidation of Nb from 400° to 800°C and from 14.7 to 605 psia. pressure. A linear rate law was found. The temperature dependence of the rate of oxidation showed a reversal in sign between 550° and 650°C. In this temperature region the rate of oxidation was very sensitive to pressure.

The thermochemical properties of the niobium oxides have been studied (4,5) and a comprehensive study of the oxides of Nb has been made (6). Three oxides, $Nb_2O_5$, $NbO_2$, and NbO exist with limited regions of homogeneity. The solid oxide $Nb_2O_5$ exists in three forms designated as (L) low, (M) middle, and (H) high. The x-ray diffraction patterns of the L form were isomorphous with $Ta_2O_5$ and were stable to 900°C. Between 1000° and 1100°C the M form was found which transforms to the H form at higher temperatures.

According to Inouye (2), Zachariasen found $Nb_2O_5$ to be isomorphous with $Ta_2O_5$. The crystal structure was pseudohexagonalorthohombic. The cell dimensions were reported as $A_1 = 6.16 \pm 0.03$Å, $A_2 = 3.65 \pm 0.02$Å, and $A_3 = 3.94 \pm 0.02$Å with the metal atoms at (0,0,0) and (½,½,0). The calculated density was 4.95 g/cc. $NbO_2$ has a crystal structure similar to that of rutile with the following lattice constants: a = 4.84Å, c = 2.99Å, and c/a = 0.618. The solubility of oxygen in Nb between 800° and 1100°C has been investigated by Seybolt (7).

The purpose of this work is *(a)* to extend earlier work to the temperature range of 350°-700°C, *(b)* to study the transition in the rate of oxidation observed by Inouye (2), and *(c)* to check the negative temperature coefficient for the reaction found by Bridges and Fassell (3).

## Experimental

The vacuum microbalance method was used in this work (8). Small strips of the metal were suspended from a sensitive microbalance operating inside a vacuum system. After removal of the gases from the vacuum system, the sample was heated to temperature and oxygen gas added. The reaction of the metal with oxygen was followed semicontinuously.

To extend the range of the study, two microbalances of different sensitivities were used and three sizes of samples. The samples weighed 0.6840 g, 0.1600 g, and 0.0780 g, and had surface areas of 6.6 $cm^2$, 1.62 $cm^2$, and 0.79 $cm^2$, respectively. The specially constructed low sensitivity microbalance had a sensitivity of $0.34 \times 10^{-3}$ cm/μg and was used with the small specimens to extend the thickness range.

Weight gains of 4.5 mg could be measured on specimens of 0.0780 g with surface areas of 0.79 $cm^2$. This was equivalent to 13% of the metal reacting with oxygen.

A gas-tight mullite furnace tube was used to enclose the sample. This tube was sealed directly to the all-glass vacuum system. No metal, rubber, grease joints, or stopcocks were used. Pressures of less than $10^{-8}$ mm Hg could be achieved in the system.

To eliminate the reaction of Nb with the gases present in the vacuum system during the heat-up period, the sample and furnace tube were pumped at room temperature for several hours at $10^{-6}$ mm Hg or less. Purified oxygen gas was added after the furnace was raised around the furnace tube and after thermal equilibrium was established.

The specimens were prepared from Fansteel high purity vacuum sintered Nb sheet. The analysis of the sheet was as follows: C, 0.0162 wt %; Ta, 0.143; Fe, 0.008; Zr, 0.65; Ti, 0.013; N, 0.028; and O, 0.107. To remove surface contamination, the specimens were abraded under purified kerosene. Each oxidation was made using a new specimen. There was no indication that decarburization was a factor in the change of weight of the specimen. The experimental results were reproducible within 10%.

## Results and Discussion

*Effect of temperature 375° to 525°C.*—Figures 1 to 5 show the results of the oxidation experiments for temperatures of 375°-525°C. In these figures the weight gain in micrograms per $cm^2$ was plotted as a function of the time in minutes. The usual oxidation experiment was for 6 hr. However, in several experiments longer times were used. All experiments were made at 0.1 atmospheres pressure of oxygen.

To convert the weight gain in micrograms per $cm^2$ to thickness in Angstroms, a factor of 67.2 was used. This factor was calculated from the oxide $Nb_2O_5$, a density of 4.5, and a surface roughness ratio of unity.

Figure 1 shows the weight gain curves for the 375° and 400°C oxidation curves. After a rapid initial reaction, the rate of oxidation decreases as the oxide thickens. Table I shows a summary of the thickness data after a given time of reaction, together with the color of the oxide film and its stability to cracking on cooling. At 375°C no evidence was observed in 6 hr for a transition in the rate of oxidation.

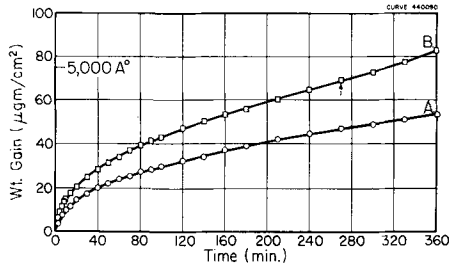


Fig. 1. Effect of temperature on oxidation of Nb abraded through 4/0, 7.6 cm Hg of $O_2$. Curve A, 375°C; curve B, 400°C.

**Table I. Thickness, color, and physical character of oxide films formed on Nb**

| Temp, °C | Time, min | Oxide thickness μg/cm² | Oxide thickness Å | Color | Character |
|---|---|---|---|---|---|
| 375 | 360 | 53.8 | 3620 | Blue-green | Stable |
| 400 | 360 | 83.5 | 5610 | Dark gray | Stable |
| 425 | 330 | 591 | 39,800 | Dark gray | Stable |
| 450 | 360 | 2780 | 187,000 | Light gray | Stable |
| 475 | 190 | 2880 | 193,500 | Light gray | Stable |
| 500 | 120 | 1818 | 122,100 | Light and dark gray | Spalled |
| 525 | 100 | 1308 | 87,900 | Dark gray + small amt. light gray | Spalled |
| 550 | 120 | 3190 | 214,500 | Light and dark gray | Spalled |
| 575 | 120 | 3610 | 236,000 | Light and dark gray | Spalled |
| 600 | 120 | 3270 | 220,000 | Dark gray + small amt. light gray | Spalled |
| 625 | 120 | 3350 | 225,500 | Dark gray + small amt. light gray | Spalled |
| 650 | 120 | 4290 | 288,000 | Dark gray + small amt. light gray | Spalled |
| 675 | 95 | 5550 | 373,000 | Dark gray + small amt. light gray | Spalled |
| 700 | 55 | 5550 | 373,000 | Dark gray | Cracked oxide film |

For the 400°C experiment of Fig. 1, the oxidation reaction follows the protective pattern for 4½ hr after which a transition occurs and the rate of oxidation increases. This transition occurs at a film thickness of about 60-80 μg/cm². Bridges and Fassell (3) state that nearly 6 hr were required before the oxidation rate became linear at 400°C and a pressure of 1 atmosphere of oxygen. This observation could be interpreted as a transition in the oxidation rate and is in agreement with the results of Fig. 1. Transitions in the rate of oxidation have been observed in other systems (9) and may be a general phenomenon for the oxidation of a wide variety of metals and alloys. What was unusual was the low thickness value at which transition occurs.

Figure 2 shows the oxidation curve at 425°C. Again the oxidation curve shows the formation of a protective oxide during the initial stage of the reaction. However, after a film thickness of 55 μg/cm² was reached, the rate of oxidation underwent a transition to a linear rate. These results confirm the transformation shown at 400°C.

Figure 3 shows the course of the 450°C oxidation curve. The curve shows a very short period of protective oxide formation followed by a transition to a linear rate of reaction. The transition thickness was about 50 μg/cm². The weight gains corresponding to 100,000 and 200,000Å of film thickness were noted on the figure. A film thickness of 100,000Å corresponds to $10^{-3}$ cm, or 0.0004 in. This was an appreciable amount of reaction for a 3-hr period at this temperature.

Figure 4 shows the results at 475°C. Here, the initial stage of the reaction was very short. The

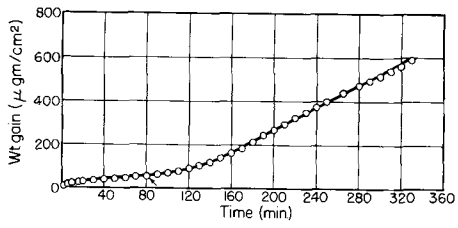


Fig. 2. Oxidation of Nb, abraded through 4/0, 425°C (797°F), 7.6 cm Hg of $O_2$.

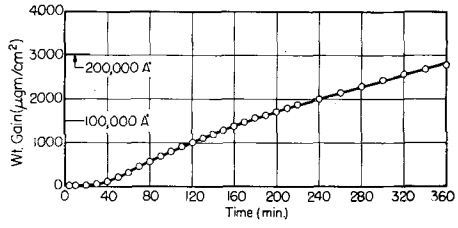


Fig. 3. Oxidation of Nb, abraded through 4/0, 450°C (842°F), 7.6 cm Hg of $O_2$.

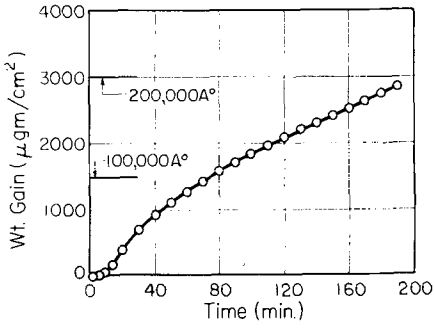


Fig. 4. Oxidation of Nb, abraded through 4/0, 475°C (887°F), 7.6 cm Hg of $O_2$.

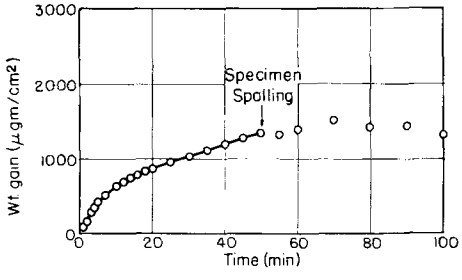


Fig. 5. Oxidation of Nb, abraded through 4/0, 525°C (977°F), 7.6 cm Hg of $O_2$.

extent of reaction after 3 hr of reaction was nearly $2 \times 10^{-3}$ cm, or 0.0008 in. Table I shows that the oxide film was cracking on cooling, and one must conclude that the oxide was unprotective for this temperature.

Figure 5 shows several new features in the course of the oxidation curve at 525°C. First, the initial period was no longer observed. Second, spalling of the oxide from the metal was interfering with the rate measurements. Third, the previously termed linear rate law region was not linear since the rate decreases with time. This could be an indication of spalling or a change in the mechanism of reaction.

*Effect of temperature* 550°-700°C.—Figure 6 shows oxidation curves for experiments between 550° and 700°C. Between 500° and 625°C the rate of oxidation was nearly independent of temperature, while above 625°C the rate of oxidation in-

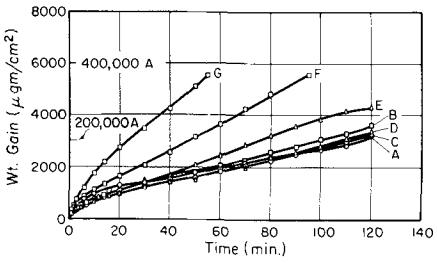


Fig. 6. Effect of temperature on oxidation of Nb, abraded through 4/0, 7.6 cm Hg of $O_2$. Curve A, 550°C; curve B, 575°C; curve C, 600°C; curve D, 625°C; curve E, 650°C; curve 7, 675°C; curve G, 700°C.

creased with temperature. After an initial period, the data approximately fit a linear rate law. Due to occasional spalling of the oxide, the linear rate law was not uniform. All of the oxide films formed in this temperature range spalled or cracked on cooling to room temperature. Table I summarizes the oxide thickness, the oxide color, and the stability data for these experiments. Figure 7 shows a photograph of the 675°C sample after oxidation, together with the spalled oxide collected from the furnace tube.

These experiments suggest that there exists a temperature region in which the rate of oxidation is nearly constant with temperature. No evidence was found for a reversal in the temperature coefficient of the oxidation reaction as noted by Bridges and Fassell (3).

*Rate law correlation.*—Both the linear and parabolic rate law have been used to explain the oxidation rate of Nb (1-3). The parabolic rate law states

$$W^2 = At + C$$

Here $W$ is the weight gain, $t$ is the time, and $A$ and $C$ are constants. Wagner and Grünewald (10) and later Mott (11) derived this equation from fundamental principles of diffusion and lattice defects. The linear rate law states

$$W = At + C$$

and suggests that diffusion processes are not rate controlling. The symbols have the same meaning as before.

To test the fitness of the parabolic rate law and to show the transition to the linear rate law, plots were made of the weight gain squared vs. time. Three plots were made for 375°, 425°, and 475°C runs. Figure 8 shows the parabolic rate law plots

**Table II. Comparison of parabolic rate constants for oxidation of Nb**

| Temp, t°C | Older work (1) parabolic constants (g/cm$^2$)$^2$/sec | Temp, t°C | This study parabolic constants (g/cm$^2$)$^2$/sec |
|---|---|---|---|
| 200 | $1.06 \times 10^{-15}$ | 375 | $1.25 \times 10^{-13}$ |
| 225 | $4.45 \times 10^{-15}$ | 400 | $2.96 \times 10^{-13}$ |
| 250 | $6.25 \times 10^{-15}$ | 425 | $6.50 \times 10^{-13}$ |
| 275 | $5.52 \times 10^{-14}$ | 450 | $1.12 \times 10^{-12}$ |
| 300 | $7.39 \times 10^{-14}$ | 475 | $1.75 \times 10^{-12}$ |
| 325 | $9.38 \times 10^{-14}$ | | |
| 350 | $2.8 \times 10^{-13}$ | | |
| 375 | $9.03 \times 10^{-13}$ | | |

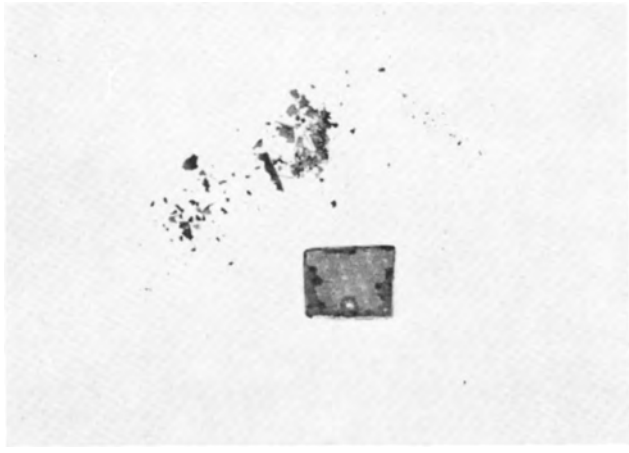

Fig. 7. Oxidation of Nb, 650°C, 7.6 cm Hg of $O_2$

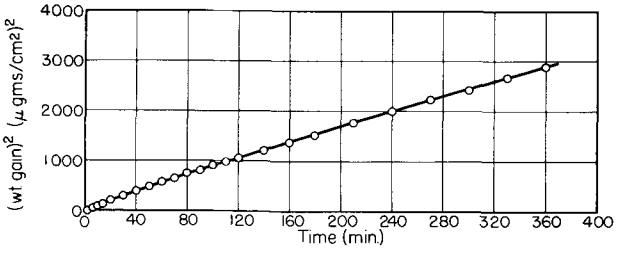


Fig. 8. Oxidation of Nb parabolic plot, abraded through 4/0, 375°C (707°F), 7.6 cm Hg of $O_2$. $A_{1\text{-}2\ hr} = 1.35 \times 10^{-13}$ (g/cm$^2$)$^2$/sec; $A_{4\text{-}6\ hr} = 1.25 \times 10^{-13}$ (g/cm$^2$)$^2$/sec.

for 375°C run. After the initial period a fairly good fit was obtained. This confirms the earlier results of Gulbransen and Andrew (1). Figure 9 for the 425°C oxidation shows the parabolic rate law to fit the initial part of the reaction. The transition to the linear rate law occurs after 80 min of reaction. Figure 10 shows a parabolic rate law plot for the 475°C experiment. No fit was obtained at this temperature.

Table II shows a comparison of the parabolic rate law constants obtained in this study with those obtained in the authors' earlier work. Results for the commercial grade of Nb show lower rates of reaction than results on a somewhat purer grade of Nb used in our earlier study.

Figure 11 shows a logarithmic plot of the parabolic rate law constant vs. $1/T$. The results of the earlier study were included. The figure shows that the temperature coefficients of the parabolic rate

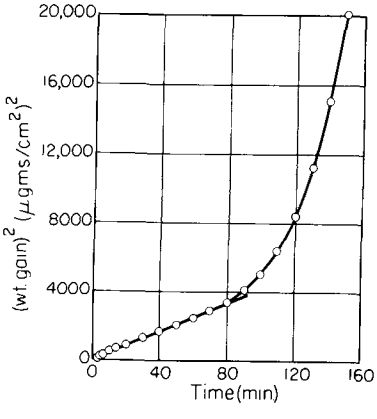


Fig. 9. Oxidation of Nb parabolic plot, abraded through 4/0, 425°C (797°F), 7.6 cm Hg of $O_2$. $A = 6.95 \times 10^{-13}$ (g/cm$^2$)$^2$/sec.

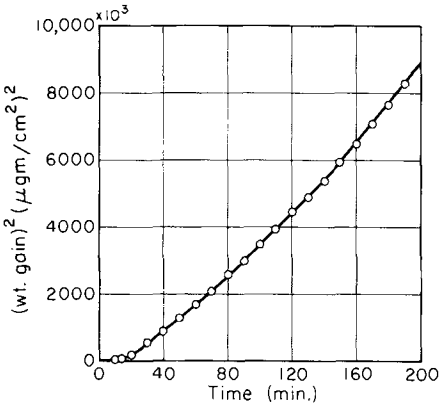


Fig. 10. Oxidation of Nb parabolic plot, abraded through 4/0, 470°C (887°F), 7.6 cm Hg of $O_2$.

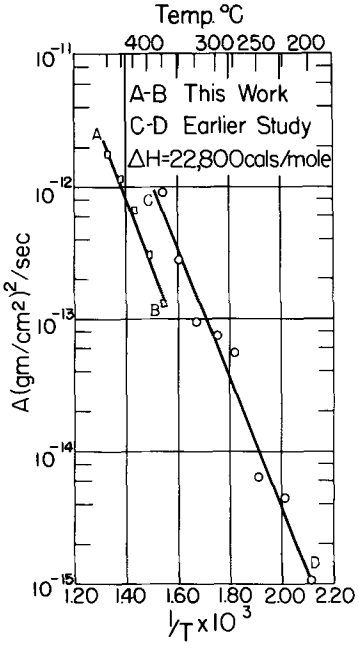


Fig. 11. Oxidation of Nb, log A vs. 1/T

law constant for the two sets of results were about the same. However, the actual constants for the commercial grade of material were smaller. A heat of activation of 22,800 ± 3,000 cal/mole was calculated. Since the studies of Inouye (2) and Bridges and Fassell (3) were for the linear range of oxidation, no comparisons can be made with their data.

Table III shows a summary of the linear rate law constants for the temperature range of 400°-700°C. The values identified as initial values were obtained immediately after transition and do not represent the long period rate of reaction.

Figure 12 shows a logarithm linear rate constant vs. 1/*T* plot of the linear rate law data, together with the data of Inouye (2) and Bridges and Fassell (3). Below 500°C the data from the three studies were in agreement, while above 500°C the three studies are not in agreement. The present study shows no evidence at 0.1 atmosphere pressure of oxygen for a negative temperature coefficient for the rate of oxidation as noted by Bridges and Fassell (3). Although Inouye only studied the reaction at 100°C intervals, his data also show no evidence for this phenomenon.

**Table III. Linear rate law constants, oxidation of Nb**

| Temp, °C | Linear rate law const g/cm²/sec | Temp, °C | Linear rate law const g/cm²/sec |
|---|---|---|---|
| 400 | $5.7 \times 10^{-9}$* | 550 | $3.3 \times 10^{-7}$ |
| 425 | $4.3 \times 10^{-8}$* | 575 | $3.76 \times 10^{-7}$ |
| 450 | $1.13 \times 10^{-7}$ | 600 | $3.81 \times 10^{-7}$ |
| 450 | $2.05 \times 10^{-7}$* | 625 | $3.88 \times 10^{-7}$ |
| 475 | $2.07 \times 10^{-7}$ | 650 | $5.53 \times 10^{-7}$ |
| 500 | $1.9 \times 10^{-7}$ | 675 | $8.8 \times 10^{-7}$ |
| 525 | $2.66 \times 10^{-7}$ | 700 | $1.39 \times 10^{-6}$ |

* Initial values.

*Transition in the rate of oxidation data.*—Niobium undergoes a transition in the rate of oxidation from the parabolic rate law to the linear rate law at film thicknesses of 50-67 μg/cm² in the temperature range of 400°-450°C. This confirms the results of Inouye (2).

After transition the oxide was not adherent to the metal. The early onset of transition is a major difficulty in the use of the material at high temperature. In the protective range of the oxidation of Nb the parabolic rate constants were considerably higher than those found for Zr, Ni, and other metals.

The data of Table I suggest that there is a definite relation between the fact that the oxide spalls at temperature or cracks on cooling and the transition to a linear rate law. However, the 400°-475°C experiments indicate that the oxide did not crack on cooling. This suggests that the oxide film had lost adhesion on a local basis long before the necessary stresses were reached for cracking of the oxide from the metal. We associate, therefore, the transition in the rate of oxidation to local loss of adhesion or to cracking or spalling of the oxide from the metal. The cracking or spalling of the oxide was a later stage of the process which starts as one involving a local loss of adhesion.

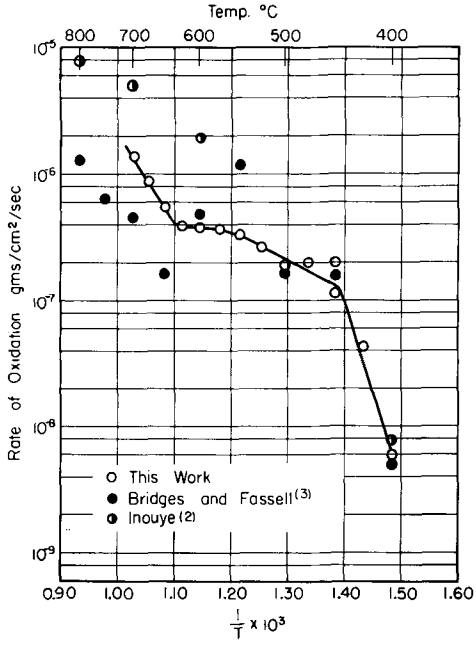


Fig. 12. Oxidation rate Nb vs. 1/T $O_2$ at 7.6 cm Hg, 400°-700°C.

Table IV. Comparison of x-ray diffraction data on spalled oxide with $Nb_2O_5$ (L-form) Ni $K_\alpha$

| 550°C Oxide $d_{hkl}$ | $I/I_o$ | 700°C Oxide $d_{hkl}$ | $I/I_o$ | $Nb_2O_5$ (L-form) (6) $d_{hkl}$ | $I/I_o$ |
|---|---|---|---|---|---|
| 3.9231 | 10 | 3.8854 | 9 | 4.0550 | 1 |
| 3.1260 | 8 | 3.1258 | 10 | 3.9482 | 8 |
| 3.0758 | 8 | 3.0575 | 5 | 3.1661 | 8 |
| 2.9199 | 1 | 2.4394 | 4 | 3.0867 | 5 |
| 2.8177 | 1 | 2.4120 | 2 | 2.4661 | 5 |
| 2.7252 | tr | 2.1051 | tr | 2.4364 | 3 |
| 2.4479 | 7 | 2.0028 | tr | 2.1319 | 1 |
| 2.4197 | 7 | 1.9626 | 7 | 2.0213 | 2 |
| 2.1136 | tr | 1.8205 | 6 | 1.9729 | 5 |
| 2.0011 | tr | 1.7852 | 7 | 1.8377 | 3 |
| 1.9585 | 7 | 1.6560 | 9 | 1.8004 | 5 |
| 1.8232 | 1 | 1.6253 | 5 | 1.6664 | 5 |
| 1.7884 | 3 | 1.5696 | 3 | 1.6380 | 3 |
| 1.6564 | 5 | 1.5375 | 1 | 1.5798 | 3 |
| 1.6267 | 2 | 1.4574 | 3 | 1.5508 | 2 |
| 1.5668 | tr | 1.3365 | 3 | 1.5276 | 1 |
| 1.5390 | tr | 1.3207 | 3 | 1.4977 | 1 |
| 1.4589 | tr | 1.2265 | 1 | 1.4687 | 3 |
| 1.4318 | tr | 1.2088 | 1 | 1.4435 | 1 |
| 1.3205 | tr | 1.1930 | 1 | 1.4029 | 1 |
| | | 1.1429 | 1 | 1.3429 | 3 |
| | | 1.1227 | tr | 1.3280 | 3 |
| | | | | 1.2333 | 2 |
| | | | | 1.2161 | 1 |
| | | | | 1.1995 | 1 |
| | | | | 1.1493 | 2 |
| | | | | 1.0084 | 1 |

*X-ray diffraction studies.*—An x-ray diffraction study was made of the oxides formed in the oxidation of Nb for the temperature range of 500°-700°C. The x-ray diffraction $d_{hkl}$ values can best be correlated with the L-form of $Nb_2O_5$, although important deviations are found. Table IV shows a correlation between the $d_{hkl}$ values for the 550° and 700°C spalled oxide films with the L-form of $Nb_2O_5$ (6). X-ray studies on the spalled oxide agree with those of Inouye (2).

Attempts were made to strip the oxide film electrochemically from the 375° and 400°C experiments where adherent oxide films were formed. These efforts were not successful.

It was concluded that the low temperature modification of $Nb_2O_5$ was formed. However, the parameters were not exactly those observed by Brauer (6). A phase diagram study of the niobium oxide system must be made to understand the observed structures and those of Brauer. Also, the important oxide films to study were those for the adherent scales. Methods must be developed for removing the base metal from the oxide film.

Manuscript received May 27, 1957. This paper was prepared for delivery before the Washington Meeting, May 12-16, 1957.

Any discussion of this paper will appear in a Discussion Section to be published in the December 1958 JOURNAL.

REFERENCES

1. E. A. Gulbransen and K. F. Andrew, *Trans. Am. Inst. Mining Met. Engrs.*, **188**, 586 (1950).
2. H. Inouye, A.I.M.E. Reactive Metal Conference, Buffalo, New York, March 19-21, (1956). To be published.
3. D. W. Bridges and W. M. Fassell, Jr., *This Journal*, **103**, 326-350 (1956).
4. G. Grube, O. Kubaschewski, and K. Zwiaur, Z. *Elektrochem.*, **45**, 885 (1939).
5. O. Kubaschewski, *ibid.*, **62**, 818 (1940).
6. G. Brauer, Z. *anorg. u. allgem. chem.*, **248**, 1 (1941).
7. A. U. Seybolt, *J. Metals*, **6**, 774 (1954).
8. E. A. Gulbransen, *Trans. Electrochem. Soc.*, **83**, 301 (1943).
9. E. A. Gulbransen and K. F. Andrew, Unpublished work.
10. C. Wagner and K. Grünewald, *Z. Phys. Chem.*, **40B**, 455 (1938).
11. N. F. Mott, *Trans. Faraday Soc.*, **36**, 472 (1940).

# The Action of Lead Pigments and Lead Soaps on Aluminum

**M. J. Pryor, R. J. Hogan, and F. B. Patten**

*Department of Metallurgical Research, Kaiser Aluminum & Chemical Corporation, Spokane, Washington*

ABSTRACT

Aqueous extracts from metallic lead and litharge are corrosive to aluminum due to their initially high *p*H and to the galvanic corrosion resulting from lead deposition on the aluminum. Aqueous extracts from red lead and basic lead carbonate have lower *p*H, do not deposit metallic lead on aluminum, and are much less corrosive. Aqueous extracts from lead linoleate, lead ricinoleate, and lead laurate inhibit the corrosion of aluminum and the galvanic corrosion of aluminum coupled to lead. Inhibition is believed to be due to the adsorption of fatty acid anions on the oxide covered aluminum surface. Since the diameter of the fatty acid anions is large, the electric fields accelerating aluminum ions from the metal through the oxide film are very weak. Consequently the corrosion of aluminum in lead soaps is prevented. Inhibition by lead soaps is easily broken down by the simultaneous presence of small quantities of chloride ions.

The question of whether organic coatings pigmented with lead compounds accelerate or reduce the corrosion of aluminum has never been fully resolved. It has been argued (1) that paints containing lead pigments should accelerate corrosion due to deposition of metallic lead which forms damaging galvanic cells. However, Wagner (2) has suggested that red lead primers may be used safely on aluminum provided all alkaline cleaning compounds are first removed. This uncertainty has been accen-

tuated by the varied service experience with aluminum which had been coated with lead based paints.

Mayne (3) demonstrated that oxygen and water pass through organic films at a relatively high rate but that the passage of other more corrosive anions such as chloride ions is largely prevented. Therefore it follows that the effectiveness of a primer depends to a considerable extent on the rate of corrosion of the base metal in an oxygen-containing aqueous extract from the pigment or from the products of interaction of the pigment with the vehicle.

Several investigations have been carried out in the past (4-6) which have shown that aqueous extracts from certain lead pigments such as litharge, metallic lead, and red lead have an inhibitive action on the corrosion of steel. Furthermore, lead linoleate (5), a product of reaction of a lead pigment with a linseed oil vehicle, is a corrosion inhibitor for steel.

These observations have been of great assistance in furthering the understanding of how lead pigmented paints control the corrosion of steel. Therefore it was considered that an investigation of the corrosion rate of aluminum in aqueous extracts from litharge, red lead, basic lead carbonate, and metallic lead pigments and in certain lead soaps might clarify the effect of lead pigmented paints on aluminum. Lead soaps of unsaturated linoleic ($C_{18}H_{32}O_2$) and ricinoleic acids ($C_{18}H_{34}O_3$) together with the lead soap of saturated lauric acid ($C_{12}H_{24}O_2$) were selected for this investigation because these acids are commonly found in the vehicles of many air-drying and baking coatings. In particular it is desirable to determine whether sufficient lead passes into aqueous solution from lead pigments or lead soaps to initiate metallic deposition on aluminum. Should this occur, the problem becomes primarily one of galvanic corrosion between aluminum and lead. Consequently, the intensity of the galvanic corrosion between aluminum and lead in the different pigment and soap extracts must be investigated in some detail.

## Experimental

*Materials.*—The aluminum used in this investigation was high purity, cold rolled sheet 0.088 cm thick. Its chemical composition together with those of the litharge, red lead, basic lead carbonate (white lead), metalic lead, and lead soaps are shown in Table I. All other solutions were prepared from C.P. chemicals and distilled water.

### *Preparation of the Aqueous Extracts*

Extracts from the four inorganic lead compounds were prepared by exposing 50 g of each compound to one liter of distilled water for eight days in a stoppered flask at 25°±0.05°C. The flasks were shaken at frequent intervals to ensure dispersion of the fine particles of pigment. After eight days the solutions were filtered rapidly through glass wool and contained in well-stoppered bottles. Since the conductivities of the extracts changed markedly with time, even after filtration, all experiments described below were carried out on fresh extracts. The extracts from lead soaps were prepared in a manner similar to that previously described by Mayne (5). The lead soaps were dispersed in hot xylene and applied to the inside of glass beakers. After drying in air for eight days the beakers were filled with distilled water at 25°C for a further eight days. After this period the solutions were decanted and stored in well-stoppered bottles.

**Table II. Properties of aqueous extracts**

| Extract | Initial *pH* | Lead content mg per liter: After filtration through glass wool | Lead content mg per liter: After filtration through Whatman #1 paper | Avg Spec Res after filtration through glass wool ohm/cm²/cm |
|---|---|---|---|---|
| Lead | 9.1 | 70.0 | 6.9 | 40,500 |
| Litharge | 9.0 | 82.5 | 2.0 | 29,500 |
| Red lead | 6.1 | 7.5 | 2.1 | 49,000 |
| Basic lead carbonate | 6.3 | 2.0 | 0.18 | 33,000 |
| Lead linoleate | 5.1 | 218.0 | — | 4,400 |
| Lead ricinoleate | 6.0 | 20.8 | — | 24,000 |
| Lead laurate | 5.5 | 296.0 | — | 4,200 |
| Distilled water | 6.0 | — | — | 1,500,000 |

*Properties of the aqueous extracts.*—The properties of the aqueous extracts are shown in Table II. The lead content of each extract was determined colorimetrically using diphenyl thiocarbazone (11). Both the litharge and lead extracts are initially markedly alkaline. However on standing in contact with the atmosphere they become less alkaline due to the absorption of carbon dioxide and the resulting precipitation of basic lead carbonate (6). Furthermore both the litharge and lead extracts after filtration through glass wool are buffered to some extent (Fig. 1). The reserve alkalinity of 100 ml of extract will be defined arbitrarily as the volume of 0.01*N* hydrochloric acid required to lower its pH to a value of 6.0. The reserve alkalinities of lead and litharge extracts are dependent not only on the quantity of lead in solution but also on the form in which it is present. Table II shows that most of the lead from litharge and lead extracts may be removed by filtration through Whatman No. 1 filter

**Table I. Compositions of the materials used**

| | | | | |
|---|---|---|---|---|
| Aluminum | Silicon 0.001% | Iron 0.001% | Copper 0.002% | Balance Al |
| Lead powder | Silicon 0.004% | Iron—trace | Magnesium—trace | Balance Lead |
| Sheet lead | Bismuth 0.06% | Silver 0.003% | Copper 0.03% | Balance Lead |
| | | Silicon 0.004% | | |
| Litharge | PbO assay 99.9% | | | |
| Basic lead carbonate | Lead carbonate 63.5% | Moisture 0.04% | | |
| Red lead | $Pb_3O_4$ assay 97.0% | | | |
| Lead linoleate | 25% Lead | | | |
| Lead ricinoleate | 25% Lead | | | |
| Lead laurate | 32.3% Lead | | | |

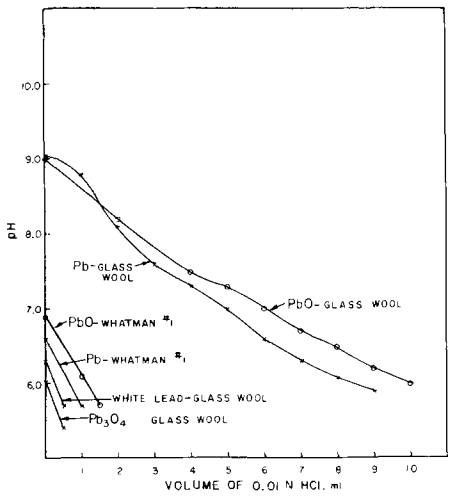


Fig. 1. Neutralization curves for pigment extracts filtered through glass wool and through Whatman No. 1 filter paper.

paper. This is probably due to the removal of massive lead hydroxide, lead dioxydihydroxide [$Pb_3O_2(OH)_2$] (12) and to the adsorption of lead compounds by the filter paper (13).

The lead linoleate extract has a relatively low pH (5.1) and specific resistance together with a high lead content similar to the value previously reported by Mayne (5). The lead laurate extract contains even higher quantities of lead but otherwise its properties are similar to those of lead linoleate. Lead ricinoleate is less soluble than the other two lead soaps and shows a correspondingly increased specific resistance and pH value.

Twenty-five ml of the inorganic extracts were filtered through glass wool and enclosed in semipermeable membranes of untreated (nonwaterproofed) cellophane. These "bags" of cellophane were then placed in 25 ml of distilled water for 48 hr in order to investigate whether detectable quantities of ionic lead were present in the aqueous extracts. Using the sensitive lead sulfide test it was found that in no case did detectable quantities of lead ions pass through semipermeable membranes into the surrounding water. In the case of the litharge extract this result differs from previous work (6) in which it was found that a substantial quantity of the lead in the litharge extract was present as $Pb(OH)^+$ ions. Evidently the properties of litharge extracts are dependent on the source of the pigment.

**Table III. Weight losses of aluminum specimens in fifteen days in aqueous extracts**

| Extract | Filtration method | Weight losses (mg/cm²) |
|---|---|---|
| Fresh distilled water | None | 0.195, 0.27, 0.29, 0.34, 0.18, 0.42 |
| Distilled water after 8 days' contact with glass | None | 0.43, 0.47, 0.40 |
| Metallic lead | Glass wool | 0.52, 0.68, 0.49 |
| | Whatman #1 paper | 0.22, 0.22, 0.235 |
| Litharge | Glass wool | 0.65, 0.65, 0.55 |
| | Whatman #1 paper | 0.23, 0.23, 0.26 |
| Red lead | Glass wool | 0.00, 0.00, 0.01 |
| | Whatman #1 paper | 0.00, 0.00, 0.00 |
| Basic lead carbonate | Glass wool | 0.00, 0.00, 0.00 |
| | Whatman #1 paper | 0.00, 0.00, 0.00 |
| Lead linoleate | None | 0.00, 0.00, 0.00 |
| Lead ricinoleate | None | 0.00, 0.00, 0.00 |
| Lead laurate | None | 0.00, 0.00, 0.00 |

*Reactions between Aluminum and Aqueous Extracts in the Presence of Dissolved Air*

Aluminum specimens measuring 5.6 x 2.5 cm were degreased in benzene, etched for 1 min in cold 10% NaOH, rinsed, dried, stored in dry air for 24 hr, and weighed. Triplicate specimens were totally immersed for fifteen days at 25°±0.05°C in 100 ml of fresh extracts which had been filtered through glass wool. The tops of the specimens were located 1 cm below the water line of the solution. Evaporation was largely prevented by covering the tops of the vessels with Saran plastic tissue. Control experiments in fresh distilled water and in distilled water that had been stored in glass vessels for eight days were also carried out.[1] At the end of the experiments the specimens were treated with nitric acid to remove the corrosion products together with any lead compounds, then they were dried in acetone and re-weighed. The weight losses[2] for these experiments are shown in Table III. This table also contains the results of similar experiments in which the extracts were filtered through Whatman No. 1 filter paper before use. Potential/time curves measured by means of a Speedomax recording potentiometer are shown in Fig. 2.[3]

Specimens immersed in litharge and lead extracts that had been filtered through glass wool rapidly developed a plating of metallic lead. However, after a short while the lead plate transformed into a white powder which was identified by x-ray diffraction as having 2 $PbCO_3 \cdot Pb(OH)_2$ as the major constituent and lead as a minor one. The quantity of lead deposited, as indicated by approximate weight gain figures, was greater in litharge extracts

[1] This was to investigate the suggestion made previously for iron (7) that silicate leached from the glass might influence the results.

[2] All weight losses in this paper are corrected by subtracting the small weight loss resulting from the chemical cleaning process itself.

[3] All potentials in this paper are expressed on the Standard Hydrogen Scale.

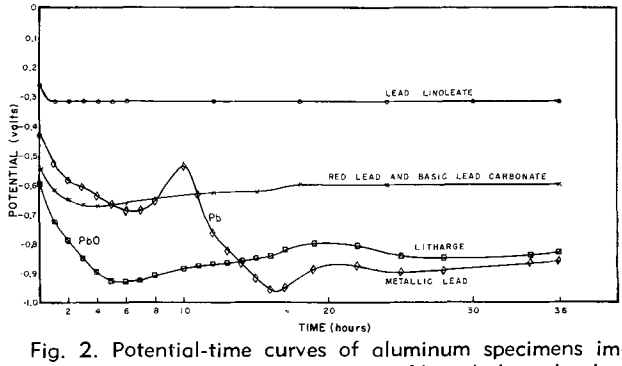


Fig. 2. Potential-time curves of aluminum specimens immersed in inorganic pigment extracts filtered through glass wool and in lead linoleate at 25°±0.05°C. All specimens carried an air-formed oxide film.

than in lead extracts. Conductivity measurements indicated that lead was not completely stripped from the solution by deposition on aluminum. When the lead-plated aluminum samples were removed from the solution, transformation of the deposited lead to basic lead carbonate was greatly hastened.

Specimens immersed in fresh distilled water remained apparently uncorroded for around six days after which time a continuous gray film and later white $\beta$ $Al_2O_3.3H_2O$ formed. Specimens immersed in distilled water that had been contained in a glass beaker for eight days before the experiment not only formed gray films and white corrosion product somewhat faster than those immersed in fresh distilled water but were more severely corroded. The silicate leached out of the glass raised the initial pH of the water by around one pH unit and evidently increased the corrosion rate of the aluminum.

Specimens immersed in the extracts of red lead, basic lead carbonate, lead linoleate, lead ricinoleate, and lead laurate were not visibly attacked and suffered no loss in weight.

### *Galvanic Experiments*

Galvanic experiments were carried out using the apparatus shown in Fig. 3. The lead (*see* Table I for composition) and aluminum electrodes had equal areas of 25 $cm^2$ immersed in 320 ml of the aqueous extract under investigation and were held firmly in place 5 cm apart by means of a Lucite holder. The back surfaces of the electrodes were masked with water-proofed Scotch pressure-sensitive tape. Surface pretreatment of lead involved degreasing in benzene, etching for 1 min in 50% nitric acid, followed by rinsing, drying, weighing, and storage in dry air for 24 hr. Surface pretreatment of aluminum was carried out in a similar manner except that etching was done in cold 10% NaOH for 1 min. The cell was contained in a water-bath thermostatted at 25°±0.05°C.

The electrodes were short-circuited for the test period for 96 hr. Current values at zero external resistance were measured periodically by introducing a zero resistance microammeter into the circuit. Potential measurements of the aluminum electrodes were made against a saturated calomel electrode using a high resistance bridge. Diffusion of the dilute chloride solution contained in the reference electrode vessel was prevented by a bentonite plug (8). The tip of the tubulus was situated 1 mm from the aluminum electrode surface since, in high resistance solutions, there is a significant potential drop across the solution in addition to localized undetermined potential changes at the double layers next to the electrodes (9). The potentials of aluminum electrodes coupled to lead were somewhat more noble than those measured during corrosion of uncoupled aluminum specimens in the same solution.

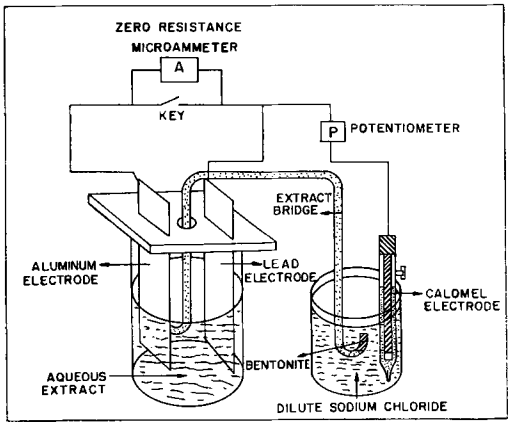


Fig. 3. Apparatus for galvanic studies in pigment and lead soap extracts.

After 96 hr the experiments were discontinued and corrosion products removed chemically so that weight loss of the electrodes could be determined. The aluminum specimens were cleaned by immersion in nitric acid whereas the lead specimens were cleaned by 10-min immersion in boiling 1% acetic acid (10). The total number of coulombs flowing in each experiment was calculated from the appropriate current/time curve. By knowing the weight loss of uncoupled specimens in the appropriate extract, the decrease in weight loss of the cathodic member of the couple and the current efficiency of the anodic process can be calculated. The weight losses of lead specimens immersed in the four inorganic pigment extracts for 96 hr are shown in Table IV.

Current/time curves for the aluminum/lead couple in aqueous extracts from lead, litharge, red lead, basic lead carbonate, and in distilled water were erratic. The total number of coulombs flowing in triplicate experiments together with the weight losses of the aluminum and lead are shown in Table V. However, aluminum invariably behaved as the anode in the galvanic studies of the aluminum-lead couple.

Initial values of current flow in aqueous extracts from the four inorganic lead compounds were primarily dependent on the resistance of the extract. Later however the resistance of the extracts decreased as the lead cathodes corroded. In these experiments the greatest proportion of the corrosion of the aluminum was the result of the deposition of metallic lead on the aluminum anodes. Lead is fairly readily attacked by extracts from the inorganic lead compounds and the galvanic currents are insufficiently strong for complete cathodic protection. Therefore the extracts may be regarded as providing a reservoir of lead ions from which metallic lead may be deposited on the aluminum. Substantial quantities of basic lead carbonate were precipitated from the extracts over a period of four days and the lead cathodes also became blanketed with this compound.

**Table IV. Weight losses of lead specimens in 96 hr in aqueous inorganic extracts filtered through glass wool**

| Extract | Weight loss of lead specimens ($mg/cm^2$) |
|---|---|
| Distilled water | 2.8, 2.3, 2.6 |
| Metallic lead extract | 3.4, 2.7, 2.6 |
| PbO extract | 3.9, 2.5, 2.4 |
| $Pb_3O_4$ extract | 3.1, 2.6, 2.7 |
| Basic lead carbonate extract | 3.2, 2.9, 2.7 |

Table V. Galvanic corrosion data for the aluminum-lead couple in aqueous extracts filtered through glass wool

| | Wt loss of lead cathode mg/cm² | Wt loss of Al anode mg/cm² | No. of coulombs flowing in 96 hr | Calculated Al wt loss due to galvanic current flow mg/cm² | Al wt loss due to local action mg/cm² |
|---|---|---|---|---|---|
| Distilled water | 5.2 | 0.33 | 17.7 | 0.085 | 0.245 |
| | 5.5 | 0.31 | 11.8 | 0.055 | 0.255 |
| | 4.2 | 0.31 | 14.2 | 0.065 | 0.24 |
| | 4.3 | 0.36 | 20.2 | 0.095 | 0.265 |
| Metallic lead | 5.15 | 0.205 | 11.3 | 0.055 | 0.15 |
| | 3.0 | 0.23 | 12.5 | 0.065 | 0.165 |
| | 5.4 | 0.155 | 11.5 | 0.055 | 0.10 |
| PbO | 4.1 | 0.20 | 29.9 | 0.14 | 0.06 |
| | 3.1 | 0.165 | 18.2 | 0.085 | 0.08 |
| | 3.0 | 0.12 | 12.1 | 0.060 | 0.06 |
| $Pb_3O_4$ | 5.6 | 0.09 | 8.4 | 0.04 | 0.05 |
| | 4.2 | 0.09 | 11.1 | 0.05 | 0.04 |
| | 4.8 | 0.06 | 8.0 | 0.035 | 0.025 |
| Basic lead carbonate | 5.9 | 0.095 | 14.1 | 0.065 | 0.030 |
| | 3.5 | 0.05 | 8.6 | 0.04 | 0.01 |
| | 4.1 | 0.05 | 8.4 | 0.04 | 0.01 |
| Lead linoleate | 2.4 | 0.00 | 0.06 | 0.00 | 0.00 |
| | 2.3 | 0.00 | 0.19 | 0.00 | 0.00 |
| | 2.4 | 0.00 | 0.05 | 0.00 | 0.00 |
| Lead ricinoleate | 3.4 | 0.00 | 0.4 | 0.00 | 0.00 |
| | 4.6 | 0.00 | 0.9 | 0.00 | 0.00 |
| Lead laurate | 1.2 | 0.00 | 0.04 | 0.00 | 0.00 |
| | 1.5 | 0.00 | 0.03 | 0.00 | 0.00 |

Table V also contains the results of experiments on the aluminum/lead couple in lead soap extracts. In this case, little galvanic current flow was observed (Table V) and such minute currents that could be detected were very constant (Fig. 4). The minimum galvanic current flow was observed in lead laurate and the maximum current flow in lead ricinoleate. Weight loss determinations showed that galvanic corrosion of the aluminum and metallic lead deposition were completely prevented in all lead soap solutions despite the high soluble lead content of the extracts and their lower specific resistance. The corrosion rates of the lead cathodes were lower than in distilled water and were lowest in lead laurate extract.

*Electrochemical Studies in Lead Soaps*

Potential/time curves for initially "film-free" aluminum specimens were determined by first removing the air-formed oxide film by abrading the specimen with fine, high purity aluminum oxide in a high pressure stream of helium and then introducing the specimens immediately into the soap extract which had been presaturated with dissolved air. Alternatively the oxide film may also be removed by similar alumina/helium abrasion under the lead soap extract. In either case the results are identical and are shown in Fig. 5. Bubbling purified helium through the lead linoleate extract did not alter the potential of an aluminum specimen that originally carried an air formed oxide film and shifts the potentials of originally "film-free" specimens in the soap solutions only slightly in the less noble direction.

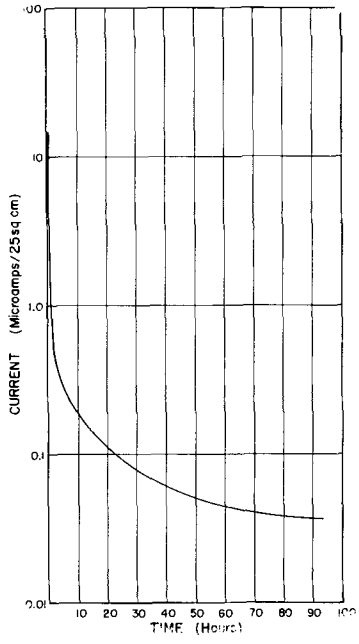


Fig. 4. Current vs. time curve at zero external resistance for the aluminum-lead couple in lead linoleate extract at 25°C.

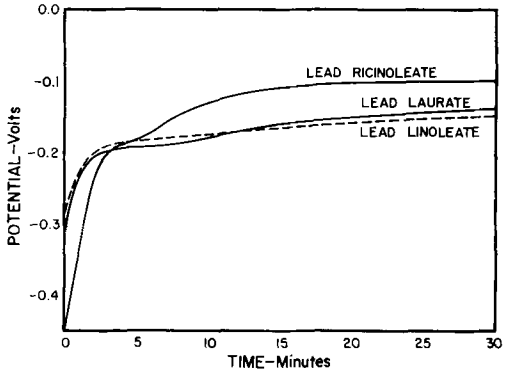


Fig. 5. Potential-time curves for initially "film-free" aluminum in lead soap extracts at 25°±0.05°C. The air-formed oxide film on the aluminum specimens was removed by abrasion with aluminum oxide in a high pressure stream of helium.

Anodic polarization curves for aluminum after 24-hr immersion in lead soap extracts are shown in Fig. 6. The aluminum specimens carried an initial air-formed oxide film before immersion in the solutions. Polarization curves were obtained by applying small constant currents for a fixed 5-min period and recording the potential at that time. The actual values of potential, although not the shape of the curves, are purely arbitrary since the potentials, except at the inflections in the curves, show a steady and reproducible shift with time to more noble potentials. An anodic polarization curve in normal sodium chloride solution is included for comparison.

## Discussion

*Composition of Inorganic Pigment Extracts*

Examination of the pigment extracts by dialysis shows that there is no evidence of appreciable quantities of lead being present in the ionic form. Therefore it is probable that the inorganic pigment extracts contain lead mainly in the form of colloidal

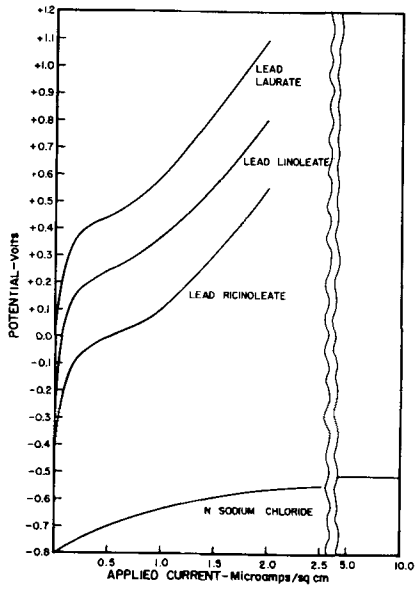


Fig. 6. Anodic polarization curves for aluminum in lead soap extracts and in normal sodium chloride at 25°±0.05°C. The specimens initially carried an oxide film formed in dry air for one day and were immersed in the solutions for 24 hr before the curves were determined.

lead hydroxide as had been found previously for metallic lead extracts (6). On standing, the colloidal lead hydroxide may subsequently age to the more insoluble lead dioxydihydroxide $Pb_3O_2(OH)_2$ (12). In the presence of atmospheric carbon dioxide insoluble basic lead carbonate will also be precipitated. The presence of colloidal lead hydroxide together with the other two reaction products evidently gives rise to some considerable buffering action as shown in Fig. 1. The values of reserve alkalinity for the four pigment extracts are approximately proportional to the total quantities of lead in solution. Since the rate of interaction of hydrogen ions with massive and colloidal lead hydroxide must be quite rapid, lead need not be present in the ionic form for buffering of an extract. Because lead is present largely as hydroxide in the massive and/or colloidal forms it is relatively easily removed by filtration (Fig. 1). Filtration through Whatman No. 1 paper removes the lead dioxydihydroxide and basic lead carbonate together with any residual pigment particles. Filtration also removes much colloidal lead hydroxide by adsorption on the paper (13). Consequently the buffering action in metallic lead and litharge extracts is almost destroyed by filtration (Fig. 1).

### *Corrosion of Aluminum in Inorganic Pigment Extracts*

The results contained in Table III demonstrate that the weight losses of all aluminum specimens immersed in inorganic pigment extracts are fairly low. Metallic lead and litharge extracts alone corrode aluminum more rapidly than distilled water. In part, the stimulation of corrosion may be attributed to deposition of metallic lead. However, the higher initial *p*H values of the lead and litharge extracts must also contribute to the increased corrosion rate, since distilled water which had been contained for eight days in a Pyrex glass beaker corroded aluminum somewhat more rapidly than fresh distilled water (Table III). This effect is probably associated with the slow leaching of sodium silicate from the glass which raises the initial *p*H value of the solution. That higher initial *p*H values of lead pigment extracts stimulates corrosion of aluminum is consistent with previous suggestions of Wagner (2).

Evidently in the immersion tests, metallic lead is deposited on the aluminum from lead and litharge extracts. Initially gas bubbles, presumably of hydrogen, form on the lead plate. However the carbon dioxide contained in the extracts reacts rapidly with the finely divided lead deposit, forming relatively insoluble basic lead carbonate. Since basic lead carbonate is not an efficient electronic conductor it should not be capable of acting as a preferential cathode and should not stimulate corrosion of the aluminum. Undoubtedly, in the absence of carbon dioxide, deposited lead would act as a more efficient cathode than in the present experiments. Consequently, under $CO_2$-free conditions a greater rate of corrosion of the aluminum might be anticipated in litharge and metallic lead extracts.

The very low rates of corrosion of aluminum in red lead and basic lead carbonate extracts are probably due to a combination of low dissolution rate of the two pigments combined with control of *p*H within the range 5-6 (Table II). Although the degree of buffering resulting from the very slight dissolution of both compounds is small (Fig. 1) it is sufficient to result in a marked decrease in corrosion rate. Whereas the results in Table III suggest that extracts from red lead, basic lead carbonate, and lead soaps are inhibitive towards aluminum, the subsequent galvanic experiments (Table V) indicate that only lead soaps are truly inhibitive. Therefore the negligible weight losses of aluminum in red lead and basic lead carbonate extracts are probably due to a lengthening of the induction period before corrosion of the aluminum begins. In distilled water the induction period is around 100 hr, and in red lead and basic lead carbonate extracts it must be in excess of 360 hr. Thus the aluminum specimens exhibit the phenomenon of metastable passivity in red lead and basic lead carbonate extracts.

### *Galvanic Corrosion of the Aluminum-Lead Couple in Inorganic Pigment Extracts*

Results of galvanic experiments in which aluminum invariably behaves as the anode are contained in Table V and Fig. 4. For distilled water and the four inorganic pigment extracts, comparison of Tables IV and V shows that the corrosion rate of lead is somewhat stimulated by coupling to aluminum, possibly on account of the increased local *p*H values at the cathodes. The current flow values in the galvanic cells are generally low and erratic; therefore only the total number of coulombs flowing are recorded. The generally low value of current flow is attributed to the high resistance of the solution and the moderately high value of hydrogen overpotential on lead (14). Initially the current flow appears to be controlled by the specific re-

sistance of the electrolyte (Table II), but after appreciable corrosion of the lead cathodes the current in the cells involving red lead and basic lead carbonate extracts increases to approximately that in the litharge and metallic lead extracts. However, Table V shows that the corrosion rates of aluminum anodes in distilled water, litharge, and metallic lead extracts are generally higher than those in red lead and basic lead carbonate extracts. In the first three solutions calculation from Faraday's Law shows that the weight loss due to the galvanic current flow constitutes only a small portion of the total weight loss of the anode. In red lead and basic lead carbonate extracts a greater proportion of the total aluminum weight loss is due to the galvanic current flow.

When aluminum is coupled to steel in sodium chloride appreciable quantities of aluminum are corroded by local action (9). This was attributed to incomplete suppression of the local cathodes on active aluminum anodes. The weight loss of an aluminum anode due to local action was independent of the area of steel cathode and decreased with decreasing area of the aluminum anode. At equal areas of steel and aluminum about 10% of the total aluminum weight loss was due to local action. In the aluminum-steel couple there was, of course, no question of metallic deposition on the aluminum anode.

It is evident that, in distilled water and in extracts from metallic lead and litharge, as much as 80% of the total weight loss is due to local action, whereas in basic lead carbonate and red lead extracts up to 50% of the total weight loss is due to local action. The much higher local action weight losses of aluminum coupled to lead are clearly due to deposition of metallic lead on the local cathodes on an active aluminum anode. Previous work (15) has demonstrated that the cathodes on aluminum in neutral solutions are small and that high cathodic polarization exists primarily because of the high electronic resistance of the air-formed aluminum oxide film. The high cathodic polarization at local cathodes on aluminum undoubtedly explains why the local action weight losses on aluminum anodes are much less than those on zinc anodes under similar experimental conditions (9). When metallic lead is deposited at these local cathodes local action corrosion is greatly intensified despite the relatively high hydrogen overvoltage on lead (14). An even higher intensification of local action corrosion would be anticipated if a metal of lower hydrogen overpotential such as copper was deposited.

### *Inhibition of the Corrosion of Aluminum by Lead Soaps*

The weight loss experiments (Table III) and galvanic experiments (Table V and Fig. 4) demonstrate that lead linoleate, ricinoleate, and laurate completely inhibit the corrosion of aluminum and the galvanic corrosion of aluminum coupled to lead. The potential of aluminum initially freed from oxide is strongly ennobled (Fig. 5) in these extracts and the anodic polarization curves (Fig. 6) suggest an anodic form of inhibition. The negligible values of galvanic current in lead soap extracts cannot be attributed to high values of electrolyte resistance since Table II shows that, with the exception of lead ricinoleate, the values of specific resistance are very low. There is no evidence of lead deposition on either aluminum panels or aluminum anodes despite some dissolution of lead from the cathodes in the galvanic experiments.

More recent work by Mayne and Van Rooyen (16) has demonstrated that the water-soluble degradation products of lead linoleate are responsible for inhibition of the corrosion of steel. The effect of oxygen is to increase the apparent solubility of lead linoleate in water from around 0.002 to 0.07%. A saturated solution of lead linoleate prepared in the absence of air does not inhibit the corrosion of steel. Mayne and Van Rooyen identified lead salts of formic acid, azelaic acid, and an unsaturated hydroxyacid derived from pelargonic acid as comprising the primary degradation products of lead linoleate. Small quantities of acetic, propionic, butyric, and suberic acid were also detected. Lead azelate, lead suberate, and lead pelargonate inhibited the corrosion of steel at concentrations of around 35 ppm within the *p*H range 4.5-6.0. Lead salts were more inhibitive than calcium salts which in turn were more effective than sodium salts.

It would be anticipated that some degradation of lead ricinoleate might occur in the presence of oxygen since ricinoleic acid is also unsaturated. However from the solubility measurements (Table II) it is evident that degradation by oxygen occurs to a lesser extent in lead ricinoleate than in lead linoleate. Since lauric acid is saturated, lead laurate probably does not degrade in a similar manner in the presence of oxygen. Instead its high solubility must be attributed mainly to the shorter carbon chain length.

Inhibition of corrosion of aluminum by lead soaps must be associated with the adsorption of fatty acid anions since small quantities of basic lead carbonate are precipitated when large areas of aluminum are immersed in small volumes of lead soap extracts; similar precipitation is not observed in the absence of an aluminum surface. Because, under most conditions examined in this investigation, the aluminum is covered with an oxide film, adsorption of long chain fatty acid anions must occur on the surface of the oxide. Furthermore it is considered that the oxide film is continuous rather than containing holes or cracks which penetrate to film-free metal. Since adsorption is involved as part of the inhibition process it becomes easier to understand why lead soaps are more effective inhibitors for steel than calcium or sodium soaps (16). The *p*H value of sodium and calcium soaps will be higher than those of lead soaps (5.1-6.0). In the more alkaline solutions less acid soap will exist and above *p*H values of 8.0 it should be virtually absent. Since —COONa has a much greater attraction for water than —COOH (17) it follows that an acid soap should be more strongly adsorbed at an interface than a neutral soap. The undeniably weaker inhibitive action of lead ricinoleate must therefore be attributed to a combination of somewhat higher *p*H

and lower concentration (Table II) which makes the anions less readily adsorbed.

If fatty acid anions are adsorbed on oxide covered aluminum as a condensed film, each anion should occupy an area of 20.5 sq Å at zero compression (18). However it is somewhat more likely that laurate would be adsorbed as an expanded film, which, at low compressions, should show an area of around 48 sq Å per ion. Unsaturated acids exhibit larger limiting areas which increase with increasing number of double bonds (20). For instance, elaeostearic acids with three double bonds may exhibit limiting areas of 100 sq Å or more which probably means that the ions are lying almost flat on the surface. If such unsaturated acids are permitted to oxidize, as in the case in this investigation, the adsorbed films still remain coherent with a limiting area of around 125 sq Å per ion. This figure is probably close to the effective areas of adsorbed linoleate and ricinoleate ions or their degradation products.

It follows that if fatty acid anions of large effective areas are adsorbed on an oxide surface, the electric field[4] accelerating aluminum ions through the oxide will be very weak—much weaker than those fields resulting from the adsorption of smaller ions such as the chloride ion. Therefore the corrosion rate of aluminum will be negligible as is in fact observed. Furthermore since considerable energy must be supplied to transport aluminum ions through the oxide film and the adsorbed fatty acid anion layer, the potential of the aluminum is strongly ennobled. Assuming this model of an electrode surface, which is described later in more detail, the actual value of the "corrosion" potential will depend on the thickness and defect structure of the oxide film on the aluminum and on the energy required to transport aluminum ions through the adsorbed fatty acid anion layer. Experiments not reported in this paper demonstrate that lead soaps and their degradation products have no appreciable solvent action on aluminum oxide. Therefore, local intensification of the adsorption field cannot be obtained by local film thinning as is the case with fluoride and chloride ions.

When soaps are adsorbed on initially film-free aluminum, Fig. 5 shows that there is first an ennobled potential which increases with increasing time. This progressive ennoblement is not observed to anything like the same degree in lead linoleate when the aluminum initially carries an oxide film resulting from the exposure to dry air for 24 hr (Fig. 2). The initial ennoblement of potential in the virtual absence of oxide must be due to the high energy required for transport of aluminum ions through the adsorbed layer of fatty acid anions. Evidently this energy is lower when film-free aluminum is immersed in more weakly adsorbed ricinoleate solutions. Clearly the magnitude of this energy is sufficiently high that adsorption must be considered to be the primary cause of inhibition. The subsequent ennoblement of potential with time shown in Fig. 5 is attributed to the formation of aluminum oxide primarily by discharge of fatty acid anions at anodic areas on the aluminum; the fatty acid anions are probably reduced to complex alkyne or possibly ketonic compounds. The formation of oxide is apparently not dependent on the presence of dissolved oxygen in solution since the extracts may be saturated with helium without markedly altering the corrosion rate or potential. Neither is oxide formation believed to occur uniformly over the surface but instead occurs locally at areas of maximum ionic conductivity, i.e., at the local anodes. Oxide formation by adsorption of dissolved oxygen is probably of some importance in the presence of more weakly adsorbing anions such as ricinoleate. This would serve to explain the higher rate of ennoblement of potential of initially film-free aluminum in lead ricinoleate extract (Fig. 5). Thus the additional formation of aluminum oxide films in these systems is an important secondary cause of inhibition. Work to be reported elsewhere shows that at current densities of 0.5-1.0 $\mu a/cm^2$ the formation of oxide by anodic discharge of fatty acid anions proceeds at current efficiencies in the region of 85-92%. Since oxide is not formed in similar experiments in distilled water, its formation in lead soap solutions may be attributed with some certainty to discharge of fatty acid anions. That aluminum oxide is formed by anodic discharge of fatty acid anions at potentials of the order of 0.0 v on the Hydrogen Scale indicates that the oxygens in the $RCOO^1$ groups are in intimate contact with the electrode surface.

Since some small local corrosion currents are presumed to flow initially during the inhibition of corrosion of aluminum in lead soaps, these corrosion currents should result in local thickening of the oxide film by the mechanism outlined above at areas of higher ionic conductivity in any initial oxide film. Since the local currents are presumably very small the current efficiency of aluminum oxide formation may be less than at higher current densities. Local thickening of the oxide film will result in a further decrease in the electric fields accelerating aluminum ions into solution. Thus inhibition must be due to a combination of adsorption and oxide film formation. If aluminum is coupled to a lead cathode in the soap extracts the somewhat higher initial galvanic currents (Fig. 4) are considered to result in the formation of oxide at higher efficiencies on the aluminum anodes. Thus as the oxide film progressively thickens it becomes steadily more difficult to pass further current and so the galvanic current rapidly decays (Fig. 4).

That oxide formation due to very small local corrosion currents may proceed at lowered current efficiencies is supported by the polarization curves in Fig. 6. These all show a marked inflection at a current density of around 0.5 $\mu a/cm^2$ which is not observed in similar polarization curves measured in distilled water. It is believed that this inflection represents the occurrence of the Kolbe reaction:

$$2RCOO^1 = R\text{-}R^5 + 2CO_2 + 2E$$

[4] The electric field across the oxide film is proportional to the adsorbed charge density and inversely proportional to the oxide thickness. The charge density is proportional to the anion valence and inversely proportional to the anion area.

[5] In electrolysis of the higher fatty acids olefines rather than paraffins are usually evolved at the anode (22).

which at very low currents may be an alternative reaction to oxide formation in these systems. Latimer (21) quotes a value of −0.16 v for the Standard Electrode Potential of the Kolbe reaction for acetic acid. Since an increase in the carbon chain length should not greatly influence the $E_o$ value, this reaction must be considered to be thermodynamically possible at the potentials shown in Fig. 6. Attempts were made to hold the potential of aluminum electrodes constant in the region of the inflection in the polarization curves with a view to collecting and, if possible, identifying the olefines which might form on the aluminum anodes. These attempts were invariably unsuccessful since in a short while oxide began to form at higher current efficiencies and the potentials of the aluminum anodes were displaced to much more noble values. Therefore it is concluded that the Kolbe reaction in the lead soap systems probably proceeds with a very high steric hindrance factor. At very low currents of less than 0.5 $\mu a/cm^2$ it must be considered as an alternative anodic reaction to the formation of aluminum oxide by discharge of soap anions. At extremely low current density the very slow leakage of aluminum ions into solution may also occur to a very limited extent although this is not detectable by microchemical analysis using the alizarin test.

Since inhibition of aluminum by lead soaps is attributed to the adsorption of large radius fatty acid anions on the oxide surface and the resultant weak electric fields accelerating aluminum ions through the oxide film, it follows that the simultaneous adsorption of even a small number of chloride ions of much smaller diameter should produce intense local fields which would effectively transport aluminum ions into solution. Accordingly the inhibition afforded by lead soaps is broken down by the addition even of 5 ppm chloride.

From the more practical standpoint of performance of lead based paints on aluminum, this implies that lead paints, particularly those pigmented with red lead or basic lead carbonate, would be expected to perform well on aluminum provided that chloride (or sulfate) ions were absent at the metal-paint interface. According to the work of Mayne (3) this condition should be realized, at least initially, since organic films can effectively prevent the passage of anions such as chloride and sulfate ions for considerable periods. Therefore, provided that the paint completely covers the aluminum, inhibition of corrosion by virtue of the presence of lead soaps should occur. However once the paint suffers breakdown or if it is discontinuous initially so that chloride or sulfate ions reach the metal surface, inhibition of corrosion would not be obtained. Particularly, in paints pigmented with litharge, rather severe corrosion of the aluminum should result. It is felt that these two opposing tendencies may be the reason for the very variable performance of aluminum covered with lead pigmented paints.

## Acknowledgments

The authors wish to acknowledge some careful experimental work by P. G. Sprang and the many helpful suggestions of J. J. McMullen. They wish to thank A. J. Eickhoff of the National Lead Company for supplying the pigments, W. J. Stewart of Nuodex Products for supplying the lead soaps, and the Kaiser Aluminum & Chemical Corporation for their support of this work and for their permission to publish the results.

Manuscript received April 2, 1957. This paper was prepared for presentation before the Cleveland Meeting, Sept. 30-Oct. 4, 1956.

Any discussion of this paper will appear in a Discussion Section to be published in the December 1958 JOURNAL.

## REFERENCES

1. H. Rohrig, *Korr. u. Metallshutz*, **5**, 85 (1929).
2. H. Wagner, *ibid.*, **16**, 329 (1940).
3. J. E. O. Mayne, *Research*, **6**, 278 (1952).
4. K. G. Lewis and U. R. Evans, *J. Soc. Chem. Ind.*, **53**, 25T (1934).
5. J. E. O. Mayne, *ibid.*, **65**, 196 (1946).
6. M. J. Pryor, *This Journal*, **101**, 141 (1953).
7. R. S. Thornhill, *J. Soc. Chem. Ind.*, **65**, 197 (1946).
8. M. J. Pryor and M. Cohen, *This Journal*, **100**, 203 (1953).
9. M. J. Pryor and D. S. Keir, *ibid.*, **104**, 269 (1957).
10. H. H. Uhlig, Editor, "Corrosion Handbook," p. 1081, John Wiley & Sons, Inc., New York (1948).
11. Snell and Snell, "Colorimetric Methods of Analysis," Vol. III, p. 1 (1949).
12. M. Pleissner, *Arb. kaiserl. Gesundh.*, **26**, 398 (1907).
13. J. C. Thresh, *Analyst*, **49**, 124 (1924).
14. J. A. V. Butler, "Electrocapillarity," p. 126, Methuen, London (1940).
15. M. J. Pryor and D. S. Keir, *This Journal*, **102**, 605 (1955).
16. J. E. O. Mayne and D. Van Rooyen, *J. Appl. Chem.*, **4**, 384 (1954).
17. N. K. Adam, "The Physics and Chemistry of Surfaces," p. 128, Oxford (1941).
18. N. K. Adam, *Proc. Roy. Soc.*, **A99**, 336 (1921).
19. N. K. Adam, "The Physics and Chemistry of Surfaces," p. 60, Oxford (1941).
20. E. K. Rideal, *Proc. Roy. Soc.*, **A140**, 253 (1933).
21. W. M. Latimer, "Oxidation Potentials," p. 123, Prentice Hall, New York (1950).
22. G. Kortum and J. O. M. Bockris, "A Textbook of Electrochemistry," Vol. II, p. 457, Elsevier Publishing Co., New York (1951).

# Analysis of Films on Copper by Coulometric Reduction

**R. H. Lambert and D. J. Trevoy**

*Research Laboratories, Eastman Kodak Company, Rochester, New York*

ABSTRACT

A technique is described for coulometric reduction of films on copper and other electropositive metals which utilizes a granular electrode for rapid and thorough pre-electrolysis of electrolyte to remove dissolved oxygen and traces of plateable cations. The sensitivity of the method has been thereby increased, and as little as a quarter of a monolayer of a reducible film can be detected readily. Results are reported for reversible cell potentials, overpotential as a function of pH and current density, and the effect of oxygen in the electrolyte, for the reduction of films of cuprous oxide, and for reduction of hydrogen ions at a copper surface. Data are also reported on the reduction of thick films of cuprous oxide formed at 125°C, and the usefulness of the coulometric method in providing information about the topography of reducible surface films is demonstrated. Other films studied included cuprous sulfide, cupric oxide, and cupric hydrogen phosphate, occurring alone or as mixed films. The effectiveness of various preparatory and rinsing techniques in eliminating phosphate contamination from copper surfaces electropolished in o-phosphoric acid has been evaluated. With the most favorable technique, the residual phosphate appears to be much less than a monolayer.

Many important operations involving the surfaces of solids, such as flotation, lithography, boundary lubrication, corrosion inhibition, and adhesion, depend ultimately on the interaction of substances with the outermost layer of atoms or molecules that constitutes the surface of the solid. In the case of certain metals, information about both the nature and the amount of inorganic films which may be present initially can often be obtained by controlled electrochemical reduction of the films *in situ*. The early experiments of Evans and Bannister (1), in which iodide films on silver foil were reduced electrochemically at constant potential, were followed by the work of Evans and Miley (2) on the reduction at constant current of oxide films on Cu and Fe. In subsequent work, the constant-current method has been preferred, and the technique has been considerably refined.

In theory, the method is capable of readily detecting and measuring very thin films, even fractions of a monolayer. When such sensitivity is desired, the problem is to decrease the concentrations of plateable cations and dissolved oxygen to sufficiently low levels, since these substances also compete for the reduction current. Campbell and Thomas (3) preboiled the 0.1*N* KCl electrolyte, bubbled $N_2$ through the solution before an experiment, and passed $N_2$ over the solution during an experiment. Prior to use, the $N_2$ was passed over hot reduced Cu.

Early experiments conducted here indicated that with such techniques the sensitivity was still limited by dissolved oxygen. To lower the oxygen level even farther, the aqueous solution was pre-electrolyzed by a modification of the pre-electrolysis technique which has found favor in studies of hydrogen overpotential (4). The present paper describes an apparatus for rapid and thorough pre-electrolysis of electrolyte by circulation of the liquid through the interstices in a large granular electrode. Films on Cu of the order of one Å have been detected, and reduction potentials observed for a variety of films agreed with theory in most instances.

## Experimental

### *Apparatus*

The apparatus consists of two interconnected cells, one for pre-electrolytic treatment of the solution, and the other for reduction of the film on a specimen. The electrical circuit is essentially the same for each cell, constant current being obtained from a 90-v dry-cell supply by placing the reduction cell in series with a large resistor. With suitable switching to change the size of the large resistor, the current may readily be varied in the range 0.008-1000 $\mu$a, and is measured with a microammeter and suitable shunts. A Ag-AgCl reference electrode with a Luggin capillary is coupled with the cathode to provide a potential signal which is amplified by an electrometer,[1] the output of which operates a recorder.[2] The recorder is connected to the output of the electrometer by a potential divider in parallel with an appropriate condenser-resistor combination which slightly damps the response of the recorder. A plot of potential as a function of time is thereby obtained without drawing appreciable current from the electrode pair. In parallel with the electrometer, a pH meter is also included to provide more accurate values of the potential when desired. The experimental points indicated in all of the figures were obtained in this way. Shielded conductors are used for all connections involved in

[1] Keithley, Model 210, input impedance $10^{14}$ ohms across a capacitance of 6$\mu\mu$f.

[2] Bristol, range 0-5 mv d.c., rate of chart travel 3/8 in./min.

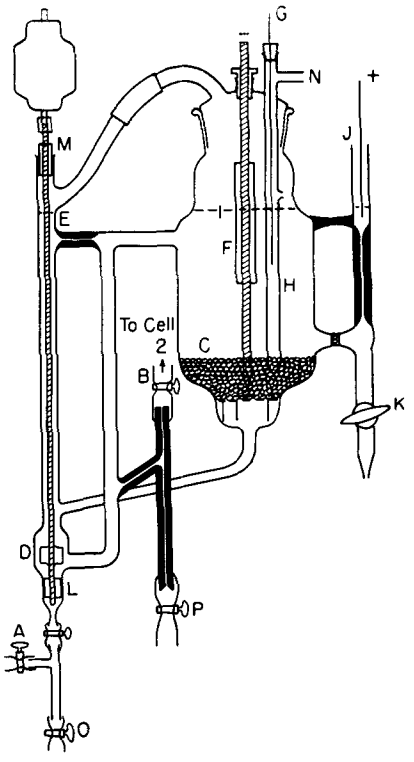


Fig. 1. Cell 1 for pre-electrolysis of electrolyte

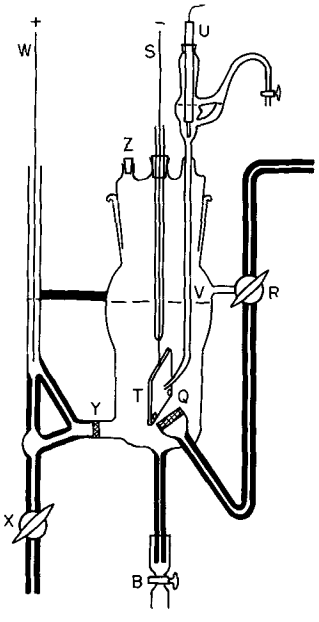


Fig. 2. Cell for reduction of films on metal surfaces

measuring or recording the potential, and the shielding is grounded.

Cell 1, shown in Fig. 1, and Cell 2, shown in Fig. 2, are similar in principle in that Cu is the cathode, and the anode and cathode sections are separated by a fritted-glass diaphragm. Cell 1 receives its solution at A from a 4-liter supply bottle through which hydrogen has been vigorously bubbled for a considerable time. After pre-electrolysis in Cell 1, a portion of the solution is passed to Cell 2 through the Tygon connection at B.

Cathode C of Cell 1 consists of a 3.2-mm Cu rod embedded in a large mass of Cu granules (Merck reagent). These granules have an average diameter of 2 mm and all are retained on a No. 18 sieve. Their total weight is 713 g, and the apparent surface area is estimated to be 1300 $cm^2$. The granules are supported on a Cu tripod, the upper plate of which is a Cu disk having many perforations. When the glass pump, D, is energized, the solution flows into the cathode chamber near the top, down through the granular electrode and Cu disk, and back to the pump in a cyclic path, thus making intimate contact with the large surface of the electrode. A small fraction of the flow passes through the capillary, E, thereby maintaining positive circulation of liquid in all parts of the cell. Around the Cu rod which forms part of the cathode a tightly fitting Teflon sleeve, F, eliminates any spurious effect which might arise at the gas-liquid interface. The Ag-AgCl reference electrode, G, passes through a cork into a glass tube, H, which extends into the granular Cu mass and has an orifice (0.05 cm in diameter) at its extremity, thus acting as a Luggin bridge. A hole in tube H just above the catholyte surface, I, permits entry of hydrogen or nitrogen gas, thereby maintaining an inert atmosphere over the solution. Anode J is at Pt wire. Diffusion of electrically formed $Cl_2$ from anode to cathode compartments is hindered by use of a fritted-glass disk and capillary tubing. Drainage of the anode compartment is effected at K. The pump shaft is supported by Teflon bearings at L and M, a slot in the upper bearing allowing for escape of gas entering at N. The volume of catholyte is about 800 ml. When the electrolyte has been sufficiently freed of oxygen and plateable cations, it is forced from Cell 1 to Cell 2 by suitably adjusting the speed of the pump and opening the clamp at B. The electrolyte may be drained from Cell 1 at O, and samples for *p*H determinations are obtained at P.

In Cell 2, Fig. 2, agitation may be secured by passing hydrogen or nitrogen through the solution in fine bubbles formed by the fritted-glass disk, Q. If agitation is not desired, the gas is passed over the solution by adjustment of the three-way stopcock, R. The Pt wire, S, is led through a sealed glass tube to a Pt saddle, T, which holds the Cu specimen. The Ag-AgCl electrode, U, is mounted in a Teflon sleeve, and the electrolyte is drawn up by suction through the Luggin capillary, V. The anode compartment with Pt anode, W, is attached with capillary tubing to allow for ready elimination of bubbles and for draining through a stopcock, X. A fritted-glass diaphragm, Y, separates the two compartments. Gas entering the cell through stopcock R escapes through a groove in the cork, Z. The volume of the cathode compartment is about 80 ml. Screw clamps on Tygon tubing are used wherever contamination of electrolyte by stopcock grease might occur, and glass stopcocks are used to control drainage from anode compartments and to regulate gas flow.

### *Method of Operation*

A 0.1*N* KCl solution is prepared in a 4-liter bottle from reagent-grade KCl and conductivity water, and is bubbled with $H_2$ for 1 hr. Bubbles are formed by a submerged, medium-porosity, fritted-glass disk. A portion of electrolyte is then allowed to

enter Cell 1 until the level is at I (Fig. 1), and a current of about 1 ma is applied while electrolyte is circulated at a moderate rate. The observed cathode potential measured against the reference electrode is about −0.25 v, corresponding to reduction of oxide, and is substantially constant for 15-30 min, after which it rapidly changes to −1.0 to −1.2 v, corresponding to reduction of hydrogen ions. By this time, most of the oxygen has been removed from the electrolyte, but traces are still present. Some measure of the amount remaining can be obtained by reducing successively the current in the circuit to determine the value at which the potential returns to about −0.25 v. This change occurs when the rate of arrival at the electrode of oxygen from the electrolyte is just equal to the rate of reduction of that oxygen (or oxide) by the imposed current. To further decrease the oxygen level in the electrolyte, reduction is continued with a moderate flow of electrolyte for approximately 1 hr, the current being just sufficient to reduce the oxygen as fast as it arrives. By this time, the oxygen content is usually sufficiently low so that the potential corresponding to evolution of hydrogen in Cell 1 does not move in the more positive direction by more than 25 mv in 30 min with a current of 20 $\mu$a through the cell. In the present work, pre-electrolysis is arbitrarily considered sufficient when such a condition is attained, and, if done correctly, the pH of the resulting electrolyte will not be above 8.5.

During pre-electrolysis of the solution in Cell 1, the Cu specimen, usually a 1-in. square of 16-gauge metal,[3] is placed in position in Cell 2 and hydrogen is passed through the cell prior to introduction of pre-electrolyzed solution from Cell 1. The film on a specimen is usually reduced without agitation, and hydrogen is passed over the surface of the electrolyte during reduction to prevent entry of oxygen from the air. The inflection point in the potential-time curve is taken as the endpoint, and the film thickness is calculated by the relation,

$$T = \frac{100itM}{aNFd} \qquad \text{(I)}$$

where $T$ is the thickness in Å, $i$ is the current in microamp, $t$ is the time in sec, $M$ is the formula weight, $a$ is the area in cm², $N$ is the number of faradays required to reduce one gram formula weight, $F$ is the faraday value in coulombs, and $d$ is the density of the film in g/cm³. The pH of the electrolyte is measured just before and just after many of the runs, and it is customary to discard the electrolyte before the pH reaches 11.0. Most of the work reported here was done in the pH range of 9.0-10.5, and the preferred current density for reduction of films in the thickness range of 20-40Å was 2.5 $\mu$a/cm². The time required for the actual reduction was 15-25 min.

## Overpotential and pH

Potential data presented below are compared with the reversible values calculated from data on free energy of formation compiled by Latimer (5), using the sign convention of Glasstone (6), a value of 0.770 for the activity coefficient of 0.1*N* KCl, and equating activity and concentration for hydrogen ions and hydroxyl ions. This procedure leads to the following relations for the reversible cathode potential with respect to the Ag-AgCl electrode in 0.1*N* KCl:

| | | |
|---|---|---|
| $Cu_2O \rightarrow Cu$ | $E = 0.181 - 0.0591\ pH$ | (II) |
| $H^+ \rightarrow \frac{1}{2} H_2$ | $E = -0.288 - 0.0591\ pH$ | (III) |
| $CuO \rightarrow Cu$ | $E = 0.281 - 0.0591\ pH$ | (IV) |
| $CuO \rightarrow Cu_2O$ | $E = 0.381 - 0.0591\ pH$ | (V) |

The change in potential with respect to current density when cuprous ion is being reduced to Cu is shown for two values of pH in Fig. 3. The curves approach the theoretical reversible values, calcu-

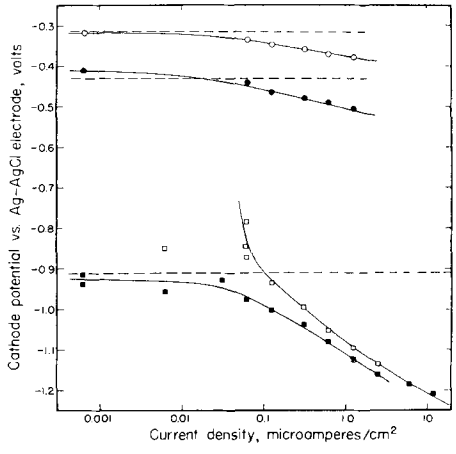


Fig. 3. Observed and calculated values of the potential for reduction of $Cu_2O$ at low current density, and for reduction of hydrogen ions at a Cu surface: open circle, reduction of oxide at pH = 8.50; closed circle, reduction of oxide at pH = 10.45; open square, reduction of hydrogen ions at pH = 10.5, with hydrogen bubbling; closed square, reduction of hydrogen ions at pH = 10.5, with no bubbling; ——— observed; — — — reversible.

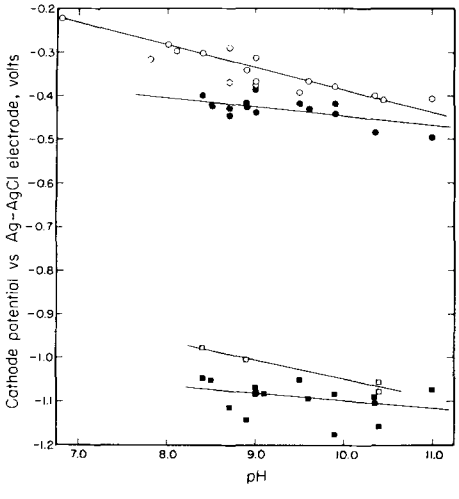


Fig. 4. Variation with pH of the potential for $Cu_2O$ reduction and for reduction of hydrogen ions at a Cu surface for various values of current density: open circle, oxide reduction at 0.00063 $\mu$a/cm²; closed circle, oxide reduction at 2.51 $\mu$a/cm²; open square, hydrogen ion reduction at 0.63 $\mu$a/cm²; closed square, hydrogen ion reduction at 2.51 $\mu$a/cm².

[3] Photoengravers' copper, Edes Manufacturing Co., Plymouth, Mass.

lated by Eq. (II), as the current density becomes small. The deviation at higher current densities may be considered to be due to the "copper overpotential" which is analogous to the more familiar hydrogen overpotential. The variation of potential with current density for reduction of hydrogen ions at a Cu surface is also shown in Fig. 3 for a pH of 10.5. As for the cuprous ion, the approach to the reversible value is satisfactory at very low values of the current density. Bubbling hydrogen through the liquid during reduction is believed to reduce concentration polarization and thereby to shift the cathode potential to more positive values. At a current density of about 0.1 $\mu a/cm^2$, bubbling had increased the rate of arrival of dissolved oxygen at the cathode to such a level that a substantial part of the current was used in reducing this oxygen. At even lower current density values, the rate of arrival of oxygen at the cathode in the agitated electrolyte exceeded that which could be taken care of by the available current, and the potential became much less negative. This effect is believed to be due not to oxygen transferred from the hydrogen bubbles but to the increased rate of arrival at the cathode of residual oxygen already present in the electrolyte. Once the oxygen content of the electrolyte is quite low, tank hydrogen may be bubbled vigorously through the solution for 2 hr without producing any measurable oxide film on the specimen, the sensitivity of measurement being about 0.5Å.

Some idea of the effect of pH on the observed potentials for reduction of cuprous oxide films and for reduction of hydrogen ions was obtained by plotting the data obtained from many months of operation; Fig. 4 is typical of the results obtained. Considerable scatter was observed, and the number of observations was insufficient, at many values of current density, to provide highly significant correlations. For very low values of current density, however, the slopes of the lines of best fit on a pH-potential plot were in fair agreement with theory (−0.0591), but, at normal values of current density, the lines were more nearly horizontal. Measurements on a single specimen were consistent within themselves, but pronounced scatter was often observed when different specimens were compared. This suggests that subtle variations may occur from one run to the next in the nature of the surface, residual stresses in surface crystals, the real surface area, the number and nature of any adsorbed molecules (7), and the topography of the surface film.

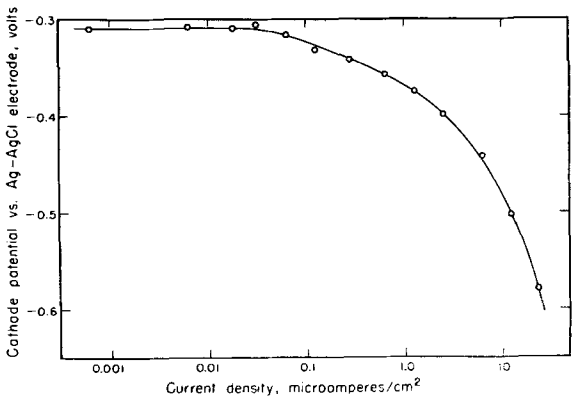


Fig. 5. Variation of reduction potential with current density for a thick $Cu_2O$ film at a pH of 9.6.

By subtracting the calculated reversible values from particular values taken from the lines of best fit, values of overpotential were obtained for the two electrode processes as a function of pH, and are given in Table I. It is observed that, for both electrode processes, the values of overpotential decrease with increasing pH at about the same rate. The overpotential for oxide reduction is much lower than that for reduction of hydrogen ions, an observation which suggests a smaller potential energy barrier in the case of oxide reduction. A slight extrapolation of the data for reduction of cuprous oxide indicates that the overpotential would become zero at pH = 11.0. In a discussion of Cu and its oxides by Pourbaix (8), a stability diagram is presented which indicates that the metal is passivated and $Cu_2O$ is the stable phase in the pH range 8.0-11.5. For more alkaline solutions, the diagram indicates that $Cu_2O$ films are not stable, and should dissolve spontaneously, in which case the overpotential would be zero. In a qualitative way, the authors' measurements of overpotential are in accord with this prediction.

In the present study, many measurements of oxide thickness on both abraded and electropolished surfaces have been made by the coulometric technique, but little difference in thickness of oxide has been observed as a result of differences in the method of surface preparation. It appears that a protective $Cu_2O$ film of 20-40Å is formed very rapidly on exposure to air, tank hydrogen, or tank nitrogen, and the particular thickness seems to depend more on rinsing and drying conditions than on the method of surface preparation.

## Thick Oxide Films on Copper and Topography of the Oxide Layer

It is generally agreed that only $Cu_2O$ is formed by aerial oxidation of Cu below 150°C, although the sensitivity limits of the diffraction techniques normally used do not exclude the possible existence of a few percent of CuO. Thick oxide films on Cu in the range of 200-400Å were prepared by storing cleaned specimens in air at 125°C for several hours or days. The films were then reduced coulometrically. With a very low current density, $6.3 \times 10^{-4}$ $\mu a/cm^2$, these specimens always showed an initial potential in the range of −0.13 to −0.20 v, substantially less negative than that observed for much

Table I. Overpotential as a function of pH at a current density of 2.51 $\mu a/cm^2$

| Electrode process | Overpotential, volts | | | |
|---|---|---|---|---|
| | pH = 8.5 | pH = 9.0 | pH = 10.0 | pH = 10.5 |
| Reduction of $Cu_2O$ to Cu | −0.095 | −0.077 | −0.038 | −0.018 |
| Reduction of hydrogen ions at a Cu surface | −0.288 | −0.265 | −0.219 | −0.198 |

thinner films (−0.30 to −0.35 v). With time, the potential became more negative, and finally became comparable to that of thin films of $Cu_2O$. The rate of change of potential with time was not accelerated by changing the current density over a wide range or by stirring the electrolyte.

As a tentative explanation for these phenomena, it is pointed out that the initial potential approximates that for reduction of CuO to $Cu_2O$, as shown by Eq. (V), and may therefore indicate traces of CuO. When immersed in the electrolyte, a change in the film occurs which is not dependent on the rate of charge transfer and which results in the attainment of the normal potential for a $Cu_2O$ film after sufficient time has elapsed. If the initial potential is actually due to traces of CuO, this oxide may be converted slowly to $Cu_2O$, or may perhaps be dissolved on standing in the KCl solution.

The phenomena observed during reduction of thick films and the uncertainty of the speculation concerning the origin of these effects led the authors to present the data on thick films separately from those for thin films formed at room temperature, the typical variation of reduction potential with current density being shown in Fig. 5 for thick films formed at 125°C.

Because the reduction potential is strongly dependent on current density in the range of current density normally used, considerable information concerning the topography or uniformity of distribution of a film over the surface of the metal can be obtained from the reduction curve. Very thin films, having a thickness of the order of 20Å, might be expected to be quite uniform in thickness, and, on reduction, such films yield a rather flat plateau, followed by a rapid change in potential when the film is exhausted. In this case, the transition from one plateau to the next probably requires the period of time needed for the reduction of the last monolayer of the almost exhausted component in the film. To prove that the shape of the curve in the transition region is not controlled by some other process, such as diffusion, a specimen having about the usual thickness of oxide was reduced at half the usual current density. The transition occupied twice as much time as previously, and, when the curve was replotted with the abscissa compressed by a factor of two, the shape of the curve was identical with that obtained by reducing at the higher current density. If one relates the change in potential with current density, shown in Fig. 5, to the shape of the curve in the transition region for a specimen having a thin film of $Cu_2O$, it is evident that 90% or more of the last monolayer of $Cu_2O$ has been reduced when the potential-time curve reaches the inflection point.

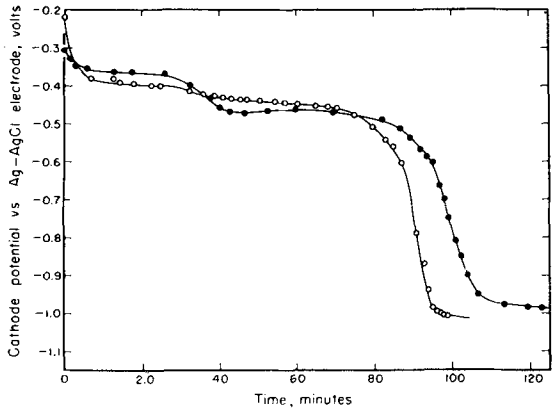


Fig. 6. Effect of variations in topography of $Cu_2O$ films on the reduction curves: open circle, thick film on 50% of area, 2.53 $\mu a/cm^2$; closed circle, thick film on 10% of area, 1.29 $\mu a/cm^2$.

A thick film, on the other hand, is often less uniform in thickness over the area of the specimen. This could conceivably result in a gradual increase in potential along the plateau, as some areas are virtually freed of film while others still have a considerable coating. When the film is almost gone, its persistence in local areas which were thicker originally might tend to produce a more gradual change in potential in the transition region. The validity of these ideas was confirmed by reducing specimens with nonuniform film distributions on which interference colors varied over the area. A further check was provided by reduction of specimens which carried both a thick and a thin film on adjacent areas of the same specimen. One of these was prepared by forming a thick oxide deposit at 125°C, then dissolving the oxide on half the specimen by dipping in 0.02*N* HCl, followed by rapid rinsing in water and in alcohol. When dry, the specimen was thereby covered over half the area with a thick oxide deposit and the remainder had only a thin film. In another case, nine-tenths of the thick film was dissolved in the dilute acid. Reduction potential curves for these specimens are shown in Fig. 6, and, in each case, one observes two plateaus arising from the fact that the effective current density changes rather abruptly when the thin film becomes exhausted.

When a thick film is prepared by a 5-min aerial oxidation at 500°C, only cupric oxide is formed, according to Dixit and Agashe (9). Such a film gave potentials generally about 0.09 v more negative than were obtained for thick films of cuprous oxide, although Eqs. (II) and (IV) indicate a potential 0.10 v more positive, as the limiting case of zero current is approached. The present experiments do not agree well with those of Miley (10), who observed for reduction of CuO a potential 0.315 v more negative than that required for reduction of $Cu_2O$.

### Other Films on Copper

Measurement of mixed sulfide and oxide films on Cu yielded results similar to those of Campbell and Thomas (3), the sulfide being formed by dipping a pumiced specimen in $H_2S$ water. When reduced at a current density of 2.51 $\mu a/cm^2$, the first plateau occurred at −0.394 v, a reasonable value for $Cu_2O$ reduction, and the second plateau occurred at −0.956 v, a value believed to correspond to the reduction of $Cu_2S$ to Cu. The mixed-film experiment demonstrates that many reducible films can be analyzed by this technique if they are relatively insoluble in the electrolyte, and if the reduction occurs at a potential less negative than the evolution of hydrogen or other limiting reaction.

The nature of electropolished surfaces is of considerable interest in other studies currently being

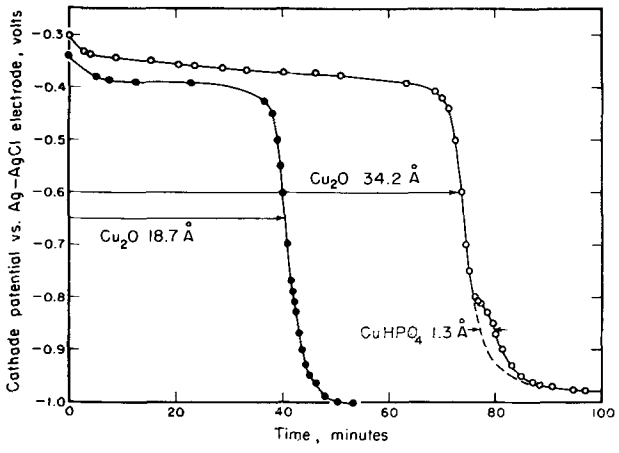


Fig. 7. Reduction at 0.62 $\mu a/cm^2$ of the film on electropolished Cu rinsed in 10% o-phosphoric acid, and for the same specimen after reoxidation in tank nitrogen: open circle, pH = 8.5; closed circle, pH = 9.0.

conducted here. When a smooth Cu specimen was prepared by electropolishing in an aqueous solution containing 63% by weight of o-phosphoric acid, followed by thorough rinsing in redistilled water and ethanol before drying, two plateaus were observed in the reduction curve. The first at −0.413 v probably indicated $Cu_2O$, while the second at −0.792 v is believed due to a phosphate salt insolubilized during rinsing of the electropolished specimen. [Following Walton (11), it is assumed that the salt is cupric hydrogen phosphate.] Allen (12) has reported similar results but claims that the phosphate film can be removed completely by a rinse with 10% o-phosphoric acid, followed by a thorough rinse with water. Our reduction experiments, which are believed to be more sensitive than Allen's, have not verified the absolute removal of phosphate by this rinsing technique. It seemed likely that the phosphate salt might reside largely in pits or irregularities in the surface, and these were minimized by polishing in a vertical plane and by filing the lower edge of the specimen to a knife-edge before polishing to eliminate attachment of bubbles and subsequent pitting. This technique reduced the estimated amount of phosphate to about 1.3Å, as shown in the upper curve of Fig. 7. [Using a radioactive tracer technique, Simpson and Hackerman (13) recently studied the elimination of phosphate contamination from electropolished Cu surfaces, but the 10% phosphoric acid rinse was not employed in their work.]

After reduction, the specimen was lifted out of the electrolyte and left for three days in nitrogen gas above the solution. The surface film was then reduced again, and the data provide the lower curve of Fig. 7, indicating complete absence of the phosphate salt. If the reduced specimen was allowed to remain in the electrolyte in which the phosphate salt had been reduced, no re-formation of a phosphate film on the specimen was observed on subsequent reduction. After reduction of a sulfide film, however, gradual re-formation of the sulfide film was observed when the reduced specimen was left in the electrolyte. This difference in behavior may be due to a difference in the solubility product constants of the sulfide and phosphate salts.

### Films on Electronegative Metals

The results just described demonstrate that coulometric reduction is a valuable tool for the study of reducible films on Cu, the sensitivity being sufficient for measurement of fractional monolayers. Application of the method to electronegative metals in aqueous solution is precluded, however, by the evolution of hydrogen at potentials less negative than are necessary for reduction of surface films. It was hoped that a nonaqueous system could be found which would avoid this difficulty without introducing other problems, but preliminary experiments have not led to the discovery of such a system.

Manuscript received Feb. 19, 1957. Communication No. 1882 from the Kodak Research Laboratories.

Any discussion of this paper will appear in a Discussion Section to be published in the December 1958 JOURNAL.

REFERENCES

1. U. R. Evans and L. C. Bannister, *Proc. Roy. Soc. (London)*, **A125**, 370 (1929).
2. U. R. Evans and H. A. Miley, *Nature*, **139**, 283 (1937).
3. W. E. Campbell and U. B. Thomas, *Trans. Electrochem. Soc.*, **76**, 303 (1939).
4. J. O'M. Bockris, *Chem. Revs.*, **43**, 544 (1948).
5. W. M. Latimer, "Oxidation Potentials," 2nd ed., Prentice-Hall Inc., New York (1952).
6. S. Glasstone, "Textbook of Physical Chemistry," 2nd ed., D. Van Nostrand Co., New York (1946).
7. R. S. Hansen and B. H. Clampitt, *J. Phys. Chem.*, **58**, 908 (1954).
8. M. J. N. Pourbaix, "Thermodynamics of Dilute Aqueous Solutions," p. 55, Edward Arnold and Co., London (1949).
9. K. R. Dixit and V. V. Agashe, *Z. Naturforsch.*, **10a**, 152 (1955).
10. H. A. Miley, *J. Am. Chem. Soc.*, **59**, 2626 (1937).
11. H. F. Walton, *This Journal*, **97**, 219 (1950).
12. J. A. Allen, *Trans. Faraday Soc.*, **48**, 273 (1952).
13. N. H. Simpson and N. Hackerman, *This Journal*, **102**, 660 (1955).

## June 1958 Discussion Section

A Discussion Section, covering papers published in the July–December 1957 JOURNALS, is scheduled for publication in the June 1958 issue. Any discussion which did not reach the Editor in time for inclusion in the December 1957 Discussion Section will be included in the June 1958 issue.

Those who plan to contribute remarks for this Discussion Section should submit their comments or questions in triplicate to the Managing Editor of the JOURNAL, 1860 Broadway, New York 23, N. Y., *not later than March 1, 1958*. All discussion will be forwarded to the author, or authors, for reply before being printed in the JOURNAL.

# Acid Copper Plating on Aluminum

J. T. N. Atkinson

*Naval Research Establishment, Dartmouth, Nova Scotia*

ABSTRACT

A method for plating copper on aluminum and its alloys is recorded that eliminates the need for special pretreatments, zincate dips, etc. A moderately acid copper solution containing oxalates, pyrophosphates, ammonia, and triethylamine has been found to be most effective. Rack and barrel plated work can be controlled to give adhesion better than the ultimate properties of tin-lead solder; continuously plated wire has been produced on a small scale.

Following an initial observation that, when a Cu-Al couple is immersed in glacial acetic acid, the Cu is attacked preferentially, an attempt was made to apply this phenomenon to useful systems for plating Cu on Al. This seemed to open the possibility of using strongly acid solutions for the direct electrodeposition of Cu or other metals on Al, in marked contrast to the normal practice of using neutral or nearly neutral solutions for the electroplating step (1, 2), except for the method of Burgess and Hambuechen (3).

Their method depends on mechanical keying for adhesion, but removes final traces of the $Al_2O_3$ film by cathodic action in the mildly acid zinc sulfate plating solution prescribed. Otherwise there has been an implicit assumption (4) that electroplating on Al from an acid solution is impossible. Only within the last few months has a reference to an acid Cu solution for direct plating on aluminum been published (5), although this process requires pretreatment steps under vacuum and its practical utility is unknown.

A review of plating various metals from acid solutions led to an interesting rediscovery of the Gauduin (6) process. Unfortunately the original patent was as vague as the brief references found, and merely established that the bath consisted of ammonium oxalate, copper oxalate, and oxalic acid and should be operated at from 40° to 60°C.

Although heating large plating tanks was difficult, the process was used for Cu plating some cast iron statuary for the Paris exhibition of 1878, the largest pieces being two cast iron bulls weighing 1600 kg each. Later, attempts to heat the plating tanks were apparently abandoned, and the process was modified to operate at room temperature but at lower current density.

This modification appears to have ruined the Gauduin process. It was not revived even when, around the turn of the century, practical methods of heating plating tanks paved the way for general acceptance of cyanide copper plating. It is indeed strange that there has been no re-examination of the Gauduin process, as there has been a good deal of interest in replacing cyanide baths by less toxic formulations of comparable usefulness, particularly in view of the technical excellence of the process in its early stages.

Once it was established here experimentally that even a moderate Cu-Al adhesion could result from direct plating methods, effort was concentrated on such methods. These would have considerable practical as well as theoretical interest. Removal of oxide film concurrently with the deposition of another metal such as Cu from a plating bath of otherwise normal characteristics should provide an elegant solution of the oxide film difficulties previously associated with plating on Al. Elimination of acid treatment and zincate immersion steps would naturally appeal to the practical plater.

## Experimental Work

Experiments showed that Al did not corrode rapidly in a wide variety of more or less conventional acid Cu plating solutions and attempts were made to use these to plate on Al. However, poor adhesion resulted from attempts to plate from standard formulations. Addition of an agent designed to increase corrosion of Al by the electrolyte resulted, in certain cases, in the marked improvement of the adhesion of the plate to the basis metal. All of these tests were conducted using commercially pure Al that had been solvent or vapor cleaned, and degreased in a conventional phosphate-carbonate cleaner.

The initial criterion of adhesion was an 180° bending test without a mandrel. The practical criterion (in spite of objections to simple testing procedure) of Ehrhardt and Guthrie (8) was later adopted. That is, an adequate test for plated Al is the mechanical destruction of a soldered joint without causing the plate to part from the basis metal. Essentially, the adhesion in shear was measured via a soldered joint of 1/16 $in.^2$ area; the final refined version of this test has been published elsewhere (9). Much of the work reported in this paper preceded this development, and adhesion is therefore characterized as good, intermediate, and poor when it exceeds 5000 psi, is between 2000 and 5000 psi, and is less than 2000 psi, respectively. Confirmatory tests of samples considered to have good adhesion showed that no plating failure by repeated bending could be detected. In the case of some such samples annealed at 350°C after plating, metallographic examination showed extensive formation of intermetallic compound at the interface.

Table I. Results of initial plating trials

| Metal plated | Other cations | Anions present | Other additions | Adhesion | Remarks |
|---|---|---|---|---|---|
| Cu | — | Acetate | Various | Poor | Solubility of Cu too low |
| Cu | — | Citrate, nitrate | — | Poor-inter. | — |
| Cu | — | Citrate, nitrate, fluoride | — | Inter. | — |
| Cu | Ammonium | Citrate, nitrate, fluoride | — | Inter. | — |
| Cu | — | Citrate, sulfate, fluoride | — | Inter. | — |
| Cu | — | Sulfate | — | Poor | — |
| Cu | — | Sulfate | Various* | Poor-inter. | — |
| Cu | Ammonium | Oxalate | — | Inter. | Gauduin's bath—pH 5 |
| Cu | Ammonium | Oxalate | Various† | Inter.-good | Approx. pH 5 |

* To increase solubility of $Al_2O_3$ film; complexing agents such as aluminon and corrodents such as grapefruit juice were helpful.
† *See* Table II.

Results of initial experiments with Cu plating are consolidated into Table I. The pH of the plating solutions, except where noted, was less than 2, and often less than 1. Similar tests with Zn, Cd, Ni, Sn, Pb, and Ag were generally less promising. In the case of Pb and Ag there was serious corrosion of the Al cathode.

### Development of Solutions Based on Oxalates

Although considerable effort was directed toward development of plating solutions related to the conventional acid sulfate bath and the systems including citric acid, only in the case of the oxalate solutions were the best results obtainable. Since the published information on Gauduin's bath was so meager, work had to start with solubility studies. The preferred bath composition consisted of 20 g of cupric oxide dissolved in a hot solution of 100 g of ammonium oxalate crystals and 60 g of oxalic acid crystals, the final volume being made up to 1 liter. This bath gives a fully adherent immersion deposit on steel in addition to giving good matt electrodeposits at about 2 amp/dm$^2$ at 50°-60°C. By modern standards the rate of deposition is too low and the anode corrosion inferior. For direct plating on Al the adhesion was as good as the best obtained in alternative systems referred to in Table I.

Limitations of the Gauduin bath appeared to be twofold: low solubility of ammonium oxalate and/or a Cu complex; insufficient reactivity with aluminum oxide to develop good adhesion. Modifications were made to overcome these defects, and are summarized in Table II.

Table II. Modifications to Gauduin bath

| Anion replacing or added to oxalate: | Other addition | Adhesion | Comments |
|---|---|---|---|
| Sulfate, nitrate, Citrate, acetate, Tartrate, malate, Salicylate, sulfo Salicylate, or succinate | | Not improved | |
| Boric acid | — | Slight improvement | 10 g/l |
| Fluoride | — | Slight improvement | 0.2 g/l |
| | Aluminon | Slight improvement | Up to limit of solubility |
| Pyrophosphate | — | Major improvement | |

Without question, the most effective of the initial modifications was the replacement of all the ammonium oxalate in the original formulation by a like amount of ammonium pyrophosphate. This definitely overcomes the solubility limitations noted earlier and also puts the adhesion on Al consistently in the good range for the relatively thin deposits employed. Anode corrosion was still somewhat inferior, however, so attempts were made to remedy this.

Since the adhesion of Cu to Al fell off as pH was increased, this method of improving anode corrosion was not acceptable. The influence of a large number of amines on anode corrosion was then studied, and it was found that those with soluble Cu complexes were generally helpful in promoting adhesion. However, only the tertiary alkyl amines were stable to extended electrolysis, and triethylamine appeared to be the preferred addition.

The solution composition which has been tested most extensively is: ammonium pyrophosphate, 100 g; oxalic acid crystals, 60 g; copper oxide, 20 g; triethylamine, 50 g; water to make 1 liter; initial pH, 5.6-5.8.

The ammonium pyrophosphate was prepared by reaction of ammonia and pyrophosphoric acid at or near 0°C to avoid excessive hydrolysis. In view of this complication, and the difficulty of dissolving copper oxide, the use of copper pyrophosphate as starting material may be superior, particularly for large-scale use.

### Details of Plating Procedure

The bulk of the work with this solution has been performed on rack plated work, in solution batches ranging up to 55 gal and using the same batch of solution for periods of up to the order of months. Barrel plated work has been, so far as can be judged with the limited adhesion test used, fully satisfactory, while wire plated in the low speed continuous wire plating device developed intermediate adhesion only.

Typical procedure is as follows: the work, following vapor degreasing, is cleaned by immersion for

about 45 sec in a solution containing 3% each, by weight, of trisodium phosphate and soda ash, at a temperature of about 65°C. The time of immersion cleaning is varied slightly according to the alloy used, being greater for the more corrosion resistant alloys. The work is then rinsed and immersed in the plating solution, with the plating current being applied at up to a minute or two after the immersion of the work. Plating then proceeds at 2.7 amp/dm$^2$ at a temperature of 60°C with cathode bar agitation at 90 in./min. Under these conditions, deposits of good adhesion, according to the solder adhesion test, can be obtained at least up to 0.0005 in. in thickness.

The step requiring closest control in the above sequence appears to be the immersion cleaning step. This step is not drastic enough to remove any appreciable contamination, yet adhesion can suffer from overcleaning. Wide variations in solution composition seem to be acceptable for the plating bath, and satisfactory results have been obtained with compositions running from one half to three times that of the example given. Too high a ratio of pyrophosphate to Cu appears to be undesirable, as it appears to lead to more rapid hydrolysis of the pyrophosphate, but otherwise there seems to be considerable leeway in solution formulation. As would be expected, the more concentrated solutions give good plating at higher current densities and temperatures.

An interesting series of observations is connected with the relation between plating adhesion, plating conditions, plating thickness, and a number of possible intermediate treatments. Some inconsistencies in adhesion had been noted, but appeared to correlate with the observation that good adhesion could only be obtained for thin deposits, unless effective cathode agitation was employed. Without such agitation, good adhesion could only be obtained for deposits below 0.0001 in. in thickness, with the Cu-Al adhesion of deposits over 0.001 in. decidedly poor. Poor Cu-Al adhesion also resulted from transferring the work to other solutions for deposits of acid copper, cyanide copper, pyrophosphate copper, Watts nickel, etc. However, this defect could be ameliorated by leaving the work with the thin Cu strike at room temperature for a few days, or immersing it for 20 or 30 min in boiling water prior to continued plating. Adhesion of moderately thick deposits was also improved by plating with interrupted d.c., although this was not so effective as cathode bar agitation. It should be noted that Cu plated from this bath on solid surfaces and subsequently stripped was only slightly curled, suggesting that stress levels in the plate were quite low.

Aluminum wire plated continuously from this bath gave intermediate adhesion only. This is believed to be due to the inability to operate the plating device used at high wire speed. A trial on a larger, high speed device seems warranted.

## Discussion of Results

The general field of oxalate plating of Cu on Al has shown promise, a number of additives being available to enhance the performance of the ammonium oxalate-oxalic acid-copper oxalate type of bath.

The original formulation was improved by the addition of fluorides or boric acid, and by replacing all or part of the ammonium oxalate by ammonium pyrophosphate. The properties of the pyrophosphate-oxalate system noted above could be improved still further by the addition of triethylamine. Unfortunately, solubility limitations prevented the operation of these solutions at pH values below about 5, where more rapid dissolution of the aluminum oxide film could be expected. This is probably why a brief immersion period prior to plating was sometimes helpful.

The principal shortcoming noted in the experimental work was associated with attempts to produce deposits of several ten thousandths of an inch in thickness under improper conditions. The improvement in adhesion resulting from leaving plated work for a few days at room temperature or for a few hours at 100°C strongly suggests the possibility of gas accumulation at the Cu-Al interface. That this occurs with a variety of plating solutions suggests that codeposited hydrogen accumulates in molecular form at the Cu-Al interface. This hypothesis requires an abnormally high diffusion rate for hydrogen in electroplated Cu, analogous to that recently reported by Ewing, Tobin, and Foulke (11) for hydrogen in electroplated Ni.

The results obtained appear to suggest that the amine modified pyrophosphate-oxalate process for plating Cu on Al shows promise of providing a significant technical advance. The fully successful barrel plating operations and the highly promising continuous wire plating are especially noteworthy.

The concept of a plating bath for Al incorporating an acid pickling as well as a plating action also seems to be substantiated by the results obtained. It is evident, however, that the action of the pyrophosphate-oxalate baths is highly specific, since this type of bath produces so much better results than those found for other solutions.

Returning to the Gauduin process itself, there is some reason to believe that its rediscovery may lead to important practical applications in the plating of metals other than Al, notably Zn and Fe. For this, some modification of the original process would likely be more effective than to use the original three component formulation.

The successful use of acid Cu solutions for direct plating on Al implies that the corrosion of Al in acid Cu solutions is much less than expected. Since both Pb and Ag show normal acceleration of Al corrosion in acid solution, it may be speculated that Cu ions tend to behave as corrosion inhibitors for Al in acid solution. In connection with this, Cobb and Uhlig's (12) conclusion that Cu ions inhibit corrosion of Ti in acid solution should be mentioned parenthetically.

## Acknowledgments

The work reported in this paper constitutes part of Defense Research Board Project D12-75-20-01. The author is grateful to the Chairman of the Board for permission to publish this work. The author wishes to acknowledge the assistance of Messrs.

J. Bannerman, J. L. Cromwell, R. A. Stuart, R. A. Brown, J. M. Roberge, and T. Sorensen in performing parts of the experimental work.

Manuscript received Sept. 24, 1956. This paper was prepared for delivery before the Cleveland Meeting, Sept. 30-Oct. 4, 1956.

Any discussion of this paper will appear in a Discussion Section to be published in the December 1958 JOURNAL.

REFERENCES

1. H. K. Work, *Trans. Electrochem. Soc.*, **53**, 361 (1928).
2. A. G. Gray, Editor, "Modern Electroplating," John Wiley & Sons, Inc., New York (1953).
3. C. F. Burgess and C. Hambuechen, *Electrochem. Ind.*, **2**, 85 (1904).
4. J. E. Stareck (to United Chromium Inc.), U. S. Pat. 2,437,865, Mar. 16, 1948.
5. R. Kumagaya (to Fuji Industries Co.), Japan. Pat. 860, Feb. 12, 1955.
6. Gauduin, Mignon, et Rouart, French Pat. 97030, Oct. 30, 1872.
7. H. C. Schlaupitz and W. D. Robertson, *Plating*, **39**, 750, 862 (1952).
8. R. A. Ehrhardt and J. M. Guthrie, *Monthly Rev. Am. Electroplaters Soc.*, **34**, 421 (1947).
9. J. D. McIntyre and A. F. McMillan, *Can. J. Technol.*, **34**, 212 (1956).
10. S. Heiman, *J. (and Trans.) Electrochem. Soc.*, **95**, 205 (1949).
11. D. T. Ewing, J. M. Tobin, and D. G. Foulke, *This Journal*, **103**, 545 (1956).
12. J. R. Cobb and H. H. Uhlig, *ibid.*, **99**, 13 (1952).

# Energy Transfer and Sensitization in Single Crystal Phosphors

**R. Leach**

*Department of Physics, The University of Hull, England*

ABSTRACT

Previous investigations, showing that calcium fluoride activated with cerium and manganese forms a sensitized phosphor of high efficiency, are confirmed as a result of measurements on activated single crystals. Measurements of oscillator strength enable the absorptive transitions at the cerium center to be identified, and the transition giving rise to the observed manganese emission is also identified. Evidence is presented to show that the transfer involves a spin exchange interaction between the unlike impurity ions which must be situated within a few lattice sites of each other in the fluorite lattice.

In recent years the subject of sensitized luminescence has been studied extensively, both on account of the applications to the fluorescent lamp industry and also because of the great theoretical interest attached to the solution of a problem intrinsically much simpler than most others in the field of luminescence. A fundamental study of the problem involves the determination of the mechanism of interaction between the sensitizer center, which is responsible for most of the energy absorption, and the activator center, which gives rise to the main emission band.

A variety of theories has been proposed to explain the transfer mechanism, and these have been summarized in an excellent article by Botden (1). As a result of an extensive experimental study of many different sensitized systems it is possible to eliminate most of the theories, chiefly on the grounds that the dependence of the activator emission on excitation intensity is linear and not quadratic, and because sensitized systems are nonphotoconducting. The most likely explanation of the energy transfer process involves the concept of resonance between the excited states of sensitizer and activator centers, which possess a similar amount of energy with respect to the energy level scheme in the host material. Transfer of energy by a quantum mechanical resonance process will be strongly dependent on the distance over which the energy must be transferred and also on the precise nature of the optical transition at each center.

The theoretical treatment of the resonance process is directly analogous to that developed by Perrin (2) and also Förster (3) to account for certain energy transfer processes in gases. However, in the solid state the activator emission usually originates from a forbidden transition and thus the resonance process differs from that in gases where only electric dipole interactions need be considered. Dexter (4) has extended the theoretical treatment and calculates, for transitions of differing multipole order, the number of lattice sites over which transfer is possible. The transfer range is large for dipole-dipole transitions falling off to small values for exchange interactions, and becoming negligibly small for dipole-magnetic dipole interactions.

It is difficult to account for the high observed transfer efficiencies occurring with quite low activator concentrations on the basis of the above simple picture alone, and most workers have attempted to overcome the deficiency by postulating successive sensitizer-sensitizer transitions until the excitation energy reaches a sensitizer center sufficiently close to an activator center for the transfer to be possible. However, in many systems large Frank-Condon shifts occur between the maxima of the sensitizer absorption and emission bands whereas it is essential in all resonance transfers for the excited states concerned to have similar energies with respect to the level scheme of the matrix lattice. Thus transfer to a neighboring identical sensitizer center must be necessarily unlikely in view

of the considerable energy difference between the occupied and unoccupied excited states.

This paper describes the results of experiments which have been carried out on the sensitized system formed by $CaF_2$ activated with trivalent Ce and divalent Mn as sensitizer and activator, respectively. It is demonstrated that the results are in agreement with the predictions of the resonance theory of energy transfer, although in the absence of sensitizer-sensitizer transitions, the high transfer efficiencies can only be explained by assuming a nonrandom distribution of activators.

## Experimental

The $CaF_2$-Ce-Mn system has been studied by Ginther (5) who made extensive measurements of reflection spectra and luminescence excitation and emission spectra. His specimens were all in the form of microcrystalline powders. The present measurements were inspired by the availability of large, synthetic, single crystals of fluorite into which the activators could be introduced either in the melt or by subsequent diffusion processes at temperatures well below the melting point of $CaF_2$. The use of single crystals permits a wide range of physical measurements to be made and, in the present case, information obtained from measurements of absorption coefficients enabled the nature of the transitions at each center to be established. Diffusion experiments using small cleavage crystals provided important evidence in support of the existence of large localized impurity distributions.

The fluorite crystals were grown *in vacuo* by the Stockbarger method. In the cases where the impurities were introduced in the melt the luminescence characteristics indicated a uniform distribution of Ce, but a zone purification effect occurred in the case of Mn. This defect was overcome by making all measurements on a single slab of crystal cut perpendicular to the growth direction. The Mn content was determined by colorimetric analysis.

*Thermal diffusion.*—The specimens activated by thermal diffusion were produced by heating small, good-quality, cleavage crystals of fluorite in a silica tube, together with the desired quantity of manganous or cerous fluoride mixed with $CaF_2$ powder, which prevented the small quantities of the activators from being lost during the preliminary evacuation of the system and also provided a useful comparison with the resultant luminescence of the crystal after activation. The tube was heated in an electric furnace in an atmosphere of argon which served to prevent oxidation. Cathodoluminescent fluorite could be prepared by diffusion of Mn into the lattice at temperatures as low as 800°K, although at this temperature diffusion took place mainly along the direction of dislocations in the lattice and on the surface of the specimens. As the firing temperature was raised the activation, as judged by discharge excitation following cleaving and polishing, became more uniform. It was not possible to produce cathodoluminescent crystals by heating fluorites which had an evaporated layer of metallic Mn on the surface.

Cerium could be introduced into the lattice by thermal diffusion only with great difficulty and required periods of several days at temperatures of around 1300°K. Since the apparent nonexistence of a zone purification effect with Ce, in crystals grown from the melt, suggests that the mobility of Ce ions in the fluorite lattice is extremely small, the difficulty in obtaining activation with Ce by the thermal diffusion process was not unexpected. Thus most of the experiments were confined to the introduction of Mn into crystals which already contained Ce added to the original melt. However, in this case the amount of sensitization was very small, much less than obtained from crystals activated with similar impurity concentrations in the melt.

*Paramagnetic resonance.*—The paramagnetic resonance spectrum of crystals activated in the melt was compared with the spectrum of crystals and powders activated by thermal diffusion. Since Ce resonance can only be observed at 20°K (6), the only resonance observed was that due to divalent Mn. Marked differences in the fine structure of the resonance line were found according to the mode of activation. In all cases of comparable Mn content, the fine structure exhibited by crystals activated in the melt was more deeply developed than those activated by thermal diffusion. The explanation of this effect appears to be that Mn is uniformly distributed throughout the crystals activated in the melt whereas it is concentrated in aggregates, possibly along the lines of dislocations and similar faults, in crystals and powders activated by thermal diffusion. The aggregation leads to a quenching of the fine structure effect by spin exchange interaction between nearby Mn ions. Even in the unexcited state some interaction between the Ce and Mn ions, which are both paramagnetic, was found and an increase in Ce content produced a slight broadening of the six peaks in the fine structure of the Mn resonance. This effect appeared to be smaller in crystals containing Ce added to the melt and into which Mn was introduced by thermal diffusion, than in specimens activated with both impurities in the melt.

*X-ray analysis.*—Debye-Scherrer "powder" photographs of each of the samples showed that in all cases Ce produces an expansion and Mn a contraction of the fluorite lattice. This is expected from a consideration of the ionic radii.

*Optical measurements.*—Specimens used in the optical measurements were cleavage crystals 0.5 mm to 1 mm thick, polished with a commercial diamond compound. In regions far removed from any absorption bands the crystal transmission was at least 90% in all cases. No absorption was found in the wave-length region between 2 and 0.4$\mu$ and, therefore, with one exception, detailed measurements were only made in the region of the cerous ion absorption bands, between 0.2 and 0.4$\mu$. Within this region experiments were made using 800 cps "chopped" radiation from a hydrogen arc lamp in conjunction with a Leiss pattern double prism monochromator. Transmitted light intensity was measured by an EMI 5311 11-stage photomultiplier feeding into a tuned amplifier with output matched to a penrecording milliammeter. Where necessary

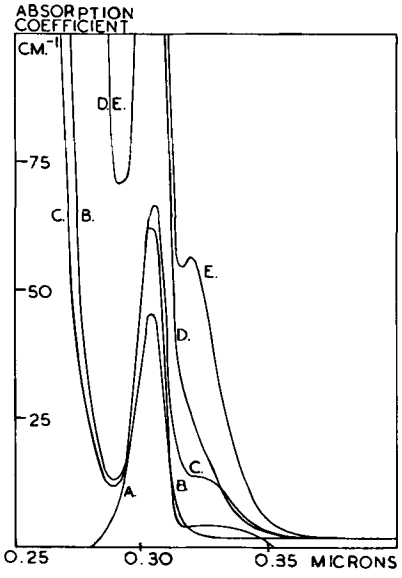


Fig. 1. Absorption spectra of activator fluorite crystals. Curve A, 0.2% Mn, 0.01% Ce; curve B, 0.45% Mn, 0.7% Ce; curve C, 0.22% Mn, 0.6% Ce; curve D, 1.1% Mn, 5.0% Ce; curve E, 5.0% Ce.

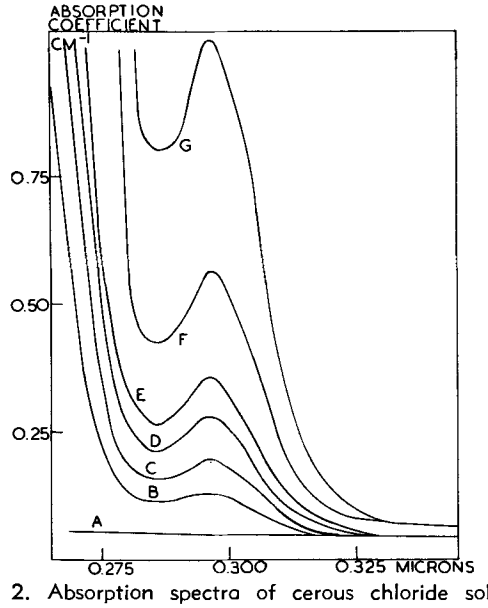


Fig. 2. Absorption spectra of cerous chloride solutions. Curve A, Zero Ce concentration; curve B, 0.00075 g/cc; curve C, 0.00126 g/cc; curve D, 0.00188 g/cc; curve E, 0.00251 g/cc; curve F, 0.00374 g/cc; curve G, 0.00753 g/cc.

correction was made for light reflected and scattered from the crystal surfaces.

*Absorption spectra.*—Figure 1 gives a family of curves of absorption coefficient vs. wave length for a series of specimens of varying impurity content. The curves show that absorption takes place in the three bands listed by Ginther (5). For all Ce concentrations greater than about 0.1% the absorption band in the region of 0.25$\mu$ was the most pronounced and the peak of this band could not be located. A second band peaking at about 0.305$\mu$ was very strong in specimens of any Ce concentration. The third band, with peak at about 0.33$\mu$, was most evident in crystals of low Mn content and diminished in intensity rapidly with increasing Mn concentration. This effect was not commented on by Ginther (5), although it can be noticed in his published data.

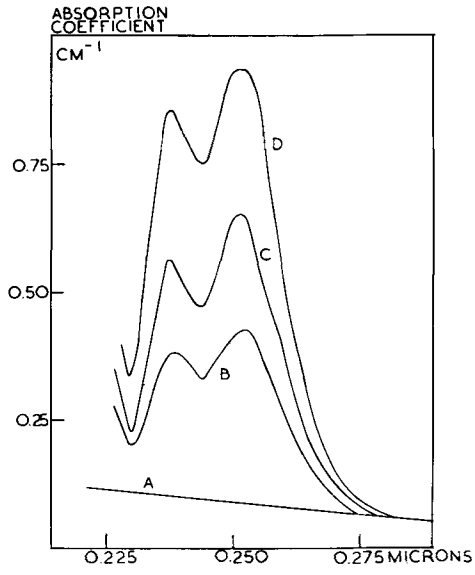


Fig. 3. Absorption spectra of cerous chloride solutions. Curve A, Zero Ce concentration; curve B, 0.000064 g/cc; curve C, 0.000096 g/cc; curve D, 0.000192 g/cc.

For the purpose of comparison, absorption coefficients of a series of solutions of cerous chloride in water were measured. These are plotted in Fig. 2 and 3. Three absorption bands were found, the first occurring with maximum absorption at about 0.305$\mu$ and the remaining two with about equal intensity at 0.2530$\mu$ and 0.2475$\mu$. For all concentrations, absorption in the two short wave-length bands was about 100 times as intense as that in the band at longer wave lengths.

Crystals containing Mn but no Ce showed no absorption in the region of the bands described. However, in a crystal specimen 0.5 cm thick activated with about 5% Mn by diffusion, very feeble absorption was found in a broad band with maximum at about 0.375$\mu$. This effect is shown in Fig. 4. The absorption band appears to correspond with the feeble excitation region which Ginther (5) observed at 0.4$\mu$ in specimens with high Mn concentration.

*Excitation and emission spectra.*—Measurements of excitation and emission spectra were not so exhaustive as those of Ginther (5) but, nevertheless, served to verify his observations. Sensitization was very pronounced in the two shorter wave-length Ce absorption bands but was extremely feeble following absorption in the 0.33$\mu$ Ce band. The broad, green, emission band attributed to the Mn ion could

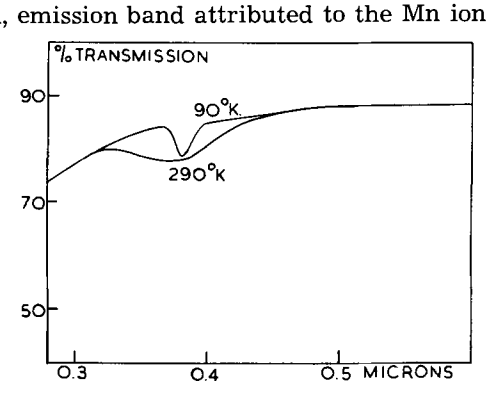


Fig. 4. Spectral transmission of $CaF_2$-5% Mn. Specimen thickness 5 mm.

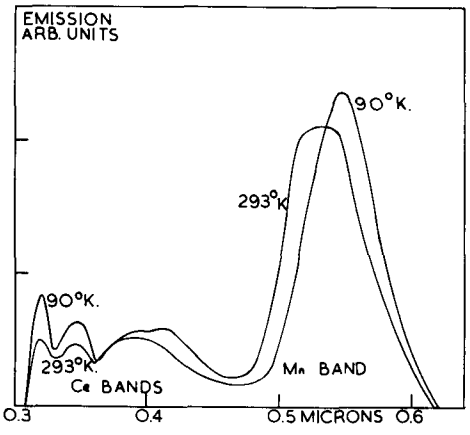


Fig. 5 Emission spectra of typical activated fluorites, at 293°K and 90°K. Impurity concentrations in this case are Ce 0.6%, Mn 0.20%.

be excited by an electrical discharge in air, in agreement with the earlier investigation. However, the sensitized emission of Mn was very feeble in crystals activated with this impurity by thermal diffusion; much less than in crystals containing a comparable amount of Mn introduced into the melt, although discharge excitation of the two types of crystal gave about equal intensities of luminescence. Measurement of emission spectra at 90°K showed little difference in form from the room temperature case, as indicated by Fig. 5. Curves of emission intensity vs. temperature are plotted on Fig. 6 as a typical crystal was allowed to warm up from 90°K.

*Lifetime investigation.*—The decay times for the various emission bands were investigated using a phosphoroscope wheel method. In every case the u.v. emission had a decay time less than $10^{-4}$ sec which was the experimental limit of measurement. The decay time for the visible Mn emission was measured at various temperatures and found to be of the order of tens of milliseconds. Figure 7 is a plot of the decay time of emission in this band as a function of Mn concentration, for a series of specimens in which the Ce concentration also varied over a wide range. The curve shows that the decay time is proportional to the Mn concentration but remains unaffected by large changes in the Ce concentration. The decrease in decay time with increasing Mn

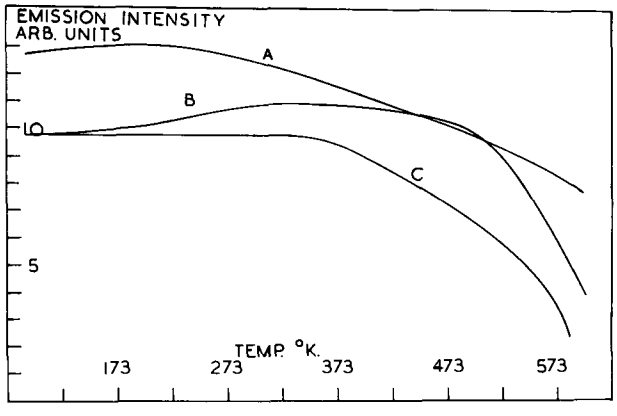


Fig. 6. Fluorescence intensity vs. temperature curves. Curve A, Ce emission, 0.254$\mu$ excitation; curve B, Mn emission, 0.254$\mu$ excitation; curve C, Mn emission, 0.313$\mu$ excitation.

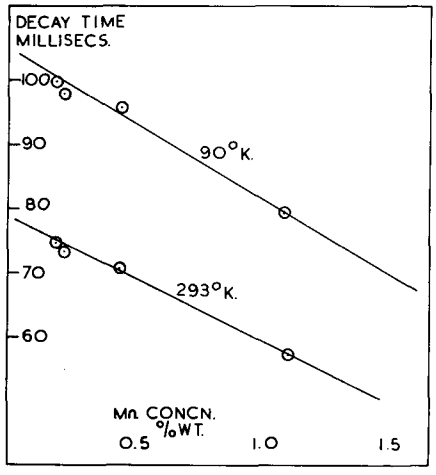


Fig. 7. Decay time for Mn emission at room temperature, and 90°K, and for varying Mn concentration.

concentration is presumably due to a spin exchange interaction between nearby Mn ions.

## Discussion

By means of other experiments not described above it was possible to show that the activated crystals were nonphotoconductors, and also that the Mn emission intensity varied linearly with the excitation intensity. Thus it can be concluded that the system is an example of sensitized luminescence. As in all other luminescent systems it is of paramount importance to identify the particular levels of the impurity centers which are responsible for the emission, and energy level schemes are suggested for both activators below. Finally, the process of energy transfer by resonance, in this system, is discussed.

### *The Cerous Ion Center*

A comparison of the absorption bands in the crystals with those for the cerous chloride solutions immediately suggests a direct correspondence between the two cases. The two dominant bands in fluorite at 0.305$\mu$ and 0.25$\mu$ appear to correspond exactly with the same two bands in the solutions (*see* Fig. 1, 2, and 3). The shape of the short wave-length absorption band, as measured in reflection spectra by Ginther (5), indicates the same form as the double peaked band in the solutions, while the band at longer wave lengths corresponds exactly.

Oscillator strengths were calculated for the 0.305$\mu$ and 0.25$\mu$ bands in the cerous chloride solutions, using Smakula's formula (7). The results are tabulated in Table I. Calculation of the oscillator strength for the 0.305$\mu$ Ce band in fluorite, assuming that all of the Ce added to the melt stays in the lattice, gives values which differ from those for the solutions by a factor of only four. This relatively good agreement serves to further verify the suggested correspondence between the transitions in aqueous solution and in fluorite activated with Ce. The 0.33$\mu$ band, which does not occur in the solutions, is assumed to be due to some interaction between a Ce ion and its surroundings in the fluorite lattice.

Because of the similarity between the absorption of cerous ions in solution and in the fluorite lattice it appears fairly certain that Ce goes into the lattice

**Table I. Oscillator strengths for transitions giving rise to 0.30$\mu$ and 0.25$\mu$ absorption bands in aqueous solutions of cerous chloride and in cerium activated fluorite**

0.30$\mu$ Absorption band in cerous chloride

| Soln. | Conc g/cc | No. of centers/cc $N_0$ | Max. abs. coeff. $cm^{-1}$ | Half width ev | Oscillator strength $(f)$ |
|---|---|---|---|---|---|
| B | 0.00075 | $1.88 \times 10^{18}$ | 0.08 | 0.28 | $1.37 \times 10^{-4}$ |
| C | 0.0013 | $2.90 \times 10^{18}$ | 0.15 | 0.28 | $1.67 \times 10^{-4}$ |
| D | 0.0019 | $4.73 \times 10^{18}$ | 0.235 | 0.26 | $1.49 \times 10^{-4}$ |
| E | 0.0025 | $6.30 \times 10^{18}$ | 0.315 | 0.28 | $1.61 \times 10^{-4}$ |
| F | 0.0037 | $9.37 \times 10^{18}$ | 0.515 | 0.31 | $1.95 \times 10^{-4}$ |
| G | 0.0075 | $18.9 \times 10^{18}$ | 0.97 | 0.31 | $1.83 \times 10^{-4}$ |
| | | | Mean value = | | $1.65 \times 10^{-4}$ |

0.25$\mu$ Absorption band in cerous chloride

| Soln. | Conc g/cc | No. of centers/cc $N_0$ | Max. abs. coeff. $cm^{-1}$ | Half width ev | Oscillator strength $(f)$ |
|---|---|---|---|---|---|
| B | 0.000064 | $1.61 \times 10^{17}$ | 0.340 | 0.30 | $7.27 \times 10^{-3}$ |
| C | 0.000096 | $2.41 \times 10^{17}$ | 0.550 | 0.30 | $8.00 \times 10^{-3}$ |
| D | 0.000192 | $4.81 \times 10^{17}$ | 0.845 | 0.30 | $6.07 \times 10^{-3}$ |
| | | | Mean value = | | $7.11 \times 10^{-3}$ |

0.30$\mu$ Absorption band in cerium containing fluorite

| Spec. | Conc atomic % | No. of centers/cc $N_0$ | Max. abs. coeff. $cm^{-1}$ | Half width ev | Oscillator strength $(f)$ |
|---|---|---|---|---|---|
| A | 0.01 | $0.024 \times 10^{20}$ | 0.93 | 0.15 | $6.67 \times 10^{-4}$ |
| B | 0.7 | $1.75 \times 10^{20}$ | 62.5 | 0.16 | $6.57 \times 10^{-4}$ |
| C | 0.6 | $1.63 \times 10^{20}$ | 66.5 | 0.14 | $6.56 \times 10^{-4}$ |
| | | | Mean value = | | $6.60 \times 10^{-4}$ |

as the trivalent $Ce^{+++}$ ion, and not in the quadrivalent form. Thus one has the situation of a trivalent ion of greater size than the Ca ion being substituted into a divalent, predominantly ionic, lattice. Applying simple ideas of localized charge compensation it appears that two $Ce^{+++}$ ions should replace two Ca ions along the 110 axis, which is the direction of least potential energy in the crystal, with a Ca ion situated midway between them. However, Bleaney (8) has stated that no axial symmetry is observed in the paramagnetic resonance spectrum of Ce in a divalent lattice and this seems to preclude the above mechanism. The alternative is to suppose that there is a direct substitution of $Ce^{+++}$ for $Ca^{++}$ with charge compensation resulting from the presence of a nearby interstitial fluorine ion. This situation will lead to severe local distortion of the lattice due to the large disparity in ion size.

In fluorite the short wave-length absorption band does not appear for very low Ce concentration but, as the concentration of Ce increases, absorption in this band rapidly becomes much more intense than that in any other. The 0.25$\mu$ absorption band is the most pronounced in cerous chloride solutions of all concentrations indicating that the nature of the Ce center changes with the concentration of this activator in fluorite. Ginther (5) postulated the existence of an aggregate or "cluster" of Ce ions to account for the increased short wave length absorption with high Ce concentrations. In this case the perturbation of the local field produced by the interaction between nearby Ce ions is presumably sufficient to permit absorption in the 0.25$\mu$ band. However, severe distortion of the surrounding lattice results from the presence of localized groups of Ce ions, each ion being compensated by an interstitial fluorine ion. A detailed investigation of the paramagnetic resonance spectrum due to Ce in fluorite should yield interesting results which might demonstrate the increasing interaction between Ce ions as the concentration of this impurity is increased.

It is somewhat surprising that the same transitions appear to occur in both solutions of cerous salts and cerium ions in crystalline media. However, this is in accord with magnetic data on the rare earths and is attributed to the shielding of the solitary 4f electron by the outer filled 5s and 5p orbitals. Hund's selection rules applied to the $Ce^{+++}$ ion give $4^2F_{5/2}$ for the ground state, since the separation of the doublet $4^2F_{5/2} - 4^2F_{7/2}$ is much greater than $kT$ at room temperature. The screening effect of the outer electrons would be expected to result in line spectra for inner shell transitions and this suggests that the excited states of the ion, corresponding to the measured absorption bands, are outer levels. Roberts, Wallace, and Pierce (9) calculated oscillator strengths for solutions of cerous sulfate, from measurements of the Faraday effect, assuming that the outer levels were $5^2D_{3/2}$ and $5^2D_{5/2}$ for the 0.305$\mu$ and 0.25$\mu$ absorption bands, respectively. The values they obtained are in substantial agreement with those quoted in Table I as a result of the present optical measurements. Thus it seems likely that the excited states concerned in these transitions are at any rate perturbed Stark levels of the $^2D$ state of this ion.

The low value of the oscillator strength is at first sight unexpected since the postulated transition is allowed by the usual selection rules. However, as pointed out by Mott and Gurney (10), the oscillator strength is essentially fixed by the product of the wave functions of the excited and ground states concerned and in this case the radial extension of the outer shell, excited state, wave function will be many times greater than that of the shielded, inner shell, ground state and thus the oscillator strength will be necessarily small. Bril, Klasens, and Zalm (11) measured the lifetime for decay of luminescence in Ce-activated phosphors and obtained values of about 1 $\mu$sec which again suggests a small oscillator strength for the lowest energy transitions of the $Ce^{+++}$ ion, in agreement with the suggested scheme.

*The Manganese Ion Center*

The divalent Mn ion possesses an outer incomplete 3d electron shell containing five electrons, and in the isolated condition the ground state would be $3^6S_{5/2}$. In the crystalline state the susceptibility of transition metal ions is given by an expression of the form $\kappa = \frac{N\beta^2}{3kT} \cdot 4S(S+1)$, which can only be explained if the orbital angular momentum is completely quenched. Van Vleck (12) states that this orbital quenching is probably due to the presence of strong assymetrical electric fields which break

down the spin-orbit coupling. This view is supported by the disappearance of all fine structure in the paramagnetic resonance spectrum of Mn at concentrations of more than a few percent. Orgel (13) has considered the spectra of transition metal complexes and the same general considerations apply to the present case where $Mn^{++}$ is assumed to enter the fluorite lattice substitutionally, by simple replacement of Ca ions. The degeneracy of the *d* orbitals completely vanishes, leaving five separate levels with transitions possible between any two of them. In general, the transitions are all forbidden, and strong associated absorption is not expected. However, some *d-p* hybridization occurs in the excited states and in certain cases this may lead to an increased transition probability between particular states. Thus for $Mn^{++}$ the ground state is a $3^6S$ level which is not significantly split by the crystalline field and the lowest excited state predicted is the $3^4G$ level (14), involving a spin reversal only. Even in the free state transitions to outer levels involve energies of many electron volts and for cubical, or octahedral, coordination in the crystalline state these separations will increase and thus may be precluded here. Orgel (13) states that the $^4G$ state in Mn is split into three and the transition responsible for the observed luminescence in the present case is probably from one of the higher pair of these states back to the $^6S$ ground state.

Very weak absorption has been reported for the hydrated Mn ion at about 0.39$\mu$ (15) and this seems to fit in with the above theoretical picture. The broad, weak, absorption band located in fluorite containing approximately 5% of Mn (*see* Fig. 4) with maximum absorption at 0.375$\mu$, and also the excitation at 0.4$\mu$ reported by Ginther (5) further support this tentative allocation of energy states. The long luminescence decay time measured in the present experiments is in agreement with the supposition that the radiative transition is one which is normally forbidden.

### *Mechanism for Energy Transfer*

In agreement with Ginther's conclusions (5), the present experiments support the view that $CaF_2$ activated with Ce and Mn forms a sensitized system of high efficiency. In view of the large spin change involved in the suggested transition at the Mn center, energy transfer by resonance must involve a spin exchange interaction between the excited states of Ce and Mn. According to the detailed theoretical calculations of Dexter (4) this type of interaction is one of extremely short range. However, exchange forces can produce the necessary strong coupling between the spins of two highly paramagnetic ions such as Ce and Mn when the ions are situated within a few lattice sites of each other.

Most previous authors have rejected the idea of a close spatial association between activator and sensitizer on the grounds that a close interaction between the two impurity centers would severely perturb the form and position of the absorption and emission spectra obtained when either activator is present alone. However, a comparison of the experimentally determined absorption and emission spectra of the present two activators with those for the same two elements in other phosphor systems and in aqueous solution shows that the surrounding lattice has little effect on the position of the energy levels. Activator pairing would not be expected to produce any large additional perturbation and therefore the principal objection to the close association of the activators is removed. Dexter (4) calculates the upper limit for energy transfer by a spin exchange interaction to be about 40 lattice sites surrounding a given excited sensitizer center. A rapid calculation shows that in a phosphor containing 1% $MnF_2$ and 1% $CeF_3$ by weight there are only approximately two Mn ions and one Ce ion for every two normal cation points and thus pairing appears to be essential in order to explain the high transfer efficiencies found with activator concentrations of a few tenths of a percent.

### *Evidence for Association of Activators in Specimens Prepared from the Melt*

The ionic sizes of Ce and Mn are, respectively, larger and smaller than that of Ca and x-ray analysis showed that addition of Ce leads to an expansion, and addition of Mn to a contraction, of the fluorite lattice. When the two ions were present together in about equal proportions little change in the fluorite lattice spacing was detected, nor was there appreciable line broadening. The introduction of Ce into the fluorite lattice will lead to a severe local lattice distortion which will be particularly marked when Ce aggregation occurs. However, the lattice distortion is minimized by the presence of a nearby Mn ion. The formation of associations of impurity ions is opposed by considerations of the statistical nature of entropy and also by electrostatic repulsion, but at the temperature at which the lattice was formed from the melt these effects are less important.

The critical dependence on temperature of the factors which tend to promote pairing of Ce and Mn is well illustrated by the diffusion experiments. It was stated in a previous section that it was possible to diffuse Mn into fluorite at quite low temperatures, and so far as could be ascertained from the luminescence properties the activation was uniform throughout the bulk of the lattice. However, diffusion of Mn into a crystal which already contained Ce added to the melt did not produce appreciable sensitization, even after prolonged diffusion periods at 1300°K. It appears that the influence favoring pairing is operative only at temperatures at, or close to, the melting point of $CaF_2$, where the cation mobility is high. Efficient sensitization is only found in crystals in which the association of activators has taken place. However, efficient powder phosphors were obtained by firing cerous and manganous fluorides with $CaF_2$ at 1100°K, but in this case it was shown by paramagnetic resonance measurements, which indicated little fine structure even for low Mn concentrations, that the impurities were mainly contained in the surface layers of the microcrystalline grains. Since this is the case for Mn which has a relatively high mobility in fluorite, the

surface distribution of Ce which has a low mobility, may be expected to be even more pronounced. Thus the local concentration in the surface of the powder grains will be high enough for interaction between Ce and Mn.

The spectral measurements provide further evidence for the formation of a nonrandom distribution of activators. Ginther's investigations (5) are in agreement with the present work in two significant respects, (*a*) the shift to longer wave lengths of the Mn emission with increasing Ce concentration, and (*b*) the diminution of the 0.33$\mu$ Ce absorption band with increasing Mn concentration. The first effect, the shift in the peak of the Mn emission band, would only be expected to result from a very close interaction between Mn and Ce ions since most reported experimental evidence shows that the spectra of transition metal elements are but little affected by their environment. The 0.33$\mu$ Ce absorption band in fluorite has been shown, by comparison with the absorption of cerous salt solutions, to be due to a transition characteristic of the Ce ion in the fluorite lattice. The disappearance of this band at high Mn concentrations suggests that the presence of a nearby Mn ion reduces, or removes, the particular field perturbation which made the transition possible in an isolated Ce center. This assumption was verified by measuring the absorption of a crystal activated with Ce in the melt, both before and after diffusion of Mn into the lattice. No diminution in the magnitude of the 0.33$\mu$ absorption band was apparent in this case, although discharge excitation showed that Mn had entered the lattice.

The data obtained from measurements of paramagnetic resonance provide strong evidence in support of the association of impurity ions in the fluorite lattice of specimens activated in the melt. For specimens activated in this way a noticeable diminution in the depth of the six fine structure peaks of the Mn resonance was found to accompany an increase in the Ce content. The effect can be attributed directly to a spin exchange interaction between Ce and Mn ions. The extremely short range of the exchange forces necessitates the assumption of a nonrandom distribution of activators since otherwise, with the activator concentrations used in the present work, an effect of observable magnitude would not be expected. It is hoped that a detailed experimental and theoretical account of the paramagnetic resonance studies will form the subject of a future communication.

## Conclusion

Ginther's observation (5) that $CaF_2$-Ce-Mn phosphors form a sensitized luminescence system of high efficiency has been verified. Measurements of absorption coefficients and emission spectra have enabled tentative spectroscopic states to be proposed for the ground states of both impurity ions, for the primary excited states of Ce and for the excited state of Mn responsible for the observed emission. Evidence in favor of a close association of Mn and Ce in the fluorite lattice has been presented. This helps to explain the high energy transfer efficiency found in this phosphor system despite the extremely short range of the spin exchange forces. It has not been possible to identify the particular excited states between which the resonance occurs, nor has the precise nature of the luminescence center been established. A limit to the size of the latter is supplied by Dexter's calculation (4) which puts 40 lattice sites as the maximum distance before the exchange interaction becomes negligibly small. However, it is likely that the separation of the impurity ions comprising the center is much less than 40 lattice sites in view of the high transfer efficiency and the magnitude of the observed spectral shifts.

## Acknowledgments

The author wishes to acknowledge with grateful thanks the active support and encouragement of G. F. J. Garlick, who suggested the problem and subsequently provided much valuable criticism. Thanks are also due to R. V. Jones and the staff of Mareschal College, University of Aberdeen, Scotland, who supplied the fluorite crystals, and to A. Cunliffe of this laboratory for his kind assistance with the measurements of paramagnetic resonance. During the course of this work the author was supported by an award from the Department of Scientific and Industrial Research.

Manuscript received April 26, 1957. This paper was prepared for delivery before the Washington Meeting, May 12-16, 1957.

Any discussion of this paper will appear in a Discussion Section to be published in the December 1958 JOURNAL.

REFERENCES

1. T. P. J. Botden, *Philip's Research Repts.*, **7**, 197 (1952).
2. F. Perrin, *J. phys. radium*, **7**, 1 (1936).
3. T. Förster, *Ann. phys.*, **2**, 55 (1948).
4. D. L. Dexter, *J. Chem. Phys.*, **21**, 836 (1953).
5. R. J. Ginther, *This Journal*, **101**, 248 (1954).
6. S. S. Bogle, A. H. Cooke, and S. Whitley, *Proc. Phys. Soc.*, **A64**, 931 (1951).
7. A. Smakula, *Z. Physik.*, **59**, 603 (1930).
8. B. Bleaney, Private communication.
9. R. W. Roberts, L. A. Wallace, and I. T. Pierce, *Phil. Mag.*, **17**, 934 (1934).
10. N. F. Mott and R. W. Gurney, "Electronic Processes in Ionic Crystals," Oxford University Press (1940).
11. A. Bril, H. A. Klasens, and P. Zalm, *Philip's Research Rpts.*, **8**, 393 (1953).
12. J. H. Van Vleck, "The Theory of Electric and Magnetic Susceptibilities," Oxford University Press (1932).
13. L. E. Orgel, *J. Chem. Phys.*, **23**, 1004 (1955).
14. M. A. Catalán and O. Garciá-Riquelme, "Atomic Energy Levels," Vol. 2, Circular 467, Washington, 1952.
15. G. Gielessen, *Annal. der Phys.*, **22**, 537 (1935).
16. P. A. Forrester and E. E. Schneider, *Proc. Phys. Soc.*, **96B**, 833 (1956).

# The Calcium-Silicate-Tungstate Phosphor

## Phase Relationships and Fluorescent Properties

**D. E. Harrison**

*Luminescent Materials Laboratories, Lamp Wire and Phosphors Department, General Electric Company, Cleveland, Ohio*

**and**

**F. A. Hummel**

*Department of Ceramic Technology, Pennsylvania State University, University Park, Pennsylvania*

ABSTRACT

An efficient phosphor can be prepared by a co-crystallization of $\beta$-$CaSiO_3$:Mn+Pb and $CaWO_4$:Pb. The fluorescence, exicted by either 2537Å or cathode radiation, is that of a mechanical mixture of $\beta$-$CaSiO_3$:Mn+Pb and $CaWO_4$:Pb. In the presence of tungstic oxide, the formation of $\beta$-$CaSiO_3$ is greatly accelerated.

Determination of the pertinent compatibility tetrahedra in the system CaO-MnO-$SiO_2$-$WO_3$ revealed that the phosphor compositions lie in the sub-tetrahedron $\beta$-$CaSiO_3$-$MnSiO_3$-$SiO_2$-$CaWO_4$. X-ray data showed that there was no solid solubility of $\beta(Ca_{1-x}Mn_x)SiO_3$ in $CaWO_4$; the fluorescence of $CaWO_4$ is adversely affected by MnO.

Working independently Froelich (1) and Merrill and Stewart (2) made the discovery that $\beta$-$CaSiO_3$ could be cooperatively activated by incorporating small quantities of Pb and Mn ions into the wollastonite structure.

The properties of the $\beta$-$CaSiO_3$:Mn + Pb phosphor have been described by Froelich (3), Merrill and Schulman (4), Schulman, Ginther, and Evans (5), Fonda and Froelich (6).

The synthesis of wollastonite ($\beta$-$CaSiO_3$) involves several intermediate stages. Landiya and Mchedlov-Petrosyan (7) showed again recently that when an equimolar mixture of CaO and $SiO_2$ was heated between 1000° and 1100°C, the first phase to form was $Ca_2SiO_4$. The orthosilicate reacted with excess $SiO_2$ to form either $Ca_3Si_2O_7$ or $\beta$-$CaSiO_3$. $Ca_3Si_2O_7$ subsequently reacted with excess $SiO_2$ to yield $\beta$-$CaSiO_3$. The final reaction product consisted entirely of wollastonite.

In the absence of mineralizers, the synthesis of wollastonite is a sluggish reaction. Steadman (8) used 100% excess silica in the preparation of $CaSiO_3$:Mn and $CaSiO_3$:Pb phosphors to help promote the rate of reaction. Schulman (9) found that 0.0025-0.0088 moles of $PbF_2$/mole Ca served as an effective mineralizer. Froelich (10) used 0.05-5.0% of an equimolar mixture of $CaF_2$ and $CaCl_2$ to produce an efficient phosphor which required only 4-5 hr firing time between 1100° and 1200°C. Froelich (1,3,11) also found that steam was an efficient catalyst during the firing of silicate phosphors.

This paper describes the phase relationships and fluorescent characteristics of a phosphor prepared by a co-crystallization of $\beta$-$CaSiO_3$:Mn + Pb and $CaWO_4$:Pb. In the presence of tungstic oxide, wollastonite can be synthesized readily without the use of $PbF_2$, $CaF_2$, steam, or excessive temperature.

### Experimental Procedure

The raw materials used for phosphor synthesis were as follows: Mallinckrodt Special Bulky silica, and Reagent Grade $PbSO_4$ and $MnCO_3$. The $H_2WO_4$ and $CaCO_3$ were prepared by Chemical Products Plant of the General Electric Company for phosphor production.

*Preparation of compositions and heat treatments.*—The components were mixed in a mortar with reagent grade acetone until it had evaporated and a dry powder resulted. Calcines were prepared in fused silica crucibles at temperatures ranging from 1000°-1200°C for periods of 2 hr to several days. For survey work in a temperature gradient, a Pt-wound furnace was used. For heat treatments at constant temperature, silicon carbide element furnaces were used.

*Apparatus and techniques.*—(*A*) X-ray patterns: x-ray data were obtained from Norelco and General Electric recording spectrometers using $CuK\alpha$ radiation ($\lambda = 1.5418$Å) filtered with Ni (Table I); (*B*) Infrared absorption measurements: data were obtained by means of a Perkin-Elmer Model 21, infrared spectrophotometer. Samples were prepared using pellets of KBr formed under pressure (Table II); (*C*) Fluorescence measurements: emission curves were obtained with an automatically recording General Electric spectroradiometer.

### Results and Discussion

Calcium fluoride serves as an effective mineralizer toward wollastonite. However, when using a batch consisting of $CaCO_3$, $SiO_2$, $PbSO_4$, $MnCO_3$, and $CaF_2$, the material produced has coarse and variable grain size. Quench experiments disclosed the presence of considerable liquid formation in the temperature region between 800° and 900°C. This liquid results

Table I. Calcium silicate, calcium tungstate, and calcium-silicate-tungstate compositions used in x-ray analysis

| Molecular ratio | | | | Weight per cent composition | | | |
|---|---|---|---|---|---|---|---|
| CaO | MnO | $SiO_2$ | $WO_3$ | CaO | MnO | $SiO_2$ | $WO_3$ |
| 1.000 | 0.010 | — | 1.010 | 19.27 | 0.246 | — | 80.59 |
| 1.000 | 0.031 | — | 1.031 | 18.86 | 0.738 | — | 80.40 |
| 1.000 | 0.064 | — | 1.064 | 18.25 | 1.47 | — | 80.28 |
| 1.000 | 0.031 | 0.757 | 0.343 | 30.59 | 1.20 | 24.79 | 43.43 |
| 1.000 | 0.064 | 0.781 | 0.354 | 29.57 | 2.39 | 24.73 | 43.32 |
| 1.000 | 0.750 | 1.777 | 0.150 | 14.39 | 13.61 | 27.37 | 44.64 |
| 1.000 | 1.331 | 2.029 | 1.331 | 9.63 | 16.23 | 20.98 | 53.15 |
| 1.000 | 0.500 | 1.500 | 0.500 | 18.84 | 11.92 | 30.28 | 38.96 |
| 1.000 | 2.000 | 2.000 | 2.000 | 7.17 | 18.14 | 15.36 | 59.33 |
| 1.000 | 1.000 | 1.000 | 3.009 | 6.35 | 8.03 | 6.80 | 78.80 |

Table II. Compositions used in infrared study

| Molecular ratio | | | Weight per cent composition | | |
|---|---|---|---|---|---|
| CaO | $WO_3$ | $SiO_3$ | CaO | $WO_3$ | $SiO_2$ |
| 1.00 | 1.00 | — | 19.47 | 80.53 | — |
| 1.00 | — | 1.10 | 45.91 | — | 54.09 |
| 1.00 | 0.08 | 1.02 | 39.86 | 13.18 | 46.96 |

primarily from eutectics in the system $PbO-CaF_2$ or $PbSO_4-CaF_2$ and also to a lesser extent from eutectics in the system $PbO-SiO_2$. The liquid formed, which serves to accelerate the reaction, has only temporary existence. However, it promotes the formation of large aggregates of $\beta$-$CaSiO_3$.

The addition of 10-15 wt % $WO_3$ to an equimolar mixture of $CaCO_3$ and $SiO_2$ facilitates the formation of wollastonite without the development of a liquid phase. In the presence of MnO and PbO, a fine-grained powder can be obtained by firing this material at 1050°C for 3 hr. A typical composition is given in Table III.

The calcium-silicate-tungstate phosphor is not a silicotungstate but an intimate mechanical mixture of $\beta$-$CaSiO_3$ and $CaWO_4$ crystals. This can be shown in several ways: (*a*) x-ray diffraction data showed two phases, $\beta$-$CaSiO_3$ and $CaWO_4$. (*b*) Microscopic examination of the composite while it was being irradiated by 2537Å excitation revealed blue fluorescing $CaWO_4$:Pb crystals situated in aggregates of orange fluorescing $\beta$-$CaSiO_3$:Mn + Pb crystals. It was not possible to separate the two phases by manipulating the aggregates with a probe. The bonding of the $CaWO_4$ and $\beta$-$CaSiO_3$ crystals was further demonstrated by noting that practically none of the co-crystallized $\beta$-$CaSiO_3$-$CaWO_4$ phosphor, which had been previously ground in a mortar, floated in tetrabromethane (sp gr 2.964) whereas much of a material prepared by mixing $CaWO_4$ and $\beta$-$CaSiO_3$ phosphors, each of which had been prepared separately, was carried in suspension because of the buoyancy of $\beta$-$CaSiO_3$.

### *Optical Properties*

The fluorescent emission of the $\beta$-$CaSiO_3$:Mn + Pb and $CaWO_4$:Pb phases in the calcium-silicate-tungstate phosphor is the same as those of the two phases when each is prepared separately. The composite is efficiently excited by 2537Å and cathode radiation and inefficiently excited by 3650Å. A relative spectral distribution curve is shown in Fig. 1.

Table III. Typical calcium-silicate-tungstate composition

| Molecular ratio | | | | | Weight per cent composition | | | | |
|---|---|---|---|---|---|---|---|---|---|
| CaO | MnO | PbO | $SiO_2$ | $WO_3$ | CaO | MnO | PbO | $SiO_2$ | $WO_3$ |
| 1.000 | 0.062 | 0.018 | 1.112 | 0.085 | 37.15 | 2.90 | 2.72 | 44.22 | 13.01 |

A comparison of the x-ray data of $\beta$-$CaSiO_3$ and $CaWO_4$, each of which had been prepared separately, with the x-ray data of the phases in the composite $\beta$-$CaSiO_3$-$CaWO_4$ material revealed no modification in either the wollastonite or scheelite patterns. However, a comparison of the infrared absorption spectrograms of 0.92 $\beta$-$CaSiO_3$ 0.08$CaWO_4$: 0.10$SiO_2$ with those of $CaWO_4$ and $\beta$-$CaSiO_3$: 0.10$SiO_2$ showed that some modifications had occurred in the $\beta$-$CaSiO_3$ spectrum. The most marked change occurred at 14.0$\mu$; smaller changes were observed between 9 and 11$\mu$. The $CaWO_4$ and $\beta$-$CaSiO_3$ + quartz absorption spectrograms were in good agreement with those reported by Miller and Wilkens (12) and by Hunt, Wisherd, and Bonham (13), respectively. Infrared absorption spectrograms are shown in Fig. 2.

Although the structural modifications in $\beta$-$CaSiO_3$ producing changes in the absorption spectrum are not known, it is suggested that they may be the result of surface forces bonding the $\beta$-$CaSiO_3$ and $CaWO_4$ crystals.

### *Phase Relationships*

The behavior of Mn in the $\beta$-$CaSiO_3$-$CaWO_4$ composite was unexpected. When the phases were examined individually, manganese oxide was found to be a severe poison toward $CaWO_4$. Kroger (14)

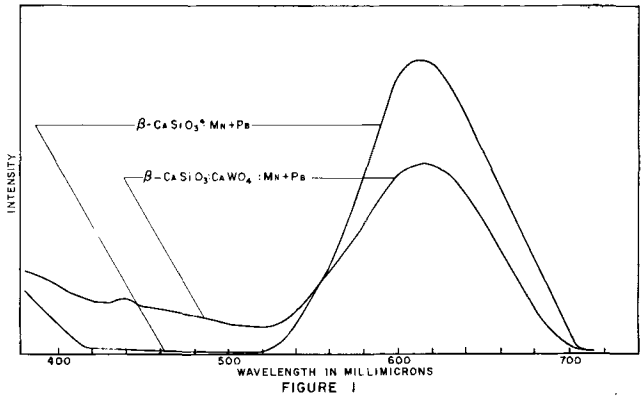


Fig. 1. Relative spectral distribution curves excited by 2537Å ultraviolet.

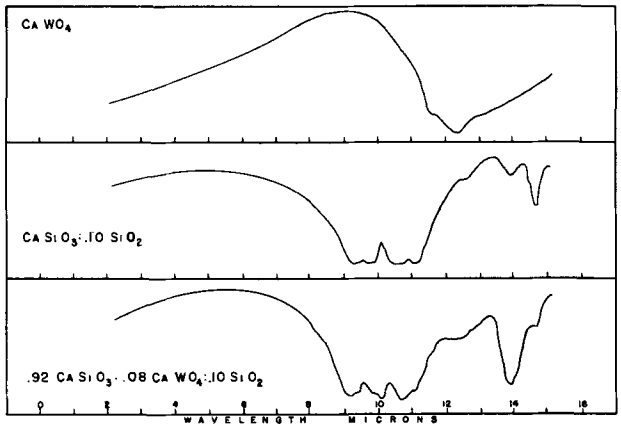


Fig. 2. Infrared absorption spectrograms

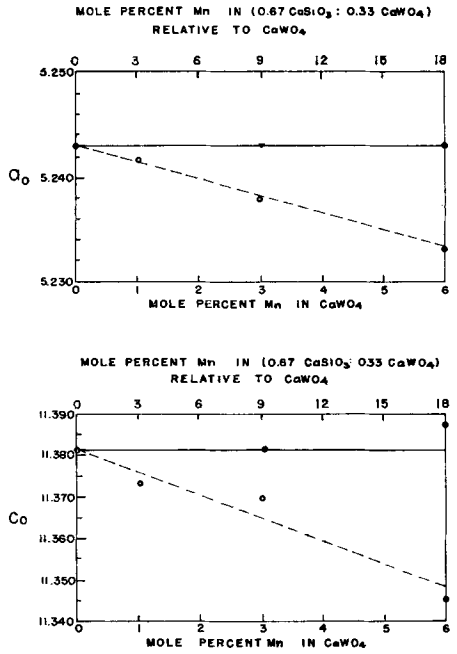


Fig. 3. Variation of unit cell dimensions of $CaWO_4$ with Mn substitutions in (0.67 $CaSiO_3$:0.33 $CaWO_4$).

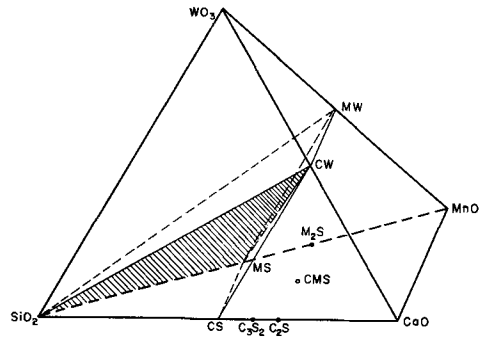


Fig. 4. The system CaO-MnO-$SiO_2$-$WO_3$ (1100°C)

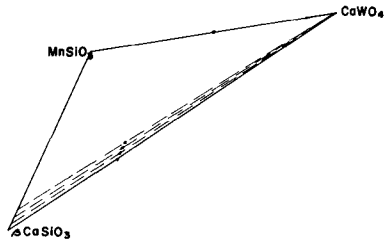


Fig. 5. The plane $\beta$-$CaSiO_3$-$MnSiO_3$-$CaWO_4$

reported that as little as 0.1 mole % Mn in $CaWO_4$ decreased the fluorescent intensity by 37%.

The distribution of Mn in the $\beta$-$CaSiO_3$-$CaWO_4$ composite was determined by measuring the changes in the lattice parameters of $CaWO_4$. The results for a sample consisting of 67 mole % $\beta$-$CaSiO_3$ 33 mole % $CaWO_4$ with up to 6 mole % substitutions of Mn for Ca are shown in Fig. 3. The dashed line indicates the changes in the (a) and (c) lattice parameters attending substitutions of Mn for Ca in $CaWO_4$. The solid line shows the results of measurements of $CaWO_4$ lattice parameters in the composite containing silica and Mn. The "d" spacings were determined to an accuracy of 0.0025%. The data show no detectable solid solubility of $MnWO_4$ in $CaWO_4$.

This rather unexpected result can be explained readily by considering the compatibility tetrahedra in the quaternary system CaO-MnO-$SiO_2$-$WO_3$. The subsolidus phase relationships in the temperature region between 1000° and 1200°C were determined using x-ray and microscopic techniques. Only the pertinent subtetrahedra in the high $SiO_2$-$WO_3$ region were investigated. A diagram of the system CaO-MnO-$SiO_2$-$WO_3$ is shown in Fig. 4.

The $\beta$-$CaSiO_3$:$CaWO_4$ phosphor compositions lie in the subtetrahedron $\beta$-$CaSiO_3$-$MnSiO_3$-$CaWO_4$-$SiO_2$. Neglecting a small excess of silica, the phosphor compositions lie in the plane $\beta$-$CaSiO_3$-$MnSiO_3$-$CaWO_4$. Since there is complete solid solubility between $\beta$-$CaSiO_3$ and $MnSiO_3$ in this temperature region (15), two phases are involved, i.e., $\beta(Ca_{1-x}Mn_x)SiO_3$ and $CaWO_4$. The $\beta$-$CaSiO_3$-$MnSiO_3$-$CaWO_4$ plane is shown in Fig. 5. X-ray data showed that there was no solid solubility of $\beta(Ca_{1-x}Mn_x)SiO_3$ in $CaWO_4$.

On the $MnWO_4$ side of the plane $SiO_2$-$CaWO_4$-$MnSiO_3$, i.e., in the subtetrahedron $CaWO_4$-$MnSiO_3$-$MnWO_4$-$SiO_2$, the situation is different, for there is considerable solid solubility between $CaWO_4$ and $MnWO_4$. This effect can be demonstrated optically. Two compositions were selected, one at 10 mole % $CaSiO_3$ on one side of the common plane $MnSiO_3$-$CaWO_4$-$SiO_2$ and the second on the other side of the plane at 10 mole % $MnWO_4$. After firing at 1100°C for 4 hr, the fluorescent characteristics were compared. The compositions containing $\beta$-$CaSiO_3$ fluoresced a bright blue whereas that containing $MnWO_4$ fluoresced only weakly.

The small addition of Pb required to sensitize the phosphor under 2537Å radiation does not appear to alter the phase relationships. Lead oxide distributes itself between the two phases. Determination of the lattice parameters of $CaWO_4$:Pb in the composite $\beta$-(Ca,Mn,Pb)$SiO_3$-$CaWO_4$:Pb showed that from 0 to 2 mole % PbO enters the tungstate phase. The retention of lead by the $CaWO_4$ phase is very dependent upon the firing conditions. Kroger (16) has presented data on the changes in luminescent emission with composition for $CaWO_4$-$PbWO_4$ solid solutions.

Manuscript received June 6, 1957. This paper is a part of a thesis submitted by D. E. Harrison in partial fulfillment of the requirements for the Ph.D. degree to the Pennyslvania State University; contribution No. 56-64 from the Mineral Industries Experiment Station, The Pennsylvania State University. This paper was prepared for delivery before the Washington Meeting, May 12-16, 1957.

Any discussion of this paper will appear in a Discussion Section to be published in the December 1958 JOURNAL.

REFERENCES

1. H. C. Froelich, British Pat. 577,694.
2. J. B. Merrill and W. E. Stewart, British Pat. 581,-951, Oct. 30, 1946; *J. Opt. Soc. Amer.*, **38**, 471 (1948).
3. H. C. Froelich, *J. (and Trans.) Electrochem. Soc.*, **93**, 101 (1948).
4. J. B. Merrill and J. H. Schulman, *J. Opt. Soc. Amer.*, **38**, 471 (1948).
5. J. H. Schulman, R. J. Ginther, and L. W. Evans, *ibid.*, **38**, 817 (1948).
6. G. R. Fonda and H. C. Froelich, *J. (and Trans.) Electrochem. Soc.*, **93**, 114 (1948).

7. N. A. Landiya and O. P. Mchedlov-Petrosyan, *Zhur. Fiz. Khim.*, **26**, 1785 (1952); *Chem. Abs.*, **47**, 6231e.
8. A. Steadman, U. S. Pat. 2,299,510, Oct. 20, 1943; *Chem. Abs.*, **37**, 1658[3].
9. J. H. Schulman, U. S. Pat. No. 2,474,193, June 21, 1949; *Chem. Abs.*, **43**, 6517g.
10. H. C. Froelich, U. S. Pat. 2,542,322, Feb. 20, 1951; *Chem. Abs.*, **45**, 5027a.
11. H. C. Froelich, U. S. Pat. 2,525,028, Oct. 10, 1950; *Chem. Abs.*, **45**, 456[b].
12. F. A. Miller and C. H. Wilkins, *Anal. Chem.*, **24**, 1253 (1952).
13. J. M. Hunt, M. P. Wisherd, and L. C. Bonham, *ibid.*, **22**, 1478 (1950).
14. F. A. Kröger, "Some Aspects of the Luminescence of Solids," p. 137, Elsevier Publishing Company, Inc., Amsterdam (1943).
15. E. Voos, *Z. anorg. u. allgem. chem.*, **222**, 213 (1935); F. P. Hall and H. Insley, *J. Am. Ceram. Soc.*, **30**, 63 (1947).
16. F. A. Kröger, *loc. cit.*, p. 123.

# The Calcium-Silicate-Tungstate Phosphor

## Preparation and Physical Properties

**Shannon Jones**

*Lamp Wire and Phosphors Department, General Electric Company, Cleveland, Ohio*

ABSTRACT

A typical formulation and method of preparation is given for the calcium-silicate-tungstate (CST) phosphor. The wave length of the peak fluorescent emission of the tungstate phase is a function of its lead content. From spectral distribution of the emission of a CST phosphor, one can determine the lead content and the luminous efficiency to be expected from the tungstate phase. The effect of calcium fluoride as a batch addition in increasing average particle diameter of CST phosphor is shown.

Finer-grained phosphors (CST, calcium silicate, calcium tungstate) are produced if the batch is preheated at about 500°C before firing the phosphor.

Beta calcium metasilicate and calcium tungstate can be cocrystallized in the presence of Pb and Mn to form $\beta$-$CaSiO_3$:Mn:Pb and $CaWO_4$:Pb. Harrison and Hummel (1) described the phase relationships and fluorescence of this composite phosphor. Their work showed that no Mn entered the $CaWO_4$:Pb phase, where it was known to be a poison (2). The fluorescent properties of this calcium-silicate-tungstate phosphor under 2537Å excitation are simply those of a mixture of $\beta$-$CaSiO_3$:Mn:Pb and $CaWO_4$:Pb. The emission spectrum of a typical composite is shown in Fig. 1.

The use of $H_2WO_4$ in place of $CaF_2$ (3) as a mineralizer in the preparation of calcium silicate phosphor permits synthesis of a finer-grained material. However, the formation of the additional fluorescent phase, $CaWO_4$:Pb, not only affects the color but also reduces the luminous efficiency, since a substantial portion of the $CaWO_4$:Pb emission occurs in the near ultraviolet and in the less luminous part of the visible spectrum.

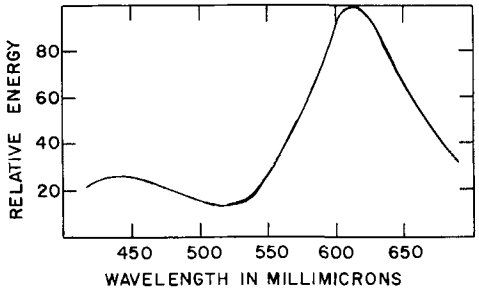


Fig. 1. Emission spectrum of CST phosphor

Fortunately an increase in the amount of $PbWO_4$ in solution in $CaWO_4$ has the effect of shifting the emission spectrum farther into the visible region. The distribution of Pb between the $\beta$-$CaSiO_3$:Mn:Pb and $CaWO_4$:Pb phases does not, in practice, reach equilibrium, but rather it is dependent on firing conditions. Under proper firing conditions it is possible to retain sufficient Pb in the calcium tungstate phase to obtain nearly maximum luminous efficiency in this phase.

### *Object*

The primary objectives of this paper are: (*a*) to present data on the effect of Pb concentration on the fluorescent properties under 2537Å excitation of the calcium tungstate phase in the calcium-silicate-tungstate (CST) phosphor; (*b*) to compare average particle sizes of calcium-silicate-tungstate phosphor and calcium silicate phosphor prepared using $CaF_2$.

The particle size of the CST phosphor or of calcium silicate or calcium tungstate phosphor is dependent on the method of preparation. It was found that a preheating technique was effective in producing finer particle size, particularly in the case of CST phosphor.

### *Preparation*

A typical CST phosphor was prepared by pebble-milling the batch given in Table I, firing it at 1140°C for 3 hr, mixing with 3 wt % of $NH_4Cl$, then refiring at 1140°C for 3 hr. Both firings were done in open "Vycor" crucibles in air in an electric resistance furnace.

Table I. Batch

| Ingredient | Moles |
|---|---|
| $CaCO_3$ | 1.10 |
| $MnCO_3$ | 0.070 |
| $PbSO_4$ | 0.025 |
| $H_2Si_3O_7$ | 0.40 |
| $H_2WO_4$ | 0.10 |
| $NH_4Cl$ * | 0.94 |

* $NH_4Cl$ was added after the first (or structure-forming) firing.

Table II. Phosphor

| Phase | Composition Oxide | Moles |
|---|---|---|
| | CaO | 1.0007 |
| Calcium | MnO | 0.068 |
| Silicate | PbO | 0.003 |
| | $SiO_2$ | 1.20 |
| — | — | — |
| Calcium | CaO | 0.0993 |
| Tungstate | PbO | 0.0007† |
| | $WO_3$ | 0.10 |

† This value was estimated from the peak wave length of the fluorescent emission band of the calcium tungstate phase.

The resulting approximate phosphor composition is given in Table II. It will be seen that the Pb content of the phosphor is much lower than that of the batch, the Mn content only slightly lower. Such variations result from selective volatilization of the compounds, particularly of the chlorides of Pb and Mn during the second (or scavenging) firing.

*Role of Lead in the Calcium Tungstate Phase*

Since the brightness of CST phosphor is partially dependent on the spectral distribution of the two phases, it is of value to know the changes in spectral distribution of each phase in the composite CST phosphor produced under various firing conditions.

First, examine in detail the calcium tungstate phase of CST phosphor. Kröger has published data on the fluorescent color of various $CaWO_4$-$PbWO_4$ solid solutions at room temperature under 2537Å excitation (2). He showed that, with increasing Pb content, the spectrum shifts toward longer wave lengths. However, his published data were not sufficiently detailed to be of value in determining the Pb content from the peak emission wave length. If one knows the relation between brightness and peak emission wave length of the tungstate phase, then one can, from its spectral distribution, determine whether the tungstate phase is potentially efficient.

Harrison and Hummel have shown that from 0 to at least 2 mole % Pb can be retained in the tungstate phase of CST. The Pb content of the tungstate phase is not determinable from the batch composition alone because one cannot predict either the distribution of Pb between the two phases or the total Pb retained in CST unless one knows the firing conditions and their effects on the retention of Pb.

However, from the peak wave length of the emission of the tungstate phase its Pb content and brightness can be determined. The emission bands of the calcium silicate phase do not overlap the peak of the tungstate emission. If one knows the Pb content of the tungstate phase from its peak wave length and the Pb content of the CST composite phosphor from chemical analysis, one can determine the Pb retained in the silicate phase of the CST phosphor.

In order to determine the effect of Pb content on the spectral distribution and other fluorescent properties of calcium tungstate phosphor, five batches were made up with various amounts of $PbSO_4$ (none, 0.0075 mole, 0.0150, 0.0225, 0.0300) added to 1.05 moles $CaSO_4$ plus 1.00 mole $H_2WO_4$. Part of each batch was fired at about 1000°C for 3 hr, another part for 15 hr. No subsequent addition of $NH_4Cl$ was made and no second firing was given the phosphor. There is no reason to believe that subsequent additions of $NH_4Cl$ and refirings have any substantial effect on the fluorescent properties of the calcium tungstate phase in CST other than those effects which are due to the reduction in Pb content.

Spectral distribution curves were run on the emission of the samples at room temperature under 2537Å radiation. Relative brightness was obtained on the samples with a barrier layer photocell corrected to the visibility function. Relative photocell outputs were obtained from the phosphors when an arbitrary blue filter was placed over the uncorrected barrier-layer cell. Each blue output, divided by the brightness of the phosphor, gave a ratio which is called "blueness". The "blueness" number should not be considered as having an easily definable quantitative significance, but rather it is a subjectively descriptive number indicating the appearance of the phosphor.

Figures 2, 3, and 4, respectively, are graphs of Pb introduced vs. peak wave length, brightness, and "blueness" for various firing times. In each figure a curve extrapolated to an estimated effective zero firing time is drawn. Points defining the extrapolated curves were determined by assuming that the loss of Pb followed first-order kinetics, i.e., $A = A_0 \exp(-bt)$, where $A$ is the amount of Pb at time $t$, $A_0$ is the amount of lead at time $t = 0$, and b is the rate constant, which is determinable from the data at 3 and 15 hr. Along these extrapolated curves one may assume that the Pb retained in the tungstate phase is determined solely by the Pb introduced in the batch. Thus the extrapolated curve in Fig. 2 pro-

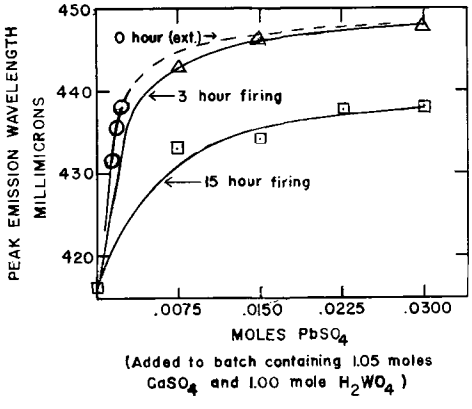


Fig. 2. Effect of Pb content and firing time on peak wave length of calcium tungstate phosphor.

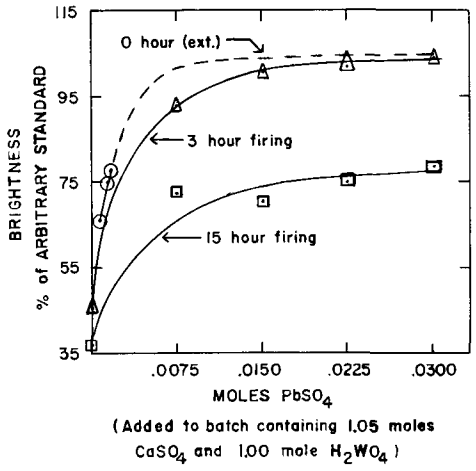


Fig. 3. Effect of Pb content and firing time on brightness of calcium tungstate phosphor.

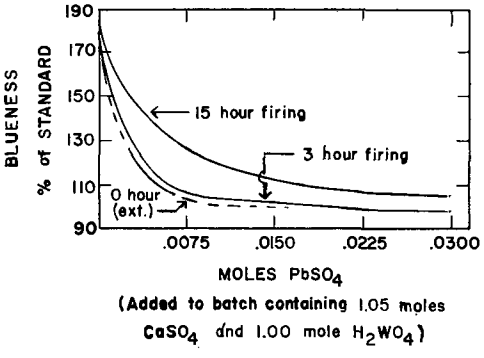


Fig. 4. Effect of Pb content and firing time on "blueness" of calcium tungstate phosphor.

vides a basis for a reasonably accurate estimate, from peak wave length of the tungstate phase, of the Pb retained in this phase. In turn, from the Pb content, one can determine the relative brightness of the tungstate phase from Fig. 3. In Fig. 3 the apparent dependence of brightness on firing time even where no Pb was introduced is probably false and the result of Pb contamination of the furnace.

### *The Calcium Silicate Phase in CST*

The optimum amount of Pb in the calcium silicate phase is not critical. In the phosphor formulation given in Table I, variations in Pb content of the calcium silicate phase from 0.0025 to 0.0035 moles do not give significant differences in brightness.

In practice an excess of Pb must be introduced initially into the CST or into straight calcium silicate phosphor, presumably to promote a sufficiently rapid formation of the proper structure. This excess of Pb in calcium silicate phosphor produces a dark phase, which probably contains some Mn. The dark phase reduces the brightness of the calcium silicate, consequently the scavenging firing with a chloride (3) is required to whiten the calcium silicate phosphor and increase its efficiency.

Firing with chloride reduces the Mn content slightly, as indicated in Table I. In the composition region of Table I, the spectral peak of the calcium silicate phase is shifted slightly away from the red by the reduction in Mn content, but the brightness is virtually constant.

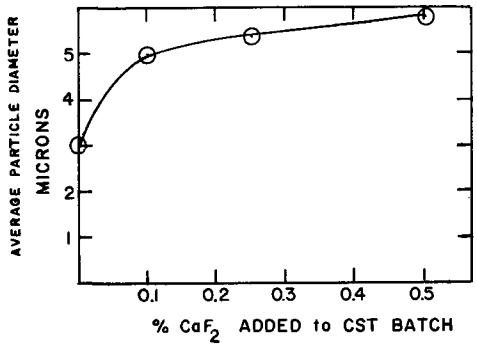


Fig. 5. Effect of $CaF_2$ on particle size of CST phosphor

### *Influence of Mineralizers on Particle Size*

The strong tendency of $CaF_2$ to cause an increase in particle size of CST phosphor is shown in Fig. 5. The average particle diameters were determined by an air permeation method ("Fisher Sub-Sieve Sizer"). Klasens, Hoekstra, and Cox recently mentioned the effect of fluorides in promoting crystal growth in silicates (4).

Similar effects of $CaF_2$ on particle size of calcium silicate phosphor have been observed. Tungstic acid in the amount given in Table I catalyzes the formation of the silicate phase about as effectively as the fluoride without causing the formation of as large grains. Harrison and Hummel have attributed the formation of large grains, particularly when using $CaF_2$, to the presence of liquid regions during firing (1).

### *Effect of Preheating on Particle Size*

In the CST formula of Table I there is no fluoride to form liquid regions. However, there is a probability of lead silicate glass being formed at certain points in the batch where the ratio of lead sulfate to silica is near a eutectic composition. It is possible to minimize the formation of these liquid regions by preheating the batch for a sufficient time below the temperature of liquid formation. Such a treatment distributes the lead compound by solid and vapor state diffusion until the small local regions of batch having compositions near the eutectic have lost their excess of lead compound.

Two experiments on typical CST batches showed average particle diameter (APD) reductions due to preheating as follows: not preheated, 4.6$\mu$ and 6.2$\mu$; preheated, 450°C, 3 hr, 2.9$\mu$ and 4.8$\mu$.

The above diameters apply to the phosphor after the structure-forming but before the addition of

**Table III. Average particle diameter (Fisher Sub-Sieve Sizer)**

| Preheating treatment | | Phosphor type | | |
|---|---|---|---|---|
| Temp, °C | Time, hr | Calcium silicate $\mu$ | CST $\mu$ | Calcium tungstate $\mu$ |
| NONE | | 7.7 | 7.2 | 6.2 |
| 400 | 3 | 5.6 | 6.7 | 4.9 |
| 400 | 16 | 5.8 | 4.5 | 4.6 |
| 400 | 64 | 5.4 | 4.4 | 4.6 |
| 500 | 3 | 6.6 | 4.5 | 5.1 |
| 500 | 16 | 6.3 | 4.5 | 5.4 |
| 500 | 64 | 6.0 | 4.3 | 5.2 |
| 600 | 3 | 6.3 | 4.3 | 5.9 |
| 600 | 16 | 6.4 | 4.3 | 5.9 |

$NH_4Cl$ and the scavenging firing. Qualitatively, differences in particle size which result from different procedures and which are apparent after the first firing tend to remain after a subsequent addition of $NH_4Cl$ and a refiring. However, the method of mixing in the $NH_4Cl$, the second firing conditions, and other factors also affect the particle size. For these reasons, it is not possible to give a single, clear-cut relationship between particle size after the second firing and either the fluoride content of the batch or the preheating treatment.

In another group of experiments it was found that preheating of the batches produced smaller particle sizes of calcium silicate phosphor and of calcium tungstate phosphor as well as of CST. For these tests, each of three batches was divided into ten parts. One part was fired directly at 1150°C for 3 hr; the other nine parts were preheated at various low temperatures for various times before taking them up to firing temperature (1150°C for 3 hr). The samples were not refired with $NH_4Cl$. Results are given in Table III.

## Summary and Conclusions

1. By using tungstic acid instead of calcium fluoride as the mineralizer, a finer grained calcium silicate phosphor phase can be obtained.
2. The introduction of tungstate produces a second fluorescent phase, $CaWO_4$:Pb whose efficiency can be determined from the spectral distribution of fluorescent emission of the composite.
3. Average particle size of CST phosphor, or of calcium silicate phosphor or calcium tungstate phosphor, can be reduced by a batch preheating technique.

Manuscript received June 6, 1957.
Any discussion of this paper will appear in a Discussion Section to be published in the December 1958 JOURNAL.

REFERENCES

1. D. E. Harrison and F. A. Hummel, *This Journal*, 105, 34 (1958).
2. F. A. Kröger, "Some Aspects of the Luminescence of Solids," Chap. III.
3. H. C. Froelich, U. S. Patent 2,542,322.
4. H. A. Klasens, A. H. Hoekstra, and A. P. M. Cox, *This Journal* **104**, 93 (1957).

# Heat of Formation of Titanium Tribromide by the Mercury Reduction of Titanium Tetrabromide

**Elton H. Hall and John M. Blocher, Jr.**

*Battelle Memorial Institute, Columbus, Ohio*

ABSTRACT

The experimentally determined heat of reaction, $\frac{1}{2}Hg_2Br_2(s) + TiBr_3(s) = TiBr_4(g) + Hg(l)$, $\Delta H_{475} = 23.0 \pm 1.2$ kcal is combined with existing data for $TiBr_4$, Hg, and $Hg_2Br_2$ to obtain for the heat of formation and standard entropy of $TiBr_3$,

$$\Delta H^\circ_{f298.2} = -130.6 \pm 1.2 \text{ kcal/mole}$$
$$S^\circ_{298.2} = 43.4 \pm 1.6 \text{ e.u.}$$

As part of a program directed toward the determination of the physical and thermodynamic properties of the titanium bromides, a study of the following equilibrium was undertaken:

$$\frac{1}{2}\ Hg_2Br_2(s) + TiBr_3(s) = TiBr_4(g) + Hg(l) \quad (I)$$

The heat of this reaction may be combined with the heats of formation of $Hg_2Br_2$ and $TiBr_4$ to calculate the heat of formation of $TiBr_3$. A study by a dew-point method of the corresponding reduction of $TiCl_4$ has been reported by Schäfer, *et al.* (1).

## Experimental

The reagents were triple-distilled Hg and $TiBr_4$ prepared from distilled Br and iodide-process Ti, and distilled in a 30-plate column, as described by Blocher, *et al.* (2).

Measurements of the equilibrium pressure of $TiBr_4$ over $Hg_2Br_2$, $TiBr_3$, and Hg were made in the apparatus shown in Fig. 1. The cell was carefully cleaned with HF, rinsed, outgassed, and charged with Hg by vacuum distillation from a reservoir attached at Point A. A small amount of pure $TiBr_4$, transferred in an ampoule provided with a break seal, was distilled into the cell and allowed to react with the Hg to form a surface coating of $Hg_2Br_2$ and $TiBr_3$, after which the cell was sealed off at A and separated from the filling apparatus. The purpose of the flexible rubber tubing connecting the cell to the vacuum and controlled-pressure system was to

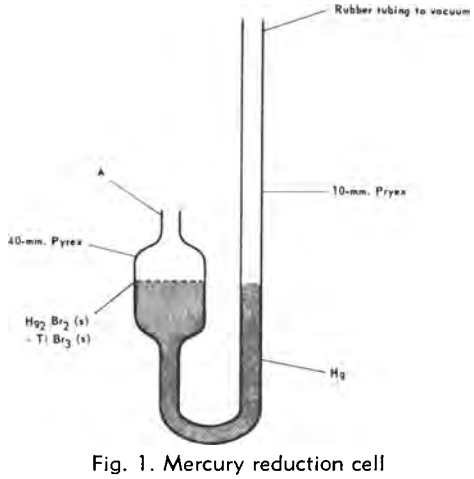


Fig. 1. Mercury reduction cell

permit outgassing by inverting the cell while evacuating the system.

The cell was used as a null indicator, the pressure above the bromides being balanced by a measured pressure of inert gas which was varied until the Hg level in the 10-mm tube was returned to the position occupied at zero pressure differential. As a check on the reliability of the technique, and of the prediction that the partial pressures of $Hg_2Br_2(g)$ and $HgBr_2(g)$ are negligible,[1] the cell was charged with Hg and Br to form a scum of $Hg_2Br_2$ over the Hg surface. The pressure-temperature data given in Table I indicate that only the partial pressure of Hg is significant, although there appears to be a small systematic error in the experimental values. In the Hg reduction of $TiBr_4$, the Hg saturation vapor pressure is exerted over the Hg at unit activity in the cell along with the equilibrium $TiBr_4$ pressure, and must be subtracted from the observed total pressure to obtain the partial pressure of $TiBr_4$.

The cell was thermostated to $\pm 0.2$°C in a salt bath whose temperature was measured by a calibrated Chromel-Alumel thermocouple. The Hg levels in the cell and the manometer were measured with a cathetometer.

The data obtained with six separate preparations are given in Tables II-IV. Figure 2 shows the results for samples E and F, which are typical. In the preparation of each of samples A through D, an undetermined amount of Br was distilled into the cell in addition to the Hg and $TiBr_4$, thus providing an excess of $Hg_2Br_2$. Samples E and F were prepared using only Hg and $TiBr_4$ so that the $Hg_2Br_2$ and $TiBr_3$ were produced in stoichiometric ratio.

## Results

The data obtained on samples C and E, when plotted in the usual manner, fell on three straight lines. The pressures exerted by a fresh sample fell on line I. However, when the sample was held at high temperature, e.g., 250°C, the pressure decreased slowly over a period of 36 hr. A new equilibrium was apparently established on line II. Finally, when the sample was cooled below 200°C, line III was obtained, the slope of which was less than the slope of I. The system was then reversible between II and III with considerable lag in the change in slope after passing the break in either direction. The intersection of II and III occurred at 238° and 218°C for samples C and E, respectively.

A similar break in the log $p$ vs. $1/T$ curve was observed in the data for sample A. At the time, this was considered to be anomalous behavior and precise data were not obtained during the early stages of the run. The points reported for sample A correspond to the system in state III.

The measurements on sample B were made over a very short period of time compared to sample A, and the run was completed before a drift in pressure was observed.

Runs D and F were purposely terminated while the system was still in the state leading to pressures on line I.

[1] Calculations based on the data given by Brewer (3) indicate a $HgBr_2$ pressure, e.g., of 0.13 mm at 225°C.

**Table I. Total pressure over Hg(l) and $Hg_2Br_2$(s)**

| Temp, °C | $P_{total}$,[a] mm of Hg | $P_{Hg(g)}$,[b] mm of Hg | $P_{total} - P_{Hg}$, mm of Hg | $\frac{\Delta P}{P}$, % |
|---|---|---|---|---|
| 236.5 | 52.3 | 51.6 | 0.7 | 1.35 |
| 238.1 | 54.4 | 54.0 | 0.5 | 0.93 |
| 246.2 | 67.3 | 67.3 | 0.0 | 0.0 |
| 254.5 | 83.9 | 83.7 | 0.2 | 0.24 |
| 257.9 | 91.7 | 91.2 | 0.5 | 0.55 |
| 274.1 | 137.1 | 136.4 | 0.7 | 0.52 |

[a] Observed pressure corrected for latitude, and for thermal expansion of Hg in the cell and in the manometer.
[b] "Handbook of Chemistry and Physics," 35th Ed., Chemical Rubber Publishing Co., p. 2147 (1953-54).

**Table II. Equilibrium $TiBr_4$ pressure in Mercury Reduction Reaction, Runs A and B**

| Run[a] | Temp, °K | $P_{TiBr_4}$, mm of Hg |
|---|---|---|
| A | 449.3 | 6.4 |
| A | 443.4 | 4.3 |
| A | 430.5 | 1.7 |
| A | 472.3 | 21.7 |
| A | 466.0 | 16.9 |
| A | 463.3 | 14.0 |
| A | 446.8 | 5.6 |
| B | 462.7 | 12.0 |
| B | 475.7 | 25.0 |
| B | 492.2 | 60.8 |
| B | 459.4 | 10.0 |
| B | 449.7 | 5.6 |
| B | 491.0 | 56.5 |
| B | 510.7 | 139.8 |
| B | 444.1 | 3.7 |

[a] Data listed in order taken.

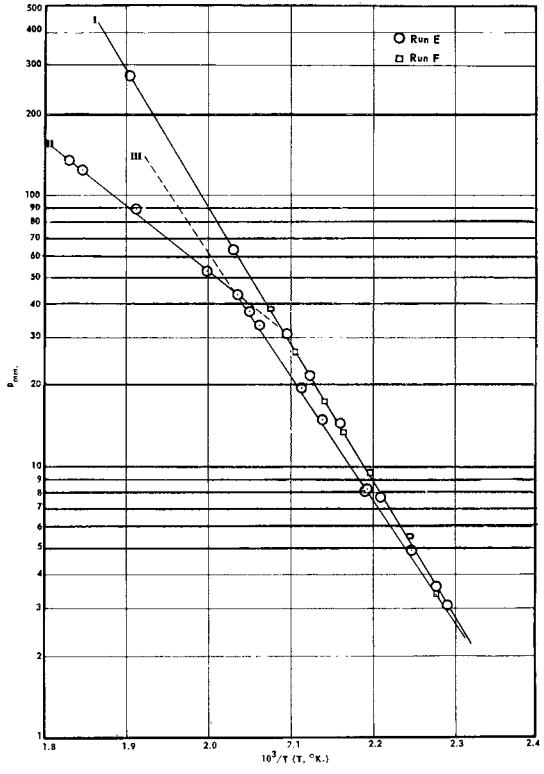


Fig. 2. $TiBr_4$ pressure in mercury reduction reaction (runs E and F)

Table III. Equilibrium $TiBr_4$ Pressure in Mercury Reduction Reaction Runs C and D

| Run C[a] | | Run D[a] | |
|---|---|---|---|
| Temp, °K | $P_{TiBr_4}$, mm of Hg | Temp, °K | $P_{TiBr_4}$, mm of Hg |
| 498.8 | 89.3 | 444.2 | 4.1 |
| 465.1 | 16.3 | 444.0 | 4.0 |
| 448.4 | 6.7 | 467.5 | 16.1 |
| 510.4 | 218.3 | 495.2 | 65.8 |
| 462.2 | 14.5 | 485.1 | 36.2 |
| 502.2 | 88.3 | 481.2 | 30.7 |
| 518.1 | 176.3 | 460.8 | 12.4 |
| 509.6 | 94.5 | 496.2 | 65.2 |
| 530.2 | 145.3 | 523.2 | 211.3 |
| 528.4 | 138.2 | | |
| 522.4 | 121.4 | | |
| 516.7 | 108.6 | | |
| 508.2 | 92.8 | | |
| 507.6 | 91.7 | | |
| 501.3 | 78.9 | | |
| 495.2 | 70.0 | | |
| 445.7 | 5.3 | | |
| 476.2 | 24.5 | | |
| 471.4 | 19.7 | | |
| 488.7 | 39.7 | | |
| 496.8 | 55.2 | | |
| 499.6 | 61.9 | | |

[a] Data listed in the order taken.

Table IV. Equilibrium $TiBr_4$ Pressure in Mercury Reduction Reaction, Runs E and F

| Run E[a] | | Run F[a] | |
|---|---|---|---|
| Temp, °K | $P_{TiBr_4}$, mm of Hg | Temp, °K | $P_{TiBr_4}$, mm of Hg |
| 477.2 | 31.0 | 467.2 | 17.3 |
| 471.2 | 21.8 | 455.2 | 9.5 |
| 463.1 | 14.4 | 439.4 | 3.4 |
| 439.2 | 3.6 | 481.9 | 38.3 |
| 452.8 | 7.7 | 462.0 | 13.3 |
| 444.8 | 4.9 | 445.2 | 5.5 |
| 492.7 | 63.8 | 475.0 | 26.8 |
| 525.6 | 279.7 | | |
| 541.2 | 125.1 | | |
| 546.6 | 135.1 | | |
| 523.3 | 89.4 | | |
| 500.4 | 53.3 | | |
| 467.7 | 15.0 | | |
| 436.7 | 3.1 | | |
| 473.5 | 19.6 | | |
| 485.1 | 33.4 | | |
| 456.2 | 8.2 | | |
| 456.6 | 8.1 | | |
| 491.4 | 43.6 | | |
| 488.0 | 33.5 | | |

[a] Data listed in the order taken.

The slope of line I varies slightly among samples B through E. This variation, which is outside the limits set by the relatively small scatter in the data for a given sample, could not be correlated with changes in conditions or technique. For samples E and F, the initial points fall on the same line, suggesting that the data are at least reproducible for stoichiometric samples. Table V gives the $\Delta H$ values calculated from the data.

*X-ray Diffraction Analysis*

The breaks in the log $p$ vs. $1/T$ curves clearly indicate a fairly energetic phase change. As an aid in the interpretation of the data, several samples were submitted to x-ray diffraction analysis. The first such sample was prepared by placing Hg and $TiBr_4$ in a quartz capillary and heating for 18 hr at 120°C. The x-ray pattern taken with the sample at 250°C showed $TiBr_3$ and $Hg_2Br_2$. At the conclusion of run C (sample in state III), a sample of the reaction product was examined. $Hg_2Br_2$ was found in addition to a few unidentified lines. However, no lines for $TiBr_3$ were seen.

Samples from runs E and F showed $Hg_2Br_2$ with no extra lines and no $TiBr_3$ lines. Two additional preparations were made by reacting $TiBr_4$ with distilled Hg. No pressure measurements were made on these samples. Only $Hg_2Br_2$ were detected in one sample, while in the other, strong $Hg_2Br_2$ and faint $TiBr_3$ lines were seen in the x-ray pattern.

No expansion of the lattice parameter of $Hg_2Br_2$ could be detected in any of the samples.

*Hot-Stage Microscopy*

The heat effect (about 12 kcal), indicated by the break in the slope of the log $p$ vs. $1/T$ curve, is of the order of a heat of fusion rather than being characteristic of a heat of solid solution which might be about 2 to 3 kcal.

To detect possible fusion, a sample of the reaction solids was observed with a hot-stage microscope. The temperature was increased from room temperature to over 300°C. No fusion process was observed. However, at one point, a crystallization from the excess Hg was observed in the cooling process.

*Solubility Experiment*

In a separate experiment designed to detect possible solution of reactants in the Hg, a sample was taken at temperature from below the surface of liquid Hg which had been equilibrated with the reaction mixture at 220°C for 72 hr. A small amount (about 0.2%) of bromide-containing scum was observed to separate from the Hg sample on cooling. No Ti (<0.5%) was detected in the scum such as might be expected if solution in Hg were the explanation of the disappearance of the $TiBr_3$ phase in the aged samples.

## Discussion

It may be assumed that the pressure-temperature data taken on a fresh sample are representative of the Hg reduction equilibrium as written in Eq. (I), since both $TiBr_3$ and $Hg_2Br_2$ were observed as sepa-

Table V. Heats of Reaction Calculated from the Slopes of Lines I, II, and III in the Temperature Range 435°K to 525°K

| Sample | $\Delta H_I$, kcal/mole | $\Delta H_{II}$, kcal/mole | $\Delta H_{III}$, kcal/mole |
|---|---|---|---|
| A | — | — | 20.6, 22.9[a] |
| B | 24.2 | — | — |
| C | 21.8 | 10.9 | 20.2 |
| D | 22.7 | — | — |
| E | 23.2 | 11.2 | 20.8 |
| F | 23.2 | — | — |
| | Mean $\Delta H_I = 23.0 \pm 1.2$ kcal/mole | | |

[a] Mercury expansion data were not taken on the cell used for run A. The corrections determined for the cells used in runs B and C, when applied to the pressure data of run A, lead to two different lines. $\Delta H_{III}$ values calculated from each slope are reported.

rate solid phases in the x-ray diffraction patterns of fresh samples. The reason for the variation of the slope of the initial line among different samples is unknown. Therefore, the average of the initial slopes for samples B through F has been used to calculate the heat of reaction with the variation in the slopes included in the ascribed uncertainty.

To extrapolate the experimental data to 298.2°K, it was necessary to obtain a value for the $\Delta C_p$ of reaction. Unfortunately, reliable values for the heat capacities of $TiBr_3$ and $Hg_2Br_2$ are not available. However, values obtained by estimation should be entirely adequate for this purpose. The heat capacity of $Hg_2Br_2$ was taken as the average (24.8 cal/mole/deg at 298.2°K) of those of $Hg_2Cl_2$ and $Hg_2I_2$ given in National Bureau of Standards Circular 500. The heat capacity of $TiBr_3$ (also 24.8 cal/mole/deg at 298.2°K) was estimated by adding 0.8 cal/deg/gram-atom to the heat capacity of $TiCl_3$ obtained by averaging the heat capacities given for $VCl_3$ and $AlCl_3$. The heat capacity of Hg is also given in Circular 500. That of $TiBr_4(g)$ was obtained by calculation from the spectroscopic data of Delwaulle, *et al.* (4). The resulting value of $\Delta C_p = -6.5$ was taken as the average over the temperature range of the measurements.

This treatment of the data gives for Eq. (I):

$$\log_{10} P_{atm} = -5706/T - 3.271 \log T + 19.291$$
$$\Delta H_{298.2} = 24.16 \pm 1.2 \text{ kcal}$$
$$\Delta S_{298.2} = 44.7 \pm 1.6 \text{ e.u.}$$

Since entropy values can be estimated with greater certainty than can heats of reaction, comparison of the entropy change obtained in the above work with that calculated from the best available information gives an indication of the reliability of the experimental data. In calculating the standard entropy of $TiBr_3(s)$, the values at 298.2°K for Hg(l) = 18.5 e.u. and $\frac{1}{2}Hg_2Br_2(s)$ = 25.45 e.u. were taken from Circular 500. The value for $TiBr_4(g)$ = 95.02 e.u. was calculated from spectroscopic data (4). The resulting value, $S^\circ_{298.2} = 43.4 \pm 1.6$ e.u., is very close to the estimated value of 43 e.u. given by Brewer (3).

Prosen and his associates (5) at the National Bureau of Standards have obtained for

$$2\ Br_2(l) + Ti(\alpha) = TiBr_4(s)$$
$$\Delta H_{298.2} = -147.40 \pm 1.1 \text{ kcal/mole}$$

This may be combined with the above results, the heat of formation of $Hg_2Br_2$ (−49.42 kcal/mole from Circular 500), and the heats of vaporization and fusion of $TiBr_4$ [13.22 kcal of Hall, *et al.* (6), and 3.08 kcal of Kelley (7), respectively] at 298.2°C, to give the heat of formation of $TiBr_3(s)$:

$$3/2\ Br_2(l) + Ti(\alpha) = TiBr_3(s)$$
$$\Delta H_{298.2} = -130.6 \pm 1.2 \text{ kcal/mole}$$

The occurrence of the break in the log $p$ vs. $1/T$ curve and the failure of the system to return to its initial state upon cooling below the break cannot be explained on the basis of the available experimental evidence. The possibility that $HgBr_2(s)$ is the stable phase above the break is dismissed, since thermodynamic calculations indicate that the invariant point [where Hg(l), $HgBr_2(s)$, and $Hg_2Br_2(s)$ coexist] lies somewhere between 1000° and 1200°C, rather than at the 225°C level of the observed break. This conclusion is confirmed by the absence of $HgBr_2(s)$ in the x-ray patterns observed at 250°C. It appears that one or both phenomena are related to the disappearance of the $TiBr_3$ lines from the x-ray diffraction patterns of aged samples taken from the pressure cell. This could result from *(a)* formation of an amorphous form of $TiBr_3$, *(b)* formation of a solid solution or complex between $TiBr_3$ and $Hg_2Br_2$ which has the $Hg_2Br_2$ crystal structure or is amorphous, and *(c)* solution of $TiBr_3$ in the liquid Hg. However, neither the formation of amorphous $TiBr_3$ nor the formation of a solid solution would be expected to contribute as large a heat effect as that observed. Furthermore, the failure to detect any expansion of the lattice parameter of $Hg_2Br_2$ indicates that no solid solution is formed. The solution of $TiBr_3$ in liquid Hg could produce the observed heat change; however, no Ti could be detected in Hg sampled at 220°C after equilibration with the reaction solids.

Since this work was concluded, it has been suggested that the disappearance of the $TiBr_3(s)$ phase may have resulted from a reaction with Pyrex which may not occur with quartz. Equilibrium determinations in quartz equipment would settle this point. However, it should be noted that in the present work no visible etching of the cell occurred such as might be expected if the Pyrex reacted appreciably with the relatively large amount of titanium bromide contained in the cell.

## Summary

In order to permit calculation of the heat of formation of $TiBr_3$, a study of the Hg reduction of $TiBr_4$ has been made. Pressure data obtained on fresh samples have been assigned to the equilibrium:

$\frac{1}{2}\ Hg_2Br_2(s) + TiBr_3(s) = TiBr_4(g) + Hg(l)$

since both $Hg_2Br_2$ and $TiBr_3$ were observed as separate solid phases in the x-ray diffraction patterns of fresh samples. The heat of reaction calculated from these data has been combined with the heats of formation of $TiBr_4(s)$ and $Hg_2Br_2(s)$ and the heats of fusion and vaporization of $TiBr_4$ to give the heat of formation of $TiBr_3(s)$.

A break in the log $p$ vs. $1/T$ curve was observed at high temperatures after prolonged heating. Furthermore, the $TiBr_3$ pattern was not seen in the x-ray diffraction studies of heated samples. A full investigation of these phenomena must be deferred. However, it is concluded that, despite these irregularities, a fairly reliable value has been obtained for heat of formation of $TiBr_3$.

## Acknowledgment

The authors are grateful for the help and interest of the Office of Naval Research who supported this work under Contract No. Nonr-1120(00). They are also indebted to the following members of the Battelle staff: Neil D. Veigel for some of the pressure measurements, George Cocks for the hot-stage microscopy and J. Robert Bridge, for the crystallographic work.

Manuscript received July 5, 1957. This paper was prepared for delivery before the Cleveland Meeting, Sept. 30-Oct. 4, 1956.

Any discussion of this paper will appear in a Discussion Section to be published in the December 1958 JOURNAL.

REFERENCES

1. H. Schäfer, G. Breil, and G. Pfeffer, *Z. anorg. u. allgem. Chem.*, **276**, 325 (1954).
2. J. M. Blocher, Jr., R. F. Rolsten, and I. E. Campbell, *This Journal*, **104**, 553, (1956).
3. L. Brewer, "National Nuclear Energy Series," Vol. IV-19B, L. L. Quill, Editor, McGraw-Hill Book Co., New York (1950).
4. M. Delwaulle and F. Francois, *Compt. rend.*, **220**, 173 (1945).
5. R. A. Nelson, W. H. Johnson, and E. J. Prosen, National Bureau of Standards Report No. 4607, November (1955).
6. E. H. Hall, J. M. Blocher, Jr., and I. E. Campbell. To be published.
7. K. K. Kelly. To be published.

# Pressure Distribution within a Vacuum Arc Furnace

**J. W. Suiter**

*Mines Branch, Department of Mines and Technical Surveys, Ottawa, Ontario, Canada*

ABSTRACT

The pressure distribution within a continuously evacuated, consumable electrode arc furnace was determined when a variable leak was placed in the melting region of the furnace. This pressure distribution agreed both with that obtained from a simplified calculation based on the kinetic theory of gases and with that obtained during the melting of mild steel electrodes.

Johnson, *et al.* (1) have shown that the arc characteristics and the melting rate in a consumable electrode, vacuum arc furnace depend on a number of variables, including the gas pressure within the furnace. In current practice the pressure is usually measured at some point in the body of the furnace and not in the region of the arc. Since gas is evolved from most metals during melting the pressure in the region of the arc will be higher than that in the body of the furnace.

In the present work the pressure in the region of the arc has been calculated and measured in a simple simulated melting system and results have been compared with similar pressure measurements obtained during the melting of steel electrodes.

## Apparatus and Experimental

The experiments were conducted in the furnace described by Rylski and Kinsey (2) and shown schematically in Fig. 1 Gas pressure was measured at the top of the mould and at a point 30 cm below the top by means of thermocouple vacuum gauges and probe tubes which passed through vacum seals in a side port of the furnace. The probes were constructed from 1 cm diameter tubing and were the same length so that their response to pressure fluctuations would be the same. The pressure in the body of the furnace was measured with an Alphatron ionization gauge. The Alphatron ionization gauge was initially calibrated against a McLeod gauge. Prior to each experiment the thermocouple gauges were calibrated *in situ* against the Alphatron ionization gauge by isolating the furnace from the pumps and admitting air to a series of static pressures. These recalibrations of the thermocouple gauges were reproducible within $\pm 1\mu$ Hg pressure.

To simulate the evolution of gas during melting, a needle valve was connected to the base of the mould. The lower probe was about 9 cm from the base plate of the mould. The leak rate for each setting of the needle valve was determined from the known volume of the furnace and the observed rate of increase in pressure when the furnace was isolated from the pumps. After each adjustment to a specified leak rate, it was necessary to allow 30 sec to elapse for the attainment of equilibrium, before measuring the pressure at the three points.

The pressure distribution within the mould was determined while melting a mild steel electrode which contained 0.13% C, 0.01% N, 0.005% O and less than 0.0001% H. During these experiments the pressure was measured only at the top and at the lower part of the mould and the temperature of the tip of the lower probe was measured by means of a thermocouple attached to it. When the arc was struck, the pressure rose quickly but, after about 90

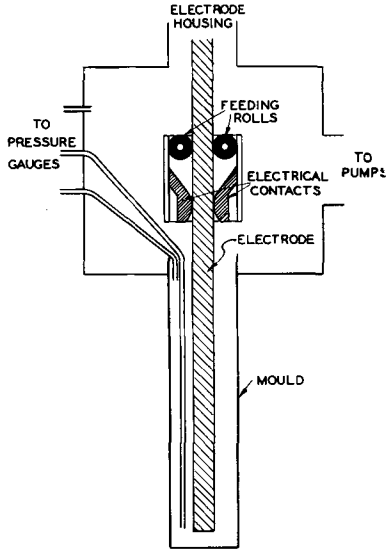


Fig. 1. Arrangement for measurement of pressure distribution with the arc furnace.

sec, dropped to a steady value when the feed rate was uniform. Before melting, the lower probe was about 4 cm from the melting zone and no melting of this probe occurred when a steady feed rate of the electrode was quickly attained and the arc length kept short.

## Results

*Simulated melting.*—The distributions of pressure, for two electrode and two mould sizes, are shown as functions of the leak rate in Fig. 2-5. When the 11.5 cm diameter mould was used the pressure difference between the top and the lower part of the mould was not very large and was only slightly affected by the electrode size. Relatively large pressure differences were obtained when the 7.5 cm diameter mould was used and these differences varied considerably with the size of the electrode.

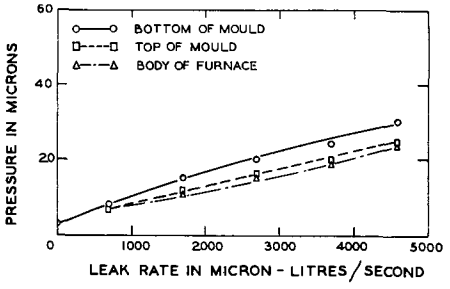


Fig. 2. Distribution in pressure for an electrode 3.2 cm x 3.2 cm in a mould of 11.5 cm diameter.

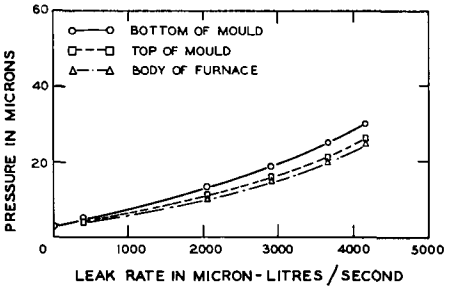


Fig. 3. Distribution in pressure for an electrode 3.2 cm x 4.9 cm in a mould of 11.5 cm diameter.

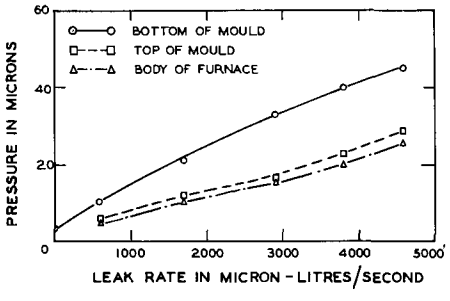


Fig. 4. Distribution in pressure for an electrode 3.2 cm x 3.2 cm in a mould of 7.5 cm diameter.

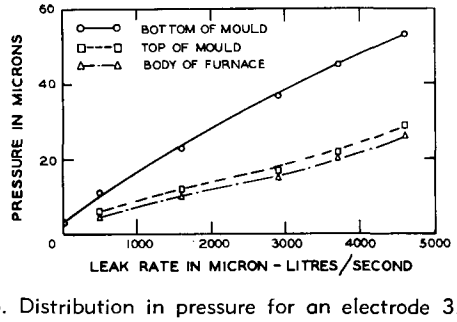


Fig. 5. Distribution in pressure for an electrode 3.2 cm x 4.9 cm in a mould of 7.5 cm diameter.

*Actual melting.*—To avoid melting the lower probe, the pressure distribution in the mould was measured only when melting a 3.2 cm square steel electrode in the 11.5 cm diameter mould. Different rates of gas evolution were obtained by melting the same steel electrode at different rates. The rate of melting was controlled by the amount of current used in the arc. Because of the temperature gradient along the lower probe, there was a pressure gradient along this probe.

If the mean free path of the molecules in the hot region of the probe is greater than the diameter of the probe, then the pressure $P_A$ in the hot region is related to the pressure $P_B$ measured at the gauge by:

$$P_A/P_B = \sqrt{T_A/T_B} \qquad (I)$$

where $T_A$ is the temperature of the tip of the probe and $T_B$ is the temperature of the gauge.

In the present case the mean free path of the molecules was approximately the same as the diameter of the probe and Eq. (I) gave too high a value for the pressure in the hot region. A correction factor, which depends on the ratio of mean free path to probe diameter, for Eq. (I) has been obtained from the results of other workers (3). Table I lists the measured pressures at the top and the lower part of the mould and also the corrected values of the pressure at the lower part of the mould. Once melting started, the temperature of the probe tip rose quickly for approximately 90 sec but in the following 30 sec, when steady pressure readings were obtained, the temperature of the probe tip increased by only 40°K. Variations in temperature of this order of magnitude have little effect on the calculated pressure in the hot region and the relatively steady temperature of the probe tip suggests that the measured temperature should be close to the gas temperature.

## Discussion

On the basis of the kinetic theory of gases, Gruber (4) has calculated the pressure at the top of a mould and then the pressure at the lower part of that mould. In calculating the pressure at the top of the mould a formula was used which is applica-

**Table I. Distribution of pressure within a mould of 11.5 cm diameter while melting a steel electrode 3.2 cm square**

| Arc current (amp) | Temperature of probe (°K) | Pressure at lower part of mold ($\mu$ of Hg) | Pressure at lower part of mould, corrected for temperature effect ($\mu$ of Hg) | Pressure at top of mold ($\mu$ of Hg) | Approx. melting rate (kg/min) |
|---|---|---|---|---|---|
| 1200 | 1200 | 9 | 15 | 13 | 0.5 |
| 1500 | 1200 | 10 | 16 | 14 | 0.6 |
| 1800 | 1200 | 13 | 21 | 19 | 0.9 |
| 2100 | 1100 | 22 | 32 | 28 | 1.3 |

ble only to a thin aperture, the dimensions of which are small compared with those of the vessel from which the flow is occurring. This leads to considerably lower pressures than are encountered in practice and thus the pressure drop along the mould as calculated by Gruber will be in error.

The following calculation of the pressure drop along the mould during the simulated melting experiments is based on an equation describing the flow of gas through a simple pipe and this is modified to allow for the presence of the electrode. The flow of gas through a circular pipe over a wide range of pressures is described by a semi-empirical equation developed by Knudsen (5) and for air flowing at 25°C may be written in the following form:

$$\frac{Q}{P_1 - P_2} = \mathrm{Cm} \left\{ 0.0145\, a(P_1 + P_2) + \frac{1 + 0.246\, a(P_1 + P_2)}{1 + 0.304\, a(P_1 + P_2)} \right\} \qquad \text{(II)}$$

where $Q$ is the quantity of gas flowing through the pipe, in micron-liters per second; $P_1$ and $P_2$ are the pressures at the ends of the pipe, in microns; Cm is the conductance of the pipe when molecular flow is occurring, in liters per second; and $a$ is the radius of the pipe, in centimeters.

For the present case of an electrode within the circular mould, the average separation between the mould and the electrode was used rather than the radius of the mould. The molecular conductance of any duct, for air flowing at room temperature, may be calculated from the following formula (6):

$$\mathrm{Cm} = 61.8\, K \frac{A^2}{BL} \qquad \text{(III)}$$

where $A$ is the cross-sectional area of the duct, in square centimeters; $BL$ is the surface area of the walls of the duct, in square centimeters; and $K$ is a constant equal to 1.1 for an annular duct (6) similar to the present arrangement of an electrode in a mould.

From the observed leak rate and the pressure at the top of the mould the pressure drop along the mould was calculated. These values are given in Table II together with those measured during the simulated melting experiments. Reasonable agreement is evident between the calculated and the experimental values. Particular attention is drawn to the close agreement between the values of the pressure difference measured in the actual melting experiments with those measured during the simulated melting experiments. It is possible to compare these two sets of results because the H content of the steel used in the melting experiments is so low. The gases evolved during the melting experiments are mainly N and O or CO. Since these gases have physical properties similar to those of air, the response of the thermocouple vacuum gauges and the conditions of flow in the mould are similar in the two sets of experiments.

**Table II. Pressure drop along mould of 11.5 cm diameter containing an electrode 3.2 cm²**

| Pressure at top of mould (μ of Hg) | Measured pressure drop during simulated melting (μ of Hg) | Calculated pressure drop for simulated melting (μ of Hg) | Measured pressure drop while melting (μ of Hg) |
|---|---|---|---|
| 13 | 3 | 2.2 | 2 |
| 14 | 3 | 2.5 | 2 |
| 19 | 4 | 2.7 | 2 |
| 28 | 4 | 3.0 | 4 |

The flow of gas depends not only on the conditions already mentioned but also on the temperature of the gas. Therefore it might be expected that, in actual melting experiments where the flow is occurring in both a pressure gradient and a temperature gradient, the pressure drop along the mould would be considerably different from that during a simulated melting experiment where the flow is occurring in a pressure gradient alone. One reason for the close agreement may be that the water cooling of the mould cooled the gas quickly and the flow of gas through the mould occurred essentially at an uniform temperature.

The present work shows that the pressure drop along the mould of a consumable-electrode vacuum arc furnace can be measured in simulated melting experiments or can be calculated if the rate of gas evolution in the region of the arc and the pressure at the top of the mould are known. It also shows that if high pressures in the melting region of vacuum arc furnaces, with the accompanying troublesome glow discharges, are to be avoided it is essential that sufficient free space be provided between the electrode and the mould to ensure rapid removal of the gases evolved during melting.

Particularly when melting Ti, and other similar metals, it is possible that some gas (mainly H) will be evolved from the electrode some distance above the melting zone in the furnace as well as in the melting zone. Such evolution above the melting zone will tend to reduce the pressure gradient along the mould.

## Acknowledgments

The work was done under the general direction of H. V. Kinsey of the Department of Mines and Technical Surveys, Ottawa, and was made possible by the award of a Fellowship by the National Research Council of Canada.

Manuscript received April 12, 1957.

Any discussion of this paper will appear in a Discussion Section to be published in the December 1958 JOURNAL.

## REFERENCES

1. E. W. Johnson, G. T. Hahn and R. Itoh, "Arcs in Inert Atmospheres and Vacuum," W. E. Kuhn, Editor, p. 19, John Wiley & Sons, Inc., New York (1956).
2. O. Z. Rylski and H. V. Kinsey, *ibid.*, p. 69.
3. S. Dushman, "Scientific Foundations of Vacuum Techniques," p. 67; John Wiley & Sons, Inc., New York (1949).
4. H. Gruber, "Arcs in Inert Atmospheres and Vacuum," W. E. Kuhn, Editor, p. 118, John Wiley & Sons, Inc., New York (1956).
5. S. Dushman, *op. cit.*, p. 115.
6. A. Guthrie and R. K. Wakerling, "Vacuum Equipment and Techniques," p. 35, McGraw-Hill Book Co., New York (1949).

# The Anodic Oxidation of Zinc and Zinc-Tin Alloys at Very Low Current Density

S. E. S. El Wakkad,[1] A. M. Shams El Din, and H. Kotb

*Department of Chemistry, Faculty of Science, Cairo University, Cairo, Egypt*

ABSTRACT

The anodic oxidation of zinc and zinc-tin alloys at very low current density was carried out in solutions of different pH values using the direct potentiometric method. In the case of zinc, the primary oxidation product was a film of zinc oxide or hydroxide less than one molecule thick. When tin was alloyed in different concentrations with zinc, the anodic process resulted in the successive formation of zinc hydroxide, stannous and stannic hydroxides before oxygen evolution. The alloys required less quantities of electricity to passivate than their pure components, thus revealing their noble character. The passivation of the alloys in 0.1*N* nitric acid is due to a chemical and not to electrochemical process. Critical current densities for passivation also revealed the noble character of the alloys.

The current theories of passivity are based largely on experiments performed with pure metals. Metallic alloys have attracted little attention despite their technical importance. In this laboratory, a systematic study of the anodic oxidation of metals at very low current density was undertaken (1-6). The work has now been extended to simple, two-component alloys. A start was made with speculum (Cu-Sn) alloys (7), and the present paper is a report on the results obtained with Zn-Sn alloys. By using a very small constant polarizing current, and an electrode of relatively large surface area, considerable time was taken by the electrode to pass from hydrogen to oxygen evolution potentials. This enabled the determination of the type and thickness of the oxides formed on the electrode during polarization. On the other hand, current-potential curves were helpful in determining the critical current densities for the passivation process. No work on Zn-Sn alloys from the present stand point has been published. In a publication from the Tin Research Institute (8) the mechanism of anode filming of the alloy in a bath containing sodium stannate and zinc cyanide was described.

## Experimental

The electrical circuit used in obtaining the variation of the potential of the anode with the current employed a pentode valve as a constant current device; so the current passing was largely independent of changes in the back emf of the electrode system. The current was supplied from a 250-v dry battery.

The electrolytic cell used was of Pyrex glass without rubber connections. It consisted of a vessel of ca. 500 ml capacity with 5 openings. Three of these, fitted with mercury sealed covers, were for the anode compartment, cathode compartment, and the compartment for the syphon of the calomel electrode, respectively. The last two compartments were fitted with sintered glass in order to prevent contaminations with the anolyte. The other openings were for the inlet and outlet of pure nitrogen.

*The zinc electrode.*—This was prepared by electrodeposition from an acidified zinc sulfate bath prepared by dissolving 145 g $ZnSO_4 \cdot 7H_2O$ in 1 liter *N* $H_2SO_4$. Electrodeposition was carried out using a current density of 12.5 ma/cm² for 40 min on a Pt foil 2 cm² apparent area. This gave a spongy deposit with relatively large area.

*Zinc-tin alloys.*—These were also electrodeposited from a bath recommended by the Tin Research Institute (8), prepared by dissolving 30 g sodium stannate, 2.5 g zinc cyanide, 27.5 g sodium cyanide, and 5 g of sodium hydroxide in 1 liter of water. Electrodeposition was carried out at 65 ± 2°C on a Pt foil of 2 cm² apparent area for 20 min with a current density of 25 ma/cm². This bath gave a deposit containing 25% Zn. A cast anode of the same composition was used and was filmed to insure the dissolution of its tin content in the quadrivalent state (8). The area of the anode was adjusted to give an anode current density of 16 ma/cm². Alloys of 12½% and 50% Zn were prepared by varying the zinc and free hydroxide content of the bath. All deposits were analyzed for their tin content by the tannin method, and the analysis was confirmed by the Tin Research Institute. Alloys prepared either by electrodeposition on a copper substrate or by casting gave exactly the same behavior.

Each experiment was carried out with a freshly prepared electrode. Whenever the bath showed signs of deterioration, a new bath was prepared.

Measurements were carried out mainly in alkaline solutions, viz., 0.1*N* sodium hydroxide (pH = 13), 0.1*N* sodium carbonate (pH = 11.2) and 0.1M sodium borate (pH = 9.2). Measurements were also extended to neutral and acid solutions; 0.1*M* sodium sulfate (pH = 7), acetate buffer of pH = 6, and 0.1*N* nitric acid (pH = 1). All solutions were pre-

[1] Deceased.

pared from AnalaR materials and conductivity water. The solution in the cell was boiled before use and cooled in an atmosphere of pure nitrogen. The detailed experimental procedure for obtaining the anodic, cathodic, and decay curves was essentially as described before (1). All measurements were performed at 25°C.

### *Current-Potential Cuves for* Zn, Sn, *and* Zn-Sn *Alloys*

When a metal electrode is polarized anodically in a solution where passivity sets in readily, the primary oxidation process will be the oxidation of the metal itself. If the current is raised, a value is reached at which the process changes to that of oxygen evolution. This critical current for passivation is a good measure of the nobility of the metal; the nobler the metal, the smaller the current at which the potential changes to that of oxygen evolution. Critical current densities for passivation for Zn, Sn, and Zn-Sn alloys of different compositions were determined. The procedure of Uhlig and Woodside (9) was followed. Measurements were carried out in 0.1M borax solution, since in such medium the oxides of Zn and Sn possess minimum solubility. The electrode was first cathodically polarized with a current of 100 μa/electrode until a steady potential was reached. This took from 15 to 30 min. The cathodic current was then disconnected and the potential was left to decay to the open circuit value till a potential was reached which did not vary more than 20 mv in a period of 5 min. A small anodic current was then imposed on the electrode and the corresponding potential was recorded. The current was again disconnected and the open circuit value awaited. Anodic polarization was started again with a higher current. The process of connecting and disconnecting the current was repeated until the potential of the electrode changed toward oxygen evolution potential.

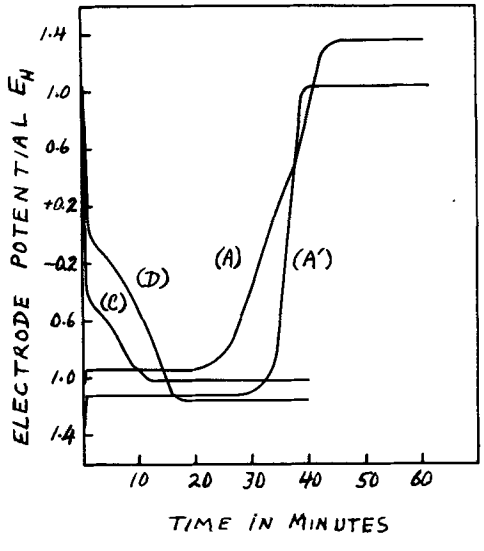


Fig. 1. Anodic polarization of Zn in: (A) 0.1M borax solution with a polarizing current of 20 μa/electrode; (A') 0.1M NaOH solution with a polarizing current of 300 μa/electrode; (C) cathodic curve in 0.1M borax with a polarizing current of 5 μa/electrode; (D) anodic decay in 0.1M NaOH solution.

## Results and Discussion

*Behavior of pure zinc.*—Curve A, Fig. 1, is the characteristic anodic polarization curve of the Zn electrode in 0.1M sodium borate solution when using a polarizing current of 20 μa/electrode. Curve A' in Fig. 1 represents the behavior of the Zn anode in 0.1N NaOH solution when using a polarizing current of 300 μa/electrode. From these curves, which show the variation of the Zn electrode potential with the quantity of electricity passed, it can be seen that, at first, there is a rapid build up of potential, ascribed by similarity to cases studied (1-7) to the charging of the double layer. This is followed by one step before oxygen evolution. Measurements from a large number of polarization curves gave an average value for the double layer capacity of 6,000 μF/electrode in the borate solution. In the hydroxide solution, the average capacity of the double layer was comparable with that in the borate solution. The arrest in the borate solution appears to start at a potential of −0.95 v, and in the hydroxide solution at −1.15 v. In Table I are shown the potentials of this arrest in the two solutions, respectively, compared with the equilibrium potentials of the system $Zn/Zn(OH)_2$ at the corresponding *p*H values. These latter were calculated as follows: Taking the free energy of $OH^-$ and $Zn(OH)_2$ as −37,595 and −132,600 calories, respectively (10), the free energy of the reaction:

$$Zn + 2\ OH^- = Zn(OH)_2 + 2\ \bar{e}$$

was calculated to be −57,410 cal and hence $E_B^\circ$ (the potential at the extreme alkaline range of *p*H) is −1.245 v. By applying the ordinary equation for the variation of the potential of the system with *p*H, the values shown in column III of Table I were obtained.

The very close agreement between the starting potential of the arrest as obtained from polarization curves and the potential of the system $Zn/Zn(OH)_2$ at the corresponding *p*H value leaves little doubt that this step corresponds to the formation of zinc hydroxide or oxide on the electrode before oxygen evolution. The standard condition of the Zn electrode was taken to be that of the borate solution. The quantity of electricity passed from the beginning to the end of this step in the borate solution was found to be reproducible and amounting to 30,000 μcoulomb/electrode. This is sufficient for the liberation of $9.37 \times 10^{16}$ atoms of oxygen. Taking the specific gravity of the Zn metal as 7.1 g/cm³, the diameter of the Zn atom was calculated to be 2.48Å, and hence there would be $1.63 \times 10^{15}$ atoms of Zn/true cm² of the Zn surface. An estimation of the ratio real/apparent area of the electrode could be determined from the capacity of the double layer

Table I

| Solution | Starting potential of the arrest (v) | Equilibrium potential of the system $Zn/Zn(OH)_2$ |
|---|---|---|
| 0.1M Sodium borate | −0.95 | −0.96 |
| 0.1N Sodium hydroxide | −1.15 | −1.18 |

before oxide formation. The capacity of the anodic double layer was recently determined by El Wakkad and Salem (11) to be 100 $\mu$F/real cm$^2$. As the capacity of the double of the Zn electrode amounts to 6,000 $\mu$F/electrode, the ratio real/apparent area will be 30/1; hence, there would be 9.78 x $10^{16}$ atoms of Zn on the whole surface of the electrode. This shows that the quantity of electricity passed during oxide formation corresponds to the formation of less than a unimolecular layer of the oxide. In NaOH solution the quantity of electricity passed during oxide formation amounted to 594,000 $\mu$ coulomb. This is sufficient for the formation of a zinc hydroxide layer ~19 molecules thick. This high value suggests that the oxide in such a medium is more soluble than in the borate solution. In 1*N* NaOH solution, using currents up to 2 ma/electrode, the potential did not rise to oxygen evolution value, but remained constant at the Zn/Zn(OH)$_2$ at the corresponding *p*H value, viz., —1.24 v, denoting anodic dissolution of the formed hydroxide to form zincate.

In 0.1*N* sodium carbonate solution of *p*H = 11.2, an arrest was recorded due to the formation of zinc oxide. However, the potential of the electrode did not reach oxygen evolution value and showed irregularities due to the probable formation of nonconducting nonadherent basic carbonate film which readily pealed away from the surface of the electrode. Similar behavior was observed in the case of the nickel electrode in borate solutions (2), and in the case of the manganese electrode in phosphate solutions (12).

Cathodic curves reveal that, on reversing the polarizing current to make the working electrode the cathode, reduction of the zinc hydroxide film takes place at more or less its reversible potential. As a representative example, the cathodic behavior of zinc in sodium borate solution with a polarizing current of 5 $\mu$a/electrode is shown by curve C, Fig. 1. In NaOH solution, the reduction step corresponds to the deposition of Zn from zincate solution.

Anodic decay curves reveal that, on interruption of the polarizing current when the electrode was at oxygen evolution value, the potential dropped to a somewhat more positive value than the Zn/Zn(OH)$_2$ system at the corresponding *p*H value, but continuously drifted with time toward the above system. The time of this drift varied from one solution to the other. Curve D of Fig. 1 is an example of the anodic decay in NaOH solution.

Anodic polarization of Zn in solutions of *p*H values less than 9 resulted in the dissolution of the Zn at the Zn/Zn(OH)$_2$ potential.

*Time-potential curves for zinc-tin alloys.*—Curves A and A′ of Fig. 2 are the characteristic anodic polarization curves for Zn-Sn alloys containing 25% and 12½% Zn, respectively, in sodium borate

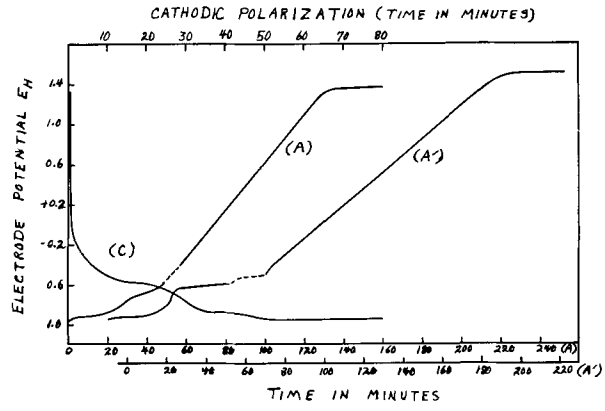


Fig. 2. Anodic polarization of 25% Zn alloy (A) and 12½% Zn alloy (A′) in 0.1M borax solution; Polarizing current = 10 $\mu$a/electrode; dotted parts at 1 $\mu$a/electrode; (C) cathodic polarization of 50% Zn alloy with a polarizing current of 5 $\mu$a/electrode.

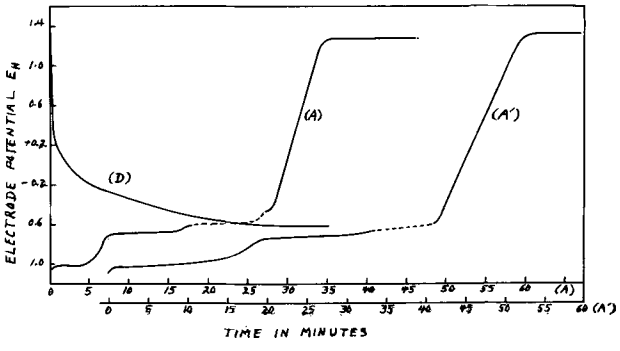


Fig. 3. Anodic polarization of 25% Zn alloy (A) and 50% Zn alloy (A′) in 0.1M sodium carbonate solution; polarizing current = 60 $\mu$a/electrode, dotted parts at 10 $\mu$a/electrode; (D) anodic decay for 12½% Zn alloy.

solution. The polarizing current was 10 $\mu$a/electrode. In the dotted parts of the curves, the polarizing current was decreased to 1 $\mu$a/electrode to decrease the rate of the anodic process to be followed by the direct potentiometric method. Curves A and A′ of Fig. 3 are the same anodic polarization curves for alloys containing 25% and 50% Zn, respectively, in 0.1M sodium carbonate solution. The polarizing current was 60 $\mu$a/electrode and the dotted parts were obtained with a current of 10 $\mu$a/electrode. From these curves, which show the variation of the alloy potential with the quantity of electricity passed, it can be seen that there is a rapid short build up of potential, due to the charging of the double layer, followed by 3 well-defined steps before oxygen evolution. It was difficult in this case to determine the exact capacity of the double layer because the potential of the electrode, when made the cathode, was very near to the first arrest. The starting potential of three steps, in the borate solution, were, respectively, —0.95 v, —0.66 v, and —0.52 v. In the carbonate solution, these were —1.04 v, —0.75 v, and —0.59 v. In Table II, the starting po-

Table II

| Solution | Starting potential of arrest 1st | 2nd | 3rd | Equilibrium potential of the system Zn/Zn(OH)$_2$ | Sn/Sn(OH)$_2$ | Sn(OH)$_2$/Sn(OH)$_4$ |
|---|---|---|---|---|---|---|
| 0.1M Borax | —0.95 | —0.66 | —0.52 | —0.96 | —0.64 | —0.47 |
| 0.1M Carbonate | —1.04 | —0.75 | —0.59 | —1.08 | —0.76 | —0.59 |

tential of the three steps in the two electrolytes are compared with the equilibrium potentials of the systems $Zn/Zn(OH)_2$, $Sn/Sn(OH)_2$, and $Sn(OH)_2/Sn(OH)_4$.[2] The last two values were obtained by taking the free energy of $Sn(OH)_2$, $Sn(OH)_4$, and $OH^-$ as −117,600, −227,500, and −37,595 calories, respectively (13). The free energy of the reactions:

$Sn + 2\,OH^- = Sn(OH)_2 + 2\bar{e}$ $\quad \Delta F^\circ = -42{,}410$ cal.

and

$Sn(OH)_2 + 2OH^- = Sn(OH)_4 + 2\bar{e}$ $\quad \Delta F^\circ = -34{,}710$ cal.

This gives $E_B^\circ$ values of −0.92 and −0.75 v, respectively.[3]

By applying the ordinary equation for the variation of the potential of the above systems with *p*H, the values in columns 5, 6, and 7 in Table II were obtained.

The very close agreement between these two sets of potentials leaves little doubt that these steps correspond to the consecutive formation of zinc oxide or hydroxide, stannous and stannic hydroxides, respectively, before oxygen evolution. Thus, on anodic polarization, the behavior of the alloy appears to be a combination of the behavior of its pure constituents. The same conclusion was reached in the case of Cu-Sn alloys (7).

The quantity of electricity consumed in the passivation of the alloy varied from one composition to the other, and also depended on the pH value of the solution. Thus, for example, whereas the first step (formation of zinc hydroxide) in the borate solution for the 25% Zn alloy consumed 15,000 μcoulomb, the corresponding step for the 50% Zn alloy in the carbonate solution consumed 86,000 μcoulomb.[4] Also in the step corresponding to the formation of $Sn(OH)_2$ in the borate solution for the 12½% Zn alloy, the quantity of electricity amounted to 18,000 μcoulomb, while in the corresponding step for the 25% Zn alloy in the carbonate solution, the same quantity was 36,000 μcoulomb.

Alloys prepared by electrodeposition are considered to have an area more or less comparable with those of the Zn and Sn alone. The standard condition for the alloy was taken to be that of the borate solution since the oxides of both Zn and Sn show minimum solubility at that *p*H. Taking the alloy containing 25% Zn, which has technical importance, as an example, the quantity of electricity that passed in the formation of zinc hydroxide amounted to 15,000 μcoulomb/electrode. Comparison of this amount with that obtained in the case of pure Zn electrode revealed that the alloy required a lesser amount of electricity to passivate. The quantity of electricity that passed in the second arrest (stannous hydroxide formation) was found to be 11,000 μcoulomb, which was less than the corresponding value for pure Sn under similar conditions. This supports the conclusion that alloys are nobler than their constituents (7,9).

In 0.1*N* NaOH solution the behavior of the alloy was rather simple. On starting the anodic polarization, a step at −1.15 v was obtained. The potential of this step is in good agreement with that of the system $Zn/Zn(OH)_2$ at the corresponding *p*H value. After a time, dependent on the Sn content of the alloy, the potential rose to −0.90 v where it remained constant. This latter value suggested that the formed stannous hydroxide is freely soluble in the hydroxide solution to give the stannite (6).

The behavior of the alloy in 0.1*N* $HNO_3$ is of extreme interest. Although the electrode was immersed in the $HNO_3$ solution with the current switched on cathodically, the potential was found to rise to more positive values, even when using a current as high as 1 ma/electrode. This behavior is shown for the alloys 25% Zn and 50% Zn in Fig. 4. An arrest was obtained at −0.44 v in close agreement with the $Zn/Zn(OH)_2$ potential at this *p*H, viz., −0.46 v. The potential then rose to give two steps whose potentials agreed well with those of the systems $Sn/Sn(OH)_2$ and $Sn(OH)_2/Sn(OH)_4$ at the same *p*H value. When the current was reduced to 400 μa/electrode and reversed to start the anodic polarization, the potential of the electrode changed directly to oxygen evolution value. The heads of the arrows in Fig. 4 show the time at which the current was reduced and reversed. Such behavior indicated that the electrode was already in the passive state. This state of affairs could be explained by taking into consideration the oxidizing effect of the $HNO_3$. The Zn in the alloy was oxidized by the acid to ZnO, and the rate of oxidation seems to be too high to be stopped by a cathodic current as high as 1 ma/electrode. Zinc oxide, being freely soluble in the acid, goes into solution leaving the Sn on the surface. This latter also is oxidized in a similar fashion to stannous hydroxide (6). However, after a short time, the potential changed to that of the $Sn(OH)_2/Sn(OH)_4$ system, where it remained constant. On reversing the polarizing current to start the anodic oxidation, the potential changed directly toward

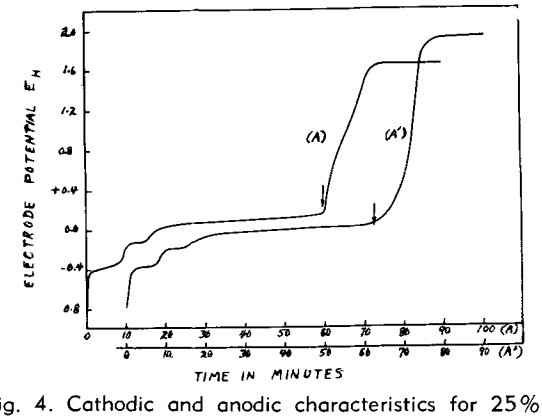


Fig. 4. Cathodic and anodic characteristics for 25% Zn alloy (A) and 50% Zn alloy (A') in 0.1N nitric acid solution; polarizing current = 1 ma/electrode; arrows point to time of start of anodic polarization with 400 μa/electrode.

[2] In this comparison, no correction of the measured potentials was made to account for the fact that the activities in the alloys are less than unity. This is because such variations are uncertain and small.

[3] Calculation based on the assumption that stannous and stannic oxides and not the hydroxides are formed gave the following interesting results:

$Sn + 2\,OH^- = SnO + H_2O + 2\bar{e}$ $\quad \Delta F^\circ = -43{,}000$ cal., $E^\circ_B = -0.932$ v

$SnO + 2\,OH^- = SnO_2 + H_2O + 2\bar{e}$ $\quad \Delta F^\circ = -44{,}200$ cal., $E^\circ_B = -0.958$ v

which directly suggest that the oxidation of stannous oxide to the corresponding stannic oxide is improbable, since the potential of the couple $SnO/SnO_2$ is more negative than that of Sn/SnO. This supports the conclusion that stannous and stannic hydroxides are formed on the oxidation of the Sn electrode.

For the Zn electrode, no noticeable difference was found in the free energy if calculations were made for $Zn(OH)_2$ or ZnO.

[4] The end of the step is taken as the point of intersection of the extrapolated lines from the bottom of the step with that obtained from the rising part of the following one.

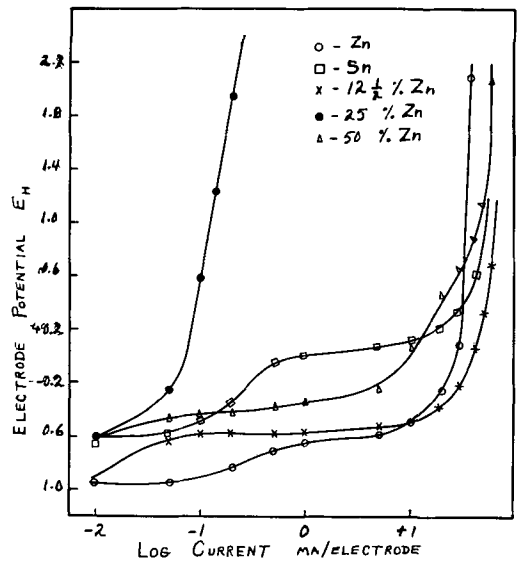


Fig. 5. Potential-log i curves for Zn, Sn, and Zn-Sn alloys in 0.1M borax.

oxygen evolution value, denoting the passivity of the electrode.

The cathodic curves reveal the reduction of both stannic and stannous hydroxides followed by the reduction of zinc hydroxide before hydrogen evolution. As a representative curve, the cathodic behavior of the 50% Zn alloy in 0.1M borax solution with a polarizing current of 5 $\mu$a/electrode is shown by curve C, Fig. 2.

The anodic decay curves reveal that, on interruption of the polarizing current, the potential dropped to a value somewhat more positive than the corresponding $Sn(OH)_2/Sn(OH)_4$, and changed slowly toward the value of this system. The decay curve for the 12½% Zn alloy in 0.1M sodium carbonate solution is shown by curve D, Fig. 3.

It is of interest to remark here on the effect of alloying on the potential of oxygen evolution. Thus, whereas oxygen evolution potential on pure Sn and pure Zn in 0.1M borax solution are, respectively, +1.21 and +1.36 v with a polarizing current of 20 $\mu a/cm^2$, the corresponding values for the 12½%, 25%, and 50% Zn alloys in the same solution are respectively +1.51, 1.36, and 1.40 v. Although no general conclusion could be drawn at the moment, it could be said that the addition of Zn to Sn raised the oxygen evolution potential on the alloy to at least that of the Zn alone. The effect of alloying over a wider range of Zn content on the oxygen evolution potential is still under investigation.

In Fig. 5 the plot of log $i$ vs. potential for pure Zn, pure Sn, and Zn-Sn alloys of compositions varying between 12½% Zn and 50% Zn is shown. This enables the determination of the critical current densities for passivation (*see* experimental section). The behavior of the electrodes on polarization varied from one case to the other. Thus, with the 25% Zn alloy, a critical current density could not be determined easily. Any applied current raised the potential to more positive values and no sudden break in the log $i$-potential curve was observed. With the other electrodes on the other hand, sharper critical currents were obtained. The noble character among the electrodes studied decreased in the order 25% Zn alloy, 50% Zn alloy, Zn, Sn, and 12½% Zn alloy. These findings are in harmony with the general conclusion that the alloys are nobler in character than their components.

## Summary and Conclusion

The anodic behavior of Zn and Zn-Sn alloys at very low current density was studied in solutions where passivity readily sets up. Two anodic processes occur at a Zn electrode when the current is reversed from cathode to anode: (*a*) the charging of an anodic double layer, and (*b*) the formation of zinc hydroxide film less than one molecule thick.

The anodic polarization of Zn-Sn alloys resulted in the consecutive formation of zinc hydroxide, stannous and stannic hydroxides before oxygen evolution. These oxides formed at their reversible potentials; thus the behavior of the alloys on polarization is the combined behavior of its constituents. The quantities of electricities consumed in bringing the electrode from hydrogen evolution to oxygen evolution potentials in the case of the alloys were less than those used by either Zn or Sn. This demonstrated the noble character of the alloys. The same conclusion was also reached from current potential curves.

Manuscript received Feb. 1, 1957. This paper was prepared for delivery before the Cincinnati Meeting, May 1-5, 1955.

Any discussion of this paper will appear in a Discussion Section to be published in the December 1958 JOURNAL.

REFERENCES

1. S. E. S. El Wakkad and S. H. Emara, *J. Chem. Soc.*, **1952**, 461.
2. S. E. S. El Wakkad and S. H. Emara, *ibid.*, **1953**, 3504.
3. S. E. S. El Wakkad and S. H. Emara, *ibid.*, **1953**, 3508.
4. S. E. S. El Wakkad and A. M. Shams El Din, *ibid.*, **1954**, 3094.
5. S. E. S. El Wakkad and A. M. Shams El Din, *ibid.*, **1954**, 3098.
6. S. E. S. El Wakkad, A. M. Shams El Din, and J. A. El Sayed, *ibid.*, **1954**, 3103.
7. S. E. S. El Wakkad, T. M. Salem, A. M. Shams El Din, and Z. Hanafi, *ibid.*, **1956**, 2857.
8. Tin Research Institute, Technical Publication, March, 1952.
9. H. H. Uhlig and G. E. Woodside, *J. Phys. Chem.*, **57**, 280 (1953).
10. W. M. Latimer, "The Oxidation States of the Elements and their Potentials in Aqueous Solutions," Prentice-Hall, New York, p. 168 (1953).
11. S. E. S. El Wakkad and T. M. Salem, *J. Chem. Soc.*, **1955**, 1489.
12. S. E. S. El Wakkad and A. M. Shams El Din, Unpublished work.
13. Reference (10), p. 148.

# The Anodic Oxidation of Cadmium

## I. Mechanism of Film Formation

**Phyllis E. Lake and E. J. Casey**

*Defence Research Chemical Laboratories, Ottawa, Canada*

ABSTRACT

Cadmium oxidizes anodically in hydroxide solutions to form films of reaction products which control the subsequent anodic processes. The electrometrics of film formation and reduction were determined, and various other definitive experiments were done which permit an interpretation of the general mechanism of oxidation to be made. The film forms as CdO which is converted into $Cd(OH)_2$ at a rate dependent upon various experimental factors.

Interest in the Ni-Cd battery has focused our attention on the behavior of Cd during electrolytic oxidation and reduction in KOH electrolyte, both with and without $K_2CO_3$ impurity.

The purpose of this work was to establish the nature of the anodic reactions on Cd metal in caustic electrolytes, and to try to determine the general mechanism of the process.

### Experimental Materials and Methods

The Cd electrodes were prepared by casting reagent grade Cd into rectangular blocks, and painting all but a known apparent area with stop-off lacquer; thus the sample had a polycrystalline surface. The electrode was rinsed with dilute $HNO_3$ and running distilled water. It was then placed in the test cell and reduced at 0.5 ma $cm^{-2}$ until hydrogen was evolved. Even with these precautions to insure a clean surface by removal of all oxide, reproducibility was poor. The real area of the electrodes probably varied from sample to sample. In addition, a finite thickness of metal was removed from the electrode face during each oxidation and cleaning, so that the crystal faces presented to the electrolyte at the beginning of each experiment were different. These factors lead to variations in current density and therefore in measured passivation times. Values plotted in Fig. 2, 3, and 4 are average values for several determinations.

To keep the current distribution as uniform as possible a cylindrical cell of which the anode and cathode formed the ends was used in most experiments. For measurement of gas evolution a bell shaped cell was used with the electrodes placed one above the other. Experiments were done in both air-free and air-saturated solutions, but no significant differences were noted in the amount of Cd oxidized before passivation occurred.

Using solutions freshly prepared from reagent grade chemicals, oxidation studies were done at 25°, 0°, and −40°C; gas evolution and rate of depassivation were measured at 25° only. Oxidation current densities ranged from 10 $\mu$a to 5 ma $cm^{-2}$. The KOH and $K_2CO_3$ solutions ranged from 0.72 to 7.2*N*; mixed solutions were always 7.2*N* with respect to potassium ion and contained varying proportions of $OH^-$ and $CO_3^=$.

The operating voltage of the Cd was measured against an Hg/HgO/KOH reference electrode and the recorded potential values are given with reference to this electrode. The additional liquid junction potential introduced was constant throughout each experiment and was therefore disregarded.

To prepare samples of film material for x-ray diffraction studies, the electrode was removed from the solution immediately after the oxidizing current was switched off, washed quickly with distilled water to remove the electrolyte clinging to the film, then rinsed with absolute methanol. The electrode was then air dried and the film scraped off. All samples were prepared from passivated electrodes. During the early part of the oxidation the film was too thin to be removed mechanically from the metal. For all photographs the Unicam rotation camera S25 was used (radius 30 mm, copper radiation, 40 kv, 15 ma, and a nickel filter).

### Results

*Electrometrics.*—Figure 1 is a typical voltage vs. time curve for anodic oxidation of Cd at constant current in a caustic electrolyte. The potential remained flat near the reversible value for Cd/Cd $(OH)_2$ while the electrode became covered with film. The voltage then rose and oxygen started to evolve. The voltage continued to rise quickly to ~1

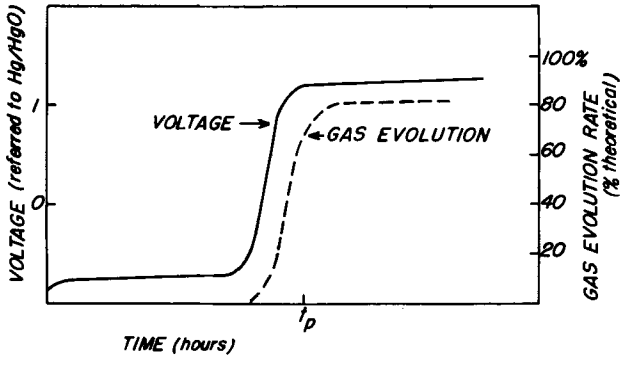


Fig. 1. Variation of voltage with time for oxidation of Cd at constant current.

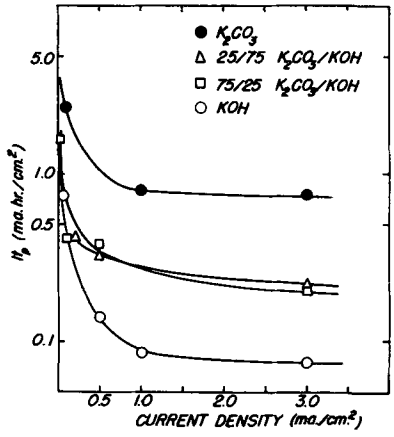


Fig. 2. Variation of $It_p$ with current density at 25°C

v, then flattened off ($E_p$) and rose very slowly (a few mv/hr) for periods of up to 24 hr. The voltage vs. time curve for the mixed and carbonate electrolytes was similar in shape, except that $E_p$ was higher and more constant. Gas evolution started slowly and rose to a steady value which depended on the current density and electrolyte composition. In $K_2CO_3$ solutions at high current densities, it was very close to 100% of theoretical (based on total current); it was somewhat less in hydroxide solutions and at lower current densities.

The amount of Cd oxidized before passivation occurred ($It_p$, where $I$ is current density in ma cm$^{-2}$ and $t_p$ is the time in hours taken to reach a relatively constant potential at which oxygen is evolved) is dependent on current density, temperature, and composition of the electrolyte (Fig. 2, 3, 4). At low current densities at room temperature the curves $It_p$ vs. composition follow the "U" shape of the curve solubility of CdO vs. composition. Increasing the current density decreases $It_p$, the effect being most marked in pure hydroxide solutions. Decreasing the temperature also decreases $It_p$ but the effect is most pronounced in high carbonate solutions. These results are considered in detail later.

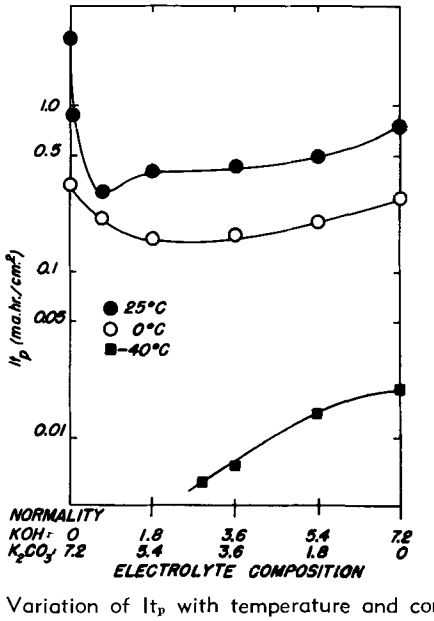


Fig. 3. Variation of $It_p$ with temperature and composition at 0.07 ma/cm².

To determine the efficiency of the oxidation process, reductions were carried out at the same current density as the preceding oxidation and the time taken to reach a constant potential at which hydrogen was evolved ($t_r$) was measured. If the oxidation time ($t_{ox}$) was shorter than $t_p$, then $t_r = t_{ox}$, if $t_{ox}$ was equal to or somewhat longer than $t_p$, $t_r = t_p$. If the electrolyte in which the electrode was oxidized was replaced with fresh electrolyte of the same composition before the reduction was carried out, the same values for $t_r$ were found. Thus, all the current passed (experimental error ±3%) up to time $t_p$ was utilized in the oxidation of Cd and all the Cd was present in the film. However, if oxidation was continued for a long time, i.e., $t_{ox} >> t_p$, some of the outer film sometimes fell off the electrode, and $t_r < t_p$. A small amount of Cd was also dissolved in the electrolyte, since Cd was found on the cathode after long oxidations ($t_{ox} >> t_p$).

*Film composition.*—The color of the film depends on the electrolyte and current density. At low current densities in KOH solutions interference colors

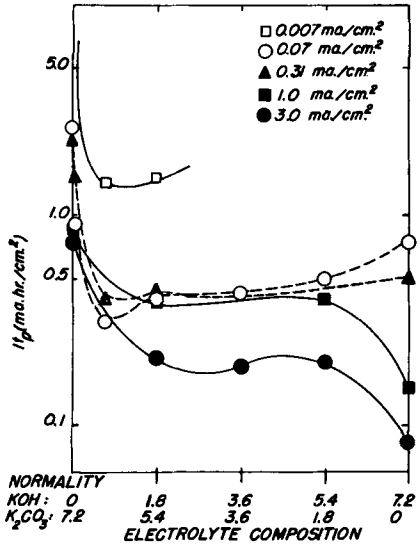


Fig. 4a. Variation of $It_p$ with electrolyte composition and current density at 25°C.

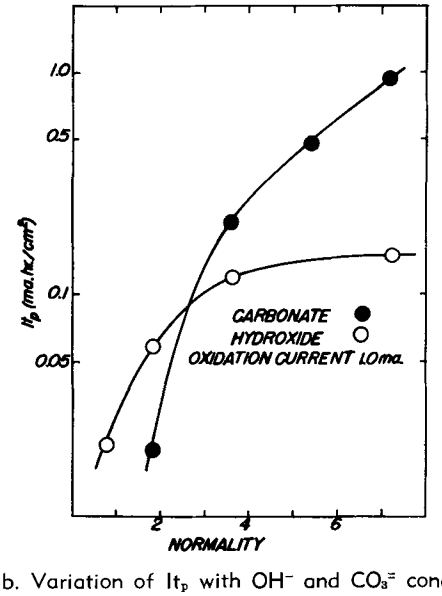


Fig. 4b. Variation of $It_p$ with $OH^-$ and $CO_3^=$ concentration at 25°C.

were noted as the film thickened, and in some cases different rates of film growth on different crystal faces could be thus observed. In mixed and carbonate electrolytes and at higher current densities these colors could not be observed, and the initial film was brown or black.

After the electrode was passivated the film consisted of a dark, tightly adherent layer next to the metal and an outer layer of a loose, scaly or powdery, yellow material which was easily scraped off. X-ray diffraction patterns showed that the outer material was essentially $Cd(OH)_2$ in all but the pure carbonate solutions. The samples taken from films formed in carbonate solutions consisted of $CdCO_3$ contaminated with $2K_2CO_3 \cdot 3H_2O$ which had not been removed during the washing. There was no evidence of other Cd compounds in the outer film, and only weak traces of unidentifiable materials in a few samples. It was not possible to remove the inner layer mechanically for x-ray studies.

Huber has shown (1) by electron diffraction photographs that the initial film formed on Cd in NaOH and $Na_2CO_3$ solutions is the oxide, and that on continued oxidation this primary product is converted to $Cd(OH)_2$ in NaOH solutions, and through basic carbonate to $CdCO_3$ in $Na_2CO_3$ solutions. Since Huber's observations of composition of the outer layer are parallel to the authors' and the inner layer was always the dark color of CdO, it is assumed that the inner layer of film was essentially cadmium monoxide.

*Autocorrosion.*—The reduction time $t_r$ was measured for samples which had been cleaned and then exposed to the solutions for varying lengths of time with no external current flowing. When the electrode was first immersed in the solution, the autocorrosion rate was equivalent to a few microamperes, but decreased with time. Therefore, it is of little importance except at very low current densities.

*The depassivating reaction.*—Passivated electrodes allowed to stand in contact with the electrolyte with no current flowing became "depassivated". That is, when the oxidizing current was turned on again, Cd oxidized at a voltage near the reversible value for a time $t_p'$ before the voltage again rose to the passivation voltage. Thus, some of the passivating film was removed or changed to nonpassivating film during the stand time ($t_s$), and the passivating film was rebuilt during $t_p'$.

The amount of Cd oxidized to repassivate the electrode ($It_p'$) should be equal to the amount of passivating film converted into nonpassivating film during the time $t_s + t_p'$. This enables one to calculate the current which would be equivalent to the average rate $R_2$ of the depassivating reaction during the time $t_s + t_p'$. These equivalent currents are plotted against time in Fig. 5a and 5b. It can be seen that the rate of the depassivating reaction decreases with time and depends on the composition of the electrolyte, being higher in carbonate solutions.

It is well known (2,3) that cadmium monoxide and hydroxide are soluble in alkaline solutions, and indeed Rozentsveig, *et al.*, (2) have evidence that the Cd is present in a negative ion complex.

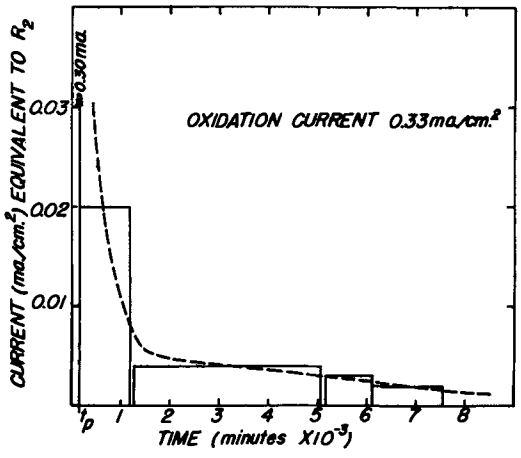


Fig. 5a. Determination of $R_2$ for $K_2CO_3$ solution

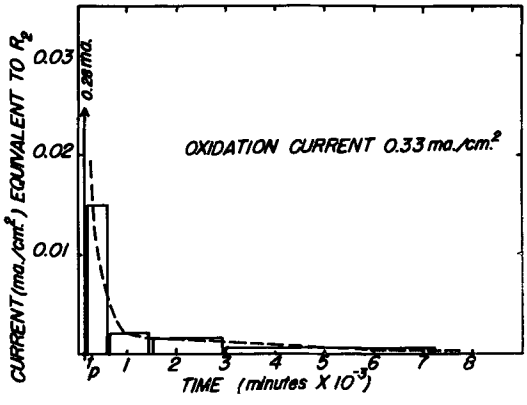


Fig. 5b. Determination of $R_2$ for KOH solution

The amount of Cd present in samples of the test electrolytes which had stood in contact with CdO for 8 days at 25°C was measured polarographically and results are plotted in Fig. 6a and b. Agreement with Rozentsveig's data is quite good. However, Dirkse (4) has shown that KOH solutions, previously saturated with respect to ZnO, continue to dissolve the reaction products formed by the anodic oxidation of Zn, and that on standing the excess eventually precipitates out as ZnO. The amount of Cd oxidized before passivation (i.e., $It_p$) in solutions which had been previously saturated with cadmium [KOH with $Cd(OH)_2$ and $K_2CO_3$ with $CdCO_3$] was smaller than in the corresponding unsaturated solution, but was much larger than would be expected if no supersaturation occurred. Rosentsveig, *et al*, (2) have estimated that 3-8 monolayers of oxide are necessary for passivation. This is equivalent to approximately 0.01 ma hr $cm^{-2}$. The measured values are shown in Table I.

Thus, it appears that the behavior of Cd with respect to alkaline and carbonate solutions is parallel to that which Dirkse found for Zn in alkaline solutions and that the depassivation reaction depends not only on the actual solubility of CdO, but also on

**Table I. Values for $It_p$**

| | Measured | | |
|---|---|---|---|
| | Unsaturated | Saturated | Calculated |
| KOH | 0.52 | 0.25 | ~0.01 |
| $K_2CO_3$ | 0.89 | 0.75 | ~0.01 |

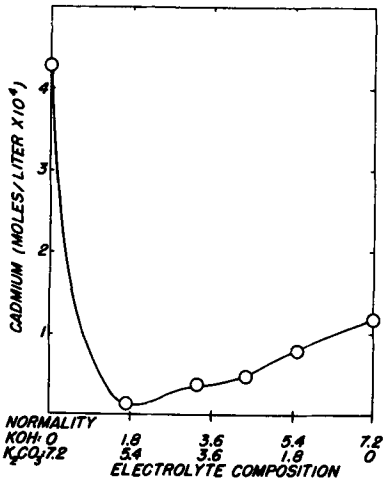


Fig. 6a. Variation of solubility of cadmium oxide with electrolyte composition.

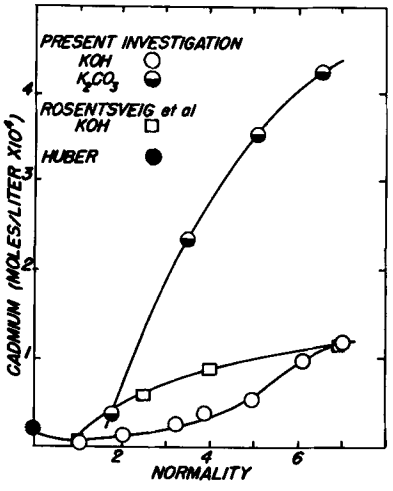


Fig. 6b. Variation of solubility of cadmium oxide with KOH and $K_2CO_3$ concentration.

the degree of supersaturation which can exist before precipitation occurs.

## Discussion

From considerations of the detailed results a mechanism has evolved. For simplicity, the mechanism is presented first, and then the experimental results interpreted in these terms.

The formation of the film must be at least a two-step process, formation of CdO and chemical conversion to $Cd(OH)_2$ or $CdCO_3$, and can be represented as

$$Cd \xrightarrow{R_1} CdO \xrightarrow{R_2} \begin{matrix}[Cd(OH)_2] \\ (CdCO_3)\end{matrix}$$

where $R_1$ depends on the anodic current and $R_2$ on the rate of supply of the converting species to the outer surface of the CdO.

There are two ways in which current may pass through the oxide film (*a*) electron transfer with $O_2$ evolution at the surface, and (*b*) ion transfer ($Cd^{++}$ out or $O^=$ in) through the film. The electronic resistance of CdO is low at room temperature and the ionic resistance would be expected to be much higher (5). But Hickling has shown that $O_2$ overvoltage on Cd is high (6). Since large amounts of Cd are oxidized before the electrode becomes passive, it appears that the high oxygen overvoltage permits ionic migration to take place during oxidation, until the CdO builds to such a thickness that $IR_{ionic} = IR_{electronic} + E_{overvoltage}$, at which time oxygen starts to be discharged.

Huber (1) observed that no carbonate precipitate was formed until after the electrode had been oxidized for some time, and the same observation was made under the present conditions. This behavior can be explained if an amount of CdO far in excess of that to be expected from solubility product considerations must be dissolved to produce the degree of supersaturation necessary to initiate precipitation. Precipitation of the carbonate or hydroxide then begins, and continues at a rate which depends on the degree of supersaturation. The degree of supersaturation, in turn, depends on the rate of precipitation and the rate of dissolution. The rate of dissolution depends on the thickness of the precipitated film through which the "dissolving agent" must pass to dissolve the CdO. Thus, the dissolution reaction goes at its maximum rate until supersaturation is reached; it then decreases as the thickness of the precipitated film increases. The precipitation reaction does not start until the critical concentration is reached. It then starts and rises until the rate of precipitation exceeds the rate of dissolution, after which it decreases in a manner which is interdependent with the decrease in rate of the solution reaction.

In summary, the over-all reaction can now be represented as three steps,

$$Cd \xrightarrow{R_1} CdO \xrightarrow{R_2'} \text{Soluble Complex} \xrightarrow{R_2''} \begin{matrix}Cd(OH)_2 \text{ or} \\ CdCO_3\end{matrix}$$

where $R_2'$ is the rate of solution and $R_2''$ the rate of precipitation. The time dependence of $R_2'$ and $R_2''$ can be roughly sketched as seen in Fig. 7,

*Nature of the Passivating Film.*—Hickling, in his studies of oxygen overvoltage on metals (6), found that below $10^{-5}$ amp $cm^{-2}$ no oxygen discharge occurred on Cd. The authors' work has shown that at $10^{-5}$ amp $cm^{-2}$ at 25°C, a Cd electrode continues to oxidize at −0.8 v for periods of at least 28 days ($It$ = 8.7 ma hr $cm^{-2}$). Figure 5 shows that, in this case, the removal rate $R_2$ is much greater than $R_1$, thus the CdO would be removed as fast as it is formed. The porous conversion product accumulates, the oxide film does not, and the electrode does not passivate. On electrodes oxidized at higher current densities, such that $R_2' < R_1$ initially or that $R_2'$ becomes smaller than $R_1$ after some accumulation of conversion product, the monoxide film builds

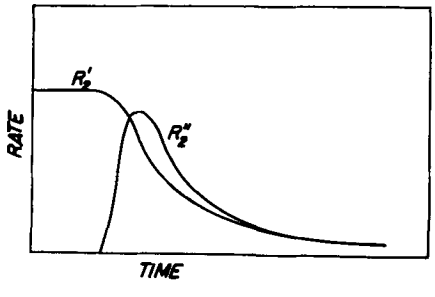


Fig. 7. Schematic representation of the variation of $R_2'$ and $R_2''$ with time.

up, and the electrodes do passivate (Fig. 2). Thus, the oxide layer appears to be the primary passivating layer, while the outer layer of conversion product affects passivation only insofar as it controls $R_2'$. The growth pattern of the cadmium monoxide film affects the amount of Cd which must be oxidized to produce a passivating layer. Further work is in progress on this problem.

*Effect of current density and temperature on $It_p$.*—(Fig. 2 and 3). These effects are similar since increasing $I$ increases $R_1$, and hence increases $(R_1-R_2')$, while holding $I$ constant and decreasing the temperature decreases $R_2$, and increases $(R_1 - R_2')$. It must be noted that, although the equations allow for the case of $R_2' >> R_1$, $R_2'$ can in fact never be greater than $R_1$, since the oxide film cannot dissolve more quickly than it is formed. That is if $R_2' >> R_1$ (at low current densities, high temperatures) the electrodes will not passivate, and $It_p = \infty$.

If $R_2' \approx R_1$ (medium $I$ at high temperature or very low $I$ at low temperature) an oxide film eventually builds up, and large amounts of conversion product form, so that $It_p$ is large. The rate of accumulation of CdO depends on $(R_1 - R_2')$: it is zero or small at first, and after critical supersaturation is reached increases as $R_2'$ decreases. If $R_1 >> R_2'$ (high current densities or low temperatures) the oxide film reaches the thickness required to produce passivation before very much conversion product is formed, and $It_p$ is small. It is interesting to note that the values of $It_p$ obtained at $-40°$ (0.1 — 0.16 ma hr $cm^{-2}$) are very close to the value calculated from Rozentsveig's (2) estimate of the thickness of the CdO which causes passivation (3-8 monolayers).

Results plotted in Fig. 3 show that the variation of $It_p$ with temperature is much larger in carbonate solutions than in hydroxide solutions. Since the rate of the depassivating reaction depends on the mobility of the ions in solution, $R_2'$ approaches zero at the freezing point of the solution. The freezing point of 7.2*N* KOH is below $-60°C$, while the freezing point of 7.2*N* $K_2CO_3$ is about $-25°C$; thus the temperature coefficient of $R_2$ (and hence $It_p$) is larger in the carbonate solutions.

*Effect of electrolyte composition.*—The value of $It_p$ in pure carbonate solutions is much higher than in mixed solutions (Fig. 4a). In pure $K_2CO_3$ the solubility of CdO is high; hence $R_2'$ can operate at its maximum rate for longer periods before supersaturation is reached. At low current densities there is a minimum in the $It_p$ vs. composition curve at a composition close to that at which the minimum in the solubility occurs. This minimum may have been masked at higher current densities, but the data are not complete enough to be sure. At low current densities $It_p$ increases as hydroxide concentration is increased, as does solubility, but at high current densities the value of $It_p$ drops sharply in pure KOH solutions. This drop can be explained by a low value of $R_2'$: if $R_2' >> R_1$ initially, the CdO film may build up even before supersaturation is reached.

Figure 4b shows the variation of $It_p$ with variations of $CO_3^=$ and $OH^-$. $It_p$ decreases with decreasing concentration as would be expected, since the solubility of CdO and $R_2'$ decrease with decreasing $OH^-$ and $CO_3^=$ concentrations. There is, in fact, a linear relation between activity and $It_p$ in solutions of varying $K_2CO_3$ concentration. However, this relation does not hold in KOH solutions, and its significance is still obscure.

*General Observations*

The passivation voltage ($E_p$) and gas evolution rate in the various solutions are of interest. In pure $K_2CO_3$ solutions $E_p$ was high (~1.4 v) and the gas rate after $t_p$ was very nearly 100% of theoretical; in mixed electrolytes the $E_p$ was lower (~1.1 v) and the gas rate was somewhat lower (~70%); in pure KOH, $E_p$ was only ~1.0 v, while the gas rate was much lower (as low as 30% at low current densities). Since the dissolution and precipitation reactions continue beyond $t_p$, a part of the current must always be utilized to maintain the passivating film.

Later work on voltage decay curves has shown that oxygen overvoltage is smaller in hydroxide solutions than in carbonate solutions. In hydroxide solutions oxygen evolution may occur before the CdO film has reached its maximum thickness. That the CdO film continues to build up after $t_p$ is indicated by the gradual increase in $E_p$ noted above.

The two essential transport processes in the oxidation mechanism have not been considered in this paper. Firstly, there is the "outer" transport process: once the conversion product has begun to form, the conversion species ($H_2O$, $OH^-$, $CO_3^=$?) must move across the final product from electrolyte to the CdO surface to permit conversion. Second, the "inner" transport process essential to the oxidation involves the movement of either $Cd^{++}$ or an oxygen-containing species across the CdO layer to permit formation of CdO.

## Summary

1. Studies have been made of the anodic oxidation of Cd in KOH, $K_2CO_3$, and mixed electrolytes. The effect of experimental conditions on electrical behavior and film composition have been examined.

2. The general mechanism has been determined: The primary reaction is the formation of cadmium monoxide. The monoxide is converted to either the hydroxide or carbonate (depending on the electrolyte) through a soluble intermediate. The rate of conversion is governed by the solubility of the monoxide and the rate of transport of the dissolving species through the conversion product from the electrolyte.

3. Cadmium monoxide is the passivating species. When resistance polarization through the film is high enough to drive the CdO surface beyond the oxygen overpotential, oxygen is evolved.

4. The following factors, which vary with experimental conditions, determine the time required to produce this passivating film: (*a*) rate of formation of CdO: *f*(current density); (*b*) solubility and rate of dissolution of CdO: *f*(temperature, composition); (*c*) rate of precipitation and degree of supersaturation necessary to initiate precipitation: *f*(temperature, composition); and (*d*) conductivity of the oxide: *f*(temperature, current density).

### Acknowledgments

The authors wish to express their thanks to L. G. Wilson and V. C. Shore of these Laboratories who did the x-ray diffraction studies, and to the Defence Research Board for permission to publish.

Manuscript received Jan. 28, 1957. Paper issued as DRCL Report No. 231.

Any discussion of this paper will appear in a Discussion Section to be published in the December 1958 JOURNAL.

REFERENCES

1. K. Huber, *This Journal*, **100**, 376 (1953).
2. S. A. Rozentsveig, B. V. Ershler, E. L. Shtrum, M. M. Ostanina, *Trudy Soveshchaniya Elektrokhim. Akad. Nauk. S.S.S.R. Otdel. Khim. Nauk*, **1950**, 571 (1953).
3. R. Scholder and E. Staufenbiel, *Z. anorg. u. allgem. Chem.*, **247**, 259 (1941).
4. T. P. Dirkse, *This Journal*, **101**, 328 (1954); *ibid.*, **102**, 497 (1955).
5. C. A. Hogarth, *Proc. Phys. Soc.*, **B64**, 691 (1951).
6. A. Hickling and S. Hill, *Disc. Faraday Soc.*, **1947**, 236.

# Technical Note

## Sedimentation Volumes of a Phosphor Powder in Potassium Silicate and Potassium Silicate-Barium Acetate Settling Media

**J. Fred. Hazel and Louis Fiorito**

*Department of Chemistry, University of Pennsylvania, Philadelphia, Pennsylvania*

The preparation of cathode ray screens for black and white television receivers involves the sedimentation of a luminescent powder through an aqueous solution containing potassium silicate and barium ions. The silicate is adsorbed on the solid surfaces and as a result the negative charge on the particles and on the glass foundation is increased (1, 2). Rapid adhesion of the particles to each other and to the glass is obtained on addition of a soluble barium salt (2). This decreases the repulsion between the silicate covered surfaces by decreasing the charge. Polymerization of the silicate and binding of the surfaces follow spontaneously.

The settling procedure for producing cathode ray screens is remarkable from the point of view of the uniformity in thickness of the screen. This conclusion is suggested from the consideration that the displacement of a layer one particle thick could cause a variation in thickness of up to 50% in a screen that averages only a few particle diameters in thickness. Another factor affecting screen thickness, in addition to the particle diameter and the number of particles per unit area, is the density of packing of the particles in the screen. The present study on sedimentation volume was designed to yield information on this factor. It is known that the charge on mineral powders has an effect on their sedimentation volume (3). This is of interest since the charge on phosphor particles depends on the composition of the liquid through which the particles settle (1, 2).

### Materials

Du Pont No. 1630 zinc sulfide-zinc cadmium sulfide phosphor was shaken with distilled water and allowed to settle, after which the liquid was decanted. Three washings were performed before the wet slurry was poured onto a large watch glass and permitted to dry in a dark cabinet.

The potassium silicate solution (Kasil No. 22, Philadelphia Quartz Co.), containing approximately 8.6% alkali calculated as $K_2O$ and 18.9% $SiO_2$ was a purified solution of $K_2O \cdot 3.45\ SiO_2$.

### Experimental

The sedimentation volumes were measured in 9 mm glass tubes. The tubes were made by cutting 20 cm lengths and sealing them at one end. A mark was etched at 1.00 ml on each tube and a linear scale was made with divisions of 0.1 ml. The scale divisions were 2.88 mm apart and readings could be estimated to 0.1 scale division, corresponding to 0.01 ml. The precision of the measurements was satisfactory after a standardized procedure was developed, the mean deviation being approximately 0.15 scale divisions.

The volume of a freshly prepared 1% or 10% stock solution of the silicate required to be added to water to bring the total volume to 10 ml and contain the desired concentration of $K_2O \cdot 3.45\ SiO_2$, in parts per million (ppm), was calculated. The potassium silicate solution was pipetted into a dry 30 ml beaker, and the water into another beaker. The silicate was added all at once to the water, and transferred from one beaker to another to mix the diluted system thoroughly. A portion of the silicate solution immediately was added to 2.00 g of phosphor powder which had been placed in the tube. The volume of solution in the tube was approximately 5 ml. The tubes were shaken vigorously after addition of the silicate and placed in a rack in an upright position to permit the phosphor to settle. Readings were taken daily until none of the samples in a given series showed a decrease in sedi-

Table I. Sedimentation volumes of phosphor powder in potassium silicate solutions. Sedimentation Time: 19 Days

| Potassium silicate, ppm | Sedimentation volume, ml | Potassium silicate, ppm | Sedimentation volume, ml |
|---|---|---|---|
| 0 | 1.03 | 1,770 | 0.89 |
| 17 | 0.91 | 2,040 | 0.89 |
| 34 | 0.94 | 2,720 | 0.88 |
| 102 | 0.92 | 4,860 | 0.89 |
| 340 | 0.90 | 6,800 | 0.92 |
| 680 | 0.91* | 13,600 | 1.03 |
| 1,360 | 0.85 | 20,400 | 1.04 |
| 1,720 | 0.89 | 34,000 | 1.08 |

* 9 day sedimentation period.

Table II. Sedimentation volumes of phosphor powder in potassium silicate-barium acetate mixtures

| Potassium silicate, ppm | Barium acetate, ppm | Sedimentation volume, ml |
|---|---|---|
| 0 | 275 | 1.02 |
| 1,720 | 275 | 0.98 |
| 1,770 | 275 | 0.98 |
| 6,800 | 275 | 1.06 |
| 20,400 | 275 | 1.13 |

mentation volume of more than 0.01 ml on successive readings. In the preparation of the systems containing barium acetate the volume of barium acetate solution required to produce a concentration of 275 ppm in the final system, was pipetted into the beaker containing the water. The potassium silicate was poured into the diluted barium acetate solution and the same procedure followed as before.

## Results and Discussion

The sedimentation volumes of the phosphor given in Table I were obtained after a 19 day sedimentation period in potassium silicate solutions of increasing concentration. The reported values are not significantly different from those measured after 12 days: in only two cases did the readings differ as much as 0.02 ml.

Sedimentation volumes of the phosphor in potassium silicate-barium acetate mixtures are given in Table II. The values correspond to a sedimentation time of 19 days.

The data in Table I indicate that the sedimentation volume of phosphor particles decreases with increasing concentration of potassium silicate. The volume occupied by the particles passes through a minimum and then increases to a value above that in water alone. The change in sedimentation volume may be attributed to the change in zeta potential as the concentration of silicate is varied. It is suggested that as the negative potential of the particles is increased they repel each other more in settling. This permits the particles to pass by one another and pack together in a small volume. They do not stick to each other or coagulate and entrap a large amount of liquid in their packing, Fig. 1, as is the case when the zeta potential has a low value.

The silicate concentration is plotted against the zeta potential of the particles in the upper part of Fig. 2 and against the sedimentation volume of the particles in the lower part of the same figure. A

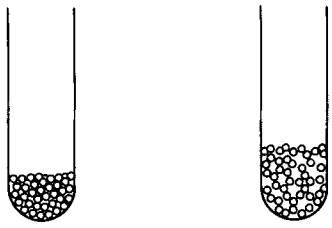


Fig. 1. The packing of particles with different zeta potentials.

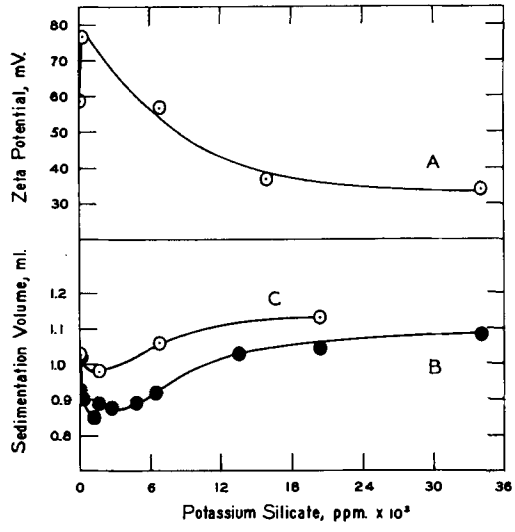


Fig. 2. Relationship of zeta potential to sedimentation volumes.

maximum in the zeta potential curve and a minimum in the sedimentation volume occur at low concentrations of silicate. Moreover, as the silicate concentration increases the zeta potential decreases and the sedimentation volume increases. That the maximum in the zeta potential curve occurs at a somewhat lower silicate concentration than the minimum in the sedimentation volume can be attributed to the fact that the former was determined by using a streaming potential diaphragm and a constant flow of silicate while the latter was determined in a static system.

The presence of barium acetate caused an increase in sedimentation volumes as shown in the bottom part of Fig. 2. The role of barium acetate in the preparation of cathode ray screens is to reduce the charge on the particles (2). The larger sedimentation volumes observed in all cases when barium acetate was employed, indicate that the charge on the particles was reduced under these conditions.

Manuscript received June 25, 1957. This paper was prepared for delivery before the Washington Meeting, May 12-16, 1957.

Any discussion of this paper will appear in a Discussion Section to be published in the December 1958 JOURNAL.

## REFERENCES

1. R. Edelberg and J. F. Hazel, *J. (and Trans.) Electrochem. Soc.*, **96**, 13 (1949).
2. J. F. Hazel and G. L. Schnable, *This Journal*, **100**, 65 (1953).
3. N. K. Adam, "The Physics and Chemistry of Surfaces," p. 202, Oxford University Press, London (1941).

# The Relation of the Conditions of Electrodeposition of Manganese Dioxide to the Discharge Characteristics

**Akiya Kozawa and W. C. Vosburgh**

*Department of Chemistry, Duke University, Durham, North Carolina*

ABSTRACT

Electrodes were prepared by electrodeposition of $MnO_2$ at various temperatures and current densities or with $NH_4^+$, $K^+$, $Zn^{++}$, $Mg^{++}$, or $Al^{3+}$ in the plating bath. The overpotential in acid electrolyte is largest when deposition is at high temperature and low current density. Variation in surface area seems to account for these effects. When $NH_4^+$ or $K^+$ is present in the plating bath, the $MnO_2$ contains $NH_4^+$ or $K^+$ and has a discharge curve in $NH_4Cl$ electrolyte different from the normal. The other cations in the plating bath had only small effects. Heating at 140°C gave discharge curves resembling those of $MnO_2$ containing $NH_4^+$ in some respects.

In the preparation of electrodeposited electrodes in this laboratory the conditions generally have been approximately those of Nichols (1). Specifically, the bath contained about 50 g/l of $MnSO_4 \cdot H_2O$ and about 65 g/l of $H_2SO_4$. The $MnO_2$ was electrodeposited on graphite rods at an apparent current density of 3.13 ma/cm² for 30 min with the bath at 80° or 90°C. The temperature of the plating bath affected the overpotential of the electrode when discharged in $NH_4Cl$ solutions (2). In the present investigation the effect of variations of temperature and current density of electrodeposition, of the presence of certain foreign ions in the plating bath, and of heating the $MnO_2$ were studied.

## Experimental

*Preparation and discharge of electrodes.*—Electrodes were prepared by electrodeposition of about 0.2 mmole of $MnO_2$ on 8 cm² of surface area of spectrochemical grade, 4.5 mm diameter graphite rods from a bath usually of the composition given above. The bath was maintained at constant temperature (±1.5°C) by a water bath and the current, furnished by dry cells and held constant manually, was measured by a milliammeter. The bath was not stirred. When not stated otherwise the temperature was 90°C, the current 25 ma, and the time 30 min. After electrodeposition electrodes were allowed to stand in water which was changed occasionally until no more acid was washed out. They were kept in water until used. Previous to discharge they were kept for several hours in the electrolyte to be used in the discharge.

Discharges (2) were carried out in vessels holding 250 ml of electrolyte with either clean lead or graphite anodes, the latter consisting of 5 rods surrounding the electrode to be discharged. Separation of cathode and anode was 2-3 cm. The cell was connected in series with four No. 6 dry cells and suitable resistance, and the discharge current was maintained constant manually. The electrolyte was stirred continuously during discharge by a magnetic stirrer. Air was not excluded. The potential of the discharging electrode was measured against a saturated calomel electrode by means of a recording potentiometer.

*Effect of temperature and current density of electrodeposition on the overpotential in acid electrolyte.*—Electrodes were made at 60°, 70°, 80°, 90°, and 97°C with a current of 25 ma for 30 min and at 90°C at current densities of 12.5, 25, 50, and 100 ma/electrode for 60, 30, 15, and 7.5 min, respectively. Overpotentials were measured in acid solutions as described previously (3). Briefly, an electrode was discharged for a short time with an electrolyte of 0.1M $H_2SO_4$ and 0.1M $MnSO_4$ and when constant potential was attained the circuit was broken and the equilibrium open circuit potential was measured. The difference between the two was the overpotential. Several measurements could be made on a single electrode. With different electrodes the overpotentials at the same current agreed within 2 mv. Measurements were made with currents of 2, 4, and 6 ma/electrode of 8 cm² apparent surface. The *iR* drop was larger than previously (3) but probably did not exceed 2 mv. No correction was made. Results are shown in Fig. 1.

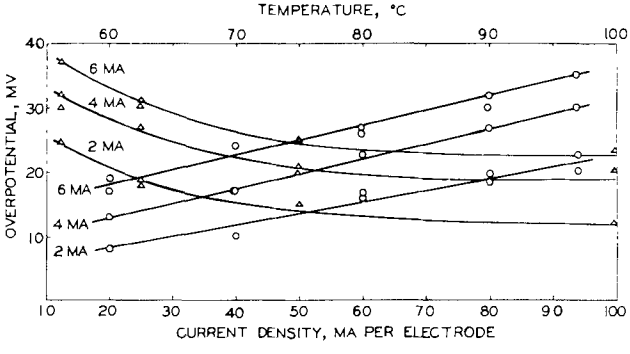


Fig. 1. Overpotentials in acid electrolyte (0.1M $H_2SO_4$, 0.1M $MnSO_4$) of electrodes made by electrodeposition at various temperatures and current densities. The straight lines and upper scale of abscissas represent electrodes made at various temperatures and constant current (25 ma). The curves and lower scale of abscissas represent electrodes made at 90°C and various current densities, but with constant total $MnO_2$.

Overpotential increases linearly with the temperature at which the $MnO_2$ was electrodeposited between 60° and 97°C. An increase of temperature of about 2° corresponds to an increase of overpotential of 1 mv. The overpotential decreases with increasing current at which the $MnO_2$ was electrodeposited. Between 12.5 and 50 ma/electrode (1.56-6.3 ma/cm$^2$) the decrease is roughly 3 mv for 10 ma increase in electrodeposition current, but from 50 to 100 ma the change is much less than this.

A number of electrodes made at various temperatures and current densities were analyzed to see whether the above results could be correlated with changes in composition. Analyses were made by dissolution in $FeSO_4$ solution at room temperature for available oxygen[1] followed by potentiometric titration of the same samples for total manganese. Incomplete washing of the porous graphite rods after dissolution of the $MnO_2$ led to a positive error in $x$ estimated as about 0.03. Between 80° and 97°C and at different current densities at 90°C the observed values of $x$ in $MnO_x$ varied between 1.97 and 2.00 erratically and could not be correlated with the conditions of electrodeposition with any assurance. At 60° and 70°C $x$ was appreciably lower, 1.94. Some other factor than composition of the $MnO_2$ must be responsible for the changes in overpotential.

*Adsorption of zinc ion by* $MnO_2$.—$Zn^{++}$ is adsorbed by $MnO_2$ from a slightly alkaline solution of $ZnCl_2$ and $NH_4Cl$. The amount of $Zn^{++}$ adsorbed by electrodeposited $MnO_2$ electrodes from a particular solution increases as the overpotential of the electrodes decreases, and suggests that both phenomena are related to the same feature of the $MnO_2$.

Previous to measurement of Zn adsorption an electrode was kept in 0.05M $H_2SO_4$ for 6 hr to remove any adsorbed $Mn^{++}$ or lower oxide on the surface. Then it was washed and immersed for 12-15 hr at room temperature in 10 ml of Zn reagent, prepared by dissolution of 0.005 mole of ZnO in a liter of 0.5M $NH_4Cl$ and having a pH of 7.2. Then the electrode was removed without washing and the excess Zn in the solution titrated with 0.01M ethylenediaminetetracetic acid disodium salt with eriochrom black T as the indicater. The difference between the amount of Zn in 10 ml of the original reagent and that in the reagent after removal of the electrode is the Zn adsorbed by the $MnO_2$ of the electrode. Because of the small quantities involved, errors may be 5-10%. The Zn adsorbed by a bare graphite rod was found to be negligible. The adsorbed Zn can be removed by keeping the electrode in 0.05M $H_2SO_4$ for several hours. After this a second trial leads to as much Zn adsorbed as in the first trial, or sometimes more.

The Zn adsorption must be dependent on the surface area of the $MnO_2$ and on the amount adsorbed per unit of surface. For $MnO_2$ samples sufficiently alike in structure the surface area is probably the more important. It will be assumed that, for similar samples of $MnO_2$, Zn adsorption is proportional to surface area. The surface area of a sample of electrolytic $MnO_2$ was found to be 52.9 meter$^2$/g by the B.E.T. method by Saito.[2] The same $MnO_2$ adsorbed 55.5 x $10^{-5}$ mole/g of $Zn^{++}$. Therefore, 1 x $10^{-5}$ mole of $Zn^{++}$ is adsorbed by approximately 1 meter$^2$ of $MnO_2$ surface and one $Zn^{++}$ occupies an area of 17 Å$^2$.

The surface area 25.4 meter$^2$/g has been reported (5) for an electrolytic $\gamma$-$MnO_2$ in apparent disagreement with the value above. However, it is shown in Table II that even larger differences than this in electrolytic $MnO_2$ can be caused by differences in current density of electrodeposition.

Some representative data are shown in Table I. Four electrodes with different thicknesses of $MnO_2$ (plated on Karbate rods at 80°C and 25 ma for different times) were treated for 15 hr with the Zn reagent and the amount of Zn adsorbed measured by difference. The adsorbed Zn was then removed by standing in 0.05M $H_2SO_4$ for 6 hr after which a second and later a third measurement was made.

It is evident that the Zn adsorption is reversible and fairly reproducible. The increase in Zn adsorbed in successive trials may indicate a real increase of surface or greater accessibility to all parts of the surface as the result of the alternating treatment with $NH_4Cl$ and acid solutions (4). The Zn adsorption by the two thinnest $MnO_2$ deposits is nearly proportional to the total $MnO_2$, indicating a porous structure with all parts accessible to $Zn^{++}$. In the thicker layers the increase in adsorption with thickness is less, the inner part of the $MnO_2$ being less accessible than the outer portion.

It would be expected from these data that a thicker $MnO_2$ deposit would show a smaller overpotential on discharge than a thinner, if the apparent surface and the apparent current density are the same. A thicker deposit with its larger true surface would have a smaller true current density. This has been shown to be true previously (3).

Zinc adsorption data for electrodes prepared at different temperatures and at different current densities are shown in Table II, and in the last column

[1] This gives more nearly correct results than the method used previously (4). Details will be published.

[2] H. Saito at Nagoya University.

**Table I. Zinc adsorption by $MnO_2$ electrodes of varying thickness**

| Time of plating, min | 1st Zn adsorption, mole x $10^5$ | 2d Zn adsorption, mole x $10^5$ | 3d Zn adsorption,* mole x $10^5$ | Surface area, meter$^2$ |
|---|---|---|---|---|
| 60 | 1.72 | 2.32 | 2.40 | 1.7 |
| 30 | 1.40 | 1.70 | 2.00 | 1.4 |
| 15 | 1.05 | 1.19 | 1.18 | 1.1 |
| 7.5 | 0.59 | 0.60 | 0.55 | 0.6 |

* The Zn of the 2d adsorption was removed by 55 hr treatment with 0.05M $H_2SO_4$ and 24 hr was allowed for the 3d adsorption.

**Table II. Variation of overpotential with surface area as measured by Zn adsorption**

| Plating conditions | | | Zinc adsorption, mole x $10^5$ | Current calc'd, ma | Overpotential | |
|---|---|---|---|---|---|---|
| Temp, °C | Current ma | time, min | | | Y and V mv | Obs. mv |
| 97 | 25 | 30 | 0.65 | 4.8 | 33 | 30 |
| 90 | 25 | 30 | 0.75, 0.80 | 4.0 | 29 | 27 |
| 80 | 25 | 30 | 0.87, 0.92 | 3.4$_5$ | 26 | 23 |
| 90 | 12.5 | 60 | 0.50, 0.63 | 4.7 | 36 | 32, 30 |
| 90 | 50 | 30 | 1.05, 1.05 | 2.9$_5$ | 25 | 20, 21 |
| 90 | 100 | 7.5 | 1.80, 1.76 | 1.7$_4$ | 19 | 20 |

some overpotentials for similar electrodes, taken from the 4 ma data of Fig. 1. To test the relation between the two, the surface area of the electrode prepared at 90°C and 25 ma for 30 min was arbitrarily taken as unity, and relative surface areas for the other electrodes were calculated from the Zn adsorption data. The good reproducibility in overpotential of electrodes prepared under these conditions (3) shows that the surface area must be well controlled by the plating conditions. Then relative current densities were calculated by dividing the current per electrode, 4 ma in each case, by the relative surface area. Finally, overpotentials at the various relative current densities were interpolated from the data of Yoshizawa and Vosburgh (3) for their electrolyte No. 3. Their current per electrode is the same as the corresponding relative current density of Table II, because their electrodes were all prepared at 90°C and 25 ma for 30 min, assumed above to give unit surface. The overpotentials so calculated, given in the 7th column of Table II, are a little higher than the corresponding observed values of this investigation. Other experiments have shown that electrolyte No. 3 which contained 0.9M $Na_2SO_4$ in addition to 0.1M $H_2SO_4$ and 0.1M $MnSO_4$ gives overpotentials a few millivolts higher than without the $Na_2SO_4$. Correction of the $Y$ and $V$ values by subtracting 3 mv leads to as good agreement with the observed as can be expected. As far as these experiments can show, variations of overpotential with the current density and temperature of electrodeposition of the $MnO_2$ can be explained as the result of variations in surface area.

*Discharge in ammonium-salt electrolyte.*—Plating conditions have only a small effect in discharges in an ammonium-salt electrolyte of *p*H in the vicinity of 7.5. Four electrodes made like those described in Table II that were plated at 90°C and different current densities were discharged under carefully controlled conditions. The electrolyte was 2M $NH_4Cl$ with enough $NH_3$ to give *p*H 7.65. The anode was five graphite rods surrounding the cathode, and the current passed was 2 ma for 100 min after which the electrode remained in the cell on open circuit for an additional 35 min. Under these conditions most of the $Mn^{++}$ passing into solution from the cathode in the discharge is deposited as an oxide on the anode rods. The amount so deposited was dissolved by $H_2O_2$ and $H_2SO_4$ and determined colorimetrically a $HMnO_4$. The small amount in the solution was determined also, and the sum of the two amounts is reported as $Mn^{++}$ formed.

The discharge curves were the same shape as the two lower curves of Fig. 2, or the upper one of Fig. 3, and showed small differences in closed-circuit potential such as would be predicted from Fig. 1. The $Mn^{++}$ formed was 0.33 x $10^{-2}$ mmole for the 12.5-ma electrode, 0.28 x $10^{-2}$ mmole for the 25-ma, and 0.19 x $10^{-2}$ mmole for the 50 ma and 100 ma electrodes. The $Mn^{++}$ was 1-2% of the total Mn on the electrode and decreased a little with increasing surface area.

Electrodes plated at 70°, 80°, and 90°C also gave similar curves and the most $Mn^{++}$ for 90°-electrodes and the least for 70°C.

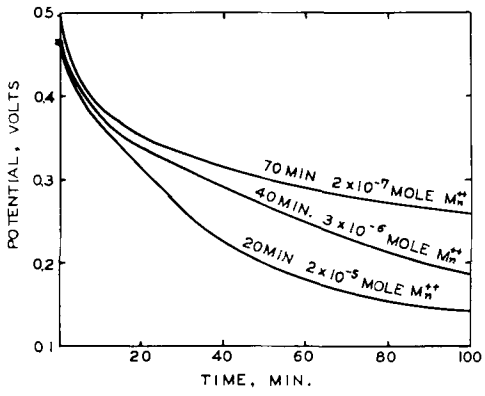


Fig. 2. Discharge curves for electrodes with different thicknesses of $MnO_2$; plating time at 25 ma for 8 $cm^2$ is a measure of thickness; $Mn^{++}$ passing into solution on discharge is given; discharges in 2M $NH_4Cl$ and $NH_3$, pH 7.42.

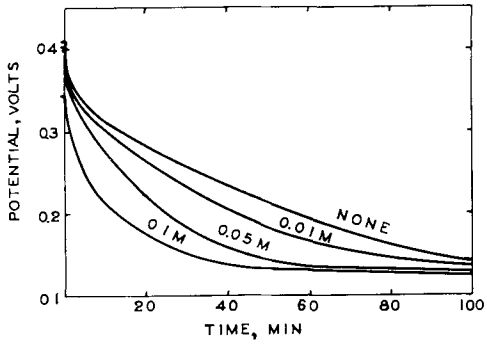


Fig 3 Discharge curves for $MnO_2$ electrodes made with 0.01, 0 05, and 0 1M $(NH_4)_2SO_4$ in the plating bath compared with a curve for an electrode plated in the usual bath without $(NH_4)_2SO_4$.

Electrodes with different thicknesses differed more. Plated at 90° and 25 ma for 20, 30, 40, 50, and 70 min, five electrodes gave 2.3, 1.2, 0.3, 0.08, and 0.02 x $10^{-2}$ mmole of $Mn^{++}$, respectively. The discharge curves at *p*H 7.56 for plating times of 20, 40, and 70 min are shown in Fig. 2. The two other curves fell in the expected places and were omitted for simplicity.

Comparison of Tables I and II shows that the variation of Zn adsorption with thickness is of the same order of magnitude as its variation with the current density of plating. However, the effect of thickness on the shape of the discharge curve and on the $Mn^{++}$ produced is much greater than the effect of current density. An increase in thickness not only brings about an increase in surface area, but also provides more $MnO_2$ for dilution of the lower oxide remaining on the electrode, if the latter diffuses into the interior of the oxide. Less lower oxide at the surface would lead to a higher closed-circuit potential and less $Mn^{++}$ going into solution. Both of these effects are observed, as Fig. 2 shows.

*$MnO_2$ electrodeposited from solutions containing foreign cations.*—$MnO_2$ electrodeposited from a bath containing $(NH_4)_2SO_4$ differs from that deposited in its absence and has been identified as $\alpha$-$MnO_2$ (6, 7). Electrodes were prepared by electrodeposition from baths containing 0.01, 0.05, 0.10, and 1.0M $(NH_4)_2SO_4$ in addition to the usual $MnSO_4$ and $H_2SO_4$ and discharged in the usual manner in an electrolyte of 2M $NH_4Cl$ and $NH_3$ with *p*H 7.8. In Fig. 3 the discharge

Table III. Zinc adsorption by electrodes prepared with 0.1 mole/l of foreign cation present and $Mn^{++}$ formed in the discharge

| Foreign cation | $NH_4^+$ | $K^+$ | $Mg^{++}$ | $Zn^{++}$ | $Al^{3+}$ |
|---|---|---|---|---|---|
| $Zn^{++}$ ads., mole/electrode x $10^5$ | 1.15 | 1.17 | 0.62 | 0.42 | 0.67 |
| $Mn^{++}$ formed, mmole x $10^2$ | 1.6 | 2.7 | 0.16 | 0.20 | 0.12 |

curves for electrodes plated in the presence of 0.01M, 0.05M, and 0.1M $(NH_4)_2SO_4$ are compared with the curve for one plated in absence of $(NH_4)_2SO_4$. The curve for 1M $(NH_4)_2SO_4$ was much like that for 0.1M. It is clear that $NH_4^+$ in the plating bath affects the shape of the discharge curve. The nearly flat portion of the lowest curve represents an approximately steady state in which the electrode surface is changing little with time, whereas there is no flat portion in the upper curve, which will arbitrarily be considered a normal curve.

The $Mn^{++}$ that went into solution during the five discharges was 0.38 x $10^{-2}$ mmoles for the normal and 0.95, 2.3, 3.4, and 3.3 x $10^{-2}$ mmoles for the four other electrodes in the order of increasing $NH_4^+$ concentration during preparation.

The lowest curve, for what was probably $\alpha$-$MnO_2$, falls much more steeply at the beginning than the normal. This may be explained as the result of slower diffusion of the lower oxide into the interior of the $MnO_2$. An alternative explanation that the surface area of the $\alpha$-$MnO_2$ is much smaller will be shown (Table III) to be improbable. With slower diffusion, the surface oxide becomes reduced to such a low potential that it can react with the electrolyte to give $Mn^{++}$. When this reaction consumes the lower oxide as fast as it is produced a steady state results, with no further decrease of potential. This hypothesis can be checked by calculation of the electrical energy equivalent to the 3.4 x $10^{-2}$ mmoles of $Mn^{++}$ produced in the discharge represented by the lowest curve in Fig. 3. This calculation gives 110 ma-min to produce the $Mn^{++}$, which may be compared with the 60 to 65-min period of constant potential with a current of 2 ma. The difference allows for production of a little lower oxide remaining on the electrode and accounting for the slight downward trend of the curve.

Electrodes were prepared from solutions containing $K_2SO_4$, $ZnSO_4$, $MgSO_4$, or $Al_2(SO_4)_3$. When the concentration of the foreign cation was 0.1M the electrodes gave the discharge curves shown in Fig. 4. The curves for $Zn^{++}$, $Mg^{++}$, and $Al^{3+}$ are little different from the normal curve for electrodes made with no foreign cation present (compare with Fig. 3). The curve for $K^+$ resembles closely the curve for $NH_4^+$. Data for Zn adsorption and the $Mn^{++}$ formed in the five discharges are given in Table III. Here also the $NH_4^+$ and $K^+$ electrodes are alike and different from the other three.

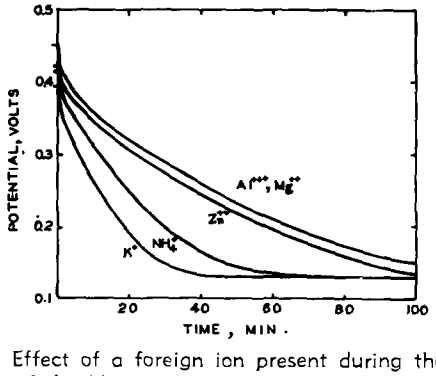


Fig. 4. Effect of a foreign ion present during the electrodeposition of the $MnO_2$ on the shape of the discharge curve; discharges in 2M $NH_4Cl$ and $NH_3$, pH 8.

The effect of $NH_4^+$ and $K^+$ in the plating bath on the overpotentials in acid electrolyte of the resulting electrodes was within the limits of variability of the electrodes except when the $NH_4^+$ or $K^+$ concentration was 0.3 to 1M. At these higher concentrations the effect was a decrease in overpotential.

*Analysis for $NH_4^+$ and $K^+$.*—Several electrodes prepared in the presence of $NH_4^+$ or $K^+$ were analyzed for these ions. The $MnO_2$ was dissolved by 10 ml of 1% $H_2O_2$ in 1M $H_2SO_4$ and the solution diluted to 100 ml. For $NH_4^+$ a 10 ml portion was treated with excess KOH and the resulting $NH_3$ distilled by heating in a slow current of air and catching in water. The $NH_3$ was then determined colorimetrically by Nessler's reagent. For $K^+$ a flame photometer was used. Both methods were checked by known solutions. Results are shown in Table IV.

The $NH_4^+$ or $K^+$ content of $MnO_2$ increases as the concentration of the foreign ion in the plating bath increases. The two ions are much alike in the relation of concentration to the mole ratio in the $MnO_2$. The mole ratio of Mn:K in the formula for a typical cryptomelane (8) is 100:8.5, and this ratio is approached by the electrolytic $MnO_2$.

*Replacement of $K^+$ in $MnO_2$ by other ions.*—It is of interest to inquire to what extent $K^+$ in $MnO_2$ can be exchanged for other ions, especially $NH_4^+$, when the $MnO_2$ is placed in a suitable medium. Electrodes were made in a bath containing 0.1M $K_2SO_4$, then

Table IV. $NH_4^+$ or $K^+$ content of electrodes made by electrodeposition in presence of $(NH_4)_2SO_4$ or $K_2SO_4$

| $(NH_4)_2SO_4$ or $K_2SO_4$ M | $NH_4^+$ in $MnO_2$ mg/electrode | $K^+$ in $MnO_2$ mg/electrode | Moles/100 g-atoms Mn $NH_4^+$ | Moles/100 g-atoms Mn $K^+$ |
|---|---|---|---|---|
| 0 | 0.01 | 0.06 | — | — |
| 0.01 | 0.10 | 0.36 | 3.6 | 4.6 |
| 0.05 | 0.18 | 0.47 | 6.5 | 6.0 |
| 0.10 | 0.20 | 0.62* | 7.3 | 7.9 |
| 0.30 | 0.22 | 0.62 | 7.8 | 7.9 |
| 0.5 | — | 0.65 | — | 8.3 |
| 1.0 | 0.24 | — | 8.6 | — |

* Average for 3 electrodes; 0.62, 0.63, 0.61.

Table V. Exchange of $K^+$ for other ions when $MnO_2$ containing $K^+$ is digested for 3 days with various solutions

| Solution | $K^+$ after treatment mg/electrode | K exchanged % |
|---|---|---|
| $H_2O$, 0.1 and 1M $MgSO_4$ | 0.60, 0.60, 0.60* | 0 |
| 0.1 and 0.3M $NH_4Cl$ | 0.32, 0.28 | 53, 48 |
| 1 and 4M $NH_4Cl$ | 0.25, 0.25 | 58 |
| 0.3 and 1M $H_2SO_4$ | 0.53, 0.48 | 12, 20 |
| 0.3 and 1M $ZnCl_2$ | 0.59, 0.58 | 3 |
| 0.1 and 1M $CuSO_4$ | 0.59, 0.57 | 3 |

* Compare 4th line of Table IV.

well washed and kept in solutions of $NH_4Cl$, $H_2SO_4$, $ZnSO_4$, $ZnCl_2$, $CuSO_4$, and $MgSO_4$ for 3 days at room temperature. They were then kept in water for a day to wash out salts and the K content determined. Results are shown in Table V.

Nearly 60% of the $K^+$ is replaced in 1M $NH_4Cl$ whereas only 20% is replaced in 1M $H_2SO_4$. The divalent cations have little or no effect.

*The minimum in the discharge curve.*—The discharge curve of a $MnO_2$ electrode often passes through a minimum potential (2, 3). The cause of the minimum is not clear and some observations on the effect of conditions of preparation of the electrodes on the minimum are recorded in the interests of its better understanding.

Electrodes plated at 90° and 97°C at 25 ma for 30 min and at 80° and 90°C at 12.5 ma for 60 min showed a pronounced minimum in the first discharge in 0.1M $H_2SO_4$ and 0.1M $MnSO_4$. Electrodes plated at 60°-80°C at 25 ma for 30 min and at 90°C at 50 or 100 ma for 15 or 7.5 min showed no minimum. The conditions of the latter group lead to larger surface areas than the conditions of the former group.

Increasing amounts of $K^+$ in the $MnO_2$ led to decreasing depth of the minimum and an electrode made with 1M $K_2SO_4$ present gave no minimum. Amounts of $NH_4^+$ in $MnO_2$ resulting from the presence in the plating bath of 0.05-1M $(NH_4)_2SO_4$ gave no minima.

In discharges in 1M $NH_4Cl$ buffered at *p*H 4 with an acetate buffer the minimum is usually much more pronounced than in acid electrolyte, 20-40 mv deep as compared with 9-14 mv in acid. Electrodes plated in solutions containing 0.1M $(NH_4)_2SO_4$, 0.1M $K_2SO_4$, and 0.1M $MgSO_4$ gave no minima, although the overpotential was the same as for a normal electrode.

*Effect of heating* $MnO_2$.—Heating some forms of $MnO_2$ decreases the electrode potential, reduces the discharge capacity, improves the crystal form, changes the iso-acidic point, and makes small changes in the available oxygen (9, 10). These changes were observed at temperatures above 100°C and mostly above 150°C. However, even below 100°C heating has an effect on the shape of the discharge curve and at 140°C a pronounced change takes place.

Electrodes after thorough washing were heated as in Table VI. They were then discharged for 100 min at 2 ma in 2M $NH_4Cl$ and $NH_3$ with *p*H 7.8. The $Mn^{++}$ which passed into the solution is shown in Table VI and the curves are shown in Fig. 5.

**Table VI. Conditions for heating electrodes and the $Mn^{++}$ produced on discharge at *p*H 7.8**

| Electrode | Manner of heating | Temp, °C | Time of heating, hr | $Mn^{++}$ mmole x $10^2$ |
|---|---|---|---|---|
| 1 | (None) | — | — | 0.32, 0.50 |
| 2 | Oven | 90 | 14 | 0.59 |
| 3 | Water | 100 | 5 | 0.77 |
| 4 | Oven | 105 | 3 | 0.69 |
| 5 | Oven | 125 | 3 | 2.96 |
| 6 | Oven | 140 | 3 | 3.86 |

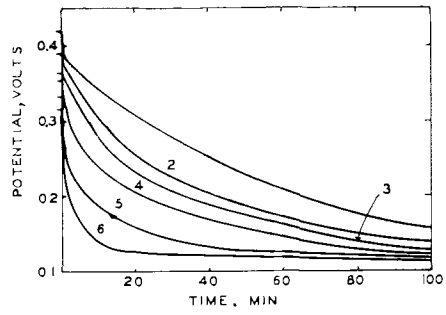


Fig. 5. Discharge curves for electrodes that were heated after preparation. The numbers refer to the electrode numbers in Table VI where the heating conditions and the $Mn^{++}$ produced in the discharges are given.

Heating, either in an oven or in hot water, has a progressively increasing effect as the temperature increases from 90° to 140°C. The discharge curve has a steeper initial portion, larger drop in potential, and is more nearly flat after the initial drop as the temperature increases. The amount of $Mn^{++}$ formed increases as the curve drops to lower and lower potentials and becomes more nearly flat in the second portion.

The curve shapes for heated $MnO_2$ are very much like those for $MnO_2$ prepared in the presence of $NH_4^+$. There is some difference between the two in discharges in 1M $NH_4Cl$ buffered at *p*H 4, however. Under these conditions no minimum in the discharge curve was found for $\alpha$-$MnO_2$ containing $NH_4^+$ whereas both normal $MnO_2$ and heated $MnO_2$ (150°C) gave pronounced minima. The $\alpha$-$MnO_2$ had about the same overpotential as normal at *p*H 4, but heated $MnO_2$ had an overpotential about 30% larger than the normal.

## Acknowledgment

This work was supported in part by the Office of Naval Research.

Manuscript received Aug. 26, 1957. This paper was prepared for delivery at the Buffalo Meeting, Oct. 6-10, 1957.

Any discussion of this paper will appear in a Discussion Section to be published in the December 1958 JOURNAL.

## REFERENCES

1. G. W. Nichols, *Trans. Electrochem. Soc.*, **62**, 393 (1932).
2. A. M. Chreitzberg, Jr., and W. C. Vosburgh, *This Journal*, **104**, 1 (1957).
3. S. Yoshizawa and W. C. Vosburgh, *ibid.*, **104**, 399 (1957).
4. S. Hills and W. C. Vosburgh, *ibid.*, **104**, 5 (1957).
5. W. Buser and P. Graf, *Helv. Chim. Acta*, **38**, 828 (1955).
6. S. Okada, I. Uei, and H. Chin, *J. Electrochem. Soc. Japan*, **15**, 79 (1947).
7. I. Nakajima, *ibid.*, **21**, 369 (1953).
8. J. W. Gruner, *Am. Mineralogist*, **28**, 497 (1943).
9. J. Brenet and A. M. Moussard-Briot, *Rev. gén. élec.*, **61**, 405 (1952).
10. A. Kozawa and K. Sasaki, *J. Electrochem. Soc. Japan*, **22**, 569 (1954).

# Cathodic Disintegration of Tin

**H. W. Salzberg**

*City College, New York, New York*

**F. Mies**

*Brown University, Providence, Rhode Island*

ABSTRACT

Disintegration of tin cathodes at high current densities was studied in neutral, acid, and alkaline solutions of sulfuric acid and alkali and ammonium hydroxides, sulfates, and chlorides. The tin left the surface as $SnH_4$ and the $i_o$'s were of the order of amp/cm$^2$. Acid decreased the disintegration rate, salts added to acid increased the rate, salts added to neutral solution decreased the rate. The cation effect was specific, disintegration rates decreasing in the order sodium, potassium, lithium, ammonium, and hydronium ion.

Previous work on Pb (1,2) and Sb (3) indicated that cathode disintegration was the result of hydride formation via reduction of water molecules. The present investigation was undertaken in the expectation that tin hydride would be formed at low current densities and so give insight into the source of the hydrogen evolved at these low current densities. Instead, tin cathodes disintegrated only at extremely high current densities and this paper reports these anomalous results. The apparatus, materials, and method were the same as used previously (2,3).

## Observations and Results

The disintegration rate was independent of time, as with Pb and Sb. Impurities seemed to have less of an effect. Critical current densities were much higher, the $i_o$'s being about an order of magnitude bigger, i.e., amperes per cm$^2$, and the cation effect was very specific. In concentrated ammonium salt solutions, small amounts of ammonia gas were given off at about 0.5 amp/cm$^2$. The most striking observation, other than the magnitude of the current density, was the fact that even though tin hydride is a fairly stable compound at room temperature (5), most of the Sn lost to the cathode appeared as metallic Sn in the electrolysis cell. Only traces of Sn were picked up from the exit gas.

Figure 1 shows that for NaOH the slopes are less than theoretical for formation of $SnH_4$ and that both slope and rate decrease as concentration increases. The rate in KOH was negligible in comparison to that in NaOH, and in $NH_4OH$ there was no disintegration at all.

For neutral solutions (Fig. 2) the following was found:

(*a*) Disintegration rates decrease in the order $Na^+$, $K^+$, $Li^+$. The rate in rubidium chloride was too small to be plotted and nothing at all was observed in either lithium chloride or ammonium sulfate.

(*b*) Increased $Na_2SO_4$ concentration decreased the rate. The intercept was increased but the slope was practically unchanged.

(*c*) Addition of KCl to $Na_2SO_4$ solution decreased the rate markedly but the reverse, adding $Na_2SO_4$ to KCl solutions, did not seem to have much of an effect.

(*d*) Adding LiCl to $Na_2SO_4$ did not seem to have any effect.

(*e*) Not shown on the graph are the results for addition of 0.02M RuCl and 0.02M CsCl to 0.1M $Na_2SO_4$. The disintegration was completely stopped up to at least 2.7 amp/cm$^2$ which was as far as the experiment went.

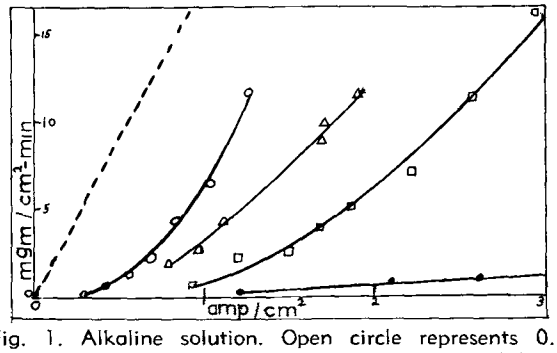


Fig. 1. Alkaline solution. Open circle represents 0.1M NaOH; open triangle, 1M NaOH; open square, 5M NaOH; closed circle, 2M KOH.

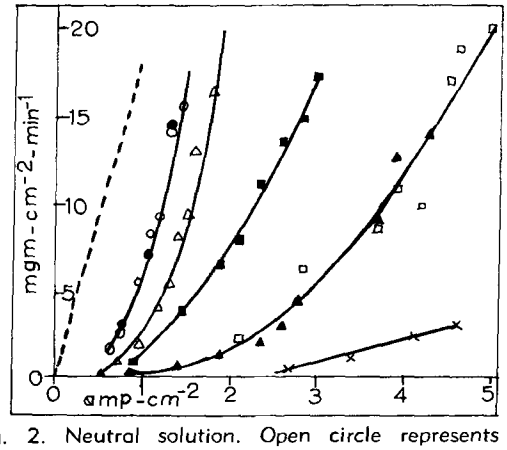


Fig. 2. Neutral solution. Open circle represents 0.1M $Na_2SO_4$; solid circle, 0.1M $Na_2SO_4$ plus 0.04M LiCl; solid square, 0.1M $Na_2SO_4$ plus 0.04M KCl; open square, 0.02M $Na_2SO_4$ plus 0.1M KCl; open triangle, 1M $Na_2SO_4$; solid triangle, 0.1M KCl; X, 0.2M LiCl.

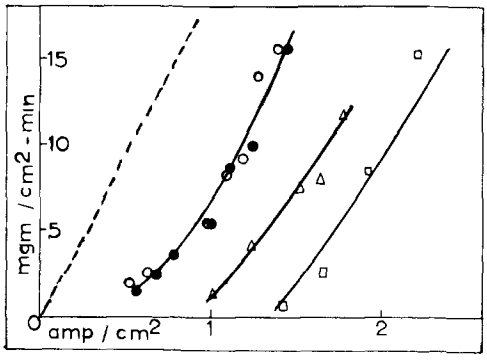


Fig. 3. 0.1M $Na_2SO_4$. Open circle represents 0.0M $H_2SO_4$; solid circle, 0.01M $H_2SO_4$; open triangle, 0.1M $H_2SO_4$, open square, 0.2M $H_2SO_4$.

In the presence of a constant amount of neutral salt, addition of acid decreased the rate sharply (Fig. 3). No decrease was noted in 0.1M $Na_2SO_4$ until the acid/salt ratio was greater than 1/10. Increased salt concentration at constant acidity increased the rates. Additional, ungraphed results showed that in more concentrated salt solutions rates were lower at the same acid/salt ratios and that the decrease began at lower acid/salt ratios. In other words, the rate depends on total ionic strength and total acidity as well as the acid/salt ratio. Also ungraphed, is the observation that in the absence of salt small amounts of acid lowered the rate drastically. For example, in 0.1M sulfuric acid the weight loss was only 0.4 mg/cm$^2$-min at 4 amp/cm$^2$.

## Discussion and Conclusions

The disintegration is due to hydride formation since (*a*) the exit gas rapidly reduces silver nitrate; (*b*) the weight loss of the Sn is linear with current density and the slope of the curve corresponds to that required for formation of the known hydride, $SnH_4$ (at weight losses greater than 30 mg/cm$^2$-min or 40 monolayers/sec the linearity disappears due to erosion as pieces fall off the surface); (c) the possibility of a tin-alkali alloy which reacts with water is ruled out because an increase in the concentration of any alkali cation either decreases the rate sharply or stops it completey. Even more to the point, disintegration was observed in dilute $H_2SO_4$ in the absence of alkali cations.

The $SnH_4$ is formed in a strained and unstable state. Since stannane is a tetrahedral molecule, it would have to be in a highly strained state (5,7) when formed at a planar surface. Even though unstrained stannane is stable at room temperature the strained variety should decompose rapidly, decomposition perhaps being catalyzed by cations in the double layer. This would explain the small amount of stannane found in the exhaust gas and the large amount of colloidal Sn found in the cell and also the low efficiency of electrolytic stannane production, reported by Paneth (6).

Figure 3 shows that the increase in hydronium ion concentration merely shifts the curve along the axis to higher current densities without change in slope. This indicates that the reaction is the same but that a higher current density is needed to start it, probably to remove the extra hydronium ions. Also, if surface hydronium ions are displaced by sodium ions, i.e., if salt is added to acid, the rate increases. The lack of disintegration in acid solutions would therefore seem to be due to the reduction of hydronium ions at potentials too low for stannane formation. Only water molecule reduction would allow the potential to rise enough to form stannane. Certainly, at the extremely high current densities used here, there is not enough surface $H_3O^+$ ion to support the current (4) and the source of the hydrogen found in the stannane must be the water molecule.

The specificity of the cation effect must be explained on the basis of competing effects in the double layer. At first glance, this seems to be in accord with the alkali-alloy hypothesis, i.e., rates increase and $E^\circ$ decreases in the same order, Li, K, Na. However, in addition to the general evidence mentioned above the alkali-alloy hypothesis is not tenable because (*a*) disintegration rates in $Li^+$ solutions are much greater than in those of $Cs^+$ or $Ru^+$, although Li has a higher $E^\circ$; (*b*) the deposition potential of Li is 0.10 v higher than that of $K^+$ and 0.3 v higher than that of $Na^+$. Assuming a Tafel slope of 0.12 for the deposition of $H_2$ on Sn, the current density needed for $Li^+$ deposition would have to be about 7 times that for $K^+$ deposition and about 400 times that for Na deposition. Since, according to the alloy hypothesis, the disintegration rate would be proportional to the alkali deposition rate, the current densities at equal disintegration rates would have to be in the approximate ratio 400/57/1 for Li, K, and Na salt solutions, respectively. Figures 1 and 2 show that this is definitely not the case.

The formation of $SnH_4$ requires both a high potential and a surface largely covered by $SnH_2$ groups adjacent to each other. A large cation would not affect the potential particularly and would not be adsorbed strongly, but if adsorbed it would cover a large surface area. A small cation, with a more intense field, would cover a smaller portion of the surface but would be more strongly adsorbed and in addition have a greater effect in lowering the potential across the double layer.

Ion hydration decreases from Li to Cs and therefore so does the ionic radius. The area covered by the ion decreases in proportion to the square of the decrease in ionic radius. On the other hand, the force of attraction between the ion and the surface, and hence the adsorption, increases as the reciprocal of the square of the radius increases. These competing effects should cause a minimum to appear in the curve of surface coverage vs. ionic radius. If the minimum were in the neighborhood of the sodium ion radius, solutions of sodium salts should show maximum disintegration rates.

Some support is lent to this picture by the fact that mixtures of lithium and sodium salts show the disintegration rate expected of the smaller and more tightly held sodium ion and mixtures of sodium and potassium salts show the rates expected of the potassium salt solution.

The effect of ammonium ion is not covered by this explanation. Here, the evidence indicates that the ammonium ion is itself reduced, probably at a lower potential than that needed for stannane formation. This statement is based on the facts that (*a*) addition of ammonium salts to a sodium salt solution almost completely stops disintegration; (*b*) small quantities of ammonia gas are observed to be given off from the solution, even in 0.1M sulfuric acid; (*c*) the surface of the tin darkens during this process, loosing its metallic luster.

At current densities above $i_o$, the surface is probably saturated with unstable $SnH_2$ molecules. The reasoning for this is as follows.

Since the 4 hydrogen atoms needed for $SnH_4$ are almost certainly not produced by consecutive reductions at the same site, at least 2 sites and therefore 2 tin atoms are involved, with some sort of disproportionation following the electrochemical reduction. The most probable disproportionation would be the one involving two tin atoms each with two hydrogen atoms. The hydrogen atoms would not be in the form of an adsorbed molecule, since at the high current densities of this reaction the molecules would be formed in such a high energy state that they could desorb immediately on formation. Instead, the two hydrogen atoms would have to be associated with the tin atom as a complex or hydride. This $SnH_2$ hydride would have to be nonvolatile, and unstable, the first because the slope of the curve shows that tin leaves in the tetravalent state, the second because no $SnH_2$ has been reported. This molecule would decompose to tin and hydrogen molecules unless it reacted with an adjacent $SnH_2$ to form $SnH_4$ and a tin atom. Since at and above $i_o$ most of the current goes into removal of tin from the surface, (one equivalent of tetravalent tin for each faraday) the surface would have to be saturated with $SnH_2$ molecules.

Below $i_o$ the surface is unsaturated and the large current densities are required to saturate the surface with the unstable $SnH_2$ molecules. This statement is based on the following considerations.

The over-all disintegration rate is determined either by the reactions involved in forming the $SnH_4$ or by the disproportionation between two $SnH_2$ groups. If the former, the rate-determining step will be either electrochemical or a chemical combination of two atoms. If the rate-determining step is electrochemical, both disintegration and the over-all current density will be semilog functions of potential and therefore linear with each other at $i_o$. However, the graphs show that the intercept at $i_o$ is curved, which eliminates an electrochemical step as the rate-determining factor. If the rate is determined by the chemical combination of two hydrogen atoms, to form an $SnH_2$ complex, the rate will be proportional to the square of the hydrogen atom concentration. Since until stannane is evolved all the hydrogen leaves the surface as $H_2$, $i = k\,H^2$, so that the disintegration rate should be linear with current. Since the figures are definitely curved, at the intercept, this possibility is also eliminated.

Finally, if the disintegration is determined by the rate of combination of two $SnH_2$ groups, each of which would have to be in equilibrium with two hydrogen atoms, the over-all rate would be proportional to the fourth power of hydrogen atom concentration and therefore proportional to the square of the current density. The graphs seem to support this possibility, within experimental error.

This picture of an over-all rate being determined by the combination of adjacent unstable complexes would explain (*a*) the very high current densities needed, (*b*) the relative insensitivity of the reaction to high overvoltage poisons such as mercury and lead, and (c) the relatively inefficient production of stannane even at high overvoltage cathodes.

## Acknowledgment

This work was done under a research contract with the Office of Naval Research. The authors wish to thank J. C. White and Sigmund Schuldiner of the Naval Research Laboratory for their encouragement and technical assistance and Saul Berman of the Office of Naval Research for his administrative assistance.

Manuscript received Nov. 15, 1956.

Any discussion of this paper will appear in a Discussion Section to be published in the December 1958 JOURNAL.

REFERENCES

1. H. W. Salzberg, *This Journal*, **100**, 146 (1953).
2. L. Gastwirt and H. W. Salzberg, *ibid.*, **104**, 701 (1957).
3. A. Andreatch and H. W. Salzberg, *ibid.*, **101**, 528 (1954).
4. S. Schuldiner, *ibid.*, **99**, 488 (1952).
5. D. Hurd, "Chemistry of the Hydrides," John Wiley & Sons, Inc., New York (1952).
6. F. Paneth and E. Rabinowitch, *Ber.*, **57B**, 1877 (1924).
7. J. W. Mellor, "Reference Book of Inorganic Chemistry," Vol. 1, p. 324, Longmans, Green and Co., London (1922).

# Oxidation of An Aluminum-3 Per Cent Magnesium Alloy in the Temperature Range 200°-550°C

W. W. Smeltzer[1]

*Aluminium Laboratories Limited, Kingston, Ontario, Canada*

ABSTRACT

A study of the oxidation and magnesium evaporation kinetics has been carried out on an aluminum-3% magnesium alloy. A metallographic examination of the surface oxide films produced was included. The alloy was oxidation resistant to 200°C. At temperatures greater than 350°C the oxidation rate was initially inversely proportional to the oxide film thickness, transforming to a constant rate for long exposures. Selective oxidation of magnesium caused formation of aluminum inclusions in the surface oxide. These inclusions imparted a black discoloration to the alloy surface. Magnesium evaporated from the alloy in a vacuum at temperatures greater than 350°C after an induction period, the duration of which was dependent on the temperature. A comparison of the magnesium evaporation and alloy oxidation rates demonstrated that the oxide film offered resistance to oxidation of the metal.

It has been shown in previous investigations that oxide film structures on alloys containing up to 10% Mg are dependent on the mode of heating, and final temperatures attained as amorphous oxide formed at room temperature may crystallize into $\gamma$-alumina or $MgAl_2O_4$ and MgO (1, 2). Magnesia forms rapidly on these alloys if they are exposed to steam (3-6). The surface of the Al-Mg alloy is discolored gray to black by high temperature oxidation and it has been suggested that this effect is associated with the MgO content of the oxide film (2). This discoloration is decreased by volatilization of $NaBF_4$ into the oxidizing atmosphere (7), pre-exposure of the alloy to HF (3), or small additions of Be to the metal (5, 8).

Although Al forms an oxide film highly resistant to oxidation (9, 10), Al additions increase the oxidation rates of Mg (11, 12). For the converse case, additions of Mg to Al, information is not available. Hence, in this investigation the oxidation rates of an Al-3% Mg alloy in pure oxygen have been investigated. Some results of studies on Mg evaporation rates from the alloy and metallographic examination of the oxide films are also included.

## Experimental

The alloy used in this investigation was prepared from high purity Al and Mg and contained 2.87% Mg and impurities of 0.002% Cu, 0.03% Fe, and 0.001% Si. The 0.063 in. gauge sheet as received was cold-rolled to 0.013 in., annealed for 30 min at 400°C, and further cold-rolled to 0.010 in. Specimens, 0.6800 g, were prepared from sections of this sheet after they had been polished to 000 emery under kerosene and then on a dry Selvyt cloth. All specimens were stored in a desiccator after preparation and prior to use.

A vacuum microbalance assembly, which has been described previously (9, 13), was employed for the measurement of the oxidation and Mg evaporation rates. Oxidation rates were determined from specimen weight increases in oxygen at 7.6 cm oxygen pressure and Mg evaporation rates were determined from specimen weight losses in a vacuum of $10^{-6}$ mm. Each specimen was suspended on the microbalance and degassed at room temperature in a vacuum for 5 hr prior to further experimentation. For oxidation tests at 200° and 350°C each specimen was degassed 30 min at 400° and 12 hr at 350°C, respectively. At higher temperatures oxygen was admitted to the specimens before the initiation of Mg evaporation.

Results of oxidation tests in the temperature range 200°-550°C for short and long exposures are illustrated in Fig. 1 and 2. These results show that the alloy was relatively oxidation resistant at a temperature of 200°C. As the temperature was elevated, the oxidation rate increased. However, rapid oxidation did not occur until a temperature

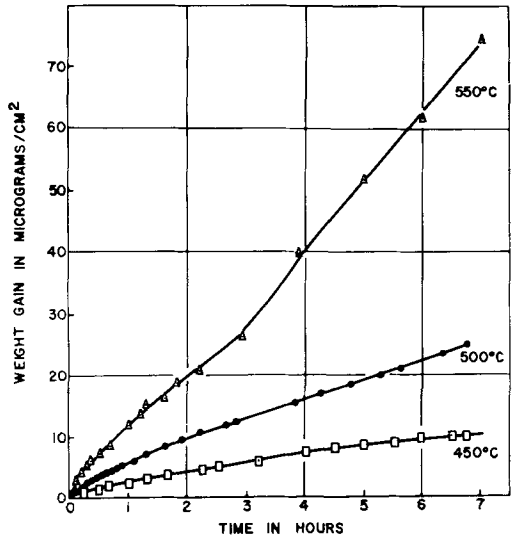


Fig 1. Oxidation of metallographically polished Al-3% Mg alloy in the temperature range 450°-550°C.

[1] Present address: Metals Research Laboratory, Carnegie Institute of Technology, Pittsburgh, Pa.

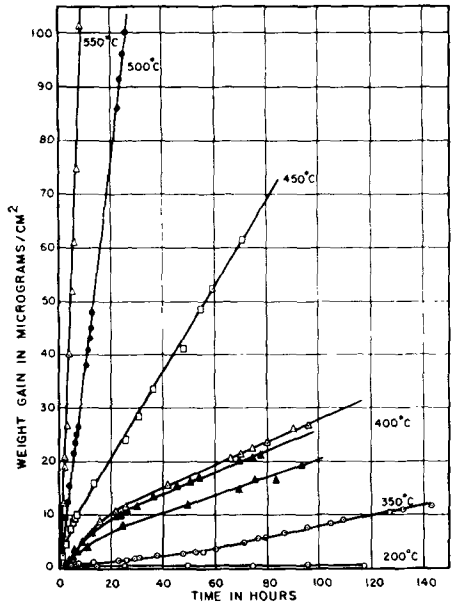


Fig. 2. Oxidation of metallographically polished Al-3% Mg alloy in the temperature range 200°-550°C.

of 400°C was exceeded. The initial rate of oxidation decreased with time but gave way to an approximately constant rate at oxygen weight gains less than 10 $\mu g/cm^2$ (less than 1000Å film thickness) over the temperature range 350°-550°C. Thus an increase in film thickness beyond a certain range did not increase oxidation resistance. The reproducibility of the measurements is illustrated by the three 400°C curves in Fig. 2.

Results of the Mg evaporation tests in the temperature range 350°-500°C are illustrated in Fig. 3. There was an initial weight loss of approximately $10\mu g/cm^2$ because of loss of gas as each specimen was heated in vacuum to the evaporation test temperature. This was followed by an additional weight loss due to Mg evaporation after an induction period which was dependent on the temperature. For example, this period was 200 min at 375°C and was of such short duration at 500°C that it could not be determined accurately. Magnesium evaporation measurements were reproducible to 10%.

Marked discoloration of the Al-3% Mg alloy occurred on exposure to oxygen above 400°C. Conversely, metallographically polished specimens and a specimen with a thick oxide layer (100$\mu$) were

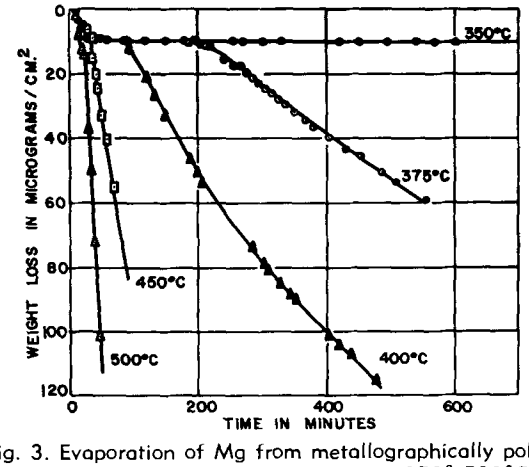


Fig. 3. Evaporation of Mg from metallographically polished Al-3% Mg alloy in the temperature range 350°-500°C.

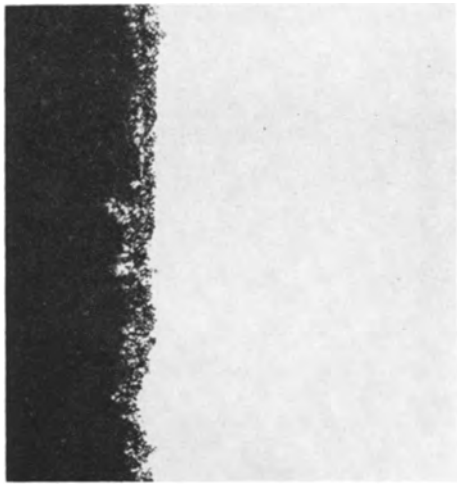

Fig. 4. Oxide film on Al-3% Mg alloy, in cross section at magnification of 500X before reduction for publication; Metal—white, oxide—black.

not discolored by vacuum anneals at 500°C. The photomicrograph in Fig. 4 illustrates the cross section of a black oxide film formed on the alloy after a 40-hr exposure at 550°C. The oxide was nonuniform in thickness (3-15$\mu$) and contained small metal particles. Further, the metal/oxide interface was serrated with many small metal inclusions nearly surrounded by oxide. Examination of metal cross sections revealed oxide penetration along grain boundaries and directly into grains.

It was doubtful if these metal inclusions resulted from metal entrainment during polishing. To confirm this, oxide films were stripped from the metal substrate and then examined. The surface of an oxidized specimen was backed with Formvar plastic by brushing on a 3% solution of Formvar in $C_4H_2O_2$. Sections, 1 $cm^2$, were outlined with razor scratches and the film stripped with a 3% solution of Br in anhydrous methanol. A section was prepared for microscopic examination by placing it between two pieces of 1/16 in. Lucite sheet and placing this sandwich vertically in a Lucite plastic mount for metallographic polishing. Such an oxide cross section is illustrated in Fig. 5. Particles of a second phase less

Fig. 5. Stripped oxide film from Al-3% Mg alloy at magnification of 1000X with oil immersion objective before reduction for publication; metal inclusions—small white spots.

than 2$\mu$ in diameter were scattered throughout the oxide. Also, powder x-ray analyses were taken of oxide stripped from an alloy which had been exposed 60 hr in dry oxygen at 500°C. All powders gave an Al diffraction pattern and the oxides identified were MgO and $MgAl_2O_4$. One powder contained silica in trace amounts. Two powders, which gave the best Al diffraction patterns, were heated 18 hr in air at 900°C. The powders changed color from black to white; x-ray analyses showed only MgO and $MgAl_2O_4$.

## Discussion

### *Alloy Oxidation*

Due to the complexity of the oxidation kinetics, quantitative conclusions cannot be deduced from the oxidation characteristics of this Al-Mg alloy. However, qualitative conclusions may be drawn by approximating the results to parabolic and linear oxidation rate equations. That is, the rate constants for the initial varying and final constant oxidation rates may be expressed, respectively, as,

$$K_P = \operatorname{Lim}_{t\to 0} \left[ \frac{d}{dt} (\Delta m/A) \right]^2 \qquad \text{(I)}$$

$$K_L = \operatorname{Lim}_{t\to \infty} \left[ \frac{d}{dt} (\Delta m/A) \right] \qquad \text{(II)}$$

where $K_P$ and $K_L$ are the parabolic and linear rate constants, respectively, and $\Delta m/A$ is the amount of oxygen per unit area at time $t$. The initial weight increments were plotted according to the parabolic equation: $(\mu g/cm^2)^2$ oxygen vs. time. These curves and linear sections of the oxidation curves illustrated in Fig. 2 show that the oxidation rates obey parabolic and linear relationships to a first approximation over the temperature range 350°-500°C. Parabolic and linear rate constant values determined from tangents to the initial and final sections of the parabolic and linear oxidation curves are recorded in Table I.

The temperature variation of these oxidation rate constants over part of the temperature range examined may be expressed by the Arrhenius relation

$$K = A \exp - E/RT \qquad \text{(III)}$$

where $A$ is the frequency factor, $E$ is the energy of activation, $R$ is the gas constant and $T$ is the absolute temperature. This is illustrated by plots of log

**Table I. Oxidation and Mg evaporation rates for the Al 2.87% Mg alloy**

| Temp, °C | Linear oxidation rate (g/cm²/sec) | Parabolic oxidation rate (g/cm²/sec)² | Mg evaporation rate (g/cm² sec) |
|---|---|---|---|
| 350 | | $3.8 \times 10^{-17}$ | |
| 375 | | | $2.6 \times 10^{-9}$ |
| 400 | $4.7 \times 10^{-11}$ | $9.2 \times 10^{-17}$ | $6.0 \times 10^{-9}$ |
| | $5.6 \times 10^{-11}$ | $2.4 \times 10^{-16}$ | |
| | $5.9 \times 10^{-11}$ | $3.8 \times 10^{-16}$ | |
| 450 | $2.2 \times 10^{-10}$ | $1.6 \times 10^{-15}$ | $1.6 \times 10^{-8}$ |
| 500 | $9.2 \times 10^{-10}$ | $3.9 \times 10^{-15}$ | $5.6 \times 10^{-8}$ |
| | | | $6.8 \times 10^{-8}$ |
| 550 | $2.8 \times 10^{-9}$ | $2.9 \times 10^{-14}$ | $1.3 \times 10^{-7}$ |

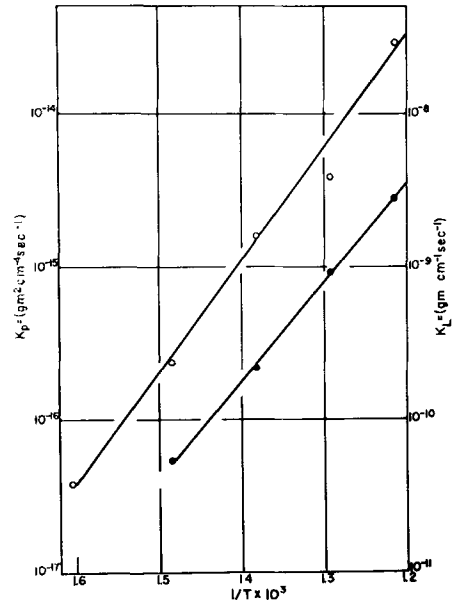


Fig. 6. Arrhenius plots of parabolic and linear oxidation rate constants; open circle = parabolic constants; solid circle = linear constants.

$K$ vs. $1/T$ in Fig. 6; the expressions for the constants are:

$$K_P \ (\text{g/cm}^2 \text{ sec})^2 = 2\text{x}10^{-5} \exp - 33{,}000/RT \qquad \text{(IV)}$$

$$K_L \ (\text{g/cm}^2 \text{ sec}) = 0.2 \exp - 29{,}000/RT \qquad \text{(V)}$$

It has been suggested by Evans (14) and Loriers (15) that transition from a parabolic to a linear oxidation rate relationship occurs for pure metals if porous oxide forms over compact oxide. The inner compact layer tends to a limiting thickness $y_{max}$ when its formation rate is equal to its transformation rate to porous oxide. Webb, Norton, and Wagner (16) express this thickness as,

$$y_{max} = f K_P/2K_L \qquad \text{(VI)}$$

where $f$ is the ratio of oxygen content per gram atom metal in the compact and porous oxide.

From electron diffraction results, De Brouckère (3) has suggested that the oxide on Al-Mg alloys, containing up to 8% Mg, consists of an inner $\gamma$-alumina or magnesium aluminate compact layer and an outer porous magnesia layer upon high temperature oxidation. If this is valid, it follows to a first approximation from Eqs. (IV), (V), and (VI) that

$$y_{max} = 5\text{x}10^{-5} \exp - 4000/RT \qquad \text{(VII)}$$

The calculated oxygen values of 3 to 5 $\mu g/cm^2$ for compact layer formation over the temperature range 400°-550°C are of the same magnitude as the experimental values of less than 10 $\mu g/cm^2$ before the onset of constant oxidation rates.

Other evidence may be advanced to support the view that the oxide film offers resistance to the reaction of metal with oxygen. Studies of Leontis and Rhines (11) and Gulbransen (17) have shown that the oxidation and evaporation kinetics of pure Mg may be represented by linear rate equations. Table II contains three different ratios: the evaporation

Table II. Comparison of oxidation and Mg rates for pure Mg and the Al 2.87% Mg alloy

| Temp, °C | Mg oxid. rate[11, 17] (g/cm² sec) | Mg evap. rate[17] (g/cm² sec) | Mg evap. Alloy evap. | Alloy oxid. Alloy evap. | Mg oxid. Alloy oxid. |
|---|---|---|---|---|---|
| 400 | $4.7 \times 10^{-11}$ | | | $7 \times 10^{-3}$ | 1.1 |
| | | | | $1.2 \times 10^{-2}$ | 0.7 |
| 450 | $5.6 \times 10^{-10}$ | $3.6 \times 10^{-8}$ | 2.3 | $2.8 \times 10^{-2}$ | 1.9 |
| | $6.3 \times 10^{-10}$ | $2.2 \times 10^{-9}$ | 1.4 | | |
| 500 | $6.3 \times 10^{-9}$ | $1.9 \times 10^{-8}$ | 0.3 | $2.5 \times 10^{-2}$ | 4.5 |
| | $2.0 \times 10^{-8}$ | | | | |

rate of pure Mg to its evaporation rate from the alloy, the oxidation rate of the alloy to the evaporation of Mg from the alloy and, finally, the oxidation rate of pure Mg to the oxidation rate of the alloy. These ratios show, first, that the oxidation rate of the alloy is very nearly the same as for pure Mg and, second, the oxidation rate of either the alloy or pure Mg is much smaller than Mg evaporation rates. This suggests that the oxide film on the alloy offers resistance to oxidation of the metal at all stages of exposure.

Although parabolic and linear rate equations give an excellent approximation to the reaction kinetics, oxidation does not proceed simply by formation of porous magnesia over a compact oxide layer of constant thickness. The oxidation mechanism is more complex as the metal/oxide interface is highly serrated and metal inclusions occur in the oxide. Perhaps, this composite film forms according to the type of alloy oxidation mechanism proposed by Wagner (18). In the temperature range of this investigation, Al oxidizes rapidly for exposures not exceeding 10 hr and after this formative stage the oxidation rate decreases to a negligible value at film thicknesses of the order of 2000Å (9, 10). On the other hand, the alloy oxidizes at a constant rate similar to Mg after the initial formative oxidation stages. Thus, the oxidation rate of the base component, Mg, exceeds that of the noble component, Al, for long exposures. Selective oxidation of Mg would produce the serrated alloy/oxide interface and inclusions of the alloy depleted with respect to Mg as the oxide moves inward to fill the space of consumed metal.

### *Magnesium Evaporation*

The weight loss curves of Fig. 3 for specimens suspended in vacuum at elevated temperatures have shown three characteristic features: *(a)* an initial weight loss due to outgassing; *(b)* an induction period; and *(c)* the onset of Mg evaporation. Values for the initial Mg evaporation rate (Table II) increase exponentially with temperature according to the Arrhenius relation:

$$K_{\text{Evap.}}\ (\text{g/cm}^2\ \text{sec}) = 0.6 \exp - 25{,}000/RT \qquad \text{(VIII)}$$

Magnesium may evaporate at an initial constant rate after the induction period by two possible mechanisms: it may diffuse through the oxide film upon establishment of a concentration gradient or evaporate from the metal/vacuum interface if the compact oxide film breaks down to porous oxide. These two mechanisms may be differentiated by a calculation based on equations for the induction period and diffusion rate of a substance through a semipermeable membrane given by Barrer (19). The diffusion rate $P$ of a substance through a semipermeable membrane of thickness $l$ is to a first approximation

$$P = \frac{lc}{6L} \qquad \text{(IX)}$$

if $L$ is the period required to establish a concentration gradient for concentrations of c and zero at the interfaces. The concentration c, which in this case represents the solubility of Mg in the oxide at the metal/oxide interface, may be estimated from the experimental data. The electron diffraction studies of De Brouckère (2) indicate that the air-formed oxide film on the alloy at room temperature does not exceed 100Å at 400°C; the initial Mg evaporation rate is $6 \times 10^{-9}$ g/cm² sec after an induction period of 200 min. Hence, $c = 432$ g/cm³. This very high value indicates that Mg evaporates from the metal/vacuum interface through porous oxide which may be produced by chemical reaction or mechanical breakdown of compact oxide. Since the duration of the induction period is strongly dependent on temperature, alumina may be reduced by Mg to give magnesia and the film would be porous as the volume ratio products/reactants for this reaction is 0.7. Consequently, the decreasing Mg evaporation rate from the alloy illustrated by the curve for vacuum exposure at 400°C is determined by its diffusion rate in the alloy and by partial resistance of porous oxide.

## Surface Discoloration

Different views as to the origin of the discoloration of Al-Mg alloys by oxidation have been expressed. De Brouckère (2) has shown by electron diffraction that black films contain magnesia which was assumed to cause discoloration. Guminski and Hines (20) have suggested that metal in atomic or particle form in the surface oxide may be the cause of discoloration as hydrogen is evolved from black oxide when it is treated with acid. This investigation indicates that metal particles embedded in the oxide are a primary cause of discoloration as microscopic and x-ray examinations have shown the occurrence of Al inclusions. Thus, the black oxide became white when exposed at 900°C, as Al was completely oxidized. Metal particles of colloidal dimensions are often colored black. However, it is not known if discoloration is caused by this effect or by multiple reflection and absorption of light by irregular surfaces of larger particles. The view that discoloration is associated with the lattice defect structure of magnesia has not been disproven in this investigation. Leontis and Rhines (11) have shown that gray magnesia, presumably due to its nonstoichiometric composition, occurs next to the metal surface of magnesium. That this effect is a primary cause of alloy discoloration is doubtful as metallographically polished specimens or a specimen with a thick anodic film were not discolored by vacuum anneals of sufficient duration to allow Mg evaporation.

### General

In the preceding discussion, the oxidation kinetics at temperatures greater than 350°C have been approximated to parabolic and linear rate equations. A comparison of oxidation and Mg evaporation rates demonstrated that the oxide film offered resistance to oxidation at all stages of exposure. Metallographic and x-ray examinations have shown that depletion of Mg by selective oxidation resulted in formation of Al inclusion in the oxide. These inclusions, in turn, caused a gray to black discoloration of the surface. Many of the views which have been expressed must remain speculative because chemical compositions and structures of the oxides in the composite film, and determinations of Mg activities and diffusivities for the alloy and oxides are required to elucidate the oxidation and Mg evaporation behavior.

### Acknowledgments

The author wishes to express his thanks to former colleagues, especially J. S. Kirkaldy and H. P. Godard, at Aluminium Laboratories, for helpful discussions.

Manuscript received Nov. 26, 1956.

Any discussion of this paper will appear in a Discussion Section to be published in the December 1958 JOURNAL.

REFERENCES

1. S. Dobinski and M. Niesluchowski, *Nature*, **144**, 510 (1939).
2. L. De Brouckère, *J. Inst. Metals*, **71**, 131 (1945).
3. R. Eborall and C. E. Ransley, *ibid.*, **71**, 525 (1945).
4. O. Kubaschewski and H. Ebert, *Metallforschung*, **2**, 232 (1947).
5. M. Whitaker and A. R. Heath, *J. Inst. Metals*, **82**, 107 (1953).
6. A. J. Swain, *ibid.*, **80**, 125 (1951).
7. P. T. Stroup, "Controlled Atmospheres," A.S.M. (1941).
8. E. A. Smith, Jr., *Light Metal Age*, **12**, 24 (October, 1954).
9. W. W. Smeltzer, *This Journal*, **103**, 209 (1956).
10. M. S. Hunter and P. Fowle, *ibid.*, **103**, 483 (1956).
11. T. E. Leontis and F. N. Rhines, *Trans. Am. Inst. Mining Met. Engrs.*, **166**, 265 (1946).
12. I. A. Makolkin, *Zhur. Priklad. Khim.*, **24**, 460 (1951).
13. E. A. Gulbransen, *Rev. Sci. Instr.*, **15**, 201 (1944).
14. U. R. Evans, *Trans. Am. Inst. Mining Met. Engrs.*, **166**, 292 (1946).
15. J. Loriers, *Compt. rend.*, **231**, 522 (1950).
16. W. W. Webb, J. T. Norton and C. Wagner, *This Journal*, **103**, 107 (1956).
17. E. A. Gulbransen, *Trans. Electrochem. Soc.*, **87**, 589 (1945).
18. C. Wagner, *This Journal*, **103**, 571 (1956).
19. R. M. Barrer, "Diffusion in and Through Solids," Cambridge University Press, p. 19 (1951).
20. R. D. Guminski and R. A. Hines, Private communication.

# Metallographic Manifestations of the Air Oxidation of Tantalum at 750°C

**Robert Bakish**[1]

*Sprague Electric Company, North Adams, Massachusetts*

ABSTRACT

The crystallographic and structural factors involved in the air oxidation of tantalum at 750°C are presented. The role of the {100} planes in the oxidation process is discussed, and a tentative mechanism for the conversion of metal to oxide under these conditions is proposed.

The oxidation of Ta has been studied by a number of investigators with emphasis on the type and structure of the oxide formed (1-4) or on the kinetics of oxidation (5-9). Work on the solubility of oxygen in Ta has also been reported (10). In all these investigations, the nature of the oxide-metal interface has been completely disregarded, and no mention of the crystallographic dependence of the tantalum oxygen reaction has been made.

Pure Ta (Ta 99.9 + Fe 0.03 max and C 0.03 max) supplied by Fansteel Metallurgical Corporation was used for this investigation.

### Experimental Procedure

It has been shown that tantalum oxide exists in a stable modification in the temperature range 650°-1300°C (3). The tantalum oxide used in the most recent structure determination was prepared by oxidation of the metal at 700°C (4). In order to avoid possible complications introduced by working with an unknown oxide, an oxidation temperature was selected on the basis of the above references. All specimens in this investigation were subjected to 45-min oxidation in air at 750°C, followed by quenching in air at room temperature.

X-ray powder technique was used to identify the oxide formed. The single crystals used in this study were grown by standard strain anneal technique and their orientations determined using Greninger's method (11). The identification of the plane of oxidation was carried out as follows: two surfaces with known angular relations were ground on crystals of known orientation, and the angles made by the planes of preferred oxidation with the common edge were measured. This information was then plotted stereographically and analyzed using a standard cubic projection, in accordance with standard procedures (12).

[1] Present address: Ciba Limited, Rare Metals Division, Basle, Switzerland.

Standard metallographic techniques were applied in this study, and a solution consisting of $H_2SO_4$ (96%), $HNO_3$ (70%), and HF (48%) in ratio (2:1:1) was used as the etching reagent.

In oxygen embrittled Ta, both inter- and transcrystalline fracture can be observed. Intergranular failure is predominant in relatively small grain size material (about 0.1 mm). The oxide distribution on grain surfaces obtained by fracturing small grained metal were examined in order to gain additional information regarding the sites of preferred oxidation. These observations were made on freshly fractured wires without any subsequent surface preparation.

## Experimental Results

Air oxidation of Ta leads to surface oxidation and crystallographically dependent internal oxidation. The latter proceeds at higher rates along certain planes and directions in the Ta lattice. The oxide-metal interface in polycrystalline Ta oxidized in air at 750°C is shown in Fig. 1. Observe here the surface oxide and the spear-like orientation-dependent platelets of the oxide. Note that no preferential oxidation exists at the grain boundary. This type of interface is typical of the large number of oxide-metal interfaces examined and is unaffected by longer oxidation treatments which only moves this interface into the metal.

X-ray study by application of powder technique indicates that the oxide formed under these conditions is $Ta_2O_5$, of the same variety as commercially produced material of this formula. The structure of this oxide has recently been reevaluated (4). X-ray lines characteristic of the oxide pattern were also detected after removal of the surface oxide in specimens which, by metallographic examination, were shown to have internal preferential oxidation.

The oxide formed on polycrystalline Ta is of very fine particle size, as indicated by diffuse x-ray patterns. This oxide has a high degree of porosity which can be detected on careful microscopic examination of the polished oxide. The same type of polycrystalline oxide seems to be formed on single crystal surfaces.

X-ray analysis of the internal oxidation occurring in single crystals shows that, within the accuracy of the measurements of about 2°, the planes of internal oxidation are parallel to the {100} planes of the bcc lattice. On successive lapping and polishing of single crystal surfaces normal to the oxidized surface, and in several cases normal to the <100> directions, it was found that quite often the solid platelet profile of {100} planes was substituted at a greater depth by a bead profile and eventually with discrete sites of oxidation. See Fig. 2 for the appearance of {100} traces at some depth from the oxide metal interface. (Observe both "bead" profile and discrete oxidation sites.) These oxide platelets do not grow appreciably in thickness normal to the {100} planes after they reach a thickness of about 0.002 mm (*see* Fig. 3). Heavier oxidation is characterized by the presence of a greater number of more narrowly spaced platelets. The porous oxide is but a thorough oxidation of the volume of the metal by oxidation along {100} planes. Figure 4, which is a taper section of an oxidized surface of a single crystal, supports this contention. Observe the islands of porous oxide, the high density of platelets in their immediate vicinity, and the relatively smaller density of platelets as the distance from the oxidized surface is increased. That this appears to be the nature of oxidation seems to be also supported by examination of polished oxide surfaces

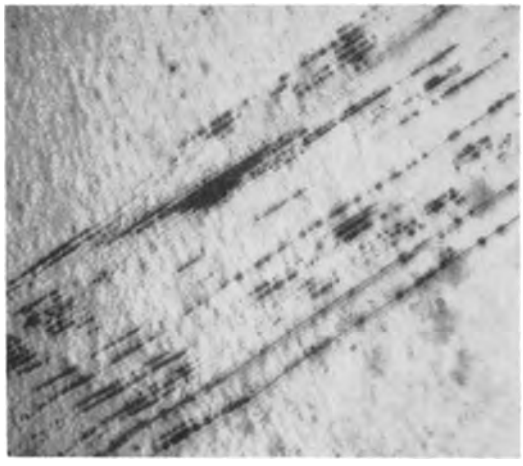

Fig. 2. Details of early stage internal oxidation. 2000X before reduction for publication.

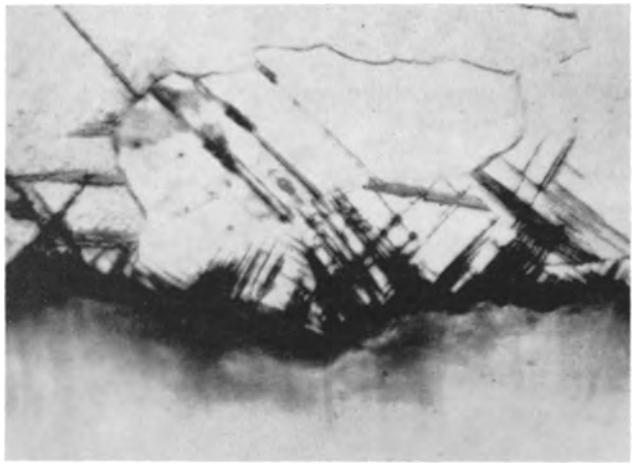

Fig. 1. Oxide metal interface, cross section normal to oxidized surface. 2000X before reduction for publication.

Fig. 3. Traces of the {100} planes. 2000X before reduction for publication.

Fig. 4. Taper section of oxidized single crystal surface. 500X before reduction for publication.

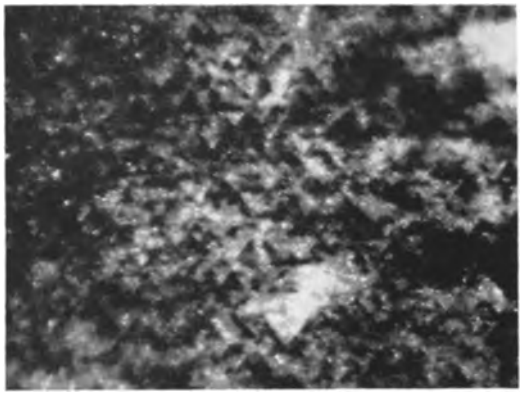

Fig. 5. Polished oxide surface (polarized light). 500X before reduction for publication.

under polarized light (*see* Fig. 5). This reveals a fine structure with elements parallel to the traces of the {100} planes of the substrate.

Another aspect in which the crystallographic dependence of oxidation manifests itself is the formation of steps bound by {100} substrate planes on the oxide-metal interface of single crystals. Figure 6 shows the appearance of such an interface as viewed on a (112) plane. When such single crystals were subjected to oxidation, it was possible to observe that the <100> directions in the {100} planes were the directions of a higher rate of oxidation. This observation and the occurrence of the {100} step formation, tend to show that the <100> directions

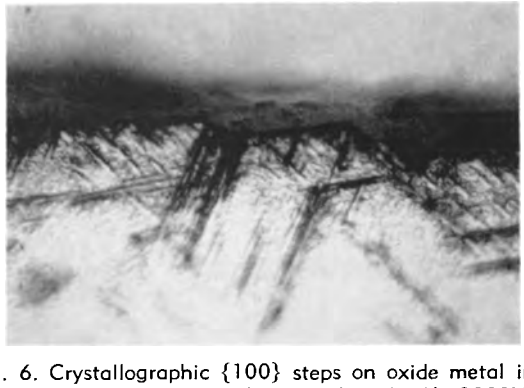

Fig. 6. Crystallographic {100} steps on oxide metal interface plane of photomicrograph parallel to (112). 2000X before reduction for publication.

Fig. 7. Fractograph showing sites of nucleation of oxygen metal reaction on a grain surface. 500X before reduction for publication.

in the {100} planes are the directions of preferred oxidation.

In addition to oxidation within the grains, evidence of internal oxidation was found on grain surfaces. This information was obtained by microscopic examination of fractured, fine grained, oxidized Ta wire. Figure 7 shows a distribution typical of those observed.

## Discussion of Results

The findings of this investigation show the presence of a set of high activity planes in the {100} planes of the Ta lattice.

Two alternatives are offered as possible explanations of the high activity of the {100} planes: it can be due either to the inherent high activity of this plane; or it can be the result of the presence of favorably oriented imperfections which could act as short circuiting paths for diffusion and oxidation. It is on these imperfections that the metal-oxide reaction appears to nucleate. No preferential grain boundary oxidation was observed in this study. The oxidation process seems to proceed by nucleation of oxidation at highly localized sites along the traces of the {100} planes, leading to the growth of oxide platelets parallel to the {100} planes. These platelets grow in thickness until they reach about 0.002 mm. Further oxidation proceeds by nucleation and the growth of additional platelets until all the metal is consumed in the reaction. The high activity usually associated with grain boundaries in oxidation reactions is not apparent from examination of metal-oxide interfaces in this study. No satisfactory explanation for this behavior can be advanced at present. Oxide-metal reaction, however, was found to nucleate at discrete sites on grain surfaces, and discrete oxide particles can be seen on observation of these surfaces. The exact nature of the sites which act as nucleating centers for the oxide-metal reaction is not known. Their appearance and distributions suggest the possibility that they are dislocations. This, however, cannot be asserted at present.

## Conclusions

On the basis of this study, it is proposed that oxidation of Ta proceeds by preferential oxidation

along the {100} planes in the <100> direction. The complete conversion of the metal to oxide is effected by the nucleation and growth of {100} plates, which eventually fill the volume of the metal. The individual plates do not exceed 0.002 mm in thickness.

On examination of tapered sections, the $Ta_2O_5$ shows clearly the crystallographic dependence of its growth process and the orientation of the traces of the {100} planes of the substrate. Lattice imperfections, believed to be dislocations, seem to act as sites for the nucleation of the metal-oxide reaction.

### Acknowledgment

The author wishes to acknowledge the assistance of D. Rogers and N. Harvin in the course of this work. Thanks are also due to W. Bernard for reading the manuscript.

Manuscript received April 22, 1957. This paper was prepared for delivery before the Buffalo Meeting, Oct. 6-10, 1957.

Any discussion of this paper will appear in a Discussion Section to be published in the December 1958 JOURNAL.

REFERENCES

1. G. Brauer, *Z. anorg. u. allgem. Chem.*, **248**, 1 (1941).
2. S. Lagergren and A. Magneli, *Acta. Chem. Scand.*, **6**, 444 (1952).
3. R. J. Wasilewski, *J. Am. Chem. Soc.*, **75**, 1001 (1953).
4. L. K. Frevel and H. W. Rinn, *Anal. Chem.*, **27**, 1329 (1955).
5. E. Gulbransen and K. F. Andrews, *This Journal*, **99**, 6 (1949).
6. E. Gulbransen and K. F. Andrews, *Trans. Am. Inst. Mining Met. Engrs.*, **186**, 586 (1950).
7. R. C. Petersen, *et al.*, *ibid.*, **200**, 1038 (1954).
8. J. T. Waber, *J. Chem. Phys.*, **20**, 734 (1952).
9. J. T. Waber, *et al.*, *This Journal*, **99**, 121 (1952).
10. E. Gebhardt and H. Preisendanz, Plansee Proceedings, 254 (1956).
11. A. B. Greninger, *Trans. Am. Inst. Mining Met. Engrs.*, **17**, 61 (1935).
12. C. S. Barrett, Structure of Metals, 40 (1952).

# Cathodic Reduction of Oxide Films on Iron

## II. Determination of $\alpha$-$Fe_2O_3$ and $Fe_3O_4$

**K. H. Buob, A. F. Beck, and M. Cohen**

*National Research Council, Ottawa, Ontario, Canada*

ABSTRACT

A study of the cathodic reduction of $\alpha$-$Fe_2O_3$ on iron has been made with the object of using the technique for the accurate determination of both the $\alpha$-$Fe_2O_3$ and $Fe_3O_4$ formed during the oxidation of iron. The films were examined after oxidation and after various stages of cathodic reduction. Examination was made by weight change, electron diffraction, x-ray diffraction, and chemical analysis of the films. Some evidence for the existence of a thin layer of $\gamma$-$Fe_2O_3$ between the layers of $Fe_3O_4$ and $\alpha$-$Fe_2O_3$ was found. A standard pattern for $Fe_3O_4$ was obtained.

When Fe is oxidized in oxygen at temperatures up to about 450°C a duplex film of $Fe_3O_4$ next to the metal and $\alpha$-$Fe_2O_3$ is formed. The over-all growth of the oxide film should be related to the rates of growth of these two layers. In a previous paper (1) there was described a technique for the cathodic reduction of $\alpha$-$Fe_2O_3$. In this paper the application of this technique to the determination of $\alpha$-$Fe_2O_3$ and $Fe_3O_4$ is described.

The method proposed was to weigh the oxidized specimen and to reduce it cathodically until the potential of the Fe indicated a change in the cathodic process. The specimen was reweighed and the $Fe_2O_3$ determined by difference. The $Fe_3O_4$ was calculated from the total weight gained and the weight of $Fe_2O_3$.

To check on the validity of this method, reflection electron diffraction identification of the oxide was made during various stages of the cathodic reduction process. Films were stripped for identification by both diffraction and chemical analysis, and the effect of cathodic reduction on magnetite films was determined.

### Experimental

*Preparation of oxidized specimens.*—The specimens measuring 5 x 1 cm with a handle 2.5 x 0.2 cm were cut from rolled Armco Iron sheet 0.150 mm thick. The Fe contained 0.113% total impurities. The specimens were degreased in benzene, wiped dry with Kleenex, stored in a desiccator for 1 hr, and weighed on a microbalance to $\pm 2 \times 10^{-6}$ g. They were then supported in a quartz tube over which a

furnace could be drawn. The temperature of the furnace was regulated to ±0.5°C. The Fe surface was reduced in purified hydrogen at 400°C for 1 hr. The hydrogen was pumped off and the Fe outgassed for 3 hr, during which time the desired oxidation temperature was set. Oxygen was admitted to the oxidation chamber to a pressure of 20 mm Hg. At the end of the desired oxidation time, the furnace was removed, the outside of the quartz tube was cooled rapidly with water, the specimens placed in a desiccator for 1 hr, and reweighed on the microbalance.

*Cathodic reduction of* $\alpha$-$Fe_2O_3$.—The cathodic reduction was carried out in the cell described by Oswin and Cohen (1). Optimum results were obtained in a borate-HCl buffer of *p*H 7.65, with a current density of 15 $\mu a/cm^2$. The specimens were dried and weighed after cathodic reduction.

*Isolation of oxide films.*—A modified version of the film stripping apparatus of Vernon, Wormwell, and Nurse (2) was used. This was of all-glass construction and employed a vacuum and purified nitrogen for deoxygenation and movement of solutions. A solution of 12% iodine in methanol was used. All reagents were well dried and free of oxygen. The time of treatment varied from 30 to 90 min, depending on the nature of the films. It was found that the duplex film or a film of $Fe_3O_4$ alone could be stripped equally well.

After treatment the film was washed and floated on methanol. This film could then be used for chemical analysis or examination by diffraction.

*Electron diffraction.*—For electron diffraction examination the oxide film was mounted on a 12 mesh grid supported by a thin Formvar film. This film was prepared by spreading one drop of a 0.3% w/v Formvar in ethylene dichloride solution on water, and mounting on the grid. This combination forms a tough mounting substrate for the somewhat brittle oxide film, yet the Formvar film is thin enough to be practically transparent to the electron beam. The "hole" area of the 12 mesh grid is larger than the area of the electron beam, hence eliminating interference by the grid. Reflection electron diffraction examination was also made on the specimens at various stages of reduction.

*Chemical analysis.*—The thin stripped films were thoroughly washed with water and then dissolved in 1:1 HCl. The magnetite dissolved readily while the $Fe_2O_3$ dissolved only very slowly. Ferrous ion was determined by the $\alpha$ $\alpha'$ dipyridyl method (3) and total Fe by the thioglycollic acid method (4).

## Results and Discussion

A series of specimens were oxidized in quadruplicate. These were then reduced cathodically and the amounts of $\alpha$-$Fe_2O_3$ and $Fe_3O_4$ determined. A typical set of results is shown in Table I. As can be seen from the table the deviation from the average is less than 7%. The $Fe_3O_4$ value, of course, is obtained by difference. As pointed out in the previous paper, the current efficiency estimated from either weight loss or Fe in solution is about 95%.

A cathodic reduction curve is shown in Fig. 1. The normal points at which the specimens are weighed

**Table I. Iron oxidized at 320°C**

| Time min | Total wt gain $\mu g/cm^2$ | Weight loss on C.R.* $\mu g/cm^2$ | $O_2$ $\alpha$-$Fe_2O_3$ $\mu g/cm^2$ | $O_2$ as $Fe_3O_4$ $\mu g/cm^2$ |
|---|---|---|---|---|
| 2413 | 21.0 | 45.1 | 13.5 | 7.5 |
| 2413 | 21.3 | 46.8 | 14.0 | 7.3 |
| 2413 | 23.1 | 50.7 | 15.1 | 8.0 |
| 2413 | 21.8 | 50.8 | 15.2 | 6.6 |
| Average | 21.8 | 48.4 | 14.4 | 7.4 |

* Cathodic reduction.

**Table II. Effect of cathodic reduction on $Fe_3O_4$**

| Reduction time min | Weight loss $\mu g/cm^2$ | Current efficiency % |
|---|---|---|
| 53 (Point A) | 39.2 | 98 |
| +5 | 0.60 | — |
| +5 | 0.66 | — |
| +10 | 0.73 | — |
| +20 | 0.60 | — |

are at the beginning and at Point A, just after completion of the inflection. Reflection electron diffraction showed that the surface was composed of $\alpha$-$Fe_2O_3$ at the end of the oxidation. After cathodic reduction up to Point A only $Fe_3O_4$ was present.

A series of experiments was made to determine whether $Fe_3O_4$ was reduced under the conditions used in the cathodic reduction. A specimen was reduced to Point A and weighed. It was then reduced under the same conditions for further periods of 5, 5, 10, and 20 min, with weighings between each reduction period. The results on a specimen which had been heated for 24 hr at 320°C are shown in Table II. It was also shown that cathodic reduction for periods up to at least 1 hr past Point A did not change the $Fe_3O_4$ diffraction pattern.

It can be seen that, once the $\alpha$-$Fe_2O_3$ has been removed at Point A, there is a small but constant

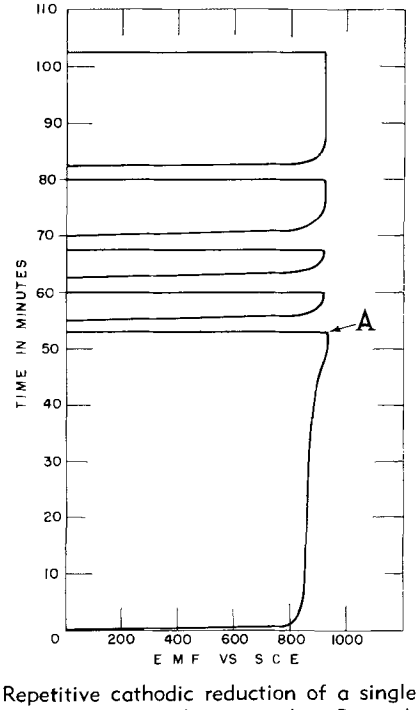


Fig. 1. Repetitive cathodic reduction of a single specimen. Complete reduction is usually assumed at Point A.

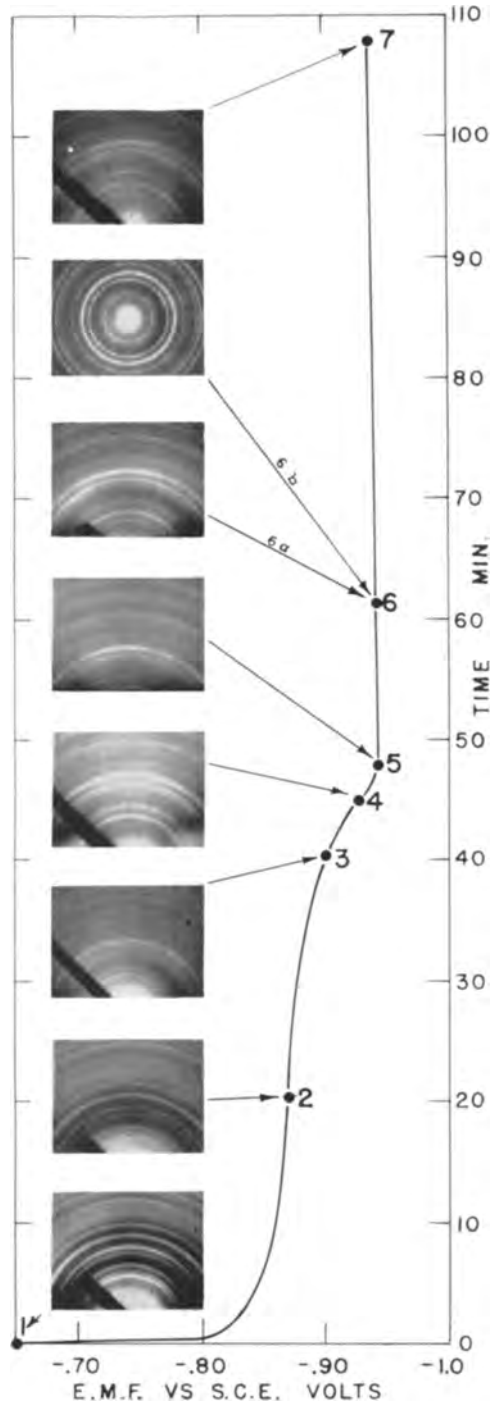


Fig. 2. Diffraction patterns of specimens removed at various stages of cathodic reduction.

weight loss on re-exposing the specimen to further reduction. This is probably caused by corrosion loss in the short period that the specimen is first immersed until it is cathodically protected. A part of the weight loss may be due to a small amount of oxidation of $Fe_3O_4$ to $Fe_2O_3$ on exposure to air with subsequent reduction of this $Fe_2O_3$. In a continuous run, the weight change after Point A should be negligible. It would thus appear that $Fe_3O_4$ is not reduced under the conditions used in these experiments.

As a further check on the process, reflection patterns were obtained from specimens which had been cathodically reduced to the points indicated in Fig. 2. In Table III typical interplanar spacings and the estimated intensities of the patterns are tabulated. Only those spacings, and their intensities, unique to the particular oxide are tabulated.

*Reduction curve.*—The specimen at point 1 in Fig. 2 gave a reflection pattern only of hexagonal $\alpha$-$Fe_2O_3$, indicating the thickness of this oxide to be greater than the depth of penetration of the electron beam. At point 2 enough of the $\alpha$-$Fe_2O_3$ had been removed to allow the beam to diffract from a cubic oxide beneath, producing a pattern of $\alpha$-$Fe_2O_3$ plus a trace of cubic oxide. The pattern from point 3 was similar to that from point 2. Of these last three patterns, the intensity of the characteristic 2.69 line has been decreasing as the reduction progresses, being absent at point 4. No material, other than the cubic oxide, was detected during the reduction, indicating that no intermediate product was formed by the reduction. Reflection diffraction patterns from thicker oxide films showed no $Fe_3O_4$ until point 4 was reached, thus eliminating the possibility of formation of $Fe_3O_4$ as a reduction product of $\alpha$-$Fe_2O_3$.

The pattern from point 4 did not contain the characteristic $d = 2.69$Å reflection, indicating almost total disappearance of $\alpha$-$Fe_2O_3$. The pattern, however, differed from that of $Fe_3O_4$ by extra reflections not possible by a true $Fe_3O_4$ structure. This pattern is very similar to Brindley's (5) $\gamma$-$Fe_2O_3$. Davies and Evans (6) find that $\gamma$-$Fe_2O_3$ can be distinguished from $Fe_3O_4$ by the presence of these and other additional lines; also that the $\gamma$-$Fe_2O_3$ pattern appears in adjacent layers of $\gamma$-$Fe_2O_3$ and $Fe_3O_4$ when the ratio of these oxides is approximately 4:1, respectively. The presence of these extra lines, and the slight shift of the remaining lines in point 4 toward the higher angle of diffraction indicate a high probability of the presence of $\gamma$-$Fe_2O_3$.

The patterns from specimens at points 5, 6, and 7, (there is also a transmission pattern at point 6) all give a strictly $Fe_3O_4$ pattern, with no anomalies. It would appear that if $\gamma$-$Fe_2O_3$ is present, it is only present as a very thin layer.

*Chemical analysis.*—Stripped films were dissolved in HCl and analyzed for both ferrous and total Fe. Pure $Fe_3O_4$ would have a total $Fe/Fe^{++}$ ratio of 3/1, while mixtures of $Fe_3O_4$ and $Fe_2O_3$ would have a ratio greater than 3/1.

Films which had been stripped without initial reduction gave ratios greater than 3, indicating the presence of both ferric and ferrous ions. Specimens which had been cathodically reduced before stripping gave ratios of $2.73 \pm 0.10$. This would indicate too high a concentration of ferrous ion for pure $Fe_3O_4$. X-ray diffraction of these films showed the presence of small amounts of $\alpha$-Fe and $Fe_3C$, which probably consisted of particles which adhered to the stripped film. Approximately 5% of extraneous Fe in the film would account for this lowering in ratio.

Some specimens were oxidized in the ordinary way and then annealed in vacuum until only an $Fe_3O_4$ pattern was obtained. Films stripped from

**Table III**

| d [1] | I/I₀ | d [2] | I/I₀ | d [3] | I/I₀ | d [4] | I/I₀ | d [5] | I/I₀ | d [6a] | I/I₀ | d [6b] | I/I₀ | d [7] | I/I₀ |
|---|---|---|---|---|---|---|---|---|---|---|---|---|---|---|---|
| | | | | | | 3.00 | 40 | 2.97 | 40 | 2.97 | 33 | 2.97 | 40 | 2.98 | 50 |
| 2.69 | 100 | 2.72 | 80 | 2.70 | 5 | | | | | | | | | | |
| | | | | | | [1]* | | | | | | | | | |
| | | | | | | 2.64 | 20 | | | | | | | | |
| 2.50 | 50 | 2.50 | 100 | 2.50 | 100 | 2.50 | 100 | 2.54 | 100 | 2.52 | 100 | 2.53 | 100 | 2.51 | 100 |
| | | | | | | [2]* | | | | | | | | | |
| 2.20 | 35 | 2.20 | 65 | 2.19 | 33 | 2.19 | 20 | | | | | | | | |
| | | | | | | 2.09 | 40 | 2.09 | 20 | 2.08 | 33 | 2.09 | 20 | 2.09 | 50 |
| | | | | | | | | 1.87 | 14 | 1.88 | 3 | 1.87 | 4 | | |
| 1.85 | 25 | 1.85 | 33 | 1.84 | 17 | | | | | | | | | | |
| | | | | | | [3]* | | | | | | | | | |
| | | | | | | 1.81 | 13 | | | | | | | | |
| 1.68 | 80 | 1.69 | 65 | 1.68 | 33 | 1.70 | 17 | 1.70 | 17 | 1.70 | 10 | 1.71 | 13 | 1.69 | 25 |
| 1.60 | 8 | 1.61 | 25 | 1.60 | 13 | 1.61 | 40 | 1.61 | 50 | 1.61 | 50 | 1.62 | 33 | 1.60 | 65 |
| | | | | | | 1.09 | 33 | 1.08 | 40 | 1.09 | 25 | 1.09 | 20 | 1.09 | 30 |

* Spacings [1] and [3] belong neither to $\alpha$-$Fe_2O_3$ nor $Fe_3O_4$. The $\gamma$-$Fe_2O_3$ pattern, as given by Brindley, however, contains these 2 lines, as well as line [2]. The absence of the 2.70 spacing of $\alpha$-$Fe_2O_3$ in the pattern reduces the probability of line [2] being that of $\alpha$-$Fe_2O_3$.

these specimens gave a total $Fe/Fe^{++}$ ratio of $2.93 \pm 0.05$. X-ray diffraction of these specimens showed only a trace of the Fe lines. This lowering in ratio would be accounted for by about 1% of extraneous Fe.

$Fe_3O_4$ *standard.*—The annealed specimens described above gave extremely good $Fe_3O_4$ patterns both by reflection and transmission. Some of the film was mounted on a glass fiber with C.I.L. Duco cement for x-ray diffraction. The patterns obtained contained more lines than those reported by Brindley (5) or any other source. The electron diffraction patterns are shown in Fig. 3 and the tabulated spacings are given in Table IV. It can be seen that there is very good agreement between the reflection and transmission patterns. This indicates that there is no significant change during the stripping of the film. The transmission pattern gives the more accurate values, because the diameters of whole cir-

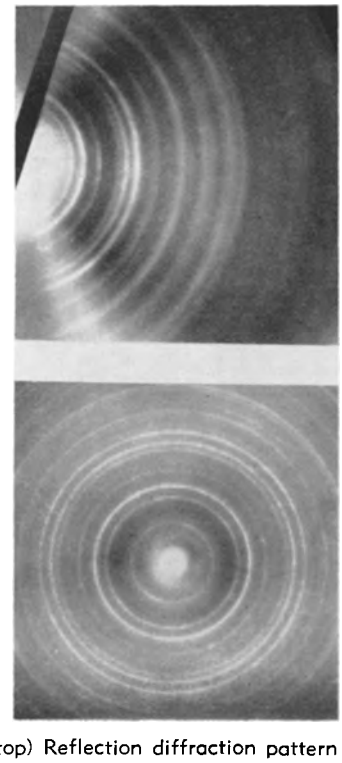

Fig. 3. o. (top) Reflection diffraction pattern of $Fe_3O_4$; Fig. 3b. (bottom) transmission diffraction pattern of $Fe_3O_4$.

**Table IV. Standard $Fe_3O_4$ Patterns**

| hkl | Reflection d | Reflection I/I₀ | Transmission d | Transmission I/I₀ | X-ray d | X-ray I/I₀ |
|---|---|---|---|---|---|---|
| 111 | 4.93 | 20 | 4.81 | 25 | 4.78 | 20 |
| 200 | | | 4.20 | 4 | | |
| 220 | 2.95 | 40† | 2.97 | 40 | 2.95 | 70 |
| | | | | | 2.70 | 10 |
| 311 | 2.53 | 100 | 2.53 | 100 | 2.53 | 100 |
| 222 | 2.42 | 5 | 2.43 | 20 | 2.42 | 5 |
| 400 | 2.09 | 33 | 2.09 | 25 | 2.09 | 75 |
| | | | | | 2.04* | 10 |
| 331 | 1.91 | 10 | 1.92 | 8 | | |
| 420 | | | 1.87 | 6 | 1.85 | 2 |
| 422 | 1.72 | 20 | 1.71 | 25 | 1.71 | 20 |
| 511 / 333 | 1.62 | 50† | 1.62 | 40 | 1.61 | 70 |
| 440 | 1.48 | 80† | 1.48 | 50 | 1.48 | 80 |
| 531 | 1.42 | 10 | 1.42 | 13 | | |
| 620 | 1.34 | 10 | 1.32 | 13 | 1.33 | 10 |
| 533 | 1.28 | 20 | 1.28 | 20 | 1.28 | 20 |
| 444 | 1.22 | 10 | 1.21 | 17 | 1.21 | 7 |
| 711 / 551 | 1.18 | 10 | 1.17 | 13 | | |
| 642 | 1.12 | 20 | 1.12 | 20 | 1.13 | 5 |
| 731 / 553 | 1.10 | 25 | 1.09 | 25 | 1.09 | 25 |
| 800 | 1.05 | 17 | 1.05 | 8 | 1.05 | 10 |
| 820 / 644 | | | 1.02 | 6 | | |
| 822 / 660 | 0.986 | 20 | 0.983 | 8 | 0.985 | 2 |
| 751 / 555 | 0.966 | 25 | 0.966 | 17 | 0.970 | 20 |
| 840 | 0.938 | 20 | 0.938 | 13 | 0.938 | 5 |
| 842 | | | 0.917 | 10 | | |
| 664 | | | 0.892 | 5 | | |
| 931 | 0.877 | 17 | 0.877 | 13 | | |
| 844 / (10)00 860 | 0.854 | 25 | 0.854 | 20 | | |
| | | | 0.839 | 5 | | |
| (10)20 862 | | | 0.821 | 5 | | |
| 951 / 773 | 0.815 | 17 | 0.810 | 13 | | |

* Strongest Fe line.
† Broad.

cles can be measured more accurately than the radii of semicircles.

The lattice parameter of $Fe_3O_4$ was calculated from the x-ray data and was found to be 8.394 ± 0.002Å.


### Summary

It has been shown that the cathodic reduction technique can be used to obtain an accurate measure of the amounts of $Fe_3O_4$ and $\alpha$-$Fe_2O_3$ found in a two scale layer on Fe. Positive identification of the two layers has been made. There is some diffraction evidence for the existence of a very thin layer of $\gamma$-$Fe_2O_3$ between the two layers which is also reduced and measured as $\alpha$-$Fe_2O_3$.

In the course of the work a standard pattern for $Fe_3O_4$ was obtained.


Manuscript received May 29, 1957. This paper was prepared for delivery before the Buffalo Meeting, Oct. 6-10, 1957.

Any discussion of this paper will appear in a Discussion Section to be published in the December 1958 JOURNAL.

REFERENCES

1. H. G. Oswin and M. Cohen, *This Journal*, **104**, 9 (1957).
2. W. H. J. Vernon, F. Wormwell, and T. J. Nurse, *J. Chem. Soc.*, **1939**, 621.
3. E. Schulek and I. Floderer, *Z. anal. Chem.*, **117**, 176 (1939).
4. J. W. Swank and M. G. Mellon, *Ind. Eng. Chem.*, Anal. Ed., **30**, 7 (1938).
5. G. W. Brindley, "X-ray Identification and Crystal Structure of Clay Material," The Mineralogical Society, London (1951).
6. D. E. Davies and U. R. Evans, *J. Chem. Soc.*, **1956**, 4373.

# Temperature Characteristics of Barium Strontium Lithium Silicate Phosphors

**A. H. McKeag**

*Research Laboratories, General Electric Company, Ltd., Wembley, England*

ABSTRACT

The changes in spectral emission, efficiency, and temperature stability are discussed which result from changes in the following variable parameters in phosphor preparation: the barium:strontium ratio, lithium content, base:acid ratio, activator concentrations, and firing conditions. For practical application in jacketed high pressure mercury vapor lamps, compositions within a critical base:acid ratio of 3RO : 1.8 to 1.9 $SiO_2$ have produced the best results.

The temperature dependence of the luminescence of various phosphors has been studied by a number of workers (1,2). The wide variation in behavior between the same activator in different matrices and between different activators in the same matrix suggests that temperature dependence characteristics are determined by the nature of the matrix-activator combination. The effect of activator concentration has also been studied and Fonda has shown that in Willemite high Mn concentrations produce a lowering of the quenching temperature (2). Similar effects have also been observed when certain harmful impurities, such as Fe, are added to sulfides and silicates. Kroeger (1) has also noted that phosphors which are badly crystallized have a low quenching point.

Recently, attention has been directed to the improvement in both color rendering and efficiency of high pressure Hg vapor lamps by the application of improved phosphors to the outer glass envelopes of these lamps. As a result of this work (3-8), a number of new phosphors have been found which maintain their fluorescence at high temperatures. The present paper gives details of the preparation of improved barium strontium lithium silicate phosphors for use at high temperatures and shows that the method of preparation can have a marked effect on the temperature characteristics of the phosphor.

## Barium Strontium Lithium Silicates—Activated with Cerium and Manganese

This family of phosphors have been described previously (6,7). Trivalent Ce, produced by firing in reducing conditions, gives a characteristic blue emission by itself, and acts as a sensitizer for the secondary activator, Mn. The broad excitation spectrum and freedom from appreciable body color makes these "triple silicate" phosphors attractive for use in color-corrected high pressure Hg vapor (H.P.M.V.) lamps.

A marked improvement in the temperature characteristics of these phosphors, obtained by the methods described below, has led to a corresponding improvement in the color rendering properties of commercial H.P.M.V. lamps utilizing these phosphors.

### *Preparation Conditions, Barium to Strontium Ratio*

As Ba is replaced by Sr in these phosphors, the color of the fluorescence changes from orange-yellow to red with a given Mn content and this change is also associated with a decrease in the response to short u.v. radiation. The brightest phosphors have not been obtained with a pure barium lithium silicate composition, as might be expected from color considerations, but with phosphors containing an appreciable proportion of Sr corresponding to an

approximate molar ratio of 4BaO:1SrO. This effect may be associated with differences in ionic size between Ba and activator ions which would tend to make substitution of activator ions more difficult in phosphors of pure barium lithium silicate composition.

*Lithium Content*

The lithium oxide content is not critical and can be varied over a wide range without altering the color or intensity of the fluorescence markedly. The most useful range lies between one fifth and one half the combined molar proportions of the alkaline earth oxides, and within this range x-ray examination shows that the crystal structure is basically unchanged. At higher Li contents, a phase of different crystal structure can be formed (7) and the spectral emission becomes modified; these phosphors show poorer temperature characteristics as the lithium oxide is increased. Although Li may be regarded as a major constituent of the complex silicate lattice, it is interesting to note that Klasens (5) has observed an improvement in the temperature characteristics of magnesium arsenate phosphors, following the addition of Li.

*Silica Content*

Silica content appears to exercise a marked effect on both chemical stability and temperature response characteristics of these phosphors. Phosphors can be prepared in the range 3RO:1.7$SiO_2$ to 3RO:2.3$SiO_2$ (where RO represents the combined basic radicals), but the best results have been obtained within the much narrower range 3RO:1.8$SiO_2$ to 3RO:1.9$SiO_2$. These ranges, which are modified by the activator content, refer to phosphors containing 0.25 additional moles of the combined oxides of Ce and Mn.

With this proportion of activators the range of silica from 1.8 to 1.9 moles appears to cover a critical balance point in the chemical stability of these phosphors. At ambient temperatures, the brightest phosphors are obtained with silica contents ranging from 1.8 to 1.85 moles of silica (Fig. 1) and these phosphors are initially somewhat whiter in body color than those with higher silica ratios. If, however, a range of phosphors with varying silica contents are heated in air to about 400°C, a marked discoloration occurs in phosphors containing about 1.8 moles of silica or less, whereas much smaller changes take place with higher silica ratios. As might be expected phosphors with low silica contents are more susceptible to lamp processing conditions.

Changes in body color, which occur when phosphors with low silica content are heated, begin to develop markedly at temperatures slightly higher than the temperature break point and are thought to be associated with displacement of activator atoms from the phosphor lattice followed by surface oxidation. X-ray examination shows that, after prolonged heating at 400°C, small amounts of a second phase may be formed. This second phase, referred to later, is believed to correspond to a triple silicate which is deficient in Ce.

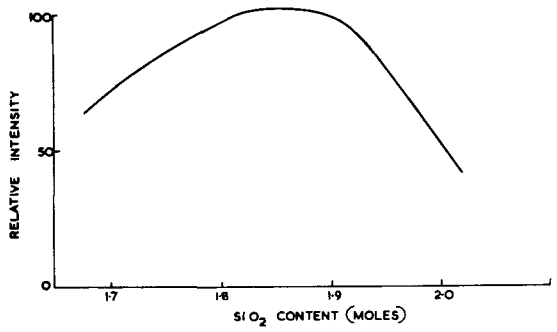


Fig. 1. Variation of brightness of triple silicate phosphor with silica content (at ambient temperature).

The temperature response curves of phosphors prepared with a range of silica contents also show a marked progression in properties as the silica content is increased (Fig. 2). At low temperatures (below 200°C) phosphors with lower silica ratios are brighter, but as the silica content is increased the maximum is reached at progressively higher temperatures. The temperature break point for phosphors with lower silica content corresponds roughly to the temperature at which darkening sets in and suggests that the silica content (base to acid ratio) may determine the readiness with which the activators are displaced from the lattice, evidenced by the discoloration produced by heating in air.

**Effect of Activator Concentration**

In common with calcium orthophosphate phosphors activated with Ce and Mn (9), comparatively large quantities of Ce of the order of 10% by weight of the matrix, give the brightest fluorescence at ambient temperatures. Although the temperature characteristics of these phosphors are not critically dependent on the Ce content, increase in Ce lowers the temperature at which optimum brightness occurs while the rate of depreciation beyond this point is reduced. Results are similar to those observed by Kroeger (1) for lanthanum silicate activated by Ce.

Manganese content influences the color and intensity of fluorescence but, even in amounts which

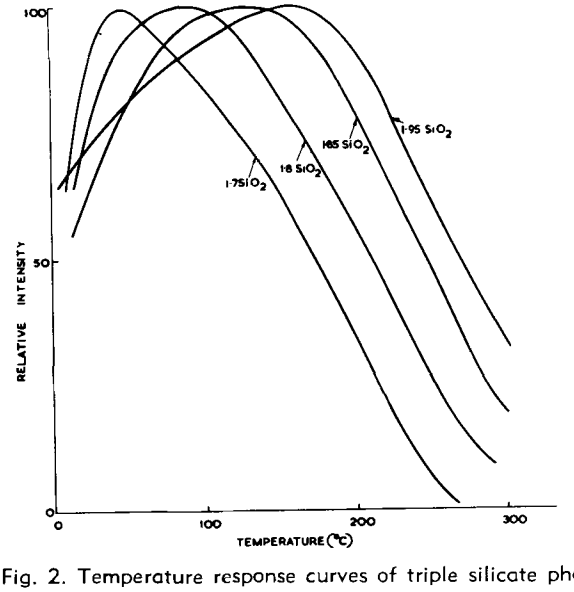


Fig. 2. Temperature response curves of triple silicate phosphor with varying silica content.

reduce the initial brightness, does not alter markedly the shape of the temperature dependence curves, provided optimum silica ratios are maintained.

Cerium also appears to assist in the formation of the crystalline phase associated with fluorescence (7). Nonfluorescent materials, prepared without Ce, are usually of a distinct crystal structure.

*Effect of Firing Treatment*

Triple silicate phosphors are fired in a reducing atmosphere to retain Ce in the cerous state necessary for activation. The optimum firing temperature is fairly critical and the best results have been obtained at temperatures close to the sintering temperature which may vary between 800°-900°C for compositions described earlier. As the firing time is increased a marked improvement in temperature dependence occurs. This effect is illustrated in Fig. 3, which compares phosphors with the same initial composition fired for 3 hr and 100 hr, respectively. X-ray examination shows that the only crystal phase in these two samples is that normally associated with the barium strontium lithium silicate phosphors. The crystal size of the material fired for the longer period ranged from 5 to 30$\mu$, while the 3-hr firing period gave a crystal size range of approximately 1-10$\mu$. These results confirm those of Kroeger (1), that the temperature characteristics depend on the perfection of the crystal lattice.

## Effect of Temperature on Spectral Emission Characteristics

The triple silicate phosphor shows a marked change in color of fluorescence as its temperature is raised. This is due to a shift in the position of the Mn emission band toward shorter wave lengths, which occurs most markedly below about 150°C (*see* Fig. 3). This shift also accounts, at least partly, for the observed increase in brightness of fluorescence between these temperatures (Fig. 2). At higher temperatures, modification of the color is less marked and is due mainly to a relative decrease in the blue emission band due to Ce.

At liquid air temperatures there may be some tendency to a head in the red emission band which occurs at 6,400Å for a phosphor containing equimolecular proportions of Ba and Sr.

## Performance in Lamps

Color corrected H.P.M.V. lamps were first introduced in Great Britain in 1937 using zinc cadmium sulfide phosphors. These lamps gave a red ratio of about 5% where red ratio is defined as the percentage of the total lumens from the lamp passing through an orange Wratten No. 25 filter. In 1953, triple silicate phosphors were introduced in place of the sulfide phosphors in 125-w quartz lamps. Red ratios of about 6-7% were obtained with these early phosphors which had relatively poor temperature response characteristics. Improvements in temperature characteristics of these phosphors, of the type described above, have led to an improvement in red output of some 20%, so that red ratios of about 8% are now obtained. The improvement in color rendering over sulfide-coated lamps is not fully reflected by the increase in red ratio measurements. The blue emission from the silicate phosphor together with its relative freedom from body color gives a marked improvement in the blue and blue-green regions of the spectrum. The luminous efficiency and lumen maintenance characteristics of these lamps follow closely that of the lamp without fluorescent coating and lamps of 125 w rating give 100 hr efficiencies of about 40 lpw.

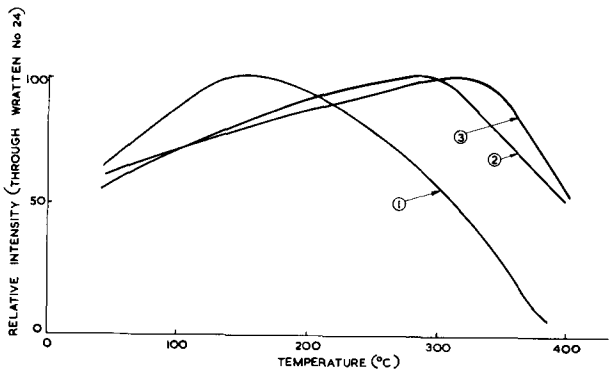


Fig. 3. Effect of firing time on temperature response of triple silicate phosphor. Curve 1, triple silicate (3-hr firing); curve 2, triple silicate (100-hr firing); curve 3, 3 MgO·1 $MgF_2 \cdot GeO_2$(Mn).

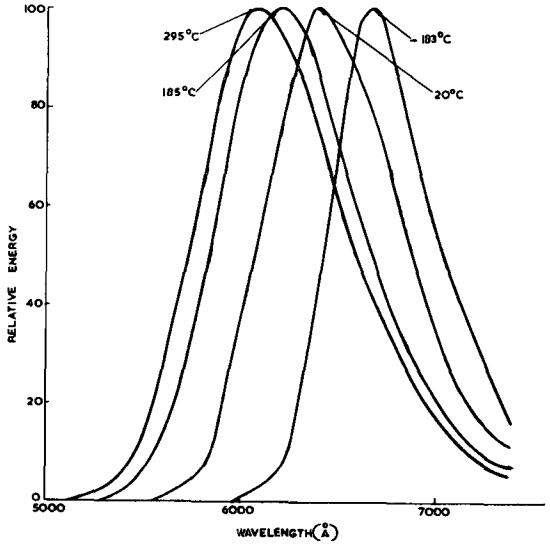


Fig. 4. Change of spectral energy distribution of triple silicate phosphor (Mn band) with temperature.

These results are obtained with triple silicate phosphors having equimolecular proportions of Ba and Sr. If phosphors with higher Ba to Sr ratios are used, additional yellow light is added and efficiencies some 10% higher can be obtained. Although the color rendering properties are slightly degraded, the red ratio figures are not materially reduced. This may be due to the increased sensitivity of these phosphors to short u.v. radiation, which results in a higher proportion of fluorescence emission in lamps coated with these phosphors.

## Discussion

The addition of comparatively minor constituents to improve the temperature characteristics of several phosphor systems is well known. Froelich and Margolis (9), for example, have shown that certain

alkali metals can improve the temperature characteristics of calcium phosphates activated with Ce and Mn, and have suggested that these additives may produce a lattice with fewer vacancies or defects. Klasens (5) has observed similar improvements with Mn-activated magnesium arsenate phosphors containing Li. The effect of silica content, in the triple silicates, represents a further example of the importance of small changes in phosphor composition on temperature characteristics.

As described above, increase in silica content improves temperature dependence characteristics and reduces the tendency to discolor during low temperature air bake. The onset of marked discoloration in phosphors with low silica content appears to occur at temperatures somewhat higher than those at which peak brightness of fluorescence is attained. This discoloration is believed to correspond to a displacement of activators from lattice positions at elevated temperatures which is followed by a superficial oxidation. Such conditions may be expected to obtain in a lattice which is constrained and the function of additional silica may be to relieve such constraints. It may, for example, provide more readily for the incorporation of activators into the lattice or indirectly by creating lattice vacancies by the incorporation of additional Li ions into the lattice. In either case, conditions may be created in the lattice equivalent to a lowering of activator concentration, and which might, therefore, be expected to give improved temperature characteristics. The results thus lend some support to the views of Klement (10) that in a given phosphor system temperature quenching is dependent on the degree of isomorphism of the activator and the matrix lattice.

Manuscript received June 3, 1957. This paper was prepared for delivery before the Washington Meeting, May 12-16, 1957.

Any discussion of this paper will appear in a Discussion Section to be published in the December 1958 JOURNAL.

REFERENCES

1. F. A. Kroeger, "Some Aspects of the Luminescence of Solids," Chap. VI, Elsevier Publishing Co., Amsterdam (1948).
2. G. R. Fonda, *J. Phys. Chem.*, **43**, 561 (1939).
3. L. Thorington, *J. Opt. Soc. Amer.*, **40**, 579 (1950).
4. M. Travnicek, F. A. Kroeger, Th. P. J. Botden, and P. Zalm, *Physica*, **18**, 33 (1952).
5. H. A. Klasens, *Philips Research Repts.*, **9**, 377 (1954).
6. H. G. Jenkins and A. H. McKeag, *Lux*, **21**, 87 (1953).
7. A. H. McKeag and E. G. Steward, *Brit. J. Appl. Phys.*, Suppl. No. 4, p. S26 (1954).
8. M. J. B. Thomas, K. H. Butler, and J. M. Harris, Illum. Eng. Soc. Conf., 1956, Preprint No. 30.
9. H. C. Froelich and J. M. Margolis, *This Journal*, **98**, 400 (1951).
10. F. D. Klement, *Izvest. Akad. Nauk. S.S.S.R. Ser. Fiziol*, **15**, 651 (1951).

# Zone Purification of Silicon

**E. A. Taft and F. H. Horn**

*Research Laboratory, General Electric Company, Schenectady, New York*

ABSTRACT

A procedure is described for the zone purification of high purity silicon using thin-walled quartz boats. Data are given that show that improved lifetime and more uniform electrical resistivity result from the zone purification of commercially available silicon.

The zone purification (1) of high purity Si in a boat presents problems not encountered in processing the less chemically reactive Ge for which zone refining is almost a routine purification procedure. It is not necessary to use a boat as in floating zone purification (2); however, in such a case one is limited to one molten zone per pass. It is the purpose of this report to (*a*) describe a procedure that has been used successfully to zone refine high purity Si in quartz, (*b*) present data to indicate what is accomplished thereby, and (*c*) suggest some of the present limitations to the process.

In order to work out a process one is faced with a certain number of variables that after some exploration must be arbitrarily fixed. In the case of zone refining these are (*a*) materials for the boat and related apparatus, (*b*) working atmosphere, (*c*) source of heat, and (*d*) the form of starting material.

## Experimental

Tests using selected refractory sulfides, nitrides, carbides, and oxides indicated that because of direct attack by molten Si and/or because of the impurities in the refractories obtainable, fused clear quartz was the best available material for the boat. There are certain chemical limitations to the use of quartz that are discussed later. The first serious difficulty involved in the use of quartz is mechanical. Molten Si wets quartz. If molten Si is allowed to freeze in boats of quartz of commercially available thickness, cracking of the quartz and Si takes place on cooling the solid Si since the coefficient of thermal expansion of quartz is considerably smaller than that for Si. Nevertheless quartz may be employed for handling Si if use is made of the plastic properties of quartz and Si. At and above the freezing point of Si, quartz is plastic; below the freezing point of Si to about 1000°C (3), in which temperature range

quartz is negligibly plastic, solid Si itself is plastic. The solution to the problem of using quartz to handle molten and solid Si is to use as thin quartz as possible, in practice from 5 to 15 mils thickness[1] depending on the size of equipment, and to maintain the temperature of the solid Si in the plastic range throughout a process. This latter requirement may be met by a proper distribution of heat.

No very marked differences in the final product have been observed whether the Si during zone refining is maintained in a vacuum or in atmospheres of H, He, or A. The use of A requires less power than H or He for heating. A lower power input may be reflected in a somewhat lower temperature of the molten silicon-quartz interface. This is important as is discussed below. The use of A is preferred for this reason.

Induction heating has been used throughout this work. The source of power has been a 15-kw 450-kc General Electric Induction heater. The power output was filtered to remove low frequency components that cause agitation of the liquid zones. It is not essential to do this in order to zone melt the Si; however, crystal grains grow to a significantly larger size if the agitation is removed by the use of a filter.

High purity Si is obtainable in either small crystalline aggregate or "densified" form.[2] With direct induction coupling the fusion of aggregates or densified material in a boat is very difficult to accomplish. It is easier to have a single solid rod of Si to place in the boat. Such rods were prepared by melting together the crystalline aggregates.

Premelting is carried out in a thin wall quartz tube in the apparatus shown schematically in Fig. 1. The molten Si is blanketed by argon gas. As the Si is added, the heating coils are moved upward keeping about 1 in. of molten Si on top of the solid. The quartz tube adheres to the Si and must be removed (HF solution) before proceeding with the zone refining. Typical premelt rods are shown in Fig. 2, both before and after removing the quartz tube.

[1] Available through General Electric Company, Cleveland Quartz Works, Cleveland, Ohio.

[2] E. I. du Pont de Nemours Company, Pigments Division, was the major supplier of the high purity Si used in these experiments.

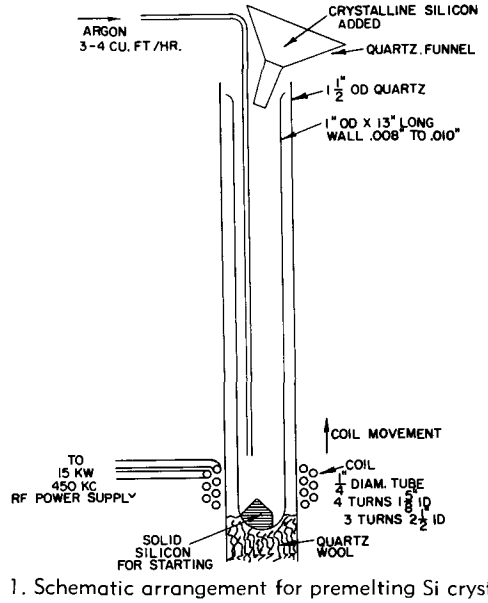


Fig. 1. Schematic arrangement for premelting Si crystals

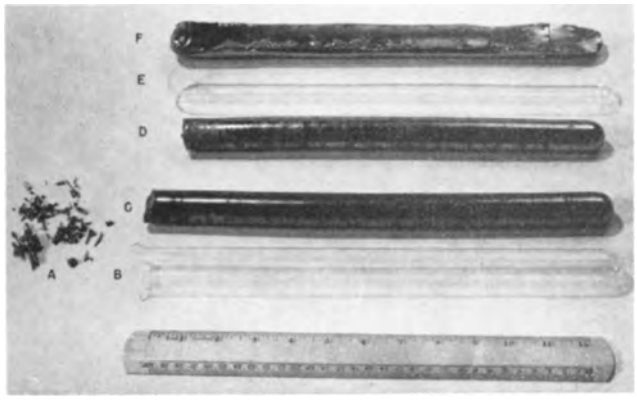


Fig. 2. Photograph of (A) crystalline aggregate of Si; (B) thin quartz premelt tube; (C) premelt rod of Si with quartz tube adhering to surface; (D) premelt rod of Si with quartz removed; (E) thin quartz zone melt boat; (F) zone melted billet of Si.

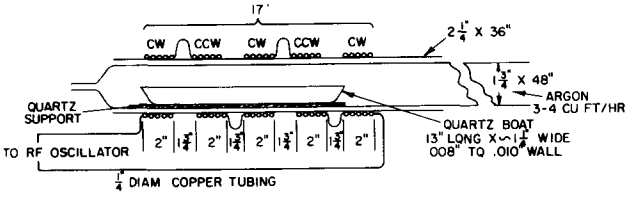


Fig. 3. Schematic arrangement for zone refining Si

The arrangement for zone refining Si is shown schematically in Fig. 3. Approximately 400 g of Si is handled at a time and five zones are carried through the solid in one pass. Movement of the zones at the rate of about 5½ in./hr has been found satisfactory. The appearance of a zone refined billet is shown in the photograph of Fig. 2. Before use, the quartz adhering to the Si must again be removed by solution in HF.

## Discussion

In order to assess what is accomplished by the zone purification, single crystals were grown from quartz crucibles using portions of the zone refined ingot. Lifetime and resistivity measurements were made along the length of the single crystal. Some of these data are given in Tables I and II. The con-

**Table I. Lifetime and resistivity of crystals grown from zone refined Si ingot**

| Crystal No. | Description | Type | Resistivity ohm cm* $\rho_{10}$ | Resistivity ohm cm* $\rho_{90}$ | Lifetime μsec $\tau_{10}$ | Lifetime μsec $\tau_{50}$ | Lifetime μsec $\tau_{90}$ |
|---|---|---|---|---|---|---|---|
| 91 | Premelt only | *P* | 80 | 56 | 90 | 50 | — |
| 82 | Zone melt—front | *P* | 90 | 40 | 200 | 400 | 150 |
| 83 | 2nd—10% | *P* | 90 | 40 | >1000 | 750 | 400 |
| 84 | 3rd—10% | *P* | 90 | 40 | 800 | 150 | — |
| 85 | 4th—10% | *P* | 90 | 40 | 200 | 100 | 60 |
| 86 | Zone melt—50% | *P* | 90 | 40 | 140 | 100 | 60 |

* Subscript denotes percentage of grown crystal.

**Table II. Lifetime and resistivity of crystals grown from separate zone refined ingots from same lot of Si**

| Crystal No. | Description | Type | Resistivity ohm cm* $\rho_{10}$ | Resistivity ohm cm* $\rho_{90}$ | Lifetime μsec $\tau_{10}$ | Lifetime μsec $\tau_{90}$ |
|---|---|---|---|---|---|---|
| 127 | Densified Si | *n* | 20 | 2 | 100 | 100 |
| 193 | Zone melt 133 | *P* | 76 | 34 | 300 | 200 |
| 195 | Zone melt 134 | *P* | 90 | 50 | 300 | 200 |
| 198 | Zone melt 135 | *P* | — | — | 300 | 150 |

* Subscript denotes percentage of crystal grown.

clusions reached based on these data are valid for all of the work done on zone refining.

All data in Table I are derived by using the same lot of Si. Crystals grown directly from the crystal aggregates of this lot contain barriers which make resistivity measurements unreliable as an index of purity. The lifetime as determined for regions of the crystals not including a barrier was less than 20 $\mu$sec. It is seen that the premelting operation alone improves the quality of the Si. A more significant improvement is obtained after zone purification. In particular, the concentration of impurities that shorten the lifetime of the crystal appears to be reduced. The resistivity is not appreciably altered. The resistivity profiles of the crystals are consistent with an assumption of the presence in the crystals of an acceptor impurity with a segregation coefficient near unity such as is the case for boron. If no B is introduced during the processing of the Si, the results suggest that the donors originally present are either volatile or are readily segregated during growth of the evaluation crystal. This situation is more apparent from the results of Table II.

The data in Table II are all for the same lot of Si but the evaluations were made on crystals grown from the Si taken from the same region of different zone melt ingots. These data are compared with those from an evaluation crystal grown from densified Si (without zone refining) from the same lot. The dominant impurity in the densified material was a donor, the dominant impurity after premelting and zone refining was an acceptor. Processing apparently removes the donor impurities. Lifetime is again seen to improve. The consistency of the results from separate operations suggests that the final resistivity level results from an impurity whose segregation coefficient is near unity.

These results of Si quality are indicative of what is accomplished by zone refining, namely *(a)* increased lifetime resulting from a substantial reduction in the concentration of lifetime suppressors in Si, and *(b)* reduction of the concentration of donors with resultant increased uniformity of material from an ingot, or a lot, and even among lots.

It was considered desirable to learn, particularly with respect to boron, the extent to which the use of commercially available quartz may control the results of zone purifying Si. In order to assess this possible limitation it is necessary to know the rate of attack of fused quartz by molten Si. This was done by determining the loss in weight from cubes of fused quartz left in contact with molten Si at several temperatures. The area of contact between the quartz and Si is clearly indicated by the reaction. The weight loss per cm$^2$ per hour is plotted as a function of the Si temperatures in Fig. 4. Using the value of 5 mg/cm$^2$/hr for the rate of reaction between quartz and molten Si it is estimated that about $10^{14}$ boron at./cc of Si may be dissolved during zone melting for each part per million of B in the quartz. The B concentration in the quartz used is of the order of tenths of parts per million. In practice, material with a resistivity in excess of 300 ohm cm, or less than 5 x $10^{13}$ carriers/cc has been realized. The reaction between the quartz and molten Si can be kept at a minimum by keeping the liquid Si at a temperature as near the melting temperature as is consistent with conducting the process.

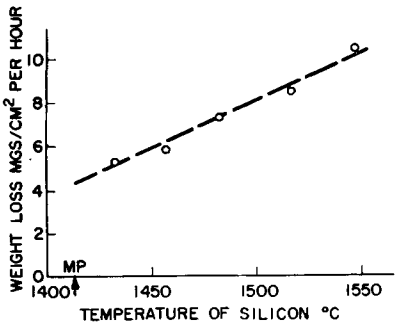


Fig. 4. Removal of quartz by molten Si

In addition to the problem of possible B contamination by the quartz, Si melted in quartz apparatus also contains some oxygen (4). In this respect the Si zone refined in quartz differs from the material obtainable by a procedure such as the floating zone. If Si relatively free from oxygen is required, the Si zone refined in quartz represents a convenient form of starting material for applying the floating zone technique.

## Summary

1. A procedure for zone refining Si in thin-walled quartz is described.

2. Zone refining Si has been found to improve lifetime.

3. Silicon of more consistent resistivity is realized within an ingot or within a lot after zone purification. The remaining impurity behaves like B.

4. The use of commercially available quartz does not necessarily constitute a limitation on the purity of the zone refined Si if the initial concentration of the poorly segregating impurity in the Si (presumed B) is larger than approximately 5 x $10^{13}$ carriers/cm$^3$ (300 ohm cm). It should be borne in mind, however, that Si processed in quartz is not free of oxygen.

Manuscript received Aug. 19, 1957.

Any discussion of this paper will appear in a Discussion Section to be published in the December 1958 JOURNAL.

REFERENCES

1. W. G. Pfann, *Trans. Am. Inst. Mining Met. Engrs.*, **194**, 747 (1952).
2. P. H. Keck, W. Van Horn, J. Soled, and A. MacDonald, *Rev. Sci. Instr.*, **25**, 331 (1954).
3. C. J. Gallagher, *Phys. Rev.*, **88**, 721 (1952).
4. W. Kaiser, P. H. Keck, and C. F. Lange, *ibid.*, **101**, 1264 (1956).

# A Fused Bath for Electrodeposition of Molten Cadmium-Indium Alloy

**George L. Schnable and John G. Javes**

*Philco Corporation, Lansdale Tube Company Division, Lansdale, Pennsylvania*

ABSTRACT

A fused salt bath for electrodeposition of molten cadmium-indium alloy is described, from which ellipsoidal beads of molten alloy are plated onto wires used as leads to emitter and collector electrodes of transistors. Electrodeposition of molten metals can be very rapid, and the deposits are smooth, dense, and nonporous. The fused salt bath, containing 6% cadmium chloride, 56% indium monochloride, and 38% zinc chloride, by weight, is operated at about 260°C. Tungsten anodes are used. With 6 v d.c. applied, a 2 mg ellipsoidal bead of cadmium-indium alloy of approximately eutectic composition can be deposited on a 0.5 mm wire that is immersed a depth of 1.5 mm into the plating bath in about 4 sec. Under these conditions, current density is of the order of 40 amp/cm$^2$. The effect of bath composition and of plating conditions on alloy composition and plating rate is discussed.

In the fabrication of transistors, for example, alloyed-junction and surface-barrier types, electrical connections must be made to the emitter and collector electrodes. If the transistor electrodes are indium metal, In cannot be used as a solder since it is not desirable to melt the electrodes during soldering. Cadmium-indium eutectic alloy (25% Cd, 75% In, by weight) melts at 123°C. The molten alloy readily wets In in the presence of a suitable flux and can be used to solder whisker wires, ribbons, stem leads, or other electrical connections to the emitter and collector electrodes without melting the In electrodes (mp 157°C). The soldering operation is performed in a few seconds at 140°C in the presence of a mild flux. The alloy is harder than In metal, with the result that joints soldered with it are considerably stronger than joints soldered with In alone. Transistors having In electrodes soldered with Cd-In alloy, in contrast to those soldered with Sn-In alloy, can be clean-up etched in acids such as aqueous solutions containing $HNO_3$ and HF. $Cd^{++}$ and $In^{+++}$ ions do not deposit chemically on the Ge during the clean-up etching process. Since both Cd and In are more negative than Ge in the electromotive series (1-3) (less noble), chemical deposition would not be expected.

### *Electrodeposition of Molten Cd-In Alloys*

Several milligrams of Cd-In alloy are required on the ends of emitter and collector leads of transistor stems. (The stem consists of three lead wires hermetically sealed in an equilateral triangular configuration in a glass base.) Because of the sensitivity of transistors to contaminants, the Cd-In solder must be free of entrapped fluxes, plating solutions, or other impurities. A rapid process was required for production line use.

Experiments indicated that hot dip "tinning" of stems in molten Cd-In alloy produced coatings too thin to be satisfactory. Electrodeposition of solder was considered the most suitable approach. With electrodeposition any or all of a group of lead wires simultaneously immersed in the plating solution can be plated and different amounts can readily be plated on emitter and collector leads.

Electrodeposition of Cd-In alloys from aqueous solutions resulted in rough, porous deposits. Plating rates were too low for production use.

Electrodeposition of molten metals results in smooth, dense, nonporous deposits which are free of plating bath constituents (occlusions). The high surface tension of the molten deposits in plating baths having a fluxing action tends to affect the surface area and location of the molten metal or alloy deposit. For example, on wires held vertically during plating, the molten deposit flows downward, forming a smooth ellipsoidal bead of molten metal or alloy at the end of the wire.

Since molten deposits in an effective flux are characterized only by composition and temperature, plating quality is unaffected by many of the variables which must be carefully controlled in ordinary aqueous plating processes. For example, the limiting current density which can be employed is not determined by plating quality as with aqueous plating baths, where dendritic growths are formed at higher current densities.

A number of methods have been developed at this laboratory for electrodepositing molten metals and alloys from plating baths operated at temperatures above the melting point of the metal or alloy.

Baths developed for electrodeposition of molten Cd-In alloys are of two general types: *(a)* Cd and In salts dissolved in high-boiling polar organic solvents such as glycerol; *(b)* fused salt solutions containing Cd and In salts.

In general, the plating baths developed are effective fluxes for base metals such as Ni as well as for

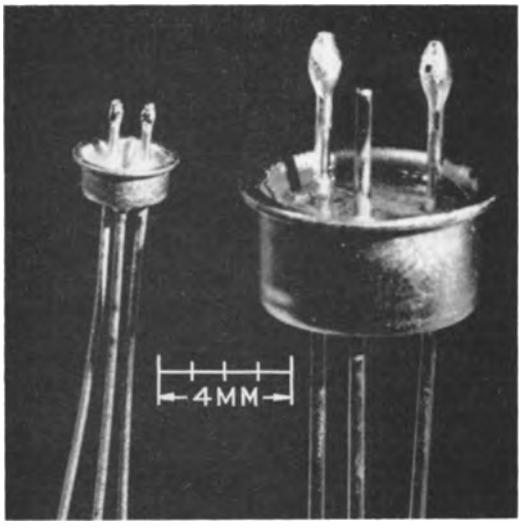


Fig. 1. Typical transistor stems having leads plated with Cd-In alloy.

the deposited metals and alloys. Thus good wetting of the base metals is obtained.

*Typical Operating Conditions*

The fused salt bath is particularly suitable for plating wires 5-40 mils in diameter, where a few milligrams of Cd-In alloy are desired on each wire or lead. The preferred bath, containing 6% $CdCl_2$, 56% InCl, and 38% $ZnCl_2$ by weight, plates molten Cd-In alloy several hundred times as fast as aqueous baths. Under typical operating conditions the plating bath is maintained at 255°±5°C; a plating potential of 6 v d.c. is applied between the cathode and a tungsten anode. For 60 mil immersion of stem leads 20 mils in diameter (1.5 mm immersion of leads 0.5 mm in diameter), plating times of roughly 2 and 4 sec are suitable for electrodeposition of 1 and 2 mg of Cd-In alloy on emitter and collector leads, respectively. Plating current averages about 2 amp/lead. Under these conditions, current density is of the order of 40 amp/$cm^2$.

Typical plated whiskers and stems are shown in Fig. 1.

No Zn has been detected in Cd-In alloys plated from $CdCl_2$-InCl-$ZnCl_2$ fused salt baths.

## Experimental Results

*Cadmium-Indium Alloys*

The Cd-In system has been investigated by Betteridge (4), Carapella and Peretti (5), Valentiner (6), and Wilson and Wick (7). Cadmium (mp 321°C) and indium (mp 157°C) form a eutectic alloy containing 25% Cd and 75% In by weight, melting at 123°C. Cadmium-indium alloys in the range from nearly 100% Cd to about 18% Cd-82% In by weight have structures showing the eutectic, and thus have a solidus temperature of 123°C; liquidus temperatures vary from 321° to 123°C. Alloys containing less than about 18% Cd by weight have solidus temperatures from 123° up to 157°C as In content increases. Alloys in the approximate range from 50% Cd-50% In to 20% Cd-80% In have been found to flow at temperatures below 130°C. Although some of these alloys have a liquidus temperature above 130°C, all have a solidus temperature of 123°C and all would consist of at least 67% liquid phase at 130°C. Therefore, any alloy in this composition range flows below 130°C and is considered a satisfactory solder for In metal.

The temperature at which deposited alloys flow was determined by flattening ellipsoidal beads of alloy plated on the ends of wires and immersing them in a heated flux bath which was stirred vigorously. Alloys were considered to flow if the flattened alloy returned to an ellipsoidal bead of molten alloy within 3 sec after immersion in a flux bath at the particular temperature chosen. A flux consisting of 2% by volume concentrated HCl (37%) in glycerol is suitable.

Breaking load experiments have indicated that Cd-In eutectic alloy at any temperature from 25° to 110°C has a greater tensile strength than In metal at the same temperature; indeed the alloy has a greater tensile strength at 110°C than In metal at room temperature. Cadmium-indium alloys might be expected to have a greater tensile strength than In metal since binary alloys of In with Pb, Ag, Cd, Bi, and Sn have been reported to have tensile strengths greater than that of In at room temperature (8-10).

Hundred-hour creep strength measurements made at 100°C have shown that Cd-In eutectic alloy has a somewhat higher creep strength than In metal at 100°C.

*Fused Salt Bath for Electrodeposition of Molten Cadmium-Indium Alloys*

The requirements of a fused salt bath for electrodeposition of molten Cd-In alloys on Ni wires are rapid plating rate, practical operating temperature, freedom from objectionable crust formations, reasonable bath life, minimum evolution of fumes, and ability to act as a satisfactory flux for Ni as well as for molten Cd-In alloy.

The most obvious choice as a source of In ions for a fused salt bath is $InCl_3$, which melts at 586°C but sublimes below 400°C. The only alkali or alkaline earth chloride system which could serve as a solvent for $InCl_3$ was the LiCl-KCl eutectic, mp 352°C. A solution of $InCl_3$ in molten LiCl-KCl eutectic fumed too much to be practical.

Indium trichloride was found to dissolve in molten $ZnCl_2$. However, electrolysis of a molten solution of $InCl_3$ in $ZnCl_2$ at 320°C resulted in cathodic reduction of $In^{+++}$ to $In^{++}$ and/or $In^{+}$ (indicated by formation of In metal by disproportionation when an electrolyzed bath was treated with water) but no In metal (or Zn) was deposited on the cathode. This is in agreement with the work of Coyle (12), who, upon electrolysis of a fused solution of $InCl_3$ in $ZnCl_2$, obtained no deposit of In metal at the cathode.

Molten InCl, mp 225°C, was found to deposit molten In metal upon electrolysis. However, InCl is a relatively poor solvent for anhydrous $CdCl_2$, tends to form crusts (oxides), and was a relatively poor flux for Ni.

Molten InCl (mp 225°C) and molten $ZnCl_2$ (mp 275°C) are miscible in all proportions. Cooling curves run on fused salt solutions of InCl and $ZnCl_2$,

containing 50, 57, and 60% by weight InCl, indicated that the InCl-$ZnCl_2$ system forms a eutectic containing about 55-60% InCl by weight, melting at roughly 145°C.

Cadmium chloride appears to be more soluble in molten solutions containing both InCl and $ZnCl_2$ than in either of these alone. A solution containing 60% InCl and 40% $ZnCl_2$ dissolves roughly 10% by weight of $CdCl_2$ at 200°C, and dissolves more than 15% $CdCl_2$ at 260°C. [Molten $ZnCl_2$ dissolves only 15% by weight $CdCl_2$ at 305°C (11).]

The presence of $ZnCl_2$ in the fused salt plating bath minimizes crust formations and makes the bath a more effective flux for base metals such as Ni as well as for the molten Cd-In alloy.

A $CdCl_2$-InCl-$ZnCl_2$ bath containing 6% $CdCl_2$, 56% InCl, and 38% $ZnCl_2$, by weight, may be operated at temperatures from 200° to about 320°C. At temperatures above 300°C fuming may be objectionable.

Electrolysis of molten $CdCl_2$-InCl-$ZnCl_2$ solutions at 250°C results in electrodeposition of molten Cd-In alloys at the cathode; no Zn has been detected in spectrographic analyses of the electrodeposited alloys. Thus, in the solutions investigated, $Zn^{++}$ is sufficiently negative in the electromotive series compared to $Cd^{++}$ and $In^{+}$ (or $In^{++}$ and $In^{+++}$) that $ZnCl_2$ is capable of serving as an inert solvent for $CdCl_2$ and InCl without any reduction of $Zn^{++}$ ions to Zn metal occurring during electrolysis. This might be expected from the data of Hamer, Malmberg, and Rubin (13), who calculated the theoretical decomposition voltages of fused metal chlorides at various temperatures.

### *Preparation of Plating Baths*

The InCl used in the plating solution is prepared by reacting anhydrous $InCl_3$ with an excess of In metal at 300°C in an inert atmosphere to form molten InCl (mp 225°C). Indium monochloride prepared by this method has a monovalent In content, as determined by the disproportionation method, averaging 96-98% of theoretical. Minimum assay for acceptable InCl is 95%.

Some InCl has also been prepared by reaction of anhydrous HCl gas with excess molten In metal at about 300°C.

It is necessary for fused salt baths which are operated at high current densities to be essentially anhydrous. Otherwise excessive bubbling occurs at the cathode, caused by evolution of water vapor as a result of local heating at the cathode during electrolysis and/or by evolution of hydrogen gas at the cathode. A considerable amount of water was found to be present in $CdCl_2$-InCl-$ZnCl_2$ baths prepared by heating the constituent salts to 250°C. The principal source of the water is the $ZnCl_2$; reagent-grade zinc chloride has an assay of about 95% $ZnCl_2$.

While water can be removed from fused salt baths by heating to about 450°C, this procedure results in the formation of some insoluble material since in the presence of water the metal chlorides are to some extent converted to oxides and/or oxychlorides with evolution of HCl. It was found that completely clear, anhydrous $CdCl_2$-InCl-$ZnCl_2$ fused salt solutions could be prepared by bubbling anhydrous HCl gas through the molten bath at about 360°C. Any excess HCl in the treated melt is removed by bubbling dry nitrogen through the fused salt solution.

The InCl is treated with anhydrous HCl during preparation. Cadmium chloride and zinc chloride in the proper proportions are heated to 360°C and treated with anhydrous HCl to remove water, at which time the correct amount of InCl is added, and the $CdCl_2$-InCl-$ZnCl_2$ solution at 360°C is treated with anhydrous HCl for a short time.

The fused salt bath, analyzed for monovalent In content by disproportionation, should assay not less than 93% of the theoretical amount of InCl.

### *Plating Apparatus*

Stirring of fused salt baths during rapid electrodeposition of Cd-In alloy is essential in order to insure reproducible plating of the correct amount of alloy of suitable composition. Stirring minimizes local depletion of ions at the electrodes and minimizes local heating at the cathode during electrolysis. It also enables immersed wires, which are to be plated, to attain bath temperature quickly. This is especially important when immersion depth is only slightly greater than the diameter of the wire to be plated.

A magnetic stirring apparatus was used during all plating experiments described below. The magnetic stirring bar was sealed in a Pyrex tube. Average velocity of plating bath past cathodes and anodes was estimated to be of the order of 10 cm/sec. Baths were contained in Pyrex vessels.

Inert anodes are used in the fused salt bath for electrodepositing molten Cd-In alloy. Carbon anodes (spectroscopic graphite) may be used at low currents but disintegrate rather rapidly at high currents, and, therefore, are not recommended. Rhodium appears to be a satisfactory material for anodes. Tungsten has been entirely satisfactory as an anode material, and was used in all of the experiments described below.

The anode should be large enough to minimize anodic polarization. Using a spiral tungsten wire (0.1 cm diameter) with an effective length of about 30 cm as an anode, no appreciable polarization was evident at currents up to 4 amp.

The anode should be located symmetrically with respect to each of the stem leads to be plated so that, with equal potentials applied between the anode and each lead to be plated, equal currents will flow through each stem lead. Under these conditions the plating rate will be the same for each stem lead. Anodes were located roughly 1 cm from the wires to be electroplated.

If different amounts of Cd-In alloy are desired on emitter and collector leads, this should be accomplished by employing different plating times rather than by applying different potentials to emitter and collector leads. This is done in order to obtain alloy of the same composition on both leads.

An inert atmosphere such as dry nitrogen gas is passed over the surface of the plating bath to minimize oxide formation and air oxidation of monovalent indium.

Several plating baths, protected by a nitrogen atmosphere, have been maintained at 250°C for 1 week without appreciable change in the alloy composition as determined by the flow temperature of alloy plated from the bath.

*Relationship between Bath and Plated Alloy Composition*

Successive increments of $CdCl_2$ were added to a fused salt solution consisting of 60% InCl and 40% $ZnCl_2$ by weight. Bath composition versus plated alloy composition, as determined by EDTA titrations, is shown in Table I for a bath operated at 255°C. Six volts d.c. were applied. Plating currents were about the same in each case. The approximate amounts of Cd-In alloy plated in 10 sec on a 20-mil wire immersed 60 mils into the bath are given in the table. All percentages are by weight.

The cathode area of immersed stem leads increases rapidly as ellipsoidal beads of molten Cd-In alloy are electrodeposited on the immersed stem leads. Under typical operating conditions (60 mil immersion of a 20 mil lead in the preferred bath at 255°C, 6 v d.c. applied) the surface area of the molten Cd-In alloy at the end of a 3-sec plating period is 2 to 3 times as great as the original surface area of the immersed lead. As the area of the molten Cd-In alloy increased during plating, the current drawn (at constant applied voltage) also increased. For this reason accurate measurements of current density were not possible. Current density under the typical operating conditions described above is of the order of 40 amp/cm$^2$.

In repeat tests, baths operated under the same conditions as those described above (255°C, 6 v, tungsten anode) showed good reproducibility of deposited alloy composition.

Decrease in deposition rate (amount of alloy deposit obtained in a given time) with increase in cadmium chloride content in the bath, as shown in Table I, is ascribed in part to the fact that the reduction reaction at the cathode involves an increasing proportion of $Cd^{++}$ ions, which have an equivalent weight only half as great as that of $In^+$ ions. As a result, even if the cathode current efficiency does not change, the weight of metal deposited would drop somewhat as the alloy deposit becomes richer in Cd.

*Effects of Plating Voltage on Alloy Composition*

In experiments where a bath containing 6% $CdCl_2$, 56% InCl, and 38% $ZnCl_2$, operated at a temperature of 255°C, was electrolyzed at various potentials from 1.5 to 12 v, alloys flowing below 130° were obtained in all cases. Analysis showed that alloys plated at 1.5 v contained 24% Cd, 76% In; alloys plated at 6 v contained 27% Cd, 73% In.

Potentials of 10 v or more cause a considerable amount of fuming due to local heating at the cathode.

**Table I. Effect of bath composition on electrodeposited alloy composition and deposition rate; bath at 255°C; 6 v applied**

| Bath composition | | | | Deposited alloy | |
|---|---|---|---|---|---|
| %$CdCl_2$ | %InCl | %$ZnCl_2$ | $\frac{Cd}{Cd+In}\times 100$ | Composition %Cd | Approximate quantity, mg |
| 0 | 60 | 40 | 0 | 0 | 95 |
| 3 | 58 | 39 | 4 | 13 | 77 |
| 6 | 56 | 38 | 8 | 28 | 63 |
| 9 | 55 | 36 | 12 | 38 | 50 |

*Anode Reactions and Plating Bath Depletion*

Depletion tests on a bath containing 9% $CdCl_2$, 55% InCl, and 36% $ZnCl_2$ by weight indicated that about 5 g of Cd-In alloy (equivalent to about 1600 transistor stems having 1 mg of alloy on the emitter lead and 2 mg on the collector lead) can be plated from a 160-g bath before the plating rate decreases noticeably. Plating was done at 260°C using 6 v d.c. Over 7 g of Cd-In alloy was deposited with little change in plated alloy composition, as indicated by flow temperature determinations and by EDTA titrations. Plating current remained essentially constant during depletion tests.

The anode reaction during electrolysis of fused $CdCl_2$-InCl-$ZnCl_2$ baths involves oxidation of monovalent In ions to $In^{++}$ and/or $In^{+++}$ ions. While this reaction decreases the operating life of the bath, it completely eliminates evolution of chlorine gas at the anode, which would be very undesirable in many applications of the bath. The gradual increase in multivalent In ions in the bath during electrolysis leads to lower plating rates.

Tests in which successive increments of $InCl_3$ were added to a bath consisting of 9% $CdCl_2$, 55% InCl, and 36% $ZnCl_2$ indicated that plating rate decreased because the cathode reaction $In^{+++} + e^- \rightarrow In^{++}$ and/or the cathode reaction $In^{++} + e^- \rightarrow In^+$ competed with the desired reactions $In^+ + e^- \rightarrow In$ and $Cd^{++} + 2e^- \rightarrow Cd$. A solution containing 8% $CdCl_2$, 46% InCl, 15% $InCl_3$, and 31% $ZnCl_2$ plated Cd-In alloy less than half as fast as a bath containing 9% $CdCl_2$, 55% InCl, and 36% $ZnCl_2$, although plating currents were about equal.

If indium dichloride is formed at the anode during electrolysis, electrodeposition of 1 g of eutectic alloy (containing 25% Cd, 75% In, by weight) results in oxidation of 1.26 g of $In^+$ to $In^{++}$ at the anode; if $InCl_3$ is formed, 0.63 g of $In^+$ is oxidized to $In^{+++}$. There is considerable evidence (14) that indium dichloride actually exists as $In^+InCl^-_4$.

*Cleaning of Stems Plated in the Fused Salt Baths*

Stems plated in the fused salt bath can be cleaned by immersion in $ZnCl_2$-$NH_4Cl$ eutectic flux at about 250°C to remove the thin coating of solidified plating bath on the Cd-In alloy. Stems should be immersed deeper into the flux than they had been immersed in the fused salt bath. Gentle stirring is helpful in removing all of the plating bath from the surface of the Cd-In alloy. The $ZnCl_2$-$NH_4Cl$ eutectic flux (75% $ZnCl_2$, 25% $NH_4Cl$, by weight, mp 180°C) is prepared by heating the mixture of $ZnCl_2$ and $NH_4Cl$ at about 300°C until a clear solution is formed.

The $ZnCl_2$-$NH_4Cl$ eutectic flux rinse is followed by successive rinses in 3% acetic acid (3% by volume glacial acetic acid in deionized water), cold

deionized water, and hot deionized water (about 80°C). Stems are dried in air.

In some applications dilute HCl can be used to remove the thin coating of solidified plating bath from Cd-In alloys. In the presence of dilute HCl the In sponge resulting from disproportionation of the fused salt bath in water is dissolved with evolution of hydrogen gas. Concentrations from 0.01*N* to 0.1*N* HCl are suitable.

*Analytical Methods*

In the presence of water InCl undergoes disproportionation (14,15) to In metal and $InCl_3$ according to the reaction $3InCl \xrightarrow{H_2O} 2In + In^{+++} + 3Cl^-$. This reaction is the basis of the disproportionation method for determining the monovalent In content of InCl samples and of $CdCl_2$-InCl-$ZnCl_2$ baths.

A weighed sample of InCl or of fused salt bath is placed in stirred water to bring about the disproportionation reaction. The aqueous solution is decanted from the resulting spongy lumps of In metal. The In is melted in a mild flux such as 10% $NH_4Cl$ in glycerol to form a single, dense lump of metal, which is cooled and weighed.

Experiments have indicated that the disproportionation reaction is quantitative. Since both Cd and Zn are more negative than In in the electromotive series (3,16), the presence of $CdCl_2$ and $ZnCl_2$ in the fused salt bath does not interfere with the reaction in any way; the resulting In metal is spectroscopically free of Cd and of Zn.

Indium dichloride also undergoes disproportionation (14,15) according to the reaction $3InCl_2 \xrightarrow{H_2O} In + 2In^{+++} + 6Cl^-$.

Since, within the range of alloy compositions from 50% Cd-50% In to 20% Cd-80% In, determination of flow temperature is not suitable for estimating alloy compositions, a procedure was developed for titrating In in the presence of Cd with ethylenediaminetetraacetic acid (EDTA) solution. In this procedure, a modification of that described by Flaschka and Amin (17), the $Cd^{++}$ is complexed with excess KCN and the $In^{+++}$ is titrated with standard EDTA solution. Cadmium was determined by difference based on the total weight of the Cd-In alloy and based on titration of both $Cd^{++}$ and $In^{+++}$ with EDTA. No KCN was used during the titration of $Cd^{++} + In^{+++}$.

No Zn has been detected in spectrographic analyses of Cd-In alloys plated from $CdCl_2$-InCl-$ZnCl_2$ baths. Detection limit was 0.0001% for Zn.

*Indium Recovery from Depleted Baths*

Since the bath containing 6% $CdCl_2$, 56% InCl, and 38% $ZnCl_2$ contains 43% In metal by weight, methods of recovery of depleted plating baths have been investigated.

In the method now used the depleted bath is heated to about 280°C and slowly poured into a large beaker containing rapidly stirred deionized water (at room temperature). In the resulting disproportionation reaction, two-thirds of the monovalent In and one-third of the divalent In in the bath is converted to In metal. The aqueous solution is decanted from the In sponge, which is then melted under a flux of $NH_4Cl$ in glycerol to form a single globule of In. The In is allowed to cool until solidified and is rinsed with deionized water. No Zn or Cd was detected in spectrographic analyses of In metal samples recovered in this way. Other impurities were at the same level of concentration as those present in the In metal and in the $InCl_3$ used to prepare the InCl used in the formulation of the fused salt bath.

The recovered In metal can be used to prepare InCl.

The aqueous solution from the disproportionation reaction, containing $Cd^{++}$, $In^{+++}$, $Zn^{++}$, and $Cl^-$, can be treated with Zn dust to recover In scrap.

## Acknowledgment

The authors gratefully acknowledge the interest and encouragement of T. J. Manns and M. Sadowsky.

Manuscript received Oct. 10, 1956. This paper was prepared for delivery before the Cleveland Meeting, Oct. 1-4, 1956.

Any discussion of this paper will appear in a Discussion Section to be published in the December 1958 JOURNAL.

REFERENCES

1. F. Jirsa, *Z. anorg. u. allgem. Chem.*, **268**, 84 (1952).
2. O. H. Johnson, *Chem. Rev.*, **51**, 431 (1952).
3. W. M. Latimer, "The Oxidation States of the Elements and Their Potentials in Aqueous Solutions," 2nd ed., Prentice-Hall, Inc., New York (1952).
4. W. Betteridge, *Proc. Phys. Soc., London*, **50**, 519 (1938).
5. S. C. Carapella, Jr., and E. A. Peretti, *Trans. Am. Soc. Metals*, **43**, 853 (1951).
6. S. Valentiner, *Z. Metallkunde*, **35**, 250 (1943).
7. C. L. Wilson and O. J. Wick, *Ind. Eng. Chem.*, **29**, 1164 (1937).
8. "Intermediate 'Indalloy' Solders," Indium Corp. of America, New York (1954).
9. R. I. Jaffee and M. G. Weiss, cited in "Indium" by J. R. Mills, R. C. Bell, and R. A. King in "Rare Metals Handbook," edited by C. A. Hampel, pp. 199-200, Reinhold Publishing Corp., New York (1954).
10. R. I. Jaffee and S. M. Weiss, *Materials & Methods*, **36**, (3), 113 (1952).
11. Herrmann, *Z. anorg. Chem.*, **71**, 257 (1911).
12. J. Coyle, *Trans. Electrochem. Soc.*, **85**, 223 (1944).
13. W. J. Hamer, M. S. Malmberg, and B. Rubin, *This Journal*, **103**, 8 (1956).
14. N. V. Sidgwick, "The Chemical Elements and Their Compounds," Vol. I, pp. 458-481, Oxford University Press, London (1950).
15. "Gallium and Indium," Chapter 8 in "Chapters in the Chemistry of the Less Familiar Elements," Vol. I, pp. 13-22, by B. S. Hopkins, Stipes Publishing Co., Champaign, Ill. (1939).
16. T. Moller and B. S. Hopkins, *J. (and Trans.) Electrochem. Soc.*, **93**, 84 (1948).
17. H. Flaschka and A. M. Amin, *Z. anal. Chem.*, **140**, 6 (1953).

# The Relationship between Thermal Decomposition in Vacuum and the Macrostructure of Alkaline Earth Carbonates

**B. Wolk**

*Physics Laboratory, Sylvania Electric Products Inc., Bayside, New York*

ABSTRACT

The control of quality in electronic tubes processed by production equipment depends on numerous factors. Among these factors are those involving the time and temperature conditions for effective conversion of the cathode coating from the carbonate to the emitting oxide. A technique is described for evaluating the relative thermal decomposition properties of different cathode carbonates under simulated tube processing conditions. Various observations on the relationship between the macrostructure of cathode carbonates and the thermal decomposition behavior are described.

One of the fundamental chemical reactions involved in the processing of a coated cathode tube is the dissociation of the emission carbonate. The temperature range over which this is carried out influences a variety of other phenomena such as crystal growth, evaporation and diffusion of impurity elements in both the base metal and bulk oxide, and the formation of interface compounds. Some preliminary studies of carbonate breakdown have been carried out and this paper reports on the method employed and the results obtained.

Work on the double carbonates (1) (Ba, Sr) $CO_3$ and on dolomite (2,3), (Ca, Mg) $CO_3$, indicates that a multistep process is involved in the conversion to the corresponding oxides. Studies of magnesite (4), $MgCO_3$, decomposition in a variety of gaseous atmospheres revealed the mechanism of the reaction. Wooten (5) has studied decomposition of single carbonates in nitrogen and in hydrogen atmospheres. Investigations of $CaCO_3$ decomposition (6) and $BaCO_3$ breakdown (7), as well as double and triple carbonates under vacuum conditions, have also been reported. In no instance have two investigators employed identical techniques for the study of these reactions, and the data reported are not adequate in terms of the objectives in the current program. Among the earliest work attempting to relate thermionic emission with the size of the carbonate was that of Benjamin (8), who reported that small carbonate size favors higher emission levels. Shimazu (9), using small-angle scattering x-ray methods, concluded that small oxide size yields higher emission levels than do larger sizes. Generally the decomposition rate itself is only introduced in terms of its dependency on chemical composition, whereas the growth of the oxide crystal is examined in relation to processing time and temperature conditions. Recently both the carbonate and oxide crystal sizes have been studied in terms of their effect on emission levels. Wright (10) reported that superior emission characteristics can be expected from the smaller oxide crystal size originally produced from larger carbonate crystals. This relation applies to carbonates precipitated by $Na_2CO_3$, but holds only to a lesser extent for different sizes of carbonates prepared by $(NH_4)_2CO_3$ precipitation owing to a "wider size distribution" in the latter case.

The several kinds of double and triple carbonates currently in general use differ from one another both chemically and physically. The proper choice of processing schedules for any one of these is invariably dictated by the necessity for obtaining complete breakdown in minimum time without destroying the ability of the coating to respond favorably to subsequent activation. However, qualitative consideration is given to the influence of such factors as coating composition, density, weight, particle size, and even the presence of reducing gases during breakdown.

Here the processing performance of coatings has been studied to establish relations between such properties as particle size, size distribution, particle shape, and coating density. Performance in this case means the relative ease with which thermal decomposition occurs under a set of fixed temperature and time conditions.

The general procedure employs a constant rate of increase in temperature of Pt strips coated with the carbonate. An analysis of the resulting pressure-time-temperature relationships provided by each of the materials ultimately made it possible to introduce a method of ranking the carbonates according to their decomposition performance. In addition to relating this performance to the macrostructure of the carbonates, primarily characterized by Fisher sub-sieve sizer (F.S.S.) measurements, it was also possible to evaluate the unique role of coating density.

## Experimental Procedure

A hot-filament ionization gauge technique made possible direct measurement of the pressure of the thermal decomposition products and provided relatively simple data for analysis of the resulting pressure-time-temperature profile. This method provided a practical means for studying carbonates

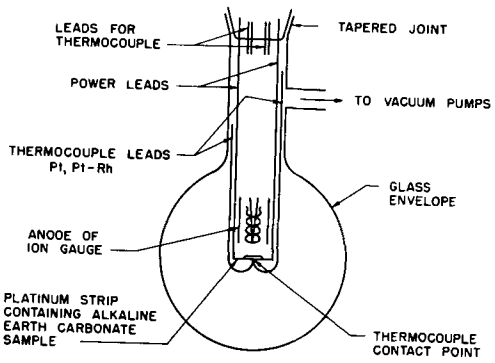


Fig. 1. Vacuum chamber containing sample and ionization gauge.

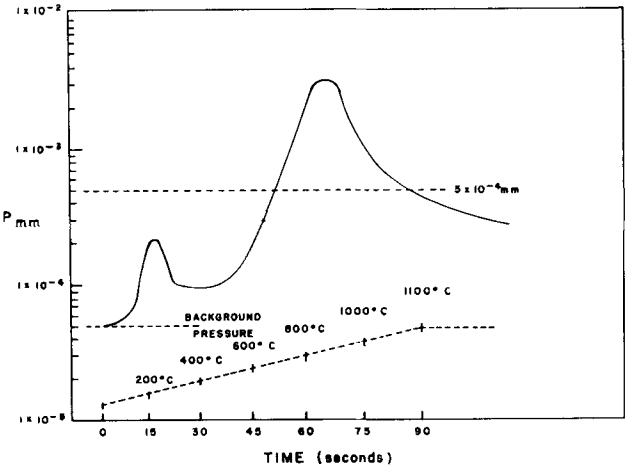


Fig. 2. Typical pressure-time-temperature curves

taken directly from production sources as well as from those prepared here. The apparatus in Fig. 1 contains an ion gauge built into a demountable glass envelope provided with power and thermocouple (Pt, Pt-Rh) leads. The cylindrical anode was of Ta. The glass connection to the oil diffusion pump was located near the upper portion of the envelope. The various carbonates, in standard lacquer suspensions, were sprayed on the central section of 0.002 in. Pt strips. A thermocouple junction was made at the midpoint of the opposite side with 0.004 in. wires. These were welded to 0.020 in. wires of the same materials after the Pt strip was welded securely to the power leads of the demountable stem structure with the coated side facing the ion gauge.

The experimental method had to approximate the breakdown speed normally employed in processing experimental or production tubes to be of greatest value. To do this systematically a servo-controlled linear temperatures scan rate of 13°C/sec was employed. Maximum variation in the rate of temperature rise under these conditions was about ±2%. Other essential requirements included rigid control of coating density, a reliable thickness measuring technique, and use of a relatively small mass, thickness and area of the coating under test.

Conventional micrometric methods were replaced by microscopic examination (with a bifilar microscopic eye piece) of the sprayed-coating profile and projection of the resultant image on a ground-glass screen. The calibrated lines and adjustable reference line were projected on the screen simultaneously with the coating profile. This method eliminates uncertainty that might be due to appreciable sample compression, usually about 15%. The largest observable error, about ±5%, is an unavoidable consequence of both restricted thickness (about 0.001 in.) and the high degree of surface roughness inherent in low-density coatings, i.e., less than 1 g/cc.

The main reason for employing a small coating thickness was to minimize the thermal gradient through the bulk of the sprayed coating during decomposition. Thinner coatings are more uniform and are less likely to chip away from the Pt strip.

## Pressure-Time-Temperature Curves

The usual pressure-time-temperature relation observed when carbonates are heated at linear temperatures scan rates is illustrated in Fig. 2. Starting at room temperature and at a fixed background pressure of $5 \times 10^{-5}$ mm, the first peak in the pressure-time curve, about $2 \times 10^{-4}$ mm, occurs as the temperature approaches 200°C due to partial decomposition of the binder. The pressure falls, then starts to rise at about 600°C, and continues until a maximum, usually $1\text{-}3 \times 10^{-3}$ mm, is reached at from 800° to 1000°C. From then on, the temperature is permitted to rise to 1100°C and is maintained at that value until the final pressure of $5 \times 10^{-4}$ mm is reached.

The comparison of the breakdown behavior of various carbonates shown in Table I is based on several characteristics in the decomposition curve just described. Of considerable interest is the temperature at which the maximum pressure occurs. These curves constitute a relative measure of the rate at which decomposition proceeds; they should not, however, be interpreted as true breakdown temperatures. The pressure-time curve width is reported in terms of the number of seconds required for the filament, starting at a temperature equiva-

**Table I. Thermal decomposition data obtained for a variety of triple carbonates precipitated under different conditions**

| Type | Fisher size (μ) | BET size (μ) | Peak press. temp °C | Decomp. time (sec) |
|---|---|---|---|---|
| C-3 | 3.05 | 0.97 | 871 | 68.6 |
| C-4 (1829)* | 2.76 | 0.86 | 867 | 67.3 |
| C-4 (1698)* | 2.63 | 0.89 | 863 | 66.5 |
| C-4 (1903)* | 2.55 | 1.06 | 868 | 65.9 |
| C-4 (1904)* | 2.40 | 0.64 | 869 | 66.9 |
| C-3,4 | 2.5 | 0.16 | 872 | 68.3 |
| C-3,4 | 1.92 | 0.27 | 873 | 71.6 |
| C-3,4 | 1.41 | 0.87 | 860 | 67.0 |
| C-3,4 | 13.5 | 0.63 | 945 | 77.7 |
| C-3,4 | 14.0 | 1.20 | 960 | 76.4 |
| C-10 (1455)* | 1.21 | 0.64 | 843 | 66.0 |
| C-10 (1813)* | 0.95 | 0.73 | 864 | 67.7 |
| C-10 (1948)* | 1.20 | 0.83 | 859 | 66.4 |
| C-3,4 | 1.9 | 0.55 | 864 | 67.3 |
| C-3,4 | 1.4 | 0.26 | 858 | 66.3 |
| C-3,4 | 4.2 | 1.21 | 884 | 69.5 |
| C-3,4 | 4.0 | 1.16 | 883 | 68.0 |
| C-3,4 | 5.5 | 1.3 | 916 | 71.0 |
| C-3,4 | 6.3 | 1.7 | 900 | 69.6 |

* These samples were obtained from production batches of Sylvania's Towanda Tungsten and Chemical Division. The remaining specimens were laboratory preparations.

lent to a thermocouple emf of 1 mv, to reach a pressure of $5 \times 10^{-4}$ mm once maximum pressure has been attained. The estimated pumping speed of the system is 3 liters/sec. Conditions affecting pumping speed remain the same from one test to another; consequently the data are strictly comparative. Subsequent experiments showed that the peak pressure reflected primarily the differences in sample weight; the time required to reach the peak reflected primarily differences in the other variables.

*Average Particle Size of Carbonates before and after Ball-Milling*

It is known that ball milling deagglomerates carbonates in suspension; in this connection Fig. 3 is of interest. Microscopic observations indicate this effect to be especially evident for spherical particles, but much less apparent when the original carbonate is in the form of needlelike particles. However, when deagglomerated suspensions were examined after they had been sprayed on Pt filaments and heated in vacuum to 500°C, the carbonate consisted once again of essentially reagglomerated particles as shown in Fig. 3c. Thus, the similarity between initial and final physical states provided evidence that no permanent alteration in the degree of aggregation results from ball milling.

Routine F.S.S. average particle size determinations reveal a high degree of uniformity among batches of a particular species. However, surface area measurements do not show this same consistency for these same carbonates—a fact presumably due to much greater variation in the microstructure of the surface than in the macrostructure of the carbonate aggregates which the sieve observes. The decomposition-particle size relationship is more generally observed to be consistent with Fisher size values than with particle size values estimated from Brunauer-Emmett-Teller (BET) gas adsorption surface-area measurements.

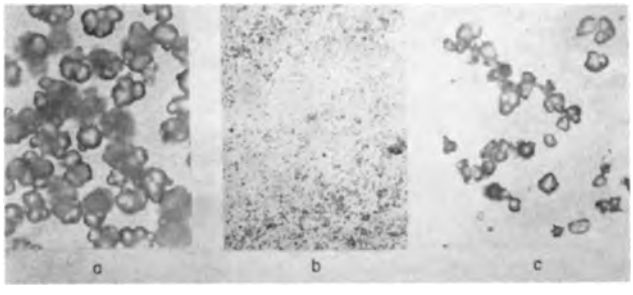


Fig. 3. (a) A large agglomerate specimen of triple carbonate (450 x); (b) same specimen shown after ball milling (450 x); (c) same material shown after being sprayed on a platinum filament and heated to 500°C in vacuum (450 x).

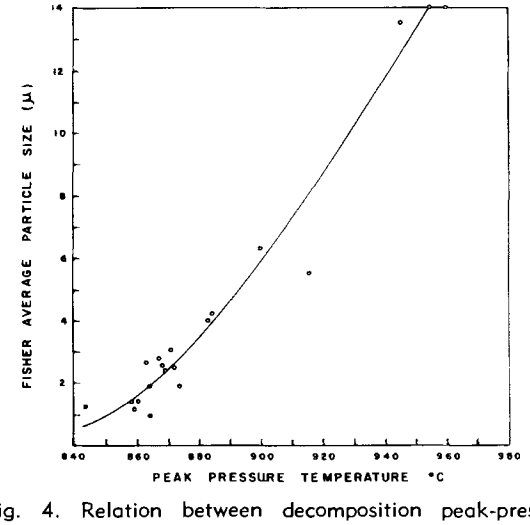


Fig. 4. Relation between decomposition peak-pressure-temperature and average particle size for various triple carbonates.

Some of the original laboratory preparations were based on certain desired BET size ranges obtained under different conditions of precipitation. However, results on the basis of BET analysis were completely different from those based on F.S.S. measurements. Low power microscopic examination confirmed the presence of large aggregates that were influencing the sieve measurements. A series of carbonates prepared at different precipitation temperatures but under otherwise uniform conditions, gave better qualitative agreement between the BET and F.S.S. average particle size values. However, electron microscopic examination using carbon replicas revealed very little difference in the microstructure of these specimens. Differences of a macroscopic nature were confirmed by low power microscopy. Figure 4 illustrates the relation between decomposition (peak pressure) temperature data and the sieve mean particle diameters of several production and laboratory triple carbonates. On the other hand, the absence of correlation between these decomposition data and mean particle diameters based on BET measurements (Table I) points out the lesser importance of the microstructure as a factor in determining the decomposition rate.

Thermal decomposition data and corresponding Fisher values obtained for different lots of the same type of production carbonate were consistently reproducible. This leads one to suspect that reported instances of poor cathode processing reliability are related to factors other than particle size variation. Other possible explanations of observed nonreproducible cathode breakdown performance are discussed later.

## Effects of Differences in Coating Density, Weight, and Thickness on Thermal Decomposition of Triple Carbonates

In addition to the fact that small particles decompose more readily than the larger ones, coating density is an influencing factor under certain conditions.

A coating density limit of 1 g/cc±0.05 was maintained throughout the previously described tests because there were no data on the effect of density variation on thermal decomposition. For this reason the study of carbonate decomposition as a function of coating density was included. The relation between bulk density and thermal decomposition was studied on one batch of small-size triple carbonate and one of large size. Table II illustrates two points of considerable interest. First, variations in bulk density for small average particles significantly affect all decomposition characteristics; second, the decomposition of large average particles is unaffected by coating density variations of 30%. The carbon

Table II. Effect of bulk coating density on experimentally observed peak-pressure temperatures for chemically identical carbonates composed of large and small average particle diameters

| Fisher average particle size $\mu$ | Sample weight x$10^3$ g | Sample thickness x$10^3$ in. | Coating density g/cc | Temperature (°C) at peak pressure |
|---|---|---|---|---|
| 1.85 | 0.33 | 1.23 | 0.895 | 848 |
| 1.85 | 0.37 | 1.21 | 1.02 | 863 |
| 1.85 | 0.43 | 1.23 | 1.17 | 889 |
| 1.85 | 0.33 | 1.23 | 1.17 | 894 |
| 6.3 | 0.44 | 1.77 | 0.83 | 912 |
| 6.3 | 0.31 | 1.25 | 0.83 | 913 |
| 6.3 | 0.37 | 1.25 | 0.99 | 917 |
| 6.3 | 0.45 | 1.15 | 1.30 | 920 |

replica electron micrographs reveal no significant difference in their microstructures; the differences are in the sizes of the aggregates.

Peak-pressure temperatures observed for the 1.85$\mu$ (F.S.S.) carbonate were found to be independent of sample weight. Several samples were coated to the same weight and density, then some of the coating was removed from some of the samples. Although the pressure variations during decomposition reflected the lower sample weight, the temperature at peak pressures remained unchanged.

The influence of coating thickness variations was subsequently demonstrated for one small (Fisher mpd = 1.85$\mu$) and one large particle size (Fisher mpd = 6.3$\mu$) carbonate; two groups of the 6.3$\mu$ carbonate were sprayed to different coating weights of constant density (0.83 g/cc). The heavier samples were also thicker as indicated by the original dimensions as shown in Table II. By removing approximately one third of the coated area it was possible to eliminate the weight difference. No effect due to thickness differences was noted, since the temperature for peak pressure remained the same as in the original tests. On the other hand, when two groups of small particle size carbonates were sprayed to the same density, but with different thicknesses (0.00121 in. and 0.00137 in.), the peak-pressure temperature was significantly higher for the thicker samples. The thermal decomposition behavior of the smaller particles thus appears to be highly sensitive to both thickness and density variations.

### Decomposition of Individual Carbonate Particles

Reduced particle size usually results in increased decomposition, as noted by Bircumshaw and Newman (11) in their studies of the thermal decomposition of ammonium perchlorate. Generally speaking, this is the result of shorter diffusion paths. The special problem of decomposition gas flow impedance due to the relatively small pore dimensions found in coatings composed of small sized particles must be considered. Here the rate of heat transfer by "gaseous conduction" becomes dependent on the dimensions of the pores which make up about 75% of the total volume of a 1 g/cc density coating. For a given spray condition, the packing factor depends largely on such properties as particle size, degree of agglomeration, particle shape, and particle distribution. The random nature of the packing resulting from spraying means that, for a given bulk density, the smaller particles form a close-packed array. Moreover, this close packing is extremely sensitive to spray conditions and bulk density; consequently breakdown speed is related to both factors. When the pore dimensions produced by larger agglomerates are sufficiently large, the same coating density limitations do not apply and diffusion of the decomposition gases is not so seriously impeded.

### Conclusions

1. Despite macrostructure irregularities observed in laboratory and production carbonates, the Fisher size determination method appears to characterize the average particle size in a manner that is related to the thermal decomposition characteristics. Carbonates other than those with needlelike and rodlike forms appear to be highly aggregated. Each portion of any such aggregate is itself composed of still smaller structures which are not yet the ultimate crystallites. This complex microstructure apparently accounts for the large surface area values generally obtained by the BET method.

2. Small aggregates decompose more readily than do the larger aggregates under the experimental conditions described here.

3. Sprayed coatings of normal bulk densities made from carbonates precipitated as rod-shaped, well-ordered crystals exhibit a more sluggish response during thermal decomposition than do the conventional carbonates. The effect is measurable, but, at the same time, can only be explained tentatively on the basis of the higher stability inherent in well-ordered crystals.

4. Ball milling procedures deagglomerate aggregates of spherical carbonate particles, but the shearing forces involved are insufficient to appreciably fracture rods or needles. Subsequent spraying appears to reagglomerate those with spherical habits so that the resulting sprayed coating essentially resembles the original macrostructure.

5. Under the conditions of measurement employed, a coating of high density comprised of small size particles alters those decomposition characteristics which normally distinguish the smaller size materials from the larger ones (Table II). Cathodes using larger particles break down more slowly at rates which are relatively insensitive to coating density variations.

6. The observed differences in thermal decomposition between particles of different sizes persist even when the linear temperature scan rates are decreased or increased by factors of two. Such consistent differences can become potentially critical, from a practical point of view, as a direct consequence of the increased tube processing rates and accompanying reduction in the time available for breakdown.

### Acknowledgments

The author is indebted to James G. Buck, for the substantial contribution of discussions and suggestions, and to C. F. Tufts, of the Metallurgy Laboratory, for carbon-replica electron photomicrographs of sample materials used in the experiments. The work was supported by U.S. Navy Contracts Nobs-5359 and Nobs-8023.

Manuscript received June 24, 1957. This paper was prepared for delivery before the Washington Meeting, May 12-16, 1957.

Any discussion of this paper will appear in a Discussion Section to be published in the December 1958 JOURNAL.

REFERENCES

1. A. Eisenstein, *J. Appl. Phys.*, **17**, 434 (1946).
2. O. A. Esin, P. V. Gel'd, and S. I. Popel, *J. A. Chem. (Russian)*, **22**, 354 (1949).
3. H. G. F. Wilsdorf and R. A. W. Haul, *Nature*, **167**, 945 (1951).
4. E. Kremer, Solid-State Reactions in Various Atmospheres, University of Innsbruck, Austria. Lecture given at Bayside, December 1953.
5. L. A. Wooten, Bell Lab. Report made to ACS Meeting in 1943.
6. J. Zawadski and S. Bretsznajder, *Bull. intern. acad. polon. sci., Classe Sci. Math. Nat. Ser. A*, 1940-46, pp. 60-64 (1948).
7. J. J. Lander, *J. Am. Chem. Soc.*, **73**, 5794 (1951).
8. M. Benjamin, R. J. Huck, and R. O. Jenkins, *Proc. Phys. Soc.*, **50**, 345 (1938).
9. J. Shimazu, *J. Phys. Soc. Japan*, **6**, [6] 479 (1951).
10. D. A. Wright, *Le Vide*, **51**, 58 (1954).
11. L. L. Bircumshaw and B. H. Newman, *Proc. Roy. Soc. A*, **227**, pt. 1, 115, pt. 2, 228 (1955).
12. F. Feakes, Quarterly Report of $H_2O_2$ Laboratories Prep. for ONR Contract No. N5 ori-07819 Sept. 1955, MIT.

APPENDIX

A series of reproducibility tests was carried out, early in the program, using one of the production triple carbonates. The batches of coated filaments were prepared at different times from individually ball-milled suspensions of the same powder. The two coatings differed with respect to their bulk densities by 4.3%. The sample weights had a 2.2% difference, and the coating thickness variation was 2.5%. Examination of the pressure-time curves for six samples in each test batch revealed that the average peak pressures were $1.82 \times 10^{-3} \pm 0.05 \times 10^{-3}$ mm and $1.83 \times 10^{-3} \pm 0.09 \times 10^{-3}$ mm, respectively. The corresponding average temperatures at these pressure peaks were 878° and 876°C. The decomposition times (*see* text) were 70.6 and 67.3 sec. While individual results in each batch showed deviations from the average of 1 to 5%, the difference between batches was only about 1%. The production carbonate used in these tests continued to serve as a control material with which the reliability of the over-all test equipment and procedure were checked periodically.

# Zone Melting and Crystal Pulling Experiments with AlSb

**W. P. Allred, Bernard Paris, and M. Genser[1]**

*Battelle Memorial Institute, Columbus, Ohio*

ABSTRACT

It has been found that high-resistivity AlSb ingots result from the zone refining of the compound in $Al_2O_3$ crucibles. Distribution coefficients of the spectroscopically observed impurities in AlSb were found to be 0.1 and smaller. Resistivity and Hall coefficients have been determined for some single-crystal specimens cut from the zone-melted ingots. Single crystals of AlSb have been grown by pulling from the melt. These crystals exhibited low resistivities. The mobility for holes in the crystals has been found to range between 300 and 500 $cm^2$/v-sec.

Of the nine Group III-V semiconducting intermetallic compounds, AlSb, GaAs, and InP are of major interest for use in the fabrication of solid-state rectifiers and transistors. A considerable amount of work has been done recently on the purification and growth of single crystals and on the study of the electrical properties of the compounds (1). In this paper, the preparation of AlSb by zone melting and the growth of AlSb crystals by crystal pulling are described.

## Zone Melting of AlSb

Zone melting is considerably more difficult to apply to AlSb than to Ge because AlSb tends to wet commercially available crucible materials. A slow reaction between AlSb and graphite at high temperatures results in the formation of $Al_4C_3$ and free Sb. The continued passage of a molten zone along the length of the melt distributes these reaction products throughout the ingot. Materials other than graphite that have been studied for use as crucibles are BN, $Si_3N_4$, Ta, MgO, and $Al_2O_3$. Except for dense $Al_2O_3$, these crucibles either reacted with the melt or caused excessive doping of the ingot.

The AlSb was zone melted in the apparatus illustrated in Fig. 1. This arrangement is similar to that used by Schell (2). The wire-wound furnaces provide an ambient temperature of approximately 800°C. Heating of the surroundings prevents cracking of $Al_2O_3$ boats because of sudden temperature changes during the course of the zone melting and also prevents the condensation of Sb vapor on the

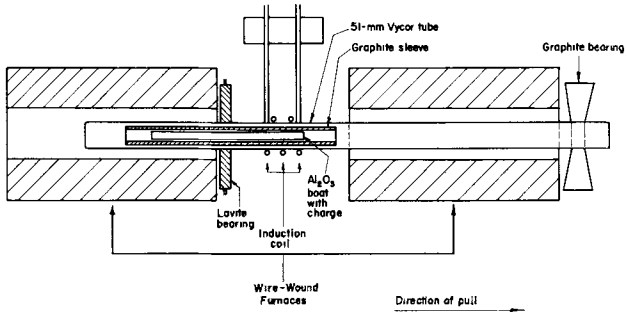


Fig. 1. Apparatus for zone melting AlSb

[1] Present address: International Business Machines, Inc., Poughkeepsie, N. Y.

cold walls of the enclosing Vycor vessel. Special equipment drew the tube containing the graphite sleeve, boat, and contents through the induction coil, returned the tube to start another pass, and counted the number of passes.

The compound was prepared by heating stoichiometric proportions of Al and Sb slightly above the melting point of AlSb. At this temperature, the reaction proceeds rapidly. At the end of the experiment, the ingot of AlSb adheres strongly to the boat; large lumps of AlSb could be cut away from the boat with a SiC wheel.

The Al and Sb used for the preparation of the compound were zone melted prior to use. Spectrographic analysis indicated that the concentration of such impurities as Mg, Si, Fe, and Cu varied in an Al ingot from 1-2 ppm near the front of the ingot to 10-20 ppm near the rear. The Sb contained less than 20 ppm impurities.

The ingots are polycrystalline since the material wets the boat, and crystal growth can be seen to start at the sides of the crucible and proceed toward the center. However, if the last zone-melting pass is carried out slowly (1-2 in./hr) and if the freezing interface is properly shaped (convex into the melt) in the center of the crucible, single crystals can be found which are suitable for Hall specimens. Unfortunately, these large crystallites seldom occur near the front of the boat where the highest resistivity material is found.

Resistivity profiles were measured by the four-probe method. Resistivities determined by this method are generally an order of magnitude greater than those measured on single-crystal Hall specimens. This is thought to be caused by the grain boundary resistance of the zone-melted polycrystalline ingot.

Figure 2 is the resistivity profile of a typical zone-melted ingot. The resistivity decreases from over $10^3$ ohm-cm at the front to $10^{-1}$ ohm-cm at the rear. The entire ingot was $p$-type, as shown by the sign

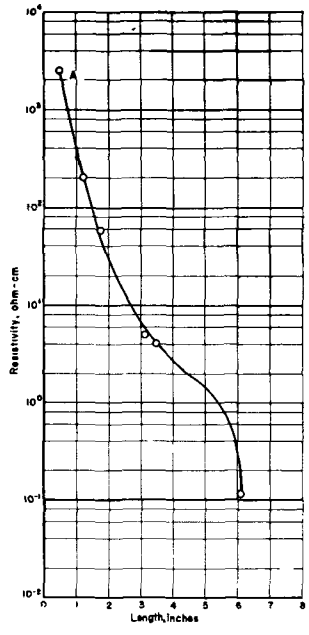


Fig. 2. Resistivity profile of an ingot of AlSb after twenty zone-melting passes.

Table I. Electrical properties of some single-crystal specimens cut from a zone-refined AlSb ingot

| Specimen No. | Resistivity, ohm-cm | Hall coefficient, cm³/coulomb | Hall mobility, cm²/v-sec | $N_h$ holes/cm³ |
|---|---|---|---|---|
| H-1 | 5.5 | 1650 | 250 | $4.3 \times 10^{15}$ |
| H-2 | 3.0 | 1100 | 310 | $6.5 \times 10^{15}$ |
| H-3 | 1.6 | 530 | 280 | $1.3 \times 10^{16}$ |
| H-4 | 1.0 | 360 | 310 | $2.0 \times 10^{16}$ |
| H-5 | 0.15 | 79 | 450 | $9.0 \times 10^{16}$ |
| H-6 | 0.35 | 190 | 460 | $3.8 \times 10^{16}$ |

of the thermoelectric effect. This ingot was given 20 passes of zone melting; the zone width was about 5 cm and the ingot length was 20 cm.

The resistivity profiles of many zone-melted ingots were shaped as in Fig. 2. However, the resistivities of the front portion of the ingot varied between 10 ohm-cm and more than $10^4$ ohm-cm. These variations in resistivity profiles may be attributed to the variation in purity of the Al used in preparing the ingots. Likewise, because Al of higher purity was used in preparing the compound prior to zone melting, the considerably higher resistivities which were observed over those reported by Schell may be explained. Spectrographic analyses of specimens of the compound cut from the front, center, and rear regions of a zone-melted ingot revealed Mg in a concentration of 2 ppm in the rear of the ingot. It is known that the boats used for the zone melting contained a few tenths of a per cent of MgO. This could be the source of the Mg in the ingot.

Table I shows some typical resistivities and Hall coefficients determined on single-crystal specimens cut from a zone-refined ingot. Samples were cut from the front (first to crystallize) half of the ingot with H-1 being the sample nearest the front of the $Al_2O_3$ boat. The general decrease in Hall mobility as the resistivity increases suggests that the extremely high-resistivity material often observed near the front of the ingot may be due to compensation. The resistivity and Hall coefficient of Specimens H-2, H-3, and H-4 were determined as a function of temperature (Fig. 3 and 4).

## Distribution Coefficients of Some Impurities in AlSb

Impurities normally found in the Al were studied to determine if the high-resistivity material observed in the zone-refined ingots was the result of compensation due to an $n$-type impurity with a distribution coefficient greater than unity. Pfann's equation (3) describes the distribution of a solute along the length of a zone-melted ingot after one pass, when the solute is added to the first zone.[1] The equation is

$$C = kC_o e^{-kx/L}$$

where $C$ is the concentration of solute in the solid, $k$ is the distribution coefficient, $C_o$ is the concentration of solute added to the first zone, $L$ is the zone width, and $x$ is the distance along the ingot. In cases where $k$ is small, the exponential reduces to unity and $k$ can be determined simply as the ratio of the concentration in the solid to the initial liquid

[1] This process is referred to as "zone leveling".

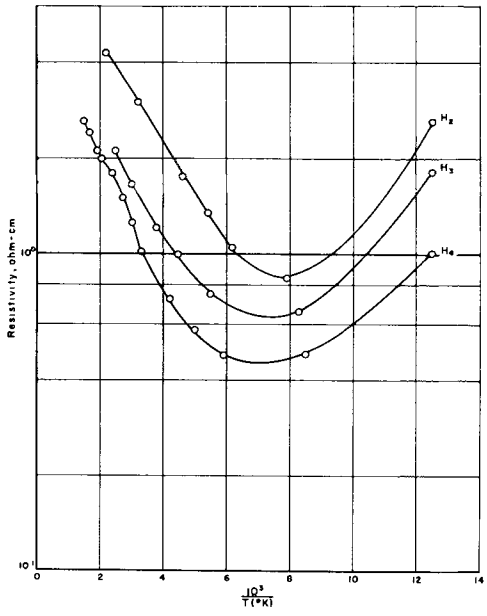


Fig. 3. Variation of resistivity of zone-melted AlSb with reciprocal temperature.

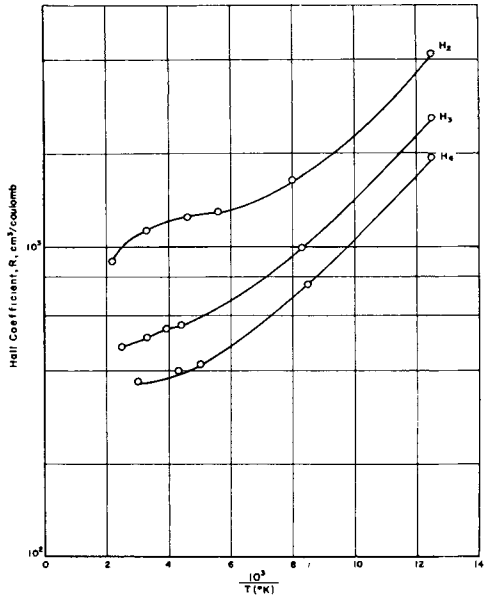


Fig. 4. Variation of Hall coefficient of zone-melted AlSb with reciprocal temperature.

concentration. Where $k$ is appreciable ($>0.01$), the concentration of solute will be higher in the first zone and will decrease toward the rear of the ingot. By plotting ln C as a function of $x/L$, the negative of the slope of the line is the distribution coefficient.

In impure AlSb, the following impurities are usually observed spectrographically: Mg, Si, Fe, Cu, B, Ag, Pb, V, Ni, Mn, Ti. Therefore, these metals were added to the front zone in a zone-leveling experiment. Specimens of the doped ingot were analyzed spectrographically and the distribution coefficients were determined as above. Order of magnitude values for $k$ were obtained and are given in Table II.

The distribution coefficients of Mg, Si, Fe, and Cu which are usually present in a few ppm are significantly less than one and, hence, these impurities

Table II. Approximate distribution coefficients of some impurity elements in AlSb

| Element | Distribution coefficient, $k$ |
|---|---|
| Mg | 0.1 |
| Si | 0.1 |
| Cu | 0.02-0.1 |
| Fe | 0.01-0.1 |
| B | 0.01-0.02 |
| Ag | 0.1 |
| Pb | $<0.01$ |
| V | $<0.01$ |
| Ni | $<0.01$ |
| Mn | $<0.01$ |
| Ti | $<0.01$ |

segregate to the rear of the ingot. The other impurities listed in the table are usually present in smaller concentrations. They also segregate to the rear of the ingot. It is important that such transition elements as V and Ti have a small distribution coefficient and segregate to the rear of the ingot. If such elements segregated to the front of the ingot, they could cause the high resistivity in the AlSb, as do Fe and Co in Ge (4).

Unfortunately, elements such as Se and Te cannot be studied by the spectrographic technique. These elements are donor elements in AlSb and if they moved to the front of the ingot in zone melting, they could compensate for the acceptor impurities yielding a high-resistivity region. Crystal pulling work with these elements has shown qualitatively that their distribution coefficients are less than unity.

## Effects of Dissociation of AlSb at the Melting Point on the Resistivity

The effects of the dissociation of the compound at the melting point were investigated. It could be hypothesized, for example, that some dissociation in the liquid would occur. Since at the melting point of the compound the free Sb would have a higher vapor pressure than the Al, the melt could become rich in Al if the Sb continued to escape. In a crystal pulling furnace, for example, it is difficult to maintain a high, even temperature in an enclosed system. In fact, in crystal pulling work traces of free metal, presumably Al, have been observed in the crucible after a crystal is withdrawn.

An experiment was carried out in which the melt was doped indirectly with an excess of Al. The ingot of aluminum antimonide was zone melted in an $Al_2O_3$ boat inclosed in a Vycor tube. The temperature of the entire system was the usual 800°C. Prior to the final pass, the temperature was lowered to 450°C, a condition that permitted the condensation of Sb. The net result was the enrichment of the melt with Al. Figure 5 shows the resistivity profile of this ingot. Some decrease in resistivity is apparent. However, the decrease is not so large as might be expected. Ingots with no higher resistivities after a similar number of passes of zone melting at 800°C ambient temperature have been prepared. The experiment suggests that Al is quite insoluble in the solid compound.

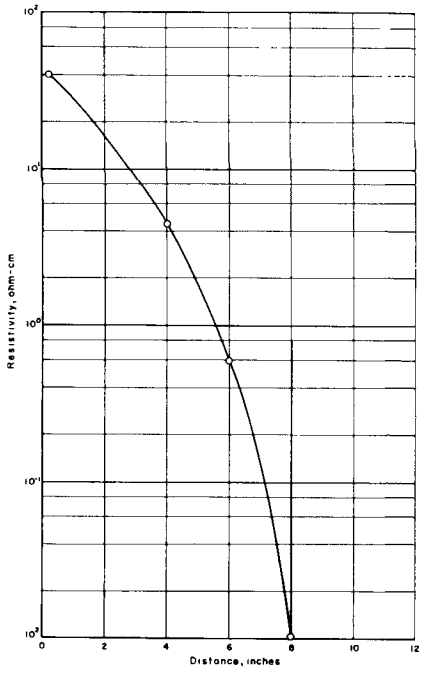


Fig. 5. Resistivity profile of a zone-refined AlSb ingot doped with Al.

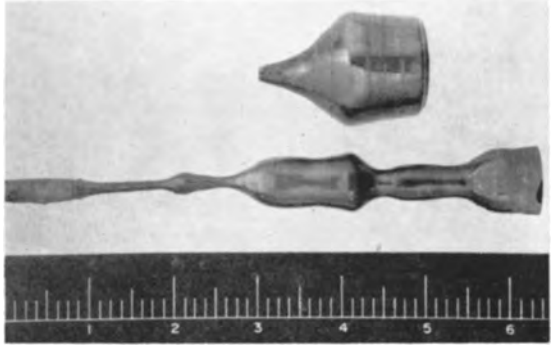

Fig. 6. Crystals of AlSb grown from the melt

## Growth of Crystals of AlSb

Single crystals of AlSb were grown in a typical crystal pulling apparatus by the Czochralski technique. Because oxide on the surface of molten AlSb could nucleate the development of new crystals, the melt was skimmed with an $Al_2O_3$ probe to clear the surface for crystal growth. Figure 6 shows a photograph of typical AlSb crystals grown from the melt. When crystals were pulled from the melt, only low-resistivity *p*-type crystals resulted. In some of the experiments, the AlSb was melted in pure graphite crucibles. Although graphite boats will not suffice for zone melting, graphite crucibles are satisfactory for crystal pulling, provided the temperature of the melt does not greatly exceed the melting point of the compound for long periods of time.

Crystals pulled from zone-refined AlSb exhibited slightly higher mobilities than did crystals pulled from melts prepared directly from the elements. Likewise, the pulled crystals exhibited higher mobilities than did crystals prepared by zone melting, even though the zone-refined crystals were of higher resistivity.

Failure to pull higher resistivity crystals from zone-refined AlSb was surprising, in view of the zone-melting work where it was observed that excess Al is not greatly soluble in solid AlSb. Spectrographic analysis of a portion of the crystal pulled from an $Al_2O_3$ crucible showed the presence of Mg and Si. Thus, it is likely that impurities are being introduced by the crucible. The graphite crucible likewise probably introduces impurities into the melt. For example it has been found that a solid solution between AlSb and $Al_4C_3$ forms on the surface of the graphite in contact with the melt.

An experiment was carried out in which a crystal was drawn from a melt of aluminum antimonide containing an excess of Sb. The excess of Sb was such that, as it was removed from the melt by volatilization, the melt composition passed through the regions of excess Sb, stoichiometry, and finally excess Al, as the crystal was withdrawn. However, the resulting crystal exhibited no resistivity maximum, which would have been expected if stoichiometry effects were controlling the crystal resistivity.

## Conclusions

From the work reported here, it can be seen that most impurities found in AlSb segregate readily to the rear during zone refining. Single crystals can be grown by the Czochralski technique. However, the growth of high purity crystals seems to be limited by the purity of the alumina crucible and to the purity of the Al rather than by the effect of deviations from stoichiometry, since both excess Al and Sb are apparently insoluble in AlSb.

## Acknowledgment

The authors wish to acknowledge the advice and suggestions of H. L. Goering, Chief of the Physical Chemistry Division. The comments of A. C. Beer are also appreciated. This work was supported by the Wright Air Development Center, Air Research and Development Command, United States Air Force.

Manuscript received Jan. 31, 1957. This paper was prepared for delivery before the Pittsburgh Meeting, Oct. 9-13, 1955.

Any discussion of this paper will appear in a Discussion Section to be published in the December 1958 JOURNAL.

REFERENCES

1. *See* papers by H. Welker, especially *Physica*, **20**, 893 (1954). For early work on AlSb see R. K. Willardson, A. C. Beer, and A. E. Middleton, *This Journal*, **101**, 354 (1954).
2. H. A. Schell, *Z. Metallkunde*, **46**, 58 (1955).
3. W. G. Pfann, *J. Metals*, **4**, 747 (1952).
4. W. W. Tyler, H. H. Woodbury, and R. Newman, *Phys. Rev.*, **94**, 1419 (1954).

# Transport Numbers in Pure Fused Salts

## Lead Chloride, Lead Bromide, Thallous Chloride, and Silver Nitrate

**Richard W. Laity[1] and Frederick R. Duke**

*Institute for Atomic Research and Department of Chemistry, Iowa State College, Ames, Iowa*

ABSTRACT

The application of the authors' moving bubble cell to the measurement of transport numbers in four pure fused salts is described. From the experimental results it is shown that the anion carries approximately three-fourths of the current in lead chloride, and one-fourth in silver nitrate. Except for lead bromide, in which this figure increases by about 3% when the temperature is raised 100°C, little, if any, temperature dependence is observed.

A radiotracer experiment in fused lead chloride is shown to indicate that long-lived complex anions do not carry any appreciable fraction of the current in this salt. The limitations of the method used are discussed.

The authors' method for measuring the transference numbers of the ions in pure molten salts has already been described (1, 2). The present paper deals with the application of this procedure, or slight modifications of it, to four different salts.

A recent paper by Bloom and Doull described a cell for measuring transport numbers in fused salts in which the possibility of the results being influenced by flow of the liquid under gravity is minimized by making the whole system horizontal (3). The transport numbers for $PbCl_2$ reported by Bloom and Doull, however, correspond to only a small fraction as much $PbCl_2$ being transferred from catholyte to anolyte per faraday as was observed in the author's moving bubble cell. Lorenz and Janz (4) have shown that leakage through the membrane was very likely in the experiment of Bloom and Doull, and at the same time point out some limitations of the moving bubble cell; chiefly these limitations center around the fact that certain salts in some types of capillaries form "sticky" bubbles which do not move under small pressure differentials. They showed, however, that $PbCl_2$ was not one of these salts.

Sundheim (5) has pointed out that the salt can gain no net momentum from the electrode processes, and he further states correctly that, regardless of the nature of complex ions which might be present, $t^+ = M_-/(M^+ + M_-)$ providing no momentum is transferred to the cell. His view that no momentum is transferred to the cell appears to be an extreme one, since, with no net preferential adsorption of one ion, there could still be frictional interaction between an anion tending to move and an anion held to the surface; the same sort of interaction between cations might be expected.

It was pointed out previously that in order to calculate transport numbers from the data obtained in measurements of this type it is necessary to assume formulas for the current-carrying ions. In the light of no evidence to the contrary, the simplest formulas, e.g., $Pb^{++}$ and $Cl^-$, were assumed.

### Experimental

*Materials.*—Fisher certified reagent $PbCl_2$ was used. In addition, $PbCl_2$ containing labeled cation was prepared by dissolving thorium B ($Pb^{212}$) in nitric acid, adding PbN carrier and precipitating with HCl. The salt was recrystallized from 0.01*N* HCl, filtered, and dried at 110°C.

Fisher purified $PbBr_2$ was recrystallized twice from 0.1*N* HBr. The dried product melted sharply at 370°C.

Fisher purified thallium (ous) chloride was recrystallized from 0.01 HCl. Spectrographic analysis revealed no appreciable amounts of metal impurities.

"Bakers Analyzed" $AgNO_3$ was recrystallized from water.

The lead metal used for electrodes was "Bakers Analyzed" reagent grade. Thallium electrodes were of Sargent CP Tl metal. Silver electrodes were plated onto the tungsten wires in the cell from an aqueous cyanide bath, using Fisher certified reagent silver metal as anodes in the electroplating.

*Apparatus.*—The moving bubble cell and accompanying apparatus have already been described (1, 2). These were used in unmodified form in the experiments on $PbCl_2$, $PbBr_2$, and TlCl. In the tracer experiment on $PbCl_2$ a much smaller version was used. The electrode compartments were again joined by a 10-mm tube containing an "ultrafine" porosity fritted Pyrex disk, but no capillary tube was used in the smaller cell. The moving bubble cell was modified only slightly for the work on $AgNO_3$. In these experiments one vertical arm of the cell was fitted with a glass stopper at the top so that the electrolyte could be sealed tightly into that compartment.

*Procedure.*—The procedure already described for $PbCl_2$ was used for $PbBr_2$ and for TlCl (1, 2). In the case of $PbBr_2$ an unfavorable combination of

[1] Present address: Department of Chemistry, Princeton University, Princeton, New Jersey.

surface properties and viscosity prevented rapid equilibration of the liquid levels below about 480°C. At higher temperatures, however, good reproducibility was obtained. Thallium chloride was found to undergo a slow hydrolysis or exchange reaction with oxygen on standing molten in the cell. The progress of this conversion to $Tl_2O$ could be followed by noting the change with time of the rate and, eventually, the direction of bubble movement for a given current. A corresponding increase in the activation energy of conductivity from about 3.4 to 10.1 kcal was observed during a 48-hr period. For this reason the salt was freshly purified before filling each cell, and only the initial runs were considered valid. Excellent reproducibility was obtained in this way from one cell to the next.

Rather than test each salt with a variety of membranes, as had been done for $PbCl_2$, the "activation energy of conductivity" criterion proposed earlier (2) was applied to determine whether the membrane might be affecting the mechanism of the conductivity process in each case. This was done by allowing the furnace to cool slowly while measuring the resistance of the transport cell containing the salt with a 1000-cycle conductivity bridge. The slope of log $1/R$ vs. $1/T$ was then compared with literature values for cells without membranes.

Silver nitrate was the first salt for which the use of solid electrodes was required. This introduced the problem of keeping the silver "trees," which rapidly grew out from the cathode during electrolysis, from growing right into the anode compartment before sufficient current to make a measurement has been passed. The problem was solved when it was found that superimposing a 60-cycle alternating current of about 350 ma on the 25 ma direct current used for the electrolysis changed the nature of the growth to a bushy deposit which grew out much more slowly. A further modification in these measurements was the stoppering of one compartment of the cell. The purpose of this was to increase the sensitivity of the measurements by magnifying the effect of any volume change developing during electrolysis, the bubble movement being forced in this case by a pressure difference rather than by gravity flow. This procedure was necessitated by the fact that no appreciable bubble movement could be observed for $AgNO_3$ in an unstoppered cell. In the stoppered cell, however, it was found that the passage of current caused a slight initial displacement of the bubble away from the stoppered compartment, after which the bubble came to rest and showed no further tendency to move. The initial displacement was, of course, due to the expansion of liquid in the stoppered side caused by the electrical heating as could be shown by passing a-c current only. This observation established the fact that the bubble was indeed sensitive to small volume changes, so that the accumulating liquid was not escaping back through the membrane, as had been suspected at first. The subsequent stopping of the bubble when the heating effect reached a steady state thus proved that in $AgNO_3$ the transport numbers happened to have just those values for which the volume of salt accumulating in the anode compartment is equal to the volume of Ag being transferred from anode to cathode in the temperature range studied. The accuracy of the measurements was, however, considerably reduced by the modifications imposed. The small d-c currents used meant less electrolysis per unit time, while the sealed compartment greatly increased the sensitivity of the bubble to small thermal fluctuations in the furnace.

In the tracer experiment on $PbCl_2$, two identical cells of the small type described above were placed close together in a sand bath inside the furnace. Each cell contained lead electrodes and molten lead chloride in the usual way. The system was allowed to stand several hours at constant temperature, so that thermal and gravitational equilibrium of the electrolyte in each compartment was assured. A few hundred milligrams of the labeled $PbCl_2$ were now introduced into one compartment of each cell. The system was again left standing for about half an hour, a period which was found adequate to permit the labeled salt to become uniformly distributed throughout the compartments containing it. A direct current of about 0.3 amp was now passed through one cell, while an equal alternating current was passed through the other, the electrode in contact with the labeled salt being the cathode in the d-c cell. After about an hour of electrolysis the cells were removed from the furnace, chilled, and broken open at the membrane. The salt in each compartment was dissolved in a solution of sodium acetate and acetic acid. Aliquots of each solution were treated with excess HCl and the resulting precipitates of $PbCl_2$ collected on filter paper, weighed, and counted with a Geiger counter by standard methods.

## Results and Discussion

The results of transport number determinations on the four salts are summarized in Table I. The figures for $PbCl_2$ represent no new measurements, but are included here for purposes of comparison. The second column in the table, headed $E_m$, gives the activation energy of conductivity found for these membrane-containing cells over at least a 70° temperature range encompassing the temperatures of the transport measurements, which are listed in the

**Table I. Results of transport number determinations**

| Salt | $E_m$ kcal | $E_n$ kcal | $T_t$ °C | No. of expts. | $t_-$ (avg.) | $t_+$ |
|---|---|---|---|---|---|---|
| $PbCl_2$ | 3.9 | 3.5[a] | 565 | 22 | 0.758 ± 0.014 | 0.242 |
| | | | 635 | 7 | 0.757 ± 0.009 | 0.243 |
| $PbBr_2$ | 4.1 | 4.1[b] | 500 | 11 | 0.653 ± 0.013 | 0.347 |
| | | | 600 | 5 | 0.674 ± 0.003 | 0.326 |
| TlCl | 3.4 | 3.0[c] | 475 | 3 | 0.496 ± 0.004 | 0.504 |
| | | | 505 | 2 | 0.492 ± 0.001 | 0.508 |
| | | | 525 | 2 | 0.493 ± 0.000 | 0.507 |
| | | | 225 | 2 | 0.24 ± 0.05 | 0.76 |
| | | | 275 | 2 | 0.24 ± 0.05 | 0.76 |

[a] H. Bloom and E. Heymann, *Proc. Roy. Soc. (London)*, **A188**, 392 (1947).
[b] "International Critical Tables," Vol. VI, p. 148, McGraw-Hill Book Co., Inc., New York, (1926).
[c] P. Drossbach, "Electrochemie geschmolzener Salze," p. 73, Julius Springer, Berlin, (1938).
[d] J. Byrne, H. Fleming, and F. E. W. Wetmore, *Can. J. Chem.*, **30**, 922 (1952).

fourth column under $T_t$. Values of $E_m$ are probably accurate to better than ± 0.5 kcal. In column three, headed $E_n$, are listed the activation energies found for the same salts in conductivity cells with no membranes, as calculated from data in the references cited. The transport numbers found for the negative ions, $t_-$, are listed in the sixth column along with the average deviation for the number of experiments shown in column five. The cationic transport number $t_+$ ($= 1 - t_-$) is also tabulated in the last column for discussion purposes.

In the tracer experiment less than 2% of the labeled cations were found to have diffused into the opposite compartment in the blank (a-c) cell, showing the diffusion correction to be small for this method. The activity found in the anode compartment of the d-c cell, however, represented an even smaller fraction of the total activity. This is exactly the result to be expected for a salt in which a negligible fraction of the current is carried by complex anionic species, since the electrolytic migration of cations carries some of the diffusing activity back into the cathode compartment. If, on the other hand, an appreciable fraction of the ions passing through the membrane from catholyte to anolyte consisted of lead ions bonded to chloride, then the amount of activity found in the anode compartment should have exceeded that found for the blank run. The results of this experiment were sufficiently accurate to warrant the conclusion that such lead-containing anions carried less than 1% of the total current in this experiment on pure $PbCl_2$ at 550°C.

It should first be pointed out that tracer experiments on $PbCl_2$ very similar to the type described here had already been carried out by Wirths (7). His results also indicated the lack of nondissociating current-carrying complex anions, but the experimental error was too large to permit the definite conclusion. Wirth's paper also includes data on $PbCl_2$-KCl mixtures which seem to bear out the observation of complex anions in the more dilute (in $PbCl_2$) mixtures. Again, however, the deviations seem extraordinarily large for this type of measurement. Since it is highly probable that equilibration among the possible anionic and cationic radioactive species is very rapid under the conditions of the experiment, and since the average residence time in the membrane is of the order of 10 sec or longer, the probability of a complex anion, even though it exists, getting through the membrane is exceedingly small unless the equilibrium concentration of such complex ions is such as to cause the gross migration of the lead ions toward the anode. Thus, the radiotracer method at such high temperatures would be expected to measure the net motion of lead ions toward the cathode, unless the melt contains anionic complexes of unexpectedly long life. The results of the authors' experiments, as well as those of Wirth, therefore, still leave open to a considerable extent the question of the existence of complexes in the pure salt.

The transport numbers obtained indicate roughly that the larger the ion, the less mobile it is; the bromide ion, for example, carries less current relative to lead ion than does chloride. More striking is the effect of the charge on the ion, the relatively small $Pb^{++}$ carrying less current than even the very large bromide ion; in the cases of the univalent salts, however, the cations compete well with the anions. Aside from pointing out these obvious indications, the authors feel that much more data are needed before attempting to arrive at a theory for electrical conductivity in fused salts.

Manuscript received Feb. 11, 1957. Contribution No. 593; work was performed in the Ames Laboratory of the U. S. Atomic Energy Commission.

Any discussion of this paper will appear in a Discussion Section to be published in the December 1958 JOURNAL.

REFERENCES

1. F. R. Duke and R. W. Laity, *J. Am. Chem. Soc.*, **76**, 4046 (1954).
2. F. R. Duke and R. W. Laity, *J. Phys. Chem.*, **59**, 549 (1955).
3. H. Bloom and N. J. Doull, *ibid.*, **60**, 620 (1956).
4. M. R. Lorenz and G. Janz, Armed Services Technical Information Agency Technical Note 57-240, ASTIA Document Service Center, Dayton 2, Ohio, 1957.
5. B. R. Sundheim, *J. Phys. Chem.*, **60**, 1381 (1956).
6. R. Lorenz and W. Ruckstuhl, *Z. Anorg. Chem.*, **58**, 41 (1907).
7. G. Wirths, *Z. Elektrochem.*, **43**, 486 (1937).

# Lead Dioxide Anode for Commercial Use

J. C. Grigger, H. C. Miller, and F. D. Loomis

*Research and Development Department, Whitemarsh Research Laboratories,*

*Pennsalt Chemicals Corporation, Wyndmoor, Pennsylvania*

ABSTRACT

Results are presented on one phase of a research carried out under an Office of Naval Research contract for the development of an electrode to replace platinum in the perchlorate cell. Electrodeposition of massive lead dioxide is preferably carried out from a lead nitrate bath. Uniquely, anodic deposition on tantalum is possible without polarization or erosion of the base. In the subsequent anodic process use, this tantalum acts as a polarized, inert filler. Sprayed silver permits the formation of an operable, low resistance current contact to the lead dioxide. Operation of a 100 amp perchlorate cell with a lead dioxide anode is described. Current efficiency of the lead dioxide anode is compared to platinum, and the effect of $K_2S_2O_8$ addition is shown.

The chemical and electrical properties of $PbO_2$ suggest that it should be an ideal material for anodes in electrolytic processes. With a resistivity as low as 40 to 50 x $10^{-6}$ ohm-cm, it is a better electrical conductor than many metals, and a much better conductor than carbon or graphite. Chemically, $PbO_2$ is inert to most oxidizing agents and strong acids. Although it has been suggested as an anode material for several electrolytic processes (1-7), up to the present time no commercially practical anode has been advanced. Electrodes reported to date have been weak; they have been formed in odd shapes difficult to adapt to commercial cells, and methods of making the electrical contact have not been satisfactory.

The purpose of this investigation was to develop a practical $PbO_2$ anode that could be used in industrial electrolytic processes. It was hoped that a suitable electrode would be developed that would replace Pt in the perchlorate cell.

## Experimental

### *Electrodeposition of Massive* $PbO_2$

Several baths (3, 8, 9) are known for the electrodeposition of $PbO_2$ on common metals. The compositions of three bath types modified to give improved $PbO_2$ deposits are shown in Table I. In this work, the $Pb(NO_3)_2$ bath was preferred because it gives the highest quality of deposit. The addition of copper nitrate to this bath serves to suppress Pb deposition on the cathode, which is preferably carbon or graphite. In order to deposit $PbO_2$ of high strength, density, and surface smoothness, an addition agent is necessary such as Igepal CO-880[1] which is a nonionic surface-active agent of the class of "alkyl phenoxy polyoxyethylene ethanol." Addition to the bath of a natural hydrophilic colloid such as gelatin resulted in the formation of a $PbO_2$ deposit with a high surface smoothness, but which was very weak and was laced throughout its cross section with many fine fissures.

[1] Trade Name of Antara Chemical Division of General Dyestuff Corp.

**Table I. Lead dioxide plating baths**

1. Alkaline lead tartrate
   100 g potassium sodium tartrate, $KNaC_4H_4O_6 \cdot 4H_2O$
   50 g sodium hydroxide, NaOH
   96 g lead oxide, PbO
   Dissolve in the order listed in distilled water to make 2 liters of solution. Heat to 60°C to complete solution of lead oxide. Cool and filter through sintered glass. Bath *p*H is about 13.
2. Lead perchlorate
   108 ml of 60% perchloric acid (100 g $HClO_4$)
   167 ml distilled water
   111.0 g lead oxide, PbO
   Dissolve the lead oxide in the diluted perchloric acid. Make up to 2 liters with distilled water. Heat to boiling for 2-3 min to dissolve any white precipitate. Cool and use. Bath *p*H is about 5.
3. Lead nitrate
   269 ml of 69.9% nitric acid (266.5 g $HNO_3$)
   1000 ml distilled water
   472 g lead oxide, PbO
   Add the lead oxide slowly to the diluted nitric acid with stirring. Dilute to 2 liters and heat to 75°C with stirring. Cool and filter through sintered glass. To this bath add:
   $Cu(NO_3)_2 \cdot 3H_2O$—0.75 g/l
   Igepal CO-880*—0.75 g/l
   Bath *p*H is about 3.5.

* Trade Name of Antara Chemical Division of General Dyestuff Corp.

Using the acid baths mentioned above, it is difficult to form good deposits on thin attackable base sheets because of the serious anodic dissolution of the metal base. This problem was overcome by using Ta as the base metal. Sound, adherent deposits of $PbO_2$ 2 cm or more in thickness could be formed without any signs of erosion of the base Ta. This plating on Ta was unexpected, since Ta polarizes in most electrolytes when operated as the anode.

Electrodeposits of $PbO_2$ were made readily on Ta wire, rod, and sheet without any nodular growth, using the $Pb(NO_3)_2$ bath at an anode current density

of 0.016-0.032 amp/cm² (15-30 amp/ft²) and a temperature of 70°C. Figure 1 shows a rod of massive $PbO_2$ formed on a single wire. The wire core was withdrawn by a sharp pull with pliers. In plating flat base-free deposits by blanking off one side of the starting sheet and stripping away this base after a thick deposit had formed, it was difficult to secure unbroken specimens. Therefore, this approach was discontinued in favor of plating on permanent base sheets.

Flat, massive $PbO_2$ deposits of surprising strength were made by plating on both sides of rectangular sections of Ta screen in the mesh range of 10-50. The use of baffles around the edges of flat, rectangular anodes permitted the formation of nodular free deposits to within rather close tolerances, as shown in Fig. 2. Using a 14 mesh (0.064 cm wire) Ta screen, a $PbO_2$ electrode measuring 36.8 x 8.9 x 1.6 cm and weighing 4500 g was plated in 142½ hr from the $Pb(NO_3)_2$ bath. Current was maintained at 0.016 amp/cm² on the anode and the bath temperature at 70°C throughout the electrolysis.

If the *p*H of the nitrate plating bath is not carefully controlled, the bath drifts strongly acid during electrolysis and is very corrosive to all of the common metals. However, by very careful maintenance of the *p*H in the range of about 2-4 during electrolysis by the frequent addition of lead oxide, and by protecting the base metal at the surface of the electrolyte, it is possible to plate $PbO_2$ on such metals as Ni and Fe. Even with these precautions, the base is slowly eroded away and by the time a thick plate has formed most of the base metal (in contrast to Ta) will have been eroded away, leaving voids (which are not always objectionable) in the center of the $PbO_2$ deposit.

### *Current Contacts to* $PbO_2$ *Anode*

Whenever $PbO_2$ with a conventional Cu current contact is used as anode in electrolytic cells, severe heating is observed in the contact area. If Ag current contacts are used, no heating occurs. The contact resistance between a number of the common metals and lead dioxide was measured[2] and it was found that all metals tested with the exception of Ag show high contact resistance to $PbO_2$ as seen in Table II. It is suggested that the resistance is caused by an oxide layer forming between the contact metal and the $PbO_2$. Most metal oxides being poor electrical conductors show high resistance. Silver, on the other hand, forms a conducting oxide and therefore has a low contact resistance.

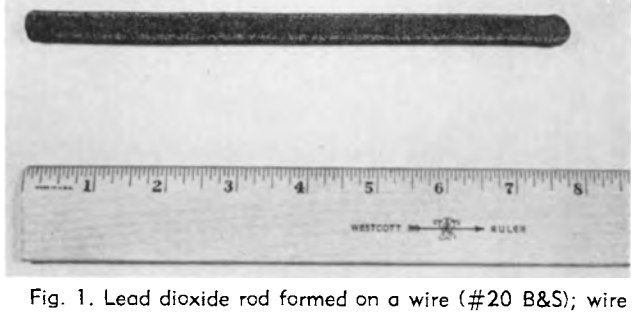

Fig. 1. Lead dioxide rod formed on a wire (#20 B&S); wire core withdrawn.

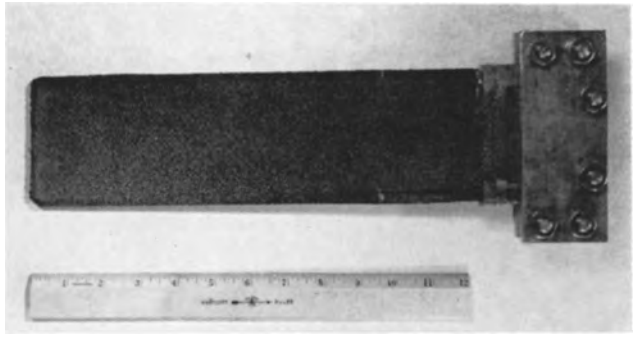

Fig. 2. Massive $PbO_2$ plated on a Ta screen base, and having a sprayed Cu over Ag current contact.

**Table II. Contact resistance of electrodeposited $PbO_2$ to various metals sprayed thereon**

| Metal | Contact potential at 1 amp Volts |
|---|---|
| Tin | 0.65 |
| Lead | 0.52 |
| Copper | 0.04 |
| 18-8 Stainless steel | 0.69 |
| Zinc | 0.5 |
| Aluminum | 0.19 |
| Silver | 0.0002 |
| Copper over silver | 0.0002 |
| Tin over silver | 0.0002 |
| Aluminum over silver | 0.0002 |

A coating of Ag only 0.002 cm or less in thickness applied by a metal spray technique was sufficient to produce low resistance and to overcome completely the heating previously observed in these electrode connections. In order to protect the Ag and to provide a rugged electrical contact to the $PbO_2$, the Ag-coated area is sprayed with a heavy layer of Cu, 0.16 cm or more in thickness. Preferably, the Ag and Cu are sprayed to form a jacket over the top end of the $PbO_2$ electrode, as in Fig. 2. The combination is sufficiently adherent to the base oxide so that it can be machined to fit in a mechanical current contact or it can be soldered directly to the power bus without injury to the $PbO_2$.

### *Testing the* $PbO_2$ *Anodes*

Electrodes formed by plating a thin coat of $PbO_2$, 0.04 cm or less, on a base metal proved unsatisfactory when used as anode in a perchlorate cell. With such a thin coating on Ta there was poor electrical contact and poor adhesion. The $PbO_2$ coating on Ni and other base metals proved to be extremely porous and did not protect the base metal from rapid anodic erosion when used in the perchlorate cell.

Thick $PbO_2$ deposits, 0.16 cm or more, on Ta proved to be efficient anodes in the perchlorate cells. The Ta base polarizes rapidly and then acts as an inert filler. Thick deposits on Fe and Ni also proved satisfactory after they had operated sufficiently long to leach out all traces of the base metal that were left after the original plating operation. It is, therefore, desirable when electrodepositing $PbO_2$ on metals such as Fe and Ni, to keep the weight of the base to a minimum.

[2] Test specimens were prepared by spray coating 2.5 cm of each end of electrodeposited $PbO_2$ rods about 1 cm in diameter and 10 cm long with the given metal. The rods were clamped at the metal coated ends and 1 amp was passed from a direct current source. The potentials across the metal-$PbO_2$ contact were measured on a potentiometer using manual pressure test probes.

**Table III. Current efficiencies in electrolysis of $NaClO_3$ with $PbO_2$ and Pt anodes (no additives)**

| Anode | Test No. | $NaClO_3$ conc. range over which eff. is calculated Initial g/l | Final g/l | Current efficiency, % |
|---|---|---|---|---|
| Pt | 1 | 602 | 100 | 85.2 |
| | | 293 | 39.8 | 82.4 |
| | 2 | 602 | 100 | 87.4 |
| | | 197.6 | 3.9 | 65.4 |
| $PbO_2$ | 1 | 606 | 100 | 75.0 |
| | | 198 | 1.8 | 27.1 |
| | 2 | 612 | 100 | 61.2 |
| | | 186 | 49.1 | 33.9 |

Anode current density = 0.3 amp/cm²; cell temperature = 25°-35°C; cell potential = 5-6.5 v.

**Table IV. Effect of $K_2S_2O_8$ additive on current efficiency in electrolysis of $NaClO_3$ with $PbO_2$ anode**

| g $K_2S_2O_8$ per liter of electrolyte | Test No. | $NaClO_3$ conc. range over which eff. is calculated Initial g/l | Final g/l | Current efficiency, % |
|---|---|---|---|---|
| 2.08 | 1 | 606 | 7.1 | 73.3 |
| | | 204 | 7.1 | 52.0 |
| 2.08 | 2 | 606 | 30.3 | 68.2 |
| | | 200 | 44.9 | 49.2 |
| None | 1 | 606 | 28.9 | 46.5 |
| | | 200 | 28.9 | 27.1 |
| | | 126 | 28.9 | 20.3 |
| None | 2 | 606 | 31.0 | 43.4 |
| | | 200 | 31.0 | 30.5 |
| | | 128.4 | 31.0 | 22.9 |

Anode current density = 0.3 amp/cm²; cell temperature = 25°-35°C; cell potential = 5-6.5 v.

The large $PbO_2$ electrode formed on the Ta screen, and described above, was used with a sprayed Cu over Ag contact in a 100 amp perchlorate cell at a current density of 0.28 amp/cm² and a temperature of 30°-50°C. The cathodes were type 430 stainless steel and the electrolyte was 5 liters of $NaClO_3$ solution having an initial concentration of 600 g/l. This cell was operated for 24 batches for a total running time of 860 hr without noticeable erosion of the anode, and with less than 0.25 ppm of Pb in the recovered $NaClO_4$.

The current efficiency of $PbO_2$ anodes in the conversion of chlorate to perchlorate, although less than that of Pt, is reasonably high when the concentration of $NaClO_3$ in the electrolyte is above 100 g/l. Below this concentration of chlorate, the current efficiency drops sharply. In Table III, the current efficiencies of $PbO_2$ and Pt anodes are compared for various chlorate concentration ranges when operated in 10-amp cells.

In order to obtain higher current efficiencies with the $PbO_2$ anode, especially in the lower chlorate concentration range, the use of additives becomes necessary. Sugino (10) has reported using NaF additive at a concentration of 2 g/l. In the present work, $K_2S_2O_8$ was found (11) to be even more effective, and the increase in current efficiency due to this additive is shown in Table IV.

## Acknowledgments

This paper includes the results of one phase of a research carried out under the Office of Naval Research Contracts Nonr 372(00) (2/19/51-8/31/51) and Nonr 807(00) (2/1/52-1/31/54).

The authors wish to express their thanks to J. F. Gall under whose supervision this work was done, and to E. Eitelman and W. Barry for their excellent assistance in the laboratory work.

Manuscript received June 24, 1957.

Any discussion of this paper will appear in a Discussion Section to be published in the December 1958 JOURNAL.

## REFERENCES

1. J. Mizuguchi, *J. Electrochem. Soc. Japan*, **17**, 294 (1949).
2. J. Mizuguchi, *ibid.*, **17**, 258 (1949).
3. G. Angel and H. Mellquist, *Z. Elektrochem.*, **40**, 702 (1934).
4. E. Andreoli, U. S. Pat. 598,193, Feb. 1, 1898.
5. V. Engelhardt and M. Huth (to Siemens & Halske, A.-G.) U. S. Pat. 935,250, Sept. 28, 1909.
6. M. Huth (to Siemens & Halske, A.-G.) U. S. Pat. 1,043,937, Nov. 12, 1912.
7. K. Sugino and M. Yamashita, *J. Electrochem. Soc. Japan*, **15**, 61 (1947).
8. Y. Kato and K. Koizumi, *J. Electrochem. Assoc. (Japan)*, **2**, 309 (1934).
9. F. Mathers, *Trans. Am. Electrochem. Soc.*, **17**, 261 (1910).
10. K. Sugino, *Bull. Chem. Soc. Japan*, **23**, 115 (1950).
11. H. C. Miller and J. C. Grigger, U. S. Pat. 2,813,825, Nov. 19, 1957.

# Technical Notes

## Enhanced Surface Reactions

### II. Oxygen Adsorption on Several Metals

**Manfred J. D. Low**

*Nichols Laboratory, New York University, New York, New York*

Recently, interesting experiments have been reported (1, 2) on the influence of high-frequency induced gaseous discharges on rates of chemisorption. In a previous paper (3) the enhancement of the rate and extent of adsorption in four adsorbate-adsorbent systems were reported, and a general mechanism was proposed. That investigation was extended to the adsorption of oxygen on seven metals and is here reported.

#### Experimental

A Tesla coil was applied in a manner previously described (3) to a standard constant volume adsorption system. Over desired periods of time a continuous discharge barely visible in a darkened room could be caused to persist. It was found that, under the conditions prevailing in actual runs, but in the absence of the adsorbent, the discharge had no noticeable effect on the pressure of the system.

The adsorption of tank oxygen on the following adsorbents is described: *(a)* 3.07 g gold foil "cohesive cylinders"; *(b)* 14.23 g C.P. aluminum foil; *(c)* 136 g N.F. 20 mesh iron filings; *(d)* 28 g 200 mesh 99.8% Mo powder; *(e)* 28 g 200 mesh Ni-free C.P. Co powder; *(f)* 42 g "Baker Analized" Cu foil; *(g)* 18 g "Baker Purified" 30 mesh Mg powder. In order to preclude any effects due to adsorbed hydrogen, the metals were not cleaned by the customary hydrogen reduction and evacuation procedure, but were merely degassed. It was found that a pressure of $10^{-6}$ mm Hg, or less, could be obtained and maintained by pumping at 400°±10°C for 16 hr for all metals except gold, which required 170 hr until release of gas ceased. The adsorption of oxygen was thus measured on surfaces covered partially or wholly with oxide films.

#### Results and Discussion

*Gold.*—Slight, instantaneous up-takes of oxygen were detected at 0°, 100°, 147°, and 257°C at oxygen pressures of 39-46 mm Hg. An estimate of the amount adsorbed was obtained by pumping, at the adsorption temperature, in 4 min to $10^{-4}$ mm Hg after the Au had been in contact with oxygen for periods up to 5 hr, and then heating the adsorbent to 400°C. Desorption of gas was detected at approximately 350° during the heating. Pressure increases of up to 0.94 mm Hg within the system indicated that about 0.02 ml NTP of gas had been evolved. It was concluded that a small amount of oxygen was strongly adsorbed by the Au under the conditions of the experiments, and that at least a part of it remained on the solid while the pressure was decreased and was caused to desorb under the influence of increasing temperature. Causing a discharge in the oxygen for periods up to 4 hr after the adsorption process had taken place had no effect on the oxygen take-up.

*Molybdenum, copper, magnesium, aluminum.*—Figure 1 is a plot of the data of experiments on the adsorption of oxygen by Mo and by Co. The enhancement in the rate of adsorption on causing the discharge ("ON") is quite detectable and remarkably large in view of the small energizing action of the Tesla coil. On stopping the discharge ("OFF"), the adsorption is seen to approximate its previous rate.

A much larger enhancement is depicted by curve I of Fig. 2, showing the adsorption of oxygen on Mg. At P the adsorbent was heated to 400°C and evacuated for 16 hr to a final pressure of $10^{-6}$ mm Hg. The experiment described by curve II was then made. It is seen that the rate, extent, and enhancement of adsorption are smaller than those shown by

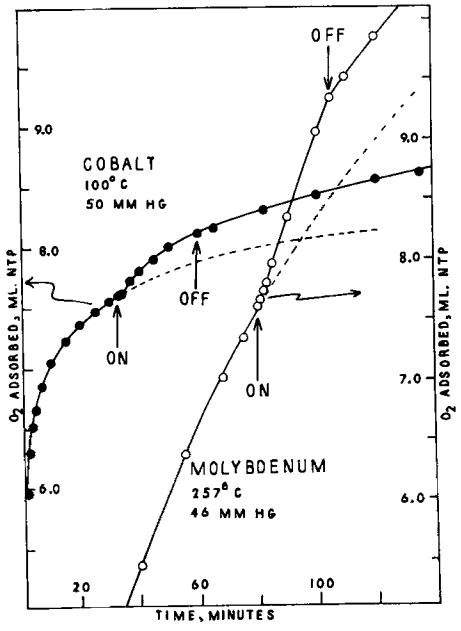


Fig. 1. Adsorption of oxygen on Co and on Mo

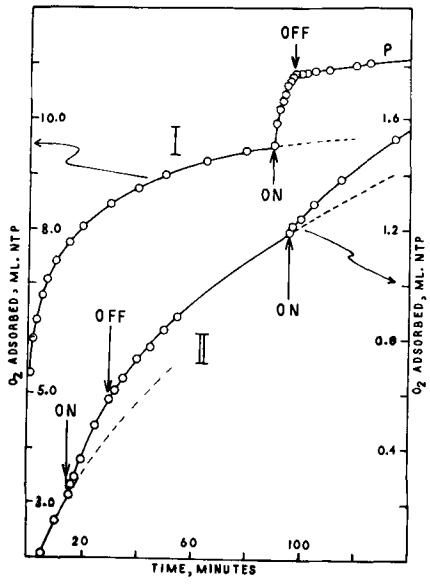


Fig. 2. Adsorption of oxygen on Mg at 100°C, 46 mm Hg

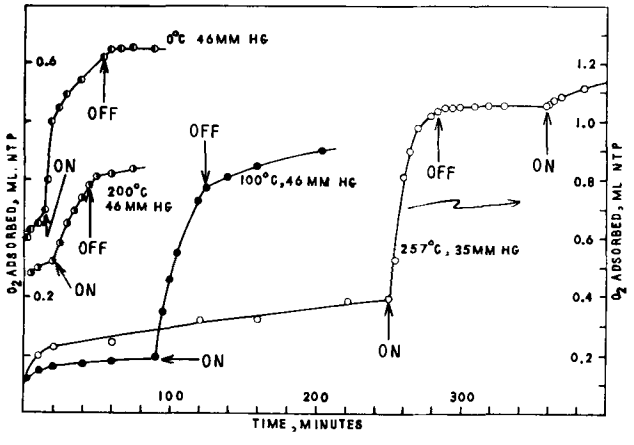


Fig. 3. Adsorption of oxygen on Al

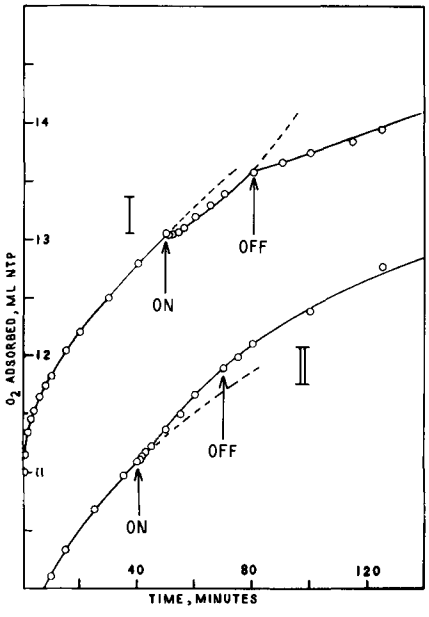


Fig. 4. Adsorption of oxygen on Fe at 257°C, 50 mm Hg

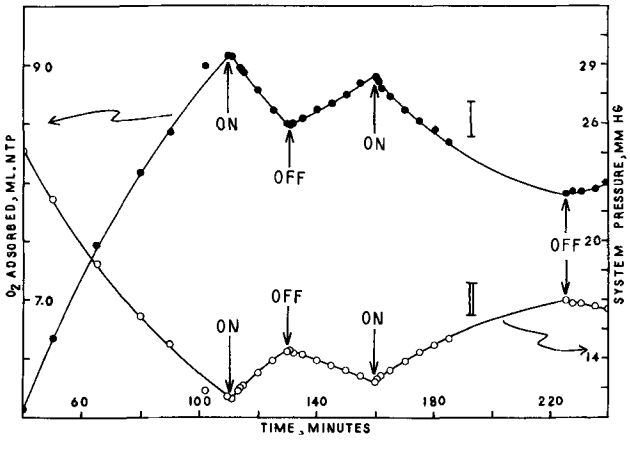


Fig. 5. Adsorption of oxygen on Cu at 257°C, 50 mm Hg

curve I. At the end of the experiments the metal had taken on a deep blue sheen confined to the surface of the adsorbent, and a transparent deep blue coating had appeared on the walls of the adsorbent chamber.

In Fig. 3 the enhanced adsorption of oxygen on Al is shown. The data of four consecutive experiments made at 257°, 100°, 0°, and 200°C in that order are shown, the metal having been pumped at 400° for 16 hr to $10^{-6}$ mm Hg after each experiment. It is seen that the adsorption rate falls off in a relatively short time, and that adsorption may be caused to occur on almost "saturated" surfaces.

*Iron and copper.*—Figure 4 shows two plots of adsorption of oxygen on Fe at 257°C. Curve I is an experiment with a fresh surface and curve II after this same adsorbent had been pumped on at 400° for 16 hr to $10^{-6}$ mm Hg. Desorption, manifested by an increase in system pressure, was found when the discharge was caused, shown by curve I. A slight enhancement effect, however, was detected during the second run, shown by curve II.

A more pronounced desorption effect was found to occur with Cu, Fig. 5. The magnitude of the measured effect is shown by the system pressure-time plot II of that figure.

*General theory.*—A general theory capable of accounting for enhancement of chemisorption, oxidation, and other phenomena, by activation of heterogeneous systems was presented previously (3). It was suggested that the relatively large effects instigated by a minute activating disturbance in the gas phase occur via a branching chain mechanism. If an active particle, G, strikes a surface atom, S, a "dissociation" of the latter may occur with formation of adsorption sites, V, the over-all process being written,

$$G + nS \rightarrow GV + (2n-1)V \qquad (I)$$

The remaining $(2n-1)$ sites may be active for further adsorption, causing enhancement, or may suffer bimolecular decay (4). It is suggested that this mechanism is operative in all cases described, with the exception of Au. The enhancements of adsorption which were detected, especially in the case of the almost "saturated" Al surfaces, together with previously discussed enhancement effects (3), tend to support this theory, which is also capable of explaining the interesting desorption phenomena described above.

The oxidation of Cu in activated oxygen has been studied by Dravnieks (5,6) in the pressure range

0.5-2.0 mm Hg and at temperatures ranging from 500° to 690°C. Enhancements of oxygen up-take were found to occur at 0.5, 1.0, and 2.0 mm Hg at 500°C, and at 0.5 mm at 600° and 690°C. At higher pressures at the last two temperatures, however, the enhancement disappeared, and at 2.0 mm and 600°C a retardation in oxygen up-take was found. At 500°C the oxidation curves, plotted according to the parabolic rate law, appeared as two straight lines with an intermediate region of rapidly changing slope. The first parabolic rate was identified with oxidation to $Cu_2O$, the region of rapidly changing slope with beginning of precipitation of CuO on the surface of the $Cu_2O$, and the second parabolic region with oxidation occurring in the presence of both oxides. At higher temperatures the oxidation curves could not be resolved into two distinct parabolas. The observations that activation may accelerate or retard the oxidation and may change the composition of the oxide scale were explained in terms of lower permeability of CuO than $Cu_2O$ to reactants, and of rate of precipitation of CuO.

Tylecote (7) found that the CuO content of scales formed on high purity Cu in dry air increased with reduction in temperature from 7% at 850°C to about 100% at 420°C, and that for the majority of temperatures, the CuO content decreased to a constant temperature dependent value as the film increased in thickness. Under the conditions of the experiments reported here, it may be expected, then, that a film of CuO formed on the Cu surface. Similarly, the retardations noted by Dravnieks occurred under conditions at which CuO would predominate, whereas enhancement was found when $Cu_2O$ would predominate.

It is suggested the evolution of gas observed during activation was caused by the transition,

$$2CuO \rightarrow Cu_2O + \tfrac{1}{2}\ O_2 \qquad (II)$$

Because the observed effect was large in comparison to the magnitude of the stimulus, it may be postulated that a chain disturbance was initiated on the surface, causing unstable CuO to give up oxygen. The initial step of the mechanism may be the collision of an active oxygen particle, perhaps a metastable oxygen molecule (8), with a surface CuO, causing reaction (II) to occur. The local disturbance then spreads through the film, permitting the gas evolution to occur. The chain propagator may be activated CuO-oxygen complexes, Cu atoms, or the oxygen atoms produced by the process.

The action of active oxygen on iron may be explained similarly by an enhanced transition of a surface film (9) of $\gamma$-$Fe_2O_3$ to cubic $Fe_3O_4$ with attendant release of oxygen when $\gamma$-$Fe_2O_3$ predominates. At higher $Fe_3O_4$ concentrations, the normal enhancement effect occurs (Fig. 4).

The influence of active oxygen on Cu and Fe, at least, is thus twofold if more than one oxide can be formed. (*A*) If a change in oxidation state can occur, that change may be enhanced by causing an increase in the active particle concentration. The effect appears as an actual gas evolution, as described above, or as a retardation of oxidation rate resulting, in either case, in a change in the oxide composition. (*B*) If no change in oxidation state is possible, or if such a change has occurred, then an enhancement of oxygen adsorption may occur, probably via the site-creating mechanism (I). It seems plausible that an enhancement of adsorption occurs simultaneously with the enhanced change of oxidation state, but may be overshadowed by the latter.

The relatively large enhancements detected (1-3) and the generality of the effect lend credence to the proposed theory. A similar high degree of plausibility is inferred for the application of that theory to the retardation effect. The proposed generation of sites for the enhancement of chemisorption as well as the retardation or enhanced transition of oxidation states must be considered to be operative through a self-perpetuating surface disturbance, of electronic or particulate nature, of considerable chain-length in order to explain the relatively large effects instigated by a small stimulus.

Manuscript received May 29, 1957.

Any discussion of this paper will appear in a Discussion Section to be published in the December 1958 JOURNAL.

REFERENCES

1. H.-J. Engell and K. Hauffe, *Z. Elektrochem.*, **57**, 773 (1953).
2. T. J. Gray and P. W. Darby, *J. Phys. Chem.*, **60**, 209 (1956).
3. M. J. D. Low and H. A. Taylor, *This Journal*, **104**, 439 (1957).
4. H. A. Taylor and N. Thon, *J. Am. Chem. Soc.*, **74**, 4169 (1952).
5. A. Dravnieks, *ibid.*, **72**, 3761 (1950).
6. A. Dravnieks, *J. Phys. Colloid Chem.*, **55**, 540 (1951).
7. R. F. Tylecote, *Metallurgia*, **53**, 191 (1956).
8. S. N. Fouer and R. L. Hudson, *J. Chem. Phys.*, **25**, 601 (1956).
9. D. E. Davies and U. R. Evans, *J. Chem. Soc.*, **1956**, 4373.

# Photodeposition of Luminescent Screens

**M. Sadowsky and P. D. Payne, Jr.**

*Lansdale Tube Division, Philco Corporation, Lansdale, Pennsylvania*

In the Philco color tube, the phosphor is deposited (1) as a line array on the inside surface of the cathode ray tube bulb panel. The array consists of red-, blue-, and green-emitting phosphor stripes, between each line of which there is a black, nonluminescent line (2,3). The screen is backed by a reflective film of aluminum, on the back of which is a set of magnesium oxide powder stripes applied in

strict reference to the phosphor lines on the face. These phosphor lines vary in width in a controlled manner between the center and the edge for electrical reasons. The total triplet of red, blue, and green lines plus the three dark guard lines averages 61 mils.

The exact procedure for depositing a color screen is as follows: The bulb is picked up automatically from an indexing conveyor. 200 ml of a clear photoresist solution, containing 25g PVA grade 52-22, and 2.75 g ammonium bichromate dissolved in 600 ml water with 290 ml denatured ethanol, is introduced by a dispenser. The bulb face is flow-coated by tilting and rotating. The excess solution is drained off, and the bulb returned to the conveyor. There it is dried for 35 min using filtered, dried air. It is then placed face down in the projector for a 3½-min exposure through the appropriate line master. It is then returned to the conveyor for automatic flow-coating and drying of the phosphor slurry. 100 ml of a mixture of 80 ml denatured alcohol, 60 ml water, and 50 g phosphor is normally used. Drying takes 13 min. The final step of washing off the unexposed photoresist and phosphor is done on a turntable with water directed against the inside funnel wall and flowing up and across the screen for 1 min. The same procedure is used for guard lines, color lines, and index lines. The screen is treated with 0.5% aqueous lithium hydroxide after the first and second color lines are applied. This prevents subsequently applied phosphors from contaminating the previously applied lines. The suggested mechanism for photofixation is shown in Fig. 1.

When the phosphor slurry is superimposed on the film with its latent image of hardened lines, the water in the phosphor slurry goes into the crosslinked film, softening it for penetration. The alcohol on the other hand tends to remove the water, making it possible to control penetration by proper control of the water-to-alcohol ratio. A compromise is effected between maximum phosphor occlusion (thicker screens) and penetration of the phosphor to the glass which might result in adhesion in the

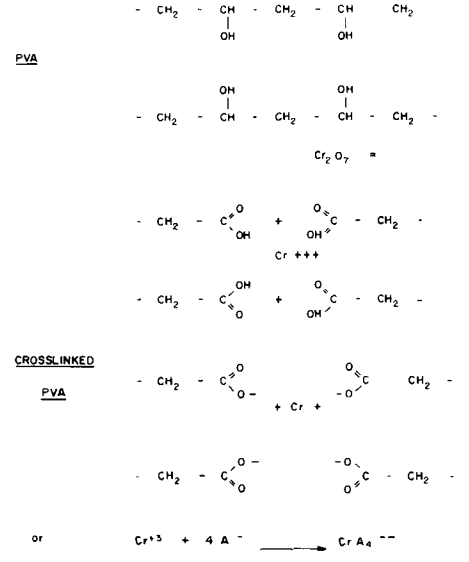


Fig. 1. Suggested mechanism for photofixation of the lines on the screen.

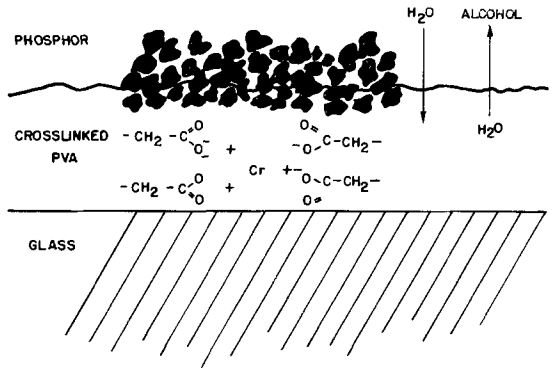


Fig. 2. Mechanism for phosphor imbedment

nonexposed areas. The mechanism for phosphor imbedment is shown in Fig. 2.

The problems encountered in photodeposition of multicomponent screens are: adhesion, control of screen weight, cross contamination and fogging.

To be practical, the process should be a water system, and must also be reasonably fast (short exposure times), must not affect deleteriously the phosphors, MgO, or Al used; agents used must bake off so as not to leave a significant residue in the completed tube, which might damage the cathode.

Addition of $H_3PO_4$ to the sensitized PVA solution promotes adhesion to the glass, but is difficult to control and deteriorates rapidly with age. Urea formaldehyde gives similar results with slower deterioration. PVA of lower per cent hydrolysis has better adhesion to glass, but is not sufficiently photosensitive. Consistently good adhesion is best obtained by drying the PVA film to equilibrium with air of 1% RH.

### *Parameters in Control of Screen Weight*

*Thickness of sensitized PVA film on glass.*—As the coating thickness is increased, the total depth of the phosphor layer increases. If exposure takes place from the surface to be coated, through to the glass, too thick a film will result in insufficient light reaching the glass-film interface to provide adequate fixing to the glass. If the exposure time is then increased, the surface to be coated will be insolubilized to such an extent that the phosphor particles will not penetrate it, and a thin screen will result. This effect can be overcome by leaching a portion of the sensitizer out of the surface of the film with a solvent, such as ethyl alcohol, which will dissolve the sensitizer, but not the film.

*Phosphor slurry formulation.*—A suspension of phosphor in water provides maximum softening of the exposed film, allowing maximum phosphor penetration and screen weight. However, such a slurry is difficult to apply uniformly because it dissolves and carries along much of the unexposed water-soluble portion of the film and dries too slowly. Also, this allows phosphor to reach the glass between the image lines and adhere there. Addition of ethyl alcohol to the slurry reduces its effect on the water-soluble film, and promotes more rapid drying, resulting in a more uniform screen. Addition of the alcohol, however, reduces the penetration of the image lines by the phosphor, causing a

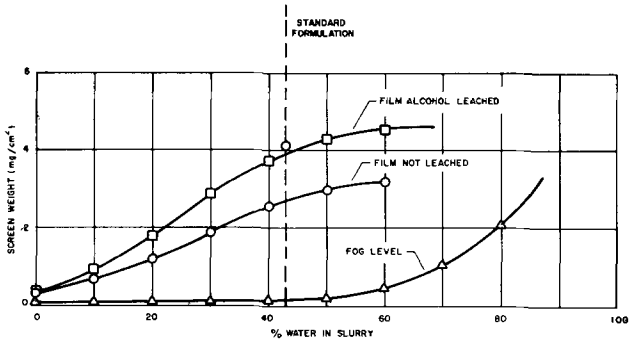


Fig. 3. The screen weight vs. per cent of water in slurry. The three curves show fog level (triangle), film leached with alcohol (square) and film not leached (circle).

drop in screen weight, so these factors are balanced to provide the best combination of screen weight, uniformity, and freedom from fogging between the lines. A typical slurry will contain 80 parts alcohol and 60 parts water by volume, with from 40 to 90 g of phosphor, depending on the particular phosphor used. The weight of phosphor used is set at that value which produces the best flowing characteristics. The compromise is shown on the graph in Fig. 3.

### *Cross Contamination*

Cross contamination is the presence of phosphor of one color in screen lines of another color.

*Causes.*—(*a*) Trapping of particles by the PVA line of a previous color which was not thoroughly covered with phosphor; (*b*) trapping of particles in the rough phosphor surface of a previous line.

*Cures.*—First, post-harden the PVA to prevent any further phosphor being trapped. Materials used include: titanium lactate, Quilon (chrome organic complex), DMU, glyoxal, diazocyanates, hydroxyadipaldehyde, aqueous ammonium dichromate (exposed to light), heat at 110°C for 15 min. All of these aid in reducing cross-contamination, but none is sufficient.

Retreat the phosphor lines with the same color slurry prior to application of the next color. This works, but is too costly.

Second, coat the screen with an impervious layer (*a*) lacquer film; this protects completely, but causes wrinkling of subsequent lines; (*b*) aqueous potassium silicate; this reduces contamination but produces fog.

Treat the screen with aqueous lithium hydroxide to repel subsequent phosphor. This treatment has produced good results most consistently and is currently in use.

### *Fog*

Fog is the term used to describe phosphor particles which deposit on the glass between the lines and fail to wash off.

*Causes.*—(*a*) Electrostatic attraction of particles to the glass; (*b*) trapping of particles in partially fixed PVA which has dried between the lines after washing.

*Cures.*—(*a*) Use of phosphor with few superfines; particles which tend to adhere to bare glass are those of low density and particle size below 1$\mu$; (*b*) prevent penetration of particles through unexposed portion of film to the glass by keeping the water content of the slurry low enough; (*c*) wash the exposed and coated screen before drying is completed, where very fine particles must be used, and water content must be kept high.

The process described above has been used to make thousands of tubes. The precision is built into the equipment, rather than into hardware incorporated in the tube. The chemical processes are controllable and practical, giving high reproducibility with little more care than is exercised in the preparation of screens for monochrome cathode ray tubes.

Manuscript received June 27, 1957. This paper was prepared for delivery before the Washington Meeting, May 12-16, 1957.

Any discussion of this paper will appear in a Discussion Section to be published in the December 1958 JOURNAL.

REFERENCES

1. M. Sadowsky, *J. (and Trans.) Electrochem. Soc.*, **95**, 112 (1949).
2. H. Colgate, C. Comeau, D. Kelley, D. Payne, and S. Moulton, 1957 IRE National Convention Record, Part 3, pp. 238-241.
3. G. S. Barnett, F. J. Bingley, S. L. Parsons, G. W. Pratt, and M. Sadowsky, *Proc. IRE*, **44** [9], 1115 (1956).

## June 1958 Discussion Section

A Discussion Section, covering papers published in the July–December 1957 JOURNALS, is scheduled for publication in the June 1958 issue. Any discussion which did not reach the Editor in time for inclusion in the December 1957 Discussion Section will be included in the June 1958 issue.

Those who plan to contribute remarks for this Discussion Section should submit their comments or questions in triplicate to the Managing Editor of the JOURNAL, 1860 Broadway, New York 23, N. Y., *not later than March 3, 1958.* All discussion will be forwarded to the author, or authors, for reply before being printed in the JOURNAL.

# Convection and Film Instability

## Copper Anodes in Hydrochloric Acid

R. S. Cooper and J. H. Bartlett

*Department of Physics, University of Illinois, Urbana, Illinois*

ABSTRACT

In the Cu/HCl system, when natural convection occurs, there are two steady-state current plateaus. On the first of these ($-0.28<V<-0.05$), copper dissolves only in the cuprous form, and the value of the current agrees with that predicted by the Tobias theory of natural convection. On the second plateau, up to 30% of the copper is dissolved as cupric ions. When the circuit is interrupted, the resistance of the CuCl layer decays primarily due to opening of its pores, the pore area increasing linearly with time. Oscillations are found at the anode voltage region below which there is no layer and above which the layer can remain on the electrode indefinitely. A kinetic explanation of oscillations is proposed, and is in accord with the observations.

In the study of the anodic behavior of Cu in HCl, it has been shown (1) that the phenomena of overshoot and oscillation, as well as the existence of a nonzero steady-state current, are possible only if convection is allowed to take place.

The process of convection is a complicated one, and at first sight one might suppose that quantitative conclusions would be difficult to obtain. Nevertheless, progress has been made in the theory (2), at least as regards the steady-state behavior. If the composition of the convection layer is known, perhaps by deduction from schlieren and other information, then the rate at which the reaction products are removed by diffusion and convection may be calculated, and thus the value of the steady-state current. In the present paper, it is shown that theory and experiment agree well.

The manner of approach to the steady state is more difficult to explain, but even here one can at least clarify some aspects of it. Initially the main process is the deposition of $Cl^-$ from solution to form a cuprous chloride layer, and this has precedence until the layer is complete. Any material which has been convected downward during this stage (time less than 3 sec) is not sufficient to form a stream from the bottom of the anode. However, once the layer is complete, or almost so, the current is reduced by the layer resistance, and the bulk removal process becomes predominant. The initial thickness of the CuCl layer is a function of the plateau current $i_f$. If this thickness is greater than the steady-state value, one may expect an adjustment to occur such that the thickness decreases, with pore area constant, and the current will rise from a minimum value. On the assumption that the thickness decreases at a rate proportional to the excess of removal current over actual current, it is possible, as will be shown, to account for the shape of the current vs. time curve after the minimum.

It had previously been a puzzle as to what is responsible for the higher current on the second steady-state plateau. Accordingly, weight-loss determinations were made, and showed that a new reaction involving cupric ions comes in. On the basis of a simple model, it now seems possible to account for the value of the above-mentioned current.

Also, previous measurements (3) of the decay of layer resistance had not been made for times sufficiently short so that one could draw good conclusions about the mechanism. This has now been remedied, and it seems certain that the process which is most important electrically is the opening of the pores.

The mechanism underlying oscillations has been uncertain. Bonhoeffer and Gerischer (4) tried to construct a theory in which a $Cu_2O$ layer was involved. In the previous work (1), the second current-time plateau was found to be much more prominent at lower concentrations, and it seemed therefore that the $OH^-$ ion is involved. Subsequent observations reveal that CuCl is also deposited during this plateau, and there still is no direct evidence for $Cu_2O$ formation, even though electron diffraction techniques allow the detection of very small quantities. The above theory remains, therefore, very much in doubt, especially since our observations show the oscillations to be confined to the boundary region between where a layer exists and where it does not. Hence the present article contains a discussion of how one can expect oscillations even in the absence of a $Cu_2O$ layer.

*Experimental arrangement.*—The experimental apparatus and methods, as well as the associated nomenclature, are the same as described in previous studies (1,3,5). These consisted of a simple cell with an 0.1*N* calomel reference electrode and the necessary equipment for applying and measuring voltages and currents. Circular anodes (0.02 $cm^2$) were

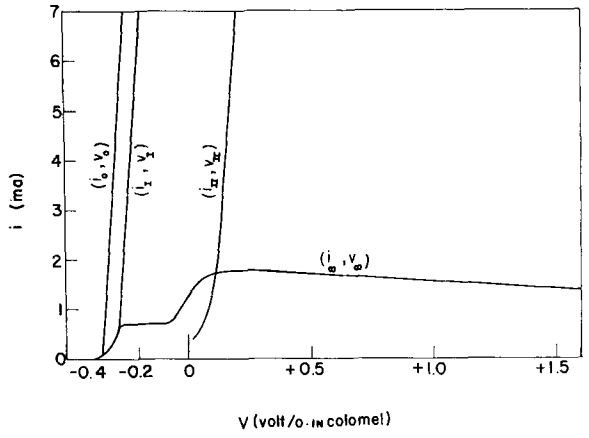


Fig. 1. Characteristic curves for an unshielded anode (0.02 cm²) with exposed face vertical, in 2N HCl, showing locus of initial current and voltage ($i_0$,$V_0$), of stationary values of current and voltage for the first plateau ($i_I$,$V_I$), for the second plateau ($i_{II}$,$V_{II}$), and for the steady state ($i_\infty$,$V_\infty$).

used for the most part, the electrolyte being 2*N* HCl.

## Results

### *The Steady State*

As may be seen from Fig. 1, the steady-state current-voltage curve is similar in shape to a polarogram, having two plateaus,[1] i.e., regions where the current is approximately independent of voltage. The steady state (indicated by the subscript $\infty$) is usually reached in from 1 to 5 min, except at high voltages where the time may be longer. The curve for $i_\infty$ vs. $V_\infty$ does not depend on the choice of external parameters ($E$ and $R$), nor on the values of the initial current or initial layer thickness.

*The low-voltage region.*—The region below −0.24 v is governed by a polarization equation of the form

$$V = a + b \log i \qquad \text{(I)}$$

This is the form expected according to the reaction rate theory of Glasstone, Laidler, and Eyring (6), applied to anodic dissolution of a metal; with

[1] These are not to be confused with the current-time plateaus of ref. (1).

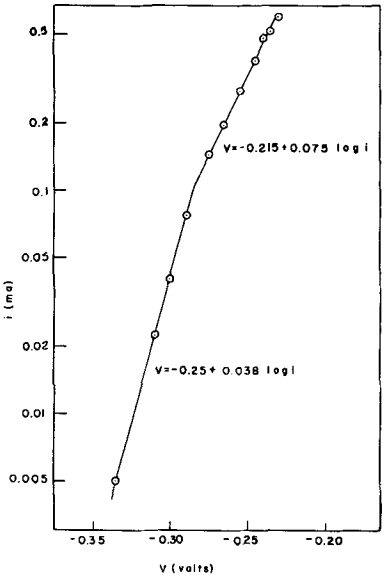


Fig. 2. Current vs. voltage in the steady state, at low voltages for a Cu anode (0.02 cm²) in 2N HCl.

$$b = \frac{0.059}{Z\alpha} \qquad \text{(II)}$$

where $Z$ is the charge transferred and $\alpha$ is a constant lying between 0 and 1. Alpha is sometimes found to be greater than one, and this has been interpreted as due to mechanisms involving more than one ion (7). The results (Fig. 2) show a break in the curve at −0.28 v, corresponding to the potential of Cu in CuCl-saturated 2*N* HCl (1). Below −0.28 v, $b = 0.038$, and above that voltage $b$ abruptly doubles, becoming 0.075. The value for $b$ below −0.28 v yields a value for $\alpha$ (= 1.55) greater than 1, which indicates a mechanism involving at least two ions, and thus favors the reaction

$$Cu + 2Cl^- \rightarrow CuCl^-_2 + e^- \qquad \text{(III)}$$

as a mechanism rather than direct formation of $Cu^+$ ion, followed by complex ion formation in solution. The fact that $b$ exactly doubles may mean that the effective $\alpha$ is the same in both cases, and that the larger value of $b$ (corresponding to $\alpha = 0.785$) is associated with a reaction involving only one ion. The reaction

$$Cu + Cl^- \rightarrow CuCl + e^- \qquad \text{(IV)}$$

is such a reaction, and all our available evidence indicates that it is the one which occurs.

*The first steady-state plateau.*—For $V \geqq -0.28$ v, an anodic film, which was identified as CuCl by means of electron diffraction, was observed on the electrode. On the first plateau, i.e., for the range $-0.28 \leqq V_\infty \leqq -0.05$, no $Cu^{++}$ enters the solution (shown by weight-loss determinations). In the steady state, the current is thus accounted for wholly by the entrance of cuprous ions into solution in the form of the complex $CuCl^-_2$, which is removed from the anode region by convection and diffusion. If one assumes reasonable values for viscosity and density of the convection layer, then, as is shown below, it is possible to calculate from theory a value for the steady-state current, as well as a value for the maximum thickness of the convection layer, which is in good agreement with the experimental value.

*Application of convection theory.*—Tobias and coworkers (2) and Wagner (8)[2] have recently developed a theory of natural convection control at electrodes and soluble slabs, treating the mass transfer problem in the same fashion as the well-studied problem of heat transfer. A relation is developed in terms of three dimensionless groups, which written out in familiar terms is

$$\frac{i}{S} = 0.66 \frac{zFD\,\Delta c}{y(1-t_-)} \left(\frac{\mu}{\rho D}\right)^{1/4} \left(\frac{gy^3\,\Delta\rho}{\mu^2}\right)^{1/4} \qquad \text{(V)}$$

where $S$ is the anode area, $\mu$ is the average viscosity of the solution in the convection layer, and is approximately that of 2*N* HCl (= $10^{-2}$ poise); $g$ is the acceleration of gravity; and $\rho$ is the average density, 1.045 g/cc. $\Delta c$ and $\Delta\rho$ are the differences between the bulk and interphase concentrations and densities, respectively. (These two quantities serve as

[2] In the author's case, the condition of Wagner that $|\Delta c| << c_0$ is not met. Instead, $|\Delta c|$ is about $\Delta c_{max}$ and this leads to $x^{-1/4}$ dependence, where $x$ is the distance from the leading edge of the electrode.

the driving force of the mass transfer process). $F$ is the Faraday, and $z$ the valence (= 1 here). The concentration referred to is that of the $CuCl_2^-$ complex ion. It is zero in the bulk phase and $0.24N$ at the CuCl layer surface, if there is saturation in the approximately $2N$ $Cl^-$ solution. [That the $Cl^-$ concentration is close to the bulk value can be seen from the schlieren photos of the steady state (11), and from a calculation (Appendix I) which shows that even under pure diffusion a small $Cl^-$ gradient (about $0.2N$ across the layer) is sufficient to supply the steady-state $Cl^-$ demand.] From solubility data (9), and using the densities as determined by Engle (10), $\Delta\rho = 0.026$ g/cm. $y$ is the height of the electrode, and must be suitably averaged for one with a circular cross section. The precise evaluation is made in Appendix II and the result is $y = 0.121$ cm for the case considered here. $t_-$ is the transport number of the $CuCl_2^-$ ion, and may be taken as zero, since the $CuCl_2^-$ ion must move against the current, and is at most one-tenth as numerous as the $Cl^-$ and $H^+$ ions. $D$, the diffusion coefficient of $CuCl_2^-$, is estimated to be $1 \times 10^{-5}$ cm²/sec, from the value for similar ions. Putting these values in Eq. (V) one obtains 32.7 ma/cm² as the limiting current density, which falls in the observed range of 30-35 ma/cm². This is strong evidence that the current on the first plateau is controlled by natural convection of the $CuCl_2^-$ away from the electrode. It is to be noted that this process is almost entirely independent of electrochemical influences, being mainly mass transfer from a solid slab of a soluble material. When the circuit is opened, this process continues unchanged as long as there is a CuCl layer on the anode surface, as is proven by schlieren observations. This fact, that the removal process is relatively independent of current fluctuations, will prove to be important for subsequent discussions of oscillations and overshoot.

The thickness of the convection layer varies along the height of the electrode, being zero at the top and a maximum at the bottom. The maximum thickness was found to be independent of current density once convection had become stabilized, and was of the order of 0.02 mm as measured from schlieren photographs (11). This agrees with the recent theoretical result of Keulegen (12) for the maximum convection layer thickness:

$$\delta_c = 3.33 \left( \frac{\mu D y}{g \Delta\rho} \right)^{1/4} \qquad \text{(VI)}$$

which yields a value for $\delta_c$ of 0.185 mm, for an electrode 2.5 mm high in $2N$ HCl.

*The Second Steady-State Plateau.*—Electrochemical experiments show that the increase in current above −0.05 v is at least partially due to the formation of $Cu^{++}$ ions, which go directly into solution through the pores in the CuCl layer. Weight loss determinations were carried out at −0.02, 0.4, 0.5, and 0.96 v, and the fractions of cupric ion formed were found to be 13%, 29%, 32%, and 28%, respectively. The first result corresponds to a point about half-way up on the rise between −0.05 and +0.1 v (Fig. 1), and the following three to points on the second plateau. Thus the relative $Cu^{++}$ formation reaches a limiting value of approximately 30% of the Cu lost (equivalent to 46% of the current).

Since $Cu^{++}$ is highly favored in concentrated solutions of copper ion, one might expect $Cu^{++}$ formation exclusively, instead of its being limited to 30%. However, a closer analysis shows how this limiting current may come about. Assume that in the steady state there exists a porous CuCl layer with pore area $S_p$, that the production of more CuCl occurs according to Eq. (IV) at the Cu surface, the $Cl^-$ passing in through the pores, and that the CuCl layer dissolves by a purely chemical action at the interface of the layer and the solution. Under these conditions the $Cl^-$ flux through the pores will be equal to the current due to Eq. (IV). Because there is a source of $Cu^{++}$ at the anode surface the $H^+$ ions (being 8 times as mobile as the $Cu^{++}$) will tend to migrate out of the pores, which will then be filled with a solution consisting mainly of $CuCl_2$. If the concentration of the $CuCl_2$ in the pores is uniform (molarity = $c$) which is reasonable on the grounds that there are appropriate sources and sinks at the end of the pores and that the mobilities, $\mu$, are comparable, then the currents carried by the respective ions are due only to migration and are:

$$i_{Cu^+} = i_{Cl^-} = eS_pF\left(\frac{dN}{dt}\right)_{Cl^-} = eS_pF\mu_{Cl^-}E\,2c \qquad \text{(VII)}$$

$$i_{Cu^{++}} = 2eS_pF\left(\frac{dN}{dt}\right)_{Cu^{++}} = 2eS_pF\mu_{Cu^{++}}Ec \qquad \text{(VIII)}$$

where $dN/dt$ is the ion flux and $E$ is the electric field. Thus the ratio of the currents due to $Cu^{++}$ and $Cu^+$ formation is equal to the ratio of the $Cu^{++}$ and $Cl^-$ ion mobilities (or ionic conductances). Using values at infinite dilution from Conway (13),

$$\frac{i_{Cu^{++}}}{i} = \frac{\lambda_{Cu^{++}}}{\lambda_{Cu^{++}} + \lambda_{Cl^-}} = 41.5\%$$

$$\frac{[Cu^{++}]}{[Cu^{++}] + [Cu^+]} = 26\%$$

compared to 46% and 30% experimentally, which is very good agreement considering the crude assumptions and approximations involved.

It may be possible to account for the magnitude of the current increase from the first plateau to the second. Adding the percentage of current due to $Cu^{++}$ would increase the 0.65 ma to only 1.2 ma. If Eq. (V) is used uncritically, the added $Cu^{++}$ (estimated to be at least 0.2 molar from schlieren data from preceding papers) approximately doubles the density difference ($\Delta\rho$) and consequently increases the convection current to about 1.4 ma, as against the observed value of 1.8 ma. However, Eq. (V) only holds for one current-carrying ionic species, so that the agreement is reasonably good.

*Resistance and potential.*—By breaking the circuit and observing the voltage change one can determine the open-circuit electrode potential and the electrode resistance associated with the steady state. At voltages below −0.05 v, it was found (3) that the electrode resistance is small compared to the solution resistance of about 14 ohms, and that the electrode potential varies, adjusting to the applied

voltage. The anode film is so thin or porous as to have a resistance negligible as compared to that of the solution. The variation in electrode potential is due to concentration polarization of the $Cl^-$ ions in the pores of the layer, as was shown for the first temporal plateau (1). For applied voltages above —0.05 v the resistance increases with $V_\infty$, while the electrode potential remains constant, being in the range of —0.05 to —0.03 v. The resistance increase is associated partly with the observed (3) increase in the steady-state layer thickness ($\delta_\infty$). That the electrode potential remains near the standard potential of the $Cu|Cu^{++}$ half-cell (—0.05 v) indicates that the $Cu^{++}$ is the potential determining ion. A twofold increase of $Cu^{++}$ concentration is equivalent to a polarization of only 0.01 v, and the maximum solubility of $CuCl_2$ (7M) limits the total polarization to 0.03 v above the standard potential. Thus, until the initiation of a new reaction with a higher electrode potential, the electrode potential must remain below —0.02 v.

*Break transients.*—The decay of layer resistance has been studied previously (3), but most of the data were for times greater than 30 msec, when the resistance has already dropped to less than one-tenth of its steady-state value. To obtain the missing information, it was found convenient to use the rapid-acting interruption switch (1) to obtain data for short off-times. This switch, which was motor driven, would operate from 2 to 6 times/sec, opening the circuit for periods of from 0.4 to 10 msec. Since the period between interruptions was sufficiently long for the electrode to recover completely, a complete resistance decay curve could be obtained during one run. The result for V = 2.5 v (Fig. 3) shows $\sigma$, the conductance of solution plus layer, to be a linear function of time in the early stages of the decay, namely,

$$\sigma = 0.36 \times 10^{-3} + 0.24t \qquad \text{(IX)}$$

Extrapolating this to the end of the —0.05 v potential plateau (0.29 sec) gives 14 ohms, which is the value of the solution resistance alone. Thus the linear relation for $\sigma$ holds throughout the resistance decay.

It is to be noted that, while the data cover only 2% of the time of the decay, this corresponds to

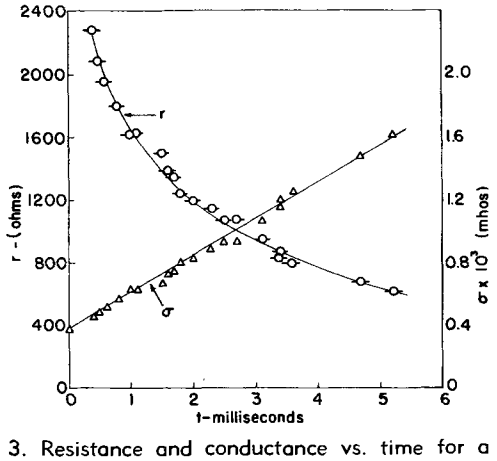


Fig. 3. Resistance and conductance vs. time for a break from the steady state (V = 2.5v). Copper anode (0.02 $cm^2$) in 2N HCl.

75% of the resistance drop, after which the percentage uncertainty in $\sigma$ becomes high. The fact that the layer resistance becomes of the order of $r_0$ (14 ohms) or smaller does not mean that the layer has dissolved to any great extent, but rather that the pores have widened. Assuming the layer in question to be $10^{-3}$ cm thick, then the resistance would be 14 Ω if the pore area were as much as only 1% of the surface. Furthermore the rate of solution is not sufficient to dissolve an appreciable portion of the layer in the short times associated with the resistance decay. The film resistance ($r_1$) is given by:

$$r_1 = \frac{\delta}{\kappa S_p} \qquad \text{(X)}$$

Since $\delta$ cannot change so rapidly and $\kappa$ cannot be expected to vary much (in going from that for a $CuCl_2$ solution to that for HCl) then the major change in $r_1$ must be due to variation in $S_p$, the pore area. Comparing (IX) and (X) one sees that $S_p$ increases linearly with time. Therefore

$$S_p(t) = (S_p)_\infty + kt \qquad \text{(XI)}$$

where $k$ is a constant.

### *Overshoot*

Overshoot is defined to be the situation where the current or voltage passes beyond its steady-state value before finally arriving there. For definiteness, the following discussion will be confined to the case where the current goes through a minimum after the completion of a plateau.

Shielded electrodes with no convection display no minimum, but rather a monotonically decreasing current. Also, unshielded vertical electrodes in low acid concentrations (small removal currents) do not show appreciable overshoot. Finally, such current minima never occur before 3 sec have passed, regardless of the duration of the plateau. Since this is approximately the time required for the initiation of convective fluid flow, this type of overshoot appears to be associated with the convection process, which removes material from the layer.

Several examples, taken with an unshielded electrode in 2*N* HCl, are reproduced in Fig. 4. The transient in Fig. 4a is typical of those with low applied voltages such that the steady state lies on the first plateau, between —0.27 and —0.05 v. As the applied voltage is increased the overshoot, ($i_\infty - i_{min}$), becomes at first greater, and then smaller, finally disappearing altogether (Fig. 4d).

The thickness ($\delta_1$) of the layer originally formed during the first current plateau *depends only on the value of the current on the plateau* ($i_1$), and may be larger[3] than the steady-state layer thickness ($\delta_\infty$) which depends only on $V_\infty$. If there were no convection, the thickness would increase indefinitely once the pore area had reached its lowest value. Obviously, if $\delta_1 > \delta_\infty$, the steady state will be approached only if the thickness decreases due to dissolution of the layer.

[3] The value of $\delta_1$ is a function of $i_1$, and ranges from $10^{-2}$ cm at low current densities to $10^{-4}$ cm or less at high current densities. $\delta_\infty$ varies with $V_\infty$ and has been estimated (3) to be of the order of $2 \times 10^{-4}$ cm in the steady state.

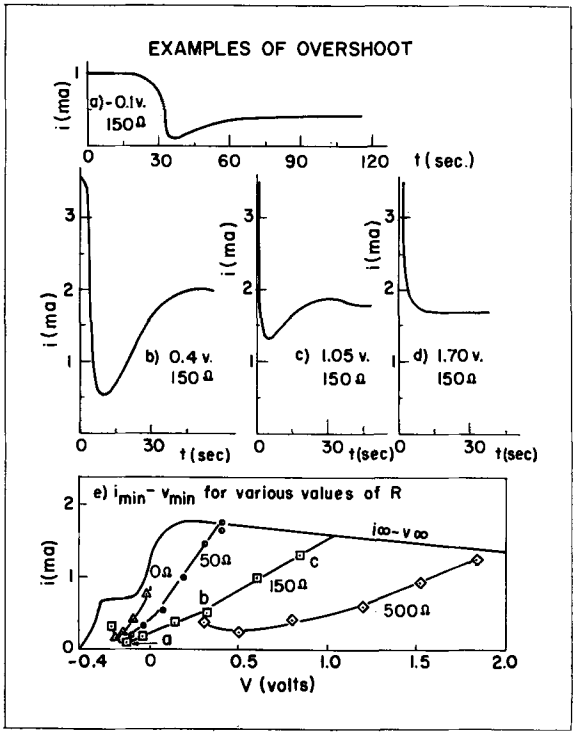


Fig. 4. (a) — (d) Current vs. time curves for a Cu anode (0.02 cm²) in 2N HCl. R = 150Ω and E is indicated on each graph. (e) Curves showing $i_{min}$ vs. $V_{min}$ for various values of R. The steady-state curve $i_\infty$ vs. $V_\infty$ is also shown, and an unshielded Cu anode (0.02 cm²) is used, in 2N HCl.

To obtain a quantitative relation for the current rise after the minimum, assume that the transient has reached the current minimum through the process of layer formation, and that sufficient time has passed for the solution and removal of the layer by convection to reach its steady-state value of $i_r$ ($= i_\infty$). The layer will be removed by solution at a net rate proportional to $(i_r - i)$, the difference between formation and removal, assuming no complication due to varying rate of formation of $Cu^{++}$. If any $Cu^{++}$ is formed, its rate of formation may vary during the overshoot, and its appearance in solution will alter the removal rate of the CuCl. Thus the following analysis is strictly valid only for $V < -0.05$ v, where $CuCl_2^-$ and CuCl are the only reaction products. The rate of solution of the layer is given by

$$\frac{d\delta}{dt} = \frac{-M(i_r - i)}{\rho SF} \qquad \text{(XI)}$$

The layer thickness may be approximated by:

$$\delta(t) = \delta_{max} - \frac{M(i_r - i)\ (t - t_{min})}{\rho SF} \quad (t \geqq t_{min}) \qquad \text{(XII)}$$

The symbols $\delta_{max}$, $r_{max}$, $i_{min}$, and $t_{min}$ refer to those quantities at the current minimum. The current at any time is given by:

$$i = \frac{E - \epsilon}{R + r_0 + r_1} \qquad \text{(XIII)}$$

where $r_1 = \frac{\delta(t)}{\kappa S_p}$, the layer resistance, and $\epsilon$ is the open-circuit potential. Combining Eqs. (XII) and (XIII) we have the behavior of the current after the minimum:

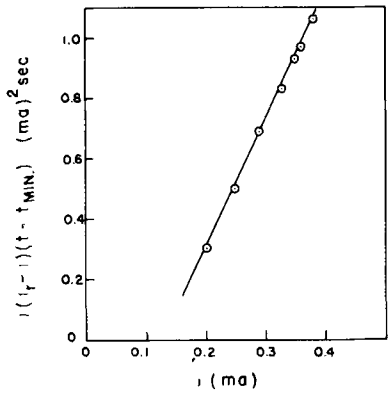


Fig. 5. Plot of $i\ (i_r - i)\ (t - t_{min})$ vs. $i$ to test Eq. (XV). Cu anode, 0.02 cm², 2N HCl, E = —0.1 v, R = 150Ω, and $t - t_{min}$ ranges from 6 sec to 40 sec. Data from curve 4(a).

$$i = \frac{E - \epsilon}{R + r_0 + \dfrac{\delta\ \max}{\kappa S_p} - \dfrac{M(i_r - i)\,(t - t_{min})}{S_p\,\kappa\rho\,SF}} \qquad \text{(XIV)}$$

According to Eq. (XIV) $i$ will increase with time, asymptotically approaching $i_r$. To compare Eq. (XIV) with experiment it is most convenient to rearrange it to

$$i(i_r - i)\,(t - t_{min}) = \frac{F\rho\kappa SS_p}{M}\,[(E - \epsilon) + (R + r_{max})i] \qquad \text{(XV)}$$

This is of the form $f\ (i, t) = a + bi$, and thus a plot of $i(i_r - i)\ (t - t_{min})$ vs. $i$ must be a straight line if Eq. (XIV) is correct, and $\epsilon$, $\kappa$, and $S_p$ are constant during the overshoot. In the example of Fig. 4a no cupric ion is formed and it may be used as a test of Eq. (XIV). The result (Fig. 5) was a line with a slope of $4.2 \times 10^{-3}$ amp-sec and an intercept of $-0.6 \times 10^{-6}$ amp² sec. $a$ and $b$ can be estimated only to an order of magnitude because of the lack of precise knowledge of $(E - \epsilon)$, $\kappa$, and $S_p$. Assuming values of $10^{-1}$ v, $10^{-2}$ (ohm-cm)$^{-1}$, and $10^{-4}$ cm², respectively, for these quantities gives $a = -0.7 \times 10^{-6}$ amp²-sec and $b = 5.4 \times 10^{-3}$ amp-sec, in good agreement with experiment. Thus the model, which pictures overshoot as due to the reduction of the initial layer thickness ($\delta_I$) to a value determined by steady-state condition, appears to be applicable in certain cases.

Although the model used above based on the relative values of $\delta_I$ and $\delta_\infty$ is not quantitatively accurate in the cases involving $Cu^{++}$ ion, it is consistent with the observed behavior of overshoot. On this model one would expect that the value of the minimum current would increase with decreasing $\delta_I$, for at the current minimum the pore area has reached its minimum value, and the resistance of the layer is proportional to its thickness. The expected result is observed to be the case for $R$ constant and $i_I > 2$ ma (Fig. 6), as can be seen from the fact that $\delta_I$ varies inversely with $i_I$. That the trend is reversed for $i_I < 2$ ma may be due to the partial solution of the layer which takes place (1) during the long plateaus associated with the low values of $i_I$. The dependence of $i_{min}$ upon $R$ at constant $i_I$ may be related in part to the variations in amount of current carried by $Cu^{++}$; e.g., at $i_I = 4$ ma (Fig. 6) the lowest value of $i_{min}$ is for a transient with no

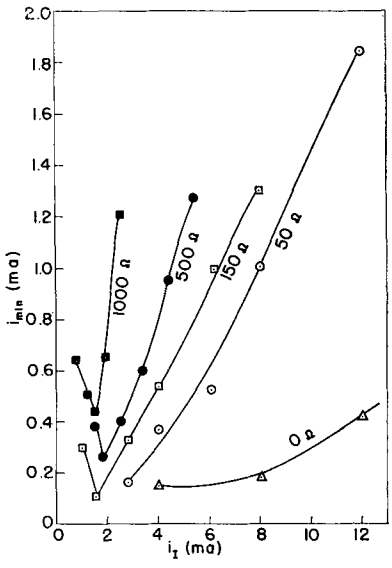


Fig. 6. Minimum current vs. current on first plateau, for various values of the external resistance R (shown on curve). Cu anode, 0.02 cm², 2N HCl.

$Cu^{++}$ formed, and the higher values of $i_{min}$ are associated with voltage in the range of increasing percentage of $Cu^{++}$. Next consider the limiting cases of overshoot (Fig. 4d) where the current assumes its steady-state value immediately after the current drop. This implies that $\delta_I$ plus the growth in depth (1) is equal to $\delta_\infty$, the steady-state layer thickness. The limiting cases of overshoot associated with larger values of $\delta_I$ correspond to larger values of $\delta_x$, as would be expected if the growth in depth is relatively independent of $\delta_I$. Finally, with very high initial currents, and consequently extremely thin initial layers, no overshoot is observed.

### *Oscillations*

Under certain conditions, with a fixed d-c voltage applied, the cell current and electrode potential undergo periodic fluctuations after approaching a quasi-stationary state, which is called here the steady state. Such oscillations have been observed and studied by Hedges (14) and Bonhoeffer (4) using large applied voltages (6 to 200 v). In this work, oscillations have been observed for low applied voltages, (Fig. 7) in the region below $Cu^{++}$ or $O_2$ formation and apparently below that for oxide production. These oscillations have a period which varies in the Cu|HCl system from 10 sec to 1 min or more, and may continue indefinitely, damp out slowly, or cease abruptly after a number of cycles. Usually they have the form of relaxation oscillations, with periods of relatively constant current interrupted by sudden changes. After the current rises from the initial minimum and approaches the steady-state value, it may suddenly rise to $i_I$, the current on the first plateau, remain there for a time shorter than the duration of the first plateau, and fall to a minimum in a manner similar to the drop after the plateau. After passing through this minimum the current rises at a rate more rapid than that from the first overshoot, until it again becomes approximately equal to the steady-state value. The interval when $i < i_\infty$ is denoted by Bonhoeffer as the passive phase (Fig. 7), although considerable current is flowing. Following the passive period the current rises rapidly to $i_I$ (active phase) and the cycle repeats. In certain cases each phase is distinctly separate, while in others the oscillations appear almost sinusoidal. Periodic phenomena do not appear if the electrode is shielded to prevent convection, but are found in systems with natural convection or stirring. The major condition necessary for the occurrence of oscillations in this geometry and concentration is that the steady-state voltage lies in the range of −0.27 to −0.25 v, which is at the beginning of the first current-voltage plateau (Fig. 1). This is the voltage at which a solid layer of CuCl first appears. Subject to this very restrictive condition, oscillations have been found with any value of applied voltage $E > -0.26$ and external resistance $R \geqq 20$. The current fluctuates above and below the steady-state current, and when the potential is too low for the production of $Cu^{++}$ ions, the average current is exactly $i_\infty$ ($V_\infty = -0.26$). In any one period the amount of CuCl removed during the passive period will be equal to the amount deposited during the active period. When no $Cu^{++}$ is produced, this means area 'a' (Fig. 7) will be equal to area 'b', as is found experimentally for $E < 0$ v.

Interruption experiments were performed to observe the variation of electrode resistance and potential during the oscillations. The results (Fig. 8)

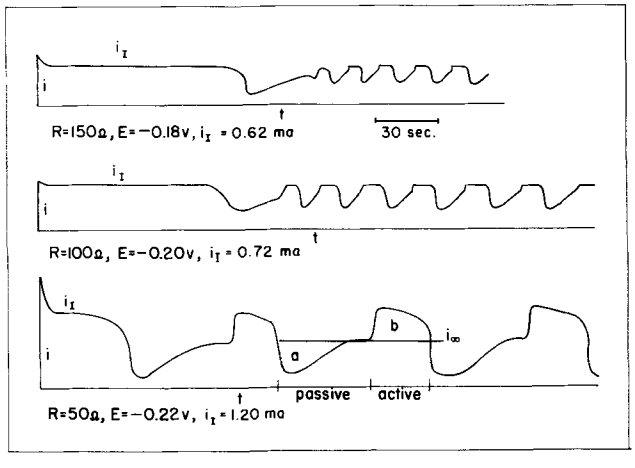


Fig. 7. Current vs. time oscillations for a Cu anode 0.02 cm² in 2N HCl.

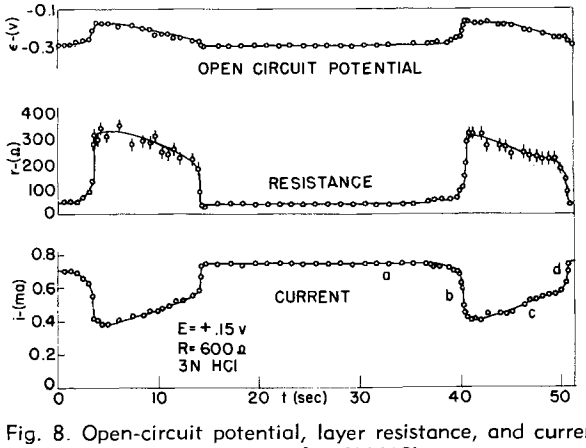


Fig. 8. Open-circuit potential, layer resistance, and current vs. time for a Cu anode 0.02 cm² in 3N HCl.

indicate that the major portion of the current change is due to variations in electrode resistance, while the potential alters by a small amount.

## Discussion

The role of natural convection in determining the steady-state current-voltage characteristic has been demonstrated for a case involving a solid anode film. This process is apparently effective in controlling the current even in the presence of an additional, soluble, reaction product. Convective removal of the CuCl layer also alters the duration of current-time plateaus, which has been discussed elsewhere (1).

Overshoot has been explained on the basis of a model which assumes the completion of a relatively thick initial layer and the subsequent reduction of this layer to one with thickness determined by the steady-state conditions. This model is in general qualitative agreement with the experimental results, and quantitatively predicts the form of the current rise after the minimum. [Its general quantitative applicability is limited by the appearance of $Cu^{++}$, which not only adds to the current directly but also increases the rate of solution of the CuCl layer (by altering the density in the convection layer). It should be possible to investigate overshoot without this complication by choosing a suitable singly-valent system (involving a moderately soluble salt), such as $Ag|H_2SO_4$.] The difficulty in developing a single equation which gives the current both before and after the minimum is that there apparently are at least two distinct processes occurring. The first process is that of layer formation, which usually involves both sideways growth and growth in depth, even when there is only one reaction product. The process tending to increase the current is the solution of the layer, which is strongly dependent on the removal of the dissolved salt by natural convection. The calculation of the steady-state configuration of a natural convection layer is a very complicated mathematical problem, and that of its development in time is even more complex, and so analysis from first principles will have to await further work.

An examination of the shape of the oscillations can yield important clues as to the processes which are taking place. At first, there is a current plateau followed by a drop, which has been identified as due to the formation of a CuCl layer. The current rises from the minimum and levels off. During this interval the resistance decreases, which is to be expected when the layer is being removed. At the same time, the open-circuit potential decreases, as would be the case if the $Cl^-$ concentration should increase. This continues rather slowly for a time, and then there is a small but rapid change in the potential, which occurs because the Cu surface is suddenly exposed to $Cl^-$ with concentration roughly the bulk value. The simultaneous rapid decrease in resistance is probably due to widening of the pores. Since the duration of the active phase is not as great as that of the first plateau, it is probable that not all of the solid layer is removed. (A similar breakdown of the layer occurs for Fe in $H_2SO_4$, at the lower limit for stability of the passive layer. After the minimum, the current rises slowly for a long time, and then the potential drops suddenly, as does the resistance. Current flows at a high rate, and it is some time before the passive layer is restored.)

It is now in order to consider the variation in concentration of $Cl^-$, the potential-determining ion. As the CuCl surface layer is formed, this concentration decreases, as is evidenced by schlieren observations. Upon completion of the layer, $\epsilon$ increases suddenly and by a large amount, indicating that the concentration at the base of the pores has decreased still more. Since the total current is now much less, the gradient of the anolyte concentration must decrease, and the concentration at the layer-solution interface must increase (to a value about that in bulk). The current density, however, is presumably just a function of $\epsilon$ and stays relatively constant, as does the gradient in the pores. Consequently, the concentration at the base of the pores rises to keep pace with that outside, and the value of $\epsilon$ goes down. When it becomes les than $\epsilon_I$, layer can no longer be formed. However, the removal continues until the layer has been eaten away, and the cycle repeats itself.

Oscillations occur when the system can exist in two possible states neither one of which is permanently stable. The current cannot remain at its minimum value because the initial thickness of the layer is more than needed to maintain a balance between the processes of formation and removal, when the $Cl^-$ concentration has reached its steady-state value. After the overshoot, the current can maintain a steady-state value only if enough new layer is being formed to offset the amount removed by dissolution. No new layer can be formed below $V = -0.28$ v, and it can be presumed that, in a limited range above this potential, the rate of formation is not sufficient to keep pace with the removal. Under these circumstances, the layer cannot stay on the electrode and no steady state is possible. Hence, sustained oscillations will take place.

The above oscillations represent only one extreme case of nonlinear oscillations, namely, where there are practically discontinuous jumps between two possible states. The other extreme is characterized by oscillations which are sinusoidal and of small amplitude (15), and has been found with the systems $Cu|KCl$ and $Fe|H_2SO_4$. It would seem that it represents a situation where there is a more delicate balance between the two states, but further work is necessary in order to elucidate the details.

## Summary

Natural convection, which aids in the solution of the layer, causes the appearance of a nonzero steady-state current, overshoot, and oscillations.

The steady state is characterized by two regions where the current is independent of voltage. In the first of these ($-0.28 < V < -0.05$) CuCl and $CuCl^-_2$ have been found to be the only reaction products, and the current is in agreement with that predicted by Tobias' theory of mass transfer by natural con-

vection. The removal process is that of a solution of a soluble slab, the CuCl being chemically dissolved by formation of the $CuCl^-_2$ complex ion, which is convected away due to the increased density of the solution. The dependence of $i_\infty$ on anode area and on bulk acid concentration, as well as the diffusion layer thickness, is given correctly by the convection theory.

For $V > -0.05$, the current increases, with $V_\infty$ corresponding to increasing proportions of $Cu^{++}$ ion formed, up to a limit of 30% at $V = +0.1$ v. At higher voltages the current is approximately independent of voltage. The limiting current and proportion of cupric ion has been explained on the basis of the mass transfer rate of CuCl and the relative mobilities of the $Cu^{++}$ and $Cu^-$ ions.

The steady-state electrode potential was found to be given by the same conditions holding for transients (1), i.e., for $\epsilon$ is given by the $Cu|CuCl^-_2$ potential; for $-0.28 \leqq V \leqq -0.05$, $\epsilon$ is determined by the chloride ion polarization. For $V_\infty > -0.05$, $Cu^{++}$ is observed as a product and $\epsilon$ is within 0.03 v of the $Cu\text{-}Cu^{++}$ standard potential. The decay of the layer resistance has been found to be due to the opening of the pores, a process different from the bulk removal of the layer. Overshoot has been explained by noting that the initial layer thickness may be greater than that in the steady state, and thus that the current flowing on completion of the initial layer will then be less than $i_\infty$. Convection acts to reduce the layer thickness and thus increase the current. Using this model it has been possible to account quantitatively for the current rise after the minimum in certain cases, and to understand qualitatively other features of overshoot.

The oscillations which are found in the Cu|HCl system have been investigated and most phases of the oscillations are understood in terms of events occurring during the ordinary transients. After the layer is complete, the decrease of total current causes an increase in anolyte concentration. This drags up the concentration at the base of the pores and lowers the electrode potential there. Below the critical value, layer formation will cease and the existing layer will continue to dissolve until the surface is bare enough for the cycle to begin again.

## Acknowledgment

This reasearch was supported by the Office of Ordnance Research under Contract DA-11-022-ORD-939 to whom the authors are sincerely grateful.

Manuscript received June 6, 1957.

Any discussion of this paper will appear in a Discussion Section to be published in the December 1958 JOURNAL.

## REFERENCES

1. R. S. Cooper, *This Journal*, **103**, 307 (1956).
2. C. W. Tobias, C. R. Wilke, and M. Eisenberg, *Chem. Eng. Progr.*, **49**, 663 (1953); C. R. Wilke, M. Eisenberg, and C. W. Tobias, *This Journal*, **100**, 513 (1953).
3. J. H. Bartlett and L. P. Stephenson, *This Journal*, **101**, 571 (1954).
4. K. F. Bonhoeffer and H. Gerischer, *Z. Elektrochem.*, **52**, 149 (1948).
5. J. H. Bartlett and L. P. Stephenson, *This Journal*, **99**, 504 (1952).
6. S. Glasstone, J. Laidler, and H. Eyring, "The Theory of Rate Processes," Chap. 10, McGraw Hill Book Co., New York (1941).
7. S. Glasstone, "Introduction to Electrochemistry," p. 461, D. Van Nostrand Co., New York (1951).
8. C. Wagner, *This Journal*, **104**, 129 (1957).
9. H. Le Chatelier, *Compt. rend.*, **98**, 814 (1884).
10. M. Engle, *Ann. Chem. et Phys.*, (6), **17**, 372 (1889).
11. R. S. Cooper, To be published.
12. G. Keulegan, *J. Research Nat. Bur. Standards*, **47**, 156 (1951).
13. B. E. Conway, "Electrochemical Data," Elsevier Publishing Co., Amsterdam (1955).
14. E. S. Hedges, *J. Chem. Soc.*, **1926**, 1533.
15. B. van der Pol, *Phil. Mag.*, **2**, 978 (1926).

## APPENDIX I

The upper limit for the chloride ion concentration difference across the convection layer may be estimated by applying Fick's law to a stagnant diffusion layer of the same thickness. This gives

$$\Delta c = \frac{lo}{SFDZ}$$

where $l$ is the convection layer thickness which is approximately 0.02 cm from schlieren observations (3) or a current density of 30 ma/cm$^2$, as found in the steady state, this gives $\Delta c = 0.2N$, which is small compared to the bulk acid concentration ($2N$). In the presence of convective flow the actual value of $\Delta c$ will be even less.

## APPENDIX II

In order to compute the average current density for a circular electrode using Eq. (XIV), it is only necessary to average the dependence of the current density on the anode height ($y$) over a circle. Since $i$ varies as $y^{-1/4}$ we want

$$y^{-1/4} = \frac{1}{R}\int_0^R (2\sqrt{R^2 - x^2})^{-1/4}\, dx$$

$$= (2R)^{1/4}\,\frac{\sqrt{\pi}\,\Gamma(7/8)}{2\,\Gamma(11/8)} = 1.08\,(2R)^{-1/4}$$

For the anodes used in this study this results in $y = 0.121$ cm.

# A Reaction Rate Study of the Corrosion of Low-Hafnium Zirconium in Aqueous Hydrofluoric Acid Solutions

**Tennyson Smith[1] and George Richard Hill**

*Department of Fuel Technology, University of Utah, Salt Lake City, Utah*

ABSTRACT

Zirconium dissolves readily in HF solutions leaving a smooth unpitted surface. The rate of dissolution of Zr in aqueous HF solutions has been studied over a temperature range of 7°-78°C using a radioactive tracer $Zr^{95}$. The rate was found to be directly proportional to the un-ionized HF concentration. In order to control the equilibrium concentrations of un-ionized HF, $HF^{-}_{2}$, $H^{+}$, and $F^{-}$ ions, most of the solutions contained another component such as HCl, $HNO_3$, KF, or $HClO_4$. For a given un-ionized HF concentration, the rate was independent of the $HF^{-}_{2}$, $H^{+}$, $F^{-}$, $Cl^{-}$, $NO^{-}_{3}$, $K^{+}$, or $ClO^{-}_{4}$ concentrations over a wide range.

A discussion of the Zr complex ions in solution is given. The gaseous product of the reaction between Zr and aqueous HF with HCl is $H_2$. When $HNO_3$ is used in place of HCl the gaseous products are $H_2$ and $N_2O$. The diffusion of un-ionized HF from the bulk solution through a diffusion film to the solid surface is postulated as the slow step, the energy of activation being 3.3 kcal/mole. At 25°C the rate constant for the case of rapid stirring is $5.19 \times 10^{-3}$ g $cm^{-2}$ $min^{-1}$ (moles HF)$^{-1}$ liter.

The wide interest in research and development of Zr is a result of its favorable properties as a construction material in nuclear reactors. Some of these properties are: low neutron absorption cross section of 0.18 barn; corrosion resistance to acids, bases, and water; ductility and ability to be fabricated.

The literature consists of reports concerned primarily with corrosion rates useful as engineering data. This work was undertaken to study the corrosion of Zr from a fundamental point of view, i.e., to determine the mechanism of the corrosion of Zr in acid solutions. Two systems have been studied; Zr in HF solutions, which is reported in this paper, and Zr in $H_2SO_4$ solutions which will be reported in a later paper.

Baumrucher (1) studied the possibility of using dissolution of Zr by HF for analysis of diffusion specimens requiring handling by remote control. A rough estimate of the activation energy from runs made at two temperatures by Baumrucher is 4 kcal/mole, as compared to 3.3 kcal/mole reported here. He found a linear relation between the weight of Zr dissolved and time, also as reported here. Since he made all of his runs at one concentration and did not report rates of stirring of the solution, no further correlation could be made.

## Experimental

The Zr samples supplied by the Atomic Energy Commission were 5 cm x 5 cm x 0.32 cm. Four samples were irradiated to an activity of 10 millicuries each. The irradiation was accomplished by neutron bombardment at the Oak Ridge National Laboratory.

[1] Present address: Atomics International, Canoga Park, Calif.

The isotope $Zr^{95}$ with a half life of 65 days, emits a $\beta$ particle to become $Nb^{95}$, the $Nb^{95}$ emits a 0.73 mev $\gamma$ and then a $\beta$ particle to become stable Mo. The decay scheme is more complicated than this, but the fairly strong $\gamma$ rays can be detected easily with a scintillometer. Specimens were tested for uniformity of activity by taking samples at various depths through the specimen thickness and measuring the activity of each sample with the counting equipment. The activity proved constant within experimental error through three-eighths of the specimen thickness from either side, then rose to a maximum at the center. The activity at the center was about twice that at the surface. Only the outer part of the specimen was used in these runs.

In order to detect any change in the true surface area, control runs were made periodically as the specimens were used. Since the rate of reaction remained constant within experimental error, under the same experimental conditions each time, it was concluded that the ratio of the true to the apparent surface area remained constant.

The AEC supplied the analysis (Table I) and the following history with the samples. The Zr was

**Table I. Analysis of zirconium samples**

| Concentration of contaminants in parts per million | | | | | |
|---|---|---|---|---|---|
| Hf | 80-100 | Fe | 300 | Si | 50 |
| B | 0.5 | Mn | 20 | Sn | 20 |
| Cd | 1.0 | Al | 30 | Ti | 50 |
| Co | 10.0 | C | 100-200 | V | 20 |
| Cr | 50.0 | N | 48 | Zn | 50 |
| Ca | 50.0 | Ni | 5 | Mo | 50 |
| Mg | 20.0 | Pb | 50 | | |

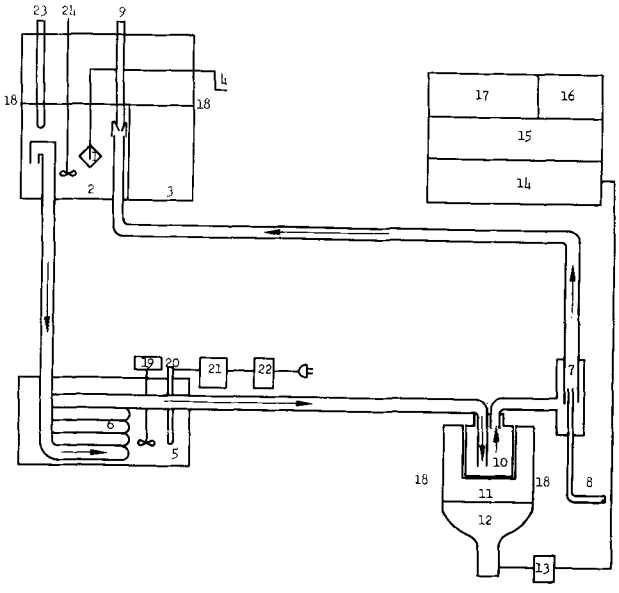


Fig. 1. Schematic diagram of the apparatus: 1, zirconium sample; 2, reaction cell; 3, cleaning cell; 4, sample manipulator; 5, constant temperature bath; 6, heat exchanger coil; 7, air lift pumps; 8, gas intake; 9, baffle filler tube; 10, sample cell; 11, scintillation solution; 12, photomultiplier tube; 13, preamplifier; 14, amplifier; 15, scaler; 16, recorder; 17, counting rate computer; 18, lead shielding (not shown); 19, stirring motor; 20, thermoregulator; 21, current reducer; 22, relay; 23, thermocouple well; 24, stirring rod.

fabricated from 300 to 500 lb, double-arc melted ingots. They were then: forged at 1800°F, blasted to remove oxide, hot-rolled to size, cold-rolled to about 25% reduction, annealed in air at 1550°F, and pickled in a HF solution.

In this study all solutions were made with conductivity water and reagent grade chemicals.

### *Apparatus*

The equipment had to comply with a number of requirements due to the nature of this work. The samples, being radioactive, had to be shielded to protect the investigators and to keep the background count to a minimum. Since HF, $H_2SO_4$, and other acids were to be used, a material resistant to these was needed. Polyethylene fulfilled this requirement very well. The temperature of the solution had to be controlled and numbers 5, 6, 20, 21, and 22 in Fig. 1 indicate the apparatus used for this purpose. Although a temperature drop existed between the reaction cell and the constant temperature bath, the temperature in the cell remained constant within ±0.1°C during a run.

The reaction cell (No. 2, Fig. 1) was approximately 11 cm long by 6 cm wide by 11 cm high, and had an inlet and outlet tube by which the solution could be circulated through a constant temperature bath (No. 5 Fig. 1), through a scintillation counter unit (Nos. 10, 11, 12, Fig. 1) and back to the cell with the help of the airlift pump (No. 7, Fig. 1). The other cell shown was for the purpose of cleaning and storing the sample. Although Fig. 1 is not to scale, it gives a close description of the way each part of the equipment was arranged relative to each other part. The container for the reaction cell was made of Lucite and was surrounded by lead bricks. Number 4, Fig. 1, is a rod covered with polyethylene used as a manipulator. It allowed the radioactive sample to be transferred from one cell to another without exposing the operator. The Lucite container was made air tight so that the desired atmosphere of air, oxygen, or argon could be maintained in contact with the solution in order to test the effect of oxygen partial pressure on the reaction rate. Lead was also placed around the scintillation unit (Nos. 10, 11, 12, Fig. 1) to lower the background.

The sample cell (No. 10, Fig. 1) was placed in a specially made container filled with scintillation fluid (toluene + 4 g/liter of 2, 5 diphenyloxazole). This container was attached to a 5 in. diameter Dumont photomultiplier tube No. 6365. The Dumont tube was connected to a preamplifier which was in series with an amplifier, scaler, count rate computer, and recorder in that order. As the solution containing the radioactive $Zr^{95}$ passed through the cell, a permanent record of the activity was made on the recorder. To determine the weight of Zr dissolved in the solution from the counts per minute as read on the recorder at any given time, a standard was made for each specimen. This was done by taking a small representative sample from each specimen, weighing it, dissolving it in HF solution, and placing it in a polyethylene bottle the same size as that used for circulating the solution through the scintillometer (No. 10, Fig. 1). A correction factor to account for any change in the efficiency of the counting equipment, or the activity of the specimens, was determined by counting the radiation from the standard before and after each run.

The reaction cell (No. 2, Fig. 1) held 600 ml of solution, the sample cell (in the scintillometer) contained 140 ml and the rest of the system contained 160 ml, making a total of 900 ml.

### *Reactant Solutions*

The stoichiometric concentrations, the concentration of undissociated hydrofluoric acid, $(HF)_{un}$, and the observed dissolution rates per mole of hydrofluoric acid, Rate/$(HF)_{un}$, for a few of the runs at 33° and 34°C, are given in Table II. The concentra-

**Table II. Observed rates of dissolution of Zr at 33° and 34°C with stirring 1200 rpm**

| Stoichiometric conc., *M* | | | Initial rate*, g cm$^{-2}$ min$^{-1}$ divided by $(HF)_{un}$ |
|---|---|---|---|
| HF | Other | $(HF)_{un}$ | $\times 10^3$ |
| 0.27 | 1.5 HCl | 0.27 | 4.30 |
| 0.27 | 0.61 KF | 0.05 | 3.57 |
| 0.27 | 1.0 $HNO_3$ | 0.27 | 4.12 |
| 0.27 | 0.5 $HClO_4$ | 0.27 | 4.02 |
| 0.27 | — | 0.248 | 3.40 |
| 0.27 | — | 0.248 | 4.12 |
| HF $\times 10^3$ | | $(HF)_{un} \times 10^3$ | |
| 6.0 | 1.25 $HNO_3$ | 6.0 | 4.49 |
| 1.1 | 1.52 $HNO_3$ | 1.1 | 4.40 |
| 0.275 | 1.52 $HNO_3$ | 0.275 | 2.84 |
| — | 1.52 $HNO_3$ | — Rate = $3.2 \times 10^{-7}$ | |

* Multiply (g cm$^{-2}$ min$^{-1}$) by $1.44 \times 10^8$ to get mdd (milligrams per dm$^2$ per day).
Multiply (g cm$^{-2}$ min$^{-1}$) by $3.23 \times 10^4$ to get ipy (inches penetration per year).

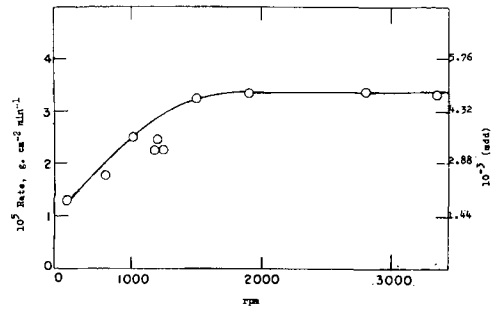


Fig. 2. Relationship between the rate of stirring in rpm and the rate of dissolution of Zr. The molarity of HF is 0.00613 and $H^+$ is 1.50M; T, 33°C.

tions of undissociated HF, fluoride and hydrogen bifluoride ions were calculated by interpolating and extrapolating equilibrium constants from the following data of Broene and deVries (2).

| | Temperature°C | 12 | 15 | 25 | 35 |
|---|---|---|---|---|---|
| $HF \rightleftharpoons H^+ + F^-$ | $K_1 \times 10^4 =$ | 8.3 | 7.9 | 6.7 | 5.6 |
| $HF + F^- \rightleftharpoons HF_2^-$ | $K_2 =$ | | 3.92 | 3.96 | 4.33 |

With foreign acids present and in very dilute solutions, fluoride and hydrogen bifluoride ion concentrations are small, and, in some cases, difficult to calculate. Their values were estimated until it became obvious that they bore no relation to the rate.

At 0°C the activity coefficient for $(HF)_{un}$ is essentially unity to 0.1M HF, increasing to 1.06 at 1M HF (3). Similar values are to be expected at higher temperatures and no attempt was made to substitute the activity for the concentration of HF. While the concentrations of $H^+$ ion and accompanying ($NO_3^-$, $Cl^-$, $F^-$, $HF_2^-$, $ClO_4^-$) ions were varied over a wide range, the values of, Rate/$(HF)_{un}$ remained essentially constant. It was concluded that at constant temperature the rate is a function of nothing but the $HF_{un}$ concentration.

## Results

*Stirring effect.*—Figure 2 shows a pronounced effect of stirring on the rate, with a leveling off above 2,000 rpm. This is typical for transport-controlled heterogeneous reactions, with the type of stirring used; the rate is proportional to a fractional power of the rpm. The absolute velocity of the solution past the Zr sample was not measured.

*Effect of various ions on the rate.*—Analysis of 32 runs at about 33°C (rpm 1200) gave an average value for the Rate/$(HF)_{un}$ as $4.11 \times 10^{-3}$ g cm$^{-2}$ min$^{-1}$ per mole liter$^{-1}$ with or without the use of foreign acids. The average error is $0.46 \times 10^{-3}$ g cm$^{-2}$ min$^{-1}$ per mole liter$^{-1}$.

As shown in Table II, a run made in 1.52M $HNO_3$ gave a rate of $3.2 \times 10^{-7}$ g cm$^{-2}$ min$^{-1}$ which was appreciable when the most dilute HF solutions were used. It is concluded that the variations in the Rate/$(HF)_{un}$ are due to a combination of experimental errors, error in calculating the concentration of $(HF)_{un}$ in some cases, lack of correction for $HNO_3$, etc.

*Effect of hydrofluoric acid on the rate.*—A plot of all the rates at ca. 33°C and 1200 rpm vs. the concentration of $(HF)_{un}$ is given in Fig. 3. The circles

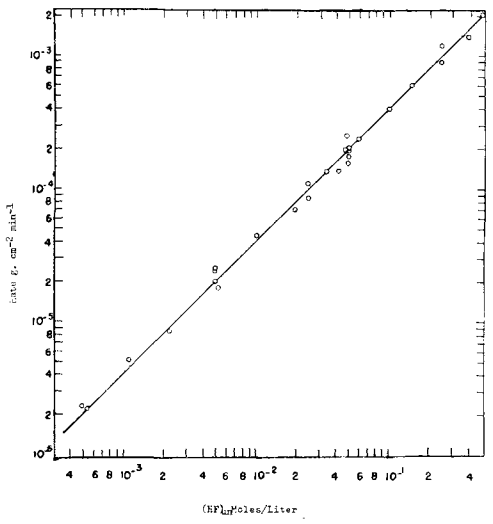


Fig. 3. Relationship between the equilibrium concentration of un-ionized HF and the rate of dissolution of Zr. T≈33°C, rpm = 1200.

are experimental values, the curve is drawn with a slope of 1 on the log-log scale, corresponding to a first order reaction with respect to $(HF)_{un}$. These are initial rates determined from the slopes of plots of g (Zr dissolving) per cm$^2$ (of surface area) vs. time.

*Effect of oxygen on the rate.*—In order to determine the effect of oxygen on the reaction rate, a number of runs were made with a Zr, aqueous HF, HCl system in which the partial pressure of oxygen in equilibrium with the solution was varied. The oxygen partial pressure ranged from one to zero atmospheres in a series of experiments, the partial pressure being varied by mixing oxygen with purified argon. No variation in the rate was observed as the oxygen partial pressure was changed from run to run. The remainder of the runs were made with air to pump the solution.

*Effect of temperature on the rate.*—Figure 4 is an Arrhenius plot; the circles represent the data tabulated in Table III and the line is the best eye fit of these points. The symbol $k$ is the rate constant defined by $k = R/(HF)_{un}$, where $R$ is the rate in g cm$^{-2}$ min$^{-1}$ and $(HF)_{un}$ is the concentration of un-ionized HF in moles/liter. All of the runs in Table III were made with stirring greater than 2000 rpm, where the stirring effect had reached its limit. The

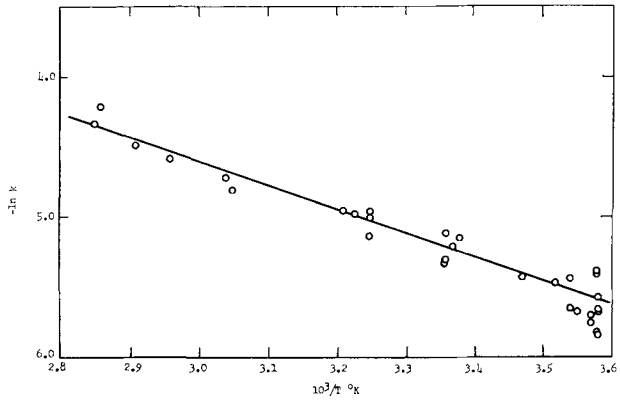


Fig. 4. Plot of ln k vs. 1/T, showing the temperature coefficient of the rate constant, (rpm > 2000).

Table III. Variation of the rate constant with HF concentration* and temperature, (rpm > 2000, (HCl) = 0.5-1.5)

| $t$°C | $(HF)_{un}$ | $-\ln k$ | $t$°C | $(HF)_{un}$ | $-\ln k$ |
|---|---|---|---|---|---|
| 6.0 | 0.0005 | 5.42 | 24.0 | 0.050 | 5.22 |
| 7.0 | 0.0005 | 5.69 | 25.0 | 0.0005 | 5.34 |
| 7.0 | 0.0010 | 5.58 | 25.0 | 0.0050 | 5.30 |
| 7.0 | 0.0050 | 5.40 | 25.0 | 0.0050 | 5.11 |
| 7.0 | 0.050 | 5.69 | 35.0 | 0.0005 | 5.15 |
| 7.0 | 0.050 | 5.85 | 35.0 | 0.0050 | 4.96 |
| 7.0 | 0.50 | 5.84 | 35.0 | 0.50 | 5.02 |
| 7.5 | 0.50 | 5.76 | 37.0 | 0.050 | 4.99 |
| 7.5 | 1.00 | 5.71 | 38.5 | 0.0005 | 4.96 |
| 8.5 | 0.50 | 5.68 | 55.3 | 0.0005 | 4.73 |
| 9.0 | 0.050 | 5.66 | 55.0 | 0.050 | 4.81 |
| 9.0 | 0.50 | 5.43 | 65.0 | 0.0005 | 4.00 |
| 11.0 | 0.0090 | 5.48 | 71.0 | 0.0090 | 4.50 |
| 15.0 | 0.050 | 5.43 | 73.0 | 0.0050 | 4.21 |
| 23.0 | 0.0090 | 5.16 | 78.0 | 0.0090 | 4.35 |

* The stoichiometric HF concentration is essentially equal to $(HF)_{un}$ at (HCl) 0.5M or greater.

temperature coefficient is seen to be small; the activation energy was calculated to be 3.34 kcal/mole.

*Reaction products.*—There has been some question as to whether the majority of the Zr complex ions in aqueous HF is $ZrF_3^+$, $ZrF_4$, or $ZrF_6^=$. A qualitative determination of the complex ions in solution can be made as follows: let $A$ be the initial concentration of HF and $X$ be the moles of HF per liter that have reacted at time $t$. Consider the over-all reaction:

$$Zr + (4-b)H^+ + bHF \rightarrow ZrF_b^{(4-b)+} + 2H_2$$

where $b$ is the average number of fluorine atoms associated with a Zr atom in solution. The number of moles of Zr per liter that have reacted at time $t$ is just $X/b$. Since in the experiments the rate that Zr enters the solution is measured and not the rate that HF is depleted, the rate equation is written, $R = d(Zr)/dt = k(HF)_{un} = k(A-X) = -d(X/b)/dt$. Although $b$ varies slowly with $X$, if one makes the approximation that $b$ is constant, and makes the well-known integration of the first order rate expression, one gets: $\ln(1-X/A) = bkt$ if $X = 0$ at $t = 0$. The $\ln(1-X/A)$ plotted vs. $t$ gives a straight line only with the proper choice of $b$, and therefore suggested a method of evaluating $b$. A plot of the $\ln(1-X/A)$ vs. $t$ for various choices of $b$ is given in Fig. 5. It is seen that a choice of $b \approx 3.3$ gives a straight line. However, rather than remain constant as was assumed, $b$ must decrease as the HF is used up. This is shown by the following equilibrium constants at 25°C reported by Connick and McVey (4):

$$Zr^{+4} + HF \rightleftharpoons ZrF^{+3} + H^+ \qquad K_1 = 6.3 \times 10^5$$
$$ZrF^{+3} + HF \rightleftharpoons ZrF_2^{+2} + H^+ \qquad K_2 = 2.1 \times 10^4$$
$$ZrF_2^{+2} + HF \rightleftharpoons ZrF_3^+ + H^+ \qquad K_3 = 6.7 \times 10^2$$

Consequently, the concentration of $ZrF_4$, $ZrF_6^=$, or $ZrF_7^=$ must be very small in this particular solution, the majority of the complex being $ZrF_3^+$. Plots similar to Fig. 5 for runs in which higher concentrations of HF were used showed a shift to higher values of $b$ as was expected. For example, a run with an

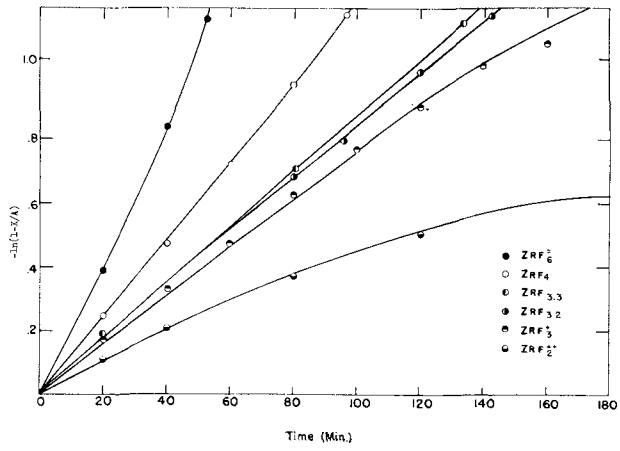


Fig. 5. Curves to determine the correct formula for the Zr complex ion in solution.

aqueous solution 0.009M in HF, 0.5M in hydrogen ion and at 71°C gave $b \approx 4.5$.

Gas samples for the reaction of Zr in aqueous HF were analyzed by infrared spectroscopy and with an Orsat gas analyzer. For the system Zr, aqueous HF, and HCl, only $H_2$ was detected. For the system Zr, aqueous HF, and $HNO_3$, $H_2$ and $N_2O$ were detected, the majority being hydrogen. Comparing the amount of gas evolved with the weight of Zr dissolved showed that just enough $H^+$ ions were reduced to oxidize Zr to the +4 state.

## Discussion

The following observations have been made: The amount of hydrogen evolved is that which is expected if Zr is oxidized to the +4 state. The over-all reaction is: $Zr + (4-b)H^+ + bHF \rightarrow ZrF_b^{(4-b)+} + 2H_2$ or $Zr + 4HF \rightarrow ZrF_b^{(4-b)+} + 2H_2 + (4-b)F^-$ when no excess $H^+$ ion is available. The reaction is first order with respect to un-ionized HF. The rate does not drop off at high HF concentrations as might be expected if the slow step was one of adsorption. The stirring rate greatly influences the rate of reaction, but does come to a limit as shown in Fig. 2. The activation energy for the reaction is 3.34 kcal/mole.

From Fig. 2 one would expect that above 2000 rpm the diffusion step would be eliminated as the slow step. However, this is not necessarily true. The effect of stirring, in Fig. 2, is very similar to that for the dissolution of Fe in solution recorded by King (5). It would appear that a diffusion film is established very close to the surface, the thickness of which reaches a limit as the turbulence in the bulk liquid is increased. A great deal of study (6-8) has been made concerning the nature of such a boundary layer.

Assuming the diffusion of un-ionized HF across a boundary layer of thickness $\delta$ to be rate controlling, a comparison of the rate equation with Fick's first low (S1C), for the case of steady state, can be made.

Consider the equations: $-d(HF)/dt = bk(HF)_{un}$ and $-J = Ddc/dx$, where $J$ is the flux (mass passing unit area per second) and $dc/dx$ is the differential concentration gradient at the plane the particles are diffusing across. The term $d(HF)/dt$ is the moles of

HF reaching 1 $cm^2$ of the Zr surface/sec. Then, $J = d(HF)/dt$ and $bk(HF)_{un} = Ddc/dx$. Assuming $D$ to be a constant, it follows that the concentration gradient $dc/dx$ is constant, since $J$ is constant for steady state. Therefore, $dc/dx$ can be written $\Delta c/\Delta x$ or $(c - c_o)/\delta$, where $c$ is the concentration in the bulk solution, $c_o$ is the concentration at the metal surface and $\delta$ is the boundary layer thickness. Since the reaction at the surface is probably much faster than the rate the HF diffuses to the surface, it may be assumed that $c_o = 0$, then $\delta = D/bk$. From Fig. 4, at 298°K, $k = 5.19 \times 10^{-3}$ g $cm^{-2}$ $min^{-1}$ $moles^{-1}$ liter or $k = 0.95 \times 10^{-3}$ cm $sec^{-1}$. The diffusion coefficients for most small molecules in water vary between $1 \times 10^{-5}$ and $5 \times 10^{-5}$ $cm^2$ $sec^{-1}$ at room temperature. Assuming $D = 1 \times 10^{-5}$ $cm^2$ $sec^{-1}$ for HF in water, and $b = 3$, it is seen that $\delta = 3.5 \times 10^{-3}$ cm. From calculations for typical runs given in King's (5) data (S1C), $\delta$ varies between $3 \times 10^{-3}$ cm and $5 \times 10^{-3}$ cm.

From these facts and the observation that the rate constant and activation energy are of the same magnitude as many other dissolution reactions that are diffusion (5, 9) controlled, it was concluded that the slow step is the diffusion of un-ionized HF through an effective diffusion layer to the metal surface.

Manuscript received March 22, 1956. This paper was prepared for delivery before the Cleveland Meeting, Sept. 30-Oct. 4, 1956.

Any discussion of this paper will appear in a Discussion Section to be published in the December 1958 JOURNAL.

REFERENCES

1. J. E. Baumrucker, AEC Report ANL 5020.
2. H. H. Broene and T. de Vries, *J. Am. Chem. Soc.*, **69**, 1644 (1947).
3. D. J. Anthony and L. J. Hudleston, *J. Chem. Soc.* **127**, 1122 (1925).
4. R. E. Connick and W. H. McVey, *J. Am. Chem. Soc.* **72**, 3182 (1949).
5. C. V. King, *ibid.*, **57**, 828 (1935); **59**, 63 (1937); **61**, 2290 (1939).
6. Kamenetskii, D. A. Frank, "Diffusion and Heat Exchange in Chemical Kinetics," Princeton University Press, Princeton (1955).
7. J. Laufer, *Nat. Advisory Comm. Aeronaut., Repts, Tech Note* 2945, June (1953).
8. R. G. Deissler and C. S. Eian, *Nat. Advisory Comm. Aeronaut., Repts, Tech. Note* 2629, Feb. (1952).
9. R. G. Van Name and G. Edgar, *Am. J. Sci.*, **29**, 237 (1910); R. S. Bosworth and R. G. Van Name, *ibid.*, **32**, 207 (1911); D. U. Hill and R. G. Van Name, *ibid.*, **42**, 307 (1916).

# Metal-Water Reactions

## VI. Kinetics of the Reactions of Water Vapor with Strontium and Barium

**Harry J. Svec and H. Gene Staley**

*Institute for Atomic Research and Department of Chemistry, Iowa State College, Ames, Iowa*

ABSTRACT

Strontium and barium were reacted with water vapor and the kinetics determined in the temperature range 40°-66°C for water vapor pressures from 17.5 to 92.5 mm Hg. The stoichiometry varied according to the reaction conditions. For the strontium reactions the products were $H_2$ and $Sr(OH)_2$. For vapor pressures below 44 mm the products of the barium reactions were $H_2$ and $Ba(OH)_2$ while for pressures above 44 mm they were $H_2$ and $Ba(OH)_2 \cdot H_2O$.

Manometric and gravimetric methods were employed in the kinetic studies. Both the Sr and lower vapor pressure Ba reactions followed the parabolic rate law. At higher pressures the Ba reaction followed a linear law. An activation energy of $-5.2 \pm 0.2$ kcal/mole was found for the Sr reactions. The activation energy for the Ba reactions was found to depend on reaction conditions.

Higher temperature studies of the reactions between water vapor and Sr, Ba, and Ca indicated that in certain temperature ranges above 100°C completely protective coatings were formed similar to those observed in the oxidation of Al or Cr.

The kinetics of gas-metal reactions involving $N_2$, $O_2$, and $H_2$ have been studied for many years and numerous references are available (1). In recent years there has been interest in reactions between metals and water vapor. It has been shown that lithium (2), thorium (3), and calcium (4) follow a logarithmic rate law and that magnesium (5) follows the linear rate law.

Strontium and barium were studied in order to compare the other alkaline earth metals with calcium. Because of the nature of the reaction and the products, the rate was followed by observing the evolution of $H_2$ and/or the weight gain of a specimen of the reacting metal as a function of time. Conditions of temperature and water vapor pressures were regulated carefully to determine their effect on the rate of reaction.

### Experimental

Strontium and barium rods were obtained from the Mackay Company of New York. Spectrographic analysis showed that the impurities totalling ap-

proximately 1% occurred in the Sr mainly as a mixture of Ca, Ba, Mn, Mg, Fe, and Al; in the Ba, 1% occurred mainly as Sr, Mn, Fe, Mg, and Al. Cylindrical specimens of the metals were prepared in the manner described (4) for Ca. Because of the greater reactivity of Sr and Ba, special care was required in handling and transporting the specimens in their final prepared form from the controlled atmosphere box, in which the machining was done, to the reaction apparatus. Flushing the apparatus with purified argon or helium prevented contamination with atmospheric $CO_2$. The apparatus used in this work has already been described (3, 4).

### *Results for Strontium*

The reactions between Sr and water vapor were carried out in the temperature range 40°-66°C and water vapor pressures of 17.5-92.5 mm Hg. During some of the kinetic experiments careful measurements were made of the amounts of Sr and $H_2O$ consumed and the amounts of $Sr(OH)_2$ and $H_2$ formed. As a result of these measurements, which attained a precision of ±1%, the stoichiometry of the reaction was established to be according to the equation

$$Sr + 2H_2O \rightarrow Sr(OH)_2 + H_2$$

The uniqueness and the identity of the products were determined by chemical, x-ray, and mass spectrometric methods.

The weight of water consumed in mg $H_2O/cm^2$ of Sr was plotted against various functions of time in order to determine the rate law. In all cases, the data indicated that the reaction follows the parabolic rate law more nearly than any other law. Several plots of the reaction data obtained at various temperatures and a water vapor pressure of 55 mm Hg are shown in Fig. 1.

The rate constant $k$, [mg $H_2O/cm^2Sr)^2hr$] was determined for each reaction condition. A plot of $k$ vs. temperature is shown in Fig. 2, where the $k$'s obtained at different but constant water vapor pressures are plotted against the reaction temperature. As is indicated, the value of the rate constants decreased as the temperature increased. At about 51°-56°C the rate constants of the reactions at 17.5 and 32 mm Hg water vapor pressure appear to become independent of temperature.

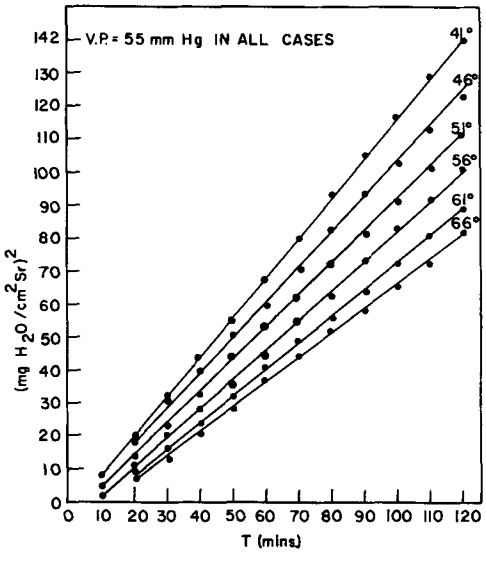


Fig. 1. Parabolic plots of strontium-water vapor data at 55 mm water vapor pressure in the low temperature range 41°-66°C.

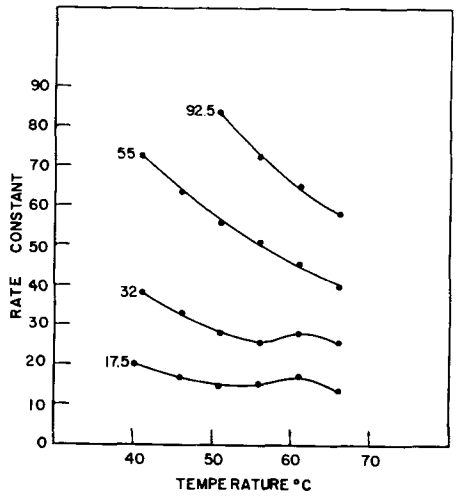


Fig. 2. Effect of temperature on the rate constants of the strontium-water vapor reaction. The units of k are [mg $H_2O/cm^2Sr]^2/hr$. The plotted points represent the average of several runs under each experimental condition. The general precision obtained was from ± 5 to 10% with the higher range generally applying to low pressure, low temperature experiments.

Arrhenius plots were made for each isobar over the temperature dependent range. The plots were linear with positive slopes, indicating an apparent negative energy of activation. The calculated activation energy was independent of water vapor pressure and had a value of $-5.2 \pm 0.2$ kcal/mole.

### *Results for Barium*

The reactions between Ba and water vapor were observed in the temperature range 41°-66°C and at water vapor pressures of 17.5, 32, 55, and 92.5 mm Hg. Two different reaction stoichiometries were observed. These were established by measuring the liquid water consumed and the hydrogen formed, in addition to x-ray diffraction analysis of the solid product. For water vapor pressures of 17.5 and 32 mm Hg, the stoichiometry is according to the equation

$$Ba + 2H_2O \rightarrow Ba(OH)_2 + H_2$$

At water vapor pressures of 55 and 92.5 mm Hg the stoichiometry is according to the equation

$$Ba + 3H_2O \rightarrow Ba(OH)_2 \cdot H_2O + H_2$$

Both manometric and gravimetric procedures indicated that the reactions at 17.5 and 32 mm Hg pressure followed the parabolic rate law. Manometric reactions at 55 and 92.5 mm pressure did not follow any of the known rate laws. The general pattern of these reactions is shown in Fig. 3. When the reactions were observed in the gravimetric apparatus (3) at 55 and 92.5 mm Hg, after an initial period of very rapid reaction rate during which time no law was determinable by the method available, the kinetics approached the linear rate law. A typical

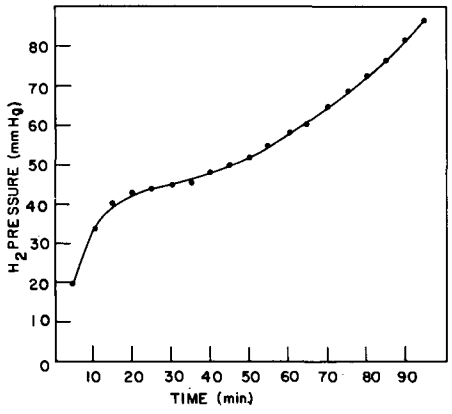


Fig. 3. General pattern of the manometric data for the barium-water vapor reaction. The curve illustrated is from data at 55 mm water vapor pressure and 56°C.

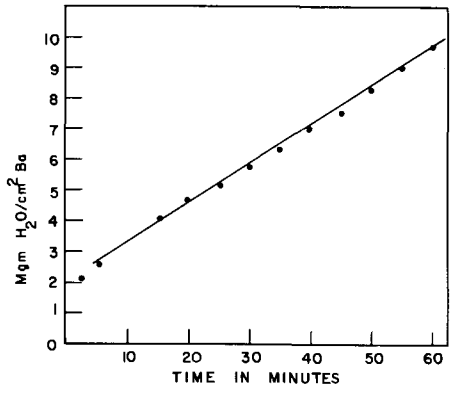


Fig. 4. Lineor plot of the gravimetric data for the barium-water vapor data obtained at 55 mm water vapor pressure ond 41°C. Other data at 55 mm and 92.5 mm and other temperatures cited here follow the same general pattern as these data.

gravimetric reaction is plotted in Fig. 4. It is significant that flaking occurred after 4 or 5 min in the reactions at 55 and 92.5 mm Hg water vapor pressure.

The vapor pressure at which water combines with $Ba(OH)_2$ to form the monohydrate is $44 \pm 2$ mm Hg. This was measured by following the weight gained by anhydrous $Ba(OH)_2$ in contact with water vapor at known pressures. It was also shown that formation of the octahydrate also takes place in this vapor pressure range, but only after all of the anhydrous $Ba(OH)_2$ has been converted to the monohydrate.

The rate constants for both manometric and gravimetric reactions are plotted against temperature of reaction in Fig. 5 and 6. Arrhenius plots of the data for the reactions at 32 mm in the temperature range 41°-56°C indicated an apparent activation energy of $-5.1 \pm 0.3$ kcal/mole. At 17.5 mm the apparent activation energy is zero. Similar plots of the linear data for the 55 mm reaction indicate no linear relationship in the temperature range 41°-56°C; so, no activation energy was deduced. If such were possible, however, it would be negative in sign. The data at 55 mm from 56° to 66°C give a linear plot and the activation energy is $9.5 \pm 1.0$ kcal/mole.

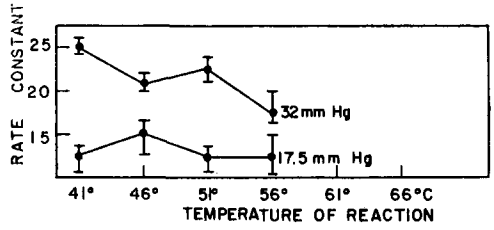


Fig. 5. Effect of temperature on the rate constants of the barium-water vapor reaction where kinetics are described by the parabolic rate law. Data were obtained manometrically. Units of k are [mg $H_2O/cm^2Ba]^2/hr$.

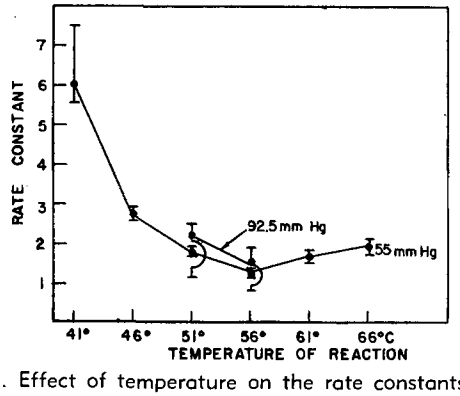


Fig. 6. Effect of temperature on the rate constants of the barium-water vapor reaction where kinetics are described by the linear rate law. Data were obtained gravimetrically. The units of k are [mg $H_2O/cm^2Ba]/hr$.

## High Temperature Reactions of Ca, Sr, and Ba with Water Vapor

Calcium, strontium, and barium reactions were carried out at higher temperatures in an apparatus similar to the one used above but modified to permit higher reaction temperatures. The reactions were carried out at vapor pressures of $25 \pm 1.5$ mm Hg. It was found that in certain temperature ranges these reactions would start and then apparently stop, due to the formation of protective coatings similar to those involved in the air oxidation of Al or Cr. In all the reactions described below, in which there was a protective coating formed, the hydrogen pressure increased steadily for about 15 min after the initiation of the reaction and then the increase stopped. No further evolution of $H_2$ took place, even after 5 hr of contact between the metal specimens and water vapor.

It was observed that for Ca the reaction was of this type in two temperature ranges, one from 100° to 255°C and the second from 400° to 500°C, above which temperature no observations were made. The reaction below 100°C is that reported by Svec and Apel (4). The reaction rate as determined manometrically went through a maximum at around 85°C and then apparently decreased to zero at 100°C. Similar behavior was again observed between 255° and 330°C. From 330° to 400°C the reaction was approximately the same as described by Gibbs and Svec (6). The differences of temperature range described here and those obtained in the earlier work are probably due to the fact that the Ca used in these experiments was the redistilled material (4) prepared in the Ames Laboratory of the A.E.C., while that used by Gibbs and Svec was ordinary commercial metal.

In the 100°-250°C range, the specimens maintained their original shiny, metallic luster. In the 400°-500°C range, the specimens were covered by a thin whitish coating. X-ray diffraction studies of the protective coatings in both upper and lower regions indicated the presence of Ca, $Ca(OH)_2$, and CaO with possible small amounts of $CaH_2$ at the higher temperatures. The x-ray lines were very sharp compared to those produced by the reaction product formed at temperatures below 70°C (4). The presence of strong lines due to Ca reflections in the x-ray diffraction patterns was taken as *a priori* evidence that the reaction product coating was very thin, although no attempt was made to measure its thickness.

Reactions involving Sr and Ba showed only one temperature range for each metal in which the completely protective type of coating was formed. For Sr this range was 175°-375°C while for Ba it was 100°-400°C. The upper limit in both cases coincides with the mp of the respective anhydrous hydroxides. Both Sr and Ba specimens maintained their metallic appearance.

## Discussion of Results

The separation of the reactants in the metal-water vapor reaction by the solid product indicates some diffusion process must take place within the coating. In both the Sr and Ba reactions, under each set of conditions, markers, which were small chips of Mg incorporated into the metal surfaces during the machining of the sample, stayed flush with the surface of the coating being displaced from the Sr and Ba metal after reaction by a layer of hydroxide. This is strong evidence that inward diffusion of some species takes place in both reactions. Similar observations with marker experiments have been made for the reactions of water vapor with Ca and with Th which follow a logarithmic rate law. The same observation was made in marker experiments with the Mg reactions although it was expected since the rate of reaction is linear. These limited observations suggest that inward diffusion of some species may be a general characteristic of water vapor-metal reactions. Experiments with less active metals than the alkaline earths will be necessary to record these phenomena microphotographically.

A comparison of the reaction rates of Ca, Sr, and Ba cannot include the Ca reaction because of the logarithmic nature of the kinetic law. However, comparison of Sr and Ba at 17.5 mm and 32 mm water vapor pressure where both reactions appear to be parabolic indicates (Fig. 5 and 2) that Sr is more reactive than Ba, which is contrary to general observations and expectations. This apparent difference based only on manometric data might be explained on the basis of hydride formation. However, comparison of gravimetric data still indicated that the Sr reaction is faster than the corresponding Ba reaction. No evidence for hydride was obtained by x-ray diffraction analyses. No reasonable explanation is apparent at this time.

In an exact comparison of the gravimetric with the manometric data, some difficulty was first observed due to the change in size of the cylindrical specimens for the two types of experimental conditions. In order to gain greater sensitivity in the manometric experiments a larger sample was used. All data were consistent and reproducible as long as the size did not change appreciably. In the gravimetric experiments the diameter of the sample specimens was about ½ that of the manometric samples. Despite the fact that no changes were made in tool position on the lathe used to prepare the samples, the data, which were again consistent and reproducible, indicated a rate of reaction higher than in the manometric experiments. Comparative data between the two types of experiments were obtained only after experiments were made using samples with similar dimensions.

The assumption was always made in the past that a reproducible surface was obtained by close control of the machining operations. Reaction rates given in weight of $H_2O$ reacted/$cm^2$ of metal surface were assumed to be minimum rates. Now it appears that in order to reproduce a machined surface, the dimensions of the machined specimen must be comparable. This is probably related to the exact tool-to-metal angle which changes as the diameter of the machined bar is reduced. As the diameter is decreased, the surface roughness increases, thereby causing an increase in available metal surface. It was fortuitous that during the Li(2), Ca(4), Th(3), and Mg(5) work the specimen size was kept constant, thereby accounting for the consistency of these data.

The apparent negative activation energy observed for the Sr reactions can be explained in the same manner as that observed for Ca(4) as involving a heat of desorption. Except for the change in rate law, Sr reactions follow a pattern similar to that of Ca throughout the temperature range in which kinetics were studied. In the heterogeneous reactions of concern here, this presumes that a prior fast equilibrium exists in a chain of reactions. This is then followed by a slow, rate-governing reaction. For example, if the equilibrium involves some interaction of $H_2O$ vapor with the surface, one can write

$$H_2O_{(g)} + S \underset{\text{fast}}{\overset{K_{eq}}{=}} H_2O \cdot S \qquad (I)$$

where $K_{eq}$ is the equilibrium constant and S some property of the surface. The slow step might then follow according to some relationship as

$$\frac{d(H_2O)}{dt} = k\,[H_2O \cdot S] \qquad (II)$$

or

$$\frac{d(H_2O)}{dt} = k\,K_{eq}[H_2O_{(g)}][S] \qquad (III)$$

If the value of $K_{eq}$ is temperature sensitive and decreases in value sufficiently to make the product $k \cdot K_{eq}$ become smaller as the temperature increases, then the apparent activation energy, computed from the Arrhenius relationship, becomes negative. This condition is attained when the forward reaction in (I) is slower than the reverse reaction. In the case of water vapor-metal systems it involves desorption

of $H_2O$ molecules from the coating surface. That this has not been observed in oxidation reactions involving $O_2$ or $N_2$ is probably due to the difference in the character of the adsorption compared to water molecules.

The apparent negative activation energies observed for the Ba reactions are also explainable as involving heats of desorption. The value of −5.1 kcal/mole found for the 32 mm Ba reactions indicates that the processes in this and the Sr reactions are similar. The apparent zero value for the activation energy at 17.5 mm is similar to the same Sr reaction at temperatures above 51°C and can be explained on the basis of a change in the predominant character of the rate-limiting processes. If the constants in equations (I) and (II) are decreasing and increasing at such a rate as to make their product remain at a fixed value, the rate of reaction then appears to be independent of temperature. As the temperature increases further, the product $k \cdot K_{eq}$ increases in value and the apparent activation energy should become positive. This was observed in the 55 mm reactions from 56° to 66°C. It is significant that the activation energy of 9.5 kcal/mole for this linear Ba-$H_2O$ reaction is the same as that for the Mg-$H_2O$ reaction (5) at 425°-500°C and 208 mm (11.1 ± 2.7 kcal/mole) which appears to depend on the rate of adsorption of gas molecules on the reacting surface.

The high temperature reactions were followed only by the manometric technique. The observations of Svec and Gibbs (6) on Ca made the appearance of a completely protective coating in these reactions unexpected, especially at the high temperatures. It was not possible to deduce what rate law was followed during the initial stages of these high temperature reactions. The experimental difficulties of characterizing precisely the coatings at the elevated temperatures involved make it impossible to educe an explanation for these phenomena based on experimental fact. The most significant observation remains the sharpening of the x-ray diffraction patterns of the high temperature coating compared to the low temperature coatings.

Manuscript received June 4, 1957.

Any discussion of this paper will appear in a Discussion Section to be published in the December 1958 JOURNAL.

REFERENCES

1. O. Kubaschewski and B. E. Hopkins, "Oxidation of Metals and Alloys," Academic Press Inc., New York (1953).
2. H. J. Svec and B. E. Deal, *J. Am. Chem. Soc.*, **75**, 6173 (1953).
3. H. J. Svec and B. E. Deal, *This Journal*, **103**, 421 (1956).
4. H. J. Svec and C. A. Apel, *ibid.*, **104**, 346 (1957).
5. H. J. Svec and D. S. Gibbs, *ibid.*, **104**, 434 (1957).
6. H. J. Svec and D. S. Gibbs, *J. Am. Chem. Soc.*, **75**, 6052 (1953).

# Phase Equilibria in the System ZnO-$P_2O_5$

**Fred L. Katnack and F. A. Hummel**

*College of Mineral Industries, Pennsylvania State University, University Park, Pennsylvania*

ABSTRACT

Phase relationships in the system ZnO-$P_2O_5$ were determined in air in the range between ZnO and $Zn(PO_3)_2$, using solid state and quenching methods. Three congruently melting compounds exist, $Zn_3(PO_4)_2$, $Zn_2P_2O_7$, and $Zn(PO_3)_2$. The orthophosphate has a sluggish, reversible inversion at 942° and melts at 1060° ±8°C. The pyrophosphate undergoes a rapid, reversible inversion at 132° and melts at 1017°C. The irreversible inversion in the metaphosphate takes place in air in the range between 600° and 700°C, depending on the rate of heating of the sample. The low temperature form of the metaphosphate cannot be obtained by heating the high temperature form in air, but glass of the metaphosphate composition will yield a mixture of low and high temperature forms if held at 550°C for 16 hr. $Zn(PO_3)_2$ melts at 872°C. Simple eutectic relationships exist between ZnO and $Zn_3(PO_4)_2$, $Zn_3(PO_4)_2$ and $Zn_2P_2O_7$, and $Zn_2P_2O_7$ and $Zn(PO_3)_2$.

The phase relationships in the system ZnO-$P_2O_5$ were investigated because the system was known to contain at least two compounds of interest as host lattices for luminescent preparations, and it was thought that a determination of the properties of the crystals and glasses in the system might be of some interest to allied fields.

Numerous references to hydrated and anhydrous zinc phosphate minerals and synthetic preparations are available, e.g., (1), but the paper by Smith (2) on luminescence of zinc phosphates appears to be the only high temperature study which is closely related to the present work. Smith claimed three forms of $Zn_3(PO_4)_2$, $\alpha$, $\beta$, and $\gamma$. The $\alpha$ form was said to be stable up to the fusion point if no Mn was present. To produce a pure $\beta$ form, 1% Mn and temperatures above 800°C were required. Therefore, it was inferred that the $\beta$ form would not appear if less than 1% Mn were present. The $\gamma$ form was produced by the addition of 2 mole % $Mg_3(PO_4)_2$ with or without the addition of Mn. Gamma could be produced by the addition of $Zn_2P_2O_7$ to $Zn_3(PO_4)_2$. It was not clear whether or not Mn was present in the latter experiment. Pyrophosphates were said to prevent the formation of $\beta$-$Zn_3(PO_4)_2$.

It was felt that a detailed study of the phase relationships in the systems ZnO-$P_2O_5$, ZnO-MnO-$P_2O_5$, and ZnO-MgO-MnO-$P_2O_5$ would be necessary

in order to understand the luminescent properties of these compositions. This paper is confined to a clarification of the relationships between ZnO and $P_2O_5$. The other systems will be dealt with in a later paper.

## Experimental Procedure

### *Techniques, Equipment, and Materials*

*Quench technique.*—The quench technique followed essentially that described by Hill, Faust, and Reynolds (3) in the system $P_2O_5$-$2CaO \cdot P_2O_5$. Since their work was concerned with the $P_2O_5$-rich end of the system, elaborate methods of minimizing $P_2O_5$ volatilization were used. Such techniques did not appear necessary in the ZnO-$P_2O_5$ system, since chemical analyses of some of the zinc phosphate glasses did not indicate a significant loss of $P_2O_5$ through volatilization.

The quench furnace consisted of a Pt wound tube furnace. Temperature was controlled by a Tagliabue Celectray indicating potentiometer controller. A separate Pt-Pt 10% Rh thermocouple for the controller was inserted inside the tube so that this control thermocouple could be positioned manually near the quench packet.

Actual quench packet temperatures were measured by a L&N portable precision potentiometer using a second Pt-Pt 10% Rh thermocouple placed next to the quench packet. The accuracy of the second thermocouple was checked periodically against the melting point of gold at 1063°C.

*X-ray diffraction.*—Room temperature x-ray diffraction data were recorded with a Norelco Geiger counter diffractometer. Nickel-filtered CuK$\alpha$ radiation was used with the x-ray tube operating at 40 kv at 15 ma current. For routine identification, a scanning rate of 1 deg/min was used while the initial patterns used as a reference throughout this work were recorded at ½ deg/min.

High temperature x-ray diffraction data were obtained on a General Electric XRD-3 Geiger counter diffractometer also using Ni-filtered CuK$\alpha$ radiation. The x-ray furnace[1] was of ceramic construction with Pt heating elements and sample holder. An Al foil window in the furnace served as an entrance and exit for the x-radiation. The temperature of the specimen was maintained at ±5°C.

*Differential thermal analyses.*—Differential thermal analyses were done on an apparatus described by Gruver (4).

*Polarizing microscope.*—A Bausch and Lomb polarizing microscope was used to examine the crystalline and glass phases in the ZnO-$P_2O_5$ system. Index oils accurate to 0.004 were used for the index of refraction measurements of the glasses.

*Heat treating furnaces.*—All heat treatment other than quench work was done in electrically heated furnaces using silicon carbide heating elements. The temperature was controlled manually by an autotransformer. Because of the large size of the heating chamber, temperatures were considered accurate to only ±10°C. Such processes as formation of large amounts of glass, dehydration of zinc phosphate crystalline materials, weight loss measurements, and the preliminary work in determining the phase equilibrium relationships were done in these furnaces.

*Raw materials.*—The ZnO used in this investigation was obtained from the Chemical Products Plant of the General Electric Company. It is manufactured by the New Jersey Zinc Company and is a luminescent grade raw material with a purity comparable to a C.P. grade in commercially available chemicals. The ZnO was used as received with no weight loss correction.

The phosphoric acid used was a Baker Analyzed Reagent of C.P. grade. This acid contained approximately 85% orthophosphoric acid, $H_3PO_4$, the remaining 15% being water. To determine exactly the amount of $P_2O_5$ in the acid, gravimetric quantitative analysis of $P_2O_5$ described by Pierce and Haenisch (5) was used. This analysis consisted briefly of precipitation of the $P_2O_5$ as $MgNH_4PO_4 \cdot 6H_2O$ and finally weighing as $Mg_2P_2O_7$. Two 7-lb bottles of $H_3PO_4$ were analyzed separately. The following results were obtained:

| Bottle #1 (g of $P_2O_5$/ml of acid) | | Bottle #2 (g of $P_2O_5$/ml of acid) | |
|---|---|---|---|
| 1.0665 | | 1.0305 | |
| 1.0660 | | 1.0340 | |
| 1.0665 | | 1.0325 | |
| Average analysis | 1.066±.001 | Average analysis | 1.032±.002 |

### *Compositions and Heat Treatments*

*Compound preparation.* — Zinc orthophosphate was prepared by reacting ZnO with $H_3PO_4$. The acid was slowly added to a water slurry of the ZnO. To insure homogeneity the resulting batch was hand mixed in a glass mortar for 1 hr. The acid reacted quite readily with the ZnO and water had to be added continually as the $Zn_3(PO_4)_2$ that was formed became hydrated. The final material was then dried at 110°C.

A sample of the dried batch which was heated to 640°C for 5 hr underwent a 9.14% weight loss. The theoretical weight loss in dehydrating $Zn_3(PO_4)_2 \cdot 2H_2O$ is 9.34%; therefore, it was concluded that this material was zinc orthophosphate dihydrate, and the x-ray data presented in Table IV as $Zn_3(PO_4)_2 \cdot 2H_2O$ were recorded from this material.

This $Zn_3(PO_4)_2 \cdot 2H_2O$ was then fired to 800-950°C for 12 hr. X-ray analysis indicated that the fired material consisted mainly of $\alpha$-$Zn_3(PO_4)_2$ with some $\beta$-$Zn_3(PO_4)_2$ present. Further heat treatment of this mixture of $\alpha$ and $\beta$ $Zn_3(PO_4)_2$ produced the pure forms of this compound. Refiring to 750°C for 4 hr produced all $\alpha$-$Zn_3(PO_4)_2$, while refiring to 1000°C for 12 hr produced all $\beta$-$Zn_3(PO_4)_2$ (Table IV).

Three chemical analyses were run on each of two samples of the $Zn_3(PO_4)_2$. The average value obtained was 36.59±0.2% $P_2O_5$ compared to the theoretical value of 36.79% $P_2O_5$ in $Zn_3(PO_4)_2$. An independent analysis[2] gave a value of 36.48% $P_2O_5$.

[1] Furnace designed by H. A. McKinstry of the Mineral Constitution Laboratory of the Pennsylvania State University.

[2] Chemical Products Plant, General Electric Co., Cleveland, Ohio.

Zinc pyrophosphate was made by the well-known analytical procedure used for both ZnO and $P_2O_5$ analysis. A C.P. grade of $ZnCl_2$ was reacted with C.P. $(NH_4)_3PO_4$ to form $ZnNH_4PO_4$. The Zn $NH_4PO_4$ produced in this manner was fired to 900°C for 12 hr. A $P_2O_5$ analysis[2] indicated 47.3% $P_2O_5$ present compared to the theoretical amount of 46.59%. This indicated that a small amount of $Zn(PO_3)_2$ was present in the $Zn_2P_2O_7$.

Zinc metaphosphate could not be made by the reaction of ZnO with $H_3PO_4$. $Zn_3(PO_4)_2$ would form preferentially and even at elevated temperatures would not react readily with the remainder of the acid.

The $Zn(PO_3)_2$ finally used in the phase equilibrium investigation was obtained from the Monsanto Chemical Company. A chemical analysis[2] gave a value of 63.34±0.07% $P_2O_5$ as compared with the theoretical amount of 63.58% $P_2O_5$ in $Zn(PO_3)_2$.

*Intermediate compositions and glasses.*—The intermediate compositions between ZnO and $Zn_2P_2O_7$ were made by reacting ZnO with $H_3PO_4$ while the compositions between $Zn_2P_2O_7$ and $Zn(PO_3)_2$ were made from ZnO and $Zn(PO_3)_2$.

All solid-state reactions were done in Pt crucibles. The batches were given an initial low temperature firing between 600° and 700°C and then stored for later use.

Since the batches in the composition range between $Zn_2P_2O_7$ and $Zn(PO_3)_2$ were made from ZnO and $Zn(PO_3)_2$, $Zn_3(PO_4)_2$ rather than $Zn_2P_2O_7$ formed in some cases during the low temperature firing. This nonequilibrium existence of $Zn_3(PO_4)_2$ in this composition range did not affect the over-all chemical compositions or the glasses that were later made from these batches. As firing temperatures increased the $Zn_3(PO_4)_2$ disappeared.

After the intermediate compositions were made, portions of these batches were used to determine the extent of glass formation in this system. About 10-g samples were melted between 1100° and 1200°C for 30 min in a Pt crucible and quenched to a glass. The glass was removed from the crucible and crushed to −100 mesh particle size with a steel mortar and pestle. A magnet was used to remove any Fe particles introduced by the grinding. Table I lists the compositions made in the study of the ZnO-$P_2O_5$ system.

*Chemical analyses.*—To check the accuracy of the compositions made in the ZnO-$P_2O_5$ system, $P_2O_5$ analyses were run on various crystalline samples and glasses. Table II lists these analyses, some of which were mentioned previously in the section on compound formation.

*Heat treatment of compositions.*—All crystalline and glass compositions used for the phase equilibrium study in the ZnO-$P_2O_5$ system were heat treated in quench furnaces. This assured accurate temperature control and a minimum of $P_2O_5$ volatilization because of the sealed quench packet.

The preliminary investigations in the system were done using only crystalline batches as starting materials. Glasses were later used for liquidus and solidus determinations and for checking various points in the system.

One group of glasses in the composition range between $Zn_2P_2O_7$ and $Zn(PO_3)_2$ was devitrified in a Globar furnace. The purpose of this study was to crystallize the low form of $Zn(PO_3)_2$ from the

**Table I. Compositions used for investigation of the system ZnO-$P_2O_5$**

| No. | Weight % ZnO | Weight % $P_2O_5$ | Mole ratio | Initial heat treatment Time, hr | Initial heat treatment Temp, °C |
|---|---|---|---|---|---|
| 1 | 74.12 | 25.88 | 5:1 | 12 | 924 |
| 2 | 72.00 | 28.00 | | 19 | 700 |
| 3* | 69.62 | 30.38 | 4:1 | 12 | 836 |
| 4* | 68.00 | 32.00 | | 19 | 700 |
| 5* | 66.00 | 34.00 | | 24 | 700 |
| 6 | 64.50 | 35.50 | | 18 | 700 |
| 7 | 63.22 | 36.78 | 3:1 | | |
| 8 | 62.00 | 38.00 | | 19 | 700 |
| 9* | 61.00 | 39.00 | | 48 | 712 |
| 10 | 60.00 | 40.00 | | 18 | 700 |
| 11* | 58.89 | 41.11 | 5:2 | | |
| 12* | 58.00 | 42.00 | | 24 | 600 |
| 13* | 57.00 | 43.00 | | 12 | 750 |
| 14* | 55.00 | 45.00 | | 12 | 710 |
| 15* | 53.40 | 46.60 | 2:1 | | |
| 16* | 51.00 | 49.00 | | 12 | 650 |
| 17* | 48.85 | 51.15 | 5:3 | 24 | 650 |
| 18* | 46.22 | 53.78 | 3:2 | 12 | 650 |
| 19* | 43.31 | 56.69 | 4:3 | 24 | 650 |
| 20* | 41.73 | 58.27 | 5:4 | 24 | 650 |
| 21 | 40.4 | 59.6 | | 24 | 600 |
| 22* | 39.00 | 61.00 | | 24 | 650 |
| 23 | 37.6 | 62.4 | | 24 | 650 |
| 24 | 36.42 | 63.58 | 1:1 | | |

* Composition melted to glasses for use in quench determinations.

**Table II. Chemical analyses of ZnO-$P_2O_5$ compositions**

| Sample No. | Description of sample | Weight per cent $P_2O_5$ Calculated | Analyzed Sample No. 1 | Analyzed Sample No. 2 |
|---|---|---|---|---|
| 1 | ZnO and $P_2O_5$ reacted in a 5:1 molar ratio and fired to 924°C/12 hr. | 25.88 | 25.21 | 25.21 |
| 2 | ZnO and $P_2O_5$ reacted in a 3:1 molar ratio and fired to 900°C/12 hr. | 36.78 | 36.51 | 36.32 |
| 3 | ZnO and $P_2O_5$ reacted and fired to 700°C/19 hr. | 38.00 | 37.20 | 37.26 |
| 4 | ZnO and $P_2O_5$ reacted and melted to a glass at 1200°C/30 min. | 43.00 | 42.96 | 42.89 |
| 5 | $Zn_2P_2O_7$ made from zinc ammonium phosphate and fired to 900°C/12 hr. | 46.60 | 46.18 | 46.17 |
| 6 | $Zn_2P_2O_7$ made from ZnO and $H_3PO_4$, fired to 800°C/12 hr. | 46.60 | 45.66 | 45.62 |
| 7 | $Zn_2P_2O_7$ melted to a glass at 1200°C/30 min. | 46.60 | 47.10 | 47.12 |
| 8 | ZnO and $Zn(PO_3)_2$ reacted in solid state at 650°C/24 hr. | 62.40 | 62.30 | 62.37 |
| 9 | Monsanto Chemical Company zinc metaphosphate, dried 110°C. | 63.58 | 63.27 | 63.41 |

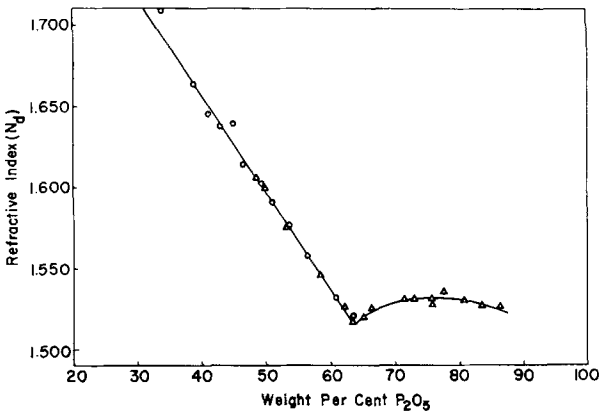


Fig. 1. Refractive indices of zinc phosphate glasses (sodium D light).

glasses. Since temperatures were not critical, the quench furnaces were not used in this investigation.

## Experimental Results and Discussion

### *Zinc Phosphate Glasses*

The index of refraction curve of the zinc phosphate glasses for sodium light is presented in Fig. 1. A break in the curve occurs at the $Zn(PO_3)_2$ composition according to the data of Kordes (11). Since the present work was concerned only with compositions ranging from ZnO to $Zn(PO_3)_2$, no glasses were made with a higher $P_2O_5$ content, and the data of Kordes were not checked.

The composition of $Zn_3(PO_4)_2$, 63.22% ZnO and 36.78% $P_2O_5$, could not be quenched to a glass. However, glasses could be formed on the ZnO side of $Zn_3(PO_4)_2$. This presents an unusual situation, since glasses could be formed on both sides of a compound composition, but not exactly on the compound composition.

The glasses with a $P_2O_5$ content greater than that in the $Zn_2P_2O_7$ composition, 53.40% ZnO and 46.60% $P_2O_5$, were attacked by the moisture in the air after a two month period.

### *Zinc Phosphate Compounds*

*Zinc orthophosphate.*—The differential thermal analyses of the low and high forms of $Zn_3(PO_4)_2$ are presented in Fig. 2.

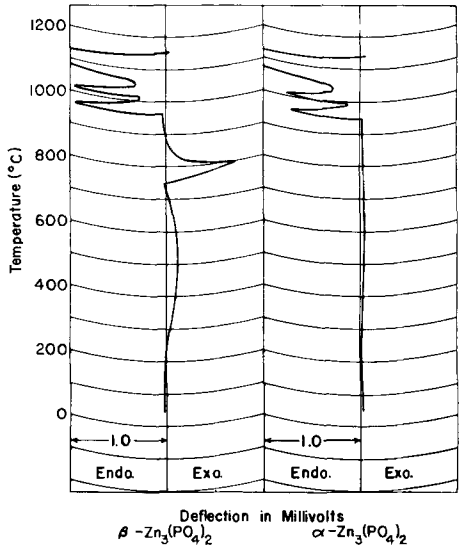


Fig. 2. Typical differential thermal analysis curves for β-$Zn_3(PO_4)_2$ and α-$Zn_3(PO_4)_2$.

The DTA of the α-$Zn_3(PO_4)_2$ showed three endothermic peaks. The first peak was due to an inversion in this compound. High temperature x-ray diffraction data indicated that this was the change from the α to the β form.

The inversion temperature was measured exactly by inserting samples of both α- and β-$Zn_3(PO_4)_2$ together in the quench furnace and examining the samples after heat treatment by x-ray analysis. At 938°C α-$Zn_3(PO_4)_2$ was stable and the β-$Zn_3(PO_4)_2$ was partially converted to α-$Zn_3(PO_4)_2$. This conversion was not complete even after 27 hr at this temperature. After 20 hr at 942°C, both the samples of α- and β-$Zn_3(PO_4)_2$ remained in their original form. At 944°C for 4 hr β-$Zn_3(PO_4)_2$ was stable, and the α-$Zn_3(PO_4)_2$ was partially converted to β-$Zn_3(PO_4)_2$. An inversion temperature of 942°C was concluded on the basis of these data.

The second endothermic peak in α-$Zn_3(PO_4)_2$ was due to the formation of some liquid in the sample. The chemical analysis indicated that the $P_2O_5$ content was about 0.3% low, indicating that the composition lies between the ZnO and $Zn_3(PO_4)_2$ end members. The eutectic temperature in this region is 1005°C. Above this temperature $Zn_3(PO_4)_2$ would be in equilibrium with a small amount of liquid phase if the composition deviated from the exact $3ZnO:P_2O_5$ ratio.

The third peak was due to the melting of $Zn_3(PO_4)_2$. Since $Zn_3(PO_4)_2$ could not be quenched completely to a glass, the melting point was measured by examining the material with a binocular microscope after heat treatment. As indicated, a small amount of liquid formed below the melting point. The effect of this liquid was to form the sample into a hard, dense mass. Above the melting point the $Zn_3(PO_4)_2$ flowed completely to the bottom of the quench packet. This difference in appearance above and below the melting temperature was used to determine the melting point. At a temperature of 1062°C, the sample had definitely melted, and there was a trace of glass present, while at 1056°C the sample was unmelted. A melting point of 1060°C was concluded from these data with an error of ±8°C because of the relatively poorer accuracy obtainable by this technique as compared to the regular quench technique using a glass.

The DTA of the high form of $Zn_3(PO_4)_2$ showed the three peaks present in the low form plus a fourth exothermic peak. The three endothermic peaks correspond to the three peaks in the α-$Zn_3(PO_4)_2$ DTA curve and are caused by the α-β inversion, eutectic liquid formation, and melting. However, the exothermic peak was unique for the DTA of the high form. Numerous runs showed that the temperature at which this peak occurred was not consistent and varied between 800° and 900°C. This peak is due to the return of β-$Zn_3(PO_4)_2$, which is unstable in this temperature range, to α-$Zn_3(PO_4)_2$.

Thermal expansion curves of α-$Zn_3(PO_4)_2$ indicated that the compound undergoes a substantial contraction during the inversion to β-$Zn_3(PO_4)_2$.

Conversely, the $\beta$ form expands as it returns to the stable $\alpha$ form.

It was concluded that $Zn_3(PO_4)_2$ has a sluggish inversion at 942°C. The $\beta$ form which is desired as a phosphor is metastable at room temperature which explains its poor chemical and thermal stability.

The x-ray diffraction data for $\alpha$ and $\beta$-$Zn_3(PO_4)_2$ shown in Table III reveal some differences when compared to those of Smith (2). It is believed that the data given in Table III are for pure phases, not contaminated with each other, or with "$\gamma$ zinc phosphate."

**Table III. X-ray diffraction potterns for the compounds in the system $ZnO$-$P_2O_5$**

$Zn_3(PO_4)_2 \cdot 2H_2O$ (dried 110°C)*

| 2θ | d | I/I₀ | 2θ | d | I/I₀ |
|---|---|---|---|---|---|
| 9.8° | 9.03 | 10 | 38.6° | 2.33 | — |
| 11.3° | 7.83 | 100 | 39.5° | 2.28 | — |
| 17.1° | 5.19 | — | 41.3° | 2.19 | — |
| 18.6° | 4.77 | 5 | 42.9° | 2.11 | — |
| 19.5° | 4.55 | 10 | 43.2° | 2.09 | — |
| 20.9° | 4.25 | 10 | 46.4° | 1.96 | 15 |
| 22.7° | 3.92 | 75 | 47.0° | 1.93 | 15 |
| 24.6° | 3.62 | 5 | 48.4° | 1.88 | 5 |
| 25.5° | 3.49 | — | 50.4° | 1.81 | 5 |
| 25.9° | 3.44 | — | 53.3° | 1.72 | — |
| 26.4° | 3.38 | — | 54.2° | 1.69 | — |
| 27.9° | 3.20 | 30 | 55.3° | 1.66 | — |
| 29.2° | 3.06 | 5 | 56.6° | 1.63 | — |
| 29.6° | 3.02 | 10 | 58.1° | 1.59 | 5 |
| 30.5° | 2.93 | 15 | 59.0° | 1.57 | 10 |
| 31.5° | 2.84 | 5 | 60.9° | 1.52 | 5 |
| 32.2° | 2.78 | — | 62.7° | 1.48 | — |
| 32.7° | 2.74 | — | 65.7° | 1.42 | — |
| 34.4° | 2.61 | 5 | 68.5° | 1.37 | 5 |
| 34.9° | 2.57 | — | 69.5° | 1.35 | — |
| 35.8° | 2.51 | 5 | 70.9° | 1.33 | 5 |
| 36.9° | 2.44 | — | Other reflections | | |
| 37.5° | 2.40 | 5 | * Pattern recorded at 1°/min. | | |

Low (α) $Zn_3(PO_4)_2$

| 2θ | d | I/I₀ | 2θ | d | I/I₀ |
|---|---|---|---|---|---|
| 12.4° | 7.14 | 5 | 44.6° | 2.03 | 5 |
| 19.5° | 4.55 | 40 | 45.1° | 2.01 | 10 |
| 21.3° | 4.17 | 35 | 46.2° | 1.96 | 10 |
| 22.7° | 3.92 | 40 | 46.5° | 1.95 | 10 |
| 24.8° | 3.59 | 90 | 47.1° | 1.93 | 5 |
| 28.6° | 3.12 | 75 | 49.2° | 1.85 | 10 |
| 29.2° | 3.06 | 100 | 50.0° | 1.82 | 20 |
| 31.9° | 2.81 | 15 | 50.8° | 1.80 | 10 |
| 32.5° | 2.75 | 10 | 51.3° | 1.78 | 10 |
| 33.9° | 2.64 | 10 | 54.9° | 1.67 | 10 |
| 34.3° | 2.61 | 25 | 55.6° | 1.65 | 10 |
| 36.9° | 2.44 | 40 | 57.9° | 1.59 | 5 |
| 37.4° | 2.40 | 35 | 59.8° | 1.55 | 20 |
| 37.9° | 2.37 | 5 | 60.9° | 1.52 | 15 |
| 38.4° | 2.34 | 5 | 61.5° | 1.51 | 10 |
| 39.4° | 2.29 | 40 | 63.2° | 1.47 | 5 |
| 40.3° | 2.24 | 25 | 64.6° | 1.44 | 15 |
| 40.8° | 2.21 | 20 | 66.2° | 1.41 | 10 |
| 42.7° | 2.12 | 10 | | | |
| 43.6° | 2.07 | 10 | Other reflections | | |

High (β) $Zn_3(PO_4)_2$

| 2θ | d | I/I₀ | 2θ | d | I/I₀ |
|---|---|---|---|---|---|
| 20.6° | 4.31 | 5 | 38.1° | 2.36 | 5 |
| 21.3° | 4.17 | 15 | 39.1° | 2.30 | 5 |
| 22.2° | 4.00 | 10 | 39.6° | 2.28 | — |
| 22.6° | 3.93 | 15 | 41.0° | 2.20 | 5 |
| 22.8° | 3.90 | 10 | 41.5° | 2.18 | — |
| 23.3° | 3.82 | — | 42.0° | 2.15 | 10 |
| 24.2° | 3.68 | 10 | 43.3° | 2.09 | 15 |
| 25.2° | 3.53 | — | 44.7° | 2.03 | 5 |
| 27.1° | 3.29 | 100 | 45.1° | 2.01 | 5 |
| 28.4° | 3.14 | 20 | 45.5° | 1.99 | 5 |
| 28.9° | 3.09 | 60 | 46.4° | 1.96 | 5 |
| 29.1° | 3.07 | 35 | 47.2° | 1.93 | — |
| 29.6° | 3.02 | 20 | 47.6° | 1.91 | 15 |
| 30.5° | 2.93 | 15 | 48.7° | 1.87 | 15 |
| 31.2° | 2.87 | 75 | 48.9° | 1.86 | 15 |
| 31.5° | 2.84 | 60 | 50.4° | 1.81 | 15 |
| 31.9° | 2.81 | 5 | 51.4° | 1.78 | 5 |
| 32.4° | 2.76 | — | 53.7° | 1.71 | — |
| 33.7° | 2.66 | — | 54.7° | 1.68 | 10 |
| 34.1° | 2.63 | 5 | 55.5° | 1.66 | 5 |
| 35.0° | 2.56 | 10 | 56.0° | 1.64 | 5 |
| 35.3° | 2.54 | 5 | 57.4° | 1.61 | 15 |
| 36.0° | 2.49 | 20 | 58.8° | 1.57 | 5 |
| 36.6° | 2.46 | 5 | | | |
| 37.6° | 2.39 | 20 | Other reflections | | |

Low (α) $Zn_2P_2O_7$

| 2θ | d | I/I₀ | 2θ | d | I/I₀ |
|---|---|---|---|---|---|
| 9.2° | 9.61 | — | 35.3° | 2.54 | 45 |
| 15.8° | 5.61 | 10 | 36.2° | 2.48 | — |
| 17.4° | 5.10 | 10 | 38.1° | 2.36 | — |
| 18.4° | 4.82 | — | 39.1° | 2.30 | 10 |
| 18.8° | 4.72 | — | 41.2° | 2.19 | 5 |
| 19.4° | 4.58 | — | 42.8° | 2.11 | 20 |
| 19.8° | 4.48 | — | 43.2° | 2.09 | 45 |
| 20.3° | 4.37 | 15 | 43.5° | 2.08 | 5 |
| 21.3° | 4.17 | 15 | 45.0° | 2.01 | 10 |
| 22.5° | 3.95 | — | 47.0° | 1.93 | 5 |
| 23.3° | 3.82 | — | 47.6° | 1.91 | — |
| 23.7° | 3.75 | 5 | 48.5° | 1.88 | 10 |
| 24.7° | 3.60 | 5 | 51.6° | 1.77 | — |
| 25.4° | 3.51 | — | 52.1° | 1.76 | — |
| 25.8° | 3.45 | — | 53.5° | 1.71 | 5 |
| 26.5° | 3.36 | — | 54.1° | 1.70 | 5 |
| 26.8° | 3.33 | — | 55.0° | 1.67 | 5 |
| 27.7° | 3.22 | — | 55.8° | 1.65 | 5 |
| 28.3° | 3.15 | — | 56.8° | 1.62 | 5 |
| 28.9° | 3.09 | 5 | 57.2° | 1.61 | 10 |
| 29.5° | 3.03 | 60 | 57.4° | 1.61 | 10 |
| 29.7° | 3.01 | 100 | 58.7° | 1.57 | 25 |
| 31.2° | 2.87 | 5 | 59.6° | 1.55 | 5 |
| 31.4° | 2.85 | 10 | 60.0° | 1.54 | 5 |
| 31.8° | 2.81 | — | 61.8° | 1.50 | 5 |
| 32.9° | 2.72 | 5 | 63.1° | 1.47 | 15 |
| 34.6° | 2.59 | — | Other reflections | | |

High (β) $Zn_2P_2O_7$*

| 2θ | d | I/I₀ | 2θ | d | I/I₀ |
|---|---|---|---|---|---|
| 17.5° | 5.07 | — | 57.0° | 1.62 | 10 |
| 20.3° | 4.34 | 5 | 58.4° | 1.58 | 15 |
| 24.7° | 3.60 | — | 59.8° | 1.55 | 5 |
| 27.3° | 3.27 | — | 61.5° | 1.51 | 5 |
| 28.7° | 3.11 | — | 62.0° | 1.50 | — |
| 29.6° | 3.02 | 100 | 62.8° | 1.48 | 10 |
| 34.9° | 2.57 | — | 63.6° | 1.46 | — |
| 35.2° | 2.55 | 30 | 70.0° | 1.34 | 5 |
| 39.0° | 2.31 | 5 | 70.7° | 1.33 | 5 |
| 41.1° | 2.20 | 5 | 71.4° | 1.32 | — |
| 43.0° | 2.10 | 25 | 71.7° | 1.32 | 5 |
| 43.6° | 2.08 | 5 | 75.4° | 1.26 | 5 |
| 44.9° | 2.02 | 5 | 78.3° | 1.22 | — |
| 46.8° | 1.94 | 5 | 78.9° | 1.21 | — |
| 48.5° | 1.88 | 15 | | | |
| 51.9° | 1.76 | 5 | Other reflections | | |
| 53.5° | 1.71 | 5 | * Pattern recorded at 1°/min | | |
| 54.1° | 1.70 | 5 | with specimen at 850°C. | | |

Low (α) $Zn(PO_3)_2$

| 2θ | d | I/I₀ | 2θ | d | I/I₀ |
|---|---|---|---|---|---|
| 13.5° | 6.56 | 5 | 38.2° | 2.36 | 25 |
| 13.7° | 6.46 | 15 | 42.4° | 2.13 | 10 |
| 13.8° | 6.42 | 55 | 42.9° | 2.11 | 10 |
| 14.4° | 6.15 | 5 | 43.8° | 2.07 | 25 |
| 19.3° | 4.60 | 5 | 45.1° | 2.01 | 10 |
| 20.0° | 4.44 | 55 | 45.4° | 2.00 | 10 |
| 20.8° | 4.27 | 50 | 46.8° | 1.94 | 5 |
| 25.2° | 3.53 | 5 | 47.9° | 1.90 | 20 |
| 25.8° | 3.45 | 55 | 50.1° | 1.82 | — |
| 26.4° | 3.38 | 5 | 50.6° | 1.80 | — |
| 27.1° | 3.29 | — | 51.0° | 1.79 | 10 |
| 27.6° | 3.23 | 5 | 52.0° | 1.76 | — |
| 28.1° | 3.18 | 5 | 52.4° | 1.75 | 5 |
| 29.3° | 3.05 | 15 | 53.5° | 1.71 | 5 |
| 30.1° | 2.97 | 95 | 56.6° | 1.63 | 10 |
| 30.7° | 2.91 | 100 | 56.9° | 1.62 | 10 |
| 31.2° | 2.87 | 5 | 57.5° | 1.60 | 10 |
| 31.7° | 2.82 | 20 | 59.6° | 1.55 | 10 |
| 34.8° | 2.58 | 5 | 60.1° | 1.54 | 50 |
| 35.5° | 2.53 | 5 | 60.7° | 1.53 | 5 |
| 37.3° | 2.41 | 45 | | | |
| 37.7° | 2.39 | 10 | Other reflections | | |

Table III. X-ray diffraction patterns for the compounds in the system $ZnO-P_2O_5$ (Cont.)

| High ($\beta$) $Zn(PO_3)_2$ | | | | | |
|---|---|---|---|---|---|
| $2\theta$ | $d$ | $I/I_o$ | $2\theta$ | $d$ | $I/I_o$ |
| 16.5° | 5.37 | 5 | 35.4° | 2.54 | — |
| 17.3° | 5.13 | 5 | 36.3° | 2.47 | 5 |
| 17.6° | 5.04 | 5 | 37.4° | 2.40 | 10 |
| 19.6° | 4.53 | 10 | 37.7° | 2.39 | 10 |
| 20.1° | 4.42 | 10 | 39.6° | 2.28 | 10 |
| 21.8° | 4.08 | 40 | 40.0° | 2.25 | 5 |
| 23.1° | 3.85 | 10 | 40.8° | 2.21 | 5 |
| 23.4° | 3.80 | 30 | 41.2° | 2.19 | 10 |
| 24.0° | 3.71 | 15 | 41.5° | 2.18 | 5 |
| 25.5° | 3.49 | 45 | 44.1° | 2.05 | 5 |
| 25.8° | 3.45 | 100 | 44.3° | 2.04 | 15 |
| 26.2° | 3.40 | 25 | 47.8° | 1.90 | 5 |
| 27.2° | 3.28 | 10 | 48.2° | 1.89 | 5 |
| 27.8° | 3.21 | 15 | 48.7° | 1.87 | 5 |
| 29.8° | 3.00 | — | 49.6° | 1.84 | 5 |
| 31.8° | 2.81 | 10 | 51.4° | 1.78 | 5 |
| 32.5° | 2.75 | 10 | 53.9° | 1.70 | 10 |
| 33.6° | 2.67 | 10 | Other reflections | | |

*Zinc pyrophosphate.*—The differential thermal analysis curve of $Zn_2P_2O_7$ is given in Fig. 3. The curve showed two peaks, one at about 130° and the other at about 1020°C.

The first peak was due to an inversion in $Zn_2P_2O_7$. Duplicate runs on the same sample indicated that this inversion was reversible. Quenches of $Zn_2P_2O_7$ heated to temperatures above the inversion temperature did not freeze in a high form of the material. These data indicated that the inversion was very rapidly reversible.

High temperature x-ray methods were used to measure the inversion temperature. A sample was heated above the inversion temperature and then cooled in 10°C increments until the x-ray pattern showed a change to another form. This change took place between 127° and 137°C. An inversion temperature of 132°±8°C was concluded from these data.

The major peaks in the x-ray data of the high form of $Zn_2P_2O_7$ closely resembled those for the low form, Table III. The inversion to the high form was accompanied by the disappearance of about one-half of the x-ray peaks present in the low form. This suggests that the inversion of $Zn_2P_2O_7$ was due to a change from a lower to a higher symmetry

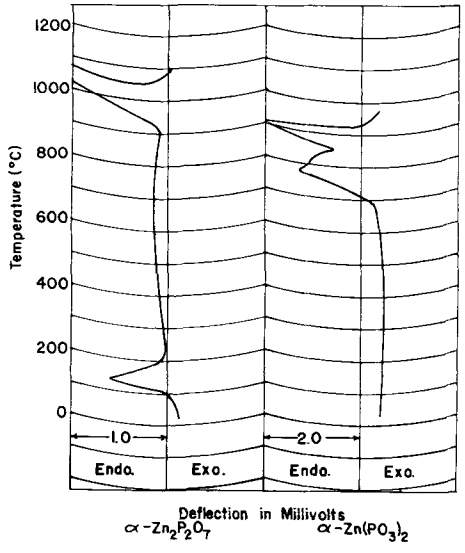


Fig. 3. Typical differential thermal analysis curves for $\alpha$-$Zn_2P_2O_7$ and $\alpha$-$Zn(PO_3)_2$.

structure. The low form of $Zn_2P_2O_7$ gave biaxial interference figures under the polarizing microscope.

The second peak at 1020°C in the DTA curve was due to the melting of $Zn_2P_2O_7$. The melting point of $Zn_2P_2O_7$ as determined accurately by quench techniques is 1017°C.

*Zinc metaphosphate.*—The differential thermal analysis curve of $Zn(PO_3)_2$ is presented in Fig. 3. This curve showed two peaks, one at approximately 780° and the other at 900°C.

The first peak is due to a polymorphic inversion in $Zn(PO_3)_2$. This peak has an unusual contour showing a slow rounding effect after the initial sharp peak. This rounding effect was probably due to the formation of a very small amount of liquid in the sample. The chemical analysis indicated the $P_2O_5$ content was about 0.3% below that of pure $Zn(PO_3)_2$, or that the actual composition of this material lies between $Zn_2P_2O_7$ and $Zn(PO_3)_2$. The eutectic temperature in this region is 834°C which is approximately where this rounding effect takes place. This peak is about 120°C above the inversion temperature of 650°C as measured by quench techniques. This is to be expected since differential thermal analysis is a dynamic measurement and this inversion is sluggish.

The second peak was due to the melting of $Zn(PO_3)_2$ and corresponds roughly to the melting point of 872°C as measured by quench techniques.

A sample of $\alpha$-$Zn(PO_3)_2$ was heated to 630°-650°C for 54 hr to confirm the stability of the low form in this temperature range. X-ray analysis of the above sample indicated that only the low form of $Zn(PO_3)_2$ was present.

Since heating the high form of $Zn(PO_3)_2$ at a temperature below its inversion at 650°C did not produce the low form, an attempt was made to form $\alpha$-$Zn(PO_3)_2$ by devitrifying a glass of the $Zn(PO_3)_2$ composition. The first experimental run consisted of heating a sample of $Zn(PO_3)_2$ glass for 1, 4, and 16 hr at 650°C. X-ray analysis indicated that these glasses divitrified to only the high form. A second set of glasses heated for 1, 4, and 16 hr at 550°C devitrified to a mixture of the high and low forms of $Zn(PO_3)_2$. Temperatures below 450°C were found to be not high enough to produce devitrification. This study indicated that the low form of $Zn(PO_3)_2$ could be formed by devitrifying $Zn(PO_3)_2$ glass. However, complete devitrification to the low form could not be obtained. This eliminated the technique of measuring the inversion temperature by devitrifying glasses. Consequently, the inversion temperature measurement was determined only by going from the low to the high form.

It was concluded that $Zn(PO_3)_2$ has an irreversible inversion when heated in air. This inversion is reasonably slow in a temperature range near the inversion. Temperatures 90°-140°C above the arbitrarily selected inversion temperature of 650°C produce complete transition to the higher form in about a one-hour firing time.

### *Phase Equilibrium Relationships*

*Quench data.*—The experimental data obtained by quench method are presented in Table IV. The

Table IV. Quench data for the system $ZnO-P_2O_5$

| No. | Composition weight % ZnO | Composition weight % $P_2O_5$ | Mole ratio | Starting material | Heat treatment Time, hr | Heat treatment Temp, °C | Phases present | Method of direction |
|---|---|---|---|---|---|---|---|---|
| 1 | 74.12 | 25.88 | 5:1 | CR | 1 | 1015 | GL + CR | M |
| | | | | CR | 1 | 1004 | CR | M |
| | | | | CR | 3 | 1012 | ZnO (+GL) | X |
| | | | | CR | 20 | 941 | ZnO + α3:1 | X |
| | | | | CR | 2 | 932 | ZnO + α3:1 | X |
| | | | | CR | 4 | 916 | ZnO + α3:1 | X |
| 3 | 69.62 | 30.38 | 4:1 | GL | ½ | 1179 | GL | M |
| | | | | GL | ½ | 1170 | GL + CR | M |
| | | | | CR | 1 | 1003 | GL + CR | M |
| | | | | CR | 1 | 992 | CR | M |
| | | | | CR | 15 | 1028 | ZnO (+GL) | X |
| | | | | CR | 3 | 959 | ZnO + β3:1 | X |
| | | | | CR | 2 | 948 | ZnO + β3:1 | X |
| | | | | CR | 2 | 932 | ZnO + α3:1 | X |
| | | | | CR | 20 | 892 | ZnO + α3:1 | X |
| 4 | 68.00 | 32.00 | — | GL | ½ | 1110 | GL | M |
| | | | | GL | ½ | 1104 | CR | M |
| 5 | 66.00 | 34.00 | — | CR | 4 | 1013 | GL | M |
| | | | | CR | 4 | 1008 | GL + CR | M |
| 7 | 63.22 | 36.78 | 3:1 | CR | 14 | 1062 | GL + CR | M |
| | | | | CR | 3 | 1056 | CR | M |
| | | | | CR | 15 | 1030 | β3:1 | X |
| | | | | CR | 15 | 990 | β3:1 | X |
| | | | | CR | 15 | 954 | β3:1 | X |
| | | | | CR | 21 | 949 | β3:1 | X |
| | | | | CR | 20 | 942 | β3:1 | X |
| | | | | CR | 20 | 942 | α3:1 | X |
| | | | | CR | 27 | 938 | α3:1 | X |
| | | | | CR | 24 | 928 | α3:1 | X |
| 8 | 62.00 | 38.00 | — | CR | 2 | 954 | α3:1 + β2:1 | X |
| | | | | CR | 2 | 900 | α3:1 + β2:1 | X |
| | | | | CR | 2 | 850 | α3:1 + β2:1 | X |
| 9 | 61.00 | 39.00 | — | CR | 1½ | 1045 | GL | M |
| | | | | CR | 2 | 1041 | GL + CR | M |
| | | | | CR | 8 | 1024 | β3:1 (+GL) | X |
| | | | | CR | 8 | 990 | β3:1 (+GL) | X |
| | | | | GL | 2 | 954 | α3:1 + β2:1 | X |
| | | | | CR | 15 | 948 | α3:1 + β2:1 | X |
| | | | | GL | 2 | 897 | α3:1 + β2:1 | X |
| | | | | GL | 2 | 849 | α3:1 + β2:1 | X |
| 11 | 58.89 | 41.11 | 5:2 | CR | ½ | 1026 | GL | M |
| | | | | CR | ½ | 1016 | GL + CR | M |
| | | | | CR | 12 | 1032 | (GL) | X |
| | | | | CR | 15 | 989 | β3:1 (+GL) | X |
| | | | | GL | 2 | 954 | α3:1 + β2:1 | X |
| | | | | CR | 15 | 948 | α3:1 + β2:1 | X |
| | | | | GL | 2 | 897 | α3:1 + β2:1 | X |
| | | | | GL | 2 | 849 | α3:1 + β2:1 | X |
| 12 | 58.00 | 42.00 | — | CR | ½ | 1007 | GL | M |
| | | | | CR | ½ | 995 | GL + CR | M |
| | | | | CR | 1½ | 958 | β3:1 + β2:1 | X |
| 13 | 57.00 | 43.00 | — | CR | ½ | 982 | GL | M |
| | | | | CR | ½ | 972 | GL + CR | M |
| | | | | CR | 20 | 1029 | (GL) | X |
| | | | | CR | 20 | 939 | α3:1 + β2:1 | X |
| 14 | 55.00 | 45.00 | — | CR | ½ | 1006 | GL | M |
| | | | | CR | ½ | 997 | GL + CR | M |
| | | | | CR | 12 | 976 | β2:1 (+GL) | X |
| | | | | CR | 1½ | 967 | β3:1 + β2:1 | X |
| 15 | 53.40 | 46.60 | 2:1 | CR | 2 | 1018 | GL | M |
| | | | | CR | 2 | 1015 | CR | M |
| 16 | 51.00 | 49.00 | — | GL | 2½ | 1006 | GL | M |
| | | | | GL | 2½ | 1001 | GL + CR | M |
| | | | | CR | 10 | 902 | β2:1 (+GL) | X |
| | | | | CR | 16 | 820 | β2:1 + β1:1 | X |
| 17 | 48.85 | 51.15 | 5:3 | CR | ½ | 1020 | GL | M |
| | | | | CR | ½ | 1014 | GL + CR | M |
| | | | | GL | 3 | 837 | β2:1 (+GL) | X |
| | | | | GL | 1 | 827 | β2:1 + β1:1 | X |
| | | | | GL | 2½ | 818 | β2:1 + β1:1 | X |

Table IV. Quench data for the system $ZnO-P_2O_5$ (Cont.)

| | | | | | | | | |
|---|---|---|---|---|---|---|---|---|
| 18 | 46.22 | 53.78 | 3:2 | GL | ½ | 1004 | GL | M |
| | | | | GL | ½ | 997 | GL + CR | M |
| | | | | CR | 6 | 895 | β2:1 (+GL) | X |
| | | | | CR | 22 | 836 | β2:1 (+GL) | X |
| | | | | CR | 8 | 820 | β2:1 + β1:1 | X |
| | | | | CR | 22 | 755 | β2:1 + β1:1 | X |
| | | | | CR | 9 | 711 | β2:1 + α1:1 | X |
| 19 | 43.31 | 56.69 | 4:3 | GL | ½ | 962 | GL | M |
| | | | | GL | ½ | 957 | GL + CR | M |
| | | | | GL | 3 | 837 | β2:1 (+GL) | X |
| | | | | GL | 1 | 827 | β2:1 + β1:1 | X |
| | | | | GL | 2½ | 818 | β2:1 + β1:1 | X |
| | | | | GL | 1½ | 717 | β2:1 + α1:1 | X |
| 20 | 41.73 | 58.27 | 5:4 | CR | ½ | 938 | GL | M |
| | | | | CR | ½ | 932 | GL + CR | M |
| | | | | CR | 4 | 859 | β2:1 (+GL) | X |
| | | | | CR | 6 | 818 | β2:1 + β1:1 | X |
| | | | | CR | 15 | 722 | β2:1 + α1:1 | X |
| | | | | CR | 6 | 699 | β2:1 + α1:1 | X |
| 22 | 39.00 | 61.00 | — | GL | ½ | 844 | GL | M |
| | | | | GL | ½ | 840 | GL + CR | M |
| | | | | GL | 1 | 827 | β2:1 + β1:1 | X |
| | | | | GL | 2½ | 818 | β2:1 + β1:1 | X |
| | | | | CR | 19 | 707 | β2:1 + β1:1 | X |
| 24 | 36.42 | 63.58 | 1:1 | CR | 2 | 874 | GL | M |
| | | | | CR | 1 | 870 | CR | M |
| | | | | CR | 16 | 745 | β1:1 | X |
| | | | | CR | 22 | 694 | β1:1 (Trace α1:1) | X |
| | | | | CR | 9 | 690 | β1:1 + α1:1 | X |
| | | | | CR | 20 | 687 | α1:1 | X |
| | | | | CR | 20 | 676 | α1:1 | X |
| | | | | CR | 20 | 658 | α1:1 | X |

α3:1 = Low (α) $Zn_3(PO_4)_2$
β3:1 = High (β) $Zn_3(PO_4)_2$
β2:1 = High (β) $Zn_2P_2O_7$
α1:1 = Low (α) $Zn(PO_3)_2$
β1:1 = High (β) $Zn(PO_3)_2$

GL = Glass
CR = Crystals
M = Microscope
X = X-ray

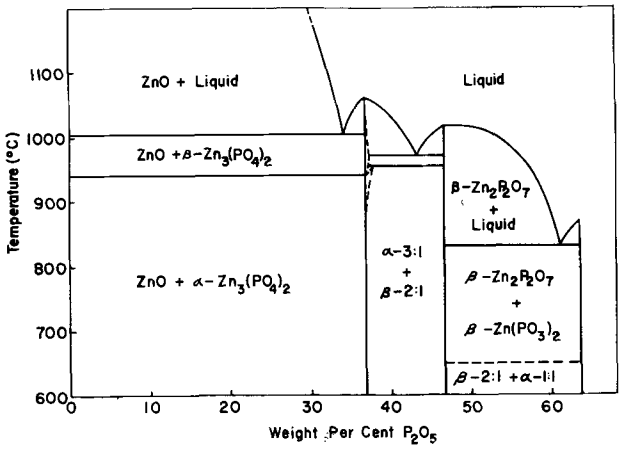


Fig. 4. Phase equilibrium diagram for the system $ZnO-Zn(PO_3)_2$.

phase diagram of the $ZnO-Zn(PO_3)_2$ portion of the $ZnO-P_2O_5$ system was drawn from these data and is presented in Fig. 4.

The five crystalline modifications of the zinc phosphates obtainable at room temperature all produced biaxial interference figures under the polarizing microscope. The high and low forms of $Zn_3(PO_4)_2$ particularly resembled one another under the light microscope. Since all these materials produced distinct and characteristic x-ray diffraction patterns, x-ray diffraction techniques were used for all crystal indentification. This single method of identification proved to be completely adequate throughout the system.

$ZnO-Zn_3(PO_4)_2$ *portion.*—The presence of excess ZnO with $Zn_3(PO_4)_2$ had no effect on the inversion temperature of the pure $Zn_3(PO_4)_2$, indicating no solubility of ZnO in the orthophosphate.

The eutectic temperature is 1005°C, and the eutectic composition is approximately 66% ZnO and 34% $P_2O_5$. No experimental difficulty was experienced in obtaining ZnO in equilibrium with α-$Zn_3(PO_4)_2$, β-$Zn_3(PO_4)_2$ or glass.

$Zn_3(PO_4)_2-Zn_2P_2O_7$ *portion.*— An enlarged view of the $Zn_3(PO_4)_2-Zn(PO_3)_2$ portion of the system is presented in Fig. 5. The presence of $Zn_2P_2O_7$ with $Zn_3(PO_4)_2$ had a definite effect on the inversion temperature of $Zn_3(PO_4)_2$. The quenched compositions in this portion showed that α-$Zn_3(PO_4)_2$ was stable in the presence of $Zn_2P_2O_7$ to at least 955°C, 13° above the inversion temperature of pure $Zn_3(PO_4)_2$. This increase in inversion temperature implies the existence of a solid solution of $Zn_2P_2O_7$ in $Zn_3(PO_4)_2$ to the extent of approximately 5% $Zn_2P_2O_7$. A composition with a chemical analysis of 37.23% $P_2O_5$, which is about 0.5% more $P_2O_5$ than the pure $Zn_3(PO_4)_2$, always showed the presence of two phases when heat treated.

There was no difficulty in obtaining α-$Zn_3(PO_4)_2$ in equilibrium with $Zn_2P_2O_7$. However, it was very difficult to obtain β-$Zn_3(PO_4)_2$ in equilibrium with $Zn_2P_2O_7$. Only two quenches presented in Table IV

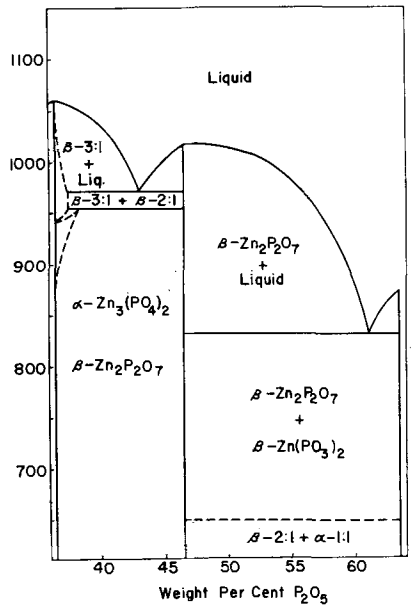


Fig. 5. Enlarged diagram of the equilibrium relationships in the range between $Zn_3(PO_4)_2$ and $Zn(PO_3)_2$.

contain these two phases. Numerous other quenches in this very small temperature range usually showed the nonequilibrium existence of three phases, $\alpha$-$Zn_3(PO_4)_2$, $\beta$-$Zn_3(PO_4)_2$, and $Zn_2P_2O_7$. The eutectic temperature in this region is at 972°C, and the eutectic composition is approximately 57% ZnO and 43% $P_2O_5$.

$Zn_2P_2O_7$-$Zn(PO_3)_2$ *portion.*—Since glasses in this portion of the system could not be devitrified completely to the low form, the $Zn(PO_3)_2$ inversion in the presence of $Zn_2P_2O_7$ was measured using crystalline starting material.

The $Zn(PO_3)_2$ inversion appeared to be inhibited by the presence of $Zn_2P_2O_7$ and occurred at temperatures of 65°-80°C above the 650° observed for the pure $Zn(PO_3)_2$. Since the lowest temperature at which pure $\alpha$-$Zn(PO_3)_2$ crystallized from glass was 650°C, the inversion is shown at this temperature in Fig. 4 and 5. The actual equilibrium inversion temperature may be considerably below 650°C.

The eutectic temperature is 832°C, and the eutectic composition is approximately 39% ZnO and 61% $P_2O_5$.

## Summary and Conclusions

1. Equilibrium relationships have been established for the system $ZnO-Zn(PO_3)_2$.

2. The conclusion of Smith that $Zn_3(PO_4)_2$ does not show any phase change up to the point of fusion has been proven incorrect. A relatively sluggish reversible inversion of $\alpha$-$Zn_3(PO_4)_2$ to $\beta$-$Zn_3(PO_4)_2$ occurs at 942°C.

3. $Zn_2P_2O_7$ and $Zn(PO_3)_2$ exist in two polymorphic forms.

## Acknowledgment

The authors wish to thank members of the analytical laboratory of the Chemical Products Plant of the General Electric Co., Cleveland, Ohio for their assistance with the chemical analyses. The financial support of the General Electric Company during the course of the work was deeply appreciated.

Manuscript received July 15, 1957. Contribution No. 57-1 from the College of Mineral Industries, The Pennsylvania State University.

Any discussion of this paper will appear in a Discussion Section to be published in the December 1958 JOURNAL.

## REFERENCES

1. H. Insley, G. W. Morey, F. D. Rossini, and A. Silverman, Editors, *Bull. Nat. Research Council. (U. S.)*, No. 118, U. of Pittsburgh (1949).
2. A. L. Smith, *This Journal*, **98**, 363 (1951).
3. W. L. Hill, G. T. Faust, and D. S. Reynolds, *Am. J. Sci.*, **242**, 457 (1944).
4. R. M. Gruver, *J. Am. Ceram. Soc.*, **31**, 323 (1948).
5. W. C. Pierce and E. L. Haenisch, "Quantitative Analysis," 2nd ed., John Wiley & Sons, Inc., New York (1937).

# The Luminescence of Self-Coactivated ZnS:Cu

**M. H. Aven and R. M. Potter**

*Lamp Development Department, General Electric Company, Nela Park, East Cleveland, Ohio*

ABSTRACT

Phosphors prepared by firing ZnS with Cu in purified $H_2S$ show a simple orange emission band, with no other bands in evidence even at 90°K. Excitation by ultraviolet, cathode rays, and electric field gives identical emission spectra. The emission band peaks at the same wave length for samples with either hexagonal or cubic crystal structure, but is shifted to longer wave lengths by addition of CdS. The orange luminescence is strongly decreased by traces of $H_2O$ in the $H_2S$ firing atmosphere, but quite stable to firing in oxidizing or reducing atmospheres.

Addition of Al to ZnS:Cu gives a series of phosphors showing various proportions of orange, blue, and green emission. Firing ZnS with Ag in pure $H_2S$ gives a new yellow-emitting phosphor with properties very similar to the orange Cu-activated phosphor. Possible models for the orange center are discussed.

A few years ago, Froelich (1) described a new ZnS:Cu phosphor exhibiting a yellow-red emission under ultraviolet or electroluminescent excitation. It was prepared by firing mixes containing from $10^{-5}$ to $10^{-2}$ atom fraction Cu at temperatures above 1000°C in an $H_2S$ atmosphere which was free of oxygenous impurities. The emission spectra of Froelich's products varied somewhat with the firing conditions, and also with the mode of excitation. The emission occurred in a broad band peaking around 6500Å, and was believed to consist of a strong red band at 6700Å, and a weaker yellow band at 5800Å. The relative intensity of the latter under ultraviolet depended on the wave length of the exciting radiation.

Recently Bowers and Melamed (2) reported that a blue (4400Å) emission band was always found in their ZnS:Cu phosphors showing the 6700Å band (referred to by them as the "red" emission), although in some of their products, the blue band showed up only at liquid air temperatures. Since they found no temperature-dependent magnetic susceptibility in these products they concluded that the "red" centers did not involve any unpaired electrons. They therefore proposed that the "red" center was an interstitial copper coactivated by a zinc vacancy, which in turn was responsible for the 4400Å band.

In the present work it was possible, by scrupulous elimination of oxygenous and coactivator type impurities from the $H_2S$ firing atmosphere, to prepare "self-coactivated" ZnS:Cu with only the 6700Å band present with all types of excitation used. This band is referred to in this paper as the "orange band" because "orange" describes the color of its luminescent emission as perceived by the eye better than "red".

## Preparation of Phosphors

The phosphors were prepared from precipitated ZnS which had been prefired in pure $H_2S$ to remove oxygen and halide impurities. Froelich (1) had found that, in preparing the orange phosphors, comparable results were obtained with pure $H_2S$ gas directly from a cylinder and with gas that was first washed with $Ba(OH)_2$ solution and then freed from water vapor. In the present work, however, it was found to be impossible to obtain bright orange phosphors, using the best available grade $H_2S$ gas directly from a cylinder. Therefore the above-mentioned method of purification was employed in all $H_2S$ firings. The residual quantity of oxygenous and coactivator impurities after such treatment was estimated to be less than 10 ppm (possibly much less than 10 ppm).

The phosphors were fired in small bottle-shaped tubes in an arrangement very similar to that described by Froelich (1). In this set-up, fresh $H_2S$ gas is passed continually over the phosphor sample, thus sweeping out any gaseous reaction products.

The phosphor mixes were prepared by adding Cu or Al as dilute solutions of the nitrate or sulfate to ZnS powder, along with enough deionized water to give a stiff paste. This paste was dried, sieved, and transferred to the firing tube. The firing tubes were inserted into the furnace at 600°C, and the temperature raised quickly to the firing temperature, usually 1100°C. After the firing period, usually 1 hr, the tube was removed from the furnace and allowed to cool to room temperature. The flow of pure $H_2S$ was maintained from the time before inserting the tube into the furnace until the time the firing tube had cooled to room temperature. The cooled phosphors were removed from the firing tube and washed in NaCN solution to remove free $Cu_2S$.

It is of theoretical interest to know the minimum temperature needed to form a phosphor. When attempts were made to prepare the orange phosphor by the method described above, but using firing temperatures lower than 1000°C, the products showed very weak or no luminescence. It was sus-

pected that these lower temperature firings failed to remove the oxygen which was present in the starting materials. This residual oxygen then prevented the formation of orange centers. Therefore a preparation method was developed in which oxygen was removed from the starting materials. A portion of ZnS, prefired as described above, was further fired for ½ hr at 1100°C in pure $H_2S$. A sample of $Cu_2S$ was prefired for 20 min at 600°C in $H_2S$. With $H_2S$ passing through both tubes, the $Cu_2S$ was shaken into the tube containing the ZnS, avoiding contact with air. After mixing by rotating the tube, the mix was put back into the furnace at 900°C for 1 hr. This experiment was repeated except that the final firing was (*a*) 2 hr at 800°C, (*b*) 2 hr at 700°C. In each case the orange luminescence appeared, although not as bright as in normally prepared samples. A sample fired for 2 hr at 600°C did not fluoresce. Thus it appears that orange centers can form at comparatively low temperatures provided oxygen is carefully excluded.

In some preparations, the phosphor mix was fired in $H_2S$ to which $H_2O$ had purposely been added in certain proportions. This wet $H_2S$ was prepared by passing pure $H_2S$ through water or over ice maintained at a series of temperatures to give the desired vapor pressure of $H_2O$. In these products, the orange emission was much weaker than in samples fired in dry $H_2S$. The intensity of the orange band could be brought back to normal by refiring at 1100°C for approximately 1 hr in dry $H_2S$. However, once this good phosphor was formed, firing for several hours at 1100°C in wet $H_2S$ caused very little dimming of the fluorescence. Refiring at 1200°C or higher in wet $H_2S$ again destroyed the orange luminescence. Apparently, the activation energy for destroying orange centers with $H_2O$ is appreciably higher than that for forming them from nonluminescing material.

Some experiments were carried out which indicated stability of the orange centers to firing in oxidizing atmospheres. Some preformed (unwashed) ZnS:$10^{-3}$ Cu orange phosphor was placed in a thick-walled quartz tube and fired in $H_2S$ at 1100°C for ½ hr to remove any adsorbed air or water. After cooling, enough pure sulfur was added to give about 15 atm of $S_2$ at 1100°C (assuming perfect gas laws), and the tube was sealed off under vacuum. It was then placed in a furnace and brought up to 1100°C for 1 hr, cooled slowly, and removed. The product appeared essentially unchanged in fluorescent color and brightness from the starting material.

In order to determine the stability of the orange centers to reducing atmospheres, some firings were performed in $H_2$ and in Zn vapor. Firings of ZnS:$10^{-4}$ Cu carried out in a flow of pure $H_2$ (similar to $H_2S$ firing technique) gave a product showing the orange emission. However the fluorescent color depended, at least in part, on the number of similar firings carried out in the same quartz tube. A series of three firings in one tube gave products which were in time sequence, blue (with some weak orange), pink (blue plus orange), and pink (even less blue). The part of the sample next to the walls was blue in each case. The blue fluorescence probably corresponds to under-coactivated Cu blue emission (*see* Fig. 3). A single firing in another tube gave a green-fluorescing product. Analogous experiments, using enough pure Zn to give 15 atm, gave nonuniform products which were sometimes quite green, but sometimes largely pink under u.v. excitation. Apparently some coactivating impurity, like Al, is present in the quartz walls of the firing tube, and a reducing atmosphere like Zn or $H_2$ causes it to leach out into the ZnS:Cu. Repeated firings seem to deplete this impurity from the walls and allow the normal orange fluorescent color to develop. It was difficult to reproduce these results, apparently because of a variability in the quartz firing tubes.

These results indicate that orange centers are stable to reducing or oxidizing conditions. They suggest a different interpretation of the results of Riehl and Ortmann (3), who reported a green-fluorescing product from firing ZnS:Cu in $H_2$. It seems quite possible that their product was contaminated with a coactivator impurity.

### Methods of Spectral Measurements

The emission spectra were measured with a Perkin-Elmer Double Pass Monochromator, Model 99. The detector used for the visible region of the spectrum was a 1P22 photomultiplier tube. In one special measurement, a DuMont infrared photomultiplier tube, which gives response out to about 1.1$\mu$ was used. For 3650Å excitation, the output of an AH4 mercury lamp, passed through a 7-37 Corning filter, was focussed on the sample. For 3000-3500Å excitation, an erythemal fluorescent lamp was used; the intensity of excitation was much lower with this source. The electroluminescent excitation was produced by a 60 cps 500 v rms field across a 0.005 in. phosphor-dielectric layer. The cathode ray spectrum was measured using a 16 kv, 510$\mu$ nonfocussed raster (130 $cm^2$). The spectrometer used here was not calibrated beyond 7000Å.

The monochromator (used for all spectra except the cathode ray spectrum) was calibrated with an incandescent lamp whose spectral distribution was known. The calibration was expressed in a form to give fluorescent emission spectra as a plot of the relative energy per unit photon energy interval vs. photon energy rather than the conventional relative energy per unit wave-length interval vs. wave length. When simple fluorescent emission spectra are plotted in the former units, they usually assume, to a good degree of accuracy, a symmetrical bell-shape or Gaussian form (4, 5). Complex emission spectra can be resolved usually into a set of Gaussian curves. The positions of the emission peaks of spectra plotted in this fashion are, of course, slightly shifted relative to their positions on conventional plots. For example, the emission peak of the orange phosphor occurs at 1.84 e.v. (6750Å) on the energy per unit photon energy interval plot and at 1.91 e.v. (6500Å) on the energy per unit wavelength interval plot.

The excitation spectrum of the orange phosphor was determined by mounting the sample as a thin layer in front of the photomultiplier detector of the

Perkin-Elmer spectrophotometer. A red filter next to the photomultiplier transmitted only the fluorescent emission. A projection lamp was focussed on the entrance slit. First pass and stray radiation were eliminated at the exit slit by means of suitable filters. Two runs were made; in the first, the radiation from the exit slit was deflected to the internal thermocouple detector by means of a mirror. The signal from the thermocouple as the spectral region of interest was scanned gave the intensity $I_E$ of the exciting radiation. In the second run, the light from the exit slit was allowed to fall on the sample. The signal from the photomultiplier gave the intensity $I_F$ of the fluorescent emission. The excitation spectrum is a plot of $I_F/I_E$ vs. photon energy.

## Results

In Fig. 1 is shown the emission spectrum of ZnS:1.5 x $10^{-3}$ Cu[1] (fired at 1100°C for ½ hr) under four different methods of excitation. The solid line is the Gaussian fitting the equation $I = I_0 \exp[-C(E - E_0)^2]$, where $I$ is the emitted energy per unit photon energy interval, $E$ is the photon energy, $E_0$ is the photon energy at the peak of the emission band, $I_0$ is a normalization constant, and $C$ is related to the half-width, $2(E_{1/2} - E_0)$, of the band by the relation

$$C = \frac{\ln 2}{(E_{1/2} - E_0)^2}$$

For the emission band in Fig. 1, $E_0 = 1.84$ e.v. and $2(E_{1/2} - E_0) = 0.62$ e.v. The experimental points for 3650Å, 3000-3500Å, cathode ray, and electroluminescent excitation are plotted to show the accuracy of fit to a Gaussian curve and to show the near identity of results for different methods of excitation. The portion of the 3650Å plot for photon energies less than 1.7 e.v. was obtained in a separate measurement with the infrared sensitive photomultiplier tube.

[1] In all formulas in this paper, the number preceding the impurity symbol refers to the atom fraction of added impurity; in the case of ZnS:Cu with no Al, the atom fraction retained in the phosphor after the NaCN wash is about 30-40% of that added.

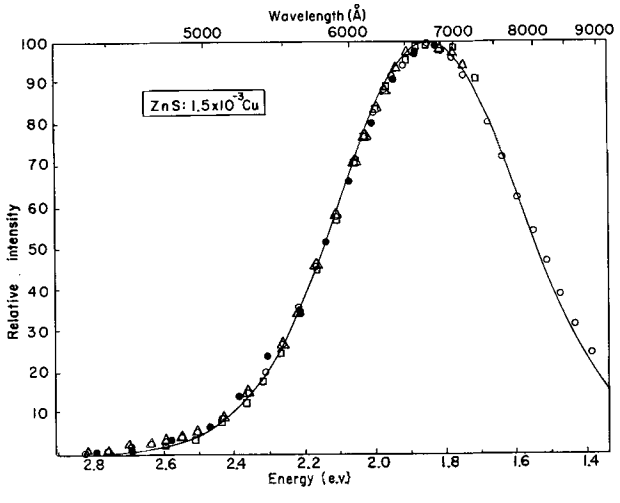


Fig. 1. Emission spectrum of orange fluorescing ZnS:1.5 x $10^{-3}$ Cu, fired at 1100°C. Solid line, Gaussian function fitted through the experimental points; open circles, 3650 Å u.v. excitation; full circles, cathode ray excitation; squares, electroluminescent excitation; triangles, 3000-3500Å u.v. excitation.

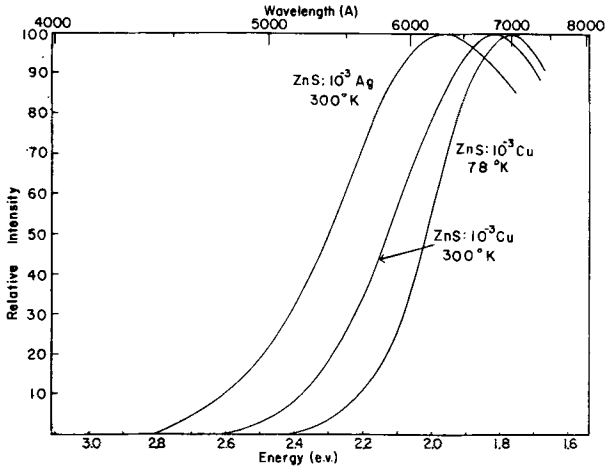


Fig. 2. Emission spectra of ZnS:$10^{-3}$ Cu at 78°K and at 300°K, and the emission spectrum of ZnS:$10^{-3}$ Ag at 300°K.

There is no detectable change in emission spectrum when the frequency of electroluminescent excitation is changed from 60 to 5000 cps. The electroluminescent emission spectra of a few samples with higher than average electroluminescent response showed a shift of the whole orange emission band by a few hundredths of an electron volt toward higher energies compared to the u.v. excited spectrum. This effect is due presumably to a perturbation of the energy levels in the activator centers by the high local electric fields present during electroluminescent excitation.

The spectrum of ZnS:Cu at 78°K is shown in Fig. 2. This, as well as all other spectra discussed below, was obtained under 3650Å u.v. excitation. Here the peak is shifted to 1.78 e.v. and the half-width is decreased from 0.62 e.v. to 0.48 e.v. It still approximates a single Gaussian band and no blue emission band is observed.

Since ZnS phosphors activated with Ag and Au and coactivated with Al or Cl exist and are similar to coactivated Cu phosphors, it was decided to attempt to prepare self-coactivated ZnS:Ag and ZnS:Au. The ZnS:Ag firing produced a yellow-emitting phosphor with a weak afterglow, whose spectrum is shown in Fig. 2. It is seen that the half-width of the band is about the same as that of the ZnS:Cu band, but the emission peak occurs at a higher photon energy (1.97 e.v.). This shift of the peak to higher photon energies is analogous to the shift from green to blue in coactivated ZnS:Cu and ZnS:Ag phosphors, and indicates that the Cu and Ag atoms are integral parts of the emission centers. The ZnS:Au firing produced a nonluminescent product.

The series ZnS: $10^{-4}$ Cu, x Al was prepared in order to investigate the action of various concentrations of Al when these are below that of the Cu. The emission spectra are presented in Fig. 3. The sample without Al shows emission only in the orange band. The addition of as little as $10^{-5}$ Al is sufficient to give a blue band of greater peak intensity than the orange. Further addition of Al almost completely eliminates the orange band and produces a green band in addition to the blue. With equivalent Al or greater, both the orange and blue bands become negligible compared to the green band.

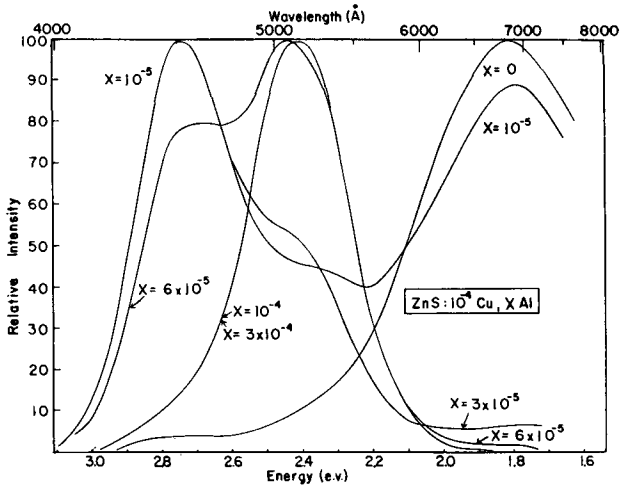


Fig. 3. Emission spectra of ZnS:$10^{-4}$ Cu x Al, with x ranging from 0 to 3 x $10^{-4}$.

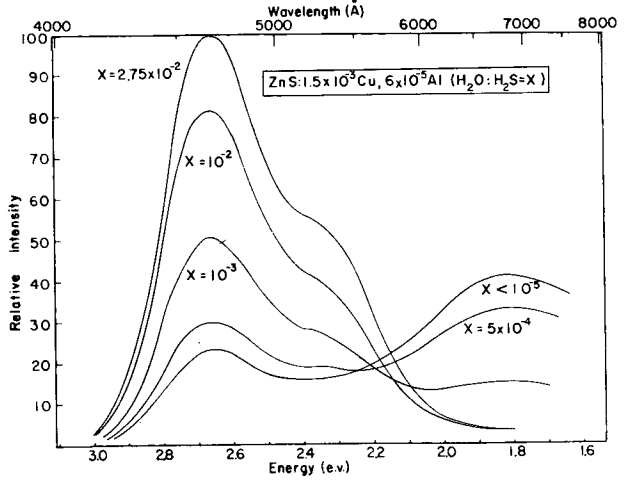


Fig. 5. Emission spectra of ZnS:1.5 x $10^{-3}$ Cu, 6 x $10^{-5}$ Al fired in $H_2S$ containing variable amounts of $H_2O$.

In Fig. 4, the spectra of ZnS:9 x $10^{-4}$ Cu fired in $H_2S$ containing an increasing mole fraction of water are shown. It can be seen that the presence of water strongly inhibits the orange emission. This action of water on the orange centers might be due to one of two causes: the water may somehow inhibit the formation of orange centers, or it may introduce a large concentration of killer centers. The choice between these two hypotheses will become clear in the light of the results reported next.

In Fig. 5, the emission spectra of ZnS:1.5 x $10^{-3}$ Cu, 6 x $10^{-5}$ Al fired in $H_2S$ containing an increasing mole fraction of water are shown. These plots are drawn so that the area under each curve is proportional to the relative total emitted energy. Several things are apparent from the plots. First, with increasing water content, the orange emission band is strongly reduced, while the blue and green bands are increased. Second, the total emitted energy increases somewhat with increasing water content. A replot of these data on the basis of number of photons vs. photon energy showed that the total number of photons emitted remains constant, indicating a constant quantum efficiency. Third, the ratio of blue to green emission remains constant. Apparently the inhibiting effect of water is specific for orange centers; the hypothesis of water causing the formation of killer centers, which should lower the over-all quantum efficiency, must be ruled out.

The excitation spectrum of ZnS:$10^{-3}$ Cu, shown in Fig. 6, peaks around 3.3 e.v. (3750Å), thus falling between that of self-coactivated blue at 3.65 e.v. (3400Å) (6) and green-emitting ZnS:Cu, Cl at 3.1 e.v. (4000Å).

The diffuse reflection spectra of two samples of ZnS:$10^{-4}$ Cu, one fired in dry $H_2S$ and the other fired in $H_2S$ saturated with water at room temperature are shown in Fig. 7. Both products show a very broad absorption band extending to about 2.1 e.v. (6000Å); this band is broader in the wet-fired sample. The dry-fired sample shows in addition a narrower absorption band extending to about 3.0 e.v. (4200Å). This band seems to correspond to the excitation band for dry-fired ZnS:$10^{-3}$ Cu, which indicates that absorption in the narrower band leads to the excitation of orange centers. The absorption between 3.0 e.v. (4200Å) and 2.1 e.v. (6000Å) cannot be explained at present. The absence of the narrower absorption band in wet-fired samples further supports the idea that wet $H_2S$ firing inhibits the formation of the orange centers. The presence of killer centers would not be expected to destroy an absorption band.

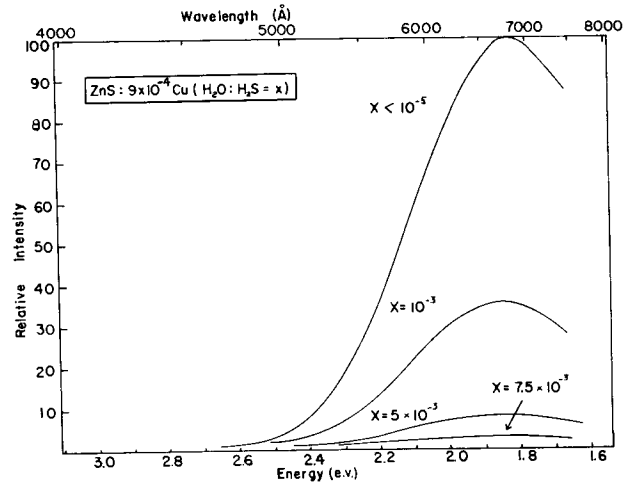


Fig. 4. Emission spectra of ZnS:9 x $10^{-4}$ Cu fired in $H_2S$ containing variable amounts of $H_2O$.

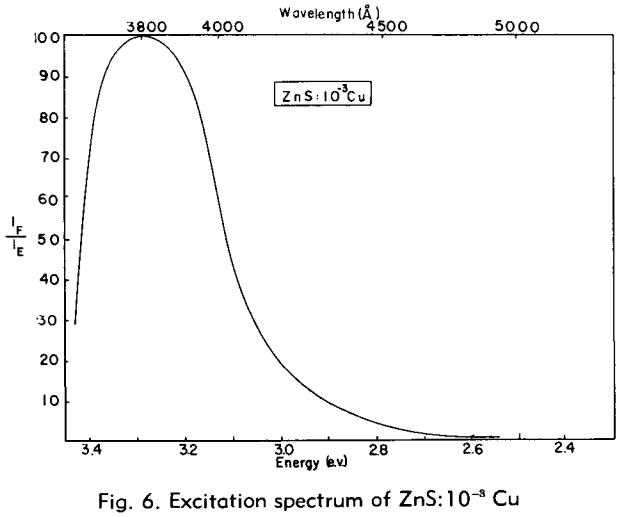


Fig. 6. Excitation spectrum of ZnS:$10^{-3}$ Cu

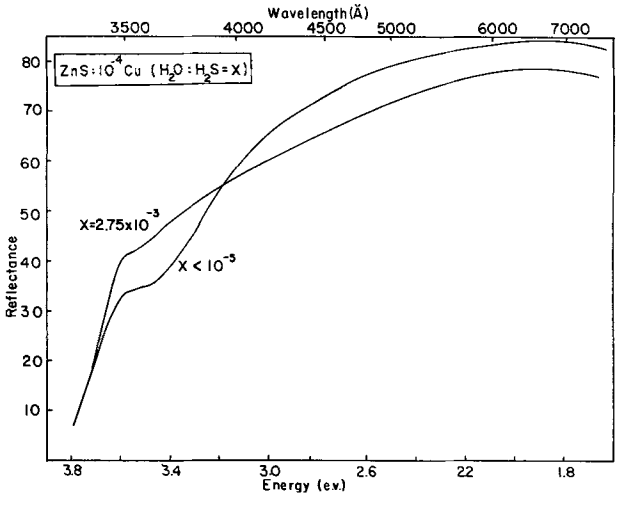


Fig. 7. Diffuse reflectance spectra of ZnS:$10^{-4}$ Cu fired in pure $H_2S$ and in $H_2S$ saturated with water vapor at room temperature.

Orange-fluorescing ZnS:Cu shows no afterglow but does show moderate infrared stimulability (1). Preliminary glow curve work (7) reveals a principal peak at around 400°K (about 0.5 e.v.), which is shifted to lower temperatures by the addition of CdS. In under-coactivated ZnS:Cu, Al phosphors with the main emission in the green band but with some orange band emission, the phosphorescence is much stronger than in over-coactivated ZnS:Cu, Al showing only the green band. This phosphorescence is presumably due to the 400°K trap associated with the orange centers.

Investigation of the crystal structure of the orange phosphors showed that samples of ZnS:Cu with high (around $10^{-3}$ or more) Cu, fired at 1100°C and cooled normally are largely cubic in crystal structure. This is in contrast to samples containing low ($10^{-4}$) Cu or those with high Cu in which the Cu is completely coactivated by Cl or Al, which are hexagonal (8). Preparations of ZnS:$10^{-4}$ Cu, which are almost pure hexagonal, show a fluorescent emission spectrum which is almost identical to that of cubic ZnS:$10^{-3}$ Cu (compare Fig. 1 and 3). This absence of a shift in emission peak with change in crystal structure from cubic to hexagonal is in contrast to the well-known shift of about 150Å to shorter wave lengths found for the blue and green Cu emission bands. The fact that ZnS:Cu with high Cu is largely cubic in spite of being fired above the hexagonal-cubic transition point (1040°C) is believed due to the excess $Cu_2S$ promoting the hexagonal-cubic transition during the cooling of the sample.

A shift of the orange band to longer wave lengths has been found for ZnS:$10^{-3}$ Cu prepared under very special conditions, i.e., cooled rapidly from 1300°C. The shift amounts to about 0.1 e.v. (400Å). The sample was fired in a special firing tube with a thin bottom, which was held in the hot zone of a vertical tube furnace. To achieve the high cooling rate (about 1000°C/sec.) the firing tube was released and fell out of the furnace onto a metal point just above the surface of a container of water. The tube shattered, allowing the powdered phosphor to disperse rapidly into the water. The origin of this shift is not yet known.

## Discussion

The variance of emission spectrum with method of excitation, the nonappearance of more than one band at low temperature, and the good fit to a Gaussian curve strongly support the idea that the orange band is due to a single species of emission center. An additional piece of evidence was provided by measuring the buildup and decay of the 3650Å u.v. excited emission of ZnS:Cu with and without a deep red filter at the detector. With the filter in place, only the long wave-length part of the emission band could reach the detector, while without the filter the entire emission band was passed. The time constants for buildup and decay were found to be nearly identical for the two cases, which would not be expected if the orange band were a composite of two bands due to two species of emission center.

The temperature dependence of brightness of the orange emission was measured and found to be about the same as that of self-activated blue emission (9). In terms of the Schön-Klasens (10) theory of hole migration, this can be interpreted as meaning that the ground states of the self-activated blue centers and of the orange centers must have about the same position with respect to the top of the filled band (about 0.4 e.v. above it). The excitation spectrum qualitatively supports this conclusion, the peak lying about 0.4 e.v. from the ZnS absorption edge.

In forming a theory of the orange center, it is reasonable to compare the properties of the orange phosphor with those of the class of ZnS phosphors produced by "indirect activation", discussed by Klasens (11). Self-coactivated ZnS:Cu and ZnS:Ag resemble this class in certain aspects. The relatively small difference of 0.13 e.v. between their emission peaks suggests that the emission is more a property of the lattice itself than of the activator. Also, a preliminary experiment showed that the emission peak of ZnS:Cu is shifted from 1.84 e.v. to 1.71 e.v. by addition of 10% CdS. This shift of 0.13 e.v. for the first 10% of added CdS is very close to that observed in the well-known indirectly activated phosphors. However, the self-coactivated phosphors differ from this class in other respects. The half-width of the emission band is unusually great, as is the energy difference between excitation and emission peaks. Also, there is no difference in the position of the emission peak between essentially hexagonal and essentially cubic products, as is found for the better known indirect activators. It is concluded that the self-activated phosphors can be considered to be indirectly activated but to differ in some details from the better-known members of this class of ZnS phosphors.

The specific effect of $H_2O$ (and other oxygenous agents) in inhibiting the formation of orange centers is not completely understood. Some preliminary observations indicate that the $H_2O$ actually prevents the $Cu_2S$ from dissolving in the ZnS. Careful comparison of a sample of ZnS:$10^{-4}$ Cu fired in dry $H_2S$ with one fired in wet $H_2S$ showed the latter to have

a lower reflectance to visible light, presumably because of the presence of a greater amount of undissolved $Cu_2S$. When the two samples were ground in NaCN solution to remove excess $Cu_2S$ and refired at 1100°C in dry $H_2S$, the sample originally fired in wet $H_2S$ was the dimmer, indicating less Cu available for formation of orange centers. The wet-fired sample was found by chemical analysis to contain only about half as much Cu as the dry-fired sample. Thus at least part of the decrease in orange emission in wet-fired samples can be correlated with a decrease in the concentration of dissolved Cu.

It is probable that a small amount of ZnO is formed in solid solution in the ZnS during a wet $H_2S$ firing. A semiquantitative chemical analysis of wet-fired ZnS:$10^{-3}$ Cu indicated that the concentration of ZnO must amount to less than $10^{-4}$ mole fraction. Since the concentration of orange centers, while being unknown, is expected to be of the order of $10^{-4}$, it is conceivable that this amount of dissolved oxygen may associate with the Cu or the coactivating species so as to prevent the formation of orange centers. A better oxygen analysis should help clear up this question.

There is not yet sufficient evidence to decide on the identity of the orange center in ZnS:Cu. It may be of some value, however, to list all the models which seem reasonably likely; this has been done below. Models (II) and (IV) have been suggested previously by Kröger (12), and model (I), by Bowers and Melamed (2). All the models will here be assumed to adhere to the rule that no species may have unpaired electrons. This rule is based on the conclusion of Bowers and Melamed (2) that no unpaired electrons are involved in the orange centers.

(I) $Cu_i^+ \cdot V_C^{--} \cdot Cu_i^+$
(II) $Cu_s^- \cdot V_A^{++} \cdot Cu_s^-$
(III) $Cu_s^- \cdot Zn_i^{++} \cdot Cu_s^-$
(IV) $Cu_s^- \cdot Cu_i^+$
(V) $Cu_s^- \cdot Cu_s^+$

The convention used in the above list for labeling imperfection or impurity centers in ZnS is as follows: subscripts s and i are used to designate substitutional and interstitial positions. Zinc and sulfur vacancies are written as $V_C$ and $V_A$, respectively. The superscript is the excess charge in the region of the species arising from donor or acceptor action in the sense used by Prener and Williams (13) or Bowers and Melamed (2). For instance, substitutional Cu, having one less electron than Zn, must act as a single acceptor. It accepts one electron from the donor and thus takes on a single negative charge compared to substitutional Zn. A sulfur vacancy or an interstitial Zn acts as a doubly ionized donor and therefore takes on a double positive charge, while interstitial Cu acts as a singly ionized donor. The positive charge on a substitutional Cu in model (V) will be explained in a later paragraph.

In all the above models, the different species are considered as associated, that is, occupying positions in the close neighborhood of each other. This comes out of the following reasoning.

It is generally agreed that the green center in coactivated ZnS:Cu is $Cu_s^-$, with the coactivator, such as $Cl_s^+$ or $Al_s^+$, (*a*) randomly distributed with respect to the $Cu_s^-$, or (*b*) associated with it (11). The former has been tacitly assumed in the past. A model in which the $Cu_s^-$ and $Cl_s^+$ occupy second or third nearest neighbor positions was proposed by Prener and Williams (13). This association was predicted on the basis of the electrostatic attraction between the $Cu_s^-$ and the $Cl_s^+$. It will be shown that whichever case is the truth, the species of the orange center must be associated.

Now models (II) to (V) each involve a $Cu_s^-$. Therefore, if the species are not associated, each model would yield $Cu_s^-$, with the positively charged species randomly distributed. According to postulate (*a*), this $Cu_s^-$ should then behave as a green center. Since self-coactivated ZnS:Cu does not emit in a green band, one would conclude that the species are associated.

If, however, it is true that electrostatic attraction between $Cu_s^-$ and the coactivator leads to association, then the species in models (II) to (V) should also be associated for the same reason. In this case, the peculiar nature of the self-coactivator must account for the emission spectrum differing so radically from the green band found for the usual coactivators.

An analogous argument can be developed for model (I), where the $V_C^{--}$ could lead to blue emission band like self-activated ZnS, if postulate (*a*) is true.

Theoretically, it should be possible to choose among the models by predicting the free energies of formation of the various species and choosing the model which represents the smallest (positive) free energy charge. This would entail a careful estimation of the energy associated with interstitial atoms, vacancies, missing bonds, coulombic terms, entropy, etc. The ZnS lattice can probably be considered as largely covalent in these estimates, although an ionic contribution may be important. The concept of donors and acceptors can be borrowed from semiconductor theory to help understand some of the relationships (2). However, a limited exploration of this method indicates no very great energy differences among the different models.

It does seem that model (I) can be eliminated because of the following considerations. Model (I) involves the same species as that proposed by Bowers and Melamed (2), but is associated, whereas they apparently assumed a completely dissociated model with the $V_C^{--}$ accounting for the blue emission band they found in their samples. Since the blue band has been shown by this work to be due to impurities, their argument for this dissociated model is unsatisfactory. This model also seems improbable because it is likely that energy could be gained by the reaction

$$Cu_i^+ \cdot V_C^{--} \cdot Cu_i^+ \rightarrow Cu_s^- \cdot Cu_i^+$$

Here the energy of the system can be decreased by a Cu atom moving from an interstitial position (which may represent a strain) into a vacancy

where it can form bonds to the surrounding S atoms.

Model (V) involves oxidation of the ZnS as can be seen by writing the formal steps necessary to convert model (II) into model (V).

$$2\,Cu_s^- \cdot V_A^{++} \rightarrow 2\,Cu_s^\circ \cdot V_A \xrightarrow{\frac{1}{2}S_2} 2\,Cu_s^\circ \rightarrow Cu_s^- + Cu_s^+$$

In the first step, each $Cu_s^-$ acceptor transfers its electron back to the $V_A^{++}$ donor. A neutral S atom from the atmosphere then fills the $V_A$. Then one of the $Cu_s^\circ$ atoms acts as a donor, giving an electron to the other $Cu_s^\circ$, which acts as an acceptor. The $Cu_s^+$ then is a substitutional Cu (with *d* shell filled), with both electrons missing from one of its bonds to a neighboring S atom. This model is attractive because no vacancies or interstitial atoms are necessary. In addition, when associated in neighboring positions, the pair of Cu atoms may lower the energy of the system by the resonance represented by the equation

$$Cu_s^- \cdot Cu_s^+ \rightleftharpoons Cu_s^+ \cdot Cu_s^-$$

This resonance might result in a set of energy levels quite different from those of a hypothetical system with $Cu_s^+$ and $Cu_s^-$ separated, with no resonance occurring. These levels might account for the peculiar properties of the orange center. The weakness of this model is the fact that the orange centers are stable to firing in a reducing atmosphere, a condition which should inhibit the necessary oxidation step shown above.

## Conclusions

1. The emission of self-coactivated ZnS:Cu consists of a single broad band peaking at 1.84 e.v.; the presence of other emission bands can be attributed to coactivator type impurities.
2. An analogous silver-activated phosphor can be prepared with an emission peak at 1.97 e.v.
3. The position of the self-coactivated ZnS:Cu emission peak does not change with crystal structure, but does shift with CdS addition.
4. Orange centers are insensitive to oxidizing and reducing atmospheres.
5. Orange centers do not form in the presence of traces of oxygenous impurities in the firing atmosphere; once formed at 1100°C, however, they are stable to these impurities at 1100° or lower.
6. The orange center is probably completely associated, has a ground level about 0.4 e.v. from the top of the filled band and a trapping level about 0.5 e.v. below the bottom of the conduction band.

## Acknowledgments

The authors wish to acknowledge the contribution of Miss M. Brines of the General Electric Chemical Products Plant, who measured the cathode ray spectrum, of Miss J. R. Cooper of this laboratory, who carried out the crystal structure investigation, and of Dr. F. F. Morehead, also of this laboratory, who performed the buildup and decay measurements.

Manuscript received Aug. 19, 1957. This paper was prepared for delivery before the Washington Meeting, May 12-16, 1957.

Any discussion of this paper will appear in a Discussion Section to be published in the December 1958 JOURNAL.

## REFERENCES

1. H. C. Froelich, *This Journal*, **100**, 280 (1953).
2. R. Bowers and N. T. Melamed, *Phys. Rev.*, **99**, 1781 (1955).
3. N. Riehl and H. Ortmann, *J. phys. radium*, **17**, 620 (1956).
4. Brinkman and Vlam, *Physica*, **14**, 650 (1949).
5. P. W. Ranby, *et al.*, *Brit. J. Appl. Phys.*, Supplement No. 4, S18 (1954).
6. H. W. Leverenz, "Luminescence of Solids," p. 163, John Wiley & Sons, Inc., New York (1950).
7. F. F. Morehead, Extended Abstracts of the Electronics Division, ECS, Washington Meeting, p. 2 (1957).
8. H. C. Froelich, *This Journal*, **100**, 496 (1953).
9. H. W. Leverenz, *loc. cit.*, p. 344.
10. M. Schön, *Z. Physik*, **119**, 463 (1942); H. A. Klasens, *Nature*, **158**, 306 (1946).
11. H. A. Klasens, *This Journal*, **100**, 72 (1953).
12. F. A. Kröger, *Brit. J. Appl. Phys.*, Supplement No. 4 S58 (1954).
13. J. S. Prener and F. E. Williams, *J. phys. radium*, **17**, 667 (1956); *Phys. Rev.*, **101**, 1427 (1956); *This Journal*, **103**, 342 (1956).

# Conductivity and Energy Gap Measurements of Some Relatives of Phthalocyanine

**Wolfgang Felmayer and Irving Wolf**

*Materials and Processes Laboratory, General Electric Company, Syracuse, New York*

ABSTRACT

The electrical resistance of samples of powdered copper-phythalocyanine, platinum phthalocyanine, highly chlorinated copper-phthalocyanine, and of two polymers of copper-phthalocyanine were measured at various temperatures in a nitrogen atmosphere.

All of the compounds showed semiconductive behavior. The highly chlorinated copper-phthalocyanine and the platinum-phthalocyanine had approximately the same resistance as the copper-phthalocyanine, whereas both polymers had lower resistances—one of the polymers having a resistance of about $10^{-3}$ that of copper-phthalocyanine at various temperatures. Some theoretical implications of the above facts are mentioned in this report.

In 1935 and 1936 Robertson (1) reported the crystal structure of several metal substituted phthalocyanines, as well as phthalocyanine itself. These compounds are well-known pigments which are structurally related to the naturally occurring porphyrins. The structures of phthalocyanine and copper phthalocyanine are shown in Fig. 1.

Vartanyan (2) and Eley (3), working independently, found the exponential relationship between conductivity and the reciprocal of the temperature for phthalocyanines; from this and other observations, they each concluded that phthalocyanines act like intrinsic semiconductors.

Kleitman (4) reported temperature-conductivity measurements for single crystals of phthalocyanine and copper phthalocyanine, as well as absorption spectra and photoconductivity measurements of "smeared films" of phthalocyanine. He compared "energy gaps" determined from the different measurements, in addition to making a photosensitive point contact rectifier from a pressed pill of phthalocyanine.

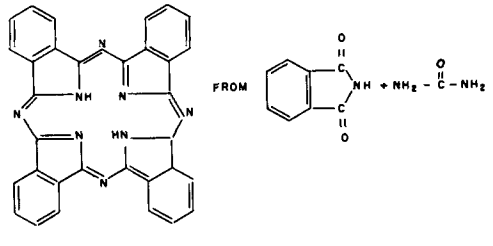


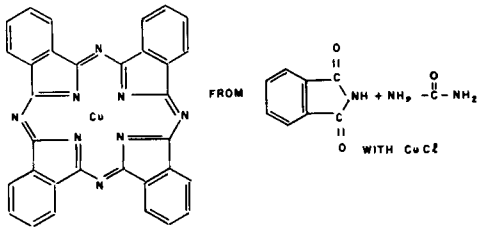


Fig. 1. Structural formulas and starting compounds

Many, Harnik, and Gerlich (5) made rough calculations of the "mobility" of the carriers in phthalocyanine, copper phthalocyanine, and many other polynuclear organic materials. The values they estimated were 1 $cm^2/v/sec$ for phthalocyanine and 10 $cm^2/v/sec$ for the copper substituted compound.

In this work, temperature-conductivity measurements have been made on powder samples of copper phthalocyanine and a number of relatives of these compounds differing only in crystalline arrangement or molecular structure.

The results on each material can be expressed by a relation of the form

$$\sigma = \sigma_0 e^{-\epsilon/2kT}$$

where $\epsilon$ may be considered the apparent energy gap and $\sigma_0$, the conductivity extrapolated to infinite temperature which may be presumed to depend on the total carrier concentration and on the carrier mobility. The various materials are thus conveniently compared in terms of these parameters.

The compounds studied besides copper phthalocyanine were chlorinated copper phthalocyanine, platinum phthalocyanine, and the two polymers of copper phthalocyanine. This was done in an attempt to discover what effect the differences between the compounds might have on the "energy gap" and "relative mobility" of the carriers. It was felt that through this, some insight into the nature of the conductivity might be gained.

*Chlorinated copper phthalocyanine.*—The chlorinated copper phthalocyanine molecule has chlorine in place of the hydrogens which surround the molecule. On the average, 15 out of the 16 hydrogens were replaced by chlorine. If the energy gap or mobility depends on activity at the edges of the molecule, the replacement of the hydrogen should vastly affect it.

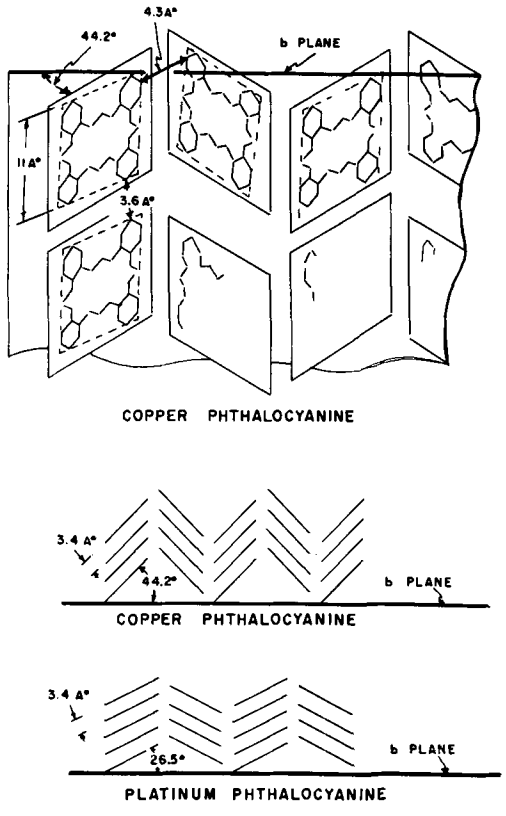


Fig. 2. Geometric positioning of molecular planes in crystal

*Platinum phthalocyanine.*—The platinum phthalocyanine differs in crystalline arrangement from the copper compound in that the angle with the b plane (*see* Fig. 2) differs from that of the latter considerably. Thus, if the energy gap or mobility depends on specific atoms in one molecule in a "stack" being lined up with specific atoms of a neighbor in front of or behind it, the variation in angle should greatly affect it.

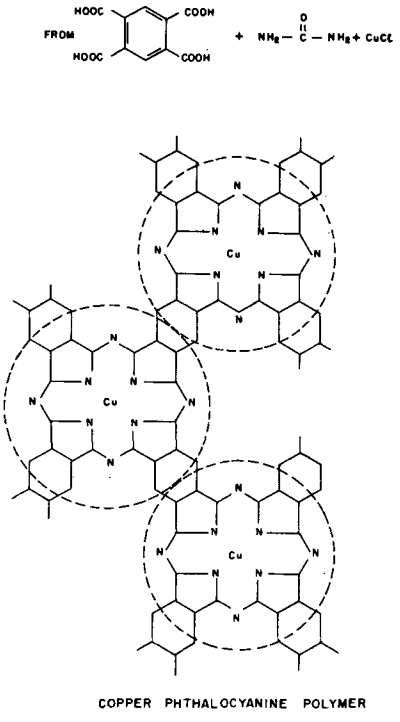


Fig. 3. Structure of polymer and starting compounds

*Polymers.*—The polymers (*see* Fig. 3) differed from the monomer in size; the molecules of the former probably "stacking" just as the latter. As in the chlorinated compound, if the activity were edge to edge, some very substantial effects should be noted on energy gap and mobility.

Thus, it was felt that the comparisons described above would provide some early indications of the nature of the charge motion from molecule to molecule.

## Experimental Results

*Copper-phthalocyanine.*—The first step was to take resistance vs. temperature measurements on multiply vacuum-sublimed copper-phthalocyanine crystal powder. The purpose of this measurement was to compare the results with existing measurements and thus test the procedure and equipment used in this work (*see* Fig. 4). The samples measured were all loose powders under low compaction pressure (about 8 psi). It was noted that the resistance did not vary appreciably with minor pressure variations. The resistances given throughout were for samples 20 mm in diameter and approximately 1 mm thick. The electrodes were gold disks. To avoid irregularities of measurements during the first run (4), the samples were heated directly up to 340°C in a nitrogen atmosphere; then the resistances were measured while the temperature was decreasing constantly at a rate of about 10°C/min in intervals of 10°C (Fig. 5, curve a). Measurements taken during constantly increasing temperature showed slightly higher resistances (Fig. 5, curve b). For final data the samples were reheated to at least three different temperatures—for the sake of accuracy each of these temperatures was maintained for approximately half an hour before the resistance was measured. This method led to readings (Fig. 5 curve c) which lay between those of the first two runs. Graphically all linear curves in the log Ω vs. $1/T$ diagram showed the same slope, while their resistances differed by a constant factor due to temperature lags in the sample. Therefore, the middle curve was considered to be the most accurate one.

It should be mentioned that copper-phthalocyanine synthesized from different materials (phthalic acid, phthalamide, phthalonitrile) showed the same semiconductive behavior. The only deviations were due

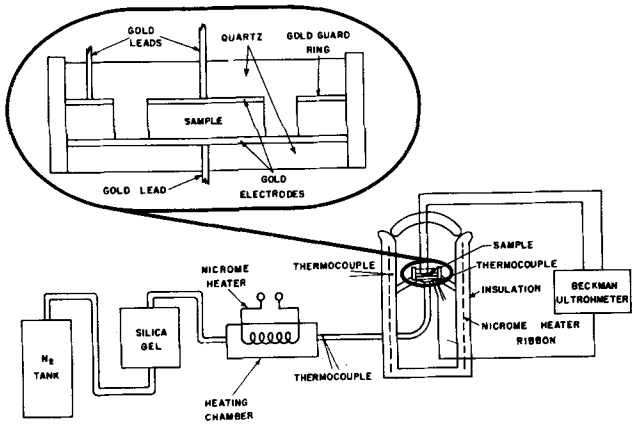


Fig. 4. Measurement apparatus

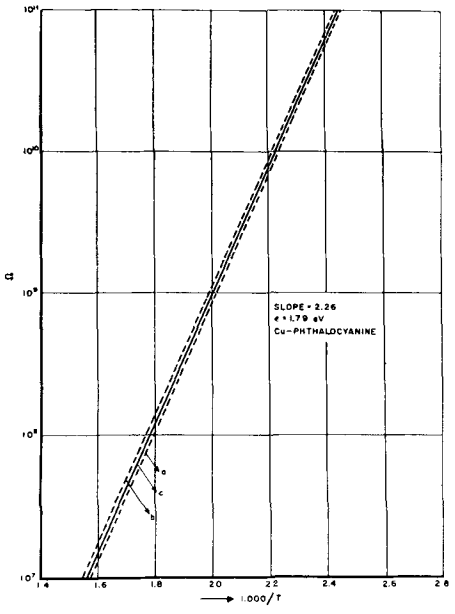


Fig. 5. Resistance of Cu-phthalocyanine vs. reciprocal of temperature.

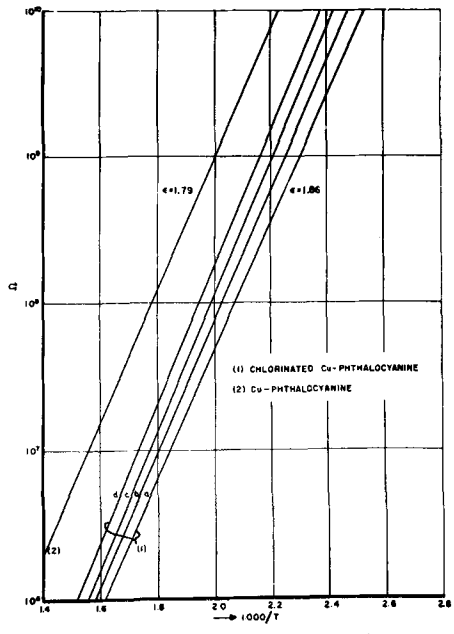


Fig. 6. Comparison of results for Cu-phthalocyanine with its chlorinated counterpart.

to poor purity of the pigment. Even after the first vacuum sublimation certain irregularities were sometimes found, while the results after a second and third sublimation were always in good agreement.

In order to study the most effective purification methods for nonsublimable phthalocyanines, a series of purification experiments were performed on nonsublimed copper-phthalocyanine. Even multiple reprecipitation or recrystallization from concentrated sulfuric acid proved to be insufficient. Bringing the sample up to 400°C and holding it there for several hours in nitrogen atmosphere resulted in a product, of which the resistance vs. temperature measurements were in good agreement with those of sublimed copper-phthalocyanine. Hourly checks showed a constant approach to the ideal curve, which was reached after 5 hr. A further heating of up to 10 hr brought no change.

*Chlorinated copper-phthalocyanine.*—Highly chlorinated (about 15 Cl-atoms per phthalocyanine molecule) copper-phthalocyanine (du Pont Monastral Fast Green G) was purified carefully at first by treatments with HCl and NaOH. In addition, the product was extracted with boiling alcohol. A treatment at 350°C in vacuum still gave some sublimation of a white material. After some hours the first resistance vs. temperature measurements were taken (Fig. 6, curve a). Further heat treatment in vacuum up to 500°C, however, resulted in an approach of this curve toward the normal copper-phthalocyanine log Ω over $1/T$ curve. (Fig. 6, curve b, c). Since a sublimation of copper-phthalocyanine was found in the tube, it is assumed that chlorinated copper-phthalocyanine splits off some or all of its chlorine atoms. The residue, also, looked much bluer than the original sample and had characteristics given in curve d of Fig. 6.

Thus, for this compound, indications were that decomposition accompanied purification and the data obtained should be understood to be that of a partially dechlorinated molecule. In general, it may be said that chlorinated copper-phthalocyanine shows the same activation energy as copper-phthalocyanine itself and about 1/10 the resistance (*see* Fig. 6).

*Platinum-phthalocyanine.*—By x-ray examination of platinum-phthalocyanine crystals, Robertson (1) found that the molecular structure of platinum-phthalocyanine is very similar to the other phthalocyanines. As for its crystalline structure, however, even though the molecules are arranged in a similar "stacked" fashion, they are at an angle to the (b) plane of only 26.5° instead of 44.2° as in copper-phthalocyanine. All the other phthalocyanines examined were similar to the copper in this respect.

In order to study the effect of the crystal structure on semiconductive properties of phthalocyanines, some resistance vs. temperature measurements on multiply sublimed platinum-phthalocyanine were made. Results are given in Fig. 7 and compared with

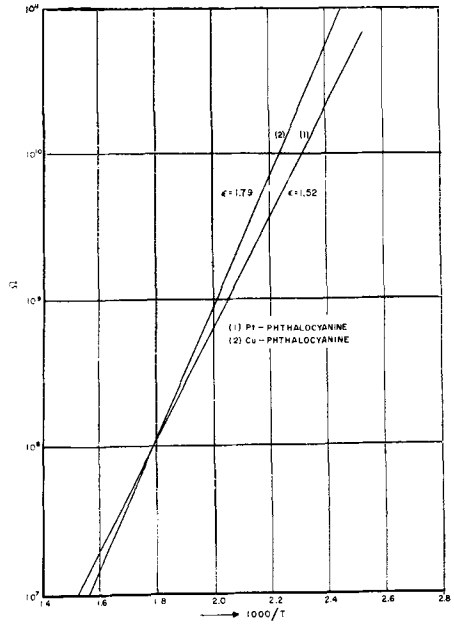


Fig. 7. Comporison of results for Cu-phthalocyanine with Pt-phthalocyanine.

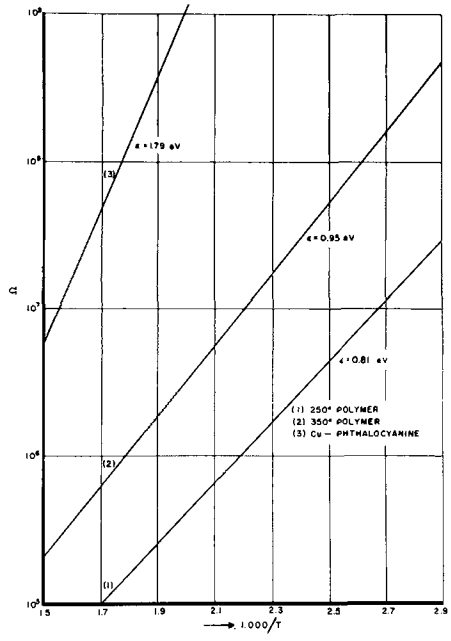


Fig. 8. Comparison of results for Cu-phthalocyanine monomer with two polymers.

those of copper-phthalocyanine. As the difference in absolute resistance values is small, the conclusion was reached that the angle with the (b) plane—which governs the way atoms in one molecule line up with those in another, behind or in front of it—has no important influence on the mobility of the charge carriers.

A slight difference in slope of both curves is not very surprising, as the same effect was known for phthalocyanine, magnesium-phthalocyanine, and similar compounds when compared with each other or with copper-phthalocyanine. Thus, a certain influence of the central atom on the band gap is to be expected.

*Polymer copper-phthalocyanine.*—Although it is not possible to give definite statements about the structure of the polymer phthalocyanines, chemical and physical examinations indicate that the four carboxyl groups of pryomellitic acid react with molten urea in a way similar to the reaction of the two carboxyl groups of phthalic acid when phthalocyanine is formed. In this way a polymer phthalocyanine is built up. A combination of elementary analysis and theoretical calculations lead to the indication of a model of at least ten closely packed phthalocyanine molecules.

Since former experiments have shown that the reaction temperature has considerable influence on this kind of phthalocyanine condensation and also affects the polymolecularity, two parallel condensations were started, one at 250°C and the other at 350°C.

*Comparison of the 250° polymer and the 350° polymer.*—All of the experiments led to the conclusion that the 250° polymer had a higher molecular weight than the 350° polymer. The chief indications were resistance vs. temperature measurements, viscosity measurements in solution, and copper-analyses. A further confirmation might be expected from total elementary analysis. The importance of the latter, however, is rather small since the data for C, H, N, and O show smaller changes with the polymolecularity than the copper data.

Table I

| Compound | $\epsilon$ (e.v.) | $\Omega_0$ (ohms) | $\sigma_0$ (ohm-cm)$^{-1}$ $\times 10^{-3}$ |
|---|---|---|---|
| Copper phthalocyanine | 1.79 | 0.83 | 3.82 |
| Platinum phthalocyanine | 1.52 | 13.92 | 0.229 |
| Chlorinated copper phthalocyanine | 1.86 | 0.09 | 35.0 |
| Lower polymer (350°C) | 0.95 | 31.9 | 0.10 |
| Higher polymer (250°C) | 0.81 | 50.2 | 0.063 |

*Resistance vs. temperature measurements.*—Figure 8 shows that both the slope and conductivity for the 350° polymer lie between respective data for the 250° polymer and the monomer copper-phthalocyanine. The comparison of the band gaps of the three compounds shows that they are subject to an expected decreasing sequence (7-10).

According to the results of the copper analysis, the two polymers should be considered as tight molecular nets. This configuration results in a number of new resonance possibilities which are responsible for the compound's extremely dark color.

Results indicate that the energy gaps of such polymers decrease as the number of condensed rings and hence the resonance possibilities increase. A similar result has been obtained in studies by Akamatu and Inokuchi (7-10) who found lower activation energies for such higher condensed aromatics as violanthrons and isoviolanthrone than for anthracene. It appears that the increase in the number of condensed rings results, in general, in a decreasing energy gap.

## Comparative Results

In Table I are listed for each of the materials the values of $\epsilon$ and $\sigma_0$, together with $\Omega_0$, the extrapolated sample resistance corresponding to $t = \infty$. A comparison of these values indicates no vast difference in $\sigma_0$. It is true that the chlorinated substituted compound has about 10 times the $\sigma_0$ of the unsubstituted, and the high polymer a value 60 times lower than the monomer, but these differences are thought to be much smaller than would be expected if the actual mechanism of charge transfer were altered.

Since the carriers are probably pi-electrons, whose density is roughly proportional to the density of the materials, and since these densities vary only slightly compared to the variation of $\sigma_0$'s observed, the relative values for $\sigma_0$ might also be considered a good indication of the relative values of carrier mobility.

Manuscript received Jan. 11, 1957. This paper was prepared for delivery before the San Francisco Meeting, May 1-5, 1956.

Any discussion of this paper will appear in a Discussion Section to be published in the December 1958 JOURNAL.

REFERENCES

1. J. M. Robertson, *J. Chem. Soc.*, **1935**, 615; **1936**, 1195.
2. A. T. Vartanyan, *Zhur. Fiz. Khim.* **22**, 769 (1948).

3. D. D. Eley, *Nature*, **162**, 819 (1948).
4. D. Kleitman, Electrical Properties of Phthalocyanine, U. S. Dept. of Commerce, Office of Technical Services, Report PB111419 (1953).
5. A. Many, E. Harnik, D. Gerlich, *J. Chem. Phys.*, **23**, 1733 (1955).
6. W. Felmayer, Dissertation, University of Vienna, (1954).
7. H. Akamatu and H. Inokuchi, *J. Chem. Phys.*, **20**, 1481 (1952).
8. H. Akamatu, H. Inokuchi, T. Handa, *Nature*, **168**, 520 (1951).
9. H. Akamatu and H. Inokuchi, *J. Chem. Phys.*, **18**, 810 (1950).
10. H. Inokuchi, *Bull. Chem. Soc. Japan*, **24**, 222 (1951).
11. H. Inokuchi, *ibid.*, **24**, 28 (1952).

# The Concentration of Hydrogen in Nickel under Hydrogen Ion Bombardment

**J. Morrison and J. J. Lander**

*Bell Telephone Laboratories, Inc., Murray Hill, New Jersey*

ABSTRACT

Concentrations of hydrogen dissolved in nickel under hydrogen ion bombardment have been measured using a nickel diffusion tube as the cathode in a glow discharge. No increase above the normal was observed when clean nickel was bombarded. Increases of several orders of magnitude were obtained in the range near 200°C when the nickel was coated with nickel oxide or barium oxide. It is believed that energetic ions penetrate the outer surfaces of these materials efficiently and are then trapped in the interior by surface barriers. These data show that normal values of concentration cannot be applied to nickel and probably many other metals operating under hydrogen ion bombardment if their surfaces are contaminated.

It has been found that high concentrations of hydrogen can be produced in ZnO by hydrogen ion bombardment (1). For example, bombardment at 200°C with hydrogen ions can produce a concentration five orders of magnitude higher than the concentration obtained when an equal number of normal hydrogen molecules strike the surface. This behavior results from two factors: *(a)* ions of sufficient velocity penetrate efficiently a surface barrier to normal reaction, and *(b)* the barrier to escape of dissolved hydrogen is high. In general it is expected that in systems where such surface barriers are high, relatively large internal pressures of hydrogen can be generated by hydrogen ion bombardment.

In the work on ZnO concentrations of hydrogen were determined by measurements of conductivity. This was possible because hydrogen forms a donor with convenient properties. In this work steady-state diffusion rates of hydrogen through a Ni tube under hydrogen ion bombardment were measured.

In the steady state the quantity of hydrogen flowing through such a tube is

$$Q = CDtA/d \qquad \text{(I)}$$

where $Q$ is the quantity in cc mm (a cc mm is 1 cc at 1 mm pressure), $C$ is the concentration in cc mm/cc of Ni, $D$ the diffusion coefficient in cm²/sec, $t$ the time in seconds, $A$ the area of the tube in cm², and $d$ the thickness of the tube in cm. The concentration at the exit side is assumed to be relatively low. Bombardment by hydrogen ions was accomplished by using the Ni tube as cathode in a glow discharge.

This work has shown the importance of oxide films on Ni under hydrogen ion bombardment. Large increases in concentration of hydrogen in Ni were obtained with NiO on Ni and with BaO on Ni. Following the previous work on ZnO, it is proposed that the surfaces of these oxides are easily penetrated by energetic ions, but they act as effective barriers to the escape of hydrogen molecules. No increase in concentration was detected when the Ni was "clean."

## Apparatus

The work was carried on with the system shown schematically in Fig. 1. Hydrogen from a tank was introduced through a stop-cock to a spiraled tube of Ni. This Ni spiral was formed of six turns of approximately 3 cm diameter from tubing measuring 45 mils outside diameter and 2 mils wall thickness. An electrode of 60 mil Ni rod was mounted parallel to the spiral and about 1 cm distant from the top of the spiral. An oil manometer using Octoil S and a Pirani gauge were used to measure the hydrogen pressure. A small cold trap was in the line near the

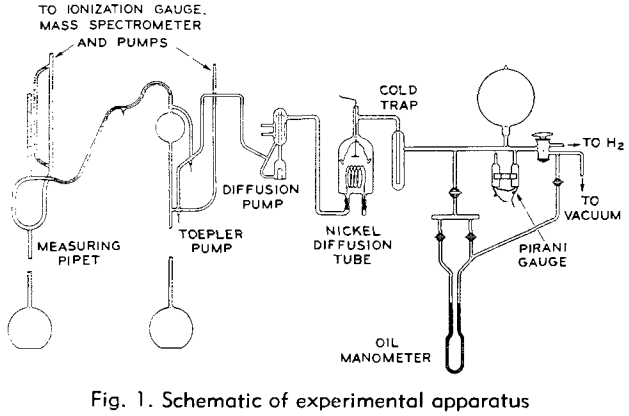


Fig. 1. Schematic of experimental apparatus

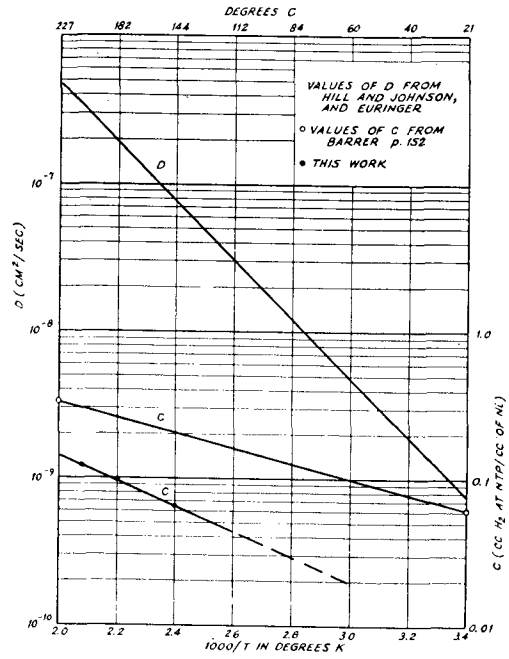


Fig. 2. Diffusion coefficient and normal concentration of hydrogen in Ni as a function of temperature.

tube containing the Ni spiral. This part of the system could be evacuated to a good fore pump pressure before flushing and filling with hydrogen.

One of the ends of the spiral was sealed and the other end connected to the gas measuring system in which a small Hg diffusion pump was used to evacuate the inside of the Ni tubing. The gas removed was pumped by a Toepler pump into a calibrated volume.

## Techniques of Measurement

*Quantity of gas.*—The quantity of gas collected in a 3-min interval was measured in the calibrated volume. After measurement it was pumped away through a system to which a mass spectrometer and an ionization gauge were sealed. The background pressure in this vacuum system was 2-3 x $10^{-7}$ mm.

*Temperature.*—Change in the average temperature of the Ni spiral was determined by measuring its change in resistance with a calibrated ammeter and voltmeter. A curve was drawn using data obtained from the International Critical Tables for the temperature coefficient of resistivity and the observed value of resistance of the spiral at room temperature. The spiral was heated by either the glow discharge, by passing current through it, or by a combination of the two.

*Blank determination.*—The gas evolved by the Ni spiral and associated equipment at room temperature after it had been outgassed and conditioned was collected for a 3-min period. This quantity was near 0.01 cc mm and was relatively steady. This figure is also near the limit of sensitivity of the apparatus since it corresponds to 3 min of Hg on the measuring pipet. The blank was frequently checked, not only with the Ni at room temperature but also when it was at much higher temperatures in hydrogen at very low pressure.

*Pressures of water vapor.*—Four different pressures of water vapor were used during the experimental determinations. A drop of water was placed in the cold trap located near the experimental tube. Liquid Ni was used to attain what is called zero pressure. A $CaCl_2$ bath at −51°C was used to hold the pressure of water vapor at 0.026 mm. An alcohol-ice mixture was used to attain a temperature of −24°C and a vapor pressure of 0.53 mm. Finally an ice water bath at 0°C gave a vapor pressure of 3.8 mm.

*Oxide films.*—During the course of these studies it was found desirable to oxidize the Ni spiral and later a Ba film which was deposited on the clean Ni. The Ni was heated to about 400°C in air to obtain a visible NiO film. This could be removed by heating in hydrogen. The evaporated Ba was converted to a visible oxide film by admission of air.

*Diffusion coefficient.*—Exploratory measurements of initial transients gave values from which hydrogen diffusion coefficients were calculated. These were in agreement with Euringer (2), and Hill and Johnson (3). Their values have been used to draw the curve given in Fig. 2 which has been used in the calculations of concentration.

*Concentration.*—Hydrogen concentration was calculated from the steady state quantity of gas flowing through the tube using Eq. (I). The concentration is

$$C = \frac{1.36 \times 10^{-6} Q}{D} \text{ cc mm/cc Ni} \qquad \text{(II)}$$

where the values $t$ = 180 sec, $A$ = 20.5 cm², $d$ = 0.0050 cm have been substituted. Results of measurements made with hydrogen at 0.67 mm of Hg, no bombardment and various temperatures are given in Fig. 2. These are to be compared with values given by Barrer (4), which have been corrected to 0.67 mm of hydrogen by assuming that concentration is proportional to the square root of hydrogen pressure. The authors' values are lower by a factor of about two. The reason for this discrepancy was not discovered. The results were very reproducible and independent of the cleanliness of the Ni tubing.

## Results of Hydrogen Bombardment

*"Clean" nickel.*—After the concentration of normal hydrogen was determined the effect of a glow discharge in dry hydrogen was studied. The results were not reproducible. There was a tendency for large quantities of hydrogen to flow during an initial period of bombardment, but on prolonged bombardment the flow would ultimately drop to that obtained without the discharge. Since the effect of bombardment should be to clean the surface of the Ni by chemical reduction and by sputtering, it was concluded that the initial effects were due to surface contamination and that effects due to bombardment of clean Ni were too small to be measured.

*Nickel plus nickel oxide.*—Since there was no increase in concentration under hydrogen ion bombardment of clean Ni at temperatures up to 182°C, it was decided to bombard oxidized Ni. An objective was to determine if the initial results could be repeated and made reproducible. Bombardment of oxidized Ni in the same temperature range increased the initial flow but again the flow could not be main-

tained. During these tests liquid nitrogen had been on the cold trap. The liquid nitrogen was removed, a few drops of water were placed in the trap and it was surrounded by an alcohol-ice bath. Hydrogen was admitted to a pressure of 0.67 mm and the glow discharge started. Immediately the quantities collected were much larger than those collected at the same temperature in the absence of the discharge and the results obtained were reproducible. Apparently the two conditions necessary for this higher concentration were the oxide film and enough water vapor or other oxidizing gas to maintain the oxide in the presence of the reducing action of the glow discharge. The flow of hydrogen through the Ni was measured for a range of temperatures and pressures of water vapor as well as different current densities of the glow discharge.

*Nickel plus barium oxide.*—The tube containing the Ni spiral was opened and two 5-mg Ba getters were attached to the upper electrode with tungsten wires. They were in such a position, one on each side of the tube, that when flashed the Ba evolved coated most of the tubing. The system was pumped and the Ni brought to a clean state. The getters were flashed until there was a visible film of Ba on the glass walls. After oxidation a thin white film of BaO could be seen on the Ni. It was found that the oxide had no effect on the normal flow of hydrogen, but that under bombardment higher concentrations were found than with NiO on Ni. In all these tests with BaO dry hydrogen was used and the results were reproducible.

It was found that a series of cyclic treatments such as heating to 600°-700°C and bombarding at high current densities produced a state resulting in concentrations three to four times greater than those found previously. However, this was an unstable condition and could be maintained for only a few minutes.

## Summary of Results

*Temperature.*—A representative picture of the over-all results is shown in Fig. 3, where the concentration in cc mm/cc of Ni is plotted as a function of the reciprocal of temperature. The lowest curve shows the reference line or the concentration of hydrogen molecules by 0.67 mm of dry hydrogen. The other two curves show the concentrations obtained with bombardment by hydrogen ions under the conditions noted. In the temperature range studied there is a definite increase in concentration as the temperature is lowered. The BaO on Ni resulted in somewhat higher concentration than for NiO on Ni.

*Water vapor pressure.*—The effect of water vapor on the concentration of hydrogen ions in the system NiO on Ni is shown clearly in Fig. 4 where curves for the increase in concentration ($\Delta C$) are plotted for temperatures of 115° and 182°C. Effects of pressures higher than about 4 mm could not be determined because a proper glow could not be maintained.

The question might be raised as to the effect of the water vapor alone on the Ni. This condition was studied and at 3-4 mm pressure of water vapor and temperatures as high as 450°C, no reaction was observed which resulted in the diffusion of hydrogen through the Ni. At 24 mm pressure of water vapor and 450°C the diffusion of hydrogen was observed but it was completely stopped if the Ni was oxidized visibly.

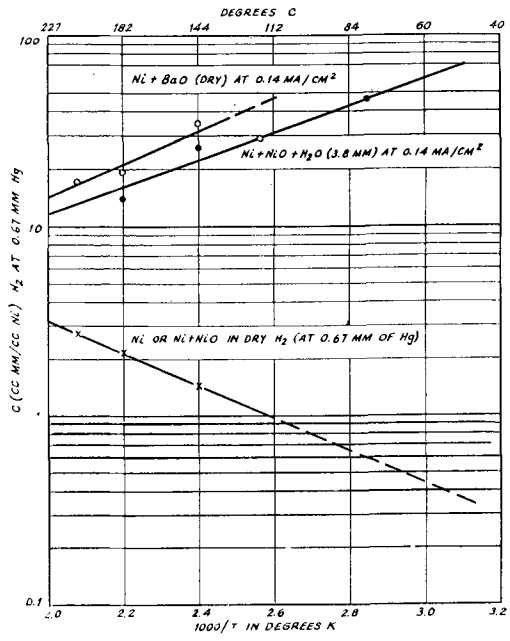


Fig. 3. Concentrations of hydrogen in Ni produced by bombardment compared with normal concentration as a function of temperature.

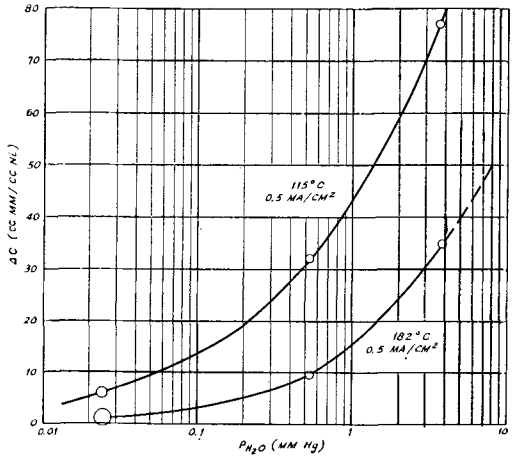


Fig. 4. Effect of water vapor on bombardment enhanced concentration of hydrogen in Ni.

*Current density of glow discharge.*—The effect of the current density of the discharge on the concentration is shown in Fig. 5. Concentration increased linearly with increasing current density at low current densities but saturated ultimately. For BaO on Ni in dry hydrogen at a pressure of 0.67 mm, saturation was observed in the range from 0.1 to 0.5 ma/cm$^2$.

## Conclusions

1. In order to relate results obtained by ion bombardment with normal concentration, concentrations are compared for equal numbers of atoms striking the surface. On this basis bombardment has increased the concentration by about four orders of magnitude in the range near 100°C.

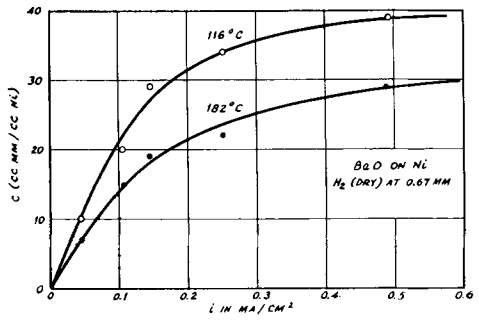


Fig. 5. Effect of current density of the glow discharge on concentration.

2. Bombardment also produces a reversal in the temperature coefficient of concentration. The difference in slopes is a measure of the barrier to escape of hydrogen. This barrier is found to be about 0.35 e.v. for both NiO and BaO on Ni under the conditions of these experiments.

3. Because no effect was observed with clean Ni, it is concluded there is no large barrier to the escape of hydrogen from a clean Ni surface.

4. It is interesting to note that in flowing through the system the hydrogen must pass through the oxide to Ni interface. If a high barrier to flow existed here the very large increases in concentration could not have been obtained.

5. These experiments do not tell the state of hydrogen in the films. It is not unlikely that part or all of the film of BaO was converted to $Ba(OH)_2$ by bombardment, since this is a relatively stable compound under the conditions of these experiments, and because the small amount of oxygen required to form the hydroxide was probably present in the system. Where NiO was the starting material relatively high pressures of water were required to produce the enhanced diffusion rates, and under these conditions $Ni(OH)_2$ is expected to form. Thus the transport mechanism in both surface films is believed to have been proton migration in imperfect hydroxides. It is believed (because of the work with ZnO) that proton migration in the oxides can also take place.

6. These results show conditions for concentrating much larger quantities of hydrogen in Ni than can be obtained by exposure to normal hydrogen. From these data it is clear that normal values of concentration cannot be applied to Ni and probably many other metals operating under hydrogen ion bombardment if their surfaces are contaminated.

Manuscript received Aug. 27, 1957. This paper was prepared for delivery before the Washington Meeting, May 12-16, 1957.

Any discussion of this paper will appear in a Discussion Section to be published in the December 1958 JOURNAL.

REFERENCES

1. J. J. Lander, *J. Phys. and Chem. Solids*, **3**, 87 (1957).
2. G. Euringer, *Z. Physik.*, **96**, 37 (1935).
3. M. L. Hill and E. W. Johnson, *Acta Met.*, **3**, 6 (1955).
4. R. M. Barrer, "Diffusion In and Through Solids," p. 152, Cambridge Press, London (1951).

# Iron and Phosphate Slag from Byproduct Ferrophosphorus

**J. M. Potts, W. C. Scott, Jr., J. U. Campbell, and J. A. Wilbanks**

*Tennessee Valley Authority, Wilson Dam, Alabama*

ABSTRACT

A process and furnace were developed for converting byproduct ferrophosphorus into high-grade iron for metallurgical purposes and phosphatic slag that might be used as a fertilizer or animal-feed supplement. The process consists in continuously smelting ferrophosphorus with calcined, siliceous iron ore and burnt lime in an electric furnace. The furnace has a two-component lining: walls of graphite, which resist corrosion by molten phosphate slag, and a hearth of magnesite, which resists attack by iron of low phosphorus content. In pilot-plant tests in a 2-meter diameter by 1.5-meter furnace operated at a power input of 350 kw, best results were obtained with about 100 v between the two electrodes. The product iron contained 0.5% P and the slag contained 22% citrate-soluble $P_2O_5$.

The Tennessee Valley Authority has developed a process and a furnace for the utilization of byproduct ferrophosphorus in the production of high-grade iron for metallurgical purposes and phosphatic slag that should be satisfactory for use as fertilizer or animal-feed supplement. The process involves smelting ferrophosphorus, siliceous iron ore, and burned lime in an electric furnace. The reaction approximates the following equation:

$$6Fe_2P + 5Fe_2O_3 \cdot 3SiO_2 + 15CaO = 22Fe + 3(5CaO \cdot P_2O_5 \cdot SiO_2) \quad (I)$$

This process was identified a number of years ago (5). However, it was not considered technically feasible at that time because of the severe attack of the molten iron and slag on the lining of the furnace. No single refractory material, including rammed magnesite, magnesite brick, chrome ore, zircon brick, and graphite, resisted the corrosive action of both the slag and iron. Work by the Bureau of Mines (2) and others (3) interested in processing ferrophosphorus also failed to define a satisfactory refractory.

In recent work here, the refractory problem was solved through the use of a two-component furnace lining. Graphite, which is resistant to corrosion by molten phosphate slag, was used to line the walls of the furnace, and magnesite, which resists attack by

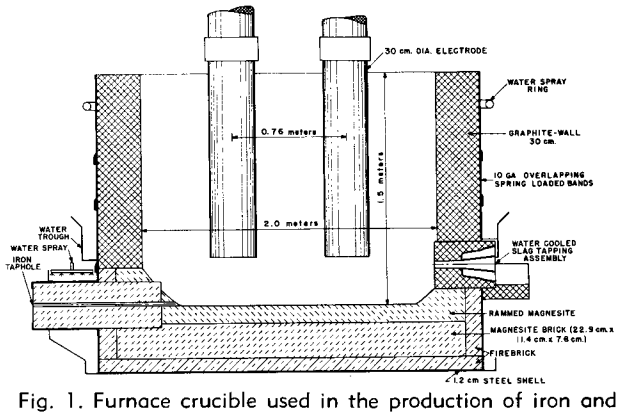


Fig. 1. Furnace crucible used in the production of iron and phosphate slag from byproduct ferrophosphorus.

iron of low-phosphorus content, was used to line the hearth.

This paper briefly describes the new pilot-plant furnace and the results of tests made for the production of iron and phosphate slag.

## The Furnace

A sectional view of the new pilot-plant furnace is shown in Fig. 1. The inside diameter of the furnace was 2 meters and the depth was 1.5 meters. The side wall was made of 30-cm thick graphite shapes, which were supported on the hearth with dry joints. Overlapping spring-loaded bands held the shapes in place. A water-spray ring was located around the top of the furnace and a water-collection trough was located just above the hearth section.

The hearth, which was contained in a steel shell, consisted of 7.6 cm of firebrick in the bottom and around the sides of the steel shell, 22.9 cm of magnesite brick, and 15.2 cm of rammed magnesite. At the walls, the rammed magnesite extended 25.4 cm above the floor of the hearth to approximately the slag-tapping level. It was recognized that a small area of the magnesite lining would be exposed to molten slag; however, it was anticipated that the expected high rate of heat transfer to the adjacent graphite would prevent excessive corrosion.

The tapping block for slag was made from a section of 30-cm graphite electrode with a 5-cm taphole in the center. It was fitted with a water-cooled bronze tapping monkey. The tapping block for metal was made from magnesite brick and was water cooled.

Two 30-cm graphite electrodes were located on 76-cm centers an equal distance from the furnace center line. Single-phase power was supplied to the furnace through a voltage regulator, an autotransformer, and a power transformer. The electrodes were connected to opposite ends of the secondary winding of the power transformer. Operation with 50 to about 100 v between electrodes, or 25 to about 50 v between each electrode and ground, was possible. The electrical system used has been described previously in an article on the pilot-plant production of aluminum-silicon alloy (4).

Table I. Compositions of raw materials used in pilot-plant tests

| | Analysis, % by weight | | | | |
|---|---|---|---|---|---|
| Ferrophosphorus | | Lime | | Calcined iron ore | |
| P | 24.4 | CaO | 95.0 | $Fe_2O_3$ | 78.3 |
| Fe | 68.6 | $CO_2$ | 1.1 | FeO | 3.8 |
| Mn | 3.0 | MgO | 1.5 | $SiO_2$ | 13.3 |
| Ti | 2.4 | $SiO_2$ | 0.9 | $P_2O_5$ | 1.4 |
| Si | 1.3 | $Al_2O_3$ | 0.3 | CaO | 0.1 |
| S | 0.3 | $Fe_2O_3$ | 0.1 | $H_2O$ | <0.1 |
| | | Ignition loss | 1.1 | Other | 3.0 |

## Pilot-Plant Tests

*Procedure.*—Six tests, which totalled 563 hr of operation, were made with the new furnace. The raw materials consisted of ferrophosphorus containing 24.4% P, lime containing 95% CaO, and calcined iron ore containing 59% Fe (Table I). Calcined iron ore was used because, in exploratory tests, uncalcined ore caused boiling of the slag and poor furnace operation. The ore was calcined in a 0.76-meter diameter by 12-meter long gas-fired, pilot-plant rotary kiln at a temperature of 1300°C. The ferrophosphorus and the calcined iron ore were crushed to minus 1½ in. before being used. The lime was purchased as minus 1-in. material. The materials were premixed in the desired proportions before being charged to the furnace.

The power input was kept at about 350 kw. Although this power input may have been somewhat less than optimum, the pilot plant was not equipped to handle the larger quantities of molten slag and iron that would have been produced with more power.

Best results were obtained with about 100 v between electrodes. Operation also was satisfactory with 75 v. When less than 75 v were used, the electrodes rode too low in the furnace and caused boiling of the slag. Also, carbon from the electrodes was absorbed by the iron with the result that dephosphorization was poorer because of preferential oxidation of the carbon.

The furnace operated continuously and was charged through a feed chute as required to keep the level near the top. Molten slag and iron were tapped at 2-hr intervals. The slag, at about 1620°C, was tapped into a cast-iron chill pan in which it was permitted to cool before it was ground to the desired size. The iron was tapped into a preheated crane-type ladle and then was cast into 34-kg pigs.

## Effect of Burden Composition

Equation (I) indicates that, for dephosphorization of ferrophosphorus, the stoichiometric requirement of iron oxide is that necessary to oxidize the phosphorus to $P_2O_5$. Also, the equation calls for 5 moles CaO and 1 mole $SiO_2$ per mole of $P_2O_5$, which is the relationship for silicocarnotite (6). Since the proportion of $SiO_2$ supplied in the charge material was in excess of 1 mole per mole of $P_2O_5$, it was assumed that 1 mole of CaO should be provided per mole of $SiO_2$ and 4 moles should be provided per mole of $P_2O_5$. However, in the pilot-plant tests, excesses of iron ore and lime were required to obtain satisfactory furnace operation and products of the desired chemical composition. Exploratory tests showed that 135% of the stoichiometric proportion of iron ore was required, and this amount was used in most of the subsequent work.

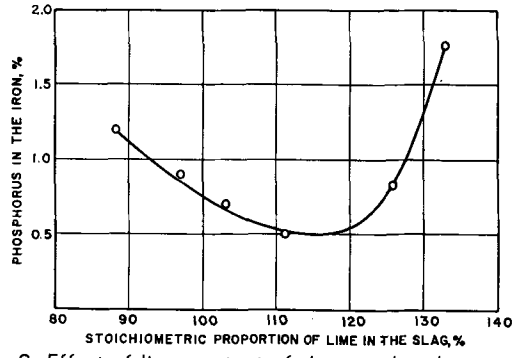


Fig. 2. Effect of lime content of slag on phosphorus content of the iron.

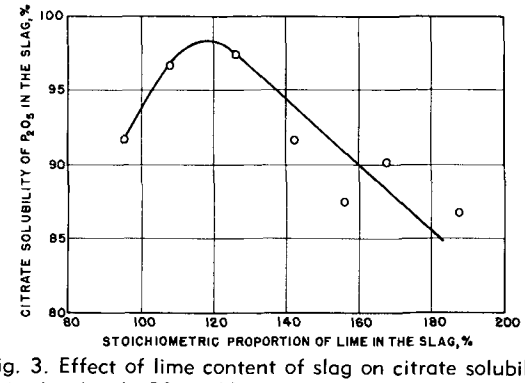


Fig. 3. Effect of lime content of slag on citrate solubility of $P_2O_5$ in the slag (—80 mesh).

Figure 2 shows that the phosphorus content of the iron decreased to 0.5% as the proportion of lime was increased to about 110% of the stoichiometric requirement. When the proportion of lime was increased to above 120% of stoichiometric, the viscosity of the slag in the furnace increased, with the result that furnace operation was poor and the phosphorus content of the iron increased.

Figure 3 shows that the citrate solubility of the $P_2O_5$ in the slag was at a maximum of 98% when it contained 120% of the CaO required to form silicocarnotite and was over 95% when the CaO content was in the range 105 to 135% of stoichiometric.

## Operating Results

Best results were obtained when the furnace was operated at 75-100 v and 350 kw and the charge was proportioned to contain 110% of the stoichiometric amount of lime required to provide 4 moles of CaO per mole of $P_2O_5$ and 1 mole of CaO per mole of $SiO_2$, and 135% of the stoichiometric amount of iron ore required to oxidize the phosphorus present. Data from a typical test are given in Table II. By weight, the charge contained 1.8 metric tons of calcined iron ore (59% Fe) and 1.3 metric tons of lime (95% CaO) per metric ton of ferrophosphorus (24.4% P). From this charge, the products, per ton of ferrophosphorus, were: 1.3 tons of iron containing 0.8% P and 2.5 tons of slag containing 22.1% $P_2O_5$ of which 99% was soluble in neutral ammonium citrate solution when the slag was ground to pass an 80-mesh screen. Presumably, 0.3 ton was lost as spillage of raw materials and products. Power consumption averaged 1761 kwhr and electrode consumption averaged 29.1 kg per metric ton of ferrophosphorus charged.

The graphite lining of the furnace showed very little attack by molten slag. The magnesite hearth was satisfactorily resistant to attack by molten iron of low phosphorus content. No apparent damage to the hearth was observed after tests in which the iron produced contained less than 1% of phosphorus. However, after one test in which the composition of the charge was not controlled satisfactorily and 12 of 40 taps contained more than 1% phosphorus,

Table II. Summary of data on production of phosphate slag and iron from byproduct ferrophosphorus

| | | | | | |
|---|---|---|---|---|---|
| **Operating Conditions** | | | | | |
| Length of period, hr | 117.5 | Electrode voltage (between electrodes) | | | 101.5 |
| Total time of operation, hr | 110.4 | Current, amp | | | 3644 |
| Operating time, % | 94.0 | Electrode current density, amp/cm² | | | 5.0 |
| Charge proportions, kg | | | | | |
| Lime | 1275 | Average kva | | | 369.9 |
| Ore | 1800 | Average kw | | | 350 |
| Ferrophosphorus | 1000 | Power factor | | | 0.946 |
| **Operating Results** | | | | | |
| Consumption of charge | | Iron composition, % | | | |
| Lime, kg/hr | 229 | Fe | 99.0 | C | 0.07 |
| Ore, kg/hr | 322 | P | 0.8 | Cr | 0.03 |
| Ferrophosphorus, kg/hr | 179 | Si | 0.01 | Mo | 0.01 |
| Lime, kg/metric ton of ferrophosphorus charged | 1275 | Mn | 0.07 | Sn | <0.10 |
| Ore, kg/metric ton of ferrophosphorus charged | 1800 | S | 0.01 | Pb | <0.10 |
| Ferrophosphorus, kg/metric ton of iron produced | 760 | Cu | <0.10 | Zn | <0.40 |
| Iron production rate, kg/hr | 236 | Ti | <0.02 | Ni | <0.10 |
| Slag production rate, kg/hr | 443 | | | | |
| Power consumption, kwhr/metric ton of ferrophosphorus charged | 1941 | Slag composition, % | | | |
| | | $SiO_2$ | 12.0 | MgO | 0.9 |
| Graphite electrode consumption | | $Fe_2O_3$ | 12.1 | MnO | 2.0 |
| kg/hr | 5.2 | CaO | 49.2 | $Al_2O_3$ | 2.7 |
| kg/metric ton of ferrophosphorus charged | 29.1 | $P_2O_5$ | 22.1 | $TiO_2$ | 1.1 |
| Temperature of iron as tapped, °C | 1540 | C.I. $P_2O_5$ | 0.2 | F | 0.02 |
| Temperature of slag as tapped, °C | 1620 | | | As | <0.001 |
| Iron recovery, kg/metric ton of ferrophosphorus charged | 1316 | | | | |
| Slag recovery, kg/metric ton of ferrophosphorus charged | 2467 | | | | |

drillings of the hearth showed that it had been penetrated about 8 cm by the metal.

### Acknowledgment

The authors wish to acknowledge the advice and encouragement received from M. M. Striplin, Jr., and T. P. Hignett. A. W. Beinlich, Jr., M. R. Burns, H. W. Elder, J. L. Graham, A. B. Harrison, and other members of the TVA Development Branch helped carry out the experimental work.

Manuscript received July 8, 1957.

Any discussion of this paper will appear in a Discussion Section to be published in the December 1958 JOURNAL.

REFERENCES

1. G. L. Bridger, J. W. Moore, and H. M. McLeod, Jr., *Ind. Eng. Chem.*, **41**, 1391 (1949).
2. R. C. Buehl and M. B. Royer, *Bur. Mines Rept. Investigations 5102*, February 1955.
3. Private correspondence.
4. M. M. Striplin, Jr. and W. M. Kelly, *Chem. Eng. Prog.*, **43**, 569 (1947).
5. Tennessee Valley Authority, Chemical Engineering Report No. 10. Analytical Index of Chemical Engineering Publications, Patents, and Reports. Compiled by E. L. Newman and L. D. Copeland. U. S. Government Printing Office, Washington, D. C. (1954).
6. G. Tromel, *Stahl u. Eisen*, **63**, 21 (1943).

# Electrolytic Production of Sodium Perchlorate Using Lead Dioxide Anodes

**Joseph C. Schumacher, David R. Stern, and Paul R. Graham**

*American Potash & Chemical Corporation, Whittier, California*

ABSTRACT

Lead dioxide was investigated as an anode substitute for platinum in the production of sodium perchlorate. Rod shaped deposits were prepared on nickel and platinum clad tantalum wires. The plate was dense, heavy, metallic-like in appearance and not too fragile for ordinary handling. The first phase of experimentation was performed in small laboratory cells to determine approximate electrolyses data. Larger bench-scale production cells were also run simulating plant operating conditions. Lead dioxide anodes produce sodium perchlorate at high cumulative current efficiencies. One lead dioxide anode was used in cell operation for 3,000 hr. Cumulative current efficiency for a given anodic current density is a function of the cathode material, cathodic current density, and the additive used. Perchlorate can be produced using nickel, copper, stainless steel, and carbon steel cathodes. Energy requirements, under identical experimental conditions, indicate that stainless steel and nickel are the best cathode materials. A current efficiency of 91.5% was obtained with a stainless cathode at anodic and cathodic current densities of 15.5 amp/dm$^2$ and of 7.25 amp/dm$^2$, respectively. No unusual metallic contamination could be detected in the ammonium perchlorate prepared from the sodium perchlorate.

Increased demand for $NaClO_4$ as an intermediate for the production of ammonium and potassium perchlorates resulted in a search for a replacement for the Pt anode. Previous investigations have shown that $PbO_2$ might be a satisfactory substitute for Pt. Lead dioxide electrodes in various sizes and shapes may be prepared from suitable electrolytic baths (1-4). The rod-shaped electrodes used in these experiments were prepared by plating $PbO_2$ on Ni and Pt clad Ta wires. Platinum clad Ta as a conductor on which to deposit the $PbO_2$ had the advantage of being corrosion resistant to the $HNO_3$ liberated during electrolysis from the $Pb(NO_3)_2$ electrolyte. The $PbO_2$ deposit is dense, heavy, and metallic in appearance. Perchlorates can be produced on $PbO_2$ deposits from 8-10 mm thick (4). Thin deposits are fragile and erode easily during electrolysis. When a thickness of at least 20 mm is obtained, the electrode is not too fragile for ordinary handling and erosion is not significant.

The over-all chemical equation for the electrochemical oxidation of chlorate to perchlorate has been reported by other investigators (5-9).

The investigation was divided into two phases. The first dealt with exploratory experiments in small laboratory cells designed to determine feasibility, to approximate electrolyses data, and to evaluate different cathodes with small $PbO_2$ anodes. On the basis of these experiments, larger cells were operated simulating actual plant conditions. The first phase of the investigation is referred to as laboratory cell experimentation and the latter phase as bench-scale production.

Three methods for measuring current efficiencies have been used by other investigators and were used in this study. They were:

*Gas collection.*—If a standard coulombic cell with Pt electrodes containing a 5% NaOH electrolyte is connected in series with a perchlorate cell, the ratio of gas volumes in the coulombic cell to that of the

perchlorate is 3:2. Thus, the gas volumes from the coulombic and perchlorate cells give an approximate measure of the instantaneous current efficiency. This may not be too accurate if there are appreciable side reactions.

*Chlorate depletion.*—If side reactions are negligible, then the $NaClO_3$ disappearing can be used as an approximation to current efficiency.

*Perchlorate determination.*—This measurement is the most accurate determination of current efficiency, but necessitates a time consuming perchlorate analysis. Moreover, this is a cumulative and not an instantaneous current efficiency.

Gas collection and chlorate depletion are easily and rapidly obtained and may indicate the trend of a variable. Gas collection was utilized for the small laboratory cells, recognizing that it was only an approximation, which would be checked by direct analyses later on the bench-scale production cell.

Data obtained by analyses on the bench-scale cell indicate that inefficiencies due to side reactions are of small magnitude with some cathodes and that the current efficiency measurement used for the laboratory cells has some validity.

## Laboratory Cell

*Cell construction.*—Laboratory cells were constructed of ⅛ in. Lucite. They were cylindrical in shape, 2½ in. I.D. x 5 in. high. The electrodes, a thermometer, and a ¼ in. diameter x 1½ in. gas outlet tube were sealed through the cell cover. A rubber gasket was fitted to a ½ in. flange around the top of the cells. Wing nuts through the flange secured the cover, creating a gas-tight fitting.

Evolved gas was directed to 50 ml burets. Volumes were measured by the displacement of water in the burets.

Electrolyte levels in both cells were maintained 1 in. from the top; this gave a small equal volume. Electrolysis time, while the gases were being collected, was short. Since a ratio of volumes was utilized, no corrections for pressure and temperature were necessary; it was assumed that the burets remained under identical conditions, even though volumes of different magnitude were involved.

Lead dioxide was employed as the anode in the laboratory cell except for the initial experiments. A Pt anode was used in these experiments to establish reference data. Two cathodes connected in parallel were used. The initial concentration of the electrolyte was approximately 500 g/l of reagent grade $NaClO_3$ with various additives. New electrolyte was used for each series of experiments.

Temperatures of both cells were controlled with external water cooling within 5°C.

*Experimental procedure.*—The coulombic and laboratory cell were connected in series to a Se rectifier. Current and voltage across the laboratory cell were measured during electrolysis. These cells were operated until the coulombic cell had evolved 50 ml of gas. Comparison of this volume to that evolved from the laboratory cell gave the current efficiency. Each experiment was made under a controlled current density. The *p*H of the electrolyte was controlled within a given range and was adjusted with HCl or NaOH.

The cells were operated a sufficient length of time after reaching thermal equilibrium to purge the dead air space. During this time gas was evolved to the atmosphere. When a steady rate of evolution existed, the gas was collected in the burets and data recorded during the collection of the gas samples. Current was varied from 1.33 to 5.30 amp, while the voltage across the laboratory perchlorate cell covered the range of 4.0-6.1 v. A temperature range of 20°-40°C was investigated.

### *Experimental Results*

To establish reference data, the initial experiments utilized a Pt anode in the laboratory perchlorate cell. After this, experiments were conducted using $PbO_2$ as the anode with Cu, carbon steel, Ni, and stainless steel as the cathodes. Variables observed were current efficiency, current density, cell temperature, electrolyte concentration, *p*H, cathode material, and additives. Some of these data are presented in Table I. The most satisfactory values of cell operating conditions were selected from these data for subsequent verification in the larger bench-scale production cell.

**Table I. Experimental results of laboratory perchlorate cells**

| Material | | Anodic current density | Voltage | Current | Temp range | | Initial concentration (g/l) | | | Current* efficiency |
|---|---|---|---|---|---|---|---|---|---|---|
| | | | | | | | Electrolyte | Additive | | |
| Anode | Cathode | (amp/dm²) | (volts) | (amp) | (°C) | *p*H | $NaClO_3$ | NaF | $Na_2Cr_2O_7$ | (%) |
| Pt | Carbon steel | 31.0 | 5.2 | 2.90 | 20-25 | 6.0 | 484.5 | — | 5 | 92.8 |
| $PbO_2$ | Carbon steel | 15.5 | 4.6 | 2.46 | 30-35 | 6.5 | 484.5 | — | 5 | 37.7† |
| $PbO_2$ | Copper | 15.5 | 4.4 | 4.71 | 30-35 | 6.0 | 484.5 | — | 5 | 36.3 |
| $PbO_2$ | Copper | 15.5 | 5.0 | 1.47 | 35-40 | 6.5 | 500.0 | 0.5 | — | 92.4 |
| $PbO_2$ | Nickel | 7.25 | 4.0 | 1.33 | 35-40 | 6.5 | 500.6 | 0.5 | — | 93.5 |
| $PbO_2$ | Nickel | 15.5 | 5.0 | 1.47 | 35-40 | 6.5 | 493.5 | — | — | 84.8 |
| $PbO_2$ | Nickel | 15.5 | 5.0 | 1.47 | 35-40 | 6.5 | 493.5 | 0.5 | — | 92.3 |
| $PbO_2$ | Nickel | 15.5 | 5.3 | 1.47 | 35-40 | 6.5 | 493.5 | 1.5 | — | 92.7 |
| $PbO_2$ | Nickel | 15.5 | 5.2 | 1.47 | 35-40 | 6.5 | 493.5 | Saturated | — | 93.0 |
| $PbO_2$ | Nickel | 15.5 | 4.9 | 2.65 | 35-40 | 6.5 | 500.6 | 0.5 | — | 93.7 |
| $PbO_2$ | Nickel | 23.25 | 5.8 | 2.21 | 35-40 | 6.5 | 493.5 | 0.5 | — | 92.7 |
| $PbO_2$ | Stainless steel (302) | 31.0 | 6.1 | 5.30 | 25-30 | 6.5 | 495.2 | 0.5 | — | 97.5† |

* Approximate instantaneous current efficiency based on gas collection technique.
† Discoloration of evolved cell gases during electrolysis indicated that side reactions were taking place.

*Conclusions.*—Examination of the data in Table I indicates that the following conclusions may be made:

1. Sodium perchlorate can be made by electrolysis using a $PbO_2$ anode with Cu, carbon steel, Ni, or stainless steel cathodes.
2. Current efficiencies appear to be higher with Ni, stainless steel, and Cu cathodes than with carbon steel.
3. Data obtained with carbon steel are not conclusive because of side reactions.
4. Sodium fluoride appears to be a better additive than sodium dichromate. The minimum effective NaF concentration is 0.5 g/l.
5. Data obtained with a $PbO_2$ anode, Ni cathodes, and a NaF additive indicate that the current efficiency is practically independent of current density, temperature, and pH in the range of variables investigated. An instantaneous current efficiency of 93.7% was obtained at an anodic current density of 15.5 amp/dm$^2$.
6. Lower voltages appear to be possible using $PbO_2$ anodes.

## Bench-Scale Production Cell

The first phase of the investigation had set up sufficient design criteria to proceed with the construction of a larger unit which could be operated semicontinuously and for longer periods of time. All the variables could be evaluated based on the current efficiency, which could be determined by a direct chemical analysis. In order to proceed with this unit, larger $PbO_2$ anodes were made.

*Bench-scale cell construction.*—The cell was a 4-liter resin reaction kettle with a bottom outlet (Fig. 1). Current was provided by a Se rectifier and voltages and current measurements obtained. Temperature was controlled by circulating water through a glass coil immersed in the electrolyte. When pH control was necessary, 18% HCl was added.

The anode consisted of a rod-shaped, rough surfaced $PbO_2$ electrode and was immersed in solution so that, at a current of 26 amp, the anodic current density was 15.5 amp/dm$^2$. This value was maintained constant in all experiments. It proved to be the best value obtained in the smaller laboratory cells and simulates approximate plant operating conditions. Cathodes were U-shaped metal rods of varying diameters by 15 in. in length. The anode, cathodes, cooling coil, and thermometer were inserted through the top of the cell into the electrolyte. An electrical connection was made at the top of the anode with a Ag-plated Cu clamp. Cathodes were on 3 in. center to center spacing, with the anode centered between them or 1½ in. from the cathodes. Figure 2 is a picture of a typical $PbO_2$ anode with the cathodes used.

Electrolyte could be removed from the bottom of the cell and returned to the top to insure adequate mixing.

*Experimental procedure.*—At the start, the cell was filled with 4 liters of solution containing approximately 500 g/l $NaClO_3$ plus the additive. The pH and temperature were recorded. A value of 6.9 was considered to be the maximum limiting pH while the temperature was controlled within the range of 30°-45°C. Current was adjusted to the desired anodic current density, and voltage noted.

Electrolyte was removed during electrolysis from the bottom of the cell and returned through the top. About 2 liters were removed in from 2 to 3 min in 500 ml increments. This served to keep the electrolyte well circulated and was repeated every half hour. After recirculation was completed, a 100 ml sample was secured and the pH measured. This sample was returned to the cell and the pH adjusted, if necessary.

A 15 ml sample was taken for chemical analysis every 2 hr after recirculation. Then 15 ml of make-up solution were added to maintain constant volume.

The addition of make-up solution is important, since no drastic concentration changes in the electrolyte could be introduced. During the initial phases of the experiment the make-up solution contained 300 g/l $NaClO_3$. This solution was used until the concentration of the electrolyte in the cell dropped to 150

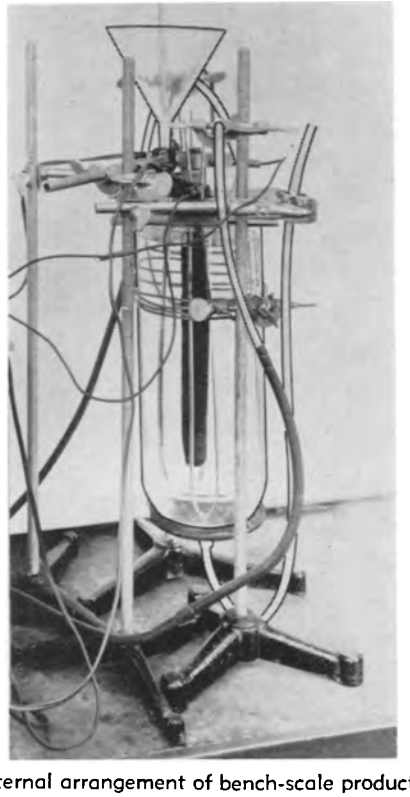

Fig 1. Internal arrangement of bench-scale production cell

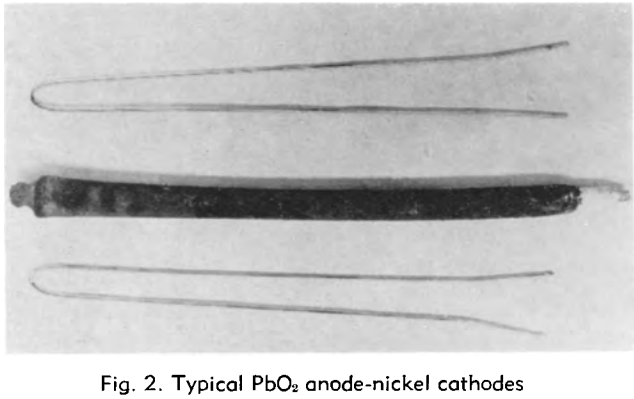

Fig. 2. Typical $PbO_2$ anode-nickel cathodes

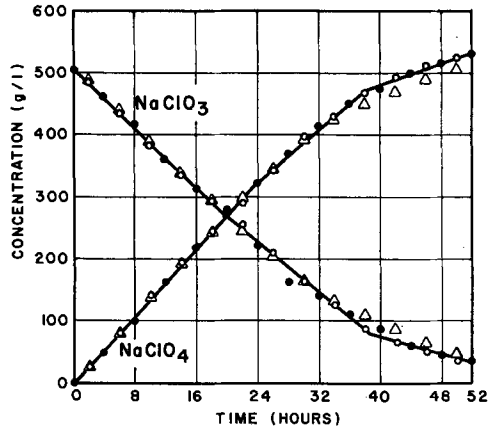


Fig. 3. Effect of $PbO_2$ conductor wire. Electrolysis conditions: anodic C. D. = 15.5 amp/dm²; cathodic C. D. = 7.25 amp/dm²; temp. range = 30°-45°C; cell voltage = 5.2-5.3 v; pH = 5.2-5.7; NaF conc. = 0.5 g/l. Anode: solid circle, $PbO_2$ plated on Ni wire; open circle, $PbO_2$ plated on Pt clad Ta; open triangle, $PbO_2$ plated on Ni wire.

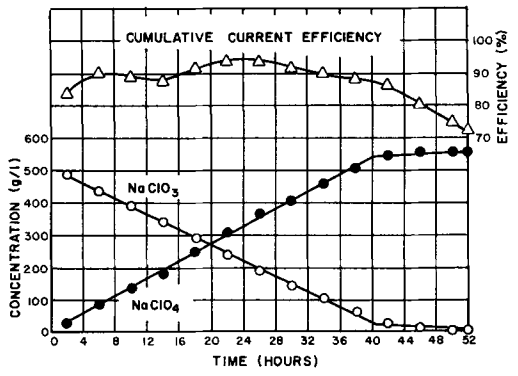


Fig. 4. Effect of nickel cathodes on cumulative current efficiency. Electrolysis conditions: anodic C. D. = 15.5 amp/dm²; cathodic C. D. = 7.25 amp/dm²; temp. range = 35°-45°C; cell voltage = 5.0 v; pH = 5.3; NaF conc. = 0.5 g/l; anode: rough surface rod-shaped, 2.06 cm dia. x 45.72 cm long; cathode: two U-shaped Ni rods, 0.95 cm dia. x 38.10 cm long.

g/l of chlorate. From this point, make-up solution of 150 g/l was added until the concentration dropped to 100 g/l. Then solution adjusted to the chlorate composition of the electrolyte was added until the completion of the experiment.

Every 2 hr a 15 ml sample was analyzed immediately for its sodium chloride and chlorate concentrations. Since the perchlorate determination was time consuming, samples were taken only every 4 hr for analyses.

Experiments were carried out for 52 hr continuously, except when side reactions or chlorate analyses indicated that the obtained efficiencies were too low.

### *Experimental Results*

Two different $PbO_2$ anodes were used in the experiments with the bench-scale production cell. One

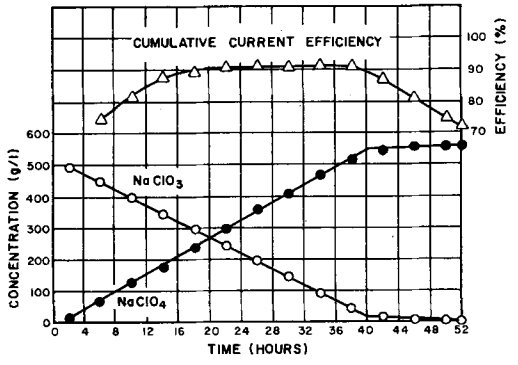


Fig. 5. Effect of stainless steel cathodes on cumulative current efficiency. Electrolysis conditions: anodic C. D. = 15.5 amp/dm²; cathodic C. D. = 7.25 amp/dm²; temp. range = 35°-45°C; cell voltage = 4.75 v; pH = 5.7; NaF conc. = 0.5 g/l; anode: rough surface rod-shaped, 2.06 cm dia. x 45.72 cm long; cathode: two U-shaped stainless steel (302) rods, 0.95 cm dia. x 38.10 cm long.

**Table II. Experimental results of bench-scale production cells**

| Cathode | Cathode current density (amp/dm²) | Additive | Voltage (volts) | Current[a] (amp) | Time, (hr) | Kw-Hr | Final[b] concentration (g/l) $NaClO_4$ | Final[b] concentration (g/l) $NaClO_3$ | Cumulative current efficiency (%) | Unit energy[c] (kw-hr/lb) |
|---|---|---|---|---|---|---|---|---|---|---|
| Nickel | 21.4 | NaF[d] | 5.1 | 26.0 | 41.6 | 5.51 | 510 | 50 | 83.0 | 1.23 |
| Nickel | 21.4 | NaF and $Na_2Cr_2O_7$[e] | 5.3 | 26.0 | 52.0 | 7.16 | 240 | 280 | 31.1 | 3.38 |
| Nickel | 7.25 | NaF | 5.0 | 26.0 | 38.6 | 5.02 | 514 | 50 | 88.2 | 1.11 |
| Stainless steel (302) | 21.4 | NaF | 5.2 | 26.0 | 49.2 | 6.52 | 493 | 50 | 68.0 | 1.50 |
| Stainless steel (302) | 7.25 | NaF | 4.75 | 26.0 | 37.6 | 4.64 | 505 | 50 | 91.5 | 1.04 |
| Stainless steel (302) | 7.25 | NaF and $Na_2Cr_2O_7$[f] | 4.75 | 26.0 | 24.0 | 2.96 | 235.5 | 287.6 | 66.0 | 1.43 |
| Copper | 21.4 | NaF | 5.7 | 26.0 | 42.8 | 6.36 | 492 | 50 | 78.5 | 1.47 |
| Carbon steel | 21.4 | NaF | 5.1 | 26.0 | 52.0 | 6.89 | 264 | 214 | 34.2 | 2.96 |
| Carbon steel | 14.1 | $Na_2Cr_2O_7$[g] | 4.9 | 26.0 | 48.0 | 6.13 | 68 | 445 | 9.9 | 10.23 |

[a] Anodic current density = 15.5 amp/dm².
[b] Volume = 4 liters.
[c] Commercial production requires 1.5-1.9 kw-hr/lb at 6.2-6.8 v, and anodic current densities of 31.1-52 amp/dm² (11).
[d] NaF as an additive = 0.5 g/l concentration.
[e] $Na_2Cr_2O_7$ concentration = 0.5 g/l.
[f] $Na_2Cr_2O_7$ concentration = 0.003 g/l.
[g] $Na_2Cr_2O_7$ concentration = 5.1 g/l.

Table III. Spectrographic analyses of unpurified ammonium perchlorate

| Cathode material | Nickel | Stainless steel (302) | Copper |
|---|---|---|---|
| Major constituent* ** | Sodium | Sodium | Sodium |
| Intermediate constituent | Potassium | Potassium | Potassium |
| Minor constituent | Approximate % | Approximate % | Approximate % |
| Calcium | 0.10 | 0.10 | 0.10 |
| Aluminum | 0.05 | 0.05 | 0.01 |
| Iron | 0.05 | 0.01 | 0.005 |
| Magnesium | 0.01 | None found | None found |
| Silicon | 0.01 | 0.01 | None found |
| Barium | 0.01 | 0.01 | 0.01 |
| Chromium | 0.005 | 0.001 | 0.001 |
| Copper | 0.005 | 0.01 | 0.005 |
| Vanadium | 0.005 | 0.001 | 0.001 |
| Nickel | 0.005 | None found | None found |
| Manganese | 0.001 | None found | None found |
| Lead | 0.001 | Trace | Trace |
| Wt of Ash (g) | 1.62 | 1.39 | 3.03 |

* Mother liquor hold-up.
** Based on spectrographic analyses of ash.

anode consisted of $PbO_2$ plated on Pt clad Ta and the other was plated on Ni wire. Experimental results obtained when $PbO_2$ is plated on these two different conductors are presented in Fig. 3. When sodium dichromate was used as an additive, a thin yellow deposit was formed on the surface of the $PbO_2$ anode. Cathodes were constructed of Ni, Cu, carbon steel, and 302 stainless steel. The effects of cathodic current density and additives were also investigated. Some experimental results are presented in Table II.

A typical result, using Ni cathodes, illustrating the change in electrolyte concentration as a function of time and the cumulative current efficiency is presented in Fig. 4. Figure 5 presents results with stainless steel cathodes.

Sodium perchlorate produced in these bench-scale experiments was converted to ammonium perchlorate to determine purity and for evaluation purposes. Only the first crop of unwashed crystals was selected for chemical and spectrographic analyses. Table III presents spectrographic data on the ammonium perchlorate prepared, and indicates that no unusual quantity of metallic impurities was introduced into the perchlorate.

*Conclusions.*—The following conclusions may be reached from the experimentation, utilizing $PbO_2$ anodes as a substitute for Pt in the production of sodium perchlorate:

1. Lead dioxide anodes produce sodium perchlorate at high cumulative current efficiencies.
2. The cumulative current efficiency for a given anodic current density is a function of chlorate concentration, the cathode material, the cathodic current density, and the additive used.
3. The wire on which the $PbO_2$ was plated for an anode appears to have no effect on the production of sodium perchlorate.
4. Sodium perchlorate can be produced using cathodes of Ni, Cu, stainless steel, and carbon steel. However, efficiencies with carbon steel are very low.
5. Sodium dichromate has a detrimental effect on the current efficiency by forming a thin deposit on the surface of the $PbO_2$ anode.
6. Decreasing the cathodic current density increased the current efficiency when utilizing Ni and stainless steel cathodes.
7. One $PbO_2$ anode was used in the cell operation for 3,000 hr.
8. Ammonium perchlorate was prepared from the sodium perchlorate produced in these experiments. No unusual metallic contamination was present and the ammonium perchlorate meets present commercial specifications.
9. Comparison of energy requirements calculated for identical experimental conditions indicates that Ni and stainless steel are the best cathode materials and that $PbO_2$ offers energy advantages over Pt as an anode.
10. Energy results of 1.04 kw-hr/lb of sodium perchlorate with a cumulative current efficiency of 91.5% were obtained. These results were attained with stainless steel cathodes at a cathodic current density of 7.25 amp/dm$^2$ and a final sodium chlorate concentration of 50 g/l.

Manuscript received May 6, 1957. This paper was prepared for delivery before the Washington Meeting, May 12-16, 1957.

Any discussion of this paper will appear in a Discussion Section to be published in the December 1958 JOURNAL.

REFERENCES

1. G. Angel and H. Mellquist, *Z. Elektrochem.*, **40**, 702 (1934) (Ger. 140,317; 195,117; 206,329).
2. Y. Kato and K. Koizumi, *J. Electrochem. Assoc. Japan*, **2**, 309 (1934).
3. K. Sugino and Y. Shibazaki, *ibid.*, **16**, 9 (1948).
4. K. Sugino, *Bull. Chem. Soc. Japan*, **23**, 115 (1950).
5. F. Foerster, *Z. Elektrochem.*, **4**, 386 (1898).
6. W. Oechsli, *ibid.*, **9**, 807 (1903).
7. J. G. Williams, *Trans. Faraday Soc.*, **15**, 134 (1919).
8. N. V. S. Knibbs, *ibid.*, **16**, 402 (1921).
9. C. W. Bennett, *ibid.*, **29**, 323 (1916).
10. N. H. Furman, "Scott's Standard Methods of Chemical Analyses," Vol. 1, p. 272-275, D. Van Nostrand Co., Inc., New York (1950).
11. C. L. Mantell, "Industrial Electrochemistry," 3rd ed., p. 135, McGraw-Hill Book Co., Inc., New York (1950).

# Dissolution of Metals in Aqueous Acid Solutions

## II. Depolarized Dissolution of Mild Steel

A. C. Makrides and N. Hackerman

*Department of Chemistry, University of Texas, Austin, Texas*

ABSTRACT

Dissolution rates of mild steel cylinders rotated in 2*N* HCl solutions containing ferric chloride, benzoquinone, and tolu-*p*-quinone are reported. At high velocities the dissolution rate depends linearly on velocity of rotation. The dissolution rate also depends on the roughness of the metal surface.

In a previous paper (1) current-potential relations for dissolution of mild steel in acid solutions containing depolarizers were interpreted on the assumption that dissolution was under diffusion control. A kinetic study of dissolution is presented here. In particular, the dependence of rate on depolarizer concentration, stirring velocity, temperature, and surface roughness of the metal is examined. Results are consistent with the postulate that dissolution is limited by the rate of diffusion of depolarizer to the interface.

### Experimental

The experimental arrangement and procedure have been described previously (1). Mild steel cylinders, polished with 2/0 emery paper and degreased with benzene in an extractor, were rotated in 2*N* HCl solutions containing depolarizer at speeds up to 11,000 rpm (1000 cm/sec linear velocity). Only the lateral surface of the cylinder was exposed to the solution, the top and bottom parts as well as the edges being covered with paraffin. All solutions were deaerated by passing nitrogen through the solution before a run.

The reaction vessel was a 600 ml beaker loosely fitted with a Lucite cap. The cap had openings through which the specimen and a calomel electrode with a saturated KCl-agar bridge were inserted. The center of the cylinder was 2 cm from the center of the beaker. This arrangement was chosen to avoid separation of flow along the shaft observed when the cylinder was concentric with the beaker.

The surface of the cylinder was 1.5 cm from the wall of the beaker and 4 cm from the tip of a calomel electrode placed opposite the cylinder and next to the wall of the container. The top of the cylinder was immersed to a depth of 4 cm when the cylinder was stationary. The diameter of the cylinders varied from 1.70 to 1.90 cm and the height of the lateral surface exposed to solution was between 1.8 and 2.1 cm. These last two dimensions were measured for each run.

Ferric chloride was of C. P. grade and was used without further purification. The quinones were of highest commercial purity available and were twice recrystallized from ethanol.

### Results and Discussion

Dissolution rates are expressed in terms of the specific rate constant $k$, given by

$$k = \frac{2.30\ V_s}{At} \log \frac{x_\infty}{x_\infty - x} \qquad (I)$$

Here $V_s$ is the volume of the solution (400 ml), $A$ the projected exposed metal surface area, $x$ the weight loss (mg) in time $t$ (sec), and $x_\infty$ the calculated weight loss for $t \to \infty$.

Generally, the weight loss at the end of a specified time (600 sec) was measured and $k$ calculated from Eq. (I). In some cases the solution was analyzed for iron at measured time intervals and $k$ obtained from a first order kinetic plot.

For purposes of discussion a differentiation is made between results obtained at average dissolution rates less than 0.020 mg/sec/cm$^2$ of projected area and those at higher rates. Results for the former interval are given in Tables I and II and are plotted in Fig. 1. In this range, $k$ is independent of initial depolarizer concentration. At greater average dissolution rates, $k$ increases with initial depolarizer concentration. It is shown below that the dependence of $k$ on $C_o$ in the latter case is caused by excessive surface roughening brought about by dissolution.

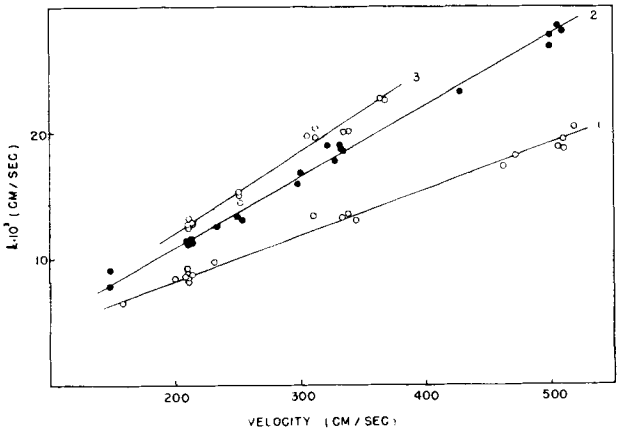


Fig. 1. Specific rate constant as a function of velocity: curve 1, ferric chloride; curve 2, tolu-p-quinone; curve 3, benzoquinone.

Table I. Dissolution rates of mild steel cylinders in 2N HCl solutions containing depolarizers; T = 30 ± 0.5°C

| Ferric chloride | | | Tolu-p-quinone | | | Benzoquinone | | |
|---|---|---|---|---|---|---|---|---|
| Velocity (cm/sec) | Conc (moles/l) | $k \cdot 10^3$ (cm/sec) | Velocity (cm/sec) | Conc (moles/l) | $k \cdot 10^3$ (cm/sec) | Velocity (cm/sec) | Conc (moles/l) | $k \cdot 10^3$ (cm/sec) |
| 158 | 0.0431 | 6.62 | 147 | 0.0100 | 7.88 | 209 | 0.0056 | 13.0 |
| 200 | 0.0432 | 8.36 | 149 | 0.0100 | 9.25 | 210 | 0.0050 | 12.6 |
| 210 | 0.0700 | 8.60 | 211 | 0.0050 | 11.4 | 211 | 0.0094 | 12.6 |
| 211 | 0.0102 | 9.32 | 212 | 0.0100 | 11.5 | 211 | 0.0204 | 13.3 |
| 211 | 0.0103 | 9.20 | 212 | 0.0200 | 10.9 | 211 | 0.0301 | 13.1 |
| 211 | 0.0318 | 8.50 | 234 | 0.0100 | 12.7 | 212 | 0.0108 | 13.0 |
| 211 | 0.0446 | 8.19 | 250 | 0.0100 | 13.4 | 212 | 0.0150 | 12.3 |
| 213 | 0.0191 | 8.73 | 254 | 0.0100 | 13.1 | 213 | 0.0300 | 12.6 |
| 232 | 0.0431 | 9.83 | 299 | 0.0100 | 15.9 | 245 | 0.0100 | 15.3 |
| 311 | 0.0432 | 13.5 | 300 | 0.0100 | 16.8 | 251 | 0.0100 | 15.3 |
| 333 | 0.0450 | 13.3 | 322 | 0.0049 | 19.0 | 253 | 0.0050 | 14.6 |
| 339 | 0.0450 | 13.6 | 328 | 0.0046 | 17.7 | 253 | 0.0050 | 15.1 |
| 345 | 0.0194 | 13.1 | 332 | 0.0092 | 18.7 | 305 | 0.0051 | 19.8 |
| 463 | 0.0200 | 17.4 | 332 | 0.0098 | 19.2 | 312 | 0.0103 | 19.6 |
| 472 | 0.0200 | 18.2 | 334 | 0.0200 | 18.4 | 312 | 0.0106 | 20.4 |
| 506 | 0.0200 | 18.9 | 424 | 0.0100 | 23.4 | 335 | 0.0200 | 20.1 |
| 512 | 0.0194 | 18.7 | 488 | 0.0050 | 27.7 | 339 | 0.0200 | 20.2 |
| 512 | 0.0194 | 19.4 | 500 | 0.0050 | 26.7 | 364 | 0.0050 | 22.7 |
| 520 | 0.0312 | 20.4 | 506 | 0.0100 | 28.6 | 368 | 0.0050 | 22.6 |
| | | | 510 | 0.0100 | 28.0 | | | |

Table II. Dependence of rate constant on velocity

| Depolarizer* | Slope† | Intercept† | Estimated Deviation† ‡ |
|---|---|---|---|
| 2N HCl solutions containing depolarizers. $T = 30.0° \pm 0.5°C$. | | | |
| Ferric chloride | $3.50 \times 10^{-5}$ | $+1.38 \times 10^{-3}$ | $\pm 0.74 \times 10^{-3}$ |
| Tolu-p-quinone | $5.56 \times 10^{-5}$ | $-0.09 \times 10^{-3}$ | $\pm 0.88 \times 10^{-3}$ |
| Benzoquinone | $6.39 \times 10^{-5}$ | $-0.70 \times 10^{-3}$ | $\pm 0.60 \times 10^{-3}$ |

Note: * Range of Reynolds numbers: 30,000 to 100,000.
† From results given in Table I. The slope and intercept were calculated by the least squares method.
‡ The estimated deviation is given by $S_k(\text{estim}) = S_k(1-r^2)^{1/2}$ where $S_k$ is the standard deviation and $r$ the correlation coefficient. The average deviation is ±6.0% for ferric chloride, ±4.5% for tolu-p-quinone, and ±4.0% for benzoquinone.

*Dependence of the Specific Rate Constant on Velocity*

Heat and mass transfer in turbulent flow are of considerable theoretical as well as practical interest and have been the subject of numerous investigations (2). The work of King and collaborators (3), of Agar (4), and of Eisenberg, Tobias, and Wilke (5, 6) is of particular interest since it is directly applicable to the rotating cylinder-turbulent flow system.

Agar (4) has suggested that the effective thickness, $\delta$, of the boundary layer at the solid surface is given by an expression of the form[1]

$$\delta = \frac{L}{B} (R_d)^{-\alpha} (Pr)^{-\beta} \qquad \text{(II)}$$

Here $L$ is the characteristic length, the diameter, $d$, of the cylinder in this case; $B$, $\alpha$, and $\beta$ are constants; $(R_d)$ is the Reynolds number; and $(Pr)$ Prandtl's number. The last two are given by

$$(R_d) = \frac{Vd}{\nu} \qquad \text{(III)}$$

$$(Pr) = \frac{\nu}{D} \qquad \text{(IV)}$$

[1] The effective thickness of the boundary layer is equivalent to that calculated on the basis of a model of a stationary layer of liquid adjacent to the solid. Through this layer, the concentration of diffusing species is assumed to change linearly with distance from a value of zero, at the surface, to that in the bulk of the solution. $\delta$ is not, in general, equal to the physical thickness of the hydrodynamic boundary layer, but it is related to this thickness.

where $\nu$ is the kinematic viscosity and $D$ the diffusion coefficient. Equation (II) assumes that for forced convection $\delta$ is independent of the concentration of diffusing species and that electrolytic transport is negligible. Agar (4) notes that experimentally

$$\delta = (\text{const})\ V^{-q} \qquad \text{(V)}$$

where $0.5 < q < 1.0$. If a reaction is controlled by diffusion

$$k = D/\delta \qquad \text{(VI)}$$

and Fig. 1 shows that in this case $q$ [and hence $\alpha$ in Eq. (II)] is unity.

*Comparison with Results of Previous Investigators*

The linear dependence of $k$ on velocity of stirring found with the present system is in agreement with the results of King and co-workers (3) and of Frank-Kamenitskii and co-workers (7), but is, at first sight, in variance with the results of Roald and Beck (8), and of Eisenberg, Tobias, and Wilke (5, 6) who find that the rate of mass transfer increases as the 0.70 power of velocity. The latter authors correlate their results through the function $j'_D = (k/V)(Pr)^{-0.644}$. From a plot of $j'_D$ vs. Reynolds number they find

$$k = 0.0791\ V\ (R_d)^{-0.30}\ (Pr)^{0.644} \qquad \text{(VII)}$$

The experimental system studied by these authors (6) was oxidation and reduction of the ferri-ferrocyanide couple at inert (nickel) electrodes.

The velocity exponent given in Eq. (VII) is a "best value" for the range of Reynolds number 1,000 to 100,000 (6). Actually, the exponent depends on Reynolds number. Thus, the slope of the correlation curve ($j'_D$ vs $R_d$) was −0.32 for the interval $R_d$ = 1,000 to 10,000, while it was only −0.23 for $R_d$ = 30,000 to 100,000 [Table II of ref. (6)]. To be exact, therefore, comparisons must be made in the same range of Reynolds numbers.

In the work reported here, Reynolds number varied from 30,000 to 100,000. A least squares' analysis of the data of Eisenberg, Tobias, and Wilke (6)

in this interval shows that the limiting rates for reduction and oxidation depend on the 0.72 and 0.77 power of velocity, respectively.

Table II gives an analysis of the data of Table I by the least squares method. As noted above, a linear relation exists between $k$ and $V$. The possibility that a log-log function gives a better fit was examined and rejected. In the case of $FeCl_3$, for example, the correlation coefficient was 0.988 for a linear relation and 0.92 for a logarithmic one.

Hydrodynamic considerations, based on a model of a liquid layer of finite thickness through which convective diffusion is absent, show that for the limiting case of large Reynolds and Prandtl's numbers the rate of mass transfer is linearly related to the flow velocity (7). However, it is unlikely that the Reynolds and Prandtl's numbers involved here are sufficiently large to attain this case.[2] In the absence of complicating effects, the dissolution rate is expected to increase as the 0.70 to 0.80 power of velocity (6). The higher value of the velocity exponent must therefore be attributed either to a difference in geometrical arrangement, or to an effect of the dissolution process on the hydrodynamic conditions under which mass transfer occurs.

*Hydrodynamic conditions.*—The different velocity exponents found in this work and that of Eisenberg, Tobias, and Wilke (5, 6) may be the result of different geometric arrangements. These authors (5, 6) used cylinders concentric with the wall (outer cylinder), a length to diameter ratio from 3.0 to 11.6, and complete end-baffling. In this work the cylinder was not concentric with the vessel and the length to diameter ratio was 1.0 to 1.2.

The differences noted above are probably not responsible for the different velocity exponents observed. The length to diameter ratio, $l/d$, does not appear to be significant. Eisenberg, Tobias, and Wilke (5, 6) found no effect for an almost fourfold change in this ratio. If, as pointed out below, a correlation exists between dissolution rate and friction factors derived from measurements of the drag on cylinders rotating in fluids, the experiments of Theodorsen and Regier (9) also support the view that the $l/d$ ratio is without influence. These authors (9) found no effect on the dependence of the drag coefficient, $f/2$, on $R_r$ for a change of $l/d$ from 20:1 to 3:1. Further, the functional dependence of $f/2$ on $R_r$ was the same for cylinders and disks,[3] which suggests that even extreme variation of the $l/d$ ratio does not alter the velocity dependence.

The effect of baffling and of concentric arrangement is more difficult to evaluate. Eisenberg, Tobias, and Wilke (5, 6) found no dependence on the gap between the rotating cylinder and the outer tube (gaps of 0.5-12.5 cm). However, all of their experiments were done with a concentric arrangement. It has been suggested (8) that increased baffling gives values of the velocity exponent closer to unity. On this basis, our results should have shown probably a smaller, rather than larger, velocity exponent.

Proposed correlations [*see* (14-17)] between heat or mass transfer and hydrodynamic parameters are based generally on Reynolds' analogy (13) and assume the validity of the momentum transfer theory of turbulence. With other theories, e.g., the vorticity transfer theory (10), there is no direct correlation between the velocity and temperature distributions. It is probable that the success of proposed relations is to be ascribed to the fact that the momentum transfer theory gives the correct velocity distribution near a wall (11).

Even in cases where the velocity distribution in the core of the flow agrees with the vorticity transfer theory, Reynolds analogy may still be applicable. An example is the system of concentric cylinders. Eisenberg, Tobias, and Wilke (5, 6) find that an extended Reynolds' analogy (the Chilton-Colburn analogy) describes correctly the dependence of the mass transfer coefficient on Reynolds number. The work of Taylor (10) and of Pai-Shih I (12) shows that in this case, the momentum transfer theory fails in the core of the flow. However, in the neighborhood of the wall, the momentum transfer theory is valid and the skin friction coefficient is given by a von Kármán logarithmic equation (9, 10, 12). These observations support the view that the type of core flow is of secondary importance when mass transfer is controlled by the hydrodynamic conditions near a wall. If this supposition is correct, the nature of secondary flows, the presence of other surfaces at distances of the order of 1000 times the thickness of the boundary layer, a concentric or eccentric arrangement, and the extent of end-baffling are not expected to influence the rate of mass transfer.

One possible difficulty with dissolution experiments may be mentioned here. Dissolution is frequently accompanied by evolution of hydrogen. Although depolarizers reduce hydrogen evolution, it is unlikely that they suppress it entirely. The stirring effect of bubbles moving in the boundary layer must therefore be considered.

Roald and Beck (8) found for magnesium dissolving in HCl solutions that the stirring effect of bubbles was negligible at small dissolution rates but became dominant at high rates. The dissolution rate at which the stirring effect of hydrogen first becomes detectable increases with stirring velocity. At 150 cm/sec, this rate is equivalent to 1.9 cc $H_2/cm^2/min$. The maximum rate of hydrogen evolution in the experiments reported here was 0.01 cc $H_2/cm^2/min$.[4] Since the rate here is 100 times smaller than the rate threshold found by Roald and Beck (8), it may be concluded that stirring by bubbles is negligible.

It is believed that the linear dependence of rate on velocity usually found in dissolution experiments is the result of surface roughening caused by the

[2] These statements refer to smooth surfaces. As shown below, the rate of mass transfer may become a linear function of velocity at relatively small Reynolds numbers if the surface is hydrodynamically rough.

[3] Theodorsen and Regier (9) find for cylinders $1/\sqrt{f} - 4.07 \log\sqrt{f} = -0.6 + 4.07 \log R_r$ and for disks $1/\sqrt{f_x} - 4.07 \log\sqrt{f_x} = -2.05 + 4.07 \log R_x$, where $f_x$ and $R_x$ refer to the drag coefficient and Reynolds number at a distance $x$ from the center of the disk. $R_r$ is Reynolds number based on the radius of the cylinder.

[4] An upper bound for the rate of hydrogen evolution is given by the rate in solutions without depolarizers. This is calculated from the dissolution rate in 2*N* HCl.

dissolution process. Eisenberg, Tobias, and Wilke (6) took special pains to prepare smooth surfaces. In the present study it was impossible to avoid surface roughening during a run. Surface irregularities of height comparable to the thickness of the laminar sublayer give rise to a "hydrodynamically rough" surface. The rate is expected then to be a linear function of velocity when a critical value of Reynolds number is exceeded. The effect of surface roughness on rate of mass transfer is considered below.

*Mass transfer in turbulent flow.*—Proposed correlations (14-17) between rates of heat or mass transfer and hydrodynamic parameters are generally based on Reynolds' analogy which suggests that in turbulent flow momentum and heat are transferred in the same way (13). Reynolds' analogy fails for fluids for which Prandtl's number is not unity because of the existence of a layer near the wall through which the transfer of heat and momentum by conduction and viscosity is important. Kármán's extension (16) of Reynolds' analogy leads to the following expression for the rate of heat transfer

$$1/k_H = \frac{2}{f} + 5\sqrt{2/f}\,[(Pr-1) + \ln\{1+0.83(Pr-1)\}] \qquad \text{(VIII)}$$

where

$$k_H = \frac{Q_0}{V(T_0 - T_m)c\rho}$$

with $Q_0$ the rate of heat transfer per unit area of the wall, $T_0$ the temperature at the wall, $T_m$ the mean temperature for the region of flow considered, c the specific heat capacity, and $\rho$ density.

For small values of Prandtl's number (Pr~1-10), Eq. (VIII) is in reasonably good agreement with experiment (11). At large values of Prandtl's number, however, Eq. (VIII) reduces to

$$\frac{1}{k_H} = \frac{2}{f} + 5\sqrt{2/f}\,(Pr) \qquad \text{(VIIIa)}$$

The indicated linear dependence of $1/k_H$ on $(Pr)$ for constant $f/2$ is contrary to observation (17). Good agreement with experiment is observed with

$$k_H = \frac{f}{2}(Pr)^{(\beta-1)} \qquad \text{(IX)}$$

where $\beta \approx 0.35$. Colburn (17) and Chilton and Colburn (18) use $\beta = 1/3$, while Eisenberg, Tobias, and Wilke (5, 6) find from mass transfer experiments with cylinders $\beta = 0.356$.

Theodorsen and Regier (9) find for rotating cylinders with smooth surfaces

$$\frac{1}{\sqrt{f/2}} = -1.72 + 5.76 \log R_d\sqrt{f/2} \qquad \text{(X)}$$

As pointed out by Eisenberg, Tobias, and Wilke (5), Eq. (X) is closely approximated by

$$f/2 = 0.0794\, R_d^{-0.30} \qquad \text{(Xa)}$$

in the range $1000 \leqq R_d \leqq 100{,}000$. Substitution of this value of $f/2$ in an equation for mass transfer similar to Eq. (IX) gave good agreement with experiment (5, 6).

For rough surfaces, Theodorsen and Regier (9) find $\sqrt{f/2}$ to be a function of relative roughness and independent of $R_d$ once a critical value of $R_d$ is exceeded[5]

$$\frac{1}{\sqrt{f/2}} = 1.25 + 5.76 \log (d/\epsilon) \qquad \text{(XI)}$$

where $d$ is the diameter of the cylinder and $\epsilon$ the height of surface irregularities.[6] The value of $\epsilon$ at which relation (XI) holds is given by

$$\epsilon/L \geqq 3.3$$

where $L$ is the friction length

$$L = \nu/V_\tau = \nu/\sqrt{\tau_0/\rho}$$

with $V_\tau$ the friction velocity, $\tau_0$ the shear per unit area at the surface, and $\rho$ the density.

But

$$d/L = R_d\sqrt{f/2}$$

and from (Xa)

$$d/L \cong 0.282\, R_d^{0.85}$$

At the lowest $R_d$ used here (30,000) and with $d = 1.8$ cm

$$L \cong 3.55\,(d)\,R_d^{-0.85} \cong 1.0 \times 10^{-3}\ \text{cm}$$

If surface irregularities of height

$$\epsilon \geqq 3.3\,L \geqq 3.3 \times 10^{-3}\ \text{cm}$$

are present, the Chilton-Colburn analogy predicts a linear dependence on velocity since substitution in

$$k_M = \frac{k}{V} = \frac{f}{2}(Pr)^{-0.644}$$

of Theodorsen and Regier's value for $f/2$ gives

$$k = (1.25 + 5.76 \log [d/\epsilon])^{-2}\,(Pr)^{-0.644}\,V \qquad \text{(XII)}$$

Microscopic examination after polishing of the cylinders used here showed that, on the average, the height of surface irregularities was about $1 \times 10^{-3}$ cm. Examination after a run revealed irregularities of height 5 to $15 \times 10^{-3}$ cm. As shown below, it is probable that surface roughening occurs in the first minute of a run. Taking as an average height $10 \times 10^{-3}$ cm, the value of $f/2$ is 0.00493 and[7]

$$k = 0.00493\,(Pr)^{-0.644}\,V \qquad \text{(XIIa)}$$

An accurate comparison of the present results with Eq. (XIIa) is not possible because reliable values for the diffusion coefficients are lacking. General agreement with Eq. (XIIa) was found using estimated values for the diffusion coefficients (Table III). It should be noted that the calculated

[5] This result refers to a "saturation" condition for the spacing of surface irregularities. In this case the drag coefficient remains constant and equal to its critical value. A saturation condition exists with specimens undergoing dissolution.

[6] A similar equation has been found by Nikuradse (19) from experiments with pipes.

[7] For $\epsilon = 5\text{x}10^{-3}$ cm, $f/2 = 0.00392$, while for $\epsilon = 15\text{x}10^{-3}$ cm, $f/2 = 0.00580$.

Table III. T = 30.0° ± 0.5°C

| Depolarizer | Observed slope | D·10⁶ (cm²/sec) | (ν/D) [4] | Calculated[5] slope |
|---|---|---|---|---|
| Ferric chloride | $3.50 \times 10^{-5}$ | 3.5[1] | $2.48 \times 10^{3}$ | $3.2 \times 10^{-5}$ |
| Tolu-p-quinone | $5.56 \times 10^{-5}$ | 7.0[2] | $1.24 \times 10^{3}$ | $5.0 \times 10^{-5}$ |
| Benzoquinone | $6.39 \times 10^{-5}$ | 8.0[3] | $1.09 \times 10^{3}$ | $5.5 \times 10^{-5}$ |

[1] Estimated from the data of King and Weidhenhammer (20). Since $D_{FeCl_3}$ depends on the HCl concentration, the estimate given may be in error appreciably.
[2] Estimated from the diffusion coefficient of hydroquinone.
[3] The value given is that for hydroquinone (21). The value for benzoquinone is probably less.
[4] The kinematic viscosity used (0.87 x $10^{-2}$ cm²/sec) is for 2N HCl solutions. The value of $\nu$ for solutions containing depolarizers at concentrations employed here is estimated to deviate less than 2% from this value.
[5] Calculated from Eq. (XIIa).

slopes in Table III are uncertain within rather wide limits.

*Surface Roughness and Dissolution Rate*

Figure 2 shows weight loss in 600 sec as a function of velocity. The linear increase of weight loss with velocity is contrary to expectation since it suggests that the velocity exponent in Eq. (V) is considerably greater than unity. Examination of the cylinders after each run showed that at the higher velocities, the surface had become exceedingly rough. Numerous elongated pits appeared. Their long dimension was approximately parallel to the axis of the cylinder and their width was about 1/30 to 1/40 their length. Their depth varied, but was generally of the order of tenths of a millimeter. It was apparent that during the run the surface area had increased greatly.

Surface irregularities, in addition to their effect on flow conditions discussed in the previous section, may alter both the (apparent) magnitude and the (apparent) velocity dependence of rate constants calculated with the aid of Eq. (I).

Surface irregularities of height comparable to the thickness of the laminar sublayer may change the effective surface area of the cylinder. In using Eq. (I) it was assumed that the cross-sectional area for diffusion was equal to the projected geometric area. This may not be true for hydrodynamically rough surfaces. Consequently, $k$'s calculated from Eq. (I), which may be termed "apparent rate constants", may be numerically larger than the actual rate constants for rough surfaces.

The extent of surface roughening is, in general, a function of dissolution rate and of the metal specimen and its metallurgical history. If, therefore, in any given velocity and concentration interval, the extent of surface roughness increases with dissolution rate, the effective surface area may be a function of velocity, and the apparent dependence of $k$ on velocity greater than expected from flow conditions alone.

In the velocity interval 150-550 cm/sec, and for the range of concentrations given in Table I, the specific rate constant was independent of initial depolarizer concentration, and, consequently, also independent of dissolution rate. The effective surface area was therefore constant and the surface roughness approximately the same in all cases. The surface roughening observed in this interval probably occurred in approximately the first minute of a run during which time the dissolution rate is greatest.

In general, it was found that for average dissolution rates (in 600 sec) less than 0.020 mg/sec/cm² of projected area, specific rate constants calculated from Eq. (I) were independent of initial depolarizer concentration. The opposite was true for rates greater than 0.025 to 0.030 mg/sec/cm² of projected area. It should be noted that at any given velocity, the average dissolution rate increases with concentration. Accordingly, in compiling Table I, the concentration ranges were restricted to values giving average dissolution rates less than the stated limiting value.

*Experiments with roughened cylinders.*—The rate of dissolution was determined as a function of time at the higher velocities by withdrawing small portions of the solution and analyzing for iron (Fig. 3). With initially polished cylinders, the specific rate constant, given by the slope of the log $x_\infty/(x_\infty - x)$ vs. $t$ curve, increased continuously at small times and eventually became constant (curve 1, Fig. 3). If the

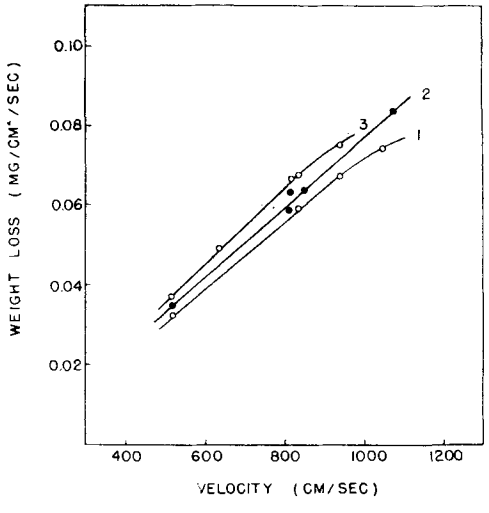


Fig. 2. Weight loss as a function of velocity: curve 1, 0.020M tolu-p-quinone; curve 2, 0.0431M ferric chloride; curve 3, 0.020M benzoquinone.

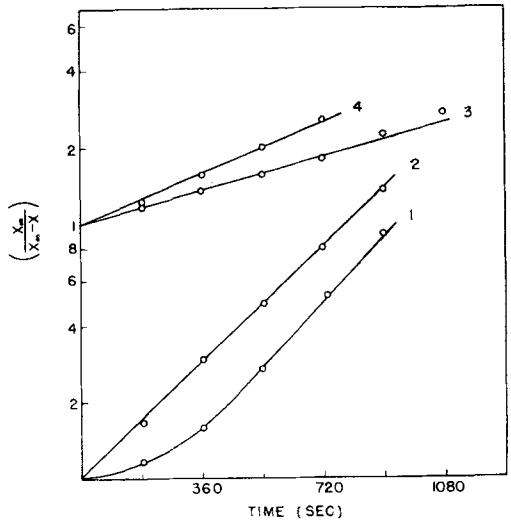


Fig. 3. First order kinetic plot with 0.0431M ferric chloride: curve 1, polished specimen, V = 820 cm/sec; curve 2, roughened specimen, V = 820 cm/sec; curve 3, roughened specimen, V = 200 cm/sec; curve 4, roughened specimen, V = 312 cm/sec. The log $x_\infty/(x_\infty - x)$ values have been corrected for volume changes during the run.

cylinder was used again without polishing, curve 2 was obtained. The slope was constant throughout the time interval studied and was equal to the slope of curve 1 at large times. It is apparent that in the former case the effective surface area increased during the course of the run until it attained a constant value. This value was not changed by repeating the run with the roughened cylinder.

Cylinders whose surface had been roughened by runs at 820 cm/sec in 0.0431M $FeCl_3$, were used without repolishing at smaller velocities. Curves 3 and 4 of Fig. 3 gave for the rate constants $k_{200} = 41.0 \times 10^{-3}$ cm/sec and $k_{312} = 61.5 \times 10^{-3}$ cm/sec. The value of $k$ obtained with roughened cylinders at 820 cm/sec (curve 2, Fig. 3) was $140 \times 10^{-3}$ cm/sec.

*Effective surface area for dissolution.*—In the velocity interval 150 to 550 cm/sec and for average dissolution rates less than 0.020 mg/sec/cm$^2$, observed values of $k$ agree within 20% with those calculated from Eq. (XIIa) (*see* Table IV). It is evident, therefore, that the effective surface area for dissolution is, in this case, essentially equal to the projected surface area used in Eq. (I).

At high velocities and dissolution rates, the apparent values of $k$ are larger than calculated, even after allowance is made for the increase in the friction coefficient because of increased roughness. From Eq. (XI) with $\epsilon \approx 0.05$ cm,

$$f/2 \approx 0.01$$

and from (XII)

$$k \approx 0.01\ (Pr)^{0.644}\ V \qquad \text{(XIIb)}$$

Values of $k$ calculated from (XIIb) are compared with observed values in Table IV. The observed (apparent) values are from 2.9 to 3.2 times larger than calculated from Eq. (XIIb). This result agrees with the authors' interpretation of the dissolution rate-time curves (Fig. 3).

The suggestion that with roughened specimens the effective surface area is larger than the projected area is not inconsistent with the physical interpretation of the hydrodynamic boundary layer. In Kármán's model (9), the thickness of the laminar sublayer is about $11.5(L)$. While irregularities of the order of $3(L)$ cause the friction coefficient to become independent of $R_a$, they do not change, apparently, the effective area for dissolution from that of a hydrodynamically smooth surface. Irregularities of height larger than $12(L)$ may alter however the effective surface area. The large apparent values of $k$ observed with roughened cylinders indicate that, in this case, the ratio of the effective to the projected area is about 3.

Table IV. $C_{FeCl_3} = 0.0431M$

| Velocity (cm/sec) | Polished cylinders $k$ (obs) (cm/sec) | Polished cylinders $k$ (calc) * (cm/sec) | Roughened cylinders $k$ (obs) (cm/sec) | Roughened cylinders $k$ (calc) ** (cm/sec) |
|---|---|---|---|---|
| 200 | $8.2 \cdot 10^{-3}$ | $6.4 \cdot 10^{-3}$ | $41.0 \cdot 10^{-3}$ | $12.8 \cdot 10^{-3}$ |
| 318 | $12.5 \cdot 10^{-3}$ | $10.2 \cdot 10^{-3}$ | $61.5 \cdot 10^{-3}$ | $20.5 \cdot 10^{-3}$ |
| 820 | —— | $(27.2 \cdot 10^{-3})$ | $140 \cdot 10^{-3}$ | $52.5 \cdot 10^{-3}$ |

* Calculated from Eq. (XIIa).
** Calculated from Eq. (XIIb).

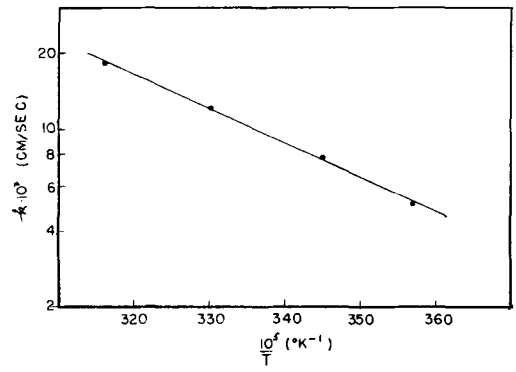


Fig. 4. The specific rate constant as a function of temperature: 0.0431M $FeCl_3$, $V = 312$ cm/sec.

### *Temperature Coefficient*

Figure 4 shows the temperature dependence of the specific rate constant at 312 cm/sec in 0.0431M $FeCl_3$ solutions. The Arrhenius energy of activation is 6100 cal.

The observed temperature dependence is within the range expected for diffusion controlled reactions. It is in good agreement with the values 5500 cal ($V =$ 33 cm/sec, 0.050M $FeCl_3$) and 6100 cal ($V = 167$ cm/sec, 0.025M $FeCl_3$) reported by Abramson and King (22).

## Conclusions

1. The dependence of dissolution rate on stirring velocity, depolarizer concentration, and temperature indicates diffusion-controlled kinetics.
2. The specific reaction rate constant depends on the stirring velocity to a power close to unity. This is probably a result of the effect of surface irregularities on flow conditions near the surface.
3. When surface irregularities or height comparable to the thickness of the laminar sublayer are present, the effective surface area for dissolution may be larger than the projected geometric area.

## Acknowledgment

The authors thank N. Komodromos and J. J. Bordeaux for carrying out some of the measurements given in Table I. The authors also gratefully acknowledge financial assistance from the Office of Ordnance Research under contract DA 23-072-ORD-216 and the Office of Naval Research under contract Nonr-375 (02).

Manuscript received Jan. 9, 1957. This paper was prepared for delivery before the Pittsburgh Meeting, Oct. 9-13, 1955.

Any discussion of this paper will appear in a Discussion Section to be published in the December 1958 JOURNAL.

## REFERENCES

1. A. C. Makrides, N. Komodromos, and N. Hackerman, *This Journal*, **102**, 363 (1955).
2. L. Prandtl, "Essentials of Fluid Dynamics," Hafner Publishing Co., New York (1952).
3. C. V. King and W. H. Catchart, *J. Am. Chem. Soc.*, **59**, 63 (1937); C. V. King and P. L. Howard, *Ind. Eng. Chem.*, **29**, 75 (1937).
4. J. N. Agar, *Disc. Faraday Soc.*, **1**, 26 (1947).
5. M. Eisenberg, C. W. Tobias, and C. R. Wilke, *Chem. Eng. Progr.*, **51**, [16] (1955).
6. M. Eisenberg, C. W. Tobias, and C. R. Wilke, *This Journal*, **101**, 306 (1954).

7. D. A. Frank-Kamenitskii, "Diffusion and Heat Exchange in Chemical Kinetics," Princeton University Press, Princeton (1955).
8. B. Roald and W. Beck, *This Journal*, **98**, 277 (1951).
9. T. Theodorsen and A. Regier, *Nat. Advisory Comm. Aeronaut., Rept* **793** (1944).
10. G. I. Taylor, *Proc. Roy. Soc. (London)*, **A151**, 494 (1935).
11. "Fluid Dynamics," S. Goldstein, Editor, Vol. II, p. 650—4, Oxford Press (1938).
12. Pai Shih-I, *Nat. Advisory Comm. Aeronaut., Tech. Note* **892** (1943).
13. O. Reynolds, *Proc. Manchester Lit. and Phil. Soc.*, **14**, 7 (1874).
14. L. Prandtl, *Physik. Z.*, **29**, 487 (1928).
15. G. I. Taylor, *Aeronaut. Res. Comm., Reports and Memoranda*, No. 272 (1919).
16. T. von Kármán, *Proc. 4th Intern. Congress for Applied Mechanics*, p. 77, Cambridge (1934).
17. A. P. Colburn, *Trans. Am. Inst. Chem. Engrs.*, **29**, 174 (1933).
18. T. H. Chilton and A. P. Colburn, *Ind. Eng. Chem.*, **26**, 174 (1933).
19. J. Nikuradse, *Ver. deutsch. Ing., Forschungsheft*, 361 (1933).
20. C. V. King and L. Weidenhammer, *J. Am. Chem. Soc.*, **58**, 602 (1936).
21. International Critical Tables, Vol. V, 70 (1929).
22. M. B. Abramson and C. V. King, *J. Am. Chem. Soc.* **61**, 2290 (1939).

# Anodic Polarization of Titanium in Nonaqueous Base Etching Solutions

**Morris Eisenberg[1] and Robert E. DeLaRue**

*Stanford Research Institute, Menlo Park, California*

ABSTRACT

Results of systematic studies of the anodic polarization of titanium in essentially nonaqueous electrolytic etching baths of hydrogen fluoride are described. Solvents included ethylene glycol, dioxane, and tetrahydrofuran. A direct method using nickel reference electrodes was employed. The studies covered a current density range from 0 to 100 ma/cm$^2$ at temperatures ranging from 25° to 65°C. Plots of current density vs. net anode polarization show an interesting rapid rise of the polarization (by an incremental change ranging from 1.3 to 4.1 v) at a "critical" current density whose value depends on bath composition and temperature. The critical current density, which varied from 6.5 to 15 ma/cm$^2$ (when working with ascending current densities), has been found, in the course of experiments designed to test the applicability of Faraday's law, to correspond to a point at which chemical (local action) attack by the hydrofluoric acid is essentially eliminated and the linear rate of anode dissolution corresponds to the requirements of Faraday's law.

For a completely nonaqueous solution (including both HF and $H_2SO_4$) a cathodic polarization curve was also determined. A linear relationship between the polarization and the current density was found and interpreted to be due both to the dissolution of the titanium cathode and to the hydrogen discharge process.

For each of the six solutions studied, the parameter $L/k$ $(dE/dI)$ was evaluated and compared with the observed nonuniformity of the etching as manifested by electropolishing in areas of high current density. This parameter was found to be a valuable criterion of the uniformity of current distribution only within the range of conditions at which a desirable anodic process can take place. Anodic polarization and dissolution rate studies offer a valuable method for determination of the optimum conditions for anodic etching of titanium without causing hydrogen embrittlement.

In studies of electrodeposition of protective coatings of Cu and Ni on Ti and Zr, it has been found that the usual methods for removal of the oxide film do not necessarily assure satisfactory adhesion of the coatings to the underlying substrate. Furthermore, the cohesive forces between Ti and coatings of Cu or Ni cannot be expected to be large in view of the different crystal structures of the metals involved. The room temperature stable phase of Ti (alpha) has a hexagonal, close-packed structure with lattice constants $a = 3.228$Å and $c = 5.120$Å. On the other hand, Cu and Ni have face-centered cubic structures with lattice constants of 3.608Å and 3.517Å, respectively. To obtain an acceptable adherence, Colner, Feinleib, and Reding (1) found it necessary to produce electrolytically a pocket-type roughening of the Ti surface in order to assure a mechanical bonding by means of keying and anchoring of the deposit on the Ti substrate. On this basis an essentially mechanical "as-plated" adhesion was sought. Hydrofluoric acid solutions proved necessary for electrolytic etching, and to reduce the local action of the bath Colner and co-workers had to resort to essentially nonaqueous baths with small amounts of water added to increase the d-c conductivity of the

[1] Present address: Lockheed MSD, Palo Alto, California.

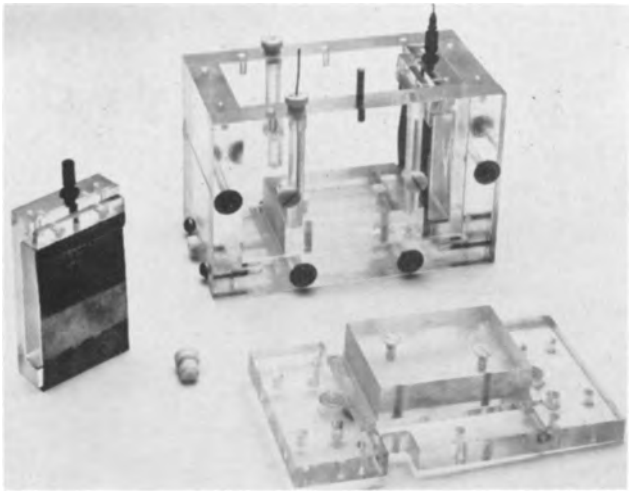

Fig. 1. Cell and electrodes for polarization studies

bath. In ethylene glycol baths containing as little as 6% water, they still found that local action persisted up to current densities of 18 ma/cm$^2$. From this point on, a rate of dissolution linear with increasing current was observed.

Earlier work in this laboratory on problems of preparation of Ti surfaces for electrodeposition by means of anodic etching has pointed toward difficulties in obtaining adhesion and toward a necessity for elucidating the mechanism of the anodic etching. It was expected that a study of this mechanism would yield valuable information relating to the optimum conditions for obtaining the type of surface etching most desirable for electrodeposition purposes.

A systematic study was initiated of the anodic polarization of Ti in essentially nonaqueous baths employing ethylene glycol, p-dioxane, and tetrahydrofuran.

### Experimental Studies and Results

A Lucite cell was constructed with suitable electrode assemblies designed to allow accurate determination of the polarization of single electrodes as a function of applied current density, without polarizing the reference electrodes (Fig. 1). The reference electrodes were built into the walls of the cell and connected to the main compartment by means of small capillary openings. Nickel wires were found to be quite suitable as reference electrodes. Two were used in the cell walls near the Ti anode and a Ni cathode of the same size was placed parallel to the anode in the cell. Titanium metal Ti 75A[2] cleaned by mechanical abrasion and degreasing was employed throughout these experiments. The electrodes were mounted in special Lucite holders (Fig. 1), and were insulated on the back side by means of epoxy resins. They had an exposed surface area of 50 cm$^2$. The cell was thermostated in a large bath. A stirrer with a constant speed of 415 rpm was employed between the cathode and the anode throughout all experiments. Sometimes it was necessary to employ a Ni cathode, which was perforated to facilitate a better heat transfer through the cell when an additional stirrer was placed behind it. This was necessary because in the dissolution of Ti, the anodic

[2] Supplied by Titanium Metals Corporation.

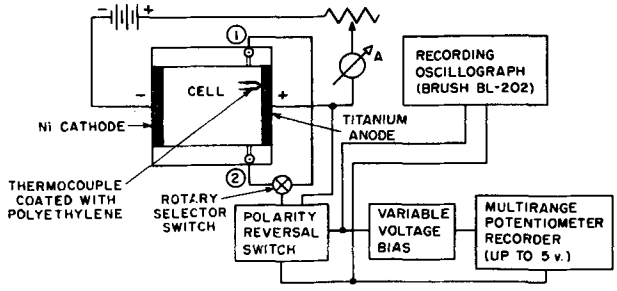


Fig. 2. Schematic diagram of cell and circuit

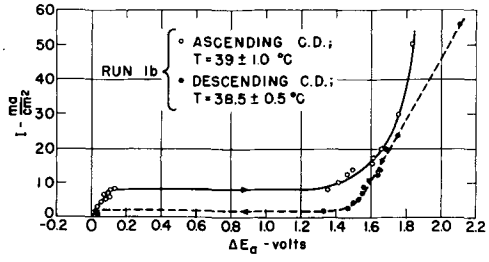


Fig. 3. Net polarization of Ti anode (Ti 75A) as a function of apparent c.d. Solution D-4: 11.9% HF, 6.6% $H_2O$, 81.5% ethylene glycol.

reaction is highly irreversible, with an estimated free energy for reaction of −109 kcal/mole (for the formation of the $TiF_6^{-2}$ ion). The circuit is shown in Fig. 2. By means of a rotary switch it was possible to measure the anode potential vs. reference 1 and also vs. reference 2 successively twice a minute. A variable voltage bias was employed, when necessary, to measure potentials over 5 v. A specially designed multirange potentiometer recorded simultaneously the potentials of a Ti anode against both references and thus provided the basis for calculation of the $iR$-drop between reference 1 and the anode according to the direct method (2). In addition, a recording oscillograph (Brush BL202) was employed to record rapid potential changes. A small iron-constantan thermocouple with a thin coating of polyethylene was placed in the vicinity of the anode, thus permitting temperature measurements to be made.

The resulting data were used to calculate the net anode polarization, i.e., the departure of anode potential at various set current densities from the zero current potential determined prior to the experiment. Figure 3 shows a typical plot.

Essentially nonaqueous solutions of HF in ethylene glycol were used. The solutions were prepared from a base of pure ethylene glycol in which gaseous HF had been dissolved. Water was added as desired to a maximum content of 10 wt %. The glycol base assured low chemical attack of the Ti by the electrolyte; the water improved the d-c conductivity of the bath. In one case, however, an entirely nonaqueous solution was used successfully with an $H_2SO_4$ addition serving to improve conductivity. The compositions of all solutions employed are given in Table II.

Polarization runs were carried out with both successively increasing and successively decreasing current densities. Slight changes in the anode potential occurred after each current setting, and within a

Table II. Compositions and Properties of Etching Solutions

| | D-4 | D-8 | K-2 | M-5 | K-6 | N-1 |
|---|---|---|---|---|---|---|
| 1. Composition: | | | | | | |
| % HF | 11.9 | 18.0 | 11.5 | 12.0 | 11.0 | 15 |
| % KF | — | — | — | — | 0.5 | — |
| % $H_2O$ | 6.6 | 6.2 | 6.2 | 10.0 | 6.2 | — |
| % $H_2SO_4$ | — | — | — | — | — | 15 |
| % Dioxane | — | — | — | 15.0 | — | — |
| % THF | — | — | 15.0 | — | 15 | — |
| (Balance ethylene glycol) | | | | | | |
| 2. Rate of chem. dissolution at 55°C at no current (415 rpm) $\frac{\text{moles}}{\text{cm}^2\,\text{sec}} \times 10^7$ | 1.35<br>1.39 | 1.81<br>1.90 | 1.80<br>1.87 | 1.01<br>1.10 | 0.0348 | 0.0157 |
| C.d. at min. anode losses ma/cm² | 10.5 | 5.0 | 12.0 | 5.0 | — | — |
| $n$ average (in Faraday's Law) | 3.11 | 3.29 | 3.50 | 3.63 | 3.68 | 3.73 |
| 3. Min. rate of loss by chem. dissolution at 55°C (calc.) $\frac{\text{moles}}{\text{cm}^2\,\text{sec}} \times 10^7$ | 0.15 | 0.18 | 0.20 | 0.08 | — | — |

minute or two the values became constant. The rapid rise of potential on ascending current densities or drop in potential on descending current densities were investigated for each run by means of the Brush recording oscillograph. An example of this rise is given in Fig. 4, which shows that practically the entire change took place within about 10 sec. As shown in this figure, such a change could take place with an overshoot of as much as 0.1 v compared to the final value which occurred after an additional 30 sec. The current remained essentially constant during such a rise. In other cases, however, no such overshoot was observed, as shown in Fig. 5 in which solution M-5 containing 15% p-dioxane was employed. Here the bulk of the potential rise occurred within 25 sec. The entire change from the initial constant value to the final constant value rarely exceeded 60 sec. No attempt was made to replot the shape of these potential rise-time curves to the bath composition, as it is believed that the shape of these curves depends, among other factors, on the manner in which the particular applied current density was set.

It should be noted that the current density value at which the sudden potential rise occurred (from here on denoted as the critical c.d.) depended to a small extent on the experimental procedure. Thus in an auxiliary experiment it was found possible to obtain this potential rise at a c.d. somewhat below the one accepted as the critical c.d. However, the time it took to arrive at the rise of potential, as well as the time period for the rise itself, were quite long, in one case as long as 40 min. For this reason it was decided to accept arbitrarily as the critical c.d. the value at which the rise of potential took place within a period not exceeding 5 min after the setting of the

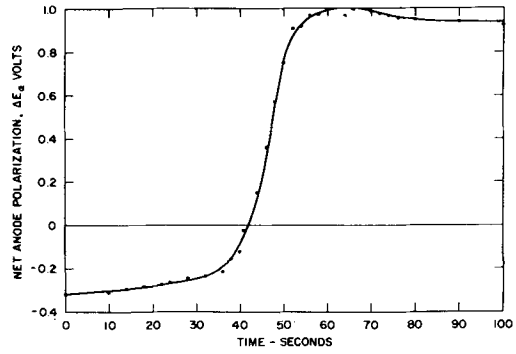


Fig. 4. Rise of net anode polarization of Ti (Ti 75A) at the breakthrough c.d. of 10.5 ma/cm². Solution D-4: 11.5% HF + 6.2% $H_2O$ + glycol. Run 1a, T = 43° ± 1°C.

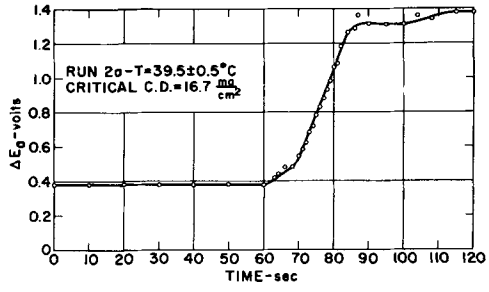


Fig. 5. Rise of net anode polarization of Ti (Ti 75A) at the "critical" c.d. of 16.7 ma/cm² (ascending c.d.'s). Solution M-5: 12% HF, 10% $H_2O$, 15% dioxane, 63% ethylene glycol.

current. This was justified by the fact that the potential rise usually took place quickly (within less than 1 min) when the critical c.d. was reached or exceeded. By applying small enough increments of current, particularly in the region at which the transition could be expected (on the basis of preliminary experiments), it was possible to determine the critical c.d. in a fairly reproducible manner. This can be seen, for instance, in Fig. 6, in which for a solution containing 18% HF the various branches of the polarization curves are well reproduced. An important feature of these curves is that the critical c.d. obtained with ascending current was always higher than the value obtained with descending currents. Another important feature is the dependence of the critical c.d. on the temperature, illustrated in Fig. 7 for three temperatures: 26°, 39.5°, and 55.5°C. With ascending currents, the corresponding critical c.d. values are 11, 17, and 32 ma/cm², respectively. The values of the critical c.d.'s obtained with descending

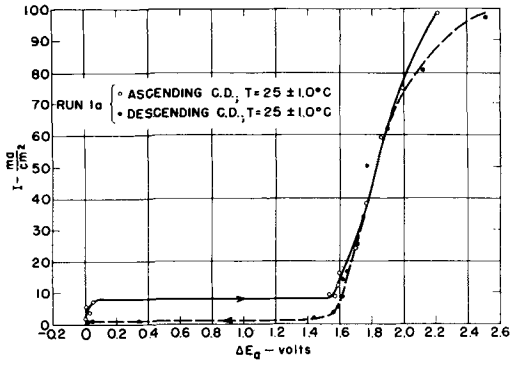


Fig. 6. Net polarization of Ti anode (Ti 75A) as function of apparent c.d. Solution D-8: 18% HF, 6.2% $H_2O$, 75.8% ethylene glycol.

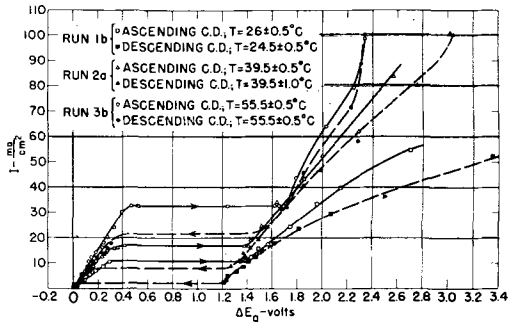


Fig. 7. Net polarization of Ti anode (Ti 75A) as function of apparent c.d. Solution M-5: 12% HF, 10% $H_2O$, 15% dioxane, 63% ethylene glycol.

applied currents are lower, but remain in approximately the same ratio. The critical c.d. increases generally with the chemical activity of the electrolyte, which depends on its acid and water content as well as the temperature of the bath. For instance, with solution K-2 a change from about 40° to about 55°C accounted for a rise in the critical c.d. (on ascending currents) from 8.5 to about 17 ma/cm².

In the initial phase of these studies, anodic polarization curves were taken up to very high c.d.'s with the result that anodic limiting current plateaus were obtained (usually in the region of 0.05-0.12 amp/cm² depending on the temperature and the solution). The upper part of Fig. 12 illustrates the achievement of such a limiting c.d. plateau at 0.078 amp/cm². Normally the anodic curves were not taken up to the limiting conditions.

Values of critical c.d.'s obtained with ascending and descending applied currents at various temperatures (in the range 25°-55°C) for the six electrolytes covered by this study are given in Table I.

As has already been reported (1), Ti undergoes chemical attack even in glycol solutions of HF when the applied current is too small. Under such conditions chemical etching takes place, resulting in a uniformly roughened surface. However, as pointed out previously, in preparing Ti for electrodeposition purposes a deep pocket-type roughening is desirable. This could be achieved only by electrolytic etching in low-activity, essentially nonaqueous, baths of composition representing a compromise between a desirable low chemical activity and satisfactory d-c conductivity. In such baths Colner and co-workers (1) found it necessary to apply a certain minimum c.d. to suppress the desirable chemical action. This minimum current increased with acid concentration of the bath, its water content, and temperature.

Since the critical c.d.'s obtained from anodic polarization curves showed a similar dependence on temperature and acid concentration it was suggested that these critical c.d.'s are related or equal to the current values required for suppressing local action by chemical attack.

It was thought that studies of the rate of metal dissolution as a function of applied c.d. (with particular attention to the low c.d. range) would lead to the determination of the minimum current required to stop chemical attack as the point beyond which the metal dissolution proceeds according to a

**Table I. Critical Current Densities**

| Solution | Run No. | Critical c.d. Ascending ma/cm² | Critical c.d. Descending ma/cm² | Temperature Ascending °C | Temperature Descending °C |
|---|---|---|---|---|---|
| D-4 | 1a | 6.89 | 1.78 | 41 | 43 |
| | 1b | 8.14 | 1.40 | 39 | 38.5 |
| | 2a | 13.7 | 3.65 | 53.5 | 55 |
| | 2b | 14.9 | 3.66 | 54.5 | 56 |
| D-8 | 1a | 8.83 | 0.87 | 25 | 25 |
| | 1b | 8.88 | 0.65 | 25 | 25 |
| | 2a | 16.6 | 3.76 | 55 | 54.5 |
| | 2b | 20.2 | 3.79 | 55.5 | 54 |
| K-2 | 1a | 8.60 | 2.82 | 40.5 | 43.5 |
| | 1b | 8.60 | 2.79 | 40.5 | 42.5 |
| | 2a | 14.80 | 4.45 | 55.5 | 55 |
| | 2b | 17.20 | 4.39 | 57 | 55.5 |
| M-5 | 1a | 10.3 | 1.81 | 25.5 | 25.5 |
| | 1b | 11.5 | 1.91 | 26 | 24.5 |
| | 2a | 16.7 | 7.17 | 39.5 | 39.5 |
| | 2b | 20.2 | 7.43 | 40 | 39 |
| | 3a | 27.2 | 18.2 | 55 | 55 |
| | 3b | 32.7 | 17.8 | 55.5 | 55.5 |
| K-6 | 1a | 0.033 (15 min*) | 0.061 | 25 | 25 |
| | 2a | 0.105 (20 min) | 2.76 (14 min) | 55 | 54 |
| N-1 | 1a | 0.028 (18 min) | 0.004 (21 min) | 23 | 24 |
| | 2a | 1.61** | 1.25 | 53 | 55 |
| | 2b | 0.925-0.687 | — | 49.5 | — |
| | 2c | 0.924-0.656 | — | 49 | — |

* Potential transition usually occurred within 150 sec or less. Whenever longer time periods were involved, these are indicated in parentheses.

** This transition required only 53 sec, obviously due to the overrun over the Run 1a current density value. This underscores the importance of relating the critical c.d. to the transition time.

linear Faradaic relationship. With this in mind additional experiments were undertaken in which Ti anodes were subjected to a constant current at a given temperature and for periods ranging from 10 to 20 min. From the resulting weight losses and the known number of coulombs passed, a check on the applicability of Faraday's law was carried out for the six solutions employed in these studies (*see* Table II). The results for solution D-4, containing 11.9% HF, are shown in Fig. 8 in the form of a plot of the rate of dissolution in moles/cm²/sec against the applied c.d. Each point in this plot represents a separate experiment with a new Ti anode. The rate of metal dissolution by local chemical action, which takes place with liberation of hydrogen, gradually

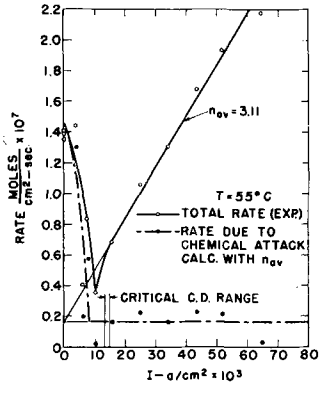


Fig. 8. Rate of Ti anode dissolution vs. c.d. Solution D-4: 11.9% HF, 6.6% $H_2O$, 81.5% ethylene glycol.

decreases until a minimum is reached at a value of 10 ma/cm$^2$. From then on the rate of Ti dissolution follows a linear law increasing with the applied c.d. along a straight line with a slope corresponding to an average number of 3.11 equivalents in Faraday's law. With the value of this slope one can calculate the amount of Ti that should have dissolved if no other process but the anodic dissolution took place. Extrapolation of the straight line portion to the zero current axis gives the value of the residual chemical attack which still persists after the anodic dissolution essentially becomes the major mechanism. The results of such calculations are shown at the bottom of Table II. Using the correction for residual chemical attack, the net total chemical rate can be calculated (as shown in Fig. 8 by a dashed line) with the assumption that the residual chemical rate remains constant once the Ti is anodically polarized. The validity of this assumption is subject to some dispute.

For comparison the range of critical c.d. values obtained with the same solution at the same temperature (55°C) is indicated in Fig. 8. These values generally coincide with the c.d.'s at which the anodic electrochemical dissolution becomes the predominant reaction.

Sometimes (*see* Fig. 9 and 10), the critical c.d. values, derived from polarization runs, were larger than the c.d. at which reversal in the rate of dissolution curve occurred. Such deviations were due to the different techniques used in the two types of experiments. In the study of dissolution rates, a new specimen was used for each point; however, a single anode was employed in a polarization run with the result that the surface of the anode was already roughened when the critical c.d. point was reached. If, as it happened in some runs, the roughening significantly increased the true anode surface area, the observed (apparent) critical c.d. values were larger than normal.

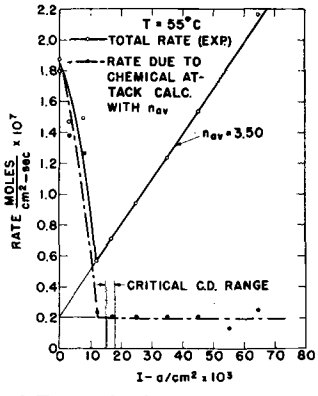


Fig. 9. Rate of Ti anode dissolution vs. c.d. Solution K-2: 11.5% HF, 6.2% $H_2O$, 15% tetrahydrofuran, 67.3% ethylene glycol.

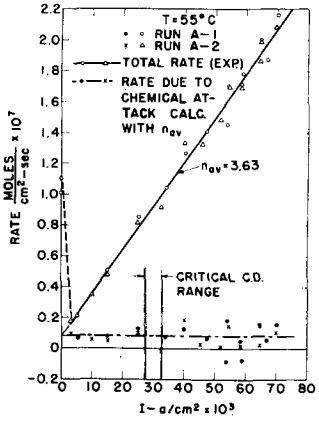


Fig. 10. Rate of Ti anode dissolution vs. c.d. Solution M-5: 12% HF, 10% $H_2O$, 15% dioxane, 63% ethylene glycol.

The experimental value of 3.11 Faradays per mole of metal, shown in Fig. 8, suggests that Ti dissolves in the form of two ions, the +3 and the +4 titanium ions. It is believed that both of these ions complex readily in solution, forming primarily $TiF_6^{-2}$ and $TiF_6^{-3}$. Since the solutions employed in these experiments were essentially saturated with air, all Ti would eventually be oxidized to the +4 state. Indeed, preliminary polarographic studies gave only reduction waves for solution samples taken near the anode at the end of a run, thus indicating the presence of reducible species. Reduction potentials of approximately 0.44 v (half-wave potential vs. the mercury pool) were obtained with diffusion currents suggesting $Ti^{+4}$ concentrations ranging from 3 to 8 millimoles per liter. Reduction of $Ti^{+3}$ would require much higher potentials.

It should not be surprising that Ti can dissolve simultaneously in the +3 and the +4 state. If the values for standard potentials in aqueous solutions given by Latimer (3) can be used as an approximation, one finds that the oxidation potential for the formation of the $TiF_6^{-2}$ ion is 1.19 v and that of the $Ti^{+3}$ (and probably of $TiF_6^{-3}$) formation would be 1.21 v. While these values do not apply directly to the systems employed, they give a fair approximation of the free energy and standard potential relationships that might be involved in the two dissolution reactions. On this basis it can be expected that the actual electrode potentials at which Ti can go into solution in either ionic form are fairly close and the two processes occur simultaneously.

As mentioned above, the extension of the linear portion of the anode dissolution curve to intersection with the zero current intercept should indicate the value of the minimum rate of chemical attack on Ti that still persists, at least at this transition point. In the calculation used for Fig. 8 through 11 this minimum value was assumed to apply throughout up to high c.d.'s. A value of 3.50 Faradays/mole (*see* Fig. 9) would indicate that half of the Ti dissolves in the +3 and the other half in the +4 state. However, if with increasing c.d. this minimum rate of chemical attack should in reality still decrease, then the actual slope of the line (from which $n$ is calculated) as plotted in Fig. 9 or 10 would increase and therefore would decrease the number of Faradays/mole in the direction of the value of 3.0. It can thus be safely said that in most of the cases studied at least half of the Ti went into solution in the +3 state rather than in the +4 state. Attempts to carry out calculations with the assumption that the +2 state is favored showed the latter reaction to be improbable. The standard oxidation potential estimated by Latimer for the formation of the +2 ion is larger

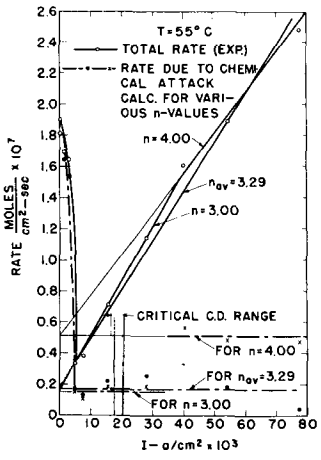


Fig. 11. Rate of Ti anode dissolution vs. c.d. Solution D-8: 18% HF, 6.2% $H_2O$, 75.8% ethylene glycol.

than for the other ions, namely, about 1.63 v. Figure 10 shows results of similar calculations performed for solution M-5, in which two sets of runs are given; the general agreement is found to be quite satisfactory. It should be noted, however, that in this case the c.d. at which inversion of the rate took place was significantly lower than the critical c.d. range determined through the polarization measurements. A similar discrepancy is shown in Fig. 11 for solution D-8.

It is interesting to note that in all cases (for a given solution and temperature) the critical c.d. values were larger than the c.d. at which the inversion of the dissolution rate occurred.

While these discrepancies cannot be accounted for quantitatively, a satisfactory qualitative explanation becomes available when the difference in the procedures in the two types of experiments is considered. In the dissolution rate vs. c.d. studies, a fixed total current was applied to a new, smooth Ti anode and kept constant. Each point on the plot represents a separate specimen. The apparent c.d. value for inversion in the rate found from such a plot is thus fairly close to that of the true c.d. On the other hand, in the polarization experiments complete curves were taken on one anode, which thus underwent progressive suface roughening (to a major or minor extent depending on the number of coulombs passed) with the result that the measured apparent c.d. values were significantly larger than the true current densities. Thus the observed critical (apparent) c.d. value was also larger than the value one would expect on a new, smooth Ti surface. The latter should obviously be smaller and coincide with the c.d. at which inversion of the rate takes place. The soundness of this explanation was confirmed when a polarization curve was taken with a fresh anode at which current was passed for a short time (compare Fig. 8).

For Solution D-8 (Fig. 11) in addition to the average value of $n$, slopes corresponding to $n = 3$ and $n = 4$ were found. This shows that in the lower c.d. range the +3 state is favored while at higher c.d.'s the +4 state is predominant.

Another problem investigated was whether a previous or simultaneous anodic treatment of a Ti specimen affects the rate of chemical dissolution itself. This was of interest because it was thought that passage of current removes the protective oxide from the Ti and facilitates the rate of chemical local action. Experiments carried out with specimens treated at 5-40 ma/cm$^{-2}$ for 1 min and then left in the same electrolyte with no applied current for 10 min indicated that the rate of chemical action was essentially the same as the one obtained without any previous passage of current. Hence the chemical activity of the electrolytes is sufficiently large to remove any $TiO_2$ films which might interfere with the metal dissolution process.

In the solutions discussed above, small amounts of water were used to improve their conductivity. It was thought desirable to investigate the behavior of a completely anhydrous electrolyte in which $H_2SO_4$ (100%) (instead of the water) was used. The ethylene glycol solution of 15% HF and 15% $H_2SO_4$ (N-1 in Tables III and IV) was found to have the

**Table III. Slope of Polarization Curves**

Assuming straight line from critical c.d. value on:

| Solution | Run No. | Ascending $dE/dI$ volt cm² a | Ascending Temp, °C | Descending $dE/dI$ volt cm² a | Descending Temp, °C |
|---|---|---|---|---|---|
| D-4 | 1a | 12.1 | 41 | 12.6 | 43 |
| | 1b | 10.5 | 39 | 11.1 | 38.5 |
| | 2a | 0 | 53.5 | 1.78 | 55 |
| | 2b | 0.7 | 54.5 | 0.024 | 56 |
| D-8 | 1a | 6.4 | 25 | 6.31 | 25 |
| | 1b | 4.5 | 25 | 3.28 | 25 |
| | 2a | 0 | 55 | 2.34 | 54.5 |
| | 2b | 0.5 | 55.5 | 3.32 | 54 |
| K-2 | 1a | 6.3 | 40.5 | 8.00 | 43.5 |
| | 2a | 2.9 | 55.5 | 1.11 | 55 |
| | 2b | 2.4 | 57 | 1.78 | 55.5 |
| M-5 | 1a | 29.8 | 25.5 | 27.3 | 25.5 |
| | 1b | 26.8 | 26 | 32.7 | 24.5 |
| | 2a | 16.8 | 39.5 | 19.7 | 39.5 |
| | 2b | 16.4 | 40 | 17.4 | 39 |
| | 3b | 10.4 | 55.5 | 11.1 | 55.5 |
| K-6 | 1a | 33.7 | 25 | 35.7 | 25 |
| | 2a | 7.37 | 55 | 11.9 | 54 |
| N-1 | 1a | 0 | 23 | 0 | 24 |
| | 2a | 6.30 | 53 | 9.01 | 55 |
| | 2c | 0 | 49 | — | 49 |

**Table IV. Throwing Power in Etching Baths at 55°C**

| | D-4 | D-8 | K-2 | M-5 | K-6 | N-1 |
|---|---|---|---|---|---|---|
| Conductivity, k mhos/cm × $10^3$ | 4.42 | 10.7 | 3.8 | 6.32 | 17.9 | 235 |
| $h_c = k \cdot dE/dI$, volt cm / amp ohm × $10^3$ | 1.72 | 2.70 | 8.2 | 99.8 | 132 | 740 |
| Parameter: $L/h_c$ (dimensionless) ($L$ = width of electrode = 1.52 cm) | 885 | 565 | 186 | 15.2 | 11.5 | 2.05 |
| Dimension, a (average electropolished length near edges, i.e., high c.d. area), at applied average c.d. of 45 ma/cm², microns | 270 | 225 | 50 | 115 | —* | —** |

* The value for this solution was excessively large and difficult to determine. The useful etching range was limited and the pit depths were low (up to 15$\mu$).

** Insufficient and non-uniform etching at 15-25 ma/cm². At 45 ma/cm² complete polishing occurred.

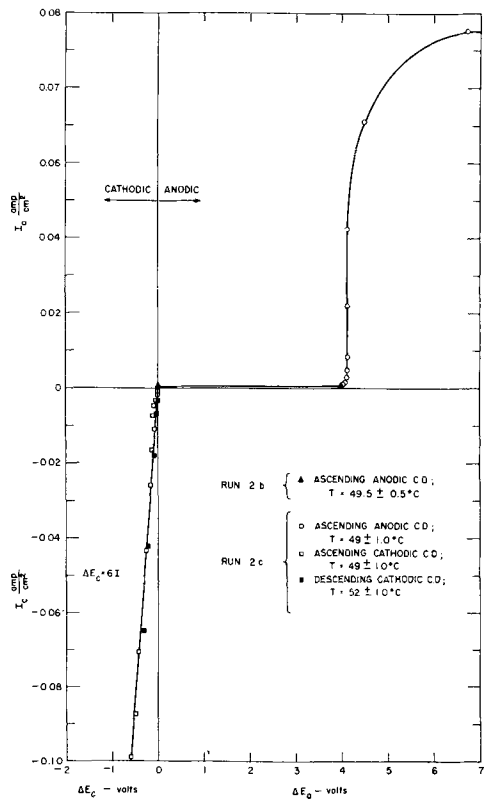


Fig. 12. Net anodic and cathodic polarization of Ti vs. apparent c.d. Solution N-1: 15% HF, 15% $H_2SO_4$, 70% ethylene glycol.

highest conductivity among the solutions studied (0.235 mhos/cm). Both cathodic and anodic polarization studies were carried out on Ti in this system, as shown in Fig. 12. Several interesting features can be noted. The anodic behavior was analogous to that in the other solutions except that Ti polarized much stronger (by about 4.1 v) already at a very low (critical) c.d. (less than 1 ma/cm$^2$). This agreed with the practical observations that Solution N-1 gave poor etching of the Ti anodes and tended to cause electropolishing at c.d. values as low as 20 ma/cm$^2$.

The cathodic polarization of Ti in Solution N-1 was remarkable because the usual logarithmic dependence on the c.d. (as called for by the Tafel equation) was not followed. Instead a perfectly linear relation was found between the cathodic polarization and the applied c.d. From the results shown in Fig. 12, the following relation for the net cathodic polarization is obtained.

$$\Delta E_c = 6\,I \qquad (I)$$

where $\Delta E_c$ = total net cathode polarization, volts, and $I$ = current density, amp/cm$^2$. A similar straight line relationship, although with a different slope value, was observed by Straumanis and co-workers (4) in aqueous solutions of HF. In comparing the behavior of Ti in aqueous solutions of various acids they concluded that the linear dependence takes place if the cathodic metal, Ti, dissolves with hydrogen evolution in the HF acid solution, whereas a logarithmic relation is obtained if it does not dissolve, e.g., in HCl solutions, but behaves as a noble metal. In the nonaqueous solution (N-1) employed in the present study, in addition to the cathodic reduction of hydrogen ($H^+ \rightarrow \frac{1}{2}H_2$), the chemical dissolution of Ti takes place, due to the presence of HF ($Ti + 3H^+ \rightarrow Ti^{+++} + 3/2H_2$), as confirmed by observed weight losses of the electrode.

No cathodic polarization studies were carried out on the solutions containing a small amount of water; however, in view of the behavior of completely aqueous systems (4) and the results of the present study, it is reasonable to expect that linear cathodic polarization curves would result for all of the solutions employed in this study. The slopes of such curves may differ from case to case due to varying HF acid activities.

## Discussion and Conclusions

The anodic behavior of Ti in essentially nonaqueous electrolytes is dominated by the presence of a "critical c.d."—a particular value of the apparent c.d. at which the incidental chemical attack of the metal by the electrolyte is suppressed and the anodic reaction becomes the controlling process. Values of the critical c.d. were found to be usually larger when obtained with ascending, than with descending, applied currents. This "hysteresis" can be explained, at least in part, by: (*a*) increased surface roughness, i.e., lowering of the true current density in the descending runs which followed the ascending runs; and (*b*) the natural tendency to overshoot the applied current in ascending runs and to undershoot in descending runs.

In general, the critical c.d. increased with temperature and the chemical activity of the bath. The latter increased with the content of HF and of water in the glycol base solutions. The combined effect of these two is to increase the thermodynamic activity of the acid in the solution and the rate of metal attack with the resulting evolution of hydrogen according to:

$$Ti + 3H^+ \rightarrow Ti^{+3} + 3/2H_2 \qquad (II)$$

This reaction involves a flow of electrons from the metal to the electrolyte and results in discharge of protons; it is thus essentially a cathodic process. When the critical c.d. value is reached the anodic dissolution of the metal becomes the dominant process according to either:

$$Ti \rightarrow Ti^{+3} + 3\bar{e} \qquad (IIIa)$$

or

$$Ti \rightarrow Ti^{+4} + 4\bar{e} \qquad (IIIb)^3$$

and the cathodic reaction (II) is then suppressed. Since reaction (II) involves evolution of atomic hydrogen capable of severe embrittlement of the Ti, the critical c.d. is also an important concept in practical consideration of anodic cleaning or etching of the metal.

The magnitude of the critical c.d. in anodic polarization runs can be considered a measure of the chemical activity of the bath. Comparison of critical c.d. with the compositions of Solutions D-4, D-8, and H-5 (Table II) indicates that an increase in water content (from about 6.4% to 10%) causes a

[3] The actual form of the metal ions is probably $TiF_6^{-3}$ and $TiF_6^{-2}$.

much larger increase in critical c.d. values than results from an increase of the acid concentration. The presence of cyclic ethers such as dioxane and tetrahydrofuran apparently does not affect the chemical activity of the solutions.

The rapid potential shift at the critical c.d. represents the onset of the polarization of the Ti electrode associated with the normal electrochemical dissolution reaction. This rise in potential must therefore be clearly differentiated from limiting current plateaus which, incidentally, are rarely observed in such a form for anodic metal dissolution processes. In supplementary experiments it was found that by carrying out the reaction to large enough c.d.'s an actual plateau was obtained. The latter corresponded to the discharge of oxygen. However, such reactions could not be studied very satisfactorily because of the extreme amount of heat involved at very high c.d.'s and because of the difficulty of controlling the current and the temperature.

From the studies of the rate of metal dissolution with and without applied current, the rate was found to decrease from the zero current value to a minimum at a c.d. ($I_{min}$) close to the critical c.d. ($I_{crit}$) obtained from anodic polarization studies in the same solution. From the $I_{min}$ value on the rate vs. c.d., plots follow a linear relationship according to Faraday's law. The slopes of the straight line portions correspond to values of $n$ (number of equivalents/mole) ranging from 3.11 to 3.73 (Table II), thus indicating that the relative amounts of $Ti^{+3}$ and $Ti^{+4}$ formed through anode dissolution depend on the composition of the electrolyte.

Through extrapolation of the straight line portions of the rate vs. c.d. plots the minimum residual rates due to chemical attack (persisting simultaneously with the anodic dissolution) were estimated. These residual minimum rates were found to be, by an order of magnitude, smaller than the zero current rate (compare Table II). The persistence of a residual chemical attack rate and its value are important in determining the suitability of a given electrolyte for anodic treatment of Ti from the hydrogen embrittlement point of view.

Generally in electrolytic etching it is important to obtain as uniform a c.d. distribution as possible. Otherwise, in the high c.d. areas near edges and corners, electropolishing takes place while the central area of the specimen is at the optimum etching conditions. For this reason it was interesting to investigate how the various baths compare in respect to the uniformity of the secondary current distribution, i.e., throwing power. In a special set of experiments Ti specimens were etched at several c.d.'s in the various baths and examined metallographically in cross section. The extent of smoothing due to electropolishing near the edges was measured in terms of an electropolished length adjacent to the outer edge. These values are shown as dimension "a" in Table IV. As is known (5, 6) the throwing power of a bath can be best described in terms of a dimensionless parameter ($L/h_c$) which represents a ratio of a characteristic length dimension over the product of the conductivity and the slope of the polarization with respect to the applied current. Using the slope values from Table III the values of the dimensionless parameter were calculated at 55°C for the six solutions under study and compared with the measured electropolished length "a". Inspection shows that with decreasing value of the parameter the electropolished length "a" diminishes as the theory would require. Strictly speaking, throwing power should be evaluated experimentally by means of the Haring method or according to the method of sectioned electrodes (7). However, when out of practical considerations one is concerned with a uniform etching of the surface, direct observation and measurement provide a satisfactory way for correlating uniformity of etching with theory and for determining the suitability of a given etching bath.

The criterion that the parameter, $L/h_c$, should be at a minimum for optimum throwing power cannot be used, of course, without limitations. In some solutions, it is possible to obtain a fairly good secondary current distribution (and low values of $L/h_c$) without a satisfactory etching. Thus Solutions M-5, K-6, and N-1, which showed the lowest values of $L/h_c$ (*see* Table IV) tended to cause electropolishing even at c.d.'s below 45 ma/cm$^2$ (in most cases, dimension "a" could not even be determined). Of the entire group, Solution K-2 was definitely the most suitable for etching purposes on the basis of the most uniform and deep surface roughening. However, Solutions K-6 and N-1 (of low parameter values) were not suitable for etching at all. This demonstrates that the magnitude of the parameter $L/h_c$ is primarily a criterion of the uniformity of the secondary c.d. in a cell and by itself is not sufficient to determine the suitability of a given solution for a desirable anodic process. Its usefulness for prediction of throwing power is thus limited to a range of conditions within which the desirable electrode processes can take place.

The anodic polarization studies for Ti in essentially nonaqueous solutions, coupled with rate studies as a function of c.d., represent a reliable method for determination of the suitability of an electrolyte and of the optimum operational conditions, e.g., temperature and c.d., for anodic etching of Ti without causing a deterimental hydrogen embrittlement of the metal.

Manuscript received July 16, 1956. This paper was prepared for delivery before the Cincinnati Meeting, May 1-5, 1955.

Any discussion of this paper will appear in a Discussion Section to be published in the December 1958 JOURNAL.

## REFERENCES

1. W. H. Colner, M. Feinleib, and J. N. Reding, *This Journal*, **100**, 485 (1953).
2. M. Eisenberg, C. W. Tobias, and C. R. Wilke, *ibid.*, **102**, 415 (1955).
3. W. M. Latimer, "Oxidation Potentials," 2nd ed., p. 269, Prentice Hall, New York (1952).
4. M. E. Straumanis, S. T. Shih, and A. W. Schlechten, *J. Phys. Chem.*, **59**, 317 (1955).
5. C. Wagner, *This Journal*, **98**, 116 (1951).
6. T. P. Hoar and J. N. Agar, *Disc. Faraday Soc.*, **1**, 162 (1947).
7. E. Mantzell, *Z. Elektrochem.*, **39**, 10 (1935).

# Technical Note

## Junction Delineation in Silicon by Gold Chemiplating

S. J. Silverman and D. R. Benn

*Allentown Laboratory, Bell Telephone Laboratories, Inc., Allentown, Pennsylvania*

In recent years there has been an increased demand for a simple, straightforward technique to analyze junctions in Si. These junctions may occur as an uncontrolled series of striations during the growth of single crystals for raw material evaluations. They may also be created purposely by doping during growth or by alloy or diffusion processes on wafers. In the first case one may wish to determine qualitatively the degree of homogeneity in the single crystal. This observation can be used to appraise the extent of removal of *N*-type impurities by observing a cross-sectioned single crystal after refining the raw material. In the other two cases junction depths may be measured and the degree of planarity examined.

Several methods have been used for this type of analysis. Originally one used finely divided particles of $BaTiO_3$ (1) which concentrated along a junction barrier under the influence of an external electric field. A second procedure, highly successful in Ge, has been copper electroplating using a pulsed field in an appropriate electrolytic solution of $CuSO_4$ (2). A third process, perfected by Fuller (3), involves staining of the surface using a suitable combination of $HNO_3$ and HF. A preferential oxidation stains the *P*-type region darker than the *N*-type. The gold chemiplating technique is analogous to the Fuller stain. It is believed that this plating action in the vicinity of the junction is accomplished by preferential reduction, gold first appearing on the *N*-type region relative to a *P* region. The advantages of this technique lie in the relative simplicity of sample preparation and subsequent processing. The resultant pattern shows excellent definition enabling one to detect junctions readily.

Originally, Au chemiplating was used in making ohmic contacts on Si diodes. A discussion of this process is given in detail by Pudvin (4). During the course of plating disks prior to device fabrication, it was noticed that initially Au did not plate uniformly. This observation prompted a more complete investigation, the results of which are herein described.

### Experimental

The sample is prepared by lapping with 600 mesh carborundum powder, rinsing well with deionized water, and drying quickly with an air blast. It is then immersed in the plating solution. Care is taken not to contaminate the surface during handling; otherwise, spurious patterns may develop. The following plating solution is identical to that described by Pudvin (5): (*a*) 10 g $KAu(CN)_2$ (67% Au content); (*b*) 200 g KOH; (c) deionized $H_2O$ for one liter of solution.

In order to obtain reproducible results, both heat and light are necessary. This requirement is easily satisfied by using an infrared lamp. A solution temperature range of 30°-70°C is desirable, depending on the type of junction. The reaction is seriously hampered by the precipitation of KOH at temperatures below 5°C. Those junctions having a less pronounced change in the net impurity concentration, $|N_D - N_A|$, across the junction require higher temperatures and longer exposure times in the solution. After the pattern shows sufficient definition the chemical action is stopped by removing the sample from the bath. It is rinsed immediately with tap water and dried with an air blast.

Various surfaces have been examined for the production of an optimum pattern. Attempts to plate an etched surface have been unsuccessful in that the resulting deposit is neither reproducible nor adherent. Although sharply defined striations appeared, the color contrast is decreased and the pattern is easily obliterated by additional Au which soon plates the surface indiscriminately. A delicately adherent film, however, can be plated on a Linde A polished surface. It is felt that this type of surface preparation is more desirable when investigating thin junction depths of the order of 0.5 mil because of better resolution under a microscope. Such a smoothly abraded surface requires a longer plating time than a coarse one. For purposes of rapid, reproducible analyses, however, 600 mesh carborundum powder is satisfactory. Figure 1 shows individual striations whose widths have been measured to be about 1 mil on a single crystal lapped in the latter manner.

### Mechanism

The over-all process may be classified as a displacement reaction described by the following reaction:

$$2KAu(CN)_2 + 4KOH + Si \rightarrow 2Au + K_2SiO_3 + 4KCN + H_2 + H_2O$$

Although the electrochemical action causes Au to plate on a Si surface according to this equation, it is

Fig. 1. Striations in a single-crystal cross section

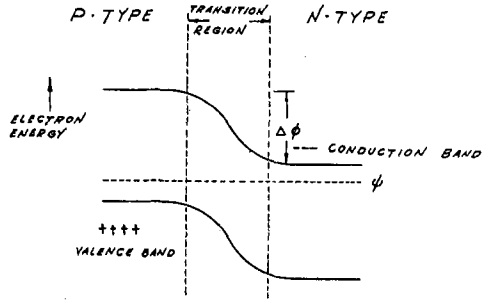


Fig. 2. Potential distribution in a typical PN junction

only in the presence of light that one can obtain consistently predictable results in which the Au plates first on the more negative side of a junction (6). A brief explanation of the possible mechanism responsible for this phenomenon is presented.

If one considers the simplified energy diagram of a typical *P-N* junction, one notes the potential difference associated with the difference in carrier concentration on either side, as indicated in Fig. 2. Psi represents the Fermi level and $\Delta\phi$ is the change in electron energy when going from the *N* region to the *P*. Neglecting possible complications due to surface states, one can, by the following equation, represent $\Delta\phi$ as a function of $p$ and $n$, where $p$ is the density of excess holes in the *P* region; $n$ is the density of excess electrons in the *N* region; and $n_i$ represents the density of intrinsic carriers.

$$\Delta\phi = \phi_n - \phi_p = \frac{KT}{q} \ln \frac{pn}{n_i^2}$$

This equation then represents conditions in the vicinity of the junction which satisfy requirements of thermal equilibrium and charge neutrality throughout the specimen.

If, now, one shines light on the junction, hole-electron pairs are created. The minority carriers in either region diffuse across the transition region under the influence of the built-in field created by $\Delta\phi$. A photovoltage then is created on the surface near the junction. Positive Au ions resulting from dissociation of the $Au(CN)_2^-$ complex in the solution above the surface are attracted to the more negative region and plate on the *N* side. The photovoltage is more pronounced the greater the potential difference across the junction. It has been observed that the rate of plating increases with this difference; the greater the concentration of excess carriers in the *P* and *N* regions, respectively, the faster the Au plates onto the more negative region.

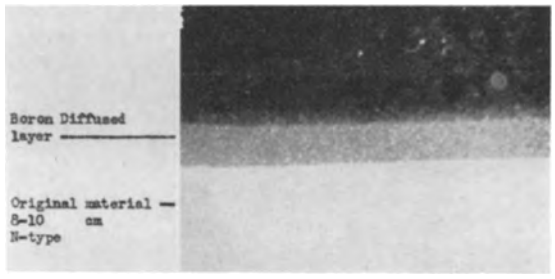


Fig. 3. $NP^+$ junction. Magnification 30X before reduction for publication.

In order to approximate conditions wherein one could vary the deposition rate with the potential difference across a junction, several single conductivity crystals with different *N*-type concentrations were prepared. These were measured by standard two-probe resistivity techniques, cut into samples of equal size, and diffused simultaneously with the same amount of $P^+$ type (boron) diffusant to form the junctions ($^+$ denotes the high concentration in the diffused layer). After diffusion the specimens were prepared by the previously described experimental procedure and simultaneously immersed in the plating solution. Figure 3 is a typical example of an $NP^+$ junction. Measurements were made of the average times required for the Au to become sufficiently thick that the junction became delineated. Table I shows that those specimens with the higher *N*-type concentration and, hence, the larger potential difference across the junction exhibited the faster deposition rate.

An additional experiment illustrated the effect of the potential difference of the junction on the deposition rate. Part of a grown *NP* junction was cut in half. The *N* region and the *P* region were separated and then immersed in the plating solution together with the original junction. The plating times were observed as follows: (*a*) the *N* region of the junction, 30 sec; (*b*) the isolated *N* region, 4 min; (c) the isolated *P* region, 7 min; (*d*) and the *P* region of the junction, 40 min. These results indicated that, although one can plate Au on any Si surface, the presence of a junction can be detected more rapidly, thus making this technique a very positive method of junction delineation.

Table II is a summary of the relative ease in getting positive results for various types of junctions. It can be seen that this technique is applicable to all types of junctions with varying degrees of suc-

**Table I. A comparison of plating times for the same junction types**

| Group | Specimen | Cond. type | $N_D$-$N_A$ in at./cc | Junction type | Avg. plating time, min |
|---|---|---|---|---|---|
| I | A | *N* | $1.1 \times 10^{13}$ | $NP^+$ | 3.8 |
| | B | *N* | $5.2 \times 10^{16}$ | $NP^+$ | 1.8 |
| II | C | *N* | $1.6 \times 10^{14}$ | $NP^+$ | 5.8 |
| | D | *N* | $5.8 \times 10^{16}$ | $NP^+$ | 2.4 |

Table II. A comparison of the plating times for different junction types

| Junction type | Avg. plating time, min | Reproducibility |
|---|---|---|
| $PN$ | ≦ 6 | Excellent |
| $PN^+$ | ≦ 6 | Excellent |
| $NP^+$ | ≦ 6 | Excellent |
| $PN^+P^+$ | ≦ 7 | Good |
| $PP^+$ | ≦ 20 | Good |
| $NP^+N^+$ | ≦120 | Fair |
| $NN^+$ | ≦ 10 | Questionable |

cess. The reason for the poor reproducibility on $NN^+$ is not known. It is possible that surface states so alter the potential difference as to render the effect undetectable.

When one attempts to duplicate these general observations at the same temperature without exposing the samples to the light source, the results are not reproducible. A simple experiment was devised to compare the plating action on a given junction in the light and then in the dark. The same specimens were immersed for equal times in the same plating solution, first in the light and then in the dark. In the light Au always deposited on the more negative regions first. In the dark, however, several of the previously examined junctions plated in the opposite manner, on the $P$-type regions first; whereas, on the other surfaces Au plating was randomized. Therefore, it has been concluded that the photovoltaic effect is essential to obtain results that can be predicted reliably from theory.

Examination of the foregoing results leads one to suggest that Au chemiplating, essentially a reduction process, complements the Fuller etch (3), an oxidation process. Whereas Pudvin (4) has adequately described the chemistry for Au chemiplating in the dark, the present study offers a model to explain the reaction in the presence of light.

## Conclusions

It has been shown that the Au chemiplating technique has been highly successful for simple, rapid qualitative analyses of junctions in Si. The results are permanent until the Au is removed by dissolving or lapping.

## Acknowledgment

The authors are indebted to B. Sawyer, J. F. Pudvin, and other members of the staff for their interest and encouragement in this study.

Manuscript received June 10, 1957. This paper was prepared for delivery before the Cleveland Meeting, Sept. 30-Oct. 4, 1956.

Any discussion of this paper will appear in a Discussion Section to be published in the December 1958 JOURNAL.

## REFERENCES

1. "Transistor Technology," Vol. I, Chap. 12, p. 290, D. VanNostrand Co. (1958).
2. P. R. Camp, *J. Appl. Phys.*, **25**, 459 (1954).
3. C. S. Fuller, *ibid.*, **27**, 553 (1956).
4. J. F. Pudvin, "Transistor Technology," Vol. II, Chap. 15, D. VanNostrand Co. (1958).
5. J. F. Pudvin and J. E. McNamara, Semiconductor Symposium, Electrochemical Society, Pittsburgh, October 1955.
6. D. R. Turner, Private communication.

Technical Review

# A Review of the Measurement of the Quantum Efficiency of Inorganic Phosphors

J. Tregellas-Williams

*Research Laboratories, The General Electric Company, Limited, Wembley, England*

The importance of the knowledge of the quantum efficiency of any phosphor is widely accepted; apart from its theoretical importance in the consideration of the mechanism of the processes involved in luminescence, it is a valuable guide to the luminous efficiency which may be expected from a phosphor when incorporated in a lamp. Discrepancies between the precise values given by various authors for particular phosphors are still rather wide, as are the differences in the methods of measurement. This paper is intended to review both the published data and the methods used, in the light of original work on various phosphors by some of these methods.

The quantum efficiency of a phosphor is defined as the ratio of the number of quanta emitted to the number absorbed; it is thus a measure of the energy loss due to the failure of all absorbed photons to lead to emission. In general, this includes emission in the near infrared, since it is absolute quantum efficiency rather than the quantum efficiency in the visible which is under consideration. When measurements of emitted radiation are taken only in the range of about 4000-7000 Angström units, that is, when the ratio of the number of quanta of visible radiation emitted to the number of quanta absorbed is quoted, a fall in quantum efficiency might be observed when a range of phosphors is examined, if the spectral energy distributions overlap increasingly into the ultraviolet or infrared regions. This observation might imply a change in the process leading to luminescence although, in fact, the quantum efficiency, as defined above, may be unaltered. The value corresponding to the more precise definition may be rather more difficult to measure in some cases, due to the difficulties involved in changing photocells at the ends of the spectrum in optical methods, but this would seem to be overcome when the determination of the non-emitted energy is made thermally, when no differentiation occurs between visible and near visible radiation.

The quantum efficiency of a phosphor may vary both with the wave length (1, 2) and the intensity of the exciting radiation; for example, some phosphors have broad excitation spectra and are strongly excited by both 2537Å and 3650Å radiation, but most phosphors have a comparatively narrow excitation spectrum. For certain sulfide phosphors, the quantum efficiency is reported (2) to be constant at the fundamental absorption frequency, thereafter falling as the anti-Stokes region is entered. Most measurements have been made at the wave lengths of the strong mercury lines, e.g., at 3650Å for sulfides and at 2537Å for halophosphates. A nonlinear dependence of quantum efficiency on the intensity of excitation has been observed in sulfide phosphors (3-6); the effect is more marked when nickel is present and varies with temperature and the concentration of the nickel. The intensity of the source in use is rarely, if ever, quoted when quantum efficiency results are published, however, and in comparing results, one must assume that the conditions of excitation do not differ widely in intensity.

The measurement of quantum efficiency has been carried out in four different ways: by direct optical measurements, from measurements of lamp efficiencies, by comparison with a fluorescent powder having a known quantum efficiency, and by a calorimetric method. These are discussed below.

## Methods

*Direct optical measurement.*—In the method used by Fonda (7), the spectral energy distribution of the phosphor emission under monochromatic radiation was determined by the use of a spectrophotometer, the intensity of the emitted lines being compared with that of a standardized tungsten lamp. The efficiency of excitation, given by the ratio of visible fluorescence energy to the energy of the exciting radiation, was obtained, the fluorescence energy being measured in an integrating sphere with a photovoltaic cell and correcting filter. Conversion to lumens was achieved by calibrating the sphere for light of known wave lengths, and measuring the radiant energy with a thermopile. Values for the quantum yield were obtained for zinc and cadmium silicates, zinc sulfide and zinc cadmium sulfide, but quantum efficiences were not derived in the absence of data on the absorption of the exciting radiation by the phosphor. However, since

$$\text{Quantum yield, } \phi, = \frac{\text{No. of quanta of radiant energy falling on sample}}{\text{No. of quanta of fluorescent energy emitted}}$$

$$\text{and Quantum efficiency } \eta = \frac{\text{No. of quanta emitted by sample}}{\text{No. of quanta absorbed by sample}}$$

$$\eta = 1/\phi \cdot \frac{1}{1-r}$$

where $r$ is the reflection coefficient for exciting light. Values of $1/\phi$ give minimum values of quantum efficiency of 0.77 for zinc silicate:Mn, 0.36 for zinc sulfide:Cu and 0.24 for zinc cadmium sulfide:Cu. A similar method has been used by Kröger (21).

In a later paper (8) the quantum efficiency of magnesium tungstate, measured by a similar method, was reported to be unity. This is higher than other published values from 0.70 to 0.90 (9-11).

The quantum efficiency of zinc sulfide:Cu and zinc silicate:Mn has been determined by Antonov-Romanovsky and Epstein (12); the phosphor occupied the space between two concentric quartz spheres, fitted with ports for the exciting and emitted radiation. The energy of the former was measured by interposing a calibrated thermopile and the latter by a photocell. The energy absorbed was determined by comparing the brightness of a luminescent screen when exposed to the incident radiation with that obtained when the screen was placed at the exit port of the sphere.

The quantum efficiency of ZnS:Cu was found to be a maximum of 0.50 at 3600Å; $Zn_2SiO_4$:Mn had a maximum value of 0.60 from 2200Å to 2600Å, falling to zero at 3100Å. This is lower than the minimum efficiency computed above and may be due to the particular sample used.

This method, which is capable of giving absolute values of quantum efficiency, involves measuremental difficulties and other, more convenient methods have been used for the determination of quantum efficiency.

*Comparison method.*—The method (13) consists of evaluating the quantum output of a phosphor relative to magnesium tungstate by integrating the product of fluorescence energy and wave length over the visible range and expressing this as a percentage of the quantum output of magnesium tungstate obtained under identical conditions. Division of this value by the phosphor absorption for the exciting radiation gives the quantum efficiency related to magnesium tungstate. Since, as mentioned above, a quantum efficiency of unity has been reported for this phosphor (8), the relative quantum efficiency is taken to equal the absolute value.

Results were reported (13) for calcium halophosphate phosphors containing optimum amounts of manganese and antimony and antimony alone: the reported value of 0.85 for the former is somewhat lower than most published values.

The measurements required by this method take much less time than in the previous method, but a disadvantage may lie in the reliance on the value for magnesium tungstate. The method is very useful, however, where series of phosphors are to be compared, although it leads to a "visible quantum efficiency" rather than the absolute quantum efficiency as defined above. A variant of this method has been used by the author for the determination of the quantum efficiency of four standard phosphors. From spectral energy distributions, plots were made of the variation of the energy function $E\lambda$ and the luminosity function $\bar{Ey}$ with wave length and integrating over the wave-length range from 3600Å to 7300Å, thus including the whole spectral emission. Since the measurements were made over a period, values of $E$ were not necessarily consistent; the curves were normalized by determining the brightness of the phosphors relative to magnesium tungstate in a simple powder photometer which employed a circular quartz lamp and selenium cell with correcting filter.

The observed integral $\int E\lambda d\lambda$ is normalized by the application of the factor $F$

$$F = \frac{B}{B_o} \cdot \frac{\int E_o \bar{y} d\lambda}{\int \bar{Ey} d\lambda}$$

where $B$ = brightness and subscript $_o$ refers to $MgWO_4$. Then

$$\text{Q.E.} = F \cdot \frac{\int E\lambda d\lambda}{\int E_o \lambda d\lambda}$$

Values obtained are given in Table I. The fact that the general level of these figures is rather high may be attributable to the assumption of a higher efficiency for magnesium tungstate than is justifiable; the agreement with published data for halophosphate is within ±5% which is the expected variation although, when phosphors are compared under the same conditions, as in normal use, the results might be expected to have a smaller spread, say ±2%. The last column in Table I shows values computed for a quantum efficiency of 0.90 for magnesium tungstate as deduced from lamp efficiency measurements.

If, as seems reasonable, spectral energy distributions can be assumed to vary little with small variations in composition, the relative brightness of a phosphor becomes a useful measure of the quantum efficiency.

*Lamp efficiencies.*—The method of deducing quantum efficiencies of lamp phosphors from the luminous performance of fluorescent lamps was introduced by Thayer and Barnes (9); it is based on correcting the theoretical maximum performance of a lamp for losses incurred in the phosphor during processing and for lamp losses, e.g., at the ends, then relating the observed initial luminous efficiency to

**Table I. Quantum efficiencies by comparison method**

| Phosphor | Q.E. ($MgWO_4$ = 1.0) | Q.E. ($MgWO_4$ = .90) |
|---|---|---|
| Warm white halophosphate | 0.96 | 0.87 |
| Daylight halophosphate | 0.99 | 0.89 |
| Cadmium borate | 0.73 | 0.66 |
| Zinc silicate | 1.02 | 0.92 |

this, the ratio giving the quantum efficiency of the phosphor. The method gave efficiencies of 0.53 and 0.70 for zinc beryllium silicate and magnesium tungstate, respectively. Later, more exhaustive corrections were applied (11), resulting in new values of 0.9 in both cases. This was partially attributed to improved manufacturing techniques. The corrections considered included coating absorption, end losses, utilization of 2537Å radiation, bulb absorption, and the approximate brightness loss on milling; of these, the latter is greatest and varies from lamp to lamp according to the method of lamp manufacture used. The method has been applied to halophosphates and blended phosphors, using a single factor of 75% for the corrections above.

The theoretical efficiency then became

$$\text{lpw} = \frac{K\int \bar{E}\bar{y}d\lambda}{\int E\lambda/2537 \cdot d\lambda} + C$$

where $K = 281$ and includes the above corrections, and $C = 5$ lpw which is the contribution to the output by the visible mercury lines. Quite good agreement with values from the tungstate comparison method were obtained, although this phosphor was found to be only 84% efficient which was thought to be due to a higher loss in lampmaking than in the case of halophosphates.

This method has been used by the author and comparison with the published data is interesting (*see* Table II). It will be seen that there is good agreement for daylight halophosphate, and that for warm white halophosphate, the value obtained approaches more nearly the figure for the comparison method. The use of factor $K$ for phosphors other than halophosphate may cause some error, since the corrections are computed for halophosphates. The value obtained for magnesium tungstate is higher than the previous figure, which is due, perhaps, to the measurement of the quantum output over the whole of the emission spectrum, including, in this case, the ultraviolet. Results obtained by this method for zinc silicate are likely to be somewhat unreliable due to the difficulties in obtaining accurate initial luminous efficiencies with this phosphor.

The method is attractive to the lamp-maker since, when results are compared with those obtained by the comparison method, a direct measure of the efficiency of the lamp manufacturing process is made available; if the values are close, improvements should be sought in the phosphor, but if the efficiency by the comparison method is greater, then improvements should be possible in the lamp making process. For accurate measurements, the method suffers from the disadvantage that some of the corrections accumulated into the factor $K$ apply to a particular phosphor made into one batch of lamps; extension to include other phosphors, even within the same general class, e.g., the halophosphates, may lead to inaccuracies.

*Calorimetric method.*—The measurement of the light absorbed by a layer of phosphor may be made (14) by measuring the temperature change of the layer on irradiation. By repeating the experiment with a similar layer of carbon black, a measure of the total light falling on the phosphor is obtained, which, combined with reflection measurements, makes possible the calculation of the quantum efficiency of a phosphor. Since the exciting and emitted radiation are both determined in terms of heat energy, the quantum output obtained includes radiation emitted in the near visible regions of the spectrum, and the quantum efficiency deduced conforms to the definition in absolute terms given in the introductory paragraphs above.

The apparatus used by Bodo consisted of two copper disks, coated with phosphor and carbon black, respectively, supported on a tray which was thermally isolated from a massive base, in an insulated enclosure, the temperature of the tray being measured with respect to the base by a series of 40 thermocouples. Radiation from germicidal lamps was admitted through a water filter with a quartz window.

A modified version of the microcalorimeter is shown in Fig. 1. A copper disk, D, which is coated with phosphor on one side and blackened on the other, rests on a copper tray, T, which is supported in a cylindrical copper box, B, internally blackened, in an evacuable enclosure, E, by insulators A and G. Cooled water is circulated over the quartz disk, Q, to remove heat radiated by the source. The difference in temperature between the tray and the box is measured by the current flowing in three germanium-copper thermocouples, C, connected in par-

Table II. Quantum efficiency of phosphors from lamp efficiencies

| | Daylight | Warm white | Blue halophosphate | Magnesium tungstate | Cadmium borate | Zinc silicate |
|---|---|---|---|---|---|---|
| QE (G.E.C.) | 92 | 91 | 95 | 90 | 79 | 83 |
| QE (Jerome) | 92 | 86 | | 84 | | |
| QE (Comparison) | 90 | 94 | | 100 | | |
| QE (Bodó) | 84 | | | | 58 | 71 |

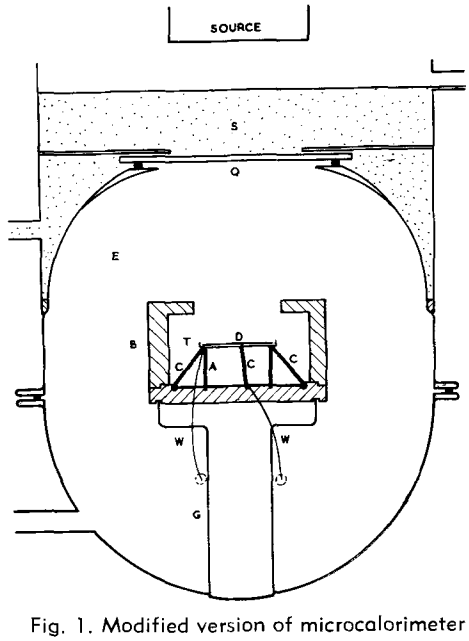


Fig. 1. Modified version of microcalorimeter

allel, which passes out of the enclosure through fine copper wires.

Measurements on phosphors excited by 2537Å radiation are difficult to make since, ideally, a compact monochromatic source of high power is required for imaging onto the phosphor-coated disk. In the practical case, very high sensitivity is required to measure the temperature rise obtained when an efficient phosphor is irradiated by a practical, extended source.

For experiments on long wave u.v. excited phosphors a 125W H.P.M.V. lamp with Woods glass outer bulb, suspended in a reflector very close to the water surface, raises the temperature of the disk and the maximum current flowing in the thermocouples is recorded. Emitted or reflected light leaving the disk is absorbed by the blackened box and spurious heating effects caused by reflection onto the disk are avoided. The disk is then reversed and the procedure repeated. From the maximum values, and from separate reflection measurements, the luminous efficiency and hence the quantum efficiency may be found.

After Bodó, the quantum efficiency $\eta'_2$ uncorrected for absorption by the phosphor of its own radiation is

$$\eta'_2 = \frac{1}{\eta_1}\left[1 - p/b \cdot \frac{(1-r_b)}{(1-r_p)}\right]$$

where $\eta_1$ is the quantum conversion (the ratio of the mean absorbed wave length to the mean emitted wave length); $p$ and $b$, respectively, are the galvanometer readings for phosphor and black surface uppermost; $r_p$ and $r_b$ are the respective reflection coefficients for ultraviolet radiation.

The true quantum efficiency is given by

$$\eta_2 = \eta'_2 \cdot \frac{2}{r+1}$$

(where $r$ is the reflection coefficient of the phosphor for light of the same spectral composition as its emission), which makes correction for the absorption of emitted radiation by the phosphor.

The low quantum efficiency of the sulfide phosphor (Table III) is in agreement with published values; higher efficiencies may be expected for oxygen-dominated phosphors excited by long wave ultraviolet and have been reported for many of this class. The higher quantum efficiency of barium strontium lithium silicate is in accord with results obtained for oxygen-dominated phosphors.

## Conclusion

The relative merits of the methods outlined above vary according to what use is to be made of the information obtained. For fundamental work of high accuracy it seems probable that a painstaking series of measurements by a direct optical method would be preferred, since all the other methods require subsidiary optical measurements. For routine evaluation of phosphors, a rapid and simple method is required and the comparison method would seem to be suitable, provided that the quantum efficiency of the standard phosphor chosen had been measured by as many methods as possible. It is important that the whole spectral emission of the phosphors and standard be measured; otherwise errors may arise due to the energy emitted at the extremes of the spectral energy distribution curves. Magnesium tungstate is perhaps the most suitable primary standard since its characteristics are independent of activator concentration.

The lamp efficiency method is useful for determining the quantum efficiency of a phosphor, but some of the factors involved are variable, even within one class of phosphors, and one should be cautious in extending the method to purely experimental phosphors.

The novel principle applied in the calorimetric method makes it attractive for confirmation of results obtained by more conventional methods and for measurements on phosphors emitting in the near visible regions; the limitations on sensitivity are not easily surmounted especially for very efficient phosphors excited by short u.v. radiation.

Table IV summarizes the reported values of quantum efficiencies for various phosphors. It will be noted that existing figures for sulfide phosphors appear to be variable but that, in general, efficiencies of about 50% appear to be the rule. In oxygen-dominated phosphors the agreement between various authors is much better; figures obtained by the calorimetric method are sometimes at variance with those obtained from more conventional techniques; this may be due to the difference in principle involved.

Much more work remains to be done to clarify the position; the only group where agreement is reasonable is the halophosphates: other phosphors require further study to resolve anomalies.

Table III. Quantum efficiencies by calorimetric method (3650Å)

| | $p$ | $b$ | $r_p$ | $r_b$ | $\eta_1$ | $\eta'_2$ | $r$ | $\eta_2$ |
|---|---|---|---|---|---|---|---|---|
| Zinc cadmium sulfide: Cu | 72 | 129 | 0.12 | 0.01 | 0.61 | 0.61 | 0.95 | 0.63 |
| Barium, strontium lithium silicate Ce, Mn | 75 | 155 | 0.08 | 0.01 | 0.57 | 0.84 | 0.8 | 0.93 |

## Acknowledgment

Acknowledgment is due to J. Fryer, who made the measurements of spectral energy distributions and reflection coefficients.

Manuscript received June 3, 1957. This paper was prepared for delivery before the Washington Meeting, May 12-16, 1957.

Any discussion of this paper will appear in a Discussion Section to be published in the December 1958 JOURNAL.

## REFERENCES

1. R. Nagy, R. W. Wollentin, and C. K. Lui, *J. (and Trans.) Electrochem. Soc.*, **95**, 187 (1949).
2. V. V. Antonov-Romanovsky, *J. phys. radium*, **17**, 694 (1956).
3. N. Riehl, *Z. Tech. Physik.*, **20**, 152 (1939).
4. J. H. Gisoff and F. A. Kröger, *Physica*, **6**, 1101 (1939).
5. N. R. Nail, D. Pearlman, and F. Urbach, Cornell Symposium of Amer. Phys. Soc., p. 190, John Wiley & Sons, Inc., New York (1948).

Table IV. O-Dominated phosphors

| Phosphor | Excited by | Q.E. | Method | Reference |
|---|---|---|---|---|
| Aluminum oxide: Cr | 3650 | 0.35 | | Leverenz 1950 (20) |
| (Ca,Mg) Aluminum oxide: Mn | 3650 | 0.39 | Direct | Kröger 1948 (21) |
| Barium strontium lithium silicate: Ce,Mn | 3650 | 0.93 | Calorimeter | This paper |
| Cadmium borate: Mn | 2537 | 0.58 | Calorimeter | Bodó 1953 (14) |
| | | 0.73 | Comparison | This paper |
| | | 0.79 | Lamp efficiency | This paper |
| | | 0.79 | Lamp efficiency | Shklover 1947 (26) |
| Cadmium silicate: Mn | 2537 | 0.56 | Direct | Fonda 1939 (7) |
| | | 0.55 | Lamp efficiency | Thayer and Barnes (9) |
| Calcium halophosphate: Sb | 2537 | 0.87-0.96 | Comparison | Fonda, 1954 (13) |
| | | 0.95 | Lamp efficiency | This paper |
| : Sb,Mn | 2537 | 0.52-0.76 | Comparison | Fonda, 1954 (13) |
| | | 0.85 | Comparison | Fonda, 1954 (16) |
| (Warm white) | | 0.86 | Lamp efficiency | Jerome, 1953 (11) |
| | | 0.91 | Lamp efficiency | This paper |
| | | 0.94 | Comparison | Jerome, 1953 (11) |
| (Daylight) | | 0.92 | Lamp efficiency | Jerome, 1953 (11) |
| | | 0.92 | Lamp efficiency | This paper |
| | | 0.90 | Comparison | Jerome, 1953 (11) |
| | | 0.84 | Calorimeter | Bodó, 1953 (14) |
| Calcium molybdate: Sm | 2537 | 0.26 | Direct | Botden, 1951 (22) |
| Calcium phosphate: Ce | 2537 | 0.7 | Lamp efficiency | Froelich, 1947 (23) |
| : Tl | 2537 | 0.9 | Lamp efficiency | Froelich, 1947 (23) |
| : Ce,Mn | 2537 | 0.74 | Lamp efficiency | Froelich, 1951 (24) |
| | | 0.65 | Direct | Botden and Kröger, 1948 (17) |
| | | 0.50 | | Ouweltjes, 1952 (15) |
| : Ce,Th | 2537 | ca. 0.8 | Lamp efficiency | Froelich, 1947 (23) |
| Calcium silicate: Pb,Mn | 2537 | 0.55 | Lamp efficiency | Thayer and Barnes, 1939 (9) |
| | | >0.8 | Lamp efficiency | Froelich, 1948 (25) |
| Calcium tungstate: | 2537 | 0.7 | Lamp efficiency | Thayer and Barnes, 1939 (9) |
| | | 0.7 | Direct | Kröger, 1948 (21) |
| : Sm | | 0.28 | Direct | Kröger, 1948 (21) |
| | | 0.58 | Direct | Botden, 1951 (22) |
| Magnesium arsenate: Mn | 2537-3650 | | | |
| | | 0.85 | | Ouweltjes et al, 1952 (19) |
| Magnesium tungstate | 2537 | 0.7 | Lamp efficiency | Thayer and Barnes, 1939 (9) |
| | | 1.0 | Direct | Fonda, 1944 (8) |
| | | 0.9 | Lamp efficiency | Thayer, 1945 (10) |
| | | 0.84 | Lamp efficiency | Jerome, 1953 (11) |
| | | 0.90 | Lamp efficiency | This paper |
| | | 0.82-0.98 | Lamp efficiency | Shklover, 1947 (26) |
| Zinc beryllium silicate: Mn | 2537 | 0.53 | Lamp efficiency | Thayer and Barnes, 1939 (9) |
| | | 0.9 | Lamp efficiency | Thayer, 1945 (10) |
| | | 0.53-0.74 | Lamp efficiency | Shklover, 1947 (26) |
| | | 0.77-0.84 | | Schulman, 1946 (27) |
| Zinc silicate: Mn | 2537 | ≈0.77 | Direct | Fonda, 1939 (7) |
| | | 0.71 | Calorimeter | Bodó, 1953 (14) |
| | | 0.83 | Lamp efficiency | This paper |
| | | 0.92 | Comparison | This paper |
| | | 0.91 | Lamp efficiency | Shklover, 1947 (26) |
| | 2200-2600 | 0.60 | Direct | Antonov-Romanovsky, 1949 (12) |

Sulfide phosphors

| Phosphor | Exciting wave length | Q.E. | Method | References |
|---|---|---|---|---|
| Zinc sulfide: Ag (Hex) | 3650 | 0.90-0.94 | Calorimeter | Gergely, 1956 (18) |
| (Cub) | 3650 | 0.89 | Calorimeter | Gergely, 1956 (18) |
| : Cu | 2200->3650 | 0.50 (Max) at 3600Å | Direct | Antonov-Romanovsky, 1949 (12) |
| | 3600-4000 | 0.6 | Direct | Antonov-Romanovsky, 1956 (2) |
| | 3650 | 0.36 (Min) | Direct | Fonda, 1939 (7) |
| : Zn | 3400 | 0.6 | Direct | Antonov-Romanovsky, 1956 (2) |
| Zinc Cadmium Sulfide | 3650 | 0.24 (Min) | Direct | Fonda, 1939 (7) |
| : Cu | | 0.50 | — | Ouweltjes, 1952 (15) |
| | 2537 | 0.25 | — | Ouweltjes, 1952 (15) |
| | 3650 | 0.63 | Calorimeter | This paper |
| | 3650 | 0.55 | Calorimeter | Gergely, 1956 (18) |

6. N. R. Nail, F. Urbach, and D. Pearlman, *J. Opt. Soc. Amer.*, **39**, 690 (1949).
7. G. R. Fonda, *J. Phys. Chem.*, **43**, 574 (1939).
8. G. R. Fonda, *ibid.*, **48**, 303 (1944).
9. R. N. Thayer and B. T. Barnes, *J. Opt. Soc. Amer.*, **29**, 131 (1939).
10. R. N. Thayer, *Trans. Electrochem. Soc.*, **87**, 413 (1945).
11. C. W. Jerome, *This Journal*, **100**, 586 (1953).
12. V. V. Antonov-Romanovsky and M. T. Epstein, *C. R. Acad. Sci. U.R.S.S.*, **64**, 483 (1949).
13. G. R. Fonda, *Brit. J. Appl. Phys. Suppl.*, **4**, S69 (1954).
14. Z. Bodó, *Acta. Phys. Acad. Sci. Hung.*, **3**, 23 (1953).
15. J. L. Ouweltjes, *Phillips Tech. Rev.*, **13**, 346 (1952).
16. G. R. Fonda, *Brit. J. Appl. Phys. Suppl.*, **4**, S17 (1954).
17. P. J. Botden and F. A. Kröger, *Physica*, **14**, 553 (1948).
18. Gy. Gergely, *J. phys. radium*, **672**, 698 (1956).
19. J. L. Ouweltjes, W. Elenbaas, and K. R. Labberté, *Phillips Tech. Rev.*, **13**, 109 (1952).
20. H. W. Leverenz, "An Introduction to the Luminescence of Solids," John Wiley & Sons, Inc., New York (1950).
21. F. A. Kröger, "Some Aspects of the Luminescence of Solids," Elsevier Publishing Co., New York (1948).
22. P. J. Botden, *Phillips Res. Repts.*, **6**, 425 (1951).
23. H. C. Froelich, *Trans. Electrochem. Soc.*, **91**, 241 (1947).
24. H. C. Froelich, *This Journal*, **98**, 402 (1951).
25. H. C. Froelich, *J. (and Trans.) Electrochem. Soc.*, **93**, 101 (1948).
26. A. A. Shklover, *J. Tech. Phys. (USSR)*, **7**, 1239 (1947).
27. J. H. Schulman, *J. Appl. Phys.*, **17**, 902 (1946).

# An Investigation of Some New Cathode Depolarizer Materials

A. B. Tripler, Jr., and L. D. McGraw

*Electrochemical Engineering Division, Battelle Memorial Institute, Columbus, Ohio*

ABSTRACT

A stable trivalent manganese compound, manganic phosphate, has been found to have good cathode depolarizer properties in strongly acid electrolytes. Manganic phosphate-carbon cathodes of the type used in this work delivered up to 8.5 amp-min/g of $MnPO_4$. This corresponds to over 80% utilization. When coupled with lead in excess $HBF_4$ electrolyte, the watt-minute capacity per gram of $MnPO_4$ was 8. The electrochemical behavior, and charge retention of the cathodes are described. Manganic phosphate and another less stable depolarizer, $BaFeO_4$, furnish cathodes which can be discharged at 200 ma/in.$^3$ (16.4 cc) without severe polarization. The maximum nonpolarizing currents for the $MnPO_4$ are discussed in terms of the surface area of carbon admixed with it to form cathodes. The depolarizing properties of a strongly oxidizing, insoluble organic compound chloranil are reported.

Inorganic compounds containing metals in unusual valence states and organic compounds of high oxidizing power are of interest as potential cathode depolarizers. Tervalent manganese compounds and hexavalent iron compounds have not been investigated in this connection, although they are known to have excellent oxidizing power. A literature search disclosed that manganic orthophosphate might have desirable properties. The material is very slightly soluble in water, and is not attacked by 6*N* HCl. In the case of iron, the most promising choice for a reasonably stable and insoluble compound containing the element in the hexavalent state was barium ferrate. Among the organics, chloranil (tetrachloroquinone) is attractive because of its insolubility and its high oxidation potential (1). Accordingly, these three materials were investigated.

## Materials

*Manganic phosphate.*—Manganic phosphate was successfully prepared chemically, and also by anodic oxidation of the metal. The electrochemical method was devised in the course of this work. The chemical method is a modification of a reported preparation (2). Electrolytic Mn was oxidized anodically in a solution of 7 parts by volume water to 6 parts by volume sirupy phosphoric acid (85 wt % $H_3PO_4$) at 82°-93°C. The temperature was maintained by the electrolytic current between the anode and a platinum cathode. At an apparent anode current density of about 6 amp/in.$^2$ (0.93 amp/cm$^2$), 40 amp-min of current produced 1.06 g $MnPO_4$. This corresponds to about 28% current efficiency. Electrolysis was accompanied by rhythmic polarization of the anode and by current fluctuation. The first product of electrolysis was a pink solution. With the formation of powdery $MnPO_4$, the pink color disappeared and further $MnPO_4$ appeared to form directly at the anode without formation of the intermediate pink manganic solution.

For the chemical preparation, a mixture of 185 ml of sirupy phosphoric acid and 20 g $MnO_2$ was heated slowly to 250°C. The $MnO_2$ reacted to form a purple viscous solution. The temperature of the solution was held at 250°C for ½ hr after which it was lowered to 150°-200°C. Then 200 ml distilled water were added while the solution was stirred. The $MnPO_4$ precipitated as a gray-green powder.

Samples of $MnPO_4$, prepared by the above chemical method, had an equivalent weight of 165 (theor. 150), as determined by titrating the iodine liberated from acid iodide solutions. The apparent density of the material was 3.024 g/cc, as determined by the displacement of water.

The solubility of the salt was measured in various electrolytes by analysis for the total amount of Mn dissolved when 1.000 g of the salt was stirred with 100 ml of the electrolytes for 1 hr at room temperature (24°-27°C). There was no detectable amount of $MnPO_4$ dissolved by 30 wt % $HBF_4$ and only a trace dissolved by 60 wt % $HClO_4$. Water dissolved 0.9 mg Mn/100 ml, and 30 wt % $H_2SO_4$ dissolved 6.1 mg Mn/100 ml. It is possible that these results are not properly called solubilities. They may be only indicative of the rate of hydrolysis of the phosphate.

Because solubility tests had indicated the possibility of hydrolysis of $MnPO_4$, observations were made on the stability of the compound over a range of *p*H. The product retained its gray-green color when suspended in solutions of *p*H below 5.3, changed to tan at *p*H 5.3, and changed to dark brown at *p*H 8.8. At *p*H 10.6 the material was black, indicating a change to $MnO_2$. Possibly the trivalent Mn disproportionates to divalent and tetravalent Mn. In any event, erratic results were expected and were found when the material was used as a depolarizer in electrolytes of *p*H above 5.

*Barium ferrate.*—$BaFeO_4$ was prepared by a double decomposition reaction between sodium ferrate solution and crystalline $Ba(OH)_2 \cdot 8H_2O$. The sodium ferrate solution was prepared by oxidation of ferric nitrate solution with caustic hypochlorite solution (3). The assay of the precipitated $BaFeO_4$ was not high but was raised to 90% or better by washing

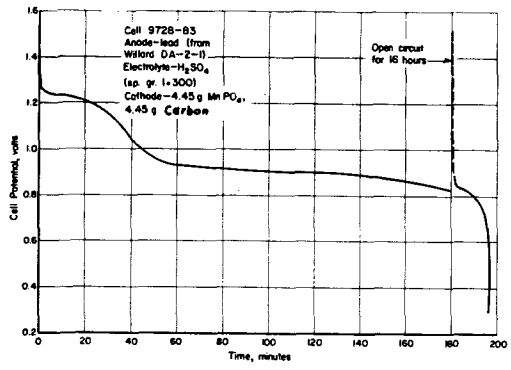


Fig. 1. Discharge characteristics for a cell of the type $Pb/H_2SO_4/MnPO_4$, C drained at 220 ma.

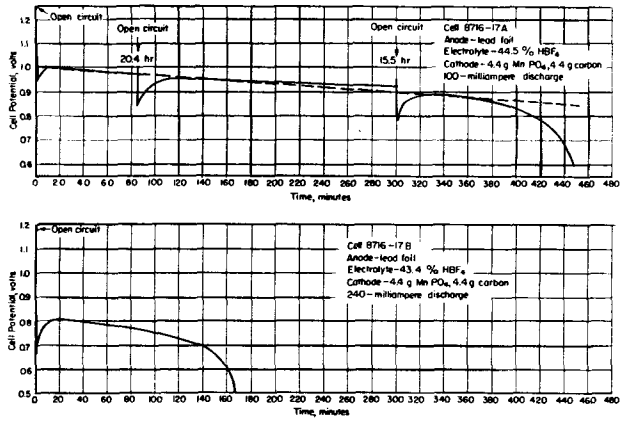


Fig. 2. Discharge characteristics for cells of the type $Pb/HBF_4/MnPO_4$, C.

with glacial acetic acid followed by drying with alcohol and ether.

The solubility of $BaFeO_4$ was measured in 0.18*M* $Ba(OH)_2$ at 27°C. The concentration of ferrate found, 0.0068 g/l, furnished a rough value for the solubility product of $BaFeO_4$, $4.75 \times 10^{-6}$.

*Chloranil.*—Chloranil was used as purchased from Eastman.

## Apparatus

In most cases, the electrochemical behavior of the new materials was studied by discharge of cells containing a large excess of electrolyte, a large unpolarizable anode, and a cathode consisting of an Alundum thimble or a double Dacron bag into which a mixture of depolarizer and acetylene black[1] was packed. A pointed carbon rod was driven into the depolarizer mix to make electrical contact. The Alundum thimble was 19 mm (¾ in.) OD x 90 mm (3½ in.) long, and had a wall thickness of 1.6 mm (1/16 in.). The Dacron bags were made to approximately the same dimensions as the Alundum thimbles. When the cells had to be stored for a period of time, a thin layer of mineral oil was poured on top of the electrolyte. This was effective in preventing evaporation of water. The container for the cell was a Pyrex or polyethylene beaker. The cathodes had a volume of about 1 in.$^3$ (16.4 cc). All cells were discharged at constant current.

[1] Shawinigan Acetylene Black, 100% compressed, Shawinigan Chemicals, Ltd., Montreal, Quebec, Canada.

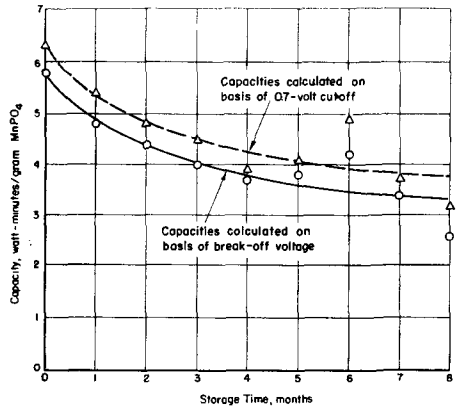


Fig. 3. Decrease in capacity with storage time for $MnPO_4$ cells calculated on basis of break-off voltage and on basis of a 0.7-v cutoff.

## Electrochemical Characteristics of Chemically Prepared Manganic Phosphate

An anode from a commercial lead-acid storage battery (Willard DA-2-1) was coupled with a $MnPO_4$ cathode to determine the characteristics of the new cathode depolarizer in 1.300 sp gr $H_2SO_4$ (nominally 40% by weight). The cell had an open circuit potential of 1.61 v. It was discharged at 220 ma to an 0.8 v cutoff; its characteristics are illustrated in Fig. 1. The cell had a capacity of 37.8 watt-min, or 8.5 watt-min/g $MnPO_4$. The 8.9 amp-min/g capacity of the cathode was 83% of theoretical.

Sheet lead anodes were used in cells for evaluation of the $MnPO_4$-carbon cathodes in a $HBF_4$ electrolyte. Beaker-type cells having 45 wt % $HBF_4$ as electrolyte were assembled and tested. Figure 2 shows typical discharge characteristics at 100 and 240 ma for the 1 in.$^3$ (16.4 cc) cathodes containing 4.4 g $MnPO_4$. Cell 8716-17A had a capacity of 7.8 watt-min/g $MnPO_4$ and Cell 8716-17B had a capacity of 5.5 watt-min/g $MnPO_4$.

The $MnPO_4$ cathode was evaluated for shelf life in $HBF_4$. Figure 3 presents preliminary capacity-storage data. The lower curve of Fig. 3 is based on capacities calculated from end voltages corresponding to sharp breaks in the individual polarization curves. For some cells, sharp breaks were not apparent, so all capacities were recalculated for a 0.7 v cutoff (upper curve). The same conclusions regarding shelf life can be made from either curve. Approximately 50% of the capacity of the cathodes was lost in 8 months in the shelf-life test. At the end of the 8-month period, however, the rate of loss of capacity had been reduced to a low value. The bobbins were 1.9*M* in divalent Mn at the end of an 8-month storage by virtue of the fact that half of the Mn had been reduced. The following calculations illustrate that the cathode potential would be too low to oxidize water when the concentration of divalent Mn reached 1.9*M*, and explain the arrest in the rate of loss of capacity after 8 months.

The measured potential of the manganic-manganous couple is given by Latimer (4):

$$Mn^{+2} = Mn^{+3} + e, E^\circ = 1.51 \text{ v} \qquad (I)$$

From the approximate solubility of $MnPO_4$ (less

Table I. Effect of Divalent Mn on the Retention of Capacity of $MnPO_4$ Cathodes

| Group | Electrolyte | Average open-circuit potential immediately after makeup, v | Average open-circuit potential after 1 month, v | Average capacity immediately after makeup, watt-min/g $MnPO_4$ | Average capacity after 1 month, watt-min/g $MnPO_4$ | Loss in capacity, % |
|---|---|---|---|---|---|---|
| 1 | 50% $HBF_4$ solution | 1.51 | 1.53 | 8.0 | 5.65 | 29 |
| 2 | 29% $HBF_4$ solution | 1.48 | 1.45 | 6.5 | 4.75 | 27 |
| 3 | 29% $HBF_4$ plus 0.01*M* $Mn_3(PO_4)_2$ | 1.48 | 1.48 | 6.9 | 5.0 | 27.5 |
| 4 | 29% $HBF_4$ plus 0.10*M* $Mn_3(PO_4)_2$ | 1.46 | 1.46 | 6.65 | 5.9 | 11 |

than $7 \times 10^{-5}$M), the potential of the $MnPO_4$ electrode must be at least:

$$Mn^{+2} + PO_4^{-3} = MnPO_4 + e, E^\circ = 1.265 \text{ v} \quad \text{(II)}$$

In order to bring the potential of the $MnPO_4$ electrode to 1.229 so it can no longer decompose water, it is necessary to have a $Mn^{+2}$ and $PO_4^{-3}$ concentration of 2.02*M* according to the Nernst equation applied to (II). This corresponds to a 0.67*M* concentration of $Mn_3(PO_4)_2$. This is in good agreement with the fact that the $MnPO_4$ cathodes lost capacity very slowly after 50% was, presumably, reduced to form a 1.9*M* solution of divalent Mn.

Attempts were made to improve the shelf life of the electrode by incorporation of $Mn_3(PO_4)_2$ in the $HBF_4$ electrolyte. From the data of Table I, it appears that manganous phosphate of 0.10*M* concentration has effected a reduction in the rate of loss of capacity. The manganous salt did not appear to be more soluble than 0.1*M*, so no attempts were made to check the complete arrest of loss of capacity expected with 0.67*M* solution.

### *Fabrication of a* Pb-$MnPO_4$ *Dry Cell*

All the experiments described thus far on $MnPO_4$ were performed with excess electrolyte. For practical application, a dry-type cell would have advantages. Therefore, the following experiments were performed.

By using materials immediately at hand, cells were fabricated which did not contain excess electrolyte and yet had fairly good characteristics. The cell construction was patterned after the common LeClanché cell. The anode consisted of a lead-alloy can supplied in the form of an unfilled collapsible tube made from an alloy containing 2¼% Sb, ¼% Sn, with the balance Pb. Whatman filter-paper extraction thimbles which fitted snugly into the lead tubes were used as separators. When wetted with 2 g 50 wt % $HBF_4$, they swelled to make intimate contact with the lead. Approximately 13 g of a mix of $MnPO_4$ and Shawinigan acetylene black was wetted with $HBF_4$ electrolyte and was placed into the lined can. A carbon rod was inserted into the center of the wet mix, and molten Pyseal[2] was poured into the vacant space at the top of the can, thus sealing the cell. The external dimensions of the cells were 1 in. in diameter by 3 in. long (2.5 cm x 7.5 cm).

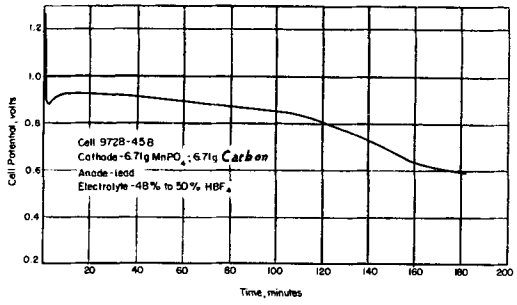


Fig. 4. Discharge characteristics for a $MnPO_4$ dry cell at 220-ma discharge.

A characteristic discharge curve is shown for such a cell in Fig. 4 (220-ma discharge). The initial dip and recovery were present in this dry cell as in the cells with excess electrolyte. The relatively flat discharge was also present. The sharp break-off was not observed, however, in the case of dry cells. For the cell of Fig. 4, the break-off was taken as 110 min. The capacity was 3.2 watt-min/g $MnPO_4$ or 3.6 amp-min/g $MnPO_4$.

The dry cells had virtually no shelf life because of the rapid attack of the electrolyte on the very thin walls of the lead cans (about 5 mils or 0.125 mm thick). It was because of this wall thinness that the discharge tests had to be run shortly after the cells were made. This was of no concern in evaluating the cathode material.

### *Discussion of the Electrochemical Characteristics of* $MnPO_4$

Data on the manganic-manganous system (5) show that, on the basis of a measured exchange current on Pt of $10^{-5}$ amp/cm$^2$, activation polarization should not exceed 30 mv for 200 ma currents on 4 g of Shawinigan Acetylene Black having a true surface area of $2.8 \times 10^6$ cm$^2$. Polarization was much more severe than this in experimental cells. The actual polarization must be due either to concentration polarization owing to slow rate of dissolution of $MnPO_4$ or to the fact that carbon is a poor surface for the electrochemical reaction to take place. The latter alternative corresponds to different exchange currents on platinum and carbon electrodes.

It is concluded that slow dissolution of $MnPO_4$ is responsible for ultimate polarization because polarization is less severe in the electrolytes in which $MnPO_4$ dissolves more rapidly (30% $H_2SO_4$). The over-all effect of slow dissolution of $MnPO_4$ is a form of concentration polarization.

## Electrochemical Characteristics of Barium Ferrate

Barium ferrate cathodes polarize strongly when drained in simple alkaline electrolytes. Polarization is probably due to a coating of insoluble ferric oxide on the ferrate particles. The reduction of hexavalent

[2] A proprietary sealing compound distributed by Fisher Scientific Company, Pittsburgh, Pennsylvania.

Table II. Preliminary Evaluation of $BaFeO_4$ Cathodes as Components of Alkaline Cells

| | Cell I | Cell II | Cell III | Cell IV |
|---|---|---|---|---|
| Anode | Zinc | Zinc | Zinc | Zinc |
| Electrolyte | $K_4P_2O_7$, 40% KOH, 10% | $K_4P_2O_7$, 40% KOH, 10% | $K_4P_2O_7$, 40% | $K_4P_2O_7$, 40% KOH, 20% |
| Cathode | | | | |
| Weight of $BaFeO_4$ (78%), g | 4 | 4 | 4 | 4 |
| Weight of Carbon Black, g | 4 | 4 | 4 | 4 |
| Theoretical capacity, amp-min | 58.5 | 58.5 | 58.5 | 58.5 |
| Open-circuit voltage, v | 1.65 | 1.61 | 1.49 | 1.72 |
| Discharge potential range, v | 1.16-1.10 | 1.00-1.00 | 1.49-1.0 | 1.03-1.00 |
| Discharge current, ma | 100 | 220 | 220 | 220 |
| Measured capacity | | | | |
| amp-min | 18.3 | 11.4 | 3.96 | 14.7 |
| amp-min/g 78.0% $BaFeO_4$ | 4.6 | 2.9 | 1.0 | 3.7 |
| Per Cent utilization of $BaFeO_4$ | 32 | 19.5 | 6.8 | 25 |

iron produces trivalent iron which is insoluble in alkaline media.

Far less polarization of the $BaFeO_4$ cathodes occurred when the alkaline electrolyte contained an agent such as potassium pyrophosphate which could complex and solubilize the reduction products.

Four electrolytes, each having a different ratio of $K_4P_2O_7$ to KOH, were tested in beaker cells having 3 x 3-in. (7.5 x 7.5-cm) zinc foil anodes. The make-up of the cells and their performances are given in Table II.

The importance of free alkali in the electrolyte may be seen from the poor discharge characteristics of Cell III, Table II, and the superior performance of Cell IV, Table II, and Fig. 5. The former cell had no free alkali and the latter had 20% free alkali. The flat discharge curve of the latter cell illustrates how effectively the pyrophosphate prevents cathodic polarization.

### *Stability of* $BaFeO_4$

In lieu of shelf-life tests on cells with $BaFeO_4$ cathodes, quantitative chemical tests were made to determine the stability of $BaFeO_4$ in the alkaline electrolytes. These tests indicated an activated stand life of 24 hr and an unactivated stand of 6 weeks.

The stability of $BaFeO_4$ was not increased by the use of materials such as acetanilide which are used to stabilize other oxidizing agents. A more stable ferrate than $BaFeO_4$ is required for a storageable cell.

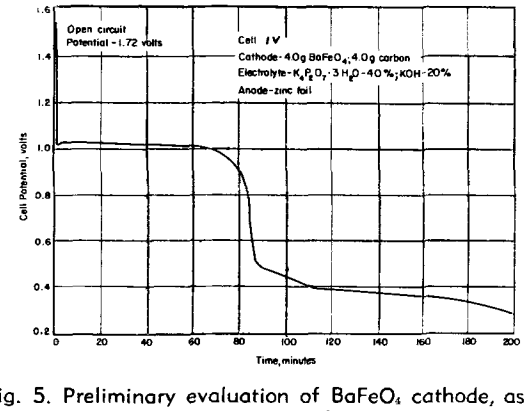


Fig. 5. Preliminary evaluation of $BaFeO_4$ cathode, as component of alkaline cell containing 20% KOH, by discharge at 220 ma (see Table II).

## Electrochemical Characteristics of Chloranil (Tetrachloroquinone)

Chloranil (tetrachloroquinone) is a strong oxidizing agent used as an intermediate in the dye industry. Its oxidation potential is rather high, as indicated by Conant and Fieser (1). Chloranil is stable in oxidizing acids such as sulfuric and nitric acids, and has a low solubility. It has been suggested previously as a cathode depolarizer material (6).

*Evaluation of chloranil as a cathode depolarizer.*— Chloranil was evaluated in preliminary tests as a cathode depolarizer material in beaker-type cells.

The electrolytes in the preliminary tests were 5 wt % KOH, 48 to 50 wt % $HBF_4$, and dry cell electrolyte.[3] They were used with zinc, lead, and zinc anodes, respectively. The open circuit potential of the cells and their discharge capacities at a 100-ma drain rate were measured. The results are shown in Table III.

[3] Weight per cent composition: $NH_4Cl$-26, $ZnCl_2$-8.8, $H_2O$-65.2.

Table III. Evaluation of Cells with Chloranil Cathodes

| | Cell I* | Cell II | Cell III* |
|---|---|---|---|
| Anode | Zinc | Lead | Zinc |
| Electrolyte | KOH, 5% | $HBF_4$, 50% | Dry cell |
| Cathode | | | |
| Weight of chloranil, g | 3.86 | 3.90 | 3.50 |
| Theoretical capacity, amp-min | 50.4 | 50.9 | 45.7 |
| Open-circuit potential, v | 1.50 | 0.99 | 1.19 |
| Discharge potential, v | 1.2-1.15 | 0.85-0.80 | 1.04-0.99 |
| Measured capacity (100-ma drain) | | | |
| amp-min | 20 | 30 | 26 |
| amp-min/g chloranil | 5.1 | 7.8 | 7.4 |
| watt-min/g chloranil | 5.9 | 6.4 | 6.1 |

* The tabulated data on these cells are only approximations. Cell I was not discharged to its break-off point. The test was discontinued because the chloranil was obviously hydrolyzing and dissolving in the alkaline electrolyte. Cell III discharged erratically because the anode did not corrode uniformly.

This quinone was electrochemically active in alkaline solution (Cell I). However, it hydrolyzed in the alkali so it would not have good shelf-life. Chloranil was also electrochemically active in highly and moderately acid electrolytes (Cells II and III).

The cell containing dry cell electrolyte (III) did not discharge at a steady potential until the zinc anode was activated by treatment with 1 to 1 (Vol) HCl. Prior to such treatment, three zinc foil anodes failed by corrosion at the solution level, one prior to discharge of the cell and two during discharge of the cell. Also, when the fresh anodes were placed in the electrolyte, they corroded at only a few spots during discharge. This accounts for the fluctuations in potential during discharge until the last anode (activated by HCl) was added. It is characteristic of anodic inhibitors to aggravate the local corrosion (7) when they are not present in sufficient concentration.

In spite of the unexpected behavior of the chloranil toward the anodes of these cells, the two electrochemical systems in acid electrolytes showed inclination toward flat discharge curves, good capacity, and resistance to anode corrosion during open-circuit storage. Taking all the observations on these preliminary tests into consideration, chloranil offers interesting prospects as a cathode depolarizer and an anodic corrosion inhibitor for zinc.

**Acknowledgment**

Financial support for this program from the Power Sources Branch of Signal Corps Engineering Laboratories under Contract No. DA-36-039-SC-42682 is gratefully acknowledged. The authors wish to express their thanks to the sponsoring agency for permission to publish portions of the work done under that contract.

Manuscript received March 18, 1957. This paper was prepared for delivery before the Buffalo Meeting, Oct. 6-10, 1957.

Any discussion of this paper will appear in a Discussion Section to be published in the December 1958 JOURNAL.

REFERENCES

1. J. B. Conant and L. F. Fieser, *J. Am. Chem. Soc.*, **45**, 2207 (1923).
2. J. W. Mellor, "A Comprehensive Treatise on Inorganic and Theoretical Chemistry," Longmans, Green and Co., London, Vol. **12**, Chapter LXIV, p. 429 (1932).
3. *Ibid.*, Vol. **12**, Chapter LXVI, pp. 931 and 934.
4. W. M. Latimer, "Oxidation Potentials," 2nd ed., p. 237, Prentice-Hall, Inc., New York (1952).
5. K. Vetter and G. Manecke, *Z. physik., Chem.*, **195**, 270 (1950).
6. W. O. Arsem, U. S. Pat. 2,306,927, Dec. 29, 1942.
7. U. R. Evans, "Metallic Corrosion, Passivity and Protection," 2nd ed., p. 545, Longmans, Green and Co., London (1946).

# Kinetics of Reaction of Steel with Hydrogen Sulfide-Hydrogen Mixtures

**Andrew Dravnieks and Carl H. Samans**

*Engineering Research Department, Standard Oil Company (Indiana), Whiting, Indiana*

ABSTRACT

The kinetics of the reaction of steel with pure hydrogen sulfide at 250°-500°C may be interpreted in terms of consecutive linear and parabolic rates. In hydrogen sulfide-hydrogen mixtures similar reactions exist, but the reaction rate decreases as the thermodynamic equilibrium line ($Fe + H_2S \rightleftharpoons FeS + H_2$) is approached, in a manner which is approximately proportional to the decrease in the thermodynamic driving force. Increase of pressure up to 20 atmospheres increases the reaction rate by a fractional power of the pressure. In the presence of traces of oxygen, the linear rate component is minimized. The observed kinetics can be explained in terms of three steps: adsorption, rate of formation of diffusing species, and diffusion.

Iron reacts readily with sulfur and with sulfur compounds to form iron sulfides. The kinetics of the reaction of low carbon steel with elemental S has been investigated (1-4) and has been found to obey a parabolic law, with a deviation in long-range corrosion vs. time curves, believed to be due to microcracking of the scale. In the reaction of low carbon steel with $H_2S$, the reaction mechanism is complicated by the presence of hydrogen, since hydrogen is one of the reaction products and must leave the surface of the sulfide scale before the reaction can proceed. These complications are even more pronounced in the reaction of low carbon steel with mixtures of $H_2S$ and $H_2$. The thermodynamics of the steel-hydrogen sulfide reaction has been clarified by the recent work of Rosenqvist (5), among others. The kinetics has been studied by many investigators (6-14) for various sets of conditions. Sorell and Hoyt (15) have summarized this work well and have made some correlations. However, the field has not yet been explored over a sufficient range of experimentally comparable conditions to obtain a

clear picture of the rate processes involved. The present work was undertaken to amend this shortcoming.

## Experimental Methods

Several experimental techniques were used.

For experiments with pure $H_2S$-$H_2$ mixtures, electrolytic hydrogen was passed through a commercial catalyst cartridge to change oxygen to water, and through a silica gel tower to remove water vapor.

To introduce $H_2S$ at various concentrations, three methods were used: (*A*) for the higher concentration, metered quantities of $H_2S$ and hydrogen were taken from gas cylinders; (*B*) for the lower concentrations, purified hydrogen was bubbled through molten sulfur at a constant temperature to charge it with a constant amount of sulfur vapor; the resulting hot mixture of hydrogen and sulfur vapor then was passed through an alundum column at 510°-540°C to react the sulfur vapor completely with the hydrogen, producing a corresponding amount of $H_2S$ (5); (*C*) for still lower concentrations, the most dilute mixture prepared by the above molten sulfur procedure was diluted still further with pure hydrogen. In most cases, continuous mixing was employed. For experiments at higher pressures, $H_2S$ and $H_2$ were premixed in a steel gas cylinder.[1]

Reaction vs. time curves were obtained by two methods: (*a*) electrical resistance measurements on corroding strips of metals (1, 16); and (*b*) weight-gain measurements with specimens hung on a quartz spring balance suspension in the flowing gas mixture in a furnace. In addition, rates of reaction were measured by the conventional weight-loss method.

In all cases, the linear flow of the gas mixture past the specimens was maintained sufficiently high, of the order of 150-450 cm/min, to prevent any slowdown of corrosion by exhaustion of the $H_2S$ in the mixture. The drag on the specimens hung on the quartz spring was found to produce a lift of 0.10-0.15 mg. To minimize the effect of the error caused by the drag, gas flow velocities were kept constant. Most samples were run at least in duplicate.

Figure 1 represents the equipment used for tests at atmospheric pressures. For the continuous weighing method, a quartz spring was used instead of the specimen holder shown. Figure 2 represents the equipment used for tests at pressures up to 21 atm. The end of the reaction tube was modified to carry sealed electrodes so that measurements of the change in electrical resistance could be made on the specimens, for continuous studies of the reaction.

Temperatures constant to ±2°C were maintained by means of heated Al cylinders with holes for inserting the reaction tubes. Specimens were made of low carbon steel with a nominal percentage composition of: C 0.06; Mn 0.37; P 0.018; S 0.031; Si 0.002; Cu 0.02; Ni 0.06; Sn 0.25. Annealing seemed

[1] It was found that oxygen had to be removed in making such mixtures. In the presence of oxygen, which occurs in small quantities in commercial bottled hydrogen, $H_2S$ at low levels slowly disappeared from the mixture, apparently by reaction with the oxygen to form water and sulfur. Also, to accelerate mixing of the $H_2S$ and the hydrogen in the cylinder, the cylinders were laid flat and lifted in succession several times. Without this procedure, an interval of 2-3 days was required to homogenize the contents of the cylinder.

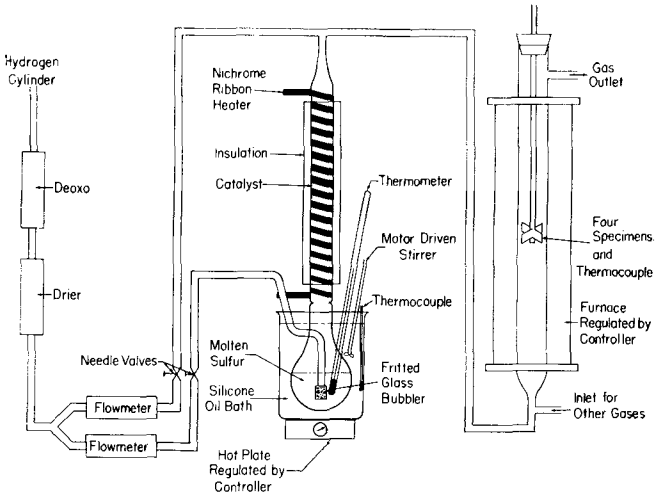


Fig. 1. Experimental setup for corrosion studies in $H_2S/H_2$ mixtures at atmospheric pressures.

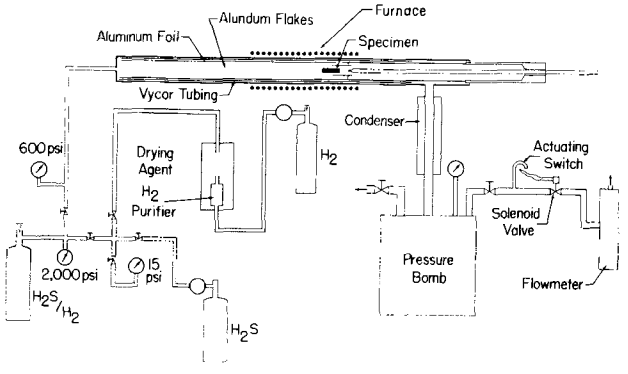


Fig. 2. Experimental setup for corrosion studies in naphtha, $H_2S$, and hydrogen mixtures at elevated pressures.

to have no pronounced influence on the reaction rates. However, to avoid possible strain effects, annealed specimens (1 hr at 650°C, in vacuum) were used in obtaining all reaction vs. time curves.

To obtain weight losses on single specimens, the sulfide layer was pealed off mechanically and the sulfide still adhering to the specimen was dissolved by pickling in inhibited 15% HCl for 2 min. With the commercial pickling inhibitor used, the weight loss by acid attack of the steel itself was found to be less than 0.1 mg per specimen.

Gases were analyzed by passing a metered quantity through a bubbler containing aqueous NaOH, and titrating the resultant $Na_2S$ potentiometrically with ammoniacal $AgNO_3$ solution, using a silver sulfide-coated silver wire and a calomel cell as electrodes.

## Results and Discussion

### *Initial Reaction Kinetics*

Figure 3 gives the initial range for a number of typical time-sulfidization reaction curves. Data were obtained in pure $H_2S$ and in $H_2S$-$H_2$ mixtures, at atmospheric pressures and at elevated pressures. In all cases, the reaction rates decrease with time. This decrease, however, is slower than if only the parabolic law were obeyed, indicating that a more complex form of corrosion reaction is involved.

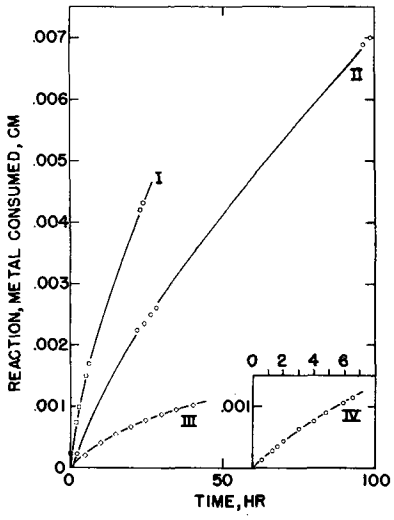


Fig. 3. Initial range of typical reaction curves of steel with $H_2S$ and with $H_2S/H_2$ mixtures.

| Curve | Temp, °C | Pressure atm. | $H_2S/H_2$ | Technique |
|---|---|---|---|---|
| I | 530 | 1 | pure $H_2S$ | Cont. weighing |
| II | 450 | 1 | $7.5 \times 10^{-4}$ | Elect. resist. |
| III | 250 | 1 | pure $H_2S$ | Elect. resist. |
| IV | 530 | 21 | $8 \times 10^{-4}$ | Elect. resist. |

The data were analyzed by the graphic-kinetic technique of Fischbeck (17) and Wagner (18). According to this method, the corrosion reaction is assumed to proceed by two consecutive reaction steps: a linear interface reaction, followed by a diffusion through the scale.

Each of these reaction steps has its own "resistivity" defined as $1/k_1$ for the interface reaction, where $k_1$ is a linear reaction constant, and as $y/k_2$ for the diffusion step, where $k_2$ is the parabolic rate constant, and $y$ is the thickness of the reaction product scale through which the diffusion occurs. The total reaction rate is then:

$$\frac{dy}{dt} = \frac{C}{1/k_1 + y/k_2} \qquad (I)$$

where $C$ is a constant. Integrated and rearranged, this becomes

$$\frac{t}{y} = \frac{1}{Ck_1} + \frac{y}{2Ck_2} \qquad (II)$$

Consequently, a plot of $t/y$ vs. $y$ should be linear, with $1/Ck_1$ as the intercept, and $1/2Ck_2$ as the slope. Such a plot of typical data is given in Fig. 4. Thus, the initial kinetics may be explained in terms of two consecutive rate-limiting steps: a linear step, presumably limited by an interface reaction; and a parabolic step, probably controlled by the rate of diffusion of the reactants through the sulfide layer.

If a small amount of $O_2$ is introduced into the $H_2S$-$H_2$ mixture just ahead of the specimen exposure tube, it reacts readily with the $H_2S$ to form sulfur vapor and water vapor. The reaction rate of sulfur with $H_2$ is relatively slow under these conditions so that the sulfur vapor is carried through the experimental equipment and has been observed to deposit on the cooler parts beyond the furnace. In the presence of this sulfur vapor the reaction becomes faster (Fig. 5) but the linear component, characterized by the intercept on the time/reaction axis of the Fischbeck-Wagner plot, either becomes quite small or disappears. The addition of water vapor alone did not influence the rate of sulfide scale growth. The previously found parabolic rate curves for the corrosion of steel in molten sulfur (1, 2), similarly, did not show any intercepts on the time/reaction axis. Thus the sulfidization of Fe follows effects similar to those found for the sulfidization of Ag (19) where the parabolic law is observed principally in the Ag-S system, but a linear law is followed in the Ag-$H_2S$ system.

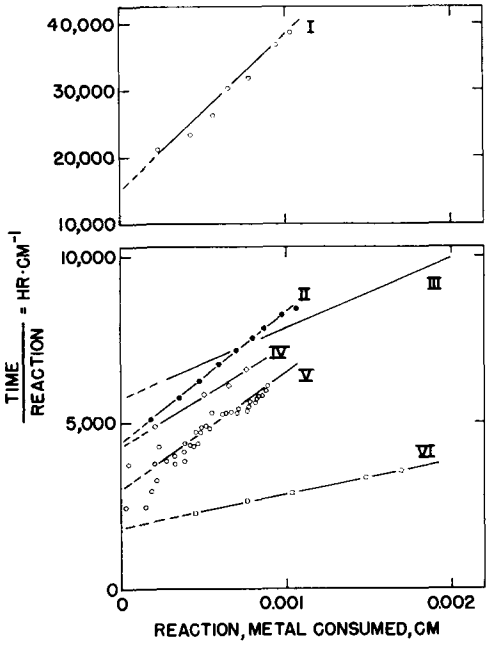


Fig. 4. Graphic kinetic analysis of reaction curves, initial range.

| Curve | Temp, °C | $H_2S/H_2$ | Pressure, atm. |
|---|---|---|---|
| I | 250 | Pure $H_2S$ | 1 |
| II | 315 | Pure $H_2S$ | 1 |
| III | 450 | $8 \times 10^{-4}$ | 1* |
| IV | 480 | Pure $H_2S$ | 1 |
| V | 530 | $5.5 \times 10^{-4}$ | 21 |
| VI | 530 | Pure $H_2S$ | 1 |

* Curve III is an extrapolation of Curve II from Fig. 5.

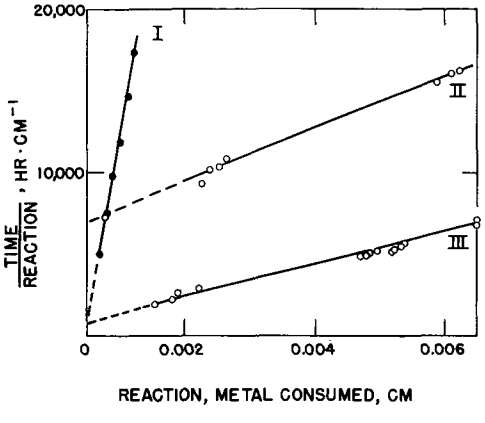


Fig. 5. Graphic kinetic analysis of the influence of oxygen on the reaction of steel with $H_2S$ mixtures. Curve I, steel in molten sulfur ot 325°C; II, steel in $H_2S/H_2 = 8 \times 10^{-4}$ at 450°C; III, same as II but with 0.1% $O_2$ added to the gas stream ahead of the specimen.

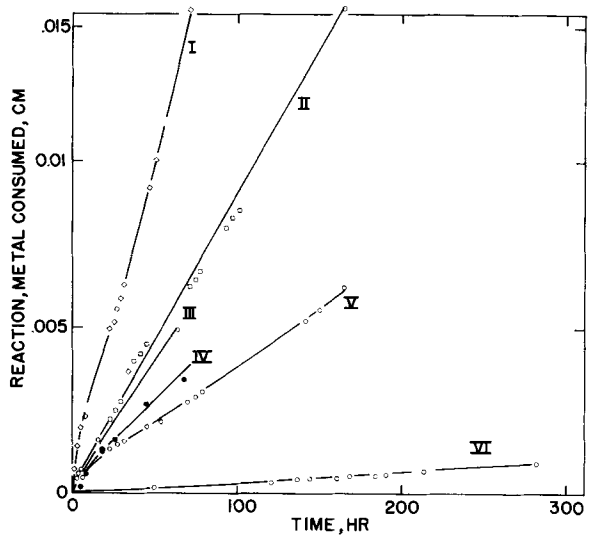


Fig. 6. Typical long-time reaction curves—I, pure $H_2S$, 530°C; II, pure $H_2S$, 480°C; III, $H_2S/H_2 = 0.33$, 440°C; IV, $H_2S/H_2 = 1 \times 10^{-3}$, 520°C (weight loss on separate specimens); V, pure $H_2S$, 380°C; VI, $H_2S/H_2 = 512 \times 10^{-4}$, 370°C. All pressures atmospheric.

These observations indicate, therefore, that the surface of the sulfide scale is the most likely site of the rate-limiting linear step. It must be noted that in a certain fraction of the experiments the parabolic element was poorly defined.

### *Long-Time Reaction Kinetics*

The initial kinetics discussed above held only for a limited period, up to an extent of reaction corresponding approximately to a metal loss in thickness of $2\text{-}3 \times 10^{-3}$ cm. Typical long-time reaction curves are shown in Fig. 6. As a first approximation, these may be considered to be linear after a short initial stage. Thus, the initial linear-parabolic kinetics cannot be used with validity to extrapolate to reactions of long duration.

The long-time average rates were approximately those established at the time when the usual linear-parabolic kinetics broke down.

*Variation of reaction rates with hydrogen sulfide: hydrogen ratio and temperature.*—To obtain a complete quantitative picture of the separate variation of the linear and the parabolic rates with the $H_2S:H_2$ ratio and with temperature is a formidable experimental task. Most of the work was conducted with 16 to 18-hr exposures and was interpreted as an average rate of metal consumption in centimeters per hour. This simplification still permitted some generalization of the kinetics.

Figure 7 gives isokinetic curves for a field covering a wide range of temperatures and $H_2S:H_2$ ratios. The two solid straight lines represent the thermodynamic existence limits for FeS and for $FeS_2$ taken from the work of Rosenqvist (5). Between these lines, FeS of varying composition is stable thermodynamically. Three of the isothermal cross sections, which served to prepare the plot, are shown in Fig. 8. Toward the low concentration end, these curves were drawn so as to be consistent with the thermodynamic data of Rosenqvist (5). The decrease in the reaction rates as the limit of existence of the FeS phase is approached is clear. Therefore, at a constant $H_2S:H_2$ ratio, the reaction rates first increase and then rather abruptly decrease with increasing temperature. From the data of Fig. 7, a rough estimate of the over-all activation energy (Arrhenius) gave a value of 19.3 kcal/mole, at constant $H_2S:H_2$ ratio and in the ratio-temperature range sufficiently far away from the equilibrium line to give a linear relationship.

*Effect of oxygen on reaction rates.*—Table I illustrates the effect of $O_2$ on the rates of reaction at various locations of the plot of Fig. 7. Oxygen, introduced into the $H_2S$-$H_2$ mixtures, forms elemental sulfur as discussed previously. This accelerates the sulfidization rates, and initiates and supports sulfidic attack in a range where, in the absence of $O_2$, i.e., from $H_2S$-$H_2$ mixtures alone, the formation of FeS is impossible thermodynamically. The presence of elemental sulfur vapor accounts for this effect.

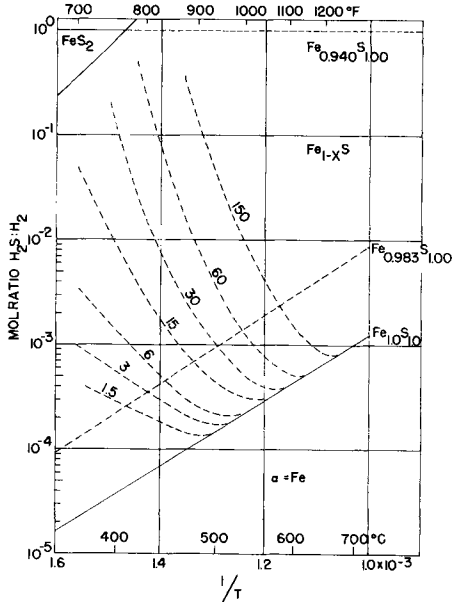


Fig. 7. Isokinetic curves and phase existence limits for the reaction of steel with $H_2S$ mixtures at atmospheric pressure. The existence fields of Fe, $Fe_{1-x}S$, and $FeS_2$ are from the work of Rosenqvist (4). The numbers on the isokinetic curves indicate rates of reaction in units of $cm \cdot 10^{-6} \cdot hr^{-1}$ of metal consumed; 1.5 $cm \cdot 10^{-6} \cdot hr^{-1}$ corresponds approximately to 0.005 ipy.

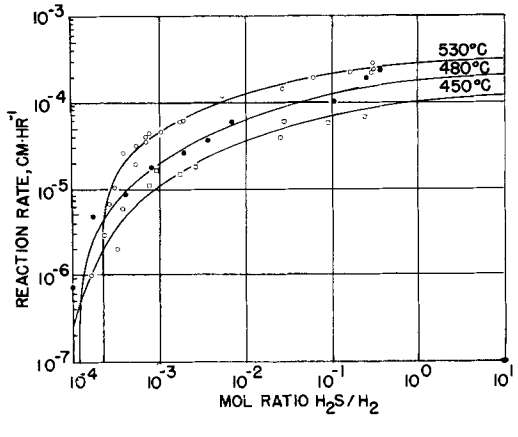


Fig. 8. Three typical experimental isothermal cross sections of Fig. 7.

Table I. Influence of Oxygen on Rates of Reaction of Steel with Hydrogen Sulfide-Hydrogen Mixtures

| Temp, °C | Mole ratio, $H_2S:H_2$ | Reaction rate, $cm \cdot 10^{-6} \cdot hr^{-1}$ | |
|---|---|---|---|
| | | No $O_2$ | 0.1 vol. % $O_2$ added |
| 330 | $7.5 \times 10^{-4}$ | 17 | 30 |
| 375 | $7.5 \times 10^{-4}$ | 17 | 100 |
| 560 | $11 \times 10^{-4}$ | 48 | 440 |
| 530 | $1 \times 10^{-4}$ | 0 | 88 |
| 530 | $0.5 \times 10^{-4}$ | 0 | 30 |

A quantitative evaluation of the $O_2$ effect was not attempted since this would require detailed knowledge of the rates of reaction of $H_2S$ with $O_2$ and of S with $H_2$ in the flowing gas mixture in order to determine the specific concentrations of S at the point of specimen exposure.

*Variation of reaction rates with pressure.*—Increasing the total pressure without changing the $H_2S:H_2$ ratio accelerates the sulfidization rate of steel, as shown in Fig. 14. This acceleration, however, is less than directly proportional to the total pressure. The data available, if analyzed by the Fischbeck-Wagner method (cf. Fig. 4), indicate that the rate change occurs principally by acceleration of the linear surface reaction, and that the parabolic rate constant is relatively unchanged.

Small amounts of $O_2$, if not excluded meticulously, distort the pressure-sulfidization rate relationship considerably, since concurrently with the partial oxidation of $H_2S$ to water vapor and S, which promotes the sulfidization rate, there proceeds the slower reaction of S with $H_2$ to form $H_2S$. Under these conditions increased pressure, by causing a longer exposure of the flowing gas mixture to high temperatures in the experimental equipment, occasionally decreases the concentration of free S vapor at the specimen site. Consequently, the rate of sulfidization of steel at a certain site may even decrease with pressure if $O_2$ is not eliminated meticulously.

*Physical structure of sulfidic scale.*—Metallographic examination of the sulfidic scales shows that they may consist of several layers. However, during the early stages there appears to be only two layers, as illustrated in Fig. 9. Layer A, next to the metal, is dense and fine grained. Layer B, between layer A and the gas, is composed predominantly of coarse columnar grains which have their longest dimension roughly normal to the scale surface. The grains in layer B are separated by relatively large pores which extend from layer A to the free surface. During the early stages, layer A is approximately one-half to one-third as thick as layer B.

After the reaction is more advanced, evidence has been noted in some specimens of a third layer, C, lying between the other two. This layer also is porous and relatively coarsely crystalline although not so much so as layer B. Layer C may be nothing more than a variation of layer B. The ratio of the thickness of layer A to that of layer B (and C) decreases as the reaction advances. Apparently the outer layer increases in thickness whereas the thickness of layer A approaches a limiting value.

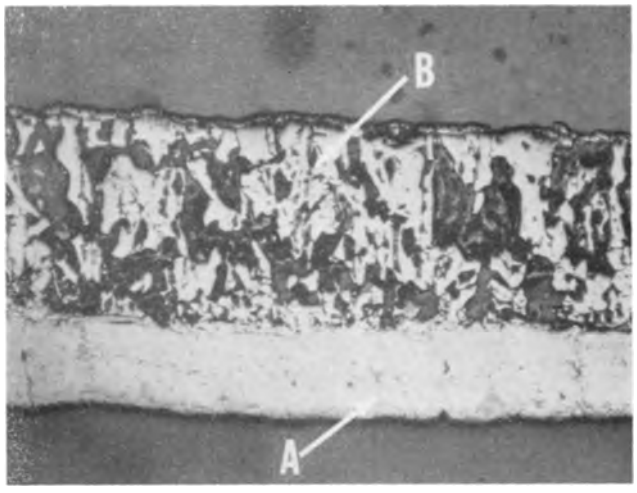


Fig. 9a. Cross section through FeS scale on iron showing the two main layers. Layer A (lower) is the dense, fine crystalline material formed next to the metal. Layer B (upper) is the porous, columnar-crystalline material found between the dense layer and the gas. Photograph taken with sensitive tint plate (X100) so pores and cavities appear gray.

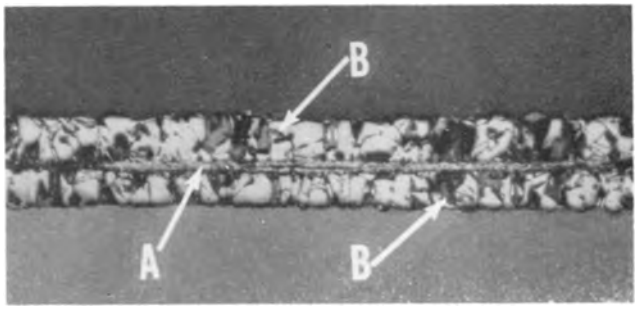


Fig. 9b. Structure of cross section of thin specimen of low carbon steel after 18-hr exposure to pure $H_2S$ at 530°C. The metal has been completely consumed and the two layers, (A) dense fine-crystalline and (B) porous coarsely crystalline, appear on either side of the center line. Photograph taken with sensitive tint plate (X100) so pores and cavities appear gray.

The striking difference in the texture of layer A, as compared with that of layers B and C, points to different modes of nucleation and growth. Both layers were FeS.

## Mechanism of the Sulfidization of Steel

The following sequence of reaction steps seems to be the simplest consistent with the experimental observations; there may be other possibilities.

*Step 1. Surface adsorption:* $(H_2S)_{gas} \rightleftharpoons (H_2S)_{adsorbed}$ This step may be assumed to be fast, so that an equilibrium exists essentially between the adsorbed and the gaseous $H_2S$, at least at the higher temperatures. The surface concentration of $H_2S$ molecules then is determined (through an adsorption isotherm) by the partial pressure of $H_2S$ in the gas phase.

*Step 2. Formation of diffusing species at the gas-iron sulfide interface:* According to the usually accepted concepts (3, 20) the diffusing species in FeS is a cation vacancy. For such a mechanism, the re-

action for Step 2 may be written, at least for a sulfur-rich composition range:

$$H_2S_{adsorbed} + 2Fe^{++}{}_{scale} + 2S^{=}{}_{scale} \rightarrow H_2 + 2Fe^{+++}{}_{scale} + V_c + 3S^{=}{}_{scale}$$

where $V_c$ denotes a cation vacancy. For this step, the rate may be written

$$\frac{dV_c}{dt} = \dot{y} = a[H_2S_{adsorbed}] \qquad (III)$$

where $a$ is a constant and $y$ is the amount of reaction in terms of metal thickness consumed, and is assumed to be, as the simplest form, of first order with respect to the adsorbed $H_2S$. Hauffe and Pfeiffer (21, 22) used a similar concept in explaining the linear law found in the oxidation of Fe by $CO_2$-CO mixtures.[2] If the diffusing species is of a different kind, Eq. (III) still would apply since it is not committed to any definite species.

*Step 3. Diffusion through the sulfide scale*: Cation vacancy diffusion, with $Fe^{++}$ ions moving from the metal through the scale to the gas-scale interface, is the usually accepted mechanism (4). However, it is not possible to explain the coexistence of two distinctly different types of layers in the scale by means of this particular diffusion mechanism alone. Also it cannot explain the long-range linear rates satisfactorily. Hence it is postulated that two diffusion mechanism act:

(*a*) In the porous columnar layer, B, the diffusion, so far as the FeS phase is concerned, is by the mechanism of cation vacancies. Of course, gaseous diffusion in the pores also occurs.

(*b*) In the dense fine-crystalline layer, A, the diffusing species is different; sulfur ions or atoms may be the diffusing species there. Thus, layer A would grow at the metal-scale interface, filling the zone of metal consumption (24), whereas layer B would grow at the gas-scale interface, by diffusion of $Fe^{++}$ ions through vacancies from the boundary between A and B to this interface.

The diffusion limitation resides mainly in layer A.

*Excursus on support for the second postulate in Step 3.*—The second postulate given above may be supported by several arguments.

The total driving force of the reaction is

$$G = +RT \log \frac{r}{r_o} \qquad (IV)$$

where $r$ is the $H_2S$:$H_2$ ratio for the given experimental conditions, and $r_o$ is the same ratio for the equilibrium conditions at the temperature, $T$, in the FeS/Fe system, and $R$ is the gas constant. This driving force is applied across the sum of all of the reaction steps. Thus, a fraction of this driving force may be assigned to each of the consecutive steps. Since, as further discussion will show, Step 2 probably is the principal rate-limiting step, it may use up most of the driving force available, leaving only a relatively small remainder to be applied across the sulfide phase proper. This would place the composition of the growing sulfide film, layer A, in the immediate vicinity of the FeS/Fe equilibrium line shown in Fig. 7. Now:

(*A*) If the surface reaction, Step 2, uses up most of the driving force for the reaction, the composition of the dense layer, while it is growing, is close to that of FeS in equilibrium with Fe; thus, very few cation vacancies exist, and another diffusing species could take over easily.

(*B*) FeS in equilibrium with Fe appears to have a slight S deficiency (5) thus indicating the possible existence of some mode of disorder other than the cation vacancy.

(*C*) Pfeiffer and Ilschner (25) report considerable S mobility in the FeS scale. The mobility of anions in a divalent oxide (MgO) also is apparent from the work by Winters and Houghton (26, 27).

The first argument hinges on a large decrease in driving force across the surface reaction step. Figure 10 compares the data of Hauffe and Rahmel (3), obtained at 10 mm S vapor pressure, with the parabolic rate constant derived from the slopes of curves, such as those in Fig. 4, for the reaction of steel with pure $H_2S$. The chemical potential, that is, the partial molar free energy, of S in pure $H_2S$ at 530°C corresponds approximately to a sulfur ($S_2$) vapor pressure of 5 mm. The dashed line (III) in Fig. 10 shows the present experimental data curve after correction to a constant $S_2$ pressure of 5 mm by means of the $p^{1/4}$ relation found by Hauffe and Rahmel. The extrapolated curve of Hauffe and Rahmel would predict a very much higher reaction rate. Hence, sulfide film growth in pure $H_2S$ occurs as if the chemical potential of S on the gas phase side of the sulfide film were very much lower than that which actually exists in the gas phase. In other words, the outer layer of the sulfide film "sees" a much lower chemical potential of S than that which

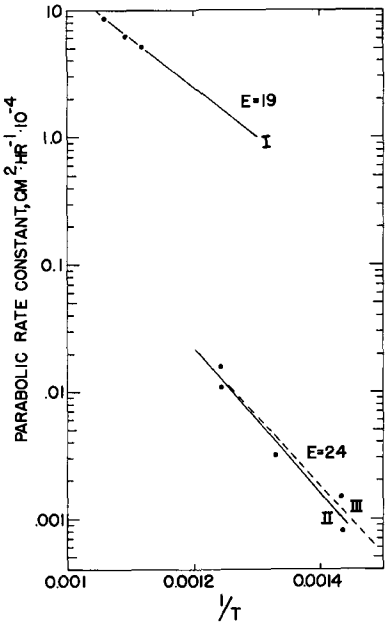


Fig. 10. Comparison of parabolic rate constants in S vapor and in $H_2S$. Curve I, Hauffe and Rahmel's results in S vapor at $P_{S_2}$ = 10 mm; II, present results in pure $H_2S$; III, curve II corrected to one (4.7 mm) equivalent S pressure.

[2] Wagner (23) has proposed a dissociation of adsorbed $CO_2$ into CO and adsorbed O or $O^{=}$ as the rate-limiting step in this case; such treatment also leads to a correct mathematical form.

exists in the gas, a stituation also observed, for example, in the sulfidization of Ag by $H_2S$ (19). This indicates a sizable decrease in the available driving force in Step 2. At the same time, the activation energies (Arrhenius) are roughly the same, viz., 19-24 kcal/mole.

A cursory x-ray examination of the sulfidic scale both for layer A and for layer B supported the thesis that the composition of the scale, even that formed by the sulfidization of steel in pure $H_2S$, indeed corresponds to FeS with a composition in the vicinity of the Fe-FeS equilibrium line. The following x-ray findings may be cited: (*a*) Even when $H_2S$ alone was used, no $FeS_2$ was found. (*b*) Interplanar spacings, computed from planes with Miller indices: (100), (002), (101), and (102), which could be identified beyond doubt by comparison with the data of Hagg and Sucksdorff (20), were within a fraction of a per cent the same for scale formed in pure $H_2S$ and for scale formed in a mixture in which the $H_2S$:$H_2$ ratio was $1.1 \times 10^{-3}$. This indicates that, even in pure $H_2S$, the scale does not contain more than a per cent or so of surplus S. (c) Besides the basic cell spacings, extra lines were present in the pattern of the scale formed in pure $H_2S$; some of the lines approximating Hagg's superlattice lines. According to Hagg, the existence of a superlattice is confined to the compositions between $Fe_1S_1$ and approximately $Fe_{0.95}S_1$; this is to be compared with compositions of the order of $Fe_{0.85}S_1$ which are thermodynamically possible in pure $H_2S$. (*d*) The lines in the x-ray patterns were not broad, and thus were more representative of a homogenous narrow range of composition than of a wide continuous composition range.

Aside from lines which could be clearly identified with Hagg's data, other lines were present, and some of Hagg's lines were absent. This might be the result of certain minor changes in the lattice cells of FeS and indicates that a more thorough x-ray investigation of the reaction products would aid in explaining the diffusion mechanisms.

Similarly, the scale formed in pure $H_2S$ contained only very slightly magnetic or nonmagnetic fractions as tested by a hand magnet. The fractions described as "magnetic" did not exceed, by a crude comparison, on gently crushed scale, the paramagnetic susceptibility which was observed for $MnCl_2$ ($\kappa = 107 \times 10^{-6}$ cgs e.m. units). This would place the scale composition in the range close to stoichiometric FeS on the basis of Haraldsen's data (28, 29).

*Step 4. Reaction at the metal-sulfide interface*: There appears to be no immediate need to consider the reaction at the metal-sulfide interface to be rate-limiting. In the light of the postulates discussed under Step 3, this reaction may be one of sulfur atoms in the FeS lattice forming bonds with the iron atoms on the metal surface and then gradually penetrating into the metal.

*Step 5. Processes in the contact zone between layers A and B*: Occurrences in the contact zone between layers A and B also should be considered. With the above postulates, in this zone the transport process changes from that of S diffusion to that of Fe diffusion by means of cation vacancies. As sulfur atoms move through layer A toward the metal, iron ions, becoming surplus in the outer part of layer A, migrate through the columnar crystals of layer B toward the gas-scale interface. The cation diffusion coefficient should increase in this zone quite rapidly as the cation vacancies become more numerous. Formation of cation vacancies also causes a lattice shrinkage (Fig. 11).

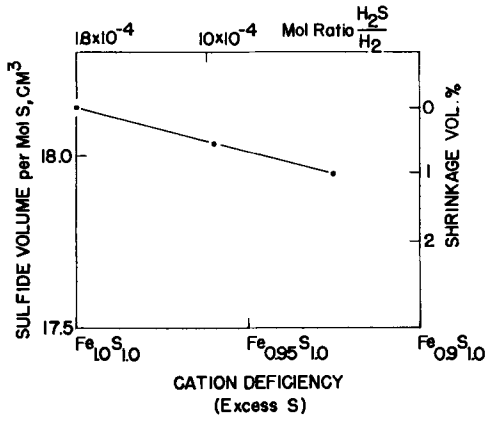


Fig. 11. Shrinkage of FeS volume with $H_2S/H_2$ mole ratio and with S content at 530°C (based on data of Hagg and Sucksdorff and of Rosenqvist).

Layer B should become prominent as soon as the increasing retardation of the diffusion rate through the scale by Step 3 brings the chemical potential of S in the outer regions of layer A into the existence range of cation vacancies. Accordingly, the long-time linear growth rates should become established as soon as layer A reaches a certain thickness. This is in at least qualitative agreement with the observations.

In the presence of Cr, e.g., in a 5% Cr-½% Mo steel, the linear long-range rate becomes established at a much smaller scale thickness. On the basis of a vacancy diffusion mechanism, the incorporation of $Cr^{+++}$ ions into the FeS lattice will generate vacancies, since $Cr^{+++}$ can act like $Fe^{+++}$ in the equation shown in Step 2. Therefore, layer B can start forming at a lower chemical potential of S.

*Cavity stabilization in Layer B.*—The persistence of cavities in layer B is readily understood. The cavities communicate with the gas phase, and $H_2S$ is consumed and $H_2$ generated in the cavities, thereby decreasing the $H_2S$:$H_2$ ratio. The cavity cannot close, since, if arrival of fresh $H_2S$ is hindered, the gas phase in the cavity rapidly approaches the FeS/Fe equilibrium line and becomes less and less sulfidizing. On specimens prepared in S vapor, cavities were not observed.

On the basis of this and previous considerations, the composition of FeS in the columnar layer should be quite uniform, with a relatively small cation vacancy concentration gradient over the thickness of the layer.

### *Influence of Hydrogen Sulfide:Hydrogen Ratio and of Pressure*

The kinetic relations are explainable on the basis of the above steps. The sum of the resistances im-

posed by Steps 2 and 3 determine the sulfide film growth rate. Under the conditions for which the kinetics is mixed linear-parabolic it may be considered, by analogy with Ohm's law (Fischbeck), that:

$$\dot{y} = \frac{E}{R_1 + R_2} \qquad (V)$$

where $\dot{y}$ is the reaction rate, $E$ is a constant proportional to the driving force for the reaction, $R_1$ is the resistance (proportional to $1/k_1$) imposed by the gas-scale interface reaction, and $R_2$ is the resistance (proportional to $y/k_2$) imposed by the diffusion step. The reaction resistances, of course, are proportional to the reciprocals of the reaction rate constants. The resistance $R_1$ is dependent only on the surface concentration of adsorbed $H_2S$ [Eq. (III)], but the resistance $R_2$ is proportional to the amount of reaction, $y$, since the length of the diffusion paths increases with $y$.

Once layer A has attained a substantially constant thickness as was observed in the case of the long-time rates, the resistance $R_2$ is limited predominantly by the diffusion in layer A; $R_2$ then becomes substantially constant. Under these conditions, Eq. (V) may be combined with Eq. (III) and (IV) and rewritten:

$$\dot{y} = \frac{A \cdot RT \log (r/r_o)}{\frac{B}{(H_2S_{adsorbed})} + C}$$

$$\approx \text{const} \cdot (H_2S_{adsorbed}) \cdot (\log r/r_o) \qquad (VI)$$

where $A$, $B$, and $C$ are constants. For a constant temperature, the logarithmic term now gives the driving force, and the rate of the linear reaction has been made proportional to, i.e., the resistance is made inversely proportional to, the surface concentration of adsorbed $H_2S$. This new reaction rate, however, will be smaller than that controlled by the linear component alone, as was the case during the initial stages of the growth of layer A. This is consistent with the results obtained.

To test the compliance of the experimental data with the above mathematical form (VI), three curves of Fig. 4 are replotted in Fig. 12 in terms of log $r/r_o$ as the abscissa, without any correction for the adsorption isotherms. At 530°C the plot is almost linear and, thus, the reaction rate is almost directly proportional to the driving force. For the two other temperatures, the lines are curved. These two, however, can be straightened out, cf. Fig. 13, by correcting for the adsorption isotherm. A Freundlich type function:

$$s = \text{const} \cdot p^{1/n} \qquad (VII)$$

has been used, with $n = 10$, to account for adsorption. This magnitude of $n$ suggests a relatively high coverage of the surface with adsorbed $H_2S$.

The increase in the reaction rate with pressure at constant $H_2S$:$H_2$ ratio, shown in Fig. 14 (a) on a logarithmic scale, replots well in terms of the Langmuir adsorption isotherm, cf. Fig. 14 (b). The Langmuir isotherm was not used in making the correction in Fig. 13 because of its more complex form.

Thus, the variation of the reaction rate with the $H_2S$:$H_2$ ratio, and with the pressure, follows kinetics explainable in terms of adsorption, surface reaction, and diffusion steps. The short-time rate has a linear component, explained by the reaction of adsorbed $H_2S$ to form a diffusing species at the gas-scale interface, and a parabolic component, ex-

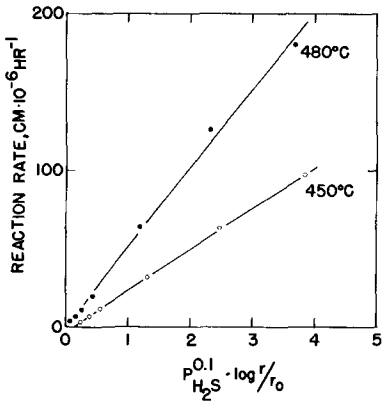


Fig. 13. Data of Fig. 12 modified by introduction of adsorption term.

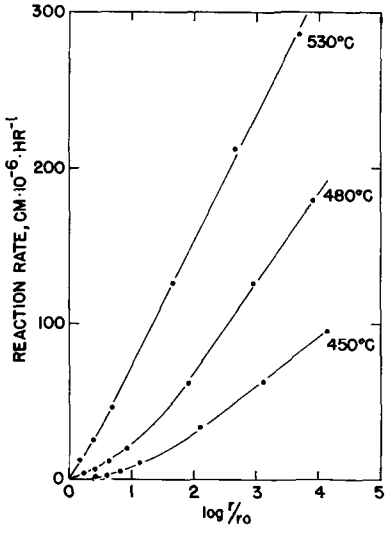


Fig. 12. Variation of reaction rate with driving force

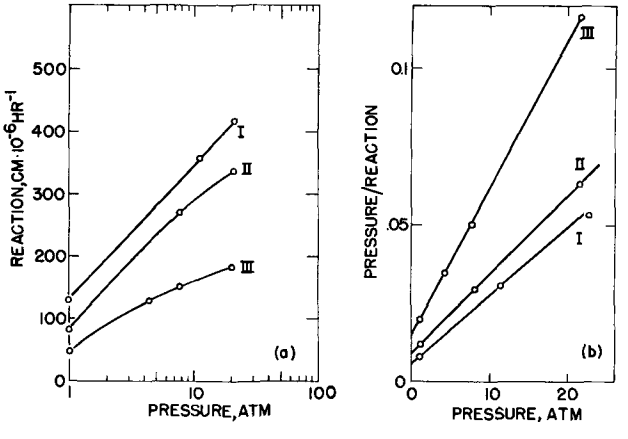


Fig. 14. Variation of the reaction rates at 530°C with total pressure, at a constant $H_2S/H_2$ mole ratio. (a) (left): semilogarithmic plot; (b) (right): plot for an isotherm of the Langmuir type. $H_2S/H_2$ mole ratios: curve I, 22 x $10^{-4}$; II, 11 x $10^{-4}$; III, 8 x $10^{-4}$.

plained by the diffusion resistance of a growing dense layer of FeS. The long-time linear rate may be explained, at least qualitatively, by the coexistence of two diffusion mechanisms and the consequent formation of two layers—a porous one which presents no diffusion barrier and a dense one which becomes substantially constant in thickness and thus presents substantially a constant diffusion barrier.

### Acknowledgment

The authors are indebted to Bernard Ostrofsky for his x-ray interpretations. The experimental help of Cecelia Husen and Gerald Van Hees is gratefully acknowledged.

Manuscript received Dec. 10, 1956. This paper was prepared for delivery before the Cleveland Meeting Sept. 30-Oct. 4, 1956.

Any discussion of this paper will appear in a Discussion Section to be published in the December 1958 JOURNAL.

REFERENCES

1. A. Dravnieks, *Ind. Eng. Chem.*, **43**, 2897 (1951).
2. A. Dravnieks, *This Journal*, **102**, 435 (1955).
3. K. Hauffe and A. Rahmel, *Z. Physik. Chem.*, **199**, 152 (1951).
4. R. A. Meussner and C. E. Birchenall, Metallurgy Report No. 7, Princeton University (1956).
5. T. Rosenqvist, *J. Iron Steel Inst. London*, **176**, 37 (1954).
6. M. Farber and D. M. Ehrenberg, *This Journal*, **99**, 427 (1952).
7. R. E. Wilson and W. H. Bahlke, *Ind. Eng. Chem.*, **17**, 355 (1925).
8. E. Dietrich, *Chem. Fabrik*, **6**, 25 (1933).
9. E. Dietrich, *ibid.*, **10**, 145 (1937).
10. C. F. Prutton, D. Turnbull, and G. Dlouhy, *Ind. Eng. Chem.*, **37**, 1092 (1945).
11. E. B. Backensto, R. D. Drew, and C. C. Stapleford, *Corrosion*, **12**, 22 (1956).
12. E. B. Backensto, R. D. Drew, R. W. Manuel, and J. W. Sjoberg, *Corrosion*, **12**, 235 (1956).
13. C. Phillips, Jr., "High Temperature Sulfide Corrosion in Catalytic Reforming of Light Naphthas," presented at South Central Region meeting of N.A.C.E., San Antonio, Texas (Oct. 1956).
14. F. J. Bruns, "Effect of Hot $H_2S$ Environments on Various Metals," *ibid.*
15. G. Sorell and W. B. Hoyt, *Corrosion*, **12**, 213 (1956).
16. A. Dravnieks, *J. Am. Chem. Soc.*, **72**, 3761 (1950).
17. K. Fischbeck, L. Neundenbel, and F. Salzer, *Z. Elektrochem.*, **40**, 517 (1934).
18. C. Wagner and K. Grunewald, *Z. Physik. Chem.*, **B40**, 455 (1938); cf. W. Jost, "Diffusion in Solids," p. 353, Academic Press, Inc., New York (1952).
19. H. Reinhold and H. Seidel, *Z. Elektrochem.*, **41**, 499 (1953).
20. G. Hägg and I. Z. Sucksdorff, *Z. Physik. Chem.*, **B22**, 444 (1933).
21. K. Hauffe and H. Pfeiffer, *Z. Elektrochem.*, **56**, 390 (1952).
22. K. Hauffe and H. Pfeiffer, *Z. Metallkunde*, **44**, 27 (1953).
23. C. Wagner, Private communication.
24. A. Dravnieks and H. J. McDonald, *J. (and Trans.) Electrochem. Soc.*, **94**, 139 (1948).
25. H. Pfeiffer and B. Ilschner, *Z. Elektrochem.*, **60**, 424 (1956).
26. E. R. S. Winters and G. Houghton, *Nature*, **164**, 1130 (1949).
27. E. R. S. Winters and G. Houghton, "Mass Spectrometry," p. 127, The Institute of Petroleum, London (1952).
28. H. Haraldsen, *Z. anorg. u. allgem. Chem.*, **246**, 169, 195 (1941).
29. P. W. Selwood, "Magnetochemistry," p. 246, Interscience Publishers, New York (1943).

# Corrosion Inhibition by Organic Amines

**Helmut Kaesche[1] and Norman Hackerman**

*Department of Chemistry, The University of Texas, Austin, Texas*

ABSTRACT

The corrosion of pure iron in 1*N* HCl is discussed in terms of the theory of mixed potentials and the theory is applied to inhibition by organic compounds. Corrosion rates with and without inhibition by aniline, several aniline derivatives, and alkylamines were determined by cathodic polarization measurements as well as by colorimetric analysis of the solution. It is shown that all compounds show a maximum inhibitor efficiency at a concentration of approximately 0.1 mole/l, that with one exception all are cathodic as well as anodic inhibitors, and that in most cases they are predominantly anodic inhibitors. An interpretation of the data on cathodic inhibition is suggested on the basis of the assumption of a uniform metal surface and uniform adsorption. The interpretation of anodic inhibition is found to be difficult due to a lack of satisfactory experimental data.

There is little question that organic compounds acting as inhibitors of wet corrosion do so by forming an adsorbed layer at the metal-solution interface. There is still considerable difference of opinion as to the details of the mechanism of inhibition. Also, while an extensive literature on inhibition exists, detailed knowledge of the influence of the nature of the inhibitor is still lacking. Therefore it is desirable to accumulate more data on the inhibition efficiency of simple organic compounds with fairly well-known molecular properties. It is for this reason that some experiments with simple aniline derivatives and

[1] Present address: Bundesanstalt fuer Materialpruefung, Berlin-Dahlem, West Germany.

alkylamines have been carried out and are presented in this paper.

The corrosion of pure Fe in air-free 1*N* HCl was chosen for the investigation. The over-all corrosion reaction may be split into the anodic and cathodic "partial" reactions:

$$Fe \rightarrow Fe^{++} + 2e^-; \qquad 2H^+ + 2e^- \rightarrow H_2$$

The electrochemical behavior of the Fe specimen as an electrode, including corrosion, is then determined by the kinetics of the partial reactions, these being characterized by their overvoltage curves. This leads to the concept of the superposition of the "partial overvoltage curves" to the "total current-voltage curve" originally given by Wagner (1) and recently applied to the corroding Fe electrode by Uhlig (2), Stern (3), Bonhoeffer (4), and Heusler (5). The following two paragraphs give a short summary of the terms involved. For more detail the papers cited above should be used.

Neglecting the reverse reactions (Fe deposition and H dissolution), the two partial reactions are assumed to have exponential overvoltage curves of the form

$$j_{Fe} = (j_o)_{Fe} \exp\left[-\frac{1}{b'_{Fe}}(E_{Fe} - E)\right] \qquad (I)$$

$$j_H = (j_o)_H \exp\left[\frac{1}{b'_H}(E_H - E)\right] \qquad (II)$$

Here $j_{Fe}$ and $j_H$ are the apparent anodic and cathodic current densities based on projected surface area; $(j_o)_{Fe}$ and $(j_o)_H$ are the current values at the equilibrium potentials $E_{Fe}$ and $E'_H$, $b'_{Fe}$, and $b'_H$ are the "Tafel" slopes; and $E$ is the measured electrode potential. Regardless of their actual physical significance $(j_o)_{Fe}$ and $(j_o)_H$ are called exchange currents.

At any value of a polarizing current, $j$

$$j = j_{Fe} - j_H \qquad (III)$$

This is the equation of the total current-voltage curve which can be measured by external polarization. At $j = 0$, $E = E_{corr}$ and

$$|j_{Fe}| = |j_H| = j_{corr}$$

Here $j_{corr}$ is the corrosion rate in terms of an apparent current density, and $E_{corr}$ the corrosion potential (open circuit potential). With Eqs. (I), (II), and (III) both the corrosion rate and the corrosion potential are completely determined by the overvoltage properties of the partial reactions. The simultaneous measurements of $j$, $j_{Fe}$, and $j_H$ should therefore yield complete knowledge of the electrode behavior in a given surrounding medium. This procedure involves laborious analytical determinations of the amount of dissolved iron or deposited hydrogen. Alternatively the electrode may simply be polarized to potential regions where either $j_{Fe}$ or $j_H$ becomes very small so that $j \cong j_H$, or $j \cong j_{Fe}$. Then the total current voltage curve becomes practically identical with one or the other of the partial overvoltage curves. Provided no change of the rate-determining step of the partial reaction occurs between this potential region and $E_{corr}$, the partial curve in the vicinity of the latter potential can then be obtained by extrapolation.[2] This simple geometrical operation is illustrated by Fig. 1. Moreover, extrapolation to $E_{corr}$ yields the value of $j_{corr}$. Stern (3) has shown that the corrosion rates obtained by extrapolation of the cathodic partial overvoltage curve check well with those determined by analysis of the amount of dissolved Fe. The same method is used throughout the present investigation. So far it appears to be difficult to measure the anodic partial curve in this way, but in the vicinity of $E_{corr}$ a part of this curve may be obtained from corresponding values of $j$ and $j_H$ by application of Eq. (III).

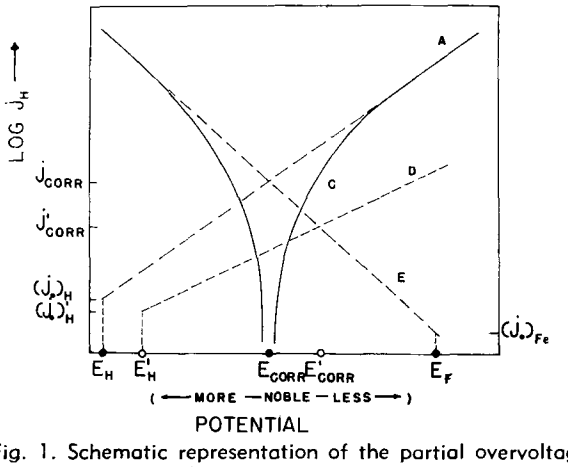


Fig. 1. Schematic representation of the partial overvoltage curves (dashed curves) and the total current voltage curve (solid curve C) of iron corroding in nonoxidizing acids. (A)—cathodic partial curve; (D)—cathodic partial curve in the presence of a cathodic inhibitor; (E)—anodic partial curve. Other symbols as defined in the text.

The organic inhibitors used for the present investigation do not change the over-all reaction. The lowering of the corrosion rate must therefore be brought about either by a decrease of the difference between the equilibrium potentials $E_H$ and $E_{Fe}$, which can only be brought about by changes of the bulk concentration of the species taking part in the corrosion reaction, or by an increase of the overvoltage of one or both partial reactions. With respect to their action on one or both partial reactions, inhibitors are often classified as being of an anodic, cathodic, or mixed type. The general result of strictly cathodic inhibition is shown in Fig. 1 by the shift of the cathodic partial curve (A) without inhibition to (D) with inhibition. The inhibition is assumed to decrease the H-equilibrium potential from $E_H$ to $E'_H$, the exchange current from $(j_o)_H$ to $(j_o)'_H$ and to increase the Tafel slope. At the same time the corrosion rate decreases from $j_{corr}$ to $j'_{corr}$. Whether one, two, or all the possible changes occur, $E_{corr}$ must always change to a less noble value $E'_{corr}$. Similarly, a reverse change of $E_{corr}$ indicates some anodic inhibition. However, observation of the decrease of $j_{corr}$ and the shift of $E_{corr}$ alone simply indicates predominance of anodic or cathodic inhibition since a small effect on the opposite partial reaction may also exist. That is, the inhibition is actually of the mixed type.

Local cell action between fixed anodic and cathodic areas cannot be affected seriously by the ohmic resistance of the adsorbed layer as long as this polarization method gives the same value for the

[2] This also requires that no other oxidation or reduction process becomes operative in this potential span.

corrosion rate as does a direct analytical method. The former is based on the assumption of a virtually uniform electrode potential and must lead to serious errors if $iR$ drops of the order of $\geqq 5$ mv exist along an average current path between local electrodes. Correct polarization values of $j_{corr}$ indicate either very short local current paths or low values of the specific resistance of the adsorbed layer. Hoar (6) has suggested that practically the whole electrode surface is capable of acting as a cathodic area, whereas the anodic area should be represented by the sum of all atomic sites undergoing dissolution at any given moment, e.g., where the sites might be the ends of incomplete atom rows. With any nonideal crystal, lattice distortions and impurity atoms may also give rise to anodic spots. Thus, with respect to the relative size of anodic and cathodic areas, as well as to the distribution of anodic spots, the condition of the corroding iron surface is similar to the condition of the surface of a corroding liquid amalgam. In the latter case the cathodic area is identical with the total surface and the anodic area is given by the sum of atoms of the amalgamated metal in the surface of the Hg. Since at any moment predictions can be made that the next Fe atom being transferred across the phase boundary should come from the same incomplete atom row or lattice distortion, Fe dissolution is still not as truly statistical as the dissolution of an amalgamated metal. Nevertheless, the condition of the corroding amalgam surface should be a better model for the condition of the surface or corroding Fe, especially in acid solutions, than is the frequently used model of a checkerboard-like pattern of local electrodes. Therefore, the concept of a uniform metal surface undergoing statistical dissolution is used for the discussion of inhibition. It is obvious that this concept, if justified for pure Fe, is not immediately applicable to steel surfaces where secondary phases may have considerable influence.

If the electrode surface is uniform, inhibitor adsorption should be general. As has been pointed out by Hoar (7), and Hackerman and Makrides (8), the theory of adsorption of cationic inhibitors on cathodic sites only, for some time widely accepted (9), is objectionable even if local cells are operating on the corroding surface, the obvious argument being the uniformity of the electrode potential. The possibility of cation adsorption by means of electrostatic forces is determined by the electric charge of the electrode with respect to the solution, i.e., by the position of the electrocapillary maximum with respect to $E_{corr}$, not by the charge of one electrode with respect to another electrode, as with local anodes and cathodes. Little is known about the electrocapillary maximum of Fe, and Frumkin's value of 0.37 v in $10^{-3}N$ $H_2SO_4$ (10) does not indicate that Fe corroding in $1N$ HCl ($E_{corr} = 0.25$ v) has a positive charge at the corrosion potential. The electrocapillary maximum may be shifted to considerably more noble potentials by chemisorption of $Cl^-$, analogous to observations reported by Iofa and coworkers (11) for $I^-$ and $Br^-$ at very low concentrations. At present, therefore, the possibility of strong cation adsorption on corroding Fe is undecided. This is important with respect to the theory of chemical rather than physical adsorption suggested by Hackerman and Makrides (8). According to this concept, cationic organic inhibitors are deionized at the metal-solution interface; therefore, in the case of amine-hydrochlorides the adsorbed species should be the free amine. The establishment of a more or less well-defined chemical bond between the inhibitor and the Fe should result in a decrease in apparent reactivity of the Fe in the electrode surface [Hackerman (12)]. This leaves $E_{Fe}$ unchanged, but it may greatly decrease the exchange current of the anodic partial reaction.

### Material and Apparatus

Iron electrodes were cut out of 99.99% Armco iron sheets, 1 mm in thickness, in the shape of little flags of about 4-5 $cm^2$ geometric surface area. The handle of these flags was soldered to a copper wire and sealed into a glass holder with polyethylene. Before immersion, the electrodes were abraded with No. 1 through 4/0 emery paper, and rinsed with benzene, acetone, and water.

$1N$ HCl solutions were prepared from C.P. concentrated HCl and double-distilled water. No change of the corrosion rate was observed when gaseous HCl distilled into water was used instead.

Except for methylamine- and ethylamine-hydrochloride, which were used without further purification of the high-grade compound, all inhibitors were redistilled one to three times under reduced pressure, until a colorless product of constant boiling point was obtained. The inhibitors were then dissolved in the appropriate amount of concentrated HCl to give a $1N$ HCl solution of the hydrochloride. No inhibitor solution was used later than three days after preparation.

Electrolytic hydrogen was passed through pyrogallic acid in alkaline solution, sodium plumbite in alkaline solution, concentrated $H_2SO_4$, a trap cooled with liquid nitrogen, and finally a 50-cm column of $1N$ HCl before being bubbled through the test solution. Omitting this procedure resulted in a marked decrease of the corrosion rate.

The apparatus used throughout the experiments is shown in Fig. 2. All parts were made of Pyrex, with stoppers and stopcocks very lightly greased with silicone grease. The test vessel A, the Ag/AgCl-electrode B, and the Pt-electrode C, were filled with $1N$ HCl up to the dotted lines. Three iron electrodes, D, of which only one is shown, were used at the same time.

The outlet of burette F was sealed into the ground joint E and on top of F a flask G served as a reservoir for inhibitor solutions. A second burette H was also sealed into E and was extended via capillary tubing into the test solution. Hydrogen entered the apparatus at I and left it at K, thus keeping all parts air-free and also slightly agitating the solution. If hydrogen was bubbled through the solution more vigorously the corrosion potential and the corrosion rate did not change by more than 1 mv and 1 $\mu a/cm^2$. The test vessel was placed in a thermostat kept at $30 \pm 0.5°C$. The volume of the test solution in A

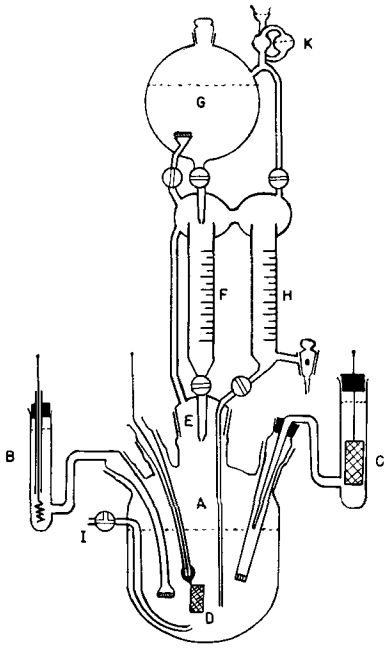


Fig. 2. Apparatus used for the measurement of overvoltage properties and corrosion rates.

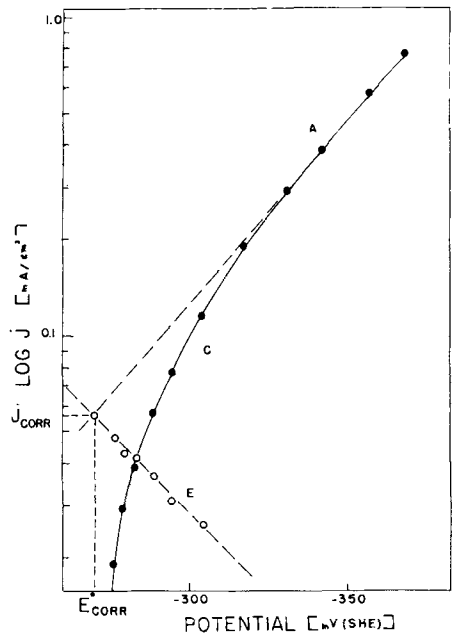


Fig. 3. Total current-voltage curve and partial overvoltage curve determined by cathodic polarization of an iron electrode in 1N HCl without inhibition. Symbols as given in the caption of Fig. 1; other symbols as defined in text.

was 500 cc; all pH changes due to the corrosion reaction were negligible.

The potential difference between the Fe-electrode and the Ag/AgCl-reference electrode was measured with a student-type potentiometer within ±1 mv. In order to be able to make quick readings during polarization measurements, an oscilloscope was used as zero indicator. Polarizing currents were applied between the Fe- and the Pt-electrode, using a 220 v dry battery in series with a resistance box and a milliammeter. Current readings were taken with a precision of ±5 $\mu$a at currents between 1 and 3 ma and ± 2$\mu$a at currents less than 1 ma. The resistance of the electrode system was small compared with the external ohmic resistance, the polarizing currents were therefore constant during the polarization time.

## Procedure and Results

After the electrodes had been immersed in air- and inhibitor-free 1*N* HCl, a period of 3-5 hr was required for both $E^{\circ}_{corr}$ and $j^{\circ}_{corr}$[3] to become constant. After 5 hr, $E^{\circ}_{corr}$ and $j^{\circ}_{corr}$ were constant in most cases except for random changes of ±1 mv/hr and ±3 $\mu$a/cm²/hr, respectively. The polarization behavior of all electrodes was checked at one-hour intervals throughout the immersion time, but only the readings taken between 5 and 7 hr after immersion were used for the final determination of the overvoltage properties. A considerable number of runs had to be discarded because of (*a*) corrosion rates more than 5 $\mu$a/cm² lower or higher than the average of all measurements, (*b*) nonconstant values of $E_{corr}$ and $j_{corr}$ after 5 hr, (*c*) potential drifts during polarization. Any drift greater than 1 mv/10 sec observed later than 10 sec after switching on the polarizing current was regarded as abnormal and attributed to contamination of the acid. In all cases of erratic behavior the electrodes were freshly sealed to the glass holder, freshly abraded and rinsed, and the test solution replaced by freshly prepared solution. No inhibition experiment was carried out until a given set of electrodes exhibited "normal" behavior, with $E_{corr} = -260 \pm 10$ mv (vs. S.H.E.), $j_{corr} = 50 \pm \mu$a/cm² and nondrifting potentials during cathodic polarization.

A typical example of a single polarization measurement with an uninhibited specimen is shown in Fig. 3. $E_{corr}$ was measured immediately before the first polarization (immediately afterwards $E_{corr}$ is usually 1-2 mv more noble than before, but the original value is reestablished within a minute). Cathodic currents of various strength were applied at 30-sec intervals and the polarized potentials $E$ measured with the potentiometer (solid circles) 5-10 sec after switching on the current. The total current-voltage curve obtained as $E$ vs. log $j$ (solid curve) was always found to have a linear section in the current range $0.2 \leqq j \leqq 0.7$ ma/cm² which could easily be extrapolated to $E^{\circ}_{corr}$ (dashed curve). From this curve, presumably the cathodic partial overvoltage curve, $j^{\circ}_{corr}$ and $b^{\circ}_{H}$ ($=b^{\circ\prime}_{H}/2.303$) were determined graphically. In a few cases the nonlinear part of the logarithmic total current voltage curve was also measured to obtain examples of the anodic partial overvoltage curve by application of Eq. (III) (open circles and broken line). Thus the slope $b^{\circ}_{Fe}$ of the anodic curve was found to be of the order of 0.075 ± 0.01 v/log $j$ which may be compared with Stern's (13) value 0.068, determined by the same method in NaCl + HCl solution of pH 1.5 at 25°C. The exchange current $(j_o)^{\circ}_{Fe}$ was calculated to be of the order of 0.04 to 0.1 $\mu$a/cm² which agrees fairly well with Stern's value of 0.04 $\mu$a/cm². However, any single determination of $(j_o)_{Fe}$ is good only to ±0.02 and any attempt to calculate the change of the exchange current due to weak inhibitor action is useless.

[3] o designates uninhibited properties.

Table I. Comparison of the average total corrosion rate of 3 electrodes obtained by cathodic polarization ($i_1$) and by colorimetric analysis ($i_2$)

| Inhibitor | C (mole/l) | $i_1$ ($\mu$a) | $i_2$ ($\mu$a) |
|---|---|---|---|
| — | 0 | 820 ± 20 | 840 ± 50 |
| *N*-Methylaniline | 0.06 | 720 ± 20 | 700 ± 20 |
| *N*-Ethylaniline | 0.05 | 490 ± 10 | 490 ± 10 |
| *N*-Propylaniline | 0.12 | 355 ± 10 | 350 ± 20 |

In order to avoid erroneous results caused by slow drifts of the electrode properties during immersion over several days, all electrodes were again abraded and rinsed before addition of inhibitors to the solution. Also, usually after two complete series of experiments for one inhibitor new electrodes were prepared. Otherwise the measurements in inhibited solutions were carried out exactly as were those without inhibitors. In these systems the cathodic partial current of the inhibited electrode at $E^{\circ}_{corr}$, $j'$, was also determined.

Especially after addition of the more effective inhibitors a slow drift of the potential of externally-polarized electrodes to less noble potentials could not be eliminated. It was probably caused by changes of the adsorption concentration of the inhibitor. Nevertheless, correct values of $j_{corr}$ were obtained by using the potentials obtained 5-10 sec after switching on the polarization current, allowing 1-min intervals between two consecutive polarizations, and also limiting the polarizing currents to 0.5 ma/cm² in cases where the logarithmic total current-voltage curve became linear at 0.15-0.17 ma/cm² because of the lowered $j_{corr}$. This was shown by independent analytical measurements. For this control, polarization measurements were carried out between 2 and 8 hr after immersion in separate runs at one-hour intervals, and samples of the solution were taken at the same time. The $Fe^{++}$ concentration of the samples was then determined colorimetrically, using o-phenanthroline. The average values of the corrosion rate obtained by polarization checked well with the corrosion rate determined by analysis (Table I).

Usually 3-4 runs at inhibitor concentrations between 0.05 and 0.2 mole/l were carried out. For each inhibitor concentration final values of $j_{corr}$, $j'$, $b_H$, and $E_{corr}$ were obtained by obtaining the algebraic mean of six single measurements, two per electrode. A typical example of the resulting curves of the electrode properties as a function of concentration is shown in Fig. 4 for *m*-toluidine. At $C \geqq 0.08$ to 0.1 mole/l, all inhibitors showed a maximum effect on the electrode properties independent of further increase of concentration up to 0.2 mole/l, the highest concentration investigated. As no attempt was made to measure fully the changes of the electrode properties at concentrations $0 \leqq C \leqq 0.1$, Table II lists only the electrode properties at maximum inhibitor effect obtained graphically from plots of the experimental values against concentration. With propylamine as inhibitor the slope $b^{m}_{Fe}$ of the anodic partial overvoltage curve was determined at maximum inhibitor effect and found to be of the order of 0.080 ± 0.01 v/log *i*.

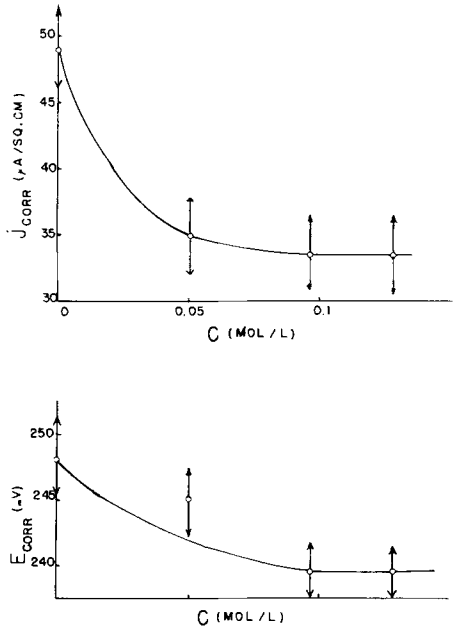


Fig. 4. The variation of the corrosion potential $E_{corr}$ and the corrosion rate $j_{corr}$ of a set of 3 Fe electrodes as function of the concentration of m-toluidine hydrochloride.

The error limits given in the tables are caused by differences in the behavior of different electrodes. Compared with these differences the limited precision of the measurements has little significance. This includes the error introduced by the resistance between the tip of the reference electrode and the iron electrodes about 2 cm away. It does not include the error limit of the colorimetrically determined values of $j_{corr}$.

## Discussion

*Inhibition of the cathodic partial reaction.*—Table II shows that $j'$ is lower than $j^{\circ}_{corr}$ for all the inhibi-

Table II. Average value of the corrosion potential $E_{corr}$, the corrosion rate $j_{corr}$, and the cathodic Tafel slope $b_H$ of three electrodes with no inhibition (O) and at maximum inhibition (m), also the cathodic current at maximum inhibition at $E^{\circ}_{corr}$

| Inhibitor | | $E^{\circ}_{corr}$ $E^{m}_{corr}$ (mv) | $b^{\circ}_H$ $b^{m}_H$ (v/log i) | $j^{\circ}_{corr}$ $j^{m}_{corr}$ ($\mu$a/cm²) | $j'$ ($\mu$a/cm²) |
|---|---|---|---|---|---|
| Aniline | O | −249 | 0.091 | 47 | |
| | m | −237 | 0.090* | 30 | 40 |
| *m*-Toluidine | O | −248 | 0.092 | 48 | |
| | m | −239 | 0.093 | 33 | 42 |
| *o*-Toluidine | O | −257 | 0.086 | 51 | |
| | m | −240 | 0.091 | 29 | 44 |
| *N*-Methylaniline | O | −249 | 0.092 | 51 | |
| | m | −241 | 0.089 | 38 | 46 |
| *N*-Ethylaniline | O | −269 | 0.088 | 53 | |
| | m | −260 | 0.094 | 37 | 46 |
| *N*-*n*-Propylaniline | O | −267 | 0.089 | 49 | |
| | m | −258 | 0.095* | 32 | 38 |
| *N*-Dimethylaniline | O | −249 | 0.085 | 53 | |
| | m | −231 | 0.085 | 31 | 47 |
| *N*-Diethylaniline | O | −268 | 0.083 | 54 | |
| | m | −255 | 0.093 | 25 | 34 |
| *N*-Di-*n*-propylaniline | O | −266 | 0.084 | 53 | |
| | m | −252 | 0.093 | 24 | 29 |
| Methylamine | O | −265 | 0.086 | 52 | |
| | m | −268 | 0.086 | 45 | 43 |
| Ethylamine | O | −268 | 0.091 | 54 | |
| | m | −268 | 0.091 | 42 | 42 |
| Propylamine | O | −269 | 0.085 | 55 | |
| | m | −267 | 0.091 | 42 | 44 |
| Error limit | | ±2 | ±0.002-3 | ±2 | ±3 |

* To ±0.004 in these cases.

tors and in many cases $b^m_H$ (inhibited) is larger than $b^o_H$. Therefore, all inhibitors investigated exhibit cathodic inhibitor action. To obtain a quantitative measure of this action recall that, with $b_H$ constant, $j'/j_{corr}$ must equal $(j_o)^m_H/(j_o)^o_H$, and therefore be a measure of the decrease of the cathodic exchange current. Even for small values of $\Delta b_H$ ($= b^m_H - b^o_H$) the same relationship holds to a first approximation and was therefore calculated for each inhibitor. Following common usage in inhibitor research, instead of $j'/j^o_{corr}$ itself, Table III lists the quantity $(I - j'/j^o_{corr}) \cdot 100\% = I_c$. Neglecting the influence of $\Delta b_H$ this quantity is called the "cathodic inhibitor efficiency" (not identical with the inhibitor efficiency which would be observed with a given $I_c$ in the absence of all anodic inhibition). The values of $\Delta b_H$ and the "total inhibitor efficiency" $I_T = (1 - j^m_{corr}/j^o_{corr}) \cdot 100\%$ are also tabulated. It is seen that $I_c$ is practically constant for the first group and the last group (the alkylamines). With increasing chain length of the substituent of *N*-alkylanilines, inhibition increases, more noticeably in the *N*-dialkylanilines than in the *N*-monoalkylaniline series.

Remembering that all numbers are limiting values for maximum inhibition and therefore probably maximum adsorption, it can be expected that the adsorbed molecules are oriented nearly perpendicularly to the surface. If this is true, then the observed tendencies of the change of $I_c$ strongly suggests an effect of the projected area per molecule. For perpendicularly oriented molecules the projected area of straight chain alkylamines is independent of the chain length and equals the projected area of the amine group. On the other hand, perpendicular adsorption of a *N*-substituted aniline means that all substituents form an angle smaller than 90° with the metal surface. An increase of chain length consequently increases the projected area. Also, with *N*-dialkylanilines a larger increase of the projected area is to be expected since two alkyl groups are added instead of one as in the case of *N*-monoalkylanilines. While no quantitative interpretation is possible it is clear that, for alkylamines and *N*-alkylamines, changes of $I_c$ parallel changes of the projected area within each group. As $I_c$ is the same for aniline and the toluidines it follows that only substitution for H on the amino group is effective, that is, close to the surface of the underlying metal. It is also possible that a smaller effect would be observed on increasing the chain length of the substituent on the benzene ring.

If all types of aniline derivatives investigated have the same maximum number of moles adsorbed per sq cm of the metal, then the total projected area should increase in the series aniline, *N*-methylaniline, *N*-dimethylaniline, and $I_c$ should also increase. Actually $I_c$ is greater for aniline than for either *N*-methyl- or *N*-dimethylaniline, and is about the same for these two compounds. Experimental data for the maximum adsorbed amount are not available, but it is reasonable to predict a decrease with increasing branching of the substituents due to steric hindrance. Therefore it is likely that, while the projected area per molecule increases, the total projected area decreases from aniline to *N*-methylaniline because of a decrease of the number of adsorbed moles. Thus the decrease of $I_c$ here is not contradictory.

The decrease of $(j_o)_H$ is usually ascribed to a decrease of the true surface area available for hydrogen deposition (6, 7, 9). The observed changes of $b_H$, neglected in the discussion just above, is of importance here. In principle, changes of $b_H$ can indeed be caused by mere changes of the true surface area available. This follows not only for the case of competing adsorption of inhibitor and H-atoms but also because of competing parallel reaction paths for H-deposition, depending to different degrees on the H-concentration of the surface. However, this requires very special assumptions not justified by experimental evidence.

A preferable less elaborate assumption is that both partial reactions are controlled by an energy barrier at the phase boundary which requires a slow discharge mechanism for the cathodic partial reaction. According to the H-overvoltage theory, $b_H$ should then be of the form $2.303RT/\alpha z\mathbf{F}$, where $R$ is the gas constant, $T$ the absolute temperature, $\alpha$ a factor between 0 and 1, $z$ the electron number, and $\mathbf{F}$ the Faraday. For Fe in different inhibitor-free solutions values of $b_H$ between 0.08 and 0.15 v/log $i$ have been observed by different authors (3, 5, 13, 14) indicating values of $\alpha$ ranging from 0.7 to 0.4. The average value of $b_H$ found during the present investigation is $0.088 \pm 0.004$; $\alpha$ therefore is 0.66. The theory of slow discharge predicts $\alpha = 0.5$ for the case that exactly half of the overvoltage is used to lower the activation energy of the forward reaction, the other half being used to increase the activation energy of the reverse reaction. However, this ideal symmetry need not be followed in every case and, with a different $\alpha$, slow discharge (or the electrochemical mechanism) may still be rate-determining. If this is accepted for the cathodic partial reaction it follows that an increase of $b_H$ indicates a decrease of $\alpha$ and therefore a decrease in the fraction of the cathodic overvoltage used to lower the activation energy of the $H^+$ transfer across the phase boundary. This requires a distortion of the potential distribu-

**Table III. Total, cathodic, and anodic inhibitor efficiency calculated for each inhibitor from $j^m_{corr}$, j', and j'', respectively; and $j^o_{corr}$ as found in uninhibited solution with the same set of electrodes; also $\Delta b_H = b^m_H - b^o_H$ calculated in the same way.**

| Inhibitor | $I_T$ (%) | $I_c$ (%) | $\Delta b_H$ (v/log i) | $I_a$ (%) |
|---|---|---|---|---|
| Aniline | 36 | 15 | −0.001 | 55 |
| *m*-Toluidine | 31 | 13 | +0.001 | 46 |
| *o*-Toluidine | 43 | 14 | +0.005 | 65 |
| *N*-Methylaniline | 25 | 10 | −0.003 | 41 |
| *N*-Ethylaniline | 30 | 13 | +0.006 | 47 |
| *N*-*n*-Propylaniline | 36 | 26 | +0.006 | 53 |
| *N*-Dimethylaniline | 41 | 11 | 0.000 | 66 |
| *N*-Diethylaniline | 54 | 37 | +0.010 | 68 |
| *N*-Di-*n*-propylaniline | 57 | 40 | +0.008 | 71 |
| Methylamine | 13 | 18 | 0.000 | 0 |
| Ethylamine | 17 | 20 | +0.002 | 20 |
| Propylamine | 23 | 20 | +0.006 | 29 |
| Error limit | 4 | 4 | 0.003-4 | 4 |

tion in the phase boundary. It is then reasonable to assume that the cause of this distortion is the establishment of an additional energy barrier due to inhibitor adsorption. Consequently, the inhibitor layer is treated as a uniform film which leaves the available surface unchanged but increases the activation energy of $H^+$ transfer, thus decreasing the probability of this transfer. While distortion of the potential distribution may be responsible for the change of $b_H$ lowering the transfer probability is responsible for the decrease of $(j_o)_H$. The observed influence of the total projected area is then not that of increasing surface coverage but of increasing density of the uniform inhibitor layer. The increase in density should cause a proportional increase in the activation energy. In view of the considerable error limit of the $\Delta b_H$ values, a similar interpretation cannot be attempted for $b_H$ as a function of the molecular structure of the inhibitor.

*Inhibition of the anodic partial reaction.*—Except for the single pair of data of $b_{Fe}$ before and after addition of propylamine as inhibitor no other information on anodic inhibition has been obtained except the shift of $E_{Fe}$. Assuming $b_{Fe}$ = constant = 0.075 for inhibited and uninhibited electrodes, an anodic partial current $j''$ of the inhibited electrode at $E^\circ_{corr}$ can be obtained from $I_{corr}$ and $I_c$ and a quantity $(1 - j''/j^\circ_{corr}) \cdot 100\% = I_a$ can be calculated which is comparable to $I_c$. This has been done graphically and the resulting values of $I_a$ (Table III) are used instead of the shift of $E^\circ_{corr}$ for the discussion of anodic inhibition. In view of the arbitrary assumption $b_{Fe}$ = constant the same error limit has to be attributed to the $I_a$ values as to those of $I_c$. Within this limit $I_a$, if not a measure of the decrease of $(j_o)_{Fe}$, is at any rate a measure of the anodic inhibition and therefore justly called the "anodic inhibitor efficiency". Table III shows that, with the exception of methylamine, all inhibitors investigated exhibit anodic as well as cathodic inhibition and are therefore inhibitors of the mixed type. Furthermore it is also seen that all aniline derivatives are of a predominantly anodic type.

$I_a$ is zero for methylamine and increases rapidly with increasing chain length of alkylamines. It has already been argued that the total projected area for alkylamines is constant with respect to the cathodic partial reaction. Within the concept of general adsorption and uniform electrode surface, the same must be true for the anodic partial reaction. An explanation of the increase for $I$, in spite of constant total projected area, is offered by the theory of chemisorption. It has been pointed out by Hackerman and Makrides (8) that chemisorption of amines should increase with electron donor properties and that, lacking other data, the basicity of the free amine should be considered representative of these properties. As the basicities of the alkylamines used here are practically constant (15), this suggestion gives no clue to the variation of the chemisorption of these compounds. Therefore, it can only be assumed tentatively that the contribution of chemisorption to the total adsorption may increase with increasing chain length, while the total adsorbed amount, and therefore the total projected area, remains constant because of the existence of a saturated monolayer of adsorbed amines. As has been mentioned before, this can be expected to result in a decrease of the apparent reactivity of Fe in the electrode surface. If slow charge transfer across the interface is rate-determining for the anodic partial reaction, the anodic exchange current $(j_o)_{Fe}$ may then be treated as the product of the true surface area (which is constant if the concept of uniform adsorption is correct), a transfer probability (the probability of the penetration of the activation barrier across the double layer by $Fe^{++}$), and the iron surface reactivity. The predominance of anodic inhibition can then be interpreted as being due to the lowering of the reactivity by chemisorption, where the lowering of the transfer probability by inhibitor adsorption is roughly the same as that for the cathodic inhibition.

Aniline derivatives are much less basic than straight chain alkylamines, but they are none the less the better anodic inhibitors. The *N*-alkylanilines show a comparatively small increase of $I_c$ with increasing chain length of the aliphatic substituent, but it is doubtful whether this can be attributed to the basicity. Basicity constants of aniline derivatives (15) in dilute solutions show that the basicity does not increase regularly with chain length of aliphatic substituents. The difference in basicity of different compounds is usually small, so that no predictions as to the basicity in concentrated solutions are possible. Both the total amount and the differences of anodic inhibition observed with aniline derivatives are therefore difficult to explain. Considering that within each group of *N*-alkylanilines the changes of $I_a$ parallel the changes of $I_c$, it may be assumed tentatively that this indicates an influence of the energy barrier similar to that of the cathodic partial reaction. Whether the large total value of $I_a$ is caused by additional strong chemisorption of the aniline derivatives cannot be decided here.

## Acknowledgment

The authors are grateful to the Office of Naval Research for the financial support of this work under Contract Nonr 375(02). The authors also wish to express their appreciation to A. C. Makrides for his contributions through helpful discussions.

Manuscript received April 17, 1957.

Any discussion of this paper will appear in a Discussion Section to be published in the December 1958 JOURNAL.

## REFERENCES

1. C. Wagner and W. Traud, *Z. Elektrochem.*, **44**, 391 (1938).
2. H. H. Uhlig, *Proc. Nat. Acad. Sci. U.S.*, **40**, 276 (1954).
3. M. Stern, *This Journal*, **102**, 609 (1955).
4. K. F. Bonhoeffer, Lecture given at Electrochemical Society Meeting, San Francisco, 1956.
5. K. F. Bonhoeffer and K. Heusler, *Z. physik. Chem.* (N.F.), **8**, 390 (1956).
6. T. P. Hoar and R. D. Holliday, *J. appl. Chem.*, **3**, 502 (1953).
7. T. P. Hoar, Pittsburg International Conference on Surface Reactions, 1948, pp. 127-134.

8. N. Hackerman and A. C. Makrides, *Ind. Eng. Chem.*, **46**, 523 (1954).
9. Shih-Jen Chiao and C. A. Mann, *ibid.*, **39**, 910 (1947).
10. A. Frumkin, *Z. Elektrochem.*, **59**, 807 (1955).
11. S. Iofa, *et. al., Doklady Akad, Nauk SSSR*, **69**, 213 (1949); **84**, 543 (1952); **91**, 1159 (1953).
12. N. Hackerman, *Trans. N. Y. Acad. Sci.*, [2] **17**, 7 (1954).
13. M. Stern and R. M. Roth, *This Journal*, **104**, 390 (1957).
14. A. G. Pecherskaja and V. V. Stender, *Zhur. Priklad. Khim.*, **19**, 1303 (1946).
15. N. F. Hall and M. R. Sprinkle, *J. Am. Chem. Soc.*, **54**, 3469 (1932).

# Local Cell Action during the Scaling of Metals, I

**Christa Ilschner-Gensch[1] and Carl Wagner[2]**

*Department of Metallurgy, Massachusetts Institute of Technology, Cambridge, Massachusetts*

ABSTRACT

When a tantalum wire partly covered by silver is exposed to iodine vapor at 174°C, a AgI layer is formed not only on silver but also rapidly along the tantalum surface by virtue of local cell action involving migration of silver ions in AgI and migration of electrons in the tantalum wire and across the AgI layer. The observed rate of sidewise growth of the AgI layer along the tantalum surface is in accord with theoretical calculations. By and large, local cell action may increase the rate of dry corrosion when there are different phases, one of which involves easy flow of ions and another involves easy flow of electrons.

Corrosion of metals in aqueous solutions at room temperature, as well as corrosion of metals in oxygen or sulfur at elevated temperatures, has been interpreted in terms of electrochemical reactions and, accordingly, the rates of both types of reactions may be calculated from electrical measurements. There are, however, significant differences between these two types of reactions. The rate of corrosion in aqueous solutions is frequently determined by the magnitude of activation polarization, and cathodic and anodic reactions may occur at different interfaces corresponding to local cell action. In contradistinction, the rate of oxidation of metals at elevated temperatures is frequently determined by the rate of diffusion in the solid reaction product rather than by the rate of phase boundary reactions, and diffusion of ions and electrons occurs in the same phase.

It is already known that local cell action takes place in solid-state reactions of type A + B = C + D, e.g., Cu + AgCl = CuCl + Ag at 230°C (1). Likewise, it can be anticipated that local cell action will be operative when metals are oxidized at elevated temperatures under conditions involving several phases, with easy flow of ions in one phase and easy flow of electrons in another phase. In particular, when the main product of an oxidation reaction has a high electronic but a low ionic conductivity, addition of another phase providing easy flow of ions may result in a much higher over-all corrosion rate. The same is true if, conversely, the main product has a high ionic but a low electronic conductivity and another phase providing easy flow of electrons is added. As an example for the latter case, the reaction between silver and iodine vapor has been investigated. According to Reinhold and Seidel (2) and Jost and Weiss (3), the rate of formation of AgI is determined by transport of electrons rather than ions across the AgI layer since AgI is mainly an ionic conductor.

[1] Present address: Zentralforschunganstalt Fried. Krupp, Essen, Germany.
[2] Present address: Max Planck Institute for Physical Chemistry, Goettingen, Germany.

## Experimental

To make local cell action possible, Ta wires were covered by Ag by immersing the ends of the Ta wires in molten Ag contained in a vycor tube. After cleaning the surface, the Ta wires were placed together with dried iodine in Pyrex tubes cooled by means of dry ice. The Pyrex tubes were evacuated, sealed off, heated in boiling decane at 174°C for 15-150 min, and placed again in dry ice in order to terminate the reaction. At 174°C the vapor pressure of iodine amounts to 575 mm Hg.

It was observed that a AgI layer grows not only on the Ag surface but also spreads along the Ta surface as is shown schematically in Fig. 1. Supposedly, silver ions migrate in the AgI layer and electrons migrate in the Ta wire and across the AgI layer. The distance X' between the tip of the AgI layer and the step next to the Ag slug was measured and the estimated thickness δ of the AgI layer on the silver slug was added in order to obtain the length $X = X' + \delta$ of the AgI layer on Ta.

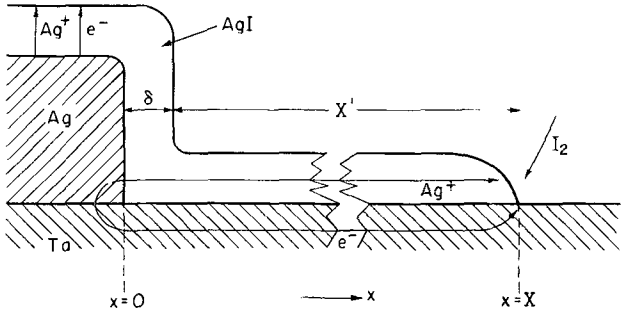


Fig. 1. Reaction of iodine vapor with Ag on Ta

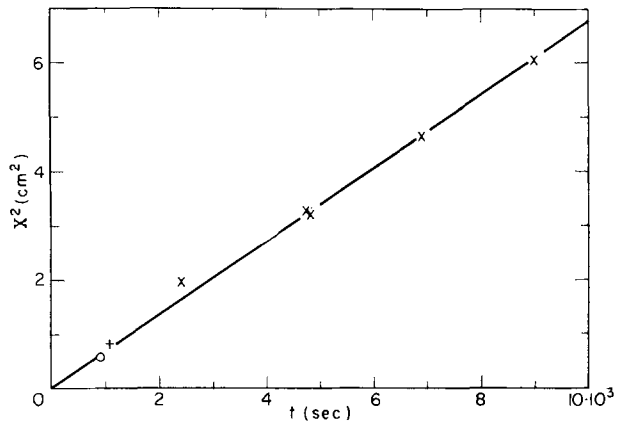


Fig. 2. Square of the length X of a AgI layer on Ta (x), Pt (o), and graphite (+) vs. time.

Results are shown in Fig. 2. In accord with Eq. [25] derived below, a plot of the square of length $X$ vs. time $t$ yields a straight line. Figure 2 also shows results obtained with Pt and graphite instead of Ta. These results show no significant difference, although Pt itself reacts to a minor extent with iodine vapor and yields a very thin blackish film which can be distinguished easily from the much thicker yellow AgI layer.

Some samples were sectioned and examined microscopically. The thickness of the AgI layer on Ag was found to be 0.046 cm for $t = 4740$ sec. The thickness of the AgI layer on Ta was found to decrease with increasing distance $x$ from the Ag slug, qualitatively in accord with Eq. [20] derived below.

## Theoretical Calculations

The location of the three-phase boundary Ag-Ta-AgI at $t = 0$ is supposed to be at $x = 0$ (*see* Fig. 1) and moves at $t > 0$ with respect to a hypothetical marker inside the Ta wire since Ag is consumed by the sidewise growth of the AgI layer. If the thickness of the Ag layer on the Ta wire is much greater than the thickness of the AgI layer, the shift of the location of the three-phase boundary with time is only minor and will be disregarded in what follows.

In principle, migration of silver ions, iodine ions, and electrons denoted as particles of type 1, 2, and 3 is to be considered. Practically, the migration of iodine ions is insignificant (4).

The flux $j_1$ of silver ions in the AgI layer on the Ta wire along the surface ($x$-direction) may be calculated as (5)

$$j_1 = -(\kappa_1/\mathbf{F}^2)\ (\partial\eta_1/\partial x) \text{ at } 0 < x < X \qquad [1]$$

where $\eta_1$ is the local electrochemical potential of the silver ions, $\mathbf{F}$ is the Faraday constant, $x$ is distance as shown in Fig. 1, and $X$ denotes the location of the tip of the AgI layer at time $t$. The partial conductivity $\kappa_1$ for silver ions in AgI may be written as the product of their concentration $c_1$, their electrical mobility $u_1$, and the Faraday constant,

$$\kappa_1 = c_1 u_1 \mathbf{F} \qquad [2]$$

From Eq. [2] the mobility $u_1$ may be calculated as

$$u_1 = \kappa_1/c_1\mathbf{F} = \kappa V_{AgI}/\mathbf{F} \qquad [3]$$

where $V_{AgI} = 1/c_1$ is the molar volume of AgI and $\kappa$ is the total conductivity which is virtually equal to the cationic conductivity $\kappa_1$.

The electrochemical potential $\eta_1$ is the sum of the chemical potential $\mu_1$ of the silver ions and the product $\phi\mathbf{F}$ where $\phi$ is the local electrical potential. In view of the high degree of disorder of the cations in AgI above 146°C, their chemical potential $\mu_1$ is virtually constant. Thus the gradient of the electrochemical potential $\eta_1$ is essentially equal to the product of the gradient of the electrical potential and the Faraday constant,

$$\partial\eta_1/\partial x \cong \mathbf{F}(\partial\phi/\partial x) \qquad [4]$$

In view of Eqs. [2] and [4], Eq. [1] may be rewritten as

$$j_1 \cong -u_1 c_1(\partial\phi/\partial x) \qquad [5]$$

i.e., the driving force for the migration of silver ions in AgI results mainly from an electrical field.

The formation of AgI from silver and iodine vapor follows the parabolic rate law (2, 3)

$$\delta = (2k't)^{1/2} \text{ at } x < 0 \qquad [6]$$

where $\delta$ is the thickness of the AgI film at time $t$ and $k'$ is the rate constant of Tammann's rate law. Since the rate is determined essentially by migration of electrons, the rate depends virtually only on the gradient of the electrochemical potential $\eta_3$ of the electrons. In view of the high conductivity of Ag and Ta, $\eta_3$ is practically constant along the entire metal-AgI interface ($x >< 0$). Thus the thickness $\delta$ of the AgI layer on the Ta wire follows the same rate law after time $t_x$ at which the tip of the AgI layer has arrived at $x$,

$$\delta = [2k'(t - t_x)]^{1/2} \text{ at } 0 < x < X \qquad [7]$$

corresponding to the differential equation

$$\partial\delta/\partial t = k'/\delta \text{ at } t > t_x \qquad [8]$$

and the boundary condition

$$\delta = 0 \text{ at } t = t_x \qquad [9]$$

The continuity condition requires that the amount of AgI formed per unit width is equal to the negative value of the divergence of the flow of silver ions per unit width. Thus

$$c_1(\partial\delta/\partial t) = \partial(j\delta)/\partial x \qquad [10]$$

Substitution of Eqs. [1], [2], and [8] in Eq. [10] yields

$$\frac{u_1}{\mathbf{F}}\frac{\partial}{\partial x}\left(\delta\frac{\partial\eta_1}{\partial x}\right) = \frac{k'}{\delta} \qquad [11]$$

At the tip of the AgI layer the average velocity of the silver ions equal to $j_1/c_1$ must be equal to the rate of advancement of the tip, $dX/dt$. In view of Eqs. [1] and [2] it follows that

$$\frac{dX}{dt} = \left(\frac{j_1}{c_1}\right)_{x=X} = -\frac{u_1}{\mathbf{F}}\left(\frac{\partial\eta_1}{\partial x}\right)_{x=X} \qquad [12]$$

At the two-phase boundary Ag-AgI at $x = 0$, equilibrium for the reaction

$$Ag(s) = Ag^+ (\text{in AgI}) + e^- \quad [13]$$

is supposed to be established. Thus

$$\mu_{Ag}^\circ = \eta_1(x = 0) + \eta_3 \quad [14]$$

where $\mu_{Ag}^\circ$ is the standard chemical potential of Ag.

Along the three-phase boundary Ta-AgI-gas at $x = X$, equilibrium for the reaction

$$Ag^+(\text{in AgI}) + e^- + \frac{1}{2} I_2(g) = AgI \quad [15]$$

is supposed to be established. Thus

$$\eta_1(x = X) + \eta_3 + \frac{1}{2}\mu_{I_2} = \mu_{AgI}^\circ \quad [16]$$

where $\mu_{I_2}$ and $\mu_{AgI}^\circ$ denote the chemical potentials of iodine in the gas phase and solid silver iodide, respectively, and the electrochemical potential $\eta_3$ of the electrons has the same value as in Eq. [14] in view of the high electronic conductivity of the metallic phases.

Upon adding corresponding sides of Eqs. [14] and [16] and regrouping, it follows that

$$\eta_1 (x = 0) - \eta_1(x = X) = -\left[ \mu_{AgI}^\circ - \mu_{Ag}^\circ - \frac{1}{2}\mu_{I_2} \right]$$

$$= -\Delta F = EF \quad [17]$$

where $\Delta F$ is the free energy of formation of AgI and $E$ is the emf of a galvanic cell involving formation of one mole AgI from the elements on passing one faraday as virtual cell reaction.

Since this is a semi-infinite diffusion problem, the location of the tip of the AgI layer is supposed to be proportional to the square root of time $t$,

$$X = 2(\gamma t)^{1/2} \quad [18]$$

where $\gamma$ is a constant parameter which has the dimension of a diffusion coefficient.

In view of Eq. [18], the value of $t_x$ introduced in Eq. [7] is

$$t_x = x^2/4\gamma \quad [19]$$

whereupon Eq. [7] becomes

$$\delta = [2\,k't(1 - x^2/X^2)]^{1/2} \quad [20]$$

Substitution of Eq. [20] in Eqs. [11] and [12] yields

$$\frac{u_1}{F}\frac{\partial}{\partial x}\left\{ \left[ 2\,k't(1 - x^2/X^2) \right]^{1/2} \frac{\partial \eta_1}{\partial x} \right\} = \frac{k'}{[2\,k't(1 - x^2/X^2)]^{1/2}} \quad [21]$$

$$\left(\frac{\partial \eta_1}{\partial x}\right)_{x=X} = -\frac{2F\gamma}{u_1 X} \quad [22]$$

Upon integrating Eq. [21] once with respect to $x$ at constant $t$ and using Eq. [18] and [22]

$$\frac{\partial \eta_1}{\partial x} = -\frac{2\gamma F}{u_1 X}\frac{\cos^{-1}(x/X)}{(1 - x^2/X^2)^{1/2}} \quad [23]$$

Upon integrating Eq. [23] between $x = 0$ and $x = X$, using Eq. [17], and solving for $\gamma$, it follows that

$$\gamma = (4/\pi^2) u_1 E \quad [24]$$

In view of Eqs. [18] and [24], the location $X$ of the tip of AgI layer at time $t$ is found to be

$$X = (4/\pi)(u_1 E t)^{1/2} \quad [25]$$

Equation [24] has been evaluated by using the numerical values $V_{AgI} = 38.4$ cm³/mole (6), $\kappa_{AgI}$ 1.5 ohm$^{-1}$ cm$^{-1}$ (7), $u_1 = 6.0 \times 10^{-4}$ cm² volt$^{-1}$ sec$^{-1}$ calculated from Eq. [3], $\Delta F = -16{,}135$ cal/mole calculated from the heat of formation at 25°C, enthalpy increments, and entropy values (8, 9) corresponding to $E = 0.70$ v. Thus $\gamma$ has been found to be $1.7 \times 10^{-4}$ cm²/sec. The straight line in Fig. 2 has been drawn in accord with this value and agrees closely with the observed values. This confirms the principles of the theoretical analysis.

## Concluding Remarks

The results of the foregoing experiments may be generalized. Sidewise growth of tarnishing layers may also be expected when Ta wires partly covered by Ag are exposed to chlorine or bromine gas. In view of the lower ionic conductivity of AgCl and AgBr corresponding to a lower average mobility $u_1$ of silver ions in AgCl and AgBr, however, sidewise growth will be less spectacular.

Especially high oxidation rates may result when an alloy yields a composite scale consisting of a melt providing easy flow of ions and a solid phase providing easy flow of electrons. Experimental investigations are in preparation.

## Acknowledgment

This investigation was sponsored by U. S. Atomic Energy Commission under Contract AT(30-1)-1903.

Manuscript received July 25, 1957.

Any discussion of this paper will appear in a Discussion Section to be published in the December 1958 JOURNAL.

## REFERENCES

1. C. Wagner, *Z. anorg. u allgem. Chem.*, **236**, 320 (1937).
2. H. Reinhold and H. Seidel, *Z. Elektrochem.*, **41**, 499 (1935).
3. W. Jost and K. Weiss, *Z. physik. Chem. N.F.*, **2**, 112 (1954). According to a private communication from the authors, values of the rate constants and transference numbers need to be corrected, but the main conclusions are not affected thereby.
4. C. Tubandt, *Z. anorg. u. allgem., Chem.*, **115**, 105 (1921).
5. C. Wagner, *Z. Elektrochem.*, **60**, 4 (1956).
6. E. Cohen and W. J. D. van Dobbenburg, *Z. physik. Chem.*, **A137**, 289 (1928); L. W. Strock, *ibid.*, **B25**, 441 (1934).
7. C. Tubandt and E. Lorenz, *ibid.*, **87**, 573 (1914).
8. National Bureau of Standards Circular *500* (1952).
9. K. K. Kelley, Bulletin Bureau of Mines 476 (1949).
10. C. Wagner, *Z. physik. Chem.*, **B32**, 447 (1936).
11. C. Wagner, *ibid.*, **B21**, 25 (1933).

# The Effect of Temperature and Thickness on the Electrical Resistivity of Ceramic Coatings

**Wm. H. Fischer**

*General Engineering Laboratory, General Electric Company, Schenectady, New York*

ABSTRACT

Tests show that the electrical resistivity of ceramic coatings less than 3 mils thick vary with thickness, although the variation of resistivity with temperature is normal. It is believed that the resistivity-thickness variation is due to surface irregularities and metal-ceramic interface factors which together produce nonuniform, nonhomogenous coatings. Consequently, electrical characteristics of ceramic coatings intended for electrical insulation use should be evaluated only from measurements made on coatings closely approximating actual service thicknesses.

Recent demands for electrical and electronic components capable of operation at temperatures as high as 500°C have led to the investigation of ceramic materials applied in thin coatings for electrical insulation. Such coatings are of the order of 0.0005 in. or less in thickness. However, the electrical properties, particularly the resistivity, of such thin coatings are frequently lower than those reported for the same or similar material in massive forms or when applied in thicker coatings. Consequently it was thought wise to explore the resistivity vs. thickness relationship for thin coatings on the theory that factors operating at the metal-ceramic interface as well as outer surface irregularities might be expected to affect the measured resistance of very thin coatings. If this were true, it would be unwise to evaluate ceramics for design purposes on the basis of resistivity measured on thick coatings.

Strauss, Richards and Moore (1) applied ceramic type coatings to Inconel strips by dipping and studied the effects of temperature on resistivity. They concluded that the resistivity of ceramic coatings is independent of thickness over the thickness range 0.003 in. to 0.020 in.

## Experimental

The experimental technique used in this investigation was similar to that of Strauss, *et al.* (1). Inconel plates 2½ in. by 1½ in. by 1/16 in. were polished and oxidized to give a surface suitable for the application of a ceramic coating. The oxidation was performed in a controlled wet hydrogen atmosphere to secure the proper type and amount of oxide to form a strong ceramic to metal bond (as determined in previous work here). Ten of these plates were coated with each of two kinds of ceramic. The nominal oxide compositions for the coatings are given in Table I. In each group two plates were coated at each of the following thicknesses: 0.005 in., 0.003 in., 0.001 in., 0.0005 in., and 0.00025 in. The ceramic frit was suspended in isopropanol and sprayed from a De Vilbiss atomizer onto one side of the plates. After air drying the coating was fired for 3 min at 1050° or 1195°C depending on formulation. A ¾ in. diameter electrode was formed on the ceramic by brushing silver paint on through a template centered on the plate. After air drying the silver paint was baked to form a smooth, adherent electrode of known area. This is essentially the same as the Bureau of Standards technique (1). Additionally, resistance measurements were made using a conducting rubber electrode. Measurements were made with direct voltage at 24°C and 50% relative humidity using a Keithley variable voltage power supply and a Keithley electronic voltmeter with a shunt which converts it to a micromicroammeter. No polarity effect was observed, nor did the resistance vary with the voltage applied. Voltage varied from 10 v on the thinnest specimens to 500 on the thickest, the increase in the voltage being necessary to achieve measurable currents with the thicker specimens. The resistance of

Table I. Ceramic coatings composition

| | G-6 (1) | G-6G (1) | I-2 (1) | 5210 | H-147 |
|---|---|---|---|---|---|
| $SiO_2$ | 27.73 | 28.40 | 49.48 | 48.16 | 39.30 |
| $B_2O_3$ | 4.36 | 4.46 | 15.24 | 7.85 | 8.71 |
| $Al_2O_3$ | 1.90 | 1.90 | 7.37 | 3.62 | 0.98 |
| $Cr_2O_3$ | 28.76 | 28.76 | — | — | — |
| BaO | 29.53 | 30.29 | — | 18.26 | 33.24 |
| CaO | 2.68 | 2.75 | 5.21 | 1.06 | 2.95 |
| ZnO | 3.36 | 3.44 | — | 4.32 | 3.75 |
| BeO | 1.68 | — | — | — | — |
| $Na_2O$ | — | — | 13.75 | 2.58 | 2.24 |
| $K_2O$ | — | — | 3.54 | 1.08 | 1.60 |
| $F_2$ | — | — | 3.44 | 0.10 | 0.77 |
| MnO | — | — | 0.76 | — | — |
| CoO | — | — | 0.56 | — | — |
| NiO | — | — | 0.65 | — | — |
| $TiO_2$ | — | — | — | 8.40 | 3.46 |
| ZrO | — | — | — | 4.67 | 2.08 |
| MgO | — | — | — | — | 0.17 |
| $P_2O_5$ | — | — | — | — | 0.62 |
| $Co_2O_3$ | — | — | — | — | 0.03 |
| $MnO_2$ | — | — | — | — | 0.05 |
| $Ni_2O_3$ | — | — | — | — | 0.05 |

the specimens varied so widely that it was necessary to vary the voltage in order to maintain the current within the range of the measuring equipment. Consequently, neither constant voltage nor constant voltage gradient was maintained. The conditions more nearly approximated constant current.

In order to assess the effect of surface irregularities better, the 0.005 in. specimens were reduced progressively in ceramic thickness. This procedure would further show whether resistance was uniform throughout the thickness of the film. The specimens were ground on a metallurgical polishing wheel to successive approximate thicknesses of 0.004, 0.003, 0.002, 0.001, and 0.0005 in. Resistance measurements were made with conducting rubber electrodes at each stage.

For high temperature application, the resistivity at temperature is obviously the important property. To establish this the 0.001, 0.003, and 0.005 in. specimens were used to determine the resistivity at temperatures from 25° to 500°C.

## Results

Figure 1 shows resistivity vs. thickness from this study and from that of Strauss, Richards, and Moore (1). The present data were gathered at room temperature (except for points E and F) and the others were measured at elevated temperatures. In the original resistivity vs. thickness curves of (1), there are several points scattered below the G-6, G-6G line between 0.003 and 0.005 in. which might indicate the beginning of a downward trend.

The author's data show that both ceramics decrease in resistivity as thickness decreases, the major decline being at thicknesses below 0.001 in.

Figure 2 is a plot of the resistivity vs. thickness for the ground samples. For the 5210 ceramic, the ground specimens follow the original curve closely, whereas as soon as the H-147 coating was ground from 0.005 to 0.004 in. the resistivity decreased by 3 decades.

The curves for resistivity vs. temperature obtained in this study as well as that from the Bureau of Standards (1) are all similar in shape and slope (Fig. 3). The decrease of 1½ to 2 decades in resistivity per 100°C increase in temperature indicates that the ceramics are normal at usual thicknesses and that the variation of resistivity with thickness is not peculiar to the special ceramics used in this work.

## Discussion

It is apparent from Fig. 1 that the resistivities of applied ceramics are not independent of coating thickness when the thickness is below 0.003 in. While the resistivity of a tiny section of the ceramic encompassing only a few molecules in any direction may be constant, the measured resistivity must include many such sections as well as sections which are not free from the effects of the ceramic-metal interface or surface irregularities. As the over-all ceramic thickness decreases these disturbing effects must manifest themselves to an increasing degree. In thicknesses of the order of 0.0005 in. the application technique which has an effect on surface roughness and the interface characteristics overbalance the internal electrical characteristics of the ceramic. Such interface characteristics as ceramic to metal bonding (interpenetration of the ceramic and metal by each other), metal oxide characteristics, and roughness of the substrate surface, all influence the measured resistance from which resistivity must be calculated. This calculation has to be made on the basis of a nominal or general thickness measurement with a micrometer which touches only the high spots of the ceramic surface. As ceramic surface roughness increases, the actual surface area of the measuring electrode varies from the apparent

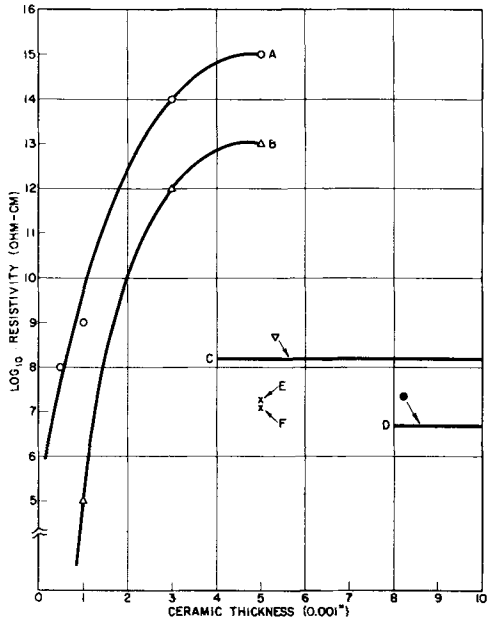


Fig. 1. Resistivity vs. ceramic thickness, measured with silver electrodes. A, 5210, room temperature; B, H-147, room temperature; C, G-6 and G-6G, 400°C (1); D, I-2, 300°C (1); E, 5210, 400°C; F, H-147, 400°C.

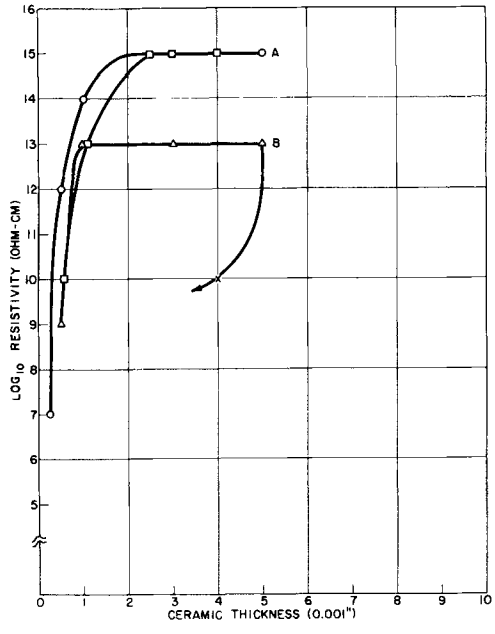


Fig. 2. Resistivity vs. ceramic thickness, measured with rubber electrodes at room temperature. A, open circle, 5210, as applied, open square, 5210, applied at 5 mils, then ground to plotted thickness; B, open triangle, H-147, as applied, x, H-147, applied at 5 mils, then ground to plotted thickness.

area based on a diameter measurement and the ceramic thickness also varies, being always less than that indicated by a micrometer measurement. As a consequence of these considerations, the electrical characteristics of ceramics intended for electrical insulation use should be evaluated only from measurements on coatings closely approximating actual service thickness.

It is believed that the explanation for the variation of resistivity with thickness lies in two effects, ceramic surface irregularities and ceramic-metal interface factors. The larger thicknesses show a higher and more constant resistivity with the rubber electrode than with the silver paint electrode (compare Fig. 1 with Fig. 2), indicating that the surface irregularities are more important at these thicknesses, since the rubber electrode does not follow these irregularities as well as does the silver paint electrode.

However, at very small thicknesses, the interface factors become more important, and these affect the resistivities determined with either electrode.

The sudden drop with only a slight decrease in thickness observed with the H-147 ceramic is related to the manner in which the ceramic was fired. This material was developed for firing in a protective atmosphere, but it was fired in air to assess the effect of such treatment. The air firing increased the substrate oxidation and hence the amount of oxide dissolved in the ceramic coating. This oxide-rich ceramic was overlain by a normal ceramic layer. Once this low oxide layer was removed, the remaining oxide rich layer exhibited its markedly lower electrical properties.

There was considerable variation in the resistance of the thinnest samples at temperatures between 25° and 200°C. Some of them showed higher resistances at 100° and 200°C than at 25°C. A second series of measurements gave a fairly good duplication of this performance.

It is believed that this behavior was caused by the penetration of the thin and imperfect ceramic films by the moisture in the 50% humidity room where the samples were conditioned and tested at 25°C. The moisture was removed by heating to 100°-200°C after which the resistance of these samples followed a normal course. When the specimens were cooled to 25°C for the repeat test moisture again penetrated the ceramic and the curves were repeated for these moisture sensitive samples. The thicker samples, of course, showed a smoothly decreasing resistance vs. temperature curve, as depicted in Fig. 3.

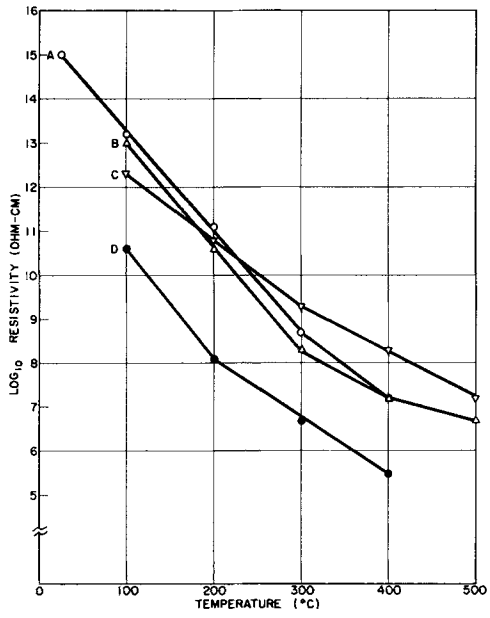


Fig. 3. Resistivity vs. temperature measured with silver electrodes. A, 5210; B, H-147; C, G-6 and G-6G (1); D, 1-2 (1).

## Conclusions

1. The resistivity of ceramic coatings decreases with increasing temperature, as is to be expected.
2. The resistivity of thin ceramic coatings is affected by surface irregularities and factors existing at the metal-ceramic interface which operate to produce a nonhomogenous coating of nonuniform thickness.
3. Electrical characteristics of ceramics intended for use as electrical insulation should be evaluated only from measurements on coatings closely approximating actual service conditions.

## Acknowledgments

The author wishes to thank Mr. G. R. Sewell for sample preparation, Messrs. A. Soris, J. Francoys, and R. D. Wagner who made the measurements, and Mr. H. T. McLean who suggested that the work be done and participated in the analysis of the results.

Manuscript received Nov. 4, 1957. This paper was prepared for delivery before the New York Meeting, April 27-May 1, 1958.

Any discussion of this paper will appear in a Discussion Section to be published in the December 1958 JOURNAL.

## REFERENCE

1. S. W. Strauss, L. E. Richards, and D. G. Moore in "Symposium on Porcelain Enamels and Ceramic Coatings as Engineering Materials", p. 101, ASTM Special Technical Publication No. 153, Philadelphia (1954).

# A New Approach to the Measurement of Coating Thickness by Fluorescent X-Ray Absorption

**Fred A. Achey and Earl J. Serfass**

*Department of Chemistry, Lehigh University, Bethlehem, Pennsylvania*

ABSTRACT

Absorption of x-ray fluorescence from the base metal of a plated sample is the most frequently used x-ray method for coating thickness determinations. If both coating and base metal yield fluorescent x-rays, it is necessary to isolate the base metal fluorescence before measurement.

Balanced filters are used for isolating the fluorescence from the base metal, and results show close agreement with crystal reflection techniques. Simplicity of the method, together with low equipment cost and high accuracy, recommend it as a useful tool in measuring plating thicknesses.

The method of measuring coating thicknesses by fluorescent x-ray absorption involves irradiating a sample with an incident x-ray beam of sufficient energy (1) to excite base metal fluorescence. The thickness of the coating layer is determined by observing, with a Geiger counter, the absorption of base metal fluorescence as it passes through the coating.

If the base metal is of lower atomic number than the coating, interference from coating fluorescence can be eliminated by adjustment of the incident x-ray tube potential (1). This was demonstrated by Beeghly (2) in his determination of tin coating thickness on steel, where the x-ray tube potential was held below that required to excite tin.

In samples where the coating is of lower atomic number than the base metal, both coating and base metal will be excited by the incident x-ray beam. Therefore, it is necessary to isolate base metal fluorescence from that of the coating before measurements are taken. Zemany and Liebhafsky (3) have shown that coating thicknesses can be determined by absorption procedures using good collimation and crystal reflection for isolation of base metal fluorescence.

The proposed technique, based on absorption of base metal fluorescence by the coating, is independent of atomic number relationships between coating and base metal, and completely eliminates the need for precise crystal reflection procedures. A differential filter system, first developed by Ross (4) and recently used in coating fluorescence measurement (5), isolates the base metal fluorescence from any interfering radiation. This affords a simple method of monochromatization with a great gain in intensity over crystal reflection procedures (6), and its use corrects for background errors normally encountered using other methods of monochromatization.

## Apparatus

A General Electric XRD-3 x-ray unit was used for the coating thickness determinations. The x-ray tube was a tungsten target Machlett AEG-50T, used in conjunction with the General Electric fluorescent sample chamber. The Geiger counter of the unit was placed directly opposite the collimator of the sample chamber, and an accurately machined slide used to place the filters alternately in the fluorescent beam. No crystal reflection was employed, and only soller-type collimators were used [*see* (5) for more details].

## Experimental

To test the use of a differential filter system for coating thickness determinations, samples were prepared using iron foil as the coating, and zirconium and silver as the base metals (Table I). These choices were made so that a direct comparison could be obtained with recent experiments by Zemany and Liebhafsky who utilized crystal reflection procedures (3). The use of iron foil simplified the preparation of accurate thickness coatings, and provided an example where the fluorescence from the coating could not be eliminated by selection of x-ray tube potential.

Before making measurements it is necessary to select and prepare the filters used for isolation of the characteristic radiation of the base metal. The

**Table I. Experimental data**

| Thickness of iron coating (mils) | Silver fluorescence (cps) | Zirconium fluorescence (cps) |
|---|---|---|
| 0.0 | 9654 | 36680 |
| 0.5 | 6404 | 12320 |
| 1.0 | 4250 | 3502 |
| 1.5 | 2029 | 1107 |
| 2.0 | 1370 | 342 |
| 2.5 | 868 | 104 |
| 3.0 | 535 | 35 |
| 3.5 | 339 | 11 |
| 4.0 | 199 | 3 |
| 4.5 | 122 | 1 |
| 5.0 | 69 | — |
| 5.5 | 47 | — |
| 6.0 | 24 | — |

elements selected for filters are chosen so that their K edges fall on both the long and short wave length side of the characteristic K radiation to be measured (base metal fluorescence). These filter elements, in elemental or compound form, are mixed thoroughly with polystyrene flour and pressed in a die heated to 350°F, forming a rigid filter disk with the element or compound uniformly dispersed throughout. The appropriate filters are balanced by sanding so that they transmit the unwanted radiation (coating fluorescence) equally. Filters used in this experimental work were balanced to ±0.3%, and their selection was based on data given in Table II. The balancing procedure eliminated the interference from coating fluorescence and background radiation.

In taking a measurement of a particular sample, filters are placed alternately in the beam consisting of fluorescent radiation from both the coating and base metal. Since previous filter balance equalized transmission of coating fluorescence, the difference in observed intensity with the two filters in the beam is due to the characteristic K radiation from the base metal, which falls in the wave-length interval, or pass band, between the two filter K edges. The high transmission of the filters reduced the power requirements of the x-ray tube to 35 kvp, 20 ma.

## Discussion

As shown in Fig. 1, straight line relationships between observed base metal intensity and coating thicknesses are obtained directly by experiment and do not involve any corrections for background interference. This is possible because of the balancing procedure, which involves equalizing the transmission of the two filters for both the coating fluorescence and the background radiation. Subtraction of intensities obtained with the two filters eliminates the effects of coating fluorescence and background radiation, and yields only the net intensity of the radiation in the previously selected pass band. The high transmission of the differential filter system reduced the power requirements to 35 kvp, 20 ma.

**Table II. Filter selection**

Iron coating on silver base metal (Ag fluorescence = 0.56Å)

| Filter | K edge (A) |
|---|---|
| Mo | 0.618 |
| Rh | 0.533 |

Iron coating on zirconium base metal (Zr fluorescence = 0.78 Å)

| Filter | K edge (A) |
|---|---|
| Rb (as RbCl) | 0.814 |
| Sr (as $SrSO_4$) | 0.768 |

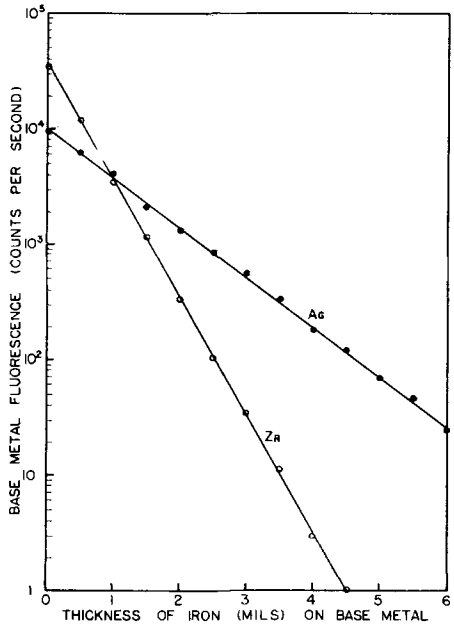


Fig. 1. Experimental results for the measurement of base metal fluorescence with balanced filters.

The straight line logarithmic relationships obtained in measurements of both the silver and zirconium base metal fluorescent intensities indicate adherence to the well known x-ray absorption laws, confirming that the intensity difference obtained with the two filters is essentially monochromatic beam.

A comparison of the proposed balanced filter method and the crystal reflection technique of Zemany and Liebhafsky (3) shows close agreement obtained between the two methods of analysis. Ultimately, however, balanced filters do not afford as critical a wave-length isolation as reflection methods, but their use in coating thickness determinations reduces equipment costs, simplifies power requirements, and automatically compensates for background radiation with no significant loss in accuracy.

Manuscript received Sept. 20, 1957.

Any discussion of this paper will appear in a Discussion Section to be published in the December 1958 JOURNAL.

## REFERENCES

1. W. T. Sproull, "X-Rays in Practice," 1st ed., McGraw-Hill Book Co., New York (1946).
2. H. F. Beeghly, *This Journal*, **97**, 152 (1950).
3. P. D. Zemany and H. A. Liebhafsky, *ibid.*, **103**, 157 (1956).
4. P. A. Ross, *Phys. Rev.*, **28**, 425 (1926).
5. F. A. Achey and E. J. Serfass, 43rd Annual Technical Proceedings, American Electroplaters' Society, p. 41 (1956).
6. P. Kirkpatrick, *Rev. Sci. Instr.*, **10**, 186 (1939).

# The Lead Oxide-Lead Sulfate and Lead Oxide-Lead Selenate Systems

**R. O. Jones and S. Rothschild**

*Mullard Research Laboratories, Cross Oak Lane, Salfords, Nr. Redhill, Surrey, England*

ABSTRACT

The lead oxide-lead sulfate and lead oxide-lead selenate systems have been investigated using the room temperature x-ray powder method. The two systems are very similar and the preparation and x-ray powder patterns are given of lead sulfate $PbSO_4$, lead monoxysulfate $PbO.PbSO_4$, lead tetroxysulfate $4PbO.PbSO_4$, lead selenate $PbSeO_4$, lead monoxyselenate $PbO.PbSeO_4$, and lead tetroxyselenate $4PbO.PbSeO_4$. The lead oxyselenates are isomorphous with the corresponding lead oxysulfates and the pattern of lead monoxyselenate has been indexed on the basis of a monoclinic unit cell of dimensions. a = 13.94Å, b = 5.78Å, c = 7.25Å, $\beta$ = 115.9°.

The lead oxide-lead sulfate system has been investigated by a number of workers but without much agreement as to the chemical formulae of the various lead oxysulfates present. The compounds reported by the various authors are listed in Table I.

The x-ray powder patterns of the lead oxysulfates detected have been published by Clark, *et al.* (3), Lander (4), and by the Shell Petroleum Co., Ltd. (5).

The structures of lead sulfate, $PbSO_4$, and lead monoxysulfate, $PbO.PbSO_4$, which occur naturally as anglesite and lanarkite, respectively, have been described (6,7).

The lead oxide-lead selenate system has not been investigated previously. The present work was carried out to re-investigate the compounds present in the lead oxide-lead sulfate system and their x-ray patterns, and to determine the compounds present in the lead oxide-lead selenate system and their powder patterns.

## Experimental

Series of lead oxide-lead sulfate and lead oxide-lead selenate materials of known compositions were prepared. X-ray powder patterns were recorded at room temperature using a Philips 114.83 mm diameter cylindrical camera and CuK $\alpha$ radiation, the specimen being coated on a thin glass fiber at the center of the camera. Suppose materials of $x$, $y$, and $z$ molecular % $PbSO_4$ show on the x-ray powder patterns the presence of PbO + compound A, compound A + compound B, and compound B + $PbSO_4$, respectively. It follows that pure A must contain between $x$ and $y$ % $PbSO_4$ and pure B similarly lies in the range $y - z$. Other materials in the range $x - y$ can now be selected until a composition is found which gives only the lines associated with A: this will be the composition of pure A. It should be noted that the method detects only those compounds that are stable at room temperature.

The x-ray powder patterns are given below in the form of tables of the interplanar spacing $d$ (in Å) and intensity $I$ of each line of the pattern. The interplanar spacings were determined by measurement of the distance between lines on the film and the estimated accuracy of $d$ is given in Table II.

The intensities of the lines were generally estimated visually and are given in terms of the scale vvs (100-90), vs (90-70), s (70-40), ms (40-30,) m (30-20), mw (20-15), w (15-10), vw (< 10). The figures in brackets denote the approximate relative intensities.

In some cases the lines were also microphotometered and the values of relative intensities obtained in these cases are given as figures in the intensity column of the tables.

## Results

### *Lead Oxide PbO (red)*

The red (tetragonal) form of lead oxide was prepared by heating lead nitrate in air at 500°C for 30

**Table I**

| Authors | Compounds reported | | | |
|---|---|---|---|---|
| Jaeger and Germs (1) | | $3PbO.PbSO_4$ | $2PbO.PbSO_4$ | $PbO.PbSO_4$ |
| Schenck (2) | | $3PbO.PbSO_4$ | $2PbO.PbSO_4$ | $PbO.PbSO_4$ |
| Clark, *et al.* (3) | $4PbO.PbSO_4$ | $3PbO.PbSO_4$ | $2PbO.PbSO_4$ | |
| Lander (4) | $4PbO.PbSO_4$ | | $2PbO.PbSO_4$ | $PbO.PbSO_4$ |

Table II

| | | | | | |
|---|---|---|---|---|---|
| d, Å | 8.0 | 4.00 | 3.00 | 2.00 | 1.500 |
| ±Δd, Å | 0.1 | 0.05 | 0.02 | 0.01 | 0.005 |

min, the x-ray powder pattern observed being in agreement with that of Swanson and Fuyat (8).

*Lead Oxide-Lead Sulfate System*

*Lead sulfate $PbSO_4$—Preparation.*—Lead acetate was dissolved in water and dilute $H_2SO_4$ added to the solution. The mixture was allowed to stand until precipitation was complete; the precipitate was then filtered off, washed, and dried.

Chemical analysis of the material so prepared gave $PbO/SO_3 = 1.00$ in agreement with the formula $PbSO_4$.

*X-ray data.*—The x-ray powder pattern obtained from the lead sulfate so prepared is given in Table III.

Heating the lead sulfate at 600°C in air and then cooling to room temperature resulted in no change in the x-ray pattern, so that lead sulfate is stable under these conditions.

*Lead oxide-lead sulfate compounds.*—For the preparation of known composition lead oxide-lead sulfate materials the following general method was employed, values of $x$ and $y$ being chosen to give the required composition. $x$ g of lead nitrate were dissolved in water, $y$ g of ammonium sulfate added to the solution, and the mixture evaporated to dryness. The product was heated in air at 500°C for 30 min and, when cool, was ground and reheated in air at a temperature between 600° and 700°C for 60 min.

A series of such materials of different composition was prepared and the results of the x-ray analysis are given in Table IV. PbO(r) denotes the red (tetragonal) form of lead oxide.

Under the conditions of preparation employed, in addition to lead oxide and lead sulfate two other definite compounds which are stable at room temperature occur in the system. These compounds A and B occur at compositions corresponding to formulas $4PbO.PbSO_4$ and $PbO.PbSO_4$, respectively.

*Lead tetroxysulfate $4PbO.PbSO_4$—Preparation.*—General method with $x = 66.0$, $y = 5.2$. Chemical analysis of the material so prepared gave $PbO/SO_3 = 4.95$ (calc. for $4PbO.PbSO_4$, 5.00).

*X-ray data.*—The x-ray powder pattern obtained from the lead tetroxysulfate so prepared is given in Table V.

Table III

| d | I | d | I | d | I |
|---|---|---|---|---|---|
| 4.3 | vs 90 | 2.40 | m 25 | 1.88 | w — |
| 3.80 | s 45 | 2.37 | vw — | 1.79 | m 30 |
| 3.62 | m 25 | 2.28 | m 25 | 1.74 | mw 15 |
| 3.47 | m 30 | 2.24 | vw — | 1.70 | m 25 |
| 3.32 | vs 80 | 2.16 | m 30 | 1.65 | mw 20 |
| 3.21 | s 60 | 2.12 | vw — | 1.61 | m 30 |
| 3.00 | vvs 100 | 2.07 | vvs 100 | 1.57 | w — |
| 2.78 | ms 40 | 2.02 | vs 80 | 1.54 | vw — |
| 2.70 | ms 40 | 1.97 | m 30 | 1.49 | m — |
| 2.62 | mw — | 1.90 | vw — | | |

Table IV

| Composition molecular % $PbSO_4$ | X-ray powder pattern corresponding to |
|---|---|
| 0 | PbO (r) |
| 10.0 | PbO (r) + Compound A |
| 16.7 | PbO (r) + Compound A |
| 20.0 | Compound A |
| 25.0 | Compound A + Compound B |
| 33.3 | Compound A + Compound B |
| 50.0 | Compound B |
| 66.7 | Compound B + $PbSO_4$ |
| 75.0 | Compound B + $PbSO_4$ |
| 80.0 | Compound B + $PbSO_4$ |
| 83.3 | Compound B + $PbSO_4$ |
| 90.0 | Compound B + $PbSO_4$ |
| 100 | $PbSO_4$ |

*Lead monoxysulfate $PbO.PbSO_4$—Preparation.*—*(a)* General method with $x = 66.2$, $y = 13.2$; *(b)* 50 g of basic lead acetate.

$(CH_3COO)_2Pb.Pb(OH)_2$ were dissolved in water and the turbid solution poured into a warm solution of 200 g of sodium sulfate in water. The mixture was allowed to stand until precipitation was complete; the precipitate was then filtered off, washed, and dried.

Chemical analysis of the material prepared by method *(b)* gave a value of $PbO/SO_3 = 1.95$ (calc. for $PbOPbSO_4$, 2.00).

*X-ray data.*—The x-ray powder patterns obtained for the lead monoxysulfate prepared by the two methods were identical and the pattern is given in Table VI.

Table V. $4PbO\ PbSO_4$

| d | I |
|---|---|
| 8.3 | m — |
| 7.2 | w — |
| 6.3 | w — |
| 5.8 | vw — |
| 5.5 | vw — |
| 4.3 | w — |
| 3.23 | vvs 100 |
| 3.10 | ms — |
| 3.06 | ms — |
| 2.97 | w — |
| 2.88 | ms 35 |
| 2.68 | S 65 |
| 2.60 | vw — |
| 2.45 | vw — |
| 2.35 | vw — |
| 2.20 | vw — |
| 2.14 | vw — |
| 2.06 | vw — |
| 1.97 | ms 30 |
| 1.95 | ms 40 |
| 1.86 | w — |
| 1.83 | mw 15 |
| 1.72 | m 20 |

Table VI. PbO $PbSO_4$

| d | I |
|---|---|
| 6.4 | m 30 |
| 5.9 | mw — |
| 5.3 | vw — |
| 4.4 | m 20 |
| 3.70 | m 25 |
| 3.52 | m 30 |
| 3.34 | vvs 100 |
| 3.19 | w — |
| 2.96 | vs 85 |
| 2.85 | s 45 |
| 2.60 | vw — |
| 2.48 | m 25 |
| 2.43 | mw 15 |
| 2.35 | mw — |
| 2.28 | m 20 |
| 2.24 | vw — |
| 2.17 | vw — |
| 2.12 | vw — |
| 2.05 | m 25 |
| 1.96 | w — |
| 1.91 | mw — |
| 1.85 | ms 35 |
| 1.76 | w — |
| 1.72 | mw — |

Table VII

| d | I | d | I | d | I |
|---|---|---|---|---|---|
| 5.5 | w — | 2.78 | m 25 | 1.99 | m 30 |
| 5.0 | ms 35 | 2.61 | m 30 | 1.97 | mw 15 |
| 4.4 | m 30 | 2.59 | w — | 1.93 | w 10 |
| 3.74 | m 25 | 2.49 | w 10 | 1.86 | ms 40 |
| 3.49 | s 50 | 2.31 | m 25 | 1.79 | w 10 |
| 3.38 | vw — | 2.27 | m 25 | 1.74 | vw — |
| 3.28 | vvs 100 | 2.21 | w — | 1.72 | w — |
| 3.16 | mw — | 2.10 | ms 40 | | |
| 3.08 | vvs 95 | 2.07 | w — | | |

*Lead Oxide-Lead Selenate System*

*Lead selenate $PbSeO_4$—Preparation.*—38 g of lead acetate were dissolved in water and the solution added to a solution of 19 g of sodium selenate in water. The mixture was allowed to stand until precipitation was complete; the precipitate was then filtered off, washed, and dried. Chemical analysis of the material so prepared gave $PbO/SeO_3$ = 1.03 (calc. for $PbSeO_4$, 1.00).

*X-ray data.*—The x-ray powder pattern obtained from the lead selenate so prepared is given in Table VII.

Heating of the lead selenate at 600°C in air and then cooling to room temperature resulted in a change in the x-ray pattern indicating that the lead selenate is unstable under these conditions. The decomposition product is usually complicated; lead oxide and lead oxyselenates have been detected. When the heating was carried out below about 500°C for the periods used in practice (30-60 min) decomposition of the lead selenate did not occur to any appreciable extent.

*Lead oxide-lead selenate compounds.*—For the preparation of known composition lead oxide-lead selenate materials the following general method was employed, values of $x$ and $y$ being chosen to give the required composition. $x$ g of lead nitrate were dissolved in water, $y$ g of lead selenate (prepared as above) added to the solution and the mixture evaporated to dryness. The product was heated in air at 450°C for 30 min and when cool was ground and reheated in air at $T$ °C for 60 min. The value of $T$ was chosen so that decomposition of the lead selenate did not occur. It was found that in the range 0-50 molecular % lead selenate $T$ = 600 was satisfactory, but in the region 50-100 molecular % lead selenate it was necessary to reduce $T$ to 450.

Table VIII

| Composition molecular % $PbSeO_4$ | X-ray powder pattern corresponding to |
|---|---|
| 0 | PbO (r) |
| 10.0 | PbO(r) + Compound C |
| 16.7 | PbO(r) + Compound C |
| 20.0 | Compound C |
| 25.0 | Compound C + Compound D |
| 33.3 | Compound C + Compound D |
| 50.0 | Compound D |
| 66.7 | Compound D + $PbSeO_4$ |
| 75.0 | Compound D + $PbSeO_4$ |
| 80.0 | Compound D + $PbSeO_4$ |
| 83.3 | Compound D + $PbSeO_4$ |
| 90.0 | Compound D + $PbSeO_4$ |
| 100 | $PbSeO_4$ |

A series of lead oxide-lead selenate materials of different composition were prepared and results of the x-ray analysis are given in Table VIII.

Under the conditions of preparation employed, in addition to lead oxide and lead selenate, two other definite compounds which are stable at room temperature occur in the system. These compounds C and D occur at compositions corresponding to formulas $4PbO.PbSeO_4$ and $PbO.PbSeO_4$, respectively.

*Lead tetroxyselenate $4PbO.PbSeO_4$—Preparation.*—General method with $x$ = 33.00, $y$ = 8.75, $T$ = 600. Chemical analysis of the material so prepared

Table IX. 4PbO $PbSeO_4$

| d | I |
|---|---|
| 8.3 | m — |
| 7.5 | w — |
| 6.3 | w — |
| 5.9 | w — |
| 5.5 | vw — |
| 4.4 | vw — |
| 3.27 | vvs 100 |
| 3.18 | ms — |
| 3.11 | ms — |
| 3.00 | vw — |
| 2.91 | ms 40 |
| 2.71 | S 60 |
| 2.62 | vw — |
| 2.49 | vw — |
| 2.39 | vw — |
| 2.35 | vw — |
| 2.28 | vw — |
| 2.22 | vw — |
| 2.16 | vw — |
| 2.07 | vw — |
| 2.00 | ms 30 |
| 1.96 | ms 40 |
| 1.86 | m 20 |
| 1.75 | m 20 |

Table X. $PbOPbSeO_4$

| d | I | Indices |
|---|---|---|
| 6.5 | m 25 | 001 |
| 6.0 | mw — | $20\bar{1}$ |
| 4.5 | mw 15 | $11\bar{1}$ |
| 3.79 | w 10 | $111$ $201$ |
| 3.57 | vw — | $31\bar{1}$ |
| 3.41 | vvs 100 | 310 |
| 3.27 | mw 15 | 002 |
| 3.01 | vs 80 | $11\bar{2}$ $40\bar{2}$ |
| 2.89 | s 40 | 020 |
| 2.62 | vw — | $220$ $22\bar{1}$ |
| 2.50 | m 20 | 202 |
| 2.39 | w — | $51\bar{2}$ $20\bar{3}$ |
| 2.33 | mw — | 403 |
| 2.28 | mw — | $221$ $60\bar{2}$ |
| 2.20 | vw — | $31\bar{3}$ |
| 2.16 | vw — | $022$ $003$ |
| 2.09 | m 25 | 600 |
| 2.01 | vw — | 312 |
| 1.96 | vw — | 511 |
| 1.89 | m 20 | $402$ $222$ |
| 1.79 | mw 15 | $20\bar{4}$ |
| 1.75 | m — | |

gave $PbO/SeO_3$ = 4.89 (calc. for $4PbO.PbSeO_4$, 5.00).

*X-ray data.*—The x-ray powder pattern obtained from the lead tetroxyselenate so prepared is given in Table IX.

*Lead monoxyselenate $PbO.PbSeO_4$—Preparation.*—*(a)* General method with $x$ = 11.30, $y$ = 12.00, $T$ = 600. *(b)* Two g of basic lead acetate were dissolved in water and the turbid solution poured into a solution of 12 g sodium selenate in water. The mixture was allowed to stand until precipitation was complete; the precipitate was then filtered off, washed, and dried. Chemical analysis of the material prepared by method *(b)* gave a value of $PbO/SeO_3$ = 2.04 (calc. for $PbO.PbSeO_4$, 2.00).

*X-ray data.*—The x-ray powder patterns obtained for the lead monoxyselenate prepared by the two methods were identical and the pattern is given in Table X.

## Discussion

The work on the lead oxide-lead sulfate system confirms that of Lander (4) in that two lead oxysulfates, namely, lead monoxysulfate $PbO.PbSO_4$ and tetroxysulfate $4PbO.PbSO_4$, exist under the conditions employed. The lead dioxysulfate $2PbO.PbSO_4$ reported by Lander to be unstable below 450°C was not detected in the present work, but this is understandable since only compounds stable at room temperature would be detected.

The x-ray powder pattern given for lead sulfate $PbSO_4$ is in good agreement with that of Swanson, Fuyat, and Ugrinic (9), while the patterns of lead monoxysulfate $PbO.PbSO_4$ and lead tetroxysulfate $4PbO.PbSO_4$ are in reasonable agreement with those of Lander (4) and the Shell Petroleum Co. (5).

The lead oxide-lead selenate system is very similar to the lead oxide-lead sulfate system, two lead oxyselenates, namely, lead monoxyselenate $PbO.PbSeO_4$ and lead tetroxyselenate $4PbO.PbSeO_4$, being stable at room temperature. The x-ray patterns of these are very similar to the corresponding oxysulfates, and the lead oxyselenates are therefore isomorphous with the corresponding lead oxysulfates.

Binnie (7) found the unit cell of lead monoxysulfate to be monoclinic of dimensions, a = 13.75Å, b = 5.68Å, c = 7.05Å, $\beta$ = 116.2°, and since the present work shows lead monoxyselenate to be isomorphous with lead monoxysulfate, the x-ray powder pattern of lead monoxyselenate can be indexed from that of lead monoxysulfate. The unit cell dimensions of lead monoxyselenate then become a = 13.94Å, b = 5.78Å, c = 7.25Å, $\beta$ = 115.9°, that is the sides of the unit cell are all increased and the angle decreased from those of lead monoxysulfate.

## Acknowledgments

Permission of the Directors of Mullards Research Laboratories to publish this work is gratefully acknowledged by the authors.

Manuscript received May 29, 1957. This paper was prepared for delivery before the New York Meeting, April 27–May 1, 1958.

Any discussion of this paper will appear in a Discussion Section to be published in the December 1958 JOURNAL.

## REFERENCES

1. F. M. Jaeger and H. C. Germs, *Z. anorg. u. allgem. Chem.*, **119**, 145 (1921).
2. R. Schenck, *Metall. u. Erz*, **23**, 408 (1926).
3. G. L. Clark, J. N. Megudick, and N. C. Schieltz, *Z. anorg. u. allgem. Chem.*, **229**, 401 (1936).
4. J. J. Lander, *This Journal*, **95**, 174 (1949).
5. "X-ray Diffraction Patterns of Lead Compounds", pp. 47-51, The Shell Petroleum Co. Ltd., Chester (1954).
6. "Strukturbericht 1913-1928," Von P. P. Ewald and C. Herman, Editors, pp. 344, 384, Leipzig (1931) [Edward Brothers, Inc., Ann Arbor (1943)].
7. W. P. Binnie, *Acta Cryst.*, **4**, 471 (1951).
8. H. E. Swanson and R. K. Fuyat, "Standard X-ray Diffraction Powder Patterns," N.B.S. Circular 539, II, p. 30.
9. H. E. Swanson, R. K. Fuyat, and G. M. Ugrinic, "Standard X-ray Diffraction Powder Patterns," N.B.S. Circular, 539, III, p. 67.

# Equilibria between Titanium Metal and Solutions of Titanium Dichloride in Fused Magnesium Chloride

**K. Komarek and P. Herasymenko**

*Department of Metallurgical Engineering, Research Division, College of Engineering, New York University, New York, New York*

ABSTRACT

A method has been developed for collecting vapors over solid $TiCl_2$ or over mixtures of $TiCl_2$ and $MgCl_2$ in a specially designed titanium pipette at elevated temperatures. The reaction of titanium tetra- and trichloride with Ti metal could not be prevented on cooling, but the analytical total content of chlorine could be used to determine the apparent total concentration of titanium in the vapor phase. The study indicated strong positive deviations from Raoult's Law for liquid $MgCl_2$-$TiCl_2$ solutions and limited solubility of $TiCl_2$ in liquid $MgCl_2$ in the range from 720° to 800°C. This was confirmed by thermal analyses of mixtures. The system $MgCl_2$-$TiCl_2$ is of the peritectic type. The peritectic point lies at about 0.3 wt % $TiCl_2$ and at 716°C. The melting point of $TiCl_2$ is 1025°C. Salt mixtures in equilibrium with Ti metal contain only $TiCl_2$, and no measurable quantities of $TiCl_4$ or $TiCl_3$.

In Kroll's method of Ti metal production, $TiCl_4$ reacts with Mg at temperatures above 700°C. Solutions of $TiCl_3$ and $TiCl_2$ in liquid $MgCl_2$ are likely to occur as intermediate stages of this reaction. The present work proposes to investigate the nature of such solutions in the presence of Ti metal. Two experimental methods were used: (*a*) a specially designed method of measuring the vapor pressure of volatile constituents over molten mixtures, and (*b*) thermal analysis of molten salts.

## Measurements of the Apparent Vapor Pressure

The following method appeared to be promising in determining the composition of the gas phase over fused salt mixtures. If a known volume of vapor over the molten salt could be collected by means of a pipette without disturbing the vapor-liquid equilibrium, and the closed pipette were rapidly cooled, the salt vapors would condense on the inside walls of the pipette and could be analyzed for the different molecular species present in the vapor, and their relative amounts could be determined. The partial pressures could then be calculated, assuming ideal behavior of the gas phase. For practical reasons the volume of the pipette cannot be very large, and therefore an accurate microanalytical method is required to analyze the salts condensed from the vapor on the pipette walls. The analytical results will be correct only if no reaction between the vapors and the pipette material takes place during cooling. Here, the choice of the pipette material was limited to Ti metal, because any other material would affect the equilibrium between liquid and vapor. As shown below, the reaction between $TiCl_3$ or $TiCl_4$ and metal could not be prevented. This fact, and other difficulties inherent in the system under study, did not allow determination of the values of partial pressures of different titanium chlorides. However, the apparent values of the vapor pressure derived from the authors' measurements permitted drawing some conclusions on the nature of the $MgCl_2$-$TiCl_x$ mixtures.

The final design of the apparatus used for the study of the vapor phase is shown in Fig. 1. After assembly of the apparatus, the whole system is evacuated at room temperature, and then transferred into a furnace preheated to a temperature at which the vapor pressure

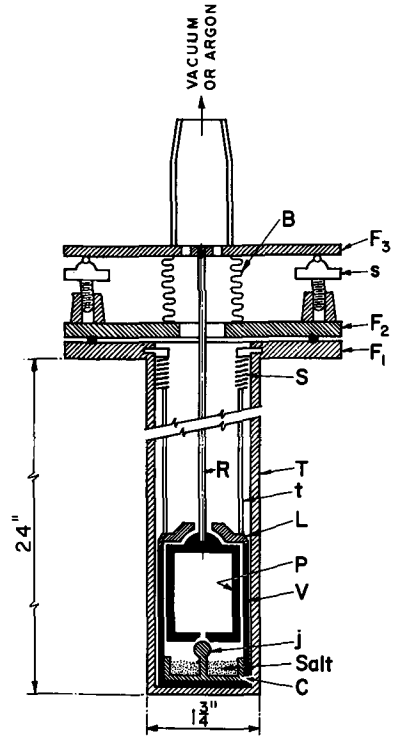


Fig. 1. Apparatus for collecting salt vapors. B, bellows; $F_1$, $F_2$, $F_3$, flanges; s, screw; S, spring; T, t, stainless steel tubes; R, Ti tube; L, Ti lid; P, pipette; J, Ti vessel; j, ground ball joint; C, salt container.

of the salts is negligible. The evacuation of the system is continued and the temperature slowly increased. When the temperature of the Ti vessel approaches the desired level, the pipette is raised to close the lid L. The vapors of the salts saturate the space inside vessel V, and pipette P. The closed vessel is then held for the desired time to equalize the temperature in the vessel and to attain equilibrium between salt, vapor, and metal parts. The temperature in the upper part of the vessel in which the pipette is located is maintained about 2° to 3°C above the temperature of the salt container. This was thought necessary to prevent condensation of salts in the pipette due to small fluctuations of temperature.

When the space inside the closed vessel V and pipette P had equilibrated with the vapor of salt in the salt container, the pipette was lowered until its opening was closed by the ball joint j attached to the salt container. Then the whole stainless steel tube was withdrawn from the furnace and cooled. After complete cooling, argon at atmospheric pressure was introduced into the apparatus so that it could be opened and the pipette removed from the tube for analysis.

The ball joint j sealed the pipette quite tightly. It was frequently observed that, when the pipette was carefully removed from the tube, the salt container, hanging on the ball joint, was also lifted from the tube. The difference in pressure—partial vacuum inside the pipette and atmospheric pressure outside it—could be preserved for at least 1 hr.

The polarographic method was used for microanalysis. The salts condensed on the inner walls of the pipette were dissolved in a small volume of 1$N$ $H_2SO_4$. It was found that this acid does not dissolve Ti from the vessel at room temperature in a polarographically detectable amount. Only the total content of Ti, Mg, and Cl could be determined polarographically.

The convenient concentration range of $Ti^{4+}$ and $Cl'$ ions for polarographic analysis is from about $5 \times 10^{-5}$ to $10^{-3}$ moles per liter. If the total pressure of titanium chlorides is about 1 mm Hg at 1000°K, the amount of Ti salt condensed on the inner walls of the pipette (22.4 ml) will be about $4 \times 10^{-7}$ moles. In order to obtain the final concentration of $Ti^{4+}$ in the analyzed solution of the order of $10^{-4}$ moles per liter, the required volume of the final solution is about 4 ml. For larger amounts of condensed titanium chlorides, correspondingly larger volumes of acid solution can be used for leaching.

This method was applied first to determine the composition of the vapor phase over solid $TiCl_2$ in equilibrium with metal. The dichloride was prepared by disproportionating solid $TiCl_3$ under vacuum at 450°C for about 30 hr. The reaction was carried out in the apparatus shown in Fig. 1 except that the pipette was not introduced. From 0.2 to 0.5 g of solid $TiCl_3$ was charged into the salt container. The trichloride was covered by a layer of iodide titanium chips to reduce the tetrachloride formed during the reaction to dichloride. After this treatment, the Ti pipette was introduced into the apparatus, and the vapor pressure determined as described above.

Denoting the number of moles of di-, tri- and tetrachloride in the gas phase over the salt at the temperature of the experiment as $n_2$, $n_3$, and $n_4$, respectively, the total content of Ti atoms is

$$n_2 + n_3 + n_4 = \Sigma n_{Ti} \qquad (I)$$

and the total content of chlorine atoms:

$$2n_2 + 3n_3 + 4n_4 = \Sigma n_{Cl} \qquad (II)$$

Assuming that the gas condensed in the pipette can be cooled and condensed so that the reaction of higher chlorides with the walls of the pipette can be neglected, the analysis will give the values of $\Sigma n_{Ti}$ and $\Sigma n_{Cl}$. Equations (I) and (II) are not sufficient to determine all three unknown values, $n_2$, $n_3$, and $n_4$, unless one of them is negligibly small or unless one of them can be determined by an independent method.

The ratio Cl/Ti in the condensed salt was found to be equal to 2 within experimental error (±0.05). Two interpretations of this fact are possible: (*A*) the vapor consists predominantly of $TiCl_2$ molecules, the content of $TiCl_3$ and $TiCl_4$ being negligibly small; (*B*) tri- and tetrachloride react with metal of the pipette on cooling to form $TiCl_2$. The latter interpretation seemed more probable. In this case, the total number of Ti atoms, $\Sigma n'_{Ti}$, as determined analytically, will be given by the equation:

$$\Sigma n'_{Ti} = \tfrac{1}{2}\,\Sigma n_{Cl} = n_2 + 1.5n_3 + 2n_4 \qquad (III)$$

The "apparent" total pressure, i.e., $\Sigma P'_{Ti} = p_2 + 1.5\,p_3 + 2p_4$, calculated from the analysis of the condensed salt, will be higher than the equilibrium pressure $\Sigma P_{Ti} = p_2 + p_3 + p_4$. The values of the apparent pressure for the experiments reported in Table I are given in the third column.

The disproportionation of lower titanium chlorides was studied recently by Skinner and Ruehrwein (1). They measured the total pressure of vapors over solid dichloride and calculated the partial pressures of di- tri- and tetrachloride from other thermodynamic data and estimated entropies and specific heats. Their values for $p_2$, $p_3$, and $p_4$ are shown in Fig. 2. Sanderson and MacWood (2) measured the heats of formation of $TiCl_2$ and $TiCl_3$ and the disproportionation equilibria of trichloride. From these measurements and from the estimated entropies and specific heats they deduced a consistent set of thermodynamic data for titanium chlorides. The values of partial pressures of tri- and tetrachloride over solid $TiCl_2$ calculated from their data are also shown in Fig. 2. Uncertainties in the estimated thermodynamic data are responsible for considerable differences in the calculated values of the partial pressure derived from both investigations.

Table I. Disproportionation of $TiCl_2$

| Temp, °C | G-atoms × $10^{-6}$ chlorine in 22.5 ml | $\Sigma P'_{Ti}$ mm Hg |
|---|---|---|
| 652 | 3.64 | 5 |
| 670 | 6.04 | 8.5 |
| 682 | 6.3 | 9.0 |
| 687 | 8.9 | 12.5 |
| 695 | 10.4 | 15 |
| 703 | 14.5 | 21 |
| 704 | 9.7 | 14 |
| 730 | 20.8 | 31 |
| 733 | 26.1 | 39 |
| 735 | 22.0 | 33 |
| 737 | 32.0 | 48 |
| 762 | 45.6 | 70 |

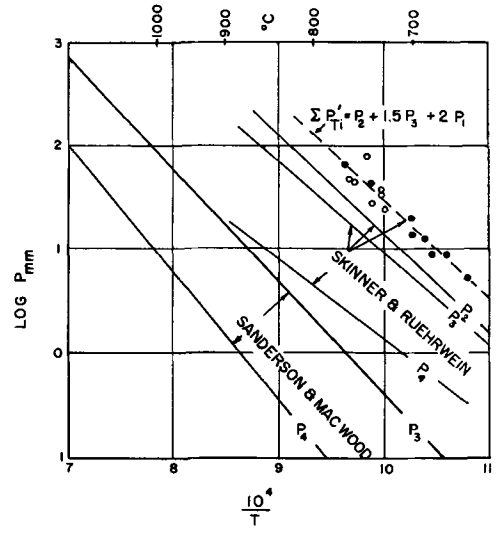


Fig. 2. Comparison of experimental $\Sigma P'_{Ti}$ values with the values derived from Skinner's and Sanderson's papers.

The broken line in the diagram, Fig. 2, represents the sum $\Sigma P'_{Ti} = p_2 + 1.5p_3 + 2p_4$, calculated from the data by Skinner and Ruehrwein to make a comparison with our experimentally found values, shown in the same figure as full circles. The agreement is good, but may be fortuitous. Sanderson and MacWood have not estimated the value of $p_2$ (the sublimation pressure of $TiCl_2$). If their values for $p_3$ and $p_4$ are taken to be more correct than those estimated by Skinner and Ruehrwein, then—in order to conform with present measurements—one has to assume that the sublimation pressure of $TiCl_2$ should be only slightly lower than the apparent pressures. Further experimental studies will be necessary to decide this matter.

Further measurements of the apparent total pressure $\Sigma P'_{Ti}$ were made over mixtures of $TiCl_2$ and molten $MgCl_2$. Results for mixtures containing more than 40 mole % $TiCl_2$ are shown in Table II. At the time when these experiments were carried out, a suitable dry box was not available to remove the salt from the reaction tube for analysis. When the salt container was removed from the argon-filled stainless steel tube the salt reacted violently with moist air with evolution of light. In only three cases was it possible to obtain approximate analyses of the salt by introducing an acid solution directly into the argon-filled titanium vessel. The accuracy was probably not greater than ±1% Ti by weight.

Since the salt mixtures were always prepared in similar proportions, one can conclude that the content of $TiCl_2$ varied within the limits found in three analyzed mixtures, i.e., from about 40 to 60% $TiCl_2$. The values of $\Sigma P'_{Ti}$ found by the analysis of vapors entrapped in the pipette are plotted in Fig. 2 as open circles. It is seen that within the limits of experimental accuracy, the points fall on the same line as for pure $TiCl_2$. This fact indicates that the activity of $TiCl_2$ in salt mixtures containing more than about 40 molar % of Ti is practically the same as that of pure $TiCl_2$. In other words, it can be safely stated that the solubility of $TiCl_2$ in molten $MgCl_2$ at about 750°C is less than 40 mole % $TiCl_2$.

Experiments with dilute solutions of $TiCl_2$ in molten $MgCl_2$ also pointed to the same conclusion. A few experiments carried out in the range up to about 2.4 mole % $TiCl_2$ are shown in Table III.

The activity of $TiCl_2$ in these dilute solutions can be taken as approximately equal to the ratio of the apparent pressure, $\Sigma P'_{Ti}$, for the given solution to the apparent pressure of the $MgCl_2$-free $TiCl_2$ at the same temperature (extrapolated from the data of Tables I and II and designated by $P_o$ in Table III). The activity coefficient, $\gamma$, calculated in this manner is about 5, indicating a strong positive deviation from Raoult's Law.

Further determinations with the described method were not carried out. Although the accuracy of the method could be improved by further experimentation, measurements of the apparent total vapor pressure for the sole purpose of determining the solubility of $TiCl_2$ in $MgCl_2$ were not justified.

## Thermal Analysis in the System $MgCl_2$-$TiCl_2$

*Experimental procedure.*—Materials used for this investigation were anhydrous $MgCl_2$ and $TiCl_2$. The $MgCl_2$ was obtained from the Bureau of Mines Experimental Station in Albany, Oregon, in a pure anhydrous form as received as a by-product from the production of zirconium metal by the Kroll process. The salt dissolved in water without any residue. Its melting point was determined to 715°C, which agreed well with the value of 714°C reported in the literature (3).

The $TiCl_3$ was obtained by reacting high purity $TiCl_4$ with Ti metal. The $TiCl_4$ was furnished in part by the Bureau of Standards and the rest was purchased from the Fisher Scientific Company. The former was 99.99% pure and the latter was purified according to NBS

Table II. Values of the apparent vapor pressure of $TiCl_x$, $\Sigma P'_{Ti}$, over mixtures of $MgCl_2$ with over 40 mole % $TiCl_2$

| Temp, °C | Approximate mole % $TiCl_2$ | G-atoms × $10^{-6}$ Ti in 22.5 ml | $\Sigma P'_{Ti}$ mm Hg | $P_{MgCl_2}$ mm Hg |
|---|---|---|---|---|
| 720 | 42 | 8.1 | 24 | — |
| 726 | — | 14.0 | 42 | 0.5 |
| 730 | — | 11.7 | 35 | 0.4 |
| 737 | 63 | 15.4 | 46 | 0.5 |
| 740 | — | 9.6 | 29 | — |
| 742 | — | 25.8 | 78 | — |
| 751 | 45 | 13.8 | 42 | 0.6 |
| 757 | — | 15.0 | 46 | 1.2? |
| 763 | — | 34.1 | 105 | — |

Table III. Values of the apparent vapor pressure of $TiCl_x$ ($\Sigma P'_{Ti}$) over mixtures of $MgCl_2$ with small contents of $TiCl_x$

| Temp, °C | Approximate mole % of $TiCl_2$* | G-atoms × $10^{-6}$ Ti in 22.5 ml | $\Sigma P'_{Ti}$ mm Hg | $P_{Mg}$ mm Hg | $P_o$ mm Hg | $\gamma$ |
|---|---|---|---|---|---|---|
| 760 | 1.8 | 2.3 | 7.0 | — | 75 | 5.2 |
| 791 | 1.4 | 3.2 | 10.3 | — | 142 | 5.2 |
| 800 | 2.4 | 5.5 | 17.5 | 1.7 | 170 | 4.3 |
| 839 | 1.3 | 7.6 | 25.0 | — | 390 | 4.9 |
| 846 | — | 8.0 | 26.5 | 3.3 | 450 | — |
| 857 | 1.2 | 9.3 | 31 | 3.4 | 550 | 4.7 |

The molar percentage of $TiCl_2$ was calculated on the assumption that only this species is present in the molten salt.

Report 3874 by addition of $Cl_2$ to the refluxing liquid. The $TiCl_4$ was transferred by distillation to avoid exposure to humid air. The Ti metal used was either iodide-grade with 99.98% Ti or an electrolytic product (Bureau of Mines, Boulder City) with 99.53% Ti.

The reaction between the tetrachloride and the metal was carried out in a quartz apparatus. A quartz flask of 250 ml capacity served as a container for the tetrachloride. The neck of the flask was connected to a quartz tube 1 3/16 in. in diameter and approximately 15 in. long. The tube was constricted about 5 in. above the flask to keep the solid piece of Ti metal in place, and then tetrachloride was distilled into the flask in excess of the amount required to react with the metal to form $TiCl_3$. The tetrachloride was cooled to —70°C, the apparatus evacuated to about 1$\mu$ and the quartz tube was finally sealed close to the upper end. The flask had a thin sealed side tube through which the excess of $TiCl_4$ could be distilled off after the run. The quartz tube with the metal was then inserted in a furnace and the metal heated to 750°C, while the temperature of the liquid $TiCl_4$ was maintained at 80°-100°C. The reaction was allowed to proceed for about 14 days. Titanium trichloride condensed in the wider parts of the quartz tube above and below the metal in the form of dense, deep violet crystal masses which would gradually fill the whole diameter of the tube. When no decrease in the volume of tetrachloride was noticeable, the temperature of the furnace was slowly lowered to convert $TiCl_2$ to $TiCl_3$. The side tube of the flask was then broken, the excess of tetrachloride distilled off, and finally the $TiCl_3$ was heated to about 200°C and the whole apparatus evacuated to remove all tetrachloride. The quartz tube was then cut off from the flask in a dry box; the trichloride was removed and stored in glass bottles. One run produced about 110 g of very dense $TiCl_3$.

For the thermal analysis, mixtures of $MgCl_2$ and $TiCl_3$ were prepared in a dry box in argon atmosphere. The crucibles and the thermocouple protection tubes which were in direct contact with molten salt were made of commercial Ti. In one modification, the crucible was open at the top and a thin Ti tube closed at the lower end served as the thermocouple well. The latter carried also at its lower end a perforated Ti disk to make the stirring of the melt more efficient. The crucible was covered with a screwed-in lid provided with an opening for the thermocouple well. To prevent excessive evaporation of salt at temperatures above 950°C, an entirely closed crucible was employed. The cap of the crucible with the thermocouple well was machined from one piece of Ti. The cap could be tightly screwed on the top of the crucible, with a thin annealed Ti sheet serving as a gasket.

The crucibles were placed in a stainless steel tube of a design similar to that shown in Fig. 1. The Ti thermocouple protection tube was screwed to a thin stainless steel tube which served as an extension of the thermocouple well, and was connected with the upper brass flange. The brass bellows permitted raising or lowering of the thermocouple well to stir the melt in the open crucible or to shake the closed type crucible. The large stainless steel tube with two brass top flanges was connected with the argon purification train by a series of movable glass elbows with ground joints so that the tube could be inserted into the preheated vertical furnace and quenched in cold water after the run without disconnecting it. The chromel-alumel thermocouple wires were sealed, vacuum tight, into the glass part of the top of the stainless steel tube with black Apiezon wax. The wires were insulated by a double-bore, hard porcelain tube. This tube reacted at elevated temperatures with Ti parts: a shiny coating, presumably of titanium silicide, was formed on its surface which could further contaminate the thermocouple. Frequent calibrations of the thermocouple with pure NaCl (Baker, analytical grade) and pure $MgCl_2$ have shown that the change in the thermocouple readings amounted to only 1°-2°C after two or three runs.

Magnesium chloride and titanium trichloride were mixed in the desired proportions in a dry box filled with argon, and were charged in Ti crucibles. In some cases, a certain amount of Ti powder was added to avoid excessive corrosion of Ti crucibles, especially at higher contents of $TiCl_3$ in the charge. The amount of salt charged in the crucibles was always about 20 g. The crucibles were transferred into the stainless steel tube under argon. The tube was connected with the vacuum system, evacuated, filled with argon, and then put into the preheated furnace. The salt was heated well above the expected freezing point and the melt was stirred or shaken frequently to homogenize the melt during an hour, the time sufficient to attain equilibrium. The power input of the furnace was then gradually lowered by means of a Variac transformer to obtain a constant cooling rate of 1-2°C/min. Readings were taken at intervals of 1 min, and between the readings the melt was stirred. Since no thermal arrests were found below 700°C, the stainless steel tube was taken out of the furnace and quenched in a water tank. The crucibles were then opened in the dry box and samples taken for analysis.

For the determination of total soluble Ti a sample was dissolved in a titration flask which was continuously flushed with hydrogen to prevent oxidation of trivalent Ti. Then, 200 ml 0.5*N* HCl and 5 ml 85% $H_3PO_3$ were added, and the trivalent Ti was oxidized with 50 ml 0.1*N* ferric ammonium sulfate solution. Eight drops of a 0.2% aqueous barium diphenylamin sulfonate solution were added as an indicator and the ferrous ions were titrated with 0.1*N* potassium dichromate solution.

For the determination of $TiCl_2$ the following procedure is suggested in literature (4). Titanium dichloride on dissolving in dilute acid reacts according to the equation

$$TiCl_2 + HCl = TiCl_3 + \tfrac{1}{2} H_2$$

The content of dichloride can thus be obtained from the volume of hydrogen formed in this reaction. The resulting solution of $TiCl_3$ can be titrated for the total content of Ti, and the initial content of trivalent Ti in the analyzed salt is then obtained from the difference,

$$\%\ Ti_{total} - \%\ Ti_{TiCl_2} = \%\ Ti_{TiCl_3}$$

Most of the salt mixtures were analyzed for divalent and trivalent titanium according to this scheme. Titanium dichloride and trichloride were always found together, the ratio being about 7.5. The fair reproducibility of the analyses led the author to believe that the knowledge of the sum of di- and trichloride was sufficient to define completely the salt composition. Therefore, the content of $MgCl_2$ and total chlorine were not determined. However, the final experiments with $MgCl_2$-free titanium chloride cast considerable doubt on the accuracy of determinations of $TiCl_2$ from the volume of hydrogen. The $MgCl_2$-free salt which solidified at 1025°C gave

Table IV.

| Position in the crucible | $TiCl_2$ % | $TiCl_3$ % | $TiCl_2 + TiCl_3$ % | Total soluble Ti % | $TiCl_2$ calculated from total soluble Ti % |
|---|---|---|---|---|---|
| Top | 84.20 | 20.60 | 104.8 | 40.30 | 99.9 |
| Bottom | 88.25 | 16.57 | 104.8 | 40.75 | 101.2 |

the values shown in Table IV. The melt contained from 9.4 to 19.7% of finely dispersed Ti metal which was separated by filtration after dissolving the samples in dilute HCl, and after the volume of hydrogen had been measured. The percentages of $TiCl_2$ and $TiCl_3$ given in Table IV refer to the composition of the metal-free salt.

The above analyses show that the sum, ($TiCl_2$ + $TiCl_3$), was about 105%. This high result could be due to the fact that not all hydrogen formed during the dissolution of samples in HCl had been collected. This failure of the exact determination of divalent Ti from the volume of hydrogen can be explained by the formation of titanium hydride in the reaction between the nascent hydrogen and Ti metal dispersed in the solid salt.

When, in the case considered here, the total soluble Ti was assumed to be present exclusively in the divalent form, the calculated percentage of dichloride was found to be close to 100%, which is a more reasonable analytical result than the 105% obtained for the sum, ($TiCl_2$ + $TiCl_3$). In other words, it appeared probable that the salt did not contain $TiCl_3$. In order to prove this conclusion, two further preparations of the $MgCl_2$-free salt were made under widely different conditions of cooling from the liquid state, and were analyzed several times for total Ti and Cl. Sample N 15 was prepared by heating $TiCl_2$ at about 1050°C, cooling slowly in the furnace to about 675°C, and then rapidly cooling. Sample V 16 was heated to 1050°C in a closed Ti crucible inserted in a sealed quartz tube, and then quenched in water. Portions of the samples were dissolved in dilute (2.5%) $H_2SO_4$, the Ti particles removed by filtration, and the total soluble Ti content determined by precipitation with cupferron or with acetic acid. Both methods gave the same results. The chlorine content was determined as silver chloride.

Gravimetric analyses gave the results shown in Table V.

The results show that the solidified salt contained only $TiCl_2$. The content of trichloride, if it was at all present, must be negligibly small. There are no reasons to suppose that trivalent Ti would be more stable in $MgCl_2$-$TiCl_2$ mixtures which solidified as heterogenous mixtures of $MgCl_2$ and $TiCl_2$. Therefore, the total contents of soluble Ti as found by titration of samples dissolved in HCl were recalculated to $TiCl_2$. Table VI gives the summary of analytical results and of thermal analyses.

Table V.

| | V 16 | | | N 15 | | Theoretical composition of pure $TiCl_2$ |
|---|---|---|---|---|---|---|
| Wt % Ti | 40.2 | 40.3 | 40.2 | 40.3 | 40.9 | 40.32 |
| Wt % Cl | — | 59.5 | 57.8 | 58.3 | 59.1 | 59.68 |
| Total % | — | 99.8 | 98.0 | 98.6 | 100.0 | 100.00 |

These experiments show that measurements of the content of $TiCl_2$ from the volume of hydrogen evolved during dissolution in acids in the samples containing dispersed metal particles are not reliable. We suspect that errors similar to those experienced here could occur in the work of other investigators who reported analyses for di- and trichloride in melts containing dispersed metal particles.

The phase diagram of the system $TiCl_2$-$MgCl_2$ shown in Fig. 3 indicates that the system is of the peritectic type. The peritectic point lies close to the melting point of pure $MgCl_2$ at about 0.29 mole % (0.35 wt %) $TiCl_2$ and 716°C. The observed peritectic temperature shows a tendency to increase with increasing content of $TiCl_2$ reaching about 725°C near the $TiCl_2$-end of the diagram. The reason for this increase is not known.

The solubility of $TiCl_2$ in solid $MgCl_2$ is below 0.35 wt % $TiCl_2$ at 715°C; the solubility of $MgCl_2$ in solid $TiCl_2$ was not determined, but it is believed to be small.

The solidified salt low in $TiCl_2$ had an emerald green color which deepened to a dark green at about 50 wt % $TiCl_2$. Further increase of the concentration of the dichloride changed the color from a grayish dark green to black with a violet tinge. The salt also changed in physical appearance, and it was more and more difficult to remove it from the crucible. The magnesium-chloride-free salt was a graphite-like substance which had to be scraped out of the crucible and which "smeared" when it was crushed with a pestle in a mortar. It was not pyrophoric and not particularly sensitive to moisture when in compact form. Much longer time was required to dissolve a sample of pure $TiCl_2$ in acid solution than samples containing $MgCl_2$.

The Ti powder was mostly deposited as a spongy mass on the walls and on the thermocouple protection tube. At higher concentrations the top part of the salt contained more Ti powder than the bottom part, and sometimes a layer of pure salt was observed at the bottom with almost no metallic Ti.

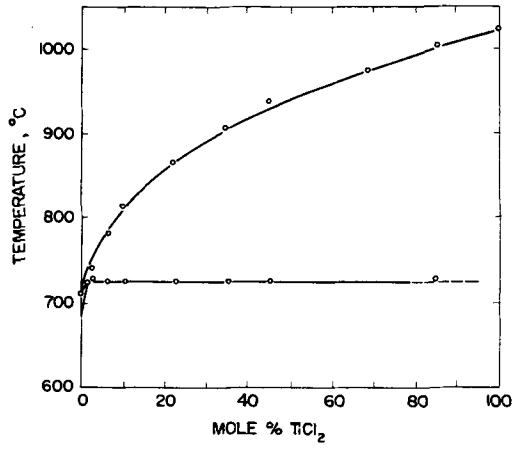


Fig. 3. Phase diagram of the $MgCl_2$-$TiCl_2$ system

Table VI. Summary of experimental results[1]

| Run No. | Charge wt, g | Wt loss, g | Ti metal (insoluble residue) wt % | Total soluble Ti, wt %[2] | $TiCl_2$ Wt %[2] | $TiCl_2$ mole % | Thermal arrests, °C |
|---|---|---|---|---|---|---|---|
| | | | Open Crucibles | | | | |
| 1 | — | — | — | 0 | 0 | 0[3] | 714 |
| 2 | — | — | — | 2.68 | 6.6 | 5.35 | 769 718 |
| 3 | 24.4 | — | 0.41 | 4.28 | 10.57 | 8.64 | 795 719 |
| 4 | 17.05 | — | 1.1 | 10.21 | 25.18 | 21.22 | 848.5 720 |
| 5 | 22.06 | Apprec. | 2.26 | 10.08 | 25.03 | 21.18 | 851 719 |
| 6 | 19.16 | — | 1.24 | 15.96 | 39.5 | 34.32 | 897 722 |
| 7 | 19.75 | — | 13.64 | 19.82 | 49.1 | 43.58 | 929 722 |
| | | | Closed Crucibles | | | | |
| 12 | — | — | — | 0 | 0 | 0[3] | 714 |
| 11 | — | — | — | 0.02 | 0.05 | | 715.5 |
| 10 | — | — | — | 0.14 | 0.35 | 0.29 | 722 716 |
| 9 | — | — | — | 0.38 | 0.94 | 0.76 | 722 716 |
| 8 | — | — | — | 0.75 | 1.86 | 1.50 | 732 716 |
| 13 | 17.32 | 0.1 | 41.1 | 29.55 | 73.2 | 68.63 | 977 — |
| 14 top | | | 14.4 | 36.10 | 89.2 | | |
| 14 middle | 16.26 | 0.2 | 10.4 | 34.50 | 85.4 | 84.59 | 1001 726 |
| 14 bottom | [4] | | 0.15 | 35.10 | 87.2 | [7] | |
| 15 top | | | 19.7 | 40.30 | 99.9 | | |
| | 20.85 | 3.4 | | | | 100.0 | 1025 — |
| 15 bottom | [5] | | 11.8 | 40.75 | 101.2 | [8] | |
| V 16 | —[6] | — | 5.2 | 40.25 | 98.9 | 100.0 | |
| N 15 | —[6] | — | 4.0 | 40.55 | 99.3 | 100.0 | |

Remarks: [1] Determinations of $TiCl_2$ content from the volume of hydrogen collected after dissolving samples in dilute acid are not given here because they were found to be inaccurate.
[2] The percentages of total soluble Ti and of $TiCl_2$ were calculated from analyses after subtracting the insoluble (metallic) Ti dispersed in the salt.
[3] 100% $MgCl_2$.
[4] 1.15 g metallic Ti powder added to the charge.
[5] 3.9 g metallic Ti powder added to the charge.
[6] Average values.
[7] Average value.
[8] Accepted value.

It has to be pointed out that appreciable amounts of metallic Ti dispersed in the melts were found in all cases, whether Ti powder was added to the charge or not. As it is seen from Table VI, the percentage of dispersed metal generally increased with increasing content of soluble Ti. The origin of the dispersed metal was certainly the material of the crucible. The dispersions were formed through the corrosive action of $TiCl_3$ in the charge which strongly attacked the inner walls of the crucibles. Some metallic particles were coarse (up to 0.5 mm in cross section); they were probably metal crystals loosened from the crucible walls. Similar formation of metallic dispersions ("pyrosols") was observed by Straumanis (5) in the melts exposed to air or when the metal immersed in a halide melt contained oxygen. The material of our crucibles was commercial grade Ti with about 0.3% oxygen: it did not form Straumanis' "pyrosols" in pure magnesium or sodium chloride melts, under argon atmosphere, but could do so when exposed to the corrosive action of $TiCl_3$ in the charge.

The formation of metal dispersion by some disproportionation reaction on cooling, e.g.,

$$2TiCl \rightarrow Ti + TiCl_2$$

does not seem probable. Our data do not lend any tangible support for the assumption that titanium monochloride could form in the melts and disproportionate on cooling.

## Acknowledgments

B. L. Dunicz participated in the early development stages of the vapor pressure measurements method. Arnold Veinbachs did most of the analytical work. The study was supported by the Office of Naval Research Contract No. Nonr 285(13) as a part of the research program on the Extraction Metallurgy of Titanium.

Manuscript received April 15, 1957. This paper was prepared for delivery before the Cleveland Meeting, Sept. 30-Oct. 4, 1956.

Any discussion of this paper will appear in a Discussion Section to be published in the December 1958 JOURNAL.

## REFERENCES

1. G. B. Skinner and R. B. Ruehrwein, *J. Phys. Chem.*, **59**, 113 (1955).
2. B. S. Sanderson and G. E. MacWood, *ibid.*, **60**, 314 (1956).
3. O. Kubaschewski and E. Ll. Evans, "Metallurgical Thermochemistry," p. 255, Pergamon Press, New York, 2nd ed. (1956).
4. W. C. Kreye, C. J. B. Fincham, L. Nanis, M. Jaworsky, and H. Kellogg, Final Report, Nonr 266(24), Columbia University, June, 1956.
5. S. T. Shih, M. E. Straumanis, and A. W. Schlechten, *This Journal*, **103**, 395 (1956).

# Equilibria between Titanium Metal and Solutions of Titanium Dichloride in Fused Sodium Chloride

K. Komarek and P. Herasymenko

*Department of Metallurgical Engineering, New York University, New York, New York*

ABSTRACT

Thermal analyses of $TiCl_2$ and NaCl in closed titanium metal crucibles were made in the range from 0 to 100 wt % $TiCl_2$. The melting point of $TiCl_2$ was confirmed to be 1025°C. The phase diagram of the system has two compounds and one eutectic. The eutectic point lies at 50.0 wt % $TiCl_2$ and 605°C. One compound, $NaCl \cdot TiCl_2$, is formed by a peritectic reaction at 628°C; the other one, $2NaCl \cdot TiCl_2$, decomposes in the solid state at 548°C.

The free energy curves derived from the phase diagram indicate that liquid NaCl-$TiCl_2$ melts have the highest stability at temperatures up to about 800°C at the composition 2Na + 1 Ti + 4Cl, thus making probable the existence of $[TiCl_4]^{2-}$ complex ions. At higher temperatures or in the presence of large cations, more complex ionic clusters are likely to exist.

Results of an investigation of the $MgCl_2$-$TiCl_2$ system were reported in a previous paper (1). Information on other salt systems containing titanium tri- and di-chloride is rather scarce. Mixtures of NaCl and $TiCl_3$ or $TiCl_2$ are of special interest because they are formed transitionally in the Na reduction process, and may also be used in the electrolytic production of Ti metal.

## Thermal Analysis in the System NaCl-$TiCl_2$

This paper gives the results of an investigation of the phase diagram in the system NaCl-$TiCl_2$ by thermal analysis. The charge consisted of NaCl and $TiCl_3$. The NaCl was of the AR grade and was dried by heating *in vacuo* at 500°C. Titanium trichloride was prepared in this laboratory. The materials were charged under argon into Ti crucibles made of commercial Ti. The crucibles were provided with lids which permitted them to be closed tightly. The lid carried a thermocouple-well tube made of Ti, which projected into the salt mixture. The experimental procedure and the analysis of salt mixtures have been already described (1). On heating, $TiCl_3$ reacted with the metal of the crucible, giving $TiCl_2$. The weight of the mixture was about 20 g. It was rather difficult to attain complete tightness of the crucible lid, so that in most cases some loss due to evaporation was observed. The average amount lost from mixtures containing NaCl was 0.5 g or about 2.5% of the charge. The mixtures were heated about 100°C above the expected melting point, and thermal arrests were determined on cooling. Chemical analyses of solidified salts presented similar difficulties as were observed in the case of $MgCl_2$-$TiCl_2$ mixtures. The salts contained dispersed Ti metal powder in varying amounts (from 1 to 5 g/melt). There was no correlation between the amount of dispersed Ti metal and the chemical analysis of the salt soluble in dilute HCl. The most probable origin of this metallic dispersion was the crucible material. The crucibles were made of commercial grade Ti which contained about 0.3% oxygen. Straumanis and co-workers have shown recently (2) that oxygen-bearing Ti tends to form fine dispersions of metal ("pyrosols") in molten halides. In the present case, the formation of such dispersions was assisted by corrosive action of $TiCl_3$ in the charge which strongly attacked the inner walls of the crucible. Some metallic particles were rather coarse, up to 0.5 mm in cross section; they were most probably metal crystals loosened from the inner surface of the crucibles by the corrosive action of $TiCl_3$.

The solidified salt was scraped out of the crucible in a dry box under argon. The mixture was then dissolved in HCl and the total analyzed content of soluble Ti was calculated as $TiCl_2$. It was shown previously (1) that $TiCl_2$ solidifying at 1025°C in closed Ti crucibles contained titanium and chlorine atoms in the ratio 1:2. This ratio was found in several preparations of the salt made under different conditions of cooling from the molten state and containing different amounts of suspended metal. In the present work it was assumed that fused mixtures of NaCl and TiCl obtained in contact with Ti metal also contained only divalent Ti. A direct determination of divalent Ti from the volume of hydrogen evolved during the dissolution of salts in acids was found to be unreliable in the presence of fine metallic particles. As already mentioned (1), part of the hydrogen reduced by $TiCl_2$ from dilute acid reacts with finely dispersed Ti metal to form solid titanium hydride. Therefore, the measured volume of hydrogen gas is lower than would correspond to the content of $TiCl_2$.

Values of $TiCl_2$ as found by titration are given in Table I and were used in construction of the phase diagram shown in Fig. 1.

Table I. Summary of results

| Charge weight in g | Weight loss in g | $TiCl_2$ wt % | $TiCl_2$ mole % | Thermal arrests in °C | | | |
|---|---|---|---|---|---|---|---|
| 22.0 | — | 0 | 0* | 801 | — | — | — |
| 21.1 | 0.6 | 15.84 | 8.46 | 762.5 | — | 605.5 | — |
| 19.1 | 0.8 | 21.75 | 12.02 | 740 | — | 611.5 | — |
| 24.3 | 0.0 | 30.32 | 17.62 | 709.5 | — | 612.5 | 566.5 |
| 24.5 | 0.3 | 40.3 | 24.92 | 656.5 | — | 611 | 549 |
| 16.5 | 0.9 | 46.2 | 29.68 | 621 | — | 603 | 547.5 |
| 21.7 | 0.2 | 49.9 | 32.9 | — | — | 608 | 552 |
| 21.2 | 0.2 | 52.7 | 35.3 | 680 | 629 | 605 | 548 |
| 19.7 | 0.2 | 61.25 | 43.75 | 822 | 628 | 605 | 546 |
| 20.8 | 1.3 | 76.8 | 61.9 | 938.5 | 625 | (597.5)† | (548)† |
| 18.9 | 0.1 | 83.15 | 70.8 | 969 | 626.5 | (598)† | (543)† |
| 19.0 | 3.6 | 100 | 100 | 1025 | — | — | — |

* 100% NaCl; † Faint arrests.

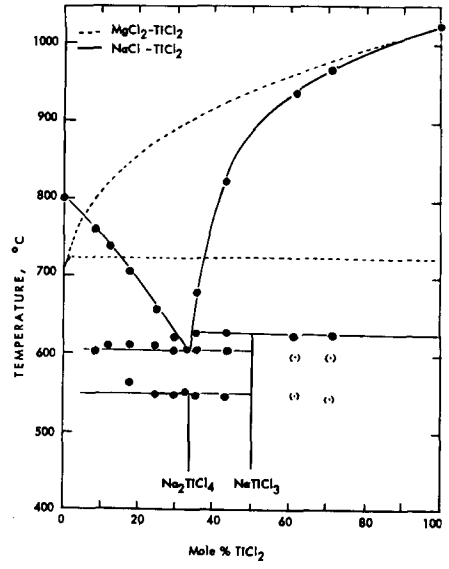


Fig. 1. Phase diagrams of the NaCl-$TiCl_2$ and $MgCl_2$-$TiCl_2$ systems.

## Discussion

The phase diagram of the system has one eutectic at 605°C and at 50.0 wt % (33.3 mole %) $TiCl_2$.

The solid phase in equilibrium with the melt on the NaCl-rich side of the diagram is a solid solution of $TiCl_2$ in NaCl. The extent of this solid solution was not determined. The curve of primary crystallization rises steeply on the side of higher concentrations of $TiCl_2$ to the melting point of $TiCl_2$. The melting point of $TiCl_2$ was redetermined twice and was found to be, respectively, 1027° and 1023°C which is in good agreement with the previously reported value of 1025°C. The composition of the solid phase in equilibrium with the liquid on the $TiCl_2$-rich side was not investigated, but the formation of extensive solid solutions of NaCl in $TiCl_2$ seems to be improbable.

At 628°C, a peritectic reaction takes place; the melt reacts here on cooling to form a compound. The composition of this compound was not determined. A tentative formula of NaCl·$TiCl_2$ was assigned to this compound.

On further cooling below the eutectic temperature another reaction takes place at 548°C. This can be interpreted as a peritectoid reaction: a compound, probably 2NaCl·$TiCl_2$, disproportionates at 548°C into two solid phases, the solid solution of $TiCl_2$ in NaCl and the above mentioned compound NaCl·$TiCl_2$. The formula 2NaCl·$TiCl_2$ is very probable, since the arrests are strongest around 33.3 mole % $TiCl_2$. Analogous compounds, 2KCl·$TiCl_2$ and KCl·$TiCl_2$, have been found in the KCl-$TiCl_2$ system by Ehrlich (3). The existence of these compounds was confirmed by x-ray studies.

The solidified salt low in $TiCl_2$ had a bluish-green color which deepened with increasing content of $TiCl_2$. At about 50 wt % the salt was gray-green. At higher contents of $TiCl_2$ the color changed to a black-violet and the physical appearance became like that described previously for $TiCl_2$.

Figure 1 shows a comparison of the phase diagrams for the two systems—$MgCl_2$-$TiCl_2$ and NaCl-$TiCl_2$—on the molar concentration basis. A qualitative discussion of thermodynamic properties of these systems will be helpful for a general explanation of the behavior of $TiCl_2$ in molten salts.

Figure 2 shows schematic curves of the free energy of formation of liquid NaCl-$TiCl_2$ solutions from solid NaCl and solid $TiCl_2$ at three temperatures: just above the eutectic temperature, just above the decomposition temperature of NaCl·$TiCl_2$,

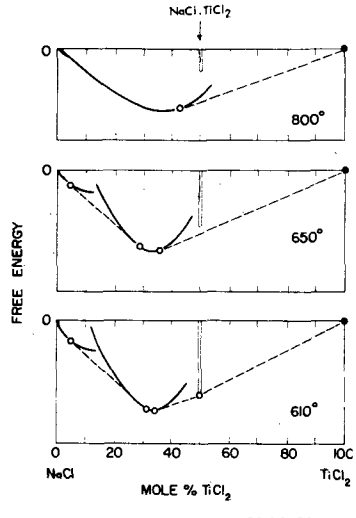


Fig. 2. Free energy curves for NaCl-$TiCl_2$ system at 610°, 650°, and 800°C. Open circles correspond to two-phase boundaries.

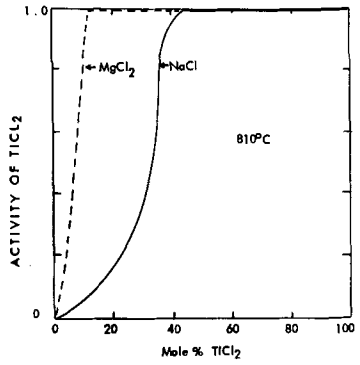


Fig. 3. Activities of $TiCl_2$ in NaCl-$TiCl_2$ and $MgCl_2$-$TiCl_2$ mixtures at 810°C.

and at 800°C. It is seen that the free energy of liquid NaCl-$TiCl_2$ solutions is the lowest near the eutectic composition, i.e., at 33.3 mole % $TiCl_2$. It is evident also that this conclusion is not affected by the existence of the compound NaCl·$TiCl_2$ at temperatures below 650°C, because the free energy of formation of this compound should be more positive than that of the liquid at temperatures above the eutectic point.

Figure 3 shows a qualitative comparison of $TiCl_2$ activities in both systems at 810°C, i.e., above the melting points of NaCl and $MgCl_2$ but below the melting point of $TiCl_2$. An appreciable solid solubility of either $MgCl_2$ or NaCl in $TiCl_2$ is improbable. Therefore, the activity of $TiCl_2$ in the two-phase regions, liquid + $TiCl_2$, should be very close to unity. In the liquid phase, the activity should decrease with decreasing content of $TiCl_2$. It is evident that the activity of $TiCl_2$ in liquid NaCl-$TiCl_2$ solution will be considerably lower at all concentrations below about 42 mole % $TiCl_2$ at 810°C than in $MgCl_2$-$TiCl_2$ mixtures. Thus, $TiCl_2$ is more strongly bound in NaCl liquid solutions than in $MgCl_2$ melts. The fact that the free energy of formation of NaCl-$TiCl_2$ melts has a minimum at the composition of 2NaCl·$TiCl_2$ was used in construction of the activity curve in Fig. 3 to indicate that the activity of $TiCl_2$ in NaCl melts should have an inflection point at this composition.

The highest stability of the liquid at the composition 2Na + 1Ti + 4Cl makes the assumption of stable complex ions $[TiCl_4]^{2-}$ very probable. Thus the main structural units of the melt on the NaCl-rich side of the phase diagram appear to be $Na^+$, $Cl^-$, and $[TiCl_4]^{2-}$ ions.

The liquidus on the $TiCl_2$ side of the NaCl-$TiCl_2$ system rises steeply above the eutectic temperature and begins to deflect toward the temperature axis at a perceptibly accelerated rate only above 800°C. Thus, it can be concluded that NaCl-$TiCl_2$ melts can dissolve $TiCl_2$ in excess of 33.3 mole % only at the expense of an increase of the free energy in the system. The dichloride dissolving in the melt in excess of 33.3 mole % should be present in a form different from that of the complex ions, $[TiCl_4]^{2-}$; it may be either undissociated molecules of $TiCl_2$ or large ionic clusters composed of

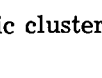

sub-units with direct bonds between Ti atoms. The existence of undissociated molecules in ionic melts is rather improbable. On the other hand, by postulating the existence of large ionic clusters, the general behavior of $TiCl_2$ can be explained and partly predicted on the basis of the electrostatic theory of bonding in molten electrolytes.

For clarity of further discussion, the term "complex ion" is reserved here for units containing only one metallic ion in the center, e.g., $[TiCl_4]^{2-}$, $[MgCl_4]^{2-}$, and the like. The bonding between the central atom and chlorine atoms is largely ionic. The "ionic clusters" are defined as structural units containing more than one metallic atom per unit, e.g.,

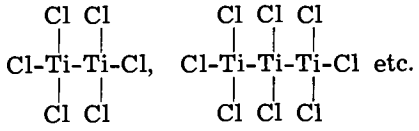

The bonding between Ti ions is nonionic.

The large clusters represent a transition to solid $TiCl_2$ which is known to possess a layer structure with direct bonds between Ti atoms. The activity of $TiCl_2$ in melts containing such large clusters should be higher than in melts containing only $[TiCl_4]^{2-}$ ions; it approaches the value of unity on approaching the phase boundary between the liquid solution and solid titanium dichloride. The structural units of the $MgCl_2$-$TiCl_2$ melts are mainly large clusters composed of

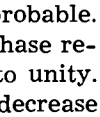

and

sub units. (Solid $MgCl_2$ has also a layer structure, and it is reasonable to suppose that the structure of liquid $MgCl_2$ at not very high temperatures does not differ substantially from that of the solid.) Since divalent Mg and Ti atoms have approximately the same ionic radii, Cl ions are attracted to them roughly to the same degree: neither Ti nor Mg cations possess a marked tendency to form preferentially complex ions, $[TiCl_4]^{2-}$ or $[MgCl_4]^{2-}$. On the other hand, the electrostatic field of force of Na ions, which have a larger size and a smaller charge than Mg ions, is weaker than that of divalent ions. Therefore, chloride ions in the NaCl-$TiCl_2$ melts are more strongly attracted by bivalent Ti ions than by Na ions with the formation of complex ions of the type $[TiCl_4]^{2-}$. The stability of these complex ions is strongly influenced by the charge and size of the solvent cations. Thus, the activity of divalent Ti in molten chlorides should decrease when Mg ions are replaced by larger divalent cations ($Ca^{2+}$, $Sr^{2+}$, or $Ba^{2+}$); this decrease should be even more pronounced when Mg ions are replaced by monovalent cations ($Na^+$, $K^+$, $Rb^+$, or $Cs^+$).

A similar effect of different cations on the activity of AgBr in molten alkali bromides was observed by Salstrom and Hildebrand (4). They found that Li and Na cations which have a smaller size than Ag ions increased the activity of AgBr, whereas K and Rb cations having larger diameters decreased it. Analogous effects of the solvent cation size are observed in molten basic steelmaking slags. The activity of P, which is present in the slags in form of

$[PO_4]^{3-}$ complex ions decreases by several orders of magnitude when small $Fe^{2+}$ or $Mg^{2+}$ ions are replaced by large $Ca^{2+}$ ions (5, 6).

Large clusters composed of two or more Cl-Ti-Cl sub-units can be held in solution when the structure of the melt is sufficiently open. (An increased openness of the melt structure can be attained either by expansion due to temperature increase or in the presence of large cations.) Sodium ions are evidently not large enough to make the structure of $NaCl$-$TiCl_2$ melts sufficiently open to permit the dissolution of $TiCl_2$ much in excess of 33.3 mole % at temperatures below about 800°C, i.e., the melt cannot accommodate much of the large cluster ions. The solubility of $TiCl_2$ in these melts increases rapidly at temperatures above 800°C; thermal expansion becomes a predominant factor here. Monovalent cations of larger size than Na ions should permit the accommodation of more of such clusters in the melt; in other words, they should extend the range of liquid solutions to the $TiCl_2$ side more than is observed in the $NaCl$-$TiCl_2$ system. This conclusion is in agreement with observation. The solubility of $TiCl_2$ in NaCl melts at 800°C is 42 mole % (present work), and in KCl melts it is 67 mole % [Ehrlich's work (3)]. One can safely predict that this solubility will be considerably lower in $LiCl$-$TiCl_2$ melts and appreciably higher in $RbCl$-$TiCl_2$ and $CsCl$-$TiCl_2$ melts. In the binary systems with alkaline earth chlorides the solubility of $TiCl_2$ will increase with increasing radius of solvent cation in the sequence Mg, Ca, Sr, Ba.

Analogous conditions are found in other binary systems where one of the components has a layer structure in the solid state. Thus, the solubility of solid $CdCl_2$ (or of $MgCl_2$) in binary melts with alkali chlorides increases when Na ions are replaced by K ions. Similarly, the solubility of solid silica in silicate melts (7) increases in binary oxide systems in the direction of the increasing size of alkali or alkaline-earth cations:

Cs>Rb>K>Na>Li>Ba>Sr>Ca>Mg

(Silica dissolved in silicate melts forms large ionic units, i.e., chains, networks and even more complex spacial structures, in which some oxygen atoms are shared by two Si atoms and which require an open structure for their accommodation in the melt.)

### Acknowledgments

This study was supported by the Office of Naval Research, Contract No. Nonr 285(13), as part of the Research Program on the Extractive Metallurgy of Titanium. The authors gratefully acknowledge the assistance of A. Veinbachs in carrying out chemical analyses.

Manuscript received May 22, 1957.

Any discussion of this paper will appear in a Discussion Section to be published in the December 1958 JOURNAL.

REFERENCES

1. K. Komarek and P. Herasymenko, Submitted for publication.
2. M. E. Straumanis, et al., *This Journal*, **103**, 395 (1956).
3. P. Ehrlich, *Z. anorg. u. allgem. chem.*, **292**, 146 (1957).
4. E. J. Salstrom and J. H. Hildebrand, *J. Am. Chem. Soc.*, **54**, 4252 (1932).
5. P. Herasymenko, *J. Iron and Steel Inst.*, **166**, 169 (1950).
6. H. Flood and K. Grjotheim, *ibid.*, **171**, 64 (1952).
7. F. C. Kracek, *J. Am. Chem. Soc.*, **52**, 1436 (1930).

# Equilibria in the Niobium-Hydrogen System

**W. M. Albrecht, M. W. Mallett, and W. D. Goode**

*Battelle Memorial Institute, Columbus, Ohio*

ABSTRACT

Equilibria in the niobium-hydrogen system were determined in the range 100°-900°C, 10-1000 mm of mercury hydrogen pressure, and atomic ratios of hydrogen to niobium of 0.01-0.85. A single phase solid solution of hydrogen in niobium was produced throughout most of the system. In no region did the equilibrium solubility exactly follow a simple pressure dependency. The heat of solution increased with hydrogen content, which behavior may be related to an expansion in the niobium lattice.

Until recently, the chief interest in niobium was its use as an alloying constituent of steels. Now in the nuclear reactor field, Nb *per se* is attractive because of its potential high temperature properties. In order to evaluate these properties, a knowledge of the behavior of Nb in various environments is essential. In the present study the equilibria in the Nb-H system were determined.

An early study of the solubility of hydrogen in rather impure Nb was reported by Hagen and Sieverts (1). Later, Sieverts and Moritz (2) determined the solubility at 1 atm pressure using a purer (98.5%) metal. The major impurity was Ta. It is considered that the later study is more reliable. McKinley (3) recently presented an equilibrium-solubility study for low hydrogen compositions.

Gulbransen and Andrew (4) investigated the reaction of hydrogen with Nb in the range 200°-900°C at pressures up to 5.7 cm Hg. These investigators stated that there were probably two hydrides of Nb which formed at low hydrogen pressures. In a few kinetic experiments performed at this laboratory no

Table I. Summary of room temperature x-ray studies of the Nb-H system

| Composition, H/Nb | Body-centered cubic lattice parameter, kX | | Reference |
|---|---|---|---|
| | Alpha | Beta | |
| 0.39 | 3.300 to 3.306 | 3.416 to 3.420 | (5) |
| 0 | 3.302 ± 0.004 | — | (6) |
| 0.11 | 3.327 ± 0.003 | — | (6) |
| 0.49 | 3.323 ± 0.003 | Complex* | (6) |
| 0 | 3.295 | — | (7) |
| 0.11 | 3.307 | — | (7) |
| 0.11 to 0.41 | 3.303 | Orthorhombic† | (7) |
| >0.41 | — | Orthorhombic† | (7) |
| 0.091 | 3.297 ± 0.005 | 3.420 ± 0.005 | (8) |
| 0.098 | 3.302 ± 0.005 | 3.410 ± 0.010 | (8) |
| 0.63 | — | 3.410 ± 0.005 | (8) |
| 0.82 | — | 3.440 ± 0.005 | (8) |
| 0.09 | 3.301 ± 0.002 | — | This work |
| 0.20 | 3.305 ± 0.002 | 3.43 | This work |
| 0.68 | 3.301 ± 0.002 | 3.41 | This work |

* Close packed hexagonal structure believed by Brauer and Hermann (7) to be nitride.
† a = 4.718, b = 4.768, c = 3.421. This structure was also considered to be a distended BCC structure, $a_o$ = 3.44 kX.

surface product was formed at 400°-700°C at 1 atm of hydrogen pressure.

Several limited, room temperature x-ray studies have been reported for the Nb-H system. Umanski (5) found a two-phase structure in Nb containing H at an atomic ratio of H to Nb of 0.39. Both phases were given as body-centered cubic having different lattice constants. Horn and Ziegler (6) studied the system at concentrations up to 0.49 atomic ratio and reported a single phase (alpha phase) and a two-phase (alpha plus gamma prime) region. Brauer and Hermann (7) report two single-phase regions with a two-phase region in between 10 and 41 a/o hydrogen (0.11 to 0.70 H/Nb ratio). Knowles (8), likewise, reports two single phases and a two-phased region over the range of atomic ratios of H to Nb of 0.091-0.83. The results of the various room temperature x-ray investigations are summarized in Table I. In general, these studies show that there is a lattice expansion in each single-phase region as the H content increases.

### *Material*

Bar niobium having a Vicker's hardness of 113 was fabricated into rod approximately 0.3 cm in diameter and into a 0.03 cm sheet. Analysis of the fabricated Nb, shown in Table II, was obtained by spectrographic, chemical, and vacuum-fashion techniques.

Pure hydrogen was obtained from the thermal decomposition of uranium hydride prepared from dry, tank hydrogen and degreased uranium chips.

### *Method*

A micro-Sieverts' apparatus, shown in Fig. 1, having a double-walled reaction tube was used for the pressure-temperature-composition equilibria determinations. The total volumes of the reaction section at room temperature and at several selected elevated temperatures were measured with helium. From these, the effective volumes of the hot zone (at furnace temperature) and cold zone (at room temperature) were calculated for each furnace temperature. Reference curves were plotted of the variation of the volumes of the hot and cold zones over the temperature range of the study.

Table II. Analysis of Nb

| Element | PPM by weight |
|---|---|
| Ta | 1500 |
| Fe | 200 |
| Sn | 200 |
| Mo | 50 |
| Si | 50 |
| V | 50 |
| Cr | 20 |
| Al | 20 |
| Ti | 20 |
| C | 120 |
| $O_2$ | 430 |
| $N_2$ | 120 |
| $H_2$ | <3* |

* After degassing.

Specimens consisted of 3-4 g of sheet Nb in pieces 1-2 cm long, 0.6 cm wide, and 0.03 cm thick. Also, small pieces of 0.3 cm diameter rod were used in one experiment. Samples were dry abraded with 240-grit silicon carbide paper and placed in the calibrated inner chamber of the reaction tube. A Pt-Pt + 10% Rh thermocouple was inserted into the reaction tube so that the bead was in close proximity with the specimen. The reaction tube was then evacuated and the specimen degassed for 1 hr at 800°C and 0.02$\mu$ of Hg.

Equilibrium data were obtained in the following manner. An initial measured quantity of H was added to the inner reaction tube at the desired temperature. The system was allowed to come to a constant pressure as measured on a Hg manometer. This pressure was considered to be the equilibrium pressure. The equilibrium composition was calculated from the equilibrium pressure, specimen weight, the gas addition, and volume of the reaction system. The temperature was increased and equilibrium points determined at various temperatures. Another gas addition was then made and the process repeated by decreasing temperature. This was continued until the entire ranges of pressure, tempera-

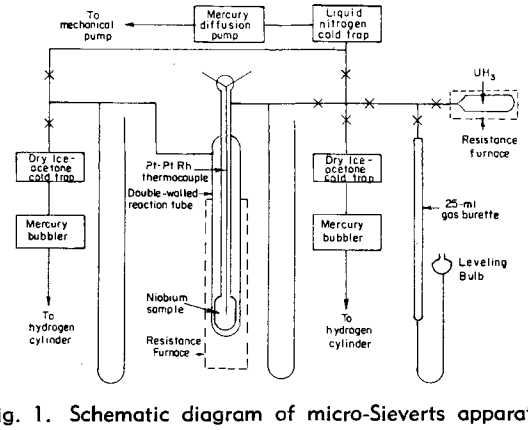


Fig. 1. Schematic diagram of micro-Sieverts apparatus

ture, and composition were covered. Equilibrium data were obtained in a comparable manner by making gas extractions from the system. Also, H additions and extractions were made isothermally at 400°, 450°, and 500°C to note whether hysteresis occurs. No hysteresis was noted.

Throughout the experiments, a pressure close to that in the system was maintained in the outer chamber of the furnace tube with dry, tank H. This was done to prevent diffusion of H out of the reaction system.

Vacuum-fusion analysis of the Nb specimens after the runs showed that there was little or no change in the oxygen content of the metal. The Nb that originally contained 430 ppm oxygen by weight analyzed 460 ppm by weight, after an equilibrium experiment. This is within the normal reproducibility limit for oxygen analyses.

## Results

The pressure-temperature-composition equilibria of the Nb-H system were determined in the range 100°-900°C, 10-1000 mm Hg, and atomic ratios of H to Nb of 0.01-0.85. Determinations were made with three different samples of 0.03 cm Nb sheet and one of 0.3 cm diameter rod. Figures 2 and 3 show isotherms for all the equilibrium data. Figure 2 is a plot of equilibrium pressure against the H/Nb ratio, while Fig. 3 is a logarithmic plot of the same variables. The 300°C isotherm (Fig. 2) is invariant at about 8 mm Hg, indicating the presence of a two-phase region. No other invariant pressures were obtained for any of the isotherms at 350°C and above. Therefore, the results show that nearly all of the equilibrium data were obtained in a single-phase region. This is also shown in Fig. 4, in which the equilibrium temperature is plotted against the H/Nb ratio to show isobars at 10, 100, and 1000 mm Hg. It is seen that only a small portion of the 10 mm isobar is invariant in the range of H/Nb ratios of 0.21-0.42.

To determine room-temperature structures, x-ray diffraction patterns were obtained and metallographic examinations were made on several Nb specimens having compositions of H/Nb of 0.09, 0.20, and 0.68. These samples were water quenched from equilibrium at 700°, 500°, and 400°C, respectively. The sample containing 0.09 H/Nb showed primarily a body-centered cubic Nb structure, alpha phase, with lattice parameter, $a_o = 3.301 \pm 0.002$ kX. A very small amount of a second phase was also detected. This phase can be seen as needles in the photomicrograph of the material shown in Fig. 5. The alpha matrix phase of the microstructure appears the same as that of the original hydrogen-free Nb. Two phases were found in the specimen containing 0.20 H/Nb, an alpha niobium phase ($a_o = 3.305 \pm 0.002$ kX) and another body-centered cubic structure, beta phase, with $a_o = 3.43$ kX. The two-phase structure of this material can be seen in Fig. 6. The specimen containing 0.68 H/Nb contained primarily the beta phase, $a_o = 3.41$ kX, and a small amount of alpha phase, $a_o = 3.301 \pm 0.002$ kX. This structure is shown in Fig. 7. These data are in agreement with the published results

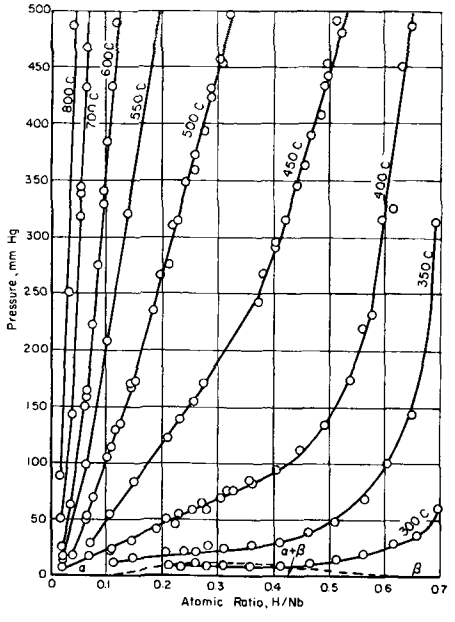


Fig. 2. Isotherms in the Nb-H system

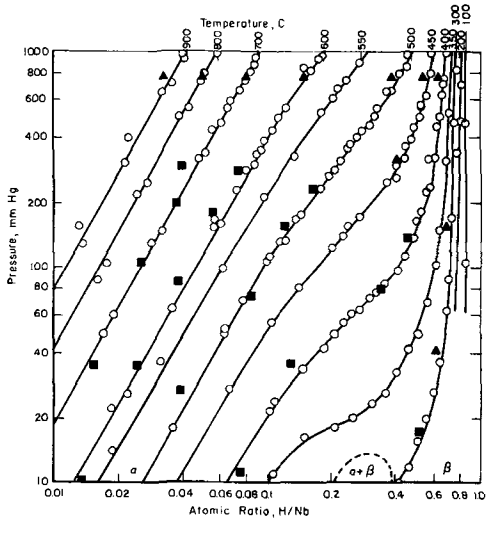


Fig. 3. Logarithmic plot of isotherms in the Nb-H system. Open circle, present study; solid square, McKinley (3); solid triangle, Sieverts and Moritz (2).

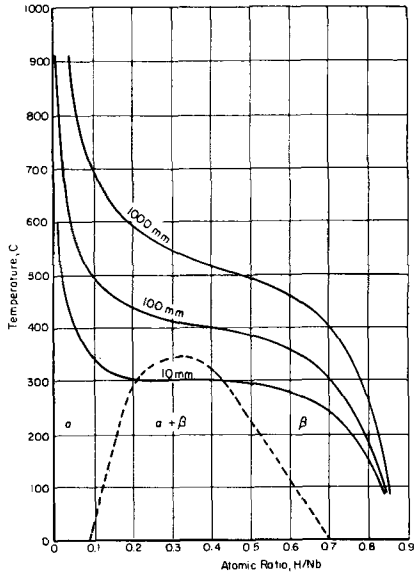


Fig. 4. Representative isobars for the Nb-H system

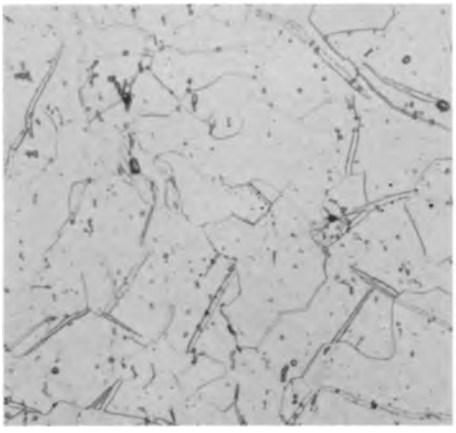

Fig. 5. Niobium containing 0.09 H/Nb quenched from equilibrium at 700°C. Magnification, 250X before reduction for publication.

Fig. 6. Niobium containing 0.20 H/Nb quenched from equilibrium at 500°C. Magnification, 250X before reduction for publication.

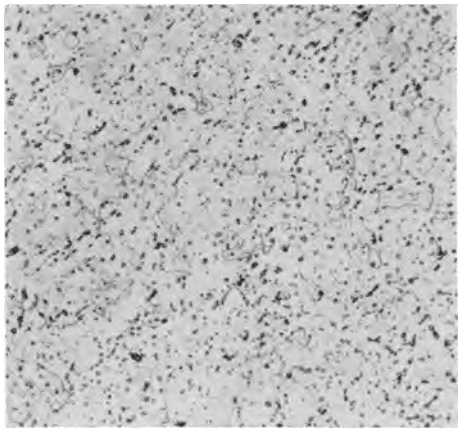

Fig. 7. Niobium containing 0.68 H/Nb quenched from equilibrium at 400°C. Magnification, 250X before reduction for publication.

from room temperature x-ray investigations (5-8) shown in Table I. If all the x-ray data are considered, the two-phase region extends from about 0.09 to 0.7 H/Nb at room temperature. These limits were used with those obtained at 300°C in the present equilibria study to outline the probable two-phase boundary in the Nb-H system shown in Fig. 4. Apparently, the temperature of the critical point where the two phases, alpha and beta, become identical lies somewhere between 300° and 350°C. Above the critical temperature, S-shaped isobars were obtained. This is also indicated in the experimental isotherms in Fig. 2 and Fig. 3. In equilibrium diagrams S-shaped isotherms are usual in single-phase regions immediately above the critical point. Similar curves have been shown in the palladium-deuterium system reported by Gillespie and Downs (9).

Figure 3 shows that the isotherms from a logarithmic pressure-composition plot were straight at concentrations up to 0.1 H/Nb. At higher hydrogen contents the S-shaped curvature of the isotherms is quite evident. Similar curves fit the limited data for the Nb-H equilibrium reported by Sieverts and Moritz (2) and McKinley (3). As shown in Fig. 3, their data corroborate those of the present study. However, at high H/Nb ratios Sieverts and Moritz show a lower equilibrium hydrogen concentration at the same temperature and pressure than the present work. Since they used Nb that was less pure (98.5%) this would be expected. Impurities in the metal would probably decrease the hydrogen solubility. This effect would be more pronounced in the high hydrogen concentration range. McKinley reports that at concentrations up to H/Nb of 0.055 the equilibrium solubility follows the square root of pressure or Sieverts law and a heat of solution of 18.5 kcal/mole was obtained. In the present study, a plot of square root of equilibrium pressure against composition deviated from Sieverts law. Deviations were observed at lower compositions than expected. However, a heat of solution estimated from a Sieverts type plot for compositions below about 0.085 H/Nb agrees very well with that of McKinley. It would not be expected that the equilibrium solubilities at higher compositions necessarily follow a square root of pressure dependency since the published x-ray investigations show lattice expansions in Nb as the hydrogen content increases. This constitutes another variable which may affect equilibrium solubility.

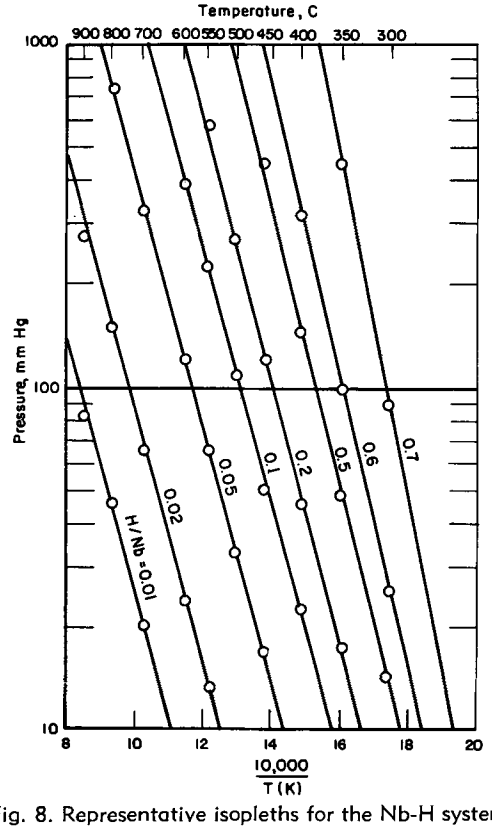


Fig. 8. Representative isopleths for the Nb-H system

Table III. Thermodynamic data for various Nb-H compositions

| Composition H/Nb | Constants in $\log_{10}P_{mm} = -A/T + B$ A | B | ΔH, cal/mole |
|---|---|---|---|
| 0.01 | 3509 | 4.92 | 16,050 ± 380 |
| 0.02 | 3628 | 5.54 | 16,600 ± 170 |
| 0.05 | 3674 | 6.30 | 16,810 ± 170 |
| 0.10 | 3693 | 6.83 | 16,900 ± 190 |
| 0.20 | 3908 | 7.49 | 17,880 ± 240 |
| 0.50 | 4131 | 8.33 | 18,900 ± 450 |
| 0.60 | 4503 | 9.21 | 20,610 ± 190 |
| 0.70 | 5093 | 10.80 | 23,300* |

* Calculated from two points.

To put the equilibrium in the Nb-H system on a sound basis, it is necessary to consider the equilibrium of formation of various products (solid solutions) having definite H/Nb ratios. Therefore, various isopleths were plotted, logarithm of equilibrium pressure against reciprocal temperature, in Fig. 8. It is seen that a series of straight lines were obtained which increase in slope with hydrogen content. The equation for these lines is

$$\log_{10}P_{mm} = -\frac{A}{T\,(K)} + B$$

The values of the constants, A and B, in this equation and the heats of solution for the various compositions are given in Table III. It is seen that the heat of solution increases with hydrogen content.

## Conclusions

The Nb-H system has been investigated in the ranges 100°-900°C, 10-1000 mm Hg, and H/Nb ratios of 0.01-0.85. The absorption of hydrogen resulted in the formation of a single-phase solid solution throughout most of the system. However, at about 300°C and a pressure of 8 mm Hg, the presence of a two-phase region was indicated between H/Nb ratios of 0.21-0.42. In the equilibrium diagram, the critical point where the two phases become identical probably lies just within the ranges of this work.

At low hydrogen compositions the equilibrium solubility follows approximately a square root of pressure relationship. This indicates that hydrogen is absorbed as atoms. At the higher hydrogen compositions, no simple pressure dependency was evident. Lattice expansion of the niobium causes deviations from a strict square root of pressure dependency. Both lattice parameter and heat of solution increase with hydrogen concentration.

Manuscript received Sept. 10, 1957. Work performed under AEC Contract W-7405-eng-92.

Any discussion of this paper will appear in a Discussion Section to be published in the December 1958 JOURNAL.

REFERENCES

1. H. Hagen and A. Sieverts, *Z. anorg. u. allgem. Chem.*, **185**, 225 (1930).
2. A. Sieverts and H. Moritz, *ibid.*, **247**, 124 (1941).
3. T. D. McKinley, Paper presented before the Regional AIME Meeting, Cleveland, Ohio (April 1957).
4. E. A. Gulbransen and K. F. Andrew, *J. Metals*, **188**, 586 (1950).
5. Y. S. Umanski, *J. Phys. Chem. U.S.S.R.*, **14**, 332 (1940).
6. F. H. Horn and W. S. Ziegler, *J. Am. Chem. Soc.*, **69**, 2762 (1947).
7. G. Brauer and R. Hermann, *Z. anorg. u. allgem. Chem.*, **274**, 11 (1953).
8. D. R. Knowles, Report No. IGR-R/C-190, United Kingdom Atomic Energy Authority (March, 1957).
9. L. J. Gillespie and W. R. Downs, *J. Am. Chem. Soc.*, **61**, 2496 (1939).

# Electromotive Force Measurements in Cerium-Cerium Chloride Liquid Systems

**Seymour Senderoff and G. W. Mellors**

*National Carbon Research Laboratories, National Carbon Company, A Division of Union Carbide Corporation, Cleveland, Ohio*

ABSTRACT

The emf of the cell $Ce|CeCl_3(1-x)Ce(x)||CeCl_3|Cl_2$ (graphite) has been measured over a temperature range from the melting point of $CeCl_3$ to about 950°C. Preliminary conductance measurements indicate that the saturated solution of cerium in cerium chloride is an ionic conductor. The potential results indicate the presence of a subhalide, $Ce^+[CeCl_4]^-$, in which both monovalent and trivalent cerium exist. Further, it is suggested that cerium chloride may exist in a highly associated state in which the following formula may represent the dominant species, viz., $[CeCl_2]^+$ $[CeCl_4]^-$. The addition of cerium to this system may result in the reduction of the less highly complexed cation as follows:

$$[Ce^{3+}Cl_2]^+ [Ce^{3+}Cl_4]^- + Ce \rightarrow\rightarrow \frac{3}{2} Ce^+[Ce^{3+}Cl_4]^-$$

In the course of the work a reversible chlorine electrode, satisfactory at temperatures up to 950°C, has been developed and will be reported elsewhere.

Few investigations of metal-metal halide liquid systems have been reported. Some information exists in the form of phase diagrams by Cubicciotti and co-workers (1, 2, 3). Conductance work in alkali metal-alkali halide melts has been reported by Bronstein and Bredig (4); phase equilibria have been studied in these systems by Bredig, *et al.* (5, 6). Corbett and Winbush (7) have reported the solubility of some metals in their molten halides, while Grjotheim, Gronwold, and Krogh-Moe (8) studied cryoscopy in Cd-$CdCl_2$ melts.

Various theories have been presented regarding the structure of the molten metal-metal halide systems; the first was that of Lorenz (9), who called them "pyrosols" and considered them to be emulsions or colloidal dispersions of the metal in the metal halide. Cubicciotti (1-3) showed that this could not be true in the systems he studied, since definite freezing point depressions were observed, which could only be ascribed to true solution formation. The nature of these solutions, however, has been a matter of controversy and three approaches have been used to describe them:

(*A*) The metal dissolves by entering the liquid as atoms which occupy vacancies or interstitial sites in the liquid.

(*B*) The metal dissolves as cations occupying normal cationic sites. The electrons are considered either to occupy anionic vacancies or to be more or less free electrons in a postulated band structure in the liquid analogous to the conditions in a nonstoichiometric crystal.

(*C*) The metal reduces the salt to a lower halide. The system may then be considered as the solution of a subhalide in the normal halide.

Emf studies of metal-metal halide systems appear to be a promising method of distinguishing among these alternatives, since each would produce distinctly different effects on the emf of a reversible metal electrode immersed in the molten salt solution. The first model would be equivalent to simple dilution and the change in emf on the addition of metal to the salt should be of the order of magnitude predicted by the Nernst equation for the appropriate changes in activity of the components of the system. The second model should result in considerable electronic conductivity in the system which should cause changes in the emf which depend on the degree of electronic conductivity as discussed by Wagner (10). Wagner showed that when electronic conductance is small $\Delta E/E_o = t_e$, where $E_o$ is the emf of the system in the absence of electronic conductance, $\Delta E$ the difference between the observed emf and $E_o$, and $t_e$ the "transference number" for electrons. The third model would introduce a new ionic species, which may produce a widely different emf from that of the higher valence ion. If both the higher and lower valence ions exist, they should also exhibit a characteristic redox potential.

The system selected for study was cerium metal dissolved in cerium trichloride, the phase diagram for which has been reported by Cubicciotti (3), who found a rather large solubility of cerium, up to a maximum of 33 mole %. There are no reports in the literature of previous emf measurements in this system.

## Experimental

### *Materials*

$CeCl_3$ was prepared from $Ce_2S_3$ as follows: Pellets of $Ce_2S_3$ were charged into a previously chlorinated graphite crucible; the crucible was tightly closed with a fitted graphite cover containing graphite tubes for gas inlet and outlet and thermowell. This

was placed in a quartz tube and the entire assembly put into a pot furnace. The outer quartz tube was fitted with a "Transite" cover. Purified argon was continually passed through the quartz tube and a mixture of argon and chlorine through the graphite crucible containing the $Ce_2S_3$. On heating the charge, the reaction started at about 300°C with the evolution of sulfur chlorides and sulfur. The temperature rose rapidly to about 700°C and was controlled by varying the ratio of $Cl_2$ to argon in the feed gas. When, after several hours, the evolution of sulfur compounds almost stopped, the temperature of the charge was raised to 900°C. When the charge melted (at about 820°C) sulfur compounds again appeared in the exit gases and the reaction was continued until these were eliminated. Finally, the apparatus and contents were cooled slowly in an argon atmosphere. The material was stored in a dry box. Analysis indicated the theoretical Ce:Cl ratio and over-all purity of 99.2%. No foreign metals were observed by spectrographic analysis and no water-insoluble material (i.e., CeOCl) was noted.

Creium metal was prepared by electrolysis of a LiCl-KCl eutectic mixture containing 40 wt % $CeCl_3$ by a method based on that described by Eastman, *et al.* (11). Analysis indicated that the cerium was 99.6% pure. All weighings and transfers were performed in a dry box.

Chlorine electrodes were prepared by inserting the end of a 2-ft length of high-density graphite base tubing, 10.4 mm O.D., 5.4 mm I.D., to the bottom of a porous graphite cylinder (National Carbon Company, Grade 60), 4 in. high and 15 mm O.D., a seal being made with F-cement (National Carbon Company). The base of the porous cylinder was about 3-4 mm thick. The electrodes were purified by treatment with chlorine at 2300°C for 2 hr. In use chlorine was passed into the tube and allowed to emerge through the porous cylinder into the electrolyte. The electrode, its reversibility, and its other properties are described more fully elsewhere (12).

Argon was purified by passage through titanium chips at 900°C. Chlorine was dried by passage through a column of "Drierite" desiccant. Spectroscopic examination of chlorine showed no significant traces of impurities, water, CO, and $CO_2$ being absent.

*Furnace and cell.*—The furnace was a tensile test type made by Marshall Products. The bore was 3½ in. and an iron tube 3¼ in. O.D. ¼ in. wall thickness served as a baffle between the furnace windings and the "Vycor" glass tube containing the cell and electrodes. The cell envelope was a 51 mm O.D. "Vycor" glass tube, 30 in. in length, closed at each end with a 10½ rubber stopper. Each stopper was protected by an Alundum thermal radiation shield. Through the lower stopper passed a 9 mm "Pyrex" glass tube, which served as entry tube for argon and as guide for the pedestal, the latter being a ¼ in. diameter iron rod. A short piece of molybdenum rod (⅛ in. diameter) threaded 6/32 screwed into the top of the iron rod and was secured by a Mo collar (inner) and a stainless nut (outer) through the base of a "Morganite" ΔRR XN100 recrystallized alumina crucible. A liquid-tight seal was always obtained by

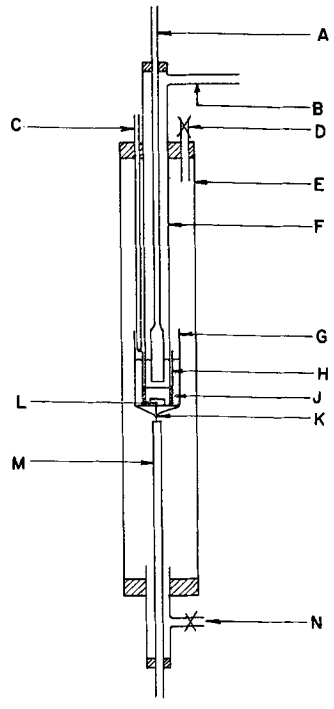


Fig. 1. Cell envelope and contents. A, chlorine electrode; B, chlorine exit; C, thermocouple sheath; D, argon exit; E, 51 mm O.D. Vycor glass envelope; F, 25 mm O.D. Vycor glass sheath; G, XN100 alumina crucible; H, XN20 alumina crucible; J, ΔRR alumina pedestal; K, molybdenum rod, threaded 6/32; L, molybdenum collar; M, iron pedestal; N, argon entry tube.

this method. Inside the XN100 crucible an XN20 crucible was mounted on a ΔRR alumina collar. Communication between the melts in the two crucibles was established through a 1/32 in. diameter hole, drilled through the base of the XN20 crucible, packed with asbestos and prefired. Through the upper 10½ rubber stopper, passed an argon exit tube, (provided with a tap), a "Vycor" thermocouple sheath and a 25 mm O.D. "Vycor" glass tube, provided with a side arm for exit of chlorine. This tube fitted snugly inside the XN20 crucible and, with the apparatus charged with molten salts, a good "liquid seal" between the $Cl_2$ and A atmospheres was maintained. The $Cl_2$ electrode passed through a No. 4 stopper in the top of the 25-mm tube. The upper part of the electrode was protected from atmospheric oxidation as follows: chlorine passed through a glass entry tube, the O.D. of which was equal to the I.D. of the graphite tube, and a pressure tubing sleeve gripped both members. Electrical contact was maintained by a copper band, tightened into a groove around the graphite: the whole was coated with "Unichrome" stop-off (Metal and Thermit Corporation) and no portion of the electrode was exposed to the atmosphere. A schematic diagram and a photograph of the apparatus are shown in Fig. 1 and 2.

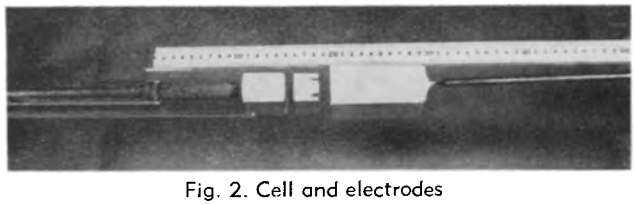

Fig. 2. Cell and electrodes

*Temperature.*—Chromel-alumel thermocouples were used, protected by 6 mm "Vycor" glass sheaths, closed at the lower end. The thermocouple was positioned at the top of the XN20 crucible, ¼ in. above the melt in the outer (XN100) crucible. It was shown that there was less than 1° difference in temperature between this portion and a point immediately beneath the base of the outer (XN100) crucible. An L&N potentiometer was used to measure thermocouple output. The temperature of the furnace was controlled by a "Wheelco" controller with an independent thermocouple adjacent to the furnace winding.

*Measurement of potential.*—A "Rubicon" galvanometer and potentiometer were used, the latter reading from 0 to 1.6 v in steps of 0.05 mv. Since the potential to be measured was of the order of 2.2 v, it was necessary to include a source of "bucking" potential in the circuit. An "Eveready" "Air Cell" (National Carbon Company) battery was employed, shunted permanently across a 200 ohm resistor; the potential was ascertained accurately each time a measurement was made.

*General procedure.*—The apparatus was charged with an amount of $CeCl_3$ previously calculated to give a satisfactory depth of melt in the crucibles. A large excess of cerium metal was used, since it was necessary for there to be sufficient (*a*) to saturate the $CeCl_3$ in the outer crucible and (*b*) to cover completely the molybdenum collar in the base of the XN100 crucible. (This was usually of the order of 40 g.) All joints in the apparatus were sealed with a "Unichrome" stop-off prior to commencement of a run. The apparatus was flushed with argon for several hours and then heated slowly overnight to about 900°C. The $Cl_2$ was then bubbled slowly (¼ c.f.h.) through the melt. After two to three hours a steady, reproducible value of potential was obtained and measurements were made, cooling and heating, between 810° and about 950°C. The argon supply was stopped during potential measurements, since the flow cooled the lower electrode, leading to inaccurate results.

## Results

Potential values as a function of temperature for the cell $Ce|CeCl_3$ (saturated with Ce)$||CeCl_3|Cl_2$ (graphite) (I) are shown in Fig. 3. The chlorine electrode was the + electrode in all the measurements.

Over the temperature range 820°-920°C, $dE/dT$ has the value −0.68 mv/°C. The curve of Fig. 3 represents the average of three runs, the maximum deviation being 2 mv at low temperatures (820°C) and 3 mv at high temperatures (920°C and above). It will be observed that the values obtained here are about 0.7 v less than those calculated from thermal data by Hamer, *et al.* (13). Since the departure of 0.7 v (equivalent to approx. 48 kcal) from the theoretical decomposition potential of $CeCl_3$ suggests that the reaction $2Ce + 3Cl_2 \rightarrow\rightarrow 2CeCl_3$ is not the one which is responsible for the observed potential, a series of experiments was performed to determine whether a lower valence state of cerium may be the potential-determining species. In this case the solution of cerium in cerium chloride would form a redox system and its potential could be studied by

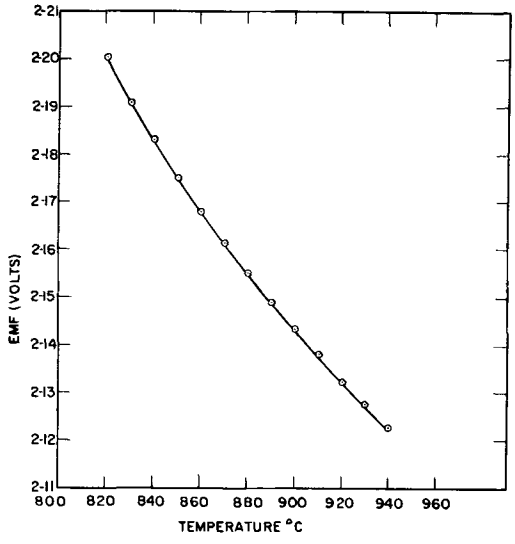


Fig. 3. Emf as a function of temperature in saturated solution.

varying the concentration of added cerium metal and observing the potential on an inert electrode in a cell which can be written as follows:

Mo, $Ce^{3+}$, $Ce^{(3-x)+}||CeCl_3|Cl_2$ (graphite) Cell (II)

In most experiments, molybdenum electrodes were used, but in two cases identical potentials were obtained using tungsten electrodes, thus establishing the inert character of both of these elements in the system.

In Table I, the weight of Ce and $CeCl_3$ in the outer crucible are shown, together with $Ce^{3+}/Ce^{2+}$ and $Ce^{3+}/Ce^{1+}$ [1] hypothetical ratios calculated on the assumption that such are the valence states exhibited by the Ce ions in these systems. The last column gives the value of the observed emf of Cell II at a number of compositions.

## Discussion

The first important result to consider is the departure of 0.7 v in the observed potential of Cell (I) from the calculated value of Hamer, *et al.* (13). The uncertainty in the thermal data of Brewer (14) may be of the order of 150 mv. A measurement of the Cell $Ce|KCl$ (0.95) $CeCl_3$ (0.05)$||KCl$ (0.95) $CeCl_3$ (0.05)$|Cl_2$ (graphite) (III) gave a potential of 2.8 v

[1] $Ce^{3+}/Ce^{2+} = [0.189\ y/x - 0.667]$
$Ce^{3+}/Ce^{1+} = [0.379\ y/x - 0.333]$
where $x$ = wt of Ce in grams and $y$ = wt of $CeCl_3$ in grams.

Table I.

| Wt Ce (g) | Wt $CeCl_3$ (g) | Mole ratio $Ce/CeCl_3$ | $Ce^{3+}/Ce^{2+}$ | $Ce^{3+}/Ce^{1+}$ | $E$ (880°C) |
|---|---|---|---|---|---|
| Excess | — | — | 0 | 1. | 2.1550 |
| 12.56 | 72.00 | 0.307 | 0.446 | 1.84 | 2.1583 |
| 12.55 | 72.00 | 0.307 | 0.446 | 1.84 | 2.1586 |
| 11.30* | 83.90 | 0.237 | 0.736 | 2.48 | 2.1562 |
| 9.00* | 83.90 | 0.189 | 1.098 | 3.20 | 2.1580 |
| 6.95 | 83.90 | 0.146 | 1.620 | 4.25 | 2.1571 |
| 4.13 | 83.90 | 0.0867 | 3.160 | 7.36 | 2.1540 |
| 2.91 | 83.90 | 0.0611 | 4.790 | 10.61 | 2.1478 |
| 1.48 | 72.00 | 0.0362 | 8.550 | 18.12 | 2.1024 |
| 1.18 | 72.00 | 0.0289 | 10.890 | 22.77 | 2.0904 |
| 0.871 | 83.90 | 0.0183 | 17.57 | 36.09 | 2.0372 |
| 0.8557 | 83.90 | 0.0180 | 17.94 | 36.87 | 2.0882 |

* Tungsten electrodes.

at 922°C. The solubility of cerium in the electrolyte of Cell (III) is very small (probably of the order of 0.1%), so in this case it is the $Ce^0/Ce^{3+}$ couple that is being measured. Using concentration instead of activity in the Nernst equation to correct for the dilution of $CeCl_3$ in Cell (III), the potential of Cell (III) with pure $CeCl_3$ as the electrolyte would be about 2.7 v, in fair agreement with the value of 2.87 v calculated from the approximate thermal data. The departure then is real and not ascribable to the uncertainty in the literature value.

An obvious source of error in the potential measurement is the liquid junction potential in Cell (I) between the cerium-saturated $CeCl_3$ and the pure cerium chloride. The liquid junction potential between silver chloride and cerium chloride has been found by the authors to be less than 60 mv over the temperature range 820°-920°C. Since the cerium-saturated solution of $CeCl_3$ has a lower conductance than that of silver chloride, the liquid junction potential in Cell (I) should be substantially less than this value and must be considered as not significant. A formal calculation of the activity of $CeCl_3$ in the cerium-saturated solution based on the observed potential value and the $E_0$ of Hamer (14) gives a value of $10^{+6}$ for the activity at a mole fraction of 0.67. This indicates the essential absence of $CeCl_3$ in its usual state.

Ascribing the deviation to electronic conductance is impossible on two grounds. First, the interposition of pure $CeCl_3$, generally considered to be a pure ionic conductor, as an electrolyte in Cell (I) "filters out" any electronic current which may be supported by the cerium-containing electrolyte on the other side of the cell, and thus eliminates any effect on the cell potential of electronic conduction (15). Second, preliminary conductance measurements which the authors have made indicate that the almost saturated solution of cerium in cerium chloride is a typical ionic conductor having a conductance of 3.76 mhos at 840°C and 3.57 mhos at 810°C, a positive temperature coefficient of conductance, which is also a property of ionic conductance. The conductance of $CeCl_3$ at 840°C is about 0.92 mhos and no evidence for electronic conductance may be deduced from this comparatively small change in conductance on adding 32 mole % cerium, especially in view of the results of Bronstein and Bredig (4), who showed that addition of 20 mole % K to KCl increased the conductance by a factor of 70. To explain the deviation of 0.7 v on the basis of Wagner's (10) equation would require about 24% electronic conductance.

Another alternative would be to consider the Ce-$CeCl_3$ mixture not as an electrolyte with either ionic or mixed conduction, but as a semiconducting electrode. In this case, however, the cell would be essentially $Ce|CeCl_3|Cl_2$ and, in the case of the saturated solution of Ce in $CeCl_3$, the potential would be expected to approximate the calculated value for this cell. As noted above, it is actually found to be 0.7 v lower. The assumption of semiconduction of the Ce-$CeCl_3$ system is apparently not in accord with the observed emf.

There remains, then, the formation of subhalides by reduction of $CeCl_3$ with cerium to explain the observed result. The stoichiometric reduction of $CeCl_3$ to the "dichloride" may be expressed by either of the following equations:

$$2CeCl_3 + Ce \rightarrow\rightarrow 3CeCl_2 \qquad (a)$$

$$4CeCl_3 + 2Ce \rightarrow\rightarrow 3Ce^+ [CeCl_4]^- \qquad (b)$$

The "dichloride" of equation (a) is written to indicate the cerium is present as $Ce^{2+}$ and the "dichloride" of equation (b) indicates the cerium is present in two valence states, $Ce^{1+}$ and $Ce^{3+}$. The existence of $Ce^{+1}$ in the absence of $Ce^{3+}$ (i.e., a net valence state less than +2) may be disregarded because of insufficient "solubility" of cerium in cerium chloride.[2]

The preponderance of evidence derived from the emf measurements suggests equation (b) as the description of the "solution" of cerium in $CeCl_3$. It was noted in Table I that no appreciable change in potential was observed on changing the concentration of cerium metal in the system from that containing excess cerium (in which a pool of cerium formed the electrode) to one containing only 8.7 mole % cerium (in which molybdenum or tungsten rods were the electrodes). This indicates that in these solutions a redox potential between two valence states in solution was being measured in which the cerium, molybdenum, or tungsten electrodes were inert electrodes. If reaction (a) described the 33 mole % cerium solution, then a rapid decrease of potential with decreasing cerium content should have been observed, with the initial increments of $Ce^{3+}$ resulting from cerium concentrations just below this value. However, if reaction (b) describes the 33 mole % cerium solution, then the ratio of oxidant to reductant in this solution is unity and increments of either oxidant or reductant at this concentration would have only a small effect on the potential. In Fig. 4 the observed potentials are plot-

[2] The phase diagram for the system published by Cubiciotti (3) indicates the maximum solubility of cerium as 33 mole %, with a temperature coefficient close to zero over a range of at least 100°C. This would correspond exactly to the stoichiometry of equations (a) and (b). Work now in progress in this laboratory indicates some modification of the phase diagram may be necessary, but the "solubility" of cerium certainly is not greater than this value.

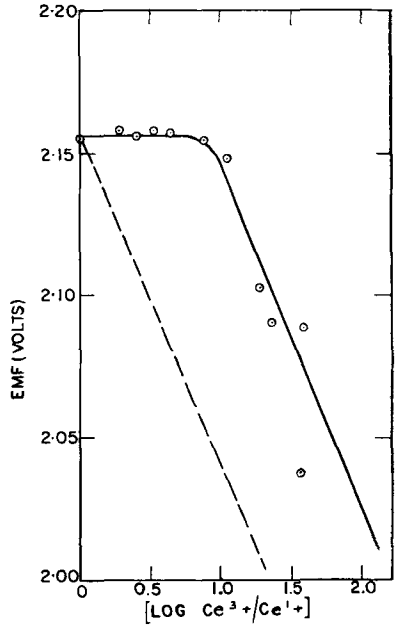


Fig. 4. Emf as a function of cerium metal concentration, 880°C (Cell II). Dotted circles, experimental results; dashed line, theoretical Nernst plot for n = 2.

ted against the logarithm of the concentration ratios using $Ce^{3+}/Ce^{1+}$ as the potential-determining couple. Also indicated on the curve is the ideal Nernst plot using $n = 2$, the slope of which at 880°C is 0.115 v. It will be noted that, in the region of dilute $Ce^{+}$, the slope approaches the Nernst value for $n = 2$.

It seems reasonable, then, to conclude that the cerium "dichloride" present in solutions of Ce in $CeCl_3$ is actually $Ce^{+}[CeCl_4]^{-}$, in the temperature range between 820° and 920°C. Consistent with this is the work of Woodward, *et al.* (16), who showed by Raman Spectra studies that liquid gallium dichloride is $Ga^{+}[GaCl_4]^{-}$ and the work of Garton, *et al.* (17), who showed by x-ray studies that solid gallium dichloride has the structure $Ga^{+}[GaCl_4]^{-}$ in the crystal. Further subsidiary evidence is the fact that cerium metal cannot be obtained by electrolysis of pure cerium chloride from a cell without a diaphragm, while it is easily obtained from a solution of $CeCl_3$ in alkali halides. If $CeCl_3$ is an associated liquid which may be described by a formula such as $[CeCl_2]^{+}[CeCl_4]^{-}$ then electrolysis will produce initially $Ce^{+}[CeCl_4]^{-}$, probably by reduction of the less completely coordinated cations, and not cerium, since the $Ce^{3+}\rightarrow\rightarrow Ce^{1+}$ potential is noble by about 0.7 v to that of $Ce^{3+}\rightarrow\rightarrow Ce^{0}$. However, dilution with alkali halides (i.e., KCl) would probably give a liquid which may be formulated $K^{+}[CeCl_4]^{-}$ and allow the direct reduction of $[CeCl_4]^{-}$ to $Ce^{0}$. Taking the literature value (13) for the potential of the $Ce^{3+}/Ce^{0}$ half-cell (−2.9 v)[3] and the authors' value for the $Ce^{3+}/Ce^{1+}$ half-cell (−2.2 v), then the potential for the $Ce^{1+}/Ce^{0}$ half-cell should be −4.3 v, a value much less noble than either of the other two reactions. This indicates that where oxidation-reduction cycling of $Ce^{1+}\rightarrow\rightarrow Ce^{3+}$ in a cell is possible, cerium metal cannot be expected to be formed by reduction of either the monovalent or trivalent ion.

The formulation of $CeCl_3$ as $[CeCl_2]^{+}[CeCl_4]^{-}$ while purely speculative at this time is in line with suggestions by Yaffe and Van Artsdalen (18) regarding other rare earth halides, and also consistent with the increase in conductance to approximately that of NaCl, which is observed on adding cerium to the trihalide.

The flattening of the curve in Fig. 4 at high concentrations of monovalent cerium in the solution is apparently a buffering effect which the authors have not yet been able to explain. A suitable explanation would involve the postulation of a reservoir for $Ce^{1+}$ in a complex ion in an un-ionized particle or as suggested by Flood and Hill (19) for $Fe_2O_3$-FeO systems in vacancies in the structure. Alternatively, the buffering effect may merely result from the variation of activity of the potential-determining ions with concentration, so that at high concentrations the ratio of the activities of the oxidized and reduced ions remains constant. The buffering would also be found if the system in this region were not actually a single phase as is indicated by the published phase diagram. Studies of the phase diagram, of conductance, and of density now in progress may assist in accounting for the behavior in this buffered region.

[3] If one considers the chlorine electrode as a reference zero in metal/metal chloride/chlorine, graphite cells, then the measured emf or the calculated decomposition potential for the chloride is numerically equal to the potential of the half-cell appropriate to the metal electrode.


## Summary

The emf of the cell $Ce|CeCl_3(1-x)Ce(x)||CeCl_3|Cl_2$ (graphite) has been measured over the temperature range 820°-940°C from a mole ratio of cerium to cerium chloride of 0.018-0.333. The potential of the saturated cell is 2.2005 v at 820°C and 2.1225 v at 940°C, the temperature coefficient of emf being −0.68 mv/°C over this temperature range. Over a concentration range from 33.3 molar % to 8.67 molar % Ce, the emf of the cell remains constant, while with less cerium a decrease in potential in agreement with a Nernst slope for a 2-electron change is observed. It is concluded that the solution of Ce in $CeCl_3$ contains a subhalide consisting of monovalent and trivalent cerium ions, the probable formula of which is $Ce^{+}[CeCl_4]^{-}$. Preliminary measurements indicate that the saturated solution is a typical ionic conductor with a conductance of 3.76 $ohms^{-1}$ $cm^{-1}$ at 840°C.



## Acknowledgments

The authors wish to express their thanks to E. R. Van Artsdalen, R. Didchenko, and L. M. Litz for many enlightening discussions, and to B. Flashman for considerable experimental assistance during the course of the work.

Manuscript received Sept. 3, 1957. This paper was prepared for delivery before the New York Meeting, April 27-May 1, 1958.

Any discussion of this paper will appear in a Discussion Section to be published in the December 1958 JOURNAL.


## REFERENCES


1. D. D. Cubicciotti, *J. Metals*, **5**, 1106 (1953).
2. D. D. Cubicciotti and C. D. Thurmond, *J. Am. Chem. Soc.*, **71**, 2149 (1949).
3. D. D. Cubicciotti, *ibid.*, **71**, 4119 (1949).
4. H. R. Bronstein and M. A. Bredig, Abstract of paper presented at AIME Convention, New Orleans, Feb. 1957.
5. M. A. Bredig, J. W. Johnson, and W. T. Smith, *J. Am. Chem. Soc.*, **77**, 307 (1955).
6. M. A. Bredig, H. R. Bronstein, and W. T. Smith, *ibid.*, **77**, 1454 (1955).
7. J. D. Corbett and S. Von Winbush, *ibid.*, **77**, 3964 (1955).
8. K. Grjotheim, F. Grönwold, and J. Krogh-Moe, *ibid.*, **77**, 5824 (1955).
9. R. Lorenz. "Die Electrolyse Geschmolzener Salze," W. Knapp-Halle A-S (1906).
10. C. Wagner, *Z. Physik. Chem.*, **21B**, 36 (1933).
11. E. D. Eastman, B. S. Fontana, *et al.*, USAEC TID-5212 14-24 (1955).
12. S. Senderoff and G. W. Mellors, To be published.
13. W. J. Hamer, M. S. Malmberg, and B. Rubin, *This Journal*, **103**, 8 (1956).
14. L. Brewer, *et al.*, Paper 6, page 76 et seq. "Chemistry and Metallurgy of Miscellaneous Materials: Thermodynamics," L. L. Quill, Editor, National Nuclear Energy Series.
15. K. Kiukkola and C. Wagner, *This Journal*, **104**, 308 (1957).
16. L. A. Woodward, G. Garton, and H. L. Roberts, *J. Chem. Soc.*, **1956** 3723.
17. G. Garton and H. M. Powell, *J. Inorg. and Nucl. Chem.*, **4**, 84 (1957).
18. I. S. Yaffe and E. R. Van Artsdalen, To be published.
19. H. Flood and S. G. Hill, *Z. Elektrochem.*, **61**, 18 (1957).

# Kinetics of the Thiosulfate-Bromoacetate Reaction in the Presence of Electrolytes

**Gerald Corsaro and Ronald W. Smith**

*Department of Chemistry, The University of Akron, Akron, Ohio*

**and**

**Howard L. Stephens**

*Institute of Rubber Research, The University of Akron, Akron, Ohio*

ABSTRACT

The reaction between thiosulfate and bromoacetate ions in solvent mixtures of different dielectric constant and in the presence of added salts fails to give results conforming to the predictions of the Brönsted primary salt effect. The deviation from theory is particularly high in solvents of low dielectric constant and in the presence of higher valence type electrolytes. A mechanism for the over-all reaction is proposed to account for the apparent abnormalities. New experimental data are added to those previously obtained and are correlated with the Brönsted-Christiansen-Scatchard theoretical expressions which relate the log of the molar reaction rate constants to the dielectric constant of the solvent mixture in which reaction takes place, the ionic strength of the solutions making up the reaction mixture, and the size and charge of the intermediate complex assumed to be formed in ionic reactions. The essential condition in the postulated mechanism is that the reaction proceeds through the formation of a complex or ion pair between the added cation and thiosulfate ion, followed by reaction of this complex with bromoacetate ion.

The reaction between bromoacetate and thiosulfate ions in several solvent systems has been investigated extensively (3-10). The conclusions reached by Ciapetta and Tomilinson (10) are pertinent to the remarks to be made in the present discussion. They may be summarized as follows.

(*A*) Specific solvent effects are minor. Observed rate constant data obtained with different isodielectric constant solvents, but with identical concentrations of reactants and added salt, are of the same order of magnitude.

(*B*) Strontium and calcium nitrate mixed with reactants produce high rate constants. Rate constants level off to almost constant values when these salts are present in excess of the reactants.

(C) When lanthanum nitrate is the added salt, reaction rate constants are as high as one hundredfold times those anticipated from the Brönsted-Christiansen-Scatchard theoretical expressions (1,2). When the reaction is allowed to take place in solvents of low dielectric constant, the rate constants increase in value with increase in the added salt concentration, reaching a maximum when the added salt concentration equals that of reactants, then fall off with further increases in added salt.

(*D*) LaMer and Davis (3) have shown that when solvents range in dielectric constant from 20 to 35 so that constant DT values are obtained, the observed energies of activation for the reactions with added salt are the same as those in which salt addition is absent. They concluded that abnormal rate constants were the result of certain electrostatic attractions leading to possible ion pair formations. Ciapetta and Tomilinson postulated an ion pair $(LaS_2O_3BrAc)^\circ$ since they observed that the maximum in the rate constant value was usually obtained when the salt concentration added with reactants was equal to that of the reactants. They concluded further that rate constants were lower in the presence of greater concentrations of added salt because lanthanum ions would compete with each other for the formation of this complex.

If electrostatic attractions influence the course and rate of reaction, it is also reasonable to assume that a complex or ion pair could form between the added cation of the salt and thiosulfate ion, and this in turn would react with bromoacetate ion. Furthermore, the complex postulated by Ciapetta and Tomilinson would be specific for those reaction studies involving only lanthanum nitrate additions, and thus would provide no over-all explanation for the effect of other valence type salts which also produce deviation from predicted results.

A reaction mechanism can be written:

$$M^{+n} + S_2O_3^{=} \rightarrow (M\,S_2O_3^{=})^{n-2} \qquad \text{(I)}$$

$$(M\,S_2O_3^{=})^{n-2} + BrAc^{-} \rightarrow [\text{Complex}]^{Z_a+Z_b} \qquad \text{(II)}$$

$$[\text{Complex}]^{Z_a+Z_b} \rightarrow Br^{-} + CH_2COOS_2O_3^{-} + M^{+n} \qquad \text{(III)}$$

$M^{+n}$ is the cation of the added salt with valence charge $+n$, and $Z_a$, $Z_b$ the valence charge of the ion pair and bromoacetate ion, respectively. Since, according to this mechanism, the cation is regenerated

in the slow step of the over-all reaction, a rate expression can be written:

$$\frac{-d[S_2O_3^=]}{dt} = Kf(M) \cdot [\text{Reactant}]^2 = k[\text{reactant}]^2 \quad \text{(IV)}$$

In this expression the term [reactant] represents equimolar concentration of thiosulfate and bromoacetate ions, $k$ the observed second order rate constant, and $f(M)$ a function of the added salt concentration. This function should represent [M] raised to a fractional power $1/X$, representing the extent to which the added cation concentration takes part in ion pair formation with thiosulfate ion concentration. Then $K$ equals $k/[M]^{1/x}$.

If one assumes that [M] in the above expressions is limited to salt concentrations less or equal to that of reactants, then the constancy represented by $k/f(M)$ will be limited to added salt concentrations equal to that of reactants, or less. There is no specific way of predicting the actual fraction of salt which enters into ion pair formation, but this fraction may be approximately deduced from the rate constant data.

The discussion in this paper includes some of the data reported by Ciapetta and Tomilinson whose work involved the use of solvent mixtures containing 72.2% by weight isopropyl alcohol with water which corresponds to a dielectric constant value of 30. The present reported results involve mixtures of 10 and 40% ethyl alcohol by weight with water and dielectric constant values of 72 and 55, respectively. To avoid repetition of solvent description, only the dielectric constant value is designated hereafter.

## Experimental

The reaction rate between thiosulfate and bromoacetate was followed by titration of residual thiosulfate with 0.01$N$ iodine solution. The reaction mixture was prepared by mixing weighed amounts of bromoacetic acid in the chosen solvent mixture, equilibrating this with previously standardized NaOH solution, also prepared in the same solvent mixture, and then diluting the solution to twice the molar concentration for the bromoacetate ion concentration used in the run. The sodium thiosulfate was prepared from a standard thiosulfate solution and mixed with the appropriate concentration of the salt investigated. After bringing the two separate solutions to thermal equilibrium, they were mixed and the reaction rate was followed by taking samples at specified intervals of time. The latter procedure involved tripping the stop watch at the instant of mixing the two prepared solutions. About one minute before a specified interval of time, a sample analysis was withdrawn from the reaction vessel. At the instant the time interval was completed excess 0.01$N$ iodine solution was run into the sample. Back titration with 0.01$N$ thiosulfate was then carried out. Blank runs with iodine on samples of solvent were made to make corrections for end point detection using the starch indicator. Volume ratios between thiosulfate and iodine solutions were made at the beginning of each separate run. Rate constants were calculated using the expression:

$$k = \frac{x}{at[a-x]}$$

where $a$ is the initial reactant concentration of thiosulfate ion and $x$ is the amount reacted in time $t$.

For thorium nitrate additions, it was observed that only plots of $1/[S_2O_3^=]^2$ vs. time, where $[S_2O_3^=]$ is the residual thiosulfate concentration, gave linear plots. Rate constants were calculated by the expression for third order reactions:

$$k = \frac{x}{2at[a-x]^2}$$

The average values of second and third order calculated rate constants were compared with the values of $1/[S_2O_3^=]$ vs. time and $1/[S_2O_3^=]$ vs. time plots from whose slopes the rate constants can be evaluated. Typical rate data with lanthanum and thorium nitrate are summarized in Tables I and II. Al-

**Table I. Typical rate data with lanthanum nitrate additions ($D$=72)**

| | $[BrA\bar{c}] = [S_2O_3^=] = 0.002M$ | | | [La] = 0.0015M | |
|---|---|---|---|---|---|
| $t$ Min | $I_2$ ml | $S_2O_3^=$ ml | $I_2$ ml net | $[S_2O_3^=]$ | $k$ Liter/moles × sec |
| 5 | 12.67 | 3.66 | 9.23 | 0.001957 | 3.25 |
| 15 | 12.77 | 4.33 | 8.70 | 0.001844 | 3.22 |
| 30 | 11.41 | 3.65 | 7.78 | 0.001678 | 3.19 |
| 45 | 9.56 | 2.30 | 7.40 | 0.001569 | 3.05 |
| 60 | 9.41 | 2.70 | 6.87 | 0.001456 | 3.12 |

Blank with 0.01$N$ $I_2$ = 0.14 ml. Results above corrected.

**Table II. Typical rate data with thorium nitrate additions ($D$=72)**

| | $[BrA\bar{c}] = [S_2O_3^=] = 0.002M$ | | | [Thorium] = 0.0015M | |
|---|---|---|---|---|---|
| $t$ Min | $I_2$ ml | $S_2O_3^=$ ml | $I_2$ ml net | $[S_2O_3^=]$ | $k \times 10^{-4}$ |
| 5 | 6.85 | 1.30 | 5.55 | 0.001187 | 2.90 |
| 15 | 4.82 | 1.18 | 3.72 | 0.000796 | 3.19 |
| 30 | 4.76 | 2.20 | 2.71 | 0.000579 | 3.50 |
| 45 | 3.35 | 1.15 | 2.27 | 0.000466 | 3.52 |
| 60 | 3.26 | 1.21 | 2.13 | 0.000456 | 3.09 |

**Table III. Data from Ciapetta and Tomilinson. Calcium and strontium nitrate additions (D=30)**

| | $[S_2O_3^=] = [BrA\bar{c}] = 0.005M$ | | 0.003M Reactants | | |
|---|---|---|---|---|---|
| M ($C_a$) | $k$ Liter/moles × sec | M ($S_r$) | $k$ Liter/moles × sec | M ($C_a$) | $k$ Liter/moles × sec |
| 0.00236 | 1.98 | 0.00204 | 1.62 | 0.00293 | 2.76 |
| 0.00580 | 3.17 | 0.01206 | 3.04 | 0.00597 | 3.60 |
| 0.01452 | 3.82 | 0.01917 | 3.77 | 0.01019 | 3.70 |
| 0.01885 | 4.01 | 0.02893 | 4.09 | 0.01451 | 3.89 |
| 0.02320 | 3.85 | 0.03624 | 3.82 | 0.02327 | 3.54 |
| 0.04352 | 3.85 | 0.04826 | 3.92 | 0.03480 | 3.48 |

though times up to 60 min are shown in these tables, in some cases times of reaction up to 1300 min were taken. A titration error of 0.05 cc 0.01*N* iodine is equivalent to the average deviation shown.

Data in Tables III-VII represent results of the present investigation and those taken in part from the work of Ciapetta and Tomilinson (10). Data summarized in the remaining tables are those used for the plots in Fig. 1-8.

## Discussion of Results

According to Brönsted-Christiansen-Scatchard (1, 2) the molar rate constant for an ionic reaction in dilute solution for reaction between ions of $Z_a$ and $Z_b$ charges is given by:

$$\log k = \log k'_o - \frac{Z_a Z_b E^2 N}{DRT} \cdot \frac{1}{r_a + r_b} + \frac{Z_a Z_b E^2 N}{DRT} \cdot \frac{\kappa}{1 + ai\kappa} \qquad (V)$$

where $\kappa$ is the Debye-Hückel constant given by:

$$\kappa = \left[ \frac{8\pi \ E^2 u}{DRT \cdot 1000} \right]^{1/2} \qquad (VI)$$

and the remaining terms have their usual significance. According to Amis (13) the Debye first approximation parameter $ai$, and the term $r_a + r_b$, the distance of closest approach for ions before they react, may be taken as equal in magnitude.

The term, log $k'_o$ represents the reaction rate constant at infinite dielectric constant. The Brönsted salt effect is included in this expression since log $k$ vs. $u^{1/2}$ should give a linear relation according to expression (V). The Brönsted equation for primary salt effect alone may be written in its limiting form as:

$$\log k = \log k_o + 2A \cdot Z_a \cdot Z_b (u)^{1/2} \qquad (VII)$$

where $A$ is the Debye-Huckel constant obtained from

$$A = \frac{1.824 \times 10^6}{(DT)^{3/2}} \qquad (VIII)$$

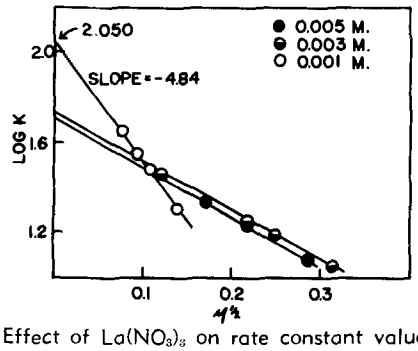


Fig. 1. Effect of $La(NO_3)_3$ on rate constant values in solvents, D = 30. [La] equal and in excess of [reactants]. Data from Table VIII.

**Table IV. Data from Ciapetta and Tomilinson. Effect of lanthanum nitrate additions (*D*=30)**

| M (La) | [BrAc⁻] = [$S_2O_3^=$] = 0.005M $k$ | $k/M \times 10^{-3}$ |
|---|---|---|
| 0.00180 | 9.78 ± 0.04 | 5.43 |
| 0.00299 | 17.4 ± 0.4 | 5.67 |
| 0.00354 | 19.7 ± 0.1 | 5.56 |
| 0.00474 | 23.3 ± 0.2 | 5.00 |
| 0.00596 | 22.7 ± 0.3 | — |
| 0.00956 | 17.7 ± 0.2 | — |
| 0.01194 | 15.4 ± 0.1 | — |
| 0.01792 | 11.1 ± 0.1 | — |
| | [BrAc] = [$S_2O_3^=$] = 0.003M | |
| M (La) | $k$ | $k/M \times 10^{-3}$ |
| 0.00095 | 9.34 ± 0.01 | 9.83 |
| 0.00237 | 24.8 ± 0.1 | 10.40 |
| 0.00343 | 29.9 ± 0.1 | 9.00 |
| 0.00473 | 22.6 ± 0.1 | — |
| 0.00593 | 21.9 ± 0.3 | — |
| 0.00953 | 14.8 ± 0.2 | — |
| 0.01480 | 12.1 ± 0.3 | — |
| 0.02621 | 9.19 ± 0.05 | — |

**Table V. Effect of lanthanum nitrate additions on the bromoacetate-thiosulfate reaction in 10% ethyl alcohol (*D*=72)**

| M (La) | $u^{1/2}$ | (BrAc⁻) = ($S_2O_3^=$) = 0.002M $k$ | log $k$ | $k/M^{1/2}$ |
|---|---|---|---|---|
| 0.0005 | 0.097 | 1.51 ± 0.04 | 0.179 | 67.4 ± 1.8 |
| 0.00075 | 0.101 | 2.24 ± 0.06 | 0.350 | 81.7 ± 2.2 |
| 0.0010 | 0.104 | 2.56 ± 0.05 | 0.408 | 84.1 ± 1.6 |
| 0.0015 | 0.111 | 3.28 ± 0.06 | 0.516 | 84.8 ± 1.7 |
| 0.00175 | 0.115 | 3.69 ± 0.22 | 0.567 | 88.3 ± 5.2 |
| 0.002 | 0.119 | 3.78 ± 0.18 | 0.577 | 84.6 ± 4.0 |

**Table VI. Effect of lanthanum nitrate additions on the bromoacetate-thiosulfate reaction in 40% ethyl alcohol (*D*=55)**

| M (La) | $u^{1/2}$ | (BrAc⁻) = ($S_2O_3^=$) = 0.002M $k$ | log $k$ | $k/M^{1/2}$ |
|---|---|---|---|---|
| 0.0005 | 0.097 | 6.32 ± 0.19 | 0.801 | 282 ± 8.4 |
| 0.00075 | 0.101 | 9.70 ± 0.06 | 0.987 | 354 ± 2.1 |
| 0.0010 | 0.104 | 11.19 ± 0.04 | 1.049 | 354 ± 1.2 |
| 0.00125 | 0.108 | 12.65 ± 0.11 | 1.102 | 357 ± 3.1 |
| 0.00175 | 0.115 | 14.49 ± 0.23 | 1.161 | 352 ± 5.5 |
| 0.0019 | 0.117 | 15.48 ± 0.31 | 1.499 | 355 ± 2.1 |
| 0.004 | 0.161 | 13.51 ± 0.27 | 1.131 | 213 ± 4.2 |
| 0.006 | 0.194 | 11.87 ± 0.06 | 1.074 | 153 ± 0.9 |
| 0.008 | 0.223 | 10.47 ± 0.21 | 1.029 | 117 ± 2.3 |

**Table VII. Effect of thorium nitrate additions on the bromoacetate-thiosulfate reaction in 10% ethyl alcohol (*D*=72)**

| M (Th) | [BrAc⁻] = [$S_2O_3^=$] = 0.0005M $k$, $\frac{\text{Liter}^2}{\text{mole} \times \text{min}}$ | log $k$ | $k/M \times 10^{-7}$ |
|---|---|---|---|
| 0.0005 | 1,150,000 | 6.060 | — |
| 0.001 | 1,030,000 | 6.012 | — |
| 0.002 | 660,000 | 5.819 | — |
| | [BrAc⁻] = [$S_2O_3^=$] = 0.001M | | |
| 0.0005 | 16,000 | 4.204 | 32.0 |
| 0.0001 | 34,000 | 4.532 | 34.0 |
| 0.0002 | 65,000 | 4.813 | 32.5 |
| 0.0005 | 152,000 | 5.185 | 30.4 |
| 0.001 | 318,000 | 5.502 | 31.8 |
| 0.002 | 303,000 | 5.482 | 15.1 |
| 0.006 | 148,000 | 5.170 | 2.8 |
| | [BrAc⁻] = [$S_2O_3^=$] = 0.002M | | |
| 0.0005 | 9,300 | 3.968 | 18.6 |
| 0.001 | 21,100 | 4.324 | 21.1 |
| 0.0015 | 31,000 | 4.491 | 20.6 |
| 0.00175 | 36,800 | 4.566 | 21.0 |
| 0.002 | 41,500 | 4.618 | 20.7 |
| 0.004 | 27,700 | 4.443 | 6.9 |
| 0.006 | 18,000 | 4.255 | 3.0 |
| 0.008 | 15,400 | 4.215 | 2.0 |

The term log $k_o$ in the Brönsted equation represents the log of the reaction rate constant at zero ionic strength and therefore zero $\kappa$. The log $k_o$ may be obtained from the experimental data by extrapolating the linear plots of log $k$ vs. $u^{1/2}$ to zero ionic strength. According to expression (V) a plot of these extrapolated log $k_o$ values for solvents of different dielectric constant plotted against $1/D$ should give linear curves.

By the new mechanism described in expressions (I), (II), and (III), reaction rates should increase when the ion pair concentration increases. The portion of a plot involving the log of the molar reaction rate constant vs. the square root of the ionic strength up to ionic strengths equivalent to added salt concentrations equal to that of reactants cannot then be interpreted as the influence of ionic strength increase on the thiosulfate-bromoacetate ion reaction. This portion of the plot reflects only the increase in rate as a function of increase in reactant concentration represented by increasing amounts of ion pair formed as more and more salt is added. Once the maximum concentration of ion pair has formed, further increases in salt addition then provide the increase in ionic strength which may influence the reaction taking place between ion pair and bromoacetate ion. The Brönsted salt effect manifests itself by reduction in rate constants if the ion pair is opposite in charge from that of the bromoacetate ion, or rate constant values should remain constant with increase in ionic strength if the ion pair has a zero net charge. Hence, the slopes of the portion of the log $k$ vs. $u^{1/2}$ plots, starting with reactants and added salt at equal concentrations, should be given by expression (VII), namely $2A \cdot Z_a \cdot Z_b$.

Ionic strength values associated with all of the plotted data described in this paper have been calculated by assuming that the ion pair is a distinct ion species. For solvents of $D$ equal to 30, the concentration of the ion pair was assumed equal to that of the added lanthanum nitrate. Thus, for example, when 0.0005M lanthanum nitrate is mixed with 0.001M reactants, it is assumed that 0.0005M ion pair has been formed leaving 0.0005M thiosulfate and the remaining ions. With solvents $D$ equal to 55 and 72, for reasons which will be given, it is assumed that only half the added lanthanum participates in ion pair formation. In these cases a 0.001M addition of salt with 0.001M reactant concentration would produce 0.0005M ion pair leaving 0.0005M lanthanum ion, 0.0005M thiosulfate ion, and the remaining ionic concentrations.

Figure 3 drawn with the data taken from Table VI shows a typical plot of log $k$ vs. $u^{1/2}$ when solvents with $D$ equal to 55 are used with lanthanum nitrate salt additions.

The extent to which added cation takes part in ion pair formation should be greater the lower the dielectric constant of the solvent, the smaller the cation size, and the greater the valence charge of the cation (11, 12).

The fraction, $1/x$, of the added cation concentration which participates in ion pair formation may be determined approximately by noting the fractional power of (M) which gives constant values of $k/(\mathrm{M})^{1/x}$.

With solvent mixtures ($D$ equal to 30), the limited data available in the low salt concentration range from the results of Ciapetta and Tomilinson indicate that almost all the added cation concentration is involved in ion pair formation. Table IV shows that $k/(\mathrm{M})$ values are almost constant. Again it should be emphasized that $k/(\mathrm{M})$ does not give constant values when cation concentration is in excess of reactant concentration. The regeneration of the cation in the slow step of the reaction process provides the means of continuing the reaction so as to give $k/(\mathrm{M})$ constant values.

Tables V and VI show data which indicate that about one-half the added cation concentration takes part in ion pair formation. The first result in each of these tables is low, suggesting that some minimum salt concentration must be present to form the ion pair to its maximum extent.

It has already been stated that, when thorium nitrate is added with reactants, a third order reaction process is apparent. The over-all reaction may be written:

$$2(\mathrm{Th}\,S_2O_8)^{++} + \mathrm{BrA\bar{c}} \rightarrow (\mathrm{Complex}) \rightarrow \mathrm{Products} \quad (\mathrm{IX})$$

Plots of the log of the third order rate constants vs. $u^{1/2}$ also produce maxima as illustrated by Fig. 4. The data in Table VII show that, although the solvent mixture represented by these data is that for $D$ equal to 72, $k/[\mathrm{M}]$ values are constant. The effect of high valence charge and small cation size for the Th ion is probably a strong factor in ion pair formation and in changing the over-all reaction process from second to third order. The intermediate complex formed in this reaction may be quite different from that produced with the other salt additions. The size factor is also manifest in the results obtained with strontium or calcium nitrate additions with reactants. First, although the solvent mixture corresponds to D = 30, the rate constants are not as high as when lanthanum nitrate is used. Further, Table III shows that 0.00580M concentration of the smaller calcium ion produces reaction rates which give almost the same rate constant as 0.01206M strontium ion, although both salts eventually give about the same rate constant values at higher concentrations. When log $k$ values are plotted against $u^{1/2}$, therefore, one obtains slopes which are almost zero in value in the region of ionic strengths equiva-

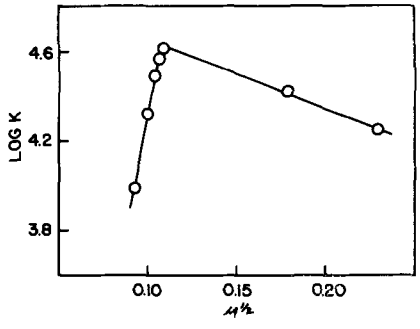


Fig. 4. Effect of $Th(NO_3)_4$ on third order reaction rate constants in solvents, D = 72. Data from Table VII.

lent to concentration in excess of reactants. This result conforms to the views postulated in this paper since the ion pair between Sr or Ca and thiosulfate ion should have a zero net charge. The slight maximum noted from Table III suggests that the reaction between thiosulfate and bromoacetate ions alone, as well as that between ion pair and bromoacetate, contributes to the over-all rate, because of the small fraction of salt participating in ion pair formation.

The preceding discussion should make it apparent that the Brönsted salt effect must be limited to reaction rates obtained when the added salt is equal to or in excess of the reactant concentration. Consider, for instance, the data of Table VIII and Fig. 1. The ionic strengths used are those calculated in the manner described and are for concentrations of added lanthanum nitrate, equal and in excess to that of the reactants. The log $k$ vs. $u^{1/2}$ plots are linear with negative slopes. Values of these slopes are not too different from those calculated by the expression $2A \cdot Z_a \cdot Z_b$.

Figure 2, on the other hand, employs data (Table IX) for the reaction rates obtained when using only those concentrations of added lanthanum nitrate equal to reactants at 0.001, 0.003, and 0.005M concentration. In this case the plot of log $k$ vs. $u^{1/2}$ gives a slope of −4.31 which happens to be identical with that calculated in the manner given.

Following a procedure similar to that employed in making the plot of Fig. 2, the data of Tables X

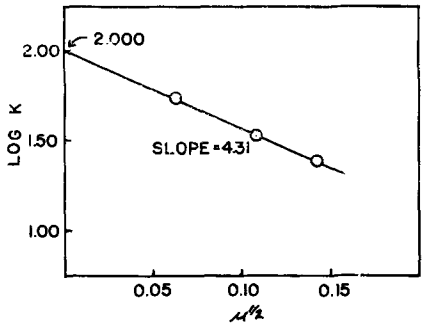


Fig. 2. Effect of $La(NO_3)_3$ on rate constant values in solvents, D = 30. [La] = [reactants] = 0.001, 0.003, and 0.005M. Data from Table IX.

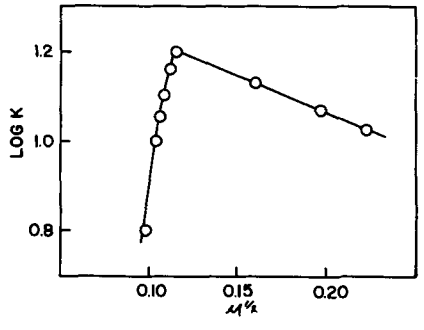


Fig. 3. Effect of $La(NO_3)_3$ on rate constant values in solvents, D = 55. Data from Table VI.

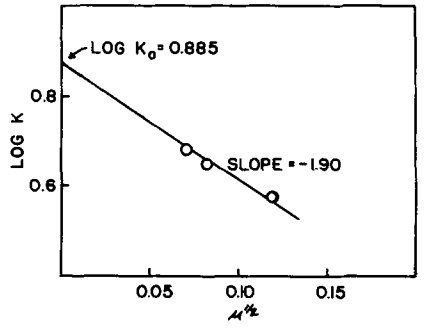


Fig. 5. Effect of $La(NO_3)_3$ on rate constant values in solvents, D = 72. [La] = [reactants] = 0.0005, 0.001, and 0.002M. Data from Table X.

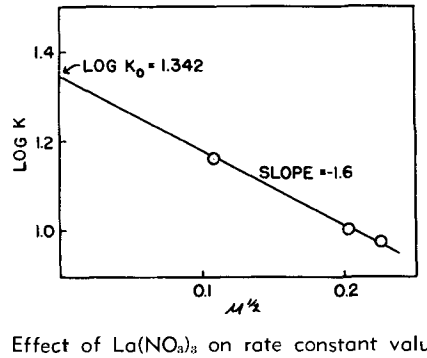


Fig. 6. Effect of $La(NO_3)_3$ on rate constant values in solvents, D = 55. [La] = [reactants] = 0.002, 0.006, 0.008M. Data from Table XI.

**Table VIII. Data for Fig. 1. Effect of lanthanum nitrate on the bromoacetate-thiosulfate reaction ($D$=30) La in excess of reactants.**

| Reactants [.005M] | | Reactants [.003M] | | Reactants [.001M] | |
|---|---|---|---|---|---|
| $u^{1/2}$ | log $k$ | $u^{1/2}$ | log $k$ | $u^{1/2}$ | log $k$ |
| 0.1207 | 1.476 | | | | |
| 0.1496 | 1.352 | 0.1605 | 1.356 | 0.0773 | 1.656 |
| 0.1720 | 1.340 | 0.2176 | 1.248 | 0.0932 | 1.552 |
| 0.2262 | 1.170 | 0.2483 | 1.188 | 0.1100 | 1.480 |
| 0.2878 | 1.083 | 0.3120 | 1.049 | 0.1385 | 1.350 |
| 0.3889 | 0.964 | | | | |

**Table IX. Data for Fig. 2. Effect of lanthanum nitrate on the bromoacetate-thiosulfate reaction ($D$=30); [La] = [BrAc] = [$S_2O_3$]**

| $u^{1/2}$ | log $k$ | [La] = [Reactants] |
|---|---|---|
| 0.141 | 1.396 | 0.005 |
| 0.109 | 1.520 | 0.003 |
| 0.063 | 1.730 | 0.001 |

Extrapolated value of log $k_o$ = 2.000, slope = −4.31

**Table X. Data for Fig. 5. Effect of lanthanum nitrate on the bromoacetate-thiosulfate ($D$=72), [La] = [Reactants]**

| M (La) (Reactant) | $u^{1/2}$ | log $k$ |
|---|---|---|
| 0.0005 | 0.0598 | 0.680 |
| 0.0010 | 0.083 | 0.645 |
| 0.0020 | 0.119 | 0.577 |

Extrapolated value of log $k_o$ = 0.885, slope = −1.90

**Table XI. Data for Fig. 6. Effect of lanthanum nitrate on the bromoacetate-thiosulfate reaction ($D$=55). [La] = [Reactants]**

| M (La) (Reactant) | $u^{1/2}$ | log $k$ |
|---|---|---|
| 0.002 | 0.119 | 1.161 |
| 0.006 | 0.205 | 1.012 |
| 0.008 | 0.237 | 0.973 |

Extrapolated value of log $k_o$ = 1.342, slope = −1.60

Table XII. Data for Fig. 7. Effect of thorium nitrate on the bromoacetate-thiosulfate reaction ($D$=72). [Th] = [Reactants]

| M (Th) (Reactant) | $u^{1/2}$ | log $k$ |
|---|---|---|
| 0.0005 | 0.054 | 6.060 |
| 0.0010 | 0.077 | 5.500 |
| 0.0020 | 0.109 | 4.060 |

Slope = −11.7

Table XIII. Data for Fig. 8. Log $k_o$ vs. $1/D$

| log $k_o$ | $D$ | $1/D$ | Solvent |
|---|---|---|---|
| 0.885 | 72 | 0.0137 | 10% EtOH-$H_2O$ |
| 1.342 | 55 | 0.0182 | 40% EtOH-$H_2O$ |
| 2.000 | 30 | 0.0333 | 72% Isopropanol-$H_2O$ |

Per cent compositions are by weight.

and XI are plotted in Fig. 5 and 6. The linear plots of log $k$ vs. $u^{1/2}$ have slopes of −1.90 and −1.60 compared to calculated values of −1.14 and −1.74. These data correspond to solvents of $D$ equal to 72 and 55, respectively. Although these values do not coincide with theory, the signs of the slopes are significant, and deviation from theory may be accounted for by the fact that, in solvents of high dielectric constant, the ion pair participation is not as complete as with cases of low solvent dielectric constant values. Similar data taken for reactions carried out with thorium nitrate additions as given in Table XII and plotted in Fig. 7 show that log of the third order rate constants vs. $u^{1/2}$ also give negative slopes, but of much higher magnitude than the others. However, the present Brönsted theoretical effect is derived on the basis of a bimolecular mechanism and cannot be applied to third order reactions. The similarity of results between lanthanum and thorium nitrate additions is striking, and suggests that similar rate expressions can be derived for reactions, described by expression (IX).

Expression (V) indicates that for log $k_o$ vs. $1/D$, linear plots with slopes equal to

$$S = \frac{-Z_a \cdot Z_b \cdot E^2 N}{2.303 \cdot r \cdot RT} \qquad (X)$$

should be obtained. The values of log $k_o$ are those obtained by extrapolating the plots of log $k$ vs. $u^{1/2}$ to zero ionic strength. These values are listed with the tabulated data already described and are also shown in the Fig. 2, 5, and 6. Since as stated, the value of $a_i$ and $r_a + r_b$ may be taken equal, the value of $r$ in expression (X) is equal to the size of the intermediate complex assumed to be formed in ionic reactions. $E$ is the electronic charge, $Z_a$ and $Z_b$ the valence charge of the ion pair and bromoacetate ion, respectively, and the remaining symbols have their usual significance.

The plot of the log $k_o$ values vs. $1/D$ is shown in Fig. 8. This is not strictly linear because of the character of the deviations mentioned above, but the average slope is positive at a value of 75. The value of $r$ using this slope is $3.3 \times 10^{-8}$ cm. This value compares with values of $r$ calculated for the ammonium ion-cyanate ion reaction carried out in sol-

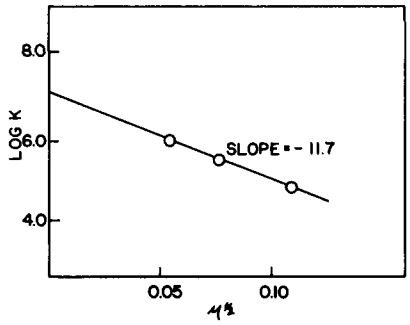


Fig. 7. Effect of $Th(NO_3)_4$ on third order reaction rate constant values in solvents, D = 72. [Th] = [reactants] = 0.0005, 0.001, and 0.002M. Data from Table XII.

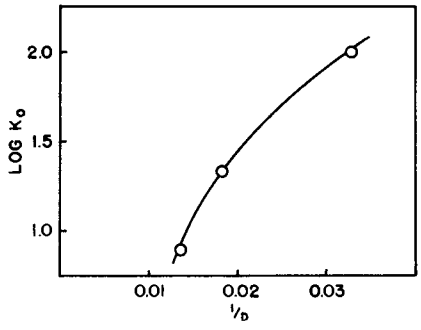


Fig. 8. Log $k_o$ vs. 1/D. Log $k_o$ values obtained by extrapolation to u = o. See Fig. 2, 5, and 6.

vent mixtures of methyl and ethyl alcohol with water. Results reported by Svirbely and Schramm and Lander and Svirbely (14, 15) are $2.2 \times 10^{-8}$ and $2.5 \times 10^{-8}$ cm for the two solvent mixtures, respectively. The effect of univalent cations on the reaction has been investigated by several workers and is included in most of the reference work already cited. The general conclusions seem to indicate that the order of departure from theory is Li > Na > K > Cs. Results, particularly with solvents of low dielectric constant, show that the largest unsolvated ion size gives results which best approach theory. If solvation of the smaller alkali ion is diminished in solvents of low dielectric constant, then ion pair participation would have the effect of reducing the net negative charge of the thiosulfate ion. The larger ions, K and Cs, should produce more closely the theoretical effect of ionic strength increases on the thiosulfate-bromoacetate reaction without ion pair formation. Results obtained by the present authors with tetramethyl ammonium salts and ammonium chloride do show that the values of slopes predicted by the Brönsted expression (V) are approached. This work is incomplete however, and will be reported in a later publication.

## Conclusions and Summary

The high rate constants observed for the reaction between bromoacetate and thiosulfate ions in the presence of higher valence electrolytes may be attributed to the fact that the actual reaction is between a complex, formed by the addition of cation with thiosulfate ion, and bromoacetate ion. Since the cation is regenerated during the slow step of the reaction, the rate of the reaction is proportional to concentrations of added cation, or some function of

concentration of cation, until the latter concentration is equal to that of equimolar reactants. Increases in cation concentration beyond this value then cause the reaction rate to decrease in conformity with the Brönsted effect since the reactant species are oppositely charged. All of the observed rate constants and plots of log $k$ vs. $u^{1/2}$ give slopes of the proper sign when the reaction mechanism is viewed in this manner; the values of slopes obtained are, in some cases at least, very close to the theoretical values. It is emphasized however, that these slopes show good agreement with theory only when the ionic strength is increased by equimolar increases in reactants and added salt. This suggests that the ionic strength principle, when mixed electrolytes are involved, may be inadequate to express the true ionic strength of such mixtures.

The observed data also demonstrate that ion pair formation, complex formation, or the increase in covalent nature of the bond between cation and anion, is favored by low dielectric constant of the solvent, small cation size, and high charge on the cation. The over-all mechanism outlined in this paper explains the previously observed conclusions of several investigators that deviations from theory were always greater, the lower the dielectric constant of the solvent in which reaction takes place.

The use of ionic reaction rates of this type may be used as a tool to detect possible ion association, although this obviously would be limited to ionic species capable of undergoing measurable reaction rates.

Manuscript received May 8, 1957. This paper was prepared for delivery before the Washington Meeting, May 12-16, 1957.

Any discussion of this paper will appear in a Discussion Section to be published in the December 1958 JOURNAL.

REFERENCES

1. G. Scatchard, *J. Am. Chem. Soc.*, **52**, page 52 (1930), *Chem. Revs.* **10**, 229 (1932).
2. J. A. Christiansen, *Z. Physik. Chem.*, **113**, 35 (1924).
3. H. G. Davis and V. K. LaMer, *J. Chem. Phys.*, **10**, 585 (1942).
4. A. N. Kappana, *J. Indian Chem. Soc.*, **51**, 3341 (1929).
5. V. K. LaMer, *J. Franklin Inst.*, **225**, 709 (1938).
6. V. K. LaMer and R. W. Fresden, *J. Am. Chem. Soc.*, **54**, 2351 (1932).
7. V. K. LaMer and N. E. Kammer, *ibid.*, **57**, 2669 (1935).
8. J. Slator, *J. Chem. Soc.*, **87**, 481 (1905).
9. H. M. Tomilinson and F. G. Ciapetta, *Ind. Eng. Chem. Anal. Ed.*, **13**, 539 (1941).
10. F. G. Ciapetta and H. M. Tomilinson, *J. Phys. Chem.*, **55**, 429 (1951).
11. K. Fajans, *Naturenissenschafren*, **11**, 165 (1923).
12. G. H. Cartledge, *J. Am. Chem. Soc.*, **50**, 2855 (1928).
13. E. S. Amis, "The Kinetics of Chemical Change in Solution," Chap. IV, MacMillan, New York (1949).
14. W. J. Svirbely and A. Schramm, *J. Am. Chem. Soc.*, **60**, 330 (1938).
15. J. Lander and W. J. Svirbely, *ibid.*, **60**, 1613 (1938).

# Technical Note

## Analysis of Manganese Dioxide with Special Reference to Electrodeposited Oxide on Graphite

**Akiya Kozawa and W. C. Vosburgh**

*Department of Chemistry, Duke University, Durham, North Carolina*

There is reason for questioning the analytical data in previous investigations (1, 2) for electrodes of electrodeposited $MnO_2$ on graphite. The analyses have led to the formula $MnO_{1.9}$ for freshly prepared and well washed electrodes. This is poorer in available oxygen than expected for electrolytic $MnO_2$ (3, 4). Also, the available oxygen as determined by the $H_3AsO_3$ method varies with the concentration of the reagent. The data obtained with 0.1$N$ $H_3AsO_3$ were accepted because the results were reproducible, and the $FeSO_4$ method gave similar results, and because a sample of $MnO_2$ from the National Bureau of Standards was correctly analyzed.

The preparation of the electrodes has been described elsewhere (5). Briefly, they consisted of a graphite rod of 4 mm diameter covered for 51 cm of its length with about 0.2 mmole of electrodeposited $MnO_2$. Most of the rod above the seal was covered with a glass tube sealed to the graphite by glyptal cement, with only the top portion exposed for contacts. The area covered by $MnO_2$ was 8 cm$^2$.

*Evidence of error*—That the previous analyses of electrodes were in error was indicated when some $MnO_2$ which had been electrodeposited on Karbate rods gave $MnO_{2.0}$ on analysis. This pointed to the graphite rods as the source of the error. The significant difference between the two kinds of rod seems to be that graphite is porous, while Karbate is not.

The volume of the pores in the graphite rods used was estimated by determining the $Cl^-$ retained from a chloride solution of known concentration after superficial washing. The volumes ranged from 12 to 20% of the volumes of the rods, and the presence of electrodeposited $MnO_2$ made no measurable difference.

Another indication of error in the previous results is that when the available oxygen is determined in $MnO_2$ on graphite by treatment with an

Table I. Analysis of electrodeposited $MnO_2$ on graphite rods after standing 15 hr in solutions of various salts

| Solution in pores | No. of samples | $x$ in $MnO_x$ |
|---|---|---|
| 4M $NH_4Cl$ | 2 | $1.81 \pm 0.02$ |
| 0.2 to 1M $NH_4Cl$ | 3 | $1.95 \pm 0.01$ |
| 4M NaCl | 1 | 2.00 |
| 2M $(NH_4)_2SO_4$ or 1M $Na_2SO_4$ | 2 | 2.00 |
| 1M KOH | 1 | 1.67 |
| 4M $NH_4Cl$ or 1M KOH, washed | 2 | $1.96 \pm 0.01$ |

excess of standard $FeSO_4$ at room temperature instead of at boiling temperature the results are higher. This is illustrated in Table I. Electrodes that had been immersed in various salt solutions for 15 hr were analyzed, because certain salts lead to very low results when the $MnO_2$ is dissolved by a hot reducing agent unless washed out previous to analysis (2). After titration of the excess $FeSO_4$ by $KMnO_4$, the total Mn was determined by the bismuthate method, with correction for the $KMnO_4$.

In the available oxygen determination the $MnO_2$ was dissolved by 10 ml of 0.1*N* $FeSO_4$ and 1.8M $H_2SO_4$ at room temperature (about 25°C) with no protection from air. The electrodes were allowed to stand in test tubes with the $FeSO_4$ solution for 1 or 2 hr, without stirring. Under these conditions the surface has the appearance of bare graphite after 40 min. One minor source of error for which no correction was made at this time was the $FeSO_4$ and $MnSO_4$ retained by the graphite rod after ordinary washing. This would lead to high values of $x$.

Table I shows that this procedure gives reasonable results for electrodes containing NaCl, $(NH_4)_2SO_4$, and $Na_2SO_4$ when an estimated 0.03 is allowed for the above error, but $NH_4Cl$ and KOH cause low results. When the $NH_4Cl$ and KOH are washed out, the results are much better, in agreement with previous experience (2). Apparently the combination of $NH_4^+$ and $Cl^-$ is more harmful than either alone.

Similar experiments using hot $FeSO_4$ (80°-90°C) for the dissolving of the $MnO_2$ gave lower results varying from 1.57 to 1.98 for $x$, and $(NH_4)_2SO_4$ gave a considerably lower result than $Na_2SO_4$ and NaCl. An increase in temperature increases the error from some of the salts, and gives lower results for all.

It may be postulated that a solution of relatively high pH is trapped in the pores of the graphite while the exterior of the $MnO_2$ is in contact with a strongly acid solution. A local-action cell is formed with a high potential cathode. Reduction of the $MnO_2$ takes place if anything in the pores is oxidizable. Increase in temperature should decrease the overpotentials and favor the local action. If hot 0.025M arsenious acid is the reagent, the local-action cell seems to be able to oxidize considerable water before the $MnO_2$ is dissolved.

In the analyses of Table I it was observed that 0.4 to 2 ml of gas was evolved when electrodes that had been kept in either $NH_4Cl$ or KOH solution were put into the acid $FeSO_4$ solution. The gas was considered to be the product of the anodic reaction of the local-action cell. Analysis showed that from $NH_4Cl$ the gas was predominantly $N_2$ and from KOH it contained more $O_2$ than $N_2$.

*Analysis of* $MnO_2$ *on graphite.*—The accuracy of the analysis with cold $FeSO_4$ solution when applied to $MnO_2$ on graphite was tested. The available oxygen was determined as for the data of Table I except that following the dissolution of the $MnO_2$ the graphite rod was kept in 1M $H_2SO_4$ for an hour for the recovery of $Fe^{++}$ and $Mn^{++}$ in the pores. The two solutions were combined for the titration. Then the total Mn was determined by potentiometric titration (6, 7) and a correction made for the Mn added as $KMnO_4$ in the first titration.

In preparing a solution containing Fe for potentiometric titration of Mn it is best if neutralization of any acid present is done by $Na_4P_2O_7$ alone. However, if there is much acid, it may be partially neutralized by NaOH before addition of $Na_4P_2O_7$. Addition of NaOH after the $Na_4P_2O_7$ is likely to introduce an error.

The result for $x$ in $MnO_x$ for 5 electrodes was 1.955 $\pm$ 0.005. The $MnO_2$ was scraped from seven similar electrodes and analyzed by the same method giving $x = 1.947 \pm 0.005$. The two results are not significantly different and, since the graphite rod could not have affected the second, it is probable that the first is correct.

A third set of analyses was made of $MnO_2$ deposited on a Pt surface of the same size and shape as the graphite surface. Three samples gave $x = 1.976 \pm 0.002$. This may represent a real difference since the true Pt surface area was less than that of the graphite and the true current density higher, at least initially.

*Analysis of precipitated* $MnO_2$ *and ores.*—It would be expected that the use of $FeSO_4$ at room temperature for reduction of $MnO_2$ would require excessive time. However, if the $FeSO_4$ solution and sample are stirred vigorously, the time for dissolution is less than with a hot solution not stirred. Five different samples of precipitated $MnO_2$ of 200 mg each were treated with 25 ml of a solution of 0.25M $FeSO_4$ and 1.8M $H_2SO_4$ at 28°C with stirring by a magnetic stirrer until the last visible particles disappeared. The times required varied from 2 to 10 min.

To test the accuracy of the method, Standard Sample No. 25b, battery grade $MnO_2$ from the National Bureau of Standards, was analyzed. Seven samples of about 200 mg each were dissolved by 25 ml portions of a solution of 0.25M $FeSO_4$ and 1.8M $H_2SO_4$ at room temperature. The excess $FeSO_4$ was titrated with 0.02M $KMnO_4$. The solution was then brought to pH 6 to 7 either by about 35 g of $Na_4P_2O_7 \cdot 10H_2O$ or partly by KOH and then $Na_4P_2O_7$ and titrated potentiometrically with 0.02M $KMnO_4$. The available oxygen was found to be $16.66 \pm 0.015\%$ and the total manganese $58.40 \pm 0.07\%$ as compared with the certified values 16.67 and 58.35%.

To test the effect of $NH_4Cl$ on the analysis in the absence of graphite, three samples of 25b were treated with 2 ml each of 1M, 2M, and 4M $NH_4Cl$ for 24 hr. Then, without removal of any of the $NH_4Cl$ solution, the $FeSO_4$ reagent was added and the analysis carried out as before, except that $HgSO_4$ was added before titration of the excess $FeSO_4$ to mask the $Cl^-$. It had been shown that $Hg_2SO_4$ has

no effect on the potentiometric titration of $Mn^{++}$. The results of the three analyses showed no effect of the $NH_4Cl$, the average being $16.64 \pm 0.003\%$ available O and $58.45 \pm 0.08\%$ Mn.

### Acknowledgment

This work was supported in part by the Office of Naval Research.

Manuscript received Aug. 12, 1957.

Any discussion of this paper will appear in a Discussion Section to be published in the December 1958 JOURNAL.

REFERENCES

1. W. C. Vosburgh, R. S. Johnson, J. S. Reiser, and D. R. Allenson, *This Journal*, **102**, 151 (1955).
2. S. Hills and W. C. Vosburgh, *ibid.*, **104**, 5 (1957).
3. G. W. Nichols, *Trans. Electrochem. Soc.*, **62**, 400 (1932).
4. W. Buser and P. Graf, *Helv. chim. Acta*, **38**, 828 (1955).
5. A. M. Chreitzberg, Jr., and W. C. Vosburgh, *This Journal*, **104**, 1 (1957).
6. J. J. Lingane and R. Karplus, *Ind. Eng. Chem., Anal. Ed.*, **18**, 191 (1946).
7. R. F. Stalzer and W. C. Vosburgh, *Anal. Chem.*, **23**, 1880 (1951).

# Indium as an Anode Material

**T. L. Boswell**

*Research and Development Division, Elgin National Watch Company, Elgin, Illinois*

ABSTRACT

Indium and its alloys with bismuth and lead are evaluated as energy producing electrodes for use in small sealed cells. The value of bismuth as an alloying element in promoting the ability of the electrode to function at high current densities is discussed and the electrical capacity, voltage stability, and temperature voltage coefficient of alkaline cells with mercuric oxide cathodes are given.

Indium possesses a high hydrogen overvoltage (1), near that of Hg and its standard potential is close to that of Cd. These two properties indicated that it might be useful as an energy producing anode and might show less tendency toward parasitic reactions which promote deterioration of commercial cells during storage.

For instrument applications where weight and volume are at a premium it was desirable to know how In would compare with other commonly used metals. On a per Faraday basis: Zn, 32.69 g, 4.57 cc; In, 38.27 g, 5.24 cc; Cd, 55.48 g, 6.42 cc; thus In is within the range of weight and volume for useful commercial anodes.

Data on the alkali resistance of indium-containing solders (2) indicated that In alloys could remain in contact with alkaline electrolytes without an appreciable reaction rate. While that work was performed on alloys of low In content (50% or less), it was not unreasonable to expect the same or lower rates of attack on alloys richer in In. Some work in this laboratory, although not yet complete, indicates that In base alloys are much more resistant to attack by alkali electrolytes than more commonly used metals, even when these other metals are protected with inhibitors.

Little consideration has been given to the use of In as an anode prior to the present work (3). Latimer (4) estimated the standard potential to be 1.18 v for the reaction in which the oxide is formed and 1.0 v for the reaction in which the hydroxide is formed (5).

For purposes of this experimental work the following equation has been assumed to be correct:

$$2In + 3HgO + 5H_2O \xrightarrow{KOH} 2In(OH)_3 \cdot H_2O \cdot 3Hg$$

While the exact composition of the In compound formed is not known precisely, there is analytical evidence that it approaches the composition given above and that, within the experimental error, the quantity of electricity obtained agrees with the combining ratios represented in the above equation.

## Experimental Results

It was recognized that one of the most serious problems to overcome was indium's lack of hardness and strength. Its tendency to flow under low stresses made it difficult to maintain tight connections at the anode terminal. An examination of the available equilibrium diagrams in the literature showed that a number of binary systems existed containing single phase areas rich in In and that an appreciable increase in hardness could be obtained by using these alloys. Several of these alloys have been studied as anodes with some gratifying results. Jaffe and Weiss (6) had reported that the strongest alloys could be obtained with Pb, but that Bi was the most potent hardening element when added to In in small quantities. As it was desirable to keep In content as high as possible, consistent with the strength requirements, the Pb and Bi alloys were studied concurrently.

The binary In-Pb alloys were complete failures as anodes due to polarization at low current densities. It is quite possible that this effect is caused by the formation of $PbO_2$ on the electrode surface during cell action. This might subsequently be reduced to spongy Pb by local action, because when such an electrode is polarized and then permitted to recover there is a voltage plateau which corresponds to the lead potential.

Quite the opposite effect is found for the In-Bi alloy anodes. Pure In serves well as an anode at low to moderate current densities, but polarizes at higher current densities, making it undesirable for high-current applications. When Bi is added to In the resulting alloy has the ability to maintain its voltage at considerably higher current densities. An additional advantage is gained from use of the In-Bi alloy anodes in that many metals which poison In are present in the commercial grades and their deleterious effect can be neutralized by intentionally adding Bi in sufficient quantities.

The ternary alloys containing Bi have not yet been properly evaluated, but preliminary experiments indicate that they will be useful as anodic materials. They are stronger than either pure In or the binary alloys, thus overcoming one of the most serious limitations to the use of In anodes.

In order to evaluate the performance of In and In alloy anodes, a series of experiments was made with small sealed cells using HgO cathodes and

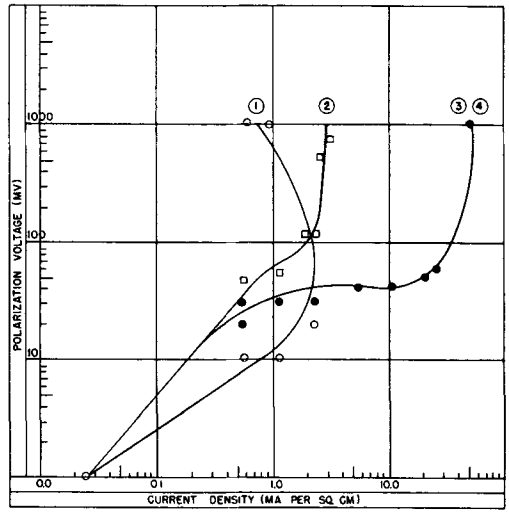


Fig. 1. Polarization of In and In alloy anodes. Each value represents the average of 5 cells. 1, commercial In; 2, 2.5% Pb-In; 3, 5% Bi-In; 4, 1.5% Pb, 2.5% Bi-In.

containing a third electrode of the anode material. By measuring the voltage between this reference electrode and the working anode or cathode, one can differentiate between anodic and cathodic polarization effects.

Successive loads were placed across the cells and voltage measurements were taken after the current had been flowing for 15 min for each load. The voltage between the reference and working anode is then a measure of the decrease in potential of the working anode due to the current flow. These data are plotted in Fig. 1.

At low current densities (2.3 ma/cm$^2$) pure In shows lower polarization characteristics than any of the alloys but quickly polarizes to an unusable extent if higher current densities are attempted.

When Pb is added to In these polarization effects are increased and the electrode ceases to be useful even at the lower current densities.

When Bi is present either in binary alloys or in the ternary alloy with lead, the electrode can function at much higher current densities, remaining useful up to about 31 ma/cm$^2$.

For evaluation tests a small sealed cell was designed using a HgO cathode and an alkaline electrolyte. This cell was 5/8 in. square x 2/10 in. thick. The electrodes were arranged facing one another and attached to the square faces of the cell. Such cells had a 400 ma-hr theoretical capacity and an apparent electrode area of 1.88 cm$^2$.

Figure 2 shows the discharge curves for a group of these evaluation cells at various current densities. The end points were taken at first polarization under continuous drain. An appreciable fraction of this theoretical service is obtained at current densities up to 5.3 ma/cm$^2$. If the cells were permitted to recover, further capacity could be obtained, especially from those cells discharged at the higher currents. The constancy of their voltage during discharge is quite noteworthy. At intermediate to high current densities a slight rise in voltage is noted during discharge. At present an adequate explanation for this characteristic cannot be given. The cell potential also rises during storage under open circuit conditions.

To determine the variation of potential with storage time, groups of the evaluation cells were stored at room temperature, some under open circuit conditions and some with small currents being drawn continuously. Voltage measurements were made with an L&N type K-2 potentiometer. At first, readings were taken each day, then on three days each week, and finally on two days each week. The results of these tests over an 18 month period are shown in Fig. 3.

The tendency of In cells to maintain their voltage is well illustrated by these data. These first results indicate that the In electrode has an excellent inherent possibility as a secondary voltage standard. While no study has been made to achieve the optimum design, it was noted that small voltage fluctuations were superimposed on the curves shown in the figure which could be correlated to room temperature changes. Of particular interest is the fact that reversal of the direction of voltage fluctuation with temperature changes occurred between unloaded cells and those where current was flowing. This suggests a possible means of compen-

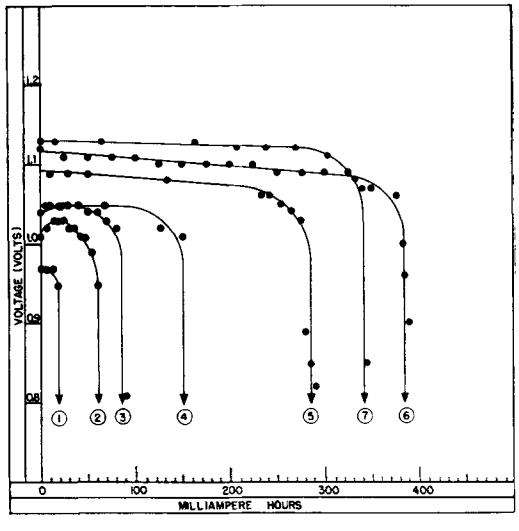


Fig. 2. Discharge curves for 5% Bi-In-HgO cells with an alkaline electrolyte. Theoretical capacity of these cells is 400 ma/hr. Each value represents the average on 5 cells. 1, 80 ma; 2, 60 ma; 3, 40 ma; 4, 20 ma; 5, 10 ma; 6, 5 ma; 7, 2 ma.

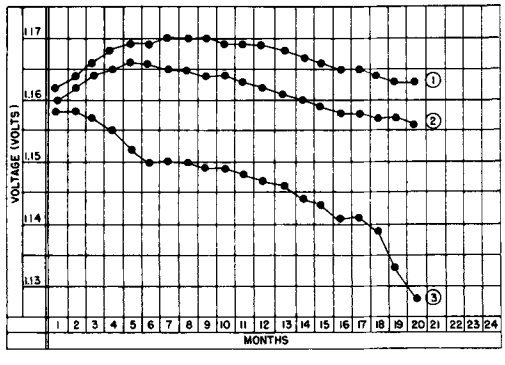


Fig. 3. Voltage stability at continuous loads indicated. Each value represents the average of at least 8 readings on 5 cells. 1, no current; 2, 1 $\mu$a; 3, 10 $\mu$a.

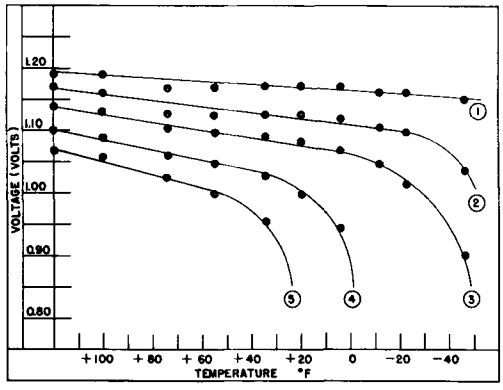


Fig. 4. Voltage-temperature-current density relationship of 5% Bi-In-HgO alkaline cells. Each value represents the average of 10 cells. 1, 0.003 ma/cm$^2$; 2, 0.12 ma/cm$^2$; 3, 0.68 ma/cm$^2$; 4, 3.29 ma/cm$^2$; 5, 6.36 ma/cm$^2$. Current densities were calculated at 23.3°C.

sating for room temperature changes when using this type of cell as a voltage reference.

Another important aspect of a cell containing this electrode is its operation at various temperatures. Figure 4 shows the voltage-temperature relationship at various current densities for a group of the same evaluation cells.

These data represent the average results obtained on 10 cells. The cells were placed in a temperature chamber and permitted to come to temperature. Voltage readings were then taken after the current had been flowing for 15 min. Some values were taken after the cells had been at temperature for just 3 hr and then rechecked after 24 hr. Excellent agreement between the two sets of readings was obtained.

From the linear relationship shown in Fig. 4, the temperature coefficient of voltage varied between 0.00080 to 0.00232 v/°C (0.00044 to 0.0013 v/°F) between 12.8 and 37.8°C (+55 and +100°F) with the larger coefficient associated with the larger current density as expected.

## Conclusion

These preliminary results indicate that In can be stored in alkaline electrolytes without deterioration and yet function usefully at the proper time. It is believed that these characteristics make further studies desirable.

Manuscript received Sept. 23, 1957. This paper was prepared for delivery before the Buffalo Meeting, Oct. 6-10, 1957.

Any discussion of this paper will appear in a Discussion Section to be published in the December 1958 JOURNAL.

REFERENCES

1. T. Moeller and B. S. Hopkins, *J. (and Trans.) Electrochem. Soc.*, **93**, 84 (1948).
2. S. M. Grymko and R. I. Jaffe, *Materials & Methods*, **31**, 59-60, March (1950).
3. T. L. Boswell, U. S. Pat. 2,683,184, July 6, 1954.
4. W. M. Latimer, "The Oxidation States of the Elements and their Potentials in Aqueous Solutions," pp. 149-151, Prentice-Hall Inc., New York (1938).
5. W. M. Latimer, "The Oxidation States of the Elements and their Potentials in Aqueous Solutions," pp. 161, Prentice-Hall Inc., New York (1952).
6. R. I. Jaffe and S. M. Weiss, *Materials & Methods*, **36**, 113-15, September (1952).

# Effect of Amines on Polarization of Iron Electrodes

**Alfred F. Schram, and Lawrence Raymond Burns**[1]

*Chemistry Department, Agricultural and Mechanical College of Texas, College Station, Texas*

ABSTRACT

An apparatus has been designed and constructed which gives a measure of the effect of organic amine salts on the polarization of iron cathodes in 1.0*N* sulfuric acid solution. The apparatus consists essentially of a Wheatstone Bridge circuit in which two of the ratio arms are electrolysis cells with a common anode and separate iron cathodes. The elements of the bridge are arranged in such a way that the electrolysis currents through the two cathodes can be measured simultaneously when the cathodes are at the same potential.

The effect of the amine salts on the polarization of the iron cathodes has been interpreted in terms of the apparent area changes brought about by adsorption of the amines on the surface of the cathodes. These apparent area changes have then been compared with the per cent inhibitor efficiencies of the amines, as measured by corrosion rate studies. Over the concentration ranges employed, the per cent inhibitor efficiency for each amine is a linear function of the apparent per cent surface area masked by that amine. Since the different amines showed considerable specificity in the relationship between per cent efficiency and apparent per cent area masked, it is concluded that the action of the amine as a corrosion inhibitor is more than a simple masking of certain portions of the surface of the corroding metal.

In the past few years considerable attention has been given to the effect of various substances, both organic and inorganic, on polarized electrodes and on corroding metals. Many organic colloids such as agar, egg albumen, and gum tragacanth, are known to retard the action of acids or pure water upon zinc or iron. The salts of arsenic, antimony,

[1] Present address: The Texas Company, Port Arthur, Texas.

and mercury, as well as many organic nitrogen and sulfur compounds, inhibit the attack of acids on metals. Different explanations have been proposed for the mechanism of these phenomena.

Some investigators have shown that organic amines in general affect the cathodic polarization of various metals, and have little or no effect on the anodic polarization (1, 4). They assert that these materials increase the hydrogen overvoltage at the cathodic areas and thus hinder the discharge of hydrogen ions. Others hold that the inhibitors are adsorbed over the entire surface, but are held more strongly at the anode areas where, by increasing the effective electron density, they prevent the dissolution of the metal from these areas (5).

A detailed theory of the mechanism of the inhibiting action of nitrogen-containing organic compounds was proposed by Mann (6) as a result of investigations carried out by himself and co-workers on the acid corrosion of steel.

Mann and Shih-Jen Ch'iao (4) investigated the possibility of a quantitative relationship between the rise in cathode potentials of polarized electrodes and the decrease in corrosion rates as determined by actual corrosion rate studies.

Mann and his co-workers investigated fourteen different amines by this method. They found that the two methods could be correlated quantitatively, and that the potential rise method was satisfactory as a means of estimating the effectiveness of the amines as corrosion inhibitors.

The purpose of the present investigation was to design and construct an apparatus which could test the theory proposed by Mann (6) that the effect of amine inhibitor ions on the surface of the corroding metal could be explained in terms of the fraction of metal surface effectively shielded by the inhibitor.

The amines used in the present work were compounds that differed from one another in structural configuration or in molecular weight. Two aliphatic amines, di-*n*-propylamine and di-*n*-butylamine; one aromatic amine, dimethylaniline; and one substituted aliphatic amine, beta-bromoethylamine, were investigated.

## Apparatus

### *The Dual Cathode Bridge*

The apparatus employed (Fig. 1) was essentially a Wheatstone bridge circuit in which the two lower arms of the bridge were branches of a three-compartmented electrolysis vessel, each compartment being separated from the others by fritted disks. A platinum anode in the center compartment of the vessel was contained within a glass sleeve. A hole approximately 1 cm$^2$ in area in the wall of the sleeve enabled current to flow from the anode to the two cathodes mounted in the two end compartments of the vessel. By rotating the glass sleeve it was possible to vary the effective path lengths between the common anode and the two cathodes, and thus, by compensating for any difference in porosity between the two fritted disks,

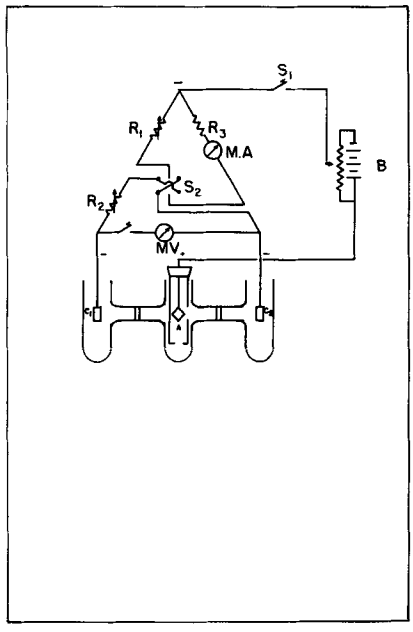


Fig. 1. Dual cathode bridge. $S_1$, Knife blade switch; B, 6 v d-c source; $R_1$, 100±0.1 Ω heliopot; $R_2$, 100±0.1 Ω heliopot; $R_3$, 15 Ω fixed resistor; M.A., milliammeter; M.V., millivoltmeter; $C_1$, left cathode; $C_2$, right cathode; A, anode.

to maintain the same solution resistance in both branches of the cell.

The electrolytic paths through each branch of the cell constituted the two lower resistance arms of the bridge circuit. The two upper resistance arms consisted of the following: a pair of 100-ohm precision variable resistances in series formed one of the arms; and a milliammeter connected in series with a 15-ohm fixed resistance formed the other arm. A millivoltmeter was connected across the two cathodes and served as the null indicator for the bridge.

A double-pole-double-throw switch was connected in the upper part of the bridge circuit in such manner that when the total resistance of the arm containing the milliammeter was carefully matched by means of one of the variable resistances in the opposing arm of the bridge, the milliammeter could be connected alternately in series with either cathode without upsetting the balance of the bridge. This enabled one to read the current flowing in either branch of the electrolysis vessel with the bridge at balance.

The two cathodes were cut from the same piece of metal stock and machined to the same shape and size, with a tolerance of less than 0.001 in. being allowed in any linear dimension. A projection of the cathode metal left on one side of each cathode allowed them to be sealed into Pyrex glass tubes by means of Dekotinsky cement. The metal projection extending through the cement was soldered to a strip of copper wire. The back and sides of each cathode were masked off with a Tygon base primer and then coated with paraffin. The electrodes were mounted in the two end compartments of the electrolysis vessel in such a way that the unmasked face of each cathode was parallel with, and directed toward, the common anode contained in

the center compartment. Special V-slotted electrode holders make it possible to remove the electrodes from the vessel and to replace them again in nearly identically the same positions. Immediately before each run, the cathodes were freshly sanded with 6/0 garnet paper, rinsed with conductivity water, and dried with filter paper.

*Operation of the bridge.*—In operation, $R_1$ (Fig. 1) was first adjusted so that its resistance was equal to the sum of $R_3$ plus the internal resistance of the milliammeter. This was accomplished by setting $R_2$ to zero and replacing the two branches of the electrolysis cell with a pair of L&N standard wire-wound resistances, each having a resistance of 10 ohms. Switch $S_1$ was then closed and $R_1$ was adjusted until the millivoltmeter was at null. At this point the resistance of $R_1$ was equal to the total resistance of the milliammeter-containing arm of the bridge, and the switch $S_2$ could be reversed without changing the balance of the bridge.

One normal sulfuric acid was placed in all three compartments of the cell, and the prepared iron cathodes and the platinum anode were connected in the circuit and placed in their respective compartments. Electrolysis was carried on until the cathodes reached equilibrium. The glass sleeve surrounding the anode was rotated until, with the bridge balanced, the current was the same in the two branches of the cell. At this point, the resistance across the left branch of the cell was equal to the resistance across the right branch, and the apparatus was ready for use. Once set in this fashion, it was found that the cathodes could be interchanged in the two end compartments with a resulting change of less than 1/10 ma in the difference between the two values of current flowing in the two branches of the cell.

With the bridge balanced as described above, the effect of amine inhibitors on the polarized iron cathode was studied by replacing the solution in the left compartment of the vessel with inhibited acid, waiting until a steady state was reached, and then rebalancing the bridge by adjusting $R_2$ until the millivoltmeter indicated that left and right cathodes were at the same potential. Current readings were then taken in the two branches of the cell at a number of different current levels. Data were obtained in this manner for various concentrations of the four different amines investigated. For each amine, at each concentration, the per cent decrease caused by the presence of the inhibitor in the left branch of the cell proved to be independent of the current level at which the bridge was operated. This fact is shown graphically in Fig. 2-5, in which the decrease in current in each case is plotted against the current in the uninhibited branch of the cell. The plots are straight lines, the slopes of which represent the percentage decrease in current caused by the presence of the inhibitor.

*Use of the dual cathode bridge.*—To determine the response of the bridge to known changes in the area of exposed surface of one cathode, the area of

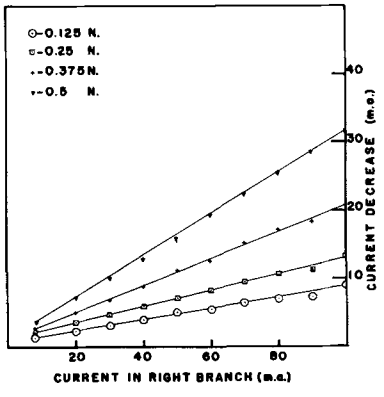


Fig. 2. Response of the dual cathode bridge to di-n-butylamine.

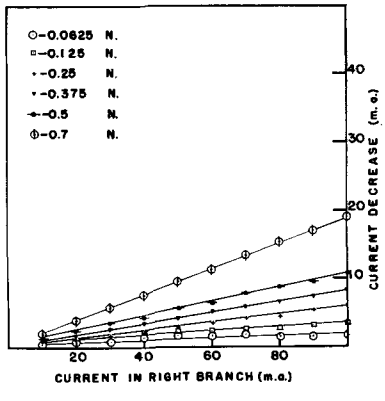


Fig. 4. Response of the dual cathode bridge to dimethylaniline.

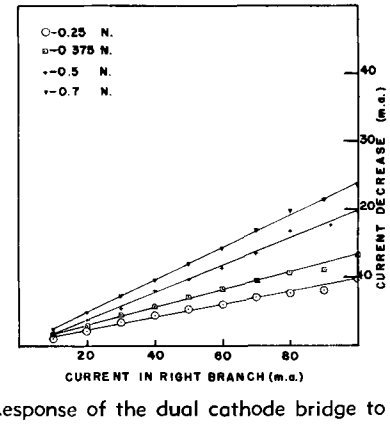


Fig. 3. Response of the dual cathode bridge to di-n-propylamine.

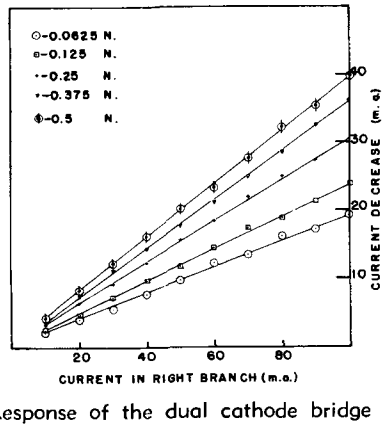


Fig. 5. Response of the dual cathode bridge to β-bromoethylamine.

exposed surface of the other cathode being held constant, the following experiment was performed.

Uninhibited 1*N* $H_2SO_4$ was placed in all compartments of the electrolysis vessel, and the bridge was balanced in the manner previously described. One of the cathodes was then removed, washed, sanded, dried, and one-third of the exposed surface was coated carefully with paraffin. The electrode was replaced in the cell and current readings in the two branches were taken at different current levels. This procedure was repeated with different fractions of the area of the electrode face being masked with paraffin. It was found that the percentage decrease in current in the left branch was independent of the current level used, and depended only on the fraction of electrode face masked by the paraffin. A graph of per cent of cathode face masked vs. per cent current decrease in the left branch was prepared (Fig. 6) and was used in the later experiments with the amine inhibitors to derive a value for the per cent decrease in surface area caused by adsorption of the amine onto the surface of the cathode. Because of the many factors involved, this value as read from Fig. 6 may not represent the true percentage decrease in surface area in the case of the shielding of the surface by the adsorbed amine. But because the percentage decrease in electrolysis current upon shielding one cathode—either by paraffin coating or by adsorbed amine—was always independent of the current level at which the bridge was operated, the values obtained from Fig. 6 must be related in some simple fashion to the true area decrease in each case. Thus the values read from Fig. 6 may be taken as at least an indirect measure of the relative amount of shielding of the electrode surface by the adsorbed amine. In this sense, the effect of each amine could be interpreted in terms of the relative or apparent area changes at the electrodes. The effectiveness of the amines in shielding the surface could then be compared in a relative fashion to their effectiveness in inhibiting corrosion, the latter being measured by the corrosion rate method.

In studying the effect of the amine inhibitors on the polarized iron electrode, the cathodes were freshly sanded before each run, rinsed with conductivity water, dried, and all but one face of each were freshly coated as previously described. Inhibited acid solution was put into the left compartment, and uninhibited acid solution into the other two compartments. All solutions had been previously subjected to electrolysis with platinum electrodes in order to remove traces of metallic impurities, and all water used in preparation had been previously distilled from alkaline permanganate and stored in Pyrex bottles.

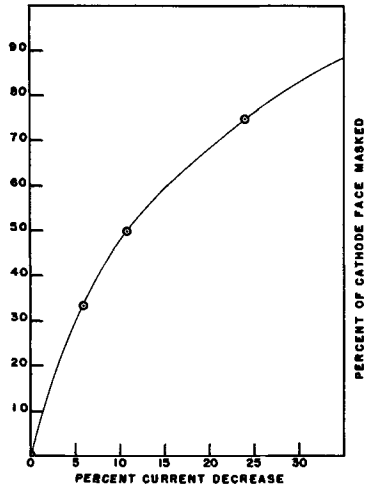


Fig. 6. Per cent current decrease vs. per cent of cathode face masked.

The electrodes were placed in the electrolysis vessel, and electrolysis was carried out until the electrodes reached equilibrium or a steady state. The bridge was balanced, and readings of current taken in both branches of the cell. In all cases it was found that the percentage decrease in current caused by the presence of the inhibitor was essentially independent of the current level at which the bridge was operated.

## Discussion

In determining the per cent inhibitor efficiencies of the four amines used in the polarization studies, mild steel coupons were cut from the same metal stock as the cathodes, and were used in measuring the inhibitor efficiencies of the amines. The per cent inhibitor efficiencies are shown in Table I.

Table I shows the value of the per cent electrode area masked, as read from Fig. 7, compared with the corresponding per cent inhibitor efficiencies as determined by the corrosion rate method. The same data are shown graphically in Fig. 7. Both the table and the graph show that the per cent inhibitor efficiency for a given amine seems to be a linear function of the amount of masking of the metal surface by the adsorbed amine ion. However, it is not directly proportional to the amount of masking,

**Table I. Comparison of apparent cathode area masked with inhibitor efficiency of amine salts**

| Inhibitor | Normality (of amine salt) | % Current decrease | % Apparent cathode area masked (from Fig. 6) | % Inhibitor efficiency (by corrosion rate method) |
|---|---|---|---|---|
| Di-*n*-propylamine | 0.25 | 10 | 47 | 75.3 |
| | 0.375 | 14 | 59 | 78.0 |
| | 0.5 | 20 | 70 | 80.0 |
| | 0.7 | 24 | 75 | — |
| Dimethylaniline | 0.0625 | 3 | 17 | 60.5 |
| | 0.125 | 4.5 | 25 | 62.3 |
| | 0.25 | 6 | 33 | 67.0 |
| | 0.375 | 8.5 | 42.5 | 71.5 |
| | 0.5 | 11 | 50 | 73.0 |
| | 0.7 | 19 | 68 | — |
| Di-*n*-butylamine | 0.125 | 9 | 44 | 78.4 |
| | 0.25 | 14 | 58 | 79.1 |
| | 0.375 | 22 | 73 | 81 |
| | 0.5 | 33 | 82 | 82.2 |
| Beta-bromoethyl-amine | 0.0625 | 20 | 70 | 83.2 |
| | 0.125 | 24.5 | 75.5 | 84.5 |
| | 0.25 | 33.15 | 81 | 89.2 |
| | 0.375 | 35.5 | 84 | 90.8 |

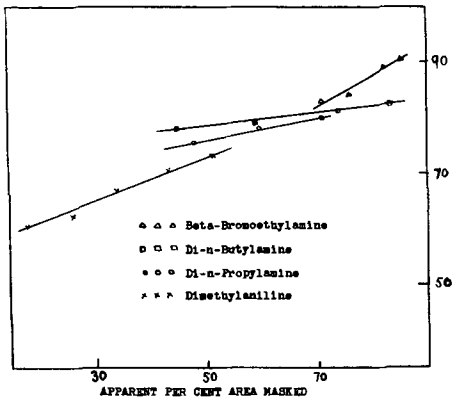


Fig. 7. Apparent per cent cathode area masked vs. inhibitor efficiency of amine salt.

and hence it is to be concluded that the action of amine salts in inhibiting corrosion is more complex than a simple percentagewise blocking off of portions of the metal surface. The fact that considerable specificity is shown by the individual amines helps to confirm further that conclusion.

Manuscript received July 8, 1957. This paper is based on a thesis presented to the faculty of the Graduate School, A. and M. College of Texas by L. R. Burns in partial fulfillment of the requirements for the M.Sc. degree.

Any discussion of this paper will appear in a Discussion Section to be published in the December 1958 JOURNAL.

REFERENCES

1. E. L. Chappell, B. E. Roetheli, and B. Y. McCarthy, *Ind. Eng. Chem.*, **20**, 582 (1928).
2. J. C. Warner, *Trans. Electrochem. Soc.*, **55**, 287 (1929).
3. F. H. Rhodes and W. E. Kuhn, *Ind. Eng. Chem.*, **21**, 1066 (1929).
4. C. A. Mann and Shih-Jen Ch'iao, *ibid.*, **39**, 910 (1947).
5. N. Hackerman and A. C. Makrides, *ibid.*, **46**, 523 (1954).
6. C. A. Mann, B. E. Lauer, and C. T. Hultin, *ibid.*, **28**, 159 (1936).

# Corrosion of Anodically and Cathodically Polarized Magnesium in Aqueous Media

**G. R. Hoey and M. Cohen**

*Division of Applied Chemistry, National Research Council, Ottawa, Ontario, Canada*

ABSTRACT

The effect of current density, pH, and temperature on the anodic behavior, cathodic behavior, and corrosion of magnesium in aqueous solutions has been studied. A tentative mechanism for the anodic oxidation of magnesium is postulated. Local corrosion and/or undermining of metallic magnesium at the anode are appreciable and may, in fact, account for the observed low anodic current efficiencies of magnesium. An intergranular type of corrosion occurs at cathodically polarized magnesium at elevated temperatures. A hydrogen embrittlement theory is proposed to explain intergranular cathodic corrosion.

The magnesium electrode, Mg; $Mg^{++}$, behaves as an irreversible electrode in aqueous solutions. The potential of Mg is considerably more noble than the electrochemical potential calculated from thermodynamic data and is practically independent of the magnesium ion concentration (1, 2). The possible causes of the wide departure from reversibility are: (*a*) the electrochemical process involves magnesium ions with abnormal valencies; (*b*) self-corrosion; (*c*) film formation; and (*d*) activation and concentration overpotential. The last of these four possibilities is relatively unimportant for Mg. To determine the importance of the various processes the electrode is studied under nonreversible operating conditions, that is, under experimental conditions of anodic and cathodic polarization.

The anodic dissolution of Mg has been studied extensively (3-8). The outstanding experimental facts of the dissolution which, as yet, are not satisfactorily explained are: (*a*) the anodic current efficiency in aqueous solutions is less than 100% (the anodic current efficiency is defined as the ratio of the actual coulombs passed to the theoretical coulombs obtainable from the actual weight loss assuming a magnesium valency of two); (*b*) the amount of hydrogen produced in the absence of added oxidizing agents is equivalent to the excess Mg dissolved at the anode; and (*c*) the corrosion film formed on Mg is composed of Mg, MgO, and $Mg(OH)_2$ (9-13).

The electrochemical formation of monovalent Mg (3, 4, 5, 8, 14) has been postulated by various workers to account for the low current efficiencies; solution reactions of $Mg^+$ were postulated to account for the hydrogen and corrosion product formation. Robinson (6) has suggested that the low current efficiencies may be due to an enhanced corrosion rate at the anode since in an unbuffered solution the acidity at the metal-solution interface is higher than in the bulk of the solution for anodically polarized Mg.

Müller has studied the anodic passivity of Mg in $H_2SO_4$, $HNO_3$, NaOH, and $MgCl_2$ solutions (15). In $H_2SO_4$ solutions the current-time curves were simi-

lar to those obtained with other metals. Magnesium becomes passive in $HNO_3$ solutions, but side reactions complicate the phenomenon. Passivity is not reached in $MgCl_2$ solutions. Passivity in NaOH solutions results quickly, beyond which stage the current rises slowly. At cell potentials >6 v only low current values are attained, whereas, at cell potentials <6 v, values of almost half of the initial current are attained. The anodic polarization curves of Mg are flat at current densities up to 1 ma $cm^{-2}$ in solutions containing ions which form soluble Mg salts; in the presence of ions such as $OH^-$, $F^-$, $CO_3^=$, $BO_2^-$, and $PO_4^{\equiv}$ the anode polarizes (6).

Evans, *et al.*, (16) and Phelps (17) have measured the cathodic polarization curves of Mg at room temperature. These authors observed a break in the potential-current curve similar to the cathodic polarization curves for iron. Phelps correlated the value of the current at this break with the corrosion current for a rotating Mg cathode.

The open circuit potential of Mg is practically constant in the *p*H range 3-11 and the corrosion rate increases slightly in this *p*H range in unbuffered solutions (18). At *p*H's >11, the potential curve shows a sharp bend toward more noble potentials and the corrosion rate shows a corresponding decrease. In buffered solutions (19) the sharp increase in potential occurs at *p*H = 9.2. A marked increase in potential and corrosion rate also occurs at *p*H's <3. The acid dissolution of Mg is probably diffusion controlled (20-24). Casey and Bergeron (25) interpreted the acid dissolution of Mg in terms of the physical control of diffusion by surface films of $Mg(OH)_2$ and/or by oxide.

The effect of temperature on the electrochemical behavior of Mg has received comparatively little attention. The current efficiency of Mg in 3% NaCl solution assuming a Mg valency of two is approximately 50% and is independent of temperature in the range 0°-50°C (8). The activation energy for dissolution of Mg in acids varies from 3-5 kcal $mole^{-1}$ (20, 23). Electron diffraction data indicate a hexagonal $Mg(OH)_2$ is formed at room temperature, whereas a film of $Mg(OH)_2$, presumably rhombic, is formed at 100°C which is more protective than the film formed at room temperature (12).

In this paper a study of the effect of temperature, *p*H, and current density on the anodic, cathodic, and open circuit behavior of Mg is presented.

## Experimental

Commercially pure distilled Mg obtained from Dominion Magnesium Ltd. was used. This material is reported to have a minimum purity of 99.96% with a total Fe, Ni, and Cu content not greater than 0.005%. Solutions were prepared from reagent grade salts. Experiments were performed using unbuffered and buffered solutions of 110 ppm NaCl. Sodium hydroxide-sodium borate, boric acid-sodium borate, and sodium carbonate-sodium bicarbonate buffers were used for *p*H's up to 10. Sodium hydroxide was used to obtain *p*H's >10. The *p*H's of the NaOH solutions were calculated using values of the dissociation constant of water $k_w = 1.0 \times 10^{-14}$ at 25°C and $k_w = 1.9 \times 10^{-13}$ at 75°C (26). The *p*H's

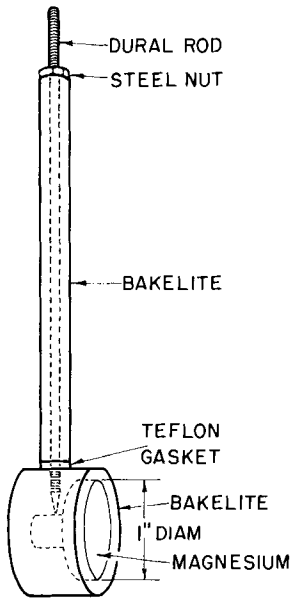


Fig. 1. Magnesium electrode

of the buffered solutions at 75°C were determined using a calibrated Ag; AgCl-glass electrode assembly and a Beckman *p*H meter. Standard buffer solutions were used for the calibration of the electrode assembly (27).

The electrolytic cell consisted of a Mg cathode and a Mg anode with a Ag;AgCl probe reference electrode (thermal electrolytic type) at both Mg electrodes immersed in aqueous solution. Potentials of the Ag;AgCl half-cell were calculated using the data of Bates and Bower (28). The Mg electrode used for most experiments is illustrated in Fig. 1. The Mg specimen was annealed at 300°C for 2 hr in an argon atmosphere, polished on 1/0 emery paper, degreased, etched in 0.1*N* HCl for 1 min, weighed, and moulded in bakelite. The bakelite button was then machined and the electrode assembled. In basic solutions (>0.01*N* NaOH) Mg rods (¼ in. diameter x 7 in. long) were used as electrodes since the bakelite decomposed in these solutions at the higher temperatures.

A constant temperature oil-bath regulated to within 1°C was used. Fresh solution was continuously supplied to the cell solution (½ l) at the rate of ¼ l/hr using an overflow system. The cells were maintained at constant current by discharging a d-c voltage supply (112.5 v) through an appropriate variable resistance, a calibrated ammeter, and the cell. Potentials were recorded on a L&N Speedomax recorder. Experiments were from 5 to 7 days duration.

The Mg specimen could be cracked from the bakelite by pressing it between the jaws of a vice. Corrosion products were removed from the Mg in boiling 15% chromic acid containing 1% silver chromate and the weight loss of the Mg determined.

The corrosion products of the Mg were analyzed by x-ray analysis. The corroded Mg specimens were examined metallographically.

## Results

The current efficiencies (%) of Mg anodes, the corrosion rate (m.d.d.) at the cathodes, the anodic

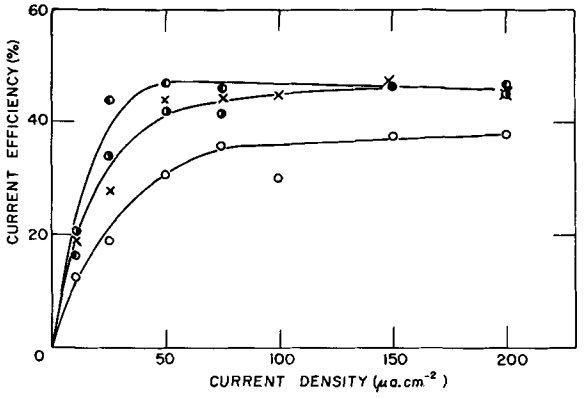


Fig. 2. Dependence of the current efficiency (%) of Mg anodes in 110 ppm NaCl solution on the current density: pH = 10 to 9; open circle, ca. 25°C; circle, right half solid, 58°C; circle, left half solid, 75°C; X, 92°C.

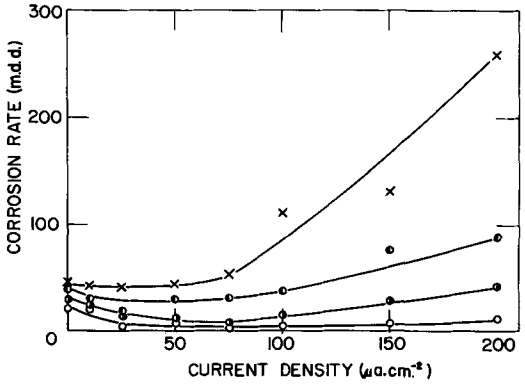


Fig. 3. Dependence of the corrosion rate of magnesium cathodes in 110 ppm NaCl solution on the current density: pH = 10 to 9; open circle, ca. 25°C; circle, right half solid, 58°C; circle, left half solid, 75°C; X, 92°C.

and cathodic polarization curves of Mg (steady potentials attained after several days immersion) in 110 ppm NaCl solutions are plotted vs. the current density ($\mu$a cm$^{-2}$) for the temperatures 25°, 58°, 75°, and 92°C in Fig. 2, 3, and 4, respectively. It was found that the current efficiency of the Mg anode and the corrosion rate at the Mg cathode at a current density of 500 $\mu$a cm$^{-2}$ at 75°C in 110 ppm NaCl solutions is independent of time in the range 2-10 days.

The effect of pH on the current efficiency of Mg at a current density of 500 $\mu$a cm$^{-2}$ and the temperatures 25°C and 75°C is shown in Fig. 5. Log [Corrosion Rate (m.d.d.)] of Mg cathodes polarized at 500 $\mu$a cm$^{-2}$ and unpolarized Mg is plotted vs. the pH for the temperature 25°C in Fig. 6 and for the temperature 75°C in Fig. 7. Photographs demonstrating the various types of attack of the Mg which was observed are shown in Figs. 8, 9, 10 and 11.

Magnesium hydroxide was identified by x-ray diffraction analysis on the cathodes, anodes, and locally corroding specimens of Mg in 110 ppm NaCl solutions at the various temperatures studied. Free Mg metal particles were observed by the microscope in the corrosion products.

Cathodic polarization of Mg does not affect the lattice parameters of Mg. The values of a nonetched Mg specimen annealed in vacuum at 350°C are $a_o = 3.203$ and $c_o = 5.199$. The values after cathodic polarization at 2.3 ma cm$^{-2}$, for 10 hr at 92°C in a

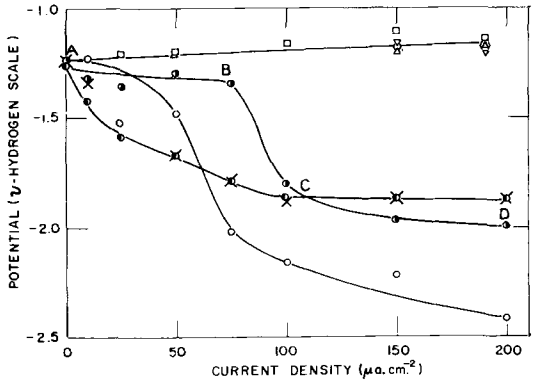


Fig. 4. Anodic polarization curve of magnesium in a 110 ppm NaCl solution: pH = 10 to 9; square, 25°C, diamond, 58°C; triangle, 75°C; inverted triangle, 92°C. Cathodic polarization curves of magnesium in 110 ppm NaCl solution: pH = 10 to 9; circle, 25°C; circle, right half solid, 58°C; circle, left half solid, 75°C; X, 92°C.

boric acid-sodium hydroxide solution with 110 ppm NaCl buffered at pH = 9.25 are $a_o = 3.202$ and $c_o = 5.200$. The change in the parameters is within experimental error.

A Mg electrode in the form of a tube with the immersed end closed and the open end joined to a gas buret was cathodically polarized at 92°C in a 110 ppm NaCl solution. No passage of $H_2$ through the Mg was observed.

## Discussion

### *Anodic Behavior of Magnesium*

A tentative mechanism for the anodic oxidation of Mg including secondary reactions is:

$$Mg = Mg^{++} + 2e \quad \text{(I)}$$

$$Mg = Mg^{+} + e \ (3,4,5,8,14) \quad \text{(II)}$$

$$2Mg = Mg^{++}\cdot Mg + 2e \quad \text{(III)}$$

$$Mg^{+} = Mg^{++} + e \ (4) \quad \text{(IV)}$$

$$2H^{+} + 2e = H_2 \ (6, 22) \quad \text{(V)}$$

$$2Mg^{+} + 2H_2O = 2Mg(OH)^{+} + H_2 \ (3) \quad \text{(VI)}$$

$$Mg^{++}\cdot Mg + 2H_2O = Mg^{++} + Mg(OH)_2 + H_2 \quad \text{(VII)}$$

$$2Mg^{+} = Mg^{++} + Mg \ (8) \quad \text{(VIII)}$$

$$Mg^{++} + 2OH^{-} = Mg(OH)_2 \quad \text{(IX)}$$

$$Mg = Mg_a \quad \text{(X)}$$

Reaction (III) is energetically possible; the bond energy of $Mg^{++}\cdot Mg$ would probably be about equal to the heat of sublimation of Mg (ca. 42 kcal mole$^{-1}$

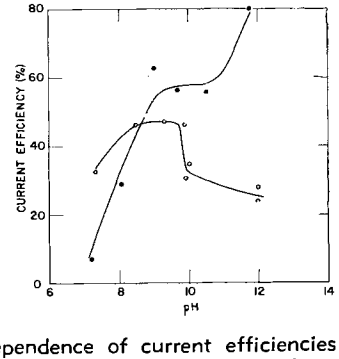


Fig. 5. Dependence of current efficiencies (%) of magnesium anodes polarized at 500 $\mu$a cm$^{-2}$ on the pH: open circle, ca. 25°C; solid circle, 75°C.

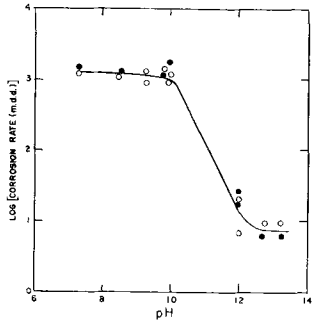


Fig. 6. Dependence of log [corrosion rate (mdd)] of magnesium cathodes polarized at 500 $\mu$a cm$^{-2}$ and nonpolarized specimens on the pH at 25°C; open circle, cathodes: solid circle, local corrosion.

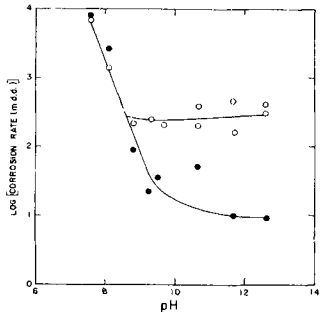


Fig. 7. Dependence of log [corrosion rate (mdd)] of magnesium cathodes polarized at 500 $\mu$a cm$^{-2}$ and nonpolarized specimens on the pH at 75°C; open circle, cathodes; solid circle, local corrosion.

at 25°C). Reaction (V) corresponds to the cathodic reaction of local corrosion on the anode. The reaction of $Mg^{+}$ and $Mg^{++}\cdot Mg$ with water is written purely formally in Eqs. (VI) and (VII), respectively. Monovalent Mg would be expected to have a short life time somewhat comparable to that of a free radical; the relatively long-lived reducing activity of the anolyte observed by Kleinberg, *et al.*, (3) is probably due to $Mg^{++}\cdot Mg$ or colloidal Mg. $Mg_s$ represents undermined Mg.

An expression may be derived for the anodic current efficiency of Mg in terms of the rates of the reactions postulated in the mechanism. Assuming Faraday's laws and a homogeneous current density over the entire anode for the electrochemical reactions.

$$\text{C.E. } (\%) = 100/[1 + (i_2+i_3+i_5+i_s-i_4)/i_T] \qquad \text{(XI)}$$

where

$$i_T = i_1 + i_2 + i_3 + i_4 - i_5 \qquad \text{(XII)}$$

$i_T$ is the total external current in amperes; $i_1$, $i_2$, $i_3$, $i_4$, and $i_5$ are the currents due to the reactions (I), (II), (III), (IV), and (V), respectively. $i_s/i_T$ is defined as the ratio of the weight loss due to undermining to the weight loss at an anode with 100% current efficiency. Magnesium metal formed by Eq. (VIII) would not effect Eq. (XI). Assuming a steady-state concentration of monovalent Mg and a uniform concentration of ions throughout the solution:

$$i_2 - i_4 = FR \qquad \text{(XIII)}$$

and

$$\text{C.E. } (\%) = 100/[1 + (i_3+i_5+i_s+FR)/i_T] \qquad \text{(XIV)}$$

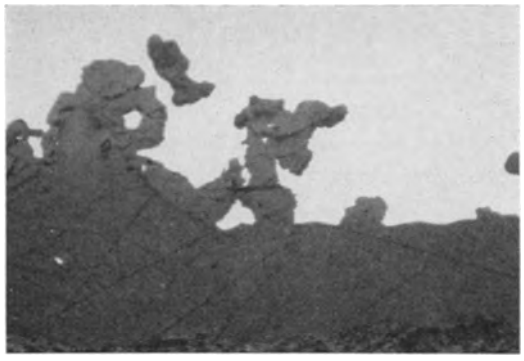

Fig. 8. Metallographic cross section of magnesium anode: polarization current = 100$\mu$a cm$^{-2}$; temperature = 75°C; time = 7 days; solution = 110 ppm NaCl. Magnification 150X before reduction for publication.

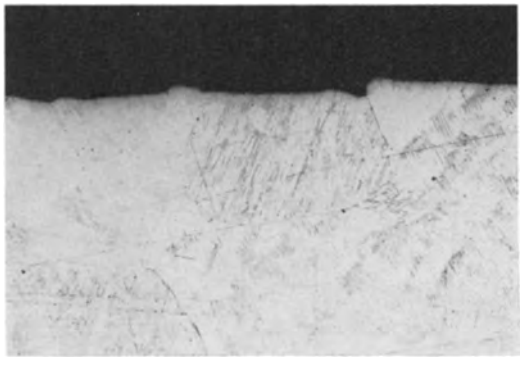

Fig. 9. Metallographic cross section of magnesium electrode demonstrating acid attack, etched. Magnification 150X before reduction for publication.

$F$ (coulombs) is the Faraday constant and $R$ (moles sec$^{-1}$) is the sum of the rates of disappearance of monovalent Mg by solution reactions.

At very low pH's and current densities the rate of the anodic dissolution of Mg which supplies external current ($i_T$) is small compared to the rate of local corrosion ($i_5$). This explains the experimental facts that the current efficiency is an increasing function of the current density and of pH in the low ranges (Fig. 2 and Fig. 5). Within experimental error the current efficiency is independent of the current density at high current densities, and, therefore,

$$(i_3 + i_5 + i_s + FR)/i_T = C \qquad \text{(XV)}$$

where C is a constant which depends on temperature and pH. If reactions (II) and (III) are the only anodic reactions which occur, the minimum value of C is unity. Since $C > 1$ in unbuffered solutions (Fig. 2), local corrosion and/or undermining ($i_s$) must be important. Reaction (I) and/or reaction (IV) must be important since at 75°C in buffered solutions at high pH's $C < 1$. The thermodynamics of reaction (I) are indistinguishable from the thermodynamics of the process which takes place by the consecutive reactions (II) and (IV), but, of course, there is a marked difference in electrode kinetics.

Low current efficiencies may possibly be due to an enhancement of local corrosion by anodic polarization. Current efficiencies in buffered solutions are higher than in the unbuffered solution at

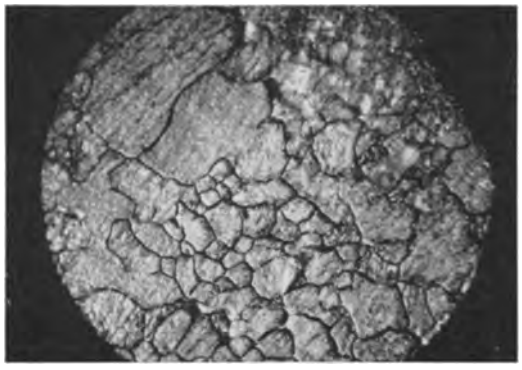

Fig. 10. Metallographic top view of magnesium cathode with corrosion products removed: polarization current = 200$\mu$a cm$^{-2}$; temperature = 58°C; time = 7 days; solution = 110 ppm NaCl. Magnification 50X before reduction for publication.

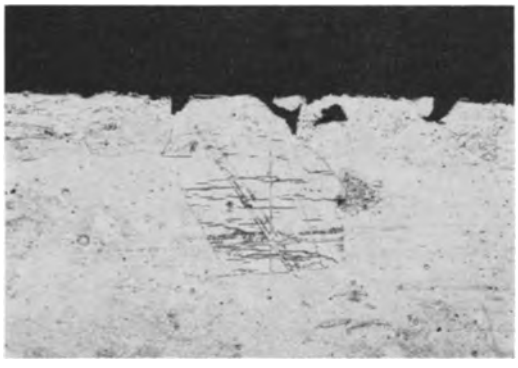

Fig. 11. Metallographic cross section of magnesium cathode with corrosion products removed, etched: polarization current = 200 $\mu$a cm$^{-2}$; temperature = 58°C; time = 7 days; solution = 110 ppm NaCl. Magnification 150X before reduction for publication.

the same bulk pH at 75°C (compare Fig. 2 and Fig. 5). This may be considered to be experimental verification for Robinson's suggestion (6) that the corrosion rate at the anode is enhanced due to the excess acidity formed at the pits as a result of anodic polarization. However, this explanation is probably not satisfactory for buffered solutions.

An alternate theory may be suggested by considering the effect of buffered pH on the current efficiency. The nature and extent of attack on Mg is strongly affected by pH. An acid type of attack (Fig. 9) occurs at the Mg anodes and locally corroding specimens at pH's $< 10$ at 25°C and at pH's $< 9$ at 75°C without visible film formation; above these pH's a pitting type of attack occurs similar to that observed in unbuffered 110 ppm NaCl solution (Fig. 8) and thick white films of $Mg(OH)_2$ containing free Mg are formed. There is evidence for thin films of MgO and/or $Mg(OH)_2$ on Mg in acid solution, the mechanism of formation of which is obscure (11). The thick film of $Mg(OH)_2$ is probably formed by reaction (IX). Further corrosion of the magnesium in the $Mg(OH)_2$-Mg film undoubtedly occurs. In strong NaCl solution the corrosion products were observed to flake off and fall to the bottom of the container. Gas evolution from the corrosion products at the bottom of the container continued for several minutes. Anodic passivity (C.E. $> 100\%$) was observed at the higher pH's at room temperature and 75°C.

The formation of thick films of $Mg(OH)_2$-Mg on anodically polarized Mg may possibly lead to an enhancement of the rate of local corrosion at the anode if it is assumed that: (*a*) the film on the anode, $Mg(OH)_2$-Mg, is cathodic to the pits or anodic areas; and (*b*) the amount of Mg in the film, and, hence, the resistance of the film reaches a steady value which is proportional to the current density. The resistance of the film is therefore inversely proportional to the anodic current density, and the rate of corrosion at the anode is directly proportional to the current density. Thus, local corrosion could conceivably account for the sharp decrease in current efficiency at pH = 10 at room temperature (Fig. 5). Since the current efficiencies observed at room temperature are considerably lower than at the elevated temperatures, it must be assumed that at elevated temperatures the resistance between local cathodic and anodic areas is increased. This may be accomplished in two ways: (*a*) $Mg(OH)_2$ is less soluble at higher temperatures and stifling of the local corrosion at the anode would be more important; and (*b*) cathodic corrosion of the free Mg in the film would occur (Fig. 3). Shishakov (12) has observed that the film formed on Mg in boiling water is more protective than the film formed at room temperature.

It is not possible to ascertain the importance of undermining in the mechanism for the anodic oxidation of Mg. On comparison of Fig. 8 and Fig. 9 it can be seen that film formation enhances undermining of Mg at least on the macro scale. Dissolution of a Mg anode by cathodic corrosion at the higher temperatures and current densities may be important. Cathodic corrosion will be discussed in the next section.

The measured potential of the Mg anode which is about 1 v more cathodic than the equilibrium potential of reaction (I) can probably not be identified with the potential of any of the three remaining anodic reactions. The equilibrium potential of the process consisting of the consecutive reactions (II) and (IV) is the same as the equilibrium potential of reaction (I). As pointed out previously either reaction (I) or reactions (II) and (IV) must occur. Since large overpotentials are not usually associated with anodic processes involving metal ions (29), the measured potential is either a composite potential of local anodic and local cathodic areas on the anode or the measured potential contains a large ohmic potential drop contribution. The experimental potential cannot be identified with that of reaction (III) since this would entail large potential differences between the various crystal faces of Mg.

### *Cathodic Behavior of Magnesium*

The salient facts of the cathodic polarization experiments are: (*a*) cathodic polarization inhibits the corrosion of Mg in 110 ppm NaCl solutions at 25°C and 58°C (Fig. 3); (*b*) at 75° and 92°C cathodic protection is not attained due to the occurrence of an intergranular type of cathodic corrosion (Fig. 10 and Fig. 11); (*c*) intergranular attack of cathodically polarized Mg ocurs at pH's $> 9$

at 75°C with formation of thick films of $Mg(OH)_2$ and acid attack (etching-type attack) without visible film formation occurs at pH's < 9 at 75°C and at pH's < 10 at room temperature on both unpolarized and cathodically polarized Mg; (*d*) the rate of intergranular cathodic corrosion is dependent on temperature and current density, and at 75°C is independent of pH at pH's > 9 (Fig. 7); (*e*) the rate of acid corrosion is dependent on temperature and pH and independent of cathodic current density at room temperature and 75°C (Fig. 6 and Fig. 7); (*f*) the lattice parameters of Mg are not significantly affected by cathodic polarization at 92°C; and (*g*) hydrogen produced at the cathode at 92°C does not diffuse readily through the Mg.

It is evident that under the experimental conditions studied in this work the mechanism of acid corrosion at room temperature and intergranular corrosion of cathodically polarized Mg are different; intergranular cathodic corrosion becomes significant only at elevated temperatures, whereas, the acid corrosion of Mg is quite appreciable at room temperature. Acid corrosion and intergranular corrosion on Mg cathodes probably occur simultaneously at elevated temperatures, although it appears that film formation greatly diminishes the acid corrosion relative to the intergranular corrosion. The mechanism for the acid dissolution of Mg has been studied extensively and is not discussed here (20-25).

The phenomenon of the intergranular cathodic corrosion of Mg may be interpreted in terms of the hydrogen embrittlement theory for steel (30, 31) with some modification. The hydrogen embrittlement theory for Mg may be based on the following assumptions: (*a*) hydrogen is occluded in Mg at the dislocations near the solution-metal interface by cathodization; (*b*) deep penetration of cathodic hydrogen into the Mg lattice does not occur (diffusion of hydrogen through Mg during cathodization was not observed and cathodization does not increase significantly the amount of interstitial hydrogen); and (c) the dislocations are "sprung" forming embrittled Mg at the solution-metal interface when the hydrogen pressure at the dislocation exceeds the elastic strength of Mg. The mechanically weakened lattice of Mg is subject to corrosion by mechanical undermining or by electrochemical corrosion. The degree of embrittlement and, hence, the rate of cathodic intergranular corrosion, would be dependent on temperature and current density.

The general shape of the cathodic polarization curves of Mg (Fig. 4) at room temperature and 58°C are similar to the cathodic polarization curves obtained for iron (32). AB represents depolarization by oxygen; CD represents evolution of hydrogen; and the current at B is the current required for cathodic protection (16). The data are insufficient to explain the absence of the inflection at B in the polarization curves at 75° and 92°C and the fact that the hydrogen overvoltage is considerably lower at the higher temperature than that at room temperature. Probably, the contribution of the ohmic p.d. to the hydrogen overpotential at the elevated temperature is smaller.

## Acknowledgment

The authors wish to express their appreciation to Mrs. A. F. Beck and Dr. L. D. Calvert for the x-ray results and to Mr. P. E. Beaubien for the metallographic work reported in this paper.

Manuscript received Aug. 1, 1957. This paper was prepared for delivery before the Buffalo Meeting, Oct. 6-10, 1957.

Any discussion of this paper will appear in a Discussion Section to be published in the December 1958 JOURNAL.

## REFERENCES

1. A. Smits, *Z. Elektrochem.* **30**, 223 (1924).
2. S. Bodforss, *Z. Physik. Chem.*, **153**, 83 (1931).
3. M. D. Rausch, W. E. McEwen, and J. Kleinberg, *J. Am. Chem. Soc.*, **76**, 363, 3622 (1954); **77**, 2093 (1955).
4. W. E. McEwen, J. Kleinberg, D. L. Burdick, W. D. Hoffman, and J. Y. Yang, *ibid.*, **78**, 4587 (1956).
5. P. Brouillet, I. Epelboin, and M. Froment, *Compt. rend.*, **239**, 1795 (1954).
6. H. A. Robinson, *Trans. Electrochem. Soc.*, **90**, 485 (1946); "Cathodic Protection, A Symposium," p. 104, N.A.C.E., Houston (1949).
7. H. A. Robinson and P. I. George, *Corrosion*, **10**, 182 (1954).
8. J. H. Greenblatt, *This Journal*, **103**, 539 (1956).
9. R. Faivre and A. Michel, *Compt. rend.*, **208**, 1008 (1939).
10. C. Brouchere, *J. Inst. Metals*, **71**, 131 (1943).
11. K. Huber, *This Journal*, **100**, 376 (1953).
12. N. A. Shishakov, *Zhur. Fiz. Khim.*, **26**, 358 (1952).
13. S. Yamaguchi, *J. Appl. Phys.*, **25**, 1437 (1954); *J. Chem. Soc. Japan*, **61**, 887 (1940).
14. W. Beetz, *Pogg. Ann.*, **27**, 115 (1866).
15. W. J. Müller and E. Nachtigall, *Monatsh.*, **69**, 1 (1936); *Korrosion u. Metallshutz*, **14**, 198 (1938).
16. U. R. Evans, L. C. Bannister, and S. C. Britton, *Proc. Royal Soc. (London)*, **A131**, 367 (1931).
17. E. H. Phelps, Thesis, Case Institute of Technology, Cleveland, Ohio (1955).
18. G. V. Akimov and I. L. Rozenfeld, *Compt. rend. acad. sci. U.R.S.S.*, **44**, 193; *Doklady Akad. Nauk, S.S.S.R.*, **44**, 211 (1944).
19. F. E. W. Wetmore, Private communication.
20. C. V. King and W. H. Cathcart, *J. Am. Chem. Soc.*, **59**, 63 (1937)
21. J. H. James, *ibid.*, **65**, 39 (1943).
22. G. E. Coates, *J. Inst. Metals*, **71**, 457 (1945).
23. A. B. Garret and R. R. Cooper, *J. Phys. and Colloid Chem.*, **54**, 437 (1950).
24. B. Roald and W. Beck, *This Journal*, **98**, 277 (1951).
25. E. J. Casey and R. E. Bergeron, *Can. J. Chem.*, **31**, 849 (1953).
26. Int. Critical Tables, **6**, 152 (1929).
27. H. T. S. Britton, "Hydrogen Ions," Vol. I, Chapman and Hall Ltd., London (1955).
28. R. G. Bates and V. E. Bower, *J. Research Nat. Bur. Standards*, **53**, 283 (1954).
29. A. Hickling, *Quarterly Revs.* (London), **3**, 95 (1949).
30. C. A. Zapffe and C. E. Sims, *Am. Inst. Mining Met. Engrs.*, **145**, 225 (1941).
31. C. A. Zapffe, *Materials & Methods*, **32**, 74 (1950).
32. G. R. Hoey and M. Cohen, *Corrosion*, To be published.

# Investigations in the $CuGaS_2$-ZnS and $AgGaS_2$-ZnS Systems

**E. F. Apple**

*Research Laboratory, General Electric Company, Schenectady, New York*

ABSTRACT

$CuGaS_2$ and ZnS form solid solutions over the entire range with some evidence for compound formation at 33 1/3 mole % $CuGaS_2$. Emission under 3650Å excitation shifts from green to red with increase in $CuGaS_2$ concentration. Samples with more than 20% $CuGaS_2$ do not luminesce at room temperature but, at −195°C, fairly bright emission is observed with up to 95% $CuGaS_2$. $AgGaS_2$ is soluble in ZnS to about 5-10 mole %, above which separation of $Ag_2S$ is observed. Emission under 3650Å excitation shifts from the blue (0.01% $AgGaS_2$) to yellow (10% $AgGaS_2$).

The ternary sulfides, $CuGaS_2$ and $AgGaS_2$, have the chalcopyrite structure which is closely related to the zinc blende structure of cubic ZnS (1). In these compounds, two different atomic species occupy equivalent lattice sites on the zinc blende lattice. In $CuGaS_2$, a = 5.34Å and c = 10.47Å (c/a = 1.96) while in $AgGaS_2$, a = 5.74Å and c = 10.26Å (c/a = 1.79) (2).

Because of the similarities in structure, unit cell dimensions, and bond type, the ternary sulfides may form solid solutions with ZnS. In such solid solutions, the ternary compounds would not only change the unit cell dimension of ZnS, but may also affect the observed luminescence in ZnS:Cu,Ga and ZnS:Ag,Ga phosphors. Cu and Ag are activators and Ga is a coactivator in normal ZnS phosphors with green and blue emission.

The solubility of these activators in ZnS is dependent on the presence of charge-compensating ions which usually function as coactivators (3). For instance, in ZnS:Cu with no chemical coactivator added, Froelich reported that only about $4 \times 10^{-3}$ g-atoms Cu/mole ZnS is retained in the lattice after firing (4). In contrast, at least $9 \times 10^{-3}$ g-atom Cu/mole ZnS is retained in the ZnS:Cu,Al phosphor with orange emission (5). Incorporation of the larger concentration of Cu in the latter case is possible because of the simultaneous incorporation of Al as $Al_2S_3$. In this phosphor, the Al was added to ZnS as an oxy-salt and converted to $Al_2S_3$ during the firing process in $H_2S$ at 1100°-1200°C. It is questionable whether a large amount of $Al_2O_3$ would be converted completely to $Al_2S_3$ when fired in the presence of ZnS in an $H_2S$ stream. Equimolar mixtures of ZnS and $Al_2O_3$, for instance, when so fired do not yield $ZnAl_2S_4$, the compound expected on complete conversion of the oxide to the sulfide. In all probability, addition of Al as the oxide or oxy-salt limits the solubility of Cu because of incomplete conversion to $Al_2S_3$. However, if the activator and coactivator are added as the ternary sulfide, the oxide conversion is circumvented. Further, activator and coactivator are added in exactly stoichiometric amounts in a form which facilitates incorporation in the lattice.

It is the purpose of this paper to report results of studies in the systems $CuGaS_2$-ZnS and $AgGaS_2$-ZnS. Of special interest will be the structural data, limits of solubility, and luminescent properties. In these systems the concentrations of Cu or Ag in ZnS far exceed those reported in the literature, and with the increased concentrations of activators incorporated new luminescent properties are observed.

## Experimental Results

### $CuGaS_2$-ZnS *System*

A stoichiometric mixture of $Cu_2S$ (made from 99.999% Cu) and $Ga_2S_3$ (made from 99.97% $Ga_2O_3$) was heated in a sealed, evacuated ampoule for 12 hr at 900°C. The body color of the mixture changed from gray to orange as a result of this firing process and an x-ray diffraction pattern of the powder indicated that $CuGaS_2$ had formed (diffraction lines due to $Cu_2S$ or $Ga_2S_3$ were absent).

Weighed mixtures of $CuGaS_2$ and ZnS (G.E. luminescent grade) were ground and ballmilled together and then fired at 975°C for 1 hr in $H_2S$. [The $H_2S$ used throughout this work was passed through a $Ba(OH)_2$ solution, then through drying columns containing silica gel and phosphorus pentoxide, and finally through a trap held at −50°C before coming in contact with the sample.] The entire range of concentrations from 0.01 mole % to 99.9 mole % $CuGaS_2$* was covered. The body color changed from near-white in the 0.01% sample through green to orange in the 30-40% region; between 50-90% it went from orange to green; above 90% the body color was orange. In no case was free $Cu_2S$ observed or did the powders have a dark body color.

X-ray diffraction patterns of the powders indicate that the structure is cubic in mixtures with up to and including 40% $CuGaS_2$. The unit cell dimension, as plotted in Fig. 1, decreases from 5.404Å (pure ZnS) to 5.350Å (40% $CuGaS_2$) with Vegard's law being obeyed approximately. Diffraction lines characteristic of tetragonal $CuGaS_2$ are absent in this range and it is concluded that $CuGaS_2$ and ZnS are miscible up to and including 40 mole % $CuGaS_2$.

* Concentrations throughout paper are in mole % $CuGaS_2$ or $AgGaS_2$ unless otherwise indicated.

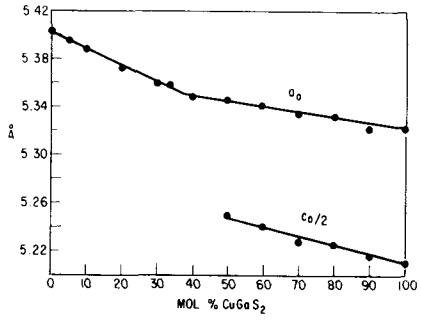


Fig. 1. Unit cell dimensions in the system ZnS-$CuGaS_2$

Above 40% $CuGaS_2$, the structure is tetragonal with the $a_o$ and $c_o$ dimensions decreasing nearly linearly with increase of $CuGaS_2$. The c/a ratio remains about the same and in all probability solid-solution formation occurs throughout the tetragonal region also. It is thus concluded from the x-ray data and also from the orderly, if not continuous, change in physical properties throughout, that $CuGaS_2$ and ZnS are completely miscible.

Samples with 20% and less $CuGaS_2$ luminesce at room temperature under 3650Å excitation (which excitation appears to be in the optimum wavelength region). The emission moves from the green into the red and, in general, the spectral distribution of emission at room temperature broadens and the brightness drops with increasing $CuGaS_2$ content. No visual afterglow occurs when excitation is removed in all samples except 0.01% $CuGaS_2$ where a long bright green afterglow is observed. Emission spectra at room temperature are shown in Fig. 2 and peak values are plotted in Fig. 3. At −195°C, luminescence is observed under 3650Å excitation in all samples in the series including $CuGaS_2$ in which the spectral distribution of emission extends beyond 7000Å and is too weak to record accurately on the spectroradiometer used. As indicated in Fig. 3, the emission peak at −195°C shifts from the characteristic green in low $CuGaS_2$ samples to a maximum wave length in the 30-40% range with the peak in the 33 1/3% sample being shifted abnormally to above 7000Å. Above 40% the peak shifts back gradually to shorter wave lengths until at 70% $CuGaS_2$ a sudden shift to a longer wave length is observed. Samples with 70% and above show evidence of two emission bands and the peaks of these bands are in fact resolved in the 90% sample as shown in Fig. 4. The half-width of the emission spectra at −195°C shows a minimum in the 30-40% region.

Thermoluminescent experiments indicate the presence of two principal glow peaks in all samples in the series. After excitation at −195°C with a BH-4 lamp and using a 10°/min heating rate, one glow peak falls in the −160° to −180°C region and the other peak occurs at −90° to −110°C.

Cathodoluminescence in samples with more than 1% $CuGaS_2$ is very weak and the spectral distribution of emission is about the same as that for 3650Å excitation.

The diffuse reflectivity, (*see* Fig. 5) moves to longer wave lengths with increasing $CuGaS_2$ content. The reflectivity edge shows a maximum in wave length in the 30-40% region with the edge in

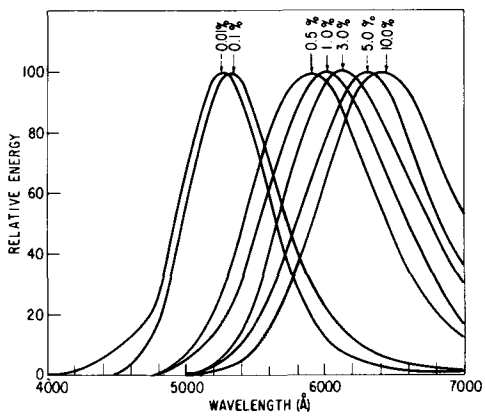


Fig. 2. Emission spectra (normalized) of ZnS-$CuGaS_2$ at room temperature under 3650Å excitation. Percentages indicate $CuGaS_2$ content. Samples fired in $H_2S$ for 1 hr at 975°C.

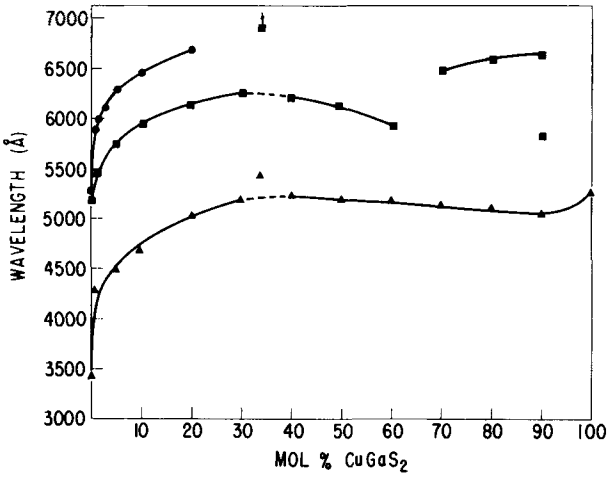


Fig. 3. Emission peak at room temperature and at −195°C, and diffuse reflectivity in ZnS-$CuGaS_2$ system. Circle, emission peak at room temperature; square, emission peak at −195°C; triangle, diffuse reflectivity (10% R reference).

the 33 1/3% $CuGaS_2$ sample being at a longer wavelength range than that of pure $CuGaS_2$. Change in diffuse reflectivity and peak emission at −195°C closely parallel each other as shown in Fig. 3. Ten per cent reflectivity is used as the point of reference.

Firing the samples containing less than 20% $CuGaS_2$ in $H_2$, $N_2$, $S_2$, or in sealed, evacuated tubes instead of in $H_2S$ has no effect on the spectral distribution of emission or the diffuse reflectivity. However, firing in $O_2$ or air for a few minutes causes the samples to darken and deadens the luminescence in most cases. Presumably, oxygen destroys the solid solution by precipitating Ga as $Ga_2O_3$ thus lowering the solubility of $Cu_2S$ in ZnS. The temperature of preparation or, more specifically, the crystal structure of the lattice has a marked effect on the luminescent properties. Samples with 1 to 10% $CuGaS_2$ prepared at 1150°C in $H_2S$ have the hexagonal structure and give a dim orange-red emission under 3650Å excitation as compared to the yellow to red emission of the samples fired at 975°C. In the 20% sample fired at 1150°C, the structure is cubic and the brightness and spectral distribution of emission are about the same as in the corresponding sample fired at 975°C. Structure, apparently, is very important in the luminescent processes involved, a

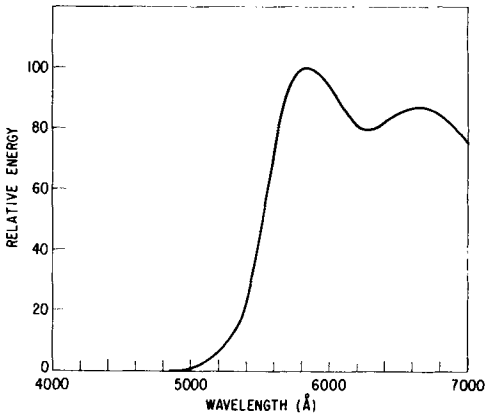


Fig. 4. Emission spectra of 0.1 ZnS·9CuGaS$_2$ at —195°C under 3650Å excitation.

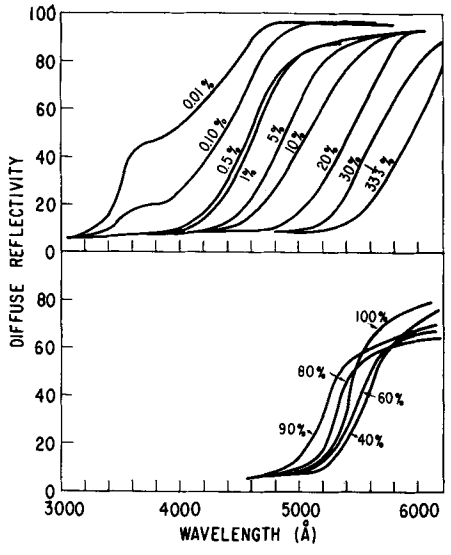


Fig. 5. Diffuse reflectivity spectra of ZnS-CuGaS$_2$

fact which is observed even in the 0.01% CuGaS$_2$ material.

ZnS:0.01% CuGaS$_2$ prepared in H$_2$S or in a sealed, evacuated ampoule at 975°C shows a green emission under 3650Å excitation at room temperature and a blue-green emission at —195°C. However, the same material fired at 1150°C under either condition gives a green emission at room temperature but a red emission at —195°C (*see* Fig. 6). In the first case, the structure is cubic and in the latter case, it is hexagonal. As will be discussed later, this effect of structure on emission is observed in a fairly large number of systems under study at the present time.

### AgGaS$_2$-ZnS *System*

AgGaS$_2$ was made by heating a stoichiometric mixture of Ag$_2$S and Ga$_2$S$_3$ in an evacuated, sealed tube at 900°C for 12 hr. The product obtained was light green in color. Mixtures of ZnS and up to 20 mole % AgGaS$_2$ were fired in H$_2$S at 900°C for 1 hr. In samples with over 5% AgGaS$_2$, black specks were observed throughout the fired material indicating separation of Ag$_2$S. For this reason, the study was terminated at 20 mole %.

Using 3650Å excitation, photoluminescence is observed at room temperature over the entire range studied. The emission shifts from the blue into the yellow as the AgGaS$_2$ content is increased. Too, the spectral distribution of emission widens and the brightness decreases. Emission spectra are shown in Fig. 7. At —195°C, the emission peak of a given sample shifts 400-500Å to shorter wave lengths as is shown in Fig. 8 and the luminescence becomes much brighter than at room temperature. Cathodoluminescence is observed in all samples, but the peak emission occurs 50-100Å shorter in wave length than that in photoluminescence.

Diffuse reflectivity spectra shown in Fig. 9 also shift to longer wave length with increasing AgGaS$_2$ content. Most of the samples containing Ag were light sensitive, and darkened on exposure to sunlight.

With 5% and below AgGaS$_2$, the structure in the system is cubic (in samples prepared at 900°C), it is a mixture of cubic and hexagonal in the 10% region, and is hexagonal in the 20% sample. This change in structure is explained by assuming a solid solution of Ga$_2$S$_3$ and ZnS forms in the region where Ag$_2$S precipitates. Such a solid solution of Ga$_2$S$_3$ in ZnS is hexagonal in this concentration range when prepared at 900°C (6).

As in ZnS:CuGaS$_2$ a marked effect of structure on luminescent properties was observed. In ZnS: 0.01% AgGaS$_2$ prepared in H$_2$S at 900°C, the emission under 3650Å excitation both at room temperature and at —195°C is blue. However, the emission

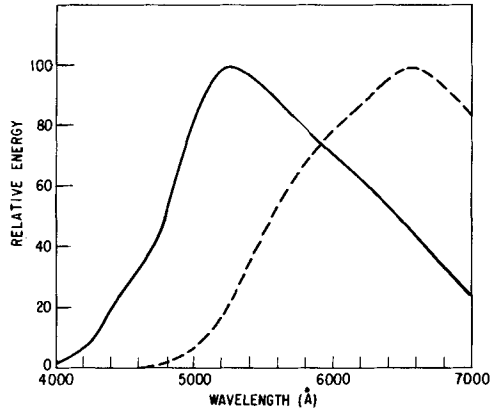


Fig. 6. Emission spectra (normalized) of ZnS:0.01% CuGaS$_2$ using 3650Å excitation. Sample fired at 1150°C in H$_2$S for 1 hr. ——— Room temperature; - - - - - - - —195°C.

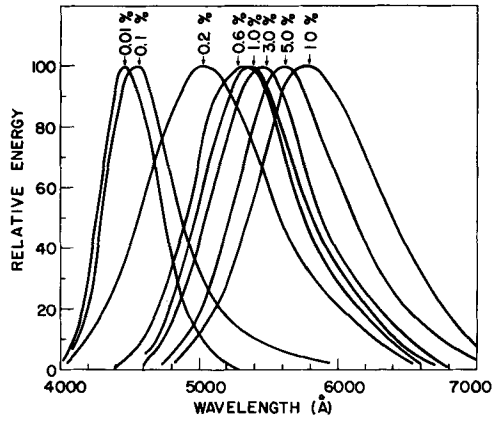


Fig. 7. Emission spectra (normalized) of ZnS-AgGaS$_2$ at room temperature under 3650Å excitation. Percentages indicate AgGaS$_2$ content. Samples fired in H$_2$S for 1 hr at 900°C.

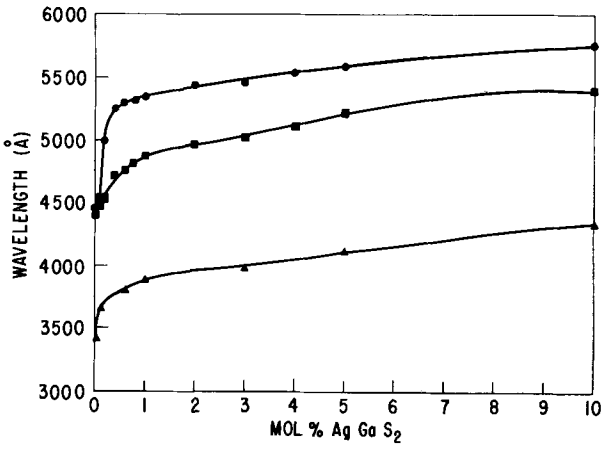


Fig. 8. Emission peak at room temperature and at —195°C, and diffuse reflectivity in ZnS-AgGaS$_2$ system. Circle, emission peak at room temperature; square, emission peak at —195°C; triangle, diffuse reflectivity (10% R reference).

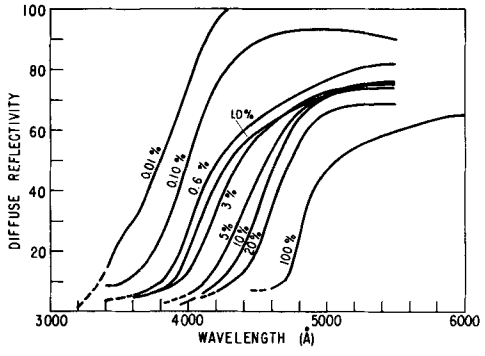


Fig. 9. Diffuse reflectivity spectra of ZnS-AgGaS$_2$

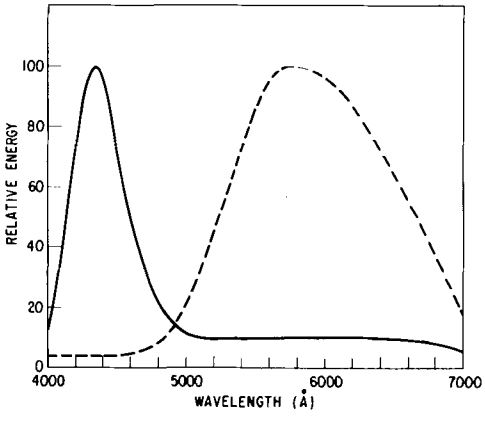


Fig. 10. Emission spectra (normalized) of ZnS:0.01% AgGoS$_2$ using 3650Å excitation. Sample fired at 1150°C in $H_2S$ for 1 hr. ———— Room temperature; - - - - - —195°C.

of a sample fired in $H_2S$ at 1150°C is blue at room temperature but yellow at —195°C as shown in Fig. 10. The structure in the sample fired at 900°C is cubic and it is hexagonal in the one fired at 1150°C.

## Discussion

Two compounds whose structures are similar sometimes are miscible over a wide concentration range. For instance, InAs and InP form mixed crystals in which the relations between the unit cell dimensions or energy gap (optical) and the composition parameter are linear (7).

CdS and ZnS form a like series of solid solutions, in which the diffuse reflectivity spectra shifts from that of pure ZnS to CdS as CdS substitutes in the lattice. CdS substitution in the ZnS:Ag,Cl phosphor shifts the emission spectra uniformly from blue into the red (8).

In the ZnS-CuGaS$_2$ system, however, some of the physical properties are not a linear function of composition even though structural data indicate solid-solution formation over the entire range. Maxima in the wave lengths of the diffuse reflectance edge and peak emission (under 3650Å excitation) and a minimum in the half-width of emission spectra occur in the 30-40% CuGaS$_2$ region. This suggests the possibility of compound formation or ordering in the structure in this region. In fact, at 33 1/3% CuGaS$_2$, where marked shifts in emission spectra and diffuse reflectance are observed, the compound Zn$_2$CuGaS$_4$ may form, in which case each S atom would be surrounded by two Zn atoms, one Cu atom, and one Ga atom. However, such an ordered arrangement would give a tetragonal structure whereas the structure of the 33 1/3% sample is cubic. Unfortunately compound formation or ordering in this system is difficult to detect by ordinary x-ray diffraction methods because of the similarity in atomic scattering factors of Cu, Zn, and Ga. However, the extreme sharpness of the $K\alpha_1$ and $K\alpha_2$ lines in the back reflection region of the x-ray diffraction pattern of 33 1/3% CuGaS$_2$ indicates virtually no tetragonal distortion. Superstructure lines are not observed in the diffraction pattern even with very long exposure times. The compound, if formed, must have a pseudocubic structure (c/a = 2.00).

Above 40% CuGaS$_2$, the diffuse reflectivity shifts to shorter wave lengths and the emission spectra become a composite of two emission bands. X-ray data shows a linear decrease in tetragonal cell dimensions in this region. Again compound formation or ordering would be difficult to detect by x-ray diffraction methods.

It should be pointed out that some solid solutions between two compounds exhibit properties which are not linear with composition. For instance, GaP and GaAs form mixed crystals but the relationship between the energy gap $\Delta E$ and the composition parameter is not linear. This has been attributed to a difference in band structures for GaAs and GaP (7). Such a difference in band structures in ZnS, Zn$_2$CuGaS$_4$, and CuGaS$_2$ would explain the observed variation in properties throughout the ZnS-CuGaS$_2$ system.

The nature of the luminescent systems in ZnS phosphors has received considerable attention (9). In these phosphors, the activator (Cu, Ag, Au) and coactivator (Cl, Al, Ga, etc.) concentrations are in the $10^{-4}$ g-atoms/mole ZnS range where departures from random distribution of the added impurities undoubtedly affect the luminescent properties. In fact the observed photoluminescent properties, including edge emission, in ZnS-type phosphors can be explained by an associated donor-acceptor luminescent center (10). It is thought that an understanding of the luminescent processes in the ZnS-CuGaS$_2$ (above 0.1%) system where Cu and Ga are by necessity highly associated may lead to a better

understanding of the activator system in normal ZnS phosphors.

A comparison of emission under 3650Å excitation with Froelich's yellow- and orange-emitting ZnS phosphors (containing up to about 9 x $10^{-3}$ g-atom Cu/mole ZnS and 5 x $10^{-2}$ g-atom Al/mole ZnS) shows that ZnS:$CuGaS_2$ has about the same spectral distribution of emission as its ZnS:Cu,Al counterpart (5). This would indicate that the emission is relatively independent of the Group III element but apparently is due to levels introduced by Cu.† S or Zn vacancies are probably not involved in the luminescent process since preparation of a particular sample in reducing ($H_2$, $N_2$) or oxidizing ($S_2$) atmospheres give identical emission spectra.

Above 40% $CuGaS_2$, where the system is tetragonal, the Zn atoms have two choices for substitution, either in place of a Cu atom or for a Ga atom. In the former case Zn will be an electron donor and in the latter case it will have acceptor properties. These two different substitutions may give rise to levels producing the two emission bands observed in this part of the series. A preferential substitution by Zn on one type of lattice site would be evidenced by changes in relative intensities of the two emission bands.

In view of the complete miscibility of $CuGaS_2$ in ZnS, it is rather striking that the solubility of $AgGaS_2$ is limited to 5-10 mole %. Certainly size considerations of Ag alone could not preclude a greater solubility since CdS has been shown to be soluble in ZnS, and Cd and Ag are similar in size. As was mentioned earlier, the unit cell dimension ratio c/a in $AgGaS_2$ is 1.79 indicating a greater distortion than is observed in $CuGaS_2$ (c/a = 1.96). This greater deviation from pseudocubic (c/a=2.00) may lower the solubility of $AgGaS_2$ in ZnS. $Ga_2S_3$ is completely miscible in ZnS and, in contact with $AgGaS_2$, would form a solid solution with ZnS when the concentration limit of the ternary sulfide is exceeded.

In the 0.01-10% $AgGaS_2$ range, uniform changes in properties such as emission and diffuse reflectance are observed. It appears from the photoluminescent spectra that the longest wave-length emission at room temperature in this system peaks at 5800-5900Å. The effect of trace impurities in the $AgGaS_2$ starting material must be considered in evaluating the spectra. The copper content of the $AgNO_3$ used in preparation of $Ag_2S$ was about $10^{-4}$ wt % which corresponds to Cu contents in the $AgGaS_2$-ZnS system studied of approximately $10^{-8}$ to $10^{-7}$ g-atom Cu/mole ZnS. This impurity may contribute slightly to the green emission observed in some samples, but several factors indicate that the over-all emission is a function of something other than Cu. First, the phosphorescence is very weak and of short duration in comparison to the long afterglow observed in, for example, ZnS: 0.01%$CuGaS_2$. Second, Cu present in such a low concentration as $10^{-6}$ g-atom/mole ZnS would give rise to blue or green emission only, whereas yellow emission is observed in the ZnS-$AgGaS_2$ system. For these reasons the observed luminescence is thought to arise from Ag and Ga impurities probably in highly associated configurations.

Of particular interest in the study of the $AgGaS_2$-ZnS system is the observation of the effect of structure on the emission spectra of the 0.01% sample. When fired in $H_2S$ or in a sealed, evacuated tube at 1000°C or below, the normal blue emission (under 3650Å excitation) is observed both at room temperature and at −195°C. However, when the same starting material is fired at 1050°C or above, the emission is blue at room temperature but yellow at −195°C. A similar shift from green to orange-red is observed in the ZnS-0.01% $CuGaS_2$. In fact, shifts due to structure changes have been observed in a number of systems including ZnS:0.01% $CuInS_2$, ZnS:0.01% $AgInS_2$, ZnS:0.01% Au,In, and ZnS:0.005% $Ga_2S_3$. In the systems containing In, the spectral shifts are observed at room temperature. The results of these studies will be included in a future communication. Suffice it to mention here that the effect is dependent on the crystal structure of the host lattice, ZnS, is reversible with change in structure from cubic to hexagonal or hexagonal to cubic, and is independent of firing atmosphere. It is thought that this effect of structure on luminescence may be related to a change in association of activator and coactivator in the ZnS host lattice.

† It should be pointed out that ZnS:$CuInS_2$ does not give the same spectral distribution of emission as its ZnS:Cu,Al or ZnS:$CuGaS_2$ counterpart.


## Acknowledgments

The author wishes to acknowledge the assistance given him by the following: Mr. A. A. Carlson for preparation of some of the samples used; Miss G. P. Lloyd and Dr. F. J. Studer for the optical measurements; Mr. F. C. Mostek and Dr. P. D. Johnson for the thermoluminescent measurements.

Manuscript received Nov. 7, 1957. This paper was prepared for delivery before the Washington Meeting, May 12-16, 1957.

Any discussion of this paper will appear in a Discussion Section to be published in the December 1958 JOURNAL.


## REFERENCES


1. A. F. Wells, "Structural Inorganic Chemistry," p. 403, Oxford Press, London (1950).
2. H. Hahn, G. Frank, W. Klinger, A. Meyer, and G. Störger, *Z. anorg. u. allgem. Chem.*, **271**, 153 (1953).
3. F. A. Kröger and J. Dikhoff, *Physica*, **16**, 297 (1950).
4. H. C. Froelich, *This Journal*, **100**, 280 (1953).
5. H. C. Froelich, *ibid.*, **100**, 496 (1953).
6. H. Hahn, G. Frank, W. Klinger, A. Störger, and G. Störger, *Z. anorg. u. allgem. Chem.*, **279**, 260 (1955).
7. O. G. Folbreth, *Z. Naturforsch.*, **10a**, 502 (1955).
8. S. Lasof, R. Shrader, and H. Leverenz, "Preparation and Characteristics of Solid Luminescent Materials," p. 224, John Wiley & Sons, Inc., New York (1946).
9. *See*, for instance: J. S. Prener and F. E. Williams, *This Journal*, **103**, 342 (1956); R. Bowers and N. T. Melamed, *Phys. Rev.*, **99**, 1781 (1955); H. A. Klasens, *This Journal*, **100**, 72 (1953).
10. J. S. Prener and F. E. Williams, *Phys. Rev.*, **101**, 1427 (1956).

# The Effect of Impurities on the Plaque Brightness of a 3000°K Calcium Halophosphate Phosphor

A. Wachtel

*Research Department, Westinghouse Lamp Division, Bloomfield, New Jersey*

ABSTRACT

The killing action of 27 elements has been investigated at 1, 10, 100, 1000, and 10,000 ppm addition to a specially purified 3000°K calcium halophosphate phosphor mix. At 1% addition, the observed reduction in output increases in the order: Al, Zr, Ce, La, Pb, Y, In, Sm, Cs, S, Pr, Nd, Na, Ag, Sn, W, Si, Mo, U, Ga, Cr, Ni, Fe, Cu, Co, V, and Ti. In the neighborhood of 100 ppm, the first five elements listed showed a slight enhancing effect. None of the elements tested had an appreciable effect on the color of the fluorescence, except where killing of the luminescence became very pronounced. Purification of chemicals for preparation of the unfired mix involved difficulties with respect to Fe and was more successful with certain organic reagents. The use of capped silica tubes enabled firings with a reproducibility of ±0.3%.

In view of the widespread use of calcium halophosphate phosphors in the fluorescent lamp industry, it appeared desirable to obtain practical limits governing the permissible impurity content of commercial raw materials. Some previous publications (1,2) dealing with calcium halophosphate phosphors in a more general manner indicate the necessity of maintaining a certain degree of purity, but no specific information with respect to the individual effects of a large number of possible killers could be found.

While it is understood that, for practical purposes, only the performance of the phosphor in lamps is of interest, it is also known that the laborious and somewhat less reproducible nature of lamp testing may be due to factors other than intrinsic phosphor performance under simple conditions of 2537Å excitation in air. Thus, the measurement of plaque brightness was believed to be capable of yielding more fundamental information, as well as of enabling the testing of a larger variety of impurity additions. Inasmuch as one may safely assume that an appreciably impaired plaque output of a phosphor will be similarly reflected in the zero-hour performance of a fluorescent lamp made with this phosphor, this type of investigation could be employed to effect a considerable elimination of samples for future lamp testing. This study was undertaken mainly for this purpose and involves only the plaque output of the calcium halophosphate phosphors.

## General Considerations

*Composition of the unfired mix.*—Inasmuch as at the time at which this project was undertaken, some increased demand for 3000°K phosphor was anticipated a 3000°K (Warm White) formulation was chosen. Its composition before firing, exclusive of $CO_2$ and residual traces of $H_2O$, is shown below:

| | |
|---|---|
| CaO | 44.29% |
| $P_2O_5$ | 41.87 |
| $SrCl_2$ | 3.74 |
| $CaF_2$ | 6.02 |
| Mn (as metal) | 1.67 |
| $Sb_2O_3$ | 2.41 |

Since the normal "white" halophosphate compositions differ from each other only in minor respects, it was assumed that the results obtained here would be reasonably representative for most similar species of this system.

*Nature of raw materials employed.*—In order to interpret small variations in phosphor output with confidence, a high degree of reproducibility of phosphor synthesis was desirable. The unfavorable influence of $H_2O$ and reducing gases such as $NH_3$ has already been pointed out by Jenkins, McKeag, and Ranby (1). Therefore, prefired $Ca_2P_2O_7$ was preferred over the more usual $CaHPO_4$. Preliminary experiments have shown that reacting $CaCO_3$ with $(NH_4)_2HPO_4$ yields a coarser and more free-flowing material than if $H_3PO_4$ is used as a source of $P_2O_5$. In spite of this, phosphor formation takes place as readily and yields similar products in each case. Incorporation of the Sb in a valence state greater than three (3) was shown to decrease the dependence of phosphor brightness on Sb addition. Since $Sb_2O_4$ or $Sb_2O_5$ was found to be gritty and difficult to admix with the rest of the ingredients, it was formed from $Sb_2O_3$ on a $CaCO_3$ carrier by heating to 500° and 600°C in air. Stronger heating was avoided to prevent the formation of calcium antimonates (4) with loss of $CO_2$, so as to avoid subsequent

chemical absorption of $H_2O$ when small amounts of impurities are added in aqueous solution. The other ingredients ($SrCl_2$, $CaF_2$, $MnCO_3$) were used in the usual form.

*Purity of raw materials.*—Purification procedures involving acid and alkaline $H_2S$ precipitations (5) were found to work satisfactorily for most impurity elements originally present, except Fe. Using $SrCl_2$ as a representative substance for most of the purification experiments, it was found that a great variety of procedures, including precipitation with collectors or firing in $HCl$-$Cl_2$ mixtures, resulted in products whose chemically determined Fe content was very low and corresponded to the efficiency of the (chemical) purification procedures employed (which for the most part were based on known analytical reactions), while the spectrographically determined Fe content was invariably higher and of the order of 10-15 ppm. No satisfactory explanation for this phenomenon could be offered, except the hypothesis that part of the spectrographically detectable Fe is present in anionic, complexed, or otherwise less reactive form. In connection with this, it was interesting to note that nitrates or acetates were easier to free of Fe than chlorides.

The best results for Ca and Sr nitrates were obtained by partial precipitation with mixtures of ammonium carbonate and $(NH_4)_2S$, followed by diphenylthiocarbazone in excess with a $Zn(NO_3)_2$ collector at $pH = 8$ to 8.5, filtration and chloroform extraction. $Mn(CH_3COO)_2$ and ammonium carbonate (for preparation of Ca and Mn carbonates) were purified similarly, except for the use of 8-hydroxyquinoline instead of the dithizone, and the use of a $Ca(NO_3)_2$ collector for ammonium carbonate, and no collector for the $Mn(CH_3COO)_2$. $SbCl_3$ was slowly distilled at atmospheric pressure from a Pyrex retort (air cooled) and the distillate hydrolized and decomposed with doubly distilled $H_2O$ and $NH_3$ gas. Reagent grades of $NH_4F$ (for reaction with $CaCO_3$) and $P_2O_5$ were found to be of sufficient purity.

It should be mentioned that inasmuch as Fe and Cu are known to be particularly harmful in calcium halophosphate phosphors, a very logical choice for the removal of these elements appeared to be ammonium-*N*-nitrosophenylhydroxylamine (cupferron). This turned out to be particularly ineffective with respect to Fe. Generally speaking, while the chemical detection of Fe is much more sensitive than the spectrographic method, the former appears to be limited to that portion of Fe which in most cases is easily removable. To a lesser degree, similar difficulties prevailed with Al. Thus, such parameters as solubility products of precipitates and known degrees of efficiency of separation and filtration techniques became almost meaningless and could not serve as more than an intuitive guide in this phase of the project.

## Experimental Procedure

*Preparation of unfired phosphor mixes.*—The impurity elements were added in aqueous solution of concentrations adjusted so as to contain 50 mg, 5 mg, 0.5 mg, 0.05 mg, and 0.005 mg of the element per 0.8 ml of solution. In order to avoid upsetting the metal:P:halide ratio of the phosphors, all elements of valence less than four were added as orthophosphates with enough $HNO_3$ to maintain solubility. Where this was not possible, the stoichiometric equivalent of $H_3PO_4$ was added separately with the nitrate. The introduction of Cl could not be avoided with Si (as $SiCl_4$ in $CCl_4$), so as to effect a higher degree of reactivity than that caused by the contact of the sample with the $SiO_2$ firing container. Elements of valence greater than four were added as anions in the form of ammonium salts, together with the stoichiometric equivalent of Ca $(NO_3)_2$ added separately.

The experimental procedure consisted of slurrying 1 g aliquots of the unfired mix with 0.8 ml aliquots of impurity solution of each of the five concentrations respectively, drying, and dry mixing the residues with 4 g aliquots of the same unfired mix. Thus, 5 g samples with additions of 1, 10, 100, 1000, and 10,000 ppm impurity element were obtained. In the case of Si, the 1 g aliquot was first moistened with 80% alcohol so as to effect hydrolysis of the $SiCl_4$ *in situ*. The precaution against $H_2O$ could have been extended further by adding the solutions to the $CaCO_3 + Sb_2O_4$ part of the mix only, followed by drying and then mixing with the rest of the phosphor components. However, preliminary tests showed this to be unnecessary.

*Phosphor firing.*—A particularly efficient closure which still permitted the dissipation of internal pressure consisted of 75 mm long tubes of 15 mm I.D., 17 mm O.D. transparent silica, closed at one end, and capped by similar tubes of 18 mm I.D., 20 mm O.D. Five such tubes containing 1, 10, 100, 1000, and 10,000 ppm impurity in the phosphor mix were arranged side by side in a covered silica firing pan and confined by fire brick so as to prevent movement of the caps due to internal pressure.

Two firings were conducted at 1100°C for 1 hr in air each. Between firings, the phosphors were screened through a 100 mesh screen. In duplicate series for each impurity tested, the tubes were aligned in reverse order in the firing pan. Using a uniform supply of an unfired calcium halophosphate mix, the reproducibility of brightness under 2537Å excitation of averaged duplicates was found to be of the order of ±0.3%.

*Brightness measurements.*—The apparatus used was very similar to the one described by Butler and Mooney (6) and is shown in Fig. 1. A U-shaped low-pressure mercury lamp whose output was not filtered served as the exciting source; made of Vycor tubing, the ultraviolet component of the lamp output could be removed by insertion of a glass plate by means of which blank readings for each individual sample could be performed. The fluorescent light was measured by a Weston Photronic cell over which three color filters (blue, Viscor, amber) could be positioned by means of a sliding carriage. Three 50 mm diameter sample cells were also available for positioning in a sliding carriage, although only two of these cells were used here. The exposed area of the plaques could be varied by insertion of apertures of different diameters.

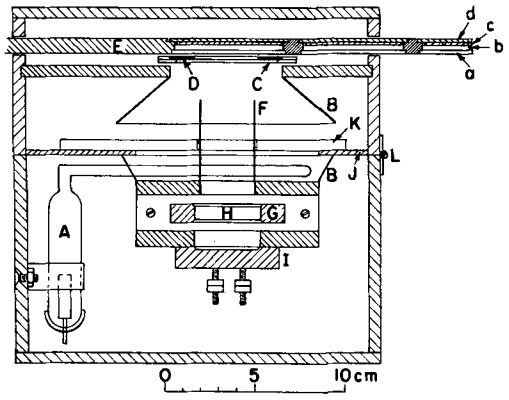


Fig. 1. Cross-sectional view of apparatus for measuring brightness of phosphor plaques: A, mercury arc lamp; B, aluminum reflectors; C, sliding carriage for apertures, D; E, sliding carriage with sample cells (a) quartz plate, (b) phosphor, (c) cardboard insert, (d) aluminum cover; F, aluminum tube; G, sliding carriage with color filters, H; I, photovoltaic cell; J, aluminum plate; K, glass plate inserted for blank readings; L, hinge. G and C slide perpendicular to the plane of the page.

The output of the Photronic cell was measured with a bridge circuit by means of the resistance selected to balance the cell output against that of a dry cell, using a multiple reflection galvanometer as null-indicator.

The measuring technique consisted in filling the first sample cell with a calcium halophosphate phosphor available in uniform supply, and placing the 1 ppm impurity sample in the second cell. The instrument was then normalized for this sample, and a reading was taken of cell No. 1. Subsequent samples were filled into cell No. 2 only, while cell No. 1 remained untouched and served only to restandardize the instrument at frequent intervals. Fatiguing of the Photronic cell became pronounced upon changing of color filters, requiring the establishment of equilibrium between individual readings. Individual blank readings were taken similarly after insertion of the glass plate to remove the 2537Å radiation. All results reported here refer to the differences of total minus blank readings, normalized to 100 for the 1 ppm impurity samples.

Preliminary tests with a uniform supply of a calcium halophosphate phosphor indicated a reproducibility of brightness readings between subsequent charges of phosphor in any one sample cell of ±0.15%.

## Results and Discussion

*Commonly occurring impurity elements.*—Figure 2 shows the effect of eight impurity elements (Fe, Cu, Ag, Na, Al, Si, Pb, and Sn) whose presence was usually detected in commercially available S.L. grade raw materials. It can be seen that only Fe exerted enough influence so that, at commonly occurring concentrations of about 15-30 ppm, appreciable interference may be expected. The usual concentration of Cu in S.L. grade raw materials is only of the order of 1-3 ppm. The effect of Fe and Cu at low concentrations as determined in separate trials is more clearly shown in Fig. 3. It should be mentioned that, while the emission of all phosphors was measured through each of the tricolor filters in the instrument, no appreciable effect on color was

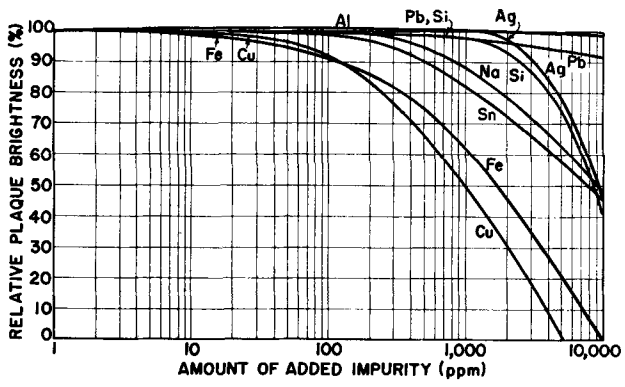


Fig. 2. Effect on brightness of eight commonly occurring impurity elements.

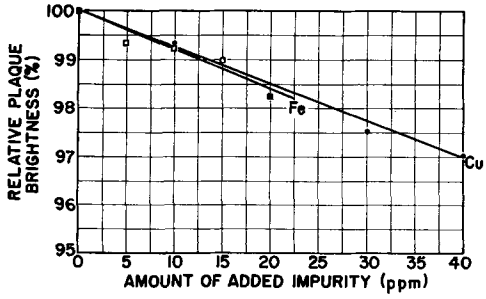


Fig. 3. Effect on brightness of Fe and Cu at low concentrations.

noted, except in cases of strong killing of the luminescence. Therefore, all figures show relative brightness only.

Enhancing effects which were sufficiently pronounced to be meaningful within the reproducibility of phosphor syntheses and measurements were noted only on Pb and Al. The results of separate trials with Pb and Al in the neighborhood of the observed emission maxima are shown in Fig. 4. The use of about 100 ppm Al has already been reported (7), while Pb (and Sn) have been used for the preparation of yellow or orange-emitting calcium halophosphates (8).

*The mechanism of enhancement by* Al.—While no investigations were made here pertaining to the mechanism (9) of the killer effect of Fe, it has been suggested (10) that Fe may enter the apatite lattice by charge compensation with alkalies, notably Na. Since the Fe and Na content of even highly purified raw materials cannot be neglected, one may expect that an appreciable concentration of Al may compete for charge compensation with such residual

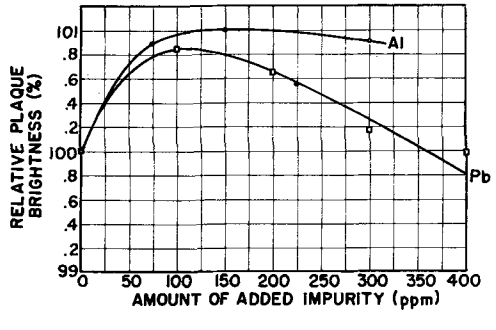


Fig. 4. Effect on brightness of Pb and Al in the neighborhood of enhancement maxima.

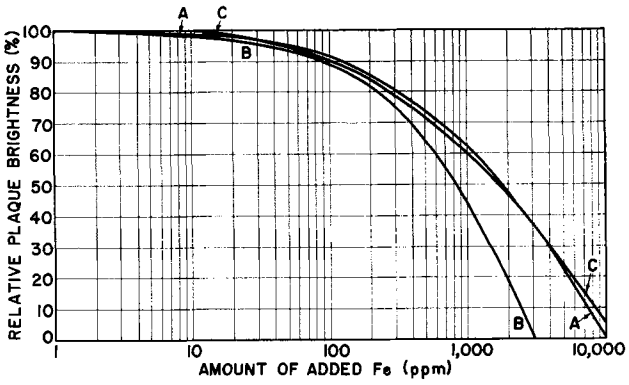


Fig. 5. Effect on brightness of Na or Al in combination with Fe. Curve A, Fe alone; curve B, Fe with 0.1% Na; curve C, Fe with 1.0% Al.

alkalies. This was investigated by firing variable concentrations of Fe in the presence of either 1% Al or 0.1% Na. A comparison with the effect of Fe alone is shown in Fig. 5, where all values have been normalized to 100 for the 1 ppm Fe addition. It can be seen that the effect of Fe was increased by the presence of Na. However, since, because of the strong effect of large concentrations of Na alone, not enough could be used to charge compensate more than about 0.24% Fe, the continued effect of Na above this Fe concentration cannot be explained. The effect of Al does not appear as pronounced, except in the neighborhood of 1% Fe, where the production of more than a very small background emission could be considered significant.

The behavior of presumably divalent Ni under similar conditions is shown in Fig. 6. Here again, Al and Na show opposite effects over most of the range, although at 1% Ni, neither Al nor Na appears to influence the output of the phosphor. It was felt that the results obtained here were inconclusive. It should also be mentioned that Wanmaker and Tak (11) have reported recently on mutually opposite effects of Na and Al on calcium halophosphates in the absence of heavy metal impurities.

*Trivalent elements other than* Al.—Examination of Fig. 7 shows that for the other trivalent impurities tried, with the exception of Ga which shows a rather sharp break around 0.1% and In which probably volatilized to a great extent, any enhancing effect noted (Ce, La) decreased with increasing

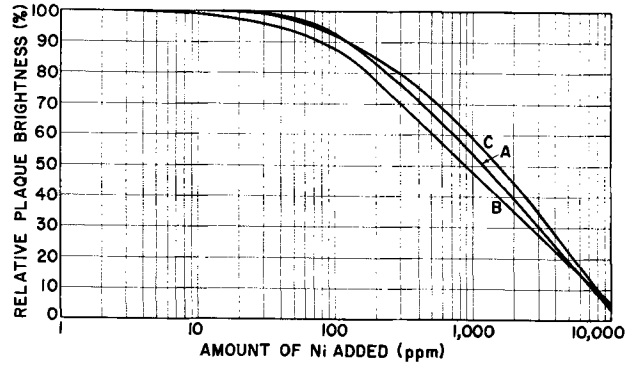


Fig. 6. Effect on brightness of Na or Al in combination with Ni. Curve A, Ni alone; curve B, Ni with 0.1% Na; curve C, Ni with 1.0% Al.

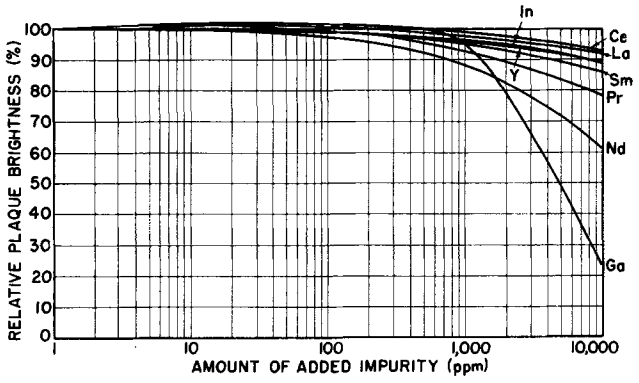


Fig. 7. Effect on brightness of some trivalent elements.

killer action of the element. On the basis of this, Al may still be considered as the best choice. Only the effect of Ce was sufficiently pronounced to be significant. Since these phosphors were not fired in a reducing atmosphere (12) it is possible that at least part of the Ce existed in tetravalent form.

*Miscellaneous impurities.*—The effect of several miscellaneous impurities tested is shown in Fig. 8. It can be seen that some elements are strong killers primarily at higher concentrations; Co and V, however, have an influence even at very low concentrations (10 ppm) which exceeds that of any other element tested. A slight enhancing effect was noted in the neighborhood of 100 ppm for Zr. Inasmuch as there is no apparent correlation between the observed killing action and other more general parameters of any of these elements, these particular results require no further comment. However, it should be stressed that any small effects (of the order of 1%) observed in this study are necessarily uncertain, and may have resulted from differences in particle size distribution as well as possibly other parameters caused by the particular impurity. Such influences might be eliminated during further processing of such phosphors in lamp making.

## Summary

The effect on plaque brightness of a number of impurity elements in a 3000°K calcium halophosphate phosphor has been investigated. Results for 100 ppm, 1000 ppm, and 1% impurity concentrations are summarized in Table I. Among those impurities which normally occur in S. L. grade raw materials in concentrations of 10-30 ppm, only Fe

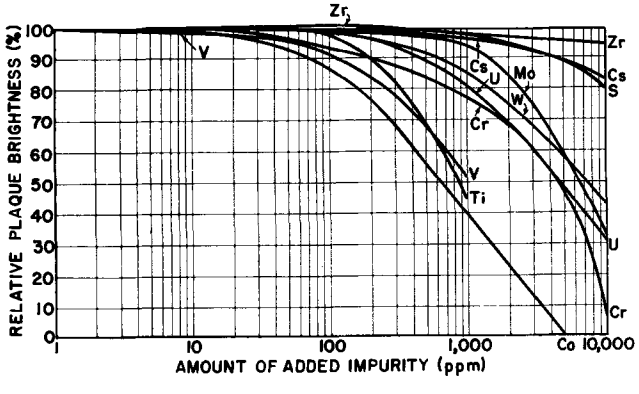


Fig. 8. Effect on brightness of some other less commonly occurring impurity elements.

Table I. Effect of impurity additions at 100 ppm, 1000 ppm, and 10,000 ppm on the plaque brightness of a 3000°K calcium halophosphate phosphor. All values are normalized to 100 for 1 ppm added impurity and arranged according to increasing killer effect.

| 100 ppm added | | 1000 ppm added | | 10,000 ppm added | |
|---|---|---|---|---|---|
| Impurity | Output | Impurity | Output | Impurity | Output |
| Ce | 101.1 | Al | 100.5 | Al | 99.5 |
| Al | 100.9 | Ce | 98.8 | Zr | 95.2 |
| Zr | 100.9 | Ag | 88.8 | Ce | 93.2 |
| Pb | 100.8 | S | 97.8 | La | 92.5 |
| Ga | 100.8 | Pb | 97.7 | Pb | 91.7 |
| La | 100.6 | Zr | 97.6 | Y | 89.6 |
| S | 100.2 | Si | 97.5 | In | 89.2 |
| Na | 100.2 | La | 97.0 | Sm | 86.2 |
| Si | 100.1 | In | 96.9 | Cs | 83.5 |
| Sm | 99.8 | Cs | 96.7 | S | 79.7 |
| Ag | 99.7 | Y | 95.3 | Pr | 78.8 |
| Cs | 99.5 | Sm | 95.1 | Nd | 61.0 |
| Mo | 99.5 | Mo | 95.0 | Na | 48.5 |
| Pr | 99.5 | Ga | 94.8 | Ag | 46.7 |
| Sn | 98.9 | Pr | 92.5 | Sn | 45.8 |
| Y | 98.8 | Nd | 88.5 | W | 42.7 |
| In | 98.5 | Na | 88.5 | Si | 41.8 |
| U | 98.5 | W | 85.7 | Mo | 32.3 |
| W | 98.3 | Sn | 81.8 | U | 31.3 |
| Nd | 98.2 | U | 81.7 | Ga | 18.1 |
| Ti | 98.1 | Cr | 77.9 | Cr | 7.57 |
| Cr | 93.5 | Fe | 62.3 | Ni | 3.96 |
| Cu | 92.5 | Ni | 53.6 | Fe | 0.72 |
| Ni | 92.3 | V | 51.3 | Cu | — |
| V | 91.8 | Cu | 50.7 | Co | — |
| Fe | 91.7 | Ti | 44.9 | V | — |
| Co | 87.3 | Co | 39.6 | Ti | — |

is believed to exert a sufficient influence to affect the phosphor output appreciably. Enhancing effects of the order of 1% or slightly less were noted for Al, Ce, Ga, La, Zr, and Pb. The results of some preparatory work on purification procedures for raw materials, as well as a reproducible technique for firing, have also been described. It is believed that any reduction in fluorescent brightness observed would probably be reflected in zero-hour lamp readings. Because of this, the results obtained allow a reasonable selection of impurities and concentration ranges for lamp testing.

## Acknowledgments

The author is indebted to Miss I. Walinski and Mr. G. Scanlon for the purification of chemicals and the preparation and measurements of the phosphors, as well as to Mr. R. W. Wollentin who helped in the design of the plaque tester. Messrs. I. Meister and T. Ellis performed the spectrographic analyses, and Messrs W. Lilliendahl and E. Biter performed chemical analyses for iron to correlate with the spectrographic results. Helpful discussions with Professor E. Banks are gratefully acknowledged. Thanks are also due to Dr. H. F. Ivey for reading and suggesting improvements in the original manuscript.

Manuscript received Oct. 3, 1957. This paper was prepared for delivery before the New York Meeting, April 27-May 1, 1958.

Any discussion of this paper will appear in a Discussion Section to be published in the December 1958 JOURNAL.

## REFERENCES

1. H. G. Jenkins, A. H. McKeag, and P. W. Ranby, *This Journal*, **96**, 1 (1949).
2. R. Nagy, R. W. Wollentin, and C. K. Lui, *ibid.*, **96**, 187 (1949).
3. K. H. Butler, U. S. Pat. 2,755,254, July 17, 1956.
4. K. H. Butler, M. J. Bergin, and V. M. B. Hannaford, *This Journal*, **97**, 117 (1950).
5. R. Ward, R. K. Osterheld, and R. D. Rosenstein, "Inorganic Syntheses," L. F. Audrieth, Editor, Vol. III, p. 11, McGraw Hill Book Co., Inc., New York (1950).
6. K. H. Butler and R. W. Mooney, *Sylvania Techn.*, **9**, #4, (October, 1956).
7. Sylvania Electric Prod. Inc., Brit. Pat. 691,140, May 6, 1953.
8. A. H. McKeag and P. W. Ranby, General Electric Co., Brit. Pat. 580,363, Sept. 5, 1946.
9. J. L. Ouweltjes, *J. phys. radium*, **17**, 641 (1956).
10. E. Banks, Polytechnic Institute of Brooklyn, Private communication.
11. W. L. Wanmaker and M. G. A. Tak, Electrochem. Soc. Enlarged Abstract #45, Electronics Division, Washington Meeting (1957).
12. S. T. Henderson and P. W. Ranby, *This Journal*, **104**, 612 (1957).

# Polorgraphic Reduction of Delta-4-3-Ketosteroids in Well-Buffered Media

**Peter Kabasakalian and James McGlotten**

*Research Division, Schering Corporation, Bloomfield, New Jersey*

ABSTRACT

The polarographic reduction of progesterone, testosterone, methyltestosterone, testosterone propionate, 17-hydroxyprogesterone, 11-deoxycorticosterone, 11-deoxycorticosterone acetate, and 11-deoxy-17-hydroxycorticosterone has been studied in relation to the changes in the wave effected by *p*H, temperature, concentration, and mercury pressure. The system used was 50% aqueous alcohol with organic buffers. Testosterone was also examined at *p*H 7 and above in phosphate and borate buffers. Wave splitting was found in these buffers that was nonexistent at comparable pH values in organic buffers.

The need for adequate buffering in the polarographic reduction of many organic compounds has by now been firmly established. Just what constitutes a good polarographic buffer in the alcoholic solutions so often necessary in the polarography of organic compounds has not been clarified. The problem of buffer choice seems to be most troublesome in the basic regions.

The polarographic buffering ability (in water-alcohol solutions) of the phosphate and borate buffers often used to obtain a *p*H of 7 or higher is open to question in view of the results obtained with azobenzene (1) in these buffers. Quite different results have been obtained for this compound by other workers (2,3) using different buffer components. Zuman, *et al.* (4), have published some work on the polarographic reduction of $\Delta^4$-3-ketosteroids in water-ethanol solutions buffered with Britton and Robinson buffers (acetic, phosphoric, and boric acids). These authors reported that the steroids investigated gave two waves in basic solutions. The relative heights of these two waves varied as the *p*H of the solutions was varied, with the total height remaining relatively constant. The presence of these two waves was attributed to forms interconvertible with *p*H. Recently Lund (5) has reported the polarographic behavior of progesterone and androsta-1, 4-diene-17$\beta$-ol-3-one in 75% methanol-25% water solutions containing 0.5*M* LiCl and 0.05*M* buffer. He reported having obtained only one wave for these compounds over the basic region.

This work presents, primarily, the polarographic behavior of eight steriods [progesterone (I), testosterone (II), methyltestosterone (III), testosterone propionate (IV), 17-hydroxyprogesterone (V), 11-deoxycorticosterone (VI), 11-deoxycorticosterone acetate (VII), 11-deoxy-17-hydroxycorticosterone (VIII)] in what is believed to be adequately buffered 50% ethanol solutions containing organic buffering materials which cover the *p*H range from *p*H 1.3 to 10.5 without any large gap between *p*H values such as was present in an earlier paper (6). Some work with testosterone in phosphate and borate buffers is also presented.

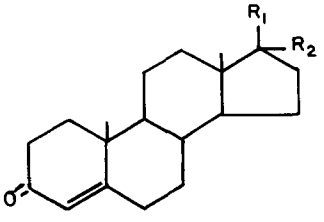


| COMPOUND | $R_1$ | $R_2$ |
|---|---|---|
| I | $-COCH_3$ | --H |
| II | --OH | --H |
| III | --OH | $-CH_3$ |
| IV | $--OCOC_2H_5$ | -H |
| V | $-COCH_3$ | --OH |
| VI | $-COCH_2OH$ | --H |
| VII | $-COCH_2OCOCH_3$ | --H |
| VIII | $-COCH_2OH$ | --OH |

## Experimental

*Apparatus and materials.*—All of the experimental work was performed on the Sargent Model XXI recording polarograph. The cells used for most of the work were small H-type cells (3-ml sample volume) containing a normal calomel electrode separated from the sample compartment by an agar plug and fritted glass diaphragm. However, 10 ml cells employing a mercury pool anode were used in the diffusion current vs. temperature studies. These cells permitted a small Anschutz precision thermometer to be immersed directly in the sample solution along with the capillary.

The electrode capillary delivered 1.768 mg of Hg/sec at a column height of 44.5 cm. The drop time was 4.01 sec and the capillary constant, $m^{2/3}t^{1/6}$, was 1.842 $mg^{2/3}$ $sec^{-1/2}$. The constants were determined

at an open circuit with the mercury dropping into a 0.1*N* potassium chloride solution.

The apparatus used in the diffusion coefficient experiments was essentially that of Stokes (7).

The absolute ethanol and buffer components were found to be polarographically inert in the desired voltage range. The steriods used in this investigation were obtained from the Schering Laboratories. The Triton X-100 was obtained from Rohm and Haas.

*Procedure.*—Electrolysis solutions for all of the qualitative work were prepared by pipetting 5 ml aliquots of an alcoholic steroidal solution into a 10 ml volumetric flask, adding 0.1 ml of 0.2% Triton X-100 and diluting to the mark with the appropriate aqueous buffer solution. Portions of the electrolysis solution were used to rinse the sample cell, a final portion was deaerated with nitrogen for 10 min and then electrolyzed. The pH of the solutions was determined after electrolysis. For the current-concentration work the sample was weighed directly into the 10 ml volumetric flask using a micro balance and dissolved in 5 ml of alcohol. Diffusion currents were determined by the method of intersecting lines. The buffer system used for the major part of this work is presented in Table I.

## Results and Discussion

*Effect of pH on half-wave potentials.*—The half-wave potentials of each steroid investigated decreased linearly with an increase in pH throughout the pH range from 1.3 to 10.5. The slopes of the $E_{1/2}$ vs. pH plots varied between 0.059 and 0.063 v/pH unit with a mean value of 0.060 v/pH unit. There were no deviations from this pH dependency observed for methyltestosterone, testosterone, or progesterone as had been observed in Britton and Robinson buffers. A comparison of the testosterone $E_{1/2}$ vs. pH plot obtained by Zuman, *et al.* (4), and that obtained in this investigation is presented in Fig. 1. The experimental data for all the steroids are compiled in Table II. The data presented by Lund (5) for progesterone show that the half-wave potentials at the basic pH values (9.80, 10.16, and 11.0) are more negative than would be expected from the slope of the line determined by the half-waves at the acidic pH values (1.05, 4.00, and 5.08). In an attempt to extend the $E_{1/2}$ vs. pH data for borate buffers, testosterone was examined in borate buffers at pH 7.7, 8.5, 10.0, and 11.1 as well as a citric acid-disodium phosphate buffer pH 4.7 for comparison. The $E_{1/2}$ vs. pH relationship was complicated by the fact that wave splitting similar to that described by Zuman (4) occurred in the solutions of pH 7.7 and 8.5. However, the one wave obtained at pH 4.7 and the small first waves obtained at pH 7.7 and 8.5

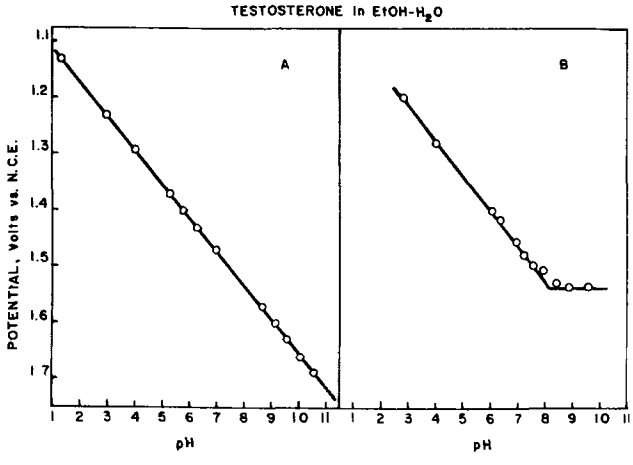


Fig. 1. Variation of $E_{1/2}$ with pH for testosterone using (A) buffers used in this study and (B) buffers used by Zuman and co-workers.

Table I. Composition of buffers* in 50% ethanol

| pH | Buffer components | | |
|---|---|---|---|
| 1.3 | 0.100 M | HCl | |
| 3.0 | 0.100 M | malonic acid | +0.025M KOH |
| 4.0 | 0.100 M | malonic acid | +0.075M KOH |
| 5.2 | 0.075 M | acetic acid | +0.025M NaOAc |
| 5.7 | 0.050 M | acetic acid | +0.050M NaOAc |
| 6.2 | 0.025 M | acetic acid | +0.075M NaOAc |
| 6.9 | 0.100 M | malonic acid | +0.170M KOH |
| 8.6 | 0.100 M | trimethylamine | +0.075M HCl |
| 9.1 | 0.100 M | trimethylamine | +0.050M HCl |
| 9.5 | 0.100 M | triethylamine | +0.075M HCl |
| 10.0 | 0.100 M | triethylamine | +0.050M HCl |
| 10.5 | 0.100 M | triethylamine | +0.025M HCl |

* Potassium chloride was added as an ionic strength agent.

Table II. Effect of pH on half-wave potential and diffusion current

| pH | Progesterone $-E_{1/2}$* | Progesterone $k$** | Testosterone $-E_{1/2}$ | Testosterone $k$ | Methyltestosterone $-E_{1/2}$ | Methyltestosterone $k$ | Testosterone propionate $-E_{1/2}$ | Testosterone propionate $k$ |
|---|---|---|---|---|---|---|---|---|
| 1.3 | 1.11 | 2.01 | 1.13 | 1.76 | 1.13 | 1.78 | 1.13 | 1.93 |
| 3.0 | 1.21 | 1.92 | 1.23 | 1.74 | 1.23 | 1.71 | 1.23 | 1.91 |
| 4.0 | 1.27 | 1.82 | 1.29 | 1.76 | 1.30 | 1.61 | 1.29 | 1.78 |
| 5.2 | 1.35 | 1.81 | 1.37 | 1.63 | 1.37 | 1.62 | 1.36 | 1.74 |
| 5.7 | 1.38 | 1.77 | 1.40 | 1.78 | 1.41 | 1.53 | 1.39 | 1.68 |
| 6.2 | 1.41 | 1.70 | 1.43 | 1.69 | 1.44 | 1.56 | 1.43 | 1.72 |
| 6.9 | 1.46 | 1.73 | 1.47 | 1.68 | 1.47 | 1.43 | 1.46 | 1.63 |
| 8.6 | 1.57 | 1.82 | 1.57 | 1.53 | 1.57 | 1.58 | 1.57 | 1.52 |
| 9.1 | 1.59 | 1.74 | 1.60 | 1.62 | 1.60 | 1.42 | 1.60 | 1.52 |
| 9.5 | 1.62 | 1.60 | 1.63 | 1.49 | 1.62 | 1.46 | 1.62 | 1.46 |
| 10.0 | 1.65 | 1.68 | 1.66 | 1.50 | 1.65 | 1.46 | 1.65 | 1.40 |
| 10.5 | 1.68 | 1.70 | 1.69 | 1.46 | 1.68 | 1.48 | 1.68 | 1.47 |
| Slope† | = 0.063 | | 0.061 | | 0.059 | | 0.060 | |

| pH | 17-Hydroxy-progesterone $-E_{1/2}$ | 17-Hydroxy-progesterone $k$ | 11-Deoxy-corticosterone $-E_{1/2}$ | 11-Deoxy-corticosterone $k$ | 11-Deoxy-corticosterone acetate $-E_{1/2}$ | 11-Deoxy-corticosterone acetate $k$ | 11-Deoxy-17-hydroxy-corticosterone $-E_{1/2}$ | 11-Deoxy-17-hydroxy-corticosterone $k$ |
|---|---|---|---|---|---|---|---|---|
| 1.3 | 1.14 | 2.09 | 1.12 | 2.31 | 1.11 | 1.92 | 1.15 | 2.10 |
| 3.0 | 1.24 | 2.02 | 1.22 | 1.80 | 1.21 | 2.06 | 1.24 | 1.74 |
| 4.0 | 1.31 | 1.90 | 1.29 | 1.58 | 1.28 | 1.64 | 1.31 | 1.76 |
| 5.2 | 1.37 | 1.78 | 1.36 | 1.57 | 1.35 | 1.43 | 1.38 | 1.71 |
| 5.7 | 1.40 | 1.72 | 1.39 | 1.58 | 1.38 | 1.43 | 1.41 | 1.68 |
| 6.2 | 1.44 | 1.70 | 1.42 | 1.58 | 1.43 | 1.43 | 1.45 | 1.63 |
| 6.9 | 1.48 | 1.53 | 1.46 | 1.65 | 1.46 | 1.61 | 1.49 | 1.54 |
| 8.6 | 1.57 | 1.62 | 1.57 | 1.83 | 1.55 | 1.84 | 1.58 | 1.60 |
| 9.1 | 1.60 | 1.61 | 1.60 | 1.86 | 1.58 | 1.76 | 1.60 | 1.62 |
| 9.5 | 1.62 | 1.54 | 1.62 | 1.66 | 1.62 | 1.54 | 1.63 | 1.36 |
| 10.0 | 1.65 | 1.61 | 1.64 | 1.50 | 1.64 | 1.47 | 1.66 | 1.41 |
| 10.5 | 1.68 | 1.57 | 1.67 | 1.51 | 1.67 | 1.45 | 1.69 | 1.36 |
| Slope | = 0.059 | | 0.059 | | 0.060 | | 0.059 | |

* Half-wave potentials in volts measured against a normal calomel electrode.
** $k$ = microamperes per millimolar.
† Slope at 25°C in v/pH units.

Table III. Testosterone in 75% $CH_3OH$

| pH | Buffer composition | $-E_{1/2}$ v | $-E_{1/2}$ v |
|---|---|---|---|
| 4.7 | 0.050M citric acid<br>0.060M disodium phosphate | 1.29 | — |
| 7.7 | 0.075M hydrochloric acid<br>0.050M sodium tetraborate | 1.45 | 1.63 |
| 8.5 | 0.045M hydrochloric acid<br>0.050M sodium tetraborate | 1.50 | 1.63 |
| 10.0 | 0.068M sodium hydroxide<br>0.050M sodium tetraborate | — | 1.66 |
| 11.1 | 0.100M sodium hydroxide<br>0.050M sodium tetraborate | — | 1.72 |
| | 0.5M LiCl added | | |

fall on a straight line whose slope is approximately 0.059 v/pH unit. The $E_{1/2}$ of the second and main wave at pH 7.7 and 8.5 was invariant at both pH values. This wave began to shift to more negative potentials at pH 10.0 and 11.1. The data are listed in Table III.

*Effect of pH on diffusion current.*—The diffusion currents obtained with eight steroids were substantially pH independent. However, the currents obtained in acid solutions were slightly larger than those obtained in basic solutions for all of the steroids examined with the exception of deoxycorticosterone and deoxycorticosterone acetate. The diffusion current constants obtained at the various pH values are listed in Table II.

*Effect of concentration on diffusion current.*—The diffusion currents obtained with progesterone, testosterone, methyltestosterone, 11-deoxy-17-hydroxycorticosterone, and testosterone propionate were found to be directly dependent upon concentration from approximately $2 \times 10^{-4}M$ to $1 \times 10^{-2}M$. With deoxycorticosterone and deoxycorticosterone acetate the current-concentration relationship appears to deviate from linearity at the lower end of this concentration range. However, the diffusion plateau for those two compounds at this point was so steep that the deviation may be due more to the method of measurement than to any change in diffusion properties.

*Effect of temperature on diffusion current.*—The variation of diffusion current with temperature was determined for the eight steroids over a temperature range from 7° to 50°C. The temperature coefficients for these $\Delta^4$-3-ketosteroids averaged 1.94± 0.08% per degree with respect to the 25°C value. The coefficients are in keeping with diffusion-controlled processes.

*Effect of mercury height on diffusion currents.*—The effect of mercury pressure on the diffusion currents obtained with these steroids was studied in 50% ethanol solutions buffered at pH 5.5 with acetic acid-sodium acetate buffer. The ratios of the currents obtained at two different mercury heights averaged 1.34± 0.01. Ratios of 1.00, 1.38, and 1.92 would be expected for kinetic, diffusion, and adsorption control, respectively, for the two mercury heights employed.

*Determination of diffusion coefficients by the diaphragm cell technique.*—Diffusion coefficients of 2.37, 2.31, 2.53, 2.25, 2.22, 2.54, 2.33, and 2.07 (in units of $10^{-6}$ $cm^2$ $sec^{-1}$) were obtained for progesterone, testosterone, methyltestosterone, testosterone propionate, 17-hydroxyprogesterone, 11-deoxycorticosterone, 11-deoxycorticosterone acetate, 11-deoxy-17-hydroxycorticosterone, respectively. On substitution in the modified Ilkovic equation (8) these diffusion coefficients yield $n$ values of 1.04, 1.02, 0.93, 1.01, 1.06, 0.90, 0.83, and 1.02 for the reduction of the steroids as listed above. This indicates that the reduction mechanism is the same as that reported earlier (6), i.e., bimolecular reduction to a pinacol.

*Wave form.*—Essentially the reduction of each of the steroid compounds is characterized by a single, regular S shaped curve. Three compounds exhibit an additional wave at pHs 3.0 and 4.0. This wave, apparently catalytic in nature, is observed with progesterone, 11-deoxycorticosterone, and 11-deoxycorticosterone acetate. It is interesting to note that this wave is not observed with 17-hydroxyprogesterone or 11-deoxy-17-hydroxycorticosterone. The addition of the 17-hydroxy group seems to have an inhibitory effect on this catalytic wave.

There was no double wave observed for any of these compounds in basic media contrary to previous reports. Zuman, *et al.* (4), observed two waves with testosterone, methyltestosterone, progesterone, and deoxycorticosterone in ethanol-water systems buffered with Britton and Robinson buffers. The heights of the two waves were found to vary with pH, the total height remaining relatively constant. The pH interval over which two waves were obtained varied for the different steroids; however, no wave splitting was found below pH 5 or above pH 11 for any of the compounds. Since no wave splitting was evidenced by the four steroids listed above anywhere in this pH range in the organic buffers used here, it would appear that the double waves observed by Zuman and his co-workers were due to the buffers used rather than the pH of the solution as had been postulated.

If equation (I)

$$S + H_2PO_4^- \rightleftharpoons SH^+ + HPO_4^= \qquad (I)$$

where S = unsaturated ketosteroid and $SH^+$ = steroid-hydrogen ion complex, represented a reaction between a steroid and a *specific buffer acid* (rather than a generalized acid-base reaction) then an equilibrium constant could be written

$$K = \frac{[SH^+]\,[HPO_4^=]}{[S]\,[H_2PO_4^-]}$$

which, with appropriate K and $HPO_4^=/H_2PO_4^-$ values, could account for two waves observed in buffer solutions which contain excess acid component providing the equilibrium at the electrode surface is reestablished slowly. The fact that the first wave increases directly with steroid concentration, decreases with increasing salt ($HPO_4^=$) concentration at constant acid concentration, and remains relatively constant upon increasing buffer concentration while maintaining $HPO_4^=/H_2PO_4^-$ constant would be understandable if such an equilibrium existed for phos-

Table IV. Effect of steroid concentration, buffer concentration, and salt to acid ratio on the two waves in phosphate buffered solutions. 50% Ethanol solutions of testosterone

| Steroid conc | Buffer conc | $i$(obs) | $i$(theory) |
|---|---|---|---|
| | (*a*) Varying steroid conc | | |
| 0.33mM | 0.030 M $KH_2PO_4$ + 0.045 M $K_2HPO_4$ | 0.31$\mu$a | 0.55$\mu$a |
| 0.65mM | 0.030 M $KH_2PO_4$ + 0.045 M $K_2HPO_4$ | 0.61$\mu$a | 1.01$\mu$a |
| 1.62mM | 0.030 M $KH_2PO_4$ + 0.045 M $K_2HPO_4$ | 1.47$\mu$a | 2.69$\mu$a |
| 3.25mM | 0.030 M $KH_2PO_4$ + 0.045 M $K_2HPO_4$ | 2.86$\mu$a | 5.40$\mu$a |
| | (*b*) Varying salt to acid ratio | | |
| 1.0mM | 0.025 M $KH_2PO_4$ + 0.050 M $K_2HPO_4$ | 0.83$\mu$a | 1.66$\mu$a |
| 1.0mM | 0.050 M $KH_2PO_4$ + 0.050 M $K_2HPO_4$ | 1.12$\mu$a | 1.66$\mu$a |
| 1.0mM | 0.075 M $KH_2PO_4$ + 0.050 M $K_2HPO_4$ | 1.25$\mu$a | 1.66$\mu$a |
| 1.0mM | 0.075 M $KH_2PO_4$ + 0.025 M $K_2HPO_4$ | 1.44$\mu$a | 1.66$\mu$a |
| | (c) Varying buffer conc | | |
| 1.0mM | 0.006 M $KH_2PO_4$ + 0.004 M $K_2HPO_4$ | 1.04$\mu$a | 1.66$\mu$a |
| 1.0mM | 0.015 M $KH_2PO_4$ + 0.010 M $K_2HPO_4$ | 1.16$\mu$a | 1.66$\mu$a |
| 1.0mM | 0.030 M $KH_2PO_4$ + 0.020 M $K_2HPO_4$ | 1.25$\mu$a | 1.66$\mu$a |
| 1.0mM | 0.060 M $KH_2PO_4$ + 0.040 M $K_2HPO_4$ | 1.27$\mu$a | 1.66$\mu$a |

$i$(obs) = current observed for the pH controlled first wave; $i$(theory) = current obtained for same wave in well-buffered solutions.

Table V. Determination of the equilibrium constant for the proposed steroid-hydrogen ion complex in phosphate and borate buffers. 50% Ethonol solutions of 1.0mM testosterone

| Buffer Composition | $i/i'$ | $K$ |
|---|---|---|
| 0.025 M $KH_2PO_4$ + 0.050 M $K_2HPO_4$ | 1.0 | 2.0 |
| 0.050 M $KH_2PO_4$ + 0.050 M $K_2HPO_4$ | 2.1 | 2.1 |
| 0.075 M $KH_2PO_4$ + 0.050 M $K_2HPO_4$ | 3.0 | 2.0 |
| 0.075 M $KH_2PO_4$ + 0.025 M $K_2HPO_4$ | 6.5 | 2.2 |
| 0.208 M $H_3BO_3$ + 0.012 M $NaH_2BO_3$ | 0.2 | 0.013 |
| 0.212 M $H_3BO_3$ + 0.008 M $NaH_2BO_3$ | 0.4 | 0.015 |
| 0.214 M $H_3BO_3$ + 0.006 M $NaH_2BO_3$ | 0.5 | 0.014 |
| 0.216 M $H_3BO_3$ + 0.004 M $NaH_2BO_3$ | 0.9 | 0.018 |
| 0.2 M KCl added | | |

$i$ = current observed for pH controlled first wave; $i'$ = current observed for pH independent second wave.

phate solutions (*see* Table IV). The slight increase in current occasioned by the increase in buffer constituents is not nearly as great as would be predicted by the equation developed by Koutecky (9) for the average current of an electrode reaction governed by the rate of diffusion of reactants and by the rate of dissociation of the buffer. Similar results were obtained with borate buffers. Table V shows values of K calculated for a series of phosphate and borate buffers.

In summary it can be said that the double wave obtained in the one electron reduction of $\Delta^4$-3-ketosteroids in 50% ethanol solutions buffered with phosphate or borate buffers (and combinations of the two) is not due to the pH of the solution, but to the buffer components. It has been shown that this wave splitting can be avoided by using tertiary amines as the buffer constituents for the higher pH range, rather than the inorganic phosphates and borates.

Manuscript received July 5, 1957. This paper was prepared for delivery before the Buffalo Meeting, Oct. 6-10, 1957.

Any discussion of this paper will appear in a Discussion Section to be published in the December 1958 JOURNAL.

REFERENCES

1. A. Foffani and M. Fragiacomo, *Ricerca sci.*, **22**, 139 (1955).
2. C. R. Castor and J. H. Saylor, *J. Am. Chem. Soc.*, **75**, 1427 (1953).
3. S. Wawzonek and J. D. Fredrickson, *ibid.*, **77**, 3985 (1955).
4. P. Zuman, J. Tenygl, and M. Brezina, *Collection Czechoslov. Chem. Communs.*, **19**, 46 (1954).
5. H. Lund, *Acta Chem. Scand.*, **11**, 283 (1957).
6. P. Kabasakalian and J. McGlotten, *J. Am. Chem. Soc.*, **78**, 5032 (1956).
7. R. H. Stokes, *ibid.*, **72**, 763 (1950).
8. J. J. Lingane and B. A. Loveridge, *ibid.*, **72**, 438 (1950).
9. J. Koutecky, *Collection Czechoslov. Chem. Communs.*, **19**, 857 (1954).

# Glow-Discharge Electrolysis in Aqueous Solutions

**A. R. Denaro and A. Hickling**

*Department of Inorganic and Physical Chemistry, University of Liverpool, Liverpool, England*

ABSTRACT

An investigation has been carried out of the reactions occurring when an electric discharge is passed from a positive electrode to the surface of an aqueous electrolyte containing oxidizable substrates such as ferrous, azide, ferrocyanide, and cerous ions. Electrolysis is accompanied by oxidation arising from the breakup of water molecules due to the bombardment of the solution by gaseous ions, and the chemical phenomena are analogous to the effects produced by ionizing radiations. An attempt has been made to develop a general mechanism of the process which will account quantitatively for the oxidation yields and their dependence on experimental conditions.

If an electrolytic cell is arranged so that one electrode is in the gas space above the electrolyte, then, on working at reduced pressure and applying a moderately high voltage, substantial currents can be passed to the liquid surface in the form of a glow discharge. The technique was developed long ago (1), and many features of glow-discharge electrolysis have been investigated, particularly by Klemenc and his co-workers (2). It has been established that, in addition to the expected electrolytic reaction, additional chemical reactions are initiated, probably by radicals produced in the discharge and, where a suitable substrate is present, oxidation yields greatly in excess of those expected from Faraday's Laws can occur. In much of this work, however, rather complex conditions have been employed, and no integrated view of the mechanism of the process has emerged which accounts quantitatively for the experimental results.

The present series of investigations was undertaken with a view to elucidating the fundamental mechanism by studying the process using a glow-discharge anode in very simple chemical systems. Initially the reactions occurring in inert electrolytes were investigated (3), where the formation and subsequent decomposition of hydrogen peroxide is the main process observed; this was followed by a study of the glow-discharge oxidation of ferrous sulfate solutions (4). This work showed that the chemical results of glow-discharge electrolysis are closely similar to those brought about by ionizing radiations such as $\alpha$, $\gamma$, and x-rays, suggesting that a similar sequence of reactions might follow a common primary step. The results indicated that with a glow-discharge anode the current is conveyed across the gas-liquid interface by positive gaseous ions derived from water vapor; these are driven into the aqueous phase under the high potential gradient which exists in the discharge near the liquid surface and may bring about dissociation of water molecules before they are discharged. The primary result of the passage of current might therefore be represented in conventional terms as follows:

$$\text{Charge transference} \quad H_2O - e^- \rightarrow H_2O^+ \rightarrow OH + H^+$$
$$\text{Dissociation} \quad H_2O \rightarrow OH + H$$

On this view the oxidation reactions which occur are due to the OH radical and in specific cases the experimental results could be interpreted quantitatively by supposing there to be a definite yield of OH radicals per faraday which are used up in competing oxidation, dimerization, and recombination reactions. The work described in the present paper was designed to test this idea using oxidizable substrates of different types, and it has led to further development and modification of the basic hypothesis.

## Experimental Technique

The method of investigation is to pass known quantities of electricity under controlled conditions to the surface of the electrolyte in the form of a glow discharge, and by subsequent analysis of the solution to express the oxidation yield in equivalents per faraday.

The type of cell used is shown in Fig. 1. It consisted of two cylindrical glass vessels, which formed the anode and cathode compartments, joined by

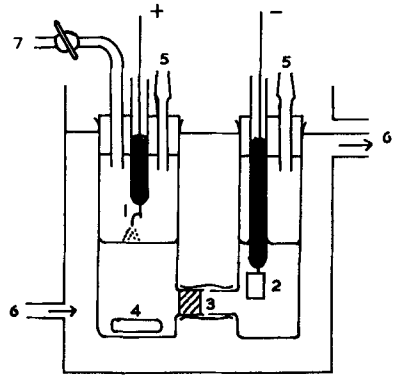


Fig. 1. Electrolytic cell: (1) glow-discharge anode; (2) cathode; (3) filter paper plug; (4) magnetic stirrer; (5) connections to vacuum line; (6) cooling water; (7) gas supply.

short side tubes near the bottom. The anolyte and catholyte were prevented from mixing by a filter paper plug in the side tube of the anode compartment, and the two halves of the cell were connected by a short length of rubber tubing. The compartments were closed by rubber bungs which carried the cell components. The anode, from which the discharge occurred, was of platinum wire connected to a tungsten rod sealed into a glass holder; the cathode was a small sheet of platinum foil. The anode and cathode compartments were connected separately to the vacuum line through small ground glass joints which permitted easy removal of the cell. The anolyte was stirred during electrolysis by a magnetic stirrer. To remove the considerable heat dissipated in the discharge, the cell was almost completely immersed in a bath through which a rapid stream of tap water was passed.

The vacuum system was of a conventional type but included a float manostat so that the pressure in the apparatus could be kept constant over long periods. Before each electrolysis the cell was evacuated to the vapor pressure of the solution. It was then filled with the gaseous atmosphere to be used (usually hydrogen) at atmospheric pressure and the system pumped down to the pressure to be used in the experiment; during electrolysis a slow stream of the gas was admitted to the anode compartment. Current was supplied from a Leland rectifier unit of adjustable voltage (0-1500 v) through a calibrated milliammeter and suitable ballast resistance (2000-10,000 ohms). The discharge was initiated by a pulse from an induction coil; once started it required about 600 v and the current could be kept steady at any desired value between 25 and 100 ma. The standard conditions of electrolysis were to use a current of 75 ma in an atmosphere of hydrogen at a pressure of 50 mm, the anode being 0.75 cm from the surface of 50 ml of anolyte, and the average temperature about 23°C.

The medium used for electrolysis has usually been either 0.8*N*-sulfuric acid (for ferrous and cerous sulfate experiments), or a phosphate buffer (0.1M-$KH_2PO_4$ + 0.1M-$Na_2HPO_4$) where a neutral medium was desirable (for ferrocyanide and azide experiments). The anolyte was made from a weighed quantity of the substrate dissolved in the medium; the catholyte was the medium alone. Analar grade reagents were used throughout. Standard volumetric methods could be employed in most cases for the analysis of the solutions. Ferrous ion was estimated by titration with permanganate; azide was found by oxidation with excess ceric sulfate followed by addition of potassium iodide and back titration with thiosulfate; ceric ion was assessed by reduction with excess ferrous sulfate and back titration with ceric sulfate; hydrogen peroxide when formed was usually determined colorimetrically with titanic sulfate. The analysis of mixtures containing ferro and ferricyanides and hydrogen peroxide presented a difficult problem. It was solved by estimating hydrogen peroxide + ferrocyanide by oxidation with ceric sulfate, while ferricyanide + hydrogen peroxide were found iodometrically; finally, by combination of the two procedures, total ferro + ferricyanide could be obtained.

The substrates had been chosen to give simple oxidation reactions and this was found generally to be the case, although some slight disintegration of ferricyanide occurred on prolonged glow-discharge electrolysis; small quantities of ammonia accompanied the nitrogen which was the main oxidation product from azide. In all cases by complete analysis of both gaseous products and those in solution a satisfactory weight and oxidation/reduction balance was established.

### Characteristics of the Discharge

The discharge took the form of a sharply defined cone between the tip of the anode and the electrolyte surface. By photographing it under different conditions of current, pressure, electrode distance, etc., it was possible to determine the variation of current density at the surface with the above factors. Variation of current produced no significant change, the spot area increasing linearly with increase of current. With decrease of pressure, current density decreased and the relation $I\,p^{-1} = 0.03$ held over the pressure range 3-10 cm of mercury, where $I$ was the current density in amp/cm$^2$ and $p$ the pressure in cm of mercury. Current density was found to vary inversely with electrode distance from the surface, but the effect was relatively slight.

To determine the fall of potential near the liquid surface a probe of platinum wire was inserted in the discharge and the voltage between it and the cathode measured on a valve voltmeter. Under the conditions of operation it was expected that the fall would occur very close to the surface of the solution, certainly within 1 mm. In practice it was not possible to have the probe nearer to the surface than this and a process of extrapolation was applied to determine the cathode fall. The probe voltage was measured at various probe-surface distances at various pressures. The results are shown in Fig. 2 whence it can be seen that the cathode fall is 415 v and occurs at a distance of less than 0.05 cm from the surface of the solution. This value was unaffected by the gaseous atmosphere, by the pressure, by the current, by the electrode-surface distance, or by the nature of the electrolyte.

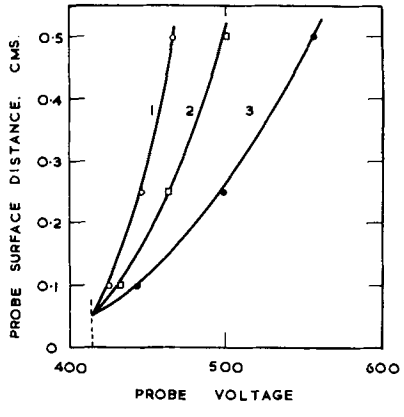


Fig. 2. Determination of potential drop near liquid surface: pressures (1) 27, (2) 50, and (3) 100 mm mercury.

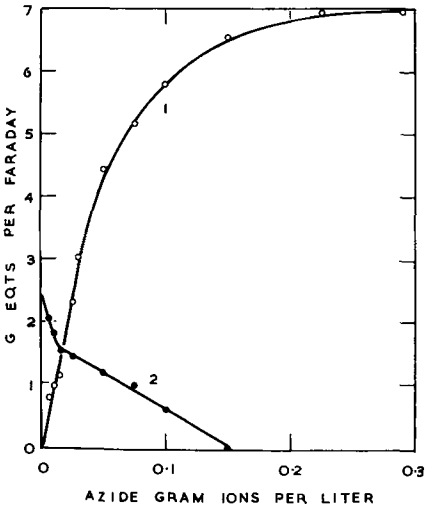


Fig. 3a. Variation of yield with concentration of substrate: curve 1, substrate oxidized; curve 2, hydrogen peroxide formed.

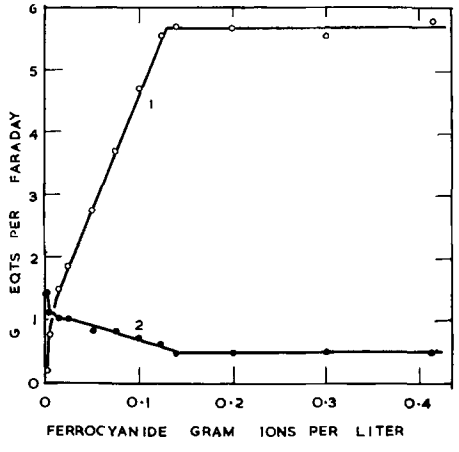


Fig. 3b. Variation of yield with concentration of substrate: curve 1, substrate oxidized; curve 2, hydrogen peroxide formed.

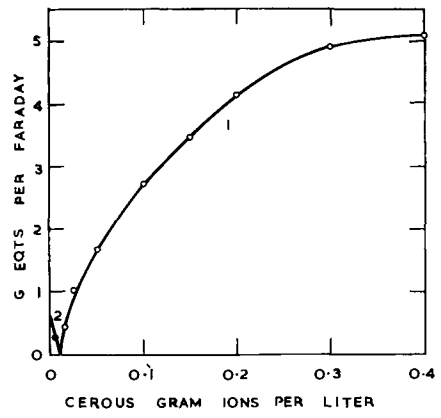


Fig. 3c. Variation of yield with concentration of substrate: curve 1, substrate oxidized; curve 2, hydrogen peroxide formed.

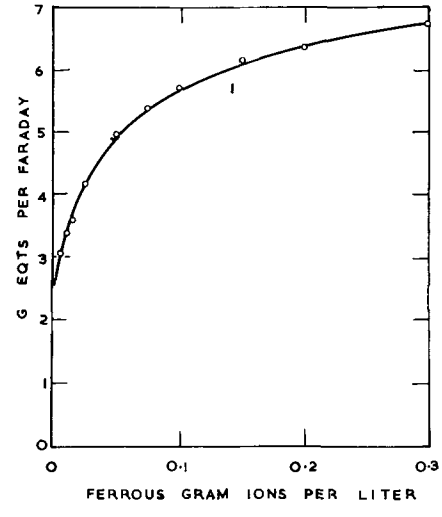


Fig. 3d. Variation of yield with concentration of substrate: curve 1, substrate oxidized.

The glow was examined using a Hilger Medium Quartz Spectrograph but, apart from showing the presence of the OH radical and diffuse absorption bands in the near ultraviolet probably due to some polyatomic hydrogen-oxygen species, the spectrograms furnished little specific information on the discharge.

## Results

Experimental variables fall into two categories. Of prime importance are the quantity of electricity passed, the concentration of the substrate, the pressure of the gas in the cell, and in some cases the presence of chloride ion in solution. Factors such as current, electrode distance, and the nature of the gas in the cell, although they may affect the power dissipated in the discharge considerably, usually have only a trivial influence on the yield of chemical products. The most useful way of summarizing the results of glow-discharge electrolysis is by quoting the instantaneous or differential yield of the product at the initial concentration of substrate. This quantity is denoted in this paper by $G$ and is given in equivalent/faraday; it is analogous in some ways to the quantity used in radiation chemistry where the yield is expressed in molecules/100 ev. Values of $G$ in the present work have been obtained from experimental curves of yield plotted against quantity of electricity passed under different experimental conditions; the slope of the tangent to such a curve at the origin gives the corresponding $G$ value. The general results obtained in the glow-discharge electrolysis of sodium azide, cerous sulfate, and potassium ferrocyanide are compared below, together with those obtained using ferrous sulfate in an earlier study (4).

*Influence of concentration.*—In Fig. 3a-d are shown graphs of the differential yield of oxidation product plotted against the concentration of substrate in the four cases; where hydrogen peroxide was formed the yield of this is also indicated (Curve 2).

In general it is seen that the differential yield increases with increasing concentration of substrate and approaches a limiting value asymptotically; the ferrocyanide case is abnormal here in that, over a substantial range of concentrations, the yield is accurately proportional to the concentration, and the limiting value is attained abruptly when the concentration is 0.125M. The behavior at low concentrations depends on the reaction of the substrate or its oxidation product with hydrogen peroxide. Where the substrate is readily oxidized by hydro-

gen peroxide, as is the case with ferrous sulfate, there is a finite oxidation yield even at zero concentration. On the other hand, where the oxidation product can be reduced by hydrogen peroxide, e.g., ceric sulfate, a certain minimum concentration of substrate is necessary for any oxidation to occur. Where hydrogen peroxide cannot react in either way, its formation accompanies the oxidation of the substrate, the hydrogen peroxide yield diminishing with increasing substrate concentration. This is seen in the azide and ferrocyanide examples, although it is noteworthy that even at the highest ferrocyanide concentrations there is still a small yield of hydrogen peroxide.

*Effect of pressure.*—With rise of pressure, i.e., increase of current density in the glow-spot, oxidation yields were found in general to fall. This is illustrated by the following figures which refer to a concentration of substrate of 0.025M in each case.

| Pressure mm | G equivalents/faraday | | | |
|---|---|---|---|---|
| | $Fe^{2+}$ | $N_3^-$ | $Fe(CN)_6^{4-}$ | $Ce^{3+}$ |
| 30 | 4.3 | 2.7 | 2.4 | 1.5 |
| 50 | 4.2 | 2.3 | 1.9 | 1.0 |
| 75 | 4.2 | 1.8 | 1.6 | 0.6 |

The effect seems most marked where the oxidation yield is low, and is relatively slight in the ferrous case.

*Influence of chloride.*—In the glow-discharge electrolysis of inert electrolytes the presence of chloride ion at concentrations greater than 0.02M seems to inhibit the formation of hydrogen peroxide, although it is not appreciably consumed, and its effect has therefore been tested in the present oxidation studies. With ferrous sulfate, sodium azide and cerous sulfate the presence of 0.02M-sodium chloride in the electrolyte decreased the oxidation yields appreciably, but with potassium ferrocyanide the oxidation yield of ferricyanide was scarcely affected, although that of the accompanying hydrogen peroxide was reduced.

*Miscellaneous factors.*—Variation of temperature is possible over a limited range of about 20°-40°C. The oxidation yield has usually been found to increase somewhat with rise of temperature, but this is not invariably so and, in the case of azide, an appreciable decrease was noted. Working with oxygen-saturated solutions of ferrous sulfate and with an oxygen atmosphere in the cell, the limiting G value at high concentrations was notably increased from about 7.0 to 12.5 equivalents/faraday; with all the other substrates investigated, however, the presence of oxygen had little effect. In the investigation of the formation of hydrogen peroxide in inert electrolytes (3) a salt effect was noted whereby the yield was increased by raising electrolyte concentration. In the present work it has been found that where the substrate is oxidized by hydrogen peroxide, as in the ferrous case, a similar rise in oxidation yield occurs, but where the substrate is fairly stable to hydrogen peroxide, as in the ferrocyanide and azide cases, little salt effect is apparent, and with cerous sulfate where the oxidation product is reduced by hydrogen peroxide the addition of sodium sulfate to the medium decreased the oxidation yield.

## Discussion

Since it seems improbable that electrons can be emitted directly from the surface of a liquid electrolyte, it follows that in experiments with a glow-discharge anode the current must be conveyed by positive gaseous ions which are driven into the liquid from the gas phase and subsequently discharged. The fact that the nature of the gas present has usually little influence on the process suggests that the discharge may well pass ultimately through water vapor in all cases and this is not unlikely since the local temperature under the glow spot must be relatively high. We have no certain knowledge of the nature of the ions present in ionized water vapor at pressures corresponding to those used in the present work, but observations made with the mass spectrometer at much lower pressures (5) have shown that the main positive ion present is $H_2O^+$, and for simplicity this will be assumed to be the species carrying the charge across the interface in the present experiments. Now, as previously mentioned, the main drop of potential is some 415 v and occurs in the discharge within about 0.05 cm of the liquid surface, and hence the maximum energy which the ions could have on entering the solution would be 415 ev. In practice, of course, much of this energy will be dissipated in collisions in the vapor phase and the average energy will depend on the mean free path of the ions in the discharge which cannot be calculated with any accuracy. Thus the particles are likely to have energies less than 415 ev and, while these are minute compared to those of most ionizing radiations, they may well be adequate to bring about dissociation of water molecules.

Thus in the primary reaction zone in the glow spot interaction of the gaseous ions with solvent molecules might be expected to produce dissociation by collision

$$H_2O \rightarrow H_2O^+ + e^- \rightarrow OH + H^+ + e^- \qquad (a)$$

or possibly

$$H_2O \rightarrow OH + H \qquad (b)$$

and to produce also 1 equivalent of OH per faraday by charge transference

$$H_2O^+_{gas} + H_2O_{liq.} \rightarrow OH + H_3O^+ \qquad (c)$$

Within this primary zone, interaction of the radicals among themselves is likely to be governed very largely by spatial considerations and is not amenable to treatment by conventional kinetics (6). However, once the active species have diffused out it should be possible to consider their reactions by ordinary kinetic methods. The OH radical may be expected to oxidize any suitable substrate S by the general reaction

$$OH + S \rightarrow S^+ + OH^- \qquad (d)$$

In an inert electrolyte hydrogen peroxide is always formed, and this may be represented by the dimerisation

$$2\,OH \rightarrow H_2O_2 \qquad (e)$$

In addition there will be a back reaction which may be represented

$$OH + H \rightarrow H_2O \qquad (f)$$

Thus oxidation by glow-discharge electrolysis on this scheme will be determined by the competition of reactions ($d$), ($e$), and ($f$). Thus if $n$ equivalents of OH are formed per faraday by the primary reactions ($a$), ($b$), and ($c$), and if $v_1$, $v_2$, and $v_3$ are the velocities of reactions ($d$), ($e$), and ($f$) in the stationary state, then the oxidation yield in equivalents per faraday will be given by

$$G(1) = n\cdot(v_1 + v_2)/(v_1 + v_2 + v_3) \qquad (I)$$

where the substrate is completely oxidized by hydrogen peroxide.

$$G(2) = n\cdot v_1/(v_1 + v_2 + v_3) \qquad (II)$$

where the substrate and product are inert toward hydrogen peroxide.

$$G(3) = n\cdot(v_1 - v_2)/(v_1 + v_2 + v_3) \qquad (III)$$

where the oxidized product is completely reduced by hydrogen peroxide. If now the velocities are expressed in terms of the concentrations of the reacting species and rate constants $k_1$, $k_2$, and $k_3$ the corresponding relations are

$$G(1) = n\cdot([S] + A)/([S] + A + B) \qquad (IV)$$

$$G(2) = n\cdot[S]/([S] + A + B) \qquad (V)$$

$$G(3) = n\cdot([S] - A)/([S] + A + B) \qquad (VI)$$

where $A = k_2[OH]/k_1$ and $B = k_3[H]/k_1$. A and B would only be expected to be constant for a particular substrate in a particular set of conditions, but $B/A = k_3[H]/k_2[OH]$ might be hoped to have some general significance if the stationary OH concentration does not vary widely with different substrates; $n$ should, of course, be constant throughout. Ferrous sulfate, sodium azide, and cerous sulfate approximate to these three limiting cases (although sodium azide in concentrated solutions is slowly oxidized by hydrogen peroxide) and it is interesting to see how the experimental data fit the above relations. On taking reciprocals of the above expressions they become

$$\frac{1}{G(1)} = \frac{1}{n}\cdot\frac{B}{[S] + A} + \frac{1}{n} \qquad (VII)$$

$$\frac{1}{G(2)} = \frac{1}{n}\cdot\frac{A + B}{[S]} + \frac{1}{n} \qquad (VIII)$$

$$\frac{1}{G(3)} = \frac{1}{n}\cdot\frac{2A + B}{[S] - A} + \frac{1}{n} \qquad (IX)$$

Hence the plot of $1/G$ against $1/[S]$ should be a straight line in each case at high concentrations of substrate and the intercept on the $1/G$ axis should be the same. In Fig. 4 the graphs are plotted; it is seen that they are linear at concentrations greater than $0.05N$ and converge to approximately a common point. From the slopes, values of $B/n$, $(A+B)/n$, and $(2A+B)/n$ can be obtained in the respective cases. To analyze these further, supplementary data are required and these are provided by the extrapolated behavior at very low substrate concentrations. In each case, the yield of hydrogen

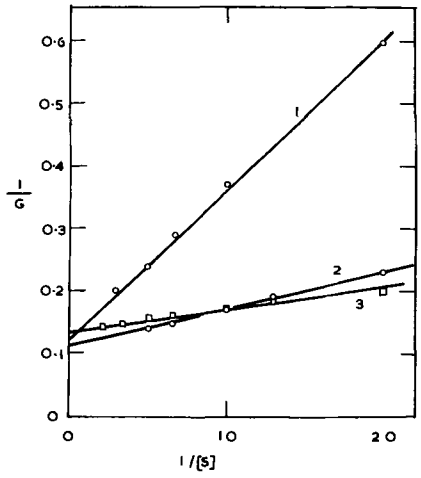


Fig. 4. Graphs of reciprocal yields against reciprocal concentrations of substrate: curve 1, $Ce_2(SO_4)_3$; curve 2, $NaN_3$; curve 3, $FeSO_4$.

peroxide in this limit should be $n\cdot A/(A + B)$; in the ferrous sulfate case this will of course correspond to the limiting oxidation at zero substrate concentration (2.5 equivalent/faraday), while in the azide and cerous cases it will be the actual yields of hydrogen peroxide obtained, i.e., approximately 2.3 and 0.6 equivalent/faraday. Utilizing these data, the values of $n$, A, B, and B/A in the three cases have been evaluated and are summarized below; values of $n$ are obtained from the intercepts on the $1/G$ axis in Fig. 4, and the values of A and B are obtained from the slopes of the graphs combined with the yields at zero substrate concentration.

| Substrate | $n$ | A | B | B/A |
|---|---|---|---|---|
| $FeSO_4$ | 7.3 | 0.011 | 0.026 | 2.4 |
| $NaN_3$ | 8.3 | 0.012 | 0.032 | 2.7 |
| $Ce_2(SO_4)_3$ | 7.6 | 0.013 | 0.152 | 11.7 |

The values of $n$ are approximately constant and B/A is of the same order of magnitude in the first two cases, although it is relatively high in the cerous oxidation. It is noteworthy that the treatment predicts that, with increasing concentration of substrate, a limiting yield should be approached asymptotically, as is found in practice, and it further indicates that in the cerous case a minimum concentration of $0.013N$ is necessary for any net oxidation yield; the experimental value is ca. $0.01N$.

With increase of pressure the area of the glow spot diminishes and it would be expected that [OH] and [H] might increase. In general, therefore, G should diminish with rise of pressure, but the effect will be very dependent on the concentration of substrate chosen, sensitivity to pressure change being only marked at low concentrations. Furthermore from the expressions deduced, the effect should be least with ferrous sulfate and greatest with cerous sulfate. Qualitatively these predictions seem to be in agreement with experimental results.

Thus the above scheme seems able to account in general terms for many features of oxidation in glow-discharge electrolysis but it encounters very great difficulties in the potassium ferrocyanide case. This oxidation shows a number of peculiar features; in particular, G is linearly dependent on ferrocy-

anide concentration over a considerable range, and the limiting value is not approached asymptotically but is attained abruptly at a ferrocyanide concentration of 0.125*N*. Furthermore the presence of chloride ion does not materially diminish the oxidation yield, whereas in other cases it always seems to interfere with oxidation by the OH radical (7). A hypothesis which would go some way toward explaining these features might suggest that by virtue of its high negative charge the $Fe(CN)_6^{4-}$ ion can act as a scavenger within the primary zone for $H_2O^+$ ions which, as indicated in Eq. (*a*), may be precursors of the OH radicals produced by dissociation of water molecules. On this basis the probability of a $H_2O^+$ ion reacting before decomposing would be directly proportional to the ferrocyanide concentration, and at a particular concentration all the $H_2O^+$ ions might react within their average life period. This can only be regarded as highly speculative at present, but in view of its peculiar features a study of the ferrocyanide system using the ordinary methods of radiation chemistry might prove highly rewarding.

The scheme of reactions put forward above to account for the mechanism of glow-discharge oxidation must obviously be a somewhat arbitrary simplification of the actual position. Thus in the radiation chemistry of aqueous systems in recent years it has been realized (8) that in addition to the OH and H radicals formed a "molecular" yield of $H_2O_2$ and $H_2$ may emerge from the primary zone. This may possibly be so in glow-discharge electrolysis also; indeed the assumption of a primary yield of $HO_2$ (rather than $H_2O_2$) accompanying the OH radical, which has been regarded as the main oxidizing agent, will explain some of the fine details of the present results which are otherwise obscure; $HO_2$ radicals might also arise, of course, by interaction of OH radicals with $H_2O_2$ molecules. It may also be noted that in the reactions suggested no reducing properties have been attributed to the hydrogen atoms formed in the dissociation of water molecules. This is in agreement with what has generally been found in glow-discharge electrolysis; thus the oxidation of a ferrous salt proceeds to completion independently of the concentration of ferric ions present and, even when a glow-discharge cathode is used, very little reduction of a ferric sulfate solution can be brought about. This absence of reducing power in a system in which the existence of hydrogen atoms is postulated has been noted frequently in the radiation field, and much ingenuity has been directed to explaining it (9).

The striking analogy between the results of glow-discharge electrolysis and the action of ionizing radiations is apparent from the previous discussion. Although the energies of the bombarding particles in glow-discharge electrolysis are relatively small, it is to be noted that the dose-rate can be extremely high. Thus with a current of 75 ma, the number of univalent gaseous ions reaching the solution surface per minute is $2.8 \times 10^{19}$ and, assuming them to have an average energy of 100 ev, this corresponds to a dose-rate of $2.8 \times 10^{21}$ ev/min. In view of the low energy of the particles very little penetration of the solution will occur, and the reaction zone immediately under the glow-spot will have a very small volume; thus the dose-rate per unit volume will probably be much greater than the above figure. The ionizing radiations employed in conventional radiochemistry are of much higher energies ($10^4$ to $10^9$ ev) than the positive ions in glow-discharge electrolysis, but the dose-rates which can be attained are much lower, being of the order of $10^{16}$-$10^{20}$ ev/cc-min. In spite of these differences the chemical effects appear to be closely similar and, if the bombarding particles in glow-discharge electrolysis are assigned energies of about 100 ev, the yields are quantitatively comparable with those produced by $\alpha$-particles. This illustrates very forcibly the indirect nature of the chemical reactions produced.

In the present work the study of glow-discharge electrolysis has been limited deliberately to very simple systems in order to clarify the fundamental mechanism, but it is apparent that the method may provide a useful tool for electro-organic preparations. It gives a means of producing and maintaining a very high local concentration of OH radicals in aqueous systems, although the considerable heat dissipated in the discharge may cause experimental difficulty where thermally unstable substances are to be used. There is the possibility also of adapting the technique to nonaqueous media where the reactions of different radical fragments of solvent molecules might be utilized.

Manuscript received Oct. 30, 1957. This paper was prepared for delivery before the Buffalo Meeting, Oct. 6-10, 1957.

Any discussion of this paper will appear in a Discussion Section to be published in the December 1958 JOURNAL.

## REFERENCES

1. J. Gubkin, *Ann. Physik*, **32**, 114 (1887); K. Klüpfel, *ibid.*, **16**, 574 (1905); A. Makowetsky, *Z. Elektrochem.*, **17**, 217 (1911).
2. A. Klemenc, *et al.*, *Z. Elektrochem.*, **20**, 485 (1914); **37**, 742 (1931); *Z. physik. Chem.*, **130**, 378 (1927); **154**, 385 (1931); **166**, 343 (1933); **27B**, 369 (1935); **179**, 1 (1937); **182**, 91 (1938); **40B**, 252 (1938); **183**, 217, 297 (1938); *Z. anorg. Chem.*, **240**, 167 (1939); *Monatsh.*, **75**, 42 (1944); **76**, 38 (1946); **78**, 243 (1948); **81**, 122 (1950); **82**, 708, 869, 1041 (1951); **84**, 365, 498, 1053 (1953); *Chimia*, **6**, 177 (1952); *Z. Elektrochem.*, **56**, 198, 634, 917 (1952); **57**, 615 (1953); *see* also, W. R. Cousins, *Z. physik. Chem.*, **4B**, 440 (1929); N. Thon, *Compt. rend.*, **197**, 1114 (1933); W. Braunbek, *Z. Physik.*, **91**, 184 (1934); A. Hickling, *J. Chem Soc.*, **1934**, 1772; F. Fichter and K. Kestenholz, *Helv. Chim. Acta*, **23**, 209 (1940); V. I. Pavlov, *Compt. rend. Acad. Sci. U.S.S.R.*, **43**, 236, 383, 385 (1944); P. de Beco, *Compt. rend.*, **207**, 623 (1938); **208**, 797 (1939); *Bull. soc. chim.*, **12**, 779, 789, 795 (1945); A. Muta, *J. Electrochem. Soc. Japan*, **17**, 265, 298 (1949).
3. R. A. Davies and A. Hickling, *J. Chem Soc.*, **1952**, 3595.
4. A. Hickling and J. K. Linacre, *ibid.*, **1954**, 711.
5. H. A. Barton and J. H. Bartlett, *Phys. Rev.*, **31**, 823 (1928); H. D. Smyth and D. W. Mueller, *ibid.*, **43**, 116 (1933); M. M. Mann, A. Hustrulid, and J. T. Tate, *ibid.*, **58**, 340 (1940).
6. Cf. R. M. Noyes, *J. Am. Chem. Soc.*, **77**, 2042 (1955).
7. Cf. M. Haissinsky, *J. Chim. phys.*, **53**, 542 (1956); T. J. Sworski, *Radiation Research*, **2**, 26 (1955).
8. A. O. Allen, *Disc. Faraday Soc.*, **12**, 79 (1952).
9. Cf. M. Haissinsky, *ibid.*, 133.

# Vapor Pressure of Titanium Tetrabromide

**Elton H. Hall, John M. Blocher, Jr., and Ivor E. Campbell**

*Battelle Memorial Institute, Columbus, Ohio*

ABSTRACT

Measurements were made of the vapor pressure of $TiBr_4(l)$. The following results were obtained:

$$TiBr_4(l) = TiBr_4(g)$$

$$\log P_{atm} = \frac{-3706.29}{T} - 6.2424 \log T + 24.199$$

$P$ = 1 atm at 506.6°K

$\Delta H_{298.2} = 13.22 \pm 0.10$ kcal

$\Delta H_{506.6} = 10.60 \pm 0.10$ kcal

$\Delta S_{298.2} = 27.58 \pm 0.22$ e. u.

$\Delta S_{506.6} = 20.93 \pm 0.22$ e. u.

Combination of the above data and thermal data with the calculated entropy of $TiBr_4(g)$ gave the standard entropy:

$TiBr_4(s)$, $S°_{298.2} = 57.6 \pm 0.22$ e. u.

This value agrees with Kelley's value $57.2 \pm 0.9$ e. u. obtained from low temperature heat-capacity measurements.

Data in the literature on the vapor pressure of $TiBr_4$ are inconsistent. Seki (1) measured the vapor pressure of solid and liquid $TiBr_4$ over a limited range.[1] However, when his equation for the liquid vapor pressure is corrected for the $\overline{\Delta C_p}$ of vaporization, −12.4 cal/mole/deg,[2] and extrapolated to 760 mm, 241°C is obtained for the boiling point. This is inconsistent with the various measured boiling points which converge around 230°C.[3] Of these, the value of Bond and Crone, 230°C at 751 mm of Hg, appears to be the most reliable.

Also in disagreement with Seki's results are data obtained in early work at Battelle (8). These data, taken with an isoteniscope (9), were subjected to a statistical analysis which indicated a high degree of precision, but gave a value of $\overline{\Delta C_p} = -7.574$, indicated by the coefficient of log $T$ in the best fit equation, which did not agree with the expected value of $\overline{\Delta C_p} = -12.4$.

Later, Kato and Abe (10) measured the vapor pressure of the liquid in the range 40 to 366 mm with a glass spoon (Bourdon) gauge.[4] Their pressures are significantly lower than either the isoteniscope data or the extrapolation of Seki's data. The data of Kato and Abe are too scattered and the range too narrow to draw any conclusions concerning the magnitude of the $\overline{\Delta C_p}$ term.

[1] Those referring to Seki's paper should note that several of the vapor pressure tables are mislabeled. The vapor pressure data for $CBr_4$, $TiBr_4$, $SnBr_4$, and $SnI_4$ are actually presented in Tables I through VIII in the same order as listed in Table IX. Furthermore, the $\Delta F$ and $\Delta S$ values listed in Table IX are misleading, having been obtained by multiplying the log $P$ equation by 2.303 $R$ without having first converted from mm of Hg to atmospheres. Thus, they imply a standard-state pressure of 1 mm of Hg. The glass-spring manometer used for these measurements is described by Nitta and Seki (2).

[2] *See* calculation of $\Delta C_p$ below.

[3] Values have been reported by Biltz and Jeep (3), 230°C at 761 mm; Bond and Crone (4), 230°C at 751 mm; Baxter and Butler (5), 230°C (760 mm ?); Young and Schumb (6), 230°C (760 mm); and by Olsen and Ryan (7), 228°C (761 mm).

[4] It should be noted that the value $\Delta S$ = 35.73 e.u. shown in Table I of Kato's paper was obtained by multiplying the log $P$ equation by 2.303 $R$ without having first converted from mm of Hg to atmospheres.

A source of error in the spoon-gauge data of Kato and Abe was thought to be the existence of a temperature differential between the bath and the convection-cooled spoon. It was also suspected that the observed $\overline{\Delta C_p}$ discrepancy in the isoteniscope data might be explained by the possible presence of small amounts of residual moisture in the glass equipment resulting in volatile hydrolysis products.

In order to determine the magnitude of these effects, new data were obtained with a Pyrex spoon gauge. The new data show that the conflicting results can be explained adequately on the above bases.

### *Heat Capacity and Standard Entropy of* $TiBr_4$ *Vapor*

The entropy and heat capacity of $TiBr_4$ vapor were calculated from the vibrational frequencies in $cm^{-1}$ given by Delwaulle, *et al.*, (11). Only the translational, rotational, and vibrational contributions to the energy were considered to be significant. No correction was made for anharmonicity, the effect having been considered to be negligible.

In calculating the rotational contributions, the value given by Lister and Sutton (12) for the Ti-Br distance (2.31Å) was used. The calculations led to

$$S°_{298.2} = 95.02 \text{ e. u.}$$

and the heat capacities given in Table I. At 298.2°K and above, the calculated heat capacity can be expressed to within ±0.02 cal/mole/deg over most of the range by the equation

$$C°_p = 25.77 - 1.58 \times 10^5 T^{-2} \qquad (I)$$

where

$$T \geqq 298.2°K$$

At 400°K, the equation is in error by 0.04 units.

Since these calculations were made, similar calculations by Skinner, Johnston, and Beckett have

Table I. Heat Capacity of $TiBr_4(g)$

| Temp, °K | $C_p$, calculated cal/mole/deg | $C_p$, Eq. (I) |
|---|---|---|
| 200 | 22.35 | (21.82) |
| 300 | 24.02 | 24.01 |
| 400 | 24.74 | 24.78 |
| 500 | 25.12 | 25.14 |
| 700 | 25.45 | 25.45 |

Table II. Vapor Pressure of Liquid $TiBr_4$

| Sample | T, °K | $P_{TiBr_4}$*, mm Hg | log $P_{obs}$ − log $P_{calc}$† |
|---|---|---|---|
| A | 352.1 | 5.9 | +0.1144 |
| A | 383.7 | 21.4 | +0.0441 |
| A | 413.0 | 62.8 | +0.0188 |
| A | 336.8 | 3.1 | +0.1927 |
| A | 362.5 | 9.3 | +0.0889 |
| A | 372.9 | 14.6 | +0.0764 |
| A | 393.2 | 31.5 | +0.0409 |
| A | 428.1 | 101.5 | +0.0109 |
| B | 446.3 | 175.7 | +0.0062 |
| B | 431.8 | 113.7 | +0.0099 |
| B | 453.0 | 211.6 | +0.0076 |
| B | 465.8 | 290.4 | −0.0042 |
| B | 480.5 | 424.4 | +0.0014 |
| B | 472.7 | 347.6 | −0.0023 |
| B | 459.0 | 246.4 | +0.0024 |
| B | 441.0 | 150.6 | +0.0098 |
| D | 372.6 | 11.5 | −0.0199 |
| D | 387.3 | 22.3 | −0.0068 |
| D | 402.2 | 40.3 | −0.0018 |
| D | 416.0 | 65.7 | −0.0069 |
| D | 403.7 | 43.4 | +0.0061 |
| D | 390.9 | 26.0 | −0.0034 |
| D | 448.1 | 181.8 | +0.0018 |
| D | 472.3 | 345.9 | 0.0000 |
| D | 498.5 | 634.7 | −0.0025 |
| D | 488.4 | 508.2 | −0.0010 |
| D | 476.4 | 381.0 | −0.0021 |
| D | 464.6 | 283.2 | −0.0013 |
| D | 450.8 | 194.2 | −0.0027 |
| D | 446.3 | 171.0 | −0.0024 |
| D | 436.3 | 126.9 | −0.0029 |
| D | 418.2 | 71.2 | −0.0011 |
| D | 402.5 | 41.1 | +0.0019 |
| D | 387.4 | 23.1 | +0.0067 |
| D | 376.4 | 13.7 | −0.0174 |
| D | 371.1 | 10.7 | −0.0257 |
| D | 366.4 | 8.6 | −0.0271 |
| D | 392.9 | 28.2 | −0.0012 |
| D | 398.0 | 34.4 | −0.0013 |
| D | 414.3 | 62.5 | 0.0000 |
| E | 401.6 | 39.4 | −0.0018 |
| E | 365.2 | 8.7 | +0.0023 |
| E | 349.8 | 3.9 | −0.0162 |
| E | 356.4 | 5.4 | −0.0204 |
| E | 374.5 | 13.5 | +0.0125 |
| E | 419.2 | 73.0 | −0.0050 |
| E | 452.9 | 206.4 | −0.0019 |
| E | 472.4 | 345.8 | −0.0012 |
| E | 463.4 | 273.9 | −0.0023 |
| E | 434.2 | 120.0 | +0.0009 |
| E | 413.2 | 60.6 | +0.0032 |
| E | 407.6 | 49.4 | +0.0012 |
| E | 395.6 | 31.5 | +0.0007 |
| E | 346.6 | 3.5 | +0.0098 |
| E | 355.0 | 5.5 | +0.0179 |
| E | 363.6 | 7.8 | −0.0123 |
| F | 358.6 | 6.6 | +0.0197 |
| F | 369.3 | 10.7 | +0.0138 |

Table II. Vapor Pressure of Liquid $TiBr_4$ (Continued)

| Sample | T, °K | $P_{TiBr_4}$*, mm Hg | log $P_{obs}$ − log $P_{calc}$† |
|---|---|---|---|
| F | 374.5 | 13.5 | +0.0125 |
| F | 392.2 | 27.6 | 0.0000 |
| F | 404.4 | 44.6 | +0.0067 |
| F | 417.9 | 70.1 | −0.0034 |
| F | 429.5 | 104.2 | +0.0035 |
| F | 422.2 | 82.2 | +0.0033 |
| F | 413.3 | 60.4 | +0.0003 |
| F | 400.6 | 37.9 | −0.0023 |
| F | 376.7 | 14.5 | +0.0014 |
| F | 457.4 | 234.0 | −0.0010 |
| F | 456.4 | 228.1 | −0.0014 |
| F | 468.4 | 314.3 | +0.0012 |
| F | 489.0 | 516.0 | −0.0002 |
| F | 481.8 | 435.5 | −0.0007 |
| F | 452.1 | 203.2 | +0.0010 |
| F | 441.4 | 150.2 | +0.0035 |
| F | 354.1 | 5.1 | +0.0048 |
| F | 341.2 | 2.5 | −0.0097 |
| F | 385.8 | 21.9 | +0.0121 |
| F | 354.5 | 5.1 | −0.0039 |
| F-II | 404.2 | 44.2 | +0.0060 |
| F-II | 444.5 | 164.4 | +0.0032 |
| F-II | 432.2 | 112.8 | +0.0008 |
| F-II | 487.1 | 494.6 | +0.0005 |
| F-II | 474.8 | 368.6 | +0.0005 |
| F-II | 460.6 | 256.2 | +0.0009 |
| F-II | 359.4 | 6.9 | +0.0220 |
| F-II | 370.2 | 11.0 | +0.0079 |
| F-II | 376.8 | 14.9 | +0.0112 |
| F-II | 384.5 | 20.2 | +0.0026 |
| F-II | 395.5 | 31.8 | +0.0065 |

* Data listed in the order taken. Pressure corrected for thermal expansion of Hg in the manometer and for latitude.
† Calculated from the equation: log $P_{atm}$ = −3706.29/$T$ − 6.2424 log $T$ + 24.199.

been published (13) which are in essential agreement.

Recent determinations by Kelley (14) show that the heat capacity of liquid titanium tetrabromide is essentially constant between the melting and boiling points. His value, 37.3 cal/mole/deg, is the result of careful determinations and should be quite reliable. Using this value with the heat capacity of the gas obtained from the above equation, one finds a $\Delta C_p$ of vaporization of −12.4 cal/mole/deg at 420°K, near the middle of the range of vapor-pressure measurements.

## Experimental

The Pyrex spoon gauge, with sample reservoir attached, was submerged in an oil bath thermostat (±0.2°C) whose temperature was measured with a chromel-alumel thermocouple calibrated at the boiling point of water and the melting point of tin.

After the initial bake-out of the gauge and appendages at 450°C and 0.05$\mu$ pressure overnight, a break seal was broken, and some $TiBr_4$ was distilled under vacuum through the system. A sample was then condensed in the reservoir and Willard valves (15) on either side were closed. Pressure measurements were made with the spoon gauge used as a null instrument. After the desired data were obtained, proper manipulation of the Willard valves

permitted either partial removal of the sample and re-examination of the residue, or complete removal and replacement by a fresh sample. During Runs D, E, F, and F-II, a heating tape wrapped around the upper part of the outer envelope of the spoon gauge was heated strongly enough to prevent condensation of liquid $TiBr_4$ in the spoon itself. For Runs F and F-II, the Willard valves were replaced by capillary tubes which served as valves on condensing and freezing plugs of $TiBr_4$.

The titanium tetrabromide used in Runs A and B was obtained from the National Bureau of Standards. Another sample of the same lot was reported by NBS to have an over-all purity of 99.998 as measured by analysis of the melting curve. The triple point temperature was reported to be 311.50° ±0.01°K. The sample was transferred by vacuum distillation into small ampoules from the large ampoule in which it was shipped. Liquid nitrogen was used to cool the pump trap and the glass was outgassed by flaming with a hand torch. Samples A and B were successive cuts from one small ampoule.

A second lot of tetrabromide, received from the Bureau of Standards having the same purity specifications, was also transferred to small ampoules. In order to eliminate, if possible, any traces of residual moisture, a seasoning technique was adopted. The transfer system was evacuated to $<0.01\mu$ and heated to about 150°C for 24 hr, after which it was then flushed out with a sample of redistilled tetrabromide so that all of the glass was in prolonged contact with the liquid. The material was all distilled out before the NBS sample was transferred. The first fraction, Sample C, from one small ampoule was used to precondition the glass surfaces of the gauge. After being heated for 48 hr, the $TiBr_4$ was entirely removed by volatilization. Samples D and E were subsequent cuts from the same ampoule, while Sample F was from a second ampoule. F-II designates the sample remaining after about half of F was removed by distillation.

Pressure vs. temperature data for the six separate samples are presented in Table II. The mutually consistent data from Samples D, E, F, and F-II were subjected to a $\Sigma$-calculation in which the coefficient of log $T$ in the vapor-pressure equation was assigned the value −6.2424 ($\overline{\Delta C_p} = -12.4$). This treatment leads to the equation:

$$\log P_{atm} = -3706.29/T - 6.2424 \log T + 24.199$$

In the fourth column of Table II are listed the deviations of each point from the above equation. A plot of the deviations vs. $T$, °K is shown in Fig. 1. It may be seen that the data for Samples D, E, F, and F-II are randomly scattered about zero deviation; hence, the value of $\overline{\Delta C_p} = -12.4$ is consistent with these data. Data for Samples A and B do not agree with the other four samples. For purposes of comparison, it may be noted that the best equation through the data of A and B is actually a straight line, i.e., the apparent $\overline{\Delta C_p} = 0$. Also shown in Fig. 1 are the deviations of the data of Seki, Kato, and Abe, the isoteniscope data, and the boiling point of Bond and Crone.

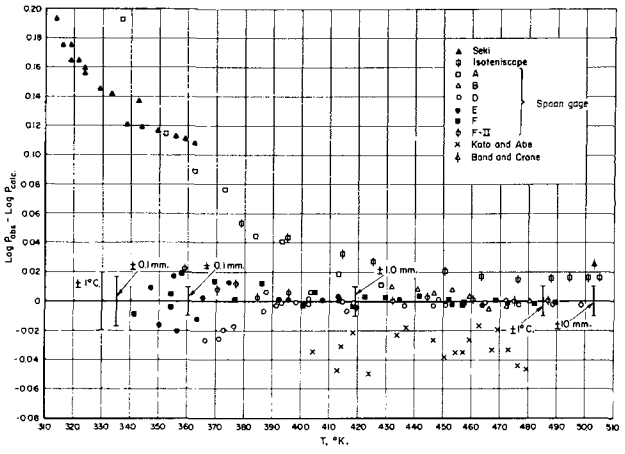


Fig. 1. Vapor pressure of liquid $TiBr_4$. Deviation from log $P_{atm} = -3706.29/T - 6.2424 \log T + 24.199$.

## Discussion

Two differences in the experimental technique have significance in the interpretation of the results: (*a*) prevention of condensation of $TiBr_4$ in the spoon portion of the system during pressure measurements, and (*b*) preconditioning of all glassware with $TiBr_4$. These precautions were employed for Samples D, E, F, and F-II, but not for A and B.

If liquid is permitted to condense in the spoon as a result of circulation of cool inert gas within the envelope, the equilibrium temperature may be noticeably lower than the bath temperature. In an experiment at constant bath temperature, the observed pressure dropped from 626.4 to 609.9 mm of Hg when the heated envelope was allowed to cool toward room temperature. This pressure difference is equivalent to a temperature difference of 1.2°C. In the low temperature range of the data, no pressure difference could be observed between a cool and a heated envelope because of the reduced convective effect at low pressure. Kato and Abe do not indicate that any precautions were taken to prevent condensation. However, as can be seen from the deviation plot, correction of their data by the above amount would bring them into better correlation with the data reported here for Samples D, E, F, and F-II. The actual magnitude of the correction would, of course, vary with the geometry of the particular apparatus.

If routine vacuum bakeout of glassware were not successful in removing sorbed moisture completely, subsequent hydrolysis of the tetrabromide would be expected to produce small amounts of volatile hydrolysis products, such as HBr, dissolved in the tetrabromide. This would introduce a rather large positive error in the observed pressure in the low-pressure range, but a much smaller relative error in the high-pressure range. The deviation plot shows that the data from Samples A and B vary in such a manner. Since the differences in sample handling technique should have reduced the possibility of moisture contamination for Samples D, E, F, and F-II, it is likely that residual moisture was indeed

the source of error in the data from Samples A and B. Since Seki's data and the isoteniscope data deviate in the same manner as Samples A and B, the same explanation probably applies.[5]

The fact that the deviation of the data from Sample B in the high-pressure range is smaller than that of the isoteniscope data is probably the result of compensating errors. The impurity error would lead to positive deviation, while the condensation error would lead to negative deviation.

The absence of volatile or soluble nonvolatile impurities in Sample F is shown by the fact that after volatilization of about half of the sample the vapor pressure remained unchanged.

## Results

One has a choice of two methods for treatment of the data. The free energy and enthalpy functions may be constructed from the $C_p$ data of Kelley (14) and the spectroscopic data of Dewaulle, *et al.* (11), which permit the calculation of values of $\Delta H^\circ_0$ for each experimental vapor-pressure point. The consistency of the data is then judged by the absence of scatter and of trend with temperature in the $\Delta H^\circ_0$ values.

For the present purpose, and in view of the fact that the $C_p$ data of Kelley are as yet unpublished, the authors prefer the $\Sigma$-function treatment which gives convenient analytical expressions for the results. The consistency with the Third Law can be tested by comparing the entropies of vaporization calculated from the vapor-pressure data and from the thermal data. Agreement of the thermodynamic quantities calculated by the two methods is well within the precision of the data.

Treatment of the data from Samples D, E, F, and F-II by the method of least squares leads to the following results for

$$TiBr_4(l) = TiBr_4(g)$$

$$\log P_{atm} = -3706.29/T - 6.2424 \log T + 24.199$$

$$P = 1 \text{ atm at } 506.6^\circ K \ (233.4^\circ C)$$

The indicated normal boiling point, 233.4°C, is 2.6° above the 230.8°C (corrected) given by Bond and Crone (4), i.e., about 3°C above the several values previously reported. However, recent unpublished results of Johannesen (16) at the National Bureau of Standards tend to confirm the higher value obtained in the present work. In the distillation of a sample of $TiBr_4$, Johannesen obtained a final boiling point of 232°C at 765 mm of Hg with a calibrated thermometer totally immersed in the vapor. Since the boiling point had risen 1°C during the distillation, it was suspected that the $TiBr_4$ contained some residual $TiCl_4$ from the preparation and that the value 232°C is somewhat low.

The ratio of fugacity[6] to pressure as a function of temperature may be approximated in the range of the data by the equation

$$\log f/p = -0.0738 \log T + 0.1908$$

By addition to the above equation one obtains,

$$\log f_{atm} = -3706.29/T - 6.3162 \log T + 24.390$$

from which the following thermodynamic quantities are derived:

$$\overline{\Delta C_p} = -12.54 \text{ cal/mole/deg}$$
$$\Delta H_{298.2} = 13.22 \pm 0.10 \text{ kcal}$$
$$\Delta H_{506.6} = 10.60 \pm 0.10 \text{ kcal}$$
$$\Delta S_{298.2} = 27.58 \pm 0.22 \text{ e. u.}$$
$$\Delta S_{506.6} = 20.93 \pm 0.22 \text{ e. u.}$$

The uncertainties are expressed as the maximum deviation from the mean of the values obtained by separate treatment of the data from each sample.

It is recognized that the coefficient of $\log T$ in the fugacity equation is the $\overline{\Delta C_p}/R$ which should be compared with that obtained from the $C_p$ of the gas and liquid as previously described. The indicated value $\overline{\Delta C_p} = -12.54$ is the difference between the gas and liquid at 400°K. Since this temperature is still near the middle of the range of the data and the temperature taken for the $\overline{\Delta C_p}$ calculation is somewhat arbitrary in any case, the $\overline{\Delta C_p}$ indicated by the fugacity equation is considered to be as appropriate for the present purpose.

The above data can be used to obtain an equation for the vapor pressure of the solid. In addition to its inherent interest, this permits a comparison of the entropy of the solid with that obtained calorimetrically by Kelley (18). The heat of fusion of $TiBr_4(s)$, $\Delta H_m = 3080$ cal/mole (14) is added to the heat of vaporization of the liquid at the melting point, $\Delta H_{v_{311.4}} = 13{,}051$ cal/mole, as calculated from the fugacity equation above, to obtain the heat of sublimation at the melting point, $\Delta H_{s_{311.4}} = 16{,}131$ cal/mole. This value is extrapolated to 0°K with the value $\overline{\Delta C_p} = -7.5$ cal/mole/deg[7] to give $\Delta H^\circ_0 = 18{,}467$ cal/mole.

The above values can be substituted in an equation of the form:

$$4.575 \log P = -\Delta H^\circ_0/T + 2.303 \Delta C_p \log T - I$$

the value of $I$ being determined by substituting, for $P$, the value calculated at the melting point from the equation for the vapor pressure of the liquid.

This treatment leads to the following results for

$$TiBr_4(s) = TiBr_4(g):$$
$$\log P_{atm} = -4036.5/T - 3.776 \log T + 19.106$$
$$\overline{\Delta C_p} = -7.5 \text{ cal/mole/deg}$$
$$\Delta H_{298.2} = 16.2 \text{ kcal}$$
$$\Delta H_{311.4} = 16.1 \text{ kcal}$$
$$\Delta S_{298.2} = 37.2 \text{ e. u.}$$
$$\Delta S_{311.4} = 36.8 \text{ e. u.}$$

The derived equation for solid $TiBr_4$ gives pressures about 50% lower than those observed by Seki for the vapor pressure of the solid. The difference may be attributable to the presence of hydrolysis products in Seki's material.

[5] It may be noted that the deviation of the isoteniscope data, for example, is not quantitatively accounted for at both ends of the pressure range on the basis of an ideal solution of HBr in $TiBr_4$. However, since the qualitative explanation appears adequate, consideration of uncertain departure from ideality in an effort to improve the agreement did not seem to be justified.

[6] Estimated by the method of Brewer and Searcy (17).

[7] Kelley (18) gives 31.43 cal/mole/deg for the heat capacity of solid $TiBr_4$ at 298.2°K. At the same temperature $C_p(g) = 23.9$ cal/mole/deg is obtained from spectroscopic data, as discussed above.

The above value of $\Delta S_{298.2}$ may be combined with the standard entropy of $TiBr_4(g)$, $S^\circ_{298.2} = 95.02$ e. u., corrected by −0.2 e.u. for nonideality,[8] to give for $TiBr_4(s)$ at 298.2°K

$$S^\circ_{298.2} = 57.6 \text{ e. u.}$$

The agreement with Kelley's (18) value of 57.2 ± 0.9 e. u., obtained from low temperature heat-capacity measurements, is within the ascribed uncertainty.

### Acknowledgment

The authors are grateful for the help and interest of the Office of Naval Research who supported this work under Contract Nonr-1120(00) as part of their program on the extractive metallurgy of titanium.

Manuscript received Oct. 14, 1957. This paper was prepared for delivery before the Cleveland Meeting, Sept. 30-Oct. 4, 1956.

Any discussion of this paper will appear in a Discussion Section to be published in the December 1958 JOURNAL.

REFERENCES

1. S. Seki, *J. Chem. Soc. Japan*, **62**, 789 (1941).
2. I. Nitta and S. Seki, *ibid.*, **62**, 581 (1941).
3. W. Biltz and K. Jeep, *Z. anorg. Chem.*, **162**, 32 (1927).
4. P. A. Bond and E. B. Crone, *J. Am. Chem. Soc.*, **56**, 2028 (1934).
5. G. P. Baxter and A. Q. Butler, *ibid.*, **50**. 408 (1928).
6. R. C. Young and W. C. Schumb, *ibid.*, **52**, 4233 (1930).
7. J. B. Olsen and E. P. Ryan, *ibid.*, **54**, 2215 (1932).
8. J. M. Blocher, Jr., R. F. Rolsten, N. D. Veigel, and I. E. Campbell, Technical Report on "The Preparation and Properties of Titanium Tetrabromide" to ONR from Battelle Memorial Institute, Contract Nonr-1120(00) July 1, 1955.
9. A. Smith and A. W. C. Menzies, *J. Am. Chem. Soc.*, **32**, 1412 (1910).
10. H. Kato and M. Abe, *J. Chem. Soc. Japan*, **76**, 1182 (1955).
11. M. L. Delwaulle and F. Francois, *Compt. rend.*, **220**, 173 (1945).
12. M. W. Lister and L. E. Sutton, *Trans. Faraday Soc.*, **37**, 393 (1941).
13. G. Skinner, H. L. Johnston, and C. Beckett, "Titanium and Its Compounds," p. 111, Herrick L. Johnston Enterprises, Columbus, Ohio (1954).
14. K. K. Kelley, Quarterly Status Report to ONR from the U. S. Bureau of Mines, Project NR 037-054, October-December, 1955.
15. J. Willard, *J. Am. Chem. Soc.*, **57**, 2328 (1935).
16. R. B. Johannesen, Private communication, Sept. 30, 1957.
17. L. Brewer and A. W. Searcy, *J. Chem. Ed.*, **26**, 548 (1949).
18. K. K. Kelley, Quarterly Status Report to ONR from U. S. Bureau of Mines, Project NR 037-054, July-September 1955.

[8] On the basis of comparison with tin tetrachloride, for which a correction of −0.16 e.u. is estimated from the critical constants, as suggested by Kelley, private communication, April, 1956.

# Vapor Pressure of Titanium Tetrafluoride

**Elton H. Hall, John M. Blocher, Jr., and Ivor E. Campbell**

*Battelle Memorial Institute, Columbus, Ohio*

ABSTRACT

Measurements were made of the vapor pressure of $TiF_4(s)$. The following results were obtained:

$$TiF_4(s) = TiF_4(g)$$
$$\log P_{atm} = -5331.51/T - 2.567 \log T + 16.631$$
$$P = 1 \text{ atm at } 556.3°K$$
$$\Delta H_{298.2} = 22.87 \pm 0.28 \text{ kcal}$$
$$\Delta H_{556.3} = 21.55 \pm 0.28 \text{ kcal}$$
$$\Delta S_{298.2} = 41.92 \pm 0.40 \text{ e. u.}$$
$$\Delta S_{556.3} = 38.74 \pm 0.40 \text{ e. u.}$$

Combination of the above data and thermal data with the calculated entropy of $TiF_4(g)$, $S^\circ_{298.2} = 73.2$ e. u., gave the standard entropy:

$$TiF_4(s), S^\circ_{298.2} = 31.3 \pm 0.40 \text{ e. u.}$$

Ruff and Plato (1) obtained 284°C as the normal sublimation point of $TiF_4$ by measuring the temperature of the vapor subliming at atmospheric pressure in a platinum flask, but no other experimental data relative to the vapor pressure of $TiF_4$ are available in the literature.

To provide these data and to derive related thermodynamic quantities, the vapor pressure has been measured over the temperature range 430° to 560°K.

## Materials

The $TiF_4$, obtained from General Chemical Division, Allied Chemical and Dye Corporation, was purified by high vacuum ($p = 0.01\mu$) sublimation from a Pyrex boiler to a Pyrex receiver fitted with a break seal. The trap to the vacuum system was cooled in liquid nitrogen.[1]

Analysis of a sample of commercial $TiF_4$ sublimed in this manner gave a F/Ti ratio of 3.93. The 1.7% deviation from the theoretical value is within the uncertainty of the fluorine analysis and in the direction of the expected error. Spectrographic analysis showed less than 0.005% Si and less than 0.015% total metallic impurity.

The absence of reaction between dry $TiF_4$ and Pyrex glass in the temperature range employed is

[1] It should be noted that cooling the trap with dry ice-acetone is an insufficient precaution against hydrolysis and subsequent discoloration of the $TiF_4$ on heating.

indicated by (*a*) absence of visible etching, (*b*) low (0.005%) Si content of the $TiF_4$, (*c*) reproducible pressure data, (*d*) absence of noncondensable gases on condensation of the $TiF_4$, and (*e*) agreement of the pressure data obtained in glass and in copper systems.

Transfer of the $TiF_4$ to the measuring cell was made by sublimation under vacuum or directly under an inert gas blanket.

### Vapor Pressure Measurements

Four methods were employed in the measurement of the vapor pressure; spoon (Bourdon) gauge method, the Ruff-Fischer method summarized by Kubaschewski and Evans (2), the transpiration, or gas-saturation method, and the method of Rodebush and Dixon (3). The first is a static method while the others are dynamic methods.

The Pyrex spoon gauge was used as a null instrument, the vapor pressure of $TiF_4$ on the inside of the gauge being balanced by a measured pressure of argon on the outside. The gauge was immersed in a salt bath thermostat (±0.2°C) the temperature of which was measured with a calibrated chromel-alumel thermocouple.

In spite of an initial bakeout in vacuum, some outgassing sometimes occurred during the first stages of a run. The residual gases were pumped out through a Willard valve (4) provided for the purpose. Data were not retained unless zero residual pressure was observed on cooling the cell.

The data obtained for two different samples (Runs A and B) are given in Table I and Fig. 1.

The second method employed was first used by Ruff (5) and later improved by Fischer (6). The determination is made by varying the pressure over a sample held at constant temperature. A sharp change in the observed rate of evaporation determines the point at which the measured opposing pressure equals the vapor pressure.

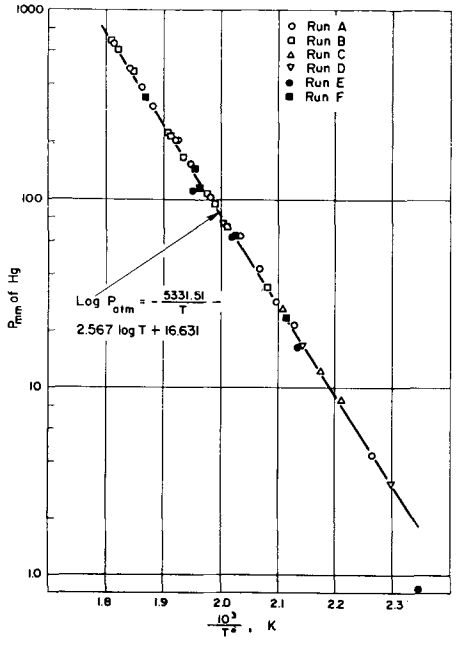


Fig. 1. Vapor pressure of $TiF_4$

Table I. Vapor pressure of $TiF_4$

| Sample | Method | Temp, °K | $P_{TiF_4}$,* mm Hg | log $P_{obs}$ − log $P_{calc}$† |
|---|---|---|---|---|
| A | Spoon gauge | 492.4 | 63.6 | +0.031 |
| A | Spoon gauge | 520.8 | 203.7 | +0.008 |
| A | Spoon gauge | 520.4 | 201.0 | +0.009 |
| A | Spoon gauge | 537.4 | 382.7 | +0.001 |
| A | Spoon gauge | 551.7 | 653.6 | +0.005 |
| A | Spoon gauge | 543.7 | 479.9 | −0.003 |
| A | Spoon gauge | 532.0 | 308.1 | −0.004 |
| A | Spoon gauge | 513.7 | 149.8 | +0.001 |
| A | Spoon gauge | 504.3 | 101.4 | +0.005 |
| A | Spoon gauge | 483.7 | 42.4 | +0.029 |
| A | Spoon gauge | 476.7 | 28.4 | +0.002 |
| A | Spoon gauge | 470.2 | 21.6 | +0.021 |
| A | Spoon gauge | 441.4 | 4.3 | −0.013 |
| B | Spoon gauge | 480.4 | 33.7 | −0.002 |
| B | Spoon gauge | 516.1 | 163.9 | −0.003 |
| B | Spoon gauge | 496.9 | 69.7 | −0.017 |
| B | Spoon gauge | 505.8 | 105.7 | −0.006 |
| B | Spoon gauge | 523.0 | 213.0 | −0.011 |
| B | Spoon gauge | 535.2 | 343.0 | −0.010 |
| B | Spoon gauge | 493.2 | 62.9 | +0.010 |
| B | Spoon gauge | 502.4 | 92.4 | 0.000 |
| B | Spoon gauge | 522.2 | 212.5 | +0.002 |
| B | Spoon gauge | 531.8 | 303.6 | −0.007 |
| B | Spoon gauge | 542.2 | 459.1 | +0.002 |
| B | Spoon gauge | 549.9 | 603.3 | −0.001 |
| B | Spoon gauge | 552.6 | 666.5 | 0.000 |
| C | Ruff-Fischer | 474.3 | 26.0 | +0.013 |
| C | Ruff-Fischer | 452.4 | 8.4 | +0.017 |
| C | Ruff-Fischer | 460.2 | 11.6 | −0.025 |
| D | Ruff-Fischer | 435.4 | 3.1 | −0.004 |
| D | Ruff-Fischer | 466.9 | 16.5 | −0.023 |
| D | Ruff-Fischer | 498.8 | 74.2 | −0.027 |
| E | Transpiration | 426.2 | 0.83 | −0.333 |
| E | Transpiration | 468.2 | 16.1 | −0.063 |
| E | Transpiration | 512.2 | 109.0 | −0.111 |
| F | Rodebush | 472.9 | 23.5 | −0.015 |
| F | Rodebush | 493.5 | 63.5 | +0.008 |
| F | Rodebush | 495.7 | 63.5 | −0.035 |
| F | Rodebush | 512.0 | 144.0 | +0.014 |
| F | Rodebush | 509.5 | 115.0 | −0.038 |
| F | Rodebush | 537.4 | 387.0 | +0.005 |

* Pressures corrected for thermal expansion of mercury in the manometer and for latitude.
† From the equation: $\log_{10} P_{atm} = -5331.51/T - 2.567 \log T + 16.631$.

The data obtained for two different samples (Runs C and D) are given in Table I and Fig. 1.

The third method employed an all-metal transpiration system. The three points (Run E), given in Table I and Fig. 1, were determined by Sense of Battelle. Details of the technique have been reported by Sense, *et al.* (7).

An additional correlation was sought in data taken in a metal system by the "quasi-static" method of Rodebush and Dixon (3, 8). All parts of the Rodebush cell in contact with $TiF_4$ vapor were made of copper. Waxed tapered seals to Pyrex were made at the cooled appendages.

The cell was heated in an air bath and the temperature measured with a calibrated chromel-alumel thermocouple. Power to the furnace was hand controlled to a temperature variation of less than ±0.8°C.

The $TiF_4$ vaporizing from the cell was totally condensed in the copper tube outside the furnace and, therefore, did not come in contact with the glass portion of the system.

In the experiments reported, it was not found possible to obtain a permanent difference in the levels of the differential manometer. It was observed, however, that the magnitude of the inert pressure relative to the vapor pressure caused considerable variation in the length of time required for the manometer to return to zero differential after a given volume of inert gas had been removed from one side. The slow recovery is attributed to evaporative cooling of the sample. This is not noticed when dealing with liquids because of the much more efficient heat transfer to the sample.

The following modification of the Rodebush technique was adopted. With the sample at constant temperature and the inert pressure greater than the expected vapor pressure, a small controlled amount of inert gas was pumped out, and the time required for the manometer to return to zero (recovery time) was determined. The procedure was repeated three or four times and the average recovery time and the inert pressure recorded. The inert gas pressure was then reduced by about 5 mm and the average recovery time determined at the new pressure. The process was repeated at successively lower pressures until the inert pressure was below the vapor pressure, as indicated by the increased recovery time. The pressure was then plotted against the recovery time and the points joined by two intersecting lines. The pressure at the point of intersection was taken as equal to the vapor pressure. The data, Run F, are given in Table I, and Fig. 1.

## Discussion of Results

In Fig. 1, the data from all four methods are shown on a log $P_{mm.}$ vs. $1/T°K$ plot, while in Fig. 2 the deviation ($\log P_{obs.} - \log P_{calc.}$) is plotted vs. temperature. The Ruff-Fischer data are seen to be in good agreement with the spoon-gauge data. It is to be noted that the most probable errors in the spoon-gauge method, namely formation of HF(g) or $SiF_4$(g) by residual water in the $TiF_4$, or outgassing of the sample, would tend to make the observed pressures too high since it is a total pressure method, while the largest error in the Ruff-Fischer method, which is thought to be the temperature differential between the bath and the evaporation-cooled sample, would lead to values which are too low. The fact that both sets of data fall on the same line strongly indicates that these systematic errors are smaller than random errors from other sources.

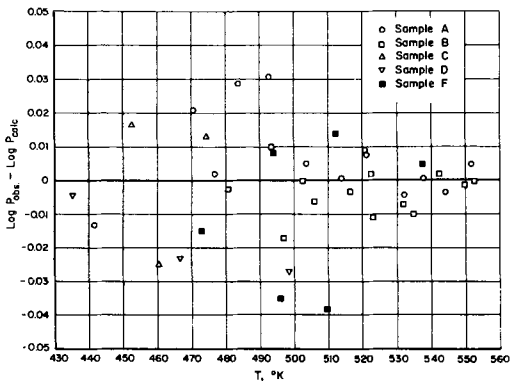


Fig. 2. Vapor pressure of $TiF_4$. Deviation from log $P_{atm}$ = −5331.51/T − 2.567 log T + 16.631.

The transpiration data are in general agreement with the other, although all three values are low. At the high-pressure point, the condenser tended to clog, while, at the lower points, the loosely adherent condensate was subject to entrainment in the inert-gas stream. Both conditions would lead to low results and it was concluded that the experimental error was large enough to account for the deviations observed. Further refinement of the technique as applied to $TiF_4$ did not appear to be warranted.

It will be noted that the data obtained by the Rodebush method are in good agreement with the spoon-gauge data, indicating that errors introduced by contamination in using a glass system are insignificant. Since the Rodebush method was employed primarily as a check on the spoon-gauge data, the precision sought was not high. Therefore, these data were not included in the statistical analysis.

A sample correction of vapor pressure to fugacity by an approximate method suggested by Brewer and Searcy (9) was found to alter the calculated heat of vaporization by about 65 cal. Since this is well within the experimental uncertainty in the heat of vaporization, the correction to fugacity was not thought to be justified.

In order to extrapolate the data, a value for $\Delta C_p$ must be obtained. To calculate an approximate value for the heat capacity of the gas, the vibrational frequencies of $TiF_4$(g) were estimated to be, 192[2],[2] 232[3], 704[1], and 804[3], by comparing those given by Kelley (10) for $CBr_4$, $CCl_4$, $CF_4$, $SiBr_4$, $SiCl_4$, $SiF_4$, and $TiCl_4$, and by Delwaulle, *et al.* (11) for $TiBr_4$. From the estimated frequencies, the heat capacity of the gas at 500°K was calculated [*see*, for example, Rossini (12)] to be 22.9 cal/mole/deg. For the solid, the variation of the heat capacity as a function of the ratio, $T/T_{m.p.}$, was compared for $TiBr_4$ (13) and $TiCl_4$ (14). The curves were roughly coincident, and the value, 28.0 cal/mole/deg, for $TiF_4$(s) at 500°K was taken to be 1 cal/mole/deg less than the corresponding $TiCl_4$ value to allow for the smaller mass of the fluorine. The resulting $\Delta C_p = -5.1$ was taken as the average over the range of the data.

The spoon-gauge and Ruff-Fischer data, representing four separate samples, were subjected to a Σ-calculation yielding the following results for

$TiF_4$(s) = $TiF_4$(g):[3]

$\overline{\Delta C_p} = -5.1$ (estimated)

$\log P_{atm.} = -5331.51/T - 2.567 \log T + 16.631$

$P$ = 1 atm at 556.3°K, 283.1°C

$\Delta H_{298.2} = 22.87 \pm 0.28$ kcal

$\Delta H_{556.3} = 21.55 \pm 0.28$ kcal

$\Delta S_{298.2} = 41.92 \pm 0.40$ e. u.

$\Delta S_{556.3} = 38.74 \pm 0.40$ e. u.

The uncertainties attached to the experimental heats and entropies of vaporization represent the differences in the values resulting from individual treatment of the data from Runs A and B. The deviations of the experimental data from the equation obtained above are shown in Fig. 2.

[2] The multiplicities are given in brackets.

[3] Vapor density determinations by Ruff and Plato (15) show that $TiF_4$ vapor is monomeric at 444°C.

The extrapolated temperature at which the vapor pressure equals one atmosphere may be compared with the value, 284°C, reported by Ruff (1).

The standard entropy of $TiF_4(s)$ may be obtained by combining the above data with the standard entropy of $TiF_4(g)$ at 298.2°K which can be estimated with reasonable certainty. The rotational contribution to the entropy was calculated by estimating a value of $1.8 \times 10^{-8}$ cm for the Ti-F distance from comparison of the tetrahalides of carbon, silicon, and titanium. The vibrational frequencies for $TiF_4$ estimated above were used to calculate the vibrational contribution to the entropy.

The calculations give for $TiF_4(g)$:

$$S^\circ_{298.2} = 73.2 \text{ e. u.}$$

which may be combined with the above value for the entropy of sublimation to give for $TiF_4(s)$:

$$S^\circ_{298.2} = 31.3 \text{ e. u.}$$

### Acknowledgment

The authors are grateful for the help and interest of the Office of Naval Research who supported this work under Contract Nonr-1120(00) as part of their program on the extractive metallurgy of titanium.

Manuscript received Oct. 14, 1957. This paper was prepared for delivery before the Cleveland Meeting, Sept. 30-Oct. 4, 1956.

Any discussion of this paper will appear in a Discussion Section to be published in the December 1958 JOURNAL.

REFERENCES

1. O. Ruff and W. Plato, *Ber.*, **37**, 673 (1904).
2. O. Kubaschewski and E. L. L. Evans, "Metallurgical Thermochemistry," 2nd ed., p. 150, John Wiley & Sons, Inc., New York (1956).
3. W. H. Rodebush and A. L. Dixon, *Phys. Rev.*, **26**, 851 (1925).
4. J. Willard, *J. Am. Chem. Soc.*, **57**, 2328 (1935).
5. O. Ruff and B. Bergdahl, *Z. anorg. chem.*, **106**, 76 (1919).
6. W. Fischer and O. Rahlfs, *ibid.*, **205**, 1 (1932).
7. K. A. Sense, J. J. Snyder, and R. B. Filbert, Jr., *J. Phys. Chem.*, **58**, 995 (1954).
8. E. F. Fiock and W. H. Rodebush, *J. Am. Chem. Soc.*, **48**, 2522 (1926).
9. L. Brewer and A. W. Searcy, *J. Chem. Ed.*, **26**, 548 (1949).
10. K. K. Kelley, U. S. Bureau of Mines Bull. No. 477 (1950).
11. M. L. Delwaulle and F. Francois, *Compt. rend.*, **220**, 173 (1945).
12. F. D. Rossini, "Chemical Thermodynamics," Chap. 19, John Wiley & Sons, Inc., New York (1950).
13. K. K. Kelley, Quarterly Status Report to ONR from U. S. Bureau of Mines, Project NR 037-054, July-September 1955.
14. W. M. Latimer, *J. Am. Chem. Soc.*, **44**, 90 (1922).
15. O. Ruff and W. Plato, *Ber.*, **37**, 677 (1904).

# Mechanisms of Hydrogen Producing Reactions on Palladium

## V. The Deuterium-Palladium System

**Sigmund Schuldiner and James P. Hoare**[1]

*U. S. Naval Research Laboratory, Washington, D. C.*

ABSTRACT

Anodic and cathodic polarization curves for the $\alpha$-Pd-D system were determined on a palladium bielectrode. The equilibrium potential of the $(Pd\text{-}D)_\alpha/D^+$ electrode was observed as $+0.029 \pm 0.001$ v vs. the $Pt/D_2$, $D^+$ reference electrode (Stockholm sign convention), in good agreement with the thermodynamic data of Gillespie and Downs (2). The rate constant $di/d\eta$ of the over-all deuterium-producing reaction on an $\alpha$-Pd-D electrode surface in the linear $\eta$ vs. $i$ region was found to be about one-half that of the hydrogen-producing reaction on $\alpha$-Pd-H. In this region, and at constant overvoltage, the rate of transport of protons through the bielectrode was 1.7 times faster than that of deuterons. It was also found that at low current densities 90% of the deuterium formed on the cathode side migrated through the bielectrode and was ionized on the anode side.

For a $\beta$-Pd-D cathode-diaphragm, it was shown that the reaction mechanisms were the same as for a $\beta$-Pd-H diaphragm. A calculation was made which showed that at a given atomic concentration gradient the rate of diffusion of hydrogen through a $\beta$-Pd diaphragm was $2\frac{1}{2}$ times faster than that of deuterium.

It was also shown that on a simple $\beta$-Pd-D cathode the rate of deuterium production was about one-fourth the rate of hydrogen production on a $\beta$-Pd-H cathode. This agrees with the separation factor of 4 found by Farkas (8).

An extensive investigation of the hydrogen-producing reactions on palladium was carried out at this laboratory. These studies have led to a detailed discussion of the mechanisms and thermodynamic properties of the hydrogen-palladium system. It was felt that a supplementary study of the deuterium-palladium system would provide an interesting comparison and would also add to a more complete understanding of the electrochemical properties of such systems.

[1] Present address: Ford Scientific Laboratory, Ford Motor Company, Dearborn, Michigan.

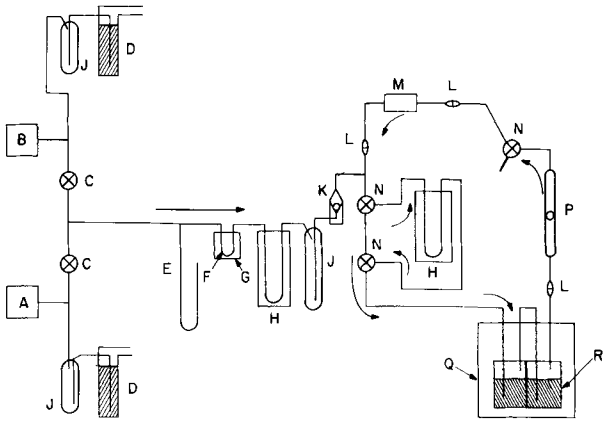


Fig. 1. Gas purification and circulation system: A, deuterium cylinder; B, helium cylinder; C, needle valve; D, mercury safety trap; E, manometer; F, palladium catalyst; G, electric heater; H, liquid nitrogen trap; J, safety trap; K, check valve; L, frittered-glass disc; M, "aquarium type" circulating pump; N, three-way stopcock; P, flowmeter; Q, polyethylene sealed box; R, electrolytic cell.

## Palladium Bielectrode

### *Experimental*

The experimental technique was the same as that used for the study of the bielectrode in the $\alpha$-Pd-H system (1) with the following modifications. In order to conserve deuterium gas a closed system was used as shown in Fig. 1. The deuterium gas was circulated with a specially constructed stainless-steel "aquarium-type" circulating pump. To protect the cell from contaminants and to prevent acid spray from reaching the pump, frittered glass discs were inserted in the inlet and outlet sides of the cell. Further protection was given by placing the pump about 3 ft above the cell.

The deuterium gas and deuterium oxide were obtained from the Stuart Oxygen Company and were better than 99.5% pure. Sulfur trioxide was prepared in an all-glass apparatus by dehydrating fuming sulfuric acid with phosphorus pentoxide (both chemicals were of reagent quality). The sulfur trioxide was distilled and condensed in deuterium oxide. In all the following experiments a $2N$ solution of deuterium sulfate in deuterium oxide was used. A 0.002-in. thick palladium foil was used as the bielectrode. Purified deuterium gas was circulated through the deuterium sulfate solution.

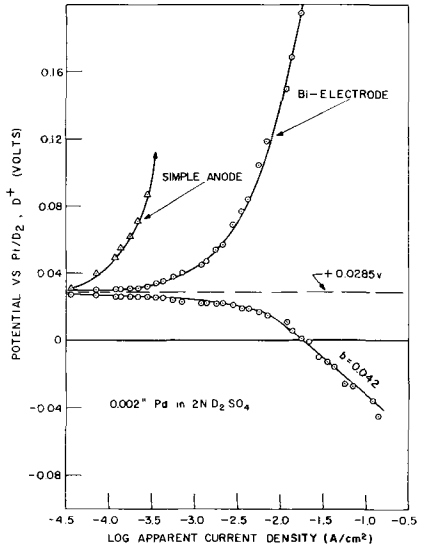


Fig. 2. Overvoltage measurements on the anode and cathode sides of a palladium bielectrode.

The following procedure was used. Before adding the $2N$ $D_2SO_4$ to the rigorously cleaned Teflon cell, the cell and the entire system was thoroughly dried by circulating purified, liquid nitrogen-dried-helium[2] through it for at least 24 hr. Deuterium sulfate solution was then added to only one compartment of the cell. The solution was pre-electrolyzed overnight and the palladium foil was cleaned by anodization under an atmosphere of helium. Deuterium gas was then passed through the system until the helium was flushed out, after which the system was closed and the circulating pump turned on. Small losses of deuterium gas were replaced by manually maintaining a positive pressure of 1 to 2 mm of mercury above atmospheric on the system.

The side of the palladium foil in the compartment containing the deuterium sulfate solution was made a simple anode. The anodic polarization curve was then determined. The average of three runs are shown in Fig. 2.

Deuterium sulfate solution was then added to the second compartment, the solution was pre-electrolyzed overnight and that side of the palladium foil was cleaned by anodization. Both compartments were stirred with deuterium gas until the open-circuit reversible potential of the palladium/deuterium system was reached.. This value at 32° ± 2°C was +0.029 ± 0.001 v. vs. the $Pt/D_2$, $D^+$ reference electrode in the same solution (Stockholm sign convention). Overvoltage data were then obtained exactly as before (1). Average results are shown in Fig. 2. The experimental points were reproducible to within ±2.5 mv.

### *Discussion*

The anodic and cathodic polarization curves for the $\alpha$-Pd-D system were very similar to those for the $\alpha$-Pd-H system. This indicated that the electrode mechanisms were the same as before (1). Gillespie and Downs (2) determined the pressure-concentration isotherms of the deuterium-palladium system, and gave the temperature dependence of the partial pressure $P$ of deuterium (in atmospheres) at the plateau (two-phase region) as $\log P_{atm} = 4.633 - 1696.11/T$. At 32°C, the plateau pressure of deuterium is 0.117 atm.

From the thermodynamic data, the equilibrium potential for the system

$$D^+ + e^- = \frac{1}{2} D_2(0.117 \text{ atm})$$

at 32°C referred to a $Pt/D_2$(0.11 atm) electrode in the same solution is $E = -(RT/2F) \ln 0.117 = 0.028$ v. The equilibrium isotherm of the deuterium-palladium systems at 32°C (Fig. 3) shows that the maximum $\alpha$-phase composition is attained at a partial pressure of 0.117 atm. By analogy to the $\alpha$-Pd-H system (3), an equilibrium is expected between deu-

[2] For the drying procedure, the liquid nitrogen trap in the circulation loop shown in Fig. 1 was used to dry the cell. During a run, this trap was removed from the system with stopcocks N.

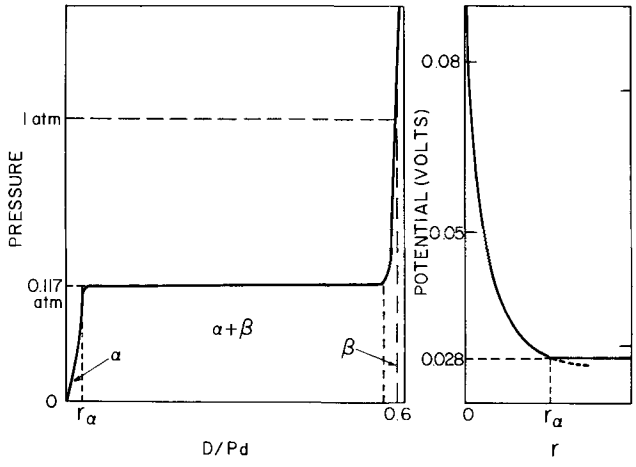


Fig. 3. (left) Phase diagram for the $Pd/D_2$ system; (right) potential-composition diagram for the $Pd/D_2$ system (r = atomic ratio D/Pd).

terium ions in solution and deuterium dissolved in the palladium, independent of the partial pressure of deuterium gas. Here $D^+ + e^- = (Pd\text{-}D)_\alpha$ is the potential determining reaction. The observed reversible potential of +0.029 v for the Pd-D system compared to a $Pt/D_2$ reference electrode in the same solution saturated with gaseous deuterium at one atmosphere pressure can be considered as the equilibrium potential for this reaction for the maximum deuterium concentration in the α-Pd-D system. Figure 3 shows the potential vs. D/Pd relationship.

At low current densities there is a linear relation between current density and anodic and cathodic overvoltages (Fig. 4). The slope $d\eta/di$ for the α-Pd-D system is twice as large as that for the α-Pd-H system. The reciprocals of these slopes measure the rate constants of the over-all electrode processes (4). For hydrogen $di/d\eta$ is 0.143 amp/cm² volt while for deuterium it is 0.065 amp/cm² volt. This shows that the catalytic activity of α-palladium for the hydrogen-producing reaction is about twice that for deuterium-producing reactions. The fact that the anodic and cathodic overvoltage for the deuterium forms a continuous linear curve which passes through the point of zero current at 0.0285 v indicates that, as in the case of the hydrogen system, the palladium/deuterium electrode is reversible.

From Fig. 2 a comparison of the simple anode curve with the anode side of the palladium bielectrode in the low current density range can be made. For a given overvoltage a difference in the current density values represents the amount of depolarizing current which flows through the palladium bielectrode. This depolarizing current is a deuteron current density, to be designated by $j$, which represents the amount of deuteron current density necessary to reduce the overvoltage of a simple anode to the same value as that found on the anodic side of the bielectrode. A plot of $j$ vs. $i$ is given in Fig. 5, where $i$ is the applied current density on the bielectrode, and obeys the linear relation $j_D = 0.9i_D$. For the hydrogen system (1), the same relation is $j_H = 0.7i_H$. The difference in the transfer coefficients of the hydrogen and deuterium systems is due to the fact that the rate constant of the hydrogen-producing reaction on the α-palladium surface is about twice that of the deuterium-producing reaction in the linear $i$ vs. $\eta$ range. Since atoms are removed on a palladium bielectrode by surface reaction to form gaseous molecules and by diffusion through the metal to the anode side, and since the surface reaction is slower for deuterium than for hydrogen, then at a given current density, more deuterium diffuses through the metal than does hydrogen. This is shown by the increase in value of the transfer coefficient for deuterium. These results indicate that the magnitude of the transfer coefficient is determined by the rate of the surface reaction.

It is possible to find a set of conditions for 100% transmission of hydrogen or deuterium through a palladium bielectrode. An experiment to show this was carried out as follows. In 2$N$ $H_2SO_4$ solutions, bielectrode measurements were made as before, except that the solutions were stirred with helium rather than hydrogen. A simple palladium anode in a helium-stirred solution is completely polarizable, that is, there is no hydrogen oxidation reaction because the partial pressure of this gas is nil and the potential rises as the double layer in the ideally polarized electrode becomes charged to a point where an oxygen or oxide-producing reaction takes place. This can be seen in Fig. 6.

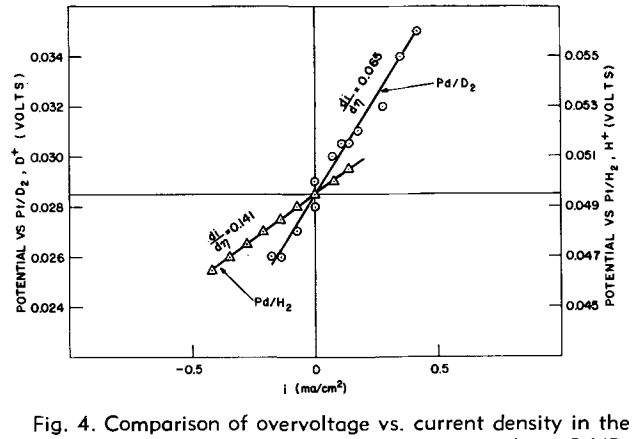


Fig. 4. Comparison of overvoltage vs. current density in the anodic and cathodic low current density region for α-$Pd/D_2$ and α-$Pd/H_2$ systems in 2N $D_2SO_4$ and $H_2SO_4$ solutions. Positive currents are anodic, negative, cathodic.

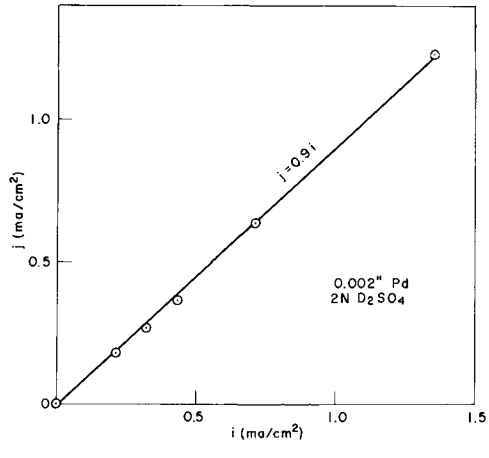


Fig. 5. Relationship between the diffusion current density, j, and the applied current density, i, on a palladium bielectrode in 2N $D_2SO_4$ solution.

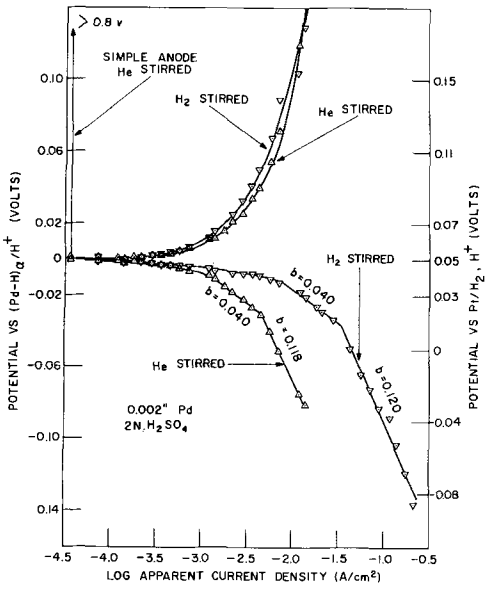


Fig. 6. Effect of replacing $H_2$ with He stirring on the overvoltage on the anode and cathode sides of a palladium bielectrode.

Since the anode side of the bielectrode in helium-stirred solution is not completely polarizable, the oxidation reaction must consist of the ionization of hydrogen atoms. The cathode and anode sides of the bielectrode being in series demands that all of the atoms formed on the cathode side be transferred to the anode side, otherwise there would be an unbalanced reversible electrode system and part of the oxidation reaction on the anode side would result in the formation of oxide or oxygen with a resulting large increase in the polarization. The fact that at low current densities the anodic branch is the same as that for hydrogen flowing through the cell means that there is a negligible oxygen-producing reaction. Hence it must be concluded that, in the case of helium flow through the compartments, $j = i$.

In the low current density range the relations between the depolarizing proton or deuteron current densities and the ratio of their rate constants when $\eta_D = \eta_H$ can give a measure of the relative transport rates of deuterons and protons. Since $j_H/j_D = 0.7i_H/0.9i_D$ and $di_H/di_D = 2.2$ for $2N$ $H^+$ and $D^+$ solutions, protons will migrate through Pd 1.7 times faster

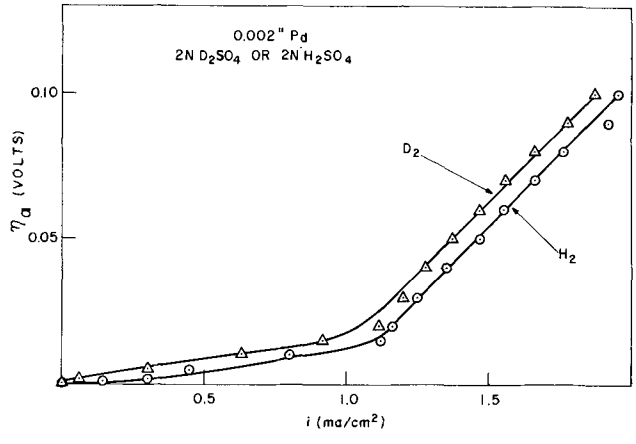


Fig. 7. Comparison of anodic polarization curves of the $Pd/H_2$, $H^+$ system with the $Pd/D_2$, $D^+$ system.

than deuterons in these solutions. Under these conditions the polarization on both the anode and cathode sides for both the $D_2$ and $H_2$ systems is small and of comparable magnitude. Hence it can be considered that these relative migration rates are essentially per unit of potential gradient.

In a previous paper (1), it was postulated that the rate of transport of hydrogen through the bielectrode was controlled by the rate of entry (solution) into or exit of hydrogen atoms from the interior of the metal through its skin. It would then follow that in these $2N$ acid solutions hydrogen dissolves in Pd about 1.7 times faster than deuterium. A comparison of the anodic bielectrode polarization curves for the H and D systems on the same Pd bielectrode is shown in Fig. 7. These curves show that the overvoltage at a given current density is always higher for the $D_2$ system. This is so because the activation energy for the ionization of molecular $H_2$ is lower.

The cathode branch in Fig. 6 is of interest because it shows that the mechanisms are the same as for the case of hydrogen flow. In addition, it should be noticed that, in comparison to a cathode curve with hydrogen flow, the Tafel, b = 0.12, slope is reached at a considerably lower current density. This may be explained as follows: In the case of hydrogen flow, hydrogen gas is oxidized to hydrogen ions at the Pt anode, but when the solution is stirred with helium, oxygen is formed at this anode. The oxygen is rapidly transferred to the cathode side of the Pd bielectrode where it poisons the hydrogen-producing reaction with the result that the 0.12 slope is reached at a relatively low current density. The effect of oxygen poisoning on the change in slope is explained in reference (1). These results support the oxygen poisoning mechanism postulated there.

A few measurements were made in a helium-stirred deuterium sulfate solution which indicated that this system was analogous to the sulfuric acid system.

It should be mentioned that the reversible hydrogen or deuterium reference electrode used in the above helium-flow experiments was one which was independent of hydrogen or deuterium partial pressure. It was shown in this laboratory (3) that the potential-determining reaction on an $\alpha$-hydrogen-palladium electrode is $H^+ + e^- = (Pd\text{-}H)_\alpha$. Similarly it was indicated above that an analogous potential-determining reaction holds in deuterium solutions. Hence a reference electrode can be prepared by placing a palladium wire in hydrogen or deuterium solution and passing their respective gases through the solution until the maximum hydrogen or deuterium concentration in the $\alpha$-phase is reached. It has been shown (5) that under these conditions hydrogen will be spontaneously absorbed in the palladium until this maximum $\alpha$-phase is reached, at which time the rate of solution of hydrogen in the metal becomes immeasurably slow. These reference electrodes were very suitable for the helium-stirred solutions since they are very stable, reproducible, and are independent of the partial pressure of either hydrogen or deuterium. In addition, they represent the reversible electrode systems for the $\alpha$-palladium-

hydrogen or -deuterium electrodes at zero current density. Using these reference electrodes to measure polarization gives the displacement from the reversible condition directly and, hence, the overvoltage of the $\alpha$-palladium electrodes.

## Palladium Diaphragm

### *Experimental*

As before (6), the palladium cathode was in the form of a diaphragm separating two isolated bodies of the same solution ($2N$ $D_2SO_4$). The current density-overvoltage relations of the polarization and diffusion sides of the diaphragm were determined with deuterium gas flowing through each compartment of the cell as described above (*see* Fig. 1).

The experimental technique was the same as reported in reference (6) with the exception that the reference electrodes were $Pt/D_2$ electrodes in the same solution. The temperature was 34°C. The thickness of the palladium foil was 0.002 in.

The average results of a run in which the current was alternately decreased and then increased for three cycles is given in Fig. 8. The reproducibility of the points was within ±2 mv.

### *Discussion*

Figure 8 shows that the shape of the polarization, $\eta_p$, and the diffusion, $\eta_d$, overvoltage vs. log $i$ curves was the same as for the corresponding $\beta$-Pd-H system. However, since it was postulated (6) that a diffusion mechanism controls the overvoltage on the diffusion side, one would expect that the rate of diffusion of deuterium through the diaphragm should be $(\frac{1}{2})^{\frac{1}{2}}$ times the hydrogen rate, at equal atomic concentration gradient, since the mass of deuterium is twice that of hydrogen. This was verified as follows: the potentials considered are diffusion overvoltages and no current flows on the diffusion side of the diaphragm; it can therefore be assumed that the concentration of $H^+$ in the double layer is constant for the potential-determining reactions on the diffusion side. These are

$$H^+ + e^- = H$$
$$H + H = H_2$$

Both steps are virtually at equilibrium and the Nernst potential equation can be used to approximate the activity of hydrogen atoms. Since,

$$E_{Pt} = E^\circ + (RT/F) \ln (H^+)/(H_o)$$

and

$$E_{Pd} = E^\circ + (RT/F) \ln (H^+)/(H)$$

then by definition,

$$(\eta_d)_H = E_{Pd} - E_{Pt} = -(RT/F) \ln (H)/(H_o)$$

and at 34°C,

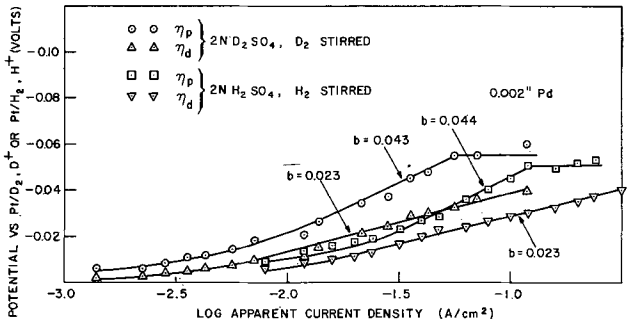


Fig. 8. Hydrogen and deuterium cathodic overvoltage curves on the polarization and diffusion sides of a palladium diaphragm.

$$(\eta_d)_H = -0.060 \log (H)/(H_o) \qquad (I)$$

Similarly for the deuterium-palladium electrode:

$$(\eta_d)_D = -0.060 \log (D)/(D_o) \qquad (II)$$

$(H_o)$ and $(D_o)$ are the activities of hydrogen and deuterium atoms on the respective platinum reference electrodes; (H) and (D) are the activities of these atoms on the diffusion side of the $\beta$-palladium diaphragm. Even though no electrolytic current flows on the diffusion side there is an effective atomic diffusion current density through the palladium which causes a polarization of this side of the palladium diaphragm because the concentration of hydrogen or deuterium atoms is a function of the current flow on the polarization side.

At a given current density the $(\eta_d)_H$ and the $(\eta_d)_D$ were determined from the curves in Fig. 8. By using relations (I) and (II), the ratio $(D)/(D_o) : (H)/(H_o)$ was determined. This ratio represents the relative rates of deuterium flow to hydrogen flow. If one assumes that the same relation between the atomic diffusion current density, $\bar{j}$, and the polarizing current density, $i$, found in (6) holds for the deuterium system, then, for a 0.002-in. diaphragm in $2N$ $D_2SO_4$:

$$\bar{j}_D = k_D\, i^{0.53} \qquad (III)$$

From (6) $k_H$ is known and therefore $\bar{j}_H$ can be calculated. The ratio $(D)/(D_o) : (H)/(H_o)$ multiplied by $\bar{j}_H$ gives $\bar{j}_D$, then $k_D$ can be found from Eq. (III). Data used for two determinations of $k_D$ are shown in Table I.

Because of the high concentration of $H^+$ or $D^+$ in their $2N$ solutions, the difference in the polarization and diffusion overvoltages in the Tafel b = 0.04 range essentially represents the concentration gradient of hydrogen or deuterium atoms across the diaphragm. From Fig. 8 the polarization current densities, $i_H$ and $i_D$, can be determined for any given $\Delta\eta = \eta_p - \eta_d$. From these polarization current densities,

Table I. Calculation of $k_D$

| log $i$ | $\eta_H$ | $\eta_D$ | $(H)/(H_o)$ | $(D)/(D_o)$ | $\frac{(D)/(D_o)}{(H)/(H_o)}$ | $\bar{j}_H$ | $\bar{j}_D$ | $k_H$ | $k_D$ |
|---|---|---|---|---|---|---|---|---|---|
| −1.4 | −0.019 | −0.028 | 2.073 | 2.929 | 1.41 | 0.0197 | 0.0278 | 0.109 | 0.154 |
| −1.0 | −0.0285 | −0.0375 | 2.986 | 4.217 | 1.41 | 0.0321 | 0.0452 | 0.109 | 0.154 |

Table II. Calculation of $\bar{j}_H/\bar{j}_D$

| $\Delta\eta$ | log $i_H$ | log $i_D$ | $\bar{j}_H$ | $\bar{j}_D$ | $\bar{j}_H/\bar{j}_D$ |
|---|---|---|---|---|---|
| 0.018 | —0.90 | —1.46 | 0.0363 | 0.0259 | 1.40 |
| 0.015 | —1.04 | —1.61 | 0.0306 | 0.0216 | 1.42 |
| 0.012 | —1.2 | —1.76 | 0.0251 | 0.0180 | 1.40 |
| 0.010 | —1.3 | —1.86 | 0.0223 | 0.0159 | 1.40 |

the atomic diffusion current densities, $\bar{j}_H$ and $\bar{j}_D$, can be determined. These values and their ratio are given in Table II. The ratio $\bar{j}_H/\bar{j}_D$ is equal to 1.4 for the cases where the concentration gradients of these respective atoms across the diaphragm are the same. This is approximately equal to $2^{1/2}$, the value predicted by classical diffusion laws. This result supports the postulate that the overvoltage mechanism on the diffusion side of the diaphragm is controlled by the diffusion of either hydrogen or deuterium atoms, respectively.

It is interesting to note that, as shown in Table I, at a given current density in the Tafel b = 0.04 range, the rate of flow of deuterium across the diaphragm is 1.41 times faster than the rate of flow of hydrogen. This can be explained if the deuterium combination reaction on the polarization side is slower than the hydrogen combination reaction. As a result, for a given current density there will be a larger concentration gradient for deuterium than for hydrogen and consequently the deuterium will flow through the diaphragm at a faster rate. From the experimental data on the bielectrode it is seen that, since the cathodic overvoltage for the deuterium-palladium system is consistently higher than that for the hydrogen-palladium system at the same current densities, the rate of removal of deuterium atoms is appreciably slower than that of hydrogen atoms. This offers supporting evidence for results found on the diaphragm. Additional evidence is given below.

## Simple Palladium Cathode

### *Experimental*

In this series of experiments the same clean palladium bead (electrolytically charged to the $\beta$-phase) of apparent area 0.0274 cm² was cathodized in pre-electrolyzed 2*N* $D_2SO_4$ in $D_2O$, 50% 2*N* $D_2SO_4$ in $D_2O$ + 50% 2*N* $H_2SO_4$ in $H_2O$, and 2*N* $H_2SO_4$ in $H_2O$, respectively. During all these runs, a flow of purified hydrogen ($H_2$) was passed through the cell. Within our experimental time limits (<24 hr) the exchange between $H_2$ and $D^+$ is negligible because of the relatively small area of exposed metal surface. The reference electrode was always a platinum electrode in the same solution. The temperature was 30° ± 2°C. The experimental details were the same as those described in earlier work (7). The cathodic overvoltage curves obtained are shown in Fig. 9. Figure 10 shows the overvoltage vs. $i$ relationship at low current densities. In all cases the palladium bead was electrolytically charged with hydrogen or deuterium to the $\beta$-phase before overvoltage measurements were taken.

### *Discussion*

The curves in Fig. 9 indicate that the mechanisms for the deuterium-producing reactions are the same as those described for hydrogen (7). As hydrogen ion is replaced with deuterium ion the exchange current, $i_o$, for the b = 0.04 range, is decreased and the value of the overvoltage plateau increases. Figure 10 shows that as the deuterium concentration is increased the rate constant, $-di/d\eta$, decreases in about a linear fashion. The ratio of the rate constants for pure $H^+$ compared to pure $D^+$ is about 4:1 which gives a separation factor consistent with that found by other investigators (8). All of these results confirm the findings above that the catalytic activity of palladium for hydrogen-producing reactions is greater than for deuterium-producing reactions.

These results contradict the conclusion of Farkas (8) that the rate of the removal of deuterium atoms from the palladium cathode is faster than the removal of hydrogen atoms to form molecules. His conclusion may be considered to be in error for the following reasons. Farkas assumed that the removal of atoms from the palladium surface was by combination, whereas our work has shown that removal is normally both by combination and electrochemical desorption. In strong acid solutions, electrochemical desorption predominates. His experimental results are actually consistent with our findings. If hydrogen is generated four times faster than deuterium on the cathode (as shown in Fig. 10) and if it dissolves in palladium 1.7 times faster than deuterium (as shown above), then the ratio H/D dis-

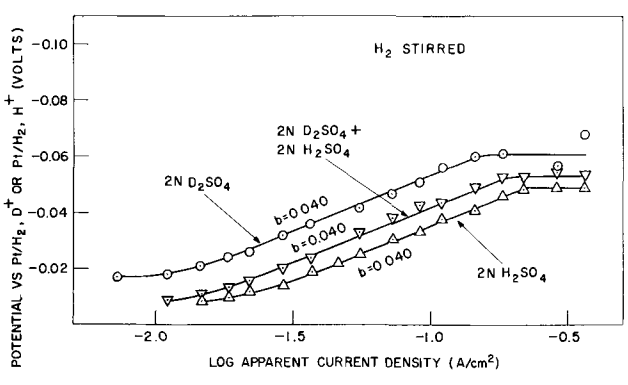


Fig. 9. Hydrogen, deuterium, and a 50-50 mixture overvoltage curve for a simple palladium cathode.

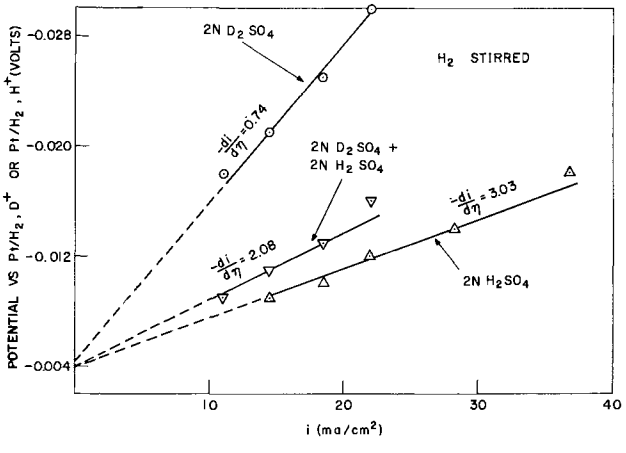


Fig. 10. Comparison of the relative rates of the hydrogen- and deuterium-producing reactions at a $\beta$-palladium cathode.

solved in the Pd is about 6.8. This compares favorably with the experimental value of 6.6 found by Farkas.

## Conclusions

1. The electrochemical mechanisms of deuterium-producing reactions on Pd are the same as those of the hydrogen-producing reactions on Pd. This statement holds true for the cases where the Pd was investigated as a bielectrode, as a cathode diaphragm, or as a simple cathode.

2. In all cases it is found that the catalytic activity of Pd is greater for $H_2$-producing reactions than for $D_2$-producing reactions.

3. It was found that: (*a*) in the linear $\eta$ vs. $i$ range $H_2$ is produced at an $\alpha$-Pd cathode about twice as fast as $D_2$; (*b*) in 2*N* acid solutions hydrogen ions are transferred through a Pd bielectrode 1.7 times faster than deuterium ions in the very low current density range; (*c*) in the linear $\eta$ vs. $i$ range $H_2$ is produced at a $\beta$-Pd cathode about 4 times faster than $D_2$; (*d*) for a given polarizing current density, H diffuses (in the Tafel b = 0.04 region) through a Pd diaphragm 1.41 times slower than D (because of item 2 above); (*e*) For a *given value* of $\Delta\eta = \eta_p - \eta_d$ (same atomic concentration gradient across diaphragm) H diffuses through a Pd diaphragm $2^{1/2}$ times faster than D.

4. An $\alpha$-Pd electrode is a stable and acceptable reversible atomic hydrogen reference electrode for systems in which $H_2$ or $D_2$ gas is not available and in which oxidizing agents are absent.

## Acknowledgments

The authors are indebted to Dr. J. C. White for many helpful discussions. They also wish to thank Professor R. A. Marcus of the Brooklyn Polytechnic Institute for his valuable comments.

Manuscript received Feb. 26, 1957. This paper was prepared for presentation before the New York Meeting, April 27-May 1, 1958.

Any discussion of this paper will appear in a Discussion Section to be published in the December 1958 JOURNAL.

## REFERENCES

1. J. P. Hoare and S. Schuldiner, *This Journal,* **104** 564 (1957).
2. L. J. Gillespie and W. R. Downs, *J. Am. Chem. Soc.,* **61**, 2496 (1939).
3. S. Schuldiner, G. W. Castellan, and J. P. Hoare, *J. Chem. Phys.,* **28**, 16 (1958).
4. P. Dolin, B. Ershler, and A. Frumkin, *Acta Physicochim. USSR,* **13**, 782 (1940).
5. J. P. Hoare, S. Schuldiner, and G. W. Castellan, *J. Chem. Phys.,* **28**, 22 (1958).
6. J. P. Hoare and S. Schuldiner, *This Journal,* **103**, 237 (1956).
7. J. P. Hoare and S. Schuldiner, *ibid.,* **102**, 485 (1955).
8. A. Farkas, *Trans. Faraday Soc.,* **33**, 552 (1937).

# Uncommon Valency Ions and the Difference Effect

**M. E. Straumanis**

*Department of Metallurgy, University of Missouri School of Mines and Metallurgy, Rolla, Missouri*

ABSTRACT

It is shown that in evaluating the rates of anodic dissolution processes it is necessary to consider the influence of the positive and negative difference effects; otherwise ions going into solution with uncommon valency may be found. Scale fragments detached from an aluminum anode by the current passing through it could be seen. The hypothesis of valence change of ions while a current is passing through the anode does not explain all observed facts, but they can be well explained by the theory developed for the positive and negative difference effects.

It has been found not only in the past but also recently that in certain anodic processes ions with an uncommon valency went into solution. For instance, the formation of monovalent Mg ions, which subsequently reacted with water under hydrogen evolution, has been discussed (1-3). Occasionally an increase of the charge of ions going anodically into solution could also be calculated.

To study the anodic dissolution phenomena and the valency of ions formed anodically, a very simple device can be used (Fig. 1). The driving force of the cell is provided by the anodic metal itself. In the case of a Mg or Al anode one easily can observe that, on closing the switch of the circuit, hydrogen evolution starts not only at the Pt cathode, but also at the anode (or the rate of evolution increases at the anode). If the current is then turned off, $H_2$ evolution ceases, or decreases strongly, at both electrodes. However, quantitative measurements show that the total amount of $H_2$ developed and the weight loss of the anode is larger than that calculated from the current by Faraday's law. It was concluded from this that the anodic metal went into solution with lower valency (1-4).

Two explanations have been proposed for this effect: (*a*) the lower or changed valency hypothesis, which explains the simultaneous $H_2$ development on the cathode and anode, for instance in case of Mg:

$$\text{Anode: } Mg \rightarrow Mg^+ + e$$
$$Mg^+ + H^+ \rightarrow Mg^{2+} + \tfrac{1}{2}H_2$$
$$\text{Cathode: } e + H^+ \rightarrow \tfrac{1}{2}H_2$$

but does not explain the larger total amount of $H_2$

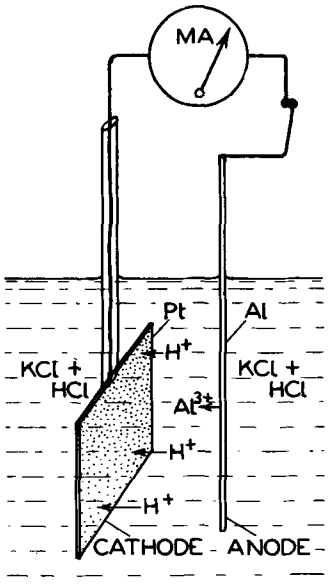


Fig. 1. Device to observe the negative and positive Δ effects

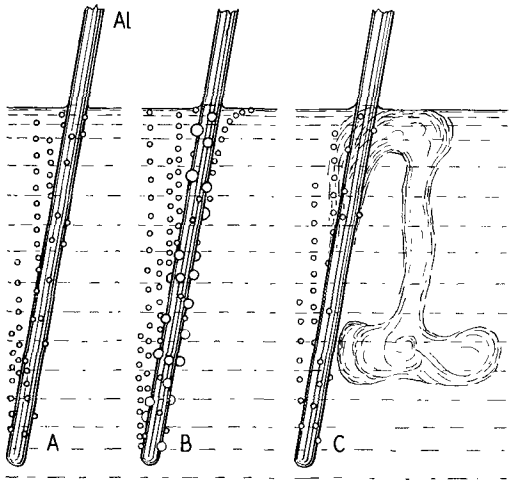


Fig. 2A. Aluminum wire as an anode in a KCl-HCl solution with the switch (Fig. 1) open. Fig. 2B. The self-dissolution of the Al wire increases with the switch closed. Fig. 2C. After interruption of the current, $H_2$ evolution decreases and a cloud of white dust, sinking down, appears.

developed; (b) the difference (Δ) effect theory explains all the phenomena observed (5-8) and besides the development of hydrogen in addition to that produced by the current flowing through the cell, Fig. 1. Unfortunately, the Δ-effect was not taken into consideration by the previous investigators (1-4) and formation of lower valency ions was assumed.

According to the theory of the negative Δ-effect (8) the very active metals (Mg, Al, Ti) react with the electrolyte (self-dissolution) in places where the protective scale is broken off from their surface. The scale can be spalled off the metal, more or less completely by passing an anodic current through the surface of the metal. If this current is interrupted the scale regenerates more or less slowly and rate of self-dissolution reduces or even ceases. All the phenomena observed are explained by this mechanism including the reducing power of the anolyte (9) during passage of the current. In case of Mg reaction in a KCl solution, the external current produces the soluble and the self-dissolution reaction (on the stripped areas of the metal) the insoluble reaction products. As the extension of these areas is roughly proportional to the anodic current (9), the ratio of the insoluble and of the soluble products is nearly constant. Occasionally, depending on the purity of the Mg, this ratio may approach 1:1, a possibility overlooked by Tomashov (10).

However, the stripping of the scale by the passing anodic current needs some additional evidence. The appearance of scale fragments can easily be observed by a device shown in Fig. 1, if, as anodic metal, an Al wire and, as an electrolyte, KCl (about 100 g/l) dissolved in an about 0.1*N* HCl solution are used. Observing the wire through a magnifying glass, nearly no development of hydrogen (with the switch open) can be seen (Fig. 2). Upon closing the switch the rate of self-dissolution of the wire clearly increases and fragments of the scale are torn off by the anions going into solution and carried up by the hydrogen bubbles (Fig. 2B). The fragments at that stage are not observable directly. However, they can be noticed as soon as the current is interrupted and the intense hydrogen evolution decreases. The particles now sink down in the form of a cloud of whitish dust (Fig. 2C). The sinking cloud can be observed best when the wire is tilted. Very small hydrogen evolving metallic particles can also be seen floating in the electrolyte, which evidently were separated from the wire together with the scale. The white particles cannot be $Al(OH)_3$ formed later ($Al^{3+} + 3\ OH'$), because the solution was strongly acidic the entire time. Thus, the particles could originate only from the scale which is difficultly soluble in diluted HCl. No such dust clouds could be observed in a solution of HF, evidently because the scale is easy soluble in this acid.

If these arguments are not regarded as being strong enough to disprove the lower valency theory, then there is also a reverse phenomenon, the positive Δ-effect (8-11). Using HF (~0.1*N*) instead of the KCl-HCl mixture one will observe a sudden decrease in the rate of dissolution (Δ-effect) of the Al wire as soon as the circuit (Fig. 1) is closed. However, after interruption of the current, the previous rate will be restored. Having subtracted this self-dissolution rate from the total rate obtained with the current on, one nevertheless will find that less Al went into solution as calculated from the current. This effect of sudden decrease in rate can never be explained by the presence of oxygen in and above the acid. So, disregarding the positive Δ-effect, one has to postulate the formation of Al ions with a valency higher than 3. While Mg or Al ions with a valency lower than the normal are still possible, the formation of ions of higher valency in aqueous solutions is theoretically unreasonable (12). Besides, why, during the passage of an anodic current, should $Al^+$ or $Al^{2+}$ be formed in HCl solutions and $Al^{4+}$ in HF solutions? Ions of uncommon valency [sometimes even lower than one (9)] will always be found in anodic dissolution processes, if the Δ effects influencing the self-dissolution rates are disregarded. Besides, the fact that the effects are

functions of current density has always to be considered. If, after all the corrections for the rates are made, some positive or negative rate being outside the limits of error still remains, this may be attributed to the appearance of ions of uncommon valency.

Manuscript received April 8, 1957. This paper was prepared for delivery before the Washington Meeting, May 12-16, 1957.

Any discussion of this paper will appear in a Discussion Section to be published in the December 1958 JOURNAL.

REFERENCES

1. R. L. Petty, A. W. Davidson, and J. Kleinberg, *J. Am. Chem. Soc.*, **76**, 363 (1954).
2. J. H. Greenblatt, *This Journal*, **103**, 539 (1956).
3. E. H. Phelps, Electrochem. Soc. Cleveland Meeting, Abstr. 61 (1956).
4. P. Brouillet, G. Epelboin, and M. Froment, *C.R.*, **239**, 1795 (1954).
5. A. Thiel and J. Eckell, *Z. Elektrochem.*, **33**, 370 (1927).
6. M. A. Streicher, *J. (and Trans.) Electrochem. Soc.*, **93**, 304 (1948).
7. W. O. Kroenig and V. N. Uspenskaja, *Korrosion u. Metallschutz*, **11**, 10 (1935); **12**, 123 (1936).
8. M. E. Straumanis and Y. N. Wang, *This Journal*, **102**, 304 (1956).
9. M. D. Rausch, W. E. McEwen, and J. Kleinberg, *J. Am. Chem. Soc.*, **77**, 2093 (1954).
10. N. D. Tomashov, V. S. Komissarova, and M. A. Timinova, *Tr. Fiz. Khim. Inst. Akad. Nauk, USSR*, **4**, 172 (1955).
11. M. E. Straumanis and P. C. Chen, *This Journal*, **98**, 351 (1951).
12. *See* also, E. Lange in H. Fischer, K. Hauffe, and W. Wiederholt, "Passivierende Filme und Deckschichten," pp. 385, 387, Springer-Verlag, Berlin (1956).

# Technical Note

## A Technique for Purifying Electrolytic Solutions

**D. A. Vermilyea**

*Research Laboratory, General Electric Company, Schenectady, New York*

One of the most difficult problems which arises in studies of surface reactions in solutions is that of contamination by adsorbed impurities. Vahramian (1) suggested a method for rendering ineffective the impurities responsible for the passivation[1] of silver electrodes in nitrate solutions, and it may be that the same method is applicable in other situations. It therefore seemed worthwhile to verify the method and to call it to the attention of people studying crystal growth and electrode reactions in solutions.

[1] Passivation means prevention of growth or solution of a crystal exposed to a supersaturated or undersaturated medium.

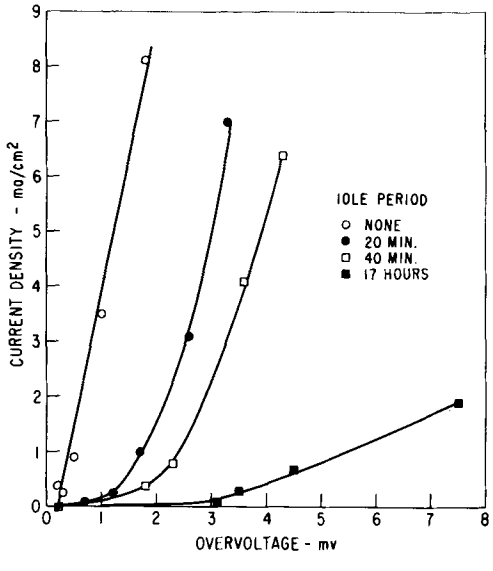


Fig. 1. Electrodeposition from nonoxidized solution

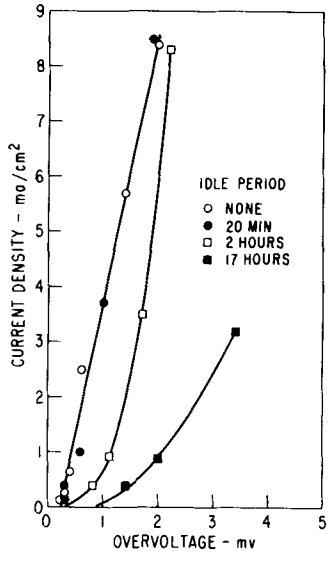


Fig. 2. Electrodeposition from oxidized solution

The suggestion was that the impurities responsible for the passivation of silver electrodes in silver nitrate solutions could be oxidized by bubbling oxygen through the solutions for 24 hr in the presence of platinumized platinum. The temperature recommended by Vahramian was 60°C; the writer has obtained equally good results at 60° and 100°C. Figures 1 and 2 show current voltage curves for

functions of current density has always to be considered. If, after all the corrections for the rates are made, some positive or negative rate being outside the limits of error still remains, this may be attributed to the appearance of ions of uncommon valency.

Manuscript received April 8, 1957. This paper was prepared for delivery before the Washington Meeting, May 12-16, 1957.

Any discussion of this paper will appear in a Discussion Section to be published in the December 1958 JOURNAL.

REFERENCES

1. R. L. Petty, A. W. Davidson, and J. Kleinberg, *J. Am. Chem. Soc.*, **76**, 363 (1954).
2. J. H. Greenblatt, *This Journal*, **103**, 539 (1956).
3. E. H. Phelps, Electrochem. Soc. Cleveland Meeting, Abstr. 61 (1956).
4. P. Brouillet, G. Epelboin, and M. Froment, *C.R.*, **239**, 1795 (1954).
5. A. Thiel and J. Eckell, *Z. Elektrochem.*, **33**, 370 (1927).
6. M. A. Streicher, *J. (and Trans.) Electrochem. Soc.*, **93**, 304 (1948).
7. W. O. Kroenig and V. N. Uspenskaja, *Korrosion u. Metallschutz*, **11**, 10 (1935); **12**, 123 (1936).
8. M. E. Straumanis and Y. N. Wang, *This Journal*, **102**, 304 (1956).
9. M. D. Rausch, W. E. McEwen, and J. Kleinberg, *J. Am. Chem. Soc.*, **77**, 2093 (1954).
10. N. D. Tomashov, V. S. Komissarova, and M. A. Timinova, *Tr. Fiz. Khim. Inst. Akad. Nauk, USSR*, **4**, 172 (1955).
11. M. E. Straumanis and P. C. Chen, *This Journal*, **98**, 351 (1951).
12. *See* also, E. Lange in H. Fischer, K. Hauffe, and W. Wiederholt, "Passivierende Filme und Deckschichten," pp. 385, 387, Springer-Verlag, Berlin (1956).

# Technical Note

## A Technique for Purifying Electrolytic Solutions

**D. A. Vermilyea**

*Research Laboratory, General Electric Company, Schenectady, New York*

One of the most difficult problems which arises in studies of surface reactions in solutions is that of contamination by adsorbed impurities. Vahramian (1) suggested a method for rendering ineffective the impurities responsible for the passivation[1] of silver electrodes in nitrate solutions, and it may be that the same method is applicable in other situations. It therefore seemed worthwhile to verify the method and to call it to the attention of people studying crystal growth and electrode reactions in solutions.

[1] Passivation means prevention of growth or solution of a crystal exposed to a supersaturated or undersaturated medium.

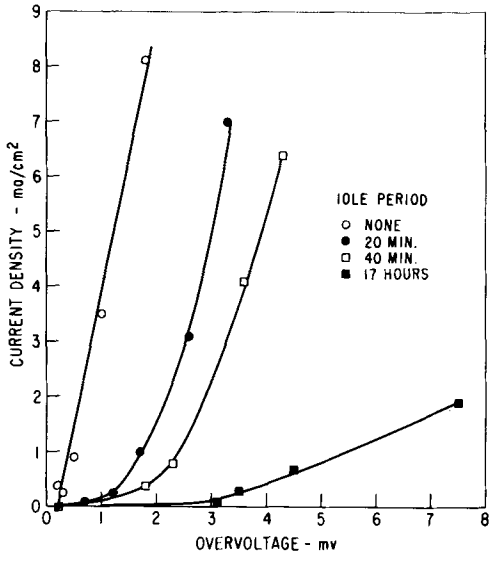


Fig. 1. Electrodeposition from nonoxidized solution

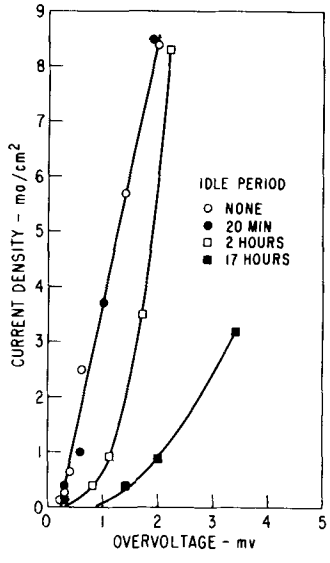


Fig. 2. Electrodeposition from oxidized solution

The suggestion was that the impurities responsible for the passivation of silver electrodes in silver nitrate solutions could be oxidized by bubbling oxygen through the solutions for 24 hr in the presence of platinumized platinum. The temperature recommended by Vahramian was 60°C; the writer has obtained equally good results at 60° and 100°C. Figures 1 and 2 show current voltage curves for

silver electrodes allowed to remain idle for various periods of time in N $AgNO_3$ solutions before and after "oxidation" as suggested by Vahramian. While an idle period of 1 or 2 min resulted in serious passivation in the solution before oxidation, it was possible to leave electrodes idle for periods of at least 30 min in the solution after oxidation without noticeable contamination. Even the electrode left overnight was not as badly contaminated as the one left 20 min in the solution as prepared. The method thus works very well indeed.

This writer has also found that very strong oxidizing treatments, such as boiling the solution after adding $KMnO_4$ or $K_2S_2O_8$, eliminated passivation. These other treatments had undesirable results such as the formation of a precipitate or the formation of divalent silver, and introduced unwanted ions into the bath. For this reason the simple oxidation with oxygen is preferable. Activated alumina and activated charcoal were also tried, both with and without oxygenation, but these treatments did not eliminate passivation. Also, when oxygen free nitrogen or helium (instead of oxygen) was used as the atmosphere in the cell while the solution was heated in contact with platinized platinum passivation was not eliminated. It thus appears that either oxygen plus a catalytic surface or a very strongly oxidizing condition is required to eliminate passivation. It seems likely that the explanation given by Vahramian—that passivation is eliminated in "oxidized" solutions because of the oxidation of organic impurities—is correct.

Manuscript received Dec. 23, 1957.

Any discussion of this paper will appear in a Discussion Section to be published in the December 1958 JOURNAL.

REFERENCE

1. A. T. Vahramian, *Acta Physicochim.*, **19**, 148 (1944).

# Silver, Cobalt, and Positive-Grid Corrosion in the Lead-Acid Battery

J. J. Lander

*The Electric Auto-Lite Company, Toledo, Ohio*

ABSTRACT

Positive-grid corrosion rates measured at several temperatures over a range of potentials corresponding to overcharge conditions show that voltage depression at the positive plate of but a few hundredths of a volt can result in corrosion rates decreasing by factors of one-third to one-half or more. Silver and cobalt when added directly to the electrolyte of batteries on SAE Overcharge Life Test depolarize the positive plate overcharge voltage, resulting in increased overcharge life. An identical series of reactions is proposed to explain the depolarizing effects of silver and cobalt. Overcharge corrosion does not play a major role in governing the service life of passenger car batteries. The SAE Overcharge Life Test cannot be expected to evaluate the effects of silver and cobalt on service life.

In the past year or so there has been an intense reawakening of interest in the effects of silver and cobalt on positive-grid corrosion in the lead-acid battery, especially in automotive types. Considerable evidence exists to show that the addition of cobalt to the battery electrolyte is quite effective in reducing grid corrosion under certain overcharge conditions (1-3). More evidence is presented in this paper. A patent covering this protective aspect of Co was issued in 1931 (4). The use of Ag in grid alloys for the purpose of decreasing overcharge corrosion, first studied by Fink and Dornblatt (5), was suggested by earlier work in which Ag-Pb alloy anodes were used in various electrolytic processes (6). Several patents have been issued for the use of Ag in grid metal (7). Older and less well known, perhaps, is the claim that Ag, even as Co, is effective as an additive to the electrolyte in extending life (8). Under current-regulated overcharge conditions only, this claim is supported herein. An interesting feature of the use of Ag is that it does not seem to be effective except under overcharge conditions (5, 9, 10). There is some evidence that this is true of Co (2).

Along with the similarities between Co and Ag already noted, another effect has been observed, i.e., addition of Co to the electrolyte results in a lowering of the oxygen overvoltage at the positive plate (2, 3, 11). Silver does so as will be shown.

These parallels between the action of Co and Ag, in conjunction with thermodynamic data and measured corrosion rates of Sb alloys, lead to a simple, consistent explanation for their protective effect. Mechanisms of protection are identical for each element; they can be expected to be protective only under overcharge conditions; and, more specifically, they are especially protective under conditions imposed by the SAE Overcharge Test.

A tentative explanation for the effect of Ag has been offered (9) which tried to relate decreased corrosion to the catalytic activity of Ag in decomposing persulfate ion. No supporting evidence was offered. Other work (2, 3) attempted to treat the theory of the effect of Co, but led to proposals of conflicting and ill-defined mechanisms because the proper corrosion data were lacking and because part of the thermodynamic data was neglected.

Table I gives the standard electrode potentials (12) for the reactions concerned.

In this way, $Co^{++}$ and $Ag^{+}$ would be returned to solution and the concentration of $Co^{+++}$ and $Ag^{++}$ would not be allowed to build up to shut off the reaction. $Co^{+++}$ does in fact oxidize water at appreciable rates (13). When a battery is on overcharge, substantially all the current that passes through the positive plate goes to evolution of oxygen. The higher the current, the higher is the overcharge

**Table I**

| | | |
|---|---|---|
| $PbSO_4 + 2H_2O = PbO_2 + SO_4^{=} + 4H^{+} + 2e$ | +1.685 | (I) |
| $Co^{++} = Co^{+++} + e$ | +1.82 | (II) |
| $Ag^{+} = Ag^{++} + e$ | +1.98 | (III) |

Reaction (I) takes place at the positive plate of the lead-acid cell. On charge, as this reaction nears completion, the evolution of oxygen commences and, at the same time, positive plate potentials become more positive to extents sufficient for reactions (II) or (III) to go when $Co^{++}$ or $Ag^{+}$ is present in the electrolyte. If these reactions occur, $Co^{+++}$ and $Ag^{++}$ can oxidize water to $H_2O_2$ as in reactions (IV) and (V)

$$2H_2O + 2Co^{+++} = H_2O_2 + 2Co^{++} + 2H^{+}, \quad F^\circ = -1.5 \text{ kcal} \quad \text{(IV)}$$

$$2H_2O + 2Ag^{++} = H_2O_2 + 2Ag^{+} + 2H^{+}, \quad F^\circ = -9.5 \text{ kcal} \quad \text{(V)}$$

$H_2O_2$ decomposes in acid solution to give oxygen:

$$2H_2O_2 = O_2 + 2H_2O, \quad F^\circ = -50.4 \text{ kcal} \quad \text{(VI)}$$

potential at the positive plate, according to often observed empirical relationships. The effect of Ag and Co is to supply an alternate path for the evolution of oxygen; therefore, their presence should result in a decreased oxygen overvoltage, as has been mentioned. It will be shown that small amounts of either Ag or Co in the electrolyte produce voltage decreases of several hundredths of a volt at the positive plate on overcharge. It will also be shown that voltage depressions of this order of magnitude can lower corrosion rates of antimonial alloys by factors of 30-90% in the SAE Overcharge Life Test range of potential. Cobalt should be the more effective depolarizer according to the potentials of reactions (II) and (III).

The possibility of this depolarization mechanism for the effect of Co on corrosion has been pointed out in substance (3), but because the corrosion work was done with Pb rather than antimonial alloys, it has been concluded (2) that the voltage lowering produced by Co was incapable of decreasing corrosion to any appreciable extent. This led to favorable entertainment of an adsorption theory. In these works (2, 3) the mechanistic identity of the function of Ag and Co in overcharge protection was not considered.

## Experimental

Corrosion rates of an antimonial alloy (6.75% Sb, 0.4 As, 0.35 Sn, balance Pb) were obtained by corroding bare grids at several constant potentials in the overcharge range in acid of 1.260 sp gr. Three temperatures were used and potential was measured with reference to a mercury-mercurous sulfate electrode in the electrolyte. Rates were obtained by stripping the corrosion product in a mannitol solution 10 g hydrazine dihydrochloride, 20 g mannitol, 100 g sodium hydroxide, per liter of solution, and obtaining weight losses as a function of time on test. Typical weight loss curves are shown in Fig. 1 for several potentials at 37.8°C and rates obtained for all potentials and temperatures are shown in Fig. 2. The potential scale has been converted to the cadmium reference electrode in all charts. The 26.6°C data is extended to lower voltages by including data on 6-8% Sb alloys obtained from other sources (14).

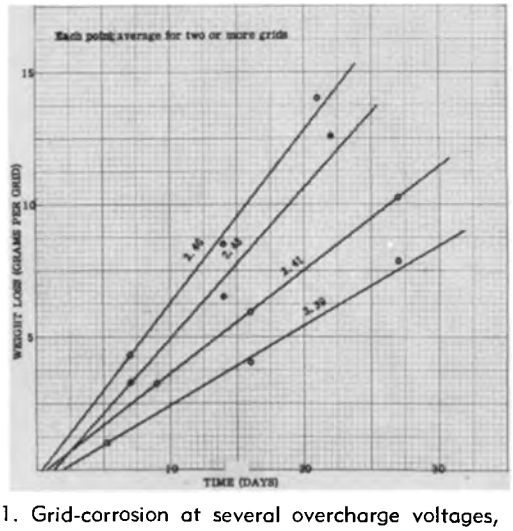


Fig. 1. Grid-corrosion at several overcharge voltages, 100°F

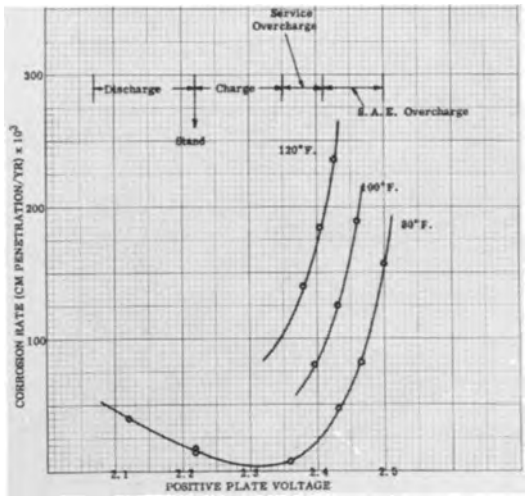


Fig. 2. Positive-grid corrosion rate vs. positive plate voltage

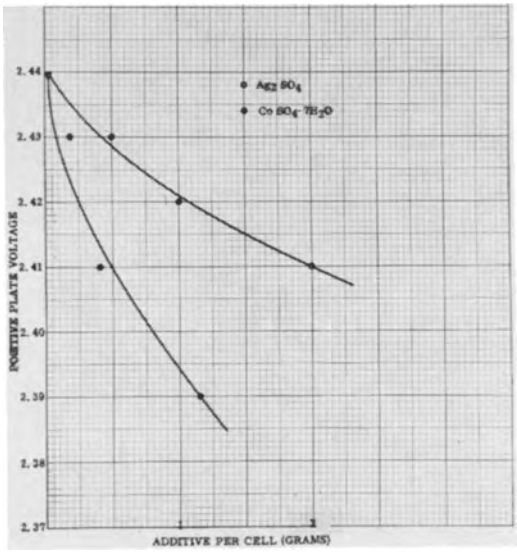


Fig. 3. Effect of Co and Ag on positive plate overcharge voltage. Group 1 Battery at 9 amp.

In another test, silver sulfate and cobalt sulfate were added in varying amounts to the electrolyte of Group 1—6-v batteries at the time they started on SAE Overcharge Life Test (15). The effect of these elements on the positive plate overcharge voltage is shown in Fig. 3. The voltage decreases exhibited persisted throughout the life test. The overcharge life of these batteries is given in Table II.

All batteries failed by positive grid corrosion.

Table II. Effect of silver and cobalt on SAE Overcharge Life

| $Ag_2SO_4$ added/cell g | SAE Overcharge Life (Avg of 2 batteries) weeks |
|---|---|
| None | 10 |
| 0.5 | 11.5 |
| 1.0 | 12.0 |
| 2.0 | 15.0 |
| $CoSO_4 \cdot 7H_2O$ added/cell | |
| None | 9.5 |
| 0.17 | 10.0 |
| 0.46 | 12.5 |
| 1.14 | 17.0 |

Table III. Estimated vs. actual increase in SAE Overcharge Life

| $Ag_2SO_4$ added/cell g | Voltage depression v | % Life increase (Est'd.) | % Life increase (Expt'l.) |
|---|---|---|---|
| 0 | 0 | 0 | 0 |
| 0.5 | 0.01 | 14 | 15 |
| 1.0 | 0.02 | 29 | 20 |
| 2.0 | 0.03 | 45 | 50 |
| $CoSO_4 \cdot 7H_2O$ added/cell | | | |
| 0 | 0 | 0 | 0 |
| 0.17 | 0.01 | 14 | 5 |
| 0.46 | 0.03 | 45 | 32 |
| 1.14 | 0.05 | 85 | 79 |

## Discussion

### *SAE Overcharge Life Test*

The positive cadmium voltages of various battery types on the SAE Overcharge Life Test fall in the range marked on Fig. 2. Internal temperatures of batteries on this test range around 43°-49°C. The slopes of the curves of Fig. 2 show that voltage depressions of but a few hundredths of a volt are quite sufficient to decrease the corrosion rate by 30-90%. From the measured decreases in voltage resulting from the use of Ag and Co shown in Fig. 3 the life increase can be estimated; for example, a voltage depression of 0.06 v at 49°C (2.43 to 2.37) cuts the corrosion rate in half which should double the SAE Overcharge life. Estimated increases for Ag and Co additions are compared with those actually obtained in Table III.

The calculated and experimental life increases are in as good agreement as can be expected considering that the usual variation in overcharge life runs about ±0.5 week when hand-pasted selected grids are used for positives. There is no doubt that voltage depressions of the values measured are quite capable of extending SAE Overcharge Life by the values found.

Whether or not the reactions go as explained in the theory needs demonstration of one step, i.e., that $Co^{+++}$ and $Ag^{++}$ are formed electrochemically at rates sufficient to by-pass appreciable amounts of current from the usual oxygen-producing reaction. The voltage depression is an indirect indication that they are formed at sufficient rates. In the absence of direct knowledge, however, it is not impossible that another mechanism could be operating. Regardless of the mechanism of voltage depression, the relation between voltage depression and increased overcharge life has been demonstrated quantitatively within experimental error, i.e., if other factors were operating in appreciable measure to decrease corrosion and increase life, this quantitative agreement would not have been produced. This is further illustrated by Fig. 4 which shows life increase as a function of voltage depression for both Ag and Co; it seems to be immaterial which element does the job. Therefore, it may be concluded that Ag and Co act to increase overcharge life by depressing the positive plate overcharge voltage at constant current, thus reducing the grid corrosion rate under constant current conditions.

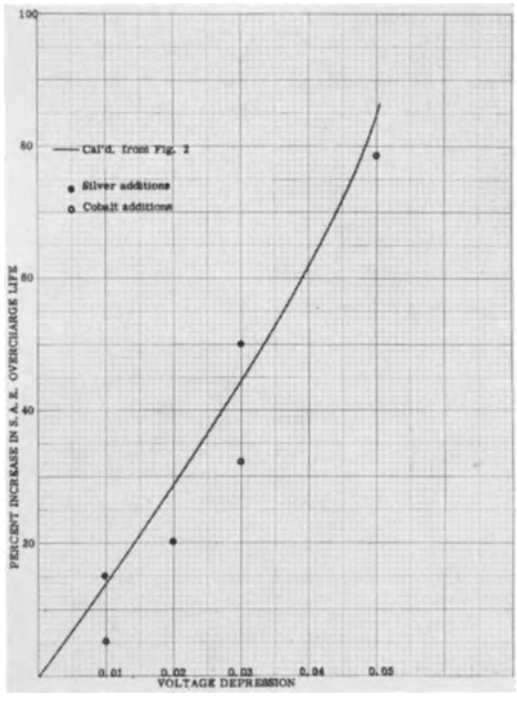


Fig. 4. SAE Overcharge Life vs. positive-plate voltage depression. Calculated vs. experimental.

### *Automobile Battery Service*

At one time it was more or less generally accepted in the automobile battery industry that in-service failure of positive grids was due to overcharge corrosion. It has been pointed out (16) that, because of the large fraction of time spent in idle periods, positive grids of automobile batteries should approach the life of the same batteries on float, their life being governed largely by grid corrosion rates on stand. There is still disagreement, however, as to which area or areas of service operation affect grid corrosion most importantly (17). This question can be resolved using the data of Fig. 2. Inasmuch as the ordinate of this graph is a rate, the curves of the graph show the important variables affecting grid corrosion to be: time, potential, and temperature. If it were known what fractions of time are spent by the positive plate in the various voltage ranges, the relative effects of the various operating conditions could be determined.

For purposes of calculation, the time distribution for passenger car service can be fixed if it is supposed that the ordinary car travels to and from work once a day for two hours, six days a week. For city driving, perhaps 20% of this time will be spent in overcharging the battery. Also let the car be driven for two hours in the country once a week, during which the battery is on overcharge, say, 75% of the time. The remainder of time the car is parked and the battery is idle. If the driving time not spent on overcharge is arbitrarily divided into 10% discharge time and 90% charge time, the above breakdown per week results in the time distribution shown in the first column of Table IV.

If these percentages of time are multiplied by their corresponding corrosion rates as determined from Fig. 2, an index of corrosion for each condition is

Table IV. Voltage-time corrosion of positive grids in service

| Voltage condition | % of time | Corrosion rate | Index | % Corrosion |
|---|---|---|---|---|
| Discharge | 0.6 | 35 | 21 | 2.1 |
| Charge | 5.4 | 6 | 32 | 3.1 |
| Overcharge | 2.3 | 25 | 58 | 5.6 |
| Stand | 91.7 | 10 | 917 | 89.2 |

obtained. These results are shown in Table IV for 26.6°C.

On the basis of this analysis only 6% of the total grid corrosion occurs during overcharge; 89% occurs while the battery is idle. Certainly, the time schedule on which this analysis is based can be varied within limits for passenger car service, but it is clear that the bulk of the grid corrosion will occur while the battery is standing idle, because the stand time far outweighs the driving time.

It can be shown in another way that overcharge corrosion is of minor influence on positive grid life. Twelve-volt, 50 A.H. batteries containing 60 mil positive plates exhibited an average of 16 weeks on the SAE Overcharge Life Test. On this test, about five days a week are spent on overcharge; therefore, the overcharge life of these batteries is about 1920 hr. In the previous time analysis, overcharge time was estimated to be about 4 hr/week. If it is true that batteries fail in service by overcharge corrosion, the service life of this battery should be $1920 \div 4 =$ 480 weeks or 9.2 years. This is a minimum value because overcharge conditions of potential and temperature are not nearly so severe in service as they are on the overcharge test. The warranty on this battery is three years.

The foregoing analysis shows that elements which act as depolarizers at the positive plate can have little or no favorable effect on grid corrosion in service life in passenger cars; indeed, there is some reason to believe that both Ag (9) and Co (10) may hasten grid corrosion at the stand potential and thus shorten grid life. The simple addition of Co may be expected to increase self-discharge at the positive plate (18) and it definitely does decrease charging efficiency at the positive plate (19).

While it has been concluded that service life of positive grids can be affected but slightly by overcharge conditions in passenger car service, it may be worthwhile to consider the implications arising from the voltage regulator system. Depolarization at either plate will result in logarithmic increases in overcharge current and, since water-loss and temperature increase are linearly related to overcharge current, these will increase logarithmically also. If both Ag and Co were to depolarize the negative as well as the positive and if the effect were equal at the negative, no decrease in positive plate voltage could occur and hence no improvement in overcharge corrosion could accrue, because current would have to increase enough to make up the voltage loss. If Ag and Co were to stay at the positive plate, a decrease in overcharge corrosion would result which might contribute as much as 2-3% increase in life, based on Table IV, unless heating caused by the extra current due to depolarization should increase corrosion enough to overbalance the beneficial effect of depolarization.

On the basis of the conclusion that overcharge corrosion is incapable of a large influence on service life and the considerations arising from the voltage-regulated system, the SAE Overcharge Test cannot be expected to evaluate the effect of Ag and Co on service life.

## Acknowledgments

Mr. Dwayne Spoon obtained the grid corrosion data and the Battery Test Section, under Mr. P. A. Cherenzia, obtained the SAE Overcharge Life data.

Manuscript received June 26, 1957. This paper was prepared for delivery before the Buffalo Meeting, Oct. 6-10, 1957.

Any discussion of this paper will appear in a Discussion Section to be published in the December 1958 JOURNAL.

## REFERENCES

1. G. W. Vinal, *et al.*, R.P. 1335, *J. Research Nat'l. Bur. Standards*, **25**, 417 (1940).
2. E. V. Krivolapova and B. N. Kabanov, *Trudy Soveshchaniya Elektrokhim, Akad. Nauk S.S.S.R., Otdel. Khim. Nauk*, **1950**, 539 (1953).
3. L. I. Antropov, *et al., ibid*, **1950**, 549 (1953).
4. F. Booss and R. N. Chamberlain, U.S. Pat. 1,826,724, Oct. 13, 1931.
5. C. G. Fink and A. J. Dornblatt, *Trans. Electrochem. Soc.*, **79**, 269 (1941).
6. C. G. Fink and L. C. Pan, *ibid.*, **46**, 349 (1924); **49**, 85 (1926); C. G. Fink and R. E. Lowe, U.S. Pat. 1,740,291, Dec. 17, 1929. Many references quoted in footnotes 17 and 18 in reference 5.
7. L. E. Lighton, U.S. Pat. 2,333,072, Oct. 26, 1943; H. Stoertz, U.S. Pat. 2,678,340, May 11, 1953; A. Kawabe, Japanese Pat. 3459 ('54) (1954); W. P. Carroll, U.S. Pat. 2,694,628, Nov. 16, 1954.
8. J. Luthy, U.S. Pat. 1,161,398, Nov. 23, 1915.
9. W. H. Power, *et al.*, Naval Research Laboratory Report P-2908 (1947).
10. J. J. Lander, Unpublished work, Naval Research Laboratory.
11. H. M. Wood, CEO 22545, Sept. 1953. The Electric Auto-Lite Company.
12. W. M. Latimer, "Oxidation Potentials," 2nd ed., p. 345, Prentice-Hall, New York (1952).
13. R. S. Young, "Cobalt," p. 61, A.C.S. Monograph No. 108, Reinhold Publishing Corp., New York (1948); C. E. H. Bawn and A. G. White, *J. Chem. Soc.*, **1951**, 331.
14. J. J. Lander, *This Journal*, **99**, 467 (1952); reference 10; and unpublished work in this laboratory.
15. G. W. Vinal, "Storage Batteries," 4th ed., p. 347, John Wiley & Sons, Inc., New York (1954).
16. J. J. Lander, *This Journal*, **103**, 1 (1956); Naval Research Laboratory Report 4475, Jan. 1955.
17. E. Willihnganz, Discussion, p. 86, in "Life Testing of Automobile Batteries and Related Subjects," The Electrochemical Society, New York (1956).
18. M. Rey, *et al.*, *Trans. Electrochem. Soc.*, **73**, 324, (1938).
19. W. T. Abel, ED-5496, Aug. 1957. The Electric Auto-Lite Company.

# A Film Lining for High-Capacity Dry Cells

**N. C. Cahoon and M. P. Korver**

*National Carbon Research Laboratories, National Carbon Company,*

*A Division of Union Carbide Corporation, Cleveland, Ohio*

ABSTRACT

The use of cereal paste is shown to contribute, to a considerable degree, to the deterioration observed in experimental dry cells made with synthetic $MnO_2$ depolarizers. The mechanism involves the hydrolysis of the cereal to form a reducing compound which then reacts chemically with the $MnO_2$ to consume a part of the available oxygen content of the depolarizer. A group of chemically inert hydrophilic colloids, including methyl cellulose, was selected for evaluation as separators. The application of methyl cellulose in a two-film lining for a dry cell is described. The anode film, to be placed next to the anode, is formulated from methyl cellulose and a mercury salt. The barrier film used to separate the anode from the depolarizer mix is formulated from methyl cellulose insolubilized to a limited degree with citric acid. Experimental cells incorporating the composite film lining show keeping qualities far surpassing those of paste-type cells.

Since the introduction of the commercial dry cell in the middle 1880's the cell liner has shown a gradual evolution through cloth, papers and pasted papers to the cereal paste used in many present-day cells. The trend has continually been toward thinner liners as a means both of reducing the internal resistance of the cell and of increasing the quantity of active depolarizer.

During recent years, the use of active electrolytic manganese dioxide has become widespread (1). However, certain early types of experimental cells prepared with this material have shown unexpected cell deterioration during storage. Table I shows the service levels of experimental cells assembled with an electrolytic $MnO_2$ depolarizer and cereal paste separators. It is clear that a serious drop in battery capacity (22-31%) occurs in the relatively short storage period of about two months at 70°F. The cells made with both flour and starch showed such a significant decrease in service that it caused serious concern.

The investigation of the cause of cell deterioration established that the hydrolysis of the separator was responsible for the reduced battery capacity. To correct this condition, a separator medium was needed which would not hydrolyze and react with the active $MnO_2$ depolarizer.

**Table I. Service of experimental "D"-size cells made with electrolytic $MnO_2$ and paste***

| Cell age† | Separators: Minutes service to 0.9 v on 4-ohm HIF test at 70°F — 3 Weeks | 3 Months | 6 Months |
|---|---|---|---|
| Separator Cereal | | | |
| Flour | 928 | 635 | 640 |
| Cornstarch | 1108 | 866 | 792 |

* The cells described above were experimental units designed only for the study of the reaction between the depolarizer and the cereal content of the paste.
† These cells were stored at 70°F.

## Experimental

Experimental attention was, therefore, directed to other hydrophilic materials which could be considered for dry-cell separators. A considerable number of materials were selected which, in general, were synthetically prepared and free of many of the variations that develop in naturally occurring materials. The alkyl cellulose ethers, the hydroxy alkyl cellulose ethers, the salts of cellulose glycolic acid, and a number of vinyl compounds, e.g., polyvinyl alcohol, were the most attractive of the groups studied. It was found that no reaction occurs between the above materials and electrolytic $MnO_2$ under simulated dry-cell conditions.

The film-forming properties of methyl cellulose permitted the easy preparation of sheets. A horizontal glass plate was coated with an aqueous solution of this material and allowed to dry. Such sheets or films were well suited to the manufacture of experimental dry cells.[1] A comparison of the performance of cells made with methyl cellulose and cereal paste separators showed that, until the cells were about six weeks old, similar results were obtained. A sudden voltage drop in the methyl cellulose cells, beginning at this point, was found to result from the slow solution of the methyl cellulose film in the electrolyte followed by its absorption into the cathode mix. This left the anode unprotected and resulted in serious corrosion.

One method of attaining the desired film permanence appeared to be a treatment which could be applied to only one surface of the methyl cellulose film. Such a protective layer should be insoluble in electrolyte, yet still permit rapid diffusion of

[1] Methyl cellulose also appeared applicable as an improvement over the cereal coatings frequently applied to cellulosic or paper layers.

Table II. Effect of the tannic acid content of methyl cellulose films on the performance of "D" size cells

| Amount of tannic acid in film liner* g | | 70°F 4-Ohm HIF† service to 0.9 v % of control |
|---|---|---|
| Control | 0 | 100 |
| | 0.10 | 104 |
| | 0.20 | 98 |
| | 0.40 | 98 |
| | 0.60 | 100 |
| | 0.80 | 91 |

* The amount of tannic acid combined with 14.0 g methyl cellulose is given above.
† The abbreviation HIF is used to indicate the Standard Heavy Industrial Flashlight test, accepted throughout the industry.

zinc chloride from anolyte to catholyte. At the same time, it should prevent the migration of the dissolved methyl cellulose from the anode surface. A large group of substances (2), including tannic, trichloroacetic, and phosphotungstic acids, will react with methyl cellulose to reduce its solubility. Tannic acid was chosen for study. Experimental films were surface-tanned by exposing one surface to a tannic acid solution for a definite time and at a given temperature. However, the precise control of conditions necessary to attain the desired result from this process appeared difficult and alternative methods were investigated.

An improvement on the above process was the incorporation of the tannic acid into the methyl cellulose solution used for the preparation of the film lining. A series of films were prepared in which amounts of tannic acid ranging from 0.10 g to 0.80 g were combined with 14.0 g of methyl cellulose in solution. The dry films were used in the preparation of experimental cells which were placed on test with the initial results shown in Table II. These data illustrate that the presence of tannic acid in the film lining does not materially reduce the initial service capacity of the cell on the 4-ohm HIF test at 70°F. Cells made with the above films have given satisfactory shelf and service maintenance for periods up to several months. However, these films lacked the desired permanence, since the insolubilizing agent dissolved slowly, and other materials were investigated.

A considerable number of reagents, in addition to those mentioned previously, have been described for insolubilizing alkyl cellulose ethers and related compounds. These include organic polybasic acids (3) such as citric, tricarballylic, tartaric, malic, phthalic, and similar compounds. Another group of reagents is that including aldehydes, such as glyoxal (4) and formaldehyde, aldehyde resins such as phenol formaldehyde (5), condensation products such as urea or melamine with formaldehyde (6) and isocyanates (7). Citric acid was chosen as representative of the first group for an experimental study.

It was found expedient to incorporate the citric acid into the aqueous solution of the methyl cellulose used for film preparation. The dry film, formed by the evaporation of the water, was exposed to heat to react the acid with the methyl cellulose. It was desired to employ the minimum amount of acid and to react it as completely as practical to prevent residual amounts of acid in the film from reacting with the $MnO_2$. It was soon found that, when mercuric chloride was incorporated with citric acid and methyl cellulose, heat treatment gave a charred useless material. Apparently the mercury salt catalyzed the thermal decomposition of methyl cellulose in some manner. This observation suggested the development of two separate films for a composite lining. That portion of the film to be placed next to the anode, formulated from methyl cellulose and a mercury salt, was termed the "anode film." The other portion of the separator, visualized as a partially insolubilized methyl cellulose layer, was termed the "barrier film." Whereas, the earlier films had been about 0.0076 cm thick, each layer of the improved film was made 0.0038 cm thick. This division of the separator into two parts with separate functions permitted a direct approach to the formulation of each part of the separator.

The requirements of a suitable barrier film now could be defined. A film was needed which would be highly permeable to electrolyte salts and ions, and yet which would prevent the migration of the methyl cellulose from the anode layer under a wide variety of dry cell discharge conditions. This film should be highly bibulous and yet retain an elastic gel structure which would not itself be dispersed in electrolyte. A great deal of experimental work was required to establish the conditions under which the above desired properties would be obtained. The composition chosen consists of a combination of 0.0025 equivalent, (1.52 g) of citric acid per $C_6$ unit (182.5 g) of methyl cellulose. An aqueous solution of these ingredients is cast on a glass plate to give a dry film 0.0038 cm thick. Heat treatment for 8-10 min at 205°C (401°F) produces the desired barrier film characteristics. Cells made with this barrier film and an anode film comprising methyl cellulose with an appropriate amount of mercury salt give excellent initial and delayed service as shown in Table III. For comparison with the data on the film-lined cells, service levels of paste cells of comparable composition are also given. It may readily be seen that the maintenance of service, voltage, and amperage of the film-lined type is far superior to that of the paste-separator cells.

## Discussion

The double film lining, described herewith, features two film layers which together contribute greatly to the maintenance of high service levels of the dry cell described in this paper. The anode film, although dry when used in the cell assembly process, absorbs electrolyte to become a viscous, highly adhesive layer. The zinc anode is thoroughly wetted by this adhesive and an efficient metal-electrolyte contact is obtained. Determinations of wasteful corrosion in experimental cells made with film linings show lower values than those found in comparable cells made with cereal paste construction. The concentrated corrosive attack at the air-separator-zinc interface, so characteristic of cells made with cereal

Table III. A comparison of the service and keeping quality of "D"-size citric acid insolubilized barrier film-lined cells with paste-lined cells containing electrolytic $MnO_2$

| Separator type | | 70°F Shelf Readings | | | | | | |
|---|---|---|---|---|---|---|---|---|
| | | Initial | 3 Months | 6 Months | 12 Months | 18 Months | 24 Months | 30 Months |
| Cereal paste | Volts | 1.74 | 1.58 | 1.53 | 1.48 | 1.45 | — | — |
| | Amperes | 7.4 | 5.7 | 4.9 | 3.3 | 1.6 | — | — |
| Film lining | Volts | 1.80 | 1.66 | 1.63 | 1.61 | 1.63 | 1.60 | 1.60 |
| | Amperes | 6.7 | 6.5 | 6.1 | 5.8 | 5.5 | 5.2 | 4.9 |

| Separator | Minutes on 4-Ohm HIF* to 0.9 v | | | | Minutes on 4-Ohm LIF* to 0.9 v | | | |
|---|---|---|---|---|---|---|---|---|
| | Initial | 3 Months | 6 Months | 12 Months | Initial | 3 Months | 6 Months | 12 Months |
| Film lining | 922 | 719 | 750 | 591 | 623 | 616 | — | 433 |
| Cereal paste | 1072 | — | 1122 | 1084 | 1372 | — | 1179 | 896 |

* The abbreviations HIF and LIF are used to indicate the Standard Heavy Industrial Flashlight and Light Industrial Flashlight tests, respectively.

paste, is greatly lessened by the use of the film lining. Zinc can perforation is also reduced as a result of the lessened wasteful attack on the anode.

The success of the film lining in providing a high-capacity cell of good keeping quality seems due in part to the unique properties of the barrier film. The reaction between methyl cellulose and an insolubilizing reagent, such as citric acid, appears to be the formation of a complex involving both materials. The resulting insolubilized film is an elastic, gelatinous layer when saturated with electrolyte and shows some evidence of cross-linkage. Because of the reduction in solubility, it can be concluded that a considerable increase in molecular size is obtained by the reaction. The behavior of the cells containing the double film lining is considered strong evidence for the ready diffusion of electrolyte salt solutions and ions through the film during discharge and rest periods.

The early indications of stability of methyl cellulose films in contact with $MnO_2$ have been confirmed by the excellent keeping quality of experimental film-lined cells stored at 35°C (95°F) and 45°C (113°F). The maintenance of service levels under such severe conditions probably indicates a trend toward the use of such linings in cells destined for tropical and similar applications. It is probable that the success of methyl cellulose film linings in this application is, in part, related to the reduced solubility of this material at the elevated temperatures. In contrast to cereal paste which becomes less viscous at elevated temperatures, methyl cellulose coagulates when the temperature exceeds the "gel point." Even when so coagulated, the separator maintains an excellent adhesive contact with the anode and effectively prevents air access to the anode surface.

The techniques developed in this work have provided an easier method of commercial manufacture (8, 9) of certain small sizes of cells than those customarily used with conventional paste separators. Thus, in the present trend toward small cell sizes, the film-type lining appears destined to play an important role.

## Acknowledgment

The authors gratefully acknowledge the valuable help and assistance given by Mr. G. W. Heise, who directed the work described in this paper.

Manuscript received Nov. 7, 1955. This paper was prepared for delivery before the Boston Meeting, Oct. 3-7, 1954.

Any discussion of this paper will appear in a Discussion Section to be published in the December 1958 JOURNAL.

## REFERENCES

1. J. A. Lee, *J. (and Trans.) Electrochem. Soc.*, **95**, 2P-13P (1949).
2. L. Lilienfeld, U. S. Pat. 1,505,044, Aug. 12, 1924.
3. R. M. Upright, U. S. Pat. 2,270,200, Jan. 13, 1942.
4. A. E. Broderick, U. S. Pat. 2,329,741, Sept. 21, 1943.
5. D. D. Lanning, U. S. Pat. 2,467,436, April 19, 1949.
6. R. M. Upright and S. L. Bass, U. S. Pat. 2,270,180, Jan. 13, 1942.
7. G. D. Jones, U. S. Pat. 2,467,832, April 19, 1949.
8. N. C. Cahoon, U. S. Pat. 2,534,336, Dec. 19, 1950; M. R. Hatfield, U. S. Pat. 2,551,799, May 8, 1951.
9. G. W. Heise, E. A. Schumacher, and N. C. Cahoon, *J. (and Trans.) Electrochem. Soc.*, **94**, 99 (1948); N. C. Cahoon and G. W. Heise, U. S. Pat. 2,612,-538, Sept. 30, 1952; H. M. Zimmerman and N. C. Cahoon, U. S. Pat. 2,572,296, Oct. 23, 1951.

# Cathode Reactions in the Leclanche Dry Cell

N. C. Cahoon, R. S. Johnson,[1] and M. P. Korver

*National Carbon Research Laboratories, National Carbon Company,*

*A Division of Union Carbide Corporation, Cleveland, Ohio*

ABSTRACT

The reactions at the cathode of the Leclanché-type dry cell are considered in terms of three heterogeneous chemical reactions for which there is advanced a plausible mechanism, leading to a unified theory of the cathode process. When reviewed in terms of this theory, the numerous observations of others that formerly have appeared to be incongruous are correlated and rationalized in terms of the over-all cathode reaction.

The identification of the reaction products formed in the dry cell cathode during cell discharge has been the subject of considerable work. An examination of the literature indicates that perhaps more effort has been spent on the identification of the products of the electrolyte reaction than on those involving manganese compounds. Until recently, the over-all reaction in the Leclanché cell was written thus:

$$Zn + 2MnO_2 + 2NH_4Cl \rightarrow ZnCl_2 \cdot 2NH_3 + Mn_2O_3 + H_2O \quad (I)$$

Although the above reaction indicates the reduced product is trivalent manganese oxide, the representation of it as bixbyite, $Mn_2O_3$, is now considered incorrect. Both manganite (1), MnOOH, and hetaerolite (2), $ZnO \cdot Mn_2O_3$, have been identified by x-ray diffraction techniques as the solid reaction products formed in cathodic reaction. In addition to these solid products, soluble manganese has been found in the electrolyte of a discharged cathode (3). It is the purpose of this paper to extend the co-ordination of part of these findings already presented (4) to include all the above reaction products and to offer a rational theory of the cathodic reaction process.

## Experimental

The analysis of the cathode mix of discharged dry cells for manganite, hetaerolite, and dissolved manganese was undertaken. Briefly, the analytical procedure involves the suspension of a weighed aliquot portion[2] (e.g., 25 g of the total cathode mix) in a 500 ml volume of a 25% aqueous solution of ammonium chloride buffered at a *p*H of 5.2-5.4, followed by stirring of the suspension at about 40°C for 2 hr. This step insures the solution of the soluble manganese together with the diammino zinc chloride and/or zinc oxychloride usually present.

It has been reported (5) that the zinc content of hetaerolite, $ZnO \cdot Mn_2O_3$, is not soluble in ammonium chloride solution under these conditions. The authors' findings confirm this observation. Thus, leaching the cathode mix with the ammonium chloride solution removes the soluble zinc compounds without attacking the hetaerolite and permits their separate determinations.

The *p*H of the slurry is initially adjusted to between 5.2 and 5.4 by the addition of a 40-45% aqueous zinc chloride solution in quantity sufficient to prevent the soluble manganese from reacting with any residual $MnO_2$ (1) during the course of the analysis. At the end of the leaching step the slurry is then filtered and the filter cake well washed, first with ammonium chloride solution and finally with water. The combined filtrate and washings are diluted with water or ammonium chloride solution to an appropriate standard volume, e.g., 1 liter. Aliquot samples of this solution are quantitatively analyzed for manganese.

From the manganese content of the aliquot sample, the dilution involved, and the sample weights, the amount of divalent manganese in the discharged bobbin can be calculated. From the reaction,

$$MnO_2 + 4H^+ + 2e \rightarrow Mn^{++} + 2H_2O \quad (II)$$

it can be calculated that 1 amp-hr of electrical energy involves the consumption of 1.62 g of $MnO_2$ and the formation of 1.02 g of divalent manganese. The latter value enables the conversion of the divalent manganese content of the cathode to equivalent ampere hours of energy represented by the formation of this product and is designated as item (a). From the above ratio the divalent manganese content of the cathode can also be calculated as an equivalent loss of $MnO_2$ in grams per cell, shown as item (b).

The filter cake is dried at 110°C and its weight and composition determined. Standard methods of quantitative analysis (6) for manganese, zinc, and available oxygen are employed. From the content of manganese and available oxygen in the filter cake, the weights of the ingredients involved and the initial weight and composition of the manganese dioxide used in the cell, the loss in available oxygen which occurred in the cathode of the cell during the particular discharge can be calculated. This can be expressed conveniently as the loss of an equivalent

[1] Present Address: Riegel Textile Corporation, Ware Shoals, South Carolina.

[2] The cell being studied is removed from test when it reaches its cutoff voltage and is immediately subjected to analysis.

weight of $MnO_2$ and designated item (c). From the reaction,

$$2MnO_2 + 2H^+ + 2e \rightarrow 2MnOOH \qquad (III)$$

it can be calculated that 3.24 g of $MnO_2$ are required to produce 1 amp-hr of energy. From the zinc content of the filter cake and the aliquot weights, the total zinc content of the discharged cathode can be calculated. On the basis of the reaction (2),

$$2MnO_2 + Zn^{++} + 2e \rightarrow ZnO \cdot Mn_2O_3 \qquad (IV)$$

and the fact that the $MnO_2$ is reduced to a trivalent oxide, 3.24 g of $MnO_2$ are converted to 4.46 g hetaerolite in which 1.22 g of zinc are combined for each ampere hour of electrical energy obtained. The zinc content of the discharged cathode can thus be converted readily to equivalent ampere hours output, and designated item (f).

The results of the cathode analysis are expressed in the following manner: (*a*) ampere hour output equivalent of $Mn^{II}$ found in the cathode; (*b*) weight of $MnO_2$ consumed equivalent to $Mn^{II}$ found in the cathode; (c) weight of $MnO_2$ consumed during the discharge of the cell; (*d*) weight of $MnO_2$ converted to trivalent oxides, (*d*) = (c) − (*b*); (*e*) ampere hour output in form of trivalent manganese oxides, (*d*) ÷ 3.24; (*f*) ampere hour equivalent of hetaerolite; (*g*) ampere hour equivalent of manganite, (*g*) = (*e*) − (*f*).

Total chemically determined output of cell, (*h*) = (*a*) + (*f*) + (*g*).

Typical analytical data for a group of representative cells appear in Table I. Item (*k*), the electrical output of the cell, is mathematically calculated from the discharge curve, and is expressed in ampere hours.

## Discussion

It has been suggested (4) that two types of reactions occur at the cathode in a Leclanché dry cell. The first is the electrochemical reaction by which electrical energy is produced; it is given as (II) above. This reaction operates only during the actual delivery of current by the cell. The divalent manganese formed in this reaction, present as a soluble manganous salt in the electrolyte, then reacts with residual manganese dioxide thus,

$$MnO_2 + Mn^{++} + 2OH^- \rightarrow 2MnOOH \qquad (V)$$

to form the product manganite.

A parallel reaction,

$$MnO_2 + Mn^{++} + 4OH^- + Zn^{++} \rightarrow ZnO \cdot Mn_2O_3 + 2H_2O \qquad (VI)$$

forming hetaerolite appears a distinct possibility. Both reactions (V) and (VI) are chemical reactions and may occur during both cell discharge and rest periods.

If the above reasoning is correct, the total energy output calculated from the amounts of chemical products found in a discharged cell will agree with the energy output measured electrically. The data presented in Table I show that a reasonable correlation exists between these two values given by items (h) and (k), respectively, for cells with two different oxides discharged on three types of tests. Further argument for this viewpoint is added by the fact that it has been found previously that the energy which would be derived simply from the reduction of $MnO_2$ to the trivalent stage does not account for all the energy actually produced. The possibility of air depolarization to explain this discrepancy has been suggested (8). However, in the present case, it is believed that air depolarization was not a factor since the difference is readily accounted for by the divalent manganese that is produced during reaction (II) and not reacted to form trivalent oxides of manganese, shown in Table I as item (b).

The fact that this correlation exists between outputs as determined by both chemical and electrical means strongly suggests that reactions (V) and (VI) may occur simultaneously. The final product usually found is a mixture of the two oxides rather than either component alone. The relative quantities of the two types of trivalent oxide appear to be the result of several factors.

### *The Manganite-Hetaerolite Ratio*

Examples of typical cell analyses are shown in Table I. A "D" size cell made with a cathode mix containing African ore and discharged on a 4 ohm continuous test forms a solid product that is substantially all manganite. On lighter drains, represented by the HIF and LIF (7) tests, the quantity of hetaerolite formed amounts to one-thirteenth and one-sixth, respectively, of the amount of maganite developed. Although the amounts of hetaerolite present are still small, the fact that the quantity increases with a reduction in the severity of the test appears significant.

Tests have shown that, if zinc salts are present in solution in the cathode mix, hetaerolite, $ZnO \cdot Mn_2O_3$, may be formed (1). If this is not the condition, then MnOOH will be the final reduction product. The amount of dissolved zinc salts in the cathode mix is determined by such factors as original cell composi-

**Table I. A comparison of the chemically determined and electrical outputs of "D" size experimental cells**

| Oxide type | 4 Ohm test (7) | Chemically determined output values: Soluble manganese ($Mn^{++}$) Item (a) | Hetaerolite ($ZnO \cdot Mn_2O_3$) Item (f) | Manganite (MnOOH) Item (g) | Total Item (h) | Electrical output Item (k) |
|---|---|---|---|---|---|---|
| African | Continuous | 0.06 | 0.001 | 1.27 | 1.33 | 1.33 |
| African | HIF* | 0.43 | 0.13 | 1.74 | 2.30 | 2.15 |
| African | LIF* | 1.15 | 0.61 | 3.16 | 4.92 | 4.91 |
| Electrolytic | HIF | 2.02 | 4.41 | 1.65 | 8.08 | 8.19 |

Data above expressed in ampere hours.
* The abbreviations HIF and LIF are used to indicate the standard Heavy Industrial Flashlight and Light Industrial Flashlight tests, respectively.

tion, diffusion from the anode, and solution pH (9). Also, the type of $MnO_2$ determines, to a certain extent, the pH of the operating cathode. It has been pointed out that the primary reaction consumed hydrogen ions. This tends to increase the pH. The secondary reactions consume hydroxyl ions and thus increase the acidity in the electrolyte at the cathode. This restoration of the pH will be faster with the more efficient types of $MnO_2$, such as electrolytic oxide.

The equations presented herewith seem to apply to all types of manganese dioxide: natural oxides, beneficiated ores, and the various types of synthetic depolarizers. Although the formation of hetaerolite is generally associated with highly reactive oxides (2), the oxide type will not necessarily determine the nature of the final product. The African Ore cells in Table I show how the hetaerolite to manganite ratio is altered when the type of test is changed.

*Stoichiometry of the Electrode*

At an operating $MnO_2$-carbon electrode, it is obvious that the system is not at equilibrium. Furthermore, during most of the time the electrode is not even under conditions of steady state. Hence, any application of the Nernst equation and similar thermodynamic relationships are totally invalid. The one rule that is applicable is Faraday's law. This can be correctly applied to the primary reaction (II). Although the final solid products, manganite and hetaerolite, are represented as MnOOH and $ZnO \cdot Mn_2O_3$, they rarely appear in the true stoichiometric proportion (2). For example, it is possible for the manganese-oxygen ratio in manganite to range from 1.4 to 1.6 and the solid can still be considered to be manganite (10). Recent work in the field of solid-state physics shows that these nonstoichiometric solids are real entities and such studies may throw further light on the mechanism of their formation.

It should be noted that the three equations used to describe the cathode process involve solids and ions in solution. Due recognition is thus given to the fact that the reactions occur in a heterogeneous system. Although $Mn^{++}$ and $Zn^{++}$ are discussed as ions, they are no doubt actually present as hydrated complex ammines of varying composition. However, the mechanism of the reactions is the same in both cases, so that simplification of the ions does not invalidate the presentation.

**Acknowledgment**

The authors gratefully acknowledge the valuable help and assistance given by Mr. G. W. Heise, who directed the work described in this paper.

Manuscript received Nov. 7, 1955. This paper was prepared for delivery before the Boston Meeting, Oct. 3-7, 1954.

Any discussion of this paper will appear in a Discussion Section to be published in the December 1958 JOURNAL.

REFERENCES

1. H. F. McMurdie, D. N. Craig, and G. W. Vinal, *Trans. Electrochem. Soc.*, **90**, 509 (1946).
2. L. C. Copeland and F. S. Griffith, *ibid.*, **89**, 495 (1946); H. F. McMurdie, *ibid.*, **86**, 313 (1944).
3. J. M. Cowley and A. Walkley, *Nature*, **161**, 173 (1948); D. T. Ferrell Jr., and W. C. Vosburgh, *This Journal*, **98**, 334 (1951).
4. N. C. Cahoon, *This Journal*, **99**, 343 (1952).
5. E. Otto, discussion H. F. McMurdie, *Trans. Electrochem. Soc.*, **86**, 325 (1944).
6. W. W. Scott, "Standard Methods of Chemical Analysis," 5th ed., D. Van Nostrand and Co. (1939).
7. American Standard Specifications for Dry Cells and Batteries, Circular of the National Bureau of Standards, No. C435, U. S. Government Printing Office, Washington, D. C. (1942); No. C559 (1955).
8. K. Arndt, H. Walter, and E. Zender, *Z. Angew. Chem.*, **39**, 1426 (1926); C. Drotschmann, "Trockenbatterien," 3rd ed., p. 10, Akademische Verlagsgesellschaft, Becker and Erler Kom.—Ges., Leipzig (1945); R. C. Kirk, P. F. George, and A. B. Frey, *This Journal*, **99**, 323 (1952).
9. N. C. Cahoon, *Trans. Electrochem. Soc.*, **92**, 159 (1947).
10. W. Feitknecht and W. Marti, *Helv. Chim. Acta*, **28**, 129 (1945).

# Investigation of the Electrochemical Properties of Organic Compounds

## I. Aromatic Nitro Compounds

R. Glicksman and C. K. Morehouse

*RCA Laboratories, Radio Corporation of America, Princeton, New Jersey*

ABSTRACT

A study of the electrochemical characteristics of aromatic nitro compounds shows that the cathode potential of these compounds during current flow is dependent on the type and position of substituent groups on the aromatic ring, as well as the composition and pH of the electrolyte.

The high theoretical ampere-minute capacity of the aromatic dinitro compounds, along with their practical operating potentials, high electrode efficiencies, and favorable physical and chemical properties, show these materials to have considerable promise for use as cathode materials in primary cells, when coupled with a magnesium anode.

Previous work by the authors (1) disclosed a class of organic compounds, the N-halogens, which had many of the desirable electrochemical characteristics of a cathode material for primary cells. A further consideration of organic oxidizing agents suggested the use of aromatic nitro compounds as cathode materials in primary cells because of their high theoretical electrode potentials and coulombic capacities.

For example, from the free energy values of aniline and nitrobenzene (2), Latimer (3) calculates the potential of the $C_6H_5NO_2$-$C_6H_5NH_3^+$ couple to be:

$$C_6H_5NO_2+7H^++6e^-=C_6H_5NH_3^++2H_2O,\ E^\circ=+0.87 \quad (I)$$

This potential compares favorably with those of inorganic oxidizing agents. In addition, it has been shown that the aromatic nitro compounds can be reduced to the amino stage by both chemical and electrolytic methods in both acid and neutral electrolyte. This indicates the possibility of attaining high coulombic capacities from these compounds through the high resultant electron change per molecule of nitro compound undergoing reduction.

In this paper a systematic study of the electrochemical characteristics of aromatic nitro compounds is presented, with a view toward employing these compounds as cathodes in primary cells.

### Experimental Data and Discussion of Results

*Apparatus and technique.*—Because of the irreversible nature of the electrode reaction and polarization effects encountered during current flow, the electrochemical characteristics of many inorganic and organic compounds cannot be predicted by thermodynamic calculations and a knowledge of their physical and chemical properties. A technique, previously described by the authors (4), has been used to measure the operating potential during current flow and the coulombic capacity of various aromatic nitro compounds. This technique consists in discharging at a constant current, in a large volume of electrolyte, a 0.5-g sample of the aromatic nitro cathode material mixed with 0.05 g of Shawinigan acetylene black. The change in cathode potential with time was measured with a L&N Type K potentiometer using a saturated calomel reference electrode. The measured potentials were corrected for the *IR* drop associated with the apparatus and electrolyte by means of an oscillographic technique (5).

All half-cell potential data reported in this paper are referred to the normal hydrogen scale and include a liquid junction potential, which in most cases is small and can be neglected. The variation of the saturated calomel electrode potential with temperature over the course of the measurements was less than 0.01 v, usually lower than 0.005 v, and no correction was made for this factor, i.e., all measured results were calculated using a value of 0.246 v for the potential of this reference electrode.

For most of the measurements an aqueous magnesium bromide electrolyte and a magnesium anode were used, while, in studying the effect of pH on potential, a zinc anode was employed with the acidic $NH_4Cl$-$ZnCl_2$-$H_2O$ and basic NaOH-$H_2O$ electrolytes.

#### *Half-Cell Studies of Nitrobenzene and Its Reduction Products*

Comprehensive studies have been made of the process of electrolytic reduction of nitrobenzene by Haber and Schmidt (6); they proposed a scheme, which, with subsequent modification (3), became the following:

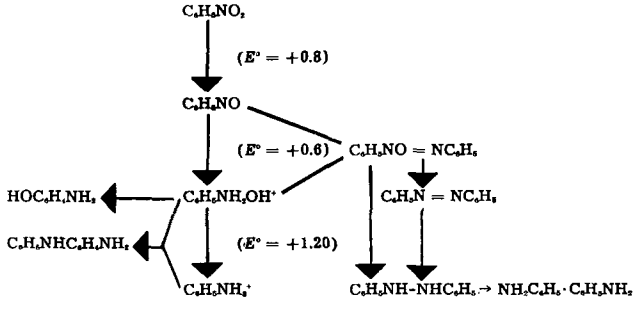

The results reported indicate that, in acid solution, the sequence of primary reduction is through the nitrosobenzene and phenylhydroxylamine stage to aniline. In strongly basic solution, nitrosobenzene can react with both phenylhydroxylamine and aniline to form azoxybenzene and azobenzene, respectively, so that a number of side products are possible. Products such as azobenzene and hydrazobenzene are also made possible by the reduction of azoxybenzene itself, as indicated by the vertical lines in the above scheme. Aniline is formed on prolonged reduction only, hydrazobenzene being the main product obtained when nitrobenzene is reduced in an alkaline solution.[1]

Half-cell discharge studies made on nitrobenzene and some of its reduction products, in various electrolytes, are shown in Fig. 1. These compounds were discharged as cathode materials in three electrolytes of different pH at a rate of 0.030 amp/g of material.[2] The data show that only nitrobenzene and nitrosobenzene operate at sufficiently high potentials to enable these materials to be coupled with a compatible anode, to yield a galvanic cell which operates at practical voltages.[3] In addition, these two compounds exhibit a desirable flat voltage discharge curve and have high theoretical coulombic capacities.

Among the lower oxidation state compounds, only azoxybenzene gives some capacity in the $MgBr_2$ and $NH_4Cl$-$ZnCl_2$ electrolytes, while its reduction products, azobenzene, hydrazobenzene, and aniline, have discharge potentials of —0.75 v or lower in the $NH_4Cl$-$ZnCl_2$ electrolyte, and —0.95 v or lower in the $MgBr_2$ electrolyte. The —0.75 and —0.95 v values are the potentials characteristic of the discharge of hydrogen ions on the carbon electrode in these electrolytes at a current drain of 0.030 amp/g of cathode material. In the NaOH electrolyte, capacity is obtained from both azobenzene and azoxybenzene, the azobenzene operating at a lower potential than the azoxybenzene. Despite the low potentials of the azoxybenzene in these three electrolytes, it exhibits a desirable flat voltage discharge curve, and might be useful if coupled with an anode of higher potential than magnesium.

Of most interest, however, are nitrobenzene and nitrosobenzene. Since each of these compounds represents only one of a large class of materials, extensive studies were made of the electrochemical properties of both classes. This paper deals with the work on the aromatic nitro compounds, while a subsequent paper will treat the data obtained on the aromatic nitroso compounds.

### *Effect of Substituted Groups on the Electrode Potential of Aromatic Nitro Compounds*

The effect of para substituted groups on the electrode potential of aromatic nitro compounds was studied at a current drain of 0.030 amp/g of cathode material in an aqueous magnesium bromide electrolyte. From the data presented in Fig. 2 and 3,

[1] An extensive review has been given by Swann (7) for the whole field of electrolytic organic oxidation and reduction reactions, which includes the reduction of aromatic nitro compounds in various media.

[2] Liquid compounds, such as nitrobenzene, were tested by mixing 0.5 ml of the compound with Shawinigan acetylene black, and discharging the resultant mix at a rate of 0.030 amp/ml of material, and making half-cell potential measurements in the usual manner.

[3] Magnesium in a $MgBr_2$ electrolyte operates at a potential of approximately 1.3 v, while zinc operates at potentials of approximately 0.7 and 1.3 v in $NH_4Cl$ and NaOH electrolytes, respectively.

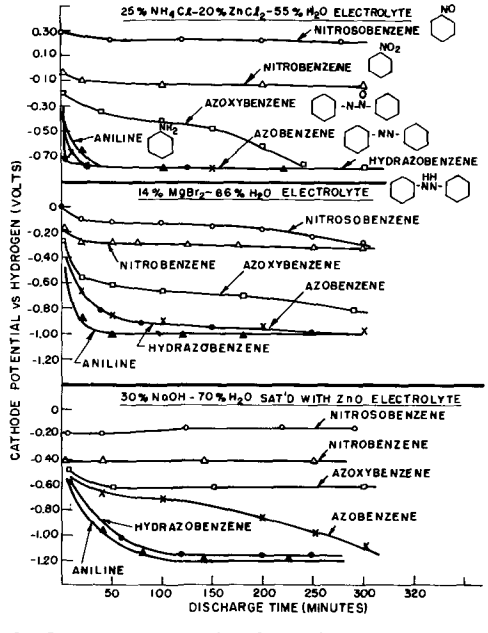


Fig. 1. Cathode potentials of nitrobenzene and its derivatives discharged in various electrolytes at 0.030 amp/g.

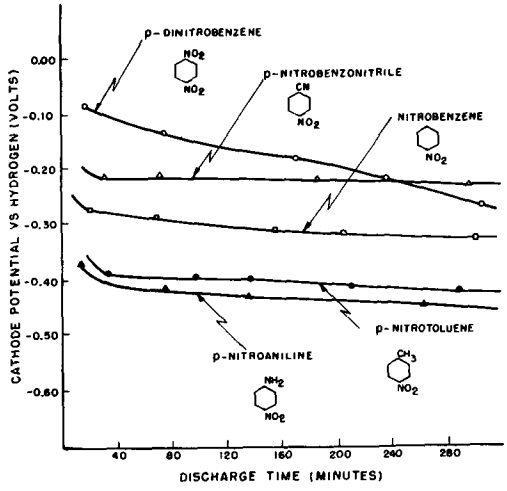


Fig. 2. Effect of para substituted groups on the cathode potential of nitrobenzene discharged in 250 g/l $MgBr_2 \cdot 6H_2O$ electrolyte at 0.030 amp/g.

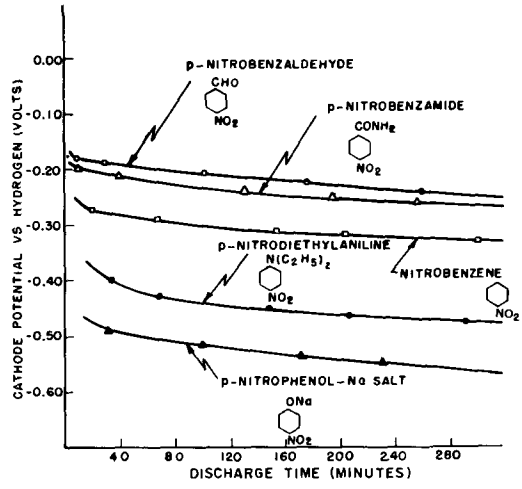


Fig. 3. Effect of para substituted groups on the cathode potential of nitrobenzene discharged in 250 g/l $MgBr_2 \cdot 6H_2O$ electrolyte at 0.030 amp/g.

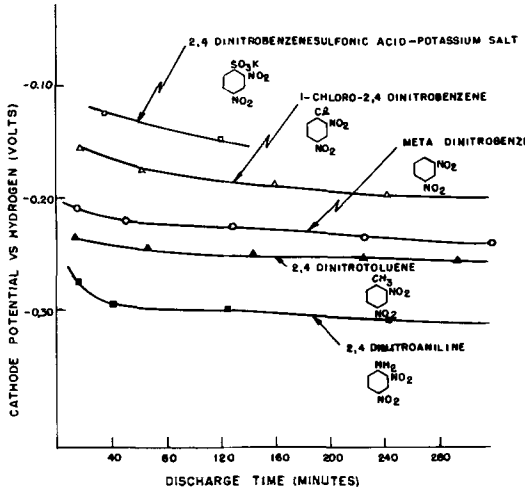


Fig. 4. Effect of substituted groups on the cathode potential of m-dinitrobenzene discharged in 250 g/l $MgBr_2 \cdot 6H_2O$ electrolyte at 0.030 amp/g.

it is seen that those compounds having electron-attracting groups, such as $-NO_2$, -CN, -CHO, and $-CONH_2$ substituted in the para position, initially operate at potentials 0.05-0.20 v higher than that of nitrobenzene. Conversely, electron-repelling groups, such as $-NH_2$, $-N(C_2H_5)_2$, $-CH_3$, and -ONa substituted in the para position, result in compounds having 0.10-0.20 v lower operating potentials than the parent nitrobenzene. In addition, it is seen that a strongly electron-attracting group, such as $-NO_2$, raises the operating potential to a greater extent than the more weakly electron-attracting groups such as -CN, -CHO, and $-CONH_2$, while the strongly electron-repelling $-NH_2$ and -ONa groups lower the operating potential to a greater extent than the weakly electron-repelling $-CH_3$ group.

The same type of behavior is noted for substituted dinitrobenzene compounds, as evidenced by the discharge curves presented in Fig. 4. However, it is significant to note that the potential lowering effect of the $-CH_3$ and $-NH_2$ groups on meta dinitrobenzene is less than that found for their addition to nitrobenzene.

The addition of more than one electron-attracting or electron-repelling group to nitrobenzene affects the potential still further, as seen by the data in Fig. 5. The effect is especially noticeable in the case

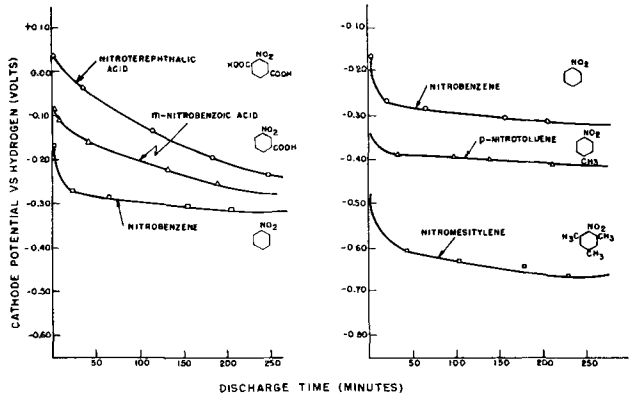


Fig. 5. Effect of the substitution of successive electron attracting and repelling groups on the cathode potential of nitrobenzene discharged in 250 g/l $MgBr_2 \cdot 6H_2O$ at 0.030 amp/g.

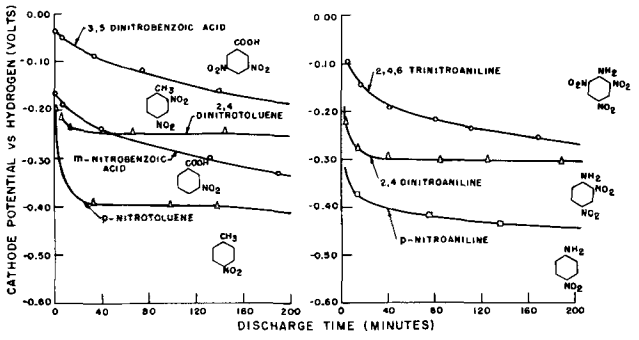


Fig. 6. Effect of an added nitro group on the cathode potential of aromatic nitro and dinitro compounds discharged in 250 g/l $MgBr_2 \cdot 6H_2O$ at 0.030 amp/g.

of nitromesitylene, which operates at a potential 0.3 v lower than nitrobenzene and 0.2 v lower than p-nitrotoluene. Conversely, the addition of successive -COOH groups to nitrobenzene, to form m-nitrobenzoic acid and nitroterephthalic acid, respectively, results in compounds with successively higher operating potentials.

In Fig. 6, it is seen that the effect of an added nitro group on the potential of p-nitrotoluene and m-nitrobenzoic acid is to raise the potential approximately 0.15 v. The further addition of a nitro group to a dinitro compound raises the potential still more, as evidenced by the discharge curves for mono, di, and trinitroaniline.

The addition of another nitro group to an aromatic nitro compound has a further advantage in that the theoretical ampere-minute capacity is increased through the addition of another reducible group. For example, assuming a six-electron change per nitro group, nitrobenzene has a theoretical capacity of 78.4 amp-min/g, as compared to 114.9 for dinitrobenzene and 136 for trinitrobenzene. Thus it would appear that, on the basis of their high electrode potential and coulombic capacity, the aromatic trinitro compounds show the most promise for use as cathode materials in primary cells. However, despite their attractive electrochemical properties, trinitro compounds in general are difficult to handle, and for that reason their use in primary cells would be limited.

*Theoretical interpretation of data.*—In order to explain the effect of substituted groups on electrode potential it is necessary to use some of the current theories of electronics, resonance, and molecular structure (8-10) pertaining to organic reactions. These theories show that the activation of an organic molecule is largely through active or incipient electron displacements leading to the development of a center of high or low electron density.

In a benzene molecule the six carbon atoms are equal to each other with respect to electron distribution. However, the addition of certain groups to the benzene ring results in an increase or decrease of electron density in the ring, depending on the substituted group. This change in electron density affects the various ring positions unequally. It has been verified by quantum-mechanical calculations that the ortho and para carbons are about equally affected, the meta carbon atoms being affected to a much smaller extent. This distribution of electron

density can be explained by theories involving the inductive and resonance effects.

Since the cathodic reaction of an electrochemical cell involves the ability of the material to accept electrons, it would be expected that the distribution of electron density in an aromatic nitro compound would have a distinguishable effect on its discharge potential. For example, in substituted nitrobenzenes the introduction of electron-attracting groups should decrease the electron density in the vicinity of the nitro group, thus increasing its affinity for electrons and facilitating its reduction. On the other hand, electron-repelling groups would increase the electron density around the nitro group, thus resulting in compounds which are reduced with more difficulty.

It is recognized that the reduction of aromatic nitro compounds involves the acceptance of hydrogen ions as well as electrons, and either or both might be involved in the rate-determining step. However, the data presented in Fig. 2-7 can be explained readily on the basis of a rate-determining electron transfer step.

This effect was first pointed out by Shikata and Tachi (11), who studied the polarographic reduction of ketones and nitro compounds and found that the ease of reduction of these compounds depends on the electronegativity of the groups combined with the reducible groups. It has been verified subsequently by other polarographic studies (12, 13). A similar effect was observed by Fieser (14) in the oxidation-reduction potentials of quinone type compounds.

*Effect of Position of Substituted Groups on the Electrode Potential of Aromatic Nitro Compounds*

According to theory, electron-attracting groups such as -CHO, -CN, and -$NO_2$ lower the electron density in the ring, but they affect the various positions unequally, the density in the ortho and para positions being decreased to the greatest extent. Therefore, one would expect compounds having a nitro group ortho or para to an electron-attracting group to be reduced more easily than those having a nitro group in the meta position, and they should thus have a higher cathodic electrode potential. The half-cell discharge data for the para and meta isomers of nitrobenzaldehyde, nitrobenzonitrile, and dinitrobenzene presented in Fig. 7 confirm the above reasoning. In each case the para substituted compound has a higher potential than the corresponding meta isomer.

Conversely, electron-repelling groups such as -$NH_2$, -OH, and -$CH_3$ increase the electron density in the ortho and para position to a greater extent than in the meta position. In this case, one would expect a nitro group in the meta position to be reduced more readily than one in an ortho or para position, and, therefore, the meta isomer should have a higher cathodic electrode potential. Half-cell discharge data for the meta and para isomers of nitroaniline, nitrophenol, and nitrotoluene are presented in Fig. 8 and, as expected, the meta isomers have higher potentials than their corresponding para compounds.

This effect is further illustrated by the discharge curves of 2,5 and 3,5 dinitrobenzoic acid and 2,5 and 2,4 dinitrophenol shown in Fig. 9. It is seen that in both cases the para dinitro compounds have higher potentials than their corresponding meta dinitro isomers.

From these data, it is seen that the position of a substituent group can alter the cathode potential of an aromatic nitro compound by 0.05-0.15 v, the effect being greatest with the more strongly electron-attracting and repelling groups, such as -$NO_2$ and -$NH_2$.

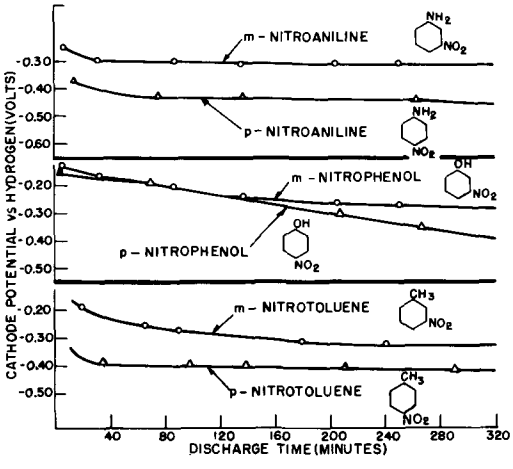


Fig. 8. Effect of the position of various groups on the cathode potential of aromatic nitro compounds discharged in 250 g/l $MgBr_2 \cdot 6H_2O$ electrolyte at 0.030 amp/g.

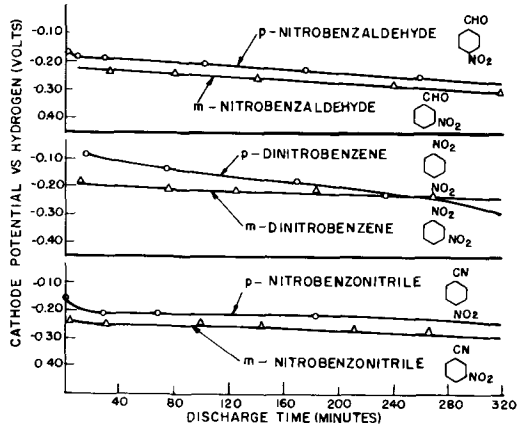


Fig. 7. Effect of the position of various groups on the cathode potential of aromatic nitro compounds discharged in 250 g/l $MgBr_2 \cdot 6H_2O$ electrolyte at 0.030 amp/g.

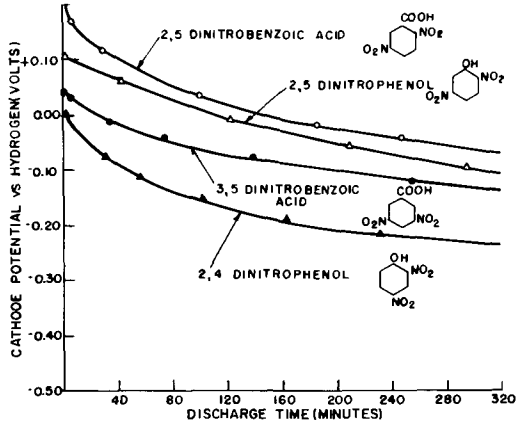


Fig. 9. Effect of the position of the nitro groups on the discharge potential of various dinitroaromatic compounds discharged in 250 g/l $MgBr_2 \cdot 6H_2O$ electrolyte at 0.030 amp/g.

*Effect of Electrolyte pH on the Electrode Potential of Aromatic Nitro Compounds*

Since hydrogen ions participate in the reduction of aromatic nitro compounds, it would be expected that the electrode potentials of these compounds are pH dependent. In Fig. 10 are presented discharge curves of 2,4 dinitroaniline and 2,4 dinitrotoluene in three different dry cell electrolytes of varying pH. It is seen that the cathode potentials of the nitro compounds increase as the pH of the electrolyte is decreased, a result in agreement with theory. This type of behavior is typical of the aromatic nitro compounds in general; however, the true effect of pH on the potential is, in some cases, masked by chemical reactions between the cathode material and the electrolyte or the discharge products.

For example, the pH of the medium often influences the intensity and direction of the inductive and resonance effects operating in a molecule by changing the nature of the molecule which is reduced. A case in point is the amino group, which is electron attracting in acid media because it acquires a proton and becomes positively charged, $-NH_3^+$, while in an alkaline medium it is a strongly electron-repelling group.

Another example of how the effect of pH on potential of a nitro compound is altered by the reaction between the electrolyte and the compound is shown in Fig. 11, where it is seen that the discharge potentials of p-nitrophenol and p-nitrophenol-Na salt are approximately the same in the acidic $NH_4Cl$-$ZnCl_2$ and basic NaOH electrolytes. It is reasoned that in a strongly basic solution p-nitrophenol reacts with the electrolyte to give the Na salt, whereas in acid solution the p-nitrophenol-Na salt hydrolyzes to give p-nitrophenol. The difference between the behavior of the two compounds in a magnesium bromide electrolyte is believed due to a neutralization reaction which occurs with time between p-nitrophenol and the magnesium bromide electrolyte, which has become saturated with $Mg(OH)_2$ as a consequence of the cathodic reduction reaction. The neutralization of the aromatic hydroxyl group could lower the potential in two ways: first, through the removal of the acidic hydrogen ion and corresponding rise of pH at the electrode surface; second, the formation of the very strongly electron-repelling phenoxide ion would lower the discharge potential of the parent nitro compound by replacing the more weakly electron-repelling hydroxyl group (15).

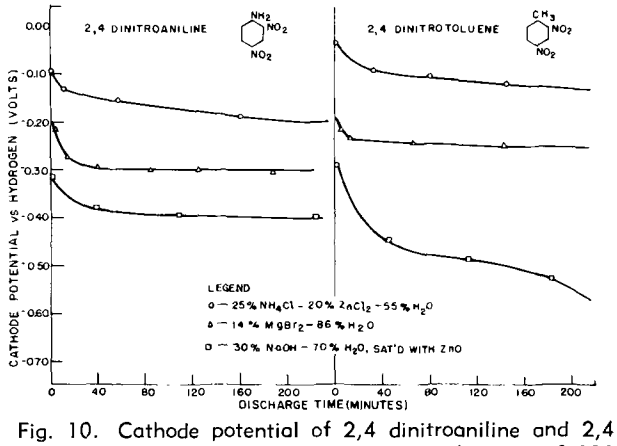


Fig. 10. Cathode potential of 2,4 dinitroaniline and 2,4 dinitrotoluene discharged in various electrolytes at 0.030 amp/g.

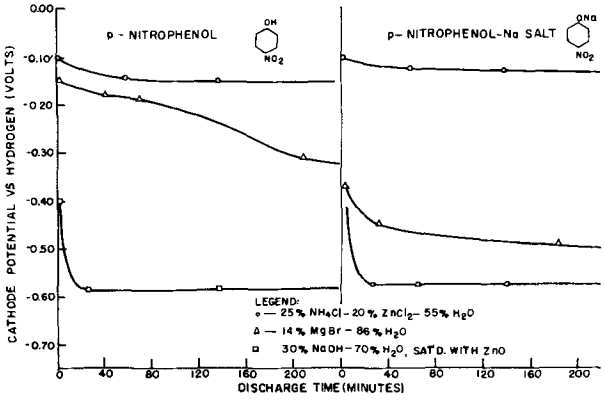


Fig. 11. Cathode potential of p-nitrophenol and its sodium salt discharged in various electrolytes at 0.030 amp/g.

The acidity of the cathode material itself can also influence the operating potential as evidenced by the discharge curves for p-nitrobenzenesulfonic and p-nitrobenzoic acids shown in Fig. 12. It is seen that these acidic compounds operate initially at higher potentials than comparable nitro compounds containing a more strongly electron-attracting group on the ring. These anomalous results are attributed to an increased hydrogen ion concentration at the electrode surface, caused by the ionization of these acidic compounds. As a result of the decreased pH at the electrode surface, the electrode potential is initially high. However, the potential of these compounds falls off with time and soon reaches a steady value, which corresponds more closely to what one would expect from these groups on the basis of their electron-attracting and repelling strengths. It is reasoned that the drop of potential with time as these compounds are discharged is due to the neutralization of the acidic groups by the hydroxide ion, formed as a consequence of the cathodic reduction reaction.

The high potential of p-nitrobenzenesulfonyl chloride may be explained by a combination of effects. The first is the inherently strong electron-attracting property of the $-SO_2Cl$ group, while the second is

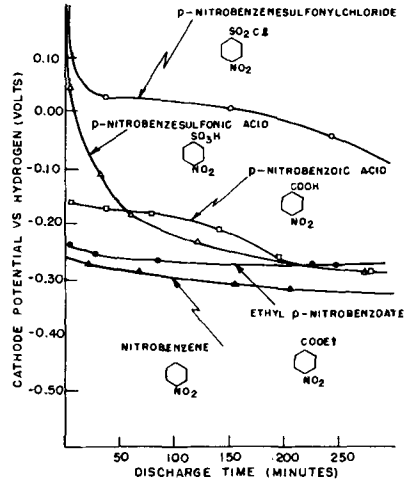


Fig. 12. Effect of acidic groups on the cathode potential of aromatic nitro compounds discharged in 250 g/l $MgBr_2 \cdot 6H_2O$ electrolyte at 0.030 amp/g.

Table I. Theoretical capacities and physical properties of various cathode materials

| Cathode material | Physical properties | Melting* point, °C | Boiling* point, °C | Density* | Theoretical capacity amp-min/g | Theoretical capacity amp-min/cm³ |
|---|---|---|---|---|---|---|
| *Conventional dry cell cathode materials* | | | | | | |
| Manganese dioxide | Solid | —0, 230 | — | 5.03 | 18.5 | 93.1 |
| Mercuric oxide | Solid | d. 100 | — | 11.14 | 14.9 | 166 |
| *Aromatic nitro compounds* | | | | | | |
| Nitrobenzene | Liquid | 5.7 | 210.9 | 1.2 | 78.4 | 94.1 |
| m-Dinitrobenzene | Solid | 89.8 | 300-2 | 1.58 | 114.9 | 181.5 |
| 1,3,5 Trinitrobenzene | Solid | 121 | Decomposes | 1.69 | 136 | 229.8 |
| 2,4 Dinitrobenzaldehyde | Solid | 69-70 | 190-210 | — | 98.6 | — |
| 2,4 Dinitrotoluene | Solid | 70 | sl.d.300 | 1.32 | 105.8 | 139.6 |
| 2,4 Dinitroaniline | Solid | 187-8 | — | 1.62 | 105.8 | 171.4 |
| 2,4 Dinitroanisole | Solid | 94-5 | — | 1.341 | 97.4 | 129.5 |

* Lange's Handbook of Chemistry, 8th edition.

the decreased pH at the electrode surface, caused by the hydrolysis of the sulfonyl chloride compound, with the formation of p-nitrobenzenesulfonic acid and HCl.

In addition to the above considerations, the formulation of a pH-potential relationship for aromatic nitro compounds is dependent on a knowledge of the electrode reaction as well as the activities of the reactants and products. Since these reduction reactions are irreversible, the nature of the reduction product is often unknown and identification of the resultant products along with kinetic studies are needed in interpreting the electrode reaction.

Thus it is seen that the effect of the medium on cathode potential is a complex one and has to be considered anew for each individual case.

*Coulombic Capacity of Aromatic Nitro Compounds*

Tabulated in Table I are theoretical capacity and physical property data for a few aromatic nitro compounds compared with two of the cathode materials now used in commercial dry cells. The theoretical capacities of the nitro compounds were computed by means of Faraday's law, with the assumption that each nitro group is reduced to the amino stage with a corresponding 6-electron change.

It is seen that the listed nitro compounds have from 4 to 7 times greater theoretical ampere-minute capacity per unit of weight than manganese dioxide, and 5-9 times greater capacity than mercuric oxide. Because of the low densities of the nitro compounds, their theoretical capacities per unit of volume range from the same as to twice that of $MnO_2$, while some are even slightly superior to HgO, despite the high density of the latter compound. In addition most of the aromatic dinitro compounds are stable solids with sufficiently high melting and boiling points to enable them to be used as cathode materials in primary cells.

Coulometric studies made on meta and para dinitrobenzene and meta and para nitroaniline in a $MgBr_2$ electrolyte are shown in Fig. 13. The results were obtained by discharging 0.5-g samples of these compounds at a constant current drain of 0.005 amp/g, and measuring the change in half-cell potential with time by the same technique as described previously. Also included for purposes of comparison are curves of electrolytic manganese dioxide and mercuric oxide, discharged at a similar rate in aqueous $MgBr_2$ and NaOH electrolytes, respectively.

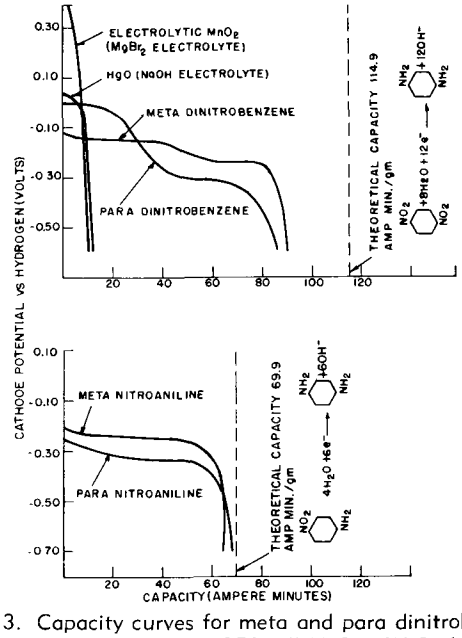


Fig. 13. Capacity curves for meta and para dinitrobenzene and nitroaniline discharged in 250 g/l $MgBr_2 \cdot 6H_2O$ electrolyte at 0.005 amp/g.

The reduction of meta and para dinitrobenzene is seen to take place stepwise, corresponding to two stages of reduction, the para dinitrobenzene having the higher cathode potential for the first stage of reduction and the meta dinitrobenzene having a greater cathode potential for the second reduction step. This is in agreement with the previous findings, relating the cathode potential of aromatic nitro compounds with the type and position of group substitution on the aromatic ring.

Although analyses were not made of the reduction products, it is believed that the reduction goes to the amino stage, as evidenced by the fact that the potentials of para and meta nitroaniline have approximately the same value as the cathode potentials corresponding to the second reduction step of para and meta dinitrobenzene. In addition, the capacities of the nitroaniline compounds indicate reduction takes place with a 6-electron change per nitro group.

Calculations based on Fig. 13 show para and meta dinitrobenzene to have capacities[4] of 78 and 88 amp-min/g, corresponding to efficiencies of 68% and

[4] Capacities reported are to a —0.40 v end point.

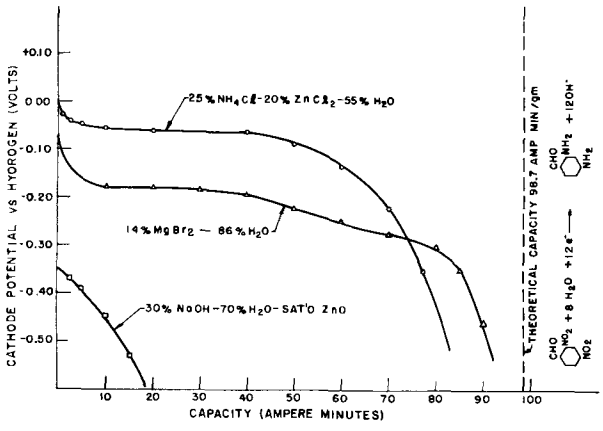


Fig. 14. Capacity curves for 2,4 dinitrobenzaldehyde discharged in various electrolytes at 0.002 amp/g.

77%, respectively, while under similar conditions of discharge the capacities of electrolytic $MnO_2$ and HgO are 10.3 and 10.4 amp-min/g, which correspond to efficiencies of 66%[5] and 70%. For the nitroaniline compounds, capacities of 61 and 63.5 amp-min/g were obtained for the para and meta isomers, respectively, corresponding to efficiencies of 87% and 91%. Thus it is seen that, under the aforementioned conditions of discharge, para and meta dinitrobenzene give 7 to 8 times greater ampere-minute capacity per unit of weight than HgO or electrolytic $MnO_2$ at comparable cathode efficiencies.

Additional coulometric studies were made on 2,4 dinitrobenzaldehyde in electrolytes of different *p*H in order to study the effect of *p*H on capacity. From the scheme of Haber and Schmidt previously described, it would be expected that the use of a strongly basic electrolyte should result in a loss of capacity due to the formation of side products such as azoxybenzene and azobenzene, which are formed by the condensation of the primary reduction products in the alkali electrolyte. The data presented in Fig. 14 for 2,4 dinitrobenzaldehyde discharged at a 0.002 amp/g rate in various electrolytes support this reasoning, as it is seen that little capacity is obtained from this compound in the strongly alkaline electrolyte. In the $MgBr_2$ and acidic $NH_4Cl$ electrolytes, reduction apparently takes place to the diamino stage as evidenced by the fact that efficiencies of 80.5% and 88.9% were obtained.

It is seen from Fig. 14 that the use of a compatible zinc anode in either the acidic $NH_4Cl$-$ZnCl_2$ or strongly basic NaOH electrolytes would result in galvanic couples which operate at voltages too low for practical use. Coupling the aromatic nitro compound with an anode of higher potential, such as magnesium, however, would result in a couple which operates at practical voltage levels. Since magnesium corrodes too readily in an acid solution and polarizes in strongly basic solution, the most favorable anode-electrolyte combination to use with these aromatic nitro compounds appears to be magnesium with a $MgBr_2$ electrolyte. In a 2*N* $MgBr_2$ electrolyte, magnesium operates at a potential of approximately 1.3 v and when coupled with a compound such as 2,4 dinitrobenzaldehyde would give galvanic couples having operating voltages of 1.00-1.10 v during current drain.

[5] Efficiency calculation based on an 85% $MnO_2$ content.

## Summary

1. A theory based on the effect of substituent groups on the electron density in the vicinity of a reducible nitro group is presented, which explains the effect of these groups on the operating potential of aromatic nitro compounds.

2. The cathode potential during current flow of mononitrobenzene compounds containing para substituted groups such as $-NO_2$, -CN, -CHO, and $-CONH_2$, which can cause a displacement of electrons toward the added group, is 0.05 to 0.20 v higher than the unsubstituted nitrobenzene, whereas mononitro compounds containing para substituted groups such as $-NH_2$, $-N(CH_3)_2$, -ONa, and $-CH_3$, which result in displacement of electrons away from the substituted group, operate at potentials 0.10 to 0.20 v lower than nitrobenzene.

3. The cathode potential is also affected by the position of the substituent group, and differences of 0.05-0.15 v are found for various meta and para isomers of the aromatic nitro compounds. For substituted electron-attracting groups, the para isomer is found to operate at higher potentials than the meta isomer, while the converse is found to hold for substituted electron-repelling groups.

4. In general, the cathode potentials of the aromatic nitro compounds increase as the *p*H of the electrolyte is decreased. However, the effect of the medium on the cathode potential is often a complex one and has to be considered for each individual case.

5. Coulometric reduction studies of various mono and dinitroaromatic compounds indicate that reduction of these compounds takes place to the amino stage, with a resultant 6-electron change per-$NO_2$ group, at electrode efficiencies of 70-90%.

6. On the basis of the data presented in this paper, the aromatic nitro and dinitro compounds show considerable promise for use as cathode materials in primary cells, the most outstanding feature of these compounds being their high theoretical ampere-minute capacities, both on a weight and volume basis.

Manuscript received Oct. 2, 1957. This paper was prepared for delivery before the Buffalo Meeting, Oct. 6-10, 1957.

Any discussion of this paper will appear in a Discussion Section to be published in the December 1958 JOURNAL.

## REFERENCES

1. C. K. Morehouse and R. Glicksman, *This Journal*, **104**, 467 (1957).
2. G. S. Parks and H. M. Huffman, "Free Energies of Some Organic Compounds," Chemical Catalogue Co., New York (1932).
3. W. M. Latimer, "Oxidation Potentials," p. 136, Prentice-Hall, Inc., New York (1952).
4. C. K. Morehouse and R. Glicksman, *This Journal*, **103**, 94 (1956).
5. R. Glicksman and C. K. Morehouse, *ibid.*, **102**, 273 (1955).
6. F. Haber and C. Schmidt, *Z. physik. Chem.*, **32**, 271 (1900).
7. S. Swann, Jr., *Trans. Electrochem. Soc.*, **69**, 287 (1936); **77**, 459 (1940); **88**, 103 (1945); **99**, 219 (1952).
8. C. K. Ingold, *Chem. Revs.*, **15**, 225 (1934).

9. L. Pauling, Gilman's "Organic Chemistry," Vol. II, pp. 1975-1979, John Wiley & Sons, Inc., New York (1943).
10. G. W. Wheland, "The Theory of Resonance," pp. 256-272, John Wiley & Sons, Inc., New York (1947).
11. M. Shikata and I. Tachi, *J. Chem. Soc. Japan*, **53**, 834 (1932); *Collection Czeckoslov. Chem. Commun.*, **10**, 368 (1938).
12. J. Pearson, *Trans. Faraday Soc.*, **44**, 683 (1948); **45**, 199 (1949).
13. S. F. Dennis, A. S. Powell, and J. Astle, *J. Am. Chem. Soc.*, **71**, 1484 (1949).
14. L. F. Fieser, *ibid.*, **51**, 3101 (1929); L. F. Fieser and M. Fieser, *ibid.*, **57**, 491 (1935).
15. C. R. Noller, "Chemistry of Organic Compounds," p. 441, W. B. Saunders Co., Philadelphia, and London, England (1951).

# Dry Cells Containing Various Aromatic Nitro Compounds as Cathode Materials

**C. K. Morehouse and R. Glicksman**

*RCA Laboratories, Radio Corporation of America, Princeton, New Jersey*

ABSTRACT

The class of aromatic nitro compounds has been found to have properties suitable for the design of improved dry cells when coupled with a magnesium anode. The performance characteristics of these cells are dependent on the type of aromatic nitro compound used as a cathode material.

The AA-size magnesium-meta dinitrobenzene dry cell has been fully characterized and shown to give superior performance to the commercial Leclanché cell on a number of discharge tests.

The use of organic nitro compounds in primary batteries was first mentioned in the patent literature by Bauer (1). He describes a wet-type battery, similar to the Lalande cell, composed of a zinc anode, an alkaline electrolyte, and a cathode consisting of a metal oxide such as copper oxide, and a nitro compound. More recently Arsem (2) and Sargent (3) make reference to the use of nitro compounds as organic oxidizing agents in dry cells. Arsem describes a cell consisting of a zinc anode, an electrolyte of an aqueous solution of boric acid and sodium chloride, and a nitro compound as a cathode. Sargent, on the other hand, employs an organic nitro compound as cathode with an aluminum anode, and an electrolyte composed of an aqueous solution of an alkali metal hydroxide and an alkali metal zincate.

Despite the references to the use of organic nitro compounds in the patent literature, no practical dry cell containing these compounds has been reported. From previous data gathered by the authors (4), one can attribute this to several factors: First, an aromatic nitro compound coupled with a zinc or an aluminum anode would result in a dry cell which would operate at too low a voltage to be competitive with existing commercial cells. Second, it has been found that electrolytes such as strongly alkaline solutions do not enable the aromatic nitro compound to be used at optimum efficiency. In addition, half-cell discharge studies have shown that certain types of aromatic nitro compounds have better cell operating characteristics than others. Finally, it has been found that the cathode mix formulation differs from the usual practice for conventional dry cells in that greater amounts of conductive carbon and electrolyte per quantity of cathode material are required.

In this paper, the performance characteristics of cells containing a magnesium anode coupled with various aromatic nitro and dinitro compounds as cathodes are presented.

## Experimental

Experimental dry cells containing various aromatic nitro and dinitro cathodes were assembled using an impact extruded magnesium AA-size (height 1.82 in., O.D. 0.521 in., I.D. 0.441 in.) can, composed of an AZ10A Dow Chemical Company alloy. The magnesium cans were lined with a piece of Nibroc salt-free paper (2¼ in. x 2¼ in. x 0.002 in. thick), after which an extruded slug of cathode mix (weighing approximately 5 g) was inserted and consolidated in the lined can. A carbon rod (ht 1.787 in., diam. 0.159 in.) containing a brass cap was then inserted in the center of the cathode mix, and the cells sealed in the conventional manner with a rosin base wax seal. Two cathode mix formulations listed below were used in this study, the first describing the formulation of the cells discussed in the first section of this paper, and the second describing that of the magnesium-m-dinitrobenzene cells discussed in the second section.

*Cathode Mix Formulation No. 1*

| | % by weight |
|---|---|
| Aromatic nitro or dinitro compound | 26.5 |
| Shawinigan acetylene black | 13.3 |
| Barium chromate | 1.2 |
| Electrolyte (aqueous solution of 500 g/l $MgBr_2 \cdot 6H_2O$ and 1.0 g/l $Li_2CrO_4 \cdot 2H_2O$) | 59.0 |

*Cathode Mix Formulation No. 2*

| | % by weight |
|---|---|
| m-Dinitrobenzene | 14.6 |
| Darco carbon black G-60 | 29.2 |
| Barium chromate | 1.3 |
| Electrolyte (aqueous solution of 500 g/l $MgBr_2 \cdot 6H_2O$ and 1.0 g/l $Li_2CrO_4 \cdot 2H_2O$) | 54.9 |

The voltage-discharge and capacity data shown in the following sections were obtained by discharging the cells through fixed resistances, and measuring the closed circuit voltage after various time intervals of discharge. All capacity data were gathered at 70° ± 2°F, 50 ± 5% relative humidity (R.H.).

## Voltage-Discharge Characteristics of Dry Cells Containing Various Aromatic Mono- and Dinitro Compounds as Cathodes

A previous paper (4) dealt with the effect of various functional groups and their positions on the operating potential of the aromatic nitro and dinitro compounds. It was shown that when electron-attracting groups such as $-NO_2$, $-CO_2H$, $-CONH_2$, $-CN$, etc., are substituted in an aromatic nitro or dinitro molecule, the cathode potential of the parent compound during current flow is raised, the effect being more pronounced when the substitution is in the ortho or para position. Conversely, the substitution of electron-repelling groups such as $-CH_3$, $-NH_2$, etc., lowers the cathode potential during current flow.

The 150-ohm continuous-discharge data obtained on AA-size dry cells containing a magnesium anode and various substituted dinitrobenzene compounds as cathodes are shown in Fig. 1. These data illustrate the effects of substituted groups on the cell discharge potential. For example, cells containing m-dinitrobenzene with electron-attracting -Cl, and $-SO_3K$ groups substituted in the position which is both ortho and para to the nitro groups operate at voltages 0.03 and 0.06 v higher than comparable cells containing the unsubstituted m-dinitrobenzene as the cathode reactant. The addition of an electron-repelling $-CH_3$ group lowers the cell potential 0.05 v below that of the m-dinitrobenzene cell, while the substitution of an $-NH_2$ group lowers the cell potential approximately 0.14 v. This difference in magnitude of effect is expected, since the $-NH_2$ group is more strongly electron repelling than the $-CH_3$ group.

The effect of group substitution is further illustrated in Fig. 2 by the discharge data for cells containing m-dinitrobenzene compounds with electron-attracting $-COOC_2H_5$ and $-CONH_2$ groups in a position meta to the nitro groups. The pronounced two-step voltage-time discharge curve for these cells indicates that the reduction of the dinitro compound

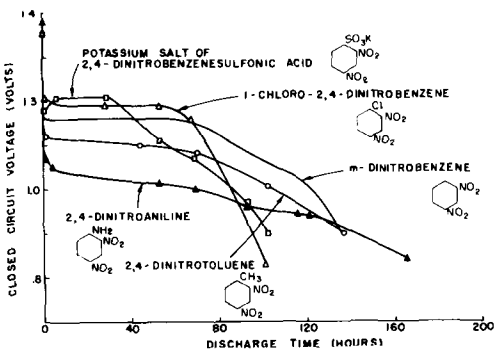


Fig. 1. AA-size dry cells containing a magnesium anode and various substituted dinitrobenzene cathodes discharged continuously through 150-ohm resistances.

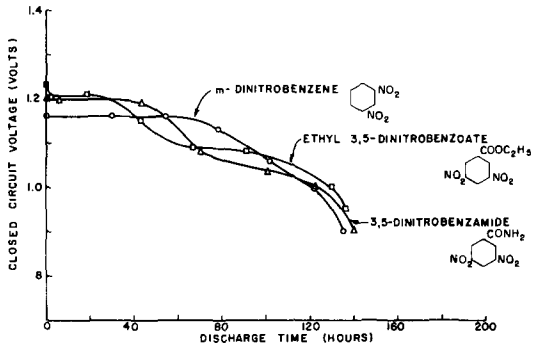


Fig. 2. AA-size dry cells containing a magnesium anode and substituted dinitrobenzene compounds as cathodes discharged continuously through 150-ohm resistances.

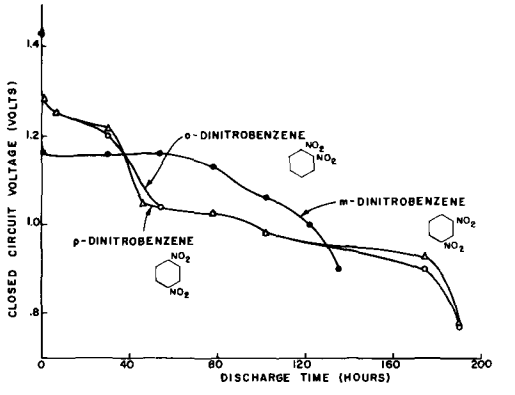


Fig. 3. AA-size dry cells containing a magnesium anode and various isomers of dinitrobenzene as cathodes discharged continuously through 150-ohm resistances.

takes place one nitro at a time. The lower operating potential of the second step is attributed to the formation of a strongly electron-repelling $-NH_2$ group as a result of the reduction of the first nitro group.

The effect of group position on the discharge potential of aromatic nitro compounds is shown in Fig. 3 by the discharge data obtained on cells containing the three isomers of dinitrobenzene. It is evident from the data that the cells have a two-step discharge curve, giving additional evidence that the nitro groups in the molecule are reduced one at a time. In accordance with theory, cells containing the ortho and para isomers have comparable discharge curves and operate at higher potentials than those with the meta isomer during the first part of the discharge. If one assumes that the first nitro group is reduced to the amino stage, the lower potential level of the second step can be explained. It has been shown (4) that a cathode of meta nitroaniline operates at a higher potential during current flow than para nitroaniline.

The effect of both position and type of substitution on operating potential is further illustrated by the discharge data in Fig. 4 for dry cells containing mono nitrobenzene derivatives. The voltage levels of the nitroaniline isomers are seen to correspond to those of the second discharge step of their corresponding dinitrobenzene isomers, giving evidence that the initial cathode reaction involves the reduction of one nitro group to the amino stage, with subsequent reduction of the second nitro group. Also

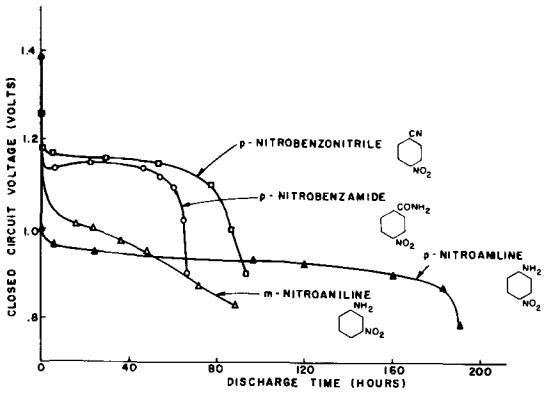


Fig. 4. AA-size dry cells containing a magnesium anode and various substituted nitrobenzene compounds as cathodes discharged continuously through 150-ohm resistances.

shown in Fig. 4 are the different voltage levels obtained when the electron attracting -CN and $-CONH_2$ groups and an electron-repelling $-NH_2$ group are substituted in the para position of nitrobenzene. A curve for a comparable cell containing nitrobenzene is not included, since nitrobenzene is a liquid, which property presents some difficulties in cell assembly. However, from half-cell discharge data (4) it would be expected that a magnesium-nitrobenzene cell would operate at approximately 1.05 v.

## Performance Characteristics of Magnesium-m-Dinitrobenzene Dry Cells

There are a large number of aromatic nitro compounds which are stable solids and have theoretical ampere-minute capacities per unit of weight several times greater than the manganese dioxide and mercuric oxide cathode materials used at present in commercial dry cells (4). In addition, when these nitro compounds are coupled with a magnesium anode, dry cells can be made which have a flat discharge curve and operate over a wide range of current drains within the voltage limits of conventional dry cells.

It is beyond the scope of this paper to characterize fully all types of magnesium-aromatic nitro dry cells because of the vast number of such electrochemical systems. Instead, the magnesium-m-dinitrobenzene couple was selected for a more thorough study to determine some of the factors which affect cell performance, as well as to compare its cell characteristics with those of known dry cells.

*Cell reactions.*—m-Dinitrobenzene, which is produced at present at low cost in tonnage quantities, theoretically has more than 6 times the ampere-minute capacity per unit of weight of manganese dioxide, and 7 times that of mercuric oxide. In addition, it has been found from half-cell coulometric studies, that m-dinitrobenzene cathodes operate at efficiencies in excess of 75%. On this basis, together with the discharge data of the meta and para dinitrobenzene dry cells presented in the previous section, the electrode reactions which are believed to occur during the discharge of a magnesium-m-dinitrobenzene dry cell are shown below.

Although the detailed mechanism has not been worked out for the cathodic reaction, the above

*Cathode reaction:*

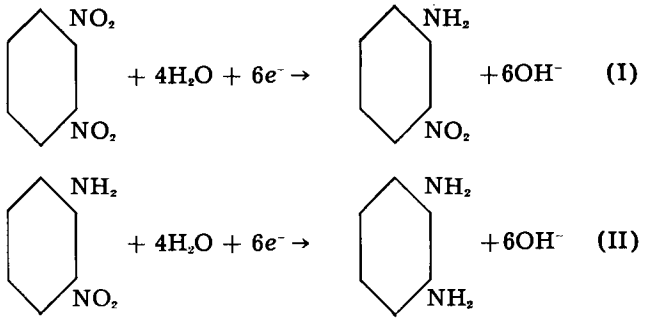


*Anode reaction:*

$$Mg \rightarrow Mg^{++} + 2e^- \qquad \text{(III)}$$

*Over-all energy producing reaction:*

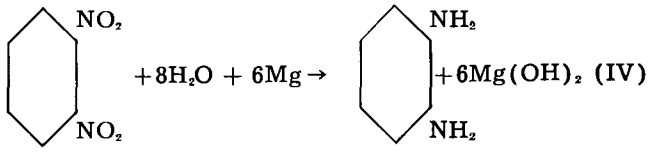


equations offer an explanation for the two-step voltage-discharge curve obtained from these dry cells, showing that reduction takes place one nitro group at a time. In addition, the over-all reduction of an aromatic nitro compound involves a six electron transfer per nitro group which accounts for the high theoretical ampere-minute capacity per unit of weight of these compounds.

*Cell discharge data.*—Experimental magnesium-m-dinitrobenzene AA-size dry cells were assembled using an impact-extruded AZ10A magnesium alloy can. It was found from a cathode mix formulation study that the type of carbon mixed with the m-dinitrobenzene affects cell performance, as well as the ratio by weight of carbon and electrolyte to m-dinitrobenzene. A formulation, previously described, containing a 1 to 2 ratio by weight of m-dinitrobenzene to Darco G-60 carbon black has been found to give favorable results. The performance characteristics of cells of this formulation are discussed below.

Initial capacity data obtained on these cells discharged continuously through 4- and 150-ohm re-

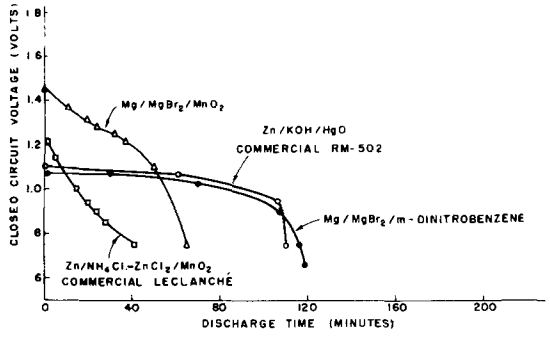


Fig. 5. AA-size dry cells discharged continuously through 4-ohm resistances.

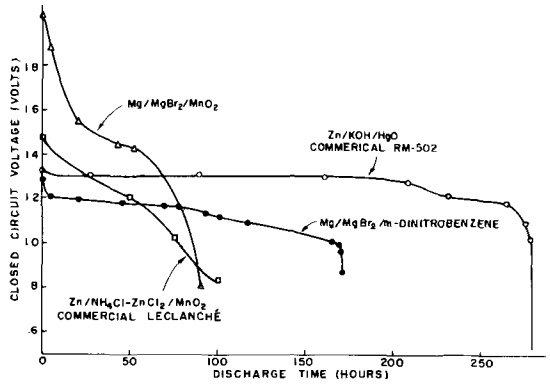


Fig. 6. AA-size dry cells discharged continuously through 150-ohm resistances.

sistances are shown in Fig. 5 and 6. The 4-ohm test represents a drain encountered in a flashlight application, while the 150-ohm test simulates a current drain encountered in a "B" battery or a transistor radio receiver application. Included in Fig. 5 and 6 are discharge data for comparable size Leclanché, zinc-mercuric oxide, and magnesium-manganese dioxide dry cells. The latter cells contained an impact extruded AZ10A magnesium alloy can and are of the type under development by the Dow Chemical Company (5).

The 4-ohm continuous-discharge data show that the m-dinitrobenzene dry cells have a flatter discharge curve than the two manganese dioxide dry cells, being comparable to that of the mercuric oxide cell. It is also seen that, on this test to a 0.90-v end voltage, the m-dinitrobenzene cells give comparable minutes of service to the mercuric oxide cell, and approximately 2 and 4 times the service of the magnesium-manganese dioxide and Leclanché dry cells, respectively.

The data for the 150-ohm continuous-discharge tests also illustrate the flat discharge curve of the m-dinitrobenzene dry cell. On this test, the organic cell gives approximately 90% more hours of service to a 0.90-v end voltage than the two manganese dioxide dry cells, and 38% less hours of service than the mercuric oxide cell.

Capacity data for the four cells obtained from continuous-discharge tests are summarized in Fig. 7 and 8. In Fig. 7 the capacity in hours of service to a 0.90-v end voltage is plotted against load resistance. It is seen that the m-dinitrobenzene cells give considerably more hours of service over a wide range of current drains than the two manganese dioxide dry cells, but are inferior to the mercuric oxide cell, except at high continuous-discharge rates.

In order to normalize the voltage differences between the four cells, watt-minute capacities per unit of weight and volume to a 0.90-v end voltage were plotted vs. average power output. The data in Fig. 8 show that under these conditions of evaluation the m-dinitrobenzene cells have a comparable watt-minute capacity per unit of volume to the magnesium-manganese dioxide dry cell, and 25-230% higher capacity than the commercial Leclanché cell over an average power output range of 5 to 270 mw. At low power output levels, the organic cell gives approximately 45% of the capacity

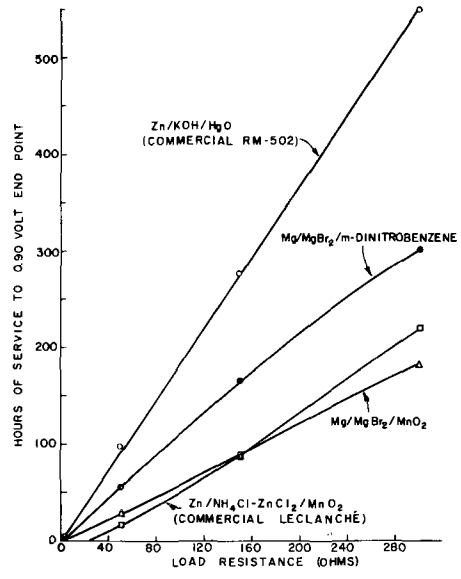


Fig. 7. Capacity in hours of service vs. load resistance of AA-size dry cells discharged continuously through various resistances.

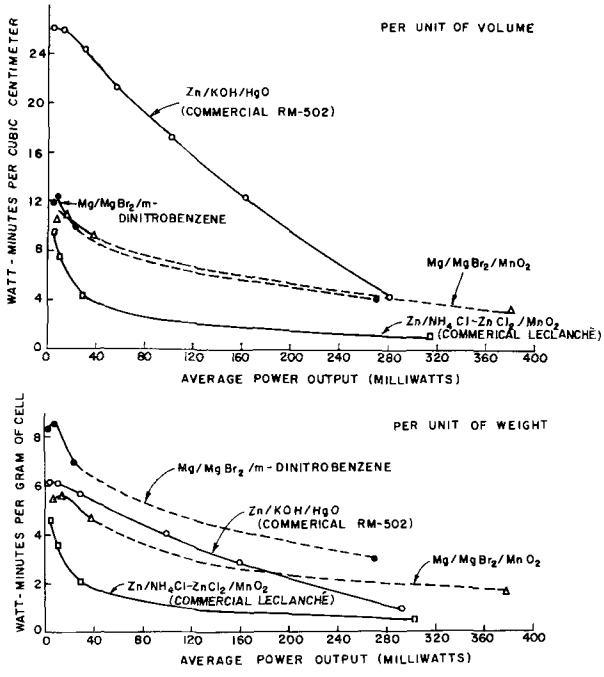


Fig. 8. Capacity in watt-minutes per unit weight and volume vs. average power output for AA-size dry cells discharged continuously through various resistances. (Watt-minute capacity and average power computed to 0.90 v end voltage.)

of the mercuric oxide cell and comparable watt-minute capacities at a power output level of 270 mw.

On the weight basis the m-dinitrobenzene cells give approximately 30% more capacity than the mercuric oxide and magnesium-manganese dioxide cells, and 80-400% greater capacity than the Leclanché cells over a wide range of power output levels.

An additional analysis of the four cells is shown in Table I in which are presented the approximate theoretical ampere-minute capacities and cathode efficiencies computed from the continuous cell discharge data. These data were calculated with the assumption that the cathode material is the limiting cell component.

Table I. Theoretical capacity and cathode efficiency of various AA-penlight size cells

| | Theoretical capacity per gram of cathode material | Approx. wt of cathode material in cell | Approx. theor. cell capacity | Cathode efficiency* of cells discharged continuously through following resistances (ohms) | | | |
|---|---|---|---|---|---|---|---|
| | | | | 4 | 50 | 150 | 300 |
| | (amp-min) | (g) | (amp-min) | % | | | |
| $Zn/NH_4Cl\text{-}ZnCl_2/MnO_2$ | | | | | | | |
| Commercial Leclanché | 18.5 | 3.3 | 60.5 | 11.1 | 40.5 | 60.6 | 89.3 |
| Zn/KOH/HgO | 14.9 | 10. | 149. | 19.3 | 94.6 | 95.2 | 95.4 |
| $Mg/MgBr_2/MnO_2$ | 18.5 | 3.9 | 72.2 | 25.6 | 62.9 | 72.6 | 71.9 |
| $Mg/MgBr_2$/m-Dinitrobenzene | 114.9 | 0.73 | 83.9 | 33.1 | 76.5 | 91.2 | 84.4 |

* Data based on ampere-minute capacity to 0.90-v end voltage.

It is seen from the efficiency data in Table I that the m-dinitrobenzene cathode operates at high efficiencies approaching its theoretical limit on the 150-ohm continuous-discharge test, followed by a slightly lower efficiency on the 300-ohm test. This fall-off in cathode efficiency is also observed with the magnesium-manganese dioxide cell and is attributed to a decrease in magnesium efficiency at the lower current densities. The wasteful corrosion of magnesium consumes water in the cell, which component is essential to the cathodic reaction [Eq. (I) and (II)].

In addition, it is seen that the m-dinitrobenzene cell has a higher theoretical capacity than the two manganese dioxide cells, despite the fact that it has considerably less cathode material. Further performance gains should be possible if a way can be found to put more m-dinitrobenzene in the cell and still obtain the same cathode efficiency.

A significant feature of the m-dinitrobenzene cathode is its high efficiency advantage over the manganese dioxide cathode on heavy continuous-drain tests as seen in Table I. The favorable high-drain characteristics are illustrated also for C-size cells by the 4-ohm continuous and intermittent discharge data presented in Fig. 9. On the continuous test to a 0.90 v end voltage the m-dinitrobenzene cells last 2 and 4 times as long as the comparable size magnesium-manganese dioxide and Leclanché cells, respectively. Some of this capacity advantage, however, is lost on the intermittent test, as the manganese dioxide electrodes become more efficient under these discharge conditions.

## Shelf Life Data for Various Magnesium-Aromatic Dinitro Compound Dry Cells

Listed in Table II are shelf life data for some AA-size dry cells containing various organic dinitro compounds as cathodes. These cells comprised an impact extruded magnesium can, a Nibroc salt-free paper separator, a $MgBr_2$ electrolyte, and were sealed with a rosin wax seal. The data presented in Table II represent single cell results. Each cell

Table II. Shelf life data obtained on "AA"-penlight size cells containing a magnesium anode and various aromatic dinitro compounds as cathodes

| | Hr of service to 0.90 v* | Storage time at 70°F 50% R. H. | | | Storage time at 113°F 90% R. H. (Cells packaged in 6 mil polyethylene bags) | |
|---|---|---|---|---|---|---|
| | | 6 Mos. | 9 Mos. | 12 Mos. | 3 Mos. | 6 Mos. |
| | | Capacity retention in % of initial | | | | |
| **Cells containing various unsubstituted aromatic dinitro cathodes** | | | | | | |
| m-Dinitrobenzene | 147 | 94 | 95 | — | 93 | 80 |
| o-Dinitrobenzene | 139 | — | 93 | 95 | 92 | 114(5)† |
| p-Dinitrobenzene | 176 | 90 | — | 100 | 93 | 72 |
| Crude dinitrobenzene (Mixture of isomers) | 110 | 110 | 72 | 112 | 97 | 100 |
| **Cells containing cathodes of various aromatic dinitro compounds with electron-repelling substituted groups** | | | | | | |
| 2,4-Dinitroaniline | 117 | 114 | 91 | 90 | 100 | 108(83@11 mos.)† |
| 2,4-Dinitrotoluene | 123 | 100 | 111 | 92 | 93 | 100(5) (73@11 mos.)† |
| 2,4-Dinitroanisole | 131 | 106 | 90 | — | — | 100 |
| 2,4-Dinitrophenetole | 142 | 49 | 106 | 95 | 100 | 88 |
| **Cells containing cathodes of various aromatic dinitro compounds with electron-attracting substituted groups** | | | | | | |
| 3,5-Dinitrobenzamide | 140 | 102 | 100 | 98 | 91 | 94(5)† |
| 3,5-Dinitrobenzonitrile | 107 | 33 | 28 | 57 | 85 | 100(5)† |
| Ethyl-3,5-dinitrobenzoate | 136 | 71 | 79 | — | — | — |
| 2,4-Dinitrobenzaldehyde | 120 | 83 | — | 69 | 100 | 100(5)† |
| 2,4-Dinitrobenzene sulfonate, potassium salt | 97 | 78 | 54 | 92 | 100 | 100 |
| 1-Chloro-2,4-dinitrobenzene | 80 | 115 | 88 | 75 | 115 | — |
| 1-Bromo-2,4-dinitrobenzene | 128 | 83 | 94 | 83 | — | — |
| 6,8-Dinitro-2,4-(1H,3H) quinazoline dione | 110 | 80 | 55 | 36 | 100 | 55 |

* Capacity measured at 70°F as hours of service to 0.90 v on 150-ohm continuous-discharge test.
† Figures in parentheses are storage time in months.

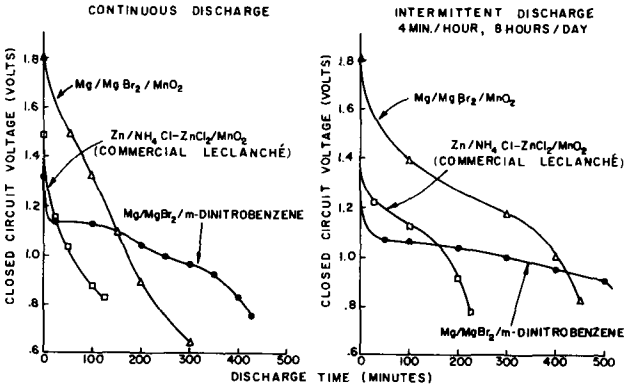


Fig. 9. C-size dry cells discharged through 4-ohm resistances.

tested was from a large group of cells assembled under controlled conditions. It is recognized that a larger test sample is preferred in order to make firm quantitative conclusions by normal statistical methods. However, the results while qualitative do indicate that many of these organic dry cells will have a satisfactory shelf life when stored at temperatures of 70° and 113°F. In several cases there is a difference between the 70°F and high temperature storage data, the cells showing a more favorable shelf life when stored at the elevated temperature. This difference is due to poor seal efficiency which resulted in greater drying out of cells stored at the lower relative humidity. The loss in water would be expected to result in a drop in capacity as water is essential to the cathode reaction as shown in Eq. (I) and (II).

## Conclusions

At the present stage of development, the magnesium-aromatic nitro dry cells have problems primarily associated with the magnesium anode. These are loss in capacity on light intermittent tests, "delayed action," and higher impedance than comparable size commercial dry cells.

## Acknowledgment

The authors wish to express their appreciation to Mr. G. R. Ganges and Dr. G. S. Lozier for assisting in gathering some of the cell data and their many helpful comments made during this study.

Manuscript received Oct. 2, 1957. This paper was prepared for delivery before the Buffalo Meeting, Oct. 6-10, 1957.

Any discussion of this paper will appear in a Discussion Section to be published in the December 1958 JOURNAL.

REFERENCES

1. W. C. Bauer, U.S. Pat. 1,134,093, April 6, 1915.
2. W. C. Arsem, U.S. Pat. 2,306,927, Dec. 29, 1942.
3. D. E. Sargent, U.S. Pat. 2,554,447, May 22, 1951.
4. R. Glicksman and C. K. Morehouse, *This Journal*, **105**, 299 (1958).
5. R. C. Kirk, P. F. George, and A. B. Fry, *ibid.*, **99**, 323 (1952).

# Corrosion of the Zinc Electrode in the Silver-Zinc-Alkali Cell

**T. P. Dirkse and Frank De Haan**

*Department of Chemistry, Calvin College, Grand Rapids, Michigan*

ABSTRACT

A study has been made of the factors that affect or bring about the corrosion of the zinc electrode in a silver-zinc-alkali cell. Cells containing 30% potassium hydroxide as electrolyte were used and kept at room temperature. Special attention was centered on open circuit or stand conditions. This corrosion is affected primarily by oxygen and by dissolved silver oxides.

Although the silver-zinc-alkali cell has been produced for a relatively short time, its applications are increasing and it is becoming a rather widely used system. It is now being marketed as a secondary cell having a fairly good life. It is especially remarkable that these advances and developments have been made without a thorough understanding of the mechanisms of the electrode reactions. Relatively little work of a more or less theoretical or fundamental nature has been reported on this system.

It has been noted (1) that the anodic dissolution of zinc in KOH solutions proceeds in two steps. However, when this reaction takes place in a silver cell the mechanism is undoubtedly more complex since there is then the additional complicating factor of the presence of the silver oxides. It was the purpose of this study to investigate the effect of silver oxides and other factors on this anodic zinc process.

The effect of the silver oxides on the anodic dissolution of zinc in KOH solutions is especially obvious when one studies the relationship of this process to Faraday's laws. Two solutions, 15% and 30% KOH, were used as the electrolyte in cells containing zinc anodes and nickel screen cathodes. Two silver coulometers were connected in series with these cells and a small current density was used for about 2 hr. Comparing the amount of zinc oxidized (dissolved) with that prescribed by Faraday's laws, there were deviations of +4% and +0.1%. When a similar test was made on a cell containing a silver oxide cathode in place of the nickel screen and 30% KOH as the electrolyte, the deviation was +93%, i.e., the loss of zinc was about twice as great as that expected from Faraday's laws. A good deal of this

loss was due to the fact that during passage of current a heavy coating of spongy material formed on the anode (zinc) and fell off when the electrode was removed from the solution. This latter fact, aside from the deviation from Faraday's laws, prompted a further investigation of this process or phenomenon. A similar phenomenon was produced under open circuit conditions, and x-ray analysis showed that the spongy metallic product was the same in each case. Therefore an attempt was made to determine the origin and nature of this deposit. This was done by using only open-circuit conditions.

## Experimental

Samples of zinc sheet, better than 99.9% pure, furnished by the New Jersey Zinc Sales Company, were cut into strips about 1 cm wide. These were degreased and then treated briefly with dilute HCl. In some cases such a zinc electrode, together with another electrode made by pasting silver oxide on a silver screen, was placed in a large test tube containing about 50 ml of 30% KOH solution. The electrodes were electrically insulated from each other, about 2 cm apart. After being in the cell for 24 hr, the zinc was withdrawn, briefly immersed in 6M acetic acid, then in distilled water, in ethanol, and finally in acetone. Following this the electrode was dried by heating for a short while. Each run was carried out in a constant temperature bath held at 25° ± 0.1°C. The loss of zinc was determined by the difference in weight. The surface area of the immersed zinc was about 10 $cm^2$. In some runs the silver oxide electrode was omitted, and in others a smaller test tube and a smaller volume of electrolyte were used. X-ray diffraction patterns were obtained by the use of copper radiation with a nickel foil filter.

## Results

It soon became apparent that even on open circuit several factors were involved in the corrosion of the zinc. When cells were assembled using silver oxide, the zinc sheet, and 30% KOH solution, the zinc electrode always became covered with a dark black film. This film had a velvety appearance when viewed with a microscope. A black film is sometimes noted on the zinc electrodes after a discharge; then it is often due to a form of zinc oxide (1). In this case, however, the black film did not appear to be the zinc oxide. It did contain varying, but appreciable, amounts of silver or its oxides. This was noted by dissolving a portion of the electrode in nitric acid and then adding HCl to precipitate the silver as the chloride. X-ray diffraction patterns obtained from this film contained the lines due to zinc, but there were other additional lines as well, particularly at about 2.25 and 2.15Å. These extra lines were found in all such samples. Furthermore, these same lines were found in the spongy material that peeled off the zinc electrode when it was removed from the solution after having received a 24-hr anodic treatment. They were also produced by the dark colored film that forms on the zinc shortly after the discharge of a silver oxide-zinc-alkali cell is begun. These two lines are not due to silver or its oxides. The indications then, are that, although silver or its oxides were found on the zinc electrode, they were not present in appreciable quantities as metallic silver or oxides of silver. This black film was formed only when the silver oxide was present in the cell, not when zinc alone was immersed in the KOH solutions. Thus the silver oxide electrode is in some manner related to this film on the zinc. However, the effects of other conditions were also studied.

Table I gives a summary of the results obtained. Column 2 indicates the conditions under which each run was made. In some runs no electrode of silver oxide was present, but rather some silver oxide powder was placed in the test tube with the electrolyte and the zinc was placed on glass beads in the bottom of the test tube. This is indicated in column 3. In other cases the zinc specimen was given a silver coating by dipping it in a silver nitrate solution before it was assembled in the cell. This is indicated in Column 5. Column 7 refers to the nature of the coating formed on the zinc specimen. The term "light black" indicates a thin deposit of the black material.

From these results several conclusions can be drawn as to the nature of the process taking place. First of all it appears that under the conditions prevailing in these experiments the amount of electrolyte had but little effect (*see* runs 17 and 21).

A significant factor is oxygen, either dissolved in the electrolyte, or present in the atmosphere above

**Table I. Factors contributing to the corrosion of zinc in 30% KOH at 25°C**

| No. | Conditions* | Silver present as: silver oxide powder in electrolyte | Silver present as: silver oxide electrode | Silver present as: metallic coating on zinc | Wt loss of zinc in mg | Color of film |
|---|---|---|---|---|---|---|
| 1 | a, g | | x | | 337 | spongy |
| 2 | a, c, g | | x | | 130 | black |
| 3 | g | | x | | 52 | black |
| 4 | c, g | | x | | 55 | black |
| 5 | c, f, g | | x | | 26 | black |
| 6 | b, g | | x | | 136 | black |
| 7 | b, c, g | | x | | 145 | black |
| 8 | e, g | | x | | 138 | black |
| 9 | h | x | | | 18 | light black |
| 10 | h | x | | | 31 | light black |
| 11 | f, h | x | | | 3 | light black |
| 12 | d, h | | | x | 78 | clear |
| 13 | d, f, h | | | x | 29 | clear |
| 14 | d, h | | | x | 65 | clear |
| 15 | a, g | | | | 46 | clear |
| 16 | h | | | | 39 | clear |
| 17 | h | | | | 43 | clear |
| 18 | b, g | | | | 8 | clear |
| 19 | e, h | | | | 31 | clear |
| 20 | d, h | | | | 6 | clear |
| 21 | g | | | | 43 | clear |

* The various conditions are: a, air bubbled through electrolyte throughout experiment; b, nitrogen bubbled through electrolyte throughout experiment; c, electrolyte saturated with zinc oxide; d, zinc completely submerged, i.e., no "water line" effect; e, electrolyte contains 0.2% hydrogen peroxide; f, electrolyte was not fresh but had just been used for another run; g, 50 ml of electrolyte used; h, 6 ml of electrolyte used.

the electrolyte. There is no doubt that such oxygen affects the corrosion of zinc. In these experiments white deposits of zinc oxide were sometimes formed at the electrolyte surface. This oxide is soluble in KOH solutions and hence such oxide formation offers no protection against corrosion. The effect of oxygen is noted by comparing run 1 with 3 and run 2 with 4. In each pair all the conditions were alike except for the bubbling of air through the electrolyte. However, even when air was not bubbled through the solution, the effect of oxygen could be noted. Comparison of run 4 with 5, 10 with 11, and 13 with 14, shows the effect of dissolved oxygen. In runs 5, 11, and 13, the electrolyte was not fresh. Consequently, dissolved oxygen had already been consumed. Comparing these with otherwise identical runs it is seen that in each case the corrosion of zinc was considerably less with the oxygen-deficient electrolyte. This was true whether silver oxide was present or not.

Still more evidence for this is found by comparing runs 17 and 20. In run 20 the zinc was completely submerged, whereas in 17 part of the zinc was out of the electrolyte. The zinc was attacked to a greater extent in the latter case where atmospheric oxygen as well as dissolved oxygen was available for reaction. Furthermore, in run 18 nitrogen was bubbled through the electrolyte thus removing the oxygen. Here again the weight loss of zinc was less than in run 21.

Thus the oxygen does attack the zinc. The mechanism of this reaction probably involves local cells containing zinc and oxygen electrodes. In effect, the oxygen transforms the zinc to zinc oxide or hydroxide which then dissolves in the KOH solution. If this is the course of the process, then, if the electrolyte were saturated with zinc oxide, the oxidation product of the zinc would not dissolve as readily and this product might then offer some protection to the remaining zinc. In run 2 an electrolyte saturated with zinc oxide was used and the attack on zinc was definitely less than in run 1. In both these runs air was bubbled through the electrolyte, thus heightening the effect of oxygen. Where this was not done the effect of zinc oxide-saturated potassium hydroxide was negligible, e.g., runs 3 and 4, runs 6 and 7.

However, under certain conditions, passing air through the electrolyte made very little difference. In run 15 the loss in weight of zinc was about the same as that in run 21. This may indicate that the oxygen attack is primarily by the dissolved oxygen. This difference may have been more pronounced if the run had continued longer.

Oxygen attacks and corrodes the zinc electrode, but this attack by itself does not produce the black film referred to earlier. Silver oxide is necessary for this and it produces the black film even in the absence of oxygen, run 6. Thus the actions of oxygen and of silver oxide are different, but they often occur simultaneously.

The effect of silver oxide electrodes on the corrosion of zinc is readily seen by comparing run 1 with 15, 3 with 21, and 6 with 18. In each case the corrosion of zinc was greater in the presence of the silver oxide electrodes. The difference was not the same in each of these three cases. The reasons for this are: (*a*) the weight loss is not accurate in each case since, especially in run 1, a large amount of spongy metallic material was formed which fell off when the electrode was removed; (*b*) in some cases the electrolyte was agitated with air or with nitrogen. When no agitation was used, runs 3 and 21, the difference was significant but not large. When the electrolyte was agitated by bubbling nitrogen through it, the corrosion loss of zinc due to the presence of silver oxide electrodes was greater (runs 6 and 18). In each case the zinc received a velvety black coating or a spongy metallic deposit.

An explanation for this phenomenon involves the ready dissolution of silver oxide in KOH solutions. This is shown on Fig. 1. Small amounts of silver oxide were placed in stoppered flasks containing 25% KOH solution. These mixtures were kept at room temperature and shaken occasionally; from time to time samples were withdrawn, filtered through glass wool, and analyzed for silver by titrating potentiometrically with a potassium iodide solution. The results show that the silver oxide dissolves rapidly in KOH solutions. When zinc was added to these solutions the dissolved silver was removed rather rapidly.

Quite likely then, the silver oxide from the electrode dissolves in the KOH electrolyte. When this dissolved silver oxide reaches the zinc electrode it reacts with the zinc and precipitates there, the reactions probably being

$$Ag_2O + H_2O + 2\,OH^- \rightarrow 2\,Ag(OH)_2^- \qquad (I)$$

$$2\,Ag(OH)_2^- + Zn \rightarrow Zn(OH)_2 + 2\,Ag + 2\,OH^- \qquad (II)$$

$$Zn(OH)_2 + 2\,OH^- \rightarrow Zn(OH)_4^{--} \qquad (III)$$

This mechanism accounts for the presence of silver found in the black film or metallic deposit on the zinc specimens. It also accounts for the effect of agitation, e.g., compare run 3 with 6 where no oxygen was present but the solution was agitated with nitrogen. This agitation hastens the diffusion

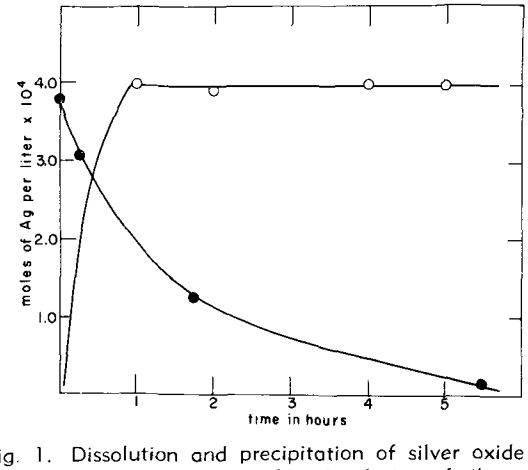


Fig. 1. Dissolution and precipitation of silver oxide from 25% KOH solution. Open circles, dissolution of silver oxide; closed circles, precipitation of dissolved silver oxide by metallic zinc.

of silver oxide to the zinc specimen; thus reaction (II) takes place more rapidly. Comparison of run 4 with 7 supports this hypothesis.

Further support for this mechanism is found in the fact that the appearance of the dark film on the zinc when the silver-zinc cell is discharged is more rapid as the temperature increases and as the concentration of the KOH increases. Increasing the temperature would increase the solubility of silver oxide and also the rate of diffusion of dissolved ions. The solubility of silver oxide also increases with increasing hydroxyl ion concentration (2).

When a little silver oxide was added to the electrolyte in the absence of silver oxide electrodes, the effect was slight (runs 9 and 10). This was undoubtedly due to the fact that the silver oxide rested on the bottom of the test tube with the zinc specimen suspended above it. In this case the dissolved silver oxide would have had to diffuse upward. That some of it did was shown by the fact that the zinc did become covered with a light black film. This was heaviest at the bottom of the electrode.

The dissolved silver oxide is largely in the form of a negative ion. Therefore, it is obvious that reaction (II) will be hastened during the discharge of the cell, since then the zinc functions as the anode. The silver ions will then migrate more rapidly to the zinc. For this reason too the same kind of film is formed on the zinc during discharge of the cell as during stand.

There still remains the question of the origin of the spongy metallic deposit on the zinc, especially in run 1. As has been noted, this deposit contained silver, but no silver lines were found in the x-ray pattern. Instead there were zinc lines plus others. A possible mechanism for this phenomenon is given below.

When reaction (II) takes place it may do so only at certain sites in the zinc lattice. The reduced silver atom then replaces the oxidized zinc atom. This gives the ordinary zinc lattice with silver atoms substituted for zinc atoms at certain points. The result is a solid solution of silver in zinc. Many studies have been made of the silver-zinc system. Of particular help is the work of Westgren and Phragmen (3), Owen and Pickup (4), and Owen and Edmunds (5), where the zinc-rich phases are discussed. Westgren and Phragmen give much information on the x-ray patterns of this system. The designation of the various phases differs, so such phases will be designated here by composition.

On Fig. 2 are given the x-ray lines for zinc, some silver-zinc alloys or solid solutions, and for a representative film obtained in our work. The lines obtained from the black film on the zinc specimens consist of those of zinc plus some of those of the silver-zinc solid solution having a composition varying from 50 to 80% zinc. The lines in Fig. 2b vary somewhat with the amount of zinc present (3). The region 51-60% zinc consists of a mixture of the two phases represented in Fig. 2b and 2c (4). These x-ray data lend support, then, to the hypothesis that, when the dissolved silver oxide reacts with the

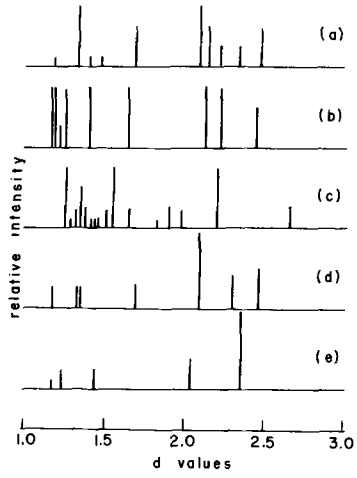


Fig. 2. X-ray patterns: (a) representative dark film obtained in this work; (b) Ag-Zn solid solution ranging from 60 to 78% Zn, ref. (3); (c) Ag-Zn solid solution ranging from 48 to 51% Zn, ref. (3); (d) zinc, ref. (6); (e) silver, ref. (6).

zinc, a solid solution of silver in zinc is formed on the surface of this zinc.

Furthermore, with this hypothesis one also has an explanation for the spongy metallic deposit formed on the zinc specimen in a few of the runs. As has been noted, analysis showed that this deposit contained zinc and silver. The potential of the silver-zinc solution is less anodic than that of zinc and hence the solid solution can be deposited by the emf of zinc itself. This explanation was also suggested by Straumanis and Fang (7) who studied a similar phenomenon in acid solutions.

There is also other evidence that metallic silver as such is not involved in this process. When zinc was covered wtih silver before being assembled in the cell (runs 12, 13, and 14) there was an increase in corrosion (compare with run 20) but there was no visible film on the zinc. Furthermore, when a silver electrode and a zinc specimen were electrically connected in a 30% KOH solution the zinc dissolved and hydrogen was evolved, vigorously at first, on the silver, but after 24 hr no zinc appeared on the silver electrode. The reaction probably was

$$Zn + 2\,H_2O + 2\,OH^- \rightarrow Zn(OH)_4^= + H_2 \qquad (IV)$$

Two runs were also made to test the effect of hydrogen peroxide on this corrosion of zinc. The presence of the $HO_2^-$ ion increases the corrosion of zinc considerably when silver oxide is present (*see* runs 3 and 8). On the basis of thermodynamic considerations this could be expected since the free energy decrease for reaction (V) is about 25 kcal greater than for reaction (VI).

$$Ag_2O + HO_2^- + 2Zn + 2H_2O \rightarrow 2Ag + 2Zn(OH)_2 + OH^- \qquad (V)$$

$$2Ag_2O + 2Zn + 2H_2O \rightarrow 4Ag + 2Zn(OH)_2 \qquad (VI)$$

However, the mechanism is likely not as simple as indicated.

In the absence of silver oxide, the effect of hydrogen peroxide is less, (*see* runs 17 and 19). In fact, the presence of the $HO_2^-$ ion seems to reduce the corrosive loss of zinc. The effect, however, is small.

## Conclusion

In a silver-zinc-alkali cell the zinc electrode is attacked and oxidized by oxygen. When no diaphragm is present to reduce or eliminate diffusion, dissolved silver oxide migrates to the zinc electrode where it is reduced and forms a solid solution with the zinc, or else is deposited as such. This enables zinc or silver-zinc solid solution to precipitate from the electrolyte in a spongy form on the zinc electrode during open-circuit conditions and this may act as a short between the plates.

## Acknowledgment

The authors wish to express thanks to the Office of Naval Research for sponsoring this project, to the New Jersey Zinc Sales Company for furnishing some of the materials, and to Mrs. Jeanne Burbank for her help in interpreting the x-ray work.

Manuscript received Nov. 4, 1957.

Any discussion of this paper will appear in a Discussion Section to be published in the December 1958 JOURNAL.

REFERENCES

1. T. P. Dirkse, *This Journal*, **102**, 497 (1955).
2. H. L. Johnston, F. Cuta, and A. B. Garrett, *J. Am. Chem. Soc.*, **55**, 2311 (1933).
3. A. Westgren and G. Phragmen, *Phil. Mag.*, **50**, 311 (1925).
4. E. A. Owen and L. Pickup, *Proc. Roy. Soc. London*, **140A**, 344 (1933).
5. E. A. Owen and I. G. Edmunds, *J. Inst. Metals*, **57**, 297 (1935); **63**, 265, 279, 291 (1938).
6. H. E. Swanson and E. Tatge, "Standard X-ray Diffraction Powder Patterns," National Bureau of Standards Circular 539, Vol. I, Washington, D. C. (1953).
7. M. E. Straumanis and C. C. Fang, *This Journal*, **98**, 9 (1951).

# Diffusion of Oxygen in Zirconium and Its Relation to Oxidation and Corrosion

**J. Paul Pemsler**

*Nuclear Metals, Inc., Cambridge, Massachusetts*

ABSTRACT

The diffusion of oxygen in zirconium and dilute zirconium alloys has been studied in the temperature range of 400° to 585°C by observing the rates of dissolution of anodically deposited interference oxide films. The diffusion coefficient of oxygen in zirconium depends on the grain orientation and varies by a factor of two among different orientations. Macroscopically observed average values obey the equation

$$D, \text{cm}^2/\text{sec} = 9.4 \exp [(-51{,}780 \pm 220)/RT]$$

where the activation energy for the diffusion of oxygen in zirconium is 51.78 kcal/mole. No macroscopic differences were observed in the diffusion coefficients of the various dilute alloys. Oxidation and corrosion rates have been observed to have an orientation dependence similar to that observed in the diffusion study. The mechanism of oxidation and corrosion is discussed in terms of diffusion of oxygen and adherence of oxide films.

Zirconium shares with titanium and hafnium the unusual ability to dissolve large amounts of oxygen in interstitial solid solution. The oxygen is strongly bound to the lattice, as evidenced by the fact that the metal can be heated beyond its melting point without oxygen evolution. Few data exist concerning the rate of diffusion of oxygen in zirconium metal, especially at temperatures where its corrosion properties are of interest in nuclear reactor applications.

Investigators have defined the zirconium-oxygen phase diagram and made observations on the nature of the oxygen in the zirconium lattice. De Boer and Fast (1) studied the solution of oxygen in the zirconium lattice and concluded that all the oxygen in the metal is present in solid solution. They observed the migration of oxygen as negative oxygen ions under the influence of a potential drop. The binary phase diagram of the zirconium-oxygen system has been studied by Hansen, McPherson, and Domagala (2), who showed that the equilibrium solubility of oxygen in alpha zirconium is independent of temperature and has a value of 29 at. %.

The only other definitive study on the diffusion of oxygen in zirconium was carried out simultaneously with this work by Mallett, Albrecht, and Wilson (3) who determined the diffusion coefficient of oxygen in alpha and beta Zircaloy by the moving boundary and concentration gradient techniques, respectively. Over the temperature range studied, 1000°-1500°C, the equations for diffusion coefficients in the alpha and beta phase were:

$$D_\alpha = 0.196 \exp [(-41{,}000 \pm 1500)/RT]$$

and

$$D_\beta = 0.0453 \exp [(-28{,}200 \pm 2400)/RT]$$

Misch (4), whose technique was similar to that used here, studied the rate of oxide film dissolution over a temperature range of 450°-600°C. He reported a linear rate of dissolution at 450°C cor-

responding to 0.6 Å/min, and measured an energy of activation for the process of 43.5 kcal/mole. The results and interpretation in this investigation differ from those of Misch.

## Experimental

In this investigation the diffusion of oxygen in zirconium and zirconium alloys was studied by following the rate of dissolution of anodically deposited interference oxide films when annealed *in vacuo*. The thickness of the oxide film was determined periodically during the experiment by observing its color.

*Materials.*—The alloys used in this study are listed below.

Zirconium—high purity, low hafnium crystal bar
Zircaloy-2 (1.5 weight per cent [w/o] Sn, 0.12 w/o Fe, 0.05 w/o Ni, 0.10 w/o Cr)
Zircaloy-3A (0.25 w/o Sn, 0.25 w/o Fe)
Zirconium—0.62 w/o Ni
Zirconium—0.93 w/o Cr
Zirconium—0.82 w/o Fe, 0.13 w/o Ni, 0.95 w/o Cr

*Sample preparation.*—Samples of zirconium and alloys, about 7 cm x 1 cm x 0.2 cm, were cut from rolled stock, annealed for 1 hr at 800°C, and furnace cooled. They were then polished on 400 grit Carborundum on a wet wheel and etched for 2 min in a bath of 50% $HNO_3$, 5% HF, and 45% $H_2O$.

*Anodic deposition of oxide film.*—Oxide films were deposited anodically from a 1% KOH solution in distilled water, with the sample as anode and a platinum wire as cathode. Samples were anodized for 15 min in steps of the desired voltage increment in a manner similar to that used by Misch in his study (4). Except for one end attached to an alligator clip, the suspended specimen was entirely submerged in the bath. After anodizing for 15 min the current was stopped, the sample withdrawn, rinsed with distilled water, and reimmersed to within 1 cm of the previous immersion. The voltage was increased by the desired increment and anodization started. In this way a step gauge strip was produced with a number of successively thicker oxide films. Table I lists the colors observed for different increasing voltages. In order to study the variation in thickness of anodically deposited oxide films with applied voltage, samples were weighed on a microbalance between successive anodizations. In these cases the same length of sample was immersed during each anodization.

Table I. Variation of color with applied voltage for anodically deposited $ZrO_2$ films

| Voltage | Color |
|---|---|
| 5 | Light yellow |
| 7½ | Amber |
| 15 | Dark blue |
| 22½ | Light blue |
| 30 | Silver |
| 37½ | Yellow |
| 50 | Orange |
| 65 | Wine |
| 80 | Green |
| 95 | Yellow |

*Film dissolution.*—Film dissolution was carried out in two different systems. In the first, a dynamic vacuum was maintained throughout the experiment. The specimen was contained in a tantalum or zirconium boat placed in a Vycor tube which was sealed at one end and had a ground glass joint at the other end. The tube was attached to a vacuum system and evacuated for at least 1 hr after a pressure of $10^{-6}$ mm Hg was attained. A thermocouple sealed into the tube was in contact with the specimen. A ball and socket ground glass joint enabled the tube to be swung into a horizontal tube furnace which had been preheated to the desired temperature and controlled to ±3°C by a temperature controller. The thermocouple indicated that the sample reached temperature in about 5 min. Periodic examination of the specimen was made under fluorescent light by lifting the top half of the furnace. The examination could be made quickly so that the temperature of the specimen, as indicated by the thermocouple, was not affected at all, or only slightly affected for a brief period. The color of each zone changed with time in the direction of decreasing film thickness, so that any given color corresponding to a particular oxide thickness would go through all the colors in Table I corresponding to films thinner than it. At any given time, the decrease in film thickness was found to be independent of the original thickness of a particular zone; thus, identical results were obtained using any one of the color zones as indicator. However, certain colors corresponding to a narrow range of thickness, and easy to detect, were used to decide when a given film thickness was reached within a smaller range of error. The approach to these colors could be estimated to within as little as ±0.5 v or 15Å.

The second system used for film dissolution involved a static vacuum. The sample, contained in a boat, and a wad of zirconium turnings were placed at opposite ends of a 15-in. Vycor tube sealed at one end. The tube was evacuated to $10^{-6}$ mm Hg or better and sealed off. The end containing the zirconium turnings was placed into the tube furnace and kept at 800°C for 1 hr, while the end containing the specimen extended far enough out of the furnace to prevent it from becoming heated. This treatment served to getter any remaining atmosphere in the tube. From this point on, the procedure was similar to the dynamic vacuum system, except that the thermocouple was external to the tube and the time required for the sample to reach temperature could not be estimated with the accuracy attainable in the first method.

## Results and Discussion

### *The Anodic Film*

The relation between the weight gain and applied voltage during the anodization of three different zirconium specimens was determined. The weight gain is linear with applied voltage from 0 to 65 v. An increase in slope corresponding to a higher rate of weight gain with voltage was obtained above 65 v. This latter increase may have been due to impurities in the anodizing bath. The majority of

studies were made using a maximum film thickness corresponding to values less than 65 v. Assuming a value of 5.7 for the density of $ZrO_2$, the oxide film thickness deposited during anodization corresponds to 29.0Å/v in the range of 0-65 v. This result is in good agreement with studies by Polling and Charlesby (5) and Misch (4), who obtained conversion factors of 27Å/v and 30Å/v, respectively.

Difficulty was observed during the anodization of several iron-containing alloys when there occurred an appreciable "creepage" of oxide film from the water line into the color zone above. Anodizations of these specimens at high voltages produced a dull film, and there was a great deal of bubbling compared to that observed while pure zirconium was being anodized. Further, during the subsequent vacuum anneal of these alloys, there was a dullness and fading of color compared to the bright reflecting film on pure zirconium and other alloys. The failure to form a suitable anodic film in these alloys is believed to be due to the low oxygen overvoltage on iron intermetallics. The vigorous liberation of oxygen in many areas during anodization prevented the formation of an adherent oxide film. Alloys containing appreciable amounts of iron present as finely divided second-phase particles are not amenable to this type of investigation.

Polling and Charlesby (6) report that, with respect to rate effects, anodically formed films are equivalent to air-formed films. Misch (7) criticizes this viewpoint, stating that anodic films are formed under high field strength which subjects the film to a very large pressure. In the corrosion reaction the formation field is much lower than in anodization except when anodizing at very low voltages.

In order to ascertain whether anodically deposited films are comparable to oxidation films, a zirconium sample was oxidized slowly in an oxygen atmosphere until a thin interference film oxide was formed. Subsequent vacuum annealing of this sample gave results in good agreement with the data obtained using anodically deposited films. While these anodic oxide films may differ initially from corrosion films, it appears that at elevated temperatures, in a short time compared to the time of the diffusion experiment, the mobility of oxygen in the metal and oxide causes the anodic film to behave similarly to a corrosion film, at least insofar as its dissolution rate is concerned.

### *Diffusion Coefficients*

Data obtained using the dynamic vacuum suffered from a lack of reproducibility. Samples run side by side and at the same time gave identical results, but repetitions at a different time did not always agree with the previous data. During certain runs, a yellow tinge on some of the samples was noticed, especially at the end that had no original anodic deposit. This was undoubtedly due to the formation of yellow zirconium nitride, with the sample acting as a continuous getter for the residual atmosphere in the system. The nitride persisted during the diffusion, indicating that the mobility of nitrogen in zirconium is small compared to that of oxygen at the temperatures used in the diffusion anneal. On one occasion when the vacuum system suffered a small leak during an experiment, there was actually a reversal in the film dissolution process and the film thickened with time. However, in cases where the surface was free from nitride, results of the dynamic and static methods were in good agreement. The second technique of gettering the remaining atmosphere in a static system provided a method of obtaining consistently reproducible data.

Microscopic examination of samples which have been anodized and subsequently vacuum annealed revealed that the dissolution process was not homogeneous, and that, macroscopically, an average process was being observed. A wide range of colors, sharply defined by grain boundaries, was observed under a microscope. Under similar magnification an anodized specimen, before vacuum annealing, was homogeneous in color, except for small differences in the tints of some grains. These differences may have been due to small differences in the reactivity or reflectivity of the variously oriented grains. The results presented in this section are then based on a macroscopic, average estimate of color. Variation in diffusion coefficient from grain to grain depending on orientation is discussed in detail in the next section.

The decrease in thickness of oxide film as a function of time has been measured at five different temperatures. The results are plotted in Fig. 1, 2,

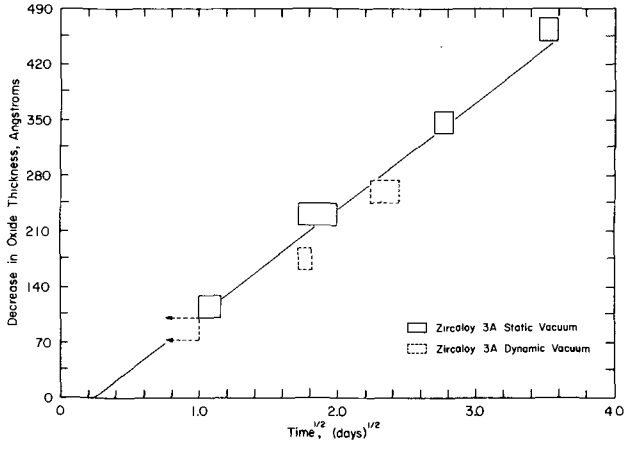


Fig. 1. Decrease in thickness of oxide film as a function of time, at 400°C.

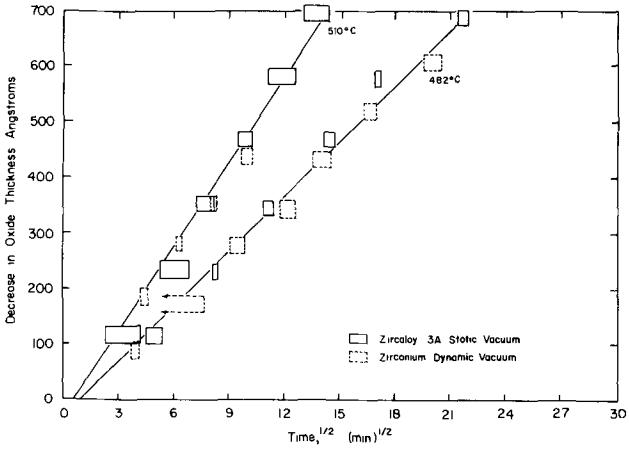


Fig. 2. Decrease in thickness of oxide film as a function of time, at 482° and 510°C.

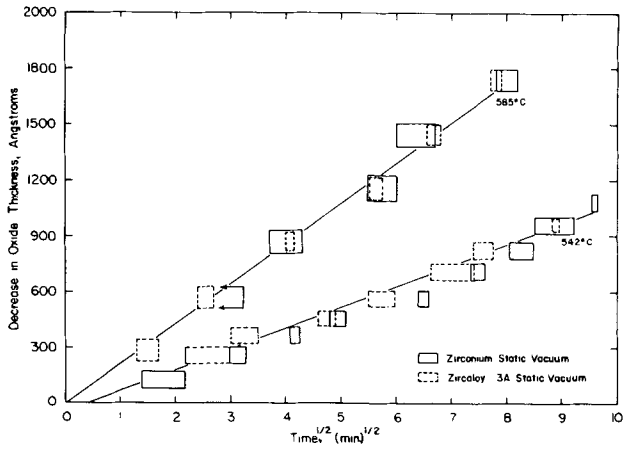


Fig. 3. Decrease in thickness of oxide film as a function of time, at 542° and 585°C.

and 3. Since the samples were examined intermittently, and the thickness estimated visually, each experimental observation is indicated by a rectangle whose dimensions correspond to estimates of the error in the observation. A plot of the decrease in film thickness vs. the square root of time is linear. Extrapolations of some of these lines miss the origin by a small amount, possibly corresponding to very small errors in estimation of the time when the sample came to temperature. Since the equilibrium partial pressure of oxygen over $ZrO_2$ is of the order of $10^{-56}$ atm at 600°C, the disappearance of oxide film must be due to solution of oxygen in zirconium metal, with a consequent growth of metal at the expense of oxide. Misch (4) measured the time dependence of dissolution of anodic oxide films at a single temperature. His points, based on a single observation of each sample after a given time interval, show appreciable scatter. Although he suggests a linear rate of dissolution, his data when replotted appear to fit a parabolic function about as well as they fit a straight line. The reproducibility in this study is better than is Misch's, and repeated observation of the same sample shows that a linear time-dissolution relationship is definitely excluded.

The parabolic rate of disappearance of the oxide film on zirconium suggests that the rate-determining step in the dissolution process is the diffusion of oxygen in zirconium metal. An alternative rate-determining step, the transfer of oxygen across the oxide-metal interface, would be expected to lead to a linear rate of disappearance of oxide. The consumption of oxide, generating additional metal, is accompanied by an outward motion of the oxide-metal boundary until the oxide is entirely consumed. Mathematically, this case falls within a limited class of moving-boundary diffusion problems, for which solutions are readily found. The diffusion equation is discussed in detail elsewhere (8). From the solution found on the assumption of constant diffusivity, $D$ can be found as

$$D = \frac{1}{4b^2}\left(\frac{x'}{\sqrt{t}}\right)^2$$

where $b$ is found to satisfy the equation

$$b\,(1 + \operatorname{erf} b) = \frac{1}{\sqrt{\pi}}\frac{C_o}{m_o}e^{-b^2}$$

Here in time $t$, there is a displacement of the oxide-metal boundary $x'$, which is related to the observed decrease $\Delta L$ in thickness of oxide film by the following expression involving the respective molecular volumes:

$$x' = \frac{\rho ZrO_2}{\rho Zr \text{ saturated}}\,\frac{\text{Formular weight (Zr sat)}}{\text{Formular weight } (ZrO_2)}\,\Delta L$$

The quantity $\rho$ is the density, and $C_o$ is the difference between the saturated concentration $C_s$, and the initial concentration, of oxygen in the metal. The quantity $m_o$ represents the weight of oxygen removed from the $ZrO_2$ consumed in the generation of unit volume of saturated zirconium ($ZrO_{0.41}$). It may be expressed as

$$m_o = \frac{\text{Formular weight } (O_{1.59})}{\text{Formular weight } (ZrO_{0.41})}\,\rho_{Zr\ sat}$$

In this work the values used are: $C_o = C_s = 0.450$ g/cm³ (the initial concentration was taken as zero); $m_o = 1.75$ g/cm³; $x' = 0.676\ \Delta L$, cm; $\rho_{Zr\ saturated} = 6.72$ g/cm³ (9); $\rho_{ZrO_2} = 5.73$ g/cm³ (10); $b = 0.126$. The densities of saturated zirconium and $ZrO_2$ were taken as the best available data at room temperature. No effort was made to correct these data to higher temperatures.

The solution is unique if $D$ is constant. The agreement of the experimental results with the expression derived on the basis of constant $D$ does not establish that $D$ is, in fact, independent of concentration. Evidence for the constancy of $D$, at least in beta zirconium, is found in the work of Mallett, *et al.* (3). They found that the concentration distribution of oxygen diffused into specimens of beta zirconium could be fitted with constant-diffusivity solutions of the diffusion equation.

The diffusion coefficients of oxygen in zirconium at five temperatures are listed in Table II. A plot of the logarithms of the diffusion coefficient vs. the reciprocal of the absolute temperature over the range studied here is shown in Fig. 4. The resulting straight line is in excellent agreement with an Arrhenius temperature dependence, and an energy of activation of 51.8 kcal/mole is calculated. The equation for the diffusion coefficient of oxygen in zirconium in the temperature range of 400°-585°C is given by $D$, cm²/sec $= 9.4 \exp\,[(-51{,}780 \pm 220)/RT]$.

In the results of Mallett, *et al.* (3), the diffusion coefficient of oxygen in alpha Zircaloy-2 has been determined over the temperature range 1000°-

**Table II. Diffusion coefficients of oxygen in zirconium**

| $D$, cm²/sec | T, °C |
|---|---|
| $1.34 \times 10^{-16}$ | 400 |
| $1.21 \times 10^{-14}$ | 482 |
| $2.79 \times 10^{-14}$ | 510 |
| $1.38 \times 10^{-13}$ | 542 |
| $5.62 \times 10^{-13}$ | 585 |

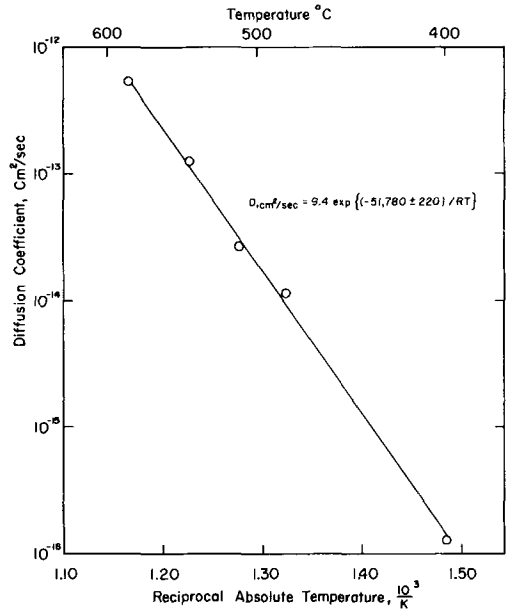


Fig. 4. Temperature dependence of the diffusion coefficient of oxygen in zirconium.

1500°C by the moving boundary technique, which makes use of the stabilization of alpha zirconium at high temperatures. The Arrhenius plot of Mallett's data together with the results of this study are presented in Fig. 5. Mallett calculated an energy of activation for diffusion of 41.0 kcal/mole. The agreement between these data is excellent considering the large differences in temperature ranges studied and in the techniques used. Extrapolation of Mallett's equation to the temperature range studied here would estimate a value for the diffusion coefficient which is high by a factor of about ten. Extrapolation of the equation obtained here to high temperatures gives excellent agreement with Mallett's data. One is tempted to draw a single least squares line through all the data from 400°-1500°C which is represented by the following equation:

$$D, \text{ cm}^2/\text{sec} = 5.2 \exp\ (-50{,}800 \pm 870)/RT$$

The activation energy obtained using all the data is in excellent agreement with that derived from the low temperature data alone.

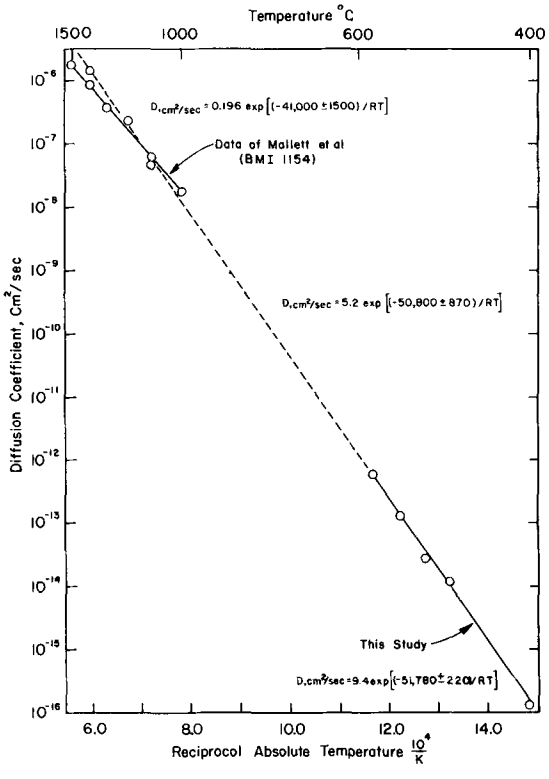


Fig. 5. Combined data for the temperature dependence of the diffusion coefficient of oxygen in zirconium.

*Orientation Dependence of the Diffusion Coefficient*

The results presented above are based on a visual estimation of the over-all extent of the diffusion. Microscopic examination of a particular color zone on a sample, after the diffusion anneal was completed, showed that a wide variation of colors was visible. For example, an area that appeared homogeneously light blue to the naked eye resolved under magnification into an approximately equal number of areas of dark blue, medium blue, light blue, silver, and light yellow color. These colors are sharply defined by grain boundaries. As previously discussed, the anodization produced a homogeneously colored oxide film.

The relation of grain orientation to diffusion coefficient was studied with the aid of a zirconium strip with very large grain size. Twenty-five separate grains, with an average grain size of 4 mm, were counted on one face of the strip. The strip was anodized, diffusion annealed, and examined with a low power microscope. The variation in color from grain to grain was very sharply defined by grain boundaries, and corresponds to a variation in the diffusion coefficient by a factor of two. Examination of numerous other specimens diffused over the range of temperatures examined in this study reveal the variation in diffusion coefficients by a factor of about two to be a constant. The orientations of eight grains exhibiting wide differences in oxygen diffusion coefficients were determined by x-ray diffraction. The continuity of these grains could be traced visually around the edges of the original face to the sides perpendicular to it. From a knowledge of the orientations of one face of the eight grains, the orientations of eight additional perpendicular faces could be calculated. The results of the examination of the relative diffusion coefficients of fifteen areas (one being the area used to attach the sample to the source of potential) are presented in Fig. 6, which shows one-twelfth of the stereographic projection of the hexagonal crystal system. The symmetry properties of the hexagonal system make this sufficient to describe all orientations.

In orientation, the c-axes of the grains range from being parallel to being within 28° of perpendicular to the plane of the sample. Relative diffusion coefficients of oxygen in zirconium are indicated by the degree of darkening of the circles indicating the orientation; the darkest circle is given a value of unity. The diffusion coefficient is a minimum when the c-axis is parallel to the reference plane, rises to a maximum when the c-axis is about 70° from the normal to the reference plane, and has inter-

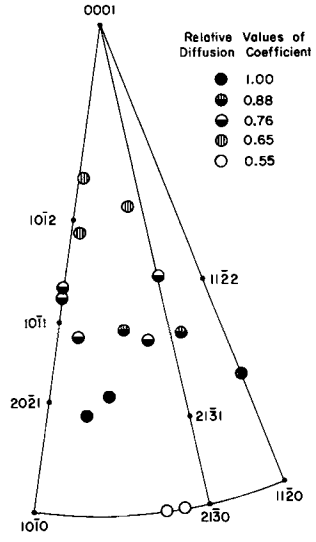


Fig. 6. Effect of orientation on the diffusion coefficient of oxygen in zirconium.

mediate values as it approaches the normal to the reference plane.

Oxygen has been postulated to diffuse through the hexagonal zirconium lattice interstitially. Size considerations (1) lead to the belief that the oxygen must be contained in octahedral rather than tetrahedral interstices. These octahedral interstices run parallel to the c-axis of the hexagonal lattice, and for this reason one would expect a maximum rate of diffusion when the c-axis is perpendicular to the plane of the sample, falling to a minimum rate when it is parallel to the sample plane. Experimental observations do not agree with this simple picture, and no explanation for the experimental observations is offered at this time.

### *Effect of Alloying Additions and Heat Treatment on the Diffusion Coefficient*

No difference could be detected in the macroscopically observed rate of diffusion of oxygen in the various alloys listed in the Materials section. Microscopic examination revealed differences in rates of diffusion of different grains in accordance with observations of the orientation dependence as discussed above. The variation of diffusion coefficients for different grains was identical for the different specimens tested.

No difference could be detected in the macroscopically observed oxygen diffusion rate of alloys annealed in the alpha and water quenched from the beta region. Microscopically, annealed specimens showed the typical color variation due to orientation differences sharply defined by grain boundaries. In the water quenched alloys the macrostructure determined the over-all tint of the macrograin, but the structure within the grains showed additional color variations. The effect on the diffusion coefficient of the fine structures due to the water quench was therefore superimposed on the effect of the orientation of the macrograins resulting from the heat treatment in the beta region.

### *Anisotropy of Oxidation and Corrosion*

In order to determine whether there is an orientation dependence on the rate of oxidation, similar to that observed in diffusion, a zirconium alloy was heated to 415°C in an oxygen atmosphere and examined periodically. An interference film formed quickly and the color changed with time in a manner analogous to that of anodic film growth with increasing voltage. Microscopic examination of the sample after the experiment was completed revealed a situation similar to that observed after a diffusion anneal: a distribution of color sharply defined by grain boundaries, indicating a variation of oxide thickness from grain to grain. The oxidation temperature used here was too low for any color changes due to anisotropic oxygen diffusion to occur in the time interval of the experiment. Such variations in interference color films on different grains have been observed previously by Schwartz, Vaughan, and Cocks (11) during the corrosion of zirconium samples in 316°C water. In order to compare the results obtained in oxygen with those in water the above experiment was repeated in a water vapor atmosphere at 415°C and in liquid water in an autoclave at 316°C. In both water vapor and liquid water the results were similar to that obtained in oxygen. However, in the latter two cases there was a decided tendency for certain areas to stain, i.e., preferentially oxidize so as to mask out any effects due to orientation. This phenomenon was not noticed during oxidation by oxygen gas.

The effect of grain orientation on the extent of oxidation was studied using the large grain zirconium sample used in the diffusion study. The sample was oxidized in an oxygen atmosphere for about 1 hr at 415°C. The effect of orientation on the extent of oxidation is shown in Fig. 7, which is a stereographic projection of the zirconium lattice as discussed above. The results parallel those observed for the orientation dependence of the oxygen diffusion coefficient: the rate of oxidation is a minimum when the c-axis is parallel to the plane of the sample, rises to a maximum when the c-axis is inclined about 20° from the sample plane, and decreases again at higher inclinations. An orientation effect similar to this has been observed in the extent of growth of anodic films on zirconium in nitric acid (12). In order to determine whether the orientation dependence of the corrosion rate persists be-

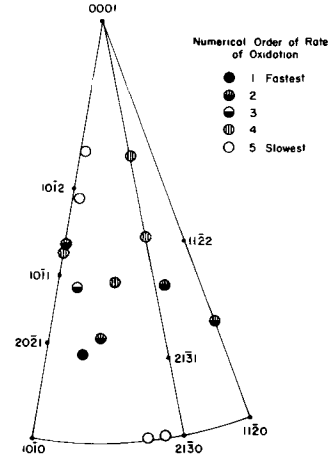


Fig. 7. Effect of orientation on the rate of oxidation of zirconium.

yond the initial stages of the reaction, a sample of pure zirconium of fairly large grain size was placed in 400°C steam at 1500 psi in an autoclave. After 20 hr the thickness of the oxide layer varied enormously from grain to grain in this single sample: some grains had interference film oxide layers of the order of a few thousand angstroms thick, while others had films ranging from dense black oxide to white blistering oxide, presumably spalling.

During the useful life of zirconium alloys in water at high temperature, before spalling occurs, weight gains of the order of 100 mg/dm$^2$ are obtained. Assuming an average grain size of the order of 0.05 mm, this weight gain corresponds to the formation of the entire oxide film from a fraction of the depth of the uppermost grains. In samples with good corrosion properties one must then reconcile the formation of a single continuous adherent oxide film (before spalling) from oxides growing at different rates on neighboring grains. The effect of this differential growth rate may lie in either of two directions:

1. Additional strains may develop between films on neighboring grains, resulting in spalling at a smaller weight gain than if there was no anisotropy of growth rate.

2. Some of the strain caused by the oxide having a greater molar volume than the metal (Pilling-Bedworth ratio 1.56) may be alleviated. A thick oxide layer under compression growing on one grain might relieve some of its stress by spreading over an adjacent grain having a thinner oxide layer under less compression. This merging of oxide above different metal grains might relieve the stress in those oxide zones under greatest compression. This relief would increase the weight gain before spalling occurred. Any mechanism purporting to explain the oxidation or corrosion of zirconium and zirconium alloys must account for the anisotropic nature of the reaction. It is obvious that more experimental work is needed before conclusions may be drawn regarding differential film growth.

*Effect of Alloying Elements on Oxidation*

The effect of alloying elements on the corrosion resistance of zirconium has been discussed in terms of the conductivity of the oxide according to the Wagner mechanism by other authors (13), and no attempt is made to evaluate these ideas. It is desired, however, to call attention to the role that second-phase inclusions may play in the film building process. Intermetallics such as $Fe_2Zr$ and $Zr_2Ni$ have been shown in themselves to have poor corrosion resistance, and yet it has been observed that a fine dispersion of these particles in an alpha matrix enhances the corrosion resistance of zirconium (14). These inclusions may serve in some way to anchor the oxide film to the metal, or alleviate stresses in the growing oxide film. Here, too, much experimental work remains.

*Relation of Diffusion to Oxidation and Corrosion*

In the initial stage of oxidation or corrosion a freshly exposed zirconium surface will dissolve oxygen in solid solution until an oxygen concentration is established at the interface which is in equilibrium with the composition of zirconium oxide. After that time, in the presence of an oxidizing atmosphere, an oxide scale will exist on the metal. As the reaction proceeds, oxygen will react with metal saturated with oxygen at the interface, and will continue to dissolve in the metal beyond the interface. If the solution to the diffusion equation given above is examined and one assumes that: (*a*) the concentration of oxygen at the metal-oxide interface is a constant, representing the solubility limit of oxygen in metal, (*b*) the concentration of oxygen is constant at the oxide-gas or liquid interface, probably representing a saturation value, and (c) the dimensions of the sample are very large compared to $\sqrt{Dt}$, several conclusions about the oxygen content of corroding zirconium may be drawn:

(*a*) Oxygen will be diffusing into metal at all times.
(*b*) The flux in the oxide will decrease with time as oxide thickness increases.
(c) The flux in the metal will decrease with time.
(*d*) The "depth of penetration", which is the distance beyond the metal-oxide interface that the oxygen has penetrated and reached some arbitrary concentration, will increase with time.

The ratio of the molar volumes of $ZrO_2$ to Zr (Pilling-Bedworth number) is 1.56 so that the growing oxide film is considered to be under compression. As the oxidation proceeds, the increasing extent of oxygen penetration in advance of the metal-oxide interface will lead to an increasing extent of embrittlement of the metal supporting the oxide film. This embrittlement may lessen the ability of the metal substrate to withstand the stress necessary to constrain the oxide film. At some point when the depth of penetration reaches a critical value, the metal may no longer be able to support the oxide and spalling will ensue.

The interpretation of weight-gain data for zirconium oxidation and corrosion should be re-examined in view of: (*a*) the appreciable dissolution of oxygen in zirconium during oxidation, (*b*) the anisotropy of the oxidation of zirconium grains, and (c) the agreement between the orientation dependence of diffusion and oxidation.

## Acknowledgments

The author is indebted to Dr. Wayne Lees for valuable discussions on the theory of diffusion. Appreciation is also expressed to Dr. Erwin Parthé of the Massachusetts Institute of Technology for the x-ray diffraction determination of grain orientation in the coarse grain zirconium sample. This work was performed under AEC Contract No. AT(30-1)-1565.

Manuscript received Aug. 14, 1957. This paper was prepared for delivery before the Buffalo Meeting, Oct. 6-10, 1957.

Any discussion of this paper will appear in a Discussion Section to be published in the December 1958 JOURNAL.

## REFERENCES

1. J. H. de Boer and J. D. Fast, *Rec. trav. chim.*, **59**, 161 (1940).

2. M. Hansen, D. J. McPherson, and R. F. Domagala, "Phase Diagrams of Zirconium-base Binary Alloys," Report COO-123 (1953).
3. M. W. Mallett, W. M. Albrecht, P. R. Wilson, "The Diffusion of Oxygen in Alpha and Beta Zircaloy-2 and Zircaloy-3 at High Temperatures," Report BMI-1154 (1957).
4. R. D. Misch, *Acta Met.*, **5**, 179 (1957).
5. J. J. Polling and A. Charlesby, *Proc. Phys. Soc.*, **67B**, 201 (1954).
6. J. J. Polling and A. Charlesby, "The Inhibition of Gas-phase Reactions of Zirconium by Anodic Oxide Films," Report AERE M/R-1040 (1953).
7. R. D. Misch, "Electrode Reactions of Zirconium Metal," in "The Metallurgy of Zirconium," p. 663, McGraw-Hill Book Co., New York (1955).
8. J. Paul Pemsler, "The Diffusion of Oxygen in Zirconium and Its Relation to Oxidation and Corrosion," Report NMI-1177 (1957).
9. W. Rostoker, "Phase Diagrams of Zirconium-base Binary Alloys," Report COO-181 (1953).
10. C. Curtis, Oak Ridge National Laboratory, Private communication.
11. C. M. Schwartz, D. A. Vaughan, and G. G. Cocks, "Identification and Growth of Oxide Films on Zirconium in High-Temperature Water," Report BMI-793 (1952).
12. R. D. Misch, *Acta Met.*, **4**, 222 (1956).
13. J. Chirigos and D. S. Thomas, "The Mechanism of Oxidation and Corrosion of Zirconium," Report WAPD 53 (1952).
14. W. K. Boyd, D. J. Maykuth, R. S. Peoples, and R. J. Jaffe, "Compositional Factors Affecting Corrosion Resistance of Zirconium in High-Temperature Water and Steam," Report BMI 1056 (1955).

# The Reaction between Iron and Water in the Absence of Oxygen

**V. J. Linnenbom**

*Naval Research Laboratory, Washington, D. C.*

ABSTRACT

The reaction between pure iron and oxygen-free water has been investigated at 25°, 60°, and 300°C. At room temperature, the primary product of reaction appears to be $Fe(OH)_2$; no evidence was found to indicate the presence of $Fe_3O_4$. Formation of $Fe_3O_4$, however, occurs readily in the iron-water system at both 60° and 300°C. The possibility that this $Fe_3O_4$ is produced via formation and subsequent decomposition of $Fe(OH)_2$ is discussed; the conclusion is reached that the mechanism of formation of $Fe_3O_4$ from the reaction of iron and water cannot be decided definitely at this time.

The nature of the product which results when pure iron reacts with water in the absence of oxygen is a matter of fundamental importance in corrosion studies. At elevated temperatures, there is general agreement that the end product is $Fe_3O_4$. However, conflicting reports have appeared in the literature as to whether this product at room temperature is $Fe(OH)_2$ or $Fe_3O_4$. A number of investigators (1-3) have employed the reaction of iron with oxygen-free water to measure the solubility of ferrous hydroxide, on the assumption that this compound is the end product of the reaction, and that the *p*H and solubility values obtained are characteristic of a saturated solution of $Fe(OH)_2$. On the other hand, it has also been reported (4-6) that $Fe_3O_4$ is the end product of the reaction. In this connection, Schikorr (7) also claimed that ferrous hydroxide at room temperature slowly transforms into magnetite, according to what is now known as Schikorr's reaction:

$$3Fe(OH)_2 \rightarrow Fe_3O_4 + H_2 + 2H_2O \qquad (I)$$

The occurrence of such a reaction would appear to confirm the claim that $Fe_3O_4$ is the end product of the iron-water reaction. However, Evans and Wanklyn (8) and Shipko and Douglas (9) found no evidence that reaction (I) occurs at room temperature unless certain substances are present to catalyze the reaction.

It is the purpose of this communication to report some experimental work carried out here on the iron-water reaction in the absence of oxygen, the results of which indicate that $Fe(OH)_2$ is formed by this reaction at room temperature, and that $Fe_3O_4$ is formed only at higher temperatures.[1]

## Experimental

The samples of iron used in this work came from three different sources. One was a specimen of pure iron foil obtained from the National Bureau of Standards, containing less than 0.01% impurities. The second was an iron powder prepared by the reduction of reagent grade ferric oxide. The third was a commercially available reduced iron powder, also certified to be reagent grade; however, an aqueous suspension of this latter material as received was found to be slightly alkaline, and it was necessary to wash it exhaustively by decantation before use to remove this impurity. In all cases the powder samples just prior to use were reduced in purified hydrogen at 900°C for a period of 24 hr; this produced a sintered mass of reduced iron powder which was bright and silvery in appearance and which tarnished very quickly if exposed to air. The iron foil was alternately oxidized and reduced several times to produce a very reactive surface, the final reduction with purified hydrogen again being

[1] These experiments are reported in more detail in Naval Research Laboratory Report 4824, September 1956.

carried out at 900°C for 24 hr. All water used in the experiments was doubly distilled and stored in quartz containers, the second distillation being made from an alkaline permanganate solution.

The reaction was investigated at three different temperatures, 25°, 60°, and 300°C. At room temperature the reaction was carried out in both Pyrex and quartz containers, since Corey and Finnegan (5) reported different results for these two materials. Each flask was fitted with an internal filter through which samples could be withdrawn at periodic intervals for solubility and pH measurements. Before adding the iron, the water was first deoxygenated by bubbling purified hydrogen through the water for a period of 48 hr. The transfer of the freshly reduced iron to the flask containing the oxygen-free water was then carried out in a dry box under an atmosphere of purified helium. During the course of the experiment a stream of hydrogen was passed continuously through the solution; it was allowed to exit through a mercury trap to prevent back diffusion of air into the flask. The mercury trap thus produced a slight positive pressure inside the flask for the entire duration of the experiment.

The experiments at 60°C were carried out in the same apparatus by encasing the flask in a heating jacket and controlling the heat input manually by means of a voltage regulator.

The experiments at 300°C were carried out in a gold-plated nickel autoclave equipped with an internal gold filter element. The doubly distilled water was deoxygenated as described above, the reduced iron sample added under a helium atmosphere, and the autoclave sealed off. During the initial period of heating from room temperature up to 300°C, a vent plug was opened periodically to flush excess helium and hydrogen from the system with the steam being generated inside the autoclave.

## Results

At room temperature there was no visible evidence that magnetite was formed. The surface of the reduced iron remained bright and silvery in appearance, even after 42 days contact with water. The solution after only a few hours showed a strong Tyndall effect (absent at the start), indicating the presence of suspended colloidal material. In some of the experiments a definite trace of turbidity developed. After four days' reaction time, samples of solution withdrawn through the filter showed a pH of 9.30 and a soluble Fe content of 0.4 ppm. These results agree with those reported by Murata (3) for the same reaction time interval. The pH remained constant with time; however, the soluble iron content showed a slow decrease, finally reaching a constant value of 0.08 ppm Fe after approximately 30 days. This may have been due to (a) increased filtering efficiency with time due to particle size growth of the colloidal ferrous hydroxide, or (b) a change in the nature of the colloidal species due to aging, with a consequent change in solubility. The visible absence of any black magnetite in the system, together with the pH and solubility values, indicate that $Fe(OH)_2$ is the species existing in contact with oxygen-free water at 25°C. In one or two cases where some magnetite did form, the reason was traced to leakage of air into the system. This was confirmed by experiments in which, after several days reaction time, the hydrogen flow was stopped and air was deliberately admitted to the flask. The flask was then sealed, and after a sufficient time lapse to allow diffusion of air through the water, the submerged sintered mass of iron powder began to darken. Eventually, an appreciable quantity of loose, black $Fe_3O_4$ powder was formed. However, when oxygen was carefully excluded, no visible signs of magnetite formation were noticeable at room temperature. There was no significant change in experimental results when quartz reaction flasks were substituted for Pyrex, contrary to the report of Corey and Finnegan (5).

At 60°C the formation of black $Fe_3O_4$ proceeded fairly rapidly, even in the absence of oxygen. Experiments which had been allowed to proceed at room temperature for several days showed almost immediate formation of the black oxide on the surface of the submerged iron when the temperature was raised to 60°. At this temperature the soluble iron content was found to be approximately 0.008 ppm after 10 days' contact between iron and water.

During the course of the experiments carried out at 300°C visual observations could not be made. However, at the conclusion of all of the experiments the autoclave was always found to contain large quantities of black $Fe_3O_4$. Solubility values in these high temperature runs showed a definite decrease with time and tended to approach a lower limit of about 0.05 ppm Fe.

## Discussion

Thermodynamic data (10) show that both $Fe(OH)_2$ and $Fe_3O_4$ may be formed spontaneously in the reaction between iron and oxygen-free water at room temperature, and that $Fe(OH)_2$ can further react spontaneously to form $Fe_3O_4$:

$$Fe+2H_2O \rightarrow Fe(OH)_2+H_2 \quad \Delta F^\circ_{298^\circ K} = -2190 \text{ cal} \quad \text{(II)}$$

$$3Fe+4H_2O \rightarrow Fe_3O_4+4H_2 \quad \Delta F^\circ_{298^\circ K} = -15{,}640 \text{ cal} \quad \text{(III)}$$

$$3Fe(OH)_2 \rightarrow Fe_3O_4+2H_2O+H_2 \quad \Delta F^\circ_{298^\circ K} = -9070 \text{ cal} \quad \text{(I)}$$

However, these data tell us nothing about the relative rates of the reactions, nor of the mechanism by which $Fe_3O_4$ may be formed. From the experimental work described here it would appear likely that reaction (II) predominates at room temperature. Solubility and pH values, as well as visual evidence, indicate that $Fe(OH)_2$ is the solid species in equilibrium with solution at 25°C. The absence of $Fe_3O_4$ would indicate that reactions (I) and (III), although thermodynamically favored, are too slow to be measurable at room temperature within the time (40 days) of these experiments.

Heat capacity data as a function of temperature (11, 12) allow calculations to be made on the free energy change of reaction (III) at 60° and 300°C. At both temperatures this reaction is still thermodynamically possible; hence, direct formation of

$Fe_3O_4$ via (III) remains possible. Unfortunately, heat capacity data on $Fe(OH)_2$ necessary to make similar calculations for reactions (I) and (II) at these temperatures are lacking, so that the possibility of $Fe_3O_4$ formation via prior formation of $Fe(OH)_2$ cannot be eliminated. Such calculations, therefore, offer no significant clues as to the reaction mechanism. In this particular case, further experimentation is needed in order to learn the mechanisms involved.

One further point should be emphasized. This is the extreme sensitivity of reaction (I) to the presence of other materials. Excess hydroxyl ion, for example, markedly inhibits the reaction, even at elevated temperatures (9). On the other hand, Evans and Wanklyn (8) reported the decomposition of precipitated ferrous hydroxide at room temperature in the presence of nickel powder, copper powder, colloidal platinum, platinum chloride, and nickel sulfate; in the absence of these materials, no decomposition occurred. Similarly, Shipko and Douglas (9) found it necessary to co-precipitate nickel hydroxide with the ferrous hydroxide in order to observe decomposition of the latter at room temperature; in the absence of the nickel hydroxide, reaction (I) did not proceed at a measurable rate below 100°C. The formation of $Fe_3O_4$ at 60°C in this work may therefore have been due to the catalyzing effect of excess iron powder in promoting reaction (I). It is appropriate to mention here a report by Gould and Evans (13) that in the absence of oxygen boiling water reacts with steel to first form $Fe(OH)_2$, which then decomposes to give $Fe_3O_4$ as the end product. These observations are pertinent to the problem of the corrosion of iron and steel in oxygen-free water. Any impurity or added substance which is effective in promoting reaction (I) might well affect corrosion rates by preventing formation of a possible protective film of ferrous hydroxide.

To summarize, the evidence reported here (solubility, *p*H, and visual observation) indicates that $Fe(OH)_2$ is the primary product of the reaction between pure iron and oxygen-free water at room temperature. No evidence was found to indicate the presence of $Fe_3O_4$. The mechanism of the formation of $Fe_3O_4$ at higher temperatures cannot be definitely decided. Whether magnetite formation is necessarily preceded by the formation of $Fe(OH)_2$, or whether it is formed directly from the water reacting on the iron, is not clear.

## Acknowledgment

The writer wishes to acknowledge the assistance of Howard S. Dreyer in performing some of the experimental work described.

Manuscript received Aug. 8, 1957.

Any discussion of this paper will appear in a Discussion Section to be published in the December 1958 JOURNAL.

## REFERENCES

1. J. W. Shipley and I. R. McHaffie, *Canadian Chem. Met.*, **8**, 121 (1924).
2. W. G. Whitman, R. P. Russell, and G. H. Davis, *J. Am. Chem. Soc.*, **47**, 70 (1925).
3. K. Murata, *J. Soc. Chem. Ind. Japan,* (Suppl. Binding), **35**, 523 (1932).
4. G. Schikorr, *Z. Elektrochem.*, **35**, 62 (1929).
5. R. C. Corey and T. J. Finnegan, *Proc. Am. Soc. Testing Materials,* **39**, 1242 (1939).
6. M. Thompson, *Trans. Electrochem. Soc.*, **78**, 251 (1940).
7. G. Schikorr, *Z. anorg. u. allgem. Chem.*, **212**, 33 (1933).
8. J. R. Evans and J. N. Wanklyn, *Nature,* **162**, 27 (1948).
9. F. J. Shipko and D. L. Douglas, *J. Phys. Chem.*, **60** 1519 (1956).
10. F. D. Rossini, D. D. Wagman, W. H. Evans, S. Levine, and I. Jaffe, *Nat. Bureau Standards Circ. 500* (1952).
11. K. K. Kelley, "Data on Theoretical Metallurgy, X. High-Temperature Heat-Content, Heat-Capacity, and Entropy Data for Inorganic Compounds," Bureau of Mines Bull. 476 (1949).
12. U.S.A.E.C., "The Reactor Handbook," Vol. 2, Chap. 2, AECD-3646, U.S. Govt. Printing Office (1955).
13. A. J. Gould and U. R. Evans, *J. Iron Steel Inst. London,* **155**, 195 (1947).

# Chemical Factors Affecting Stress Corrosion Cracking of 18-8 Stainless Steels

**H. H. Uhlig and John Lincoln, Jr.**[1]

*Corrosion Laboratory, Department of Metallurgy, Massachusetts Institute of Technology, Cambridge, Massachusetts*

ABSTRACT

Transgranular stress corrosion cracking of 18-8 Type 304 specimens in boiling 42% $MgCl_2$ does not depend on rate of stressing (<1 sec to 10 min) nor on small variations in degree of plastic deformation. Cold worked specimens fail in shorter times than annealed, sheared specimens. Addition of HCl to $MgCl_2$ decreases cracking time whereas addition of NaOH increases the time. Pre-exposure of unstressed specimens to $MgCl_2$ slightly decreases cracking times of the same specimens subsequently stressed. Cracks occur along sheared edges of unstressed specimens despite stress relief anneal at 375°C for 2 hr.

Cracks propagate along sheared edges of U-bend specimens at 0.5 to 1 cm/hr through that portion of the specimen cross section in tension, the rate being much slower through the remaining cross section. No induction time for cracks to initiate was observed.

Sizeable pits are not necessary for cracking in $MgCl_2$, but appear to be essential in media like NaCl which in absence of pitting is not particularly active in causing cracking. The pitting mechanism produces concentrated low *p*H metal chlorides (e.g., $FeCl_2$) within the pit, which like $MgCl_2$ cause immediate cracking. Oxygen is required for pitting of 18-8 by NaCl solutions as shown by Uhlig and Morrill, and hence also for stress corrosion cracking as observed by Williams and Eckel, but oxygen is not necessary in $MgCl_2$ or $FeCl_2$.

Cracking can be prevented by cathodic protection at a C.D. of 0.03 ma/cm$^2$ or higher. Anodic C.D. up to 0.01 ma/cm$^2$ were found to have no effect on cracking tendency, nor did coupling of 18-8 to Pt.

Transgranular cracking of austenitic stainless steels occurs whenever the alloys stressed in tension are exposed simultaneously to a critical chemical environment. Failures of this kind occur with all the common 18-8 stainless steels, including the stabilized (A.I.S.I. Type 321 and 347), molybdenum-containing (Type 316), and low carbon (ELC Type 304) grades, and also the higher nickel grades (Types 309 and 310). The time required for cracking can be a matter of hours under severe conditions, or of years for less severe exposures. Avoidance of failure can be approached by changing the environment, which is discussed herewith, or by certain metallurgical alterations which will be discussed in another paper. Relief of residual stress does not appear to be more than a temporary expedient because cracking occurs eventually at applied stresses, for example in a $MgCl_2$ solution, no greater than 10,000 psi (1), or in water at elevated temperatures at a stress as low as 5,000 psi (2).

Chemical media most apt to cause cracking are those containing chlorides at a *p*H slightly on the acid side of neutral. Hence boiling concentrated magnesium chloride constitutes a severe environment and cracking occurs within a few hours. General corrosion in such media is only slight. In media for which general corrosion is pronounced, cracking may not occur at all.

Although chlorides are the common constituent of a variety of environments which induce cracking, their presence does not seem to be altogether necessary. Transgranular cracking of 18-8 has been observed, for example, in caustic soda solutions at 350°C (660°F) under pressure (1), in acid sulfite cooking liquors (1), in 12% hydrofluoric acid plus 0.2% fluosilicic acid at 80°C (180°F) (3) and in molten NaOH (4) at 370°C (700°F). Furthermore, cracking of 18-8 has been observed in hot water containing very little chloride (5), in steam condensate containing less than 0.5 ppm total solids (6), and in cooling waters containing 25 ppm or more of chloride (7). Williams and Eckel (2) report that oxygen is necessary for cracking of 18-8 in hot water or in steam containing small quantities of chloride. They also report an instance of cracking in a severely cold worked 18-8 exposed to hot pure water.[2] Many additional examples are cited in the literature.

[1] Present address: Esso Standard Oil Company, Everett, Massachusetts.

[2] There is a possibility that the mechanism of transgranular cracking in chloride-free environments occurring with 18-8 that is severely cold worked, and hence has been transformed in part from austenite to ferrite, differs from that occurring with totally austenitic alloys in chloride solutions. The mechanism, for example, may be related to cracking of ferritic and martensitic stainless steels in chloride-free environments by a mechanism that appears to require interstitial hydrogen rather than electrochemical reaction at the apex of a growing crack. This particular matter requires further study.

The object of the present investigation was to outline chemical factors affecting time of cracking of 18-8 stainless steel in a boiling 42% magnesium chloride test solution, and to correlate these effects with a plausible mechanism of cracking.

### *Test Apparatus*

Spring-loaded, U-bend, Type 304 stainless steel specimens stressed beyond the elastic limit were used for all the tests. The test solution was boiling 42% $MgCl_2$ at 154°C, as suggested by Scheil (8), in which complete failure by cracking occurred in about 4 hr.[3]

Our choice of test specimens stressed beyond rather than below the elastic limit was based on the observation by several investigators and by our own work that specimens so stressed are more susceptible to cracking, they fail in a shorter time, and reproducibility from one run to another is reasonably good. Furthermore, any steps which can be taken to avoid stress corrosion cracking are more significant if they succeed with specimens stressed sufficiently to cause plastic deformation.[4]

The test apparatus was constructed of 5/16-in. square 18-8 stainless steel stock to which was attached a sliding arm of ⅛ x ⅜ in. 18-8 stainless steel strip, both stress relieved. The test specimen was held under stress by a strong compression spring and an adjustable screw located at the top of the holder. Two notched porcelain blocks insulated the specimen itself from the sliding arm. An adjustable screw attached to the sliding arm operated a normal-open microswitch which, in turn, stopped an electric time recorder when the specimen failed.

Two types of test cells were constructed from 2-liter, wide-mouth Erlenmeyer Pyrex flasks which were fitted at the neck with 71/60 ground glass outer joints. Condensers of ⅞-in. I.D. were fitted with 71/60 ground glass inner joints to permit easy removal from the cells.

The first type of test cell was adapted to the study of weight loss and cracking of stressed specimens (Fig. 1); the other was adapted to the study of cracking when specimens were anodically or cathodically polarized. Heat was supplied to both types of cells by electric hot plates.

The polarization cell contained platinum foil electrodes in the side arms separated from the center portion by means of sintered glass disks. For electrical contact with the test specimen, a piece of platinum wire, 0.016 in. in diameter, was spot welded to the upper surface of the stressed specimen and then led up through the condenser. In order to minimize current flow through electrolyte to the wire, the latter was almost totally encased in sections of 2 mm Pyrex glass tubing. The lower portion of the test apparatus (that part immersed in the solution), although insulated from the specimen, was tightly wrapped with thin Teflon ribbon in order to avoid any slight current leakage both onto and off the metal components.

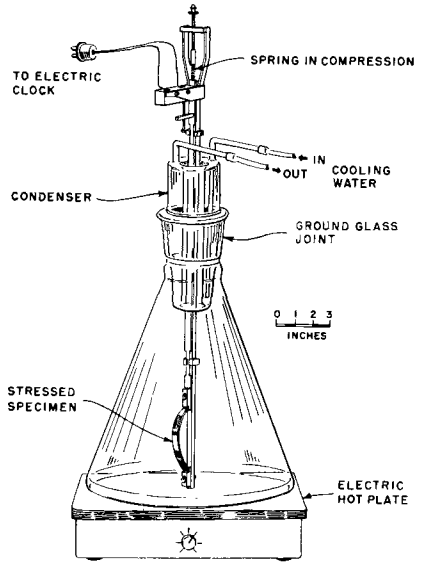


Fig. 1. Apparatus for study of stress corrosion cracking

The test solutions were prepared by using reagent grade $MgCl_2 \cdot 6\,H_2O$ crystals which were melted and dissolved in their own water of crystallization. Just enough distilled water was added to lower the boiling point of the solution to 154°C. Although very little evaporation loss was encountered, more distilled water was added daily, if necessary, so as to maintain this boiling point.

Since the $MgCl_2$ solutions gradually became contaminated with corrosion products, the solutions could be used for only a limited time. The main contaminant was probably ferric ion which is known to accelerate stress corrosion cracking of stainless steels in $MgCl_2$ (9). In general, it was found possible to use a single solution for 30-40 hr of actual test, during which time the solutions acquired a yellowish or orange color.

Different batches of fresh analytical grade $MgCl_2 \cdot 6\,H_2O$, particularly from different suppliers, were in themselves found to vary in performance. This necessitated correcting the results to take care of the variations. Corrections were made by running 5 or 6 specimens in a given new batch of salt, and determining the average time for cracking compared with the average time for many batches of salt (4.0 ± 1 hr). Data of Fig. 3 and 5, for example, were corrected in this manner. Maximum corrections amounted to 1.5 hr, and average corrections for Fig. 3 were 1.3 hr and for Fig. 5 were 1.2 hr.

### *Specimen Preparation and Stressing*

The 18-8 stainless steel, Type 304, was supplied by courtesy of the Carnegie-Illinois Steel Corporation, who also provided the following analysis: 18.42% Cr, 8.63% Ni, 1.16% Mn, 0.08% C, 0.024% P, 0.018% S, 0.30% Si, balance Fe. The rolled 1/16-in. thick sheet, as received, was sheared into specimens measuring 5 in. long and ⅜-in. wide. Each specimen was stenciled at the extreme end with an identifying number.

[3] Other boiling solutions were tried, e.g., [1] ethylene glycol containing 2.5% to 12% $MgCl_2$ or [2] ethylene glycol, 0.1*N* in HCl, [3] 65% aqueous $CaCl_2$, [4] ditto with 2 ml/l concentrated HCl, [5] glycerine, 0.7*M* in $NH_4Cl$, [6] 9*M* aqueous $NH_4Cl$. However, of all these, only $CaCl_2$ produced cracking in 6.0 hr for solution [3] and in 4.0 hr for solution [4].

[4] Since surface stresses alone determine susceptibility to initiation of stress corrosion cracking, and these cannot be measured easily, a specimen stressed beyond the elastic limit defines surface stresses in general more satisfactorily than is the case for a totally annealed specimen. This probably explains the authors' observation that reproducibility is better for plastically deformed specimens.

Specimens were cleaned by first removing any edge burrs with a metal file. They were then degreased in boiling benzene for 3-5 min, after which they were ready for heat treatment or pickling.

The majority of the specimens were used either in the as-sheared condition, or they were stress relieved at 375°C for approximately 2 hr, followed by air cooling. Some specimens were heat treated by annealing for 20-30 min at 1050°C, followed immediately by water quenching. A helium atmosphere was used during the annealing to prevent excessive surface oxidation.

Specimens after heat treatment were pickled in a 15 vol % $HNO_3$-5 vol % HF, based on the commercial acid concentrations, at a temperature of 90°C. To achieve optimum surface reproducibility, specimens were pickled individually for exactly 5 min in Pyrex test tubes immersed in a water bath at 90°C after which they were brushed under tap water to remove any loose scale. This was followed by rinsing in acetone, then in benzene, and drying in warm air.

The 5-in. test specimens were stressed beyond the yield point by bending in a vise until the ends of the specimen just fitted into a notched stainless steel holder which allowed a span of 4⅛ in. The specimen was then transferred to the test apparatus by sliding the two ends into the porcelain holding blocks and the sliding arm tightened until the notched holder was just released. The specimen was finally centered and adjusted to a span of exactly 4 in.

In all of the bending operations, extreme care was taken not to allow any spring-back. Once the specimens were loaded in the test apparatus, they were immediately immersed in the test solution.

## Results

*Corrosion rate determinations in 42% $MgCl_2$.*—The weight losses of both stressed and unstressed 18-8 test specimens, previously stress relieved, then pickled and weighed, and immersed into the boiling 42% $MgCl_2$, were determined as a function of time. Upon removal from the test solution, the specimens were brushed under tap water, rinsed in acetone, next in benzene, dried in air, and again weighed. Fresh $MgCl_2$ solutions were used in all these tests.

Results are given in Fig. 2 showing corrosion rates in mg/dm²/day (mdd) as a function of hours of exposure to $MgCl_2$, each point representing an average of 2-3 specimens. For unstressed specimens, a high initial corrosion rate falls off to a lower relatively steady state after about 4 hr. The same trend takes place for stressed specimens except that weight loss is somewhat higher and failure occurs before steady-state conditions are achieved. A few similar measurements by D. Triadis of this laboratory on specimens previously annealed at 1050°C and water quenched also showed a high initial rate followed by a lower final rate after about 4 hr exposure.

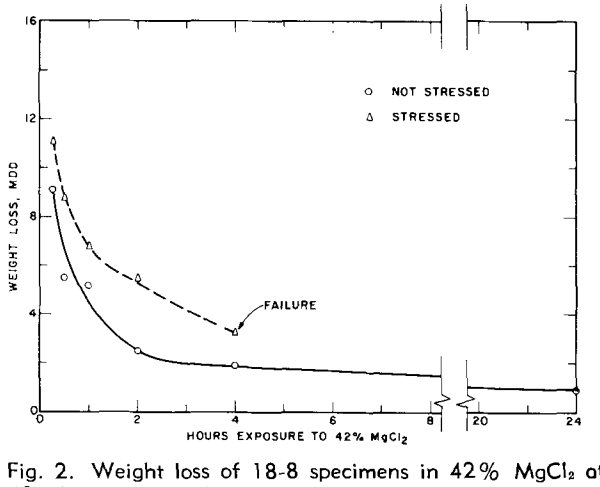


Fig. 2. Weight loss of 18-8 specimens in 42% $MgCl_2$ at 154°C (spec., previously stress relieved).

*Rate of stressing on cracking time.*—In order to determine effect of rate of stressing, 18-8 test specimens, stress relieved as usual after shearing, were bent to a 4-in. span in times of 10 sec, 5 min, and 10 min, and then immediately tested in $MgCl_2$. Results are summarized in Table I, showing no effect.

Additional but smaller size specimens bent at higher velocity by impact of falling weights held in a specially constructed jig also cracked within times normal for slowly deformed specimens.

*Degree of bending and cold work on cracking time.*—Stress-relieved specimens were bent to spans ranging from 3½ to 4⅞ in. In all cases the applied stress was above the yield strength (approx. 30,000 psi). Data of Table II show no trend, and, hence, small variations in stresses beyond the yield strength are not important. The higher average time to cracking in Table II (4.8 hr) reflects behavior of the particular batch of $MgCl_2$ employed, but this value, too, falls within the experimental variation of all tests.

Severe cold work is another story. Several as-sheared specimens were cold rolled to an average cross-sectional reduction of 30%. These specimens were then cut to a 5-in. length, pickled, bent to the usual 4-in. span, and tested in boiling 42% $MgCl_2$. The observed average time to failure for six such specimens was $1.0 \pm 0.2$ hr, which is significantly

**Table I. Time to failure of 18-8 specimens for various rates of stressing**

| Rate of stressing (Time to bend specimen to 4-in. span) | No. of specimens | Time to failure (hr) | Av |
|---|---|---|---|
| 10 sec | 3 | 4.6, 4.3, 3.7 | 4.2 |
| 5 min | 2 | 3.9, 4.2 | 4.1 |
| 10 min | 2 | 3.6, 4.1 | 3.9 |

**Table II. Time to failure of 18-8 specimens for various degrees of bending**

| Span of stressed specimens (in.) | No. of specimens | Time of failure (hr) | Av |
|---|---|---|---|
| 3½ | 2 | 4.9, 4.8 | 4.9 |
| 4 | 3 | 5.8, 3.5, 4.0 | 4.4 |
| 4¼ | 2 | 4.6, 5.6 | 5.1 |
| 4½ | 2 | 6.4, 4.5 | 5.5 |
| 4⅝ | 2 | 4.1, 4.0 | 4.1 |
| 4¾ | 2 | 4.3, 5.4 | 4.9 |
| 4⅞ | 2 | 4.8, 4.7 | 4.8 |

less than the usual 4 hr. The decrease of cracking time, probably caused by high residual stresses or microstructural changes, is in accord with similar experiments on mild steel by Parkins (10) and on 18-8 by Franks, Binder, and Brown (11) or by Hoar and Hines (12).

*Effect of adding acid or base to 42% $MgCl_2$.*— Since values of *p*H could not be measured at the boiling temperature of 42% $MgCl_2$ test solution (154°C), known amounts of HCl and NaOH solutions were added to the $MgCl_2$ test solution without reference to measured hydrogen ion activity. A 10*N* HCl solution was added before rather than after bringing the solutions up to temperature in order to minimize volatilization of the HCl on mixing with hot $MgCl_2$. General corrosion of the stressed 18-8 test specimens became significant at 8 ml 10*N* HCl/liter, and, hence, no quantitative tests were carried out for additions of acid beyond this amount. Additions of alkali were limited to 2 ml 5*N* NaOH/liter, since it was found that further additions caused precipitation of $Mg(OH)_2$.

The plot of Fig. 3 shows time to failure vs. ml/liter of added acid or base. Additions of acid decreased the cracking time to a minimum of about ½ the normal time, whereas additions of alkali increased the time slightly. These results proved that shorter times for cracking in used test solutions did not result from decrease in acidity caused by reaction of the metal with $MgCl_2$ solution. Instead the effect is undoubtedly caused by ferric chloride accumulation (9) through corrosion of specimens and test apparatus.

*Effect of anodic and cathodic polarization.*—The range of anodic current densities employed was from 0.0001 to 0.01 ma/cm² based on the measured total surface area of the test specimens (28.5 cm²). The cathodic current densities ranged from 0.0017 to 0.04 ma/cm². It was necessary to start each test in freshly prepared $MgCl_2$ solution in order to obtain consistent results. Gradually accumulating impurities, e.g., ferric ion from corrosion products, potentially caused a lowering of the effective current density by continuous reduction at the cathode and oxidation at the anode. Current through the cell

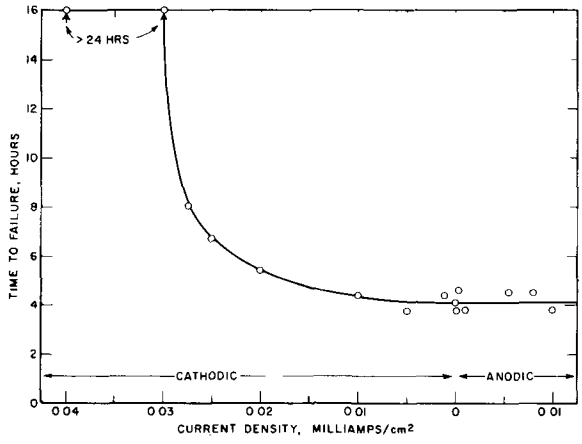


Fig. 4. Effect of anodic and cathodic polarization on time to failure of 18-8 specimens in 42% $MgCl_2$ at 154°C (spec. previously stress relieved).

varied 5% or less, which in view of the large average deviation in the time to failure (approximately ±1.0 hr) was inconsequential. A plot is provided in Fig. 4 for time to failure vs. applied current density. All points for anodic polarization are values averaged for 2-4 specimens at each current density, and similarly for 2-5 specimens for cathodic polarization, with the exception that only single runs are reported for cathodic values of 0.0017 and 0.02 ma/cm². No cracking occurred within the maximum time of the test (24 hr) for cathodic current densities above 0.03 ma/cm². On the other hand, anodic current densities of small magnitude up to 0.01 ma/cm² had no measurable effect on cracking time. In line with the anodic polarization results, 4 separate experiments in which platinum (4 cm²) was coupled to 18-8 specimens showed normal average cracking time.

*Effect of pre-exposure to 42% $MgCl_2$.*—It was desirable to know whether pre-exposure of unstressed specimens to 42% $MgCl_2$ would aid in the initiation of cracks, or produce surface areas susceptible to crack formation. An effect of this kind was reported by Hoar and Hines (13). Unstressed 18-8 test specimens, previously stress relieved, with surface prepared as usual, were pre-exposed to 42% $MgCl_2$ for

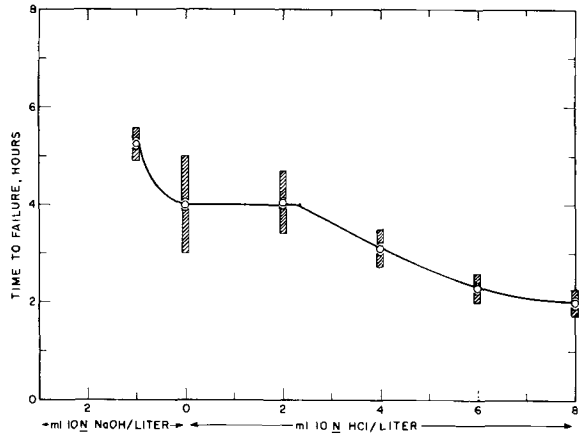


Fig. 3. Effect of acid and alkali additions to 42% $MgCl_2$ at 154°C on time to failure of stressed 18-8 specimens (spec. previously stress relieved). Spread of each point is standard deviation.

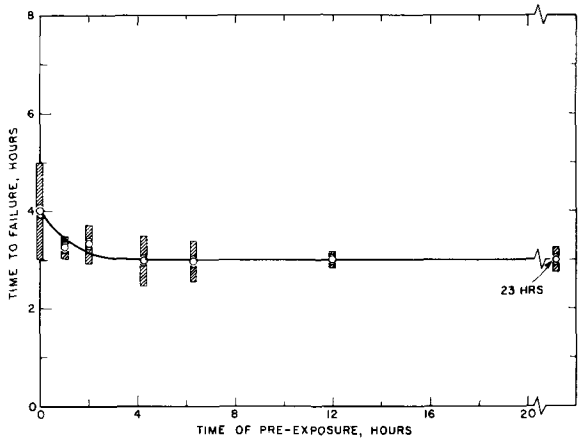


Fig. 5. Effect of pre-exposure of 18-8 specimens in unstressed condition on time to failure when stressed in 42% $MgCl_2$ at 154°C (spec. previously stress relieved). Spread of each point is standard deviation.

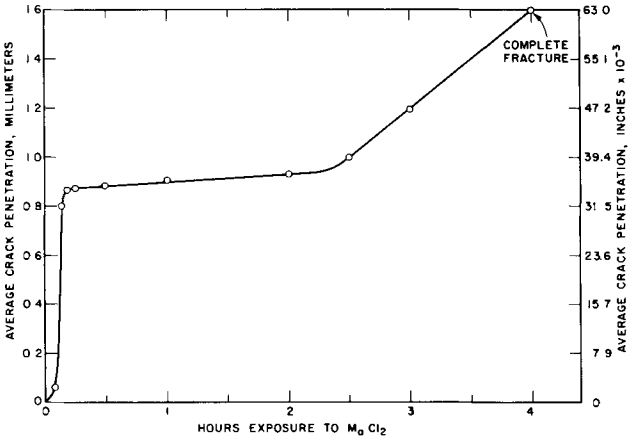


Fig. 6. Average visible rate of crack propagation for stressed 18-8 specimens in 42% $MgCl_2$. Total specimen thickness approx. 1.6 mm (spec. previously stress relieved).

various times, then immediately immersed in a beaker of distilled water. While still wet they were stressed, loaded into the test apparatus, and quickly placed in the $MgCl_2$ test solution. Times of pre-exposure varied from 0.5 to 24 hr, the corresponding cracking times being plotted in Fig. 5. The effect is one of slight decrease in the time for cracking after pre-exposure for 3 or more hours, with no further effect for longer times.

*Rate of crack propagation.*—In order to obtain data on the rate with which cracks propagate through stressed 18-8 test specimens, a metallographic inspection and photomicrographic study were made. Stressed specimens were immersed in the test solution for periods ranging from 5 min to 4 hr. Upon removal they were cleaned under tap water, mounted in Bakelite, polished, and etched. The average depth of cracks was measured from photomicrographs of known magnification and plotted vs. time of exposure to $MgCl_2$ in Fig. 6.

Crack propagation at the edges was very rapid (0.5-1 cm/hr) [5] through ½ the specimen thickness, corresponding to the tension side. Cracks stopped momentarily when they reached the midsection, corresponding to the compression side of the U-bend specimen. At this stage, thin cracks in the form of tortuous channels through the metal grew wider, eventually merging to produce one or more major cracks. Consolidation of thin cracks both at and away from the edges required about 2-2½ hr, whereupon one or more major cracks proceeded through the entire specimen cross section within another 1½ hr. This behavior clearly demonstrated that the alloy must be stressed in tension and not in compression in order to favor stress corrosion cracking.

No induction time for cracks to start was found. Tiny transgranular edge cracks were observed after the shortest time of exposure (5 min) to $MgCl_2$, still allowing time for thermal equilibrium. These cracks grew much deeper within a matter of additional minutes. The initial cracks began usually at the sheared edges, despite stress relief heat treatment, growing rapidly normal to the surface, and more slowly laterally from both edges toward the center of the convex surface. Hoar and Hines (13) found an induction time for initiation of cracks in 18-8 wire stressed below the elastic limit, except when they added HCl to the $MgCl_2$ solution, whereupon they stated that the induction time disappeared. No acid was added in our experiments.

The accompanying photomicrographs (Fig. 7 through 11) show the typical appearance of sheared edges of bent specimens after various times of exposure to $MgCl_2$.

## Discussion

### *Corrosion Rates*

The slightly higher weight losses of stressed specimens compared with unstressed specimens (Fig. 2) is probably accounted for by growing cracks on the convex surface of the stressed specimens, which do not develop in absence of stress. The higher cor-

Fig. 7. Sheared edge of bent, stress-relieved specimen after 8-min exposure to 42% $MgCl_2$. Electrolytic etch, 50X.

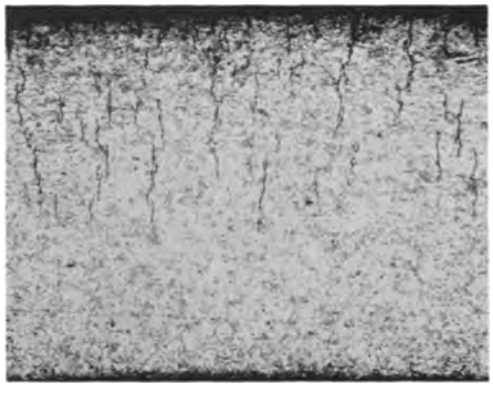

Fig. 8. Sheared edge of bent, stress-relieved specimen after 10-min exposure to 42% $MgCl_2$. Electrolytic etch, 50X.

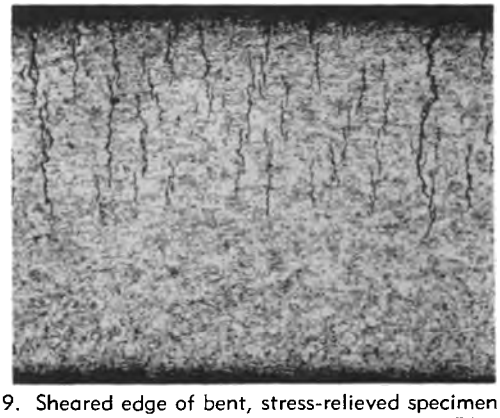

Fig. 9. Sheared edge of bent, stress-relieved specimen after 30-min exposure to 42% $MgCl_2$. Electrolytic etch, 50X.

[5] Hoar and Hines found 0.1-0.4 cm/hr (14).

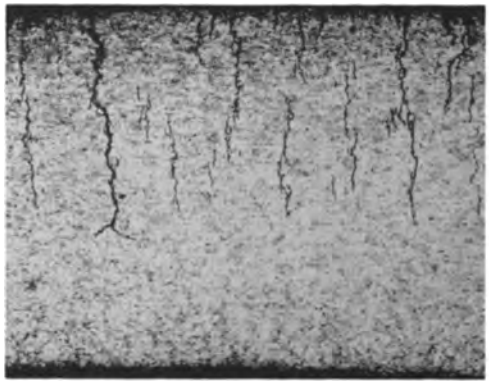

Fig. 10. Sheared edge of bent, stress-relieved specimen after 2-hr exposure to 42% $MgCl_2$. Electrolytic etch, 50X.

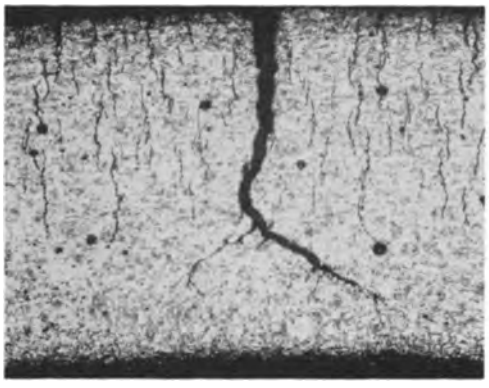

Fig. 11. Sheared edge of bent, stress-relieved specimen which failed at 3.8-hr exposure to 42% $MgCl_2$. Electrolytic etch, 50X.

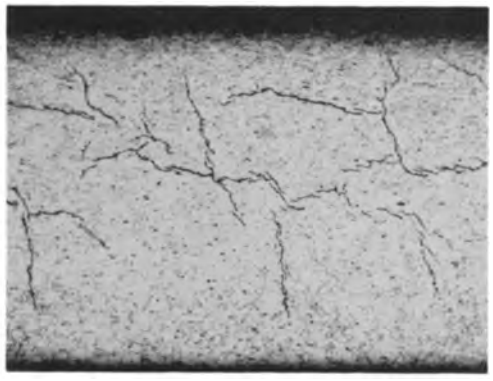

Fig. 12. Sheared edge of unbent, stress-relieved specimen exposed to 42% $MgCl_2$ for 2 hr. Electrolytic etch, 50X.

Fig. 13. Sheared edge of unbent specimen, annealed 1050°C, W.Q., exposed to 42% $MgCl_2$ for 2 hr. Electrolytic etch, 50X.

rosion rates can be explained both by formation of additional alloy surface opened up by cracks and by electrochemical action causing metal to dissolve at the apexes of opening fissures.

A high initial compared to a final constant corrosion rate, for both stressed and unstressed specimens, can be explained in part by cracks that develop rapidly at sheared edges despite stress relief heat treatment (Fig. 12), and which stop growing after tension stresses are relieved by crack formation. Such cracks indicate that heat treatment at 375°C for 2 hr is not effective in reducing residual stress to a level that precludes stress corrosion cracking.

It is also likely that oxygen dissolved in the test solution causes a high initial rate, diminishing to a final steady state as the oxygen is consumed or boiled off. A third factor is the preferential corrosion of those specific crystal faces of polycrystalline test specimens exhibiting highest corrosion rates. Examination of test specimens under the microscope confirmed that crystal facets were well developed after exposure to $MgCl_2$, these representing presumably residual crystal faces that corrode least. The effect of both dissolved oxygen and crystal orientation explains why annealed and water-quenched specimens, whose edges are not crack sensitive (Fig. 13), also show a higher initial corrosion rate.

### *Effect of Pre-exposure*

It is plausible that cracking of sheared edges during pre-exposure, despite stress relief treatment, caused part of the observed effect of pre-exposure on cracking times. Since specimens annealed at 1050°C and water-quenched, similarly pre-exposed, showed no surface cracks at either edge, pre-exposure of specimens free of residual or applied stresses would presumably have less effect on cracking times of such specimens subsequently bent. Lack of reproducibility for annealed-quenched specimens has delayed an experimental check of this conclusion and the matter is now under further study. Absence of an effect of pre-exposure on cracking times of mild steel in nitrates has been reported by Parkins (10). The effect found by Hoar and Hines for 18-8 wires pre-exposed to $MgCl_2$ may perhaps have been the result, as in our tests, of residual surface stresses causing superficial cracks.

### *Relation of Pits to Cracks*

There is no evidence that deep pitting must precede initiation of a crack when $MgCl_2$ is the test medium. Photomicrographs, such as those of Fig. 7, indicate that, within a time of exposure as short as 8 min, surface cracks form without evidence of surface cavities having dimensions greater than the cracks themselves.

However, there is good reason for believing that in waters containing neutral chlorides, e.g., NaCl, pit formation may always precede stress corrosion cracking.[6] The evidence for this comes from various in-

[6] Leu and Helle (15) demonstrate that small elongated pits of microscopic dimensions form on slip bands of stressed 18-8, and these act as nuclei for subsequent cracks. Localized attack of this kind probably always precedes stress corrosion cracking of 18-8. The pits discussed above are orders of magnitude larger than the dimensions of slip bands, and occur only under specific conditions.

stances of service failures where cracks are associated with pits, for example, at welded areas where natural crevices occur, or beneath inorganic scale formations, or at other types of crevices favorable to the initial action of oxygen-concentration cells. As was shown in an earlier paper on mechanism of pitting in stainless steels (16), interior surfaces of pits are the anodes of passive-active galvanic cells, with dissolution of anodic metal serving to fill such pits with concentrated low *p*H metal chlorides, in particular ferrous chloride. Concentrated ferrous chloride is one of the active chemical media causing stress corrosion cracking, behaving in this respect like magnesium chloride. For example, two stressed commercial 18-8 specimens exposed to boiling (114°C) concentrated ferrous chloride solution in a $N_2$ atmosphere were found to crack transgranularly within an average of 7.4 ± 0.5 hr. (A similar specimen exposed to boiling concentrated NaCl did not pit nor crack within the maximum test period of 250 hr.)

Pits, therefore, act as reservoirs for concentrated metal chlorides, the latter in turn being directly active in causing stress corrosion cracking. With magnesium chloride, the necessary crack-inducing medium is already at hand, hence pitting is not necessary, and cracks in plastically deformed metal initiate as rapidly as the metal comes into contact with the test solution.

Dissolved oxygen is necessary for pitting to occur in NaCl (17) because the cathodic reaction occurring on the large exterior surface of alloy surrounding the pit requires presence of a depolarizer. It is significant in this regard that Williams and Eckel (2) report dissolved oxygen is also necessary for stress corrosion cracking of 18-8 in NaCl solutions at elevated temperatures, from which one can conclude that since boiling concentrated NaCl did not cause cracking, pitting always precedes cracking in this medium. Following the reasoning above, dissolved oxygen should not be necessary for cracking in $MgCl_2$ or $FeCl_2$ solution. This is confirmed for $FeCl_2$ by the previously cited experiment and for $MgCl_2$ by an experiment in which two sheared Type 304 small size test specimens were exposed to 42% $MgCl_2$ test solution, the latter being thoroughly deaerated with purified nitrogen before and during the test, and observing cracking within 3.2 ± 0.6 hr.

### *Effect of pH and Depolarizers*

Decrease of cracking time by additions of acid may conceivably have a complex cause associated with supposed films on the metal surface, but it also seems reasonable that the effect may be no more than to increase electrical conductivity of $MgCl_2$ through additional hydrogen ions. The acid also increases the operating emf of metal electrode-hydrogen electrode cells, presumably responsible for crack propagation, to the extent of 42 mv (154°C) for every unit *p*H change. Ferric salts, on the same basis, decrease cracking time because they are active depolarizers serving to accelerate the cathode reaction. Any similar depolarizer is expected to behave in the same way. Continuous bubbling of oxygen through the $MgCl_2$ test solution, for example, was found to decrease cracking time about 40%.

### *Effect of Anodic and Cathodic Polarization*

The minimum cathodic current density of 0.03 ma/cm² found to protect against cracking for at least 24-hr exposure is in good agreement with values reported by Hoar and Hines (14) of 0.03 ma/cm² for protection extending to 50 hr, and of 0.05 ma/cm² for protection up to at least 250 hr and probably for an indefinite period. Results of longer test periods during which cathodic protection is applied probably mean very little because of the accompanying change in test-solution composition, particularly increase of *p*H, brought about by cathodic reaction products.

The initial over-all corrosion rate for stressed specimens is about 12 mdd (Fig. 2), corresponding to a current density of 0.005 ma/cm². From electrochemical theory, the applied current density for complete cathodic protection must always be greater than the equivalent current density corresponding to the corrosion rate in a given environment, other things being equal. The present data are in line with this conclusion. Correspondingly, in a less active medium than $MgCl_2$, the required current density for protection would be less than the values cited above.

The appreciable difference in the current density for protection and that corresponding to the corrosion rate indicate that the anodic areas of electrolytic cells responsible for cracking are appreciably polarized by the prevailing small corrosion currents (Fig. 14), assuming that cathodic polarization follows a Tafel relation. For a concentrated chloride solution such as $MgCl_2$ in which anodic passivation does not occur, and for which anodic polarization per unit area, therefore, is not pronounced, this means that the effective anodic areas must be very small. Small anodic areas correspond, logically, to the relatively limited anodic areas of metal corroding at the apexes of incipient growing cracks.

Anodic polarization of specimens presumably should affect cracking time only if applied positive current leaving the metal surface is focussed mostly

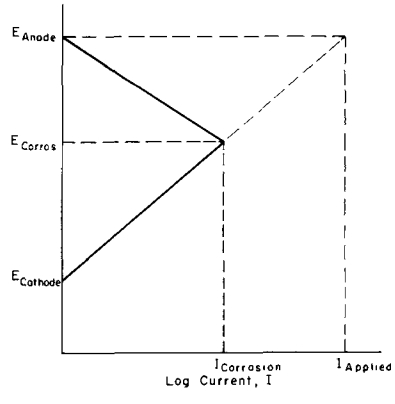


Fig. 14. Schematic polarization diagram for cell accounting for stress corrosion cracking. Applied current for cathodic protection is considerably larger than the corrosion current because of pronounced polarization of small area anode.

at nuclei for cracks.[7] This condition might obtain if supposed surface films largely exclude current from all parts of the surface except at specific defects in the film. Since an effect of anodic polarization is not found, it must be concluded that distribution of current in this manner does not occur. Lack of an effect by anodic currents does not support Edeleanu's (9) statement that coupling of platinum to stainless steel accelerates cracking, and that of Hoar and Hines (14) to the effect that anodic polarization increases rate of crack propagation. Reasons for the difference in results are not apparent.

### Acknowledgment

The authors are pleased to acknowledge assistance of Louis Bogar in carrying out several supplementary experiments.

This research was supported by the United States Air Force through the Air Force Office of Scientific Research of the Air Research and Development Command, under contract No. AF 18(600)-1221. Reproduction in whole or in part is permitted for any purpose of the United States Government.

Manuscript received July 15, 1957. This paper was prepared for delivery before the Buffalo Meeting, Oct. 6-10, 1957.

Any discussion of this paper will appear in a Discussion Section to be published in the December 1958 JOURNAL.

[7] A decrease of cracking time can result indirectly from contamination of $MgCl_2$ by accumulation of anodic dissolution products.

### REFERENCES

1. M. A. Scheil in "Corrosion Handbook," H. H. Uhlig, Editor, p. 174, John Wiley & Sons, Inc., New York (1948).
2. W. Williams and J. Eckel, *J. Am. Soc. Naval Engrs.*, **68**, 93 (February 1956).
3. H. Copson, *Welding J.*, Supplement, p. 3 (February 1953).
4. J. Heger, *Metal Prog.*, **69**, 109 (1955).
5. R. A. Lincoln, American Iron and Steel Inst., N.Y.C., May 26, 1954.
6. F. W. Davis, *Trans. Am. Soc. Metals*, **42**, 1233 (1950).
7. W. Rion, Jr., *Ind. Eng. Chem.*, **49**, 73A (1957).
8. M. Scheil, "Symposium on Stress Corrosion Cracking of Metals," ASTM and AIME, pp. 395-410, Philadelphia (1945).
9. C. Edeleanu, *J. Iron Steel Inst.*, **173**, 140 (1953).
10. R. N. Parkins in "Stress Corrosion Cracking and Embrittlement," p. 146-7, W. D. Robertson, Editor, John Wiley & Sons, Inc., New York (1956).
11. R. Franks, W. Binder, and C. Brown, Ref. 8, p. 411.
12. T. Hoar and J. Hines, *J. Iron Steel Inst.*, **184**, 166 (1956).
13. T. Hoar and J. Hines, *ibid.*, **182**, 124 (1956).
14. T. Hoar and J. Hines, Ref. 10, p. 107.
15. K. Leu and J. Helle, "On the Mech. of Stress Corros. of Austenitic Stainless Steels in Hot Aqueous Chloride Solutions". Koninklijke/Shell Lab., Amsterdam. Presented at Nat. Assoc. Corros. Engrs., St. Louis, Mar. 1957.
16. H. H. Uhlig, *Trans. Am. Inst. Mining Met. Engrs.*, **140**, 411 (1940).
17. H. H. Uhlig and M. Morrill, *Ind. Eng. Chem.*, **33**, 875 (1941).

# A Study of the Effect of Chloride Ion on Films Formed on Iron in Sodium Nitrite Solutions

G. W. Mellors,[1] M. Cohen, and A. F. Beck[2]

*Division of Applied Chemistry, National Research Council, Ottawa, Canada*

ABSTRACT

The effect of chloride ion on the potential of iron in sodium nitrite solutions has been measured. This has been related to the surface composition and topography by the techniques of electron diffraction and electron microscopy. The effect of initial surface preparation has also been investigated.

It is shown that in the absence of chloride ion the potential is noble and steady and that the surface remains practically unchanged. A film of $\gamma$-$Fe_2O_3$ is shown to be present by electron diffraction. When chloride ion is added to the system the potential becomes unsteady and less noble. Inclusions of a second phase grow in the oxide layer. This is shown to be $\gamma$-$Fe_2O_3 \cdot H_2O$ or lepidocrocite. The lower and unsteady potential is probably due to the decrease in resistance of the anodic areas, which correspond to the inclusions in the oxide layer.

The present research was initiated to confirm the nature of the oxide film formed on iron by sodium nitrite solutions (1) and to investigate more fully the effect of chloride ions on these films. It has been shown in previous work by electron diffraction that the films formed in sodium nitrite solutions are composed of $\gamma$-$Fe_2O_3$ with a small amount of $\gamma$-$Fe_2O_3 \cdot H_2O$ (lepidocrocite). The films were examined *in situ* by reflection, and transmission patterns were obtained from films stripped from the metal by the method of Vernon, Wormwell, and Nurse (2).

Although electron diffraction results have been published for films stripped from iron passivated in potassium chromate solutions (3-5) and in concentrated nitric acid (4), the above work (1) constitutes the only reflection diffraction results on films formed in sodium nitrite solutions.

It was thought desirable to employ the reflection method, despite the poorer quality of the patterns

[1] Present address: National Carbon Research Laboratories, Cleveland, Ohio.

[2] Olin Mathieson Chemical Corporation, New Haven, Conn.

obtained, since reorientation and recrystallization of the film substance may occur during the process of stripping specimens for transmission work. It is also possible that inclusions in the oxide film will be removed during the process of stripping.

Potential measurements were made of iron exposed to a range of concentrations of sodium nitrite solutions containing various amounts of chloride ions. Parallel electron diffraction examinations of the surface to identify the surface composition and electron microscope pictures to determine the surface topography were made. Specimens were also passivated in de-aerated solutions in order to determine the effect of dissolved oxygen. The effect of various surface preparations on both the electrode potential and film formation was also measured.

## Experimental and Results

The "Armco" iron was in the form of annealed sheet, 1.5 mm thick and had the following analysis:—C-0.012, Mn-0.015, P-0.005, S-0.025, Si-trace.

Sodium nitrite, potassium chloride, and all other chemicals used were of C. P. quality. The silver wire used in the preparation of the silver-silver chloride electrodes was of 99.999% purity. The electrodes were formed by anodizing in a dilute HCl solution.

### *Potential Measurements*

The specimens for potential measurements were 5 cm x 1.5 cm of which 1.5 cm x 1.5 cm was exposed to the solution. The remainder was insulated with "Apiezon" W wax. All specimens were first ground flat and then polished through 4/0 emery paper. Some of these specimens were exposed for potential measurements in this condition, while others were first exposed to dry air for 24 hr or etched with *N* HCl for 1 min.

Potential measurements were made using a reference electrode of a chloridized silver wire connected to the inhibitor solution through a salt bridge. No correction was made for junction potentials. All runs were made in the presence of air. All potentials are on the saturated Ag-AgCl scale.

The effect of surface pretreatment on the potential of iron in *N*/10 sodium nitrite is shown in Fig. 1. It can be seen that the etched specimen has a much lower potential than the unetched specimens, although all are passive.

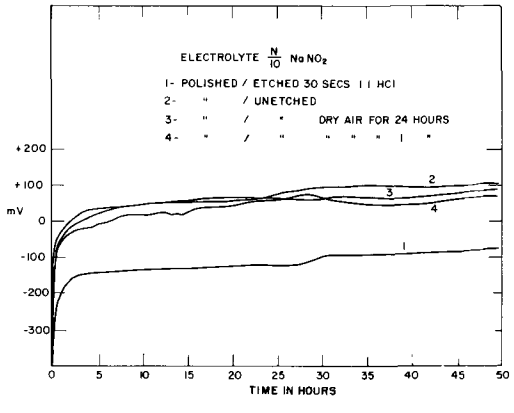


Fig. 1. Effect of pretreatment on potential of iron in N/10 $NaNO_2$ solutions.

Potentials of iron in various concentrations of nitrite solution with or without additions of chloride are shown in Fig. 2-7. Figure 8 shows the effect of small additions of "Versene" (ethylene-diamine-tetra-acetic acid) a strong complexing agent for cations, on the potentials of etched and unetched specimens in *N*/10 air-exposed solutions of sodium nitrite. In other experiments with etched iron it was noted that the time required for passivity to be attained increased with increasing Versene concentration.

The following general observations can be made:

1. In pure sodium nitrite solutions the unetched specimens attain a more positive potential than the etched specimens.
2. Differences in potential due to differing surface preparation decrease with decreasing inhibitor concentration and/or the addition of chloride.

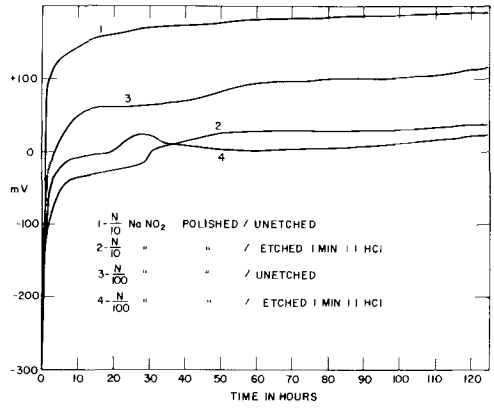


Fig. 2. Effect of concentration and etching on potential

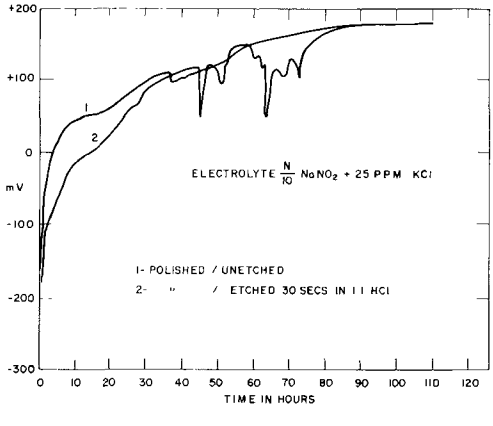


Fig. 3. Potential of iron in N/10 $NaNO_2$ + 25 ppm KCl

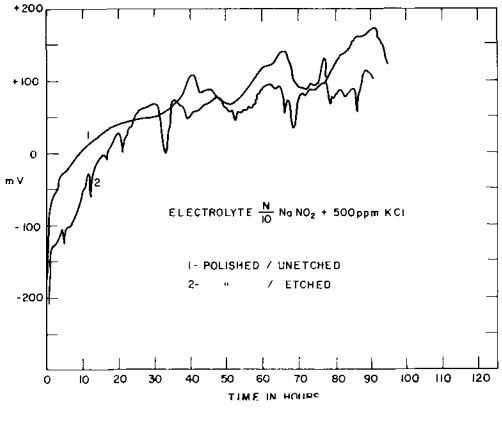


Fig. 4. Potential of iron in N/10 $NaNO_2$ + 500 ppm KCl

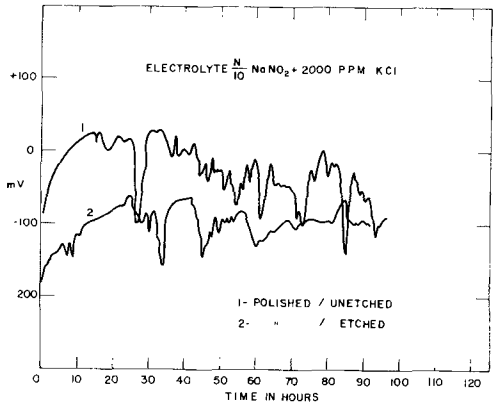


Fig. 5. Potential of iron in N/10 $NaNO_2$ + 2,000 ppm KCl

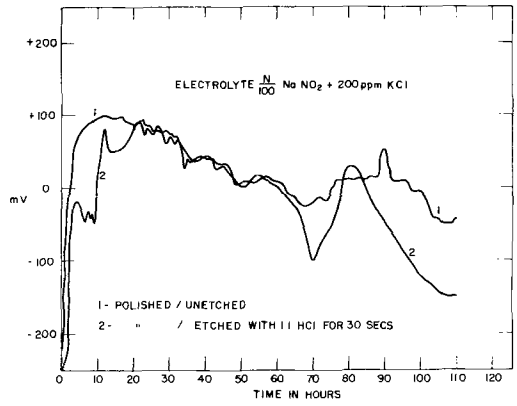


Fig. 7. Potential of iron in N/100 $NaNO_2$ + 200 ppm KCl

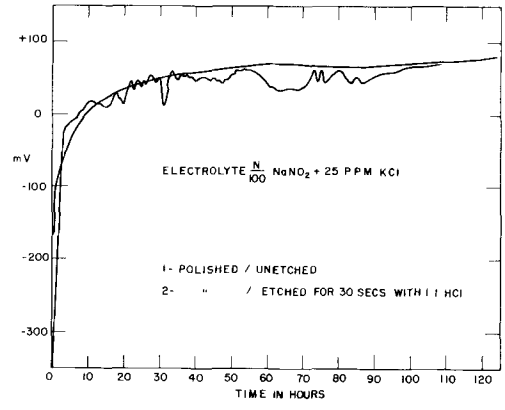


Fig. 6. Potential of iron in N/100 $NaNO_2$ + 25 ppm KCl

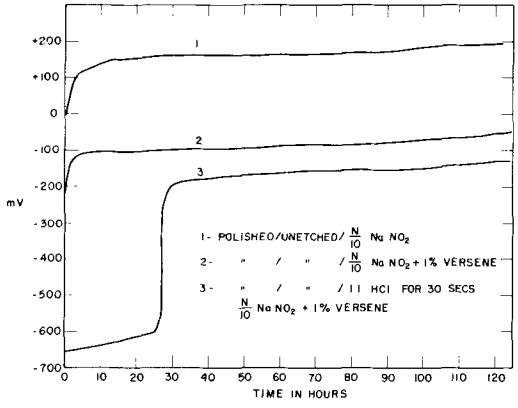


Fig. 8. Potential of iron in N/10 $NaNO_2$ + 1% Versene

3. The presence of chloride ion leads to unstable potentials. A sufficiently high concentration of chloride ion breaks down passivity completely.

4. The presence of a complexing agent (Versene) lowers the potential of etched specimens at the beginning, but after some time passivity is attained. With unetched specimens passivity is attained in the usual manner.

*Electron Diffraction Experiments*

All specimens for electron diffraction were ground flat on a belt grinder and then polished through 4/0 emery paper. All patterns were obtained by reflection in a General Electric electron diffraction machine Model No. G2. Finely divided magnesium oxide was used as a standard. After calculation of "d" values and estimation of line intensities, identification was made using the A.S.T.M. Card Index system.

It was found that specimen preparation was critical in obtaining measureable patterns. Specimens which had been given a fine polish only always gave diffuse patterns, probably due to a very finely crystalline or amorphous "Beilby" layer. When this amorphous layer was removed by etching good patterns characteristic of the metal could be obtained.

*Electron diffraction results in aerated solutions.*— A general summary of the results obtained by diffraction in aerated solutions is presented in Table I.

In Table II "d" values and relative intensities for a typical specimen are collected. The "d" values and intensities for $\gamma$-$Fe_2O_3$ and $\gamma$-$Fe_2O_3 \cdot H_2O$ are presented for identification. The treatment of the specimen was as follows: it was polished through 4/0 emery, etched for 2 min with *N*/10 HCl, and immersed in air-exposed *N*/100 sodium nitrite plus 200 ppm potassium chloride solution for 10 days.

The good numerical and intensity match of the observed lines with that of $\gamma$-$Fe_2O_3 \cdot H_2O$ and the absence of the 1.61 lines of $\gamma$-$Fe_2O_3$ leads to the conclusion that the unknown is $\gamma$-$Fe_2O_3 \cdot H_2O$ together with some $\gamma$-$Fe_2O_3$ since several lines can be matched to this latter substance. The diffuse 2.47 line is a combination of the 2.53 $\gamma$-$Fe_2O_3$ and 2.46 $\gamma$-$Fe_2O_3 \cdot H_2O$ lines.

Reproductions of some diffraction patterns obtained in air-exposed solutions are shown in Fig. 9.

The following conclusions may be drawn from the patterns:

1. Iron polished through 4/0 emery paper yields a pattern consisting of 2 or 3 diffuse haloes.

2. Iron polished through 4/0 emery and etched with *N*/10 or *N* HCl for periods of from 30 sec to 3 min, yields a pattern consisting mainly of iron plus some $\gamma$-$Fe_2O_3$ (Fig. 9a).

3. Iron treated as in [2] above, immersed in aerated *N*/10 or *N*/100 sodium nitrite yields $\gamma$-$Fe_2O_3$ together with a small amount of $\gamma$-$Fe_2O_3 \cdot H_2O$ (Fig. 9b).

4. The addition of chloride ion to sodium nitrite solutions increases the amount of $\gamma$-$Fe_2O_3 \cdot H_2O$ present. At a concentration of 25 ppm chloride ion in *N*/10 sodium nitrite, (Fig. 9c) the pattern is pre-

Table I

| Surface cond. | Mech. pol. to 4/0 | Pol. & etch. | Pol. & etch. | Pol. & etch. | Pol. & etch. | Pol. to 2/0 |
|---|---|---|---|---|---|---|
| Conc. $NaNO_2$ | — | — | N/10 | N/10 | N/10 | N/10 |
| Conc. KCl | — | — | — | 25 ppm | 2000 ppm | — |
| Patterns: Fe | Diffuse | Largely | — | — | — | Some |
| $\gamma$-$Fe_2O_3$ | — | Some | Largely | Largely | Some | Some |
| $\gamma$-$Fe_2O_3 \cdot H_2O$ | — | — | Very little | Some | Largely | — |
| Time of exposure | — | 30 sec —2 min etch | 3 hr —5 days | 9 days | 10 days | 6 days |

dominantly $\gamma$-$Fe_2O_3$, while at 2000 ppm chloride ion the pattern is almost entirely $\gamma$-$Fe_2O_3 \cdot H_2O$ (Fig. 9d).

*Effect of Deaerated Solutions on Reduced Iron Specimens*

The apparatus for the reduction of specimens in hydrogen and subsequent treatment consisted of a quartz tube connected to a vessel for de-aeration of the inhibitor. The hydrogen purification train consisted of a magnesium perchlorate drying tower and a platinized asbestos furnace that was operated around 450°C. The entire apparatus could be evacuated by means of a mercury diffusion pump supported by a backing pump.

The cycle of operations in the apparatus was as follows:

[1] An etched specimen, previously polished to 4/0 grade, was placed in the quartz vessel and the inhibitor in the connecting vessel frozen with liquid air.

[2] The entire apparatus, including the hydrogen purification train, was evacuated to about $10^{-4}$ mm Hg.

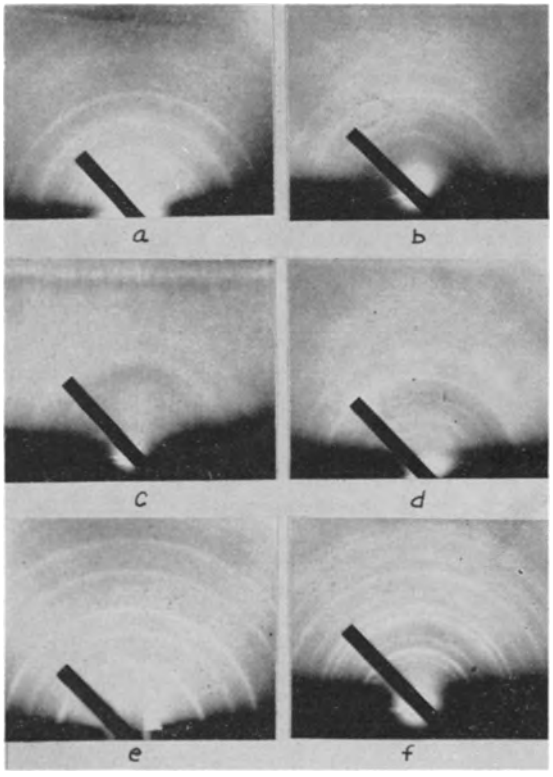


Fig. 9. Electron diffraction: (a) etched specimen; (b) etched or reduced and N/10 $NaNO_2$; (c) as (a) — N/10 $NaNO_2$ + 25 ppm KCl; (d) as (a) — N/10 $NaNO_2$ + 2000 ppm KCl; (e) reduced specimen; (f) reduced — N/100 $NaNO_2$.

Table II

| "d" Exp. | $I/I_1$ Exp. | "d" $\gamma$-$Fe_2O_3$ | $I/I_1$ | "d" $\gamma$-$Fe_2O_3 \cdot H_2O$ | $I/I_1$ |
|---|---|---|---|---|---|
| 3.23 | 80 | | | 3.29 | 90 |
| 2.47 | 90D* | 2.53 | 100 | 2.46 | 70 |
| 2.08 | 10 | 2.08 | 24 | 2.08 | 20 |
| 1.90 | 80 | — | — | 1.93 | 70 |
| 1.71 | 10 | 1.70 | 12 | 1.73 | 40 |
| 1.49 | 100 | 1.48 | 53 | — | — |
| 1.37 | 20 | | | 1.37 | 40 |
| 1.17 | 50 | | | 1.19 | 30 |
| 1.08 | v. faint | 1.09 | 19 | 1.07 | 40 |

* D—Diffuse.

[3] The inhibitor solution was de-aerated by alternate freezing and melting three or four times.

[4] The inhibitor was frozen with liquid air and a slow stream of hydrogen passed through the apparatus.

[5] The temperature of the furnace around the quartz tube was raised to 550°-600°C and the specimen reduced overnight.

[6] After cooling in hydrogen, the inhibitor solution was melted and, by rotation of the solution vessel transferred into the quartz vessel, covering the reduced specimen.

[7] The specimen was allowed to stand in contact with the inhibitor for various periods of time and a reflection diffraction pattern was obtained.

To insure that the specimen was in fact reduced by operation [5], several "dry" runs (runs with no inhibitor) were conducted. The specimen was reduced and removed from the apparatus; a reflection diffraction pattern showed lines characteristic of iron, together with two weak lines due to $\gamma$-$Fe_2O_3$, probably formed on exposure to air. If the specimen had not been reduced completely, then $\alpha$-$Fe_2O_3$ would be expected since this is the oxide stable at the high temperatures of reduction.

In all experiments conducted with de-aerated inhibitors the iron was reduced in hydrogen at 550°-600°C prior to treatment with the solution.

*Results of diffraction experiments in de-aerated solutions.*—A summary of these results is presented in Table III.

Reproductions of some diffraction patterns obtained in de-aerated solutions are shown in Fig. 9. The following conclusions may be drawn from the patterns.

(*A*) Iron polished through 4/0 emery paper, etched with *N*/10 or N HCl for from 30 sec to 3 min and reduced in hydrogen at 550°-600°C yields lines characteristic of iron with one faint line that may be ascribed to $\gamma$-$Fe_2O_3$ (Fig. 9e).

Table III

| All specimens reduced in hydrogen at 550°-600°C. Surface cond. | 40 Polish & etch. | 40 Polish & etch. | 40 Polish & etch. | 40 Polish & etch. |
|---|---|---|---|---|
| Conc. $NaNO_2$ | — | N/10 | N/100 | N/10 |
| Conc. KCl | — | — | — | 2000 ppm |
| Patterns: Fe | All | — | — | — |
| $\gamma$-$Fe_2O_3$ | (1 faint line) | All | All | Little |
| $\gamma$-$Fe_2O_3 \cdot H_2O$ | — | (1 faint line) | — | Largely |
| Time of Exposure | — | 3 hr-2 days | 2 days | 10 days |

(*B*) Iron treated as above with de-aerated N/10 or N/100 sodium nitrite yields $\gamma$-$Fe_2O_3$ plus a little $\gamma$-$Fe_2O_3 \cdot H_2O$ (identical with Fig. 9b).

(*C*) The addition of chloride ion to the nitrite solutions results in the production of $\gamma$-$Fe_2O_3 \cdot H_2O$, but some $\gamma$-$Fe_2O_3$ is present.

An experiment was made in which reduced iron was exposed to de-aerated *N*/700 (100 ppm) nitrite solution for 4 hr. A film of interference color thickness grew on the iron. A diffraction pattern (Fig. 9f) showed that this was probably $Fe_3O_4$, as the film pattern obtained has a sufficiently large number of sharp lines to distinguish it from $\gamma$-$Fe_2O_3$.

### *Electron Microscope Experiments*

Micrographs were made using an R.C.A. Model E.M.T. transmission microscope. The negative replica technique with Formvar as described by Caule and Cohen (6) was used. Metal surfaces were washed and dried with redistilled methanol prior to the application of the 0.75% solution of Formvar. The replicas were shadowed with chromium metal uni-directionally at an angle of incidence of 9°. Direct positive paper was used in order to make the shadows look dark. The iron used in these experiments was the same as that described above. The magnification was × 6700.

The micrographs, in Fig. 10, are of the shadowed replicas of the iron subjected to the following treatment: (*a*) polished to 4/0 emery paper, under ethanol, no etch; (*b*) polished to 4/0 emery paper, under ethanol, etched with N/10 HCl for 30 sec; (c) as for (*a*), then immersed into a solution of air exposed N/10 $NaNO_2$ for 120 hr; (*d*) as for (*b*), then immersed into a solution of air exposed N/10 $NaNO_2$ for 120 hr; (*e*) as for (*b*), then immersed into a solution of air exposed *N*/10 $NaNO_2$ + *N*/100 KCl for time intervals of: 70 hr, 116 hr, and 133 hr; (*f*) as for (*b*), then immersed into an air-exposed solution of 100 ppm $NaNO_2$ + 100 ppm KCl for [1] 45 hr, [2] 93 hr.

In the photographs shown in Fig. 10 one can estimate the size and height of the bumps in the film from the magnification and shadowing angle. In the micrographs the width of the light areas is equivalent to the width of the inclusions, while the length of the shadows is 6.34 (shadowing angle = 9°) times the height. The large inclusion in the center of *f*[2] is therefore $2.3 \times 10^{-4}$ cm wide and $0.5 \times 10^{-4}$ cm high. The smaller inclusion at the top of *f*[1] is $0.25 \times 10^{-4}$ cm wide and $0.1 \times 10^{-4}$ cm high. In general the inclusions protrude well above the film and are wider than high. This would account for their fairly easy detection with the 1° reflection angle of the electron diffraction machine.

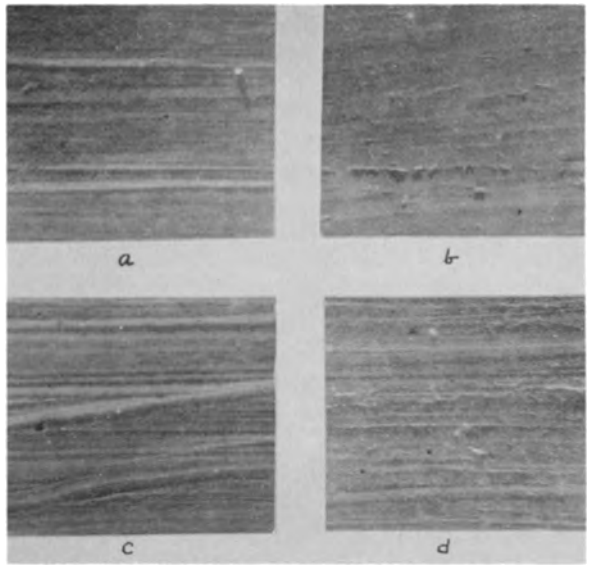


Fig. 10. Electron microscope results: (a) polished surface; (b) polished surface exposed to N/10 $NaNO_2$; (c) etched surface; (d) etched surface exposed to N/10 $NaNO_2$.

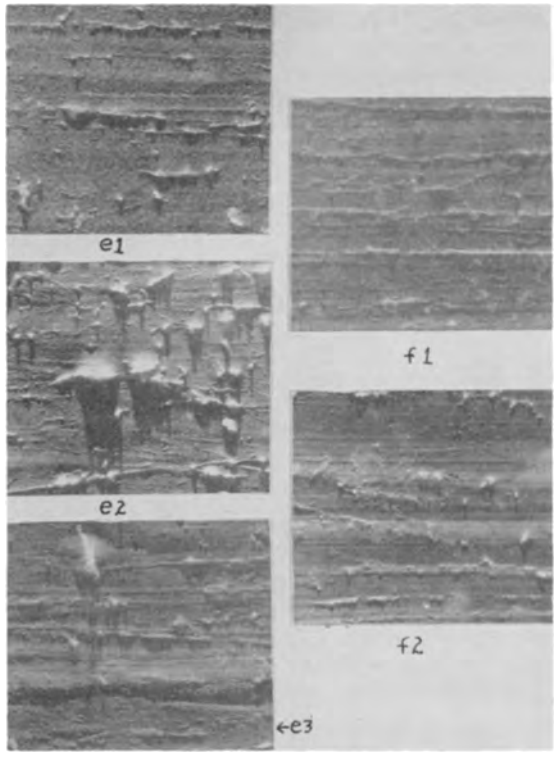


Fig. 10 (cont'd). (e) N/10 $NaNO_2$ + N/100 KCl (1) 70 hr, (2) 116 hr, (3) 333 hr; (f) 100 ppm $NaNO_2$ + 100 ppm KCl (1) 45 hr, (2) 93 hr.

## Discussion

Previous investigation had indicated that a film of $\gamma$-$Fe_2O_3$ is formed on iron in the presence of sodium nitrite solutions. There was also some evidence for the additional formation of a hydrated oxide. This has been confirmed and expanded in this work.

Surface preparation has a very marked effect on both the potential behavior and appearance of the

iron. Potentials tend to be more positive and more stable on polished than on polished and etched surfaces. This can be related to a difference in the surface which is shown both by the electron micrographs and electron diffraction. Specimens which were polished to 4/0 paper showed only diffuse iron patterns which were obscured by contact of the metal with nitrite solutions. However, specimens which were etched gave mainly iron patterns, and these on exposure to nitrite gave $\gamma$-$Fe_2O_3$ patterns. It is probable that the etched specimens, which were exposed to air before insertion into the nitrite solutions, already had a thin oxide film on them. However, this oxide film was too thin to show in the diffraction patterns and exposure to nitrite thickened the film considerably. The film after exposure to nitrite was probably at least 40Å thick.

The diffuse pattern obtained from a polished surface indicates that the metal at the surface is very finely crystalline or "amorphous." This may lead to the formation of an oxide film with very small crystals well packed together. This film would be of both small pore size and low porosity, which would lead to higher potentials than those obtained with etched specimens. The "amorphous" iron probably has a lower density than crystalline iron; this should lead to an oxide-metal interface under less strain than the interface formed on crystalline iron.[1] It should be pointed out that there is only a very small change in surface appearance as shown by the electron microscope when either polished or etched iron is exposed to $N/10$ nitrite solutions.

Intermediate air exposure or the presence of oxygen in the solution is not necessary for the formation of the $\gamma$-$Fe_2O_3$. This is shown in the experiments in which specimens were polished, etched, and then reduced by hydrogen and exposed in de-aerated nitrite solutions in the absence of air. A good $\gamma$-$Fe_2O_3$ pattern was obtained. Specimens treated in this manner without exposure to nitrite gave iron patterns, although, as stated above, there was probably a very thin oxide formed in air during transfer to the diffraction machine.

The electron microscope showed that there was very little change in the appearance of either etched or polished surfaces on exposure to nitrite solutions. This would indicate that the main function of nitrite is to thicken and repair the film.

### *Films in the Presence of Chloride*

The presence of chloride ions in the solutions both lowered the final potential and led to unsteady potentials. The electron diffraction experiments showed that there was an increasing amount of hydrated oxide present in the films formed in these solutions when both the relative amount of chloride ion or time of exposure was increased. The electron micrographs confirmed these observations by showing that inclusions were formed in the film and that these inclusions also increased in height and area with time. It is very probable that the inclusions are composed mainly of hydrated oxide. The fact that the bumps became obscured at high relative concentrations of chloride ion would appear to indicate that under the conditions leading to very unsteady potentials some of the hydrated oxide precipitates over the whole surface, thus covering the original oxide layer. This would account for the almost complete absence of anhydrous oxide lines in the diffraction patterns of these specimens.

The behavior of the potential of iron in these solutions can be explained most easily in terms of an oxide film with inclusions (7), as observed by the electron microscope technique. Inclusions of hydrated oxide have a fairly good permeability to ferrous ions and are the sites of the anodic reaction, while the oxide covered surface provides the cathodic areas. The measured potential is determined by the relative resistances of the inclusions, the electrolyte, and the cathode film, as well as the polarization characteristics of the cathodic and anodic reactions. At low chloride ion concentration the inclusions are small and their resistance is high. This leads to high anodic polarization with consequent low current and small cathodic polarization. The observed potential is then close to that of the cathodic reaction and "noble" or passive. The effect of chloride ion on breaking down the passive potential is due to three factors. Chloride ion has a relatively high transport number and small size and tends to carry a large amount of the current to the anodes. This leads to the presence of both nitrite and chloride ions in the anodic pores, which favors the formation of ferric chloride. The hydrolysis of ferric chloride decreases the *p*H of the electrolyte in the anodes, leading to conditions which are conducive to either undermining or autoreduction of the oxide film. Chloride ion is also a complexing agent for iron and tends to prevent precipitation of a healing hydrate or hydrated oxide. These factors allow the pores to grow in size. Under near passive conditions, precipitate forms, but it is thicker than the oxide film because of a higher permeability for ferrous ions. The unsteady potentials in the presence of chloride indicates that there is a continuous formation and repair of pores. This explains the necessity of the continued presence of an inhibitor for maintaining passivity.

The effect of a strong complexing agent on the potential is shown in the experiments with Versene in Fig. 8. Here it can be seen that the potential remains active until a balance between iron ions in the complex and in the solution is reached, at which point the hydrated oxide precipitates in the pores and the metal becomes passive. This would indicate that the complexing ability of the chloride ion plays only a small part in the mechanism of the breakdown of the films. It is interesting to observe that the Versene has a much smaller effect on a polished surface than on one that has been both polished and etched. This is in line with other observations that the concentration of chloride required to break down a polished surface is greater than that required to break down an etched surface. Both these effects may be explained in the following manner. The

[1] The surface of "polished" iron can be considered as having a high concentration of defects, which would lead to a lower density. The oxide formed has a lower density than iron and the strain of the metal-oxide interface is in part, at least, determined by the difference in density between the oxide and metal. Because of the small crystal size (many grain boundaries) the oxide film may grow thicker than on etched metal.

metal surface is disrupted by polishing and the oxide formed on this very finely crystalline or amorphous metal has a smaller crystal size and is possibly thicker than oxide formed on the more perfect etched metal surface. The oxide film formed on the polished metal may also contain some of the oxide formed during the polishing. It was observed that the potential of polished iron in nitrite solutions is always higher than that of etched iron. This indicates that the films on polished iron have smaller pores than those on etched iron. If the effect of chloride and/or the complexing agent is to break down the film by acting at the pores, then it would be expected that the oxide film on the polished surface would be more stable than the film on the etched metal. In this connection the major effect of the chloride is to lead finally to the breakdown of the film by undermining or autoreduction while the Versene prevents the plugging of the pores by removing iron ions before they form a precipitate.

The mechanism for nitrite inhibition would appear to be much the same as that proposed in previous papers (7, 8). The nitrite solution reacts directly with the iron surface to form an oxide film which, due to nonhomogeneity of the surface, is not perfect and does not protect completely. Full protection is obtained by the formation of inclusions in the discontinuities of the film which grow somewhat thicker than the oxide film itself until reaction substantially ceases. If there is present in the solution a material which prevents the formation of inclusions or changes their physical character, such as a complexing agent or chloride ion, then the discontinuities in the film can grow by either undermining or autoreduction of the film when the anodes become sufficiently acid, and if these disruptive agents are at a sufficiently high concentration, then passivity will not be obtained.

Manuscript received Feb. 26, 1957. This paper was prepared for delivery before the Pittsburgh Meeting, Oct. 9-13, 1955.

Any discussion of this paper will appear in a Discussion Section to be published in the December 1958 JOURNAL.

REFERENCES

1. M. Cohen, *J. Phys. Chem.*, **56**, 451 (1952).
2. W. H. J. Vernon, F. Wormwell, and J. T. Nurse, *J. Chem. Soc.*, **1939**, 621.
3. I. Itaka, S. Miyake, and T. Imori, *Nature*, **139**, 156 (1937).
4. P. D. Dankov and C. R. Shushakov, *Acad. Sci. URSS*, **24**, 553 (1939).
5. J. E. O. Mayne and M. J. Pryor, *J. Chem. Soc.*, **1949**, 1831.
6. E. J. Caule and M. Cohen, *Can. J. Chem.*, **31**, 237 (1953).
7. M. J. Pryor and M. Cohen, *This Journal*, **100**, 203 (1953).
8. R. Pyke and M. Cohen, *ibid.*, **93**, 63 (1948).

# The Protective Value of Tin-Nickel Alloy Deposits on Steel

**F. A. Lowenheim**

*Metal & Thermit Corporation, Rahway, New Jersey*

**W. W. Sellers**

*Development and Research Division, International Nickel Company, New York, New York*

**F. X. Carlin**

*Research Laboratory, International Nickel Company, Bayonne, New Jersey*

ABSTRACT

Outdoor exposure tests of the comparative value of the Sn-Ni alloy and conventional Ni/Cr deposits on steel, with and without a copper undercoat, are reported. It is shown that Sn-Ni is comparable in protective value to Ni/Cr, not quite so good in marine but superior in industrial atmospheres. The type of corrosion behavior of the two deposits differs considerably. In general, the protective value of the Sn-Ni deposit is of a high order.

A process for plating an alloy of tin and nickel from a chloride-fluoride electrolyte was developed by the Tin Research Institute in 1951 (1). Since that time several papers have appeared dealing with various aspects of the process and the resulting deposit: it has been shown that the deposit is an intermetallic compound of the formula SnNi (2); the function of fluoride ion in complexing the tin in solution has been elucidated (3); the throwing power of the bath has been determined (4); the electrode potential of the alloy and its resistance to many chemical reagents have been studied (5); the hardness has been measured (6); the original bath formulation has been modified (7); and the behavior of the deposit in outdoor weathering tests has been reported (8, 11).

The tin-nickel deposit is of exceptional interest, both theoretically and practically, for several reasons, among which may be mentioned:

1. The intermetallic compound SnNi (65% Sn, 35% Ni) does not appear on the thermal equilibrium diagram of the nickel-tin system and apparently

cannot be prepared by standard metallurgical techniques. It is thus in effect a new metal, so far preparable only by electrodeposition, having properties which cannot necessarily be predicted from those of its constituents.

2. The plating bath is of a relatively new type, being particularly unusual in that it is the first practical example of an acid tin-plating electrolyte which does not require organic addition agents for the production of sound deposits.

3. In spite of its acid nature the bath exhibits exceptionally good throwing and covering power.

4. The deposit possesses several unusual properties which give promise of useful applications in both the decorative-protective and industrial or engineering phases of metal finishing. It is hard, smooth, and almost bright as plated, and according to published reports shows exceptional chemical resistance to a wide variety of reagents as well as to outdoor weathering. It can be soldered with ordinary soft solder using mild (rosin-alcohol) fluxes. In ease of solderability the tin-nickel deposit is not so good as tin, tin-zinc alloy, etc., but the remarkable feature is that a hard, bright deposit can be soldered at all with noncorrosive fluxes.

5. When the process was first introduced, nickel was in extremely short supply, and the new deposit offered the possibility that one pound of nickel could be made to do the work of three, assuming that performance was equivalent. Although such considerations are of only ephemeral importance, they do help in lending impetus to the investigation of new processes.

Since corrosion resistance appeared to be one of the most interesting properties of the deposit, both of the companies represented by the present authors instituted programs to investigate it further, by means of outdoor exposure tests. These were designed to supplement the English results already published in several respects: several additional variables were included, the exposure times involved are considerably longer, and the exposures represent American rather than English conditions. The tests here reported are still in progress, but have proceeded far enough to permit conclusions to be drawn.

*Scope and purpose of tests.*—It was desired to investigate the performance of tin-nickel alloy deposits on steel under outdoor weathering conditions. The plating systems used in the exposure were designed to test the following variables.

**Table I. Weathering of tin:nickel-alloy coatings at Kure Beach**

Exposed on ASTM-type racks facing south in lot 800 ft from mean shore line; type of steel: mild, cold-rolled; size of panels: 4x6 in.; dates of exposure: Lots I-1 thru I-12 exposed 2-2-55. Lots M-1 thru M-23 exposed 3-24-55.

| Lot No. (3 panels per lot) | Type and thickness (mils) of coating | | | | | Rating | | | | | |
|---|---|---|---|---|---|---|---|---|---|---|---|
| | | | | | | Approximately 7 months | | 12 Months | | 24 Months | |
| | Total thickness exclud. Cr | Cu | Ni | Sn-Ni | Cr | Rating No. | Defects | Rating No. | Defects | Rating No. | Defects |
| I-1 | 0.75 | | 0.75B | | 0.01 | 2 | iS,xpR,xRs,xcR | 0 | | 0/0 | xcR,xRs |
| I-11* | | | 0.25B | 0.50 | 0.01 | | | 7 | scR,sRs,xS,xeRs | 4/0† | icR,sRs,iecR |
| I-7* | | 0.25B | | 0.50 | 0.01 | | | 6 | iS,icR,xeRs,sRs | 6/0 | icR,iRs,xecR |
| I-5 | | 0.25B | | 0.50 | — | 4 | xcR,xeRs,xS,iRs | 4 | xcR,xeRs,xS,iRs | 2/0 | xcR,iRs,xS,xecR |
| M-14 | 1.00 | | 1.00B | | 0.01 | 9 | vscR | 6 | sRs,vspR,xS | | |
| M-4 | | | | 1.00 | — | 1 | xcR | 0 | xpR,xRs,xS | | |
| M-5 | | 0.01 | | 1.00 | — | 9 | vscR | 6 | iS,iRs,spR | | |
| M-11 | | 0.25B | 0.75B | | 0.01 | 8 | vsRs,scR | 3 | iRs,xS,spR | | |
| M-3 | | 0.25 | | 0.75 | — | 5 | icR | 3 | sS,ipR,iRs | | |
| M-12 | | 0.50B | 0.50B | | 0.01 | 5 | icR,iRs | 1 | xS,spR,xRs,scR | | |
| M-2 | | 0.50 | | 0.50 | — | 3 | iRs,icR | 2 | xS,xRs,ipR | | |
| M-13 | | 0.75B | 0.25B | | 0.01 | 3 | xcR,xRs | 1 | xS,icR,xRs | | |
| M-1 | | 0.75 | | 0.25 | — | 2 | xRs,xcR | 1 | xRs,xpR | | |
| I-2 | 1.25 | | 1.25B | | 0.01 | 6 | spR,iRs,sS,icR | 5 | spR, iRs,sS,icR, seRs. | 1/1 | xpR,icR,xRs |
| I-12* | | | 0.25B | 1.00 | 0.01 | | | 8 | icR,iRs,iS,xeRs | 5/0† | icR,iRs,xecR |
| I-8* | | 0.25B | | 1.00 | 0.01 | | | 8 | iS,xeRs | 8/0 | icR,iRs,xecR |
| I-6 | | 0.25B | | 1.00 | — | 9 | xS,vsRs,xeRs | 8 | xS,vsRs,sC,xeRs | 6/0† | icR,iRs,xS,xecR |
| M-18 | 1.50 | | 1.50B | | 0.01 | 9 | vsRs | 7 | sRs,vspR,iS | | |
| M-9 | | | | 1.50 | — | 0 | xcR | 0 | xRs(100%),xpR | | |
| M-10 | | 0.01 | | 1.50 | — | 9 | vscR | 6 | iRs,iS,spR | | |
| M-15 | | 0.50B | 1.00B | | 0.01 | 9 | vscR | 7 | sS,sRs,vspR | | |
| M-8 | | 0.50 | | 1.00 | — | 7 | icR | 5 | iS,iRs,ipR | | |
| M-16 | | 0.75B | 0.75B | | 0.01 | 9 | vscR | 7 | xS,sRs,spR | | |
| M-7 | | 0.75 | | 0.75 | — | 2 | xcR,iRs | 2 | xS,ipR | | |
| M-17 | | 1.00B | 0.50B | | 0.01 | 9 | scR | 4 | xS,sRs,spR | | |
| M-6 | | 1.00 | | 0.50 | — | 4 | icR,iZ | 3 | iS,iRs,ipR | | |

NOTES: * All the chromium applied to the tin-nickel coatings had completely flaked off in less than 6 months. This is not considered in rating numbers. Ratings are an average for the lot.
† = following rating indicates a spread greater than two rating numbers from average given.
B = buffed
Lots designated with prefix "I" were prepared by the International Nickel Co.
Lots with prefix "M" were prepared by the Metal and Thermit Corp.
Abbreviations used to describe defects are identified in Table III.
Ratings for 7 and 12 months were made with single-number system. Ratings for 24 months were made with two-number system. First numeral denotes protective values; second numeral general appearance.

1. Effect of total thickness of deposit. Thicknesses from 0.75 to 1.5 mils are included.

2. Effect of proportion between copper undercoat and tin-nickel. Copper undercoats from 0.25 to 1.0 mils are used.

3. Effect of type of undercoat. Tin-nickel is plated (*a*) direct on steel, (*b*) over a copper flash, (*c*) over substantial thicknesses of copper, (*d*) over nickel.

4. Direct comparison of tin-nickel vs. nickel/chromium, thickness for thickness, over various thicknesses of copper. The nickel is in all cases buffed Watts', which is generally agreed to be at least as good as and in most cases better than bright nickel in corrosion resistance.

5. Effect of chromium over tin-nickel. As will appear, this purpose of the experiment was not fulfilled because, at the time these exposures were initiated, the method used for chromium plating over tin-nickel turned out to be unsatisfactory. Panels were prepared but the chromium flaked off soon after exposure. Later tests still on exposure give preliminary indication that this problem has been solved.

6. Possible application of tin-nickel as a final flash coat, used similarly to the conventional thin chromium. Thin plates of tin-nickel (0.01 mil or so) were deposited on copper and bronze undercoats. This phase of the program is omitted from the tables and subsequent discussion; it need only be said that tin-nickel used in this way proved unsatisfactory as a decorative finish.

7. All of the foregoing comparisons and tests are conducted in the two principal types of atmospheres, marine and industrial.

The actual plating systems used are included in Tables I and II along with the results of the exposures.

### Preparation of Panels for Exposure

Panels were prepared by International Nickel Company (designated in Tables I and II with an "I") and by Metal & Thermit Corporation (designated in the same tables with an "M").

This basis metal for all panels was cold-rolled mild steel cut to standard 4 x 6 in. size. Standard commercial practices for polishing, degreasing, electrolytic cleaning, and pickling the steel in preparation for plating were employed.

Nickel and copper were plated according to accepted methods (9). Nickel was deposited from a conventional low-*p*H Watts-type bath. Copper cyanide and copper sulfate baths were used to deposit

**Table II. Weathering of tin:nickel-alloy coatings at Bayonne**

Exposed on ASTM-type racks facing south; type of steel: mild, cold-rolled; size of panels: 4x6 in.; date of exposure: 3-24-55.

| Lot No. (3 panels per lot) | Type and thickness of coating (mils) | | | | Rating | | | | | | | |
|---|---|---|---|---|---|---|---|---|---|---|---|---|
| | | | | | 6 Months | | 12 Months | | 24 Months | | 29 Months | |
| | Cu | Ni | Sn-Ni | Cr | Rating | Defects | Rating | Defects | Rating | Defects | Rating | Defects |
| I-1 | | 0.75B | | 0.01 | 3 | xpR,xRs | 1 | xpR,xRs | 2/0 | xpR,xRs | 2/0 | xcR,xRs,xpR |
| I-11* | | 0.25B | 0.5 | 0.01 | 8 | icR | 7 | icR,iRs | 8/8 | scR | 6/4 | icR,xLS |
| I-7* | 0.25B | | 0.5 | 0.01 | 8 | vsSp,icR | 8 | vsSp,icR | 8/8 | scR | 9/7 | scR,xLS |
| I-5 | 0.25B | | 0.5 | | 7 | scR,xecR | 4 | scR,xecR | 6/6 | icR,xecR | 5/3 | icR,xLS, vxecR. |
| M-14 | | 1.0B | | 0.01 | 7 | ipR,iRs | 2 | xRs,iSp,ipR | 1/0 | vxRs | 1/0 | vxRs,xpR |
| M-4 | | | 1.0 | | 3 | iRs,xcR | 2 | xcR,xRs | 3/3 | xcR,xecR | 2/1 | xcR,xecR, xRs,xLS. |
| M-5 | 0.01 | | 1.0 | | 9 | vscR | 9 | vscR | 9/9 | vscR | 9/7 | vscR,vsSp, ieR,xLS. |
| M-11 | 0.25B | 0.75B | | 0.01 | 4 | xpR,iRs | 4 | iRs,iS,ipR | 3/1 | xpR,xSp,xRs | 2/0 | xpR,xcR,xRs |
| M-3 | 0.25 | | 0.75 | | 9 | vscR,vsRs | 8 | vscR,vsRs | 8/8 | scR | 7/5 | scR,iRs,ipR, xLS. |
| M-12 | 0.5B | 0.50B | | 0.01 | 3 | xpR,Rs,xS | 2 | xS,xpR,xRs | 2/0 | xpR,xSp,xRs | 1/0 | xpR,xcR,vxRs |
| M-2 | 0.5 | | 0.5 | | 6 | sSp,icR,sZ | 6 | sS,scR,sRs | 4/4† | icR,xRs,ipR | 3/2† | icR,xRs,xLS |
| M-13 | 0.75B | 0.25B | | 0.01 | 3 | xpR,xSp,scR,iRs | 1 | xRs,xS,xpR,icR | 1/0 | xpR,xSp,xRs | 0/0 | xcR,xRs |
| M-1 | 0.75 | | 0.25 | | 5 | sRs,icR | 4 | iRs,icR | 4/4† | icR,iRs,ipR | 4/2† | icR,xRs,xLS |
| I-2 | | 1.25B | | 0.01 | 7 | ipR,xRs | 7 | spR,sRs | 2/1 | xpR,xRs | 3/1 | xcR,xRs,xpR |
| I-12* | | 0.25B | 1.0 | 0.01 | 8 | icR | 7 | icR,iRs | 7/7 | icR | 5/3 | icR,xLS |
| I-8* | 0.25B | | 1.0 | 0.01 | 9 | scR | 9 | vscR | 9/9 | vscR | 10/8 | xLS |
| I-6 | 0.25B | | 1.0 | | 10 | | 10 | | 10/9 | sSp | 10/8 | xLS |
| M-18 | | 1.5B | | 0.01 | 8 | iSp,spR | 5 | ipR,iRs | 2/1 | xpR,xRs | 1/0 | xpR,xRs,iMS |
| M-9 | | | 1.5 | | 0 | xRs | 0 | xRs | 0/0 | xRs | 0/0 | xRs |
| M-10 | 0.01 | | 1.5 | | 8 | iZ,sRs | 8 | iZ,iRs | 8/7 | ipR,iZ,iB,sS | 7/3† | icR,iZ,iRs,xLS |
| M-15 | 0.5B | 1.0B | | 0.01 | 8 | iSp,spR,sS | 6† | iS,sRs,sSp | 4/2 | ipR,iZ,xS | 5/2 | ipR,xRs,xMS, iW |
| M-8 | 0.5 | | 1.0 | | 9 | vspR,vsSp | 9 | vspR,vsSp | 9/9 | vspR | 10/8 | xLS |
| M-16 | 0.75B | 0.75B | | 0.01 | 7 | ipR,iSp | 5 | iS,sRs,ipR | 3/2 | xpR,xS | 3/0 | xpR,xRS,xSp |
| M-7 | 0.75 | | 0.75 | | 9 | vspR,vsZ | 8 | iS,iZ,vscR | 9/9 | spR | 8/6 | vscR,ipR, iRs,xLS. |
| M-17 | 1.0B | 0.5B | | 0.01 | 7 | spR,xSp | 3 | xpR,sRs,iS | 3/1† | xpR,xRs | 4/3† | ipR,xRs,iSp |
| M-6 | 1.0 | | 0.5 | | 9 | sSp,ipR,sS | 7 | vscR,vsRs,iS | 8/8 | spR | 7/5 | spR,iRs,xLS |

NOTES: * All the chromium applied to the tin-nickel coatings had completely flaked off in less than 6 months. This is not considered in rating numbers. Ratings are an average for the lot.
† = following rating indicates a spread greater than two rating numbers from average given.
B = buffed.
Lots designated with prefix "I" were prepared by the International Nickel Co.
Lots with prefix "M" were prepared by the Metal and Thermit Corp.
Abbreviations used to describe defects are identified in Table III.
Ratings for 6 and 12 months were made with single-number system. Ratings for 24 months and 29 months were made with two-number system. First numeral denotes protective value; second numeral, general appearance.

copper. Thickness of coating on each panel was determined with a Magne-Gage at several predetermined points. Panels were rejected if any measurement deviated by more than 10% from the desired thickness.

Tin-nickel alloy was plated from the bath originally recommended by Parkinson (1). Thicknesses of coatings over copper were measured with a Magne-Gage. By measuring the time and current density required to deposit a prescribed thickness of the alloy over copper, a plating rate was determined. This rate was used to calculate plating times for the various thicknesses over nickel.

All nickel and copper coatings were buffed. The tin-nickel alloy required color buffing or wiping to remove a slight "haze" present in the as-plated coating.

Chromium was deposited as a final flash coating on panels of some lots. Thickness of chromium deposits was measured on trial panels by an anodic solution method. Although the chromium coatings on tin-nickel appeared sound initially, they powdered soon after exposure.

*Exposure sites and conditions.*—Panels were exposed at three sites, one marine and two industrial, as follows.

Kure Beach, N. C.: the test lot, 800 ft from the ocean, of the International Nickel Company's atmospheric exposure station. The atmosphere is purely marine, there being little or no industry nearby.

Bayonne, N. J.: the test lot at the laboratories of the International Nickel Company. This is a heavily industrialized area, with much chemical industry, gasoline refining, and small foundries and smelters, in the immediate neighborhood.

Pittsburgh, Pa.: the roof of a downtown office building. This area is too well-known to require description. The results of the Pittsburgh exposure are not included in the tables or discussion: trends of deterioration and relative merit of the various panels proved to be the same at Pittsburgh as at Bayonne except that Pittsburgh was less corrosive. (The I-series of panels was not included in the Pittsburgh exposure.)

All panels were exposed on standard ASTM-type racks facing south at an angle of 30° to the horizontal. The panels were not cleaned except when light brushing or rinsing became necessary during inspections to distinguish between defects and dirt.

*Methods of inspection and rating.*—Panels were rated as nearly as possible in accordance with methods used by ASTM Committee B-8 (10). In this system a rating number is assigned corresponding to the percentage of the area which is covered by defects (*see* Table III). In addition to the numerical rating, descriptions of the type of defect encountered are noted in shorthand abbreviations, the meanings of which are explained in the table.

During the time these panels were on exposure, one of the authors (F.A.L.) began experimenting with a modified scheme for assigning rating numbers which is now being tried out by Committee B-8. This involves the separation of defects into two categories: those which cause or are caused by basis metal corrosion (rusting) and those which affect only the coating. In the first category are all forms of rusting; in the second are such defects as surface pitting, flaking or peeling of topcoats which does not penetrate to the steel, tarnish, and the like. Two rating numbers are assigned to the panel, one for each category of defect, separated by a slash; thus 10/5 would indicate a panel free of rust (first number) but down-graded to 5 (second number) for one or another surface defect affecting its appearance.

The fact that rating methods were changed during the course of this exposure inevitably introduces a complication into the orderly interpretation of the results. Nevertheless this complication is more apparent than real: meaningful comparisons among various groups of panels can be drawn and significant conclusions reached.

A further complication is introduced by the tendency of tin-nickel coatings, unprotected by a chromium finish, to acquire in the atmosphere a film which might be variously described as light stain,

**Table III. Identification of rating numbers and symbols used in Tables I and II**

| Numerical rating | % of Area Defective |
|---|---|
| 10 | 0 |
| 9 | 0-0.1 |
| 8 | 0.1-0.25 |
| 7 | 0.25-0.5 |
| 6 | 0.5-1.0 |
| 5 | 1.0-2.5 |
| 4 | 2.5-5.0 |
| 3 | 5.0-10.0 |
| 2 | 10.0-25.0 |
| 1 | 25.0-50.0 |
| 0 | over 50.0 |

Where two number system is used, first number denotes protective value, second number denotes general appearance.

"Shorthand" symbols used in rating exposure panels

| Symbol | Meaning |
|---|---|
| R | Rusting of the basis metal (permanent or massive type of rust such as that in pinholes, bare or flaked areas, or in craters or broken blisters). |
| Rs | Rust staining which can be removed readily with a damp cloth or chamois and mild abrasives revealing a sound, bright surface. |
| S | Stains or spots other than obvious rust stains. |
| Sp | Surface pits (corrosion pits probably not extending through to the basis metal: i.e., absence of obvious basis metal corrosion products bleeding therefrom). |
| B | Blister |
| Z | Crazing |
| p | Pinpoint |
| c | Crater or "pustular" |
| e | Edge |
| s | Slight or small |
| i | Intermediate or moderate |
| x | Excessive or severe, or large |
| f | Few |
| m | Many |
| v | Very (to modify above adjectives) |
| L | Light |
| M | Medium |
| H | Heavy |
| L, M, H | Used to denote degree of staining |

mild tarnish, slight discoloration, or the like. Because the tarnish is readily removable by light abrasion, this defect was arbitrarily assigned a penalty of only two points in the appearance (second number) rating, e.g., a panel otherwise perfect but exhibiting the aforesaid light stain would be rated 10/8. This property of tin-nickel is discussed further below.

A characteristic of the rating method should be borne in mind in appraising and interpreting the results. Since the numbers are based on a logarithmic scale, differences in absolute area defective are far greater between two adjacent numbers at the low than at the high end of the scale. In spite of this, however, differences at the high end of the scale are far more significant practically and commercially. This is because panels with ratings below about 5 have deteriorated beyond any practical utility, so that it is of little real interest whether they rate 3 or 1. On the other hand, there is a significant difference between a 10 and a 9: the former has no defects at all, while the latter is beginning to exhibit some failure.

*Replication.*—Nine panels of each lot (Tables I and II) were prepared, so that exposures at each of the three sites were in triplicate. Since it would unduly complicate the tables of results to include ratings for all panels, lot ratings were arrived at by simply averaging the individual ratings. (Where the two-number system is used, each number is treated separately.)

When the three panels were within ±2 numbers of the lot average, the figure in the tables is given without comment. When one or more panels differed by more than two numbers from the lot average, a dagger in the table so indicates. The practical significance of this notation is that too much reliance should not be placed on the particular rating: with only three replicates one is not justified in discarding any result no matter how divergent.

## Results

The ratings of the lots on exposure at Kure Beach are given in Table I; those at Bayonne in Table II. As already explained, detailed results for the Pittsburgh exposure are omitted. The Kure Beach exposure has been discontinued; panels are still out at Bayonne and Pittsburgh.

The ratings given in the tables are plotted in Fig. 1 and 2. Where the two-number system was used, the value used for the plot is the second number since it corresponds closely to the rating that would result from the single-number method. The value of graphical presentation is twofold: it offers a readily assimilated summary of the results, and it enables calculation of an index of performance which is essentially more meaningful than the rating numbers themselves, viz., the useful service life of a given coating system. This may be defined as the time on exposure before a panel has deteriorated to a given rating.

As will be seen from an inspection of the graphs, occasionally panels seem to improve between inspections instead of deteriorating. This anomaly is explicable on the basis that the subjective element has, unfortunately, not been entirely eliminated from the

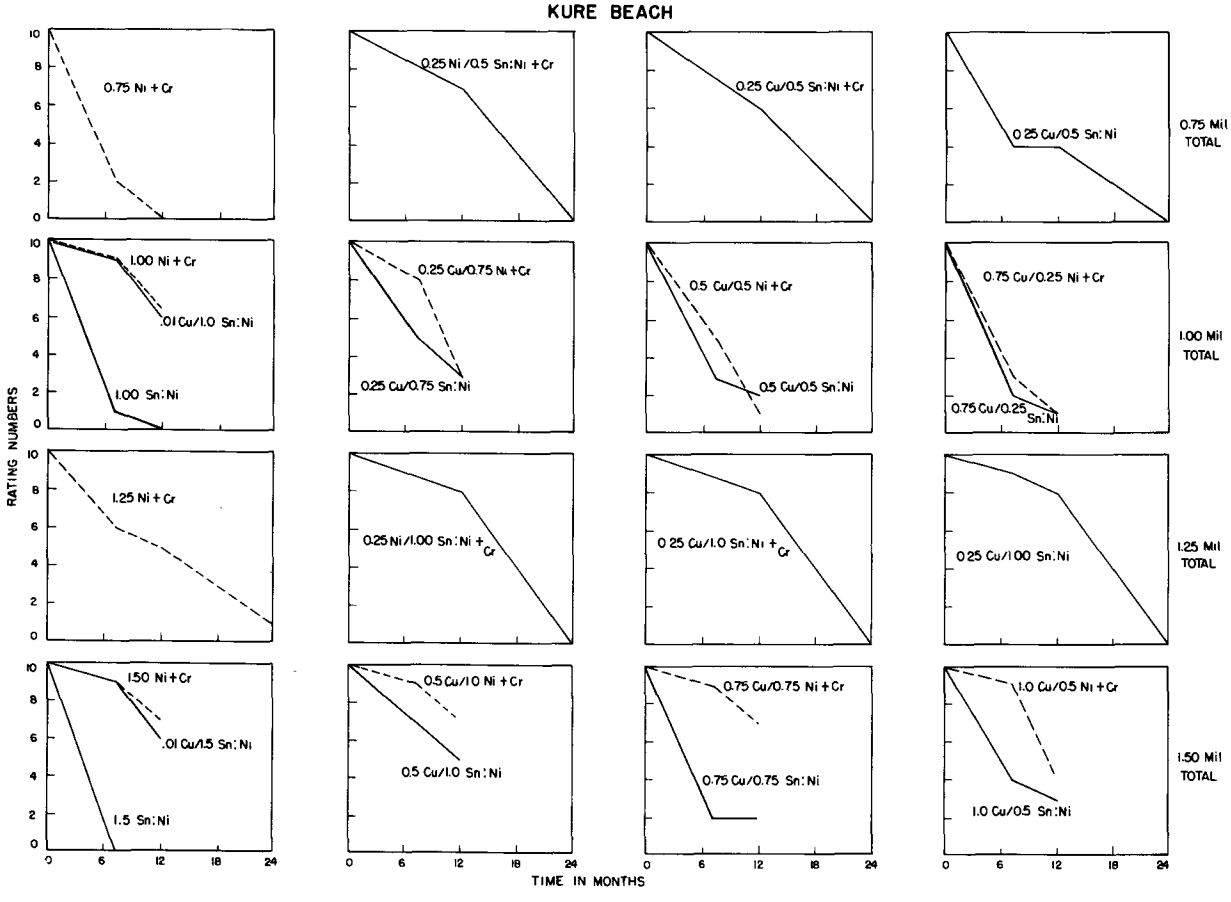


Fig. 1. Rating vs. time at Kure Beach. Solid lines, tin-nickel coatings; dashed lines, nickel/chromium coatings.

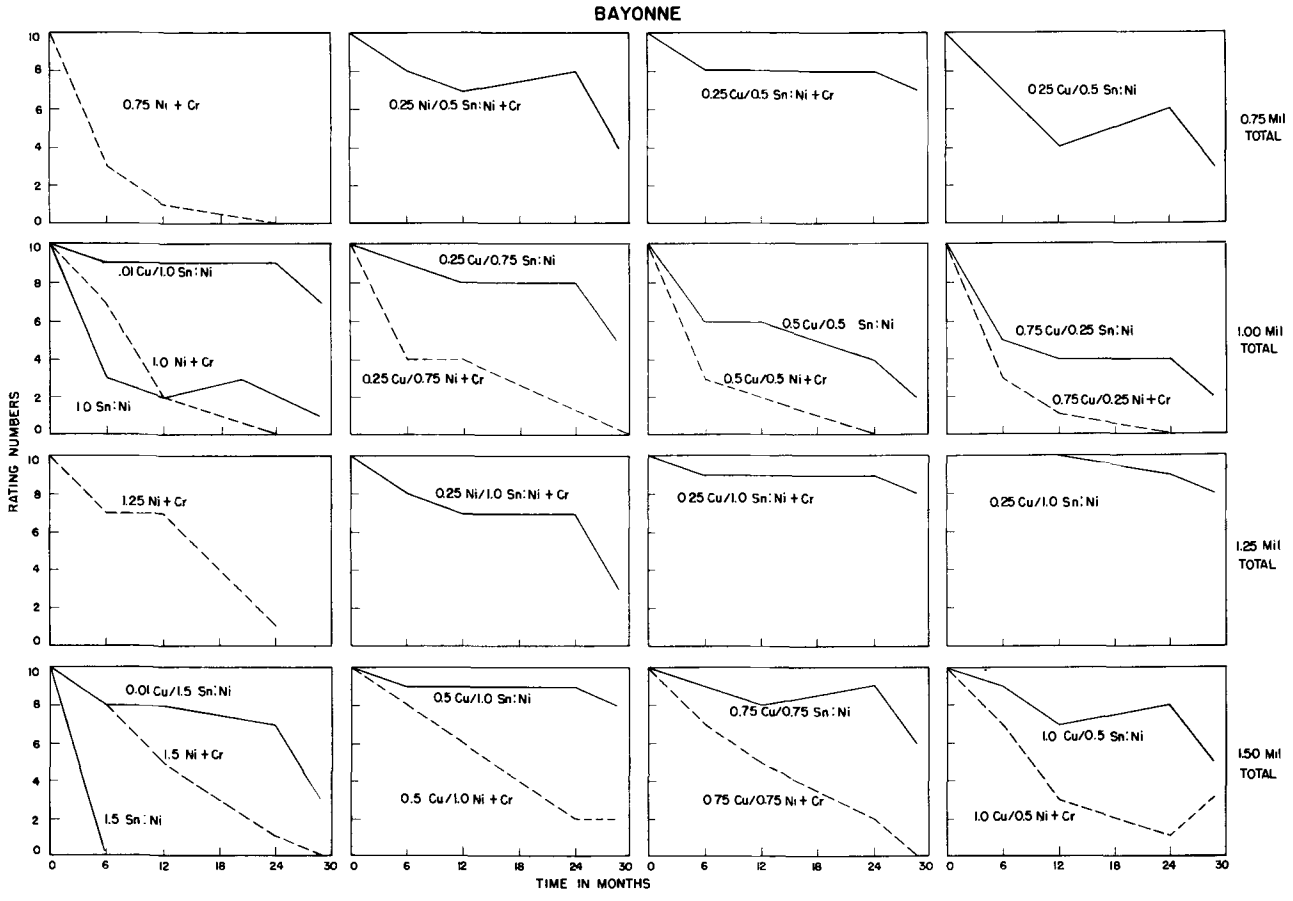


Fig. 2. Rating vs. time at Bayonne. Solid lines, tin-nickel coatings; dashed lines, nickel/chromium coatings

rating system; each inspection is independent and in many cases different inspectors were involved. Another factor may be the occurrence of heavy rain immediately before inspection, having the effect of cleaning the panels and causing them to improve in appearance.

## Discussion

It is apparent that the relative merit of the various lots is quite different under the two conditions of exposure. It therefore becomes necessary to discuss the Kure Beach and the Bayonne results separately.

*Marine atmosphere (Kure Beach).*—All the panels in the present program deteriorated relatively rapidly. For long-time service in such a location, thicker coatings than were used in this program would be required.

*Tin-nickel.*—The useful service life of the tin-nickel coatings in this test was almost independent of the thickness or nature of the undercoat (with one exception noted below). In order to obtain reasonably good performance at least 1.0 mil of tin-nickel appears to be required, but it does not seem to matter appreciably whether this is plated over 0.01, 0.25, or 0.5 mils of copper (Table I, Lots M-5, I-6, M-8 and Fig. 3). Similarly 0.5 mil tin-nickel coatings failed fairly rapidly whether they were on 0.25, 0.5, or 1.0 mil of copper (Lots I-5, M-2, M-6).

In spite of the early powdering off of the chromium from the chromium-plated tin-nickel coatings, the performance of these panels was noticeably better than that of nonchromium plated ones. (This has been noted in other tests not recorded here.)

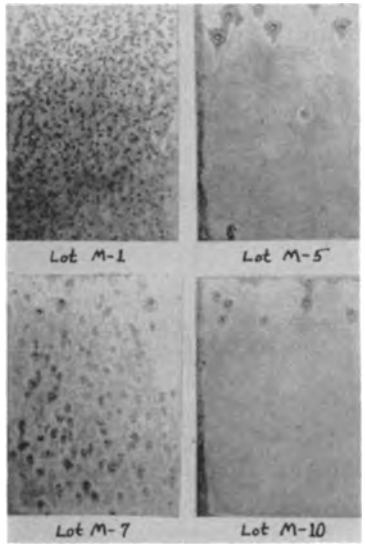


Fig. 3. Effect of thickness of tin-nickel on the protective value at Kure Beach. Total thickness of coatings: top row, 1.0 mil; bottom row, 1.5 mil. Lot M-1, 0.75 Cu/0.25 Sn:Ni; Lot M-5, 0.01 Cu/1.0 Sn:Ni; Lot M-7, 0.75 Cu/0.75 Sn:Ni; Lot M-10, 0.01 Cu/1.5 Sn:Ni.

Tin-nickel plated direct on steel failed very rapidly, but even a very thin flash of copper was sufficient to effect a dramatic improvement in performance (Lots M-4, M-5, M-9, M-10).

*Tin-nickel vs. nickel/chromium.*—Results for the thinner coatings are not entirely consistent, some showing tin-nickel to be superior, others showing an advantage for nickel. In the heavier coatings, the two appear to be roughly equivalent in performance.

Some further generalizations can be made which are applicable to the Bayonne results as well and are therefore considered later.

*Industrial atmosphere (Bayonne).*—The industrial atmosphere of Bayonne appears in these tests to be of the same order of corrosiveness toward nickel/chromium or copper/nickel/chromium coatings as is the marine atmosphere of Kure Beach. Duplicate sets of these panels failed at about the same rate in both exposures. But the industrial atmosphere was far less corrosive toward the tin-nickel coatings than was the marine. As a consequence, the tin-nickel coatings consistently outperformed the nickel/chromium coatings at Bayonne. This is illustrated in Fig. 4. This is true of all the tests, so that detailed consideration of the results is not necessary.

As at Kure Beach, for a given coating thickness performance improves as the proportion of the total which is tin-nickel increases and the proportion of the copper undercoat decreases. This statement is made principally on the basis of the data for the 1 mil coatings. Although a similar trend is observable in the 1.5 mil coatings, deterioration has not proceeded far enough to permit definite confirmation (*see* Fig. 5). The exception, as before, is the case of no undercoat at all: tin-nickel direct on steel fails very quickly; but the insertion of a mere flash of copper improves the corrosion resistance many fold. There is little to choose between nickel and copper as undercoats for tin-nickel; slight differences in comparable lots favor copper.

*Results at both locations.*—There remain to be discussed two differences in the behavior of tin-nickel coatings as compared with nickel/chromium coatings, which became evident at both locations and which are not obvious from the ratings and descriptions in Tables I and II.

1. Type of failure. When a nickel/chromium and a tin-nickel plated panel have failed to the same extent as measured by the rating numbers, they will in all probability not be similar in appearance. Nickel coatings normally fail in a multitude of small spots (pinhole rusting), of which more and more appear as deterioration proceeds until a typically low-rated panel is almost covered with thousands of small rust spots; some of these spots may of course become enlarged and develop into craters or pustules of rust. Pinhole rusting is, on the other hand, a relatively rare defect in tin-nickel coatings. Most often failure starts in a few spots which then gradually grow in size, so that a typically low-rated

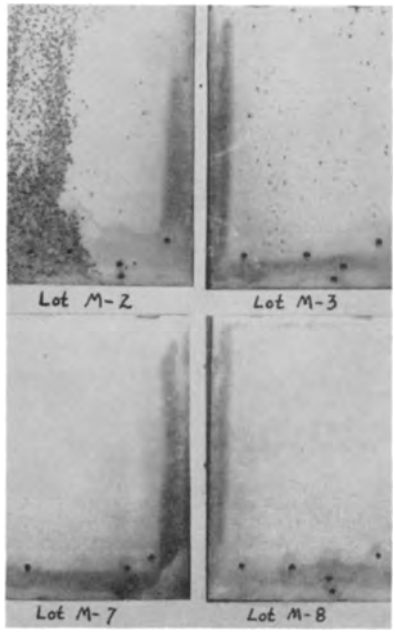


Fig. 5. Effect of thickness of tin-nickel on the protective value at Bayonne. Total thickness of coatings: top row, 1.0 mil; bottom row, 1.5 mil. Lot M-2, 0.5 Cu/0.5 Sn:Ni; Lot M-3, 0.25 Cu/0.75 Sn:Ni; Lot M-7, 0.75 Cu/0.75 Sn:Ni; Lot M-8, 0.5 Cu/1.0 Sn:Ni.

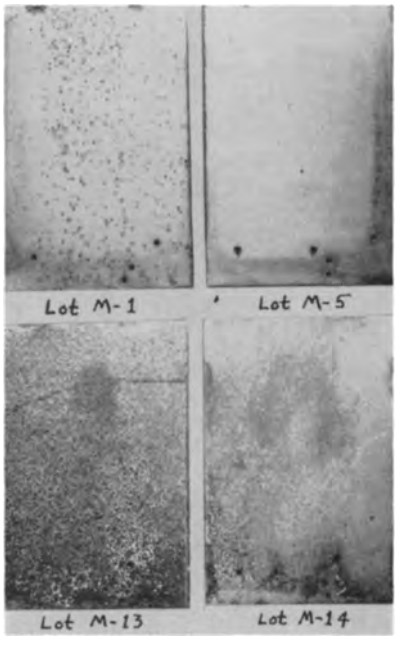


Fig. 4. Weathering of the various coatings at Bayonne. Total thickness of coatings: 1.0 mil. Lot M-1, 0.75 Cu/0.25 Sn:Ni; Lot M-5, 0.01 Cu/1.0 Sn:Ni; Lot M-13, 0.75 Cu/0.25 Ni/0.01 Cr; Lot M-14, 1.0 Ni/0.01 Cr.

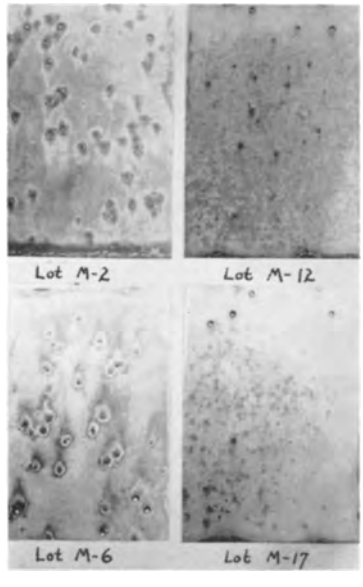


Fig. 6. Differences in the type of failure of tin-nickel and copper-nickel-chromium coatings. Kure Beach exposure. Total thickness of coatings: top row, 1.0 mil; bottom row, 1.5 mil. Lot M-2, 0.5 Cu/0.5 Sn:Ni; Lot M-12, 0.5 Cu/0.5 Ni/0.01 Cr; Lot M-6, 1.0 Cu/0.5 Sn:Ni; Lot M-17, 1.0 Cu/0.5 Ni/0.01 Cr.

tin-nickel panel may have relatively few very large rust craters, with large areas of the panel being entirely free of defects. This type of failure is illustrated in Fig. 6.

2. Stain and discoloration. If the typical "blue" color of bright chromium is taken as "standard" for a decorative finish, the tin-nickel coatings fail to meet that standard after a relatively short time of exposure. The alloy coatings, which are even as plated of a somewhat different, more reddish hue than chromium, gradually darken in color, presumably by the formation of an oxide or other film. Very soon the color difference is sufficiently obvious so that a mere glance is enough to pick out the tin-nickel panels on a rack from the chromium plated panels.

The formation of this film posed a problem in the inspection and rating of the panels, a problem which was handled differently by different inspectors. It cannot be considered a serious defect and since it usually covers the whole panel, various inspectors either ignored it entirely or penalized one or two points. It has been tentatively decided that where the tarnish film is light, two points will be attributed to this defect.

This behavior was expected from previous experience and prompted the inclusion in the present test of several lots of tin-nickel panels with a final flash coat of chromium. Unfortunately, as already stated, the chromium soon flaked off these panels so that the question whether tin-nickel can be protected from tarnishing by the conventional chromium overlay remains unanswered so far as the present test is concerned. See the remarks below on a supplementary test recently initiated.

*Supplementary program.*—The results above reported pose two problems:

1. The nature of the corrosion of tin-nickel strongly suggests that it is quite noble and that corrosion takes place through pores already present. If these pores can be avoided, the performance should be greatly improved.

2. Further efforts to chromium plate tin-nickel should be made in an attempt to avoid the tarnishing and discoloration already noted.

To investigate these questions, further panels were prepared and exposed at Kure Beach and Newark, N. J. The plating systems and results are shown in Tables IV and V.

This supplementary program has obviously not proceeded far enough to permit sweeping conclusions. But even at this early date the following can be said.

Lot S-1 (very similar to Lot M-5) is failing at about the same rate as M-5, so far.

Lot S-2: chromium has not flaked in 6 months; previously chromium flaked in a few weeks. The problem of chromium plating over tin-nickel appears nearer solution.

Lot S-3: so far indicates excellent performance by the use of the "double plate" technique, tending to confirm suspicions that corrosion of tin-nickel plated steel takes place principally through preexisting pores.

**Table IV**
**Kure Beach, Exposed 2/14/57**

| Lot | Thickness, mils Cu | TN | Cr | 4 Months | 10 Months |
|---|---|---|---|---|---|
| S-1 | 0.1 | 0.9 | — | 8/8 vf large cR, xeR | 7/4 vf large cR, iS |
| S-2 | 0.1 | 0.9 | .01 | 9/9 vscR | 9/9 vf large cR |
| S-3 | 0.1 | 0.5 + 0.4* | — | 10/10 | 10/10 |

* Buffed after 0.5 TN, then replated with additional 0.4 "Double plate".

**Table V**
**Newark, Exposed 2/28/57**

| Lot | 7 Months | 12 Months |
|---|---|---|
| S-1 | 10/10 | 10/8 iS |
| S-2 | 10/10 | 10/10 |
| S-3 | 10/10 | 10/8 iS |

## Conclusions

The principal result of this exposure program is to show that the tin-nickel deposit gives excellent resistance to corrosion, in which respect it is quite comparable to Watts' nickel plus a flash of chromium. It is roughly equivalent to nickel in marine but definitely superior to it in industrial atmospheres.

The tin-nickel alloy should not be applied direct to steel for corrosion-resistant service. Copper, even if only as a flash coating, between the steel and tin-nickel, improves performance many fold. Other undercoats including nickel and bronze may be used.

The corrosion of tin-nickel alloy coated steel takes place in a different manner, probably denoting a different mechanism, from that of nickel coatings.

Although it has excellent properties as a decorative-protective coating, tin-nickel forms on outdoor exposure a tarnish film which may be considered objectionable in appearance even though it can be easily removed. Preliminary indications from a recently begun and still continuing exposure program are that this objection can be obviated by the application of a final thin chromium plate; early problems encountered in successfully plating bright chromium over tin-nickel appear to have been solved.

## Acknowledgment

The authors are indebted to their respective companies for permitting publication of this paper. Particular thanks are due the Jones & Laughlin Steel Corporation for allowing use of their Pittsburgh exposure site.

Manuscript received Nov. 25, 1957. This paper was prepared for delivery before the Buffalo Meeting, Oct. 6-10, 1957.

Any discussion of this paper will appear in a Discussion Section to be published in the December 1958 JOURNAL.

REFERENCES

1. N. Parkinson, *J. Electrodepositors Tech. Soc.*, **27**, 129 (1951).
2. H. N. Rooksby, *ibid.*, **27**, 153 (1951).
3. A. E. Davies, *Trans. Inst. Met. Finishing*, **31**, 401 (1954).

4. F. A. Lowenheim, *Proc. Am. Electroplaters' Soc.*, **41**, 276 (1954).
5. S. C. Britton and R. M. Angles, *J. Electrodepositors Tech. Soc.*, **27**, 293 (1951).
6. V. R. Ramanathan, *Trans. Inst. Met. Finishing*, **34**, 1 (1957).
7. Metal & Thermit Corporation Data Sheet No. 140 (1956).
8. S. C. Britton and R. M. Angles, *Trans. Inst. Met. Finishing*, **29**, 26 (1953).
9. A. G. Gray, Editor, "Modern Electroplating," John Wiley & Sons, Inc., New York (1953).
10. H. A. Pray, *Proc. ASTM*, **49**, 231 (1949).
11. F. A. Lowenheim, *Proc. Amer. Electroplaters' Soc.*, **44**, 42 (1957).

# Studies of Natural Convection at Vertical Electrodes

**N. Ibl and R. H. Müller**

*Department of Physical Chemistry and Electrochemistry,*
*Swiss Federal Institute of Technology, Zurich, Switzerland*

ABSTRACT

The hydrodynamic flow near vertical electrodes in electrolysis with natural convection was studied optically. The velocity distribution was measured for various experimental conditions. The flow velocities are calculated for the case of a constant current density along the electrode by the von Kármán-Pohlhausen integral method and compared with the experimental data. In the theoretical derivation various assumptions are made concerning the shape of the velocity and concentration profiles, and their influence on the computed values of the maximum flow velocities is discussed.

Mass transfer to or from the electrodes plays an important role in electrolysis. It is accomplished in general by diffusion, migration, and convection.

A hydrodynamic flow is usually present even in a solution which is not artificially stirred. This flow is called natural or free convection. It is due to the density differences between the electrode layer and the bulk of the bath, which cause, with vertical electrodes, an upward or downward flow of the solution, depending on whether the density of the electrode layer is smaller or greater than in the bulk.

Velocity distribution near the electrode is shown schematically in Fig. 1. The velocity is zero at the electrode surface, increases until a maximum is reached, then decreases again. The comparatively small region near the interface in which the upward or downward flow occurs primarily is called the hydrodynamic (or velocity) boundary layer. Similarly, the diffusion layer is defined as the region in which the concentration is significantly different from that in the bulk.

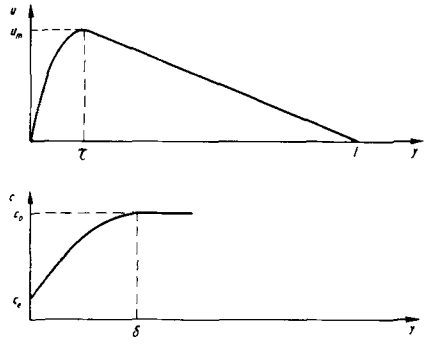

Fig. 1. Concentration and velocity distribution near the electrode (schematic).

The theory of mass transfer by natural convection to plane vertical electrodes has received much attention in recent years (1-7). The limiting current and the thickness of the diffusion layer under free convection conditions have been studied experimentally by various authors (7-13). However, no investigation of the convective flow itself has been made so far. In the present paper, measurements of the hydrodynamic boundary layer at plane vertical electrodes are reported and compared with the theory. The velocities of the flow are calculated according to the method of von Kármán-Pohlhausen (28, 27). Generalized concentration and velocity profiles are used in the calculation, and some general aspects of the application of von Kármán-Pohlhausen's method are discussed.

## Theoretical

Mass transfer calculations are usually carried out along the same lines as heat transfer computations, since the basic differential equations of the problem are formally the same in both cases. In order to be able to carry out the integration of these equations, however, the boundary conditions must be known. In the case of heat transfer to a vertical plate it is usually assumed that the temperature, and therefore the density of the fluid, is the same along the surface of the plate. In the electrolysis problem a constant fluid density means that the concentration of the bath remains the same along the surface of the electrode. This condition is realized in the case of the limiting current, where, in a cathodic process, the concentration of the ions reduced at the electrode is practically zero everywhere at the surface of the electrode. It follows from the theory that under such conditions the local current density should vary from the lower to the upper edge of

a vertical electrode; this has been confirmed by the experiment (1). However, when the current density is smaller than about one half of the limiting value, the local current density (rather than the concentration) was found to remain constant from bottom to top (15, 29). These experimental results are in agreement with a recent calculation made by Wagner (2). In electrolysis problems, therefore, two typical cases may be distinguished, according to whether the liquid density or the current density is the same along the interface.

*Constant Liquid Density*

The velocity of the flow for a constant liquid density has been calculated by various authors (1, 5, 7). The maximum velocity $u_m$ (*see* Fig. 1) in the direction parallel to the electrode is given by (for the case of a metal deposition from a pure salt solution, without addition of supporting electrolyte):

$$u_m = K \left( \frac{g\alpha D x (c_o - c_e)}{\nu} \right)^{1/2} \qquad (I)$$

where $g$ is the gravitational acceleration, $D$ the diffusion coefficient, $\nu$ the kinematic viscosity, and $x$ the distance from the lower end of the cathode. $\alpha$ is the densification coefficient[1] [$\alpha = (1/\rho)(d\rho/dc)$], and $c_o - c_e$ is the concentration difference between the electrode surface ($c_e$) and the bulk of the solution ($c_o$). In the case of the limiting current, $c_e$ is zero. $K$ is a numerical constant, the value of which depends somewhat on the kind of the approximation used in the derivation of Eq. (I). Keulegan (5) has integrated the basic differential equations of convective mass transfer with the help of Prandtl's boundary layer simplifications in a way similar in principle to that used by Pohlhausen for heat transfer [*see* (16)], whereas Wagner (1) and Wilke, Tobias, and Eisenberg (7) employed the von Kármán-Pohlhausen integral method (22a, b). Values of $K$ derived from the calculation of these authors are shown in Table I.

Ostrach (14) has integrated the differential equations of natural convection heat transfer by means of an IBM Card Programmed Electronic Calculator and has thus obtained the most nearly rigorous solution available at present. Owing to the analogy between heat and mass transfer Ostrach's results for high Prandtl numbers can be used to calculate the flow velocities involved in mass transfer in aqueous solutions. The value of $K$ thus obtained has also been entered in Table I.

If the current density is smaller than the limiting one, $c_o - c_e$ is not known and must be calculated from the mean current density $i$ over the whole electrode surface. If the relation connecting $c_o - c_e$ with $i$ is combined with Eq. (I) the following relation is obtained

$$u_m = K' \left( \frac{g\alpha i n_A}{zF\nu} \right)^{2/5} D^{1/5} x^{1/2} h^{1/10} \qquad (II)$$

where $F$ means Faraday's constant, $z$ the valence of the cations reacting at the electrode, $n_A$ the transference number of the anion, and $h$ the total height of the electrode. The values of the numerical constant $K'$ depend again on the method used in the integration of the basic differential equations of the problem and are also indicated in Table I.

Relation (II) is again valid for the case of a constant liquid density. This condition, as has been pointed out above, is in general not realized at current densities well below the limiting.

*Constant Current Density*

The case of a constant current density (in the electrolysis problem) and of a constant heat flux (in the corresponding heat transfer problem) has been considered by Wagner (2)[2] and by Sparrow (17, 18), respectively. They have not calculated, however, the velocities of the hydrodynamic flow at high Prandtl numbers.

The following derivation will be carried out for the case of a cathodic deposition from a pure salt (without addition of supporting electrolyte).[3] It can, however, be easily extended to other cases, especially to that of an anodic process.

In the derivation the von Kármán-Pohlhausen integral method (28, 27) as used by Eckert (22a, b), Wagner (2, 1), Wilke, Tobias, and Eisenberg (7) will be employed. In this method one refrains from fulfilling Prandtl's boundary layer equations for each infinitesimal volume element of the boundary layer and fulfills them instead only as a mean over the whole breadth of the boundary layer.

A volume of liquid limited by the control planes shown in Fig. 2 is considered. Plane ABCD is parallel to the electrode surface and is located at distance 1 from the electrode where the velocity of the flow can be assumed to be zero. The volume is further limited by the surface A'B'C'D' located at the interface electrode solution and by the two horizontal planes of unit width BCB'C' and ADA'D' separated by the small vertical distance $dx$ ($x$ means in the

[1] A summary of the symbols used and of the corresponding dimensions is given at the end of the paper.

**Table I. Values of $K$ and $K'$**

| $K$ | $K'$ | Method |
|---|---|---|
| 1.83 | 1.99 | Wagner (1) |
| 0.82 | 0.99 | Keulegan (5) |
| 0.98 | 1.15 | Ostrach (14) |
| 0.77 | 0.90 | Wilke, Tobias, and Eisenberg (7) |

[2] The authors are indebted to C. Wagner for having kindly sent them the manuscript of this paper.

[3] Further assumptions, which must be made in the derivation, are discussed later, together with the possibilities to realize them experimentally.

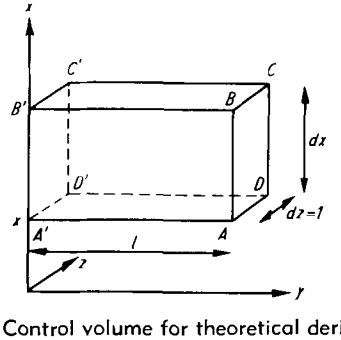


Fig. 2. Control volume for theoretical derivation

following the vertical direction, $y$ the direction perpendicular to the electrode surface).

Under steady-state conditions the change in momentum per unit time of all the liquid particles entering and leaving the volume thus defined must be equal to the external forces acting on the volume, i.e., the buoyancy force and the shear stress at the electrode surface. This leads to the equation:

$$\frac{d}{dx}\int_0^1 u^2\,dy = \alpha g \int_0^1 \theta dy - \nu \left(\frac{du}{dy}\right)_e \qquad \text{(III)}$$

with

$$\theta = c_o - c$$

where $u$ and c mean the velocity in the $x$ direction and the concentration at the distance $y$ from the electrode, respectively. $(du/dy)_e$ is the velocity gradient at the interface.

The corresponding equation for mass transfer is obtained by equating the rates at which the cations reacting at the electrode enter and leave the volume. This gives the relation:

$$\frac{d}{dx}\int_0^1 u\,\theta dy = -D\left(\frac{d\theta}{dy}\right)_e \qquad \text{(IV)}$$

where $(d\theta/dy)_e$ is equal to $-(dc/dy)_e$, i.e., to the negative concentration gradient at the interface.

To carry out the integration some assumptions must be made concerning the velocity and concentration profile. In the application of the von Kármán-Pohlhausen method to natural convection heat and mass transfer the concentration (or temperature) distribution has been usually approximated by (1, 7, 18, 22b)

$$\theta = \Theta\left(1 - \frac{y}{\delta}\right)^2 \qquad \text{(V)}$$

where in our case $\Theta$ means the concentration reduction at the interface ($\Theta = c_o - c_e$). $\delta$ is the thickness of the diffusion layer, i.e., the distance at which the concentration is equal to the value in the bulk solution.

Concerning the velocity distribution the two following assumptions have been hitherto made (1, 7, 18, 22b)

$$u = U_1\left[2\frac{y}{\delta} - \left(\frac{y}{\delta}\right)^2\right] \qquad \text{for } o < y < \delta \qquad \text{(VI)}$$

$$u = U_1\frac{y}{\delta}\left(1 - \frac{y}{\delta}\right)^2 \qquad \text{for } o < y < \delta \qquad \text{(VII)}$$

In the first case [Eq. (VI)] it is postulated that the velocity reaches its maximum at the outer limit of the diffusion layer (at $y = \delta$) and falls off very slowly afterward. The assumption is therefore made, that the thickness l of the hydrodynamic boundary layer is much greater than that of the diffusion layer. In the case of Eq. (VII) the velocity reaches its maximum at $y = \delta/3$ and is equal to zero at $y = \delta$. This means that the thicknesses of the diffusion layer and of the hydrodynamic boundary layer are now supposed to be the same.

In the case of a constant liquid density along the interface the values obtained for the maximum velocities when using Eq. (VI) ($1 >> \delta$) are more than twice as large as those computed with Eq. (VII) ($1 = \delta$).[4] The limiting current is also substantially different in both cases. Substantially different values for the maximum flow velocities are similarly obtained in the case of a constant local current density depending on whether one assumes $1 >> \delta$ or $1 = \delta$. This can be easily derived from the calculations made below.

Theoretical considerations (1) show that it is very likely that the hydrodynamic boundary layer is much thicker than the diffusion layer and this has been confirmed by the authors' experiments (19). Nevertheless, the maximum velocities (and also the limiting currents) calculated with Eq. (VII) ($1 = \delta$) fit the experimental data much better than those obtained with Eq. (VI). The unsatisfactory situation therefore arises that the wrong assumption leads to results which are in better agreement with the experiment.

In order to get a better insight into the influence exerted by the velocity and concentration profiles assumed in the derivation, the following calculation is carried out with profiles represented by more general functions than those given by Eqs. (V) to (VII). The velocity distribution is approximated by

$$u = U_1\left[\lambda\frac{y}{\tau} - \left(\frac{y}{\tau}\right)^\lambda\right] \qquad \text{for } o \leqq y \leqq \tau \qquad \text{(VIII)}$$

and

$$u = U_1\left[1 - \frac{y-\tau}{\epsilon\tau}\right](\lambda - 1) \quad \text{for } \tau \leqq y \leqq (\epsilon+1)\tau \qquad \text{(IX)}$$

where $\tau$ means the distance at which the maximum velocity is located (*see* Fig. 1).

The concentration profile is approximated by

$$\theta = \Theta\left(1 - \frac{y}{\eta\tau}\right)^\omega \quad \text{with} \quad \eta\tau = \delta \qquad \text{(X)}$$

$\epsilon$, $\eta$, $\lambda$, and $\omega$ are parameters whose variation allows the assumed profiles to change considerably. $\omega$ influences the shape of the concentration distribution. Variation of $\lambda$ allows the shape of the velocity profile to change up to the maximum velocity [whose value is given by $u_m = U_1(\lambda - 1)$]. For values of $y$ greater than $\tau$ the velocity profile is assumed to be a straight line, whose slope depends on the value of $\epsilon$. Finally, variation of $\eta$ allows the position of the velocity maximum to change with respect to $\delta$.

Insertion of Eqs. (VIII) to (X) into the momentum equation (III) yields upon integration[5]

$$\frac{d}{dx}(\Lambda U_1^2\tau) = \frac{\alpha g\eta\tau\Theta}{\omega+1} - \frac{\nu U_1\lambda}{\tau} \qquad \text{(XI)}$$

with

$$\Lambda = \frac{\lambda^2}{3} - \frac{2\lambda}{\lambda+2} + \frac{1}{2\lambda+1} + \frac{\epsilon}{3}(\lambda-1)^2 \qquad \text{(XIa)}$$

In the same way one obtains from Eq. (IV) (for values of $\eta \geqq 1$)

$$\Phi\frac{d}{dx}(U_1\Theta\tau) = \frac{D\omega\Theta}{\eta\tau}$$

[4] It is interesting to note that when using Eq. (VII) the von Kármán-Pohlhausen method yields values which differ by less than 10% from those calculated by Keulegan (5), who employed a more involved method, but also assumed $1 = \delta$.

[5] For details, *see* Müller (20).

with

$$\Phi = \frac{\lambda(\eta-1)^{\omega+2}}{\eta^{\omega}(\omega+1)(\omega+2)}\left[\left(\frac{\eta}{\eta-1}\right)^{\omega+2} - \frac{\lambda-1}{\lambda\epsilon} - \frac{\omega+2}{\lambda(\eta-1)} - 1\right] - \eta^{\lambda+1} B_{1/\eta}(\lambda+1,\omega+1) \quad \text{(XII)}$$

where

$$B_a(b,c) = \int_0^a t^{b-1}(1-t)^{c-1}\,dt$$

means the incomplete beta function, whose numerical values have been tabulated by Pearson (21).

Let $j_D$ denote the mass transfer rate per unit area due to diffusion at the interface

$$j_D = -D\left(\frac{d\theta}{dy}\right)_e = \frac{\omega\Theta D}{\eta\tau} \quad \text{(XIII)}$$

Values of $\tau$, $U_1$, and $\Theta$ must be determined. In a way similar to that used in the case of a constant liquid density along the interface [*see*, for instance, Eckert (22b)] we try solutions of the form

$$U_1 = C_1 x^m \quad \text{(XIV)}$$

$$\tau = C_2 x^n \quad \text{(XV)}$$

$$\Theta = C_2 \frac{j_D \eta}{\omega D} x^n \quad \text{(XVI)}$$

Equation (XVI) takes into account that in our case the local current density, and therefore $j_D$, is constant over the whole electrode surface.

Standard calculating procedures lead then to the result

$m = 3/5 \quad n = 1/5$

$$u_m = U_1(\lambda-1) = (\lambda-1)\,C_1 x^{3/5} =$$

$$\underbrace{(\lambda-1)\left(\frac{\omega\eta}{\Phi^3\lambda^2(\omega+1)^2}\right)^{1/5}\left(\frac{Sc}{Sc+\frac{7\omega\Lambda}{5\eta\Phi\lambda}}\right)^{2/5}\left(\frac{g\alpha j_D}{\nu D}\right)^{2/5} D^{3/5}x^{3/5}}_{A'} \quad \text{(XVII)}$$

$$\tau = C_2 x^{1/5} = \underbrace{\left(\frac{(\omega+1)\omega^2\lambda}{\Phi\eta^3}\right)^{1/5}\left(\frac{Sc+\frac{7\omega\Lambda}{5\eta\Phi\lambda}}{Sc}\right)^{1/5}\left(\frac{\nu D^2}{g\alpha j_D}\right)^{1/5}}_{E'} x^{1/5} \quad \text{(XVIIa)}$$

where $Sc = \nu/D$ = Schmidt number. Equation (XVII) relates the maximum velocity $u_m$ to the mass transfer rate $j_D$ and to the height $x$ at which it is measured. It allows one to calculate $u_m$ for various values of the parameters $\epsilon$, $\eta$, $\lambda$, $\omega$.

Equation (XVII) holds true too for the case of heat transfer with a uniform heat flux if $\alpha$ is replaced by the thermal expansion coefficient (degrees$^{-1}$), $D$ by the thermal diffusivity (cm$^2$/sec) and $j_D/D$ by $q/k$ where $q$ means the heat flux (cal/cm$^2$ sec) and $k$ the thermal conductivity (cal/cm sec degree).

If $Sc$ is greater than about 1000, as is usually the case for mass transfer in aqueous solutions (in our experiments $Sc$ was ca. 2800) $7/5\ (\omega\Lambda)/(\eta\Phi\lambda)$ can be neglected against $Sc$ for all the values of $\epsilon$, $\eta$, $\lambda$, $\omega$ indicated in Table II (except for the last line).

**Table II. Numerical values of $A$, $E$, and the auxiliary function $\phi$ for various combinations of the parameters $\epsilon$, $\eta$, $\lambda$, $\omega$**

| $\omega$ | $\lambda$ | $\eta$ | $\epsilon$ | $\phi$ | $A$ | $E$ |
|---|---|---|---|---|---|---|
| 2 | 1.2 | 1.8 | 7 | 0.078 | 0.71 | 2.03 |
| 3 | 2 | 1.8 | 7 | 0.227 | 1.41 | 2.24 |
| 2 | 1.2 | 1 | 7 | 0.032 | 1.08 | 3.42 |
| 2 | 2 | 1 | 7 | 0.133 | 1.87 | 2.86 |
| 3 | 1.2 | 1.8 | 7 | 0.052 | 0.88 | 2.72 |
| 2 | 2 | 1.8 | 7 | 0.347 | 1.19 | 1.64 |
| 2 | 2.5 | 1.8 | 7 | 0.511 | 1.29 | 1.58 |
| 2 | 2.5 | 2.5 | 7 | 0.802 | 1.05 | 1.19 |
| 3 | 2.5 | 2.5 | 7 | 0.539 | 1.29 | 1.60 |
| 2.5 | 1.8 | 2.2 | 7 | 0.306 | 1.10 | 1.65 |
| 2.5 | 1.5 | 2.2 | 7 | 0.199 | 0.96 | 1.74 |
| 2.5 | 1.8 | 1.9 | 7 | 0.248 | 1.21 | 1.88 |
| 2.5 | 1.8 | 1.5 | 7 | 0.174 | 1.31 | 2.32 |
| 2 | 1.8 | 2.2 | 7 | 0.378 | 0.98 | 1.40 |
| 3 | 1.8 | 2.2 | 7 | 0.253 | 1.20 | 1.89 |
| 2.5 | 1.8 | 2.2 | 12 | 0.306 | 1.10 | 1.65 |
| 2.5 | 1.8 | 2.2 | 20 | 0.307 | 1.10 | 1.65 |
| 2.5 | 2.5 | 2.5 | 7 | 0.639 | 1.19 | 1.40 |
| 2.3 | 1.7 | 2.1 | 10 | 0.277 | 1.04 | 1.63 |
| 5 | 5 | 5 | 10 | 2.02 | 1.28 | 1.24 |
| 5 | 1.5 | 1.5 | 10 | 0.049 | 1.9 | 4.24 |
| 2 | 1.5 | 5 | 10 | 0.648 | 0.55 | 0.74 |
| 2 | 5 | 1.5 | 10 | 0.876 | 1.84 | 1.83 |
| 5 | 5 | 1 | 10 | 0.119 | 4.10* | 6.4* |

* In this case $7/5\ (\omega\Lambda)/(\eta\phi\lambda)$ is not negligibly small in comparison to Sc and $A'$ [Eq. (XVII)] instead of $A$ [Eq. (XVIII)] is to be used to calculate $u_m$. The values indicated in the table are in this case $A'$ instead of $A$ and $E'$ [Eq. (XVIIa)] instead of $E$ [Eq. (XIX)], for a Schmidt number of 1000.

Furthermore, in the case of electrolysis $j_D$ is connected with the current density $i$ by the relation

$$j_D = \frac{in_A}{zF}$$

where $z$ means the valence of the cation deposited and $n_A$ is the transference number of the anion.

Equation (XVII) thus takes the form

$$u_m = \underbrace{(\lambda-1)\left(\frac{\eta\omega}{\Phi^3\lambda^2(\omega+1)^2}\right)^{1/5}}_{A}\left(\frac{g\alpha i n_A}{zF\nu}\right)^{2/5} D^{1/5}x^{3/5} \quad \text{(XVIII)}$$

The flow velocity is proportional to the $(2/5)^{\text{th}}$ power of the current density and to the $(3/5)^{\text{th}}$ power of the height.

The distance $\tau$ from the electrode at which the velocity maximum is located is given by

$$\tau = \underbrace{\left(\frac{(\omega+1)\omega^2\lambda}{\Phi\eta^3}\right)^{1/5}}_{E}\left(\frac{zF\nu D^2}{g\alpha i n_A}\right)^{1/5} x^{1/5} \quad \text{(XIX)}$$

In Table II $A$ and $E$ have been calculated for various values of $\epsilon$, $\eta$, $\lambda$, and $\omega$. It is seen that the assumed profiles have a great influence on the results obtained by the von Kármán-Pohlhausen method. Relatively small changes in $\eta$, $\lambda$, and $\omega$ alter $u_m$ and $\tau$ to a rather great extent. The value of $\epsilon$, however, is not critical. Therefore it can be said that the result of the calculation is strongly affected by the relative location of the velocity maximum ($\eta$) and by the shape of the velocity profile up to the maximum ($\lambda$), but not by the slope of the profile beyond the maximum (toward the bulk solution).

The velocity profiles experimentally determined in this study (Fig. 7 and 8) are in approximate

agreement with the following values of $\epsilon$, $\eta$, and $\lambda$: $\lambda = 1.2\text{-}2$; $\eta = 1.4\text{-}2.2$; $\epsilon = 5\text{-}15$. The interferometrically measured concentration profile corresponds to a value of $\omega$ of 2-3 (12).

Use of the following profiles is suggested in the application of the von Kármán-Pohlhausen method to the uniform mass transfer rate problem

$$\omega = 2.3 \qquad \eta = 2.1 \qquad \theta = \Theta\left(1 - \frac{y}{2.1\tau}\right)^{2.3} \qquad \text{(XX)}$$

$$\lambda = 1.7 \qquad u = U_1\left[1.7\frac{y}{\tau} - \left(\frac{y}{\tau}\right)^{1.7}\right] \quad \text{for } o \leqq y \leqq \tau \qquad \text{(XXI)}$$

$$\epsilon = 10 \qquad u = 0.7\,U_1\left(1 - \frac{y-\tau}{10\tau}\right) \quad \text{for } \tau < y < 11\tau \qquad \text{(XXII)}$$

These profiles are in reasonable agreement with the measured profiles and the values of $u_m$ and $\tau$ calculated with Eqs. (XX) to (XXII) fit the experimental data fairly well.

For the comparison with the experiment it is convenient to write Eqs. (XVIII) and (XIX) in dimensionless form

$$\frac{u_m x}{D} = A\,(Sc\,Gr^*)^{2/5} \qquad \text{(XXIIa)}$$

$$\frac{\tau}{x} = E\,(Sc\,Gr^*)^{-1/5} \qquad \text{(XXIIb)}$$

where

$$Gr^* = \frac{j_D g \alpha x^4}{\nu^2 D} = \frac{g \alpha i n_A x^4}{2zF\nu^2 D} \qquad \text{(XXIII)}$$

The dimensionless Group Gr* is the modified Grashof number, which plays the same role in the case of a uniform mass transfer rate as the usual Grashof number in the case of a uniform fluid density.

## Experimental

### *Experimental Procedure*[5]

Flow velocities were measured by means of a suspension of a suitable fraction of colophonium, whose particles hovered in the solution without sedimenting. The colophonium fraction was prepared by sedimentation analysis.

The particles dragged along by the stream were made visible by a dark field method shown in Fig. 3. Because of the small extent of the hydrodynamic boundary layer and the relatively low light-intensity of the small moving particles, lens D must provide (in plane B) an image of great brightness, good correction, and suitable magnification (about 10 times). Special care in the optical arrangement had to be given to prevent reflections of the illuminating light beam.

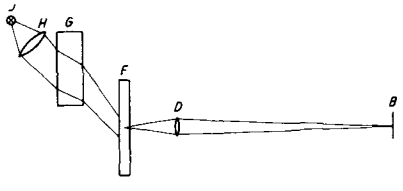


Fig. 3. Experimental arrangement for the study of the hydrodynamic boundary layer. B = image plane (camera); D = microlens (f = 46, 25, or 16 mm); F = electrolysis cell; G = liquid heat filter (6 cm $CuSO_4$ 0.1 m); H = condenser; J = light source (6 v, 6A lamp).

Fig. 4. Visualization of flow velocities. Both pictures were obtained with cell No. 1 4 min after the beginning of electrolysis (i = 1 ma/cm², exposure time 1 sec). Height: (a) (left) x = 7 cm; (b) (right) x = 1.5 cm.

The particles appear as bright spots on a dark background. Flow velocity can be measured either visually with the help of a suitable scale or photographically from the length of the lines obtained on the photographic plate and the exposure time (Fig. 4). Under optimum illuminating conditions the velocities in the experiments of Fig. 6 to Fig. 8 could be determined down to an electrode distance of 0.01 mm. At higher current densities the large refractivity gradient within the diffusion layer causes a blurring of the particles and a changed magnification within the diffusion layer in comparison to that of the bulk solution. The measurements in the vicinity of the electrode are then more difficult and less accurate.

Because of the friction of the liquid at the cell walls the velocities must be measured at some distance from the latter (and therefore at some distance from the edge of the electrode). The electrode position cannot then in general be precisely located on the image in B without the help of additional devices. One of these consisted of a sheet of acryl glass of suitable design whose sharp edge was pressed against the electrode surface. The glass sheet was provided with a scale which allowed, by extrapolation, the location of the electrode surface within a hundredth of a mm.

At great current densities the velocities are high and the particles disappear rapidly from the field of view, so that measurements by the visual method become tedious. This difficulty can be circumvented by the use of two cylindrical lenses with axes perpendicular to each other, instead of the spherical lens D. This allows different magnifications in the vertical and horizontal directions, permitting the use of a horizontal magnification large enough for an accurate determination of the electrode distance and reducing the vertical magnification to such an extent that the velocity can be measured conveniently.

All the experiments were carried out with pure 0.6*M* $CuSO_4$ solutions (*p*H = 3.35) with plane copper cathodes and anodes. The electrode arrangement and the cell form were in principle the same as in a previous study (10), but the dimensions were different (Table III). Furthermore, in cells 3 and 5 the upper and lower edge of the electrode did not reach the free liquid surface and the cell bottom, respectively.

**Table III. Dimensions of electrolysis cells (in mm)**

| Cell No. | Inside dimensions with electrodes mounted in cell | | | Electrode dimensions | | Electrode position |
|---|---|---|---|---|---|---|
| | Width | Breadth* | Height | Width | Height | |
| 1 | 5 | 48 | 140 | 5 | 140 | Fills whole cross section |
| 2 | 18 | 54 | 140 | 18 | 140 | Fills whole cross section |
| 3 | 20 | 170 | 450 | 20 | 150 | At mid height |
| 4 | 5 | 3, 15, 45 | 30 | 5 | 30 | Fills whole cross section |
| 5 | 4 | 12 | 150 | 4 | 30 | At various heights |

* i.e., distance cathode-anode.

Some measurements were made at the anode but all the experiments reported hereafter were carried out at the cathode.

*Deviations from the Ideal Flow Pattern*

In the theoretical considerations, idealized flow conditions are assumed. In the first part of the authors' experimental work deviations from these idealized conditions were studied and the circumstances under which the assumptions made in the theory are fulfilled were investigated.

1. In the theory it is postulated that the electrodes are infinitely large, i.e., that the friction at the cell walls as well as the influence of the free liquid surface and of the cell bottom can be neglected. Furthermore, it is admitted that the flow at the anode does not affect that at the cathode. The influence of these factors was studied with the help of various electrode arrangements and cells of various dimensions (*see* Table III).

Figure 5 shows velocity profiles measured with cells of various widths.[6] It is seen that down to a cell width of 5 mm no significant difference is observed. Further measurements showed that at a distance from the wall of 1 mm the velocity is practically the same as in the middle of the cell.

The free liquid surface causes a backward streaming, which starts some time after the beginning of electrolysis and substantially changes the shape of the whole hydrodynamic boundary layer. This effect has been described in more detail in an earlier paper (19) [*see* also (20)].

The influence of the cell breadth was studied with cell No. 4.

2. In the theory in its present state only steady-state conditions are considered. The time which elapses after switching on the current until steady-state conditions are reached increases with height and decreases with current density. Figure 6 shows velocity profiles measured at various times after the beginning of electrolysis. In this case the steady state was reached after 2 min.

3. In the theory it is assumed that the liquid is at rest when no electric current passes through the cell. This is not strictly realized in practice. Even hours after the solution has been filled into the cell a not negligible motion of the liquid is generally observed. It is due to small inhomogeneities in density caused by various reasons (evaporation of the solution, variations of the room temperature). Even small but rapid variations of the room temperature can give rise to flow velocities as large as 0.5 mm/sec. By careful elimination of evaporation and all causes of temperature inhomogeneities, it was possible to reduce the residual motion of the solution (i.e., the motion present without electric current) to 0.005 to 0.05 mm/sec. All the experiments reported in Fig. 5 to 10 were carried out under such conditions.

[6] In Fig. 5 to 10 $x$ means the height (over the lower cathode edge) at which the velocity is measured.

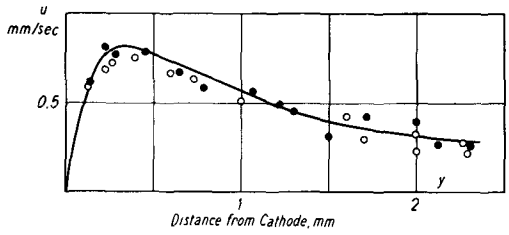


Fig. 5. Velocity profiles measured with cells of various widths with i = 1 ma/cm²; solid line, cell No. 1, x = 70 mm;[6] open circle, cell No. 2, x = 67 mm; solid circle, cell No. 3, x = 67 mm.

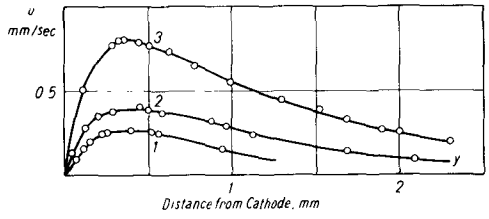


Fig. 6. Velocity profiles measured 0.5 (curve 1), 1 (curve 2), and 2 (curve 3) min after the beginning of electrolysis; cell No. 1, x = 70 mm, i = 1 ma/cm².

4. Finally, a laminar flow is postulated in the derivation of section on Constant Current Density. It was found that this condition is not realized at high current densities and great heights. A turbulence of the natural convective flow (clearly different from the backward streaming mentioned above) was for instance observed in cell No. 3 at a height of 80 mm, when the current density was greater than 20 ma/cm². The eddies which then form are similar to those which are described by Eckert (22c) for heat transfer to air.

*Quantitative Results and Discussion*

The experiments of Fig. 7 to 10 were carried out with cell No. 1. Conditions were such that the devi-

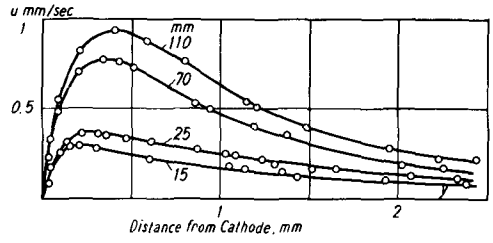


Fig. 7. Velocity profiles at heights of 15, 25, 70, and 110 mm; i = 1 ma/cm².

ations from the ideal flow pattern discussed in the preceding section were as small as possible.

Figure 7 shows the velocity profiles for various heights at a current density of 1 ma/cm² and Fig. 8 shows profiles for various current densities at a height of 70 mm.

The reproducibility of the measurements depended to some extent on the location in the cell. It was somewhat better at mid height than at the top or bottom of the electrode. It was also better near the maximum than in the outer part of the boundary layer (toward the bulk solution). In the case of the outer boundary this was probably due to the small remainders of the residual flow mentioned above.

The maximum velocity and the distance of the velocity maximum are given in Fig. 9-10 and in Table IV for various heights and current densities. The dimensionless groups $(u_m x)/D$ and $\tau/x$ are plotted logarithmically against Sc and the modified Grashof number Gr* in Fig. 9 and 10. Calculated values were computed from Eqs. (XXIIa) and (XXIIb) with $A$ and $E$ equal to 1.04 and 1.63, respectively (column 4 of Table IV, full lines of Fig. 9 and 10). These values of $A$ and $E$ are those which

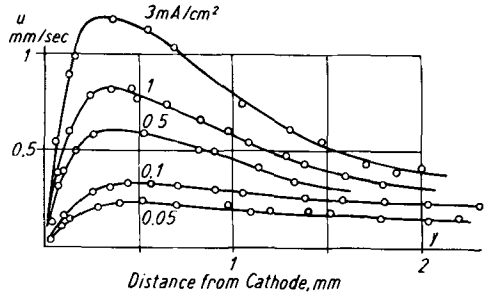


Fig. 8. Velocity profiles at current densities of 0.05, 0.1, 0.5, 1, and 3 ma/cm²; x = 70 mm.

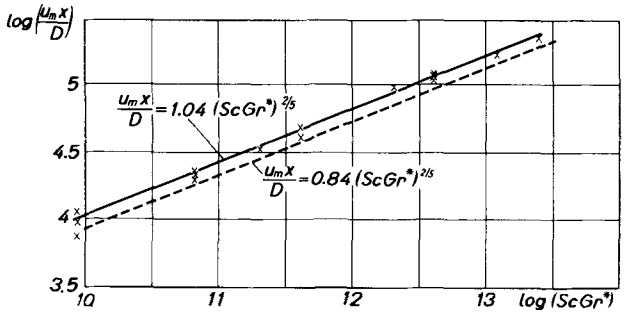


Fig. 9. General correlation of the maximum flow velocity; x = measured values.

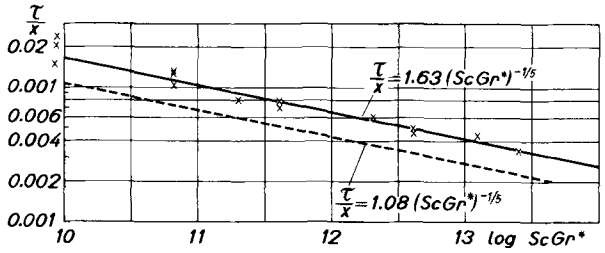


Fig. 10. General correlation of the distance of the velocity maximum from the electrode; x = measured values.

Table IV. Maximum flow velocities

| $i$ (ma/cm²) | $x$ (cm) | $u_m$ (mm/sec) measured | $u_m$ (mm/sec) calculated from Eq. (XXIIa) with $A$ = 1.04 |
|---|---|---|---|
| 0.05 | 7 | 0.22 | 0.24 |
| 0.1 | 7 | 0.32 | 0.31 |
| 0.5 | 7 | 0.60 | 0.59 |
| 1 | 7 | 0.83 | 0.78 |
| 3 | 7 | 1.2 | 1.21 |
| 1 | 1.5 | 0.36 | 0.31 |
| 1 | 2.5 | 0.44 | 0.42 |
| 1 | 11.0 | 1.02 | 1.02 |

Total electrode height: 14.0 cm.

are obtained when the profiles represented by Eqs. (XX) to (XXII) are used in the von Kármán-Pohlhausen's integral method. The dotted lines were calculated with $A$ and $E$ values of 0.84 and 1.08, respectively, which correspond to the profiles given by Eqs. (V) and (VII). It is seen that the values calculated with the profiles suggested above [Eqs. (XX) to (XXII)] fit the experimental data better.[7] Finally, a rather poor agreement is observed when the profiles of Eqs. (V) and (VI) are used in the von Kármán-Pohlhausen method. Then $u_m$ is about two times greater and $\tau$ is about 1.7 times greater than the experimental values.

The physical properties of $CuSO_4$ 0.6 m at 20°C used in the above computations were $z = 2$, $D = 4.74 \times 10^{-6}$ cm²/sec [intrapolated from data of Oeholm (24)], $\nu = 1.33 \times 10^{-2}$ cm²/sec [intrapolated from data from (23)], $\alpha = 140$ cm³/mole [calculated from the densities given in (25)], and $n_A = 0.71$ (26).

Manuscript received Aug. 19, 1957. This paper was prepared for delivery before the Cleveland Meeting, Sept. 30-Oct. 4, 1956.

Any discussion of this paper will appear in a Discussion Section to be published in the December 1958 JOURNAL.

[7] In the case of $u_m$ the difference, however, is not large.

## Notation

$A, A', E, K, K'$ = numerical coefficients (*see* text).
$c$ = concentration (moles/cm³) at distance $y$.
$c_e$ = concentration (moles/cm³) at the electrode surface.
$c_o$ = concentration (moles/cm³) in the bulk solution.
$D$ = diffusion coefficient (cm²/sec).
$F$ = Faraday's constant (coulomb/gr. equiv.).
$g$ = acceleration of gravity (cm/sec²).
Gr* = modified Grashof number = $\dfrac{g \alpha i n_A x^4}{z F \nu^2 D}$.
$h$ = total height of cathode (cm).
$i$ = current density (amp/cm²).
$j_D$ = mass transfer rate/cm² due to diffusion (moles/cm² sec).
$l$ = thickness of hydrodynamic boundary layer (cm).
$n_A$ = transference number of anion.
Sc = Schmidt number = $\nu/D$.
$u$ = velocity of hydrodynamic flow in $x$ direction (cm/sec).
$u_m$ = maximum velocity of hydrodynamic flow in $x$ direction (cm/sec).
$U_1$ = proportionality factor in assumed velocity profile [Eqs. (VI) to (IX)].
$x$ = distance from lower end of cathode (coordinate in the vertical direction) (cm).
$y$ = distance from the electrode (coordinate in the direction perpendicular to the electrode surface) (cm).
$z$ = valence of deposited cation (gr. equiv./mole).
$\alpha$ = densification coefficient (cm³/mole) = $1/\rho$ ($d\rho/dc$).
$\delta$ = thickness of diffusion layer (cm).
$\nu$ = kinematic viscosity (cm²/sec).
$\rho$ = density (g/cm³).
$\theta$ = $c_o - c$.
$\Theta$ = $c_o - c_e$ = concentration reduction at interface.
$\tau$ = distance of velocity maximum from electrode (cm).
$\phi, \Lambda$ = auxiliary functions defined by Eq. (XIa) and (XII), respectively.
$\epsilon, \eta, \lambda, \omega$ = variable parameters (*see* text).

REFERENCES

1. C. Wagner, *J. (and Trans.) Electrochem. Soc.*, **95**, 161 (1949).
2. C. Wagner, *This Journal*, **104**, 129 (1957).
3. C. W. Tobias, M. Eisenberg, and C. R. Wilke, *ibid.*, **99**, 359C (1952).
4. J. N. Agar, *Disc. Faraday Soc.*, **1**, 31 (1947).
5. G. H. Keulegan, *J. Research Nat. Bur. Standards*, **47**, 156 (1951).
6. B. Levich, *Acta Physicochim. U.R.S.S.*, **19**, 125 (1944).
7. C. R. Wilke, C. W. Tobias, and M. Eisenberg, *Chem. Eng. Progr.*, **49**, 663 (1953).
8. C. R. Wilke, M. Eisenberg, and C. W. Tobias, *This Journal*, **100**, 513 (1953).
9. A. Brenner, *Proc. Am. Electroplaters' Soc.*, **1940**, 95; **1941**, 28.
10. N. Ibl, Y. Barrada, and G. Trümpler, *Helv. Chim. Acta*, **37**, 583 (1954).
11. N. Ibl, *ibid.*, **37**, 1149 (1954).
12. N. Ibl, R. Müller, and K. Frei, Proceedings of 8th meeting of the International Committee for Electrochemical Thermodynamics and Kinetics (in press).
13. R. E. Wilson and M. A. Youtz, *Ind. Eng. Chem.*, **15**, 603 (1923).
14. S. Ostrach, *Nat. Advisory Comm. Aeronaut: Tech. Note*, 2635 (February, 1952).
15. N. Ibl, W. Rüegg, and G. Trümpler, *Helv. Chim. Acta*, **36**, 1624 (1953).
16. H. Schlichting, "Grenzschicht-Theorie," p. 257, G. Braun, Karlsruhe (1951).
17. E. M. Sparrow and J. L. Gregg, *Trans. Am. Soc. Mech. Eng.*, **78**, 435 (1956).
18. E. M. Sparrow, *Nat. Advisory Comm. Aeronaut. Tech. Note* 3508 (July, 1955).
19. N. Ibl and R. Müller, *Z. Elektrochem.*, **59**, 671 (1955).
20. R. Müller, Dissertation, Eidgenössische Technische Hochschule, Zürich (1956).
21. K. Pearson, Tables of the Incomplete Beta-Function, Cambridge (1934).
22. E. R. G. Eckert, "Introduction to the Transfer of Heat and Mass," McGraw-Hill Book Co., New York (1950) (*a*) p. 66 ff. (*b*) p. 158 ff, (*c*) p. 169-170.
23. International Critical Tables, **5**, 14 (1929).
24. L. W. Oeholm, *Soc. Sci. Fennica, Comm. Phys.-Math.*, **12**, 1 (1943).
25. "Handbook of Chemistry and Physics," **37**, 1836 (1955).
26. Landolt-Börnstein, *Hauptwerk*, **2**, 1104.
27. Th. v. Kármán, *Z. ang. Math. Mech.*, **1**, 233 (1921).
28. K. Pohlhausen, *ibid.*, **1**, 252 (1921).
29. N. Ibl and L. Ramalhete, Proceedings of 8th meeting of the International Committee for Electrochemical Thermodynamics and Kinetics (in press).

# The Preparation of Uranium Metal by the Electrolytic Reduction of Its Oxides

**L. W. Niedrach[1] and B. E. Dearing**

*Knolls Atomic Power Laboratory,[2] General Electric Company, Schenectady, New York*

ABSTRACT

The background work is described for a new continuous process for the production of uranium by electrolytic reduction of its oxides in fused salt electrolytes. Unlike past electrolytic processes for uranium production, the present one is operated at temperatures which are above the melting point of the metal. The effect of current, salt bath composition, and other variables on efficiency and cell operation are discussed.

An electrolysis bath containing 20 mole % $UF_4$ diluted with a 50:50 mole % mixture of $BaF_2$ and $MgF_2$ was found to be satisfactory. With this bath anode current densities as high as 3.6 amp/cm$^2$ are feasible without encountering "anode effect." Any of the oxides of uranium can be used as the feed, but $UO_3$ appears to be preferable. The advantages of the new process are outlined, and the areas requiring additional development work are indicated.

Although electrochemical reduction of uranium halides and $UO_2$-$UF_4$ mixtures was employed for the preparation of the initial U used on the Manhattan Project (1, 2), this process was soon superceded by the bomb reduction of $UF_4$ with Mg metal (3). The latter process is still in active use and electrochemical methods have never seriously threatened to displace it as the production method. This is at least partially related to the fact that the electrochemical procedure and other similar procedures (4-7) have been operated at temperatures below the melting point of U. The bulky, dendritic deposits, which are produced by such processes, trap large quantities of the salt bath, and a series of steps is required before the metal can be separated from the salt and compacted. These steps are inherently expensive for labor, and result in losses and considerable recycle of material to the electrolysis cell.

In spite of the success of the Hall process for producing molten Al from its oxide, no serious effort at developing a similar process for U has been reported. The attractiveness of such a process has been recognized before, but only a few isolated experiments have been reported in which $UO_2$ was electrolyzed successfully at temperatures above the melting point of U to produce beads of metal (8, 9). These results were never exploited further.

[1] Present Address: Research Laboratory, General Electric Co., Schenectady, N. Y.

[2] Operated by the General Electric Company for the U. S. Atomic Energy Commission under Contract No. W-31-109 Eng-52.

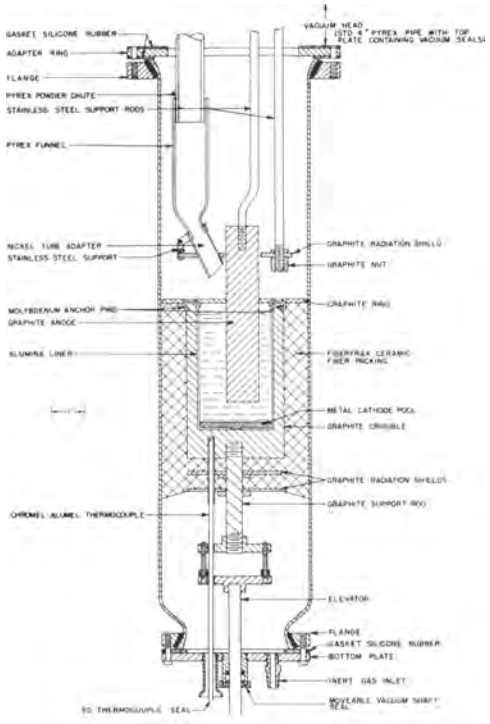

Fig. 1. Details of the electrolysis cell arrangement

It is with the development of a Hall-type process for U that the present work has been concerned. Studies of the variables connected with the electrolysis step itself are detailed in this paper. An engineering evaluation of the full process has been described in a separate report (10).

## Experimental

*Equipment and materials.*—The principal features of the electrolysis cell and its enclosure are shown in Fig. 1, and additional details relating to the equipment are summarized in Table I. Not shown in detail in the drawing is the metal plate covering the top of the cell enclosure. Vacuum seals attached to this plate permitted the insertion of a powder chute for charging solids to the cell and the ¼ in. stainless steel support rods used for the electrodes, radiation shield, and other moveable parts. Cooling fans were positioned around each joint to prolong the life of the gaskets. While several alternate cell designs were employed during the course of the investigation, all were eventually discarded.

During a run inert gas was used to blanket the cell and sweep gaseous reaction products away from

**Table I. Cell Specifications**

| | |
|---|---|
| Material of construction | Graphite, National Carbon AUC Grade |
| Diameter of crucible, in. | 3 |
| Height of crucible, in. | 4. 5 |
| Operating temperature, °C | 1200°-1250°C |
| Sparge gas | He or A |
| Sparge gas flowrate, 1/min | 1 |
| Power supply | Opad selenium rectifier 0-12 v at 150 amp |
| Heating unit | Ajax 6 kw induction heater |
| Cell liner | Morganite recrystallized alumina |
| Cathode | Molten uranium pool |
| Anode | Graphite—1 in. diameter |

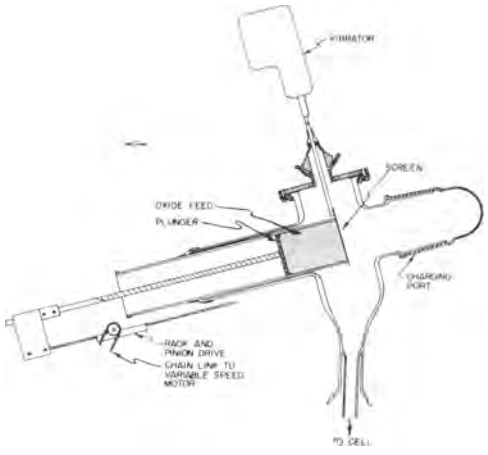

Fig. 2. Details of feed mechanism

the cell for sampling and analysis. Flowmeters were installed in both the inlet and outlet lines, and suitable arrangements were provided for obtaining grab samples of the exhaust gases.

In some of the preliminary runs oxide was fed to the cells intermittently, but in most of the work a continuous feed was used. The positive displacement mechanism shown in Fig. 2 was employed for this purpose. When the oxide was loaded into the reservoir it was tamped frequently to insure uniform packing. Feed rates were then found to be uniform to within 5%. The vibrating screen was required across the face of the discharging oxide in order to obtain the uniform feed rate. Otherwise the oxide broke away in packed lumps and feeding was very irregular.

All chemicals other than the U compounds were standard C.P. materials. The U compounds were analyzed materials obtained from AEC sources. All salts used in the preparation of the baths were predried by heating in vacuo to about 350°C. The oxides were used without further treatment.

*Operating procedure.*—The graphite crucible and its liner were first degassed at 1200°C in vacuo to remove volatile products. Sufficient U was then added to form a 0.5 cm thick layer in the cell and melted at low pressure, preferably less than 10 $\mu$. After filling the system with an inert gas, a mixture of the dry salts was sifted into the hot crucible and melted. The cell was then cooled and the system was cleaned because a thin opaque layer of salt dusted and spattered onto the walls of the furnace envelope during the salt charging procedure and interfered with observation of the cell.

The system was again evacuated and then filled with an inert gas atmosphere, the feed hopper was attached to the feed chute over the cell, and the cell was heated and placed into operation. At regular intervals during the electrolysis, grab samples of the off-gases were taken for mass spectrometric analysis.

At the completion of a run, the electrolysis circuit was opened, the electrodes were raised out of the salt bath, the feed flow was stopped, and the cell was allowed to cool slowly to room temperature. When cold, the crucible was opened, the contents

were examined, and appropriate samples were taken for analysis.

## Results and Discussion

When molten U is desired as the product, the severity of the operating conditions imposed by the high melting point and the chemical reactivity of the U metal limit the number of operating parameters that can be varied appreciably. Those which were considered important and therefore studied in detail were current, bath U content, and the properties of the oxide feed.

In addition some attention was given to the behavior of various fluorides as bath diluents. In this work NaF, LiF, $BaF_2$, and $MgF_2$ were studied. The former was unsatisfactory because of Na production, and LiF was found to be too volatile. The most satisfactory diluent material, and the one used in all of the detailed studies, was found to be a 50:50 mole % mixture of $BaF_2$ with $MgF_2$. In this system both components have low volatilities, and a wide range of liquidus compositions exists at the operating temperature of 1200°C (11).

The greatest difficulty throughout the course of the work was associated with the low solubility of $UO_2$ (the only important oxide in the bath because all higher oxides spontaneously decomposed) in the salt baths. Solubilities of the order of 2 wt % were measured in two widely different baths containing 9 and 84 wt % $UF_4$, respectively.[3] Coupled with this low solubility, the high density of the oxide resulted in rapid settling so that a dense sludge tended to form in the bottom of the cell. This interfered with coagulation of the product metal. As a result, it generally was not possible to produce a massive agglomerate. Instead, the product metal was usually in the form of small beads embedded in a matrix of salt and oxide. Typical examples of such beads are shown in Fig. 3. In addition to the material shown a considerable quantity of finer material was also always present.

In order to obtain the agglomerated product which is shown in the bottom of Fig. 3, special precautions were needed. In this case the product metal was collected in a suspended basket positioned in such a way that no unreacted oxide feed could settle in the basket. The cell design was considered too elaborate to be practical, and work with this type of cell was not pursued further.

[3] The authors are indebted to H. R. Hoekstra and I. Sheft of the Chemistry Division of Argonne National Laboratory for these analyses. Treatment of the samples with $BrF_3$ and $KBrF_4$ was employed to release the $O_2$ which was then measured manometrically (12).

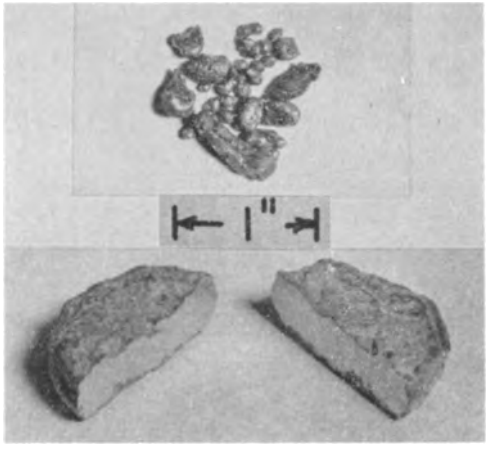


Fig. 3. Typical examples of product metal as produced in cell.

*Effects of Current and Salt Bath Uranium Content*

The effects of current and salt bath U content as variables were investigated concurrently. In this work the 50:50 mole % mixture of $MgF_2$ and $BaF_2$ was used as the bath diluent. The $UF_4$ content of the baths was varied from 10 mole % up to 40 mole %. Micronized $UO_2$, which was used as the feed, was added continuously. The feed was adjusted to supply oxide at a rate such that its complete electroreduction could be accomplished by 50% of the current flowing in the cell. It was hoped in this way to circumvent the oxide settling problem by driving the reduction reaction more toward completion.

A family of curves relating anode efficiency to salt-bath composition and electrolysis current (Fig. 4) shows that the efficiency increases as the $UF_4$ content of the bath is reduced. This may well be related to the fact that the U ion can exist in several different valence states. Then, when present at high concentrations one might expect a fair portion of the electrolysis current to be carried by cyclic oxidation and reduction between two such valence states, presumably $U^{+3}$ and $U^{+4}$. The U content of the bath cannot be reduced indefinitely, however. When the U concentration becomes relatively low, one finds that it is impossible to operate with high currents because of the polarization that occurs. This is illustrated by the curves in Fig. 5 (polarization curves for 30 and 40 mole % $UF_4$ baths are essentially identical with that for the 20 mole % bath and were therefore omitted for clarity).

Polarization is attributed to the "anode effect" often observed during electrolysis of fluoride baths (13). Normally oxide is added to a bath to eliminate the effect, but a depolarizer such as $U^{+3}$, which can be oxidized to a higher valence state without production of a gaseous product, should also prevent its occurrence. It is probably through the latter mechanism that the anode effect is eliminated in the baths containing the higher concentrations of $UF_4$.

It is evident from Fig. 4 that the current has a somewhat lesser effect on the anode efficiency than that of the bath composition. The apparent maximum occurring at 50 amp does not appear to be real,

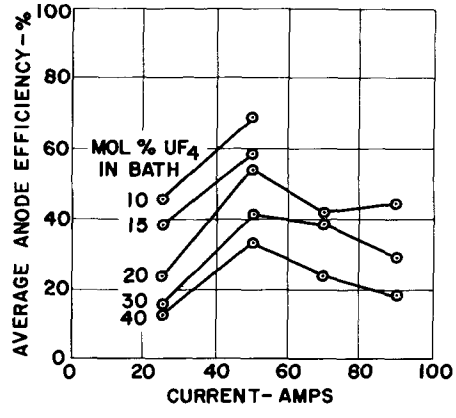


Fig. 4. Effect of current and salt bath composition on efficiency.

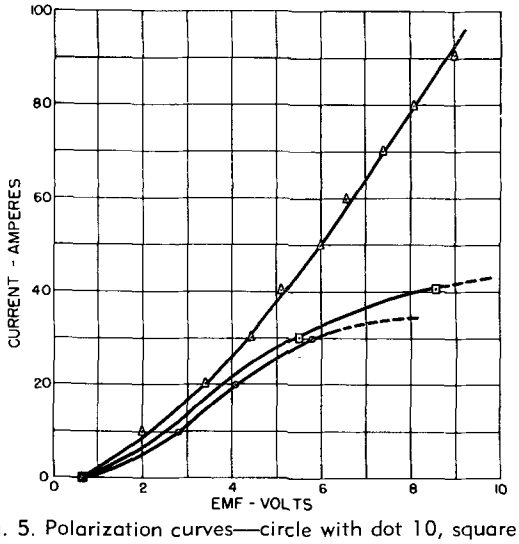


Fig. 5. Polarization curves—circle with dot 10, square with dot 15, triangle with dot 20 mole % $UF_4$ in bath.

but is related to the fact that the data for operation at 50 amp were always obtained at the start of a series of tests with a new bath. As a result any oxide originally present in the salt bath as an impurity was also available for reduction at that time and added to the apparent efficiency of operation. The data for the other currents are, however, reliable, and there is a real advantage to operating at the higher currents in preference to operation at 25 amp.

In addition to their effect on efficiency, the influence of current and bath composition on the composition of the off-gases was examined. In all cases, except that employing the 10 mole % $UF_4$ bath, CO and $CO_2$ were the major gaseous products with the CO content falling in the range 75-82%. In the run with the 10 mole % $UF_4$ bath the CO content averaged 50%. While $CO_2$ was again the other major constituent, in this case $CF_4$ contents beween 5 and 10% were also found. The $CF_4$ content of the gas from the run with the 15 mole % $UF_4$ bath averaged slightly less than 1%, and in all other cases the $CF_4$ content of the off-gases was equal to or less than 0.1%. Neither $O_2$ nor $F_2$ were ever detected in the off-gases.

For practical purposes, operating conditions can be optimized. In order to avoid polarization effects at the anode as well as to minimize $CF_4$ formation, $UF_4$ bath contents in excess of 15 mole % are desirable. On the other hand, because high $UF_4$ contents result in decreased efficiencies, it would appear that a bath containing about 20 mole % $UF_4$ would be a practical compromise.

Since there seemed to be no serious decrease in efficiency associated with cell operation up to 90 amp (about 1.5 amp/cm$^2$) and since higher current densities result in smaller cell sizes, it was of interest to determine the maximum current density that could be tolerated at the anode with a 20 mole % $UF_4$ bath. This was found to be 3.6 amp/cm$^2$.

*Behavior of Several Oxides in the Process*

The history of a U oxide has a marked effect on its ease of conversion to $UF_4$ (14). To test whether a similar effect is present in the electroreduction of U oxide, a number of runs were performed with oxide feeds having variations in physical and chemical characteristics. For this purpose various samples of $UO_2$, $U_3O_8$, and $UO_3$ were used. It was felt that the $UO_3$ might well have considerable advantage over $U_3O_8$ or $UO_2$ as a feed because it is prepared from uranyl nitrate by reactions occurring at lower temperatures than subsequent reduction operations. Reactivity would therefore be expected to be higher because there is less chance for sintering to occur.

This series of runs was made using a continuous feed of oxide to the cell. On the basis of the previous data, the bath containing $MgF_2$, $BaF_2$, and 20 mole % $UF_4$ was used. Operation was at 70 amp, and the oxide feed rate was again adjusted to correspond to about 50% current efficiency. With the exception of the short run with $U_3O_8$, all were continued for a period of about 4 hr during which time approximately 400 g of oxide was fed to the cell. A charge of U metal weighing about 250 g was added at the start of each run to serve as a molten metal cathode.

Data obtained during runs with micronized $UO_2$, peroxide $U_3O_8$, and denitration $UO_3$ are plotted in Fig. 6 to give an indication of the efficiencies obtained as well as the stability of operating conditions. It was observed qualitatively that the oxide settling problem persisted in all cases, and the typical sludge intermixed with metallic beads was found in the bottom of the cell at the end of each run. The $CF_4$ content of the off-gases was invariably less than 0.1%.

Some effort was made in these runs to determine whether gross changes in bath composition occurred during extended electrolysis. Samples of the frozen salts were therefore analyzed at the end of the runs. Because of segregation that occurred during the slow cooling of the melt, considerable scatter in the data was observed. On the average, however, the final concentrations were within 10% of those at the start for each of the cations in the bath.

In calculating the efficiencies shown in Fig. 6, a correction was first applied to the off-gas data to allow for any gases produced by thermal decomposition of the higher oxides. The remainder of the anode gases were then assumed to have been formed during the electrolytic reduction of $UO_2$ to metal. The efficiency then corresponds to the per cent of the feed oxide that was reduced to metal, which is the parameter of greatest interest in this work.

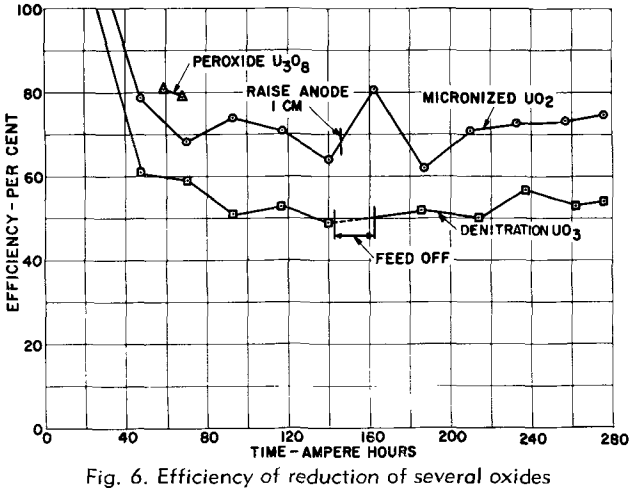


Fig. 6. Efficiency of reduction of several oxides

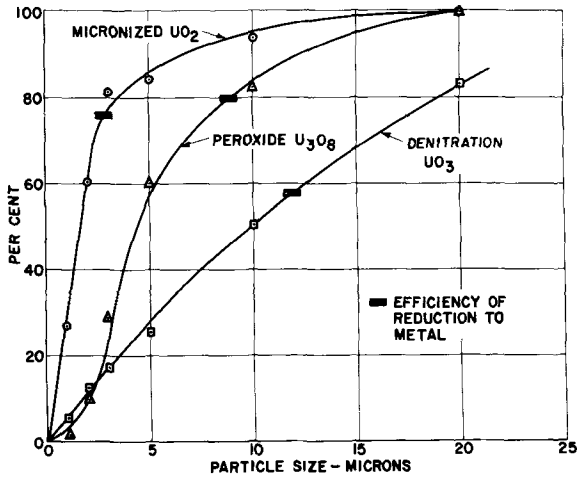


Fig. 7. Particle-size distributions for several oxides

From the results for the runs with different oxides, there does not appear to be any strong indication that one is preferable to another. If anything, the data indicate that $UO_3$ is a poorer feed than the other oxides. Since this was not expected, it is of interest to consider the efficiencies in the light of the particle size distributions of the three oxides. This can be done by referring to Fig. 7. On each of the curves a bar has been drawn at the percentage corresponding to the average efficiency of reduction of the feed to metal. One can then make the reasonable assumption that the smaller particles are reduced rapidly, while those above the line of demarcation are reduced more slowly and, therefore, settle out to form the sludge. When considered in this light, the $UO_3$ does appear to have advantages over the other oxides because much larger sized particles were present in the feed and a high percentage of the larger sized particles was actually reduced.

In view of the results obtained, it would appear desirable to perform a series of experiments employing a single feed, but with different particle size distributions. For such a series, it might be useful to feed directly from the size reducer into the cell. It might also be useful to correlate efficiencies with the reactivity of the feed as indicated by some of the common reactivity tests (15).

### *Purity of Product Metal*

Six representative product samples were analyzed. Of greatest interest is the fact that low analyses for oxygen (4-6 ppm), barium (<200 ppm), magnesium (7-20 ppm), and hydrogen (<1 ppm) were obtained because all were macro constituents of the baths. The hydrogen was present as a small amount of water impurity in the salts and the oxide feeds. The major impurities in the samples were Al and Si (both >1000 ppm), but these were undoubtedly obtained from structural materials and could be avoided. Carbon contents of about 600 ppm were felt to be reasonable in view of the use of graphite cells.

## Summary and Conclusions

This work suggests that electrolytic reduction of U oxides is feasible at temperatures above the melting point of U metal. A continuous process should therefore be possible. While U has not been produced in high yield by this method, sufficient metal has been obtained to indicate that such production is possible. Higher, more practical efficiencies should be obtainable in larger scale operations than were realized in the laboratory operations to date. This is indicated by the fact that, in the aluminum industry, efficiencies increase as one increases the spacing between electrodes (16), and such increases in spacing are possible in going to larger cells.

The major remaining problems are associated with the settling of the oxide in the electrolysis cell due to its low solubility and high density. In addition, materials of construction for the electrolysis cell must be thoroughly investigated. At present, graphite looks suitable.

The present work indicates that a bath containing $MgF_2$, $BaF_2$, and $UF_4$ is satisfactory as the solvent electrolyte. From an investigation of such baths in the range 10 to 40 mole % $UF_4$, it is concluded that a bath containing about 20 mole % $UF_4$ is most satisfactory. Lower $UF_4$ concentrations result in polarization effects at the anode which preclude the use of high currents. Higher concentrations of $UF_4$ in the bath have resulted in low current efficiencies for the electrolysis process of interest. With the 20 mole % bath an anode current density of 3.6 amp/cm$^2$ has been used without difficulty. Such high current density seems desirable for good yields. Any of the major U oxides, $UO_3$, $U_3O_8$, or $UO_2$, can be used as feed, but because $UO_3$ is the direct product of denitration of uranyl nitrate it is the most desirable for a production process.

## Acknowledgments

The authors wish to acknowledge the assistance from others at the Knolls Atomic Power Laboratory. They are particularly grateful to Mr. C. F. Pachucki and Mr. L. F. Yetter who performed the many mass spectrographic analyses of gas samples that were required, to F. P. Landis for the spectrographic work, to L. M. Osika for x-ray diffraction analyses, and to E. L. Shirley for particle-size determinations. They are also grateful to Mr. C. M. Henderson of the Mallinckrodt Chemical Works and to Dr. D. S. Arnold and Dr. W. C. Manser of the National Lead Company of Ohio for valuable discussions.

Manuscript received May 29, 1957. This paper was prepared for delivery before the Washington Meeting, May 12-16, 1957.

Any discussion of this paper will appear in a Discussion Section to be published in the December 1958 JOURNAL.

## REFERENCES

1. H. D. Smyth, "Atomic Energy for Military Purposes," p. 93, Princeton University Press, Princeton (1945).
2. J. W. Marden, W. C. Lilliendahl, G. Meister, R. Nagy, D. M. Wroughton, and N. C. Beese, AECD-3687 (1946).
3. H. A. Wilhelm, "The Preparation of Uranium Metal by the Reduction of Uranium Tetrafluoride with Magnesium," in "International Conference on Peaceful Uses of Atomic Energy," Vol. 8, p. 162, United Nations, New York (1955).
4. F. H. Driggs and W. C. Lilliendahl, *Ind. and Eng. Chem.*, 22, 516 (1930).
5. F. H. Driggs and W. C. Lilliendahl, U. S. Pat. 1,861,625, June 7, 1932.

6. R. Rosen, U. S. Pat. 2,519,792, Aug. 22, 1950.
7. S. K. Kantan, N. Shreenivasan, and G. S. Tendolkar, *Chem. Eng. Prog. Symposium Ser. No. 12,* **50**, Pt. II, 63 (1954).
8. J. M. Marden, *et al., op. cit.*, p. 161.
9. M. Kolodney, LA-40 (1943).
10. L. W. Niedrach and A. C. Schafer, KAPL 1668 (1957).
11. F. P. Hall and H. Insley, "Phase Diagrams for Ceramists," p. 108, American Ceramic Society, Inc., Columbus, Ohio (1947).
12. H. R. Hoekstra and J. J. Katz, *Anal. Chem.,* **25**, 1608 (1953).
13. C. L. Mantell, "Industrial Electrochemistry," 3rd ed., p. 477 and 497, McGraw-Hill Book Co., Inc., New York (1950).
14. B. A. Lister and G. M. Gillies, "The Conversion of Uranyl Nitrate to Uranium Dioxide and to Uranium Tetrafluoride," in "Progress in Nuclear Energy," Series 3, "Process Chemistry," Vol. I, Ch. 1.2, McGraw-Hill Publishing Co., Inc., New York (1956).
15. K. E. Rapp, J. S. Fox, N. C. Orrick, and E. J. Barber, TID 5295 (1956), p. 199.
16. J. Wleügel and O. C. Böckman, *This Journal,* **101**, 145C (1954).

# Discussion Section

This Discussion Section includes discussion of papers appearing in the JOURNAL of the Electrochemical Society, 104, No. 4 and 7-12 (April and July-December 1957). Discussion not available for this issue will appear in the Discussion Section of the December 1958 JOURNAL.

## The Potential of an Electrode of a Voltaic Cell; A New Definition with Justification for the Use of Two Sign Conventions

J. B. Ramsey (pp. 255-260, Vol. 104)

**A. J. deBethune**[1]: Professor Ramsey's paper does three things of value for the electrochemist: (*A*) It defines explicitly the thermodynamic state of the *electron* intended, but never previously defined, in such familiar half-cell reactions as $Fe = Fe^{++} + 2e^-$ or $Ag^+ + e^- = Ag$. In all such half-cell reactions, the thermodynamic state of the electrons is that of electrons in the metallic phase of the usual standard hydrogen electrode (S.H.E.). (*B*) It introduces the concept of the *electron chemical potential* $\mathcal{E}$ of any electrode, defined as the *partial molal electrochemical free energy (electrochemical potential)* of the electrons in the metallic phase of that electrode, divided by the faraday. This concept provides a physically meaningful and very illuminating description of what is commonly, but erroneously, known as the "American sign convention" (the Zn positive, Cu negative convention), first used by Walter Nernst in Germany in 1889. (*C*) Ramsey's paper also discusses the electrostatic properties of electrodes and of voltaic cell terminals (ignored in most chemistry texts) and thus establishes the electrostatic definition of the electrode potential, denoted by Gibbs' symbol $V$, which leads to the opposite "European sign convention" (the Zn negative, Cu positive convention), first used by Willard Gibbs in America in 1875-78 and by Wilhelm Ostwald in Germany in 1887, and internationally accepted by the I.U.P.A.C. at Stockholm in 1953.

The whole-cell and half-cell electromotive force $E$ changes its sign upon a reversal of the cell reaction and cell diagram. In contrast, both $\mathcal{E}$ and $V$ are sign invariant. The thermodynamic equations to be used in conjunction with $\mathcal{E}$ and $V$ are worth noting. They are:

| | with $\mathcal{E}$ | with $V$ |
|---|---|---|
| for oxidations | $\Delta F = -n\mathbf{F}\mathcal{E}$ | $= +n\mathbf{F}V$ |
| for reductions | $\Delta F = +n\mathbf{F}\mathcal{E}$ | $= -n\mathbf{F}V$ |

For whole-cells, the free energy is given, as before, by $\Delta F = -n\mathbf{F}E(\text{cell})$, where $E(\text{cell}) = \mathcal{E}_{\text{left}} - \mathcal{E}_{\text{right}} = V_{\text{right}} - V_{\text{left}}$, for the reaction which accompanies the passage of $n$ faradays of positive electricity through the cell (as written) from left to right. [*See* A. J. deBethune, *This Journal*, **102**, 288*C* (1955); T. S. Licht and A. J. deBethune, *J. Chem. Educ.*, **34**, 433 (1957)].

[1] Dept. of Chemistry, Boston College, Chestnut Hill 67, Mass.

**M. O. Davies**[2]: I wish to state emphatically that I do *not* use the left-right convention. This convention is *not* being taught at Western Reserve University and has not been taught here for years. Any students who wish to use it are allowed to do so. We do not feel that in the near future any one system will be used and agreed on by all scientists throughout the world.

We feel that no subject should be divorced from physical reality unless definite advantages are to be obtained by so doing. As we see it, the left-right convention tends to confuse the issue more often than it helps. Students tend to use it as a crutch to avoid thinking about what they are doing, and thus are often led unwittingly to false conclusions.

It is essential in discussing the left-right convention to consider what arbitrariness is involved when one attempts to divorce the subject of cell voltages from physical reality. Thus I feel that the illustrations presented below are not trivial criticisms of the left-right convention but, on the other hand, are essential in showing what troubles are involved with the convention.

Let us suppose that as a teacher you are introducing the subject of the experimental determination of cell voltages and have placed an electrochemical cell in front of you. Your left electrode is the right electrode to the class and thus, based on the physical picture, they would get the opposite sign for the cell voltage. In addition, if you were to turn the cell upside down and the contents of the cell did not spill out onto the table, you would get the sign that they originally obtained and vice versa. Yet the same process is still taking place inside the cell. For a cell consisting of concentric cylindrical electrodes, some additional designation is necessary. To avoid such difficulties, the left-right convention must divorce itself from physical reality; but, in so doing, it finds additional difficulties. The cell is represented on paper. Here enters the difficulty of how one looks at the paper.

Experimentally determined cell voltages ($E$) in our system are obtained without sign. Some of the questions that have arisen from my original comments have resulted because the words "experimentally determined cell voltages" have apparently been interpreted to mean experimentally determined open circuit cell voltages. In order to obtain currents from an experimental cell, it is essential to have spontaneous reactions taking place within the cell. A negative cell voltage would have no meaning whatsoever. An open circuit cell voltage is really nothing more than a cell voltage measured under conditions which reduce the current output to a small value. However, the cell is acting less reversibly when it is being measured (even with a potentiometer) than when it is on true open circuit.

[2] Morley Chemical Lab., Western Reserve University, Cleveland 6, Ohio.

We always measure the + and − terminals of the cell. This, plus the cell voltage (possessing no sign), is completely adequate to specify which electrode has a greater tendency to be oxidized or reduced. The absence of a sign on the experimentally determined open circuit cell voltage is not equivalent to treating a $10.00 debit as the same thing as a $10.00 credit. The − lead to the potentiometer indicates that there is an excess of electrons on the electrode to which it is connected and, thus, that its electrode reaction has a greater tendency to proceed in the oxidation sense than the electrode reaction at the electrode connected to the + lead of the potentiometer. Cell voltages are not dependent on whether some particular half-cell is being used as an anode or as a cathode. If the cell voltage is the same in magnitude and the resistances of the circuit are the same, the same amount of current will flow, whether a given half-cell is acting as an anode or as a cathode. The + lead of the cell will be hooked up to the external circuit in the same way.

It would be satisfying if all cell reactions (both at cathodes and anodes) were fully understood. This, unfortunately, is not the case. Often a cell is really nothing more than a black box with two terminals sticking out. For years, oxygen cathodes on active carbon in basic solutions were considered to be acting in accordance with the equation:

$$O_2 + 2H_2O + 4e^- \rightarrow 4OH^-$$

This misunderstanding led to many faulty interpretations of these electrodes. Actually, if the carbon does not possess a large ability to decompose peroxides, it will follow the equation:

$$O_2 + H_2O + 2e^- \rightarrow OH^- + O_2H^-$$

If the carbon is a fairly good decomposer of peroxides, its open circuit potential will lie somewhere between the expected potentials for the two reactions quoted above. Another example comes from metal-metal oxide electrodes. Their potentials often lie between the values expected for the metal-metal ion potential and the oxygen electrode potential.

Whether or not you know what cell reactions are going on inside the cell has no influence on the measurement of its voltage. As I have said before, experimentally determined cell voltages cannot be negative. Thus, in our system, no sign need be attached to them. Actually, we consider them without sign.

In our system, thermodynamically determined potentials ($\mathcal{E}$) are associated with specific reactions only, and these potentials apply only for the reaction equations as written. The thermodynamic data are used normally only for predictions of what cell voltage to expect under given conditions. In order to do so, one must know what reactions are involved, or make reasonable guesses. As stated above, this is often not simple. Only with hypothetical, thermodynamically obtained half-cell or cell reaction potentials will there be signs attached. The sign to be attached is that to be expected from the value for the free energy change for the half-cell or cell reaction, as written. In other words, if the reaction as written tends to proceed, and possesses a negative free energy change, then the reaction potential is given a positive sign and vice versa. If one obtains for the over-all cell reaction, as written, a negative value for $\mathcal{E}$, this indicates that the reaction in the cell proceeds in the opposite direction to that indicated by the written equations, and that these equations should be reversed. I agree with Dr. deBethune in stating that this aspect of electrochemistry is somewhat arbitrary. I need to define which direction a reaction is expected to follow. I feel, however, that experimentally determined cell voltages need not be divorced from physical reality as is done with the left-right convention. If experimentally determined cell voltages are treated by our system, they never need confuse the student of physical chemistry as he is confused by the multiple sign conventions for experimentally determined cell voltages. We feel that we have removed as much arbitrariness as possible by the above approach and have a sound, workable system.

It is the merits and demerits of a system that are important, not how long the system has been used or who uses it. Since I have been attempting to explain the system that I honestly believe is best, I have purposely used the symbolism that I normally use: $E$ = the experimentally determined cell voltage; $\mathcal{E}$ = the thermodynamically determined cell or half-cell reaction potential. No confusion need arise over this symbolism so long as what it signifies is clearly indicated.

## Anodic Corrosion and Hydrogen and Oxygen Overvoltage on Lead and Lead Antimony Alloys

P. Ruetschi and B. D. Cahan (pp. 406-413, Vol. 104)

**Jeanne Burbank**[3]: (*A*) The authors have failed to comprehend much published information, and have seriously misrepresented reported work. The following listing, by no means complete, gives a few examples of the unfortunate kind of misrepresentation profusely present in the paper.

1. Contrary to the statement of Ruetschi and Cahan (R. and C.), the x-ray diffraction peaks of published patterns for $\alpha$-$PbO_2$[4-7] may be accounted for by the standard patterns of PbO (tetragonal), $PbSO_4$, and $\beta$-$PbO_2$.[8] Positive identification by diffraction techniques of $\alpha$-$PbO_2$ in the possible presence of these other materials must be made with care; orientation effects are particularly to be avoided.

2. R. and C. state that "conventional cooling rates" produce considerable solid solution of antimony in lead, citing Hofmann.[9] The reference clearly states that very little antimony is retained in solid solution in as-cast lead antimony alloys; that interdendritic segregation is apparent in alloys as low as 0.1% Sb; and presents a micrograph to illustrate the point.

[3] Naval Research Lab., Washington 25, D. C.
[4] N. Kameyama and T. Fukumoto, *J. Soc. Chem. Ind., Japan*, **49**, 154 (1946).
[5] T. Katz, *Ann. de Chim.*, **5**, 5 (1950).
[6] A. I. Zaslavskii, J. D. Kondrashev, and S. S. Tolkachev, *Doklady Akad. Nauk S.S.S.R.*, **75**, 559 (1950).
[7] A. I. Zaslavskii and S. S. Tolkachev, *J. Phys. Chem. (U.S.S.R.)*, **26**, 743 (1952).
[8] X-ray Powder Data File, ASTM, Philadelphia, Pa.
[9] W. Hofmann, "Blei und Bleilegierungen," p. 16, Julius Springer, Berlin (1941).

3. Large hard black nodules were not observed by Burbank[10] on grids of storage batteries removed from service, and no mention of such examination appears in the reference cited by R. and C.

4. The studies of Burbank and Lander[10-12] on the anodic corrosion of lead in sulfuric acid comprise a determination of the corrosion kinetics, identification of anodic products, and coordination of thermodynamically possible reactions at defined anodic potentials. R. and C. have failed to comprehend the manner in which the work was carried out, and the importance of potential as a controlling factor in electrochemical reactions. R. and C. misrepresented the reports by stating that results were presented from experiments other than those described in the published papers.

(*B*) It is common analytical practice to decompose $PbO_2$ by the action of acids and $H_2O_2$. What "purification" was obtained by treating electroplated $\alpha$-$PbO_2$ with such a mixture?

(*C*) Was no antimony pattern observed in the x-ray diffraction examination of the alloys? Normally a 10.98% Sb alloy would be expected to give a strong pattern for antimony, and the strongest line in the pattern of antimony metal lies very close to the strongest lines in x-ray patterns of $\alpha$-$PbO_2$ and PbO (tetragonal).

(*D*) What potential measurements are referred to in the next-to-last paragraph in column 1, p. 408?

**J. J. Lander**[13]: The paper is of very great interest from both practical and theoretical viewpoints. The presence of $\alpha$-$PbO_2$ in the corrosion product of lead and lead alloys may be particularly significant.

There are possible misconceptions which the reader might entertain without a full knowledge of some of the work referred to in the paper. Thus, in the introduction and in the discussion one might get the idea that tetragonal PbO will not be formed as a corrosion product of lead in acid solution. The works of Wolf and Bonilla,[14] and Lander[15] referred to in the paper clearly show that it can be formed under certain potential conditions which are different from those obtaining in the paper under discussion and in the work of Wynne-Jones and co-workers[16] also of reference. The authors, and Wynne-Jones and coworkers, employed constant current techniques whereby after the formation of lead sulfate the potential rose beyond that for the lead dioxide-lead sulfate couple, i.e., a condition under which tetravalent reaction products would be preferred. In my work, constant-voltage techniques were used and the voltage was held at levels below that of the lead dioxide-lead sulfate couple, a condition whereby divalent lead reaction products would be preferred, as was borne out by the application of Faraday's law to the amount of weight loss. Moreover, examination of the corrosion products showed that lead sulfate was the smaller part.

The authors point out, as I have already done,[17] that the formation of lead dioxide is thermodynamically possible at potentials well below that for the lead dioxide-lead sulfate couple. However, I have also pointed out that, if its formation occurred under such potential conditions, it would be thermodynamically unstable, which is practically attested to by the application of Faraday's law, already mentioned. The work in footnote 17 of this discussion considered reactions whereby lead-dioxide formed low potentials could go to divalent products. The tacit implication that the x-ray analysis of corrosion products in my work, which showed the presence of tetragonal PbO, resulted from confusion or ignorance of the pattern for $\alpha$-$PbO_2$ is, therefore, unfounded.

The authors state in their discussion that $\alpha$-$PbO_2$ occurs as a grid corrosion product and had been reported as tetragonal PbO by myself[15] and other workers. My work of the reference was concerned only with corrosion of cold-rolled lead sheet at controlled potentials.

The authors' method of determining total corrosion by accounting for the $PbO_2$ present by discharge, self-discharge, and titration of residual $PbO_2$ is no doubt good for pure lead, but must be in error for lead-antimony alloys because it can take no account of the antimony loss. This would be especially true in a constant-current system if the antimony corrosion reaction were much faster than the lead corrosion reaction. Thus, Fig. 5 in the authors' paper would indicate that the antimony exerts a protective function in the alloy; however, it is open to the very obvious interpretation that with increasing antimony concentration the corroding current went preferentially to oxidation of the antimony phase of the alloy.

**Hans Bode**[18]: We have found that the rhombic modification of the lead dioxide ($\beta$-$PbO_2$) is formed in the formation process in the positive plate.* On the surface, only the tetragonal form ($\alpha$-$PbO_2$) is newly developed, whereas both forms ($\alpha$-$PbO_2$ and $\beta$-$PbO_2$) are found inside, in a proportion of about 50:50%. It seems that the $\beta$-$PbO_2$ is formed from the PbO, and the $\alpha$-$PbO_2$ from the lead sulfate or the basic lead sulfate. The beta-modification is the more stable one.

**P. Ruetschi and B. D. Cahan:** The authors have read the foregoing comments with great interest.

With regard to J. Burbank's remarks, the authors are aware that their list of references on x-ray data of $PbO_2$ is not complete. A large amount of work has been done in this field but much of the published data is unclear and contradictory.

The authors have pointed out in their paper that the major peak in the x-ray patterns of $\alpha$-$PbO_2$ coincides with a major peak of the pattern for tetragonal PbO. Similarly, other peaks of the $\alpha$-$PbO_2$ pattern are obscured, as J. Burbank points out, by the presence of other lead compounds like $PbSO_4$ and $\beta$-$PbO_2$. This is exactly the reason why $\alpha$-$PbO_2$ has remained unknown until recently. There exist, however, as pointed out in the paper, several peaks

[10] J. Burbank, *This Journal*, **103**, 87 (1956).
[11] J. J. Lander, *This Journal*, **98**, 213 (1951).
[12] J. J. Lander, *This Journal*, **103**, 1 (1956).
[13] Electric Auto-Lite Co., Toledo 1, Ohio.
[14] E. Wolf and C. Bonilla, *Trans. Electrochem. Soc.*, **79**, 307 (1941).
[15] J. J. Lander, *This Journal*, **98**, 213 (1951).
[16] W. W. Beck, R. Lind, and W. F. K. Wynne-Jones, *Trans. Faraday Soc.*, **50**, 147 (1954).
[17] J. J. Lander, *This Journal*, **103**, 1 (1956).
[18] Research Lab., Accumulatoren-Fabrik Aktiengesellschaft, Neue Mainzer Strasse 54, Frankfurt/Main, West Germany.
* H. Bode and E. Voss, *Z. Elektrochem.*, **60**, 1053 (1956).

of the $\alpha$-$PbO_2$ pattern which do not coincide exactly with any other known compound of Pb. Furthermore, some of the peaks, which do coincide in angular position with peaks of other compounds, can be differentiated by relative intensity measurements and by differences in profile of the diffraction peaks.

The second point of J. Burbank is not well taken for, although some segregation of Sb is indeed observed with 0.1% Sb alloys, this does not prove that with higher Sb concentrations a higher concentration of Sb does not remain in solid solution. This becomes particularly evident if, e.g., a 2% alloy is heat-treated below the eutectic temperature, at 245°C, in order to assure that all the Sb is homogeneously distributed in solid solution. Cooling this tempered alloy at "conventional" rates does not produce any precipitation of Sb. According to Hofmann "ist dies in dem Sinne zu deuten dass bei Luftabkühlung homogener Legierungen alles Sb in fester Lösung bleibt." In actual castings there exists a concentration gradient for Sb in the solidified lead grains such that the first portions to be precipitated are low in Sb, and the cast portions are rich in Sb.

With regard to J. Burbank's third point it should be mentioned that J. J. Lander [Ref. (27) in the authors' paper] describes a condition of positive plates, *which had been cycled around the* $PbO_2/PbSO_4$ *potential, as follows:* "Whenever the corrosion film had been built up for a week or so, even after long discharge periods there existed a black, shiny, hard, brittle, adherent film underneath the outer $PbSO_4$ film. This film was shown by x-ray analysis to be $PbO_2$ containing small amounts of PbO." No mention of the existence of an $\alpha$-$PbO_2$ is made in the cited paper. J. J. Lander also has reported [Ref. (1) in the authors' paper] that electrodes which had been anodized between 0.7 and 1.6 v vs. $H_2$ (this is below the $PbO_2/PbSO_4$ potential which is at 1.7 v) had a "grayish-white surface film consisting almost entirely of $PbSO_4$. It was loosely adherent and could be wiped off with cotton, whereupon a brown to black underfilm was exposed which x-ray analysis proved to be tetragonal PbO."

We agree with J. Burbank that Ref. (4) in the authors' paper should be omitted at the particular place referred to. The authors feel that there is no reason for J. Burbank to feel that her results have been misinterpreted. The authors have pointed out that "the existence of PbO in a strong $H_2SO_4$ solution is difficult to picture thermodynamically or kinetically and in no case has any tetragonal PbO been detected in this laboratory by x-ray diffraction of Pb corroded in $H_2SO_4$."

As stated in the authors' paper, the corrosion experiments were performed at potentials above the $PbO_2/PbSO_4$ potential. However, the authors agree with J. Burbank that under certain voltage and *p*H conditions PbO can exist underneath a partially protecting sulfate layer. The authors are aware of the difference between constant voltage and constant current techniques.

The authors also would like to point out that in none of J. J. Lander's or J. Burbank's papers on this subject (up to the publication date of the authors' paper) has the existence of $\alpha$-$PbO_2$ as a modification of $PbO_2$ been considered. In 1956, J. Burbank stated [Ref. (4) in the authors' paper] that "an unidentified material believed to be a form of lead oxide was also present in some anodic coatings. Unpublished work with several lead monoxides indicates that this may be a form of lead monoxide rather than a higher oxide." Since the publication of the authors' paper, J. Burbank has reported that this unknown material is actually $\alpha$-$PbO_2$. With regard to points (*B*), (*C*), and (*D*) in J. Burbank's comment, the acid and peroxide treatment was applied to remove possible impurities of lower oxides. Since the $\alpha$-$PbO_2$ plating solution at times contained a very fine crystalline precipitate of $Pb_3O_4$ and possibly other lead compounds, and since on washing the plating solution from the electrode some $Pb(OH)_2$ was precipitated, the nitric acid-$H_2O_2$ treatment was intended to remove these surface impurities. No Sb patterns were observed on the anodized Pb-Sb alloys. At the time of publication of the authors' paper, potentials for pure $\alpha$- and $\beta$-$PbO_2$ were not yet measured successfully. Since then the authors have reported values for $\alpha$-$PbO_2$ and $\beta$-$PbO_2$. According to these measurements, the potential of $\alpha$-$PbO_2$ is 7 mv higher than that of $\beta$-$PbO_2$ at 30°C in 1.250 sp gr sulfuric acid.

The authors are in complete agreement with the comments of J. J. Lander with regard to constant current and constant voltage techniques. He never mentions, however, the existence of $\alpha$-$PbO_2$ in his papers.

In reference to the last comment of J. J. Lander, it can be stated that the technique applied to determine the amount of corrosion, measures indeed the amount of $PbO_2$ formed. However, no error is introduced by this condition. The corrosion of Sb and Pb must be strongly coupled since corrosion occurs only at the surface of the electrode. The Sb in the alloy is enclosed by lead and can only be attacked after the surrounding lead has been oxidized. It is not conceivable that Sb moves out of unattacked bulk electrode material. The actual depth of attack can be evaluated by taking into account the density of Pb-Sb alloys, as suggested in the authors' papers. The amount of electricity, applied during the constant current oxidation (at $3ma/cm^2$) was orders of magnitude larger than the amount of electricity actually required to produce the corrosion film. Most of the current was used for gas production. If the oxidation of the Sb phase would be faster than the oxidation of the lead phase, the latter process would determine the penetration rate and the growth of the oxide film. In Fig. 5, the decrease in discharge time with increasing Sb concentration is due to an increased rate of self discharge. This is brought out in more detail in new papers which are in the course of publication.

With regard to Dr. Bode's comment, the authors are in complete agreement with his experimental findings. However, the authors have reason to suspect that (orthorhombic) $\alpha$-$PbO_2$ is formed in the plates of storage batteries by nucleation with metallic lead particles, and (tetragonal) $\beta$-$PbO_2$ by oxidation of $PbSO_4$. It would be helpful if the nomenclature for the tetragonal and orthorhombic modification of

$PbO_2$ could be made uniform. The authors, together with Zaslavsky, *et al.*, use the term $\alpha$-$PbO_2$ for the orthorhombic form, while Bode and Voss use the name $\beta$-$PbO_2$ for this modification. The respective designations for $\alpha$ and $PbO_2$ were originally chosen because of the parallelism to the orthorhombic and tetragonal modifications of $MnO_2$ which have been named $\alpha$ and $\beta$, respectively.

## High Temperature Oxidation of High Purity Nickel between 750° and 1050°C

E. A. Gulbransen and K. F. Andrew (pp. 451-454, Vol. 104)

**Stanislaw Mrowec and Teodor Werber**[19]: The mechanism of oxidation of nickel at high temperatures has been the subject of many investigations. Applying a sensitive gravimetric method, Gulbransen and Andrew measured the rate of nickel oxidation and have found that the heat of activation of this process in the atmosphere range 750°-1050°C amounts to 41.2 cal/mole. In this region no cracks were observed in the nickel oxide layer and the parabolic rate law was obeyed. This value does not differ from the former one obtained by the same authors for the temperature range 400°-750°C.[20] Using theoretical considerations and comparing the activation energy of the oxidation process with the activation energy of diffusion of nickel in nickel oxide (which was determined by Moore[21] by aid of the tracer method), Gulbransen and Andrew as well as Moore[21] conclude that the oxidation process proceeds only by the outward diffusion of nickel ions and electrons via cation vacancies and electron holes.

The mechanism of the oxidation of nickel at high temperatures has been investigated also by the marking method.[22-24] The results of these investigations cannot be conciliated with the nickel oxidation mechanism proposed by Gulbransen and Andrew and Moore.

L. Czerski[22] used as the marker a platinum wire $\phi = 1.0 \times 10^{-2}$ cm and Ilschner and Pfeiffer[23] also a Pt-wire $\phi = 0.3 \times 10^{-2}$ cm. Czerski, Mrowec, and Werber[24] used platinum wire $\phi = 7 \times 10^{-3}$ cm and submicroscopic layers of platinum. Nickel specimens were wrapped with platinum wire and then oxidized at temperatures of 1000° and 1200°C. When submicroscopic platinum films were used as markers, the specimens before oxidizing were covered with a layer of ammonium chloroplatinate which instantaneously decomposes in the temperature of reaction, forming on the surface of the specimen an ideally dispersed platinum layer. After the reaction, the specimens were cut vertically to the wire axis, the cross sections polished and microphotographed. In the case of marking with submicroscopic platinum layers, their position in the scale was determined by spectral analysis. It was found that the position of the markers does not depend on the type of marker and on the temperature. After reaction, the marker is always situated in the middle part of the scale layer on the interface between two microscopically discernible scale layers with different structure. This position of the marker in the scale indicates that the growth of scale is a result of two simultaneous and opposite processes consisting in diffusion of both reagents: nickel and oxygen through the scale. Therefrom it results that the external layer grows owing to the outward diffusion of nickel ions and the inner one owing to the inward diffusion of oxygen. (As it was stated, the plastic flow of the scale must not be taken into account in this case.) Quantitative calculations have proved that the share of the inward diffusion of oxygen in the process of scale formation amounts to 50%. If the scale should grow owing to the outward diffusion of metal only (according to the proposition of Gulbransen and Moore) the marker would be found at the interface scale/metal.

Thus, good conformity between the activation energies of diffusion and of oxidation is not, in our opinion, a sufficient condition for drawing conclusions about the mechanism of the oxidation process of a given metal. The investigations carried out by aid of markers are very necessary since they allow one to state directly the extent of diffusion of the metal and of the oxidizing agent during the process of scale formation. The marker method makes it possible to check the correctness of the supposed oxidation mechanism which was proposed on the base of the results of indirect investigations (type of ion defect of the oxide forming the scale, parabolic course of the oxidation process, etc.)

**E. A. Gulbransen and K. F. Andrew:** We are very pleased to have the interesting comments of Drs. Mrowec and Werber. The role of marker experiments in oxidation processes on metals needs a thorough examination for each metal. In particular, one needs to know the thickness range over which the parabolic rate law can be applied before "breakaway" conditions occur. Many workers apply marker tests for oxidation thicknesses far past "breakaway" where submicroscopic cracking and other types of failure occur in the scale. One must realize also that oxidation is not the formation of a uniform structureless film covering the metal surface.

Let us consider the application of markers to the oxidation of nickel as presented by Drs. Mrowec and Werber. The platinum wires used ranged in size from $7 \times 10^{-3}$ to $1.0 \times 10^{-2}$ cm while the platinum film was of undetermined thickness. A $10^{-3}$ cm wire is $10^5$ Å in diameter. To make experiments using a wire of such size one must oxidize the metal to a scale thickness of $10^6$ to $10^7$ Å. Here the wire thickness would be 1/10 to 1/100 of the oxide thickness. In our study on the oxidation of nickel, we found the parabolic rate constants to increase at temperatures above 900°C for film thickness of the order of $2 \times 10^4$ Å. We concluded that submicroscopic cracking occurred in the film at this thickness. Scales of over $7.6 \times 10^4$ Å cracked away from the metal on

[19] Dept. of General Chemistry, School of Mining and Metallurgy, Aleja Mickiewicza 30, Cracov, Poland.
[20] E. A. Gulbransen and K. F. Andrew, *This Journal*, **101**, 128 (1954).
[21] W. J. Moore and M. T. Shim, *J. Chem. Phys.*, **26**, 802 (1957).
[22] L. Czerski and F. Franik, *Arch. Górnictwa i Hutnictwa*, **3**, 43 (1955).
[23] B. Ilschner and H. Pfeiffer, *Naturwissenschaften*, **40**, 605 (1953).
[24] L. Czerski, S. Mrowec, and T. Werber, *Arch. Hutnictwa*, **3**, 25 (1958).

cooling. If submicroscopic cracks develop, oxygen penetrates to the new reacting interface.

If oxidation consists in a diffusion-controlled mechanism operating below $2 \times 10^4$ Å followed by cracking and re-oxidation, it would be impossible to study the initial reaction mechanism using wires $10^5$ Å in diameter. When cracking occurs on extended oxidation, one would expect to find the platinum wire in the middle of the oxide scale no matter what the initial mechanism of oxidation.

To use marker experiments to study the initial oxidation mechanism for nickel, the marker must be of the order of $2 \times 10^3$ Å or 1/50 of the size actually used. This would require electron microscope observations to locate the marker.

The use of submicroscopic platinum films together with spectral analyses has much merit if the technique were applied to experiments at 900°C and lower and for film thicknesses of less than $2 \times 10^4$ Å. However, the analytical difficulties in sectioning a film of this thickness have not been solved. If used on thick scales at 1000° and 1200°C, the method suffers from the same criticism as given for the use of wires.

We hope that marker experiments will be tried in the thinner film range of oxidation. With present techniques, we feel the macroscopic experiments may give a false idea as to the initial mechanism of oxidation.

## The Equilibrium between Titanium Metal, $TiCl_2$, and $TiCl_3$ in NaCl-KCl Melts

W. C. Kreye and H. H. Kellogg (pp. 504-508, Vol. 104)

**Kai Grjotheim**[25]: The mentioned paper is a welcome contribution to those engaged in a study of equilibria involving a metal and two of its salts of different valency, thus leading to the possibility of complex formation by the higher valent ion in salt melts. However, it may be of interest to comment on some of the statements made by the authors. Their calculation of the equilibrium constant for the reaction:

$$TiCl_3(\text{solution}) + 1/2\ Ti^\circ(\text{solid}) = 3/2\ TiCl_2(\text{solution}) \qquad (I)$$

on a molecular basis, by putting:

$$K_x = N^{3/2}_{TiCl_2}/N_{TiCl_3}$$

where $N_i$ = mole fraction of $(i)$ based on the constituents:

$TiCl_2$, $TiCl_3$, NaCl, and KCl

gives an "equilibrium constant" which varies with the total concentration of titanium dissolved in the melt.

Assuming ideal ionic melts, an equilibrium constant, $K$, for each of the reactions:

$$Ti^{3+} + 1/2\ Ti^\circ = 3/2\ Ti^{2+} \qquad (II)$$

$$TiCl_4^- + 1/2\ Ti^\circ = 3/2\ Ti^{2+} + 4\ Cl^- \qquad (III)$$

$$TiCl_6^{3-} + 1/2\ Ti^\circ = 3/2\ Ti^{2+} + 6\ Cl^- \qquad (IV)$$

[25] Dept. of Metallurgy, University of Toronto, Toronto, Ont., Canada.

was also calculated by Kreye and Kellogg, but the values so obtained, however, still showed the same trend with concentration displayed by $K_x$. [It may here be remarked that, using molar ionic-fractions, the constant for reaction (II) is numerically identical with $K_x$ and, with the small concentrations of titanium in the melts, the constants of reactions (III) and (IV) have almost the same numerical value as for reaction (I).]

Mellgren and Opie[26] have measured the same equilibrium between $TiCl_2$, $TiCl_3$, and Ti° in the presence of $SrCl_2$-NaCl melts. Their results indicate that there might be a slight tendency for the "equilibrium constant" to increase with increasing total titanium content in the melt. Mellgren and Opie also measured the effect of varying the NaCl to $SrCl_2$ ratio, keeping the total amount of dissolved titanium fairly constant. The equilibrium was then markedly effected in a way corresponding to a decreasing $K_x$ with increasing NaCl content in the melt.

The obvious conclusion from both these investigations must be that the solutions are not ideal when considered as simple molecular mixtures. By assuming different types of complex-molecule formation of the titanium chlorides, the authors find that relatively constant $K$ values may be obtained.

However, it seems to be rather well established by now that molten salts may be considered as completely ionized.[27-29] The "best" ideal behavior would therefore be expected by treating the solutions as ionic mixtures. When applying the ionic point of view to these solutions, however, it must be remembered that the ionic reactions (II), (III), and (IV) are taking place in a mixed ionic milieu. The ideal ionic equilibrium constant for these reactions must therefore theoretically be expected to vary with the composition of the melts.

A qualitative explanation of the variation of this "constant" may be given in the following way. When a given reaction takes place with each component in its standard state, the change in the Gibbs function is the standard change, $\Delta G^\circ$. Between the thermodynamic equilibrium constant $K$ (expressed in terms of activities of the components at equilibrium) and the standard change in Gibbs' function, one has the well-known important relationship $\Delta G^\circ = -RT \ln K$. The standard states used in equilibria involving molten salts are most conveniently selected as the pure molten salts at the given temperature. Reaction between standard states can then occur only between *neutral molecules*.

For reaction (I), therefore, the deviation from constancy of the ideal equilibrium constant calculated with use of mole fractions obviously shows that the solution is not an ideal molecular mixture.

Looking on the ionic reactions, however, the reaction between neutral molecules may be formulated in different ways for varying concentrations in the mixtures used by Kreye and Kellogg.

For the ionic reaction (III), we may assume that

[26] S. Mellgren and W. Opie, *J. Metals*, 9, 266 (1957).
[27] P. Herasymenko, *Trans. Faraday Soc.*, 34, 1245 (1938).
[28] M. Temkin, *Acta Physicochim. U.R.S.S.*, 20, 411 (1945).
[29] H. Flood, T. Förland, and K. Grjotheim, "The Physical Chemistry of Melts," p. 46, Institution of Mining and Metallurgy, London (1953).

the following reactions between neutral molecules are taking place:

$$NaTiCl_4 + 1/2\ \underline{Ti} = 3/2\ TiCl_2 + NaCl \quad (IIIa)$$

with $\Delta G^\circ_{Na}$, and

$$KTiCl_4 + 1/2\ \underline{Ti} = 3/2\ TiCl_2 + KCl \quad (IIIb)$$

with $\Delta G^\circ_K$, and

$$1/2\ Ti^{II}(Ti^{III}Cl_4)_2 + 1/2\ \underline{Ti} = 2\ TiCl_2 \quad (IIIc)$$

with $\Delta G^\circ_{Ti}$.

If either $\Delta G^\circ_{Na} \neq \Delta G^\circ_K$

or/and $\Delta G^\circ_{Na} \neq \Delta G^\circ_{Ti}$, two or all three of the thermodynamic equilibrium constants $K_{Na}$, $K_K$ and $K_{Ti}$ must differ for these reactions.

However, if ideal ionic solutions are assumed, the salt activities can be replaced by Temkins' activity terms for ideal ionic mixtures, as for example

$$a^{ideal}_{TiCl_2} = N_{Ti^{2+}} \cdot N^2_{Cl^-} ,$$

where the $N$'s are the molar ionic-fractions.[28] Then

$$K = K^{ideal}_{mix}$$

for all three reactions (III, *a*, *b*, and *c*), as well as for a reaction in a mixture involving all of them, will have the same form:

$$K^{ideal}_{mix} = \frac{N^{3/2}_{Ti^{2+}} \cdot N^4_{Cl^-}}{N_{TiCl_4^-}}$$

since the cationic fractions ($N_{Na^+}$, $N_{K^+}$ and partly $N_{Ti^{2+}}$) of the "inactive" cations cancel out. Thus in a mixed melt containing both $Na^+$, $K^+$, and $Ti^{2+}$ cations, $K^{ideal}_{mix}$ must be expected to vary with the concentrations of the cations. This is obvious due to the variation in the standard states accompanying concentration changes. A complete thermodynamic derivation of the relationship between $K^{ideal}_{mix}$ and the composition of the mixture is to be published elsewhere.[30]

## Potential-pH Diagram of the Antimony-Water System; Its Applications to Properties of the Metal, Its Compounds, Its Corrosion, and Antimony Electrodes

A. L. Pitman, Marcel Pourbaix, and Nina de Zoubov
(pp. 594-600, Vol. 104)

**A. L. Pitman, M. Pourbaix, and N. de Zoubov:** It has been found that errors appear in the reference to the paper of Piontelli and Fagnani (22) on p. 598, column 2, paragraph 4, lines 4-12. This material is hereby deleted from our paper; i.e., "It was concluded that metallic Sb displaces Fe in the stronger solutions and this action is in accordance with predictions which may be made from the thermodynamic emf of the process, a statement which is readily verified. They pointed out that because the overvoltage of hydrogen is higher on Sb than on Fe, corrosion is lessened as the deposited Sb film spreads."

Substitute in its place: "It was concluded that metallic iron displaces antimony from these solutions. This action is in accordance with predictions which may be made from a comparison between the equilibrium diagram for antimony (Fig. 4) and the equilibrium diagram for iron [*see loc. cit.* (1), p. 89, Fig. 20b.] Piontelli and Fagnani pointed out that the inhibiting influence is decided by the structure of the separated antimony. For a given concentration of dissolved antimony, the inhibiting action only exists in solutions sufficiently concentrated in HCl (for which the separation of Sb occurs in the form of a practically invisible but uniform film); for lower concentrations of HCl, Sb separates as a spongy coating which does not exert a protection action."

[30] K. Grjotheim and J. M. Toguri, To be published.

## Optical Measurement of Film Growth on Silicon and Germanium Surfaces in Room Air

R. J. Archer, (pp. 619-622, Vol. 104)

**Arthur B. Winterbottom**[31]: This application of the polarimetric technique to the study of films on Si and Ge was of special interest to the discussor as the possibilities of just this kind of study had been raised some time ago by Dr. J. O'M. Bockris.[32] It was then felt that for a profitable application it would be desirable to use single crystal surfaces, as, although both base and film might be optically isotropic, the film-forming reaction might be dependent on orientation. Further, it was considered that it should be possible to compute reflection parameters $\bar{\Delta}$ and $\bar{\Psi}$ for film-free Ge surfaces from the optical constants determined by O'Bryan[33] for vacuum-evaporated coatings. From such computed parameters, together with determinations made on surfaces with growing films, it was felt that interpretation of observations in terms of optical constants and thickness of film should be feasible on the lines expounded in the discussor's papers.[34] It is therefore somewhat puzzling to note that the author's tentative values for the optical constants of Ge, apparently, based on determinations with an immersion technique, differ considerably from O'Bryan's determinations on evaporated Ge surfaces in vacuum, viz., $N = 3.47$ and $K = 0.40$. An immersion technique involving measurement on evaporated mirrors through the quartz support was used by the discussor in the case of aluminum,[34] when it gave results in fair agreement with front surface determinations in vacuo by O'Bryan and also by Hass. As the author points out, errors in optical constants of base will have a relatively minor effect on the interpretation of relative changes in $\Delta$ in terms of film thickness, but the effect on estimates of total thickness might be considerable. This all points to the necessity of

[31] Dept. of Metallurgy, Norways Institute of Technology, Trondheim, Norway.
[32] Private communication, J. O'M. Bockris, Dec. 1956.
[33] H. M. O'Bryan, *J. Opt. Soc. Am.*, 26, 122 (1936).
[34] A. B. Winterbottom, *Kgl. Norske Videnskab. Selskabs, Skrifter*, No. 1 (1954).

reliable estimates of constants for film-free surfaces. An alternative to the immersion technique with film-covered surfaces and determinations on evaporated mirrors in vacuo might be to make measurements on clean single-crystal surfaces (of the orientation exposed by etching) while immersed in deaerated hydrofluoric acid in a plastic cell with Perspex windows. In the case of Ge it is also possible that film-free surfaces might be obtained by suitable vacuum treatments.

With regard to the curious effect of rinses in organic liquids, it seems significant that the immediate effect of the rinses gradually disappears with almost complete recovery to the original trend of the optical data. This seems rather suggestive of a gradual loss of loosely bound solvent from a swollen film.

**R. J. Archer:** There is in press[35] a paper by the writer which reports measurements of the optical constants of single-crystal Ge by the ellipsometric technique throughout the wave-length range of the visible. The paper compares these results with the five previous measurements in the literature, including O'Bryan's. It is concluded that O'Bryan's values represent least accurately the optical constants of single-crystal Ge. This fact is attributed to a difference between the optical properties of his evaporated films and bulk Ge.

The suggestion that reflection from Ge immersed in hydrofluoric acid would yield $\bar{\Delta}$ and $\bar{\Psi}$ is an interesting possibility but there is some evidence that an insoluble film, possibly a suboxide, forms under these conditions. The other suggestion that $\bar{\Delta}$ and $\bar{\Psi}$ could be measured on atomically clean surfaces in high vacua is a current experimental project of the writer. One problem associated with such measurements is the surface irregularities that result from the severe cleaning techniques in current use (e.g., ion bombardment). Such irregularities with dimensions small compared to the wave length of the reflected light constitute a surface film and effect a perturbation in $\bar{\Delta}$ and $\bar{\Psi}$. Further, the problem of strain double refraction in windows is a source of error when closed cells are used. Although problems of the nature mentioned here are not insurmountable, they make the direct measurement of $\bar{\Delta}$ and $\bar{\Psi}$ a difficult experimental undertaking.

## Stoichiometric Numbers and Hydrogen Overpotential

A. C. Makrides (pp. 677-681, Vol. 104)

**Roger Parsons**[36]**:** It is useful to have a derivation of the stoichiometric number ($\nu$) from the general concept of the proportionality of the rate to the affinity of the reaction. The difference between this and previous procedures[37,38] is perhaps more apparent than real, for, in the latter, the extrapolation from states far removed from equilibrium is necessary only in practical determinations of exchange current from current-voltage curves, not in the theoretical derivation of the relation equivalent to (VII) in the discussed paper.

Separation of the total work of transfer across an interface into "electrical" and "chemical" terms is possible in terms of a model[39] and causes no difficulty, provided that these quantities are used merely as an aid in the derivation of equations relating measurable quantities. This was the procedure used in the earlier paper.[38]

It is satisfying that the conclusions reached for hydrogen overpotential in the present paper confirm those of the previous paper.[38] The only exception is that of the dual mechanism 4($b$). [Dual mechanisms were specifically excluded in footnote 38 and their significance was discussed elsewhere.[40]] Here an unjustified approximation appears to have been made: that the exchange velocity $V^e$ of the over-all reaction is equal to that of each partial reaction ($V^e_{\text{i}}$ and $V^e_{\text{iii}}$) when these are equal. In fact, in this very special case $V^e = V^e_{\text{i}}/2 = V^e_{\text{iii}}/2$. In general, the three equations at the bottom of the first column of p. 681 of the discussed paper can be solved to obtain

$$V = \frac{V^e_{\text{i}}\, V^e_{\text{iii}}}{V^e_{\text{i}} + V^e_{\text{iii}}} \cdot \frac{A}{RT} \qquad \text{(I)}$$

Now the quotient $V^e_{\text{i}}\, V^e_{\text{iii}}/(V^e_{\text{i}} + V^e_{\text{iii}})$ is the general expression for $V^e$ for this reaction scheme[41] (compare the expression for the conductance of two conductances in series). Thus, comparison of Eq. (I) here with the general Eq. (VI) in the discussed paper shows that $\nu$ is unity for reaction scheme 4($b$) whatever the relative values of $V^e_{\text{i}}$ and $V^e_{\text{iii}}$.

If consideration is restricted to the three partial reactions: (i) discharge, (ii) combination, and (iii) ion + atom, then nonintegral stoichiometric numbers would be obtained under equilibrium conditions when two types of dual mechanisms occur: $V^e_{\text{i}} \cong V^e_{\text{ii}} >> V^e_{\text{iii}}$ and $V^e_{\text{i}} >> V^e_{\text{ii}} \cong V^e_{\text{iii}}$. In each $1 < \nu < 2$. Neither is considered in the present paper. The fact that chain and photochemical reactions have fractional values of $\nu$ has already been recorded.[42]

**A. C. Makrides:** The differences between the present approach and Dr. Parsons' derivation have been noted in the paper. Briefly, our development (i) is not based on any particular reaction rate model, (ii) avoids use of quantities $\Delta\phi$, $p$, and $q$, and (iii) is applicable to competing reaction mechanisms.

(i) Dr. Parsons employed transition state theory in setting up the basic equation for the reaction rate. The two treatments are, of course, equivalent for states neighboring equilibrium since absolute reaction rate theory expressions reduce to linear relations in this region.

(ii) The difficulties encountered with $\Delta\phi$, $p$, and $q$ are exemplified by Dr. Parsons' decomposition of the dependence of $p$ and $q$ on $\Delta\phi$ and solution composition (p. 1336 of work cited in footnote 38).

[35] R. J. Archer, *Phys. Rev.*, In press.
[36] Dept. of Physical and Inorganic Chemistry, The University, Bristol 8, England.
[37] J. Horiuti, *J. Research Inst. Catalysis, Hokkaido Univ.*, I, 8 (1948).
[38] R. Parsons, *Trans. Faraday Soc.*, **47**, 1332 (1951).
[39] R. Parsons, Chap. III, "Modern Aspects of Electrochemistry," J. O'M. Bockris, Ed., Academic Press Inc., New York (1954).
[40] R. Parsons, *J. chim. phys.*, **49**, 82 (1952).
[41] *See*, for example, J. A. Christiansen, *Z. physik. Chem.*, **28B**, 303 (1935).
[42] J. Horiuti, *Proc. Japan Acad.*, **29**, 160 (1953).

(iii) Dr. Parsons has examined the kinetics of "dual" mechanisms in the reference he cites. However, stoichiometric numbers for such mechanisms were not discussed. In general, it is difficult to see how Dr. Parsons' development could be modified for application to competing reaction mechanisms.

The observation in the paper that stoichiometric numbers may be smaller than unity was thought necessary in view of Dr. Parsons' definition, ". . . $\nu$ is an integer equal to or greater than unity" (p. 1333 of work cited in footnote 38).

Dr. Parsons' remarks on mechanism 4(*b*) are appreciated. It was assumed in the paper that the exchange velocity of the over-all reaction is equal to the exchange velocities of each partial reaction where these are equal. As Dr. Parsons notes, this is incorrect. The expression given by Dr. Parsons leads to $\nu = 1$ independently of the relative magnitude of $v^e_i$ and $v^e_{ii}$. The remarks in the last paragraph of the paper should be modified by deleting reference to mechanism 4(*b*).

We thank Dr. Parsons for his interest and particularly for his remarks on mechanism 4(*b*).

## The Influence of Surface Pretreatment on the Atmospheric Oxidation of 2S (U. S. Alloy 1100) Aluminum

P. M. Aziz and H. P. Godard (pp. 738-739, Vol. 104)

**R. C. Plumb**[43]: The studies made by Drs. Aziz and Godard are of great interest to us since we have been concerned for several years with the specific surface area or roughness factor of aluminum. In 1956[44] we described a technique for measuring the specific surface area of aluminum. Measurements were made on samples which had a variety of surface preparations, including some similar to those used by Aziz. It was found that surface areas on specimens abraded with coarse alumina or silicon carbide powders range from 2 or 3 up to as high as 20.

In a second paper which has been transmitted to Dr. Aziz in preprint form,[45] the results of a further investigation of the surface area of aluminum are described. In that work, coulometric measurements were made when barrier layer anodic oxide coatings were applied to a variety of aluminum surfaces and the apparent surface area as a function of the oxide thickness (resolution) was determined. The application of a thick barrier layer oxide on a rough surface serves to smooth the protuberances. Roughness factors measured independently on identical samples by the radiochemical technique[44] and the anodic oxidation technique[45] agreed quantitatively on samples having roughness factors as high as 20.

Aziz and Godard stated that it is hard to conceive of the geometry of a surface with a roughness factor higher than 2 or 3. A simple model for such a surface is one in which smaller asperities are built on top of large asperities. For example: One set of asperities 1000Å in size might give a specific surface area of 3. If another set of asperities 100Å in size is built upon the larger asperities, it will give a specific surface area of 9. If another set of asperities 10Å in size is added, the roughness factor will be 27.

I believe that the differences in weight gain of samples which have had different surface treatments as described by Aziz and Godard can be explained completely in terms of the specific surface area.

It is very gratifying to find that Aziz and Godard did, in fact, observe differences in weight gain which would be anticipated from our work.

**P. M. Aziz and H. P. Godard:** The authors agree with Dr. Plumb that there is no conceptual problem in visualizing a surface with roughness factors as high as 20-30, although we do have some difficulty in understanding how an abrasion process can produce a topography such as that presented by him. Nor do we feel that the research presented in the reference cited clarifies the problem, for the following reasons.

(*A*) In footnote 44, roughness factors as high as 19.9 were measured by a radiochemical method on aluminum surfaces abraded with 3/0 emery paper. Imbedded abrasive will certainly influence the results, as the authors state.

They feel that since no seizing or staining of the surface was noted during the abrasion process the surfaces were free of imbedded abrasive. It has been our experience that even under these conditions abrasive will be imbedded in the surface although a light metallographic polish is necessary before its presence can be detected; in fact, this was the case in our work.

(*B*) In footnote 45 roughness factors somewhat over 20 were measured by an anodizing technique. Young[46] has pointed out that the anodization of a rough surface will lead to the smoothing of the asperities, and thus the inner surface of the oxide over these asperities will be constrained to cover progressively decreasing areas, introducing local compressive stresses which can produce local failure of the film. This phenomenon will lead to high values of the roughness factor when measured by the anodizing technique, especially on surfaces containing asperities small enough to result in large roughness factors.

In view of this we feel that, while high values of the roughness are by no means excluded, their existence has not been conclusively demonstrated, and consider that contamination by abrasive particles can influence the behavior of the surface.

[43] Alcoa Research Labs., Aluminum Co. of America, New Kensington, Pa.

[44] J. E. Lewis and R. C. Plumb, *Intern. J. Appl. Radiation and Isotopes*, 1, 33 (1956).

[45] R. C. Plumb, "The Specific Surface Area of Aluminum as Determined with Continuously Variable Resolution from 20Å to 1000Å," *This Journal*, In review.

[46] L. Young, *Acta Met.*, 5, 711 (1957).

# Electrochemical Properties of $PbO_2$ and the Anodic Corrosion of Lead and Lead Alloys

**Paul Rüetschi and Boris D. Cahan**

*The Electric Storage Battery Company, Philadelphia, Pennsylvania*

ABSTRACT

The total amount of anodic corrosion of Pb and Pb-Sb alloys in sulfuric acid under conditions of $O_2$ evolution can be evaluated by measuring the length of the potential plateau (transition time) during the electrochemical reduction of the $PbO_2$ layers, with a constant current, taking into account self-discharge and degree of utilization of the $PbO_2$. Using high resolution techniques, a characteristic step in the potential plateau during discharge of the $PbO_2$ layer was discovered. This step can be attributed to a difference in discharge overvoltage between $\alpha$- and $\beta$-$PbO_2$. For alloys of the Pb-Sb system, constant current corrosion increases slightly with increasing Sb concentration, whereas oxygen overvoltage decreases and constant potential corrosion strongly increases with increasing Sb concentration.

Precise electrode potential measurements of the $\alpha$-$PbO_2/PbSO_4$ and the $\beta$-$PbO_2/PbSO_4$ couple gave $1.7085 \pm 0.0005$ v and $1.7015 \pm 0.0005$ v, respectively, vs. $H_2$ in 4.40*M* sulfuric acid at 31.8°C. These two oxides have different oxygen overvoltage characteristics.

Removal of oxygen from $\beta$-$PbO_2$ results in a new crystalline compound $PbO_x$ with $x$ 1.4 to 1.6, with a pseudo-face-centered cubic orthorhombic lattice. This new compound is a nonconductor. The influence of the oxygen content of the lead oxides on their electrochemical behavior is discussed.

A constant current technique has been used recently to study anodic corrosion of lead and lead alloys in $H_2SO_4$ (1). It involves evaluating the amount of $PbO_2$ formed during anodization by measuring the transition time for the discharge of the $PbO_2$ layer. Very small amounts of corrosion products can be determined accurately this way, therefore, and the corrosion resistance of an alloy can be evaluated in a relatively short time. The major corrosion product produced on lead and lead alloy anodes under conditions of oxygen evolution is $\alpha$-$PbO_2$, a new crystalline modification of lead dioxide. This new compound has been found independently in several laboratories (1-6).

The electrochemical properties of the corrosion layers depend on the relative amounts of the two lead dioxide modifications and on their oxygen content. The present paper is a study of the electrochemical properties of the corrosion layers and of their oxygen content.

It is well known that $PbO_2$ never has the stoichiometric composition but always shows an oxygen deficiency. Palmaer (7) measured the electric properties of tetragonal ($\beta$)-$PbO_2$ obtained by electrodeposition and found a resistivity of $(0.95 \pm 0.03) \cdot 10^{-4}$ ohm cm, with a positive temperature coefficient of 0.06%/degree in the range of 22°-84°C. The chemical analysis indicated that these samples had a composition $PbO_{1.99}$. The analytical results here, however, always show a lower oxygen content for both $\beta$- and $\alpha$-$PbO_2$, namely $PbO_{1.94}$ to $PbO_{1.96}$.

Thomas (8) has reported values of the resistivity of tetragonal $\beta$-$PbO_2$ produced electrolytically in a hard and dense form. He found a value of $0.94 \cdot 10^{-4}$ to $4.05 \cdot 10^{-4}$ ohm cm, with a temperature coefficient of 0.07%/degree of the room temperature value in the range −190° to −90°C. According to Thomas, the Hall coefficient is $-3.7 \cdot 10^{-2}$ to $-1.7 \cdot 10^{-2}$ cm³/coulomb. The negative sign of the Hall coefficient indicates that the carriers are electrons. The high concentration of free electrons in $PbO_2$ arises from the departure from the stoichiometric composition in the direction of oxygen deficiencies, although it is not firmly established whether $PbO_2$ is a metal excess or an anion defect type of conductor.

It has been reported that oxygen can be removed by thermal decomposition *in vacuo* to $PbO_{1.66}$ (9) or to $PbO_{1.9}$ (10) without phase change. If these results are correct, it should be possible to make $PbO_2$ even more conducting by heating *in vacuo*. Kittel, however, has shown (11) that the conductivity decreases as oxygen is removed by thermal decomposition. At the same time the Hall coefficient increases, indicating a decrease in the "free electron concentration." Kittel's data are summarized in Table I.

These results indicate the formation of a new insulating lattice as oxygen is removed. The fact that a phase change occurs has been described by several authors (11-16), although their interpretations are not at all in agreement.

According to Kittel the mean electric resistance of $PbO_2$ is $1.18 \cdot 10^{-4}$ ohm cm and the temperature coefficient in the range between −180° and 20°C is about 0.07%/degree. The mean value for the Hall coefficient is $-7.8 \cdot 10^{-3}$ cm³/amp sec. Oxygen over-

Table I. Conductivity and Hall coefficient of lead dioxide as a function of amount oxygen removed (in per cent of the initial oxygen content), Kittel's data

| Oxygen removed in % of initial amount of oxygen present | Sample No. | Conductivity ohm$^{-1}$ cm$^{-1}$ | Hall coefficient cm$^3$/amp sec |
|---|---|---|---|
| 0 | 1 | $0.74 \cdot 10^4$ | $-7.8 \cdot 10^{-3}$ |
| | 2 | 0.89 | −8.6 |
| | 3 | 0.74 | −8.5 |
| | 4 | 1.01 | −7.7 |
| | 5 | 0.82 | −8.0 |
| 0.4 | 4 | $0.13 \cdot 10^4$ | $-13.5 \cdot 10^{-3}$ |
| | 5 | 0.24 | −14.4 |
| 2.4 | 1 | $0.34 \cdot 10^4$ | $-10.7 \cdot 10^{-3}$ |
| | 2 | 0.26 | −11.3 |
| | 3 | 0.16 | −12.4 |
| 3 | 4 | $0.10 \cdot 10^4$ | $-15.7 \cdot 10^{-3}$ |
| | 5 | 0.22 | −13.2 |
| 4.4 | 2 | $0.22 \cdot 10^4$ | $-11.6 \cdot 10^{-3}$ |
| | 3 | 0.12 | −13.7 |
| 6.3 | 1 | $0.24 \cdot 10^4$ | $-13.5 \cdot 10^{-3}$ |
| 8.0 | 2 | $0.16 \cdot 10^4$ | $-13.1 \cdot 10^{-3}$ |
| | 3 | $0.10 \cdot 10^4$ | $-14.5 \cdot 10^{-3}$ |
| 13 | 3 | $0.04 \cdot 10^4$ | $-20.2 \cdot 10^{-3}$ |

voltage and anodic corrosion are related to the oxygen content of the $PbO_2$ layers during anodization, as shown below.

## Experimental

The electrolytic cell, the electric circuit, and the sample preparation for anodization and polarization studies have been described (1). Anodic corrosion was evaluated by recording the potential of $PbO_2$ layers formed at 3 ma/cm$^2$ for 20 hr at 30°C in $H_2SO_4$, sp gr 1.225 (at 20°C) during discharge with constant current, using a Minneapolis-Honeywell ½ second recorder, Model Y 153X(19)V-X-156, operated in conjunction with a General Radio Voltmeter amplifier type 1230-A. Potentials were measured against a $H_2$ electrode in the same electrolyte at the same temperature. Alloy samples for the corrosion experiments were cast, applying identical casting conditions for all the alloys, namely, a metal temperature of 900°F and a mold temperature of 400°F. It is known that grain size is an important factor in anodic corrosion of lead alloys (17).

An RCA electron microscope, type EMU-3, was used to study the surface structure of the corrosion layers. Portions of the corrosion products were stripped by imbedding in low molecular weight polystyrene. These samples were lightly covered with an evaporated carbon film to hold the crystals together. The polystyrene was dissolved with toluene and samples of corrosion products of approximately 1 mm$^2$ area were collected on copper screens for investigation under the electron microscope.

A series of batteries containing some grid alloys of Table II were built and SAE overcharge life tests were run.[1]

Baker C.P. tetragonal ($\beta$-)$PbO_2$ was used for the thermal decomposition experiments. Samples of about 2 g were heated in 7 mm Pyrex tubing in an electric tube furnace. Temperatures were controlled to ±2°C using a Sola CVH-500VA constant voltage transformer and a Variac, and measured with an iron-constant an thermocouple. Samples were heated for 3 hr at 1 mm or at 3 atm of oxygen pressure, and then removed from the furnace and air cooled. No change in the oxygen content of any sample was observed after cooling and storage in a dry atmosphere.

Samples were chemically analyzed for active oxygen by thiosulfate titration of the iodine liberated from a KI solution in sodium acetate (18). Evaporation of the liberated iodine was prevented by continuous addition of thiosulfate as the iodine was liberated by the reaction. The results of the analysis were reproducible to ±0.3%.

Small samples of the prepared oxides were mounted in collodion on a glass slide and x-rayed with a GE-XRD-3 Geiger diffractometer.

For electrode potential measurements, samples were pressed into a strip of perforated lead sheet, with a pressure of 80,000 lb/in.$^2$ using a Carver Laboratory Press. The holes in the lead strip were spaced 1.5 mm and had a diameter of 1.2 mm. The prepared and immersed part of the strip was about 1 cm$^2$. The electrode potentials were measured in $H_2SO_4$, sp gr 1.225 (at 20°C), prepared from C.P. $H_2SO_4$ and triple distilled water. The potentials were measured with a Rubicon Type B high precision potentiometer, against a hydrogen electrode in the described electrolyte.

Electrode potentials of pure orthorhombic ($\alpha$)$PbO_2$ and pure tetragonal ($\beta$)$PbO_2$ were measured by the same technique. $\alpha$-$PbO_2$ was prepared by electrolysis on a Pt screen of a concentrated solution of KOH, saturated with $Pb(OH)_2$ at a current density of 1 ma/cm$^2$. The adhering film sample was ground, washed with hot ammonium acetate solution and with conductivity water. Baker C.P. tetragonal ($\beta$)$PbO_2$ was used for the electrode potential measurements of $\beta$-$PbO_2$.

Electrode potentials of electrodeposited layers of $\alpha$- and $\beta$-$PbO_2$ were also measured. The layers were electrodeposited on a Pt wire, which was rigidly mounted between the ends of a U-shaped glass rod to prevent vibration and cracking of the $PbO_2$ film. The wire had a diameter of 0.6 mm; the length exposed to the electrolyte was 2.5 cm.

The $\alpha$-$PbO_2$ layer was electrodeposited in a two compartment cell at 50°C, at 1 ma/cm$^2$ for 20 hr. After this time period the layer had reached a thickness of about 0.1 mm. $\beta$-$PbO_2$ layers were deposited at the same current for the same time period but at 30°C. Electrode potentials were measured after washing the electrodes and immersing them in 4.40M acid.

$\beta$-$PbO_2$ was prepared by electrodeposition from 30% perchloric acid saturated with litharge, according to the procedure described by Thomas (8). The electrolytic bath for deposition of $\alpha$-$PbO_2$ was prepared by adding 50 cc of water, 50 cc of saturated sodium acetate solution, and 10 cc of saturated lead acetate solution to 100 cc of carbonate-free, saturated KOH solution.

[1] In this SAE test, a 100 amp-hr, 6 v automotive battery is overcharged at 100°F at a rate of 9 amp for a total of 1000 amp-hr each week. At the end of each week, the battery is discharged at 300 amp at 100°F. The battery has reached the end of life when the capacity is less than 0.5 min.

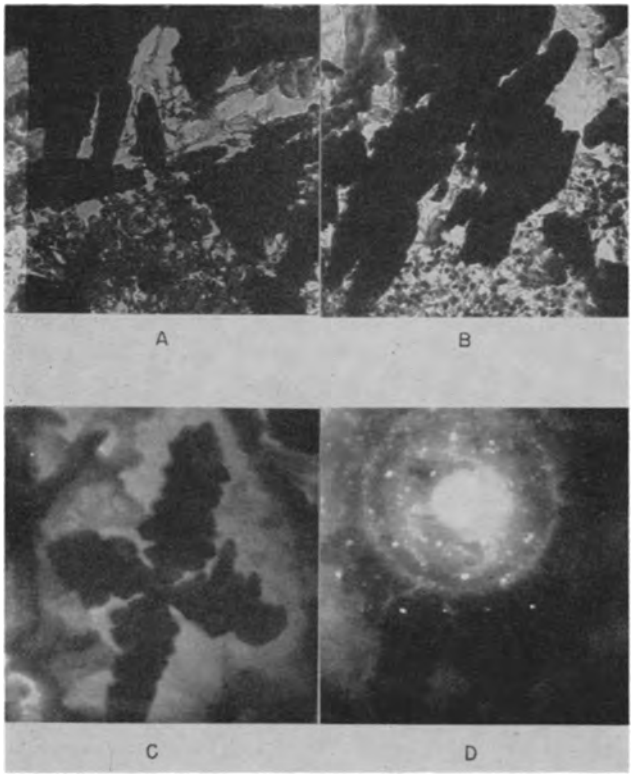


Fig. 1. Electron microscope pictures of an anodized lead surface at 30,000 x magnification.

Oxygen overvoltages were measured on these electrodeposited layers of $\alpha$- and $\beta$-$PbO_2$ in $H_2SO_4$ under very pure conditions.

## Results

The corrosion products formed by anodization of lead and lead alloys were in a fine crystalline state. Figure 1 shows electron microscope pictures of crystals of the corrosion products at 30,000 X magnification. The pictures of Fig. 1 refer to a pure lead sample which had been anodized for 4 hr with 3 ma/cm$^2$ at 30°C in $H_2SO_4$, sp gr 1.225. Single crystal diffraction patterns were obtained by selected area diffraction. Figure 1D shows such a pattern for the remarkable cross-shaped lead sulfate crystal shown in Fig. 1C. The crystal can be recognized in the background of Fig. 1D. With selected area diffraction the material of microscopic crystals can be identified. More work using this technique for studying corrosion products is anticipated.

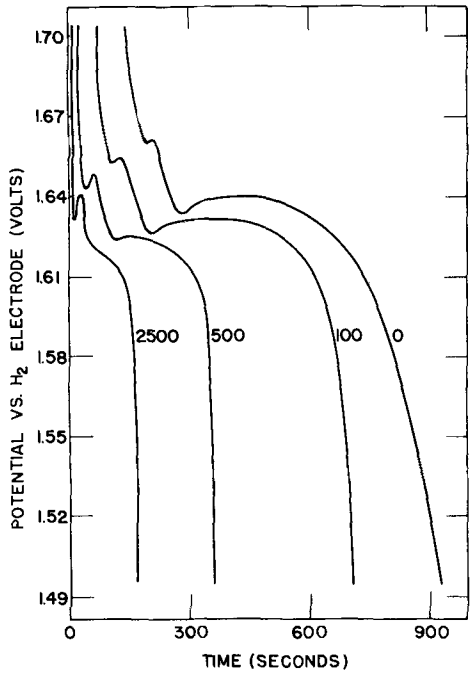


Fig. 2. Electrode potential transients during discharge at 0, 100, 500, and 2500 $\mu$a/cm$^2$ of $PbO_2$ layers formed at 3 ma/cm$^2$ for 20 hr in 53M $H_2SO_4$ at 30°C.

Figure 2 shows the potential transients during discharge with 0, 100, 500, and 2500 $\mu$a/cm$^2$ of $PbO_2$ layers which were produced by anodization for 20 hr at 3 ma/cm$^2$ of a lead alloy containing 11% Sb [alloy #8 in reference (1)]. Due to the high resolution of the potential recording equipment, interesting details of the discharge process are revealed. On interruption of the anodizing current and start of the discharge, the potential drops from the oxygen overvoltage value to a first minimum. This initial minimum has also been observed by other investigators (19). During the time period from start of discharge to the first minimum, the excess oxygen on and in the layer is desorbed. The potential then recovers to a first plateau and drops thereafter to a second plateau, about 30 mv below the first plateau. It is shown later that the two plateaus could possibly correspond to the two modifications of lead dioxide, the tetragonal $\beta$-$PbO_2$ and the orthorhombic $\alpha$-$PbO_2$.

Discharge curves as shown in Fig. 2 were taken and the discharge times (down to a fixed potential of 1.55 v vs. $H_2$) were measured at 0, 100, 500, and 2500 $\mu$a/cm$^2$ discharge current for a large series of lead alloys of the binary system PbSb (alloys No. 1 to 8) and of other lead alloys containing the elements Ca, Sb, Sn, As, and Ag (alloys No. 9 to 14). The chemical analyses of all the alloys are given in Table II.

The technique for evaluating the total amount of corrosion has been described (1). The product $i \times t$, where $i$ is the discharge current and $t$ is the discharge time, increases with decreasing discharge time. Extrapolation to zero discharge time gives the total available capacity since self-discharge is then eliminated (1, 20). The amount of $PbO_2$ left in the layer after discharge was determined by microtitration. This amount of $PbO_2$ increased only very slightly with decreasing discharge time for all of the alloys, and it was easy to extrapolate the values to zero discharge time. Adding the extrapolated values for the available capacity and the amount of $PbO_2$ left in the layer after discharge gave the total amount of corrosion. The total extrapolated capacity (total amount of corrosion) expressed in amp sec/cm$^2$, after anodization at 3 ma/cm$^2$ for 20 hr at 30°C in 1.225 sp gr $H_2SO_4$, is shown for the binary system Pb-Sb (alloys No. 1 to 8) as a function of the Sb-concentration in Fig. 3. Constant current corrosion increases slightly with increasing Sb-concentration for Sb-concentrations above 1%, although the discharge time decreases with increasing Sb-concentration particularly at small discharge currents, as shown in Fig. 4. This decrease in discharge time

**Table II. Analysis of lead alloys used for corrosion studies**

| Alloy No. | Per cent by weight | | | | | | | | |
|---|---|---|---|---|---|---|---|---|---|
| | Sb | As | Sn | Cu | Bi | Ag | Fe | Ni | Ca |
| 1 | 0.0001 | — | 0.0001 | 0.0001 | 0.0005 | 0.0001 | — | 0.0001 | — |
| 2 | 1.08 | — | 0.0001 | 0.003 | 0.05 | 0.0003 | 0.0005 | 0.0003 | — |
| 3 | 2.16 | 0.008 | 0.0001 | 0.003 | 0.01 | 0.0004 | 0.0005 | 0.0003 | — |
| 4 | 3.48 | 0.03 | 0.0001 | 0.003 | 0.018 | 0.0005 | 0.0005 | 0.0003 | — |
| 5 | 5.76 | 0.025 | 0.0002 | 0.01 | 0.015 | 0.004 | 0.0005 | 0.0003 | — |
| 6 | 7.26 | 0.015 | 0.0001 | 0.008 | 0.008 | 0.005 | 0.0005 | 0.0008 | — |
| 7 | 8.76 | 0.015 | 0.0001 | 0.01 | 0.003 | 0.004 | 0.0005 | 0.001 | — |
| 8 | 10.98 | 0.015 | 0.0001 | 0.005 | 0.008 | 0.002 | 0.0005 | 0.001 | — |
| 9 | 0.0001 | — | 0.0001 | 0.0001 | 0.0005 | 0.0001 | — | 0.0001 | 0.0495 |
| 10 | 0.0001 | — | 0.0001 | 0.0001 | 0.0005 | 0.0001 | — | 0.0001 | 0.0785 |
| 11 | 5.70 | 0.48 | 0.22 | 0.003 | 0.020 | 0.009 | 0.0005 | 0.0005 | — |
| 12 | 5.70 | 0.48 | 1.70 | 0.003 | 0.020 | 0.009 | 0.0005 | 0.0005 | — |
| 13 | 5.94 | 0.48 | 0.27 | 0.005 | 0.022 | 0.112 | 0.0005 | 0.0005 | — |
| 14 | 4.14 | 0.48 | 0.26 | 0.005 | 0.022 | 0.116 | 0.0005 | 0.0005 | — |

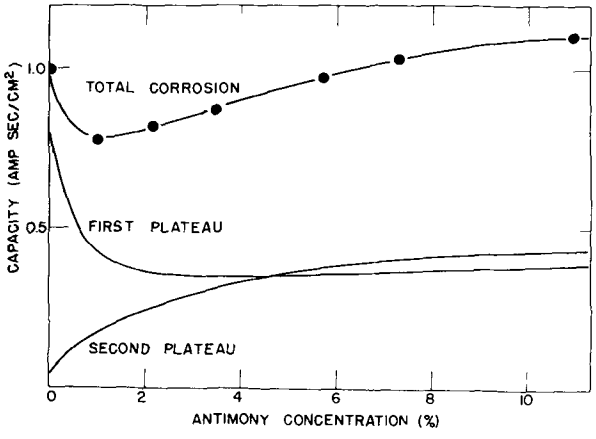


Fig. 3. Constant current corrosion of Pb-Sb alloys as a function of the Sb concentration. The amount of corrosion product is expressed in terms of equivalent capacity in amp sec/cm².

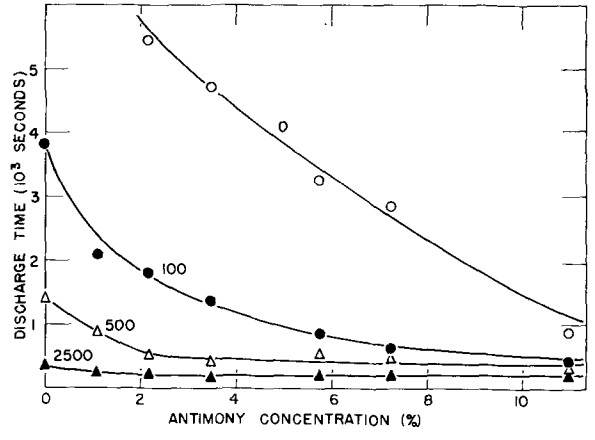


Fig. 4. Total discharge time at discharge currents of 0, 100, 500, 2500 μa/cm² of $PbO_2$ layers formed at 3 ma/cm² for 20 hr in 4.53M $H_2SO_4$ at 30°C.

with increasing Sb-concentration is due to an increased rate of self-discharge with increased Sb-concentration.

It is important to keep in mind that the corrosion values shown in Fig. 3 correspond to constant current conditions. A comparison at constant voltage would show a stronger increase of corrosion with increasing Sb-concentration. This can be shown from the curve of oxygen overvoltage vs. Sb-concentration. The solid circles in Fig. 5 show oxygen overvoltage values at 3 ma/cm² after anodization for 20 hr at 30°C in $H_2SO_4$, sp gr 1.225. The sample containing 11% Sb corroded at a potential which was about 40 mv less positive than the potential of a pure lead sample at the same current density and after the same time period. Since corrosion increases with increasing electrode potential, more corrosion would have been observed for the 11% Sb alloy if it had been maintained at a potential identical to that of the pure lead sample.

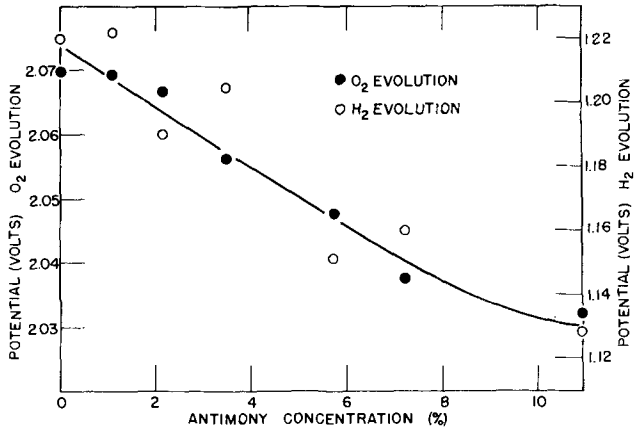


Fig. 5. Hydrogen overvoltage and oxygen overvoltage of Pb-Sb alloys at 3 ma/cm² in 4.53M $H_2SO_4$. Potentials are given vs. $H_2$.

It is interesting to compare the length of the various parts of the potential transient during discharge, as they vary with Sb-concentration and discharge current. The capacity corresponding to the time period from start of discharge to the first minimum is practically independent of the Sb-concentration. The electrode process prevailing during this time period is accompanied by a relatively small self-discharge rate. As will be discussed later, the potential-determining reaction during this period may be the removal of excess oxygen from the surface.

For a given alloy, the electrode process of the first plateau is accompanied by a higher rate of self-discharge than the electrode process corresponding to the second plateau. This is evident from the fact that the capacity during discharge decreases more

strongly with increasing discharge time for the first plateau than for the second plateau. The total available capacity as determined by extrapolation to zero discharge time has been obtained for both plateaus and has been plotted in Fig. 3. The total available capacity from the first plateau decreases with increasing Sb-concentration, whereas the amount of available capacity from the second plateau increases with increasing Sb-concentration. The rate of self-discharge of both plateaus increases with increasing Sb-concentration.

If the two plateaus are due to the presence of two different corrosion products, the product corresponding to the first plateau has a smaller discharge overvoltage (higher exchange current) and a higher rate of self-discharge than the product corresponding to the second plateau. From the fact that oxygen overvoltage and the relative amount of product corresponding to the first plateau decreases with increasing Sb-concentration, one cannot necessarily anticipate that this product has a higher oxygen overvoltage than the product corresponding to the second plateau. Figure 5 shows that hydrogen overvoltage decreases with increasing Sb-concentration. This decrease is due to free Sb metal which has a low hydrogen overvoltage. Polarization was started immediately after immersion of the microtomed metallic surface into the electrolyte in order to prevent adsorption of sulfate ions (1). Tafel slopes and $i_o$ values for oxygen and hydrogen overvoltage on lead and lead alloys were reported earlier (1).

The total amount of corrosion after anodization for 20 hr at 3 ma/cm² as determined by the extrapolation technique is plotted for a series of alloys in Fig. 6. A good correlation exists between the corrosion figures and the overcharge life of batteries containing the various alloys in the positive grids, as determined by the standard SAE overcharge test. Figure 6 demonstrates that the SAE overcharge life test is a fair measure of anodic constant current corrosion.

In order to study the influence of the oxygen concentration in more detail, a large series of lead oxides with varying oxygen content were prepared by

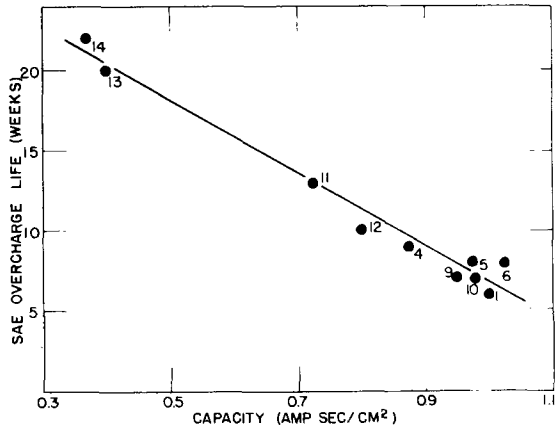


Fig. 6. Corrosion of various lead alloys vs. SAE overcharge life of batteries. The numbers identify various alloys from Table II. The ordinate gives the number of weeks a battery will perform on the SAE overcharge test. The abscissa gives the capacity of the corrosion film built up in 20 hr at 3 ma/cm² at 20°C in 4.53M $H_2SO_4$.

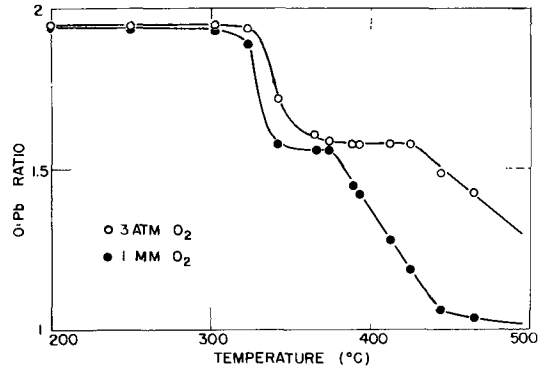


Fig. 7. Thermal decomposition of $\beta$-$PbO_2$. Oxygen content of the decomposition product as a function of temperature. Open circles refer to samples heated under an oxygen pressure of 3 atm; solid circles refer to samples heated at 1 mm oxygen pressure.

thermal decomposition of tetragonal ($\beta$)$PbO_2$. Figure 7 shows the oxygen content of samples which were heated for 3 hr at the indicated temperatures.

The decomposition temperature of $PbO_2$ strongly depends on the oxygen pressure. A first loss of oxygen occurs at about 330°C. A compound with the composition $PbO_{1.57}$ seems to form. This composition corresponds to a compound $Pb_2O_3$, or more accurately to $Pb_7O_{11}$. This composition has also been found by Holtermann and Lafitte (15). At higher temperatures apparently no equilibrium was established and the oxygen content decreased continuously down to $PbO_{1.0}$. Figure 8 shows the relative amounts (%) of the observed compounds in the heated samples as determined by x-ray analysis. Small samples of the prepared oxides were finely ground and mounted in collodion on a glass slide and x-rayed with a GE XRD-3 Geiger diffractometer. The $PbO_2$ patterns had completely disappeared after removal of oxygen down to $PbO_{1.6}$. Instead, a new pattern became apparent. This new pattern corresponds to a crystalline compound with a pseudo-face-centered cubic, orthorhombic lattice. This compound has a composition $PbO_x$ with $x = 1.6$ to 1.4 (Fig. 8). X-ray analysis shows that it undergoes a change in the lattice parameters as the oxygen content in the sample decreases below $PbO_{1.5}$. It appears that this new crystalline compound has a variable oxygen content as indicated by the shift in the lattice constants. Samples with oxygen contents smaller than $PbO_{1.4}$ showed the lines of $Pb_3O_4$ and finally PbO simultaneously with the patterns of $PbO_x$. Figure 8 also shows the colors of the produced oxide samples.

Electrodes were prepared by pressing the oxides in perforated lead foil. Electrode potentials of the prepared samples were measured in 1.225 sp gr $H_2SO_4$ against a hydrogn electrode at 20°C in the same solution. The electrode potentials usually increased over a period of 1-4 hr for several millivolts and dropped then at a slowly increasing rate to less positive potentials. This drop in potential became increasingly faster with decreasing oxygen content in the sample. Figure 8 shows the maximum positive electrode potentials reached by the various samples.

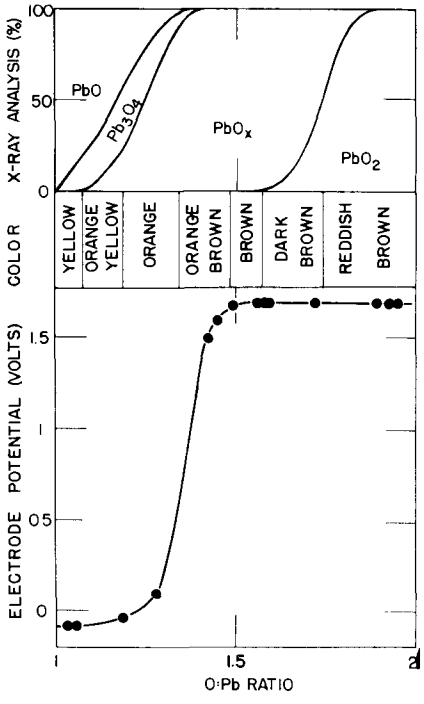


Fig. 8. Electrode potentials, colors, and x-ray analysis data of lead oxide samples with varying oxygen content produced by thermal decomposition of $\beta$-$PbO_2$.

It is interesting to note that a sample with an oxygen content as low as $PbO_{1.5}$, which showed no sign of the presence of $PbO_2$ in the x-ray pattern, still showed a $PbO_2$ potential, although only for a relatively short time. It was also observed that the maximum potential measured on samples with low oxygen content $PbO_{1.4}$ to $PbO_{1.6}$ was 1.698 v vs. $H_2$ or several millivolts higher than the value observed on pressed electrodes with untreated $\beta$-$PbO_2$ (1.692 v vs. No. 2).

In order to explain this phenomenon a sample of $PbO_{1.45}$, obtained by heating $\beta$-$PbO_2$ at 1 mm oxygen pressure at 389°C, was ground in a mortar and was placed in $H_2SO_4$, sp gr 1.225, for a period of 2 days. The sample was then carefully washed with hot and cold concentrated ammonium acetate solution in order to dissolve the lead sulfate. X-ray examination of the sample after this treatment showed that the $PbO_x$ pattern which was originally observed had disappeared completely and had been replaced by a pattern of $\alpha$-$PbO_2$. It can be concluded that the compound $PbO_x$ undergoes a disproportionation in $H_2SO_4$ into $PbSO_4$ and $\alpha$-$PbO_2$. The experiment described above suggests a simple method of preparation of $\alpha$-$PbO_2$ by heating $\beta$-$PbO_2$ *in vacuo* at 390°C and treating the product with $H_2SO_4$. The higher electrode potential of the heat treated sample is due to the fact that $\alpha$-$PbO_2$ has a higher electrode potential than $\beta$-$PbO_2$. Potential measurements in $H_2SO_4$ more dilute than sp gr 1.225 indicated that self-discharge strongly increased with decreasing acid concentration. The electrode potentials started to drop soon after immersion of the electrodes into the electrolyte.

Precise electrode potential measurements of $PbO_2$ electrodes are very difficult because of passivation due to self-discharge. Electrode potentials of $\alpha$-$PbO_2$, stable to ±1 mv over a period of 12 hr, were obtained by pressing powdered $\alpha$-$PbO_2$ into perforated pure lead sheet. However, these electrodes suffered self-discharge and the potential dropped rapidly after 2 days. The highest potential for $\alpha$-$PbO_2$ obtained by this technique was 1.707 ± 0.001 v. This potential was measured in $H_2SO_4$, sp gr 1.225, against a hydrogen electrode in the same solution at a temperature of 25°C.

Electrodeposition of $\alpha$-$PbO_2$ on a Pt wire according to the procedure described in the experimental section lead to a stable electrode potential of 1.7085 ± 0.0005 v against a hydrogen electrode at 31.8°C in 4.40*M* $H_2SO_4$. This potential can be considered as a very reliable value for $\alpha$-$PbO_2$.

Electrode potential measurements of $\beta$-$PbO_2$ using pressed lead dioxide in perforated lead strips were not stable over extended time periods and showed a high rate of self-discharge. Maximum potentials of 1.692 ± 0.002 v were obtained in $H_2SO_4$, sp gr 1.225. This value might be too low because of self-discharge effects. Generally it was observed that electrodes showing a low electrode potential were only stable over short time periods.

Electrodeposited layers of $\beta$-$PbO_2$ on Pt wires showed electrode potentials of 1.7015 ± 0.0005 in 4.40*M* $H_2SO_4$ against a hydrogen electrode in a 31.8°C temperature bath. The potential was stable over extended time periods and can be considered to be a reliable value for $\beta$-$PbO_2$. The electrode potential of the electrodeposited $\alpha$-$PbO_2$ electrode showed excellent stability. After anodization or partial discharge, the potential always returned to the stable value given above. After standing in $H_2SO_4$ for periods of several weeks the potential was observed to drop. Microscopic examination revealed a surface layer of well-developed lead sulfate crystals. After stripping the sulfate layer with ammonium acetate the potential returned to its original value. After prolonged anodization of the electrodeposited $\beta$-$PbO_2$ electrode, the potential dropped very slowly on open circuit and did not show a distinct plateau at the reversible potential (1.7015 v). However, after stripping the sulfate layer from the electrode with ammonium acetate the potential returned to the reversible value. It is interesting to note that these results show a higher electrode potential for $\alpha$-$PbO_2$ than for $\beta$-$PbO_2$ under the conditions described above, the difference being 7 mv.

The electrode potential of 1.7015 ± 0.0005 v for $\beta$-$PbO_2$ agrees with the data given by Hamer (21). If his values are extrapolated to 4.40*M* $H_2SO_4$ and 31.8°C, a potential of 1.701 v is calculated.

The temperature dependence of the potential difference between $\alpha$- and $\beta$-$PbO_2$ will be studied in the future in order to determine entropy and enthalpy for the $\beta$-$\alpha$ transition. The reversibility for the couples $\alpha$-$PbO_2$/$PbSO_4$ and $\beta$-$PbO_2$/$PbSO_4$ will be determined by measuring discharge overvoltages.

Figure 9 shows oxygen overvoltage data at 31.8°C on the electrodeposited layers. Voltages given in Fig. 9 refer to the theoretical reversible oxygen electrode in the same electrolyte as the $PbO_2$ electrode, namely 4.40*M* $H_2SO_4$. The reversible oxygen

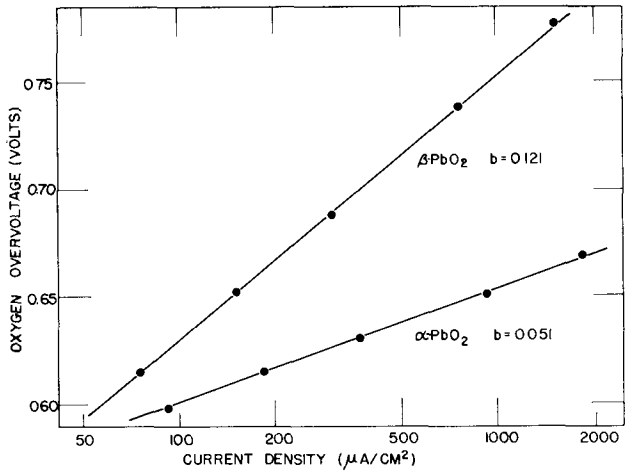


Fig. 9. Oxygen overvoltage data for α- and β-$PbO_2$

potential in this electrolyte is 1.260 v vs. $H_2$. The Tafel slope is 0.121 for β-$PbO_2$ and 0.051 for α-$PbO_2$, indicating a different mechanism for the oxygen evolution reaction on the two different $PbO_2$ modifications. These oxygen overvoltage measurements were performed in highly purified solutions. The high acid concentration prevented errors due to ohmic resistance. The curves shown were followed in both directions and were very reproducible.

The "exchange currents" $i_o$ for oxygen evolution calculated from the data shown in Fig. 9 are $1.7 \cdot 10^{-16}$ amp/cm² for α-$PbO_2$, and $6.2 \cdot 10^{-10}$ amp/cm² for β-$PbO_2$. Results for β-$PbO_2$ are in close agreement with the overvoltage data for anodized lead samples (1), indicating that oxygen is evolved primarily on the β-$PbO_2$ sites.

## Discussion

The high electrical conductivity of $PbO_2$, approaching that of metallic conductors, is caused by an apparent oxygen deficiency producing free electrons. It is possible that this is caused in part by OH groups replacing oxygen in the lattice. This viewpoint is supported by the observation that small amounts of water are produced on heating $PbO_2$ samples. However, this could be adsorbed water on the surface of the sample. Further work is anticipated on this problem.

The thermodynamically stable form of $PbO_2$ at room temperature apparently departs from its nominal composition. Chemical analysis shows a composition of $PbO_{1.94}$ to $PbO_{1.96}$. During anodization under conditions of oxygen evolution the $PbO_2$ corrosion layers must contain a higher oxygen content than at equilibrium. It has been shown that oxygen overvoltage is related to the strength of the bond M-O or M-OH in the oxide (22). The strength of this bond decreases with increasing amount of oxygen in the surface. This decreased bond strength is the cause of the high oxygen overvoltage on $PbO_2$. This interpretation of the overvoltage corresponds to the thermodynamic point of view, i.e., the formation of an intermediate oxide with a higher free energy. Thermodynamic considerations of electrochemical properties of oxide electrodes with varying oxygen content have been given by various authors (23-25). From the thermodynamics of ordered mixed phases it is possible to derive how the number of oxygen defects in $PbO_2$ should depend on the oxygen pressure. Assuming that the stoichiometric oxygen deficiency is caused by vacancies, the formation of the thermodynamically stable lead dioxide (at room temperature and atmospheric pressure oxygen content $PbO_{1.95}$) can be expressed by the equation:

$$Pb^{++++} + \square_o^{--} + \tfrac{1}{2}\, O_2\ (\text{gas}) \rightleftarrows Pb^{++++} + O^{--} \qquad (I)$$

where $Pb^{++++}$ are four valent lead ions and $\square_o^{--}$ are the oxygen vacancies. If the chemical potential of each of the components of (I) is given by

$$\mu_i = \underline{\mu_i} + RT \ln C_i \qquad (II)$$

(using to a first approximation concentrations instead of activities), the concentration of oxygen vacancies is given by

$$[\square_o^{--}] = \frac{1}{P_{O_2}^{1/2}} \exp\left(\frac{\Delta g}{Z\,RT}\right) \qquad (III)$$

where $P_{O_2}$ is the oxygen gas pressure and $\Delta g$ is the free enthalpy for reaction (I). Thus the oxygen vacancy concentration in $PbO_2$ is not very sensitive to $O_2$ pressure. Figure 7 shows that the oxygen content of $PbO_2$ and $PbO_x$ depends slightly on the oxygen pressure.

Removal of oxygen below a Pb/O ratio of 1.94 results in a decrease in conductivity due to the formation of a new, nonconductive compound. The decrease in conductivity is accompanied by an increase in the negative Hall coefficient, due to a decrease in the free electron concentration. The new compound has a variable oxygen content ($PbO_x$ with $x = 1.4$ to 1.6), and the x-ray lattice parameters change with oxygen content. A high self-discharge rate and fast passivation are observed with electrodes consisting largely of this compound. The electrode potential for these electrodes is established by the presence of α-$PbO_2$ produced by disproportionation of the original $PbO_x$ in $H_2SO_4$. This α-$PbO_2$ is rapidly passivated by the $PbSO_4$ formed during the reaction. The fact that α-$PbO_2$ is formed is very interesting. Note that the lattice structures of α-$PbO_2$ and $PbO_x$ are quite similar. Both compounds form an orthorhombic lattice; $PbO_x$ is a distorted α-$PbO_2$ lattice. Thermal decomposition of β-$PbO_2$ probably starts with a transition to an α-$PbO_2$ lattice which then looses oxygen. It seems that oxygen might be removed from α-$PbO_2$ down to an oxygen content of $PbO_{1.4}$ without a drastic phase change.

According to Bode and Voss (3) the tetragonal (β)$PbO_2$ has a higher electrode potential than the orthorhombic (α)$PbO_2$. Our measurements definitely show a higher electrode potential for α-$PbO_2$. Discharge overvoltages for α- and β-$PbO_2$ are unknown at the present time, however, and further proof seems necessary to decide definitely if the first plateau corresponds to the discharge of α-$PbO_2$ and the second plateau to the discharge of β-$PbO_2$. Since the first plateau shows a higher self-discharge rate, one could anticipate that the material corresponding

to this plateau is in more immediate contact with the underlying metal.

The mechanism of formation of the two oxides must be different. $\alpha$-$PbO_2$ is formed in alkaline solution by anodic deposition on inert electrodes and in $H_2SO_4$ solution by direct oxidation of the metallic lead. $\beta$-$PbO_2$ is formed in acid solution by anodic deposition. It is possible that in the formation of $\alpha$-$PbO_2$ an intermediate complex of tetravalent lead with (OH) groups is formed, whereas formation of $\beta$-$PbO_2$ proceeds over a complex of tetravalent lead with other groups such as $SO_4$. The size of the participating group probably determines which oxide modification is formed. The presence of any nuclei of either modification at the beginning of formation can also have an influence (3).

It has been observed that formation of positive storage battery plates begins at the surface of the grid members. This is to be expected since the active material of an unformed plate has extremely low conductivity. As formation progresses, $H_2SO_4$ is liberated at the formation boundary (the interior of the plates remains basic even after prolonged immersion of the plates in $H_2SO_4$) and becomes available for sulfation of PbO and basic lead sulfates. In plates made from sublimed litharge or in thoroughly conditioned plates (no free lead) formation of $\alpha$-$PbO_2$ is not observed. It is to be concluded that the formation of $\alpha$-$PbO_2$ in the interior of storage battery plates is probably not nucleated by PbO but rather by the direct oxidation of metallic lead particles. That further production of $\alpha$-$PbO_2$ is induced by these nuclei is evident from the fact that even after prolonged periods of cycling $\alpha$-$PbO_2$ is found in the plates.

The oxygen overvoltage data on $\alpha$- and $\beta$-$PbO_2$ shown in Fig. 9 indicates that a different mechanism takes place on the two oxides. $\alpha$-$PbO_2$ shows a Tafel slope of 0.05, like a large series of electrodes in alkaline solution. This slope corresponds to a process where two electronic charges are involved when the rate-determining reaction occurs once (22). $\beta$-$PbO_2$ has a Tafel slope of 0.12 indicating that only one electronic charge is involved in the rate-determining reaction. Therefore, $\alpha$-$PbO_2$ in $H_2SO_4$ behaves like an oxygen-evolving electrode in alkaline solution, where $\beta$-$PbO_2$ shows the normal Tafel slope of 0.12 like most of the other electrode materials in acid solution. This difference is apparently due to a difference in the lattice spacing of two oxides, $\alpha$-$PbO_2$ having the smaller spacing.

Anodic corrosion in the potential region where oxygen is evolved increases strongly with the electrode potential (26). Therefore, electrodes with a low oxygen overvoltage should withstand corrosion better under constant current conditions. Certain additives to the electrolyte such as $Co^{++}$ ions can reduce oxygen overvoltage and anodic corrosion. Oxygen overvoltage is, of course, not the only factor determining the rate of anodic corrosion. In particular, the nature of the electrode material has a strong influence (27). The fact that constant current corrosion increases wtih increasing Sb concentration for Pb-Sb alloys has also been described by Krivolapova and Kabanov (28).

Oxygen overvoltage and anodic corrosion are influenced by the amount of $SO_4''$ ions adsorbed on the electrode surface. Since in all of these corrosion experiments the anodizing current was kept at 3 ma/$cm^2$ the electrode potential during the period of anodic corrosion was considerably higher than the zero-charge potential, according to Fig. 5, always above 2 v. At this potential the electrode surface is covered with specifically adsorbed anions (29). The zero charge potential on a lead dioxide electrode has been determined at 1.80 v by Kabanov, *et al.* (30).

The relative ratio of the amounts of $\alpha$- and $\beta$-$PbO_2$ in the corrosion layer changes with the time of anodization. X-ray examination shows that as anodization progresses the $\alpha$-$PbO_2$ pattern becomes more and more pronounced. At the same time oxygen overvoltage decreases.

## Acknowledgments

The authors are indebted to H. Stoertz, J. F. McGivern, Jr., and A. F. Pippel, of the Metallurgy Division, for their assistance in preparing the microtomed samples used for the corrosion studies. They are also indebted to Dr. Bode for drawing the Kittel reference (8) to their attention and providing a copy of the article.

The electron microscope pictures were taken with the assistance of Mr. Kelsch of the RCA Laboratories in Camden to whom they owe many thanks. They would also like to thank Mr. C. G. Grimes, Director of Research of the Electric Storage Battery Company, for permission to publish this paper.

Manuscript received Oct. 2, 1957. This paper was prepared for delivery before the Buffalo Meeting, Oct. 6-10, 1957.

Any discussion of this paper will appear in a Discussion Section to be published in the June 1959 JOURNAL.

## REFERENCES

1. P. Rüetschi and B. D. Cahan, *This Journal*, **104**, 407 (1957).
2. A. I. Zaslavsky, Y. A. Kondrashov, and S. S. Tolkachev, *Doklady Akad. Nauk. SSSR*, **75**, 559 (1950).
3. H. Bode and E. Voss, *Z. Elektrochem.*, **60**, 1053 (1956).
4. J. Burbank, *This Journal*, **103**, 87 (1956); **104**, 693 (1957).
5. N. Kameyana and T. Fukumato, *J. Soc. Chem. Ind. Japan*, **49**, 154 (1946).
6. T. Katz, *Ann. chim.*, 12th Ser., **5**, 5 (1950).
7. K. H. Palmer, *Z. Elektrochem.*, **29**, 415 (1923).
8. U. B. Thomas, *This Journal*, **94**, 42 (1948).
9. M. LeBlanc and E. Eberius, *Z. Phys. Chem.*, **A160**, 69 (1932).
10. T. Katz and R. LeFaivre, *Bull. Soc. Chim. France*, **16**, D124 (1949).
11. A. Kittel, Breiträge Zum Mechanisms der elektrischem Leitung in $PbO_2$ and Se, Diss. Prag, Czechoslov (1944).
12. A. Bystrom, *Arkiv Kemi Mineral. Geol.*, **20A**, 1 (1945).
13. E. Rencker, *Bull. Soc. Chim.*, 5e serie, **3**, 981 (1936).
14. B. Allessandro, *Gazz. chim. ital.*, **68**, 387 (1938).
15. C. Holtermann and P. Lafitte, *Compt. rend.*, **204**, 1813 (1937)
16. G. Butler and J. L. Copp, *J. Chem. Soc.*, **1956**, 725.
17. M. A Dasoyan, *Doklady Akad. Nauk. USSR*, **107**, 863 (1956).

18. K. Topf, *Z. anal. Chem.*, **26**, 296 (1944).
19. W. H. Beck, R. Lind, and W. F. K. Wynne-Jones, *Trans. Faraday Soc.*, **50**, 147 (1954).
20 W. H. Beck, P. Jones, and W. F. K. Wynne-Jones, *ibid.*, **50**, 1249 (1954).
21. W. J. Hamer, *J. Am. Chem. Soc.*, **57**, 9 (1935).
22. P. Rüetschi and P. Delahay, *J. Chem. Phys.*, **32**, 556 (1955).
23. W. Schottky, *Z. Elektrochem.*, **45**, 33 (1939).
24. H. J. Engell, *Arch. Eisenhüttenw.*, **28**, 109 (1957).
25. P. D. Lukovtsev and S. A Temerin, *Trudy Sov. Elektrokhim 1950, Akad. Nauk SSSR, Otdel Khim Nauk*, 494 (1953).
26. J. J. Lander, *This Journal*, **98**, 213 (1951); **103**, 1 (1956).
27. G. Z. Kiryakov and V. V. Stender, *Izv. Akad. Nauk Kazakliskai SSSR*, **5**, 91 (1954).
28. E. V. Krivapolova and B. N. Kabanov, *Trudy Sov. Elektrokhim. Akad. Nauk SSSR, Otdel Khim Nauk 1950*, 539 (1953).
29. I. G. Kiseleva and B. N. Kabanov, *Doklady Akad. Nauk SSSR*, **108**, 864 (1956).
30. D. I. Leikis, *ibid.*, **99**, 805 (1954).

# A Contribution to the Theory of Stress Corrosion in Al-4% Cu Alloys

**William H. Colner and Howard T. Francis**

*Armour Research Foundation of the Illinois Institute of Technology, Chicago, Illinois*

ABSTRACT

Stress cracking of Al-4% Cu alloys was found to be greatly influenced by exposed area of the specimen (small areas showed long time-to-failure). Experiments with grain boundary-grain center couples showed that neither potentials nor couple current were influenced sufficiently by stress to account for the acceleration of failure by stress. At constant applied anodic current, however, stress was found to direct the attack perpendicular to applied stress. The theory of Champion and Logan is substantiated. A refinement is suggested in which the last stages of failure result from direct and rapid local attack on film-free metal.

Many theories have been proposed to account for the conjoint action of stress and corrosion in destroying metals and alloys. These have been reviewed adequately in the corrosion literature (1-4). One notes in examining these theories that there is general agreement on the mechanism of the beginning of the attack; there is lack of agreement, however, centered around the role of the stress in the mechanism of failure. It was the purpose of this study to shed some light on the mechanism of the stress effect.

The general approach was first to show that a susceptible alloy, 2024, exhibited an area effect (the dependence of the time to stress-corrosion failure on the amount of area exposed to the corrodent). It was felt that the establishment of this property would give information regarding the nature of the corroding cell. The phenomenon has been noted in other alloys (5-7). The second phase of the study was to make certain electrochemical measurements on cells in which the anodes were separated from the cathodes and to determine the effect on these measurements of certain variables: stress, $H_2O_2$ concentration, relative areas, etc. A mechanism is proposed to account for the results obtained in the study; it is essentially that suggested by Champion (8) and Logan (9), with some refinement.

## Area Effect in 2024 Al

*Apparatus and materials.*—Four-point loading was selected as the means for stressing ¾ in. x 3⅜ in. x 0.035 in. (1.9 cm x 8.6 cm x 0.089 cm) specimens. This type of loading places the surface of the specimen between the inner supports in a state of uniform stress (10). The method is simple in load application and calculation of stress.

Figure 1 shows the test fixture, constructed almost entirely of Lucite. It consists of two inner knife-

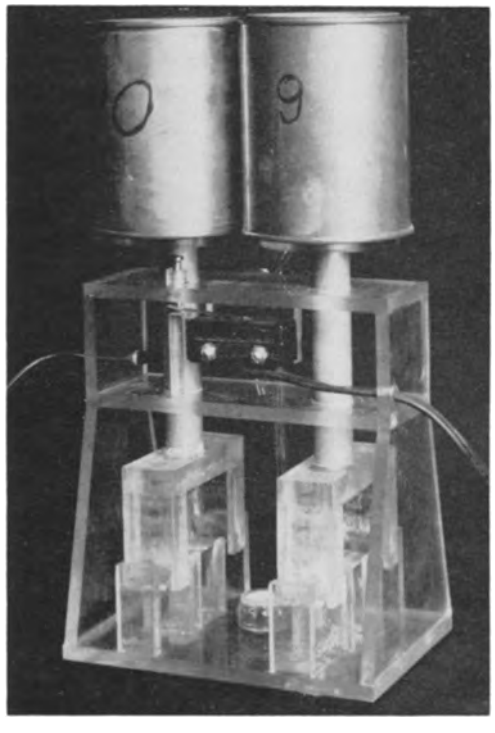

Fig. 1. Stress corrosion fixture

Table I. Compositions of alloys

| | Cu | Mg | Mn | Fe | Si | Al |
|---|---|---|---|---|---|---|
| H. P. Al. | 0.000 | 0.001 | —— | 0.001 | 0.002 | Bal. |
| Al-4 % Cu | 4.07 | 0.001 | <0.001 | 0.001 | 0.006 | Bal. |
| 2024 | 4.70 | 1.20 | 0.94 | 0.16 | 0.08 | Bal. |

edge supports cemented to the base of the fixture 1 in. (2.54 cm) apart. The outer knife-edges, 3 in. apart (7.62 cm), are inverted and fixed to the weight stage by a post. These apply the load to the specimen. The switch, actuated by the weight stage, shuts off a timer when the specimen deflection increases by a certain increment due to corrosion. These increments were either ¼ in. (0.63 cm) or ⅛ in. (0.31 cm) and were defined as "failure" for the purpose of this work. Loads were calculated from the equation

$$S = \frac{3Lx}{bd^2}$$

where $S$ is the stress in the outer fibers, $L$ is the load, $x$ is the distance between inner and outer supports (1 in. with the fixture shown), $b$ is the specimen width, and $d$ is the specimen thickness.

The fixtures (each accommodating two specimens) were placed in individual glass troughs when a variable in composition of corrodent was being observed, or in a long Lucite trough when variables other than the medium were being studied. When using the long trough, the solution was circulated from a 12-gal reservoir which was kept at constant temperature.

Commercial 2024 alloy was used in most of the experiments reported in this work; however, a few experiments involved high-purity aluminum and a high-purity aluminum-copper alloy. The compositions of these are shown in Table I. The high-purity alloys were furnished by Aluminum Research Laboratory, Aluminum Company of America; the H. P. Al as 0.064 in. sheet, and the Al-4% Cu as 1½ in. forged bars, which were first hot and then cold rolled to 0.035 in. strip. The 2024 alloy was purchased as 0.032 in. annealed sheet.

Experiments were conducted to determine the correlation, if any, between the total area exposed on a stressed specimen and the time to failure. Sensitized[1] specimens were masked completely on the bottom surfaces; the top surfaces were partially masked to expose certain areas. The masking material was a commercial plating stop-off compound. Quadruplicate specimens were used for each area. These specimens were stressed in the fixtures to 80% yield strength (Y.S. was 42,500 psi) and placed in the trough with 53 g/l NaCl + 2.5 g/l $H_2O_2$ at room temperature (72°F). The results of the run are shown in Fig. 2 (upper curve) and indicate a definite correlation between area exposed and time to failure.

Failure mechanisms based on mechanical considerations only have been proposed to explain area effect. To show that the effect is electrochemical in nature the above experiment was conducted in the same manner, but with each specimen electrically connected to an unstressed immersed specimen. The unstressed specimen was masked to expose an area such that the total area (stressed plus unstressed) was 13.3 cm² (equal to the largest specimen of the previous run, 7 x 1.9 cm). The results of this experiment are shown as the lower curve in Fig. 2. It should be noted that the area effect is no longer in evidence, and all specimens failed in essentially the same time, namely, that of the 7 x 1.9 cm stressed and uncoupled specimen.

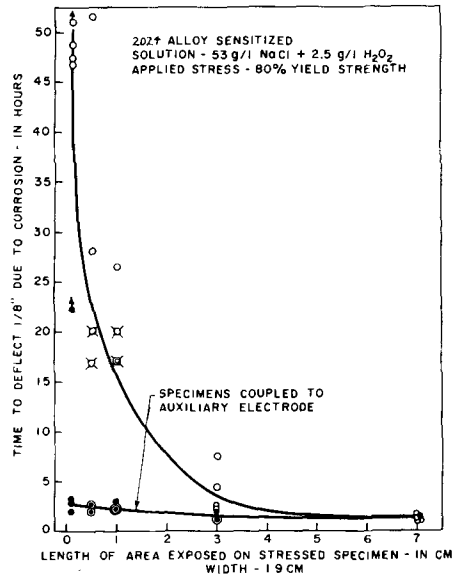


Fig. 2. Area effect for 2024 alloy and the influence of an auxiliary electrode.

It appears from the results shown in Fig. 2 that time to failure is a function of the total area exposed (stressed plus unstressed). This would be difficult to explain purely on mechanical grounds. Electrochemically, the results are a confirmation of the fact that the corroding cell is under cathodic control. The total attack is strongly dependent on the total cathodic area, stressed or unstressed; that is, where large cathodic areas are exposed, attack is great, where small cathodic areas are exposed, attack is less. Since grain centers constitute the bulk of specimen surface, the cathodic area can be taken as being roughly equal to the total area.

*Effect of Hydrogen Peroxide on Time to Failure*

Early in the program it was found that the hydrogen peroxide concentration fell rapidly during a test. Investigation showed that the peroxide decomposed at a rate proportional to specimen size when 2024 was involved, but that pure aluminum caused no detectable peroxide loss. It was quickly established that the peroxide decomposition was catalyzed by cupric ion, produced by the corrosion of the 2024. This is a well-known effect sometimes neglected in corrosion testing.

The dependence of the time to failure on peroxide concentration was determined. Sensitized 2024 specimens, masked to expose 7 x 1.9 cm, were stressed to 80% yield strength and each fixture (carrying duplicate specimens) was placed in a

[1] Sensitizing treatment for 2024 specimens consisted of holding specimens at 350°F for 6 hr after solution treatment (910°-930°F: cold water quenched).

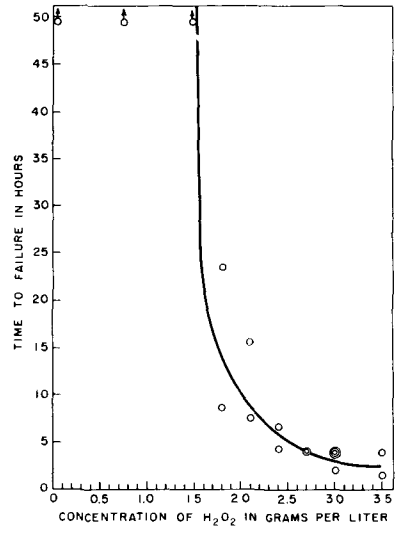


Fig. 3. Effect of $H_2O_2$ concentration on time to failure in 53 g/l NaCl. Specimens were 2024 alloy, quenched and aged at 350°F for 6 hr, stressed to 80% yield strength.

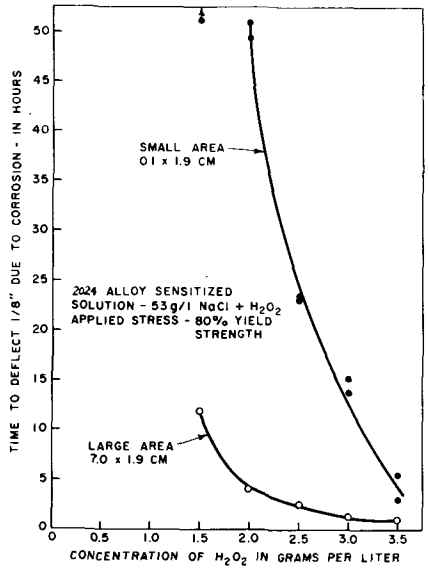


Fig. 4. Influence of $H_2O_2$ concentration on area effect

separate glass trough. Each trough was filled with 53 g/l NaCl, with varying concentrations of $H_2O_2$. The results of the experiment are shown in Fig. 3. Great sensitivity to the peroxide concentration in the range 1.5-3.0 g/l is noted. Above this critical range, specimens failed in a few hours; below about 1.5 g/l, the failure time increased rapidly.

The data illustrate the importance of good peroxide concentration control during the course of a stress corrosion test, a factor which may not have been fully recognized in earlier work.

The fact that the time to failure is sensitive to peroxide concentration (a cathodic depolarizer) is further verification that the cell is under cathodic control.

Runs were made using oxygen gas instead of peroxide in an effort to stabilize the depolarizer concentration. The gas dispenser can be seen in Fig. 1. No failure was noted after exposure of 337 hr (14 days). This result is consistent with other experience (11) in which oxygen saturation has been found equivalent to about 0.02 g/l $H_2O_2$. Referring to Fig. 3 and 4, it is seen that this level is well below that causing rapid failure. The use of peroxide was therefore continued.

### *Influence of $H_2O_2$ on Area Effect*

Having shown the critical dependence of time to failure on peroxide concentration, the area effect was reinvestigated as a function of peroxide concentration. Large (7.0 x 1.9 cm) and small (0.1 x 1.9 cm) sensitized specimens were exposed to different concentrations of peroxide, stressed at 80% yield strength. Figure 4 shows the results of these runs. As might be expected, the area effect became more pronounced as the depolarizer concentration was decreased. Due to the long times to failure, the region below 1.5 g/l $H_2O_2$ was not investigated. Runs identical with those shown in Fig. 2, substituting 2.0 g/l $H_2O_2$, were made; the largest area (7.0 x 1.9 cm) failed in a few hours; the smaller areas had not failed in 65 hr (confirming the data of Fig. 4).

## Grain Boundary-Grain Center Cell Study

Mears, Brown, and Dix studied the area effect for a magnesium base-6Al alloy (5). They concluded that cracking time was controlled by the total available cathodic activity. The area effect for 2024 described above was approached from the same point of view. Studies were made of potentials and currents involved in the corrosion process. These were followed by a set of experiments designed to clarify the role of stress in the mechanism of failure.

*Specimen preparation.*—The example of the classical experiments of Dix and associates (12) was followed in this phase of the study. Grain boundaries and grain centers were masked on identical specimens of copper-aluminum binary alloy (composition shown in Table I).

The high purity of the alloy permitted easy growth of large grains by the strain-anneal method. Final grain size was in the range ½-1 cm[2]. Following grain growth, specimens were given a caustic pickle and solution treated. Anode specimens were sensitized following solution treatment; cathode specimens were used in the solution-treated condition. Following heat treatment, all specimens were etched in Flick's reagent[2] and then masked.

Masking compound was made by thinning Duco[3] cement with Cellosolve[4] and colored with fuchsin dye. Masking of grain boundary specimens was performed under a low power microscope (30X) so that exposed grain boundary zones could be held to 0.5 mm. Since the grain center specimens were used in the solution-treated condition, it was felt that the entire surface of the specimen would be sufficiently homogeneous to obviate the need for masking the grain boundary zones. Electrical connections were made by peening the bared end of 30 gauge Teflon-covered wire into a slit in the specimen; the entire joint was then covered by stop-off.

[2] HCl (conc.) 15 ml, HF (48%) 10 ml, $H_2O$ 90 ml.

[3] E. I. du Pont de Nemours & Co.

[4] Carbide & Carbon Chemical Co.

*Effect of Hydrogen Peroxide, Anode Area, and Cathode Area on Current and Potential*

Pairs of specimens prepared as described above (anode and a cathode) were exposed unstressed to media containing various peroxide concentrations plus 53 g/l NaCl, a fresh pair of specimens for each peroxide concentration. Open-circuit potentials of grain boundary and grain center specimens were measured and then shorted through an electronic self-balancing zero-resistance ammeter (13). The current was observed until it reached a steady value (about 1 min). Data derived from these experiments are shown in Fig. 5 and 6.

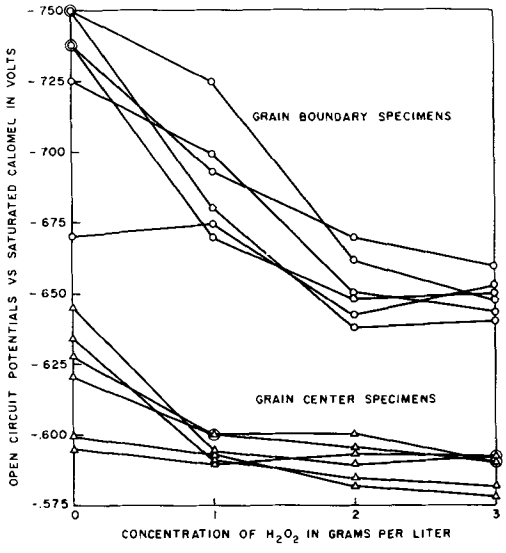


Fig. 5. Open-circuit potentials of grain center and grain boundary specimens in solutions containing 53 g/l NaCl and various levels of $H_2O_2$.

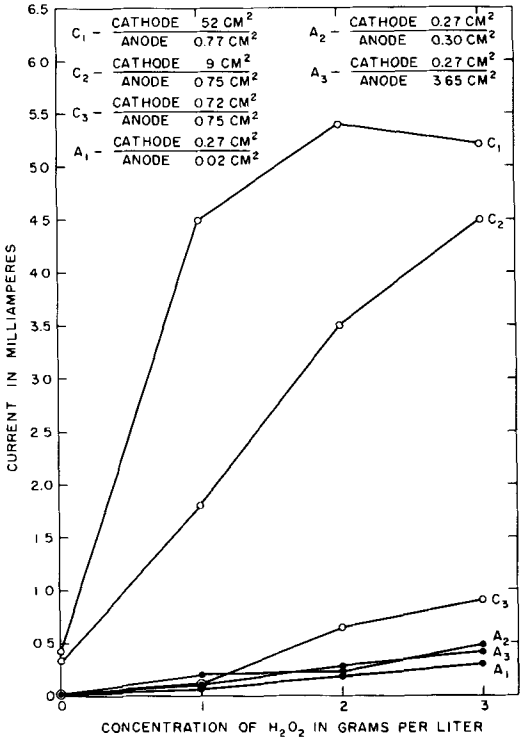


Fig. 6. Current flow between various areas of anode and cathode specimens at different $H_2O_2$ concentrations and 53 g/l NaCl.

Several observations may be made from the data shown in Fig. 5. It is to be noted that in all cases the grain boundary specimens showed open-circuit voltages more anodic than those of the grain centers. This indicates clearly that grain boundaries are anodic to grain centers at all concentrations of peroxide.

It is interesting to note that the anode curves shift in the cathodic direction with increasing peroxide concentration. This shift might be caused by a depolarization of the local cathodes on the anode specimen (the 0.5 mm exposed width would include considerable cathode area); it might also be caused by a passivation of the anode regions by the oxidizing peroxide. The cathode curves show a much less marked change in open-circuit potential with increasing peroxide. The spread of the potentials at zero peroxide for both anodes and cathodes is characteristic of aluminum in straight salt solutions.

Figure 6 shows the current flowing between various areas of anodes and cathodes at different peroxide concentrations. The $C_1$, $C_2$, and $C_3$ curves vary in cathode area (with fixed anode area); the $A_1$, $A_2$, and $A_3$ curves vary in anode area (with fixed cathode area). It should be noted that in all cases the couples are under cathodic control. Thus, with actual corroding specimens a greater total current (hence more rapid penetration) would be expected for large area specimens than for small area specimens, in agreement with the experimental data of Fig. 2.

*Effect of Peroxide Concentration on Polarization of Anodes and Cathodes*

It has been shown that the magnitude of the couple current in the above cells is strongly dependent on the concentration of the cathodic depolarizer, hydrogen peroxide. To assess this effect quantitatively, polarization curves ($E$ vs. $I$) were determined for the anode and cathode specimens prepared as described above, using three different peroxide concentrations, 0, 1.5, and 3.0 g/l $H_2O_2$.

Potential measurements were made using a saturated calomel reference cell equipped with a small tubulus. The opening was placed just above the

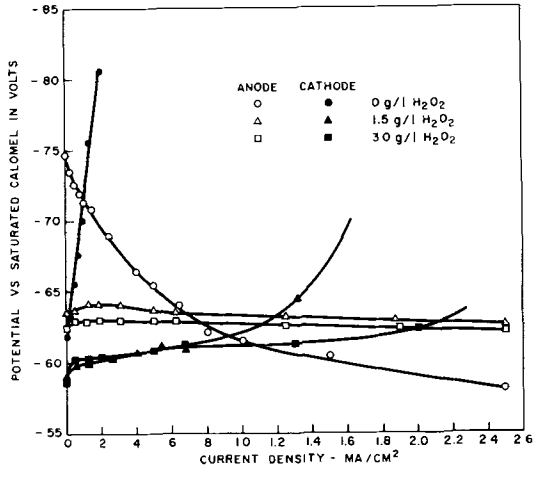


Fig. 7. Potential vs. current curves for anode and cathode specimens for various $H_2O_2$ concentrations with 53 g/l NaCl (Cu-Al binary alloy).

specimen, held in the stress jig but not stressed. Current was obtained from a voltage divider connected across a 6-v battery. Grain boundary specimens were polarized anodically and grain center specimens cathodically. The inert electrode was a platinum screen.

The polarization curves are shown in Fig. 7. The depolarization effect of peroxide is seen to be great in the case of the cathode.

The anode open-circuit potentials show a shift in the cathodic direction with increasing peroxide and, surprisingly, anode polarization is found to be less at the higher peroxide levels.

Thus, the corrosion process is stimulated by peroxide, acting chiefly as a cathodic depolarizer. This effect is most pronounced in the low concentration range (0-1.5 g/l).

### *Effect of Stress on Polarization of Anodes and Cathodes at Varying Peroxide Concentrations*

Having established the polarization curves for unstressed anodes and cathodes, the question then arises as to the effect of stress on these curves and in turn on the couple current. The experiments used to obtain the curves in Fig. 7 were repeated; in this case, however, both grain boundary and grain center specimens were stressed to 80% yield strength. The results of these runs are shown in Fig. 8 for 0, 1.5, and 3.0 g/l $H_2O_2$.

The difficulty of obtaining accurate data on polarization curves of this type limits the extent to which they can be interpreted quantitatively. It is possible, however, to reach certain general conclusions from the data Fig. 8: (*a*) anodic activity appears to be increased consistently by stress at all peroxide levels; the cathodic effect is not clear cut; (*b*) the increase in anodic activity produced by stress does not appear to be sufficient to account for the very marked effect of stress on the penetration rate in actual stress corrosion.

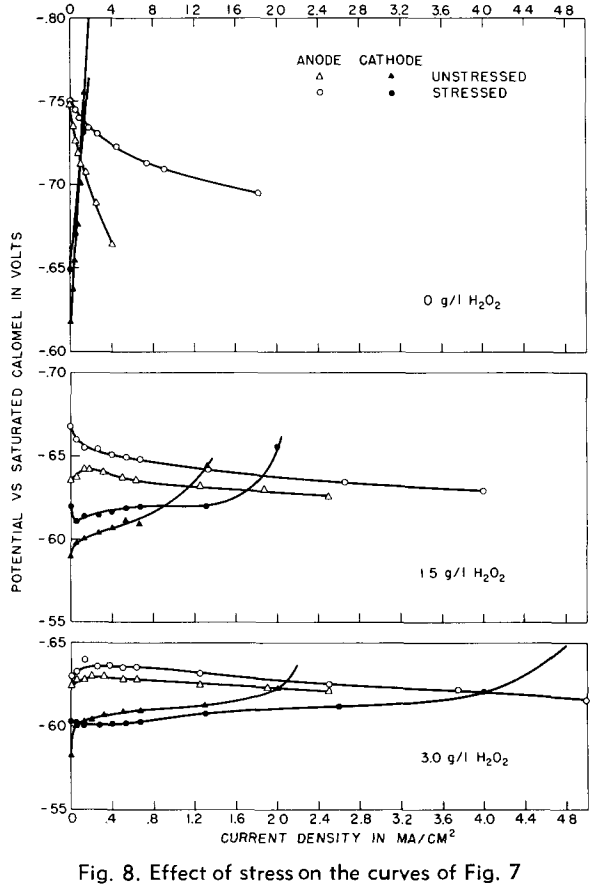


Fig. 8. Effect of stress on the curves of Fig. 7

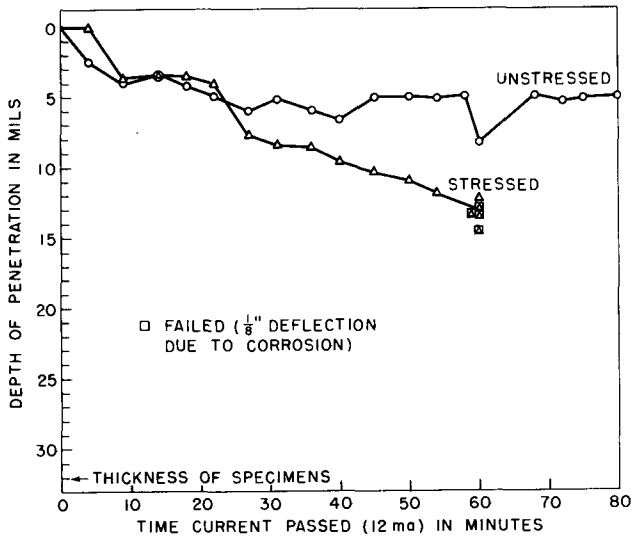


Fig. 9. Effect of stress on rate of penetration of 2024 specimens by applied anodic current (53 g/l NaCl).

### *Effect of Stress on Rate of Penetration*

The data presented thus far have shown that the stress does not increase the corrosion current sufficiently to account for the marked acceleration of failure. To further clarify the role of stress, the rate of penetration was measured.

Specimens of sensitized 2024 alloy masked to expose 0.3 x 1.9 cm areas were made anodic in a solution of 53 g/l NaCl. The anodic current was held constant at 12 ma, and both stressed and unstressed specimens were exposed. Specimens were removed after certain times of exposure, and cross sections were examined metallographically to determine the depth of penetration. The results are shown in Fig. 9.

The curves for both stressed and unstressed specimens follow the same course up to 25 min, at which point the unstressed specimens suffer no further penetration, while the stressed specimens undergo continued penetration, reaching failure at about 60 min. It should be remembered that "failure" is defined as an increase in deflection—due to cor-

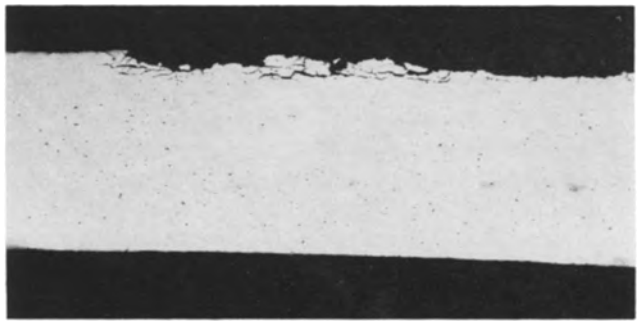

Fig. 10. Sensitized unstressed 2024 specimen after exposure to 53 g/l NaCl with 12 ma anodic current for 54 min.

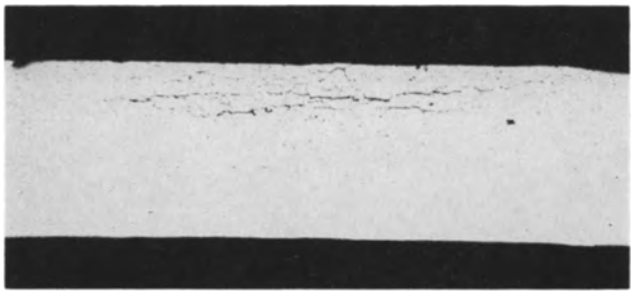

Fig. 11. Sensitized, stressed 2024 specimen after exposure to 53 g/l NaCl with 12 ma anodic current for 54 min.

rosion—of ⅛ in. This observation has been noted by others (6, 7, 14), viz, the stress is important only in the latter stages of exposure.

Photomicrographs of the unstressed and stressed specimens after 54-min exposure (just before failure of the stressed specimen) are shown in Fig. 10 and 11, respectively. These microstructures show the greater penetration for the stressed specimen and, although not too clearly, the greater total attack in the case of the stressed specimen. Both stressed and unstressed specimens were exposed to the same (externally applied) current for the same time, but it was observed that hydrogen was evolved from the stressed specimen only. This indicates that local action was initiated by the stress and accounts for the greater total attack of the stressed specimen.

Some workers (1, 4, 5) feel that this local action is induced by the creation of essentially film-free metal in the base of the crack, which, because of its greatly increased anodic activity, increases the couple current between the cathodic specimen surface (or crack walls) and the base of the crack. It seems more likely, however, that, if film-free metal is produced in the crack, the nature and site of the cathodic action are altered to include reduction of $H^+$ to H in the crack apex, as well as the reduction of peroxide on the crevice walls. This is discussed further below.

A similar experiment was performed using the high-purity binary alloy. The penetration-time curve for a stressed specimen is shown in Fig. 12. It should be noted that complete penetration occurred in 5 min as compared to 60 min for failure of stressed 2024 specimen. Figure 13 shows the unetched microstructure of the binary specimen just before complete penetration.

The differences in cracking time and in appearance between the 2024 and the high-purity binary alloy are possibly due to differences in grain size and grain boundary purity.

## Discussion

The above experiments demonstrate that the stress corrosion cracking of Al-4% Cu type of alloys is dependent on the area exposed to the corrosion medium. This area effect is electrochemical in nature and has been related to the total cathodic activity of the corrosion cell. Furthermore, hydrogen peroxide has a great influence on the time to failure of these alloys and at high concentrations tends to minimize the effect of area.

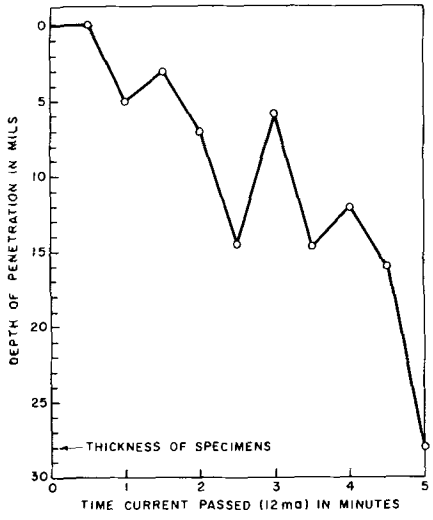


Fig. 12. Penetration of stressed Al-4% Cu binary alloy by applied anodic current.

Fig. 13. Stressed Al-4% Cu binary alloy after exposure to 53 g/l NaCl with 12 ma anodic current for 4½ min.

Experiments with partially masked specimens showed that the grain boundaries of sensitized alloy are anodic to the grain centers at all concentrations of peroxide tested. It was also shown that the grain boundary/grain center cell is under cathodic control. Hydrogen peroxide functioned as an active cathodic depolarizer, but had little effect on anodic action. Saturation by molecular oxygen was found to be far less effective in depolarization than peroxide.

Some increase in anodic activity was observed when stress was applied, but the effect was relatively small compared to the cathodic effect produced by peroxide. It appeared that the stress exerted no influence on the rate of penetration of the specimen until about half the total time-to-failure had elapsed.

The course of attack of a stressed specimen might be as follows: when first immersed in the medium, a cell is set up between the grain centers and grain boundaries of the piece. The magnitude of the current flow depends on the area of cathode, its composition, composition of the anode, and the composition of the medium. As the current flows, the grain boundaries are oxidized preferentially, resulting in the formation of trenches. As the trenches deepen with time and their apices become sharper, the stress increases due to notch effect. When the yield strength of the grain boundary (depleted zone) is reached, the specimen rapidly fails.

It is the mechanism of the last stage of the cracking process (when the effect of stress is noted) that is felt to be inadequate in present theories. Most of

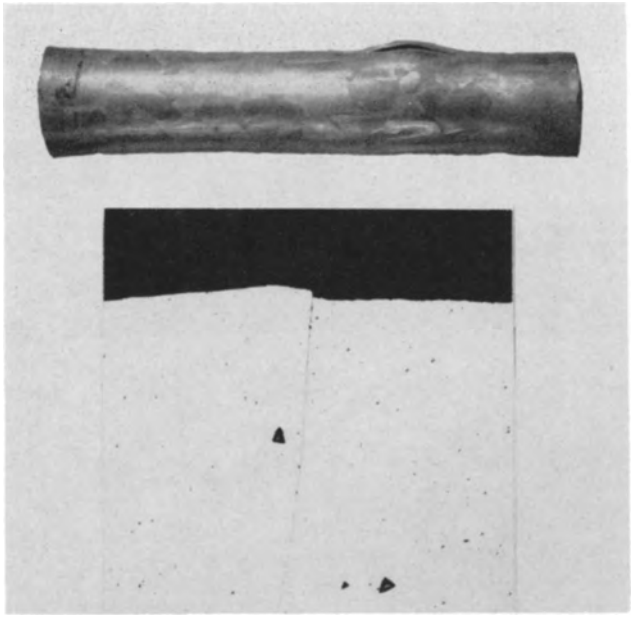

Fig. 14. Tube of Al-4% Cu alloy, quenched and sensitized, subjected to hydraulic internal pressure to bursting. Above, full size photograph before reduction for publication. Note greater deformation in grain boundaries than in grain centers. Below, photomicrograph of a grain boundary near the failure zone. Note grain boundary deformation. Etchant: 20 parts $HNO_3$, 20 parts HF, 60 parts glycerin. Magnification 150X before reduction for publication.

these postulate an increase in grain boundary-grain center couple current, due to film rupture or metal rupture which expose fresh unfilmed metal.

In the present work, however, the effect of stress on the anodic polarization curves for grain boundary zones does not appear sufficiently great to support the above mechanism. An alternative mechanism is suggested which appears to fit better the observed effect of stress on cracking rate.

Champion (8) and Logan (9) suggest that when the yield strength of the grain boundary material is exceeded (by the stress concentration effect), plastic flow begins which ruptures the film. This suggestion is reasonable since it has been demonstrated adequately elsewhere that in sensitized alloys the grain boundary zones are depleted in copper and magnesium, and, further, that alloys with lower copper contents show lower yield strength and higher ductility than those with the nominal 2024 composition (15). Evidence of this fact is shown in Fig. 14, where grain boundary flow[5] is obvious.

When the 2024 specimen reaches the stage where the grain boundaries begin to flow, the film will be broken, thus exposing fresh metal. There will be a constant tendency to refilm this naked metal. If the flow is slow (low stress), the metal will remain relatively inactive due to rapid healing of its oxide film. If the deformation is rapid, however, the medium will be unable to maintain the film, the grain boundary metal will go into solution with evolution of hydrogen, and the crack will propagate rapidly.

Thus, in effect, the propagation of a crack consists of a continuous reaction in which extremely active aluminum is exposed through film rupture and oxidized by direct reaction with the corrosion medium. This occurs only after electrochemical attack has proceeded to the point where the notch effect has increased the stress level in the grain boundary zones beyond the yield strength of the depleted zone. When the strain rate in this region is sufficient to prevent film maintenance, the extremely rapid (almost explosive) penetration occurs. It is felt that hydrogen evolution largely replaces peroxide reduction as the cathodic reaction during this phase of cracking.

Summarizing then, penetration by stress-corrosion occurs by two mechanisms; first, a galvanic dissolution of the depleted grain boundaries in which the rate depends on the area and composition of the anodes and cathodes, and second, a hydrogen evolution type of dissolution of the depleted grain boundary beginning when the strain rate of the grain boundary is too great to permit refilming, this stage being independent of cathodic area. The triggering of the second mechanism, whose rate is much faster than the first, depends on the orientation of grain boundaries relative to the direction of stress application and the sharpness of the grain boundary trench apices.

[5] Grain boundary flow in this study refers to flow of the depleted metal adjacent to the grain boundary.

## Acknowledgments

The work described above was part of a project on Stress Corrosion of Aircraft Alloys carried out at Armour Research Foundation under the sponsorship of the National Advisory Committee for Aeronautics (16, 17). The authors also wish to acknowledge the helpful advice of Dr. Max Hansen and assistance of Messrs. Donald Makar, Cornelius A. Johnson, and Edward Klimek.

Manuscript received Jan. 21, 1957. This paper was prepared for delivery at the Cleveland Meeting, Sept. 30-Oct. 4, 1956. The work reported herein was submitted by one of the authors (W. H. C.) to the Department of Metallurgical Engineering, Illinois Institute of Technology in partial fulfillment of the requirements for the Ph.D. degree.

Any discussion of this paper will appear in a Discussion Section to be published in the June 1959 JOURNAL.

## REFERENCES

1. J. J. Harwood, *Corrosion*, **6**, 249, 390 (1950).
2. L. R. Standifer, F. H. Beck, and M. G. Fontana, Summary Tech. Rept., ONR Cont. N6ori-17 Task Ord. II, Proj. NR 031 029, Proj. 266, Ohio State Univ. Res. Fndn., April 1952.
3. P. Brenner, *Z. Metallkunde*, **44**, 85 (1953).
4. W. D. Robertson, "Stress Corrosion Cracking and Embrittlement," (Electrochemical Society Monograph), John Wiley & Sons, Inc., New York (1956).
5. R. B. Mears, R. H. Brown, and E. H. Dix, Jr., "Symposium on Stress-Corrosion Cracking of Metals," ASTM-AIME, 323-337 (1944).
6. E. C. W. Perryman and S. E. Hadden, *J. Inst. Met.*, **77**, 207 (1950).
7. E. L Jones, *J. Appl. Chem.*, **4**, 1 (1954).
8. F. A. Champion, "Symposium on Internal Stresses in Metals," Inst. Met. (London), p. 468 (1948); *J. Inst. Met.*, **83**, 385 (1955).
9. H. L. Logan, *J. Research Nat. Bur. Standards*, **48** RP2291, 99 (1952).
10. F. A. Champion, "Corrosion Testing Procedures," p. 144, Chapman and Hall, London (1952).

11. J. E. Draley, Private communication.
12. E. Dix, Jr., Inst. Metals Lecture, AIME, **137**, 11 (1940).
13. D. R. Makar and H. T. Francis, *This Journal*, **102**, 669 (1955).
14. C. Edeleanu, *J. Inst. Met.*, **80**, 188 (1951-2).
15. E. H. Dix, Jr., and J. J. Bowman, "Metals Handbook," ASM, Fig. 2, p. 804 (1948 Ed.).
16. Final Report, NACA Contract No. NAw-6313, Oct. 25, 1954.
17. W. H. Colner and H. T. Francis, NACA Technical Note 3292, Nov. 1954.

# Grain Growth and Flecking in Electroplated Copper Caused by Cyclic Stress

**H. Okubo and N. Nozaki**

*Nagoya University, Nagoya, Japan*

ABSTRACT

Microscopic investigation has been made on microflecks produced by cyclic stress on the surface of electroplated copper. Examination of the surface and cross section of the plated copper after stressing reveals that some of the micrograins constituting the plated metal grow to a considerable size.

It is ascertained that the flecks are always produced when grain growth occurs in the plated metal and can never be produced when grain growth does not occur.

The electroplating method originated by one of the present authors proved useful for an accurate determination of the surface stress (1). The method is based on the sensitive color change on the surface of a copper-plated specimen made by microflecks produced by cyclic stress. There is little information available on the detailed process as to how flecks are produced by cyclic stress. For an improvement of the electroplating method, however, it is most essential that the mechanism of producing the flecks be found.

## Experimental

*Conditions for deposition.*—Specimens used in this experiment are conical rods of carbon steel. They are prepared by treatment in dilute $H_2SO_4$ and caustic alkali after a fine polishing and then receive a preliminary deposit of copper from a cyanide copper vat.

The conditions for deposition are as follows:

| | | |
|---|---|---|
| Solution: | $CuSO_4 \cdot 5H_2O$ | 250 g |
| | $H_2SO_4$ | 80 g |
| | $H_2O$ | 1 l |

Current density: 3 amp/dm$^2$; temperature: 23°C; Bath voltage: 0.5 v; duration of deposition: 15 min.

*Microscopic examination.*—Examining the surface of a specimen undergoing color change, as shown in Fig. 1, by microscope, microgroups of fine flaws mixed among the flecks are found and these flaws run almost parallel to the planes of maximum shear (2).[1] Figure 2 is a micrograph of the flaws produced on the surface of a specimen by rotary bending test; Fig. 3 is a micrograph of flaws produced by torsion test; the arrows indicate the axial direction of the specimens. Close examination shows that a fleck is not a mass of flaws and that the group of flaws is not always situated exactly in a fleck.

When a specimen is exposed to a flow of hydrogen gas at 300°C during the comparatively short interval of 5 min, the flecks disappear, leaving only a trace, while the groups of flaws suffer no change whatever. Figure 4 is an original fleck and Fig. 5 its trace deoxidized by a flow of hydrogen gas. When a specimen is exposed to a flow of carbon dioxide at the same temperature, the flecks suffer no change. This indicates that the flecks are not produced by a mechanical change on the surface as are the flaws, but that they are produced by a chemical change occurring in the surface layer of the plated metal.

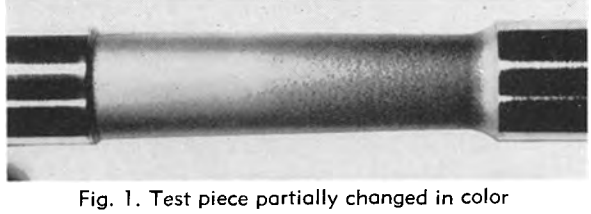

Fig. 1. Test piece partially changed in color

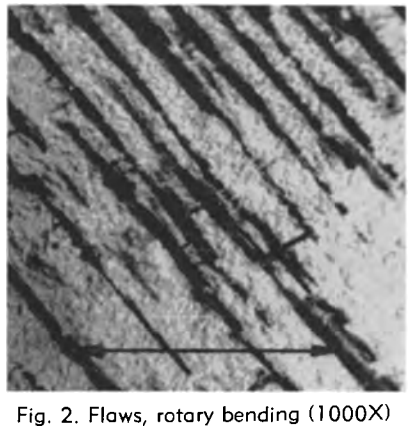

Fig. 2. Flaws, rotary bending (1000X)

[1] Similar flaws are also found when brass is used as the ground metal instead of steel.

Being only in the surface, the flecks are readily removed by slight electropolishing.

*Grain growth in plated metal.*—Microscopic examination of the surface and cross section of a specimen having been color-changed, electropolished, and etched, reveals the nature of grain growth in the plated metal. Figures 6 and 7 are cross sections of specimens showing the initial status of grain growth, namely, the number of repetitions of cyclic stress has been below one million, the flecks have not as yet appeared, and the surface of the specimen has not changed in color, while the physical change as shown in the figures is already found in the plated metal.

With sufficient increase in the number of repetitions of cyclic stress, the grains grow up to the surface of the plated metal, as shown in Fig. 8 and 9, and the flecks are produced.

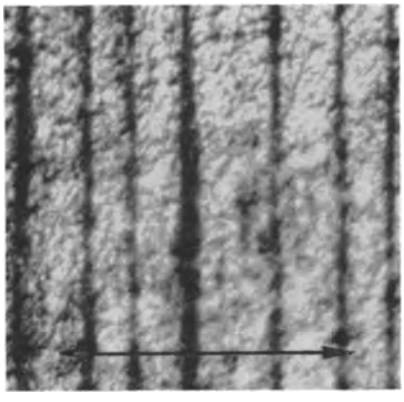

Fig. 3. Flaws, torsion (1000X)

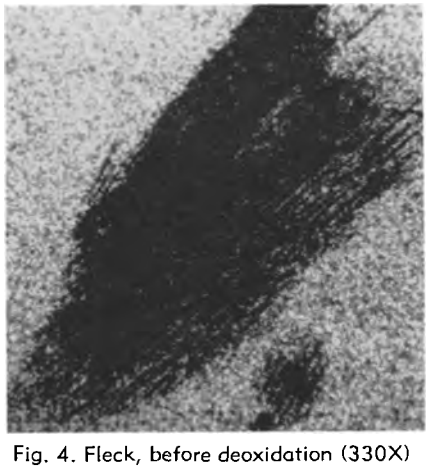

Fig. 4. Fleck, before deoxidation (330X)

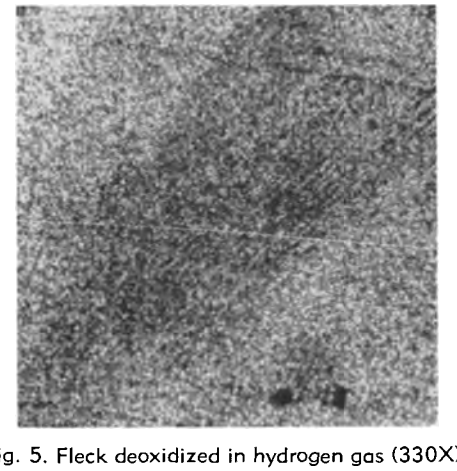

Fig. 5. Fleck deoxidized in hydrogen gas (330X)

Fig. 6. Initial status of grain growth, after direct stress of $\pm 18$ kg/mm$^2$ for $9 \times 10^5$ cycles (1000X).

Fig. 7. Initial status of grain growth, after direct stress of $\pm 18$ kg/mm$^2$ for $9 \times 10^5$ cycles (1000X).

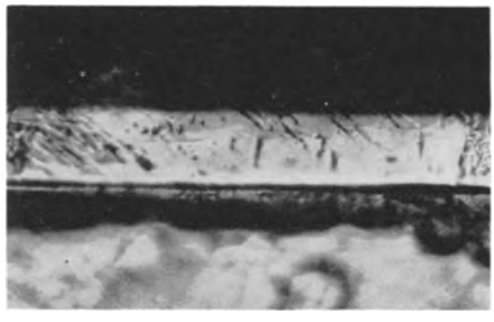

Fig. 8. Grown grain, after direct stress of $\pm 18$ kg/mm$^2$ for $5 \times 10^6$ cycles (1000X).

Figures 10 and 11 are micrographs, the former of a fleck and the latter of a figure on the etched surface after slight electropolishing. By means of etching, one can distinguish easily between the part changed in physical constitution and the remaining part, namely, between a large grown grain and the neighboring micrograins.

Comparison of the x-ray patterns before and after stressing also suggests grain growth in the plated metal. X-ray patterns are shown in Fig. 12 and 13.

These results show that, when a specimen plated with copper is submitted to reversals of cyclic stress, if the magnitude of the stress exceeds the "proper stress",[2] some of the micrograins in the plated metal gradually grow to a considerable size with increase of the number of repetitions. Then the microgroups of fine flaws appear on the surface of these grown grains.

[2] In a previous paper, the limit value of the cyclic stress within which the flecks are not produced by fatigue is termed "proper stress" of the plated metal. The value of the proper stress, however, is a nominal one and is not the true value of the stress arising in the plated metal since it is calculated from the bending moment or the twisting moment acting on a specimen and ignores the difference between the elastic moduli of copper and steel; the value of the proper stress is based on the elastic modulus of the underlying steel. The proper stress is usually much smaller than the endurance limit of the steel.

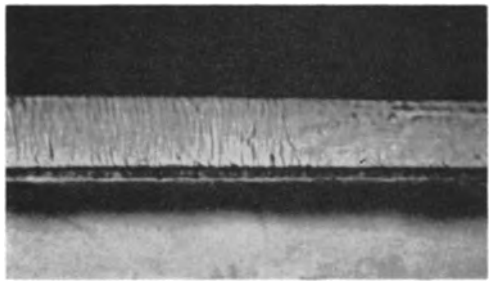

Fig. 9. Grown grain, ofter direct stress of $\pm 20$ kg/mm$^2$ for $5 \times 10^6$ cycles (1000X).

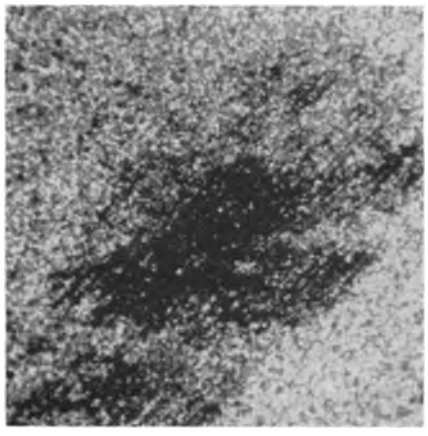

Fig. 10. Fleck (330X)

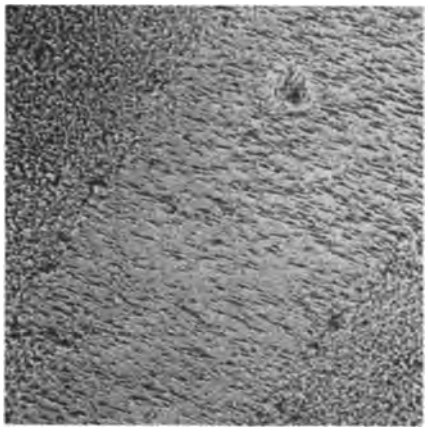

Fig. 11. Etched figure after electropolishing, showing a grown grain and the neighboring micrograins (330X).

*Size of grown grains.*—The size of grown grains is almost equal to the size of flecks and often to the grain size of the underlying steel. The grain size of the ground metal may affect the size of grown grains, but the definite relation between them is not yet known.

The size of grown grains is considerably affected by various conditions even though the same ground steel is used, for example by a slight difference in plating solution, by the temperature of deposition, by the heat treatment of specimens, and other factors.

The size of grown grains is much smaller when the plating solution is made with cupric oxide instead of commercial copper sulfate, when the temperature of deposition is much higher than room temperature, and when specimens are annealed at a temperature near 250°C.

In cases where the size of grown grains is quite small, the grain growth generally occurs at a lower value of cyclic stress than usual and the value of the proper stress is appreciably reduced. The microgroups of fine flaws described usually are not found in this case.

Figure 14 is a surface view showing grown grains in the plated metal when the plating solution is made with commercial grade copper sulfate. Figures

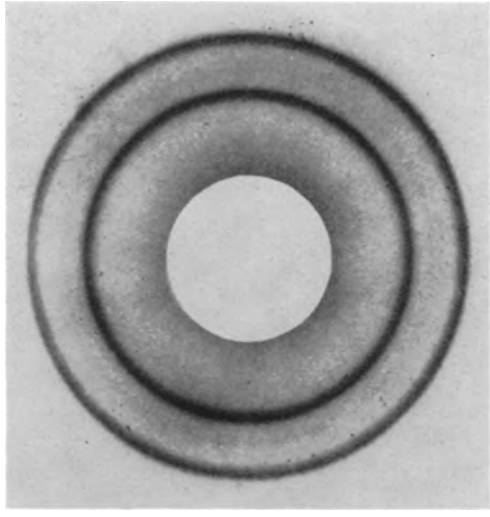

Fig. 12. X-ray pattern, before stressing

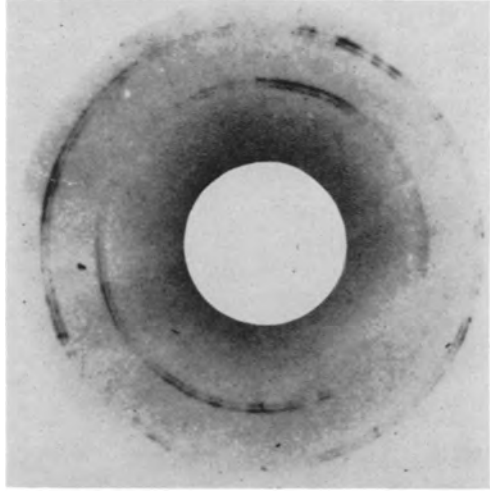

Fig. 13. X-ray pattern, after direct stress of $\pm 22$ kg/mm$^2$ for $16 \times 10^6$ cycles.

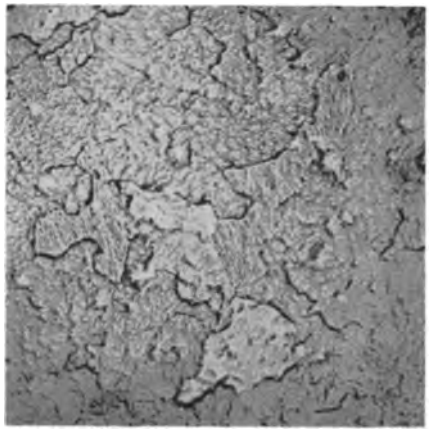

Fig. 14. Grown grains, plating solution made with cupric oxide (330X).

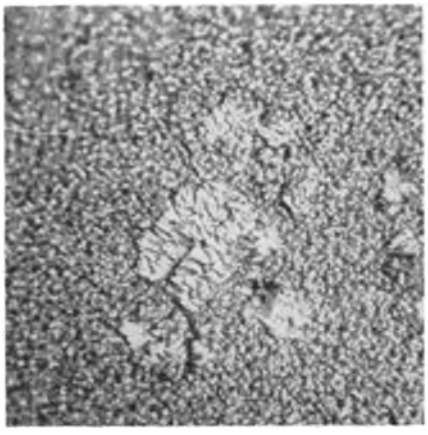

Fig. 15. Annealed at 250°C, before stressing (1000X)

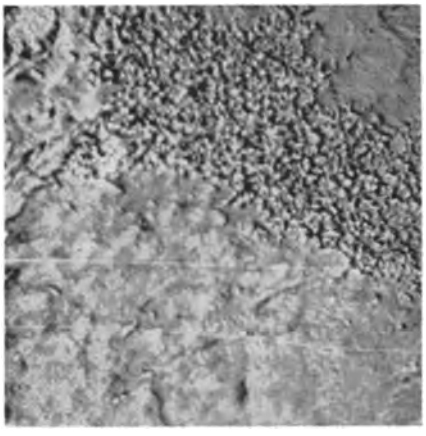

Fig. 16. Annealed at 250°C, after stressing (1000X)

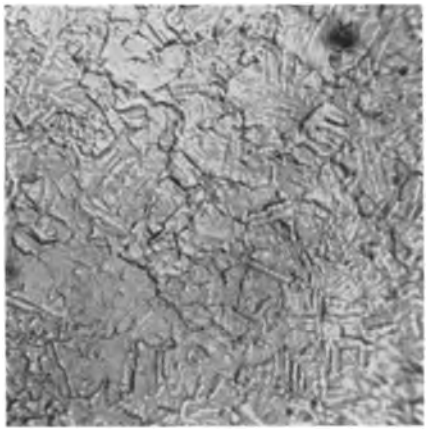

Fig. 17. Annealed at 350°C, before stressing (1000X)

15 and 16 are surface views showing the constitution of the plated metal before and after stressing, respectively, when the specimen is annealed at 250°C for 1 hr in vacuum. As is shown in Fig. 15, the recrystallization of copper occurs in part by the heat treatment. Comparing Fig. 14, 16, and 11, it would appear that the size of grown grains becomes much smaller than in the usual case.

*Effect of heat treatment.*—Figures 17 and 18 show the surface of the plated metal annealed at 350°C before and after stressing, respectively. In this case, since the progress of recrystallization of copper is considerably advanced, the grain growth caused by cyclic stress does not occur and the flecks described

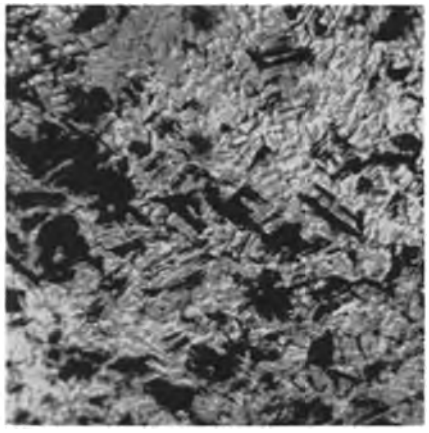

Fig. 18. Annealed at 350°C, after stressing (1000X)

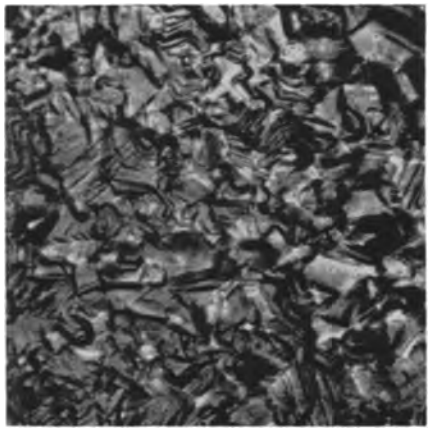

Fig. 19. Annealed at 600°C, before stressing (1000X)

are not produced. The surface of a specimen submitted to cyclic stress, however, becomes tarnished owing to the appearance of microflaws, as shown in Fig. 18.

Figures 19 and 20 are views of the surface and cross section of the plated metal annealed at 600°C, where the recrystallization of copper is complete. The endurance limit of annealed copper (3) almost agrees with the true value of the proper stress of the plated metal. Consequently, when the magnitude of the cyclic stress passes the proper stress, fatigue cracks appear instead of the flecks, as shown in Fig. 21.

## Conclusion and Remarks

The experimental results described indicate that the flecks are produced only when the grains constituting the plated metal develop in sufficient size to reach its surface and can never be produced when grain growth does not occur.

The mechanism of the flecking and the substance which causes the chemical change creating the flecks have not been definitely known until now. It may be concluded that the chemical change is due to some substance contained in the plated metal and not to oxygen in the atmosphere. This is verified by the fact that, when a specimen is isolated from the air by a coating of vinyl prior to stressing, it changes as usual in color while there is no discernible change in the appearance of the flecks.

As was described in a previous paper, the predominating stress producing the flecks is shearing

Fig. 20. Annealed at 600°C, before stressing (1000X)

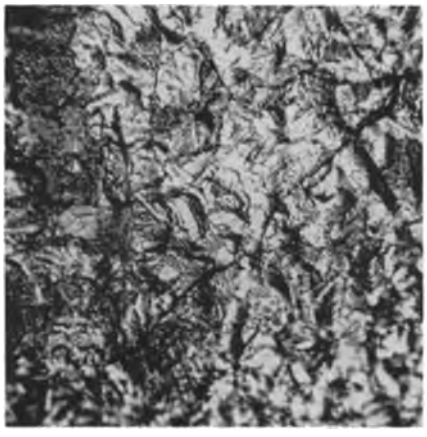

Fig. 21. Annealed at 600°C, after stressing (1000X)

stress (4). Consequently, the physical change in the constitution of the plated metal can be attributed to the reversals of shearing strain.

It is known that a very small quantity of gelatine mixed in the plating solution raises the value of the proper stress remarkably (4). The gelatine, mixed with the micrograins of the plated metal, prevents the grains from growing and resists orientation of flecks.

The temperature rise on the plated metal during stressing has been measured by Kikuchi[3] by means of the electrostrain gauge. According to his findings, the temperature rise begins at the point of proper stress, but amounts to only several degrees even for stressing in considerable excess over the proper stress. It is concluded that such a small temperature rise cannot be the cause of grain growth, which then must be attributed to a purely mechanical cause.

### Acknowledgment

The authors express their thanks to Mr. K. Hosono for his help in preparing the micrographs. Their thanks are also due to the Ministry of Education of Japan for their Grant-in-Aid for Fundamental Scientific Research.

Manuscript received March 4, 1957.

Any discussion of this paper will appear in a Discussion Section to be published in the June 1959 JOURNAL.

REFERENCES

1. H. Ōkubo, *J. Appl. Phys.*, **24**, 1130 (1953); H. Ōkubo and S. Satō, *J. Appl. Mechanics*, **22**, 193 (1955); H. Ōkubo and K. Takai, *ibid.*, **23**, 478 (1956); H. Ōkubo, *Mem. Fac. Eng., Nagoya Univ.*, **6**, 23 (1954); H. Ōkubo and S. Kikuchi, *J. Appl. Mechanics*, **24**, 313 (1957).
2. M. Suzuki, paper presented at Annual Meeting, Japan Society of Mechanical Engineers, Tokyo, 1955; *Z. Metallk.*, **48**, 395 (1957).
3. N. Thompson, N. Wadsworth, and N. Louat, *Phil. Mag.*, **1**, 113 (1956).
4. H. Ōkubo, *Science of Machine* (in Japanese), **7**, 431 (1955).

[3] S. Kikuchi, graduate student at Nagoya University.

# Surface Phenomena Associated with Application of Organic Films to Phosphor Screens

**R. W. Dudding and D. J. Finnett**

*Research Laboratories, The General Electric Company Limited, Wembley, England*

ABSTRACT

The production of aluminized screens for cathode ray tubes involves the formation of a temporary organic barrier film on the phosphor coating on which the aluminum may be deposited. Defects in this film produce undesirable blemishes on the finished screen. Certain inherent defects encountered when employing a "flow filming" technique are described, and the fundamental factors governing their formation and prevention are considered.

The use of aluminized cathode ray tube screens has become almost universal in the manufacture of television picture tubes and to a lesser extent in the manufacture of instrument and radar tubes. The well-known technique of aluminizing screens involves the production of a temporary organic barrier layer or film upon which the reflecting aluminum coating may be deposited, usually by evaporation in vacuum. The success of the aluminizing process depends largely on the production of this organic film free from variations in thickness and imperfections which would allow the aluminum to penetrate round the phosphor crystals and so cause local undesirable reductions in the light output from the screen. It is also necessary for this layer to be extremely thin (less than 1$\mu$) and to be composed of a material that may be removed from the screen during subsequent baking treatment. Nitrocellulose and methacrylic resins have been found to be suitable film forming materials.

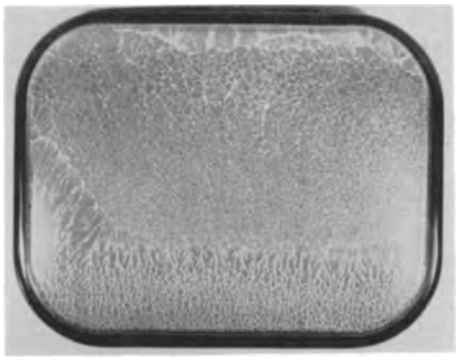

Fig. 1. Generol appearance of lace pattern in the lacquer film on a 14-in. screen.

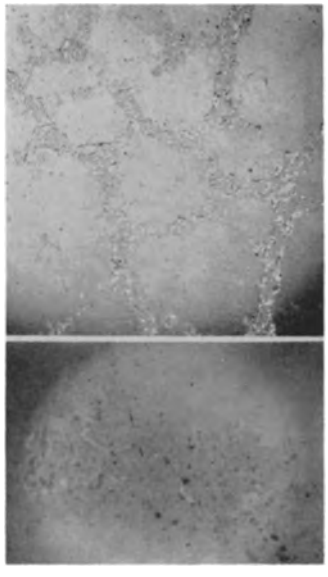

Fig. 2. Areas of laced film showing tendency to globulization and lens formation. Magnification, top 50X, bottom 100X before reduction for publication.

The barrier layer has been prepared by several different techniques, each presenting its own particular problems and producing characteristic defects. It is proposed to limit this paper to a brief description of a "flow filming" technique, as it has come to be called, and to a study of some associated surface phenomena.

Although a complete quantitative explanation of all aspects of the phenomena has not been possible, an outline will be given of the fundamental factors involved, together with appropriate results of more empirical investigations. In the investigations, phosphor screens have been produced by a potassium silicate settling process with barium nitrate as the precipitant and electrolyte.

### *Flow Filming Process*

The flow filming technique consists essentially of the following operations:

1. An excess of a dilute solution or lacquer of a film forming resin in a water immiscible solvent, for example butyl methacrylate in toluene, is spread over the surface of the water-moistened screen. A water-moistened screen is here considered to be a screen wherein the capillaries between the phosphor grains are filled or partially filled with water or other aqueous solution.
2. Excess lacquer is drained off.
3. The resultant liquid film is allowed to solidify by evaporation of the solvent, thus forming a solid film.

### *Defects in the Film Structure*

When the lacquer is applied under specific conditions of screen wetness and substrate pH and also when particular lacquers are used, the liquid film so produced breaks up and the resultant solid film forms a lacelike pattern, as shown in Fig. 1. These patterns consist of regions of varying film thickness or absence of film and vary in size from small starlike shapes to large irregular areas. A closer examination of solid films removed from screens indicates that the regions of laced films do themselves consist of a minute structure of thick and thin film as shown in Fig. 2.

It has been found that this structure does not occur on phosphor screens only, but may be produced with the same materials on any porous surface such as moistened filter papers and sintered glass plates.

## Basic Theoretical Considerations

Factors governing the stability of surface films of one liquid on another have been studied by many workers (1-5). Consider the conditions that govern the spreading of a liquid A of surface energy $\gamma_A$ per unit area on a denser liquid B of surface energy $\gamma_B$ per unit area. Liquid A spreads spontaneously, producing a liquid-liquid interface of energy $\gamma_{BA}$ per unit area and a liquid-gas interface of energy $\gamma_A$ per unit area if

$$\gamma_B > \gamma_{BA} + \gamma_A$$

Further, if the volume of liquid A is not so great as to maintain gravitational spreading, liquid A contracts to a lens leaving only a nonduplex thin film (probably a monolayer) at the original interface of energy $\gamma_{BA}$ per unit area if

$$\gamma_{Ba} < \gamma_A + \gamma_{BA}$$

All known liquid pairs having $\gamma_B > \gamma_{BA} + \gamma_A$ have $\gamma_{Ba} < \gamma_A + \gamma_{BA}$. The tendency is therefore for all spreading liquids to contract to a lens-monolayer equilibrium of minimum free energy.

If it were possible to find suitable liquids having initially

$$\gamma_B > \gamma_A + \gamma_{BA}$$

and finally

$$\gamma_{Ba} > \gamma_A + \gamma_{BA}$$

then liquid A would remain in stable equilibrium as a duplex film of multimolecular thickness.

Consider the relation between these fundamental factors and the flow filming technique. When the wetted screen is flow filmed, spreading is achieved initially by an excess of lacquer flowing over the surface. That is, the spreading of a multimolecular liquid film is promoted by gravitational forces. When the excess lacquer is drained off and the solvent begins to evaporate the tendency will be for the still fluid system to resolve into the state of minimum free energy, that is, a lens-monolayer state in the case of an initially spreading lacquer or a lens only in the

case of a nonspreading lacquer. The degree to which this is accomplished and the particular form it takes depends on the magnitude of the resultant contractile forces, the viscosity of the lacquer, and the structure and water content of the phosphor screen.

### Influence of Water Content

The quantity of water held in the screen has an important influence on the stability of the film of liquid lacquer. The two extreme conditions are (*a*) a screen in which the phosphor crystals are coated with a thin film of water only, as shown in Fig. 3(a), and (b) a screen in which the majority of the phosphor crystals are submerged in water, as shown in Fig. 3(b).

In the first condition, the lacquer is held in the screen capillaries; if only contraction occurs, it is within the capillaries. In the second condition, the lacquer film should contract, while it is still fluid, to a single lens in equilibrium with a monolayer. Between these two extremes there is "lacing," the formation of a multitude of lens-monolayer or lens systems of varying sizes.

Further, as shown in Fig. 3(a) condition (*a*) provides a much larger lacquer-water interface area than is provided by condition (*b*), (*see* Fig. 3a and 3b). This also has an important influence on the stability of the lacquer film.

Assuming that the surface of the lacquer is substantially at the same level initially with respect to the phosphor for all conditions of wetness of the screen, then the surface area of the lacquer will be constant.

Thus, if the ratio of the interface area to the surface area is $m$, then initially the free surface energy $E_1$ of a completely spread duplex film of area $S$ is given by

$$E_1 = S(\gamma_A + m\,\gamma_{BA})$$

where $\gamma_A$ is the surface energy of lacquer per unit area; $\gamma_{BA}$ is the interfacial energy of lacquer per unit area.

If the film contracts to an area $(S - S')$ leaving a monolayer at the original interface of area $S'$ $m$ then the free energy $E_2$ is now given by

$$E_2 = (S - S')(\gamma_A + m\gamma_{BA}) + S'\,m\gamma_{B_2}$$

where $\gamma_{B_2}$ is the monolayer energy per unit area. Contraction to a lens-monolayer equilibrium will not occur if

$$E_2 > E_1$$

i.e.,

$$(S - S')(\gamma_A + m\gamma_{BA}) + S'\,m\gamma_{B_2} - S(\gamma_A + m\gamma_{BA}) > 0$$

or

$$m\gamma_{B_2} > \gamma_A + m\gamma_{BA}$$

That is,

$$\frac{\gamma_{B_2}}{\gamma_{BA}} > 1 + \frac{\gamma_A}{m\gamma_{BA}}$$

By increasing the water content, which reduces $m$, contraction to a lens-monolayer formation and therefore lacing should be more likely to occur.

In practice these findings are confirmed. Screens drained for different times before filming with a lacquer known to be prone to lacing are found to exhibit lacing to a varying degree as shown in Fig. 4. It is therefore desirable to work with the

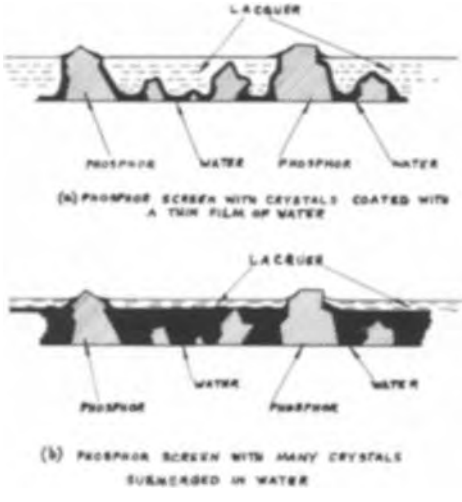


Fig. 3. Diagram of section of screen structure indicating the effect of the quantity of water held in the screen on the lacquer/water interface area.

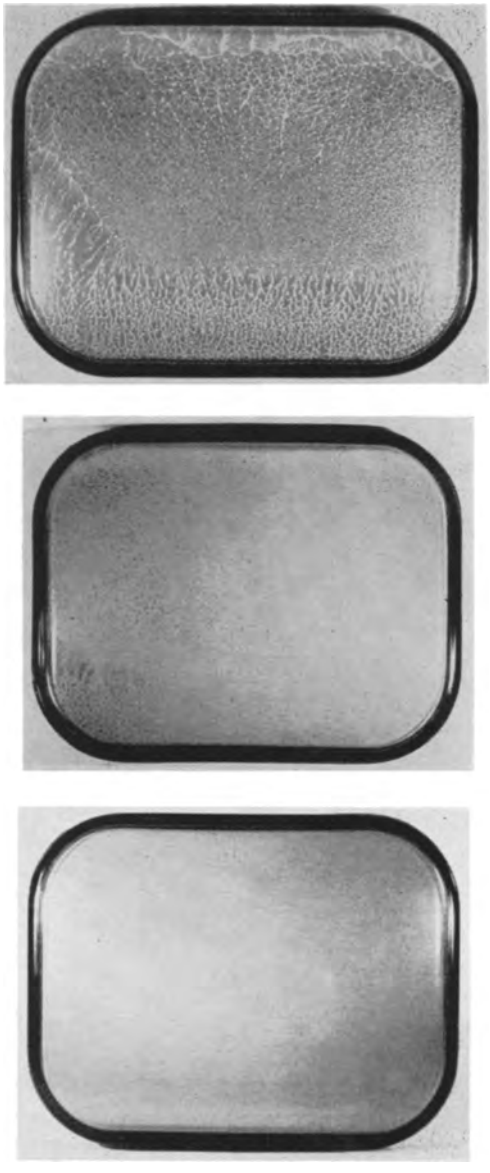

Fig. 4. Effect of water draining time on the lacing of lacquer films: top, 20 min draining; center, 1½ hr draining; bottom, 6 hr draining.

longest possible draining time, provided a state is not reached when too little water is present, which results in lacquer penetrating the phosphor layer and thus screen darkening after aluminizing. A compromise between these two conflicting requirements is generally necessary.

### Influence of Lacquer Viscosity and Composition

Immediately the lacquer has spread on to the surface of the moistened screen the solvent commences to evaporate and the viscosity of the still fluid film increases. It is desirable that the viscosity of the lacquer film should rise to a level sufficient to prevent migration of the lacquer and the formation of lace patterns. This may be achieved either by working with a high solid concentration, for example greater than 10% resin in solvent, or by using a polymeric resin of high molecular weight. The latter is preferable as it possesses the advantage of being able to achieve the high viscosity at low concentrations which in turn produces dried films of low thickness, a desirable feature when considered in relation to the subsequent bake-out and processing of the tube.

The constitution of the lacquer and also of the substrate has been found to influence the degree of the lacing defect. For example, a lacquer composed of iso-butyl methacrylate, toluene, and a poly-alkylene glycol derivative plasticizer was found to lace to a very much greater extent than the same lacquer plasticized with dibutyl phthalate or tri-cresyl phosphate. Additions of a nonionic surface active agent such as polyethylene glycol monoleate or an ionic surface active agent such as dioctyl sodium sulfosuccinate (Aerosol OT) to the lacquer caused very bad lacing and in the extreme cases an apparent complete inability of the lacquer to wet the screen surface. An example of such a case is shown in Fig. 5. This probably occurs because a very thin film of the surface active constituent spreads out rapidly over the moistened surface of the screen and in so doing reduces the surface energy $\gamma_A$ to an extremely low value so that initial spreading of the lacquer is prevented.

### Influence of *p*H

Water substrates of different *p*H produce different degrees of lacing; the higher the *p*H the less is the tendency toward lacing. This is shown in the difference in the results obtained when filming is carried out on either nondried silicate settled screens after decanting or on screens rewetted with de-ionized water. In the former case at *p*H 11 the lacing is less than in the latter case at *p*H 8. Depression of the *p*H to below 4 by the use of buffer solutions for rewetting produces an even greater tendency toward lacing.

The interfacial tension of toluene-butyl methacrylate lacquers on substrates of varying *p*H has been determined, according to Antonow's rule, from the difference between the surface tensions of the mutually saturated phases, the surface tensions being measured by the well-known capillary rise method. The interfacial tension is found to decrease as the *p*H increases, as shown in Fig. 6. From earlier considerations this would be expected to promote spreading of the lacquer. Changes in the monolayer energy might likewise be expected, but measurements of the monolayer tension have been rendered difficult and the results unreliable on account of the presence of solid resin which produces rigid layers. The mechanism of the reduction in interfacial energy is likely to be similar to that reported by Zisman (6) on the spreading of oil drops containing long chain acids.

Fig. 5. Effect of the addition of surface active agents to lacquer showing the nonwetting of the moistened screen by the lacquer.

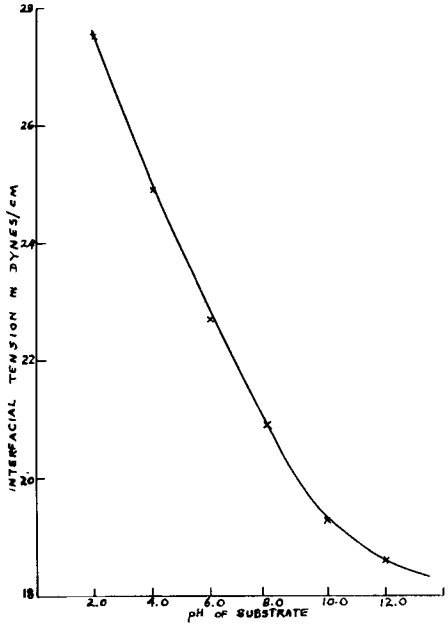


Fig. 6. Variation in interfacial tension of 8% butyl methacrylate in toluene with increasing pH of substrate.

### Surface Tension of Substrate

Changes in the surface tension of the rewetting water due to accidental or intentional contamination would be expected to alter two factors: (*a*) the quantity of water held in the screen capillaries, and (*b*) the spreading characteristics of the lacquer. These two factors would be expected, as indicated previously, to affect lacing. In order to confirm this the surface tension of the rewetting water was reduced by adding a detergent, Teepol X (Shell Chemicals) and ethyl alcohol, respectively.

Addition of 1% by volume of Teepol X, resulting in a drop in the surface tension of the water to 34 dynes/cm, was found to cause very bad lacing and inability of any lacquer to wet the surface.

The following observations were made on normally nonlacing lacquers applied on rewetting water containing various concentration of ethyl alcohol.

| Surface tension of water/alcohol solution, dynes/cm | Observations |
|---|---|
| 52 | No lacing observed |
| 45 | Slight tendency toward lacing and globulization |
| 37 | Very bad lacing and considerable globulization |
| 30 | Lacquer did not appear to wet surface at all and remained as globules. |

## Spreading of Lacquers on Aqueous Substrates

The foregoing considerations and a study of the lacing defect indicate that it is allied to the problem of the spreading of lacquers on free aqueous surfaces. In order to study the spreading properties of lacquers more closely, known small volumes of various lacquers have been spread on the surface of various aqueous solutions. The diameter of the liquid lens produced has been considered a guide to the spreading properties of the system.

Considering the conditions when a drop of liquid A of volume $V$ is spread on the surface of a liquid B of surface area $S$. If $\alpha$ is the initial surface area of the drop resting almost on B and $F(g)$ its initial gravitational energy, then the initial free energy of the system is given by

$$E_1 = \alpha\gamma_A + S\gamma_B + F(g) \qquad (I)$$

where $\gamma_A$ is the surface energy of A per unit area and $\gamma_B$ is the surface energy of B per unit area. If, on spreading, the lens is assumed to approximate to a flat cylinder, i.e., its radius is large compared with its height, then if $H$ is the height of and $\alpha'$ the area of the lens,

$$V = h\alpha'$$

and the final free energy $E_2$ is given by

$$E_2 = (S - \alpha')\gamma_{Ba} + \alpha'(\gamma_A + \gamma_{BA}) + f(g) \qquad (II)$$

where $\gamma_{Ba}$ is the surface energy of a monolayer of A on B and $f(g)$ the final gravitational energy of the lens. Then the free energy decrease $\delta E$ is $E_1 - E_2$. Therefore

$$\delta E = S(\gamma_B - \gamma_{Ba}) + \alpha\gamma_A + F(g) - f(g) - \alpha'(\gamma_A + \gamma_{BA} - \gamma_{Ba}) \qquad (III)$$

For equilibrium

$$\frac{d(\delta E)}{d\alpha'} = 0$$

i.e.,

$$-\frac{df(g)}{d\alpha'} - (\gamma_A + \gamma_{BA} - \gamma_{Ba}) = 0 \qquad (IV)$$

but $f(g) = (V\rho gh)/2$ and $h = V/\alpha'$
where $\rho$ = density of liquid A

$$\therefore f(g) = \frac{V^2\rho g}{2\alpha'} \text{ and } \frac{df(g)}{d\alpha'} = \frac{-V^2\rho g}{2\alpha'^2} \qquad (V)$$

from Eq. (IV) and (V)

$$\gamma_A + \gamma_{BA} - \gamma_{Ba} - \frac{h^2\rho g}{2} = 0$$

Thus it is seen that the thickness of the lens is dependent on the surface, interface, and monolayer energies, and anything that alters these energies would be expected to alter the height and therefore the diameter of the lens.

Numerous experiments were carried out to determine in practice the effect of changes in these parameters. It was noted that in all cases where the surface of the water was not previously contaminated, a thin film (probably a monomolecular layer) spread out in front of the main body of lacquer. The latter in many cases spread considerably initially but then contracted to a stable lens in equilibrium with the confined monolayer. Other lacquers spread more slowly initially but retained a larger lens diameter without contraction. It was found that lacquers prone to lacing exhibited the phenomena of initial spreading followed by contraction to a small diameter lens, whereas nonlacing lacquers spread without contraction to a lens of much greater diameter. Spreading was found to be greater on aqueous solutions of high $p$H than on solutions of low $p$H.

Spreading was greatest when the atmosphere over the lens and monolayer was saturated with solvent vapor.

These effects serve to indicate, without considering their mechanism, the type of phenomena that may be expected when changes are made in the various parameters of the system.

## Summary and Conclusions

Some of the problems relating to the formation of stable films have been outlined.

It has been shown that these problems are fundamental to the nature of the materials involved. The development of a satisfactory filming process depends on the choice of the solvents, resins, and aqueous substrates having the correct surface energy characteristics and on the control of the water content in the screen. The importance of avoiding contamination from surface active impurities has been shown.

Manuscript received Sept. 26, 1957. This paper was prepared for delivery before the Washington Meeting, May 12-16, 1957.

Any discussion of this paper will appear in a Discussion Section to be published in the June 1959 JOURNAL.

REFERENCES

1. W. D. Harkins, *J. Chem. Phys.*, **9**, 552 (1941).
2. I. Langmuir, *ibid.*, **1**, 756 (1933).
3. W. D. Harkins, "Physical Chemistry of Surface Films," p. 94, Reinhold Publishing Corp., New York (1952).
4. Freundlich, "Colloid and Capillary Chemistry," p. 96, Methuen, London (1926).
5. R. S. Burdon, "Surface Tension and the Spreading of Liquids," pp. 33, 53, Cambridge University Press (1949).
6. W. A. Zisman, *J. Chem. Phys.*, **9**, 534 (1941).

# Melted Layer Crystal Growth and Its Application to Germanium

**F. H. Horn**

*Research Laboratory, General Electric Company, Schenectady, New York*

ABSTRACT

Single-crystal material of constant impurity distribution may be grown conveniently from a doped melted layer maintained above solid retained in a crucible. As crystal is withdrawn from the melt, fresh material is supplied to the melted layer by moving the melted layer downward through the solid. A single crystal may be grown using direct high-frequency coupling to heat the melted layer if fluctuating components of the field are removed. Data are given for resistivity profiles of germanium crystals doped with antimony and grown with manual operation of the heaters.

The growing of a single-crystal material is usually performed to obtain "good" crystal containing the desired concentrations of specific impurities. The Czochralski method (1) for growing crystals from a melt yields "good" crystal. With doping, however, the fraction of crystal containing a certain range of impurity concentration is governed by the segregation coefficient. This fraction of crystal is smaller, the smaller the allowable range of impurity concentration for a particular use and the smaller the segregation coefficient for the impurity. The problem becomes particularly acute if one desires a high concentration of an impurity with a very small segregation coefficient, for in such a case a significant fraction of the material grown may be polycrystalline.

A more uniform distribution of impurity may be obtained by zone levelling in a boat (2) or by the floating zone (3) procedure. Single-crystal germanium grown in a boat appears to require special annealing in order to reduce the number of crystalline imperfections introduced by constraint by the boat during growth (3). These studies also indicate that the after-anneal may drastically reduce the lifetime. The properties of germanium render difficult the application of the floating zone technique for single-crystal growth although this technique would obviate the problems involved in using boats and crucibles. With the availability of crucible materials that do not react with the molten semiconductor, such as quartz or graphite for germanium, the unconstrained growth of a crystal having an impurity distribution such as is realized by zone levelling may be obtained by a "melted layer" procedure.

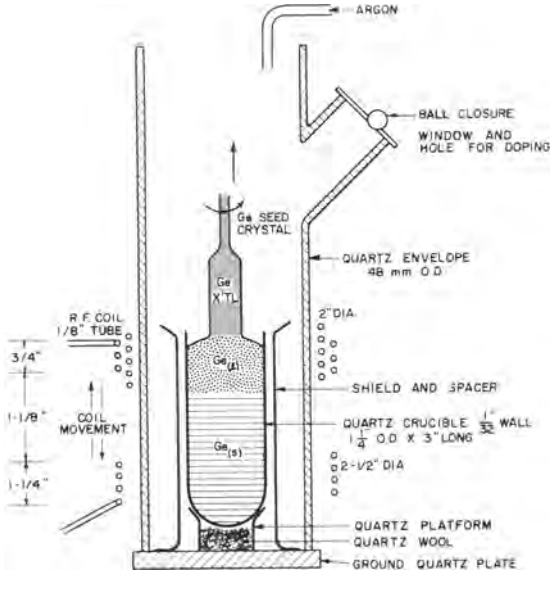


Fig. 1. Schematic arrangement of parts for growing crystal by a "melted layer" procedure.

In the melted layer arrangement, shown diagrammatically in Fig. 1, homogeneous solid is retained in a vertical crucible. A layer of melt is established at the top of the original solid. This may be inoculated with one or more impurities. A monocrystal seed is introduced into the melt and, after attention to making a good splice, a single crystal of the material is withdrawn gradually. As crystal is withdrawn, the volume of melt is regulated by melting the solid below the melted layer. This is readily accomplished by lowering the heating coils.

The principles governing the distribution of impurities follow those decribed by Pfann (2). Attention must be given to impurities present accidentally or intentionally in the solid as well as to those that may be added intentionally to the melt. In the application of the principles of zone levelling to the melted layer procedure, allowance must be made for the fact that the crystal will in general be smaller in diameter than the original solid. In practice, the diameter of the growing crystal is surprisingly constant for a given diameter of crucible and for a particular rf coil arrangement; it appears to be controlled by the rounded shape of the melt surface rather than by growth rate or power input. The fact that the diameter of the growing crystal is quite insensitive to factors other than those arising out of the original design is convenient for programming the rate at which the rf coil must move downward in order to maintain a constant volume of melt. The rate, $L$, for downward movement of the coil may be derived from simple considerations to be

$$L = \frac{P}{(D^2/d^2) - 1}$$

where $P$ is the linear rate at which the crystal is raised and $D$ and $d$ the diameters of the crucible and crystal, respectively. This relation is adequate if the

segregation coefficient is very small (e.g., $< 0.01$). The rate must be reduced if the segregation coefficient is large enough that the concentration in the crystal reduces substantially the concentration in the melt. This situation can also be taken care of by using a conical shaped crucible. In practice in order to maintain a constant melt volume it has been found necessary to decrease the power or reduce the rate of coil movement as the melted layer approaches the bottom of the crucible.

## Experimental

There are several problems encountered in conducting the melted layer procedure satisfactorily; two arise from the use of rf power for melting and the other from the expansion of germanium on freezing if a quartz crucible is used. Quartz is particularly convenient to use when programming by viewing. With automatic programming, a graphite crucible is satisfactory and then this problem peculiar to the use of quartz is obviated. The problem of obtaining a good splice is more difficult using directly coupled rf heating rather than conventional radiative heating. The seed crystal (usually small) is relatively cold. Of several ways to overcome this difficulty the easiest is to raise the melt temperature substantially. This can be done without increasing the width of the melted layer by temporarily increasing the rf power and raising the rf coils at the same time. A second difficulty arising from the use of ordinary rf power is the agitation of the melt which is usually severe enough to prevent single-crystal growth. By filtering the rf output of a standard electronic oscillator with a choke-capacitor combination, most of the fluctuating components of the rf field are removed, and agitation of the melt is reduced to a degree where there is no interference to single crystal growth.

In order to start with homogeneous solid in the crucible, it is desirable to freeze rapidly the initially molten charge. When quartz is used this ordinarily results in cracking of the crucible. No cracking need be experienced if the solid is maintained at a temperature at which it is plastic, for germanium above about 600°C (5). This situation may be realized by winding the single rf coil in two sections, a tightly wound portion for maintaining the melted layer, and an auxiliary section of more open winding to keep the solid in its plastic temperature range.

## Procedure and Results

Although the crystal pulling and rotation mechanism is automatic, the mechanism for moving the rf coils—a simple screw thread—was operated manually. The power source was a standard 5KW 450kc General Electric oscillator with the output filtered as described, using a 5000 v, d-c, 20.5 $\mu$f capacitor and large choke coil of several henrys. A typical charge for the crucible was 300 g of zone-refined germanium. After melting and rapid freezing, a melted layer approximately 5/8 in. wide was established. The volume of melt was readily estimated from the diameter of the crucible. The amount of doping was computed on the simple basis that $C = K C_i$, where $C_i$ is the concentration of added impurity necessary in the melt to produce the concentration, $C$, of that impurity in the solid, and $K$ is the segregation coefficient. After doping, the seed is introduced into the melt and crystal growth initiated. As the crystal is grown, the coil is lowered at a rate to preserve the width of the melted layer. The width of the layer was estimated from visual observation and consequently fluctuations were of the order of $\pm$ 1/16 in.

Two typical results will be reported that have a bearing on (*a*) the quality of crystal, and (*b*) the uniformity of impurity distribution under a normally adverse condition of high concentration of impurity for which the segregation coefficient is small.

In order to check that crystals grown by the melted layer procedure are substantially the same as those grown by the Czochralski method, zone-refined germanium was grown into a single crystal without any doping. The lifetime of crystal grown under the melted layer condition ranged from 1.2 $\mu$sec near the splice to 850 $\mu$sec in the region just prior to normal growth. Crystals grown by the standard Czochralski method on this material bracketed closely 1 $\mu$sec for lifetime. To the extent that lifetime is an index for crystal perfection at a given level of purity, there does not appear to be any significant difference between the quality of crystals grown by the melted-layer procedure or by the Czochralski method. The lifetime of these crystals is substantially better than those reported grown in a boat with after anneal (4).

Using antimony ($K = 0.001$) as the doping agent, in obtaining a concentration of about $3 \times 10^{17}$ carriers/ccm in a crystal grown by the Czochralski method, approximately the last third of the crystal is usually polycrystalline. Figure 2 shows resistivity plotted as a function of the crystal length for two crystals grown by the melted layer procedure in which the melted layer was doped with antimony to produce 0.01 ohm-cm germanium. In the crystal A, although mechanical difficulty was encountered, 75% of the crystal shows a variation of $\pm$20% in resistivity. Twenty-seven grams or about 10% of the initial 300 g was lost due to polycrystalline material. This situation is to be compared (dashed line) with the 30% loss by normal growth and the

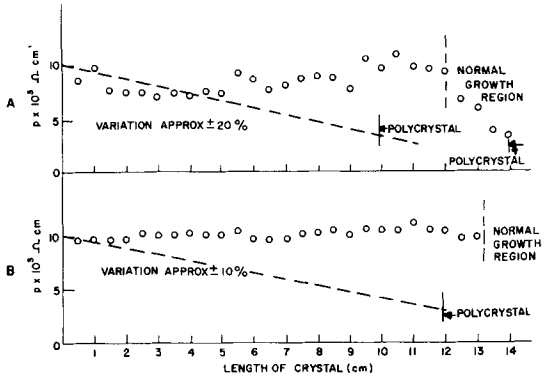


Fig. 2. Resistivity profiles for antimony-doped germanium crystals. Open circles experimental, melted layer growth; dashed line estimated for normal growth from melt.

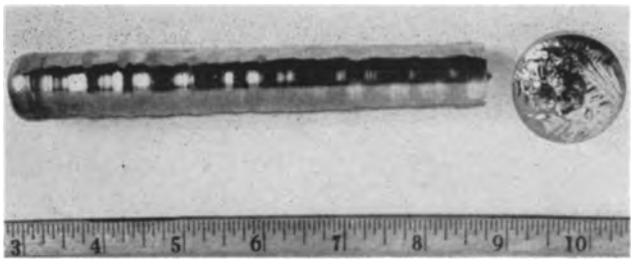

Fig. 3. Photograph of typical crystal from melted layer growth.

fact that only 50% of the original germanium would yield crystal within a factor of two for resistivity. In (B) of Fig. 2 is shown a resistivity plot for crystal grown reflecting only the variations introduced by manual operation of the coils. It may be seen that about 75% of this crystal has no more than a ± 10% variation in resistivity. A photograph of crystal B is seen in Fig. 3.

### Acknowledgments

The author is indebted to E. A. Taft and R. L. Watters for recognizing the source of difficulty of melt agitation using rf power, and for providing the filter to remove this difficulty.

Manuscript received Oct. 18, 1957.

Any discussion of this paper will appear in a Discussion Section to be published in the June 1959 JOURNAL.

### REFERENCES

1. J. Czochralski, *Z. physik. Chem.*, **92**, 219 (1918).
2. W. G. Pfann, *Trans. Am. Inst. Mining Met. Engrs.*, **194**, 747 (1952).
3. P. H. Keck, W. Van Horn, J. Soled, and A. MacDonald, *Rev. Sci. Instr.*, **25**, 331 (1954).
4. D. C. Burnett and B. Sawyer, *Bell Syst. Tech. J.*, **35**, 637 (1956)
5. C. J. Gallagher, *Phys. Rev.*, **88**, 721 (1952).

# A Study of the Molded Nickel Cathode

**C. P. Hadley and W. G. Rudy**

*Electron Tube Division, Radio Corporation of America, Lancaster, Pennsylvania*

**and**

**A. J. Stoeckert**

*Electron Tube Division, Radio Corporation of America, Harrison, New Jersey*

ABSTRACT

Research work on the molded nickel cathode is described. Results are given regarding the effects on emission and life of variations in nickel powder, alkaline-earth carbonates, reducing agents, sintering, and aging. Data on pulsed emission are presented.

This paper describes testing methods used in the evaluation of molded nickel cathodes and discusses the effect on cathode emission and life of various materials and processing techniques. Some of the early work on such cathodes was done by MacNair, Lynch, and Hannay (1). These authors discussed the fabrication of the cathodes, some of the useful properties, and gave a comparison between the emission of the molded cathode, oxide cathodes, and L cathodes. Other studies on the molded cathode were reported by Beck, Brisbane, Cutting, and King (2), Bell and Brewer (3), and by Haas and Jensen (4). In spite of the considerable previous work, only meager results have been presented regarding materials, processing, or life.

### Description of Molded Cathode

The structure of a typical molded nickel cathode is shown in Fig. 1. The cathode sleeve is a nickel cylinder having an outer diameter of 0.125 in., a length of about 0.33 in., and a wall thickness of 0.004 in. The cathode pellet is composed of two layers. The lower layer, about 0.045 in. thick, contains nickel powder and an activator ($ZrH_2$) in the weight proportions of 99:1. The upper part of the pellet, which is 0.003 to 0.005 in. thick, contains nickel powder (69% by weight), alkaline earth carbonates (30%) and an activator (1%). The nickel powder is fired at 600°C for 15 min in a hydrogen atmosphere (−10°C dew point). All powders are thoroughly dried before use.

The cathode pellet is formed and pressed into the sleeve at a pressure of 80 tons/in.$^2$ in a single step by use of a hardened steel die and hydraulic press. Active material is then removed from the edge of the cathode sleeve by rubbing with aluminum-oxide

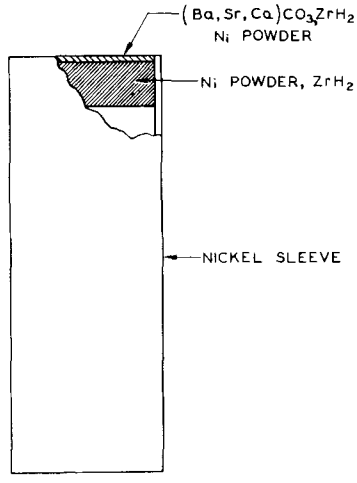


Fig. 1. Structure of a molded nickel cathode

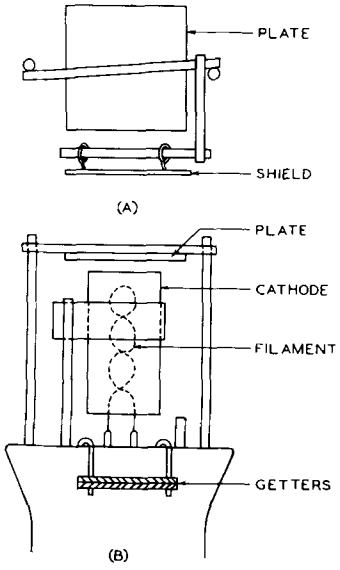


Fig. 2. Construction of test diode

paper. The most important step in the processing of the cathode is sintering, which is discussed in detail later. After sintering, the cathodes are stored in evacuated ampules until ready for use.

## Test Diode

Figure 2 is a drawing of the test diode used for emission measurements on molded nickel cathodes. The cathode is welded to a tantalum strip which, in turn, is welded to a stem lead. The plate, which is a flat piece of nickel or tantalum, is mounted at a suitable distance above the cathode so that the spacing between them is about 0.015 in. when the cathode is hot. The upper surface of the plate is sandblasted to promote radiation.

A tantalum evaporation shield [shown only in Fig. 2(A)] is mounted between the cathode and the glass envelope to keep the glass clean. This shield can be moved aside to permit pyrometric observation of the cathode temperature through the glass. Temperatures are measured near the top of the nickel cathode and are not corrected for either the emissivity of the nickel or the transmission of the glass. The temperatures quoted are, therefore, close to brightness temperatures.

No attempt is made to achieve an extremely high vacuum in the test diode. A typical evacuation schedule, which is more or less characteristic of industrial techniques, is given below.

1. The tube is baked at a temperature of 400°C for ½ hr.

2. All metal parts are heated by radio-frequency induction.

3. Heater voltage is applied in half-volt steps, each held long enough to insure that the pressure does not exceed $10^{-4}$ mm Hg. The maximum temperature to which the cathode is raised is 1000°C (brightness); this temperature is maintained until the pressure falls below $10^{-6}$ mm Hg.

4. With the cathode temperature at 1000°C (brightness), the plate voltage is slowly increased to 50 v. The plate is held at this maximum voltage for about 15 min, at the end of which time the cathode-current density is about 0.5 amp/cm$^2$.

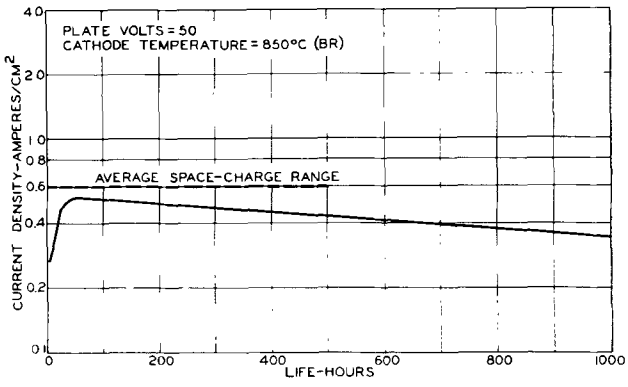


Fig. 3. D-C emission during life

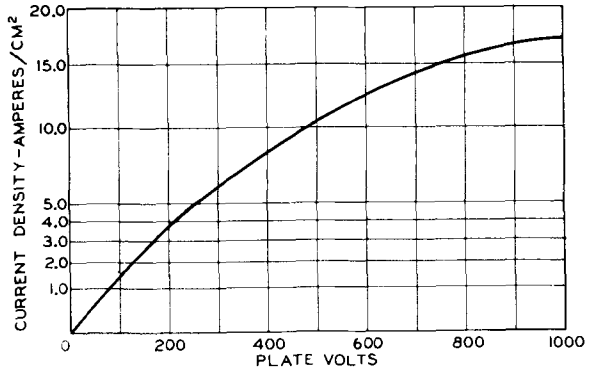


Fig. 4. Pulse-emission characteristics

5. All voltages are removed, the getter is partially fired, the tube is sealed off, and the getter is then completely fired.

After the tube is removed from the exhaust system, the cathode is aged for about 15 min at a temperature of 1000°C (brightness) and a plate voltage of 50 v. The effect of aging schedules is described later.

## D-C Life Test and Pulse Emission

All cathodes are life-tested for 1000 hr at a cathode temperature of 850°C (brightness) and a plate voltage of 50 v. Figure 3 shows the typical current densities during 1000 hr of life. The average space-charge-limited current, calculated from the dimensions of the tube by means of elementary space-charge theory, is also indicated. The average current density throughout life is about 0.4 amp/cm$^2$, which is slightly less than that predicted by space-charge theory.

The life test is interrupted periodically, and the pulse emission of the cathodes is measured at a cathode temperature of 850°C (brightness), a peak plate voltage of 1000 v, a pulse length of 2.5 $\mu$sec, and a repetition rate of 60 pulses/sec. Figure 4 shows the peak current density as a function of peak plate voltage. At the 1000-v measuring condition, the field at the cathode is clearly accelerating. Field-free emission is less than the 1000-v emission by a factor which varies between 2 and 6, depending on the activity of the cathode and the cathode-plate spacing. For many cathodes, the maximum peak emission throughout life (usually reached after 24 to 100 hr) is between 16 and 20 amp/cm$^2$ at the 1000-v condition. These values are equivalent,

therefore, to an emission of about 2 to 10 amp/cm$^2$ under field-free conditions.

Bell and Brewer (3) discussed the necessity of preventing emission which can result from high fields at the edges of the active cathode pellet. Because the pellet they used extended beyond the cathode sleeve, they shielded the cathode edges by an additional electrode structure held at cathode potential. No such shield is necessary with the cathode shown in Fig. 1 because the active cathode material does not migrate appreciably to the edge of the cathode sleeve, as evidenced by the fact that the emission never exceeds that predicted by space-charge theory. Furthermore, if a space-charge plot is made at moderate voltages, a straight line results, with a slope which indicates that only about 70% of the surface is emitting.

Some comment is in order on the result that only about 70% of the cathode surface emits, a conclusion also reached by Beck, *et al.* (2), but obtained by different experimental techniques. It is believed that at least two sources of emission are required to explain the above fact: (*a*) alkaline-earth-oxides contained within the pores of the matrix; (*b*) a monolayer of alkaline-earth-oxide (probably barium oxide), which has migrated onto a small area of the nickel which surrounds each pore. The following facts are cited to support this explanation.

1. From geometrical considerations and the proportions of carbonate and nickel used in the active pellet, one concludes that less than 70% of the active surface is composed of alkaline-earth-oxide.
2. The pulsed emission of the cathode is greater than the d-c emission, but by a factor much smaller than that usually reported for an alkaline-earth-oxide cathode.

## Cathode-Pellet Composition

Although a complete study of cathode pellet materials was not made, various compositions were tried. The most useful emissive material is a triple carbonate, designated RCA-33C-311-B, containing 57% by weight barium carbonate, 39% strontium carbonate, and 4% calcium carbonate. Cathode pellets were also made from a triple carbonate containing 13% calcium carbonate and from barium carbonate alone. Satisfactory emission was obtained from all the cathode pellets, but the ones containing barium carbonate alone were somewhat gassy.

Three nickel powders having particles of different sizes were tried: Type B carbonyl nickel (1-3$\mu$), standard carbonyl nickel (9-14$\mu$), and Sherritt-Gordon nickel (60$\mu$). Although the emission from cathodes using type B material was best, the difference was not necessarily significant.

Three reducing agents were tested as activators: zirconium hydride, carbon, and titanium hydride. Carbon is gassy and results in short-lived emission. Zirconium hydride gives satisfactory results and is used in the cathodes for which data are reported. Titanium hydride is satisfactory but has no particular advantage over zirconium hydride.

**Table I. Time-temperature schedule during sintering**

| Temp, °C* | Atmosphere | Time (min) |
|---|---|---|
| Room to 600 | $H_2$ | 8 |
| 600 to 1000 | $N_2$ | 7 |
| 1000 to 600 | $N_2$ | 7 |
| 600 to Room | $H_2$ | 8 |
| Room | $N_2$ | 10 |

* Temperature is held constant during change of atmosphere from one gas to another, which may take as much as a minute.

## Sintering and Aging

The most important step in the processing of molded nickel cathodes is sintering. During this process, the cathodes are held in a nickel boat within a Vycor tube, which in turn is within a muffle furnace. Nitrogen and hydrogen are passed in series through a deoxidizer, an electrodryer, a liquid-nitrogen trap, and finally the Vycor tube. The hydrogen flows at the rate of 200 cm$^3$/sec, the nitrogen at 50 cm$^3$/sec. The time-temperature schedule during sintering, which is quite critical, is given in Table I.

Figure 5 shows pulse current density (measured periodically during life) as a function of hours of life for both sintered and unsintered cathodes. The remarkable improvement in life performance due to sintering is obvious.

The mechanism of the sintering process is not completely understood. Presumably it includes deoxidization of the nickel powder, decomposition of the zirconium hydride, and diffusion of a small amount of free zirconium into the nickel matrix. The zirconium which diffuses into the matrix later diffuses out and acts as a reducing agent throughout the life of the emitter. During sintering, at least part of the carbonate is broken down, as evidenced by the fact that sintered cathodes give off considerably less gas during exhaust than unsintered ones.

The effect of aging on cathodes is shown in Fig. 6. Pulse emission is plotted as a function of life for cathodes which are (*a*) not aged, (*b*) aged for 15 min, and (*c*) aged for 30 min. The best performance was obtained with cathodes aged for 15 min. However, uncontrolled variations in construction and processing of cathodes may require different aging times for optimum results. The optimum aging time can be determined by observation of the current during aging. Most cathodes show a slump of current during initial phases and then recover. The

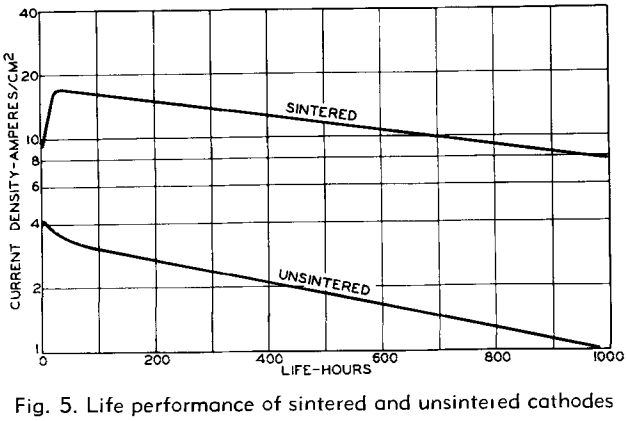


Fig. 5. Life performance of sintered and unsintered cathodes

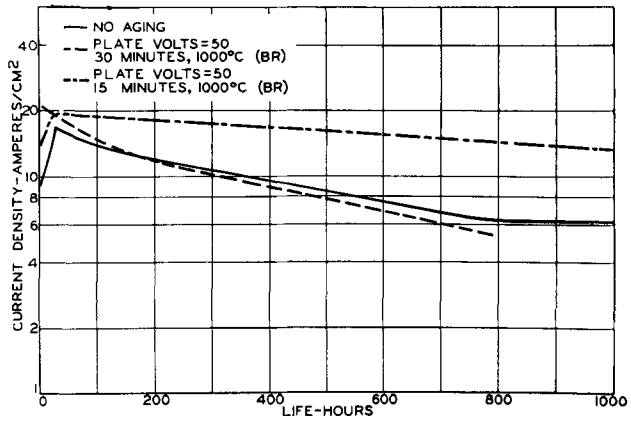


Fig. 6. Effect of aging on life

optimum aging time is reached when the recovery is essentially complete.

## Applications

Molded nickel cathodes have been used in several practical applications. Their use is most advantageous when the cathode must be exposed to air (as in demountable systems) or when it is expected to deliver large amounts of current in the presence of positive ion bombardment, a poor vacuum, or a large electric field. A comparison between the performance of molded nickel cathodes and that of oxide-coated cathodes in three applications demonstrated the superiority of the molded cathodes.

In the first application, a typical cathode ray gun was mounted in a demountable vacuum system for the purpose of evaluating phosphors. Cathode-current requirements are fairly low, about 1.5$\mu$a. However, the demountable system is opened to air several times a day for varying periods of time. A typical molded nickel cathode survives 80-100 such cycles and is still able to deliver the required current. In contrast, typical oxide-coated cathodes last only 10-20 cycles.

In the second application, a similar electron gun was mounted in a demountable vacuum system for the purpose of evaluating electron-optical structures. In this gun, however, the beam current was about 150$\mu$a. A molded nickel cathode performed satisfactorily through about 30 openings of the demountable system, but an oxide cathode lasted through about 3 such openings. In this application, the cathode is not heated while the system is open to air, as described by Haas and Jensen (4).

In the third application, a molded nickel cathode was used in a developmental projection kinescope. In this structure, the aperture of grid No. 1 is 0.035 in. in diameter, the accelerating voltage is 40 kv, and the beam current is 1000$\mu$a. Because the gun structure has no ion trap, the cathode is subjected to heavy ion bombardment. After 1500 hr of operation under these conditions, the emission from the molded cathode was still satisfactory. A typical oxide cathode lasts only about 600 hr under such conditions.

## Acknowledgment

The authors wish to thank Messrs. MacNair, Lynch, and Hannay for their helpful private communications concerning sintering techniques.

Manuscript received Jan. 8, 1958. This paper was prepared for delivery before the Washington Meeting, May 12-16, 1957.

Any discussion of this paper will appear in a Discussion Section to be published in the June 1959 JOURNAL.

## REFERENCES

1. D. MacNair, R. T. Lynch, and N. B. Hannay, *J. Appl. Phys.*, **24**, 1335 (1953).
2. A. H. Beck, A. D. Brisbane, A. B. Cutting, and G. King, *Le Vide*, **9**, 302 (1954.)
3. J. J. Bell and G. R. Brewer, Paper presented at Electrochemical Society Meeting, Cincinnati, May 1955.
4. G. A. Haas and J. T. Jensen, Jr., NRL Report No. 4856, Nov. 9, 1956.

# Equilibrium Reduction of Tungsten Dioxide by Hydrogen

**Robert C. Griffis**

*Refractory Metals Laboratory, General Electric Company, Cleveland, Ohio*

## ABSTRACT

A study has been made of the heterogeneous equilibrium involving $H_2$-W-$WO_2$-$H_2O$ in the temperature range 500°-1000°C, using a static equilibrium-type of apparatus. The standard heat of formation and entropy of $WO_2$, as calculated from the equilibrium data, was found to be $\Delta H^\circ = -135.0 \pm 0.3$ kcal and $17.1 \pm 1.0$ e.u. The heats of formation of $WO_2$ and the two higher suboxides were determined by direct combustion. $\Delta H^\circ$ of $W_{18}O_{49}$ ($WO_{2.72}$) = $-183 \pm 1$ kcal/mole W, $\Delta H^\circ$ of $W_{20}O_{58}$ ($WO_{2.90}$) = $-193 \pm 1$ kcal/mole W, and $\Delta H^\circ$ of $WO_2 = -137 \pm 1$ kcal/mole W.

The oxide analyses of Glemser and Sauer (1) and the single crystal studies by Magneli, *et al.* (2) have established the existence of the following tungsten oxide phases which are stable at room temperature:

$\alpha$ $WO_3$ — yellow — triclinic pseudo-orthorhombic (stable below 740°C)

$\beta$ $W_{20}O_{58}$—blue—($WO_{2.90}$) monoclinic

$\gamma$ $W_{18}O_{49}$—violet—($WO_{2.72}$) monoclinic

$\delta$ $WO_2$—brown—monoclinic

The homogeneity ranges of the above oxides are very narrow according to Magneli, *et al.* The exist-

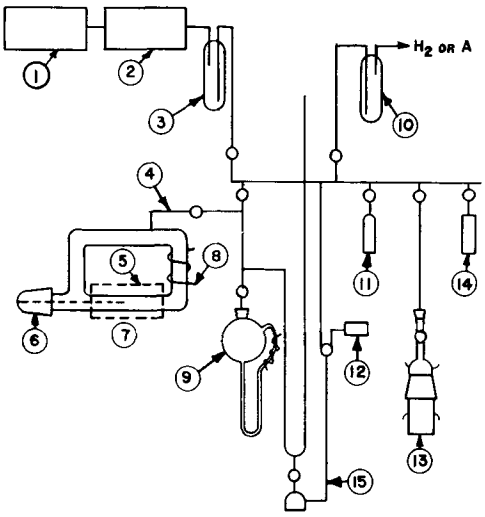


Fig. 1. Equilibrium Apparatus. 1, mechanical forepump; 2, diffusion pump; 3, liquid $N_2$ trap; 4, quartz-Pyrex seal; 5, reaction furnace; 6, thermocouple well; 7, quartz reaction chamber; 8, auxiliary circulating heater; 9, condensing bulb; 10, liquid $N_2$ trap; 11, vacuum gauge; 12, drier; 13, $H_2O$ vessel; 14, drier; 15, constant volume manometer.

ence of a stable tetragonal form of $WO_3$ above 720°-740°C has been reported (3-5). There is increasing evidence of an oxide phase $W_3O$ (beta tungsten) (6-8). This point has been in dispute (9-11) and the question remains a point of controversy.

However, the thermodynamic data that are available for the tungsten oxides are based in most part on studies (12-17) made prior to these oxide phase investigations. In addition to the uncertainties concerning the oxide phases, it has been pointed out (18) that considerable errors, due to thermal diffusion effects, are encountered in the use of a Deville (19) type of apparatus such as was almost universally used in earlier studies. The purpose of the paper is to present a redetermination of the W-$WO_2$-$H_2$-$H_2O$ equilibria as a first step in the study of the possible equilibria involved in the reduction of $WO_3$ to W by $H_2$.

## Experimental

Figure 1 shows the experimental apparatus designed to avoid the separation of the equilibrium mixture of $H_2$ and $H_2O$ by thermal diffusion. The apparatus consists of a square doughnut-shaped 1 in. quartz tubing reaction chamber into which a small quartz boat, 4 cm long, 1 cm wide, and 0.8 cm high, containing the solid phases (W and $WO_2$), is placed. The reaction chamber is sealed off from the atmosphere by a standard taper 24/40 joint containing the thermocouple well. The reaction furnace windings are spaced so that there is no appreciable radial temperature gradient, and the constant temperature (±1°C) zone is approximately 3 cm long. All chromel-alumel thermocouples and lead extensions were calibrated, over the entire range, against a Bureau of Standards Certified platinum-platinum 10% rhodium thermocouple to ± 1°C. Aluminum foil is used as a heat shield to help reduce the large end losses and to keep the entire reaction chamber at an elevated temperature to prevent condensation of water present in the reaction gases. The thermocouple serves both to control and indicate the temperature since the response of the detector to the addition or loss of heat is almost instantaneous due to the quartz construction. A small auxiliary heater on the vertical leg assures a circulation of the gases by convection currents. The chamber is connected by a quartz-Pyrex seal to the condensing bulb, constant volume mercury manometer, and vacuum manifold. The vacuum system includes a mechanical forepump, a two-stage mercury diffusion pump, liquid $N_2$ trap, and thermocouple vacuum gauge. The condensing bulb includes a cold finger and circulating tube. The small heater in the circulating side arm causes the gas to rise and thus maintains a convection current which causes all of the $H_2O$ vapor in the system to be frozen out in the cold portion immersed in liquid $N_2$. The manometer readings were made with a precision cathetometer to ± 0.05 mm. All manometer readings were corrected, when necessary, for the cooling effect of liquid $N_2$.

All equilibrium measurements were made by alternate reduction and oxidation of the samples. This alternating procedure yielded consistent values for $K_p$ after 2 to 3 conditioning runs. The presence of both phases (W and $WO_2$) enabled establishment of equilibrium in as short a time as possible which prevented surface depletion of either phase and sintering effects. This time varied from 2 hr for lower temperatures to less than ½ hr for higher temperatures. A 2-g sample was placed in the reaction chamber and the system evacuated to less than 0.1 micron for a period of 2 hr. $H_2$ and/or $H_2O$ vapor was introduced into the chamber which was then closed off from the rest of the system. The temperature of the chamber was raised to the desired point and the equilibrium run made while the condensing bulb and manometer were being pumped down. Upon completion of the run, the hot gases were expanded into the condensing bulb and manometer. The total pressure and the pressure after the $H_2O$ was frozen out were then noted.

All reagents were prepared from purified $WO_3$, which was made by firing $H_2WO_4$[1] at 900°C for 1½ hr. Spectrographic analysis of the $WO_3$ is given in Table I.

The $H_2$ gas was purified by passage through a Deoxo catalytic unit to remove $O_2$ and then through a liquid $N_2$ trap to remove traces of $H_2O$. The $H_2$ gas was obtained directly from manufacturing facil-

[1] Obtained from Chemical Products, General Electric Co., Cleveland, Ohio.

Table I. Analysis of $WO_3$ starting material

| | Metallic elements | | | | | | | | | | |
|---|---|---|---|---|---|---|---|---|---|---|---|
| | Al | Mo | Si | Ca | Fe | Ni | Cu | Cr | Mr | Ti | Sn,Co,Pb |
| % by wt | 0.002 | 0.002 | 0.020 | 0.001 | 0.001 | 0.001 | 0.001 | 0.001 | 0.001 | trace | absent |

ities providing a highly purified gas. Pure W metal was obtained by the reduction of $WO_3$ with dry $H_2$ (400 cc/min) at 650°C for a 24-hr period. Material balance and x-ray analysis showed the product to be $\alpha$-W. 100 grams of tungsten was made. There are two primary methods for producing $WO_2$ and the other sub oxides (1, 2). Both yield the same product as evidenced by x-ray analysis. The bulk of the $WO_2$ used for equilibrium samples was prepared by reduction of 15-g charges of $WO_3$ at 700°C by $H_2$ gas (200 cc/min), saturated with $H_2O$ vapor at 45°C, for ½ hr. Approximately 160 g of $WO_2$ was so prepared. 60 g each of $W_{20}O_{58}$ ($WO_{2.90}$) and $W_{18}O_{49}$ ($WO_{2.72}$) were prepared by heating stoichiometric quantities of W and $WO_3$ in evacuated sealed quartz tubes as described by Magneli, *et al.* (2).

The standard heat of formation of $WO_2$ was also determined (as well as values for $WO_{2.90}$ and $WO_{2.72}$) by combustion methods. The bomb assembly consisted of a single-valve Parr oxygen bomb and Series 1300 Plain Calorimeter. The bomb was flushed at 25 atm with $O_2$ once to reduce the $N_2$ content. The $O_2$ contained 0.3% argon with about 0.001% hydrocarbon impurities. The calorimeter run was carried out according to the manufacturer's recommendations. Temperatures were measured with a Parr Calorimeter thermometer supplied with a test certificate which enabled scale correction to within ±0.005°F to be made. The thermometer readings were made with a cathetometer to avoid parallax. No. 34 B & S gauge nickel-chromium alloy wire was used as a fuse. The combustion capsules were made of 25-20 stainless steel and were lined with a 10-g layer of $WO_3$ for each run with the exception of the determination of the water equivalent by standardized benzoic acid. A correction was made for the difference in heat capacity. The samples were pressed into pellets 1 in. diam x ⅛ in. thick. Tungsten was pressed at 12,000 psi while the other three oxides were pressed at 51,000 psi. The samples consisted of pieces of these broken pellets. Complete combustion was not obtained for samples of W and $WO_2$, but the higher oxides $WO_{2.72}$ and $WO_{2.90}$ reacted completely when mixed with W metal pellets. The residues of all runs were crushed and digested in 5% NaOH at 85°C for 24 hr, the hot solutions filtered and the metallic W weighed. X-ray examination of the treated residues showed only W present for the runs involving W, $WO_{2.72}$, and $W_{2.90}$. Tungsten dioxide samples were reacted without any addition of W metal; residues were treated as above, and only $WO_2$ was found after filtration. Other laboratory techniques showed that if 130 mg of $WO_2$ is so treated, the recovery is close to 123 mg or better. This loss could be attributed to either the solution of the $WO_2$ or, as has been reported (20), the reaction of the $WO_2$ with $(OH)^-$ to yield a higher oxide and metallic W. In either case the correction involved is less than the final estimated error. The combustion values for $WO_{2.72}$ and $WO_{2.90}$ have been corrected for the energy supplied by the combustion of the added W metal.

The $\Delta E$ values from the combustion runs were corrected to unit fugacity of $O_2$ by reference to the work of Rossini and Frandsen (21). The conventional conversion of $\Delta E$ to $\Delta H$ was made and all results were calculated on the basis of 1 mole of W, for reasons of comparison.

## Results and Discussion

The experimental techniques described above were first used to determine the $Fe\text{-}H_2O\text{-}H_2\text{-}Fe_3O_4$ equilibrium over the temperature range 400°-550°C. The data of Emmett and Schultz (18) was used for comparison. Reagent grade $Fe_2O_3$ (red) was used as a starting material. Twenty g of $Fe_3O_4$ was prepared by reduction of $Fe_2O_3$ at 700°C by wet $H_2$($H_2O/H_2$ ratio 1.8:1) for 1 hr: x-ray and material balance analysis indicated $Fe_3O_4$. Metallic Fe was prepared by reduction at 700°C with dry $H_2$ for 3½ hr. Experimental results checked very favorably with the literature values.

The equilibrium values for the reaction:

$$\tfrac{1}{2}\ WO_2 + H_2 \leftrightharpoons \tfrac{1}{2}\ W + H_2O$$

in the temperature interval 500°-1000°C are given in Table II and Fig. 2.

$\Delta Cp$ for the reaction,

$$WO_2 + 2H_2 \rightarrow W + 2H_2O (500°\text{-}1000°C)$$

was calculated on the basis of literature values for $H_2$, $H_2O$(22), W(23), and using Cp = 14.0 cal°/C

Table II. Equilibrium data for the system $WO_2$-$H_2$-W-$H_2O$

| Run No. | Temp, C° | $K_p = P_{H_2O}/P_{H_2}$ | Initial conditions |
|---|---|---|---|
| 64A | 500 | 0.112 | reducing |
| 68 | 500 | 0.118 | reducing |
| 82 | 500 | 0.120 | oxidizing |
| 83 | 500 | 0.121 | oxidizing |
| 88 | 500 | 0.120 | reducing |
| 83A | 600 | 0.214 | reducing |
| 83B | 600 | 0.212 | reducing |
| 83C | 600 | 0.210 | oxidizing |
| 88A | 600 | 0.208 | reducing |
| 88B | 600 | 0.218 | oxidizing |
| 90 | 600 | 0.206 | oxidizing |
| 86A | 700 | 0.356 | oxidizing |
| 86B | 700 | 0.346 | reducing |
| 86C | 700 | 0.348 | oxidizing |
| 87 | 700 | 0.340 | oxidizing |
| 91A | 700 | 0.351 | reducing |
| 91B | 700 | 0.355 | reducing |
| 88 | 800 | 0.507 | reducing |
| 90A | 800 | 0.460 | reducing |
| 90B | 800 | 0.460 | oxidizing |
| 90C | 800 | 0.515 | reducing |
| 90D | 800 | 0.520 | oxidizing |
| 90E | 800 | 0.510 | oxidizing |
| 72A | 900 | 0.694 | oxidizing |
| 72B | 900 | 0.684 | reducing |
| 73 | 900 | 0.705 | oxidizing |
| 75A | 900 | 0.690 | reducing |
| 75B | 900 | 0.709 | oxidizing |
| 75C | 900 | 0.695 | reducing |
| 94A | 1000 | 0.931 | reducing |
| 94C | 1000 | 0.935 | reducing |
| 94D | 1000 | 0.935 | oxidizing |
| 95A | 1000 | 0.945 | oxidizing |
| 95B | 1000 | 0.937 | oxidizing |
| 95C | 1000 | 0.934 | reducing |

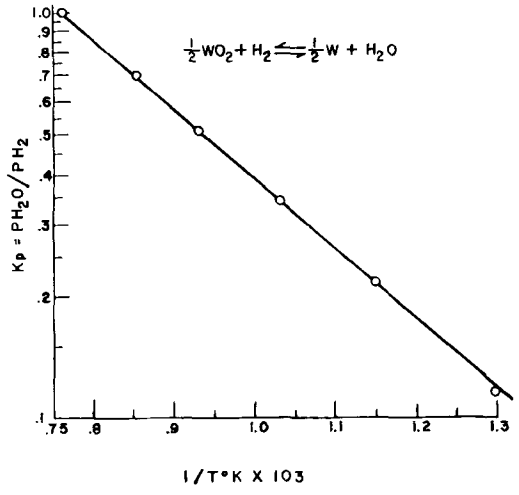


Fig. 2. Plot of log $K_p = \frac{P_{H_2O}}{P_{H_2}}$ vs. 1/T°K for the system $WO_2$-$H_2$-W-$H_2O$.

(Kopp's rule) for $WO_2$ since no literature values are available.

$$\Delta Cp = 6.96 + 4.32 \times 10^{-3}T - 0.08 \times 10^{5}T^{-2} \quad (I)$$

The equilibrium values in Table II were treated by means of Sigma functions and the method of least squares, using the value for ΔCp, to yield the following equations for this reaction:

$$\Delta H^\circ = 21{,}000 - 6.96T + \frac{4.32}{2} \times 10^{-3}T^2 + 0.08 \times 10^{5}T^{-1} \quad (II)$$

$$\Delta F^\circ = 21{,}000 + 6.96\,T\ln T - \frac{4.32}{2} \times 10^{-3}T^2 + \frac{0.08}{2} \times 10^{5}T^{-1} - 63.1T \quad (III)$$

From these were calculated,

$$\Delta H^\circ_{298} = +19.4 \pm 0.2 \text{ kcal/mole W}$$

$$\Delta F^\circ_{298} = +13.9 \pm 0.2 \text{ kcal/mole W}$$

Literature values of $\Delta F^\circ_{298}$ and $\Delta H^\circ_{298}$ (24) for the reaction $2H_2 + O_2 \rightarrow 2H_2O$, were used to calculate the following values of $\Delta F^\circ_{298}$ and $\Delta H^\circ_{298}$ for the reaction,

$$W + O_2 \rightarrow WO_2$$

$$\Delta F^\circ_{298} = -123.1 \pm 0.3 \text{ kcal/mole W}$$

$$\Delta H^\circ_{298} = -135.0 \pm 0.3 \text{ kcal/mole W}$$

The standard entropy values for W and $O_2$ (25) were used to calculate the standard entropy of $WO_2$.

$$S^\circ_{298}\, WO_2 = 17.1 \pm 1.0 \text{ e.u.}$$

Table III. Bomb calorimeter results

| Reaction | $-\Delta H^\circ_{298}$ kcal/mole W |
|---|---|
| $W + 3/2\ O_2 \rightarrow WO_3$ | 199.5 |
| $W + 3/2\ O_2 \rightarrow WO_3$ | 198.5 |
| $W + 3/2\ O_2 \rightarrow WO_3$ | 199.1 |
| $WO_2 + 1/2\ O_2 \rightarrow WO_3$ | 62.0 |
| $WO_2 + 1/2\ O_2 \rightarrow WO_3$ | 61.4 |
| $WO_2 + 1/2\ O_2 \rightarrow WO_3$ | 60.8 |
| $WO_2 + 1/2\ O_2 \rightarrow WO_3$ | 62.3 |
| $WO_{2.72} + 0.28/2\ O_2 \rightarrow WO_3$ | 15.0 |
| $WO_{2.72} + 0.28/2\ O_2 \rightarrow WO_3$ | 16.2 |
| $WO_{2.72} + 0.28/2\ O_2 \rightarrow WO_3$ | 17.1 |
| $WO_{2.72} + 0.28/2\ O_2 \rightarrow WO_3$ | 15.8 |
| $WO_{2.90} + 0.10/2\ O_2 \rightarrow WO_3$ | 4.7 |
| $WO_{2.90} + 0.10/2\ O_2 \rightarrow WO_3$ | 5.9 |
| $WO_{2.90} + 0.10/2\ O_2 \rightarrow WO_3$ | 6.2 |
| $WO_{2.90} + 0.10/2\ O_2 \rightarrow WO_3$ | 6.4 |

There is no literature value available for comparison, but it is reasonable since $S^\circ_{298}$ of $WO_3 = 19.9$ e.u. (26). The heat of formation of $WO_2$ was also obtained by direct combustion technique. The results of the bomb calorimeter runs are tabulated in Table III.

The data in Table III can be used to determine the heats of formation of the oxides as summarized in Table IV.

## Summary

The equilibrium values obtained for the system W-$WO_2$-$H_2O$-$H_2$ are slightly lower than the experimental data available in the literature for this system. $\Delta H^\circ$ of $WO_2 = -135.0 \pm 0.3$ kcal as calculated from these data and $\Delta H^\circ$ of $WO_2 = -137.0 \pm 1$ kcal as calculated from combustion experiments also reported here. $S^\circ_{298}$ of $WO_2 = 17.1 \pm 1.0$ e.u. (from equilibrium data). $\Delta H^\circ WO_{2.72}$ ($W_{18}O_{49}$) = $-183 \pm 1$ kcal and $\Delta H^\circ WO_{2.90}$ ($W_{20}O_{58}$) = $-193 \pm 1$ kcal. These values were obtained by combustion experiments and no literature values are available for comparison.

## Acknowledgments

The author wishes to thank many members of the Refractory Metals Laboratory, and other Divisions of the General Electric Company for their helpful assistance.

Manuscript received Sept. 19, 1957. This paper was prepared for delivery before the Buffalo Meeting, Oct. 6-10, 1957.

Any discussion of this paper will appear in a Discussion Section to be published in the June 1959 JOURNAL.

Table IV. Heats of formation of tungsten oxides

| Oxide | Heat of formation $\Delta H^\circ$ kcal/mole W | Method of determination | Literature value kcal/mole W | |
|---|---|---|---|---|
| $WO_3$ | $-199 \pm 1$ | combustion | $-200.2 \pm 0.10$ | (20) |
| $WO_2$ | $-137 \pm 1$ | combustion | $-135$ | (27) |
| $WO_2$ | $-135.0 \pm 0.3$ | equilibrium | $-134 \pm 2$ | (27) |
| $WO_{2.72}$ ($W_{18}O_{49}$) | $-183 \pm 1$ | combustion | ——— | |
| $WO_{2.90}$ ($W_{20}O_{58}$) | $-193 \pm 1$ | combustion | ——— | |

REFERENCES

1. O. Glemser and H. Sauer, *Z. anorg. u. allgem. Chem.*, **252**, 144 (1943).
2. A. Magneli, G. Anderson, B. Blomberg, and L. Kihlborg, *Anal. Chem.*, **24**, 1998 (1952).
3. W. Kehl, R. Hay, and D. Wahl, *J. Appl. Phys.*, **23**, 212 (1952).
4. R. Ueda and T. Ichinokawa, *Phys. Rev.*, **82**, 563 (1951).
5. S. Sawada, *ibid.*, **91**, 1010 (1953).
6. G. Hagg and N. Schonberg, *Acta. Cryst.*, **7**, 351 (1954).
7. M. Charlton, *Nature*, **169**, 109 (1952).
8. M. Charlton, *ibid.*, **174**, 703 (1954).
9. H. Hartmen, F. Ebert, and O. Bretschneider, *Z. anorg. u. allgem. Chem.*, **198**, 116 (1931).
10. G. Mannella and J. Hougen, *J. Phys. Chem.*, **60**, 1148 (1956).
11. A. Hegedus, T. Millner, J. Neugebarer, and K. Sasvari, *Z. anorg. u. allgem. Chem.*, **281**, 64 (1955).
12. G. Chaudron, *Compt. rend.*, **170**, 1056 (1920).
13. G. Chaudron, *Ann. Chem.*, **16**, 221 (1921).
14. J. Van Liempt, *Z. anorg. u. allgem. Chem.*, **126**, 183 (1923).
15. J. Van Liempt, *ibid.*, **120**, 267 (1922).
16. Frederick and Sittig, *ibid.*, **145**, 127 (1925).
17. L. Wohler and R. Gunther, *Z. Elektrochem.*, **29**, 276 (1953).
18. P. Emmett and J. Schultz, *J. Am. Chem. Soc.*, **55**, 1376 (1933).
19. St. C. Deville, *Compt. rend.*, **70**, 1105, 1201 (1870).
20. G. Ruff, E. Squittieri, and P. Snyder, *J. Am. Chem. Soc.*, **70**, 3380 (1948).
21. F. Rossini and M. Frandsen, *J. Research Nat. Bur. Standards*, **9**, 733 (1932).
22. O. Kubaschewski and E. Evans, "Metallurgical Thermochemistry," pp. 312, 320, John Wiley & Sons, Inc., New York (1956).
23. K. K. Kelley, Bureau of Mines Bulletin 476 (1949).
24. O. Kubaschewski and E. Evans, *op. cit.*, p. 248, 334.
25. K. K. Kelley, Bureau of Mines Bulletin 434 (1948).
26. H. Seltz, F. Dunkerley, and B. DeWitt, *J. Am. Chem. Soc.*, **65**, 600 (1943).
27. L. Brewer, *Chem. Rev.*, **52**, 29 (1953).

# Electropolishing Silicon in Hydrofluoric Acid Solutions

**Dennis R. Turner**

*Bell Telephone Laboratories, Incorporated, Murray Hill, New Jersey*

ABSTRACT

Silicon is electropolished in hydrofluoric acid solutions if a critical current density is exceeded. Below the critical c.d., silicon dissolution is largely divalent, and a thick solid layer forms. This film is unstable and reacts slowly with the electrolyte to form tetravalent silicon and hydrogen gas. In the electropolishing region, silicon dissolution is mainly tetravalent with the formation of a very thin high resistance type of film.

Experimental results on the effect of HF concentration, viscosity, and temperature indicate that electropolishing begins when the HF concentration at the silicon becomes limited by the rate of "mass transfer" of HF from the solution bulk to the surface.

Silicon is a semiconductor material used in making solid-state electronic devices. In their manufacture, it is necessary to employ chemical and electrochemical techniques to remove damaged surface material and/or shape the silicon to a particular geometry. The principle advantage of electrochemical over chemical methods of removing silicon is that the amount and the place where the material is to be removed can be controlled more easily. It is usually desirable that the surface of the silicon be polished after processing.

The technique of electropolishing involves making the metal to be polished anode in a suitable electrolyte at a current density sufficient to produce a thin continuous anode film on the surface. The anode film must be soluble in the electrolyte, but not too soluble or no appreciable electropolishing film will be built up at a reasonable current density. The electropolishing anode film is described by various workers as either a solid or highly viscous liquid layer. Polishing requires both brightening and smoothing. Hoar and Mowat (1) have proposed that the brightening effect is due to a random transfer of metal atoms into vacant cation sites in the anode film. Smoothing is due to preferential dissolution of the film at high points on the surface.

Previous work on electropolishing silicon is almost nonexistent. Uhlir (2) was able to electropolish *p*-type silicon in a largely nonaqueous electrolyte of ethylene glycol containing some HF.

Electropolishing silicon appears practical only for *p*-type material at the present time since an internal voltage barrier is formed in *n*-type semiconductors (3) which causes excessive heating of the electrode before the required polishing current is attained. Methods of breaking down the voltage barrier by introducing hole-electron pairs with heat and/or light is effective with germanium, but this is difficult if not impossible with silicon because of its higher energy gap.

The experimental work was done in two parts. First, a number of exploratory experiments were performed to determine the best electrolyte and general conditions for electropolishing. This work was done with silicon electrodes held vertically in solution and without temperature control. The second part was done more carefully with the silicon positioned horizontally facing up and the temperature controlled.

### Preliminary Experiments

Most of the preliminary experiments were carried out with 1 ohm cm single-crystal $p$-type silicon electrodes. A number of electrolytes were investigated to determine one suitable for electropolishing silicon.

Strong alkaline solutions chemically attack silicon, forming a soluble silicate and hydrogen gas. The rate of reaction increases rapidly with temperature. If a piece of silicon is made anodic in hot 1$N$ KOH, however, the chemical attack stops above a critical anode potential. The surface is passivated. Furthermore, after the cell current is interrupted, the hot alkaline solution requires several minutes to break through the passive layer and resume chemical attack of the silicon. A brief cathodic treatment reactivates the silicon immediately. Alkaline solutions do not appear promising for electropolishing silicon. The passivating anodic film formed, however, may be of value in stabilizing the surface electronically (4).

Electrolytes containing the fluoride ion were considered since they can be made to form soluble fluosilicate complexes with silicon. The most successful electrolyte found for electropolishing silicon was hydrofluoric acid. For a given set of conditions of HF concentration, temperature, viscosity, and stirring, there is a critical current density which must be exceeded before electropolishing can take place. Below this critical current density, a thick solid anode film forms on the silicon. For example, Uhlir (2) reported that silicon does not electropolish in 24 to 48% HF solutions up to 0.5 amp/cm$^2$ because of a thick anode deposit. As will be seen later, higher current densities are required to electropolish silicon at these HF concentrations.

The HF concentration range in which a vertical $p$-type silicon electrode is electropolished at 400 ma/cm$^2$ current density is shown in Fig. 1. There was no temperature control in this experiment. The effective resistance of the electrolytic cell and the power dissipated in the cell were measured at the same time. These data are included only to show the qualitative effect of HF concentration on the cell resistance and power dissipation. At low HF concentrations the cell resistance is high, the power dissipated as heat is large, and the silicon is anodically etched but not electropolished. A clear polished silicon surface is not obtained until the HF concentration is at least 2.5%. More concentrated solutions of HF decrease the effective cell resistance and thus the power dissipated in the cell. The thick film begins to form at about 8.5% HF under the conditions of this experiment.[1] There is no discontinuity in the cell resistance with film formation which indicates that the thick film is probably porous.

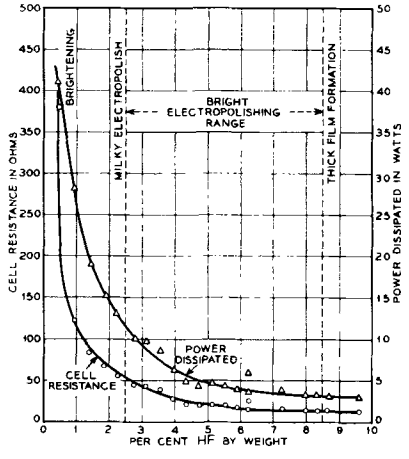


Fig. 1. Cell resistance and power dissipated in an electropolishing cell vs. HF concentration using a vertical p-type silicon anode at 400 ma/cm$^2$ density.

Anode efficiency measurements were made during electropolishing in 5% HF using a vertical $p$-type silicon electrode. Since there was a tendency for the current to oscillate in the electropolishing range, it was necessary to employ a copper coulometer to integrate the current used. Assuming a silicon valence of 4, an anode efficiency of 105 ± 2% was obtained which indicates that about 5% of the current formed divalent silicon. The anode efficiency appears to be independent of current density over the range studied between 110 and 850 ma/cm$^2$. The rate of silicon dissolution by electropolishing in 5% HF calculated from the observed anode efficiency and the electrochemical equivalent for silicon is $3.3 \times 10^{-5}$ cm$^2$/coulomb. At 500 ma/cm$^2$, the etching rate is $1.7 \times 10^{-5}$ cm/sec (0.0004 in./min).

A silicon electrode held vertically in the solution without temperature control requires a relatively high minimum current density of about 300 ma/cm$^2$ to start electropolishing in 5% HF. A high current density promotes rapid electropolishing which is often desirable. However, the $I^2R$ heat generated in the silicon at these current densities can be excessive and cause the solution around the electrode to boil and even melt the soft solder connection made to a copper wire. It was of a practical interest, therefore, to investigate the various parameters of the silicon electropolishing process to determine how the minimum current density for electropolishing could be reduced.

### Experimental Arrangements Using a Horizontal Electrode

A cross-section view of the electrolytic cell designed for these experiments is shown in Fig. 2. The silicon electrode was mounted horizontally facing up

[1] Since this paper was submitted for publication, P. Wang, of Sylvania, in an oral presentation at the Buffalo Meeting of the Society reported that p-type silicon could be electropolished in 1-10% aqueous HF solutions.

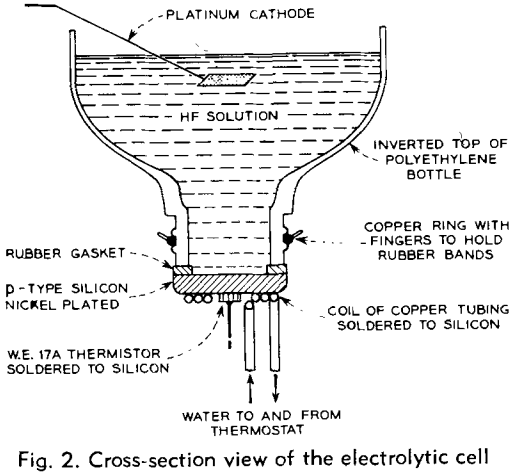


Fig. 2. Cross-section view of the electrolytic cell

to minimize stirring by convection. The arrangement also provides for a fairly uniform primary current distribution over the silicon and permits a visual examination of the surface at all times. A circular piece of single crystal 3.5 Ω cm *p*-type silicon about 2.5 cm in diameter and 0.5 cm thick was used in most of the experiments. After the silicon was nickel plated by the "electroless" process (5), a coil of 3-mm diameter copper tubing was soft soldered to the back side. This served the dual purpose of forming an ohmic contact to the silicon and a convenient means of controlling the silicon temperature. The temperature of the silicon during an electropolishing experiment was usually controlled to ±0.3°C by pumping water through the coil at the rate of about 400 cc/min from a 1-gal thermostat reservoir. A Western Electric thermistor type 17A was also soldered to the back side of the electrode to measure temperature. The thermistor was connected in series with a 5 ma milliammeter and a 1.5 v No. 6 dry cell and calibrated in terms of current as a function of temperature.

Prior to each experiment, the top surface of the silicon was lapped with No. 600 mesh silicon carbide. The electrode was held tightly against the rubber gasket by two rubber bands (not shown) attached to the fingers of the copper ring.

Also not shown is the polyethylene syphon used to make electrode potential measurements against a saturated calomel reference electrode. One end of the syphon was heated and drawn to a fine capillary tip. The syphon was filled with the HF solution and plugged at the large end with rolled-up filter paper. The plugged end of the syphon dipped into a saturated solution of KCl which contained the reference electrode, while the capillary tip end dipped into the electrolytic cell and was positioned so that only one corner touched the silicon. This arrangement produces a negligible amount of masking by the capillary tip and yet insures sufficient proximity to avoid including an appreciable solution *IR* drop in the potential measurement. An error of 10 or even 100 mv in the potential is not important in this study. Considerable difficulty was encountered in obtaining potential data when gas was being evolved at the electrode. Gas bubbles have a tendency to enter the capillary tip when close to a gassing electrode. This often produces an open circuit. The best procedure was to lower the tip to touch the silicon for each potential measurement and then withdraw it some distance away.

The cathode was a 1 cm square sheet of platinum welded to a platinum wire. All the HF solutions were made up using 48% by weight reagent grade hydrofluoric acid. About 100 cc of solution was used in each experiment as this was the cell capacity. The power supply consisted of one or two large 45-v dry batteries with two slide wire rheostats in series to adjust the current.

### Anode Potential—Current Density Characteristic

A typical anode potential-current density curve for a horizontal *p*-type silicon electrode facing up is shown in Fig. 3. The curve was obtained by slowly decreasing the rheostat resistance while the anode

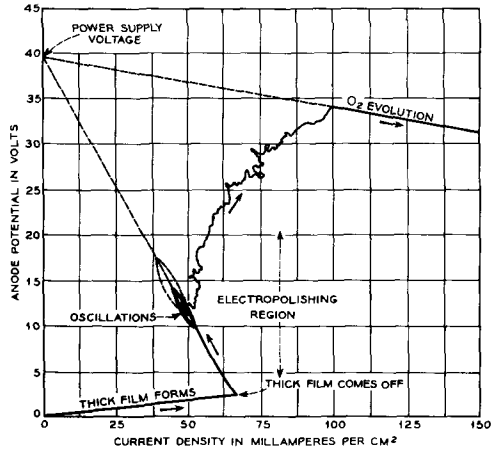


Fig. 3. Typical anode potential-current density curve for a horizontal p-type silicon anode facing up in 5% HF at 25°C.

potential and current were recorded an a L&N X-Y Recorder. In the initial portion of the curve, a thick film forms and there is considerable gassing. At a critical current density, the thick film suddenly starts coming off and floats to the surface. Gassing virtually ceases. If no change is made in the rheostat setting, the current slowly decreases while the anode potential increases. This is due to a high resistance film being formed on the silicon. The negative slope in the anode potential-current density curve above the critical c.d. is determined by the power supply voltage and the rheostat resistance. If the straight line sections are projected back to zero current, they intersect the potential axis at the power supply voltage as shown in Fig. 3. When the anode potential reaches about 10 v, oscillations in current and potential occur. It may take several minutes to reach this condition. The transition can be hastened by raising the voltage applied to the cell. If the transition stage in Fig. 3 had been allowed to continue, the current and potential would have changed further along the same straight line; however, the oscillations would have stopped at about 17 v. In one experiment, the transition stage was allowed to continue for about 1 hr and the anode potential rose to about 30 v while the current density dropped to 20 ma/cm. The anode potential-current density curve above the initial transition stage is erratic as seen in Fig. 3. It is interesting to note that above 20 v anode potential, if the current is interrupted, a burst of gas is given off the surface of the horizontal silicon electrode. At a second critical current density, continuous oxygen evolution begins and the anode potential decreases while the current increases in a runaway process.

The E-I curve for a vertical electrode (with convection stirring) differs from the curve shown in Fig. 3 in that there is no abrupt change in the current and potential when electropolishing starts. Perhaps this is due to electropolishing beginning at only some areas at first and gradually spreading to the entire surface with increasing current.

If a voltage is suddenly applied to the cell which is sufficient to pass more than the critical current density initially, the anode potential and current will pass quickly into the electropolishing region.

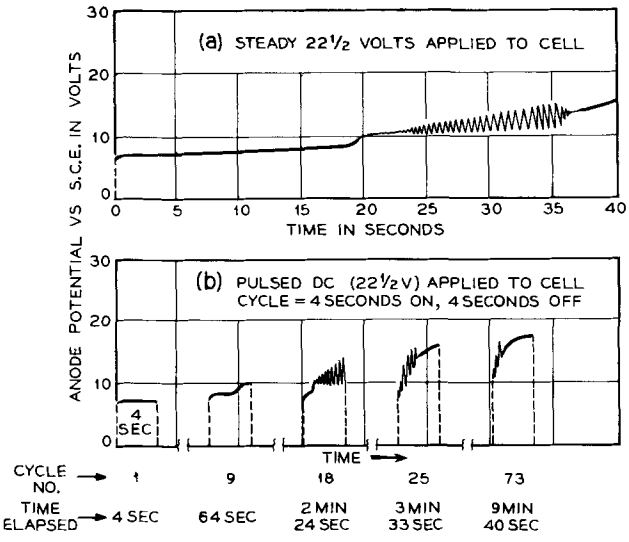


Fig. 4. Anode potential-time curves for p-type silicon in 5% HF at 30°C: (a) steady 22½ v applied to cell; (b) pulsed D.C. (22½ v) applied to cell cycle: 4 sec on, 4 sec off.

A short induction period is required before the transition takes place, however, as shown in Fig. 4a which is a record of the anode potential change with time. A 22½-v battery was connected directly across the cell with no external resistance. Electropolishing does not begin until after 20 sec, at which time there is a step in the curve. Oscillations also begin and tend to increase in amplitude with time. Eventually the oscillations stop and the anode potential rises to a fairly steady value approaching the supply voltage.

Another technique employed was to apply a pulsed d-c voltage to the cell. The anode potential-time curves obtained under these conditions are shown in Fig. 4b. A cycle of 4 sec on and 4 sec off was used. The first appearance of the step in potential comes during the ninth cycle or about 1 min after the start. In successive pulses, the E-t curve changes so that a greater portion of the pulse time is occupied in the electropolishing region.

The simplest means of electropolishing silicon in aqueous hydrofluoric acid solutions is to apply a constant voltage between 10 and 20 v directly across the cell. Initially the current is large and is limited mainly by the electrolyte resistance. As the high resistance electropolishing film forms, the current drops and an increasing amount of the applied voltage appears across the electropolishing film. The potential between the silicon and the electrolyte thus automatically stays in the electropolishing region.

## Nature of Thick Anode Film Prior to Electropolishing

The most reproducible and stable part of the E-I curve for silicon in HF solutions is the initial section where a thick, solid film forms. The film is removed easily for study by briefly raising the current above the critical value. It comes off in large flakes and floats to the surface. The film is a brown color when formed on a surface lapped with No. 600 mesh silicon carbide. If the silicon is electropolished beforehand, several orders of interference colors can be seen as the film thickens. Thick pieces grown on an electropolished surface are an orange-red color and glassy in appearance. Electron and x-ray diffraction studies show the film to be amorphous. This is characteristic of anodically grown films. The film appears to be a good insulator since it holds a static charge well. Pieces of the film react with explosive violence when put in contact with a strong oxidizing agent such as nitric acid. This result and the fact that Uhlir (2) obtained an effective valence of about two for the dissolution of silicon with the thick anode film being formed means that the film contains divalent silicon. Brouillet and co-workers (6) also found that in perchloric acid solutions, if a metal has several valence states, the anodic dissolution process favors the lowest one. The gas evolved during the thick film formation is hydrogen (2). Hydrogen evolution at an anode is unusual. In this case it is due to the chemical reduction of hydrogen ions by divalent silicon in the anode film. Hydrogen has also been observed from anodized aluminum (7) and magnesium (8) as the result of a similar chemical reduction process.

Fluoride ion has also been detected in the thick anode film by means of a spot test. This could be due to some HF being trapped inside but it also could mean that the film is composed of silicon subfluoride. Subfluorides of silicon have been reported in the literature. Attempts by Ruff (9) to repeat this work were unsuccessful, nor could he obtain evidence of a subfluoride by means other than those previously tried. Recently, however, Schmeisser (10) has reported forming subfluorides of silicon by the reduction of $SiF_2Br_2$ or $SiFBr_3$ with magnesium in an ether solution.

On the basis of the experimental results it appears likely that some silicon subfluoride $(SiF_2)_x$ is formed anodically. This is unstable in water solutions and is oxidized to tetravalent silicon with hydrogen gas evolved as follows:

$$x\mathrm{Si} + 2x\mathrm{HF} = (\mathrm{SiF_2})_x + 2x\mathrm{H^+} + 2xe^-$$

$$(\mathrm{SiF_2})_x + 2x\mathrm{H_2O} = x\mathrm{SiO_2} + 2x\mathrm{HF} + x\mathrm{H_2}\uparrow$$

## Critical Current Density for Electropolishing

In order to enter the current-potential region where the electropolishing of silicon takes place, a critical current density, $i_c$, must be reached. The effects of temperature, HF concentration, viscosity, and the concentration of the final anode product, fluosilicic acid ($H_2SiF_6$), on $i_c$ were determined. All of the data were obtained starting with a lapped surface.

*Effect of temperature.*—The E-I curve in Fig. 3 was obtained at 25°C. If the temperature of the silicon is varied, it is found that the critical current required to start electropolishing silicon also changes. The critical current density $i_c$, is defined as the current density at which the thick anode film starts coming off and the transition to the electropolishing region takes place. Higher temperatures require higher current densities. This is illustrated in Fig. 5. At a given current density, the anode potential decreases with increasing temperature. It can be seen from Fig. 5, however, that the anode potential at

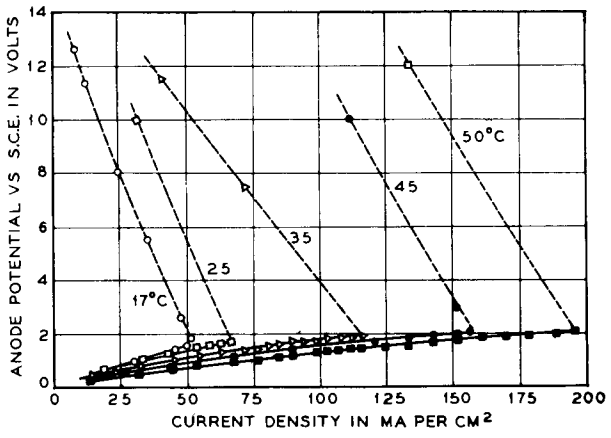


Fig. 5. Anode potential-current density curves for p-type silicon in 5% HF at various temperatures.

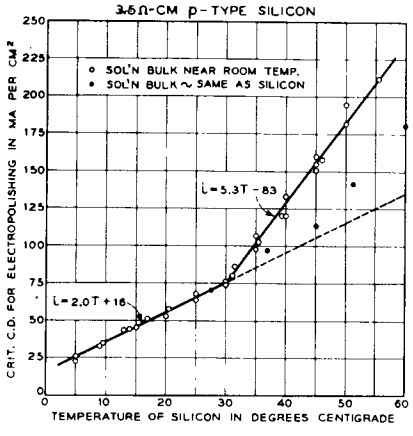


Fig. 6. Effect of temperature on the critical current density required to start electropolishing silicon in 5% HF.

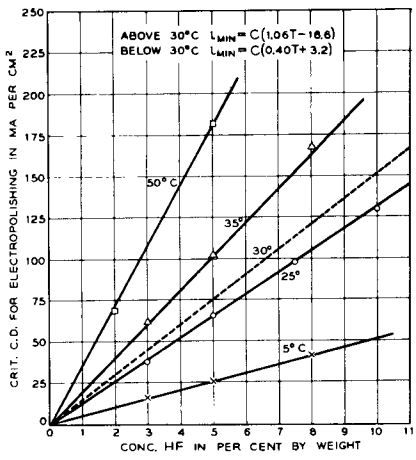


Fig. 7. Effect of HF concentration on the critical current density required to start electropolishing silicon at various temperatures.

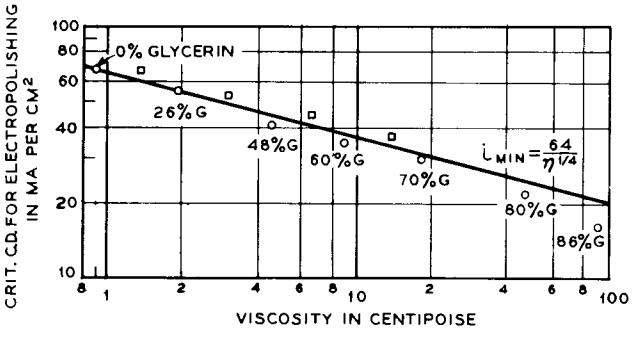


Fig. 8. Effect of viscosity on the critical current density required to start electropolishing silicon in 5% HF and glycerin at 25°C.

which electropolishing starts, increases with temperature.

The critical current density required to start electropolishing silicon in 5% HF from 5° to 60°C is shown in Fig. 6. Most of the data were obtained with the bulk of the solution near room temperature. The points fall along two straight lines which intersect near room temperature. The critical current density is reproducible within ±2 ma/cm² below 30°C. Above 30°C, the reproducibility decreased with an increasing temperature difference between the silicon and the solution bulk. A few additional points were obtained under conditions where the solution temperature was about the same as that of the silicon. These results will be discussed later.

*Effect of* HF *concentration.*—At a constant silicon temperature, the $i_c$ is linearly related to the HF concentration. Data obtained at four temperatures, two below and two above 30°C, are shown in Fig. 7. The straight lines drawn are obtained from the empirical equations derived from the $i_c$-$T$ data in Fig. 6. These equations were modified to include the effect of HF concentration, assuming that $i_c$ is directly proportional to the HF concentration. The data obtained in the two experiments agree rather well.

*Effect of viscosity.*—The viscosity of the solution is known to be a factor in electropolishing metals. To test the effect of viscosity alone, it is necessary that an inert material be used to change the viscosity. Glycerin is often used and was chosen for this work. All solutions contained 5% by weight HF. Solution viscosities were obtained from published data on glycerin-water solutions (11). The data obtained in two series of experiments are presented on a log-log plot in Fig. 8. The straight line drawn for the empirical equation $i_c = 64\eta^{1/4}$ is a reasonable fit to the data. It shows that $i_c$ is inversely proportional to the fourth root of the viscosity. Large deviations from this relation occur only at high viscosities, i.e., solutions 80 and 86% by weight glycerin.

*Effect of* $H_2SiF_6$ *concentration.*—Some workers (12) have found that the critical c.d. for electropolishing certain metals is decreased when the concentration of the metal in solution is increased. A series of six solutions were made up containing 5% HF and from 0 to 25% by wt fluosilicic acid ($H_2SiF_6$). The critical current density required to start electropolishing silicon in aqueous HF was not affected by the addition of fluosilicic acid.

## Electropolishing *n*-Type Silicon

A few attempts were made to electropolish *n*-type silicon at 5°C where low polishing current densities can be used (~25 ma/cm²). The silicon was always pitted after the anodic treatment. This is due to the voltage barrier in the surface layer of the silicon which breaks down only at the points of pitting. It may be possible to obtain uniform breakdown of the voltage barrier by illuminating the silicon with a strong light. Even with a very strong light, however,

it will not be possible to electropolish $n$-type silicon rapidly since this requires a high current density.

## Discussion

The experimental results suggest that silicon begins to electropolish in hydrofluoric acid solutions when the HF concentration at the anode surface decreases to a critical value. Hydrofluoric acid is consumed in the anode process. The supply of HF at the anode surface is determined by its rate of "mass transfer," i.e., by diffusion, convection, and migration from the bulk to the electrode surface. The nature of "mass transfer" of the reacting species to a horizontal silicon anode in HF solutions prior to electropolishing is complicated by the fact that an anode film is formed and gas is evolved. The contribution due to ion migration probably can be neglected. There are, however, several sources for "free convection" at the surface as a result of density differences in the solution near the surface. The thick anode film that forms consumes HF which tends to make the solution layer at the surface less dense than the bulk. The anode film reacts slowly with the electrolyte, however, to form fluosilicic acid and hydrogen gas. Fluosilicic acid should tend to counter the decrease in density due to the consumption of HF. The hydrogen gas that comes off produces a stirring effect like that due to density differences in fluids. Bubble size is probably an important factor in determining the effectiveness of stirring due to gassing. Thermal gradients in solutions also produce convection stirring. If the horizontal silicon electrode is colder than the solution above it, the solution layer at the surface is more dense than the bulk and there is no tendency for convection stirring due to thermal effects. When the silicon electrode becomes warmer than the bulk solution, however, the surface layer becomes less dense than the bulk and convection stirring results. The break in the $i_c - T$ curve in Fig. 6 shows this effect very clearly. Above 30°C the silicon is warmer than the bulk solution and the thermal gradient contributes to the "free convection." An attempt was made to thermostat the solution to the same temperature as the silicon. The few experimental points obtained under these conditions lie between an extension of the lower line and the upper line in Fig. 6. The results are in the right direction, but apparently thermal gradients have not been entirely eliminated.

If the reacting species reaches the electrode only by diffusion under steady-state conditions, the critical (or limiting) current density may be given by:

$$i_c = \frac{nFDC_b}{\delta} \qquad \text{(I)}$$

where $n$ = the number of electrons involved in the electrode reaction, $F$ = Faraday's constant, amp sec/g equivalent, $D$ = diffusion coefficient, $C_b$ = bulk concentration of reacting species, and $\delta$ = thickness of hypothetical diffusion layer. The diffusion layer thickness $\delta$ is not a constant under conditions that are nonsteady state and where "free convection" contributes to the "mass transfer" of the reacting species. Tobias, Eisenberg, and Wilke (13) have shown that the diffusion layer thickness depends on the electrolyte composition, viscosity, diffusion constant, density coefficient, electrode reaction, electrode height, shape, and orientation. With vertical electrodes under conditions of "free convection",

$$\delta = 1.91\left[\frac{x\,\eta\,D\,\rho_b}{g(\rho_b - \rho_i)\rho}\right]^{1/4} \qquad \text{(II)}$$

where $x$ = vertical height on electrode surface, $\eta$ = viscosity, $\rho_b$ = bulk solution density, $\rho_i$ = solution density at the surface, $\rho$ = average solution density, and $g$ = acceleration due to gravity. It is convenient to relate the density difference to the concentration difference by a specific densification coefficient, $\alpha$, defined by:

$$\alpha = \frac{\rho_b - \rho_i}{\rho_b(C_b - C_i)} \qquad \text{(III)}$$

where $C_i$ is the reacting species concentration at the surface. At $i_c$, $C_i = 0$, then from Eqs. (I)-(III)

$$i_c = 0.52\,nFD^{3/4}C^{5/4}\left[\frac{g\,\alpha\,\rho}{x\eta}\right]^{1/4} \qquad \text{(IV)}$$

The general form of this equation has been verified experimentally by Wagner (14) and Wilke, *et al.* (15).

A similar mathematical analysis for horizontal electrodes has not been developed because of the complexity of the problem. However, empirical studies by Schmidt (16) on heat transfer and Fenech (17) on copper deposition under free convection conditions indicate that the critical or limiting current density on horizontal electrodes is proportional to the 4/3 power of the bulk concentration and is inversely related to the 1/3 power of the viscosity.

The critical current density at which electropolishing starts on a horizontal silicon electrode in HF solutions was found experimentally to vary linearly with HF concentration and temperature and inversely with the fourth root of viscosity. The diffusion constant and viscosity in Eq. (IV) are both temperature sensitive. Over a short range of temperatures, $i_c$ should be approximately a linear function of temperature since $D \propto T$ and $\log \eta \propto 1/T$. These effects of HF concentration, viscosity, and temperature are in the right order of magnitude to assume that the $i_c$ for electropolishing silicon in HF solutions is controlled by the rate of "mass transfer" of HF from the bulk to the surface. The sudden change in the slope of the $i_c - T$ curve in Fig. 6, signifying the start of convection stirring due to thermal effects, is also indicative that $i_c$ is controlled by the "mass transfer" of HF to the silicon surface.

The mechanism for electropolishing silicon in HF solutions involves an understanding of the significance of the critical current density required to start electropolishing. Experimental results, while not extensive, do suggest that $i_c$ is determined by the rate of "mass transfer" of HF from the bulk to the surface. As long as the HF concentration at the surface remains above a critical value, silicon dis-

solution is divalent and a solid anode film is formed, presumably $(SiF_2)_x$. At $i_c$, there is insufficient HF at the anode surface to continue this process and the next anode reaction begins. This involves dissolution of silicon in the tetravalent form. The anode product formed under these conditions produces the electropolishing film. The most likely assumption is that it is some form of $SiO_2$. Silicon dioxide is readily dissolved in HF which is consistent with the observation that the electropolishing film on silicon is always very thin—less than interference-color thickness.

### Acknowledgment

The author is grateful to U. B. Thomas and J. F. Dewald for their helpful comments and discussion of this work.

Manuscript received June 24, 1957. This paper was prepared for delivery before the New York Meeting, April 27-May 1, 1958.

Any discussion of this paper will appear in a Discussion Section to be published in the June 1959 JOURNAL.

REFERENCES

1. T. P. Hoar and J. A. S. Mowat, *Nature*, **165**, 64 (1950).
2. A. Uhlir, *Bell System Tech. J.*, **35**, 333 (1956).
3. D. R. Turner, *This Journal*, **103**, 252 (1956).
4. R. J. Archer, Private communication.
5. M. V. Sullivan and J. H Eigler, *This Journal*, **104**, 226 (1957).
6. P. Brouillet, I. Epelboin, and M. Fromet, *Compt. rend.*, **239**, 1795 (1954).
7. P. Brouillet, *Metaux Corrosion Ind.*, **30**, 243 (1955).
8. J. H. Greenblatt, *This Journal*, **103**, 539 (1956).
9. O. Ruff, "Die Chemi des Fluors," p. 119, J. Springer, Berlin (1920).
10. M. Schmeisser. I.U.P.A.C. Colloquim, Munster, p. 28 (1954).
11. M. L. Sheely, *Ind. Eng. Chem.*, **24**, 1060 (1932).
12. A. Hickling and J. K. Higgins, *Trans. Inst. Metal Finishing*, **29**, 274 (1953).
13. C. W. Tobias, M. Eisenberg, and C. R. Wilke, *This Journal*, **99**, 359C (1952).
14. C. Wagner, *J. (and Trans.) Electrochem. Soc.*, **95**, 161 (1949).
15. C. R. Wilke, M. Eisenberg, and C. W. Tobias, *This Journal*, *100*, 513 (1953).
16. E. Schmidt, *Chimie Ingeniueur Technik*, **28**, 175 (1956).
17. E. J. Fenech, "Correlation of Limiting Currents at Horizontal Electrodes Under Free Convection Conditions," M.S. Thesis, University of California, Berkeley, Calif. (1956).

# Electrochemical Measurement of Oxide Formation

**Douglas G. Hill, Bernard Porter,[1] and Arthur S. Gillespie, Jr.[2]**

*Duke University, Durham, North Carolina*

ABSTRACT

Measurements have been made of the potential developed between a metal wire covered with its oxide and a platinum wire over which air or oxygen was passed. The electrolyte was the eutectic mixture of $Li_2SO_4$ and $K_2SO_4$, containing dissolved CaO and operated at various temperatures between 550° and 750°C. Heavy metal oxides are only very slightly soluble in this melt, so that the measured potential corresponds to the formation of metal oxide from the elements. Iron probably formed FeO, nickel formed NiO below 658° and probably a solid solution of $LiNiO_2$ in NiO at higher temperatures, while copper formed $Cu_2O$. Gold showed only the thermoelectric potential expected. The values found are in agreement with the free energy of formation of the oxides as determined by other methods.

An electrode reversible to oxygen gas and oxygen ion is useful both for thermodynamic measurements involving oxide formation and for determining the oxide ion activity in reactions of metallurgical interest. Such an electrode has not been possible in water solution, but it was shown many years ago that molten metal in contact with oxygen gas appeared to serve as such an electrode in fused salts at high temperatures (1). More recently a study of solid metal electrodes with oxygen gas in fused salts has been published by Lux (2), whose work has been critically reviewed and extended by Flood, Forland, and Motzfeldt (3). These last workers showed that a platinum wire surrounded by oxygen and immersed in a fused salt gave reproducible potentials, depending on the oxide ion concentration in the melt. The dependence of the potential on the concentration was discussed by Flood and Forland (4).

The authors combined this electrode with one made from a heavy metal covered with its oxide. The cell may be represented as

$$M/MO/\text{Fused Salt}/O_2/Pt \quad (O^{=}\text{in})$$

The metals studied form oxides which are only very slightly soluble in the molten salt, the melt giving no chemical test for the metal after use. The authors assume saturation with the metal oxide and, therefore, assume that the reaction measured is the formation of the metal oxide from its elements. In such a reaction, the oxide ion concentration should have no effect on the measured potential, which was found to be the case, save in one experiment to be

[1] Present address: Kaiser Aluminum & Chemical Corp., Permanente, Calif.

[2] Present address: Research Laboratories, Aluminum Company of America, New Kensington, Pa.

discussed below. The only variable is the oxygen pressure, to which the measured potential showed the proper relation.

## Experimental

*Solvent.*—The fused salt solvent was the eutectic mixture of $Li_2SO_4$ and $K_2SO_4$, with 28.4% $K_2SO_4$. This has the high temperature stability of the other alkali sulfates, and the advantage of a lower melting point, 535°C. The lower melting point permitted study at temperatures at which corrosion by the oxide-containing melt was less severe, and lowered the vapor pressure of alkali oxides to a negligible value. Lux was forced to operate at 950°, where both problems were accentuated. The salts were reagent grade and were used without purification other than drying at 110°. Calcium oxide was added to establish the oxide ion concentration, which was varied from 0.1% to saturation. The latter is only approximately known, but is not far from 1%.

*Cell and furnace.*—The cell was heated in a Lindberg Pot Furnace with a controller operated by a thermocouple which measured air temperature in the furnace. This was constant only to ±4°, but the large heat capacity of the cell itself reduced the variation as measured in the electrolyte to ±1°, while installation of a stainless steel pot later reduced it to a few tenths of a degree.

A thick insulating top for the furnace was constructed of Marionite asbestos, which was covered on the bottom with a stainless steel sheet when the metal pot was used. The top was mounted on a Transite board with guides, support rods, and pulleys so that it could be raised and lowered while remaining aligned with the furnace. All electrodes and other fittings were mounted rigidly on the top, and raised and lowered into the melt by this means. Where the metal reflector was not used, the top was painted with water glass to prevent loose asbestos from falling into the melt.

The cell itself was a fused alumina crucible, Morganite, which was not attacked by the fused sulfates or even by moderate oxide concentrations. Tubing of this grade alumina was not available, so thermocouple well and gas inlet tubes were of less resistant alumina containing some silica. There is no evidence that a very small silica or alumina content in the fused salt was objectionable.

In the most successful cell the simplicity of the electrode system is noteworthy. The heavy metal electrode was a stout wire of the metal arranged to project into the melt when the top was lowered. An alundum shield was tried, but appeared to make no difference in the emf, and not as much as hoped in the corrosion. Preoxidation of the wire surface did not change the ultimate voltage but decreased the time required to reach equilibrium.

The most successful type of oxygen electrode was modelled on the Hildebrand hydrogen electrode long used in aqueous solution. An alundum tube 8 mm OD, 3 mm ID immersed 1 cm in the fused salt and extending through the top admitted the gas, either air or oxygen. A platinum wire was inserted through this tube and allowed to extend about 1 cm further into the liquid. Alundum appears to be a good enough insulator up to our highest temperatures so that no electrical losses were observed.

*Gases.*—Air from a regulated pressure line or oxygen from a cylinder was dried with sulfuric acid and filtered through glass wool.

*Potential measurement.*—Potentials were measured on a L&N Student Potentiometer, which was sufficiently precise for the experiments where "equilibrium" potentials might vary by several millivolts. There was no correlation between the random variations in voltage and the temperature variations in the cell. This would be expected to be the case from the measured temperature effect in Table I.

## Results

The potentials observed when a metal wire and an oxygen electrode are inserted in a sulfate eutectic with dissolved oxide approach stable values at rates differing for the various metals. Iron at times was stable after 1 hr, although usually several hours were required. Copper required at least 24 hr, while nickel at the lowest temperature took even longer. Special care is needed to avoid a dependence on the rate of flow of the gas, whether air or oxygen, at the oxygen electrode. Flood, Forland, and Motzfeldt found that the rate of flow caused a change in measured potential when using oxygen electrodes in an oxide-ion concentration cell, but were able to eliminate it by insuring that the furnace atmosphere was identical to the entering gas. This source of error did not explain our variations when using air as the gas in a cell exposed to air, and investigation of each electrode was required.

The heavy metal-metal oxide electrodes change their potential when stirring takes place around them, the reason probably being the same as in the case of the poisoned oxygen electrode to be discussed below. However, it was possible to show by physically moving the electrode that, when located as much as 2 cm from the gas stream, no appreciable stirring took place. The emf reported is measured when the metal oxide is in a region essentially quiescent.

The potentials measured at these electrodes might be expected to be incorrect due to the occurrence of "mixed potentials." It was observed that the metal wires were heavily oxidized above the solution level by direct reaction with the gas present in the cell. In some cases the wire was led in through an alundum tube just dipping into the melt, which should much decrease the rate of chemical oxidation. The potentials were the same as with a bare wire exposed to the gas throughout, so the practice was discontinued in order to simplify the experimental arrangement. The fact that the potentials measured agree reasonably well with those calculated from the free energies of formation of the metal oxides appears to mean that mixed electrode conditions were not present. It is suggested that the solubility of oxygen in the melt is quite low, and that the diffusion of oxygen gas through a metal oxide layer is very slow. Under these circumstances, the conditions for mixed potential due to direct reaction would only be attained very close to the surface of the melt. The greater part of the wire be-

low the surface could react only in the electrochemical sense, so that the standard potential would be observed. It would seem to be of considerable interest that such simple experimental arrangements may be used without the appearance of mixed potentials.

At the oxygen electrode conditions are different since stirring occurs, and stirring caused potential changes in some cases. The observation that deposits were formed on the platinum wire of the oxygen electrode in all cells which showed a stirring potential at that electrode provided the explanation for it. The deposits gave an iron test on solution in HCl, so that iron compounds, presumably oxide, are the cause of the variability. Occasional cells in which no deposit formed were free of stirring potential. It proved very difficult to keep the iron content of the melt low enough to prevent formation of the deposit, since even reagent grade chemicals usually have a trace of iron. When an iron wire electrode was being measured, it was at first considered that stirring potentials were unavoidable. However, it was found that if the gas stream was shut off, the observed potential rose to a steady and reproducible value, and maintained it for many hours, finally falling off as the dissolved oxygen concentration in the cell decreased. Many observations were made with this technique, and some of the values given are open, therefore, to the objection that, although reproducible, they may not represent true equilibrium for the reaction postulated. These potentials are indicated as such.

Later in the work a method was developed which prevented the formation of the deposits on the platinum wire. Addition of active aluminum oxide or zirconium oxide, both of which have very low solubilities, to the cell contents before inserting the electrodes precipitates the small amount of dissolved iron (as a reddish brown solid on the powdered oxide), and prevents the deposition on the platinum of any which may be dissolved later, so that stable potentials are obtained, independent of stirring rate. With an iron electrode in the cell, a porous alundum filter thimble surrounding the oxygen electrode serves to protect it from the very low iron concentration which is present in the melt. Many tests on used melts have shown that the equilibrium concentration of iron in the presence of dissolved CaO is too low for detection, but unless it is made still lower by a method like that indicated, deposits form on the oxygen electrode. It should also be mentioned that no substance has been found which is able to remove a deposit once formed. It is essential to keep the oxygen electrode free of iron at all times.

The poisoning observed for the Pt-$O_2$ electrode might be described equally well as a "mixed potential," as Wagner (5) has shown for similar poisoning at a Pt-$H_2$ electrode in aqueous solution. The aim in the present experiments has been to find a chemical explanation and means for preventing the deposit of poison.

The effect of iron oxide is to raise the apparent potential of the oxygen electrode, while stirring lowers it, makes it less positive. Sufficiently rapid stirring might bring the emf down to that of an unpoisoned wire, but an impractical rate would be required. Using two poisoned platinum wires and stirring with oxygen around one, it has been possible to measure a potential as much as 200 mv between them although no voltage is found for unstirred wires. We propose that an iron oxide deposit absorbs cations from the melt, thus raising its positive potential, and that stirring disrupts this layer, thus lowering the voltage.

Table I. Standard potentials for metal oxide formation

| Metal | Temp, °C | $E_0$, v | $E_0$ (litt) | Ref. |
|---|---|---|---|---|
| Fe | 584 | 1.111* | | |
| | 588 | 1.085 | 1.070 (FeO) 1.079 ($Fe_3O_4$) | (6) |
| | 616 | 1.097* | 1.058 (FeO) 1.062 ($Fe_3O_4$) | |
| | 667 | 1.089* | 1.043 (FeO) 1.043 ($Fe_3O_4$) | |
| Cu | 714 | 0.520 | 0.540 ($Cu_2O$) | (6) |
| Ni | 658 | 0.788 | 0.792 (NiO) | (6-8) |
| | 682 | 0.884* | | |
| | 692 | 0.932* higher valence | (black oxide) | |
| | 708 | 1.032* nickel oxide | | |
| Au | 617 | 0.025-0.008 | | |
| | 716 | 0.025-0.008 | | |

* Steady emf after turning off gas.

The potentials measured with several metal/metal oxide electrodes against a Pt-$O_2$ electrode in $Li_2SO_4$-$K_2SO_4$ eutectic containing CaO are given in Table I. Most of the measurements were made with air rather than oxygen, since corrosion of the metals was much reduced. Enough use was made of pure oxygen to show the expected obedience to the Nernst equation in terms of oxygen pressure. The values given are the standard potentials for the formation of solid metal oxide from the elements at 1 atm oxygen pressure. The literature values given for comparison are calculated from the standard free energies of formation of the oxides as determined from heat capacities or from equilibria such as the reduction of the oxide with CO. The potentials are reproducible to ±0.005 v, which would be considered very poor in aqueous solution. However, variations as large or larger than this are common and so far unexplained in all high temperature cells. Some discussion of the individual cells follows.

*Iron-oxygen cell.*—Equilibrium was rapidly established between either an initially bright iron wire or one superficially oxidized and an oxygen electrode, usually operated with air. Considerable oxidation of the wire occurred outside the liquid, shortening the life of a wire as the temperature was raised. Although iron reduces alkali sulfates at high temperatures, test of solids, melt, and exhaust gas showed that no reduction had occurred in an experiment.

The emf at 588° was obtained with an unpoisoned oxygen electrode protected with an alundum filter thimble. The other values were all obtained earlier

with poisoned electrodes, and the steady voltage after turning off the air stream as recorded. These latter values are therefore too high.

Attempts were made to determine the formula of the oxide formed on the wire. The oxide was cracked off a wire after use in a cell, and the ratio of Fe(II) to Fe(III) determined by the method of Cheesbrough (9). The ratio varied from 2 to 5, averaging 3.2 over ten samples, and no correlation between length of time in the cell and oxide composition could be found. We believe that FeO is the oxide primarily formed, and that the higher oxides are formed by direct oxidation, which is not electrochemical in nature. In no case could any iron be found in the melt after a run.

*Copper-oxygen cell.*—At the one temperature studied this cell gave a potential for the formation of $Cu_2O$. Since at this temperature CuO is less stable by about 6 kcal, there seems little doubt that the reaction measured was the formation of the lower oxide. Both oxides were found on the wire, with the red adhering closely and the black on the outside as is often found in the air oxidation of copper. The reaction was not studied with pure oxygen, since the cell was much slower than the iron cell to reach equilibrium and destruction of the metal occurs with too long exposure. No copper was found in the used melt.

Stirring potentials were found in some, not all, cases in these cells, apparently caused by iron impurities. The cells quoted were free of stirring potentials, but the voltage was rather lower than calculated, so that it is possible that true equilibrium had not yet been attained. An attempt to prevent stirring potentials with alumina demonstrated that this was possible, but the cell failed to reach an equilibrium potential in 12 hr.

*Nickel-oxygen cell.*—At 658° this cell gave a potential agreeing very closely with that expected for NiO. The oxide was greenish in color and formed as a tight layer with an extremely high resistance. Presumably because of this property, it was not possible to reach equilibrium starting with a bright nickel wire. It was necessary to equilibrate at higher temperatures, forming "black oxide" (*see* below) and then to reduce the temperature. The compound then turned green rapidly, and the potential fell as rapidly to that given for NiO. The high electrical resistance of NiO layers has been noted by Verwey (10). Perhaps by accident, stirring potentials were not encountered in the measurements at 658° giving green oxide, and no deposits formed on the platinum wire. This was not the case with the higher temperature "black oxide" experiments.

At the higher temperatures a black material formed on the nickel wire. It was a good conductor, but still came to equilibrium very slowly. It gave a much higher potential than did green NiO and showed pronounced stirring potentials; the emf rose with the temperature. The substance appears to contain nickel in a higher valence state, since it was able to oxidize HCl to $Cl_2$, and, slowly, water to $O_2$. Verwey prepared a black material with a high oxidation potential and a low electrical resistance by

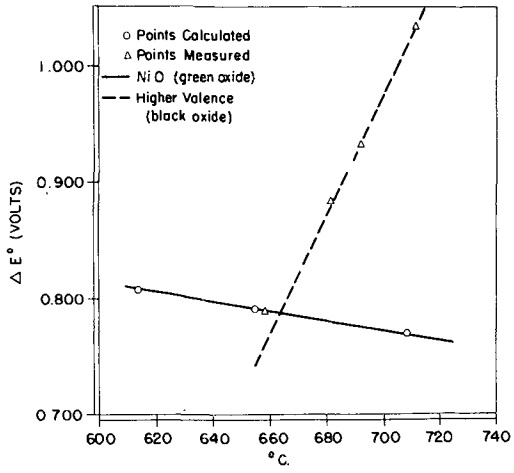

Fig. 1

the reaction of NiO with $Li_2O$ at 1200°C. It is described as having the same crystal lattice as NiO, (NaCl), but with a slightly smaller unit cell. In the crystal, $Li^+$ ions fill some of the positions of $Ni^{++}$ ions at random and, for each lithium, one nickel must become trivalent to keep charge balance. This might be described as a solid solution of $LiNiO_2$ in NiO.

Our experiments are consistent with the hypothesis that this solid solution is formed above 663° in contact with our sulfate eutectic containing $Li^+$ and $O^=$ ions. Below this temperature it decomposes to solid NiO, while $Li_2O$ dissolves in the melt. If our measured $E_0$ values are plotted against temperature, including the $E_0$ values calculated for NiO from free energies, a transition at 663° seems to be indicated (*see* Fig. 1). The open circles are calculated from the thermal data (5).

We have attempted to obtain evidence for this transition by means of cooling curves. A mixture of Ni, NiO, sulfate eutectic and a small amount of CaO (dissolved) was heated at 800° until equilibrium was presumed to have been reached, and then allowed to cool slowly, following the temperature on a thermocouple recorder. Halts were not obtained in every trial, but they were found between 660° and 663° in a number of cases. Probably the transition is not fast enough for unambiguous thermal analysis, but the results lend confidence to the theory.

The "black oxide" was obtained with either air or oxygen at the oxygen electrode, and the potential followed the Nernst law, (observed increase in emf from air to oxygen, 31 mv, calc 33 mv). The potential in this case should also be dependent on the oxide ion concentration, but the changes in the latter were unfortunately not large enough to provide unambiguous evidence. In no case was nickel found in the melt, nor in the deposit on the platinum wire.

We therefore suggest that nickel in a fused sulfate bath containing both $Li^+$ and $O^=$ ions reacts with $O_2$ below 663° to form NiO, while above this temperature the product is a solid solution of $LiNiO_2$ in NiO. The possibility of similar reactions with other heavy metals and alkalies may depend on ionic diameters.

This explanation would imply that our emf values above the transition are not true $E_0$ values, both be-

cause the oxide ion was not at unit activity and because a solid phase transition might require a very long time to reach equilibrium. Under these circumstances, the rise of apparent emf with temperature is not surprising.

*Gold-oxygen cell.*—Gold is not expected to form a stable oxide at the temperatures of our experiments. The only potential to be expected is the thermoelectric potential between Au and Pt, which should amount to about 10 mv. Although the potentials were erratic, those found were of the correct order of magnitude.

### Acknowledgment

This work was supported in part by Research Contract AT-(40.1)-1526 between Duke University and the Atomic Energy Commission, whose assistance the authors thankfully acknowledge.

Part of this work was presented at a meeting of the American Chemical Society in New York, September, 1954.

Manuscript received Oct. 4, 1956.

Any discussion of this paper will appear in a Discussion Section to be published in the June 1959 JOURNAL.

REFERENCES

1. E. Baur and H. Ehrenburg, *Z. Elektrochem.*, **18**, 1002 (1912); W. D. Treadwell, *Z. Elektrochem.*, **22**, 414 (1916).
2. H. Lux, *Z. Elektrochem.*, **45**, 303 (1939) and subsequent papers.
3. H. Flood, T. Forland, and K. Motzfeldt, *Acta Chem. Scand.*, **6**, 257 (1952).
4. H. Flood and T. Forland, Farad. Soc. Discussion No. I, 302 (1947).
5. C. Wagner and W. Traut, *Z. Elektrochem.* **44**, 391-402 (1938).
6. F. D. Richardson and J. E. Jeffes, *J. Iron Steel Inst.* (London) **160**, 261 (1948).
7. A. F. Kapustinski and M. J. Nowesselezew, *J. Phys. Chem.* (USSR) **11**, 61 (1938).
8. D. P. Bogatski, *J. Gen. Chem.* (USSR) **21**, 1 (1951).
9. E. W. Cheesbrough, *Chemist Analyst*, **20**, No. 3, 14 (1931).
10. E. J. Verwey, *"Semi-Conducting Materials"*, Academic Press, New York, 1951, p. 151.

# Equivalent Conductivities of $AgNO_3$-$KNO_3$ Mixtures

**F. R. Duke and R. A. Fleming**

*Institute for Atomic Research and Department of Chemistry, Iowa State College, Ames, Iowa*

The specific conductivities and the densities of $AgNO_3$-$KNO_3$ mixtures have been determined by Polyakov (1). The densities have also been determined by Bloom and Rhodes (2). The density data of the two investigators agree within 1% where comparison is possible, except at the higher $AgNO_3$ concentrations. Bloom and Rhodes agree with Spooner and Wetmore (3) on the density of pure $AgNO_3$. Thus, at higher $AgNO_3$ concentrations, the data of Bloom and Rhodes were used. Polyakov's data on the specific conductivity of pure $AgNO_3$ differ from those of Spooner and Wetmore. Thus, the present work is a redetermination of the specific conductivities of the mixtures, the values at high concentrations of $AgNO_3$ being significantly different from those of Polyakov.

### Experimental

The apparatus and techniques used were identical with those used by Duke and Fleming in a previous study (4). The thermocouple used for the measurement of the temperature of the cell was calibrated at the tin and lead freezing points, using especially purified samples of the metals.

The salts used were CP reagent grade, and the mixtures were prepared by mixing carefully weighed amounts of each salt. In addition, the salt mixtures were partially analyzed, silver being determined by the Volhard method.

### Results

Results are listed in Table I.

It is of interest to note that, when a plot of equivalent conductivity vs. composition is made, a very slight negative deviation from a straight line is observed at all temperatures. Thus, $AgNO_3$-$KNO_3$ mixtures are, in this sense, "regular" solutions.

Manuscript received Jan. 21, 1958. Work was performed in the Ames Laboratory of the U. S. Atomic Energy Commission.

Any discussion of this paper will appear in a Discussion Section to be published in the June 1959 JOURNAL.

REFERENCES

1. V. D. Polyakov, *Akad. Nauk S.S.S.R., Izvest Sekt. Fiz. Khim. Anal.*, **26**, 147 (1955).
2. H. Bloom and D. C. Rhodes, *J. Phys. Chem.*, **60**, 791 (1956).
3. R. C. Spooner and F. E. W. Wetmore, *Can. J. Chem.*, **29**, 777 (1951).
4. F. R. Duke and R. A. Fleming, *This Journal*, **104**, 251 (1957).

Table I. Densities, specific and equivalent conductivities of $AgNO_3$-$KNO_3$ mixtures at various temperatures

| T<br>Mole fraction $AgNO_3$ | 350°C | | | 325°C | | | 300°C | | | 275°C | | | 250°C | | |
|---|---|---|---|---|---|---|---|---|---|---|---|---|---|---|---|
| | $\rho$ | $L$ | $\lambda$ | $\rho$ | $L$ | $\lambda$ | $\rho$ | $L$ | $\lambda$ | $\rho$ | $L$ | $\lambda$ | $\rho$ | $L$ | $\lambda$ |
| 1.00 | 3.81 | 1.230 | 54.8 | 3.84 | 1.138 | 50.4 | 3.87 | 1.038 | 45.6 | 3.89 | 0.938 | 40.9 | 3.92 | 0.836 | 36.2 |
| 0.832 | 3.42 | 1.127 | 52.2 | 3.45 | 1.028 | 47.1 | 3.48 | 0.927 | 42.2 | 3.50 | 0.824 | 37.4 | 3.53 | 0.723 | 32.6 |
| 0.700 | 3.15 | 1.033 | 48.9 | 3.17 | 0.935 | 44.0 | 3.19 | 0.840 | 39.3 | 3.22 | 0.744 | 34.5 | 3.25 | 0.650 | 29.9 |
| 0.475 | 2.67 | 0.900 | 45.0 | 2.69 | 0.811 | 40.3 | 2.72 | 0.718 | 35.4 | 2.74 | 0.624 | 30.5 | 2.77 | 0.531 | 25.7 |
| 0.295 | 2.36 | 0.798 | 41.1 | 2.38 | 0.719 | 36.7 | 2.40 | 0.634 | 32.1 | 2.43 | 0.545 | 27.2 | 2.44 | 0.470 | 23.4 |
| 0.149 | 2.10 | 0.715 | 37.9 | 2.12 | 0.641 | 33.6 | 2.15 | 0.561 | 29.1 | — | — | — | — | — | — |
| 000 | 1.86 | 0.670 | 36.4 | — | — | — | — | — | — | — | — | — | — | — | — |

$\rho$ taken from Ref. (2) for pure $AgNO_3$ and 0.832 mole fraction $AnNO_3$, and from Ref. (1) in the other cases.

# Electrolytic Iron Powders—Production and Properties

W. M. Shafer and C. R. Harr

*Plastic Metals, Division of National-U. S. Radiator Corporation,*

*Johnstown, Pennsylvania*

A thorough discussion of all aspects of the production and use of electrolytic iron powder obviously would require more space than is available here. Consequently, after a brief historical review, we shall describe the production and properties of electrolytic iron powder as it is now prepared for the market by this corporation.

## Historical Background

The first recorded laboratory production of electrolytic iron in any form was by the French scientist, Becquerel, in 1831. The first practical use of electrolytic iron plating appears to have been in making iron electrotypes for printing bank notes by the Russian Mint in 1868 (1). This process, developed by Klein, used a cold ferrous sulfate bath at very low current densities. The process was quite successful and it was still in use at the time of the Russian Revolution in 1917.

Hot iron chloride baths were developed for commercial production of electrolytic iron sheet and tubes in France in 1910 (2). This French plant operated successfully for 15 to 20 years, after which it was forced to close because of economic reasons. Two ambitious, but unsuccessful, attempts were made in this country during 1920-1930 to electroform iron sheets and tubes, using hot chloride baths (3, 4). These attempts were made by the Milford and Niagara Electrolytic Iron Companies. An improved hot iron chloride bath was developed in 1930 by Thomas and Blum for the production of electrolytic iron printing plates by the U. S. Bureau of Engraving and Printing (5). So far as we know, this process is still in use. The first known commercial production of electrolytic iron powder was by the Western Electric Company in 1921. This was before the era of powder metallurgy as we now know it. A mixed ferrous sulfate, ferrous chloride, and ammonium sulfate bath was used, at a current density of 12 amp/ft$^2$. A description of the process is found in the literature (6). The Western Electric plant had a capacity of 100,000 lb of iron powder per month. The powder was used by this firm chiefly in the construction of loading coils for telephone circuits. Electrolytic iron powder has since been replaced by Permalloy in this application because of its higher magnetic permeability. The era of modern iron powder metallurgy began in the early 1930's. The new industry received much publicity and extravagant claims were made for it by enthusiastic sponsors. As frequently happens in such situations, more people were attracted to the industry than it could support. United States firms who have engaged in the commercial production of electrolytic iron powder since 1930 and the approximate periods of their activity follow:

| | | |
|---|---|---|
| Plastic Metals Division of The National-U. S. Radiator Corporation | — | 1934 to Present |
| The National Lead Company | — | 1940 to 1945 |
| Bu-El Metals Company | — | 1947 to 1949 |
| Tacoma Powdered Metals Company | — | 1948 to 1954 |

The only one of these firms in production today is The Plastic Metals Division of The National-U. S. Radiator Corporation. The main reason for this high mortality is probably failure of the demand for electrolytic iron powder to grow at the rate expected by many. There has been a steady growth in its applications, but it has met severe competition from nonelectrolytic iron powders which sell at 30 to 40% as much. At present, one domestic and two foreign firms are actively selling electrolytic iron powder in this country. The foreign firms are Husqvarna Vapenfabrik of Sweden and George Cohen Sons and Company, Ltd., of England.

Frequent inquiries are made about how our corporation, whose main products are boilers, radiators, and other heating equipment, became involved in the production of electrolytic iron powder. The story is as follows. The National Radiator Company, now the National-U. S. Radiator Corp., established a Fellowship at Mellon Institute in 1929, for the purpose of developing a process for electroforming iron radiators. It soon became evident that electroformed iron radiators could not compete in cost with conventional cast iron and nonferrous radiators and convectors. The production of electrolytic iron sheet was investigated, but also was abandoned for economic and technical reasons. At this time the new iron powder metallurgy appeared on the scene. Efforts were then directed toward salvag-

Fig. 1. Electrolytic iron cells

ing the knowledge and experience gained, in developing a process for the production of electrolytic iron powder.

## Production

The first pilot plant was built in Johnstown in 1934, and commercial shipments of electrolytic iron powder were made that year. Production and sale has increased manyfold in the years since then.

A description of the present process for producing electrolytic iron powder follows.

### *Electrolytic Iron Deposition*

Cell dimensions, inside, 10 ft long x 2.5 ft wide x 2.5 ft deep; cell composition, Haveg No. 42; electrolyte, mixed ferrous and ammonium sulfates; pH of electrolyte, 5.0-6.0; anode material, Armco ingot iron plates; cathodes, 16 gauge Type 430 stainless steel; current density, 25 amp/ft$^2$; number of anodes per cell, 17; number of cathodes per cell, 16; source of current, d-c motor-generators; temperature of electrolyte, 120°-140°F; plating time, 3½ days; plating thickness, 3/32 in. to ¼ in.; kilowatt hours/lb of iron produced, 1.50; quantity of iron produced per cell per day, 100 lb. View of the electrolytic iron cells with cathodes and anodes in position is shown in Fig. 1.

### *Cell Operation*

The cathode efficiency of 95 to 99% is high, but not quite as high as the anode efficiency. This causes a gradual increase of iron in the cell, and there is some sludge formation. The sludge settles to the bottom of the cell and is removed about every 3 weeks.

Use of the usual low-carbon steel plates as anodes instead of Armco plates results in an increase of carbon, sulfur, and manganese in the deposits.

Some ferric iron is produced by the surface oxidation of the electrolyte and is helpful in producing brittle deposits.

Cell solutions are analyzed weekly and adjusted to specified levels of pH, $NH_3$, and $Fe^{++}$.

### *Washing and Stripping*

The cathodes, with their deposits, are given cold and hot water rinses to remove as much of the electrolyte as possible. This washing is especially important in achieving low values of total sulfur. Deposits are allowed to dry and are removed from the cathodes by flexing and striking against a table top. Stripped cathodes are sanded, straightened when necessary, and returned to the cells.

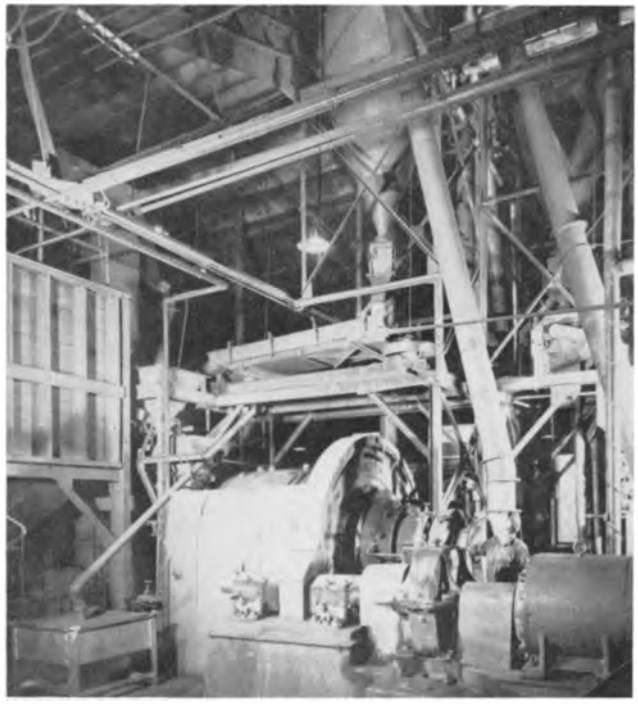

Fig. 2. Ball mill which grinds chips to powder of the desired mesh.

### *Crushing and Grinding of Deposits*

The stripped deposits, made brittle by their hydrogen content, are broken to approximately 1 in. chips in a spike roll crusher. Samples of the chips are analyzed for total sulfur, total carbon, and oxygen. Some iron is sold in this form as melting stock. Melting stock is analyzed further by chemical and spectrographic methods for total sulfur, carbon, oxygen, manganese, nickel, copper, silicon, and lead.

The chips are ground to powder of the desired mesh size in large ball mills such as shown in Fig. 2. The ball mills contain 11,000 lb of 2 in. steel balls and 3,000-4,000 lb of grinding stock at a time. Closed-type mills are used since it is generally necessary to use an inert atmosphere, such as nitrogen, to prevent firing and excessive oxidation.

Batch-type mills with 1 in. diameter steel balls are used in grinding powders to 200 mesh and finer. These mills must be kept tight during grinding, and precautions must be taken in discharging in order to prevent firing.

### *Classification*

The next step after grinding the powder is to separate it into the desired mesh. This is done by both screens and air classifiers. In some cases the classifier is attached to the mill; this is preferred because of the obviously lower costs. This combination of mill and classifier is not always possible especially in producing finer mesh powders, because of fire hazards.

### *Annealing*

The powder is hard, due to work hardening, and contained hydrogen as it leaves the ball mill or

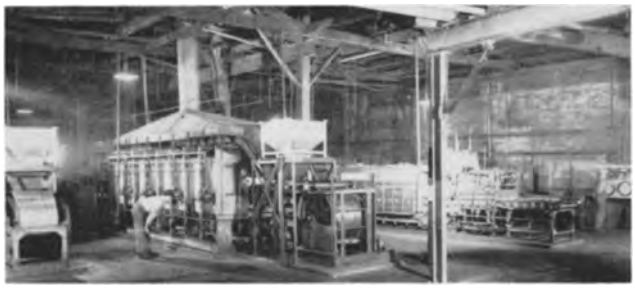

Fig. 3. Annealing furnaces

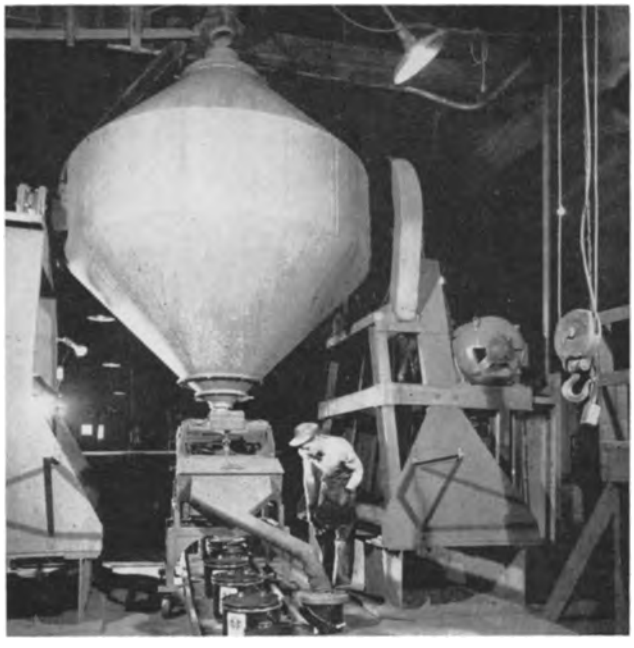

Fig. 4. 25,000 lb capacity mixers

classifier; it is dark in color because of surface oxidation. The powder can be used in this form for a few chemical and pharmaceutical applications. A combination annealing and reducing operation is required to soften it and remove the surface oxide for satisfactory use in powder metallurgy pressing and sintering operations. The annealed powder is soft and bright. Annealing is carried out at 1200°-1500°F for 30-45 min, in hydrogen or cracked ammonia, in furnaces such as the one shown in Fig. 3. The annealing temperature and time are adjusted to the mesh of the powder to prevent formation of an excessively hard sinter cake. Fine powders require lower temperatures than coarse powders. The sinter cake is given a light break-up in a crusher and reclassified.

*Mixing and Packing*

As a final step in processing, the powder is mixed to insure uniformity. The operation is carried out in mixers of 25,000-lb capacity as shown in Fig. 4. Samples of powder are taken during packing for chemical and physical tests and checking against specifications.

## Properties of Electrolytic Iron Powder

The superior properties of electrolytic iron powder are due mainly to its high purity. Table I shows a comparison of the chemical analysis of Armco Ingot Iron with that of two grades of electrolytic iron grinding or melting stock. Grade A-101 is the usual, lower cost, grinding or melting stock. It is made by electrolytic refining of Armco Ingot Iron. Note the reduction of impurities. Grade A-104 was developed for those interested in unusually pure iron, who are willing to pay for it. This grade is made by further refining of Grade A-101.

Table I. Typical chemical analyses of Armco ingot iron and electrolytic iron

| Analysis, % | Armco ingot iron | Electrolytic iron Grade A-101 | Electrolytic iron Grade A-104 |
|---|---|---|---|
| Carbon | 0.03 | 0.015 | 0.004 |
| Manganese | 0.02 | 0.002 | <0.001 |
| Sulfur | 0.025 | 0.004 | 0.003 |
| Phosphorus | 0.006 | 0.004 | 0.002 |
| Silicon | 0.020 | 0.005 | 0.001 |
| Nickel | 0.030 | 0.010 | 0.005 |
| Cobalt | 0.007 | 0.005 | 0.002 |
| Chromium | 0.005 | 0.002 | <0.002 |
| Lead | 0.005 | Nil | Nil |
| Arsenic | 0.012 | Nil | Nil |
| Boron | — | Nil | Nil |
| Copper | 0.040 | 0.008 | 0.003 |
| Total iron | — | 99.840 | 99.900 |

Table II shows comparative data on typical 100 mesh electrolytic and nonelectrolytic commercial iron powders, excluding carbonyl powder. Note the superior purity of the electrolytic product. It is not, however, quite as pure as the grinding stock from which it is made because of impurities picked up in grinding and classifying.

Table III shows a comparison of the pressing and sintering properties of electrolytic and nonelectrolytic iron powders. Note especially the higher pressed densities and better sintering properties of the softer and purer electrolytic powder. This makes possible the production of "high density" sintered iron parts with good physical properties.

Table IV shows properties of electrolytic iron sinterings obtained under various processing conditions. Note especially the properties achieved at unusually high densities and with the use of carbon. The National Cash Register Company has been particularly successful in the production of high

Table II. Comporative data on typical 100 mesh electrolytic and nonelectrolytic iron powders

| Property | Electrolytic | Nonelectrolytic |
|---|---|---|
| Chemical analysis, % | | |
| Total Carbon | 0.02 | 0.08 |
| Sulfur | 0.008 | 0.03 |
| Silicon | 0.01 | 0.15 |
| Oxygen | 0.40 | 0.60 |
| Manganese | 0.002 | 0.20 |
| Phosphorus | 0.005 | 0.03 |
| All Others | 0.03 | 0.25 |
| Physical Properties | | |
| Apparent density, g/cc | 2.45 | 2.40 |
| Flow (Hall) | 35.00 | 30.00 |
| Screen, % | | |
| On 100 mesh | 1.00 | 1.00 |
| On 150 mesh | 17.00 | 25.00 |
| On 200 mesh | 14.00 | 30.00 |
| On 250 mesh | 8.00 | 7.00 |
| On 325 mesh | 15.00 | 15.00 |
| <325 mesh | 45.00 | 22.00 |

Table III. Some comparative pressing and sintering properties of 100 mesh electrolytic and nonelectrolytic iron powders

| Pressing properties | Electrolytic | Nonelectrolytic |
|---|---|---|
| At 30 tsi pressure: | | |
| Pressed density, g/cc | 6.70 | 6.25 |
| Green strength of Transverse bar, psi | 3000 | 2000 |
| At 50 tsi pressure: | | |
| Pressed density, g/cc | 7.10 | 6.65 |
| Green strength of Transverse bar, psi | 5000 | 4000 |
| **Sintering properties** | | |
| At 30 tsi pressure: | | |
| Ultimate tensile strength, psi | 22,000 | 16,000 |
| Elongation, % | 7.00 | 4.00 |
| Hardness, RH | 55.00 | 70.00 |
| At 50 tsi pressure: | | |
| Ultimate tensile strength, psi | 30,000 | 24,000 |
| Elongation, % | 12.00 | 6.00 |
| Hardness, RH | 60.00 | 75.00 |

Note: One per cent zinc stearate was mixed with powders as a lubricant for pressing and sintering was at 2050°F for 45 min in hydrogen. tsi equals tons per square inch.

density, high strength parts, with a resulting saving in costs.

As mentioned previously, the first commercial use for electrolytic iron powder was in a magnetic core application by Western Electric Company. Some magnetic applications for cores, pole pieces, etc., still exist. Serious competition is met, however, from the ferrites, carbonyl iron powder, and Permalloy. Table V shows some of the magnetic properties of electrolytic iron in solid, powder, and flake form.

The use of electrolytic iron in flake form permits the achievement of higher magnetic permeabilities and lower core losses than when powder is used, because the flakes become somewhat oriented during pressing. Maximum permeability and minimum core losses are achieved when the long axes of the flakes are parallel to the magnetic flux.

## Concluding Remarks

It has been shown how electrolytic iron powder is produced and some of its properties have been discussed. Electrolytic iron powder is both superior in quality and higher in cost as compared with nonelectrolytic iron powders, excluding carbonyl iron. Its characteristics suit it to the production of high density sinterings with superior physical properties. These applications will increase in number and volume as the quality is increased and the relative cost is reduced.

Manuscript received March 6, 1958. This paper was prepared for delivery before the Buffalo Meeting, Oct. 6-10, 1957.

Any discussion of this paper will appear in a Discussion Section to be published in the June 1959 JOURNAL.

Table IV. Some properties of electrolytic iron sinterings obtained under various processing conditions

| Processing conditions | Density | Ult. tensile strength, psi | Elongation in 2 in., % | Rockwell hardness | Source of information |
|---|---|---|---|---|---|
| 1. Ingot iron — hot rolled rods or plates | 7.87 | 42,000 to 48,000 | 22.00 to 28.00 | 39 to 55 RB | A.S.M. Handbook |
| 2. Pressed at 50 tsi, sintered at 2050°F for 45 min | 7.10 | 30,000 | 12.00 | 60 RH | P.M.* |
| 3. Pressed at 50 tsi, sintered at 2050°F for 45 min, re-pressed at 50 tsi, re-sintered at 2050°F for 30 min | 7.60 | 44,000 | 23.00 | 36 RB | P.M. |
| 4. Pressed at 160 tsi, sintered at 2012°F, 1 hr | 7.79 | 47,700 | 37.50 | 44 RB | (7) |
| 5. Mixed with 0.8% C, pressed at 30 tsi, sintered 1 hr at 2050°F, quenched and tempered | 6.65 | 105,000 | — | 88 RB | P.M.* |
| 6. Mixed with 0.40% C, pressed at 50 tsi, sintered 1 hr at 2050°F | 7.00 | 65,000 | 5.00 | — | P.M.* |
| 7. Pressed, sintered at 2070°F for 30 min, sized, carburized to depth of 0.05 to 0.06 in., quenched, and hardened | 7.00 | 170,000 | 2.00 | — | (8) |

* P.M.—Plastic Metals Div. Data.

Table V. Typical magnetic values

| | Solid electrolytic iron | Armco iron | Sintered electrolytic iron | Cores from insulated electrolytic iron | |
|---|---|---|---|---|---|
| | | | | 16 Mesh flakes | 100 Mesh powder |
| Maximum permeability (D.C.) | 20,000 to 41,000* | 7,250 | 1,200 to 15,000* | 380 | 120 |
| Initial permeability | 410 | 250 | 450 | | |
| Saturation induction, gauss | 23,050 | 22,000 | — | 18,000 | — |
| Core loss ergs/cc/cycle | — | — | 15,000 | 1,600 | — |

* Value depends on purity, heat treatment, and density.

REFERENCES

1. M. Klein, *Chemical News*, **18**, 133 (1868).
2. L. Guillet, *Iron Age*, **94**, 1390 (1914).
3. D. Belcher, *Trans. Am. Electrochem. Soc.*, **45**, 455 (1924).
4. Anon., *Iron Age*, **116**, 675 (1925).
5. C. T. Thomas and W. Blum, *Trans. Am. Electrochem. Soc.*, **57**, 59 (1930).
6. Speed and Elmen, *JAIEE*, **40**, 596 (1921).
7. C. W. Balke, A.S.T.M. Symposium on Powder Metallurgy 1943.
8. W. J. Doelker and H. T. Harrison, M.P.A. Proc. 1953.

# Electromagnetic Forces in Large Aluminum Furnaces

**O. Chr. Bockman and J. Wleügel**

*Elektrokemisk A/S, Oslo, Norway, and A/S Norsk Aluminium Company, Oslo, Norway, respectively*

The heavy direct currents used in large aluminum furnaces produce strong magnetic fields in the whole volume of the furnace. Of particular interest to the problem is the magnetic field produced in the volume of molten cryolite and aluminum, because these magnetic fields, by interaction with the electric currents present in this volume, produce electromagnetic forces acting on the two liquid layers. It has been observed that, under unfavorable conditions, the interface between cryolite and aluminum layers may be distorted. The anode-cathode distance may thus get out of control, which is harmful to the smooth operation of the furnace (1). In addition, the liquids may yield to the forces and flow, and the stirring action produced may influence the electrolysis adversely by mixing anolyte and catholyte and reduce the current efficiency.

A complete description of the system would require a tracing of the forces set up and an evaluation of the effects of these forces on the flow system. The hydraulic aspect of the problem need not be considered, however, except for the obvious effect that a reduction of the forces necessarily reduces the flow. The main purpose of the analysis is to demonstrate how the forces are set up, to indicate how they affect the interpolar distance, and to show the possible ways of reducing the harmful electromagnetic forces.

The distance between the anode and the metal layer acting as cathode is small compared with the size of the furnace, and the magnetic field in neighboring volumes of the two liquid layers may be considered to be equal, both in magnitude and in direction. An evaluation of the distribution of magnetic flux in the two liquid layers is the first part of the analysis. This distribution is strongly influenced by steel parts in the furnace structure and does not lend itself readily to any calculation. Therefore, scale models of the furnace have been used to determine the distribution of magnetic flux.

The forces are set up by interaction of magnetic fields with electric currents. The next part of the analysis, therefore, is the evaluation of electric current distribution in the two liquid layers. Measurements on furnaces in operation are extremely difficult or even impossible, so one must rely on calculations based on the design features and the assumed electric resistivities of the parts in question.

Such calculations show that the current distribution in the aluminum layer differs largely from that in the cryolite layer. In the two liquid layers, therefore, quite different patterns of forces are set up. The difference in densities of the two liquids being small, the interface is unstable and any difference in forces acting on the two liquids may distort the interface and thus influence the anode-cathode distance.

The evaluation of electromagnetic forces is thus seen to be divided into three parts: (*a*) evaluating magnetic flux distribution; (*b*) evaluating electric current distribution in cryolite and aluminum layers; and (*c*) combining magnetic flux and electric current distributions to show the pattern of electromagnetic forces acting on the two liquid layers.

Aluminum furnaces differ largely in design and in the arrangement of the furnaces in pot lines. This work deals only with furnaces equipped with vertical contact stud Söderberg anodes with one central anode bus bar, the furnaces being arranged end to end in the pot line.

### *Magnetic Flux Distribution*

Without regard to the effect of steel parts, the distribution of magnetic flux may be calculated and some information obtained (2). However, models to a linear scale of 1:16 of a 100 ka furnace have been operated at room temperature to show the effect of steel parts on magnetic flux distribution (3). The models are designed to give close approximation to the anode and cathode bus bar current distribution of the prototype, and hence the magnetic field produced by these currents is closely reproduced in the models. To obtain the correct magnetic flux, the current of the model is made proportional to linear scale. This produces a high current density in the model, and water-cooled copper tubing is used for the conductors in the model. The magnetic flux density is measured at appropriate points with a ballistic galvanometer and a coil, the method of commutation being used.

It has been found that the current of the anode bus bar most significantly contributes to the dangerous magnetic field in the liquid layers. Two aspects of the furnace design have turned out to influence the magnitude of this magnetic field profoundly, viz., the method of feeding the current to the anode and the arrangement of steel parts in the vicinity of the anode bus bar, especially the vertical contact studs and the arrangement for suspending the anode.

REFERENCES

1. M. Klein, *Chemical News*, **18**, 133 (1868).
2. L. Guillet, *Iron Age*, **94**, 1390 (1914).
3. D. Belcher, *Trans. Am. Electrochem. Soc.*, **45**, 455 (1924).
4. Anon., *Iron Age*, **116**, 675 (1925).
5. C. T. Thomas and W. Blum, *Trans. Am. Electrochem. Soc.*, **57**, 59 (1930).
6. Speed and Elmen, *JAIEE*, **40**, 596 (1921).
7. C. W. Balke, A.S.T.M. Symposium on Powder Metallurgy 1943.
8. W. J. Doelker and H. T. Harrison, M.P.A. Proc. 1953.

# Electromagnetic Forces in Large Aluminum Furnaces

**O. Chr. Bockman and J. Wleügel**

*Elektrokemisk A/S, Oslo, Norway, and A/S Norsk Aluminium Company, Oslo, Norway, respectively*

The heavy direct currents used in large aluminum furnaces produce strong magnetic fields in the whole volume of the furnace. Of particular interest to the problem is the magnetic field produced in the volume of molten cryolite and aluminum, because these magnetic fields, by interaction with the electric currents present in this volume, produce electromagnetic forces acting on the two liquid layers. It has been observed that, under unfavorable conditions, the interface between cryolite and aluminum layers may be distorted. The anode-cathode distance may thus get out of control, which is harmful to the smooth operation of the furnace (1). In addition, the liquids may yield to the forces and flow, and the stirring action produced may influence the electrolysis adversely by mixing anolyte and catholyte and reduce the current efficiency.

A complete description of the system would require a tracing of the forces set up and an evaluation of the effects of these forces on the flow system. The hydraulic aspect of the problem need not be considered, however, except for the obvious effect that a reduction of the forces necessarily reduces the flow. The main purpose of the analysis is to demonstrate how the forces are set up, to indicate how they affect the interpolar distance, and to show the possible ways of reducing the harmful electromagnetic forces.

The distance between the anode and the metal layer acting as cathode is small compared with the size of the furnace, and the magnetic field in neighboring volumes of the two liquid layers may be considered to be equal, both in magnitude and in direction. An evaluation of the distribution of magnetic flux in the two liquid layers is the first part of the analysis. This distribution is strongly influenced by steel parts in the furnace structure and does not lend itself readily to any calculation. Therefore, scale models of the furnace have been used to determine the distribution of magnetic flux.

The forces are set up by interaction of magnetic fields with electric currents. The next part of the analysis, therefore, is the evaluation of electric current distribution in the two liquid layers. Measurements on furnaces in operation are extremely difficult or even impossible, so one must rely on calculations based on the design features and the assumed electric resistivities of the parts in question.

Such calculations show that the current distribution in the aluminum layer differs largely from that in the cryolite layer. In the two liquid layers, therefore, quite different patterns of forces are set up. The difference in densities of the two liquids being small, the interface is unstable and any difference in forces acting on the two liquids may distort the interface and thus influence the anode-cathode distance.

The evaluation of electromagnetic forces is thus seen to be divided into three parts: (*a*) evaluating magnetic flux distribution; (*b*) evaluating electric current distribution in cryolite and aluminum layers; and (*c*) combining magnetic flux and electric current distributions to show the pattern of electromagnetic forces acting on the two liquid layers.

Aluminum furnaces differ largely in design and in the arrangement of the furnaces in pot lines. This work deals only with furnaces equipped with vertical contact stud Söderberg anodes with one central anode bus bar, the furnaces being arranged end to end in the pot line.

### *Magnetic Flux Distribution*

Without regard to the effect of steel parts, the distribution of magnetic flux may be calculated and some information obtained (2). However, models to a linear scale of 1:16 of a 100 ka furnace have been operated at room temperature to show the effect of steel parts on magnetic flux distribution (3). The models are designed to give close approximation to the anode and cathode bus bar current distribution of the prototype, and hence the magnetic field produced by these currents is closely reproduced in the models. To obtain the correct magnetic flux, the current of the model is made proportional to linear scale. This produces a high current density in the model, and water-cooled copper tubing is used for the conductors in the model. The magnetic flux density is measured at appropriate points with a ballistic galvanometer and a coil, the method of commutation being used.

It has been found that the current of the anode bus bar most significantly contributes to the dangerous magnetic field in the liquid layers. Two aspects of the furnace design have turned out to influence the magnitude of this magnetic field profoundly, viz., the method of feeding the current to the anode and the arrangement of steel parts in the vicinity of the anode bus bar, especially the vertical contact studs and the arrangement for suspending the anode.

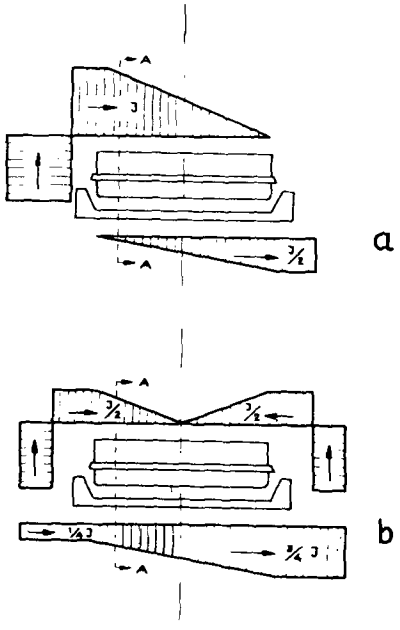


Fig. 1

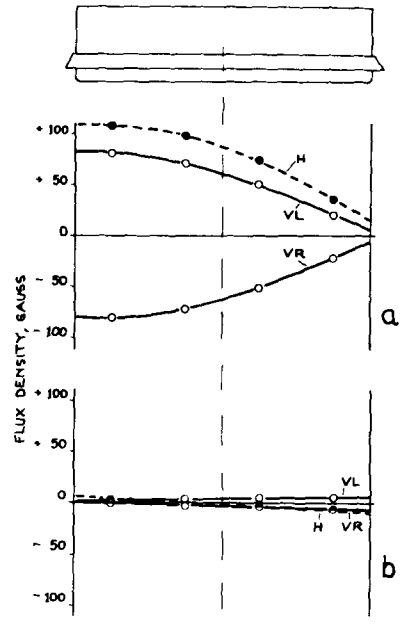


Fig. 3

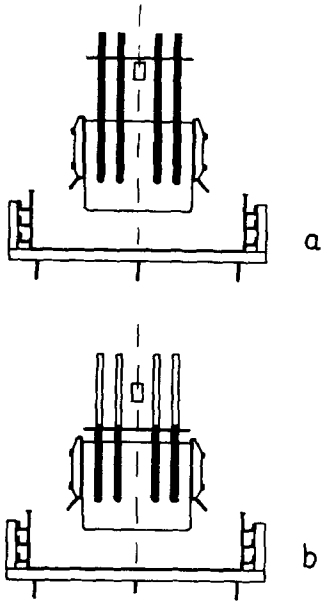


Fig. 2

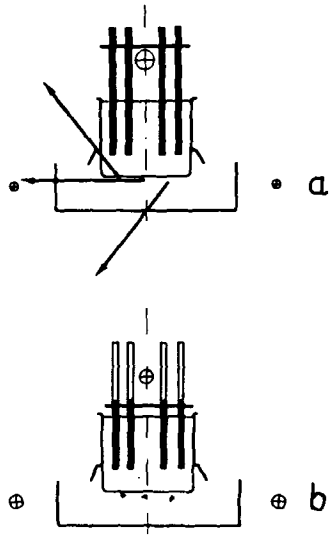


Fig. 4

Two methods of feeding the current to the anode, as illustrated in Fig. 1, have been tested: (*a*) total current fed to one end of the anode, and (*b*) half the total current fed to each end of the anode. As may be expected, the latter method gives a less intensive magnetic field. Several arrangements of steel parts have been tested; only two extreme cases will be reported, as illustrated in Fig. 2. The one arrangement (*a*) is found to be especially unfavorable as far as magnetic fields are considered, the other (*b*) especially favorable.

Figure 3 and 4 show magnetic field measurements on models of two extreme combinations: (*a*) a furnace designed unfavorably both with respect to method of feeding the current to the anode (Fig. 1a) and with respect to the arrangement of steel parts (Fig. 2a); (*b*) a furnace designed favorably in both respects (Fig. 1b and 2b). Magnetic flux densities are given in Fig. 3 for three lengthwise cuts of the anode. The horizontal transverse component (H) is given for a central cut, the vertical component in cuts on the left (VL) and right (VR) side of the anode. Transverse cuts A-A of Fig. 1 are shown in Fig. 4. The magnitude and direction of the magnetic flux density are shown in this figure by arrows.

It may be concluded that the magnetic flux density in the volume of interest is greatly influenced by the design of the furnace.

The importance of the arrangement of steel parts may be explained by some simple experiments. In Fig. 5 a conductor perpendicular to the plane of the paper carries a heavy direct current, and the magnetic flux density is measured at two diametrically opposed points. When the conductor is surrounded by a steel tube, no change in flux density is observed. When a part of the tube is cut away, leaving an air gap, the flux density is seen to be increased at

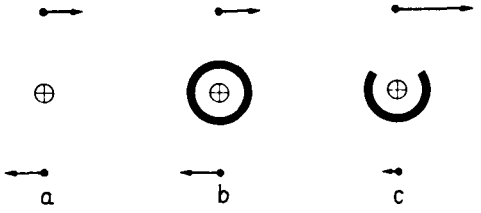

Fig. 5

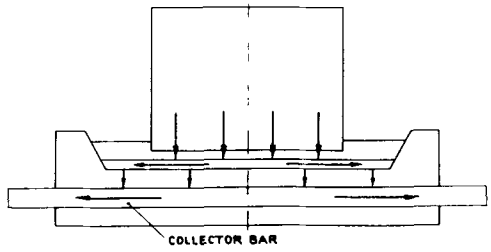

Fig. 6

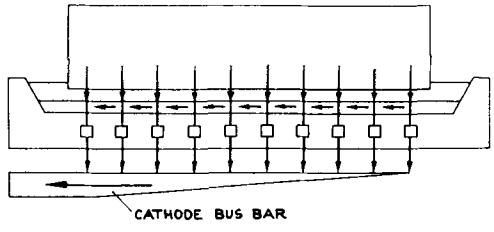

Fig. 7

the side of the air gap and reduced at the opposite side.

Thus it is not possible to reduce the total flux but, according to the design of the steel parts, the flux is pushed to one side or the other. In this way, the design given in Fig. 2a is seen to increase the flux density below the anode by setting up a magnetic circuit with steel parts on three sides and the air gap pointing downward. By arranging the steel structure for suspending the anode below the anode bus bar, a magnetic bridge is set up, short circuiting the air gap between the rows of vertical studs. By making the upper parts of the studs of nonmagnetic material an additional reduction in flux density below the anode is obtained.

*Current Distribution*

The electric current flows from the anode through the cryolite and aluminum layers to the carbon lining. The current is then collected by the steel collector bars and led to the cathode bus bars, by which the total current is passed to the next furnace.

The current thus flows in all three directions when passing from the anode bus bar of one furnace, through the furnace, and to the anode bus bar of the next furnace. In this flow several parallel circuits are set up. Compared with the other parts of the furnace, the aluminum layer is a good electric conductor and may carry large currents without appreciable voltage drop. In the transverse direction of the furnace, the aluminum layer is seen (Fig. 6) to be electrically connected in parallel to the collector bars, and in the lengthwise direction (Fig. 7) parallel to the cathode bus bars. Therefore, the aluminum layer may carry current in the horizontal direction, both transverse and lengthwise of the furnace. Calculations have been made on reasonable assumptions as to electric resistivities of the various parts of the furnace, and the horizontal currents have been found to be considerable under certain conditions.

In addition, when the normal operation of the furnace is disturbed, e.g., by a partly frozen bottom, the aluminum layer is bound to carry large currents in the horizontal direction.

In the cryolite layer no horizontal current will be set up because of the poor conductivity. In this way the current distribution in the two fluid layers differs significantly.

*Pattern of Forces*

The electromagnetic force acting on a volume element is equal to the vectorial product of the electric current and magnetic flux flowing through the element. If the volume element is taken to be a cube, the side being 1 cm, and if the directions of the electric current and magnetic flux are those of Fig. 8, the force will have the direction indicated on the figure and numerically, in dynes/cm$^3$, will be equal to the product of current density in amp/cm$^2$ and flux density in gauss (and multiplied by 0.1). When the distributions of electric current and flux density have been determined, they may in this way be combined to give the pattern of forces.

In the volume of molten cryolite only horizontal forces are set up because the direction of the current is purely vertical. In the metal layer, forces may be set up in the vertical as well as in the horizontal direction. The horizontal forces, however, are considered more important because their action is cumulative in the direction of the forces. No doubt the vertical forces play a part, but as a test of the quality of a design only the pattern of horizontal forces need be considered.

The unfavorable furnace design which has given the strong magnetic field of Fig. 3a and 4a, combined with a reasonable distribution of electric current in the aluminum layer, will turn out to give the pattern of forces of Fig. 9a in this layer. In the cryolite layer, however, much weaker forces are set up, as shown by Fig. 9b.

The much weaker magnetic field, shown in Fig. 3b and 4b, produced in a well designed furnace, gives rise to electromagnetic forces so small that they would need another scale of plotting to be readable.

*Methods of Reducing the Electromagnetic Forces*

In principle, the electromagnetic forces may be reduced by lowering the electric current density or the magnetic flux density, or by reducing both of them. Reduction of current density is considered first.

The vertical current through the cryolite layer is the electrolyzing current, the density of which is determined by other considerations. The horizontal currents in the aluminum layer, however, may be influenced by the furnace design. These currents, being in parallel to the currents of collector bars

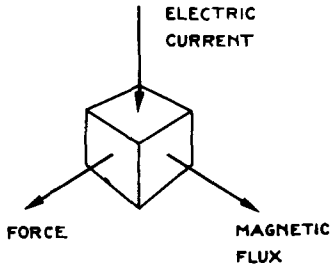


Fig. 8

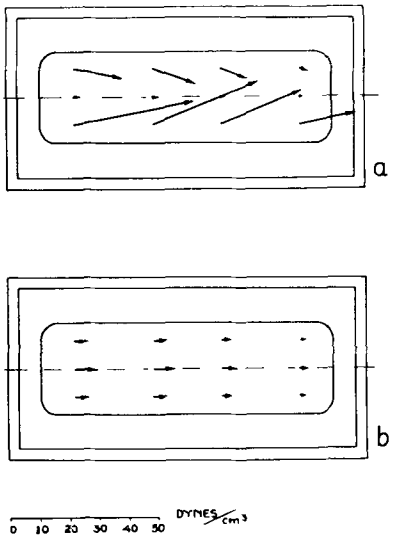


Fig. 9

and cathode bus bars, in the transverse and longitudinal directions, respectively, may be reduced by using heavy cross-sectional areas of these bars. More generally, a design of collector bar and bus bar arrangements that insures that no large potential drop is set up along the bars will give only small horizontal currents in the aluminum layer.

The forces set up in the aluminum layer may be reduced most significantly by increasing the thickness of this layer. In this way the density of horizontal currents in the aluminum layer may be kept at a low level—when the furnace is in good operation. Any disturbance of the good operation, e.g., a partly frozen bottom, will cause heavy horizontal currents to be set up in the aluminum layer. Such disturbances normally occur in the operation of a pot line, and unpredictable wild currents in the aluminum layer must be taken as a more or less normal condition.

This fact makes it the more important to reduce the magnetic flux density as far as possible. As has been seen, the magnitude of the flux density may be influenced largely by furnace design. By feeding half the total current to each end of the anode the flux density is reduced. When, in addition, the steel structure is designed to produce a screening effect, a further reduction in flux density is obtained. Figure 2a and b may be taken as examples of poor and good designs, respectively, as far as the screening effect of steel parts is concerned.

Manuscript received Feb. 24, 1958. This paper was presented at the Washington Meeting, May 12-16, 1957.

Any discussion of this paper will appear in a Discussion Section to be published in the June 1959 JOURNAL.

REFERENCES

1. J. Wleügel and O. C. Böckman, *This Journal*, **101**, 145C (1954).
2. J. Wleügel, *Aluminio*, **12** (6), 759 (1953).
3. O. C. Böckman, Congrés international de l'aluminium, Paris, June 1954, Vol. 1, p. 151.

# Fundamentals of the Theory of Electrodes and Galvanic Cells

**Erich Lange**

*Institute of Physical Chemistry, University of Erlangen, Erlangen, Germany*

**and**

**Pierre Van Rysselberghe**

*Department of Chemistry and Chemical Engineering, Stanford University, Stanford, California*

Present day electrochemistry is in a rather peculiar state. On the one hand there have been, particularly during the last two decades, important theoretical developments based on fundamental principles of thermodynamics and kinetics, as well as considerable progress on the experimental side on account of the availability of many new and ingenious methods and devices. On the other hand there is repeated evidence in textbooks and in research publications of a continued confusion with regard to fundamental concepts, definitions, matters of nomenclature, etc., which had originated in the early stages of the development of electrochemistry, but for the persistence of which there is no valid reason. The conflict between the so-called American and the so-called European signs for electrode tensions is but one example of this situation. Constantly recurring discussions of this particular problem have not settled it yet [*see*, for instance, the recent articles of deBéthune (1), Ramsey (2), Licht and deBéthune (3)].

In this connection, the recommendation made at Stockholm in 1953 by the International Union of Pure and Applied Chemistry (IUPAC) and formulated by Christiansen and Pourbaix (4) constituted a first step toward the removal of these unnecessary difficulties. This recommendation was in favor of the European signs and, in spite of a presentation judged unsatisfactory even by some of the Commission members involved in its preparation, it is to

be hoped that universal adoption of the recommendation itself will take place. The problem, however, requires a more fundamental approach and a better formal presentation of its solution. This has been done over a period of eight years in the successive editions of the report on Electrochemical Nomenclature and Definitions of the International Committee of Electrochemical Thermodynamics and Kinetics (CITCE), now an affiliated IUPAC Commission (5).

The purpose of the present communication is to outline the fundamental ideas which have been serving as guides for the work of CITCE's Commission of Electrochemical Nomenclature and Definitions (identical with the Sub-Commission of Electrochemical Symbols and Terminology of IUPAC's Commission of Electrochemistry). In addition the authors present some points beyond the contents of the latest CITCE report but within its spirit, details about these being available elsewhere (6-11).

The authors had the benefit of oral or written discussions with many electrochemists in the United States, with their CITCE colleagues, and with numerous other electrochemists in Europe. They feel that large areas of agreement have thus been established. It is their hope that the outline offered here will help in bridging certain gaps between points of view and methods of reasoning and in promoting greater interest toward the elaboration of a better presentation of electrochemical fundamentals.

The outline starts with some essential points concerning single electrodes and continues, practically and intentionally in the same language, with the corresponding aspects of the theory of galvanic cells. Some expressions used in this paper will be new for most readers. This will be the case in particular with the various uses of the word *tension* which we are adopting as the exact equivalent of the French "tension" and of the German "Spannung" and which we are recommending for general adoption. So far there has been no "official" IUPAC recommendation for the use of "tension" in English and our use of it here must be regarded as a suggestion. This is also the case with the various symbols, since no list of electrochemical notations has so far been recommended officially.

## Electrochemical Two-Phase Systems—Single Electrodes

[2.1] The phases of an *electrode* are numbered in the sequence I, II in the following manner. Taking as a typical example a zinc-zinc ion solution electrode, we may represent it by the diagram $Zn/Zn^{+2}$, which we shall designate as x, phase I being Zn and phase II being $Zn^{+2}$; or we may represent it by the diagram $Zn^{+2}/Zn$, which we shall designate as y, phase I being now $Zn^{+2}$ and phase II being Zn.

The direction in which the phases are counted and in which they are read from the diagram will normally be from left to right, independently of whether or not a current is flowing through the electrode and, in the case of current flow, independently of the direction of this current. A current flowing in the direction of the counting, i.e., from phase I to phase II, will be regarded as positive, while a current flowing in the opposite direction, i.e., from II to I, will be regarded as negative.

[2.2] An *electrode reaction* is a heterogeneous chemical reaction involving thermodynamically defined reagents and products (ions, electrons, atoms, and molecules) in the two phases of the electrode and transferring a corresponding electrical charge from one phase to the other.

The electrode reaction is completely represented, with respect to both extent and direction, by writing, in the case of our example, either electrode reaction $\alpha$:

$$Zn^{+2}\ (\text{metal}) \rightarrow Zn^{+2}\ (\text{solution})$$

or its reverse, electrode reaction $\beta$:

$$Zn^{+2}\ (\text{solution}) \rightarrow Zn^{+2}\ (\text{metal})$$

The electrode reaction is written in a direction independent from that of the counting of the phases because, according to the direction of the current, we shall have either reaction $\alpha$ or reaction $\beta$ occurring at either electrode x or at electrode y.

[2.3] The *chemical affinity* A of the electrode reaction and its *free enthalpy change* $\Delta G$ (G = G. N. Lewis' "free energy" F) are related to the chemical potentials $\mu_i$ of the reactants and products and to their stoichiometric coefficients $\nu_i$ as follows:

$$\text{for } \alpha\text{: } A_\alpha = -\Delta G_\alpha = -\Sigma \nu_{i,\alpha} \cdot \mu_i$$

$$\text{for } \beta\text{: } A_\beta = -\Delta G_\beta = -\Sigma \nu_{i,\beta} \cdot \mu_i = -A_\alpha = +\Delta G_\alpha$$

If chemical forces were alone effective (i.e., in the absence of electrostatic forces) a positive $A_\alpha$ would indicate that the corresponding reaction is spontaneous, a negative $A_\alpha$ that it is nonspontaneous.

[2.4] The *reaction charge* z.F or the *number of charges transported* z corresponds to one occurrence of the electrode reaction, F representing one equivalent of positive charge or one Faraday. If the charge transported across the interphase in the direction of the counting, i.e., from I to II, is positive, z is positive; if a positive charge is transported against the direction of the counting, i.e., from II to I, z is negative.

Since the electrode reaction can be either $\alpha$ or $\beta$ and the electrode can be either x or y, we have the following four possibilities and the corresponding values of z:

| | Electrode reaction $\alpha$ | Electrode reaction $\beta$ |
|---|---|---|
| Electrode x, $Zn/Zn^{+2}$ | $z_{\alpha,x} = +2$ | $z_{\beta,x} = -2$ |
| Electrode y, $Zn^{+2}/Zn$ | $z_{\alpha,y} = -2$ | $z_{\beta,y} = +2$ |

A number of charges such as $z_{\alpha,x}$ is related to the stoichiometric coefficients $\nu_{i,\alpha,I}$ of the reactants i of reaction $\alpha$ located in phase I and to their charge numbers $z_i$ as follows:

$$z_{\alpha,x} = -\Sigma \nu_{i,\alpha,I} \cdot z_i$$

It is similarly related to the stoichiometric coefficients $\nu_{i,\alpha,II}$ of the products i of reaction $\alpha$ located

in phase II and to their charge numbers $z_i$ as follows:

$$z_{\alpha,x} = + \Sigma \nu_{i,\alpha,II} \cdot z_i$$

[2.5] The *chemical tension*[1] $\epsilon = A/(z \cdot F)$ of an electrode represents, in magnitude and in sign, the force with which the electrode reaction tends to move *positive* charges through the interphase in the direction of the counting of the phases on account of *chemical* (or, more generally, nonelectrostatic) causes, *no other forces being effective.*

Applying the general relation $\epsilon = A/(z \cdot F)$ to electrodes x and y and to reactions $\alpha$ and $\beta$, we have:

$$\epsilon_x = A_\alpha/(z_{\alpha,x} \cdot F) = A_\beta/(z_{\beta,x} \cdot F)$$

$$\epsilon_y = A_\alpha/(z_{\alpha,y} \cdot F) = A_\beta/(z_{\beta,y} \cdot F) = -\epsilon_x$$

The practical unit of tension is the volt.

[2.6] The *Galvani tension* or *inner electric tension* of an electrode is defined as being equal to the inner electric potential $\phi_I$ of phase I minus the inner electric potential $\phi_{II}$ of phase II. It represents, in magnitude and in sign, the force with which the electrode reaction tends to move *positive* charges through the interphase in the direction of the counting of the phases on account of purely *electric* causes, i.e., on account of the electrostatic distribution of space charges, *no forces other than the electrostatic ones being effective.*

We shall designate these nonmeasurable Galvani tensions by g:

$$g_{I,II} = \phi_I - \phi_{II}$$

At electrode x we have $g_x$ and at electrode y we have $g_y$.

[2.7] The *electrochemical affinity* of an electrode reaction $\alpha$ or $\beta$ (as defined in [2.2]) at an electrode with a Galvani tension g (defined in [2.6]) is given as follows:

$$\text{for } \alpha: \tilde{A}_\alpha = A_\alpha + z_{\alpha,x} \cdot F \cdot g_x \quad \text{at electrode x}$$

$$= A_\alpha + z_{\alpha,y} \cdot F \cdot g_y \quad \text{at electrode y}$$

$$\text{for } \beta: \tilde{A}_\beta = A_\beta + z_{\beta,x} \cdot F \cdot g_x \quad \text{at electrode x}$$

$$= A_\beta + z_{\beta,y} \cdot F \cdot g_y = -\tilde{A}_\alpha \quad \text{at electrode y}$$

If $\tilde{A}_\alpha$ is positive, reaction $\alpha$ is spontaneous under the influence of the existing chemical *and* electric forces. If $\tilde{A}_\alpha$ is negative, reaction $\alpha$ is nonspontaneous.

[2.8] The *electrochemical tension* $\tilde{\epsilon}$ of an electrode I/II is defined as follows:

$$\tilde{\epsilon}_x = \tilde{A}_\alpha/(z_{\alpha,x} \cdot F) = \tilde{A}_\beta/(z_{\beta,x} \cdot F) \quad \text{for electrode x}$$

$$\tilde{\epsilon}_y = \tilde{A}_\alpha/(z_{\alpha,y} \cdot F) = \tilde{A}_\beta/(z_{\beta,y} \cdot F) = -\tilde{\epsilon}_x \quad \text{for electrode y}$$

[2.9] When reaction $\alpha$ or $\beta$ at electrode x or y is at *electrochemical equilibrium*, i.e., when no current is flowing through the electrode, the electrochemical affinities are equal to zero:

$$\tilde{A}_\alpha = 0 \quad \text{and} \quad \tilde{A}_\beta = 0$$

and the electrochemical tensions are likewise equal to zero:

$$\tilde{\epsilon}_x = 0 \quad \text{and} \quad \tilde{\epsilon}_y = 0$$

This state of equilibrium can be regarded as resulting from the compensation exerted by a "reversible" Galvani tension g acting as a counterforce against a chemical tension $\epsilon$:

for electrode x :

$$g_{x,\alpha} = -A_\alpha/(z_{\alpha,x} \cdot F) = g_{x,\beta} = -A_\beta/(z_{\beta,x} \cdot F) = -\epsilon_x$$

for electrode y :

$$g_{y,\alpha} = -A_\alpha/(z_{\alpha,y} \cdot F) = g_{y,\beta} = -A_\beta/(z_{\beta,y} \cdot F) = -\epsilon_y$$

The reversible Galvani tension of a given electrode x is the same whether the electrode reaction is regarded as being $\alpha$ or $\beta$, but it is equal to minus the reversible Galvani tension of the "reverse" electrode y:

$$g_{x,\alpha} = g_{x,\beta} = -g_{y,\alpha} = -g_{y,\beta}$$

The sign of the corresponding chemical tension $\epsilon$ of the electrode depends on the chosen direction of the counting of the phases, but it does not depend on whether reaction $\alpha$ or $\beta$ is used for the calculation of $\epsilon$.

In the case of the $Zn/Zn^{+2}$ electrode at equilibrium the electrochemical potentials of the $Zn^{+2}$ ion have the same value in two phases:

$$\tilde{\mu}_{Zn^{+2},I} = \tilde{\mu}_{Zn^{+2},II}$$

[2.10] At a Galvani tension $g_x$ different from the reversible value $g_{x,\alpha} = g_{x,\beta}$ (defined in [2.9]) the measurable *overtension* (or overvoltage) $\Delta g$ of electrode x has the same value whether reaction $\alpha$ or reaction $\beta$ is being considered:

$$\Delta g_{x,\alpha} = g_x - g_{x,\alpha} = \Delta g_{x,\beta} = g_x - g_{x,\beta}$$

When $g_x > g_{x,\alpha}$, we have $\Delta g_{x,\alpha} = \Delta g_{x,\beta} > 0$, and when $g_x < g_{x,\alpha}$, we have $\Delta g_{x,\alpha} = \Delta g_{x,\beta} < 0$.

The overtensions at electrode x under the actual tension $g_x$ are related to the corresponding electrochemical affinities of electrode reactions $\alpha$ and $\beta$ as follows:

$$\tilde{A}_\alpha = z_{x,\alpha} \cdot F \cdot \Delta g_{x,\alpha} \quad \text{and} \quad \tilde{A}_\beta = z_{x,\beta} \cdot F \cdot \Delta g_{x,\beta} = -\tilde{A}_\alpha$$

They are related to the electrochemical tension $\tilde{\epsilon}_x$ of electrode x as follows:

$$\tilde{\epsilon}_x = \tilde{A}_\alpha/(z_{x,\alpha} \cdot F) = \Delta g_{x,\alpha} = \tilde{A}_\beta/(z_{x,\beta} \cdot F) = \Delta g_{x,\beta}$$

[2.11] With current flowing through the electrode the *face* of the metallic phase of an electrochemical two-phase system into which the positive current *enters* from the adjacent nonmetallic phase (a solution, for instance) is called a *cathode.* If the positive current *leaves* the face of the metallic phase toward the adjacent nonmetallic phase, this face is called an *anode.*

[1] A "tension" ("tension" in French, "Spannung" in German) between the initial point I and the final point II of an interval is a force tending to move positive charges from I to II, regardless of the particular nature of the tension and of the signs of the ions or electrons actually set in motion. The expression "electric tension" is synonymous with such expressions as "voltage," "potential drop," and sometimes "potential difference."

[2.12] An electrode reaction taking place at a cathode, with electrons and metallic ions moving in the appropriate directions defined in [2.11], is sometimes called a *reduction*. An electrode reaction taking place at an *anode* is sometimes called an *oxidation*.

[2.13] The minimum Galvani tension g (more positive than the reversible value $g_\alpha$ or $g_\beta$) of an electrode metal I / nonmetal II able to produce an arbitrarily fixed minimum velocity of the electrode reaction in the direction of oxidation may be called *oxidation tension*, while the maximum Galvani tension g (more negative than the reversible value $g_\alpha$ or $g_\beta$) of the same electrode able to produce an arbitrarily fixed minimum velocity of the electrode reaction in the direction of reduction may be called *reduction tension*.

[2.14] Let us consider electrode x and reaction $\alpha$, with the stationary current J flowing through the electrode during time t. The change $\Delta n_{i,II}$ in the number of moles of ion i (*electrolytic change of mole number*) in the end portion of phase II in contact with phase I and affected by the electrode reaction and by migration is given by the following equation (10):

$$\Delta n_{i,II} = \left( \frac{\nu_{i,II}}{z_\alpha} - \frac{\delta_{i,II}}{z_i} \right) \cdot \frac{J \cdot t}{F}$$

in which $\nu_{i,II}$ is the stoichiometric coefficient of i in II, $z_\alpha$ is the number of charges transported, $\delta_{i,II}$ is the transference number of i in II, $z_i$ is the charge number of i.

Similarly, for the change $\Delta n_{i,I}$ in the end portion of phase I in contact with phase II we have:

$$\Delta n_{i,I} = \left( \frac{\nu_{i,I}}{z_\alpha} + \frac{\delta_{i,I}}{z_i} \right) \cdot \frac{J \cdot t}{F}$$

[2.15] The *Volta tension* or *outer electric tension* of an electrode is defined as being equal to the outer electric potential $\psi_I$ of phase I minus the outer electric potential $\psi_{II}$ of phase II.

The inner and outer electric potentials of a phase, I for instance, are related by the formula

$$\phi_I = \psi_I + \chi_I$$

in which $\chi_I$ is the surface electric tension of the phase.

### Overtensions at Electrodes with Diffusion Layers (11)

[3.1] The concepts and definitions developed above for single electrodes metal I / nonmetal II or nonmetal I / metal II do not take into account the possible presence of diffusion layers. We shall now give some additional definitions applying to cases in which a diffusion layer occupies the end portion of the nonmetal phase (usually a solution) and is being taken into account. Such a situation in general will be the result of the passage of current through single or multiple electrodes (i.e., electrodes at which, respectively, one or several reactions may occur), but it may also be the result of corrosion processes at multiple electrodes with zero net current.

[3.2] Moving from the bulk of the solution toward the outer surface of the metal phase we find the *diffusion layer* starting at some last *homogeneous layer* c and finishing at the *end layer* b of solution in contact with the metal. Between positions b and c the chemical potentials of the constituents of the solution may differ from their values in the bulk of the solution, but the standard chemical potentials in b-c are the same as those in the bulk of the solution.

[3.3] All intensive quantities and concepts already considered as pertaining to the bulk solution can be regarded as pertaining also to the homogeneous layer c. We may designate them as *bulk quantities* or *bulk concepts* and represent them by the bulk symbols without any c specification:

the *bulk* chemical potential $\mu_i$,
the *bulk* inner electric potential $\phi_{II}$,
the *bulk* electrochemical potential
$\tilde{\mu}_i = \mu_i + z_i \cdot F \cdot \phi_{II}$,,
the *bulk* electrode reaction $\alpha$,
the chemical affinity of the *bulk* electrode reaction
$A_\alpha = -\Sigma \nu_i \cdot \mu_i$,
the *bulk* chemical tension $\epsilon = A_\alpha/(z_\alpha \cdot F)$,
the *bulk* Galvani tension $g = \phi_I - \phi_{II}$,
the *bulk* reversible Galvani tension
$g_\alpha = -A_\alpha/(z_\alpha \cdot F)$,
the *bulk* overtension $\Delta g_\alpha = g - g_\alpha$,
the electrochemical affinity of the *bulk* electrode reaction $\tilde{A}_\alpha = -\Sigma \nu_i \cdot \tilde{\mu}_i =$
$A_\alpha + z_\alpha \cdot F \cdot g = z_\alpha \cdot F \cdot \Delta g_\alpha$,
the *bulk* electrochemical tension
$\tilde{\epsilon} = \tilde{A}_\alpha/(z_\alpha \cdot F) = \Delta g_\alpha$,
the *bulk* electrode polarization $\Delta g = g_{J \neq 0} - g_{J=0}$; at simple electrodes $\Delta g = \Delta g_\alpha$.

[3.4] Some quantities and concepts pertaining to the end layer b may be designated as *end quantities* or *end concepts* and represented by symbols with, for instance, an asterisk (*) as a specification:

the *end* chemical potential $\mu_i^*$,
the *end* inner electric potential $\phi_{II}^*$,
the *end* electrochemical potential
$\mu_i^* = \mu_i^* + z_i \cdot F \cdot \phi_{II}^*$,
the *end* electrode reaction $\alpha^*$,
the chemical affinity of the *end* electrode reaction
$A_\alpha^* = -\Sigma \nu_i \cdot \mu_i^*$,
the *end* chemical tension $\epsilon^* = A_\alpha^*/(z_\alpha \cdot F)$,
the *end* Galvani tension $g^* = \phi_I - \phi_{II}^*$,
the *end* reversible Galvani tension
$g_\alpha^* = -A_\alpha^*/(z_\alpha \cdot F)$,
the activation overtension of the *end* electrode reaction $\Delta g_\alpha^* = g^* - g_\alpha^*$,
the electrochemical affinity of the *end* electrode reaction $\tilde{A}_\alpha^* = -\Sigma \nu_i \cdot \tilde{\mu}_i^*$ (including $\tilde{\mu}_{i,I}$) =
$A_\alpha^* + z_\alpha \cdot F \cdot g^* = z_\alpha \cdot F \cdot \Delta g_\alpha^*$,
the *end* electrochemical tension
$\tilde{\epsilon}^* = \tilde{A}_\alpha^*/(z_\alpha \cdot F) = \Delta g_\alpha^*$,
the *end* electrode polarization $\Delta g^* = g_{J \neq 0}^* - g_{J=0}^*$; at mono or single electrodes $\Delta g^* = \Delta g_\alpha^*$.

[3.5] We now have to consider several important *bulk-end concepts* and *bulk-end relations* involving simultaneously properties of the bulk layer c and of the end layer *b*:

the diffusion tension in the diffusion layer
$g_{diff.} = \phi_{II}^* - \phi_{II} = g - g^*$,
the concentration overtension
$\Delta g_{ak} = g_a^* - g_a = -(A_a^* - A_a)/(z_a \cdot F)$,
the following *general* relation between the various overtensions at single electrodes:
$\Delta g = \Delta g_a = \Delta g_{ak} + \Delta g_a^* + g_{diff.}$, which can be simplified to the following relations under special conditions: $\Delta g = \Delta g_a = \Delta g_{ak} + g_{diff.}$, if $\Delta g_a^* = 0$, $\Delta g = \Delta g_a = \Delta g_{ak} + \Delta g_a^*$, if $g_{diff.} = 0$, for instance in the presence of an excess of foreign electrolyte in the solution,
$\Delta g = \Delta g_a = \Delta g_{ak}$, if $\Delta g_a^* = 0$ and $g_{diff.} = 0$.

## Ideal Galvanic Cells

[4.1] A typical *ideal galvanic cell* is that represented by the following diagram in which the successive phases are counted from left to right as indicated, and in which eventual irreversible diffusion phenomena (for instance at the II/III interphase) are neglected:

$$\begin{array}{ccccccc} \text{Ag} & / & \text{AgCl} & / & \text{PbCl}_2 & / & \text{Pb} & / & \text{Ag} \\ \text{I} & & \text{II} & & \text{III} & & \text{IV} & & \text{I}' \end{array}$$

which we shall designate as galvanic cell v, or by the following diagram:

$$\begin{array}{ccccccc} \text{Pb} & / & \text{PbCl}_2 & / & \text{AgCl} & / & \text{Ag} & / & \text{Pb} \\ \text{I} & & \text{II} & & \text{III} & & \text{IV} & & \text{I}' \end{array}$$

which we shall designate as galvanic cell w.

In both cases the chemically identical terminal phases I and I′ are the *ideal poles* or *terminals* of the *open* cell. In accordance with current practice we may also designate the chemically different metallic phases I and IV as the *real poles* of the cell. Besides the open galvanic cell it is useful, for many practical purposes, to consider the corresponding *closed* cell which, in addition to phases I and I′, also includes a metallic connection between poles I and I′ (*see* [4.14] below).

The mode of representation of the cell and the order of the counting of the phases must be independent of whether a current is flowing or not and, in the case of current flow, of whether this current flows in the direction of the counting or against this direction. The current J is positive in the former case and negative in the latter, whether the actual reaction is known or not known.

[4.2] The *cell reaction* is a heterogeneous chemical reaction between thermodynamically defined reagents and products (ions, electrons, atoms, or molecules) present in the homogeneous interiors of the phases of the cell, while a simultaneous transfer of a corresponding electrical charge takes place through the cell.

The cell reaction is completely represented, with respect to both extent and direction, by writing, in the case of our example, either cell reaction $\gamma$:

$$2\text{Ag} + \text{PbCl}_2 \rightarrow 2\text{AgCl} + \text{Pb}$$

or the reverse cell reaction $\delta$:

$$\text{Pb} + 2\text{AgCl} \rightarrow \text{PbCl}_2 + 2\text{Ag}$$

Depending on the direction of the current, reaction $\gamma$ or reaction $\delta$ will occur in cell v or in cell w.

There must be independence of the direction of the cell reaction from the fixed direction of the counting of the phases.

[4.3] If we wish to consider the corresponding transfer of electrons through the external metallic connection between I and I′, we may designate this transfer as the *pole reaction*. Adding this pole reaction to the *open cell reaction* in the *open galvanic cell* we obtain the *closed cell reaction* in the *closed cell*. It thus becomes clear that no essential difference needs to be introduced between the treatments of open and closed cells and cell reactions (*see* [4.14] below).

[4.4] The *chemical affinity* A of the cell reaction and its *free enthalpy change* $\Delta G$ are related to the chemical potentials $\mu_i$ of the reactants and products and to their stoichiometric coefficients $\nu_i$ as follows:

for reaction $\gamma$: $A_\gamma = -\Delta G_\gamma = -\Sigma \nu_{i,\gamma} \cdot \mu_i$

for reaction $\delta$: $A_\delta = -\Delta G_\delta = -\Sigma \nu_{i,\delta} \cdot \mu_i = -A_\gamma$

According to whether cell reaction $\gamma$ is chemically spontaneous or nonspontaneous its chemical affinity is positive or negative.

[4.5] The *reaction charge* z.F and the *number of charges transported* z correspond to one occurrence of the cell reaction. If the charge transported through the cell in the direction of the counting, i.e., from I to I′ is positive, z is positive; if a positive charge is transported against the direction of the counting, i.e., from I′ to I, z is negative.

Since the cell reaction can be either $\gamma$ or $\delta$ and the cell can be either v or w, we have the following four possibilities and corresponding values of z:

| | Cell reaction $\gamma$ | Cell reaction $\delta$ |
|---|---|---|
| Galvanic cell v: | $z_{\gamma,v} = +2$ | $z_{\delta,v} = -2$ |
| Galvanic cell w: | $z_{\gamma,w} = -2$ | $z_{\delta,w} = +2$ |

[4.6] The open cell reaction, the pole reaction, and the closed cell reaction, when written in terms of the same stoichiometry, have the *same* number of charges transported z.

[4.7] The *chemical tension* or *electromotive force* $E = A/(z \cdot F)$ of a galvanic cell represents, in magnitude and in sign, the force with which the cell reaction tends to move *positive* charges through the cell in the direction of the counting of the phases on account of *chemical* (or, more generally, nonelectrostatic) causes, *no other forces being effective*. The chemical tension E is given in units of tension, for instance in volts.

Applying the general relation $E = A/(z \cdot F)$ to galvanic cells v and w and to cell reactions $\gamma$ and $\delta$, we have:

$$E_v = A_\gamma/(z_{\gamma,v} \cdot F) = A_\delta/(z_{\delta,v} \cdot F)$$

$$E_w = A_\gamma/(z_{\gamma,w} \cdot F) = A_\delta/(z_{\delta,w} \cdot F) = -E_v$$

[4.8] The *cell tension* $U = \phi_I - \phi_{I'}$, sometimes called "cell voltage," of an open galvanic cell (with

a chosen direction I to I′ for the counting of the phases) is defined as being equal to the inner electric potential of pole I minus the inner electric potential of pole I′. This quantity is *measurable*. It represents, in magnitude and in sign, the force with which the cell reaction tends to move *positive* charges through the cell in the direction of the counting of the phases on account of purely *electric* causes, i.e., on account of the electrostatic distribution of space charges, no other forces being effective.

This definition of the cell tension is in agreement with the general definition of a tension: $U = \phi_{in.} - \phi_{fin.}$ between the initial and the final points of an interval, while the "electric potential difference" is, on the other hand, defined as $\Delta\phi = \phi_{fin.} - \phi_{in.}$. It follows therefore that, in general,

*electric tension = — electric potential difference*

The expression "cell potential" is sometimes used in place of "cell tension," but this easily leads to confusion with other kinds of potentials (chemical, electrochemical, surface, outer electric, etc.) and cannot be recommended.

[4.9] The *electrochemical affinity* of the cell reaction $\gamma$ or $\delta$ of an open cell with a cell tension $U_v$ or $U_w$ is given as follows:

$$\tilde{A}_\gamma = A_\gamma + z_{\gamma,v} \cdot F \cdot U_v = A_\gamma + z_{\gamma,w} \cdot F \cdot U_w$$

$$\tilde{A}_\delta = A_\delta + z_{\delta,v} \cdot F \cdot U_v = A_\delta + z_{\delta,w} \cdot F \cdot U_w = -\tilde{A}_\gamma$$

[4.10] The *electrochemical tension* $\tilde{E}_v$ or $\tilde{E}_w$ of an open galvanic cell v or w is defined as follows:

$$\tilde{E}_v = \tilde{A}_\gamma/(z_{\gamma,v} \cdot F) = \tilde{A}_\delta/(z_{\delta,v} \cdot F)$$

$$\tilde{E}_w = A_\gamma/(z_{\gamma,w} \cdot F) = \tilde{A}_\delta/(z_{\delta,w} \cdot F) = -\tilde{E}_v$$

[4.11] When reaction $\gamma$ or $\delta$ of an open cell v or w is at *electrochemical equilibrium*, i.e., when no current is flowing through the cell, the electrochemical affinities are equal to zero:

$$\tilde{A}_\gamma = 0 \quad \text{and} \quad \tilde{A}_\delta = 0$$

and the electrochemical tensions are likewise equal to zero:

$$\tilde{E}_v = 0 \quad \text{and} \quad \tilde{E}_w = 0$$

This state of equilibrium can be regarded as resulting from the compensation exerted by the "reversible" cell tension U acting as a counterforce against the chemical tension (or electromotive force) E:

for cell v: $U_{v,\gamma} = -A_\gamma/(z_{\gamma,v} \cdot F) = U_{v,\delta} = -A_\delta/(z_{\delta,w} \cdot F) = -E_v$

for cell w: $U_{w,\gamma} = -A_\gamma/(z_{\gamma,w} \cdot F) = U_{w,\delta} = -A_\delta/(z_{\delta,w} \cdot F) = -E_w$

with: $U_{v,\gamma} = -U_{w,\gamma}$; $U_{v,\delta} = -U_{w,\delta}$; $E_v = -E_w$

The sign of the reversible cell tension U, as well as that of the corresponding chemical tension (or electromotive force) E, depends on the chosen direction of the counting of the phases of the cell, but it does not depend on whether reaction $\gamma$ or $\delta$ is used for the calculation of U and E.

It is most important to make a sharp distinction, both as to denomination and as to symbol, between U and E, their respective electrostatic and chemical natures being emphasized by the fact that they have opposite signs.

Even when the cell reaction, its affinity, and the number of charges transported are unknown, we always have $U = -E$. On account of the definition $U = \phi_I - \phi_{I'}$ it follows mathematically, but not by definition, that $E = \phi_{I'} - \phi_I$.

[4.12] The reversible cell tension of an open ideal galvanic cell I/II/III/IV/I′ is the resultant of the reversible Galvani tensions at the successive interphases:

$$U_v = \phi_I - \phi_{I'} = g_{I,II} + g_{II,III} + g_{III,IV} + g_{IV,I'}$$

It is clear that the Galvani tension between the two metallic phases IV and I′ must fully be taken into account (12).

[4.13] For some practical purposes, especially if the sign of the cell tension is not ambiguous, or if it happens to be of no importance, one may, as a simplification, use the absolute value of the reversible cell tension or that of its chemical tension (or electromotive force). However, for purposes of tabulation and calculation, the signs are essential.

[4.14] Let us consider a certain *cell reaction* $\gamma$ in an *open* galvanic cell v. The corresponding *pole reaction* $\pi$ with the same number of charges transported, $z_\pi = z_\gamma$, consists of the transfer of electrons from pole I to pole I′ through an external metallic connection (*see* [4.3]):

$$z_\gamma e^-(I) \rightarrow z_\gamma e^-(I')$$

By adding $\pi$ to $\gamma$ we transform the open cell reaction $\gamma$ into the *closed cell reaction* $\lambda$ of the *closed* cell I/II/III/IV/I′/I (the phases being counted by rotation from I back to I). We can also consider a *real pole reaction* $\rho$ with the same number of charges transported as $\gamma$ or $\pi$, $z_\rho = z_\gamma$, consisting of the transfer of electrons from pole I to phase IV through the external metallic connection and pole I′:

$$z_\gamma e^-(I) \rightarrow z_\gamma e^-(IV)$$

The quantities z, A, E, U, $\tilde{A}$ and $\tilde{E}$ for reactions $\gamma$, $\pi$, $\lambda = \gamma + \pi$ and $\rho$ at electrochemical equilibrium may be tabulated as follows:

| $\gamma$ | $\pi$ | $\lambda = \gamma + \pi$ | $\rho$ |
|---|---|---|---|
| $z_\gamma$ | $z_\pi = z_\gamma$ | $z_\lambda = z_\gamma$ | $z_\rho = z_\gamma$ |
| $A_\gamma$ | $A_\pi = 0$ | $A_\lambda = A_\gamma + A_\pi = A_\gamma$ | |
| $E_\gamma = A_\gamma/(z_\gamma \cdot F)$ | $E_\pi = 0$ | $E_\lambda = E_\gamma + E_\pi = E_\gamma$ | |
| $U_\gamma = \phi_I - \phi_{I'} = -E_\gamma$ | $U_\pi = -U_\gamma$ | $U_\lambda = U_\gamma + U_\pi = 0$ | |
| $\tilde{A}_\gamma = A_\gamma + z_\gamma \cdot F \cdot U_\gamma = 0$ | $\tilde{A}_\pi = z_\gamma \cdot F \cdot U_\pi$ | $\tilde{A}_\lambda = \tilde{A}_\gamma + \tilde{A}_\pi = \tilde{A}_\pi$ | $\tilde{A}_\rho = \tilde{A}_\lambda = \tilde{A}_\pi$ |
| $\tilde{E}_\gamma = \tilde{A}_\gamma/(z_\gamma \cdot F) = 0$ | $\tilde{E}_\pi = -U_\gamma = E_\gamma$ | $\tilde{E}_\lambda = \tilde{E}_\gamma + \tilde{E}_\pi = -U_\gamma$ | $\tilde{E}_\rho = \tilde{E}_\lambda = -U_\gamma$ |

It is practically important that the electrochemical tension $\tilde{E}_\pi$ between I′ and I, as well as the electrochemical tension $\tilde{E}_\rho$ between IV and I, are equal but (on account of the counting of the phases by rotation) of opposite sign to the cell tension $U_\gamma$.

[4.15] At a cell tension $U_v$ different from the reversible value $U_{v,\gamma} = U_{v,\delta}$, the measurable *cell po-*

*larization* of cell v, with cell reaction $\gamma$ or $\delta$, is given by

$$\Delta U_{v,\gamma} = U_v - U_{v,\gamma} = \Delta U_{v,\delta} = U_v - U_{v,\delta}$$

This polarization of the cell, under the cell tension $U_v$, results in general from the passage of current and is related to the corresponding electrochemical affinities of cell reactions $\gamma$ and $\delta$ as follows:

$$\tilde{A}_\gamma = z_{\gamma,v} \cdot F \cdot \Delta U_{v,\gamma} \text{ and } \tilde{A}_\delta = z_{\delta,v} \cdot F \cdot \Delta U_{v,\delta} = -\tilde{A}_\gamma$$

and to the electrochemical tension $\tilde{E}_v$ of cell v resulting from cell reaction $\gamma$ or $\delta$ as follows:

$$\tilde{E}_v = \tilde{A}_\gamma/(z_{\gamma,v} \cdot F) = \Delta U_{v,\gamma} = \tilde{A}_\delta/(z_{\delta,v} \cdot F) = \Delta U_{v,\delta}$$

[4.16] If the actual Galvani tensions g and the actual cell tension U differ only on account of the passage of current from the reversible values of the g's and of U in the same cell at zero current, the polarization values being then such that

$$\Delta g = g_{J \neq 0} - g_{J=0} \quad \text{and} \quad \Delta U = U_{J \neq 0} - U_{J=0}$$

and if ohmic tensions $U_\Omega$ occur in each homogeneous phase, we have the general relation

$$\Delta U = \Sigma \Delta g + \Sigma U_\Omega$$

In other words, the cell polarization $\Delta U$ is the algebraic sum of the electrode polarizations $\Delta g$ and of the ohmic tensions $U_\Omega$ within the phases.

[4.17] A distinction is often made, particularly in the Anglo-American electrochemical literature, between a "galvanic cell" able to produce a spontaneous current (for which $J < 0$ corresponds to $U > 0$ and $J > 0$ to $U < 0$) and an "electrolytic cell" in which the cell reaction results from a nonspontaneous current (for which $J > 0$ corresponds to $U > 0$ and $J < 0$ to $U < 0$).

The recommendations put forward in the CITCE report on Electrochemical Nomenclature and Definitions (5) do not make such a distinction, the single expression *galvanic cell* being used for both types of cases, whether or not a current is flowing and, in the event of current flow, whether its direction is spontaneous or nonspontaneous.

[4.18] Let us consider a galvanic cell in which a constant current J flows between time $t_0$ and time $t_1$. The cell tension $U_J = \phi_I - \phi_{I'}$ will in general vary with time during the interval $t_1 - t_0$ .The outside circuit, under the tension $U'_J = \phi_{I'} - \phi_I = -U_J$, receives, in this *primary* performance of the cell, the quantity of electric work [*see* (10)]:

$$W_{0,1} = \int_{t_0}^{t_1} U'_J \cdot J \cdot dt = -\int_0^{\Delta q} U_J \cdot dq$$

with $\Delta q = J \cdot (t_1 - t_0)$. If, from time $t_1$ to time $t_2$, with $t_2 - t_1 = t_1 - t_0$, the constant current $J_r = -J$ is made to flow through the cell in the direction *opposite* to that of J, the total charge transported by this reverse current will be $\Delta q_r = J_r \cdot (t_2 - t_1) = -J \cdot (t_1 - t_0) = -\Delta q$, and the outside circuit, under the tension $U'_{J_r} = -U_{J_r}$, will receive, in this *secondary* performance of the cell, the quantity of electric work

$$W_{1,2} = \int_{t_1}^{t_2} U'_{J_r} \cdot J_r \cdot dt = \int_0^{\Delta q} U_{J_r} \cdot dq$$

The material changes produced in the cell during the primary performance are exactly compensated by those produced during the secondary performance. At given temperature and pressure the cell may thus be regarded as having accomplished a cyclic process and the total external work done by the cell must, in accordance with thermodynamic principles, be either negative or equal to zero:

$$W = W_{0,1} + W_{1,2} = -\int_0^{\Delta q} U_J \cdot dq + \int_0^{\Delta q} U_{J_r} \cdot dq \leqq 0$$

In the case of over-all *irreversible* performance there is a dissipation of external work, $W < 0$ (as in the case of a resistance), while in the limiting case of *reversible* performance we have $W = 0$ (as in the case of a condenser).

[4.19] When, at each instant between $t_0$ and $t_2$, the galvanic cell can be regarded as having a *tension at rest* $U_R$ which is a determinable function of the charge q transported up to that instant and which remains unchanged at each value of q to which the cell will return after further performance and current reversal, we may add to, and subtract from the foregoing equation the integral

$$\int_0^{\Delta q} U_R \cdot dq$$

Introducing the polarizations

$$\Delta U = U_J - U_R \quad \text{and} \quad \Delta U_r = U_{J_r} - U_R$$

we then obtain:

$$W = -\int_0^{\Delta q} \Delta U \cdot dq + \int_0^{\Delta q} \Delta U_r \cdot dq \leqq 0$$

The primary performance may be *spontaneous,* in which case we have:

$$U_R > 0 \text{ with } U_J < U_R, \Delta U < 0, \text{ and } J < 0;$$

$$\text{or } U_R < 0 \text{ with } U_J > U_R, \Delta U > 0, \text{ and } J > 0,$$

or it may be *nonspontaneous,* in which case we have:

$$U_R > 0 \text{ with } U_J > U_R, \Delta U > 0, \text{ and } J > 0;$$

$$\text{or } U_R < 0 \text{ with } U_J < U_R, \Delta U < 0, \text{ and } J < 0.$$

At vanishing polarization, i.e., as $\Delta U$ tends toward zero, the performance of the cell becomes *reversible.*

## Real Galvanic Cells—Reference Cells

[5.1] Real galvanic cells differ from ideal ones on account of the fact that the former exhibit certain irreversible chemical changes even when no current is flowing. Typical cases of this sort are those of galvanic cells in which phases II and III are solutions of electrolytes between which irreversible diffusion processes occur. An example is the real galvanic cell v:

$$Zn \,/\, Zn^{+2} \,//\, Cu^{+2} \,/\, Cu \,/\, Zn$$

In this case there is, strictly, a small diffusion tension $g_{II,III}$ between the two electrolyte solutions II and III. If we neglect it, the relation given in [4.12] can be simplified to

$$U_v = \phi_I - \phi_{I'} = g_{I,II} + g_{III,IV} + g_{IV,I'}$$

$$= g_{I,II} - g_{IV,III} + g_{IV,I'}$$

We see that $U_v$ does not represent only the difference of the two Galvani tensions $g_{I,II}$ and $g_{IV,III}$, but that it also includes the Galvani tension $g_{IV,I'} = g_{Cu,Zn}$ which specifically depends on the properties of the two metals in contact.

[5.2] We designate as *reference cells* such real galvanic cells as

$$Zn \,/\, Zn^{+2} \,//\, H^+,\ H_2 \,/\, Pt \,/\, Zn \text{ and}$$

$$Cu \,/\, Cu^{+2} \,//\, H^+,\ H_2 \,/\, Pt \,/\, Cu$$

In each one of these cells the electrode on the right is the reference electrode Pt / $H^+$, $H_2$ taken at standard conditions. It is thermodynamically and experimentally established that the *reference cell tensions* $U_{h,Zn}$ and $U_{h,Cu}$ are related to the cell tension $U_v$ of the cell considered above as follows:

$$U_v = U_{h,Zn} - U_{h,Cu}$$

These reference cell tensions $U_h$, listed according to their increasing or decreasing values, constitute the so-called electrochemical series.

[5.3] An incorrect interpretation of the foregoing important difference relations originates in the erroneous assumption that, in the exact relations for the cell tension given in [5.1], i.e.,

$$U_{h,Zn} = g_{Zn/Zn^{+2}} - g_{Pt/H^+,H_2} + g_{Pt/Zn}$$

$$U_{h,Cu} = g_{Cu/Cu^{+2}} - g_{Pt/H^+,H_2} + g_{Pt/Cu}$$

$$U_v = g_{Zn/Zn^{+2}} - g_{Cu/Cu^{+2}} + g_{Cu/Zn}$$

the individual Galvani tensions between the corresponding two metals, $g_{Pt/Zn}$, $g_{Pt/Cu}$ and $g_{Cu/Zn}$ can be neglected. Indeed, in this manner, we would obtain the formally simpler but incorrect relations:

$$U_{h,Zn} = g_{Zn/Zn^{+2}} - g_{Pt/H^+,H_2}$$

$$U_{h,Cu} = g_{Cu/Cu^{+2}} - g_{Pt/H^+,H_2}$$

$$U_v = g_{Zn/Zn^{+2}} - g_{Cu/Cu^{+2}}$$

[5.4] A further incorrect step consists of putting $g_{Pt/H^+,H_2} = 0$, with the deceptively simple but again incorrect result:

$$U_{h,Zn} = g_{Zn/Zn^{+2}} \quad \text{and} \quad U_{h,Cu} = g_{Cu/Cu^{+2}}$$

We find here the reason for the denomination "electrode potentials" which is sometimes used to designate the reference cell tensions $U_h$. Even among those who know the arbitrariness of this last hypothesis, there are many who overlook the error made in neglecting the individual Galvani tensions between metals in contact (12) when they consider that the sequence of the $U_h$ values as given by the electrochemical series is also the sequence of the corresponding Galvani tensions such as $g_{Zn/Zn^{+2}}$.

## Some Remarks Concerning Multiple Electrodes

[6.1] The foregoing fundamental considerations apply to simple (or mono-) electrodes and to galvanic cells constituted of such electrodes. It is important to add some remarks concerning *multiple* (or *poly-*) *electrodes*, which are frequently encountered in real galvanic cells.

[6.2] A *bi-electrode* is the seat of *two* different electrode reactions. A *poly-electrode* is the seat of *several* different electrode reactions.

[6.3] Among the bi-electrodes we further distinguish two important types of cases: (i) The 2-2 electrodes whose metallic phases I contribute *one* ionic species to one of the electrode reactions and *another* ionic species to the other electrode reaction. For instance, the metallic ion $Me^+$ in I is involved in reaction 1 and the electron $e^-$ in I is involved in reaction 2. (ii) The 1-2 electrodes whose metallic phases I contribute the *same* ionic species, for instance $Me^+$ or $e^-$, to both reactions.

[6.4] A frequent complication with bi-electrodes is the occurrence of an inner reaction in the solution phase II between the reactants or products of the two electrode processes without the formation of a new solid phase. Certain additional material changes will then superpose themselves to the diffusion phenomena in the diffusion layer, concentrations and overtensions being thus markedly affected.

A further complication resulting from an inner reaction is the formation of one or several new solid phases. In addition to material disturbances within the diffusion layer the electrode end reactions will now be affected and their respective barriers modified.

[6.5] Some particular concepts, magnitudes and relations applying to a bi- or to a poly-electrode result directly from those pertaining to each of the two or of the several separate electrode reactions and which have been examined in the foregoing treatment of mono-electrodes. For instance, the total current is the sum of the partial currents: $J = J_1 + J_2$.

[6.6] A simple case is that of the *double electrochemical equilibrium* in which the equilibrium Galvani tensions of the two electrode reactions of a bi-electrode are equal to each other: $g_1 = g_2$.

[6.7] A more complicated case is that of a *mixed electrode* for which the equilibrium Galvani tensions of the several reactions are different from one another: for instance, $g_1 \neq g_2$ for a bi-electrode.

At zero net current we then have a *mixed Galvani tension* $g_{J=0}$ and a *local current* $J_1 = -J_2$, concepts applying for instance both to *corrosion* and to *passivity*.

With a net current different from zero we have a *mixed Galvani tension* $g_{J\neq 0}$, a *polarization* $\Delta g_J = g_{J\neq 0} - g_{J=0}$, and such phenomena as *difference effects* in the material changes at phase ends and *changes in the signs of the polarizations* of the separate electrode reactions, all of these resulting from the shapes and relative positions of the polarization curves of these separate reactions.

### Concluding Remarks

In view of the rapid development of electrochemistry in recent times, only a rational system of concepts, definitions, symbols, etc., can provide a firm basis for further research and for teaching. The carefully worked out recommendations contained in the yearly reports of CITCE's Commission No. 2 on Electrochemical Nomenclature and Definitions (5) should go a long way toward the fulfillment of this goal.

It is to be hoped that all electrochemists interested in the fundamentals of their subject, and especially the younger students in the field, will display the same spirit of cooperation and mutual understanding which has presided over the work of the international CITCE group and that considerable benefits for the future of electrochemistry will thereby ensue.

Manuscript received March 10, 1958.

Any discussion of this paper will appear in a Discussion Section to be published in the June 1959 JOURNAL.

REFERENCES

1. A. J. de Béthune, *This Journal*, **102**, 288C (1955).
2. J. B. Ramsey, *ibid.*, **104**, 255 (1957).
3. T. S. Licht and A. J. de Béthune, *J. Chem. Educ.*, **34**, 433 (1957).
4. J. A. Christiansen and M. Pourbaix, *Compt. rend. XVIIth conf. union intern. chim. pure et appli.*, Stockholm, 1953, p. 82, Baison de la Chimie, Paris (1954).
5. P. Van Rysselberghe, *Z. Elektrochem.*, **58**, 530 (1954); Proc. 6th Meeting Intern. Comm. Electrochem. Thermodynam. and Kinet., Butterworths, London, 1955, p. 20; *ibid.*, 8th and 9th meetings, in press.
6. E. Lange, "Handbuch der Experimentalphysik," Vol. XII, Part 2, p. 263, Akademische Verlagsgesellschaft, Leipzig (1933).
7. E. Lange, *Z. Elektrochem.*, **55**, 76 (1951); **56**, 94 (1952).
8. E. Lange, *Z. physik. Chem.*, **200**, 97 (1952).
9. P. Van Rysselberghe, "Electrochemical Affinity," Hermann, Paris (1955).
10. E. Lange, *Z. Elektrochem.*, **61**, 1301 (1957).
11. E. Lange, *Z. physik. Chem.*, in press (1958).
12. E. Lange and K. Nagel, *Z. Elektrochem.*, **42**, 50 (1936).
13. E. Lange, presented at CITCE's 4th meeting in London and Cambridge, 1952, Unpublished.

# The Fuel Cell Round Table

**A Report by Ralph Roberts**

*Office of Naval Research, Washington, D. C.*

A round-table discussion of fuel cells was held on October 10, 1957, as part of the Battery Division program of the 112th Meeting of The Electrochemical Society in Buffalo, N. Y. The discussion was organized by George Heise, National Carbon Laboratories (retired), who also acted as panel chairman. Other members of the panel were: Ernest Yeager, Western Reserve University; George E. Evans, National Carbon Research Laboratories; Howard L. Recht, Pittsburgh Consolidation Coal Co.; and Ralph Roberts, Office of Naval Research. The attendance at the discussion was approximately 175.

In his opening remarks Mr. Heise indicated that the objectives of the panel were to review the status of fuel cell development and the potentialities of fuel cells as a power source. He read a letter from Professor Farrington Daniel, University of Wisconsin, who indicated that a solution to the solar energy problem might be a combination of the fuel cell with the photochemical decomposition of water. It was further suggested that the storage of hydrogen might be accomplished by adsorbing it at one temperature and releasing it at a higher one.

Dr. Yeager reviewed some of the theoretical considerations regarding fuel cells, which he defined as electrochemical systems in which the direct or indirect oxidation of conventional fuels occurs. In the comparison of the fuel cell with methods of power generation based on the Carnot cycle, one should account for any energy losses due to reactions in preparing the fuel for utilization in the cell. The heat of reaction in the cell itself is given by:

$$Q \text{ cell} = nF(E_{rev} - E_{cell}) + T\Delta S \qquad (I)$$

where the terms all have their usual significance.

In most fuel cells the gas-consuming electrodes are semilyophobic. The reactant diffuses through the electrode pores to the electrode-electrolyte interface. The life-time of the electrode depends on its rate of wetting by the electrolyte or, for high-temperature cells, on the deterioration of the porous plate. The internal losses due to the resistance of the cell are related to the bulk properties of the materials within the cell and their method of assembly. To overcome activation polarization Dr. Yeager suggested the use of large effective areas of electrode, catalysts, and increasing the temperature of cell operation. For example in the Bacon cell, which utilizes a nickel electrode at 200°-250°C, the activation polarization is an important factor. In the high-temperature fuel cells, i.e., those operating above 500°C, there is very little activation polarization. Mass or concentration polarization can be reduced by increasing the porosity of the electrode through which the gas reactants diffuse. The reactants should not diffuse into the electrolyte, as this not only leads to poor efficiency in their utilization,

but can lead to dangerous mixtures of fuel and oxidant.

Available evidence indicates that the oxygen electrode, on an active carbon surface in alkaline media and at temperatures below 100°C, is reversible with respect to the hydroperoxide ion, $HO_2^-$:

$$O_2 + H_2O + 2e = HO_2^- + OH^- \qquad (II)$$

However, it is possible to obtain a four-electron process in terms of coulomb efficiency, utilizing both atoms of oxygen in the oxygen molecule by the incorporation of a good catalyst for the decomposition of the hydroperoxide ion in the carbon electrode. Thus, the loss of oxygen by the diffusion of the hydroperoxide ion away from the electrode is prevented. Silver has been found to be a very effective catalyst for this purpose, but the addition of the catalyst does not assure a four-electron process in terms of free energy or voltage. In the use of metal electrodes with oxygen it is necessary to have the interaction between the metal and oxygen and the electron transfer process highly reversible if the potential of the oxygen electrode is to be realized.

In low-temperature cells utilizing hydrogen at the anode, the addition of metals, especially platinized platinum, to the carbon electrode helps overcome the activation polarization. In the high-temperature fused electrolyte fuel cells, utilizing hydrocarbons, it appears that the hydrocarbon is cracked to carbon and hydrogen and the latter reacts at the electrode.

Dr. Yeager referred to the possibility of closed cycle battery systems. In such a system the reactants are regenerated from the products formed during the discharge of the cell. In a semi-closed system only one of the reactants would be regenerated from the cell products. The following methods of reactant regeneration were suggested: (*a*) chemical; (*b*) photochemical; (*c*) radiochemical; (*d*) thermal; (*e*) electrolytic. The process involved in the case of thermal regeneration is shown in Fig. 1 and the maximum efficiency is given by the Carnot cycle. In the case of electrolytic regeneration, the regenerating cell would be operated at a temperature higher than the energy-producing one. The efficiency of such a system is given by:

$$\frac{nF(E_{T_1} - E_{T_2})}{Q_{T_1}} = \frac{T_1 - T_2}{T_1} \qquad (III)$$

where $T_1$ is the higher temperature and $T_2$ the lower one.

Dr. Evans defined the fuel cell as "an electrochemical system in which the oxidant and reductant

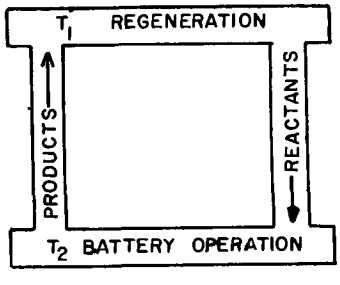


Fig. 1. Closed cycle system

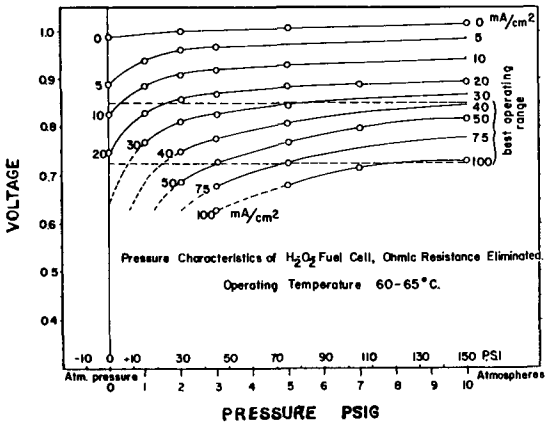


Fig. 2. Pressure characteristics of hydrogen-oxygen fuel cell

are introduced continuously and the products withdrawn continuously, with the composition of the system remaining invariant during the generation of electricity."

Research at the National Carbon Research Laboratories is concerned with the low-temperature hydrogen-oxygen cell, below 100°C. The electrodes are specially prepared carbon and the electrolyte is potassium hydroxide solution. The water formed due to the electrochemical reactions is evaporated at the same rate that it is produced. The low operating temperature makes the use of air more practical than in the high-temperature systems as heat loss to the nitrogen is negligible. Because of the polarization of the cathode in the presence of air such a cell is limited to low power densities. For high power outputs it is necessary to increase air pressure above atmospheric or to use oxygen. The effect of oxygen pressure on cell performance is shown in Fig. 2. When the pressure is above three atmospheres the curves become nearly linear. No real difficulty is presented until the pressure exceeds five atmospheres; up to this pressure conventional construction can be used.

The anode utilizes commercial tank hydrogen. It is insensitive to sulfur-containing impurities, carbon monoxide and other impurities, and has operated on natural gas and then returned to hydrogen without loss in its operating characteristics. Because of the storage problem, an inexpensive source of hydrogen would be advantageous. The actual source and method of storage would be determined in part by the use conditions. Research is being continued to obtain more information regarding the optimization of the cell parameters and the effect of temperature and pressure on its operation. The low operating temperature permits greater flexibility in the selection of materials of construction and leads to low maintenance cost. Battery lifetime depends largely on the rate at which the electrode is wetted. To date the National Carbon Company has operated the same electrodes for 300 days, drawing current during the day and allowing the system to stand on open circuit overnight. This cell is still in operation.

The present status of the Bacon cell, a hydrogen-oxygen fuel cell which operates at elevated pressure and temperatures above 200°C, was reviewed by Dr. Roberts. This was based on published informa-

Table I. Operating data for the Bacon cell

| Temp, 200°C Voltage | Pressure 600 lb/in² Amp/ft² |
|---|---|
| 1.10 | open circuit |
| 0.89 | 90 |
| 0.83 | 180 |
| 0.72 | 360 |
| 0.62 | 540 |

tion (1). The electrodes are of porous nickel about 4 mm thick, and have a pore size of about 30 microns on the gas side, and a thin layer with much smaller pores on the liquid side. The oxygen electrode, which initially controlled the cell lifetime, has been improved by a preoxidation treatment. Lithium atoms are incorporated into the crystal lattice of the nickel oxide, thus converting the ordinary green nickel oxide into a black double oxide of nickel and lithium, which is a good semiconductor. Using this method of preparation, oxygen electrodes have now been in operation for up to 1500 hr at 200°C. Specimens of the preoxidized nickel have been exposed to oxygen and caustic potash, the electrolyte, at 200°C for more than 8000 hr without visible deterioration. Each cell in this battery is approximately ½ in. thick. Because of the vapor pressure of water over the caustic potash solution at 200°C, it is essential to operate this system at elevated pressure. Table I presents characteristic operating data.

The system requires high purity hydrogen, being more sensitive to contaminants in the anode feed gas than reported above for the National Carbon low-temperature battery. It presents similar problems regarding hydrogen sources, with the additional high purity requirement.

Bacon has suggested that the high-pressure hydrogen-oxygen cell would be primarily used as a storage battery. In this case, the gases for use in the cell would be generated electrochemically from water. The use of hydrogen obtained from the reaction between water and coal and with oxygen obtained from air also has been mentioned. An application noted by Bacon is in the field of railway traction, particularly for rail cars, on lines where it is uneconomic to electrify completely with overhead wires or a third rail. This type of operation, with storage batteries, is in use in the German state railway.

Dr. Recht discussed the high-temperature fuel cell. The primary reason for development of such a system is the wider range of fuels that it can accommodate. The low-temperature cells which have been studied to date can utilize only hydrogen. The high cost of this gas and the difficulties associated with its transport rule out its economic application except in highly specialized situations. The high-temperature cell can accommodate gases containing mixtures of hydrogen, carbon monoxide, and carbon dioxide which can be generated directly from coal, natural gas, and petroleum. It is even likely that hydrocarbon fuels could be used either directly or indirectly in these cells. The integration of the high-temperature fuel cell with a coal gasification unit is possible. The high-temperature cells also offer the possibility of higher output at comparable gas pressures due to the reduced electrode polarization and higher diffusion rates in the electrolyte.

One of the major drawbacks in the high-temperature cell is the severely corrosive conditions encountered. This affects not only the containing structure of the cell, but also the materials of which the cell itself is constructed. Another problem is the maintenance of cell stability i.e., the prevention of loss of electrolyte through seepage from the cell, attack on the electrodes or the matrix by the electrolyte, and the accumulation of corrosion products within the electrolyte.

The discussion of Dr. Recht was on the work of the Pittsburgh Consolidation Coal Co., which is under the sponsorship of the Army Signal Corps. The electrolyte section of the cell consists of a porous magnesium oxide matrix containing the molten electrolyte and an equi-molar mixture of sodium and lithium carbonates. It has been found necessary to use an extremely pure grade of magnesium oxide for the matrix. For the fuel electrode a porous nickel metal sheet has been found to be satisfactory. The air electrode has presented a more difficult problem. The most promising result to date has been obtained with the use of nickel oxide with additives to produce a semiconducting material. Carbon dioxide is added to the air supply to reduce concentration polarization and maintain a stable system.

The work at Pittsburgh Consolidation Coal Company has been in the temperature range of 500°-800°C, mainly to simplify solution of the problem of materials of construction. Due to the disproportionation of carbon monoxide at the lower end of this temperature range, fuels containing carbon monoxide are difficult to use. Therefore, hydrogen has been used in the low-temperature range. At the higher temperatures, in the order of 800°C, carbon monoxide and mixtures of carbon monoxide and hydrogen can be used without carbon deposition. The open-circuit voltages obtained, of the order of one volt, are usually within 50 mv of the theoretical value, and often closer. A power output of 30 w/ft² of electrode has been achieved. With proper cell assembly, the open-circuit voltage and the performance level do not change appreciably over a period of several days with the cell maintained at operating temperatures. The ultimate operating life of the unit has not been determined.

In addition to the chemical nature of the cell components, the physical form has a great effect on the performance obtained. Good contact between the electrodes and the electrolyte, as well as good electrical contact from the electrodes to the external circuit are not always easy to obtain. These problems, and that of retaining the molten electrolyte within the cell, will prove major problems for the engineer, if a commercial high-temperature fuel cell is to be developed. In addition, the operating life of a commercially satisfactory fuel cell must be of the order of several years because of the expected high capital cost.

Dr. Recht noted the lack of knowledge of the mechanism of the electrode reactions occurring in the high-temperature fuel cell. He indicated that the understanding of the fundamental mechanism of the fuel cell reactions is extremely important to the attainment of the practical goals.

The work in Great Britain on the Redox fuel cell was reported by Dr. Roberts. The information was based on a report which was made available through the courtesy of the United Kingdom Electricity Council (2). The work was under the general direction of Sir Eric Rideal at Kings College, London.

This type of cell is one in which the electrode reactants are regenerated outside the cell, but the net reaction is equivalent to that of fuel combustion. This is illustrated in the following summary:

Negative electrode:

Internal to cell

$$M^{+2} = M^{+3} + e^- - E_1$$

External to cell

$$4M^{+3} + C + 2H_2O = 4M^{+2} + CO_2 + 4H^+ - E_1^r$$

Positive electrode:

Internal to cell

$$R^{+3} + e^- = R^{+2} - E_2$$

External to cell

$$4R^{+2} + O_2 + 4H^+ = 4R^{+3} + 2H_2O - E_2^r$$

Net reaction:

$$C + O_2 = CO_2 - E_3$$

$$E_1^r > E_1 \ , \ E_2^r > E_2$$

$$E_1 + E_2 < E_1^r + E_2^r$$

$$E_1 + E_2 < E_3$$

The electromotive force of the cells studied by this group is limited by the free energy of the carbon, oxygen reaction or approximately 1.02 v. It is further reduced because each regeneration reaction must have a negative free energy, thus giving a net effective voltage, as noted above, less than that of the carbon-oxygen cell. The thermodynamic efficiency of this system is given by Eq. (IV):

$$\text{Eff} = \frac{E_1 + E_2}{E_3} \times 100\% \qquad \text{(IV)}$$

$E_1$–anode potential; $E_2$–cathode potential; $E_3$–carbon-oxygen cell potential.

Two general types of redox fuel cells have been studied. In the first, the same element in different oxidation states is used as the anode and cathode reactants. An example of this is the ferrous-ferric couple. This, as expected by the Nernst equation, is limited to low voltages (~0.25 v). In the second type, different elements are used in the anode and cathode compartments.

The best of the anodic materials studied to date has been stannic chloride in a hydrochloric acid solution. However, it has not been found possible to regenerate this from the cell product by use of coal. Even at temperatures of 100°-180°C, in an autoclave, only a small amount of reduction of the stannic ion occurs. The sulfur dioxide-sulfate ion couple is more rapidly regenerated; however, few cell performance data were reported for this couple. As much as 30% of the coal has been utilized for the reduction of the sulfate ion and the results have given interesting information on coal chemistry. More success has been obtained with the positive electrode. Using bromine in a solution of hydrobromic acid as the cathodic material, it has been found possible to regenerate the bromine at room temperature using oxygen in the presence of nitrogen dioxide as a catalyst. The group has reported on the kinetics of this reaction (3).

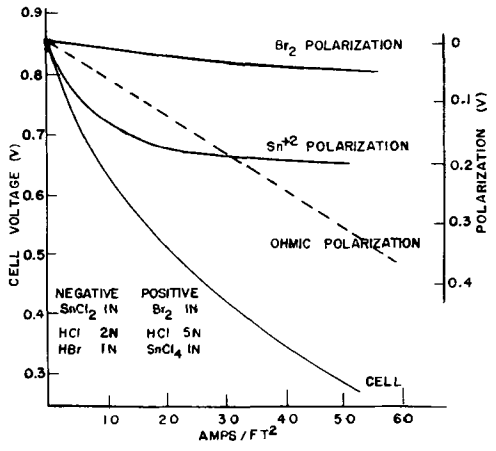


Fig. 3. Operating characteristics of stannous ion-bromine cell

The operating characteristics of the stannous ion, bromine cell are shown in Fig. 3.

The concept of the redox fuel cell is a very interesting one, but a complete working system has not been developed. The regeneration problem, especially of the negative reactant with coal, has only been attained with low coal utilization efficiency. The investigators are of the opinion that the material efficiencies that can reasonably be expected, on the basis of the present stage of development, are about 70% for fuel consumption, 90% for the cell, and 60% over-all.

During the discussion Dr. George J. Young, Pennsylvania State University, reviewed some of the recent work in his laboratory on electrodes related to fuel cells. In the metal-oxygen electrode system he indicated the importance of the equilibrium between the chemically adsorbed state and the solution, the potential of the oxygen electrode depending on the nature of the chemisorbed state. The ultimate limitation in current density is the chemical kinetics of the system, which includes the activated adsorption of reactants, activated desorption of products, and the activation energy for surface mobility. He also reviewed some work on the relationship between the heat of chemisorption of hydrogen on metals as related to the d-band vacancies of the latter. The chemical adsorption energies are greatest where there is binding between the bonding orbital of the metal and the adsorbed substance. He has concluded that the best catalysts for the hydrogen anode are the metals of Group 8b.

Although there was considerable discussion of potential applications very few specific ones were

noted. Dr. Evans pointed out that the portability and availability of power on demand from fuel cells make them of interest in nonmilitary parts of the economy. However, it appears that certain military applications are more immediate. Dr. R. C. Shair and Dr. H. L. Foote of the Bell Telephone Laboratories indicated that there may be a possible application of the fuel cell in the telephone system. With the decrease in the nominal power required for telephone operation through the greater use of transistors, a small reliable power generator of 1-100 w may be required. Such power generators are either not available or are inefficient and uneconomic. A reliable fuel cell that could be operated in remote areas as required would therefore be of interest to this telephone application.

It was the general consensus that a fuel cell symposium should be held within two to three years.

The writer wishes to acknowledge the assistance of the members of the panel and Mr. U. B. Thomas.

Manuscript received Feb. 12, 1958.

Any discussion of this paper will appear in a Discussion Section to be published in the June 1959 JOURNAL.

REFERENCES

1. F. T. Bacon, *The Times Science Review Quarterly*, No. 20, p. 6, *The Times*, London, England (Summer 1956).
2. A. L. Benjamin, B. E. M. Bingham, and A. M. Posner, "On the Production of Electrical Energy From Redox Processes", Final Report to the Central Electricity Authority, United Kingdom, dated Nov. 25, 1955.
3. B. E. M. Bingham and A. M. Posner, *J. Am. Chem. Soc.*, **77**, 2634 (1955).

# Brief Communication

## ZnS:Sn,Li Phosphor

**A. Wachtel**

*Research Department, Westinghouse Electric Corporation, Bloomfield, New Jersey*

Garlick and Mason (1) have described the use of Sn as an activator in ZnS, resulting in a red photoluminescence peaked at 6450Å. During the course of some investigations of this system, it was noted that the use of Li salts (and to a lesser degree, Na salts) results in the formation of a yellow-emitting photo- and cathodoluminescent phosphor. The best results were obtained by the use of Li halides, of which only very small concentrations (of the order of 100 ppm) are necessary to effect the conversion to this system, although about 4 mole % were found practical so as to obtain additional fluxing action.

Figures 1 and 2 show the excitation and emission spectra at room temperature of a typical hexagonal ZnS:Sn,Li phosphor prepared with 1 mole % Sn and 4 mole % LiBr. It can be seen that, in this case, the emission at 4380Å of Li in ZnS as reported by Kröger (2) for cubic ZnS is not apparent. The excitation spectrum, especially that of ZnS:Sn (not shown here), has the appearance of being due to Cu (presumably present as a contaminating impurity) so that even in this case an energy transfer could be visualized (3).

It has been suggested (4) that Sn, replacing Zn, can act as a double donor center. In the red-emitting ZnS:Sn phosphor, the Sn may be neutralized by a Zn-vacancy. On the other hand, charge compensation by monovalent cations such as Li would require two such atoms for each atom of Sn present. If the energy levels of these are not equivalent to each other, then the presence of the double peak in the emission spectrum of ZnS:Sn,Li may thus be explainable.

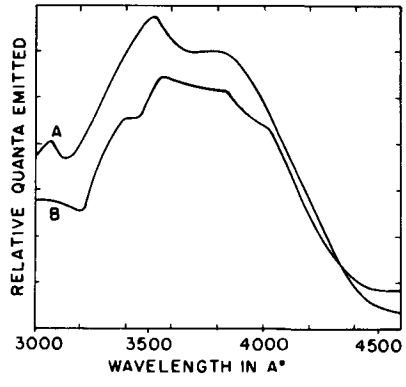


Fig. 1. Excitation spectra of ZnS:Sn,Li. Curve A, 5800Å peak, not corrected for overlap; curve B, assumed peak at 6300Å, corrected for assumed 5800Å overlap.

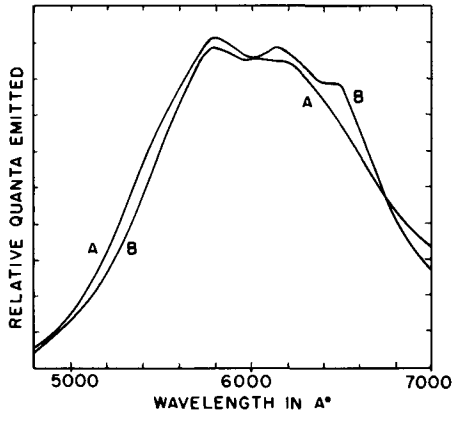


Fig. 2. Emission spectra of ZnS:Sn,Li. Curve A, 3650Å excitation; curve B, 4048Å excitation.

# A New Zinc-Iodate Primary Battery

**J. L. Jones and A. B. Arranaga**

*U. S. Naval Ordnance Test Station, Pasadena Annex, Pasadena, California*

ABSTRACT

A new primary battery has been developed comprising a zinc anode, a potassium iodate cathodic reactant, and an electrolyte consisting substantially of sulfuric acid. A reserve battery of this type is capable of comparatively high current drain rates, typically 0.092 amp/cm$^2$ (0.6 amp/in.$^2$) at a discharge potential of 1.6 v for 7 min. A typically self-contained battery capable of operating at the above performance level has an energy output of 2.32 watt min/cm$^3$ and watt min/g output of 1.88. Procedures have been developed for manufacturing low cost cells in a simplified type of mechanical battery construction. Prototype batteries have been constructed and experimental data are given on their performance.

An experimental program has been carried out at the U. S. Naval Ordnance Test Station to develop new high drain rate primary batteries for ordnance applications. As a result of this investigation, a new electrochemical couple has been developed to a practical stage for primary battery application.

The couple consists of potassium iodate as the cathodic reactant, and zinc metal as the anodic reactant in the presence of sulfuric acid as the electrolyte. Two possible equations for the reaction may be written as follows:

$$5Zn + 2KIO_3 + 6H_2SO_4 \rightarrow 5ZnSO_4 + I_2 + K_2SO_4 + 6H_2O \quad [1]$$

$$3Zn + KIO_3 + 3H_2SO_4 \rightarrow 3ZnSO_4 + KI + 3H_2O \quad [2]$$

The standard half-cell reactions of the zinc anode, reaction [3], and the iodate cathode, reaction [4], as combined below in acid solution yield a standard open cell potential of 1.958 v, reaction [5] (1).

$$Zn \rightarrow Zn^{++} + 2e \qquad E^\circ = 0.763 \text{ v} \quad [3]$$

$$IO_3^- + 6H^+ + 5e \rightarrow 1/2I_2 + 3H_2O \qquad E^\circ = 1.195 \text{ v} \quad [4]$$

$$5Zn + 2IO_3^- + 12H^+ \rightarrow 5Zn^{++} + I_2 + 6H_2O \qquad E^\circ = 1.958 \text{ v} \quad [5]$$

Analytical results on the nature of actual cell reactions clearly indicate that both reactions [1] and [2] occur, reaction [1] being the dominant cell reaction at room temperature and higher, while reaction [2] becomes more important at temperatures down to 0°C. It is interesting to note that the experimental cell develops approximately 1.6 v at high current drains, e.g., 0.092 amp/cm$^2$ (0.6 amp/in.$^2$) as compared to the standard open-circuit voltage of 1.958 v.

A review of the literature indicates that there has been no systematic cell investigation of the zinc-iodate couple. A passing reference in a British patent of 1884 mentions the use of iodate solutions in galvanic batteries as a depolarizing agent (2). A patent application is pending on the now developed zinc-iodate battery (3).

The battery developed from the above cell reaction has been of interest for ordnance application problems in view of its high available current drain rates for limited periods of time. The zinc-iodate battery, as it has been developed mechanically, is a reserve type of primary battery in which the electrolyte is rapidly forced into the dry cell structure by compressed carbon dioxide gas, aided by a partial vacuum previously created in the dry plate structure.

Early work in this experimental program also applied the bromate ion as a cathodic reactant. Cells containing bromate ion cathodes tended to yield cell voltage vs. discharge time curves considerably less flat than cells utilizing the iodate cathodes. Bromate and iodate cathodes produced cells capable of discharging at comparable current density; however, the bromate cells tended to produce more hydrogen gas. As a result of the deficiencies of the bromate cathode as compared to the iodate cathode, a decision was made to develop the iodate cell.

## Experimental

### *The Zinc-Iodate Cell*

The basic element in the cell construction is an electrode, approximately 0.10 cm (0.04 in.) thick, which has the following structure: A zinc sheet, 0.020 cm (0.008 in.) thick, is coated on one side with a silver pigmented paint, approximately 0.002 cm (0.0007 in.) thick. Bonded to the silver layer is a cathodic reactant mix in which potassium iodate is the active ingredient, made electrically conducting by the addition of graphite and acetylene black. In principle, the electrodes can be stacked, the anode side of one electrode facing the cathode side of the next electrode, separated by a 0.10 cm (0.04 in.) gasket and round spacers to provide room for the electrolyte (*see* Fig. 1). The battery is activated and made electrically conducting by introducing the electrolyte rapidly into the dry cell plate structure of the battery. All of the experimental program has been designed to produce a cell capable of discharging within a second or less at high drain rate after introducing the electrolyte.

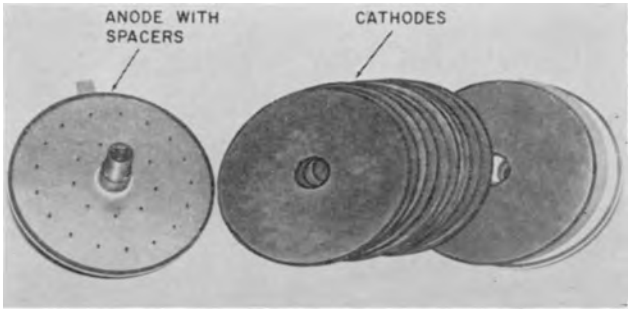


Fig 1. Exploded view of eleven-cell battery

The cathode dry mixture consists of the following [for 645 $cm^2$ (100 $in.^2$) surface]:

| | Grams | Per cent |
|---|---|---|
| Potassium iodate (−120 mesh) | 29.5 | 57.1 |
| Graphite (Acheson No. 38) | 21.1 | 40.8 |
| Acetylene black, 50% compression | 1.1 | 2.1 |
| | 51.7 | 100.0 |

The dry mixture was blended for 1 hr in a rotary mixer and then blended for approximately 5 min with a prescribed amount of polyvinyl acetate binder. In a typical cell construction, the thickness of the cathodic reactant [0.080 cm (1/32 in.)] thick was easily regulated by cementing on a rubber gasket of the proper thickness to the periphery of the zinc sheet (Fig. 1), providing an interior area which was covered with the pasty cathode mix to the top level of the gasket. After air drying for ½ hr, the wet cathode was baked for 1 hr at 105°C. The proportion of dry cathode mix ingredients of graphite and acetylene black were arrived at experimentally to provide a mixture of proper electrical conductivity for the cathode plate structure. The function of the silver surface coating is to provide an electrically conducting layer which physically and chemically separates the zinc anode and the potassium iodate cathode and prevents their direct reaction in the presence of the sulfuric acid electrolyte. The electrolyte volume was provided by cementing typically 0.119 cm (3/64 in.) thick neoprene rubber gaskets and spacers to the clear zinc surface of the electrode.

The dry plate structure of a battery was simply completed by cementing the zinc anode face of one electrode, fitted with an electrolyte gasket and spacers, to the iodate cathode face of an adjacent electrode. The cell formed was nominally 0.203 cm (0.080 in.) thick. Cell structure thus assembled into packs formed electrical series of cells when filled with electrolyte. The power was withdrawn from tabs on the end plates. The maximum number of cells placed in series to date is 25, but there is no reason the number cannot be much larger.

The electrolyte consisted of 8.0*N* $H_2SO_4$ + 0.5*N* HCl + 2% $HgCl_2$. It was found that mercuric chloride was very effective in reducing the formation of hydrogen gas to a low level. The use of 0.5*N* HCl in conjunction with 8.0*N* $H_2SO_4$ increased the voltage of the battery at low temperature, i.e., 0°C.

### *The Cell Reaction*

Cells of the following construction were discharged at various temperatures from 0°-65°C:

Zinc/8*N* $H_2SO_4$ + 0.5*N* HCl + 3% $HgCl_2/KIO_3$

The cells were discharged at constant external resistance to a 1-v cut-off at current densities of approximately 0.0853 amp/$cm^2$ (0.55 amp/$in.^2$). The average voltages produced were approximately 1.5 v, except for the 0° discharge, which produced an average 1.16 v.

The spent electrolyte was removed and saved and the cell rinsed thoroughly with distilled water. The electrolyte with rinsings was analyzed for total hydrogen ion, iodine, iodide ion, chloride ion, and zinc ion. A 1.3 × 15 cm (½ × 6-in.) strip was cut vertically from the center portion of the cathode [originally 15 × 15 cm (6 × 6 in.)] and the cathode material scraped from the zinc and extracted with water. The extract and rinsings were analyzed for iodine and iodate.

In both the electrolyte and cathode analyses, iodine was extracted with carbon tetrachloride and determined by titration with standard sodium thiosulfate. To determine the quantity of iodate present, an aliquot portion of the solution obtained in the cathode extractions was treated with an excess of KI and titrated with standard sodium thiosulfate.

The total activity was measured potentiometrically by titration with standard sodium hydroxide solution.

Iodide and chloride were analyzed together volumetrically and gravimetrically by precipitation with silver nitrate. In the volumetric analysis an excess of standard silver nitrate was added and the excess back-titrated with standard potassium thiocyanate solution. The results of the volumetric and gravimetric analyses were expressed in the form of two equations which were solved simultaneously for the quantities of the halides.

Zinc was determined gravimetrically by treatment of aliquot portions of the spent electrolyte with diammonium hydrogen phosphate and weighing as the pyrophosphate.

According to Table I less that 10% of the zinc consumed entered into side reactions. This indicates that the predominant side reactions do not involve zinc.

The values in Table I indicate that, except for the 0° discharge, the unused acid remaining after the discharge was 16-29% of the original. The 46.1% acid remaining at 0° is indicative of the slowness of the cell reaction at this temperature. The hydrogen ion consumed in side reactions varied between 14-41%, depending on which current-producing reaction is postulated, being greater at 40°, 55°, and 65° than at 26° and 0°C.

The results in Table I show that, except for the 0° discharge, the amount of potassium iodate remaining unreacted in the cell was 14-29% of the original amount. All cells were discharged to the 1-v end point. In the 0° discharge the unreacted iodate was approximately one-half of the original. The percentage of potassium iodate consumed in the production of current also represents the electrical efficiency of the cell. The efficiency is greatest at room temperature (26°C), and becomes less as the ambient temperature rises toward 65°C, or falls toward 0°C. The

Table I. Distribution of reactant consumption
(Per cent of original cell reactants)

| Exp. | Temp, °C | Zn consumed in side reaction | Reaction [1] | | Reaction [2] | | Unreacted $KIO_3$ in cathode | $KIO_3$ used in producing current | $KIO_3$ unaccounted for |
|---|---|---|---|---|---|---|---|---|---|
| | | | $H^+$ used in cell react. | $H^+$ used in side react. | $H^+$ used in cell react. | $H^+$ used in side react. | | | |
| 1 | 65 | | 45.5 | 32.9 | 37.9 | 40.5 | 14.3 | 38.4 | 47.3 |
| 2 | 55 | 9.7 | 55.0 | 28.4 | 45.8 | 37.6 | 25.8 | 40.6 | 33.6 |
| 3 | 40 | 5.5 | 51.8 | 19.5 | 43.1 | 28.2 | 23.5 | 40.6 | 35.9 |
| 4 | 26 | | 60.1 | 14.9 | 50.0 | 25.0 | 29.0 | 57.6 | 13.4 |
| 5 | 0 | 5.1 | 39.9 | 14.0 | 33.2 | 20.6 | 51.5 | 36.1 | 12.4 |

tendency of the cathodic reactant to engage in side reactions increases as the temperature rises. The most favorable ambient temperature for discharge appears to be about 26°C.

From Table I the quantity of potassium iodate unreacted in the cell discharge is known, and this value subtracted from the amount originally present gives the amount of potassium iodate consumed. The quantity of potassium iodate consumed may also be calculated from the iodide and iodine found by chemical analysis, provided the recovery is 100%.

Iodide ion and iodine were probably partially unrecovered for several reasons. Mercuric chloride, present in the electrolyte, can react with iodide or iodine.

Although the quantities of iodine and iodide recovered in the chemical analyses did not approach the theoretical values, the quantities of iodine determined were fairly consistent with each other at the various temperatures. However, the values for iodide ion at 0° and 26°C were considerably greater than those at the higher discharge temperatures. This seems to indicate that at the lower temperatures the current-producing reaction tends more toward the formation of iodide ion rather than iodine, that is, Eq. [2] rather than Eq. [1].

### *Power Output of the Cell*

The power output of the cell is shown in Fig. 2, which illustrates a typical discharge for a 232 $cm^2$ (36 $in.^2$) cell. The zinc-iodate cell had a typical current density of 0.104 amp/$cm^2$ (0.67 amp/$in.^2$); however, current densities as high as 0.155 amp/$cm^2$ (1.0 amp/$in.^2$) could be obtained for short periods of time. The flat voltage characteristics of the cell discharge is particularly desirable for operation of electronic equipment. For design purposes in testing the cell, power was usually withdrawn from the cell until there was a 15% voltage drop.

Although the development work was directed primarily toward high discharge rates for short intervals of time, sufficient information was gathered to indicate that the battery is probably capable of discharging over periods of several hours. Figure 3 illustrates the typically developed cell voltage as a function of current density for varying discharge periods of time. As would be expected, the average cell voltage is higher for the longer discharge time. In these cells the zinc anode was 0.013 cm (0.005 in.) thick and the iodate cathode was 0.080 cm (1/32 in.) thick. The electrode spacing for the electrolyte is as indicated in Fig. 3.

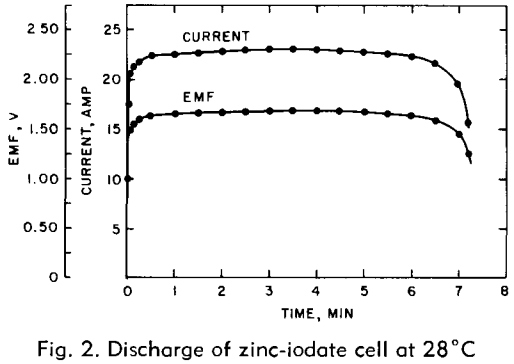


Fig. 2. Discharge of zinc-iodate cell at 28°C

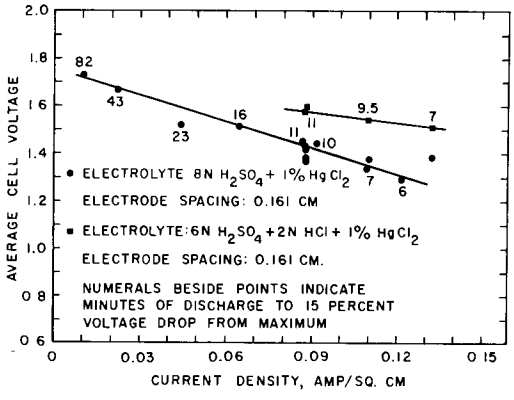


Fig. 3. Cell voltage vs. current density

### *A Prototype Battery*

A zinc-iodate primary battery for a military application was designed to the following specifications:

| | |
|---|---|
| Average emf, v | 26.5 ± 1 |
| Average current, amp | 135 ± 2 |
| Discharge time, min | 8 |
| Weight, kg | 14.1 (31 lb) |
| Length, cm | 27.2 (10.7 in.) |
| Diameter, cm | 23.1 (9.1 in.) |

The battery consists of a dry-plate section (Fig. 4, lower) and an electrolyte chamber (Fig. 4, upper). The battery case is made of 0.025 cm (0.010 in.) steel sheet. The electrolyte, consisting of 8*N* $H_2SO_4$ + 0.5*N* HCl + 2% $HgCl_2$, is contained in a rubber bag. The dry-plate structure is housed in an electrically insulated and vacuum-sealed container. The power terminals are located beneath the plate structure and are brought out of the case through glass-insulated connectors. The electrolyte bag is connected to the lower half of the battery through an assembly consisting of an acid-resistant fitting, an O-ring seal, and a plastic diaphragm which is in-

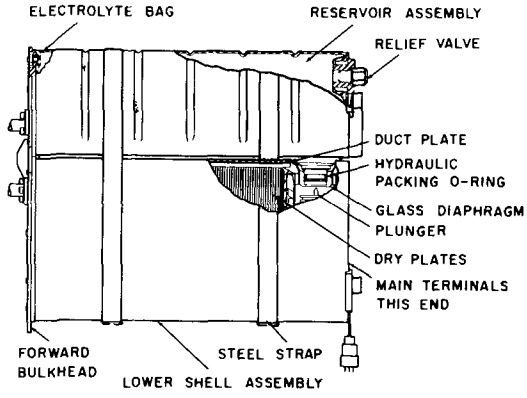


Fig. 4. Partial sectional elevation view of a prototype battery

tegral with the evacuated section of the battery. Upon activation, gas under pressure forces a plunger to break the glass diaphragm, whereupon the electrolyte is drawn rapidly into the cells through a set of ducts located at the top of the cells. Simultaneously, $CO_2$ gas pressure is exerted on the outside of the rubber bag to assist in rapid filling of the cells.

The dry-plate structure consists of six cell packs connected in parallel. Each pack consists, in turn, of 17 cells in series, and is designed to produce 22.5 amp at 26.5 v. A pack is fabricated as a unit by first assembling the cell bipole plates, using rubber O-ring stock for spacing and insulation purposes, then potting the assembly with resin. The top is left open. Six packs are potted together in a mold to form a block and the duct plate is cemented to the open side of the cell block. Next, the bus bars are attached to the bottom of the cell block and the whole assembly inserted into the battery case. Remaining operations consist of attaching fittings, filling dead space with resin, sealing the can, and attaching heating units and the electrolyte section. The electrolyte bag is filled in the field just before field-check of the torpedo.

A feature not incorporated in the design of the battery was a means which has been devised for leveling the electrolyte in a cell pack should some of the cells not fill completely. However, there is at present no reason to believe that the cells will not fill completely. A slight excess of electrolyte will insure this fact. Figure 5 shows a typical battery discharge of the construction illustrated in Fig. 4. A well-constructed battery of the type described discharged for 7.3 min to a 23-v end point. The average potential of the discharge was 26.9 v and the average current was 134.2 amp. These values compare favorably with the specification requirement for a

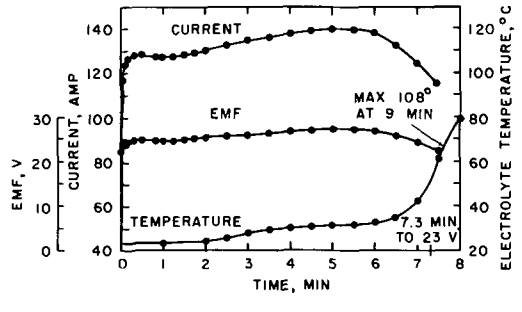


Fig. 5. Discharge of a zinc-iodate battery

potential of 26.5 ± 1 v and a current of 135 ± 2 amp. The discharge time of the battery favorably approached the 8-min discharge time design limit. The activation time of the battery was 2.1 sec to a rising transient 20-v discharge potential under load, well within the specification requirements of 5 sec. It is expected that some further improvement can be made in the performance of the battery by further changes in design.

## Discussion

A typical type of battery design has been illustrated in the previous discussion, being cylindrical in general configuration. There is little doubt that this battery can be constructed inexpensively in a variety of sizes and shapes to meet varying military and commercial requirements. The mechanical design of the battery can be made far more flexible than the typical rectangular shape of commercial batteries. The rapid activation time under load of the battery is another distinct advantage, being of the magnitude of 1-2 sec, to a voltage approximating the working level. The battery is of the primary type and was designed for high-current drain applications. A typical reserve battery of this type is capable of producing a discharge potential of 1.6 v, for 7 min, at a current drain rate of 0.092 amp/cm$^2$ (0.6 amp/in.$^2$). A self-contained battery of this type, operated at the above performance level, has an energy output of 2.32 watt min/cm$^3$ and a watt min/g output of 1.88. The battery has been operated at current drains of as high as 0.140 amp/cm$^2$ (0.9 amp/in.$^2$). Considering a single cell structure alone, composed of a zinc anode, a typical iodate cathode (without a zinc sheet backing), and sulfuric acid electrolyte, the energy output of a single cell without auxiliary mechanical structures is 5.38 watt min/cm$^3$ and 2.61 watt min/g for a typical discharge time of 7 min. The inexpensive chemicals used in this battery are important for basic over-all low battery costs. The inexpensive tin can type of mechanical battery construction is also important for rapid manufacture of low-cost batteries.

There are indications that the battery can be adjusted to different environmental temperature conditions by changing the composition of the electrolyte. Sulfuric acid electrolyte is suitable at high temperature applications. Increasing amounts of hydrochloric acid should be added to the electrolyte as the environmental operating temperature drops toward 0°C.

There are, of course, limitations in the applications of the battery. This battery, like other electrochemical systems, is ineffective at very low ambient temperatures, i.e., below 0°C. There is a tendency for the battery to overheat and lose electrolyte by boiling at high current drain rates. In a one-shot device such as a missile, if the discharge time of the battery is adjusted to the lifetime of the desired missile application, this is of less importance. The fragmentary information available from preliminary research indicates that this primary battery has a comparatively short life after activation with electrolyte, i.e., hours rather than days, due to self-discharge.

As far as the writers are aware, this battery represents the first practical demonstration of this electrochemical couple. On this same type of technical basis, the performance of the zinc-bromate couple should also be studied.

Manuscript received Jan. 3, 1958.
Any discussion of this paper will appear in a Discussion Section to be published in the June 1959 JOURNAL.

REFERENCES

1. W. M. Latimer "Oxidation Potentials," Prentice-Hall, Inc., New York (1952).
2. John Rapieff, British Pat. 5922, Jan. 5, 1884.
3. J. L. Jones, U. S. Patent Application, Serial No. 342,761, March 16, 1953.

# Halogen-Activated Solid Electrolyte Cell

**J. L. Weininger**

*Research Laboratory, General Electric Company, Schenectady, New York*

ABSTRACT

A new type of silver halide solid electrolyte cell consists of a small bead of silver halide with tantalum and silver wires, cathode and anode, respectively. The mechanism of the electrochemical reaction of this cell has been determined. When the cell is exposed to bromine or iodine vapor, it is a promising primary cell for elevated temperatures. With silver iodide as electrolyte, the cell can be recharged several times.

Historically, electrochemical cells with solid electrolytes were first used by Reinhold (1). He studied thermocells as an outgrowth of his work on chemical equilibria between solid salts. Likewise Wagner used solid electrolytes in galvanic cells in his study of the conductance of solids (2). These cells have come into prominence recently because of the development of electronic equipment, such as ion chambers, scintillation counters, or photomultiplier tubes, which requires high voltages and very small currents.

Generally, solid electrolyte cells, as distinguished from cells with liquid electrolytes, have the advantage of simpler construction. By reducing their weight and size, batteries can be miniaturized. Their disadvantage is that the solid electrolyte has a high internal impedance, which results in short-circuit currents or flash currents of the order of a few microamperes at room temperature.

## Cells with Silver Halide Electrolytes

The solid electrolytes of the present work are silver halides, because they have relatively large ionic conductivities. Their use in solid-state cells has been described by Lehovec and Broder (3) and van der Grinten (4). The cells developed by van der Grinten consist of the following:

| ⊕ | ELECTROLYTE | ⊖ |
|---|---|---|
| CATHODE | AgBr | ANODE |
| $CuBr_2 + C$ | | Ag |

The reactions as postulated by van der Grinten are:

Electrode reactions: $CuBr_2 \rightarrow \frac{1}{2}Cu_2Br_2 + \frac{1}{2}Br_2$, $Ag \rightarrow Ag^+ + e^-$; $\frac{1}{2}Br_2 + Ag^+ + e^- \rightarrow AgBr$

Cell reaction: $\frac{1}{2}Br_2 + Ag \rightarrow AgBr$

Over-all reaction: $CuBr_2 + Ag \rightarrow \frac{1}{2}Cu_2Br_2 + AgBr$

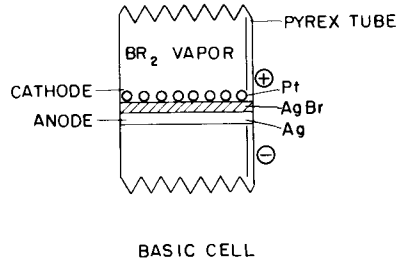


BASIC CELL

Fig. 1. Basic cell

In this cell it is possible to replace the cathode mix, the source of bromine vapor, with an inert metallic conductor, at which the halogen vapor reacts directly, e.g., in the cell

$$\oplus \text{Pt (or Ta)} + Br_2 / AgBr / Ag \ominus$$

Figure 1 indicates the basic structure of such a cell, which is in the form of a thin disk. A brominated silver foil (anode and electrolyte) is placed against a platinum screen (cathode). A simple stack of these cells could be assembled to form a battery, but firm electrical contact between the silver foil of one cell and the platinum screen of the next would have to be maintained. It is also convenient to use a bimetallic strip of silver and tantalum in which tantalum provides very satisfactory protection from thermal tarnishing of silver as contrasted to the desirable electrochemical consumption of silver in the cell reaction.

## Bead Cell

*Construction and mechanism.*—More recently "bead" cells have been constructed in order to elucidate the mechanism of these solid electrolyte cells. Figure 2 shows the basic structure and explains the name. Beads with diameters ranging in size from 0.075 to 0.15 cm are formed by melting the chemically pure halide in a stream of dry nitrogen. The electrodes are inserted into the solid beads by heat-

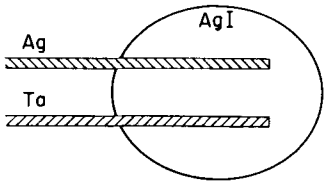


Fig. 2. Halide "bead" cell

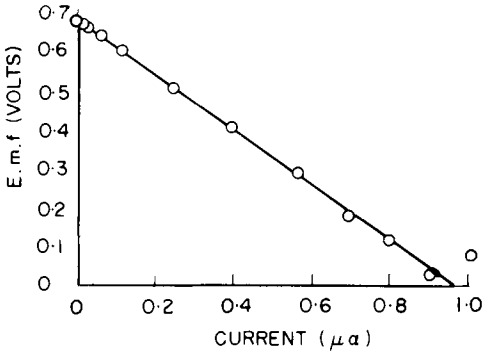


Fig. 3. Current-voltage plot of a silver iodide bead cell at room temperature.

ing the wires (0.012 to 0.05 cm diameter) while they are touching the beads. This melts the electrolyte at the point of entry of the wires only. By continuing this process the wires are submerged substantially in the bead and should be situated side by side as indicated in Fig. 2. Either platinum or tantalum can be used as the inert electrode on which the cathode reaction takes place. If halogen vapor is present, e.g., iodine, it would be reduced at the cathode: $\frac{1}{2}\ I_2 + e^- = I^-$, while, at the anode, silver is oxidized: $Ag = Ag^+ + e^-$. Thus, the over-all cell reaction is the formation of more electrolyte: $Ag + \frac{1}{2}\ I_2 = AgI$. The same cell can be used as a secondary cell in the absence of halogen. The cell is charged by application of an external voltage larger than the decomposition potential of the halide. In the case of silver iodide at room temperature this is 0.685 v. Silver is plated out on the cathode and iodine vapor is produced at the anode. Removal of the externally applied voltage leaves the cell in a charged condition. On discharge, the reaction will be the reverse of the original decomposition reaction.

*Bead cell as primary cell.*—Figure 3 is a typical current-voltage plot of the silver iodide bead cell at room temperature. The open cell voltage corresponds to the theoretical voltage derived from the thermodynamic free energy of formation of silver iodide. Application of Ohm's law gives an impedance of 700KΩ. The straight line indicates that at room temperature the internal impedance of the cell is so large that the *IR* drop overshadows all other polarization phenomena.

A similar cell was maintained at open cell voltage for 47 days at room temperature. The impedance of this cell increased to about 5MΩ and then remained constant. This is shown by the current-voltage diagrams of Fig. 4. After 50 days the cell broke down because the protruding silver anode had been severely attacked by the iodine vapor. The cell design of Fig. 5 illustrates, however, one method of eliminating the thermal attack on the silver wire.

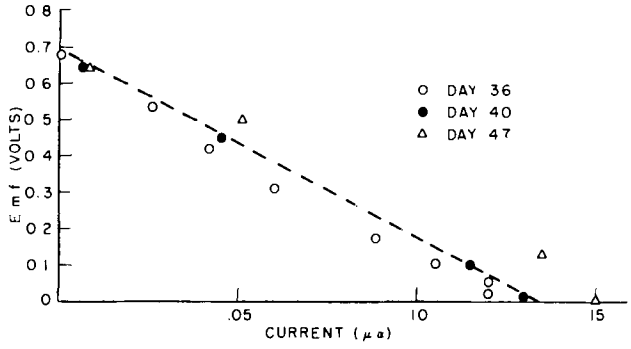


Fig. 4. Current-voltage measurements during life test of a silver iodide bead cell. Cell was stored at 80°C, measured at room temperature.

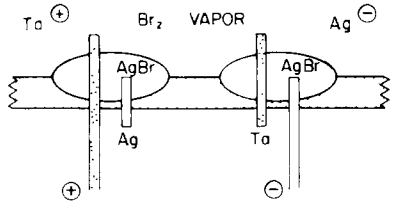


Fig. 5. Series connection of bead cells

In this battery the halogen vapor again activates the tantalum cathode, but it is physically separated from the silver anode by an insulating Pyrex sheet. Individual cells are connected in series as shown. They have very long lifetimes. Thus, one iodine cell retained theoretical voltage at 75°C for one year. Another cell, tested at room temperature with 1 MΩ load, yielded 0.145 coulombs over a period of 32 days.

More favorable results are obtained with bead cells at elevated temperatures because the conductivity of silver iodide increases rapidly with temperature. Figure 6 illustrates the improved cell output with increased temperature. The dashed line is the room temperature long-life behavior of Fig. 4. As the temperature increases, the internal impedance of the electrolyte decreases and correspondingly larger currents are obtained. Whereas at room temperature the cells exhibit only resistance polarization as described above, below 120°C they are subject to another type of polarization, presumably concentration polarization. This, in turn, disappears at 120°C with the first of two phase transformations of AgI. Due to changes of crystal structure at 120° and 145°C the conductivity of silver iodide, which is only slightly larger than those of other silver halides at room temperature, in-

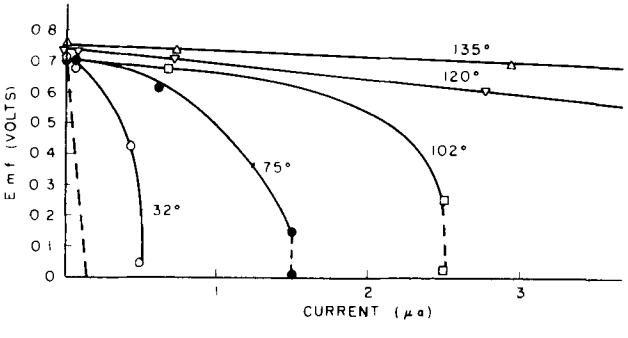


Fig. 6. Current-voltage curves as function of temperature

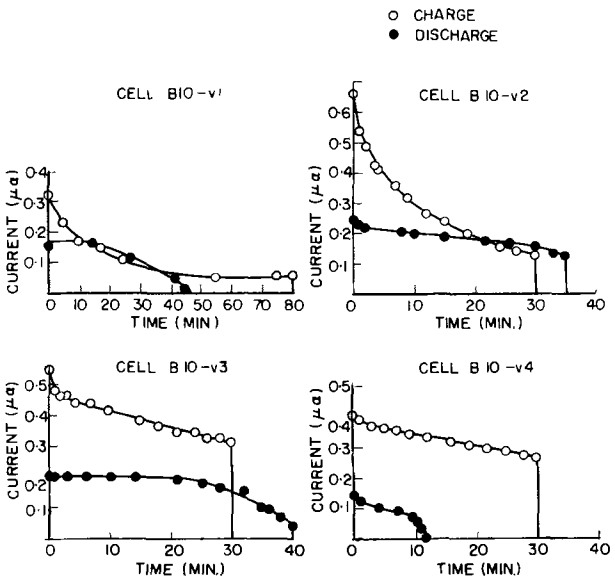


Fig. 7. First charge-discharge cycles of AgI cells at different temperatures and periods of storage. B10-v1, no storage, 73% of charge recovered; B10-v2, B10-v3, and B10-v4 stored 90 min each at —210°, 0°, and 25°C, after which 73, 63, and 15% of charge recovered, respectively. Open circle, charge; solid circle, discharge.

creases very rapidly, first at 120°, from an order of $10^{-6}$ to $10^{-4}$ $ohm^{-1}$-$cm^{-1}$, then to 1 $ohm^{-1}$-$cm^{-1}$ at 145° (5,6). In fact, at the melting point, 552°, the conductivity is larger in the solid phase than in the melt. This is explained by the crystal structure, which is cubic in the high temperature alpha-modification (7). The large iodine ions form the big building blocks among which the smaller silver ions move freely. The application of the bead cell to higher temperature, therefore, became obvious. This work is still in progress.

*Bead cells as secondary cells.*—Bead cells could be charged to the theoretical open cell voltage and discharged several times without deterioration. Better yields were obtained with the iodine system than with the comparable bromine system; data obtained with four identical silver iodide cells in their first cycle are shown in Fig. 7. The cells were charged and discharged at 0°C. Duration and temperature of storage, before discharge, was varied. Charge was best retained at the lowest temperature and is lost on storage at room temperature.

These observations are consistent with the hypothesis that diffusion of iodine to the surface of the electrolyte bead determines the loss of charges in the bead. However, the published diffusion data indicate that anion diffusion through the ionic lattice is very slow. Thus, Teltow (8) estimates a diffusion coefficient of bromine in silver bromide of the order of $10^{-20}$ $cm^2$/sec at 20°C. This implies that the anions are immobile because the diffusion path per day would be less than one lattice parameter. Jordan and Pochon (9) have given an upper limit of $10^{-15}$ $cm^2$/sec for the diffusion coefficient of iodine at 20°C in either of the two modifications of silver iodide that are stable at room temperature. This would also be too slow to account for loss of charge in the present experiments. But the magnitude of diffusion clearly depends on the structure of the halide. By analogy, in the case of conductivity of silver bromide it is known that in single crystals in the absence of bromine the conductivity is electronic (10), but when the pure single crystal is exposed to bromine, or dislocations are introduced, silver ion conduction will completely account for charge transport. In the present cells the diffusion path of iodine to the surface of the electrolyte is open to speculation. It may be along dislocations at grain boundaries or gross faults in the bead; or, since about 0.5 μg of iodine is formed in charging the bead cell, it has been suggested (11) that solid iodine is produced at the cathode to a thickness of about 100 atomic layers, and that in the process of depositing iodine some free space develops at the cathode. Thus, an alternative diffusion path lies along the tantalum wire cathode. No explanation is offered why only 73% charge was recovered with zero storage time. Although some energy losses in overcoming cell impedance and in the cathode reaction are feasible the possibility of submicroscopic leaks seems more likely. As in the discussion of diffusion paths this again emphasizes the importance of the solid electrolyte structure.

## Acknowledgment

The author would like to thank Dr. W. T. Grubb for valuable discussions during the course of this work.

Manuscript received Dec. 18, 1957. This paper was prepared for delivery before the Buffalo Meeting, Oct. 6-10, 1957.

Any discussion of this paper will appear in a Discussion Section to be published in the June 1959 JOURNAL.

## REFERENCES

1. H. Reinhold, *Z. anorg. u. allgem. Chem.*, **171**, 181 (1928); H. Reinhold and A. Blachny, *Z. Elektrochem.*, **39**, 290 (1933).
2. C. Wagner, *Z. physik. Chem.*, **B21**, 25 (1933); *Z. Elektrochem.*, **60**, 4 (1956).
3. K. Lehovec and J. Broder, *This Journal*, **101**, 208 (1954); K. Lehovec, Proc. 10th Annual U.S.A. Signal Corp. R. & D. Conf., Asbury Park, May 1956.
4. W. J. van der Grinten, *This Journal*, **103**, 201C, (1956).
5. C. Tubandt and E. Lorenz, *Z. physik. Chem.*, **87**, 513 (1914).
6. K. H. Lieser, *Z. physik. Chem. (n.F.)*, **9**, 216, 302 (1956).
7. L. W. Strock, *Z. physik. Chem.*, **B25**, 441 (1934).
8. J. Teltow, *Z. Elektrochem.*, **56**, 767 (1952).
9. P. Jordan and M. Pochon, *Helv. Phys. Acta*, **30**, 33 (1957).
10. I. Pfeiffer, K. Hauffe, and W. Jaenicke, *Z. Elektrochem.*, **56**, 728 (1952).
11. A. F. Daniel, Private communications.

# The Microtopography of Oxide Films on Niobium

J. V. Cathcart, J. J. Campbell, and G. P. Smith

*Metallurgy Division, Oak Ridge National Laboratory, Union Carbide Nuclear Company, Oak Ridge, Tennessee*

ABSTRACT

An electron microscopic study of the oxide films formed on niobium permits the apparently anomalous oxidation rate behavior of niobium to be explained in terms of the formation of small, blister-like cracks in the oxide film. An oxidation model, based on the idea that an oxidation process which is maintained by interstitial-anion or anion-vacancy diffusion leads to the generation of stresses in the oxide film, is proposed to account for these results. The observation of similar blister-like cracks in oxide films on tantalum is also reported.

This paper is a report of an electron optical investigation of the microtopography of oxide films formed on niobium at temperatures ranging from 325° to 450°C. It was found that small, blister-like cracks tended to form in the oxide while the film was still relatively thin and that the onset of this blistering could be correlated with an increase in the oxidation rate. A similar phenomenon was observed in oxide films on tantalum.

As a preliminary to the main study, a series of rate measurements was made on niobium at temperatures in the vicinity of 400°C. A typical result is shown in Fig. 1. Characteristically, these oxidation rate curves showed an initial protective stage of oxidation followed by a transition period in which the oxidation rate increased. Finally, a nonprotective stage of oxidation ensued in which the oxidation rate became essentially constant. A manometric technique similar to that used in a previous study of the oxidation of alkali metals (1) was utilized for these rate measurements.

The above results are in general agreement with the data of Inouye (2) and of Gulbransen and Andrew (3). The latter authors reported that protective oxidation continued for at least 7 hr at 375°C. At higher temperatures, however, their rate curves had the same qualitative form as that shown in Fig. 1, the protective stage of oxidation becoming shorter and shorter as the temperature was increased to 500°C. At 600°C and above, Inouye reported the existence of linear rate curves throughout his experiments.

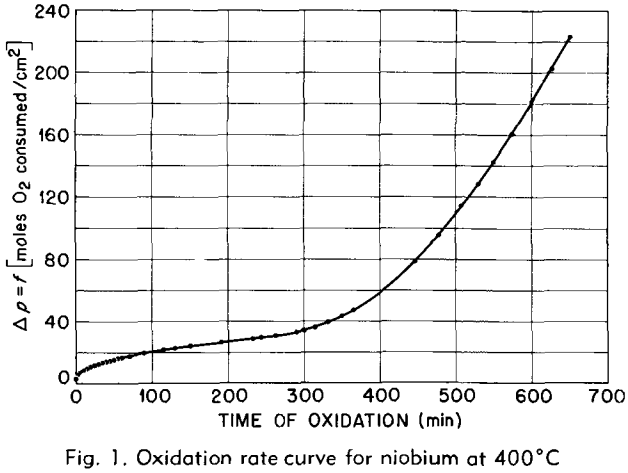


Fig. 1. Oxidation rate curve for niobium at 400°C

## Procedure and Results

Electron microscope specimens were prepared from niobium[1] coupons 1 x 2 cm on a side and 0.05 cm thick. The coupons were hand ground through 4/0 emery, polished with 0.3-micron levigated alumina, and electrolytically polished in a 90% $H_2SO_4$ —10% HF solution. Prior to oxidation the polished specimens were annealed in a Pyrex glass apparatus overnight at the oxidation temperature under a pressure of approximately $10^{-6}$ mm Hg. All specimens were oxidized in purified $O_2$ at 1 atm pressure. Carbon replicas, preshadowed with a gold-Manganin alloy, were then made of the surfaces of most of the oxidized specimens, but in a few instances Formvar replicas were prepared.

Several additional specimen pretreatments were also tested. For example, some specimens were mechanically polished only, and these along with electropolished specimens were oxidized both with and without prior vacuum annealing. In a few instances specimens were annealed at 1000°C at a pressure of 1 x $10^{-6}$ mm Hg before oxidation at 400°C. Speci-

[1] Chemical analysis of Nb specimens: C, 0.007%; Si, 0.10%; Ti, 0.025%; Fe, less than 0.005%; Ta, less than 0.16%; $H_2$, 0.002%; $O_2$, 0.010%; $N_2$, 0.017%.

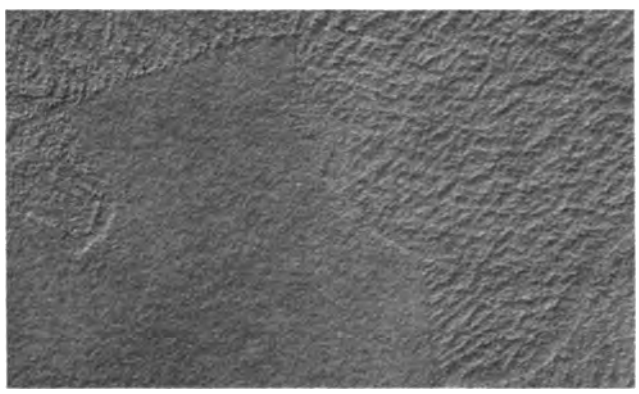

Fig. 2a. Carbon replica, preshadowed with gold-Manganin, of Nb specimen oxidized for 30 min at 140°C. Magnification 12,000X before reduction for publication.

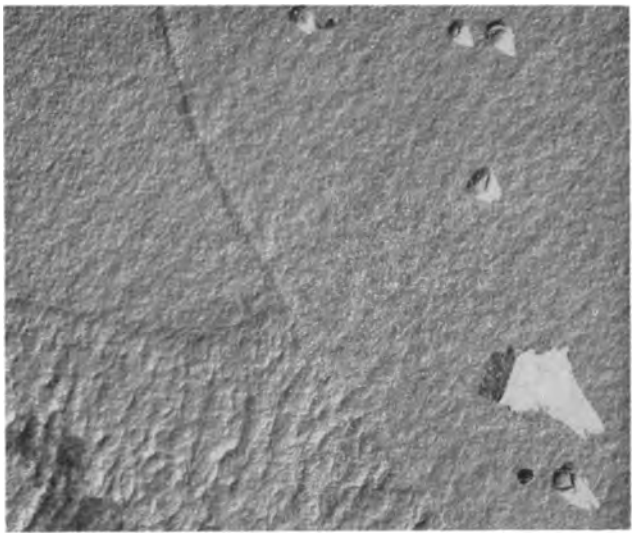

Fig. 2b. Carbon replica, preshadowed with gold-Manganin, of Nb specimen oxidized for 120 min at 400°C. The irregular white area in the lower right hand corner is a tear in the replica produced when the replica was removed from the specimen. Note that the shadowing indicates that a blister had formed at this point in the oxide. Magnification 22,700X before reduction for publication.

Fig. 2c. Formvar replica, shadowed with gold-Manganin, of Nb specimen oxidized for 210 min at 400°C. Magnification 5,000X before reduction for publication.

mens prepared by these different methods all exhibited essentially the same oxidation behavior; however, the method described in the preceding paragraph gave the most consistently reproducible results and, therefore, was adopted as a standard procedure.

The changes in oxide topography as a function of time at a constant oxidation temperature are illustrated in Fig. 2a, b, and c. These electron micrographs show the surface topography of the oxide film after times ranging from 30 to 210 min for oxidation at 400°C. Optical examination of the specimen which had been oxidized for 30 min, corresponding to the protective stage of oxidation, revealed only the presence of the oxide interference colors usually associated with protective oxide films. In the related electron micrograph (Fig. 2a), the oxide film appeared to be essentially smooth and coherent; no cracks could be observed in the film. The most striking feature of the specimen was the variation of oxidation rate with crystal plane as was shown by the different thicknesses of oxide over different grains in the metal.

The 120-min specimen corresponded to the beginning of the transition zone in the oxidation rate curve. Again optical examination showed only interference colors in the oxide film. However, a few blister-like cracks were apparent in the electron micrograph, Fig. 2b, although most of the oxide still appeared to be quite coherent.

The approximate center of the transition zone in the oxidation rate curve was reached with the 210-min specimen. Optical examination of this specimen revealed areas of oxide interference colors interspersed with small rough areas of white oxide. Electron micrographs (*see* Fig. 2c) showed that these white areas were regions of the oxide in which a large increase in blister density had occurred.

When oxidation was continued until the linear portion of the oxidation rate curve had been reached, the entire specimen surface became covered with a rough white oxide. These surfaces were too rough to permit replication, since particles of oxide adhered to the replica. For this reason, the electron optical portion of this study had to be limited to cases where the oxidation of the specimens had not proceeded beyond the approximate center of the transition zone of the rate curves.

The surface topography of the niobium-oxide films also reflected the decrease, reported by Gulbransen and Andrew (3), in the duration of the initial, protective stage of oxidation with increasing temperature. As judged on the basis of blister density, the transition region between the protective and nonprotective stages of oxidation occurred after 10, 60, 240, 480, and 2900 min for oxidation temperatures of 450°, 420°, 400°, 380°, and 350°C, respectively. A typical result from these experiments is illustrated in Fig. 3 which shows the surface topography of the oxide film formed in 480 min at 380°C. At 325°C no blisters were seen in the oxide films in experiments lasting up to 144 hr (*see* Fig. 4).

It was also observed that, as the oxide films thickened, their surfaces tended to become rougher. This phenomenon occurred at all temperatures investi-

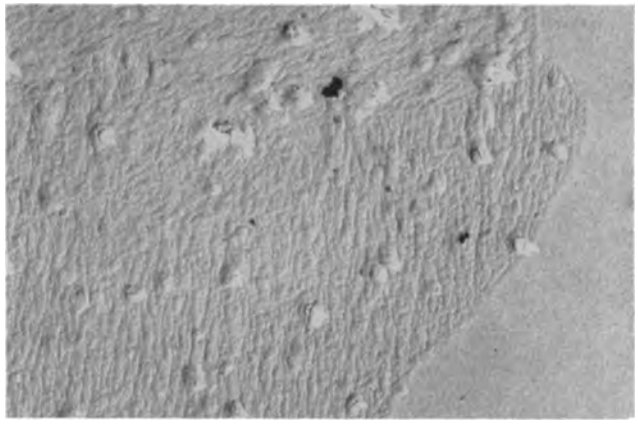

Fig. 3. Carbon replica, preshadowed with gold-Manganin, of Nb specimen oxidized for 480 min at 380°C. Magnification 7,500X before reduction for publication.

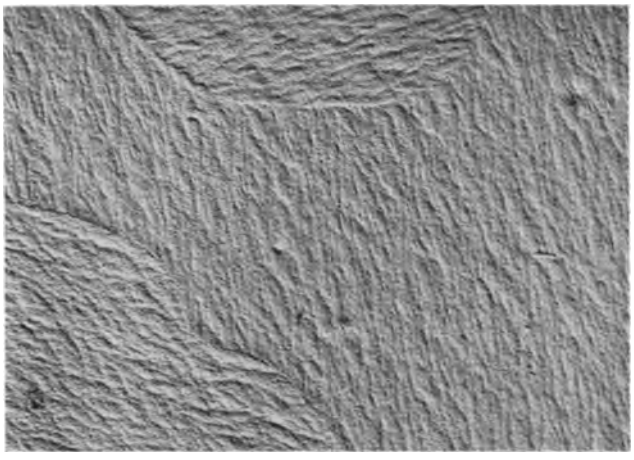

Fig. 4. Carbon replica, preshadowed with gold-Manganin, of Nb specimen oxidized 48 hr at 380°C. Magnification 12,000X before reduction for publication.

gated, but it can be seen most clearly in Fig. 3 and 4. The oxide surface had a "rippled" texture, the direction of the "ripples" varying with crystallographic direction. As discussed below, it is thought that this effect may be related to plastic deformation of the oxide film.

The oxide films formed on niobium were studied both by x-ray and electron diffraction methods. Only the low temperature form of $Nb_2O_5$ was detected. However, this result does not preclude the presence of one of the lower oxides of niobium, especially if such an oxide were present as a thin layer at the oxide-metal interface.

## Discussion

A clear correlation appeared to exist between oxide topography and the oxidation rate curves (cf., Fig. 1 and 2). Both the rate curves and the electron micrographs showed that in the initial stages the oxide film was nonporous and protective. After a period of time which depended inversely on the temperature of oxidation, blister-like cracks formed in the oxide, and the film became less protective. Further increase in blister density produced a corresponding increase in oxidation rate until finally a steady-state condition was attained in which the rate curve was linear. Thus, it is evident that blister formation was related to an increase in the porosity of the oxide film, and in the latter stages where a linear rate curve was observed, the oxidation was either an interface-controlled process or else the rate of oxidation was determined by diffusion across a thin layer of oxide which statistically maintained a constant thickness.

While it is plain that the nonprotective stage of the oxidation of niobium is related to the formation of blister-like cracks in the oxide, the source of the stress which leads to such blister formation is much less obvious. The oxide-to-metal volume ratio for $Nb_2O_5/Nb$ is high (2.7), but it is to be expected that any stresses produced in the oxide on account of its epitaxial misfit with the substrate metal should be confined to a very thin layer at the oxide-metal interface as a result of the formation of an array of dislocations or other lattice defects at this interface. If such be the case, differences in volume of equivalent amounts of oxide and parent metal cannot, *per se*, produce a significant stress in any but the thinnest oxide films.

Blister formation could, perhaps, be accounted for in terms of the recrystallization of the oxide films in accord with the mechanism proposed by Vermilyea (4) to explain crack formation during the early stages of the "field crystallization" of anodically formed, amorphous tantalum oxide films. This mechanism does not, however, appear to explain the continued linearity of the oxidation rate curves for niobium after long periods of oxidation (2), nor does it account for the "rippled surface texture" (*see* above) which developed as the niobium oxide films thickened.

A possible alternative explanation, somewhat similar to that proposed by Jenkins (5) for the oxidation of titanium, of the results observed is provided by a consideration of the diffusion mechanism associated with the oxidation of niobium. A marker experiment was performed in which a fine platinum wire was tied around a 0.25-in. diameter niobium rod, and the rod was oxidized for 4 hr at 450°C. The specimen was then sectioned and examined metallographically. The platinum wire was found at the oxide-gas interface while the oxide-metal interface had receded from the wire, indicating that oxidation has proceeded by either anion-vacancy or anion-interstitial diffusion. This result was consistent with the known electrical properties of $Nb_2O_5$ (6) and with the fact that thick oxide films on Nb exhibit re-entrant edges and corners (2). It was concluded, therefore, that new oxide was formed at the oxide-metal interface rather than at the oxide-gas interface.

On the basis of this observation, a model for the oxidation of Nb has been devised. The basic assumption made is that cation diffusion within the oxide film is insignificant compared to anion diffusion. It follows then that new oxide must be formed at the oxide-metal interface. When a segment of the metal lattice at this interface is converted to oxide, a three-dimensional expansion of the metal lattice is required to bring the metal ions into their new positions in the oxide. This expansion is resisted by the overlying layer of previously formed oxide and can occur only through the deformation of this layer. Thus, an important conclusion of the above argument is that, in an oxidation reaction where new oxide is formed at the oxide-metal interface, the oxidation process itself continually produces stresses in the oxide film.

The observed increase in surface roughness of the oxide with film thickness may be cited in support of this argument. The surface topography of the niobium-oxide films (*see* especially Fig. 3 and 4) resembles in many respects the type of surface texture which might be expected for a highly deformed film.

Sufficient plastic deformation would, of course, eventually lead to fracturing of the oxide. However, the blister-like nature of the cracks actually observed suggests that the stresses producing them were much more highly localized than the stresses discussed in connection with the plastic deformation of the entire oxide film. The development of a

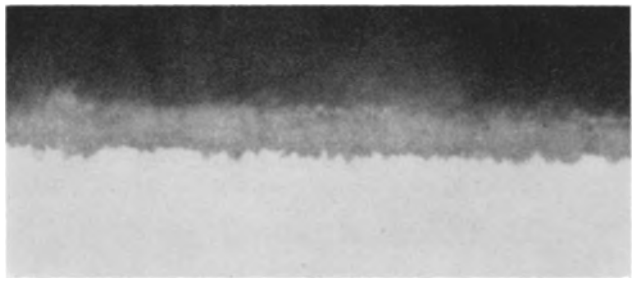

Fig. 5. Edge of a transverse section of a Nb specimen oxidized 4 hr at 400°C. Magnification 2000X.

locally highly stressed region leading ultimately to blister formation can be rationalized in terms of any mechanism which would produce a localized acceleration of oxidation. Such a condition would lead to the formation of a pit in the metal at the metal-oxide interface. Then, because of the volume difference between equivalent amounts of oxide and metal, the oxide produced in forming the pit would exert a substantial force normal to the surface of the oxide film. When the stress so generated exceeded the fracture strength of the oxide, a blister-like crack would form. It should also be noted that, once the surface of the metal becomes pitted, this same mechanism would permit continued crack formation in newly formed oxide. If the breakdown of the new film occurred at different moments at different sites over the specimen surface, the various "rate curves" for each such microscopic area must blend into a straight line, thus accounting for the linear portion of the macroscopic rate curve.

Figure 5 shows an optical micrograph of the edge of a transverse section through a niobium specimen which had been oxidized for 4 hr at 400°C. The white area at the bottom of the photograph is a portion of the unoxidized part of the metal specimen, while a cross section through a heavily blistered region of the oxide film appears as a narrow, slightly irregular band of gray just above the metal. As may be seen, the metal surface under this blistered area was badly pitted, in agreement with the mechanism outlined above.

It is realized that much of the argument presented above is speculative, and the authors regard this oxidation model only as a working hypothesis. It is an hypothesis which has, nevertheless, proved very helpful in suggesting a new approach to the problem of determining the factors which produce non-protective oxide formation on many metals. Thus, the model requires that any metal for which oxidation is maintained primarily by some form of anion diffusion should exhibit a tendency toward non-protective oxidation, especially if its oxide-to-metal volume ratio is significantly different from unity.

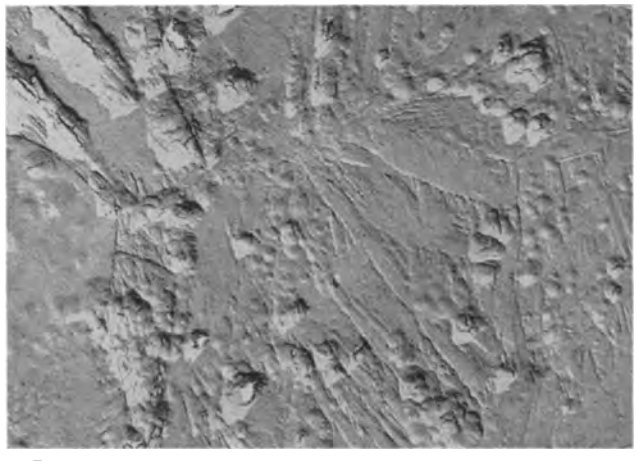

Fig. 6. Carbon replica, preshadowed with gold-Manganin, of Ta specimen oxidized for 4 hr at 500°C. Magnification 7,500X before reduction for publication.

The selection of another oxide-metal system with which to test this postulate is difficult because very little unequivocable information is available concerning the mode of diffusion in metallic oxides. For example, $Ta_2O_5$ has been shown to contain an excess of metallic ions (7), but it is not known whether this fact is attributable to the presence of interstitial cations on anion vacancies. However, from the point of view of its oxidation rate behavior (8), the structure and composition of its oxides (9), and its general chemical and physical properties, tantalum is similar to niobium. The oxide-to-metal volume ratio for $Ta_2O_5/Ta$ is also large (2.5). Preliminary studies of the microtopography of oxide films on tantalum have shown results in many respects like those observed for niobium oxide. Figure 6 is an electron micrograph of the surface of a tantalum specimen oxidized for 4 hr at 500°C. Blister-like cracks, similar to those observed in niobium oxide, are clearly evident. Thus, it is to be expected that the oxidation mechanisms of the two metals are analogous and involve anion-vacancy diffusion. Moreover, the oxidation results obtained with tantalum appear to be explainable in terms of the oxidation model devised for Nb.

## Summary

Previous measurements of the oxidation rates of niobium in a temperature range from about 350° to 500°C indicated that the oxidation process consisted of an initial stage in which protective oxidation occurred, a transition period marked by a gradual increase in the oxidation rate, and finally, a non-protective stage in which the oxidation rate was constant. An electron microscopic study of oxide films on niobium has permitted these rate changes to be correlated with the formation of small, blister-like cracks in the oxide film. An oxidation model, based primarily on the idea that an oxidation process which is maintained by interstitial-anion or anion-vacancy diffusion leads to the generation of stresses in the oxide film, was proposed to explain the experimental results obtained with niobium. The formation of similar blister-like cracks in oxide films on tantalum was cited as an example of a second case explainable in terms of this model.

## Acknowledgment

The authors gratefully acknowledge the assistance rendered in this research by E. L. Long and W. H. Bridges of the Electron Microscopy Section of the Metallurgy Division at the Oak Ridge National Laboratory.

Manuscript received Oct. 18, 1957.

Any discussion of this paper will appear in a Discussion Section to be published in the June 1959 JOURNAL.

REFERENCES
1. J. V. Cathcart, L. L. Hall, and G. P. Smith, *Acta Met.*, **5**, 245 (1957).
2. H. Inouye, "Scaling of Niobium in Air," ORNL-1565 (1953).
3. E. A. Gulbransen and K. F. Andrew, To be published.
4. D. A. Vermilyea, *This Journal*, **102**, 207, (1955); *ibid.*, **104**, 537 (1957).
5. A. E. Jenkins, *J. Inst. Met.*, **82**, 215 (1953-54).
6. K. Hauffe, "Oxydation von Metallen und Metallegierungen," pp. 200-204, Springer-Berlin (1956).
7. W. Hartmann, *J. Physik.*, **102**, 709 (1936).
8. W. McKewan and W. M. Fassel, Jr., AECU, 1918; "Corrosion Handbook," H. H. Uhlig, Editor, pp. 720-721, John Wiley & Sons, New York (1948).
9. G. Brauer, *Z. anor. u. allgem. Chem.*, **248**, 1 (1941).

# Higher Oxides of Silver

**William S. Graff**[1]

*American Machine & Foundry Company, Raleigh, North Carolina*

**and**

**Hans H. Stadelmaier**

*Department of Engineering Research, North Carolina State College, Raleigh, North Carolina*

ABSTRACT

Samples of higher oxides of silver were prepared by several chemical and electrochemical procedures. Two distinct higher oxides were produced. The first, argentic oxide, AgO, is a black powder and has a monoclinic structure for which lattice constants are derived. There is no evidence of the existence of other crystalline forms of AgO. The second oxide, with silver in a valence state higher than plus two, is present in some preparations along with AgO. The stoichiometry was not determined. It is also black and has a face-centered cubic lattice. It decomposed to AgO gradually over a period of months.

The only commonly recognized silver oxide is $Ag_2O$. Its existence and crystal structure have been definitely established.

The existence of a higher oxide with silver in the plus two state appears to be definitely established (1-10). Silver oxide with silver in the plus two state is sold to the battery industry by Merck and Company under the trade name of "Divasil." The structure of the divalent oxide has not been established conclusively. McMillan (11) reported AgO to be monoclinic and isomorphous with Tenorite (CuO), and he proposed lattice constants based on powder analysis. On the other hand Conn (12) reported that AgO exhibited three crystalline modifications: cubic, face-centered cubic, and orthorhombic.

The existence of even higher oxides of silver, notably $Ag_2O_3$, has been reported (10, 13-22). The only structure information is that reported by Braekken (23), who claimed that $Ag_2O_3$ is face-centered cubic and reported lattice constants for preparations from several silver salts. However, this information is clouded by the reports of Zvonkova and Zdanov (24) and Swanson, Fuyat, and Ugrinic (25) who claim that preparations yielding diffraction data indentical with Braekken's are silver peroxynitrate ($Ag_7NO_{11}$).

## Experimental

Samples of higher silver oxides were prepared by the following methods:

1. *Reaction of potassium peroxydisulfate with silver nitrate.*—The procedure essentially duplicates that described by deBoer (18) and Jirsa (20) except that the reaction was carried out between 80°-90°C.

2. *Anodic oxidation of silver perchlorate-perchloric acid solution.*—A spiraled platinum wire anode and cathode were used. The anode was rotated at 60 rpm. A plastic bucket was installed underneath the anode to catch the sample. The cathode was surrounded by a Coors porous porcelain cup to prevent silver from treeing to the anode. Ranges of bath concentrations (from 0.4 to 5.3*N* $AgClO_4$ and from 0.005 to 4.7*N* $HClO_4$), anode current densities (from 0.6 to 185 amp/dm$^2$), and bath temperatures (from 2° to 28°C) were investigated in an unsuccessful attempt to grow large single crystals. Only fine black powder samples (minus 150 mesh) could be formed. The samples were washed in 25°C water followed by air drying at 55°C for 1 hr. During initial washing the samples gave off some gas with a faint chlorine odor but presumably consisting mainly of adsorbed oxygen.

3. *Anodic oxidation of silver fluoride-hydrofluoric acid solution.*—The apparatus described above was used except that a sheet polyethylene shield was used instead of the Coors cup. The samples contained considerably coarser particles than those formed with the perchlorate bath. The coarsest particles were obtained with a bath concentration of 9.0*N* AgF and 0.75*N* HF, an anode current density of 1 amp/dm$^2$, and a bath temperature of 29°C. Microscopic examination evidenced a fraction of larger crystals (up to 0.8 mm) with octagonal symmetry plus a fraction of fine black powder. In some cases the larger crystals were joined together to build up dendritic structures. The dendrite branches always formed at 90° to the stem with a fourfold symmetry

[1] Present address: International Business Machines Corporation, Poughkeepsie, New York.

Table I. Argentic oxide samples powder diffraction data

| Reaction of $K_2S_2O_8 + AgNO_3$ | | Anodic oxidation of perchlorate bath | | Boiled sample from anodic oxidation nitrate bath | | Surface of overcharged silver plaque | | Merck & Co. "Divasil" | | Accepted values | | | Observed | Calculated | |
|---|---|---|---|---|---|---|---|---|---|---|---|---|---|---|---|
| $2\theta$ | $I/I_0$ | $2\theta$ | $I/I_0$ | $2\theta$ | $I/I_0$ | $2\theta$ | $I/I_0$ | $2\theta$ | $I/I_0$ | $2\theta$ | d | $I/I_0$ | $\sin^2\theta$† | $\sin^2\theta$† | hkl |
| 30.30° | 3 | — | — | — | — | 30.30° | 3 | — | — | 30.30° | 2.950 | 3 | 0.0682 | 0.0681 | 110 |
| 32.15 | 52 | 32.30° | 80 | 32.15° | 60 | 32.10 | 49 | 32.15° | 60 | 32.15 | 2.783 | 65 | 0.0765 | 0.0764 | 200 |
| 32.40 | 100 | 32.45 | 100 | 32.30 | 100 | 32.35 | 100 | 32.35 | 100 | 32.35 | 2.768 | 100 | 0.0775 | 0.0776 | $\bar{1}11$ |
| 34.25 | 34 | 34.40 | 41 | 34.25 | 31 | 34.25 | 46 | 34.30 | 35 | 34.25 | 2.618 | 32 | 0.0866 | 0.0866 | 002 |
| 37.30 | 80 | 37.30 | 77 | 37.25 | 65 | 37.25 | 75 | 37.30 | 88 | 37.25 | 2.414 | 80 | 0.1018 | 0.1020 | 111 |
| 39.55 | 29 | 39.60 | 22 | 39.45 | 29 | 39.50 | 47 | 39.50 | 35 | 39.50 | 2.281 | 32 | 0.1140 | 0.1142 | $\bar{2}02$ |
| 52.55* | 10 | 52.75 | 8 | 52.55 | 6 | 52.65 | 9 | 52.55* | 7 | 52.55* | 1.740 | 8 | 0.1960 | 0.1960 | 020 |
| 54.05 | 19 | 54.00 | 21 | 53.95* | 17 | 54.00 | 16 | 53.95* | 20 | 53.95* | 1.698 | 20 | 0.2058 | 0.2060 | $\bar{3}11$ |
| 54.80 | 11 | 54.80 | 8 | 54.80* | 8 | 54.85 | 10 | 54.80* | 11 | 54.80* | 1.673 | 10 | 0.2118 | 0.2118 | 202 |
| 56.75* | 19 | 56.80 | 22 | 56.80* | 16 | 56.85 | 21 | 56.75* | 17 | 56.80* | 1.621 | 18 | 0.2268 | 0.2264 | $\bar{1}13$ |
| 62.95* | 11 | 62.90* | 18 | 62.90* | 9 | 62.90 | 9 | 62.95 | 11 | 62.90* | 1.476 | 11 | 0.2722 | 0.2724 | 220 |
| 63.80* | 11 | 63.60* | 16 | 63.80 | 7 | 63.90 | 11 | 63.75* | 10 | 63.75* | 1.459 | 12 | 0.2789 | 0.2792 | 311 |
| 64.20* | 11 | 64.20* | 18 | 64.20* | 8 | 64.30 | 8 | 64.20* | 9 | 64.20* | 1.449 | 9 | 0.2824 | 0.2826 | 022 |
| 65.65 | 4 | 65.90 | 11 | 65.70* | 3 | ——— | | 65.80* | 6 | 65.80* | 1.418 | 7 | 0.2950 | 0.2946 | $\bar{4}02$ |
| 66.40 | 8 | 66.40 | 11 | ——— | | | | 66.30* | 7 | 66.35* | 1.408 | 7 | 0.2994 | 0.2996 | 113 |
| 67.05 | 10 | 67.05 | 11 | | | | | 67.05* | 14 | 67.05* | 1.395 | 14 | 0.3050 | 0.3056 | 400 |
| 67.70 | 6 | 67.80 | 14 | | | | | 67.60* | 9 | 67.65* | 1.384 | 8 | 0.3099 | 0.3102 | $\bar{2}22$ |
| 69.45* | 4 | 69.50* | 8 | | | | | 69.50* | 3 | 69.50* | 1.351 | 4 | 0.3249 | 0.3252 | $\bar{2}04$ |
| 72.15 | 4 | ——— | | | | | | 72.20 | 4 | 72.10* | 1.309 | 4 | 0.3463 | 0.3464 | 004 |
| 79.50 | 3 | | | | | | | 79.40* | 4 | 79.40* | 1.206 | 4 | 0.4080 | 0.4078 | 222 |
| 86.50 | 3 | | | | | | | 86.40* | 3 | 86.45* | 1.125 | 3 | 0.4690 | 0.4696 | $\bar{1}31$ |

Notes:
* Cu $K\alpha_1$ lines. † All positions converted to Cu $K\alpha_1$.

around the stem. The samples were washed in 25°C water followed by air drying at 55°C for 1 hr. During initial washing most samples gave off a small amount of odorless gas, presumably adsorbed oxygen.

4. *Anodic oxidation of silver nitrate-nitric acid solutions.*—The apparatus described in 2 above was used. The electrolyte used for the first preparation was that given by Noyes (10) (1.5*N* $AgNO_3$ and 1.5*N* $HNO_3$). The largest crystals were obtained with the $HNO_3$ reduced to 0.75*N*, an anode current density of 0.4 amp/dm$^2$, and a bath temperature of 2°C. Samples were washed in 25°C water followed by drying over $P_2O_5$. Microscopic examination indicated the same type of crystal formations as obtained from the fluoride bath except that the dendritic growth did not have simple 90° symmetry. A portion of one sample was heated in a water bath for 2 hr at 98°-100°C to attempt the decomposition to AgO reported in the literature (1, 2, 10). The sample remained black. Under the microscope, however, it was observed that the once hard single crystals, while still in the same shape, had transformed to fine powder easily broken apart.

5. *Anodic oxidation of porous sintered silver in potassium hydroxide solution.*—Three porous sintered silver plaques were prepared by pasting a mixture of $Ag_2O$ and water on a silver screen and firing in air at 425°C for 20 min followed by pressing. The resultant plaques were 24.2 cm$^2$ x 0.61 mm thick and contained 4.15-4.19 g of porous sintered silver. The plaques were anodized in 5% KOH at 0.14 amp for 22 hr. They were then discharged at 25°C in 32% KOH at 1.00 amp to a cut-out at 1.00 v taken against a zinc reference electrode. Recharging followed at 0.10 amp. Two plaques were charged for 16.50 and 15.25 hr to 2.00 v. The third plaque was overcharged for a total of 27.75 hr to a charge voltage of 2.17 v. One of the plaques charged to 2.00 v was discharged again at 27°C in 32% KOH at 0.20 amp and delivered 1.66 amp-hr to a cut-out at 1.00 v. The other two were washed and dried over $P_2O_5$.

The samples were analyzed for total oxygen and total silver by thermally decomposing the oxide at 480°C to silver and determining oxygen by weight change. Samples were dried to constant weight over $P_2O_5$. It is to be noted that this procedure does not necessarily constitute a complete and accurate analysis since additional analyses for other possible constituents (e.g., nitrogen or fluorine) were not included.

X-ray diffraction powder patterns and, where possible, single crystal rotation patterns were obtained using nickel filtered copper radiation.

## Results and Discussion

*Argentic oxide,* AgO.—Preparations 1, 2, 4 (after boiling in water for 2 hr), and 5 gave an identical and unique powder diffraction pattern. Merck and Company's "Divasil" also gave the same powder pattern.

No $Ag_2O$ lines were present in any of the patterns. The sintered silver plaque charged to 2.00 v contained some weak silver lines; the plaque charged to 2.17 v evidenced a pure pattern of the oxide.

The relative line intensities for all the samples appear to be in good agreement (*see* Table I). Therefore, it is considered that the pattern is singular and is not a mixture of two or more individual oxides. It is to be noted that three extra trace lines appeared at 19.2°, 29.2°, and 33.7° 2 $\theta$ for some of the samples. These lines can be accounted for by postulating the

Table II. Higher silver oxide powder diffraction data

| Anodic oxidation of fluoride bath | | | Anodic oxidation of nitrate bath | | | Swanson, *et al.* (25) data Anodic oxidation of nitrate bath | | | Assigned hkl |
|---|---|---|---|---|---|---|---|---|---|
| Obs. *d* | Calc. *a* | $I/I_0$ | Obs. *d* | Calc. *a* | $I/I_0$ | Obs. *d* | Calc. *a* | $I/I_0$ | |
| Å | Å | | Å | Å | | Å | Å | | |
| 5.66 | 9.80 | 31 | 5.70 | 9.87 | 10 | 5.73 | 9.92 | 10 | 111 |
| 4.90 | 9.80 | 16 | 4.94 | 9.83 | 3 | 4.96 | 9.92 | 6 | 200 |
| 3.47 | 9.80 | 25 | 3.49 | 9.86 | 3 | 3.498 | 9.894 | 4 | 220 |
| 2.96 | 9.80 | 6 | — | | — | 2.980 | 9.884 | 2 | 311 |
| 2.836 | 9.824 | 100 | 2.855 | 9.890 | 100 | 2.856 | 9.893 | 100 | 222 |
| 2.457 | 9.828 | 80 | 2.472 | 9.888 | 32 | 2.474 | 9.896 | 45 | 400 |
| 2.254 | 9.825 | 20 | 2.27 | | 12 | 2.270 | 9.895 | 12 | 331 |
| 2.19 | | 3 | — | | — | 2.213 | 9.897 | 4 | 420 |
| 2.00 | | 3 | 2.02 | | 3 | 2.019 | 9.891 | 3 | 422 |
| 1.90 | | 2 | — | | — | 1.903 | 9.888 | 2 | 511, 333 |
| 1.740 | 9.843 | 89 | 1.747 | 9.883 | 30 | 1.749 | 9.894 | 42 | 440 |
| 1.66 | | 5 | — | | — | 1.672 | 9.892 | 4 | 531 |
| 1.641 | 9.846 | 5 | — | | — | 1.649 | 9.894 | 4 | 600, 442 |
| 1.56 | | 2 | 1.56 | | 1 | 1.564 | 9.892 | 1 | 620 |
| 1.50 | | 1 | 1.50 | | 5 | 1.508 | 9.892 | 1 | 533 |
| 1.483 | 9.837 | 66 | 1.491 | 9.900 | 14 | 1.491 | 9.890 | 37 | 622 |
| 1.42 | | 2 | | | | 1.428 | 9.893 | 15 | 444 |
| 1.378 | 9.841 | 6 | | | | 1.385 | 9.891 | 2 | 711, 551 |
| 1.36 | | 3 | | | | 1.372 | 9.894 | 2 | 640 |
| 1.32 | | 2 | | | | 1.322 | 9.893 | 1 | 642 |
| 1.28 | | 2 | | | | 1.288 | 9.892 | 3 | 731, 553 |
| 1.230 | 9.840 | 5 | | | | 1.237 | 9.896 | 7 | 800 |
| 1.20 | | 3 | | | | 1.209 | 9.896 | 2 | 733 |
| 1.19 | | 3 | | | | — | | — | 820, 644 |
| 1.150 | 9.834 | 3 | | | | — | | — | 822, 660 |
| 1.13 | | 30 | | | | 1.1425 | 9.894 | 1 | 751 |
| 1.1261 | 9.817 | 20 | | | | 1.1348 | 9.893 | 14 | 662 |
| 1.0988 | 9.837 | 20 | | | | 1.1062 | 9.894 | 9 | 840 |
| Av lattice spacing, *a* | 9.834±0.009 | | | 9.890±0.006 | | | 9.893±0.003 | | |

formation of a trace surface film of $Ag_2CO_3$ during air drying.

It was not possible to index the pattern as tetragonal, hexagonal, or orthorhombic (using the Lipson method). The pattern was indexed by trial and error using the monoclinic structure of Tenorite (CuO) as a starting point. The observed and calculated $\sin^2\theta$ values are compared in Table I. Their agreement is excellent with most differences less than 0.0002 and with no greater difference than 0.0006. The calculated line positions establish the following monoclinic lattice constants for the oxide:

$$a = 5.842\text{Å} \qquad c = 5.487\text{Å}$$
$$b = 3.480\text{Å} \qquad \beta = 107° 27'$$

This indexing confirms that of McMillan (11).

The chemical analyses for total oxygen in the samples are as follows: boiled sample from anodic oxidation of nitrate bath, $AgO_{1.05}$; anodic oxidation of perchlorate bath, $AgO_{1.15}$, $AgO_{1.18}$; reaction of $K_2S_2O_8$ and $AgNO_3$, $AgO_{1.09}$; Merck and Co. "Divasil", $AgO_{1.005}$, $AgO_{1.01}$. These results indicate fairly close agreement with the formula AgO. The excess above the stoichiometric ratio could be due to absorbed salts, excess oxygen in the lattice, and/or a small amount of higher silver oxide that did not show up in the diffraction pattern.

This compound has variously been referred to as an oxide and a peroxide. Yost (14) reported that the structure was not a peroxide since it did not give a hydrogen peroxide reaction when dissolved in acid. It can be added to this evidence that the electrical capacity of the charged sintered silver plaque (1.66 amp-hr for 4.17 g of Ag) is equivalent to 80% of the theoretical capacity based on a plus two valence state. Hence, the plus one state is impossible, and the compound cannot be a peroxide. The oxide, therefore, is AgO, argentic oxide, and not $Ag_2O_2$, silver peroxide, as it has often been referred to in the literature.

*Higher silver oxide.*—Preparations from the anodic oxidation of the silver fluoride and silver nitrate baths gave powder diffraction patterns that were mixtures of the AgO pattern and another pattern which will be tentatively referred to as a higher silver oxide.

Rotation patterns of the large crystals described above were identical for rotations in three mutually perpendicular axes, thus establishing cubic symmetry. The first and third layer lines were very weak. The extra pattern in the powder samples was then readily indexed as face-centered cubic. Table II summarizes our powder data for this higher oxide. The data is identical with that reported by Braekken (23) for $Ag_2O_3$, and with that reported by Zvonkova (24) and Swanson (25) for $Ag_7NO_{11}$.

Three points should now be considered. First, Braekken's work and our work present evidence that the same structure is obtained regardless of the salt contained in the anodizing bath, i.e., whether or not nitrogen compounds are present. Second, the powder diffraction pattern for a sample prepared from the nitrate bath evidenced a small but definite amount of separately crystallized $AgNO_3$. Third, Noyes (10)

established by solubility measurements that a complex of silver oxide and silver nitrate (e.g., $Ag_7NO_{11}$) existed in solution; however, this should not be considered to establish the fact that the same complex or compound exists after precipitation and drying. Both Zvonkova (24) and Swanson (25) did not perform chemical analysis of their samples, but followed Noyes (10) preparation and assumed his analysis to hold for their precipitates. On the basis of these considerations it is postulated that on formation at the anode, and/or on drying, the anode product is converted to a higher silver oxide, and that in the case of the nitrate bath, as a consequence of the intermediate nitrate complex, a measurable amount of $AgNO_3$ is absorbed.

A series of powder diffraction patterns was obtained for these samples to investigate aging effects. The data are often inconsistent because the large crystal size of the higher oxide fraction presented preferred orientation difficulties. The samples were not ground to a smaller particle size because it was thought that the higher oxide, and possibly AgO, would suffer some decomposition. It can be stated qualitatively that over a five month period of storage at 22°-30°C the higher oxide decomposed to some extent with a resultant increase in AgO. As mentioned above, there was complete decomposition to AgO after 2 hr of heating in water at 98°-100°C. There was no evidence of line shifting in either the higher oxide or the AgO patterns with aging, indicating no range of solid solubility of oxygen in the lattices.

It is now of interest to consider the stoichiometry of this higher oxide. This task is made difficult by the fact that AgO was present in all the samples regardless of variations in bath composition and concentration, temperature, and current density. Jirsa (3) reported the same difficulty. The total oxygen analyses for the preparations ranged between $AgO_{1.52-1.67}$ for aging up to one month, and $AgO_{1.23-1.33}$ for aging between 4½ to 5½ months. Therefore, even though the stoichiometry of the higher oxide cannot be determined, it appears that the silver is in a higher valence state than plus two.

## Summary

Argentic oxide, AgO, was prepared by several different procedures resulting in all cases in a black powder that gave a unique powder diffraction pattern. This pattern was indexed to establish monoclinic symmetry and cell dimensions. These results confirm the work of McMillan and tend to reject the possibility that AgO exists in other crystalline modifications. Crystals of AgO suitable for single crystal diffraction studies could not be prepared.

The anodic oxidation of both silver fluoride and silver nitrate baths gave samples that were a mixture of AgO and another substance, sometimes present as fairly large (0.8 mm) single crystals. This other substance has a face-centered cubic lattice with very weak first and third layer lines. It is concluded that the substance is a higher silver oxide with silver in a valence state higher than plus two. Unfortunately the exact stoichiometry could not be determined. The substance is evidently not $Ag_7NO_{11}$ as proposed by other investigators (24, 25) since it can also be prepared from a silver fluoride bath. This oxide decomposes to AgO slowly (longer than five months) at normal temperatures but within 2 hr in 98°-100°C water.

## Acknowledgment

One of the authors (W. S. Graff) wishes to thank Professor R. Maddin, Acting Director of the School of Metallurgical Engineering of the University of Pennsylvania, for his guidance and encouragement; Mr. H. F. Bauman, associated at present with Armour Research Foundation, for his advice concerning the chemical preparations; and the Raleigh Laboratory of the American Machine and Foundry Company for making available laboratory facilities for portions of this work.

Manuscript received Sept. 25, 1957. This paper is based on a thesis submitted by W. S. Graff to the Faculty of the School of Metallurgical Engineering of the University of Pennsylvania in partial fulfillment of the requirements for the M.S. degree in metallurgical engineering.

Any discussion of this paper will appear in a Discussion Section to be published in the June 1959 issue of the JOURNAL.

## REFERENCES

1. O. Sulc, *Z. anorg. Chem.*, **12**, 89 (1896).
2. E. R. Watson, *J. Chem. Soc.*, **89**, 578 (1906).
3. F. Jirsa, *Chem. Listy*, **19**, 3 (1925).
4. F. Jirsa, *Z. anorg. u. allgem. Chem.*, **158**, 33 (1926).
5. F. Jirsa and J. Jelinck, *ibid.*, **158**, 61 (1926).
6. A. A. Noyes, *et al.*, *J. Am. Chem. Soc.*, **57**, 1221 (1935).
7. A. A. Noyes, *et al.*, *ibid.*, **57**, 1229 (1935).
8. A. A. Noyes, *et al.*, *ibid.*, **57**, 1238 (1935).
9. A. A. Noyes, *et al.*, *ibid.*, **59**, 1316 (1937).
10. A. A. Noyes, *et al.*, *ibid.*, **59**, 1326 (1937).
11. J. A. McMillan, *Acta Cryst.* (abstract), **7**, 640 (1954).
12. J. B. Conn, Abstracts, 8th Annual Battery Research and Development Conference (Signal Corps Engineers Labs.) Asbury Park, N. J. (1954).
13. P. C. Austin, *J. Chem. Soc. Trans.*, **99**, 262 (1911).
14. D. M. Yost, *J. Am. Chem. Soc.*, **48**, 152 (1926).
15. G. A. Barbieri, *Ber.*, **60B**, 2427 (1927).
16. G. A. Barbieri, *Atti accad. Lincei*, **13**, 882 (1931).
17. P. C. Carman, *Trans. Faraday Soc.*, **30**, 574 (1934).
18. J. H. deBoer and J. Van Ormondt, British Pat. 579, 817, Aug. 16, 1946.
19. F. Jirsa, *Chemie (Prague)*, **3**, 4 (1947).
20. F. Jirsa, *Czech. Chem. Communs.*, **14**, 445 (1949).
21. G. A. Barbieri and A. Malaguti, *Atti accad. nazl. Lincei*, **8**, 619 (1950).
22. A. Malaguti, *Ann. chim.*, **41**, 241 (1951).
23. H. Braekken, *Kgl. Norske Videnskab. Selskabs Forh.*, **7**, 143 (1935).
24. Z. V. Zvonkova and G. S. Zdanov, *Zhur. Fiz. Khim*, **22**, 1284 (1948).
25. H. E. Swanson, R. K. Fuyat, and G. M. Ugrinic, *Nat. Bur. Standards Circ. 539*, Vol. IV (1955).

# Protection of Molybdenum from Oxidation at Elevated Temperatures

**Dwight E. Couch, Harold Shapiro, John K. Taylor, and Abner Brenner**

*National Bureau of Standards, Washington, D. C.*

ABSTRACT

Molybdenum may be protected against oxidation at 1100°C by composite coatings of chromium and nickel. Adhesion of chromium to molybdenum was obtained by anodically etching the molybdenum in a solution of sulfuric and phosphoric acids (1:1 by volume) before plating.

Chromium was deposited from a conventional chromic acid bath operated at 75°-80°C and at a current density of 120 amp/dm$^2$. A coating consisting of 0.001 in. of chromium followed by 0.007 in. of nickel protected molybdenum at 980°, 1100°, and 1200°C for 1200, 500, and 100 hr, respectively. Shot peening and ball milling of the coatings did not increase their life. Oxidation and diffusion phenomena were studied to explain ultimate failure of the coatings, and both mechanisms are shown to be contributing causes.

The engineer and metallurgist have in molybdenum a material possessing high strength at elevated temperatures. The chemical nature of this metal, however, precludes its use under oxidizing conditions. The work reported here was an attempt to protect molybdenum from oxidation by electroplating it with composite coatings of chromium and nickel.

Alloys of molybdenum with nickel or cobalt (1) form protective coatings of molybdates when oxidized at 900°-1000°C. However, these alloys are not satisfactory when thermocycling is necessary because of severe spalling of the molybdates. The addition of nickel or cobalt to molybdenum in percentages large enough to prevent oxidation also causes a loss in the hot strength of molybdenum. Molybdenum-chromium alloys with as much as 36% chromium have been studied (2) but were not recommended for use above 980°C because of rapid oxidation. Cladding of molybdenum with nickel and nickel alloys was investigated by Bruckhart and Jaffee (3).

Korbelak (4) used chromium as an initial deposit and electrodeposited other metals on the chromium strike. Brenner (5) obtained adhesion by using a brass strike. Vaaler (6) reported that adhesion of the chromium to molybdenum was improved through the use of Murakami's etching solution (7). Whitfield (8) electrodeposited several metals on molybdenum but gave no procedure or indication of the degree of adhesion he obtained. Runck (9) has published a metallographic study of chromium-plated molybdenum.

## Experimental Methods

*Sample preparation.*—Fastening electrical leads to the molybdenum samples presented some difficulty since the sample failed at the point where the lead joined the molybdenum because of access of oxygen at these points. This difficulty was overcome by welding a nickel wire to a sharp tip of the molybdenum piece with Colmonoy[1] (*see* Fig. 1). The welded area was ground to give a smooth continuous metal surface so that subsequent plating operations completely covered this area with coating. The sharp edges of molybdenum left by shearing or machining operations were ground smooth to prevent treeing and edge buildup during plating. These samples were then degreased and the scale removed by anodic treatment in 70% sulfuric acid.

*Plating and adhesion.*—Preliminary studies showed that good adhesion of chromium to molybdenum could be obtained fairly consistently by the use of Murakami's etching solution. The etching time in this solution required rather careful control. If insufficiently etched, poor adhesion was obtained; however, if etching were extended to 10 min, a brown film formed on the molybdenum which prevented adhesion. Murakami's etching reagent was also prepared in a more dilute solution containing 100 g of potassium ferricyanide and 100 g of sodium

[1] Hard facing alloy purchasable from Wall Colmonoy Corp., 19345 John R St., Detroit, Mich.

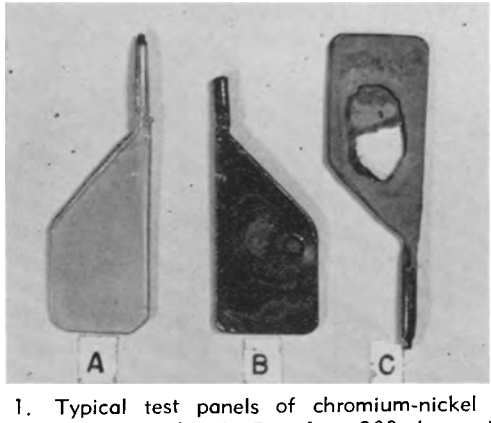


Fig. 1. Typical test panels of chromium-nickel plated molybdenum. A, as plated; B, after 300 hr, oxidation 1100°C; C, after 300 hr, oxidation 1100°C. The difference between B and C shows the variations in samples prepared under identical conditions. Magnification ¾X before reduction for publication.

hydroxide per liter and used at 80°-90°C. Agitation of the samples during the etching process tended to prevent formation of the brown films mentioned above and gave a clean, etched surface on the molybdenum. This solution was not satisfactory for cleaning alloys containing titanium because they formed more tenacious films when etched. After being etched, the samples were rinsed and plated with chromium.

A second method of preparation consisted of treating the samples anodically at 20-40 amp/dm$^2$ in 70% sulfuric acid for about 2-3 min. However, a blue film sometimes formed during rinsing which caused poor adhesion. Higher current densities in the anodic treatment usually prevented the formation of these films.

A third etching reagent that worked very well, even with alloys containing titanium, was prepared by using equal volumes of concentrated sulfuric and phosphoric acid. This solution gave a very satisfactory etch when samples were treated anodically in it at 2-10 amp/dm$^2$ for 2 to 3 min.

After etching by one of the procedures previously described, the samples were rinsed and plated with 25$\mu$ (1 mil) of chromium from a bath containing 250 g of $CrO_3$ and 2.5 g of sulfuric acid per liter. The chromium was electrodeposited under three different conditions. Low contraction chromium (10), plated at 80-120 amp/dm$^2$, at a temperature of 85°-95°C, gave excellent adhesion. Satisfactory adhesion was also obtained by plating bright chromium at 20-30 amp/dm$^2$, and at a temperature of 50°C. However, the chromium plated at low temperatures (25°C) gave poor coverage, and the adhesion was not satisfactory. Deposits made under these conditions tended to crack and peel from the molybdenum. This cracking was eliminated by initiating deposition at a temperature (50°C) which produced bright chromium, then reducing the temperature after the samples had been plated for a few minutes.

After chromium plating, the samples were etched in 1:1 hydrochloric acid until the surface appeared gray, given a nickel strike (20-60 amp/dm$^2$ for 1-3 min) in an all-chloride strike bath, and then plated with nickel from an all-chloride or a Watts nickel bath. The samples were not rinsed between the strike and plating operation. This procedure gave very good adhesion, as was indicated by bending a specimen until it fractured. The break was nearly always within the molybdenum and not between the electrodeposited layers.

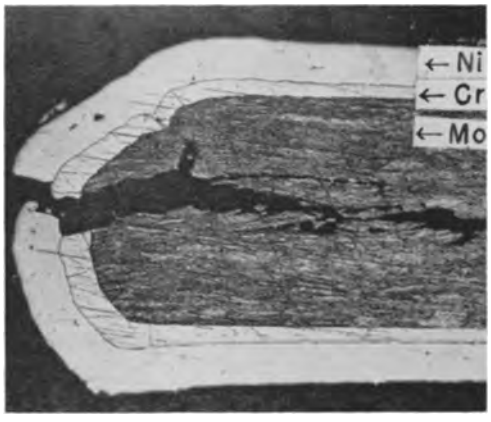


Fig. 2. Fracture of coating when heated to 900°C caused by discontinuities in the molybdenum sheet. Magnification 50X before reduction for publication.

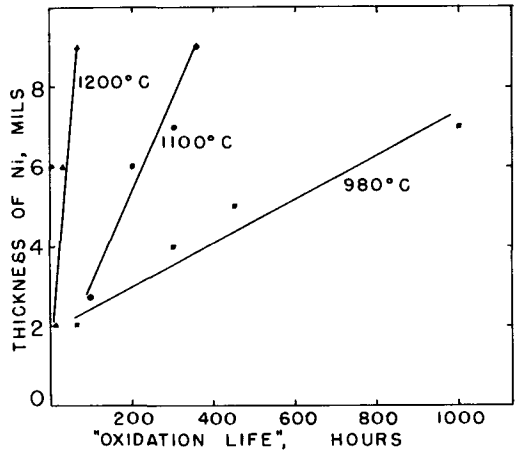


Fig. 3. Effect of temperature and nickel thickness on "oxidation life" of molybdenum plated with chromium and nickel.

*Inspection methods.*—The time to failure under oxidizing conditions is referred to hereafter as "oxidation life." It is the time the sample remains intact from the moment it is placed in the furnace, at temperature, to the first moment that molybdic oxide smoke is detected, or green nickel molybdate is observed. The early studies of the time to failure showed an appreciable amount of scattering. This led to the belief that there were flaws in the coating and a good inspection method prior to oxidation was needed.

Electrodeposited radioactive-chromium (11) was used as a possible method of detecting voids or inclusions in the nickel deposit. The chromium deposits were made from a bath that contained chromium 51 in concentrations of about 0.06 millicurie per milliliter. This method worked well and showed pores and voids in the nickel deposits when the deposits were less than 0.001 in. thick. However, with nickel thicknesses of 0.007 in., even visible pits did not produce sufficient contrast for the image to be seen.

The only satisfactory method of inspection found was to heat the plated panels in a helium or hydrogen atmosphere to 900°C, then carefully inspect them for cracks or blisters in the coating. A photomicrograph of a fracture caused by faulty molybdenum sheet is shown in Fig. 2.

## Results and Discussion

### *Effect of Coating Thickness and Temperature on Oxidation Life*

Figure 3 shows the relation between the thickness of nickel coating and the oxidation life of specimens tested at three different temperatures. The molybdenum was plated with 25$\mu$ (1 mil) of chromium prior to electrodepositing nickel. The samples tested at 1200°C oxidized very rapidly and even specimens coated with 225$\mu$ (9 mils) of nickel failed in less than 100 hr. Thus, it appeared that 1200°C was an excessive temperature for the study of these coatings.

Table I. "Oxidation lives" of molybdenum panels plated with chromium and chromium-nickel tested at 1100°C and thermocycled every 24 hr

| Exp. No. | No. of panels tested | Thickness Cr μ | Thickness Ni μ | Time to failure, hr Min | Time to failure, hr Max | Time to failure, hr Av | Comments |
|---|---|---|---|---|---|---|---|
| 1 | 4 | 60* | None | 20 | 20 | 20 | Low temperature chromium |
| 2 | 2 | 60 | None | 20 | 40 | 30 | — |
| 3 | 3 | 60 | None | 90 | 240 | 170 | Preheated 200 hr at 1100°C |
| 4 | 3 | 100 | None | 20 | 50 | 45 | Bright chromium |
| 5 | 3 | 120 | None | 20 | 70 | 55 | Low temperature chromium |
| 6 | 3 | 180 | None | 140 | 160 | 150 | Bright chromium |
| 7 | 10 | 220 | None | 40 | 600 | 330 | — |
| 8 | 3 | 25 | 60 | 40 | 240 | 130 | — |
| 9 | 6 | 25 | 120 | 170 | 350 | 250 | — |
| 10 | 37 | 25 | 170 | 120 | 640 | 360 | — |
| 11 | 9 | 25 | 200 | 160 | 700 | 350 | — |
| 12 | 3 | 25 | 220 | 300 | 360 | 340 | — |
| 13 | 4 | 100 | 100 | 160 | 160 | 160 | — |
| 14 | 4 | 100 | 170 | 400 | 920 | 780 | — |
| 15 | 4 | 220 | 170 | 540 | >800 | — | Test discontinued after 800 hr |
| 16 | 3 | 25 | 150 | 40 | 120 | 110 | Preheated 250 hr |
| 17 | 3 | 25 | 150 | 40 | 90 | 70 | Preheated 500 hr |

* Unless otherwise noted, all chromium deposits were prepared at 85°C, 100-120 amp/dm².

A temperature of 1100°C was chosen as a more practical condition for use in testing these coatings and was generally used in this investigation.

The oxidation lives of chromium-plated molybdenum, oxidized at 1100°C, were not reproducible. Some samples failed in less than 24 hr while others lasted several hundred hours. Table I shows the results for a series of panels plated with both chromium and nickel.

Generally, deposits 50μ (2 mils) or less in thickness failed in 20 hr or less, while deposits that were 220μ (9 mils) thick had widely different oxidation lives. Those samples that lasted over 50 hr usually had lives of several hundred hours. A chromium-molybdenum alloy forms at the interface and it may be that this alloy is a good oxidation barrier. To check this idea, a group of samples were chromium plated, and some of these were heated in an inert atmosphere at 1100°C for 200 hr before oxidation (experiments 2 and 3 of Table I). The controls had an average life of 30 hr while the preheated panels had an average life of 170 hr. This indicated the importance of forming the chromium-molybdenum diffusion alloy prior to oxidation.

Although chromium-plated molybdenum has desirable properties for the prevention of oxidation, if preheated prior to oxidation, one undesirable characteristic was noticed; after 2 or 3 thermocycles the chromic oxide usually scaled off in large flakes and exposed a bright chromium surface to further rapid oxidation.

The effect of the thickness of the composite chromium-nickel coating on the oxidation life of molybdenum panels is also shown in Table I.

Formation of a chromium-nickel alloy by heating the samples prior to oxidation had an adverse effect on the oxidation life (experiments 16 and 17, Table I). The type of chromium used to coat the molybdenum did not have a marked effect on the oxidation life of the panels (experiments 1, 2, 4, and 5, Table I). The low-contraction type of chromium was generally used because of its superior adhesion and covering power.

Table II. Results of oxidation tests of molybdenum panels plated with 1 mil of Cr and 7 mils of Ni

| No. of samples tested | Type Ni | Temp, °C | Oxidation life Min hr | Oxidation life Max hr | Oxidation life Av hr | Comment |
|---|---|---|---|---|---|---|
| 33 | Cl | 1100 | 70 | 360 | 150 | |
| 17 | W | 1100 | 210 | 760 | 320 | |
| 34 | Cl | 980 | 160 | >1200 | — | 3 unfailed after 1200 hr |
| 16 | W | 980 | 740 | >1200 | — | 13 unfailed after 1200 hr |

Cl—Nickel deposited from an all-chloride bath.
W—Nickel deposited from a Watts type of bath.

*Effect of Plating Conditions on Oxidation Life*

A large group of samples were prepared from molybdenum sheet 750μ (30 mils) thick. These samples, 2 x 5 cm in size, were plated with approximately 25μ (1 mil) of chromium and 175μ (7 mils) of nickel. After plating, the samples were oxidized at 980° or 1100°C in a laboratory furnace through which a slow stream of air was passed to remove the molybdic oxide that escaped from the samples which failed. The samples were thermocycled by removing them from the furnace and allowing them to cool to room temperature once every 24 hr.

Table II shows the results for 100 samples that were oxidized. The deposits from the Watts and chloride bath are shown separately in the table for the purpose of comparison. They were actually oxidized in random sequence to eliminate any differences arising from uncontrollable factors.

Panels plated under conditions that were known to give highly stressed deposits were the first to fail. Since the stress in the deposit is relieved by the heating used for inspection, it is not likely that the stress as such is a factor. However, the factors that cause high stress may also cause inclusions or other weaknesses in the deposit which could account for the early failures of these deposits. Weight gains due to oxidation were obtained for nickel electrodeposited from both the Watts and all-chloride-type baths. The results showed only small differences in oxidation rates and could not account for the differences in oxidation life that are shown in Table II.

Early failures may be due to "oxidation pathways" as illustrated in Fig. 4. Although only a small portion of the nickel deposit had been oxidized, the sample was almost ready to fail. Figure 5 is a more advanced case where the oxygen has actually reacted with the molybdenum leaving a shell of nickel around the void. Small holes of this type are usually filled with nickel molybdate.

Since molybdic oxide reacts with both nickel and nickel oxide to form nickel molybdate, the samples usually remain intact while in the furnace. However, when cooled, the nickel molybdate undergoes a transformation which causes violent spalling, thus rupturing the nickel oxide and laying open a hole where the molybdate had formed.

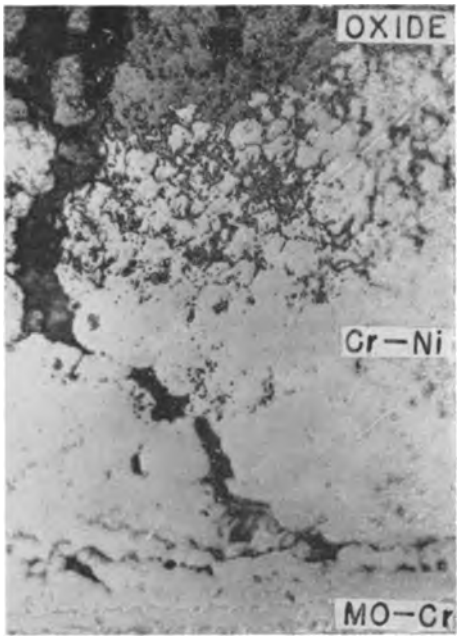


Fig. 4. Oxidation pathway through chromium-nickel coating. Magnification 500X before reduction for publication.

Typical failures are shown in Fig. 1B and 1C. Sometimes these failures could be detected in their early stages by the appearance of a small greenish spot on the outside of the black, adherent, vitreous nickel-oxide envelop. Occasionally, the nickel oxide cracked and flaked away from the sample and showed greenish areas beneath the scale.

*Diffusion Studies*

There was a possibility that the molybdenum diffusing out through these coatings would form a nickel-molybdenum alloy which would cause spalling when oxidized and thermocycled. To obtain a semi-quantitative measure of diffusion, two molybdenum bars, about ½ in. in diameter and 2 in. in length, were turned in a lathe on true centers. These bars were then plated with 25-50$\mu$ (1-2 mils) of chromium and 250-300$\mu$ (10-12 mils) of nickel, taking care to obtain uniform deposits. After plating, they were heated in hydrogen at 1100°C for 100 hr to permit diffusion of the metals, then returned to the lathe and a portion of the coating of each bar was turned off. The diameters of the bars were checked after each cut to insure that the turnings were coming from parallel layers. These lathe cuts were from 25 to 50$\mu$ (1-2 mils) per cut and were kept separate from each other for chemical analysis. Figure 6 shows the analysis of the coatings after 100 hr of diffusion, and Fig. 7 shows a photomicrograph of the bar.

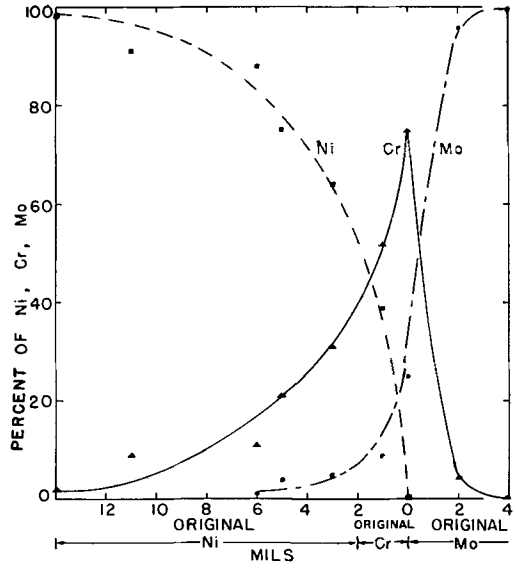


Fig. 6. Analysis of diffusion bar after heating 100 hr at 1100°C.

The remaining portion of one of these bars was again heated for a total of 600 hr at 1100°C. It was then machined as previously described, and a chemical analysis for all three components was made of these turnings. The results of the analysis are shown in Fig. 8.

The chromium was distributed throughout the region which originally consisted of two layers, one of nickel and one of chromium. Figure 8 also shows some diffusion into the molybdenum, but there was a sizable amount of molybdenum that diffused outward into the chromium-nickel alloy. X-ray analysis showed the existence of a nickel-molybdenum intermetallic compound, NiMo.

A photomicrograph of the second bar after heating for 600 hr is shown in Fig. 9. Apparently, the diffusion of the molybdenum into the chromium-nickel layer did not change its structure appreciably at

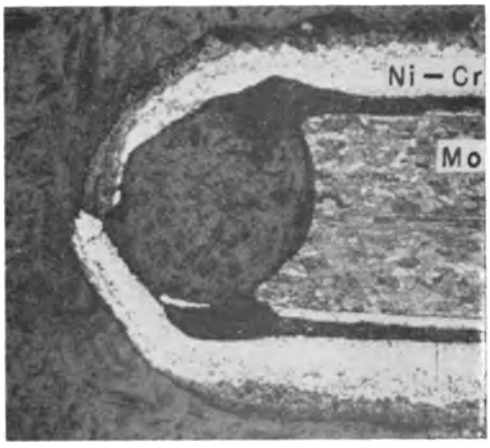


Fig. 5. Oxidation corrosion at edge of panel. Magnification 50X before reduction for publication.

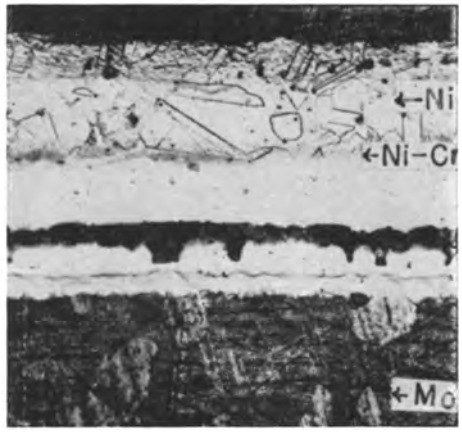


Fig. 7. Diffusion bar after heating 100 hr at 1100°C. Magnification 100X before reduction for publication.

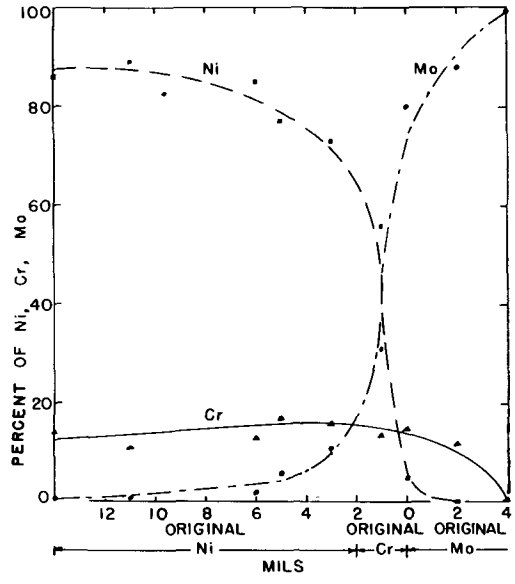


Fig. 8. Analysis of diffusion bar after heating 600 hr at 1100°C.

these concentrations. The chromium-molybdenum alloy is seen easily.

Since a wrought nichrome type of alloy is very resistant to oxidation, it was thought the formation of these alloys by heating, in an inert atmosphere, prior to oxidation would improve the protective value of the coating. To test this idea, a series of molybdenum panels were plated with 25$\mu$ (1 mil) of chromium and 175$\mu$ (7 mils) of nickel. Some of these were saved for control panels in the "as plated" condition; the others were heated for 250 and 500 hr at 1100°C in hydrogen. The results are included in Table I. Comparison of Exp. 16 and 17 with Exp. 9 and 10 shows that the formation by diffusion of these nickel-chromium-molybdenum alloys was detrimental to the life of the samples. This differs from the conclusions reached by Safranek and Schaer (12) who worked under somewhat different conditions. A rather loose oxide scale formed during oxidation and apparently permitted the oxidation to progress at a more rapid rate than would be expected from a parabolic law.

### *Effect of Mechanical Working*

Variations in the oxidation life observed for a group of specimens indicated that some flaws in the deposit allowed a direct access of the oxygen to the molybdenum and thus caused the early failures. It was thought that mechanical working of the deposit might improve it by causing some flow of the metal with a resultant closing of pores.

**Table III. Oxidation life of mechanically worked samples**

| Type of work performed on sample | Av life hr | Av life of unworked control hr |
|---|---|---|
| Shot peened | 262 | 275 |
| Heated to 1100°C then shot peened | 72 | 72 |
| Ball milled, 800°C in $H_2$ atm | 230 | 320 |

One group of plated panels was shot peened[2] using several different nozzle pressures and shot sizes. Another group of plated panels was ball milled in a 4-in. diameter steel ball mill rotated at 20 rpm and operated at 800°C in an atmosphere of hydrogen. The samples were hot worked in this way for 3 hr using ½ in. ceramic balls. Neither the peening nor the ball milling caused any significant increases in life (Table III). This showed that mechanical working of this type (ball milling and shot peening) did not affect the causes of oxidation failure.

### *Causes of Failure*

Metallographic examination and x-ray analysis of a series of specimens subjected to different periods of oxidation in air at 1100°C showed some interesting phenomena. Oxidation for 1 hr caused very little change in the samples except that the electrodeposited nickel and the molybdenum had recrystallized and some segregation of impurities had taken place at the grain boundaries of the nickel. By the end of 7 hr the nickel had started to show oxidation at the grain boundaries and a void had developed at the edge of the sample (Fig. 10). Continued oxidation and thermal cycling for from 50 to 150 hr caused a line of oxide inclusions to form such as that shown in Fig. 11. The time required for these oxides to develop was different for each sample. With nickel coatings 175$\mu$ (7 mils) thick, the inclusions could be seen as isolated spots after 50 hr and

[2] These samples were shot peened at the plant of the Pangborn Corporation, Hagerstown, Md.

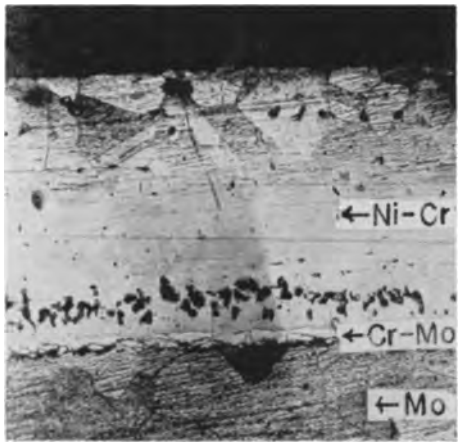


Fig. 9. Diffusion bar, after heating 600 hr at 1100°C. Magnification 100X before reduction for publication.

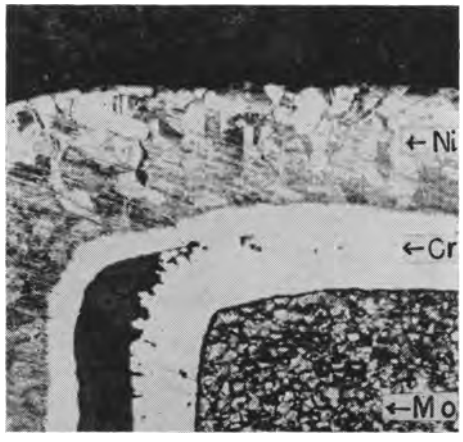


Fig. 10. Chromium-nickel-plated molybdenum panel after 7 hr of oxidation. Magnification 100X before reduction for publication.

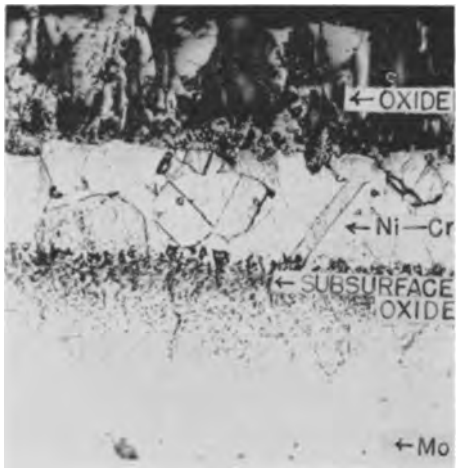


Fig. 11. Subsurface oxide shown as isolated areas after 100 hr of oxidation at 1100°C. Magnification 500X before reduction for publication.

had usually grown into a solid band of subsurface oxide after 100 to 150 hr of oxidation.

To study the cause of these three formations, i.e., subsurface oxide, grain-boundary oxidation, and edge separations, electroformed nickel sheet instead of molybdenum was plated with chromium and nickel and then oxidized and sectioned for examination. The specimens showed the same three formations that were noted with the molybdenum samples (Fig. 12). Thus, the molybdenum was not involved in any of these processes.

In other experiments, electroformed nickel sheets of two thicknesses, 150$\mu$ (6 mils) and 250$\mu$ (10 mils), were plated with 50$\mu$ (2 mils) of chromium and 150$\mu$ (6 mils) of nickel on only one side. These samples (Fig. 13B and 14B) show a series of inclusions in the area of the original chromium deposit. Similar inclusions noticed in the diffusion bar studies are shown in Fig. 7 and 9. Figure 13B shows the formation of the subsurface oxide on both sides of the original chromium layer. In the other case, Fig. 14B and 14C, the subsurface oxide is visible on one side only. The side consisting of the 20-mil thick nickel shows only isolated spots of oxide which increased in size and number with increased oxidation time.

The subsurface oxide was not detected in samples that were heated in hydrogen or helium. These

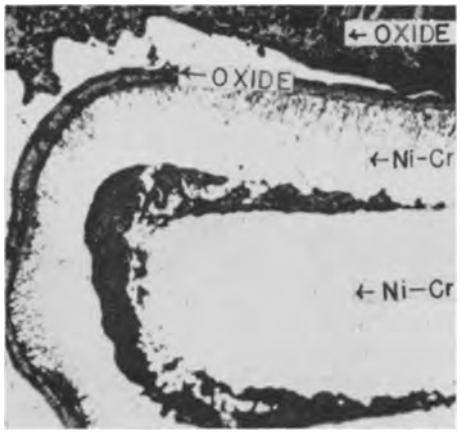


Fig. 12. Effects of 300 hr of oxidation on nickel-chromium-nickel sample.

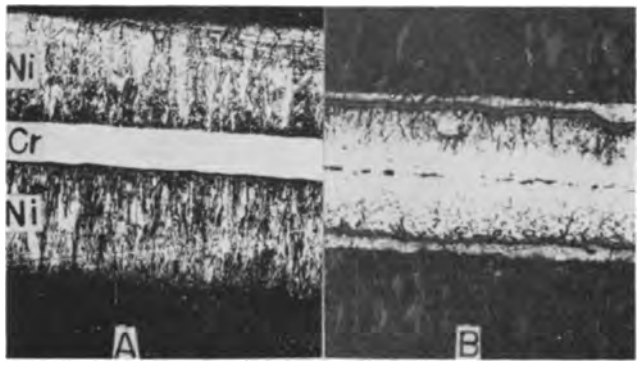


Fig. 13. Electrodeposited nickel-chromium nickel. A, as deposited; B, after 100 hr of oxidation at 1100°C. Magnification 100X before reduction for publication.

oxides were associated with atmospheric oxidation and were not a result of inclusion within the nickel deposit. Apparently, this subsurface oxide layer was caused by oxidation of the chromium-nickel alloy formed by diffusion, the oxygen either coming from dissolved oxygen in the nickel or along grain boundaries. According to Zima (13) chromium-nickel alloys that contain less than 10% chromium oxidize more rapidly than either pure nickel or alloys with over 10% chromium. The subsurface oxide layer formed through much thicker layers of nickel if it was over a curved surface. Grain boundary oxidation was also more severe at curved edges. The fact that the subsurface oxide forms at the chromium diffusion front was also demonstrated by the use of an etching solution for nickel. It etched the structure down to the subsurface oxide but not below, thus showing the alloy to be low in chromium above the subsurface oxide layer and rich in chromium below this layer (Fig. 11).

### *Comparisons of Actual and Theoretical Oxidation Life*

It was of interest to compare the actual life of the plated panel with the oxidation rates of nickel given in the literature (14-16).

Table IV shows the oxidation rates of various types of nickel, reported in the literature, and those obtained in this laboratory. The maximum oxidation

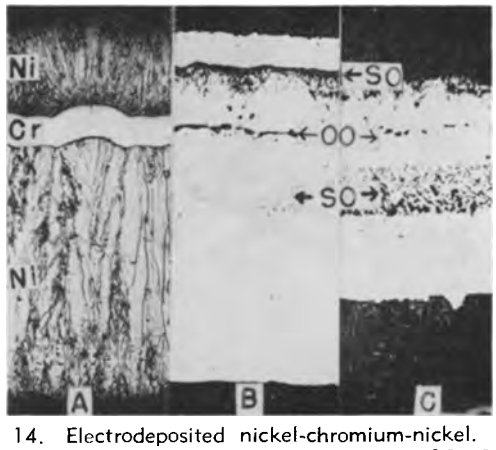


Fig. 14. Electrodeposited nickel-chromium-nickel. A, as deposited; B, after 70 hr of oxidation at 1100°C; C, after 300 hr of oxidation at 1100°C. In Band C, the subsurface oxide is shown as "SO" while the occluded oxide is marked "OO". Magnification 100X before reduction for publication.

Table IV. Oxidation rate constants of nickel ($K_p$)

| Kind of Ni | Temp of oxidation, °C | $K_p$ $g^2/cm^4/sec$ |
|---|---|---|
| 1. All-chloride bath as plated | 1100 | $8.9 \times 10^{-10}$ |
| 2. As 1 but cold rolled 10% reduced | 1100 | $20 \times 10^{-10}$ |
| 3. As 1 but cold rolled 50% reduced | 1100 | $8.1 \times 10^{-10}$ |
| 4. Wrought rod | 1100 | $24 \times 10^{-10}$ |
| 5. As plated Watts cobalt-free | 1100 | $7.6 \times 10^{-10}$ |
| 6. Carbonyl (14) | 1100 | $2.2 \times 10^{-10}$ |
| 7. Foil (15) | 1100 | $0.17 \times 10^{-10}$ |
| 8. Commercial (16) | 1100 | $1.6 \times 10^{-10}$ |

life at 1100°C of molybdenum panels coated with 25$\mu$ (1 mil) chromium and 175$\mu$ (7 mils) nickel was about 600 hr. This is reasonably close to the value of 560 hr calculated from the data for electrodeposited nickel (No. 1, 2, 3, and 5, Table IV). By using oxidation data reported in the literature (No. 6, 7, and 8, Table IV) an expected life of 2200 to 45,000 hr was obtained. These literature values were obtained from relatively short oxidation times, while that obtained in this work was for 100 to 200 hr of oxidation.

### Acknowledgments

The authors express their appreciation to the Navy Department, Bureau of Aeronautics, for financial support of the project and for permission to publish the results.

Manuscript received Nov. 15, 1957.

Any discussion of this paper will appear in a Discussion Section to be published in the June 1959 JOURNAL.

REFERENCES

1. J. W. Spretnak and R. Speiser, ONR Contract N6onr 22582, NR 039-005 Report 13, Project 467, Ohio State University.
2. H. D. Kessler and M. Hansen, *Trans. Am. Soc. Metals*, **42**, 1008 (1950).
3. W. L. Bruckhart and R. I. Jaffee, *ibid.*, **44**, 176 (1952).
4. A. Korbelak, *Tech. Proc. Am. Electroplaters' Soc.*, **40**, 90 (1953).
5. S. S. Brenner, *Plating*, **43**, 1143 (1956).
6. L. E. Vaaler, C. A. Snavely, and C. L. Faust, U.S. Atomic Energy Report BMI 813, April 1, 1953.
7. "Metals Handbook," p. 1140, Am. Soc. for Metals, Cleveland, Ohio (1948).
8. M. G. Whitfield, U. S. Pat. 2,682,101, June 29, 1956.
9. R. J. Runck, *This Journal*, **104**, 74 (1957).
10. A. Brenner, P. Burkhead, and C. J. Jennings, *J. Research Natl. Bur. Standards*, **40**, 31 (1948).
11. R. H. Wolff, M. A. Henderson, and S. L. Eisler, *Plating*, **42**, 537 (1955).
12. W. H. Safranek and G. R. Schaer, *Proc. Am. Electroplaters' Soc.*, **43**, 105 (1956).
13. G. E. Zima, Contract N6onr 24430, Proj. NR 031-355 7th tech report, Calif. Inst. Tech. April 1956, ASTIA No. 92520.
14. S. F. Frederick and I. Cornet, *This Journal*, **102**, 285 (1955).
15. W. J. Moore and J. K. Lee, *Trans. Faraday Soc.*, **48**, 916 (1956).
16. A. Preece and G. Lucas, *J. Inst. Metals (London)*, **20**, 219 (1952).

# Temperature Dependence of Fluorescence of Tin-Activated Orthophosphates

**Richard W. Mooney**

*Chemical and Metallurgical Division, Sylvania Electric Products Inc., Towanda, Pennsylvania*

ABSTRACT

Apparatus for measuring the temperature dependence of fluorescence is described. The variation of fluorescent intensity with temperature as a function of tin-activator concentration is given for the systems: strontium-zinc orthophosphate and strontium-calcium orthophosphate. In both cases, the quenching temperature is independent of activator concentration. The results are interpreted in terms of Johnson and Williams' theory of fluorescent quenching.

With the increasing use of phosphors in high-pressure mercury vapor lamps, it has become necessary to increase our knowledge of the properties of these phosphors at the elevated temperatures to which they are exposed during normal operation. One of the most important properties of such phosphors is the temperature dependence of fluorescence or the manner in which the fluorescent efficiency of the phosphor varies with temperature. This property has been measured for many phosphor systems that respond to the wave lengths present in the high-pressure mercury vapor arc and, in at least two cases, the variation of temperature dependence of fluorescence with activator concentration has been studied in some detail (1, 2). In both cases, the higher activator concentrations caused a decrease in the quenching temperature, i.e., the temperature at which the relative fluorescent efficiency begins to decrease.

Recently, it has been shown that certain tin-activated alkaline earth orthophosphate phosphors fluoresce efficiently under high-pressure mercury vapor arc excitation (3, 4), and therefore a study of the temperature dependence of fluorescence of these phosphors was undertaken. The object of the present study was to develop a method of measurement which would give reproducible results and to use this method to determine the efficiencies of these

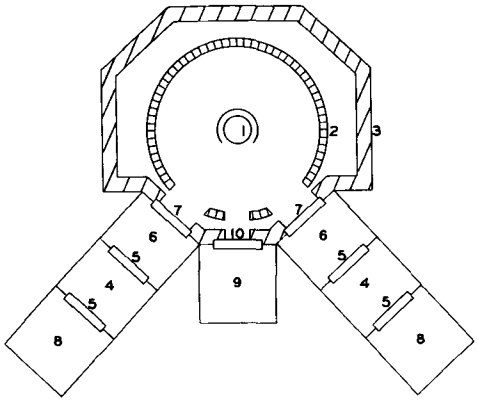


Fig. 1. Schematic diagram of apparatus for measuring temperature dependence of fluorescence.

phosphors at high temperatures. The results have been interpreted in terms of the Johnson and Williams theory of fluorescent quenching (5).

### Apparatus and Method of Measurement

To measure the temperature dependence of fluorescence, one must be able to heat the phosphor at a controlled rate while measuring its light emission. The obvious problems in obtaining meaningful measurements are (*a*) keeping the rate of heating constant, (*b*) excluding all other light from the apparatus, and (c) maintaining the intensity of ultraviolet irradiation constant.

A schematic diagram of the apparatus for making these measurements is shown in Fig. 1. The phosphor is held in a small quartz cylinder, 1, located in the center of an oven, 2. Excessive heat loss is prevented by insulating the entire heating assembly consisting of the oven and associated strip heaters with magnesia blocks, 3. Ultraviolet excitation is furnished by Sylvania G4T4 lamps (254 m$\mu$) or other suitable u.v. lamps located as shown, 4. The excitation is filtered by Corning 9863 glass filters, 5, to remove visible light. The lamps are separated from the oven by an insulating chamber, 6, to lower the amount of heat radiation reaching them. A Vycor filter, 7, at the front of this chamber adjacent to the oven also helps to cut down heat transfer. The output of the u.v. lamps is monitored by 1P28 photomultipliers, 8, while the fluorescence of the phosphor sample is picked up by a 1P21 photomultiplier, 9, located as shown. Colored filters, 10, may be inserted between the sample and the 1P21 photomultiplier.

With the phosphor sample in place and all equipment warmed up, the current through the G4T4 tubes is adjusted to slightly above the minimum operating value for each lamp. Successive readings of each of the three photomultiplier tubes are then made on a photometer (Photovolt Model 520-M). The readings of the 1P28 monitor tubes are set approximately equal and the fluorescence reading is adjusted to give a mid-scale reading on the photometer. The current through the heaters is gradually increased to maintain a rate of heating of approximately 2°C/min. Periodic temperature readings are taken on a L&N potentiometer with an iron-constantan thermocouple imbedded in the phosphor sample. The u.v. outputs of the G4T4's are monitored by the 1P28's and maintained at their room temperature values by adjustment of lamp currents. Readings of temperature and relative fluorescence of the phosphor sample are recorded.

When a dependent variable such as fluorescent efficiency is measured while an independent variable such as temperature is being varied continually, the correctness of labeling the results as true equilibrium data naturally arises. However, for true equilibrium data it would be necessary to use an infinitely slow rate of heating or to make point by point measurements. A compromise is normally arrived at, and in this case the relatively slow heating rate of 2°C/min was chosen. A check on the heating rate was conducted by following the fluorescent efficiency on both a heating and a cooling curve on several different phosphors. The greatest discrepancy was found at the highest temperatures where, when the heat was removed from the sample, the phosphor cooled very rapidly. In this region the relative efficiency varied from heating to cooling curve by as much as 5 to 7%. The difference in the measured values decreased with decreasing temperature, becoming approximately zero at room temperature.

Most of the measurements reported herein were made under 254 m$\mu$ excitation obtained from germicidal lamps due to the ease of operation of these lamps in the equipment. However, in the application of these phosphors, the exciting source is the high pressure mercury vapor arc with strong u.v. line emission at 313 and 365 m$\mu$. Therefore, some measurements of temperature dependence of fluorescence were carried out using the radiation from a high-pressure mercury vapor arc lamp as the exciting medium. The data so obtained were in substantial agreement with those obtained under 254 m$\mu$ radiation and reported herein.

Relative efficiency data at room temperature were obtained on plaque testers of the type described by Butler and Mooney (6).

### Experimental Results

In order to check the results obtained with this instrument, the temperature dependence of fluorescence of calcium halophosphate and magnesium tungstate was determined. The data so obtained were in agreement with previous measurements on the same phosphors made by Jerome (7).

A survey of the high temperature fluorescent properties of known phosphor systems was then conducted during which it was found that tin-activated calcium orthophosphate phosphors modified by strontium or barium (8) maintain or improve their room temperature efficiencies up to temperatures of about 270°C (543°K). With the calcium strontium orthophosphate system, these measurements were made with the phosphor in an atmosphere of helium, water vapor, air, and in vacuum, with the same result in all cases. Unfortunately, these tin-activated calcium orthophosphate phosphors do not respond to the wave lengths present in the high-pressure mercury vapor arc. However, an investigation of other tin-activated orthophosphates by Thomas and Butler (3) uncovered several sys-

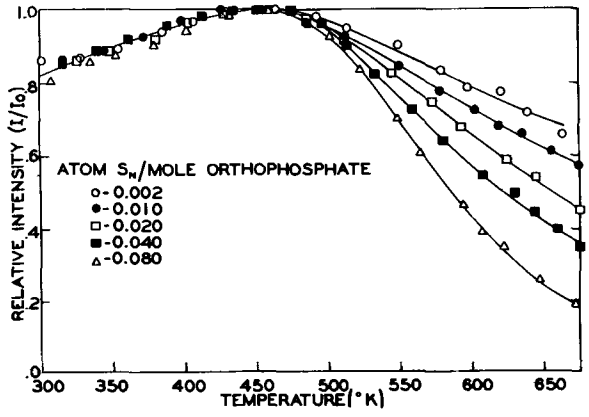


Fig. 2. Variation of fluorescent intensity with temperature for tin-activated strontium-zinc orthophosphate. Excitation $\lambda = 254$ mμ.

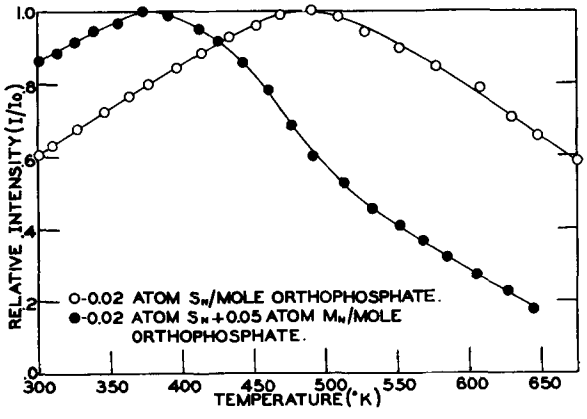


Fig. 4. Effect of Mn on the variation of fluorescent intensity with temperature for tin-activated strontium-calcium orthophosphate. Excitation $\lambda = 254$ mμ.

tems which were highly efficient under high-pressure mercury vapor arc excitation. The temperature dependence of fluorescence of some of these systems was investigated in detail, especially as regards the manner in which this property varies with activator concentration. Results on two of the systems studied are reported below.

*Tin-activated strontium-zinc orthophosphate.*—This phosphor has the approximate composition $Sr_{2.65}Zn_{0.20}(PO_4)_2$. It has been shown that the spectral energy distribution of the emission is dependent upon the wave length of excitation (3, 4). Thus when exposed to 254 mμ, the phosphor has a main emission band at about 600 mμ and a weaker band at about 390 mμ. When excited by 313 mμ the weak emission band at 390 mμ disappears, and the phosphor emits solely in the orange-red with negligible emission below 500 mμ. Therefore, the phosphor emission color when excited by the wave lengths present in the high-pressure mercury vapor arc lamp is largely orange-red with a very small blue component from the 254 mμ line.

The temperature dependence of fluorescence under 254 mμ excitation was measured for phosphors having activator concentrations of 0.002, 0.005, 0.01, 0.02, 0.04, and 0.08 gram-atoms Sn per gram-mole of the orthophosphate as given above. With the exception of the data for the phosphor containing 0.005 gram-atom Sn, the results are shown graphically in Fig. 2. The data for 0.005 gram-atom Sn were omitted due to their close proximity to the 0.002 gram-atom Sn data. All measurements were made using a Corning 3-76 filter, which absorbs 90% or more of the wave lengths below 540 mμ, in position 10, Fig. 1. Therefore, only the temperature dependence of fluorescence of the main emission band at 600 mμ was measured. Some of the measurements were checked using a Corning 3-72 sharp-cut type of filter with a wave-length "cut" (37% transmittance) equal to 460 mμ with identical results. An inspection of Fig. 2 shows that up to a temperature of 460°K the experimental results are independent of activator concentration. Above this temperature, however, an increase in the activator concentration causes a decrease in the relative intensity of fluorescence. It should be noted that the temperature at which quenching begins is independent of activator concentration.

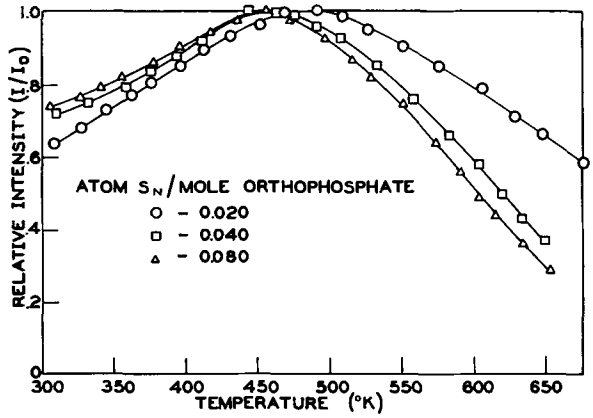


Fig. 3. Variation of fluorescent intensity with temperature for tin-activated strontium-calcium orthophosphate. Excitation $\lambda = 254$ mμ.

*Tin-activated strontium-calcium orthophosphate.*—This phosphor has the approximate composition $Sr_{2.40}Ca_{0.45}(PO_4)_2$. It has approximately the same response to 254 mμ and 313 mμ excitation as the tin-activated strontium-zinc orthophosphate phosphor described above. The variation of fluorescent intensity as a function of temperature was measured for phosphors having Sn concentrations of 0.02, 0.04, and 0.08 gram-atoms Sn per gram-mole of the orthophosphate as given above. The fluorescent emission was filtered by a Corning 3-77 filter which absorbs 90% or more of the wave lengths below 470 mμ. Results are shown graphically in Fig. 3. It is apparent that, although the relative intensity at 500°K and above falls off rapidly with increasing activator concentration, the temperature at which quenching begins is again independent of the Sn concentration.

The addition of Mn to this system as a secondary activator shifts the emission toward the red, and for phosphor applications in high-pressure mercury vapor lamps, an increase in red emission is very desirable. Unfortunately, however, the addition of manganese adversely affects the high temperature fluorescence as shown in Fig. 4 which compares the temperature dependence of fluorescence of a strontium calcium orthophosphate containing 0.02 gram-atom Sn per gram-mole of orthophosphate to one

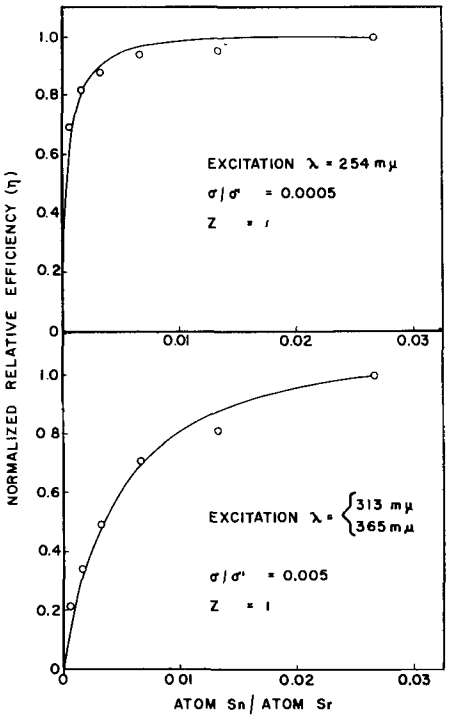


Fig. 5. Relative efficiency vs. activator concentration at 25°C (298°K).

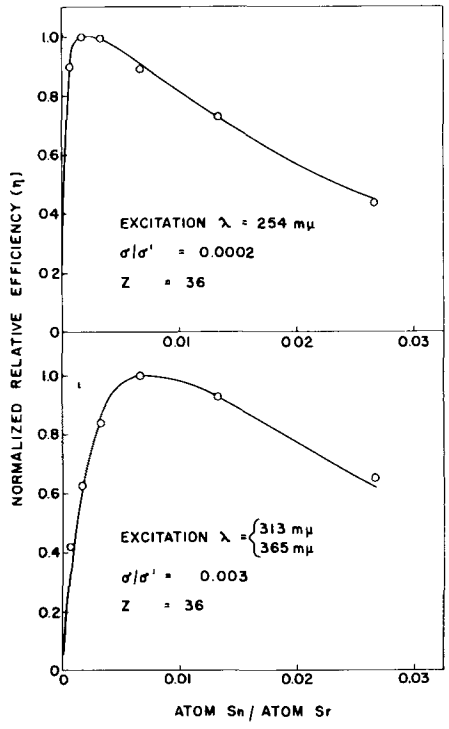


Fig. 6. Relative efficiency vs. activator concentration at 377°C (650°K).

containing 0.02 gram-atom Sn plus 0.05 gram-atom Mn per gram-mole of orthophosphate. The addition of manganese causes a marked lowering of the temperature at which quenching occurs, and therefore the red emission would not be improved at the operating temperatures of high-pressure mercury vapor lamps. The results shown in Fig. 4 were obtained using a Corning 3-72 filter (wave-length "cut" equal to 460 mμ) in position 10, Fig. 1.

## Discussion

The efficiency of emission of a phosphor as a function of temperature will depend on the effectiveness with which the absorbed energy can be protected from loss by thermal dissipation. Any interaction of the atoms comprising the "luminescent center" with another "luminescent center" increases the probability of a nonradiative dissipation of energy and quenching of the emission becomes likely. Therefore, it would be expected that an increase in the concentration of "luminescent centers," i.e., activators, would increase the probability of quenching.

Johnson and Williams (5) have derived an expression for the efficiency as a function of activator concentration which has the form

$$\eta = \frac{c(1-c)^z}{c + (\sigma/\sigma')(1-c)} \qquad [1]$$

where $c$ is the total mole fraction of activator and $\sigma/\sigma'$ and $z$ are adjustable parameters. The parameter $\sigma/\sigma'$ is the ratio of the capture cross sections of nonactivators to the capture cross sections of luminescent activators, while the parameter $z$ is defined as the number of lattice positions surrounding a given activator such that, if any one of these sites is occupied by another activator, luminescence is quenched.

By selecting appropriate values of $\sigma/\sigma'$ and $z$, Eq. [1] may be fitted to the room temperature efficiency vs. activator concentration data for the $Sr_{2.65}Zn_{0.20}(PO_4)_2$ phosphor under 254 mμ and high-pressure mercury vapor arc excitation (*see* Fig. 5). In Fig. 5, and also in Fig. 6, the activator concentration is expressed as atom Sn per atom of Sr rather than as mole fraction in order to maintain the original definition of $z$ in terms of lattice sites, in this case Sr sites, that could be occupied by Sn.

It is apparent from the experimental data that the efficiency as a function of Sn concentration varies with the type of excitation with the higher energy excitation (254 mμ) producing higher efficiencies at low activator concentrations. However, in both cases, the $z$ value which gives the best fit is 1, in agreement with the prediction that $z$ is independent of the type of excitation at a given temperature (5). The $\sigma/\sigma'$ values which best fit the data are 0.0005 for 254 mμ excitation and 0.005 for high-pressure mercury vapor excitation.

Efficiency vs. activator concentration data may be calculated from the information given in Fig. 2 and 5 for any temperature up to about 675°K (398°C). The data plotted in Fig. 6 for a temperature of 377°C were arrived at in this manner. At this temperature the shift of peak efficiency toward lower activator concentrations with increasing energy of excitation is readily observable. Once again, the curves which gave the best fit to the data had the same $z$ value, namely 36. The $\sigma/\sigma'$ values are approximately the same as before, i.e., 0.0002 for 254 mμ excitation and 0.003 for high-pressure mercury vapor arc excitation. Thus in agreement with theory, temperature has a relatively negligible effect on the $\sigma/\sigma'$ values for a given type of excitation. It is interesting that a slight trend toward lower $\sigma/\sigma'$ values with increasing temperature is found in both cases.

The theory advanced by Johnson and Williams predicts an increase in the $z$ value with increasing temperature, and it is apparent that this system behaves as expected going from a $z$ value of 1 at room temperature to a $z$ value of 36 at 377°C. The number of Sr atoms surrounding another Sr atom in the $Sr_3(PO_4)_2$ lattice may be calculated from the crystal structure work of Zachariasen (9). These values, corresponding to successively larger predicted values of $z$, are 6, 8, 14, 20, 32, 38, 50, etc. Exact agreement of the experimentally determined value of $z$ with one of these calculated values would not be expected.

The experimental values of $z$ are, however, qualitatively very interesting. The $z$ value of 1 obtained at room temperature would imply that two Sn-activator atoms would have to be nearest neighbors at a separation of 3.97Å before concentration quenching were possible. At the activator concentrations used in this study this would be extremely unlikely. This conclusion is substantiated further by the data plotted in Fig. 2 where the relative intensity of fluorescence as a function of temperature is not affected by changes in activator concentration up to a temperature of about 460°K (187°C). Even at 377°C, the $z$ value has only increased to 36. The calculated radius of a sphere containing 32 Sr atoms surrounding another is 6.8Å, while the radius of a sphere containing 38 Sr atoms is 7.4Å. However, the maximum activator concentration used, i.e., 0.080 atom Sn per mole of $Sr_{2.65}Zn_{0.20}(PO_4)_2$, corresponds to a Sn-Sn distance of 13.1Å assuming random distribution of activator atoms in a $Sr_3(PO_4)_2$ unit cell volume of 181.8Å$^3$ (9). A separation of 13.1Å corresponds to a $z$ value between 170 and 182. Therefore, the experimental $z$ value of 36 would still not give concentration quenching. It is evident, however, both from the efficiency data and the data on temperature dependence of fluorescence that concentration quenching is taking place especially at elevated temperatures. Therefore, the definition of the parameter $z$ given by Johnson and Williams does not appear to be strictly applicable to this system.

It is interesting to compare the present results to those of Klasens (2), who measured the temperature dependence of fluorescence of $6MgO \cdot As_2O_5$ at various Mn activator contents. It would appear that two different processes are operating since Klasens' curves are shifted to lower temperatures with increasing Mn content, whereas, for the tin-activated phosphors, the quenching temperature seems to be independent of the activator concentration. The data are similar in that in both cases increasing activator concentrations cause the efficiency to drop at high temperatures. The falling portions of the temperature dependence curves at high temperatures were analyzed by Klasens in terms of the well-known quenchng formula

$$\eta = \frac{1}{1 + \frac{s}{A} e^{-E/kT}} = I/I_o \qquad [2]$$

giving values of $E$, the height of the energy barrier for the radiationless process for activator atoms separated by the finite distance $r$. The values of $E$ so obtained fitted the equation

$$E = E_o(1 - e^{-ar}) \qquad [3]$$

also due to Johnson and Williams (5) if $E_o$, the height of the energy barrier for the radiationless process at infinite dilution of activator, were set equal to 1.45 e.v. and $a$ equal to 0.075. Equation [3] is obtained by assuming that the activation energy for the radiationless process in the activator center is lowered by the presence of a second activator in the close vicinity and that the amount of this energy lowering is approximately proportional to the overlap integral for the wave functions of the interacting activators. It is obvious that Eq. [3] must give decreasing values of the energy barrier $E$ for decreasing distance $r$ between activator centers.

Table I

| Sn | Av Sn-Sn distance (Å) | $Sr_{2.65}Zn_{0.20}(PO_4)_2$ $E$ (eV) | ln ($s/A$) |
|---|---|---|---|
| 0.002 | 45.0 | 0.36 | 5.9 |
| 0.010 | 26.3 | 0.37 | 6.2 |
| 0.020 | 20.9 | 0.41 | 7.3 |
| 0.040 | 16.6 | 0.46 | 8.5 |
| 0.080 | 13.1 | 0.58 | 11.6 |

If, for purposes of comparison, the data for the strontium-zinc orthophosphate phosphors are analyzed by Eq. [2], values of $E$, and ln ($s/A$) may be determined. These values are tabulated in Table I for each of the activator concentrations in the strontium-zinc orthophosphate system. The use of Eq. [2] to analyze the temperature dependence data on strontium-zinc orthophosphate is rigorously inappropriate since it has been shown experimentally that concentration quenching is taking place. However, the analysis gives a direct comparison to Klasens' (2) data taken over the same range of concentration.

The average Sn-Sn distance was calculated as before, assuming random distribution of activator atoms. In order to check the fit of these parameters to the original data, the values of $E$ and $\ln(s/A)$ for $Sr_{2.65}Zn_{0.20}(PO_4)_2$ were used to calculate values of $I/I_o$ as a function of 1/T. The logarithm of the calculated value of $I/I_o$ is plotted as a function of the reciprocal of the absolute temperature in Fig. 7, together with the experimental points. The fit of the curves to the data is quite good, especially at the higher temperatures.

However, although the experimental data on temperature dependence of fluorescence of $6MgO \cdot As_2O_5$:Mn and $Sr_{2.65}Zn_{0.20}(PO_4)_2$:Sn may both be equally well fitted to Eq. [2] over approximately the same range of activator concentrations, the meaning of the resulting values of $E$ is open to question. In one case, $E$ decreases with decreasing $r$ whereas in the other, $E$ increases with decreasing $r$. Therefore, the fit of the $E$ values for Klasens' data to Eq. [3] is thought to be fortuitous since a corresponding analysis of the data for the tin-activated phosphors would give $E$ values varying in exactly the opposite manner from that predicted by Eq. [3].

Summarizing, analysis of the efficiency data in terms of Eq. [1] yields values of $z$ and $\sigma/\sigma'$ which

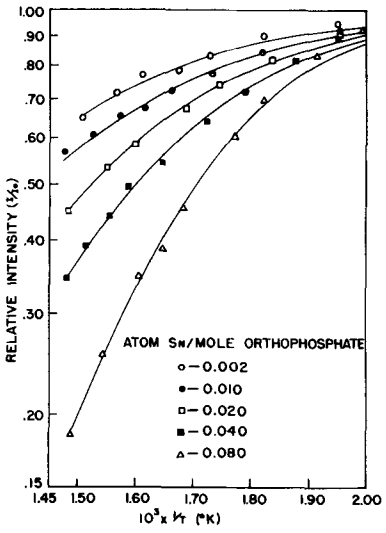


Fig. 7. The fit of the experimental data to the equation $I/I_o = 1/\left(1 + \frac{se^{-E/kT}}{A}\right)$ using the values of the parameters E and ln $\frac{s}{A}$ given in Table I for tin-activated strontium-zinc orthophosphate.

vary qualitatively in accordance with the predictions made by Johnson and Williams (5). Quantitatively, however, the derived values of $z$ are not in accord with the experimental results since the $z$ values are too small to explain the concentration quenching that is observed. The results are also compared to Klasens' data on $6MgO \cdot As_2O_5$ by the use of Eq. [2] for thermal quenching, although the use of this equation to interpret the data is not strictly appropriate since it has been shown that concentration quenching is taking place simultaneously. However, the comparison leads one to doubt the experimental verification of Eq. [3] claimed by Klasens in view of the widely differing trends of the $E$ values. It is evident that further theoretical and experimental studies of concentration and thermal quenching of fluorescence are necessary in order to develop a consistent theory of fluorescent quenching for all phosphor systems.

### Acknowledgment

The author is indebted to Dr. K. H. Butler for many helpful discussions in the course of this work and to the late Dr. E. F. Lowry for advice and encouragement. Thanks are also due to Dr. M. J. B. Thomas who supplied the phosphor samples.

Manuscript received Jan. 6, 1958. This paper was prepared for delivery before the Washington Meeting, May 12-16, 1957.

Any discussion of this paper will appear in a Discussion Section to be published in the June 1959 JOURNAL.

REFERENCES

1. G. R. Fonda, *J. Phys. Chem.*, **43**, 561 (1939).
2. H. A. Klasens, *Philips Res. Repts.*, **9**, 377 (1954).
3. M. J. B. Thomas and K. H. Butler, Paper presented at the ECS Washington Meeting, May 12-16, 1957.
4. M. J. B. Thomas, K. H. Butler, and J. M. Harris, *Illuminating Eng.*, **52**, 279 (1957).
5. P. D. Johnson and F. E. Williams, *J. Chem. Phys.*, **18**, 1477 (1950).
6. K. H. Butler and R. W. Mooney, *Sylvania Technologist*, **9**, 121 (1956).
7. C. W. Jerome, *This Journal*, **98**, 376 (1951).
8. K. H. Butler, *ibid.*, **100**, 250 (1953).
9. W. H. Zachariasen, *Acta Cryst.*, **1**, 263 (1948).

# Electron Traps and the Electroluminescence Brightness and Brightness Waveform

**Frederick F. Morehead, Jr.**

*Lamp Development Department, Lamp Division, General Electric Company, Nela Park, Cleveland, Ohio*

ABSTRACT

This work describes an investigation of the effect of temperature, voltage, and rise time on the size and shape of the brightness waves of electroluminescence; sawtooth and square pulse voltage waveforms were used to excite copper-activated ZnS phosphors in a slightly conducting medium. A model is proposed which accounts for the major features of the experiments. Electrons which have been ionized from a region of high field are trapped in another part of the phosphor particle. A field opposite in polarity to that which produced the ionization serves to sweep the conduction electrons, which are at every instant in thermal equilibrium with the traps, back into the high field region where the electrons recombine, with radiative emission. The model is successfully applied to measurements of the average electroluminescence brightness for sinusoidal excitation of a binderless phosphor layer as a function of temperature, frequency, and voltage.

Several authors have already noted in the interpretation of their experiments a connection between electronic trapping levels in ZnS phosphors and the temperature and frequency dependence of electroluminescent brightness (1-4). Neumark (5) has shown that electrons released from traps during thermoluminescence greatly enhance the d-c electroluminescence of some ZnS single crystals. Thornton (6) accounts for the shape of brightness waves produced by sinusoidal excitation on the basis of field-controlled thermal release of electrons from traps.

Although there is disagreement in the details of the various theoretical treatments in the above references, the most general consensus is the following. Electrons which originate either from trapping or donor levels or from collision-ionized emission centers are swept by the field from a region of high field into a region of low field, where they are subsequently trapped. Light emission then depends on the release of the electrons from these traps in the bulk of the phosphor particle and their return to the region from which they were ionized where recombination with the ionized emission centers occurs. A change in temperature or frequency will change the number of electrons which return and recombine per half-cycle. It is then the rate of release of electrons from trapping levels in the bulk of the phosphor particle that accounts for the major details of the temperature and frequency dependence of the electroluminescent emission of ZnS:Cu phosphors at temperatures below thermal quenching.

Notable exceptions to this point of view are those published by Johnson, Piper, and Williams (2), and Zalm (4). A change in temperature is thought to affect the number of electrons which are thermally released during one half-cycle from the region in which the high, ionizing field is produced and hence alters the configuration of the field in that region.

It is the purpose of this paper to describe experimental results that support the former picture at least in a particular temperature range, and to supply from these results the important details of this process.

## Experimental Technique

Glow curves and measurements of the temperature dependence of electroluminescence brightness and the brightness waveform were made in a vacuum-enclosed apparatus similar in structural details to that described by Johnson and Williams (7). For the electroluminescence measurements, a conducting glass plate held the phosphor layer against the heated copper block with an electrode separation of about 50$\mu$. Electrical contact was made to the conducting glass plate through an insulated thimble in the copper block. Temperature measurements were made with a copper-constantan thermocouple in the copper block.

Measurements of the brightness waveform were performed on phosphors imbedded in a slightly conducting medium, tricresyl phosphate, so that the average field across the phosphor was approximately equal to and in phase with the average field applied to the cell (8). The conductivity of the tricresyl phosphate decreases with decreasing temperature, making the above approximation less valid at the lowest temperatures. One set of measurements of electroluminescence brightness as a function of temperature, frequency, and voltage was performed on a binderless layer of the phosphor with the same apparatus. A Corning filter No. 3389 was used in front of a 1P21 photomultiplier to change the response of the photomultiplier to be more nearly uniform to green and blue light.

The output of the photomultiplier tube was either displayed together with the exciting voltage on a Tektronix 532 dual trace oscilloscope, read with a Keithley electrometer, model 210, or in the case of glow curve measurements, fed into a L&N X-Y recorder. The sawtooth and pulsed voltages were generated with various combinations of Tektronix series 160 units and amplified by a d-c amplifier which has a rise time of less than 5 $\mu$sec and which can be driven to an output of 700 v peak to peak. Sine waves were generated by a Hewlett Packard wide range oscillator.

## Experimental Results

When a repetitive d-c pulse is applied to a cell in which the phosphor (ZnS,ZnO:Cu,Cl) is imbedded in the slightly conducting medium, the light emission shown in Fig. 1 results (8). Almost no light is produced when the field is applied; the great bulk of the emission occurs when the field is removed. If another d-c pulse is added to the repetitive pattern in the opposite direction, as shown in Fig. 2, much greater light emission occurs, most of it when the field, positive or negative, is applied. The amount of light emitted when the field is removed is the same as that for the case of the single polarity pulsing, about 1/20 of the total for alternate polarity pulsing.

Note that this experiment differs from a similar one reported by Zalm (8) in which the brightness waveform and light output of a square-wave d-c field applied to a phosphor suspended in tricresyl phosphate are compared with that produced by a square-wave a-c field of the same peak to peak value and frequency. Thus the size of the ionizing field for the a-c case in Zalm's experiment is only half that for the d-c square wave. In our experiment the ionizing field is the same in both cases.

These observations suggest not only that recombination and light emission is delayed by one half-cycle following the ionization process (8) but also that most of the recombination occurs only when facilitated by a field opposite in sign to that field which produced the ionization. Obviously, a given voltage pulse will perform both of the two functions, ionizing and untrapping, but with respect to different active portions of phosphor particles which are nearer to the negative and positive electrodes, respectively.

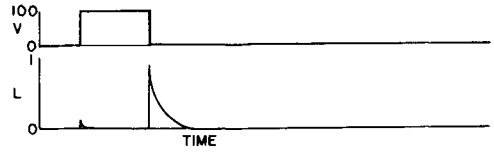


Fig. 1. Brightness waveform resulting from single polarity repetitive pulsing (ZnS,ZnO:Cu,Cl).

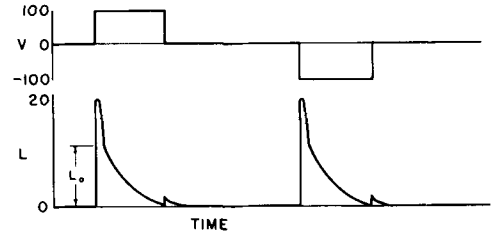


Fig. 2. Brightness waveform resulting from alternate polarity repetitive pulsing (ZnS,ZnO:Cu,Cl).

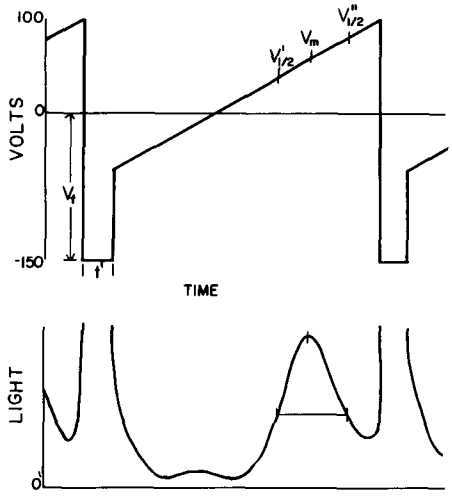


Fig. 3. Brightness waveform produced by the pulse and sawtooth voltage waveform (ZnS:Cu,Al).

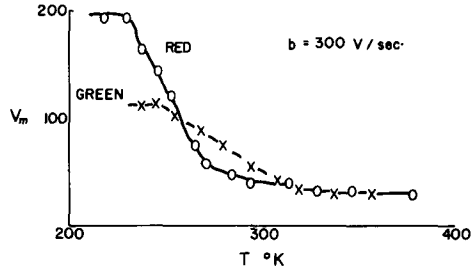


Fig. 4. The voltage of maximum light emission $V_m$ as a function of temperature for two phosphors, ZnS:Cu,Al (green) and ZnS:Cu (red).

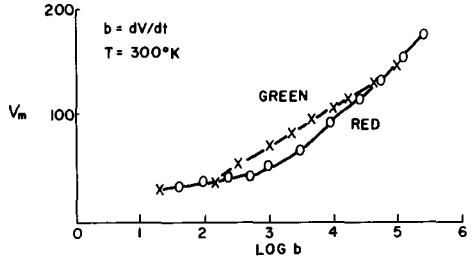


Fig. 5. The voltage of maximum light emission $V_m$ as a function of $dV/dt = b$ at 300°K for two phosphors, ZnS:Cu,Al (green) and ZnS:Cu (red).

If the untrapping field rises linearly with time, as shown in Fig. 3, the light emission rises to a maximum at a particular value of the applied voltage and then falls as the supply of trapped electrons is depleted. The small light peak which occurs before the applied field has passed through zero corresponds to the secondary peak observed with sinusoidal excitation (9) and to the smaller peak produced by alternate polarity pulsing (Fig. 2). Changing the voltage $V_f$ or the duration $t'$ of the ionizing pulse (Fig. 3) alters the size of the subsequent light peak, but does not change its position ($V_m$).

The voltage $V_m$ at which the light maximum occurs changes negligibly when the voltage waveform is moved up or down with respect to ground. $V_m$ increases with decreasing temperature and with increasing values of $b = dV/dt$. Figure 4 shows the variation of $V_m$ with $T$ for two different phosphors, one a green-blue emitting ZnS:Cu, Al and the other a self-coactivated ZnS:Cu with orange-red emission (10, 11). Figure 5 shows the variation of $V_m$ with $b$ for the two phosphors at room temperature.

The shape of the brightness wave changes with $T$ and with $b$ but not the total light output (to 15%) within the range of these measurements so long as the filling pulse (Fig. 3) remains constant and the untrapping field rises to a voltage which is high enough to return all of the trapped electrons. Figure 6 shows three typical curves of instantaneous light intensity vs. voltage for three different temperatures at constant $b$ for ZnS:Cu,Al. Figure 7 shows three similar plots for different values of $b$ at room temperature for this phosphor. The ordinate in Fig. 7 is $L/b$ so that equal areas under the three curves correspond to equal amounts of light, as they do in Fig. 6.

Figure 8 describes the change in shape of the brightness wave: the difference between the voltages at maximum and half-maximum $V_m - V'_{1/2}$ (Fig. 3) is linear with $V_m$ up to 100 v for both phosphors regardless of whether the temperature or the value of $b$ is held constant. Values of $V_m$ above 100 v occur at low temperatures or very high values of $b$ and hence are not so reliable experimentally.

The glow curve of the ZnS:Cu, Al phosphor consists of a single broad peak with a maximum at

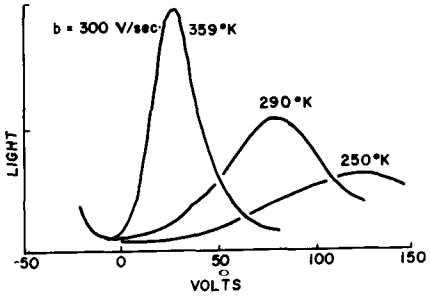


Fig. 6. Three brightness waveforms produced by sawtooth voltage at three different temperatures at a constant value of b (300 v/sec) (ZnS:Cu,Al).

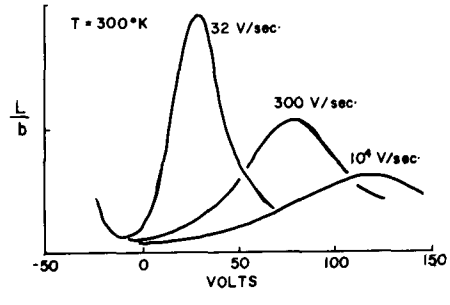


Fig. 7. Three brightness waveforms produced by sawtooth voltage for three different values of b at 300°K. Ordinate (L/b) has been chosen so that equal areas under the curves imply equal total light output (ZnS:Cu,Al).

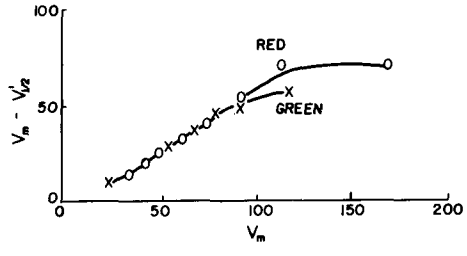


Fig. 8. The quarter width ($V_m - V'_{1/2}$) of the brightness wave produced by sawtooth voltage as a function of the voltage of maximum light emission ($V_m$). (See text.)

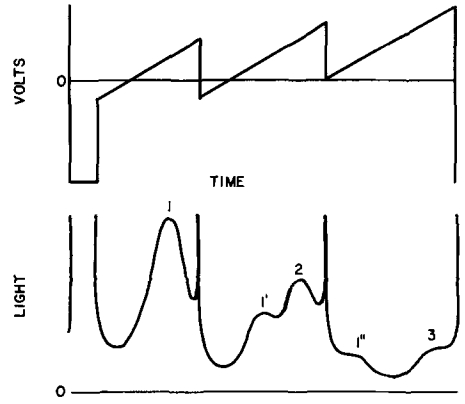


Fig. 9. Brightness waveform produced by pulse and multiple sawtooth voltage waveform, showing additional light peaks (ZnS,ZnO:Cu,Cl).

152°K. The phosphor, which was irradiated with 3650Å u.v. light at the temperature of liquid nitrogen, was heated to 136°K to empty the shallower traps, quenched with liquid nitrogen, and then the glow curve was rerun (12). Examination of the leading edge of the resulting glow peak showed an activation energy of 0.23 e.v. The glow curve of the self-coactivated ZnS:Cu shows a large, complex peak at 388°K together with several much smaller peaks between 140° and 250°K. The high temperature peak contains over 80% of the total thermoluminescence despite strong thermal quenching of the photoluminescence at that temperature. The activation energy of this peak, obtained by a procedure similar to that described above, is 0.52 e.v. The most important trap depth of ZnS,ZnO:Cu,Cl is 0.21 e.v. This phosphor was used in some of the experiments below.

Although the shape of the brightness waveform produced by alternate polarity pulsing (Fig. 2) is complicated by the effect of the fast rise time of the pulses, some measurements were made on a ZnS, ZnO:Cu,Cl phosphor of the value of the brightness intercept $L_o$ and of the time $t_{1/2}$ required for the light emission to fall to half the value. In one experiment with the pulse pattern shown in Fig. 2, the value of the negative or "filling" pulse was held constant at 100 v and that of the positive pulse varied from 25 to 250 v. The data fit the following empirical equations quite closely:

$$L_o = V_+/20 \quad (L_o \text{ in convenient arbitrary units})$$
$$V_+ t_{1/2} = 1200 \quad (t_{1/2} \text{ in milliseconds})$$

In another experiment with the same pulse pattern, both pulses were set at 100 v and $t_{1/2}$ measured as a function of temperature from 280° to 330°K. When log $t_{1/2}$ was plotted against $1/T$, a good straight line was obtained with a slope corresponding to an activation energy of 0.23 e.v.

Figure 9 shows the light pattern resulting from the application of a multiple sawtooth voltage waveform to a cell with ZnS,ZnO:Cu,Cl with conducting binder. The voltage at which light peak 1 occurs is the same for peaks 1' and 1", the voltage $V_m$ of peak 2 is larger and that for peak 3 larger still.

To measure the temperature dependence of electroluminescent brightness at different voltages and frequencies over as wide a temperature range as possible, a binderless layer of ZnS,ZnO:Cu,Cl phosphor was used. The results are summarized in Fig. 10. Figure 10a shows four brightness-temperature curves that illustrate the range of frequencies (5 cps to 50 kc) and voltages (150-700 v) which were employed and thus to point out the extremes in the variation of average brightness $B$ with temperature which were encountered. Figure 10b shows the change in the temperature variation of brightness

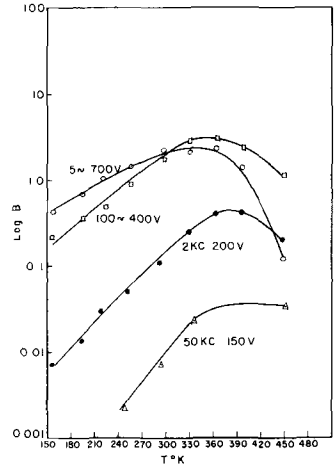


Fig. 10a. Log B as a function of temperature for several combinations of frequency and voltage (ZnS,ZnO:Cu,Cl).

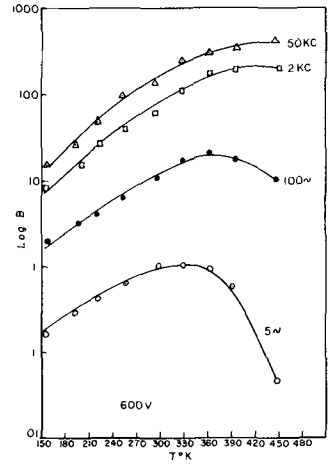


Fig. 10b. Log B as a function of temperature for different frequencies at a single voltage (ZnS,ZnO:Cu,Cl).

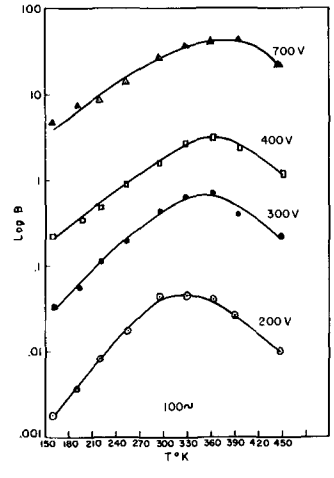


Fig. 10c. Log B as a function of temperature for different voltages at a single frequency (ZnS,ZnO:Cu,Cl).

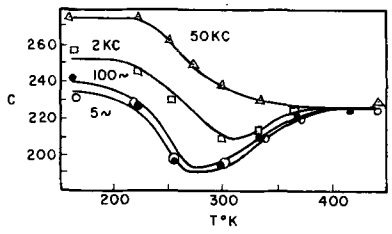


Fig. 11. Values of c (see text) as a function of temperature for several frequencies (ZnS,ZnO:Cu,Cl).

with frequency at constant voltage; Fig. 10c shows the change with voltage at constant frequency. Figure 11 is a plot of the values of c obtained at each temperature and frequency, where c is given by (4)

$$B = B_o \exp\ (-c/\sqrt{V})$$

## Discussion and Interpretation

As shown in Fig. 6 and 7, the total light emitted per half-cycle, for the voltage waveform diagrammed in Fig. 3, is approximately (15%) independent of both temperature and the value of $b$. This observation indicates quite strongly that the variation of $B/f$ with both temperature and sinusoidal frequency $f$ is not due to a frequency or temperature dependence of the excitation process but rather to the effect of these parameters in somehow limiting the number of electrons which can return from the bulk of the phosphor particles to the high field region where ionization occurs. To illustrate how this limitation can affect the average steady-state brightness, the following model is proposed. Assume and define:

1. There are $n_e$ "mobile" electrons which emerge from and return to the high field region during each cycle in the phosphor particle at a steady state.

2. There are $N_T$ electrons trapped in the bulk of the particle distant from the high field region which remain trapped there.

3. There are $N_+ = N_T + n_e$ ionized recombination centers in the high field region.

4. $\alpha n_e$ electrons recombine with ionized emission centers and this number of photons is emitted. $\alpha = N_+ X$, where $X$ is proportional to the capture cross section of the ionized recombination centers.

5. $\beta n_e$ electrons fill empty shallow traps or donor sites in the high field region. Field ionization of these electrons produces the exhaustion barrier which constitutes the high field region (4).

6. $\gamma n_e$ electrons fill empty deep traps or donor sites in the high field region (13).

7. At a steady-state condition as many recombination centers are ionized by electrons released from deep donors or traps and accelerated by the field as recombined during the previous half-cycle.

8. Of the $N \equiv N_T + n_e$ electrons in the bulk of the phosphor particle prior to the return step, only a fraction $\Psi = \Psi\ (T,f,V) = n_e/(n_e + N_T)$ have sufficient time and thermal activation to return.

9. There are many more shallow than deep donor sites or traps in the high field region, and their relative concentration is constant.

We then have the following:

$$\alpha + \beta + \gamma = 1 \qquad [1]$$

From Assumption 7, [cf. Ref. (4)]

$$\alpha n_e = \gamma n_e \exp\ (-c'/\sqrt{V}) \equiv \gamma n_e F \qquad [2]$$

From Assumption 9

$$\beta/\gamma = C\ (\text{const.}) >> 1 \qquad [3]$$

From Eqs. [1], [2], and [3]

$$\alpha = \frac{1}{1 + \dfrac{C+1}{F}} = \frac{F}{F + C + 1} \sim \frac{F}{C} \qquad [4]$$

From Assumptions 8, 3, and 4

$$\alpha = (X/\psi)\ n_e \qquad [5]$$

From Eqs. [5] and [4] we have for the equilibrium number of mobile electrons

$$n_e = (\psi/X)\ (F/C) \qquad [6]$$

Since the light emitted per half-cycle $B/f$ is proportional to $n_e$, it follows that

$$B/f \propto (\psi/X)\ (F/C)^2 \qquad [7]$$

or

$$B/f \propto (X/\psi)\ n_e^2 \text{ (Assumptions 3, 4, and 8)} \qquad [8]$$

Equation [7] shows that light output per cycle $B/f$ is proportional both to the usual ionization probability factor

$$F^2 = \exp\ (-2c'/\sqrt{V}) = \exp\ (-c/\sqrt{V})$$

and to a factor $\psi$, the fraction of trapped electrons returning from the bulk. Thus a reasonable picture based on the assumption of incomplete return of electrons trapped in the bulk of the phosphor particle is possible, consistent with the basic principle that when a steady state is reached as many electrons must return to the recombination or high field region as left that region during the previous half-cycle. It is interesting to note that this particular model also shows $B/f$ to be proportional to $n_e^2$ (Eq. [8]) provided $\psi$ is a weak function of the operational parameters under consideration, such as voltage, in agreement with the conclusions of Lehman (15) from loss measurements.

The nature of the function $\psi = \psi\ (T,f,V)$ is then an important question to be resolved, in particular the role played by the time-varying field in facilitating the return of the trapped electrons. Thornton (6) assigns to the field the function of lowering the effective trap depth $E_o$ by an amount $\mathcal{E}aV/l$, where $a$ is the average trap separation, $V$ the applied voltage, $\mathcal{E}$ the electronic charge, and $l$ the cell thickness. The rate of recombination is assumed to be proportional to the rate of field-controlled thermal release of the trapped electrons. The instantaneous light output $L$ is then given by[1] (6)

$$L \propto -\frac{dn}{dt} = sne \exp\left(-\frac{E - \mathcal{E}aV/l}{kT}\right) \qquad [9]$$

[1] Actually we have
$L \propto \alpha n_e(t) = XN_+ n_e(t)$, and
$-dn/dt \propto n_e(t)$, where $2n_e = \int_o^{1/f} n_e(t)\,dt$
Since we have assumed that only a small fraction of the returning $n_e$ electrons recombine with the $N_+$ ionized activators, $N_+$ is a weak function of time so that $L \propto -dn/dt$.

Here $n$ is the number of trapped electrons and $s$ is a frequency factor or, more simply, a porportionality constant. Substituting $V = bt$, integrating, and setting $dL/dt = 0$ we have

$$V_m = \frac{E_o}{(\mathscr{E}a/l)} - \frac{kT}{(\mathscr{E}a/l)} \ln \frac{skt}{(\mathscr{E}a/l)b} \quad [10]$$

$$V_m - V'_{1/2} = 1.46 \frac{kT}{(\mathscr{E}a/l)} \quad [11]$$

where $V_m$ and $V'_{1/2}$ are defined as shown in Fig. 3. Application of Eq. [10] to the experimental results shown in Fig. 4 and 5 for the ZnS:Cu,Al gives $E_o$ = 0.53 e.v. and $a$ = 400Å, corresponding to a trap concentration of $2 \times 10^{16}$ cm$^{-3}$; the glow curve of this phosphor shows no traps of this depth. The most important glow peak corresponds to a trap depth of 0.23 e.v. Equation [11] requires $V_m - V'_{1/2}$ to be independent of $b$ and to increase with temperature, contradicting the facts as shown in Fig. 6, 7, and 8, which show that $V_m - V'_{1/2}$ *decreases* with temperature and *increases* with $b$.

The other possible function of the field is that of simply sweeping thermally untrapped electrons back into the recombination region. This role has been used by Alfrey and Taylor (1) and by Zalm (8); the latter employed this model to construct a simple theory of the shift in phase of the brightness waves with respect to that of the exciting voltage as a function of frequency and voltage. We add to Zalm's expression, viz., $L \propto -dn/dt = nAV$, a thermal activation factor giving instantaneous light emission $L$

$$L \propto -dn/dt = nAV \exp(-E_o/kT) \quad [12]$$

where $V$ is the applied voltage and $A$ is a proportionality constant which contains a mobility factor. The factor $n \exp(-E_o/kT)$ represents the number of electrons in the conduction band which are at any instant in thermal equilibrium with the trapped electrons $n$. We assume that the time constant for establishing this equilibrium is very short compared to $1/f$, at least for ordinary frequencies. For $V = bt$ we have

$$V_m = \sqrt{b/A} \exp(E_o/2kT) \quad [13]$$

$$V_m - V'_{1/2} = 0.69\, V_m \quad [14]$$

Experimentally we find that if we replot the data from which Fig. 4 was drawn for ZnS:Cu, Al in the form of log $V_m$ vs. $1/T$, as required by Eq. [13] (Fig. 12) a straight line is obtained between 260° and 340°K, the slope of which yields from Eq. [13] a value of $E_o$ = 0.2 e.v., in good agreement with the glow curve data for this phosphor. Similar treatment of the ZnS:Cu data gives $E_o$ = 0.4 e.v., (240°-290°K) while the value obtained from the analysis of the glow curve described above is 0.52 e.v. Below the temperature range over which these activation energies apply, traps are probably ionized more often by collision with conduction electrons than thermally, hence $V_m$ does not increase with further decrease in temperature. Note that the maximum value of $V_m$ is 190 volts for ZnS:Cu and 107 for ZnS:Cu,Al; these values have roughly the same ratio

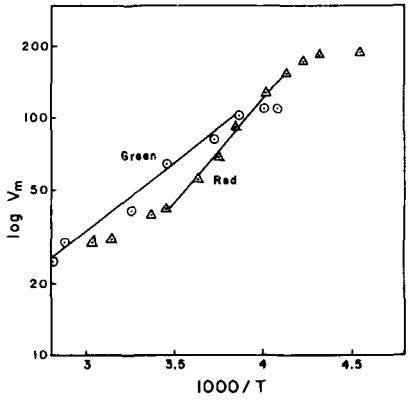


Fig. 12. Log $V_m$ vs. 1000/T for ZnS:Cu, Al (green) and ZnS:Cu (red), from the same data as Fig. 4.

as the important trap depths, in agreement with the above hypothesis. Above this temperature range for this particular value of $b$ (300 v/second) the rate-determining step leading to light emission is probably recombination in the barrier region rather than the supply of electrons to that region. Thus $V_m$ decreases much more slowly with further increase in temperature.

A plot of log $V_m$ vs. log $b$ is linear for both phosphors, but with a slope of 0.3 rather than 0.5 as predicted by Eq. [13]. We can explain this discrepancy if we assume that the mobility of the electrons (contained in the constant $A$ in Eq. [13]) is proportional to $b^{0.4}$, that is, that retrapping is diminished by evacuating the electrons faster. A similar assumption can bring the values of $E_o$ obtained from the theory of field-controlled thermal release into reasonable agreement with experiment (16). However, this theory still does not predict correctly the dependence of $V_m - V'_{1/2}$ on $T$ and $b$. The second model does predict correctly a linear relation between $V_m - V'_{1/2}$ and $V_m$ (Eq. [14]); the experimental relation is (Fig. 8) $V_m - V'_{1/2} = 0.55\, V_m$, for both phosphors; the observed constant of proportionality differs from the predicted by only 20%.

For the case in which $V = V_o$, a constant value, which is applicable to the alternate pulsing experiments described above, we have for the proposed model of thermal release followed by field assisted return, (Eq. [12])

$$L \propto -dn/dt = n_o A' V_o \exp(-A' V_o t) \quad [15]$$

where $A' = A \exp(-E_o/kT)$. Experimentally (ZnS:Cu,Cl), we found $L_o$ (Fig. 2) and $t_{1/2}$ to be linear with $V_o$ and that the temperature dependence of $t_{1/2}$ corresponded, as predicted by this model, to an activation energy of 0.23 e.v.

Having thus established a reasonable model for the return of electrons from the bulk, we can proceed to calculate a value of $\psi$ (Eq. [7]) based on this model. The model has been checked against experiments in which electron injection from the conducting medium is possible (8), while Eq. [7] and [8] have been developed from assumptions which are strictly true only for insulated phosphor particles (Eq. [1]). However, it seems unlikely that "injection" significantly alters the nature of $\psi$.

With sinusoidal excitation the substitution $V = V_o \sin 2\pi ft$ is made in Eq. [12]; integration yields (3)

$$L \propto n_o V_o A' \sin 2\pi ft \exp \mu (\sin^2 \pi ft) \qquad [16]$$

where

$$\mu = \frac{A'V_o}{\pi f} = \frac{AV_o}{\pi f} \exp (-E_o/kT)$$

also[2]

[2] $n_o$ is the total number of electrons trapped in the phosphor bulk at $V = 0$.

$$\frac{B}{f} = \int_0^{1/f} Ldt \propto 2n_o (1 - e^{-\mu}) = 2n_e$$

Therefore this model requires that the value of the factor $\psi$ in Eq. [7], the fraction of the electrons trapped in the particle bulk which are returned each half-cycle, be proportional to $(1 - e^{-\mu})$. Note that at lower frequencies, high voltages, and high temperatures the value of $\psi$ approaches unity, so that the over-all voltage dependence is exp $(-2c'/\sqrt{V}) =$ exp $(-c/\sqrt{V})$; at higher frequencies, lower voltages, and lower temperatures, $\psi$ approaches $\mu$, so that the voltage dependence of brightness is $V$ exp $(-c/\sqrt{V})$. This latter dependence gives a higher absolute value to the slope of a plot of ln $B$ vs. $1/\sqrt{V}$ which is approximately equal to $c + 2\sqrt{V}$.

For a binderless layer or for phosphor plus insulating binder, the supply of available electrons, $N_T + n_e$, can be regarded as independent of frequency since this supply is limited to sources within the particles themselves, which is, of course, not the case with conducting binder (4, 8). The excitation probability $F =$ exp $(-c'/\sqrt{V})$ is probably nearly independent of frequency for ordinary frequencies. The data in Fig. 11 indicate that the minimum value of $c = 2c'$ (*see* Eq. [2], [9]) obtained at each frequency, hence the closest to the actual value of $2c'$ is very nearly the same only at 5 and 100 cps, where $c = 195$; at 2 kc, $c = 210$, and at 50 kc, $c = 230$. Evidently the high-field region requires a small but finite build-up time. The difference between the highest and lowest values of c indicated in Fig. 11 is 44 units for 5 cps, 50 for 100 cps, 45 for 2 kc, and 50 for 50 kc. For $\overline{V} = 500$ volts, the predicted difference, $2\sqrt{V}$, is 45 units, probably within experimental error of observed values. The maximum difference in c shown in Fig. 11 is 80 units, so that we must assume that c' increases somewhat with frequency.

The increase in c (Fig. 11) with $T$ after passing a minimum at moderate frequencies probably arises from the increased diffusion of holes from the barrier, decreasing the barrier field at a given voltage (4). To show that the function $\psi = 1 - e^{-\mu}$ correctly predicts the temperature dependence of the electroluminescent brightness $B$, we multiply the data from which Fig. 10 was taken by the factor

$$\frac{e^{c(f)/\sqrt{V}}}{f}$$

Four such sets of normalized data are shown in Fig. 13. The solid lines correspond to the function

$$B = 700 (1 - e^{-\mu})$$
$$\mu = 50 (V/f^{0.6}) \exp (-E_o/kT)$$
$$E_o = 0.2 \text{ e.v.}$$

Note that the frequency appears in the fitted equations to the 0.6 power. We have assumed here that the mobility constant $A$ in Eq. [18] is proportional to $f^{0.4}$ just as it was necessary to assume that this same constant $A$ (Eq. [14], [15]) is a function of $b = dV/dt$, that is, $A = A_o b^{0.4}$.

The divergence of the experimental points toward higher brightnesses at the lower temperatures may indicate the onset with decreasing temperature of another thermally sensitive mechanism such as that proposed by Johnson, Piper, and Williams (2) or Zalm (4), which in this case overcomes somewhat the effect of the rapid decrease of the $\psi$ function and in some cases leads to a minimum in the brightness-temperature curve at low temperatures. A second possible explanation is that the emptying of very shallow traps (~0.05 e.v.) contributes appreciably to the electroluminescence at temperatures too low to empty the 0.2-0.5 e.v. traps. Evidence for the existence of such traps has been given by Haake (3).

## Summary and Conclusions

Measurements of both (*a*) the size and shape of electroluminescence brightness waves for simple voltage waveforms at different temperatures and voltage rise times, and (*b*) average brightness as a function of temperature, voltage, and frequency for sinusoidal excitation lead to the following conclusions: In agreement with most workers in the field (1, 3, 6), we find that the major effect of temperature on electroluminescence, apart from thermal quenching, is in the transfer of electrons from traps in the low field region in the phosphor particle bulk to ionized emission centers in the high field region. An increase in temperature increases the concentration of conduction electrons in thermal equilibrium with the traps in the low field region, which may then be swept by the applied field into the high field region. The applied field does not appear to lower the trap depths significantly; retrapping before recombination is probably an important factor. Although a single trapping level suffices to explain the major experimental details, Fig. 9 indicates that additional deeper levels are also involved.

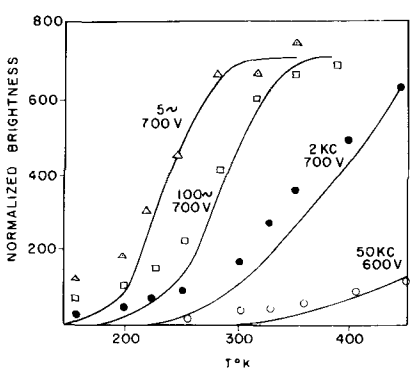


Fig. 13. Normalized brightness (see text) as a function of temperature for several frequencies (ZnS, ZnO:Cu, Cl). Plotted points are experimental; solid lines, theoretical.

Finally, a summary of the over-all trend in temperature dependence of electroluminescence in ZnS: Cu materials can be proposed. At very low temperatures the return of electrons from the phosphor bulk to the barrier is sustained by impact rather than thermal detrapping, so that finite light emission is maintained. Further, if in the barrier some of the electrons in the deeper "shallow" traps are held until the barrier field is at its maximum,[3] then their contribution to the brightness will diminish with increasing temperature so that a minimum in the brightness-temperature relation results, as found by Johnson, Piper, and Williams (2). At low to moderate temperatures the barrier field is relatively unaffected by thermal effects and brightness increases with temperature because of the increased number of electrons that can return to the barrier from the bulk in one half-cycle. This increased return current arises from increased thermal detrapping in the bulk (1). Finally at high temperatures positive holes escaping from ionized activators diffuse from the barrier, decreasing the barrier field (4) or simply become localized at killer centers (3), producing a maximum in the brightness-temperature curve.

[3] This amounts to a lower value of $C$, the ratio of shallow to deep donors, at these very low temperatures, so that if $F$ is not too much lower (because of the very slightly diminished space charge developed in the barrier), then a higher brightness results than at some slightly higher temperature; viz., Eq. [7],

$$B/f \propto \frac{\psi}{X}\left(\frac{F}{C}\right)^2$$

$\psi$ remains constant in this very low temperature range from impact detrapping. At higher temperatures the small increase in $F$ associated with complete exhaustion of the barrier (2) (more effective acceleration of fewer electrons) may cooperate with increased thermal detrapping in the bulk again to increase the brightness.

## Acknowledgment

The writer wishes to thank the following persons for much helpful discussion: Dr. M. Aven, Dr. R. M. Potter, Dr. J. S. Saby, Dr. M. A. Weinstein, and, in particular, Dr. F. E. Williams.

Manuscript received March 13, 1958. This paper was prepared for delivery before the Washington Meeting, May 12-16, 1957.

Any discussion of this paper will appear in a Discussion Section to be published in the June 1959 JOURNAL.

## REFERENCES

1. G. F. Alfrey and J. B. Taylor, *Proc. Phys. Soc.*, **B68**, 775 (1956).
2. P. D. Johnson, W. W. Piper, and F. E. Williams, *This Journal*, **103**, 221 (1956).
3. C. H. Haake, *ibid.*, **104**, 291 (1957); *J. Opt. Soc. Amer.*, **47**, 881 (1957).
4. P. Zalm, *Philips Res. Repts.*, **11**, 417 (1956).
5. G. F. Neumark, *Phys. Rev.*, **103**, 41 (1956)
6. W. A. Thornton, *ibid.*, **102**, 38 (1956); *ibid.*, **103**, 1585 (L) (1956).
7. P. D. Johnson and F. E. Williams, *J. Chem. Phys.*, **21**, 126 (1953).
8. P. Zalm, *Philips Res. Repts.*, **11**, 353 (1956).
9. S. Nudelman and F. Matossi, *This Journal*, **101**, 546 (1954).
10. H. C. Froelich, *ibid.*, **100**, 280 (1953).
11. M. A. Aven and R. M. Potter, *ibid.*, **105**, 134 (1958).
12. J. J. Hill and P. Schwed, *J. Chem. Phys.*, **23**, 652 (1955).
13. W. W. Piper and F. E. Williams, *Phys. Rev.*, **87**, 151 (1952); *Brit. J. Appl. Phys.*, **54**, 539 (1955).
14. P. Zalm, G. Diemer, and H. A. Klasens, *Philips Res. Repts.*, **10**, 205 (1955).
15. W. Lehmann, *This Journal*, **103**, 24 (1956); *Optik*, **14**, 319 (1957).
16. F. F. Morehead, Jr., Enlarged Abstracts, Electronics Div., The Electrochemical Society, Washington Meeting, p. 2 (1957) (not published).

## SYMBOLS

| | |
|---|---|
| $\alpha$ | The relative probability of the capture of returning electrons by ionized activators in the high field region. |
| $\beta$ | The relative probability of the capture of returning electrons by shallow traps in the high field region. |
| $\gamma$ | The relative probability of the capture of returning electrons by deep traps in the high field region. |
| $\mathcal{E}$ | The electronic charge. |
| $\mu$ | $AV_o \exp(-E_o/kT)/\pi f$ |
| $\psi$ | The fraction of electrons trapped in the bulk which return to the high field region. |
| $A$ | The proportionality constant in Eq. [12], a function of electron mobility. |
| $A'$ | $A \exp(-E_o/kT)$ |
| $a$ | The average separation of electron traps. |
| $B$ | The average brightness. |
| $b$ | $dV/dt$ for sawtooth excitation. |
| $C$ | $\beta/\gamma$ |
| c | An empirical constant in the relation $B = B_o \exp(-c/\sqrt{V})$ |
| c' | A constant in the expression of ionization probability $\exp(-c'/\sqrt{V})$ in Eq. [2]; $c = 2c'$ |
| $E_o$ | The trap depth. |
| $F$ | $\exp(-c'/\sqrt{V})$ |
| $f$ | Frequency in cycles per second. |
| $L$ | Instantaneous light emission. |
| $L_o$ | Instantaneous light emission at the beginning of a square pulse (Fig. 2). |
| $l$ | Cell thickness. |
| $N_+$ | The number of ionized activator centers in the high field region. |
| $N_T$ | The number of electrons trapped in the bulk of the phosphor which remain trapped throughout the voltage cycle. |
| $n$ | The number of electrons trapped in the phosphor bulk at a given instant. |
| $n_e$ | The number of electrons that go back and forth between the phosphor bulk and the high field region. |
| $t'$ | The duration of the filling pulse (Fig. 3). |
| $t_{1/2}$ | The time required for $L$ to decay to $L_o/2$ for square pulses (Fig. 2). |
| $\bar{V}$ | An "average" voltage for a given voltage range. |
| $V_m$ | The voltage at which $L$ is maximum for sawtooth excitation (Fig. 3). |
| $V'_{1/2}$ | The voltages at which $L$ is half of maximum for |
| $V''_{1/2}$ | sawtooth excitation (Fig. 3). |
| $X$ | A constant proportional to the capture cross section of the ionized activators. |

# Selective Electrolytic Etching of Germanium and Silicon Junction Transistor Structures

I. A. Lesk and R. E. Gonzalez

*Electronic Components Division, General Electric Company, Syracuse, New York*

ABSTRACT

The electrolytic dissolution of germanium and silicon has been applied to the selective etching of n-p-n and p-n-p junction transistor structures. By employing the electrical properties of p-n junctions internal to the pellet as well as the electrolytic behavior of the n- and p-type germanium or silicon, part of the emitter or collector (or both) of a transistor pellet may be etched away, leaving the rest of the pellet intact. The resulting exposure of part of the base region may be used to locate the base region and facilitate attachment of the transistor base lead.

Germanium and silicon junction transistor structures are in common use at the present time for making both high-frequency and high-power transistors. Methods for producing the n-p-n or p-n-p germanium or silicon bar include the double doped (1), rate grown (2), meltback (3-5), grown-diffused (6), surface diffused (7, 8), and diffused meltback (9, 10) processes. In order to fabricate a transistor from the bar, attachment of a base lead presents a problem common to each of the processes. For most transistors, the base region is so thin (generally 0.0001 in. to 0.0005 in.) that no practical method exists for attaching a lead to the side of it without spilling over onto emitter or collector regions, or both. Even if a contact could be made to the side of the base region only, it would generally be mechanically weak due to the small area of contact involved.

It is desirable to be able to expose part of the large dimension of the base region in a junction transistor structure. This may be used to identify the base, and permit making a base contact of convenient area (and slight penetration), minimizing or eliminating entirely overlap onto emitter and collector regions. This paper describes an electrolytic etching technique that removes germanium or silicon of one conductivity type without attacking the adjoining region of opposite conductivity type. When this etch is used to reduce the size of the emitter (or collector) of a transistor bar without etching the base, the desired geometry results. Electrolytic etching experiments were carried out on meltback [germanium n-p-n (3, 4) and silicon p-n-p (5)] and diffused meltback [germanium p-n-p (10) and silicon n-p-n (9, 10)] pellets. These particular pellet combinations were chosen because of the ease with which the structures could be made. Results should be applicable, however, to transistor bars made by any of the processes mentioned.

## Etching Characteristics of Germanium and Silicon and Experimental Techniques

The following characteristics of the electrolytic dissolution of germanium (11) or silicon apply to the selective anodic etching of p-n junction structures.

1. Hole current at the surface is required to remove material.
2. P-n junctions internal to the structure to be etched may have potentials impressed across them due to the driving voltage. Reverse biased junctions block the current flow, and forward biased junctions inject minority carriers according to well-established principles.
3. A p-type layer forms on the surface of germanium or silicon in many electrolytes.
4. When high voltages are applied to n-type material, the surface p-n junction will avalanche, supplying at the surface large numbers of holes which can remove material.
5. Holes may be injected into n-type material by a forward biased p-n junction (item 2 above), or by the application of light.

The electrolyte used must not attack germanium (or silicon), or chemical etching will proceed simultaneously with electrolytic etching. Also, a high conductivity electrolyte appears to give the best preferential attack. Hydrofluoric-acetic acid mixtures worked best of all the electrolytes tried. Glacial acetic acid and 49% hydrofluoric acid were used. The ratio of acids was not critical, so a 1:1 mixture was used for convenience.

In the electrolytic etching circuit, contact to the germanium or silicon bar may be made most conveniently by means of an alloy or solder region. However, simply holding the pellet in a pair of tweezers generally gives satisfactory results. About 50 cc of electrolyte were used.

All etching was done in a dimly lit area to minimize effects of light injection of carriers. No agitation was used, but the violent bubbling at high current densities stirred the electrolyte well and minimized heating at the interface. The etching proceeded continuously, with no passivation phenomena at high current density.

## Etching of Uniform Resistivity Pellets

To illustrate the different electrolytic etching rates of n- and p-type semiconductors, uniform re-

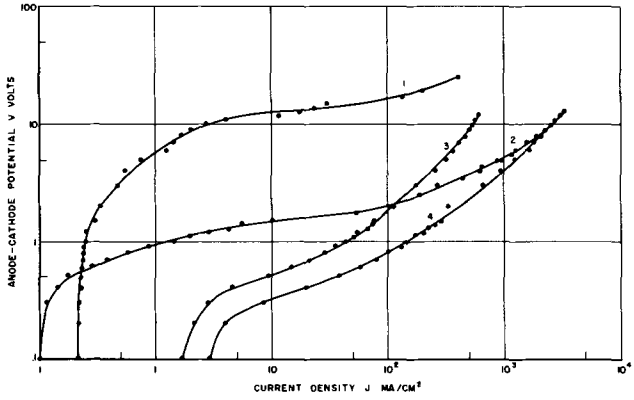


Fig. 1. Electrolytic etching of germanium. Curve 1, 4Ω-cm n-type; curve 2, 0.03Ω-cm n-type; curve 3, 12Ω-cm p-type; curve 4, 0.03Ω-cm p-type.

sistivity pellets of both types were used. Current density vs. applied (anode to cathode) voltage curves for low and high resistivity samples are shown in Fig. 1. The voltages measured in this way give no accurate information about the potential across the semiconductor-electrolyte boundary, which must be measured in order to correlate quantitatively with theory. However, all the essential features are illustrated well enough for application to p-n junction structure etching. Curve 1, for 4Ω-cm n-type Ge, shows the low current saturation and high voltage avalanche breakdown of the p-n junction formed on the surface. Curve 2, for 0.03Ω-cm n-type Ge, shows a smaller saturation current and lower voltage breakdown, as is expected for a (surface) p-n junction on a lower resistivity base. Curve 3, for 12Ω-cm p-type Ge, shows that relatively high currents may be drawn at low voltages due to the plentiful supply of holes and ineffective p-$p^+$ barrier at the surface. Curve 4, for 0.03Ω-cm p-type Ge, is much the same as curve 3, but more highly conducting due to the larger hole concentration. At high current levels, all currents are becoming limited by the bulk resistance of the pellet. Appreciable current fluctuation with time contributed to the scatter of points. At higher current levels, measurements had to be taken very quickly, because the bars were etching rapidly and hence the current changing continuously. At these levels, a loud crackling noise accompanied the rapid etching.

The results of various etching rates can be seen in Fig. 2. In each pair of pellets, the one on the left is 0.03Ω-cm n-type, the one on the right 0.03Ω-cm p-type. The pair at upper left were etched at 2 v for 15 min. The n-type pellet, drawing little current, is etched very slightly, whereas the p-type sample is severely attacked. The pair at the upper right were etched at 5 v for 4 min. In this case, the n-type sample is now being etched, but not as fast as the p-type bar. At lower left, 10 v for 3 min, and at lower right, 15 v for 1.5 min give almost equal etching rates for the n-type and p-type germanium. Irregularities in the shapes of the etched surfaces come from small voltage drops down the bars and from fluctuations in the position of the liquid surface due to severe bubbling at high current densities.

Electrolytic etching curves for silicon could not be obtained because of the excessive fluctuations

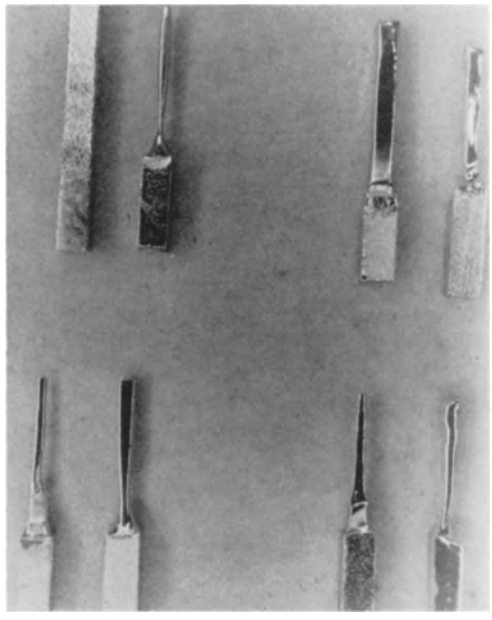

Fig. 2. Electrolytic etching of uniform resistivity pellets. For each pair, left pellet = 0.03Ω-cm n-type, right pellet = 0.03Ω-cm p-type. Unetched section of each pellet is on the bottom. Upper left, 2 v for 15 min; upper right, 5 v for 4 min; lower left, 10 v for 3 min; lower right, 15 v for 1.5 min.

with time of the current at a given voltage. However, since silicon junction structures etch in a manner much the same as those of germanium, the curves for uniform resistivity rods should be similar.

### Etching of Transistor Structures

The same techniques may be applied to the selective etching of junction transistor structures. Results are illustrated in the photographs that follow. As an aid to visualizing the contours of the etched regions, a sketch of each case is drawn in Fig. 3. The shape of a meltback or diffused-meltback bar is shown in Fig. 3-1. The unmelted end of the pellet (top) serves as the emitter, and the meltback section (bottom) as the collector. The thin central region is the base, which is generally curved to an extent controlled by the isothermal contours during the melting cycle. The emitter, collector, or both in some cases may be etched to varying degrees, as

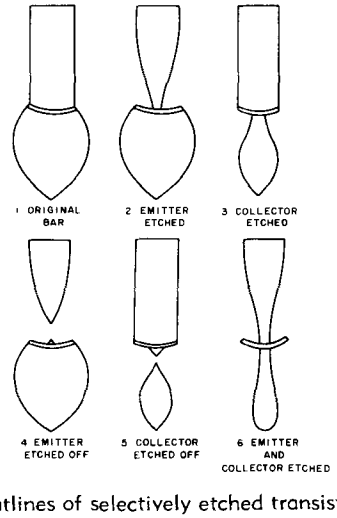


Fig. 3. Outlines of selectively etched transistor pellets

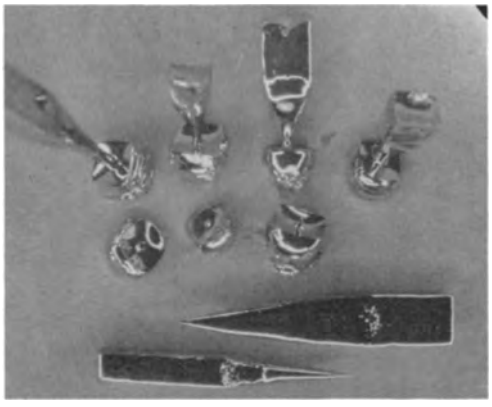

Fig. 4. Germanium n-p-n pellets. Top, emitter etched; center and bottom, emitter etched off.

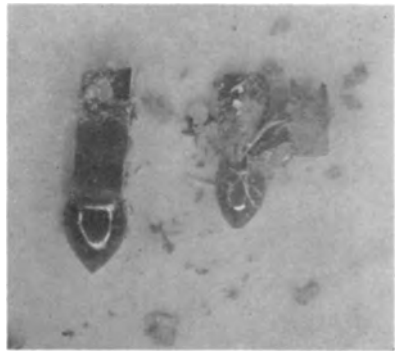

Fig. 6. Silicon n-p-n pellets. Left, immediately after electrolytic etching. Right, emitter pressed after etching to reveal flaky material, under which lies selectively etched pellet as in Fig. 5, top.

indicated in Fig. 3. Contact to the region to be etched was made by a small alloy dot using gold containing antimony for the n-type or gallium for the p-type region. The region to be etched was made the anode. Except where specifically mentioned, base widths are $<0.0015$ in. for the silicon p-n-p meltback bars, $<0.0005$ in. for all the other structures. All bars were approximately 0.030 in. square, 0.125 in. to 0.250 in. long. About 0.050 in. was melted in each case.

In order to ascertain that the base region is not attacked, the following commonly used methods of junction location were employed. (*a*) An ac voltage was applied from emitter to collector while the bar was held in a suspension of fine barium titanate particles in benzene. The titanate deposited lightly on the p-type regions and heavily on the p-n junctions. (*b*) A fine thermoelectric probe was moved over the bar surfaces. Direction of the emf determined the conductivity type. (*c*) Metallographic cross sectioning and polishing followed by a slight etch ($HNO_3$:HF = 4:1) showed up the junctions. Since the base regions were so thin, chipping of the edges limited the applicability of this method. (*d*) Completed transistors were made with base contacts alloyed to the base "shelf" only.

When measured by any of the above techniques, properly controlled electrolytic etching appeared to stop precisely at the base-emitter or base-collector junction.

Figures 4 through 6 deal with germanium and silicon n-p-n bars. The surface-induced p-n junction barrier between the (low resistivity) emitter and the electrolyte breaks down at low voltages and appreciable current flows through the emitter surface, etching it away. The emitter-base p-n junction is in the blocking direction, however, and keeps current from flowing into the base region. Hence the base is not attacked.

Figure 4 shows a group of germanium n-p-n bars. The top four have emitter regions etched (outline 4-2). The three pellets in the middle have emitters etched off (outline 4-4). A small spike of the emitter remains in the center of the base. Two of the separated emitter regions are shown at the bottom. These bars were etched at 20 v anode to cathode for about 30 sec. In Figs. 4, 5, 7, and 8 bars were given a slight chemical etch after electrolytic etching to produce shiny surfaces so that selectively attacked regions would show up better in the photomicrographs.

Figure 5 shows a group of silicon n-p-n pellets. Etching voltages and times are the same as for the germanium n-p-n bars (Fig. 4). The three pellets at the top have partially etched emitters (outline 4-2), while those in the center have emitters etched off (outline 4-4). At the bottom are two of the separated emitters.

A peculiar surface condition resulted only in the case of silicon n-p-n pellets. Visually, the pellets appeared to be unattacked by the electrolytic etch. They retained their shape and metallic appearance. However, slight mechanical pressure to the etched part of the emitter region revealed a flaky material that peeled off easily, exposing the selectively at-

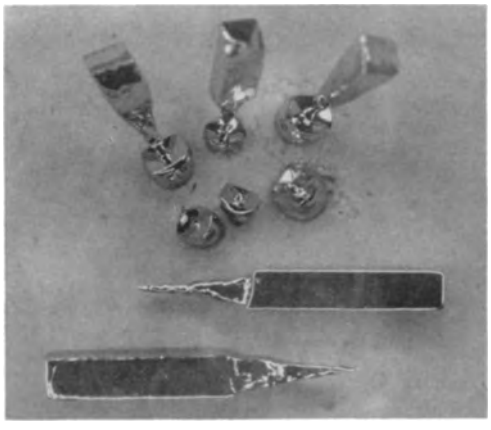

Fig. 5. Silicon n-p-n pellets. Top, emitter etched; center and bottom, emitter etched off.

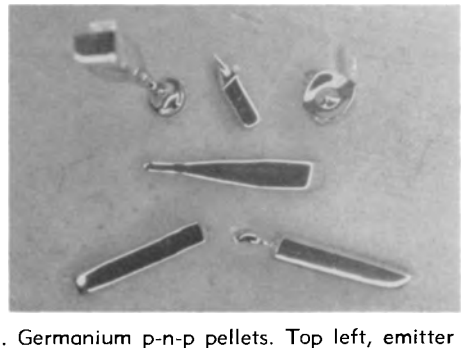

Fig. 7. Germanium p-n-p pellets. Top left, emitter etched; top right, emitter etched off; center, nonselective attack at higher voltages; bottom right, collector etched; bottom left, collector etched off.

Fig. 8. Silicon p-n-p pellets. Top, emitter etched; center and bottom, emitter etched off.

Fig. 9. Silicon p-n-p pellets with ~0.003 in. bases. Emitter and collector etched.

tacked structure below. Figure 6 shows this effect. The bar on the left appears to be unetched, but the "emitter" surface is easily ruptured, as shown in the bar on the right. Underneath is a structure as shown in Fig. 5 (top). Identification of the flaky material has not been attempted. It is possibly an oxide of silicon. It does not interfere with the selective etching, but gives a wrinkled appearance to the etched part of the emitter region, Fig. 5 bottom.

Figures 7 through 9 deal with germanium and silicon p-n-p bars. To attack preferentially the emitter of such a structure, etching must be done at a voltage low enough so that the level of injected holes into the base by the (forward biased) emitter p-n junction is not large, and the surface p-n junction of the exposed part of the base does not avalanche. If the voltage is too low, etching is very slow. The collector may be attacked selectively by making it the anode instead of the emitter. In such a case, etching can be carried out at much higher current densities because the low injection efficiency of the collector p-n junction does not produce high hole densities in the base region.

A group of germanium p-n-p pellets is shown in Fig. 7. The bar at upper left has the emitter etched (outline 4-2). The bar at upper left was etched with 2 v anode to cathode for several minutes. Longer etching at the same potential results in a separation of the emitter, as shown in Fig. 7, upper right (outline 4-4). In the middle of Fig. 7 is shown a pellet etched in the same way but at a potential of 20 v. Selective attack no longer occurs because of larger injected densities of holes into the base. The collector is on the left. At the lower right in Fig. 7 is shown a p-n-p germanium bar with the collector etched (outline 4-3). Etching in this case was done at 20 v for approximately 1 min. At lower left in Fig. 7 is a pellet with the collector etched off (outline 4-5), which took 20 v for several minutes. The remaining tip of the collector region may be seen at the right end of the pellet.

Figure 8 illustrates selective etching of silicon p-n-p bars. The three top bars have emitters attacked (outline 4-2). They were etched at 20 v for about half a minute. The base and collector are not attacked, as they were for germanium p-n-p pellets at such a high voltage. This is probably due to the low minority carrier lifetime in silicon cooled so fast from its melting point, which results in a lower concentration of holes injected into the base than for the (emitter etched) germanium p-n-p bars. The two center rows show pellets with separated emitters, etched at 20 v for about a minute. Two silicon p-n-p bars with both emitter and collector etched down (outline 4-6) are shown in Fig. 9. Base widths in this case are about 0.003 in. so as to show up in the photograph. Emitter and collector were etched separately. The small dot on the bottom (emitter) of the pellet at left is the gold-gallium alloy contact. The white film on the exposed base of the pellet on the right is deposited during the electrolytic attack. It was easily cleaned off with a slight acid etch ($HNO_3$:HF=4:1).

## Acknowledgment

The photomicrographs were taken by O. G. White and D. B. Blackwood.

Manuscript received Jan. 10, 1958. This paper was prepared for delivery before the San Francisco Meeting, April 29-May 3, 1956.

Any discussion of this paper will appear in a Discussion Section to be published in the June 1959 JOURNAL.

## REFERENCES

1. G. K. Teal, M. Sparks, and E. Buehler, *Proc. I.R.E.*, **40**, 906 (1952).
2. R. N. Hall, *J. Phys. Chem.*, **57**, 836 (1953).
3. R. N. Hall, 1955 IRE-AIEE Semiconductor Device Research Conference. June 20, 1955.
4. J. I. Pankove, 1955 IRE-AIEE Semiconductor Device Research Conference. June 21, 1955. Published Transistors I, R.C.A. Laboratories, March 1956, p. 82.
5. I. A. Lesk, AIME Semiconductor Symposium, Feb. 25, 1957.
6. H. Statz, W. Leverton, J. Spanos, 1955 IRE-AIEE Semiconductor Device Research Conference. June 20, 1955; B. Cornelison and W. A. Adcock, 1957 I.R.E. Wescon Conv. Rec. Part 3 p. 22.
7. M. Tanenbaum and D. E. Thomas, *Bell System Tech. J.*, **35**, 1 (1956).
8. C. A. Lee, *ibid.*, **35**, 23 (1956).
9. K. Lehovec and A. Levitas, 1956 AIEE-IRE Semiconductor Devices Research Conference, June 27, 1956. Also, *J. Appl. Phy.*, **28**, 106 (1957).
10. I. A. Lesk, 1956 AIEE-IRE Semiconductor Devices Research Conference, June 27, 1956. Also, I.R.E.-P.G.E.D. Conference, Nov. 1, 1957. To be published I.R.E. Transactions on Electron Devices.
11. A. Uhlir, Jr., *Bell System Tech. J.*, **35**, 333 (1956).

# Preparation and Identification of the Thorium Germanides

A. G. Tharp

*Department of Chemistry, Purdue University, Lafayette, Indiana*

and

Alan W. Searcy and Hans Nowotny

*Ceramics Laboratories, Division of Mineral Technology, University of California, Berkeley, California*

ABSTRACT

X-ray diffraction studies indicate the existence of at least six thorium germanide phases. The phase of highest germanium content is $ThGe_{3.0\pm0.4}$, tentatively identified as cubic or pseudo cubic with $a_o = 11.72$Å, $\alpha$-$ThGe_2$, isostructural with $\alpha$-$ThSi_2$ and $\alpha$-$USi_2$, is tetragonal, space group $D^{19}_{4h}$ — I4/amd, $a_o = 4.106 \pm 0.003$Å, $c_o = 14.193 \pm 0.005$Å. A phase of composition $ThGe_{1.6\pm0.3}$ ($\beta$-$ThGe_2$) has a distorted $AlB_2$ structure. ThGe is cubic, space group $O^5_h$ — Fm3m (NaCl Type), with $a_o = 6.033 \pm 0.001$Å. $Th_3Ge_2$ is primitive tetragonal, space group $D^5_{4h}$ — P4/mbm, with $a_o = 7.971 \pm 0.004$Å and $c_o = 4.170 \pm 0.003$Å. A phase of composition $ThGe_{0.3\pm0.1}$ gives a complex diffraction pattern. Reactivities with a few common chemical reagents are reported for $\alpha$-$ThGe_2$, $ThGe_{1.6}$, and $ThGe_3$.

Preparation and structure investigations for a number of silicides and for three germanides of actinon elements have been reported. Brauer and Mitius (1) prepared $ThSi_2$ and reported its structure. The preparations and structure determinations for $ThSi_{1.5}$ ("$\beta$-$ThSi_2$"), ThSi, and $Th_3Si_2$ were carried out by Jacobson, Freeman, Tharp, and Searcy (2). The thorium silicide phases are isostructural with the corresponding uranium silicides whose structures were earlier identified by Zachariasen (3). Zachariasen also found $\alpha$-$PuSi_2$ and $\alpha$-$NpSi_2$ to have the $\alpha$-$ThSi_2$ structure (3). These uranium silicides as well as $U_3Si$ and $USi_3$ had been first prepared by Kaufmann, Cullity, and Bitsianes (4). The structures of $U_3Si$ (3) and of $USi_3$ (5, 6) and an isomorphous uranium germanide (6) have also been worked out. Runnals and Boucher (7) have prepared $PuSi_{1.5}$ ("$\beta$-$PuSi_2$") and have found it to be identical in structure to $USi_{1.5}$ ("$\beta$-$USi_2$").

The present research reports the first investigation of the thorium germanides.

## Experimental

The thorium metal used in these experiments was obtained from the Fairmont Chemical Company as 200 mesh powder. Spectroscopic analysis showed trace amounts of iron and manganese and smaller amounts of a few other heavy metals. Spectroscopically pure germanium was obtained from the Eagle-Picher Company. Germanium oxide was removed by volatilization. From behavior of the thorium on ignition and toward compound formation, 20 to 30 mole % was estimated to be present as inert oxide. All stated compositions were calculated on the assumption that only 80% of the material added as thorium actually was available for reaction.

Preparations were made by direct synthesis from the powdered elements in graphite, alumina, or tungsten crucibles at 1000°-1500°C. Some samples were reground and reheated to insure obtaining equilibrium, and weight losses were assumed to be due to the vaporization of germanium. Cooling rates of different samples varied from 10°C/min to 300°C/min.

X-ray analyses were made with 114.59 mm powder diffraction cameras. Filtered copper $K_\alpha$ radiation was used for all but two preparations. Experimental procedures were similar to those described previously (8).

### *Identification and Structure of the Phases*

Preparations with a Ge:Th ratio near 3.0 (allowing for the thorium oxide present) when heated in the temperature range of these experiments gave strong diffraction patterns of a thorium germanide phase, a faint pattern of germanium, and a medium-strong pattern of $ThO_2$. Attempts to index the germanide pattern on the basis of known structures were unsuccessful. All spacings were consistent with a cubic unit cell for which $a_o = 11.72$Å, but this large cell may not be the true crystallographic unit; further investigation is contemplated. Indexing of the first 20 spacings is shown in Table I. Although the phase is almost certainly $ThGe_3$, its composition will be designated as $ThGe_{3.0\pm0.4}$ because the exact oxide content of the thorium is unknown.

Samples near composition $ThGe_{2.5}$ showed a strong pattern of a new phase and the strongest lines of $ThGe_{3.0}$. Spacings of this new phase were compared with those of the $\alpha$-$ThSi_2$ type compounds and were found to be almost identical. The $\sin^2\theta$ values were indexed on the basis of a tetragonal unit cell with $a_o = 4.106 \pm 0.003$Å and $c_o = 14.193 \pm 0.005$Å. Calculated intensities, as shown in Table II, are in good agreement with the observed intensities. The structure has group $D^{19}_{4h}$ — I4/amd symmetry.

Table I. Crystallographic data for $ThGe_{3.0\pm0.4}$

| hkl | $\sin^2\theta_{obs.}$ | $\sin^2\theta_{calc.}$ | $I^*_{obs.}$ |
|---|---|---|---|
| 110 | 0.0086 | 0.0086 | w |
| 220 | 0.0344 | 0.0344 | m |
| 221 | 0.0388 | 0.0388 | m |
| 320‡ | 0.0558 | 0.0560 | s |
| 400 | 0.0689 | 0.0689 | m |
| 410 | 0.0732 | 0.0732 | w |
| 411, 330 | 0.0772 | 0.0776 | w |
| 421 | 0.0905 | 0.0905 | vs |
| 510 | 0.1119 | 0.1121 | w⁻ |
| 520 | 0.1252 | 0.1250 | w⁻ |
| 440 | 0.1378 | 0.1380 | w⁺ |
| 522, 441 | 0.1422 | 0.1422 | w⁺ |
| 620 | 0.1720 | 0.1724 | w |
| 621 | 0.1763 | 0.1768 | w |
| 541 | 0.1814 | 0.1810 | w |
| 630 | 0.1944 | 0.1940 | w⁻ |
| 710, 550 | 0.2156 | 0.2157 | m |
| 640 | 0.2236 | 0.2241 | w |
| 641 | 0.2283 | 0.2282 | w |
| 730 | 0.2496 | 0.2500 | w⁻ |

Plus many additional lines.

* w = weak, m = medium, s = strong, vs = very strong.
‡ Coincides with a germanium reflection.

There are four molecules of $\alpha$-$ThGe_2$ per unit cell with four thorium atoms located in 0,0,0; $0,\frac{1}{2},\frac{1}{4}$; $\frac{1}{2},\frac{1}{2},\frac{1}{2}$; $\frac{1}{2},0,\frac{3}{4}$; and eight germanium atoms in $0,0,z$; $0,0,-z$; $0,\frac{1}{2},(\frac{1}{4}+z)$; $0,\frac{1}{2},(\frac{1}{4}-z)$; $\frac{1}{2},\frac{1}{2},(\frac{1}{2}+z)$; $\frac{1}{2},\frac{1}{2},(\frac{1}{2}-z)$; $\frac{1}{2},0,(\frac{3}{4}+z)$; $\frac{1}{2},0,(\frac{3}{4}-z)$. The value of $z$ is approximately 0.42. The $c/a$ ratio is 3.456, and the calculated density at room temperature is 10.47 g-cm$^{-3}$.

Samples near composition $ThGe_{1.6}$ gave the diffraction pattern of an entirely new phase. Comparison of this germanide pattern with that for $ThSi_{1.5}$ (defect $AlB_2$ structure) showed a striking similarity between the two. However, there are more reflections shown by the germanide phase than by the silicide phase. In addition, some germanide reflections are diffuse with sharp lines showing on either side of the diffuse lines. The $\sin^2\theta$ values for the germanide phase index moderately well for a hexagonal unit cell similar to that for $ThSi_{1.5}$. Intensities calculated assuming that $ThGe_{1.6}$, like $ThSi_{1.5}$, belongs to the $D^1_{6h}$ structure are compared with observed intensities in Table III.

Table II. Crystallographic data for $\alpha$-$ThGe_2$

| hkl | $\sin^2\theta_{obs.}$ | $\sin^2\theta_{calc.}$ | $I_{obs.}$ | $I_{calc.}$ |
|---|---|---|---|---|
| 101 | 0.0387 | 0.0382 | w⁺ | 139.2 |
| 004 | 0.0480 | 0.0474 | m | 41.7 |
| 103 | 0.0622 | 0.0619 | s⁻ | 49.3 |
| 112 | 0.0825 | 0.0823 | s⁺ | 295.0 |
| 105 | 0.1098 | 0.1092 | s | 125.6 |
| 200 | 0.1412 | 0.1410 | m⁺ | 26.0 |
| 116 | 0.1782 | 0.1770 | w⁻ | |
| 211 | 0.1801 | 0.1791 | s⁻ | 4.9 |
| 107 | | 0.1803 | | 50.3 |
| 204 | 0.1887 | 0.1884 | w⁺ | 25.9 |
| 008 | | 0.1894 | | 4.4 |
| 213 | 0.2027 | 0.2028 | m⁻ | 39.3 |
| 215 | 0.2501 | 0.2502 | s⁻ | 68.0 |
| 109 | 0.2749 | 0.2750 | w⁺ | 14.9 |
| 220 | 0.2807 | 0.2819 | m⁻ | 31.4 |
| 301 | 0.3207 | 0.3201 | s⁻ | 4.2 |
| 217 | | 0.3212 | | 47.8 |
| 224 | 0.3288 | 0.3292 | w⁺ | 10.8 |
| 208 | | 0.3304 | | 7.4 |
| 303 | absent | 0.3437 | | |
| 1-1-10 | 0.3639 | 0.3655 | s diffuse | 22.4 |
| 312 | | 0.3642 | | 55.4 |
| 305 | absent | 0.3912 | | |
| 1-0-11 | absent | 0.3934 | | |
| 219 | 0.4146 | 0.4151 | w | 16.3 |
| 0-0-12 | 0.4240 | 0.4248 | w⁻ | 7.8 |

Table III. Crystallographic data for $ThGe_{1.6}$

| hkl | $\sin^2\theta_{obs.}$ | $\sin^2\theta_{calc.}$ | $I^*_{obs.}$ | $I_{calc.}$ |
|---|---|---|---|---|
| 001 | 0.0341 | 0.0338 | w⁻ | 78 |
| 100 | 0.0489 | 0.0486 | m | 646 |
| 101 | 0.0822 | 0.0824 | vs | 2605 |
| 002 | 0.1344 | 0.1346 | w | 330 |
| 110 | 0.1461 | 0.1459 | m⁺ | 884 |
| 111 | 0.1796 | 0.1797 | w | 72 |
| 102 | 0.1830 | 0.1832 | m | 228 |
| 200 | 0.1960 | 0.1946 | w | 104 |
| 201 | 0.2267 | 0.2284 | m⁺ | 564 |
| 112 | 0.2796 | 0.2805 | s⁻ | 604 |
| 003 | 0.3033 | 0.3028 | w⁻ | 6 |
| 202 | 0.3259 | 0.3304 | w⁻ | 90 |
| 210 | 0.3406 | 0.3405 | w⁻ | 86 |
| 103 | 0.3503 | 0.3517 | m⁻ | 275 |
| 211 | 0.3734 | 0.3743 | m | 494 |
| 300 | 0.4400 | 0.4378 | w⁺ | 150 |
| 113 | absent | 0.4478 | | 19 |
| 301 | 0.4734 | 0.4716 | w | 18 |
| 212 | | 0.4751 | | 106 |
| 203 | 0.4934 | 0.4974 | w | 167 |

Plus several additional lines.

* w = weak, m = medium, s = strong, vs = very strong.

The pseudo-hexagonal unit cell contains one molecule of $ThGe_2$ with one thorium atom in 0,0,0 and two germanium atoms in 1/2,2/3,1/2 and 2/3,1/3,1/2. The calculated density at room temperature is 10.51 g-cm$^{-3}$.

Our data seem best explained by the assumption of a slight distortion of the ideal hexagonal cell in addition to the vacancies in the ideal $MX_2$ lattice like those noted for $USi_{1.5}$, $PuSi_{1.5}$, and $ThSi_{1.5}$ (2, 7). Assumption of an orthorhombic distortion does not appear to yield the proper calculated spacings. An attempt will be made to index the structure as a monoclinic or triclinic distortion of the hexagonal cell.

Preparations in the $ThGe_{1.25\pm0.3}$ composition range give a diffraction pattern of $ThGe_{1.6}$ and a stronger pattern of a new phase. After being recrushed and reheated at 1500°C for about 2 hr, a sample of composition $ThGe_{1.2}$ gave a diffraction pattern essentially free of $ThGe_{1.6}$. The $\sin^2\theta$ values for this new phase were indexed on the basis of a cubic unit cell. The hkl values are either all even or all odd, suggesting a sodium chloride type lattice. Relative intensities were calculated on the assumption that the symmetry was that of space group $O^5_h$-Fm3m (NaCl type) with four thorium atoms in 0,0,0,; $\frac{1}{2},\frac{1}{2},0$; $\frac{1}{2},0,\frac{1}{2}$; $0,\frac{1}{2},\frac{1}{2}$; and four germanium atoms in $\frac{1}{2},\frac{1}{2},\frac{1}{2}$; $\frac{1}{2},0,0,$; $0,\frac{1}{2},0$; $0,0,\frac{1}{2}$. Calculated intensities are in excellent agreement with observed intensities. Table IV is a tabulation of these data. The good fit to the sodium chloride lattice leads one to conclude the phase to be ThGe.

Table IV. Crystallographic data for ThGe

| hkl | $\sin^2\theta_{obs.}$ | $\sin^2\theta_{calc.}$ | $I^*_{obs.}$ | $I_{calc.}$ |
|---|---|---|---|---|
| 111 | 0.0492 | 0.0488 | s | 137 |
| 200 | 0.0654 | 0.0651 | vs | 290 |
| 220 | 0.1307 | 0.1302 | vs | 216 |
| 311 | 0.1797 | 0.1791 | s⁻ | 75 |
| 222 | 0.2697 | 0.2605 | m⁺ | 36 |
| 331 | 0.3094 | 0.3093 | m⁻ | 28 |
| 420 | 0.3260 | 0.3256 | s | 97 |
| 422 | 0.3910 | 0.3907 | s⁻ | 74 |
| 511 | 0.4402 | 0.4396 | w | 18 |
| 333 | | | | 6 |
| 440 | 0.5199 | 0.5210 | w⁺ | 26 |
| 531 | 0.5695 | 0.5698 | w⁺ | 28 |
| 600 | 0.5856 | 0.5861 | m⁺ | 11 |
| 442 | | | | 46 |
| 620 | 0.6533 | 0.6533 | m | 45 |
| 533 | 0.6995 | 0.6987 | w⁻ | 14 |
| 622‡ | 0.7154 | 0.7151 | m | 47 |
| 444 | 0.7800 | 0.7801 | w⁻ | 17 |
| 711 | 0.8290 | 0.8289 | w⁺ | 18 |
| 551 | | | | 18 |
| 641 | 0.8451 | 0.8451 | m⁺ | 61 |
| 642 | 0.9103 | 0.9101 | s | 160 |
| 731 | 0.9592 | 0.9589 | m diffuse | 76 |
| 553 | | | | 38 |

* w = weak, m = medium, s = strong, vs = very strong.
‡ Remainder of reflections are for CuK$\alpha_1$ radiation.

The lattice parameter for ThGe was calculated using the sharp reflections in the back reflection region. Calculation from three different diffraction patterns gives the value $a_o = 6.044 \pm 0.001$Å. The calculated density at room temperature is 9.17 g-cm$^{-3}$.

Samples near composition $ThGe_{0.8}$ gave diffraction patterns showing a weak ThGe phase and a higher thorium phase. This phase was never prepared in the pure state and apparently did not crystallize well. It may be thermodynamically stable over only part of the temperature range studied. The low angle reflection region of the diffraction patterns of the new phase is very similar to that for $U_3Si_2$. The $\sin^2\theta$ values could be fitted to a unit cell with tetragonal symmetry. Intensities were calculated by use of the assumption that the compound is isostructural with $U_3Si_2$ and that the atoms are located in positions corresponding to those in the silicide. Table V contains the observed and calculated data. Since agreement is good, these data confirm the formula $Th_3Ge_2$. The structure is primitive tetragonal with space group $D^5_{4h}$-P4/mbm symmetry. There are two molecules per unit cell with the thorium atoms located as follows: $2Th_I$ in 0,0,0,; ½,½,0; $4Th_{II}$ in $x,½+x,½$; $-x,½-x,½$; $½+x,-x,½$; $½-x,x,½$; with $x$ approximately equal to 0.18. The four germanium atoms are located in $x,½+x,0$; $-x,½-x,0$; $½+x,-x,0$; $½-x,x,0$; with $x$ approximately equal to 0.39. The lattice parameters are $a_o = 7.971 \pm 0.004$Å and $c_o = 4.170 \pm 0.003$Å. The $c/a$ ratio is 0.523, and the calculated density at room temperature is 10.55 g-cm$^{-3}$.

Table V. Crystallographic data for $Th_3Ge_2$

| hkl | $\sin^2\theta_{obs.}$ | $\sin^2\theta_{calc.}$ | $I_{obs.}$ | $I_{calc.}$ |
|---|---|---|---|---|
| 110 | 0.0180 | 0.0187 | w⁻ | 7.0 |
| 001 | absent | 0.0342 | | 3.1 |
| 200 | absent | 0.0374 | | 1.4 |
| 210 | 0.0464 | 0.0467 | m | 78.8 |
| 111 | 0.0527 | 0.0529 | m | 67.0 |
| 201 | 0.0706 | 0.0716 | vs | 286.1 |
| 220 | 0.0749 | 0.0748 | m⁻ | 79.6 |
| 211 | 0.0808 | 0.0809 | vs | 266.9 |
| 310 | 0.0933 | 0.0935 | s | 143.8 |
| 221 | absent | 0.1089 | | 0.9 |
| 320 | 0.1216 | 0.1215 | w | 20.7 |
| 311 | 0.1277 | 0.1277 | w⁻ | 7.9 |
| 002 | 0.1365 | 0.1368 | m | 57.4 |
| 400* | 0.1506 | 0.1497 | m | 0.7 |
| 112 | absent | 0.1555 | | 1.3 |
| 321 | absent | 0.1557 | | 0.5 |
| 410 | 0.1589 | 0.1589 | m | 58.2 |
| 330 | 0.1680 | 0.1683 | w⁻ | 7.4 |
| 202 | absent | 0.1742 | | 0.5 |
| 212 | 0.1834 | 0.1835 | w | 25.5 |
| 401 | | 0.1839 | | 7.0 |
| 420 | 0.1872 | 0.1870 | w⁻ | 14.8 |
| 411 | 0.1934 | 0.1931 | m | 63.1 |
| 331 | 0.2021 | 0.2025 | m | 78.0 |
| 222 | 0.2106 | 0.2116 | w | 34.8 |

* This reflection corresponds to a $ThO_2$ reflection.

Table VI. Nearest neighbors and interatomic distances

| Compound | Nearest Neighbors | |
|---|---|---|
| $\alpha$-$ThGe_2$ | Thorium— | 12 Ge at 3.14Å |
| | Germanium— | 6 Th at 3.14Å |
| | | 3 Ge at 2.37Å |
| $\beta$-$ThGe_2$ | Thorium— | 12 Ge at 3.15Å |
| | | 6 Th at 4.04Å |
| | | 2 Th at 4.22Å |
| | Germanium— | 6 Th at 3.15Å |
| | | 3 Ge at 2.34Å |
| ThGe | Thorium— | 6 Ge at 3.022Å |
| | | 12 Th at 4.274Å |
| | Germanium— | 6 Th at 3.022Å |
| | | 12 Ge at 4.274Å |
| $Th_3Ge_2$ | Thorium I— | 4 Ge at 3.23Å |
| | | 8 Th at 3.66Å |
| | Thorium II— | 6 Ge at 3.16Å |
| | | 4 Th at 3.66Å |
| | Germanium— | 1 Ge at 2.48Å |
| | | 2 Th at 3.23Å |
| | | 6 Th at 3.16Å |

Samples of higher thorium content give a diffraction pattern for thorium, thorium dioxide, and a new phase of complicated structure. Attempts to index the spacings for the new phase were unsuccessful. Because of the $ThO_2$ contaminant it is not possible to assign to the phase an accurate composition. On the basis of the composition of samples which gave the best patterns of the known compounds, the compound is believed to be $ThGe_{0.3\pm0.1}$. This compound is the only one found whose structure is apparently different from that of a corresponding uranium silicide.

### *Nearest Neighbor Distances and Coordination Numbers*

As can be seen from Table VI, the calculated interatomic distances are compatible with the structures determined for the different compounds. The same coordination numbers are found in $\alpha$-$ThGe_2$ and $ThGe_{1.6}$ for the theoretical $MX_2$ structures with the interatomic distances being only slightly different. This observation is interesting because the

arrangement of atoms is quite different. In $\alpha$-$ThGe_2$ the thorium atoms are contained in a three dimensional network of germanium atoms, and in $\beta$-$ThGe_2$ the thorium atoms are between a two dimensional, graphite-like layer of germanium atoms. In ThGe there is only thorium to germanium bonding. In the $Th_3Ge_2$ structure the thorium I is not equivalent to the thorium II atoms. There is thorium to thorium bonding and the germanium atoms are joined in pairs at approximately their single bond distance. The general structure is one of a layer of thorium atoms contained between layers which contain both thorium and germanium atoms.

It is interesting to note that by removing half of the germanium atoms from $\beta$-$ThGe_2$ in an alternate manner, and by shifting the atom positions only slightly, the ThGe structure is obtained. The 111 plane of $\beta$-$ThGe_2$ contains an almost identical arrangement of atoms to that found in ThGe.

*Reactivity with Common Reagents*

The reactivity at room temperature was observed for the $ThGe_{3.0\pm0.4}$ $\alpha$-$ThGe_2$, and $ThGe_{1.0\pm0.3}$ phases. The other compounds were not tested for reactivity because they were not available as pure phases.

Reactions of the three compounds tested with 5% HCl, concentrated HF, aqua regia, and 10% NaOH were vigorous. Reaction with 30% $H_2O_2$, 3M $H_2SO_4$, 18M $H_2SO_4$, 6M $HNO_3$, and concentrated $HNO_3$ proceeded rather slowly. No reaction was observed to take place with 85% $H_3PO_4$ or 0.1N $KMnO_4$. It is possible that some of the reactivities were affected by the presence of $ThO_2$ in the samples.

### Acknowledgment

This work was supported by the Office of Naval Research.

Manuscript received June 17, 1957. This paper was prepared for delivery before the Chicago Meeting, May 2-6, 1954.

Any discussion of this paper will appear in a Discussion Section to be published in the June 1959 JOURNAL.

REFERENCES

1. G. Brauer and A. Mitius, *Z. anorg. Chem.*, **249**, 325 (1942).
2. E. L. Jacobson, R. D. Freeman, A. G. Tharp, and A. W. Searcy, *J. Am. Chem. Soc.*, **78**, 4850 (1956).
3. W. H. Zachariasen, *Acta. Cryst.*, **2**, 94 (1949).
4. A. Kaufmann, B. Cullity, and G. Bitsianes, *J. Metals* **9**, *AIME Trans.* **209**, 23 (1957).
5. B. R. T. Frost and J. T. Maskrey, *J. Inst. Metals*, **8**, 177 (1953).
6. A. Iandelli and R. Ferro, *Ann. Chim. Applicata, Roma*, **42**, 598 (1952).
7. O. J. Runnalls and R. R. Boucher, *Acta Cryst.*, **8**, 592 (1955).
8. A. W. Searcy and R. A. McNees, Jr., *J. Am. Chem. Soc.* **75**, 1578 (1953).

# The Mobilities of the Ions in Fused $KNO_3$-$AgNO_3$ Mixtures

**F. R. Duke and Boone Owens**

*Institute for Atomic Research and Department of Chemistry, Iowa State College, Ames, Iowa*

ABSTRACT

The mobilities of the three ions in fused $KNO_3$-$AgNO_3$ mixtures have been determined as a function of composition. The mobility of the nitrate ion is insensitive to composition changes; the cations, however, tend toward the mobility of the main constituent cation at each end of the composition scale. Temperature variation has no significant effect on the transport numbers of these ions.

The mobilities of the ions in a $NaNO_3$-$AgNO_3$ mixture have been determined (1). This mixture was ideal in the sense that the ion mobilities are independent of composition. However, since $Na^+$ and $Ag^+$ in the pure nitrates have essentially the same mobilities, it was considered advisable to repeat the work using a pair of cations having significantly different mobilities. Thus, a mixture of $AgNO_3$ and $KNO_3$ was chosen for study.

## Experimental

C. P. Reagent Grade salts and pure silver wire were used in the study. The apparatus and techniques used were duplicates of those used in the $AgNO_3$-$NaNO_3$ work (1).

## Results and Discussion

The values for the mobility of the two cations relative to the anion are expressed in terms of $\phi$ (2), where $\phi = 1 - t_{Ag^+} - N_1^\circ t_-$, where $N_1^\circ$ is the original mole fraction of $AgNO_3$ and $t_-$ is the transport number of $NO_3^-$. If $t_-$ is taken as zero, then $\phi = t_{K^+}$. A plot of $\phi$ vs. $N_1$ is shown in Fig. 1. It can be seen that there is some deviation from linearity, the $K^+$ being less mobile than the $Ag^+$.

The results of the volume change across a membrane during electrolysis of mixtures of $AgNO_3$ and $KNO_3$ serve to fix all three of the transport numbers when combined with the $\phi$ data.

**Table I. Volume change of cathode per equivalent, $\phi$, and $t_+$ data for various mixtures of $KNO_3$-$AgNO_3$**

| Mole fraction $AgNO_3$ | $\phi$ | $V_c/Z$ (cm³/Eq.) | $t_{Ag^+}$ | $t_{K^+}$ |
|---|---|---|---|---|
| 1.00 | — | −1.5±2.6 | 0.72±.06 | 0.0 |
| 0.75 | 0.21±.01 | −0.5±0.6 | 0.56±.03 | 0.15±.03 |
| 0.50 | 0.41±.01 | −1.2±2.0 | 0.43±.04 | 0.25±.04 |
| 0.25 | 0.70±.01 | −2.9±0.5 | 0.20±.03 | 0.40±.03 |
| 0.00 | — | −0.9±1.3 | 0.0 | 0.60±.03 |

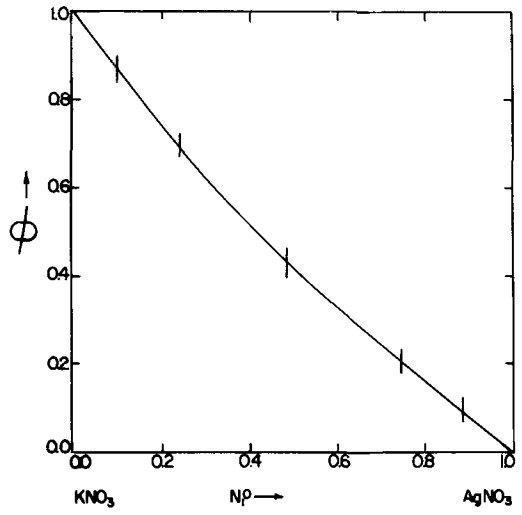


Fig. 1. $\phi$ vs. composition in the system $AgNO_3$-$KNO_3$

$$\frac{\Delta V_c}{Z} = \overline{V}_{Ag} + (t_{Ag^+} - 1)\overline{V}_{AgNO_3} + t_{K^+}\overline{V}_{KNO_3}$$

where $V_c$ is the volume change of the catholyte, $Z$ is the current, and the $\overline{V}$'s are the molar volumes of the species indicated. Molar volumes in this system are very nearly identical with partial molal volumes (3). In the pure salts, both transport numbers may be calculated from the volume-change equation (4). Table I shows values of $(\Delta V_c)/Z$ for the pure salts and salt mixtures.

The transport numbers calculated from the $\phi$ and $\Delta V_c$ equations are listed in Table I.

The ionic equivalent conductances, $\lambda_i$, are calculated from the total equivalent conductivities and the transport numbers using the equation $\lambda_i = \lambda t_i / N_i$, where $\lambda$ is the total equivalent conductance, $t_i$ the transport number, and $N_i$ the equivalent fraction. The total equivalent conductivity of the mixture

**Table II. Ionic equivalent conductivities in the system $AgNO_3$-$KNO_3$ at 350°C**

| Mole fraction $AgNO_3$ | $\lambda$ | $\lambda_{Ag^+}$ | $\lambda_{K^+}$ | $\lambda_{NO_3^-}$ |
|---|---|---|---|---|
| 0.00 | 36.4 | — | 21.7±1.1 | 14.7±1.1 |
| 0.25 | 40.7 | 32.6±4.9 | 21.7±1.6 | 16.3±1.0 |
| 0.50 | 45.6 | 39.2±3.6 | 22.8±3.7 | 14.6±1.8 |
| 0.75 | 50.3 | 37.6±2.0 | 30.2±6.0 | 14.6±1.0 |
| 1.00 | 54.8 | 39.7±3.5 | — | 15.6±3.3 |

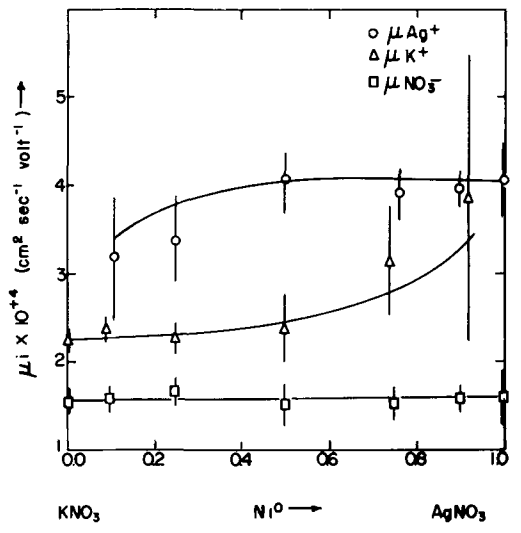


Fig. 2. Ionic mobilities in the system $AgNO_3$-$KNO_3$ at 350°C.

was calculated from the density data of Bloom and Rhodes (3) and from specific conductivity data obtained in this laboratory (5). These data are listed in Table II.

The mobilities, $\mu_i$, are calculated using the equation $\mu_i = (\lambda_i)/96500$ and are plotted as functions of composition in Fig. 2.

The precision in the determination of mobilities becomes poor at high dilution of the ions because they carry so little of the total current. However, the mobility curves for the cations suggest that, at high dilution, the mobility of the minor constituent approaches that of the major constituent; this, in turn, suggests that some sort of chain mechanism involving more than one ion of the same kind is responsible for the normal mobility in the pure salts.

Manuscript received March 24, 1958. Contribution No. 605. Work was performed in the Ames Laboratory of the U. S. Atomic Energy Commission.

Any discussion of this paper will appear in a Discussion Section to be published in the June 1959 JOURNAL.

REFERENCES

1. F. R. Duke, R. W. Laity, and B. Owens, *This Journal*, **104**, 299 (1957).
2. P. M. Aziz and F. E. W. Wetmore, *Can. J. Chem.*, **30**, 779 (1952).
3. H. Bloom and D. C. Rhodes, *J. Phys. Chem.*, **60**, 791 (1956).
4. F. R. Duke and B. Owens, *This Journal*, To be published.
5. F. R. Duke and R. A. Fleming, *ibid.*

# Mechanism of Anode Thermal Reaction in Aluminum Reduction Cells

**Harry Stern**

*State College of Washington, Pullman, Washington*

**and**

**G. T. Holmes**

*Aluminum Company of America, New Kensington, Pennsylvania*

ABSTRACT

A number of aluminum production potlines were subjected to a series of counter-emf tests wherein the decay of the reversible voltage with time was measured. Analysis of these data indicate that the reversible voltage during electrolysis is associated with an intermediate compound C*O on the anode surface which decomposes chemically to $CO_2$ by a reaction of approximately second order. At a current density of 0.95 amp/cm$^2$ and a temperature of 971°C, the reversible voltage is 1.45 v. The free energy of formation of C*O at 971°C from C and $O_2$ at 25°C is —67,150 cal/g mole.

The over all chemical reaction for the reduction of alumina as carried out normally in electrolytic cells by the Hall process is

$$2Al_2O_3 + 3C \rightarrow 4Al + 3CO_2 \qquad [1]$$

as judged from the initial reactants and final products. Experimental evidence is presented here to support the view that carbon dioxide is formed by a thermal reaction between the carbon anode and oxygen adsorbed on the carbon surface and that the actual electrochemical reaction should be written

$$2Al_2O_3 + 6C \rightarrow 4Al + 6C^*O \qquad [2]$$

where the symbol C*O represents oxygen adsorbed on the carbon surface. Specifically, it will be shown that the reversible decomposition voltage of the cell depends primarily on the concentration of adsorbed oxygen on the anode surface and not on the concentration of $CO_2$ nor on concentration gradients within the electrolyte. It is postulated that reaction [2] is followed by

$$6C^*O \rightarrow 3CO_2 + 3C \qquad [3]$$

to give the over-all reaction [1] and it will be shown that reaction [3] is a thermal reaction proceeding at a rate corresponding to approximately a second order reaction.

## Experimental

The experimental measurements consisted entirely of a number of counter-emf tests performed on a series of production potlines. In a counter-emf test, a line of normally operating cells is suddenly disconnected from its operating electrical power source, and the open-circuit voltage generated by the resulting line of voltaic cells is measured as a function of time. The result is a recorded curve of the potline counter-emf on open circuit as it decays with time. The number of volts per pot is determined by dividing the potline counter-emf by the number of pots (cells) in the line.

The tests were performed at the Wenatchee, Washington, plant of the Aluminum Company of America. Tests were performed only on potlines that showed no anode effect for a considerable period before the test, and in which all of the cells were apparently operating normally. Of course it is probable that conditions varied somewhat from cell to cell. By taking a potline voltage and dividing by the number of cells in the line, an average cell voltage is obtained.

Fig. 1 is a diagram of the electrical connections used. Before the potline is tripped (disconnected from its power source), the d-c source shown is adjusted to the approximate value of the counter-emf of the potline which is about 200 v. This puts the pointer on the voltmeter at about the desired reading and greatly reduces overswing and "hunting." When the potline is tripped, the "b" contacts on the cathode breaker close. The coil of $C_1$ is energized by the "b" contact closing. $C_1$ closes and energizes the coil of $C_2$. When $C_2$ operates, the d-c

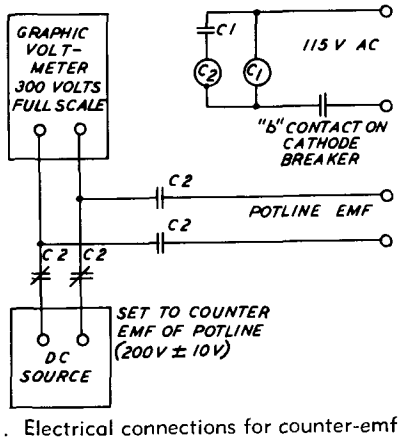


Fig. 1. Electrical connections for counter-emf tests

source is disconnected from the voltmeter and the potline counter-emf is simultaneously applied to the meter. The $C_1 - C_2$ relay chain provides a time delay which prevents the voltmeter from being placed across the potline during the inductive surge following the tripping of the potline. This surge, which was shown by oscillograph measurements to reach 1500 v, would cause the pointer to swing off scale and then "hunt." In this manner only the first few milliseconds of reading are lost, but the potline emf could not be read during this time anyway since the surge is caused by the high d-c field collapsing around the bus bars.

Time is taken as zero at the instant the potline is tripped. The counter-emf at time zero, which corresponds to the reversible decomposition voltage of the cells at the operating current density and temperature, could not be read directly for the reasons given above. Values for the reversible decomposition voltage were obtained by extrapolation of the voltage decay curves back to zero time using an analytical procedure as will be shown.

Data from these tests are given in Table I. In Table I, the time in minutes could be determined readily from the meter chart to 0.001 min and the voltage per pot to 0.01 v. An estimate of the next decimal place is given for each reading, although the correlation does not depend on this estimate. The response time of the meter was very small and would not affect the reading in view of the gradual drop of the voltage, except possibly during the first few seconds.

## Theoretical Analysis

The voltaic cells generate a voltage which corresponds to the reverse of the postulated reaction [2], that is

$$2Al + 3C^*O \rightarrow Al_2O_3 + 3C \qquad [4]$$

The open-circuit (reversible) voltage generated by reaction [4] is given by the equation

$$E = E_o + \frac{RT}{nF} \ln \frac{a^2_{Al}\, a^3_{C^*O}}{a_{Al_2O_3}\, a^3_C} \qquad [5]$$

where $E$ is the voltage of the cell, $E_o$ is the voltage that would be generated if all reactants and products of reaction [4] were in their standard states (arbitrarily chosen), and the $a$ values are the activities of the reactants and products based on these standard states. $R$ equals 8.313 joules/g mole °K; $T$ equals °K; $F$ equals 96,500 coulombs/g equiv; $n$ equals 6 g equiv/g mole $Al_2O_3$; and ln equals log to the base $e$.

Since neither the aluminum nor the carbon are in solution phase, their activities are 1 and equation [5] becomes

$$E = E_o + \frac{RT}{nF} \ln \frac{a^3_{C^*O}}{a_{Al_2O_3}} \qquad [6]$$

Since the selection of standard states is arbitrary, let us select the conditions at time $O$, that is, when the electrical circuit is broken, as the standard states. Then let

$$a_{C^*O} = \frac{p}{p_o} \text{ and } a_{Al_2O_3} = \frac{c}{c_o}$$

where $p_o$ and $c_o$ are the fugacities of $C^*O$ and $Al_2O_3$, respectively, at time $O$ (standard states), and $p$ and $c$ are the corresponding fugacities at any subsequent time $t$ when the open circuit voltage has decayed to $E$ after starting with a value of $E_o$ at time $O$. Then equation [6] becomes

$$E = E_o + \frac{3RT}{nF} \ln \frac{p}{p_o} - \frac{RT}{nF} \ln \frac{c}{c_o} \qquad [7]$$

If now $p$ and $c$ can be found as functions of the time $t$, then equation [7] will express the decay of $E$ with $t$ and can be checked against the experimental data of the counter-emf tests. Before this is done, however, let us examine possible means of simplifying equation [7].

If we assume tentatively that the decay of $E$ with time is due *entirely* to the rise in $c$ caused by the equalization of the $Al_2O_3$ concentration gradient near the electrodes, then the $p$ term can be eliminated and Eq. [7] becomes

$$E = E_o - \frac{RT}{nF} \ln \frac{c}{c_o} \qquad [8]$$

On the other hand, if we assume tentatively that the decay of $E$ is due *entirely* to the fall in $p$ caused by reaction [3], then the $c$ term can be eliminated and equation [7] becomes

$$E = E_o + \frac{3RT}{nF} \ln \frac{p}{p_o} \qquad [9]$$

To test the validity of either of these assumptions, Eqs. [8] and [9] will be tested against the experimental data. If neither [8] nor [9] fits the data, then we may conclude that both effects are important and will be forced to use the more complex Eq. [7].

### *Test of Diffusion Hypothesis*

Let us test Eq. [8] first. For the relation between $c$ and $t$, assume that the change of $c$ with time is due to the equalization of the $Al_2O_3$ concentration gradient formed near the electrodes during electrolysis. This equalization takes place by diffusion and convection after the electric current is shut off. The rate of equalization may be written in the form

$$\frac{dc}{dt} = K(c_b - c) \qquad [10]$$

where $K$ is the mass transfer coefficient and will depend on the degree of turbulence as well as on the diffusivity of the bath at the electrode surface, $c_b$ is the fugacity of the $Al_2O_3$ in the bulk of the bath, and $c$ is the fugacity of the $Al_2O_3$ at the electrode surface. If we assume that $K$ is a constant (a rough approximation especially near time $O$) we may write

$$\int_{c_o}^{c} \frac{dc}{c_b - c} = K \int_0^t dt \qquad [11]$$

where $c_o$ is the fugacity at the electrode surface at time $O$ and $c$ is the fugacity of the electrode surface at any subsequent time $t$. Integrating and rearranging Eq. [11] gives

$$c = \frac{c_b(e^{Kt} - 1)}{e^{Kt}} + c_o \qquad [12]$$

Table I. Decay of voltage with time for five counter-emf tests

| Test No. 1 Prebake anode Current density 0.93 amp/cm² (before time O) Temperature, 971°C | | Test No. 2 Prebake anode Current density 0.90 amp/cm² (before time O) Temperature, 973°C | | Test No. 3 Prebake anode Current density 1.22 amp/cm² (before time O) Temperature, 976°C | | Test No. 4 Prebake anode Current density 0.93 amp/cm² (before time O) Temperature, 967°C | | Test No. 5 Soderberg anode Current density 0.79 amp/cm² (before time O) Temperature, 968°C | |
|---|---|---|---|---|---|---|---|---|---|
| $t$ Min | $E$ Volts/pot | $t$ Min | $E$ Volts/pot | $t$ Min | $E$ Volts/pot | $t$ Min | $E$ Volts/pot | $t$ Min | $E$ Volts/pot |
| 0.0333 | 1.324 | 0.0130 | 1.437 | 0.0167 | 1.412 | 0.0319 | 1.305 | 0.0833 | 1.355 |
| 0.0639 | 1.296 | 0.0269 | 1.407 | 0.0833 | 1.303 | 0.0667 | 1.277 | 0.1667 | 1.331 |
| 0.1194 | 1.268 | 0.0425 | 1.380 | 0.1667 | 1.269 | 0.1194 | 1.248 | 0.2500 | 1.318 |
| 0.2152 | 1.239 | 0.0694 | 1.352 | 0.2500 | 1.244 | 0.1931 | 1.220 | 0.3300 | 1.289 |
| 0.3055 | 1.211 | 0.1237 | 1.324 | 0.3333 | 1.227 | 0.2569 | 1.191 | 0.4167 | 1.273 |
| 0.4444 | 1.183 | 0.2222 | 1.296 | 0.4167 | 1.202 | 0.2972 | 1.163 | 0.5000 | 1.248 |
| 0.7361 | 1.155 | 0.4053 | 1.268 | 0.5000 | 1.185 | 0.3417 | 1.135 | 0.5833 | 1.231 |
| 1.0693 | 1.126 | 0.7109 | 1.239 | 0.5833 | 1.168 | 0.4222 | 1.106 | 0.7500 | 1.223 |
| 1.764 | 1.098 | 1.4526 | 1.211 | 0.6667 | 1.151 | 0.8472 | 1.078 | 1.000 | 1.227 |
| 2.564 | 1.070 | 1.9387 | 1.183 | 0.7500 | 1.143 | 1.019 | 1.050 | 1.250 | 1.219 |
| 4.028 | 1.042 | 3.161 | 1.155 | 1.1667 | 1.118 | 1.669 | 1.021 | 1.500 | 1.204 |
| 6.030 | 1.014 | 4.792 | 1.127 | 1.6667 | 1.092 | 2.375 | 0.993 | 1.833 | 1.196 |
| 8.717 | 0.986 | | | 2.5000 | 1.067 | 3.643 | 0.965 | 2.500 | 1.192 |
| | | | | 3.5000 | 1.042 | 5.287 | 0.936 | 3.000 | 1.174 |
| | | | | 5.0000 | 1.017 | 7.249 | 0.908 | 4.000 | 1.162 |
| | | | | 7.0000 | 0.994 | 9.639 | 0.876 | 6.000 | 1.141 |
| | | | | 10.0000 | 0.967 | 11.47 | 0.862 | 7.000 | 1.134 |
| | | | | 13.5000 | 0.943 | | | 9.000 | 1.123 |
| | | | | | | | | 12.000 | 1.111 |
| | | | | | | | | 19.000 | 1.095 |

Substituting for $c$ from Eq. [12] into Eq. [8] gives

$$E = E_o - \frac{RT}{nF} \ln \left[ \frac{c_b}{c_o} \left( \frac{e^{Kt} - 1}{e^{Kt}} \right) + 1 \right] \quad [13]$$

This is the equation to be tested against the data. The data indicate that in 10 minutes' time the voltage decays by about 0.4 v. That is, $E_o - E = 0.4$ when $t = 10$. Using these values in Eq. [13],

$$E_o - E = \frac{2.303\,RT}{nF} \log \left[ \frac{c_b}{c_o} \left( \frac{e^{10K} - 1}{e^{10K}} \right) + 1 \right] = 0.4 \quad [14]$$

The average temperature of these tests was 1244°K, so that

$$\frac{2.303\,RT}{nF} = \frac{2.303 \times 8.313 \times 1244}{6 \times 96{,}500} = 0.0411 \text{ v}$$

Then, from Eq. [14]

$$\log \left[ \frac{c_b}{c_o} \left( \frac{e^{10K} - 1}{e^{10K}} \right) + 1 \right] = \frac{0.4}{0.0411} \cong 10$$

If $K$ is greater than or equal to 1, $\frac{e^{10K} - 1}{e^{10K}}$ is very close to 1, $\log \left[ \frac{c_b}{c_o} + 1 \right] = 10$, and $\frac{c_b}{c_o} = 10^{10}$. If $K$ is less than 1, $\frac{c_b}{c_o}$ must be even larger than $10^{10}$.

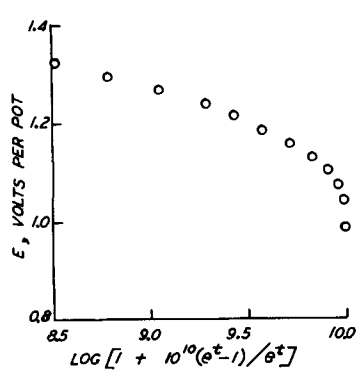


Fig. 2. Nonlinear plot showing that Eq. [15], representing diffusion, is not valid.

Thus we see that, for Eq. [13] to fit the data, it is necessary for the activity of the $Al_2O_3$ in the bulk of the bath to be at least 10 billion times the activity of the $Al_2O_3$ at the electrode surface during electrolysis (before and at time $O$). This does not seem likely. However, since we do not know the activity at the electrode surface, we may admit that this is possible at high current densities. Using $10^{10}$ for $\frac{c_b}{c_o}$ in Eq. [13] and tentatively letting $K = 1$,

$$E = E_o - 0.0411 \log \left[ \frac{e^t - 1}{e^t} \times 10^{10} + 1 \right] \quad [15]$$

If Eq. [15] fits the data, a plot of $E$ vs. $\log \left[ \frac{e^t - 1}{e^t} \times 10^{10} + 1 \right]$ would give a straight line.

The data of counter-emf test No. 1, Table I, are plotted in this way in Fig. 2 where it can be seen that the points definitely do not fall along a straight line and Eq. [15] does not represent the experimental data.

In Eq. [15], $K$ was arbitrarily set equal to 1. Let us examine the effect of taking other values of $K$. Values of $K$ greater than 1 yield curves that are even farther removed from a straight line than that shown in Fig. 2. Values of $K$ less than 1 yield curves that are straighter than that shown in Fig. 2. In fact, when $K$ is any value between 0 and 0.01, Eq. [13] can be made to represent the data. However, such representation must be regarded as trivial, for, when $K$ is between 0 and 0.01, the function $\frac{e^{Kt} - 1}{e^{Kt}}$

has essentially the same values as $Kt$ for the range of $t$ values in the tests and therefore does not represent the assumptions which led to Eq. [13]. Furthermore, the slopes of the straight lines obtained when Eq. [13] is used on the experimental tests with $K = 0.01$ are found to vary from $-0.1$ to $-0.2$. But Eq. [13] calls for a constant slope of $-0.0411$ at 1244°K. Thus Eq. [13] cannot account for either the magnitude or the variation of these slopes.

Thus it is seen that Eq. [13], and therefore Eq. [8], does not represent the data, and it can therefore be concluded that equalization of concentration gradients is not an important cause of voltage decay with time during counter-emf tests although it may have some effect.

*Test of Chemical Reaction Hypothesis*

Now let us test Eq. [9] for which the assumption was made that the only important cause of counter-emf decay is the depletion of oxygen atoms on the surface of the carbon anode caused by chemical reaction [3]. For the relation between $p$ and $t$, we may write as the rate equation for reaction [3]

$$-\frac{dp}{dt} = kp^r \qquad [16]$$

where $k$ is the reaction rate constant and $r$ is the order of the reaction.

Reaction [3] may be written

$$2C^*O \rightarrow CO_2 + C$$

This reaction may be visualized as taking place by the mechanism of 2 adsorbed oxygen atoms combining directly with one carbon atom to form carbon dioxide and thus leave a freshly exposed carbon atom on the anode surface to adsorb another oxygen atom from the fused salt bath. The molecularity of the reaction is thus 2, and if the reaction occurs by the simple mechanism outlined then the order of the reaction is also 2 (1). The order of the reaction $r$ can be determined experimentally and, if it turns out to be 2, we may consider this to be a confirming piece of evidence for our postulates.

Using limits of $p_o$ at time $O$ and $p$ at time $t$, Eq. [16] becomes

$$\int_{p_o}^{p} \frac{dp}{p^r} = -k\int_{o}^{t} dt$$

Integrating and solving for p gives

$$p = \left[ p_o^{1-r} + k(r-1)t \right]^{1/1-r} \qquad [17]$$

Substituting for $p$ from Eq. [17] into Eq. [9] and rearranging gives

$$E = E_o - \frac{3RT}{nF}\ln p_o + \frac{3RT}{nF(1-r)}\ln[k(r-1)] + \frac{3RT}{nF(1-r)}\ln\left(\frac{p_o^{1-r}}{k(r-1)} + t\right) \qquad [18]$$

Equation [18] can be written in the form

$$E = S + W \log (t + U) \qquad [19]$$

where the constants $S$, $W$, and $U$ have values as follows:

$$S = E_o - \frac{3RT}{nF}\ln p_o + \frac{3RT}{nF(1-r)}\ln[k(r-1)] \qquad [20]$$

$$W = \frac{(2.303)\,3RT}{nF(1-r)} \qquad [21]$$

$$U = \frac{p_o^{1-r}}{k(r-1)} \qquad [22]$$

If Eq. [19] fits the data, a plot of $E$ vs. log $(t + U)$ should give a straight line. The data of five counter-emf tests, given in Table I, are plotted this way in Fig. 3 to 7. As can be seen, the points do in fact fall along straight lines. Furthermore, Eq. [19] accounts for the variation and magnitude of the slopes of these lines. The slope $W$ varies from test to test because of variation in $r$, the kinetic order of reaction [3]. For the five tests, $r$ is found from Eq. [21] to have values ranging from 1.64 to 2.11. Thus reaction [3] is found to be approximately a second

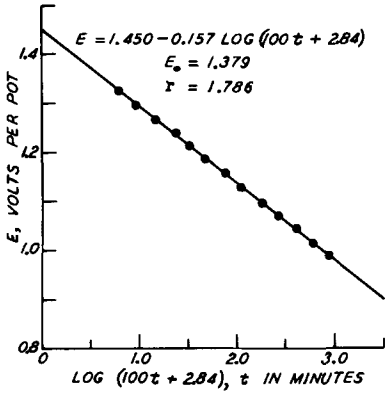


Fig. 3. Counter-emf test No. 1

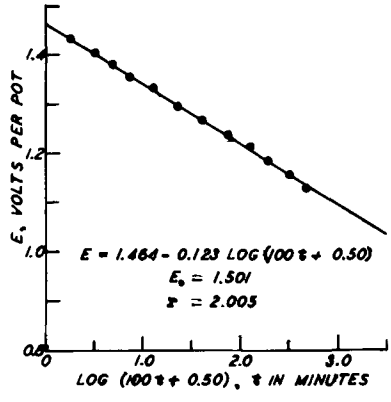


Fig. 4. Counter-emf test No. 2

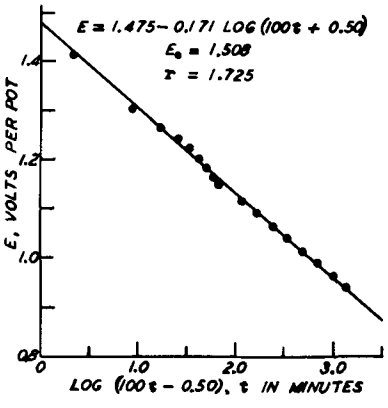


Fig. 5. Counter-emf test No. 3

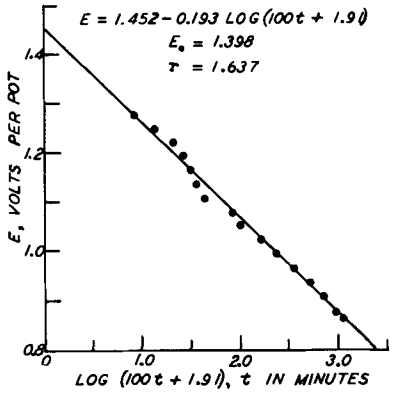


Fig. 6. Counter-emf test No. 4

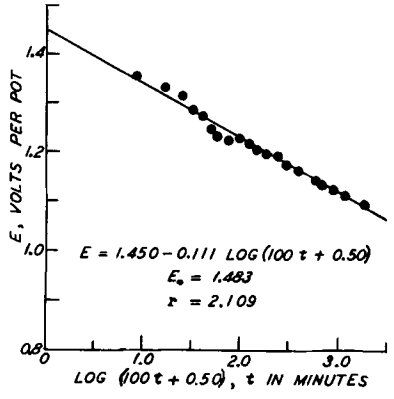


Fig. 7. Counter-emf test No. 5

order kinetic reaction, the variation in order possibly being caused by different surface characteristics of the anode carbons. The magnitude of $r$ thus confirms the assumptions made in deriving Eq. [19].

The validity of Eq. [19], and therefore Eq. [9], is thus substantiated. It may therefore be concluded that the thermal reaction of oxygen atoms with carbon at the anode is the only important cause of the voltage decay with time during the counter-emf tests. From this it follows that during normal electrolysis the depolarization must be due almost entirely to reaction [3] and depends only slightly on the rate of diffusion of $Al_2O_3$ to the electrodes. The long time constant polarization discussed by Haupin (3) is thus seen to be caused predominantly by the kinetics of the carbon-oxygen reaction rather than by equalization of concentration gradients in the electrolyte.

The fact that, in general, $r$ is not exactly 2, indicates that reaction [3] is kinetically of a somewhat complex order (4). This in turn may mean that the reaction proceeds via a chain reaction and may therefore be accelerated or inhibited by trace catalysts. Since reaction [3] is also the controlling step in the normal combustion of carbon (5) the following possibility suggests itself. A carbon anode can be made in two parts, the lower part containing a trace accelerator for reaction [3] to lower the decomposition voltage, and the upper part or stub containing a trace inhibitor to reduce air burning. A systematic search for such trace catalysts may prove fruitful.

Equation [19] may be used to find precise values for the decomposition voltage. The voltage at $O$ time, $E_o$, is virtually impossible to obtain by direct experimental observation. It can be obtained, however, by extrapolation of the data to $O$ time. This is best done by setting $t = 0$ in Eq. [19] and solving for $E$ which then becomes $E_o$, the decomposition voltage of the cell reaction. The constants for Eq. [19] together with values for $E_o$ and $r$ are given in Fig. 3 to 7. The range of $E_o$ is 1.38 to 1.51 v.

Individual values of $k$ and $p_o$ in Eq. [18] cannot be obtained from the empirical constants because there are only 3 empirical constants, $S$, $W$, and $U$ to determine 4 unknowns, $E_o$, $r$, $k$, and $p_o$. It may be possible to find $k$ and $p_o$ by running a series of counter-emf tests over a range of temperatures and using the Arrhenius equation

$$k = Ae^{-B/T} \qquad [23]$$

together with Eq. [20] and [22] and their first derivatives with respect to temperature.

It may be argued that Eq. [18] could apply to any thermal reaction such as

$$CO_2 + C \rightarrow 2CO$$

But, if this were the case, the voltage would start at 1.2 v which is the voltage corresponding to the electrochemical reaction

$$2Al_2O_3 + 3C \rightarrow 3CO_2 + 4Al$$

and decay to 1.1 v which is the voltage corresponding to the reaction

$$Al_2O_3 + 3C \rightarrow 3CO + 2Al$$

The fact is that the voltage starts at 1.4 to 1.5 v and decays steadily and indefinitely to values well below 1.1 with no sign of leveling off. This is best explained by assuming the indefinite depletion of oxygen atoms at the carbon surface, with the $CO_2$ product having no effect on the voltage.

The results of this analysis are in line with the reports of recent investigators. Pearson and Waddington (6) have shown that the primary anode gas evolved is $CO_2$ and that CO is formed as a secondary product by reduction of $CO_2$ either by the anode carbon or by metal fog. Schadinger (7) has shown that CO is not affected by contact with metal fog so that the drop in voltage below 1.1 cannot be explained on the basis of reduction of CO by metal fog. Grjotheim (8), using a platinum anode, found that no measurable overvoltage occurs for the discharge of aluminum on an aluminum cathode so that the disregard of cathode polarization in the above analysis is justified. A number of investigators (9-11) have used the hypothesis of the formation of intermediate carbon oxides on the anode surface to explain results that are related to those presented here.

*Free Energy of Formation of the Compound C*O*

If we assume that the compound C*O exists on the surface of the anode during electrolysis and that reaction [2] represents the electrochemical reaction, then the results of these counter-emf tests permit the calculation of an approximate value for the free energy of formation of C*O which may be compared with that for CO and $CO_2$. This calculation is performed as follows:

The average value of the reversible voltage $E_o$ obtained from these tests is 1.45 v and therefore the voltage associated with the electrochemical reaction

$$Al_2O_3 + 3C \rightarrow 2Al + 3C^*O$$

is −1.45 v at 971°C with the Al in the pure molten state, the carbon in the pure solid state, the $Al_2O_3$ dissolved in cryolite to give a 5% solution by weight, and the compound C*O attached to the carbon anode surface. The free energy change for the reaction as written above is then

$$\Delta G_r = -nFE = \frac{6 \times 96{,}500 \times 1.45}{4.185} = +200{,}609 \text{ cal}$$

The free energy of formation $\Delta G_f$ of each of the compounds in their above designated states as formed from their elements at 25°C was calculated from published data (12, 13) to give

for Al (molten at 971°C) $\Delta G_f = -12{,}610$ cal/g mole

for $Al_2O_3$ (in 5% solution cryolite at 971°C) $\Delta G_f = -414{,}668$ cal/g mole

for C (solid at 971°C) $\Delta G_f = -4{,}202$ cal/g mole

The free energy of formation of C*O at 971°C from its elements at 25°C is then calculated from the relation

$$\Delta G_r = -\Delta G_{Al_2O_3} - 3\Delta G_C + 2\Delta G_{Al} + 3\Delta G_{C^*O}$$

or

$$\Delta G_{C^*O} = 1/3\ (\Delta G_{Al_2O_3} + 3\Delta G_C - 2\Delta G_{Al} + \Delta G_r)$$
$$= 1/3\ (-414{,}668 - 12{,}606 + 25{,}220 + 200{,}609)$$
$$= 1/3\ (-201{,}445) = -67{,}148 \text{ cal/g mole}$$

It is interesting to compare this value with the corresponding values for CO and $CO_2$. The free energies of formation of CO and $CO_2$ in gaseous state at 971°C as formed from the elements at 25°C are listed below:

$CO_2$ $\Delta G_f = -151{,}500$ cal/g mole $CO_2$

CO $\Delta G_f = -76{,}570$ cal/g mole CO

C*O $\Delta G_f = -67{,}150$ cal/g mole C*O

Thus it appears that the compound C*O is thermodynamically less stable than either CO or $CO_2$, and its formation during electrolysis must be postulated to account for the observed reversible voltage and its decay with time on open circuit.

Manuscript received Aug. 13, 1957.

Any discussion of this paper will appear in a Discussion Section to be published in the June 1959 JOURNAL.

REFERENCES

1. O. A. Hougen and K. M. Watson, "Chemical Process Principles," Vol. 3, p. 807, John Wiley & Sons, New York (1947).
2. D. S. Davis, "Empirical Equation and Nomography," 1st ed. p. 5, Type 5, McGraw-Hill Book Co., New York (1943).
3. W. E. Haupin, *This Journal*, **103**, 174 (1956).
4. O. A. Hougen and K. M. Watson, *ibid.*, **103**, 819 (1956).
5. S. I. Rempel and L. P. Khodak, *Doklady Akad. Nauk SSSR*, **75**, 833 (1950).
6. T. G. Pearson and J. Waddington, *Disc. Faraday Soc.* **1**, 314 (1947).
7. R. Schadinger, *Alluminio*, **22**, 691 (1953).
8. K. Grjotheim, *Kgl. Norske Videnskab. Selskabs, Skrifter 2*, **5**, 1 (1957).
9. S. I. Rempel and L. P. Khodak, *Zhur. Priklad. Khim.*, **26**, 931 (1953).
10. V. P. Mashovets and A. A. Revazyan, *ibid.*, **30**, 1006 (1957).
11. A. Vajna, *Bull. soc. franc. elec.*, **2**, 85 (1952).
12. J. H. Perry, "Chemical Engineers' Handbook," McGraw Hill Book Co., New York (1950).
13. "Selected Values of Chemical Thermodynamic Properties," *Natl. Bur. Standards Circ.* 500 (1952).

# Technical Notes

## The Effect of Gamma Irradiation on the Potential Behavior of Platinum and Stainless Steel Electrodes

**Walter E. Clark**

*Chemistry Division, Oak Ridge National Laboratory, Oak Ridge, Tennessee*

The recent studies by Cartledge (1, 2) of the potential behavior of stainless steel in 0.1*N* $H_2SO_4$ have presented interpretations of almost every part of the potential-time plots in terms of reactions taking place at the electrode surface. The purpose of the present work is to determine the effect of gamma irradiation on the potential of stainless steel under the same conditions as those employed by Cartledge.

The radiation source employed was a cylindrical cobalt-60 source of the type described by Ghormley and Hochanadel (3) with 1000 curie loading. The dose rate in the center of the cylinder amounted to $8.5 \times 10^{17}$ ev/g $H_2O$/min The solution and the metal electrodes were contained in a glass cell of 20 ml capacity connected to an external silver-silver sulfate-0.1*M* $H_2SO_4$ reference electrode by means of a glass and Tygon bridge. The solution was stirred by means of a magnetic stirrer and a 300 rpm electric motor. Temperature of the solution was automatically controlled to ±1.5°C. Potentials were measured to ±2 mv by means of a vibrating reed electrometer and a Brown continuous recorder. All measurements were carried out in 0.1*N* $H_2SO_4$ solution at 85°C. These conditions were chosen because steady-state

potentials are reached with relative rapidity at this temperature (2) and because a considerable amount of experience has been acquired with various stainless steels in this system and under these conditions (4). The work reported was carried out on type 347 stainless steel. Exploratory comparative experiments were carried out on types 302, 304, 309, 310, 316, and 321. The general pattern of behavior was found to be the same in all cases.

The stainless steel electrodes consisted of cylinders 1 cm in length and 0.16 cm in diameter having a nominal area of 0.54 $cm^2$ sealed into Pyrex glass tubes. The electrode was abraded with 2/0 emery paper, rinsed, and stored in an oven at 110°C until use. A few samples were heated in air at 200°C before use, in order to build up an oxide film. Usually, however, it was felt desirable to use metal with a minimum amount of oxide film to avoid the complication of appreciable concentrations of iron in the solution during the early stages of the experiments.

In order to employ the platinum electrode as a monitor of the redox potential of the solution, it was necessary to investigate the effect of radiation on the potential of platinum. The only known study of this system was made by Veselovsky (5) and few details are given.

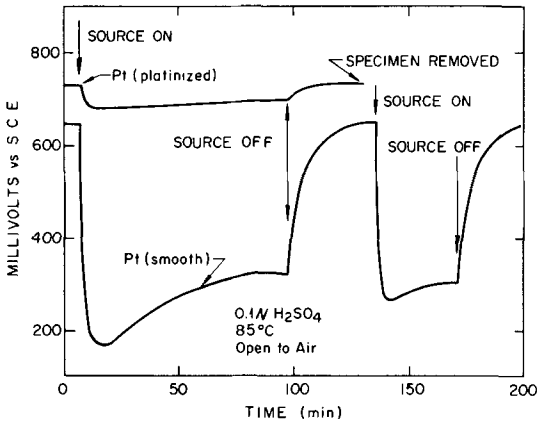


Fig. 1. Effect of gamma irradiation on the potential of smooth platinum and of platinized platinum electrodes in 0.1N $H_2SO_4$ open to air.

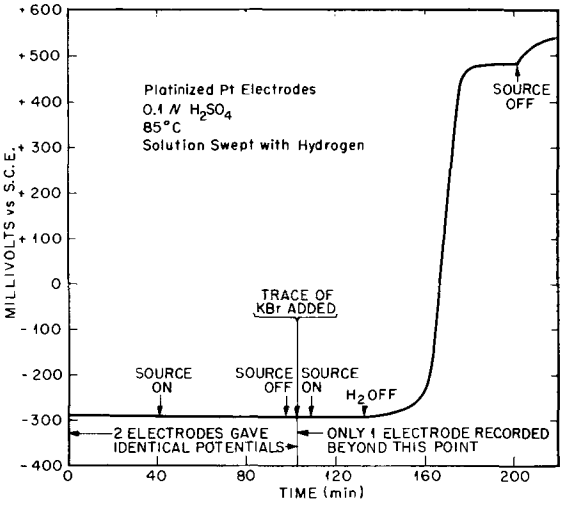


Fig. 2. Effect of gamma radiation on the potential of the hydrogen electrode in 0.1N $H_2SO_4$.

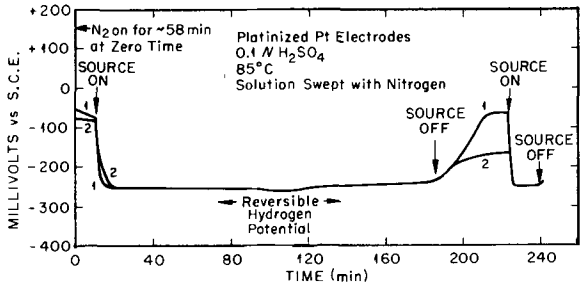


Fig. 3. Effect of gamma radiation on the potential of platinized platinum in deoxygenated 0.1N $H_2SO_4$.

Figures 1, 2, and 3 show the effect of gamma irradiation on platinum electrodes under atmospheres of air, hydrogen, and nitrogen, respectively. Although smooth platinum electrodes are much more sensitive to products of radiolysis than are platinized electrodes, the general behavior of both types is the same. Imposition of the source causes rapid debasement. Under an atmosphere of air this is followed by slow ennoblement which does not occur under hydrogen or nitrogen. Removal of the source results in rapid ennoblement. A second imposition of radiation causes a second rapid debasement. Under air the degree of this debasement appears to be somewhat a function of the time elapsed since the source was last removed, indicating a probable buildup in the solution of some oxidizing species having a finite lifetime. The addition of potassium bromide ($10^{-4}M$) to the solution as indicated in Fig. 2 produced no change in potential due to postulated changes in the reactions of the products of radiolysis. (6).

Figures 4 and 5 represent two types of behavior which were observed during exposure of type 347 stainless steel. In the first case (Fig. 4) the initial debasement was not sufficiently drastic to result in the evolution of hydrogen, and the behavior of the steel under irradiation was essentially that of an indicator electrode. In the second case (Fig. 5) even though the potential of the steel recovered from its initial debasement immediately following immersion, the imposition of irradiation caused it to drop to a value indicating active corrosion. In this particular case the steel eventually recovered its noble potential while still under irradiation. The fact that

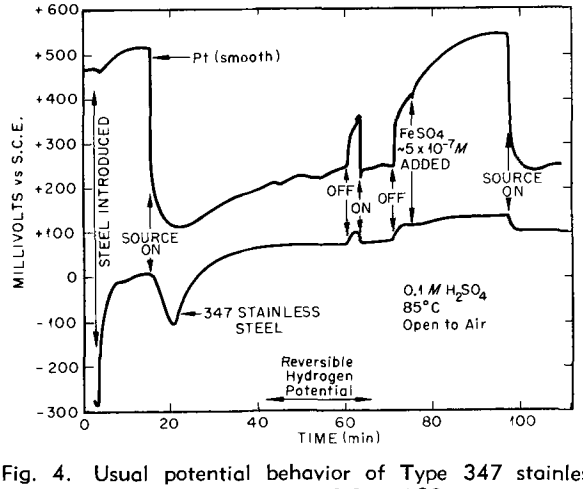


Fig. 4. Usual potential behavior of Type 347 stainless steel under gamma irradiation in 0.1N $H_2SO_4$.

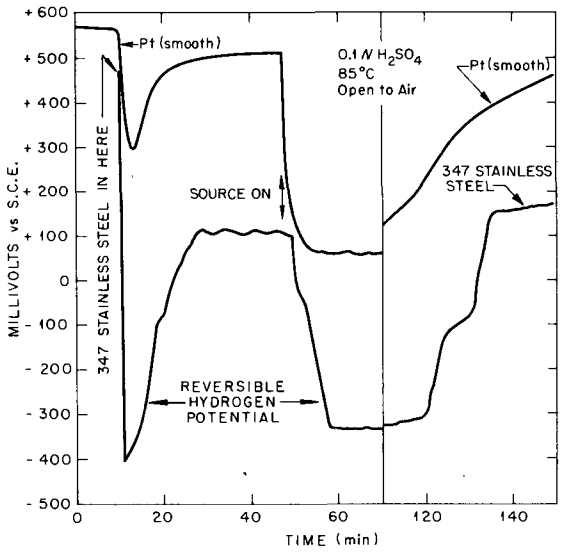


Fig. 5. Failure and subsequent recovery of Type 347 stainless steel under gamma irradiation in 0.1N $H_2SO_4$.

the potential of the smooth platinum electrode remains debased so long as the steel corrodes actively demonstrates the value of the platinum electrode as a qualitative monitor of the continuing production of Fe(II) in the solution even in the presence of the products of the radiolytic decomposition of water.

Hochanadel (7) lists the following reactions as being among those of importance in the radiolysis of water at 25°C:

$$H_2O \xrightarrow{\gamma} H_2O_2 + H_2 + H + OH \quad \text{(Net decomposition reaction)} \qquad [1]$$

$$H_2 + OH \rightarrow H_2O + H \qquad [2]$$

$$O_2 + H \rightarrow HO_2 \qquad [3]$$

$$HO_2 + HO_2 \rightarrow H_2O_2 + O_2 \qquad [4]$$

As peroxide builds up in solution:

$$H_2O_2 + H \rightarrow H_2O + OH \qquad [5]$$

$$H_2O_2 + OH \rightarrow HO_2 + H_2O \qquad [6]$$

At elevated temperatures hydrogen peroxide decomposes thermally, but even at 150°C peroxide was present at the end of irradiation.

The results reported here confirm the expected buildup of peroxide in the irradiated solution when open to air. Under hydrogen, reaction [2] will predominate, peroxide will be removed, and a platinized platinum electrode will assume the reversible hydrogen potential. Under nitrogen, both hydrogen and oxygen from radiolysis will tend to be removed and the potential will approach that of the hydrogen electrode, due to the great solubility of hydrogen in platinum and to the greater speed of the hydrogen reaction on platinum compared to the reactions involving oxidizing species.

The potential assumed by the stainless steel depends on the nature of the surface of the electrode as well as on the redox species in solution. When the steel is passivated, it tends to behave as an indicator electrode. The presence of radiolytic hydrogen causes rapid debasement of such an electrode. Since no film on stainless steel is completely protective, the "indicator electrode potential" will always be modified somewhat by the effect of a simultaneous corrosion reaction. The effect of the radiolytic oxidizing species will not be felt immediately since these species diffuse more slowly than hydrogen. If the protective film on the steel is destroyed or reduced before the effect of the oxidants is appreciable, active corrosion may continue indefinitely. At present quantitative methods for evaluating the balance between oxidizing and reducing reactions are not available for such systems.

Manuscript received Feb. 14, 1957. This work was done for the U. S. Atomic Energy Commission, under contract with the Union Carbide Nuclear Company.

Any discussion of this paper will appear in a Discussion Section to be published in the June 1959 JOURNAL.

REFERENCES

1. G. H. Cartledge, *Nature*, **177**, 1812 (1956).
2. G. H. Cartledge, *This Journal*, **104**, 420 (1957).
3. J. A. Ghormley and C. J. Hochanadel, *Rev. Sci. Instruments*, **22**, 473 (1951).
4. G. H. Cartledge, F. A. Posey, and Walter E. Clark, Unpublished work.
5. V. I. Veselovsky, A/Conf. Proc. International Conf. on Peaceful Uses of Atomic Energy, **7**, 521 (1956).
6. T. J. Sworski, *J. Am. Chem. Soc.*, **76**, 4687 (1954).
7. C. J. Hochanadel, Proc. International Conf. on Peaceful Uses of Atomic Energy, **7**, 599 (1956); cf. *ibid.*, *J. Phys. Chem.*, **56**, 587 (1952).

# The Use of Nickel-Aluminum Alloy Coatings for the Protection of Molybdenum from Oxidation

**D. E. Couch, H. Shapiro, and A. Brenner**

*Electrodeposition Section, Division of Chemistry, National Bureau of Standards, Washington, D. C.*

Recent reports (1, 2) have shown that wrought nickel-aluminum alloys are very resistant to oxidation. However, because of their hardness and brittle nature, they are difficult to fabricate.

The protective coatings described herein were prepared by plating the molybdenum with 25$\mu$ (1 mil) of chromium followed by 175$\mu$ (7 mils) of nickel. These samples were then plated with 50-75$\mu$ (2-3 mils) of aluminum.

Several methods of forming nickel-aluminum alloy coatings were studied and found unsatisfactory. Aluminum plating from the hydride bath (3) was

tried, but the adhesion to the nickel was poor and the deposits often blistered during the heating cycle at 600° to 700°C which was required to alloy the aluminum with the nickel.

Low temperature fused salt baths were also used, such as potassium bromide, aluminum bromide (4) and potassium chloride, sodium chloride, aluminum chloride (5). With these fused salt baths the limiting thickness of the aluminum deposit was about 12$\mu$ (0.5 mil) before treeing and rough deposits prevented further build up.

The most effective method of forming the nickel-aluminide layer was by electrodeposition from a fused cryolite bath operated at 1000°C.

With current densities of 50 amp/dm$^2$, aluminum deposited too rapidly for complete alloying. The excess aluminum ran to the bottom of the cathode and collected as a metal bead. At current densities of 10-20 amp/dm$^2$, the aluminum was deposited at sufficiently slow rates to allow complete alloying with the nickel. At 20 amp/dm$^2$, about 2.5 hr were required to deposit 65$\mu$ (2.5 mils) of aluminum.

Several molybdenum panels which had been previously plated with chromium and nickel were plated with aluminum from the various baths just described. The amount of aluminum deposited was determined by weight from which an average thickness was calculated. Panels with 12$\mu$ (0.5 mil) of aluminum or less oxidized at about the same rate as electrodeposited nickel, and they acquired the vitreous black nickel oxide coating typical of nickel oxidized in air at 1100°C. With aluminum thicknesses of between 12$\mu$ (0.5 mil) and 20$\mu$ (0.8 mil) the rate of oxidation during the first 24-48 hr was markedly reduced; the panels acquired a bluish coating which gradually turned black after about 100 hr of oxidation.

Samples coated with a thickness of alloy equivalent to 50$\mu$ (2 mils) of aluminum were oxidized for 400 hr at 1100°C. These samples developed white or tan oxide films and showed weight gains of only 0.005 g/cm$^2$. The nickel plated panels used as controls gave weight gains of 0.04 g/cm$^2$.

These experiments show that the aluminide layer gave a very significant improvement to the nickel coatings. Some method of reducing the rate of diffusion of aluminum into nickel would probably further improve the life of the samples since it would maintain the aluminum concentration at a higher level in the surface for a longer period of time. This might be accomplished by using a layer of nickel 75-125$\mu$ (3-5 mils) over some metal that would act as a diffusion barrier to the aluminum, possibly chromium. In this way the nickel aluminide composition could be controlled at the most oxidation resistant ratio and it would be possible to obtain the same oxidation life with much thinner coatings than are being used at the present time.

Manuscript received Dec. 9, 1957.

Any discussion of this paper will appear in a Discussion Section to be published in the June 1959 JOURNAL.

REFERENCES

1. W. A. Maxwell and E. M. Grala, Lewis Flight Propulsion Lab., Cleveland, Ohio, Tech. Note 3259.
2. J. H. Westbrook, *This Journal*, **103**, 54 (1956).
3. D. E. Couch and A. Brenner, *ibid.*, **99**, 234 (1952).
4. W. G. Lovell and N. E. Phillips, U. S. Pat. 2,373,320, April 1945.
5. W. H. Wade, G. O. Twellmeyer, and L. F. Yntema, *Trans. Electrochem. Soc.*, **78**, 77 (1940).

## Correction

In the paper "The Effect of Temperature and Thickness on the Electrical Resistivity of Ceramic Coatings" by Wm. H. Fischer which appeared on pp. 201-203 in the April 1958 JOURNAL, Vol. 105, No. 4, the last column (H-147) in Table I should read:

| | H-147 |
|---|---|
| $SiO_2$ | 49.44 |
| $B_2O_3$ | 4.84 |
| $Al_2O_3$ | 0.54 |
| $Cr_2O_3$ | 16.67 |
| BaO | 18.46 |
| CaO | 1.64 |
| ZnO | 2.08 |
| BeO | — |
| $Na_2O$ | 1.24 |
| $K_2O$ | 0.89 |
| $F_2$ | 0.43 |
| MnO | — |
| CoO | — |
| NiO | — |
| $TiO_2$ | 1.92 |
| ZrO | 1.16 |
| MgO | 0.09 |
| $P_2O_5$ | 0.34 |
| $Co_2O_3$ | 0.01 |
| $MnO_2$ | 0.03 |
| $Ni_2O_3$ | 0.03 |

H-147 (cont'd)

# The Reaction of Germanium with Nitric Acid Solutions

## I. The Dissolution Reaction

**Mary C. Cretella and Harry C. Gatos**

*Lincoln Laboratory, Massachusetts Institute of Technology, Lexington, Massachusetts*

ABSTRACT

The reaction of single-crystal germanium with $HNO_3$ was studied as a function of concentration, stirring rate, and temperature. The reaction rate increased with increasing $HNO_3$ concentration, reaching a maximum at approximately $6N$. At a given $HNO_3$ concentration the dissolution rate decreased with stirring and increased with time. The initial rate was found to be proportional to the product of the concentrations of undissociated $HNO_3$ and $HNO_2$. The dissolution potential of the germanium became more noble (cathodic) with increasing $HNO_3$ concentration. It is proposed that the rate-determining step of the dissolution process is

$$HNO_3 + HNO_2 \rightarrow 2NO_2 + H_2O$$

The germanium dissolution rate in $HNO_3$ solutions ($N < 6$) was not affected by the presence of HF unless the concentration of the latter exceeded approximately $6N$.

Chemical reactions of semiconductor surfaces with aqueous solutions have become of considerable interest in recent years. The preparation of consistently clean and reproducible surfaces, particularly those of germanium and silicon, is extremely important in many studies of semiconductor physics and in the fabrication of solid-state devices. Mechanical means of surface preparation usually result in contamination and, especially, in structural distortion of the surfaces. Chemical methods, on the other hand, have been employed satisfactorily by and large. A number of solutions have been developed for chemical polishing and etching, primarily on an empirical basis. Since germanium and silicon are generally not attacked by nonoxidizing media over a wide range of *p*H, effective etches for these two elements contain at least one oxidizing agent. Nitric acid is the principal oxidizing agent in the relatively successful and most commonly used etching or polishing solution for germanium and silicon. Known as the CP-4 etch, it contains hydrofluoric acid, acetic acid, and bromine in addition to nitric acid. The action of this chemical polishing agent or that of its individual components is little understood.

The present study represents an attempt to elucidate the action of $HNO_3$, undoubtedly the most important component of CP-4 etch, with elemental semiconductors. Germanium was chosen since it was more readily available at high purity than silicon. In order to clarify certain aspects of the action of nitric acid on germanium, nitric-hydrofluoric acid solutions were employed. Thus, to some extent, the action of hydrofluoric acid on germanium was also studied.

### Experimental

*Germanium samples.*—The samples used were prepared from single crystals grown in this laboratory from high-purity, zone-refined germanium. Slabs with uniform resistivity of about 20 ohm-cm were cut from p-type crystals and 40 ohm-cm from n-type. The crystals were grown along the <111> axis, and slabs were cut perpendicular to this axis. All samples employed were rectangular in shape and measured 1 cm x 2 cm x 0.06 cm, affording a large face-to-edge ratio. The two large faces were {111} surfaces. Unless otherwise stated, the data reported in the paper refer to p-type material.

Surface treatment consisted of grinding the faces with No. 600 Carborundum, etching for 1 min in CP-4 etch to remove the distorted layers and immediately rinsing thoroughly with doubly distilled water. This treatment resulted in smooth and reproducible surfaces. The samples were desiccated prior to weighing. Frequently the samples were reused, but their surfaces were prepared in the same manner as above prior to each run.

*Solutions.*—Stock solutions of the desired $HNO_3$ normality were prepared, and their exact concentration was determined analytically. The $HNO_3$ + HF solutions were prepared just before use by weighing standard $HNO_3$ and HF solutions into the reaction vessel. Prior to weighing, the concentrations of the individual solutions were determined analytically. All solutions were prepared from reagent grade chemicals and doubly distilled water.

*Apparatus for dissolution experiments and potential measurements.*—The apparatus employed for the dissolution experiments, potential measurements, and the effect of stirring is shown in Fig. 1. The main vessel was constructed of glass in the $HNO_3$ experiments and of "Kel-F" when HF solutions were employed. A Kel-F sample holder permitted rotation of the germanium samples and electrical connection for electrode potential measurements. Ohmic contacts between platinum leads and

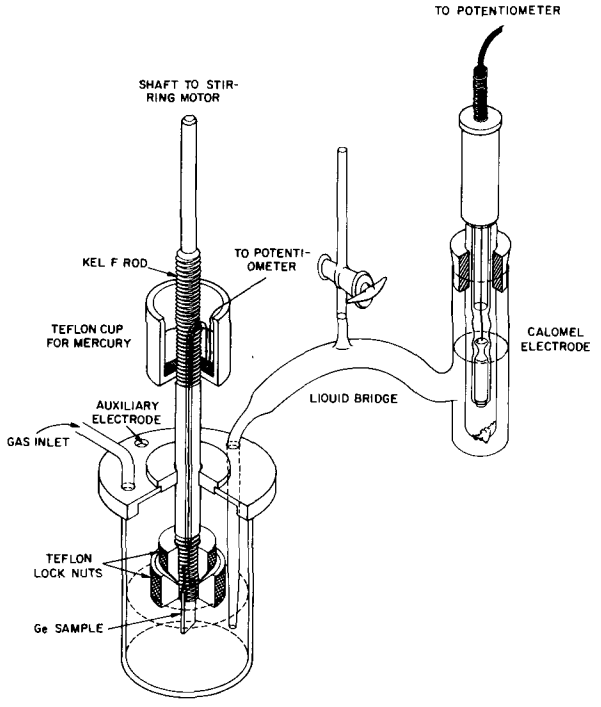


Fig. 1. Apparatus for dissolution experiments and potential measurements.

the germanium samples were obtained by soldering. In cases of vigorous or extensive dissolution the small portion of the sample masked by the holder was attacked, and its area was then included in computing the rates. Ordinarily, however, the clamped portion underwent very slight attack. Excellent agreement was found between dissolution rates determined without stirring, using the holder shown in Fig. 1, and those determined using a four-point contact sample holder made of glass rod.

Movement of solution over the sample surface was provided by coupling the Kel-F sample holder to the shaft of a stirring motor.

The apparatus was maintained to constant temperature ±0.1°C. Before sample immersion the solutions were allowed to reach the desired temperature. Unless otherwise specified the data discussed in this paper were obtained at 27.5°C.

*Rate determinations.*—The dissolution rates were determined principally from weight-loss measurements (to ±0.005 mg) employing an Oertling microbalance and the geometric area of the samples. Generally the weight losses fell between 0.06 and 200 mg for a sample area of approximately 4.5 $cm^2$. The weight-loss data were compared with data obtained by analysis of the solutions for germanium using the spectrophotometric hematoxylin method (1) suitably modified for this work. The results of the two methods were in very good agreement. It was necessary to resort to the analytical method for all samples bearing electrical connections. Since in most cases dissolution rates remained constant for the first few hours, rates were calculated from the weight loss after 1-hr immersion and are expressed throughout in units of $mg/cm^2/hr$.

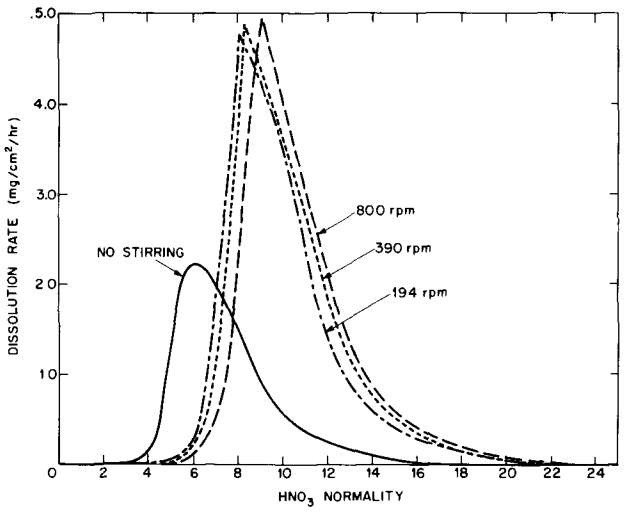


Fig. 2. Dissolution rate of germanium in $HNO_3$ as a function of $HNO_3$ concentration and stirring at 27.5°C.

*Introduction of gases into the solutions.*—Gases obtained commercially, mainly prepurified nitrogen, nitrogen dioxide, or mixtures of the two, were introduced through calibrated flow meters. In general, gas was bubbled through the solution for at least 1 hr prior to immersion of the samples; total gas flow was maintained at 80 ml/min. The agitation caused by gas bubbling could not be directly calculated in terms of sample rotation, which was the main form of agitation employed in this study. However, an estimate of equivalent stirring rate could be made by comparing dissolution rates during nitrogen bubbling with rates measured at various stirring rates. Nitrogen was used in this study since it could not chemically participate in the reaction mechanism.

## Results and Discussion

### *Dependence of Dissolution Rate on Acid Concentration and Agitation*

The dissolution rate of germanium as a function of $HNO_3$ concentration is shown for several stirring rates in Fig. 2. For all stirring rates (including zero) the dissolution rate at first increases with increasing $HNO_3$ concentration, reaches a maximum and then decreases, approaching zero at sufficiently high $HNO_3$ concentrations.

The $HNO_3$ concentration at which the dissolution rate is essentially zero in 1 hr or less is approximately 17*N* with no stirring; this value is shifted to approximately 23*N* (fuming $HNO_3$) with stirring. No hydrogen was evolved[2] during dissolution either with or without stirring. Stirring increases the dissolution rate at $HNO_3$ concentrations below about 8*N*, but it has the reverse effect above 8*N* as shown for two representative concentrations in Fig. 3. The velocities indicated are the average for all parts of the sample faces as calculated from the rpm and the geometry of the sample.

The above behavior of germanium resembles closely the behavior of some of the more common

[2] Analysis for evolved hydrogen was performed by sweeping the reaction chamber with a stream of nitrogen and employing standard oxidation and adsorption techniques.

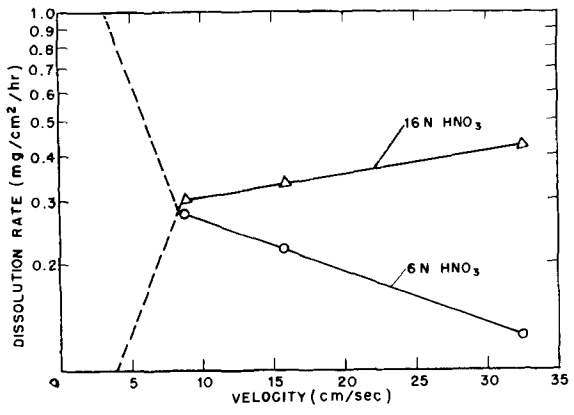


Fig. 3. Germanium dissolution in $HNO_3$ as a function of sample velocity at 27.5°C.

metals such as iron (2) and aluminum (3) in $HNO_3$ solutions. These metals are known to dissolve in dilute $HNO_3$ solutions and to become passive in concentrated $HNO_3$. Furthermore, stirring has been found to affect their dissolution rates (4) in a way similar to that observed for germanium.

The foregoing results lead to the following conclusions.

In $HNO_3$ concentrations corresponding to the ascending branch of the dissolution curves (Fig. 2) intermediate products formed by the interaction of germanium and nitric acid participate in the overall dissolution reaction. Thus, stirring decreases the dissolution rate because it brings about a lower steady-state concentration of intermediates at the germanium-solution interface than does diffusion alone.

In $HNO_3$ concentrations corresponding to the descending branch of the dissolution curves, stirring increases the dissolution rate by reducing concentration polarization, as is often the case in metal dissolution reactions.

Apparently, different mechanisms operate in the ascending and descending branches of the dissolution curves. Furthermore, the mechanism of the descending branch must lead to passivation of germanium.

The experiments described below were carried out in an attempt to clarify these two mechanisms. The semiconductor properties of germanium have been taken into consideration.

*Role of Nitrous Acid in the Dissolution Reaction*

Since $HNO_2$ is recognized as an important intermediate in the reduction of $HNO_3$, a study of the role of $HNO_2$ was considered essential to an understanding of the Ge-$HNO_3$ reaction.

In addition to $HNO_2$, $NO_2$ has been considered an important intermediate in the reduction of $HNO_3$ (5). Actually, an equilibrium exists among the species $HNO_2$, $NO_2$, and $HNO_3$ in aqueous solutions as shown in Eq. [1]

$$HNO_3 + HNO_2 \rightleftarrows 2NO_2 + H_2O \qquad [1]$$

Vetter (6) showed that the ratio $\frac{[NO_2]^2}{[HNO_2]}$ varies from $10^{-7}$ to $10^{-5}$ in $HNO_3$ solutions ranging from 7 to 14.5*N* at 25°C, and hence $[HNO_2] >> [NO_2]$. Thus,

Table I. Dissolution of germanium in dilute $HNO_3$ solutions at 27.5°C

| Dissolution rate mg/cm²/hr | $HNO_3$ Normality | $C_{HNO_2}$ mole/liter × $10^3$ | $C_{HNO_3}$* mole/liter | $C_{HNO_2} \times C_{HNO_3}$ × $10^5$ |
|---|---|---|---|---|
| With stirring, 194 rpm | | | | |
| 0.06 | 5.46 | — | 1.26 | — |
| 0.20 | 5.95 | 0.12 | 1.49 | 17.9 |
| 0.90 | 6.36 | 0.41 | 1.75 | 71.7 |
| 1.75 | 6.94 | 0.57 | 2.05 | 116.8 |
| 3.00 | 7.46 | 0.82 | 2.41 | 197.6 |
| Without stirring | | | | |
| 0.15 | 4.00 | 0.18 | 0.67 | 12.1 |
| 0.33 | 4.50 | 0.22 | 1.04 | 35.4 |
| 1.50 | 5.05 | 0.34 | 1.26 | 21.4 |
| 2.15 | 5.70 | 0.65 | 1.49 | 96.9 |

* Concentration of undissociated $HNO_3$

virtually all of the $NO_2$ introduced into a moderately concentrated $HNO_3$ solution is immediately converted to $HNO_3 + HNO_2$.

In view of this equilibrium, it is possible to determine the amount of $HNO_2$ present in $HNO_3$ solutions by means of a suitable oxidizing agent, without introducing any significant uncertainty due to the presence of dissolved free $NO_2$. Furthermore, addition of $HNO_2$ to $HNO_3$ solutions can be conveniently accomplished by bubbling $NO_2$ through the solution. This technique is preferable to adding a nitrite salt since no foreign cation is introduced into the system under study; however, it is necessary to determine both $HNO_2$ and $HNO_3$ after $NO_2$ bubbling.

In $HNO_3$ solutions resulting from dissolution runs with stirring the amount of $HNO_2$ present was determined by introducing aliquot portions of the solution into a $Ce^{+4}$ solution and titrating the excess of $Ce^{+4}$ with $FeSO_4$. The solutions resulting from runs without stirring were homogenized before aliquots were taken for analysis. The analytical results are presented in Table I. No significant change in $HNO_3$ concentration was found during the 1-hr duration of the experiments. The $HNO_2$ concentration remained essentially constant in the vicinity of one hour.

The dissolution rates tabulated in Table I pertaining to stirred solutions are plotted in Fig. 4 against the product of the concentrations of $HNO_3$ and $HNO_2$. The dependence of rate on concentration is expressed by the following relationship:

$$V = KC_{HNO_2}C_{HNO_3} \qquad [2]$$

where $V$ is the dissolution rate, and $C_{HNO_2}$ and $C_{HNO_3}$ are the concentrations of undissociated $HNO_2$ and

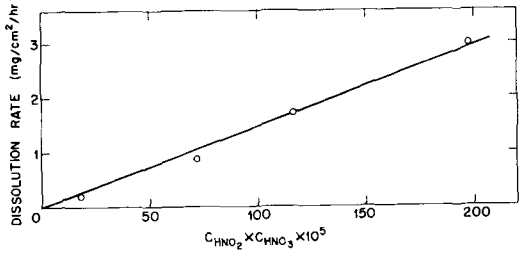


Fig. 4. Dissolution rate of germanium as a function of the product of concentrations of undissociated $HNO_2$ and $HNO_3$ at 27.5°C.

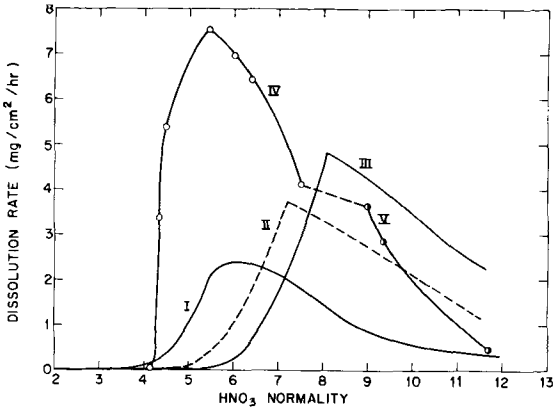


Fig. 5. Dissolution of germanium in $HNO_3$ solutions at 27.5°C. The effect of $HNO_2$. Curve 1, no stirring (as in Fig. 2); curve II, stirring resulting from $N_2$ bubbling; curve III, stirring, 194 rpm (as in Fig. 2); curve IV, mixtures of $NO_2$ + $N_2$ bubbling through $HNO_3$ solution. Initial concentration 4.29N $HNO_3$. Stirring equivalent to curve II; curve V, as in curve IV except initial $HNO_3$ concentration was 8.1N.

$HNO_3$, respectively. The values of $C_{HNO_3}$ were calculated from the $HNO_3$ normality using the data of Hood, Redlich, and Reilly (7). The values of $C_{HNO_2}$ were assumed to be the same as the corresponding $HNO_2$ normalities since the dissociation constant of $HNO_2$ is relatively small ($4 \times 10^{-4}$) and ionization is further repressed by the presence of $HNO_3$. It is of interest to note that Eq. [2] does not apply to the rates obtained without stirring (Table I). This result is not surprising since, without stirring, the average $HNO_2$ concentration in the bulk of the solution does not represent, even approximately, the concentration in the immediate vicinity of the germanium surface. In fact, if it is assumed that Eq. [2] applies to the dissolution without stirring, it can be estimated from the data of Table I that the concentration of $HNO_2$ at the germanium-solution interface may be 10 to 30 times greater than the over-all concentration.

The influence of $HNO_2$ is further brought out by the results plotted in Fig. 5. Curve II was obtained in $HNO_3$ solutions through which $N_2$ was bubbling and curve IV in solutions through which $NO_2$ and $N_2$ mixtures were bubbling. In both cases the over-all rate of gas flow and, therefore, the rate of stirring was the same. The $HNO_3$ solutions corresponding to curve IV, therefore contained appreciably more $HNO_2$ than those of curve II. Curves I and III already shown in Fig. 2, are replotted for comparison. Curve V will be discussed later.

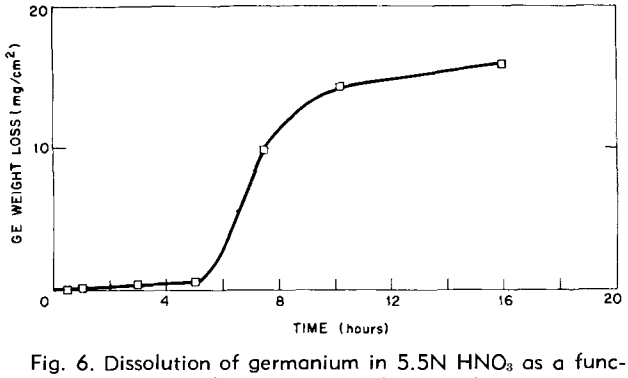


Fig. 6. Dissolution of germanium in 5.5N $HNO_3$ as a function of time at 27.5°C with stirring (194 rpm).

A comparison of curves II and IV (Fig. 5) shows that for a given $HNO_3$ concentration $HNO_2$ increases the dissolution rate and also shifts the position of maximum dissolution rate toward lower $HNO_3$ concentrations. The observed increase in dissolution rate by a factor of approximately 100 in going from curve II to curve IV for the concentrations 4.37*N* and 4.54*N* (experimental points on curve IV) resulted from an increase in $HNO_2$ concentration by a factor of approximately 200. In view of the fact that the amount of stirring in these runs was not sufficient to prevent entirely concentration polarization at the germanium-solution interface, the results are in reasonable agreement with Eq. [2].

Since $HNO_2$ is formed during the dissolution process and is itself a reactant, the dissolution rate should increase with time, i.e., the reaction should be autocatalytic. Such increase in rate has been observed for a number of common metals (4). Results obtained with germanium in 5.5*N* $HNO_3$ are shown in Fig. 6. The dissolution rate (slope) with stirring remains constant for the first 5 hr, then it increases sharply and finally decreases. Accordingly, the $HNO_2$ concentration at the end of 7½ hr was found to be approximately fives times larger than that at the end of 5 hr. The latter concentration, on the other hand, was found to be only 10% larger than that at the end of 3 hr. The reasons for the several hour interval prior to the sharp increase in $HNO_2$ concentration are not clear at this time. A sharp increase in $HNO_2$ concentration, however, is reflected in a sharp increase in dissolution rate. The subsequent decrease in dissolution rate will be discussed later.

### *Dissolution Potential*

The instantaneous electrode potential of germanium obtained within 10 sec after immersion in unstirred $HNO_3$ solutions is plotted as a function of $HNO_3$ normality in Fig. 7. In the concentration range 5 to 7*N*, where the maximum in dissolution rate occurs, the potential shifts towards more noble (positive) values by approximately 0.2 v.

The cathodic shift of the potential with increasing $HNO_3$ concentration, accompanied by an increase in dissolution rate, is indicative of a decrease in ca-

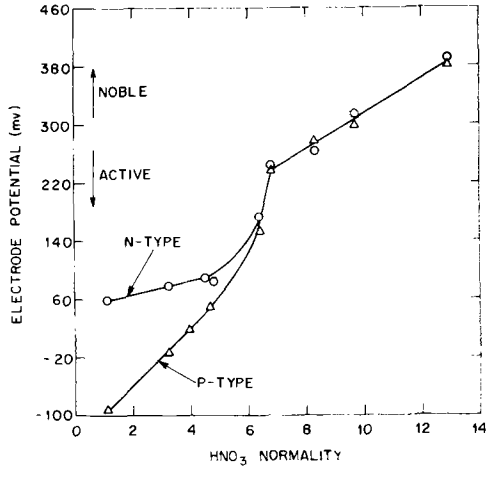


Fig. 7. Instantaneous potential of germanium in $HNO_3$ solutions at 27.5°C vs. standard hydrogen electrode; no stirring.

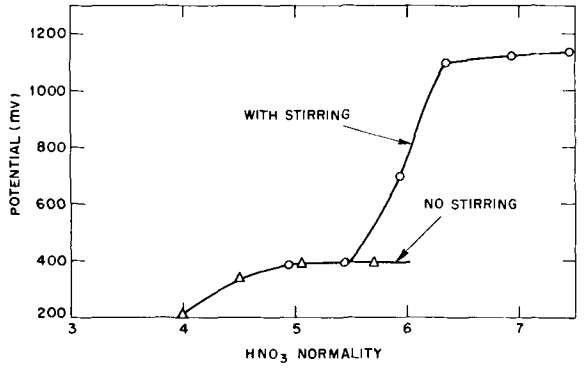


Fig. 8. Dissolution potential of germanium in $HNO_3$ solutions at 27.5°C vs. standard hydrogen electrode.

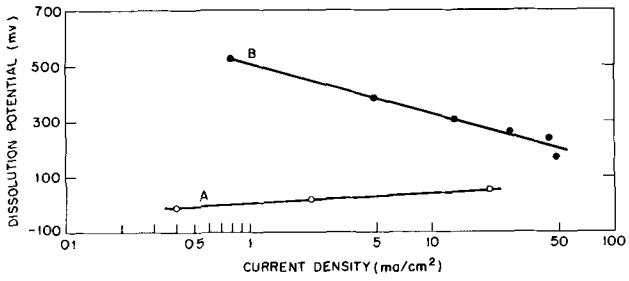


Fig. 9. Potential of germanium in $HNO_3$ solutions at 27.5°C as a function of current density. Calculated from dissolution rates. A, $HNO_3$ < 6N; B, $HNO_3$ > 6N.

thodic polarization (8). On the other hand, above approximately 7*N* $HNO_3$ the cathodic shift of the dissolution potential, associated with a decrease in dissolution rate, is indicative of an increase in anodic polarization which, at higher $HNO_3$ concentrations, leads to germanium passivity as will be discussed later.

The steady-state dissolution potential, essentially attained within 1 hr after immersion, is shown in Fig. 8 as a function of $HNO_3$ normality. In this case, both with and without stirring, the pronounced cathodic shift occurs at smaller concentrations than in the case of instantaneous potential, probably owing to the accumulation of $HNO_2$. This behavior is consistent with the observed cathodic shift of the potential with time for a given $HNO_3$ concentration. As shown in Fig. 8, in 5*N* and 5.5*N* $HNO_3$ the dissolution potential is the same with and without stirring, indicating that stirring does not significantly affect the anodic reaction. At higher concentrations, however, where the cathodic reaction controls the dissolution potential (*see* below) stirring shifts the potential toward more noble values by causing a decrease in the cathodic polarization.

It is of interest to note in Fig. 7 that in dilute $HNO_3$ solutions the instantaneous potential of n-type germanium is more noble than that of p-type. During metal dissolution in acids the dissolution potential (mixed potential) usually remains near the reversible potential of the metal (9) because the exchange current for the metal-oxidation reaction is usually much larger than the exchange current for the hydrogen-reduction reaction, or in this case the $HNO_3$ reduction reaction. Thus, the dissolution potential is usually controlled by the anodic reaction. In the present case, the over-all anodic reaction could be represented as (10):

$$Ge + 2H_2O + 2e^+ \rightarrow GeO_2 + 4H^+ + 2e^- \quad [3]$$

where $e^+$ is a positive hole, or electron deficiency in the valence band in germanium. According to this mechanism the instantaneous potential of p-type germanium should be more active than that of n-type in the same solution owing to the greater supply of holes (cf. Fig. 7). Moreover, the initial dissolution rate (averaged over the first hour of immersion) of p-type germanium has been found to be approximately twice that of n-type at $HNO_3$ concentrations up to 4*N*. In more concentrated $HNO_3$ solutions, on the other hand, where pronounced anodic polarization occurs (anodic control) and the anodic reaction no longer controls the dissolution potential, no difference in potential (Fig. 7) or in dissolution rate was observed between the two types of germanium.

In Fig. 9 the instantaneous potential is plotted against the logarithm of the current density as calculated from the dissolution rates assuming a roughness factor of 1.3 (11). This Tafel-type relationship has been observed earlier by Makrides, Komodromos, and Hackerman (12) and by Gatos (13, 14) for the potential of iron dissolving in oxidizing acid media. For the concentration range indicated (Fig. 9) straight line A *approximates* the anodic polarization of dissolving germanium since the system is under cathodic control (12) and, correspondingly, B *approximates* the cathodic polarization.

### *Interpretation of the Dissolution Process*

At low $HNO_3$ concentrations (nonpassivating) the over-all anodic reaction can be represented by Eq. [3]. No attempt was made in this investigation to determine the mechanism involved in the removal of germanium atoms from their respective lattice sites and their oxidation to the corresponding ions. Turner (15) has recently investigated this aspect in studying the anodic dissolution of germanium under the influence of an externally applied emf. In the present system, as it has been pointed out above, the dissolution process is controlled by the cathodic reaction which will be the subject of the present discussion.

In discussing the role of $HNO_2$ in the dissolution of metals in $HNO_3$, Evans (4) concludes that, in the absence of hydrogen evolution, reaction [1] leads to the formation of $NO_2$ which is responsible for the oxidation of the surface metal atoms. Similarly, Vetter (16) has found that reaction [1] is rate determining in the reduction of $HNO_3$ on a platinum electrode.

Thus, the over-all cathodic reaction involves the reduction of $HNO_3$ to $HNO_2$ and possibly, although unlikely, to NO. An effort was made to detect free hydrogen among the reaction products, under all experimental conditions, but the results were negative. The reduction of $HNO_3$ in the present system is believed to proceed according to the mechanism proposed by Vetter (16) for the cathodic reduction of $HNO_3$ on a platinum electrode:

$$H^+ + NO_3^- \rightleftarrows HNO_3 \text{ (fast)} \quad [4]$$
$$HNO_3 + HNO_2 \rightarrow N_2O_4 + H_2O \text{ (slow, rate determining)} \quad [5]$$
$$N_2O_4 \rightleftarrows 2NO_2 \text{ (fast)} \quad [6]$$
$$2NO_2 + 2e^- \rightarrow 2NO_2^- \text{ (fast)} \quad [7]$$
$$2NO_2^- + 2H^+ \rightleftarrows 2HNO_2 \text{ (fast)} \quad [8]$$
$$3H^+ + NO_3^- + 2e^- \rightarrow HNO_2 + H_2O \text{ (over-all)} \quad [9]$$

Reaction [5] is rate determining. Reaction [7] determines the cathodic potential since it is the only reaction involving electron transfer. According to Vetter, this reaction becomes rate determining at low current densities, well below these corresponding to the dissolution rates at hand (0.1 to 1 ma/cm$^2$).

Some of the experimental results described above will now be viewed briefly in the light of this mechanism.

With no stirring the concentration of $HNO_2$ becomes appreciably higher at the germanium-liquid interface than in the main body of the solution, $HNO_2$ forming faster than it can diffuse away from the interface. Stirring decreases the dissolution rate (Fig. 2) by removing the $HNO_2$ forming at the interface. Changes in stirring at high stirring rates have only a small effect on the dissolution rate, indicating that the $HNO_2$ formation rate approaches the rate of its consumption through reaction [5] and through removal from the interface by stirring. Although no electron exchange with the germanium surface takes place in reaction [5] the action of $HNO_2$ is essentially limited at the interface for two reasons. First, $NO_2$ produced in reaction [5] undergoes reduction at the germanium surface according to reaction [7], and second, reaction [5] is catalyzed by metallic surfaces as shown by Vetter (6) in the case of platinum.

On the basis of the above mechanism the $HNO_2$ concentration must increase with time and, as a result, the dissolution rate must also increase since it is controlled by reaction [5]. The decrease in $C_{HNO_3}$ corresponding to the increase in $C_{HNO_2}$ is of little significance because at time zero $C_{HNO_3} >> C_{HNO_2}$. In agreement with the above are the results shown in Fig. 6 where the $HNO_2$ concentrations, determined analytically as a function of time, were found consistent with the dissolution rates. Furthermore, the potential ($E$) of the Pt|$HNO_3$, $HNO_2$ electrode shifted during germanium dissolution, because of $HNO_2$ formation, as expected from the relationship $E = E_o - 0.0296 \log [HNO_2]$, which has been verified experimentally by Monk and Ellingham (17). Also consistent are the results reported on solutions in which the concentration of $HNO_2$ was appreciably increased by bubbling $NO_2$ (Fig. 5).

Activation energies were obtained for the dissolution process by determining the dissolution rates 27.5°, 34.4°, and 44.2°C. The results are shown in Table II.[3] Vetter (6) determined the activation energy of reaction [5] on platinum and found that it decreases from 16.5 kcal/mole (in 6.9$N$ $HNO_3$) to 14.4 kcal/mole (in 14.5$N$). Our value of 18.0 kcal/mole in 5.5$N$ solution, with stirring, is consistent with Vetter's results. In the case of 7.5$N$ solution our value of 12 kcal/mole is lower than the corresponding value by Vetter (approximately 16 kcal/mole). This is not surprising, however, since, in the present system, 7.5$N$ approaches the passivating region where the above reaction mechanism no longer holds. In 5.5$N$ and 7.5$N$, with no stirring, the activation energies are lower than those obtained with stirring (18 and 12 as compared with 10 and 9 kcal/mole). The outstanding difference between a stirred and nonstirred Ge-$HNO_3$ reaction is that the $HNO_2$ concentration at the germanium-liquid interface is appreciably less in the former than in the latter. Thus, it appears reasonable that the measured activation energy could also be a function of $HNO_2$ concentration. Consistent with this is the low value of 5 kcal/mole obtained in 6.0$N$ solutions, through which $NO_2$ had been bubbled. The $HNO_2$ concentration in this case was appreciably higher than in the previous cases.

[3] The activation energy is equal to $\left(\frac{1}{T_1} - \frac{1}{T_2}\right) R \ln \frac{V_2}{V_1}$, where $V_1$ and $V_2$ are the rates at the absolute temperatures $T_1$ and $T_2$ respectively, assuming that the concentration of the reactants is not sensitive to temperature.

## II. Passivity of Germanium

ABSTRACT

Above 6 to 8$N$, $HNO_3$, the initial dissolution rate of germanium decreased with increasing $HNO_3$ concentration and increasing stirring rate. The time required to bring about passivation of the germanium in these solutions decreased from several hours to a few seconds in going to higher $HNO_3$ concentrations. A surface oxide film (very likely $GeO_2$) is associated with the passivity of germanium. Accordingly, the presence of HF which dissolves $GeO_2$ but not germanium prevented germanium passivity. Dissolution potential measurements were consistent with the kinetic data.

### Dissolution as a Function of Time in Concentrated $HNO_3$ Solutions

Weight losses of germanium in 7.5, 10.3, and 12.0$N$ $HNO_3$ as a function of time, with no stirring, are shown in Fig. 10. The time necessary to attain a maximum weight loss is seen to decrease with increasing $HNO_3$ concentration. The gain in weight beyond this point is associated with the formation of a surface film which eventually becomes visible. At concentrations greater than 18$N$ the film forms immediately upon immersion. When sufficiently thick, the film is opaque white and exhibits the properties of the soluble hexagonal $GeO_2$.[4] Thus, it can be reremoved without affecting the substrate, since it is soluble in KOH, NaOH, and HF, solutions which do not attack germanium at room temperature in the

[4] The extremely inert tetragonal form of $GeO_2$ was not detected. This form is insoluble in water and is not attacked by HF or NaOH solutions (18).

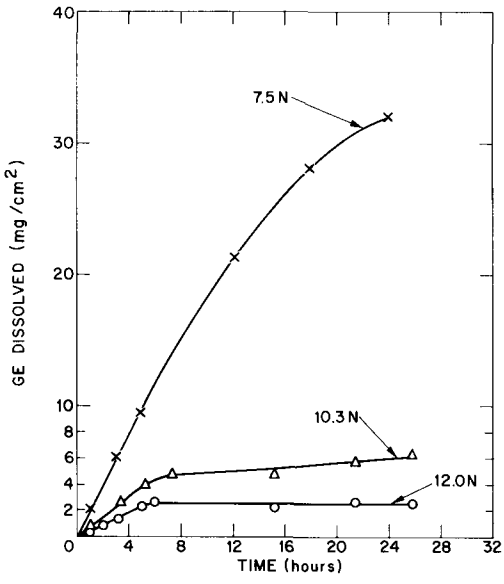


Fig. 10. Dissolution of germanium in $HNO_3$ solutions as a function of time at 27.5°C.

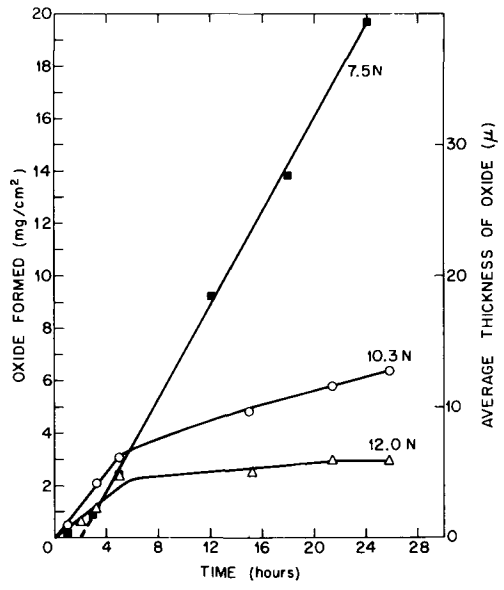


Fig. 12. Oxide film on germanium formed in $HNO_3$ solutions at 27.5°C as a function of time.

absence of dissolved oxygen (19). In this respect, the Ge-$GeO_2$ system affords a unique advantage over the more common metals.

The total amount of germanium reacted was determined from the weight losses plotted in Fig. 10 and the amount of germanium contained in the oxide film. The latter was obtained gravimetrically by immersing the oxide bearing samples in 1*N* NaOH for approximately 1 hr. Repeated immersions in 1*N* NaOH resulted in no additional weight loss. The results are shown in Fig. 11. No structural studies of the oxide film were carried out; however, analysis of the germanium oxide solutions for germanium combined with the total weight of the oxide film gave the empirical formula $Ge_xO_{2x}$. The amount of oxide present on the surface and its average thickness, assuming a density (4.7 g $cm^{-3}$) equal to that of bulk $GeO_2$, is shown in Fig. 12 as a function of time. In 7.5*N* solution an extended period of rapid growth begins after approximately 3 hr. For periods shorter than about 3 hr the average thickness of oxide in 7.5*N* $HNO_3$ is less than that formed in the more concentrated solutions, although the initial dissolution rate for the latter concentrations is smaller than for the former. Assuming that the nature of the surface film is the same in the various solutions, it is apparent that its solubility and/or rate of solution is greater in 7.5*N* $HNO_3$ than in the other two solutions. Accordingly, while the initial rate of germanium dissolution in 10.3*N* $HNO_3$ is 2.7 times smaller than in 7.5*N* solution, the initial rate of oxide growth in the former is only 1.6 times smaller than in the latter considering the linear growth beyond 3 hr. In agreement with the above, semiquantitative experiments showed that the solubility and rate of dissolution in $HNO_3$ solutions decreases appreciably with increasing $HNO_3$ concentrations. Pugh (20) has observed similar behavior for $GeO_2$ in $H_2SO_4$ solutions over a wide concentration range (0 to 16*N*).

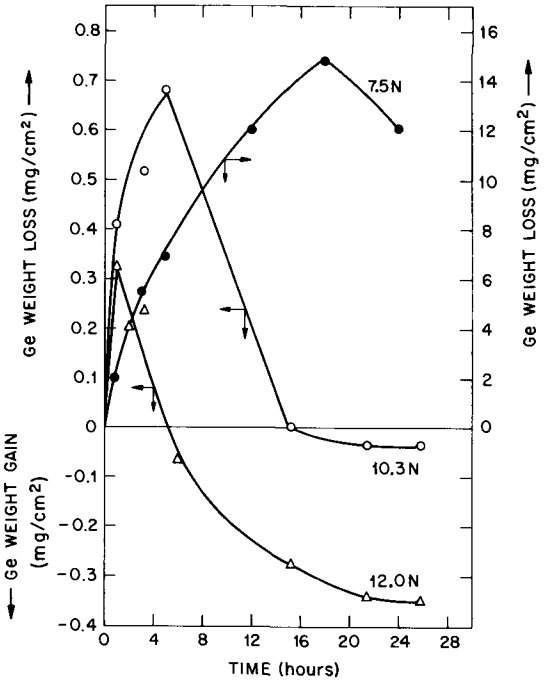


Fig. 11. Dissolution of germanium in $HNO_3$ solutions as a function of time at 27.5°C (oxide surface film removed).

In stirred concentrated $HNO_3$ solutions the behavior of germanium is similar to that in nonstirred solutions except that with stirring higher concentrations and/or longer periods are required to bring about passivity.

It should be pointed out that in concentrations lower than 6-8*N* the dissolution rate can also decrease with time, although it does not become zero. In this case, however, relatively large amounts of germanium dissolve before a surface film is formed. By decreasing the volume of a 5.5*N* $HNO_3$ solution from 90 to 20 ml, the decrease in dissolution rate set in after 6 hr rather than after approximately 24 hr. A surface film was ultimately formed in both experiments and, after an additional 24 hr, small amounts of $GeO_2$ were observed on the walls of the reaction vessel.

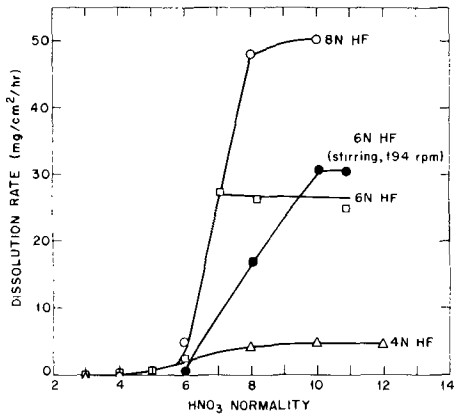


Fig. 13. Dissolution of germanium in $HNO_3$ solutions containing HF at 27.5°C. The solutions were not stirred except in the case indicated.

*Effect of Hydrofluoric Acid*

Dissolution rates pertaining to HF + $HNO_3$ mixtures are summarized in Fig. 13. A comparison of these results with those of Fig. 2 shows that, in general, the dissolution rate is not significantly affected by the presence of HF at $HNO_3$ concentrations below 6*N* without stirring and 8*N* with stirring. An increase in dissolution rate by a factor of approximately 2 is observed in nonstirred 6*N* $HNO_3$ + 6*N* HF solution over 6*N* $HNO_3$, possibly due to a decrease in the degree of dissociation of $HNO_3$. An increase in the concentration of undissociated $HNO_3$ would lead to increased rate according to Eq. [2]. Lack of suitable concentration and dissociation data under the present experimental conditions prevents a quantitative treatment of this effect.

Figure 13 shows further that in the presence of HF, as in the absence of HF (Fig. 2), stirring decreases the dissolution rate at the lower $HNO_3$ concentrations. Thus, it appears that HF does not interfere with the mechanism of dissolution and that reaction [5] remains rate determining. In accord with this result, the activation energy of the dissolution process in stirred 6*N* $HNO_3$ + 6*N* HF was determined as 19 kcal/mole which compares favorably with the value of 18 kcal/mole found in stirred 5.5*N* $HNO_3$ (Table II).

In the higher $HNO_3$ concentrations where reaction [5] is no longer rate determining, the dissolution rate increases markedly in the presence of HF and reaches a limiting value which, for a given $HNO_3$ concentration, increases with increasing HF concentration (Fig. 13). As in the absence of HF (Fig. 2), here also stirring increases the dissolution rate.

**Table II. Activation energy for the dissolution of germanium in $HNO_3$ solutions**

| $HNO_3$ Normality | Activation energy Kcal/mole |
|---|---|
| 5.5*N*, 194 rpm | 18 |
| 7.5*N*, 194 rpm | 12 |
| 6.0*N* + added $HNO_2$, 194 rpm | 5 |
| 5.5*N*, no stirring | 10 |
| 7.5*N*, no stirring | 9 |
| 6.0*N* + 6*N* HF, 194 rpm | 19 |

Inasmuch as the decrease in dissolution rate is associated with surface oxide formation, it is reasonable to assume that the increase in dissolution rate by HF is due to the greater solubility of $GeO_2$ in HF solutions due to the reaction:

$$GeO_2 + 6HF \rightarrow H_2GeF_6 + 2H_2O \qquad [10]$$

*The Nature of the Passivity of Germanium*

The facts described above point to a pronounced anodic polarization in concentrated $HNO_3$ solutions resulting from the formation of a surface oxide which can become protective and lead to passivity. The anodic reaction and related side-reactions may not be precisely described by Eq. [3]. However, in view of the predominantly acidic character of $GeO_2$, it is unlikely that ionic or molecular species other than $GeO_2$ or germanic acids are formed during oxidation of germanium with $HNO_3$. The formation of complex compounds between germanium and $HNO_3$ (or the intermediates of $HNO_3$ reduction) is essentially excluded since the solubility of $GeO_2$ decreases with increasing $HNO_3$ concentration. It is possible that $GeO_2$ is the first distinct anodic product and that $H_2GeO_3$ is formed from it by hydration. Alternatively, $GeO_2$ may form from $H_2GeO_3$ by dehydration. Knowledge of the sequence of formation of the two compounds is not essential to our argument since, in either event, formation of $GeO_2$ can take place on or near the germanium surface.

The formation of a layer of $GeO_2$ at high $HNO_3$ concentrations is explained as follows. The rate of formation of $GeO_2$ increases as the rate of the cathodic reaction increases according to [2]. At the same time, however, the solubility and/or the dissolution rate of the oxide decreases. Thus, the germanium-liquid interface becomes saturated with respect to $GeO_2$. Since diffusion of $GeO_2$ or $H_2GeO_3$ away from the interface is relatively slow, nucleation and growth of $GeO_2$ occurs on the germanium surface before $GeO_2$ precipitates out in the bulk of the solution. At very high concentrations sufficient $GeO_2$ precipitates out within a few seconds and in a suitable form to cover all of the germanium surface and bring about passivity.

In low concentrations, but not below 6*N*, $GeO_2$ at first forms adherent "patches" on the germanium surface. Thus, the surface exposed to the solution is decreased. If at any time sufficient germanium area were exposed for reaction [7] to proceed faster than [5], the dissolution mechanism should be the same as described for dilute $HNO_3$ solutions. In such a case, the rate of the cathodic reaction and hence, the average dissolution rate should not be affected by the presence of oxide patches. Thus, the attack should become localized at the bare germanium surface. Indeed, intensified local attack was observed in $HNO_3$ solutions with concentrations near those corresponding to the maximum dissolution rates. Above these concentrations, however, the average dissolution rate decreases with increasing $HNO_3$ normality. This clearly suggests that reaction [5] ceases to be rate determining. Since reaction [5] is catalyzed by metallic surfaces, the possibility exists that its average rate is a function of the

amount of the germanium surface not covered by oxide. If this were the case, the dissolution process at these concentrations should be under cathodic control and, thus, the dissolution potential should shift toward more anodic values as the dissolution rate decreased (8). Since a potential shift toward more cathodic values was observed, the system is now under anodic control and the anodic reaction [3] determines the rate of the over-all dissolution process.

The growth of thick oxide films as in the present case (of the order of microns, Fig. 12) by diffusion of oxygen inward or germanium ions outward is not plausible at room temperature and in the absence of very strong electric fields (21). On the other hand, the approximate linear growth for the first few hours in 10.3*N* and 12.0*N* can be explained on the basis of poor film adhesion, blistering, cracking or other such macroscopic defects in the film (22). Actually, in the present case, the greater the limiting thickness the more porous and the less dense the oxide film appeared under microscopic examination. In some respects the passivity of germanium resembles the passivity of metals caused by insoluble salts as described by Müller (23).

The time necessary for passivity and the limiting average oxide thickness decrease with increasing $HNO_3$ concentration. This trend extends to appreciably higher concentrations than those shown in Fig. 11 and 12. The experimental approach employed does not lend itself to establishing a quantitative expression of this trend. It was found, however, that in the concentration beyond 16*N* (without stirring) the time required for passivation is of the order of seconds and the oxide thickness approximately 150Å. Thus, it appears that the limiting oxide thickness is inversely related to the initial germanium dissolution rate and to the solubility (and/or the dissolution rate) of the oxide in the $HNO_3$ solutions. The initial dissolution rate increases and the solubility of $GeO_2$ decreases with increasing $HNO_3$ concentrations. High rates of formation of $GeO_2$ lead to adhering dense surface oxide film for reasons which are not clear at present. Extension of the passivating range to lower $HNO_3$ concentrations in the presence of $HNO_2$ (Fig. 5, curve IV) is readily understood in the light of the fact that, for a given $HNO_3$ concentration, $HNO_2$ increases the initial dissolution rate of germanium.

Our views that the behavior of germanium and its passivity in concentrated $HNO_3$ solutions are determined by the formation and presence of a $GeO_2$ surface film rather than by absorption of certain species from the solution onto the surface are consistent with the fact that in these solutions both n- and p-type germanium behave alike. In dilute solutions where no oxide film is present, distinct differences were observed between the two types of germanium. If adsorption played an important role in the passivity of germanium, the two types of germanium would probably exhibit measurable differences in their passivating characteristics. Passivity in $HNO_3$ due to adsorption and/or chemisorption was hypothesized in the case of iron (24, 25). It is not necessary that passivity in $HNO_3$ is established by the same mechanism for all metals. Thus, iron passivity may and may not be comparable to germanium passivity. The Ge-$HNO_3$ reaction, however, as pointed out earlier, lends itself to a more direct study than the corresponding behavior of iron in nitric acid.

## Summary

I. *In* $HNO_3$ *solutions below ca. 6N.*—The dissolution rate of germanium is a function of the concentration of undissociated $HNO_3$ and $HNO_2$. Since $HNO_2$ is formed during the reaction of germanium with $HNO_3$, the dissolution process is "autocatalytic." Consequently, stirring decreases the dissolution rate by removing reaction products from the germanium $HNO_3$ interface. In addition, for a given stirring rate, the dissolution rate increases with time owing to an increase in concentration of $HNO_2$.

In unstirred solutions the dissolution rate reaches a maximum in approximately 6*N* $HNO_3$; the maximum occurs at a higher concentration (8-9*N*) with stirring and at a somewhat lower concentration when relatively large amounts of $HNO_2$ are present.

The dissolution potential of n-type germanium is more noble than that of p-type. Furthermore, for a given $HNO_3$ concentration the dissolution rate of the former is smaller than that of the latter.

The dissolution potential of both n- and p-type germanium becomes more noble with increasing $HNO_3$ concentration and, hence, with increasing dissolution rate. Thus, the dissolution process is controlled by the cathodic reaction (reduction of $HNO_3$) and the dissolution potential by the anodic reaction.

The presence of HF does not affect the dissolution rate unless the HF concentration becomes sufficiently high (above ca. 6*N*) to decrease the dissociation of $HNO_3$.

II. *In* $HNO_3$ *solutions above 6N.*—The dissolution rate decreases with increasing $HNO_3$ concentration and increases with stirring. For a given $HNO_3$ concentration the dissolution rate decreases with time and eventually approaches zero; the higher the $HNO_3$ concentration, the sooner germanium acquires passivity. The time required varies from a few hours to a few seconds. A surface oxide film (very likely $GeO_2$) is associated with passive germanium. The average thickness of the oxide film can vary from a few microns to approximately 150Å.

The dissolution potential becomes more noble with increasing $HNO_3$ concentration and, hence, with decreasing dissolution rate. Thus, the reaction of germanium with concentrated solutions of $HNO_3$ is controlled by the anodic reaction (formation of $GeO_2$) and passivity is associated with pronounced anodic polarization. The decrease in solubility and/or rate of solution of $GeO_2$ with increasing $HNO_3$ concentration is of paramount importance in the passivation process.

Passivity of germanium in $HNO_3$ solutions is prevented or destroyed by the presence of HF since HF prevents the formation of a protective oxide film.

## Acknowledgment

The authors wish to express their appreciation to L. J. Gordon for his skillful assistance with many

of the experiments and Dr. W. W. Harvey for valuable suggestions.

Manuscript received Sept. 23, 1957. This paper was prepared for delivery before the Cleveland Meeting, Sept. 30-Oct. 4, 1956. The research in this paper was supported jointly by the Army, Navy, and Air Force under contract with Massachusetts Institute of Technology.

Any discussion of this paper will appear in a Discussion Section to be published in the June 1959 JOURNAL.

REFERENCES

1. H. Newcombe, W. McBryde, J. Bartlett, and F. Beamish, *Anal. Chem.*, **23**, 1023 (1951).
2. A. Portevin, *Rev. Met.*, **26**, 617 (1929).
3. U. R. Evans, "Metallic Corrosion Passivity and Protection," p. 247, Edward Arnold and Company, London (1948).
4. *Ibid*, p. 225.
5. E. Abel and H. Schmid, *Z. Physik. Chem.*, **132**, 55 (1928).
6. K. Vetter, *Z. Anorg. Chem.*, **260**, 244 (1949).
7. G. C. Hood, O. Redlich, and C. A. Reilly, *J. Chem. Phys.*, **22**, 2067 (1954).
8. R. B. Mears, *J. (and Trans.) Electrochem. Soc.*, **95**, 1 (1949).
9. J. O'M. Bockris, "Modern Aspects of Electrochemistry," p. 255, Academic Press Inc., New York (1954).
10. W. H. Brattain and C. G. B. Garrett, *Bell System Tech. J.*, **34**, 129 (1955).
11. J. T. Law, *J. Phys. Chem.*, **59**, 543 (1955).
12. A. C. Makrides, N. M. Komodromos, and N. Hackerman, *This Journal*, **102**, 363 (1955).
13. H. C. Gatos, *ibid.*, **103**, 286 (1956).
14. H. C. Gatos, *Corrosion*, **12**, 322 (1956).
15. D. R. Turner, *This Journal*, **103**, 252 (1956).
16. K. Vetter, *Z. Physik. Chem.*, **194**, 199 (1950).
17. R. G. Monk and J. T. Ellingham, *J. Chem. Soc.*, **1935**, 125.
18. O. H. Johnson, *Chem. Rev.*, **51**, 431 (1952).
19. W. W. Harvey and H. C. Gatos, to be submitted for publication to *J. Electrochem Soc.*
20. W. Pugh, *J. Chem. Soc.*, **1929**, II, 1537.
21. N. F. Mott, *Trans. Faraday Soc.*, **43**, 429 (1947).
22. U. R. Evans, *Trans. Electrochem. Soc.*, **91**, 547 (1947).
23. W. J. Müller, "Die Bedeckungstheorie der Passivitat der Metalle und ihre Experimentelle Begründung," Verlag Chemie (1934).
24. H. C. Gatos and H. H. Uhlig, *This Journal*, **99**, 250 (1952).
25. H. H. Uhlig and T. L. O'Connor, *ibid.*, **102**, 562 (1955).

# Studies of the Anodic Behavior of Aluminum

## I. The Direction of Ionic Movement

**John E. Lewis and Robert C. Plumb**[1]

*Research Laboratories, Aluminum Company of America, New Kensington, Pennsylvania*

ABSTRACT

It is demonstrated, by a series of marker experiments in which layers of nonporous anodic oxide were tagged by incorporating radioactive material in them, that nonporous anodic oxide grows at, or close to, the oxide-electrolyte interface; it is concluded that the aluminum ion is the mobile species. Similar experiments with a porous oxide may also be interpreted in terms of formation of the oxide at the oxide-electrolyte interface, but in this case the interface is at the bottom of pores filled with electrolyte.

Two distinct types of oxide films may be formed on aluminum by anodic oxidation, depending on the rate at which the oxide is dissolved by the electrolyte during the oxidation (1).

Where there is little solvent action, thin nonporous films, whose thickness is proportional to the applied voltage, are formed (2). When there is appreciable solvent action, thick porous films, whose thickness increases with the time anodized, are formed (3). It has been shown that the porous films contain a hexagonal array of pores, each of which extends from the solution inwards almost to the metal surface. The base of each pore is separated from the metal by a thin nonporous layer of oxide (4). A slight tendency toward porosity with electrolytes which do not have solvent action has been noted by Franklin (5). The classification of anodic films as "essentially nonporous" and "porous" will be retained, however.

It has not been demonstrated by experiment whether, during formation, aluminum moves outward through the film or oxygen moves inward, or if both processes take place. Depending on which of the three possibilities is in fact realized, the oxide film will be growing at the oxide-solution interface, at the metal-oxide interface, or somewhere between the two interfaces. In the case of porous-type coatings, the electrolyte probably fills the pores, making contact with the oxide at the pore bases, and the growth of further oxide must take place somewhere between the pore bases and the metal. This has, in fact, been demonstrated in numerous experiments (6, 7) by observing the movement of layers of porous oxide which were tagged by pigments incorporated in the pores. These experiments, however, do not tell whether the new oxide is being formed at the oxide-metal or the oxide-solution interface, and hence give no information about the movement of aluminum or oxygen through the oxide layer.

The experiments to be described are similar to those in which oxide layers were tagged with pig-

[1] Present address: Department of Chemical Engineering and Chemistry, Worcester Polytechnic Institute, Worcester, Massachusetts.

ments, but in this case the complication of a pore structure was avoided by using essentially nonporous oxide films tagged by forming in a radioactive electrolyte. It will be shown in a later paper (8) that during anodizing some of the anion from the electrolyte is incorporated in the oxide as an essential component of it. The tagged layer was applied either before or after applying a rather thick (700Å) nonradioactive, nonporous oxide layer. The position of the tagged layer in the composite film was determined by dissolving the oxide slowly and measuring the remaining radioactivity of the sample.

## Experimental

Sulfur-35 tagged electrolyte was prepared by adding carrier $H_2SO_4$ to radioactive $H_2SO_4$ (Oak Ridge Cat. Item S-35-P-1), fuming to remove chloride ion, and diluting to make a 0.1% electrolyte having a specific activity of 0.6 mc/mg $SO_4$. Anodizing in a sulfuric acid electrolyte for an extended time gives a porous type film. However, by very brief anodizing in such an electrolyte with a suitable applied voltage, the buildup of a porous layer can be minimized and one will obtain primarily a nonporous barrier layer (4). In this work, 99.99% Al specimens were immersed for various periods of time in the bath, at a distance of 5 cm from an aluminum cathode with an applied voltage of 15 v. Where a sulfate coating was applied after the 50-v tartrate coating, a 52-v potential was used.

The 700Å thick nonradioactive coatings were obtained by anodizing at a 50-v potential in a 3% ammonium tartrate electrolyte (2).

The radiation from the oxide films was measured with an end window Geiger-Mueller counter with a precision of 2%. The 700Å thick coating would attenuate less than 2% of the sulfur-35 radiation.

The oxide was dissolved from the specimens with a 5% $H_3PO_4$-2% $CrO_3$ solution at 50°C. This reagent does not attack the aluminum, and it should not undermine the oxide.

The activity remaining on the specimens was plotted against the total time of exposure to the oxide stripping solution.

## Results

Figure 1 shows the results on three specimens treated with (*a*) 30-sec $H_2SO_4$ coating only, (*b*) 700Å inert layer, then 30-sec $H_2SO_4$ coating, (*c*) 30-sec $H_2SO_4$ coating, then 700Å inert layer. In all cases, the $H_2SO_4$ coating was radioactive. It is apparent from these three curves that the oxide layer which is applied first is the last layer to be removed during the stripping treatments, so the oxide must have formed at the oxide-solution interface.

It is difficult, because of the possibility of nonuniform attack on the oxide by the stripping solution, to say precisely that the oxide is being formed at the oxide-solution interface rather than at some point within the oxide layer but quite close to the oxide-solution interface. In this sense, the results are qualitative, and one can only conclude that the oxide is being formed much nearer the solution interface than the metal interface. It follows that the principal material transported through the

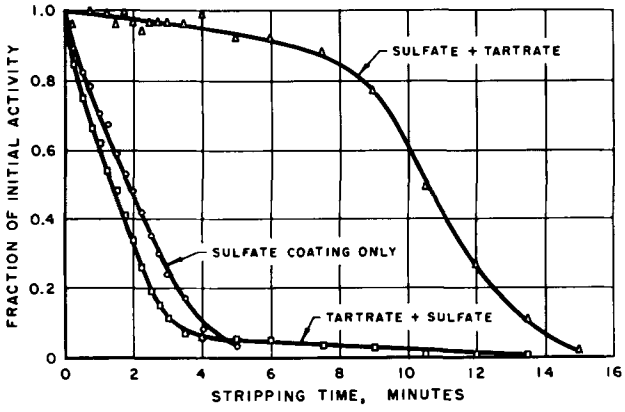


Fig. 1. Decrease in activity of sulfur-35 tagged oxide vs. time exposed to oxide stripping solution. Curves, top to bottom: 30-sec sulfate coating followed by 50-v tartrate coating; 30-sec sulfate coating only; 50-v tartrate coating followed by 30-sec sulfate coating.

oxide film during anodizing is aluminum and not oxygen. This result is consistent with work which indicates that, under forming conditions, barrier type oxides are nonstoichiometric, containing excess aluminum.

Another interesting set of curves is shown in Fig. 2. In this case, 30-sec, 3-min, and 10-min coatings were formed in the radioactive sulfuric acid. After the radioactive coatings were applied, the specimens were anodized in ammonium tartrate to give a 50-v (700Å) nonporous layer. It would be expected that the tartrate anodizing would: (*a*) form a uniform nonporous layer on top of the essentially nonporous 30-sec coating, (*b*) completely fill the pores of the 3-min coating and perhaps build a nonporous layer on top of it, and (*c*) tend to fill the pores of the 10-min coating, but to a lesser extent than with the 3-min coating. The curves in Fig. 2 are, in fact, just what would be expected with

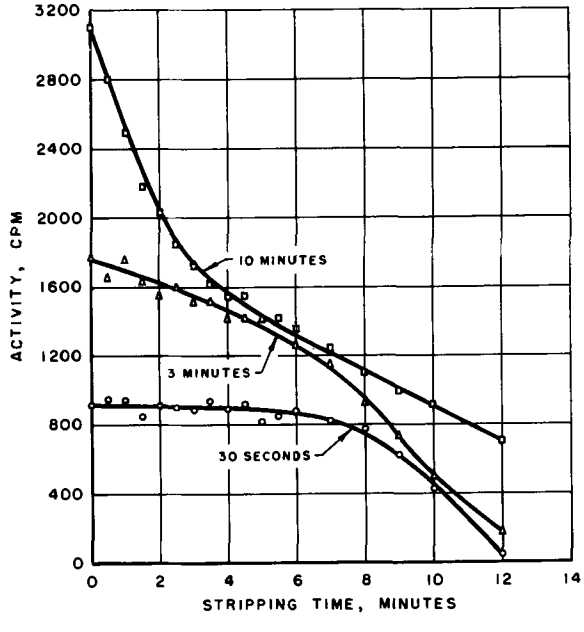


Fig. 2. Decrease in activity of sulfur-35 tagged oxide vs. time exposed to oxide stripping solution. Curves, top to bottom: 10-min sulfate coating followed by 50-v tartrate coating; 3-min sulfate coating followed by 50-v tartrate coating; 30-sec sulfate coating followed by 50-v tartrate coating.

this model. The activity of the sample which had a 10-min coating decreased rapidly, showing that the pores in the tagged oxide applied first were not filled up completely by the nonradioactive oxide. The activity of the sample which had a 3-min coating, whose pores would be completely filled by the nonradioactive oxide, decreased but at a much slower rate than the activity of the 10-min sample. The sample with the 30-sec coating of tagged oxide did not show a decrease in activity until the nonradioactive oxide on top had been dissolved away.

These marker experiments demonstrate conclusively that the aluminum ion is the mobile species in the anodic oxidation of aluminum. The result is analogous to that found in the anodic oxidation of tantalum (9).

When the electrolyte has no solvent action on the oxide, the aluminum combines with oxygen at or near the oxide-solution interface, building up the thickness of the oxide in a continuous, uniform manner. When the electrolyte has solvent action on the oxide and causes pores to be formed, the aluminum ions combine with oxygen at or near the base of the pores. This new oxide apparently fills in between the outer porous oxide layer and the metal, and must itself become a part of the porous oxide after further oxidation takes place. The details of the process by which the porous layer is built up continuously from oxide which is formed near the bases of the pores are not clear at the present time.

### Acknowledgment

The authors would like to express thanks to Mr. F. Keller and Mrs. Phyllis Towner for valuable discussions of the manuscript.

Manuscript received Jan. 20, 1958. This paper was prepared for delivery before the Ottawa Meeting, Sept. 28-Oct. 2, 1958.

Any discussion of this paper will appear in a Discussion Section to be published in the June 1959 JOURNAL.

REFERENCES

1. J. D. Edwards, *Trans. Electrochem. Soc.*, **81**, 341 (1942).
2. G. Haas, *J. Opt. Soc. Amer.*, **39**, 532 (1949).
3. J. D. Edwards and F. Keller, Tech. Publ. No. 1710, AIMME (1944).
4. F. Keller, M. S. Hunter, and D. L. Robinson, *This Journal*, **100**, 411 (1953).
5. R. W. Franklin, *Nature*, **180**, 1470 (1957).
6. Unpublished results, Alcoa Research Laboratories.
7. N. D. Pullen and B. A. Scott, *Trans. Inst. Met. Finishing*, **33**, 163 (1956).
8. R. C. Plumb, *This Journal*, **105**, 498 (1958).
9. D. A. Vermilyea, *Acta Met.*, **2**, 482 (1954).

# Studies of the Anodic Behavior of Aluminum

## II. Coulometry of Barrier Layer Production

**Robert C. Plumb**[1]

*Research Group on the Physics and Chemistry of Solids, Cambridge University, Cambridge, England*

ABSTRACT

In order to avoid solvent action by the electrolyte during anodic oxidation of aluminum, the electrolyte must have a high buffering capacity. With such an electrolyte the conversion of aluminum to aluminum oxide is essentially quantitative. The film thickness is proportional to the voltage drop across the film, and the proportionality constant does not depend on the length of time which the voltage is left applied. The film contains, as an essential part of its structure, a quantity of the anion from the electrolyte. The film appears to be nonstoichiometric, having excess aluminum during formation, the amount of excess decreasing with increased length of anodizing time. The coulombic transfer during film formation is quantitatively accounted for during formation by oxidation of aluminum to the trivalent state and liberation of oxygen gas. After the film growth has ceased, the current can be only partially accounted for by oxygen evolution, but it is thought that this is because of difficulty in nucleating oxygen bubbles.

It is now well known that an oxide film whose thickness is proportional to the voltage may be formed on aluminum by anodic oxidation in an electrolyte which has no solvent action on aluminum oxide. This paper describes several experiments designed to determine to what extent a quantitative electrochemical description of the process can be made. It considers the relationship between the thickness of the film and the potential drop across it, the composition of the film, the nature of the electrolyte, and the coulombic efficiency in forming the film. The physics of the ion transport through the film is not considered explicitly, although evidence of nonstoichiometry is presented.

Many factors may influence the coulombic efficiency in film formation. Haas (1) found by multiple beam interferometry that the film thickness per volt for anodizing aluminum in an ammonium tartrate electrolyte at a pH of 5.5 increases from 12.2Å/v in 30 sec anodizing to 13.5Å/v after 15 min anodizing and increases further at a rate of 1%/hr after that. He found that the aluminum oxide film

[1] Present address: Department of Chemical Engineering and Chemistry, Worcester Polytechnic Institute, Worcester, Massachusetts.

accounted for only 80% of the aluminum consumed, although the electrolyte itself did not attack the film. Dewald (2,3) and Young (4, 5) have discussed the role of space charge, in the form of excess metal ions, during anodic oxidation. Young (5) has demonstrated that such space charge is probably "frozen into" the oxide when current is interrupted. Direct chemical observation of "frozen in" space charge has not been made. It has been proposed (6, 7) that low valent aluminum is a direct product of anodic oxidation, and that its oxidation to the trivalent state results in hydrogen being liberated at the anode. Although hydrogen evolution does undoubtedly occur in some electrolytes, it is usually thought that oxygen is the gas evolved when aluminum is anodized in electrolytes which are suitable for the development of oxide films. It has been observed by many investigators that porous anodic oxide coatings (formed in electrolytes with solvent action on aluminum oxide) contain measurable amounts of the acid anion, e.g., 12-14% $SO_3$ from $H_2SO_4$ (8).

## Experimental

*Weighing and oxide stripping.*—The average thickness of an oxide film on aluminum was determined directly by weighing a specimen, anodizing under the appropriate conditions, reweighing, dissolving the oxide off in a reagent which does not attack aluminum, and weighing again. This gives the aluminum consumed in forming the oxide film and the total weight of the film. The reagent used was 5% $H_3PO_4$-2% $CrO_3$ at 85°C. Dissolution of ordinary anodic oxide films which have not been formed at excessively high voltages or temperatures is complete in 5 min, whereas the attack on the aluminum is less than 2Å/min, as determined by radioactive tracer experiments (9) and less than 0.06 $\mu g/cm^2/min$ as determined by direct weighing measurement in preliminary work in this investigation. The inertness of the aluminum results from the formation of a 10-20Å thick mixed phosphate-chromate film on the surface by reaction with it (9). The aluminum consumed in forming an oxide film may be determined from the weight loss of a specimen when a film is formed and then stripped off.

In this investigation, a 99.9% Al foil, with 34 $cm^2$ area, suspended from a 0.010 in. Al wire, was used. An Oertling torsion balance, counterbalanced to accommodate the foil, which weighed about 30 mg, was used. The precision of weighing was ±10 $\mu g$. The calibration of the torsion scale was not affected by the counterbalancing. Samples were rinsed twice in distilled water and twice in acetone, dried by suspending in hot air over a hot plate, and weighed. Thermal equilibrium in the balance was reached within 5 min. Electrostatic charges interfered with weighing on very dry days. No loss of precision was noted as a result of the sample washing and drying procedure.

*Anodizing.*—Two different electrolytes were used. One was a 3% tartaric acid solution, adjusted to a pH of 5.5 with ammonia, as used by Haas. The other was a solution of 1.6 wt % $H_3PO_4$ adjusted to a pH of 7.0 with KOH. The electrolytes were saturated with oxygen gas. A platinum cathode was used. The voltages across the film were measured with a vacuum tube volt meter, using an oxygen-platinized platinum reference electrode near the sample. The reference electrode and correction for its half-cell were similar to those described in a subsequent publication (10).

*Radioactive tracer experiments.*—The phosphate content of anodic oxide films formed in the phosphate electrolyte was measured by using neutron irradiated $KH_2PO_4$ and comparing the activity of the films with standards prepared by evaporation of aliquots of the electrolyte. Activities were measured with a 1.5 $mg/cm^2$ end window Geiger-Mueller detector to a precision of 1%. No self-absorption by films of the thickness employed is to be expected.

The samples in this portion of the work were 1-in. squares of 0.064-in. thick, high-purity sheet (99.99% Al), chemically polished by the Alcoa R-5 bright dip process.[2] Weighing of these samples was done with a Kuhlmann microbalance.

## Results

*The electrolyte.*—The previous observation (1), that more aluminum is consumed during anodizing in a tartrate electrolyte than can be accounted for in the film, was confirmed by weight change measurements. Up to 50% excess aluminum could be consumed in forming an 1100Å coating. The excess was variable and depended on current density and other unknown factors. This author has observed in other studies that barrier-type films cannot be formed in certain other electrolytes such as $K_2SO_4$, but that porous films similar to those formed in $H_2SO_4$ are obtained. Neither ammonium tartrate nor potassium sulfate electrolytes will dissolve $Al_2O_3$ by simple contact without current flow.

The behavior observed in the different electrolytes may be explained readily in terms of the buffering capacity of the electrolyte. By discharge of oxygen anions, through formation of $Al_2O_3$ or liberation of oxygen gas, a zone adjacent to the surface which is deficient in anions is formed. In the absence of a buffering agent this zone will be acidic. The oxide is forming at the oxide-solution interface (11), and, while in the process of forming, will not show any of the customary aging effects which are responsible for the difficulty usually encountered in oxide dissolution. Hence, it should dissolve readily if the solution adjacent to it has a pH below about 3.5 (12). Potassium sulfate has almost no buffering capacity and ammonium tartrate only little, and it is not unreasonable to expect that the pH at the oxide surface falls below 3.5 during anodizing. A suitable electrolyte for quantitative conversion of aluminum to $Al_2O_3$ should have, as the pH of maximum buffering capacity, a value close to that of least solubility of $Al_2O_3$. Of course, anions such as chloride, which have a deleterious effect on the blocking power of the oxide, should be avoided.

The phosphate electrolyte described previously (a mixture of $KH_2PO_4$ and $K_2HPO_4$-pH 7), with a high buffering capacity, has been used. The conversion of metallic aluminum to an oxide film is es-

[2] U. S. Pat. 2,650,157.

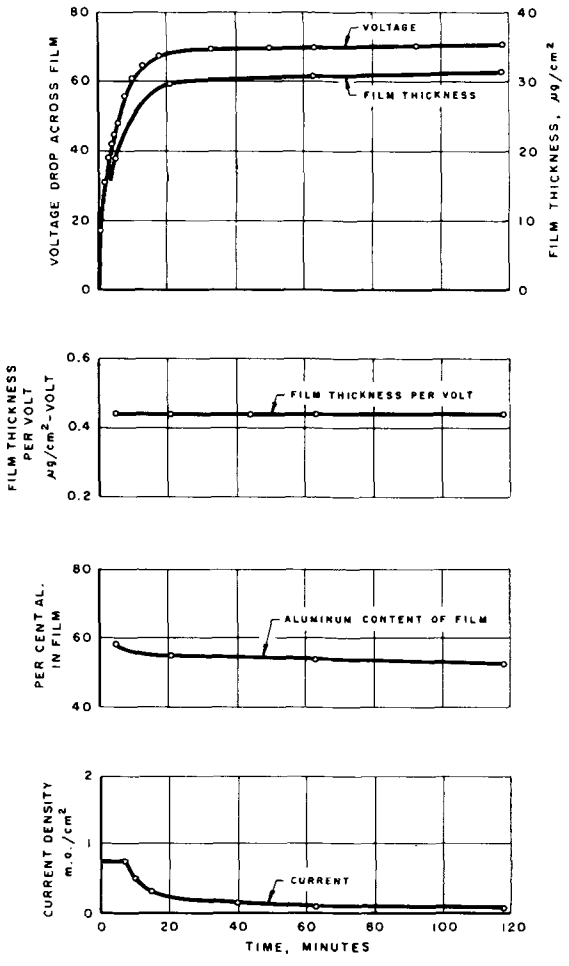


Fig. 1. Variation of voltage, film thickness, film thickness per volt, aluminum content of film, and current density with time in formation of barrier-type anodic oxide film in phosphate electrolyte.

sentially quantitative with this electrolyte. During the initial stages of film formation there is an apparent excess of aluminum over that required to form the film (e.g., as seen in Fig. 1, to be discussed later), but the apparent excess decreases with increasing length of anodic treatment. Since it is unlikely that aluminum lost to the solution could reenter the coating, the excess aluminum must be in the coating rather than lost to the solution by solvent action.

*Film thickness per volt.*—Figure 1 shows the potential drop across a film, the film thickness, and the density thickness per volt as a function of time when a film was formed in the phosphate electrolyte. The current was limited to 0.75 ma/cm² in the initial stages of film formation by an external variable resistance. A slight break in the voltage curve just above 30 v corresponds to the point at which gas starts to be liberated at the sample surface. The current density is also shown. It is seen that the thickness per volt is constant (within an experimental error of 1 or 2%) from the point where only 65% of the film thickness has been reached to the time when the film thickness is changing at a rate of only 1%/hr.

The linearity of the relationship between film thickness and voltage is shown in Fig. 2.

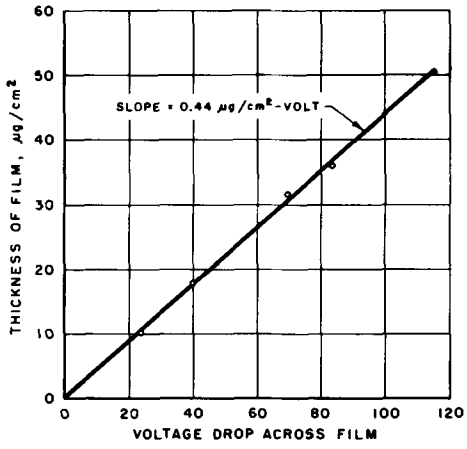


Fig. 2. Relationship between film thickness and voltage drop across barrier-type anodic oxide film formed in phosphate electrolyte.

Using a density of 3.2 for the film, which is in agreement with other investigations of anodic oxidation of aluminum, the film thickness in Å/v is 13.8 ± 0.3 which is in excellent agreement with Haas's value of 13.5 Å/v for 15 min anodizing.

Although the film thickness per volt was found to be independent of time in this work, Haas (1) did observe a dependence. Two reasons may account for this. First, cathode polarization and ohmic losses through the electrolyte were avoided in this work by measuring only the potential drop across the film by means of a reference electrode. Second, the slight tendency for the oxide to dissolve in the tartrate electrolyte may cause a previously undetected porosity in films formed in that electrolyte.

*Composition of film.*—By forming films in an electrolyte containing phosphorous-32, it was found that the film contains phosphorus equivalent to about 6% $PO_4$, as shown in Fig. 3. The amount of phosphorus in a film varies in direct proportion with its thickness, showing that the phosphorus is in the film rather than absorbed on the surface. If it is present as $AlPO_4$, then a stoichiometric film contains 8% $AlPO_4$ and 92% $Al_2O_3$. The most likely form for the phosphorus would be $P_2O_5$ with the phosphorus atoms simply substituted for aluminum atoms in the

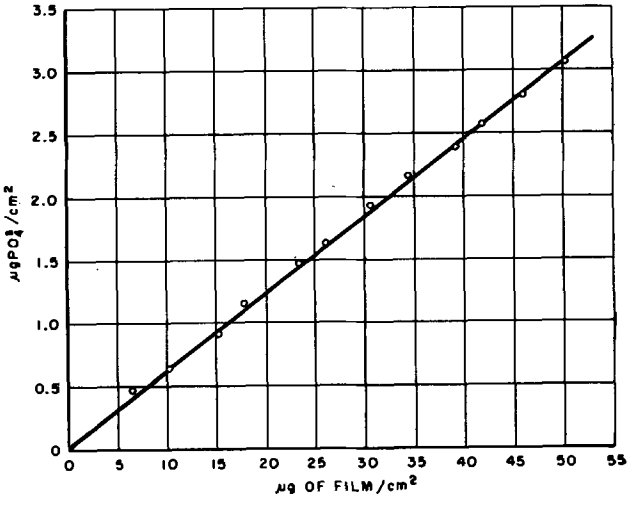


Fig. 3. Phosphate content as a function of thickness of barrier-type anodic oxide film formed in phosphate electrolyte.

oxide lattice. In this case, the composition would be 3.5% $P_2O_3$ and 96.5% $Al_2O_3$. In either case, the stoichiometric composition of the film would be 51% Al. Figure 1 shows the measured percentage of aluminum used in forming a 70-v film, as a function of time. After 5 min forming, while a current of 0.75 ma/cm$^2$ was flowing through the film, 58% Al had been consumed. The percentage of aluminum decreased with length of forming time to only 53% Al in 2 hr. There is no evidence of hydration of the barrier-type films.

A more detailed study of the composition of anodic oxide films is being pursued and a discussion of the significance of the nonstoichiometry to the mechanism of ionic transport will be postponed until further information is available. The results presented here do support, by direct chemical methods, Young's (4) prediction of excess metal ions being "frozen into" the oxide when anodizing is stopped.

*Current efficiency.*—When forming oxide films by anodic oxidation in the phosphate electrolyte, the current passing through the film may be accounted for quantitatively by the oxidation of aluminum to the trivalent ion (forming an oxide film of thickness 14Å/v, density 3.2, and containing the nonstoichiometric 55% Al) and the liberation of oxygen gas at the anode surface. After the oxide film reaches its maximum thickness for a given applied voltage, only about 80% of the residual current flowing through it may be accounted for in terms of oxygen gas liberation at the anode. These effects are illustrated by an experiment summarized in Fig. 4. Specimens were polished metallographically and chemically micropolished by the procedure given by Lewis and Plumb (9). They were then anodized in the special cell described in the next paper of this series (10). The total coulombs passed through the cell, the voltage drop across the film, and the volume of gas liberated at the anode were measured at various times during the formation of a 77 v film. Using the thickness factor (13.8Å/v), density, and composition expected from previous work, and assuming oxidation of aluminum to the trivalent state, the coulombs required to form the film were calculated. Adding to this the coulombs required to generate the observed volume of gas, the curve marked "film plus oxygen" was obtained. It is seen that the agreement with the experimental curve is quantitative while the film is forming, but less good when the film formation is almost complete. The poor agreement after film formation has practically ceased does not necessarily indicate that oxygen liberation and film formation do not quantitatively account for the current under all conditions. During formation of the oxide film at the solution-oxide interface, the surface is changing continuously and would supply sites where oxygen bubbles could nucleate readily; in contrast to this, a stationary surface would not provide as many sites for nucleation, and hence would favor discharge of oxygen without nucleation of gas bubbles producing a diffusion-type current similar to that which occurs at any anode when the oxygen overvoltage is not exceeded.

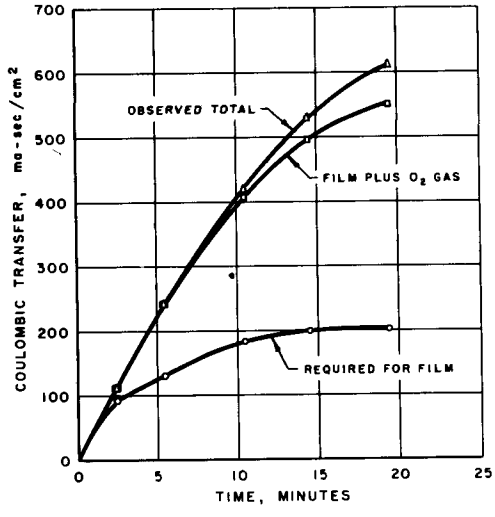


Fig. 4. Coulombic transfer in formation of 80-v barrier layer film by anodizing in phosphate electrolyte.

The coulombic efficiency, as defined by the ratio of coulombs necessary to oxidize the proper amount of aluminum to the trivalent state, to the total coulombs passed through film, varies greatly with the thickness of the film and the length of time the voltage is applied. It is generally observed that no oxygen is evolved from the anode until there is a voltage drop of 15-20 v across the film. Until then the current efficiency is close to 100%. As the film thickens, a continuously higher percentage of the total current appears as oxygen, and the efficiency drops to 50% and lower. When the film stops growing, some current (usually called leakage current) continues to flow, and the apparent current efficiency drops still lower depending on how long the leakage current is allowed to flow.

The results obtained may be explained without postulating low valent aluminum ion production. If even 10% of the aluminum were produced as a divalent or monovalent ion, these coulometric measurements should have detected it. It is possible that the low valent aluminum ions are produced to a lower extent and were detected by Davidson's (6, 7) sensitive experiments but escaped detection in this work. Further, there are probably basic differences between the electrolytes used by Davidson and those used in this work, since his electrolytes were not generally suitable for forming protective oxide coatings. It is likely that the nature of the ionic species produced will be sensitive to this difference.

## Summary

The measured potential drop across an anodic oxide film formed in a $KH_2PO_4$-$K_2HPO_4$ electrolyte at a pH of 7 appears to be a precise measure of the thickness of the film, independent of whether the film is undergoing formation or whether growth has ceased. Using a $KH_2PO_4$-$K_2HPO_4$ electrolyte, the conversion of aluminum to aluminum oxide is essentially quantitative and the coulombic transfer may be accounted for by conversion of the aluminum to the trivalent state and the liberation of some oxygen gas.

**Acknowledgments**

Work was supported by a grant from the National Science Foundation. The author wishes to thank the Aluminum Company of America for permission to include the results of the radioactive tracer measurements of the phosphate content of the anodic oxide films, performed in their research laboratories. Special thanks are expressed to Dr. F. P. Bowden for encouraging this work and providing laboratory facilities.

Manuscript received Jan. 20, 1958. This paper was prepared for delivery before the Ottawa Meeting, Sept. 28-Oct. 2, 1958.

Any discussion of this paper will appear in a Discussion Section to be published in the June 1959 JOURNAL.

REFERENCES

1. G. Haas, *J. Opt. Amer.*, **39**, 532 (1949).
2. J. F. Dewald, *Acta Met.*, **2**, 340 (1954).
3. J. F. Dewald, *J. Phys. Chem. Solids*, **2**, 55 (1957).
4. L. Young, *Acta Met.*, **4**, 100 (1956).
5. L. Young, *Trans. Faraday Soc.*, **52**, 502, 515 (1956).
6. W. E. Barnett, A. W. Davidson, and J. Kleinberg, *J. Am. Chem. Soc.*, **74**, 732 (1952).
7. E. Raijola and A. W. Davidson, *ibid.*, **78**, 556 (1956).
8. R. B. Mason, *This Journal*, **102**, 671 (1955).
9. J. E. Lewis and R. C. Plumb, *Intern. J. Appl. Radiation and Isotopes*, **1**, 33 (1956).
10. R. C. Plumb, *This Journal*, **105**, 502 (1958).
11. J. E. Lewis and R. C. Plumb, *ibid.*, **105**, 496 (1958).
12. S. P. Marion, A. W. Thomas, *J. Colloid Sci.*, **1**, 221 (1946).

# Studies of the Anodic Behavior of Aluminum

## III. The Specific Surface Area of Aluminum with Variable Resolution from 20Å to 1000Å

**Robert C. Plumb**[1]

*Research Group on the Physics and Chemistry of Solids, Cambridge University, Cambridge, England*

ABSTRACT

A new technique for studying the surfaces of metals that can be anodically oxidized is proposed. Its development and application for a variety of aluminum surfaces is described. It gives a measure of the specific area of aluminum with what may be described as a continuously variable resolution from 40Å to 1000Å. The results agree with measurements of specific surface area by a radiochemical technique which has a resolution of about 20Å and optical measurements made at resolution greater than 1000Å. The shape of a particular surface area vs. resolution curve gives information about the topography of the surface.

If one could look at an ideally prepared cross section of a metallic surface with a continuously variable magnification from less than 1 diameter to about $10^6$ diameters, more and more detail of the surface contours would be revealed as smaller and smaller asperities, cracks, fissures, etc., were resolved, until ultimately the asperities consisting of a few atoms, together with oxide layers and adsorbed molecules, were revealed. Such a detailed direct examination of surface contours over a suitable magnification range is impossible at the present stage of development of electron microscopy and sample sectioning techniques. Special techniques for revealing surface contours such as multiple beam interferometry and reflection electron microscopy are applicable only to relatively smooth surfaces. As a result, the knowledge of surface topography of rough surfaces is very limited.

One may further consider the hypothetical examination of a surface under idealized conditions. If the surface area were measured at each magnification, one would find it continuously increasing in the manner of a geometric progression since the smaller asperities, fissures, and cracks would appear as irregularities on larger asperities which had been observed at lower magnifications. The converse relationship is that, if the surface area could be measured with continuously variable resolution, the distribution of asperity sizes could be inferred from the variation of the measured surface area. Such a process is considered here.

The surface area of metals may be measured by several physical chemical techniques. Measurements by gas adsorption have recently been reviewed by O'Connor and Uhlig (1). Bowden and Rideal (2) devised the classical technique of measuring double layer capacitance of a metal in an electrolyte. This technique has been re-examined recently by Wiebe and Winkler (3). Adsorption of radioactive fatty acids from solution has been used (4). The formation of a thin radioactive barrier layer on aluminum has been used by this author (5). Each of these methods of area measurement has a characteristic resolution or resolving power corresponding to the thickness of the layer applied to the surface. Because of experimental difficulties in the measurements and the questionable validity of the results in some cases, the surface area frequently remains an unknown factor in otherwise quantitative investigations of surface phenomena.

Many metals, when anodically oxidized in a suitable electrolyte, become covered with a thin oxide

[1] Present address: Department of Chemical Engineering and Chemistry, Worcester Polytechnic Institute, Worcester, Massachusetts.

film whose thickness is in direct proportion to the voltage drop across the film. Aluminum and tantalum have been investigated in the most detail. Zirconium, uranium, silicon, chromium, niobium, and many other metals may also be anodically oxidized, although the detailed variation of film thickness with voltage has not been elucidated. With aluminum, in a suitable electrolyte (6), the film thickens until the field strength is reduced to about 0.07 v/Å, and then the film stops growing. If such a film is formed on a rough surface, the film reproduces the contours of the surface only if the height or width of the asperities exceeds the thickness of the film. By measuring the amount of a film of a known thickness formed on a surface, the area of the surface would be determined with a specified resolution (the film thickness).

This technique of measuring surface area with variable resolution has been developed for aluminum. The results have been compared at each end of the resolution curve with measurements of the specific surface made by a radioactive tracer technique (5) (resolution 20Å), and electron and optical microscopic techniques (resolution 1000-10,000Å).

### *Measurement of Specific Surface Area by Anodic Oxidation*

As shown in a previous paper (6), the thickness of the oxide film formed on aluminum by anodic oxidation in a 1.6% $H_3PO_4$ electrolyte, adjusted to a pH of 7.0 with KOH, is 0.44 mg/cm²-v or 14Å/v. The film contains about 55% aluminum under forming conditions, and the coulombic transport through the film during its formation may be accounted for to within 5% by oxidation of aluminum to the trivalent ion and the liberation of some oxygen gas. The surface area should be measurable then by forming an oxide film of a known thickness, measuring the total amount of film formed from the coulombic transfer (correcting for oxygen gas evolution), and calculating the extension of the film in area units. Dividing by the geometric area gives the specific surface area or roughness factor.

*Coulometer.*—The coulombic transfer was measured with a hydrogen gas coulometer, which also served as the cathode for anodizing. The cathode was a ⅛-in. long platinized platinum wire. The gas volume in the coulometer above the liquid was kept under 0.3 ml to minimize the effects of temperature variations. Since the electrolyte was saturated with oxygen, whenever the level of the liquid was raised the coulometer was conditioned by passing current for a short time to consume any oxygen which might combine directly with the hydrogen at the platinum surface. The response of the coulometer, as determined by comparison with a good quality ammeter, was within 1% of the theoretical volume of gas/coulomb in the range of 200 μa to 50 ma. At 175 μa the response was 95% and at 100 μa it was 70%. Day-to-day barometric changes were negligible. Gas collection after passing current was complete in 2 or 3 min, and with care the volume of gas could be measured to 0.001 ml (1λ) corresponding to a sensitivity of 0.008 coulombs.

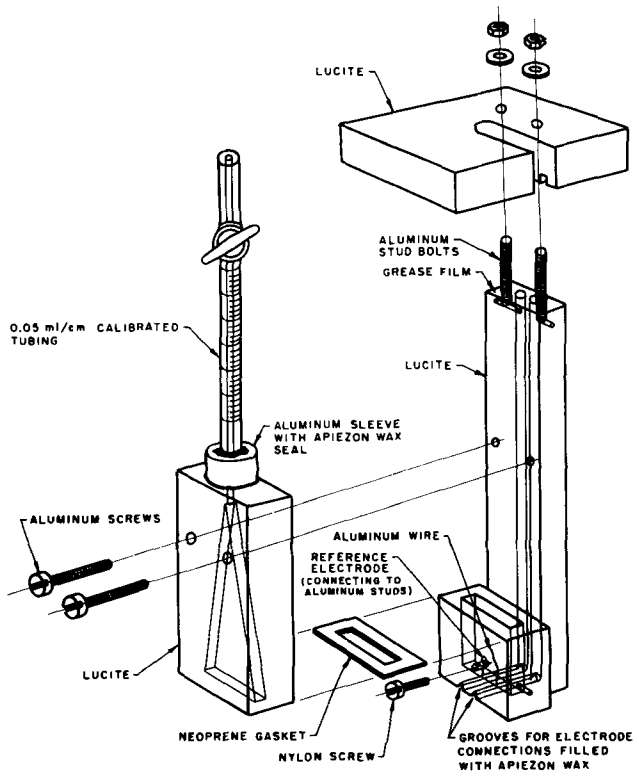


Fig. 1. Anode compartment of anodizing cell

*Cell design.*—The design was directed toward quantitative collection of oxygen gas. The cell is shown in Fig. 1. Gas bubbles were collected by tapping on the top of the cell. The addition of 1% amyl alcohol to the electrolyte greatly facilitated bubble collection without affecting the characteristics of the anodizing process. To minimize diffusion current, the electrolyte was kept saturated with $O_2$ gas that was bubbled into the electrolyte through a fine capillary at high pressure. Electrical contact with the sample was made with a 0.010 in. aluminum wire pressed into the surface of the sample by a nylon screw. Before the initial assembly of the cell, the wire was anodized to a 160-v barrier layer. In operation of the cell with a piece of plastic substituted for the sample, no detectable current was observed. A film of grease at the joint between the top and central portions of the cell prevented the accumulation of a conducting moisture film between the two electrode connections. The voltage drop across the film was measured with an $O_2$ reference electrode, consisting of a platinized platinum wire about 1 mm away from the sample. The reference electrode was kept saturated with $O_2$ from the solution and by passing current (4 ma x 15 sec) through it before each step of anodizing. $O_2$ reference electrodes show instability and lack of reproducibility in the range of tens of millivolts, but since the voltages to be measured here were large, good precision was needed only on the differences between successive voltages and not on their absolute value. The $O_2$ electrode had the special advantage that there was no risk of introducing foreign ions, such as chloride, which can be very deleterious to anodizing.

*Power supply.*—Sets of 22.5-v and 1.5-v dry cells were arranged with multiple taps to give any pre-

set voltage from 0 to 160 v in 1.5-v steps. An auxiliary circuit was used to pass the conditioning current through the platinum electrodes.

*Sample preparation.*—To limit the area of a specimen for measurement, the desired area was masked off with apiezon wax and the rest of the specimen was anodized to a 160-v coating. The wax was then removed by a thorough benzene vapor degreasing. No other procedure tried was effective because of the tendency for anodic oxide to penetrate beneath any protective coating. The procedures for obtaining the various surfaces are given in the captions for the figures.

*Measurement procedure.*—After a sample had been inserted, the electrolyte saturated with $O_2$, temperature equilibration reached, and the hydrogen coulometer conditioned, voltages were applied to the sample in 1.5 v and larger steps. Voltage drops across the film were measured and plotted against time. Since the recovery of $O_2$ did not appear to be quantitative when the film growth was very slow (6), the voltages were applied for short times (2-5 min) only, until the measured voltage across the film showed signs of leveling off. The $H_2$ and $O_2$ (if any) were collected and measured, and a new voltage step was applied. It was generally found that the first voltage at which $O_2$ was evolved was near 20 v.

*Calculation of specific surface area and resolution.*—The measured potential difference between the reference electrode and the aluminum specimen is the sum of the oxygen half-cell at the platinum (0.4 v), the potential drop across the film, and double layer and interfacial potentials which may be safely ignored because of their magnitude. The potential drop across the film is the sum of the aluminum half-cell ($Al \rightleftarrows Al^{+++} + 3e$, 1.7 v) which will be polarized to some extent by the oxide films, and that potential derived from the external source. The sum of the potentials (2.1 v) for the aluminum half-cell and the oxygen electrode were added to the observed voltage readings to obtain the total potential drop across the film. The thickness of the oxide film was then calculated at 14Å/v and this used as a measure of the resolution. Corrections are probably good to better than a volt. The resolution will then be correct to within about 10Å. The differences between the voltages at the end of two successive steps were used as a measure of the additional thickening of the film in that step. The specific surface area was then calculated from three quantities: the thickness of the film formed in the voltage step, the amount of oxide formed as determined coulometrically, and the geometric area of the specimen. The calculated area from the voltage step where $O_2$ was first evolved generally disagreed with points obtained just before and after. This measurement was discarded in all work.

### *Measurement of the Specific Surface Area by Radioactive Phosphate-Chromate Barrier Film*

This technique has been described in detail previously (5). When aluminum is treated with a solution of 5% $H_3PO_4$-3% $CrO_3$ at 85°C, the oxide is dissolved and a phosphate-chromate film is formed on the surface by reaction with the aluminum. This film, 10-20Å thick, seals the surface and prevents further reaction on the aluminum by the acid mixture. The amount of the film can be determined by using radioactive phosphoric acid (phosphorus-32), and its thickness is reproducible so that the surface area can be calculated. The resolution is thought to be 20Å. The measurements by this method were performed on portions of the samples used for the anodic oxidation work, but independently, and in separate laboratories.

### *Measurement of Specific Surface Area by Microscopic Techniques*

Specimens which had been used for the anodic oxide work were mounted face down against another specimen of aluminum with Araldite adhesive, thermally cured, mounted in plastic, and a perpendicular cross section cut and polished by metallographic methods. Araldite was used because it wets the oxide surface very well, and when cured it has a hardness close to that of aluminum. The good contact between two materials of similar hardness is essential in polishing a cross section of an edge to prevent metal flow and distortion of the edge. The specimens were photographed at the desired magnification and the photographs were enlarged 10X by projection. A soft wire 1 mm thick (corresponding to 0.1 mm on the photograph) was bent to conform to the irregularities of the cross section of the surface. The specific surface area was calculated as the ratio of the length of the wire to the extension of the wire after bending to conform

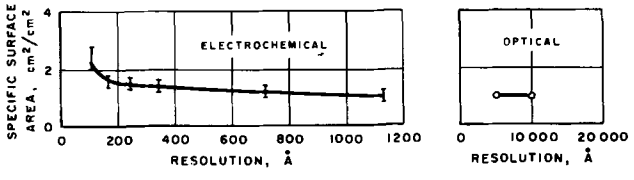


Fig. 2. Area-resolution curve for aluminum sheet chemically polished by Alcoa R-5 bright dip treatment (U. S. Pat. 2,650,157).

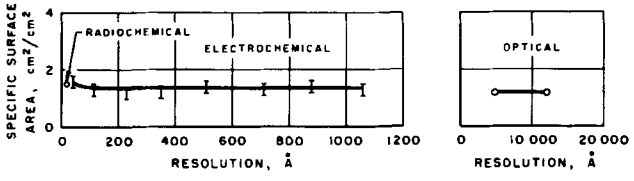


Fig. 3. Area-resolution curve for aluminum sheet specimen faced in lathe. No lubricant used but a clean cut with no tendency for stock to gall, sieze, or chatter.

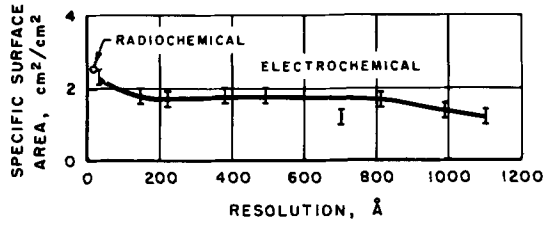


Fig. 4. Area-resolution curve for aluminum sheet specimen in "as rolled" condition.

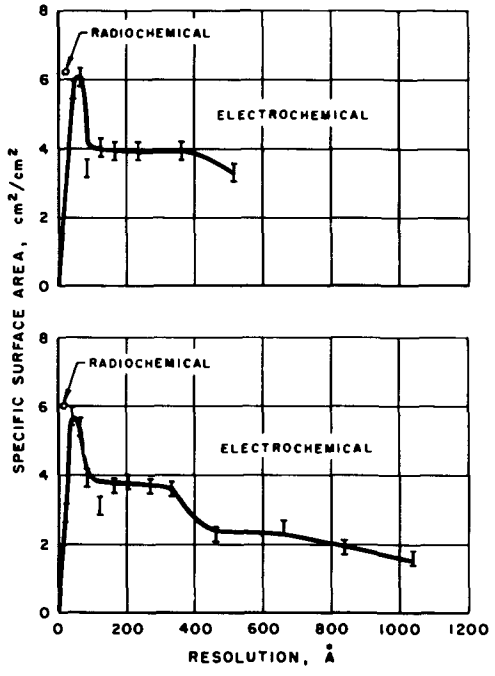


Fig. 5. Area-resolution curves for two specimens abraded separately on No. 320 "Aloxite" cloth with kerosene lubrication. Specimens were mounted in plastic. "Aloxite" cloth was mounted on metallographic polishing wheel rotating at 300 rpm light hand pressure on sample.

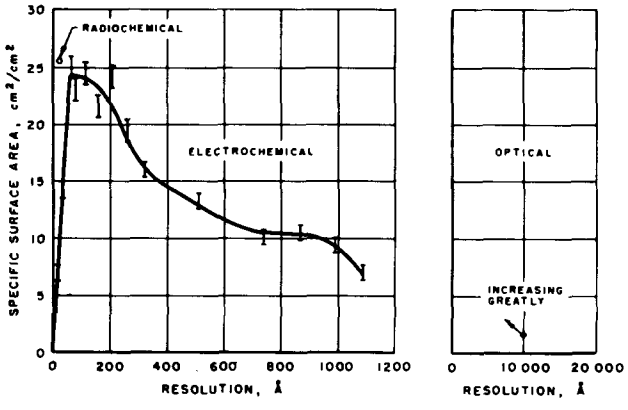


Fig. 6. Area-resolution curve for aluminum abraded successively with No. 120, No. 240, and No. 600 silicon carbide paper using kerosene lubrication but (a) using very short irregular strokes in random direction, (b) rubbing only long enough to develop scratches characteristic of the paper in use but not long enough to remove the scratches from the previous paper.

to the projected surface. The resolution was taken as the thickness of the wire divided by 10X times the magnification.

## Comparison of Results of Surface Area Measurements by Three Methods

Figures 2-6 show the results of surface area measurement on a variety of aluminum surfaces. The radiochemical result is shown to the left, the anodic oxide measurements are shown in the middle, plotted as specific surface area vs. resolution, and the optical measurements are plotted to the right, again as a function of resolution. Radiochemical results are not included for the chemically polished surface in Fig. 2 because the phosphate film left by the chemical polishing treatment interfered with the measurement. Optical measurements were made only on surfaces which were relatively smooth and which could be measured easily.

All aluminum surfaces which have been exposed to oxygen are covered with a natural oxide which is 20-30Å thick at room temperature. This natural oxide should affect the area measurements by anodic oxidation since the expected ionic current flow through the film will not occur until the measured film thickness exceeds that of the natural oxide. It is seen from Fig. 5 and 6 that the measured surface area increases as the measured film thickness (resolution) increases, until it exceeds 20 or 30Å. The surface area measured at resolutions of 30Å and lower are of course not valid, because of the natural oxide, and have been omitted from the other curves but retained on Fig. 5 and 6 for illustrative purposes. The fact that the experiments reveal the natural oxide and give an approximately correct thickness for it lends confidence to the method. The surface areas measured by anodic oxidations are absolute in the sense that they are based on the independently measured physical parameters of thickness per volt (7), density (7), and composition of the oxide (6). Most comparative surface area measurements (2, 4, 5) are based on the magnitude of a physical quantity which has been measured on a surface which is assumed to be smooth.

It is seen from Fig. 2-6 that the radiochemical measurements agree with the anodic oxide measurements within about 5% over the range of specific surface areas from 1.5 to 25. Considering the widely divergent sources of the fundamental parameters used in calculating the specific surface area from anodic oxidation, and the extreme differences between the radiochemical and the electrochemical techniques, the agreement is gratifying. Even the slight difference between two samples shown in Fig. 5, which had been prepared identically, but independently, are reproduced by the radiochemical and the electrochemical measurements. The difference in area between the two was 3.5% by the radiochemical technique and 5% by the electrochemical technique. It is thought that the area measurements at 30 to 40Å resolutions are accurate to at least 10% and possibly 5%.

Only two samples (Fig. 3 and 4) were studied in detail at resolutions greater than 1000Å by optical methods, but the agreement was good.

## Distribution of Asperity Sizes on a Surface and Observations on the Nature of Surfaces Produced by Several Treatments

The curves shown in Fig. 5 are the most interesting of the surface area resolution curves from the viewpoint of the structure of the surface which is revealed. The specific area at a resolution of 1000Å is 1.5. This is increased by about 50% by irregularities which can be detected at a resolution of 600Å but not at 1000Å. Irregularities about 300Å in size cause another 60% increase in area, and irregularities less than 90Å in size increase the area by another 50%. The rather sharp breaks in the curves such as are shown in Fig. 5 were not obtained on most of the other curves. However, a few general

trends are indicated. For example, the measurements shown on the very rough surface in Fig. 6 indicate that there is little contribution to the surface area by irregularities smaller than 200Å, but the surface area is a result of a rather continuous range of irregularities varying in size from 200Å up to more than 10,000Å. From Fig. 4 it is seen that a rolled surface has irregularities smaller than 150Å, almost no irregularities in the size range from 150Å to 700 or 800Å, but a quite significant contribution to the surface area by irregularities in the range of 1000Å. One of the most interesting surfaces was that obtained by lathe turning. This surface had macro roughness visible to the unaided eye, but within an experimental error of ±10% no micro roughness aside from a small contribution from irregularities detectable at 50Å resolution. In terms of surface area this compares very well with the best metallographically polished surfaces which have a specific surface area of about 1.3 (5).

It is apparent that the specific surface area of aluminum surfaces may vary greatly depending on the method of sample preparation. Surfaces with roughness factors between 1.25 and 25 have been observed and results by three independent methods are in excellent agreement. Further, by measuring the specific surface area with variable resolution, the dimensions of the asperities which contribute to the surface area may be deduced. It would seem that the information about the surface area and surface topography would be of value in the quantitative interpretation of oxidation and corrosion rates, and would aid in interpreting lubrication, friction, and adhesion phenomena.

### Acknowledgments

Work was supported by a grant from the National Science Foundation. To the Aluminum Company of America the author expresses thanks for a leave of absence and for supplying numerous samples of aluminum and performing the radiochemical measurements. To Dr. F. P. Bowden he expresses appreciation for making the facilities of his laboratory available and for providing continuous encouragement and suggestions.

Manuscript received Jan. 20, 1958. This paper was prepared for delivery before the Ottawa Meeting, Sept. 28-Oct. 2, 1958.

Any discussion of this paper will appear in a Discussion Section to be published in the June 1959 JOURNAL.

REFERENCES

1. T. L. O'Connor and H. H. Uhlig, *J. Phys. Chem.*, **61**, 402 (1957).
2. F. Bowden and E. Rideal, *Proc. Roy. Soc. (London)*, **120A**, 59 (1928).
3. A. Wiebe and C. Winkler, *Can. J. Chem.*, **31**, 306, 665, 111B (1953).
4. J. W. Shepard and J. P. Ryan, *J. Phys. Chem.*, **60**, 127 (1956).
5. J. E. Lewis and R. C. Plumb, *Intern. J. Appl. Radiation and Isotopes*, **1**, 33 (1956).
6. R. C. Plumb, *This Journal*, **105**, 498 (1958).
7. G. Haas, *J. Opt. Soc. Amer.*, **39**, 522 (1949).
8. M. S. Hunter and D. L. Robinson, *J. Metals*, **5**, 717 (1953).

# Schlieren Studies of Concentration Gradients at a Cu|HCl Anode

**Ralph S. Cooper**[1]

*Department of Physics, University of Illinois, Urbana, Illinois*

ABSTRACT

Schlieren optical techniques have been applied to the study of the anolyte at a Cu|HCl anode during current transients. Both the space and time dependence of the concentration gradients were quantitatively observed and correlated to the electrochemical processes occurring at the anode. The depletion of $Cl^-$ ion in solution, owing to the formation of a solid CuCl anode layer, and the entrance into solution of $Cu^{++}$ ion and the $CuCl_2^-$ complex were observed. The development and relative importance of diffusion and natural convection were studied under various conditions. In addition, using a $Cu|CuSO_4$ anode, experimental evidence was obtained, confirming the concentration distribution within the natural convection layer expected on theoretical grounds.

Detailed information concerning the concentration gradients at an electrode would be invaluable in the fields of electrodeposition, corrosion, and polarization. The purpose of this paper is to present information of this type for a Cu|HCl anode, obtained by use of the schlieren optical technique. Schlieren methods have been used previously to observe electrochemical phenomena qualitatively (1-4) and at least semiquantitatively by Stephenson (5) and Yeager and co-workers (6).

[1] Present address: Los Alamos Scientific Laboratory, Los Alamos, New Mexico.

## Experimental Arrangement

### *Design and Principles*

The schlieren apparatus used in these experiments was designed by Stephenson (5) and required only slight modification to produce quantitatively accurate results. Its resolving power ($10^{-2}$ mm) permits detailed examination of diffusion layers only 0.1 mm thick.

The schlieren apparatus produces an image in which the brightness at any point is proportional to the gradient of the refractive index at that point

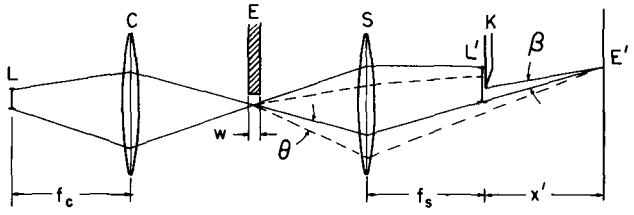


Fig. 1. The schlieren optical system

in the object space. Thus by integration one can obtain the index of refraction at any point in the solution and, consequently, obtain information concerning the ionic concentrations. The principle of the instrument is as follows (Fig. 1). A beam of light from a source (L) illuminates the solution near an electrode (E), whose image is formed on the film at E'. The lens system is arranged so that the image of the electrode (E') lies beyond the image of the light source (L'). A knife edge is placed at L' to intercept some of the rays from the electrolyte. If a concentration gradient (and, consequently, a refractive index gradient) exists in the electrolyte at some point, the bundle of rays passing through that point will be bent, e.g., as shown by the dotted lines. This will not alter the formation of the image at E' but will shift the image of the light source (S') with respect to the knife edge. Thus the amount of light reaching E' will depend upon the refractive index gradients at E. The angle $\theta$ through which the beam is bent in passing through the anolyte is given by

$$\theta = wn' \qquad [1]$$

where $w$ is the region in which the gradient lies, and this region is defined in practice by shielding the electrode with two glass cover slips. $n'$ is the value of the gradient in the $x$ direction which is perpendicular to the knife edge and in a plane parallel to the film plane. It is useful to know how far the image of the source will be shifted with respect to the knife edge under a particular gradient. Denoting this by $\Delta z$, the result is

$$\Delta z = wn'f_s = \theta f_s \qquad [2]$$

for the lens system employed here, where $f_s$ is the focal length of the schlieren lens. Note that this is independent of the exact position of the electrode and the position and focal length of the collimating lens and depends only on the fact that the image of the source lies at the focal point of the schlieren lens.

An exact analysis of diffraction phenomena in schlieren systems is very difficult and has not been carried out thus far, but simple considerations can give useful results. The critical phenomenon is the diffraction which occurs when the knife edge cuts off most of the light from the source. The main effect of this is to lower the resolution of the instrument, spreading the light from a single point in the anolyte over a region in the film plane. The half width of the diffraction pattern is approximately

$$h = \frac{\lambda}{\sin \beta} = \frac{\lambda x'}{z} \qquad [3]$$

where $\lambda$ is the wave length of light, $x'$ is the distance from the knife edge to the film, and $z$ is the height of that portion of the source image which is not intercepted by the knife edge. Thus the knife edge must not be allowed to cut off too much of the beam and reduce the resolving power of the instrument to below that required. For our apparatus, if $z = 0.05$ mm, then the resolving power is reduced to 0.04 mm, which is a considerable fraction of the field of view. The collimating lens has a focal length ($f_c$) of 48 mm, and the schlieren lens has $f_s = 24$ mm. The light source L is actually an illuminated slit, placed at the focal point of the collimating lens. Therefore, its image will be at the focal point of the schlieren lens and be half the size of the slit. The apertures in our system permit a maximum slit height of 3 mm, giving a maximum $\Delta z$ of 1.5 mm. The electrode thickness ($w$) is of the order of 1 mm, which puts an upper bound of 0.06 riu/mm on the gradient of the refractive index. This is roughly equivalent to a concentration gradient of 6 molar/mm of NaCl or a current density of 60 ma/cm$^2$.

The recording system of the schlieren apparatus was a commercial 8 mm motion picture camera, with an appropriate lens set behind the knife edge. The direct magnification was of the order of unity while the field of view was approximately 1 cm$^2$. The film could be examined microscopically to obtain the maximum resolving power of the instrument. Photographs could be taken at rates of 16-64 frames/sec to yield the temporal development of diffusion transients. To analyze the photographic data, a metallurgical microscope was modified to project a beam of light on the film which was placed in the normal viewing position on the stage of the microscope. The beam, rectangular in cross section and only 20 $\mu$ wide at the film, passed through the film to a photomultiplier tube mounted under the stage. Thus it was possible to determine the relative density of a portion of the film only $2 \times 10^{-5}$ cm$^2$ in area. The film was mounted on a movable, calibrated stage so that the density could be obtained as a function of the distance along the film which was equivalent to distance in the object space. In order to process the data automatically, the stage was driven by a constant speed motor while the output of the photomultiplier was fed through an amplifier into a Brown recording potentiometer.

### *Calibration*

The calibration of the instrument may be carried out by two distinct methods: by placing a standard in the object space, or by adjusting the knife edge. The latter method depends on the fact that the position of the slit image relative to the knife edge determines the intensity of the film. Thus by moving the knife edge by $\Delta z$ from its normal setting, one obtains the intensity corresponding to a gradient $\Delta z/wf_s$. A lens may serve as a standard schlieren or to check the other method of calibration. The angle through which a ray is bent in passing through the lens at a distance $r$ from the center of the lens is just $r/f_l$ for small angles. The ray through the center is undeviated. Thus a schlieren photo of a lens would show one side bright with the intensity

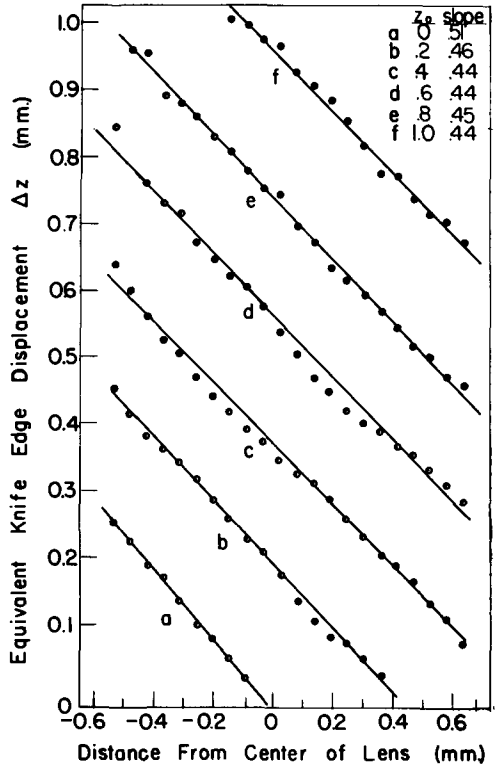


Fig. 2. Results of schlieren photographs of a lens as an object, taken with various settings of the knife edge.

decreasing linearly toward the other side. The difficulty in using a lens as a standard is that the center is not exactly known. Nevertheless, it is valuable as a check on the apparatus, including the diffraction error. Figure 2 shows the result of photographing a lens of focal length $f_l$ with various settings of the knife edge. Since

$$\Delta z = \theta f_s = \frac{r}{f_l} f_s \qquad [4]$$

one expects a straight line of slope $f_s/f_l$ for a plot of $\Delta z$ vs. distance $r$ across the lens. For all cases where the knife edge was open 0.2 mm or more, the difference between the experimental result and that predicted on the basis of the focal lengths agree to within 3%. On the other hand, the one curve which corresponds to low values of $\Delta z$ and, consequently, poor resolving power, gave a result high by 13%. In this case, the calibration was carried out by photographing the empty object space with various settings of the knife edge.

### *The Electrochemical System*

The system chosen for study was the Cu|HCl anode which had already been investigated by standard electrochemical techniques (1, 4, 7). With a fixed applied voltage, the current transients show one or more periods (current plateaus) where the current is independent of time, followed by relatively rapid decreases. The current may go through a minimum before approaching a steady state, and even may exhibit sustained oscillations. The same experimental arrangements were used in this work, using anodes which permitted natural convection to take place. Unless otherwise noted, the bulk acid concentration was 2*N*.

An anode was constructed with a vertical rectangular surface, 1 mm wide by 2.4 mm high. Thin glass cover slips were cemented to the sides of the electrode to define the region $w$ (Fig. 1) in which the concentration gradients lie. The presence of the cover slips did not appreciably affect the convection process.

Schlieren motion picture (8 mm) were taken of transients at 16 frames/sec, which is sufficiently rapid to give a continuous development in time of the diffusional processes, yet allows photographing a sufficient period (15 sec) to observe the motion of the fluid in the complete development of natural convection. The results were observed qualitatively with a standard 8 mm motion picture projector. The film was then examined frame by frame, and representative frames were selected for quantitative analysis. Intensity calibration was affected by the method of altering the knife edge position, and spatial calibration was made by photographing a reticle placed at the electrode.

## Results and Discussion

### *Schlieren Studies of the* Cu|HCl *System*

The first transient to which the schlieren technique was applied exhibited most of the phenomena of interest. The first current-time plateau ($i_l = 3.6$ ma) was completed in 3 sec, before appreciable convection was observed. After a very brief second plateau, the current reached a minimum of 0.3 ma ($t = 5$ sec) and then rose to its steady-state value of 1.5 ma. In the steady state the reaction products include $Cu^{++}$ ion, as the applied potential was sufficient for its formation (7). Schlieren motion pictures were taken from $t = 0$ to $t = 12$ sec, and during the steady state ($t = 4$ min). Frames at approximately 1, 2, 3, 4, and 7 sec, plus one in the steady state were selected for quantitative analysis. The results (Fig. 3 and 4) are presented as graphs of the refractive index gradient ($n'$) vs. the distance from the electrode face ($x$), with the convention that a positive gradient corresponds to $n$ increasing toward the anode. Since the refractive index is roughly proportional to the total ionic concentra-

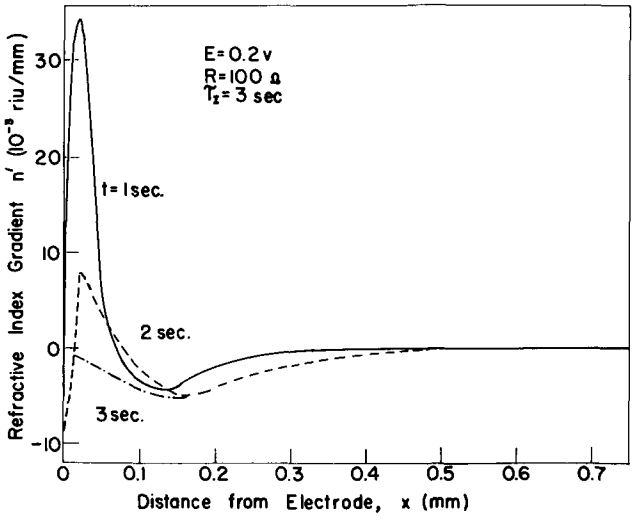


Fig. 3. Refractive index gradients near a Cu|HCl anode during the early stages of a current transient.

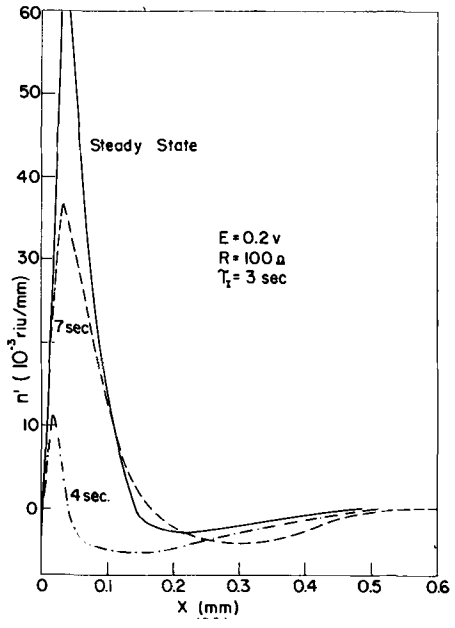


Fig. 4. Refractive index gradients near a Cu | HCl anode after the current drop, and in the steady state.

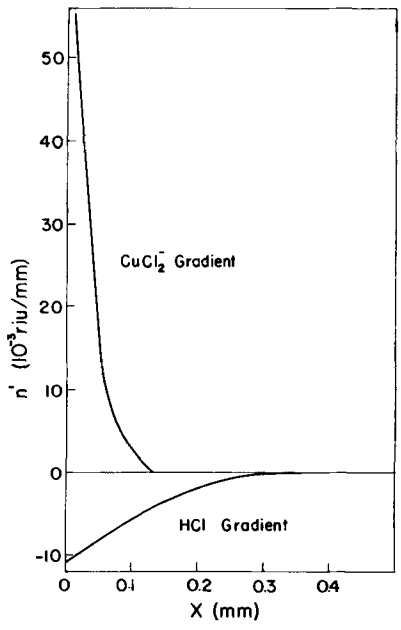


Fig. 5. A decomposition of the configuration t = 1 sec (Fig. 3) into two components refractive index gradients, a positive gradient owing to the entrance of $Cu^+$ into solution as the $CuCl_2^-$ complex, and a negative gradient due to the depletion of the $Cl^-$ ion used in the formation of the solid CuCl layer.

tion, the curves may also be thought of as plots of concentration and density gradients.

From Fig. 3 we see that after 1 sec a positive gradient has arisen in the region $0 < x < 0.065$ mm. (The apparent decrease in $n'$ for $x < 0.02$ mm is due to diffraction at the edge of the anode. The curves should be extrapolated into that region to obtain values at the anode surface.) The gradient is negative from $x = 0.065$ mm to $x = 0.04$ mm, where it approaches zero. Integrating in from the bulk,[2] we find that the index of refraction first decreases, reaching a minimum (of $n = n_{bulk} - 0.05 \times 10^{-3}$) at 0.065 mm, and then increases to $n_{bulk} + 1.2 \times 10^{-3}$ at the anode face.

It is clear that there are at least two distinct[3] concentration gradients required to produce the result observed for $t = 1$ sec. These are a large positive gradient close to the anode ($x = 0.06$ mm) and a smaller negative gradient reaching further out into the solution. Since $Cu^{++}$ has been shown not to occur at the potentials associated with the first plateau (7), and the anolyte becomes saturated with $CuCl_2^-$ prior to precipitation of CuCl, the large positive gradient must be due to saturation of the anolyte by $CuCl_2^-$. The negative gradient corresponds to a lower total ionic concentration which can be accounted for only by depletion of chlorine ions due to the formation of the CuCl layer and the $CuCl_2^-$ complex close to the anode face.

If the separation of the two gradients (Fig. 5) is valid, we may compare the concentrations computed from them to values obtained by independent means. From the area of the negative gradient in Fig. 5, we find the difference ($\Delta c$) between the bulk and anode acid concentrations to be $0.17N$. We can estimate the HCl concentration at the surface using diffusion theory (7) by the equation

$$\Delta c = \frac{it_+\sqrt{4Dt}}{FSD\sqrt{\pi}} = 6.4 \times 10^{-3} i\sqrt{t} \qquad [5]$$

where $i$ is in ma, and $\Delta c$ in moles/liter. $D$ is the diffusion coefficient of the salt; $F$ is the Faraday constant; $t_+$ is the transference number of the $H^+$ ion; and $S$ is the anode surface area. For $t = 1$ sec, this gives $c = 0.2$M, in good agreement with observation, and well within the approximations involved. Second, the presence of solid CuCl indicates that the solution at the anode face is saturated with $CuCl_2^-$, which is about $0.22N$ in $1.8N$ HCl. From the area of the positive gradient, we compute $0.25N$, again in good agreement.

Now consider the time dependence of the gradients (Fig. 3 and 4). After 2 sec, the $CuCl_2^-$ gradient has greater spatial extent but is smaller in magnitude, while the HCl gradient has become larger. This trend is continued throughout the duration of the first plateau (< 3 sec), the HCl gradient becoming so large compared to the other that the net refractive index gradient is negative everywhere (at $t = 3$ sec). This behavior is to be expected, because the total $CuCl_2^-$ concentration difference cannot be greater than the concentration of the saturated solution, while the HCl concentration decreases as $\sqrt{t}$ until its concentration has been reduced to zero at the anode face. This type of behavior is observed for all transients for which the current drop occurs before convection begins. The higher $i_l$ is, the more pronounced is the negative gradient as is to be expected from Eq. [5]. This

[2] The bulk solution serves as a reference point for the refractive index and the concentration, which is $2N$ HCl unless noted otherwise.

[3] There are at least three compounds which may appear in solution: HCl, CuCl, and $CuCl_2$. In solution, these will be ionized or complexed and will exist largely as a mixture of $H^+$, $Cl^-$, $CuCl_3^-$, and $Cu^{++}$. To a first approximation, we may consider the contributions to the refractive index by the various components to be additive and proportional to the concentrations of the respective compounds. The partial molar refractivities are $8.6 \times 10^{-3}$ for HCl, $1.44 \times 10^{-2}$ for $CuCl_2$, and estimated to be $1.0 \times 10^{-2}$ for CuCl in HCl.

region is seen (1) to convect upward, which demonstrates that it corresponds to a solution of concentration lower than the bulk. The HCl gradient does not continue to grow indefinitely but is reduced by the effect of natural convection.

After the current drop, the electrode voltage ($V$) rises into the range for $Cu^{++}$ ion formation, $V \geqq -0.05$ v (7). The entrance of a new salt into solution can be seen at $t = 4$ sec (Fig. 5) as a new positive gradient next to the electrode. This increases rapidly even while the current is passing through its minimum, and has submerged most of the HCl gradient. As the current rises to the steady state, the positive gradients increase, but convection limits the region in which they occur to about 0.17 mm. The negative gradient is also reduced because of the bulk transport of ions by convection. In the steady state, the HCl gradient must be small as can be seen by considering the $Cl^-$ concentration gradient necessary to carry the steady-state current across a stagnant layer of width $\Delta x$. By Fick's law

$$\frac{i}{SF} = D\frac{\Delta c}{\Delta x} \qquad [6]$$

Therefore, $\Delta c = 0.3M$. Convection effects will reduce this considerably, and the fact that $Cu^{++}$ ions are carrying some of the current also will decrease $\Delta c$. Thus the HCl concentration difference can be expected to be small compared to its bulk concentration ($2N$).

The positive gradient is composed of contributions from both $CuCl_2^-$ and $CuCl_2$. We know the approximate concentration of the $CuCl_2^-$ at the surface to be about $0.24N$ (saturated solution) and can subtract its effect on the index of refraction to determine the $CuCl_2$ concentration. From Fig. 4, for the steady state, this results in a value of 0.22M for the $CuCl_2$ at the anode, which value is very close to the CuCl concentration. The value of the $CuCl_2$ concentration computed this way is a lower limit, as some $Cu^{++}$ may have replaced $H^+$ from the HCl, an effect which would produce a smaller effect on the refractive index than the addition of $CuCl_2$ to the solution. However, as CuCl and $CuCl_2$ are found to be produced in roughly equal amounts (7) and undergo similar mass transfer processes, one would expect that their concentration profiles would be similar and thus their concentrations at the anode roughly equal. All transients with short plateaus (< 4 sec) exhibit schlieren similar to the one just discussed, differing only in intensity and time scale.

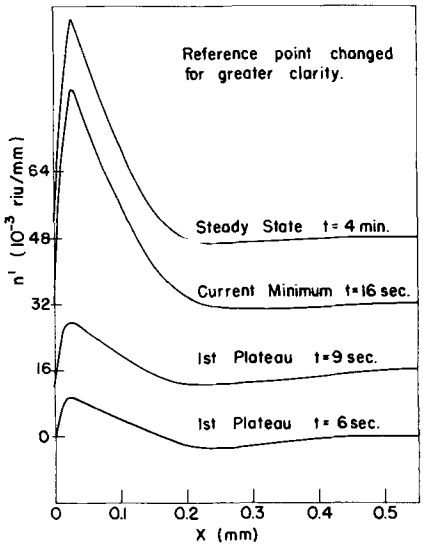


Fig. 6. Refractive index gradients near a Cu|HCl anode where convection occurs before the current drop ($\tau_1 \approx 12$ sec). A stable configuration is developed which lasts until the end of the current plateau. Afterward, a larger gradient is established and persists in the steady state.

For transients with a long first plateau, i.e., when $i_l$ is small, the $Cl^-$ is not depleted at a rapid rate, and thus large negative gradients never arise. The schlieren of such a transient (Fig. 6) shows a positive gradient which increases for the first few seconds and then becomes stabilized by convection. The concentration gradients are then constant until the current drop. If $V$ remains less than −0.05 v, then no concentration changes occur during or after the current drop, as it is observed that the convection layer has already become stabilized, and no new electrode process is found to occur (7). For those cases where $V$ increases beyond −0.05 v, an increase in the positive gradient in the convection layer is observed between the end of the first plateau and the current minimum. This increase remains until the steady state is reached (Fig. 6). It is attributed to the entrance of $Cu^{++}$ into solution as this is the only mechanism which could increase the ionic concentration beyond that of saturated CuCl and because $Cu^{++}$ is observed as a reaction product for $V \geqq -0.05$ v. In $2N$ HCl, the second current-time plateau is too short to distinguish whether the increase in $n'$ occurs during or after the plateau, but this is possible at lower concentrations. In $0.5N$ HCl, the maximum CuCl concentration is only $0.015N$, and thus only a very small positive gradient could be due to saturation of the HCl at the anode face. The second plateau is longer than the first in $0.5N$ HCl, giving ample time to determine the conditions existing during the second plateau. Visual schlieren observations were made using movement of the knife edge for quantitative estimates of the gradients. A large positive gradient (with a maximum of the order of $40 \times 10^{-3}$ riu/mm) appeared next to the anode as soon as the second plateau was initiated. This could be due only to $Cu^{++}$ entering the solution for the reasons cited above.

### *Steady State and Oscillations*

Steady-state conditions are independent of early stages of the transients, and depend only on the final electrode voltage ($V_\infty$) and current ($i_\infty$). The two types of steady-state conditions have already been discussed, the region where a CuCl layer exists and only cuprous ion is formed ($-0.27 < V_\infty < -0.05$) and the region where cupric ion forms part of the reaction products ($V_\infty \geqq -0.05$ v).

The final schlieren study in the Cu|HCl system was of the diffusion layer during current oscillations. With $E = -0.2$ v and $R = 100\Omega$, the transient displayed current oscillations as observed by Bonhoeffer (8), with a period of 26 sec (Fig. 7). This

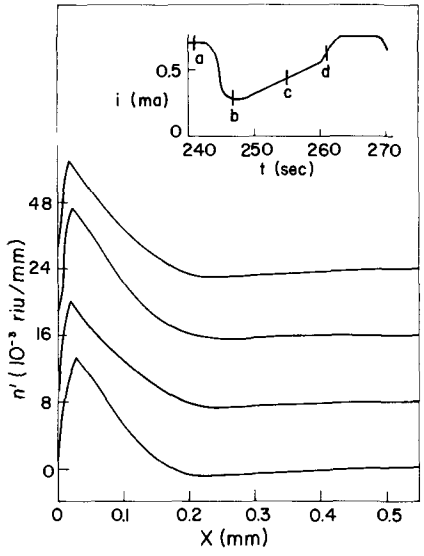


Fig. 7. The configuration of the diffusion-convection layer during current oscillations in the Cu|HCl system. The reference point has been changed for greater clarity, the curves overlapping considerably. The concentrations in the layer thus appear independent of the current fluctuations.

type of oscillation was studied with more standard electrochemical techniques by Bartlett and Cooper (7) and appears to be due to fluctuations between two quasi-steady states, one with a solid anode film and the other without it, as postulated in the above paper. The first plateau lasted 90 sec with $i_l = 0.68$ ma, and the minimum current was 0.27 ma. Upon approaching the steady state (20 sec after the current minimum), the current rose suddenly to 0.65 ma and oscillations began. They lasted only eight periods and then ceased abruptly, the current immediately becoming constant at the steady-state value. Schlieren motion pictures were taken during the first 10 sec of the transient, over one complete cycle of an oscillation (the sixth) and during the steady state. The schlieren for four significant points during the oscillation were analyzed (Fig. 7). The main fact to be noted is the similarity of the four results, the concentration gradients appearing to be relatively independent of the current. Furthermore, the result for the steady state is the same as that during oscillations. This result is to be expected if the removal rate is controlled by a mass transfer process (solution of the layer as $CuCl_2^-$, and subsequent convection away) which is essentially physicochemical rather than electrochemical, i.e., that the removal rate is determined by physical quantities such as the rates of solution and diffusion of the salt, and specific gravity differences, rather than by the rate of some step involved in the electrode reaction. As long as the electrode has sufficient solid CuCl on it to keep the solution at the anode face saturated, the solution and convection will proceed at the same rates, and the gradients will be unaltered. This can be clearly seen experimentally in schlieren motion pictures taken when the circuit is broken with the electrode in the steady state. The concentration gradients are unaltered when the current drops abruptly to zero, and they remain unchanged for about 10 sec, finally diminishing to zero in 30 sec. The 10-sec period corresponds to the time when the last solid CuCl is dissolved as determined by direct observation. The gradients are approximately linear as is to be expected on the basis of the theory of mass transfer (9) by natural convection, which is shown in the next section to be true for a system containing a single salt.

*Natural Convection at a Cu|$CuSO_4$ Anode*

The schlieren technique was applied to anodic dissolution of copper in 2*N* $CuSO_4$ as a check on the theory of natural convection. With only one salt present, the index of refraction could be unambiguously related to the concentration. Currents in the range of 25-250 $\mu a/cm^2$ were passed and schlieren photographs taken after 30 sec, which allowed enough time for a steady state to be established. The steady-state thickness of the convection layer was found to be independent of the current density in the range investigated, in agreement with the interferometric studies of Ibl, Barrada, and Trümpler (10) on the same system.

The theory of Tobias and co-workers (9) is based on the analogy between mass transfer and heat transfer and involves the assumption that the concentration distribution in the former process is the same as the temperature distribution in the latter. This distribution is a parabolic one and thus the gradient would be linear. For $CuSO_4$, the concentration is closely proportional to the increase in the index of refraction, and so the two gradients should also be proportional. Figure 8 shows that the gradient is found to be linear by direct schlieren measurement, giving direct experimental proof of this assumption.

## Summary and Conclusions

The schlieren technique has been shown to be useful as a quantitative as well as qualitative tool in the study of electrode processes and has been applied to the Cu|HCl anode. In this application it has given a quantitative development in time and space of the concentration gradients in the near neighborhood of the electrode. The depletion of the $Cl^-$ ion, owing to the formation of solid CuCl, and the entrance into solution of $Cu^{++}$ ion have been seen and measured. By the use of cinematography, the

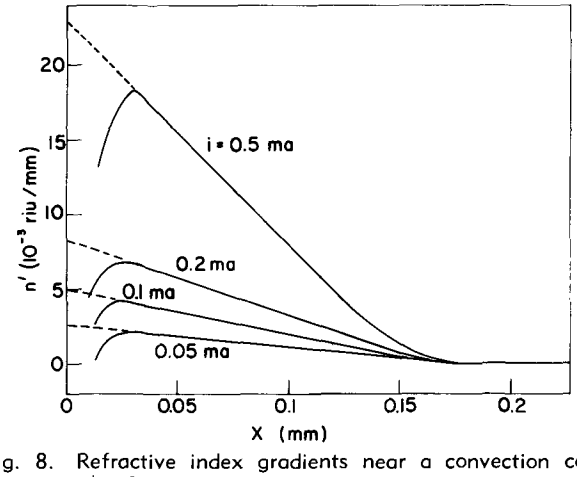


Fig. 8. Refractive index gradients near a convection controlled Cu|$CuSO_4$ anode in the steady state. For this salt, the concentration is proportional to the refractive index, and the linear relation between concentration gradient and distance from the anode is verified.

details of the convection process, including the shape and time dependence of the convection layer thickness and its relative importance under various conditions have been investigated. Finally, using the simpler system (a $Cu|CuSO_4$ anode), linear concentration distribution which is one of the underlying assumptions of present theories of convection has been experimentally verified.

We would like to point out the utility of the schlieren microscope as a research tool in the study of electrode phenomena. It is simple and relatively inexpensive to construct. Its adjustment for operation is not critical as are many interferometers, and thus qualitative observations are very easily obtained. Quantitative data can be obtained as close as $10^{-5}$ cm from an electrode without disturbing the solution in any way. Both space and time dependence of processes may be observed. By selection of the optical parameters, the sensitivity, resolving power, and field of view may be varied over wide ranges to suit various applications.

### Acknowledgments

This work was supported by the Office of Ordnance Research under contract DA-11-022-ORD-939. The author is greatly indebted to Dr. L. P. Stephenson who is primarily responsible for the design and application of this schlieren apparatus, and to Professor J. H. Bartlett for his encouragement and aid with the manuscript.

Manuscript received Dec. 11, 1957. This paper is based on a dissertation presented as partial fulfillment of the requirements for the degree of Doctor of Philosophy in Physics at the University of Illinois, Urbana, Illinois.

Any discussion of this paper will appear in a Discussion Section to be published in the June 1959 JOURNAL.

REFERENCES

1. L. Stephenson and J. H. Bartlett, *This Journal*, **101**, 571 (1954).
2. H. J. Antweiler, *Z. Elektrochem.*, **43**, 596 (1937).
3. F. H. Giles, Doctoral Dissertation, University of Illinois, Urbana, Ill. (1956).
4. R. S. Cooper, *This Journal*, **103**, 307 (1956).
5. L. P. Stephenson, Doctoral Dissertation, University of Illinois, Urbana, Ill. (1953).
6. E. Yeager, W. R. Wolfe, N. Chessin, and F. Hovorka, *This Journal*, **101**, 590 (1954).
7. J. H. Bartlett and R. S. Cooper, *ibid.*, **105**, 109 (1958).
8. K. F. Bonhoeffer and H. Gerischer, *Z. Elektrochem.*, **52**, 149 (1948).
9. C. W. Tobias, C. R. Wilke, and M. Eisenberg, *Chem. Eng. Progr.*, **49**, 663 (1953).
10. N. Abl, Y. Barrada, and G. Trümpler, *Helv. Chim. Acta*, **37**, 583 (1954).

# The Electrodeposition of Iron-Molybdenum Alloys

**L. O. Case and Albertine Krohn**[1]

*Chemistry Department, University of Michigan, Ann Arbor, Michigan*

ABSTRACT

A plating cell was designed to provide a method for the variable rotation of a cylindrical cathode between rubber wiper blades, since wiping the cathode greatly increased the efficiency of the process for plating iron-molybdenum alloys from a solution containing sodium molybdate, ferric chloride, and sodium pyrophosphate buffered to a *p*H of 8 with excess sodium bicarbonate. A complete study of the variables showed it possible to electrodeposit alloys which are bright and adherent in thicknesses of a few hundredths of a millimeter. No theoretical treatment is yet available to explain completely this type of deposition.

With increased interest in metals which have utilitarian properties at very high temperatures, molybdenum has received considerable attention because of its ready availability in this country and its valuable refractory properties (1, 2). Many attempts have been made to develop a satisfactory process for the electrodeposition of this element so that, when only surface properties were important, a coating of molybdenum could be applied. This would conserve the metal and permit one to take advantage of the structural properties of the basis metal. However, all available evidence indicates that pure molybdenum cannot be electroplated from a solvent containing oxygen in any form.

Attempts have been made by a number of investigators to plate molybdenum from aqueous solutions (3-11). None of the methods suggested produces more than a flash deposit a few microns in thickness, and there is no proof that such deposits are pure molybdenum. Organic solvents and nonaqueous systems such as liquid ammonia have failed to give molybdenum deposits (12, 13). Several moderately successful attempts to electrodeposit molybdenum from fused salt baths have been reported (14-19). The most recent of these is reported to be the first instance of the production of coherent massive electrodeposits of molydenum (20). This process uses a melt of $K_3MoCl_6$ dissolved in a mixture of alkali halides, the electrolysis being carried out in an inert atmosphere.

As in the case of other metals which cannot be deposited by themselves, a number of alloys and oxides of molybdenum have been electrodeposited from aqueous solutions (21). For many years, permanent black protective and decorative coatings

[1] Present address: Chemistry Department, University of Toledo, Toledo, Ohio.

have been applied to copper, iron, and their alloys by electrodepositing hydrated molybdenum sesquioxide, $Mo_2O_3 \cdot xH_2O$, on the object and then igniting it [(22) p. 192]. Sometimes the molybdenum oxide is deposited with an alloying metal (23, 24), and colored coatings have been reported (25).

Some patents have been granted covering the electrodeposition of certain molybdenum alloys. The deposition of cobalt-molybdenum alloys (26, 27), chromium-molybdenum alloys (28), and alloys of molybdenum with cobalt, nickel, and iron (29, 30) have been patented.

A number of studies on the electrolytic production of various alloys deposited from alkaline citrate and tartrate baths have been reported (31-36). Alloys of molybdenum with iron, cobalt, nickel, copper, or zinc were obtained using a pyrophosphate bath buffered with sodium bicarbonate (37).

All of the reports mentioning iron-molybdenum alloys indicated that it is possible to electrodeposit alloys containing up to about 60% molybdenum. This is a higher molybdenum content than appears possible with other codepositing metals. However, the plating processes were inefficient and the alloys were described as being of poor quality. Because of their comparatively high molybdenum content, these alloys were selected for more intensive study. This research was undertaken in an attempt to develop an aqueous plating bath suitable for the production of these alloys, and to investigate the possibilities of increasing the efficiency of the process.

### *Preliminary Studies*

Approximately 300 plating runs were made during the preliminary work. About 170 of the deposits were analyzed for their iron and molybdenum contents. The first experiments were carried out with a citrate solution (34), but the deposits obtained were dull, dark, and nonadherent. Attempts to modify the bath by replacing the citric acid with $NaKC_4H_4O_6$ or $KHC_4H_4O_6$ were unsatisfactory.

More promising results were obtained using a modification of the pyrophosphate bath suggested by Myers (37). The function of the sodium pyrophosphate is to form a complex with the $Fe^{+++}$ and thus prevent the precipitation of ferric hydroxide in the alkaline solution. It has advantages over the citrates and tartrates used in other baths in that the solutions are very stable and that the pyrophosphate does not produce undesirable products during electrolysis. A commercial chelating agent, Versene Fe-3 Specific, was tried as a replacement for the pyrophosphate. The deposits obtained were about the same, but the solutions were less stable particularly at higher temperatures.

Using the pyrophosphate solution, several series of plating runs were made to determine the effects of the variables on the composition of the deposits and on the cathode current efficiency. A few runs were made using the apparatus for periodic current reversal which had been designed for another study (38). The deposits produced were of inferior quality, so the experiments were discontinued. A crude setup was used to test the effect of rotating the electrode between a pair of rubber wiper blades. This process improved the efficiency so much that new apparatus was designed in order to permit a more thorough study with the incorporation of the wiping procedure.

## Experimental

*Apparatus.*—The plating cell consisted of a cylindrical Lucite container with an electrolyte capacity of about 800 ml. The cell was fitted with a plastic cover to which was attached the anode holder. The cover had an opening in the center to permit insertion of the cathode and another near one side for a calomel electrode. The details of the plating cell assembly are shown in Fig. 1. For the anode, a piece of sheet platinum was rolled and slipped inside the anode holder. Several small holes were drilled near the top of the holder to permit free circulation of the plating solution.

The cathodes were cylinders of platinum or brass 1¾ in. long, ⅝ in. OD, 9/16 in. ID. The plating area of such a cathode is 3.43 in.$^2$ (0.217 dm$^2$). Plating with cylindrical anodes and cathodes results in a more symmetrical current distribution than plating on flat cathodes.

The top of the cathode holder was machined from stainless steel to give a friction fit with the cathode cylinders. The exposed portion of the holder was protected with stop-off lacquer. The lower end of the upper holder was threaded to fit the bottom holder which was made of plastic. The bottom holder was turned to precision fit the cathodes, so that, when the cylinder was slipped over the holder and the two parts tightened, the system was leak proof. An L-shaped stirrer was threaded into the bottom cathode holder.

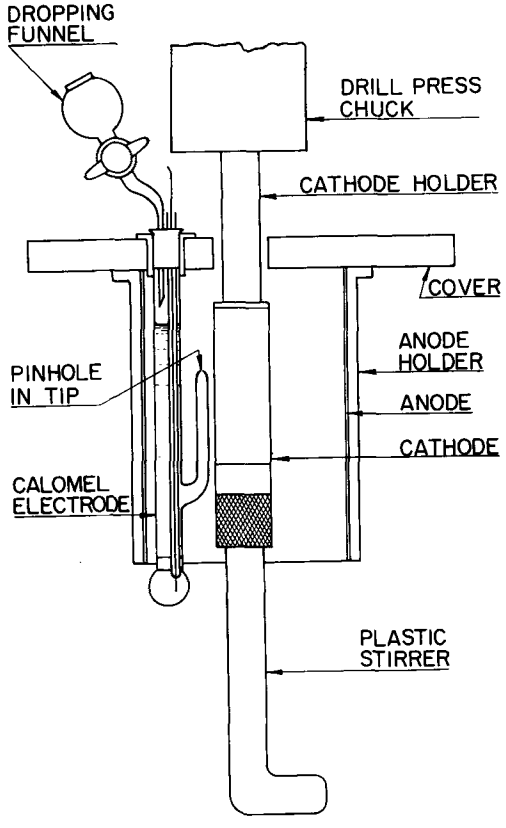


Fig. 1. Side view of plating cell assembly

A bench size drill press operated by a half-horsepower motor served as a convenient device for rotation of the cathode. Since the cathode and spindle were rotating during the plating process, a direct connection was impossible. Contact was established by means of a pool of mercury in a small hole drilled in a steel cylinder attached to the top of the spindle. A steel bar supported a piece of platinum wire which dipped into the mercury.

Provision was made for wiping the cathode during the plating run by the use of two adjustable wiper blades attached to the plating cell cover (*see* Fig. 2). The wiper blades were 2-in. lengths of 5 ply rubber windshield wiper which slipped into slotted plastic holders. The top of each holder was tapped to take a brass machine screw which passed through an opening in the cell cover. After adjusting the position of the wiper blades, the screws were tightened. The entire plating assembly was immersed in a constant temperature bath.

*Analysis of the deposits.*—Alloy deposits were washed, dried, weighed, and dissolved from the cathode in 5*N* nitric acid. They were analyzed by a colorimetric method based on the fact that both molybdenum and iron form colored compounds with mercaptoacetic acid (39-42).

## Experimental Results

Unless otherwise specified, plating runs were made at 50°C with a current density of 15.6 amp/dm$^2$ (140 amp/ft$^2$). Most plating times were 10 min. The usual composition of the bath was:

| | | |
|---|---|---|
| Sodium molybdate ($Na_2MoO_4 \cdot 2H_2O$) | 1.0*N* | (40 g/l) |
| Ferric chloride ($FeCl_3 \cdot 6H_2O$) | 0.1*N* | (9 g/l) |
| Sodium pyrophosphate ($Na_4P_2O_7 \cdot 10H_2O$) | 0.4*N* | (45 g/l) |
| Sodium bicarbonate ($NaHCO_3$) | 0.9*N* | (75 g/l) |

The effects of changes in the solution composition and plating conditions on the composition of the deposits and on the cathode current efficiency are summarized by the following graphs and discussion. Cathode current efficiencies were calculated on the basis of the deposition of iron from iron(III) and molybdenum from Mo(VI).

*Effect of cathode rotation, stirring, and wiping.*—Runs were made in a still bath; with rotation of the cathode at 1750 rpm; with rotation at the same speed with the L-shaped stirrer attached to the cathode fixture; with rotation between fixed wiper blades without the stirrer; and finally with rotation, stirring, and wiping. The efficiency of the cathode plating process is nearly tripled when rotation, stirring, and wiping are used (*see* Fig. 3). The wiping process aids in the removal of hydrogen bubbles and also decreases the oxide content of the deposits.

Deposits from a still bath were dull dark gray. Those made with the use of rotation without wiping had a frosty gray appearance, while those which were wiped had a bright metallic luster and did not tarnish.

*Effect of the rate of cathode rotation.*—Runs were made with the cathode rotating at 875, 1750, 2675, and 3500 rpm. These correspond to 143, 286, 429, and 572 ft/min. As shown in Fig. 4, the rate of cathode rotation does not affect appreciably the composition of the alloy deposits except at very high speeds when the molybdenum content increased and the oxide content decreased. At 3500 rpm the vigorous rotation threw the solution away from the top of the cathode. The deposit obtained at this rate of rotation was iridescent dark blue near the top and tended to flake off the base metal when dried. The efficiency decreased at the higher speeds also because of the tendency for the solution to be thrown away from the rotating cathode, even though the wiper blades served as baffles to some extent. The greatest efficiency was obtained at 1750 rpm, so this speed was used in all subsequent experiments.

*Effect of current density.*—Nine runs were made at current densities varied from 2.2 to 20.0 amp/dm$^2$ (20 to 180 amp/ft$^2$ in increments of 20 amp/ft$^2$). The time of each plating run was adjusted so that 2100 coulombs passed during each run. At current densities below 8.9 amp/dm$^2$ (80 amp/ft$^2$) the deposits were coarsely crystalline, the rate of growth of the nuclei exceeding the rate of nucleus formation. The molybdenum content was low and the oxide content high as shown in Fig. 5. As the current density was increased, the rate of formation of the nuclei was greater and the deposits became

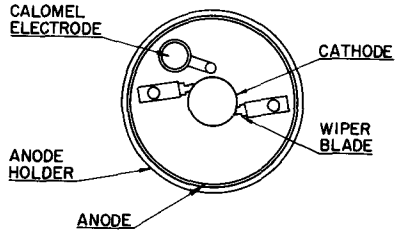


Fig. 2. Top view of plating cell

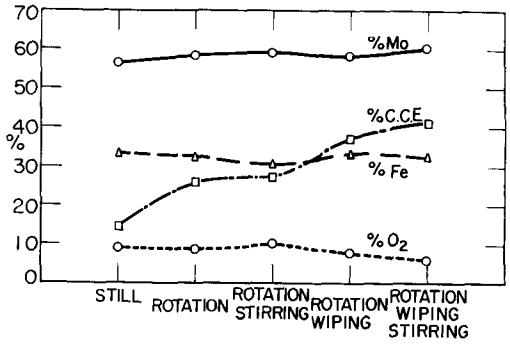


Fig. 3. Effect of rotation, stirring, and wiping

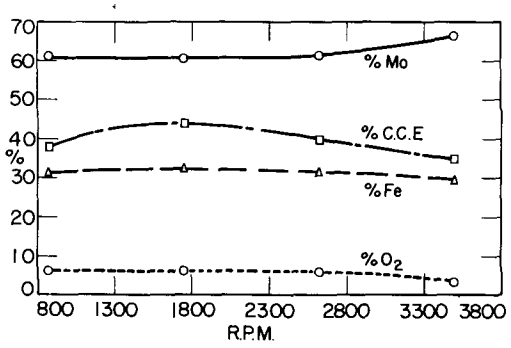


Fig. 4. Effect of the rate of cathode rotation

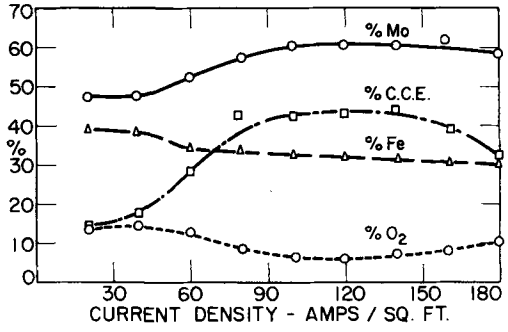


Fig. 5. Effect of current density

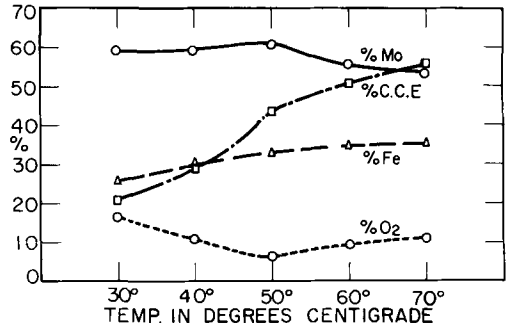


Fig. 6. Effect of temperature

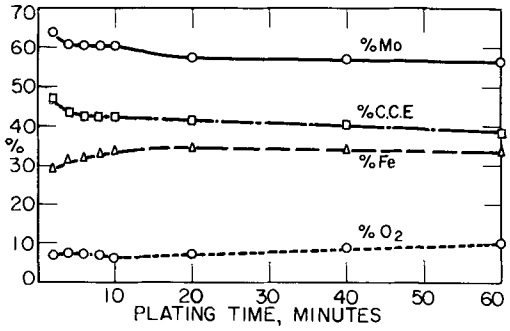


Fig. 7. Effect of length of plating time

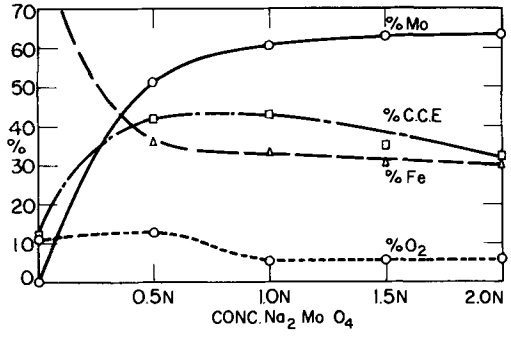


Fig. 8. Effect of Mo(VI) concentration

more fine grained. There was a decrease in the relative amount of the more noble metal (iron) since it was more rapidly depleted in the deposition zone. Current density was not critical in the range 11-20 amp/dm$^2$ (100-140 amp/ft$^2$). The deposits were good and the process was efficient. Deposits were less bright at higher current densities and the efficiency decreased. Since the metal ions could not be discharged rapidly enough, more hydrogen was evolved instead.

*Effect of temperature.*—Runs were made at 30°, 40°, 50°, 60°, and 70°C. The deposits improved in appearance, becoming more smooth and bright as the deposition was carried out at higher temperatures. The efficiency of the cathode process likewise was increased. However, the percentage of iron in the alloy deposits increased at temperatures above 50°C, while the percentage of molybdenum decreased as shown in Fig. 6. In selecting an operating temperature, a choice must be made between an increase in efficiency and a decrease in the molybdenum content of the alloy. A reasonable compromise is achieved at 50°C.

*Effect of the length of plating time.*—Runs were made of 2- to 60-min duration. Except for very short or very long plating periods, the composition of the deposits and the current efficiency did not change significantly (Fig. 7). The deposit obtained after plating for 2 min was thin, bright, and relatively high in molybdenum content. Those obtained with 4- to 10-min plating periods were nearly identical in appearance and composition and were plated with about the same efficiency. As the length of the plating time was increased, the deposits became dull and rough and were less adherent. These experiments show that, by the present method, it is possible to electrodeposit satisfactory coatings of iron-molybdenum alloy up to about 0.01 mm in thickness.

*Effect of* Mo(VI) *concentration.*—The concentration of Mo(VI) was varied from 0.0 to 2.0*N* (0 to 80 g/l $Na_2MoO_4 \cdot 2H_2O$), keeping the other bath components constant. With no $Na_2MoO_4$ in the plating bath, a very poor deposit was obtained. The iron plate was contaminated with considerable oxide which gave it a rough, dark appearance. Figure 8 shows that, as the concentration of Mo(VI) was increased, the molybdenum content of the deposits increased and the iron content decreased. However, the changes were not very great at concentrations above 1.0*N*, indicating the presence of some type of regulating mechanism which prevents the deposition of molybdenum in proportion to its concentration in the plating bath. The cathode current efficiency was greatest at 1.0*N* Mo(VI) and decreased at higher concentrations. All deposits were good except the one which contained no molybdenum.

*Effect of* Fe(III) *concentration.*—The concentration of Fe(III) was varied from 0.0 to 0.4*N* (0 to 36 g/l $FeCl_3 \cdot 6\,H_2O$). To keep the iron complexed to the same extent in each solution, the amount of $Na_4P_2O_7 \cdot 10\,H_2O$ was correspondingly varied. The normality of $Na_4P_2O_7 \cdot 10\,H_2O$ used was equal to four times the normality of $FeCl_3 \cdot 6\,H_2O$ in each case except that without $FeCl_3 \cdot 6\,H_2O$ which contained the usual 0.4*N* pyrophosphate. Although no deposit was expected in the absence of Fe(III), a run was made in order to obtain potential measurements. Much more negative values than usual were found for the static molybdenum potentials in the solution without iron, which would seem to indicate that the $Na_4P_2O_7$ forms a complex with the $Na_2MoO_4$. This is quite likely in view of the well-known complexes of molybdate with phosphates. The compound $Na(MoP_2O_7) \cdot 12\,H_2O$ has been reported (43). As the concentration of Fe(III) was increased from 0.05 to 0.4*N*, the iron content of the deposits increased and

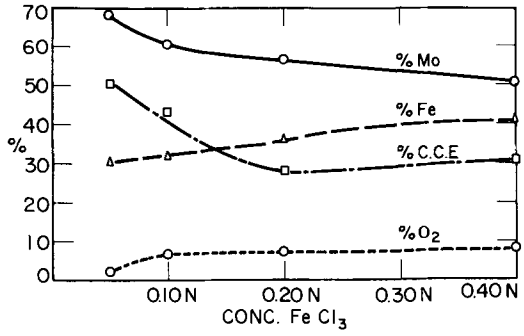


Fig. 9. Effect of Fe(III) concentration

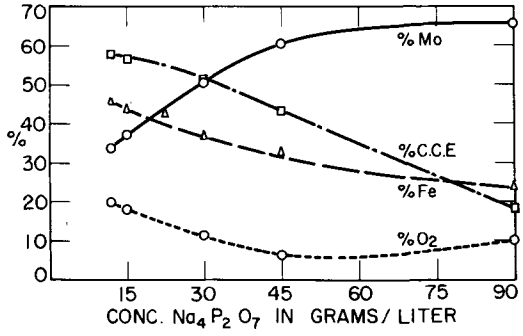


Fig. 10. Effect of sodium pyrophosphate concentration

the molybdenum content decreased (*see* Fig. 9). The cathode current efficiency decreased with increased Fe(III) concentration.

*Effect of sodium pyrophosphate concentration.*—The concentration of $Na_4P_2O_7 \cdot 10\,H_2O$ was varied from 12 g/l to 90 g/l (approximately 0.1 to 0.8*N*). According to the literature, Fe(III) forms three complexes with pyrophosphate depending on their relative concentrations (44). With 4 equivalents of Fe(III) to 3 equivalents of pyrophosphate, a precipitate of $Fe_4(P_2O_7)_3$ is obtained. This precipitate is soluble in the presence of excess pyrophosphate to form $Fe(P_2O_7)^-$ and $Fe(P_2O_7)_2^{-5}$. One run was made with just enough pyrophosphate to dissolve the precipitate $Fe_4(P_2O_7)_3$. The solution was dark red, indicating the probable presence of some dispersed $Fe(OH)_3$ since the amount of pyrophosphate present was insufficient to keep all the iron(III) in solution. The deposit obtained from this solution was low in molybdenum content and high in iron and oxygen. As the pyrophosphate content of the solutions was increased, the color changed to orange-yellow, yellow-green, and finally to blue-green. The percentage of iron in the deposits decreased as the iron was more tightly bound by the excess pyrophosphate. The efficiency of the plating process decreased markedly, as seen in Fig. 10. The static potentials of both molybdenum and iron became more negative as the concentration of pyrophosphate was increased. This supplies additional evidence to indicate that the pyrophosphate forms a complex with molybdenum as well as with iron. The alloy deposits were poor at the lower pyrophosphate concentrations.

*Effect of pH.*—Five runs were made over the *p*H range 7-10. Deposits were not obtained in acid solutions. For the first run, the $NaHCO_3$ was replaced by an equivalent amount of NaCl to maintain constant salt concentration. A few drops of dilute HCl were added to bring the *p*H to 7. The usual plating bath maintained a *p*H of 8. Higher *p*H values were achieved by the replacement of part or all of the $NaHCO_3$ by $Na_2CO_3$. A very poor deposit was formed from the neutral plating solution. As Fig. 11 shows, the alloy was low in molybdenum and high in iron and oxygen. The current efficiency increased up to *p*H 9.3. At *p*H 9.9 some $Fe(OH)_3$ was suspended colloidally in the bath, since the pyrophosphate was unable to keep the iron completely complexed at this high *p*H. The deposit was exceptionally smooth and bright because of the colloid in the bath.

*Reproducibility.*—Four identical runs were made, keeping all factors as nearly constant as possible, in order to determine the extent to which the potential measurements and the composition of the deposits were reproducible. The composition of the deposits was found to be reproducible within 0.4%, which was about the degree of accuracy attainable with the analytical method used. The four deposits obtained were nearly identical in appearance. The static molybdenum potentials were reproducible within 3 mv. The static iron potentials and the dynamic alloy potentials were not significant either through lack of reversibility or duplicability.

*Stability.*—A standard 800-ml batch of plating solution was prepared and a series of 30 consecutive 10-min runs was made from the original solution. There was no evidence of solution breakdown during this series of experiments, showing that the system is very stable.

A 3200-ml batch of standard solution was prepared. One run was made using 800 ml of the freshly prepared solution, and additional runs were made on 800 ml portions of the remainder 1 day, 26 days, and 80 days later. There was no aging effect in this plating solution during the 80-day interval. The bath gave deposits of essentially constant composition with the same efficiency whether from fresh or aged solution.

*Examination of the deposits.*—The usual iron-molybdenum alloy deposits were bright, silvery gray and did not tarnish visibly in laboratory air during periods of four months. A typical deposit is shown in Fig. 12.

The alloys were readily soluble in 5*N* $HNO_3$, but did not dissolve in dilute $H_2SO_4$, $H_2SO_4$ plus $H_3PO_4$, hot 6*N* HCl, hot or cold dilute $HClO_4$, or cold concentrated $HClO_4$. They were slightly soluble in hot

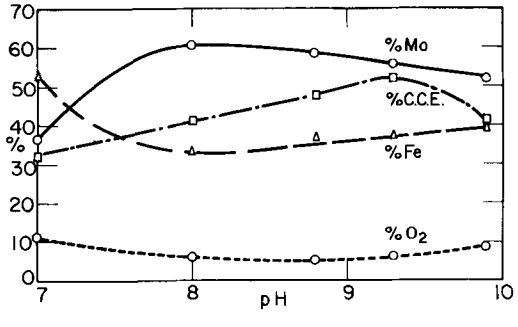


Fig. 11. Effect of pH

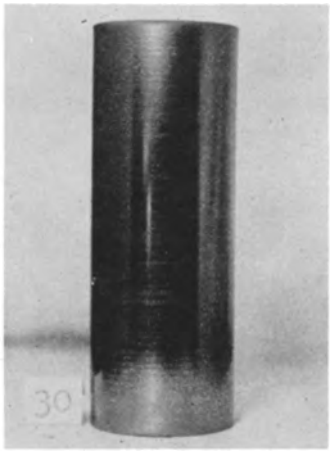

Fig. 12. A typical iron-molybdenum deposit

concentrated $H_2SO_4$. The plates appear inert toward alkaline solutions.

The deposits adhere well to the cylindrical platinum cathodes as long as the thickness is not greater than a few hundredths of a millimeter. They were found to be hard and brittle.

Microscopic examination of the deposits showed that they contain numerous cracks, as shown in Fig. 13. This is a photomicrograph of a typical iron-molybdenum alloy as plated on a brass tube and then covered with copper electrodeposited from a cyanide bath. There is no evidence of a banded structure, nor are there any large occlusions in the deposits. Neither higher magnifications up to 1200 X nor the action of etching agents gave evidence of more than a single phase.

This suggests the probable formation of an intermetallic compound or a solid solution. The epsilon phase in the iron-molybdenum system ($Fe_7Mo_6$) is well-defined, but the composition of the deposits is more indicative of the sigma phase which has the formula FeMo [(45) p. 1210]. FeMo is thermally stable above 1180°C, and therefore would be metastable under the plating conditions used. The deposits were so highly strained that attempts to identify their structures by x-ray analysis resulted in bands which were too diffuse to give any definite information. The strained condition may be due to a metastable solid solution, although hydrogen absorption may well be another factor. While not a part of the present study, an investigation of the possible effects of heat treatment in relieving these strains would be desirable. The place of oxygen in this system is not known.

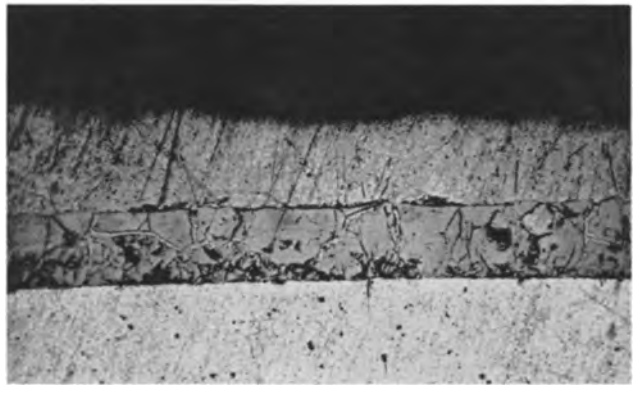

Fig. 13. Photomicrograph of a typical iron-molybdenum deposit. Magnification 500X before reduction for publication.

## Discussion

It is now realized that even single metal deposition is a complicated process for which no complete kinetic theory is yet available (46-48). However, molybdenum alloy deposition presents additional problems in any attempt to explain the mechanism of the cathodic process. The formation of these alloys is one example of a more general phenomenon whereby certain elements which cannot be deposited by themselves from aqueous solutions can be codeposited with any one of a number of other metals. Iron, cobalt, and nickel are most effective in this respect, although copper, zinc, and sometimes manganese, tin, or chromium can be the codepositing metal.

In general, metals cannot be deposited from aqueous solutions if the equilibrium of the deposition reaction lies so far on the ionic side that the electrode potential is more negative than the hydrogen discharge potential. According to Lyons (49) this occurs in the case of molybdenum because the molybdate ion is stabilized by inner orbital hybridization; that is, the 4*d* orbitals are hybridized with 5*s* and *p* orbitals. Apparently the energy required to break such hybridization exceeds that required for the cathodic discharge of hydrogen.

There is then, superimposed on the complex mechanism of direct metal deposition by cathodic reduction, a different problem in molybdenum alloy deposition, namely, that of induced codeposition. These questions then arise: (*a*) if molybdenum cannot be electrodeposited by itself from aqueous solutions, why does it deposit with certain alloying metals; (*b*) why is the molybdenum content of the alloys limited; and (c) why do the deposits always contain oxygen? Following are some of the theories proposed to answer these questions.

### *Proposed Mechanisms for Molybdenum Alloy Plating*

*Alternate layer theory.*—A mechanism proposed for the electrolytic reduction of aqueous tungstate solutions (50) might apply to the case of aqueous molybdate solutions also. According to this theory, the deposition of the alloying metal (iron) proceeds until the cathode is covered with a thin layer of iron which then reduces the activation energy for the deposition of molybdenum to occur. This reaction proceeds until the cathode surface is covered with a layer of molybdenum. Then the deposition of molybdenum ceases and the cycle is repeated.

This hypothesis fails to explain why the molybdenum alloy deposits contain oxygen, nor does it necessarily account for the laminar structure frequently encountered. Laminations also occur in single metal deposition and are not necessarily indicative of the deposition of alternate layers of two metals. Also, there is no apparent reason why only molybdenum should deposit on the initial iron layer.

*Oxide film theory.*—The oxide film theory (51) has been postulated as a mechanism for tungsten

alloy plating, but could include the similar phenomenon involving molybdenum. This theory proposes the deposition of a film of partly reduced tungstate (or molybdate) on the cathode and subsequent catalytic reduction of this film by hydrogen in the presence of freshly deposited iron, cobalt, or nickel.

This hypothesis explains the presence of oxides in the deposits on the basis of incomplete reduction and points out that the reason the iron-group metals are so effective in this type of deposition is because they are good hydrogenation catalysts. It does not explain why the molybdenum content of the alloys is limited.

*Hydroxide film theory.*—Myers (37) proposes that a mixed film of the hydrated oxides of molybdenum(III) and the carrier metal forms at the cathode during electrolysis. The presence of the carrier metal hydroxide is necessary to alter the permeability of the film so that the molybdate ions are able to penetrate it and to be discharged on the cathode surface. At the same time, the film insulates the nascent molybdenum atoms from reoxidation by the chemical action of the bath. A similar film is proposed for the reduction of sexivalent chromium at a rotated platinum cathode (52).

There is considerable experimental evidence to support this theory. First, it is important to note that no molybdenum alloy plate forms unless hydrogen is evolved. This is the same as saying that no plate forms until hydroxide ions are generated in the cathode film. (This also could be used as evidence for catalytic reduction by previously deposited hydrogen atoms.) If the solution is made acid, or if sufficient sodium cyanide is added to the bath so that the precipitation of the carrier metal hydroxide is prevented, then no alloy is deposited. By using extreme operating conditions of high temperature and very high current density, it is possible to form visible coatings of $Fe(OH)_3$ and $Mo(OH)_3$ around the cathode [(37), (53), pp. 160-165]. The presence of oxides of molybdenum and the carrier metal in the deposits is said to result from the occlusion of dehydrated portions of the diaphragm.

If such a film is present, it evidently is very thin and adherent since it is not destroyed by cathode wiping. The wiping process appears to be simply a means for the removal of accumulated hydrogen bubbles from the cathode surface, thus facilitating contact of the solution with the film.

This theory is capable of supplying explanations for many of the experimental results previously described. Figure 5 shows that the molybdenum content of the deposits increased initially with increased current density. The *p*H of the cathode film would be increased with an increase in current density, permitting the formation of a more effective hydroxide film, and an increase in efficiency and the relative amount of molybdenum deposited.

The solubility of such a film would increase at higher temperatures, which would result in a decrease in the molybdenum content of the deposits. This is borne out by the results given in Fig. 6.

The film apparently operates best when it is freshly formed (*see* Fig. 7). When the plating process is carried on for long periods of time, some film breakdown is suggested by the decreased molybdenum content and increased oxide content of the deposits.

As was pointed out in the discussion of Fig. 9, the molybdenum content of the deposits did not increase in proportion to the increase in concentration of molybdenum salts in the bath. This can be explained by assuming that too great an amount of $Mo(OH)_3$ in the film makes it less permeable to molybdate ions. Thus, the depositing ratio of molybdenum to carrier metal reaches a limiting value.

Changes in the sodium pyrophosphate concentration would be expected to affect the ease of film formation because of changes in the degree of complex formation with Fe(III). Figure 10 shows that the efficiency of the deposition process decreased with increased pyrophosphate concentration, which could be attributed to the increased difficulty of film formation. As the $Fe(OH)_3$ concentration in the film decreased, the iron content of the deposits decreased and the molybdenum content increased. However, the proportion of molybdenum in the deposits again seems to approach a limiting value.

The *p*H of the plating solution is also an important factor in film formation, but it should be pointed out that, because of the hydrogen discharge, the *p*H in the vicinity of the cathode will be higher than that in the body of the solution. When deposition was carried out from a neutral solution, the hydroxide film was less readily formed, because the only source of $OH^-$ was that resulting from hydrogen evolution. As the *p*H of the solution was increased, the film was formed more readily and the efficiency of the plating process was increased (Fig. 11). However, the molybdenum content of the deposits decreased and the iron content increased as the *p*H was increased above 8. This may be attributed to changes in the stability of the pyrophosphate complexes with increased *p*H. As was previously mentioned, $Fe(P_2O_7)_2^{-5}$ is not sufficiently stable to prevent the precipitation of $Fe(OH)_3$ at a *p*H of 9.9

Although, as has been shown in the preceding paragraphs, the hydroxide film theory can be used to explain many of the experimental data, it does not explain why the iron-group metals are the most effective in giving the film the necessary permeability.

One objection to the theory is that, if molybdenum deposition is prevented by the formation of a film containing only hydrated molybdenum oxide, then deposition at a dropping mercury electrode would be expected because such a film could not form. However, it has been reported that, while it is possible to form small amounts of molybdenum amalgam by electrolysis of an acidic molybdate solution, alkaline solutions of molybdate are not reduced at a dropping mercury electrode (54-56).

*Induced codeposition theory.*—A new theory has been proposed by Brenner (57) in which he refers to the phenomenon of molybdenum alloy deposition as an example of "induced codeposition." He refers to metals which cannot be deposited by themselves as "reluctant" metals, and the metals which aid in bringing about codeposition as "inducing" metals.

This theory proposes that the reluctant metals are actually more noble than the inducing metals and that their inability to deposit individually is due not to a highly negative electrode potential, but to a lack of electrochemical reactivity of their ions with electrons at the cathode. This is somewhat difficult to prove since the reversible potentials of the reluctant metals cannot be measured because these metals do not establish electrochemical equilibrium with solutions of their salts. If it is true that molybdenum is inherently more noble than iron, then the potential of the electrodeposited alloy would be expected to be more noble than that of iron. This was not the case, since the static potential of iron in the bath was about −0.2 v, while that of the alloys was −0.5 v.

To explain induced codeposition, Brenner postulates that the deposition of the inducing metal brings about an activation of the potentially depositable reluctant ion. He suggests that this is the result of an interaction whereby the energy of polarization of the inducing metal at the moment of deposition is transferred to the ions of the reluctant metal instead of being liberated as heat. If the reluctant ion is thus activated, it takes on its "normal" electrode potential and becomes capable of taking on electrons from the cathode, and the transferred energy then appears as heat.

It is further postulated that the energy of polarization is transferred as a unit and can aid in the acceptance of only one electron by the reluctant ion. This postulate explains the limitation of the reluctant metal content of the deposits by reasoning that the maximum content of reluctant metal in the deposit should approach a limit of one equivalent to each equivalent of inducing metal. If such calculations are made on the basis of Mo(VI) and Fe(III), then the theoretical limit of molybdenum in the electrodeposited alloys should be 46% by weight. This is considerably less than the percentage of molybdenum actually found in most of the deposits. The theoretical limit calculated on the basis of Mo(III) and Fe(III) gives a more reasonable limit of 63% molybdenum. Therefore, one might assume hydrogen reduction of Mo(VI) to Mo(III) followed by electrochemical reduction to the metal. An alternate assumption would be that hydrogen also acts as an inducing element. Still another point to consider is that if oxygen is essentially tied up with the molybdenum, then all of the molybdenum is not in the metallic state and thus has not been deposited. Calculations show that each per cent of oxygen ties up approximately 4% of molybdenum. Thus a deposit containing 60% Mo, 34% Fe, and 6% $O_2$ would contain only 36% metallic molybdenum assuming that all the oxygen is combined with molybdenum.

This theory fails to explain why the iron-group metals are most effective in bringing about induced codeposition and why deposition occurs more efficiently at elevated temperatures under which condition polarization is lowest. It does not account for the oxide content of the deposits.

## Summary and Conclusions

This summary of the experimental results is based on the fact that the primary objective of this research was to plate good quality iron-molybdenum alloys containing the highest possible percentage of molybdenum with the greatest possible current efficiency. Unfortunately, the conditions for attaining these objectives are not always the same, as shown by Table I. The first set of values for the variables lists those which favor the deposition of alloys which are high in molybdenum content, and the second set gives those which favor high efficiency. The third set of values lists those selected for practical operation of the plating system.

Deposits on a 21.7 $cm^2$ electrode using the solution composition and conditions indicated in the last column of Table I weigh about 0.17 g, contain about 61% Mo, 33% Fe, and 6% $O_2$, and are plated with an efficiency of about 44%. They are smooth, bright, and adhere well to the basis metal.

Of the several mechanisms proposed for the electrodeposition of iron-molybdenum alloys, the hydroxide film theory provides reasonable explanations for most of the experimental data. None of the postulated mechanisms is capable of a complete explanation of all the phenomena connected with this and other examples of induced codeposition. The final explanation must account for the presence in the deposits of substantial amounts of nonmetallic material, presumably oxygen.

The bridge complex mechanism for electrodeposition suggested by Lyons (49) might be extended to include this type of deposition, but to date there is insufficient knowledge of the structural nature of molybdenum ions in aqueous media to permit postulation of such a mechanism.

## Acknowledgments

The preliminary part of this investigation was supported by the Gerity-Michigan Corporation through the Research Foundation of the University

Table I. Optimum solution composition and plating conditions using cathode stirring and wiping

| Variable | Value for highest % Mo | Value for greatest % C.C.E. | Value for practical operation |
|---|---|---|---|
| Rate of rotation | 3500 rpm | 1750 rpm | 1750 rpm |
| Current density | 160 amp/$ft^2$ | 140 amp/$ft^2$ | 140 amp/$ft^2$ |
| Temperature | 50°C | 70°C | 50°C |
| Length of plating time | 2 min | 2 min | 10 min |
| Mo(VI) Conc. | 2.0$N$ (80 g/l) | 1.0$N$ (40 g/l) | 1.0$N$ (40 g/l) |
| Fe(III) Conc. | 0.05$N$ (4.5 g/l) | 0.05$N$ (4.5 g/l) | 0.1$N$ (9 g/l) |
| Sodium pyrophosphate conc. | 0.8$N$ (90 g/l) | 0.1$N$ (12 g/l) | 0.4$N$ (45 g/l) |
| pH | 8.0 | 9.3 | 8.0 |

of Toledo, with Dr. Nelson W. Hovey as project director. The authors wish to thank Dr. M. J. Sinnott of the Department of Chemical and Metallurgical Engineering of the University of Michigan for his assistance in the metallographic examination of the deposits, and the Climax Molybdenum Company for furnishing information on molybdenum and samples of molybdenum and molybdenum compounds.

Manuscript received June 20, 1957. This paper was prepared for delivery at the Washington Meeting, May 12-16, 1957. It is abstracted from a thesis presented by Albertine Krohn to the University of Michigan in partial fulfillment of the requirements for the degree of Doctor of Philosophy.

Any discussion of this paper will appear in a Discussion Section to be published in the June 1959 JOURNAL.

## REFERENCES

1. C. A. Hampel, Editor, "Rare Metals Handbook," Reinhold Publishing Co., New York (1954).
2. J. J. Harwood, *Prod. Eng.*, **23**, 121 (1952).
3. P. P. Belyaev and A. I. Lipovetskaya, *Korroziya i Bor'ba s Nei*, **6**, No. 2, 47 (1940).
4. C. G. Fink and C. H. Eldridge, Canadian Pat. 274,429, Oct. 4, 1927.
5. H. Krause, *Feinmech. u. Präzision*, **41**, 106 (1933).
6. M. J. Ksycki and L. F. Yntema, *J. (and Trans.) Electrochem. Soc.*, **96**, 48 (1949).
7. A. S. Minin, Russian Pat. 59,863, April 30, 1941.
8. K. A. Paul, Russian Pat. 53,756, Aug. 31, 1938.
9. E. Pokorny and K. Schneider (to I. G. Farbinend), German Pat. 582,528, May 22, 1934.
10. W. P. Price and O. W. Brown, *Trans. Electrochem. Soc.*, **70**, 423 (1936).
11. L. F. Yntema, *J. Am. Chem. Soc.*, **54**, 3775 (1932).
12. H. S. Booth and M. Merlub-Sobel, *J. Phys. Chem.*, **35**, 3303 (1931).
13. A. Brenner, *Record Chem. Progr.* (Kresge-Hooker Sci. Lib.), **16**, 241 (1955).
14. L. Andrieux, *Compt. rend.*, **184**, 91 (1927).
15. J. W. Beckman, U. S. Pat. 973,336, Oct. 18, 1910.
16. T. R. Forlund, U. S. Pat. 1,305,350, June 3, 1919.
17. G. Gin, *Trans. Electrochem. Soc.*, **12**, 411 (1907).
18. H. Hartmann and U. Conrad, *Z. anorg. u. allgem., Chem.*, **233**, 313 (1937).
19. A. Kratky and W. Bruckner, German Pat. 263,301, April 19, 1911.
20. S. Senderoff and A. Brenner, *This Journal*, **101**, 16 (1954); U. S. Pat. 2,715,093, Aug. 9, 1955.
21. F. W. Salt, *Murex, Ltd., Rev.*, **1** (9), 201 (1951).
22. D. H. Killeffer and A. Linz, "Molybdenum Compounds," Interscience Publishers, New York (1952).
23. R. A. Hoffman and R. O. Hull, *Proc. Am. Electroplaters' Soc.*, June **1939**, 45.
24. R. A. Hoffman (to du Pont), U. S. Pat. 2,380,044, July 10, 1945.
25. E. W. Schweikher (to du Pont), U. S. Pat. 2,351,639, June 20, 1944.
26. A. Brenner and P. S. Burkhead, U. S. Pat. 2,653,127, Sept. 22, 1953.
27. L. F. Yntema, U. S. Pat. 2,428,404, Oct. 7, 1947.
28. C. C. Ma (to Westinghouse Electric Corp.), U. S. Pat. 2,516,227, July 25, 1950.
29. M. L. Holt and H. J. Seim, U. S. Pat. 2,599,178, June 3, 1952.
30. L. F. Yntema and M. J. Ksycki, U. S. Pat. 2,499,807, March 7, 1950.
31. I. N. Frantsevich, T. F. Frantsevich-Zabludovskaya, and E. H. Zhelvis, *J. Appl. Chem. U.S.S.R.*, **25**, 387 (1952) (Engl. Trans.); *Zhur. Priklad. Khim.*, **25**, 350 (1952).
32. T. F. Frantsevich-Zabludovskaya, *J. Appl. Chem. U.S.S.R.*, **25**, 1369 (1952) (Engl. Trans.); *Zhur. Priklad. Khim.*, **25**, 1314 (1952).
33. T. F. Frantsevich-Zabludovskaya, I. N. Frantsevich, and K. D. Modylevskaya, *Zhur. Priklad, Khim.*, **27**, 413 (1954).
34. H. J. Seim and M. L. Holt, *J. (and Trans.) Electrochem. Soc.*, **96**, 205 (1949).
35. R. F. McElwee and M. L. Holt, *This Journal*, **99**, 48 (1952).
36. D. W. Ernst, R. F. Amlie, and M. L. Holt, *ibid.*, **102**, 461 (1955).
37. H. S. Myers, "The Electrodeposition of Molybdenum," unpublished Ph.D. thesis, Columbia University (1941).
38. N. W. Hovey, J. L. Griffin, and A. Krohn, *This Journal*, **102**, 470 (1955).
39. E. Lyons, *J. Am. Chem. Soc.*, **49**, 1916 (1927).
40. H. W. Swank and M. G. Mellon, *Ind. Eng. Chem., Anal. Ed.*, **10**, 7 (1938).
41. J. H. Hamence, *Analyst*, **65**, 152 (1940).
42. F. Will, III, and J. H. Yoe, *Anal. Chem.*, **25**, 1363 (1953).
43. J. W. Mellor, "A Comprehensive Treatise on Inorganic and Theoretical Chemistry," Vol. XI, 671, Longman's Green & Co., London (1930).
44. L. B. Rogers and C. A. Reynolds, *J. Am. Chem. Soc.*, **71**, 2081 (1949).
45. T. Lyman, Editor, "Metals Handbook," American Society for Metals, Cleveland (1948).
46. J. O. Bockris, Editor, "Modern Aspects of Electrochemistry," Buttersworth Scientific Publications, London (1954).
47. H. Fischer, "Elektrolytische Abscheidung und Elektrokristallisation von Metallen," Springer-Verlag, Berlin (1954).
48. A. G. Gray, Editor, "Modern Electroplating," John Wiley & Sons, Inc., New York (1953).
49. E. H. Lyons, Jr., *This Journal*, **101**, 363 (1954).
50. M. L. Holt and L. E. Vaaler, *ibid.*, **94**, 50 (1948).
51. W. E. Clark and M. H. Lietzke, *ibid.*, **99**, 245 (1952).
52. I. M. Kolthoff and A. M. Shams El Din, *J. Phys. Chem.*, **60**, 1564 (1956).
53. E. F. Smith, "Electro-analysis," 5th ed., Blakiston, Philadelphia (1911).
54. L. J. Merrill and A. S. Russell, *J. Chem. Soc.*, **1929**, 2389.
55. R. Holtje and R. Geyer, *Z. anorg. u. allgem. Chem.*, **246**, 258 (1941).
56. Y. P. Hokhshtein, *J. Gen. Chem. U.S.S.R.*, **10**, 1752 (1940).
57. A. Brenner, "A Theory of the Induced Codeposition of Metals," Private communication (1955).

# Isolation of the Diffusion Layer at an Electrode and the Determination of Concentration Polarization

**Theodore Yannakopoulos[1] and Abner Brenner**

*National Bureau of Standards, Washington, D. C.*

ABSTRACT

A method has been developed for sampling the electrolyte (concentration $C_i$) that exists during electrolysis at the interface of electrode electrolyte. Copper was electrodeposited from sulfate baths (concentration $C_b$) on to the outside surface of a hollow, microporous metal cylinder, and electrolyte was slowly drawn into the interior which contained an organic liquid immiscible with water. The electrolyte being less dense rose to the surface of the organic liquid and was collected.

The difference, $C_b - C_i = \Delta Cu$, was somewhat greater than theoretical. Also, $\Delta Cu$ was larger for baths of higher copper content.

From the values of $C_i$, the Nernst concentration polarization was calculated and shown to be about 10 mv in ordinary plating operations and hence is not significant.

A knowledge of the concentrations of ions in the vicinity of an electrode is necessary for a clear understanding of the mechanism of electrochemical processes. The concentrations of metal-containing ions affect various phenomena, such as polarization, the structure of electrodeposits, and the composition of electrodeposited alloys. The authors were particularly interested in the relation between polarization and the concentrations existing at the interface of cathode and electrolyte. There has been a considerable amount of speculation about the magnitude of concentration polarization. It has not been measured with certainty, because the methods that have been used were indirect and involved unproved assumptions.

The most direct method for determining concentration polarization would be to measure the metal ion concentration existing at the interface of the electrode and the solution and apply Nernst's formula to the data. Although several methods have been proposed for measuring concentrations at the interface, each one has certain disadvantages. A new method for isolating the interfacial solution has been developed and was applied to the study of the concentration polarization that occurs during electrolysis of copper sulfate solutions.

## Methods of Measuring the Concentrations at the Electrode-Solution Interface

Two general methods have been used for determining the concentrations that exist at the electrode-solution interface: optical and sampling techniques. The optical method was first applied to the measurement of the composition of the cathode diffusion layer by Samarcev (1) who used schlieren interferometry to determine the concentration profile of copper ion in a diffusion layer formed during electrolysis of a copper sulfate solution streaming between horizontal electrodes. The same general method was later used by Ibl and co-workers (2) and by Lin and co-workers (3). Ibl determined the concentration profile and the thickness of the diffusion layer on vertical cathodes under conditions of natural convection.

The optical method has the advantages over sampling techniques of being very sensitive and of not disturbing the diffusion layer. It has the disadvantage of being nonspecific, since it depends on a shift in the index of refraction. Hence, the optical method cannot be used to determine the concentrations of several different solutes present in one solution. Another difficulty with the method is that at high current densities large differences in the density of the diffusion layer occur and cause the diffraction bands to become diffuse. Also, the optical method cannot be used readily with deeply colored solutions such as a chromium plating bath.

Sampling techniques include the drainage, pinhole, and freezing methods. The drainage method consists of the quick removal of the electrode from the bath while the current is still flowing. The solution is allowed to drain from the vertical electrode for several seconds, and the remaining solution is removed with a squeegee and collected. It is a crude method, but gives a fair indication of the concentrations existing at the electrode solution interface. This method has been used by Brenner (4) for determining the concentrations at the cathode in several solutions and by Brenner and Wranglen (5) for measuring the pH at the cathode-solution interface of nickel baths.

In the pinhole method developed by Graham, Heiman, and Read (6) the diffusion layer is sampled by withdrawing it through a capillary tube cemented on the back-side of the cathode over a hole. The sampling rate was about 7 ml/hr through a capillary having an inside diameter of 1 mm. This corresponds to a rate of flow of about 12 cm/min

[1] Present address: University of Athens, Athens, Greece.

normal to the electrode. Since the diffusion layer in a conventional plating bath is only about 0.3 mm thick and requires about 1 min to reach equilibrium with respect to concentration, it is evident that this rate of sampling is too great. The concentration changes observed by Graham, Heiman, and Read were only about one-tenth of those observed by Brenner (4). This indicates that a large proportion of the sample of Graham, Heiman, and Read probably came from the body of the bath.

The freezing method developed by Brenner (4) involves deposition on the outer surface of a hollow cylindrical electrode. At the moment that the current is cut off, a slurry of partially frozen isopentane is poured into the cylinder causing the diffusion layer to be frozen on the cylinder. This layer is turned off in increments on a lathe and each one analyzed. The freezing method permits the measurement of both the concentration profile and the thickness of the diffusion layer. Difficulties with the method are the collection of frost during the turning operation, the occasional poor adhesion of the frozen layer to the cylinder, and the low eutectic temperature of some solutions.

## Experimental

A new method of sampling the diffusion layer has been developed which involves the use of a sheet of microporous metal to form part or the entire wall of a hollow electrode. The method will be referred to as the porous-electrode method. The electrochemical reaction takes place on the outer surface of the microporous metal, and the solution existing at the interface of the electrode and the bath is slowly withdrawn into the interior of the hollow electrode and collected. The pores of the microporous metal were about 5$\mu$ in diameter and the voids amounted to about one-half the volume of the metal.

The use of a hollow, porous electrode for separating the reaction product of an electrolysis from the bulk of the solution is not new. It was mentioned by Knobel (7). Also some patents (8, 9) have been issued on the subject. The most important work was that carried out for the National Carbon Company by Heise (10), Janes (11), and Winslow (12). All of these prior studies of porous electrodes have dealt with the use of porous graphite. In the studies of the National Carbon Company, the aim was to obtain a high yield of product, and therefore the solution at the interface was withdrawn into the interior of the cell rapidly enough to accomplish this purpose.

The technique described in this paper is an improvement over the use of graphite electrodes for the study of diffusion layers in that microporous metal has a much finer porosity than graphite and, because of its greater strength, permits it to be fashioned into vessels with much thinner walls. Some further improvements in the technique are described in a later paragraph. The rate of sampling used in our experiments was about one-tenth of that used in the experiments of the National Carbon Company. A low rate of flow was necessary to prevent inclusion of solution from the body of the bath.

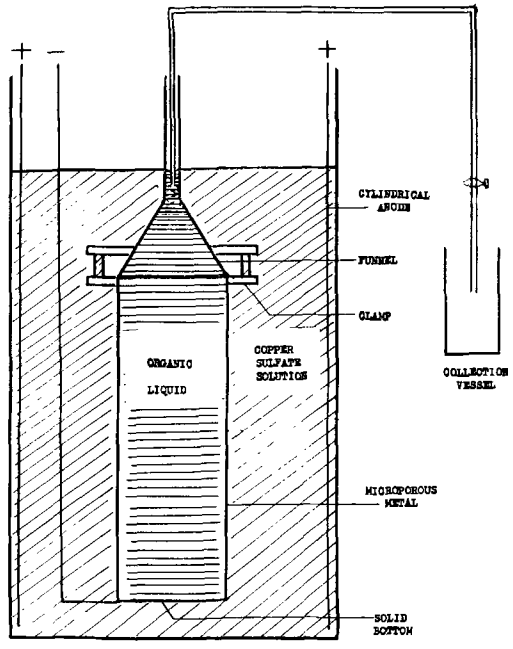


Fig. 1. Schematic diagram of hollow cylindrical cathode of microporous stainless steel and auxiliary equipment used for sampling the diffusion layer formed in the electrolysis of copper sulfate solution.

The hollow electrode vessel may take several shapes. For example, it may consist of a plane sheet of microporous metal attached to the mouth of a funnel. In the experiments described here, the electrode consisted of a vertical cylinder of microporous stainless steel, with a solid bottom, shown schematically in Fig. 1. The cylinder was 15 cm in length and 5 cm in diameter. The wall thickness was 0.07 cm. An inverted glass funnel was clamped to the top of the cylinder by two rings, the lower one of which was rigidly attached to the cylinder by a resin cement. The purpose of the funnel was to facilitate the collection of the sample which was drawn into the interior of the vessel at the rate of about 0.25 ml/min.

Two problems were encountered in the use of the vertical cylinder: (*a*) attaining a uniform hydrostatic pressure along the height of the cylinder, and (*b*) holding the solution inside the cylinder to a small volume so that a sample would not be mixed with part of a preceding one.

Since the hydrostatic pressure varied along the length of the vertical, cylindrical electrode and was greatest at the bottom, the tendency was for solution from the bath to be withdrawn into the cylinder more rapidly through the bottom walls. Various means were tried for obtaining a uniform hydrostatic pressure along the vertical length of the wall. The problem was solved by filling the interior of the cell with an organic liquid, immiscible with water, which had the same density as the body of the bath. In this manner the hydrostatic pressure was made equal on the inside and outside of the cylinder along its entire length, and a uniform flow of solution through the walls of the cylinder was obtained by reducing the pressure on the interior.

The use of the immiscible liquid had a further advantage in that it caused the less dense solution

collected at the cathode-solution interface to rise rapidly to the surface where it could be collected. Since the interior of the electrode was completely filled with the organic solvent at the start of the electrolysis, it also solved the problem of lessening the dilution of the sample with extraneous solution.

*Porosity and Wall Thickness of the Electrode*

In preliminary experiments, electrodes of different porosity were tried. The electrode with the smallest pores was the easiest to manipulate and seemed to give a more accurate sampling of the diffusion layer.

The porosity of the electrode was not uniform along its length. However, the uniformity of flow through the wall was considerably improved by pumping a suspension of alumina through the cylinder. Resistance to flow was increased about tenfold. This was desirable, since the effect of small differences in the hydrostatic pressure between the inside and outside of the electrode was diminished.

A thin electrode wall was desirable. The interstices of the wall were filled with plating bath at the beginning of the experiment, and the plating solution in the wall mixed with the sample of the diffusion layer as it passed through the wall. Consequently, the sampling had to be continued until all the bath initially in the wall had been drawn through. The thicker the wall, the longer was the time required for obtaining a representative sample of the diffusion layer. The thinnest wall commercially available was slightly less than 1 mm in thickness. Still thinner walls would be desirable.

*Procedure*

The first step in an experiment consisted in filling the pores of the cylinder with a suspension of alumina as mentioned previously. The excess was removed from the surface of the electrode by washing with a stream of water. The electrode was then immersed in a vessel of the plating solution in order to fill the pores. The interior of the electrode was next filled with a mixture of chloroform and paraffin oil having the same density as that of the bath. The organic liquid was slowly poured into the cylinder while the latter was slowly lowered into the bath at such a rate that the height of the liquids on the inside and outside of the cylinder were about the same. The siphon, also filled with organic liquid, was next attached to the inverted funnel.

After the electrolysis was started, the flow through the siphon was regulated with a stopcock to the desired rate, usually about 0.25 mil/min. At first a few milliliters of organic liquid was delivered, but soon the siphon which was of small diameter became filled with the aqueous solution and delivery of the latter began. A sampling rate of 0.25 mil/min was equivalent to a displacement of the interface layer of about $4 \times 10^{-5}$ cm/sec. This calculation is based on an area of pores of about 1 $dm^2$. It is believed that this rate of movement is too low to affect significantly the steady-state concentrations in the diffusion layer.

The electrolysis usually lasted about 1.5 to 2 hr, during which time 15 to 30 ml of solution was obtained, depending on the sampling rate. The first solution delivered contained some of the solution which was initially in the porous walls of the electrode. Consequently, the concentration of each succeeding sample of solution diminished and approached either a constant value or a flat minimum which was taken as the concentration of the solute existing at the cathode-solution interface.

Copper sulfate solutions ranging in concentration from 0.25 to 0.94M were used. No additions, such as sulfuric acid, were made to the solution, as it was desired to keep the composition of the bath simple so that the data could be more easily compared with diffusion theory. The plating was done at about 25°C without stirring. The samples were analyzed for copper by the iodide method.

## Results

*Variation of copper content of successive samples.* —The decrease in the copper content of successive samples mentioned in the previous section is illustrated in Fig. 2. This datum was taken before the technique of plugging the pores of the cylinder walls with alumina was developed. With the latter technique the upturn of the curve at the right was not pronounced. The cause of the increase in the copper content of successive samples with period of plating is not definitely known, but it is believed to be caused by the covering over of the small pores on the outer surface of the cylinder with the copper deposit. This caused a larger proportion of the sample to be drawn into the cylinder through a relatively small number of larger pores, with the result that the velocity of flow of the diffusion layer at these points was greatly increased. The upturn was less pronounced with a plugged cylinder wall probably because the large pores were eliminated.

We believe that the copper content of the sample approximates the composition of the solution at the cathode-solution interface. The latter actually has no thickness and, strictly speaking, cannot be sampled. The decrease in copper content below that of the body of the bath is not caused, as has been suggested, by deposition of copper in the interstices of

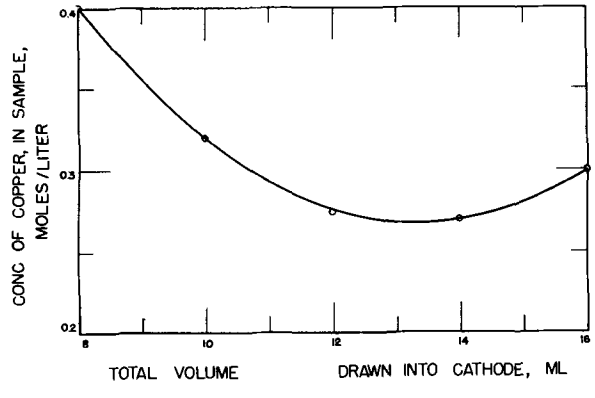


Fig. 2. Relation between the copper content of a sample drawn into the cylinder and the total volume of solution passing through the cylinder. The abscissa is the total volume of solution collected up to and including the volume of the sample used for analysis. The ordinate is the concentration of copper in a 1-ml sample individually collected. Rate of flow of liquid into cylinder, 0.25 ml/min; copper concentration in the body of both, 0.94M; current density, 2.86 amp/$dm^2$; room temperature; apparatus as shown in Fig. 1.

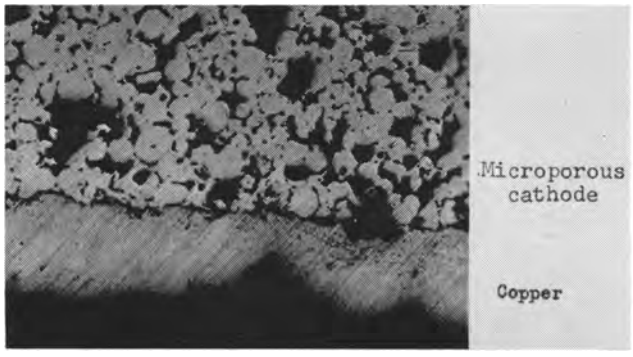


Fig. 3. Photomicrograph of a cross section of copper deposited on microporous stainless steel.

the cell wall. Deposition of copper within the interstices is improbable because of the minute current that flows into deep recesses having a cross section of the order of 5$\mu$. Definite evidence that deposition does not occur in the pores of the cylinder is given in Fig. 3, which shows that the copper coating lies only on the outside surface of the microporous cathode.

Since the internal surface of the electrode walls is very large, the possibility exists that an appreciable amount of copper would deposit within the walls without attaining a thickness sufficient to be observed microscopically. This possibility was explored by determining the amount of copper leached out of the cell walls with nitric acid. The walls of this cell were twice the thickness of those of the cell used for obtaining the values of $\Delta$Cu reported in this paper. In a blank experiment, the thick-walled cell was immersed in copper sulfate solution for 2 hr to determine if copper deposited by immersion. The copper extracted from the cell walls with nitric acid amounted to only a few milligrams and hence was negligible. In another experiment, copper was deposited at 4 amp/dm$^2$ from a 1M bath over the cylinder as in an ordinary experiment. The copper coating was then peeled from the exterior of the cylinder and any residual copper nodules were removed with a polishing wheel. The copper obtained by a nitric acid extraction amounted to only 12 mg. This copper was probably not deposited on the interior of the wall but probably existed in surface cracks too deep to be reached by the polishing wheel. This amount of copper would affect the value of $\Delta$Cu only about 1%, which is less than the experimental reproducibility.

*Rate of withdrawing samples.*—The rate of withdrawing samples was an important variable. At a high sampling rate, some of the bulk solution was drawn into the cell along with the diffusion layer. Figure 4 shows the relation between the decrease in the copper content in the collected sample and the rate of collection of the sample. At a rate of 0.25 ml/min the decrease in the copper concentration, $\Delta$Cu, differed by only 3% from the value of $\Delta$Cu obtained by extrapolating the straight line of the figure to zero rate of sampling. Each point of Fig. 4 was obtained by the method illustrated in Fig. 1.

### *Relation between Current Density and* $\Delta$Cu

The relation between $\Delta$Cu and current density is shown in Fig. 5 for copper sulfate solutions of three different concentrations. The current densities are based on the apparent area of the cylinder, considered as a continuous surface. Some observations were made at higher current densities than those recorded in Fig. 5. At the highest current density, which was above the limiting current density of metal deposition, the samples withdrawn from the electrode were virtually colorless indicating almost complete removal of copper.

One interesting aspect of Fig. 5 is that $\Delta$Cu at a given current density is larger the more concentrated the plating bath. A similar trend of metal depletion in the cathode diffusion layer was observed by Brenner (4) with nickel solutions and by Samarcev (1) with copper sulfate solutions. The explanation given by Samarcev, as well as by Brenner, was that in the dilute solution, and particularly in the still more dilute diffusion layer, the rate of diffusion of the metallic ions was greater than in

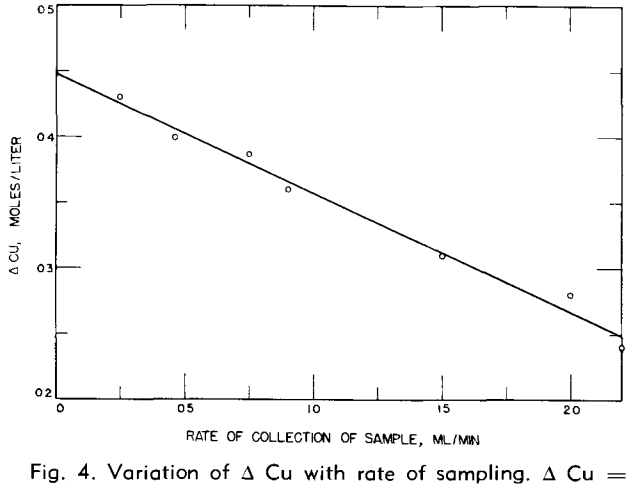


Fig. 4. Variation of $\Delta$ Cu with rate of sampling. $\Delta$ Cu = $C_b - C_i$ where $C_b$ is the concentration of copper in the body of the bath and $C_i$ is the concentration of copper in the sample of the diffusion layer. $C_b$ = 1M; current density, 1.5 amp/dm$^2$; temperature, 28°C; microporous cathode, 0.15 cm thick; apparatus as in Fig. 1.

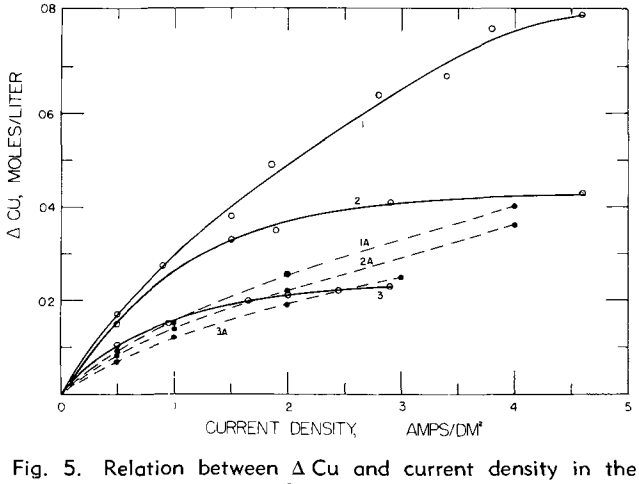


Fig. 5. Relation between $\Delta$ Cu and current density in the electrolysis of copper sulfate solutions of three different concentrations. Rate of collection of sample, 0.25 ml/min. Curve 1. 0.94M copper sulfate; Curve 2. 0.49M copper sulfate; Curve 3. 0.24M copper sulfate; Curves 1A, 2A, and 3A are calculated curves based on diffusion theory (see Table I) according to Keulegan (13), for the same bath concentrations as curves 1, 2, and 3.

the concentrated solutions. This would result in a smaller value of ΔCu for the more dilute baths. However, the variation of the diffusion constant of copper sulfate with concentration seems inadequate to explain the differences of more than twofold in the values of ΔCu obtained at a given current density for the different baths.

*Comparison of Data with Theory*

Within recent years a considerable amount of theoretical and experimental investigation has been made of the hydrodynamics of electrode diffusion layers by Ibl and co-workers (2, 21, 22), Wagner (17, 18), and Tobias, Eisenberg, and Wilke (19, 20). The various approaches lead to similar numerical results for ΔCu (23) even though they involve some different assumptions.

The values of ΔCu obtained with the porous electrode were compared with those theoretically expected. The theory of the diffusion layer developed by Keulegan (13) was used in making the calculations. This theory was used because the authors were more familiar with it, and its use does not imply that it is more correct than the other theories. Actually it involves two assumptions that did not obtain in our experiments, namely, that the depletion of metal ion was uniform over the cathode and that the hydrodynamic boundary layer coincided with the diffusion layer.

Theory based on hydrodynamics and diffusion does not predict widely separated curves, as shown in Fig. 5, for solutions of different initial concentrations. Keulegan's theory leads to the following equation for ΔC. This ΔC, like the ΔCu obtained with the porous electrode, is the value of the reduction in metal ion concentration *averaged* over the cathode surface.

$$\Delta C = \left(\frac{It_a}{0.63F}\right)^{4/5} \cdot \frac{(\rho_1 \nu\, xm)^{1/5}}{g^{1/5} D^{3/5}}$$

where $I$ = current density, amp/dm$^2$; $t_a$ = transference number of anion; $F$ = 96,500 coulombs; $\rho_1$ = density of the bulk of the bath; $\nu$ = kinematic viscosity, poises; $x$ = length of cylinder, (13.2 cm); $m = \frac{dc}{d\rho} = 0.0132$ g equiv/g, c is the concentration of the copper sulfate solution in gram equiv/ml, and $\rho$ is the density of the copper sulfate solution; $g$ = 981 cm/sec$^2$; $D$ = diffusion constant of copper sulfate, cm$^2$/sec. This equation is based on equations 89 and 118 of Keulegan's paper. For the present experiments, the above equation simplifies to the following:

$$\Delta C = 2.5 \times 10^{-5} (It_a)^{4/5} \cdot \frac{(\rho_1 \nu)^{1/5}}{D^{3/5}}$$

In using this equation, the values of the variables are those of the solution at the interface of the cathode and the solution, except for $\rho_1$ which refers to the density of the bulk of the bath.

Calculations were made using the above equation. The values of the different variables are given in Table I. The results are represented in Fig. 5 as dotted curves. The three curves based on Keulegan's equation lie close together, indicating that the effects of the variations of transference number, viscosity, and diffusion constant with concentration were not sufficient to explain the large difference in ΔCu experimentally obtained with the three different solutions at a given current density. The agreement of experiment with diffusion theory was best for the 0.24M copper sulfate solution.

We do not have a satisfactory explanation for the large difference between the three curves of Fig. 5 and the difference between curve 1 and the theoretical curve. It is possible that the roughness of the cathode surface or some other experimental detail may be responsible. Also, electrical migration may directly affect the thickness of the diffusion layer.

This latter suggestion is based on the behavior of liquid junctions in the moving boundary method of determining transference numbers. With suitably chosen solutions, the junctions remain sharp while current is passing. However, it is also possible for the current to dissipate a junction, depending on the relative mobilities of the ions involved. A similar phenomenon occurs at the junction of two solutions of different concentration. Thus, the electrical migration may have an effect on the establishment, the thickness, and the sharpness of the diffusion layer in addition to the factors of hydrodynamics.

*Concentration Polarization*

The polarization that occurs during an electrochemical reaction has been considered by electrochemists to be of two types: activation polarization and concentration polarization. The division is somewhat arbitrary since there are no direct experimental measurements for distinguishing between them. Very roughly, concentration polarization is considered to be caused by the change in concentration of the reactive ions at the electrode surface (24). The remainder of the polarization is considered to be of the other type. Various means for discriminating between them have involved different assumptions. It is assumed that stirring eliminates concentration polarization but does not affect activation polarization. Also, it is assumed that the latter type disappears more rapidly than the former when the circuit is broken. However, since nothing is known definitely about the activation type of polarization, one cannot, a priori, assume that concentration polarization is affected by a certain variable, such as stirring and the other one is not.

Concentration polarization, $P_c$, at a cathode is usually defined by the Nernst expression:

$$P_c = \frac{RT}{nF} \log \frac{A_b}{A_i}$$

where $A_b$ is the activity of the metal ion in the body of the bath and $A_i$ is the activity of the metal ion at the cathode-solution interface. That is, the concentration polarization is equivalent to the potential of a concentration cell with negligible liquid junction. In actual measurements of polarization with a capillary, a variable liquid junction potential exists between the solution of the reference electrode and

Table I

Calculations of ΔCu from the formula,

$$\Delta Cu = 2.5 \times 10^{-5} \cdot (It_a)^{4/5} \cdot \frac{(\rho_1 \nu)^{1/5}}{D^{3/5}}$$

ΔCu is given by the formula in units of $\frac{\text{g-equiv}}{\text{cm}^3}$

$I$, current density, amp/cm²; $t_c$, transference number of cation; $t_a$, transference number of anion; $\rho_1$ density of body of bath; $\nu$, kinematic viscosity, poises; $D$, diffusion constant, cm²/sec; $C_b$, concentration of copper in the body of the bath, g-equiv/cm³; $C_i$, concentration of copper at the cathode-solution interface, g-equiv/cm³.

| $C_i$ g-equiv/cm³ × 10⁴ | $t_c$ | $t_a$ | $I$ amp/cm² | $(It_a)^{4/5}$ × 10⁴ | $\nu$ × 10² | $(\rho_1\nu)^{1/5}$ | $D$ × 10⁶ | $D^{3/5}$ × 10⁴ | ΔCu g-equiv/cm³ Calc. × 10⁴ | ΔCu g-equiv/cm³ Exp. × 10⁴ |
|---|---|---|---|---|---|---|---|---|---|---|
| | | $C_b$ = 0.94M | | | $\rho_1$ = 1.130 | | | | | |
| 15.4 | 0.275 | 0.725 | 0.005 | 111 | 1.27 | 0.428 | 5.05 | 6.6 | 1.8 | 3.4 |
| 12.8 | 0.285 | 0.715 | 0.01 | 192 | 1.22 | 0.425 | 5.1 | 6.68 | 3.0 | 6.0 |
| 8.6 | 0.300 | 0.700 | 0.02 | 329 | 1.10 | 0.416 | 5.2 | 6.76 | 5.1 | 10.2 |
| 3.8 | 0.34 | 0.66 | 0.04 | 546 | 0.98 | 0.406 | 5.4 | 6.9 | 8.0 | 15.0 |
| | | $C_b$ = 0.490 moles | | | $\rho_1$ = 1.075 | | | | | |
| 6.4 | 0.307 | 0.693 | 0.005 | 108 | 1.05 | 0.408 | 5.25 | 6.80 | 1.6 | 3.4 |
| 4.6 | 0.325 | 0.675 | 0.01 | 183 | 1.00 | 0.404 | 5.30 | 6.84 | 2.7 | 5.2 |
| 2.6 | 0.370 | 0.630 | 0.02 | 302 | 0.96 | 0.400 | 5.56 | 6.98 | 4.3 | 7.2 |
| 1.2 | 0.390 | 0.610 | 0.04 | 512 | 0.93 | 0.398 | 5.6 | 7.06 | 7.2 | 8.6 |
| | | $C_b$ = 0.240M | | | $\rho_1$ = 1.035 | | | | | |
| 2.7 | 0.370 | 0.630 | 0.005 | 99.7 | 0.96 | 0.397 | 5.5 | 6.98 | 1.4 | 2.1 |
| 1.8 | 0.390 | 0.610 | 0.01 | 169 | 0.94 | 0.396 | 5.65 | 7.10 | 2.4 | 3.0 |
| 0.6 | 0.395 | 0.605 | 0.02 | 293 | 0.91 | 0.393 | 6.2 | 7.51 | 3.8 | 4.2 |
| 0.2 | 0.395 | 0.605 | 0.03 | 405 | 0.90 | 0.392 | 6.9 | 8.00 | 5.0 | 4.6 |

Data for $D$ taken from Eversole, Kindsvater, and Peterson (15) for concentration of copper sulfate up to 0.35M. Other values of $D$ were obtained by extrapolation.

Data for $t_c$ is that for $Zn^{++}$ in zinc sulfate, as given by Conway (14 B), as the transference number of $Cu^{++}$ should be about the same.

that of the bath, because with no current flowing the capillary is immersed in a solution having an ion activity $A_b$, and with the current flowing the activity of the ion is $A_i$. However, this junction potential is too small to be of consequence.

Concentration polarization as defined by the Nernst equation will be referred to in the following discussion as Nernst concentration polarization. It has a definite meaning, because it depends only on the activities of a particular species of ion. From a knowledge of the concentrations of solute, $C_i$, at the interface of the electrode and solution, and $C_b$, the concentration in the body of the bath the Nernst concentration polarization can be calculated; or it can be measured by setting up a concentration cell, with metal concentrations $C_i$ and $C_b$, provided the metal has a reversible static potential.

At a given current density, Nernst concentration polarization is a more definite and reproducible quantity than activation polarization. For example, the latter may increase greatly in the presence of a small amount of an addition agent in a solution although the basic electrode reaction has not changed. In contrast, the concentration of metal ions which determine concentration polarization is largely a function of current density and is fairly reproducible from one experiment to another.

Only one prior study has been made to calculate Nernst concentration polarization from measurements of concentration. This work was done by Samarcev (1) with a copper sulfate solution. He showed that the polarization was greater than that which could be accounted for on the basis of Nernst concentration polarization. Prior to his work many electrochemists had considered the polarization involved in the deposition of copper from a sulfate bath to be entirely concentration polarization. This work of Samarcev stands out as being the first determination of concentration polarization based on measurements of concentration.

Concentration polarization corresponding to curves 1, 2, and 3 of Fig. 5 were calculated by means of the Nernst equation using the activities for copper ion given by Conway (14A). The results of these calculations are shown in Fig. 6. To compare the magnitude of concentration polarization with the total polarization of copper deposition, curve 4 is included. This is for the deposition of copper from a 1M solution containing 0.05M sulfuric acid. A comparison of curve 1 with 4 shows that the contribution of concentration polarization to the total polarization is rather small.

Shreir and Smith (16) attempted to measure the concentration polarization of copper sulfate solu-

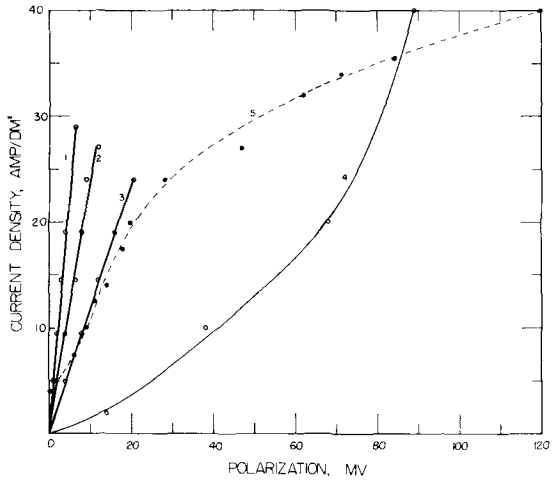


Fig. 6. Nernst concentration polarization calculated from the copper concentration, $C_i$, at the electrode interface. Curves 1, 2, and 3 refer to the like-numbered curves of Fig. 5. Curve 4 is the total polarization for a solution 1.0M in copper sulfate and 0.05M in sulfuric acid measured with a Luggin capillary. Curve 5 is the concentration polarization of a solution 0.5M in copper and 0.5M in sulfuric acid obtained by the stirring method. Data of Shreir and Smith (16). [Calculations for curves 1, 2, and 3 are based on the activities of copper ions given by Conway (14)].

tions by measuring the difference in potential of the electrode in a still and in a stirred bath. Their data for a bath 0.5M in copper sulfate and 0.5M in sulfuric acid is reproduced in Fig. 6 as a broken line. Their data indicates a considerably larger concentration polarization than was obtained by the present method. A comparison between our data and theirs is valid even though their bath contained sulfuric acid. The maximum effect of the acid would be to decrease the transport number of copper ions. If the transport number were reduced to zero, this would result in only about a 30% increase over our values of concentration polarization given in Fig. 6.

The probable reason that our values are smaller than those of Shreir and Smith is that the latter's values include some contributions due to activation polarization. Activation polarization is a function of concentration, as well as of current density, as is shown by the data of Shreir and Smith (16). Since the concentration of metal ion at the electrode surface in the still solution must have differed from that in a stirred solution, the activation polarization must also have varied under these two conditions. Thus the procedure of measuring the Nernst concentration polarization by the difference in potential between a stirred and unstirred bath is not accurate because it also includes the effect of concentration on activation polarization.

The relation between activation polarization and concentration of the solution could be determined in the following way. A series of solutions of different concentrations could be electrolyzed at the same current density and the concentration of metal at the electrode-solution interface and the total electrode polarization determined. The Nernst concentration polarization can be calculated and subtracted from the total polarization to yield the activation polarization. The latter could be related to either the metal concentration of the body of the bath or to the concentration at the interface of the electrode and the solution.

## Discussion

The porous electrode method of sampling the diffusion layer has the advantage over the freezing method of being simpler to set up and operate. Also the diffusion layer can be continuously sampled. However, it does not yield the concentration profile of the diffusion layer as does the freezing method and cannot be used to study the rate of attainment of the steady state in the diffusion layer. The drainage method is simpler than the porous electrode method but is a less precise way of isolating the solution at the electrode interface. In carrying out the drainage method, some mixing of the bulk of the bath with the diffusion layer probably occurs.

The porous electrode method yielded larger values for $\Delta Cu$ than either the freezing method or the optical method. The value of $\Delta Cu$ given in Fig. 5 for the 0.94M solution at 4 amp/dm$^2$ was twice as large as that obtained by Brenner (4) with the freezing method. The value of $\Delta Cu$ for the 0.49M solution at 0.5 amp/dm$^2$ was about three times larger than that obtained by Ibl and co-workers (2) with the interferometric method. The comparison of our results with those of the latter workers may not be strictly valid, because they measured a local $\Delta Cu$, not an average value, and the length of their electrode was only about one-fourth the length of ours.

The fact that the porous electrode method yielded larger values of $\Delta Cu$ than other methods may be evidence that it comes closer than the other methods to giving the true concentration of metal ion at the electrode interface. Experimental difficulties, such as mixing of the cathode diffusion layer with the bulk of the bath, would have led to smaller values of $\Delta Cu$. The fact that the values of $\Delta Cu$ in Fig. 5 were larger for the more concentrated solutions is further evidence that no large amount of mixing took place between the diffusion layer and the bulk of the bath.

The concentration polarizations shown in Fig. 6 are rather small compared with the total polarization. These results can be applied to electrodeposition in general, since the experiments with the copper sulfate solutions covered the usual range of concentration of metallic salts and of current density employed in conventional electroplating. The current densities used in electroplating are usually not over half of the limiting current density for metal deposition, that is, the concentration of metal ions at the cathode interface usually would not be reduced below about half that in the body of the bath. Consequently, on the basis of the results given in Fig. 6, it may be concluded that in ordinary electrodeposition the Nernst concentration polarization is small. In particular, Fig. 6 shows that the concentration polarization in the 0.49M and 0.94M solutions was less than 10 mv at a current density of 2 amp/dm$^2$, which is a current density commonly employed in plating. Since the precision of measuring electrode polarization is usually of the order of 5 mv to 10 mv, the concentration polarization

should be barely detectable at the current densities used in conventional electroplating. The directly observed polarizations, such as curve 4 in Fig. 6, must be attributed to other causes than the Nernst explanation.

## Summary

1. A method for isolating the solution at the interface of an electrode and the bath has been developed.

2. The Nernst concentration polarization has been calculated for copper sulfate solutions.

3. It is concluded that the Nernst concentration polarization probably is not significant in plating baths operated at conventional current densities.

## Acknowledgment

Theodore Yannakopoulos expresses his appreciation to the National Academy of Sciences under whose auspices he was a guest research worker at the National Bureau of Standards during 1954-1955.

Manuscript received Sept. 20, 1957. This paper was prepared for delivery before the Pittsburgh Meeting, Oct. 9-13, 1955.

Any discussion of this paper will appear in a Discussion Section to be published in the June 1959 JOURNAL.

REFERENCES

1. A. G. Samarcev, *Z. Physik. Chem.*, **A168**, 45 (1934).
2. N. Ibl, Y. Barrada, and G. Trümpler, *Helv. Chim. Acta*, **37**, 583 (1954).
3. C. S. Lin, R. W. Moulton, and G. L. Putnam, *Ind. Eng. Chem.*, **45**, 636 (1953); *ibid.*, 640.
4. A. Brenner, *Proc. Am. Electroplaters' Soc.*, **1940**, 95; *ibid.*, **1941**, 28.
5. A. Brenner and E. G. Wranglen, *Särtryck ur Svensk Kemisk Tidskrift*, **67**, 81 (1955).
6. (*a*) A. K. Graham, S. Heiman, and H. J. Read, *Proc. Am. Electroplaters' Soc.*, **1939**, 95; (*b*) H. J. Read and A. K. Graham, *Trans. Electrochem Soc.*, **78**, 279 (1940).
7. M. Knobel, *Ind. Eng. Chem.*, **17**, 826 (1925).
8. Boehringer and Sons and Messinger, German Pat. 109,051, Oct. 1898.
9. E. Schlumberger, U. S. Pat. 1,598,018, Aug. 31, 1926.
10. G. W. Heise, *Trans. Electrochem. Soc.*, **75**, 147 (1939).
11. M. Janes, *ibid.*, **77**, 411 (1940).
12. N. M. Winslow, *ibid.*, **80**, 121 (1941).
13. G. H. Keulegan, *J. Research Nat. Bur. Standards*, **47**, 156 (1951).
14. B. E. Conway, "Electrochemical Data," Elsevier Publishing Co., New York (1952), A.p.79; B.p.166.
15. W. G. Eversole, H. M. Kindsvater, and J. D. Peterson, *J. Phys. Chem.*, **46**, 370 (1942).
16. L. L. Shreir and J. W. Smith, *This Journal*, **99**, 64 (1952).
17. C. Wagner, *J. (and Trans.) Electrochem. Soc.*, **95**, 161 (1949).
18. C. Wagner, *This Journal*, **104**, 129 (1957).
19. C. W. Tobias, M. Eisenberg, and C. R. Wilke, *ibid.*, **99**, 359C (1952).
20. C. R. Wilke, M. Eisenberg, and C. W. Tobias, *ibid.*, **100**, 513 (1953).
21. N. Ibl and R. Müller, *Z. Elektrochem.*, **59**, 671 (1955).
22. N. Ibl and R. Müller. Paper delivered at the Fall Meeting of the Electrochemical Society, 1956.
23. N. Ibl, Private communication, February 1958.
24. J. V. Petrocelli, *This Journal*, **98**, 187 (1951).

# Phase Equilibria and Fluorescence in a Portion of the System ZnO-MnO-$P_2O_5$

**F. A. Hummel and Fred L. Katnack**

*Department of Ceramic Technology, College of Mineral Industries,*

*The Pennsylvania State University, University Park, Pennsylvania*

ABSTRACT

Phase equilibrium data have been obtained for compositions in the ternary system lying near the $Zn_3(PO_4)_2$ compound, particularly those on the orthophosphate join. It was found that "gamma zinc orthophosphate" is a ternary solid solution which has a region of stability on the orthophosphate join ranging from about 5 to about 25 mole % $Mn_3(PO_4)_2$. A definitive x-ray pattern characteristic of the ternary solid solution series is given.

$\beta$-$Zn_3(PO_4)_2$ forms an extended series of solid solutions with $Mn_3(PO_4)_2$ at temperatures above 940°C. The melting behavior of the $\beta$-$Zn_3(PO_4)_2$ solid solution is difficult to determine in air due to the usual change in oxidation state of manganese at temperatures above 1000°C.

Emission curves for cathode ray excitation are presented for $\alpha$ and $\beta$ zinc orthophosphate, the so-called "$\gamma$-zinc phosphate," $Zn_2P_2O_7$, and the two forms of $Zn(PO_3)_2$.

In a recent paper by Katnack and Hummel (1), the equilibrium relationships for the system ZnO-$P_2O_5$ were established, and it was shown that low- and high-temperature forms of ortho-, pyro-, and metaphosphate compounds existed.

The primary purpose of this paper was to establish the equilibrium relationships in the ternary system ZnO-MnO-$P_2O_5$ in the neighborhood of $Zn_3(PO_4)_2$ and to relate these data to the fluorescence of the $\alpha$, $\beta$, and "$\gamma$" forms of the orthophosphate. A second purpose was to obtain luminescence data on $Zn_2P_2O_7$ and the two forms of the metaphosphate.

## Compositions and Procedure

*General.*—The raw materials and experimental techniques were the same as those described in the

Table I. ZnO-MnO-$P_2O_5$ compositions on the $Zn_3(PO_4)_2$-$Mn_3(PO_4)_2$ join

| No. | Composition (Mole %) $Zn_3(PO_4)_2$ | Composition (Mole %) $Mn_3(PO_4)_2$ | Mole ratio | Equivalent ternary composition (wt %) ZnO | MnO | $P_2O_5$ | Initial heat treatment Time, hr | Temp, °C |
|---|---|---|---|---|---|---|---|---|
| 1 | 99 | 1 | | 62.64 | 0.55 | 36.81 | 24 | 826 |
| 2 | 98 | 2 | | 62.08 | 1.11 | 36.81 | 3 | 700 |
| 3 | 96 | 4 | | 60.88 | 2.22 | 36.90 | 3 | 700 |
| 4 | 95 | 5 | | 60.32 | 2.76 | 36.92 | 12 | 828 |
| 5 | 94 | 6 | | 59.72 | 3.33 | 36.95 | 3 | 700 |
| 6 | 91.67 | 8.33 | 11:1:4 | 58.35 | 4.62 | 37.03 | 3 | 700 |
| 7 | 90 | 10 | | 57.36 | 5.52 | 37.12 | 12 | 828 |
| 8 | 88.89 | 11.11 | 8:1:3 | 56.71 | 6.18 | 37.11 | 3 | 700 |
| 9 | 85 | 15 | | 54.40 | 8.36 | 37.24 | 12 | 826 |
| 10 | 83.33 | 16.67 | 5:1:2 | 53.39 | 9.32 | 37.29 | 24 | 500 |
| 11 | 80 | 20 | | 51.42 | 11.20 | 37.38 | 12 | 826 |
| 12 | 70 | 30 | | 45.36 | 16.95 | 37.69 | 12 | 818 |
| 13 | 50 | 50 | | 32.96 | 28.73 | 38.31 | 12 | 818 |
| 14 | 44.44 | 55.56 | 4:5:3 | 29.42 | 32.06 | 38.52 | 12 | 800 |
| 15 | 40 | 60 | 6:9:5 | 26.58 | 34.75 | 38.66 | 12 | 800 |
| 16 | 33.33 | 66.67 | 1:2:1 | 22.28 | 38.84 | 38.89 | 12 | 800 |
| 17 | 25 | 75 | 3:9:4 | 16.83 | 44.01 | 39.17 | 12 | 800 |

previous paper (1). C.P. $MnCO_3$ was the source of MnO. Spectral distribution curves were obtained with a demountable cathode ray tube operating at 16 kv anode potential, 0.5 $\mu a/cm^2$ beam current density on a standard scan T.V. raster of 65 $cm^2$ area. Brightness under the above conditions was measured using an eye-corrected Weston foot-lambert meter.

ZnO-MnO-$P_2O_5$ *compositions lying on the* $Zn_3(PO_4)_2$-$Mn_3(PO_4)_2$ *join.*—Since the $\beta$-$Zn_3(PO_4)_2$:Mn phosphor was thought to be of primary interest, the ZnO-MnO-$P_2O_5$ ternary system was first studied along the zinc orthophosphate-manganese orthophosphate join. The compositions on this join were made either directly from previously prepared end members, $Zn_3(PO_4)_2$ and $Mn_3(PO_4)_2$, or from a mixture of $Mn_3(PO_4)_2$, ZnO, and $H_3PO_4$.

Seventeen compositions were made on this join by substituting $Mn_3(PO_4)_2$ for $Zn_3(PO_4)_2$ on a molar basis. These compositions are given in Table I. The equivalent ternary compositions on a weight per cent basis are listed beside the molar compositions. Compositions 5-17 are presented graphically in Fig. 1. Compositions 1-4 are not included because of limited space.

ZnO-MnO-$P_2O_5$ *compositions not on the* $Zn_3(P_4O)_2$-$Mn_3(PO_4)_2$ *join.*—Eight ZnO-MnO-$P_2O_5$ compositions were made in the vicinity of pure $Zn_3(PO_4)_2$ but not lying on the $Zn_3(PO_4)_2$-$Mn_3(PO_4)_2$ join. These compositions were made at 2 and 5 wt % levels of MnO with varying amounts of ZnO and $P_2O_5$.

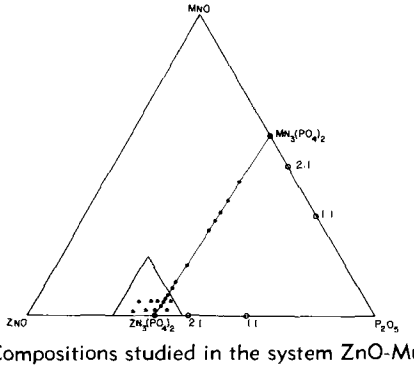


Fig. 1. Compositions studied in the system ZnO-MnO-$P_2O_5$

The raw materials used for these compositions were ZnO, $MnC_2O_4 \cdot 2H_2O$, and $H_3PO_4$. The batches were mixed at room temperature and dried at 110°C. No preliminary heat treatment was given to this group of compositions. These eight compositions are listed in Table II and shown graphically in Fig. 1.

## Experimental Results and Discussion

*Phase Relationships on the* $Zn_3(PO_4)_2$-$Mn_3(PO_4)_2$ *join.*—Compositions on the $Zn_3(PO_4)_2$-$Mn_3(PO_4)_2$ join were heat treated only in quench furnaces. The results of the quenching data are listed in Table III. In general, longer heat treatments were used in this system than in the ZnO-$P_2O_5$ binary system as crystalline batches were used as starting materials throughout the study.

A not-impossible phase diagram was drawn from these quench data and is presented in Fig. 2. This diagram reveals the existence of four different phases. The phase listed as $\alpha$-$Zn_3(PO_4)_2$ gave an x-ray pattern corresponding to the low ($\alpha$) form of pure zinc orthophosphate. The $\beta$-$Zn_3(PO_4)_2$ solid solutions gave x-ray patterns corresponding to the high ($\beta$) form of the zinc orthophosphate end member. The form listed as "$\gamma$-zinc phosphate" gave an x-ray pattern which in no way resembled the low or high form of $Zn_3(PO_4)_2$. The major peaks of this x-ray pattern generally corresponded to the x-ray pattern presented by Smith (2) for the so-called

Table II. ZnO-MnO-$P_2O_5$ compositions not on the $Zn_3(PO_4)_2$-$Mn_3(PO_4)_2$ join

| Sample No. | Composition (wt %) ZnO | MnO | $P_2O_5$ |
|---|---|---|---|
| 18 | 65 | 5 | 30 |
| 19 | 62 | 5 | 33 |
| 20 | 60 | 5 | 35 |
| 21 | 56 | 5 | 39 |
| 22 | 68 | 2 | 30 |
| 23 | 65 | 2 | 33 |
| 24 | 62 | 2 | 36 |
| 25 | 59 | 2 | 39 |

**Table III. Quench data for the system $Zn_3(PO_4)_2$-$Mn_3(PO_4)_2$**

| Composition No. | Composition (Mole %) $Zn_3(PO_4)_2$ | $Mn_3(PO_4)_2$ | Mole ratio | Heat treatment Time, hr | Temp, °C | Crystalline phases present |
|---|---|---|---|---|---|---|
| 1 | 99 | 1 | — | 24 | 937 | β |
| | | | | 24 | 912 | α,β |
| | | | | 24 | 884 | α,γ |
| | | | | 24 | 843 | α,γ |
| | | | | 24 | 826 | α,γ |
| 2 | 98 | 2 | — | 23 | 936 | β |
| | | | | 24 | 918 | β |
| | | | | 24 | 874 | α,γ |
| | | | | 20 | 858 | α,γ |
| 3 | 96 | 4 | — | 23 | 938 | β |
| | | | | 24 | 926 | β,γ |
| | | | | 23 | 907 | α,γ |
| | | | | 24 | 874 | α,γ |
| | | | | 20 | 858 | α,γ |
| 4 | 95 | 5 | — | 24 | 938 | β |
| | | | | 8 | 923 | β,γ |
| | | | | 24 | 892 | γ |
| | | | | 22 | 867 | γ |
| | | | | 12 | 828 | γ |
| 6 | 91.67 | 8.33 | 11:1:4 | 22 | 937 | β |
| | | | | 24 | 920 | β,γ |
| | | | | 10 | 901 | γ |
| | | | | 12 | 894 | γ |
| | | | | 12 | 845 | γ |
| 7 | 90 | 10 | — | 24 | 925 | β,γ |
| | | | | 9 | 900 | γ |
| | | | | 21 | 852 | γ |
| | | | | 12 | 828 | γ |
| 8 | 88.89 | 11.11 | 8:1:3 | 23 | 943 | β |
| | | | | 24 | 935 | β |
| | | | | 22 | 918 | γ |
| | | | | 24 | 884 | γ |
| 9 | 85 | 15 | — | 24 | 941 | β |
| | | | | 23 | 922 | β,γ |
| | | | | 11 | 905 | γ |
| | | | | 21 | 866 | γ |
| | | | | 12 | 826 | γ |
| 10 | 83.33 | 16.67 | 5:1:2 | 10 | 936 | β |
| 11 | 80 | 20 | — | 17 | 950 | β |
| | | | | 20 | 932 | β |
| | | | | 20 | 915 | β,γ |
| | | | | 24 | 895 | γ |
| | | | | 24 | 887 | γ |
| | | | | 24 | 883 | γ |
| | | | | 9 | 862 | γ |
| | | | | 12 | 826 | γ |
| 12 | 70 | 30 | — | 5 | 953 | β |
| | | | | 22 | 932 | β,M |
| | | | | 24 | 911 | β,M |
| | | | | 22 | 893 | γ,M |
| | | | | 24 | 859 | γ,M |
| | | | | 22 | 832 | γ,M |
| | | | | 22 | 806 | γ,M |
| 13 | 50 | 50 | — | 17 | 952 | M |
| | | | | 12 | 818 | γ,M |

α = α-$Zn_3(PO_4)_2$
β = β-$Zn_3(PO_4)_2$ solid solution
γ = γ-zinc phosphate
M = $Mn_3(PO_4)_2$

"gamma form of zinc orthophosphate." The fourth phase found in this system appeared to be the end member $Mn_3(PO_4)_2$. $Mn_3(PO_4)_2$ gave a very poorly defined x-ray diffraction pattern in comparison to the patterns of the forms of $Zn_3(PO_4)_2$ when using CuKα radiation. Consequently, the use of x-ray analysis as a method of identification was difficult above 30 mole % $Mn_3(PO_4)_2$. Therefore, this portion of the diagram was not investigated as thoroughly as the $Zn_3(PO_4)_2$ end, and the boundaries in this area are presented as dashed lines.

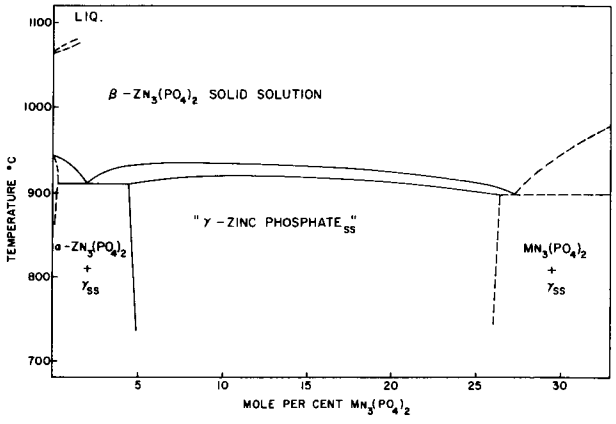


Fig. 2. Probable equilibrium relationships on the join $Zn_3(PO_4)_2$-$Mn_3(PO_4)_2$.

At the outset of the work it was postulated that γ-zinc phosphate was a ZnO-MnO-$P_2O_5$ ternary compound whose composition was on the $Zn_3(PO_4)_2$-$Mn_3(PO_4)_2$ join. In particular, a mole ratio of $8ZnO \cdot MnO \cdot 3P_2O_5$ or 88.89 mole % $Zn_3(PO_4)_2$ and 11.11 mole % $Mn_3(PO_4)_2$ was thought to be the compound. It appeared from preliminary work that this composition changed directly from γ-zinc phosphate to a β-$Zn_3(PO_4)_2$ solid solution without going through a temperature range in which both γ-zinc phosphate and β-$Zn_3(PO_4)_2$ solid solutions were in equilibrium. However, more precise work showed that the narrow band containing these two phases in equilibrium probably exists continuously from 5 to 25 mole % $Mn_3(PO_4)_2$ and does not "close up" at 11.11 mole % $Mn_3(PO_4)_2$, the $8ZnO \cdot MnO \cdot 3P_2O_5$ composition. With no other evidence supporting the existence of $8ZnO \cdot MnO \cdot 3P_2O_5$ as a compound, the identification of γ-zinc phosphate remains inconclusive and the series must simply be described as ternary solid solutions. The x-ray data for γ-zinc phosphate presented in Table IV were recorded from a sample

**Table IV. X-ray diffraction data for the ternary solid solution phase (γ-zinc phosphate)**

| 2θ | d | $I/I_0$ | 2θ | d | $I/I_0$ |
|---|---|---|---|---|---|
| 15.9° | 5.57 | 10 | 45.3° | 2.00 | — |
| 20.5° | 4.33 | 90 | 46.6° | 1.95 | 5 |
| 21.1° | 4.21 | 5 | 46.9° | 1.94 | 5 |
| 22.3° | 3.99 | 40 | 47.8° | 1.90 | 5 |
| 23.0° | 3.87 | 25 | 48.7° | 1.87 | 5 |
| 24.2° | 3.68 | 5 | 49.3° | 1.85 | 10 |
| 26.1° | 3.41 | 100 | 50.5° | 1.81 | 5 |
| 27.6° | 3.23 | 20 | 51.0° | 1.79 | 5 |
| 29.5° | 3.03 | 20 | 51.6° | 1.77 | 10 |
| 30.8° | 2.90 | 10 | 52.1° | 1.76 | 5 |
| 31.9° | 2.81 | 25 | 53.9° | 1.70 | 5 |
| 32.9° | 2.72 | 15 | 55.0° | 1.67 | 10 |
| 34.0° | 2.64 | 10 | 55.3° | 1.66 | 15 |
| 35.6° | 2.52 | 35 | 55.7° | 1.65 | 5 |
| 35.8° | 2.51 | 35 | 56.3° | 1.63 | 5 |
| 36.6° | 2.46 | 55 | 59.6° | 1.55 | 15 |
| 37.5° | 2.40 | 25 | Other reflections | | |
| 37.8° | 2.38 | 10 | | | |
| 39.1° | 2.30 | 10 | | | |
| 40.3° | 2.24 | 10 | | | |
| 41.9° | 2.16 | 5 | | | |
| 42.8° | 2.11 | 10 | | | |
| 43.2° | 2.09 | 25 | | | |
| 44.6° | 2.03 | 20 | | | |

containing 94 mole % $Zn_3(PO_4)_2$ and 6 mole % $Mn_3(PO_4)_2$, fired to 840°C for 70 hr.

The phase diagram shows that $\gamma$-zinc phosphate is probably only soluble in $\alpha$-$Zn_3(PO_4)_2$ to a very limited extent, less than could be measured experimentally by petrographic or x-ray analysis. Gamma-zinc phosphate coexists with $\alpha$-$Zn_3(PO_4)_2$ at very small concentrations of $Mn_3(PO_4)_2$. This indicates that a pure $\alpha$-$Zn_3(PO_4)_2$:Mn phosphor would be difficult to produce without some $\gamma$-zinc phosphate contamination. This is evident from the x-ray data presented by Smith (2) for pure $\alpha$-$Zn_3(PO_4)_2$. The major differences between his x-ray diffraction data and those presented in Table IV can be attributed to the presence of $\gamma$-zinc phosphate in his sample of "pure" $\alpha$-$Zn_3(PO_4)_2$. It would appear that Smith obtained his x-ray data on $\alpha$-$Zn_3(PO_4)_2$:Mn rather than on pure $\alpha$-$Zn_3(PO_4)_2$.

This work indicates that the $\beta$-$Zn_3(PO_4)_2$:Mn phosphor can be produced free from $\alpha$-$Zn_3(PO_4)_2$ or $\gamma$-zinc phosphate by firing the phosphor batches to a temperature above 942°C, the $\alpha$-$\beta$ inversion temperature in the pure zinc orthophosphate end member. However, an appreciable amount of sintering takes place at this high firing temperature, and the resultant hardening and increase in particle size would probably require a grinding operation to produce a usable $\beta$-$Zn_3(PO_4)_2$ phosphor. A pure $\beta$-$Zn_3(PO_4)_2$:Mn phosphor can be made at temperatures as low as 915°C if the eutectoid composition of 98 mole % $Zn_3(PO_4)_2$, 2 mole % $Mn_3(PO_4)_2$ is utilized.

*Phase relationships in ternary compositions surrounding* $Zn_3(PO_4)_2$.—To investigate the phase relationships in the system ZnO-MnO-$P_2O_5$ around the binary compound $Zn_3(PO_4)_2$, the eight compositions listed in Table II were heat treated in a Globar furnace in platinum crucibles at three different temperature levels. Since quench furnaces were not used, a temperature variation of ±10°C is introduced. The fired batches were air quenched and the crystalline phases identified by x-ray analysis.

The results of these analyses are listed in Table V and presented graphically in Fig. 3, 4, and 5.

The results indicate that compositions to the left of the $Zn_3(PO_4)_2$-$Mn_3(PO_4)_2$ join show ZnO and $\gamma$-zinc phosphate in equilibrium at 865°C, and ZnO and $\beta$-$Zn_3(PO_4)_2$ in equilibrium at higher temperatures. Compositions to the right of the $Zn_3(PO_4)_2$-$Mn_3(PO_4)_2$ join generally showed $Zn_2P_2O_7$ in equilibrium with $\beta$-$Zn_3(PO_4)_2$ and $\gamma$-zinc phosphate. While

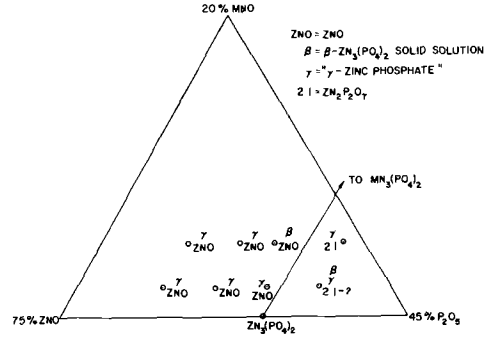


Fig. 3. Isothermal plane at 865° ± 10°C

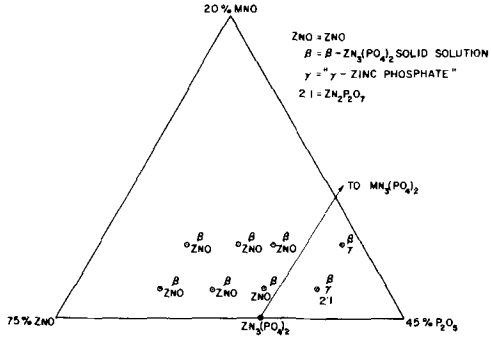


Fig. 4. Isothermal plane at 892° ± 10°C

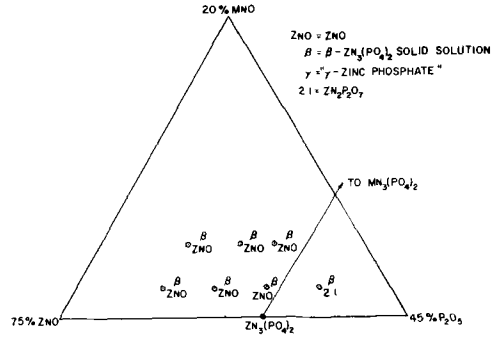


Fig. 5. Isothermal plane at 941° ± 10°C

free ZnO appeared in compositions to the left of the join and $Zn_2P_2O_7$ in compositions to the right of the join, these two phases were not detected in compositions on the join. The low ($\alpha$) form of $Zn_3(PO_4)_2$ did not appear in any of these compositions after the above heat treatments.

*Luminescence of the compounds and intermediate compositions in the* ZnO-MnO-$P_2O_5$ *system.*—The

**Table V. Phase analysis of ZnO-MnO-$P_2O_5$ compositions not on the $Zn_3(PO_4)_2$-$Mn_3(PO_4)_2$ join**

| No. | Composition (wt %) ZnO | MnO | $P_2O_5$ | Heat treatment (24 hr) | Crystalline phases present |
|---|---|---|---|---|---|
| 18a | 65 | 5 | 30 | 865 | ZnO, $\gamma$ |
| 18b | 65 | 5 | 30 | 892 | ZnO, $\beta$ |
| 18c | 65 | 5 | 30 | 941 | ZnO, $\beta$ |
| 19a | 62 | 5 | 33 | 865 | ZnO, $\gamma$ |
| 19b | 62 | 5 | 33 | 892 | ZnO, $\beta$ |
| 19c | 62 | 5 | 33 | 941 | ZnO, $\beta$ |
| 20a | 60 | 5 | 35 | 865 | ZnO-?, $\beta$, $\gamma$ |
| 20b | 60 | 5 | 35 | 892 | ZnO, $\beta$ |
| 20c | 60 | 5 | 35 | 941 | ZnO, $\beta$ |
| 21a | 56 | 5 | 39 | 865 | 2:1, $\gamma$ |
| 21b | 56 | 5 | 39 | 892 | $\gamma$, $\beta$ |
| 22a | 68 | 2 | 30 | 865 | ZnO, $\gamma$ |
| 22b | 68 | 2 | 30 | 892 | ZnO, $\beta$ |
| 22c | 68 | 2 | 30 | 941 | ZnO, $\beta$ |
| 23a | 65 | 2 | 33 | 865 | ZnO, $\gamma$ |
| 23b | 65 | 2 | 33 | 892 | ZnO, $\beta$ |
| 23c | 65 | 2 | 33 | 941 | ZnO, $\beta$ |
| 24a | 62 | 2 | 36 | 865 | ZnO, $\gamma$ |
| 24b | 62 | 2 | 36 | 892 | ZnO, $\beta$ |
| 24c | 62 | 2 | 36 | 941 | ZnO, $\beta$ |
| 25a | 59 | 2 | 39 | 865 | 2:1-?, $\beta$, $\gamma$ |
| 25b | 59 | 2 | 39 | 892 | 2:1, $\beta$, $\gamma$ |
| 25c | 59 | 2 | 39 | 941 | 2:1, $\beta$ |

ZnO = ZnO
$\beta$ = $\beta$-$Zn_3(PO_4)_2$
$\gamma$ = $\gamma$-zinc phosphate
2:1 = $Zn_2P_2O_7$

**Table VI. Characteristic luminescence of the zinc phosphate compounds activated with manganese**

| Compound | Heat treatment Time, hr | Heat treatment Temp, °C | Luminescence Brightness (ft-L) | Luminescence Peak wave length (mμ) |
|---|---|---|---|---|
| Low ($\alpha$) $Zn_3(PO_4)_2$ | 5 | 805 | 8.7 | 551 |
| High ($\beta$) $Zn_3(PO_4)_2$ | 12 | 960 | 12.0 | 638 |
| $Zn_3(PO_4)_2$ N.B.S. Std. 1025 | | | 15.3 | 638 |
| Low ($\alpha$) $Zn_2P_2O_7$ | 5 | 866 | 3.4 | 690 |
| Low ($\alpha$) $Zn(PO_3)_2$ | 72 | 600 | 0.8 | 626 |
| High ($\beta$) $Zn(PO_3)_2$ | 12 | 800 | 4.8 | 570 |

investigation of the $ZnO$-$P_2O_5$ system indicated that five forms of zinc phosphate could be obtained at room temperature. These consisted of the low temperature stable forms of $Zn_3(PO_4)_2$, $Zn_2P_2O_7$, and $Zn(PO_3)_2$, and the high temperature metastable (at room temperature) forms of $Zn_3(PO_4)_2$ and $Zn(PO_3)_2$. One weight per cent MnO was added to these compounds and the batches were fired to the proper temperature to produce the five forms as shown in Table VI. The normalized emission curves for cathode ray excitation are shown in Fig. 6.

The compounds listed in Table VI were examined by x-rays to assure that only one phase was present in each case. As was to be expected, the low ($\alpha$) $Zn_3(PO_4)_2$ contained some $\gamma$-zinc phosphate. Concentrations of MnO lower than 1.0 wt % would diminish the amount of $\gamma$-zinc phosphate formation in this phosphor. However, a 1.0% MnO level was used to maintain equal amounts of activator in all of the phosphors.

Luminescence in the $ZnO$-$MnO$-$P_2O_5$ system was also examined along the $Zn_3(PO_4)_2$-$Mn_3(PO_4)_2$ join. It is apparent from the phase diagram of this join that two series of solid solutions exist. The first series, labeled $\gamma$-zinc phosphate, exists from about 5 to 25 mole % $Mn_3(PO_4)_2$ and is stable below 900°C. The second series, labeled $\beta$-$Zn_3(PO_4)_2$ solid solution, extends from the pure $Zn_3(PO_4)_2$ end member to about 25 mole % $Mn_3(PO_4)_2$ and is stable above 942°C.

Seven $Zn_3(PO_4)_2$-$Mn_3(PO_4)_2$ mixtures were made to investigate the luminescence of these solid solutions. Four were in the $\gamma$-zinc phosphate solid solution series while the other three were in the $\beta$-$Zn_3(PO_4)_2$ solid solution series. These compositions and their heat treatments are listed in Table VII; the emission curves are presented in Fig. 7 and 8.

**Table VII. Luminescence of $\beta$-$Zn_3(PO_4)_2$ and $\gamma$-zinc phosphate solid solutions**

| Composition (Mole %) $Zn_3(PO_4)_2$ | Composition (Mole %) $Mn_3(PO_4)_2$ | Heat Treatment Time, hr | Heat Treatment Temp, °C | Luminescence Brightness (ft-L) | Luminescence Peak wave length (mμ) | $y$ |
|---|---|---|---|---|---|---|
| 96 | 4 | 70 | 840 | 13.8 | 630 | 0.2650 |
| 94 | 6 | 70 | 840 | 9.7 | 630 | |
| 91.7 | 8.3 | 70 | 840 | 5.7 | 630 | |
| 88.9 | 11.1 | 70 | 840 | 2.7 | 630 | |
| 99 | 1 | 12 | 960 | 12.0 | 638 | 0.1911 |
| 95 | 5 | 12 | 960 | 11.5 | 638 | |
| 88.9 | 11.1 | 12 | 960 | 3.2 | 638 | |

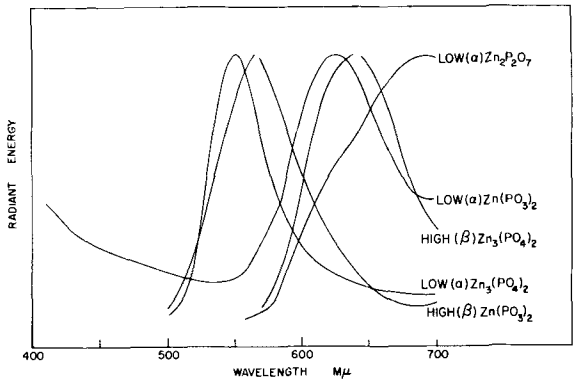


Fig. 6. Emission curves for zinc phosphate compounds under cathode ray excitation.

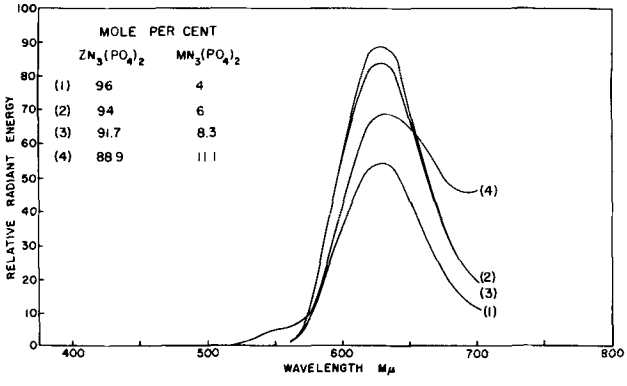


Fig. 7. Emission curves for $\gamma$-zinc phosphate solid solutions under cathode ray excitation.

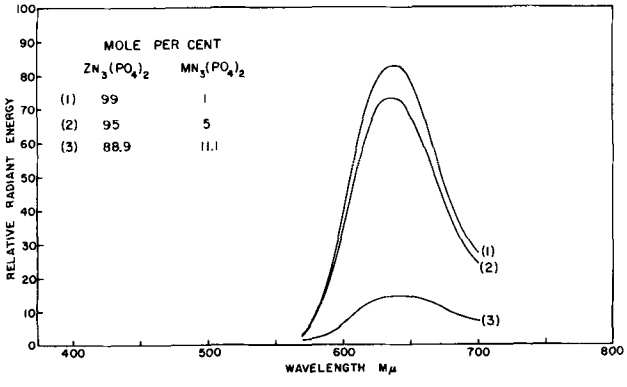


Fig. 8. Emission curves for $\beta$-zinc orthophosphate solid solutions under cathode ray excitation.

It is observed from these emission curves that the $\gamma$-zinc phosphate solid solutions have a slightly more yellow color than the $\beta$-$Zn_3(PO_4)_2$ phosphors. However, their intensities are less than those of the phosphors in the $\beta$-$Zn_3(PO_4)_2$ series. The 24-hr heat treatments used in the quench work were sufficient to produce all $\gamma$-zinc phosphate with the small quantities of material used in the quench packet. However, when larger quantities of the $\gamma$-zinc phosphate solid solutions were made for the luminescence studies, some $\alpha$-$Zn_3(PO_4)_2$ appeared with the $\gamma$-zinc phosphate when batches were fired for 24 hr. Consequently, a 70-hr firing time was used to assure the presence of all $\gamma$-zinc phosphate.

It is observed from the emission curves of the $\beta$-$Zn_3(PO_4)_2$ phosphors that the brightness falls off rapidly with greater than 5 mole % $Mn_3(PO_4)_2$

while the intensities of the phosphors with 1 and 5 mole % $Mn_3(PO_4)_2$ were quite similar. The eutectoid composition of 2 mole % $Mn_3(PO_4)_2$ can therefore be used to produce $\beta$-$Zn_3(PO_4)_2$ at the lowest possible firing temperature without suffering a significant loss in efficiency due to the presence of too much activator.

## Conclusions

1. The $\gamma$-zinc orthophosphate previously reported is not a polymorphic form of $Zn_3(PO_4)_2$. It is a ternary solid solution series which has not as yet been identified with a ternary compound of ZnO, MnO, and $P_2O_5$.
2. The $\gamma$-zinc orthophosphate ternary solid solution series will yield red phosphors which are not generally comparable in brightness with the $\beta$ series under cathode ray excitation. The compositions must be fired for relatively long times (70 hr) in order to assure equilibrium.
3. The $\beta$-$Zn_3(PO_4)_2$:Mn solid solutions yield bright red phosphors under cathode ray excitation up to 5 mole % $Mn_3(PO_4)_2$.
4. $\alpha$-$Zn_2P_2O_7$:Mn is red under cathode ray excitation, as is well known.
5. High $(\beta)Zn(PO_3)_2$ is green under cathode ray excitation, while low $(\alpha)Zn(PO_3)_2$ is orange.

## Acknowledgment

The authors wish to thank the Chemical Products Plant of the General Electric Company for financial support during the course of this work. The assistance of various members of the Chemical Products laboratory in obtaining emission curves is gratefully acknowledged, as is the permission of Mr. R. S. Mackie to publish this paper.

Manuscript received March 14, 1958. This paper was prepared for delivery before the New York Meeting, April 27-May 1, 1958. Contribution No. 57-51 from the College of Mineral Industries, The Pennsylvania State University.

Any discussion of this paper will appear in a Discussion Section to be published in the June 1959 JOURNAL.

REFERENCES

1. F. L. Katnack and F. A. Hummel, *This Journal*, **105**, 125 (1958).
2. A. L. Smith, *ibid.*, **98**, 363 (1951).

# Preparation and Properties of Aluminum Antimonide

**A. Herczog,[1] R. R. Haberecht, and A. E. Middleton[2]**

*P. R. Mallory & Co. Inc., Indianapolis, Indiana*

ABSTRACT

The high-energy gap intermetallic compound semiconductors, AlSb, GaAs, and InP, are considered as potential materials for devices operating at temperatures in excess of the limit for silicon. A comparative evaluation of these semiconductors is given which reveals some of the advantages and disadvantages of AlSb.

Aluminum and antimony of high purity were prepared by zone refining, and single crystals of AlSb were grown by the Czochralski technique. Effects of various impurities in the starting materials and crucibles on the electrical properties are discussed, and equipment for crystal growing under equilibrium vapor pressure of Sb is described. The resistivity of as-grown-P-type crystals can be decreased substantially by doping with carbon and increased by small quantities of Se and Te. A larger quantity of Te will change the crystals to N-type. P-N junctions were made by controlled doping during crystal growing. Effects of various surface treatments on the electrical properties of AlSb are discussed, and some data on point contact and P-N junction diodes are presented.

This work has been conducted in the interest of developing high-purity and preferentially doped aluminum antimonide crystals from high-purity metals using the Czochralski technique, and evaluating this intermetallic compound as a semiconductor to be used in place of germanium and silicon in devices capable of operating up to near 500°C.

This paper reports on purification, crystal growth, doping, P-N junction fabrication, electrical measurements and analysis, surface studies, device feasibility studies, and evaluation of the potential of aluminum antimonide for high-temperature semiconductor devices. In order to compare the relative potential of aluminum antimonide for high-temperature devices with that of other high-energy gap semiconductors, a comparative evaluation of important known properties of these semiconductors is given below.

## Evaluation of Potential of AlSb for Semiconductor Devices Operable at 500°C; Comparison with Other High-Energy Gap Semiconductors

Table I shows the pertinent properties of aluminum antimonide, as compared to other high-energy gap semiconductors, and assembled according to source (1-7). It can be noted in the table that, for aluminum antimonide, mobility ratios $\mu n/\mu p$, varying from 1/5 to 6/1, are reported. The only conclusion that one can draw is that these data were obtained on highly impure or polycrystalline material and, therefore, they are a poor indication of the true

[1] Present address: Corning Glass Works, Corning, N. Y.

[2] Present address: Lamp Division, General Electric Company, Cleveland, Ohio.

**Table I. Summary of data on properties of high-energy gap semiconductors**

| Compound | Source of data | Thermal energy gap, ev | Optical energy gap, ev | $\mu n$ | $\mu p$ | M.P., °C |
|---|---|---|---|---|---|---|
| AlSb | Burstein and Egli (1) | 1.6 | 1.5 | 1200 | 200 | 1060 |
| | Dunlap (2) | 1.65 | | 35 | 150 | 1060 |
| | Willardson, Beer, and Middleton (3) | 1.55 | | 100 | 100 | 1060 |
| | Welker (4) | 1.65 | 1.65 | 200 | 200 | 1060 |
| | Jenny (5) | 1.6 | | 400 | | |
| GaAs | Burstein and Egli (1) | | 1.1 | 4000 | 200 | 1240 |
| | Welker (4) | 1.38 | 1.35 | 3400 | 200 | 1238 |
| | Jenny (5) | 1.35 | | 4500 | | |
| InP | Burstein and Egli (1) | | 1.25 | 3400 | 650 | 1070 |
| | Welker (4) | 1.34 | 1.26 | 3400 | 50 | 1070 |
| | Jenny (5) | 1.25 | | | | |
| SiC (hex.) | Hall (7) | 3.1 | | | | 2200 decomp |
| | Jenny (5) | 2.8 | | 100 | | |
| | Dunlap (2) | | | 40-60 | 5-10 | |

mobilities and of the device potential of aluminum antimonide. This conclusion is supported by the data and analyses reported in this paper.

In evaluating the device potential of aluminum antimonide, an appraisal of the upper temperature and frequency limits of operation is of interest. The upper temperature limit is prescribed by the highest resistivity region adjacent to the P-N junction, since this region reaches the intrinsic region first with an increase in temperature. A conservative temperature limit for a transistor, made from germanium, is 50°C or more below the intersection of the extrinsic resistivity curve, characterizing the highest resistivity region of the device, with the intrinsic range curve. The available data for the intrinsic range resistivities of germanium, silicon, indium phosphide,

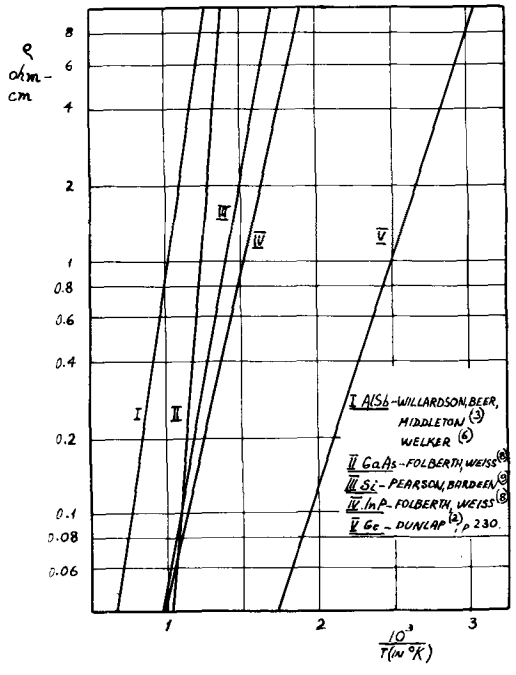


Fig. 1. Comparison of intrinsic range resistivities for Ge, InP, Si, GaAs, and AlSb vs. $10^3/T$ ( in °K).

**Table II. Maximum temperature limits for p-n junction action for high-energy gap semiconductors**

| Semiconductor | Extrinsic resistiv., ohm-cm | Temp. at intersection of intrinsic & extrinsic resistiv. curves, °C | Temp. obtained by subtraction of Hunter's (10) correction (50°C), °C | Energy gap, ev |
|---|---|---|---|---|
| Ge | 2 | 110 | 60 | 0.7 |
| | 5 | 80 | 30 | |
| Si | 2 | 390 | 340 | |
| | 5 | 350 | 300 | 1.1 |
| InP | 2 | 340 | 290 | |
| | 5 | 300 | 250 | 1.25 |
| GaAs | 2 | 490 | 440 | |
| | 5 | 450 | 400 | 1.35 |
| AlSb | 2 | 600 | 550 | |
| | 5 | 540 | 490 | 1.6 |

gallium arsenide, and aluminum antimonide are plotted as a function of temperature in Fig. 1 (2, 3, 6, 8, 9).

Table II shows the theoretical temperature limits of device operation for the cases of germanium, silicon, and the high energy gap semiconductors, for both 2 and 5 ohm-cm resistivity material. With due consideration to the limitations of the applicability of these data, it is apparent that aluminum antimonide is the most suitable material, among those given in Table II, for further development in attempting to achieve devices operable at 500°C.

A calculation of the reverse current flowing through a P-N junction, according to the equations of Shockley, yields for aluminum antimonide a theoretical leakage current of $10^{-19}$ amp/cm$^2$. In the case of silicon, a leakage current of $10^{-9}$ to $10^{-10}$ amp/cm$^2$ is obtained at room temperature, which approaches the $10^{-12}$ amp/cm$^2$ theoretical value. The theoretical leakage currents for gallium arsenide and indium phosphide are between $10^{-19}$ and $10^{-12}$ amp/cm$^2$. It can be concluded that, if surface control and structural perfection are achieved in the case of aluminum antimonide to an extent comparable to the case of silicon, the high-temperature leakage current of aluminum antimonide will be comparable with the room temperature leakage currents in silicon or germanium.

The frequency limit in transistors is controlled basically by charge carrier mobility and lifetime. Since the absolute minimum width of the base region is limited by voltage breakdown and by the accuracy of available methods of dimensional control, an approximate lower limit is imposed on the mobility of charge carriers for use in the two-junction type of transistor. This lower limit of mobility is estimated to be 1000 cm$^2$/v sec for a material of 1 $\mu$sec lifetime. Unipolar transistors, such as the field effect transistor, function by means of majority charge carriers and are not dependent in the same manner on mobility and lifetime. Jenny (5) has made a theoretical comparison of the relative frequency limits of high-energy gap semiconductors with those of germanium and silicon for unipolar transistor action using mobility values available in the literature. For the case of aluminum antimonide, his calculation is based on a mobility of 400 cm$^2$/v sec. This is a median value considering that the data

in the literature range from 1200 to 35 cm²/v sec. For this value the frequency response of aluminum antimonide has been calculated by Jenny (5) to be very similar to that of silicon.

In general, charge carrier mobilities are expected to decrease with increasing energy gap and melting point of the semiconductor. Furthermore, it has been proven by Welker and by other investigators that the group III-V intermetallic compounds generally have higher mobilities than the group IV elements for the same energy gaps and melting points. Another characteristic of group III-V compounds is that for the same energy gap the melting point is lower than is common in the group IV elements. Based on these general observations, data in the literature, calculations and analyses, the ultimate potential of high-energy gap semiconductors for high temperature rectifiers and transistors is expected to be as shown in Table III. From Table III, it appears that aluminum antimonide has potential applicability in high-temperature rectifiers and all types of high-temperature transistors, with the possible exception of the two-junction type of transistor.

Considering the expected trend of mobility with both melting point and energy gap, it appears that the electron mobility of aluminum antimonide as given by various investigators (*see* Table III) is anomalously low relative to expected values. This partially justifies the expectation of realizing considerably higher mobility with improved aluminum antimonide material.

### Purification of Aluminum and Antimony

Antimony of 99.99% purity was purified by zone refining in aluminum oxide boats. The portion of the ingot used for crystal growing experiments contained of the order of 1 ppm spectroscopically detectable impurities. The major impurity contained in the antimony was arsenic. Arsenic was eliminated by zone refining antimony to which was added a small amount of aluminum.

The segregation of arsenic in antimony by zone refining in the presence of added or contained aluminum is quite remarkable and justifies comment here, although a detailed discussion of the mechanism of segregation involved will be deferred to a later publication on this subject. Previous papers by Tanenbaum, Gross, and Pfann (11) and by Goering, *et al.* (12) indicate that the concentration of arsenic in a zone refined antimony ingot is practically constant over the whole length of the ingot. This implies that the segregation coefficient of arsenic in antimony is close to unity. The antimony metal used by these investigators did not contain any spectroscopically detectable amount of aluminum. In the present experiments, a segregation of arsenic was observed in all cases when aluminum was present. In attempting to obtain more conclusive evidence about the effect of aluminum on the segregation of arsenic, known amounts of aluminum were added to the front end of the antimony ingot before the zone refining was started. The results of these experiments showed that a strong segregation of arsenic occurs.

Aluminum of 99.99% purity was refined in aluminum oxide boats. The total impurity content of the zone refined aluminum used for crystal growing experiments was about 3 ppm, with iron as the major impurity. Since the weight of aluminum used for growing aluminum antimonide crystals was about one fourth that of antimony, the total amount of impurities in both metals (based on AlSb) was slightly above 1 ppm. In some cases, aluminum and antimony were also purified by zone refining in graphite boats.

### AlSb Crystal Preparation and Doping

The metals were reduced to a suitable size and etched to clean the fragment surfaces. The weighed quantities of the metals were placed in an aluminum oxide crucible for crystal growing. The crucibles consisted of 99.7% pure aluminum oxide made by the Morganite Co., Long Island, New York. The crystal growing was done in an atmosphere of purified helium. Helium purification was accomplished by passing the gas through magnesium perchlorate, turnings of a titanium-zirconium alloy heated to 800°C, and finally a liquid air trap.

Before growing crystals, the equipment was heated up slowly over a period of 2-3 hr. During this time a flow of dry helium gas was maintained for the purpose of eliminating traces of water vapor

**Table III. Comparison of high-temperature device potential of high-energy gap semiconductors showing trends of mobilities with melting point and energy gap**

| | SiC | GaP | AlAs | AlSb | GaAs | InP | Si | Ge |
|---|---|---|---|---|---|---|---|---|
| Energy gap in ev | ~3 | 2.4 | 2.2 | 1.6 | 1.35 | 1.25 | 1.1 | 0.7 |
| Melting point, °C | 2200 decomp. | 1350 | >1500 | 1060 | 1240 | 1070 | 1500 | 960 |
| Electron mobility at 250°C, cm²/v sec | 40-60 | — | — | 35-1200 | 3400-4500 | 3400 | 1900 | 3900 |
| Hole mobility at 250°C, cm²/v sec | 5-10 | 17 | — | 100-200 | >200 | 50 | 450 | 1900 |
| Est. max. temp. for p-n junction action, °C | 1000 | — | — | 550 | 440 | 325 | 350 | 100 |
| Rectifying action | + | 0 | 0 | + | + | + | + | + |
| Transistor (2 junction) action | — | — | — | ? | + | + | + | + |
| Unijunction transistor | × | × | × | 0 | 0 | 0 | + | + |
| Unipolar transistor | × | × | × | 0 | + | + | + | + |

+ observed; 0 not observed but expected; — not believed possible; ? doubtful; × not observed, possible at high temperature but perhaps not at low temperature.

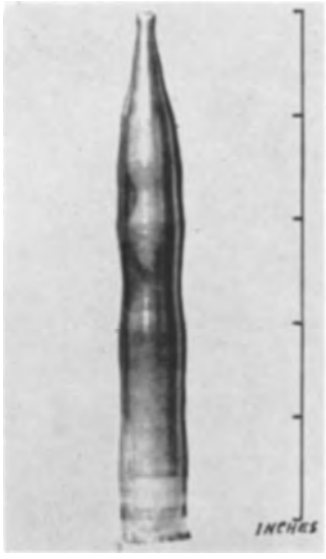


Fig. 2. AlSb crystal

and oxygen from the system. As a result of these pretreatments of the gas and the crystal growing equipment, the formation of oxide particles on the surface of the aluminum antimonide melt was minimized. Any floating particles which did appear on the melt surface were easily eliminated with a probe. The melt surface, in this mechanically cleaned state, remained clean throughout crystal growing. In the most recent work, the crucible was not rotated during crystal growing, but the seed crystal was rotated at a rate of 4 rpm.

The grown crystals have a clean metallic surface as shown in Fig. 2. Some crystals were obtained which were 80% single. Other crystals showed varying amounts of twin lines. Spectrographic data are given in Table IV for the top portion of a crystal. For comparison, the same table shows the amount of impurities contained in the zone refined metals used in growing the crystal. The amounts of copper and iron in the crystal are reduced because of segregation during crystal growing. The amount of magnesium and silicon is slightly increased because of contamination of the melt by the crucible.

Weighing was done in several cases to determine the loss of antimony by evaporation. Between 0.6 and 1.1 g was lost from approximately 122 g of antimony contained in the melt. This loss of antimony was reduced practically to zero by introducing a heated bell jar above the melt as shown in Fig. 3. The crystals grown with the heated bell jar in place were not different, however, from the crystals grown in open crucibles. As a matter of fact, they were less single in character because of difficulties encountered in skimming the surface of the melt under the bell jar.

A series of crystal growing experiments was performed under nearly identical conditions to compare the influence of small excesses of antimony or of aluminum in the melt on crystal characteristics. The data are reported in Table V. All crystals were P-type and had the same range of resistivity independent of the melt composition. It was noted that the crystals were more frequently twinned and also contained grain boundaries in the case of additions

Table IV. Analysis of aluminum antimonide crystals

| Impurities, ppm | Cu | Fe | Mg | Si | As | Ca |
|---|---|---|---|---|---|---|
| Al + Sb metals | 1.2 | 1.1 | 0.7 | 0.4 | | 0.2 |
| AlSb crystal | 0.1 | 0.15 | 2.3 | 1.4 | × | 0.5 |

× = trace.

Table V. Results of crystal growing experiments

| Crystal No. | Addition to Sb 121.76 g Al 26.98 g | Top part of crystal: Resistivity ohm-cm | Top part of crystal: Type of conductivity | Remarks |
|---|---|---|---|---|
| 26 | 0.5% Sb | 0.8 | P | Mostly single |
| 30 | 2.9% Sb | 0.8 | P | Mostly single |
| 29 | 4.0% Al | 0.4 | P | Polycrystalline |
| 28 | 0.5% Sb | 0.14 | P | Sb refined in graphite boat |
| 46 | 0.5% Sb | 0.23 | P | Al refined in graphite boat |
| 38 | 10 mg C | 0.013 | P | Frequently twinned |
| 27 | 15 mg C | 0.01 | P | Frequently twinned |
| 22 | 10 mg Te | 10.8 | P-N | Large single portions |
| 23 | 51 mg Te | 3.6 | N | Large single portions |
| 24 | 75 mg Te | 1.7 | N | Large single portions |
| 31 | 6 mg Se | 9.7 | P-N | Large single portions |
| 25 | 61 mg Se | 32.6 | N | Large single portions |

of an excess of aluminum. The resistivity of these crystals was also somewhat lower than normal. It is possible that the effects of excesses of aluminum and antimony on grown crystals might be explained by a nonstoichiometric composition of the crystal at the maximum melting point, as discussed theoretically by Hodgkinson (13).

In Table V, results of other crystal growing experiments are also reported for which either the aluminum or the antimony was purified in graphite boats. In both cases, and especially in the case of antimony refined in the graphite boat, the resistivity is considerably lower than normal. The indication that carbon contamination may cause a decrease in

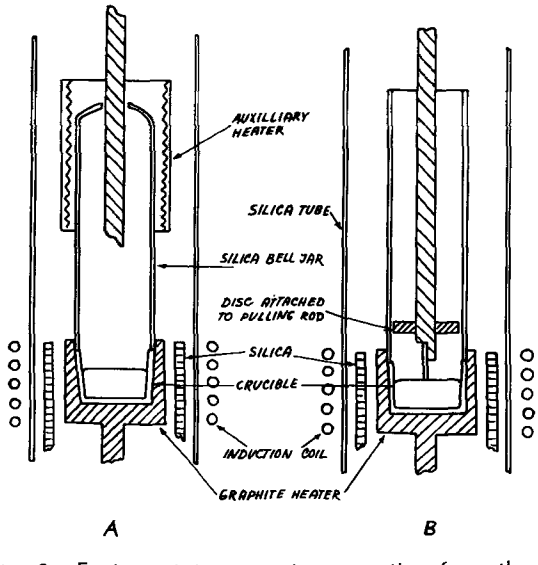


Fig. 3. Equipment to prevent evaporation from the melt during crystal growing.

resistivity is further confirmed in the case of crystals No. 38 and No. 27 where known amounts of carbon, 10 and 15 mg, respectively, were added to the metals before crystal growing. The amount of carbon actually dissolved in the melt is not known because a large portion of it was eliminated by skimming of the surface. However, the remaining quantity of carbon, which might be of the order of a few milligrams for an approximately 150-g melt, caused a great decrease in resistivity as shown in Table V.

The results of various experiments on the effect of carbon are shown in Fig. 4. Recently an analysis was made on the carbon content of antimony and of aluminum. The carbon content of aluminum was reduced by 50% by refining in an oxide boat; it was increased by 10% by refining in graphite boats. However, determinations revealed carbon contents in the range of the sensitivity of the analytical method, which was of the order of 50 ppm of carbon, and therefore cannot be considered as quantitative. Somewhat larger quantities of carbon were found in the as-received antimony. The carbon content of antimony was not appreciably reduced by zone refining.

Doping experiments were performed with various metals to gather information about type of conductivity and value of resistivity of the doped material and to evaluate their usefulness for alloyed ohmic contacts, or for rectifying junctions of any type. The impurity was added to the melt either before or during crystal growing for making P- or N-type material or P-N junctions. Figure 5 summarizes the effects of various doping agents on resistivity and type of conductivity for the available AlSb.

Of special interest are the results of doping with tellurium and selenium, both of which give N-type material. A threshold seems to exist in the quantity of the added impurity which has to be exceeded in order to obtain N-type material. The quantity below the threshold is used up in compensating existing P-type centers in the crystal. It will be noted that

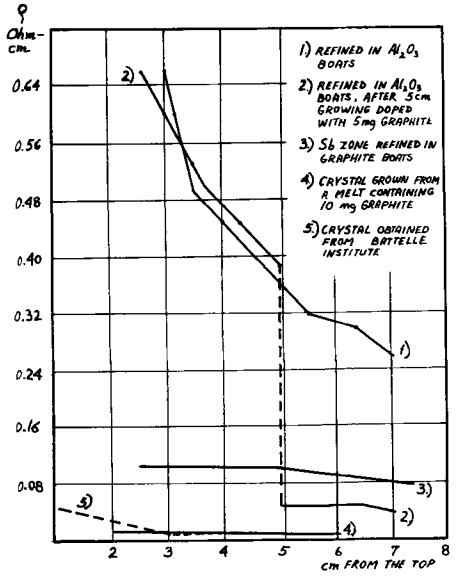


Fig. 4. Effect of carbon on the resistivity profile of AlSb crystals.

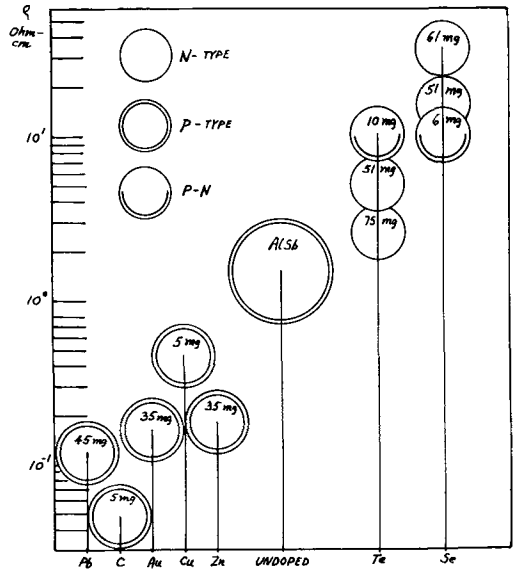


Fig. 5. Effect of various impurities on resistivity and conduction type of AlSb.

a large amount of N-type addition is required, namely about 10 mg Te or 6 mg Se, to compensate for P-type centers. The chief detectable P-type impurity in the crystal is magnesium, dissolved by the melt from the crucible. The quantity of magnesium in the crystal has been determined by spectrographic analysis to be about 2 ppm. This is almost a factor of 10 lower than the amount of Se or Te used for compensation. It is concluded, therefore, that the compensation effect is due either to another impurity of unknown quantity, possibly carbon, or to antimony vacancies. Further identification will be discussed later in connection with the interpretation of Hall effect measurements.

In the case of tellurium additions, the resistivity of the crystal increases at first until the threshold quantity for compensation and conversion to N-type is reached and then decreases with any further addition of Te. In the case of selenium addition, there is a different behavior; the resistivity increases with further additions of the impurity above the threshold value for compensation.

P-N junctions were made from P-type material by doping with tellurium or selenium. Junctions can also be made by starting from selenium containing N-type material and doping with zinc to produce the junction. A lowering of resistivity for P-type material is obtained by doping with zinc and with carbon; a smaller change is obtained for lead, copper, and gold.

## Hall Effect, Resistivity, and Tentative Identification of Extrinsic Charge Carrier Sources

Hall effect and resistivity measurements were made on an undoped P-type single-crystal section of 0.4 ohm-cm resistivity. The size of the sample was 1.6 x 0.62 x 0.13 cm. The current leads, Hall probes, and a thermocouple were soldered to the sample. The sample was kept under a vacuum of about 0.5 $\mu$ during the measurements. The magnetic field was calibrated against a 6 ohm-cm germanium sample by comparing its intrinsic range with pub-

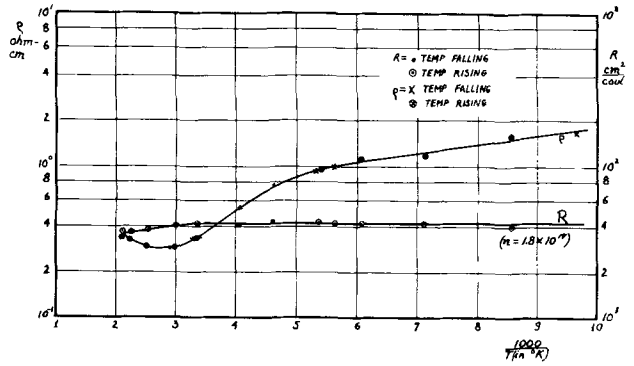


Fig. 6. Log resistivity and log Hall constant for AlSb vs. $10^3/T$ (in °K).

lished intrinsic range curves. A primary current of 1 ma was passed through the sample in a magnetic field of 7000 gauss. Measurements were made between liquid air temperature and 200°C for both rising and falling temperatures. Results are shown in Fig. 6. Although final interpretation of these results must await high-temperature data and similar runs on variously doped samples, some valuable conclusions can be drawn at this time.

Since the conduction is by extrinsic holes and the Hall constant is invariant with temperature over a long temperature range down to the lowest temperature investigated, the impurity levels controlling conduction are assumed to be exhausted. Using the relation $N = n = 7.37 \times 10^{-18}/R$, the number, $N$, of electronically active impurity centers and $n$, the total number of extrinsic holes, is found to be $1.8 \times 10^{17}$/cc. The constancy of the Hall constant over the entire low-temperature range suggests that acceptor centers due to impurities or lattice vacancies are present in the sample and that they lie very close to the valence band.

Since this sample has large positive hole extrinsic conduction, the relation $\mu p = R/\rho$ can be used to calculate the hole mobility. Figure 7 shows the resulting temperature dependence of mobility. It will be noted that the peak value of hole mobility is at 60°C and is 105 cm²/v-sec. These data on aluminum antimonide indicate that a high concentration of

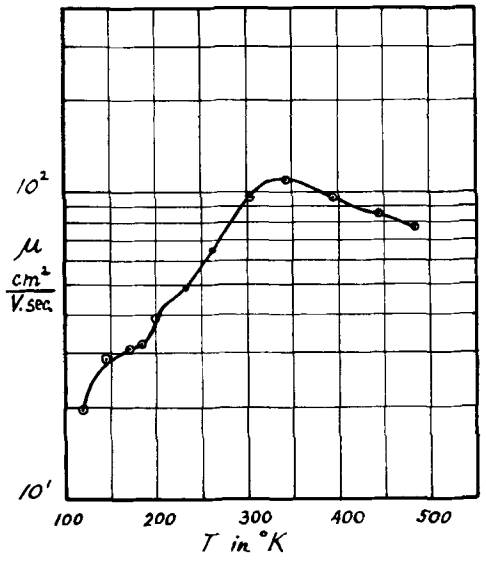


Fig. 7. Hole mobility of AlSb

centers, causing strong impurity scattering, is present in the aluminum antimonide sample. Further, it appears reasonable to conclude that the mobility of the holes in the aluminum antimonide is suppressed by the large amount of impurity scattering present.

From these data and with reference to the interpretations by Blunt and co-workers (14) of optical absorption characteristics of aluminum antimonide, some information on whether impurities or lattice defects are chiefly responsible for the observed electrical properties of aluminum antimonide can be obtained. Blunt found a deep lying level 0.75 ev above the valence band and attributed this to antimony vacancies. If Blunt and co-workers are correct in this assignment, the present Hall effect results are not easily explained on the basis of antimony vacancies, since they suggest a near-zero impurity activation energy.

With regard to the impurity which controls the electrical properties of the available aluminum antimonide, the following evidence suggests carbon as the major impurity:

1. $1.8 \times 10^{17}$/cc P-type impurity centers in undoped material are indicated by the Hall constant vs. temperature data.
2. Carbon has been shown by doping experiments to make AlSb P-type.
3. Carbon additions in small quantities produce large reductions in AlSb crystal resistivity.
4. Tellurium doping experiments indicate that large amounts of N-type doping material must be added to compensate for the P-type centers. The Te additions cause an increase in resistivity up to the compensation concentration and then the resistivity decreases as the AlSb becomes predominantly N-type. The quantitative amount of Se and Te used for obtaining compensation was about 30-40 ppm. Since $1.8 \times 10^{17}$/cc corresponds approximately to 10-50 ppm, the doping experiment observations are in agreement with the Hall effect determination of the number of acceptor impurity centers.
5. Justification of the spectroscopic analyses, considering the large quantity of impurity centers indicated by the Hall constant, is given by the fact that spectroscopic analysis is highly insensitive to carbon. Recently, however, carbon has been found by chemical analysis in the aluminum and antimony used for crystal growing at an indicated concentration of the order of 50 ppm.

## Sample Processing and Surface Treatments

Considering the well-known tendency of aluminum antimonide to oxidize in the presence of water vapor, the problem of proper surface treatments is of utmost importance. Oxidation or hydrolysis leads to the formation of a black powder, and with passage of time all the material can be converted to this state. However, the rate of this process depends to a large extent on the existing surface properties and the structural characteristics of the specific sample of material.

The highest rate of decomposition is observed for surfaces obtained by cutting with a diamond saw using water cooling. In this case the surface is not only damaged mechanically but it is also saturated

with water. The initial damage is so deep that it can hardly be improved by further treatments unless a large quantity of material is removed from the surface in a uniform manner.

If AlSb samples are cut with an oil-cooled diamond saw, the surfaces are stable enough to be kept in a desiccator, and the samples can be utilized without excessive removal of the surface layer. The surface obtained by cutting under oil can be slightly improved by lapping or by sandblasting. The material with lapped, sandblasted, or oil cut surface can be kept in a desiccator for some time without serious oxidation.

The best mechanical treatment is polishing with a fine abrasive to achieve a mirrorlike surface. Polished surfaces can be kept in open air, the only change being a development of a slight brownish color. Cleaved surfaces and the as-grown crystal behave in a manner similar to polished surfaces. This is only true for a crystal of good quality without grain-boundaries and without foreign particles such as oxide on the surface.

The best sample preparation prior to etching is either cleaving or polishing of the surface cut under oil immersion. Etching on lapped, sandblasted, or as-cut surfaces produces large etch pits and, in general, emphasizes any surface imperfections.

Various etching solutions were tried. Because of the different chemical reactivities of aluminum and antimony, it is possible to obtain surfaces with very different characteristics. Some of these surfaces show an excellent stability, not only with respect to air and water vapor, but also in contact with boiling water. It is probable that this protection is due to the presence of a slightly aluminum rich surface on which is formed an aluminum oxide layer. Surface properties were investigated by point contact rectification experiments and by four- and two-point probe resistivity measurements in order to evaluate the usefulness of various treatments for devices. The etching procedures giving best results are reported below.

A solution of HF (48%) and $H_2O_2$ (30%) in a ratio of 1:2 produces a mirrorlike surface of very high resistivity. The reaction is rather violent and is quenched by the addition of diluted $H_2O_2$ (3%) to the etch. After etching, the surface has a thin whitish layer which can be eliminated by boiling the sample in distilled water. This method has been abandoned, however, because it is not suitable for microetch or junction etch techniques. Any exposure of the sample to air after the acid treatment and before dilution of the acid causes the formation of a black deposit. The solution is unstable. It must be freshly made and used without delay.

A solution of hydrofluoric and nitric acid yields a very high resistivity surface of metallic appearance.

The best results were obtained with a solution containing hydrofluoric, nitric, and acetic acids in the ratio 2:3:0.5. The surface is bright metallic in appearance and stable in air. The same etch with a higher concentration of acetic acid is also quite satisfactory if a slower etch rate is desired.

Hydrochloric acid and potassium hydroxide, both in aqueous and alcoholic solutions, were also tried as etches. Hydrochloric acid, in the gas phase, was investigated. The resulting surface resistivity of samples treated in these ways is somewhat low and the surfaces obtained have a rather dull metallic appearance.

It is noteworthy that four-point probe resistivity measurements give much higher values on etched surfaces than on lapped or sandblasted surfaces. The large ratio of about 10 between surface and bulk resistivity is a remarkable characteristic of aluminum antimonide.

## Device Feasibility Studies

Experiments have been performed on the rectification properties of point contacts on AlSb and grown junctions in AlSb. The rectifying properties were found to depend strongly on the condition of the semiconductor surface. Owing to the near-degenerate nature of the AlSb samples, high reverse voltages were not expected nor obtained.

Rectification experiments were carried out on cleaved, polished, and variously etched surfaces. In all cases, the sample, in the form of a cut wafer or cleavage fragment, was soldered to a metal support for external contact. Thin sheets of lead solder were used.

For producing fused junctions or ohmic contacts capable of operating at high temperatures, it is of importance to know the thermal expansion coefficient of AlSb. A determination was made of the thermal expansion coefficient and the average coefficient of linear thermal expansion between room temperature and 700°C was found to be $4.9 \times 10^{-6}$.

Point contact rectifiers were made by using a small tungsten wire, 0.007 in. in diameter. This wire was bent into an S shape to provide mechanical stability. The end of it was etched electrolytically to reduce the contact area. The tungsten was welded to an external electrode. A typical unit assembly used for both point and grown junction rectifiers is illustrated in Fig. 8. The inside of the cartridge was filled with argon.

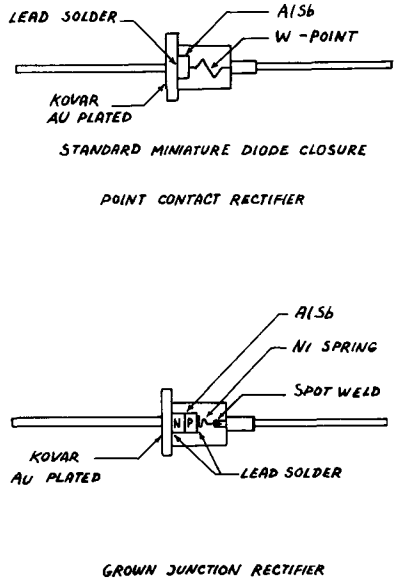


Fig. 8. Construction of point contact rectifier and junction rectifier.

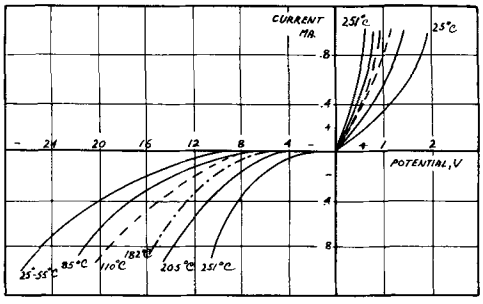


Fig. 9. Point contact rectification characteristics of AlSb as a function of temperature.

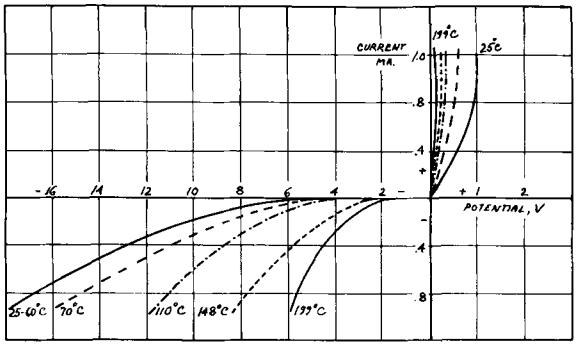


Fig. 10. Grown junction rectifier characteristics of AlSb as a function of temperature.

In the experiments, P-type material was used with 0.2-1.0 ohm-cm resistivity. Various etches were tried to improve rectification properties. Reverse voltages up to 85 v were obtained in the case of cleaved samples etched with HF-$HNO_3$ (1:9) using a dynamic reverse bias tester and 60 cycle pulsed D. C. Better reproducibility and good forward characteristics were obtained using cut wafers and HF-$HNO_3$-$CH_3COOH$ (2:3:0.5) etch.

Figure 9 shows point contact rectification curves at various sample temperatures for a P-type AlSb, etched with HF-$HNO_3$-$CH_3COOH$. Electrical tests were made up to 250°C. Failure of the units occurred at this temperature. This may have been due either to softening of the solder, to formation of a low melting point lead-antimony eutectic, or possibly to the increase with temperature of the P-N junction leakage current, characteristic of the low resistivity material.

Grown junction rectifiers were made by doping the melt with selenium during crystal growing. Selenium pellets weighing between 10 and 60 mg were dropped into the melt without exposure of the melt to the air. The sections of the crystal containing the P-N junction were encapsulated as shown previously. Figure 10 shows the rectification characteristic of a grown P-N junction rectifier as a function of temperature. Failure above 200°C is believed to be due to an increase of the leakage current of the P-N junction in the low resistivity AlSb with increasing temperature.

The AlSb material was also tested for transistor action using a soldered base connection and point contact emitter and collector. With the collector and emitter points in an almost shorted position (emitter floating potential about equal to the voltage applied between the collector and base), it was possible to modulate the collector current with the emitter current but not to the extent that any power gain could be developed.

## Acknowledgment

The authors are deeply indebted to Mr. William Hall for his services in growing the AlSb crystals.

The work was performed under Air Force Contract 33(616)-3481 which was sponsored by Wright Air Development Center, Air Research and Development Command, Wright-Patterson Air Force Base, Ohio.

Manuscript received Oct. 6, 1957. This paper was prepared for delivery before the Buffalo Meeting, Oct. 6-10, 1957.

Any discussion of this paper will appear in a Discussion Section to be published in the June 1959 JOURNAL.

## REFERENCES

1. E. Burstein and P. Egli, "The Physics of Semiconductor Materials" excerpt from "Advances in Electronics and Electron Physics," Vol. VII, Academic Press, New York (1955).
2. W. C. Dunlap, "An Introduction to Semiconductors," John Wiley & Sons, Inc., New York (1957).
3. R. K. Willardson, A. C. Beer, and A. E. Middleton, *Phys. Rev.*, **91**, 243 (1953); *This Journal*, **101**, 354 (1954).
4. H. Welker, "Intermetallic Compound Semiconductors," Techn. Rundschau Nr 50, 30. Nov. 1956, Bern, Switzerland.
5. D. A. Jenny, Biennial Electronic Materials Conference, Philadelphia, June 1957; IRE Device Conference, Boulder, Colo., July 1957.
6. H. Welker, *J. Electronics* (London), **1**, 181 (1955).
7. R. N. Hall, "SiC Rectifiers," Semiconductor Device Research Conference, Boulder, Colo., July 1957.
8. O. G. Folberth and H. Weiss, *Z. Naturforsch.*, **8**, 615 (1955).
9. G. Pearson and T. Bardeen, *Phys. Rev.*, **75**, 865 (1949).
10. L. P. Hunter, "Handbook of Semiconductor Electronics," Chap. 10, p. 9; McGraw-Hill Book Co., New York (1956).
11. M. Tanenbaum, A. J. Gross, and W. G. Pfann, *J. Metals*, **6**, 762 (1954).
12. H. A. Goering, *et al.*, Battelle Mem. Inst. Scientific Contract AF 33(616)-2338 Reports 1 & 2.
13. R. I. Hodgkinson, *J. Electronics* (London), **2**, 201 (1956).
14. R. F. Blunt, H. P. R. Frederickse, and J. H. Becker, *Phys. Rev.*, **94**, 1431 (1954).

# Anodic Polarography with a Rotating Platinum Microelectrode

## II. Oxidation of Various Indole Alkaloids

M. J. Allen and V. J. Powell

*Research Department, CIBA Pharmaceutical Products Inc., Summit, New Jersey*

ABSTRACT

The results obtained by anodic oxidation of some indole alkaloids indicate that in an acidic medium a one electron change occurs with probable hydroxyl introduction into the aromatic portion of the molecule. This reaction appears to be specific for those alkaloids containing a 6-methoxyindole nucleus. In a neutral medium a two electron change occurs with resultant N-oxide formation in those alkaloids in which the nitrogen has available an unshared pair of electrons.

In a previous report (1), a reproducible-type electrode system was described and applied to an investigation of the oxidation of the leuco base of crystal violet. Since the indole alkaloids are subject to oxidative changes of one form or another and since no previous study has been reported on the anodic oxidation of these alkaloids, it was felt that it would be of interest to determine if definite half-wave potentials could be obtained for one or more of these reactions and attempt, if possible, to correlate the results with the site of oxidative attack on the molecule. Due to possible hydrolysis of the ester groups present in many of the alkaloids investigated it was decided to use only acidic or neutral media for the study in order to avoid introduction of a competitive chemical reaction.

### Experimental

*Reagents and solutions.*—All solutions were prepared with reagent grade chemicals. The alkaloids used were of maximum purity as indicated by elementary analysis and infrared spectra.

*Apparatus.*—An H-type polarographic cell containing a centrally fused sintered disk was used in conjunction with a Leeds and Northrup Type E Electro-Chemograph. One side of the cell had its disk face covered with an agar plug and served for the standard calomel electrode. The other half of the cell was used for the sample solution. The platinum anode was identical to that described in the previous communication (1).

*Procedure.*—The cell containing a 10 ml sample was immersed in a constant temperature maintained at 30° ± 0.1°C and de-aerated for 10 min with nitrogen previously saturated with either methanol or aqueous-methanol depending on the medium used.

### Results

For comparison purposes the results obtained are given in Table I.

Coulometric analysis indicated that those alkaloids which gave a wave in the acid medium underwent a one electron change, whereas those compounds which gave a wave in the neutral medium underwent a two electron change.

Since a wave was obtained with reserpine in an acidic medium, it was possible to estimate the amount of this material in the presence of deserpidine which did not give a wave under these conditions. In Table II the *id* values are given for various concentrations of reserpine and reserpidine-deserpidine mixtures, and it can be seen that the values obtained for the mixtures do not differ significantly from those obtained for the various concentrations of pure reserpine.

### Discussion

In order to obtain a wave in the acidic medium, the presence of the 6-methoxy group in the indole nucleus is essential under our experimental conditions, and the apparent one electron change obtained with the alkaloids containing this substituent can probably be attributed to the introduction of a hydroxyl group into the aromatic portion of the molecule. The assumption that the one electron change represents the introduction of a hydroxyl group is based on the experiences of various investigators who demonstrated that generally the initial step in the anodic oxidation of an aromatic system is the introduction of a hydroxyl group (2).

Based on the aforementioned observations the authors would like to propose the following mechanism for the introduction of a hydroxyl group in the alkaloids containing the 6-methoxy substituent.

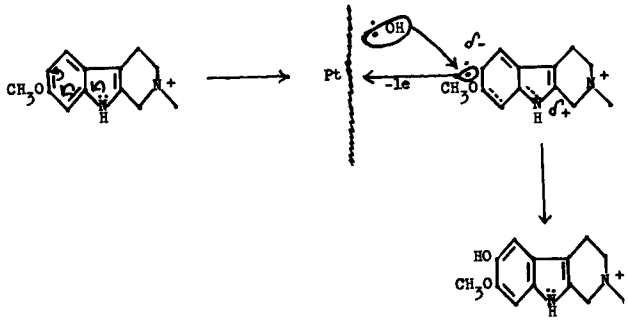


This mechanism proposes a p-quinoid intermediate due to the activating influence of the 6-methoxy substituent which is strong enough to overcome the possible deactivating effect of the positively charged nitrogen in the ring adjacent to the indole nucleus. It is possible that this form is stabilized by adsorption on the electrode surface where an electron is removed and the radical combines with a hy-

Table I

| Aklaloid | Structure | Conc. in 0.2M LiCl (Abs. MeOH) | Conc. in 0.1*N* HCl (50% aq. MeOH) |
|---|---|---|---|
| Ajmalicine | 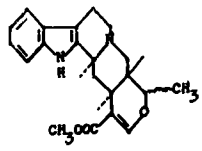 | $1.08\text{-}2.16 \times 10^{-4}$M<br>$E_{1/2} = +0.852$ | No wave |
| Alloyohimbane | 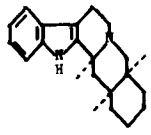 | $1.50\text{-}3.00 \times 10^{-4}$M<br>$E_{1/2} = +0.805$ | No wave |
| Corynanthine | 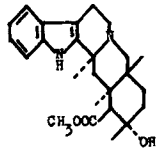 | $1.13\text{-}2.26 \times 10^{-4}$M<br>$E_{1/2} = +0.874$ | No wave |
| Deserpidine | 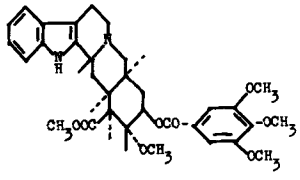 | $0.692\text{-}3.462 \times 10^{-4}$M<br>$E_{1/2} = +0.849$ | No wave |
| Deserpidine N-Oxide | 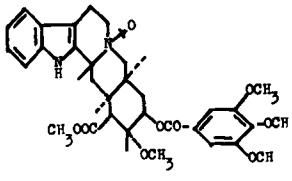 | No wave | No wave |
| Methyl Deserpidate | 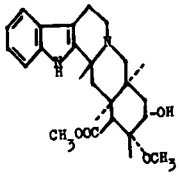 | $1.41\text{-}1.88 \times 10^{-4}$M<br>$E_{1/2} = +0.781$ | No wave |
| Yohimbine | 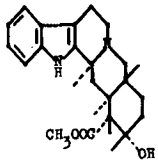 | $1.52\text{-}5.92 \times 10^{-4}$M<br>$E_{1/2} = +0.838$ | No wave |
| 3-epi-$\alpha$-Yohimbine | 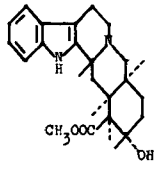 | $1.61\text{-}5.92 \times 10^{-4}$M<br>$E_{1/2} = +0.859$ | No wave |
| Serpentine Nitrate | 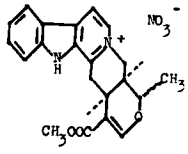 | No wave | No wave |
| Ibogaine | 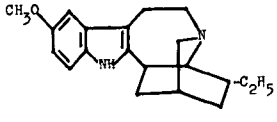 | $1.10\text{-}3.30 \times 10^{-4}$M<br>$E_{1/2} = +0.547$ | No wave |
| Ibogamine | 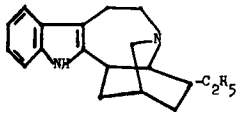 | $1.11\text{-}3.33 \times 10^{-4}$M<br>$E_{1/2} = +0.577$ | No wave |

Table I (continued)

| | | | |
|---|---|---|---|
| Tabernanthine | 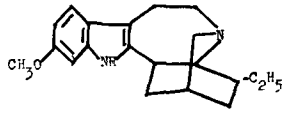 | 1.84-6.12 × $10^{-4}$M<br>$E_{1/2}$ = +0.460 | 1.84-6.12 × $10^{-4}$M<br>$E_{1/2}$ = +0.720 |
| Reserpine | 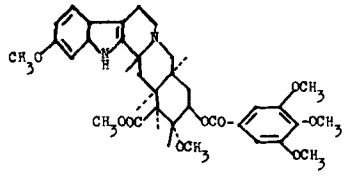 | 1.36-1.78 × $10^{-4}$M<br>$E_{1/2}$ = +0.618 | 1.46 × $10^{-4}$M<br>$E_{1/2}$ = +0.738 |
| Reserpine N-Oxide | 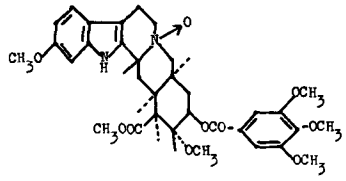 | No wave | 1.20-1.28 × $10^{-4}$M<br>$E_{1/2}$ = +0.714 |
| Methyl Reserpate | 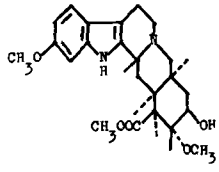 | 1.21-6.27 × $10^{-4}$M<br>$E_{1/2}$ = +0.650 | 1.25-6.27 × $10^{-4}$M<br>$E_{1/2}$ = +0.832 |
| Reserpic Acid | 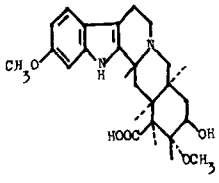 | 1.20-2.40 × $10^{-4}$M<br>$E_{1/2}$ = +0.853 | 1.20-5.99 × $10^{-4}$M<br>$E_{1/2}$ = +0.848 |
| Iso-Reserpine | 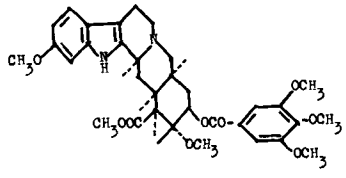 | 3.29 × $10^{-4}$M<br>$E_{1/2}$ = +0.631 | 2.95 × $10^{-4}$M<br>$E_{1/2}$ = +0.730 |
| Rescinnamine | 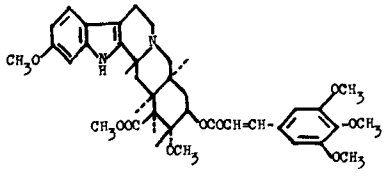 | 1.23-5.83 × $10^{-4}$M<br>$E_{1/2}$ = +0.611 | 1.23-5.83 × $10^{-4}$M<br>$E_{1/2}$ = +0.854 |
| Reserpinine | 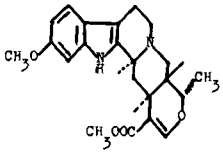 | 0.749-3.746 × $10^{-4}$M<br>$E_{1/2}$ = +0.655 | 0.644-2.576 × $10^{-4}$M<br>$E_{1/2}$ = +0.848 |

droxyl radical at the electrode with simultaneous expulsion of a proton to yield the 5-hydroxy substituted indole. That we do not detect the one electron change in going from : OH to ·OH tends to indicate that the loss of the one electron from the indole nucleus is the rate-determining step in the reaction. The possibility of the formation of a less stable o-quinoid structure must not be overlooked. If this were to occur then substitution might very well take place in position 7. As no wave is observed under our experimental conditions with the methoxy group in position 5, the indications are that the p-quinoid structure predominates, and hydroxylation in position 5 is blocked by the substituent already present in this position. The fact that we do not observe this to occur in the unsubstituted indole nucleus can possibly be attributed to the deactivating influence of the positively charged nitrogen in the adjacent ring. Removal of this possible deactivating influence, as in indole itself, resulted in a wave at $E_{1/2}$ = +0.796 v in an acidic medium.

Table II. Reserpine and deserpidine in 0.1N HCl (50% aq. MeOH)

| Reserpine conc. (moles/l) | id (μa) | Deserpidine conc. (moles/l) | Mixture of deserpidine and reserpine-id (μa) |
|---|---|---|---|
| 0.644 × $10^{-4}$ | 5.1 | 2.765 × $10^{-4}$ | 5.2 |
| 1.288 × $10^{-4}$ | 8.4 | 2.074 × $10^{-4}$ | 8.6 |
| 1.932 × $10^{-4}$ | 11.9 | 1.382 × $10^{-4}$ | 11.9 |
| 2.576 × $10^{-4}$ | 15.1 | 0.691 × $10^{-4}$ | 14.9 |

It might be of interest to point to the analogous reactivity of 6-methoxy indole alkaloids with nitrous acid as compared to the resistivity of the unsubstituted and 5-methoxy indole alkaloids to reaction with this reagent (3).

The two electron change observed in a neutral medium can be attributed to the formation of N-oxides which have also been prepared by chemical means (4). Thus, as expected, reserpine N-oxide, deserpidine N-oxide, and serpentine nitrate, the latter being a quaternary salt, do not give a wave in the neutral medium because of the unavailability of the required pair of unshared electrons on the nitrogen atom. For the same reason a two electron wave is not observed in an acidic medium with those alkaloids which do show this in a neutral medium.

The mechanism proposed as a possible explanation for the observed 2 electron change is one which is analogous to that for the formation of hydrogen peroxide, i.e., $2 : OH \rightarrow 2 \cdot OH + 2e \rightarrow H_2O_2$, except

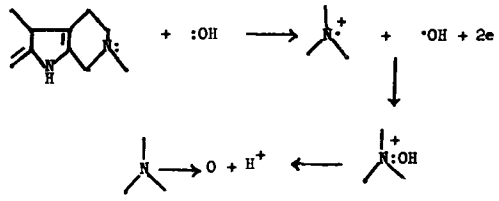

in this instance we would have at the electrode surface due to adsorption of the alkaloid molecule:

Manuscript received April 8, 1958.

Any discussion of this paper will appear in a Discussion Section to be published in the June 1959 JOURNAL.

REFERENCES

1. M. J. Allen and V. J. Powell, *Trans. Faraday Soc.*, **50**, 1244 (1954).
2. M. J. Allen, "Organic Electrode Processes," Reinhold Publishing Corp., New York (1958).
3. R. Haycock and W. J. Mader, *J. Am. Pharm. Assoc., Sci. Ed.*, **46**, 744 (1957).
4. M. Polonovski, *Bull. Soc. Chem. Belges.*, **39**, 1 (1930); C. C. J. Culvenor, *Revs. Pure Appl. Chem. (Australia)*, **3**, 83 (1953); W. I. Taylor, U. S. Pat. 2,789,-112, 2,789,113, April 16, 1957.

# The Preparation of Cadmium Niobate by an Anodic Spark Reaction

**William McNeill**

*Pitman-Dunn Laboratories, Frankford Arsenal, Philadelphia, Pennsylvania*

ABSTRACT

A new method of preparing cadmium niobate was demonstrated. This method involved the anodic spark reaction of cadmium in a niobate solution and crystallization of the anode product by heating at 650°C.

The crystallized anode product was made into a solid wafer by pressing it at 350,000 psi, and electrical measurements were made. Even though there was some evidence of impurity or porosity in the sample, a dielectric constant of about 600 was found at room temperature.

It is believed that anodic spark reactions might be employed to prepare a wide variety of complex oxides and possibly other compounds.

There are a number of metals, such as aluminum, magnesium, and tantalum, which exhibit high electrical resistances when made anodic in suitable solutions (1). This is due to the formation of an electrical barrier layer on the surface of the anode. The thickness of this layer is controlled by the voltage at which it is formed and is characteristic of the metal and solution used (2). For each such metal-electrolyte system there is a maximum voltage above which normal coating growth cannot occur. If this voltage is exceeded, electrical breakdown follows and, in many cases, sparking is observed on the anode surface (1, 3).

The high-voltage anodic processes for coating magnesium are examples of cases where sparking on the anode surface has a practical use. These coatings resemble ceramics and are composed of tiny particles of fused material. The fused material is a reaction product of the magnesium and the ions in the bath, and its properties can be controlled, to some extent, by the composition of the bath (4). For example, in the HAE process (5), aluminate in the bath reacts with the magnesium, yielding identifiable spinels in the coating. With the Cr-22 process (6), the use of an ammoniacal bath appears to prevent the retention of free magnesium oxide in the coating, even though this compound would be expected as a product.

Cadmium niobate, $Cd_2Nb_2O_7$, has been shown to be a material with a high dielectric constant (7), similar in many ways to barium titanate. As would be expected, considerable research has been done, both on methods of preparation and determination of properties of this material (8). Conventional high-temperature preparation methods are complicated by the fact that cadmium oxide volatilizes and is lost from the reaction mixture, making control of composition a problem (9). In the work referred to, it was found that weight losses of 10-20% occurred on firing $Cd_2Nb_2O_7$ in air in the temperature range of 1300°-1400°C. Although the authors were able to prevent weight losses by using a double crucible with a CdO seal, they still concluded that phase studies of the system $CdO$-$Nb_2O_5$ were ren-

dered inaccurate due to thermal decomposition of $Cd_2Nb_2O_7$.

Since it had been shown that complex oxides could be formed in anodic spark reactions, it was thought that anodizing cadmium in niobate solutions might result in the formation of cadmium niobate.

## Experimental

### *Niobate Solution Preparation*

Potassium niobate was prepared by a method which was patterned after that of Reisman, *et al.* (10). A mixture containing 50.1 mole % $K_2CO_3$ and 49.9 mole % $Nb_2O_5$ (from A. D. Mackay, Inc., 198 Broadway, New York 38, N. Y.) was placed in a platinum crucible with the $Nb_2O_5$ in a layer on the bottom. This was placed in an electric furnace at 800°C and the temperature was then raised to 1075°C at 5°C/min. This temperature was held for about 10 min and then was dropped at 2°C/min to 840°C. The fusion product was removed from the furnace at this temperature and air quenched.

After quenching, the solid cake was crushed, washed with 2% $K_2CO_3$ solution, and ground with sufficient additional $K_2CO_3$ (based on the original $Nb_2O_5$ content) to yield a mixture containing 57.5 mole % $K_2CO_3$ and 42.5 mole % $Nb_2O_5$. This mixture was heated at 960°C, held at that temperature 16 hr, cooled to 425°C at 2°C/min, held at 425°C 1 hr, cooled to 215°C at 2°C/min, and then allowed to cool overnight to room temperature.

This solid product was crushed and washed, as above, and ground with sufficient additional $K_2CO_3$ (based on the original $Nb_2O_5$ content) to yield a mixture containing 90 mole % $K_2CO_3$ and 10 mole % $Nb_2O_5$. The firing cycle for this mixture was the same as that for the 57.4 mole % mixture.

The product of this fusion, when dissolved in water, yielded a solution which was straw-yellow and clear. A sample of the solution which was allowed to stand several months remained clear and appeared to be quite stable. The solution was analyzed for niobate (10) and was found to be 0.118M in $KNbO_3$. KOH and possibly $K_2CO_3$ were also present in the solution, but their concentrations were not determined. This solution, diluted 2 to 1 (to 0.04M) was the electrolyte used for subsequent anodic oxidation studies.

### *Apparatus*

The cell used for the anodic oxidation studies was of simple design. It consisted of a 400 ml Pyrex beaker equipped with a rhodium plated copper cooling coil, a thermometer, and a magnetic stirrer. A niobium cathode and a cadmium anode were used. Niobium was used for the cathode because it was conveniently available in this laboratory. It was considered sufficiently inert for this purpose. There was no visible evidence of attack on the cathode. Protecting the anode at the electrolyte surface is usually difficult when the anode reaction involves sparking, and this case was no exception. Masks of plastic insulating tape became charred and were undercut by the electrolyte. This resulted in their rapid failure. This problem was overcome by using ¼ in. diameter cadmium anode rods, onto which were forced tight-fitting Teflon sleeves, restricting the spark reaction to the flat end of the anode surface. Direct current, having less than 5% ripple, was supplied to the cell by a variable rectifier.

### *Operating Conditions*

The operating conditions used during anodizing were selected arbitrarily for the most part, but were based on previous experience and published data on anode phenomena. An electrolyte temperature of 15°C was used because it was known that, when anodic electrical barrier effects are dependent on temperature, they are usually more pronounced at lower temperatures (1). A fairly dilute solution was used because it had been observed with magnesium anodes in chromate solutions that increasing the concentration not only lowered the spark voltage, but could stifle the spark reaction completely (11). Current densities between 0.25 and 0.75 amp/in.$^2$ were used with the niobate solutions. Agitation was used to minimize temperature and concentration gradients in the cell.

## Results and Discussion

### *Anodic Oxidation*

A number of Teflon-shielded cadmium rods were anodized using the conditions given above. In addition, one rod was anodized in 0.1*N* $K_2CO_3$ at about 1 amp/in$^2$. There were very clearly marked differences between the anode reaction of cadmium in niobate and in carbonate solutions.

In the carbonate solution, the voltage rose to 75-80 v, but would rise no higher. At this point the current increased suddenly, and this was accompanied by the formation of a bulky gelatinous film which contained about 95% water. No further work was done with this solution.

In the niobate solution, the anode voltage was initially zero, but was raised manually to maintain the anode current density in the previously stated range. From zero to 75 v, film growth seemed fairly stable and, if the voltage was not continually increased, the current dropped to nearly zero in a few minutes. The coating that formed in this range was very thin and yellow (Fig. 1A). This was thought to be some form of cadmium niobate, but it was not identified.

In the range from 75 to 85 v, the current began to increase rapidly with each small increase in voltage. In this range, a continuous evolution of gas was observed at the anode, and a faint crackling noise could be heard. This noise grew louder as the voltage was raised. Sparks were visible on the anode surface only when the cell was viewed in a darkened room. If the coating was allowed to form in this range for a few minutes, the current dropped and the smooth yellow film, formed at lower voltages, grew thicker and became darker, approaching tan (Fig. 1B).

As the voltage was raised further, the darkening and thickening of the coating continued until at 180-200 v, a third type of anode product appeared. This was a bulky, loosely held cluster of fused particles. Figure 1B shows this coating beginning

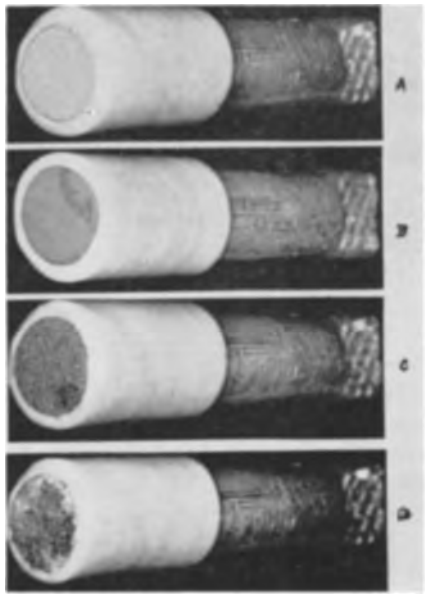

Fig. 1. Cadmium anode coatings in various stages of formation. A, 75 v; B, 75-200 v; C, 200-240 v; D, 200-240 v; prolonged anodic treatment. Magnification 4.5X before reduction for publication.

to form in one area, and in Fig. 1C the coating covers the anode surface. When the anodizing was continued and the current density was kept in the stated range, the voltage rose no higher than 240 v and fluctuated continually. Fluctuations of the current, corresponding inversely to those of the voltage, were also observed. When anodizing in this current and voltage range was prolonged, a stage was finally reached in which the fused reaction product broke away piecemeal, while the spark reaction continued at the anode surface. Figure 1D shows an anode from which material had been forming and breaking away for several hours.

Microscopic examination of all the coatings formed above 80 v in the niobate solution revealed a rough surface composed of fused particles. A sample of this is shown in Fig. 2. In this photograph, the blurred areas are due to the limited depth of focus obtainable with the magnifying camera.

An interesting phenomenon was noted in each anodizing run in niobate solution. As the anodizing continued, the solution became darker and darker. A gray-brown froth clung around the anode, and gray and yellow-brown fused solids were discharged into the solution from the anode. On standing overnight, the dark color of the solution disappeared and a small quantity of a white gelatinous product formed. This was mixed with a fused material, but was easily separated by flushing with water. The yellow-brown fused, or ceramic, material was examined as described in the following section.

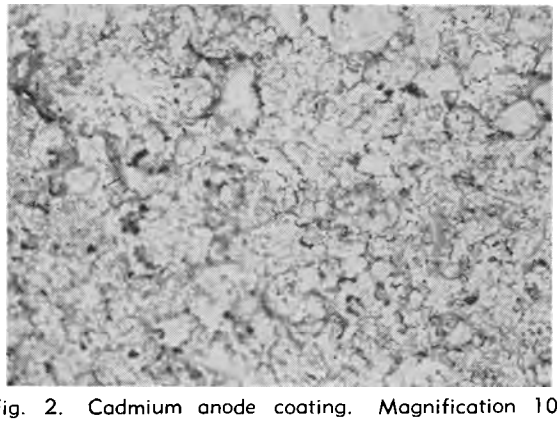

Fig. 2. Cadmium anode coating. Magnification 100X before reduction for publication.

*Anode Product Study*

A sample of the ceramic anode product was washed with distilled water and analyzed, using x-ray diffraction. No pattern was obtained. The same sample was heated for 2 hr at 650°C in an attempt to induce crystal growth. This is about 500° below the temperature at which cadmium oxide volatility becomes a problem in the usual thermal method of making cadmium niobate.

Cadmium oxide, niobium pentoxide, and a physical mixture of these two compounds were all heat treated in the same way as the anode product sample. X-ray diffraction patterns were obtained for all four materials, and also for a known sample of cadmium niobate which was obtained from the Signal Corps Laboratories at Fort Monmouth. The only pattern matching the standard was that of the crystallized anode material.

The original anode product might have been a physical mixture of cadmium oxide and niobium oxide which reacted during heat treatment to form cadmium niobate. This was discounted by the fact that the pattern for the heat-treated physical mixture of the two oxides failed to match that of the standard.

Since cadmium niobate is known to have very unusual electrical properties, attempts were made to convert the crystallized anode product to a solid wafer which could be used for electrical tests. It was desired to avoid high-temperature treatments; therefore, two samples of the crystallized anode product were pressed at room temperature, using pressures of 350,000 and 1,000,000 psi, respectively. Both samples were converted to solid brown wafers which appeared vitreous. Both wafers had small edge cracks which point in toward the center.

The central areas on both sides of each disk were painted with silver paint, and this was allowed to air dry. The wafers were dried in an oven for 24 hr at 110°C, and electrical measurements were made on them as soon as they had cooled to room temperature. The wafer pressed at 1,000,000 psi had almost zero resistance, and this appeared to be due to the silver paint having penetrated through a crack to cause a short circuit. The wafer pressed at 350,000 psi had a resistance of over 1 megohm, which was the limit of the impedance bridge. The results of the other electrical measurements on this specimen are shown in Table I.

**Table I. Electrical characteristics of pressed, anodically formed cadmium niobate**

| | | | |
|---|---|---|---|
| Frequency (cps) | 5000 | 10,000 | 20,000 |
| Capacitance ($\mu\mu$f) | 850 | 610 | 590 |
| Dissipation factor | 0.08 | 0.022 | 0.009 |
| Dielectric constant (calculated) | 890 | 639 | 618 |

d-c resistance = 1 megohm; thickness = 0.038 cm; silvered area = 0.50 cm$^2$.

Wainer and Wentworth (7) measured the dielectric constant and dissipation factor of cadmium niobate at 1000 cycles, obtaining values of 502 and 0.009. Shirane and Pepinsky (8) reported a dielectric constant of 310, measured at 10,000 cycles and room temperature. Hulm (12) obtained somewhat higher values for the dielectric constant at room temperature and noted considerable variation between samples.

The solid wafer appeared to have a strong tendency to absorb moisture. After standing for about 3 hr, exposed to a laboratory atmosphere of about 60% relative humidity, the d-c resistance was found to decrease from 1 megohm to 36,000 ohms. This and the pronounced frequency dependence of the dissipation factor were believed to indicate porosity or electrolytic impurity, or both.

### Conclusions

Crystalline cadmium niobate can be prepared by a two-step process which includes: (*a*) the anodic oxidation of cadmium in a dilute potassium niobate solution, and (*b*) the heat treatment of the anode reaction product at 650°C for 2 hr.

### Acknowledgment

This paper describes experimental work supported by the Ordnance Corps and conducted at Frankford Arsenal under project TB1-0004. The author wishes to express his appreciation to the Ordnance Corps for permission to publish this work. The author is also indebted to Dr. G. F. Nordblom, formerly of Frankford Arsenal, who first suggested the use of anodic processes to prepare ferroelectric materials.

Manuscript received Jan. 13, 1958.

Any discussion of this paper will appear in a Discussion Section to be published in the June 1959 JOURNAL.

REFERENCES

1. A. Guntherschulze, *Ann. Physik*, **34**, 657 (1911).
2. M. S. Hunter and P. Fowle, *This Journal*, **101**, 514 (1954).
3. A. Guntherschulze and H. Betz, *Z. Physik*, **78**, 196 (1932).
4. W. McNeill and R. Wick, *This Journal*, **104**, 356 (1957).
5. H. A. Evangelides, U. S. Pat. 2,723,952, Nov. 15, 1955.
6. W. McNeill, U. S. Pat. 2,778,789, Jan. 22, 1957.
7. E. Wainer and C. Wentworth, *J. Am. Ceram. Soc.*, **35**, 207 (1952).
8. G. Shirane and R. Pepinsky, *Phys. Res.*, **92**, 504 (1953).
9. L. Reed, T. Vasilos, E. D. Harris, and A. P. De Bretteville, "Dielectric and Phase Studies in the System CdO-$Nb_2O_5$," Signal Corps Engineering Laboratories, Fort Monmouth, N. J., Jan. 9, 1956.
10. A. Reisman, F. Holzberg, S. Triebwasser, and M. Berkenblit, *J. Am. Chem. Soc.*, **78**, 719 (1956).
11. W. McNeill, "Chromate Electrolytes for Anodizing Magnesium," Frankford Arsenal Report R-1191, March 1954.
12. J. K. Hulm, *Phys. Rev.*, **92**, 504 (1953).

# Technical Notes

## The Nature of Anode Slime

**D. A. Vermilyea**

*Research Laboratory, General Electric Company, Schenectady, New York*

When a metal is dissolved electrolytically the surface usually becomes covered with a dark-colored material known as "anode slime." This substance either continuously or periodically parts from the surface and falls downward through the solution. It has been thought that this anode slime comprised the impurities which were present in the metal. It is doubtful whether impurities in the metal are responsible, however, since copious quantities of anode slime are formed when silver containing less than 0.01% impurities is dissolved.

In order to determine the nature of the anode slime "high fine" silver (99.99%), obtained from Handy and Harmon Company, was dissolved anodically in a normal silver nitrate solution, pH 3, at about 1 amp/$cm^2$. The anode slime was recovered by filtration, washed, and examined. The x-ray diffraction pattern contained only the lines for metallic silver; no elements other than silver were detected

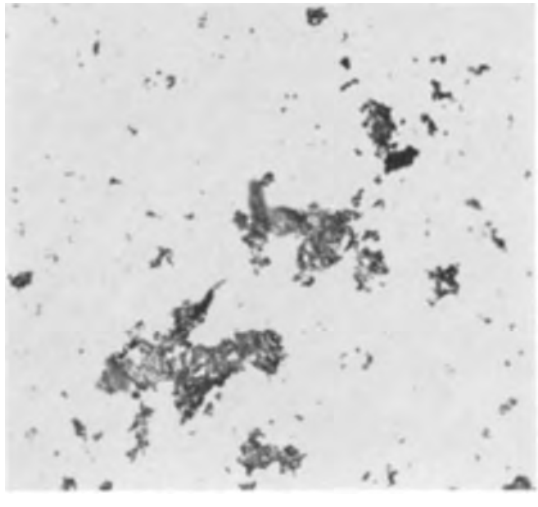

Fig. 1. Particles of anode slime from dissolution of silver. Magnification 100X.

Fig. 2. Section perpendicular to the surface of a silver electrode from which silver was dissolved anodically. Magnification 500X.

by x-ray fluorescence; and chemical analysis showed that the slime was substantially all silver.

Figure 1 shows a photomicrograph of some of the slime particles. Under the microscope they appeared shiny and looked metallic. Figure 2 shows a section perpendicular to the edge of a specimen from which some silver had been dissolved. The surface is very rough, and contains several promontories which look as though they were about to be cut off by the dissolution process.

It is concluded that the anode slime on silver consists of metallic silver; presumably the anode slime on other metals also consists of particles of the electrode metal. It seems likely that the mechanism of slime formation is as follows. Ordinary solutions contain many impurities, some of which adsorb on metal surfaces and cause "passivation." It is typical of silver particularly that electrodeposition from simple salt solutions results in the growth of only a few crystals, most of the surface of the electrode remaining inactive. It seems probable that in dissolution a similar passivation occurs, and that dissolution occurs only at isolated points. Apparently some sections of the metal surface remain passive and are cut off by dissolution from the sides, forming the silver particles which constitute the anode slime.

The experimental work described in this note was performed by W. R. Young, to whom the author is very grateful.

Manuscript received May 16, 1958.

Any discussion of this paper will appear in a Discussion Section to be published in the June 1959 JOURNAL.

# Transport Numbers of the Pure Fused Salts, $LiNO_3$, $NaNO_3$, $KNO_3$, and $AgNO_3$

**Frederick R. Duke and Boone Owens**

*Institute for Atomic Research and Department of Chemistry, Iowa State College, Ames, Iowa*

The alkali nitrates through potassium and silver nitrate were chosen for transport experiments as a series of salts similar in conductivity and charge type; the sizes and masses of the cations, however, are widely variant. Thus the series appears to be one in which the effects on mobility of size and mass of ions may be tested.

## Experimental

The transport experiments were done in a cell which has been described previously (1). In all cases the electrodes were of solid Ag surrounded by molten $AgNO_3$. When studying salts other than $AgNO_3$, cells were used which contained a capillary constriction between the alkali nitrate which filled the upper portion of the cell and the $AgNO_3$ at the bottom in contact with the silver. The mixing that did occur took place in the capillary and is not important because it has been shown that there is very little volume change when these salts are mixed with $AgNO_3$. Currents of about 50 ma for 1000 to 5000 sec were used when volume changes in the capillary were observed and several readings were taken for each salt. All salts were run at temperatures controlled to ±1°C. The salts used were A. C. S. reagent grade.

## Results and Discussion

In the cell Ag; $AgNO_3$; $MNO_3/MNO_3$; $AgNO_3$; Ag, the transport number of the cation $M^+$ is given by:

$$t^+ = \frac{1}{V_{MNO_3}}\left(\frac{\Delta Vc}{Z} + V\mathrm{AgNO_3} - V_{Ag}\right)$$

where $V$ refers to the molar volumes, $\Delta Vc$ is the volume change of the catholyte, and $Z$ is the current passed. The molar volumes were available from the literature (2-5).

The values of $\Delta Vc/Z$ and the resulting transport numbers are shown in Table I.

Since the membranes in all cases were made of sintered Pyrex, the transport numbers measured are those of the salt suspended in the pores of the glass;

Table I. Transport numbers and equivalent conductances of the ions and salts

| Salt | λ (350°C) | $V_c$ $\frac{(cm^3)}{Eq.}$ | t+ | λ+ (350°C) | λ− (350°C) |
|---|---|---|---|---|---|
| $LiNO_3$ | 53.55 | −0.5±2.2 | 0.84±0.06 | 45.0±3.2 | 8.6±3.2 |
| $NaNO_3$ | 52.46 | −2.2±0.4 | 0.71±0.01 | 37.2±0.5 | 15.3±0.5 |
| $KNO_3$ | 35.55 | −0.9±1.3 | 0.60±0.03 | 21.3±1.1 | 14.2±1.1 |
| $AgNO_3$ | 55.82 | −1.5±2.6 | 0.72±0.06 | 40.2±3.3 | 15.6±3.3 |

thus the glass takes the place of the solvent which is normally present in transport experiments, and the transport numbers are measured with respect to the glass. The rest of the apparatus and salt not in the membrane are merely conveniences to ascertain what happens in the membrane. It is assumed, in calculating mobilities of ions in fused salts, that the relative mobilities in the membrane and in the pure salt are the same; then $\lambda^{\pm} = t^{\pm}\lambda$, where $\lambda^{\pm}$ is the ionic equivalent conductivity in the pure salt, $t^{\pm}$ the transport number of the ion in the membrane, and $\lambda$ the equivalent conductivity of the salt. Table I also contains ionic equivalent conductivities.

Since, in the membrane, the ions encounter resistance to motion by the ions immobilized at the glass surface, it might be expected that the size of the ion would be important. If, on the other hand, interactions of importance occurred only between ions of opposite charge, the interaction forces would cancel, and the controlling factor should be the momentum balance which depends on the masses of the ions. Sundheim (6) has shown that the mass dependence under these special conditions would be:

$t_+ = \dfrac{m^-}{m_+ + m_-}$, where the $m$'s are the equivalent weights of the ions. This transport number is of little significance because, in the general case, one would expect the two ions to impart momentum to the membrane, due to unequal interactions with the membrane.

The effect of size can be calculated; if it is assumed, for example, that the radius of the ion is the important factor, such as in Stokes law (7), the derivation below follows.

$$F_v = k\, r\, v$$

where $F_v$ is the frictional force felt by a moving ion, $k$ is the proportionality constant, $r$ the ionic radius, and $v$ the velocity of the ion. The electrical force felt by an ion in an electric field is: $Fe = E\, z\, e$, where $E$ is the magnitude of the field, $z$ is the valence of the ion, and $e$ is the charge on the electron. Applying these equations to the case of the univalent salt, one arrives at the steady-state: $\dfrac{r_+}{r_-} = \dfrac{v_-}{v_+}$,

and since $t_+ = \dfrac{v_+}{v_+ + v_-}$, it follows that $t_+ = \dfrac{r_-}{r_+ + r_-}$.

Table II lists the experimental transport numbers and the values calculated from the equation. TlCl is included, representing a salt for which data are available (8). The agreement of experimental with calculated transport numbers is quite good, since the radii are those exhibited by certain solids rather than by liquids; and further, it is likely that, in general, the mobility depends on a more complex function of the radius than is assumed above.

Table II. Experimental and calculated transport numbers

| | $t_+$ | $r_+$ (Å) | $r_-$ (Å) | $\dfrac{r_-}{r_+ + r_-}$ |
|---|---|---|---|---|
| $LiNO_3$ | 0.84 ± 0.06 | 0.60 | 2.3 | 0.82 |
| $NaNO_3$ | 0.71 ± 0.01 | 0.95 | 2.3 | 0.71 |
| $KNO_3$ | 0.60 ± 0.03 | 1.33 | 2.3 | 0.63 |
| $AgNO_3$ | 0.72 ± 0.06 | 1.26 | 2.3 | 0.65 |
| TlCl | 0.51 ± 0.02 | 1.44 | 1.81 | 0.55 |

The values for $r_+$ and $r_{Cl^-}$ are taken from ref. (10); $r_{NO_3^-}$ is taken from ref. (11).

The mass ratio equation agrees with the experimental data in the cases of the alkali nitrates since, for those involved here, the mass of the ion is very nearly a linear function of its radius. Salts other than univalent ones have not been included because they appear to be primarily anionic conductors (9) in spite of the small cation size or mass. Thus, it appears that the transport number is strongly dependent upon the relative charge of the cation and anion.

Manuscript received Oct. 1, 1957. It is Contribution No. 546; the work was performed in the Ames Laboratory of the U.S.A.E.C.

Any discussion of this paper will appear in a Discussion Section to be published in the June 1959 JOURNAL.

REFERENCES

1. F. R. Duke, R. W. Laity, and B. Owens, *This Journal*, **104**, 299 (1957).
2. J. Byrne, H. Fleming, and F. E. W. Wetmore, *Can. J. Chem.*, **30**, 922 (1952).
3. H. M. Goodwin and R. D. Mailey, *Phys. Rev.*, **25**, 469 (1907); *ibid.*, **26**, 28 (1908).
4. H. Bloom, I. W. Knapp, J. J. Molloy, and P. Welch, *Trans. Faraday Soc.*, **49**, 1458 (1953).
5. K. Scheel, *Z. Physik.*, **5**, 167 (1921).
6. B. R. Sundheim, *J. Phys. Chem.*, **60**, 1381 (1956).
7. M. F. R. Mulcahy and E. Heymann, *J. Phys. Chem.*, **47**, 485 (1943).
8. R. W. Laity and F. R. Duke, *This Journal*, **105**, 97 (1958).
9. E. Heymann and H. Bloom, *Nature*, **156**, 479 (1945).
10. L. Pauling, "The Nature of the Chemical Bond," 2nd ed., p. 346, Cornell University Press, Ithaca, N. Y. (1948).
11. A. F. Wells, "Structural Inorganic Chemistry," 2nd ed., p. 138, Oxford University Press, London (1950).

# Report of the Chlor-Alkali Committee of the Industrial Electrolytic Division for the Year 1957

**R. B. MacMullin**

*R. B. MacMullin Associates, Niagara Falls, New York*

**Jeff C. Cole**

*Diamond Alkali Company, Cleveland, Ohio*

U. S. chlorine production in 1957 was 3,917,419 tons as compared to 3,797,702 tons for 1956. This represents an increase of only 3% above the 1956 level, whereas the trend during the past few years has been of the order of 7 or 8% increase per year. Electrolytic caustic production in 1957 increased 5% over 1956 although total caustic production increased only 2½%. Caustic soda made by the lime soda process continued to decline in 1957 and for the year represented only 7.9% of the total as compared to 10% in 1956.

The production of electrolytic potash declined somewhat in 1957. This is also true of the production of sodium metal. The total production of soda ash declined 6% in 1957, although the production of natural soda ash showed a slight gain. At the present time 87.4% of all soda ash is made by the synthetic process which now includes the manufacture of soda ash from caustic cell liquor. These results are summarized in Table I.

Chlorine produced coincidentally with caustic soda accounts for 90% of the total, as shown in Table II. Chlorine made in sodium cells accounts for 5.2%. Of the chlorine produced by brine electrolysis approximately 15.4% was made in mercury cells. In 1958 this figure is expected to increase to about 20%.

Approximately 1080 tons per day of new chlorine capacity was brought in during 1957. New chlorine capacity is expected to increase by an additional 1400 tons in 1958. Total production capacity of chlorine for the country is expected to be of the order of 13,900 tons per day by the end of 1958. Because of the current recession it is predicted that the total chlorine production for 1958 will not exceed 4 million tons. This means that by the end of the current year production facilities for chlorine will be utilized only to the extent of about 80%. So far as we are aware no new plans for increased chlorine production have been announced since early 1957. It is assumed that the normal upward trend of chlorine production will resume at the conclusion of the present business recession.

In Canada, chlorine capacity in 1957 was of the order of 790 tons per day. This is expected to increase to approximately 945 tons per day by the end of 1958. (There will then be 12 Canadian plants.) Total Canadian production of chlorine in 1957 has been estimated at 210,000 tons.

Table I. Chlor-alkali statistics, 1956 and 1957

| | 1957 | 1956 |
|---|---|---|
| Chlorine, total tons | 3,917,419 | 3,797,702 |
| NaOH, electrolytic | 3,975,609 | 3,794,963 |
| NaOH, lime soda | 341,210 | 422,034 |
| NaOH, total | 4,316,819 | 4,216,997 |
| NaOH, per cent electrolytic | 92.1 | 90.0 |
| KOH, 90% basis | 83,898 | 92,342 |
| $Na_2CO_3$, synthetic | 4,650,588 | 4,997,579 |
| $Na_2CO_3$, natural | 676,611 | 654,890 |
| $Na_2CO_3$, total | 5,327,199 | 5,652,469 |
| $Na_2CO_3$, per cent synthetic | 87.4 | 88.3 |
| Na metal | 132,977 | 136,018 |

Table II. Chlorine balance, 1957

| | Tons | % |
|---|---|---|
| $Cl_2$ equiv. of NaOH | 3,523,384 | 90.0 |
| $Cl_2$ equiv. of KOH | 47,714 | 1.2 |
| $Cl_2$ equiv. of Na | 204,958 | 5.2 |
| $Cl_2$ equiv. of electrolytic soda ash<br>$Cl_2$ equiv. of $K_2CO_3$<br>$Cl_2$ equiv. of nitrosyl process<br>$Cl_2$ equiv. of HCl oxidation | 141,363 | 3.6 |
| $Cl_2$ total gas produced | 3,917,419 | 100.0 |

## Markets and End-Use Patterns

There have been no significant changes in the end-use pattern of chlorine and caustic soda during the year 1957. Long range trends, however, have been detected and projected into the future. Tables III and IV are quoted from a paper by Theodore Sheets, Jr.[1]

The manufacture of high-energy fuels for military use could have a significant effect on the electrolytic industries. Boron fuels, for example, re-

[1] Chemical Engineering Progress, 53, 482 (1957).

Table III. Trends in chlorine use 1935-1975
(M Short Tons)

| | Chemicals | % | Pulp & Paper | % | Sanitation | % | Cotton Textiles | % | Net Exports† | % | Total Production |
|---|---|---|---|---|---|---|---|---|---|---|---|
| 1935 | 161 | 48.8 | 109 | 33.0 | 35 | 10.6 | 19 | 5.8 | 6 | 1.8 | 330 |
| 1955 | 2,745.5 | 80.6 | 510 | 14.9 | 117 | 3.4 | 5.5 | 0.2 | 30 | 0.9 | 3,408 |
| 1956 | 3,113 | 82.3 | 527 | 13.9 | 122 | 3.2 | 4 | 0.1 | 19 | 0.5 | 3,785 |
| 1965 | 6,400 | 86.5 | 800 | 10.8 | 155 | 2.1 | (7)* | (<0.1)* | 45 | 0.6 | 7,400 |
| 1975 | 9,640 | 87.7 | 1,100 | 10.0 | 200 | 1.8 | (10)* | (<0.1)* | 60 | 0.5 | 11,000 |

† Net exports = exports minus imports.
* Absorbed in chemicals.

quire sodium hydride and boron trichloride, in turn made from sodium and chlorine. Hydrazine requires chlorine. Ammonium perchlorate requires sodium chlorate as a raw material. It is also significant that a number of industrial mergers have been formed to manufacture high-energy fuels; each group includes a chlor-alkali manufacturer.

### Announcements of New Plants and Expansions

Among the new or expanded plants completed and brought into production in 1957 are the following: Allied Chemical and Dye Company, Brunswick, Ga., 260 tons per day total capacity; Columbia Southern, expansion at Lake Charles, La., 250 tons per day; Food Machinery Company, Westvaco Chemical Division, South Charleston, W. Va., rehabilitation and expansion by 90 tons to a total of 460 tons per day; Kaiser Aluminum and Chemical Corporation, Gramercy, La., 100 tons per day; Olin Mathieson Chemical Corporation, McIntosh, Ala., expansion 125 tons per day; Pennsalt Chemicals Corporation, Calvert City, Ky., expansion 100 tons per day; Weyerhaeuser Timber Company, Longview, Wash., new plant 80 tons per day.

Among the new plants scheduled to be completed in 1958 are the following: Columbia Southern, Natrium, W. Va., 160 tons per day (Uhde mercury cell); Diamond Alkali Company, Deer Park, Texas, 200 tons per day (DeNora 18 SGL); Dow Chemical Company, Plaquemine, La., 300 tons per day (Dow bipolar cell); Jefferson Chemical Company, Port Neches, Texas, 150 tons per day (Hooker S-3B cell); Wyandotte Chemical Corporation, Geismar, La., 300 tons per day (Diamond diaphragm cell); Weyerhaeuser Timber Company, Longview, Wash., expansion 80 tons per day (DeNora cells); E. I. du Pont de Nemours, Memphis, Tenn., 100 tons per day (Downs sodium cell); Allied Chemical and Dye Company, Hopewell, Va., 90 tons per day (nitrosyl process).

In Canada, Dow has announced expansion at Sarnia, Ont.; Western Chemicals, du Vernay, Alta., is doubling its capacity to 80 tons per day in 1958; and Shawinigan Chemicals at Shawinigan Falls, Que., is building a new Krebs mercury cell plant, capacity 50 tons per day. The new Hooker plant at Vancouver, B. C., capacity 100 tons per day, commenced operations in late 1957. The Electric Reduction Company has built a new chlorate plant at Vancouver, B. C.

Diamond Alkali Company announced that it will terminate its lease on the Pine Bluff, Ark., Arsenal chlor-alkali facility as of April 27, 1958.

Chemical Salt Production Company, Salt Lake City, jointly owned by Hooker Electrochemical Company and Pennsalt Chemicals Corporation, is now producing chemical grade salt which is to be shipped to the owners' plants in the Tacoma-Seattle area.

### Technical Developments

An outstanding paper describing horizontal and vertical mercury cell development in Europe and the United States was presented by Mr. H. A. Sommers, Air Products, Incorporated at the American Institute of Chemical Engineers meeting, Seattle,

Table IV. Trends in caustic soda—End-use
(M Short Tons)

| | 1935 | % | 1955 | % | 1965 | % | 1975 | % |
|---|---|---|---|---|---|---|---|---|
| Chemicals | 118 | 16.5 | 1,050 | 26.9 | 2,350 | 31.0 | 4,000 | 36.0 |
| Rayon | 158 | 22.0 | 695 | 17.8 | 680 | 9.0 | 780 | 6.9 |
| Film | — | — | — | — | 320 | 4.2 | 420 | 3.8 |
| Pulp and paper | 43 | 6.0 | 258 | 6.6 | 480 | 6.3 | 680 | 6.1 |
| Export | 71 | 9.9 | 227 | 5.8 | 330 | 4.3 | 450 | 4.0 |
| Petroleum refining | 90 | 12.6 | 215 | 5.5 | 335 | 4.4 | 460 | 4.1 |
| Lyes and cleaners | 31 | 4.3 | 160 | 4.1 | 295 | 3.9 | 390 | 3.5 |
| Cotton textiles | 34 | 4.7 | 137 | 3.5 | 190 | 2.5 | 250 | 2.2 |
| Soap | 96 | 13.4 | 82 | 2.1 | 60 | 0.8 | 55 | 0.5 |
| Reclaimed rubber | 11 | 1.5 | 27 | 0.7 | 10 | 0.1 | — | — |
| Vegetable oils | 9 | 1.3 | 24 | 0.6 | 35 | 0.5 | 45 | 0.4 |
| All others (including metallurgical uses) | 55 | 7.8 | 1,030 | 26.4 | 2,515 | 33.0 | 3,670 | 32.5 |
| Metallurgical uses | — | — | — | — | (600) | (7.9) | (1,200) | (10.7) |
| Total production | 716 | — | 3,905 | — | 7,600 | — | 11,200 | — |

Wash., June 1957. This article was published in full in the September and October issues of *Chemical Engineering Progress*, Vol. 53, p. 409 and 506. The October publication is an exhaustive tabular compilation of chlorine producing companies in the United States and Europe as of June 1, 1957 and proposed expansions by 1958. The data includes company names, plant locations, capacity, type of cells, and in some instances the number of cells and amperage.

Three important papers were presented at a symposium on "Trends in the Chlor-Alkali Industry" at the Baltimore meeting of the American Institute of Chemical Engineers in September 1957. The titles included the following: "End-Use" by T. A. Sheets, Jr., Diamond Alkali Company; "Technology" by R. B. MacMullin, R. B. MacMullin Associates; and the "Inter-relationship Between the Chlor-Alkali and the Soda Ash Industries" by M. E. Clark, Frontier Chemical Company and C. F. Gerlach, Wyandotte Chemicals Corporation. The first and third of these papers have been published in *Chemical Engineering Progress,* Vol. 53, p. 482 and 537.

Some new data on the thermodynamic properties of chlorine and hydrochloric acid were published by C. J. Dobratz, *Chemical Engineering,* Vol. 65, No. 3, p. 144 (1958).

Manuscript received May 13, 1958. This paper was prepared for delivery before the New York Meeting, April 27-May 1, 1958.

Any discussion of this paper will appear in a Discussion Section to be published in the June 1959 JOURNAL.

# Lead-Acid Storage Batteries
# Changes In Positive Active Material Density During Various Conditions of Service

J. F. Dittmann and J. F. Sams

*Research Laboratories, The Eagle-Picher Company, Joplin, Missouri*

ABSTRACT

Observations made on the lead-acid battery indicate that changes occur in the apparent density of the positive active material during service. To determine the extent of these density changes, measurements have been conducted during all usual conditions of testing. The apparent density of the positive active material has been found to decrease regardless of active material shedding. This finding appears to explain many of the observed performance characteristics of the lead-acid battery.

When observing the performance characteristics of many batteries tested under various conditions, it became evident that changes were occurring in the apparent density of the positive active material during the life of the battery. To determine the extent of these changes, density determinations were conducted periodically on positive plates during their life on each of the SAE cycling, overcharge and Emark tests, during storage, and in SLI service. Fundamental performance and life characteristics of batteries subjected to these various tests have been presented (1).

## Experimental

All data accumulated in this study were obtained from standard 15 plate 100 amp-hr battery assemblies which were tested on the various life tests. Prior to life testing, density determinations were made on representative positive plates from each group of batteries before formation, after formation, and after completion of six initial cycles.

The method used for conducting density determinations on a battery plate has been described by Dittmann and Harner (2). Briefly, the procedure is as follows: data for calculating apparent $PbO_2$ density are obtained by weighing the dry battery plate, filling the pores of active material with water, and determining the full plate volume by water displacement through use of a specially designed apparatus. The plate is again dried and weighed after first removing approximately two-thirds of its material. A second volume measurement is conducted as before on the partially filled plate. Weight and volume values are obtained by differences and used to calculate apparent density. The method has sufficient accuracy to obtain suitable values for comparison.

Starting with positive plates of known $PbO_2$ density, changes were observed by means of measurements made on representative plates periodically during the various recognized life tests (1). The consolidated data appearing in Fig. 1 are presented as indicative rather than absolute because it is evident that other conditions such as temperature, original $PbO_2$ density, grid metal and grid design, type of oxide, etc., may alter the degree of density change.

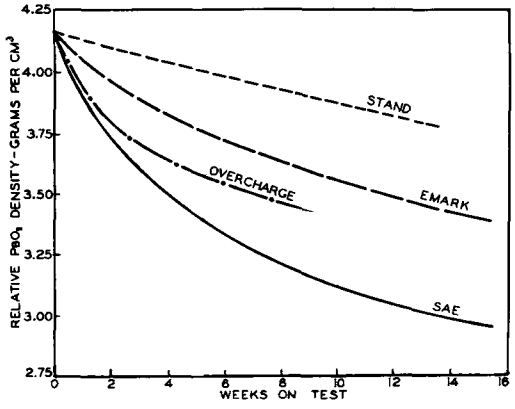


Fig. 1. Decrease in apparent $PbO_2$ density of positive plates during various conditions of testing.

## Discussion

Perhaps the most important finding disclosed by data in Fig. 1 is the fact that the apparent density of the positive active material was found to decrease regardless of conditions of testing or of the extent of positive active material shedding. More specifically it is noted that the degree of change in $PbO_2$ density is greatest for batteries subjected to the SAE "deep" cycling test. Positive plates subjected to overcharging and to the "shallow" cycling Emark test were found to decrease somewhat less in density. The fact that active material of positive plates decreased in density upon storage in sulfuric acid is also of significance. In summarizing, it may be stated that the apparent density of the active material of positive plates is caused to decrease by deep cycling, by shallow cycling, by overcharging, and by storage in sulfuric acid.

Of further significance is the fact that these characteristic decreases in $PbO_2$ density can be related to

all fundamental causes of failure commonly observed in the lead-acid battery regardless of conditions of service.

For example, the act of positive material shedding in deep cycling services can be explained simply by the fact that, as positive active material decreases in density and expands and the active material alternates between lead peroxide and lead sulfate, the crystalline bonds are disrupted causing the material to fall or be washed free from the plate.

In overcharge and shallow cycling service conditions, shedding of positive material normally does not occur because there is little or no disruption of the $PbO_2$ bonds by formation of lead sulfate. However, the act of overcharging a battery in absence of cycling also causes an appreciable decrease in $PbO_2$ apparent density, and since no appreciable shedding of material occurs, the active material must expand. This expansion exerts pressures on the grid frame and its members, causing them to break at weak points, particularly as the grid becomes weakened by electrolytic corrosion. The result is a continued loss in positive plate conductivity as the plate disintegrates.

It is recognized that the grid frame and its members also are caused to expand by products of electrolytic corrosion, and this process also contributes to ultimate positive plate disintegration. It has become evident from these investigations that the expanding forces exerted by positive active material and by products of grid corrosion are the major, if not the most important cause of battery failure in services characterized by overcharging. This is substantiated by the fact that, after a positive plate has failed by disintegration as a result of overcharging, shallow cycling, or storage, it will still contain anywhere from 50% to 80% of its original weight of grid metal.

Further evidence of the effect of $PbO_2$ expansion on positive plate disintegration is disclosed by the condition of positive plates as revealed in Fig. 2. Batteries of identical assembly, but containing positive active material at various densities, were subjected to four weeks of SAE overcharge testing. Plate No. 7, Fig. 2, contained active material lowest in initial $PbO_2$ density and was characterized by the lack of grid frame breakage. Likewise, Plate No. 8, although showing signs of complete deterioration,


Fig. 2. Effect of $PbO_2$ expansion on positive plate disintegration.

Results of four weeks SAE overcharge testing

| Positive plate No. | 7 | 8 | 9 |
|---|---|---|---|
| Original $PbO_2$ density | 4.03 | 4.27 | 4.64 g/cm³ |
| Final $PbO_2$ density | 3.54 | 3.78 | 4.09 g/cm³ |
| Final capacity efficiency | 1.31 | 1.09 | 0.49 amp-hr/28.35g |

was in better condition than No. 9 which was highest in $PbO_2$ density. The effect of stresses applied to the grid by expanding $PbO_2$ and its subsequent disintegration was also reflected by the much lower capacity output of the No. 9 plate. The appearance and condition of these plates would appear to be conclusive evidence that other factors than grid corrosion were at play. Since all plates represented in Fig. 2 were subjected to the same number of ampere-hours of overcharge, it follows that each should have developed the same amount of grid corrosion. Therefore, the obvious differences in plate appearance and degree of disintegration must be related to stresses exerted by expanding $PbO_2$ and/or other factors.

Positive plates subjected to overcharging or SLI service often warp and buckle causing wear to separators that results in battery failure. The mechanism by which a positive plate is caused to warp or buckle can, likewise, be explained by considering reduction in positive active material density during service. Seldom, if ever, is a positive plate prepared with equal distribution of paste on both sides, nor is all paste in any one plate always of the same density. Under these conditions the active material expands unequally causing stresses to be applied more in one direction than in another. As growth continues, the plates warp or buckle with the concavity toward the side of lesser active material expansion.

It is known that a lead-acid battery has a greater ampere-hour capacity after activated storage than before. This fundamental increase in capacity resulting from activated storage prior to testing was first reported by Harner and Chubb in 1935 (3). The phenomenon may be explained by consideration of changes occurring in the $PbO_2$ density during storage in sulfuric acid. As is apparent from data recorded in Fig. 1, the positive plates of a battery allowed to stand in storage for no more than a one-month period will decrease substantially in $PbO_2$ density. The increase in capacity efficiency which accompanies a decrease in positive $PbO_2$ density would explain in part, if not entirely, the reason for the observed increase in capacity which occurs as a result of storage.

A lead-acid battery in automobile service is normally subjected to shallow cycling, to overcharging, and to many hours of idleness, all of which have been shown to cause a decrease in positive active material density. From these considerations, positive plates subjected to SLI service would be expected to reveal density changes similar to those obtained upon Emark and overcharge testing. Measurements made on positive plates removed from car service disclose this to be true. Therefore, it may be concluded that stress applied to grids by expanding positive active material is a major contributing cause of failure in batteries placed in automobile service.

## Conclusions

The active material density of formed positive plates of the lead-acid battery decreases substan-

tially and progressively when subjected to deep cycling, shallow cycling, overcharging, activated storage, or automobile service. It appears that this reduction in positive active material density with service exerts a marked influence on battery performance characteristics and on the ultimate failure of the positive plate.

Manuscript received Jan. 27, 1958. This paper was prepared for delivery before the Buffalo Meeting, Oct. 6-10, 1957.

Any discussion of this paper will appear in a Discussion Section to be published in the June 1959 JOURNAL.

REFERENCES

1. J. F. Dittmann and H. R. Harner, *This Journal*, **101**, 533 (1954).
2. J. F. Dittmann and H. R. Harner, "Starting and Lighting Batteries," No. 7 in a Series, "Paste Preparation and Plate Control," The Eagle-Picher Company (1956).
3. H. R. Harner and M. F. Chubb, *Trans. Electrochem. Soc.*, **68**, 309 (1935).

# Self-Discharge Reactions In Lead-Acid Batteries

**Paul Rüetschi and R. T. Angstadt**

*Research Department, The Electric Storage Battery Company, Philadelphia, Pennsylvania*

ABSTRACT

A theoretical and experimental analysis of the self-discharge of lead-acid batteries shows that seven different reactions contribute to the process. The rate of each has been determined. It is shown that positive plate self-discharge is due primarily to a reaction between $PbO_2$ and grid metal. The rate of this reaction decreases with increasing acid concentration because of the passivating action of the $PbSO_4$ layers formed. The passivating action is decreased by the presence of antimony in the grid, producing pores in the $PbSO_4$ layers and providing further access of the electrolyte to the grid. At low acid gravities antimony compounds become almost insoluble and can act as passivators decreasing the reaction between grid metal and $PbO_2$. Other self-discharge reactions in positive plates are the decomposition of water by $PbO_2$ with evolution of oxygen and the oxidation of separator material in contact with $PbO_2$. Oxidation of hydrogen, coming from the negative plates, occurs at immeasurably small rates.

Self-discharge of the negative plates is due to the reaction between $H_2SO_4$ and lead, producing $H_2$ and $PbSO_4$. This reaction is slow in absence of foreign substances because of the high hydrogen overvoltage on lead. However, contamination of the negatives with antimony decreases the hydrogen overvoltage and greatly accelerates the self-discharge of negative plates. Furthermore, negative plates are self-discharged by oxygen dissolved in the electrolyte. The rate of reduction of oxygen is so fast on a lead electrode in sulfuric acid that the reaction is diffusion controlled.

Self-discharge, also referred to by the terms "open circuit loss," "local action," and "sulfation," of lead-acid batteries has received a great deal of attention in the past, especially in connection with standby batteries for telephone systems, with the storage of charged automobile batteries, and with special applications where the evolution of gas may be hazardous.

Battery engineers are accustomed to relate self-discharge mainly to the negative plates. It is interesting to note, however, that Vinal (1) early pointed out that self-discharge also occurs in the positive plates. He found that negative plates sulfated faster with increasing acid concentration, whereas self-discharge of the positive plates decreased with increasing acid concentration (2). He determined self-discharge rates by the method of weighing plates and this has the disadvantage of difficultly interpretable results because the weighings are made in solution and buoyancy corrections are necessary. These corrections may be different for different self-discharge reactions (see Eqs. [1] and [2]). Therefore, a correct interpretation of the weight figure is not possible without knowing the relative rate of each of the two reactions. Vinal regarded positive plate self-discharge as the result of a reaction which is the same as the cell reaction of lead acid batteries according to the double sulfation theory (3, 4). The same reaction was considered by Lander (5, 6). Positive plates sulfate faster than the negative plates in new batteries (7, 8). The influence of forming temperature on self-discharge of positive plates has also been studied (7). It had been noted before by Hatfield and Brown (9) that, on cycling test, there is an increase in the shedding of positive active material with decrease in the forming temperature. At higher temperatures, formation is more complete and less "apparent PbO" is left in the plates. Self-discharge of the positive plates decreased with increasing forming temperatures. Greenburg and Caldwell (7) attributed 50% of the self-discharge rate of positives to direct sulfation of $PbO_2$ accompanied by oxygen liberation, 25% to a "potential difference reaction" between grid metal and $PbO_2$, and 25% to sulfation of "apparent PbO." Increasing temperature caused higher

corrosion of the positive grids during formation and therefore an increase in antimony transfer to the negatives and higher self-discharge of the negatives (9).

Lander (10) found the self-discharge of the positive plate to occur at rates comparable to negative plate self-discharge. His experiments were made with cells which had previously received some overcharge and cycling. Lander suggests that the self-discharge of the positive plate is due primarily to oxidation of the Sb phase in the grid.

The self-discharge reaction occurring in the negative plate has usually been assumed to be an attack on Pb by $H_2SO_4$ with $H_2$ evolution. Contamination of the negative plate with Sb catalyzes this reaction to a high degree (11-15). A great deal of work on the self-discharge of lead-acid batteries and especially the influence of temperature on self-discharge has been done by Zachlin (16, 17), but most of his work has been concerned with full size cells and not with single positive or negative plates. In the present paper a detailed discussion of the various self-discharge reactions and a determination of their relative rates is presented.

## Experimental

Single positive plates, single negative plates, and three-plate cells with one positive and two negatives were placed in electrolytes whose gravities and temperatures were kept constant to $\pm 0.002$ g/cm$^3$ and $\pm 0.5$°C, respectively. All experiments were performed at 35°C unless otherwise noted. The specific gravities were adjusted at 26.7°C. Plates were analyzed for sulfate after 2, 4, 8, and 16 weeks. All the cells had a large excess of electrolyte, one single plate or a three-plate cell being placed in a jar with 1000 cc $H_2SO_4$ of a given gravity. The separators used were microporous rubber separators unless stated to the contrary. The positive plates had a capacity of 7.2 amp-hr at the 5 hr rate. The grids were 13.35 cm high, 10.6 cm wide and 0.17-0.18 cm thick. Positive and negative plates had identical dimensions. The composition of the grid alloys used in this study are given in Table I (18). Bismuth, iron, and nickel are not shown in the table but were all in the usual low range and without significance for this study.

The paste for the positive plates was prepared using 80% gray oxide and 20% red lead. The mix was made with 51 cc of water and 21 cc of $H_2SO_4$ (sp gr 1.400) per 453 g of active material. The negative paste contained 95% gray oxide and 5% 232 W (National Lead Company) and the mix was made using 51 cc of water and 25 cc of $H_2SO_4$ (sp gr 1.400) per 453 g of active material.

Table I. Analysis of the lead alloys used (in % per weight)

| Alloy No. | Sb | As | Sn | Ag | Cu | Ca | Al | Se | Te |
|---|---|---|---|---|---|---|---|---|---|
| 1 | 4.80 | 0.28 | 0.16 | 0.008 | 0.008 | — | — | — | — |
| 2 | 4.80 | 0.23 | 0.03 | 0.003 | 0.025 | — | — | — | — |
| 3 | 5.76 | 0.48 | 0.51 | 0.122 | 0.003 | — | — | — | — |
| 4 | 2.58 | 0.045 | 0.0001 | 0.004 | 0.010 | — | — | — | — |
| 5 | 3.36 | 0.03 | 1.66 | 0.008 | 0.003 | — | — | 0.026 | — |
| 6 | — | — | — | — | — | 0.082 | 0.006 | — | — |
| 7 | — | — | — | — | — | 0.070 | 0.010 | — | — |
| 8 | 4.20 | 0.11 | 0.62 | 0.161 | 0.040 | — | — | — | 0.040 |
| 9 | 4.26 | 0.47 | 0.51 | 0.106 | 0.005 | — | — | — | — |
| 10 | 4.20 | 0.03 | 4.36 | 0.003 | 0.008 | — | — | — | — |
| 11 | — | — | — | — | — | — | — | — | — |
| 12 | — | — | — | — | — | 0.066 | — | — | — |

Positive plates were set at room temperature and humidity for 44 hr and at completion of this time sprayed, drained, piled, and aged for 4 days. The negative plates were set for 30 hr at 51.7°C in 90% humidity, air dryed, and stored 3 days before use.

Plates with a given grid alloy were always formed against plates with the same grid alloy, the formation procedure being conventional, namely, 18 hr with 2 amp per positive plate in 1.070 sp gr acid in 11-plate cells. Then the cells were dumped and refilled and the acid adjusted to 1.250 sp gr, using a 5 hr mixing charge with 2 amp per 11-plate cell. All cells were then given one cycle consisting of a 5-hr discharge at 7.2 amp and a 9-hr charge at 5.0 amp. The cells were then taken apart and single-plate and three-plate cells were built. In the three-plate units, negative and positive plates had the same grid alloy. In order to study the influence of the separators on the rate of self-discharge, single plates covered on both sides with a separator were also placed in electrolytes of constant gravity. Three different separator types were studied, paper (phenolic-bound), spun glass with inert backing, and microporous rubber. Some of these experiments were made using electrolytes dosed with various amounts of $Sb_2(SO_4)_3$ in order to investigate the filtration action of the separators. Finally, active material was knocked out of formed plates with Sb-free grid alloy and placed in electrolytes of various gravities at constant temperature. The formation of sulfate was followed by analysis after 2, 4, 8, and 16 weeks. By this procedure the reaction of isolated active material with $H_2SO_4$ could be studied.

Samples of the active material of the plates were taken after the indicated time periods by removing the plates from the electrolyte, punching out a number of pellets of active material, grinding the active material in a mortar, and washing with water. The material was then filtered and dried. A 2-g sample of the dry material was boiled for 1 hr in a solution of 15-g of $Na_2CO_3$ in 100 cc of water. The solution was filtered, made acidic with HCl, and boiled to remove $CO_2$. Finally, the sulfate was precipitated with 20 cc of a 15% solution of barium chloride. The barium sulfate was collected in a Gooch crucible by filtration and dried over a burner at red heat until the weight was constant.

## Results

The weight percentage of lead sulfate of washed and dried samples expresses the total amount of $SO_4$ in the form of $PbSO_4$. That means that any $SO_4$ present in the form of $(SbO_2)_2SO_4$ or in the form of basic lead sulfates appears as $PbSO_4$. A detailed analysis of each self-discharge product would have been more rigorous, but, since $PbSO_4$ is the major self-discharge product, no considerable error is introduced. The results given below allow the ap-

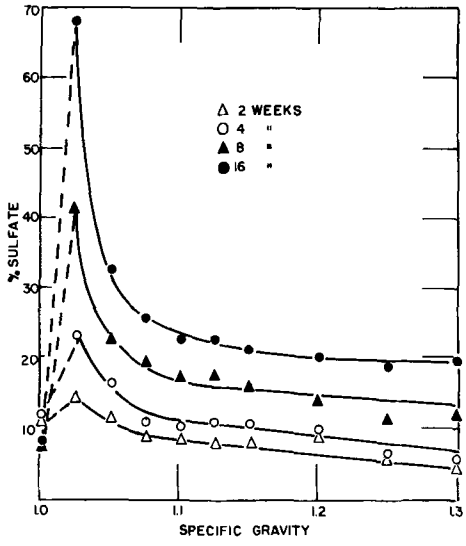


Fig. 1. Self-discharge of a single positive plate with grid alloy No. 6 at 35°C.

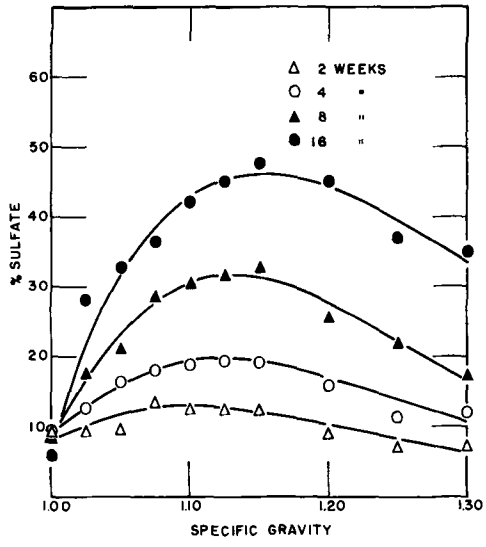


Fig. 3. Self-discharge of a single positive plate with grid alloy No. 3 at 35°C.

proximate determination of the rate of any self-discharge reaction occurring in lead-acid batteries.

The rate of self-discharge of positive plates with various grid alloys and in the absence of separators and negative plates is illustrated in Fig. 1 to 4. The self-discharge has a pronounced maximum at a gravity of about 1.100 for plates with Pb-Sb grid alloys and at a gravity of about 1.025 for plates with Pb-Ca-Al grid alloys. The maximum is shifted toward higher gravities with increasing Sb content in the grid. The maximum also seems to be displaced slightly toward higher gravities with increasing time. The results show that for the acid gravity range used in batteries the self-discharge of the positive plates increases with decreasing acid gravity. The sulfate figures for these positive plates are of the same order of magnitude as figures for negative plates for the same time periods as shown below. The $PbSO_4$ percentage shown for plates in sp gr 1 reflects the amount of $H_2SO_4$ retained in the plates when they were transferred from the forming electrolyte.

Figure 5 shows the influence of the grid alloy on positive plate self-discharge. The plots show that the reaction rate is almost independent of the sulfate content in the plates for sulfate percentages below approximately 30%. The positive plates containing Sb in the grid undergo self-discharge at a higher rate than plates with Sb-free grid alloys. Figures 6 and 7 give the rates of self-discharge reactions in positive plates under various conditions.

The rate of the self-discharge reaction of isolated positive active material depends on the acid gravity as shown by Fig. 8. The rate of the reaction between $PbO_2$ and $H_2SO_4$ increases with increasing acid concentration.

Figure 9 shows the influence of one cycle on the rate of self-discharge of single positive plates and Fig. 10 shows the influence of grid alloy on positive plate self-discharge in 3-plate cells. The negatives and the positives in each 3-plate cell had identical grid compositions. The differences between the sulfate figures are due to differences in the reaction between the grid and the active material.

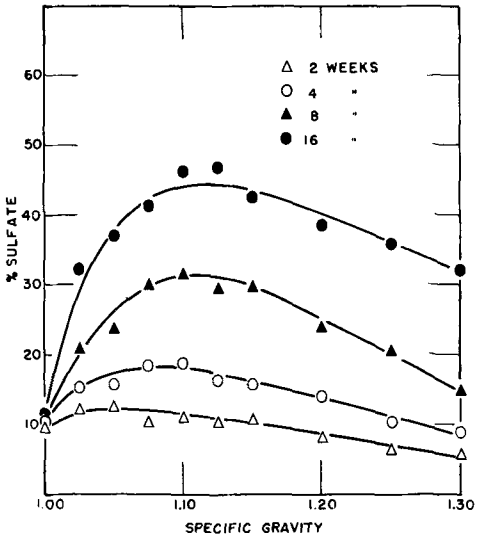


Fig. 2. Self-discharge of a single positive plate with grid alloy No. 9 at 35°C.

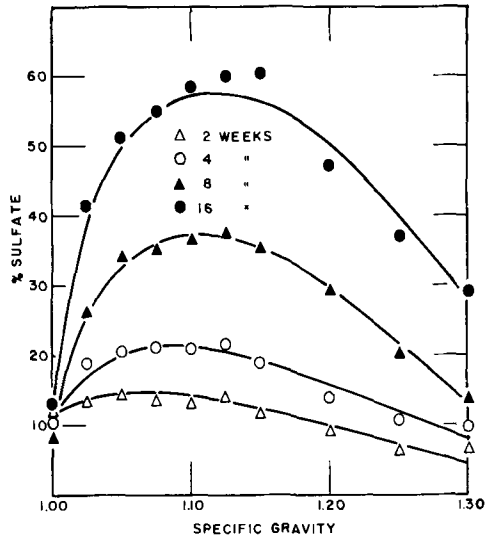


Fig. 4. Self-discharge of a single positive plate with grid alloy No. 4 at 35°C.

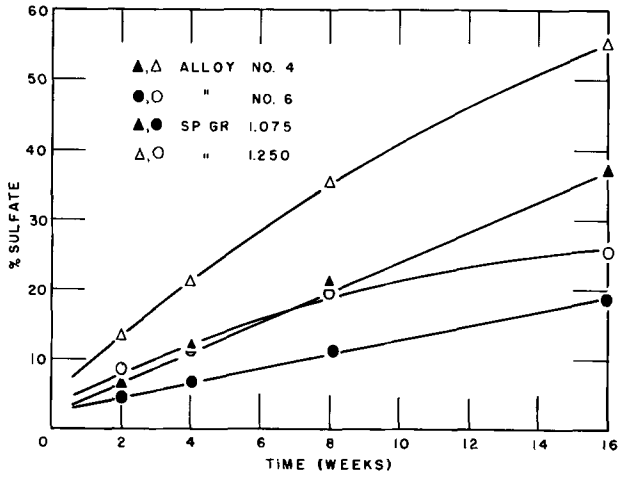


Fig. 5. Rate of self-discharge of single positive plates (grid alloy No. 4 and No. 6) in 1.250 sp gr acid and 1.075 sp gr acid at 35°C.

The results on self-discharge of negative plates are given in Fig. 11 to 15. Figure 11 shows only a small difference in self-discharge between single plates with Sb-free grids and plates with up to 4% Sb in the grids. Figure 12 and 13 illustrate the rate of the self-discharge reactions for negative plates in varying environmental conditions. Here, the open circle corresponds to the self-discharge of a single negative plate in the absence of separators and positive plates, the solid circle to the sulfation of negative plates covered on both sides with separators, the solid triangle to the self-discharge of the negative plate in 3-plate cells. The steep curve was obtained on bubbling oxygen gas through the electrolyte continuously. Enormous self-discharge rates are observed under these conditions.

Figure 14 shows the influence of different separators on negative plate self-discharge. These results were obtained with single negative plates covered with separators on both sides. A series of these plates was also placed in electrolyte dosed with 0.1 g/l and 1 g/l $Sb_2(SO_4)_3$. The presence of Sb in electrolyte accelerates negative plate self-discharge tremendously. With 1 g/l the plates without separators are 80% discharged in 4 days. In these experiments it could actually be observed how the

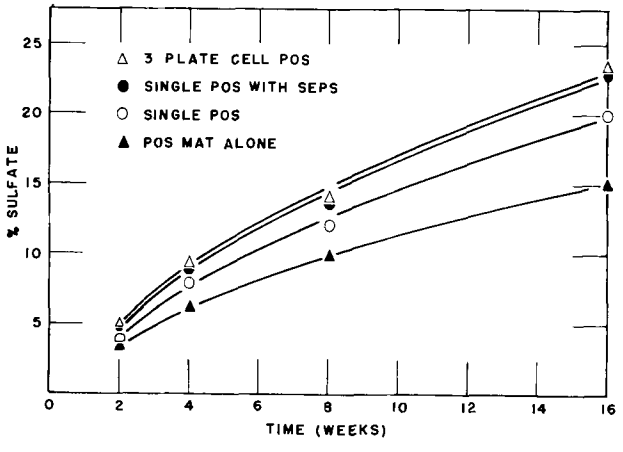


Fig. 6. Rates of self-discharge for positive plates (grid alloy No. 6) in 1.250 sp gr acid at 35°C. ▲ active material alone; O single positive plate; ● single positive plate with separators; △ positive plate in 3-plate cell.

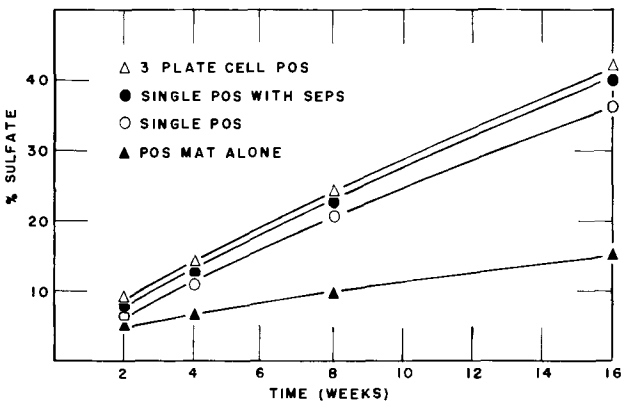


Fig. 7. Rates of self-discharge for positive plates (grid alloy No. 9) in 1.250 sp gr acid at 35°C. ▲ active material alone; O single positive plate; ● single positive plate with separators; △ positive plate in 3-plate cell.

Sb was plated on the negative plate causing increased self-discharge. The separators decrease the rate of diffusion of Sb and oxygen toward the negative plate and decrease, therefore, negative plate self-discharge.

Figure 15 shows the self-discharge of negative plates in 3-plate cells. It is interesting to note (see also Fig. 12) that negatives in Sb-free assemblies in 3-plate cells have a smaller rate of self-discharge than single Sb-free negative plates because of the protecting action of the separators against oxygen diffusion. Negatives in 3-plate cells with grid alloys of high Sb-content and particularly alloys of high corrodibility (alloy No. 4) show a higher rate of self-discharge than single negatives containing the same grid alloy because of Sb-transfer from the positives to the negatives, overcoming the benefit due to the presence of separators.

## Discussion

A large series of $PbO_2$ determinations on active material samples after 0, 2, 4, 8, and 16 weeks open-circuit stand showed that the sum of the $PbSO_4$ and $PbO_2$ percentages never added up to 100%. There was always a deficit of 5-10%. This deficit has sometimes been called "apparent PbO." However, the oxygen deficit is only partially due to actual

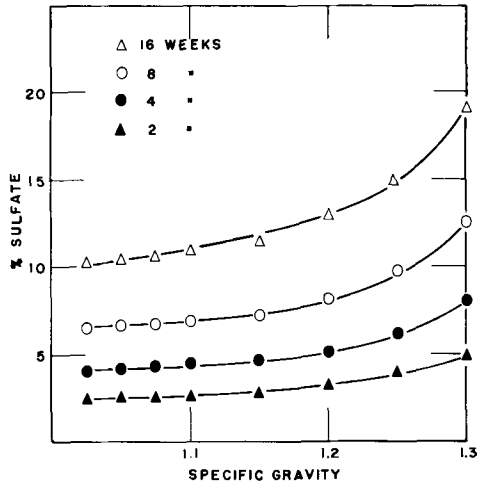


Fig. 8. Self-discharge of positive active material alone as a function of the acid gravity.

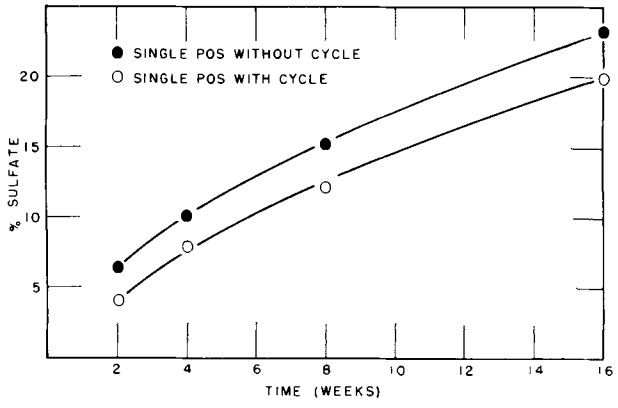


Fig. 9. Rate of self-discharge of positive plates (alloy No. 6) in sp gr 1.250 $H_2SO_4$ showing the effect of one cycle following formation.

existence of PbO. It must be kept in mind that the lead dioxide lattice always has an oxygen deficiency (19-21). The electrical conductivity of lead dioxide is very high, approaching that of metallic conductors. The oxygen deficiency produces free electrons and is responsible for high conductivity. The conductivity would be expected to increase with increasing deficit in oxygen (22). However, Kittel's thermodecomposition studies show that the conductivity decreases with increasing amount of missing oxygen, due to the formation of a new insulating compound (23). This new compound is subject to fast sulfation (24). It is not established, however, if the same compound exists in incompletely formed positive plates.

In this study all the positive plates were formed under exactly the same conditions (temperature, current rate, amount of charge) in order to form the plates to approximately the same degree of completeness. It was observed that the sulfate on freshly formed positive plates was always below 1%, using any formation procedure, but the amount of $PbO_2$ varied greatly with different formation procedures, from 88 to 95%. The rate of sulfation of positive active material in the absence of grids, separators, and negative plates increases slightly with increasing acid concentration (Fig. 8). The fact that the curves do not tend toward zero at sp gr 1.0 suggests that the sulfate ion is taking part only indirectly in

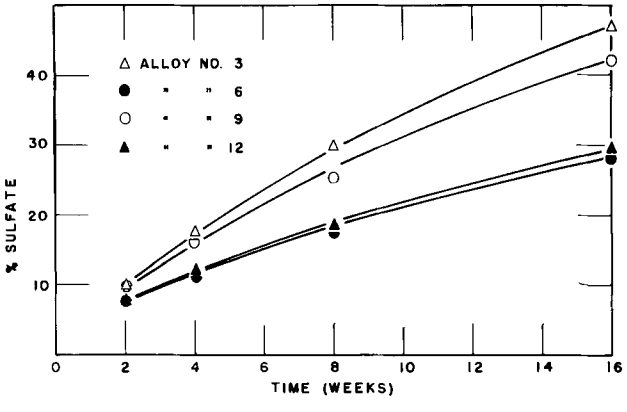


Fig. 10. Influence of the grid alloy on positive plate self-discharge in 3-plate cells (1 positive and two negatives) with sp gr 1.250 $H_2SO_4$.

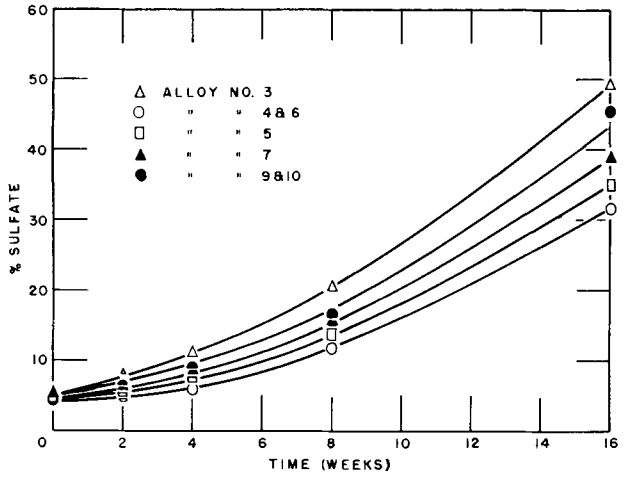


Fig. 11. Self-discharge of single negative plates in $H_2SO_4$ sp gr 1.250 at 35°C.

the reaction. Formation of persulfate $S_2O_8^=$ requires a potential of +2.01 (25), whereas the potential of the $PbSO_4/PbO_2$ couple is only 1.685 v. Persulfate is unstable in sulfuric acid and decomposes with formation of oxygen and hydrogen peroxide (26). The water-hydrogen peroxide couple has a potential +1.77 v. However, the oxygen couple in acid solution ($O_2 + 4H^+ + 4e = 2H_2O$) has a potential of only +1.229 v. This shows that persulfate and hydrogen peroxide will not be formed on a positive electrode during open-circuit stand, and that oxygen must be the reaction product.

The question of whether the oxygen evolved in the over-all self-discharge reaction

$$PbO_2 + 2H^+ + SO_4^= = PbSO_4 + H_2O + \tfrac{1}{2}O_2 \quad [1]$$

comes from the $H_2O$ in the solution or the $PbO_2$ could be answered by oxygen isotope studies. Reaction [1] is responsible for the self-discharge of isolated positive active material, and its speed can be evaluated from Fig. 6 and 7 (the curve marked with the solid triangle) and from Fig. 8. The free energy of reaction [1] is −21030 cal.

It can be shown that the oxygen content of the positive active material is related to the rate of self-discharge. Figure 9 shows a comparison of rates of

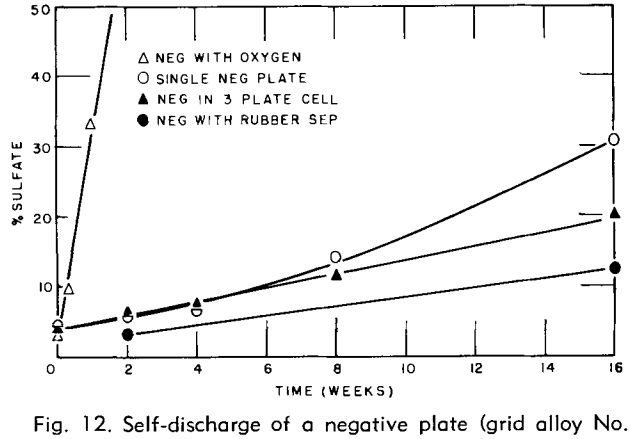


Fig. 12. Self-discharge of a negative plate (grid alloy No. 6) in $H_2SO_4$ sp gr 1.250 at 35°C. O single negative plate; ● negative plate with separators; ▲ negative plate in 3-plate cell; △ negative plate in $H_2SO_4$ saturated with oxygen.

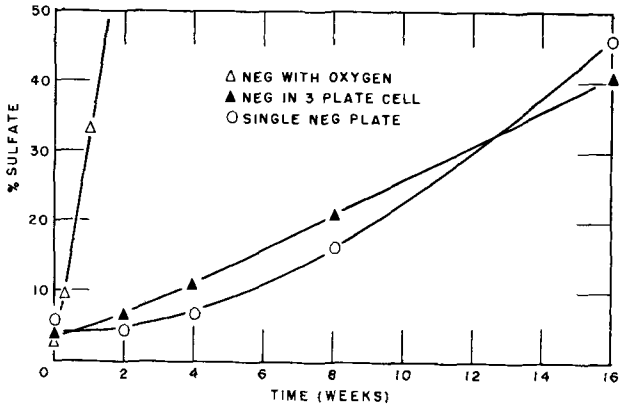


Fig. 13. Self-discharge of a negative plate (grid alloy No. 9) in $H_2SO_4$ sp gr 1.250 at 35°C. O single negative plate; ▲ negative plate in 3-plate cell; △ negative plate in $H_2SO_4$ saturated with oxygen.

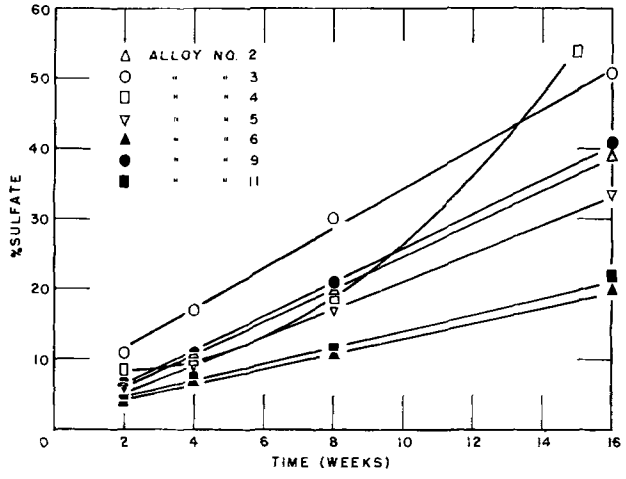


Fig. 15. Rate of self-discharge of negative plates in 3-plate cells.

self-discharge between two positives of identical grid alloy (No. 6) and which were formed in series, but one plate was discharged at the 5-hr rate for 5 hr following formation and recharged, and the other plate was not cycled. Both were left to self-discharge in 1.250 sp gr acid at 35°C with analysis made at the indicated time intervals. The analysis on these plates prior to self-discharge (after formation and one cycle for the cycled plate and after formation for the uncycled plate) showed both plates to have less than 0.5% $PbSO_4$, but the uncycled plate analyzed 92% $PbO_2$ whereas the cycled plate analyzed 94% $PbO_2$. Although these plates show a very low and nearly identical $PbSO_4$ concentration, the difference in $PbO_2$ content indicates a difference in amounts of "apparent PbO," that is, a lack of oxygen. The plate with the higher percentage of $PbO_2$ was observed to have the lower rate of self-discharge. Thus, formation of the positives should be as complete as possible to reduce stand loss. The amount of "apparent PbO" is reduced by increasing temperature during formation or by cycling after formation.

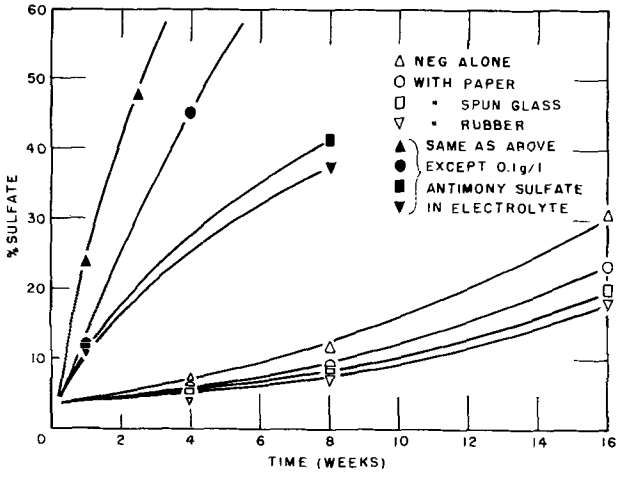


Fig. 14. Influence of the separator on self-discharge of single negative plates, △ no separator, △ microporous rubber, □ spun glass with inert backing, O paper (phenolic-bound), in $H_2SO_4$ sp gr 1.250 at 35°C. The self-discharge rates in $H_2SO_4$ sp gr 1.250 at 35°C, dosed with 0.1 g $Sb_2(SO_4)_3$ per liter are shown with black symbols.

If the positive active material is in contact with a lead or lead-antimonial grid, the following self-discharge reactions occur:

$$PbO_2 + Pb + 2H_2SO_4 \rightarrow 2PbSO_4 + 2H_2O \quad [2]$$

$$5PbO_2 + 2Sb + 6H_2SO_4 \rightarrow (SbO_2)_2SO_4 + 5PbSO_4 + 6H_2O \quad [3]$$

Reaction [2] corresponds to the discharge reaction of a lead acid cell according to the double sulfation theory. Comparing Fig. 1 with Fig. 2-4, or Fig. 6 with Fig. 7 it can be seen that reaction [2] is relatively slow in the absence of Sb in acid gravities above 1.10 and does not contribute much to the over-all rate of self-discharge. Reaction [2] involves a $\Delta F$ of −92, 300 cal and would tend to proceed spontaneously. Fortunately, the electrolyte has only very limited access to the lead metal and formation of lead sulfate passivates the reaction on the exposed areas. With increasing dilution of the acid, the solubility of lead sulfate increases as shown in Fig. 16 [data from (27)] and the passivating action of lead sulfate decreases (28-31). This situation is illustrated schematically in Fig. 17. The area of metallic lead exposed to the electrolyte is polarized anodically by the presence of $PbO_2$ to a value 2 v more positive than its reversible potential. Therefore, the lead would tend to dissolve spontaneously under formation of $Pb^{++}$ or $Pb^{++++}$ ions. The driving force for this reaction would even be expected to increase with increasing acid gravity since the potential of the positive electrode becomes more posi-

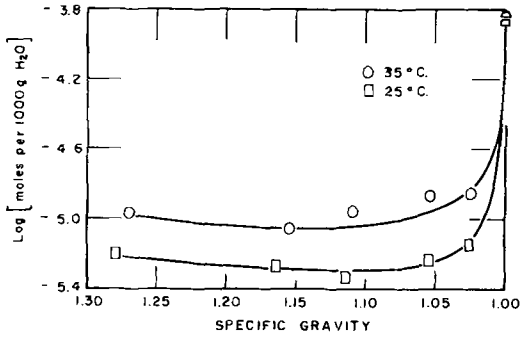


Fig. 16. Solubility of lead sulfate in sulfuric acid. [Data from (28)].

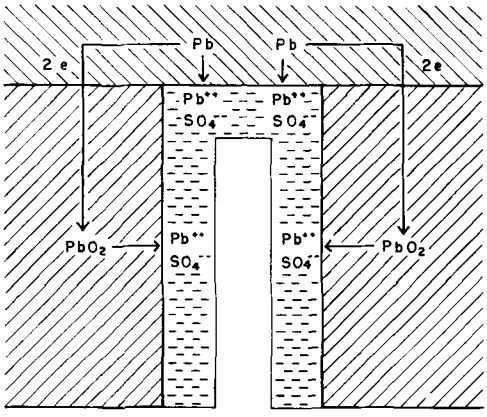


Fig. 17. Schematic diagram of the self-discharge process in a pore of a positive plate with an antimony-free grid.

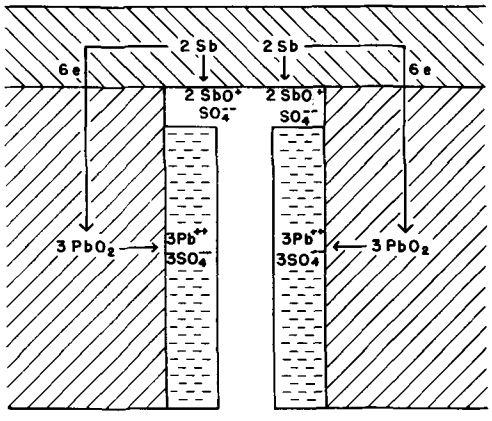


Fig. 18. Schematic diagram of the self-discharge process in a pore of a positive plate with an antimonial-lead grid.

tive at higher acid gravities. This follows from the thermodynamics of the $PbO_2/PbSO_4$ electrode.

The potential of the cell

$$Pt/H_2(1\ atm)/H_2SO_4(m)/PbSO_4/PbO_2/Pt$$

has been measured by Hamer (32) and Harned and Hamer (33). The electromotive force is given by the equation

$$E = E_o + \frac{0.05916}{2} \log a^2_{H^+} \times a_{SO_4^=} - \frac{0.05916}{2} \log a^2_{H_2O}$$

or

$$E = E_o + \frac{0.05916}{2} \log m^3_{\pm} + \frac{0.05916}{2} \log f^3_{\pm} - \frac{0.05916}{2} \log a^2_{H_2O}$$

where $m\pm$ and $f\pm$ are the mean molality $(m^2_{H^+} \cdot m_{SO_4^=})^{1/3}$ and the mean stoichiometric activity coefficient, respectively, of the sulfuric acid. At 25°C, $E_o$ equals 1.685 v. The values for the activity coefficients have been determined with fair accuracy by others (34-41).

Delahay, Pourbaix, and Van Rysselberghe (42, 43) calculated the potential of the positive electrode as follows

$$E = 1.655 - 0.0886\ pH + 0.0295 \log a_{HSO_4^-}$$

and

$$E = 1.712 - 0.1182\ pH + 0.0295 \log a_{SO_4^{--}}$$

The potential of the positive electrode increases,

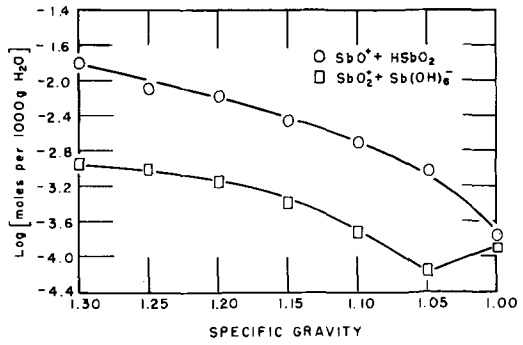


Fig. 19. Solubility of antimony sulfates in sulfuric acid

therefore, with increasing acid gravity. Nevertheless, the rate of self-discharge (anodic dissolution of Pb at the exposed areas) decreases with increasing acid concentration, due to increased passivation.

Figure 18 illustrates schematically how, in a plate with an antimonial-lead grid, the Sb may enter into the self-discharge reaction with the positive active material to form $(SbO)_2SO_4$ and $(SbO_2)_2SO_4$ which are more soluble than $PbSO_4$. This greater solubility of the Sb corrosion products creates holes or pores in the passivating layer of $PbSO_4$ and permits the self-discharge reaction between the Pb metal of the grid and the active material to continue. Figures 2 to 4 show that self-discharge in antimonial positives increases with increasing acid gravity up to a gravity of 1.1, then decreases with increasing acid gravity. This behavior can be explained by the relative solubilities of $PbSO_4$ and $(SbO_2)_2SO_4$.

Figure 19 shows the solubility of $SbO^+ + HSbO_2 + Sb(OH)_4^-$ (total amount of trivalent Sb) and of $SbO_2^+ + Sb(OH)_6^-$ (total amount of pentavalent Sb) as a function of acid gravity at 25°C. The data for trivalent Sb have been obtained in this laboratory. The values plotted for pentavalent Sb have been calculated from Ref. (44). For the acid gravity range used in storage batteries the solubility of both tri- and pentavalent Sb increases with increasing acid gravity. This opposite effect in the passivating action between the corrosion products of Pb and Sb leads to the maximum observed in Fig. 2-4. At high acid gravities, protection is due to $PbSO_4$; at low acid gravities protection is due to corrosion products of Sb. The potential-pH diagram (44) shows that pentavalent Sb will be formed preferably in the corrosion self-discharge process in positive plates.

The amount of self-discharge due to reactions [2] or [3] can be evaluated from the plots shown in Fig. 6 and 7. For positive plates without Sb in the grid alloy, the superposition of reaction [1] and [2] leads to the sulfate figures shown with the curves of Fig. 1 and with the curve marked with the open circle in Fig. 6.

From Fig. 6 and 7 it can be concluded that the reaction

$$PbO_2 + (\text{oxidizable material from separators}) + H_2SO_4 = PbSO_4 + (\text{oxidized material}) \quad [4]$$

is responsible for a slight amount of positive self-discharge. The self-discharge of the positive plates can be reduced by using separators most resistant to

oxidation. The reaction can be minimized by reducing the contact area between separators and positive plates and by the use of a small number of relatively thick plates.

In 3-plate cells, positive plate self-discharge is practically the same as with single positive plates in contact with separators. The very small difference could be due to the presence of negative plates. These evolve hydrogen on open circuit which could diffuse toward the positive plates and reduce the active material, according to the equation

$$PbO_2 + H_2 + H_2SO_4 \rightarrow PbSO_4 + 2H_2O \qquad [5]$$

The electrochemical oxidation of hydrogen on $PbO_2$ is, however, reaction controlled and extremely small. The solubility of hydrogen in $H_2SO_4$ solutions is quite low and decreases with increasing acid concentration (45). The rate of the oxidation of hydrogen has been studied recently by Frumkin (46, 47), on platinum electrodes. Similar studies for lead dioxide electrodes in this laboratory indicate that hydrogen is reduced at practically immeasurably small rates on these electrodes. The adsorption of $SO_4$ ions on the $PbO_2$ electrode probably inhibits the reaction.

The rate of self-discharge of single negative plates in the absence of separators and positive plates is of the same order of magnitude as the rate of self-discharge of positive plates. Antimony present in the grids of the negative plates accelerates the rate of self-discharge. However, the increase in self-discharge due to Sb in the negative grids is smaller than expected and only becomes important for high Sb concentrations. The self-discharge reaction

$$Pb + H_2SO_4 \rightarrow PbSO_4 + H_2 \qquad [6]$$

is catalyzed by the presence of Sb which has a much lower hydrogen overvoltage than Pb. This fact is especially evident from Fig. 14 which also shows that microporous rubber is the best separator for low self-discharge batteries. The rate of diffusion of Sb toward the negative plate is decreased in the presence of separators. The presence of the separators also decreases the rate of negative plate self-discharge in the absence of Sb. This is due to an inhibition of the diffusion of oxygen toward the negative plates. Oxygen discharges the negative plates according to the reaction:

$$Pb + \tfrac{1}{2}O_2 + H_2SO_4 \rightarrow PbSO_4 + H_2O \qquad [7]$$

This reaction is diffusion controlled since the electrochemical reduction of oxygen at the potential of the negative electrode (—0.356 v) is quite fast (48-53). This is also evident from the curves with the open triangles in Fig. 12 and 13.

The solubility of oxygen in $H_2SO_4$ solutions decreases slightly with increasing acid concentration (45). Nevertheless, the self-discharge of the negative plates normally increases with increasing acid concentration due to reaction [6].

The electromotive force of the cell

$$Pt/H_2\ (1\ atm)/H_2SO_4\ (m)/PbSO_4/Pb/Pt$$

is given by

$$E = E_o - \frac{0.05916}{2} \log a^2_{H^+}\, a_{SO_4^{--}}$$

or

$$E = E_o - \frac{0.05916}{2} \log m^3\pm - \frac{0.05916}{2} \log f^3\pm$$

The potential of the $Pb/PbSO_4$ electrode can be expressed by

$$E = -0.300 - 0.0295\ pH - 0.0295 \log a_{HSO_4^-}$$

and

$$E = -0.356 - 0.0295 \log a_{SO_4^{--}}$$

This leads to the conclusion that the potential of the $Pb/PbSO_4$ electrode is practically independent of $pH$ (31, 42).

The self-discharge of negative plates in 3-plate cells is higher than that of single negative plates covered with separators, even if the positive plate has an Sb-free grid alloy. This could be due to oxygen released from the positive plates according to reaction [1] and subsequent reduction of this oxygen according to reaction [7].

Tests with full size starter batteries with lead antimonial grids have shown that the Sb concentration in the negative active material increases from 0.003% to 0.012% during standard container formation. A further transfer of Sb takes place during open-circuit stand. The concentration of Sb in the positive active material increases from 0.002% to 0.10% during formation, whereas the concentration of Sb in the formation electrolyte never rises above 0.004 g/l. Similar conclusions have been reached recently by experiments with radioactive tracer techniques (54).

From the analysis given in the present paper it can be concluded that seven different self-discharge reactions take place in a lead-acid battery. The rate of each reaction can be determined separately.

## Acknowledgment

The authors would like to thank Mr. C. G. Grimes, Director of Research of the Electric Storage Battery Company, for permission to publish this paper.

Manuscript received Jan. 20, 1958. This paper was prepared for delivery before the Cleveland Meeting, Sept. 30-Oct. 4, 1956.

Any discussion of this paper will appear in a Discussion Section to be published in the June 1959 JOURNAL.

## REFERENCES

1. G. W. Vinal, "Storage Batteries," pp. 120-141, John Wiley & Sons, Inc., New York (1940).
2. C. Drotschmann, "Bleiakkumulatoren," pp. 34, 35, Verlag Chemie, G.M.B.H., Weinheim, Bergstrasse (1951).
3. W. H. Beck and W. F. K. Wynne-Jones, *Trans. Faraday Soc.*, **50**, 136 (1954).
4. W. H. Beck and W. F. K. Wynne-Jones, *ibid.*, **40**, 147 (1954).
5. J. J. Lander, *This Journal*, **98**, 220 (1951).
6. W. H. Power, S. W. Rabideau, R. A. Kern, R. T. Pierce, and J. J. Lander, Naval Research Lab. Report P-2G08, Washington (1947).
7. R. H. Greenburg and B. P. Caldwell, *Trans. Electrochem. Soc.*, **80**, 71 (1941).
8. R. H. Greenburg and J. A. Orsino, National Lead Co. Research Lab. Publication No. 219-50, Brooklyn (1950).

9. J. E. Hatfield and O. W. Brown, *Trans. Electrochem. Soc.*, **72**, 361 (1937).
10. J. J. Lander, *This Journal*, **99**, 339 (1952).
11. H. E. Haring and U. B. Thomas, *Trans. Electrochem. Soc.*, **68**, 293 (1935).
12. J. T. Crenell and A. G. Milligan, *Trans. Faraday Soc.*, **27**, 103 (1931).
13. J. W. R. Byfield, *Trans. Electrochem. Soc.*, **79**, 259 (1941).
14. H. E. Haring and U. B. Thomas, *ibid.*, **68**, 293 (1935).
15. C. G. Fink and A. J. Dornblatt, *ibid.*, **79**, 269 (1941).
16. A. C. Zachlin, *ibid.*, **82**, 365 (1942).
17. A. C. Zachlin, *ibid.*, **92**, 259 (1947).
18. H. Stoertz, (to the Electric Storage Battery Co.) U. S. Pat. 2,678,340 and 2,678,341 (1954).
19. M. Le Blanc and E. Eberius, *Z. physik. Chem.*, **A160**, 69 (1932).
20. A. Bystrom, *Arkiv Kemi, Mineralogi Geol.*, **20A**, 1 (1945).
21. T. Katz and R. Faivre, *Bull. Soc. Chim. France*, **16**, D124 (1949).
22. U. B. Thomas, *J. (and Trans.) Electrochem. Soc.*, **94**, 42 (1948).
23. A. Kittel, Beiträge zum Mechanismus der Elektrischen Leitung in $PbO_2$ und Se, Diss. Prag, Czechoslov. (1944).
24. P. Ruetschi and B. D. Cahan, *This Journal*, **105**, 369 (1958).
25. W. M. Latimer, "Oxidation Potentials," p. 78, Prentice-Hall, Inc., New York (1953).
26. I. M. Kolthoff and I. K. Miller, *J. Am. Chem. Soc.*, **73**, 3055 (1951).
27. A. Seidell, "Solubilities," p. 1414, D. Van Nostrand Co., Inc., New York (1953).
28. W. H. Beck, R. Lind, and W. F. K. Wynne-Jones, *Trans. Faraday Soc.*, **50**, 1249 (1954).
29. J. Jones, R. Lind, and W. F. K. Wynne-Jones, *ibid.*, **50**, 972 (1954).
30. W. H. Beck, J. Jones, and W. F. K. Wynne-Jones, *ibid.*, **50**, 1249 (1954).
31. B. N. Kabanov, D. I. Leikis, and E. I. Krepakova, *Doklady Akad. Nauk*, **98**, 989 (1954).
32. W. J. Hamer, *J. Am. Chem. Soc.*, **57**, 9 (1935).
33. H. S. Harned and W. J. Hamer, *ibid.*, **57**, 33 (1935).
34. S. Shankman and A. R. Gordon, *ibid.*, **61**, 2370 (1939).
35. R. H. Stokes, *ibid.*, **69**, 1291 (1947).
36. J. E. Kunzler and W. F. Giauque, *ibid.*, **74**, 3472 (1952).
37. R. H. Stokes, *Trans. Faraday Soc.*, **44**, 295 (1948).
38. A. Grollman and J. C. W. Frazer, *J. Am. Chem. Soc.*, **47**, 712 (1925).
39. E. Glueckauf and G. P. Kitt, *Trans. Faraday Soc.*, **52**, 1074 (1956).
40. C. N. Deno and R. W. Taft, *J. Am. Chem. Soc.*, **76**, 244 (1954).
41. E. W. Hornung and W. F. Giauque, *ibid.*, **77**, 2744 (1955).
42. P. Delahay, M. Pourbaix, and P. Van Rysselberghe, *This Journal*, **98**, 57 (1951).
43. J. Van Muylder and M. Pourbaix, Proc. of the 6th Meeting of the International Committee for Electrochemical Thermodynamics and Kinetics, Poitiers (1954).
44. A. L. Pittman, M. Pourbaix, and N. de Zoubov, *This Journal*, **104**, 594 (1957).
45. A. Geffcken, *Z. physik. Chem.*, **49**, 268 (1904).
46. A. Frumkin, *Z. Elektrochem.*, **59**, 807 (1955).
47. A. Frumkin and E. A. Aikazyan, *Doklady Akad. Nauk, SSSR*, **100**, 315 (1955).
48. M. J. Joncich and N. Hackerman, *J. Phys. Chem.*, **57**, 674 (1953).
49. S. A. Siver and B. N. Kabanov, *Zhur. Fiz. Khim.*, **1**, 53 (1948).
50. F. Tödt, *Chemiker Ztg.*, **74**, 254 (1950).
51. H. Grubitsch, *Monatsh. Chem.*, **83**, 549 (1952).
52. P. Delahay, C. L. Pillon, and D. Perry, *This Journal*, **99**, 414 (1952).
53. P. Delahay and L. J. Stagg, *ibid.*, **99**, 547 (1952).
54. W. Herrmann and G. Pröpstl, *Z. Elektrochem.*, **61**, 1154 (1957).

# The Reduction of Passive Films by Hydrogen Diffusion through Steel

**R. T. Davis, Jr., and T. J. Butler**

*Applied Research Laboratory, U. S. Steel Corporation, Monroeville, Pennsylvania*

ABSTRACT

An experimental technique is described wherein the diffusion of hydrogen through a steel specimen is followed by electrode-potential measurements. In this technique, one surface of the specimen is exposed to acid and the other surface to a sodium dichromate solution. As the hydrogen produced by acid attack at the steel surface diffuses to the other surface, the potential of the surface in contact with the $Na_2Cr_2O_7$ solution changes with time, and changes of potential ranging from 300 mv to 900 mv are observed. It is believed that the observed potential changes result from the reduction of the dichromate-produced passive film by diffused hydrogen. The effect of variations in steel composition and thickness, acid composition and concentration, and sodium dichromate concentration on the phenomenon is reported.

It is generally recognized that steel is usually permeable to hydrogen under conditions favorable to the formation of atomic hydrogen (1), i.e., high temperature, acid corrosion, or cathodic charging. When corrosion occurs on all surfaces of a steel specimen, the metal eventually becomes saturated with hydrogen. When only one surface is exposed to the corroding acid, hydrogen diffuses through the specimen and is liberated at the unexposed metal surfaces. A number of methods have been used by various workers to determine the quantity of hydrogen dissolved in steel specimens, viz., degassing techniques (2, 3) and vacuum fusion (4, 5). The permeability of hydrogen in steel has been investigated by gas-solubility (2) and gas-diffusion measurements (6, 7).

Table I. Composition of various steels used in hydrogen diffusion studies

| Specimen designation | Composition, per cent | | | | | | | | | | | |
|---|---|---|---|---|---|---|---|---|---|---|---|---|
| | C | Mn | P | S | Si | Cu | As | N | Ni | Cr | Mo | Al |
| A† | 0.071 | 0.38 | 0.009 | 0.036 | 0.001 | 0.014 | 0.011 | 0.002 | * | * | * | * |
| B | 0.078 | 0.38 | 0.010 | 0.036 | 0.001 | 0.010 | 0.010 | 0.009 | * | * | * | * |
| C | 0.050 | 0.28 | 0.005 | 0.028 | 0.001 | 0.046 | 0.009 | 0.003 | * | * | * | * |
| D | 0.074 | 0.30 | 0.005 | 0.036 | 0.001 | 0.038 | 0.013 | 0.004 | * | * | * | * |
| S | 0.088 | 0.49 | 0.006 | 0.023 | 0.002 | 0.055 | 0.010 | 0.002 | * | * | * | * |
| F | 0.100 | 0.34 | 0.006 | 0.040 | 0.001 | 0.073 | 0.015 | 0.004 | * | * | * | * |
| H-1115 | 0.21 | 0.82 | 0.013 | 0.026 | 0.032 | 0.10 | 0.002 | * | 0.03 | 0.036 | 0.009 | 0.006 |
| H-1234 | 0.20 | 0.72 | 0.009 | 0.023 | 0.063 | 0.042 | 0.006 | * | 0.03 | 0.022 | 0.018 | 0.006 |

* Not reported.

† Pairs A, B; C, D; and S, F were from the same heats of steel; members of each pair were processed in a slightly different manner. The three sets of pairs were obtained from three different Corporation mills.

Several years ago, during studies of acid corrosion of steel and hydrogen diffusion into and through steel, it was observed that the potential of the surface of a steel plate exposed to a sodium-dichromate solution changed from a cathodic (passive) potential to an anodic (active) potential when the other surface of the plate was exposed to a corrosive medium. From this we concluded that the hydrogen which diffused through the plate apparently reduced the passive surface formed by reaction with the dichromate solution. Because this phenomenon appeared to be a useful method for studying hydrogen diffusion and passive films, further research work was undertaken. We are reporting here the results of studies on the effect of variations in (*a*) steel composition and thickness, (*b*) the nature and concentration of the corroding medium, and (c) passivating conditions, on the time-potential phenomenon.

Several workers have studied the reaction of diffused hydrogen with various liquid substances or solutions (8-10) and have measured the potential of the exit surface exposed to various solutions (11, 12). However, until recently, only Uhlig (13,14) had described this phenomenon. He used the phenomenon as a means of studying passivation reactions with iron-chromium alloy surfaces and was not particularly interested in studying hydrogen diffusion. Recently, Amiot (15) studied this phenomenon and reported results somewhat similar to but not as complete as those reported here.

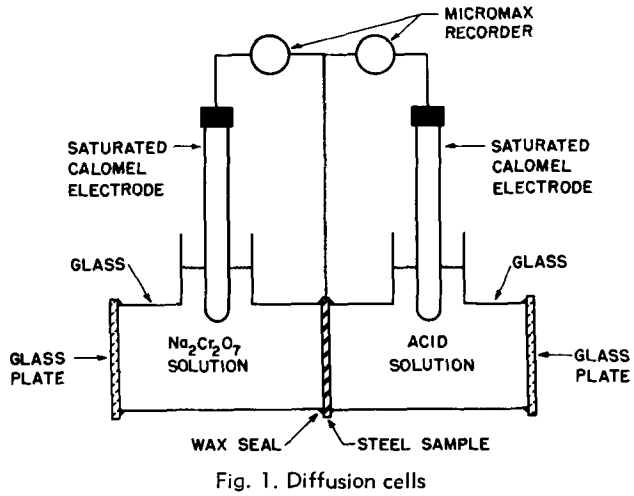


Fig. 1. Diffusion cells

## Experimental

*Steel.*—One set of specimens consisted of samples of tin-plate-gauge steel (approximately 0.25 mm thick) that had been obtained from several different sources. The other set of specimens consisted of samples of low-carbon steel (AISI C1020) that had been machined to various thicknesses ranging from 2.54 mm to 25.4 mm. The chemical compositions of the steel specimens are shown in Table I. The tin-plate steels had been box annealed. The prior processing history of the AISI C1020 steels is not known. From an examination of the microstructure of Sample H-1235 it is believed to have been annealed.

*Solution.*—All solutions were prepared from reagent-grade chemicals dissolved in distilled water. Unless otherwise specified, the corroding acid was 2*N* $H_2SO_4$, and the passivating solution was 0.05M $Na_2Cr_2O_7$. Acid solutions containing a sulfite promoter were 0.01M $Na_2SO_3$ in 2*N* $H_2SO_4$, and were freshly made prior to use.

*Instrumentation.*—All measurements of potential were made relative to the saturated calomel electrode (Leeds & Northrup Model 1199-31). The electrode potentials were recorded either on a six-point L&N Micromax Recorder that records the points at 1-min intervals, or on a L&N Speedomax Recorder having a strip speed of 10 in./min.

*Cell construction.*—Figure 1 shows a diagrammatic sketch of the cells in which the potentials were measured. The glass cells were made of 28 mm (OD) tubing, and each cell held about 30 cc. The steel samples were affixed to the cell by a wax seal (beeswax and rosin mixture). The steel acted as one electrode. Saturated calomel reference electrodes were inserted into the necks of either or both of the cells.

*Method of measurement.*—The cell unit was assembled as shown in Fig. 1. Sodium dichromate solution was poured into one of the cell compartments, the calomel electrode was inserted into the solution, and the whole unit was placed in a constant-temperature oven maintained at 40°C. The potential of the steel surface exposed to the dichromate solution was recorded as a function of time. When this potential became constant, usually after several hours, acid was poured into the other cell, and the measurement of the potential in the dichromate cell was continued. In some experiments, the potential of the

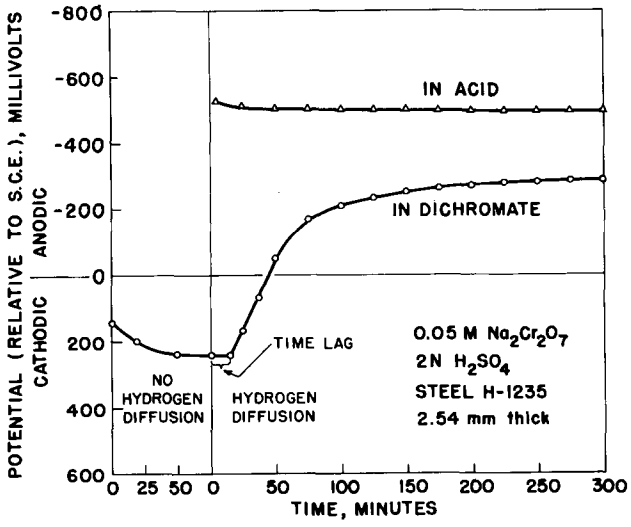


Fig. 2. Typical time-potential relation

surface exposed to the acid was also recorded as a function of time.

*General Description of the Phenomenon*

The initial potential of the steel surface exposed to the dichromate passivating solution is cathodic[1] (Fig. 2). With continued exposure to the passivating solution, the steel surface becomes more cathodic and finally, after several hours, exposure, reaches a cathodic potential of several hundred millivolts. Upon addition of acid to the adjacent cell, the potential of the passive surface remains constant for a time and then changes rapidly in the anodic direction. After a few hours, the potential of the passive surface becomes several hundred millivolts anodic, approaching in some instances a potential approximating that of the normal hydrogen overvoltage on steel.[2] The potential of the surface exposed to acid does not change appreciably with time.

[1] All potential designations in this paper are with respect to the saturated calomel electrode.

[2] "Normal hydrogen overvoltage on steel" as used in this paper is the potential approximating that observed when steel corrodes in an acid solution. See, for example, Fig. 2.

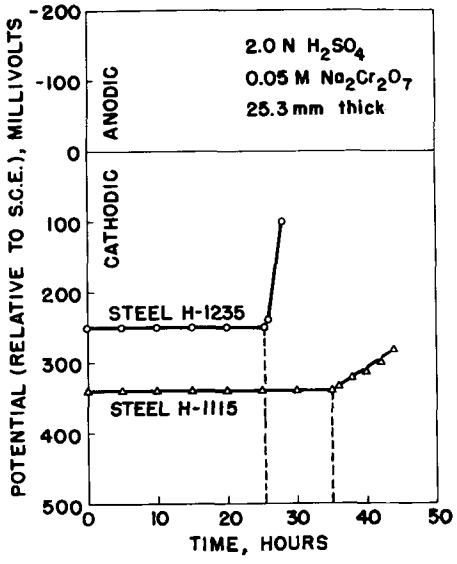


Fig. 3. Time-potential plots for two steels of same nominal composition (AISI C1020).

Table II. Time-lag values for tin-plate steels

| Steel | Thickness (mm) | Time-lag,* sec |
|---|---|---|
| A | 0.235 | 9.6 |
| B | 0.237 | 9.7 |
| C | 0.238 | 10.3 |
| D | 0.240 | 13.7 |
| S | 0.256 | 7.5 |
| F | 0.248 | 18.5 |

* Charging medium 2*N* $H_2SO_4$. Detecting medium 0.05M $Na_2Cr_2O_7$.

The reactions taking part in the phenomena described above are undoubtedly complex. Acid attack on the nonpassivated side produces hydrogen, some of which remains atomic in character and diffuses through to the passivated side. Here two reactions are possible: reduction of the passivating film on the metal surface by the diffused hydrogen, with a consequent change in surface potential

$$\text{Fe (passive)} \xrightarrow{\text{H diffused}} \text{Fe (active)} \qquad [1]$$

or recombination of the diffused hydrogen to form gaseous molecular hydrogen

$$2H_{\text{diffused}} \rightleftharpoons H \text{ (gas)} \qquad [2]$$

There is reason to believe that reaction [1] does occur (*see* later). Uhlig (13) interpreted the potential change as a result of an increase in thermodynamic "activity" of the iron and chromium components of his alloys caused by the presence of the diffused hydrogen in the lattice system. We do not believe that this is as logical an explanation as the one we proposed, which is in agreement with the suggestion made by Hoar in a discussion of Uhlig's work (13). This phenomenon is affected by variations in experimental conditions in the following manner.

## Effect of Steel Composition

Figure 3[3] presents the results of measurements made under uniform conditions for two different steel specimens of the same nominal steel type (AISI C1020) but of slightly different chemical composition. It is observed that the time-lag (time elapsing between initiation of corrosive attack and the break in the time-potential curve) is greater for one steel than for the other steel, and also that the slope is much greater for one steel than for the other. There is also a difference in the initial cathodic passive potential; however, this difference does not appear to affect the time-lag of the steel and apparently is related to nonuniform surface preparations.

Figure 4 presents the results of measurements made on six different tin-plate-gauge steel samples. Here the time-lag is so short (about 15 sec) that it does not appear in the figure. However, the time-lags have been determined by using the Speedomax recorder, and they are presented in Table II. Apparently, the nature of the steel significantly affects the shape of the time-potential curves and the time-lag value.

[3] Unless otherwise indicated, the zero of the time scale on all figures refers to the time at which acid was added to the cell.

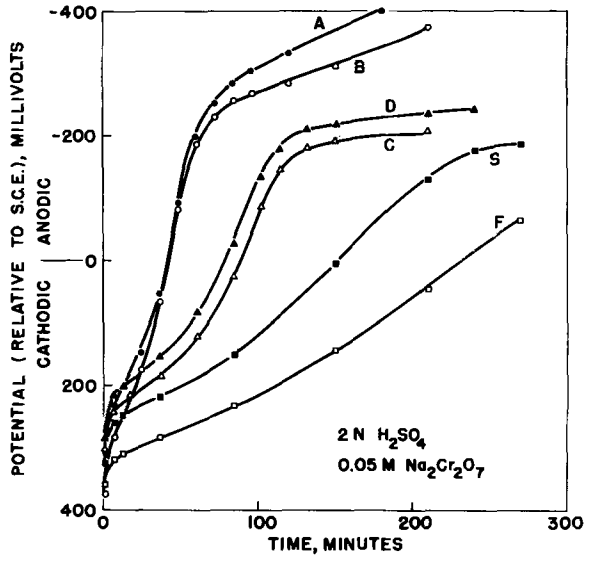


Fig. 4. Time-potential relation for tin-plate steels

It has not been possible to determine which factors, with respect to steel composition or processing history, influence these results. However, there are several ways in which variations in steel composition could effect the phenomena. For example, the chemistry of the steel can influence the rate of corrosion attack and thus increase or decrease the rate at which hydrogen is reduced at the surface. Moreover, the presence of certain alloying elements or metal impurities at the surface can catalyze or poison the recombination or surface-diffusion reactions and thus influence the ratio of hydrogen diffused to gaseous hydrogen released (effused) at the surface. Separate studies of this ratio will be made at a later date to help clarify this point.

It is also possible that variations in the steel composition or degree of mechanical work influence the rate of hydrogen diffusion, and indeed, this has been reported (2). Likewise, variations in steel composition may affect the passivation reaction in the dichromate solution and the reduction of the passive film at the dichromate-steel surface.

### *Effect of Steel Thickness*

The effect of steel thickness was investigated with two different steels and with thickness variations ranging from 2.5 mm to 25.4 mm. Figure 5 shows

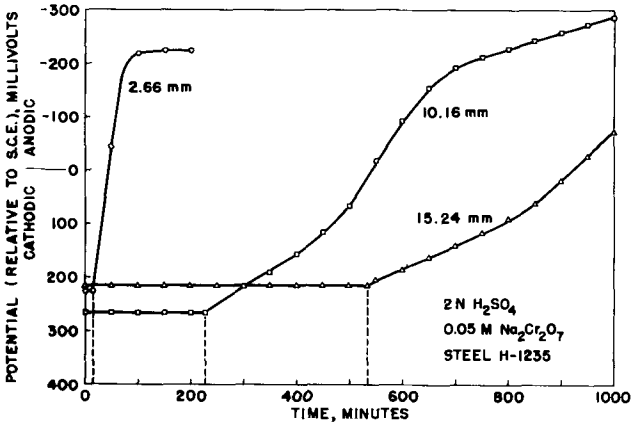


Fig. 5. Effect of sample thickness on time-potential relation

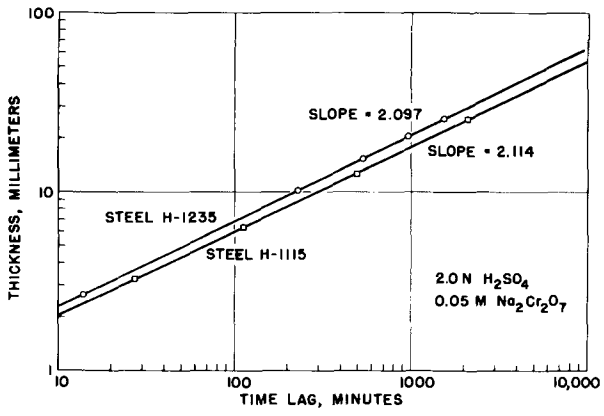


Fig. 6. Plot of thickness vs. time-lag

that as the thickness ($d$) of the steel increases the time-lag increases. A plot of the logarithm of the time-lag vs. the logarithm of thickness for the two steels investigated is shown in Fig. 6, where a straight-line relationship is observed. The lines for the two steels are parallel and have a slope of approximately 2.10. If the time-lag data are plotted against the square of thickness, $t$ vs. $d^2$, the deviation from linearity at the smaller thicknesses cannot be detected. However, calculation of $k$ of the equation $t = kd^2$ for the various sets of time-lag—thickness data shows that the $k$ is not a true constant (see Table III).

It was also observed (Fig. 5) that the initial slope of the time-potential curve decreased with increasing specimen thickness. A plot of log $(dE)/(dt)$ vs. log $d$ is shown in Fig. 7. The lines for the two steels are nearly parallel and have a slope of approximately $-1.8$.

These data indicate that the time-lag is related to the thickness of the steel by the relation $t = kd^{2.10}$ (see Table III). If it is assumed that the time-lag is a measure of the time required for hydrogen to diffuse through the specimen and appear at the steel-dichromate surface, then these results are in accord with classical diffusion theory, which would predict that the time should be proportional to the thickness squared. Whether the difference between the observed exponent 2.10 and the theoretical exponent of 2.00 is real or due to experimental error is

Table III. Time-lag vs. thickness for steel samples H-1115 and H-1235

| Thickness, $d$ (mm) | Time lag, $t$ (min) | $k_1 = \frac{t}{d^2}$ | $k_2 = \frac{t}{d^{2.1}}$ |
|---|---|---|---|
| | *Sample H-115* | | |
| 3.22 | 27 | 2.60 | 2.31 |
| 6.32 | 113 | 2.83 | 2.35 |
| 12.60 | 492 | 3.12 | 2.34 |
| 25.3 | 2100 | 3.29 | 2.35 |
| | *Sample H-1235* | | |
| 2.66 | 14 | 1.97 | 1.80 |
| 5.08 | 53 | 2.03 | 1.74 |
| 10.2 | 228 | 2.19 | 1.74 |
| 12.7 | 350 | 2.19 | 1.68 |
| 15.2 | 536 | 2.32 | 1.77 |
| 20.7 | 961 | 2.23 | 1.72 |
| 25.2 | 1527 | 2.41 | 1.72 |

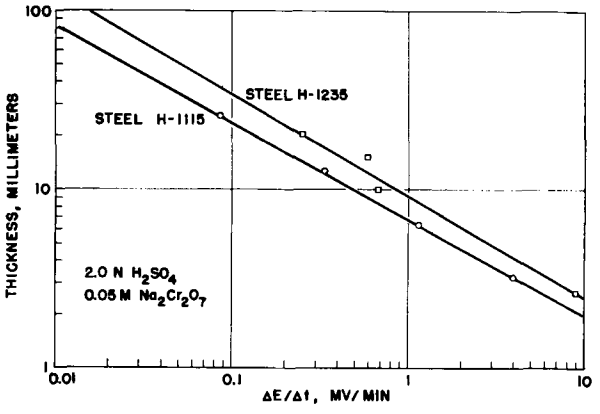


Fig. 7. Plot of thickness vs. $\Delta E/\Delta t$

not known. Indeed, it is likely that the time-lag does not correspond to the time required for the appearance of the hydrogen but perhaps to the time required for the rate of hydrogen arrival at the surface to reach a certain value.

If the change in potential $\Delta E$ is assumed to be proportional to the quantity, $Q$, of hydrogen which has diffused through the steel plate, then $\Delta E/\Delta t$ should be proportional to $dQ/dt$. However, classical diffusion theory predicts $dQ/dt$ to be inversely proportional to the thickness, $d$, of the membrane or thus, by analogy, $\Delta E/\Delta t$ should be proportional to $d^{-1}$ rather than $d^{-1.8}$ as found experimentally. Apparently $\Delta E/\Delta t$ is not proportional to the quantity of hydrogen passed through the steel, a relation which is perhaps too simple to have expected anyway. Thus, there is no explanation at this time for the $\Delta E/\Delta t = kd^{-1.8}$ relationship.

### *Effect of Acid Variations*

The effect of variations in sulfuric acid concentration is shown in Fig. 8. Note that a 1000-fold change in acid concentration markedly influences the shape of the time-potential curves. As the acid concentration decreases, the time-lag increases, and $\Delta E/\Delta t$ also decreases slightly. This is in agreement with the concept that at lower acid concentrations the rate of steel corrosion, and consequently the rate of hydrogen diffusion, decreases.

Other investigators have shown that the addition of certain compounds to the acid solution increases the rate at which hydrogen enters steel (2, 14). One

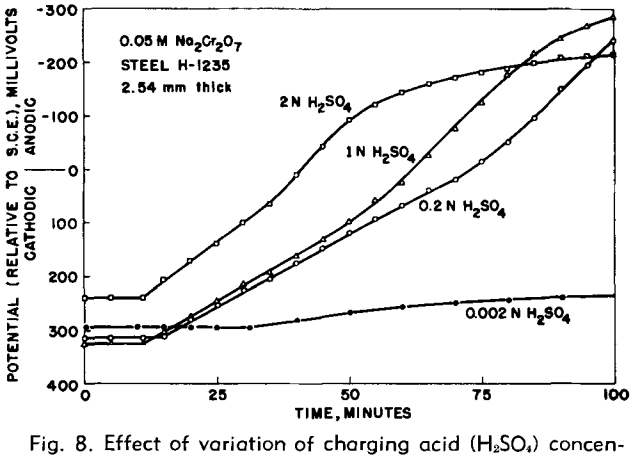


Fig. 8. Effect of variation of charging acid ($H_2SO_4$) concentration on time-potential relation.

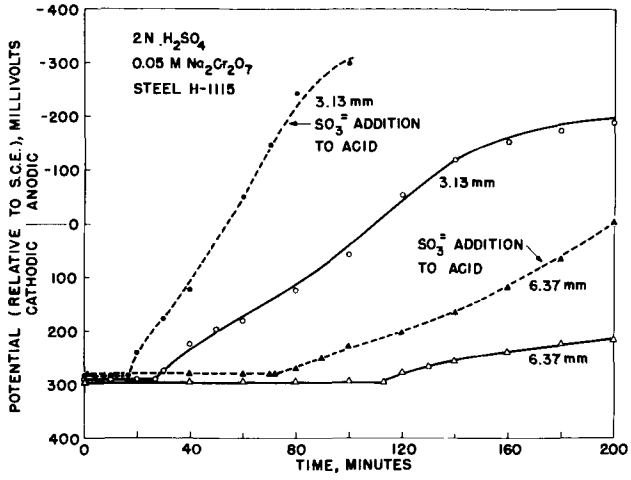


Fig. 9. Effect of $SO_3^=$ promoter action on time-potential relation.

such compound is sodium sulfite. The effect of its addition to the corroding acid on the time-potential curve is shown in Fig. 9. The addition greatly decreases the time-lag and increases $\Delta E/\Delta t$. Preliminary corrosion rate studies indicate that the presence of the sulfite increases the corrosion rate, but the change in time-lag with sulfite addition is not necessarily proportional to the change in corrosion rate.

The effect of using citric acid instead of sulfuric acid as the corroding medium is shown in Fig. 10 for the case of solutions of equal pH (1.29). Although the time-potential curves are similar when recorded over several hours, the time-lag for the sulfuric acid experiment is considerably shorter than for the citric acid experiment (19.0 vs. 27.2 sec) and the corrosion rate with sulfuric acid is almost three times greater than with citric acid.

### *Effect of Variations in Passivating Solution*

Figure 11 illustrates the changes that occurred when the concentration of the dichromate solution

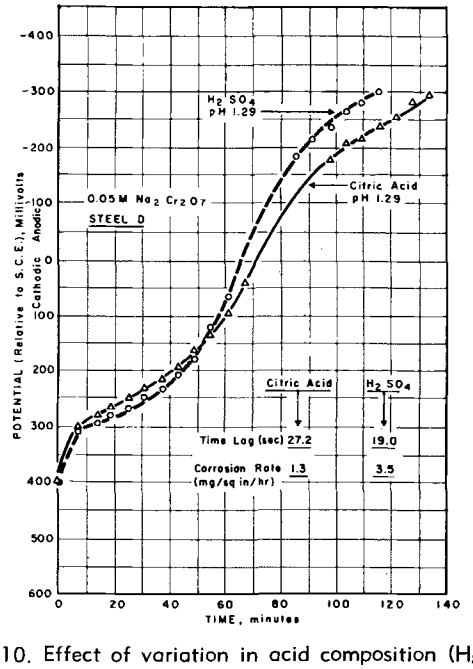


Fig. 10. Effect of variation in acid composition ($H_2SO_4$ vs. citric) at equal pH on time-potential relation.

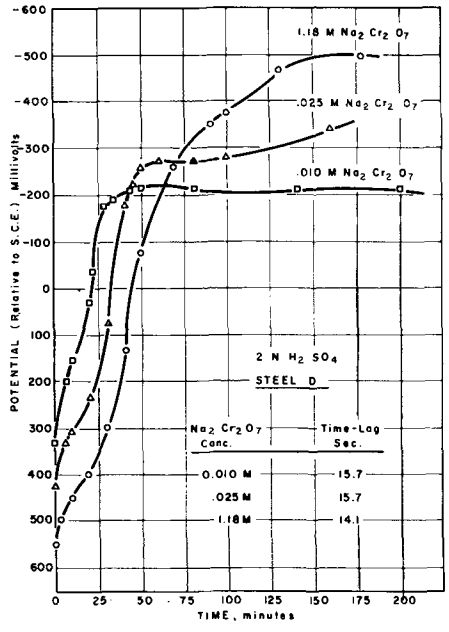


Fig. 11. Effect of variation in detecting solution ($Na_2Cr_2O_7$) concentration on time-potential relation.

was varied from 0.01M to 1.18M. As the concentration of sodium dichromate increases, the initial $\Delta E/\Delta t$ decreases; however, the time-lag remains relatively constant.

In addition to the use of sodium dichromate as a passivating solution, experiments are under way in which concentrated nitric acid, mercurous nitrate, and sodium hydroxide solutions are used as passivating agents; however, these experiments are not complete and will be reported at a later time.

## General Discussion

On the basis of the results described above, we believe that the electrode potential of the steel surface exposed to the dichromate solution is changing because of a surface reaction. The potential change does not appear to be related to the increase in dissolved hydrogen in the metal lattice or to diffusion through the lattice.

This surface reaction appears to be the reduction of the passive iron-oxide film. When this reaction occurs even to a slight extent, the surface can consist of three types of areas: the passive iron-oxide area, a reduced-iron area, and a reduced-iron area concentration-polarized by a gaseous hydrogen film. Thus, the electrode potential of the surface is no longer that of the passive iron oxide. As time proceeds, the reduced-iron area tends to increase; however, its rate of increase is influenced by the rate of passivation in the dichromate solution. Moreover, the presence of the polarizing gaseous hydrogen film on the surface tends to prevent the dichromate ions from reaching the reduced iron surface. Thus, the initial or early slope of the time-potential curve is determined by (*a*) the rate at which the hydrogen diffuses through the metal (see Fig. 5), and (*b*) the rate of passivating reaction, i.e., dichromate concentration (see Fig. 11). The final potential of the system is determined by whether the hydrogen-diffusion rate is rapid enough to completely overshadow the passivation rate, in which case the final potential is that of the normal hydrogen overvoltage on the steel surface. This actually occurs, for example, when sodium sulfite is used as a promotor, Fig. 9, or with certain steels, Fig. 4. If the hydrogen-diffusion rate is not sufficient to overshadow the passivation rate, eventually a dynamic equilibrium condition is reached wherein a constant fraction of the surface exists as a passive film and another fraction as a hydrogen polarized iron electrode. In this situation, the potential becomes steady at some value less than that of the normal hydrogen overvoltage. Numerous incidences of this have been observed (see, for example, Fig. 4 and 11). As further evidence that an equilibrium exists, it was noted that, if the acid solution is completely removed or neutralized with sodium hydroxide, the potential of the surface in the dichromate solution changes in the cathodic direction. It has also been observed that, if the corrosion reaction lowers the strength of the corroding medium, the potential in the dichromate solution will pass through a maximum.

This technique should be useful in studies of the effect of corrosion inhibitors and accelerators on hydrogen diffusion and the nature of surface passivation reactions.

## Acknowledgment

Mr. John Burke assisted in making many of the experimental measurements described above, and his assistance is gratefully acknowledged.

Manuscript received March 4, 1958. This paper was prepared for delivery before the Cleveland Meeting, Sept. 30-Oct. 4, 1956.

Any discussion of this paper will appear in a Discussion Section to be published in the June 1959 JOURNAL.

## REFERENCES

1. T. S. Fuller, *Trans. Am. Electrochem. Soc.*, **36**, 113 (1919).
2. L. S. Darken and R. P. Smith, *Corrosion*, **5**, 1 (1949).
3. T. D. McKinley, *This Journal*, **102**, 117 (1955).
4. R. A. Heaton, *Vacuum*, **2**, 115 (1952).
5. D. J. Carney, J. Chipman, and N. J. Grant, *J. Metals*, **188**, 397 (1950).
6. C. A. Edwards, *J. Iron Steel Inst. London*, **110**, 9 (1924).
7. T. N. Morris, *J. Soc. Chem. Ind., London*, **54**, 7T (1935).
8. L. D. McGraw, *et al.*, National Advisory Committee for Aeronautics, Technical Note 2696, April 1952; Technical Note 3164, March 1954.
9. M. J. N. Pourbaix, "Thermodynamics of Dilute Aqueous Solutions," p. 95, Edward Arnold and Co., London (1949).
10. J. Bernard and P. H. Albert, *Compt. rend.* **224**, 45 (1947).
11. H. Fisher and H. Heiling, *Z. Elektrochem.*, **54**, 184 (1950).
12. J. A. Bagotskaya and A. N. Frumkin, *Doklady Akad. Nauk, SSSR*, **92**, 979 (1953).
13. H. H. Uhlig, *Trans. AIME*, **140**, 387 (1940).
14. H. H. Uhlig, N. E. Carr, and P. N. Schneider, *Trans. Electrochem. Soc.*, **79**, 111 (1941).
15. P. Amiot, L'Institute de Recherches de la Siderurgie, Series A, **158**, 57, April 1957.

# An Investigation of Chemical Variables Affecting the Corrosion of Copper

W. D. Robertson,[1] V. F. Nole, W. H. Davenport, and F. P. Talboom, Jr.[2]

*Chase Brass and Copper Company, Waterbury, Connecticut*

ABSTRACT

In the presence of excess oxygen the corrosion rate of copper is a linear function of hydrogen ion concentration for each of three anions ($SO_4^=$, $Cl^-$, $C_2H_3O_2^-$). The rate is not a simple function of anion concentration, and the concentration dependence varies with *p*H. The effect of $CO_2$ is negligible. The temperature dependence of the rate, at constant oxygen concentration, for both chloride and sulfate solutions, is

$$\text{Rate} = A\, e^{-9000/RT}$$

The corrosion rate of copper in open solutions saturated with air goes through a maximum in the range 71°-77°C.

The corrosion rate of copper has been determined in dilute aqueous salt solutions, under conditions in which an attempt was made to maintain a constant, predetermined electrolyte composition throughout the test period. This was accomplished by passing solutions continuously through the corrosion vessel at a rate such that the corrosion rate was independent of the solution flow rate.

Previous investigations of the rate of solution of Cu in $H_2SO_4$ (1) and in ammonia (2) served a similar purpose by providing a large excess of reactants in a closed system. However, the present technique of a flowing system was adopted, in preference to a closed system, to avoid a significant increase in soluble corrosion products which affect the rate (3) and, at the same time, to supply an excess of reactants to the surface at a constant concentration.

The chemical variables investigated included anion concentration and type (sulfate, chloride, and acetate), hydrogen ion concentration, oxygen, free carbon dioxide, and temperature.

## Experimental Procedure

*Material.*—The material selected for the testing program was phosphorous deoxidized copper containing 0.025% phosphorus, less than 0.01% zinc, less than 0.002% iron and nickel, and less than 0.005% lead. Test specimens were prepared from cold rolled sheet, 0.032 in. thick, milled to 3.000 x 0.740 in. All edges and corners were rounded (approximate radius of curvature 0.016 in.) using an abrasive belt with No. 180 emery paper.

Prior to testing, specimens were prepared by hand scrubbing with water and pumice, rinsed in hot water, and dried immediately. Then they were weighed to the nearest tenth of a milligram and placed under test in a reproducible manner so that comparable films were formed on all specimens during the brief atmospheric exposure.

Subsequent to testing, specimens were cleaned electrolytically (4) in 5% $H_2SO_4$ containing approximately 2 ml/liter of an organic inhibitor (Rodine No. 77) for a period not exceeding 1.5 min at a current density of 0.2 amp/cm² with a Pt anode. This procedure successfully removed corrosion products without affecting the remaining metallic specimen. The specimens were then dried and again weighed to the nearest tenth of a milligram.

All plotted points are the arithmetic average of at least two determinations, and, in general, reproducibility was about ±10%.

*Corrosion cell.*—To maintain constant composition of the solution a test cell of the form shown in Fig. 1 was adopted. A continuous supply of solution was fed to the bottom of the cell through the center tube at 230 ml/hr, which was established by experiment as approximately twice the rate at which corrosion varied significantly with solution flow rate. The solution was carried up the side arm by the air-lift, mixed with solution in the tube, and aerated; the solution then passed over the specimens, and

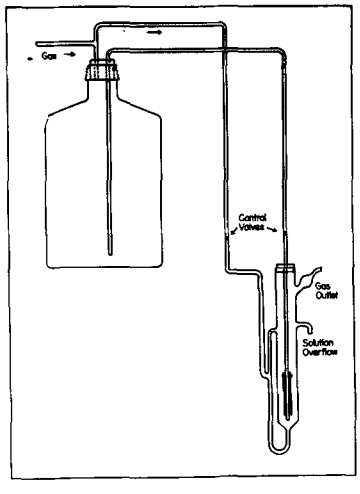


Fig. 1. Corrosion testing cell arranged for continuous renewal of solution and aeration.

[1] Yale University, New Haven, Conn., Consultant.
[2] Present address: U. S. Navy, 224 8th St., N.H.A. #1, Honolulu 18, T.H.

excess solution overflowed at the top. The pH of the air-saturated solution remained constant to ±0.1 unit, and the concentration of soluble Cu increased from zero to $3 \times 10^{-3}$M at pH 1.6, and from zero to $8 \times 10^{-6}$M at pH 6 in 48 hr.

*Preparation of solutions.*—All solutions were prepared in 10-gal quantities with laboratory distilled water and reagent grade chemicals. In the case of the chloride or sulfate ions, HCl or $H_2SO_4$ was added to the water until the desired pH was attained. By the addition of the proper sodium salt, the anion concentration was adjusted to the required value. With the acetate ion, the proper anion concentration was first obtained with acetic acid and then sodium hydroxide was added until the required pH was attained. Chloride, sulfate, and acetate concentrations were determined subsequently by titration.

*Gas atmosphere.*—When a gas atmosphere other than air was required, the gas was bubbled through the stock bottle of test solution for a period of not less than 12 hr, which was found to be sufficient to saturate the solution. During the test, gas was passed over the previously saturated solution to maintain saturation and through the corrosion cell via the gas lift. In the case of air, the solution was presaturated with air, from which $CO_2$ was removed by calcium hydroxide and the $CO_2$ free air was bubbled through the cells. The flow of gas to the side arm of the corrosion cell was maintained at 400 ml/min for all tests. Oxygen availability to the corroding surface was controlled by varying the partial pressure of $O_2$ in the gas mixture.

Gas saturation at higher temperatures was performed in the same manner. Oxygen concentrations at the various temperatures were obtained from available data (5, 6) which were verified by chemical analysis. Analyzed concentrations were found to be in agreement with the reported data.

Gases used in testing, other than air, were oxygen, carbon dioxide, mixtures of oxygen and nitrogen, and mixtures of oxygen and carbon dioxide. These gases were obtained in cylinders of commercial grade. When mixtures of gases were desired, composition was defined with flowmeters and dissolved oxygen concentrations in the solutions were determined by analysis, using a modified Winkler method.

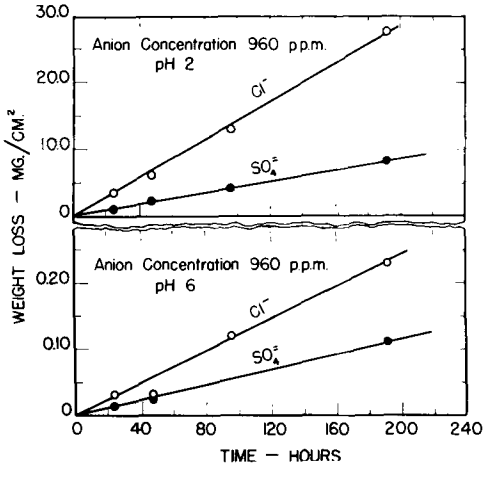


Fig. 2. Corrosion of Cu at 20°C as a function of time in chloride and sulfate solutions saturated with air at a pH of 2 and 6.

*Temperature.*—The temperature dependence of corrosion rate was determined by immersing cells in an oil bath controlled to ±0.3°C. The test solution was admitted to the cell, and the selected gas atmosphere passed through the cell in the usual manner. Upon reaching the desired temperature, the test was initiated by placing the specimens in the cell and starting the flow of solution through the cell.

Experiments involving different oxygen concentrations, defined by oxygen solubility under 1 atm of air at each temperature (the usual practical case), and experiments at constant oxygen concentration at all temperatures were performed. In the former experiments, air alone was bubbled through the cell so that the solution reached saturation with respect to oxygen in air at the temperature of the experiment.

To obtain a measure of the temperature dependence of corrosion of copper at constant oxygen concentration, tests were run with an oxygen concentration determined by the oxygen solubility at 82°C. From the oxygen solubility curve and chemical analysis it was found that the test solution contained 2.56 ppm ($8 \times 10^{-5}$M) dissolved oxygen from the air at 82°C. The oxygen concentration at this temperature was taken as the constant concentration, and oxygen and nitrogen in proper proportions were used to provide 2.56 ppm oxygen at all lower temperatures. All other tests, except those designed specifically to study temperature effects, were run at room temperature.

## Experimental Results

*Time dependence.*—Tests were conducted to determine whether corrosion rates were constant in time. Chloride and sulfate solutions of different anion concentrations, each at a pH of 2, 3, and 6 were investigated. Typical data are presented in Fig. 2.

The results of these tests show that corrosion is linear in time under the present conditions of surface preparation, constant solution composition, and pH. This was in spite of the fact that visible corrosion films are formed in the pH range of 6 to 3, but no film is evident at pH 2. On the basis of these results the exposure time chosen for subsequent tests was arbitrarily set at 48 hr.

*Anion concentration.*—Figure 3 shows the dependence of corrosion rate on sulfate and chloride concentrations at pH 2 and pH 6; at pH 2 it is impossible to extend the investigation to the low anion concentrations attainable at pH 6. Obviously, the dependence of corrosion rate on the type and concentration of anion is extremely complicated, and more extensive and detailed investigations will be necessary to separate the different factors. Almost certainly a single explanation cannot cover adequately all the observed variations.

*Dependence of corrosion rate on pH and oxygen concentration.*—The effect of pH on the corrosion rate of Cu in chloride, sulfate, and acetate solutions is shown in Fig. 4. For sulfate and acetate solutions the logarithm of corrosion rate is seen to be a linear

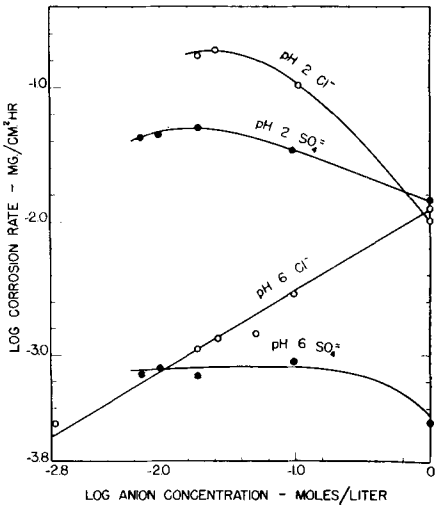


Fig. 3. Corrosion of Cu at 20°C as a function of chloride and sulfate concentration at a pH of 2 and 6, air saturation.

function of pH. In chloride solutions, below a pH of 3, the deviation from linearity is attributable to insufficient oxygen. In Fig. 5 the dependence of corrosion rate on oxygen concentration is seen to be significant in chloride solutions below pH 3. In this range corrosion rate appears to become almost independent of pH at a level defined by the oxygen partial pressure.

*Effect of carbon dioxide.*—Before investigating the effect of $CO_2$ concentration, it was necessary to determine the significance of oxygen in combination with $CO_2$. A series of experiments were conducted in sulfate and chloride solutions at pH 2, 3, and 6, saturated with free $CO_2$ in the absence of oxygen. The resulting negligible corrosion rate showed that oxygen, or an oxidizing agent, is necessary, and also that $CO_2$, by itself, does not cause corrosion of Cu.

In accordance with the preceding results, it was necessary to combine the $CO_2$ with various constant oxygen concentrations. Two constant oxygen concentrations were chosen: saturation with air (8 ppm $O_2$) and the concentration resulting from saturation with oxygen (40 ppm $O_2$).

The results are shown in Fig. 6. At pH 6 the corrosion rate appears to increase with an increase in

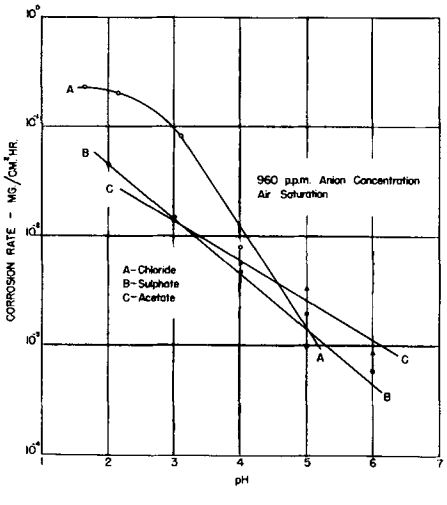


Fig. 4. Logarithm of corrosion rate of Cu at 20°C as a function of pH in sulfate, acetate, and chloride solutions.

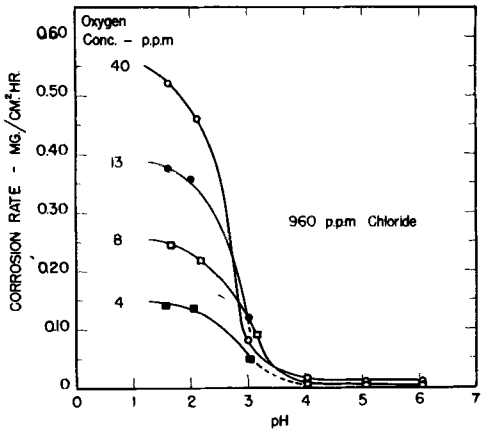


Fig. 5. Dependence of corrosion rate of Cu at 20°C on pH in a chloride solution.

$CO_2$, but this apparent increase is probably due to the difficulty of maintaining a constant pH of 6 with $CO_2$ in an unbuffered solution. At a pH of 3 the corrosion rate apparently decreases with small concentrations of $CO_2$ and then becomes essentially independent of the $CO_2$ concentration.

The lack of significant effect of $CO_2$ on the corrosion rate does not contradict general experience. In an unbuffered solution, the addition of $CO_2$ produces an increase in hydrogen ion concentration. In the present experiments, this increase is eliminated and it is demonstrated that $CO_2$, as such, has little or no effect on the corrosion rate.

*Effect of temperature.*—Figure 7 shows the dependence of corrosion rate on temperature at a pH

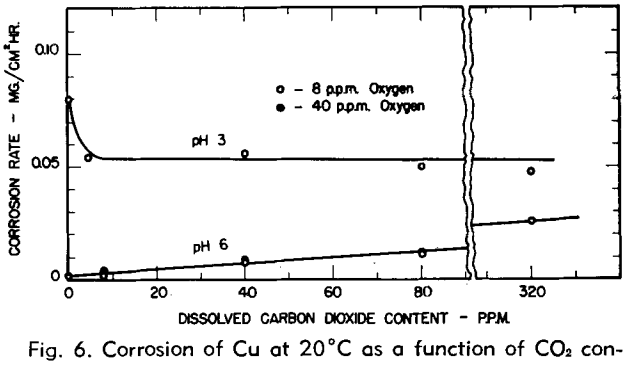


Fig. 6. Corrosion of Cu at 20°C as a function of $CO_2$ concentration.

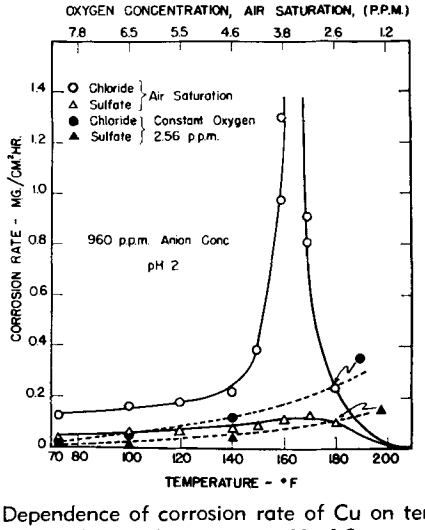


Fig. 7. Dependence of corrosion rate of Cu on temperature in chloride and sulfate solutions at a pH of 2.

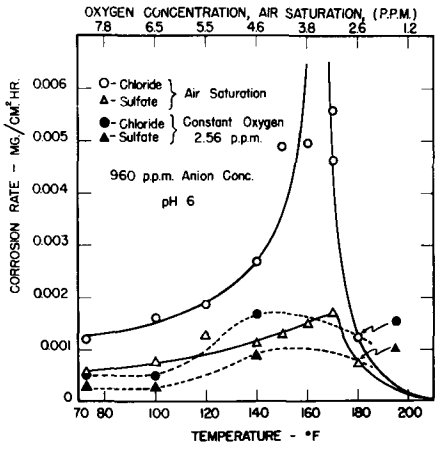


Fig. 8. Dependence of corrosion rate of Cu on temperature in chloride and sulfate solutions at a pH of 6.

of 2, in sulfate and chloride solutions (*a*) in equilibrium with air and (*b*) at constant oxygen concentration. The effect of temperature at a pH of 6, in chloride and sulfate, is shown in Fig. 8.

At a pH of 6 and a pH of 2, and constant chloride concentration of 960 ppm $Cl^-$, the corrosion rate goes through a very high maximum between 160° and 170°F (71°-77°C) in an open system. At constant sulfate concentration a maximum also appears but the corrosion rate does not become catastrophic. In both cases oxygen concentration is decreasing with temperature as shown.

The effect of temperature at constant oxygen concentration (2.56 ppm $O_2$) is also shown in Fig. 7 and 8. The lower rates are, of course, due to lower oxygen concentrations at all temperatures. In sulfate and chloride solutions at pH 6 and at the low oxygen concentration, the corrosion rates are extremely low and the data are correspondingly uncertain, but the data indicate that a maximum rate persists in the higher ranges of temperature. Subsequent tests were made in this range and the data were verified. At pH 2, the corrosion rate is shown as increasing uniformly with temperature; however, as a result of the considerations below, it is possible that a maximum may also be found in a narrow range of temperature near 71°C, where data are lacking.

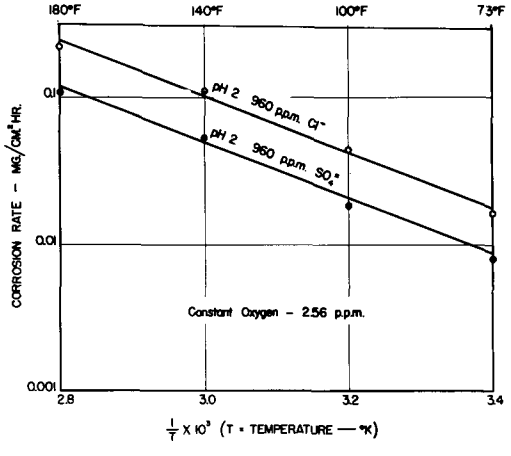


Fig. 9. Corrosion rate of Cu as a function of reciprocal absolute temperature.

## Discussion

*Time dependence.*—Since the corrosion rate at room temperature was found to be constant in time in both sulfate and chloride solutions at each pH level, it appears that the growth of visible films in time does not significantly affect the rate (which is characteristic of each ion type and pH level).

Weeks and Hill (7) have shown that the rate diminishes from a high initial value to a constant rate after about 1 min in acid chloride solutions. However, in the latter experiments, a higher order of sensitivity was employed and, while oxide films were substantially removed prior to immersion, it is possible, as suggested by those authors, that the rapid solution of traces of oxide may account for the high initial rate. In the present experiments, no attempt was made to eliminate air-formed films, and the results show that films formed during the subsequent corrosion process do not significantly affect the rate which is constant from zero time. Since a linear dependence on time was obtained in both acid and near neutral solutions, it appears that the results are quite general.

*Hydrogen ion concentration.*—If it is assumed that corrosion rate is proportional to hydrogen ion concentration, then, in accordance with the definition of pH:

$$\log \text{rate} = -k\ \text{pH} + \text{constant} \qquad [1]$$

The experimental data obtained in sulfate, acetate, and chloride solutions, Fig. 4, are in accordance with this relationship, except in chloride solutions below pH 3 where the system appears to be under oxygen control. A similar departure from linearity was observed by Weeks and Hill (7) at a lower pH. Figure 5 shows that the limiting rate is approximately proportional to the oxygen concentration which is consistent with a limiting rate defined by the diffusion-controlled transport of oxygen from the solution to the metal interfaces.

Since hydrogen ions are not reduced by the oxidation of Cu, under the present conditions, the linear dependence of corrosion rate on hydrogen ion concentration requires some explanation. Weeks and Hill (7) and Hill (8) have proposed the following net reaction for the rate-determining step:

$$2Cu + H^+ + O_2 \rightarrow 2Cu^+ + HO_2^- \qquad [2]$$

It was assumed that oxygen is first adsorbed from solution to form an "oxidized site," followed by reaction with a hydrogen ion to form the cuprous ion and the peroxide ion. The results of the present investigation appear to be generally in accord with this mechanism.

*Chloride and sulfate dependence.*—With respect to the relatively high rates observed in chloride solutions, compared with sulfate solutions, certain negative conclusions may be drawn, but the detailed mechanism is still not clear. Perhaps it should be emphasized that these data were obtained with a constant anion concentration at each pH.

In the apparent absence of rate-limiting films, particularly at pH 2, the penetrating properties of chloride ions, as demonstrated with Al and passi-

vated Fe, do not seem to have any obvious function. Furthermore, at the lower pH, the rate decreases with increasing chloride concentration, approximately parallel with the decreasing rate in sulfate solutions and the decrease is considerably larger than can be accounted for by decreasing oxygen solubility. At pH 6, the rate does increase with chloride ion concentration and it may be that film penetration is involved. However, there is no other evidence of a rate-limiting film and, since chloride ion does not appear to be involved in the net reaction, its function is not obvious.

*Temperature dependence.*—Analysis of the temperature dependence of corrosion rate can be rigorously applied only to conditions of constant oxygen concentration. However, the data obtained in air-saturated open systems is of considerable practical significance, i.e., the existence of a catastrophic phenomenon that appears in a temperature range around 71°C in chloride solution.

In conformity with general kinetic theory, the temperature dependence of reaction rate is written:

$$\text{Rate} = A \exp(-E/RT) \qquad [3]$$

and, accordingly, log Rate is shown as a function of reciprocal temperature in Fig. 9 for constant oxygen and a pH of 2. Obviously the data are in complete accord with the relationship; the apparent activation energy, $E$, is 9000 cal/mole and is the same for both chloride and sulfate solutions. It may be significant that the observed activation energy for this process, involving the reduction of oxygen, lies in the range of values observed (9) for the reduction of hydrogen ions on Pt and Pd, 6000-11500 cal/mole. Furthermore the activation energy is the same in both chloride and sulfate solutions which, again, indicates that the temperature dependence of rate is associated with a process common to both types of solution.

It is evident in Fig. 8 that at pH 6 and constant oxygen concentration the data do not conform to a simple exponential function of temperature. Assuming that the temperature dependence, as such, is exponential, the increased rate must be attributed to some extraneous factor, probably associated with the form of the corrosion products.

The presence of such an extraneous factor is indicated by the catastrophic rates observed in the open systems, particularly in the presence of chloride. After correcting for oxygen concentration, the observed rapid increase in rate in the temperature range of 62°-71°C is much greater than can be accounted for in terms of the exponential temperature dependence alone.

## Conclusions

1. The corrosion rate of Cu at room temperature is constant in time in chloride and sulfate solutions, in the range of pH 2-6, and the rate does not appear to be limited by the growth of corrosion product films.

2. In air-saturated solutions of constant anion concentration, corrosion rate is a linear function of hydrogen ion concentration except in chloride solutions at a pH less than 3, where the increasing rate is limited by the diffusion of oxygen.

3. Corrosion rate is a complex function of chloride and sulfate concentration which varies with pH in solutions of constant anion concentration.

4. In an open system, at equilibrium with air, the corrosion rate rises to a maximum between 71°-77°C. When oxygen concentration is constant at all temperatures, the rate in both chloride and sulfate solutions at pH 2 may be expressed as:

$$\text{Rate} = A\, e^{-9000/RT} \ (\text{mg cm}^{-2}\ \text{hr}^{-1})$$

## Acknowledgments

The authors wish to thank D. K. Crampton and H. L. Burghoff for their interest and suggestions concerning this investigation and to acknowledge the assistance of S. Banisky and other members of the Research and Development Dept. of the Chase Brass and Copper Co.

Manuscript received Sept. 10, 1956. This paper was prepared for delivery before the Cleveland Meeting, Sept. 30-Oct. 4, 1956.

Any discussion of this paper will appear in a Discussion Section to be published in the June 1959 JOURNAL.

## REFERENCES

1. C. Y. Lu and W. F. Graydon, *Can. J. Chem.*, **32**, 153 (1954).
2. J. Halpern, *This Journal*, **100**, 421 (1953).
3. R. J. Agnew, J. K. Truitt, and W. D. Robertson, *Ind. Eng. Chem.*, **50**, 649 (1958).
4. A.S.T.M. Standards, 1946, Part 1-B, Nonferrous Metals, p. 800, Appendix I.
5. F. N. Speller, "Corrosion Causes and Prevention," 3rd Ed., p. 167, Fig. 39, McGraw-Hill Book Co., Inc., New York (1951).
6. "Handbook of Chemistry and Physics," 37th Ed., 1955-1956, p. 1606, Chemical Rubber Publishing Co., Cleveland, Ohio (1955).
7. J. R. Weeks and G. R. Hill, *This Journal*, **103**, 203 (1956).
8. G. R. Hill, *ibid.*, **100**, 345 (1953).
9. F. P. Bowden and J. N. Agar, *Ann. Rept. Chem. Soc.*, **34**, 107 (1937).

# Some Observations on the Effect of the Interaction of Tantalum with Oxygen, Nitrogen, and Hydrogen

**R. Bakish**[1]

*Sprague Electric Company, North Adams, Massachusetts*

ABSTRACT

Experiments and results on the interaction of tantalum with $O_2$, $N_2$, and $H_2$ are presented. The {100} is shown to be the habit plane of the segregation of the reaction products which appear to be $Ta_2O_5$, TaN, and $\beta$TaH, respectively.

The role of the gas-metal interaction on the fracture behavior of single crystals has been evaluated. The observed {100} and {110} cleavage-type fractures as induced by this interaction are discussed and a hypothesis to explain occurrence advanced. Markings observed on cleavage faces are described.

The interaction of tantalum with oxygen, nitrogen, and hydrogen has been studied in some detail by a number of investigators (1-4). Several aspects of this interaction have been completely neglected, however, and an attempt to cover some of these gaps is made with this communication.

High-purity Ta in sheet and wire form from Fansteel Metallurgical Corporation (0.03 C max, 0.03 Fe max, 99.9+ Ta) was used in this investigation. Observations were made both on fine grain material and on sheet single crystals of about 0.01 in. thickness grown by strain annealing.

## Experimental Procedures and Results

Standard x-ray powder techniques were used in conjunction with the ASTM card index for the identification of compounds formed. The same technique applied to wires from which the surface reaction product was removed was also used for the identification of product of internal gas-metal reaction, i.e., the crystallographic precipitate of the oxide, nitride, or hydride, as the case might be.

All orientations were determined from Laue back-reflection photographs and stereographic analysis in accordance with standard procedures (5). Determination of the orientation of the habit plane of the internal precipitation of the gas-metal compounds were carried out as follows: two surfaces with known angular relations were ground on crystals of known orientation, and the angles made by the planes of the precipitates with the common edge were measured. This information was then plotted stereographically and analyzed using a standard projection, in accordance with standard procedures (6).

Standard metallographic techniques were applied in this study, and a solution of $H_2SO_4$ (95%), $HNO_3$ (70%), and HF (48%) in ratio (5:2:2) was used as the etchant.

### *Effect of Oxygen*

Oxygen was introduced into the specimen by oxidation in air at 750°C for 1 hr and, depending on the thickness of the material studied, complete conversion of the metal to oxide or partial conversion of the surface with internal precipitation was produced. Oxidation in pure oxygen leads in essence to the same end results even though at apparently higher rates. This fact and the inability to detect x-ray evidence of presence of TaN in specimens oxidized in air tends to indicate lack of reaction between the Ta and the $N_2$ of the air.

Possibility of dissolution of small amounts of $N_2$ is not precluded but, if present, it does not seem to affect the crystallographic factors studied. X-ray data indicate that the oxide formed is $Ta_2O_5$. It precipitates on the {100} planes of the bcc lattice, as has been discussed in detail elsewhere (7).

Single crystals oxidized in air or in $O_2$ for periods between 20 min to 1 hr are extremely brittle; in several cases, dropping a crystal to a cement floor from a distance of about 3 ft was sufficient to produce excessive cracking and disintegration along certain planes. Measurements of these elements of cleavage-type fracture revealed that oxygen-embrittled Ta single crystals cleave on the {110} and {100} planes within the error of measurement of 2°.

When noncrystallographic brittle fracture was produced in crystals by bending normal to random direction, one could always detect facets parallel to the {110} and the {100} cleavage planes on the fracture surface.

Examination of cleavage surfaces revealed the presence of markings. These are quite varied at different areas of cleaved {110} and {100} planes in a crystal and also in {110} and {100} planes in different crystals. No specific pattern associated with either of these two cleavage faces was established, yet certain patterns seemed to be characteristic and constantly appeared alone or in combinations in the large number of {100} and {110} cleavage planes examined. The most common ones are seen in Fig. 1-3.

### *Effect of Hydrogen*

Hydrogen was introduced into the Ta both by annealing in $H_2$ at 700°C for periods up to 24 hr, de-

[1] Present address: Rare Metals Division, CIBA Limited, Basle, Switzerland.

Fig. 1. Typical cleavage markings. Magnification 500X before reduction for publication.

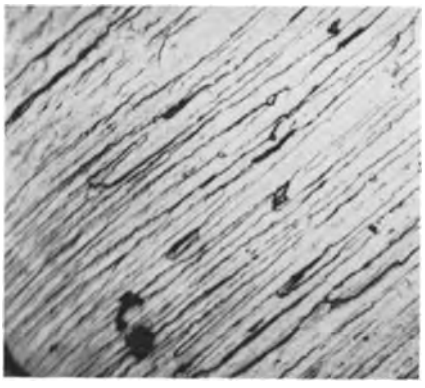

Fig. 2. Typical cleavage markings. Magnification 500X

Fig. 3. Typical cleavage markings. Magnification 2000X

pending on the extent of hydrogenation needed, and also by cathodic charging at room temperature at a current density of 0.5 amp/in.$^2$ in a solution consisting of 90% $HNO_3$ (70%) and 10% HF (48%). The cathodic charging was used for the study of the effect of $H_2$ on fracture properties and for comparison with the behavior of material in which $H_2$ was introduced at high temperature.

The product of the hydrogen-tantalum reaction also precipitates on the {100} planes. The compound believed to be segregating on the {100} plane is the $\beta$-tantalum hydride (8). This precipitation of the hydride produces distortion in the Ta which manifests itself in warping of the specimen. A polycrystalline specimen showing the crystallography dependent $\beta$-TaH precipitation can be seen in Fig. 4.

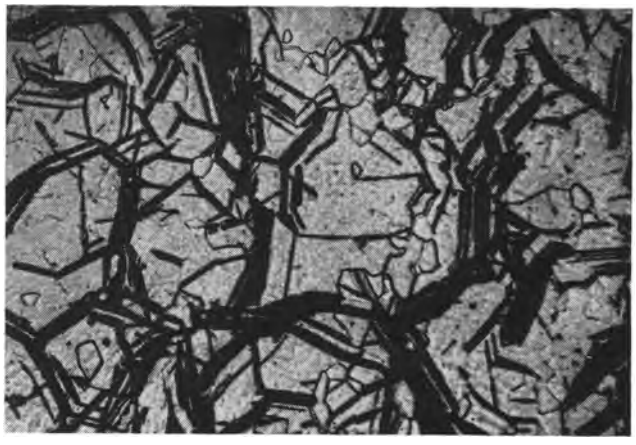

Fig. 4. $\beta$-TaH precipitate in fine-grained Ta sheet. Treatment, 24 hr, 700°C in $H_2$. Magnification 500X before reduction for publication.

Hydrogen introduced into Ta as indicated leads to cleavage-type fracture on bending. Here the {100} and the {110} type of cleavage are both observed, with the {100} type seemingly predominant.

Hydrogen introduced into Ta by cathodic charging under conditions stated above also produces room temperature embrittlement and cleavage fracture on bending. The predominant cleavage here seems to be of the {110} type; rarely was the {100} cleavage detected. Examination of cleavage faces revealed essentially the same features already referred to when discussing oxygen-induced cleavages.

*Effect of Nitrogen*

Nitrogen was introduced in the specimen by annealing in nitrogen atmosphere at 750°C. Nitrogen-tantalum reaction seems to proceed at relatively slow rates at this temperature. Five-hour nitriding was the minimum time needed for sufficient precipitation for habit-plane determination in the single crystals used, but 24-hr treatment was actually used.

The formation of the nitride in the metal must be connected with a substantial volume change, as the nitrided specimens invariably show a substantial amount of distortion and warping. Figure 5 shows the appearance of the surface of a single-crystal specimen which was nitrided for 24 hr at 750°C.

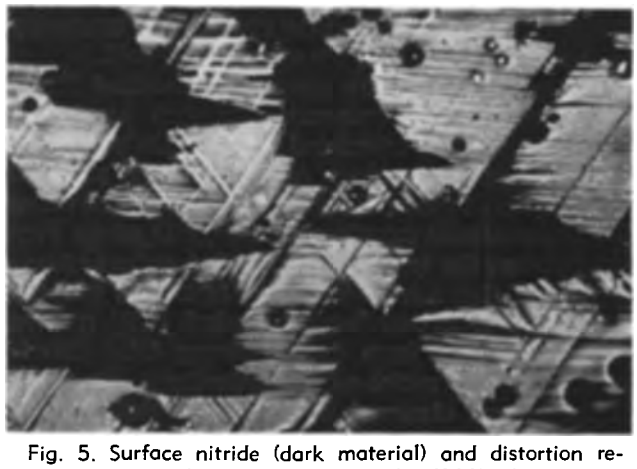

Fig. 5. Surface nitride (dark material) and distortion resulting from nitride precipitation on the (100) planes on a single crystal of Ta after 24 hr at 750°C in $N_2$ atmosphere. Magnification 500X before reduction for publication.

Fig. 6. Nitride platelets on a polished surface viewed under polarized light. Specimen treated as in Fig. 5. Magnification 500X before reduction for publication.

Fig. 7. Fracture associated with the nitride-metal interface

Observe the relief on the surface on the sites of nitride precipitation. No uniform nitride cover seems to be formed; however, bulk nitride formed at different locations is clearly visible. On metallographic polishing of the specimen normal to exposed surface and examination with polarized light, one can see that nitride platelets which form are anisotropic (Fig. 6). The habit plane of precipitation is {100}. The structure of the nitride is not known, and no study of structure was performed; in comparison with other data on tantalum nitride in the literature (9), however, it is quite likely that the compound formed both on the surface and internally on the {100} plane is of the composition TaN.

Cleavage fracture on nitrogen-embrittled Ta in the terms of the treatments described previously was always found associated with a visible precipitate. It apparently does not take place prior to segregation of the nitride phase, and it occurs along the metal-nitride interface on the {100} plane. Figure 7 shows the type of fracture that occurs associated with this nitride-tantalum interface, and the Laue back reflection shows a typical {100} pattern that one obtains from these cleavage faces associated with the metal-nitride interfaces. No {110} cleavage was observed in nitrogen-embrittled Ta.

## Discussion of Results

The gas-metal compounds resulting from the interaction of Ta with $O_2$, $N_2$, and $H_2$ all precipitate on the {100} planes of the bcc lattice. The location of the precipitate coincides with the most widely spaced atoms of this lattice. There is identity in the crystallographic factors involved in this interaction, but substantial differences exist in the kinetics of reaction of each of these three gases with the Ta.

The occurrence of cleavage-type fracture in pure Ta induced by impact at low temperature has already been discussed (10). The results of this study indicate the strong effect that $O_2$, $N_2$, and $H_2$ have in modifying this fracture behavior. The evidence presented tends to support the contention here advanced that the {100} type cleavage induced both by $H_2$ and $O_2$ must be connected with the early stages of precipitation on this plane and a direct consequence thereof. In the case of $N_2$, it takes place at a considerably later stage of precipitation and is associated with the nitride-metal interface. The {100} cleavage is the minor cleavage in high-purity Ta (10). The {110} cleavage is the major cleavage observed in Ta at low temperature (10); the {110} is also the predominant slip plane in this metal (11). The observance of this type of cleavage at room temperature under the conditions described must be a direct consequence of the presence of $O_2$ and $N_2$ in solid solution. These gases in solid solution then reduce the ductility of the Ta crystals and make it possible to produce behavior which in pure Ta takes place at −196°C at room temperature. No {110} cleavage was observed in material that was treated with $N_2$.

Markings of identical appearance as those observed and described for oxygen-embrittled Ta were also observed in hydrogen-embrittled Ta. No satisfactory hypothesis explaining their formation is advanced. It is believed, however, that they result from the interaction of the cleavage plane and screw dislocations in the crystals. Their appearance is apparently influenced by the rate and direction of the crack leading to cleavage.

## Conclusions

It has been shown that the habit plane of the precipitation of oxide, nitride, and hydride in Ta is {100} and these appear to be $Ta_2O_5$, TaN, and $\beta$-TaH, respectively.

{100} and {110} cleavages result from these gas-metal interactions. The {100} type cleavages appear to be related to the precipitation phenomena while the {110} cleavage seems to be due to gases in solid solution.

## Acknowledgment

The author wishes to acknowledge the assistance of Miss Nancy Harvin who carried out all x-ray powder work and the identification of the reaction products.

Manuscript received Nov. 4, 1957.

Any discussion of this paper will appear in a Discussion Section to be published in the June 1959 JOURNAL.

## REFERENCES

1. E. A. Gulbransen and K. F. Andrews, *J. (and Trans.) Electrochem. Soc.*, **96**, 364 (1949).
2. E. A. Gulbransen and K. F. Andrews, *This Journal*, **99**, 6 (1952).

3. E. Geberhardt and Preisdanz, *Plansee Proc.*, 254 (1956).
4. G. Brauer and R. Hermann, *Z. anorg. Chem.*, **244**, 11 (1953).
5. A. B. Greninger, *Trans. AIME*, **17**, 61 (1935).
6. C. S. Barrett, Structure of Metals, 40 (1952).
7. R. Bakish, *This Journal*, **105**, 71 (1958).
8. G. Hagg, *Z. physik. Chem.*, **11**, 433 (1930).
9. F. H. Horn and W. T. Ziegler, *J. Am. Chem. Soc.*, **69**, 276 (1947).
10. C. S. Barrett and R. Bakish, *Trans. AIME*, **208**, 122 (1958).
11. R. Bakish, *Acta Met.*, **6**, 120 (1958).

# Room Temperature Tarnishing of Silver in Bromine and Iodine

**Joseph L. Weininger**

*Research Laboratory, General Electric Company, Schenectady, New York*

ABSTRACT

Pure silver was tarnished in an atmosphere of iodine and bromine vapor at room temperature. This resulted in impervious halide surface layers, from which tarnishing rates could be deduced by means of a photomicrographic technique. It was found that the parabolic rate law, with diffusion being the rate-determining step, also holds at room temperature. The presence of water vapor reduces the rate of halogenation by a factor of two.

The tarnishing of silver by halogen vapors has attracted much attention. The reason for this interest is the relatively low temperature at which these oxidation reactions proceed and the fact that the halide produced is predominantly an ionic conductor. Hence many interesting conclusions can be drawn from tarnishing experiments (1). Wagner and his school were particularly active in connecting, by theory and experiment, the kinetics of an oxidation reaction with the ionic conductivities of the reaction products, e.g., silver halides in tarnishing reactions.

The present work arose as a problem in solid-electrolyte battery research. In the electric cell $Ta(Br_2)/AgBr/Ag$, halogen vapor reacts at the Ta cathode in the presence of a silver anode. The chemical stability of the silver anode is of great importance. One must distinguish between the thermal attack of the halogen on the silver surface, i.e., the tarnishing reaction, and the electrochemical cell reaction, the formation of silver halides. Both processes have the same over-all chemical reaction,

$$Ag + \tfrac{1}{2}Br_2 = AgBr$$

but, whereas the cell reaction is essential for the operation of the cell, the tarnishing reaction is undesirable because it consumes active cell material.

The tarnishing reaction proceeds fairly rapidly at temperatures above 200°C, and experiments performed at high temperatures are described in the literature (2-4). Only few measurements have been reported at lower temperatures and, therefore, tarnishing at room temperature was studied by the following method.

## Experimental Procedure

Jaenicke and co-workers studied the anodic formation of AgCl layers and recrystallization phenomena in aqueous solutions by means of a microscopic technique (5). In the present work, during routine photomicrographic examinations of sections of tarnished silver foils it was found that very clear reproductions could be obtained at magnification of 500. This formed the basis of an experimental technique in which the course of the tarnishing reaction would simply be followed by the observation of the microscopic increase of the tarnished layer with time.

Silver coupons of "fine" grade, supplied by Handy and Harman Company, were examined.[1] After degreasing and cleaning the coupons were exposed to

[1] The manufacturer's analysis of fine silver is: Ag 99.9+%, Cu 0.05%, Pb 0.004%, traces of Fe and other metals.

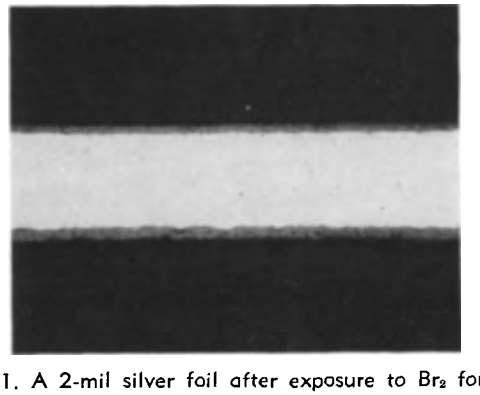

Fig. 1. A 2-mil silver foil after exposure to $Br_2$ for 7900 sec. $\Delta x_{Ag} = 1.0\ \mu$; $\Delta x_{AgBr} = 5.7\ \mu$.

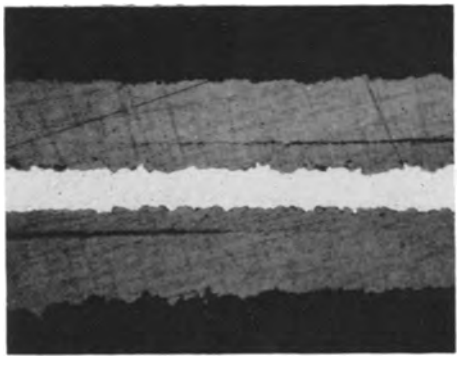

Fig. 2. A 2-mil silver foil after exposure to $Br_2$ for $1.815 \times 10^6$ sec. $\Delta x_{Ag} = 14.8\ \mu$; $\Delta x_{AgBr} = 43.3\ \mu$.

Fig. 3. A 2-mil silver foil after exposure to $Br_2$ for 5.273 $\times$ $10^6$ sec. $\Delta x_{Ag} = 22.2\ \mu$; $\Delta x_{AgBr} = 64.0\ \mu$.

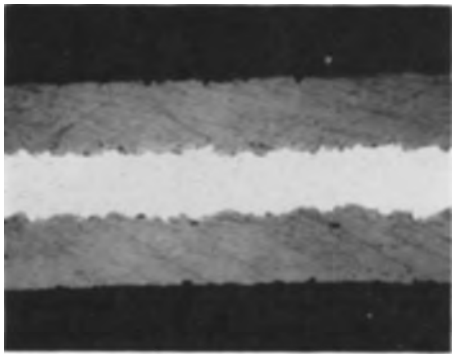

Fig. 4. A 2-mil silver foil after exposure to $I_2$ for 1.492 $\times$ $10^6$ sec. $\Delta x_{Ag} = 9.3\ \mu$; $\Delta x_{AgI} = 36.7\ \mu$.

bromine or iodine vapor at room temperature. The coupons were stored in the presence of ordinary illumination in vacuum desiccators which contained an excess of the halogen and drying agent. The desiccators were evacuated so that only the saturated halogen vapor was present. Another series of experiments was performed at 90.14% relative humidity by replacing the desiccant with a saturated aqueous solution of barium chloride. After removal from the halogen atmosphere the samples were mounted in "Selectron," a polyester (prepared from 30% styrene monomer and 70% alkyd resin) which hardens at room temperature. Samples were polished and etched. Only a very slight dichromate etch was permissible. The vertical positioning of the foils in the mount required great care in order to get photomicrographs with truly representative cross-section. Photographs were taken with a flat field objective, at a magnification of 500. For calibration, a microscale and a silver blank were added to each set of photos.

## Experimental Results

Figure 1 through 4 shows the feasibility of the method. The first three are photomicrographs of silver foils with bromide layers. These foils had been exposed to bromine in the absence of water vapor, at room temperature, for increasing periods, approximately 2 hours, 3 weeks, and 2 months, respectively. Figure 4 is an example of a cross section through a silver-silver iodide foil. Exact times of exposure in seconds and changes in the width of silver foil, $\Delta x_{Ag}$, or width of tarnished layers, $\Delta x_{AgBr}$ and $\Delta x_{AgI}$ in microns are given in the legend of the figures. It may be noted that in Fig. 2 pancake voids were formed at the original location of the silver-

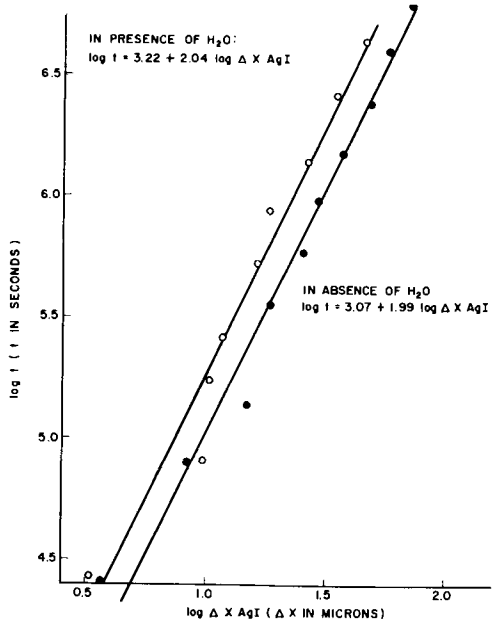


Fig. 5. Tarnshing of silver at room temperature—formation of AgI.

bromine interface (see later). Usually, large voids did not occur. Thus, in Fig. 3 the silver foil was almost completely used up in the formation of silver bromide, but only random pores existed in the halide layer.

When the course of the tarnishing reaction is plotted as the loss of silver thickness ($\Delta x_{Ag}$) and gain in thickness of the halide ($\Delta x_{Agx}$) vs. time, the graphs appeared to be parabolic. In Fig. 5 the growth of silver iodide in the presence and absence of water vapor is compared. A slope of 2 for these graphs, from a least square fit, verifies the existence of a parabolic rate law,

$$\frac{d(\Delta x)}{dt} = \frac{k'}{\Delta x}$$

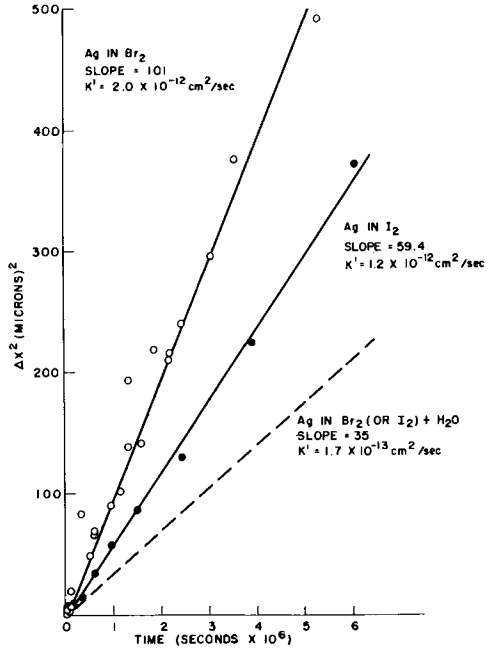


Fig. 6. Rate constants of tarnishing reaction

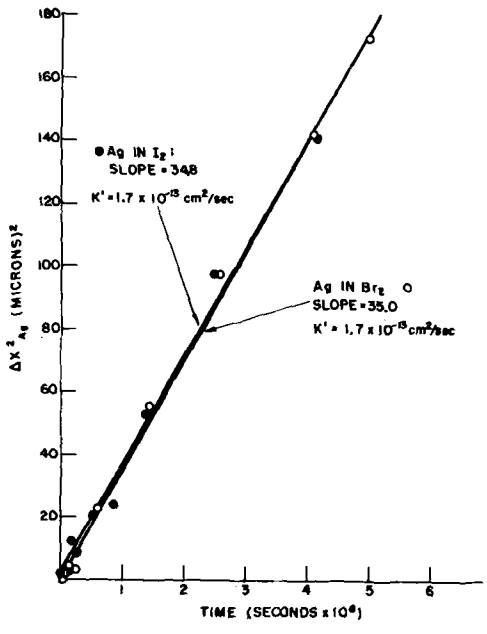


Fig. 7. Rate constants of tarnishing reaction

where $\Delta x$ is the thickness of the tarnished layer produced in time $t$ and $k'$ is the tarnishing or Tammann rate constant. If at time $t = 0$ there is no tarnished layer, then integration of the equation gives $(\Delta x)^2 = 2k' \cdot t$, and $k'$ can be evaluated from least square fits of plots as in Fig. 6. Here the constants refer to the consumption of silver in bromine and iodine, respectively. The broken line indicates the curves obtained in the presence of water vapor. This is shown in detail in Fig. 7. In water vapor the loss of silver proceeds at about the same rate in either halogen. It should be kept in mind, however, that the room temperature vapor pressures for bromine and iodine are very different and that the rate varies as the square root of the halogen pressures. These are 207 mm for bromine and 0.306 mm for iodine at 25°C. The rational rate constant, $k$, is more useful for comparison of different chemical systems because it expresses rates in terms of equivalents, thus:

$$\tilde{n} = w/\tilde{w} = (q \cdot \Delta x \cdot \rho/\tilde{v} \cdot \rho) = q \cdot \Delta x/\tilde{v}$$

where $\tilde{n}$, $\tilde{w}$, and $\tilde{v}$ are the equivalent number, weight, and volume, respectively, $q$ surface area, $\rho$ density, $w$ weight, and $\Delta x$ thickness of the reaction product. Hence, introduction of equivalents into the above rate law containing the constant $k'$ gives:

$$\frac{d\tilde{n}}{dt} = \frac{q}{\tilde{v}} \frac{d(\Delta x)}{dt} = \frac{q}{\tilde{v}} \cdot \frac{k'}{\Delta x} = k \frac{q}{\Delta x}$$

where

$$k = \frac{k'}{\tilde{v}}$$

and $k$ has the units of equivalents per centimeter per second.

The experimental results are tabulated as rate equations in Table I and rate constants in Table II.

## Discussion

From the eight rate expressions obtained in this investigation one can draw conclusions regarding the mechanism of the reaction, evaluate the rate constants of the tarnishing reaction at room temperature, and gain some insight into the structural features of the halide. As to the precision of the measurements, the probable error in the thickness of the different layers is $\pm 0.5\mu$ which is considerably smaller than the scatter of the data. The latter must be attributed to random errors in the alignment of the foils in the mount at the time of taking the photomicrograph.

### *Mechanism of the Tarnishing Reaction—Comparison with Higher Temperatures*

Consider briefly the case of silver tarnished in a bromine atmosphere. After the initial layer of silver bromide has been formed, its continued growth requires the transport of silver ions to the surface. Interstitial ions are mobile, but originate from lattice positions, therefore the following reactions are equivalent:

(A)

| ½$Br_2$ (gas) | + | $Ag'_o$ | + | $\theta$ | = | AgBr | + | $\oplus$ |
|---|---|---|---|---|---|---|---|---|
| gas molecule adsorbed on surface | | intersitial ion | | bound electron | | surface ions incorporated in lattice | | positive hole created by removal of electron |

(B)

| ½$Br_2$ (gas) | + | $Ag^+$ | + | $\theta$ | = | AgBr | + | $Ag'_{\square} + \oplus$ |
|---|---|---|---|---|---|---|---|---|
| | | lattice ion | | | | | | vacancy created by removal of lattice ion |

Note that Eq. (A) seems to have unbalanced charges. It deals with the removal of a net positive

Table I. Rate equations of tarnishing reaction at room temperature—$\Delta x$ in microns, t in seconds $\times 10^6$

| | | $H_2O$ absent | $H_2O$ vapor present (90% humidity) |
|---|---|---|---|
| (a) Parabolic relations: | | | |
| Bromination | AgBr formation | $(\Delta x)^2 = 788\,t + 103$ | $(\Delta x)^2 = 340\,t - 42$ |
| | loss of Ag | $(\Delta x)^2 = 101\,t + 7.8$ | $(\Delta x)^2 = 35.0\,t - 0.04$ |
| Iodination | AgI | $(\Delta x)^2 = 878\,t + 30$ | $(\Delta x)^2 = 442\,t + 35$ |
| | loss of Ag | $(\Delta x)^2 = 59.4\,t + 2.7$ | $(\Delta x)^2 = 34.8\,t + 1.3$ |
| (b) Logarithmic relations: | | | |
| Bromination | AgBr formation | $\log t = 2.77 + 2.14 \log \Delta x_{AgBr}$ | $\log t = 3.90 + 1.73 \log \Delta x_{AgBr}$ |
| | loss of Ag | $\log t = 3.88 + 2.13 \log \Delta x_{Ag}$ | $\log t = 4.63 + 1.80 \log \Delta x_{Ag}$ |
| Iodination | AgI formation | $\log t = 3.07 + 1.99 \log \Delta x_{AgI}$ | $\log t = 3.22 + 2.04 \log \Delta x_{AgI}$ |
| | loss of Ag | $\log t = 4.14 + 2.09 \log \Delta x_{Ag}$ | $\log t = 4.41 + 2.02 \log \Delta x_{Ag}$ |

Table II. "Rational" tarnishing rate constants (in equiv. $-cm^{-1}-sec^{-1}$)
Temp = 25° ± 5°C, $P_{Br_2}$ = 207 ± 37 mm, $P_{I_2}$ = 0.306 ± 0.016 mm

| | Ag in $Br_2$ | AgBr formation | Ag in $I_2$ | AgI formation |
|---|---|---|---|---|
| $k_{dry}$ ($H_2O$ absent) | $4.9 \times 10^{-14}$ | $1.3 \times 10^{-13}$ | $2.8 \times 10^{-14}$ | $1.1 \times 10^{-13}$ |
| $k_{wet}$ (in presence of $H_2O$ vapor, $P_{H_2O} = 21.4 \pm 5.5$ mm) | $1.7 \times 10^{-14}$ | $5.9 \times 10^{-14}$ | $1.7 \times 10^{-13}$ | $5.3 \times 10^{-14}$ |
| $k_{dry}/k_{wet}$ | 2.9 | 2.2 | 1.6 | 2.1 |
| Literature: | | | | |
| Tammann and Koester (6) ($P_{Br_2}$ = 61 mm, T = 20°, $H_2O$ present) | $10^{-14}$ | | | |
| Hauffe and Gensch (3) ($P_{Br_2}$ = 170 mm) | $1.8 \times 10^{-13}$ | (extrapolated from high temp. data) | | |
| Lehovec (7) ($p_{I_2}$ = 4.3 mm, T = 60°) | | | | $6.0 \times 10^{-13}$ |
| Wagner (theory) (2) | $10^{-16}$ | | | |

charge from the interior (interstitial Ag ion) to the surface. The ion is replaced by a positive hole, and the existence of a corresponding negative charge before and after the removal of the ion is assumed. These ions are very mobile compared to lattice ions, but holes must likewise diffuse to the surface in order that the reaction may proceed. This is the rate-determining step in the mechanism which was postulated and verified experimentally by Wagner at elevated temperatures (2). The slope of the plots of log time vs. log thickness in the present work indicates that the parabolic rate law is also valid at room temperature. It may also be assumed that the mobility of the holes is still rate-determining provided a polycrystalline but impervious layer of halide is formed. Otherwise the mechanism will depend on the gross structure of the deposit. A complication is introduced by the presence of water vapor which reduces the rates of tarnishing by a factor of two. It is known that water vapor adsorbs readily on silver halides, but its role in the tarnishing process is not yet well understood.

*Rate Constants at Room Temperature*

Table II shows a comparison of the rate constants obtained in a dry halogen atmosphere with values given in the literature. Regarding the present measurements the constants obtained from the formation of the halide or loss of silver should be the same for each of the two chemical systems. Actually there is a discrepancy of a factor of three, with the smaller rate constant being obtained from decreases of thickness of silver. Examination of the halide layers, in both cases, showed about 20% porosity of the halide, which would give a corresponding error in the rate constant. This would not account for the total discrepancy, of course, which in view of the simple experimental procedure is not surprising. In fact, comparison of the two values for each system gives a room temperature rate constant that should be more accurate than one order of magnitude. This is confirmed also by comparison with available literature values. The work of Tammann and Koester (6) was performed in an atmosphere saturated with water vapor, which may be responsible for a slightly lower value of the rate constant. In comparison to our data, their constant would also be increased by a factor of two owing to the smaller pressure of bromine in Tammann's experiment. Hauffe and Gensch (3) performed their experiments in a temperature range 200°-400°C with a quartz balance. The agreement of their extrapolated value with our rate constant is remarkable. This is also the case with the iodide determination of Lehovec who used a quartz balance too (7). Calculations of the rate constant based on Wagner's theory of tarnishing (2) depends on the knowledge of the conductivity of the tarnished layer and the transference numbers in it of both species of ions, as well as the transference number of electrons. Following Jost and Weiss (8) the sum of the ionic transference numbers, $t_1 + t_2 = 0.999$ was assumed and the electronic transference number $t_3 = 0.001$. For the conductivity of silver bromide $2.3 \times 10^{-8}$ $ohm^{-1}$ $cm^{-1}$ was chosen. The latter two values may be considerably in error, and it is therefore not surprising that the calculated rate constant is off by two or three orders of magnitude.

*Structure of the Halide*

Different views exist regarding the structure of an oxide or halide layer on a metal. The Pilling-Bedworth rule states (9) that if the volume of the oxide formed is larger than the volume of the metal, then the surface is free to expand outward, due to an increase in volume, to an extent limited only by its ability to stretch successfully. The mechanical forces on the oxide layer may eventually become great enough to cause a deviation from the parabolic rate law, or even to disrupt the uniform oxide layer. However, Vermilyea (10) has recently postulated a low-temperature mechanism of oxidation in which stresses are absent because reaction takes place only at imperfections of the oxide or halide lattice.

It may be concluded that the room temperature halogenation of silver proceeds between the two above extremes. The halide structure which is formed at room temperature, hence at a lower rate, is at least as uniform as one formed at higher temperatures. This is shown visually, by observation of photomicrographs. However, the halide structure is not perfect and pores are formed. They are located at random in the halide. As mentioned above, an estimate of the porosity based on the photomicrographs is about 20%. In a few cases agglomeration

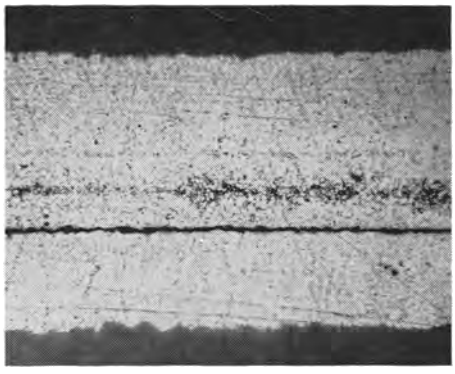

Fig. 8. A 2-mil silver foil after exposure to $Br_2$ for 3.040 $\times$ $10^6$ sec. Silver is completely brominated.

Fig. 9. A 2-mil silver foil after exposure to $Br_2$ for 8.736 $\times$ $10^6$ sec. Silver is completely brominated.

of pores into continuous voids could be observed. There are indications of such pancake pores at the original metal-vapor interface. This is most drastically seen in Fig. 8, in which a silver foil is pictured which had been completely brominated in less time than would have been required by the parabolic rate law. This is however the exception to the usual complete halogenation of a foil as pictured in Fig. 9 where again only random pores exist. It cannot be explained why the occasional silver halide shows continuous pore formation where other identically treated foils do not show this. Birchenall recently pointed out (11) that the formation of porous scales is connected with the plastic properties of oxides and therefore it is possible that some unknown factor may have entered to hinder the plastic flow of the halide in the case where large pores appear. The fact that this may occur in a few samples where a large number of others under identical conditions do not show it, only serves to point up the complexity of the study and the work that remains to be done.

## Conclusions

1. Tarnishing reactions of silver by iodine and bromine resulted in an impervious halide surface layer which contains up to 20% pores, located at random.

2. The reactions proceed according to parabolic rate law. Rate constants are given for tarnishing, in the absence of water vapor and when it was present to the extent of 90% relative humidity, at room temperature.

3. It is postulated that diffusion of defect-electrons in a direction opposite to that of silver ions, which is the rate-determining step at higher temperature, is also limiting at room temperature.

4. Presence of water vapor reduces the tarnishing rate by about a factor of two.

## Acknowledgment

The author is indebted to Dr. D. L. Douglas of the General Electric Research Laboratory for many helpful discussions. The careful metallographic work, which is the basis of this study, was performed by the Metallography group of the Research Laboratory, General Electric Company.

Manuscript received Nov. 18, 1957. This paper was prepared for delivery before the Buffalo Meeting, Oct. 6-10, 1957.

Any discussion of this paper will appear in a Discussion Section to be published in the June 1959 JOURNAL.

## REFERENCES

1. K. Hauffe, "Reaktionen in und an festen Stoffen," Springer-Verlag, Berlin (1955).
2. C. Wagner, *Z. physik. Chem.*, **B32**, 447 (1936).
3. K. Hauffe and C. Gensch, *ibid.*, **195**, 116 (1950).
4. I. Pfeiffer, K. Hauffe, and W. Jaenicke, *Z. Elektrochem.*, **56**, 728 (1952).
5. W. Jaenicke, R. P. Tischer, and H. Gerischer, *ibid.*, **59**, 448 (1955).
6. G. Tammann and W. Koester, *Z. anorg. u. allgem. Chem.*, **123**, 196 (1933).
7. K. Lehovec, *et al.*, 3rd quarterly report, February 1955, U. S. A. Signal Corps Contract No. DA-36-039-SC-63151.
8. W. Jost and K. Weiss, *Z. physik. Chem. (Frankfurt)*, **2**, 112 (1954).
9. N. B. Pilling and R. E. Bedworth, *J. Inst. Metals*, **29**, 529 (1923).
10. D. Vermilyea, *Acta Met.*, **5**, 492 (1957).
11. C. E. Birchenall, *This Journal*, **103**, 619 (1956).

# Selective Oxidation of Al from an Al-Fe Alloy

**Richard E. Grace**

*Department of Metallurgical Engineering, Purdue University, Lafayette, Indiana*

**and**

**Alan U. Seybolt**

*Research Laboratory, General Electric Company, Schenectady, New York*

ABSTRACT

The selective oxidation of aluminum from a 4.8 wt % Al-Fe alloy was studied with a microbalance at temperatures of 700°-900°C. The oxidizing gas was damp $H_2$, with dewpoints ranging from —55° to 0°C. The oxidation product was identified by electron diffraction to be the crystalline spinel, $\gamma$-$Al_2O_3$. At 800°C the parabolic oxidation constant was approximately proportional to the 1/7th power of the $H_2O/H_2$ gas ratio, and the experimental activation energy for the over-all oxidation reaction with 0°C dewpoint hydrogen gas was 72 kcal/mole.

Oxidation of alloys in damp hydrogen at elevated temperatures has been carried out recently by several investigators, Moreau and Bénard (1) and Seybolt and Alessandrini (2) on Ni-Cr alloys and Fe-Si alloys, respectively. Use of various $H_2O/H_2$ gas ratios determined by the vapor pressure of ice at subzero temperatures permits a broad coverage of oxidizing potential at very low effective oxygen pressures. When a binary solid solution is exposed to oxygen pressures which are too low to oxidize the solvent (more noble component), but which are high enough to oxidize the solute, the process is called selective oxidation. In Al-Fe solid solutions there is a wide range of oxygen pressures which permits the selective oxidation of Al without apparently affecting the Fe.

The present study was initiated in order to study the kinetics of the over-all reaction given below:

$$2Al_{\text{in Fe}} + 3H_2O \rightarrow Al_2O_3 + H_2 \qquad [1]$$

Gulbransen and Wysong (3) have studied the oxidation of Al in oxygen at various temperatures and oxygen pressures with a quartz microbalance, and the weight gain data reported herein were taken with a similar microbalance of $\pm 1$ $\mu$g sensitivity. A determination of the structure of the surface oxide films was made by reflection electron diffraction techniques on samples that were cooled to room temperature in the $H_2O/H_2$ gas in which they were oxidized.

## Experimental

Samples of a 4.8 wt % Al-Fe alloy which had been vacuum melted from electrolytic materials of 99.99+% purity and rolled to 0.014-in. sheet were cut with 5 $cm^2$ surface area. The small rectangular specimens were polished through 00 paper by hand and then washed with an 80% acetone -20% toluene degreasing solution. The samples were desiccated for 2-5 days before use. No chemical etching or polishing was attempted because it was felt that selective etching might take place or a foreign surface film might be produced. The specimens were hung on an 0.002-in. nichrome wire from one arm of a quartz microbalance in the apparatus shown schematically in Fig. 1. The system was usually flushed out overnight at room temperature with dry hydrogen (—196°C dewpoint) before the run was started. During a run the damp gas was preheated to temperature in a quartz spiral around the specimen before it was introduced into the furnace. Weight gains were followed by measuring the shift in the quartz beam away from a fixed quartz pointer with a telemicroscope. A change of 0.001 cm shift was equivalent to 1 $\mu$g, and an individual reading could be made to $\pm 0.2$ $\mu$g. The definition of the starting time for a run was arbitrarily chosen to be about 15 min after the wet hydrogen was admitted to the furnace. During this brief interval the microbalance beam oscillated, making readings erratic. While it is impossible to determine exactly the oxygen uptake of the samples during heating in the first 15 min of any run, an estimate of 2-3 $\mu$g oxygen/$cm^2$ has been made. Microbalance readings were made regularly over several hours and typical

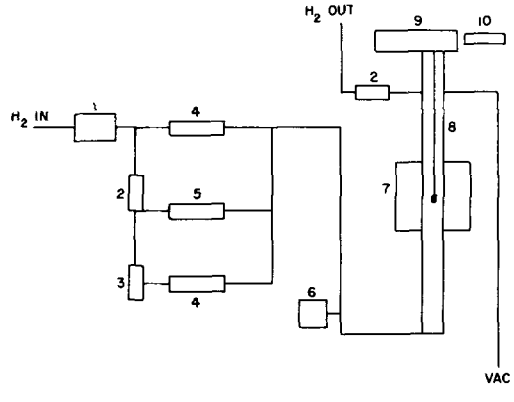


Fig. 1. Schematic representation of oxidation apparatus. 1, copper catalyst; 2, flowmeter; 3, water saturator; 4, cold trap; 5, gas mixer; 6, McLeod gauge; 7, furnace; 8, quartz tube; 9, microbalance; 10, telemicroscope.

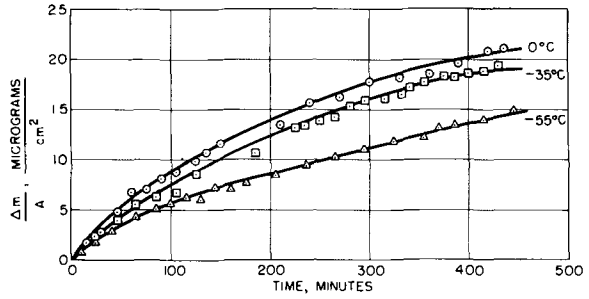


Fig. 2. Weight gain-time relations at several dewpoints for oxidation of 4.8% Al-Fe in hydrogen at 800°C.

weight gain vs. time curves are shown in Fig. 2. Two series of experiments were carried out with this technique; the first consisted of a series of runs at 800°C in which the $H_2O/H_2$ ratio was varied by changing the hydrogen dewpoint from −55° to 0°C in several steps. The second series was carried out at constant hydrogen dewpoint (0°C) at oxidizing temperatures of 700°, 800°, and 900°C.

When the runs were finished, the furnace was lowered from the sample, and it was allowed to cool to 100°C before the quartz chamber was evacuated. Generally, the samples exhibited a pastel interference color when they were removed from the furnace. This color was very uniform over the entire sample surface, indicating a smooth surface film. The films were of the order of 2000Å thick. Electron diffraction patterns were taken by reflection from the oxidized surface. Finally, the samples were measured with a metric micrometer and their areas were computed to the nearest 0.001 cm², with the assumption that the as-polished surface was perfectly plane.

## Results

The results of the weight gain-time studies fit an equation of the type

$$\left(\frac{\Delta M}{A}\right)^2 = k_p\,(t - t_o) \qquad [2]$$

where $\Delta M/A$ = weight gain per unit area; $t$ = time; $t_o$ = time constant; and $k_p$ = parabolic rate constant.

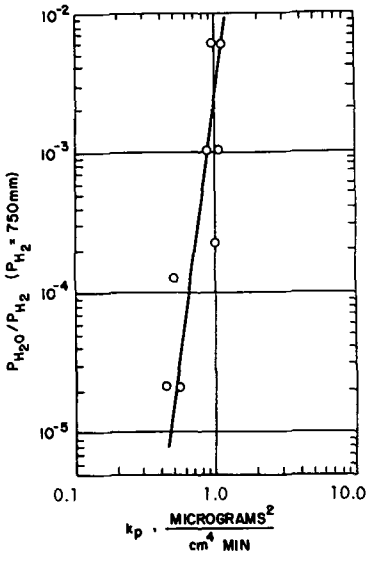


Fig. 3. Variation of parabolic rate constant with $H_2O/H_2$ ratio at 800°C.

Table I. Electron diffraction data of surface oxide on 4.8% Al-Fe alloy

| Typical unknowns* Sample No. 11 d, Å | Typical unknowns* No. 14 d, Å | (hkl) | Standards* No. 1 d, Å | Standards* No. 2 d, Å |
|---|---|---|---|---|
| 2.740 | | 220 | 2.80 | 2.79 s |
| 2.381 | | 311 | 2.39 m | 2.38 vs |
| | | 222 | 2.28 | |
| 1.946 m | 1.987 m | 400 | 1.98 m | 1.97 s |
| | | | 1.82 | |
| | | 422 | 1.62 | 1.61 |
| 1.491 | | 511, 333 | 1.52 m | 1.52 m |
| 1.37 s† | 1.410 s† | 440 | 1.40 s | 1.395 s |
| | | 533 | 1.24 | |
| 1.211 | | 622 | 1.21 | 1.19 |
| 1.163 | 1.160 m | 444 | 1.14 | 1.14 |
| 1.105 | | 711 | | |
| 1.060 | | 642 | 1.06 | |
| 1.015 | 1.016 | 553, 731 | 1.03 | 1.03 |
| 0.971 | | 800 | 0.991 | 0.988 |
| | 0.906 | 555, 751 | 0.916 | 0.912 |
| 0.897 | | 840 | 0.885 | 0.886 |
| | | | 0.844 | |
| | 0.820 | 844 | | 0.806 |
| $a_o = 7.79$ | $a_o = 7.95$ | | $a_o = 7.93$ | $a_o = 7.88$ |

* No. 11, 4.8% Al-Fe oxidized at 800°C, 20 hr, −55°C dewpoint. No. 14, 4.8% Al-Fe oxidized at 800°C, 7 hr, 0°C dewpoint. No. 1, ASTM card No. 2-1420; $\gamma$-$Al_2O_3$. No. 2, oxide on pure Al > 680°C in air [see Ref. (4)] $\gamma$-$Al_2O_3$.

† Heavily textured line.

Two preliminary runs showed that the parabolic behavior continued for at least 20 hr, but most of the runs were made only for 7 hr duration. The effect of various $H_2O/H_2$ gas ratios on the parabolic rate constant at 800°C is shown in Fig. 3. Increased water content of the gas brings about an increase in the rate of oxidation, but the effect is small. The slope of the line in Fig. 3 shows that the parabolic rate constant is approximately proportional to the $H_2O/H_2$ gas ratio to the +1/7 power.

Table I compares typical electron diffraction data from samples No. 11 and No. 14 with standard x-ray powder patterns for $\gamma$-$Al_2O_3$. The diffraction patterns for all samples indicated that the oxidation product was substantially the same at 700°, 800°, and 900°C and at all the dewpoints studied. The patterns for the samples held at 700° and 800°C for 7 hr corresponded to sample No. 14, while the patterns for the samples at 800°C (20 hr) and 900°C resembled that of sample No. 11. Longer times at temperatures and increased temperatures of oxidation increased the number and sharpness of lines appearing in the diffraction patterns.

Table II gives a summary of all the experimental data including sample treatments; parabolic rate constant, $k_p$; time constant, $t_o$; and electron diffraction results. Several preliminary experiments on the determination of the oxide structure have not been included in this table. Those results did not differ from samples 9, 11, 14, and 15. In certain experiments using dewpoints of nominally −78° and −196°C, the sample gained more weight than the amount of oxygen available in these dry gases. The water content of the hydrogen could not be reduced to a dewpoint as low as −78°C in the apparatus used.

Table II. Summary of experimental data

| Sample | Treatment All runs at 800°C except where noted | $k_p$ $\frac{\mu g^2}{cm^4\ min}$ | $t_0$ minutes | Remarks (Electron diffraction) |
|---|---|---|---|---|
| 4 | As polished 2/0 paper, acetone-toluene rinse | — | — | No oxide present |
| 11 | −55° dewpoint $H_2$ 20 hr; 200 cc/min | — | — | $a_o = 7.79$ Å Spinel |
| 17 | −55° dewpoint $H_2$ 6 hr; 200 cc/min | 0.44 | 35 | — |
| 19 | −55° dewpoint $H_2$ 6 hr; 200 cc/min | 0.55 | 70 | — |
| 24 | −40°C dewpoint $H_2$ 6½ hr; 200 cc/min | 0.50 | 60 | — |
| 16 | −35°C dewpoint $H_2$ 7 hr; 200 cc/min | 1.0 | 50 | — |
| 627 | −20°C dewpoint $H_2$ 8 hr; 200 cc/min | 1.04 | 60 | — |
| 23 | −20°C dewpoint $H_2$ 7½ hr; 200 cc/min | 0.89 | 100 | — |
| 14 | 0°C dewpoint $H_2$ 7 hr; 200 cc/min | 1.1 | 35 | $a_o = 7.95$ Å Spinel |
| 20 | 0°C dewpoint $H_2$ 7½ hr; 200 cc/min | 0.96 | 125 | — |
| 15 | Furnace at 900°C −55°C dewpoint $H_2$ 5 hr; 125 cc/min | — | — | Spinel $a_o = 7.84$ Å |
| 21 | Furnace at 900°C 0°C dewpoint $H_2$ 4 hr; 200 cc/min | 18.4 | 50 | — |
| 9 | Furnace at 700°C 0°C dewpoint $H_2$ 5½ hr; 160 cc/min | — | — | Spinel $a_o = 7.98$ Å |
| 22 | Furnace at 700°C 0°C dewpoint $H_2$ 7½ hr; 200 cc/min | 0.033 | 15 | — |

The temperature dependence of the parabolic rate constant with 0°C dewpoint hydrogen gas can be given by the equation

$$k_p = 4.0 \times 10^{14} \exp\left[-\frac{72000}{RT}\right] \frac{\mu g^2}{cm^4\ min} \quad [3]$$

This equation was determined from the plot shown in Fig. 4, which shows the temperature dependence of $k_p$ on a semilog plot. The error in the experimental activation energy is about ±2 kcal/mole. Uhlig (8) has pointed out that activation energies may be higher above the Curie temperature in some alloys in which the rate-controlling oxidation step is a surface reaction at the metal/oxide interface. However, when diffusion through the oxide film is rate controlling, magnetic effects are not important.

## Discussion

The results of this study have several things in common with the oxidation of pure Al. Preston and Bircumshaw (4), Brouckère (5), Haas (6), and Keller and Edwards (7) report $\gamma$-$Al_2O_3$ with spinel structures having a unit cell of about 7.9Å. Gulbransen and Wysong (3) have taken microbalance weighings at various temperatures and oxygen pressures and have found a slight increase in the parabolic rate constant with increasing oxygen pressure (0.76, 7.6 mm Hg), but their temperature coefficient was uncertain. Preston and Bircumshaw (4) report recrystallization of $\gamma$-$Al_2O_3$ at temperatures in excess of 680°C, while Brouckère (5) reports an amorphous and crystalline mixture of $\gamma$-$Al_2O_3$ with a tendency toward epitaxy, the cube faces being normal to the growth direction.

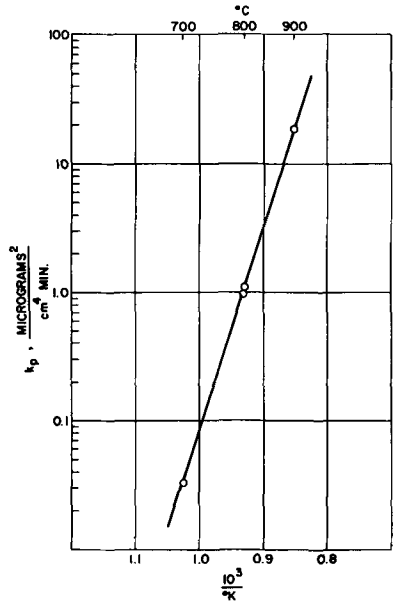


Fig. 4. Temperature dependence of the parabolic rate constant $k_p$ (0°C dewpoint gas).

The results of this investigation show that the initial stage of oxidation is different from the parabolic rate which becomes operative after 1 or 2 hr of oxidation. This effect may be due to one or more of the following: solution of oxygen in the alloy, nucleation and growth of oxide patches before film coverage is complete, or growth of an amorphous oxide which becomes crystalline upon holding at the oxidation temperature. Because of the observed appearance of new lines and sharpening of the (400) and (440) lines upon holding at temperature, the latter explanation appears plausible.

Assuming that the stoichiometric oxide composition is nearly maintained, one can attempt to account for the observed pressure dependence of the oxidation rate by postulating fast surface equilibria at the oxide interfaces and that the film grows by diffusion processes within it. Several defect equations can be written for the oxide/gas interface. These are of the type given below:

$$3H_2O = 3H_2 + Al_2O_3 + 2\square_{Al^{+++}} + 6\square_{e^-} \quad [4]$$

or

$$3\,O = Al_2O_3 + 2\square_{Al^{+++}} + 6\square_{e^-} \quad [5]^*$$

In Eq. [4] the concentration of aluminum ion vacancies varies with $H_2O/H_2$ gas ratio to a positive fractional power, +⅜. This type of pressure dependence would correspond to a cation deficient p-type semiconductor. On the other hand, if $\gamma$-$Al_2O_3$ is an n-type semiconductor having anion vacancies which permit anions to diffuse inward during oxide growth, possible equilibria at the gas/oxide interface can be written as follows:

* Equations [5], [7], and [9] may be taken as representative of the fast equilibria at the alloy/oxide interface. In Eqs. [4]-[7] diffusion fluxes will be approximately dependent on the concentration differences of vacancies per unit volume at the inner and outer interfaces, divided by the instantaneous film thickness. In Eqs. [8] and [9] diffusion fluxes will be determined by concentration differences of interstitial metal ions.

$$H_2O + \square_{O}^{--} + 2e'_i = H_2 \quad [6]$$

or

$$O + \square_{O}^{--} + 2e'_i = \text{nil} \quad [7]$$

In Eq. [6] the concentration of anion vacancies varies with $H_2O/H_2$ gas ratio to the $-1/3$ power; $e_i$ is an excess or defect electron.

If $\gamma$-alumina is an n-type semiconductor (9) with excess metal ions and electrons in interstitial positions, the following equilibria at the gas/oxide interface might apply

$$2Al_i^{+++} + 6e_i^- + 3H_2O = Al_2O_3 + 3H_2 \quad [8]$$

or

$$2Al_i^{+++} + 6e_i^- + 3\,O = Al_2O_3 \quad [9]$$

The concentration of excess metal ions in Eq. [8] would be dependent on the $H_2O/H_2$ gas ratio to the $-3/8$ power.

Because of the small positive pressure effect on the rate of formation of $\gamma$-$Al_2O_3$, it is supposed that this structure has both cation and anion vacancies. Growth must proceed by countercurrent diffusion of cations outward and anions inward through the oxide film. This kind of a structure would correspond to a transition-type semiconductor with a probable excess of cation vacancies and electron defects. The measured pressure effect agrees generally with the small positive effect demonstrated by Gulbransen and Wysong (3).

The large value of the experimental heat of activation is in agreement with the above considerations. At least four distinct processes are involved in the growth of the oxide generation and diffusion of anion vacancies and of cation vacancies. If the nature of the oxidation product varied with temperature, one would not expect the linear relation in Fig. 4 to hold. That the electron diffraction patterns were identical for all temperatures is further proof that the oxidation product in all experiments was essentially the same.

## Summary

1. Aluminum in solid solution in iron was oxidized selectively with damp hydrogen at 700°-900°C.

2. Microbalance weight gain data followed a parabolic time law after an initial time lag.

3. The surface oxidation product was identified by electron diffraction to be the crystalline spinel, $\gamma$-$Al_2O_3$.

4. The parabolic rate constants varied approximately linearly with $H_2O/H_2$ gas ratio to the $+1/7$ power.

5. The experimental activation energy for the over-all oxidation reaction was 72 kcal/mole.

## Acknowledgments

The authors wish to thank Dr. W. F. Claussen for some stimulating discussions. The help of Eileen Alessandrini and Leo Butler is also appreciated.

Manuscript received Jan. 13, 1958. This paper was prepared for delivery before the Ottawa Meeting, Sept. 28-Oct. 2, 1958.

Any discussion of this paper will appear in a Discussion Section to be published in the June 1959 JOURNAL.

REFERENCES

1. J. Moreau and J. Bénard, *J. Inst. Met.*, **83**, 87 (1954-55).
2. A. U. Seybolt and E. Alessandrini, Private communication.
3. E. A. Gulbransen and W. S. Wysong, *J. Phys. Chem.*, **51**, 1087 (1947).
4. G. D. Preston and L. L. Bircumshaw, *Phil. Mag.*, **22**, 654 (1936).
5. L. Brouckere, *J. Inst. Met.*, **71**, 131 (1945).
6. G. Haas, *Z. anorg. Chem.*, **254**, 96 (1947).
7. F. Keller and J. Edwards, Int. Conf. Surf. React., 202 (1948).
8. H. H. Uhlig, *Acta Met.*, **4**, 541 (1956).
9. W. W. Smeltzer, *This Journal*, **103**, 209 (1956).

# Particle Size and Efficiency of Electroluminescent Zinc Sulfide Phosphors

**W. Lehmann**

*Research Department, Westinghouse Electric Corporation, Bloomfield, New Jersey*

ABSTRACT

The brightness and the electric power absorption of an electroluminescent ZnS phosphor depend on the mean particle size of the phosphor. For constant amounts of phosphor by weight excited under identical conditions, decreasing particle size causes strongly decreased brightness at low voltages. However, at high voltages the brightness remains unchanged or tends to increase. At all voltages, the electric power absorption is proportional to the particle size. The efficiency, i.e., the ratio of brightness to power absorption, increases with decreasing particle size. With fine particles of a green emitting phosphor, a luminous efficiency of 14 lpw of a complete cell (corresponding to 18-19 lpw of the phosphor itself) could be measured.

Experimental data on the dependence of the emission intensity of electroluminescence on the mean particle size of zinc sulfide phosphors were presented recently by Goldberg (1). Similar experiments have also been made in our laboratory including, however, in addition the dependence of the electric power absorption on the mean particle size. A standard, green-emitting ZnS:Cu,Cl phosphor

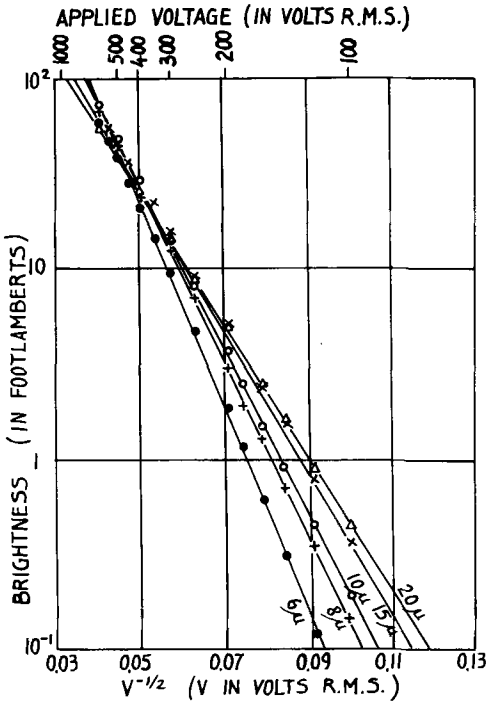


Fig. 1. Dependence of the electroluminescent brightness, L, on the exciting voltage, V, for several phosphor fractions of different mean particle diameter.

was separated by repeated sedimentation in alcohol into several fractions of different mean particle sizes. The distribution of the particle diameters of each fraction was determined microscopically. The resulting arithmetic means of the diameters and their standard deviations were: $6 \pm 2\mu$; $8 \pm 3\mu$; $10 \pm 4\mu$; $15 \pm 6\mu$; $20 \pm 6\mu$. These numbers indicate that the particle size distributions of the fractions overlap considerably. A sharper separation, i.e., smaller standard deviation, would, of course, be highly desirable but could not be obtained without losing too much phosphor. All fractions consisted mainly of separated, simple crystals and contained practically no agglomerates. The electroluminescence of these fractions was measured in the usual type of castor

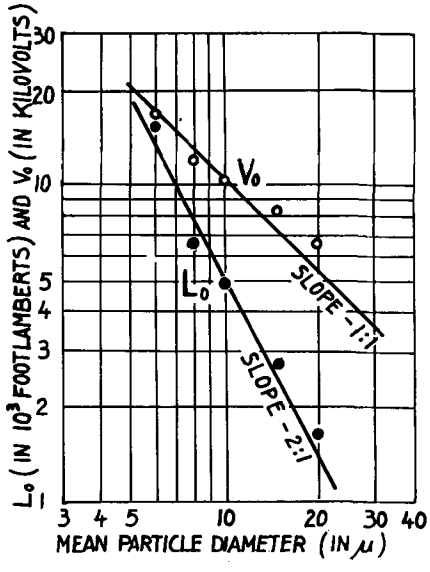


Fig. 2. Dependences of the two constants $L_0$ and $V_0$ in the equation $L = L_0 \exp [-(V_0/V)^{1/2}]$ on the mean particle diameter.

oil cell, always employing the same cell geometry and the same amount of phosphor by weight in the cell. Precautions were taken to insure that the geometrical arrangement of the phosphor particles in the liquid dielectric of the cell, i.e., bridge formation (3), was stable and did not falsify the measurements.

Figure 1 shows the dependence of the emission intensity, $L$, of the complete cells on the applied voltage, $V$, plotted as log $L$ as a function of $V^{-1/2}$. This figure is quite in agreement with Goldberg's results. The straight lines in Fig. 1 approaching the experimental points represent the familiar expression (2)

$$L = L_0 \exp [-(V_0/V)^{1/2}] \qquad [1]$$

where $L_0$ and $V_0$ are constants. Figure 2 shows the experimental dependence of $L_0$ and $V_0$ on the mean particle size, $a$, plotted on log-log scales. The points there seem to be grouped around the straight lines representing the relationships

$$L_0 = A/a^2 \qquad [2a]$$

and

$$V_0 = B/a \qquad [2b]$$

where $A$ and $B$ are two constants independent of the particle diameter. While Eq. [2b] is in agreement with Goldberg's results, he obtained an exponent of 3 for $a$ in [2a]. The reason for this disagreement may be the finite particle size distributions of all fractions investigated so far.

The dependence of the electric power absorption, $W$, on the mean particle size was determined by measuring the capacitance, $C$, and the loss angle, $\phi$, of the complete cell and calculating

$$W = 2\pi f V^2 C \sin \phi \qquad [3]$$

where $f$ and $V$ are the frequency and voltage, respectively. Details of this technique are described in an earlier publication (3). Control measurements of similar cells in two different ways, with an impedance bridge and with an electronic wattmeter, gave the same results as the measurements with the above loss angle method, so that it is believed that this method gives reliable results.

The experimentally determined dependencies of the capacitance, $C$, and the loss angle, $\phi$, are given in Fig. 3. $C$ and $\phi$ both increase with increasing particle size at finite exciting voltages, $V$. As $V$ approaches zero, $C$ approaches a constant value independent of the particle size, while $\phi$ approaches values close to zero. The term $C \sin \phi$ in Eq. [3] is that cell property which is responsible for the electric power absorption (the other two factors in [3], $f$ and $V^2$, are not cell properties). It was found that the term $C \sin \phi$ is almost proportional to the mean particle diameter, $a$. This is shown in Fig. 4 where the ratio $C \sin \phi/a$ is plotted as a function of the exciting voltage, $V$. This result is somewhat peculiar since, in all cases, the same amount of phosphor was used in the cells. The cells containing the fine particles have a lower power consumption, although they contain many more particles than the cells containing the coarse particles.

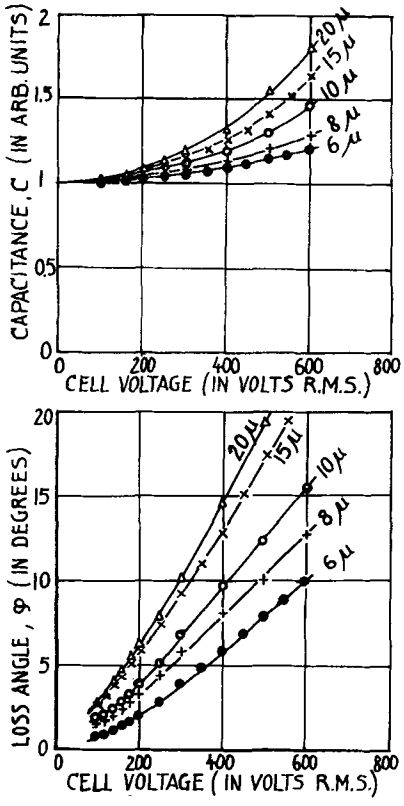


Fig. 3. Dependences of the cell capacitance, C, and the dielectric loss angle, $\phi$, of the complete cell on the exciting voltage, for several phosphor fractions of different mean particle diameter.

The efficiency of electroluminescence is essentially the ratio of the emission intensity, $L$, to the electric power absorption, $W$. The emission intensity, $L$, is not very strongly dependent on the mean particle size in the region of moderate and higher exciting voltages (Fig. 1). The electric power absorption, however, decreases with decreasing mean particle diameter (Fig. 4). Consequently, the efficiency $\eta = L/W$ increases with decreasing mean particle diameter. Experimental results are shown in Fig. 5. The highest luminous efficiency of electroluminescence observed so far in this way is 14 lpw. This is, however, the luminous efficiency of the complete cell. Estimating the energy and radiation losses in constructional parts of the cell (especially the reabsorption of light emitted from the phosphor in the cell electrodes), this value of 14 lpw corresponds to about 18 to 19 lpw for the efficiency of the phosphor itself. This is considerably above the theoretical maxima of 12 lpw predicted by Bowtell and Bate (4) and of 14 lpw calculated by Zalm (5). Furthermore, it is not believed that this value of 18 to 19 lpw is the upper limit of what is obtainable.

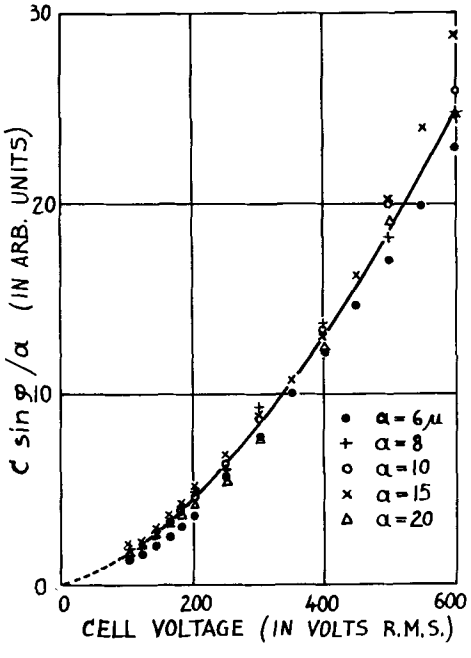


Fig. 4. Demonstration of the proportionality between C sin $\phi$ and the mean particle diameter, a.

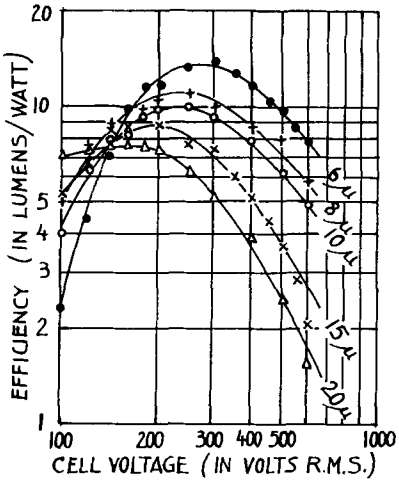


Fig. 5. Dependence of the luminous efficiency of electroluminescence on the exciting voltage for several phosphor fractions of different mean particle diameter.

The peak efficiencies of Fig. 5 are replotted in Fig. 6 on a log-log basis. The experimental points are grouped around a straight line of slope $-\frac{1}{2}$ corresponding to a dependence

$$\eta_{max} = c/a^{1/2}$$

where $c$ is a constant. Any quantitative foundation for this relationship is still missing.

Results essentially similar to those described here for a green-emitting ZnS:Cu,Cl phosphor have also been obtained for a yellow-emitting ZnS:Cu,Mn phosphor.

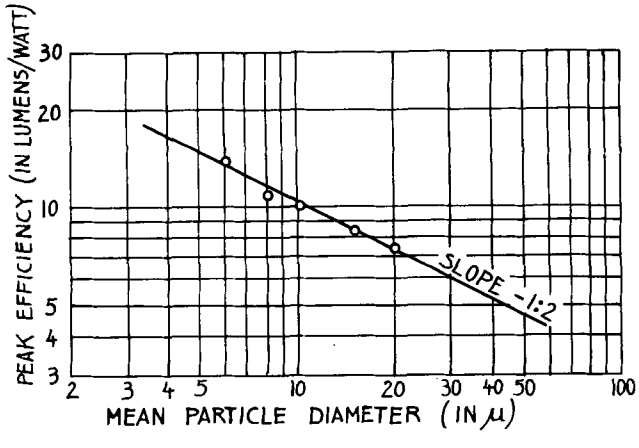


Fig. 6. Dependence of the peak electroluminescence efficiency on the mean particle diameter of the phosphor.

A qualitative explanation of all results might be possible with the familiar barrier model for electroluminescence, assuming that the excitation mechanism occurs primarily near the surface while the electric power absorption is mainly a bulk property of the phosphor particles. A decrease of the particle size increases the surface to volume ratio and hence should increase the efficiency. However, quantitative agreement of this model with the experimental data has not yet been obtained. More experiments should be made on phosphors having still more uniform particle sizes in order to obtain more information about these questions.

Manuscript received May 12, 1958. This paper was prepared for delivery before the New York Meeting, April 27-May 1, 1958.

Any discussion of this paper will appear in a Discussion Section to be published in the June 1959 JOURNAL.

REFERENCES

1. P. Goldberg, Paper presented at The Electrochemical Society Meeting, New York, April 29, 1958.
2. G. F. Alfrey and J. B. Taylor, *Proc. Phys. Soc.*, **B68**, 775 (1956).
3. W. Lehmann, *This Journal*, **103**, 24 (1956).
4. J. N. Bowtell and H. C. Bate, *Trans. Illum. Engng. Soc. (London)*, **20**, 3 (1955).
5. P. Zalm, *Philips Res. Repts.*, **11**, 438 (1956).

# Gold in Silicon

**G. Bemski and J. D. Struthers**

*Bell Telephone Laboratories, Incorporated, Murray Hill, New Jersey*

ABSTRACT

Heat treatment of silicon, both p-type and n-type, to temperatures in excess of 900°C frequently results in a decrease of lifetime and is sometimes accompanied by an increase in resistivity. In the present experiments, gold has been found to be introduced during such heat treatments in concentrations sufficient to account for the observed changes in the electrical characteristics. Gold has been observed on the surfaces of all the silicon samples examined so far. Heat treatments in the temperature range 1100°-1300°C result in a concentration of gold in the bulk material of about $10^{14}$ at./cm$^3$. A film of nickel or copper on the silicon surface during the heat treatment has a gettering action for gold. Heat treatment in vacuum can also be effective in the removal of gold.

Recently, the growth of silicon single crystals with a high minority carrier lifetime has become possible. However, in subsequent heat treatments to temperatures above 900°C, the lifetime is frequently degraded. At temperatures above 1100°C the degradation of lifetime is sometimes accompanied by the introduction of donor levels in p-type and acceptor levels in n-type Si, resulting in an increase of resistivity.

These effects could be due to either structural or chemical imperfections. It has been demonstrated that Si can be heated to high temperatures under proper conditions (in floating zone equipment), even followed by a fast cooling cycle, without significantly degrading the lifetime (1). This experiment is a strong indication that the drastic lifetime degradations normally encountered must be due to chemical impurities.

In the present experiments, neutron activation measurements were used in an attempt to correlate the electrical effects encountered in heat-treated Si with particular chemical impurities.

## Experimental

The electrical effects in heat-treated Si, that is, the change in carrier density and the change in lifetime, were studied by standard techniques. The change in carrier density was obtained from Hall effect measurements and from resistivity measurements as a function of temperature. The lifetime was measured by the injection-extraction method (2).

For the neutron activation analysis the samples were irradiated in the Brookhaven National Laboratory Reactor. Energies and decay rates were measured using a single channel scintillation spectrometer. Beta particle energies were measured by the aluminum absorber technique, and decay rates by conventional Geiger-Müller counting methods. In a few cases, radiochemical separations were made by adding inactive carriers to confirm the conclusions obtained on the basis of the measured half-life and energies of the observed radiations.

Heat treatments of the samples were performed in three different vacuum stations as well as in three different Sentry ovens in a He atmosphere. The different systems were used in order to minimize the possibility of introducing impurities due to a contamination of any one particular system. The results obtained, however, were independent of the system used.

## Results

*Surface contamination of silicon.*—It has been observed that Si wafers cut from pulled crystals, after neutron irradiation, showed an induced radioactivity other than the Si activity, or an activity due to the donor or acceptor impurities. A typical autoradiograph is shown in Fig. 1. The spotty appearance of the radioactive centers on the surface is notice-

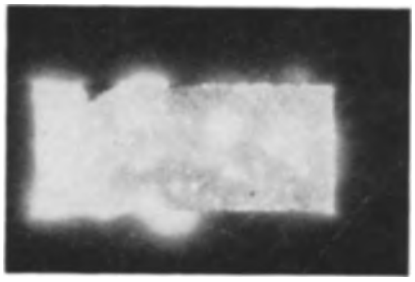

Fig. 1. Autoradiograph of an unheated Si sample (not etched after irradiation).

able in most samples. The activity is confined to the surface only; after a slight surface etch of the irradiated sample, the activity drops by orders of magnitude.

The unknown activity could be identified as $Au^{198}$, which is the isotope obtained on neutron activation from the stable isotope $Au^{197}$. This identification was obtained from the beta decay half-life of approximately 65 hr, the $\beta$ energy of 0.9 m.e.v., and the $\gamma$ energy of 0.4 m.e.v. A radiochemical separation confirmed this finding.

Several experiments have been performed in order to find a surface treatment not giving rise to Au contamination. Prior to irradiation, the following cleansing procedures have been used on the various wafers: (*a*) 48% HF (Baker) followed by a rinse in cold deionized water, (*b*) 70% $HNO_3$ (Baker) followed by a rinse in cold deionized water, (*c*) $HNO_3 + HF$, (*d*) aqua regia, (*e*) boiled deionized water, (*f*) lapped and rinsed in cold deionized water, and (*g*) HF, dried by evaporation. After all these procedures, an average Au concentration of $10^{12}$ to $10^{13}$ Au at./cm$^2$ was observed.

Even a crystal which has been pulled, then broken off at the seed, and handled with filter paper only showed Au contamination at the surface after irradiation. Polycrystalline Si material (du Pont), in the form of crystallites, has also been subjected to neutron irradiation and showed a Au concentration on the surface exceeding $10^{13}$ Au at./cm$^2$. The Al foil, used for wrapping the Si samples, showed no Au activity on irradiation. This proves that the Au was not introduced during the handling procedures.

*Volume contamination.*—As mentioned above, the activity observed on the surface disappears after slight etching. From this, one can estimate that the Au concentration in the crystal, as grown, is less than $10^{12}$ at./cm$^3$.

Gold is known to have a comparatively high-diffusion constant and a high-solid solubility in Si (3, 4); therefore, one expects a Au contamination on the surface to diffuse into the bulk of the material upon heating. Silicon wafers heated to temperatures above 1100°C have been analyzed by the neutron activation technique. After removing a surface layer to eliminate activity located at the surface, the sample still showed a $\beta$ and $\gamma$ activity uniform throughout the volume. Figure 2 shows an autoradiograph of a heated and etched sample. Figure 3 compares the $\beta$ decay observed in a gold-doped crystal with the $\beta$ decay observed in a heat-treated sample. One sees that the half-life in both samples is identical. The $\beta$ and $\gamma$ energies were also identical.

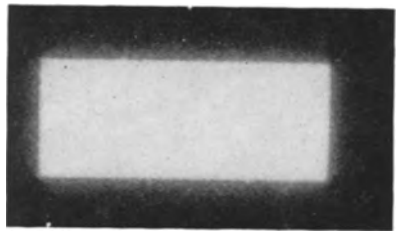

Fig. 2. Autoradiograph of a p-type Si sample heated to 1300°C (etched after irradiation).

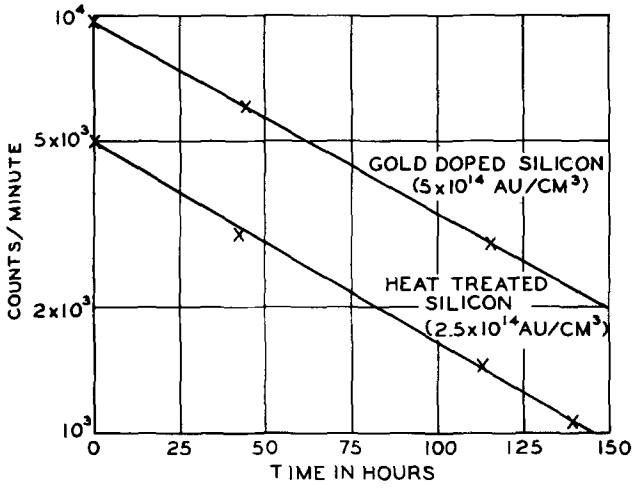


Fig. 3. Beta decay in a gold-doped Si crystal and in a heat-treated Si sample.

These findings confirm that Au had diffused into the sample during the heating cycle. The concentration of Au as found by this analysis is of the order of $10^{14}$ at./cm$^3$ and can be accounted for by the surface concentration of Au as measured prior to heating. Different samples gave similar results.

The hole concentration has been measured by the Hall effect on several p-type silicon samples of a resistivity of 20 ohm-cm or higher. Figure 4 shows the hole concentration thus found as a function of

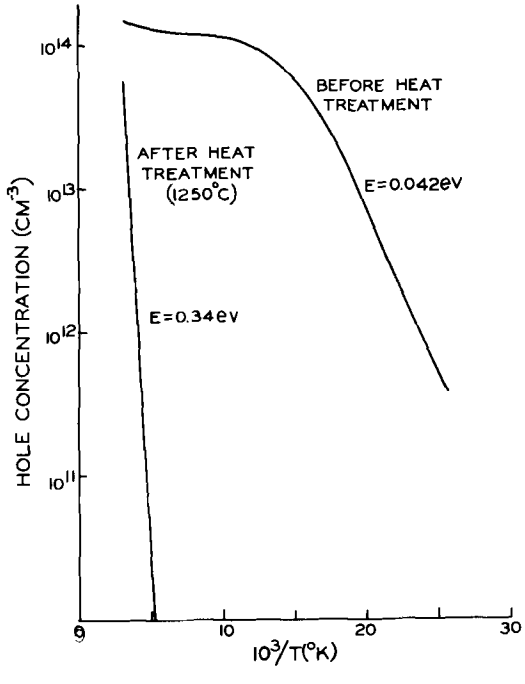


Fig. 4. Hole concentration vs. $10^3$/T in p-type Si before and after heating to 1250°C (Hall effect data).

temperature before and after heating. In this particular case the samples were heated for 1 hr at 1250°C. Results were similar in samples heated in air or in a vacuum of $10^{-5}$ mm Hg. The data in Fig. 4 indicate an introduction of donors in a concentration of $10^{14}$ at./cm$^3$ with an energy level at 0.34 ev from the valence band. This level can be observed only in fairly high resistivity Si in which the concentration of the added donor is larger than the original acceptor concentration. Among the known electrically active impurities in Si only Au, with a donor level at 0.35 ev from the valence band, comes within experimental error of the donor energy observed here.

As stated elsewhere (5), the room temperature capture cross section for minority carriers on Au levels in Si is of the order of $10^{-15}$ cm$^2$. This implies that a Au concentration of $10^{14}$ at./cm$^3$ will result in a room temperature lifetime in p-type silicon up to resistivities of 100 ohm-cm of less than 1 $\mu$sec. A room temperature, low-injection lifetime of 0.2 $\mu$sec was observed in the sample shown in Fig. 4. If one attributes this lifetime to recombination by Au centers only, one also obtains a Au concentration of the order of $10^{14}$ at./cm$^3$.

The agreement in the concentrations obtained from the neutron activation analysis, the Hall effect, and the lifetime measurement indicates that Au is the major contaminant responsible for the electrical effects observed in these samples.

*Techniques to avoid gold contamination in silicon.* —Two techniques have been reported previously which lead to an increase in lifetime during a heat treatment and in which one would suspect chemical impurities to play a role.

Baker and Bemski (6) found that vacuum heat treatment can partially restore the minority carrier lifetime in a degraded silicon sample. They suspected that chemical impurities diffused out of the bulk of the Si during such a treatment.

Silverman and Singleton (7) are reporting that the lifetime during heat treatment can be considerably increased by plating the surface of the Si with Ni, prior to the heating cycle. Nickel forms a liquid alloy on the surface of the Si at elevated temperatures. As has been shown previously for a similar system [Au-Ge liquidus on Ge (8)], such a liquidus can act as a getter for a third component if the distribution coefficient in the ternary alloy dilute in the third component is significantly less than unity. This is the case for a Ni- (or Cu-) Si alloy with Au as the dilute third component (9). Such getters can effectively prevent Au from entering the Si and they can remove Au previously introduced.

Gettering of Au by a liquidus layer has been observed whereby the Au was identified by the neutron activation analysis. Copper, as well as Ni, was used for the formation of the gettering liquidus layer. Two Si samples have been heated to 1250°C for 1 hr in an open tube furnace. One sample "A" had a Cu film on its surfaces while the other sample "B" had unprotected surfaces. After neutron activation and etching these samples gave autoradiographs as shown in Fig. 5. It is apparent that sample A shows essentially no Au concentration

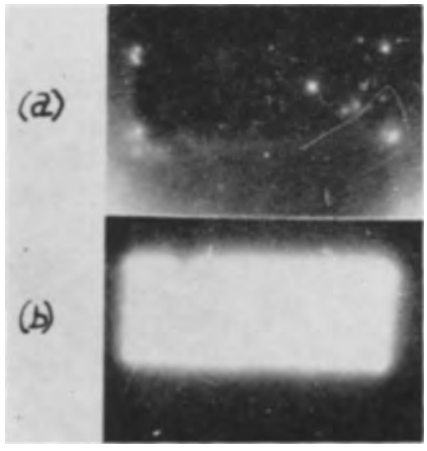


Fig. 5. Autoradiographs of Si samples heated to 1100°C. (a) in the presence of a Cu film on the surfaces; (b) without films on the surfaces. (Etched after irradiation.)

(less than $10^{12}$ at./cm$^3$), while sample B shows a strong Au concentration calculated to be $5 \times 10^{14}$ at./cm$^3$.

The results of a typical experiment, illustrating the removal of Au from the bulk, are shown in Fig. 6. Curve A shows the resistivity which has been measured as a function of temperature on samples from a gold-doped, p-type Si crystal with $5 \times 10^{14}$ Au at./cm$^3$. The 0.34 ev level is seen. Curve B was obtained on a sample which had been nickel plated and heated for 2 hr at 1100°C. These two curves indicate that the Au donor level had disappeared. Curve C was obtained on a sample after vacuum heat treatment and resembles curve B. An activation analysis showed approximately an 80% decrease in the Au concentration in the samples B and C as compared with A.

## Conclusions

The experiments so far indicate that Au is one of the major electrically active elements which are introduced in Si during heat treatment. Gold concentrations found in the material studied are sufficient to account for the changes of resistivity and lifetime. Gold contamination on the surface of the Si as well as Au in the bulk of the Si can be removed

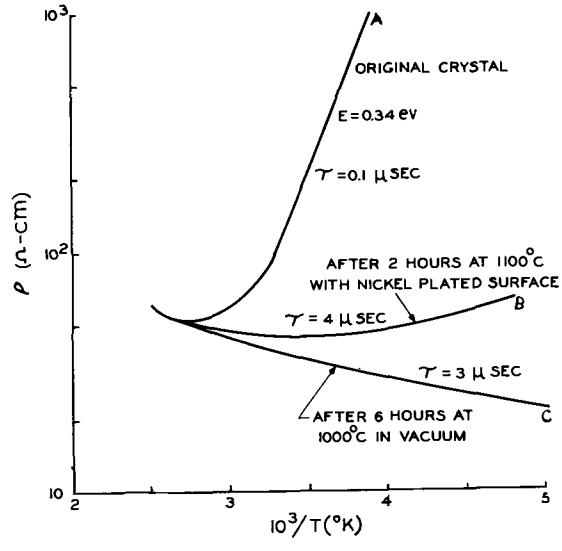


Fig. 6. Resistivity vs. $10^3$/T in gold-doped p-type Si

effectively, preferably by a Ni-Si liquidus on the surface of the samples or by a vacuum heat treatment. The crystals as grown show no Au in the bulk. This is easily understandable since the liquid Si must act as a strong getter (distribution coefficient for Au approximately $10^{-5}$). The surface film of Au observed on the grown crystals must have been deposited after the material solidified. The Au observed on etched material must have its origin in the chemicals used. One can therefore conclude that special precautions will be necessary to reduce the Au contamination to levels below those encountered here, which correspond to approximately 0.001 of a monolayer.

### Acknowledgments

The authors wish to thank Dr. F. M. Smits for helpful discussions, Miss K. Wolfstirn, Mr. F. Worthing, and Mr. R. M. Mikulyak for help in the measurements, and Mr. D. T. Lassota for growing the silicon crystals.

Manuscript received March 3, 1958. This paper was prepared for delivery before the Buffalo Meeting, Oct. 6-10, 1957.

Any discussion of this paper will appear in a Discussion Section to be published in the June 1959 JOURNAL.

REFERENCES

1. H. C. Theuerer, J. M. Whelan, H. E. Bridgers, and E. Buehler, *This Journal*, **104**, 721 (1957).
2. R. H. Kingston, *Proc. I.R.E.*, **42**, 849 (1954).
3. J. D. Struthers, *J. Appl. Phys.*, **27**, 1560 (1956).
4. C. B. Collins, R. O. Carlson, and C. J. Gallagher, *Phys. Rev.*, **105**, 1168 (1957).
5. G. Bemski, To be published.
6. A. N. Baker and G. Bemski, "Vacuum Heat Treatment of Silicon," presented at I.R.E.-A.I.E.E. Semiconductor Device Research Conference, Boulder, Colo., July 1957.
7. S. J. Silverman and J. B. Singleton, *This Journal*, **105**, 591 (1958).
8. C. D. Thurmond and R. A. Logan, *J. Phys. Chem.*, **60**, 591 (1956).
9. C. D. Thurmond, Private communication.

# Technique for Preserving Lifetime in Diffused Silicon

**S. J. Silverman and J. B. Singleton**

*Bell Telephone Laboratories, Incorporated, Allentown, Pennsylvania*

ABSTRACT

After a silicon crystal has been grown, contamination prior to and during the diffusion process is considered a significant cause of lifetime degradation. If, prior to diffusion, a suitable gettering agent is formed on the surface of a silicon slice, then the resultant average lifetime is approximately an order of magnitude greater than that in an untreated slice from the same crystal subjected to the same process. It is believed that a metal-silicon liquid phase established on the silicon surface getters recombination centers from within the bulk of the material, thereby preserving the lifetime. Nickel, silver, or bismuth has been independently applied with comparable results.

In the course of silicon device fabrication, an outstanding problem has been the maintenance of a minimum lifetime after the conventional high-temperature heat treatment, at 1000°C or above for an hour or more. If the minimum lifetime can be retained after processing, the lifetime-dependent electrical characteristics are assured. We have investigated this problem in connection with diffused, high-voltage, conductivity-modulated rectifiers. After processing the diodes, lifetimes equal to or greater than 1 $\mu$sec have been obtained in 20-60 ohm-cm Si (n- or p-type) through the gettering action of a metal-silicon liquid phase on the surface of the material. Nickel, silver, or bismuth has been used with equal success. Without this technique, the lifetime is often degraded to less than a few tenths of a microsecond.

### Experimental

The general characteristics desirable for this liquid phase metal-silicon gettering action may be postulated as follows.

(*a*) The eutectic temperature should be low enough to form a liquid phase on the surface, permitting diffusion and segregation of the impurity.

(*b*) The metal vapor pressure should be sufficiently low at the diffusion temperature to assure establishment of a permanent liquid phase on the surface.

(c) The gettering process should have no discernible electrical effect on the device other than preserving the lifetime.

It has been found that the metal can be applied to the Si surface by any of the following methods: (*a*) electroless plating, (*b*) electroplating, (c) vacuum deposition, (*d*) bulk metal in intimate contact with surface, (*e*) mixing the metal powder with the "paint-on" diffusant, or (*f*) mixing a reducible metal compound with the paint-on diffusant.

The most convenient of the above methods was the mixing of a reducible metal compound with a paint-on diffusant. This procedure consisted of mixing 2 g of $NiCO_3$ in a solution of 5 g of $P_2O_5$ and 100 cc of 2-methoxyethanol. This mixture was applied uniformly onto the Si surface with a clean camel's hair brush. The specimens, placed on a suitable quartz tray, were inserted into a resistance-heated furnace having a quartz tube open to the air and maintained at 1250°C for 16 hr. A cooling period followed at the rate of 10°C/min until 400°C, after which the specimens were removed from the

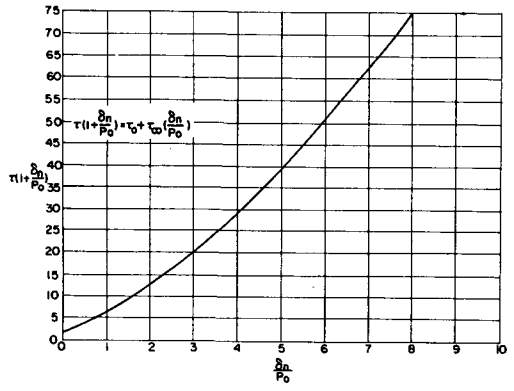


Fig. 1. Relative values of lifetime as a function of injection level.

furnace. (This slow cooling, originally considered beneficial to lifetime, will be shown unnecessary in a later section.) Under such conditions, a 1.5-mil diffusion depth of the phosphorus was obtained. The lifetime was then measured by the injection-extraction technique of Kingston (1).

It is important to stress the interpretation of lifetime values measured by this technique. One must be aware of the lifetime dependence on both (*a*) the injection level and (*b*) the composition of the material. Figure 1 is a plot of experimental data modified after the original equations proposed by Shockley and Read (2). Here, the equation is in terms of $\tau_0$ (lifetime at zero injection level) and $\tau_\infty$ (the slope in the linear portion of the curve). The relative values of $\tau$ are plotted as function of $\delta n/p_0$ (injection level). It is noteworthy that all other observations for $\tau$ were standardized at a forward current value such that $\delta n/p_0$ was approximately 8, which is well beyond saturation. This curve does not include the correction arising from the ratio of the width of the conductivity modulated region to the diffusion length (3). Such a correction would increase the value of the true lifetime relative to the observed lifetime. Emphasis is, therefore, placed not so much on the absolute value of $\tau$, but rather on the relative values of the treated and the untreated specimens when measured at the same injection level for a particular base width.

Keeping these conditions in mind, it can be shown that within certain limitations the preservation of lifetime is independent of: (*a*) material preparation, (*b*) cooling cycle, (*c*) the use of protective covering on both surfaces, (*d*) the material used in the surface-gettering liquid phase (specifically: Ni, Ag, or Bi), and (*e*) the previous heat-treatment history before the final stage in which the liquid phase mechanism is used.

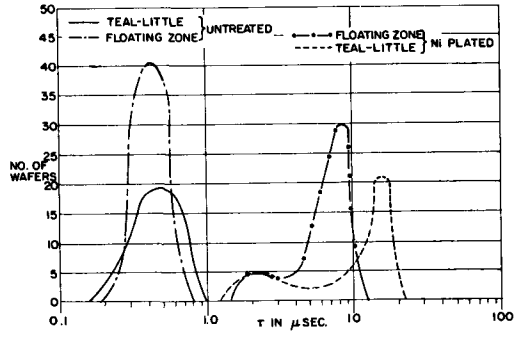


Fig. 2. Comparison of lifetime distributions between floating zone and pulled Si crystals.

In the first experiment, two crystals were doped to the same resistivity range and conductivity type. The first was grown by the floating zone technique. The original lifetime was measured by the Haynes-Hornbeck technique at 500-300 $\mu$sec. The second, grown from a quartz crucible by the Czochralski technique, gave a lifetime between 50 and 20 $\mu$sec. The two crystal sections were cut along the growth axis. The first group of half-slices were nickel-plated and their adjacent half-slices were left as controls. All were subjected simultaneously to the previously described heat treatment. Figure 2 shows that the Ni was equally effective for both types of material, whereas the controls were equally degraded.

In the next experiment, slices from the same Czochralski crystal were cut in half. The first group of half-slices was treated with Ni; the second was used as controls. All specimens were subjected to the previously described treatment except that at the end of the heating interval, they were quenched from a temperature of 1250° to 60°C by dropping them into a silicone oil bath. This change of temperature was accomplished in approximately 5 sec. Figure 3 shows that the average lifetime of the nickel-plated specimens is a factor of 10 greater than that of the controls. As a result of this experiment, the previous lengthy cooling cycle has been considerably shortened without sacrificing any of the electrical requirements of the device.

These observations on quenching (Fig. 3) compared with slow cooling at 10°C/min (Fig. 2) indicate that a metal-silicon surface liquid phase completely obscures whatever beneficial effects the latter procedure may offer under these circumstances. No apparent advantage is gained by combining the slow cooling rate with the metal-silicon liquid phase.

The question has arisen concerning the necessity of masking the entire Si surface with Ni to prevent entry of contaminants. The next experiment indicates that this precaution is unwarranted. Only a single surface covered with the gettering agent is sufficient to preserve the lifetime. Figure 4 is a comparison of units selected and processed in the same manner as in the first experiment, but divided into three groups: nickel on one surface; nickel on two surfaces; and a control. These results are of practical importance when one is restricted to single-surface treatment by the nature of the fabrication procedure.

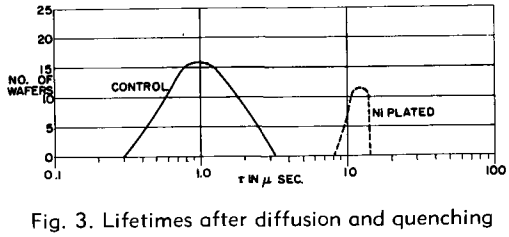


Fig. 3. Lifetimes after diffusion and quenching

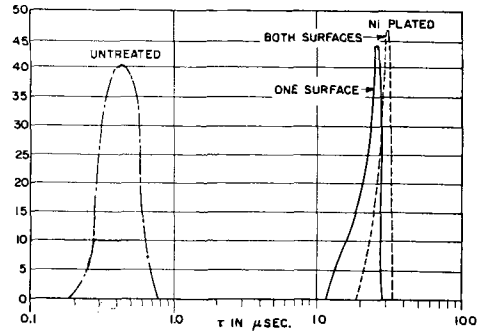


Fig. 4. Comparison of lifetimes for single and double surface treatments.

To show that Ni is not unique in this surface-gettering action, slices from the same crystal were treated independently with Ag or Bi. Silver was applied using an electroless chemiplating bath, consisting of 4 g $AgNO_3$, 0.4 cc HF, and 100 cc $H_2O$. Bismuth was introduced in the form of 2 g of $Bi_2O_3$ mixed with the previously mentioned paint-on diffusant. Figure 5 indicates that all three metals, which conform to the previously described characteristics, give substantially the same distribution groups.

The last experiment was devised to show how the lifetime, when purposely degraded beforehand, can be recovered by subsequent Ni plating on the surface and reheating above the eutectic temperature. The results are seen in Fig. 6. A slice was divided into three sections. The first was given the previously described diffusion heat cycle, then nickel-plated and reheated for 2 hr at 1250°C. The second was subjected to the same conditions as the first, without any Ni. The third was used as a control during first diffusion only. This experiment demonstrates that, regardless of the previous history of heat treatment, lifetime can still be preserved if a metal-silicon liquid phase is established during or after the final heat treatment in which the temperature at some time must be greater than the eutectic temperature. This period of heating has been as little as 1 hr.

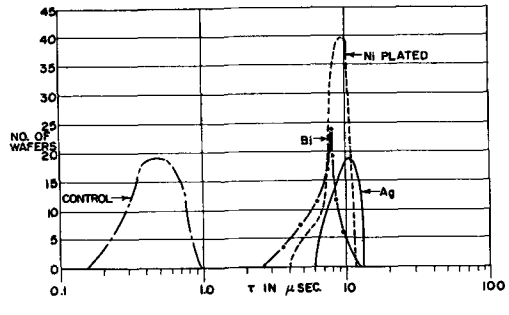


Fig. 5. Comparison of lifetimes preserved by various metals forming eutectic on Si surface.

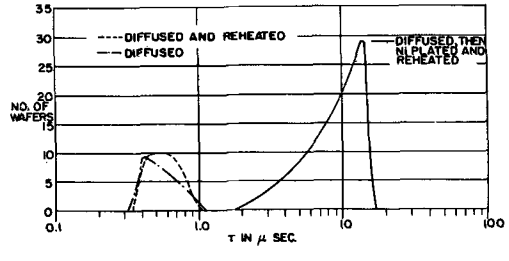


Fig. 6. Comparison of lifetimes on Si purposely degraded before final heat treatment.

## Discussion

The deterioration of lifetime as described in the previous experiments is attributed to surface contamination resulting from (*a*) the processing steps prior to heating and (*b*) the ensuing high-temperature cycle in the relatively unclean furnace environment. A significant experiment demonstrating the effect of these conditions has been successfully performed by Theuerer, *et al.* (4). A single crystal of silicon was grown by the floating zone process. The room temperature lifetime as measured by the Haynes-Hornbeck (5) technique was 500-300 μsec. The surface was then etched with CP-8,[1] rinsed with deionized water, and dried. After reheating the sample at 1100°C for 1 hr in the floating zone apparatus, the lifetime was remeasured and found to be degraded to less than 3 μsec. However, when the same heat treatment was performed without touching or treating the crystal in any manner, the original order of magnitude was retained. In an independent experiment, water ordinarily used to cool the floating zone envelope was eliminated; the interior surface of the quartz chamber was allowed to reach an elevated temperature during heat treatment, causing the same degree of degradation. In both cases the silicon surface was exposed to sufficient chemical contamination to deteriorate the lifetime. The known contaminants adversely affecting lifetime have been identified as Au, Fe, Cu, and Mn, as shown independently by Carlson (6) and others (7, 8).

Several techniques have been proposed previously to control the degradation of lifetime. They are: (*a*) slow cooling in a gaseous ambient, as originally proposed by Bemski (9); (*b*) heating and cooling under special conditions in vacuum, as suggested by Baker (10); and (*c*) the use of a surface-gettering liquid phase as discussed by Trousil (11) and by Logan and Schwartz (12).

There are two possible mechanisms associated with this last technique. Consider the case of Ni on the surface of Si. One possibility is that Ni, a fast diffuser, rapidly permeates the bulk of the material at the elevated diffusion temperature. Once within the lattice, the Ni neutralizes the recombination centers in such a manner as to reduce the capture cross section, subsequently improving the lifetime.

An attempt to verify this hypothesis experimentally was made by Buehler (13). A crystal as grown by the Czochralski technique (14) was started in the normal manner. After the first half had been solidified, Ni was added to the remainder of the melt, doping the second half of the crystal. The resistivities and lifetimes after growth did not change radically from the top to the bottom. After heat treatment, the lifetime was degraded to the same extent in both halves. The results, however, were inconclusive because of the uncertainty concerning the actual concentration of Ni successfully introduced into the lattice.

[1] 5 $HNO_3$:3 HF

To insure the maximum concentration of Ni in the material, a separate experiment was designed whereby a thin film of the metal was deposited on the surface and then diffused at $T \sim 1200°C$ for 1 hr. The layer containing the excess Ni was removed by lapping, etching, rinsing, and drying. The sample was then reheated to see if the lifetime could be preserved effectively by the Ni within the lattice. However, the lifetimes measured after this heat treatment were sufficiently degraded to show no beneficial effects from Ni employed in this manner.

Another possible role of Ni is that it forms a gettering liquid phase on the surface of the Si. This is analogous to the action of a thin film of Au on Ge, described by Logan and Schwartz (12). In the latter situation the recombination center (Cu) diffuses toward the Au-Ge liquid phase, depleting its concentration in the solid Ge and thereby improving lifetime. Logan and Thurmond (15) describe conditions under which the concentration of recombination centers can be controlled using this gettering technique. Similarly, the Ni-Si system is in a liquid state at the diffusion temperature. The equally fast-diffusing recombination centers migrate toward the liquid phase on the surface. If, as in the case of Au in Si, its effective segregation coefficient is small, this impurity becomes trapped in the liquid sink where it remains as the temperature is lowered. When the experiment was repeated at temperatures below the Ni-Si eutectic, the results were not successful. Another surface-gettering action involving diffusion and vaporization of the recombination center (Au) is described in the accompanying paper (16) by Bemski and Struthers.

## Conclusions

It is believed that the observations reported here give strong support to a surface-gettering mechanism whereby fast-diffusing recombination centers (i.e., Au, Cu, Fe, or Mn) may be effectively segregated from within the volume of Si. This action, it is felt, has been responsible for increasing lifetime by an order of magnitude or more under the previously described conditions of high-injection level in relatively high-resistivity silicon material.

Manuscript received March 3, 1958. This paper was prepared for delivery before the Buffalo Meeting, Oct. 6-10, 1957.

Any discussion of this paper will appear in a Discussion Section to be published in the June 1959 JOURNAL.

REFERENCES

1. R. H. Kingston, *Proc. IRE*, **42**, 829 (1954).
2. W. Shockley and W. T. Read, *J. Phys. Rev.*, **87**, 835 (1952).
3. J. Madigan and M. Byczkowski, *J. Appl. Phys.*, **28**, 878 (1957).
4. H. C. Theuerer, H. E. Bridgers, E. Buehler, and J. Whelan, Paper presented at the Washington, D. C. Meeting of The Electrochemical Society, May 1957.
5. J. R. Haynes and J. A. Hornbeck, *Phys. Rev.*, **97**, 311 (1955).
6. R. O. Carlson, *ibid.*, **104**, 937 (1956).
7. C. B. Collins, R. O. Carlson, and C. J. Gallagher, *ibid.*, **105**, 1168 (1957).
8. G. Bemski and H. E. Bridgers, Paper presented at the Cleveland Meeting of The Electrochemical Society, October 1956.
9. G. Bemski, *Phys. Rev.*, **103**, 567 (1956).
10. A. Baker, Paper presented at IRE Semiconductor Devices Conference, Denver, Colo., Spring, 1957.
11. Z. Trousil, *Czechoslov. J. Phys.*, **4**, 251 (1954).
12. R. A. Logan and M. Schwartz, *J. Appl. Phys.*, **26**, 1287 (1955).
13. E. Buehler, Private communication.
14. J. Czochralski, *Z. physik Chem.*, **92**, 219 (1918).
15. R. A. Logan and D. C. Thurmond, *J. Phys. Chem.*, **60**, 591 (1956).
16. G. Bemski and J. D. Struthers, *This Journal*, **105**, 588 (1958).

# Bonding Materials for Making Contacts to p-Type Silicon

**Donald R. Mason and John C. Sarace**

*Department of Chemical and Metallurgical Engineering, University of Michigan, Ann Arbor, Michigan*

ABSTRACT

Molybdenum clad on one side with aluminum, or aluminum-silicon eutectic, has been used to form structurally sound ohmic contacts to p-type silicon, although a flux was necessary when the Al-Si eutectic-clad material was used. The desired aluminum-silicon solid solution can be formed before a substantial amount of aluminum reacts with the molybdenum. The coefficients of thermal expansion are sufficiently well matched so that the silicon wafer does not crack during fabrication, and only minimal alloy penetration into the silicon is observed with the eutectic-clad material.

Nickel and iron-base metals were found to be unsatisfactory, and process troubles with indium ruled out its choice as a bonding agent. Materials produced by cladding with electroplating processes, vacuum evaporation, direct sintering, or dipping operations, either with or without a dipping flux, were unsatisfactory and only roll-clad products could be used successfully.

The necessity for making structurally sound nonrectifying contacts to the various regions of a semiconductor device is an ever recurring problem. The chemically deposited or electroless nickel plate as described by Sullivan and Eigler (1) has been developed for making broad area contacts to lapped

silicon surfaces and can be adapted readily for use on etched n-type Si surfaces. However, many devices including transistors cannot be made without using one or more controlled area contacts, and at least one alloy or bonded contact has been necessary on all junction transistors.

Low-resistance structural bonds have been made to etched n-type Si using an Sb-doped Au bond, but the low distribution coefficients of acceptors into Si from Au solutions (2) produced a high-resistance layer.

Satisfactory nonstructural contacts have been made to etched Si surfaces by alloying with a fine wire (3) or a thin film of vacuum-evaporated Al (4). Thick Al sections induce cracking because of a mismatch in the thermal coefficient of linear expansion. Peterson and McConville (5) have used Mo wire on which a layer of Al has been electroplated for making alloy junctions to n-type Si, with the aid of a post-alloy etch. Henkels (6) used a Si-Al eutectic foil to dope the n-type Si in forming flat p-n junctions, and the foil is fused to a Mo or Ta backing plate during the alloying cycle. A post-alloying etch is used.

Athough the objective of this research was limited to the formation of ohmic contacts on etched p-type Si, it was found that alloy junctions which were quite satisfactory as emitters could also be produced, even without a post-alloying etch. Similarly, there is no inherent reason which would prevent the formation of good contacts to lapped or sand-blasted silicon surfaces.

## Experimental

### *Test Specimen*

The test specimen which was used to evaluate the various base plate materials is shown schematically in Fig. 1. It comprised an n-type Si wafer having (111) major faces, into one face of which boron had been diffused to form a $p^+$-n junction. The p-layer, having a thickness of about 0.001 in. and a surface concentration of about $10^{20}$ boron atoms/cm$^3$, was placed in contact with the alloy-clad base plate which in turn had been spot-welded onto the superstructure of a solder-type, symmetrical four-pin transistor header. One wire of the header which was electroplated with Au-Sb alloy was bent around to hold the Si wafer securely against the base plate, and a satisfactory ohmic contact to the n-type region was obtained during the alloying cycle. After the alloying cycle, the superstructure could be sealed to protect the surfaces from subsequent contaminating influences, if desired, by dropping a can into the solder trough of the header. With this structure, a unitized material was simpler to use in the fabrication procedure instead of a separate solder alloy and backing plate.

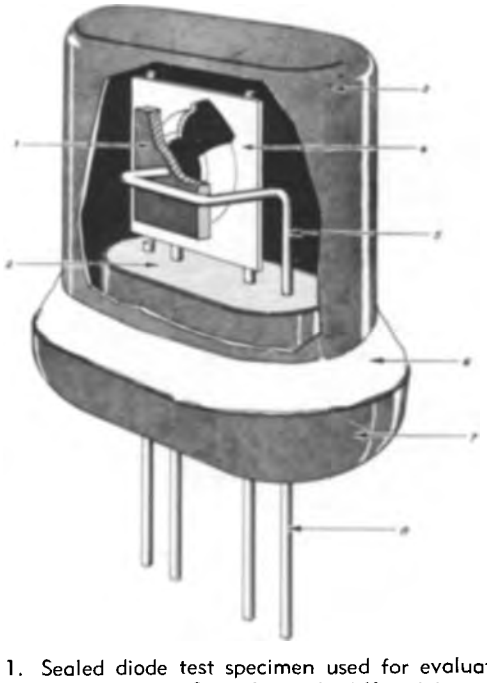

Fig. 1. Sealed diode test specimen used for evaluation of base plate materials: 1, Si wafer with diffused junction; 2, glass; 3, gold-plated can; 4, embossed alloy-clad base plate; 5, Au-Sb electroplate on this pin; 6, Sn-Ag eutectic solder; 7, Kovar eyelet; 8, Mo pins.

### *Base Plate Material*

A variety of base plate materials was obtained and evaluated.

The pertinent variables which characterize the base plate material can be classified into three categories; first, composition of the base metal; second, composition of the cladding material; and third, technique of applying the cladding material to the base metal.

Base metals of Fe, Ni, and Mo were investigated, using pure Al as the alloying film material. Aluminum-clad Fe and Ni were available from commercial sources; molybdenum samples were made to specification.

Whenever Fe was used, the reverse current of the diodes was intolerably high. A typical current-voltage characteristic is shown by diode A in Fig. 2. This result is consistent with observations by Bemski (7) that the minority carrier lifetime in Si is reduced when small traces of Fe are added to the system at high temperatures. The Fe could be acting as a recombination-generation center in the space charge region. Good uniform mechanical bonds were not formed, and other Fe-containing base metals such as Kovar were not considered.

The bonding to Si with Al-clad Ni was erratic. Good bonds were invariably accompanied by crack-

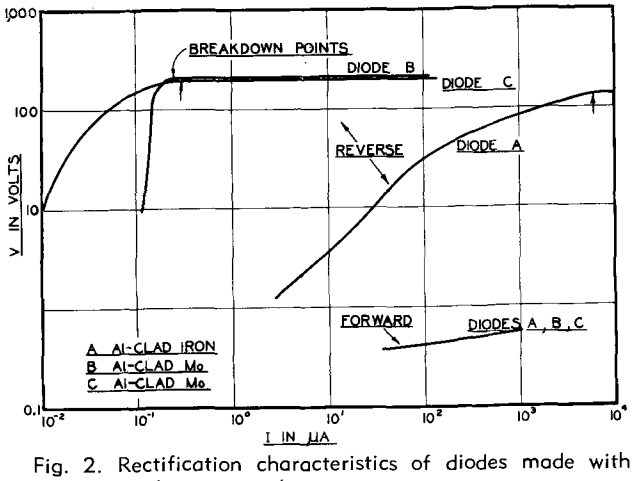


Fig. 2. Rectification characteristics of diodes made with Al-clad base plate materials.

ing of the Si wafers and hence poor electrical characteristics, because of the mismatch in the coefficients of thermal expansion. Nickel was also rejected.

Occasionally, however, satisfactory bonds and electrical characteristics were obtained using early samples of Al-clad Mo, so Mo was chosen for further investigation. Other metals, such as tungsten, having coefficients of expansion relatively close to Si could just as well have been used. However, Mo is readily available and has sufficient ductility to permit forming and manipulation in the fabrication of piece-parts for semiconductor device structures.

### *Cladding Film Compositions*

Since the cladding film must contain acceptors, the choice is almost automatically limited to Al or In in their pure forms, and Ga can be used only with a carrier alloy. In our experience Au is not a satisfactory carrier alloy because of the formation of the high-resistance film.[1]

Indium not only reacts with the molybdenum-to-molybdenum welds which were used to fabricate the test specimen but also imposes a maximum operating temperature on the device of well below 150°C; consequently, it was not considered further.

Reactions between the Al and the transition metals were observed in the preliminary work. These elements all react chemically with Al below its melting point (660°C) to form complex chemical compounds which effectively precipitate the Al from the system so that it is not available to form a solid solution alloy with the silicon. In effect, the Al is in the center of a sandwich with Mo on one side and Si on the other side. Very stable compounds of the form $Al_xM$ are known to exist, so that at equilibrium the Al may not be available to dope the Si. Perhaps as an oversimplification, it can be thought of as a reversible reaction on the Si side which is competing with an irreversible reaction on the Mo side for the utilization of the Al.

$$Al + Si \rightleftarrows AlSi \text{ (Solid solution) desired} \quad [1]$$

$$x\text{-}Al + M \rightarrow Al_xM \text{ (Precipitate) undesired} \quad [2]$$

where M is Fe, Ni, Mo, or similar element.

Since it appeared that Al was necessary for good contacts, the precipitation or diffusion of the Al into the base plate had to be overcome to permit the formation of an alloy bond to Si before all the Al was precipitated. This could be done either by interposing a barrier between the Si and the base metal to retard the precipitation reaction or by adding another component to depress the melting temperature and/or lower the Al concentration. Silver was found to be satisfactory as a third component, but the over-all results were not as good as those that were obtained with the Al-clad combinations which will be discussed in detail.

### *Aluminum Cladding Processes*

Most processes available for cladding Mo with Al also form a thin oxide film at the Al-Mo interface. Aluminum films, obtained by (*a*) electroplating, (*b*) vacuum evaporation, (*c*) direct sintering, and (*d*) dipping into molten Al without a flux, were nonadherent and could be peeled off. Films applied by dipping Mo sheets into molten Al after treatment with a sodium potassium aluminum fluoride flux were nonreproducible, but very adherent; in fact, the intimacy of contact was so good that the Al apparently reacted with the Mo before the Al-Si bond could be formed. A cross section of an attempted bond to Si using this material is shown in Fig. 3. Portions of the Si surface definitely have been dissolved, but there is no trace of the Al. The thin film that is visible on the Mo surface is probably residual Si that has been deposited there as the Al diffused into the interior of the Mo.

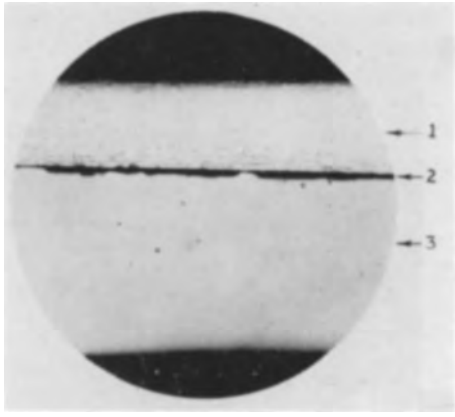


Fig. 3. Longitudinal cross section of attempted bond to Si using fluxed and Al-dipped Mo strip. 1, Mo sheet; 2, Al diffused away from here; 3, Si wafer. Magnification 200X before reduction for publication.

### *Rolled-On Aluminum*

Samples of Mo sheet having a pure Al film rolled onto one side were prepared to specifications[2] for evaluation. These comprised 0.005 in. Mo sheets having 0.0005 in. of pure Al rolled onto one side and were formed as the result of a substantial thickness reduction to promote the formation of atomic bonds between newly formed Al-Mo interfaces. Spectrochemical analyses showed the materials to be very pure.

[1] In reviewing this manuscript, M. Tanenbaum reports that he has been able to make satisfactory contacts to p-type Si using Au doped with B or Ga.

[2] From Kassel Industries, Inc., P.O. Box 432, Englewood, N. J. (Aluminum film contains ½% silicon), and General Plate Division, Metals and Controls Corp., Attleboro, Mass.

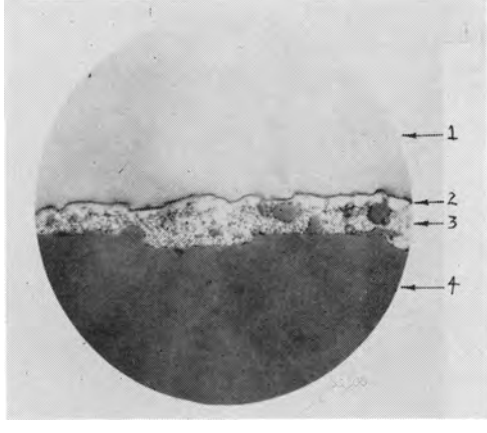


Fig. 4. Longitudinal cross section of bond to Si using Al-clad Mo. 1, Mo sheet; 2, unalloyed Al; 3, Al-Si eutectic; 4, Si wafer. Magnification 1500X before reduction for publication.

During alloying, the Al film dissolves enough of the Si wafer to form an Al-Si eutectic. A microscopic cross section of an alloyed structure is shown in Fig. 4.

Several distinct phases are distinguishable in the photomicrograph. The Si wafer has been dissolved at discrete regions over the surface, but the wetting and penetration are not uniform. During the solidification of the alloy, some of the Si redeposited on the Si surface, and some crystallites of Si remained suspended in the Al-rich phase. The grainy portion of the Al region is the Al-Si eutectic, and apparently the Al in the immediate vicinity of the Mo surface was not melted. At the same time the Al thickness is sufficiently thin to avoid cracking of the Si when alloying is carried out at temperatures around 580°-610°C. At lower temperatures no mechanical bonding occurs, while Al precipitation becomes a problem at higher temperatures.

Typical small area p-n junction characteristics are shown by diodes B and C in Fig. 2. The differences in reverse current around 0.1 $\mu$a are thought to arise from varying degrees of background contamination from the process. Minority carrier lifetimes (8) measured on these diodes by a junction recovery method were found to be in the range of from 50 to 100 m$\mu$ sec.

### *Penetration Control: Silicon-Aluminum-Clad Molybdenum*

Although these results were quite satisfactory and reproducible, the penetration into the Si wafer might be undesirable for some applications. With a 0.0005 in. thick film of Al as the alloying agent, the depth of penetration into the Si at 600°C would be about 0.0001 in. This penetration could be reduced by using a Si-Al eutectic as the alloying medium. Accordingly, a composite structure was made to specification by the rolling-on process described previously.[3] It comprised a Mo sheet 0.008 in. thick onto one side of which an Al film 0.0005 in. thick containing nominally 12% Si had been applied. During rolling, the Mo developed a micalike striated structure, and separations were observed inside the Mo sheet. In all probability this rolling texture is not inherent in the material and could be eliminated, as it was not present on the pure Al-clad material.

The alloying characteristics of this material were found to be substantially different from the pure Al material. It was impossible to form an alloy bond between the Al-Si and the Si even by heating to temperatures in excess of 700°C. These observations were corroborated in the work with the Ag carrier alloy. When as little as 4% Si was added to a Ag-Al eutectic solution, the resulting alloy would not wet spontaneously to the Si wafers.

Experiments with Al-Si clad Mo were carried out in a different furnace using flat plates instead of the formed plates as shown in Fig. 1; however, the consistency of the results with the alloys containing Si seems to indicate that the test specimen configuration and alloying furnace are of secondary importance. Since the surface properties of the system are such that wetting would not occur spontaneously, the use of a flux was indicated.

[3] From Kassel Industries, Inc., P.O. Box 432, Englewood, N. J.

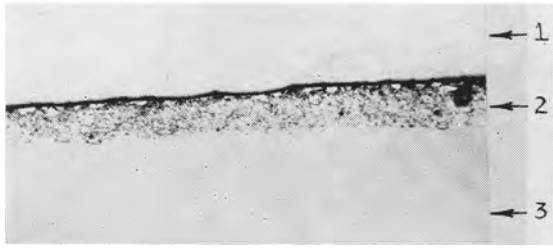


Fig. 5. Cross section of bond to Si using Mo sheet clad with Al-Si eutectic. 1, Mo sheet; 2, Al-Si eutectic; 3, Si wafer. Magnification 500X before reduction for publication.

### *Wetting*

By using various fluxes it was possible to obtain uniform wetting of the Al-Si-clad Mo to the Si slices with a minimum of penetration. In all cases the fluxes used were made from elements which either were acceptors in Si or were substantially inert, electronically, Lithium, for example, was avoided since it acts as a donor when introduced interstitially into Si (9). Although several fluxing agents were tried, the best results seemed to be obtained by painting the eutectic film with a dilute solution of boric acid in denatured alcohol immediately prior to assembling the wafer stack for alloying. Anhydrous ethyl sodamide was also used successfully, but its effectiveness decreased as the solution absorbed moisture from the atmosphere.

A photomicrograph of a boric acid-fluxed bond is shown in Fig. 5. The alloying was carried out at about 675°-700°C in an atmosphere of anhydrous, deoxidized $N_2$ for an alloying time of 5-10 min. At lower temperatures an apparent bond forms since the boric oxide acts as a glassy cement, but the bond can be ruptured by boiling in water for a few minutes. Bonds made in the alloying temperature range were mechanically sound, and on rupture, either the Mo was separated or the Si was pulled out of the Si wafer in the vicinity of the bond.

In making relatively large area contacts, it is desirable that the specimen should be cooled at a rate no greater than about 5°C/min. If substantially faster cooling rates are used, the differential thermal expansions of the system are sufficiently great to induce cracking in the Si wafers. Observations made at the corners of the specimens (silicon-eutectic-flux interfaces) indicate that the wetting angle has been reduced considerably in comparison with the Si-Al-gas interfaces.

These diodes did not have electrical characteristics quite as good as those shown in Fig. 1, presumably because it was not possible under the experimental conditions used to stabilize the ambient atmosphere around the junction with a hermetic seal subsequent to the time of alloying.

## Conclusion

Wafers of p-type Si have been bonded successfully to alloy-clad Mo to form structurally sound ohmic contacts. Molybdenum has been used as the base plate material because its coefficient in linear expansion is reasonably well-matched to that of Si and introduces no deleterious elements into the p-n

junction structure during processing. Bonding agents of pure Al or Al-Si eutectic were applied to the Mo sheet by rolling accompanied by a substantial thickness reduction to promote the formation of atomic bonds between newly formed Al-Mo interfaces. The Si bonding temperature cycle must be carried out in either an inert or reducing atmosphere. The maximum temperature is limited by the reaction of Al with the Mo, and the cooling rate is limited by the necessity for relieving stresses in the bimetallic structure without inducing fracture. When Si is added to the Al bonding material, considerably more stringent alloying conditions must be used to obtain a satisfactory bond.

### Acknowledgments

It is a pleasure to acknowledge assistance from Mr. Carl Frosch for the diffused silicon wafers, Mr. F. G. Foster and Mr. V. K. Mehra for the photomicrographs, and Mr. D. L. Hilderley for laboratory assistance. This work was made possible in part by a grant from the Faculty Research Fund of the Horace H. Rackham School of Graduate Studies at The University of Michigan. Another part of the work was carried out at the Bell Telephone Laboratories, Inc., Murray Hill, New Jersey.

Manuscript received Feb. 20, 1958. This paper was prepared for delivery before the Washington Meeting, May 13-16, 1957.

Any discussion of this paper will appear in a Discussion Section to be published in the June 1959 JOURNAL.

REFERENCES

1. M. V. Sullivan and J. H. Eigler, *This Journal*, **104**, 226 (1957).
2. D. K. Wilson, Private communication (see Footnote 1).
3. G. L. Pearson and B. Sawyer, *Proc. IRE*, **40**, 1348 (1952).
4. J. M. Goldey, Paper presented at the Washington Meeting of The Electrochem. Society, May 13-16, 1957.
5. Private communication.
6. H. W. Henkels, Private communication.
7. G. Bemski, Private communication.
8. G. Bemski, *Phys. Rev.*, **100**, 523 (1955).
9. C. S. Fuller and J. A. Ditzenberger, *ibid.*, **91**, 193 (1953).

# Electrolytic Reduction of Cyanamide

## II. The Nature of the Reduction of Cyanamide and Formamidine

**Keijiro Odo, Eiichi Ichikawa, Katsujiro Shimogai, and Kiichiro Sugino**

*Laboratory of Organic Electrochemistry, Department of Chemical Engineering,*

*Tokyo Institute of Technology, Tokyo, Japan*

ABSTRACT

Two consecutive steps in the electrolytic reduction of cyanamide have different natures from the viewpoint of organic electrode process. The first step is catalytic and the second step is voltage-controlled. Therefore, the most active cathode for one step may not be the most effective for another. Tin was an effective cathode for the over-all reduction process.

In the course of the reduction of formamidine to methylamine and ammonia, the existence of methylenediamine as second intermediate was verified.

On the electrolytic reduction of cyanamide the isolation of formamidine as intermediate and the confirmation of methylamine and ammonia as final products was reported (1). In the present work, the effect of cathode materials and other electrolytic conditions on the yield of each product was studied. Also, the reduction of formamidine at various cathodes was investigated in order to clarify the over-all reduction mechanism. The results are reported here along with some unusual phenomena observed in the course of this study.

### Experimental

The apparatus used was the same as that already described (1). However, the cell was covered in order to measure the H evolution.

Crystalline cyanamide was freshly prepared from commercial calcium cyanamide by an improved procedure (2), and its purity was determined by the usual method (as silver cyanamide) before use.

Formamidine sulfate was prepared by the catalytic reduction of cyanamide with Pd catalyst (3), mp 156°-158°C.

*Separation of the reduction products of cyanamide.*—The separation of each product was carried out more rigidly than previously (1).

After reduction, the catholyte (about 110-120 cc) was neutralized with a small amount of $H_2SO_4$ (or $NH_3$) and diluted to 200 cc; 10 cc was used as the determination of unconverted cyanamide. The remaining part was evaporated to dryness at 50°-60°C under diminished pressure and the residue was dried for 24 hr in a vacuum-desiccator over $P_2O_5$. This was extracted twice with 50 cc isopropyl alcohol to remove unconverted cyanamide. The residue was again extracted twice with 50 cc absolute

methanol. The final residue was dried at 100°C and weighed (ammonium sulfate).

The methanol extract[1] was evaporated to dryness and the residue was dissolved in 100 cc water. Then, a suitable amount of picric acid (2% excess based on converted cyanamide) was added to it, the mixture was warmed to make a clear solution, and allowed to cool overnight. The precipitate was filtered off, washed with 50 cc water, and dried. Then it was purified by extraction with absolute ether to remove free picric acid, dried at 100°C, and weighed (formamidine picrate). Solubility correction was applied.

After removing the dissolved picric acid by acidification with HCl and extraction with ether, the filtrate was concentrated to 100 cc. The concentrate of isopropyl alcohol extract was added to it, and the mixture was poured into a Kjeldahl flask and heated with 20 g NaOH/50 cc water solution. Methylamine was distilled into N-HCl and the resulting solution (100 cc) was evaporated to dryness and allowed to stand in a vacuum desiccator over $P_2O_5$ overnight. The residue was extracted twice with 50 cc butanol at 50°C. The butanol extract was concentrated to 10 cc and allowed to stand in an ice box. Methylamine hydrochloride crystals which separated out were filtered off, dried at 100°C, and weighed. Some methylamine hydrochloride was recovered from the mixture of the filtrate and the wash.

Determination was not carried out for nonnitrogeneous hydrolytic products of intermediate compounds, such as formic acid and formaldehyde.

*Separation of the reduction products of formamidine.*—After reduction, the catholyte (110-120 cc) was neutralized with a small amount of $H_2SO_4$ (or $NH_3$), evaporated to dryness at 50°-60°C under diminished pressure, and the residue was dried for 24 hr in a vacuum desiccator over $P_2O_5$. This was refluxed twice with 50 cc absolute methanol, and the insoluble residue was filtered off from the hot solution. The residue was dried at 100°C and weighed (ammonium sulfate).

The methanol extract was worked up to separate unconverted formamidine as picrate and then to collect methylamine hydrochloride just as in the separation of the reduction products of cyanamide. However, in the case, 25 g picric acid was added with 50 cc water to 100 cc aqueous solution made from the evaporation residue of the methanol extract for the separation of unconverted formamidine.

As for nonnitrogeneous hydrolytic products of starting material and the intermediate product, the determination of formaldehyde with formic acid was carried out in some cases as described later.

## Results and Discussion

### *Reduction of Cyanamide*

The yield of each reduction product at various cathode materials is shown in Table I.

[1] In the case of the reduction at Pd, the methanol extract was concentrated and allowed to cool to give formamidine sulfate. After separating these crystals, the filtrate was diluted to 100 cc with water and worked up by the same procedure.

**Table I**

Anode: Pt; anolyte: 60 cc 5% $H_2SO_4$; catholyte: 10.0 g cyanamide (purity: 96-98%) in 100 cc 8% $(NH_4)_2SO_4$. pH range adjusted at 2-7 by adding small amount of $H_2SO_4$ during the electrolysis; temp: 12°-15°C; current density: 5 amp/dm²; amount of current: 38 amp-hr (6 faradays/mole)

| Run No. | Cathode | Cyanamide converted g | Cyanamide converted % | Yield: Formamidine picrate g | Yield: Formamidine picrate % | Yield: Methylamine HCl g | Yield: Methylamine HCl % | Yield: $(NH_4)_2SO_4$ g |
|---|---|---|---|---|---|---|---|---|
| 1 | Sn | 5.1 | 53 | 4.1 | 13 | 0.7 | 9 | 2.7 |
| 2 | Pb | 1.9 | 20 | nearly zero | — | 0.2 | 7 | 0.9 |
| 3 | Hg | 2.8 | 30 | nearly zero | — | nearly zero | — | 1.0 |
| 4 | Cu | 3.1 | 32 | 0.30 | 1.5 | 0 | — | 0.8 |
| 5 | Pd black on Pd. | 8.7 | 90 | sulfate* 8.3 +picrate 7.0 | 52 | 0 | — | 3.7 |

* Of the total yield of formamidine, 8.3 g was obtained as sulfate and 7.0 g was obtained as picrate.

The reduction of cyanamide occurred at all cathodes used (1). It was confirmed that Sn was an effective cathode material for over-all reduction process. Pb and Hg, which have a high H overvoltage, were not so effective in this reduction. Especially at Hg, methylamine was scarcely obtained and ammonia was the only nitrogeneous product. It was noticed that formamidine was not obtained at these two cathodes. This is due to the effectiveness of these cathodes on the reduction of formamidine as described below. Cu, a low H overvoltage metal, was also an active cathode leaving a small amount of formamidine as product. Pd black cathode was seen to be very effective for the formation of formamidine. However, at Pd, methylamine could not be obtained at all.

*Current efficiency at various cathodes.*—Since several products were obtained in the reduction of cyanamide, H evolution at the cathodes was measured to observe the differences in current efficiency of the cathodes (except Hg[2]). The measurement was carried out at intervals of several minutes till the theoretical amount of current (6 faradays/mole) was passed. Results are shown in Fig. 1.

Palladium was the most effective from the viewpoint of current efficiency. However, even at Pd, the efficiency decreased markedly with time.[3] At Sn, the efficiency was not so high at the beginning, but it was maintained at about the same level. At Pb, the efficiency once reached to the same level as at Sn but it decreased greatly after 2 hr[4] and came down to zero after 6 hr. At Cu, the efficiency was very low and it reached to zero at the end. These observations coincided well with the results in Table I.

*Influence of pH and current density on current efficiency at tin cathode.*—The influence of pH and current density on current efficiency was then examined at the Sn cathode for a typical run. Results are shown in Fig. 2.

[2] At Hg, accurate measurement was difficult due to the formation of ammonium amalgam.

[3] This might be due to poisonous action of cyanamide on the catalyte activity of Pd.

[4] It may be possible that this is due to the formation of an insoluble film on the cathode surface, resulting from the action of cyanamide with lead.

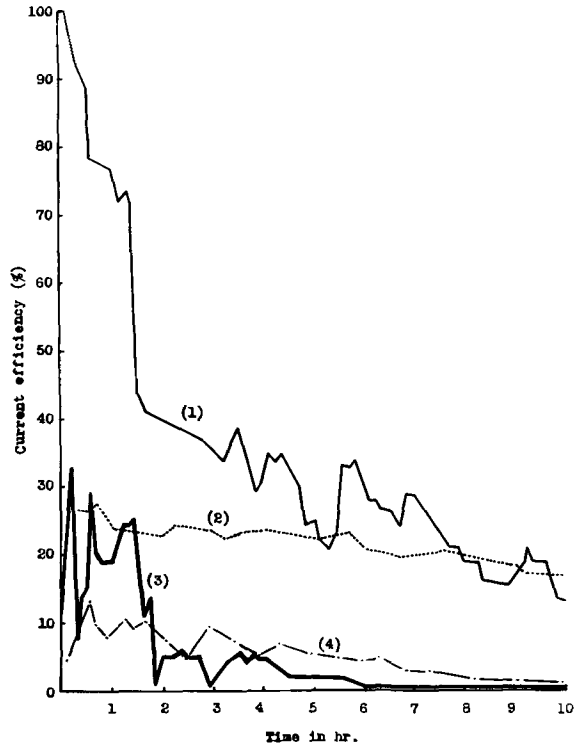


Fig. 1. Current efficiency at various cathodes (reduction of cyanamide): 1, Pd; 2, Sn; 3, Pb; 4, Cu; conditions: same as in Table I.

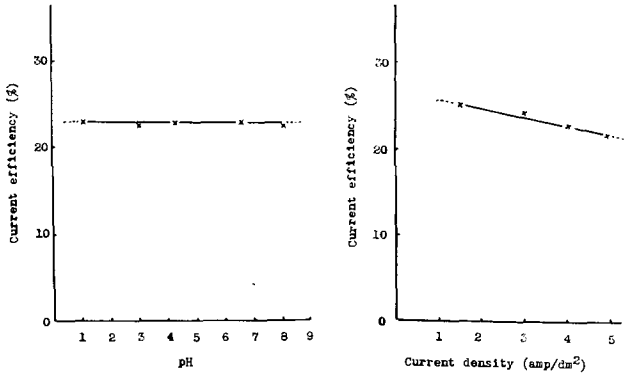


Fig. 2. Effect of pH and current density on current efficiency at Sn (reduction of cyanamide); conditions: same as in Table I.

The change of pH from 1 to 8 had no effect on the current efficiency. As for the influence of current density, the efficiency had a tendency to decrease slightly with increasing current density from 1 to 5 amp/dm$^2$.

### *Reduction of Formamidine*

The yield of each reduction product at various cathode materials is shown in Table II.

Contrary to cyanamide, the reduction of formamidine was found to occur only at cathodes having a high H overvoltage such as Sn, Pb, or Hg. The yield of methylamine based on formamidine converted was the highest at Sn, although it was relatively small. A large amount of ammonia was formed at every cathode. Especially at Hg, the largest amount of ammonia was obtained with a very small amount of methylamine. It was interesting to note that a fairly large amount (40%) of

Table II

Anode: Pt; anolyte: 60 cc 5% $H_2SO_4$; catholyte: 10.0 g formamidine sulfate in 100 cc water (almost neutral). pH range adjusted at 2-7* by adding small amount of $H_2SO_4$ during the electrolysis; temp: 12°-15°C; current density: 5 amp/dm$^2$

| Run No. | Cathode | Amount of current amp-hr | Formamidine unconverted % | Yield Methylamine HCl g | Yield Methylamine HCl % | Yield $(NH_4)_2SO_4$ g | Remarks |
|---|---|---|---|---|---|---|---|
| 1 | Sn | 57.5 | 43 | 0.8 | 18 | 6.2 | |
| 2 | Pb | 57.5† | 0 | 1.1 | 15 | 9.0 | |
| 3 | Hg | 17.3 | 0 | 0.1 | 2 | 11.0 | Urotropine obtained |
| 4 | Cu | 11.5 | 65 | 0 | — | 3.6 | |
| 5 | Pd | 11.5 | 76 | 0 | — | 1.4 | |

* It is well known that formamidine is hydrolyzed very easily to give ammonia and formic acid, especially in alkaline medium.
† In the case of Pb, this amount was more than enough to convert all of the formamidine.

hexamethylenetetramine was found in the product at Hg.[5] This is a characteristic of a mercury cathode and led us to suppose that methylenediamine was formed in the course of this reduction.

At Pd, which has the greatest activity toward the reduction of cyanamide to formamidine, no reduction products were obtained which showed its inactivity toward formamidine. At Cu, no reduction products were also obtained as well as at Pd, but the amount of ammonia formed by hydrolysis was somewhat larger than that at Pd.

*Current efficiency at various cathodes.*—Hydrogen evolution at the cathodes (except Hg)[6] was measured to observe the differences in current efficiency of the cathodes on the reduction of formamidine. The variation of pH of the catholyte was measured by pH test paper at the same time because it had a great influence on current efficiency. The measurement was carried out at intervals of several minutes till the theoretical amount of current (4 frs/mole) was passed. Results are shown in Fig. 3.

Lead showed a high current efficiency at the start, but it decreased with time and reached a small value at the end.[7] On the other hand, at Sn, a moderate efficiency was maintained, as in the reduction of cyanamide. At Pd, at which the efficiency was the highest in the reduction of cyanamide, a definite H absorption due to the reduction was not observed. At Cu, practically zero efficiency was recorded after 1 hr. These observations coincided well with the results in Table II.

*Influence of pH on current efficiency:*[8]—Using a tin cathode, the influence of pH on current efficiency was studied when[9] 17 amp-hr had passed (Fig. 4).

It was found that the current efficiency greatly decreased below pH 2. This was also observed at

[5] The electrolyte close to the cathode might be ammoniacal after ammonia had been formed by reduction or by hydrolysis.

[6] At Hg, accurate measurement was impossible due to the formation of ammonium amalgam, but H evolution could scarcely be observed during the reduction.

[7] This may be due to the disappearance of formamidine. It may be possible that the decomposition of formamidine is affected by current through its discharge.

[8] The influence of current density could not be measured due to the variation of pH with the variation of current density.

[9] At about this time, the variation of pH with current was relatively small.

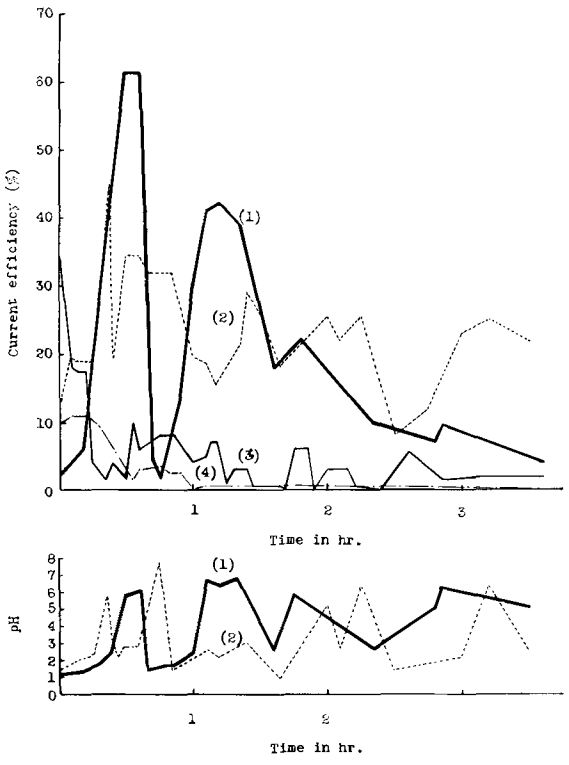


Fig. 3. Current efficiency at various cathodes (reduction of formamidine): 1, Pb; 2, Sn; 3, Pd; 4, Cu; conditions: same as in Table II.

active cathodes other than Sn, as shown in Fig. 3, and was a characteristic of formamidine reduction. This is the reason of great irregularities in current efficiency-time curves in Fig. 3.

### *Formation of Formaldehyde by Reduction of Formamidine; Indirect Confirmation of Methylenediamine as the Intermediate*

In the preceding paper, it was pointed out that in the course of the reduction of cyanamide at Sn, formamidine—the intermediate—was not only reduced to methylamine and ammonia, but hydrolyzed to ammonia and formic acid. In that case, the formation of formaldehyde was very small and barely confirmed. However, as described above, the reduction of formamidine at Hg gave a large amount of hexamethylenetetramine as follows.

Ten grams of formamidine sulfate was reduced at Hg under the same conditions as in Table II. After 13.8 amp-hr passed, the catholyte was worked up according to the procedure described above to the methanol extraction; 8.8 g ammonium sulfate was obtained. The methanol extract[10] was then concentrated to 30 cc under diminished pressure and allowed to stand until it reached to room temperature. Some crystals were separated (0.40 g). The filtrate was again evaporated to dryness to give further crops of the same crystals. The combined crystals were purified from methanol by dilution of a methanolic solution with ether, yield 1.0 g. The characteristic $HgCl_2$ compound was then prepared, mp 225°-230°C dec.

[10] When the methanol extract was allowed to cool, a small amount of brilliant crystals were separated. This was filtered off, washed with methanol, and dried in a desiccator. Yield 0.02 g, mp 215°C, picrate mp 185°-186°C. The identification of this compound has not yet been carried out.

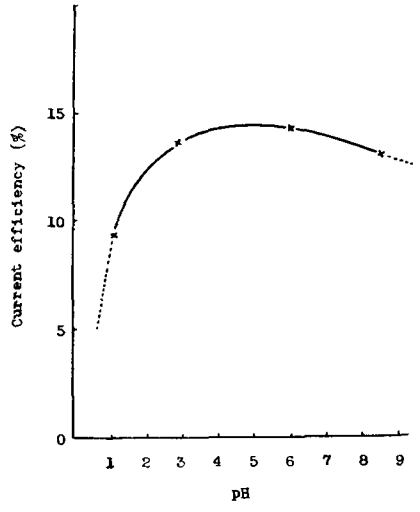


Fig. 4. Effect of pH on current efficiency at Sn (reduction of formamidine); conditions: Same as in Table II.

The isolation of hexamethylenetetramine suggested the formation of formaldehyde in the catholyte. Moreover, a small amount of formaldehyde was also recovered with formic acid from the reduction product at Pb. This may be due either (*a*) to the hydrolysis of methylenediamine which may be the intermediate from formamidine to methylamine and ammonia or (*b*) to the reduction of formic acid formed by the hydrolysis of formamidine itself. The reduction of formic acid [catholyte: 6.8 g ammonium formate in 100 cc 5% $(NH_4)_2SO_4$; other conditions: the same as in Table II] was then carried out at pH 2-7 at Sn and at Hg. Hydrogen was evolved quantitatively and no products were obtained after 11.6 amp-hr of current was passed.

It may be seen, therefore, that formaldehyde was formed by the hydrolysis of methylenediamine. To confirm it, methylenediamine was prepared by the procedure of Knudsen (4) and the hydrolysis and the reduction of it were carried out.

Methylenediamine 2HCl, needle crystal

Anal. Calc'd for $CH_8N_2Cl_2$: N, 23.9; Cl, 59.6

Found: N, 24.0; Cl, 60.9

2.3081 g sample in 100 cc water acidified with 2 cc HCl was subjected to distillation. 0.567 g, 98% formaldehyde[11] was found in the distillate (50 cc) by the $Na_2SO_3$ method. 0.648 g, 98% $NH_3$ was recovered from the residue as usual.

This indicated the quantitative formation of formaldehyde and ammonia by hydrolysis as well as the authenticity of the sample.

Then the electrolytic reduction of methylenediamine was carried out at Sn to confirm the formation of methylamine.

After reduction, the catholyte (140 cc) was acidified with HCl and subjected to distillation to give 120 cc distillate. Further distillation of the residue with 30 cc water and 3 cc HCl gave 30 cc second distillate. Formaldehyde in the combined distillate was determined by $Na_2SO_3$ method. The distillation residue was diluted with water and evaporated to

[11] Identified as dimedon derivative, mp 187°-188°C.

**Table III**

Anode: Pt
Anolyte: 60 cc 5% $H_2SO_4$
Catholyte: 5.95 g methylenediamine 2HCl, 8.0 g $NH_4Cl$, 80 cc $CH_3OH$, 50 cc $H_2O$ (initial *p*H 1.2). *p*H* adjusted at 1-7 by adding a small amount of HCl.
Temp: 6°-8°C
Current density: 3 amp/dm²
Amount of current: 7 amp-hr†
Results: Pure methylamine HCl obtained: 0.56 g, 18% (based on methylenediamine used) mp 210°C, picrate mp 200°C; methylguanidine picrate was then prepared, mp 198°C. Formaldehyde (resulted from unconverted methylenediamine and its hydrolytic product): 0.84 g, 56%.

* In the reduction of methylenediamine, keeping *p*H in a desirable range was very easy as compared with that in cyanamide or formamidine reduction.
† The electrolysis was conducted until hydrogen began to evolve quantitatively.

dryness. The solid, after drying overnight in a vacuum-desiccator over $P_2O_5$, was extracted with 50 cc hot butanol. From the extract, methylamine hydrochloride was collected by working up as described above and weighed.

Results are shown in Table III.

5.95 g methylenediamine 2HCl was also reduced at Hg and at Pb under conditions similar to those in Table III. Although the efficiency was smaller than that at Sn, the reduction occurred to give 0.1 g and 0.15 g methylamine hydrochloride after 6.12 amp-hr and 2.68 amp-hr of current was passed, respectively.[12]

These results might be proofs for existing methylenediamine as the intermediate of the reduction of formamidine.

## Polarographic Measurement[13]

Polarographic measurement was carried out for cyanamide and formamidine in order to explain the results obtained by macroelectrolysis more clearly.

[12] In these cases, formaldehyde could not be obtained from the product. At present, this is a problem we still can not understand.

[13] This was carried out by T. Sekine in our laboratory.

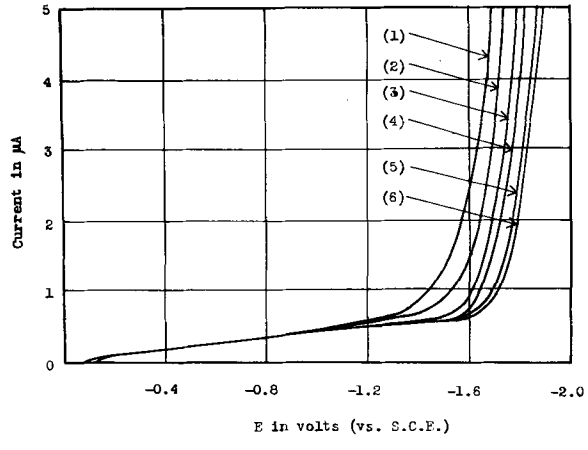


Fig. 5. Polarograms of cyanamide. Concentration of cyanamide: 1, 1.2 mole/l; 2, 2.4 × $10^{-1}$ mole/l; 3, 4.8 × $10^{-2}$ mole/l; 4, 9.5 × $10^{-3}$ mole/l; 5, 1.9 × $10^{-3}$ mole/l; 6, 0 (supporting electrolyte). Supporting electrolyte: 7.456 g KCl/l Sorensen's phosphate buffer solution (pH 6.75); sensitivity of galvanometer: 6.58 × $10^{-8}$ amp/mm; dropping mercury electrode: m = 1.67 mg/sec, t = 2.55 sec ($m^{2/3}$ $t^{1/6}$ = 1.65), h = 72 cm.

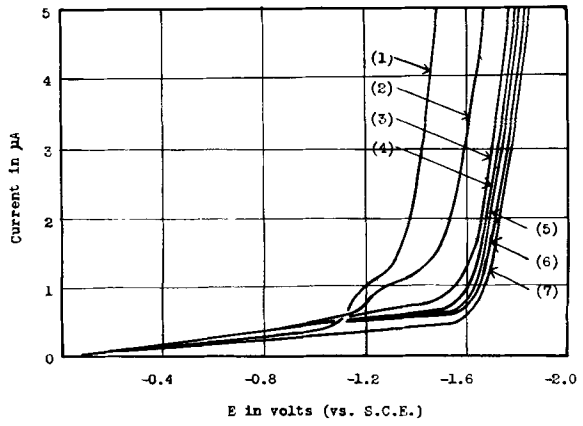


Fig. 6. Polarograms of formamidine sulfate. Concentration of formamidine: 1, 3.5 mole/l; 2, 1.2 mole/l; 3, 2.4 × $10^{-1}$ mole/l; 4, 4.8 × $10^{-2}$ mole/l; 5, 9.5 × $10^{-3}$ mole/l; 6, 1.9 × $10^{-3}$ mole/l; 7, 0 (supporting electrolyte). Supporting electrolyte: 7.456 g KCl/l Sorensen's phosphate buffer solution (pH 6.75); sensitivity of galvanometer: 6.58 × $10^{-8}$ amp/mm; dropping mercury electrode: m = 1.67 mg/sec, t = 2.55 sec ($m^{2/3}$ $t^{1/6}$ = 1.65), h = 72 cm.

Polarograms for cyanamide and formamidine sulfate are shown in Fig. 5 and Fig. 6.

Cyanamide: No distinct wave was detected prior to hydrogen discharge wave. The shift of H wave to a more positive potential with increasing concentration of cyanamide was observed.

Formamidine sulfate: No wave was detected up to the concentration of $10^{-2}$ M in Sorensen buffer (*p*H 6.75). However, in 1M solution, a wave appeared at $E^{1/2}$, —1.20 v (vs. S.C.E.). This is probably due to the reduction of undissociated molecule of formamidine, because this wave disappeared at *p*H 2.2 even in 1M solutions.[14] The shift of H wave to a more positive potential with increasing concentration of formamidine was also observed.

## Nature of Two Successive Reductions of Cyanamide

By combining the results of these studies, it is seen that two successive reductions of cyanamide have different natures from the viewpoint of electrochemical reduction. That is, the first step reduction is an exceptionally slow process and affected by the use of cathode material having catalytic action. On the other hand, the second step reduction may be a voltage-controlled one and affected by the use of cathode material having a high H overvoltage. Thus the most active cathode for one step may not be the most effective for another. For the over-all reduction process, Sn was the only effective cathode material among the cathodes used. This may be a problem in electro-organic reduction.

Moreover, the second step reduction was greatly influenced by *p*H. This is the reason for the necessity of adjusting the *p*H between 2-7 in order to carry out the reduction of cyanamide to the final state.

These gained support from the results of polarographic measurement.

## Conclusions

1. The reduction of cyanamide occurred at Pd smoothly to give formamidine in a fair yield. Tin

[14] This accounted for no occurrence of macroreduction below *p*H 2.

seems to have a mediocre activity toward this reduction, but the reduction could proceed beyond the formamidine level to methylamine and ammonia. Lead and mercury were not so effective for this reduction.

2. The reduction of formamidine, on the other hand, was effected by the use of cathodes having a high H overvoltage, such as Sn, Pb, Hg.

3. For the over-all reduction process, Sn was the only effective cathode material among the cathodes used in this study.

4. The formation of a large amount of formaldehyde at Hg suggested the existence of methylenediamine as second intermediate. This was further supported by the fact that methylenediamine gave methylamine by the reduction at Sn and other cathodes. The complete mechanism is as follows.

$$NH_2CN \xrightarrow{2H} NH_2 \cdot CH{=}NH \xrightarrow{2H}$$

$$NH_2 \cdot CH_2 \cdot NH_2 \xrightarrow{2H} NH_3 + CH_3NH_2$$

Main side reactions are

$$NH_2 \cdot CH{=}NH \xrightarrow{2H_2O} 2NH_3 + HCOOH$$

$$NH_2 \cdot CH_2 \cdot NH_2 \xrightarrow{H_2O} 2NH_3 + HCHO$$

Low yield of the final products was seen to be due to the hydrolysis of two intermediate compounds.

Manuscript received Oct. 24, 1957. This paper was prepared for delivery before the Buffalo Meeting, Oct. 6-10, 1957.

Any discussion of this paper will appear in a Discussion Section to be published in the June 1959 JOURNAL.

REFERENCES

1. K. Odo and K. Sugino, *This Journal*, **104**, 160 (1957).
2. K. Odo and E. Ichikawa, "A New Method for the Preparation of Cyanamide" given at the 9th meeting of the Chemical Society of Japan (1956).
3. K. Odo, E. Ichikawa, K. Shirai, and K. Sugino, *J. Org. Chem.*, **22**, 1715 (1957).
4. P. Knudsen, *Ber.*, **47**, 2698 (1914).

# The Measurement of Magnetic Fields in Aluminum Reduction Furnaces

**J. H. Kent**

*Research Department, British Aluminium Company Limited, Kinlochleven, Argyll, Scotland*

ABSTRACT

The efficient operation of aluminum reduction furnaces of capacities greater than about 50 KA is affected by electromagnetic forces acting in the molten bath. Measurement of the magnetic fields which give rise to these forces is made difficult because of the high temperature and corrosive nature of the molten bath. A technique is described which overcomes these difficulties. Results are given of measurements made in the baths of furnaces operating at 100 KA with different conductor layouts. It is shown how conductor layout design affects the magnetic characteristics of the furnace.

Electromagnetic forces acting in the molten bath, i.e., both metal and electrolyte, of an aluminum reduction furnace are known to affect the performance of the furnace and reduce its current efficiency (1, 2). Particularly is this so in large furnaces operating at currents above 50 KA. Briefly, their effect is to set the bath in motion and displace the molten metal layer, thus upsetting those stable conditions which are known to be essential for efficient operation. The forces can be divided into two main categories: those that arise from the interaction between the vertical component of the current and the horizontal component of the magnetic fields in the bath, and those that arise from the interaction between the horizontal component of the current in the molten metal and the vertical and horizontal components of the magnetic fields. To reduce the effect of electromagnetic forces it is necessary to reduce as much as possible and make suitably symmetrical the magnetic fields in the bath and to reduce the horizontal component of the current in the metal layer. The magnetic fields can be reduced and made suitably symmetrical by various arrangements of busbars and by magnetic shielding, such as the methods devised by Elektrokemisk (3, 4). Similarly, the horizontal component of the current in the molten metal layer can be reduced by various designs of current feed and collection such as, for instance, the methods of current collection devised by Thayer (5) or Elektrokemisk (6).

An exact calculation of the magnetic fields in the bath of a furnace is made extremely difficult by saturation and temperature effects in the steel parts of a furnace and steel structures close to it. For this reason, a design based on calculations alone may fall far short of achieving minimum magnetic fields in the bath. The use of scale models such as described by Böckman (7) overcomes many of the difficulties. However having laid down an experimental furnace in the furnaceroom to a design

based on calculation, perhaps aided by measurements on a model, a knowledge of the extent to which a reduction in the magnetic fields in the bath has been achieved can be gained only by measurement. At this stage, measurements of the fields in the bath will point the way to modifications that can be tried out on an experimental scale before standardizing the design. Such measurements present formidable difficulties owing to the extremely corrosive nature of the electrolyte and the temperature of the bath which approaches 1000°C.

### Method of Measurement

The difficulties of measuring field strength in a highly corrosive fluid at a high temperature can be overcome by using a suitably protected search coil. However, the necessary determination of field direction by the same means is far from straightforward. It was decided, therefore, to use an entirely different method to measure this quantity. A means was sought of introducing into the molten bath a soft iron needle that would first of all be free to align itself with the field direction and then set in that direction so that on removal from the bath it indicated the field direction, with respect to predetermined axes of reference, at the point at which it was placed in the bath. To achieve this, a small soft iron rod was suspended at its center in an aluminum cylinder attached to an aluminum rod (Fig. 1). The cylinder contained a synthetic resin in the liquid state. This was placed at the bottom of a graphite tube sealed at the bottom end, and alumina was packed round it to act as thermal insulation. The end of the tube containing the cylinder was then inserted under the anode of a working furnace so that the soft iron rod was freely suspended at the point at which the measurement was required and could take up the direction of the field at that point. After a predetermined time and at a predetermined temperature, the resin set hard, fixing in space the soft iron rod. The cylinder containing the rod was then removed and the field direction obtained by measuring the direction of the rod embedded in solid resin. The axis of the cylinder was used as a reference, its direction with respect to the furnace having been noted when the cylinder was in position in the furnace. Figure 1 shows the aluminum cylinder, the suspended soft iron rod and thermocouple for measuring the temperature rise. To the left is a soft iron rod set in the solid resin. Figure 2 shows the apparatus inserted under the anode of a working furnace.

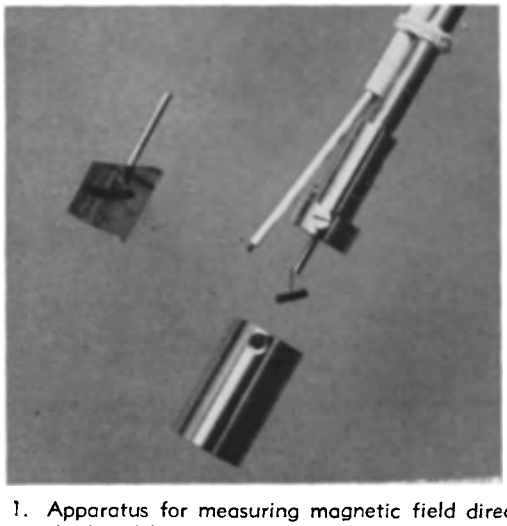

Fig. 1. Apparatus for measuring magnetic field directions in furnace baths. The suspension of the soft iron rod, its aluminum cylinder, and the rod set in the solid resin after removal from a furnace bath are shown. The thermocouple which serves to control the time of immersion in the bath is also shown.

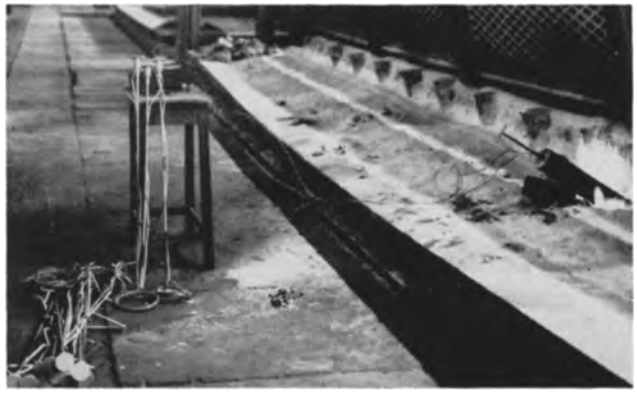

Fig. 2. Apparatus for measuring magnetic field directions in furnace baths set up beside a 100 KA furnace. To the base of the aluminum cylinders are attached asbestos disks to keep the cylinders central in the graphite tube which is shown inserted under the anode. A protected search coil is inserted into the tube to measure field strength.

The aluminum cylinder used to contain the resin is approximately 2.5 cm diameter by 4 cm deep and is bored out with a slight taper to facilitate the removal of the solid resin shape. Into the top of the lid of the cylinder is screwed an aluminum rod which protrudes from the top of the graphite tube when the cylinder is in position (Fig. 2). It has a pointer attached to it which is aligned with a mark on the cylinder. The lower end of the graphite tube is shown in Fig. 3. The rod is held centrally in the tube by a slotted Sindanyo cap fitting into the top of the tube. The resin chosen was the type that requires a catalyst and accelerator to set it. The catalyst was added some hours before the resin was required; the accelerator was stirred into the resin in the cylinder before assembling the apparatus to make a measurement. While placing the graphite tube in position in the furnace, care was taken to be sure that the tube was not making contact with the anode. When the cylinder reached the temperature at which it was known the resin would be set hard, about 3 min after insertion, the cylinder was removed and immediately placed against a current carrying busbar so that the soft iron rod would be obviously dislodged if the resin had failed to set.

Field strengths were measured in the bath with thermally insulated search coils used with a flux meter which had a full scale deflection of $7 \times 10^5$ line turns. Two coil sizes have been found necessary to measure sufficiently accurately the range of field strengths found in the baths of furnaces ranging from about 40 KA to 100 KA. Both coils measured approximately 8 cm x 1 cm x 1 cm. One carried 350 turns and the other 200 turns of fine enamelled copper wire. Figure 3 shows the details of construction

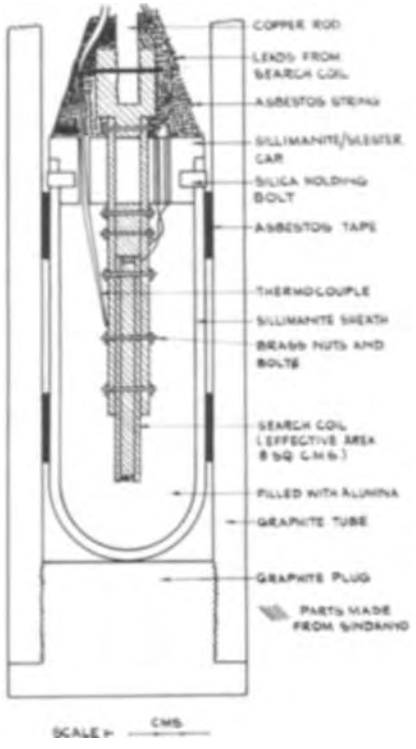


Fig. 3. Details of construction of a protected search coil

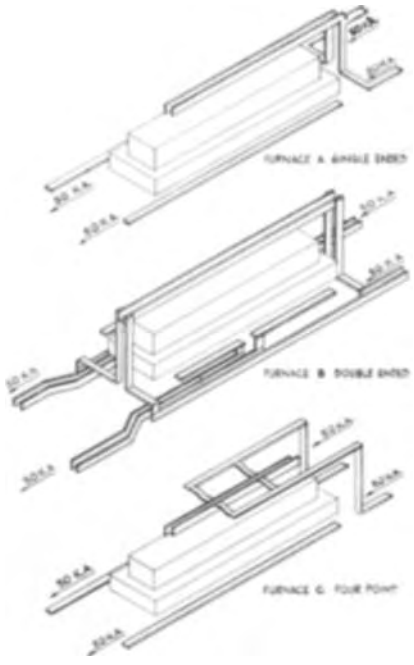

Fig. 4. Diagram of the three kinds of conductor layout of furnaces measured.

of the coils. The coil former and attachments are made of Sindanyo. A copper rod is screwed into the top of the coil assembly. The whole assembly is mounted in a ceramic cylindrical sheath packed with alumina. On rotating the copper rod about its axis the coil and its protective sheath rotate together. The sheath was made slightly smaller than the graphite tube used for holding the field direction measuring apparatus. The copper rod protrudes from the end of the graphite tube when the sheath is resting on the closed end of the tube. To make a measurement of the field strength in the bath of a furnace, the graphite tube is placed in the furnace so that the center of the coil coincides with a point at which the field direction has been measured. The coil is then rotated through 180° by twisting the copper rod. For the sake of accuracy it is best to find, by rapid trial and error, before making a measurement, that position of the coil with respect to its axis of rotation which gives a maximum deflection on the flux meter. This position must be noted so that the direction of the component of the field measured is known. Thus, knowing the total field direction, the total field strength can be calculated. To make rotation of the coil a simple and accurate operation, a circular scale was fitted to the copper rod. This scale fitted into the top of the graphite tube which had cut into it reference marks. The scale also served to keep the copper rod central in the graphite tube. A handle was fitted to the end of the rod protruding from the graphite tube.

The thermal insulation of the search coils described was sufficient to permit measurements to be made at several points in a furnace before having to cool the coils. For this reason, although the insulation could be improved upon, it was not found necessary to do so. The thermocouple shown in Fig. 3 was used to determine when the coil was getting too hot. A temperature of 250°C was found to be a suitable limit to work to. The increase in resistance of the coils did not appreciably increase the drift rate of the flux meter used.

The methods described above refer to measurements at points in the molten bath which can be reached by inserting a graphite tube under the anode. Measurements can be made on furnaces with prebaked anodes by inserting the tube from above between the anode blocks. Alternatively, in the case of Soderberg anodes, the tube can be passed down through holes in the anode. These can be made by baking in a steel tube fed from above into the soft paste so that it is gradually taken down to the working face as the anode is consumed.

### Results Obtained on 100 KA Furnaces

The field strengths and directions have been measured in the molten baths of several designs of furnaces. Figure 5 shows some results obtained on three 100 KA furnaces with different conductor layouts. Figure 4 indicates in principle the three kinds of conductor layouts chosen. Furnace A has the current fed to the anode at one end and collected from the cathode to busbars on either side of the furnace. These busbars therefore carry tapering currents building up to 50 KA each at the end opposite to that at which the current is fed to the anode. This arrangement has been termed "single-ended." In furnace B the current is divided equally, 50 KA being fed to each end of the anode. The current is collected half way down each side of the cathode so that there is a busbar extending half way down each side of the cathode carrying 50 KA. This arrangement has been termed "double-ended." Furnace C has the same cathode arrangement as furnace A but the current is fed in equal amounts to

four points of the twin anode busbar from busbars fed from one end, positioned on either side of the anode some distance above it. The points at which the anode is fed divide the anode at the quarter and three-quarter points along its length. This arrangement has been termed "four-point."

The double-ended arrangement, with various proportions of current fed to each end, is a simple and well-known means of reducing the fields at one end of the furnace and making the fields in the bath more symmetrical. It also helps to reduce horizontal currents in the metal. The four-point arrangement was designed to improve further the symmetry of the fields in the bath and at the same time to reduce the fields at the ends of the bath which were known to be responsible for unstable working conditions. It was also designed to reduce the vertical components of the field in the bath. This latter component interacts with horizontal currents in the metal which can have a very high current density, particularly when the distribution of current in the cathode or anode is temporarily upset. By reducing the vertical component of the field, those bath conditions essential to efficient operation are less easily disturbed by temporary upsets in current distribution.

The thick arrows in Fig. 5 show the direction of field in the horizontal plane. The thin arrows are vectors representing those electromagnetic forces acting at the points of measurement which are due to the interaction between the horizontal component of the magnetic field and the vertical current. It has been assumed, when calculating these vectors, that the current distribution in the cathode and anode is everywhere uniform and that the current is everywhere vertical. It will be appreciated that the vector picture so presented gives a general idea of the disposition of those forces due to the horizontal field and the vertical current acting in the metal layer of a furnace in good condition. This picture will be altered whenever the current distribution in the anode or cathode becomes uneven, to an extent dependent upon the degree of upset of current distribution.

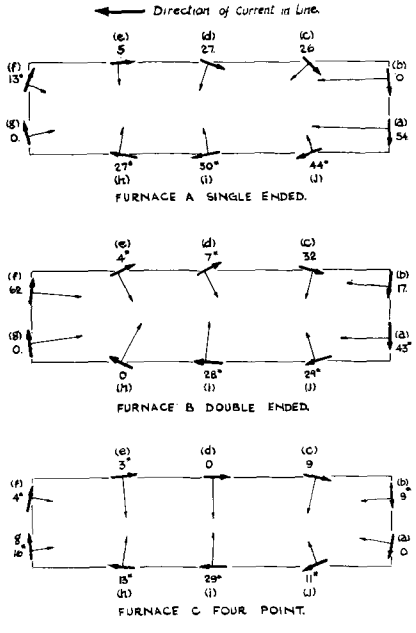


Fig. 5. Magnetic field measurements made beneath the edge of the anode in the molten metal layers of the three kinds of 100 KA furnaces shown in Fig. 4. The numbers represent the vertical components of the field in gauss. Where there is a * the conventional direction of this component is out of the paper (or upward in the furnace). Heavy arrows represent field direction in the horizontal plane; thin arrows are vectors representing those electromagnetic forces acting horizontally in the molten metal, which are due to the interaction between the horizontal field and the vertical current.

It can be seen from Fig. 5 that the forces associated with the double-ended arrangement are more suitably symmetrical than those associated with the single-ended arrangement, in that they act more toward the center of the furnace, tending to confine the metal layer within the shadow of the anode. This is achieved to a slightly better degree by the four-point arrangement. The figures shown opposite to the arrows in Fig. 5 give the strength in gauss of the vertical component of the field at the points. The forces arising from the interaction between the vertical component of the magnetic field and horizontal currents cannot, of course, be calculated without a knowledge of the horizontal currents. It should be stressed that these latter forces will only seriously upset furnace conditions and hence affect performance when there are large horizontal currents in the metal due to uneven current distribution in the anode or cathode. Such cur-

Table I*

| Busbar arrangement | Point of measurement | H (gauss) | F (gauss) | $\theta$° |
|---|---|---|---|---|
| Single-ended | a | 178 (101) | 186 | 17 |
| | b | 166 (101) | 166 | 0 |
| | c | 58 (86) | 64 | 24 |
| | d | 73 (70) | 78 | 20 |
| | e | 54 (58) | 54 | 5 |
| | f | 42 (37) | 44 | 17 |
| | g | 63 (37) | 63 | 0 |
| | h | 69 (58) | 74 | 22 |
| | i | 64 (70) | 81 | 38 |
| | j | 49 (86) | 66 | 42 |
| Double-ended | a | 106 (65) | 115 | 22 |
| | b | 98 (65) | 99 | 10 |
| | c | 69 (60) | 76 | 25 |
| | d | 68 (56) | 69 | 6 |
| | e | 79 (60) | 79 | 3 |
| | f | 107 (65) | 124 | 30 |
| | g | 113 (65) | 113 | 0 |
| | h | 96 (60) | 96 | 0 |
| | i | 92 (56) | 97 | 17 |
| | j | 67 (60) | 73 | 27 |
| Four-point | a | 74 | 74 | 0 |
| | b | 67 | 67 | 8 |
| | c | 85 | 85 | 6 |
| | d | 96 | 96 | 0 |
| | e | 94 | 94 | 2 |
| | f | 51 | 51 | 4 |
| | g | 56 | 58 | 16 |
| | h | 69 | 70 | 10 |
| | i | 76 | 81 | 20 |
| | j | 62 | 62 | 10 |

* Field strengths are given to the nearest whole number and therefore in some cases small values of $\theta$ do not show a difference between the horizontal (H) and total (F) field but the corresponding vertical component is given in Fig. 5. The numbers in parenthesis are calculated horizontal field strengths.

rents are not predictable and therefore a general pattern of the forces cannot be obtained. However, it can be seen that it is of great importance to reduce as much as possible the vertical component of the magnetic fields. It will be noticed that the four-point arrangement achieves a reduction in this component.

Table I completes the information by giving the strength in gauss of the total field F and the horizontal component H measured at the points indicated in Fig. 5. The angle $\theta$ that the field makes with the horizontal at these points is also given. All the points of measurement shown are in the molten metal layer just inside the edge of the anode. For comparison, the calculated horizontal components of the magnetic field at the points of measurement are given for the single-ended and double-ended furnaces. These values are shown in parentheses next to the measured values. The calculations were made by the usual method for fields due to finite conductors, taking into account tapering currents where applicable. Allowance was made in the calculations for the screening effect of the furnace box based on measurements made on empty furnace sites with and without the furnace box in position.

A lack of symmetry of the measured fields about the longitudinal axis will be noticed in each furnace. This is due to adjacent lines of furnaces and to the disposition of nearby steel structures. This asymmetry emphasizes the need for measurements of fields made in the baths of furnaces that have been designed to achieve certain reductions and modifications of the magnetic field characteristics in the bath. The results for the four-point arrangement, for example, point the way to further improvements in design which it would have been impossible to foresee by calculation and the need for which arises out of local conditions peculiar to the particular layout of the furnaceroom. It is of interest to note that the four-point arrangement did in fact show the expected improvement in the stability of operating conditions.

### Acknowledgments

The author gratefully acknowledges the cooperation of colleagues in the research laboratories and factories of The British Aluminium Co. Ltd.

Manuscript received March 17, 1958. This paper was prepared for delivery before the New York Meeting, April 27-May 1, 1958.

Any discussion of this paper will appear in a Discussion Section to be published in the June 1959 JOURNAL.

REFERENCES

1. R. Jötten, *Aluminio*, **22**, 751 (1953).
2. J. Wleügel, *ibid.*, **22**, 759 (1953).
3. Elektrokemisk A/S, British Pat. 740,025 Nov. 9, 1955.
4. Elektrokemisk A/S, British Pat. 754,697 Aug. 8, 1956.
5. C. S. Thayer (To Aluminum Company of America), Canadian Pat. 517,514 Oct. 18, 1955.
6. Elektrokemisk A/S, British Pat. 740,063 Nov. 9, 1955.
7. O. C. Böckman, "The Use of Scale Models for Investigating the Effect of Steel Parts on Magnetic Fields in Large Aluminium Furnaces," Rapports presentes au Congres International de l'Aluminium Paris 1954, p. 151 (La Societe Chimique de France et de l'Aluminium Francais).

# Destruction of Cyanide Wastes by Electrolytic Chlorination

**J. T. Byrne, W. S. Turnley, and A. K. Williams**

*The Dow Chemical Company, Rocky Flats Plant, Denver, Colorado*

ABSTRACT

By combining the principles of the well-known processes of alkaline chlorination and electrolytic oxidation it has been demonstrated that it is possible to obtain more effective treatment of concentrated cyanide wastes. Rock salt is added to the waste solution and hypochlorite is produced by electrolysis in the solution. Complete destruction of cyanide and destruction of most of the cyanate formed results at the rate of about 0.1 lb cyanide/kwhr. Plating metals can be recovered by cathodic deposition. During the course of the electrolysis, the discharge of cadmium ions at the cathode results in a lowering of the pH until the optimum value for cyanate oxidation is reached. Safety hazards are minimized since there is never more than a slight excess of chlorine present. A graphite anode can be used with no overvoltage problems and with a long life expectancy.

A number of methods for treating cyanide wastes from metal finishing operations have been described (1, 2). When the water supply is not adequate for dilution and ventilation limitations do not permit volatilization of hydrogen cyanide, the most widely used methods appear to be chlorination and electrolytic oxidation.

Chlorination is accomplished (3) either by the addition of chlorine gas or of hypochlorites to the waste stream. The first stage of the destruction proceeds rapidly by the reaction

$$CN^- + ClO^- \rightarrow CNO^- + Cl^-$$

or

$$CN^- + Cl_2 + 2OH^- \rightarrow 2Cl^- + CNO^- + H_2O$$

The second stage involving the oxidation of cyanate to carbon dioxide and nitrogen is considerably slower

$$2CNO^- + 3ClO^- + H_2O \rightarrow 2CO_2 + N_2 + 3Cl^- + 2OH^-$$

or

$$2CNO^- + 3Cl_2 + 4OH^- \rightarrow 2CO_2 + N_2 + 6Cl^- + 2H_2O$$

The stoichiometric reagent requirements are 2.73 parts of chlorine and 3.08 parts of sodium hydroxide per part of cyanide for the first stage and an additional 4.09 parts of chlorine and 3.08 parts of sodium hydroxide per part of cyanide for the second stage. In practice, at least 10% excess reagents are added to speed the reactions.

Either sodium hypochlorite or calcium hypochlorite could be used instead of chlorine gas for this process, but these must be added as solutions. An excessive sludge of calcium hydroxide forms when solid calcium hypochlorite is used. In cadmium cyanide solutions, the cadmium is precipitated as a carbonate sludge if either sodium or calcium hypochlorite solution is used. The alkaline chlorination process is rapid and it successfully reduces the cyanide concentration to below 1 ppm.

Electrolytic oxidation of cyanide has been attributed (4) principally to oxidation by the oxygen liberated at the anode. The method produces no sludge and plating metals can be recovered on the cathode. Available operating data are meager, but it appears that the oxidation of cyanide to cyanate takes place at the rate of about 0.3 lb/kwhr using carbon steel electrodes (5). Selection of the anode presents a problem since steel and nickel are attacked by cyanide, and graphite has a high overvoltage for oxygen evolution. The method suffers the additional disadvantage (6) that it does not result in complete destruction of the cyanide and apparently does not destroy cyanate at all.

Despite the wide use of alkaline chlorination and of electrolytic oxidation, no mention has been made of the combination of the principles of these two methods to produce a treatment combining the advantages of each.

## Experimental

*Apparatus.*—The laboratory experiments were carried out using a battery charger for the source and powerstat for control of the applied voltage. In the plant experiments (runs 4 and 5, Table I) a 150-amp full wave rectifier was used.

A graphite anode rod and a graphite, cadmium, or iron cathode rod were spaced about ¼ in. apart. The Pyrex electrolysis beaker was equipped with a peripheral cooling coil which maintained the temperature of the solution at 40°-50°C during most of the electrolysis. All runs were stirred thoroughly during electrolysis. The plant experiments (runs 4 and 5) were run without cooling, and the temperature reached about 80°C.

*Procedure.*—Prior to electrolysis, each solution was analyzed for cyanide with a p-dimethylaminobenzalrhodanine indicator (7), and for cadmium using a polarographic method. The solutions were saturated with sodium chloride by adding rock salt, and the electrolyses were carried out at the specified voltage and current. During the electrolyses, samples were taken for cadmium, cyanide, and cyanate analyses. The cyanate analyses were performed (8) by decomposing the cyanate into ammonia during a Kjeldahl digestion, distilling the ammonia, and developing color with Nessler's reagent.

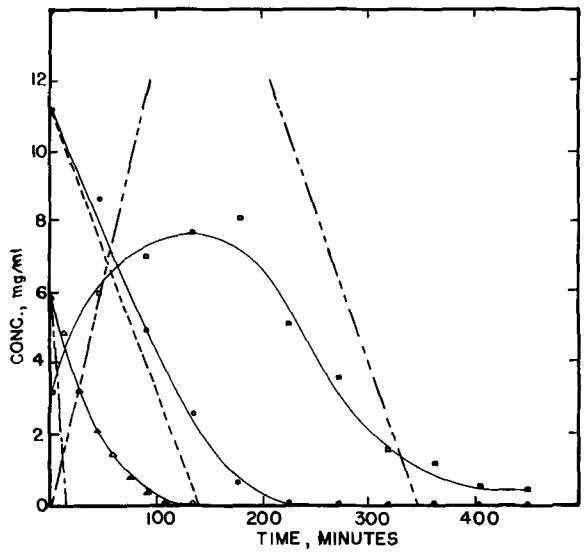


Fig. 1. Removal of cyanide, cyanate, and cadmium from plating solution during electrolytic generation of hypochlorite at 4 amp, 4.25 v, Run No. 9. O mg $CN^-$/ml (exp); □ mg $CNO^-$/ml (exp); △ mg $Cd^{++}$/ml (exp); ------ mg $CN^-$/ml (theor. at 100% current eff.); —— — —— mg $CNO^-$/ml (theor. at 100% current eff.); —— — —— mg $Cd^{++}$/ml (theor. at 100% current eff.).

*Results.*—The results of all electrolyses for which data are available are shown in Table I. Detailed studies of runs 9 and 10 were made by sampling the solution at 45-min intervals and analyzing for cyanide, cyanate, and cadmium. Results are plotted in Fig. 1. These curves show the ultimate removal of the cyanide, cyanate, and cadmium from the solution.

Cadmium proved to be the most satisfactory cathode material. When graphite was used (run No. 1), the cadmium deposit did not adhere to the cathode. When iron was used, the solution became contaminated with ferrocyanide which interfered with the cyanide analysis. Uniform and adherent deposits of cadmium were obtained in runs 4 to 11.

Current densities ranged from 72 to 470 amp/ft$^2$ as shown by the areas and currents listed in Table I.

Measurements of *p*H during run 9 showed a decrease from 10.9 at the start to 9.1 after 3.5 hr. The *p*H remained between 8.9 and 9.1 for the remaining 4 hr. The initial decrease is due to the consumption of two equivalents of hydroxyl ion per mole of chlorine in the oxidation of an equivalent of cyanide to cyanate. This is only partially compensated by the production of hydroxyl ions at the cathode, since one-third of an equivalent of cadmium is reduced per equivalent of cyanide. Qualitative confirmation of this explanation was obtained from a titration curve of the plating solution which showed a *p*H of 8.8 in a buffer region after sulfuric acid, in an amount equivalent to the cadmium, had been added.

During the oxidation of one equivalent of cyanate to carbon dioxide and nitrogen, 4/3 equivalents of hydroxyl ion are required per mole of chlorine. This would tend to lower the *p*H further if the cyanate oxidation were not so slow that an appreciable ex-

Table I. Effect of cell conditions on electrolytic chlorination of cyanide

| Run No. | Volume (ml) | Initial $CN^-$ (ppm) | Final $CN^-$ (ppm) | Time (hr) | Electrode area ($in.^2$) | Cathode | Amp | Volt |
|---|---|---|---|---|---|---|---|---|
| 1 | 300 | 1800 | 10 | 1.5 | 2 | Graphite | 1 | — |
| 2 | 300 | 1800 | 12 | 0.75 | 2 | Iron | 4 | — |
| 3 | 300 | 1800 | 16 | 0.25 | 2 | Iron | 5 | — |
| 4 | 2000 | 55,000 | 254 | 7 | 44 | Cadmium | 140 | 9–10 |
| 5a | 8000 | 55,000 | 8000 | 2 | 44 | Cadmium | 80–150 | 10–11 |
| b | 8000 | 55,000 | 4200 | 5 | 44 | Cadmium | 80–150 | 10–11 |
| 6 | 35 | 55,000 | 17 | 3 | 2 | Cadmium | 4 | 4–4.5 |
| 7 | 35 | 55,000 | 38 | 2 | 3 | Cadmium | 4 | 4–4.5 |
| 8 | 35 | 55,000 | 32 | 3 | 6 | Cadmium | 4 | 4–4.5 |
| 9 | 400 | 11,050 | <5 | 8 | 3 | Cadmium | 4 | 4–4.5 |
| 10 | 400 | 8690 | <5 | 7.5 | 3 | Cadmium | 4 | 4–4.5 |

cess of chlorine (and hydroxyl) is produced at the electrode. These *p*H changes keep the system close to the recommended ranges of 10-12.5 for the oxidation of cyanide and 7.5-9 for the oxidation of cyanate (3).

## Discussion

*Power.*—Commercial hypochlorite cells produce about 0.34 lb (3 eq.) of $ClO^-$/kwhr, while commercial chlorine cells achieve a production of about 0.8 lb (5 eq.) of $Cl_2$/kwhr (8). In the chlorine cell the product is continuously taken off as gaseous chlorine, but in the hypochlorite cell the product is held in the form of soluble hypochlorite and the yield is diminished by side reactions.

The oxidation of 1 lb of cyanide to cyanate requires 2.73 lb of chlorine, and the oxidation of the cyanate formed requires an additional 4.09 lb of chlorine. Therefore, if all the chlorine produced in a chlorine cell were used for reaction with cyanide, it would be possible to convert 0.29 lb of cyanide to cyanate per kwhr and to completely destroy 0.12 lb/kwhr.

Within the uncertainty of the current measurement, both runs 9 and 10 proceeded at the rate of 0.08-0.10 lb of cyanide destroyed per kwhr for the first 5 hr. The last stages of cyanate decomposition proceeded much more slowly. The toxicity of cyanate is reported (2) to be some 1000 times less than that of cyanide and so, in most cases, essentially complete destruction of cyanide and 90%, or less, destruction of cyanate would be sufficient.

*Cell design.*—As in the commercial production of hypochlorite and chlorine, the most satisfactory anode material is graphite. If a plating metal is to be recovered on the cathode, any material that accepts a good plate of the plating metal can be used for a cathode.

The electrodes should be arranged to give a minimum anode-cathode spacing, e.g., ¼ to ½ in. is desirable. With this spacing it should be possible to produce 1000-2000 amp by applying 3.5 to 4.5 v/cell with a current density of 100-500 amp/$ft^2$. The current density must be selected to produce an adherent cathode deposit of recoverable metal.

Each cell requires stirring and an operating temperature between 40° and 50°C. Higher temperatures favor the formation of chlorate rather than hypochlorite.

Ventilation is necessary to prevent the accumulation of hydrogen and to remove small amounts of toxic gases such as chlorine, cyanogen chloride, and hydrogen cyanide.

## Acknowledgment

The authors wish to thank L. C. Farrell and R. W. Hawley for their continued interest and encouragement.

This work was done under AEC Contract No. AT(29-1)-1106.

Manuscript received Sept. 27, 1957.

Any discussion of this paper will appear in a Discussion Section to be published in the June 1959 JOURNAL.

## REFERENCES

1. Ohio River Valley Water Sanitation Committee, "Methods for Treating Metal-Finishing Wastes," January 1953.
2. B. F. Dodge and D. C. Reams, American Electroplaters Society Research Report Serial No. 14 (1949).
3. B. F. Dodge and W. Zabban, American Electroplaters Society Research Report Serial No. 22 (1952).
4. G. H. Clevenger and M. L. Hall, *Trans. Am. Electrochem. Soc.*, **24**, 271 (1913).
5. L. B. Sperry and M. N. Caldwell, *Plating*, **36**, 343, 412 (1949).
6. R. W. Oyler, *ibid.*, **36**, 341 (1949).
7. B. F. Dodge, W. Zabban, E. J. Serfass, and R. B. Freeman, American Electroplaters Society Research Report Serial No. 19 (1952).
8. H. J. Creighton and W. A. Koehler, "Principles and Applications of Electrochemistry, Vol. II, Applications," 2nd ed., p. 275, John Wiley & Sons, Inc., New York (1944).

# Brief Communication

## Reaction of Hydrogen with Uranium

W. M. Albrecht and M. W. Mallett

*Ferrous Metallurgy Division, Battelle Memorial Institute, Columbus, Ohio*

In our paper, "Reaction of Hydrogen with Uranium," published in the July 1956 JOURNAL, pp. 404-409, certain apparent anomalies exist in the kinetics data. The following discussion may be considered an addendum to that paper. It will be noted in Fig. 6 of our paper that for each nominal pressure series the total system pressure actually was increased experimentally for runs above 250°C. In spite of this, the reaction rates decreased with increasing temperature.

It is stated in the paper that the significance of the pressure dependency of the reaction is not known. Also, it is implied that consideration of the dissociation pressure of the hydride product is important to the interpretation of the rate data. Further work with other metal-hydride systems has emphasized the great need for interpretive studies of reactions where the reaction rates are a function of both pressure and product composition. In view of this, the basic premises of kinetic studies were reviewed.

In the simplest and most often encountered case of the oxidation of metals, the kinetics of formation of a saturated phase on the metal surface is determined. Characteristic of this phase is its very low dissociation pressure, often $<10^{-6}$ mm Hg. In manometric systems where the limit of measurement is of the order of 0.1 mm Hg, such pressures are undetectable. Under these circumstances, the composition of the reaction product (if only one is formed) is constant under all experimental conditions of pressure.

In contrast with this, we have the metal hydrides which have comparatively high dissociation pressures of several millimeters of Hg or several atmospheres, depending on the hydride and the temperature. Thus, unless the system pressure equals or exceeds the dissociation pressure, the desired (saturated) reaction product is not formed. An additional complication is that many of the metal-hydride systems show wide solid-solubility regions of metal dissolved in a terminal hydride phase. In such systems, reactions carried out at constant system pressures yield products which vary in composition with temperature. Therefore, the kinetic data obtained in this manner show no recognizable relationship. However, orderly data should result if, first, the composition of the surface product (solid solution) is fixed. Then, the experiments are carried out at system pressures corresponding to the dissociation pressures of the selected product at the experimental temperatures. If experiments are carried out in this manner for several product compositions, the effect of the composition variable may be evaluated.

In the study of hydrogen and uranium, the effect of pressure on the reaction was investigated but no attempt was made to determine the effect of the composition variable on the reaction. In the range 100° to about 250°C, the reaction rate depended on $(p_{H_2})^{3/4}$. This experimental value agrees fairly well with the theoretical value of $(p_{H_2})^{2/3}$ for the dissociation of $UH_3$. Using these data and extrapolated equilibria data from the study of Gibb, *et al.* (1), calculations have been made to determine the variation of the reaction rates with temperature of certain compositions of uranium hydride. Constants for interpolated pressure equations are given in Table V.

The isopleths described by the values in Table V are plotted in Fig. 9 with the experimental rate data. An activation energy of 8600 cal/mole was obtained for the formation of $UH_{2.999}$. A similar energy was obtained for $UH_{2.991}$. Fortuitously, in all cases, two or three rate values were obtained at temperature and pressure values close to those specified by an isopleth equation. The isopleths are divergent in

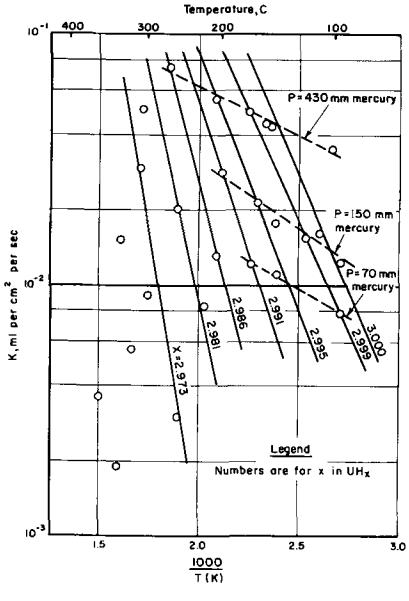


Fig. 9. Kinetics of reaction to produce constant compositions of $UH_x$.

Table V. Pressure equations for $UH_{2.97}$ to $UH_{3.0}$

| Values of $A$ and $B$ for equation, $\log_{10}P_{atm} = (-A/T) + B$ | | |
|---|---|---|
| $x$ in $UH_x$ | $A$ | $B$ |
| 2.973 | 3710 | 6.11 |
| 2.981 | 3340 | 5.70 |
| 2.986 | 3030 | 5.36 |
| 2.991 | 2660 | 4.96 |
| 2.995 | 2310 | 4.56 |
| 2.999 | 1860 | 4.02 |
| 3.000 | 1730 | 3.90 |

agreement with the data of Gibb. It is recognized that the long extrapolation from the high-pressure data of Gibb may introduce some error to this treatment. However, there appears to be no mistaking the indication that the planning and interpretation of kinetic studies of reactions producing solid solutions should be based on exact knowledge of the temperature-pressure-composition equilibria of the product involved.

Manuscript received June 16, 1958.

Any discussion of this paper will appear in a Discussion Section to be published in the June 1959 JOURNAL.

REFERENCE

1. T. R. P. Gibb, J. J. McSharry, and H. W. Kruschwitz, Jr., *J. Am. Chem. Soc.*, **74**, 6203 (1952).

## June 1959 Discussion Section

A Discussion Section, covering papers published in the July–December 1958 JOURNALS, is scheduled for publication in the June 1959 issue. Any discussion which did not reach the Editor in time for inclusion in the December 1958 Discussion Section will be included in the June 1959 issue.

Those who plan to contribute remarks for this Discussion Section should submit their comments or questions in triplicate to the Managing Editor of the JOURNAL, 1860 Broadway, New York 23, N. Y., *not later than March 2, 1959*. All discussion will be forwarded to the author, or authors, for reply before being printed in the JOURNAL.

# Investigation of Electrochemical Characteristics of Organic Compounds

## II. Aromatic Nitroso Compounds

**R. Glicksman and C. K. Morehouse**

*RCA Laboratories, Radio Corporation of America, Princeton, New Jersey*

ABSTRACT

Aromatic C-nitroso compounds operate at higher potentials than the corresponding nitro compounds, as well as the various oximes, N-nitroso, and N-oxide organic compounds tested. In addition, the electrode potential during current flow is *p*H dependent and is affected by the type and position of the substituted group on the aromatic ring. Coulometric reduction studies of various p-nitrosophenol and p-nitrosodialkylamino compounds indicate reduction of these compounds takes place to the amino stage with a resultant 4-electron change per —NO group. The high theoretical ampere-minute capacity of the aromatic C-nitroso compounds, along with their high flat operating potentials, show these materials to have considerable promise for use as cathode materials in primary cells, when coupled with a magnesium anode.

Although the majority of oxidation-reduction processes involving organic compounds are not reversible from the thermodynamic standpoint, there are some notable exceptions. Conant and Lutz (1) examined nitrosobenzene and found it to be a reversible electrode, having an electrode potential of +0.605 v in a 0.2*N* HCl-acetone solution at 25°C, while Lutz and Lytton (2) determined the potentials of a series of substituted nitrosobenzene-phenylhydroxylamine systems and found them to be generally reversible.

The favorable potential of this reversible system, along with the high theoretical ampere-minute per gram capacities of nitroso compounds, suggests the use of these materials as cathodes in primary batteries. Previous studies of the electrochemical characteristics of aromatic nitro compounds (3) and their use as cathodes in primary cells (4) have demonstrated the practicability of organic materials as electrodes in galvanic cells.

In this paper the electrochemical properties of various nitroso compounds are presented, while a subsequent paper will deal with the use of the nitroso compounds as cathodes in actual primary cells.

### *Experimental*

Because of the irreversible nature of the electrode reaction and polarization effects encountered during current flow, the electrochemical characteristics of many inorganic and organic compounds often cannot be predicted by thermodynamic calculations and a knowledge of their physical and chemical properties. A technique previously described by the authors (5) has been used to measure the operating potential during current flow and the coulombic capacity of various aromatic nitroso compounds. This technique consists in discharging at a constant current in a large volume of electrolyte a 0.5-g sample of the aromatic nitroso cathode material mixed with 10% Shawinigan acetylene black. The change in cathode potential with time was measured with a L&N Type K potentiometer using a saturated calomel reference electrode. The measured potentials were corrected for the *IR* drop associated with the apparatus and electrolyte by means of an oscillographic technique (6).

All half-cell potential data reported in this paper are referred to the normal hydrogen scale and include a liquid junction potential, which in most cases is small and can be neglected.

For most of the measurements an aqueous magnesium bromide electrolyte and a magnesium anode were used, while in studying the effect of *p*H on potential a zinc anode was employed with the acidic $NH_4Cl$-$ZnCl_2$-$H_2O$ and basic NaOH-$H_2O$ electrolytes.

### General Cathode Half-Cell Potential Relationships of Nitroso and Related Organic Compounds

*C-nitroso and nitrosamine compounds.*—Nitroso compounds contain the nitroso group —N = O attached to a carbon atom, and have two properties which distinguish them from the nitrosamines, compounds in which the nitroso group is attached to a nitrogen atom. These are, first, the blue or green color of the true monomolecular nitroso compounds in all states of aggregation and, second, the tendency of the compounds to associate to colorless bimolecular complexes according to the nature of the other groups in the molecule.

Both the N-nitroso (nitrosamines) and C-nitroso compounds can be reduced electrolytically and by chemical means using Zn or Sn in dilute acetic acid solution to the substituted hydrazine and amine respectively (7, 8).

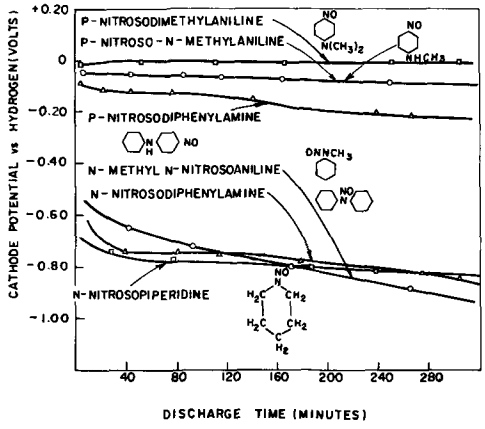


Fig. 1. Cathode half-cell potential of various C- and N-nitroso compounds discharged in 250 g/l $MgBr_2 \cdot 6H_2O$ electrolyte at a rate of 0.030 amp/g.

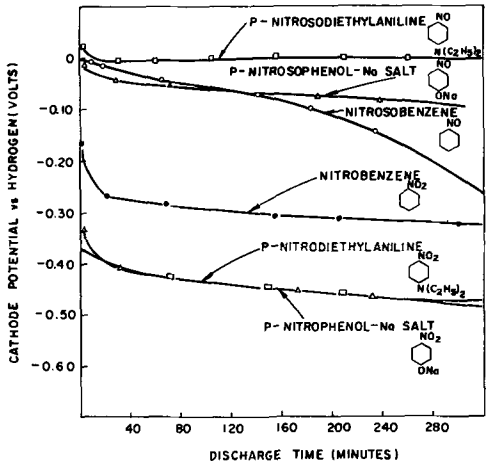


Fig. 2. Cathode half-cell potential of various C-nitroso compounds and their corresponding nitro compounds discharged in 250 g/l $MgBr_2 \cdot 6H_2O$ electrolyte at a rate of 0.030 amp/g.

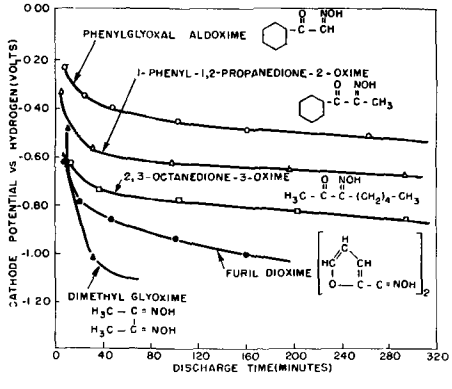


Fig. 3. Cathode half-cell potential of various oxime compounds discharged in 250 g/l $MgBr_2 \cdot 6H_2O$ electrolyte at a rate of 0.030 amp/g.

Presented in Fig. 1 are discharge data showing the change in half-cell potential with time as N-nitroso and C-nitroso compounds are discharged at a rate of 0.030 amp/g of material in an aqueous solution of 250 g/l of $MgBr_2 \cdot 6H_2O$. The N-nitroso compounds under these conditions of discharge operate at voltages of 0.6-0.7 v lower than their corresponding C-nitroso compounds. This relationship between the two types of nitroso compounds has been found to hold for all compounds tested.

*Aromatic nitro and C-nitroso compounds.*—Haber and Schmidt (9) showed that in the electrolytic reduction of nitrobenzene the basic steps of reduction are as follows:

$$C_6H_5NO_2 \rightarrow C_6H_5NO \rightarrow C_6H_5NHOH \rightarrow C_6H_5NH_2$$

The fact that nitrosobenzene was reduced to phenylhydroxylamine too readily to be capable of isolation as such indicated that nitrosobenzene was a stronger oxidizing agent than nitrobenzene.

Other evidence of the stronger oxidizing power of nitroso compounds has been reported by Glasstone and Hickling (10) who give depolarization potentials[1] of various organic compounds, which show that, as a class, nitroso compounds have potentials 0.2-0.3 v higher than nitro compounds. In addition, from polarographic studies of p-nitrosophenol and p-nitrophenol, Astle and McConnell (11) found that at a pH of 4 the half-wave potential of p-nitrosophenol is 0.48 v higher than that of the p-nitrophenol.

Presented in Fig. 2 are discharge data for various C-nitroso compounds and their corresponding nitro compounds. The C-nitroso compounds under these conditions of discharge operate at voltages of 0.2-0.4 v higher than the corresponding nitro compounds. These data show that C-nitroso compounds are stronger oxidizing agents than the corresponding nitro compounds and as cathode materials for primary batteries should operate at higher potentials during discharge.

*Oximes and N-oxide compounds.*—Aliphatic nitroso compounds RNO are known only when R is a tertiary radical;[2] consequently, reactions which would be expected to give primary or secondary nitroso compounds give oximes instead. Hence, these are sometimes called isonitroso compounds. The grouping $=CHNO$ becomes $-\overset{|}{C}=NOH$, a complete enolization.

Discharge data obtained on various oxime compounds are presented in Fig. 3. While a direct comparison cannot be made between nitroso and oxime type compounds, it is seen that the oximes operate at lower discharge potentials than the C-nitroso compounds tested under comparable conditions. It is significant that those compounds having a carbonyl group adjacent to the $-\overset{|}{C}=NOH$ group operate at higher cathode potentials than the other oximes tested. This is in agreement with the "electronegativity rule of reduction potentials" (12) which states that the organic compounds are more easily reduced as more electronegative groups are substituted in the same compound.

The amine oxides may be regarded as derivatives of the tautomeric form of hydroxylamine $H_2N \rightarrow O$. They are closely related to the tertiary amines from which they can be obtained by oxidation. Amine

[1] In the determination of "depolarization values," a definite quantity of the reducible substance is added to a given electrolyte containing a reversible hydrogen electrode, and the fall of potential of the latter is determined. The depolarization value so obtained gives an indication of the oxidizing power of the substance (10).

[2] An exception to this generalization is the compound 1-chloro-1-nitrosoethane, which exists as a colorless dimer.

Table I. Capacity data for various aromatic C-nitroso compounds

| Cathode material | Ampere-minute per gram capacity Theoretical | Obtained* | Efficiency (%) |
|---|---|---|---|
| Conventional inorganic cathodes | | | |
| Manganese dioxide | 18.5 | 10.3 | 65.6† |
| Mercuric oxide | 14.9 | 10.4 | 69.8 |
| p-Nitrosophenol cathodes | | | |
| 4-nitrosophenol | 52.2 | 48.2 | 92.3 |
| 4-nitroso-3-methyphenol | 46.9 | 40.0 | 85.3 |
| 5-nitroso-8-hydroxyquinoline | 36.7 | 31.5 | 85.8 |
| p-nitrosophenol-Na salt | 44.3 | 23.8 | 53.7 |
| p-Nitrosodialkylamino cathodes | | | |
| p-Nitrosodimethylaniline | 42.9 | 37.4 | 87.2 |
| 4-nitroso-3-methyldimethylaniline | 39.2 | 36.5 | 93.1 |
| 4-nitroso-3-hydroxyacetanilide | 35.7 | 22.5 | 63.0 |
| 4-nitroso-3-hydroxydimethylaniline | 38.7 | 30.8 | 79.6 |
| Nitrosonaphthol cathodes | | | |
| 4-nitroso-1-naphthol | 37.1 | 18.4 | 49.6 |
| 2-nitroso-1-naphthol | 37.1 | 9.8 | 26.4 |
| 1-nitroso-2-naphthol | 37.1 | 9.6 | 25.9 |
| 1-nitroso-2-naphthol-3,6-disulfonic acid—disodium salt | 17.1 | 11.8 | 69.0 |
| Mononitroso cathodes | | | |
| nitrosobenzene | 60.0 | 37.5 | 62.5 |
| o-nitrosotoluene | 53.1 | 24.2 | 45.6 |
| 4-nitrosoresorcinol | 46.2 | 2.0 | 4.3 |
| Dinitroso cathodes | | | |
| p-dinitrosobenzene | 94.6 | 26.4 | 27.9 |
| 2,4-dinitrosoresorcinol | 69.0 | 24.1 | 34.9 |
| Nitronitroso cathodes | | | |
| m-nitronitrosobenzene | 105.8 | 96.8 | 91.5 |
| 3-nitro-4-nitrosotoluene | 96.9 | 77.1 | 79.6 |
| Nitrosopyrimidine cathodes | | | |
| 2,4,6-triamino-5-nitrosopyrimidine | 41.8 | 28.8 | 68.9 |

* Computed from half-cell potential data in Fig. 5-11, using −0.40 v as cut off potential.
† Efficiency calculation based on 85% $MnO_2$ content.

oxides can be reduced to tertiary amines by reagents such as Sn and HCl. Ochiai (13) has shown that a number of pyridine-N-oxides and quinoline-N-oxides can be reduced polarographically with difficulty. Compounds of this type, such as pyridine-N-oxide and 2-piccoline-N-oxide, were found to be poor oxidizing agents and to operate at potentials too low to be measured by this experimental technique.

*Effect of electrolyte composition on the cathode half-cell potential of C-nitroso compounds.*—According to Latimer (14) the reaction involving the reduction of nitrosobenzene to phenylhydroxylamine can attain a reversible equilibrium, and the potential of the couple is as follows:

$$C_6H_5NO + 3H^+ + 2e^- = C_6H_5NH_2OH^+ \quad E^\circ = 0.60 \text{ v}$$

Phenylhydroxylamine, once formed, can react with the unreduced nitrosobenzene forming side products, or it can be reduced directly to aniline, in accordance with Haber and Schmidt's scheme.

$$C_6H_5NH_2OH^+ + 2H^+ + 2e^- = C_6H_5NH_3^+ + H_2O \quad E^\circ = 1.20 \text{ v}$$

It is seen from the above two reactions, that the electrode potential is influenced by the $H^+$ ion concentration.

Discharge data obtained on 2,4-dinitrosoresorcinol and p-nitrosodiethylaniline in three electrolytes of different *p*H are shown in Fig. 4. As expected, the discharge potentials of the nitroso compounds increase as the *p*H of the electrolyte is decreased. This behavior is typical of the aromatic C-nitroso compounds and the other N-nitroso and oxime compounds tested.

## Half-Cell Potential Studies of Various C-Nitroso Compounds

Half-cell discharge data obtained on various aromatic C-nitroso compounds discharged continuously at a 0.005 amp/g rate in a $MgBr_2 \cdot 6H_2O$ (250 g/l) electrolyte are shown in Fig. 5-11 inclusive.

The capacities obtained to an arbitrary potential of −0.40 v (vs. S.H.E.) along with their electrode efficiencies are presented in Table I together with

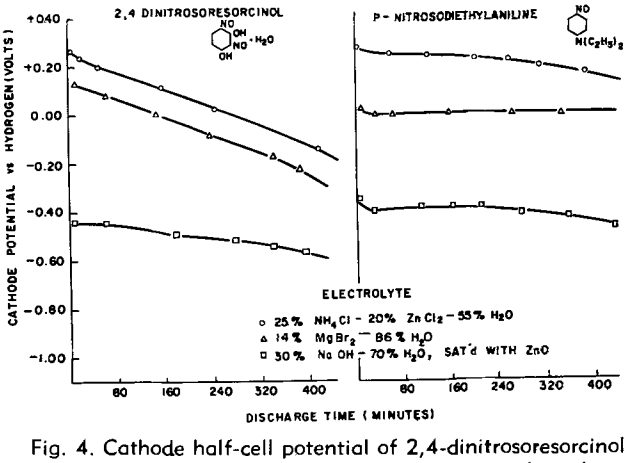


Fig. 4. Cathode half-cell potential of 2,4-dinitrosoresorcinol and p-nitrosodiethylaniline discharged in various electrolytes at a rate of 0.030 amp/g.

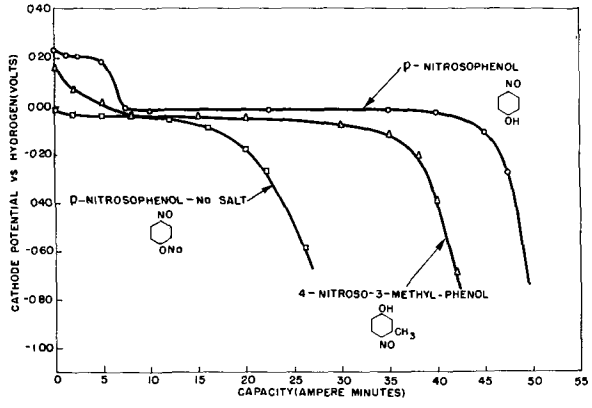


Fig. 5. Half-cell potential studies of various p-nitrosophenol derivatives discharged in 250 g/l $MgBr_2 \cdot 6H_2O$ electrolyte at a rate of 0.005 amp/g.

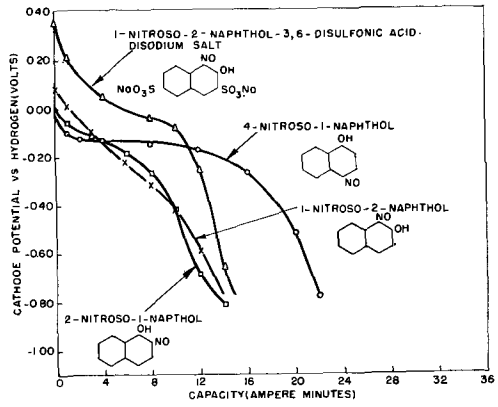


Fig. 6. Half-cell potential studies of various nitrosonaphthol derivatives discharged in 250 g/l $MgBr_2 \cdot 6H_2O$ electrolyte at a rate of 0.005 amp/g.

the theoretical capacities of these materials expressed in ampere-minutes per gram.

*Nitrosophenols and related compounds.*—Presented in Fig. 5 are half-cell discharge curves of various p-nitrosophenol derivatives. It is seen that, with the exception of the first 5-10 amp-min of discharge, these compounds have a flat operating potential throughout the course of their discharge. The high initial potential, which persists for a short time, appears to be characteristic of the hydroxyl group, as evidenced by the fact that other types of C-nitroso compounds, as well as p-nitrosophenol-Na salt, show no such behavior.

A possible explanation for this is that p-nitrosophenol is a tautomer of quinone monoxime

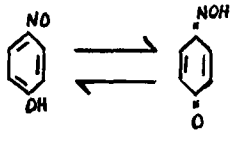


and in the free state the substance is actually present as the quinone monoxime while in the salts as derivatives of nitrosophenol, the phenolic H being more acidic than the oximic H atom. This being the case the initial potential would be due to the quinone monoxime; however, during the course of the discharge, hydroxide ion is formed and the solution becomes weakly basic, and at this stage the cathode potential would be that of the nitrosophenol salt.

The effect of adding a $-CH_3$ group to the 3 position of 4-nitrosophenol is to lower the operating potential of the parent compound by approximately 0.03 v. This type of behavior is consistent with that found for the aromatic nitro compounds (3), where the addition of an electron-repelling group to the benzene ring results in a compound having a lower discharge potential than its parent compound.

The effect of electron-attracting groups on the cathode potential is shown for the nitrosonaphthol compounds in Fig. 6. The addition of two $-SO_3Na$ groups to the naphthalene ring to form 1-nitroso-2-naphthol-3,6,-disulfonic acid disodium salt results in a compound having a discharge potential 0.2 v higher than the unsubstituted 1-nitroso-2-naphthol.

Presented in Fig. 7 are discharge curves for three types of aromatic hydroxy-nitroso compounds. It is seen that the greater the aromaticity of the ring

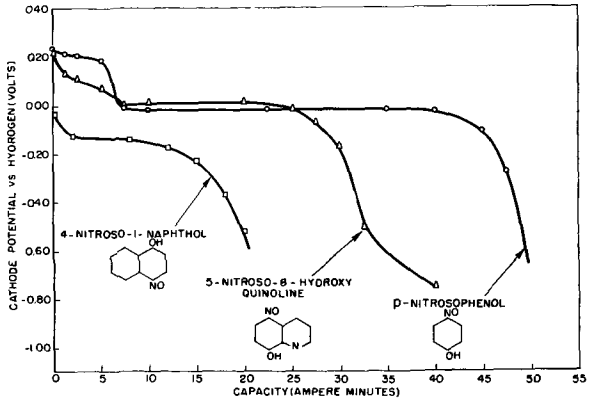


Fig. 7. Half-cell potential studies of various aromatic hydroxy-nitroso derivatives discharged in 250 g/l $MgBr_2 \cdot 6H_2O$ electrolyte at a rate of 0.005 amp/g.

structure, the higher is the cathode potential of the corresponding C-nitroso compound. This can be explained on the basis of a decreased electron density in the vicinity of the nitroso group as one goes to more aromatic ring structures. This decreased electron density results in a compound with an increased electron affinity and a higher discharge potential.

*p-Nitrosodialkylamino compounds.*—In Fig. 8, the half-cell discharge curves of various p-nitrosodialkylamino derivatives show both p-nitrosodimethylaniline and 4-nitroso-3-methyldimethylaniline to

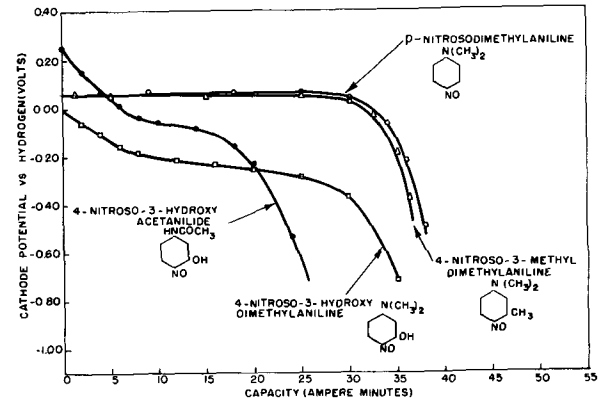


Fig. 8. Half-cell potential studies of various p-nitrosodialkylamino derivatives discharged in 250 g/l $MgBr_2 \cdot 6H_2O$ electrolyte at a rate of 0.005 amp/g.

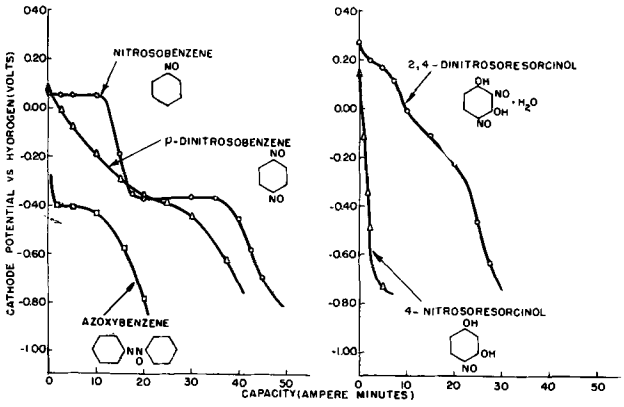


Fig. 9. Half-cell potential studies of various mono- and di-nitroso derivatives of benzene and resorcinol discharged in 250 g/l $MgBr_2 \cdot 6H_2O$ electrolyte at a rate of 0.005 amp/g.

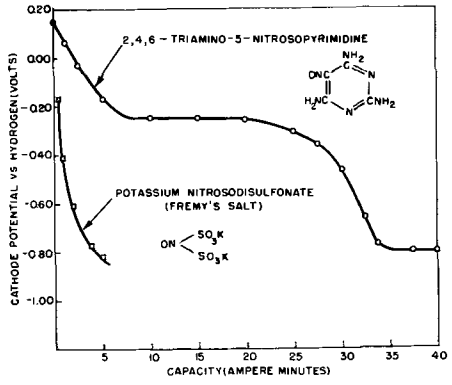


Fig. 10. Half-cell potential studies of various nitroso derivatives discharged in 250 g/l $MgBr_2 \cdot 6H_2O$ electrolyte at a rate of 0.005 amp/g.

have high, flat operating potentials throughout the course of their discharge. As with nitrosophenols, a —$CH_3$ group, ortho to the nitroso group, lowers the potential of the parent compound a very small amount. The effect of the more strongly electron-repelling —OH group in the 3 position is much more marked, resulting in a compound, 4-nitroso-3-hydroxydimethylaniline, which operates at a potential 0.3 v lower than p-nitrosodimethylaniline.

The high initial operating potential of the hydroxy compounds for the first 5-10 amp-min of discharge is again illustrated by the curves for 4-nitroso-3-hydroxyacetanilide and 4-nitroso-3-hydroxydimethylaniline. These o-nitrosophenol compounds exhibit the same type of discharge curve as the p-nitrosophenol compounds previously presented although they operate at considerably lower potentials.

*Mono- and di-nitroso compounds.*—In Fig. 9 are half-cell discharge curves of the mono and dinitroso derivatives of benzene and resorcinol. The reduction of nitrosobenzene is seen to take place stepwise, the first step occurring at a potential of +0.05 v, a value close to that of other p-hydroxy and p-dialkylamino nitroso compounds. The two step discharge may be explained by a 2 electron reduction to phenylhydroxylamine with subsequent reduction to aniline, or it can be attributed to the reduction of side products such as azoxybenzene, formed by the condensation of nitrosobenzene with phenylhydroxylamine. The discharge potential of azoxybenzene, shown in Fig. 9, is close to that of the second discharge step of nitrosobenzene, indicating the latter explanation is a distinct possibility. Additional half-cell discharge studies of azobenzene, another possible side product formed by the condensation of nitrosobenzene with aniline, indicate that this compound cannot be reduced under the experimental conditions, and it was therefore not considered further.

It was expected that the addition of another strongly electron attracting —NO group to nitrosobenzene would result in a dinitroso compound having a much higher operating potential than nitrosobenzene, similar to what one finds with the nitro and dinitrobenzene compounds (3). Actually, the potential of p-dinitrosobenzene is less than that of nitrosobenzene. For 4-nitrosoresorcinol, however, the addition of a —NO group to form 2,4-dinitrosoresorcinol results in a compound with a higher operating potential, a result in agreement with the behavior found in aromatic nitro compounds.

The apparent anomolous behavior of p-dinitrosobenzene could be due to the fact that this compound does not exhibit properties characteristic of a true nitroso compound[3] and the structure of the —NO group cannot be written as for a true nitroso compound (15).

*Nitronitroso and other nitroso compounds.*—Presented in Fig. 10 are discharge curves for potassium nitrosodisulfonate, an inorganic nitroso compound commonly known as Fremy's salt, and 2,4,6-triamino-5-nitrosopyrimidine, an example of a heterocyclic nitroso compound. Except for its high initial operating potential, the latter compound displays a flat voltage curve throughout the course of its discharge. The potassium nitrosodisulfonate gives little or no capacity under similar conditions of discharge. This is believed to be due to the instability of this compound which decomposes readily to ammonium sulfate, sulfur dioxide, and nitrous oxide (16).

Figure 11 shows discharge curves for m-nitronitrosobenzene and 3-nitro-4-nitrosotoluene. It is seen that these compounds operate at lower potentials than their corresponding mono nitroso compounds, again giving results in variance with what one would expect from the theory developed to ex-

[3] Of the three dinitrosobenzene compounds only the meta isomer has properties of a normal nitroso compound (15).

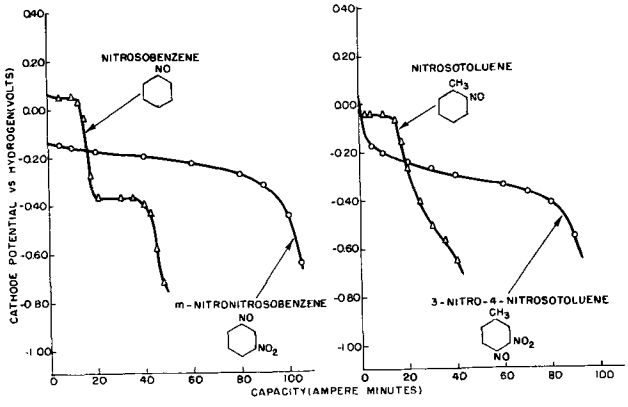


Fig. 11. Half-cell potential studies of various nitronitroso derivatives discharged in 250 g/l $MgBr_2 \cdot 6H_2O$ electrolyte at a rate of 0.005 amp/g.

plain the effect of group substitution on the operating potential of aromatic nitro compounds.

It is apparent that the type and position of the substituted group has an effect on the electrode potential of aromatic nitroso compounds. However from the data available, no definite correlations can be made, as in the case of the aromatic nitro compounds (3). The discharge data in Fig. 5-8 for various p-hydroxy and p-dialkylamino nitroso derivatives support the application of the above theory to aromatic C-nitroso compounds. However, data presented in Fig. 9 and 11 for nitrosobenzene, p-dinitrosobenzene, and m-nitronitrosobenzene cannot be explained by these theories.

The literature on the effect of group substitution on the potential of nitrosobenzene revealed some disagreement. Lutz and Lytton (2), studying the effect of added groups on the electrode potential of nitrosobenzene, contend that both electron-attracting and electron-repelling groups located ortho to the nitroso group raise the potential. In the para position, electron-repelling groups lower and electron-attracting groups raise the potential, while meta substituted groups have little or no effect on the potential regardless of the nature of the groups. The results presented in the present paper are in disagreement with those of Lutz and Lytton, whose results are difficult to understand in the light of the current theories dealing with the electron distribution in a molecule and its effect in determining the mechanism of organic reactions.

Hertel and Lebok (17) studied the electrolytic reduction of nitroso compounds and found that substitution on the ring normally increases the reactivity of the nitroso group in the order $-NO_2$, —Cl, —H, and $-N(CH_3)_2$. This is in agreement with what one finds for substituted nitrobenzene derivatives.

One of the difficulties associated with determining the effect of group substitution on the electrode potential of nitroso compounds is the tendency of these compounds to associate according to the nature of the other groups in the molecule to give bimolecular complexes. Solution favors depolymerization of these complexes, although it does not necessarily effect complete conversion to the monomeric form. As a result of this, complications may arise as with nitrosobenzene, in which the binitroso dimer is o-, p-directing, while in the monomeric form the nitroso group seems to be meta directing, as evidenced by the fact that o- and p-nitrosohalobenzenes undergo ready hydrolysis whereas the corresponding m-compounds are stable (18).

Another difficulty is the uncertainty about the exact structure of nitroso compounds, which information is necessary to develop a theory to explain the effect of structure on electrode potential during current flow.

## Coulombic Capacity Studies of Aromatic C-Nitroso Compounds

Table I gives theoretical capacity data for the aromatic C-nitroso compounds presented in Fig. 5-11 compared with two of the cathode materials now used in commercial dry cells. The theoretical

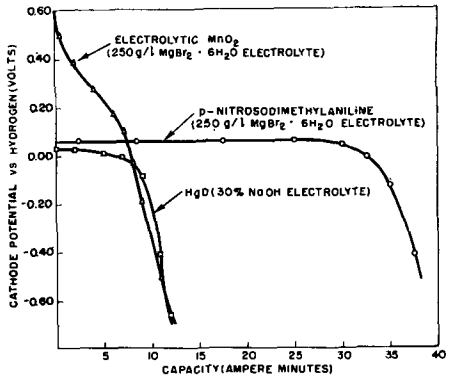


Fig. 12. Half-cell potential studies of various cathode materials discharged in compatible electrolytes at a rate of 0.005 amp/g.

capacities of the nitroso compounds were computed by means of Faraday's law, with the assumption that each nitroso group is reduced to the amino stage with a corresponding four electron change.

It is seen that most of the nitroso compounds listed have from 2 to 3 times greater theoretical ampere-minute capacity per unit of weight than manganese dioxide and mercuric oxide. However, because of the low density of the mononitroso compounds, the theoretical capacity in ampere-minutes per unit of volume is greater for the inorganic compounds.

Figure 12 shows discharge curves for p-nitrosodimethylaniline, one of the more attractive C-nitroso compounds, electrolytic manganese dioxide (85% $MnO_2$), and mercuric oxide. The p-nitrosodimethylaniline and electrolytic manganese dioxide were discharged at a rate of 0.005 amp/g in an aqueous solution of $MgBr \cdot 6H_2O$ (250 g/l), while the mercuric oxide was discharged at the same rate in a 30% solution of sodium hydroxide, saturated with zinc oxide.

On this test, to a half-cell potential of −0.4 v the manganese dioxide and mercuric oxide cathodes give capacities of 10.3 and 10.4 amp-min/g, corresponding to efficiencies of 65.6%[4] and 69.8%, respectively. At comparable conditions of discharge, p-nitrosodimethylaniline gives a capacity of 37.4 amp-min/g, corresponding to an efficiency of 87.2%. On this test, p-nitrosodimethylaniline gives more than three times the ampere-minute per gram capacity of electrolytic manganese dioxide and mercuric oxide, this capacity being greater than twice the theoretical limit of these inorganic cathode materials.

The high electrode efficiency of p-nitrosodimethylaniline is typical of that found for the p-nitrosodialkylamino and p-nitrosophenol compounds. However, poor efficiencies are also encountered among the aromatic nitroso compounds, as evidenced by the poor electrode efficiencies of the nitrosonaphthol compounds as well as of the two dinitroso compounds tested.

If the p-nitrosodimethylaniline cathode is coupled with a magnesium anode and a magnesium bromide electrolyte, it should result in a primary cell which would operate during current flow at constant volt-

[4] Efficiency calculation is 65.6% of 85% $MnO_2$ content.

age levels of 1.30-1.40 v. It is thus apparent that the aromatic C-nitroso compounds show considerable promise for use as cathode materials in primary cells, the most outstanding features of these compounds being their high constant operating potential, and their high theoretical capacity in ampere-minutes per gram.

### Acknowledgment

The authors wish to express their appreciation to Mr. W. B. Hardy of American Cyanamid Co. for supplying some of the nitroso compounds.

Manuscript received March 24, 1958. This paper was prepared for delivery before the Buffalo Meeting, Oct. 6-10, 1957.

Any discussion of this paper will appear in a Discussion Section to be published in the June 1959 JOURNAL.

REFERENCES

1. J. B. Conant and R. E. Lutz, *J. Am. Chem. Soc.*, **45**, 1047 (1923).
2. R. E. Lutz and M. R. Lytton, *J. Org. Chem.*, **2**, 68 (1937).
3. R. Glicksman and C. K. Morehouse, *This Journal*, **105**, 299 (1958).
4. C. K. Morehouse and R. Glicksman, *ibid.*, **105**, 306 (1958).
5. C. K. Morehouse and R. Glicksman, *ibid.*, **103**, 94 (1956).
6. R. Glicksman and C. K. Morehouse, *ibid.*, **102**, 273 (1955).
7. S. Swann Jr., *Trans. Electrochem. Soc.*, **66**, 287 (1936).
8. S. Glasstone and A. Hickling, "Electrolytic Oxidation and Reduction," p. 164, D. Van Nostrand Co., Inc., New York (1936).
9. F. Haber and C. Schmidt, *Z. Physik. Chem.*, **32**, 271 (1900).
10. Ref. 8, pp. 32-33.
11. M. J. Astle and W. V. McConnell, *J. Am. Chem. Soc.*, **65**, 35 (1943).
12. M. Shikata and I. Tachi, *J. Chem. Soc. Japan*, **53**, 834 (1932); *Collection Czechoslov. Chem. Comm.*, **10**, 834 (1938).
13. E. Ochiai, *J. Pharm. Soc. Japan*, **69**, 1 (1949).
14. W. M. Latimer, "Oxidation Potentials," p. 136, Prentice Hall Inc., New York (1952).
15. G. A. Stoner, Ph.D. Thesis, Tulane University (1955).
16. Therald Moeller, "Inorganic Chemistry," p. 555, John Wiley & Sons, Inc., New York (1952).
17. E. Hertel and F. Lebok, *Z. Physik. Chem.*, **(B)47**, 315 (1940).
18. E. F. Degering, "Organic Nitrogen Compounds," p. 152, University Lithoprinters (1945).

# Dry Cells Containing Various Aromatic C-Nitroso Compounds as Cathode Materials

**C. K. Morehouse and R. Glicksman**

*RCA Laboratories, Radio Corporation of America, Princeton, New Jersey*

ABSTRACT

Many aromatic C-nitroso compounds when coupled with a magnesium anode and a magnesium bromide electrolyte result in dry cells with practical features. The discharge characteristics of these cells are dependent on the particular aromatic C-nitroso compound used as a cathode. Magnesium-p-nitrosodimethylaniline dry cells operate at a flat voltage level between 1.3 and 1.4 v and give greater watt-minute capacities per unit of weight and volume than general purpose commercial Leclanché dry cells containing African manganese dioxide on a number of tests.

Previous work by the authors (1) showed that dry cells containing aromatic nitro compounds as cathodes coupled with a magnesium anode had many favorable performance characteristics. In addition, a study (2, 3) of the electrochemical properties of the reduction products of aromatic nitro and nitroso compounds indicated that the class of aromatic C-nitroso compounds also has many of the desirable properties of a cathode material for use in primary cells. For example, several of these compounds have high theoretical ampere-minute per gram capacities and flat potential-time discharge curves. These cathodes operate at high electrode efficiencies at potentials 0.2-0.4 v higher than their corresponding aromatic nitro cathode.

Arsem (4), the only reference found which refers to the use of nitroso compounds in primary cells, suggested coupling a zinc anode with an organic oxidizing agent such as p-nitrosodimethylaniline as the cathode. However, such a cell has an operating voltage of approximately 1.00 v and thus has practical limitations.

In this paper, the performance characteristics of dry cells containing a magnesium anode coupled with aromatic C-nitroso compounds as cathodes are presented.

## Experimental

Dry cells containing various aromatic C-nitroso cathodes were assembled using an impact extruded AZ10A magnesium alloy can. The magnesium cans were lined with a piece of Nibroc salt-free paper, after which an extruded slug of cathode mix was inserted and consolidated in the lined can. A carbon rod with a brass cap fitted on one end was then inserted in the center of the cathode mix and the cells sealed in the conventional manner with a rosin base wax seal. The composition of a typical cathode mix used in this study is as follows:

| | |
|---|---|
| p-Nitrosodimethylaniline | 23.3% by weight |
| Shawinigan acetylene black | 11.6% by weight |
| Barium chromate | 1.1% by weight |
| Electrolyte (aqueous solution of 500 g/l $MgBr_2 : 6H_2O$ and 1.0 g/l $Li_2CrO_4 : 2H_2O$) | 64.0% by weight |

The AA-size cells contained approximately 5 g of this mix, the C-size 15-17 g, and the D-size cells 35-40 g.

Discharge characteristics and capacity data presented in the following sections were obtained by discharging the cells through fixed resistances and measuring the closed circuit voltage after various time intervals of discharge. All capacity data were gathered at 21.1° ± 1.1°C (70° ± 2°F) and 50 ± 5% R.H.

## Voltage-Discharge Characteristics of Dry Cells Containing Various Aromatic C-Nitroso Compounds as Cathodes

Half-cell studies on various aromatic C-nitroso compounds showed that the type and position of the substituted group have an effect on their discharge potential. However, no definite correlations can be made, as in the case of the aromatic nitro compounds (2). Presented in Fig. 1-4 are discharge data obtained from AA-size dry cells containing various aromatic C-nitroso cathodes coupled with a magnesium anode. It is seen that the voltage discharge characteristics of these cells are similar to that found for the various aromatic nitroso cathodes in the half-cell studies (3).

Figure 1 shows 50- and 150-ohm continuous discharge data obtained on dry cells containing various p-nitrosodialkylamino cathodes. These cells operate at a flat voltage level above 1.30 v for most of their discharge life. The slight differences in voltage levels and capacities are attributed to variations associated with cell assembly and not to differences between structures of the cathode material.

Figure 2 gives data for some aromatic mono- and di-nitroso dry cells discharged continuously through 50- and 150-ohm resistances. It is seen that both the nitrosobenzene and o-nitrosotoluene cells have a two-step discharge curve with the nitrosobenzene cell operating at a higher voltage than the o-nitrosotoluene cells and for the first part of the discharge

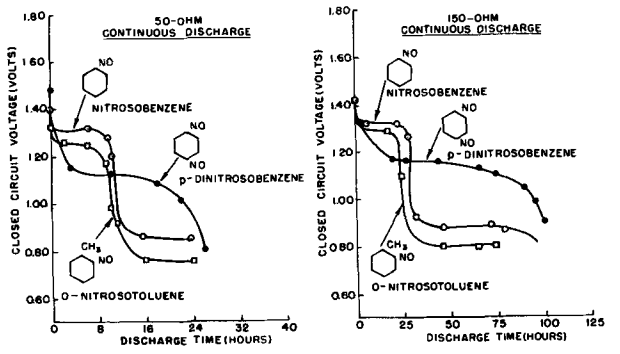


Fig. 2. Various AA-size magnesium-aromatic mono- and di-nitroso dry cells discharged continuously through 50- and 150-ohm resistances at 70° ± 2°F (50% R.H.).

at a potential close to that of the p-nitrosodialkylamino type of cells.

The p-dinitrosobenzene dry cells, although they have a higher initial closed circuit voltage, operate for most of their discharge period about 0.2 v lower than the nitrosobenzene cells. In addition, the capacity of the p-dinitrosobenzene cells is not markedly greater than that of the p-nitrosodialkylamino type cells, in spite of the greater theoretical ampere-minute capacity of the dinitroso compound.

As with the addition of the strongly electron attracting —NO group, the addition of a $—NO_2$ group to a mono nitroso compound results in a cathode with a lower operating potential. This relationship is shown by the cell discharge data in Fig. 2 and 3. The magnesium-m-nitronitrosobenzene AA-size cells operate between 1.1 and 1.2 v for most of their discharge life and give 50 and 160 hr of service to an end voltage of 0.90 v on the 50- and 150-ohm continuous discharge tests. These cells give comparable capacities to the magnesium-m-dinitrobenzene cells and are superior on these tests to the commercial general purpose Leclanché dry cells containing natural manganese dioxide and a starch-flour paste separator.

Figure 4 shows the discharge data for cells containing a magnesium anode and four aromatic hydroxynitroso compounds as cathodes. The magnesium-p-nitrosophenol cells operate for the first 6-7 amp-min of discharge between 1.40 and 1.50 v on these two tests, followed by a rapid drop to a voltage level between 1.20 and 1.30 v for most of the remaining discharge time. The second discharge

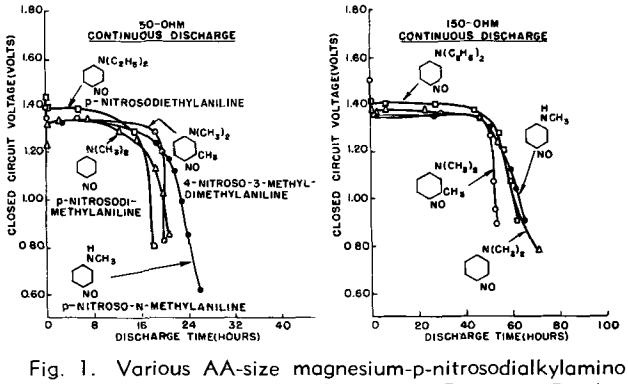


Fig. 1. Various AA-size magnesium-p-nitrosodialkylamino dry cells discharged continuously through 50- and 150-ohm resistances at 70° ± 2°F (50% R.H.).

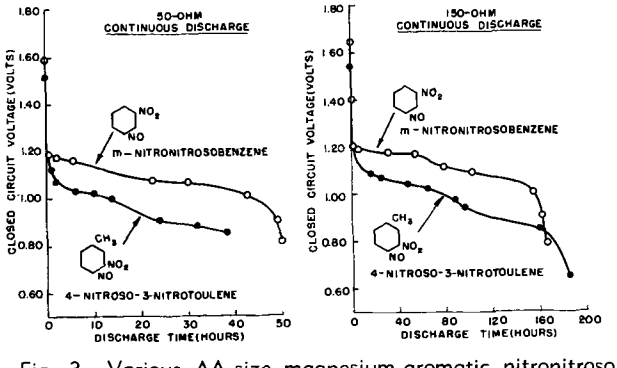


Fig. 3. Various AA-size magnesium-aromatic nitronitroso dry cells discharged continuously through 50- and 150-ohm resistances at 70° ± 2°F (50% R.H.).

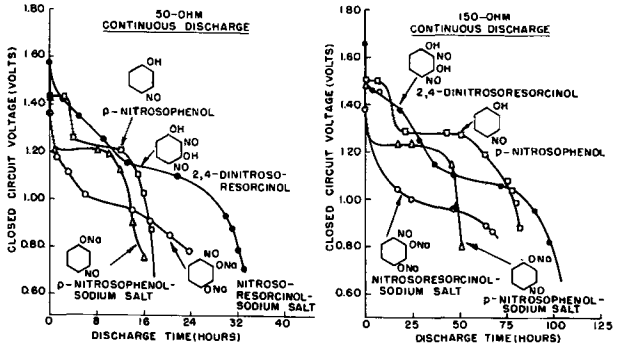


Fig. 4. Various AA-size magnesium-aromatic hydroxynitroso dry cells discharged continuously through 50- and 150-ohm resistances at 70° ± 2°F (50% R.H.).

step is close to that of the p-nitrosophenol-sodium salt. It is believed that a comparable compound is formed during discharge in a $MgBr_2$ electrolyte, as hydroxide ions are formed during discharge and neutralize the acidic phenolic H.

Figure 4 also shows the discharge characteristics of cells containing cathodes of 2,4-dinitrosoresorcinol and nitrosoresorcinol-sodium salt. As expected, the 2,4-dinitrosoresorcinol cells operate at a considerably higher voltage than the nitrosoresorcinol-sodium salt cells. It is also interesting to note that these dinitroso cells operate at a higher voltage than the mononitroso, p-dinitrosobenzene, and nitronitrosobenzene cells and exhibit a two-step voltage-discharge curve similar to the behavior found for aromatic dinitro cells.

## Performance Characteristics of Magnesium-p-Nitrosodimethylaniline Dry Cells

The class of aromatic C-nitroso compounds includes many domestically available compounds which are stable solids and have theoretical ampere-minute capacities per unit of weight several times greater than the manganese dioxide and mercuric oxide cathodes used at present in commercial dry cells.

It is beyond the scope of this paper to characterize all types of magnesium-aromatic C-nitroso dry cells because of the large number of such electrochemical systems. Instead, the magnesium-p-nitrosodimethylaniline couple was selected for a more thorough study since this organic compound is more readily available, now being used as an intermediate in the production of a number of organic dyes. In the following sections, performance characteristics of these cells are compared with those of other dry cells.

*Cell reactions.*—Half-cell coulometric studies have shown that cathodes of p-nitrosodimethylaniline operate at efficiencies in excess of 85% (3). While the products formed during the discharge of a cell have not been analyzed, the experimentally obtained cathode ampere-minute capacities indicate that the electrode reactions during cell discharge are:

Cathode reaction

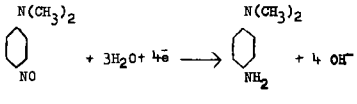


Anode reaction

$$Mg \rightarrow Mg^{++} + 2e^-$$

Over-all energy producing reaction

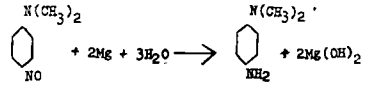


*Cell discharge data.*—From a cathode formulation study it was found that a higher ratio of carbon to p-nitrosodimethylaniline is required than is used in the manganese dioxide type of dry cells. A ratio of 2 parts of p-nitrosodimethylaniline to 1 part Shawinigan acetylene black by weight was found to give favorable results. The performance characteristics of cells of this formulation are discussed below.

Initial capacity data obtained on these cells discharged continuously through 4-, 50-, 150-, and 300-ohm resistances are shown in Fig. 5 and 6. The 4-ohm test represents a drain encountered in a flashlight application; the 150- and 300-ohm tests represent the current drains encountered in a B battery or a transistor radio receiver application. Included in Fig. 5 and 6 are discharged data for comparable size commercial Leclanché and magnesium-manganese dioxide dry cells. The commercial Leclanché dry cells were of the general purpose type and contained natural manganese dioxide and a starch-flour paste separator. The magnesium-manganese dioxide cells contained an impact ex-

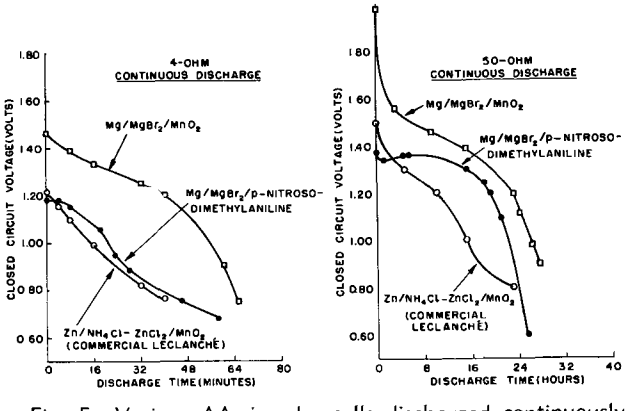


Fig. 5. Various AA-size dry cells discharged continuously through 4- and 50-ohm resistances at 70° ± 2°F (50% R.H.).

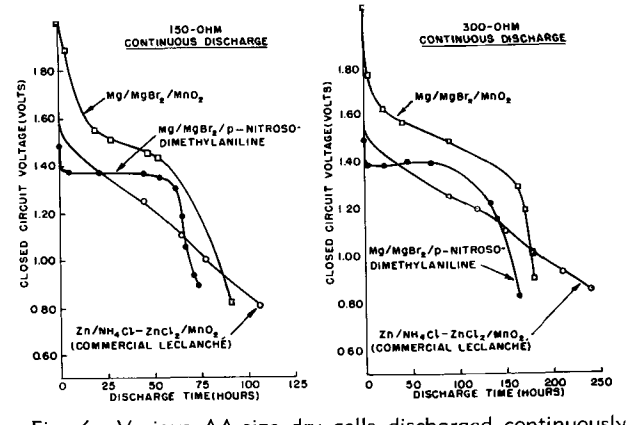


Fig. 6. Various AA-size dry cells discharged continuously through 150- and 300-ohm resistances at 70° ± 2°F (50% R.H.).

truded AZ10A magnesium alloy can, and were of the type under development by the Dow Chemical Company (5).

The 4-ohm continuous discharge test data show that the p-nitrosodimethylaniline cells have discharge characteristics comparable to the commercial Leclanché cells. On the 50-, 150-, and 300-ohm continuous discharge tests, it is seen that these organic cells have a flatter discharge curve than the two manganese dioxide dry cells and operate between 1.30 and 1.40 v for most of the discharge time.

Since performance requirements will vary depending on the application, the capacity data for the three types of AA-size cells obtained from the continuous discharge tests are summarized in several ways, as shown in Fig. 7-10 inclusive. In Fig. 7 the capacity in hours of service to 1.20 and 0.90 v end voltages are plotted against external load resistance. These data show that the p-nitrosodimethylaniline cells give more hours of service than the Leclanché cells to an end voltage of 1.20 v, but are inferior to both manganese dioxide cells to an end voltage of 0.90 v.

Since there are many applications which require maximum hours of service allowing a certain percentage voltage drop from initial closed-circuit voltage rather than maximum hours of service to specified end voltages, the capacity data are summarized in Fig. 8 in terms of hours of service vs. per cent voltage drop from initial closed-circuit voltage. The initial closed-circuit voltage was taken as the terminal voltage of the cell after 1 min of discharge through the respective resistance. The data in Fig. 8 illustrate one of the attractive properties of the p-nitrosodimethylaniline cells in that they give more hours of service than the manganese dioxide cells on the 50- and 150-ohm continuous discharge tests,

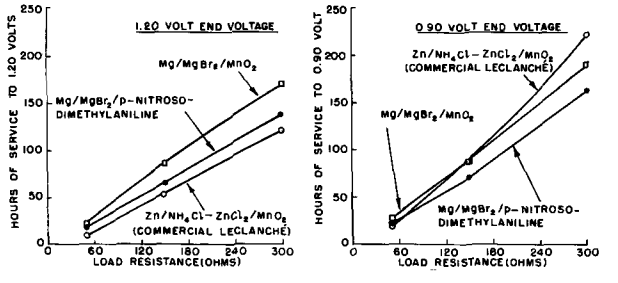


Fig. 7. Capacity in hours of service vs. load resistance of AA-size dry cells.

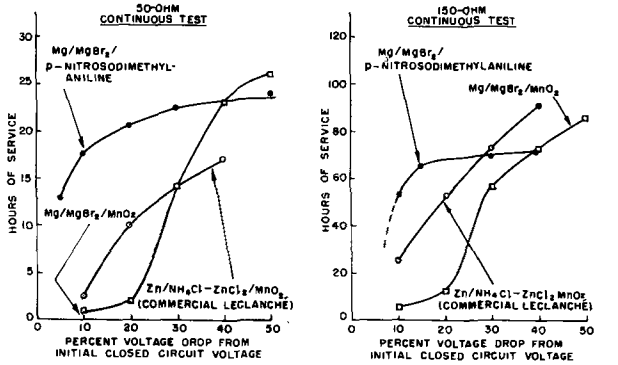


Fig. 8. Capacity in hours of service vs. per cent closed-circuit voltage drop of AA-size dry cells.

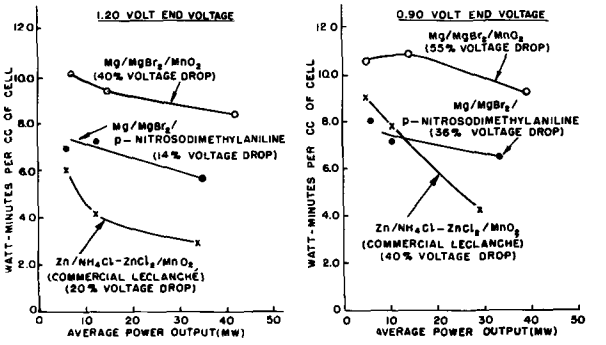


Fig. 9 Capacity in watt-minutes per cubic centimeter vs. average power output of AA-size dry cells.

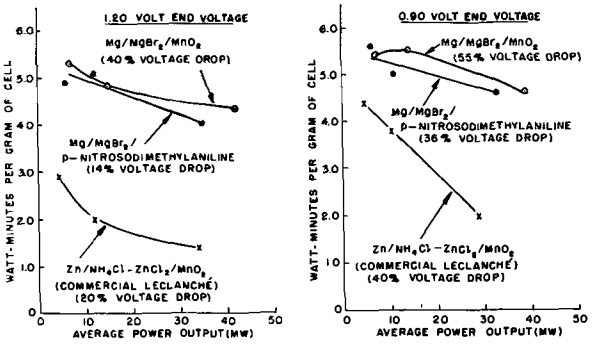


Fig. 10. Capacity in watt-minutes per gram vs. average power output of AA-size dry cells.

when the closed-circuit voltage of the cell is allowed to fall no more than 30%.

In order to normalize the voltage differences between the three cells, watt-minute capacities per unit of weight and volume to 1.20 and 0.90 v end voltages were plotted against average power output as shown in Fig. 9 and 10. The data in Fig. 9 show that the p-nitrosodimethylaniline cells give to an end voltage of 1.20 v watt-minute capacities per unit of volume between that obtained from the two manganese dioxide cells. To the lower 0.90 v end voltage the organic cells give higher capacities than the Leclanché at power output levels above 15 mw.

On the basis of watt-minute capacity per unit of weight, Fig. 10 shows that the p-nitrosodimethylaniline cells are comparable to the magnesium-manganese dioxide and superior to the Leclanché cells over a 10-40 mw range of continuous power output levels.

An additional analysis of the three cells, given in Table I, shows the approximate theoretical ampere-minute capacities and cathode efficiencies computed from their cell discharge data using a 0.90 v end voltage. These data were calculated with the assumption that the cathode material is the limiting cell component. It is seen that the p-nitrosodimethylaniline cathode becomes more efficient as the current drain is decreased, approaching its theoretical limit. In this respect it is comparable to the manganese dioxide cathodes.

Also included in Table I are comparable data obtained on p-nitrosodimethylaniline dry cells of an "inside-out construction." These cells contained a drawn steel cup coated on the inside with a conductive paint impermeable to the electrolyte. Ap-

Table I. Theoretical capacity and cathode efficiency of various AA-size dry cells

| | Theoretical capacity/g of cathode material, amp-min | Approx wt of cathode material in cell, g | Approx theoretical cell capacity, amp-min | Cathode efficiency* of cells discharged continuously through following resistances, ohms | | | |
|---|---|---|---|---|---|---|---|
| | | | | 4 | 50 | 150 | 300 |
| | | | | (per cent) | | | |
| $Zn/NH_4Cl$-$ZnCl_2/MnO_2$ Commercial Leclanché | 18.5 | 3.3 | 60.5 | 11.1 | 40.5 | 60.6 | 89.3 |
| $Mg/MgBr_2/MnO_2$ | 18.5 | 3.9 | 72.2 | 25.6 | 62.9 | 72.6 | 71.9 |
| $Mg/MgBr_2$/p-nitrosodimethylaniline (impact extruded can construction) | 42.8 | 1.2 | 51.4 | 13.9 | 69.2 | 73.5 | 83.4 |
| $Mg/MgBr_2$/p-nitrosodimethylaniline (inside-out construction) | 42.8 | 1.8 | 77.0 | — | 54.5 | 69.3 | 96.0 |

* Data based on ampere-minute capacity to 0.90 v end voltage.

proximately 7 g of cathode mix of the previously described formulation were inserted into the steel cup, and then a magnesium rod (0.20 in. diameter) wrapped with Nibroc absorbent salt-free paper was inserted into the center of the cathode mix. The cell was next sealed in the conventional manner with a pitch seal. This construction offers the advantages of (*a*) lower cost and (*b*) larger volume of cathode mix which results in greater theoretical cell capacity over the impact extruded can design. Discharge data obtained from cells of this design are shown in Fig. 11. Included for comparison are data for a comparable size Leclanché cell and a p-nitrosodimethylaniline dry cell containing an impact extruded magnesium alloy can. Cells of the inside-out design have a greater theoretical capacity (Table I) and give more hours of service than the comparable size p-nitrosodimethylaniline cells of the impact extruded magnesium alloy can design. At the present stage of development these "inside-out" cells operate at a slightly lower voltage, due to *IR* losses associated with the design. It is believed that with further development these losses can be largely eliminated, and the cells will operate at a potential close to that obtained with the impact extruded can design.

Other size p-nitrosodimethylaniline dry cells have been assembled and found to have similar relationships to comparable size Leclanché and magnesium-manganese dioxide cells. Figure 12 gives capacity data obtained on D-size cells discharged continuously and intermittently through 4-ohm resistances simulating the discharge through a 0.25-amp flashlight bulb. It is seen that the p-nitrosodimethylaniline cell has a flatter discharge curve and gives more minutes of service to a 0.90 v end voltage than either of the manganese dioxide cells on the continuous test. On the intermittent test it gives more minutes of service than the Leclanché cell but less than the magnesium-manganese dioxide cell.

## Conclusions

Many aromatic C-nitroso compounds have properties suitable for the design of improved dry cells when coupled with a magnesium anode and a magnesium bromide electrolyte. The discharge characteristics of these cells are dependent on the choice of aromatic C-nitroso cathode.

Dry cells containing various aromatic C-nitroso cathodes have been stored for 12 months at 70°F and have given 75-90% of initial capacity. However, at 113°F (90% R.H.) failure occurred after two months' storage.

The AA-size magnesium-p-nitrosodimethylaniline dry cells have been studied in greater detail. These cells have a flat voltage-discharge curve, operating for most of their discharge time above 1.30 v, and give greater watt-minute capacities per unit of weight and volume than the commercial Leclanché dry cells on a number of tests. Increased capacity can be obtained from this electrochemical system by using an inside-out construction instead of the impact extruded can design.

The magnesium-aromatic C-nitroso dry cells exhibit the same difficulties associated with other magnesium dry cells, namely, loss in capacity on light intermittent tests, "delayed action," and high impedance. It is believed that these problems can be overcome with further development.

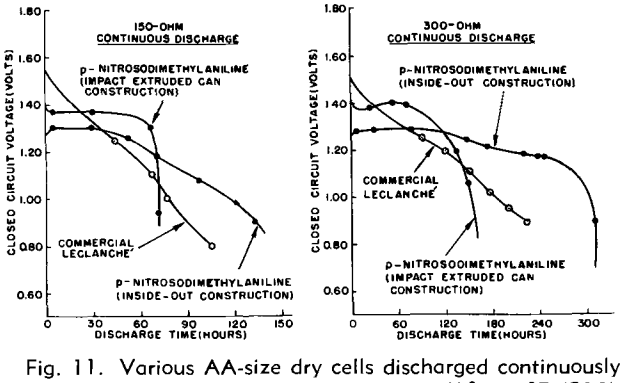


Fig. 11. Various AA-size dry cells discharged continuously through 150- and 300-ohm resistances at 70° ± 2°F (50% R.H.).

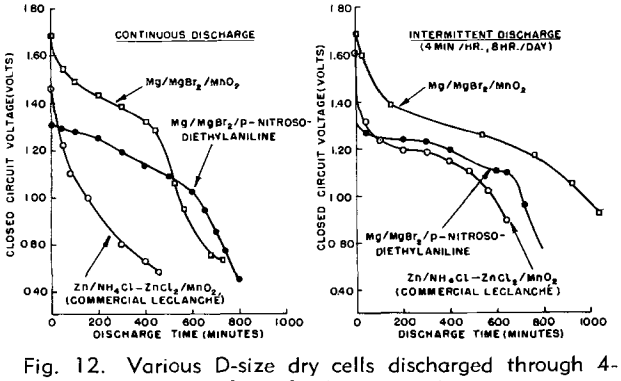


Fig. 12. Various D-size dry cells discharged through 4-ohm resistances at 70° ± 2°F (50% R.H.).

**Acknowledgment**

The authors wish to express their appreciation to Mr. G. R. Ganges and Dr. G. S. Lozier for assistance in gathering some of the cell data and their many helpful comments made during this study.

Manuscript received April 9, 1958. This paper was prepared for delivery before the Buffalo Meeting, Oct. 6-10, 1957.

Any discussion of this paper will appear in a Discussion Section to be published in the June 1959 JOURNAL.

REFERENCES

1. C. K. Morehouse and R. Glicksman, *This Journal*, **105**, 306 (1958).
2. R. Glicksman and C. K. Morehouse, *ibid.*, **105**, 299 (1958).
3. R. Glicksman and C. K. Morehouse, *ibid.*, **105**, 000 (1958).
4. W. C. Arsem, U. S. Pat. 2,306,927, Dec. 29, 1942.
5. R. C. Kirk, P. F. George, and A. B. Fry, *This Journal*, **99**, 323 (1952).

# Textures of Electrodeposited Lead Dioxide

**Yasuichi Shibasaki**[1]

*Department of Electrochemistry, Yokohama National University, Yokohama, Japan*

ABSTRACT

Slightly coarse, dull smooth, bright smooth, fibrous, columnar, rough, granular, and porous textures were found for electrodeposited lead dioxide. Textures, relative strengths, and conditions of electrodeposition of lead dioxide are discussed. The bright, smooth lead dioxide was found to be the strongest.

It has been noticed in many experiments on electrodeposition of lead dioxide under different conditions that there is a close relation between strength and texture of the electrodeposited lead dioxide. This paper describes a study of the textures of various electrodeposits.

## Experimental

*Basis materials.—Mixture of finely powdered lead dioxide and polystyrene.*—Finely powdered lead dioxide was passed through a 100-mesh screen and homogeneously mixed with polystyrene and benzene in the weight ratio of 100: (2 ~ 3): (8 ~ 20). This mixture was applied 5-10 mm thick onto a perforated hollow cylinder of stainless steel. The benzene was removed by evaporation and the mixture finished mechanically to a cylindrical rod. This rod was used as a substrate in the untreated condition or after the following treatment. The rod was made the anode for electrolysis of a 5-10% NaOH solution or a dilute $H_2SO_4$ solution at a current density of about 10 amp/dm$^2$ for 5-10 min, then washed with water, a dilute $HNO_3$ solution, and water successively. After electrodeposition the substrate could be removed easily from the electrodeposit by dissolving the polystyrene in a solvent such as benzene.

*Mixture of powdered graphite and solid paraffin.*—Powdered graphite (passed through a 100-mesh screen) and paraffin, (mp 50°-60°C) were mixed homogeneously in the weight ratio of 3.5:1 at temperatures higher than the melting point of paraffin. The mixture was applied 5-10 mm thick onto a perforated hollow cylinder of copper at the same temperatures. After cooling it was finished mechanically to a rod. The rod was cleaned by being made the anode or cathode for electrolysis of a 5-10% NaOH solution at a current density of about 10 amp/dm$^2$ until its surface was almost perfectly wet, then washed with water, a dilute $HNO_3$ solution, and water successively. The rod was used as a substrate for electrodeposition while the surface was wet. After electrodeposition it could be removed

**Table I. Samples of electrodeposited lead dioxide and electrodeposition conditions under which they were electrodeposited**

| Texture and No. | Electrodeposited lead dioxide Size (cm) When cylinder: Outside diameter | Length | Thickness | Weight (kg) |
|---|---|---|---|---|
| SC1 | Rectangular plate | 1.5 × 6 × 0.06 | | 0.005 |
| SC2 | Rectangular plate | 2 × 6.5 × 0.03 | | 0.0035 |
| DS | 4 | 6 | 0.6 | 0.35 |
| BS1 | 3 | 20 | 0.35 | 0.47 |
| BS2 | 0.6 | 7.3 | 0.04 | 0.05 |
| BS3 | 2.3 | 13 | 0.35 | 0.25 |
| BS4 | 2.5 | 13.5 | 0.3 | 0.17 |
| BS5 | 2.5 | 20 | 0.28 | 0.34 |
| BS6 | 1.8 | 10.6 | 0.4 | 0.17 |
| BS7 | 5.8 | 83 | 0.7 | 8.4 |
| BS8 | 5.5 | 82 | 0.7 | 7.3 |
| BS9 | 2.8 | 13.5 | 0.5 | 0.41 |
| BS10 | 5 | 57 | 0.85 | 5.2 |
| M(F,G) | | | 0.8 | |
| C | | | 0.57 | |
| G1 | 5.7 | 90 | 0.76 | 8.5 |
| G2 | 6 | 90 | 0.9 | 10 |
| G3 | 3.2 | 14 | 0.6 | 0.62 |
| G(S)1 | | | 0.6 | |
| G(S)2 | | | 0.6 | |
| G(R) | | | 0.6 | |
| R1 | Rectangular plate 2 × 5 | | | |
| R2 | Rectangular plate 2 × 5 | | | |
| R3 | Rectangular plate 2 × 5 | | | |
| R4 | Rectangular plate 2 × 5 | | | |
| R5 | 1.9 | 12 | 0.4 | 0.18 |
| P1 | | | 0.6 | |
| P2 | | | 0.17 | |

SS, slightly coarse; DS, dull smooth; BS, bright smooth; M(F, G), (a), mixture of lead dioxide and polystyrene; (b), mixture of

[1] Present address: Department of Chemistry, The Ohio State University, Columbus, Ohio.

easily from the electrodeposit by melting the paraffin or dissolving it in a solvent.

*Nickel cylinder; nickel plated cylindrical lead tube; or 0.15 mm thick rectangular nickel plate covered except for one surface by applying a mixture of paraffin and vaseline.*—The surfaces of these substrates were cleaned by being made the anode or cathode for electrolysis of a 5-10% NaOH solution at a current density of about 10 amp/dm$^2$ until their surfaces were almost perfectly wet, then washed with water, a dilute $HNO_3$ solution, and water successively. The tendency of electrodeposited lead dioxide to deform itself during and after electrodeposition depends on the conditions of electrodeposition (1). When lead dioxide is electrodeposited on a deformable substrate such as the nickel plate, it will deform itself and the substrate easily; stresses in the deposit will be lessened. Therefore, lead dioxide electrodeposited on a deformable substrate is usually less liable to cracking than that electrodeposited on a nondeformable substrate such as the first four substrates mentioned above. Consequently, when the tendency to crack was great, the nickel plate was used as a substrate. When there is little tendency to deformation, electrodeposited lead dioxide does not tend to crack, regardless of the type of substrate used.

If a thick layer of lead dioxide is deposited on the nickel plate, it tends to deposit not only on the over part of the substrate surface but also on the part which protrudes from the perimeter of the substrate in accordance with the progress of the electrodeposition. In this case it is quite difficult to maintain a constant current density during electrodeposition and, when the tendency is small, the other substrates are suitable.

*Electrolysis cells and electrolytes.*—Two cylindrical porcelain vessels of about 30$^\phi$ x 30 cm and 70$^\phi$ x 100 cm were used for the electrodeposition. When the substrate was cylindrical, it was placed vertically at the center of a copper cylindrical cathode which was, in turn, placed in contact with the inside of the vessel. The substrate was rotated primarily around its center axis. When the substrate was a plate, it was placed parallel to a copper plate cathode.

The electrolytes which were used for the electrodeposition are shown in Table I. Solutions were agitated. Powdery carbonates of lead and copper were dissolved in the electrolytes to control acidities and supply metal ions during electrodeposition.

Conditions for electrodeposition, such as composition and temperature of electrolyte, and current density, were maintained as constant as possible. Under extended periods, however, small fluctuations were unavoidable.

**Table I. Samples of electrodeposited lead dioxide and electrodeposition conditions under which they were electrodeposited—continued**

| Conditions of electrodeposition | | | | | | |
|---|---|---|---|---|---|---|
| Substrate | | Composition of electrolyte | | | | |
| Kind | Motion (rpm when cylinder) | Substances and their concentration in water [Pn: $Pb(NO_3)_2$, Cn: $Cu(NO_3)_2$] (m) | pH | Temperature of electrolyte (°C) | Current density (A·dm$^{-2}$) | Time of electrodeposition (hr) |
| (c) iii) | Repose | Pn: 1, Cn: 0.1 | 2 ~ 4 | 20 | 0.1 | 115.5 |
| | | | | | 1 | 5.5 |
| (b) | 60 | | 1 ~ 4 | 27 ~ 30 | 4 | 30 |
| (c) ii) | | Pn: 1 | 1 ~ 3 | 20 ~ 23 | 5.0 ~ 5.6 | 14 |
| (c) i) | Repose | Pn: 1, Cn: 0.1 | 2 ~ 4 | 20 | 5.5 | 1.5 |
| (b) | 60 | Pn: 1, $Al(NO_3)_3$: 0.1 | 1 ~ 2 | 14.5 ~ 18.5 | 4.5 | 17.5 |
| (a) | | Pn: 1, Cn: 0.1, $Mn(NO_3)_2$: 0.01 | 1.5 ~ 4 | 20 | 2 | 30 |
| (b) | | Pn: 1, Cn: 0.1, $Al(NO_3)_3$: 0.1, $CH_3(CH_2)_7CH{=}CH(CH_2)_7CH_2O(C_2H_4O)_{15}H$: 0.005 | 2 ~ 3 | 15 | 3.4 | 16 |
| (a) | 60 ~ 100 | Pn: 1, Cn: 0.1, $CH_3$-⟨⟩-$SO_2NH_2$: 0.0065 | 2 ~ 4 | 14 ~ 16 | 3.2 ~ 3.6 | 24 |
| | | | | 12 ~ 16 | 2.0 ~ 3.4 | 49 |
| | | | | 13 ~ 15 | 2.3 ~ 3.4 | 50 |
| (b) | | $Pb(NH_2SO_3)_2$: 1, $Cu(NH_2SO_3)_2$: 0.1, $C_{12}H_{25}O(C_2H_4O)_6H$: 0.002 | | 20 | 2 | 50 |
| | | | | 20 ~ 25 | 1 ~ 2 | 95 |
| (a), Reciprocation, 20 cm·sec$^{-1}$ | | Pn: 1, Cn: 0.1, $Al(NO_3)_3$: 0.3 | 1 ~ 3 | 23 | 5 | 31.5 |
| | | | | 14 | 6 | 19 |
| (a) | 60 ~ 100 | Pn: 1, Cn: 0.1 | 2 ~ 4 | 19 ~ 26 | 4.8 ~ 6.0 | 21 |
| | | Pn: 1, Cn: 0.1, $CH_3$-⟨⟩-$SO_2NH_2$: 0.003 | 1 ~ 4 | 11 ~ 18 | 2.7 ~ 4.9 | 52 |
| (b) | 50 ~ 100 (many stripes) | | 1 ~ 3 | 27 ~ 31 | 7 | 21 |
| (b) | 300 ~ 400 | Pn: 1, Cn: 0.1 | 1 ~ 2 | 28 ~ 33 | 7.0 ~ 7.7 | 16 |
| | 500 ~ 600 | | | | | |
| (c) iii) | Repose | | | 20 | 20 | 0.43 |
| | | | | | 30 | 0.27 |
| | | | | | 40 | 0.08 |
| | | | 2 ~ 4 | | 50 | 0.17 |
| (a) | | $Pb(NH_2SO_3)_2$: 1, $Cu(NH_2SO_3)_2$: 0.1, Powdery active carbon: 0.8 | | 14 ~ 15 | 1.7 ~ 2 | 37 |
| (b) | 60 ~ 100 | Pn: 1, Cn: 0.1 | 1 ~ 3 | 27 ~ 30 | 4 | 30 |
| | | | | 20 | 5 | 6.5 |

mixture of fibrous and granular; C, columnar; G, granular; G(S), stripe-shape granular; G(R), ringe-shape granular; R, rough; P, porous. graphite and paraffin; (c) i), nickel cylinder; (c) ii), nickel plated cylindrical tube; (c) iii), nickel plate.

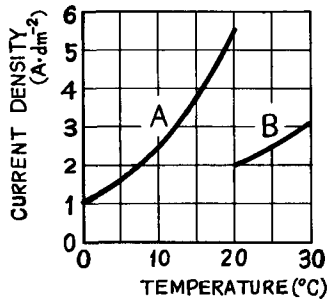


Fig. 1. Relation between current density and temperature of the electrolyte for the electrodeposition of bright, smooth lead dioxide. Curve A, 1 mole $Pb(NO_3)_2$ solution; Curve B, 1 mole $Pb(NH_2SO_3)_2$ solution.

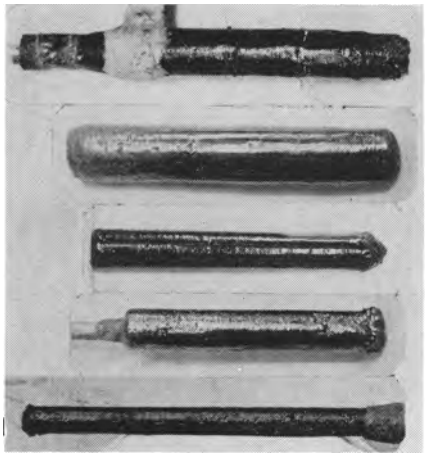

Fig. 2. Hollow cylinders of bright, smooth lead dioxide, from top to bottom: BS1, BS4, BS5, BS6, and BS7.

## Results of Experiments

Slightly coarse textured lead dioxide, whose surface is similar in nature to the surface of a very fine grain sandpaper, is deposited under the conditions of low current density and ambient temperature. It is brittle and easily cracked (see SC in Table I).

Dull, smooth lead dioxide is frequently deposited when the current density is slightly low at room temperature or when the electrolyte contains one or more of certain impurities. It has comparatively large strengths (see DS in Table I).

Bright, smooth lead dioxide is compact, strong, and most suitable for an insoluble anode. Suitable conditions found for obtaining bright, smooth deposits are:

1. The surface of the substrate should be smooth; however, when other conditions are suitable, the roughness of the deposit is less than that of the substrate.

2. The relation between current density and temperature of the electrolyte is shown in Fig. 1. Lower temperatures give more suitable conditions.

3. It is desirable that one or more of the following substances be added to the electrolyte: $Al^{3+}$, $Mn^{2+}$, polyoxyethylenealkylether, paratoluenesulfonamide. However, the desirable relations between the current density and temperature are generally effected by the addition of these substances.

4. Iron and cobalt compounds should not be present in the electrolyte. If they are present in concentrations exceeding 0.0001 mole and 0.001 mole, then a rough, weak lead dioxide is apt to be electrodeposited (2).

5. It is desirable generally that the concentration of a lead salt be high, but it must not be so high that the salt may be deposited on the electrodeposition surface as a result of a fall in the temperature of the electrolyte, an increase of the $H^+$ activity in the electrolyte, etc. (see Fig. 2 and BS in Table I).

The fibrous texture consists of a group of fibers, and the columnar texture consists of a group of columns. Under conditions that fibers or columns tend to deposit, while the electrodeposited lead dioxide layer is thin, the layer generally consists of fine crystals; however, with the increase of layer thickness, fibers or columns tend to grow up along flow lines of the electric current.

Fibrous lead dioxide tends to electrodeposit when the current density is slightly high at room temperature. Strengths of the fibrous lead dioxide rank next to those of the dull, smooth lead dioxide (see Fig. 3 and M(F,G) in Table I).

Columnar lead dioxide tends to electrodeposit when the current density is high at room temperature. In general the column has an irregularly shaped polygonal cross section, the sides of the polygon being curved lines. The cross-sectional area is generally 0.1-50 $mm^2$.

Although the column appears to be connected to its neighboring part, it is actually in contact only with the layer of the first stage of electrodeposition. In the event that a group of columns crowd, as typified in Fig. 4, the layer electrodeposited during the first period, for example, the first electrodeposited layer which is generally 1-3 mm thick, consists of fine grains which are connected more firmly to their neighboring parts. However, the layer electrodeposited at a later period consists of columns which are not connected but are instead only in contact with their neighboring parts.

Although the columns themselves in the columnar texture are comparatively strong, they are easily separated by external forces. Therefore, the columnar lead dioxide is brittle and weak, and its life for use in electrolyses is short (see Fig. 4 and C in Table I).

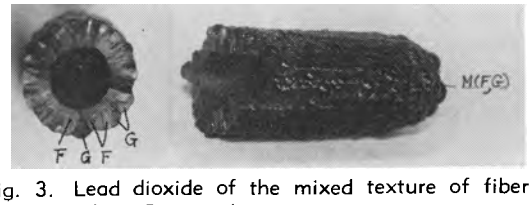


Fig. 3. Lead dioxide of the mixed texture of fiber and granule; F, fiber; G, granule.

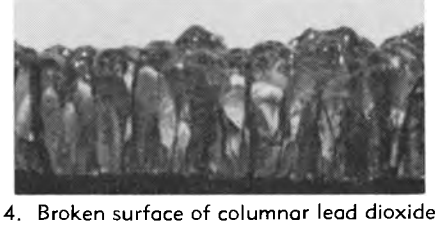

Fig. 4. Broken surface of columnar lead dioxide: C

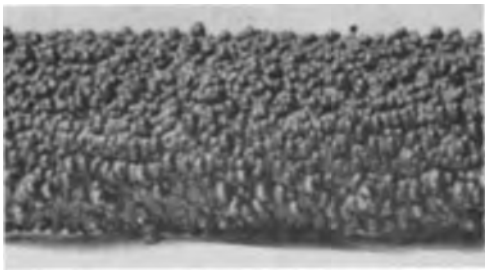

Fig. 5. Hollow cylindrical rod of granular lead dioxide: G2

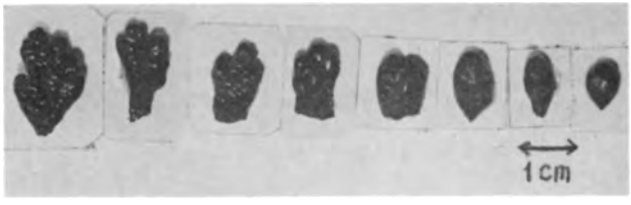


Fig. 6. Granules usually electrodeposited


Fig. 7. Electrodeposited lead dioxide whose granules were formed on projected points of the substrate. The substrate was shaped by hand with a knife to a cylindrical rod. There was many stripes parallel to the axis an the surface of the substrate.

The granular texture results from a grouping of granules (see Fig. 5 and G2 in Table I). An irregular cone or pyramid is the common shape of the granules encountered. The vertex lies near the substrate, and the base is a curved surface like a semi-sphere in the first stage and becomes a complex shape as electrodeposition progresses. For instance, some secondary granules may appear on this surface and, moreover, tertiary granules may appear on the secondary granules, etc. The granules ordinarily grow at an accelerated rate during the progress of electrodeposition. The types of granules usually electrodeposited are shown in Fig. 6.

In general, the major portion of a side of a granule appears to the naked eye to be connected to the neighboring part; however, the only connection is at the root (the part near the vertex), the remainder being merely in contact. For this reason the granule is easily removed by external forces, and the granular lead dioxide is brittle and weak.

The lead dioxide of this texture tends to be electrodeposited under one or more of the following conditions: (*a*) the surface of the substrate is rough; a granule is often formed on a projecting point on the surface of the substrate (see Fig. 7 and G3 in Table I); (*b*) high current density is at room temperature; (*c*) electrolyte composition suitable for the electrodeposition of this texture exhibits poor throwing power; (*d*) foreign particles are in the electrolyte.

If the electrolyte or electrode surface is in motion during electrodeposition, the shape of the granule is influenced. For instance, when the electrolyte flows past the electrodeposition surface during electrodeposition, the granule grows as shown in Fig. 8.

When the lead dioxide is electrodeposited on the surface of a cylinder which is rotating around its axis at high speed, the relative motion of the electrodeposition surface and the electrolyte results in the formation of stripe-shape or ring-shape protuberances in the circumferential direction instead of granules (see Fig. 9 and G(S) and G(R) in Table I).

The rough texture results from powders or fine granules which connect one another roughly. The rough lead dioxide is somewhat porous and weak. It tends to deposit under one or two of the following conditions: (*a*) current density is very high or the concentration of the $Pb^{2+}$ is very low; rough lead dioxide is more easily electrodeposited when the current density is so high or the $Pb^{2+}$ concentration is so low that oxygen is evolved simultaneously; (*b*) there are certain impurities in the electrolyte. Iron compounds, cobalt compounds, and finely powdered active carbon are examples of these (2) (see Fig. 10 and R1-R5 in Table I).

A porous texture is one that has many pits or pores. Porous lead dioxide is generally weak. This electrodeposits when gas bubbles adhere to the electrode surface and are not removed for a long time during electrodeposition or when the salt concentration of the electrolyte is so high that the salt crystallizes on the anode surface during electrodeposition. The adhering bubbles are apt to be re-

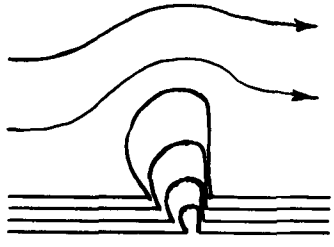

Fig. 8. Relation between growth of the granule and relative motion of the electrodepositian surface and electrolyte.

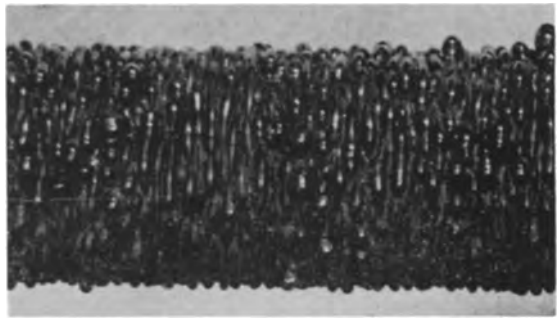

Fig. 9. Hollow cylindrical rod consisting of stripe-shape protuberances: G(S)1.

Fig. 10. Thin plate of rough lead dioxide: R4

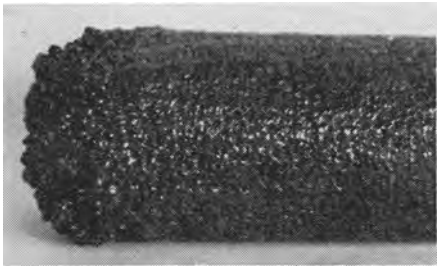

Fig. 11. Hollow cylinder of porous lead dioxide: P2

moved by adding a small quantity of a surface-active agent to the electrolyte or by brushing the surface with a nonconducting brush during electrolysis.

When the concentration of a salt in the electrolyte is high, crystals of the salt are likely to be deposited on the electrode surface, owing to the lowering of the temperature of the electrolyte or the decrease of the solubility of the salt, owing to the production of an acid on the anode surface. The crystallized salt is partly or entirely covered with the lead dioxide being electrodeposited, and pores are made when the partly covered salt is removed by washing with water (see Fig. 11 and P1 and P2 in Table I).

## Conclusions

The textures of the electrodeposited lead dioxide and the relation among the textures, the strengths of the lead dioxide, and the conditions of the electrodeposition were obtained as shown in Table II.

Bright, smooth lead dioxide was the strongest. This was electrodeposited when the substrate was smooth, when the current densities were 1 amp/dm$^2$ at 0°C, 2.5 amp/dm$^2$ at 10°C, and 5.5 amp/dm$^2$ at 20°C with concentrated lead nitrate solution, and 2 amp/dm$^2$ at 20°C with concentrated lead sulfamate solution, when one or a combination of the following substances were present in the electrolyte: aluminum salts, manganese salts, polyoxyethelene-alkylether, paratoluenesulfonamide, or when the concentrations of iron or cobalt compounds present in the electrolyte were less than 0.0001 mole and 0.001 mole, respectively.

**Table II. Textures and strengths of lead dioxide obtained under various conditions of electrodeposition**

| Texture of electrodeposited lead dioxide | Order of the strengths of lead dioxide | Conditions of electrodeposition: Current density of electrodeposition | Conditions of electrodeposition: Order of smoothness of the surface of substrate |
|---|---|---|---|
| Slightly coarse texture | 7 | Very low | |
| Dull, smooth texture | 2 | Slightly low | 2 |
| Bright, smooth texture | 1 | Medium | 1 |
| Fibrous texture | 3 | Slightly high | 3 |
| Columnar texture | 4 | Rather high | 4 |
| Granular texture | 5 | High | 5 |
| Rough texture | 8 | Very high | |
| Porous texture | 6 | Gas bubbles or crystals of a salt adhere to the surface of the electrodeposition | |

## Acknowledgment

This research was supported in part from scientific research funds granted by the Educational Department of the Japanese Government and in part by a grant from the Yokohama Battery Factory of Tohtetsu Industry Company Ltd.

Manuscript received Nov. 21, 1957. This paper was prepared for delivery before the Ottawa Meeting, Sept. 28-Oct. 2, 1958.

Any discussion of this paper will appear in a Discussion Section to be published in the June 1959 JOURNAL.

REFERENCES

1. Y. Shibasaki, *Bull. Faculty Eng. Yokohama Natl. Univ.*, **1**, 105 (1951); **2**, 69 (1953); **3**, 77 (1954); **4**, 85 (1955); **5**, 149 (1956); *J. Electrochem. Assoc. Japan*, **19**, 82 (1951); *J. Chem. Soc. Japan, Industrial Chem. Sec.*, **53**, 97 (1950); **54**, 205 (1951); **54**, 357 (1951); **54**, 713 (1951); **55**, 61 (1952); **55**, 558 (1952); **56**, 230 (1953); **56**, 398 (1953); **56**, 485 (1953); **57**, 341 (1954); **57**, 703 (1954); **57**, 794 (1954); **58**, 95 (1955); **58**, 179 (1955).
2. Y. Shibasaki, *J. Chem. Soc. Japan, Industrial Chem. Sec.*, **54**, 713 (1951); **58**, 95 (1955).

# Galvanic Corrosion

## II. Effect of pH and Dissolved Oxygen Concentration on the Aluminum-Steel Couple

M. J. Pryor[1] and D. S. Keir

*Department of Metallurgical Research, Kaiser Aluminum & Chemical Corporation, Spokane, Washington*

ABSTRACT

The effect of pH, dissolved gas composition, and deaeration on the galvanic characteristics of the aluminum-steel couple was investigated. High-purity aluminum cathodically protects steel completely in chloride solutions within the pH range 0.2-14.0. The galvanic currents and weight losses of the aluminum anodes are at a minimum from pH 4.0 to 10.0. Within this pH range the rate of galvanic corrosion is controlled by oxygen depolarization at the steel cathodes. The galvanic current fluctuates because the oxide film on the steel cathode is thickening with time in an erratic manner.

At higher and lower pH the rate of galvanic corrosion is much greater and is independent of the oxygen concentration in solution. The reaction occurring on the steel cathodes is the vigorous evolution of gaseous hydrogen. Any oxide films on the steel cathodes are subjected to rapid reductive dissolution to soluble ferrous ions. Consequently the galvanic current is extremely steady and reproducible.

In an earlier paper (1) the current flow and polarization characteristics of the aluminum-steel galvanic couple in sodium chloride solution were investigated. It was found that: (*a*) steel was cathodically protected by high-purity Al over a wide range of ratios of electrode areas, (*b*) both the galvanic current and Al weight loss were approximately proportional to the cathode area and independent of the anode area, and (*c*) the galvanic current was approximately proportional to the rate at which the solution was stirred. These results showed that the rate of galvanic corrosion in nearly neutral chloride solutions was controlled by oxygen depolarization at the steel cathodes. The Al anodes were corroded slightly more rapidly than was calculated from the galvanic current flow. This suggested that the local cathodes on active Al anodes were not completely suppressed under the conditions studied.

Experiments described in this paper represent an extension of the previous studies. The effect of pH, varying oxygen concentration in solution, and deaeration on galvanic current flow and on anodic weight loss has been investigated. The conditions under which the air-formed oxide film on the steel cathode is stable have been determined and have been correlated with the galvanic results.

### Experimental

*Materials.*—The Al and mild steel used in this investigation were in the form of cold rolled sheet 0.088 cm thick and had the same compositions as described in a previous paper (1).

All solutions were made from analytical reagent chemicals and distilled water and were presaturated with the appropriate gas before the experiment.

Steel specimens were prepared as described previously (1). Aluminum specimens were etched in 1.0*N* NaOH for 10 min, rinsed in distilled water, dried, rinsed again in benzene, and stored in dry air for 24 hr.

### Experimental Method

The closed galvanic cell used in this investigation had a solution capacity of 100 ml and is shown in Fig. 1. Two dissimilar metal electrodes (A and B) having dimensions 5 x 1 cm immersed in solution were held rigidly in place 2 cm apart by means of a small Lucite disk (C). The effective electrode area was 10 cm$^2$. The electrodes were connected to Pt wires (D) which passed out of the cell through glass seals to a zero resistance microammeter. The connections between (D) and the electrodes (A and B) were embedded in Lucite to prevent any galvanic corrosion. The cell was provided with a salt bridge (E) for measuring the potential of the couple by standard methods.

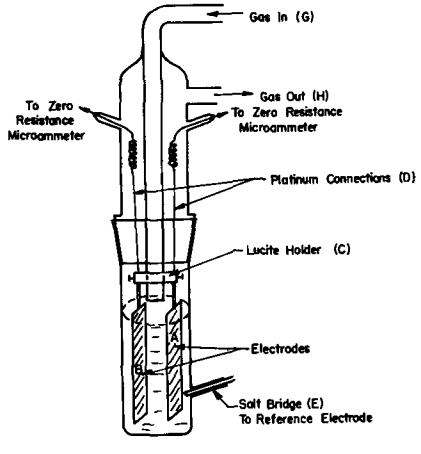


Fig. 1. Galvanic cell

[1] Present address: Metals Research Division, Olin Mathieson Chemical Corporation, New Haven, Conn.

Before any experiment, the appropriate solution was saturated in a separate vessel by prolonged bubbling with the particular gas or gas mixture under investigation. The solution was quickly transferred to the galvanic cell and the same gas, presaturated with water vapor, passed in through the tube (G) and out through (H). The rate at which the gas was passed through the galvanic cell was not critical provided the surface of the solution was not visibly agitated. The gases investigated were oxygen, air, air freed from $CO_2$, and helium.

Solutions having variable hydrogen ion concentration from $10^{-2}N$ to $10^{-12}N$ and having constant chloride ion concentration (±1%) were prepared by adjusting the pH of 1.0*N* NaCl with either HCl or NaOH. Normal HCl and NaOH, respectively, were used for pH values of 0.2 and 14.0; the latter contained no added chloride. The cell was contained in a water bath thermostatically controlled at 25° ± 0.05°C.

Current, potential, and weight loss measurements in the galvanic cells were made as described previously (1).

## Results

*Galvanic experiments at different pH values in solutions saturated with dissolved air.*—Triplicate galvanic experiments were carried out at each pH value from 0.2 to 14.0. The duration of experiments within the pH range 6.0-10.0 was 96 hr. With the exception of measurements at pH 14.0 which were carried out for 4 hr, all other experiments were carried out for 24 hr. The purpose of employing these various times was to permit the use of one experimental method while still preventing significant (a change of less than 0.5 pH units) depletion of hydrogen ions. This experimental method was considered to be less objectionable than the use of buffered solutions since these introduce specific anion effects. Although this extrapolation does not take care of change in corrosion rate, the error introduced is small in comparison with the very large change in galvanic current and weight loss with pH.

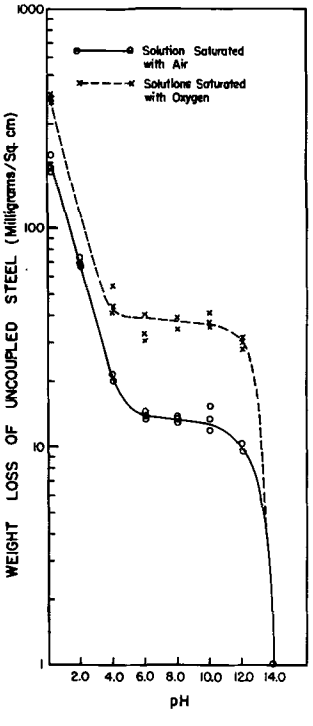


Fig. 2. Relationship between weight loss of uncoupled steel and pH of solutions saturated with air and oxygen. Calculations based on 96-hr run. Actual period for pH 14.0 was 4 hr; for pH 6.0-10.0, 96 hr; for all others, 24 hr.

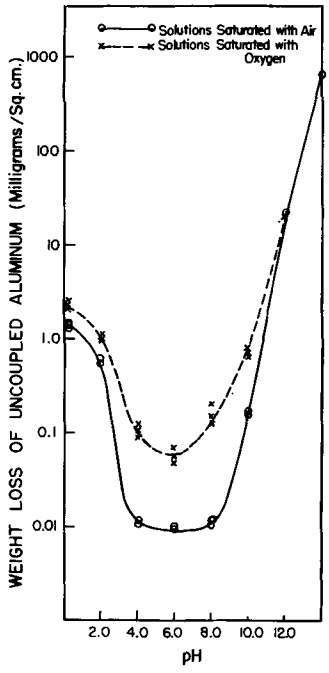


Fig. 3. Relationship between weight loss of uncoupled Al in 96 hr and pH of solutions saturated with air and oxygen at 25°C. See caption Fig. 2.

Figure 2 shows the relationship between weight loss in 96 hr and pH for uncoupled steel specimens in solutions saturated with air and with oxygen and maintained in equilibrium with these gases. The curves are of the type previously reported by Forrest, Roetheli, and Brown (2) for mild steel.

Figure 3 shows the relationship between weight loss in 96 hr and pH for uncoupled Al specimens in similar solutions. These curves exhibit minimum weight loss within the pH range of 4.0-8.0 as had been found previously by Edeleanu and Evans (3).

Steel specimens coupled to Al anodes in similar solutions were completely cathodically protected over the entire pH range studied. At the same time the weight losses of the Al anodes were increased (Fig. 4). Figure 5 shows the relation between the number of coulombs flowing and pH. The curve closely parallels the anodic weight loss vs. pH curve in Fig. 4. Table I shows the calculated anodic weight loss due to the galvanic current flow. At pH values up to 10.0 this comprises only 71-91% of the total anodic weight loss. At pH 14.0 the weight loss due to galvanic current flow is only 34-45% of the total weight loss. Evidently substantial proportions of the Al weight losses are due to local cell corrosion particularly at high pH.

*Effect of gas atmosphere.*—Figures 2-5 show experimental results on weight loss and current flow in solutions presaturated with air. Similar experiments were performed using air freed from $CO_2$.

Table I. Weight losses of Al anodes due to galvanic corrosion and local action at different pH in solutions saturated with air

| pH | No. of coulombs flowing in 96 hr | Galvanic wt loss of Al anode, mg/cm² | Total Al wt loss, mg/cm² | Wt loss due to local action, mg/cm² | % local action wt loss |
|---|---|---|---|---|---|
| 0.2 | 4916; 4270; 4870 | 45.9; 39.9; 45.4 | 53.2; 47.5; 53.7 | 7.3; 7.7; 8.3 | 14; 16; 15 |
| 2.0 | 276; 272; 256 | 2.6; 2.6; 2.4 | 3.2; 3.2; 2.9 | 0.6; 0.7; 0.5 | 20; 21; 18 |
| 4.0 | 72; 64 | 0.7; 0.6 | 1.0; 0.9 | 0.3; 0.2 | 29; 29 |
| 6.0 | 42; 41; 42 | 0.4; 0.4; 0.4 | 0.5; 0.5; 0.4 | 0.1; 0.1; 0.05 | 17; 19; 9 |
| 8.0 | 40; 40; 41 | 0.4; 0.4; 0.4 | 0.5; 0.5; 0.5 | 0.1; 0.1; 0.1 | 18; 18; 19 |
| 10.0 | 40; 44 | 0.4; 0.4 | 0.5; 0.5 | 0.1; 0.1 | 21; 18 |
| 14.0 | 23,600; 23,450 | 219; 220 | 643; 589 | 424; 368 | 66; 55 |

However, the removal of $CO_2$ in no way changed any of the results. Figures 2-5 also show that presaturation with oxygen and the maintenance of an oxygen atmosphere over the solution increase the rate of corrosion and galvanic corrosion of Al and the rate of corrosion of uncoupled steel. In the galvanic experiments the effect is only observed from pH 4.0-10.0. On uncoupled specimens of Al and steel the effect is observed over a somewhat broader pH range.

Figure 6 shows current-time curves, at zero external resistance, in normal NaCl (pH 6.0) presaturated with and maintained in atmospheres of air, oxygen, and helium. In solutions saturated with air the oxygen evidently becomes partly depleted quite rapidly and the galvanic current achieves a value of around 10 $\mu$a/cm² of cathode area. In solutions initially saturated with oxygen, the dissolved oxygen concentration is higher and so less depletion and higher galvanic currents are obtained. Only very small galvanic currents flow in solutions saturated with He. Table II shows the anodic weight losses of Al anodes and the number of coulombs flowing as a function of gas atmosphere.

Figure 7 shows the results of similar experiments in normal HCl and NaOH. Here, initial saturation of the solution with oxygen or helium (not shown in these curves) has no significant effect on the galvanic current flow or on the weight losses of Al anodes.

*Potential measurements.*—Potential measurements of the couple on closed circuit were carried out during all galvanic experiments as described previously (1). Figure 8 shows the potentials[2] of the galvanic couples at different pH values in solutions presaturated and remaining in contact with the air.

*Oxide film stability.*—The stability of the air-formed oxide film on a steel cathode has been shown to affect the current-potential relationship existing during cathodic protection (4). In order to determine whether a similar effect exists during galvanic corrosion, the stability of visible oxide films on steel cathodes coupled to Al anodes was determined at different pH values. Steel specimens were heat-tinted to the first order red interference color. A small portion of the oxide was autoreduced (5) by immersion in dilute HCl. The steel specimens were then coupled to Al anodes in solutions of different pH. The rate of reductive dissolution of the remaining red film could then be judged quite accurately

[2] Except in the first few minutes of the galvanic experiments, potentials were constant to within ±10 mv.

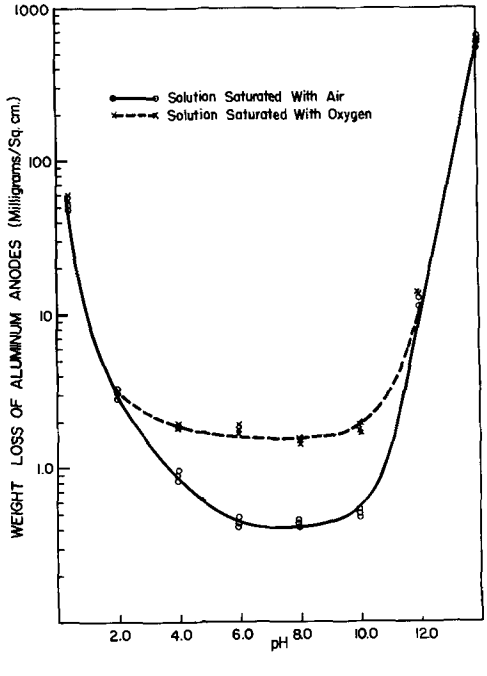


Fig. 4. Effect of pH on the weight loss in 96 hr of Al anodes in solutions saturated with air and oxygen at 25°C. See caption Fig. 2.

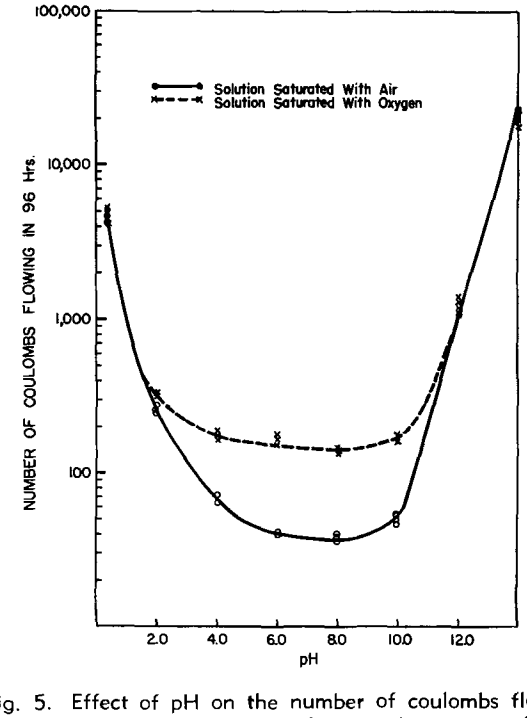


Fig. 5. Effect of pH on the number of coulombs flowing in 96 hr in solutions saturated with air and oxygen at 25°C. See caption Fig. 2.

Table II. Effect of saturation with different gases on galvanic corrosion of the Al-steel couple in 1.0*N* NaCl

| Gas environment | pH | No. of coulombs flowing | Galvanic wt loss of Al anode, mg/cm² | Total Al wt loss, mg/cm² | Al wt loss due to local action, mg/cm² |
|---|---|---|---|---|---|
| Helium | 6.0 | 6; 4 | 0.05; 0.04 | 0.07; 0.04 | 0; 0.02 |
| Air | 6.0 | 42; 41; 42 | 0.4; 0.4; 0.4 | 0.5; 0.4; 0.5 | 0.1; 0.1; 0.05 |
| Oxygen | 6.0 | 170; 166; 187 | 1.6; 1.6; 1.8 | 1.8; 1.8; 1.9 | 0.2; 0.2; 0.1 |

by observation of the time at which the boundary disappeared. The times required for reductive dissolution of the thermal oxide films at different pH values are shown in Table III.

## Discussion

This investigation shows that steel is cathodically protected by coupling to high-purity Al, not only in nearly neutral chloride solutions as was shown previously (1), but over the entire pH range. The galvanic current flow (Fig. 5) and the weight losses of the Al anodes (Fig. 4) are strongly pH dependent and follow the same general trend as the weight loss variation of uncoupled Al specimens with pH (Fig. 3).

Neither the galvanic current flow nor the anodic weight losses are affected significantly by saturation with different gases at high and at low pH values (Fig. 4, 5, 7). Consequently the cathodic reaction occurring on the steel cathodes at these pH values must be primarily the evolution of gaseous hydrogen.

Within the pH range of 4.0-10.0 both galvanic current flow and anodic Al weight losses are strongly dependent on dissolved oxygen concentration. Saturation of the solutions with dissolved oxygen increases galvanic current flow by a factor of approximately five over that obtained in solutions saturated with dissolved air (Fig. 5 and 7). These results support the previous contention (1) that the primary cathodic reaction on steel cathodes in nearly neutral solutions is the reduction of dissolved oxygen in solution. The over-all galvanic corrosion within this pH range is controlled by the rate at which dissolved oxygen can diffuse from the bulk of the solution to the cathode surface. Clearly from Fig. 7 this is controlled to a considerable degree by the oxygen content of the gas above the solution.

Removal of most of the dissolved oxygen from nearly neutral solutions by saturation with He reduces the galvanic current flow virtually to zero (Fig. 6, Table I). Since the reduction of dissolved oxygen can no longer occur, the primary cathodic reaction must now be the evolution of hydrogen.

Table III. Effect of pH on time required for reductive dissolution of first order red oxide films on steel coupled to Al

| pH | Time for reductive dissolution |
|---|---|
| 0.20 | 1 sec |
| 2.04 | 12 sec |
| 4.00 | 1 day |
| 6.15 | Incomplete reduction after 4 days |
| 7.95 | Incomplete reduction after 4 days |
| 9.95 | 2 days |
| 12.00 | 1 day |
| 14.00 | 5 sec |

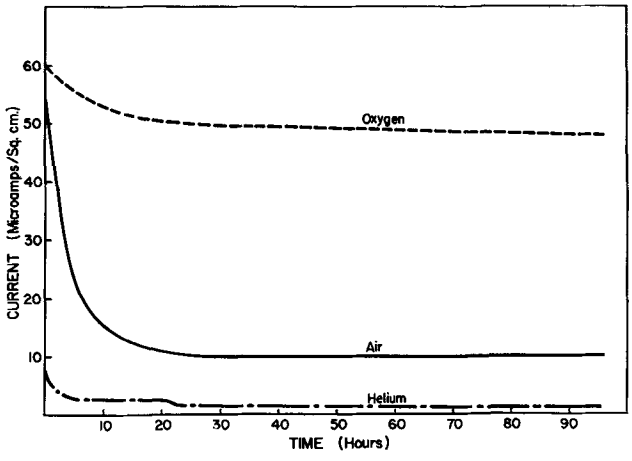


Fig. 6. Relationship between galvanic current flow and time in normal NaCl (pH 6.0) solution saturated with air, oxygen, and helium at 25°C.

Previous work (6) showed that, at potentials in the region of −0.5 to −0.6 v, the cathodic evolution of hydrogen from a steel surface is an extremely sluggish process and is highly polarized. High cathodic polarization of hydrogen evolution at potentials within the range −0.5 to −0.6 v therefore accounts for the very low values of galvanic current (Fig. 6) in nearly neutral solutions containing very little dissolved oxygen.

Figure 8 shows the relationship between the potential of the couple and pH. Potential is roughly constant up to pH 10. Consequently local action weight loss (Table I) is also roughly constant up to this pH. At higher pH values the potential of the

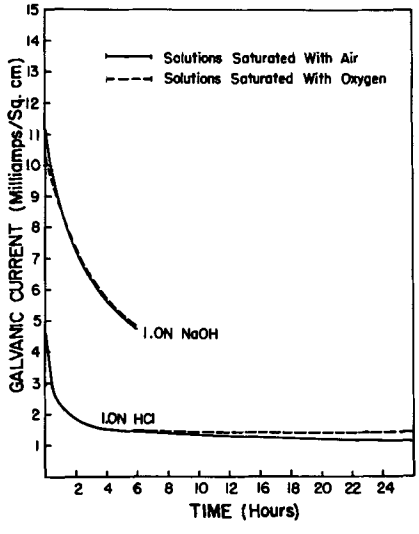


Fig. 7. Relationship between galvanic current-flow and time in normal NaOH and HCl solutions saturated with air and oxygen at 25°C.

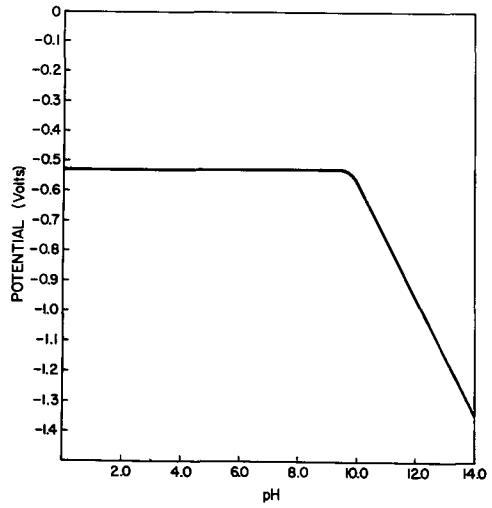


Fig. 8. Effect of pH on closed-circuit potential of the Al-steel couple at 25°C.

couple becomes less noble. Local cathodes on the Al anode should become even more active and so weight loss due to local action increases (Table I). Figure 8 closely parallels the relationship between the corrosion potential of uncoupled Al and *p*H. Therefore it is apparent that the closed-circuit potential of the galvanic couple is controlled by the corrosion potential of the Al anode. The rate of galvanic corrosion, therefore, is controlled by the current that can be drawn from a steel cathode at the potential of the Al anode.

At *p*H values up to and including 2.0 and above 12.0, hydrogen is visibly and rapidly evolved from steel cathodes. The presence or absence of dissolved oxygen has no significant effect on the rate of galvanic corrosion. Therefore the steel cathodes within these *p*H ranges may be considered to be hydrogen electrodes operating at essentially atmospheric pressure of hydrogen. Table IV shows a calculation of the reversible potential for hydrogen evolution as a function of *p*H within the range where this particular cathodic reaction occurs. Also shown in Table IV is the actual potential at which hydrogen evolution is observed on the steel cathodes (from Fig. 8) and the difference between the two values.

At *p*H values of 0.2 and 14.0 the difference between the reversible hydrogen potential and the measured potential (Table IV) is much greater than the hydrogen overpotential on steel (0.17 v) (7). Therefore hydrogen evolution from steel cathodes at *p*H values of 0.2 and 14.0 should be a very easy process. The difference between the reversible hydrogen potential and the measured potential at *p*H values of 2.0 and 12.0 is less and is more comparable with the hydrogen overpotential on steel; accordingly evolution of hydrogen from steel should be more difficult at these *p*H values. This general trend is well illustrated in the galvanic results contained in Fig. 4 and 5.

Table IV. Reversible and measured potential of $H_2$ evolution from steel cathodes

| *p*H | Reversible hydrogen electrode potential,* v | Actual potential of hydrogen evolution, v | Potential difference between two reactions, v |
|---|---|---|---|
| 0.2 | —0.01 | —0.53 | 0.52 |
| 2.0 | —0.12 | —0.53 | 0.41 |
| 12.0 | —0.71 | —0.97 | 0.26 |
| 14.0 | —0.83 | —1.34 | 0.51 |

* At 760 mm pressure of hydrogen.

At *p*H values within the range 4.0 to 10.0 hydrogen evolution is not the primary cathodic reaction on steel cathodes except when the solutions are deaerated. Instead oxygen dissolved in solution will be reduced cathodically according to an equation of the type

$$2H^+ + \tfrac{1}{2}\,O_2 + 2e = H_2O \qquad [1]$$

The $E_o$ value for this reaction is +1.27 v (8). The $E_o$ value corrected for oxygen concentration may also be calculated as a function of *p*H and compared with the measured potential at which oxygen reduction occurs. Calculation shows that the difference between the two values is also *p*H dependent and is at a minimum at *p*H 10.

However, the rate of reduction of dissolved oxygen at a steel cathode will be controlled primarily by the rate at which oxygen diffuses from the bulk of the solution to the cathode surface (1). This rate depends, with the same geometric electrode configuration, on oxygen solubility, temperature, and solution movement. In the galvanic experiments described earlier these variables, with the exception of dissolved oxygen concentration, were held constant. Dissolved oxygen concentration was held constant initially at two levels. Therefore, rate of oxygen depolarization within the *p*H range of 4-10 should be roughly constant at any one of the two levels of dissolved oxygen concentration. Reference to the galvanic results in Fig. 4 and 5 shows that this is in fact true. Both the weight losses of Al anodes and galvanic current flow are roughly constant when the solutions are initially saturated with dissolved oxygen. Galvanic current flow is somewhat increased at *p*H 4.0 in solutions initially saturated with air presumably because some hydrogen evolution occurs in these experiments.

During the previous investigation of the Al-steel couple in NaCl solutions it was noticed that the current-time curves were somewhat erratic (1). This same behavior was noticed in this investigation in solutions falling within the *p*H range of 4.0-10.0. Current-time curves at higher and lower *p*H values changed in an extremely smooth and highly reproducible manner. In order to understand this behavior it is necessary to consider in more detail the nature of the cathodic reactions occurring on a steel surface at nearly neutral *p*H values.

When the steel is first immersed in the solutions it is covered with a film of $\gamma$-$Fe_2O_3$ some 50-100 Å thick. This film either may remain stable or may be thinned uniformly and later removed entirely by reductive dissolution to soluble ferrous ions according to the equation (9):

$$Fe_2O_3 + 6H^+ + 2e = 2Fe^{++} + 3H_2O \qquad [2]$$

Table III contains information concerning the stability of somewhat thicker oxide films on steel

specimens coupled to Al anodes at different pH values. It may be seen that, in solutions having pH values of 2.0 and lower and also 12.0 and higher, reductive dissolution of oxide films on steel occurs quite rapidly. Therefore during the galvanic experiments within these two pH ranges evolution of hydrogen is taking place from film-free steel.

It was known previously that iron oxide films were readily reduced to soluble ferrous ions at low pH (5). However rapid reductive dissolution of iron oxide films at pH 14.0 has not been observed previously. Oswin and Cohen (10) reported reductive dissolution of $\alpha$-$Fe_2O_3$ films at current densities of 30 $\mu a/cm^2$ in deaerated solutions at pH 11.9. Evidently as the cathodic current density is greatly increased, reductive dissolution of iron oxide films can be achieved at even higher pH values. Normally solutions must be well deaerated to observe reductive dissolution of iron oxide films at high pH since otherwise the reduction of dissolved oxygen is the preferred cathodic process (5). This suggests that, in the present galvanic experiments, a good degree of deaeration is achieved in the vicinity of the steel cathodes within the pH range 12.0-14.0 by the very vigorous evolution of hydrogen.

Table IV shows that the oxide film on a steel cathode remains either unreduced or is only slowly reduced within the pH range 4-10. Therefore, reduction of dissolved oxygen at a steel cathode coupled to an Al anode occurs on the surface of a $\gamma$-$Fe_2O_3$ film rather than on the steel itself. Similar conditions were achieved during the application of constant impressed currents of the order of 20 $\mu a/cm^2$ to oxide covered steel cathodes in nearly neutral chloride solutions (4). Here the current was held constant and the potential of the cathode measured. The potential-time curves were extremely erratic and moved slowly in the noble direction. This suggested a process of film breakdown and repair, with film repair gradually attaining the upper hand. In the present investigation the potential of the cathode remained roughly constant and so the current could vary, provided conditions on the cathode were not constant. The same sequence of local film breakdown (due either to undermining or to highly localized reductive dissolution) and repair due to oxygen in solution should also occur in the present galvanic experiments in the nearly neutral pH range. Since the potential is roughly constant this should result in fluctuation of the galvanic current. This is in fact observed within the pH range 4-10.

At higher and lower pH where the oxide film is rapidly reduced, the steel cathode remains in the bare condition probably throughout the experiment. When the condition of the steel cathode remains constant in this manner the galvanic currents do not fluctuate in an erratic manner with time.

This implies that the mechanism of cathodic protection of a steel cathode by an Al anode is pH dependent. At high and low pH where any pre-existing oxide film on the steel is dissolved reductively, protection must be the result of depression of its potential to a value where it is difficult, on thermodynamic consideration, for iron ions to leave the metallic lattice.

In the intermediate pH range, protection of the steel cathode results largely from the thickening of the original air-formed oxide film (4) despite the fact that local breakdown of the film occurs periodically. In this connection it is significant that the potential of a steel cathode measured immediately after its contact with an Al anode had been broken is found to be ennobled by as much as 300-400 mv from its uncoupled value in the same solution (1). This noble value of potential slowly decays if the Fe remains uncoupled in the NaCl. This kinetic mechanism of cathodic protection of steel in the nearly neutral pH range (4), thus has many features common to the mechanism by which anodic inhibitors prevent the corrosion of steel (11). The action of the cathodic current is similar to that of the anodic inhibitor in that it reduces the rate at which iron ions leave the metallic lattice. This reduced rate of egress of iron ions permits the more effective adsorption of oxygen from solution onto the iron surface so that thicker and more protective films of $\gamma$-$Fe_2O_3$ may be gradually built up.

It is interesting to compare the relative behavior of high-purity Al and Zn as sacrificial anodes for steel in the nearly neutral pH range. Aluminum sacrificially protects steel by the kinetic mechanism outlined above. However, the potential of the Zn-steel couple is some 250 mv less noble than that of the Al-steel couple despite the fact that the galvanic currents are quite similar (1). At these less noble potentials any oxide film on the steel cathode is rapidly reduced (4). Consequently a Zn anode must protect steel cathodically in the neutral pH range by the same mechanism by which Al protects steel at very high and low pH. Current-time curves for the Zn-steel couple in NaCl solution are therefore much less erratic than those for the Al-steel couple (1). It is implicit that any comparison of the relative efficiencies of Al and Zn sacrificial anodes in the nearly neutral pH range should take account of the fact that the mechanism by which the two metals protect steel is different.

## Acknowledgment

The authors wish to thank the Kaiser Aluminum & Chemical Corporation for their support of this work and for their permission to publish the results.

Manuscript received Dec. 27, 1957. This paper was prepared for delivery before the Ottawa Meeting, Sept. 28-Oct. 2, 1958.

Any discussion of this paper will appear in a Discussion Section to be published in the June 1959 JOURNAL.

## REFERENCES

1. M. J. Pryor and D. S. Keir, *This Journal*, **104**, 269 (1957).
2. H. O. Forrest, B. E. Roetheli, and R. H. Brown, *Ind. Eng. Chem.*, **22**, 1197 (1930).
3. C. Edeleanu and U. R. Evans, *Trans Faraday Soc.*, **47**, 1121 (1951).
4. M. J. Pryor, *Nature*, **178**, 1245 (1956).
5. M. J. Pryor and U. R. Evans, *J. Chem. Soc.*, **1950**, 1259.
6. M. J. Pryor and M. Cohen, *This Journal*, **100**, 203 (1953).

7. J. A. V. Butler, "Electrocapillarity," p. 126, Methuen & Co., London (1940).
8. T. R. Camp, *J. New England Water Works Assn.*, **60**, 188 (1946).
9. M. J. Pryor, *J. Chem. Soc.*, **1950**, 1274.
10. H. G. Oswin and M. Cohen, *This Journal*, **104**, 9 (1957).
11. M. J. Pryor, *ibid.*, **102**, 163 (1955).

# Local Cell Action During The Scaling of Metals, II (1)

**Christa Ilschner-Gensch**[1]

*Department of Metallurgy, Massachusetts Institute of Technology, Cambridge, Massachusetts*

ABSTRACT

If nickel is covered by a borate melt under an oxygen atmosphere, practically no oxidation takes place. If, however, the nickel sample is in electrical contact with an electronic conductor, e.g., a noble metal gauze, which extends up to the melt-oxygen interface, nickel is attacked rapidly by virtue of local cell action. In this case, electron transfer is accomplished by the metal gauze and ions migrate through the borate melt. Electrochemical measurements show that the reaction is controlled mainly by polarization of the cathode where oxygen molecules are reduced to ions.

The oxidation of nickel to nickel oxide proceeds according to the over-all reaction

$$Ni(s) + \tfrac{1}{2}\, O_2(g) = NiO(s) \qquad [1]$$

If a dense oxide film is formed, as in this case, the oxidation can advance only by diffusion of the reactants across the oxide film to each other. It has been suggested (2) that the migrating particles are ions and electrons rather than atoms. In the nickel oxide, the electronic conductivity prevails, and therefore the oxidation rate is determined essentially by the ionic conductivity of the oxide. The rate constant for the nickel oxidation at 780°C and 0.1 atm $O_2$ partial pressure has been determined by different authors (3) to be $k = 10^{-12} - 10^{-11}$ g$^2$ cm$^{-4}$ sec$^{-1}$ for specimens of different purity.

When Ni is covered by a borate melt, oxidation can take place only inasmuch as oxygen dissolves in the borate melt and diffuses from the outer surface of the melt to the metal-salt interface. The relatively low solubility of oxygen molecules in a borate melt results in a low transport rate and, accordingly, in a low rate of oxidation. If, however, Ni is in electrical contact with an electronic conductor, e. g., Pt extending to the melt-gas interface, the rate of attack will be higher owing to local cell action as shown schematically in Fig. 1 and confirmed by the experiments reported below.

## Rate Measurements

In order to investigate the corrosion of Ni under a borate melt, a spiral of Ni wire of 0.068 cm diameter and 20 cm length having a geometrical surface area of 4.3 cm$^2$ was placed in a porcelain crucible and covered with a dehydrated mixture of 65M % $Na_2B_4O_7$ and 35M % $K_2B_4O_7$, which has a eutectic melting point of 666°C (4). The molten salt had a depth of about 0.3 cm. The crucible, 1.4 cm in diameter at the bottom, was introduced on a support into an electrical furnace preheated to 780°C under $N_2$ (Fig. 2). After 10-15 min, oxygen was admitted. The amount of attack after periods ranging from 30 to 1560 min was determined by measuring the weight loss of the Ni sample after dissolving the solidified borate melt in water. The observed weight

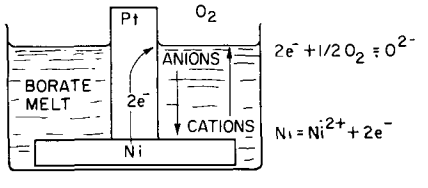


Fig. 1. Local cell action in a cell involving a Ni-Pt couple in a borate melt.

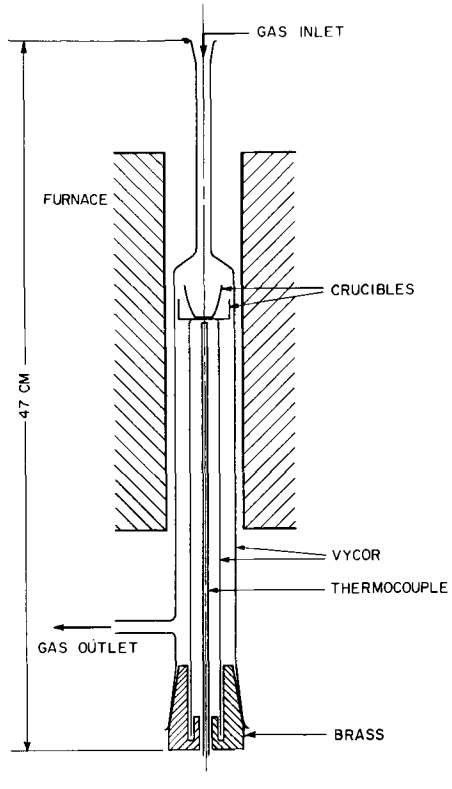


Fig. 2. Set-up for rate measurements

[1] Present address: Zentralforschungsanstalt Fried. Krupp, Essen, West Germany.

Table I. Weight losses of nickel and copper in a borate melt at 1 atm $O_2$ pressure and 780°C

| Sample | Time, min | Weight loss, mg |
|---|---|---|
| Ni | 60 | 0.1; 0.2; 0.0 |
| Ni | 1560 | 0.2 |
| Ni-Pt couple | 60 | 9.0; 7.1; 10.9 |
| Ni-Ag couple | 60 | 17.5; 10.0; 13.3 |
| Cu | 60 | 0.0 |
| Cu-Pt couple | 60 | 22.3; 21.8 |
| Cu-Ag couple | 60 | 38.0; 41.5; 35.0 |
| Ni-Pt couple + 1% FeO | 60 | 24.5; 23.1; 26.9 |

losses shown in Table I did not exceed 0.2 mg which is the limit of error.

Next, the behavior of gauzes of Ag and Pt partially immersed in the borate melt under oxygen was investigated. No appreciable weight changes were found, even after 18 hr.

In order to investigate the behavior of couples consisting of Ni wire and a gauze of Ag or Pt, a piece of noble metal gauze 2.5 cm x 4.5 cm was welded to a nickel spiral and rolled together as shown in Fig. 3. From the dimensions, the metallic surface per square centimeter gauze was estimated to be 2.24 $cm^2$ for the Ag gauze and 1.29 for the Pt gauze. Composite samples with Ni completely immersed and the noble metal gauze partly in the melt were tested as described above. After dissolving the major portion of the borate in water, there remained some greenish material which was dissolved by agitating the sample in another crucible filled with borate melt over a Bunsen burner for 2 min. As shown in Table I, the resulting weight losses of the composite samples are considerably greater than those of Ni samples without a gauze of Ag or Pt. Similar results were obtained with Cu couples, see Table I. Additional experiments with Ni-Pt composite samples were carried out, in which the noble metal did not extend through the surface but was also completely immersed. No weight loss was observed. This rules out as an explanation the assumption of a high oxygen overpotential at nickel or nickel oxide surfaces as being rate limiting in the first-mentioned experiments.

Significantly higher oxidation rates were observed on adding $FeSO_4$ corresponding to 1 wt % FeO in the presence and likewise in the absence of an electronic conductor. In this case $Fe^{2+}$ ions may be oxidized to $Fe^{3+}$ ions by molecular oxygen near the gas-electrolyte interface, the trivalent iron ions may diffuse toward the platinum-electrolyte or the nickel-electrolyte interface, respectively, where they are reduced to the divalent state, and $Fe^{2+}$ ions may diffuse backward toward the gas-electrolyte interface.

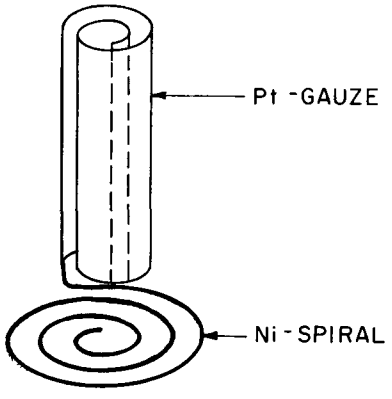


Fig. 3. Pt-Ni couple used for rate measurements

For a comparison, the rate of oxidation of Ni samples as used above under 1 atm oxygen partial pressure was determined. Weight increases from 0.8 to 0.9 mg, corresponding to loss of 3 mg Ni after 1 hr, were observed.

### Measurements of Open Circuit Potentials

The open-circuit potentials of Ni-Ag, Ni-Au, and Ni-Pt couples in a borate melt under air were determined by immersing wires of Ni and Ag, Au, or Pt in a borate melt. The potentials were initially low, increased with time, and finally reached steady-state values after about half an hour. Values are shown in Table II. The potentials observed for the Ni-Au and the Ni-Pt couple are close to the equilibrium potential of the galvanic cell

$$\mathrm{Ni(s)}, \mathrm{NiO(s)} \mid \text{borate melt} \mid \text{oxygen electrode} \quad \text{(I)}$$

involving the virtual cell reaction

$$\mathrm{Ni(s)} + \tfrac{1}{2}\,\mathrm{O_2}\ (\mathrm{g},\ 0.21\ \mathrm{atm}) = \mathrm{NiO(s)} \quad [2]$$

on passing two faradays. From data reported by Kiukkola and Wagner (5) the emf of cell (I) at 780°C is calculated to be 0.71 v. Since this value is close to the open-circuit potential of the Ni-Au and the Ni-Pt couple, it may be concluded that in these couples the Ni electrode is essentially a reversible Ni-NiO electrode in spite of the presence of oxygen, and the noble metal electrode essentially a reversible oxygen electrode. The lower open-circuit potential of the Ni-Ag couple of about 0.49 v suggests that the potential of the Ag electrode is a mixed potential resulting from the simultaneous reactions

$$\tfrac{1}{2}\,\mathrm{O_2} + 2e^- = \mathrm{O^{2-}} \quad [3]$$

$$2\mathrm{Ag^+} + 2e^- = 2\mathrm{Ag} \quad [4]$$

Likewise, the open-circuit potentials of Cu-Pt, Cu-Au, and Cu-Ag couples in a borate melt under air were determined (see Table II). In view of data reported by Kiukkola and Wagner (5), the emf of the cell

$$\mathrm{Cu(s)}, \mathrm{Cu_2O(s)} \mid \text{borate melt} \mid \text{oxygen electrode} \quad \text{(II)}$$

is estimated to be 0.45 v if the difference in the composition of the melt on the left-hand and the right-hand side of the cell is disregarded. This value

Table II. Open-circuit potentials $E$ of Ni-Pt, Ni-Au, Ni-Ag, Cu-Pt, Cu-Au, and Cu-Ag couples in a borate melt under air at 780°C

| Couple | E, v |
|---|---|
| Ni-Pt | 0.73 |
| Ni-Au | 0.74 |
| Ni-Ag | 0.49 |
| Cu-Pt | 0.47 |
| Cu-Au | 0.40 |
| Cu-Ag | 0.28 |

is not far from the potentials of 0.47 and 0.40 v observed for the Cu-Pt and the Cu-Au couple, respectively, although the melt next to the Cu electrode supposedly was not saturated with $Cu_2O$. Accordingly, the activity of $Cu_2O$ was less than unity, and elemental oxygen was not excluded. The potential observed for the Cu-Ag couple is considerably lower for reasons mentioned above for the Ni-Ag couple.

### Polarization Measurements

The current $I$ in a short-circuited cell involving a Ni and a Pt electrode as used in the rate measurements is related to the emf $E$ as driving force by the equation

$$E = \Delta E_c(I) + \Delta E_a(I) + IR \qquad [5]$$

where $\Delta E_c$ and $\Delta E_a$, respectively, are the absolute values of the polarization of the cathode and anode at current $I$, and $R$ is the resistance of the electrolyte. The conductivity of the K-Na borate melt may be assumed to be equal to that of molten $Na_2B_4O_7$, which is 0.22 $ohm^{-1}$ $cm^{-1}$ (6). The current equivalent to a weight loss of 10 mg Ni/hr is 0.01 amp. Thus the $IR$ drop is estimated to be of the order of 0.01 v, which value is much less than the available driving force $E$ in Eq. [5]. Hence, the current is controlled mainly by polarization.

To determine the value of $\Delta E_c$ accounting for polarization of the cathode, a cell involving three Pt electrodes was assembled. The cathode was a Pt gauze of the same dimensions used for the rate measurements. A ring of Pt wire as anode was located at the bottom of the porcelain crucible. In addition, there was a short Pt wire as reference electrode sidewise to the cathode. The crucible was placed in a Vycor tube with closed lower end and flushed with oxygen. The potential was predetermined with the help of a potentiometer, and the resulting current as well as the polarization potential of the cathode vs. the reference electrode was measured by a galvanometer and a tube voltmeter,

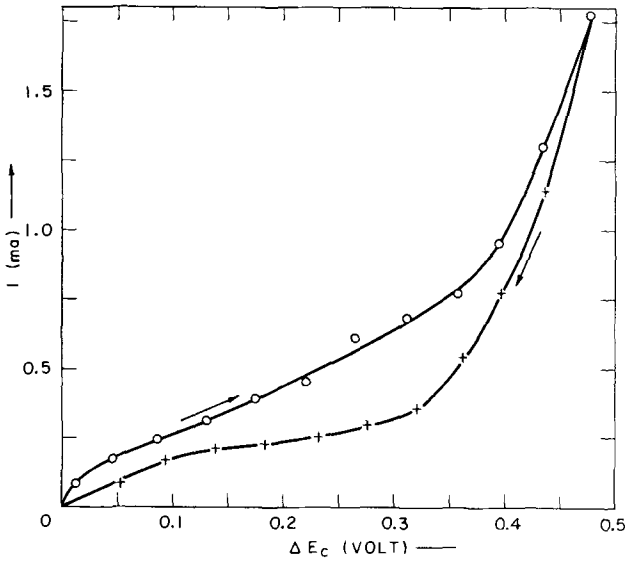


Fig. 4. Current I vs. polarization $\Delta E_c$ of a Pt gauze as cathode in a borate melt under oxygen for increasing and decreasing values of the applied potential.

respectively. The results are shown in Fig. 4. The polarization $\Delta E_c$ of the cathode is considerable and amounts to approximately 0.5 v at a current of 0.002 amp. Extrapolation of a logarithmic plot yields $\Delta E_c = 0.7$ v for $I = 0.01$ amp.

The polarization $\Delta E_a$ of a Ni anode of the same size as used in the rate measurements and covered by a borate melt was determined in a similar way. In this case, the polarization $\Delta E_a$ was measured for a current $I = 0.01$ amp applied during 1 hr. Values of $\Delta E_a$ ranging from 0.005 to 0.02 v were observed. Although results were not well reproducible, these observations indicate that the term $\Delta E_a$ in Eq. [5] is only minor.

In view of the foregoing results, it can be concluded that the current in a Ni-Pt couple is controlled mainly by polarization of the cathode at which oxygen molecules are reduced to ions. The essentially exponential shape of the curves especially for higher potentials seems to indicate a large contribution of activation polarization. The same holds supposedly for a Cu-Pt couple.

### Observations on the Wettability of Ag, Au, and Pt by a Borate Melt

At present, the individual contributions of activation and concentration polarization of a Pt electrode at which oxygen is reduced cathodically are not known precisely. Possibly concentration polarization also plays some part under the conditions employed in this research because the electrolyte was not stirred. Preliminary calculations suggest that diffusion of oxygen molecules from the gas-electrolyte interface to the portion of the cathode immersed in the melt is not sufficient in order to account for a current of 0.01 amp. Instead, the predominant mechanism of oxygen supply may be diffusion of oxygen molecules across a thin adherent layer of the borate melt wetting the Pt gauze above the general level of the melt. Subsequent migration of oxygen ions parallel to the Pt surface will be limited by resistance of the electrolyte forming the adherent layer. As a result of this, cathodic action at the Pt-electrolyte interface will be restricted to an area the height of which may be smaller than that of the adherent layer. The experimental evidence, in accordance with theoretical estimates, indicates that this is nevertheless sufficient to account for the currents observed.

The occurrence of an adherent layer of the melt on the electrodes is suggested by available observations (7), especially by recent observations by von Wartenberg (8) and Fulrath, Mitoff, and Pask (9). To obtain pertinent information for the borate melt used in the above experiments, small chunks of the solidified melt were placed on sheets of Ag, Pt, and Au in air in a tubular furnace heated to 780°C. With the help of a telescope, it was found that the borate melt spread readily on Ag and Pt, whereas in the case of Au a finite although small contact angle was observed. Thus the occurrence of an adherent layer of borate melt on Ag and Pt has been ascertained, and migration of oxygen molecules across such a layer is suggested tentatively as a mechanism accounting for relatively rapid transfer of oxygen

from the gas phase to the electrode made a cathode. Further experimental work beyond the scope of the present investigation is required in order to test this hypothesis.

### Concluding Remarks

The above results are of interest in conjunction with the catastrophic oxidation (10-12) of alloys under conditions where the scale consists of one or several solid oxides and a liquid phase. In this case, ionic conduction may take place in the liquid phase and electronic conduction in the solid oxides. The rate may be controlled by the cathodic reduction of molecular oxygen as in the experiments reported above. Possibly, the rate of oxidation may be even greater than in the foregoing experiments because the solid oxides may form a sponge involving numerous pores filled with liquid phases whereby a large cathodic area is provided. Local cell action may account for relatively high oxidation rates even without the occurrence of different valence states of elements such as iron or vanadium, but presence of such elements may lead to an even higher rate.

### Acknowledgment

The author would like to thank Professor Carl Wagner for his continuous advice and interest during this investigation. The work was sponsored by the U. S. Atomic Energy Commission under Contract AT(30-1)-1903.

Manuscript received Jan. 20, 1958.

Any discussion of this paper will appear in a Discussion Section to be published in the June 1959 JOURNAL.

REFERENCES

1. C. Ilschner-Gensch and C. Wagner, *This Journal*, **105**, 198 (1958).
2. C. Wagner, *Z. phys. Chem.*, **B21**, 25 (1933).
3. K. Hauffe, "Oxydation von Metallen und Metallegierungen," pp. 151-155, Springer-Verlag (1956).
4. A. G. Bergmann and I. N. Nikonowa, *J. allgem. Chem. USSR*, **12**, 449 (1942).
5. K. Kiukkola and C. Wagner, *This Journal*, **104**, 379 (1957).
6. B. Stalhane, *Z. Elektrochem.*, **36**, 404 (1930).
7. J. J. Bikerman, *J. Colloid Sci.*, **11**, 299 (1956).
8. H. von Wartenberg, *Angew. Chem.*, **69**, 258 (1957).
9. R. M. Fulrath, S. P. Mitoff, and J. A. Pask, *J. Am. Ceram. Soc.*, **40**, 269 (1957).
10. A. de S. Brasunas and N. J. Grant, *Trans. A.S.M.*, **44**, 1117 (1952).
11. A. de S. Brasunas, *Corrosion*, **11**, 1 (1955).
12. K. Hauffe, "Oxydation von Metallen und Metallegierungen," pp. 211-214, Springer-Verlag (1956).

# The Mechanism of Passivating-Type Inhibitors

**Milton Stern**

*Metals Research Laboratory, Electro Metallurgical Company, Division of Union Carbide Corporation, Niagara Falls, New York*

ABSTRACT

All passivating-type inhibitors are oxidizing agents. However, not all oxidizing agents are inhibitors. A passivating-type inhibitor functions by producing local-action current which anodically polarizes a metal into the passive potential region and thereby provides the means for obtaining a noble mixed potential. This mechanism is independent of whether passivity is caused primarily by oxide or adsorbed films. The major factors which determine whether a particular system will exhibit passivity are: (*a*) reversible potential of the redox system created by the oxidizing inhibitor; (*b*) electrochemical parameters for reduction of the inhibitor on the metal surface (exchange current, Tafel slope, and limiting diffusion current), and (*c*) critical anodic current and Flade potential of the metal. If oxygen is present in the system, some chemicals may function by changing its reduction kinetics. It is further shown that the amount of inhibitor found associated with the surface is not necessarily related to adsorption. Data are presented for passivation of stainless steel and titanium. The mechanism is discussed in terms of various oxidizing agents including oxygen, chromate, molybdate, and pertechnetate.

In recent years, the most active research in the field of passivity has been concerned with the nature of surface layers believed to be primarily responsible for this phenomenon. In general, the approach has been to obtain some experimental data and interpret these in terms of that type of surface film which is most consistent with the observation. It is possible, however, to explain many observations qualitatively without the necessity of postulating any specific type of surface layer. This can be done with what is now known about the electrochemistry of passive systems. The purpose of this work is to describe the behavior of systems containing passivating-type inhibitors in terms of electrochemical parameters. It is recognized that a film of some type is primarily responsible for passivity, and this description permits one to determine whether a specific type of observation is pertinent

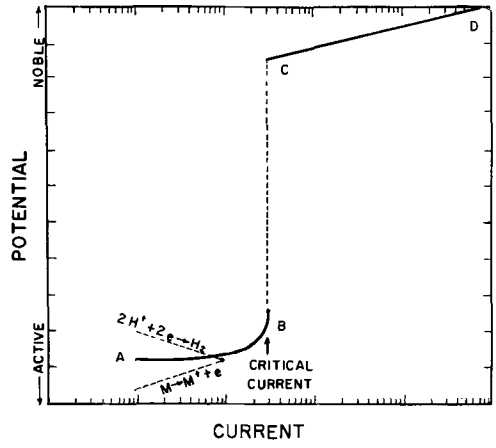


Fig. 1. Typical anodic polarization curve for metals which exhibit passivity, obtained by fixing the anodic current and measuring the potential.

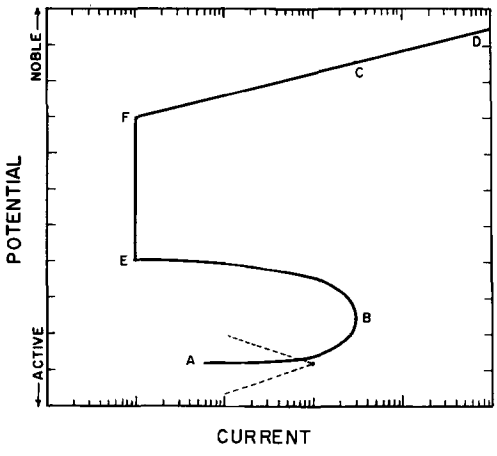


Fig. 2. Typical anodic polarization curve for metals which exhibit passivity, obtained by fixing the potential and measuring the current.

to differentiation between adsorption and oxide films.

## General Electrochemical Concepts

For metals which exhibit passive behavior, it is well known that a material in the active state can be passivated by applying sufficient anodic current. Such observations have led to the concept of a "critical anodic current" for passivity. The measurement of this characteristic has proved very useful in explaining the effect of chromium on passivity of iron-chromium alloys (1). One method of obtaining this property, used by Uhlig and Woodside (1), involves applying increasing anodic currents to the metal in the active state and observing that current which creates a marked shift of potential in the noble direction. A schematic representation of the kind of polarization curve obtained is shown in Fig. 1. On the section of the curve labeled AB, the primary anodic (oxidation) reaction is solution of metal to form metal ions in a lower valent state. In the region labeled CD, the primary anodic reaction depends upon the environment but most often involves oxygen evolution. Polarization measurements of this type, which are obtained by adjusting anodic current and measuring potential, are not completely satisfactory. First, measurements along AB are very time-dependent, particularly in the region close to the critical anodic current. Thus, the critical current one measures is dependent on the time at a given current and the current increments one uses. In addition, no information on electrode behavior can be obtained in the potential region between B and C. It is important to understand what processes occur in this region since it may extend over a range of more than 1 v and plays an important role in passivity phenomena.

To overcome some of these difficulties, a different approach has been used to obtain anodic polarization measurements. This method involves fixing the potential of the sample and measuring the current. The type of polarization curve obtained is represented schematically in Fig. 2. As the potential is changed from the active corrosion potential to B, the measured current increases. As the potential is made more noble, the current drops markedly via the route BEF and then finally increases again along FCD.

Several investigators have shown anodic polarization curves of this type for Fe-Cr alloys (2-4) and austenitic stainless steels (5-7) in $H_2SO_4$ solutions. Such behavior is not limited to alloys; for example, similar observations have been made with Ni (8), Cr (9, 10), and Fe (11, 12). There is little doubt that other metals exhibit similar characteristics under appropriate conditions. Thus, Fig. 2 may be considered as a schematic representation of the anodic polarization behavior of a metal, originally in the active state, which is passivated by anodic current. While the features of this figure may not show all the characteristics of some real systems, it is sufficiently accurate to describe most observations and is general in nature. For the purposes of this discussion, the potential region between B and E, which is usually relatively small, will be called the Flade region. There is some question at present as to whether the line between these points exhibits a finite slope or whether B and E are actually the same potential. Most experimental observations indicate that there is a real difference. The potential at point E will be called the Flade potential or the critical anodic potential, and it is considered that this potential divides the electrochemical behavior of the metal into active and passive states.

If one determines the various electrode processes which occur in the different sections of the polarization curve of Fig. 2, the following observations are made. In the potential range from A to B, the primary oxidation reaction is solution of metal to form ions in a lower valent state. The rate of this process increases from A to B. In the range from B to E, the rate of metal solution decreases markedly and finally reaches a low constant value from E to F. In this region, analysis of the solution reveals that the corrosion products are in a higher valent oxidation state. For example, if the metal contains Fe and Cr, both ferric and dichromate ions are produced in the passive region, whereas ferrous and chromic ions are corrosion products in the active region AB. The processes which occur along the polarization curve FCD depend upon both the metal and the environment. For example, in $H_2SO_4$ at a

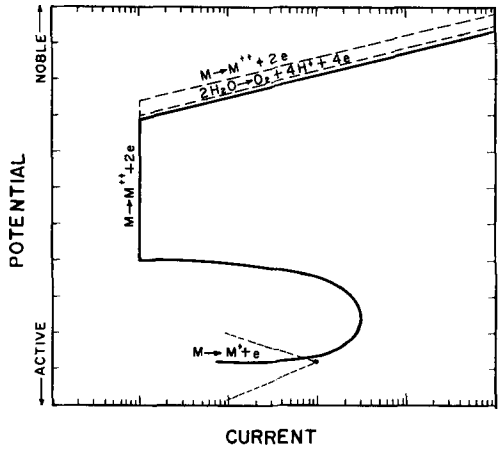


Fig. 3. Anodic polarization curve showing major oxidation reactions which occur in various potential regions.

potential more noble than the equilibrium oxygen electrode potential, oxygen evolution will be one of the primary oxidation reactions. However, metal solution still occurs and generally proceeds at a rate higher than that which exists along EF. Thus, the polarization region FCD represents the summation of more than one electrode process. At any potential along this curve, the current measured is equal to the sum of the current equivalent to oxygen evolution and the current equivalent to metal oxidation. Therefore, Fig. 2 can be changed to include the individual polarization curves of the various electrode processes which occur. This is done in Fig. 3. The two dashed lines show the current equivalent to the individual rates of metal dissolution and oxygen evolution, and the solid line represents the sum of these two processes.

## Passivating Inhibitors

### *Mechanism of Passivating Inhibitors*

Since Fig. 3 shows the rate of metal solution as a function of potential, any phenomenon which will produce a metal potential more noble than the Flade potential will create passivity. This can be accomplished by external anodic polarization as already described. There are other possibilities, however, and the question arises as to the mechanism of passivation of various inhibitors. Uhlig and Cobb (13) have shown that ferric and cupric ions inhibit Ti in $H_2SO_4$ and HCl and proposed that these ions function by adsorption on the metal surface with accompanying satisfaction of surface valences. To support this proposal, Uhlig and Geary (14) measured the potential of Ti and stainless steel in 0.2*N* $H_2SO_4$ as a function of ferric and cupric ion concentration. They assumed that the change in potential produced by inhibitor addition was the result of dipoles created at the surface by adsorbed ions and showed that their data appeared to follow a Langmuir isotherm. They also reported similar data for Fe in distilled water passivated with chromate ions. Okamoto, Nagayama, and Mitani (15), stimulated by this concept, repeated the work with Fe in chromate solutions and came to a different conclusion. They found that a critical chromate concentration exists where the potential shifts markedly in the noble direction, accompanied by a sudden drop in corrosion rate. They further showed that the passive potentials were mixed potentials, the values of which were determined by local polarization phenomena. It is quite reasonable to consider passive potentials in the light of the mixed potential theory originally treated by Wagner and Traud (16) and described in some detail by Stern (17). This concept can be used to explain many observations of the behavior of passivating inhibitors.

Consider, for example, stainless steel in an environment such as air-free dilute $H_2SO_4$ where the sample corrodes and is active. Further, consider that the anodic polarization characteristics are as illustrated in Fig. 3. If an oxidizing agent is added to the solution, an oxidation-reduction system now exists with a noble reversible potential. The oxidized species of this redox system can now be reduced on the metal surface with accompanying polarization. Since the mixed potential of the metal occurs at that potential at which the sum of the rates of all the reduction reactions equals the sum of the rates of all the oxidation reactions, a new mixed potential results from the addition of the oxidizing agent. The reversible potential and typical polarization characteristics of the redox system are illustrated in Fig. 4 along with the anodic polarization behavior of the metal. The new mixed potential is also shown. Note that now the potential is in the passive region and that the rate of solution of metal is considerably lower than that which exists at the active potential. Reduction of the oxidizing agent now constitutes the major cathodic reaction. Thus, an oxidizing agent creates passivity by producing local-action current which anodically polarizes the metal into the passive region. There are several features of this concept which warrant detailed discussion in order to show how this mechanism predicts certain characteristics of passive systems and to provide supporting evidence.

### *Nature of Passivating Inhibitors*

The picture presented above indicates that any oxidizing agent which creates a sufficiently noble redox potential should create passivity if the metal exhibits the anodic polarization behavior illustrated

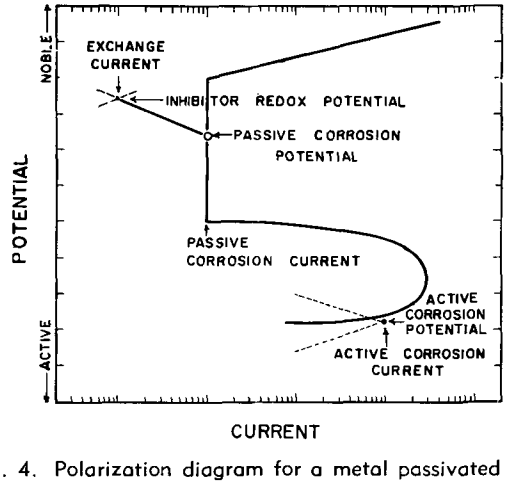


Fig. 4. Polarization diagram for a metal passivated by an oxidizing inhibitor.

in Fig. 3. To check this, seventeen readily available oxidizing agents were evaluated in regard to their ability to passivate Type 304 stainless steel in boiling 1 wt % $H_2SO_4$.[1] The results are shown in Table I, where it is evident that all were effective in producing a very marked decrease in corrosion rate when present in sufficient quantities. In this test, additions which contained chloride ions were carefully avoided because of the known effect of chloride in destroying passivity of stainless steels.[2] However, passivity of Ti is not particularly affected by chloride, and oxidizing agents can even passivate Ti in HCl. Therefore, tests similar to those described above were conducted with commercially pure Ti in boiling 1% $H_2SO_4$ and boiling 3% HCl. The results are presented in Table II. Here again, it is evident that all additions were effective in creating passivity when present in sufficient concentration. Thus, it has been demonstrated that twenty different oxidizing agents, including one organic addition, are inhibitors.[3] There appears to be little doubt that other oxidizing agents would behave in a similar manner under appropriate conditions. This is consistent with the description of the electrochemistry of passivity described above where an oxidizing addition is defined as one which produces a noble redox potential in the solution.

Figure 4 also indicates that the corrosion rate which exists when the metal is passivated with an oxidizing agent should be the same as that which occurs when the metal is passivated by anodic polarization to the same potential. Franck and Weil (18) have provided the evidence for this in studies of the passivity of Fe in $H_2SO_4$. The passive corrosion rate produced by either ceric ion or quinone has been shown to be essentially the same as that produced by anodic polarization.

[1] Tests were conducted in 1-l wide mouth Erlenmeyer flasks using finger-tip type condensers. Oxygen is probably not completely eliminated from the solution, although its concentration should be extremely low.

[2] Probably, chloride ion destroy passivity of stainless steels by markedly increasing the critical anodic current. As will be shown below, the critical anodic current is an important factor in determining whether stable passivity is possible.

[3] Potential measurements on similar systems showed that, in those cases where inhibition was obtained, passive potentials were also achieved.

**Table I. Effect of various oxidizing agents on the corrosion of stainless steel in boiling 1% $H_2SO_4$**

| Oxidizing agent | Concentration, molar | Weight loss,* mdd |
|---|---|---|
| None | — | 1150 |
| $Fe_2(SO_4)_3$ | 0.01 | 2 |
| $CuSO_4$ | 0.01 | 2 |
| $Ag_2SO_4$ | 0.01 | 0 |
| $HgSO_4$ | 0.01 | 0 |
| $Ce(SO_4)_2$† | 0.01 | 30 |
| $KAu(CN)_2$ | 0.01 | 0 |
| $HNO_3$ | 0.01 | 6110 |
| $HNO_3$ | 0.1 | 1 |
| $NaNO_3$ | 0.01 | 6030 |
| $NaNO_3$ | 0.1 | 3 |
| $NaNO_2$ | 0.01 | 1 |
| $KMnO_4$ | 0.01 | 1 |
| $Na_2Cr_2O_7$ | 0.01 | 2 |
| $Na_2MoO_4$ | 0.01 | 0 |
| $Na_2WO_4$ | 0.01 | 0 |
| $NaIO_3$ | 0.01 | 1 |
| $NaBrO_3$ | 0.01 | 15 |
| $NaClO_3$ | 0.01 | 11 |
| $H_2O_2$ | 0.1‡ | 0 |
| Quinone | 0.01 | 0 |

* 24-hr test using 500 ml of solution and approximately 20 $cm^2$ samples. A corrosion rate of 2 mdd is within the possible weighing error of these tests.
† Addition not completely soluble.
‡ 0.01*M* $H_2O_2$ decomposed too rapidly to maintain passivity.

**Table II. Effect of various oxidizing agents on the corrosion of titanium in boiling 1% $H_2SO_4$ and boiling 3% HCl**

| Oxidizing agent | Concentration, molar | Weight loss in* 1% $H_2SO_4$, mdd | Weight loss in* 3% HCl, mdd |
|---|---|---|---|
| None | — | 1130 | 670 |
| $Fe_2(SO_4)_3$ | 0.01 | 0 | — |
| $CuSO_4$ | 0.01 | 2 | — |
| $Ag_2SO_4$ | 0.01 | 0 | — |
| $HgSO_4$ | 0.01 | 0 | — |
| $Ce(SO_4)_2$† | 0.01 | 0 | 6 |
| $NaNO_3$ | 0.01 | 1 | 2 |
| $NaNO_2$ | 0.01 | 3 | 16 |
| $KMnO_4$ | 0.01 | 0 | 1 |
| $Na_2Cr_2O_7$ | 0.01 | 1 | 0 |
| $Na_2MoO_4$ | 0.01 | 0 | 0 |
| $Na_2WO_4$ | 0.01 | 0 | 0 |
| $Na_2IO_3$ | 0.01 | 0 | 1 |
| $NaBrO_3$ | 0.01 | 1 | 4 |
| $H_2O_2$ | 0.1‡ | 0 | 12 |
| Quinone | 0.01 | 0 | 0 |
| $HAuCl_4$ | 0.01 | 0 | 0 |
| $PtCl_4 \cdot 2HCl$ | 0.01 | 1 | 3 |
| $SnCl_4$ | 0.01 | — | 0 |
| $HgCl_2$ | 0.01 | — | 1 |
| $CuCl_2$ | 0.01 | — | 1 |
| $FeCl_3$ | 0.01 | — | 1 |

* 24-hr test using 500 ml of solution and approximately 20 $cm^2$ samples. A corrosion rate of 2 mdd is within the possible weighing error of these tests.
† Addition not completely soluble.
‡ 0.01*M* $H_2O_2$ decomposed too rapidly to maintain passivity.

*Effect of Concentration of Passivating Inhibitors*

Two other frequently observed phenomena in passivity are consistent with the concept that passivating inhibitors function by producing local-action current which anodically polarizes the metal into the passive region. One is concerned with the fact that an inhibitor concentration higher than some critical value is necessary to produce stable passivity. Below this critical value, the oxidizing agent may actually accelerate corrosion. The other observation is concerned with the unstable nature of passivity when the inhibitor concentration is close to this critical value. In this instance, repeated tests under apparently the same circumstances sometimes lead to passivity and sometimes to an active state. The potentials and corrosion rates are quite different for the two conditions.

When the concentration of an oxidizing agent is changed, the reversible potential of the redox system created by the inhibitor in the solution is changed. Also, the exchange current of the redox system may change, depending on the kinetics of the process. Consider first the case where a change in concentration of oxidizing agent has no effect on exchange current and only changes the reversible potential. The polarization diagram showing how such a change affects the potential and corrosion rate is illustrated in Fig. 5. As the concentration

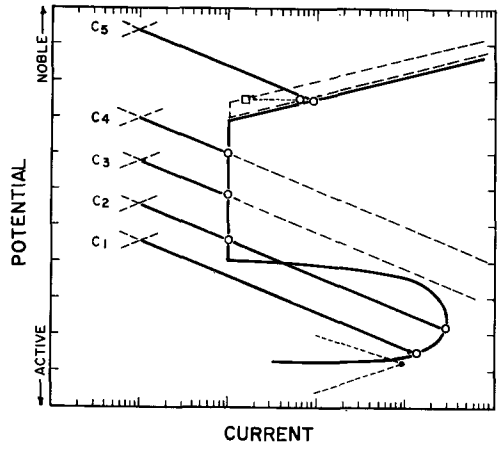


Fig. 5. Polarization diagram illustrating how a change in oxidizing agent redox potential affects corrosion current and corrosion potential.

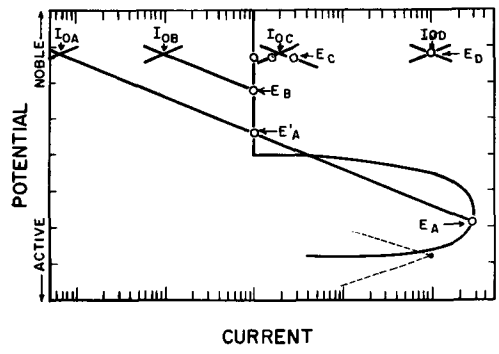


Fig. 6. Polarization diagram illustrating how a change in oxidizing agent exchange current affects corrosion current and corrosion potential.

of the oxidizing agent is increased from $C_1$ to $C_5$, the reversible potential becomes more noble in accordance with the Nernst equation. For the concentration $C_1$, the mixed potential is in the active region and the corrosion rate is increased. An example of this situation is shown in Table I where 0.01*M* nitrate additions to $H_2SO_4$ accelerated corrosion of stainless steel, whereas a 0.1*M* addition passivates. Concentration $C_2$ produces an interesting situation since there are two possible mixed potentials, that is, there are two potentials at which the sum of all the rates of oxidation equals the sum of all the rates of reduction. Which potential the metal assumes is dependent upon many intangible factors. However, the passive state is probably not very stable under these conditions. It is quite evident that appropriate conditions could exist where the metal will oscillate between the passive and active potential. It is possible that under these conditions introduction of active metal will produce an active potential, whereas if the metal is already passive, the noble potential will be evident. Concentrations $C_3$ and $C_4$ produce stable passivity, and the passive corrosion rate is independent of inhibitor concentration in this region.[4] Concentration $C_5$ also produces stable passivity although the corrosion rate is increased, as indicated by the square point on Fig. 5.[5] Note that in this case, the sum of the currents equivalent to the rate of metal dissolution and oxygen evolution equals the current equivalent to the rate of inhibitor reduction.

The exchange current of the redox system produced by the oxidizing addition also has a significant influence on behavior. For example, consider four different oxidizing agents added to an actively corroding system in appropriate concentrations necessary to produce the same redox potential. Further, consider that the oxidation-reduction kinetics for the redox systems are such that they exhibit markedly different exchange currents. This situation is shown in Fig. 6.

The system with a very low exchange current, labeled $I_{OA}$, produces unstable passivity with two possible mixed potentials as described above.

The system with the higher exchange current, $I_{OB}$, produces stable passivity. It is worth mentioning here that the conditions illustrated by this particular system are necessary in order to use an electrochemical method for measuring passive corrosion rates reported by Vetter (19). He found that the corrosion rate of passive Fe in concentrated $HNO_3$ can be determined electrochemically by polarizing the surface anodically to the potential of Pt in the same solution. The current required to polarize to the Pt potential is equivalent to the corrosion current. This can only be true if Pt exhibits the reversible redox potential of the environment and if the local anodic polarization curve for the metal is practically vertical. Also, since the applied anodic current required to polarize the passive metal to the reversible potential of the redox system is equal to the difference between the corrosion current and $I_{OB}$, the exchange current of the redox system on the passive surface should be much smaller than the passive corrosion current. If the passive corrosion potential is more than about 150 mv active to the reversible redox potential of the solution, the error in neglecting the exchange current will probably not be significant. This actually depends on the Tafel slope for reduction of the oxidizing agent on the passive surface. Thus, it is evident that this method of determining the passive corrosion rate can be applied only in special cases. For example, the system shown in Fig. 6, where the redox exchange current, $I_{OC}$, is somewhat greater than the passive corrosion rate, produces a metal potential only slightly more active than the reversible redox potential.[6] In this case, the anodic current required to polarize to the Pt potential will not be related to the corrosion rate. However, a method previously described (20) is useful here. If the oxidation-reduction kinetics of the redox system can be measured on the passive surface, then the local anodic polar-

[4] The corrosion rate of those metals which do not exhibit a Flade region will of course, increase continuously as the concentration of oxidizing agent is increased.

[5] Behavior in this region, where the metal solution rate again increases with potential, has been termed transpassivity and is an important part of the over-all passivity picture. However, this phenomenon is not pertinent to the present development and is not discussed in detail.

[6] For this condition, the rate of oxidation of the reduced species of the inhibitor becomes an important factor in determining the mixed potential. The three points in a horizontal row in Fig. 6 illustrate the fact that the mixed potential is that value at which the currents equivalent to oxidation of metal and oxidation of the reduced species of inhibitor equals the current equivalent to reduction of inhibitor.

ization curve of the metal can be determined in the region close to the passive potential. For example, it was shown that the local anodic polarization curve for Hastelloy alloy F in a ferric-ferrous chloride system was essentially vertical with a corrosion rate equivalent to only 0.02$\mu$a/cm$^2$. This system is an ideal example of the case shown in Fig. 6 where the oxidizing agent exhibits an exchange current of $I_{OC}$.

In the case where the redox exchange current, $I_{OD}$, is much greater than the passive corrosion current, the metal exhibits the reversible redox potential. This has been observed experimentally for stainless steel in ferric-ferrous sulfate solutions (21) and in two other cases which will be described below. In this instance, one cannot determine the passive corrosion rate by electrochemical means. However, if the metal exhibits the same potential as the equilibrium redox potential, the corrosion current must be at least one order of magnitude less than the redox exchange current.[7]

### *Effect of Critical Anodic Current*

There are several other tests which establish the validity of the concept that passivating inhibitors function primarily by creating local-action current which anodically polarizes the metal into the passive region. For example, this concept predicts that a metal with a high critical anodic current for passivity requires a greater critical concentration of oxidizing agent to produce stable passivity than a metal which exhibits a low critical anodic current. This is consistent with the data of Olivier (22) who measured the critical anodic current of Fe and Fe-Cr alloys in 10% $H_2SO_4$ at room temperature. In this environment, Fe exhibits a critical current of 1 amp/cm$^2$, whereas Type 304 stainless steel requires only 2.2 ma/cm$^2$ for passivity. It is well known that small additions of ferric ion or other oxidizing agents will passivate stainless steel in this environment, whereas similar additions (or much higher concentrations) accelerate the corrosion rate of iron. This principle is illustrated in Fig. 7.[8]

To obtain more quantitative data concerning the predicted effect of critical anodic current on the concentration of oxidizing agent required to passivate, measurements were conducted with commercially pure Ti in various concentrations of boiling $H_2SO_4$ containing 5% $Na_2SO_4$. Critical anodic current measurements were obtained by a method described by previous investigators (22, 23). This method involves polarizing the active metal with a fixed anodic current which is higher than the critical value. The potential of the sample is measured as a function of time as it passes from the active state to the passive state, and a critical time for passivity is selected. This is repeated for a number of anodic currents, and a plot is made of anodic current density as a function of the reciprocal of the time for passivity ($t_p$). The data fall on a reasonably straight line which is extrapolated to a value of $1/t_p$ equal to zero ($t_p = \infty$). This is considered the critical anodic current density which will produce passivity if one waits for an infinite time and, therefore, provides a convenient method for comparing different alloys or conditions. Measurements reported here were obtained with a Cary Model 31 Vibrating Reed Electrometer which drives a L&N adjustable span, adjustable zero recorder with a chart speed of 30 in./min and a full-scale pen speed of 1 sec. Current was supplied from a stable high-voltage power supply fed through high resistances to minimize current change when the sample becomes passive. The critical time for passivity was selected as the interval between the initial application of anodic current and time at the maximum slope of the potential-time curve. Potential-time curves were similar in shape to those shown by Olivier (22) except that the final passive potential assumed by Ti is considerably higher. Figure 8 shows plots of anodic current density as a function of $1/t_p$. It is evident that an increase in $H_2SO_4$ concentration increases the critical current for passivity.

To determine the effect of critical anodic current on the amount of oxidizing agent required to passivate Ti, known increments of $Fe_2(SO_4)_3$ were added to a cell in which Ti was active. The Ti potential was measured as a function of ferric ion concentration, the results of which are shown in Fig. 9. It is evident that the concentration of ferric ion required to produce a noble potential increases with increasing acid concentration in a manner similar to the increase in critical anodic current.

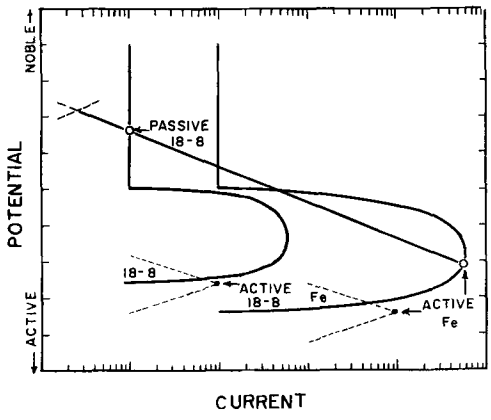


Fig. 7. Effect of critical anodic current on the behavior of passivating inhibitors.

[7] This is an important basic principle which applies not only to mixed potentials where corrosion may be involved, but also to inert electrodes which may exhibit a mixed potential in environments where more than one redox reaction can occur. Thus, Pt is a good indicating electrode for measuring the equilibrium potential of simple redox systems because exchange currents on Pt are usually very high. Side electrochemical processes which result from minor amounts of impurities occur at rates much lower than the exchange rate of the major redox process. Thus, the Pt potential is not significantly affected. However, Pt will exhibit a mixed potential if two or more major redox processes occur on the surface at rates of the same order of magnitude. For example, Pt in hydrogen-saturated 20% $H_2SO_4$ exhibits the reversible hydrogen electrode potential of $-0.20$ vs. saturated calomel. If the system is made 0.5$M$ in ferric ion and 0.1$M$ in ferrous ion, the Pt potential is $+0.50$. Finally, if the hydrogen gas is substituted by nitrogen, the Pt potential is unaffected. In this case, the exchange current for the ferrous-ferric redox system is considerably greater than the exchange current for the hydrogen electrode system so that Pt exhibits the reversible ferrous-ferric redox potential in the hydrogen-saturated solution. However, if the ferrous-ferric exchange current is reduced considerably by decreasing the ferrous ion concentration, then Pt exhibits a mixed potential. Thus, in the same acid with 0.5$M$ ferric ion and no intentional addition of ferrous ions, the Pt is $+0.62$ v vs. saturated calomel with nitrogen passed through the solution but only $+0.58$ when the system is hydrogen saturated. These two potentials are reproducible upon alternately passing nitrogen and hydrogen through the acid.

It is probable that Pt does not function as an effective oxygen electrode because the exchange current for this redox system on Pt is relatively low.

[8] This schematic figure does not consider the fact that stainless steel in many environments becomes passive at considerably more active potentials than Fe. This is also consistent with passivation of stainless steel with considerably lower concentrations of oxidizing agent than are required for Fe.

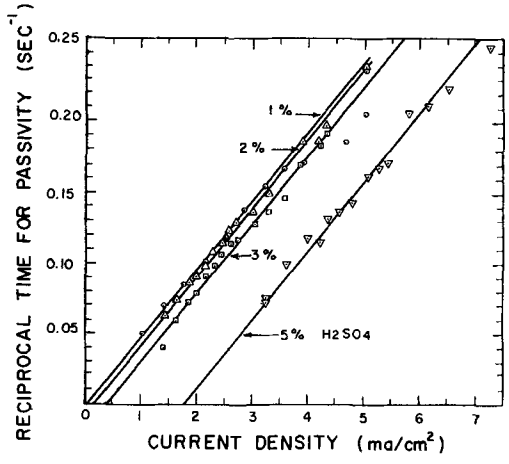


Fig. 8. Reciprocal of time for passivity as a function of applied anodic current for Ti in various concentrations of boiling $H_2SO_4$ containing 5% $Na_2SO_4$.

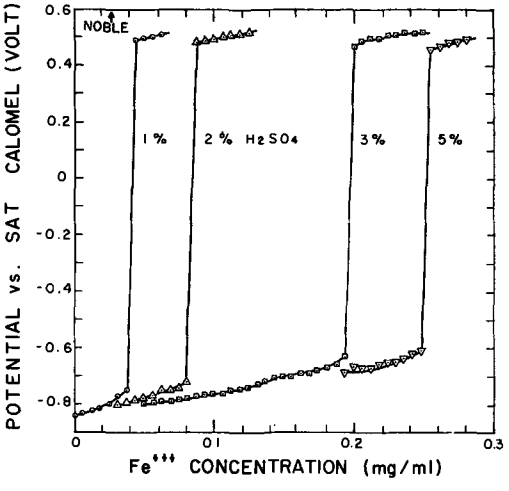


Fig. 9. The potential of Ti as a function of ferric ion concentration in boiling $H_2SO_4$ solutions containing 5% $Na_2SO_4$.

The potentials reported here are not final steady-state values, since this is an impossible condition to obtain in such a system. In the active region, the oxidizing agent is consumed in the corrosion process and thus the concentration changes with time. In the passive region, the potentials were stable and close to, but less noble than, Pt in the same solution. For ferric ion concentrations close to the critical value for stable passivity, potentials would oscillate considerably and the reported values are averages.

Corrosion tests showed that when a stable passive potential was achieved, the corrosion rate was negligible, whereas with insufficient inhibitor present, the rate was about equal to the rate with no ferric ion added. It was also found that the marked change in corrosion rate occurred at the critical inhibitor concentration shown in Fig. 9. In order to establish this last observation, it was necessary to add ferric ion to a system in which the Ti was initially active. That is, Ti was placed in the boiling solution until it was active, and then a known increment of ferric ion was added. Blank tests were conducted to determine the weight change during this initial activating period. If Ti was added to a solution in which ferric ion was initially present, then a much smaller concentration of ferric ion would maintain the original passivity created by air exposure of the sample.

Table III. Comparison of corrosion rate, critical anodic current, and critical ferric ion concentration for passivity of Ti in boiling $H_2SO_4$

| $H_2SO_4$ + 5% $Na_2SO_4$, % | Corrosion rate, mdd | Critical anodic current, ma/cm² | Critical $Fe^{+++}$ concentration, mg/ml |
|---|---|---|---|
| 1 | 280 | 0.05 | 0.040 |
| 2 | 580 | 0.2 | 0.085 |
| 3 | 1820 | 0.4 | 0.195 |
| 5 | 2880 | 1.8 | 0.250 |

Table III summarizes the effect of $H_2SO_4$ concentration on the corrosion rate, critical anodic current, and ferric concentration required for passivity. An increase in critical inhibitor concentration with an increase in critical anodic current is consistent with the mechanism of passivating inhibitors described above.

The data of Fig. 8 provide some additional information which, though not pertinent to the mechanism of passivating inhibitors, pertains to the primary cause of passivity. It can be shown that the slope of each line on this figure is inversely proportional to the number of coulombs associated with the passivation process. Since the scatter in the data is too great to determine whether the number of coulombs necessary for passivity is a function of $H_2SO_4$ concentration, the lines were intentionally drawn parallel. The data show that anodic passivation of Ti requires 0.021 coulomb/cm² where the area measurement is apparent area. Since the Ti surface is activated in the corroding environment, and it is etched, it appears reasonable to assume that the true surface area is from three to five times as large as the measured value. If one prefers to consider that the coulombs required to passivate are used in oxidizing Ti in accordance with the over-all reaction $Ti + 2H_2O \rightarrow TiO_2 + 4H^+ + 4e$, then the calculated oxide film thickness is 25Å using a surface roughness factor of 4. It should be mentioned that this kind of information has also been used to support adsorbed layers of oxygen.

*Quantity of Passivator Associated with the Surface*

It is important to note that many investigators have used radioisotopes or other sensitive analytical techniques to determine the amount of inhibitor on a passivated metal surface. This kind of information has been used to support either oxide films or adsorption as the basic cause of passivity. Data of this type have not proved particularly conclusive because the amount of material found varies considerably from system to system. For example, Cohen and Beck (25) report the passive film on Fe in chromate solutions may contain as much as 25% $Cr_2O_3$ with the remainder iron oxide. Hackerman and Powers (26), on the other hand, report that adsorbed chromate at the oxide-solution interface can be responsible for passivity even though the amount of chromate found is equivalent to about three monolayers. In addition, Cartledge (24) has shown that pertechnetate is a remarkably effective passivator for Fe even though the amount of radioactive technetium on the surface corresponds to a very small fraction of a monolayer.

When one considers that the prime function of an oxidizing inhibitor is to produce passivity by providing a redox system capable of anodically polarizing the metal to a noble mixed potential, it becomes obvious that the amount of inhibitor found on the surface is not necessarily related to the nature of the film causing passivity. The rate of reduction of the oxidizing agent is dependent upon the final mixed potential, the exchange current, and the Tafel slopes of the redox process. For example, Cartledge (24) has shown that iron passivated by either pertechnetate or osmic acid exhibits the reversible potential of the redox system in solution. Thus, under these conditions the redox system is essentially at equilibrium on the passive surface, and there is no net reduction of inhibitor. Such a system has been illustrated in Fig. 6 where the exchange current, $I_{OD}$, is considerably greater than the passive corrosion current. In most cases of passivity, where sufficient data have been reported, the passive potential is active to Pt in the same solution. This means that the passivator is being reduced at some finite rate which is equal to the rate of corrosion of metal in accordance with the theory of mixed potentials. Since the passive corrosion rate may be extremely small, the reduction rate may be quite difficult to detect. It should be mentioned, of course, that the rate of reduction of inhibitor may not be related to the amount observed on the surface, since the reduced species may not remain associated with the surface.

Thus, the mixed potential concept provides a means for explaining large variations in quantity of inhibitor found on passive surfaces without the necessity of postulating adsorption or oxide films.

## Discussion

It has been shown that many experimentally observed phenomena may be explained by considering that the prime function of passivating inhibitors is to create a stable mixed potential more noble than the Flade region. This concept was suggested by Kolotyrkin (5, 10), who wrote, "The action of passivators need not involve their direct participation in forming the passivity film. Apparently, their action may be confined to increasing the overall rate of the cathodic reaction and thereby causing a shift of the steady-state potential in the positive direction, conducive to increased passivity." Pourbaix and Van Rysselberghe (27) have suggested a similar mechanism, but the details of their proposal, which is associated with potential-pH diagrams, are quite different from those given here. The concept is also implicit in the work of many others who have treated passive potentials as mixed potentials (18-19, 28, 29). In addition, Uhlig (1) has indicated that any local-action current greater than the critical anodic value is expected to create passivity. This is consistent with the mechanism supported here.

It is of value to discuss the interesting experiments by Cartledge (24) on passivation of Fe by pertechnetate. The rather unusual ability of this ion to passivate may be attributed to a high exchange current on the metal surface in accordance with the mechanism illustrated in Fig. 5 and 6. This is consistent with several experimental observations when one considers, as Cartledge has, that passive potentials are mixed potentials. First, the quantity of inhibitor required, and the loss due to reduction, were found to be highly dependent upon the composition and surface activity of the Fe. This is consistent with the recognized fact that activation overvoltage parameters are sensitive to surface conditions. Also, as described above, the fact that the passive potential is equal to the redox potential, along with the observation that the pertechnetate observed on the surface is constant and extremely small, shows that the exchange current is considerably higher than the passive corrosion current. In addition, the exchange current for pertechnetate must be considerably higher than that for chromate because of the following reported observations: Pertechnetate is an effective inhibitor at lower concentrations than chromate in spite of the fact that chromate is a stronger oxidizing agent. The passive potential of Fe is more noble in pertechnetate solutions than in chromate solutions of equal concentration, although the redox potential of the chromate solution is more noble. These observations can only be explained by considering that pertechnetate exhibits an unusually high exchange current.

In accordance with what has already been described above, the particular behavior of a given passivating inhibitor is determined by the redox potential and oxidation-reduction parameters (particularly the exchange current) on the metal surface. Some other characteristics may be equally important. For example, a given inhibitor species may also affect the critical anodic current by some unspecified mechanism, although as yet there appears to be no direct evidence for this. Should such a situation actually exist, then that inhibitor which reduces the critical anodic current will produce stable passivity at a lower concentration, provided all other factors are the same. Cartledge has shown that the Flade potential of Fe is apparently not affected by various inhibitors, so this factor, which would also influence the amount of inhibitor required for passivity, will not be considered.

Inhibitors may also function by influencing the reduction kinetics of another oxidizing agent in solution, thus enabling the mixed potential to occur in the passive region. For example, while molybdate and tungstate are sufficiently oxidizing in nature to passivate stainless steel and Ti under essentially oxygen-free conditions (Tables I and II), oxygen is required before they will passivate Fe under the conditions described by Pryor and Cohen (30) and Cartledge (24). Thus, while it is possible that the sum of the reduction rates of these weak oxidizing agents and that of oxygen may be sufficient to polarize Fe above the Flade potential (whereas the reduction rate of oxygen alone is insufficient), it is also possible that these inhibitors raise the exchange current or decrease the Tafel slope for oxygen reduction producing a noble mixed potential. There are not sufficient data available to determine which of these possibilities is most likely.

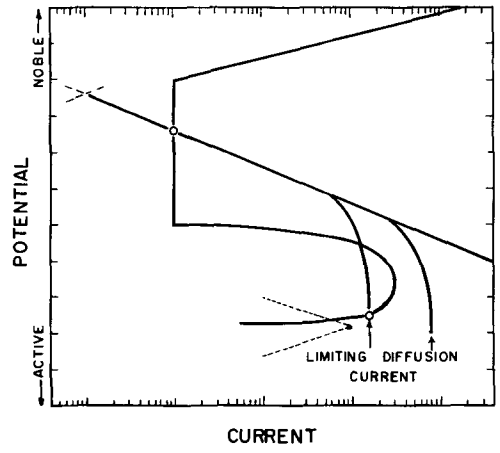


Fig. 10. The effect of concentration polarization on the behavior of passivating inhibitors.

It is possible that either or both of these may play important roles in some systems.[9]

It should be noted that oxygen has been treated in the same manner as any other oxidizing agent. In accordance with the mechanism proposed, there is no apparent need to consider that it functions in a manner different from that of other passivators. This is consistent with the observation of Uhlig and Geary (14) that the passive potential of stainless steel becomes more noble as the partial pressure of oxygen is increased, and becomes less noble as the solution is made more alkaline. Such behavior is expected, since the reversible oxygen electrode potential (determined by the reaction $O_2 + 4H^+ + 4e \rightarrow 2H_2O$) becomes more noble as the oxygen partial pressure and hydrogen ion concentration are increased. As mentioned previously, other species in solution may affect the reduction kinetics of oxygen and thus produce passivity.

The reduction kinetics of the oxidizing agent have been treated only in terms of activation polarization. However, concentration polarization undoubtedly plays an important role under some circumstances as is evidenced by the behavior of oxygen passivation of Fe in pure water (where the critical anodic current is relatively low). Under high solution velocity conditions, passivity may be achieved, whereas stagnant conditions produce an active potential and a relatively high corrosion rate (31). The effect of concentration polarization is illustrated in Fig. 10, where it is evident that when concentration polarization due to local-action currents exists, the mixed potential is active; whereas factors which raise the limiting diffusion current above the critical anodic current create only one possible mixed potential which is in the passive region.

There appears to be little doubt that passivity results from the formation of either an oxide or adsorbed film. The mechanism described here for the creation of passivity by oxidizing agents is independent of whether the unusual anodic behavior of passive metals results from an oxide or adsorbed film. However, it should be pointed out that if the principles described here are accepted, then some of the argument that adsorption is the prime cause of passivity must be re-evaluated, since a good deal of the evidence used to support this mechanism involves the behavior of passivating agents. The ability of CO to inhibit stainless steel in HCl has also been used as strong supporting evidence for adsorption as the principal cause of passivity (32). There is little doubt that CO adsorbs on stainless steel and Fe, as indicated by King and Rau (33). However, this adsorption does not lead to passivity in the electrochemical sense of the term, and it is believed that CO inhibits by the same mechanism as acid pickling inhibitors, which apparently do function by adsorption (34). For example, the potential of CO inhibited stainless steel in 2.45*N* HCl (35) is about 0.35 v more active than the saturated calomel electrode and is only about 0.1 v more noble than the same system without inhibitor. The evidence that CO should be considered in the same category as acid pickling inhibitors, and not included as a passivating inhibitor, is as follows: the inhibited potential is active; the change in potential resulting from inhibition is only about 0.1 v in the noble direction; commercial pickling inhibitors or additions like quinoline ethiodide and carbon disulfide produce similar effects, and finally oxygen passivation produces a much more noble potential.

It is believed that the final answer to passivity will come from an acceptable explanation of metal dissolution kinetics. In particular, one must explain the reason for the existence of the Flade region and also the unusual electrode kinetics which result in a metal dissolution rate which is independent of potential.

## Conclusions

1. Inhibitors which create passivity function primarily by producing a mixed potential which is more noble than the Flade region. In order to achieve this, the solution must contain a redox system with a noble reversible potential (an oxidizing agent).

2. The major factors which determine whether a particular system will exhibit passivity are the reversible potential of the redox system created by the oxidizing inhibitor; the oxidation-reduction parameters for reduction of the inhibitor on the metal surface (exchange current, Tafel slope, limiting diffusion current); and the value of critical anodic current and Flade potential of the metal. If oxygen is present in the environment, other species in solution may affect its reduction kinetics and thus produce conditions favorable to passivity.

3. Passivity is favored by high values of redox potential, exchange current, and limiting diffusion current, and by low values for the Tafel slope. A low critical anodic current for the metal and a relatively active Flade region also favor passivation.

4. While there is little doubt that passivity primarily results from either an oxide film or adsorption, the mixed potential concept proposed here is independent of which mechanism predominates. Thus, some of the argument that adsorption is the prime cause of passivity should be re-evaluated, since much of the evidence used to support this

[9] For example, Cartledge (24) has shown that in systems containing both oxygen and pertechnetate, the reversible potential of the pertechnetate system is more active than the Flade potential of Fe. Thus in this case, oxygen is the passivating inhibitor and pertechnetate probably affects the reduction kinetics of oxygen.

mechanism involves the behavior of passivating agents.

5. It is believed that a final answer to passivity will come from an acceptable explanation of metal dissolution kinetics which involves both the Flade region and the potential region where metal dissolution is independent of potential.

### Acknowledgment

The author acknowledges the skillful assistance of E J. Bartolomei and N. Darroch who conducted most of the measurements reported here.

Manuscript received Feb. 28, 1958. This paper was prepared for delivery before the Ottawa Meeting, Sept. 28-Oct. 2, 1958.

Any discussion of this paper will appear in a Discussion Section to be published in the June 1959 JOURNAL.

REFERENCES

1. H. H. Uhlig and G. E. Woodside, *J. Phys. Chem.*, **57**, 280 (1953).
2. H. J. Rocha and G. Lennartz, *Arch. Eisenhüttenw.*, **26**, 117 (1955).
3. R. Olivier, "Passivat von Eisen u. Eisen-Chrom-Legierungen," Dissertation, Leiden (1955). For summary, see T. Heumann, "Passivierende Filme und Deckschichten," p. 276, H. Fischer, K. Hauffe, and W. Wiederholt, Editors, Springer-Verlag, Berlin (1956).
4. M. Prazak, "Uber den Aufbau der Passivschicht auf Chromstählen," presented at the International Colloquium on Passivity of Metals, Heiligenberg, 1957. To be published *Z. Elektrochem.*
5. N. Y. Bune and Y. M. Kolotyrkin, *Doklady Akad. Nauk. S.S.S.R.*, **111**, 1050 (1956).
6. C. Edeleanu, *Metallurgia*, **50**, 113 (1954); *Nature*, **173**, 739 (1954).
7. C. Carius, *Arch. Eisenhüttenw.*, **27**, 401 (1956).
8. G. Okamoto, H. Kobayashi, M. Nagayama, and N. Sato, "Effect of Temperature on the Passivity of Nickel," presented at the International Colloquium on Passivity of Metals, Heiligenberg, 1957. To be published *Z. Elektrochem.*
9. T. Heumann, "Uber die Passivierung des Chroms," *ibid.*
10. Y. M. Kolotyrkin, "Electrochemical Behavior and Anodic Passivity Mechanism of Certain Metals in Electrolyte Solutions," *ibid.*
11. J. H. Bartlett and L. Stephenson, *This Journal*, **99**, 504 (1952).
12. U. F. Frank, *Z. physik Chem. (Frankfurt)*, **3**, 183 (1955).
13. H. H. Uhlig and J. Cobb, *This Journal*, **99**, 13 (1952).
14. H. H. Uhlig and A. L. Geary, *ibid.*, **101**, 215 (1954).
15. G. Okamoto, M. Nagayama and Y. Mitani, *J. Electrochem. Soc., Japan*, **24**, 69 (1956).
16. C. Wagner and W. Traud, *Z. Elektrochem.*, **44**, 391 (1938).
17. M. Stern, *This Journal*, **104**, 56 (1957); **104**, 645 (1957).
18. V. F. Franck and K. Weil, *Z. Elektrochem.*, **56**, 814 (1952).
19. K. J. Vetter, *ibid.*, **55**, 274 (1951).
20. M. Stern, *This Journal*, **104**, 600 (1957).
21. M. Stern, *ibid.*, **104**, 559 (1957).
22. R. Olivier, "Proceedings of the Sixth Meeting of the International Committee of Electrochemical Thermodynamics and Kinetics," p. 314, Butterworth's Scientific Publ., London (1955).
23. V. F. Franck, *Z. Naturforsch.*, **4A**, 378 (1949).
24. G. H. Cartledge, *Corrosion*, **11**, 335 (1955); *J. Phys. & Colloid Chem.*, **59**, 979 (1955); **60**, 28, 32, 1037, 1571 (1956); **61**, 973 (1957).
25. M. Cohen and A. F. Beck, "The Passivity of Iron in Chromate Solutions," presented at the International Colloquium on Passivity of Metals, Heiligenberg, 1957. To be published *Z. Elektrochem.*
26. N. Hackerman and R. A. Powers, *This Journal*, **100**, 314 (1953).
27. M. Pourbaix and P. Van Rysselberghe, *Corrosion*, **9**, 313 (1950).
28. K. J. Vetter, "Passivierende Film und Deckschichten," p. 72, H. Fischer, K. Hauffe, and W. Widerholt, Editors, Springer-Verlag, Berlin (1956).
29. H. Beinert and K. F. Bonhoeffer, *Z. Elektrochem.*, **47**, 536 (1941).
30. M. J. Pryor and M. Cohen, *This Journal*, **100**, 203 (1953).
31. T. P. Hoar and U. R. Evans, *ibid.*, **99**, 212 (1952).
32. H. H. Uhlig, "The Adsorption Theory of Passivity and the Flade Potential," presented at the International Colloquium on Passivity of Metals, Heiligenberg, 1957. To be published *Z. Elektrochem*; also, "Advances in Catalysis," Vol. IX, p. 379, Academic Press, New York (1957).
33. C. V. King and E. Rau, *This Journal*, **103**, 331 (1956).
34. A. C. Makrides and N. Hackerman, *J. Phys. & Colloid Chem.*, **59**, 707 (1955).
35. H. H. Uhlig, *Ind. Eng. Chem.*, **32**, 1490 (1940).

# A Study of Corrosion Films on Zirconium and Its Alloys by Impedance Measurements

**J. N. Wanklyn and D. R. Silvester**

*Atomic Energy Research Establishment, Harwell, Berkshire, England*

ABSTRACT

The oxide films formed on zirconium and some of its alloys during corrosion in steam and water at 325°C have been studied by impedance measurements made by immersion in an electrolyte. A fall in the protective character of the film is accompanied by an increase of capacity, and measurements of the latter provide a useful method of comparing films. The behavior of the resistive part of the impedance and the influence of frequency and electrolyte conductivity are complex, and only a partial interpretation can be given.

The initial reaction of zirconium and its alloys with water and steam at temperatures around 300°C is characterized by a rate of attack which falls with time. After a time which, depending on the alloy and conditions, varies from a few hours to many thousand hours, the rate increases and re-

mains constant until flaking of the oxide film prevents further accurate measurements. The phenomenon causing this change is called "breakaway" or "transition." Although Thomas and Kass (1) recently suggested that transition and breakaway are fundamentally different, the former implying only a change of kinetics, while the latter also involves loss of oxide by spalling, both conditions are explicable by cracking of the film under the compressive stresses due to the expansion (about 50% by volume) accompanying the conversion of metal to oxide. Such stresses have been directly demonstrated by Wheeler (2), and Evans (3) has discussed theoretically the types of cracking to be expected under various conditions.

It seems likely that the corrosion rate is controlled at all times by the diffusion of some species (almost certainly oxygen ions) through the oxide film, and that the change in kinetics occurs because the latter's protective character is reduced by the cracks. If cracking keeps pace with film growth, the effective rate-controlling thickness remains constant and corrosion is linear with time.

Numerous workers (4-6) have measured the capacity of oxide films on metals, generally with the aim of determining their thickness. Young (5) studied the dependence of film capacity and resistance on frequency, reaching conclusions about the structure of the films, particularly the variation of nonstoichiometry through their thickness. All this work referred to nominally crack-free films, generally produced by anodizing. Young, however, reported unduly high capacities for anodic films formed under breakdown conditions, and Misch (7), comparing anodic films formed on various metals in nitric acid found, that porous, nonprotective films had high capacities.

These high values could be due to electrolyte entering cracks, so reducing the effective thickness of dielectric and increasing the observed capacity. Cracks formed in films during corrosion and oxidation should behave similarly. The experiments described below and briefly reported elsewhere (8) were therefore carried out to study such films. This application of capacity measurements is similar to the work of Wormwell (9, 10) and co-workers, who detected the failure of paint films on metal specimens immersed in electrolyte by observing a rise of capacitance.

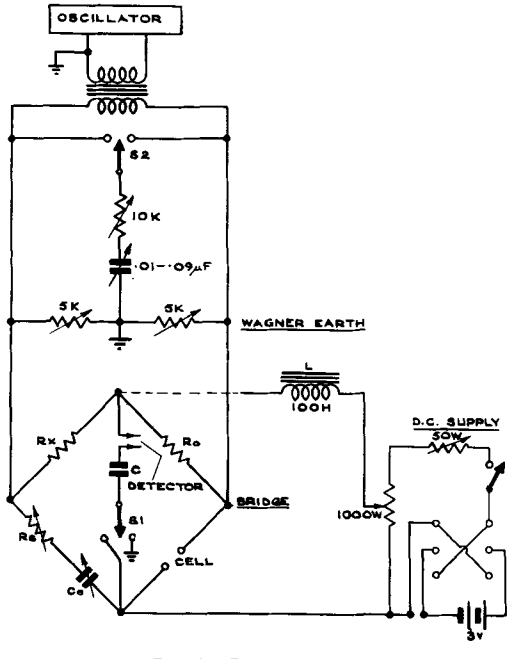


Fig. 1. Bridge circuit

## Experimental

The circuit is shown in Fig. 1. The bridge elements Rx, Ro, and Rs were Muirhead noninductive decade units and $C_o$ a Dawe three-dial decade capacitor giving 0.001 to 1.11 $\mu$F. Rx and Ro were generally kept at 10,000 ohms each and the bridge was balanced with $C_o$ and Rs which was variable in steps of 0.1 ohm up to 11,111 ohms. The oscillator (Dawe 400A) was connected to the bridge through a transformer since its output, which was earthed on one side, would be incompatible with the Wagner earthing circuit (see Fig. 1). The a-c voltage imposed on the cell during measurements was only a few tens of millivolts root mean square. Only one capacity was provided in the Wagner earth, and this was switched into whichever limb required it for balance. The 10,000 ohms series resistance provided a fine variation of the capacity adjustment. The detector was a Cossor Type 1049 oscilloscope preceded by Type TAA-16EA amplifier (MIT Radiation Laboratory) which could be turned over the range 500-5000 cps. The oscilloscope was most conveniently used with a simple time-base sweep, the amplified output being applied to the y plates. With this arrangement it was possible to distinguish visually the desired signal from background interference. Tests with standard components showed the bridge to be accurate to about 2-3%.

In the first experiments the d-c potential of the specimen was controlled by the d-c supply. The choke, L, prevented this circuit from short circuiting the a-c detector, while the condenser, C, blocked the latter's low resistance d-c path. The d-c source was adjusted by measuring the potential of the specimen against a saturated calomel electrode with a *p*H meter. When it was found that small variations of d-c potential did not influence the capacities significantly, the d-c source was disconnected and the specimen allowed to assume its natural potential.

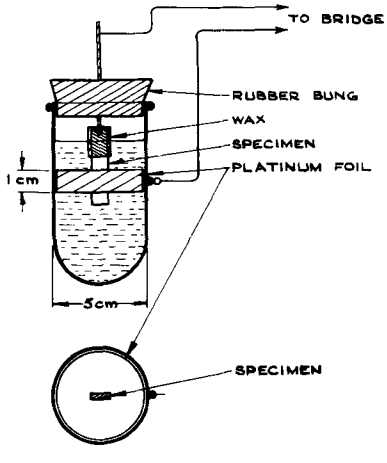


Fig. 2. Measuring cell

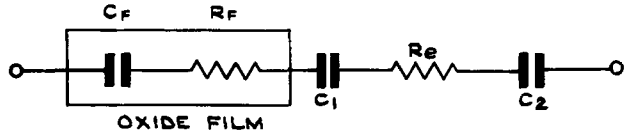


Fig. 3. Equivalent circuit of cell

The cell was as shown in Fig. 2. Specimens were attached to the supporting wire by a small nut and bolt or with a clip and were waxed so as to leave an exposed area of about 1-1½ cm². Edges cut after the corrosion experiment were always waxed, and care was taken not to scratch the surface to be measured. When d-c potentials were to be measured, the cell had a side arm leading to a saturated calomel electrode and filled with cell electrolyte, generally 1*N* $H_2SO_4$. With this solution the resistance of the cell, measured with a platinized platinum electrode of the same dimensions replacing the specimen, was about 2 ohms.

The oxide film impedance was always expressed as capacity and resistance in series. It is in series with $C_1$ and $C_2$, double layer capacities at the specimen and Pt, respectively, and with Re, the electrolyte resistance (Fig. 3). The values of Rs and $C_0$ (Fig. 1) gave the cell impedance as resistance and capacity in series and, since the capacities were always much less than typical double layer values, $C_0$ gave $C_f$ directly. The measured resistance was often much greater than Re, but when it was comparable to Re, the latter was subtracted to give $R_f$.

The materials studied were Kroll zirconium and binary and ternary alloys based on it. Analyses are given in Table I.

The preparation of the alloys and their fabrication into sheet has been described elsewhere (11). As before, all specimens were pickled in nitric/hydrofluoric acid[1] before the corrosion experiments, which were conducted either in water at 325°C, as described earlier (11), or in steam at 325°C and 1 atm. For the latter the specimens were suspended in a glass reaction chamber in a vertical tube furnace. Steam, raised in a small boiler from which all air was first expelled, was passed through the reaction chamber at about 100 cm³/min. Appropriate weighings gave the weight gain per unit area. Most of the films were adherent (experiments being stopped before the onset of flaking) so that this weight was a good measure of the extent of corrosion and of the film thickness.

**Table I. Analyses of materials**

| Unalloyed Kroll Zr | Sample No. 24, ppm | Sample No. 050, ppm |
|---|---|---|
| $N_2$ | 50 | 225 |
| C | 280 | 550 |
| Fe | 300 | 435 |
| Ni | — | 32 |
| Cr | 100 | 155 |
| Mg | 50 | 20 |
| Cl | 50 | 20 |
| Cu | — | 100 |
| $O_2$ | — | 1100 |
| $H_2$ | — | 37 |
| Al | 100 | — |

Binary alloys: 1% wt Cr, 2.5% wt Ta, 0.25% wt Al. All nominal compositions, based on Sample No. 24.
Zircaloy 2 (Nominal): 1.5% wt Sn, 0.12% wt Fe, 0.10% wt Cr, 0.05% wt Ni, balance Zr.

## Results

At first an area of exactly 1 cm² of specimen was waxed off, but, as this proved difficult to achieve, in subsequent experiments approximately 1 cm² was masked off and carefully measured. Capacity results were converted then to values for 1 cm² by dividing by the actual area, while the resistance values were multiplied by the area.

Capacity values for various alloys are given in Table II which also shows, for comparison, corrosion rates in water at 325°C. Results for specimens of unalloyed Zr after various periods of exposure to steam at 325°C and 1 atm are shown in Tables III to VI. Both these sets of measurements were made in 1*N* $H_2SO_4$ at a frequency of 1000 cps and are final steady values after at least 24 hr in electrolyte.

The effect of frequency on the impedance of several specimens in 1*N* $H_2SO_4$ is shown in Fig. 4 and 5. The results are plotted as resistance vs. 1/frequency and 1/capacity vs. log frequency. Young (5) has shown this to give straight lines for crack-free films. According to his theory, the ratio of the slope

[1] $HNO_3$ (conc), 45 cm³; HF (48% soln), 5 cm³; and water, 50 cm³.

**Table II. Capacity values for various alloys after corrosion in water at 325°C (1000 cps)**

| Alloy | Time of corrosion, hr | Weight gain W, mg/cm² | C, μF/cm² | 1/CW | Average linear corrosion rate mg/cm²/mo | Corrosion resistance |
|---|---|---|---|---|---|---|
| Zircaloy 2 | 72 | ~0.1 | 0.039 | 260 | Rate falling with time | Good |
| | 144 | 0.3 | 0.029 | 120 | | |
| | 228 | 0.3 | 0.029 | 120 | | |
| | 520 | 0.3 | 0.025 | 130 | | |
| Unalloyed | 72 | 0.5 | 0.143 | 14 | | |
| Zirconium | 144 | 1.3 | 0.135 | 5.7 | 4.4 | |
| (No. 24) | 228 | 2.1 | 0.140 | 3.4 | | Intermediate |
| | 520 | 3.7 | 0.179 | 1.5 | | |
| Zirconium | 72 | 1.0 | 0.093 | 11 | | |
| + 1% wt Cr | 144 | 2.8 | 0.257 | 1.4 | 14 | |
| | 228 | 4.7 | 0.129 | 1.7 | | |
| | 520 | 11 | 0.392 | 0.24 | | |
| Zirconium | 72 | 1.3 | 0.404 | 1.9 | ~10-20 [from | Bad |
| + 2.5% wt Ta | 520 | ? Flaking | 0.526 | — | other expts (11)] | |
| Zirconium | 72 | ~7 | 0.726 | ~0.2 | ~70 | |
| + 0.25% wt Al | | Flaking | | | | |

Table III. Capacity measurements on unalloyed zirconium (No. 050) after exposure to steam at 325°C, 1 atm for various times (1000 cps)

| Specimen No. | Time, hr | W, mg/cm² | C, μF/cm² | 1/CW | Color of oxide film |
|---|---|---|---|---|---|
| 1 | 1 | 0.058 | 0.629 | 27.4 | Blue-black |
| 2 | | 0.054 | 0.688 | 26.9 | |
| 3 | 2 | 0.051 | 0.566 | 34.6 | Blue-black |
| 4 | | 0.047 | 0.553 | 38.5 | |
| 5 | 2.5 | 0.142 | 0.960 | 7.35 | Dark gray |
| 6 | | 0.128 | 0.898 | 8.70 | |
| 7 | 3 | 0.295 | 0.744 | 4.55 | Medium gray |
| 8 | | 0.283 | 0.839 | 4.22 | |
| 9 | 4 | 0.351 | 0.890 | 3.20 | Light gray |
| 10 | | 0.319 | 0.856 | 3.66 | |
| 11 | 5 | 0.475 | 0.890 | 2.37 | Light gray |
| 12 | | 0.485 | 0.962 | 2.15 | |
| 13 | 6 | 0.497 | 0.946 | 2.12 | Light gray, |
| 14 | | 0.515 | 1.135 | 1.72 | White spots |
| 15 | 10 | 0.644 | 0.937 | 1.66 | Light gray, |
| 16 | | 0.662 | 0.892 | 1.69 | White spots |

of the "capacity" plot to that of the "resistance" plot should always be 9.2 (=4 x log e 10). (In this relation $C$ is expressed in Farads per cm².) Figure 5 gives the observed values of the ratio.

Figure 6 shows the change of capacity with time of immersion in electrolyte for cracked and uncracked films.

Table IV shows the effect of varying the electrolyte resistance from 1$N$ $H_2SO_4$ ($\rho = 5$ ohm-cm) to $N/10$ sodium sulfate ($\rho = 130$ ohm-cm), and Fig. 7 shows the frequency dependence of the resistance of typical specimens of unalloyed Zr in the two electrolytes.

## Discussion

Table II shows that, as anticipated, films of lower protective value have higher capacities. Since the capacity of a condenser is inversely proportional to the thickness of dielectric, it is convenient to take 1/capacity as a measure of the "effective thickness" of the protective part of the film. The protective character of different films may be compared by obtaining the ratio of 1/capacity to the total thickness of the film. For adherent films on Zr (which forms only one oxide) the weight gain per unit area during corrosion ($W$) is a good measure of film thickness. Protective character is thus measured by the quantity $1/CW$. Values of $1/CW$ are given in Table II and comparison with the corrosion rates shows that good alloys are sharply discriminated from bad. In Table III the fall of $1/CW$ with film growth reveals the progressive loss of protective character. This was accompanied by a change of film color usual with corroding Zr alloys, from black through shades of gray to white.

Table IV. Effect of electrolyte resistivity on film impedance (1000 cps)

| Specimen No. | W, mg/cm² | 1$N$ $H_2SO_4$ ($\rho = 5$ ohm-cm) $C_f$, μF | 1$N$ $H_2SO_4$ ($\rho = 5$ ohm-cm) $R_f$, ohm | $N/10$ $Na_2SO_4$ ($\rho = 130$ ohm-cm) $C_f$, μF | $N/10$ $Na_2SO_4$ ($\rho = 130$ ohm-cm) $R_f$, ohm | $R_f$ in $N/10$ $Na_2SO_4$ / $R_f$ in 1$N$ $H_2SO_4$ |
|---|---|---|---|---|---|---|
| 1 | 0.058 | 0.629 | 30.7 | 0.099 | 239 | 7.8 |
| 2 | 0.054 | 0.688 | 21.0 | 0.162 | 158 | 7.5 |
| 3 | 0.051 | 0.566 | 38.4 | 0.072 | 410 | 11 |
| 4 | 0.047 | 0.553 | 42.6 | 0.073 | 280 | 6.6 |
| 5 | 0.142 | 0.960 | 14.2 | 0.257 | 340 | 24 |
| 6 | 0.128 | 0.898 | 16.0 | 0.067 | 775 | 48 |
| 7 | 0.295 | 0.744 | 20.3 | 0.038 | 1630 | 80 |
| 8 | 0.283 | 0.839 | 20.6 | 0.027 | 1690 | 82 |
| 9 | 0.351 | 0.890 | 19.4 | 0.050 | 1230 | 63 |
| 10 | 0.319 | 0.856 | 16.0 | 0.233 | 357 | 22 |
| 11 | 0.475 | 0.890 | 22.3 | 0.389 | 260 | 12 |
| 12 | 0.485 | 0.962 | 20.4 | 0.235 | 595 | 29 |
| 13 | 0.497 | 0.946 | 19.7 | 0.362 | 350 | 18 |
| 14 | 0.515 | 1.135 | 18.8 | 0.316 | 472 | 25 |
| 15 | 0.644 | 0.937 | 17.5 | 0.775 | 59 | 3.4 |
| 16 | 0.662 | 0.892 | 17.4 | 0.735 | 90 | 5.2 |

Table V. Values of $R_f$ at $1/f = 0$

| Specimen No. | 1/CW | $R_f$ at $1/f = 0$ in 1$N$ $H_2SO_4$ (ohm) | $R_f$ at $1/f = 0$ in $N/10$ $Na_2SO_4$ (ohm) |
|---|---|---|---|
| 1 | 27.4 | ~1 | ~0* |
| 2 | 26.9 | ~2 | ~0* |
| 3 | 34.6 | ~5 | ~0 |
| 4 | 38.5 | ~8 | ~0* |
| 5 | 7.35 | — | ~50 |
| 6 | 8.70 | ~0 | — |
| 7 | 4.55 | ~1 | 200-300 |
| 8 | 4.22 | ~0 | ~50 |
| 9 | 3.20 | 0 | ~100 |
| 10 | 3.66 | — | ~80 |
| 11 | 2.37 | ~1 | ~100 |
| 12 | 2.15 | <1 | ~100 |
| 13 | 2.12 | — | ~100 |
| 14 | 1.72 | <1 | ~80 |
| 15 | 1.66 | ~0 | ~220 |
| 16 | 1.69 | <1 | ~30 |

* Negative intercept.

It is not possible to decide certainly whether the best material, Zircaloy 2, forms films which are entirely crack-free, but there are two reasons for supposing that it does. First, if the films are crack-free, their capacities may be calculated approximately as simple parallel plate condensers. Taking the dielectric constant (4) and density of zirconium dioxide as 27 and 5.7 g/cm³, respectively, $C = (3.5 \times 10^{-8} \sigma^2)/W$ μF/cm² where $W$ is the weight gain in mg/cm² and $\sigma$ is the ratio true surface area/apparent surface area. If calculated and observed capacities for Zircaloy 2 are equated, $\sigma$ is found to be about 1.5. Adams, *et al.* (12) found $\sigma \sim 2$ for abraded Zr and, by comparison with this, a value of 1.5 for a bright pickled surface seems reasonable. Second, films, such as those on Zircaloy 2, which have "good" values of $1/CW$ (150 or more) behave differently with time from less protective films. The final capacity of the former is established almost

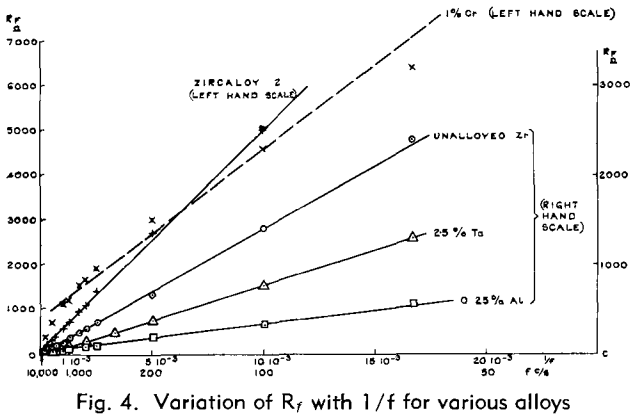


Fig. 4. Variation of $R_f$ with 1/f for various alloys

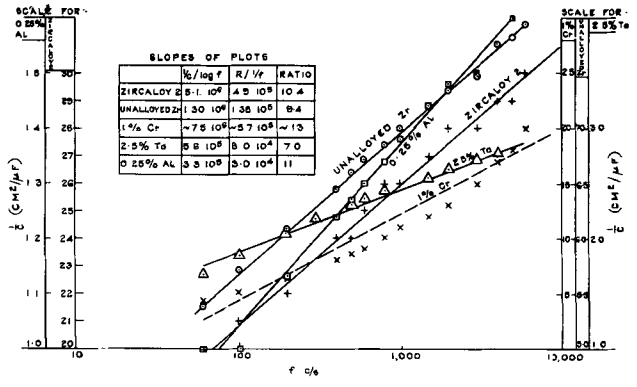


Fig. 5. Variation of 1/C with log f for various alloys

at once, but inferior films show a marked drift with time, presumably due to the slow penetration of electrolyte into cracks. Some typical cases are given in Fig. 6, which also shows that, with a very bad film ($1/CW = 1.7$) the drift diminishes again, doubtless because the cracks are large and numerous.

It was thought that extrapolation to zero time of the plots for cracked films might yield values appropriate to uncracked films of the same thickness. With extensively cracked specimens no consistent results could be obtained, the capacity changing too rapidly for accurate measurement at short times. For a few specimens, with $1/CW$ in the range 30-100, the extrapolated values approximated to the theoretical crack-free value, based on $1/CW \sim 200$.

As discussed more fully later, the film impedance obeyed approximately the relations derived by Young for crack-free films. According to the latter the film resistance is inversely proportional to the frequency and so should fall to zero at $1/f = 0$. With much-cracked films, the capacity is much larger than the uncracked value and therefore must be predominantly composed of impedance elements each connected to the bulk electrolyte by cracks filled with liquid. When, at $1/f = 0$ the resistance of the elements themselves falls to zero, there should remain a resistance characteristic of the electrolyte in the cracks. This might be expected to change by the appropriate ratio when the resistivity of the electrolyte is changed. Values of $R_f$ at $1/f = 0$ in two electrolytes are given in Table V for a number of the specimens exposed in steam at 325°C. The behavior of two specimens is illustrated in Fig. 7.

In $H_2SO_4$ the resistances are small and the accuracy low, so that one can only say that they are of

**Table VI. Mean protective thickness d and total thickness t, of films formed on unalloyed zirconium in steam at 325°C 1 atm (Sample No. 050)**

| Specimen No. | W, mg/cm² | 1/CW | d, Å | t, Å |
|---|---|---|---|---|
| 1 | 0.058 | 27.4 | 630 | 4000 |
| 3 | 0.051 | 34.6 | 730 | 3500 |
| 6 | 0.128 | 8.70 | 410 | 8800 |
| 7 | 0.295 | 4.55 | 490 | 20000 |
| 9 | 0.351 | 3.20 | 410 | 24000 |
| 11 | 0.475 | 2.37 | 410 | 33000 |
| 13 | 0.497 | 2.12 | 380 | 34000 |
| 15 | 0.644 | 1.66 | 390 | 44000 |

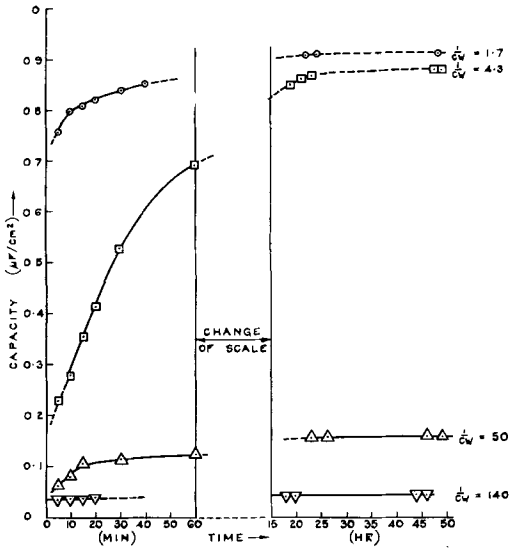


Fig. 6. Variation of capacity with time of immersion in various electrolytes. Values of 1/CW are based on final capacities.

the order of a few ohms. The sodium sulfate values are also rather imprecise, but those for specimens exposed for intermediate times (No. 5 onward) are definitely larger than in $H_2SO_4$.

Earlier specimens gave very low values, and sometimes even negative intercepts, which are recorded as "~ zero." This trend may be explained as follows: the first specimens, corroded for short periods only, have films which are only slightly cracked, so that "crack elements" contribute little to their impedance, and their series resistance is little affected by that of the electrolyte in the pores. As exposure increases, the extent of cracking increases and at about specimen No. 7 the resistance of the liquid in the cracks exerts its greatest effect. With still further exposure, however, the cross-sectional area of cracks is so much increased that their contribution to resistance again falls. Thus the increase in $R_F$ on changing to an electrolyte of higher resistivity should be least for uncracked and much-cracked films and should reach a maximum for intermediate specimens. The increase of cracking as corrosion proceeds is illustrated by the successive values of $1/CW$.

This explanation is certainly an oversimplification. For example, with the intermediate specimens

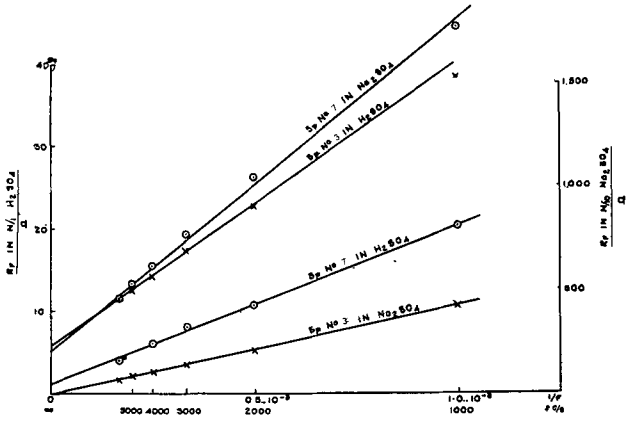

Fig. 7. Determination of $R_f$ at $1/f = 0$, for unalloyed Zr exposed to steam at 325°C, 1 atm.

of Table V, the ratio $[R_f(1/f = 0)$ in $Na_2SO_4]/[R_f(1/f = 0)$ in $H_2SO_4]$ is considerably more than the ratio of the resistivities of the electrolytes themselves, viz., 26. Table IV shows the same to be true of resistances at 1000 cps. Again, when the impedance is predominantly made up of crack elements (i.e., the capacity is much greater than the uncracked value for the thickness in question) the simple picture would suggest that the capacity should not be affected by the change of electrolyte. Table IV shows that this is by no means so, capacity values being much reduced in sodium sulfate. As with the resistances there is a tendency for the intermediate specimens to show the greatest effect.

It is thus not yet possible to explain in detail the impedance of a cracked film, and one cannot use the values to study the cracks, as fully as originally hoped. In particular, it is not possible to calculate separately their area and mean distance of approach to the metal/oxide interface. A crude estimate of the latter may however be made for much-cracked films in the following way.

A crack, although drawn in two dimensions as a line, is in fact a complicated warped surface. A simplified crack may be considered to be a plane fissure of uniform width and thickness. The latter may have any value down to that at which the proximity of the walls begins to affect the entry and properties of the electrolyte. Somewhat arbitrarily the thinnest crack may be taken as 100Å, so that the resistance of a 1 cm length of such a crack, 1 cm wide, filled with 1*N* $H_2SO_4$ is about $10^6$ ohms. Now the capacity of 1 $cm^2$ of $ZrO_2$ between electrodes 1 cm apart is about $4 \times 10^{-6}$ $\mu$F so that its impedance $(= 1/C\omega)$ at 1000 cps is about $10^8$ ohms. Thus such an element of capacity intersected by a crack perpendicular to the faces of the dielectric will have its capacitance impedance completely short-circuited by the crack. This will also be true of thinner capacity elements intersected by oblique cracks, down to elements whose thickness is about 1/100 cm. All cracks, therefore, except those almost parallel to the metal surface, short-circuit the contribution to capacity of the oxide through which they pass. Thus a cracked film constitutes a condenser, one plate of which is the metal and the other a mass of cracks filled with electrolyte, each crack short-circuiting the material above it, so that the effective area of the condenser "plate" will be that of the cracks, projected perpendicularly to the metal surface. If the film is extensively cracked, the whole area of specimen will be covered by cracking so that the projected area will be equal to the (true) area of the specimen. Knowing the area one may calculate the mean thickness of dielectric, i.e., the mean separation of the irregular surface of cracks from the metal/oxide interface. This gives the mean thickness of the protective part of the film. (Since capacity is inversely proportional to thickness, this value is the reciprocal of the mean value of 1/thickness which, compared with the arithmetic mean, gives greater weight to the lower thicknesses.) Some values of the mean thickness $d$ based on a dielectric constant of 27 and a surface roughness of 1.5 are given in Table VI.

The capacity values used are the increases over that for an uncracked film of the same total weight, i.e., they are the contributions due to cracks. For extensively cracked specimens $(1/CW <$ about 10) this is the predominant part of the capacity. The table also gives the total thickness of the film $t$, obtained from the weight gain, assuming a density of $ZrO_2$ of 5.7 $(t = 6.9 \cdot 10^4 \text{ WÅ})$. The figures show that $d$ falls to a fairly constant value of about 400Å. Considering the uncertainty of the roughness factors and dielectric constant one may conclude that the protective part of the film is of the order of 500Å thick.

The lower capacities of the earlier specimens are due either to the cracking not being so deep or to its area being less than that of the whole specimen. Some short experiments in dry oxygen (not quoted here) gave films for which, assuming unit area, $d > t$, which is impossible. On these specimens the area of cracking must have been less than the whole area of the specimen, so that $d$ could be less than $t$. It is impossible to decide whether or not the first cracks go as close to the metal as the final protective thickness. It is tempting to consider that, while the "resistance ratio" (in two electrolytes, see above) is increasing during the early part of the test, the cracks are becoming deeper and that, when the resistance ratio begins to fall again, they have reached their greatest depth and thereafter are increasing in extent. There is, however, no proof of this. Determination of the limiting protective thickness for different alloys and conditions of corrosion might be illuminating, and it is hoped to do this.

That the values of $d$ are reasonable may be seen by noting that, if diffusion through the protective part of the film controls the corrosion rate, the latter should, like the capacity, be inversely proportional to $d$. It should also, again like the capacity, be proportional to the projected area of the cracks, for it is by the latter that the corroding medium approaches the metal/oxide interface. As discussed for the capacity, the projected area approaches unity as corrosion proceeds so that the final rate should be equal to that found in the early part of the experiment when the film is still uncracked and is of thickness equal to the final protective thickness. Thus a line of slope equal to the final corrosion rate should touch the initial part of the curve at a point equivalent to the protective thickness (Fig. 8). In-

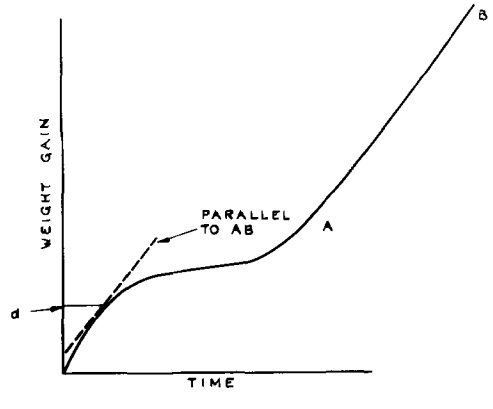


Fig. 8. Mean protective film thickness (diagrammatic)

sufficient data are available to check this point thoroughly, but a few results in oxygen at 325°C support it approximately.

It has already been said that the capacity and resistance of corrosion films follow approximately the frequency dependance derived (5) for crack-free films by considering the properties of the oxide itself. Figures 4 and 5 show that fair straight lines are obtained, and the ratio values given in Fig. 5 agree approximately with the theoretical value of 9.2, although the individual slopes vary tenfold between specimens.[2] This suggests some similarity in the "equivalent circuit" of sound and cracked oxide films, although the impedance of the latter owes much to the liquid in the cracks (cf. Table IV).

The problem may be approached by considering a cracked film not, as heretofore, as a combination of individual resistance/capacity elements, but as a block of material of constant dielectric constant whose resistivity varies through the thickness. This is how Young treats crack-free films; and in the present case conductivity due to cracks filled with electrolyte must be substituted for conductivity due to nonstoichiometry. Resistivity variation due to varying nonstoichiometry is replaced by variation due to the change of area of cracks through the thickness of the film. Formal comparison with Young's treatment shows that his relations will be obeyed if the total cross-sectional area of cracks at any plane in the film parallel to the outer surface is an exponential function of the distance from that surface.[3] Thus, if $\alpha_x$ is the fraction of the area of a plane at distance $x$ from the surface which is composed of cracks, and $\alpha_o$ is the value at the outer surface.

$$\frac{\alpha_x}{\alpha_o} = e^{-x/k}$$

k being a constant. There are at present no independent grounds for expecting an exponential variation of cracking with thickness. Possibly one might be reached by considering the mechanical properties of the film substance in which case a comparison of $k$ and $\alpha$ as between different alloys might be illuminating.

Although the results give fair straight lines when plotted according to Young's relations, further use of the latter does not yield sensible values for the resistivities of the cracked films. For example, with a dielectric constant of ~27, the above relations lead to:

$$\log \rho_d = \frac{1}{C_{1000} \times S} + 7.8$$

and

$$\log \rho_o = \log \rho_d - (2.9 \times 10^8 W)/S$$

where $\rho_o$, $\rho_d$ are the resistivities at the outside and inside of the film respectively, $W$ is the weight gain in mg/cm², $S$ is the slope of $1/C$ vs. log $f$, and $C_{1000}$ is the value at 1000 cps, in farads/cm². Conductivity being due to electrolyte in the cracks, the degree of cracking should be given by the ratio of electrolyte resistivity to film resistivity, and at the outer surface $\alpha_o$ should be equal to $\frac{\rho \text{ electrolyte}}{\rho_o}$, but most of the well cracked films ($1/CW \sim 30$ or less) gave impossibly low values of $\rho_o$, though some specimens with little cracking ($1/CW \sim 100$) gave figures which were at least plausible. This suggests that a cracked film is not well represented by a capacity shunted by a varying resistance, principally because a large part of the latter is so low as to short-circuit completely the capacity with which it is in parallel. This conclusion was also reached earlier by considering the resistance of individual cracks.

Further complications are suggested by some recent experiments in sodium nitrate solution which, though almost equal to 1$N$ $H_2SO_4$ in resistivity, gave very different results. The capacities were much less, and the resistances greater, the values departing more from those in $H_2SO_4$ than do those in $N/10$ sodium sulfate, whose resistivity is 26 times greater. This suggests that electrolytes behave specifically, more properties than their resistivity being important.

## Conclusions

The impedance of Zr specimens carrying oxide films formed by corrosion and immersed in electrolyte show higher capacities with the less protective films. This is due to penetration of electrolyte into cracks in the latter. The degree of cracking may be assessed by evaluating the quantity $1/CW$, where $C$ is the capacity and $W$ the weight gain due to corrosion. The impedance measurements also yield a resistive component which is less easy to interpret, although approximate correlation to the progress of cracking may be made. The impedances are influenced by the resistivity of the electrolyte, and other properties of the solution may be important. The frequency behavior of capacity and resistance follow approximately the relations applicable to crack-free films.

It has not been possible to use observations to determine the extent and depth of cracking in any detail, but the mean thickness of the uncracked part of the film at late stage in corrosion can be crudely estimated. The present usefulness of impedance measurements is confined to the comparison, by values of $1/CW$, of films formed on different alloys under different conditions of corrosion. Here they can be of value.

## Acknowledgments

The authors wish to thank Mr. C. N. Davey for assistance with the apparatus. They are also indebted to Dr. H. M. Finniston and Mr. R. A. U. Huddle for encouragement and criticism, and to Dr. L. Young, Dr. P. Jacobs, and Dr. A. R. Bray for helpful discussions.

[2] In this connection it is important to consider an adequate range of frequency, viz., about 50-5000 cps. Over 1000-5000 cps one can obtain fair straight lines and a slope ratio of about 10 from a simple circuit of fixed resistance and capacity in parallel, the values being chosen to give an impedance typical of films. Over the full frequency range, however, the simple model departs from these relations far more than do the film impedances.

[3] The reasonable assumption is here made that $\alpha << 1$ so that the dielectric properties of the film are independent of $x$, as Young assumes. This is not contrary to the earlier assumption that the effective area of condenser plate formed by the cracks is unity; for that area was the projected area of an irregular surface of cracks, while we are here considering the traces of individual cracks cutting an infinitely thin plane.

Manuscript received Jan. 7, 1958. This paper was prepared for delivery before the Ottawa Meeting, Sept. 28-Oct. 2, 1958.

Any discussion of this paper will appear in a Discussion Section to be published in the June 1959 JOURNAL.

REFERENCES

1. D. Thomas and S. Kass, *This Journal*, **104**, 261 (1957).
2. R. Wheeler, *U.S.A.E.C., K.A.P.L.* 39190 (Appendix) (1955).
3. U. R. Evans, *This Journal*, **91**, 547 (1947).
4. A. Charlesby, *U.K.A.E.A., A.E.R.E.*, M/R. 1176 (1953).
5. L. Young, *Trans. Faraday Soc.*, **51**, 1250 (1955).
6. Guntershulze and Betz, "Elektrolytkondensatoren," Krayn, Berlin (1937).
7. R. D. Misch and W. E. Ruther, *This Journal*, **100**, 531 (1953).
8. J. N. Wanklyn, *Nature*, **177**, 849 (1956).
9. F. Wormwell and D. Brasher, *J. Iron Steel Inst.*, **164**, 141 (1950).
10. F. Wormwell and D. Brasher, *J. Iron Steel Inst.*, **169**, 228 (1951).
11. J. N. Wanklyn and C. F. Britton, *U.K.A.E.A., A.E.R.E.*, M/R. 1924 (1956).
12. G. B. Adams, M. Maraghini, and P. Van Ryssel-berghe, *U.S.A.E.C., A.E.C.U.*, 2918 (1954).

# The Reaction of Germanium with Aqueous Solutions

## I. Dissolution Kinetics in Water Containing Dissolved Oxygen

**Walter W. Harvey and Harry C. Gatos**

*Lincoln Laboratory, Massachusetts Institute of Technology, Lexington, Massachusetts*

ABSTRACT

The dissolution of germanium in water was studied as a function of oxygen partial pressure, temperature, crystallographic orientation, and mobile-carrier density. It was found that, although thermodynamically feasible, germanium does not react with water, freed of oxygen, in the temperature range studied (up to 100°C). In the presence of oxygen the dissolution rate in pure water is a function of oxygen partial pressure, reaching a limiting value of the order of 1 $\mu$g/cm$^2$/hr at 35°C under oxygen partial pressures greater than approximately 0.5 atm. For a given oxygen pressure the dissolution rate is approximately trebled for a ten-degree temperature rise, the measured activation energy for the dissolution reaction being 19 ± 2 kcal/mole. The order of dissolution rates for the three principal crystallographic faces was found to be {100}> {110}> {111}. No effect on the dissolution rate was found to result from changes in mobile-carrier concentrations brought about by doping or illumination. From dissolution rates and potentials it is concluded that the dissolution process is under cathodic control and that the rate-determining step is the reduction of oxygen by germanium.

With the recent advances in semiconductor theory and technology, a great deal of interest has centered about the reactions of germanium surfaces with various ambients and the resulting changes in electronic properties. Chemical etching and polishing in solutions containing strong oxidizing agents have been studied extensively on a more or less empirical basis in order to meet the needs for reproducibly smooth and undistorted surfaces. However, systematic studies of the reaction of Ge with aqueous solutions containing no oxidizing agents other than dissolved oxygen have not hitherto been reported. Also lacking is an understanding of the electrochemistry of dissolution without externally applied emf.

It is known that direct interaction of Ge with water is thermodynamically possible (1)

$$Ge + 2H_2O = GeO_2 + 4H^+ + 4e^-; \quad E^\circ = -0.15 \quad [1]$$

It was found in this laboratory, however, that at ordinary temperatures (up to 100°C) this reaction does not proceed at a significant rate. In the presence of oxygen, the dissolution rate of Ge in water can be measured conveniently by analysis of the solution for Ge.

The present study was undertaken in an attempt to elucidate the role of oxygen in the dissolution of Ge in water and in aqueous solutions of nonoxidizing electrolytes. Emphasis has been placed on the kinetics and electrochemistry of the dissolution process, taking into account the semiconductor properties of Ge. This paper deals primarily with the kinetics of the dissolution of Ge in water containing dissolved oxygen.

### Experimental

#### *Materials*

*Germanium.*—Thin rectangular slabs were cut from single crystals grown in this laboratory from high purity, zone-refined Ge. The dimensions of the slabs were 15 x 20 x 1 mm. A 1-mm diameter hole was drilled ultrasonically into each slab for convenience in handling. The crystals (diamond structure) were oriented by x-ray techniques before cutting, so that the two large faces of the slabs corresponded to {100}, {110}, or {111} surfaces.

*Water.*—High resistivity water was prepared in two stages of distillation using tin-lined stills in tandem. Dissolved $CO_2$ was removed by bubbling $CO_2$-free gas ($O_2$, $N_2$, or a mixture of the two gases)

through a presaturator for several hours before forcing the presaturated water (neutral to within 0.2 pH unit) into the reaction cells.

*Gases.*—Cylinder gas was passed through a U-tube containing Ascarite for removal of $CO_2$ and then dispersed in distilled water contained in a gas-scrubbing tube before being admitted into the reaction cells. Commercial prepurified nitrogen was used.

*CP-4 etchant.*—The chemical polishing agent commonly known as "CP-4" was prepared from chemical reagent grade conc. $HNO_3$ (5 parts by volume), glacial $CH_3COOH$ (3 parts), 48% HF (3 parts), and $Br_2$ (0.06 part).

*Surface treatment.*—Gross irregularities on the surfaces of the Ge slabs were removed by lapping on a flat glass plate using a slurry of water and 1600-mesh garnet powder. The freshly abraded slabs were then treated with CP-4 for a time (usually 30 sec to 1 min) sufficient to remove all traces of the pits formed by grinding. The resulting surfaces were microscopically smooth and highly polished. The roughness factor of CP-4 treated Ge surfaces has been reported to be 1.3 (2).

Before immersion, the Ge slabs were given a brief cleansing etch in freshly prepared CP-4 and rinsed thoroughly with doubly distilled water. No Ge could be detected analytically in the last portion of rinse water. After rinsing, the slabs were transferred immediately to the reaction cells.

*Analytical.*—Samples of solution were taken during the course of an experiment (see below) and analyzed colorimetrically for Ge employing the oxidized-hematoxylin method (3). The stability of the reagents was checked by analyzing standard Ge solutions along with each set of samples. Ageing of the hematoxylin reagent for several weeks or longer before use led to enhanced color stability. Using a Beckman Model DU spectrophotometer the useful range of Ge concentration was 0-2 μg/ml with a sensitivity of 0.005 μg/ml or better and an accuracy of about 1%.

Standard solutions for analysis were prepared by bubbling oxygen gas over Ge slabs immersed in boiling water under reflux and determining the weight loss with a microbalance. The color intensities of solutions so prepared fell along the same calibration curve as for standards prepared from high purity $GeO_2$ powder, but the former values were somewhat more consistent and reproducible, possibly because of the tendency of $GeO_2$ to form colloidal solutions on dissolving in water.

### *Apparatus and Procedure*

Three to eight Ge slabs were mounted on a holder made of glass rod and separated by spacers cut from 3-mm glass tubing. The holder was suspended in a reaction cell as illustrated in Fig. 1. Three such cells were employed simultaneously. Beginning with the gas-scrubbing tubes, the apparatus was constructed entirely of glass. The stream of water-saturated gas bubbles entering the reaction cell through the capillary orifice did not come into direct contact with the Ge specimens. Continuous bubbling of gas during the runs at a rate of 80 or 100 ml/min

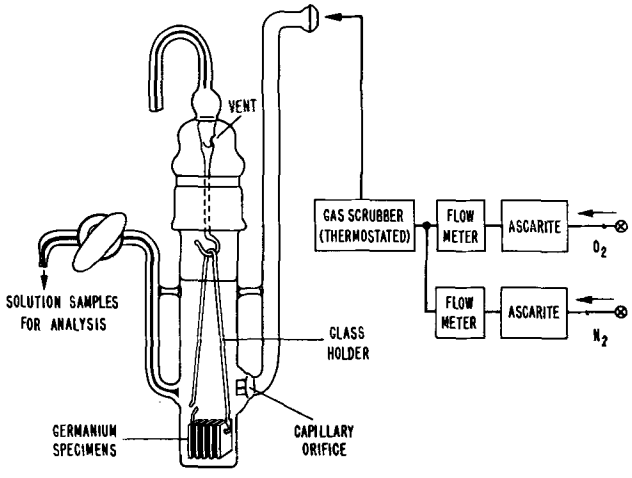


Fig. 1. Apparatus for dissolution experiments

provided vigorous agitation and maintained saturation of the solution with oxygen at the desired partial pressure. For varying the partial pressure of oxygen and, thus, the concentration of dissolved oxygen, streams of $O_2$ and $N_2$ at predetermined flow rates were mixed in the gas-scrubbing tubes and passed into the reaction cells.

The initial volume of solution in each cell was approximately 40 ml. During the course of the reaction, samples of the solution were withdrawn through the capillary sidearm by closing off the exit tube in the cap (Fig. 1). Depending on the effect being studied, 5-10 samples (generally 1.5 or 2.5 ml) from each cell were discharged into weighed vials for subsequent analysis. The amount of solution remaining in the cell at the end of the experiment was determined by pipetting into a weighed flask. A correction was made for solution retained by the specimens upon removal. Sample and residual solutions weights were determined to 0.01 g.

In studies of the effect of light on the dissolution process, illumination was provided by 40-watt incandescent lamps of tubular shape immersed in the water bath on either side of the cell. Temperature rise in the cell during illumination was prevented by adjustment of the operating temperature of the water bath. Without compensation the solution temperature increased 0.15°C as a result of thermal radiation. In all experiments reported herein the temperature was controlled to ±0.01°C.

Dissolution rates were obtained from plots of amount of Ge dissolved as a function of time. Results are reported in terms of micrograms of Ge dissolved per square centimeter of geometrical surface per hour ($\mu g/cm^2/hr$). Since the observed dissolution rates are very small, they are likely to be affected even by slight differences in surface treatment. For this reason direct comparisons of rates for different specimens were usually made by employing three sets of Ge slabs which were etched and rinsed simultaneously, and hence received nearly identical surface treatment before they were placed in individual reaction cells. The dependence of rate on temperature, oxygen partial pressure, or illumination was evaluated by changing the experimental conditions midway in a given run.

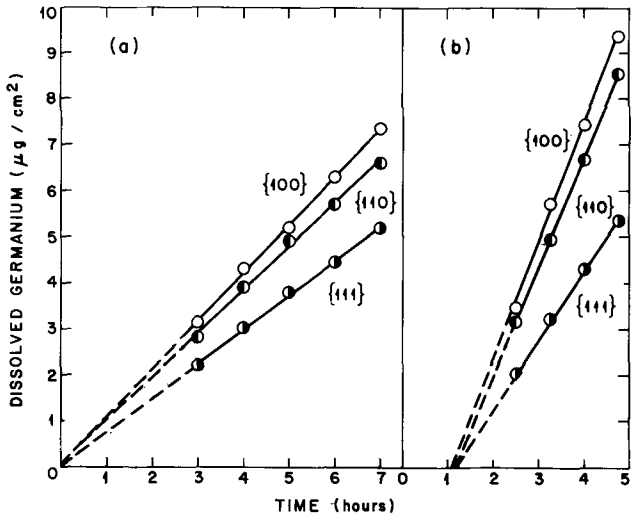


Fig. 2. Typical data showing amount of Ge dissolved in oxygen-saturated water at 35°C with and without an induction period: comparison of {100}, {110}, and {111} surfaces.

*Preliminary Experiments*

Initial measurements carried out in nitrogen-, air-, and oxygen-saturated water established that reaction [1] does not take place or proceeds at exceedingly slow rates between 30° and 40°C. In air-saturated water the average dissolution rate was 0.57 $\mu g/cm^2/hr$ at 30°C, and in oxygen-saturated water it was 0.72 $\mu g/cm^2/hr$ ({100} surfaces). One $\mu g/cm^2$ corresponds approximately to 10 atom layers of Ge. The observed dissolution rate in nitrogen-saturated water (0.024 $\mu g/cm^2/hr$) is likely the result of trace amounts of oxygen introduced with the prepurified nitrogen or not removed by nitrogen bubbling. Indeed, Ge was found to be completely inert to boiling water refluxing under a nitrogen atmosphere; even after prolonged immersion (40 hr) no detectable amounts of Ge were found in solution. It is therefore evident that dissolved oxygen is essential for the dissolution of Ge in water.

*Dissolution as Function of Time. Induction Period*

Typical data relating the amount of Ge dissolved to time of immersion in oxygen-saturated water are plotted in Fig. 2. It is seen that the rate of dissolution (slope) remains constant for rather long periods of time. This behavior was observed for the various temperatures, surface orientations, and oxygen partial pressures.

The period of induction for the reaction as determined by graphical extrapolation (Fig. 2b) varied unpredictably from experiment to experiment and is believed to be a manifestation of commonly encountered differences in surface treatment. Although apparent induction periods as long as 1.7 hr were occasionally observed, an average value of 0.5 hr was found for a number of independent runs at 35°C. Regardless of the length of the induction period, however, relative dissolution rates were satisfactorily reproducible. In general, absolute dissolution rates were higher and also less reproducible when the apparent induction period was relatively long (say more than 30 min). Thus, in 12 runs with nearly zero induction period the average dissolution rate was 1.03 ± 0.09 $\mu g/cm^2/hr$ at 35°C for {110} surfaces. On the other hand, in 28 runs with an average induction period of 0.5 hr, the average dissolution rate was 2.2 ± 1.1 $\mu g/cm^2/hr$. Samples with {100} and {111} surface orientations gave similar statistical results.

The existence of an induction period preceding Ge dissolution is believed to be associated with surface changes brought about by treatment with CP-4. With this reagent an invisible $GeO_2$ film is formed on the Ge surface; this film is believed to be several atom layers thick (4) and usually has the properties of the soluble hexagonal modification. The formation of insoluble, tetragonal $GeO_2$ is also possible, and its presence on the surface together with the soluble modification would lead to an apparent induction period preceding Ge dissolution. This difficultly soluble film is most likely formed by reaction with CP-4 vapor during transfer of the specimens to the rinsing bath. Accordingly, it was found that, by displacing the CP-4 with a large volume of dilute HF before removal of the specimens, the induction period could usually be eliminated. Treatment with HF following removal of the specimens from the CP-4 did not have this effect. The higher rates measured when Ge dissolution was preceded by an induction period are probably associated with an increase in submicroscopic surface roughness resulting from undermining of the insoluble oxide residue or may be the result of galvanic action. No attempt was made to clarify this point experimentally.

*Dependence of Dissolution Rate on Crystallographic Orientation*

For the three principal crystallographic faces the order of the observed dissolution rates was {100}>{110}>{111} (Fig. 2). Absolute and relative dissolution rates at 30° and 35°C are listed in Table I. The ratio of absolute rates corresponding to short or zero induction periods is computed from the table to be {100}/{110}/{111} = 1.00/0.91/0.70 at 35°C, in fair agreement with relative rates obtained in a large number of experiments and averaged without regard to apparent time of induction (or absolute value of rate). It is significant that electron microscopic examination of CP-4 treated Ge specimens revealed no characteristic differences in microstructure among the various surface orientations.

Comparable differences in dissolution rate were found by Camp (5) in a study of the etching of

Table I.

| | Absolute* dissolution rates ($\mu g/cm^2/hr$) | | |
|---|---|---|---|
| | {100} | {110} | {111} |
| 35°C | 1.13 ± 0.08 | 1.03 ± 0.09 | 0.79 ± 0.08 |
| 30°C | (0.68) | (0.60) | (0.41) |
| | Relative† dissolution rates | | |
| | {110}/{100} | {111}/{100} | {111}/{110}‡ |
| 30°C | 0.89 ± 0.03 | 0.63 ± 0.04 | 0.73 ± 0.04 |
| 35°C | 0.90 ± 0.03 | 0.62 ± 0.06 | 0.72 ± 0.04 |

* Averages of runs exhibiting very short induction periods. At 30°C the values listed represent the average of only two runs.
† Average ratios for all runs involving comparison of different orientations regardless of induction period.
‡ Values in this column are experimental ratios; they may be compared with values calculated from the first and middle columns.

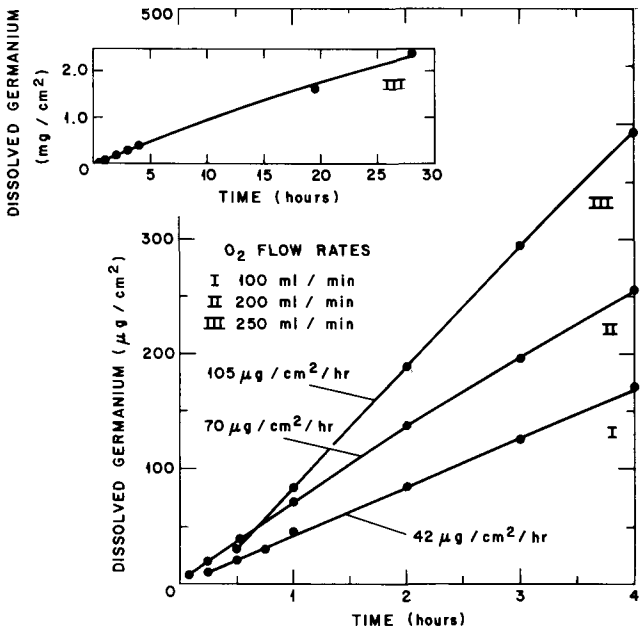


Fig. 3. Dissolution of Ge in water, 100°C, refluxing under oxygen at various flow rates.

oriented Ge surfaces in $H_2O_2$-HF-$H_2O$ solutions. The observed order for this system above 25°C was {110}>{100}>{111}; below 25°C the order of {100} and {111} was reversed. By comparison, Rösner (6) concluded from a study of the action of a number of etching media on Ge that the effect of surface orientation was not pronounced, but that {100} surfaces may be somewhat more strongly attacked.

*Temperature Dependence*

The activation energy of the dissolution process was evaluated in individual experiments by allowing the reaction to proceed for a time at a given temperature and then bringing the bath to a higher (by 5° or 10°) or lower temperature. The temperatures employed were 30°, 35°, and 40°C. In general, rates were increased threefold for a 10°C rise in temperature. No consistent variation of the calculated activation energy with surface orientation was found; the average value of $\Delta E^*$ for 15 determinations employing {100}, {110}, and {111} surfaces was found to be 19.3 ± 1.9 kcal. Moreover, since the average relative rates (Table I) do not vary appreciably in the temperature range considered, it follows that inherent differences in activation energy among the various orientations must be small, probably less than 2 kcal.

The validity of comparing the dissolution rates obtained at different temperatures might appear questionable owing to the temperature variation of oxygen solubility. However, the solubility of oxygen in water at a total pressure of 760 mm varies only from 1.112 x $10^{-3}$ to 0.964 x $10^{-3}M$ between 30° and 40° (7). Furthermore, the observed dissolution rates do not change appreciably with oxygen partial pressure in the vicinity of 1 atm (see below).

Taking the activation energy as 20 kcal and the dissolution rate at 35°C as 1.0 μg/cm²/hr, the rate at 100°C and at the same concentration of dissolved oxygen (1.0 x $10^{-3}M$), is calculated to be about 300 μg/cm²/hr. Experimental results on the dissolution of Ge at 100°C for several oxygen flow rates are shown in Fig. 3. The partial pressure of oxygen in the system can be only approximated (from the flow rate of the gas and the rate of reflux of the water); at 100 ml $O_2$/min, $p_{O_2}$ was about 0.03 atm. The observed dissolution rates (e.g., 40 μg/cm²/hr at 100 ml $O_2$/min) seem quite reasonable in terms of the rates pertaining to lower temperatures (cf. below). A dissolution rate of 22 μg/cm²/hr was reported by Rösner (6) for Ge immersed in boiling water. Considering that in the latter case the supply of oxygen was not controlled, the agreement between the two results is satisfactory.

After dissolution at 100°C the Ge specimens became visibly etched, in contrast to the experiments near room temperature where the specimens retained their high luster. Microscopic examination under polarized light revealed that the surfaces were pitted but free of bulk oxide. Etching takes place soon after immersion, which may account for the fact that the observed dissolution rates at 100°C did not vary appreciably with time (see inset in Fig. 3).

*Variation with Oxygen Partial Pressure*

Dissolution rates of {110} surfaces were determined at 40°C for various oxygen partial pressures by bubbling $N_2$-$O_2$ mixtures of known composition through the reaction cells. The data obtained are summarized in Fig. 4. In the inset of the figure, steady-state dissolution rates are plotted as a function of oxygen partial pressure. The experimental results can be expressed by the following general equation

$$r = k_1 p^n / (1 + k_2 p^n) \qquad [2]$$

where $r$ is the dissolution rate, $p$ is the oxygen partial pressure, $k_1$ and $k_2$ are constants, and $n$ is an exponent not greater than unity. Numerical values of

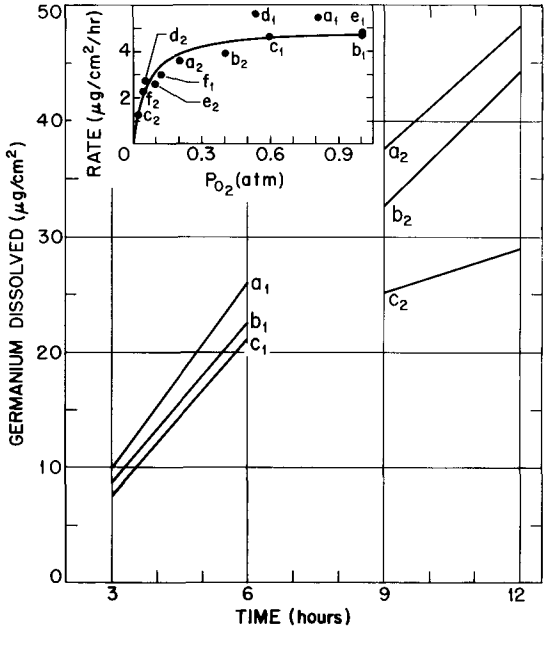


Fig. 4. Dissolution of Ge in water, 40°C, saturated with oxygen at various partial pressures. For clarity, runs d, e, and f have been omitted from the lower part of the figure. In each case, steady-state dissolution rates were measured at an initial oxygen partial pressure (subscript 1) and again, in the same run, at a lower oxygen pressure (subscript 2).

$k_1$ and $k_2$ were calculated using the method of least squares for the case $n = ½$ and $n = 1$. A better fit was obtained using $n = 1$, the correlation coefficient being 0.948 as compared to 0.899 for an assumed value of $n = ½$. Furthermore, on setting $n$ equal to unity, the calculated limiting rate ($k_2 p^n >> 1$) is 5.0 $\mu$g/cm$^2$/hr, in good agreement with observation, whereas for $n = ½$ the corresponding limiting rate is 10.4. A first-order dependence on $p_{O_2}$ is, thus, more compatible with the experimental data.

It is, of course, possible that a still better correlation could be found using some fractional power of $p_{O_2}$, between 0.5 and 1.0; the scatter of the data, however, discouraged a more detailed statistical analysis.

### *Effect of Mobile Carriers*

In the experiments described thus far, nearly intrinsic, n-type single crystals were employed; however, dissolution rates were also determined for both n- and p-type Ge of various resistivities from 3 to 40 ohm-cm. No significant variation in dissolution rate was observed with changes in sign or bulk concentration of the majority carrier.

It is well known that the densities of carriers of both types can be augmented considerably by illumination. Moreover, since the relative increase in the density of the minority carrier is comparatively large, the effect of illumination can be used to determine the role of holes or electrons in reactions involving semiconductor surfaces. Brattain and Garrett (8) have investigated the effect of light on Ge electrodes and have shown that rate of the anodic reaction is controlled by the supply of holes at the Ge/electrolyte interface. Accordingly, during anodic current flow the photoeffect was very much greater on n-type Ge than on p-type. The detailed mechanism of anodic dissolution proposed by Turner (9), viz.

$$Ge + 2e^+ + 2\,OH^- = Ge(OH)_2^{++} + 2e^- \qquad [3]$$

$$Ge(OH)_2^{++} + 2\,OH^- = H_2GeO_3 + H_2O \qquad [4]$$

or a somewhat modified form thereof, may apply to the anodic component of the over-all dissolution reaction.

In order to elucidate the role of mobile carriers in the dissolution of Ge in oxygenated water, a series of experiments was carried out in which the reaction was allowed to proceed for a time in nearly total darkness and then under strong illumination. No significant photoeffect was found in the dissolution rate for either n- or p-type material, although under the same experimental conditions the dissolution potential of n-type (but not that of p-type) Ge shifted toward a more anodic value by approximately 100 mv. This shift in potential as a result of illumination decreased with decreasing oxygen partial pressure and was essentially zero in the absence of oxygen.

## Discussion

The foregoing experimental results show that the rate of dissolution of Ge in water is determined primarily by the concentration of dissolved oxygen, temperature, and surface treatment; to a lesser extent the rate depends on the crystallographic orientation, but is not significantly affected by changes in free carrier densities, as brought about by doping or illumination.

Direct interaction of Ge with water according to Eq. [1] does not take place, or proceeds at a negligible rate in the temperature range studied (up to 100°C). In the presence of dissolved oxygen, however, Ge reacts at a measurable rate via reduction of oxygen. By employing large Ge surfaces (powdered samples) Schwab (10) was able to measure oxygen consumption in this reaction. It is generally recognized that the stable Ge species in neutral or acidic solutions and in the absence of complexing agents is metagermanic acid, $H_2GeO_3$ (11). Accordingly, the over-all dissolution reaction of Ge in water containing dissolved oxygen may be represented as follows:

$$Ge + O_{2(aq)} + H_2O\,(l) = H_2GeO_{3(aq)} \qquad [5]$$

The driving force for this reaction corresponds to a large free energy decrease, calculated from the data given by Jolly and Latimer (12) to be 113 kcal/g-atom. On the basis of the known dissociation constants of $H_2GeO_3$ (13) and the amount of Ge dissolved, pH changes were calculated for reaction [5] which were consistent with those measured in our sample solutions.

The dissolution of Ge under the present experimental conditions is activation, rather than diffusion controlled, as evidenced by the following: (*a*) for diffusion control the temperature coefficient is in general less than 1.5 per 10°C and for activation control greater than 2.0 per 10°C (14) (in the present case a temperature coefficient of approximately 3.0 per 10°C was observed); (*b*) for a given oxygen partial pressure, changes in the rate of stirring had no effect on the dissolution rate except at much lower stirring rates than those normally employed; (*c*) the observed variation of the dissolution rate with crystallographic orientation is not compatible with diffusion control.

The plot of dissolution rate as a function of oxygen partial pressure (Fig. 4) has the form of a Langmuir adsorption isotherm. The fact that Eq. [2] better describes the data for $n = 1$, rather than $n = ½$, suggests that oxygen is molecularly adsorbed. The differential heat of adsorption of water on Ge has been reported to be 16 kcal/mole at monolayer coverage (15). Thus, dissolved oxygen chemisorbs by displacing chemisorbed water. Owing to the high heat of adsorption of oxygen [found in this laboratory to be approximately 80 kcal/mole at a coverage corresponding to one monolayer (16)], displacement of water by oxygen is energetically feasible, although the present system is not directly comparable to those for which the heats of adsorption were determined.

The steady-state dissolution potential of Ge in water becomes more cathodic as the oxygen partial pressure, and therefore the dissolution rate increases (Fig. 5). Moreover, the potential is far removed from the oxygen reversible potential. This behavior indicates that the dissolution process is primarily under cathodic control. Undoubtedly the over-all dissolution process is modified by the high ohmic re-

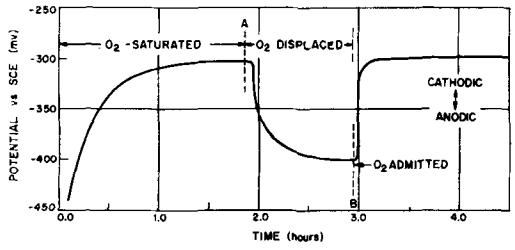


Fig. 5. Effect of oxygen on the dissolution potential of Ge

sistance of the water (combined cathodic and ohmic control). Thus, small amounts of electrolyte enhance the dissolution rate at a given oxygen partial pressure, while the process remains under cathodic control. Specific effects of added electrolytes will be discussed in a future communication.

On the basis of our findings we conclude that the Ge is in adsorptive equilibrium with dissolved oxygen and that the rate-determining step in the dissolution process lies in the reduction of oxygen. Although a detailed mechanism for the reduction of oxygen by Ge cannot be formulated at present, a mechanism which is reasonable from the point of view of solution thermodynamics involves the formation of peroxide ion, accompanied by proton exchange with water:

$$O_2 + H_2O + 2e^- = HO_2^- + OH^- \qquad [6]$$

Yeager and co-workers (17) have found a similar mechanism for the reduction of oxygen at a graphite electrode, and Handler (18) has considered formation of a peroxide structure as a possible mode of chemisorption of oxygen onto bare germanium. Rösner (6) has proposed that the etching of Ge in oxidizing liquid media proceeds by the intermediate formation of $H_2O_2$, which subsequently reacts as follows:

$$Ge + H_2O_2 \rightarrow GeO + H_2O \qquad [7]$$

$$GeO + H_2O_2 \rightarrow GeO_2 + H_2O \qquad [8]$$

Attempts were made in the present study to detect $H_2O_2$ among the soluble reaction products of the dissolution of crushed Ge samples presenting a very large surface area, but no $H_2O_2$ was detected. This result does not, of course, exclude the formation of a peroxide intermediate at the surface.

The observed variation of dissolution rate with crystallographic orientation of the Ge surface for the three principle low-index planes may be attributable to differences in the number of sites available for chemisorption. A correlation is shown in Table II between relative dissolution rates in oxygen-saturated water and densities of unfilled orbitals at the various surfaces. A significant point to be made is that the observed differences in dissolution rate are considerably smaller than one would expect on the basis of entirely different modes of oxygen chemisorption [cf. Handler (18)].

**Table II. Correlation between density of free surface bonds and dissolution rates in $O_2$-saturated $H_2O$**

| Orientation | Free bonds/cm² | Relative free bond density | Relative dissolution rates |
|---|---|---|---|
| {100} | $1.25 \times 10^{15}$ | 1.00 | 1.00 |
| {110} | $8.83 \times 10^{14}$ | 0.71 | 0.89 |
| {111} | $7.22 \times 10^{14}$ | 0.58 | 0.62 |

The absence of a photoeffect in our dissolution rates is in contrast to the results reported by Schwab (10) who found that the rate of uptake of oxygen by n-type Ge shaken with oxygen under water was accelerated by light, whereas the reaction of p-type was retarded. Schwab also noted that in the dark the rate of oxidation was somewhat lower for p-type Ge and concluded that the rate is determined by the free-electron concentration. However, his explanation in terms of separation of carriers from immobile impurity atoms by absorption of light is not consistent with the fact that donor and acceptor impurities in Ge are virtually completely ionized at room temperature (19). The shift of the dissolution potential toward more anodic values, which was observed on illumination of n-type Ge electrodes, could result from depolarization of the anodic reaction. On this basis and since the dissolution process is under cathodic control, only a very small photoeffect is to be expected in the dissolution rates. It is, thus, possible that in pure water the photoeffect lies within the limits of experimental error.

The role of electrolytes in the dissolution process and the electrode behavior of Ge under no externally applied emf will be discussed in future communications.

## Acknowledgment

The authors wish to express their sincere appreciation to A. A. Menna for his skillful assistance with the experiments.

The research reported in this paper was supported jointly by the Army, Navy, and Air Force under contract with Massachusetts Institute of Technology.

Manuscript received Jan. 27, 1958. This paper was prepared for delivery before the Buffalo Meeting, Oct. 6-10, 1957.

Any discussion of this paper will appear in a Discussion Section to be published in the June 1959 JOURNAL.

## REFERENCES

1. W. M. Latimer, "The Oxidation States of the Elements and Their Potentials in Aqueous Solutions," 2nd ed., p. 146, Prentice-Hall, Englewood Cliffs, N. J. (1952).
2. J. T. Law, *J. Phys. Chem.*, **59**, 543 (1955).
3. H. Newcombe, W. A. E. McBryde, J. Bartlett, and F. E. Beamish, *Anal. Chem.*, **23**, 1023 (1951).
4. R. H. Kingston, *J. Appl. Phys.*, **27**, 101 (1956).
5. P. R. Camp, *This Journal*, **102**, 586 (1955).
6. O. Rösner, *Z. Metallk.*, **46**, 225 (1955).
7. N. A. Lange, "Handbook of Chemistry," 5th ed., Handbook Publishers, Inc., Sandusky, Ohio (1944).
8. W. H. Brattain and C. G. B. Garrett, *Bell System Tech. J.*, **34**, 129 (1955).
9. D. R. Turner, *This Journal*, **103**, 252 (1956).
10. G.-M. Schwab, "Semiconductor Surface Physics," p. 283, R. H. Kingston, Editor, University of Pennsylvania Press, Philadelphia (1957).
11. E. Gastinger, *Fortschr. chem. Forsch.*, **3**, 603 (1955).
12. W. L. Jolly and W. M. Latimer, *J. Am. Chem. Soc.*, **74**, 5757 (1952).
13. W. Pugh, *J. Chem. Soc.*, **1929**, 1994.
14. M. B. Abramson and C. V. King, *J. Am. Chem. Soc.*, **61**, 2290 (1939).
15. J. T. Law, *J. Phys. Chem.*, **59**, 67 (1955).

16. M. Green, J. A. Kafalas, and P. H. Robinson, "Semiconductor Surface Physics," p. 349, R. H. Kingston, Editor, University of Pennsylvania Press, Philadelphia (1957).
17. M. O. Davies, M. Clark, E. Yeager, and F. Hovorka, Technical Report to ONR, No. 6 (1956).
18. P. Handler, "Semiconductor Surface Physics," p. 23, R. H. Kingston, Editor, University of Pennsylvania Press, Philadelphia (1957).
19. W. Shockley, "Electrons and Holes in Semiconductors," p. 24, D. Van Nostrand Co., New York (1950).

# Anodic Oxide Film Formation on Zirconium Kinetics with and without Concurrent Oxygen Evolution

George B. Adams, Jr., Tien-Shuey Lee,[1] Samuel M. Draganov,[2] and Pierre Van Rysselberghe[3]

*Department of Chemistry, University of Oregon, Eugene, Oregon*

ABSTRACT

Comparative studies were made with zirconium to determine whether differential formation fields measured below oxygen evolution potentials agreed with those measured at high voltages. It was found that the low-voltage field is some fifteen to thirty per cent higher than the corresponding field obtained at high voltages. However, the field lowering of the activation energy for the anodic oxidation is the same whether derived from high or low-voltage measurements. This is also true of the activation energy.

These results confirm the view that the metal is anodically oxidized to the corresponding oxide at unit current efficiency below the reversible oxygen evolution potential. Ionic current efficiencies are reported for zirconium at several current densities in the high-voltage range and for the low-voltage localized oxygen evolution process.

In previous work (1, 2) it was found that the equation

$$I = Ae^{BF} \qquad [1]$$

held for the variation of ionic current density with formation field, $F$, in the growth of anodic zirconium dioxide films. In Ref. (2) values were reported for the differential formation fields required to oxidize Zr anodically to the amorphous oxide in aqueous solution. These values were obtained by polarization with constant currents at potentials below that required for the reversible evolution of oxygen. Agreement was obtained with formation field values reported for the same process occurring at higher voltages with concurrent evolution of oxygen (1). A more recent determination of the high-voltage differential field for this process (3) casts some doubt on the agreement in the low- and high-potential field results obtained previously.

The present investigation is an attempt to clear up this point. That is, to determine whether the polarization process which occurs with Zr and Nb on low-potential anodization is actually the formation of the oxide at unit current efficiency.

Since it is known that oxide films of these metals are formed on anodic oxidation at high voltages (1), a comparison of the values of the formation fields required for the growth of the high-voltage oxide films with those derived from polarization measurements at low potentials was indicated. Quantitative agreement would be good evidence for formation of the oxide at unit current efficiency in the potential range below oxygen evolution.

The work consists of several individual investigations; each is a comparison of equivalent measurements for the low and high-potential ranges: first, Zr fields are compared at one temperature and at a single current density; then, fields, field lowerings of activation energies, and activation energies are compared.

## I—Comparison of Formation Fields (Zirconium)

### *Experimental Approach and Results*

The high-potential differential field[4] was derived from polarization measurements at constant total current over a potential range where the current efficiency remained essentially constant. The average current efficiency for each polarization run was measured polarographically from the increase in oxygen concentration which occurred over the polarization interval. From a number of these runs taken at the same total current density, an average value of the differential field was obtained for the resulting average ionic current density. Low-potential polarization measurements were then carried out with the same electrode at a current density equal to the average ionic current density which was measured for the corresponding series of high-potential runs. Differential fields obtained from the two series of runs were then compared (see Table I).

Both the Kroll process and the iodide process zirconium were used. Electrode surfaces were pre-

[1] Present address: Research Laboratories, Westinghouse Electric Corporation, Pittsburgh, Pennsylvania.

[2] Present address: United States Borax and Chemical Corporation, Los Angeles, California.

[3] Present address: Department of Chemistry, Stanford University, Stanford, California.

[4] Fields reported are apparent fields, $F/\sigma$, where $\sigma$ is the roughness factor of the electrode surface. (Values for parameters $b$ and $B$, referred to later, are also apparent, i.e., $\sigma b$ and $\sigma B$.)

Table I. Formation of anodic oxide films on zirconium. Direct comparison of differential fields measured with and without oxygen evolution (1.0N $Na_2SO_4$, 26°C)

| | Electrode | Surface | Current density, $\mu a/cm^2$ | Mean ionic current efficiency, % | Mean low-potential field,* v/cm x $10^{-6}$ | Mean high-potential field, v/cm x $10^{-6}$ | Per cent difference |
|---|---|---|---|---|---|---|---|
| 1 | E-1 (Kroll) | Abraded | 750 | 6.3 ± 4.8 | 3.49 ± 0.07 [14] | 3.56 ± 0.23 [6] | 2 |
| 2 | E-2 (Iodide) | Abraded (Emery) | 750 | 81.2 ± 0.5 | 3.46 ± 0.08 [10] | 4.17 ± 0.09 [6] | 17 |
| 3 | E-3 (Iodide) | Abraded (SiC) | 750 | 73.6 ± 8.3 | 3.65 ± 0.19 [9] | 4.20 ± 0.31 [10] | 13 |
| 4 | E-3 (Iodide) | Abraded (SiC) | 100 | 47.6 ± 6.5 | 3.30 ± 0.11 [25] | 3.60 ± 0.29 [8] | 8 |
| 5 | E-3 (Iodide) | Chemically polished | 100 | 66.0 ± 6.6 | 4.67 ± 0.17 [33] | 4.17 ± 0.16 [8] | 12 |

* Number of determinations in brackets.

pared by both abrasion and by chemical polishing. All of the results are for a single temperature, and each comparison was made at a single current density.

Typical chronopotentiograms are shown in Fig. 1-5 for both the low-and high-potential polarizations and for several electrode surface states. The break in slope observed at about 40 v for the high voltage regression lines is quite apparent and appears to be characteristic of the metal, rather than of the surface preparation.[5] Most of the curves for Kroll process metal did not show this break. Much of the data was taken above the 40-v break. A value of 5.7 was taken for the density of the oxide, following Charlesby.

Table II lists ionic current efficiencies as measured polarographically for abraded surfaces along the low-potential "flat" in the chronopotentiogram (Fig. 1). At this potential the electrode is depolarized by the passage of electronic current through low resistance paths (pores) in the oxide film. After these pores become sealed the electrode may be polarized to high voltages.

[5] Schmidt and Mickel (5) have reported chronopotentiograms for the anodic oxidation of P-type silicon which show breaks in slope at potentials between 100-250 v. They ascribe these breaks to sparking effects.
With the zirconium electrodes used in this work, visible sparking usually occurred around 150 v. This sparking so greatly affected subsequent polarographic measurements as to render them completely invalid. Since normal polarograms were obtained at the slope-break points in the chronopotentiograms and over the potential range above these break points, it does not seem likely that sparking, visible or invisible, causes the break in this case.

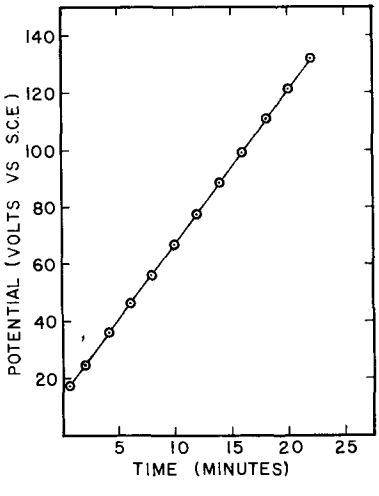


Fig. 1. Chronopotentiogram at 750 $\mu a/cm^2$. Kroll process Zr, 1.0N $Na_2SO_4$ at 26°C.

*Discussion*

From Table I it is seen that there is agreement between low- and high-potential values of the field for abraded Kroll process zirconium at 750 $\mu a/cm^2$. The agreement is rather poor, however, for abraded iodide process metal at 750 $\mu a/cm^2$, but considerably better at 100 $\mu a/cm^2$.

For abraded surfaces, the apparent formation fields determined from low-potential measurements are generally lower than those obtained at high potentials. This may be the result of a lower roughness factor for the relatively thick oxide films found at high potentials.

The ratio of the low-potential field values at 100 $\mu a/cm^2$ for chemically polished to abraded surfaces is 1.41. This ratio for the high-potential fields is 1.14. The roughness factor for the chemically polished surfaces is 1.2. This would make the roughness factors for abraded surfaces 1.7 at low potentials and 1.4 at high potentials.

The elimination of much of this uncertainty in surface roughness was the principal reason for

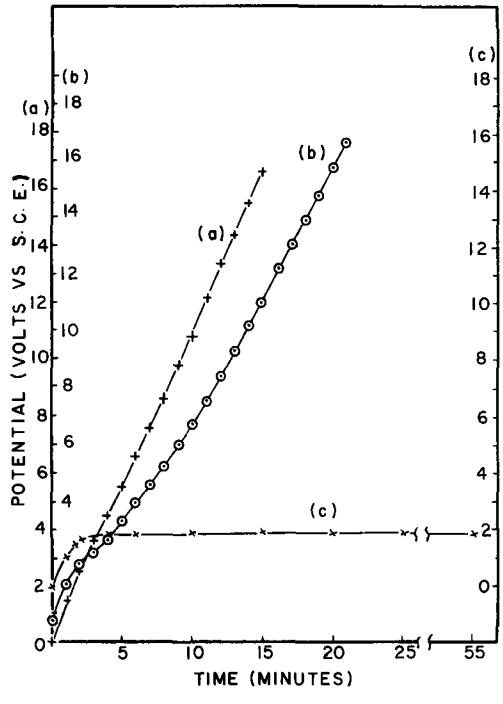


Fig. 2. Chronopotentiogram at 100 $\mu a/cm^2$. Iodide process Zr, 1.0N $Na_2SO_4$ at 26°C. (a) chemically polished; (b) abraded (#280C silicon carbide paper); (c) abraded (3/0 emery cloth).

Table II. Ionic current efficiencies along the flat of the potential-time curve (1.0N $Na_2SO_4$, 26°C)

| Current density, $\mu a/cm^2$ | Current efficiency, % |
|---|---|
| 100 | 3.0 |
| 300 | 6.0 |
| 300 | 6.3 |
| 500 | 3.3 |
| 500 | 6.0 |

working with chemically polished surfaces. However, the low-potential results here turn out to be anomalously high; the discrepancy is definitely greater than the experimental uncertainties in the measurements.

Further work along these lines has confirmed this anomaly but has also provided additional information for interpretation. This work constitutes another study and is described below.

## II—Comparison of Formation Fields, Field Lowerings of the Activation Energies, and Activation Energies

### *Experimental Approach*

The primary purpose of this work was to determine the temperature dependence of the Tafel slope for the low-potential anodization process. Another aim was to provide equivalent low-potential data for comparison with a high-potential kinetic study which was also in progress. Unfortunately, the precision of the data obtained from the low-potential work was too low to provide a valid test of Tafel slope temperature dependence. But it served as another comparative test of low and high-potential fields.

Low-potential differential formation fields were obtained from constant current chronopotentiograms taken at five current densities for each of four temperatures. Five runs were taken at each current density. Chemically polished surfaces were used exclusively in this work and in the high-potential study described below.

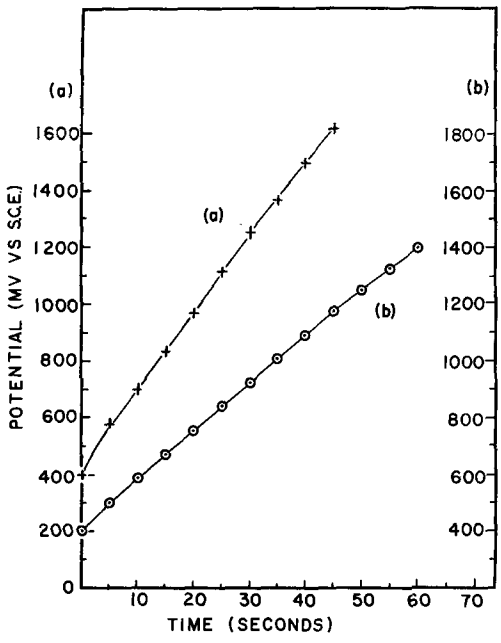


Fig. 4. Low-potential chronopotentiogram at 100 $\mu a/cm^2$, iodide process Zr, 1.0N $Na_2SO_4$ at 26°C. (a) chemically polished; (b) abraded (#280C silicon carbide paper).

The high-potential work itself constitutes an investigation which will be reported in detail later (4). Some results which are applicable to the present comparative study are included here.

The work at constant voltage proved to be the most reproducible and is used in the present equivalent high-potential comparison. In this work formation fields were measured as a function of ionic current density and temperature at constant voltage. The methods used were similar to those reported by Vermilyea (5). A standard color gauge was prepared and calibrated by means of microbalance measurements of weight increases, using ca-

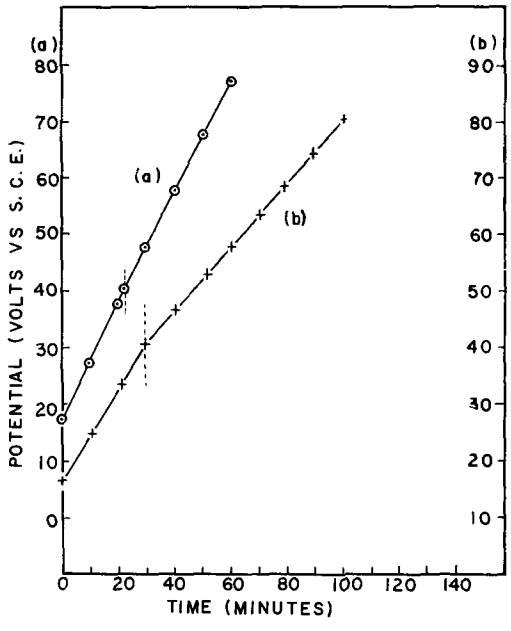


Fig. 3. Chronopotentiogram at 750 $\mu a/cm^2$. Iodide process Zr, 1.0N $Na_2SO_4$ at 26°C. (a) abraded (3/0 emery cloth); (b) abraded (#280C silicon carbide paper).

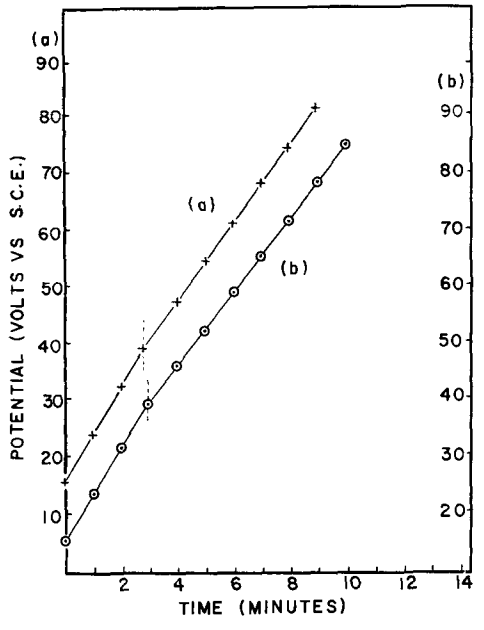


Fig. 5. Chronopotentiogram at 100 $\mu a/cm^2$, iodide process Zr, 1.0N $Na_2SO_4$ at 26°C. (a) chemically polished; (b) abraded (#280C silicon carbide paper).

Table III. Parameters in the formation of anodic oxide films on zirconium at low potentials (constant current)

| | 6.5°C | 35°C | 50°C | 65°C |
|---|---|---|---|---|
| $F_{10} \times 10^{-6}$ (volt cm$^{-1}$) | 5.17 | 4.82 | 4.24 | 4.17 |
| $F_{100} \times 10^{-6}$ (volt cm$^{-1}$) | 5.63 | 5.29 | 4.72 | 4.56 |
| $F_{1000} \times 10^{-6}$ (volt cm$^{-1}$) | 6.08 | 5.75 | 5.18 | 4.95 |
| $B \times 10^{6}$ (cm volt$^{-1}$) | 5.07 | 5.00 | 4.90 | 5.91 |
| $BF_{100}$ | 28.5 | 26.5 | 23.1 | 27.0 |
| b(Å) | 3.0 | 3.7 | 3.4 | 2.8 |

pacitance measurements as a secondary standard for determination of oxide film thicknesses. Film thicknesses were then measured as a function of time at constant potential. All measurements were made above 40 v.

*Results*

Tables III and IV[6] summarize the results of this comparison. The ratio of the low- to high-potential fields ranges from 1.17 to 1.30. But the dimensionless product $BF$ which is a measure of the lowering of the activation energy for the oxidation process by the applied field, is the same for both low- and high-potential results. This would indicate that the activation energy itself was probably the same for the oxidation, whether it occurs with or without simultaneous evolution of oxygen. This proved to be correct, as shown below.

Activation energies for both the low- and high-potential processes were obtained by plotting fields vs. absolute temperature and extrapolation to the absolute zero using the form of Eq. (1) given by the Mott and Cabrera theory (6)

$$W = bqF - k/bq \ln (I/A_o)T \qquad [2]$$

where $A = A_o e^{-W/kT}$, $B = bq/kT$, $A_o$ is a constant, $W$ is the height of the metal-oxide interfacial barrier, $q$ is the charge on metal ions crossing the barrier, and $b$ is the barrier half-width. These results are compared in Table V. A logarithmic current density dependence is apparent.[7] These values

[6] The figures in Tables III and IV are smoothed values obtained from the best straight lines through the Tafel plots. The data at 65°C, for the low-potential runs, especially, scattered rather badly. Less weight should be given to the last three figures in column four of Table III.

[7] Equation [2] requires that the regression lines for the $F$ vs. $T$ plot should extrapolate to a common intercept at the absolute zero. For both the low- and high-potential data however, the slopes for the lines at increasing constant currents remain essentially constant. The line for unit current density, however, should pass through the correct intercept since the current-dependent term drops out. The extrapolation to unit current density indicated in Table V gives the equivalent result.

Table IV. Parameters in the formation of anodic oxide films on zirconium at high potentials (constant voltage)

| | 6.5°C | 35°C | 50°C | 65°C |
|---|---|---|---|---|
| $F_{10} \times 10^{-6}$ (volt cm$^{-1}$) | 4.40 | 3.71 | 3.41 | 3.14 |
| $F_{100} \times 10^{-6}$ (volt cm$^{-1}$) | 4.81 | 4.08 | 3.78 | 3.50 |
| $F_{1000} \times 10^{-6}$ (volt cm$^{-1}$) | 5.22 | 4.44 | 4.16 | 3.90 |
| $B \times 10^{6}$ (cm volt$^{-1}$) | 5.62 | 6.31 | 6.14 | 6.06 |
| $BF_{100}$ | 27.1 | 25.7 | 23.2 | 21.2 |
| b(Å) | 3.4 | 4.2 | 4.3 | 4.4 |

Table V. Comparison of activation energies for anodic oxide film formation on zirconium at low and high potentials

| $I$ ($\mu$a/cm$^2$) | Low potentials | High potentials |
|---|---|---|
| 1000 | 1.17 | 1.19 |
| 100 | 1.12 | 1.13 |
| 10 | 1.08 | 1.08 |
| 1 | 1.05 (extr.) | 1.04 (extr.) |

are obtained for an assumed barrier half-width, $b$, of 2.5Å. This value of 1.04 ev for the activation energy is in agreement with a value of 1 ev reported by Charlesby The jump distances derived from the low-potential data are less than those obtaining at high potentials, but still rather high.

The average temperature coefficient of the field is $-1.96$ and $-2.33 \times 10^{4}$ volt cm$^{-1}$ deg$^{-1}$ for the low- and high-potential results, respectively.

## Conclusions

The agreement in both the activation energies and the field lowering of the activation energies is good evidence for the view that the metal is oxidized to the oxide at unit current efficiency below the reversible potential for oxygen evolution.

That fact that a larger field is required to pass a given current when all of that current is ionic rather than being partially electronic might be ascribed to an intrinsic difference in the jump distances for a barrier located at the metal-oxide interface and for an internal barrier located within the oxide. With both barriers the same height a shorter barrier half-width distance at the metal-oxide interface would then require a larger field to provide a field lowering of the activation energy equal to that given by the larger jump distance for the internal barrier. This interpretation is rather unattractive for several reasons.

The jump distances obtained experimentally from the kinetics for high voltage anodic oxide films are always anomalously larger than seem reasonable for the lattice parameters involved (4, 5).

It would also seem that, if there were to be a shift in rate control from an interfacial barrier to an internal barrier, the transition should be a rather gradual one. But for zirconium the observed decrease in field appears to set in abruptly as soon as an electronic component of the current through the oxide film sets in.

It would seem that a more reasonable view would be that the low-potential field is intrinsically larger than that obtained from high-potential measurements. The jump distances obtained from the low-potential kinetics agree somewhat better with what one would anticipate from the lattice parameters involved. The lowering of the field observed when concurrent oxygen evolution sets in is then to be

ascribed to the action of this electronic component of the anodic current traversing the oxide film. This leakage current probably flows through low-resistance paths in the oxide film (9). This would effectively decrease the average field across the metal-oxide interfacial barrier. An anomalously large jump distance (larger fraction of this decreased field) would then be required to provide the necessary lowering of the activation energy for the metal oxidation to proceed at a given rate.

## Experimental Details

Description of the experimental methods used in this work may be found elsewhere (4, 7, 8). Some of the more salient points are sketched here.

### *Metal Samples*

Zirconium analyses appear in Table VI. Kroll process sheet and iodide process crystal bar rod were used in the first part of this paper and 70 mil sheet, rolled from iodide process rod was used in the second part. All zirconium samples were vacuum annealed at 750°C.

### *Electrodes*

Detailed descriptions of the electrodes used in the sections on Comparison of Formation Fields and in Comparison of Formation Fields, Field Lowering, and Activation Energy appear elsewhere (4, 7). A brief description appears in Table VII.

### *Electrode Surface Preparation*

Abrasives used were 3/0 emery cloth (Behr-Manning) and #280-C silicon carbide paper (TRI-M-ITE). In the first part of this paper chemically polished surfaces were prepared by swabbing with a solution of 50% concentrated $HNO_3$, 45% water, and 5% of 48% HF (all by volume). In the second part of this paper electrodes were chemically polished by swirling in this solution until maximum brightness was obtained.

Table VI. Zirconium analyses

| Impurity | Kroll sheet ppm | Iodide rod ppm | Iodide sheet ppm |
|---|---|---|---|
| Al | 50 | 80 | 30-60 |
| C | 140 | — | 100 |
| Ca | — | — | < 50 |
| Cr | 50 | 10 | 10-20 |
| Cu | 100 | 10 | 5 |
| Fe | 800 | 300 | 400-600 |
| Hf | <500 (est.) | <300 (est.) | 100-150 |
| N | 80 | 50 | 10-25 |
| Ni | < 5 | < 5 | 25-60 |
| O | 1450 | — | 200 |
| Pb | 50 | 300 | < 10 |
| Si | 20 | 20 | 20-80 |
| Sn | 50 | 10 | < 10 |
| Ti | < 50 | < 50 | 20-40 |
| W | — | — | <100 |
| | 99.6% | 99.8% | 99.8+% |

Table VII. Construction of electrodes

| Reference | Electrode | Approximate area ($cm^2$) | Masking | Description |
|---|---|---|---|---|
| | Zr-E-1 | 5.3 | Baked enamel | Two coupled square electrodes 1.6 x 1.6 cm—from 70 mil sheet |
| Part I | Zr-E-2 | 12.0 | Baked enamel | Three coupled circular-faced electrodes—from segments of half inch rod—six faces |
| | Zr-E-3 | 13.5 | Baked enamel | Single electrode—one face—rectangular with semicircular ends 2 x 7 cm |
| Part II | Zr | 5.5 | None | Single electrode 1.6 x 1.6 cm. Both sides and edges exposed—from 70 mil sheet |

The roughness factor for a zirconium surface prepared by dry abrasion on 3/0 emery cloth as determined by Krypton adsorption was reported previously as $2.1 \pm 0.2$ (1) and is $1.2 \pm 0.1$ as determined by the same method for chemically polished surfaces prepared as in Part II.

### *Solutions*

The anolytes were 1.0*N* $Na_2SO_4$ in Part I, and 0.5*N* $Na_2SO_4$ in Part II, all made up from the AR salt and distilled water.

## Acknowledgments

This work was carried out under a contract between the University of Oregon and the U. S. Atomic Energy Commission, whose support is gratefully acknowledged.

Zirconium samples and analyses were obtained from the U. S. Bureau of Mines, Albany, Oregon, through the cooperation of Dr. E. F. Hayes and from the U. S. Atomic Energy Commission, Pittsburgh Area Office, through the courtesy of Dr. E. Epremian.

The roughness factor determination for chemically polished zirconium was carried out by Mr. E. S. Snavely, Jr., at the University of Texas, through the courtesy of Professor Norman Hackerman.

Manuscript received May 7, 1957. This paper was prepared for delivery before the Buffalo Meeting, Oct. 6-10, 1957.

Any discussion of this paper will appear in a Discussion Section to be published in the June 1959 JOURNAL.

## REFERENCES

1. A. Charlesby, *Acta Met.*, **1**, 340 (1953).
2. G. B. Adams, Jr., M. Maraghini, and P. Van Ryssselberghe, *This Journal*, **102**, 502 (1955).
3. J. J. Polling and A. Charlesby, *Proc. Phys. Soc.*, **B67**, 201 (1954).

4. G. C. Willis, "Kinetic Studies on the Electrolytic Formation of Insulating Oxide Films on Zirconium," Doctoral Thesis, University of Oregon, June, 1958.
5. D. A. Vermilyea, *Acta Met.*, **1**, 282 (1953).
6. N. Cabrera and N. F. Mott, *Repts. Prog. Phys.*, **12**, 163 (1948-49).
7. T. S. Lee, "Formation Fields and Current Efficiencies in the Anodic Oxidation of Zirconium," Master's Thesis, University of Oregon, 1956.
8. G. B. Adams, Jr., T. S. Lee, and P. Van Rysselberghe Technical Report to the U. S. Atomic Energy Commission AECU-3500, 1957.
9. D. A. Vermilyea, *J. Appl. Phys.*, **27**, 963 (1956).

# Electrochemical Calorimetry

**J. M. Sherfey and Abner Brenner**

*National Bureau of Standards, Washington, D. C.*

ABSTRACT

The heat effects of electrochemical processes have been measured calorimetrically to find those areas where such measurements might prove useful. The determination of reaction heat ($\Delta H$) is one such area. The $\Delta H$ of the reaction $W + 2H_2O + 2NaOH\ (aq) = Na_2WO_4\ (aq) + 3H_2$ was measured. The results indicate that the heat of formation of $Na_2WO_4$ (aq) given in the literature is in error by at least 12 kcal. The heat of the reaction $Cu^\circ + nCN^- + H_2O = Cu(CN)_n^{(n-1)-} + OH^- + \frac{1}{2} H_2$ was determined as a function of the cyanide to copper ratio of the electrolyte. These data confirm the existence of the $Cu(CN)_4^{\equiv}$ ion.

Another application for such measurements is in studies of electrode polarization. Equations are derived which show the relation between polarization and the other heat-producing phenomena in electrolytic cells. This treatment is extended to include simultaneous reactions, such as alloy deposition, and to compare the calorimetric measurement of polarization with the more conventional methods.

Researches on the thermodynamics of electrochemical processes are most often based on voltage measurements or on calculations which employ independently derived thermodynamic data. It is rather surprising that there have been few calorimetric measurements of the energy relations of electrochemical processes.

Most studies of this type have been concerned with the so-called electrolytic Peltier effect. These have been reviewed in a comprehensive treatment of this subject by Lange [1] who has himself contributed significantly to the field. Jahn (2-4) attempted to evaluate these energy relations by immersing in a calorimeter the battery used to drive the cell under study. Richards (5) electrolyzed a dilute solution of $H_2SO_4$ in a cell contained within a calorimeter and was able to demonstrate that the energy associated with overvoltage appears as heat in the cell.

This paper describes the initial results of a continuing research program concerned with the calorimetric measurement of the heat effects which attend electrochemical processes. The primary objective is to identify those areas in which such measurements might prove to be a useful tool. There has been no attempt to accumulate a large mass of data or to refine the measurements too highly.

The work reported here entailed the simultaneous measurement of at least three quantities; (*a*) the heat evolved by an electrochemical process; (*b*) the electrical energy necessary to effect this process; and (*c*) the extent of this process as indicated by the number of faradays passed. The necessary apparatus can be described very briefly on this basis as consisting of two parts: a calorimeter in which the reaction takes place and an electrical circuit which supplies electrical energy to the reaction and permits the measurement of both current and voltage as a function of time.

Since this apparatus is different from that of conventional calorimetry, a detailed description is given in the appendix. The two calorimetric techniques employed, the "rate method" and the "total heat method," are also given in the appendix.

## Determination of Reaction Enthalpy

The simplest application of electrochemical calorimetry is the measurement of the enthalpy change ($\Delta H$) which accompanies electrochemical reactions.

This is accomplished by measuring the electrical energy supplied to the cell and the heat energy released as a result of the electrolysis. The difference between these two quantities represents the enthalpy change of the process.

If there is no gas evolution or other pressure-volume work, this conclusion is a direct consequence of the first law of thermodynamics, $\Delta H = \Delta E = Q - W$, where $\Delta H$ is the enthalpy change, $\Delta E$ the change in internal energy, $Q$ the heat absorbed by the system, and $W$ the work done by the system. Neglecting sign, $Q$ is determined by the temperature rise of the calorimeter in which the reaction takes place, and $W$ is the electrical energy necessary to effect the reaction.

This reasoning is equally valid if the reaction produces a gas. This can be shown by dividing $W$ into two parts, $W_e$, the electrical work performed, and $W_{pv}$, the work resulting from gas evolution. Then,

$$\Delta E = Q - (W_{pv} + W_e)$$
$$\Delta H = \Delta E + W_{pv}$$

and adding

$$\Delta H = Q - W_e$$

## *Experimental*

*Heat of the reaction* $H_2O = H_2 + \frac{1}{2} O_2$.—The method and apparatus were evaluated by studying a reaction having an accurately known reaction heat. The heat of decomposition of water was chosen for several reasons. First, this reaction fulfills the above condition and, second, it presents a rather severe test in that it involves gas evolution, a complicating experimental factor. Because of the large polarization voltages at both electrodes, it involves a relatively large amount of irreversible heat, also a complicating factor.

Bright platinum was used for both electrodes and the electrolyte was 0.5*N* NaOH.

Initially the $\Delta H$ values obtained were several kilocalories low and seemed to be somewhat dependent on current density. It was believed that this difficulty was caused by recombination of dissolved hydrogen and oxygen on the platinum electrodes to give water (6). Consequently, the number of faradays passed was not an accurate measure of the over-all extent of the reaction.

This reverse reaction can be eliminated by either of two expedients: changing the electrode materials or enclosing one of the electrodes in a diaphragm in such a way as to prevent mixing of the dissolved hydrogen and oxygen by convection. The latter course was chosen because a need for such a diaphragm in future work was anticipated, and it seemed best to solve any problems involved while the apparatus was being tested.

Several diaphragm materials were tested for this application, including porous alumina and sintered glass. A synthetic membrane,[1] selectively permeable to cations, was finally chosen, not because of this selectivity, but because this type of membrane offers a relatively small resistance to the passage of ions yet is nearly impermeable to the flow of water and, presumably, dissolved gases.

[1] "Amberplex C-1", Rohm and Haas Company.

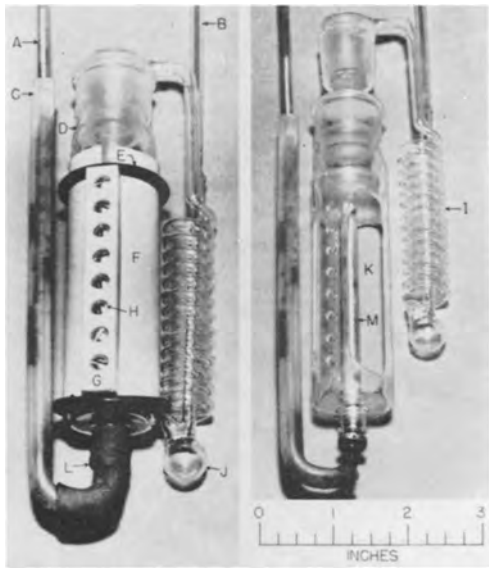


Fig. 1. Cathode compartment shown (left) assembled and (right) disassembled. A, current lead to cathode; B, hydrogen exhaust tube leading to chimney; C, plastic cover for current lead to cathode; D, electrolyte level; E, rubber compression rings (stretched "O" rings); F, membrane; G, plastic clamping block (opposing block on inside of frame not visible); H, stainless steel screws; I, spiral glass tube; J, spray trap; K, opening in glass frame; L, rubber tubing; M, cathode.

The membrane, in the form of a sheet 4 in. x 4 in. x 1/32 in., was stretched around a cylindrical glass frame to form a cathode compartment, illustrated in Fig. 1. The hydrogen generated in this compartment was carried off by a spiral glass tube which passed through the anolyte and out of the calorimeter through a chimney. This spiral brought the evolved hydrogen into thermal equilibrium with the anolyte and also acted as a spray trap. An enlargement of the tubing at the bottom of the spiral served as a reservoir for the trapped spray. Both of these functions were considered important because the catholyte was at a significantly higher temperature during the electrolysis than was the anolyte. The bright platinum anode used in previous experiments was retained, and no provision was made for trapping the spray caused by oxygen evolution.

There runs were made with this improved apparatus, all based on the total energy method. One was discarded because of experimental difficulties. The other two gave values of 68.1 and 67.8 kcal/mole. These must be corrected for the heat required to vaporize the water carried off by the evolved gases, about 0.5 kcal/mole of water decomposed. This decreases the above values to 67.6 and 67.3 kcal/mole. The accepted value is 68.317 kcal/mole (7). Recalculating to standard conditions produces a negligible change as does correcting for the heat of dilution of the 0.5*N* NaOH.

The precision of the heat capacity measurements indicates that random calorimetric errors were less than 0.1 kcal/mole. However, a significant error could have been introduced by heat lag. The cathode compartment, which had about one-tenth the volume of the calorimeter, was more or less thermally isolated from the bulk of the electrolyte. This introduced a lag which was in one direction during

Table I. Heat capacity determination

| | | |
|---|---|---|
| 1. Approx. heater current (amp) | 0.60 | 0.53 |
| 2. Approx. heater voltage (v) | 11.5 | 10.2 |
| 3. Heating period (min) | 19.00 | 20.00 |
| 4. Integrated current-voltage-time product (watt min.) | 130.16 | 108.72 |
| 5. Observed temperature rise (ohm) | 0.3071 | 0.2648 |
| 6. Calorimeter constant ($min^{-1}$) | 0.00495 | 0.00493 |
| 7. Corrected temperature rise (ohm) | 0.2866 | 0.2396 |
| 8. Heat capacity (watt min $ohm^{-1}$) | 454.1 | 453.8 |

an electrolysis run and in the opposite direction during a heater run.

Our results show that recombination of the gases was much reduced by the presence of the membrane, but the fact that the values obtained were low indicates that this effect was not completely eliminated.

The above values for the heat of decomposition of water are looked upon as being sufficiently accurate to justify confidence in both theory and method. This is especially true when considered in the light of the above difficulties. This accuracy could be greatly improved by suitable modification of the calorimeter and electrodes.

*Heat of the reaction* $W + 2NaOH(aq) + 2H_2O = Na_2WO_4(aq) + 3H_2$.—The main advantage of electrochemical calorimetry over conventional calorimetry is that it affords a direct one-step determination of certain heats of reaction instead of the devious multi-step determinations that would be otherwise necessary. For example, tungsten does not react spontaneously with aqueous sodium hydroxide, but it does dissolve readily when made the anode of an electrolytic cell. This reaction was chosen because it exemplifies this advantage of the electrochemical method and because the literature value for the heat of formation of aqueous $Na_2WO_4$ seemed to be of doubtful accuracy.

The anode current efficiency of the reaction was studied by electrolyzing a 1*N* NaOH solution between a tungsten anode and a bright platinum cathode. Both electrodes were in the form of rectangular sheets about 5 cm x 10 cm. Based on the weight loss of the anode, a value of 100.15% was obtained at an anode current density of 6 amp/$dm^2$. At 4 amp/$dm^2$ the current efficiency dropped to 99.05%. Analysis of the anode gave a tungsten content of 99.9 ±0.1%.

Calorimetric runs were made, two at the higher current density and one at the lower using the total energy method. The values obtained for the reaction as written above were −8.37, −8.04, and −5.65 kcal/mole. The data and calculations are given in abbreviated form in Tables I and II.

The agreement between the first two values for the heat of reaction is within the estimated experimental error. The difference between either of the first two and the third is about equal to the error that would be introduced if 1% of the current had been diverted to a side reaction, such as the evolution of oxygen at the anode. The current efficiency values indicate that this is very possible. In short, those results are mutually consistent and, in view of the work on decomposition of water, we have a considerable amount of confidence in a value of −7 ±1.5 kcal/mole.

The heat of formation of $Na_2WO_4$ (aq) was calculated using this reaction heat and the heats of formation of NaOH (aq) and $H_2O$ (7). A value of −368 kcal/mole was obtained. Graham and Hepler report the heat of solution of $Na_2WO_4$ to be −1.59 kcal/mole (8). This heat of solution, together with the heat of formation of $Na_2WO_4$ (c) (−395 kcal/mole) (7), gives −396.5 kcal/mole for the heat of formation of $Na_2WO_4$ (aq). This value is in serious disagreement with the literature value for $Na_2WO_4$ (aq) (−380.9 kcal/mole) and both are considerably larger than the value of −368 kcal/mole reported here.

The value −380.9 kcal/mole depends on the work of Huttig and Kurre (9) who calculated the heat of formation of $H_2WO_4$ from data on the vapor pressure-temperature relations of the system $H_2WO_4$-$WO_3$-$H_2O$. These results are uncertain because of the irreversibility of this system. Only two points of the *dp/dt* curve were related to the reaction $WO_3 + H_2O = H_2WO_4$ and one of the two temperatures used was given as "red heat."

The heat of formation of $Na_2WO_4$ (c) was obtained from Mixter's (10) measurement of the heat of reaction of tungsten powder with excess $Na_2O_2$. Mixter assumed the reaction to be $W + 3Na_2O_2 = Na_2WO_4 + 2Na_2O$ but did not demonstrate that the indicated products were obtained. It is possible that complex tungstates or peroxytungstates form in this reaction. Several experiments were performed

Table II. Determination of $\Delta H$ of the reaction $W + 2NaOH\ (aq) + 2H_2O = Na_2WO_4\ (aq) + 3H_2$

| | | | |
|---|---|---|---|
| 1. Approx. current density (amp/$dm^2$) | 6 | 6 | 4 |
| 2. Approx. current (amp) | 2.8 | 2.8 | 1.8 |
| 3. Electrolysis period (min) | 22.00 | 21.00 | 22.00 |
| 4. Integrated current-time product (amp min) | 62.29 | 59.31 | 39.55 |
| 5. Integrated current-time product (faraday) | 0.03874 | 0.03688 | 0.02459 |
| 6. Approx. cell voltage (v) | 2.0 | 2.0 | 1.7 |
| 7. Integrated current-time-voltage product (watt min) | 124.49 | 118.63 | 68.09 |
| 8. Observed temperature rise (ohm) | 0.3072 | 0.2945 | 0.1931 |
| 9. Calorimeter constant ($min^{-1}$) | 0.0491 | 0.0491 | 0.0492 |
| 10. Corrected temperature rise (ohm) | 0.2825 | 0.2689 | 0.1535 |
| 11. Heat capacity of calorimeter from Table I (watt min/ohm) | 454.0 | 454.0 | 454.0 |
| 12. Energy equivalent of temperature rise (watt min) | 128.26 | 122.08 | 69.69 |
| 13. Item 7 less item 12 (watt min) | −3.77 | −10.40 | −1.60 |
| 14. Item 13 divided by item 5 (watt min/faraday) | −97.3 | −93.5 | −64.9 |
| 15. Item 13 divided by item 5 (kcal/mole) | −8.37 | −8.04 | −5.65 |

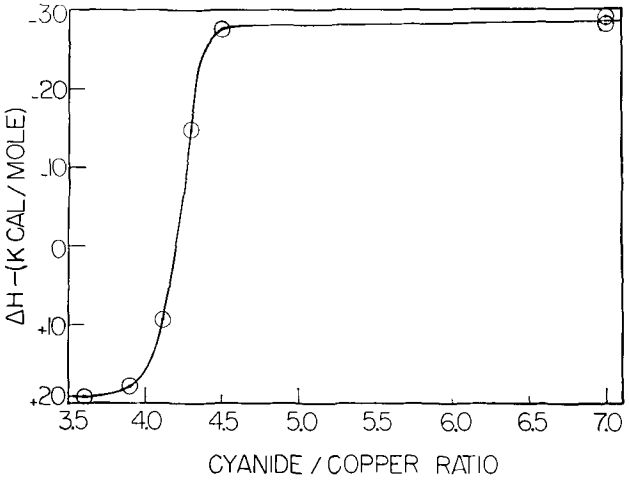


Fig. 2. Enthalpy change per equivalent of the reaction $Cu^{\circ} + nCN^{-} + H_2O = Cu(CN)_n^{(n-1)-} + OH^{-} + \frac{1}{2} H_2$ as a function of the ratio of total dissolved cyanide to total dissolved copper.

in this laboratory in order to confirm or disprove this supposition, but all were inconclusive. It must be concluded that the heats of formation of $Na_2WO_4$ and $H_2WO_4$ are not known with any degree of certainty and should be the subject of a careful redetermination. The reaction $WCl_6$ or $WF_6$ with aqueous NaOH might be suitable for this determination.

### Study of Complex Equilibria in Solution

There are several papers in the literature that deal with the calorimetric determination of the formulas and the equilibria of complex ions in solution (11-13). Such studies can be made by means of electrochemical as well as conventional calorimetry.

For example, we have studied the system CuCN-NaCN-$H_2O$. This was done by dissolving copper anodically into solutions containing various ratios of cyanide to copper and determining the enthalpy change per faraday as a function of the composition of the solution. The results of these experiments are shown graphically in Fig. 2. The pronounced change in the heat of the reaction at cyanide to copper ratios in the range 3.5 to 4.5 confirms the existence of the $Cu(CN)_4^{\equiv}$ ion.

Electrochemical calorimetry is not readily applicable to solutions containing low ratios of cyanide to copper because of poor anode corrosion. Therefore, these experiments were continued by means of conventional calorimetry. From this the formulas of the various complexes present, their heats of formation, and one of the equilibrium constants involved were determined.

A detailed discussion on this will be reported separately.

### Polarization

The voltage, $E$, of a cell operating at a finite rate differs in general from $E^e$, the voltage of the same cell operating under strictly reversible (equilibrium) conditions. The dynamic voltage, $E_D$, may be defined as $E$ less the ohmic voltage drop across the electrolyte,

$$E_D = E - IR$$

Then the polarization of the cell may be defined as

$$P = E_D - E^e \qquad [1]$$

This definition is equally applicable to a cell or an electrode.

Polarization, or overvoltage, is present when the system is operated under irreversible conditions. It represents the effect of all irreversible elements, other than Joule Heat, in the total system. Because of this its value depends on the current density. Here the system is considered under steady-state conditions only, i.e., constant current density and no concentration or thermal gradients. In practice, these gradients exist but can be minimized experimentally and their effects are undoubtedly small. The major irreversibility occurs in the region of the electrode-electrolyte interface.

A detailed theory of electrode polarization must relate the overvoltage to the various rate processes occurring at the electrode interface. However, we are concerned here primarily with the problem of measurement of polarization. In some cases $E_D$ and $E^e$ can be directly measured as voltages by means of a reference electrode and the familiar Luggin capillary.

Polarization may also be evaluated from measurements of the total heat evolved during the operation of the cell. As this method has not been used previously, it is treated here in some detail as applied to the steady-state system.

Since polarization is a voltage, the energy associated with it equals $PIt$ joules or 0.2390 $PIt$ cal, where $P$ is the polarization in volts, $I$ is the current in amperes, and $t$ the time in seconds. The relation between the heat developed in a cell and the polarization is derived as follows. If a finite number of coulombs could be passed through an electrolytic cell reversibly, the heat effect per mole of reaction would be equal to the $T\Delta S$ of the cell process. To eliminate the heat due to the resistance of the electrolyte in this hypothetical process, either the electrodes would have to be placed an infinitesimal distance apart or an infinitesimal current would have to be passed through the cell. In a real cell there are heat effects from two sources other than the entropy change, that due to the resistance of the electrolyte and that due to polarization at the two electrodes. The relation between the measured heat effect in calories and the other quantities is:

$$q = T\Delta SIt/96{,}500n + 0.2390\,[I^2Rt + (P_c + P_A)It] \qquad [2]$$

$$Q = T\Delta S/n + 23{,}060\,(IR + P_c + P_A) \qquad [3]$$

where $q$ is calories evolved in a given reaction; $Q$, calories per equivalent of reaction; $T$, absolute temperature; $\Delta S$, molar entropy change of the reaction; $I$, current, amp; $R$, resistance of the solution between electrodes, ohms; $t$, period of electrolysis, sec; $n$, number of faradays per mole of reaction; $P_A$, anode polarization, volts; and $P_C$, cathode polarization, volts.

The measurement of polarization based on Eq. [1] will be referred to as the voltage method and the indirect measurement made through its heat effect, and based on Eqs. [2] or [3], will be referred to as the heat method. The results of polarization studies are usually presented in the form of a curve

which is obtained by plotting the current density as ordinate against a voltage as abscissa. When the voltage used in plotting is the polarization, $P$, of the cell or electrode, the curve will be referred to as the polarization curve. When the voltage is the dynamic potential, $E_D$, of the cell or electrode, the curve will be referred to as the cd-ptl curve. These two curves are identical in shape but differ in their positions on the voltage axis by the value of $E^e$.

*Comparison of the Measurement of Polarization by the Voltage and by the Heat Method*

Measurement of electrode polarization by the voltage method requires that the reversible potential of the electrode be known. However, reversible electrodes are the exception rather than the rule, and most of the combinations of metals and solutions that are of interest in electrodeposition and corrosion do not form reversible systems. Since the equilibrium potentials are seldom available, the polarization ordinarily cannot be calculated, and other methods of reporting the data must be used. One such method consists of plotting the $i$ vs. $E$ curve with no attempt to estimate true polarization values, thus sidestepping the issue. The other method involves using the static potential as a basis of reference in place of the true $E^e$ of Eq. [1]. The values of polarization obtained by the latter procedure, when applied to an irreversible electrode process, have no thermodynamic significance and cannot be used to establish an energy balance for the cell.

The measurement of polarization by the heat method (see Eq. [3]) requires a knowledge of the entropy change of the reaction and the resistance of the electrolyte. The latter can be measured by conventional procedures which are described later. The former, however, often presents a difficulty. The entropies of the metals and the standard state values of many of the common ions have been determined and are tabulated in the literature (7, 14, 15). When only these known quantities are involved, the entropy change can be calculated without introducing significant error.

However, the entropies of many of the less common metallic ions, particularly the oxy- and complex ions, are not available. When this is the case, the situation is similar to that encountered when an attempt is made to use the voltage method without a knowledge of $E^e$. The curve representing current density as a function of potential can be obtained, but the position of this curve along the voltage axis cannot be established. In the one case, the unknown additive constant is the $T\Delta S$ of the cell process; in the other it is the equilibrium voltage.

In the absence of a reliable value for the equilibrium voltage of a cell and for the entropy change of the cell reaction, the heat method has an apparent advantage over the voltage method. Calculation of $E^e$ involves not only the entropy change but also the change in enthalpy. Since the latter is ordinarily about four times as large as the former, this introduces a new and probably greater uncertainty in the calculation.

*Polarization at an Electrode at Which Two or More Reactions Occur Simultaneously*

The discussion above is restricted in its application to electrodes at which only one reaction is taking place (hereinafter referred to as an OR electrode). The polarization at an alloy cathode or any electrode at which two or more simultaneous reactions are occurring (hereinafter referred to as an SR electrode) is not subject to this relatively simple theoretical treatment. This does not seem to have been recognized previously. The accepted practice when studying the polarization at an SR electrode is to use as $E^e$ the static potential of that reaction which occurs at the lowest current density, i.e., in the case of a cathode process, at the most noble potential. This method of measuring polarization is not consistent with the definition of polarization given above.

To determine the polarization of an SR electrode, the departure of each reaction from equilibrium must be measured, that is, there must be an equation similar to Eq. [1] for each reaction. Furthermore, since these reactions are occurring at different rates, the current must be prorated among the various reactions. These relations are expressed in the following equation which represents the polarization of the electrode as the sum of the partial polarizations due to each reaction.

$$\text{Polarization} = f_a(E_D - E^e_a) + f_b(E_D - E^e_b) + f_c(E_D - E^e_c) + \ldots \quad [4]$$

In this equation, $f$ represents the fraction of the current used for an electrode reaction ($\Sigma f = 1$); $E_D$ is the dynamic potential of the electrode, and $E^e$ is the static equilibrium potential of a reaction. The value of $f$ must be determined by some suitable analytical scheme.

The corresponding equation for the heat method is similar to Eq. [3], except that it contains the sum of the entropies of the various reactions prorated according to the fraction of the current used for each.

$$Q = T\left(\frac{f_a\Delta S_a}{n_a} + \frac{f_b\Delta S_b}{n_b} + \frac{f_c\Delta S_c}{n_c} + \ldots\right) + 23{,}060\ (IR + P_C + P_A) \quad [5]$$

Equations [4] and [5] are both restricted in their application to electrode processes involving no secondary reactions such as the formation of an intermetallic compound at an alloy cathode.

If Eq. [4] is applied to an SR cathode and $E^e_a$ is the equilibrium potential of the reaction which takes place at the most noble potential, then it can be seen that the conventional method for obtaining the polarization amounts to a disregard for all the terms on the right side of Eq. [4] except the first, and $f_a$ becomes unity. It can also be seen that this approach produces polarization values which are larger than the true polarization as defined by Eqs. [4] and [5]. The latter conclusion follows from the fact that the difference between the dynamic potential and the most noble equilibrum potential ($E_D - E^e_a$) must be the largest of the bracketed quantities in Eq. [4].

In the discussion of the polarization of an OR electrode, it was pointed out that $i$ vs. $E$ curve had the same shape as the true polarization curve, from which it differed only by a constant. This relation does not hold for simultaneous electrode reactions, since under these circumstances both position and shape are different. It follows that in dealing with SR electrodes the more rigorous definition of polarization assumes a correspondingly increased importance.

The discussion of polarization at an OR electrode also indicates that estimation of entropies ordinarily introduces a smaller error than does the estimation of equilibrium voltages. This advantage of the heat method over the voltage method is equally applicable to the polarization at SR electrodes.

### *Comparison of the Voltage and Heat Method with Respect to Experimental Difficulty*

The voltage method is by far the simpler to apply experimentally. The simplest technique in using this method involves the use of a Luggin capillary. This method has the advantage that it largely circumvents the $IR$ drop through the solution and yields directly the potential of a single electrode. Alternatively, as in the Haring cell, the $IR$ drop in the solution is measured with probes and subtracted from the cell potential.

The heat method is much more difficult because (*a*) measurement of heat change is inherently more difficult than measurement of a voltage; (*b*) the $IR$ drop required for Eq. [5] would in some instances be a relatively large quantity and must therefore be determined with a considerable degree of accuracy; and (c) it gives directly the cell polarization but not the polarization at only one of the electrodes.

The last difficulty can usually be overcome by means of a technique which employs as a reference an electrode through which current is flowing. In applying this method the cell consists of the electrode under study and any other counter electrode which has a reversible static potential. This will be referred to as the "dynamic counter electrode." It is necessary that this electrode have a static potential which approximates the equilibrium value because the essence of the procedure consists of measuring its polarization by the voltage method and subtracting this value from the cell polarization. This method yields at the same time the value of the IR drop in the solution.

The details of this technique for measuring the polarization of a single electrode by the heat method are as follows. The working electrodes consist of the one under study and a dynamic counter electrode. The capillary tip of a calomel half-cell or some other conventional reference electrode is pressed against the electrode under study. The potential between calomel cell and the dynamic counter electrode, with no current flowing between the working electrodes, is the equilibrium potential of the dynamic counter electrode vs. the calomel cell. With current flowing between the working electrodes, the potential between the dynamic counter electrode and the calomel half-cell is measured again. The difference between this potential and the one obtained when no current was flowing equals the sum of the $IR$ drop in the solution and the polarization at the dynamic counter electrode. The only other information required for the calculation of the polarization at a single electrode is the heat produced by the process and the entropy change involved.

The experimental work on polarization will be reported separately.

### Acknowledgment

The authors gratefully acknowledge the financial support of the Atomic Energy Commission, Research Division, which made this work possible.

Manuscript received May 16, 1958. This paper was prepared for delivery before the Cleveland Meeting, Sept. 30-Oct. 4, 1956.

Any discussion of this paper will appear in a Discussion Section to be published in the June 1959 JOURNAL.

## APPENDIX

### *The Calorimeter*

The calorimeter is made from a one-pint, cylindrical Dewar flask. Cemented to its rim is a copper flange. The lid of the calorimeter is a circular plate of copper which can be bolted against this flange to form a fluid-tight seal by means of an "O" ring. Vertical chimneys in the lid permit the introduction of the various calorimeter components: stirrer, heater, cooler, thermometer, electrode leads, and, on occasion, probes of a reference half-cell.

The relatively large currents used during electrolysis require that the electrode leads have very low resistance and No. 6 copper wire (0.41 cm diameter) was used. The low resistance thermal path formed by such heavy leads caused the temperature of the room to be reflected into the calorimeter even though the leads were passed through chimneys. To avoid this, the chimneys were reduced in length to about 2 cm and the leads were brought out through rubber stoppers. With this arrangement the bare leads pass through the constant temperature bath for a distance of at least 7 cm before coming in contact with the air. Oil is therefore required as a thermostat liquid to minimize leakage currents between the leads.

In most cases the electrodes were rectangular sheets of metal, several centimeters wide and about 10 cm long. These were attached to the current leads by a silver solder joint near the bottom of the electrode. Therefore, the lead passed through at least 10 cm of the electrolyte before passing out through the chimney. This design was adopted to prevent loss of heat along the electrode leads due to the fact that the electrodes during electrolysis are at a higher temperature than the solution that surrounds them. The copper leads and the silver solder joint were thoroughly masked to prevent attack.

In this work it is necessary to time a series of temperature readings. An ordinary stopwatch is not suitable because the accurate timing of each temperature would require stopping the watch, thus rendering impossible the timing of subsequent temperature readings. The watch used in this work is not subject to this objection and is ideally suited to this application. It is known as a "Split second timer" and is described in Federal Specification GG-W-111a under the heading "Type C."

The watch was started in synchrony with the 1-sec radio time signal and checked against it on every run. The electrical power going to the calorimeter (heater or electrolytic cell) was turned on and off manually

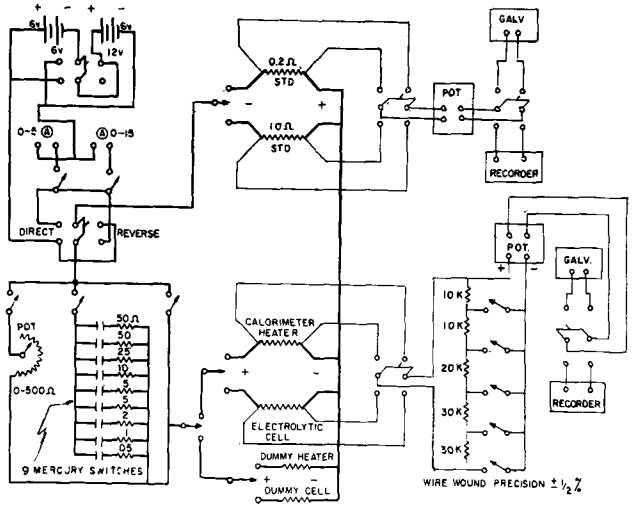


Fig. 3. Circuit diagram

and was also timed by means of the sound of this radio signal. Bath temperature, 29.6°C, was maintained with a constancy of about ±0.001°C by means of a vibrated thermoregulator. The resistance of the thermometer was read with the usual Mueller bridge and a sensitive galvanometer.

### *Electrical Circuit*

The basic circuit consists of a battery connected to the following elements in series: a variable resistor, the electrolytic cell in the calorimeter, and a standard resistor. The variable resistor controls the current. A potentiometer across the cell measures the cell voltage, and a potentiometer across the standard resistor gives, indirectly, the cell current. Numerous additions of this basic circuit are necessary to increase flexibility, accuracy, and convenience. For example, a switching arrangement makes it possible to substitute the calorimeter heater for the electrolytic cell, thus making possible an electrical determination of the heat capacity of the calorimeter. The circuit is shown in Fig. 3. Heavy lines indicate those wires that carry appreciable currents. Light lines indicate the potential measuring circuit. The two batteries in the upper left corner of the diagram are automotive-type lead cells.

The dummy heater is a coil of Manganin wire made in the same way as the heater coil. The resistances of these two elements should be approximately the same. The dummy cell is a slide wire resistor set to have about the same resistance as the electrolytic cell being studied. These dummy units make it possible to bring the batteries to a steady-state condition before activating either the electrolytic cell or the heater. There is nothing critical about the nine resistors in the parallel bank except that they should be able to withstand a 12-v drop.

All switches in that portion of the circuit indicated by heavy lines must be rugged enough so that their resistance does not change appreciably if they are subjected to vibration. Toggle switches rated at 15 amp were unsatisfactory in this application, and either 30-amp mercury switches or 100-amp airplane-type switches were used. The toggle switches were satisfactory in the voltage measuring circuit.

The total resistance of the voltage divider bank must be large enough so that the heater or electrolytic cell is not appreciably short circuited and small enough so that the potentiometers are stable. The values shown totaling 10 kohm are a satisfactory compromise. The various ratios available from this circuit must be determined accurately and must be redetermined periodically to detect any drift. An erratic variation of about 5 parts in 10,000 was noted in these ratios until they were placed in a glass well immersed in the constant temperature bath.

Two potentiometers are necessary, one to measure the drop across the standard resistor ($E_I$), thus giving indirectly the value of the current, and the other to read the voltage ($E_E$). During the first few minutes of electrolysis, both of these values change rather rapidly, sometimes as much as 20 or 30 mv, although a change of 5-10 mv is more common. Since it is necessary to know the total electrical energy delivered to the calorimeter, these changes must be known accurately as a function of time. This presents a difficulty in that the changes are too rapid to follow with a manually operated potentiometer. A recording potentiometer can follow the changes but lacks the necessary accuracy by at least an order of magnitude.

This problem was solved by using a potentiometer and a recording potentiometer in combination, one pair for $E_I$ and another for $E_E$ (Fig. 3). The potential to be determined is applied to a potentiometer, the galvanometer terminals of which are connected to either a galvanometer or a recording potentiometer with a 0-10 mv range.

Each potentiometer-recorder combination is operated as follows. The approximate value of the voltage to be measured is determined in preliminary experiments with the potentiometer connected to the galvanometer. The potentiometer is then set to a reading about 5 mv less than this voltage. When the current to the electrolytic cell (or heater) is turned on, the recorder, which has been connected in place of the galvanometer, indicates the difference between the potentiometer setting and the voltage being measured. In other words, the desired potential is the sum of the readings of the two instruments. If the recording pen goes off scale, it is only necessary to reset the potentiometer to bring it back.

The recorders have a 3 second traverse time and sometimes take almost this long to "find" the voltage. This section of the curve must be extrapolated to the instant when the current was started. The accuracy of this extrapolation is unimportant, however, and a minimum accuracy of 1 part in 1,000 (0.1 mv in 0.1 v) is easily obtained with the above arrangement. An accuracy of 1 part in 10,000 (0.1 mv in 1.0 v) is more usual.

A third standard resistor with a value of 0.5 ohm would be a very useful addition to the circuit. An addition to the potential measuring circuit which would permit measurement of the voltage across either dummy unit would also be helpful.

### *Calorimetric Technique*

Before the actual calorimetric measurements are made it is necessary to determine the current efficiency of the process as a function of current density and electrolyte composition. The nature and extent of side reactions, if any, must also be determined. Ideally the electrodes should be shaped so that the current density is constant over the entire surface of the electrodes (e.g., concentric cylinders). This latter refinement has not been observed in the present work.

The application of the two basically different techniques used to the determination of a reaction heat is given below.

*The "rate method."*—Heat leak and stirring energy both affect the temperature of the calorimeter and it is necessary to evaluate the sum of these two effects as a function of calorimeter temperature. The calorimeter is first cooled to a temperature 3° to 4°C below that of the constant temperature bath by passing ice water through a tube immersed in the electrolyte. When the desired temperature has been reached, the flow is stopped and the water in the tube is blown out with a stream of compressed air. The calorimeter is then left undisturbed except for stirring for a period of about 15 min in order to attain a steady state, after which the temperature is read every minute for a period of about 5 min. The temperature is then raised about 0.5°C by means of the heater and, after waiting

for a steady state, another series of time-temperature readings is taken. This is continued until bath temperature is reached. From the above data a "rating curve" is plotted showing the rate of temperature rise due to heat leak and stirring energy as a function of the calorimeter temperature.

The next step is the determination of the heat capacity of the calorimeter in terms of a rate of temperature rise. The calorimeter is cooled again and, without waiting for equilibrium, the heater is turned on. The current and voltage are followed by means of two recording potentiometers. When these two quantities and the time rate of temperature rise have attained constancy, another series of time-temperature readings is taken. This rate of temperature rise must be corrected by subtracting the contribution attributable to heat leak and stirring energy. This correction is obtained from the rating curve described above by noting the rate which corresponds to the average temperature during the calibration. The heat capacity is then inversely proportional to this corrected rate of temperature rise and is expressed in watt sec $ohm^{-1}$. (All temperatures are expressed in terms of the resistance of the thermometer.)

In performing the actual determination, the calorimeter is cooled and the procedure immediately above is repeated except that current is directed through the electrolytic cell instead of through the heater. It is usually necessary to start at a lower temperature than when making the determination of the heat capacity, because the cell requires a longer time to reach an approximately steady state with regard to rate of temperature rise, current, and voltage. For best precision, the temperature range over which the time-temperature readings are taken and the rate of temperature rise should be approximately the same as obtained during the heater run.

The time-rate of temperature rise observed during this run is also corrected for heat leak and stirring energy by means of the above rating curve and this corrected value (in ohm $sec^{-1}$) is multiplied by the heat capacity of the calorimeter (in watt sec $ohm^{-1}$) to get a value for the rate at which heat was being released (in watts). Subtracting this value from the power delivered to the cell under steady-state conditions and dividing the difference by the current in equivalents per second gives $\Delta H$ in joules per equivalent which is converted to kilocalories per mole.

*The "total energy" method.*—This method is based on measuring the total heat evolved by the cell process and simultaneously the total electrical energy used to effect this process.

Determination of the heat evolved, with regard to both experimental procedure and the method of calculation, has been treated fully elsewhere (16, 17).

The energy supplied to the heater during calibration or to the electrolytic cell during electrolysis is obtained by graphical integration of the charts from two recording potentiometers, one indicating voltage, and the other current (see appendix). This integration is performed in such a way that the number of faradays is obtained in the same calculation. Knowing the heat developed in the cell, the electrical energy supplied to the cell, and the number of faradays passed, the $\Delta H$ of the reaction can be calculated.

### *Sources of Error*

Calorimeters made from Dewar flasks are not ordinarily used for work requiring the utmost accuracy because the thermal lags which are characteristic of such devices introduce significant errors in the heat leak correction. This is the reason for the development of the all-metal calorimeter on which most modern precision calorimetry is based. A metal calorimeter was not used in the experiments described in this paper because such a calorimeter would have to be coated with an insulating lacquer to prevent parasitic currents. It can be seen that the demands placed on this coating would be very stringent in that it would have to be completely free of breaks, chemically inert, and, ideally, a good thermal conductor.

It is fortunate that errors due to heat lag present less of a problem in electrochemical calorimetry than in conventional calorimetry. This is a result of the fact that the former method affords complete control over reaction rate and thus makes it possible to approximate closely, during the experimental run, the temperature interval and time rate of temperature rise that obtained during the calibration run. If this approximation is sufficiently close, a correction for heat leak would be unnecessary and error due to thermal lag would be eliminated. This conclusion is equally valid for both the rate method and the total heat method. Errors due to heat lag could also be eliminated by using adiabatic calorimetry. Electrochemical calorimetry is well suited to this technique because of the above mentioned control of reaction rate.

A second source of error is applicable to only the rate method and arises from the fact that completely steady values of voltage and current are never attained, if for no other reason, because the rise in the calorimeter temperature during the experiment causes a change in the resistance of the cell. Even though these changes are slow, they result in an appreciable error and, what is more serious, there is no obvious way of correcting for such changes. There is some evidence that because of heat lag the instantaneous rate of temperature rise is a consequence of the rate of heat release about one minute prior to that instant, but this has never been demonstrated conclusively. A correction based on this supposition can only be approximate since it fails to take into account the variation of current (and reaction rate) with time.

In short, it seems that the rate method cannot be used for highly accurate work without some modification. However, the calculations involved in this method are simpler and the equipment needs are less in that the recorders are a convenience rather than a necessity. For these reasons it would be the method of choice in some situations.

So far as is known, the total heat method is free of intrinsic weaknesses and with suitable refinements should yield results as accurate as those obtained by conventional calorimetric techniques.

## REFERENCES

1. "Handbuch der Experimentalphysik," Vol. XII, Part 2, No. 7, Akademische Verlagsgesellschaft M.B.H. Leipzig (1933).
2. H. Jahn, *Z. physik, Chem.*, **18**, 399 (1895).
3. H. Jahn, *ibid.*, **26**, 385 (1898).
4. H. Jahn, *ibid.*, **29**, 77 (1899).
5. J. W. Richards, *Trans. Faraday Soc.*, **9**, 140 (1913).
6. M. J. Joncich and N. Hackerman, *J. Phys. Chem.*, **57**, 674 (1953).
7. "Selected Values of Chemical Thermodynamic Properties," Circular of the National Bureau of Standards No. 500, U. S. Government Printing Office, Washington, D. C.
8. To be published in *J. Am. Chem. Soc.*
9. G. F. Huttig and B. Kurre, *Z. anorg. Chem.*, **126**, 167 (1923).
10. W. G. Mixter, *Am. J. Sci.*, **26**, 125 (1908).
11. S. K. Siddhanta, *J. Indian Chem. Soc.*, **25**, 579 (1948).
12. S. K. Siddhanta, *ibid.*, **25**, 584 (1948).
13. S. K. Siddhanta and M. P. Guha, *ibid.*, **32**, 355 (1955).
14. W. M. Latimer, "Oxidation Potentials," 2nd ed., Prentice-Hall, Inc., New York (1952).
15. W. M. Latimer, K. S. Pitzer, and W. V. Smith, *J. Am. Chem. Soc.*, **60**, 1829 (1938).
16. F. D. Rossini, "Experimental Thermochemistry," John J. Wiley & Sons, Inc., New York (1950).
17. W. P. White, "The Modern Calorimeter," Reinhold Publishing Corp., New York (1928).

# Ten-Gram Levitation-Melted Ingots

**G. Comenetz and J. W. Salatka**

*Research Laboratories, Westinghouse Electric Corporation, Pittsburgh, Pennsylvania*

ABSTRACT

Levitation of melts of about 10 grams in a protective atmosphere is described. There is a list, based on random experience, of materials that have been melted. Change of coil permits some temperature control. Shapes can be cast. There is a comparison with the technique of arc-melting buttons, and a list of applications. An approximate formula for levitating force is given.

A scale on which electromagnetic levitation in an inert atmosphere is possible for a variety of molten metals was first described by Polonis, Butters, and Parr (1). Their method was based on the earlier work of Wroughton, *et al.* (2). The latter aimed at melts of the order of 100 g, employing a frequency of 10 kc, but succeeded only with Al. The former used 400 kc and succeeded with 5-8 g of Al, Ti, Fe, Ni, and Ti-Fe alloys.

The first to propose levitating molten metal was Muck (3). By 1953 Scheibe had levitated 4.5 cm diameter spheres of several metals at 10 kc *in vacuo*, continuing to levitate after melting (4). In 1953 Gilbert levitated 1-10 g of several metals molten in a protective atmosphere at 100 kc (5). With a dished "meander coil" Mager has floated 140 g of molten aluminum *in vacuo* and the same weight of molten magnesium in argon (6). A spoon-shaped coil at the Leningrad Polytechnic Institute is said to have handled up to 100 g of medium-density metals (7).

### *Apparatus*

The chamber, Fig. 1, is like that of Polonis, *et al.* The glass cylinder is 5 in. in ID and 7½ in. high.

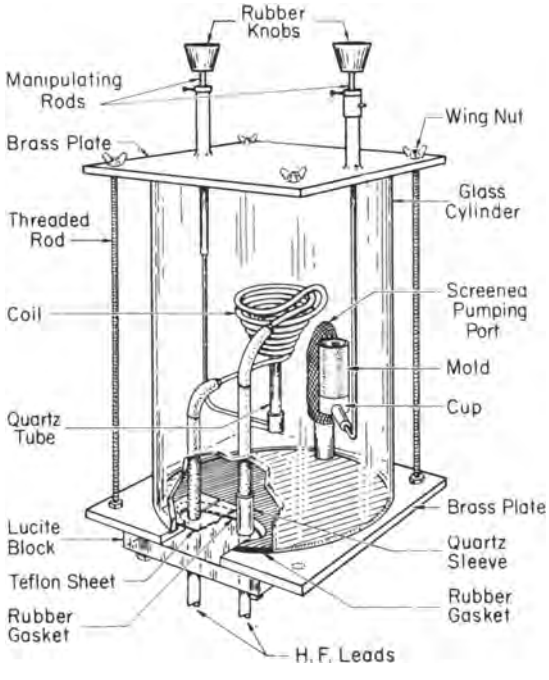


Fig. 1. Levitation chamber

The coil shown is the same as (A) in Fig. 2. It is coated with refractory cement. The left manipulating rod supports a quartz tube which can be inserted into the coil from beneath, as shown, and can be raised up within the coil. The right rod supports a cup into which a mold is set and swings the mold beneath the center of the coil after the quartz tube has been swung aside. The chamber stands on a 450 kc, 10 kw Westinghouse R.F. generator. The coil is water-cooled separately from the generator. Capacitors amounting to 0.067 $\mu$f are set on the generator and connected in parallel with the coil. An electrostatic voltmeter is connected across the leads, a little below the chamber.

Coil A, Fig. 2, has seven direct turns and one reverse turn. Coil D has seven direct and two reverse. Coils B and C, not shown, have five direct-one reverse, and five direct-two reverse, respectively.

## Procedure

The charge can have any shape that does not depart too far from spherical; a flat charge sets itself on end and falls. Generally the charge is a ½-in. diameter compact of mixed metal powders or chips, from ⅜ to ¾ in. long. Components need not be well mixed, since the melt is stirred electromagnetically. Weights have ranged from 4 to 28 g.

A ferromagnetic compact must be preheated to the Curie temperature or it will not float. Preheating is sometimes used also to set off an exothermic reaction. During preheating the compact is raised on the quartz tube, out of contact with the coil. The chamber usually contains argon or helium at atmospheric pressure, but not a vacuum.

To levitate, voltage is raised rapidly to between 500 and 900 v, depending on the charge and the coil.

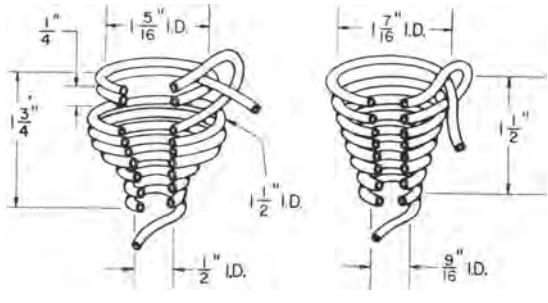


Fig. 2. Levitation coils. At left: coil D. At right: coil A, similar to that of Polonis, et al.

As much as 4 kw appears in the coil water as heat. Temperature of the floating charge is increased by lowering voltage: the charge sinks to where the field is shaped to heat better despite decreased intensity. Melting usually takes less than a minute. In coil A, Ti and lower-melting metals float not only molten, but above 2000°C. Metal vapor rises, amounting to only a small fraction of charge weight in the usual run, but sometimes so rich in a minor constituent as to alter composition.

Coils B and D are "cooler" than A, and C is cooler than B or D; Ti, for example, does not melt in C. If the tilt of A is not adjusted with care, the charge floats to one side; D requires less care.

Floating is often unsteady: the charge bobs about, although generally it does not touch the coil. Arcing sometimes occurs and may cause the charge to fall. Alloys containing Ba and Na have arced especially, perhaps owing to the low ionization potentials of those elements.

Casting is effected either by reducing voltage fairly rapidly or cutting it suddenly. If the former, some field is still present during the pour, constituting an "electromagnetic funnel" warding the melt from the bottom turn of the coil. Often the melt disappears quietly into the mold, but sometimes there is spatter.

## Results

Table I is a list of materials that have been levitation-melted in the sense of continued levitation of a complete melt, weighing between 8 and 12 g, in argon, except where otherwise stated. Alloys are in weight per cent except where a/o indicates atomic per cent.

Melts repeated under seemingly identical conditions do not all succeed. Yet the record can be good: 11 out of 14 melts of Nb, 8 out of 9 of La-Zr, 8 out of 8 Mo-Ti. On the other hand, Ba-Zr is more likely to fail than not.

### *Casting*

The levitation coil supplies a suddenly dropped melt which is small, but except for very high-melting metals can be much superheated, so that shapes can be cast.

The simplest casting is a ½-in. diameter button. The mold is a copper cup of ¼-in. wall thickness. Even if the melt is cast only a few seconds after melting becomes complete, there is at most microsegregation, which can generally be eliminated by an overnight anneal.

Flat plates ⅝ x ¾ x 1/16 or ⅛ in. thick have been cast in split Cu molds; and rods 2 in. long, ⅛ to ¼ in. in diameter, in Cu or stainless steel molds suitably vented. The rod molds do not fill quite completely. Sounder rods are cast if the mold cavity is tapered, e.g., from 3/16 in. diameter at the bottom to ⅜ in. at the top.

Tensile specimens, 1½ in. in length and 3/16 in. in gauge diameter, have been cast of Ti in a split Cu mold. A specimen was pulled, and gave reasonable values, namely, 50,000 psi yield strength, 87,000 psi ultimate strength, and 9% elongation, but a small pore could be seen at the fracture surface. Such castings of nickel-base alloys cracked transversely, no doubt owing to contraction of the cooling casting and expansion of the heating mold.

**Table I. Materials levitation-melted**

Al, 6 g. There was a skin at first, vanishing by degrees as the melt superheated, until no skin remained unless at the bottom which was not visible owing to rising vapor.

Ag, 4½ g. The melt was of carrot rather than the usual pear shape.

Au. A 4½ g mass floated 2 sec, then fell partly melted.

Si, 97% pure. (Pure Si would require preheating by other means.)

Cu, Fe, Ni, Co, Ti, Zr.

Cr, in hydrogen as well as argon, but castings in hydrogen were spongy. This is evidence that hydrogen is more soluble in liquid than in solid Cr.

Mo, Nb, 13½ g each.

C, Zr carbide, Zr nitride: floated without melting. The Zr nitride was sintered for 10 min at 2050°C by optical pyrometer, in an argon-ammonia mixture.

90 Fe-10 Al, 80 Ni-20 Fe, 90 Ni-10 Al, 50 Ni-50 Al, 65 Ni-25 Al-10 Mo, 60 Co-20 Ni-20 Cr, 40 Co-30 Ni-20 Cr, and about 30 other alloys of Al, Co, Cr, Fe, Mo, Ni. Chemical analysis of some Ni-base alloys showed nominal percentages were attained within ½% when pure Ni powder was used. With less pure powder, slag (probably alumina) floated on the melt, and the ingot proved low in Al.

Type 304 stainless steel, 20 g.

20 a/o Sn-Ti, 6 and 8 a/o Mo-Ti, 12 a/o In-Mg.

Zr with less than 5% of La, Ba or Sr. A dense white smoke rises from Ba-Zr; when it stops, the Ba is gone.

90 Cr-10 Mo, 80 Cr-20 Mo, . . . ,10 Cr-90 Mo (9 alloys).

11% Zr-Nb, 11 and 25% Cr-Nb. Loss of weight of 11% Cr-Nb was less than 0.1 g out of 11 g in a 30-sec run.

25 to 45 a/0 Mo-Mn: failed by arcing.

W, 43 g: floated solid, failed by arcing.

Ta, 10 g: would not lift.

For melts that float with high superheat, there is the possibility of welding one casting to another. Thus, 10% Al-Fe was first cast into a 3/16 in. diameter rod. A ½ in. diameter button was then poured around a ¼ in. length at the top of the rod. Welding was effected to the top ⅛ in. of the rod.

If melts were floated simultaneously in a number of coils and cast in succession into a mold which passed rapidly from one coil to another, welding of the hot strata would be more effective; in fact, the mold would receive something approaching a continuous pour from a ladle. Immediate recharging of the coils would open the way to continuous casting. Another approach to multiple casting is to dispose coils vertically, the higher coil dropping its melt into the lower one, which then casts the combined melts; or more than two coils might be used (8).

*Comparison with arc-melting.*—The technique of preparing "buttons" by arc-melting on a cold hearth is well known. It has the advantages that melts of the order of 100 g can be made, and vacuum can be employed. On the other hand, casting is not done readily, homogeneity is not always satisfactory, and

sometimes there is contamination from electrode or hearth. The power source for levitation costs more, but may be able to serve other equipment in addition to the levitation furnace.

## Applications

The following applications have turned up for levitation on the small scale described above.

Casting of buttons for hardness measurement, precipitation hardening tests, corrosion tests, and metallographic and other examination connected with phase diagram studies.

Casting of plates for x-ray diffraction and as stock to be fabricated for service trials.

Casting of rods for magnetic susceptibility measurements.

Multiple castings of Mo-Ti alloys (six ¾-in. diameter buttons cast one upon another to form a partially welded 46-g cylinder 1 5/16 in. high) for specific heat determinations.

Sintering of refractories that conduct electrically when hot.

Charging molten Ti with hydrogen (a 5-min run) for solubility studies.

Preparing castings of a series of stainless steels for which, indeed, crucibles could have been found; but levitation was simpler (given the power supply) than crucible melting and casting.

## A Levitation Formula

There has been no adequate theoretical treatment of the levitation of a liquid mass. The problem is not only that of total levitating force, but also of local support, in particular at the bottom tip of the melt, a tip which must exist with coils of nearly cylindrical symmetry. The solution should involve surface tension, and the effect of an oxide or other surface film if there is one.

There is a formula for total levitating force. While it is hedged with several limitations, it does give perspective as to the influence of some parameters. The limitations are that the charge is spherical, homogeneous and nonmagnetic, and small compared to distance over which the magnetic field can be assumed linear in the coordinates x, y, z.

The formula tells the ratio of levitating force F to charge weight $W$, a ratio which must be unity for stable levitation. The geometrical shape of the coil and the location of the center $P$ of the floating charge relative to the coil are supposed given, but not the actual dimensions.

There are six parameters; two material, determined by the composition of the charge, two electrical, and two geometrical: $\delta$ (g/cm$^3$) charge density; $\rho$ (ohm cm) charge resistivity; $\nu$ (cycles/sec) frequency; $I$ (rms amp) current; $R_1$ (cm) a selected coil dimension; $R_2$ (cm) charge radius.

The formula is

$$\frac{F}{W} = \lambda \frac{I^2 G(x)}{g \delta R_1^3}$$

$$x = 2\pi R_2 \sqrt{\frac{\nu}{10^9 \rho}}, \quad G(x) = 1 - \frac{3}{4x} - \frac{\sinh 2x - \sin 2x}{\sinh^2 x + \sin^2 x}$$

The dimensionless $x$ is ratio of charge radius to "skin depth" of the current; $G(x)$ is approximately 8 x 4/315 for $x < 1$, 0.025 at $x = 1$, 0.25 at $x = 2$, and $1 - 3/2x$ for $x > 2$; $g$ is 980 cm/sec$^2$; and the dimensionless $\lambda$ depends on coil shape, the location of $P$, and the choice of $R_1$.

For example, let the coil consist of two circular loops, each of the same radius $R_1$, having a common vertical axis. The distance between the planes of the loops is 0.81 $R_1$, and current directions are opposed. Along the axis, the largest value of $\lambda$ is 0.026, at a point $P$ located 0.15 $R_1$ above the plane of the lower loop. To float a 1-cm diameter ball of hot iron ($\rho = 120 \times 10^{-6}$, $\delta = 7.8$) at 450 kc in such a coil having loop diameter 4 cm would therefore take 1800 amp. The formula is derived by a generalization of an argument given elsewhere, whence also may be deduced the above value, both calculated and measured, of $\lambda$ (9).

At a given point $P$ in a coil of given shape, $\lambda$ can be determined by a single experiment in which the other quantities in the formula are measured. This can be done at a low current, $F$ being measured by a balance, or it may be able to be done at a current high enough to levitate, $P$ then being the point of levitation. For example, in coil A, Fig. 2, 410 amp at 450 kc would cause a 1-cm diameter hot iron ball to float at a point $P$ about ½ in. below the top turn. Choosing for $R_1$ the inside radius of the top turn, 1.9 cm, it follows that $\lambda$ is 0.42.

Voltage across the coil equals current times coil impedance. The latter is almost wholly inductive, is not decreased much by a floating charge, and depends but slightly on frequency. If scale of size ($R_1$) is changed, inductance changes proportionately. The inductances of coils A and D, Fig. 2, are 0.57 and 0.65 microhenry, respectively.

## Acknowledgment

The writers are grateful to G. M. L. Sommerman and C. S. Williams for much help with electrical problems, and to P. A. Flinn, to whom many findings and points of technique are due.

Manuscript received Aug. 30, 1957. This paper was prepared for delivery before the Washington Meeting, May 12-16, 1957.

Any discussion of this paper will appear in a Discussion Section to be published in the June 1959 JOURNAL.

## REFERENCES

1. D. H. Polonis, R. G. Butters, and J. G. Parr, *Research*, **7**, S10, 272 (1954); D. H. Polonis and J. G. Parr, *Trans. AIME*, **200**, 1148 (1954).
2. D. M. Wroughton, E. C. Okress, P. H. Brace, G. Comenetz, and J. C. R. Kelly, Jr., *This Journal*, **99**, 205 (1952). Same authors, *J. Appl. Phys.*, **23**, 545, 1413 (1952). D. M. Wroughton and E. C. Okress (to Westinghouse Electric Corp.), U.S. Pat. 2,686,-864, Aug. 17, 1954. J. C. R. Kelly, Jr. (to Westinghouse Electric Corp.), U.S. Pat. 2,686,865, Aug. 17, 1954. P. H. Brace (to Westinghouse Electric Corp.), U.S. Pat. 2,664,496, Dec. 29, 1953. J. C. R. Kelly, Jr., "High Temperature Symposium," p. 187, Stanford Res. Inst., Menlo Park, Calif. (1956).
3. O. Muck, German Pat. 422004, Oct. 30, 1923.
4. W. Scheibe, *Metall*, **7**, 751 (1953) and private communication.

5. P. T. Gilbert, Jr., Private communication.
6. A. Mager, Patentschrift Nr. 12997, Deutsche Demokratische Republik, 8 April 1957; and private communication.
7. C. G. Goetzel, Private communication.
8. F. C. Hull, Private communication.
9. Pp. 547-549 of *J. Appl. Phys.* ref. in (2). Cf. also R. Becker, "Theorie der Elektrizität," vol. I, 13th ed., p. 88, Teubner, Leipzig (1944), and I. Simon, *J. Appl. Phys.*, **24**, 19 (1953).

# High-Purity Crystalline Boron

**David R. Stern and Lahmer Lynds**

*American Potash & Chemical Corporation, Whittier, California*

ABSTRACT

Vapor phase reduction of boron trichloride with hydrogen on electrically heated filaments in flow systems was investigated as a potential method for the preparation of high-purity boron. Experiments were conducted on laboratory and bench-scale flow reactors. Conversion efficiency was a function of mole ratio of reactants, residence time, mass of deposit, and deposition temperature.

Massive deposits of crystalline boron analyzing as high as 99.6% by direct chemical analyses were obtained. Purity of boron appeared to be a function of both filament diffusion and boron trichloride purity.

Titanium filaments were found to be most satisfactory, since contamination due to titanium could be removed by chlorination at 300°C. X-ray diffraction studies indicated that titanium probably existed in solid solution with boron rather than as a boride.

Boron was first obtained by Moissan (1) in 1895 by reduction of boric oxide with magnesium in a thermite-type reaction, and appears to be the best preparational method at the present time for large quantities of relatively impure boron. Electrolysis of fused oxides, borates, or fluoborates has also produced elemental boron.

Although these primary methods are adaptable to commercial processes, it has not been demonstrated that boron of 99.0% purity, by direct analyses, could be obtained. Leaching and high-temperature degassing techniques can increase the boron purity from these processes to higher values.

Limitations on product purity focused attention on the vapor phase reduction of boron halides with hydrogen on electrically heated filaments with the objective of preparing boron of 99.0% purity or better. Filament techniques for the preparation of crystalline boron have been reported by a number of investigators (2-10).

This investigation was divided into two phases: the first dealt with relatively small deposits prepared in glass equipment; the second phase involved the formation of massive deposits in a larger stainless steel reactor.

The free-energy change for the reaction

$$BX_3(g) + 3/2H_2(g) \rightleftharpoons B(s) + 3HX(g) \qquad [1]$$

as a function of temperature was calculated for all the boron halides except the triiodide. Calculated results based on the Gibbs-Helmholtz relation and heat capacities as functions of temperature are presented in Fig. 1 (11-13). All components were assumed to behave ideally.

An examination of the mass expression

$$\frac{[HX]^3}{[BX_3]\,[H_2]^{(3/2)}} = K_p \qquad [2]$$

and the free energy equation

$$\Delta F^\circ = -nRT \ln K_p \qquad [3]$$

indicates that the reaction may go favorably in the presence of excess hydrogen even if the free-energy change is positive. Figure 1 shows that the boron trifluoride reaction requires temperatures far beyond any practical limit, while the tribromide requires a theoretically lower temperature.

*Distribution of components at equilibrium.*—The theoretical conversion and distribution for various mole ratios of hydrogen to boron trichloride were calculated and the results are presented in Table I.

Considering these equilibrium calculations and economic factors as a basis, a comparison of the respective halides can be made: (*a*) the percentage boron in the halides increases with decreasing molecular weight; (*b*) thermodynamic reduction temperature increases with decreasing molecular weight; (*c*) boron tribromide reduction theoretically requires the lowest temperature; (*d*) cost of the ha-

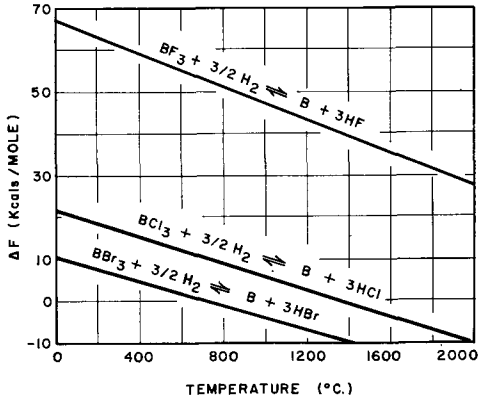


Fig. 1. Free energy of reaction as function of temperature (1 atm).

Table I. Distribution of components at equilibrium* (1100°C, 1 atm)

| Mole ratio $H_2/BCl_3$ | Mole fraction at equilibrium | | | Wt (%) conv. to boron |
|---|---|---|---|---|
| | $BCl_3$ | HCl | $H_2$ | |
| 20 | 0.009 | 0.113 | 0.878 | 80.8 |
| 16 | 0.014 | 0.131 | 0.856 | 75.6 |
| 12 | 0.024 | 0.154 | 0.823 | 68.3 |
| 8 | 0.046 | 0.184 | 0.770 | 56.9 |
| 3 | 0.161 | 0.235 | 0.604 | 32.9 |

* $BCl_3 + 3/2H_2 \rightleftharpoons B + 3HCl$.

lides decreases with decreasing molecular weight; (*e*) from the standpoint of availability, boron trichloride is potentially the cheapest halide in the group.

On this basis, the scope of research was limited to the reduction of boron trichloride with hydrogen. Although theoretical considerations give the general areas of operational conditions, it was necessary to determine the optimum conditions and the effect of metallic filaments in a laboratory flow reactor.

## Laboratory Equipment and Procedures

A schematic diagram of the reaction tube used for the laboratory investigation is presented in Fig. 2. It consisted of a Pyrex tube (38 cm in length and 10 cm in diameter) arranged vertically with standard taper joints on each side and a large joint on the bottom. Through a water-jacketed glass cap were placed two 0.25 cm tungsten leads (one 35 cm, the other 2.5 cm in length) to provide for the vertical suspension of filaments. Filaments, which were generally 8-10 cm in length, were placed between two 1.25 cm graphite rod bushings. The bottom bushing extended into a mercury well providing both mechanical freedom and an electrical contact.

*Operational procedure.*—Boron trichloride and hydrogen were continuously metered into the reactor. By-pass gas sampling networks were placed before and after the reaction tube. Hydrogen was deoxidized by passing through a Deoxo catalytic purifier followed with a dehydration column. Boron trichloride was redistilled prior to use in order to remove the silicon tetrachloride and phosgene. Surface deposition temperatures were observed with an optical pyrometer.

*Analytical procedure.*—Samples were ground to a −100 mesh, hydrochloric acid leached or treated with chlorine under conditions to be described later under Boron Upgrading. Finely ground boron was rendered water soluble by a sodium carbonate fusion and was then titrated as the mannitol complex (14). The standard deviation for 16 duplicate analyses on different samples was ±0.4%. Many samples were analyzed spectrographically which proved very effective for small quantities of impurities. However, it should be kept in mind that this is an indirect analytical method for boron and does not account for elements such as oxygen, nitrogen, and hydrogen. Comparisons between spectrographic and chemical methods indicated that spectrographic analysis consistently gave slightly higher boron values. Exhaust gases from the reactor were monitored periodically in the gas sampling network and analyzed by infrared spectrophotometry.

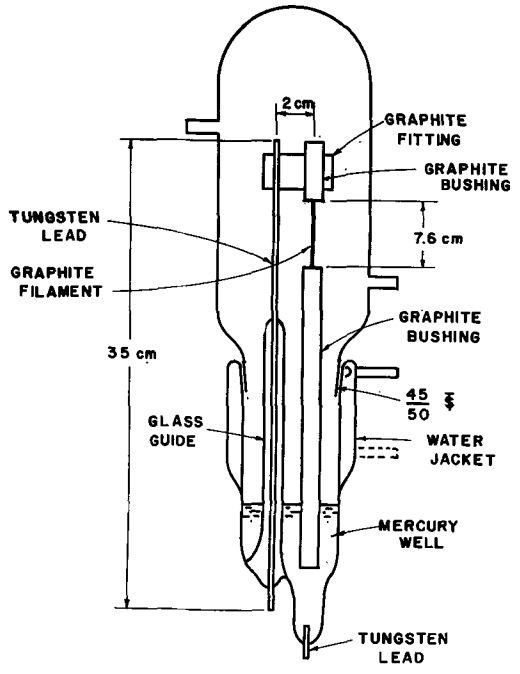


Fig. 2. Schematic diagram of laboratory flow reactor

*Laboratory Experimental Results*

Mixtures of boron trichloride and hydrogen were allowed to contact an electrically heated filament suspended in the apparatus of Fig. 2. All tests were made in an observed deposition surface temperature range of 1030°-1125°C. It was necessary to increase the filament current periodically to maintain a deposition surface temperature within the prescribed range. Effects of mole ratios of reactants and residence times on conversion percentages were studied. There was no evidence that the reaction variables effected boron purity in any way.

Major contaminants appeared to be the filament material, silicon, from the tetrahalide in the boron trichloride, and iron from the crushing operation.

*Deposition on molybdenum, tungsten, and tantalum.*—Boron was deposited on molybdenum, tungsten, and tantalum wires (8-10 cm in length, 0.15 cm in diameter). It was found that these filaments were short-lived under experimental conditions. During the first hour of operation, the filament and its deposit became extremely brittle and generally broke. Microscopic examination of the deposit showed that the boron appeared quite metallic and crystalline with a high luster. No distinct interface existed between the metal filament and boron. Analyses of some representative boron deposits on tantalum presented in Table II indicate that diffusion into boron was considerable (96.7% B and 3.2% Ta).

*Deposition on graphite.*—Boron was deposited on a spectrographic grade graphite filament (8-10 cm in length, 0.25 cm in diameter). During the first hour of operation, the filament generally developed "hot spots" which eventually healed. As deposit mass increased, it tended to crack and flake off. After cooling below 900°C, deposits became essen-

Table II. Filament data and chemical analyses for several typical tests

| Filament material | Filament temp (°C) | Reaction duration (hr) | Weight of deposit (g) | Chemical analysis weight per cent | | | | | |
|---|---|---|---|---|---|---|---|---|---|
| | | | | B | Fe | Si | Ti | Ta | Diff. |
| Ta | 1200–1250 | 10.0 | 6.7 | 97.5 | 2.1 | | | | 0.4 |
| Ta | 975–1025 | 7.0 | 3.6 | 96.7 | | | | 3.2 | 0.1 |
| Graphite | 1000–1200 | 11.0 | 5.0 | 96.1 | | | | | 3.9 |
| Graphite | 1100–1200 | 7.5 | 5.2 | 95.9 | 0.21 | | | | 3.9 |
| Graphite | 1100–1150 | 8.0 | 8.5 | 98.4 | | | | | 1.6 |
| Graphite* | 1050–1130 | 26.5 | 19.7 | 99.0 | 0.04 | | | | 1.0 |
| Graphite* | 1075–1125 | 22.0 | 20.5 | 99.5 | nil | | | | 0.5 |
| Graphite* | 1080–1120 | 16.5 | 18.5 | 99.0 | 0.45 | 0.13 | | | 0.4 |
| Graphite | 1075–1125 | 18.2 | 19.2 | 98.7 | 0.21 | 0.33 | | | 0.8 |
| Ti | 1100 | 5.5 | 3.5 | 95.0 | 0.03 | 0.13 | 2.03 | | 2.8 |

* Surface sample only.

tially nonconductive and could not be reheated. Boron has a negative temperature coefficient of resistance.

Under microscopic examination the boron appeared quite metallic and crystalline with a high luster in some areas. It was observed that deposition occurred in concentric layers and that a distinct boron-carbon interface did not exist. The latter was probably due to carbon diffusion into boron. A noticeable difference in appearance of the crystalline habit between boron produced on graphite and other filament materials was observed. Data obtained with graphite filaments are also included in Table II. Surface samples analyzed as high as 99.5% boron; however, the analysis of the entire deposit varied from 95-98.7% boron depending on the severity of carbon diffusion into boron and size of deposit.

*Deposition on titanium.*—The deposit on a titanium filament (5-6 cm in length, 0.15 cm in diameter) appeared, on microscopic examination, quite metallic and crystalline with a high luster. Cooler areas of the deposit were black and probably less crystalline. A distinct interface between the boron and a hard central core was observed. Fortunately, the boron was easily separated from the hard central core which is probably a titanium-boron system. The titanium-boron core rendered the deposit conductive such that low resistance was realized in all temperature ranges and intermittent operation was permissible. Titanium filaments appeared to resist hydriding under the experimental conditions. Chemical analysis (Table II) indicated that diffusion of titanium into the boron lattice was considerable. This product contained 95.0% boron and 2.03% titanium.

*Variables effecting deposition.*—Effects of mole ratio of reactants and residence time on deposition rate and conversion were studied. All tests were made at observed constant deposition surface temperatures of 1050°-1125°C.

Results obtained in several typical experiments are presented in Fig. 3 and 4. Figure 3 indicates that with a mole ratio $[H_2]/[BCl_3]$ of 12.0, a 38.0% conversion per pass, based on feed rate, was obtained with an average deposition rate of 0.875 g boron/hr; however, these results were obtained under flow rates varying in the range of 350-1450 cm³/min. Figure 4 presents conversion per pass as a function of residence time or total gas flow for a constant mole ratio. A mole ratio $[H_2]/[BCl_3]$ of 12.0 with a residence time of 2.75 min (800 cm³/min) resulted in a deposition rate of 0.64 g boron/hr and 39.5% conversion per pass. All tests were conducted over approximately the same time intervals in order to avoid mass effects. Results indicate that mole ratio has a greater effect than residence time (or total

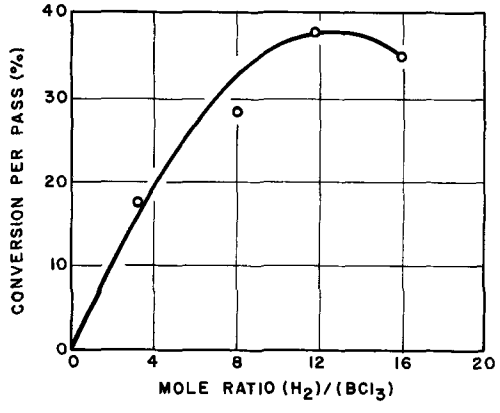


Fig. 3. Conversion per pass as a function of mole ratio. Gas reference conditions: pressure = 1 atm, temperature = 25°C. Volume of reactor = 2350 cm³. Flow rates = 365 to 1445 cm³/min. Graphite filament dimensions = 8 cm length, 0.25 cm diameter. Filament temperature = ≅1100°C.

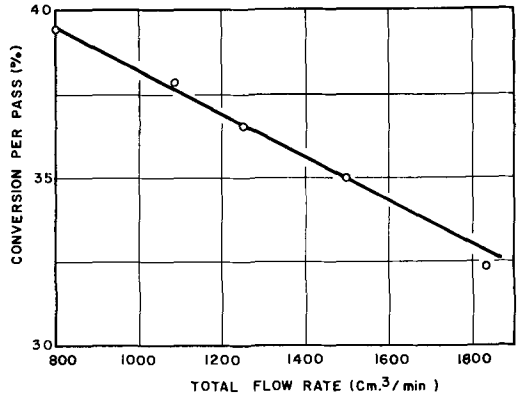


Fig. 4. Conversion per pass as a function of flow rate. Gas reference conditions: pressure = 1 atm, temperature = 25°C. Volume of reactor = 2350 cm³. Mole ratio $[H_2]/[BCl_3]$ = 12. Graphite filament dimensions = 8 cm length, 0.25 cm diameter. Filament temperature = ≅1100°C.

Table III. Deposition rates and energy requirements for graphite filaments
(Mole ratio $[H_2]/[BCl_3]$ of 12.0)

| Temp. range (°C) | Reaction time (hr) | Flow rate[a] ($cm^3$/min) Mixture $H_2 + BCl_3$ | Deposition rate (g/hr) | Conversion per pass[b] (%) | Conversion per pass based on equilibrium conditions (%) | Energy (kw-hr/g) |
|---|---|---|---|---|---|---|
| 1100–1120 | 7.0 | 800 | 0.64 | 39.5 | 57.9 | 0.72 |
| 1030–1120 | 22.0 | 1250 | 0.93 | 36.7 | 53.8 | 0.52 |
| 1080–1120 | 16.5 | 1500 | 1.12 | 36.8 | 53.9 | 0.67 |
| 1050–1125 | 19.0 | 1840 | 1.19 | 32.4 | 47.5 | 0.64 |
| 1075–1125 | 18.2 | 1500 | 1.06 | 34.7 | 50.9 | 0.69 |
| 1075–1125 | 17.0 | 1500 | 1.09 | 35.9 | 52.6 | 0.68 |
| 1100–1125 | 19.5 | 1500 | 1.07 | 35.0 | 51.3 | 0.67 |
| 1075–1125 | 15.5 | 1500 | 1.05 | 34.5 | 50.5 | 0.66 |

[a] 25°C at 1 atm.

[b] Conversion per pass (based on feed rate) $= \frac{\text{Experimental Yield}}{\text{B in } BCl_3 \text{ Feed}} \times 100.$

flow) on conversion per pass within the specified experimental range.

Table III presents some typical data on deposition rate and energy.

## Bench-Scale Reactor

### *Apparatus*

A larger reactor was designed in order to study problems associated with producing massive deposits of crystalline boron and thus reducing the degree of filament contamination.

A schematic diagram of the reactor is presented in Fig. 5. It was fabricated from stainless steel pipe (30.5 cm in diameter, 61.0 cm in length) fitted with flanges at each end. Two sight glasses in the reactor shell made it possible to measure filament temperatures with an optical pyrometer. The filament (46 cm in length) was suspended between two graphite bushings (6.5 cm in diameter). As in the laboratory reactor, the bottom bushing was suspended in a water-cooled mercury well which provided for both an electrical contact and mechanical freedom for expansion. Thus the reactor shell became one electrical contact, and the lead to the top filament bushing was inserted through a gas-tight insulated flange.

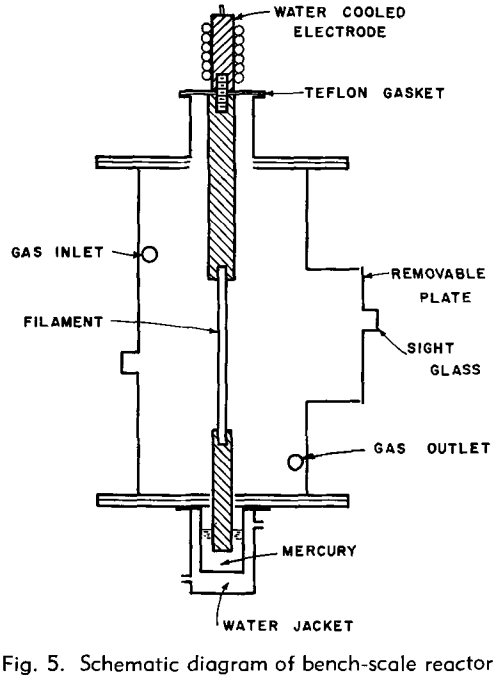


Fig. 5. Schematic diagram of bench-scale reactor

Boron trichloride and hydrogen were metered into this reactor, and the same techniques of gas monitoring and deoxidation of hydrogen were employed as in the small glass reactor. Since large quantities of unreacted boron trichloride were involved, a refrigeration system was necessary for recovery and recycling. The system consisted of a single tube heat exchanger and a condenser maintained at dry ice temperatures (−78°C) with dry ice-Methyl Cellosolve mixtures.

### *Experimental Results*

Most of the experimental work was done with vertically supported titanium filaments varying from 15.25 cm to 30.5 cm in length and having a 0.45 cm diameter. As in the smaller glass system, the deposit developed "hot spots" which eventually healed. It was necessary to increase current periodically to maintain a deposition surface temperature of 1000°-1200°C. Deposits tended to grow in length and, in some cases, up to 50% of their original length. As a result of this growth, the deposits generally became distorted, structurally weak, and eventually broke. Deposits of greater than 450 g were obtained over a 72-hr period with average deposition rates of 6-8 g/hr. Conversion per pass of 8-20% based on feed rate were obtained with overall yields (based on recycled boron trichloride) consistently near or better than 90%. A 454-g boron deposit approximately 5 cm in diameter and 20 cm long required an 8 kw power input in order to maintain a 1000°-1200°C surface temperature.

On microscopic examination, massive deposits appeared metallic and crystalline with a high luster. Cooler areas were black and probably less crystalline. The filament was generally dispersed throughout the deposit and no specific growth formations were observed. Surface samples analyzed as high as 99.7% but always contained 0.1-0.2% titanium indicating diffusion of titanium. Massive deposits, including all of the original filament, were ground to a −100 mesh in large steel mortars. Typical anal-

Fig. 6. Typical boron deposit (Scale in inches)

yses are 97.5-98.5% boron, 0.5% titanium, and the remainder was mostly iron. Further details on analyses and upgrading techniques are presented in a later section on Upgradng and in Table VII. An illustration of a typical deposit segment is presented in Fig. 6.

Some representative results obtained are presented in Table IV. These results indicate in a general way that a deposit of considerable size could be obtained with titanium filaments, if runs of sufficient duration could be maintained.

In order to study the relationship between deposit weight, instantaneous deposition rate, and time, tests were operated at constant mole ratio ($[H_2]/[BCl_3] = 8.4$), residence time (2.4 min), and with initial filament dimensions (15.25 cm in length, 0.475 cm in diameter) under as close temperature control as possible. Weight of the deposit as a function of time is presented in Fig. 7. Under the specified experimental conditions, a deposition rate of 14.0 g/hr was realized after 72 hr of operation.

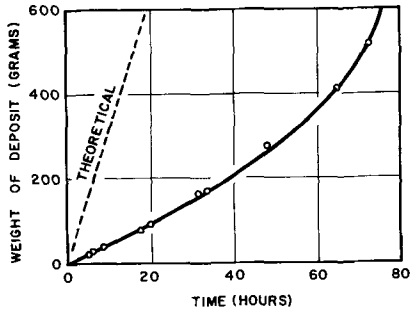


Fig. 7. Deposition weight as a function of time. Gas reference conditions: pressure = 1 atm, temperature = 25°C. Residence time = 2.4 min. Volume of reactor = 44,500 $cm^3$. Mole ratio $[H_2]/[BCl_3] = 8.4$. Titanium filament dimensions = 15.25 cm length, 0.475 cm diameter. Filament temperature = ≅1100°C. Equilibrium conversion = 58%.

If the slopes of the curve presented in Fig. 7 are plotted as a function of total deposition weight, a good linear curve is obtained up to about 72 hr or deposit weight of 500 g. An equation for this linear curve involving deposition rate and weight is:

$$\frac{dw}{d\theta} = 0.02w + 3.8 \qquad [4]$$

The solution of this differential equation results in the relation

$$w = 190\ (e^{\frac{\theta}{50}} - 1) \qquad [5]$$

$w$ = weight (g), $\theta$ = time (hr). However, this equation is empirical, and applies only for the stated conditions.

It was observed that the rate of deposition was proportional to the mass (or volume) of the deposit and not to the apparent geometric surface area. Since the rate of deposition is proportional to the mass of the deposit, it is probable that the requirements for optimum conversion are also a function of the deposit mass or time. Therefore, to maintain

**Table IV. Boron deposition on titanium filaments[a]**
**(Mole ratio $[H_2]/[BCl_3] = 8.4$)**

| Reaction duration (hr) | Ti filament dimensions (dia. × length) (cm) | Deposit temp range (°C) | Weight boron (g) | Conversion[b] per pass (%) | Average rate of deposition (g/hr) | Yield B[c] (%) |
|---|---|---|---|---|---|---|
| 126.3 | 0.475 × 15.25 | 960–1300 | 776.9 | 10.8 | 6.2 | 98 |
| 75.0 | 0.475 × 15.25 | 1080–1100 | 563.4 | 14.4 | 7.5 | 94 |
| 5.3 | 0.475 × 15.25 | 1000–1200 | 19.4 | 4.2 | 3.7 | 69 |
| 39.5 | 0.475 × 15.25 | 1025–1225 | 242.2 | 8.2 | 6.1 | 77 |
| 50.0 | 0.475 × 15.25 | 1075–1200 | 396.5 | 9.0 | 7.9 | 92 |
| 34.5 | 0.475 × 15.25 | 1050–1200 | 214.5 | 7.1 | 6.2 | 85 |
| 76.8 | 0.475 × 15.25 | 950–1225 | 568.0 | 14.5 | 7.5 | — |
| 12.0 | 0.475 × 30.5 | 1075–1500 | 103.7 | 16.1 | 8.6 | 88 |
| 7.5 | 0.475 × 30.5 | 1060–1100 | 61.7 | 15.2 | 8.2 | 73 |
| 9.8 | 0.475 × 30.5 | 1070–1100 | 79.0 | 15.5 | 8.1 | 85 |
| 40.0 | 0.475 × 30.5 | 1050–1125 | 352.5 | 16.3 | 8.1 | 84 |
| 10.3 | 0.475 × 30.5 | 1065–1085 | 96.3 | 17.1 | 9.4 | 80 |
| 50.0 | 0.475 × 61.0 | 1050–1125 | 546.0 | 20.9 | 10.8 | 96 |

[a] Residence Time = $\frac{\text{Reactor Volume}}{\text{Flow Rate (cm}^3\text{/min)}}$ = 2.4 min.
Reactor volume = 44,500 $cm^3$; reactor flow = 18,600 $cm^3$/min; reference conditions = 1 atm at 25°C.

[b] Conversion Per Pass = $\frac{\text{Experimental Yield}}{\text{B in } BCl_3 \text{ Feed}} \times 100$.

[c] Based on $BCl_3$ recovered from refrigeration cycle.

Table V. Principal x-ray diffraction "d" lines, Cu $K_\alpha$ radiation

| Reported (7) * | | Titanium filament 1075°-1125°C | | Titanium filament 1100°-1200°C | | Graphite filament 1075°-1125°C | |
|---|---|---|---|---|---|---|---|
| 5.03 | VS | 5.12 | S | 7.82 | S | 5.40 | W |
| | | 4.74 | M | 5.03 | VS | 5.03 | W |
| 4.40 | VS | | | | | | |
| 3.92 | VS | 4.00 | W | 4.67 | VS | 3.40 | VS |
| 3.56 | W | 3.25 | W | 4.44 | S | 2.88 | W |
| 3.33 | M | 3.21 | W | 3.70 | M | 2.70 | W |
| 2.70 | W | 2.87 | W | 3.54 | M | 2.55 | M |
| 2.53 | S | | | 2.86 | M | | |
| 2.42 | VS | 2.64 | M | 2.60 | M | 2.42 | VW |
| 2.34 | W | | | 2.47 | M | | |
| 2.19 | W | | | 2.40 | M | | |
| | | 2.13 | S | | | | |
| 2.02 | S | 2.05 | VS | 2.03 | M | 2.04 | VW |
| 1.74 | W | 1.77 | M | 1.76 | M | 1.76 | VW |
| 1.54 | W | 1.55 | W | 1.55 | W | | |
| | | 1.52 | M | | | 1.52 | S |
| 1.43 | S | 1.43 | W | 1.43 | M | 1.43 | W |
| 1.37 | M | 1.38 | M | 1.38 | M | | |
| | | | | 1.35 | M | | |
| 1.30 | W | 1.31 | VW | | | 1.29 | VW |

* VS—very strong line; S—strong; M—medium; W—weak; VW—very weak.

maximum conversion would necessitate constant readjustment or programming of the reaction conditions. As the reaction proceeds, it is probable that the deposition rate would approach the limit (58% theoretical equilibrium conversion or 30.3 g/hr) established by equilibrium and flow conditions.

*Crystallinity.*—X-ray diffraction studies indicated that several different samples exhibited a certain degree of crystallinity. Data in Table V compare the observed "d" values of boron deposited on graphite and titanium elements and the reported "d" values of crystalline boron whose structure has been established as a tetragonal unit with fifty atoms arranged to form four nearly regular linked icosahedra (7). In all cases no boride lines were detected, indicating that titanium or carbon and boron form mainly solid solutions rather than crystalline compounds at the deposition temperatures indicated. A wide variation in "d" line spacings was observed; however, a sample from a region in excess of 1200°C showed a resemblance to values reported in the literature. Boron deposited on titanium exhibited a considerably greater degree of crystallinity than boron deposited on graphite filaments. It has been shown previously that the crystal structure of boron is a function of temperature and may explain the differences observed in crystallinity of boron deposited on titanium filaments (15).

*Examination of reaction products.*—Exhaust gases from the reactor were monitored and analyzed with an infrared spectrophotometer. Small quantities of diborane ($B_2H_6$) were identified in the exhaust gases as well as hydrogen chloride and excess boron trichloride.

Since diborane was observed in the exhaust gases, the mechanism for the formation of boron may involve a stepwise reduction such as:

$$BCl_3 \rightarrow BH_3 \rightarrow B_2H_6 \rightarrow B$$

Borine ($BH_3$) has never been observed chemically or spectroscopically, although there is indirect evidence for borine (16-18).

## Boron Upgrading

Attempts were made to upgrade boron produced both in the laboratory and bench-scale reactors, since metal contamination appeared to be significant in all deposits. Two techniques were empolyed: density classification and a chlorine treatment.

*Density classification.*—Several boron samples containing titanium (D = 4.5) were ground to a −100 mesh, leached in 6M HCl to remove iron introduced by grinding, and were then subjected to a density classification in methylene bromide (D = 2.49). This mixture separated into high and low density components. The heavier component consisting of particles richer in titanium readily separated from the lighter boron (D = 2.33-2.39). However, there was a considerable amount of intermediate material (D = 2.39-2.49) which could not be separated by this technique. Analysis showed a slight "upgrading." Results are presented in Table VI.

This technique was also applied to boron containing tantalum (D = 11.2) which was readily separated resulting in marked "upgrading." One sample was upgraded from 81.5% to 99.8% (Table VI). Carbon (D = 2.45) could not be separated from boron by this method due to the proximity of their densities.

*Chlorination.*—One pound charges or larger of boron containing titanium were ground to a −100 mesh, and were treated with chlorine in a Pyrex tube reactor A reaction was observed between 300° and 350°C resulting in a volatile liquid which was identified as titanium tetrachloride. Small quantities of volatile iron chlorides were also detected. Infrared spectra of the reaction products proved that boron trichloride was not being formed within the prescribed temperature range. A 900-g sample (−100 mesh) analyzing 97.5% boron, 1.1% titanium, and 0.10% iron was upgraded to 99.6% boron, 0.3% titanium, and 0.07% iron by the chlorine treatment. Results obtained in several typical treatments are presented in Table VII.

## Conclusions

1. Rate of boron formation in the vapor phase reduction of boron trichloride depends mainly on four variables: mole ratio of hydrogen to boron trichloride, residence time of gas mixture in the reactor, deposition temperature, and mass of deposit. For maximum deposition rates, large hydrogen to boron

Table VI. Density classification of boron containing tantalum and titanium

| Filament impurity | Per cent boron | |
|---|---|---|
| | Before classification | After classification |
| Ti | 94.5 (5.4% Ti) | 97.0 (2.1% Ti) |
| Ta | 90.8 | 98.4 |
| Ta | 92.2 | 97.7 |
| Ta | 86.4 | 90.1 |
| Ta | 90.1 | 98.7 |
| Ta | 81.5 | 99.8 |

Table VII. Analyses of boron deposited on titanium before and after chlorination (Bench-scale reactor)

| % B | % Ti | % Fe | % Mg | % Si | % Cu | Analysis | Remarks |
|---|---|---|---|---|---|---|---|
| 95.8 | 4.0 | 0.098 | 0.0026 | 0.050 | 0.014 | Spec. | Before chlorination |
| 99.7 | 0.18 | 0.054 | 0.0024 | 0.030 | 0.0034 | Spec. | After chlorination |
| 96.9 | 1.79 | 0.04 | | 0.05 | | Chem. | Before chlorination |
| 99.6 | 0.32 | 0.026 | 0.00058 | 0.028 | 0.0017 | Spec. | After chlorination |
| 94.6 | 4.3 | 0.01 | | 0.26 | | Chem. | Before chlorination |
| 99.6 | 0.36 | 0.03 | 0.0017 | 0.022 | 0.0058 | Spec. | After chlorination |
| 97.5 | 1.1 | 0.10 | | 0.26 | | Chem. | Before chlorination |
| 99.6 | 0.28 | 0.074 | 0.0011 | 0.017 | 0.074 | Spec. | After chlorination |
| 98.0 | 1.7 | 0.24 | 0.0024 | 0.036 | 0.015 | Spec. | Before chlorination |
| 99.0 | 0.76 | 0.090 | 0.0015 | 0.12 | 0.016 | Spec. | After chlorination |
| 99.4 | 0.79 | 0.05 | | 0.06 | | Chem. | After chlorination |
| 99.4 | 0.50 | 0.052 | 0.00064 | 0.018 | 0.0036 | Spec. | After chlorination |

trichloride mole ratios on the order of 8-12 are desirable. Deposition temperatures in excess of 1000°C and low residence times are also desirable.

2. Since contamination is inevitable during the process of depositing boron on metallic filaments, it is better to use filament materials that are least objectionable from a weight standpoint and ease of removal. Titanium appears to be suitable as a filament metal, since it can be readily removed from boron by treatment with chlorine at temperatures (300°-350°C) well below the reported temperature (550°C) for boron-chlorine combination. Also, titanium forms a good conductive core in the deposit such that low resistance is realized in all temperature ranges. High deposit-to-filament-diameter ratios should be obtained in order to minimize metal contamination and this is possible with titanium as a core.

3. Crystalline boron of 99.0-99.6% purity by direct assay can be produced by vapor phase reduction followed by a chlorination step.

4. Crystallinity appears to be a function of temperature and may be a function of filament material.

5. A relationship between weight of deposit and reaction time was determined, which indicates that the rate of deposition is a function of deposit weight.

Manuscript received Feb. 10, 1958. This paper was prepared for delivery before the New York Meeting, April 27-May 1, 1958.

Any discussion of this paper will appear in a Discussion Section to be published in the June 1959 JOURNAL.

## REFERENCES

1. H. Moissan, *Ann. Chim. et phys.*, (7) **6**, 296 (1895).
2. E. Weintraub, *Trans. Am. Electrochem. Soc.*, **16**, 165 (1909).
3. L. Hackspill, A. Stieber, and R. Hocart, *Compt. rend.*, **193**, 776 (1931).
4. D. P. Mellor, S. B. Cohen, and E. B. Underwood, *Australian Chem. Inst. J. & Proc.*, **3**, 329 (1936).
5. A. E. Van Arkel, U. S. Pat. 1,774,410, Aug. 6, 1930.
6. K. Becker, "Hochschmelzende Hartstoffe und ihre Technische Anwendung," Verlag Chemie, Berlin (1937).
7. A. J. Laubengayer, D. T. Hurd, A. E. Newkirk, and J. L. Hoard, *J. Am. Chem. Soc.*, **65**, 124 (1943).
8. M. Formstecher, *Comp. rend.*, **221**, 747 (1945).
9. G. H. Fetterley, U. S. Pat. 2,542,916, Feb. 20, 1951.
10. G. M. Murphy, Separation of Boron Isotopes, U. S. Atomic Energy Commission, Oak Ridge, Tennessee (1952).
11. F. D. Rossini, D. D. Wagmen, W. H. Evans, S. L. Levine, and I. Jaffe, Selected Values of Chemical Thermodynamic Properties, Circular of the National Bureau of Standards 500, (1952).
12. K. K. Kelley, *U. S. Bur. Mines Bull. 371* (1934).
13. H. M. Spencer, *J. Chem. Phys.*, **14**, 729 (1946).
14. J. A. M. Van Liempt, *Z. anorg. u. allgem. Chem.*, **111**, 151 (1920); M. G. Mellon, and V. N. Morris, *Ind. Eng. Chem.*, **16**, 123 (1924).
15. V. P. Jacobsmeyer, L. W. Friedrich, L. J. Badar, Semiconducting Properties of Boron, Armed Services Technical Information Agency No. 52266.
16. A. Stock and E. Kuss, *Ber.*, **56B**, 789 (1923).
17. G. C. Pimentel and K. S. Pitzer, *J. Chem. Phys.*, **17**, 882 (1949).
18. H. I. Schlesinger and A. B. Burg, *Chem. Revs.*, **31**, 1 (1942).

# Methods for Preparing Pure Scandium Oxide

F. H. Spedding, J. E. Powell, A. H. Daane, M. A. Hiller, and W. H. Adams

*Institute for Atomic Research and Department of Chemistry, Iowa State College, Ames, Iowa*

ABSTRACT

A review of the techniques for isolating scandium in a pure state is presented, including the newest cation-exchange methods. These methods include elution with ethylenediaminetetraacetate and N-hydroxyethylethylenediaminetriacetate solutions and the use of copper and lead ions, respectively, as retaining ions which permit passage of scandium but retain rare earth ions. A new approach to opening thortveitite ore by treating with ammonium bifluoride and reducing the mixed metal fluorides to the metallic state with calcium is presented.

In connection with its studies of the rare earth elements, the Ames Laboratory has been interested in the isolation and purification of scandium. Methods used in the past to prepare pure Sc salts include fractional precipitation, sublimation, solvent extraction, and ion exchange.

Scandium may be precipitated as the phosphate, fluoride, oxalate, basic tartrate, basic thiosulfate, basic carbonate, basic acetate, hydroxide, and various double sulfates (1). No attempt is made here to evaluate all of these methods individually. Suffice it to say, no one precipitant isolates Sc quantitatively from all of the elements with which it is contaminated in its natural states. The great utility of precipitational methods lies in their use as concentrating steps in which the Sc is gradually upgraded. Combinations of these methods will, of course, eventually yield pure Sc with losses occurring depending on the precipitants used and proportional to the number of repetitions required to achieve the desired purity.

The sublimation of acetylacetonates (1) and the volatilization of chlorides (2), likewise, do not generally result in complete separation of Sc from all of the contaminating elements.

Solvent extraction procedures have a distinct advantage over precipitational methods in that repetitions of the extractive procedure are easily carried out. Since the materials remain in a liquid phase, no redissolution steps are necessary. Such procedures have been used frequently in the isolation of Sc and include extraction of scandium acetylacetonate by benzene or ethyl acetate (1), the chloride and nitrate by tri-n-butyl orthophosphate (3), the thenoyltrifluoroacetonate with benzene (4, 5), the cupferrate with chloroform (6, 7), and the thiocyanate with diethyl ether (1). The latter procedure will be mentioned again in connection with methods employed at Iowa State College for the purification of Sc.

Several ion-exchange techniques have been applied to the isolation of Sc. For example, an anion-exchange resin in conjunction with chloride mixtures in 12*N* HCl has been used to separate Sc from those elements which are not capable of forming anionic chloride complexes (8), and successful elutions have been made from cation-exchange resins using citric acid (9), nitrilotriacetic acid (10), glycolic acid (11), ethylenediaminetetraacetic acid (10), and hydrazine-N,N′-diacetic acid (12). Some of these methods have been demonstrated only on the tracer scale, while with larger quantities the investigators were sometimes plagued with the formation of precipitates in the resin bed. It is likely that the precipitates which formed were due to an unfortunate choice of the retaining ion, improper *p*H of the eluant, or excessive concentration. Nevertheless, it is apparent that the ion-exchange techniques used to date could be improved upon.

Recently, several hundred grams of thortveitite ore were obtained from the Norsk Feldspat Company of Norway. Marble and Glass (13) have reported that such material contains about 45% $SiO_2$, 34% $Sc_2O_3$, 11% rare earth oxides (primarily ytterbium, lutetium, thulium, erbium, dysprosium, yttrium, and gadolinium), 5% $Al_2O_3$, and 3% $Fe_2O_3$. As will be seen later, thortveitite also contains traces of many other elements. Marble has described the difficulty encountered in dissolving this ore which is occasioned by its very high silica content. The classical procedure used by Urbain and Urbain (14) involved a series of caustic fusions followed by removal of most of the resultant sodium silicate by water leachings. The residue of Sc and other insoluble metal hydroxides was then treated with dilute mineral acid to obtain the metal values in soluble form. This procedure is not entirely satisfactory owing to the difficulty encountered in filtering the slimy hydroxides from the leachate and in removing the remainder of the silica after the hydroxide residue has been dissolved in dilute acid. Other procedures used in the past for opening thortveitite ore include those of Iya (15), Vickery (16), and Adamoli (17).

Iya heated the pulverized ore with 1.2 parts of carbon for 30 min at 1800°C in order to form a mixture of carbides. The various metal carbides decomposed in dilute HCl giving a solution of chlorides which could be separated from the residue of excess carbon, silica, and silicon carbide.

Vickery obtained crude $ScCl_3$ from the ore by mixing finely ground thortveitite with carbon and heating in a tube furnace at 800°-850°C in a stream of chlorine. Since $ScCl_3$ does not volatilize below about 970°, it was finally leached from the melt with water.

Adamoli extracted Sc from its ores in a novel manner. He developed a process in which the ore was mixed with a sparingly soluble metal fluoride ($CaF_2$ for example). Next he added a solution of a mineral acid and an alkali metal salt of that acid (HCl and NaCl for example). The resulting paste was heated at a low temperature to form a water-soluble salt of the metal which was originally added in the form of a sparingly soluble fluoride ($CaCl_2$ formed in this particular instance). The liquid and the water-soluble salts were then removed and the residue was briquetted and fired at a high temperature in order to form a water-soluble complex fluoride of Sc. The resulting hexafluoscandate ion was then leached from the reaction mass.

Recent work in this laboratory on the preparation of rare earth fluorides by reaction of the oxides with ammonium bifluoride suggested a similar treatment for thortveitite which would eliminate silicon as the volatile tetrafluoride. The resulting mixture of metal fluorides, containing the Sc, could be reduced to the metallic state with an active metal such as Ca or Mg. The metals would then be easily soluble in dilute acid and the Sc could be purified by solvent extraction and/or ion exchange.

## Experimental

### *Preparation of Crude Scandium Fluoride*

The thortveitite was ground to a powder by mortar and pestle and then ball-milled. A portion weighing 307 g was mixed with 950 g of dry ammonium bifluoride (about 25% excess) and heated overnight at 375°-400°C in a platinum boat. A slow stream of air was passed through the apparatus to remove the gaseous products. The reaction may be represented as:

$$R_2O_3 \cdot SiO_2 + 10NH_4HF_2 \rightarrow 2RF_3 + SiF_4 + 10HF + 10NH_3 + 5H_2O$$

The symbol R represents Sc, Al, Fe, and rare earths. The product of this reaction was light brown in color and weighed 240 g.

### *Reduction of Crude Scandium Fluoride with Calcium*

The fluoride mixture prepared above was divided into two portions of 120 g each. Each batch was combined with 75 g of Ca metal (about 10% excess) in a Ta crucible, and reduced by heating the crucible and its contents to 1400°C under an argon atmosphere. This is the same general procedure used to prepare the rare earth metals. A clean separation was obtained between the metal and slag in each case, but the metal adhered to the Ta crucible. Consequently, the Ta foil, of which the crucibles were constructed, had to be peeled away to obtain the metal buttons. One weighed 50 g and the other 48.2 g.

*Purification of the scandium by extraction with ether from a thiocyanate solution.*—The metal buttons were dissolved separately in HCl and each solution was treated with ammonium thiocyanate and extracted with diethyl ether according to the procedure of Fischer and Bock (1). After evaporating the ether, the residues were ignited at 800°C and subjected to qualitative spectrographic analyses. The results are shown in Table I.

It is apparent that all of the contaminants, except Be, tend to concentrate in the aqueous phase, but the separation of Sc from rare earths, Fe, and many other elements is not complete after a single extraction of scandium thiocyanate with ether. Although the product undoubtedly could have been improved greatly by further extractions of this sort, it was decided to try an ion-exchange method for the separation of Sc from the remaining impurities.

*Purification of scandium by ion-exchange elution with N-hydroxyethylethylenediaminetriacetic acid.*—The enriched scandium oxide samples were combined and dissolved in HCl. The Sc was then adsorbed on a resin bed of 40-50 mesh Amberlite IR-120, 2 in. in diameter and about 4 ft long, in the hydrogen ion cycle. After rinsing the bed with distilled water, elution was begun with an eluant containing 5 g of N-hydroxyethylethylenediaminetriacetic (HEDTA) acid per liter, buffered to a pH of 7.4-7.6 with ammonium hydroxide. Two additional beds, 1 in. in diameter by about 4 ft long, in the hydrogen cycle, were used as retaining beds. A flow rate of 2-3 ml/min was maintained while consecutive fractions were being caught.

Since no band fronts were visible, the collection of samples was begun immediately after the start of elution. The first 60 l of eluate yielded almost no

**Table I. Qualitative spectrographic analysis of oxide fraction obtained after ether extraction of the thiocyanate**

| Contaminant | First Batch | | Second Batch | |
|---|---|---|---|---|
| | $H_2O$ phase (wt 19.4 g) | Ether phase (wt 44.2 g) | $H_2O$ phase (wt 18.4 g) | Ether phase (wt 44.9 g) |
| Al | M | W | M | W |
| Be | W | M | W | M |
| Ca | M | VW | M | VW |
| Co | T | — | T | — |
| Cr | W | T | W | — |
| Cu | W | FT | W | T |
| Dy | W | — | W | — |
| Er | W | — | W | — |
| Fe | S | M | S | M |
| Gd | W | — | W | — |
| Lu | M | W | M | W |
| Mg | W | VW | W | VW |
| Mn | M | W | M | W |
| Ni | VW | — | VW | — |
| Sc | M | VS | M | VS |
| Sn | VW | — | VW | VW |
| Th | T | — | T | — |
| Ti | W | T | W | T |
| Tm | M | — | M | — |
| Y | S | W | S | W |
| Yb | M | VW | M | VW |

VS, very strong; VW, very weak; S, strong; M, moderate; W, weak; T, trace; —, not detected.

Table II. Fractions obtained by elution of crude scandium with N-hydroxyethylethylenediaminetriacetic acid

| Sample No. | Vol | Solution color | Oxide color | Wt of oxide | Composition |
|---|---|---|---|---|---|
| 1 – 3 | 60 | Colorless | Brown | 0.17 | Chiefly Fe,Ca |
| 4 | 4 | Yellow | Tan | 0.07 | Chiefly Fe,Ca |
| 5 | 12 | Yellow | Brown | 1.83 | Sc with Fe |
| 6 | 6 | Yellow | Tan | 4.10 | Sc with Fe |
| 7 | 10 | Lt. yellow | Cream | 7.20 | Sc; tr. Fe; ~0.01%Y |
| 8 | 7.5 | Pale yellow | Yellowish | 5.13 | Sc; tr. Fe; ~0.03%Y |
| 9 | 10 | Colorless | Yellowish | 7.02 | Sc; tr. Fe; ~0.01%Y, Lu, Yb |
| 10 | 10 | Colorless | White | 8.13 | Sc; ~0.01%Y, Lu, Yb |
| 11 | 10 | Colorless | White | 8.36 | Sc; ~0.01%Y, Lu, Yb |
| 12 | 10 | Colorless | White | 9.41 | Sc; ~0.01%Y, Lu, Yb |
| 13 | 10 | Colorless | White | 8.43 | Sc; ~0.01%Y, Lu, Yb |
| 14 | 10 | Colorless | White | 5.11 | Sc; ~0.01%Y, Lu, Yb |
| 15 | 20 | Colorless | White | 6.35 | Sc; ~0.01%Y, Lu, Yb |
| 16 | 10 | Colorless | White | 2.94 | Sc; ~0.01%Y, Lu, Yb |
| 17 | 10 | Colorless | White | 6.26 | Sc; ~0.02%Y; ~0.01%Lu; ~0.02%Yb |
| 18 | 15 | Colorless | Dirty white | 2.64 | Sc; ~0.03%Y; ~0.9%Lu; ~0.1%Yb |
| 19 | 13 | Colorless | Tan | 3.00 | Sc&Y; rare earths; tr.Mn |
| 20 | 12 | Pink | Brown | 1.35 | Sc,Y&Mn; rare earths |
| 21 | 15 | Colorless | Tan | 0.12 | |
| | | | Total weight recovered | 84.00 g | |

residue upon evaporation and ignition.[1] At this point, the eluate turned slightly yellow and the next 22 l, spread over several individual samples, gave oxide residues varying in color from a light tan to dark brown and back to a light tan. The weights of recovered oxide over this same region increased from nothing to about 6.8 g/10-l fraction. The next three consecutive samples gave a pale cream-colored oxide weighing a little more than 7 g/10-l fraction. The next four samples, totaling 40 l, contained more than 8 g of white oxide per 10-l fraction. The weights then began tapering off and only 20.8 g of white oxide were realized from the next 50 l of eluate. The oxide recovered from the last 55 l of eluate diminished gradually in weight and also underwent a change in color ranging from cream to brownish-tan to brown with a tinge of blue and then back to light tan. Analyses of the fractions are given in Table II.

Only 84 g of residues were obtained from an original 89 g of crude oxide. Since a great deal of care was taken in evaporating down and recovering all the residues from the final purification, it is thought that the 5-g loss was due to undecomposed scandium sulfate in the crude oxide sample taken for this experiment. It is possible that some sulfate could have formed during the ignition of the scandium thiocyanate to what was thought to be scandium oxide. Sulfate would be eliminated as the scandium was loaded on the ion-exchange columns. In any event, a yield of 48.73 g of very pure $Sc_2O_3$ was obtained by this elution with HEDTA and another 19.35-g portion was obtained which showed only a trace of iron. This latter material could be freed from iron with little difficulty. Since most of the other fractions contain larger amounts of impurities, they will be resubmitted to the thiocyanate extraction process before being processed further by ion-exchange.

*Other methods for purifying scandium by ion-exchange elution.*—Two other methods have been used in preparing pure scandium oxide at the Ames Laboratory. One takes advantage of the fact that cupric ion will retain all the rare earths and many common impurities such as Ni, Pb, Zn, Co, Cd, Mn, Ca, Mg, Be, Sr, and Ba when ethylenediaminetetraacetic acid (EDTA) is used as the eluant, but will not retain Sc. By eluting a crude mixture containing Sc down a cupric-state resin bed with 0.0153*M* EDTA solution at a *p*H of 8.4, a very good yield of pure Sc has been obtained. The chief difficulty with this method is that the Sc is first obtained as a mixture with cupric ion and must be purified further either by electroplating out the Cu or by preciptating the Cu as copper sulfide. Also, cupric ion retains ferrous, but not ferric ion.

The other method is very similar, except that Pb is used as the retaining ion and N-hydroxyethylethylenediaminetriacetic acid is used as the eluant. Again, most cations, including the rare earths, are retained while Sc is not. A good yield of pure Sc has been obtained by eluting a mixture containing Sc down a lead-state resin bed with 0.018*M* HEDTA at a *p*H of 7.6 and removing lead from the Sc fractions by precipitation with $H_2S$. Copper and nickel are not retained by Pb and, therefore, must also be considered if they are present. Copper, of course, is removed along with the lead during treatment with $H_2S$ so that its presence creates no real problem. Scandium and nickel can be separated readily by the thiocyanate extraction process mentioned earlier.

## Summary

Although there are a number of alternative approaches by which Sc might be purified, the methods

[1] Recovery of all samples was accomplished by boiling the eluate to dryness and destroying the organic matter with nitric acid. From previous experience, it was found that during treatment with $HNO_3$, the residue frequently burst into flame, expelling some of the ash from the beaker. For this reason, large beakers were used and they were kept covered, since it appeared that the gaseous products evolved in the reaction were capable of controlling the burning rate if they were confined over the burning ash. Attempts to ignite material taken to dryness before destroying the organic matter resulted in the material swelling several times its size and toppling out of the crucible like "Pharaoh's Serpents" during the charring process.

described herein are quite straightforward. First of all, the removal of silicon by treatment with ammonium bifluoride is elegant in its operational simplicity. Next, the mixture is converted to soluble form by reduction to the metallic state and subsequent dissolution in HCl. Anyone who has attempted to filter silicate solutions or who has attempted to redissolve insoluble fluorides in quantity will appreciate the advantages of these procedures. The thiocyanate procedure is simple to perform and removes a major amount of the impurities but would have to be repeated a number of times in order to achieve the separation from rare earths that can be obtained by ion-exchange. Consequently, we have chosen to perform only one thiocyanate extraction before resorting to ion-exchange.

Manuscript received May 8, 1958. This paper was presented at the New York Meeting, April 27-May 1, 1958. It is Contribution No. 634; work was performed in the Ames Laboratory of the Atomic Energy Commission.

Any discussion of this paper will appear in a Discussion Section to be published in the June 1959 JOURNAL.

REFERENCES

1. W. Fischer and R. Bock, Z. *anorg. Chem.*, **249**, 146 (1942).
2. R. J. Meyer and H. Winter, *ibid.*, **67**, 398 (1910).
3. D. F. Peppard, J. P. Faris, P. R. Gray, and G. W. Mason, *J. Phys. Chem.*, **57**, 294 (1953).
4. A. Broido, A.E.C. Document No. AEC-2616, July 29, 1947.
5. H. J. Bronaugh and J. F. Suttle, A.E.C. Report No. LA-1561, June, 1953.
6. G. E. F. Lundell and J. I. Hoffman, "Outlines of Methods of Chemical Analysis," John Wiley & Sons, New York (1948).
7. C. C. Miller, *J. Chem. Soc. (London)*, **1947**, 1347.
8. K. A. Kraus, F. Nelson, and G. W. Smith, *J. Phys. Chem.*, **58**, 11 (1954).
9. P. Radhakrishna, *Anal. Chim. Acta*, **8**, 140 (1953).
10. V. K. Iya and J. Loriers, *Compt. rend.*, **237**, 1413 (1953).
11. D. C. Stewart, Proc. Intern. Conf. Peaceful Uses of Atomic Energy, Geneva, 1955, **7**, 321 (1956).
12. R. C. Vickery, *J. Chem. Soc. (London)*, **1955**, 245.
13. J. P. Marble and J. J. Glass, *Am. Mineralogist*, **27**, 696 (1942).
14. P. Urbain and G. Urbain, *Compt. rend.*, **174**, 1310 (1922).
15. V. K. Iya, *ibid.*, **236**, 608 (1953).
16. R. C. Vickery, *J. Chem. Soc. (London)*, **1956**, 3113.
17. C. Adamoli, U. S. Pat. 2,250,851, July 29, 1941.

# Cathode Potentials during the Electrodeposition of Molybdenum Alloys from Aqueous Solutions

**D. W. Ernst[1] and M. L. Holt**

*Chemistry Department, University of Wisconsin, Madison, Wisconsin*

ABSTRACT

Cathode potential measurements are used to explain the cathode reactions that result in the electrodeposition of molybdenum alloys. Potentials were measured by the direct method during the electrolysis of aqueous ammoniacal citrate solutions containing sodium molybdate and the sulfate of a codepositing metal, iron, nickel, or cobalt. The results indicate that the reduction of molybdate ion in this type of bath is probably not accomplished in one step with six electrons, but with one, two, or three electrons depending on the codepositing metal and its oxidation state in the bath. The results also indicate that hydrogen is involved in the molybdate reduction process. A two-step mechanism for the reduction of molybdate ion in the presence of a codepositing metal is proposed and an explanation of why this metal must be iron, cobalt, or nickel rather than such metals as chromium, manganese, copper, or zinc is presented.

Molybdenum readily codeposits with Fe, Co, or Ni from aqueous solutions; however, in contrast to this, the electrodeposition of appreciable amounts of pure Mo from aqueous solution has not been accomplished. The purpose of this work was to obtain experimental data that would help to explain this cathodic behavior of Mo. Cathode potential measurements made during electrolysis seemed to be a logical approach to the problem since previous studies of the effect of the various bath constituents, pH, current density, and temperature on cathode current efficiency and alloy composition did not yield sufficient information (1). Frantsevich-Zabludovskaya (2) utilized polarization curves in the recently reported results of his investigation of the deposition of Ni-Mo, Fe-Mo, and Fe-Ni alloys.

[1] Present address: National Bureau of Standards, Washington, D. C.

## Experimental Details

The cathode potentials reported here were measured by the direct method. The cell design permitted the cathode to be removed for weighing and also allowed the tip of the capillary bridge to be placed in the same position for each run. The capillary tip connecting the cathode with the reference electrode was placed near the face of the cathode, but it could have been located in other positions on or near the cathode (3-6). The cell,

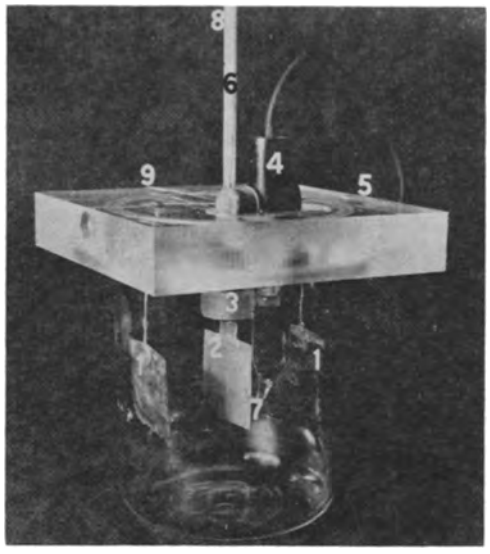


Fig. 1. Cathode potential cell showing: 1, anodes; 2, cathode; 3, Lucite nut on cathode holder; 4, calomel reference electrode; 5, anode connection; 6, Pt wire for cathode connection; 7, tip of glass bridge; 8, thermometer; 9, screw for holding cathode assembly.

Fig. 1, was made from a cut-down 500 ml tall-form Pyrex beaker fitted with a Lucite cover 10.2 cm x 10.2 cm x 1.9 cm. There were openings in the cover for two anodes, 3 cm x 3 cm x 0.03 cm, a cathode of the same size, a thermometer, and a glass bridge for the reference electrode. Each Pt anode was held in position approximately 3 cm from the centrally placed cathode held in a special holder. The removable cathode holder consisted of a fiber rod (3.8 cm x 0.64 cm) machined with a tapered thread and slot on one end; the slot was closed by tightening a Lucite nut. The Pt cathode had a tab, 0.8 cm x 0.7 cm, which fitted into the slot on the fiber rod. A Pt wire having a similar Pt tab on one end was inserted in the fiber rod to serve as the cathode connection. When the two tabs were placed in the slot and the nut tightened a good electrical connection was made. The cathode assembly was placed in the Lucite cover and held in place by a screw.

The bridge for the reference electrode was made from 12 mm Pyrex tubing with one end drawn out to a tip 1 mm in diameter and 4 cm long. Two 90° bends perpendicular to each other were made in the tip. The glass-sleeved calomel reference electrode fitted into the other end of this glass bridge. The position of the completed bridge was adjustable because it was seated into the Lucite cover with a rubber washer. It was found possible to consistently place the capillary tip to within 0.1 to 0.2 mm of the cathode surface.

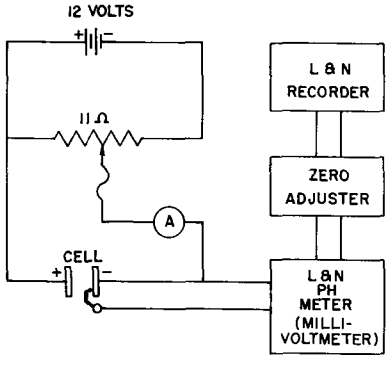


Fig. 2. Electrical circuit used for measuring cathode potentials.

This cell, Fig. 1, has the error due to *IR* drop, inherent in any direct method for measuring cathode potentials, and it does not provide a uniform current density on the cathode. A simple calculation gives the approximate magnitude of the *IR* error. The potential across the anode and cathode at the maximum current density used was approximately 5 v, and the distance over which this *IR* drop occurred was approximately 30 mm; this gives an *IR* drop of about 0.16 v/mm. Since the tip of the pickup bridge was about 0.15 mm from the cathode surface, the maximum error due to *IR* drop is approximately 20 mv. A uniform current density is obtained only with a concentric cylindrical electrode system (7), and with the parallel electrode system of this cell the current density is highest at the edges. These factors and others make cathode potential measurements somewhat uncertain so the potentials reported here are considered reproducible to ±30 mv.

The cell was used in the circuit shown in Fig. 2. The source of current was a storage battery since the rectifiers available had enough ripple to be picked up by the line-operated *p*H (millivolt) meter. The recorder was one designed for use with a chromel-alumel thermocouple, and a zero adjuster was used to set the zero point of the millivoltmeter wherever desired on the chart paper of the recorder.

The baths contained 0.3 mole per liter (m/l) of metal(II) sulfate (Fe, Co, or Ni), 0.3 m/l of sodium citrate in the Co and Ni baths and 0.45 m/l of sodium citrate in the Fe baths, and either 0.00, 0.02, or 0.75 m/l of sodium molybdate. Nickel baths containing 0.15 m/l of sodium molybdate were also studied. Each bath was adjusted to *p*H 10.5 with ammonium hydroxide. The baths were maintained at 25° ± 1°C during and after electrolysis. The Fe-Mo bath was used immediately after preparation because some iron(III) hydroxide precipitated on standing and during an electrolysis run. Two liters of each bath were made up and divided into eight 250-ml aliquots for electrolysis at currents of 0.18, 0.36, 0.54, 0.72, 0.90, 1.15, 1.45, and 1.80 amp to give cathode current densities of 1.0, 2.0, 3.0, 4.0, 5.0, 6.4, 8.0, and 10.0 amp/dm$^2$, respectively. Each 250-ml aliquot was used for two runs at each of the eight current densities. In the first run the potential was recorded up to a minute before the end of the run and when the time of electrolysis was over the cathode was removed immediately, washed, dipped in alcohol, dried, and readied for analysis. In the second run the cathode was allowed to remain in the bath after the current was shut off and the recording of the potential continued in order to obtain the formal potential, $E_f$. The same total current was used in each run at the various current densities; 1080 coulombs for the Ni-Mo and Co-Mo baths and,

because of its lower cathode current efficiency, 2160 coulombs were used with the Fe-Mo bath. No salts were added between runs, and the runs were made in no specific order. The pH of the baths after electrolysis was usually 0.1 to 0.2 pH unit lower than the initial pH.

### Experimental Data

The cathode potentials obtained in the two runs at the same current density were averaged and used in making plots on semi-log paper of current ($i$) vs. potential ($E$). The results for the three types of plating solutions studied are given in Fig. 3, 4, 5 and it can be seen that the addition of sodium molybdate lowers the cathode potential in the single metal baths. Although no potential-current plots were obtained for a molybdate solution (0.2 m/l $Na_2MoO_4$, 0.3 m/l citrate, and no codepositing metal ion) due to the fact that the cathode becomes highly polarized, it can be stated that the addition of Fe, Co, or Ni sulfate lowers the cathode potential in the molybdate solution. It should be noted that in these potential-current plots (Fig. 3-5) the lines are drawn to indicate the region of deposition and the start of the line indicates the current density where deposition was observed to begin in the plating solution being used.

The experimentally determined potentials, in addition to $E_c$ the cathode potential, were $E_d$ the discharge potential and $E_f$ the formal potential. The potentials calculated from these experimental values were $E_o$ overpotential, $E_a$ activation overpotential, and $E_p$ polarization. These various potentials are defined below and are shown pictorially in Fig. 6.

$E_c$, *cathode potential,* the potential of the cathode measured with the millivoltmeter while current is actually flowing.

$E_d$, *discharge potential of the metal ions,* the potential at which metal deposition takes place at an appreciable rate. This potential is hard to determine and is not known to have any theoretical significance.

$E_f$, *formal potential,* the equilibrium potential of the metal in the plating solution, measured while no current was flowing. It can be considered as the $E°$ of the metal corrected to the metal ion activity in the plating solution. It is the potential at which plating should begin in the absence of cathode polarization.

$E_o$, $(E_c - E_f)$ or $(E_a + E_p)$, *overpotential* or *overvoltage,* the potential in excess of the formal potential which must be impressed across the cell to cause the cell reaction to proceed at an appreciable rate.

$E_a$, $(E_d - E_f)$, *activation overpotential,* the extra potential above $E_f$ necessary to cause metal deposition at an appreciable rate. This is the metal overvoltage.

$E_p$, $(E_c - E_d)$, *electrochemical overpotential* or *polarization,* the departure of $E_c$ from $E_d$ due to the passage of current.

The formal potential, $E_f$, was difficult to measure as an equilibrium value since the deposits were continually dissolving in the plating solutions. The Co alloys dissolved completely in 1 hr and gave the most steady potential, while the Fe and Ni alloys dissolved slowly over a period of several hours. The value of $E_f$ was arbitrarily chosen as the potential ½ hr after the current had been turned off. $E_p$ values were calculated using the values of $E_c$ at 11.1

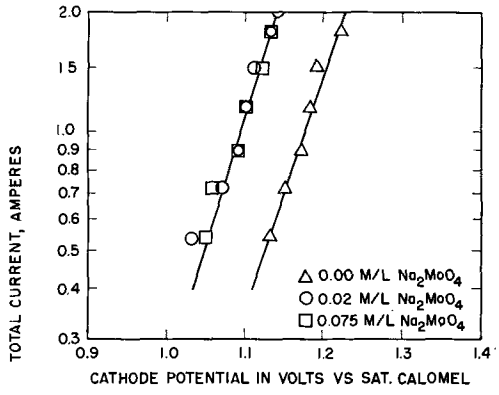


Fig. 4. Potential-current curves for the Co bath (no $Na_2MoO_4$) and for Co-Mo baths containing 0.02 and 0.075 m/l of $Na_2MoO_4$.

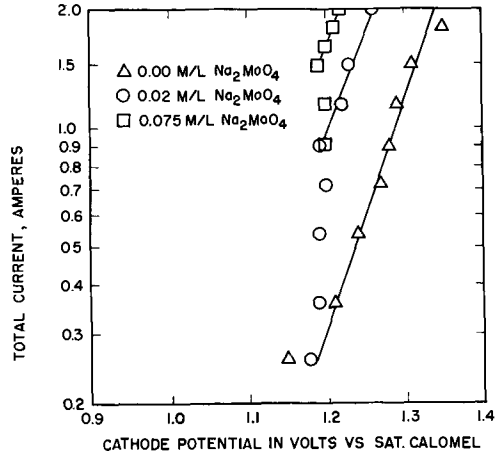


Fig. 3. Potential-current curves for the Fe bath (no $Na_2MoO_4$) and for Fe-Mo baths containing 0.02 and 0.075 m/l of $Na_2MoO_4$. (Note: In Fig. 3, 4, and 5 lines are drawn to indicate the region of deposition and the start of a line indicates the current density where deposition was observed to begin in that plating solution).

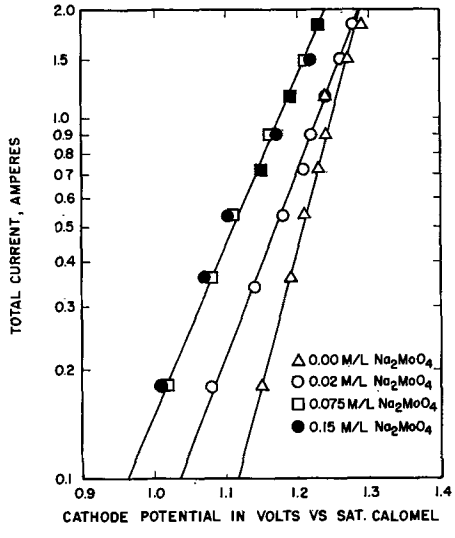


Fig. 5. Potential-current curves for the Ni bath (no $Na_2MoO_4$) and for Ni-Mo baths containing 0.02, 0.075, and 0.15 m/l of $Na_2MoO_4$.

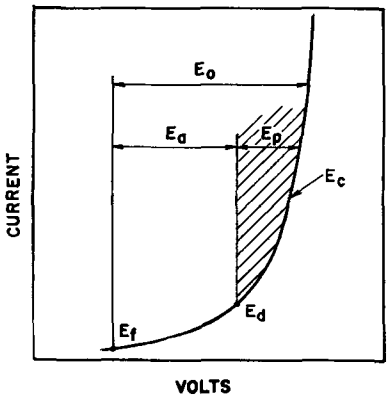


Fig. 6. Schematic diagram showing the relationship between the experimentally determined potentials, $E_c$ cathode potential, $E_d$ discharge potential, and $E_f$ formal potential, and the calculated potentials, $E_o$ overvoltage, $E_a$ activation overpotential, and $E_p$ polarization.

amp/dm$^2$ (taken directly from the graphs where $i = 2.0$ amp) and because of this the values of $E_p$ reported are maximum ones; $E_p$ ranges from zero to this maximum over the range of current densities studied. Values of $E_o$, the sum of $E_a$ and $E_p$, range from $E_a$ to $E_a + E_p$ over the same current densities. The discharge potential, $E_d$, was arbitrarily taken since it is hard to determine when plating actually begins; therefore, values of $E_a$ are less than or equal to the values reported, and values of $E_p$ are greater than or equal to those reported since, at the value of $E_d$ chosen, plating was occurring. It should be noted that no attempt was made to exclude air while these measurements were being made. Table I gives the experimental and calculated $E$ values for all baths studied.

Since Fe, Co, and their alloys with Mo do not deposit at the lower current densities, it is possible to set limits for $E_a + E_p$ in the opposite direction. For these metals it is found that at a potential 0.02 v lower than $E_d$ deposition of the metal is not occurring; however, in most cases there is deposition of a molybdenum oxide or hydroxide. Thus it is possible that the $E_a$ values may be 0.02 v lower than those reported; in terms of free energy the 0.02 v is equal to approximately 1 kcal for a two-electron reaction.

The following observations are made from the data in Table I. The formal potential of the three metals, Fe, Co, and Ni is increased by the formation of a Mo alloy indicating that Mo may be less noble than the other metals. The metal overvoltage is highest for Fe and lowest for Ni in both the single metal and alloy baths, indicating that the deposition of Ni is easier than the deposition of Fe. The metal overvoltage is lower for the alloy baths than for the single metal baths, including the sodium citrate-molybdate bath, indicating that deposition of the alloys is easier than deposition of the single metals. The cathode in the molybdate solution is highly polarized (high $E_p$) and this polarization is reduced by the addition of the sulfates of Fe, Co, and Ni. Whereas polarization in the Fe and Co baths is reduced by the addition of sodium molybdate it is increased in the Ni bath.

Table I. Experimentally determined values of $E_c$, $E_d$, and $E_f$ and calculated values of $E_a$ and $E_p$ for the plating baths studied

| Plating bath | $Na_2MoO_4$ m/l | $E_c$* v | $E_d$ v | $E_f$ v | $E_a$, $(E_d-E_f)$ † v | $E_p$, $(E_c-E_d)$ † v |
|---|---|---|---|---|---|---|
| Fe | 0.00 | 1.34 | 1.20 | 0.58 | 0.62 | 0.14 |
| Fe-Mo | 0.02 | 1.26 | 1.20 | 0.61 | 0.59 | 0.06 |
| Co | 0.00 | 1.23 | 1.11 | 0.59 | 0.52 | 0.12 |
| Co-Mo | 0.02 | 1.14 | 1.03 | 0.67 | 0.36 | 0.11 |
| Co-Mo | 0.075 | 1.14 | 1.03 | 0.63 | 0.40 | 0.11 |
| Ni | 0.00 | 1.29 | 1.12 | 0.63 | 0.49 | 0.17 |
| Ni-Mo | 0.02 | 1.29 | 1.03 | 0.84 | 0.19 | 0.26 |
| Ni-Mo | 0.075 | 1.24 | 0.96 | 0.83 | 0.13 | 0.28 |
| Ni-Mo | 0.15 | 1.24 | 0.96 | 0.84 | 0.12 | 0.28 |

* At 11.1 amp/dm$^2$.
† Potentials are given vs. the saturated calomel electrode.

The cathode deposits obtained in the various cathode potential runs were analyzed by the usual means and the results used to make calculations of current efficiency and current for each deposition reaction. From the percentages of Mo and codepositing metal in each deposit and the total current used it was possible to calculate the cathode current efficiency for each deposition reaction. The current used for each reaction ($i_{Mo}$, the current used for deposition of molybdenum and $i_{C.M.}$, the current used for deposition of the codepositing metal) was then calculated by multiplying the total current, $i_t$, by the calculated current efficiency of the reaction. Plots were then made on semi-log paper of $i_t$, $i_{Mo}$ and $i_{C.M.}$ vs. $E_c$ for each alloy bath as shown in Fig. 7, 8, and 9.

The number of electrons, $n$, involved in the reduction can be calculated from the slope $\left(\frac{n\alpha}{0.06}\right)$ of the lines in Fig. 7, 8, and 9. Alpha is the transfer coefficient and may range from 0.0 to 1.0; in many electrochemical processes it is 0.5. If a value of 0.5 is used, the expected electron changes of two for Ni and six for Mo are not obtained. If it is assumed

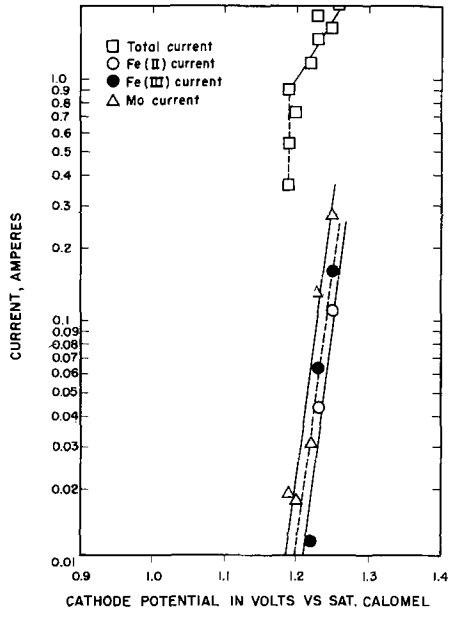


Fig. 7. Potential-current curves for the Fe-Mo bath containing 0.02 m/l of $Na_2MoO_4$. Lines show the total current (observed) as well as the current (calculated) used for depositing Mo and Fe.

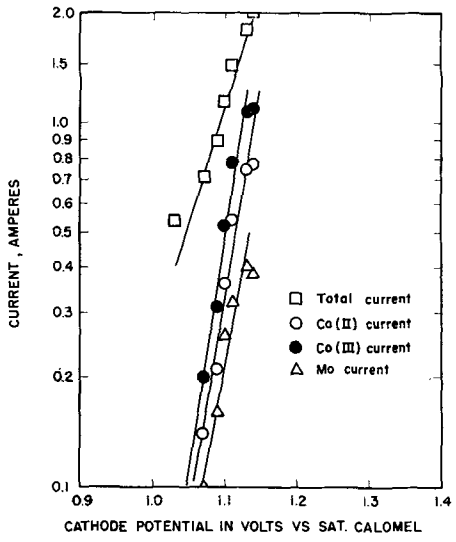


Fig. 8. Potential-current curves for the Co-Mo bath containing 0.02 m/l of $Na_2MoO_4$. Lines show the total current (observed) as well as the current (calculated) used for depositing Mo and Co.

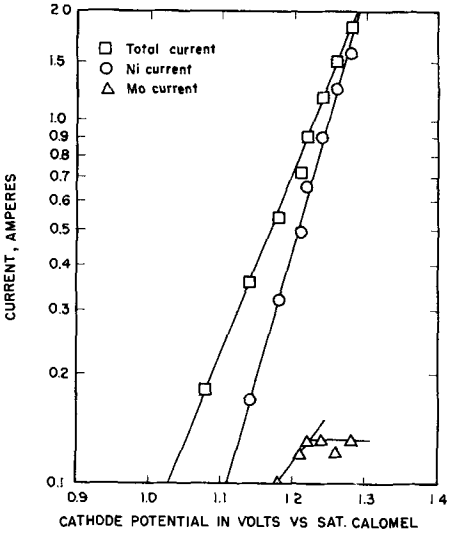


Fig. 9. Potential-current curve for the Ni-Mo bath containing 0.02 m/l of $Na_2MoO_4$. Lines show the total current (observed) as well as the current (calculated) used for depositing Mo and Ni.

that Mo and Ni are deposited from the same activated complex, then $\alpha$ can be the same for both deposition reactions. Alpha was then calculated from the slope of the $i_{c.m.}$ vs. $E_c$ plots and known values of $n$ for Fe, Co, and Ni. The $\alpha$ thus calculated was then used to calculate $n$ for the molybdate reduction using the slope of the $i_{Mo}$ vs. $E_c$ plot. Table II gives the calculated values of $\alpha$ for the three metals, Fe, Co, and Ni and $n$ for the molybdate ion.

The number of electrons involved in the Mo reaction depends on the codepositing metal and its oxidation state in the bath. The slope of the Mo reaction is nearly equal to the slope for the Co or Fe reduction so that whatever oxidation state, II or III, is used to calculate $\alpha$, that value is the number of electrons involved in the molybdate reduction. Due to the ease of oxidation of Co(II) to Co(III) in ammonical solutions, it is very likely that the Mo reaction involves three electrons when Co is the codepositing metal and this may also be true with Fe. It appears that $n$ for the molybdate reduction in a Ni bath is one.

Table II. Transfer coefficients, $\alpha$, for the Fe, Co, and Ni deposition reactions and the number of electrons, $n$, calculated for the reduction of molybdate ion

| Plating bath | $Na_2MoO_4$ m/l | Fe, Co or Ni* | | Mo | |
|---|---|---|---|---|---|
| | | $m$† | $\alpha$ | $m$† | $n$ |
| Fe | 0.0 | 0.23 | 0.13 | — | — |
| Fe-Mo | 0.02 | 0.04 | 0.75 | 0.04 | 2.0 |
| Fe-Mo | 0.075 | 0.10 | 0.30 | 0.11 | 1.8 |
| Co | 0.00 | 0.22 | 0.14 | — | — |
| Co-Mo | 0.02 | 0.09 | 0.35 | 0.09 | 1.9 |
| Co-Mo | 0.075 | 0.14 | 0.22 | 0.13 | 2.1 |
| Ni | 0.00 | 0.13 | 0.23 | — | — |
| Ni-Mo | 0.02 | 0.14 | 0.21 | 0.37 | 0.8 |
| Ni-Mo | 0.075 | 0.17 | 0.18 | 0.31 | 1.1 |
| Ni-Mo | 0.15 | 0.15 | 0.20 | 0.23 | 1.3 |

* Oxidation state is II.
† $m$ = slope.

It was also observed that the Fe, Co, and Ni single metal baths operate at different cathode current efficiencies. The efficiency of the Fe bath is between 14% and 18%; the Co bath has a peak efficiency of 65%; and the Ni bath has the highest current efficiency, 90-97%. The alloy baths operate with cathode current efficiencies which are slightly (about 10%) lower than those of the single metal baths. With an alloy bath the relative amount of Mo in the deposit decreases and the total cathode efficiency of the bath increases as the current density is increased; however, if the individual reactions are considered, the cathode current efficiency of the Mo reaction remains nearly constant throughout the full range of current densities whereas the efficiency of deposition of the alloying metal increases.

The appearance of the cathode deposits depends somewhat on the current density used. All the Ni-Mo alloys were completely metallic. All the Co-Mo alloys were metallic, except that those obtained at the lower current densities were black and nonmetallic in the center of the cathode. None of the Fe-Mo alloys were completely metallic but had a black nonmetallic center with a metallic edge. The black compound on the cathode is believed to be an oxide or hydroxide of Mo, probably $Mo(OH)_3$, since it is black and would involve a three-electron change. Observations made while washing the plated cathodes indicate that the Fe and Co deposits contain more absorbed hydrogen than the Ni deposits; this is supported by the high cathode current efficiency of the Ni baths. These observations are also in accord with data on the hydrogen content of electrodeposited metals (8).

## Discussion

On the basis of the data presented the following two step reduction of molybdate ion is proposed:

$$MoO_4^{=} + 4H_2O + ne^- \rightarrow Mo(OH)_{(6-n)} + (2+n)OH^- \quad [1]$$

$$Mo(OH)_{(6-n)} + (6-n)H + M \rightarrow M \cdot Mo + (6-n)H_2O \quad [2]$$

In these equations $n$ is one, two, or three and M is Fe, Co, or Ni. The supposition is that the metal M and the molybdate ion are deposited from the same activated complex and that hydrogen deposits simultaneously with them. The high overvoltage of the sodium citrate-molybdate bath and the fact that appreciable amounts of Mo are not deposited from it can be explained by using Eq. [1]. If the molybdate reduction is accomplished in steps by electrons according to Eq. [1], the formation of a molybdenum oxide or hydroxide such as $Mo(OH)_3$, $Mo(OH)_5$, or $MoO(OH)_3$ is possible. If this is the case, deposition is no longer occurring on the original cathode material but on the oxide, and thus the various overvoltages involved will be changed. For further reduction to occur it is necessary to overcome the Mo overvoltage which is the molybdate ion's ability to find a position in a lattice on the cathode and be discharged (9); the oxide may not supply the right lattice for deposition to continue easily causing a high overvoltage. In addition, the hydrogen overvoltage (10) could be increased since metal-hydrogen bonds[2] would not be readily established on the oxide surface. However, the reaction which occurs is the one that has the lowest potential and if the overvoltage for the deposition of Mo on its oxide is higher than the overvoltage for hydrogen deposition on the oxide, hydrogen would be liberated in preference to further deposition of Mo or an oxide. This is perhaps the situation since only a thin film of oxide is formed and large quantities of hydrogen are liberated.

It is possible, by carrying the ideas a step further, to give an explanation for the necessity of the codepositing metals Fe, Co, and Ni. The number of electrons involved in the reduction of molybdate ion has been calculated to be less than six. It is now assumed that in addition to electrons another reducing agent is needed; the agent chosen is hydrogen as given in Eq. [2]. The fact that in the deposition of Ni-Mo alloys the current for the hydrogen reaction is always larger than or equal to the Mo reduction current would seem to indicate a connection between the two. If there was no connection between Mo and hydrogen, it should be possible to deposit an alloy from the Ni-Mo bath with 100% current efficiency; this was not observed. The reason why alloy deposition is possible and the overvoltage, $E_o$, of the sodium citrate-molybdate bath is reduced may be that hydrogen reduces the molybdenum oxide or hydroxide which was formed according to the reaction given in Eq. [1]. Hydrogen is capable of doing this and is held in place for this reaction by the metal-hydrogen bond formed with the codepositing metal that has also deposited. The reduction of this oxide changes the overvoltage factors involved. Hydrogen and molybdenum are no longer depositing on the oxide but on the Mo alloy. The Mo overvoltage would be reduced since the ability of the molybdate ion to find a lattice position in an alloying metal lattice already established should be easier. The hydrogen overvoltage for Mo alloys would then be the same or nearly the same as for the codepositing metals since the hydrogen overvoltages on all metals concerned here are close together (11). A separate study of hydrogen liberation should be made and other possible side reactions checked to determine whether or not hydrogen is the reducing agent. Actually the complete reduction of molybdate ion requires six electrons regardless of the mechanism considered. It would be difficult to determine whether the reduction is accomplished by one electron followed by a five hydrogen atom reduction (which requires five electrons) or by six electrons in one step. It may be possible that hydrogen is involved only in breaking down the molybdenum hydroxide or oxide.

Molybdenum codeposits with Fe, Co, and Ni but does not codeposit in appreciable amounts with Cr, Mn, Cu, or Zn from the ammoniacal citrate type of bath. The hydrogen overvoltage factor may be one explanation for this since the overvoltage of hydrogen on Fe, Co, and Ni is lower than it is on other metals. However, due to the many factors which affect overvoltage this cannot be the complete answer. Another explanation involving the electronic configuration of the atoms of these metals can be presented. Slater, using Krutter's calculations of the zones in elemental Cu, proposed a theory for the occurrence of ferromagnetism in this group of metals (12). According to Krutter's calculations the 3d and 4s levels of the atoms are filled as given in Table III. From this table it can be seen that the

**Table III. Distribution of the outer electrons in the first row of transition elements**

| Element and At. No. | Outer electrons | | | | |
|---|---|---|---|---|---|
| | Total | 4s | +3d* | −3d* | Unpaired 3d* |
| $_{24}Cr$ | 6 | 0.6 | 2.7 | 2.7 | 0 |
| $_{25}Mn$ | 7 | 0.6 | 3.2 | 3.2 | 0 |
| $_{26}Fe$ | 8 | 0.6 | 4.8 | 2.6 | 2.2 |
| $_{27}Co$ | 9 | 0.7 | 5.0 | 3.3 | 1.7 |
| $_{28}Ni$ | 10 | 0.6 | 5.0 | 4.4 | 0.6 |
| $_{29}Cu$ | 11 | 1.0 | 5.0 | 5 | 0 |

* The 3d level can accommodate 10 electrons per atom, 5 with a plus (+) spin and 5 with a minus (−) spin. Electrons generally fill up the +3d levels first and then go into the −3d levels. The unpaired electrons which produce the ferromagnetism result because the −3d electrons cancel an equal number of +3d electrons (12).

**Table IV. Maximum atomic percentage of molybdenum in the alloys**

| Alloy | Atomic % Mo | |
|---|---|---|
| | Theoretical | Experimental |
| Fe-Mo | 42.5 | 47 |
| Co-Mo | 36.5 | 36.8 |
| Ni-Mo | 16.7 | 16.8 |
| Ni-Mo | 10.7* | — |

* Based on 5 hydrogen atoms to reduce $Mo(OH)_5$.

[2] According to Glasstone, Eyring, and Laidler (10) one possibility for hydrogen overvoltage is the ease or difficulty of the transfer of a proton from the solution to the surface of the electrode. If the cathode material forms a strong metal-hydrogen bond, the oxygen atom of the water molecule attached to the electrode surface will have an increased tendency to attract a hydrogen atom from another water molecule in the solution because one of its original hydrogen atoms is strongly attached to the metal; thus the transfer of a proton is made easier and the overvoltage is low. On the other hand if the electrode surface does not establish a strong metal-hydrogen bond, the hydrogen atom that should be attached to the metal surface will remain attached to the oxygen atom and the proton transfer is made more difficult and results in a high overvoltage.

elements with which Mo readily codeposits are the ferromagnetic elements which have unpaired 3d electrons. It was postulated previously that metal-hydrogen bond formation was necessary and that the hydrogen reduced the molybdenum oxide. The formation of this metal-hydrogen bond could be connected with the unpaired 3d electrons of Fe, Co and Ni (Table III); hydrogen having one unpaired electron in its outer shell could form a covalent bond with the unpaired 3d electrons. Thus an atom of iron with its 2.2 unpaired 3d electrons could hold an average of 2.2 hydrogen atoms, the cobalt atom with 1.7 unpaired 3d electrons could hold 1.7 hydrogen atoms and each nickel atom with 0.6 unpaired 3d electron could be expected to hold only 0.6 of a hydrogen atom. It is then possible, if these assumptions are considered to be correct, to calculate the theoretical maximum atomic percentage of Mo in each of the alloys. The results of the calculations[3] are given in Table IV. No extensive studies were made to determine the experimental maximum atomic per cent of Mo in the alloys, but the values given in Table IV are those that were obtained in this work. In the case of Fe the experimental percentage is larger than the theoretical percentage because the deposit is not completely metallic but was covered in the center with molybdenum oxide.

[3] One M atom can hold $y$ hydrogen atoms and it requires 3 hydrogen atoms to reduce one $Mo(OH)_3$ to Mo; therefore the number of atoms of $M$ required to give one atom of Mo is $3/y$. The atomic per cent of Mo is then

$$\frac{1Mo}{1Mo + \frac{3M}{y}} \text{ or } \frac{1}{1 + \frac{3}{y}} \text{ or } \frac{y}{y + 3}.$$

In summary, it is postulated that the reduction of molybdate ion in these alloy baths proceeds according to the reactions expressed by Eqs. [1] and [2] given above. In these equations the best value for $n$ seems to be three and $M$ must be a metal which has some unpaired electrons such as Fe, Co, or Ni.

Manuscript received Feb. 10, 1958. This paper was prepared for delivery before the Washington Meeting, May 12-16, 1957, and was abstracted from the thesis of D. W. Ernst submitted in partial fulfillment of the requirements for the Ph.D. degree at the University of Wisconsin.

Any discussion of this paper will appear in a Discussion Section to be published in the June 1959 JOURNAL.

REFERENCES

1. D. W. Ernst, R. F. Amlie, and M. L. Holt, *This Journal*, **102**, 461 (1955).
2. T. F. Frantsevich-Zabludovskaya, *Zhur. Priklad. Khim.*, **28**, 700 (1955); *C. A.*, **50**, 1497 (1956).
3. R. Piontelli, Trans. Inst. Met. Finishing Advance Copy No. 5, **1954**, 31.
4. S. Barnartt, *This Journal*, **99**, 549 (1952).
5. M. Eisenberg, C. W. Tobias, and C. R. Wilke, *ibid.*, **102**, 415 (1955).
6. P. Delahay, "New Instrumental Methods in Electrochemistry," Chap. 16, Interscience Publishers, Inc., New York (1954).
7. J. Kronsbein, *Plating*, **39**, 165 (1952).
8. D. P. Smith, "Hydrogen in Metals," p. 38, Univ. of Chicago Press, Chicago (1948).
9. S. Glasstone, "Introduction to Electrochemistry," pp. 462-463, D. Van Nostrand, New York (1942).
10. S. Glasstone, H. Eyring, and K. Laidler, "Theory of Rate Processes," p. 589, McGraw Hill Book Co., New York (1941).
11. J. O'M. Bockris, *Trans. Faraday Soc.*, **43**, 417 (1947).
12. C. Barrett, "Structure of Metals," p. 309, McGraw Hill Book Co., New York (1952).

# Brief Communication

# Thermally Regenerative Ionic Hydride Galvanic Cell

R. E. Shearer and R. C. Werner

*MSA Research Corporation, Callery, Pennsylvania*

Studies have been made of the electrochemical formation of ionic hydrides in fused salt media and of the thermal regeneration of the reactants. Typical reactions are:

$$H_2 + Ca \rightleftarrows Ca^{++} + 2H^-$$

and

$$\tfrac{1}{2}H_2 + Li \rightleftarrows Li^+ + H^-$$

In a calcium hydride cell with a solid calcium electrode, an open-circuit voltage of 0.56 v was obtained in the eutectic of the fluoride and the chloride of calcium at 644°C. Regeneration of the calcium and hydrogen was obtained by raising the temperature to about 1000°C. In one measurement, 89% of the hydrogen consumed reacted electrochemically with the calcium.

Widely differing open-circuit voltages were obtained with lithium hydride cells, depending on the composition of the electrolyte. With the eutectic of the bromide and the fluoride of lithium, 0.3 v was obtained. With a chloride-fluoride eutectic, 0.6 v was obtained at about the same temperature, approximately 550°C. In both cases, operating temperatures were above the melting point of lithium so that design of a simple closed cycle continuous system can readily be envisioned.

In an unoptimized cell, a current density of about 150A/ft$^2$ of lithium electrode area was obtained under maximum power output conditions. Engineering estimates indicate that a specific power output of 90 w/ft$^3$ should be readily attainable; this might be increased greatly with new development work. A similar estimate for a 2-w cell indicates a weight of 1 lb/w output. These values do not make allowances for the heat source or heat sink. Carnot cycle efficiencies of 35% are indicated for a lithium hydride cell based on cell operation at the eutectic temperature of the bromide and the fluoride of lithium (450°C) and on a regenerative temperature at which the decomposition pressure of the pure hydride is 1 atm (850°C).

### Acknowledgment

Thanks are due to J. W. Mausteller for advice and discussions and to J. C. King for his work on assembly of cells and on measurements. The authors are also indebted to C. B. Jackson, Vice-President and Director of Research of MSA Research Corporation, for his support.

Manuscript received July 21, 1958.

Any discussion of this article will appear in a Discussion Section to be published in the June 1959 JOURNAL.

## June 1959 Discussion Section

A Discussion Section, covering papers published in the July–December 1958 JOURNALS, is scheduled for publication in the June 1959 issue. Any discussion which did not reach the Editor in time for inclusion in the December 1958 Discussion Section will be included in the June 1959 issue.

Those who plan to contribute remarks for this Discussion Section should submit their comments or questions in triplicate to the Managing Editor of the JOURNAL, 1860 Broadway, New York 23, N. Y., *not later than March 2, 1959*. All discussion will be forwarded to the author, or authors, for reply before being printed in the JOURNAL.

# Diffusion Control in Silicon by Carrier Gas Composition

C. J. Frosch and L. Derick

*Bell Telephone Laboratories, Inc., Murray Hill, New Jersey*

ABSTRACT

A single heating process is described for producing controlled p-n and n-p-n diffused structures in silicon by changing the carrier gas composition during diffusion. The process is shown to depend on large changes in the rate of evaporation from a $Ga_2O_3$ source at a given temperature in carrier gases of different composition. The weight loss from a $Ga_2O_3$ source at a given temperature is quite large in reducing gases, extremely small in neutral gases, and essentially zero in oxidizing gases. The weight loss from a $Ga_2O_3$ source in reducing gases also decreases with increasing concentrations of water vapor in the carrier gas. The weight loss from a $Sb_2O_4$ source at a given temperature is relatively large in all of these carrier gases.

The diffusion apparatus consists essentially of a fused silica tube extending through separately controlled temperature zones for the location of the diffusant sources and the silicon samples. Carrier gases at controlled rates of flow carry the diffusant vapors past the silicon samples at atmospheric pressure.

Data are presented for single diffusions from $Ga_2O_3$ and $Sb_2O_4$ sources in several carrier gas compositions. P-type layers are formed in 5 ohm-cm n-type silicon in the $Ga_2O_3$ diffusions in reducing gases but not in oxidizing gases. A controlled number of gallium atoms can be introduced into silicon by heating first in a reducing gas and then in an oxidizing gas. N-type layers are formed in 5 ohm-cm p-type silicon in the $Sb_2O_4$ diffusions in all of the carrier gases studied. Data also are presented on double diffusions from $As_2O_3$-$Ga_2O_3$ and $Sb_2O_4$-$Ga_2O_3$ sources to illustrate the control of layer thickness by heating first in wet $N_2$ and then in wet $H_2$. These double diffused structures are shown to be suitable for the fabrication of high alpha transistors.

The introduction and control of impurities in semiconductors by vapor-solid diffusion techniques has been described by Fuller and Ditzenberger (1, 2) and Frosch and Derick (3). These techniques can be employed for producing controlled single and multiple diffusion layers by the proper choice of processing parameters such as temperature, time, gas flow, and gas composition. However, the control of multiple diffusion layers and often single diffusion layers generally requires more than one heating of the Si in separate diffusion apparatus. For example, a diffusion apparatus contaminated with Ga could not be employed by the older techniques for introducing Sb or As into a semiconductor to make a controlled n-p-n transistor structure.

This paper describes a new single heating process for producing controlled single and multiple diffusion layers in semiconductors by changing the carrier gas composition during the diffusion. The diffusion control is shown to depend on large changes in the volatility of certain impurities in carrier gases of different composition. However, the formation of $SiO_2$ layers on Si during heating in oxidizing carrier gases also is an important factor in the control of diffusion layers. This results from the partial masking (3) by a $SiO_2$ layer against the diffusion of certain impurities into Si at elevated temperatures. An $SiO_2$ layer on Si does not mask against Ga but does mask against Sb and As. For example, the surface concentration obtained for a Ga diffusion is essentially the same for an unoxidized or preoxidized Si sample. On the other hand, the surface concentration obtained for a Sb or As diffusion decreases with increasing thickness of a $SiO_2$ layer on the Si surface. Further discussion of these masking effects is given below.

## Apparatus and Procedure

The diffusion apparatus is shown schematically in Fig. 1. It is the same as that described previously (3) except for the addition of a third controlled temperature zone. The apparatus consists essentially of a fused silica tube extending through three separately controlled temperature zones. The first

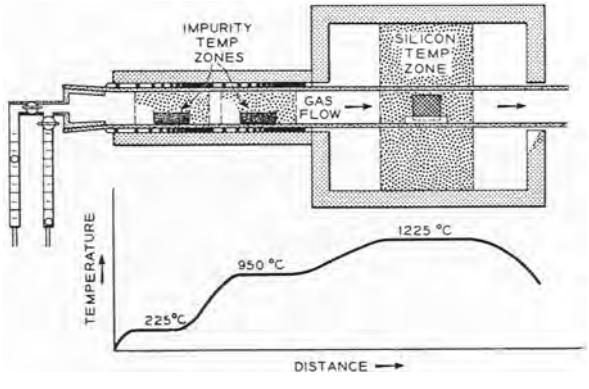


Fig. 1. Apparatus for vapor-solid diffusion at atmospheric pressure.

two temperature zones together with the carrier gases serve to regulate the volatility of the impurities placed therein. The third temperature zone is the location of the Si samples. The temperatures are regulated to ±2°C by means of Pt-Pt 10% Rh thermocouples and automatic controllers.

Flowmeters attached to one end of the furnace tube regulate the flow of the carrier gases. In this investigation flow rates of 1500 cc/min of the carrier gas were employed in furnace tubes of 2.5 cm ID. A temperature-controlled fritted-glass water bubbler is inserted between the flowmeters and the furnace tube when water vapor is being added to the carrier gas.

In the weight loss studies, a single controlled temperature zone is employed. Each carrier gas composition is allowed to flow through the apparatus for several minutes to establish a steady-state condition. Then a weighed amount of impurity (approximately 2 g) in a tared fused silica crucible is inserted into the cool end of the furnace tube. After 10 min the sample is moved quickly into the controlled temperature zone for a measured time. Then the sample is withdrawn rapidly to the cool end of the furnace tube. It is allowed to cool for 10 min before weighing. The same procedure is repeated for several successive weight losses. A new supply of impurity is employed for each carrier gas composition. The exact conditions are given on Fig. 1-3 and in the later discussion.

In the diffusion studies the impurities in fused silica or platinum crucibles are placed in the controlled temperature zones. The carrier gas composition is allowed to flow through the apparatus for several minutes to establish a steady-state condition. Then the Si samples held vertically in slotted fused-silica holders are introduced rapidly into the controlled temperature zone. Depending on the particular experiment, the carrier gas composition may be changed without removing the Si samples from the furnace. Silicon samples are removed rapidly after the heating interval. The exact process parameters are reported in Tables I-IV.

Methods for determining the electrical characteristics, surface concentrations, and diffusion depths are essentially the same as those described elsewhere (1, 2).

## Samples

The Si samples were cut from approximately 5 ohm-cm n-type (arsenic doped) or p-type (boron doped) single-crystal ingots grown in the [111] direction by pulling from the melt. The ingots were sawed perpendicular to the growth direction into slices approximately 1 mm thick. These were machine lapped on both surfaces with No. 1800 emery powder to a thickness of about $7 \times 10^{-2}$ cm. After cutting into squares of 0.75 x 0.75 cm, the samples were etched for 4-5 min in a mixture of 5 parts of concentrated $HNO_3$ to 1 part of concentrated HF. Reproducible surfaces of excellent appearance were obtained by maintaining the etchant temperature at about 20°C and employing mechanical agitation during etching. The etched samples were heated for 1 hr at 1300°C in 100% $O_2$ when preoxidized samples were employed in the diffusions.

## Impurity Volatility

The volatility of elemental diffusants or their compounds at a given temperature in carrier gases of different composition is the basic control variable in this study. Hence, volatility data are of importance in establishing diffusion process parameters. Such data are presented in this section for a single donor and a single acceptor impurity. These are sufficient to illustrate the effect of carrier gas composition on volatility. The volatility is expressed in terms of a weight loss from a heated impurity source. However, the volatile molecular species or the impurity vapor in the carrier gas stream is not necessarily of the same composition as the impurity source.

Some typical weight loss data for a $Ga_2O_3$ powder and elemental Ga are plotted in Fig. 2 and 3, respectively, as a function of heating time at 950°C in several carrier gas compositions. Note particularly the large weight losses in wet $H_2$ and the essentially zero loss in wet $N_2$ for the $Ga_2O_3$ source. The weight loss decreases rapidly with increasing $H_2O$ concentration in the $H_2$. The $Ga_2O_3$ is reduced to Ga in dry $H_2$ at these fast flow rates. Weight losses from a $Ga_2O_3$ source also are appreciable in a CO carrier gas. Volatility decreases with increasing concentrations of $H_2O$ or $CO_2$ in the CO. For com-

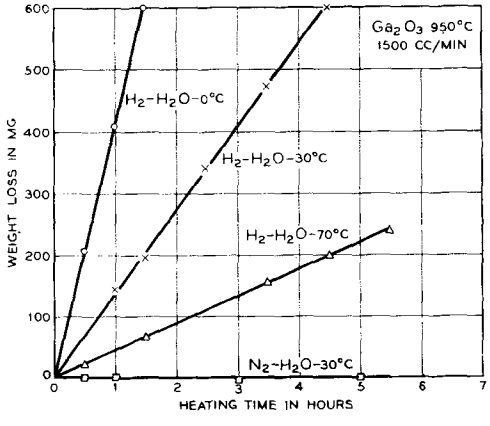


Fig. 2. Effect of carrier gas composition on weight loss from a heated $Ga_2O_3$ source.

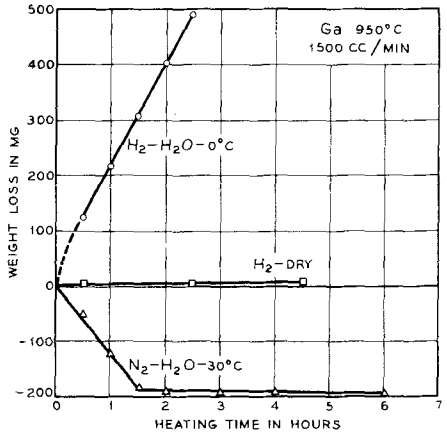


Fig. 3. Effect of carrier gas composition on weight loss from a heated Ga source.

parable conditions, weight losses in CO are from about 5 to 10 times lower than those in $H_2$. Weight losses from a $Ga_2O_3$ source are extremely small or zero over the temperature range studied up to 1200°C in gases such as $N_2$, He, A, and $O_2$ with or without added $H_2O$ or $O_2$.

In the case of the Ga source the weight losses as shown in Fig. 3 are large in wet $H_2$ but very small in dry $H_2$. A gain in weight occurs in the wet $N_2$ with a conversion of the source material to $Ga_2O_3$.

The large changes in volatility from $Ga_2O_3$ sources at a given temperature in carrier gases of different composition must depend on an increase in the concentration of a volatile molecular species in the vapor phase. Such a reaction need take place only at the evaporating surface and probably occurs rapidly. Information on these thermodynamic equilibria of impurity vapors at different temperatures in different carrier gas compositions would be helpful in establishing diffusion controls. It would lead also to a better understanding of the diffusion process.

The higher weight losses from a $Ga_2O_3$ source in reducing gases as compared to inert or oxidizing gases suggests the reduction of the impurity to a more volatile species. Unpublished vapor pressure data (4) show that the reactions can be expressed by the following equations:

$$Ga_2O_3 + 2H_2 = Ga_2O + 2H_2O \quad [1]$$

$$Ga_2O_3 + 2CO = Ga_2O + 2CO_2 \quad [2]$$

in which $Ga_2O$ is the volatile molecular species being formed. These equations explain the decrease in weight loss from a $Ga_2O_3$ source with increasing concentrations of $H_2O$ or $CO_2$ added to the $H_2$ or CO carrier gases, respectively. The weight loss for a Ga source in wet $H_2$ as shown in Fig. 3 probably occurs also as $Ga_2O$.

The weight losses from $Sb_2O_4$ and Sb sources at a given temperature are appreciable in dry or wet $N_2$, $H_2$, A, or He. For example, as shown in the second column of Table I, the weight losses from an $Sb_2O_4$ source are large at 950°C in $N_2$. They also show no definite trend or appreciable change with water content over the concentration range studied. Weight loss determinations could not be made in $H_2$ since $Sb_2O_4$ reduces to Sb even in the presence of fairly large concentrations of $H_2O$. However, the weight losses for $Sb_2O_4$ or Sb sources are known to be appreciable in all of the dry or wet carrier gases studied with the exception of $O_2$. The weight loss for an $Sb_2O_4$ source at 950°C in $O_2$ is very small as compared to that in other carrier gases such as $H_2$ or $N_2$. However, the loss at 1100°C in $O_2$ is somewhat higher than the loss in wet or dry $N_2$ at 950°C. This effect of $O_2$ might be explained by a shift upward in the transition temperature above that predicted by the equations

$$2Sb_2O_5 \underset{\leftrightarrows}{380°C} 2Sb_2O_4 + O_2 \quad [3]$$

$$2Sb_2O_4 \underset{\leftrightarrows}{930°C} 2Sb_2O_3 + O_2 \quad [4]$$

in which the $Sb_2O_3$ would be assumed to be the more volatile molecular species. It is reported elsewhere (5) that $Sb_2O_4$ is probably $Sb_4O_8$ which is a mixture of $Sb_2O_3$ and $Sb_2O_5$ below 900°C. This may account for some of the volatility effects observed with this oxide.

**Table I. Effect of carrier gas composition on the diffusion of Sb in Si. Diffusion, 1 hr; Si, 1200°C; $Sb_2O_4$, 950°C**

| Water temp, °C | $Sb_2O_4$, wt loss, mg | Ohms per square | Layer thick., cm x $10^5$ | Surface concen., at./cc x $10^{17}$ |
|---|---|---|---|---|
| | | Hydrogen | | |
| 0 | — | 263 | 15 | 30 |
| 70 | — | 495 | 13 | 12 |
| | | Nitrogen | | |
| Dry | 255 | 64 | 15 | 330 |
| 0 | 224 | 151 | 15 | 78 |
| 30 | 260 | 212 | 15 | 42 |
| 50 | — | 286 | 15 | 27 |
| 70 | 244 | 647 | 13 | 8 |

## Single Diffusion Layers

Single diffusion data are included to illustrate the relation between the previous volatility data and the diffusion depth, sheet resistance, and surface concentration. These data also provide the necessary processing parameters for the double diffusions.

In Table I single diffusion data are presented for an $Sb_2O_4$ source at 950°C in $H_2$ and $N_2$ carrier gases of different $H_2O$ content. The diffusions were made for 1 hr with 5 ohm-cm p-type Si samples at 1200°C. Note particularly the progressive increase in sheet resistance and decrease in surface concentration with increasing water content in both the $H_2$ and $N_2$ carrier gases. The measurements are not sufficiently accurate to show the probable progressive decrease in diffusion depth with increasing water content in the carrier gases. However, the weight losses in column 2 of Table I show no progressive or large change with increasing water content in the $N_2$ carrier gas. This apparent discrepancy between the weight loss and diffusion data is explained by the masking (3) effect of the $SiO_2$ layer which is being formed continuously during the introduction of the impurity. For example, no conversion layer will form under the same conditions even in dry $N_2$ if the Si samples first are preoxidized for 1 hr at 1300°C in $O_2$. This 1300°C $SiO_2$ surface layer reduces the surface concentration of Sb to below about $10^{15}$ atoms/cc. The results in Table I are explained as being due to an increase in the rate of $SiO_2$ formation and hence more effective masking with increasing water content in the carrier gas. In other words, the competition between the introduction of Sb into the Si and the formation of an $SiO_2$ layer favors the latter as the concentration of water vapor in the carrier gas is increased.

Single diffusion data for a $Ga_2O_3$ source at 950°C are presented in Table II for several carrier gas compositions. The diffusions were made for 1 hr at 1200°C using preoxidized 5 ohm-cm n-type Si. An $SiO_2$ layer does not mask (3) against the diffusion of Ga. This absence of masking by an $SiO_2$ layer against the diffusion of Ga is a necessary control

Table II. Effect of carrier gas composition on the diffusion of Ga in Si. Diffusion, 1 hr; Si, 1200°C; $Ga_2O_3$, 950°C

| Water temp, °C | $Ga_2O_3$, wt loss, mg | Ohms per square | Layer thick., cm x $10^5$ | Surface concen., at./cc x $10^{16}$ |
|---|---|---|---|---|
| | | Hydrogen | | |
| 0 | 407 | 149 | 66 | 340 |
| 30 | 136 | 361 | 61 | 150 |
| 50 | — | 1455 | 43 | 14 |
| 70 | 45 | >6000 | 25 | <6 |
| | | Carbon Monoxide | | |
| Dry | 135 | 165 | 74 | 280 |
| 0 | 45 | 1117 | 56 | 15 |
| 30 | 24 | >6000 | 20 | <6 |
| | | Nitrogen-Helium-Oxygen | | |
| 0 | 0 | N | 0 | — |

requirement in the double diffusions described later, since oxidation occurs during the introduction of the donor impurity. Preoxidized samples are preferred in Ga diffusions since surface pitting is avoided. Surface pitting of unoxidized Si by Ga is especially bad at high-diffusion temperatures.

Note particularly in Table II the absence of a conversion layer in either wet $N_2$, He, or $O_2$. The same result is obtained with dry $O_2$ or inert gases containing even a small trace of $O_2$. However, completely dry and oxygen-free inert gases such as $N_2$ and He give a conversion layer of low surface concentration. Note also in Table II the progressive increase in sheet resistance and decrease in layer thickness and surface concentration with increasing water content in the $H_2$ and CO carrier gases. The direct relation between weight loss and diffusion data also is evident from the table. The results in Table II clearly demonstrate the basic principle for controlling the introduction of Ga atoms into Si. Thus Ga atoms can be introduced by first heating in wet $H_2$ and then diffusing in wet $N_2$ to produce the desired diffusion depth without introducing more Ga atoms. The following diffusion data illustrates this principle more clearly.

The data in Table III illustrate the control of single diffusion layers by changing the carrier gas composition during the heating operation. The diffusions were made with preoxidized 5 ohm-cm n-type Si for 1 hr at 1350°C with the $Ga_2O_3$ source at 950°C. The carrier gas composition during the heating operation was either wet $H_2$ or wet $N_2$ for the time intervals shown in column 1 of Table III. Both the $H_2$ and $N_2$ were bubbled through water at 30°C in these experiments.

With the exception of the first and last experiments in Table III, note the progressive decrease in sheet resistance and increase in surface concentration with increasing time in wet $H_2$. The layer thickness also tends to increase slightly with increasing heating time in wet $H_2$. An n-p-n type structure results from the experimental conditions shown in the first row of the table. The appearance of n-type surface layers in single carrier gas Ga diffusions also occurs with unoxidized Si samples when a high water content reducing gas or pure $N_2$, He, or A are used. In other words, an n-type surface layer is formed when the Ga surface concentration falls below a limiting value which depends upon the processing conditions. The n-type surface layer is believed to result from the presence of a small concentration of a donor impurity in the $Ga_2O_3$. This seems reasonable since the diffusion conditions, which are required for the appearance of these n-type layers, differ with the source of supply of the $Ga_2O_3$. The presence of a donor impurity has not been confirmed by spectrographic analysis since it is difficult to determine small concentrations of elements such as P, As, or Sb.

The last experiment in Table III is included to illustrate the flexibility of this procedure for device development. In this case a final short heating in wet $H_2$ produces a high surface concentration (about $10^{17}$ atoms/cc) on a previously established diffusion gradient. The high surface concentration facilitates ohmic electrical contact.

The data in Table III clearly demonstrate the effectiveness of wet $H_2$ and wet $N_2$ for controlling the introduction of Ga atoms into Si at high temperatures. The method is essentially a predeposition technique. However, unlike the one described previously (3), it requires only a single heating of the Si at one temperature for both the predeposition and diffusion.

A second method for controlling the introduction of Ga atoms into Si from a $Ga_2O_3$ source is illustrated by the $H_2$ and CO experiments in Table II. In these the diffusion characteristics are determined by the water content of the reducing carrier gas rather than the time interval of heating in wet $H_2$ followed by wet $N_2$. The diffusion layers may be varied further by changing the water content of the reducing carrier gas during the heating operation. In addition, the diffusion layers may be produced by a combination of the conditions shown in Tables II and III. Thus Ga diffusion layers can be controlled over wide limits by changing the carrier gas composition during a single heating operation.

A few experimental diffusions were made with In and $In_2O_3$ sources using wet $H_2$ or wet $N_2$ as the carrier gas. Conversion layers were obtained in wet $H_2$ but not in wet $N_2$. Except for fundamental differences such as vapor pressure, diffusion constant, and surface solubility in silicon, In and $In_2O_3$ sources can be employed to produce controlled diffusion layers by varying the carrier gas composition in the manner described for the Ga and $Ga_2O_3$ sources.

Table III. Diffusion control of Ga in Si by heating first in wet $H_2$ followed by wet $N_2$. Si, 1350°C; $Ga_2O_3$, 950°C; $H_2O$, 30°C

| Time in min, $H_2$-$N_2$-$H_2$ | Ohms per square | Layer thick., cm x $10^4$ | Surface concen., at./cc x $10^{16}$ |
|---|---|---|---|
| 5—55—0 | N | 20* | — |
| 10—50—0 | 566 | 22 | 7 |
| 20—40—0 | 221 | 23 | 19 |
| 30—30—0 | 192 | 24 | 23 |
| 60— 0—0 | 112 | 23 | 95 |
| 5—50—5 | 270 | 20 | — |

* P layer.

Table IV. Control of double diffusion layers by heating first in wet $N_2$ followed by wet $H_2$. $Ga_2O_3$, 900°C; $H_2O$, 30°C

| Silicon temp, °C | Time in min $N_2$ | $H_2$ | Total | Layer thick., cm x $10^5$ N | P | N + P |
|---|---|---|---|---|---|---|
| | | $Sb_2O_4$, 900°C | | | | |
| 1300 | 30 | 90 | 120 | 51 | 130 | 181 |
| 1300 | 60 | 90 | 150 | 56 | 134 | 190 |
| 1300 | 150 | 90 | 240 | 71 | 114 | 185 |
| 1300 | 210 | 90 | 300 | 84 | 101 | 185 |
| 1300 | 330 | 90 | 420 | 97 | 81 | 178 |
| | | $As_2O_3$, 220°C | | | | |
| 1200 | 180 | 60 | 240 | 33 | 15 | 48 |
| 1200 | 120 | 120 | 240 | 36 | 46 | 82 |
| 1350 | 5 | 10 | 15 | 36 | 61 | 97 |
| 1350 | 9 | 6 | 15 | 38 | 33 | 71 |

## Double Diffusion Layers

The design of electronic devices such as transistors requires double diffused layers of controlled thicknesses and doping concentrations in semiconductors. Such layers can be produced in a single heating operation by varying the carrier gas composition in controlled time intervals as illustrated by the data in Table IV.

The diffusions were made with unoxidized 5 ohm-cm n-type Si with the $Ga_2O_3$ source at 900°C and the carrier gases bubbled through water at 30°C. The other diffusion conditions are listed in the table. A new supply of each impurity was employed in each run. The Si samples were introduced into the furnace with the wet $N_2$ carrier gas flowing. The carrier gas was changed to wet $H_2$ after a time which was predetermined from single diffusion experiments. The heating was continued in wet $H_2$ until the desired double diffused layer thicknesses were obtained.

In the $Sb_2O_4$-$Ga_2O_3$ diffusion data in Table IV, the heating time in wet $N_2$ is increased progressively while the heating time in wet $H_2$ is held constant. Note the progressive increase in the n-type layer thickness with increasing heating time in the wet $N_2$. On the other hand the Ga diffusion layer (N+P) remains essentially constant or independent of the heating time in wet $N_2$. This is in agreement with the previous single diffusion data in which Sb but not Ga is introduced into Si in wet $N_2$. Thus the Sb diffusion depth is determined by the total heating time while the Ga diffusion depth is determined by the heating time in wet $H_2$. The double diffused layers result since Sb has a higher doping level and smaller diffusion constant than Ga.

In the $As_2O_3$-$Ga_2O_3$ diffusion data in Table IV, the total heating time was held constant for each temperature while the heating time in both wet $N_2$ and wet $H_2$ was varied. Note the large changes in the p-layer thicknesses and the small changes in the n-layer thicknesses for each diffusion temperature. The control again is based on Ga since As forms conversion layers in p-type Si in both wet $N_2$ and wet $H_2$.

The data in Table IV demonstrate the control of double diffused layers in a single heating operation by changing the carrier gas composition. However, a wide range of controlled double diffusion layers can be produced by further carrier gas composition changes. For example the n-layer doping level may be increased by reducing the water content in the $N_2$. The p-layer doping level may be decreased by increasing the water content of the $H_2$ or by completing the heating in wet $N_2$ after an interval in wet $H_2$. A large number of diffusion conditions obviously are possible to meet specific structural requirements.

In order to test the suitability of the single heating process for producing transistor structures, d-c alpha measurements were made on a number of double diffused silicon samples. The contacts were applied by essentially the same evaporation and alloying techniques described by Tanenbaum and Thomas (6). The d-c measurements were made on several approximately $5 \times 10^{-2}$ cm diameter etched dots on one surface of each sample. About 90% of the d-c alpha values were 0.90-0.98 with about 50% above 0.95 at a collector voltage of 10 v and an emitter current of 5 ma. The d-c alpha values remained quite flat over an emitter current range of 0.1-15 ma.

It is possible also by this single heating process to produce controlled structures by the $SiO_2$ masking technique (3). For example, the $Sb_2O_4$ diffusions in Table IV would result in only a single p-layer if the Si was preoxidized for 1 hr at 1300°C in $O_2$. Thus controlled structures with double and single diffused layer patterns can be produced with preoxidized Si by first removing the $SiO_2$ from the regions which are to become double diffused layers.

## Summary

A single heating process has been described for the production of controlled single and double diffusion layers in Si. The process is designed to meet a large range of design parameters for electronic devices.

## Acknowledgment

The authors are indebted to M. Tanenbaum and C. D. Thurmond for their helpful suggestions during the preparation of this paper.

Manuscript received June 24, 1958. This paper was prepared for delivery before the New York Meeting, April 27-May 1, 1958.

Any discussion of this paper will appear in a Discussion Section to be published in the June 1959 JOURNAL.

## REFERENCES

1. C. S. Fuller and J. A. Ditzenberger, *J. Appl. Phys.*, **25**, 1439 (1954).
2. C. S. Fuller and J. A. Ditzenberger, *ibid.*, **27**, 544 (1956).
3. C. J. Frosch and L. Derick, *This Journal*, **104**, 547 (1957).
4. C. J. Frosch and C. D. Thurmond, Unpublished data.
5. N. V. Sidgwick, "Chemical Elements and Their Compounds," Vol. 1, p. 789 (1950).
6. M. Tanenbaum and D. E. Thomas, *Bell System Tech. J.*, **34**, 105 (1955).

# Diffusion into Silicon from Glassy Layers

J. E. Cline[1] and R. G. Seed[2]

*Semiconductor Division, Sylvania Electric Products Inc., Woburn, Massachusetts*

ABSTRACT

The diffusion of boron into silicon from glassy layers containing the system $K_2O$-$SiO_2$-$B_2O_3$ was investigated. These glassy layers can be formed by dehydrating aqueous solutions, and they are fluid at the diffusion temperature of 1200°C. Methods were explored for obtaining controllable initial concentrations and penetrations of diffusant. Uniformly flat junctions were obtained, apparently due to the solvent action of the glassy layers in preventing masking by silicon dioxide.

An important technique in the fabrication of semiconductor devices is the high-temperature diffusion of donor and acceptor impurities into single-crystal material. Diffusion is governed by the expression:

$$C_{(x,\,t)}=C_{(x=0,\,t)}\,erfc\left[\frac{x}{\sqrt{4Dt}}\right]=C_o\left[1-\frac{2}{\sqrt{\pi}}\int_0^{\frac{x}{\sqrt{4Dt}}}e^{-\alpha^2}d\alpha\right]$$

The function, *erfc y*, is plotted semilogarithmically as the solid line in Fig. 1 (1, 2).

Reproducible and uniform impurity penetration, resulting in flat junctions, can be produced only from a uniform planar source concentration.

Frosch and Derick (3) found that under special conditions of carrier-gas composition surface layers of $SiO_2$ could reduce $C_o$ by factors up to 200. Under the conditions ordinarily used in diffusion processes, it is difficult to avoid localized masking effects due to accidentally produced oxide layers.

This investigation of the effects of various glassy layers on the diffusion of boron into Si was undertaken to explore means of controlling $C_o$ in both level and uniformity.

## Precoating Procedure

The glassy layers were prepared by dehydration of aqueous solutions of silicates or borates of potassium. From the phase equilibrium diagram (4) of the binary system $K_2O$-$SiO_2$ it is apparent that a liquid phase can be maintained at temperatures above 1165°C if the $SiO_2$ concentration is below 78.8 wt %.

The following solutions were used: solution 1, potassium silicate solution, sp gr 1.25 (Sylvania Electric Products Inc.); solution 2, 10 g potassium tetraborate, $K_2B_4O_7 5H_2O$ (Fisher Scientific Co.), 3.5 g potassium hydroxide (Baker Analyzed), 15 g deionized water; solution 3, equal parts by weight of solutions 1 and 2.

It is calculated that these solutions form glassy layers, after dehydration, with the following mole ratios: solution 1, $K_2O:SiO_2 = 1:3.44$; solution 2, $K_2O:B_2O_3 = 1:1$; solution 3, $K_2O:SiO_2:B_2O_3 = 1.37:1.25:1$.

The n-type Si slices used in these experiments were oxidized by heating in air at 1200°C for 2 hr. After cooling they were each coated with one of the solutions. The coatings were then dried under a heat lamp.

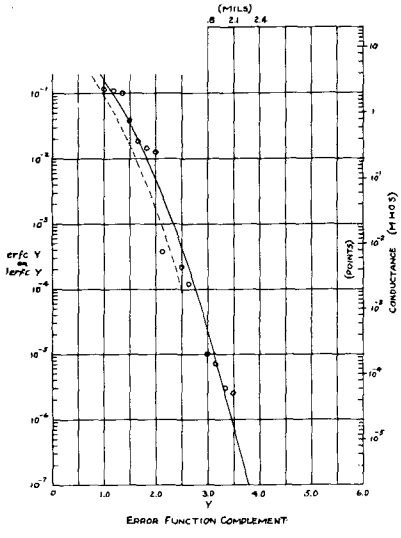


Fig. 1. The solid curve is a plot of erfc y vs. y and the dashed curve that of i erfc y vs. y. The points are experimental conductance values plotted against penetration for the 90-hr diffusion of silicon coated with solution 2.

## Diffusion Experiments

The diffusion runs were carried out in a Kanthal-wound furnace with a high-temperature combustion tube (McDanel) open to the air. Two alundum boats were placed in the hot zone; one contained $B_2O_3$ and the other the Si slices. Diffusion temperatures were in the range 1165°-1190°C. The time of a run was generally 20 hr, although one run was made for 90 hr. It is not believed that appreciable diffusion of Al occurred due to the $Al_2O_3$ in the boats used in these experiments.

The penetration of diffusant was determined after each diffusion run by carefully lapping down the Si slices and by taking electrical measurements with a linear 4-point probe (5) at thickness steps of 0.1 mil. The point at which the glassy layer was considered to be removed by the lapping was determined by the sudden increase in conductivity. The resulting measure of the ratio of volts to amperes from the probe readings is a complicated function of the resistivity

[1] Present address: Raytheon Manufacturing Co., Semiconductor Division, Newton, Mass.
[2] Present address: 258 East St., Lexington, Mass.

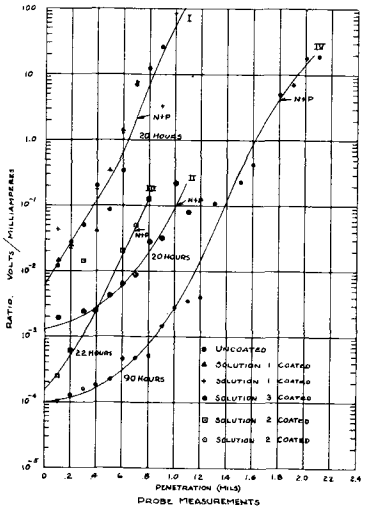


Fig. 2. Results of probe studies on 6 diffusion runs

of the material depending on how the resistivity varies with thickness in the layers below the probe. However, the ratio of amperes to volts is a direct measure of the conductance of the sample, in this case the sheet conductance. It can be shown easily that the conductance is directly proportional to the total number of carriers in the sample (sheet) which, in turn, is equal to the number of impurity atoms beneath the probe. The total number of diffused impurity atoms, $N_T$, which have penetrated beyond a depth $y$, is just

$$N_T = C_o \int_y^0 erfc \frac{x}{\sqrt{4Dt}}\, dx = \left[\frac{1}{\sqrt{4Dt}}\, i\, erfc\, y\right] C_o$$

where $i$, the commonly used symbolic representation for integration of the error function complement, is itself not a closed expression. The values, normalized to one at $x = 0$, are plotted as the dashed curve in Fig. 1. It is seen that the difference between the error function and this integral is only slight.

The position of the p-n junction was determined by hot-probe measurements on the lapped slices and also by metallographic examination of sections of the slices.

## Discussion of Results

The results of the probe studies on 6 diffusion runs are shown in Fig. 2 in which the volt-milliampere ratios are plotted against penetrations in mils. The penetrations at which the p-n junctions occurred, as determined by hot-probe measurements, are indicated by the symbol "n + p." Curve I fits the data for diffusion in uncoated Si and in two slices coated with solution 1. Curve II is for the slice coated with solution 3, and curve III for the slice coated with solution 2.

The main effect noted for the potassium silicate coating (solution 1) was to promote the formation of a flat junction as was observed by metallographic examination. Solution 3 led to an increase in $C_o$ which was indicated by the decrease in volt-milliampere ratio at zero penetration. Solution 2 caused an even greater increase in $C_o$.

A 90-hr run with solution 3, curve IV, showed both a relatively high $C_o$ and deep penetration of the diffusant. Using the same data, relative conductance was plotted against penetration in Fig. 1, the points being the experimental conductance values. The scales of ordinate and abscissa were normalized and adjusted to give the best fit to the theoretical curves. The value of $1.8 \cdot 10^{-12}$ cm$^2$/sec for the diffusion constant, $D$, was deduced from the data and agrees within experimental error of the temperature 1175°C with that reported by Fuller and Ditzenberger (6). The source-plane concentration, $C_o$ was calculated by the method of differential conductances and found to be $4.8 \cdot 10^{20}$. It would be expected that a discontinuity in the slope of the curve of conductance vs. penetration would appear at the position of the p-n junction due to the contribution of the n-type impurity to the conductance. The fact that our data do not show such discontinuities may be attributed to lack of refinement of the probe technique. The agreement of the data in the region beyond the p-n junction with the theoretical curve is fortuitous.

The flat junctions observed under the glassy coatings are apparently due to the removal of masking by localized silicon dioxide layers by the solvent action of the glasses. Increasing the boron content of the glasses increases the value of $C_o$.

## Acknowledgment

The authors are grateful to George Shaw for his contributions to the experimental work in this investigation.

Manuscript received May 20, 1958. This paper was prepared for delivery before the New York Meeting, April 27-May 1, 1958.

Any discussion of this paper will appear in a Discussion Section to be published in the June 1959 JOURNAL.

## REFERENCES

1. "Tables of Probability Functions," Vol. 1. Federal Works Agency, Work Projects Administration. New York, 1941.
2. W. Jost, "Diffusion," p. 61, Academic Press, Inc., New York (1952).
3. C. J. Frosch and L. Derick, *This Journal*, **104**, 547 (1957).
4. F. C. Kracek, N. L. Bowen, and G. W. Morey, *J. Phys. Chem.*, **33**, 1857 (1929).
5. A. Uhlir, Jr., *Bell Syst. Tech. J.*, **34**, 105 (1955).
6. C. S. Fuller and J. A. Ditzenberger, *J. Appl. Phys.*, **27**, 544 (1956).

# Diffusion Concentration Profiles by Analog Computation

**Worden Waring**[1]

*Semiconductor Division, Raytheon Manufacturing Company, Newton, Massachusetts*

ABSTRACT

Simulation of diffusion processes on an analog computer permits solutions to the diffusion equations under boundary conditions which make analytical solutions impractical. Effects on transistor structure are shown for "slumping" and "outdiffusion" of the first diffusant in a double diffusion. Diffusion from a liquid alloy dot through a regrown region is well represented by an analytical solution except for very thin regrown regions or very long diffusion times. Diffusion through two layers of material with different diffusion coefficients gives profiles which may deviate widely from the error function complement.

In order to study the various diffusion processes with semiconductor materials, an analog computer has been wired and programmed so as to simulate the actual diffusions in a one-dimensional geometry. This permits the solution of the diffusion equations under boundary conditions making an analytical solution impractical. It also permits making changes in conditions and following their effects readily. Unfortunately the analog computer can integrate with respect to only one variable, so an approximation must be used in solving the diffusion (or heat flow) equations. Also, its numerical results are limited to about 3 orders of magnitude.

The machine used is a Reeves Electronic Analog Computer (REAC), Model C400. Its behavior is directed by the wiring on a patchboard, which is varied somewhat for the different problems. Its output is obtained as a series of readings on a digital voltmeter and as curves drawn on graph paper. In the present work, integration is along the time axis and continuous curves with time may be obtained for concentration at a particular location. The variation of concentration in space is represented by concentration values at 12 equally spaced stations; curves drawn through these points are shown in the present figures.

A number of runs were made simulating simple diffusion in from a constant surface concentration. Results were tested against the error function complement, which is the correct theoretical solution (1, 2) and were found to be uniformly within about 1 percentage unit of the correct values for $C/C_o$, where $C$ is the concentration as a function of distance ($h$) and time ($t$) and $C_o$ is the constant surface concentration.

## Double Diffusion

One of the first problems was a simulation of double diffusion: silicon is heated to an appropriate temperature, gallium is diffused in from the vapor, then the sample is placed for a shorter time in phosphorus vapor at the same temperature, which diffuses in and overdopes the gallium near the surface. To simulate this, a normal indiffusion was run on the machine; then the surface concentration was set at zero and the diffusion continued. During this second diffusion the first material, which is then initially distributed according to the error function complement, tends to "slump"; its concentration tends to level out. In addition, it escapes from the surface, or "outdiffuses." Outdiffusion from an initially uniform concentration has been discussed elsewhere (3-5). The present simulation gives the results of outdiffusion from a concentration distribution initially described by the error function complement.

Runs of varying lengths of time on the REAC, as shown in Fig. 1, show successive stages in the concentration profile as these processes go on. The parameter on the curves is the ratio of the time of second diffusion to the time of first diffusion. The figure shows how the concentration near the surface drops abruptly, but further in the bulk the concentration rises gradually.

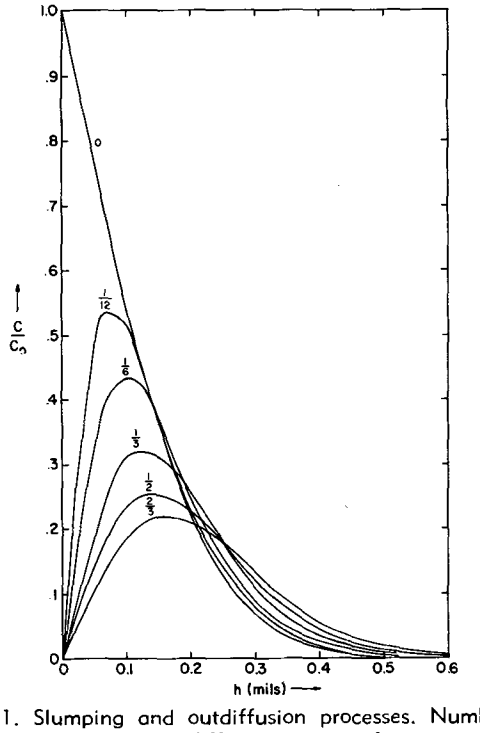


Fig. 1. Slumping and outdiffusion processes. Number on curves is ratio of second diffusion time to first.

[1] Present address: Fairchild Semiconductor Corp., Palo Alto, Calif.

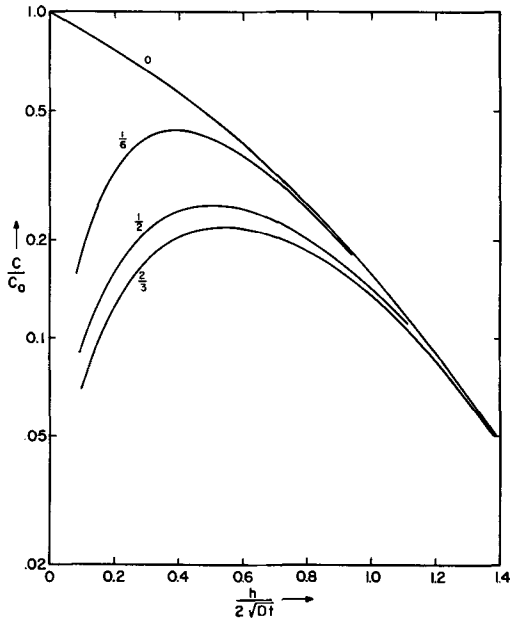


Fig. 2. Slumping and outdiffusion; reduced parameters. Number on curves is ratio of second diffusion time to first.

In order to make these results more generally useful, the concentration ratios are next plotted against a dimensionless abscissa, $h/2\sqrt{Dt}$. This would put all simple indiffusion processes on the same curve, the error function complement, which is the initial, or "0" curve in Fig. 1 and 2. In addition, in Fig. 2 a logarithmic scale is used for concentration. All the curves go down to zero (minus infinity) at zero abscissa value.

Two principal conclusions are that concentrations of the first diffusant near the surface may be considerably less than is predicted by assuming it is static during the second diffusion, and that a good approximation to concentrations of the first diffusant in the interior is to assume simple indiffusion occurs, but for the total time of both diffusions (see later).

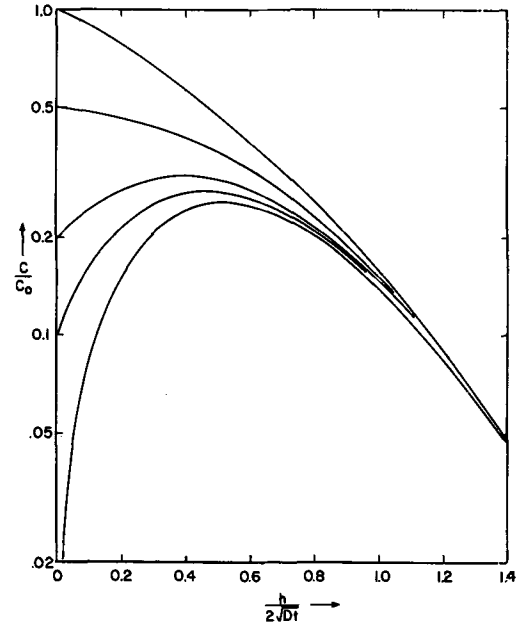


Fig. 3. Effect of surface concentration on slumping and outdiffusion.

However, the curves of Fig. 2 should be modified. It is unlikely that the surface concentration will be zero. In order to test the effects of various surface concentrations on the outdiffusion (and slumping) process, runs were made wherein the surface concentration was held constant at different values. Results are shown in Fig. 3. The second diffusion was just half the time of the first diffusion in all these runs. The bottom curve goes to zero at zero abscissa.

Rather limited data indicate that the surface concentration (in an atmosphere essentially devoid of the outdiffusing material) is several orders of magnitude less than the initial saturation value. Figure 3 shows that in such cases it should be perfectly satisfactory to assume zero surface concentration for practical outdiffusion problems.

### Application to a Transistor

The results of simulated runs such as these were applied to a hypothetical device fabrication. Gallium was diffused into n-type silicon, followed by phosphorus (with a different diffusion coefficient) in a gallium-free atmosphere. Conversion of concentrations to resistivities gave the curves of Fig. 4. The dashed curves show the resistivity and type profiles if the gallium had been static during the phosphorus diffusion, that is, using the error function complement distribution for the time of gallium diffusion alone. The junctions would be just where the vertical dashes reach the upper boundary of the figure. The solid curves show the results when outdiffusion and slumping are included; for the gallium outdiffusion, its surface concentration was set at zero, as discussed above. The junctions are located now where the lines project above the upper boundary of the figure. The inner, collector junction is seen to have moved in about 0.12 mil; the outer, emitter junction has moved out very little, 0.014 mil; the base width has thus increased by about 0.13 mil. In addition, the resistivity in the base region has decreased decidedly, and its minimum has fallen from 0.11 ohm-cm to 0.045 ohm-cm.

If the gallium distribution were calculated on the basis of simple indiffusion with constant surface con-

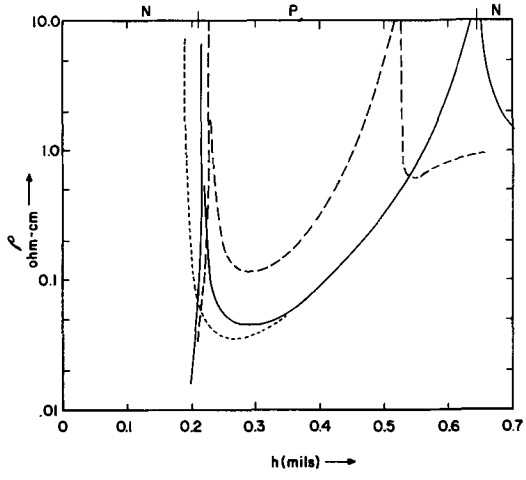


Fig. 4. Effect on device resistivity of slumping and outdiffusion. - - - - - no slumping and outdiffusion; ——— with slumping and outdiffusion; . . . . . base diffusion calculated for total time.

centration (error function complement) but for the total time of both diffusions, its distribution would be as shown by the dotted curve. This is an excellent fit for the inner junction, but introduces some error in the position of the outer, emitter junction. As mentioned before, this is a much better approximation than assuming the first diffusant is static during the second diffusion.

The effects of such changes in concentration profiles on the properties of transistors can be demonstrated readily.

### Bulk Diffusion Process

A second type of problem was to obtain the concentration profile for a material which initially had a fixed concentration of impurity in a regrown region and zero concentration in the adjacent bulk material, when the impurity diffused from the regrown region into the bulk. Transistor structures of approximately this nature have been described by various authors (6-10). The diffusion processes are similar to those in the grown-diffused technique (11, 12). The analytical, exact solution is simple for the case where both regions are of infinite extent (1). But now a liquid alloy dot is placed on the regrown region and is assumed to maintain a constant surface concentration at a fixed distance (thickness of regrown region) from the inner boundary of the regrown region. Results for this situation are compared in Fig. 5 with the analytical solution for the doubly infinite case. Solid curves are smoothed from the REAC results, and dashed curves represent the doubly infinite solution. Curves 1 are for a short time of diffusion and curves 2 for a longer time. Arrows show the boundary of the regrown region.

It is clear that the doubly infinite solution is satisfactory for a short diffusion (or, what amounts to the same thing, a thick regrown region). For a long diffusion, however, the doubly infinite solution is in error. It must always pass through the value 0.50 at the boundary of the regrown region, so it becomes poorer as time goes on. This is another example where a major value of the machine solution is in establishing limits within which simpler analytical solutions are satisfactorily accurate.

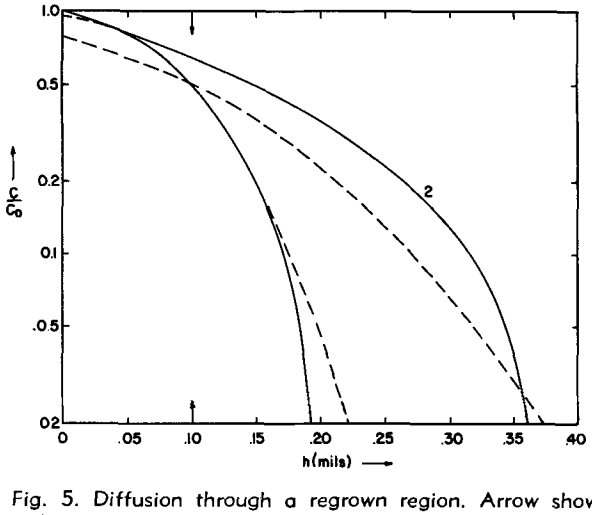


Fig. 5. Diffusion through a regrown region. Arrow shows boundary. ——————calculated by REAC; - - - - - doubly infinite solution; 1 after short time; 2 after longer time.

The abrupt dropping off of the REAC results at large distances and especially at long times is an error. It occurs because the circuitry used forces the concentration curve to go through zero just beyond the last concentration value actually read. This error is easy to recognize, however, and can be corrected by greater sophistication in directing the machine behavior. The runs shown in Fig. 5 were from unusually long machine running times, which ordinarily are rejected.

A third type of problem concerns a two-layer system, wherein there is one value of the diffusion coefficient in one layer and a different value in the other. This is not quite an oxide layer representation, because the distribution coefficient at the interface is assumed to be unity, and because the differences in coefficient values are not extreme, but it might represent a disturbed layer on a semiconductor surface.

Figure 6 shows the results when the doping material diffuses faster in the outer layer and slower in the semiconductor bulk; the ratio is 5:1. The solid curves are for two particular times, with $t_2$ later than $t_1$. The dashed curve shows what the concentration profile would have been if diffusion had occurred in the inner layer for the same length of time but with a constant "surface" concentration in the interface equal to its value at time $t_1$. The ratio of concentrations (deviation from the actual) increases with distance. The concentration at any fixed point within the material moves upward and to the left with time, on this graph.

Figure 7 shows the results when the doping material diffuses only 0.1 as fast in the outer layer as in the bulk. Again the hypothetical profile is shown for the shorter time, to indicate how the increase with time of the boundary concentration causes a profile different from the error function complement. Again,

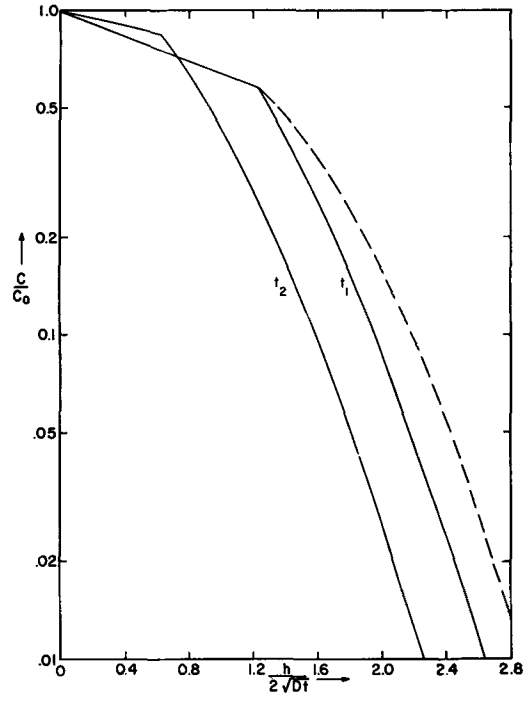


Fig. 6. Diffusion into bulk through layer with higher diffusion coefficient.

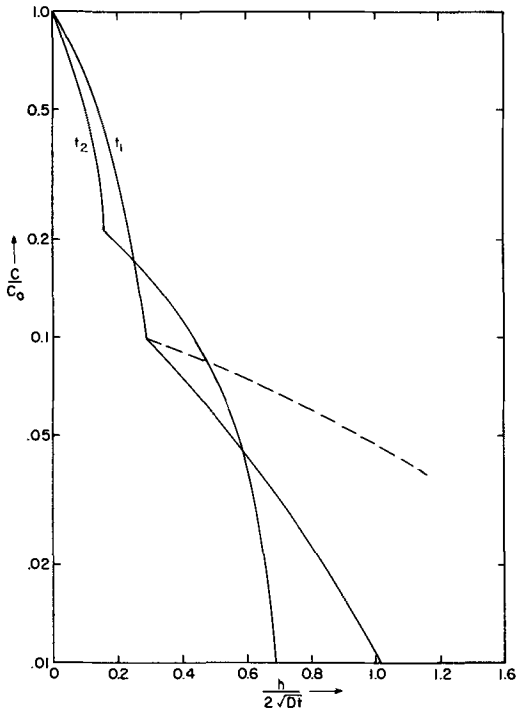


Fig. 7. Diffusion into bulk through layer with lower diffusion coefficient.

concentrations at particular locations move upward and to the left with time, on this graph. In Fig. 6 and 7 the break in each curve occurs where the diffusion coefficient changes value.

In addition to the problems discussed here, simulation of diffusion may be applied to cases where the diffusion coefficient varies with distance, as when one type of doping material is diffused through material with significant concentrations of the opposite type of dope. The diffusion coefficient may vary with time rather than with position. This will occur during the heating and cooling process involved in diffusion, and especially when slow cooling is utilized in order to maintain lifetime or resistivity of the material. Or the surface concentration may be a function of time, as when a two-temperature furnace is used and the doping material is slowly heated, or if the dope must diffuse along a rather long path in order to reach the semiconductor material.

In all such problems, a major advantage of the simulation technique is its flexibility: it is easy to represent a wide variety of diffusion conditions. It gives answers readily, when an exact analytical solution may be complex to solve or difficult to evaluate numerically. In addition to giving adequate solutions, it is also valuable in indicating limits within which simple analytical solutions are sufficiently accurate.

## Acknowledgment

The author is indebted to Norman Nicol, supervising the REAC at Raytheon's Research Division, for assistance in setting up the general problem and for stimulating discussions with regard to this and other analog computations.

The work on this paper was supported in part by Signal Corps Contract No. DA36-039-sc-72710.

Manuscript received April 29, 1958. This paper was prepared for delivery before the New York Meeting, April 27-May 1, 1958.

Any discussion of this paper will appear in a Discussion Section to be published in the June 1959 JOURNAL.

## REFERENCES

1. W. Jost, "Diffusion in Solids, Liquids, Gases," Academic Press, Inc., New York (1952).
2. H. S. Carslaw and J. C. Jaeger, "Conduction of Heat in Solids," Oxford University Press (1950).
3. K. Lehovec, K. Schoeni, and R. Zuleeg, *J. Appl. Phys.*, **28**, 420 (1957).
4. R. C. Miller and F. M. Smits, *Phys. Rev.*, **107**, 65 (1957).
5. J. Halpern and R. H. Rediker, *Proc. I.R.E.*, **46**, 1068 (1958).
6. C. E. Benjamin and R. L. Longini, I.R.E.-A.I.E.E. Semiconductor Device Research Conference, Philadelphia, June 20-22, 1955.
7. H. Statz, W. Leverton, and J. Spanos, I.R.E.-A.I.E.E. Semiconductor Device Research Conference, Philadelphia, June 20-22, 1955.
8. J. R. A. Beale, *Proc. Phys. Soc. (London)*, **B70**, 1087 (1957).
9. G. Freedman, *et al.*, I.R.E. National Convention, New York, March 24-27, 1958.
10. R. S. Schwartz and S. B. N. Slade, I.R.E. Electron Devices Meeting, Washington, D. C., Oct. 31-Nov. 1, 1957.
11. K. Lehovec and A. Levitas, *J. Appl. Phys.*, **28**, 106 (1957).
12. B.Cornelison and W. Adcock, Paper presented at WESCON; p. 22 Part 3 of Convention Record, August 1957.

# A Sensitive Method for Measuring Optical Scattering in Silicon

**G. H. Schwuttke, O. A. Weinreich, and P. H. Keck**

*Central Research Laboratories, Sylvania Electric Products, Inc., Bayside, New York*

ABSTRACT

An instrument has been developed for the observation of optical scattering in silicon and in intermetallic compounds. It is considered as a supplementary tool suitable for studying crystal imperfections in conjunction with other optical methods. Scattering patterns of heat-treated, crucible-grown silicon crystals have been discussed as examples. The observations are in complete agreement with previously published results obtained by several other investigators on the clustering of oxygen in silicon caused by heat treatment.

Optical observations on silicon in the wavelength range greater than 1.1 $\mu$, that is, in the region of its infrared transmission, have led to significant progress in the study of crystal perfection. In particular, the investigations of Dash (1) on birefringence in Si as observed in transmission between crossed polarizers have revealed many details such as strain patterns, growth rings, and multiple twinning. In his studies an infrared converter tube is used for visual observations. While this method is quite sensitive, it does not reveal certain types of imperfections, such as very finely dispersed precipitates caused by the presence of oxygen in Si crystals grown in quartz crucibles.

As Kaiser has shown, heat treatment of such crystals at 1000°C causes formation of $SiO_2$ clusters within the Si matrix, and these clusters in turn give rise to optical scattering (2). While Debye and Lederhandler (3) have reported measurements of the angular distribution of scattering, a sensitive arrangement for observing the intensity distribution of scattered light within the sample is of considerable interest in conjunction with other optical measurements such as 9-$\mu$ absorption (4) and the birefringence.

## Experimental Arrangement

A sensitive instrument for observing the scattering must use a strong light source to provide a very intense illumination of the sample and at the same time the field of view must be kept as dark as possible when the scattering sample is not in place. This condition is always easy to fulfill if the sample is illuminated through a relatively small aperture and the observation path makes a large angle with the direction of illumination, as it is done in observing the Tyndall scattering, where this angle is usually 90°. In contrast to such an arrangement, we have chosen a large illumination aperture around a conical dark field zone and the integrated scattered light is observed from inside an umbra or shadow cone (5). Figure 1 shows the optical arrangement schematically. The integrating sphere Sph is illuminated by the light source S. This sphere has a small opening, $O_2$, in front and a larger one, $O_1$, on the opposite side, which is backed by a black cone, B. The holes $O_1$ and $O_2$ define an umbra or shadow cone into which no light originating from the sphere can penetrate. If a sample is put before $O_2$ it will be illuminated with an aperture of 180°. If scattering occurs, the scattered light will penetrate into the shadow cone, which means that the sample will brighten up according to the degree of scattering when viewed from within the shadow cone.

Figure 2 shows schematically the complete arrangement of the instrument for the study of scattering in Si. This instrument actually consists of a water-cooled integrating sphere Sph of 10 cm diameter which is illuminated by a 200-w projection lamp. The inner wall of the sphere is gold plated, since gold has a high reflectivity in the infrared region. The two aligned holes $O_1$ and $O_2$ have a diameter of 60 mm and 8 mm, respectively. The black body B is a cone of 70 cm length; it is covered on

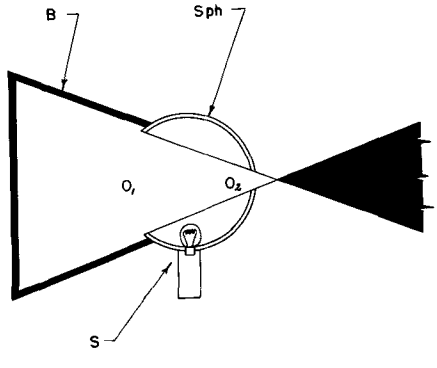


Fig. 1. Optical principle of scattering arrangement

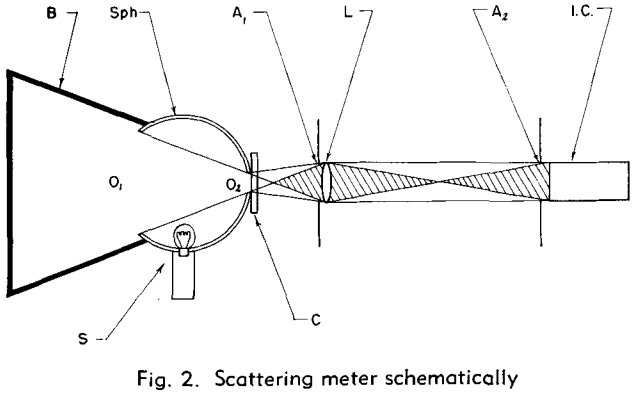


Fig. 2. Scattering meter schematically

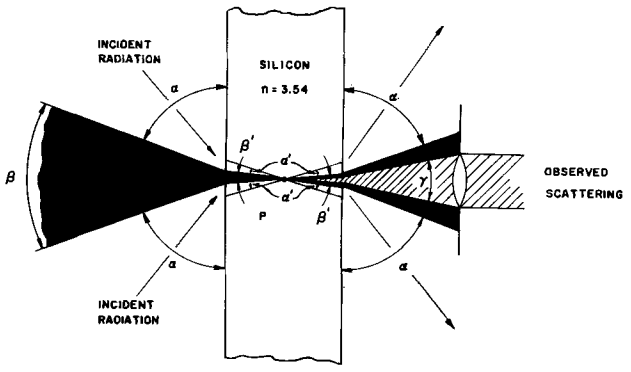


Fig. 3. Optical path in silicon samples

the inside with black velvet. The two holes in the sphere define an umbra, as explained in Fig. 1, which provides a suitable dark field for a sensitive detection of any scattering in the Si sample, which is placed in front of hole $O_2$. The sample is scanned by moving it across the hole on a microscope stage. The specimens with thickness ranging from a fraction of a millimeter to several millimeters have to have two well-polished planar faces; scratches or dust particles will show up in the scattering picture. The objective L forms a magnified image of the sample on the face of the infrared image converter tube I. C. For a sensitive observation of the scattered light from the sample, it is important that both the objective L and the image converter tube I. C. be located completely within the shadow cone. Light diffraction causes the edge of the front opening of the sphere to appear as a bright ring in the plane of the sample image. This bright ring has to be cut off by a suitable diaphragm $A_2$ in front of the image converter tube in order to keep the field of view as dark as possible. As a consequence of the dark emission of the image converter cathode, the field of view at room temperature was not very dark.

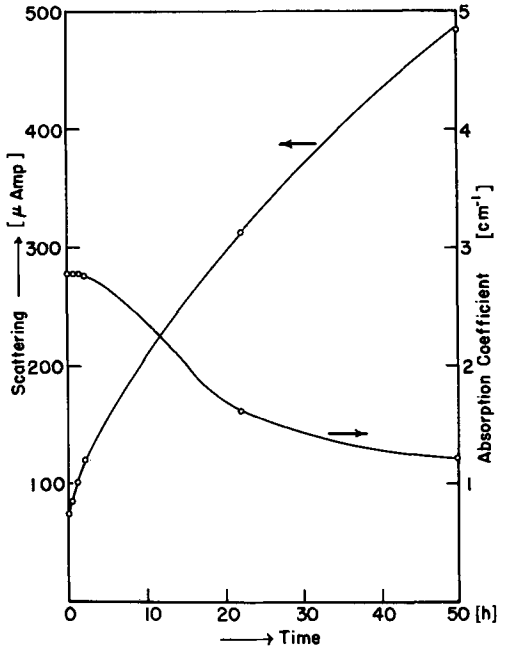


Fig. 4. Scattered intensity and 9-$\mu$ absorption vs. heat-treatment time at 1000°C for silicon (n-type, 95 ohm-cm, crucible pulled in [111] direction).

Cooling of the tube resulted in a background close to the visual threshold. For this purpose dry air cooled by liquid nitrogen was blown from a ring-shaped mouthpiece against the front window of the converter tube. For many observations it was not necessary to use cooling.

Since the refractive index of Si is relatively high, the aperture of the cone of illumination and of the cone of the observed scattering are strongly reduced within the sample in comparison to their corresponding values in air; this relation is schematically represented in Fig. 3. We are using a refractive index value of 3.54 for Si at 1.2 $\mu$ as published by Salzberg and Villa (6). For this refractive index the aperture of 180° provided by the integrating sphere shrinks to a value of 33°, or, in other words, the illuminating sphere as seen from a scattering particle P inside the Si would appear under an aperture of 33°. Similarly, the black body which appears from the front hole in the sphere under 30° is seen from P under the reduced aperture of 8° 22″. In order to preserve the dark-field arrangement the effective angle under which the scattered light is observed must be smaller than the dark cone. We have used effective observation apertures between 3° and 8°, which corresponds to 10° to 28° apertures in air. It is quite apparent that in our arrangement, due to the high refractive index of Si, essentially forward scattering within ±15° is observed.

## Results

Let us discuss some results obtained on Si single crystals. First, it should be emphasized that the described instrument serves best as a supplementary tool in conjunction with the observation of birefringence in transmission and of surface structure in reflected light. Any surface structure of Si samples shows up strongly as scattering and, in order to avoid erroneous results, the samples must be highly polished and their surface quality checked in reflected light. Twinning, lineage, and strain pattern were found to cause very little scattering and therefore are shown up more sensitively in transmission between crossed polarizers than in the scattering instrument. On the other hand, clustering of oxygen in Si caused by heat treatment of crucible-grown crystals at 1000°C produces strong effects that can readily be observed in the scattering instrument.

In Fig. 4 the intensity of scattered light in relative units is plotted against the time of heat treatment at 1000°C for adjacent slices cut from a Si crystal n-type with 95 ohm-cm resistivity. The intensity was measured with a photomultiplier tube facing the image converter tube. The background intensity as mainly caused by the image converter tube was in this case about 40 $\mu$a. Samples before heat treatment gave readings between 50 and 70 $\mu$a Also plotted is the 9-$\mu$ absorption of the samples vs. heat treatment time. The absorption coefficient before heat treatment was 2.76 $cm^{-1}$. This corresponds to an initial oxygen concentration of 4.5 x $10^{17}$ O/cc [*see* Fig. 1 in (4)]. While the decay in the 9-$\mu$ absorption takes place gradually as observed previously (2, 7), the scattered intensity increases

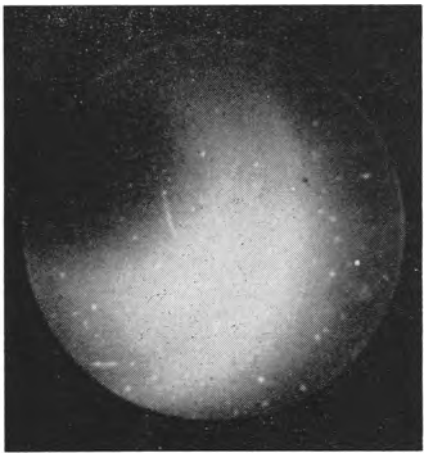

Fig. 5. Scattering pattern of silicon crystal with uniform oxygen content but with large differences in dislocation densities. The crystal was grown in the [111] direction and cut perpendicular to the growth axis. (After 130 hr of heat treatment at 1000°C, magnification 6½ times after reduction for publication.)

steeply, and after 1-2 hr of heat treatment a distinct increase in scattering is evident, while the change in the 9-$\mu$ absorption is still very small. The intensity of scattering after a certain heat-treatment period depends on the original concentration of oxygen and, of course, on the concentration of centers that serve to form the nucleus of oxygen cluster. Lederhandler and Patel (7) have shown that the decrease of the 9-$\mu$ absorption with heat-treatment time is strongly dependent on the density of dislocations, which apparently serve as nucleation centers for the precipitation of oxygen and for which further evidence was published recently (8, 9). From these results it is concluded that the intensity distribution of scattering after a short heat treatment at 1000°C is a sensitive indication of the original distribution of oxygen concentration and of the distribution of the concentration of the nucleation centers. Since the 9-$\mu$ absorption of the crystal before heat treatment provides a good measure for the oxygen concentration, the scattering pattern can be analyzed for the distribution of the nucleation center concentration. Figure 5 gives an example of a scattering pattern in a Si crystal. Before heat treatment this crystal displayed a fairly constant 9-$\mu$ absorption, which indicated that the original oxygen concentration over the region shown was uniform within 10%. In the bright area in the picture, high dislocation densities were found by etching. There precipitation of oxygen produced strong scattering, which is in general agreement with the findings of Lederhandler and Patel (7) that dislocations offer favorable sites for the clustering of oxygen.

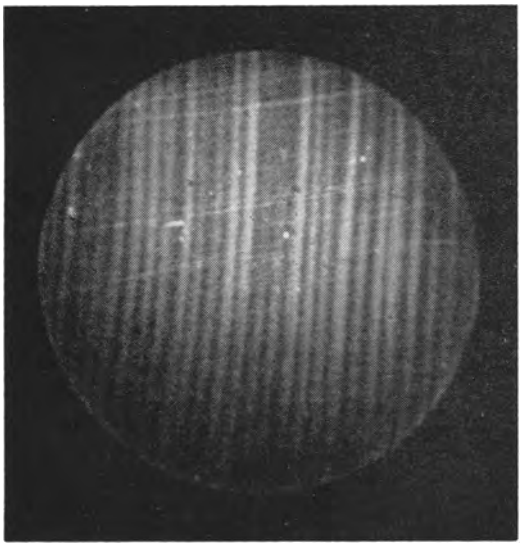

Fig. 6. Growth rings made visible by scattering. The rotated silicon crystal, p-type 130 ohm-cm, was cut parallel to growth direction [111]. (Heat treated at 1000°C for 100 hr, distance between growth rings 0.27 mm, magnification 8 times after reduction for publication.)

Growth rings can be made visible by scattering, as Kaiser (2) has already shown. Figure 6 is a scattering picture of a rotated Si crystal cut parallel to the growth direction and heat treated at 1000°C for 100 hr. The crystal was grown in the [111] direction and the sample was p-type 130 ohm-cm before heat treatment. A very distinct pattern of stripes has developed which checks with the growth rings. The picture is similar to birefringence stripes which Dash (1) has shown on rotated Si crystals to be due to small periodic temperature fluctuations during the crystal growth. Since even very small temperature fluctuations cause appreciable changes in the oxygen concentration, it is quite understandable that a distinct stripe pattern results in the scattering instrument. Heat treatment of 2-4 hr at 1000°C is sufficient to make the stripes clearly visible. Longer heat treatment was applied to the sample shown in Fig. 6 in order to produce a high contrast for reproduction purposes. No birefringence stripes were detected on this particular crystal in transmission between crossed polarizers before heat treatment; after heat treatment there was only a very faint indication of stripes. This proves that in this case the observation with scattered light is more sensitive than the observation of birefringence. In Fig. 7 the same crystal as shown in the previous figure is pictured in the lower half. In the upper half an adjacent slice of the crystal is shown that was gold plated (10) to bring out resistivity changes and junctions but was not heat treated. A close inspection indicates a good match of the two stripe patterns as is to be expected from the knowledge of the donor formation in Si (2, 9) caused by oxygen impurity at temperatures below 500°C. During the normal cooling of the sample, apparently a sufficient donor formation took place to bring out the stripe pattern after plating. This was confirmed by a second plating experiment after half-hour treatment of the sample at 450°C. The stripe pattern was essentially the same before and after this treatment.

The application of the described scattering instrument is not limited to Si, but can as well be used for other crystals which have a suitable transparency range. For instance, we have made some preliminary observations on GaAs and InP crystals that showed appreciable scattering with the appearance of a grainy structure, the understanding of which will require more detailed studies. Intermetallic compounds with a band gap larger than that

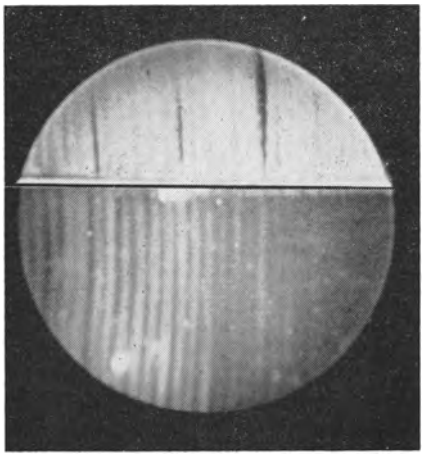

Fig. 7. Match of growth rings (same sample as Fig. 6) with junction delineation by gold plating. (Distance between growth rings 0.27 mm, magnification 6½ times after reduction for publication.)

of Si give a strongly increased sensitivity because the image-converter tube used for the observation of scattering has its maximum sensitivity at 0.8 $\mu$, while in the case of Si the tube is used only near the long wave-length limit of its sensitivity. It appears to be of interest to continue the investigation of scattering in intermetallic compounds, but it should be remembered that it is not easy with some of the materials to prepare plane, highly polished surfaces as required for the measurements.

**Acknowledgment**

It is a pleasure to acknowledge the able assistance of P. Riggio and F. Wrzesc in building the instrument and of L. Letendre and Mrs. O. Kielbasa in preparing the samples.

The research reported in this paper was sponsored by the Electronics Research Directorate of the Air Force Cambridge Research Center, Air Force and Development Command, under Contract AF19-(604)-3482

Manuscript received May 26, 1958. This paper was prepared for delivery before the New York Meeting, April 27-May 1, 1958.

Any discussion of this paper will appear in a Discussion Section to be published in the June 1959 JOURNAL.

REFERENCES

1. W. C. Dash, *Phys. Rev.*, **98**, 1536 (A) (1955).
2. W. Kaiser, *ibid.*, **105**, 1751 (1957).
3. P. P. Debye and S. Lederhandler, *Bul. Amer. Phys. Soc. Ser. II*, **2**, 66 (1957).
4. W. Kaiser and P. H. Keck, *J. Appl. Phys.*, **28**, 882 (1957).
5. P. H. Keck, *Optik*, **1**, 169 (1946).
6. C. D. Salzberg and J. J. Villa, *J. Opt. Soc. Amer.*, **47**, 244 (1957).
7. S. Lederhandler and J. R. Patel, *Phys. Rev.*, **108**, 239 (1957).
8. R. A. Logan and A. J. Peters, *J. Appl. Phys.*, **28**, 1419 (1957).
9. C. S. Fuller and R. Logan, *ibid.*, **28**, 1427 (1957).
10. S. J. Silverman and D. R. Benn, *This Journal*, **105**, 170 (1958).

# Effects of Certain Chemical Treatments and Ambient Atmospheres on Surface Properties of Silicon

**T. M. Buck and F. S. McKim**

*Bell Telephone Laboratories, Incorporated, Murray Hill, New Jersey*

ABSTRACT

Measurements of surface conductance, recombination velocity ($S$), and field effect were made on n- and p-type silicon specimens with certain surface treatments and ambient atmospheres. The conditions covered a wide range in surface potential (0.7 ev) and recombination velocity (40–$10^4$ cm/sec). Low recombination velocity occurred when the surface was strongly p-type, after treatments in boiling deionized water or sodium dichromate solution, or when the surface was strongly n-type, after treatment in concentrated hydrofluoric acid. Atmospheres which bend the energy bands back toward the middle from these extreme conditions caused $S$ to increase. Curves of $S$ vs. band position at the surface for the various treatments appear to be branches of the type of curve predicted by theory for recombination centers at a discrete energy level. The position of the Fermi level at the surface for a given treatment apparently depended to a small extent on whether the bulk material was n- or p-type. This apparent difference, which is contrary to experience on germanium, may have been caused in part by poor contact between an inversion layer and the bulk material.

Among various types of surface studies on semiconductors in recent years the dependence of surface recombination velocity ($S$) on surface potential has been used to gain considerable information on the energies, densities, and capture cross sections of surface states, particularly on Ge (1-6). On Si such studies have been hampered by the difficulty in obtaining low $S$; in fact, only a few treatments have been reported for producing low $S$ on Si (7, 8).

In the present work, three of these low $S$ treatments were studied along with a common etch which does not produce low $S$. Field-effect and sur-

face conductivity measurements showed that the low $S$ treatments produce rather large shifts in surface potential. [Moore and Nelson (7) had already reported that the dichromate treatment makes the surface p-type.] Smaller shifts were produced by atmosphere cycling of a modified Brattain-Bardeen type in which dry oxygen, wet nitrogen, and, in one case, dry nitrogen were used. The combination of chemical treatments and atmosphere cycling permitted exploration of a large range in surface potential and recombination velocity.

### Details of Chemical Treatments

The treatments studied will be identified as (*a*) dichromate (7), (*b*) boiling deionized water (8), and (c) HF soak (8). These three can produce low $S$ on both n- and p-type material. A fourth treatment, (*d*) $HNO_3$:HF, was included for comparison with the others.

*Dichromate treatment.*—The specimen was soaked in 1% sodium dichromate solution for a few minutes after a preliminary etch in 10/1 $HNO_3$-HF and a light rinse in deionized water. The dichromate solution usually has been allowed to dry on the surface. The effect is enhanced sometimes by warming the solution to 80°-90°C. Light rinsing in deionized water after this does not seem to destroy the effect. Dry oxygen is a good atmosphere for preserving the effects on surface conductivity and $S$ after this treatment.

*Boiling deionized water treatment.*—The specimen was immersed in boiling, deionized water for 30 min or longer, after preliminary etching and rinsing. After boiling, the specimen was dried by evaporation or by drawing off excess water with filter paper. It was then quickly placed in a dry oxygen atmosphere.

Conductivity of the water has usually been 0.1 $\mu$mho $cm^{-1}$ from the deionizing column and 0.5-0.6 $\mu$mho-$cm^{-1}$ after boiling, with most of the increase probably coming from sources other than the specimen. The details of this treatment are rather critical in obtaining low $S$, e.g., the water must be quite pure, it must be hot, and mere heating in air or oxygen or immersion in a number of other liquids, mostly organic, at about 100°C do not produce low $S$.

HF *treatment.*—The specimen was soaked in concentrated (48%) HF for 5 min, after a preliminary etch in 10/1 $HNO_3$:HF. It was then rinsed for about 5 sec in running, deionized water. The most pronounced effect on surface conductivity and $S$ was preserved by quickly placing the specimen in dry nitrogen (within 10-15 sec); helium, argon, etc., would probably do as well, but oxygen should be excluded, as it tends to destroy the effect.

*10/1* $HNO_3$:HF *etch followed by rinse in cold deionized water.*—This is a commonly used etch which removes Si at a moderately slow rate ($\approx$0.6 mil/min) leaving a bright smooth surface. In addition to being one of the treatments under study, this etch was used in preparing the surface for the other treatments, although the effects of the other treatments do not seem to depend critically on the nature of the preliminary etch.

### Surface Conductivity

The surface conductivity of a semiconductor is a unique function of the surface potential or surface barrier height for a given bulk resistivity. Since this function has been calculated (9-11), surface conductivity may be used to determine surface potential. The data of Kingston and Neustadter (9), which are convenient for the extrapolation necessary with Si, were used to construct curves of $\Delta\sigma_s$ vs. $U_s$ where $\sigma_s$ is the surface conductivity and $U_s = (E_F - E_i)/kT$ at the surface. $U_B$ is the corresponding quantity in the interior, $E_F$ is the Fermi level, and $E_i$ the value of $E_F$ in intrinsic material, or approximately the middle of the energy gap. No correction was made for reduced mobility near the surface, of the type calculated by Schrieffer (11); the correction is small for Ge and would be even smaller for Si because of the longer Debye length.

The specimens were thin slabs, about 0.040 cm thick, with high bulk resistivity and high volume lifetime (about 1000 $\mu$sec). Resistance was measured on a General Radio Bridge, Type 650-Pl. Temperature was controlled satisfactorily by means of a constant temperature bath at 28°C. Contacts were bonded to the ends of the specimens, gold wire for n-type material and aluminum for p-type, after first plating a small area with gold or aluminum. These contacts were found to have no significant resistance compared to the total resistance of the specimens.

The change in surface conductance, per square, was computed from

$$\Delta\sigma_s = (R_F^{-1} - R_{Max}^{-1})\frac{L}{P} + \Delta\sigma_{T.M.} \qquad [1]$$

where $R_F$ is measured resistance; $R_{Max}$ the maximum which could be observed in certain situations; $L$ the distance between contacts; $P$ the cross-sectional perimeter of the slab; and $\Delta\sigma_{T.M.}$ the minimum value (negative) on the theoretical curve of $\Delta\sigma_s$ vs. $U_s$.

It was necessary to determine experimentally (during cycling) the minimum in conductance in order to place other points on the curve. Points were placed on the n- or p-side of the minimum on the basis of the assumption that dry oxygen causes a p-type shift while water vapor causes an n-type shift, so that when $R_F$ decreases in dry oxygen or increases in wet nitrogen the surface must be on the p-side of the minimum in surface conductivity. The opposite behavior would indicate the n-side. This assumption was based on the results of separate field-effect measurements on these types of surfaces and it is in accord with the general experience of others with etched Si and Ge surfaces.

### Surface Conductivity Results

*N-type silicon.*—In Fig. 1 the ranges of surface conductivity covered during four or five cycles of alternate exposure to dry oxygen and wet nitrogen (43% R.H.) are indicated for the four different treatments. Exposures to the atmospheres were for 10 min to several hours depending on the time required for conductance to stop changing. Changes were usually more rapid in wet nitrogen than in dry

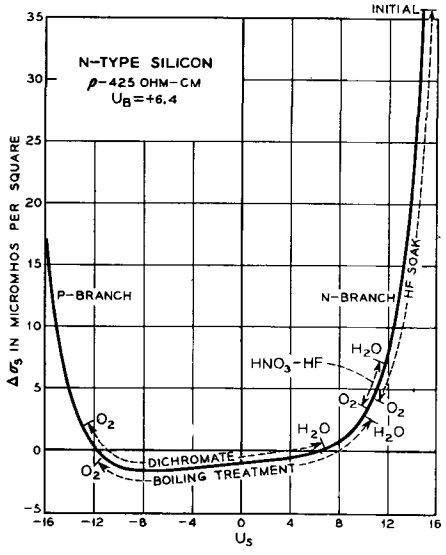


Fig. 1. N-type Si. Ranges of surface conductivity and $U_s$ for four different treatments in atmosphere cycling. Dry oxygen and wet nitrogen extremes are indicated by $O_2$ and $H_2O$.

oxygen. The extremes of conductivity reached in these atmospheres are indicated by $O_2$ or $H_2O$ in the figures.

The behavior after the 10/1 $HNO_3$:HF etch was erratic at first but after several cycles $R_F$ consistently increased in dry $O_2$ and decreased in wet $N_2$ producing the rather small range indicated on the curve, slightly on the n-side of the straight band position which is at $U_s = U_B$, $\Delta\sigma_s = 0$.

With the other treatments the bands could be bent well away from this position in both directions. The HF treatment had a strong n-type effect. Initially (in dry nitrogen) surface conductivity was over 35 $\mu$mhos per square; the specimen resistance dropped from about 70,000 to 35,000 ohms. The condition held for about 2 hr in dry nitrogen after which atmosphere cycling was started. During cycling $\Delta\sigma_s$ decreased in dry oxygen and increased in wet nitrogen, but these oscillations were superimposed on a steady downward trend in surface conductivity so that eventually after much cycling $\Delta\sigma_s$ was at the lower extreme of the range in dry $O_2$ and would not move up very far in wet nitrogen. This irreversible downward trend is probably associated with the growth of an oxide film which has been studied by Archer (12) using ellipsometry, after an HF soak. Similar behavior has been studied on Ge by Kikuchi (13), although $S$ did not behave in the manner which will be described for Si.

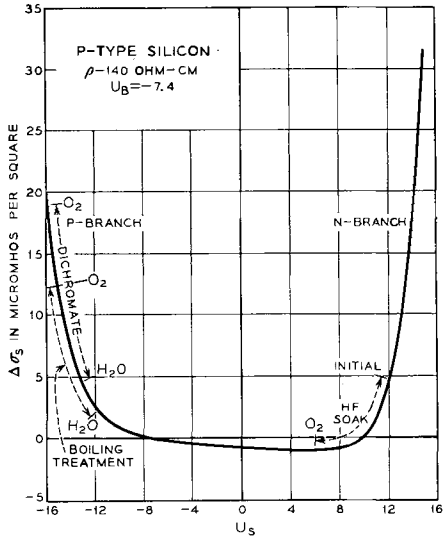


Fig. 2. P-type Si. Ranges of surface conductivity and $U_s$ for three different treatments in atmosphere cycling. Dry oxygen and wet nitrogen extremes are indicated by $O_2$ and $H_2O$.

The other two treatments allowed the surface to swing over to the p-side, the dichromate treatment producing a somewhat stronger shift than the boiling treatment. In atmosphere cycling surface conductivity traversed the ranges indicated quite reversibly, going through the minimum.

*P-type silicon.*—On a p-type specimen (Fig. 2) the treatments produced shifts in the same direction but of somewhat different magnitude. The boiling and dichromate treatments produced larger values of $\Delta\sigma_s$ and $|U_s|$ than they did on the n-type specimen while the n-type treatment (HF) produced smaller values.

On Ge, Brattain and Garrett (4) found $U_s$ the same on n- or p-type material for a given treatment; the surface states determined the position of the Fermi level at the surface regardless of the bulk resistivity or majority carrier type. In the present case, with Si, the differences are not very large but they did seem real and reproducible. Poor contact between an inversion layer and the bulk material could cause an effect in this direction; the inversion layer would not make its full contribution to the change in conductance and this would cause an underestimate of $|U_s|$, e.g., at the $O_2$ extremes for the dichromate and boiling treatments in Fig. 1. However, it does not seem that this could account entirely for the differences between the wet extremes for these same treatments on the two types of material.

Whatever the explanation of the differences in magnitude, the shifts are in the same direction on both n- and p-type material. The chemical treatments had the predominant influence in determining surface potential while the atmospheres had a secondary modulating influence. Both the chemical treatment and the ambient atmosphere are obviously important in establishing the surface potential.

The mechanisms by which these treatments cause these effects are not clear. The well-known p-type effect of oxygen (and also ozone and chlorine) has been ascribed to its high electron affinity by which it acts as an acceptor (14). Dichromate, being a strong oxidizing agent, also might be expected to provide acceptor levels. Moore and Nelson (7) proposed an electrochemical mechanism. The familiar n-type effect of water vapor is less susceptible to qualitative explanation and the same may be said for the HF soak. One wonders why the surface is so strongly n-type when it is stripped of oxide and has some HF absorbed on it, and why oxide film growth causes it to go back in the p-direction. The p-type effect of the boiling treatment may be due

to cleaning of the surface which allows oxygen to be more effective in producing its normal p-type shift.

### Surface Recombination

All the values of $S$ to be reported were computed from filament lifetimes determined by the photoconductivity-decay method (15). A simplified equation (16) was used to compute $S$ from filament lifetime for these specimens with thickness considerably smaller than width. The specimens were cut from crystals which had high volume lifetime and were relatively free of non-recombining traps. In some cases, however, especially when low $S$ was obtained together with a strong inversion layer, "tails" were observed in the photoconductivity decay curves, somewhat similar to those described by Haynes and Hornbeck for volume traps (15). This effect, when observed, was eliminated by very weak d-c light. Since it was usually, if not exclusively, associated with a strong inversion layer condition it may have been caused by surface photovoltage. All values of $S$ were determined from good exponential decay curves, usually with no ambient light but sometimes with weak d-c light when necessary to get a good exponential. The low $S$ values produced by the three special treatments, on both n- and p-type material, were confirmed, at least qualitatively and in some cases quantitatively, by the PME method (17).

It has been mentioned that the success of the low $S$ treatments depends on keeping the specimen in the proper atmosphere. A prominent feature of the behavior is that the direction in which $S$ changes in an atmosphere depends on the previous treatment.

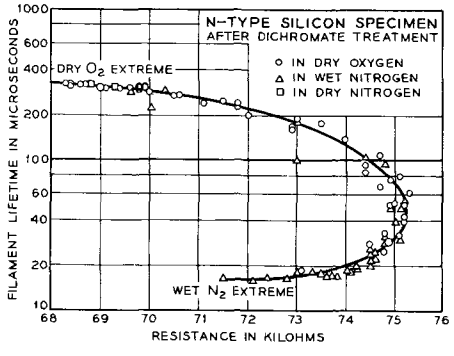


Fig. 3. Filament lifetime vs. resistance during atmosphere cycling after dichromate treatment. N-type Si, $\rho \approx 425$ ohm-cm., $\tau_B \approx 1000$ $\mu$sec. Dimensions of slab: 0.040 x 0.270 x 1.75 cm.

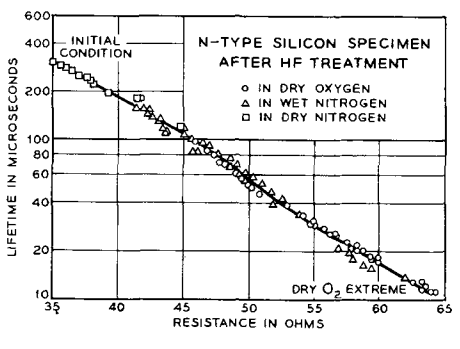


Fig. 4 Filament lifetime vs. resistance during atmosphere cycling after HF soak. N-type silicon, $\rho \approx 425$ ohm cm., $\tau_B \approx 1000$ $\mu$ sec. Dimensions of slab: 0.040 x 0.270 x 1.75 cm.

After the boiling and dichromate treatments, dry $O_2$ favors low $S$ while water vapor causes $S$ to increase drastically. The opposite is true after the HF and $HNO_3$:HF treatments.

In order to obtain $S$ as a function of $U_s$, filament lifetime measurements were made during cycling along with the surface conductivity measurements discussed above. The raw data for two such experiments are shown in Fig. 3 and 4 for the dichromate and HF treatments. After the dichromate treatment and with dry $O_2$ ambient the lifetime was high and resistance rather low. Exposure to wet nitrogen caused the values to traverse the curve in the clockwise direction down to the wet $N_2$ extreme. Dry oxygen brought them back again counterclockwise. Cycling after the HF treatment caused an oscillating shift toward higher resistance and lower lifetime. In both these cases there was very little scattering; $S$ was a well-behaved function of surface conductivity or surface potential. This was true also for the $HNO_3$-HF etch after an initial period of instability and erratic behavior. The behavior in these three cases strongly suggested that the atmospheres did not change the recombination states but merely shifted surface potential. After the boiling treatment there was some scattering and hysteresis throughout the cycling but not enough to prevent the drawing of a fairly reasonable smooth curve of lifetime vs. resistance.

Figure 5 shows the cycling data converted to $S$ and $U_s$ values. Low recombination velocity occurs when the surface is strongly n-type or strongly p-type and atmospheres which tend to bend the energy bands back toward the middle from these extreme conditions cause $S$ to increase. The behavior explains why low $S$ is not obtained with most common etches which probably leave the surface in the middle region as does the $HNO_3$:HF etch. However, it does not follow that any treatment which produces as large a shift in $U_s$ will also produce low $S$ since another treatment might cause recombination states to change in energy or density, or both. An example of this has been observed with an etch in hot sodium hydroxide[1] which caused an n-type shift even stronger than the HF treatment but did not produce very low $S$. A few measurements indicated that in this case the $S$ vs. $U_s$ curve was displaced to the right of the HF curve in Fig. 5.

Since the data of Fig. 5 represent four different chemical treatments it may be too optimistic to try to analyze the data for energies and capture cross sections of recombination centers, but an attempt has been made. For the case where $S$ varies only because of variation in surface potential without any change in the recombination centers, and where the recombination states are at one discrete energy level, current theories (3, 4) predict curves of the type given by the dashed curves of Fig. 5. Another possibility would be a curve with a broad flat top leading to two possible values of the energy level. More than one of these curves might be observed over a large range of surface potential, representing more than one set of recombination states.

[1] Suggested by I. L. Kalnins.

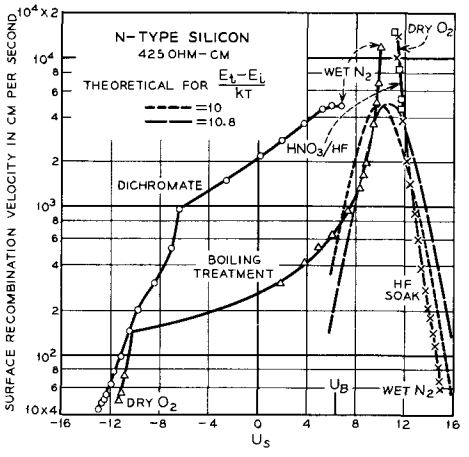


Fig. 5. Surface recombination velocity vs. $U_s$ for four different treatments, with atmosphere cycling. N-type Si. O dichromate treatment; △ boiling treatment; X HF soak; □ $HNO_3$/HF etch.

Many, et al. (3, 5) have found curves of this type in experiments on Ge in which surface potential was varied by a transverse electric field.

In the present case for Si, the data obviously do not fall on one universal curve. The chemical treatments undoubtedly do change the recombination states to some extent; for example, the density of states was apparently higher for the dichromate treatment than for the boiling treatment. However it is interesting to speculate that the HF and boiling treatment data may form two branches of the same curve and to compare them with the theoretical curves (dashed) which have been sketched in. The curve on the left is for a recombination center 0.26 ev above the middle of the energy gap with a capture cross-section ratio $\sigma_p/\sigma_n \approx 5 \times 10^8$. This is, of course, an unusually high ratio and must be regarded with suspicion in view of the piecing together of data for different treatments which was necessary to cover the range. However, the HF curve, in particular, definitely has the proper slope for one branch of the type of curve predicted by theory for a discrete trap energy and, if the whole range of $U_s$ could have been covered without changing treatments, the data might be analyzed in more detail by current theories.

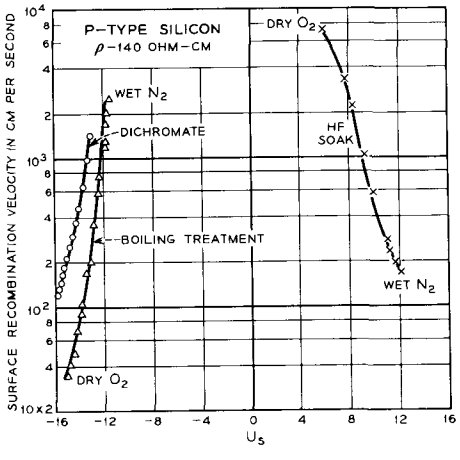


Fig. 6. Surface recombination velocity vs. $U_s$ for three different treatments, with atmosphere cycling. P-type Si.

The data for the p-type specimen, Fig. 6, again show recombination velocity low at the p- or n-type extremes and high in the middle region. And again the curves resemble outside branches of the theoretical type of curve, with $S$ falling off by $\frac{1}{e}$ in one unit ($kT$) of $U_s$.

## Field Effect

The field effect measurements are not discussed in detail. In relation to the foregoing material their chief value was that they gave qualitative indications of the n- or p-type character of the surface, as influenced by chemical treatment and atmosphere, which permitted a choice of the proper branch of the conductance curve in the d-c measurements.

The method used was that of Aigrain (18) which has been developed and used extensively by Montgomery (19) in studies of time constants of surface states on Ge. A theoretical treatment of high-frequency field-effect phenomena has been given by Garrett (20).

Field-effect mobility ($\mu_{F.E.}$) was determined as a function of frequency of the applied field, over a range of 50 cycles/sec to 60 kc/sec. The interpretation was clear in the case of a strong n-type surface on n-material or a strong p-type surface on p-material. In these cases field-effect mobility was negative or positive, respectively, and was constant over the frequency range. This is the type of behavior Montgomery found with Ge.

But anomalies occurred when strong inversion layers were evidently present. Montgomery found that with inversion layers on Ge, $\mu_{F.E.}$ had positive values at low frequency for p-type inversion layers (or negative for n-type inversion layers) and then changed in one sweep to a value having the sign of the majority carrier and considerably larger than bulk mobility; the change of sign, which occurred with an inflection at $1/(2\pi\tau_f)$ was attributed to failure of regeneration processes to keep up with the alternating field. ($\tau_f$ is the filament lifetime.) In inversion layer situations on Si the behavior was similar in that $\mu_{F.E.}$ changed sign in the same directions, but the inflection frequency was not generally equal to $1/(2\pi\tau_f)$ and there were rather sharp minima or maxima in the curves at higher frequency. The inflection frequency usually corresponded to a lifetime higher than actually measured. Again, as with the d-c conductivity measurements, there is the possibility that difficulties may arise from poor contact between the inversion layer and the bulk material. The situation is expected to be worse with Si than Ge because of the smaller reverse current across a junction in Si.

Nevertheless, in spite of the difficulty in detailed interpretation, the general features of the field-effect curves for the various treatments were quite reproducible and gave qualitative evidence of the n- or p-type effects of the various treatments and atmospheres.

## Effects on Devices

Information of this sort should be helpful in selection of surface treatments and atmospheres to

improve Si device parameters which depend on surface potential and $S$. For example, the "p-type" treatments might be expected to improve breakdown voltage in $p^+$-n diodes (higher bulk resistivity on the n-side), while all three low $S$ treatments should improve $\alpha$ in transistors which have sufficiently high volume lifetime. The HF treatment offers the combination of low $S$ with an n-type surface which in certain situations may be more desirable than the p-type surface of the other two. However, the HF-treated surfaces tend to be less stable than the other two. In some preliminary experiments with $p^+$-n grown-junction diodes the breakdown voltage increased progressively from about 140 to 310 v in going through the series from the strongest n-type (HF) treatment to the strongest p-type (dichromate) treatment. This is in accord at least qualitatively with the surface breakdown theory of Garrett and Brattain (21). However, while the dichromate treatment produced the highest breakdown voltage it also caused a large saturation current presumably because of the larger effective junction area.

## Conclusions

1. The chemical treatments had stronger effects than the atmospheres in determining surface potential. However, both the chemical treatments and ambient atmospheres were important in establishing the surface potential.

2. Low recombination velocity occurred when the surface was strongly p-type, after the dichromate and boiling deionized water treatments, or when it was strongly n-type, after the HF treatment. Atmospheres which pulled the energy bands back toward the middle from these extreme conditions caused $S$ to increase (water vapor in the case of the boiling and dichromate treatments, and dry oxygen after the HF treatment.) The extreme bending in either direction required to obtain low $S$ explains why low $S$ is not produced by most common etching treatments.

3. Curves of $S$ vs. $U_s$ for the various treatments resemble branches of theoretical curves for recombination centers at a discrete energy level. A tentative analysis made by piecing together curves for treatments on the n-type sample indicates $E_T - E_i = 0.26$ ev and a cross-section ratio $\sigma_p/\sigma_n \approx 5 \times 10^8$ for one set of recombination centers. This extremely large ratio must be viewed with suspicion because of the piecing together required to obtain it. If it had been possible to approach the maximum in $S$ from both sides without changing the chemical treatment, a more detailed and reliable analysis could be made.

4. The apparent difference between $U_s$ values for a given treatment on n- and p-type material may have been due, at least in part, to poor contact between an inversion layer and the bulk material. This would also change the shape of the $S$ vs. $U_s$ curves obtained under inversion layer conditions but would not affect the curves for enhancement layer conditions.

## Acknowledgments

A number of people have made helpful suggestions and comments during the course of this work. The authors are especially indebted to H. C. Montgomery for his advice and help in the field-effect measurements and to C. G. B. Garrett and W. H. Brattain for helpful discussions. They also wish to thank E. D. Kolb for supplying the high resistivity, high lifetime Si necessary in this work.

Manuscript received May 26, 1958. This paper was prepared for delivery before the New York Meeting, April 27-May 1, 1958.

Any discussion of this paper will appear in a Discussion Section to be published in the June 1959 JOURNAL.

REFERENCES

1. W. H. Brattain and J. Bardeen, *Bell System Tech. J.*, **32**, 1 (1953).
2. D. T. Stevenson and R. J. Keyes, *Physica*, **20**, 1041 (1954).
3. Many, Harnik, and Margoninski, "Semiconductor Surface Physics," p. 85, U. of Pennsylvania Press (1956).
4. W. H. Brattain and C. G. B. Garrett, *Bell System Tech. J.* **35**, 1019 (1956). C. G. B. Garrett and W. H. Brattain, *ibid.*, **35**, 1041 (1956).
5. A. Many and D. Gerlich, *Phys. Rev.*, **107**, 404 (1957).
6. S. Wang and G. Wallis, *ibid.*, **107**, 947 (1957).
7. A. R. Moore and H. Nelson, *RCA Rev.*, **17**, 5 (1956).
8. T. M. Buck and F. S. McKim, Paper presented Electrochem. Soc. Meeting, Cleveland, Oct. 1956.
9. R. H. Kingston and S. F. Neustadter, *J. Appl. Phys.*, **26**, 718 (1955).
10. C. G. B. Garrett and W. H. Brattain, *Phys. Rev.*, **99**, 376 (1955).
11. J. R. Schrieffer, *ibid.*, **97**, 641 (1955).
12. R. J. Archer, *This Journal*, **105**, 619 (1957).
13. M. Kikuchi, *J. Phys. Soc. Japan*, **12**, 756 (1957).
14. N. F. Mott, "Semiconducting Materials," p. 1 Butterworth Scientific Publications Ltd., London (1951); R. H. Kingston, *J. Appl. Phys.*, **27**, 101 (1956).
15. J. R. Haynes and J. A. Hornbeck, *Phys. Rev.*, **90**, 152 (1953); J. A. Hornbeck and J. R. Haynes, *ibid.*, **97**, 311 (1955).
16. J. P. McKelvey and R. L. Longini, *J. Appl. Phys.*, **25**, 634 (1954).
17. T. M. Buck and F. S. McKim, *Phys. Rev.*, **106**, 904 (1957).
18. Aigrain, Lagrenaudi, Liandrat, *J. phys. radium*, **13**, 587 (1952).
19. H. C. Montgomery, *Phys. Rev.*, **106**, 441 (1957).
20. C. G. B. Garrett, *ibid.*, **107**, 478 (1957).
21. C. G. B. Garrett and W. H. Brattain, *J. Appl. Phys.*, **27**, 299 (1956).

# Saturation Currents in Germanium and Silicon Electrodes

**John B. Flynn**

*Sylvania Electric Products Inc., Woburn, Massachusetts*

ABSTRACT

Saturation currents observed in germanium electrodes in KOH and in silicon electrodes in dilute HF solutions have been studied with a view to determining the source of generation within the electrode of the carriers involved in the reaction at the electrode solution interface. In n-type germanium anodes the generation is principally in the bulk with negligible contribution from the surface. Cathodes of p-type germanium in KOH show that surface generation is predominant. Generation in the space-charge region of silicon electrodes is probably the limiting process in dilute HF.

The phenomena of saturation current in germanium and silicon electrodes has been studied by several workers (1-5). For n-type Ge anodes in KOH solution their general conclusion is that the limiting currents observed are due to the rate of generation of holes in the bulk which diffuse to the surface and initiate the dissolution of Ge atoms. However, the role of surface generation remains somewhat obscure.

It was the purpose of this investigation to try to confirm the above findings by a more direct method and at the same time evaluate the magnitude of the contribution of surface generation. Similar studies were also carried out. on p-type cathodes and Si electrodes.

## Experimental

Figure 1 is a diagram of the cell used for the experimental work. It consisted of a three-necked 100-ml round bottomed flask; each neck was provided with a polyethylene stopper. The leads to the different electrodes passed through the stoppers. The counter electrode was a piece of platinized platinum sheet. The reference electrode for Ge was a saturated calomel electrode, connection being made by means of a bridge of saturated KCl solution.

For the work on Si electrodes a Pt wire was used as the reference electrode and the inside wall of the flask was lined with beeswax against the corrosive HF solutions. The outside of the cell was painted black because the Si electrodes were quite sensitive to light.

The HF solutions were ~5% [i.e., 1 vol of 48% HF (C.P.) diluted to 10 vol with demineralized water].[1]

The Ge or Si specimens used for electrodes were cut from single-crystal material in the form of slabs about 0.8 cm thick. The surface exposed to the solution, which was approximately on the (111) plane, varied in the area from 2 to 4 $cm^2$.

The method of mounting the Ge or Si in the cell is shown in Fig. 2. The samples were Cu plated on the back side (electrolytic for Ge, electroless for Si) which was then smeared with solder. The electrode, except for the face, was then covered with black wax to insulate it from the solution and minimize any photoeffect.

[1] Dr. P. Wang of our laboratory has found that solutions of this dilution permit smooth electrolytic etching of p-type Si.

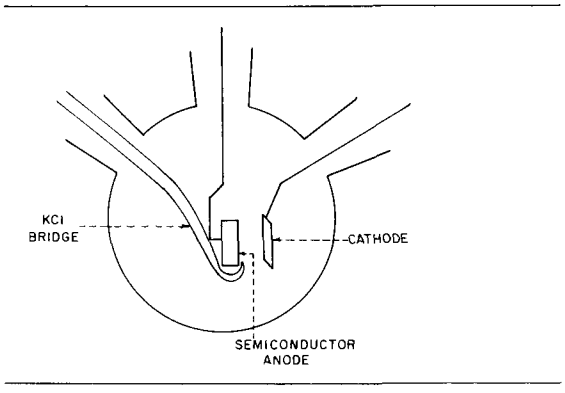


Fig. 1. Electrolytic cell diagram

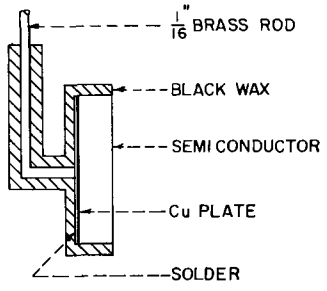


Fig. 2. Semiconductor electrode

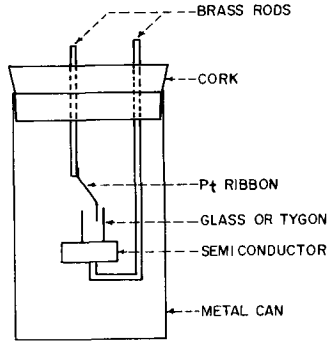


Fig. 3. Diagram of second type of cell used

A second experimental arrangement was used mainly for the purpose of checking the results obtained to see if any current leak significantly affected the results. This is shown in Fig. 3. Here the electrodes were bent in such a way that the unwaxed semiconductor surface was turned up. A glass or Tygon cylinder was mounted on this face. The solution was placed in the cylinder. This arrangement enormously reduces the chance of leakage. A platinum ribbon, serving as a counter electrode, was placed in the solution. This cell was mounted in a metal can which was covered with a cork stopper.

This metal can and the cell shown in Fig. 1 were mounted in a thermostatted water bath kept at 25.0° ±0.1°C for all of the work except where the temperature was deliberately varied.

The resistivities of the Ge and Si were measured by the four point probe method, and the lifetime on Ge was measured by the traveling light-spot technique. Lifetimes of the Si samples were not measured.

The current-voltage curves were obtained as follows. From a d-c power supply a certain voltage was applied across the cell. The voltage of the semiconductor electrode was measured against the reference electrode or counter electrode and the current through the cell was also measured at every applied voltage setting.

## Results

Using the arrangement in Fig. 3 showed that the black wax gave adequate electrical insulation between the solution and metal parts of the electrode.

Most of the work reported here deals with n-type Ge anodes. If we assume that the current in n-type Ge anodes is limited by the bulk generation of carriers, it can be shown easily that the limiting current density ($i$) should obey the relationship

$$i = q^2 D_p u_n N_i^2 \frac{\rho}{L}$$

Here $q$ is the electronic charge, $D_p$ is the diffusion coefficient of holes, $u_n$ is the electron mobility, $N_i^2$ is the product of electrons and holes at equilibrium, $\rho$ is the resistivity of the material, and $L$ is the diffusion length of holes.

In deriving this expression it is assumed that the hole concentration at the germanium-solution interface is effectively zero and that the resistivity of n-type Ge is determined by electron concentration only.

Therefore, if this relationship holds, a plot of the limiting current density for several n-type Ge specimens against the quantity ($\rho/L$) should yield a straight line of slope ($q^2 D_p u_n N_i^2$) and zero intercept.

In Fig. 4 some current voltage curves are shown which were obtained with n-type Ge anodes in a 1.35$N$ KOH solution at 25°C. The method of taking a value for the saturation current where the saturation is not perfect is shown. The portion of the curves marked A and B are extrapolated until they intersect. The current at this point is taken as the saturation current.

A plot of the saturation current densities against the ratio of resistivity to diffusion length ($\rho/L$) for several n-type Ge samples is shown in Fig. 5. Two runs were made on almost all of the samples. While the data appear to fall about a straight line passing through the origin, the value of its slope is 4.4 times the theoretically calculated value for a current multiplication of unity.

In Fig. 6 is the same data plotted a little differently, namely, the current density divided by the resistivity against the reciprocal of the diffusion length. This manner of plotting the data shows a little more clearly the dependence of the limiting current density on the bulk properties alone.

If surface generation was contributing appreciably to the current, then the plot in Fig. 6 would show a definite intercept, which it does not. Hence, in 1.35$N$ KOH and probably other electrolytic etching solutions, the saturation currents observed with

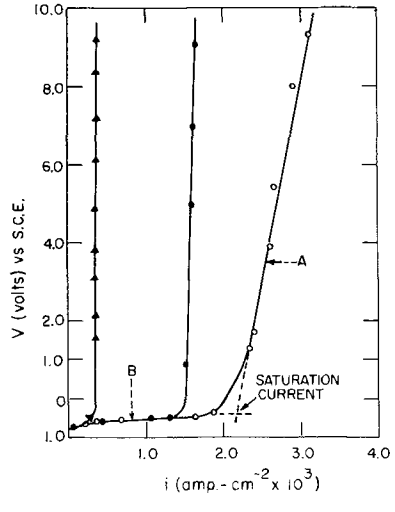


Fig. 4. Examples of voltage vs. current density curves for three n-type Ge anodes in 1.35N KOH at 25°C and method of determining "saturation current." Values of resistivity and diffusion length for these electrodes were: O, 17 ohm-cm, .07 cm; •, 14 ohm-cm, 0.07 cm; ▲, 5.8 ohm-cm, 0.13 cm.

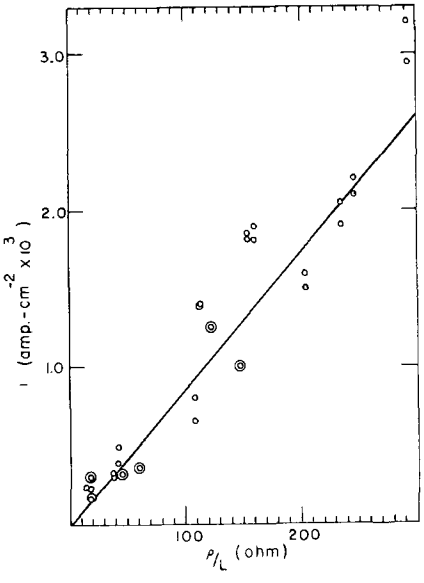


Fig. 5. Plot of i vs. ρ/L for several n-type Ge anodes in 1.35N KOH at 25°C.

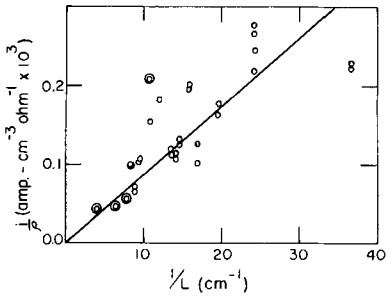


Fig. 6. Current density divided by resistivity vs. the reciprocal of the diffusion length for several n-type Ge anodes in 1.35N KOH at 25°C.

n-type Ge anodes are due to bulk generation alone with a negligible contribution from the surface.

Furthermore, the current multiplication appears to be close to 4 rather than a value of about 2 reported by others (1, 2). We are unable at this time to account for this difference in the values of current multiplication found. A possible mechanism for a current multiplication of 4 is given below:

$$\mathrm{Ge(s)} + e^{+} \rightarrow \mathrm{Ge(II)} + e^{-} \text{ rate determining}$$

$$\mathrm{Ge(II)} \longrightarrow \mathrm{Ge(IV)} + 2e^{-} \text{ rapid}$$

The Roman numerals indicate the valence state of Ge, and the role of $OH^-$ ions is not defined. This mechanism simply requires that the species formed due to the diffusion of a hole to a Ge atom at the surface is spontaneously oxidized electrolytically, and Ge ions, as $OH^-$ complexes (3), go into solution.

A final point on the n-type Ge anodes is the question of the temperature dependence of the saturation current. Since the data indicate that we may ignore the contribution from surface generation, then the temperature dependence of the saturation current should yield information on the recombination-generation levels in the bulk.

By the Shockley-Read (6) theory for the bulk lifetime of a semiconductor, it can be shown for the bulk diffusion current that

$$i \propto T^2 e^{\frac{-E_g + \frac{1}{2}\Delta E}{kT}} \frac{\sqrt{p_o + n_o}}{n_o}$$

Here $p_o$ is the hole, and $n_o$ is the electron equilibrium concentrations, respectively. $T$ is the absolute temperature, $E_g$ is the energy gap width, and $\Delta E$ is the difference between the generation center energy level and either the lowest conduction band energy level or the highest valence band level. This ambiguity arises from uncertainties regarding the relative size of quantities in the expression for bulk lifetime.

Using this expression the limiting currents were measured on two anodes; one, 30 ohm-cm; the other, 18 ohm-cm over a range of temperatures.

The quantity log $(i/T^2)(n_o/\sqrt{n_o + p_o})$ was plotted against $(1/T)$. In this plot the slope should be equal to $(-E_g + \frac{1}{2}\Delta E)/2.3k$. These two samples yielded approximately the same value of the slope, i.e., $-0.65$ ev, from which a value of $\Delta E$ of 0.28 ev can be calculated (Fig. 7). This value is consistent with a Ni or Cu recombination level (7).

Five p-type Ge cathodes were studied next in 1.35*N* KOH. The currents tended to saturate but showed no well-defined saturation current. Ellis (8) has found that a Ge specimen shows an increased surface recombination velocity after having been made a cathode in dilute acid solution as the electrolyte. He attributes this increase to deposited hydrogen.

In our case since hydrogen is deposited, the surface recombination velocity (and hence, surface generation) may be increasing because of this hydrogen and, therefore, no distinct saturation is noted.

This hypothesis was tested by replacing the KOH solution with a 1.4M $(NH_4)_2S_2O_8$ solution. The hydrogen deposition is largely replaced in this case by the reduction of persulfate ions. A more distinct saturation is obtained with this electrolyte as seen in Fig. 8. The limiting currents in 1.4M $(NH_4)_2S_2O_8$ nevertheless were still too large to be due to bulk generation alone. This can be shown by a calculation from the measured lifetimes and resistivities. Rather a surface recombination velocity of $\sim 10^{+4}$ or higher is indicated in $(NH_4)_2S_2O_8$ solution.

## Silicon

Five n-type Si anodes were used in 5% HF solutions; the currents tended to saturate fairly well and

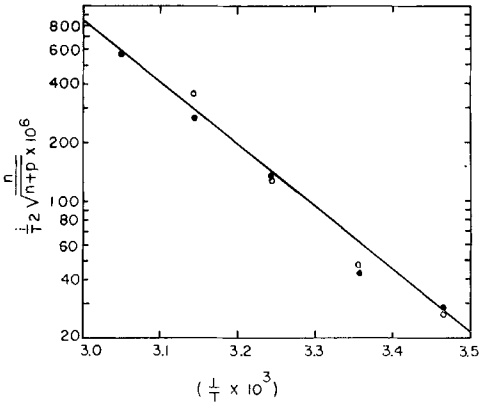


Fig. 7. Temperature variation of saturation current of two n-type Ge anodes in 1.35N KOH. O, 35 ohm-cm; •, 18 ohm-cm.

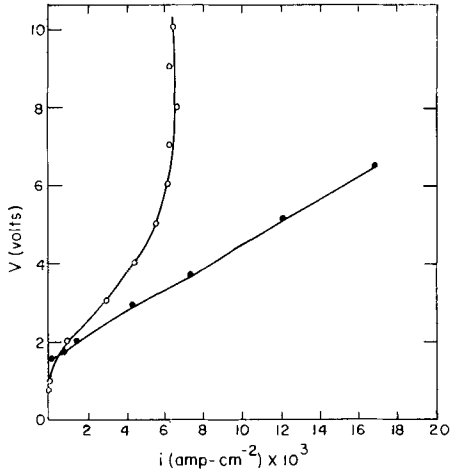


Fig. 8. Current density-voltage curve for one p-type Ge cathode at 25°C. O, 1.4M $(NH_4)_2S_2O_8$; •, 1.35N KOH.

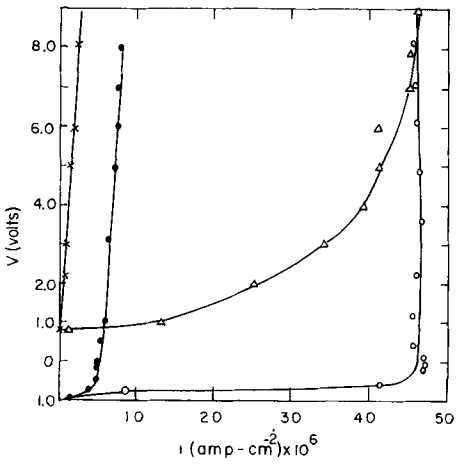


Fig. 9. Current density-voltage curves for one p-type Si cathode in dark X, and in diffuse light △, and one n-type Si anode in dark •, and in diffuse light O. In 5% HF at 25°C.

current densities in the range of 5-9 $\mu$amp-cm$^{-2}$ were observed. For bulk generation, diffusion lengths of the order of $\sim 10^{-6}$ cm would be indicated for these samples. Recent work on Si indicates diffusion lengths of the order of $10^{-3}$ cm are the rule. Moreover, surface recombination velocities of the order of $10^{+6}$ or higher would be required if surface generation was the dominant process. However, this value seems improbably high.

From the work of Sah, *et al.* (11), the current due to generation in the space charge region for p-n Si junctions under large reverse bias is given as

$$i(\text{sp. ch.}) = \frac{q\,W\,n_i}{\tau_{po}\,e^{E_t - E_i/kT} + \tau_{no}\,e^{E_i - E_t/kT}}$$

In this expression $q$ is the electronic charge, $k$ is Boltzmann's constant, $T$ is the absolute temperature, $W$ is the width of the space charge region, $n_i$ is the intrinsic carrier concentration in Si, and the quantities $\tau_{no}$, $\tau_{po}$ are the reciprocal capture probabilities of electrons and holes, respectively. The quantity $E_t - E_i$ is the difference between the recombination generation center energy level and the intrinsic level.

Values found by these authors for the unknown quantities above are: $W = 10^{-4}$ cm; $E_t - E_i = 4.6\ kT$; $\tau_{po} = 1.2 \times 10^{-8}$ sec; $\tau_{no} = 4.3 \times 10^{-6}$ sec.

Using these values in the above expression for $i$(sp. ch.) we get

$$i(\text{sp. ch.}) = 0.6 \times 10^{-6} \text{ amp cm}^{-2}$$

While this value is somewhat lower than the values of current density found, it is still of the right order of magnitude to indicate the probability that in our n-type Si anodes the source of carriers is mainly due to generation in the space charge region.

One p-type Si cathode was studied in the same solution. The current is of the same order of magnitude and indicates generation of carriers in the space charge region.

In Fig. 9 is shown the current-voltage curves for one p-type Si cathode and one n-type Si anode in 5% HF solution. Two curves are shown for each electrode. Data for one curve was taken with light excluded from the electrode; data for the other was taken with the electrode exposed to the diffuse light from the surroundings.

## Conclusion

1. Saturation currents in n-type Ge anodes in 1.35$N$ KOH are due to the generation of holes in the bulk with negligible contribution from surface generation.
2. Furthermore a current multiplication of approximately 4, instead of a value of about 2 as found by others, is reported.
3. The failure of the p-type Ge cathode to saturate distinctly in 1.35$N$ KOH can be attributed to deposited hydrogen.
4. It is probable that the limiting currents observed in Si electrodes in ~5% HF are due to generation of carriers in the space charge region of the electrode at the solution interface.

## Acknowledgment

The author wishes to express his gratitude to Drs. G. Wallis, P. Wang, S. Wang, and S. Mayburg for valuable suggestions and criticisms. Thanks are also due to Mr. I. Feinberg for assistance with the lifetime and resistivity measurements.

Manuscript received May 13, 1958. This paper was prepared for delivery before the New York Meeting, April 27-May 1, 1958.

Any discussion of this paper will appear in a Discussion Section to be published in the June 1959 JOURNAL.

REFERENCES

1. C. G. B. Garrett and W. H. Brattain, *Bell Syst. Tech. J.*, **34**, 129 (1955).
2. A. Uhlir, Jr., *ibid.*, **35**, 333 (1956).
3. D. R. Turner, *This Journal*, **103**, 252 (1956).
4. W. E. Bradley, J. W. Tiley, R. A. Williams, J. B. Angell, F. P. Keiper, Jr., R. Kansas, R. F. Schwarz, and J. F. Walsh, *Proc. I.R.E.*, **41**, 1702 (1953).
5. S. G. Ellis, *Phys. Rev.*, **100**, 1140 (1955).
6. W. Shockley and W. Read, *ibid.*, **87**, 835 (1952).
7. J. A. Burton, G. W. Hull, F. J. Morin, and J. C. Severiens, *J. Phys. Chem.*, **57**, 853 (1953).
8. S. G. Ellis, *J. Appl. Phys.*, **28**, 1262 (1957).
9. S. Mayburg and L. Cohen, *Sylvania Tech. Rept. #57-03-7.*
10. C. A. Bittman and G. Bemski, *J. Appl. Phys.*, **28**, 1423 (1957).
11. C. T. Sah, R. N. Joyce, and W. Shockley, *Proc. I.R.E.*, **45**, 1228 (1957).

# High-Pressure, High-Temperature Growth of Cadmium Sulfide Crystals

**W. E. Medcalf and R. H. Fahrig**

*The Eagle-Picher Research Laboratories, Miami, Oklahoma*

ABSTRACT

A process is described for growing cadmium sulfide crystals of uniform size, shape, and homogeneity from the melt. Structure and electrical characteristics of the crystals are discussed, and segregation data on several impurity species are given. A method is described for preparing high purity cadmium sulfide powder by the purification of cadmium and sulfur followed by direct combination of the elements.

Crystalline cadmium sulfide has risen to prominence in industry and research as a material which may be used in photovoltaic cells, radiation detection devices, infrared windows, and photosensitive elements.

The usual methods for the preparation of single crystals of cadmium sulfide have been confined to vapor phase or sublimation processes carried out at near atmospheric pressure. One such method was described by Frerichs (1, 2), in which hydrogen sulfide and a carrier gas are passed over heated cadmium metal. Crystals produced by this method are mostly ribbons or platelets. A second method described by Reynolds and Czyzak (3) is a static resublimation process in which a charge of cadmium sulfide is heated in an atmosphere of hydrogen sulfide in a sealed tube. Crystals in the form of prisms are formed directly on the charge as a result of local vaporization and crystallization. A modification of this method was reported by Reynolds and Greene (4) and involves vaporization of cadmium sulfide with recrystallization on a substrate in another part of the system. The vaporized cadmium sulfide crystallizes on the substrate in large grains, some of which weigh in excess of 50 g and are shown by x-ray measurement to be single crystals.

In the present work the development of a method of growing crystals from the melt was undertaken as another approach to the problem of growing cadmium sulfide crystals suitable for use in solar energy convertors. It was desired that the process would provide larger single crystals of cadmium sulfide with desirable photovoltaic properties and, specifically, that they would be homogeneous in respect to solute impurities and electrical characteristics.

Cadmium sulfide was first melted by Tiede and Schleede (5) and a melting point of 1750°C under 100 atm of nitrogen was reported. The experimental work was carried out in a small steel bomb containing an electrically heated graphite tube. The apparatus was operated for periods of a few minutes. Recently the melting of cadmium sulfide was carried out at the National Carbon Research Laboratories (6). This work was not published, but it is understood that a melting point of approximately 1500°C was obtained under a pressure of 200 atm of argon. More recently the melting point of cadmium sulfide was reported by Addamiano (7) to be 1475° ±15°C.

## Equipment

The initial phase of the present study was the design and construction of a furnace capable of maintaining molten cadmium sulfide for a period of several hours without excessive vaporization. The basis for the design was the available information on temperature and pressure, a consideration of the results desired, and the corrosive effects of hot cadmium sulfide vapor on various materials of construction, determined experimentally. A schematic diagram of the furnace is shown in Fig. 1.

The pressure shell is a forged steel pot with cover. The inside dimensions are 10 in. in diameter by 20 in. deep. The wall is 3 in. thick and is jacketed for water cooling. The cover, which is held down by 20-1 in. alloy steel bolts, is fitted with sight glass opening, a central vertical opening, and a pipe con-

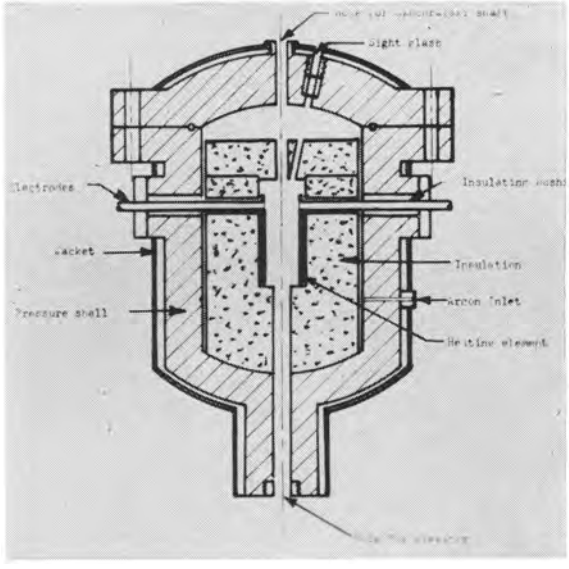


Fig. 1. Design of furnace used for growth of cadmium sulfide crystals from the melt.

nection to a gauge, safety rupture disk, and pressurizing line. The pot is equipped with insulating, pressure tight bushings around the electric power leads, and also a hydraulically operated elevator to vertically position the crucible inside the furnace. All pressure seals are Buna rubber "O" rings.

The purpose of providing the central top opening and the sight glass was for use in the Czochralski method of growing crystals, should this technique prove feasible. The elevator was provided for slow withdrawal of the melt from the hot zone.

The present method of protecting the walls of the pressure shell is by surrounding the heating element with fused stabilized zirconia brick lined with a porous carbon cylinder. The top section of the insulation is removed and replaced each time the furnace is opened for loading or unloading. The remainder of the insulation is packaged in a stainless steel container.

The heating element is a multiple split type graphite cylinder 3 in. OD x 2½ in. ID x 5 in. long. The thermal gradient along the length of the element is such that the temperature near the bottom is lower than that in the central and upper portions of the cylinder. The element is connected to the water-cooled molybdenum electrodes by threaded graphite studs.

Power for the furnace is furnished by a stepdown transformer with a variable autotransformer in the primary. The capacity of the power supply is 20 kw. Under 90% maximum heating load, the furnace draws 850 amp, at about 21.5 v. Control of the furnace temperature is by manual operation of the variable transformer.

Monitoring the temperature inside the furnace is made possible through the use of a boron graphite-graphite thermocouple (8). It is mounted on the end of a water-cooled elevator shaft. Output from the sensing device is fed to a strip chart recorder.

The p-type graphite was obtained from the National Carbon Research Laboratories.[1]

## Experimental Procedure

The pressure furnace described above cannot be used readily for either the Czochralski method or for controlled withdrawal of the melt from the hot zone. Excessive vaporization of the charge and obscurement of the sight glass occur when an uncovered crucible, necessary for the Czochralski technique, is used. Convective currents caused by chimney effect result when the crucible is withdrawn from the hot zone.

The following procedure is used in growing single crystals: Approximately 150 g of crushed, densified cadmium sulfide is introduced into a high purity graphite crucible and placed inside the furnace heating element. The crucible is supported by the thermocouple and a porous carbon stool piece which are mounted on the top end of the elevator shaft. The crucible is covered by a loosely fitting graphite lid. The hot zone of the furnace is then capped by a porous carbon cover; and the top section of the furnace insulation, a cast ceramic disk 2½ in. thick, is laid on the top. The furnace cover is next bolted down and evacuation is begun. During evacuation the pressure lines and furnace are purged with argon. After evacuation, the furnace is filled with argon to a pressure of about 1000 psi and heating is started. The temperature of the bottom of the crucible is raised rapidly to about 1500°C. This measurement lacks precision since the "cold" junction of the thermocouple varies somewhat due to conduction of heat by the pressurized gas. After the temperature reaches this point, the furnace pressure, which has been rising with the temperature, is adjusted to 1500 psi and the heating is slowed down to level off the temperature for 1 hr. This assures complete melting of the charge. The power is then reduced slowly over a period of about 6 hr so that the temperature of the crucible bottom is brought down in a linear manner.

### *Controlled Solidification of the Melt*

The thermal gradient along the heating element and conduction heat losses through the crucible support cause the lowest portion of the melt to solidify first. As the temperature is decreased by reduction of power to the element, progressive freezing of the melt takes place from the bottom upwards toward the top. A very slow advance of the solid-liquid interface encourages the formation of large crystals. Faster cooling results in smaller crystals arranged in a columnar formation.

## Results

Some of the ingots are of good crystalline structure at the bottom but have a region or pocket at the top which is noncrystalline in nature. Minute particles of elemental cadmium and voids from which sulfur and cadmium have been volatilized are often present in this pocket. This indicates that a portion of the cadmium sulfide underwent thermal decomposition while in the molten state, and that the products of decomposition were rejected by the advancing growth of crystalline material. By carefully controlling the cooling rate the size of this noncrystalline area can be diminished.

Figure 2 is a photograph illustrating the crystalline and noncrystalline areas in three ingots which have been sectioned vertically.

Cadmium sulfide crystals grown under controlled conditions are single crystals. Several ingots have been obtained which are made up of only one large crystal weighing more than 100 g. Crystallization is

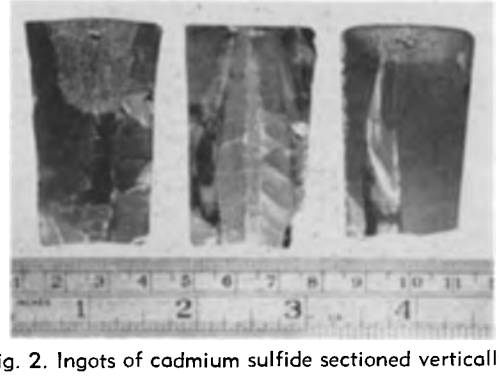


Fig. 2. Ingots of cadmium sulfide sectioned vertically

[1] Through the kindness of R. L. Shepard who, with his associates, developed the boron graphite-graphite thermocouple.

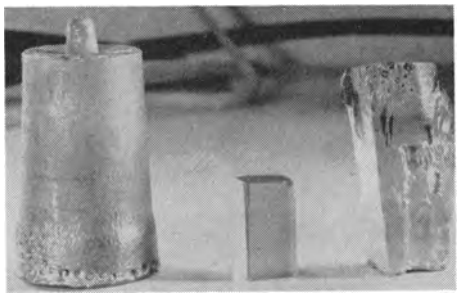

Fig. 3. Cadmium sulfide ingot with specimens cleaved and machined.

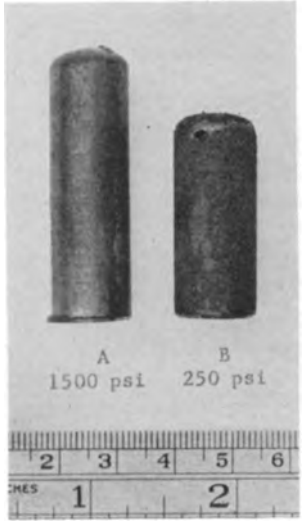


Fig. 4. Comparative size of cadmium sulfide ingots as a function of pressure.

in the hexagonal system and the vertical growth axis tends to coincide roughly with the C-axis to give an 0001 face at the top of the crystal, although in some cases the C-axis may be canted as much as 15° from the crucible axis. It is believed that this is due to unsymmetrical heat patterns existing in the hot zone of the furnace when seeding is begun in the bottom of the melt. The crystals may be cleaved, or may be machined to secure a specimen of any desired orientation.

Figure 3 is a photograph showing a single crystal ingot, a cleaved section of an ingot, and a specimen machined to a definite orientation.

*Effect of Pressure on Crystal Growth*

Several runs were carried out at pressures considerably lower than 1500 psi. With decreasing pressure the rate of volatilization of cadmium sulfide increased and the ingots were of poorer crystalline structure.

Identical weight of charge was used in the preparation of the ingots shown in Fig. 4. The charge was brought to the melting point in each case and then quick-cooled to decrease the amount of volatilization. The weight loss at 250 psi was 25.4% as compared to a 5% loss in weight at 1500 psi. There were more voids and noncrystalline areas in the ingots prepared at low pressures. Since our objective was to secure cadmium sulfide of good crystalline structure, the low pressure studies were discontinued. It is indicated, however, that low pressure melting may be used in zone-refining studies.

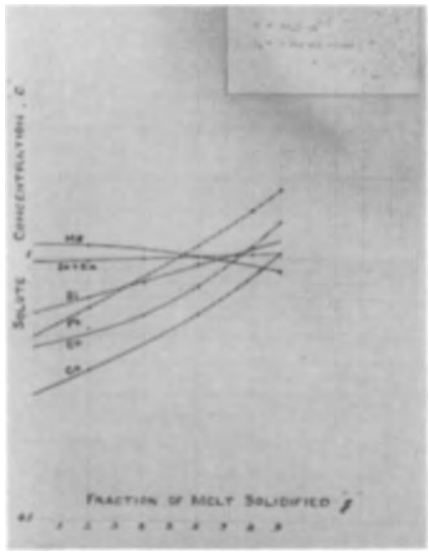

Fig. 5. Experimental concentration profiles for segregation of impurities in normal freezing of cadmium sulfide melt.

*Segregation of Solute Impurities*

Determination of effective segregation coefficients with normal freezing under a given set of experimental conditions was undertaken. Four crystals were grown under nearly identical conditions of charge, pressure, and cooling rate. The pressure was maintained at 1500 psi. The melts were caused to crystallize slowly over a period of 6 hr to provide a slowly advancing solid-liquid interface from the bottom to the top of the melt. Since the rate of movement of the interface could not be observed or precisely determined using the present equipment, the experimental coefficients obtained could not be considered as equilibrium values.

The four crystals produced were sectioned horizontally into five equal sections and analyzed spectrographically. The integrated concentration data were used to construct profiles depicting the concentration of impurities retained in the solid as a function of ($g$) the fraction of the melt solidified. The initial concentration $C_0$ was taken as the average concentration of the five segments. By plotting the solute concentration $C_s$ vs. ($g$) it is possible to determine the approximate $K_{eff}$ from the intersection of the profile with the y-axis. Figure 5 represents the experimental profiles for several impurity species in the cadmium sulfide matrix.

The profiles indicate that silicon, calcium, copper, and lead tend to be rejected by the advancing solid-liquid interface and that zinc and indium are not segregated in the normal freezing process. The profile of the magnesium species indicates a distribution coefficient slightly greater than 1.0. More recent data, not shown in Fig. 5, provide information that manganese is not segregated during the crystallization process. This is shown in Table I.

The data indicate that ($a$) normal freezing or zone refining of cadmium sulfide may be used to remove such impurities as silicon, lead, calcium, and copper; and ($b$) that certain solute impurities such as indium, zinc, and manganese can be used as doping agents homogeneously distributed throughout the crystal.

Table I
CdS crystal No. 111, doping agent $MnCl_2$

| Fraction solidified | Solute impurities, ppm Si | Mg | Cu | Ca | Mn |
|---|---|---|---|---|---|
| Top 0.9 | 500 | 5 | 1.0 | 50 | 50 |
| 0.8 | 20 | 5 | 0.5 | 10 | 50 |
| 0.6 | 20 | 5 | 0.5 | 10 | 50 |
| 0.4 | 10 | 5 | * | 10 | 50 |
| 0.2 | 10 | 5 | * | 10 | 50 |

CdS crystal No. 117, no doping agent

| Fraction solidified | Solute impurities, ppm Si | Pb | Mg | Cu | Ca | Resistivity, ohm-cm |
|---|---|---|---|---|---|---|
| 0.9 | 100 | * | 1 | 0.5 | 10 | 0.48 |
| 0.8 | 100 | 5 | 1 | 0.5 | 10 | 1.12 |
| 0.6 | 100 | * | 1 | 0.5 | 10 | 1.38 |
| 0.4 | 50 | * | 1 | * | 5 | 1.59 |
| 0.2 | 50 | * | 1 | * | 5 | 2.60 |

* Not detected.

### *Photovoltaic Cells*

Small photovoltaic cells were prepared from crystals grown by (*a*) crystallization from the melt and (*b*) the vapor phase process (3). A comparison of photovoltaic properties is shown in Table II.

### *High Purity Cadmium Sulfide*

Cadmium sulfide now available from commercial sources contains various impurities in concentrations of several parts per million. Such impurities include silicon, calcium, magnesium, zinc, lead, iron, aluminum, and copper. With the purpose of obtaining more effective control and evaluation of solute impurities in crystals grown from the melt, experimental work was carried out to provide cadmium sulfide feed material in which the impurity concentration would be not greater than 1 ppm. The procedure used in preparing cadmium sulfide of improved purity is described in the following paragraphs.

The procedure that was developed included the following steps: (*a*) purification of elemental cadmium, (*b*) purification of elemental sulfur, and (*c*) synthesis of cadmium sulfide from the purified elements. In the purification of elemental cadmium and sulfur it was found that the use of both distillation and zone melting processes was required to obtain the desired purity.

Commercial grade cadmium was given three distillations in a cast iron retort to effectively decrease the concentration of zinc and lead to approximately 20 ppm. These distillations proved to be necessary for subsequent removal of these elements to a concentration of less than 1 ppm by zone melting. The cadmium then was zone melted by the process described by Pfann (9). A graphite boat was used to provide an ingot 19 in. in length and weighing approximately 1 kg. After six molten zones of 1.0 in. length were passed horizontally through the solid ingot, the bar became monocrystalline over 90% of its length and the impurity concentration over a distance of 50% of its length was below the limits of spectrographic detection.

Four distillations of sulfur in a clear quartz unit removed iron, zinc, aluminum, and copper to near the limit of spectrographic detection. Silicon, calcium, and a trace of magnesium were still present in the sulfur after four distillations. To further purify the sulfur, zone melting techniques were investigated. These included (*a*) the conventional zone melting process in which a molten zone of approximately 1.0 in. in length was caused to traverse a horizontal solid ingot of sulfur and (*b*) a reversed zone melting procedure in which a small solid zone was caused to progress transversely through an elongated melt of sulfur. This technique of removing from a solid substance soluble impurities having a distribution coefficient greater than 1.0, was reported by Overby (10). The latter process proved to be effective in the removal of silicon and calcium from the sulfur. The zone melting procedures were carried out in a graphite boat 18 in. in length and purified ingots of sulfur weighing approximately 1 lb were produced.

The synthesis of cadmium sulfide was carried out by a vapor phase reaction in a quartz reactor. The purified sulfur and cadmium were volatilized from separate quartz boilers external to the reactor with helium used as the carrier gas. The reactor was

Table II. Comparison of photovoltaic properties of cadmium sulfide crystals grown from the melt and by a vapor phase process

| Run No. | Method crystal growth | Resistivity, ohm-cm | Mobility, $cm^2/v$ sec | Open circuit voltage, v | Conversion Efficiency* |
|---|---|---|---|---|---|
| HP-84 | From melt | 1.41 | 108 | 0.40 | 1.77% |
| HP 60 | From melt | 0.29 | 180 | 0.52 | 2.30† |
| HP-91(a) | From melt | 1.62 | 175 | 0.36 | 2.22 |
| HP-91(b) | From melt | 1.62 | 171 | 0.44 | 2.42 |
| HP-96 | From melt | 0.75 | 179 | 0.35 | 2.42 |
| HP-57 | From melt | 0.13 | 300 | 0.475 | 6.11 |
| | Vapor phase growth (average value) | — | — | — | 2.05‡ |

* RFL-2 Lamp @ 1.5 g-cal/$cm^2$/min. (In sunlight the conversion efficiency is 30-50% greater.)
† Determined by the Research Laboratories of the Harshaw Chemical Co.
‡ This value was obtained from a recent and separate study of the conversion efficiencies of a large number of cadmium sulfide crystals grown by vapor phase deposition. It is included in the table for purposes of comparison.

Table III. Spectrographic analyses

| | | Impurities, ppm Si | Pb | Mg | Fe | Cu | Zn | Ca | Al |
|---|---|---|---|---|---|---|---|---|---|
| I | Cadmium | | | | | | | | |
| | Triple distilled | 10 | 10 | 1.0 | 1 | 3.0 | 20 | 2 | 2 |
| | Zoned, 6 passes | 1 | * | 1.0 | * | * | * | * | * |
| II | Sulfur | | | | | | | | |
| | Starting sulfur | 20 | * | 1.0 | 4 | 4.0 | * | 80 | 3 |
| | 2X distilled | 20 | * | 1.0 | 2 | 2.0 | * | 50 | 2 |
| | 4X distilled | 10 | * | 0.5 | * | 1.0 | * | 30 | * |
| | 4X distilled and zone cooled | * | * | 0.5 | * | 1.0 | * | * | * |
| III | Cadmium sulfide (synthesized) | 100 | * | 0.5 | * | 0.5 | * | * | * |

* Not detected.

maintained at a temperature of 900°C during the synthesis.

The cadmium sulfide formed as small crystals having a median radius of approximately 4$\mu$. One pound of synthesized cadmium sulfide was produced per run representing a recovery of approximately 80% of theoretical based on the weight of cadmium used. The spectrographic data on the reactants and product are shown in Table III.

There was a significant increase in silicon during the synthesis due to introduction from the opaque quartz used in the reactor. There was no introduction of other impurities during the reaction.

## Conclusions

Cadmium sulfide crystals of uniform size and shape can be grown from the melt in an argon atmosphere at 1500 psi. Controlled cooling to cause a solid-liquid interface to move from the bottom to the top of the vertical cylinder of molten cadmium sulfide at a slow and controlled rate results in the formation of single crystals weighing in excess of 100 g. At pressures as low as 250 psi only polycrystalline ingots are formed.

Ingots grown from the melt are homogeneous with respect to the orientation of certain solute impurities including indium, zinc, and manganese. Silicon, calcium, copper, and lead are segregated during the normal freezing of cadmium sulfide exhibiting an effective distribution coefficient of less than one. Solar cells prepared from melt grown crystals have photovoltaic conversion efficiencies equal to solar cells prepared from vapor grown cadmium sulfide crystals.

Synthesis of cadmium sulfide from elemental cadmium and sulfur which have been purified by distillation and zone melting techniques provides a material which has, with the exception of silicon, an impurity concentration not greater than 1 ppm as determined spectrographically.

## Acknowledgment

Acknowledgment is given to the Aeronautical Research Laboratory for their sponsorship of this work and permission to publish the results. The authors also wish to express their appreciation to D. A. Hammond of Harshaw Chemical Company for check determinations on conversion efficiencies. The assistance of the following staff members of the Eagle-Picher Company in carrying out the work is also acknowledged: L. H. Garrison, J. E. Powderly, K. E. Bean, and N. H. Hemmat.

Manuscript received April 29, 1958. This paper was prepared for delivery before the New York Meeting, April 27 to May 1, 1958.

Any discussion of this paper will appear in a Discussion Section to be published in the June 1959 JOURNAL.

REFERENCES

1. R. Frerichs, *Naturwissenschaften*, **33**, 281 (1946).
2. R. Frerichs, *Phys. Rev.*, **72**, 594 (1947).
3. D. C. Reynolds and S. J. Czyzak, *ibid*, **79**, 543 (1950).
4. D. C. Reynolds and L. C. Greene, *J. Appl. Phys.*, **29**, 559 (1958).
5. E. Tiede and A. Schleede, *Ber.*, **53B**, 1717 (1920).
6. Information supplied in private communique by Dr. M. T. Jones of National Carbon Research Laboratories, Parma, Ohio
7. A. Addamiano, *J. Phys. & Colloid Chem.*, **61**, 1253 (1957).
8. R. L. Shepard, paper presented at Pittsburgh Meeting of the American Physical Society, March 15, 1956.
9. W. G. Pfann, *J. Metals*, **4**, 747 (1952).
10. S. L. Overby, U. S. Patent 2,801,192.

# Some Semiconducting Properties of HgTe

**J. Black, S. M. Ku, and H. T. Minden**

*Sylvania Research Laboratories, A Division of Sylvania Electric Products Inc., Bayside, New York*

ABSTRACT

Mercuric telluride was synthesized and single crystals were prepared both in a horizontal capsule and by the Bridgman technique. The Hall coefficient $R$ and the resistivity $\rho$ were measured as a function of temperature and magnetic field. Above 250°K the material was intrinsic with an energy gap of around 0.02 ev and a mean density-of-states effective carrier mass of about 0.04 $m_e$. Hall effect and mangetoresistance data indicated that at 300°K $\mu_n \sim 16{,}000$ cm$^2$/v sec while $\mu_n/\mu_p \sim 10$. In the intrinsic temperature range, mobilities decreased with increasing temperature.

At low temperatures $R$ decreased markedly with magnetic induction even though $R$ measured at low fields was independent of temperature for one of the ingots. In addition, the magnetoresistance fell far below a $B^2$ dependence at low temperatures. This behavior is characteristic of p-type semiconductors in the transition temperature range between intrinsic and extrinsic conduction. In HgTe this transition temperature range is quite wide because of the low energy gap.

Since all material prepared from the melt was p-type, it seems that there is either a dominating acceptor impurity in all the samples or the maximum melting point of the compound does not occur at the stoichiometric composition.

Much work has been done in recent years in determining the electrical and optical properties of semiconducting compounds with the zinc blende structure. The main effort has been concentrated on the III-V series of compounds, which are especially interesting because of their high electron mobilities.

Table I

| Crystal | Starting material | Trace impurities |
|---|---|---|
| Z21-35 | 99.8 + Te<br>Triple Distilled Hg | Ag, Cu, Fe, Pb, Si<br>No analysis |
| B51-1 | 99.999 Te<br>99.999 + Hg | Spectroscopically pure<br>Spectroscopically pure |

Comparatively little work has been done on the II-VI compounds, which have, in general, higher energy gaps but lower carrier mobilities than III-V semiconductors. Two of the compounds, however, HgSe and HgTe, have been reported to possess electron mobilities greater than 10,000 cm²/v sec at room temperature (1). Previous investigations published have been made on thin films (2, 3), pressed powders (4), pressed and sintered powders (5), or fused ingots (5). Detailed measurements of the electrical properties of single-crystal HgTe have been reported recently by Harman and Logan (6).

It is the purpose of this paper to present the results of an investigation of the electrical properties of single-crystal HgTe. The Hall effect and resistivity of a number of samples have been measured from 80° to 650°K as a function of magnetic field strength.

## Experimental Methods

Mercuric telluride was synthesized from the elements in sealed evacuated quartz capsules. The purity of the starting elements is shown in Table I. The capsule was slowly heated to 720°C, which is about 50° above the melting point of the compound; heating was done over a period of 24 hr to prevent the buildup of an excessive mercury vapor pressure. Once the capsule reached 720°C the melt was allowed to soak for an additional 2 hr with frequent agitation to insure mixing of the elements. After soaking, the material was slowly cooled to room temperature. Debye-Scherrer x-ray powder patterns of the synthesized HgTe agreed with data published previously by other investigators (7).

Two single-crystal ingots were prepared. One, Z21-35, received 35 zone refining passes and the single crystal was grown in the same boat that was used for zone refining. The other, B51-1, was grown as a single crystal by the Bridgman technique directly after synthesis.

Spectroscopic analysis of the zone-refined ingot, Z21-35, showed that all impurities observed segregated toward the last-to-freeze end. Sn, Bi, and Pb segregated rapidly while Ag, Fe, and Cu segregated slowly. The Cu and Fe concentration could not be reduced below ~5 ppm and ~50 ppm respectively in 35 passes.

Electrical measurements were made on single-crystal bars about 1 x 2 x 10 mm; samples were etched in aqua regia diluted with water. Stainless steel pressure contacts were used on some specimens; others were copper plated and soldered.

For low-temperature measurements the samples were cooled in a cryostat to about 80°K and then allowed to warm slowly to room temperature while their electrical properties were measured. Measurements above room temperature were made as the samples were being heated in a small nichrome furnace.

The Hall coefficient and resistivity were measured as a function of both temperature and magnetic field. The usual d-c technique was employed, and voltages were measured by means of a L&N Type K2 potentiometer. An Arthur D. Little 11-in. electromagnet was used. The voltage across the magnet current shunt was calibrated against the magnetic field which, in turn, was measured with a Rawson rotating coil gaussmeter.

## Experimental Results

All samples studied had a negative Hall coefficient at all temperatures which were reached in this investigation.

*Hall coefficient.*—Figure 1 shows the effect of temperature on the Hall coefficient of a sample from B51-1, at various magnetic field strengths. At high temperatures the Hall coefficient, $R$, is nearly independent of magnetic induction $B$. At low temperatures $R$ decreases with increasing magnetic field strength. In Fig. 2 data of Fig. 1 are replotted with temperature as a parameter instead of magnetic field strength to show the effect of $B$ on $R$ at various temperatures. At temperatures down to 160°K or so the Hall effect appears to be independent of $B$ below

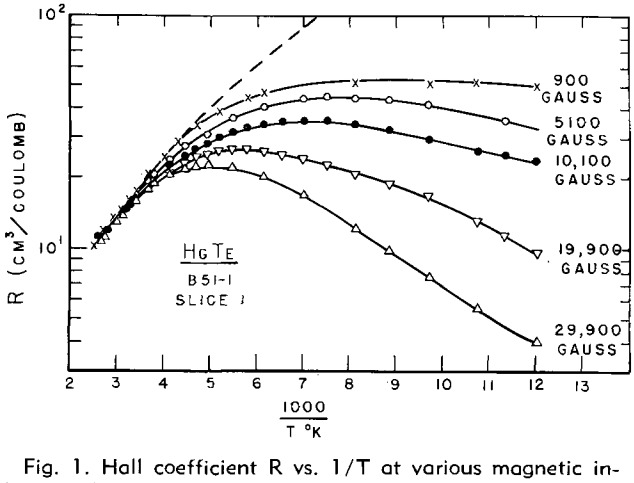


Fig. 1. Hall coefficient R vs. 1/T at various magnetic inductions for a sample cut from ingot B51-1.

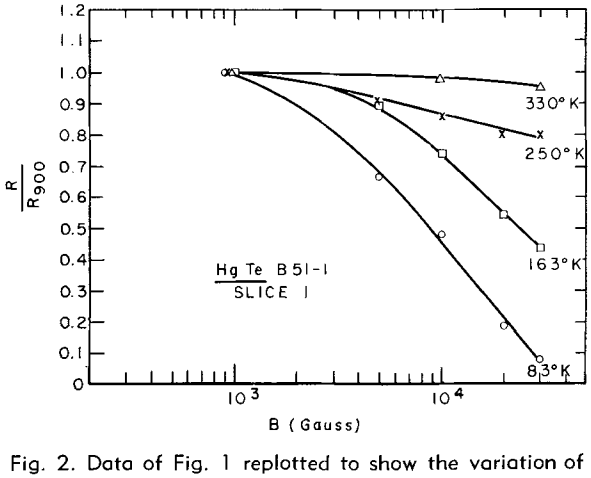


Fig. 2. Data of Fig. 1 replotted to show the variation of R (normalized to R at 900 gauss) with magnetic induction at constant temperature.

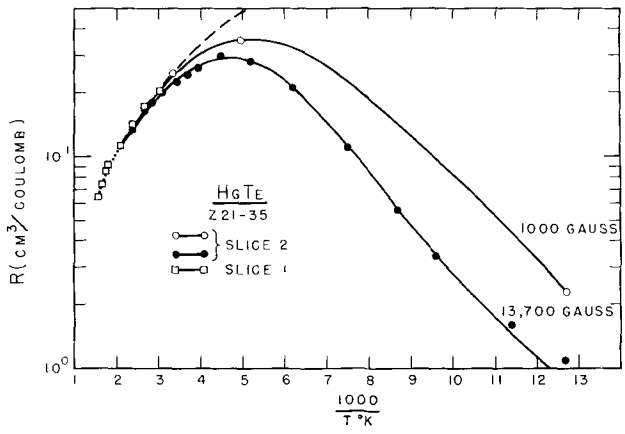


Fig. 3. Variation of R with 1/T at 1000 gauss and 13,700 gauss for two samples from ingot B51-1.

1000 gauss. At liquid nitrogen temperatures measurements below 1000 gauss are needed to determine whether $R$ varies significantly with $B$ at low field strengths.

Figure 3 shows the effect of temperature on the Hall coefficient of samples from Z21-35 at two magnetic field strengths. Irreversible changes in $R$ occurred above 500°K. These changes were probably due to decomposition; in fact, the odor of Te was noticeable above 650°K. Because of this, data above about 500°K may be in error. The variation of $R$ with magnetic field strength is shown in Fig. 4. Data for these curves were obtained from measurements of $R$ as a function of $B$ at 79°, 202°, and 296°K. It is clear that for ingot Z21-35 the Hall effect at liquid nitrogen temperatures is independent of magnetic field strength at values of $B$ below 1000 gauss. The dependence of $R$ on $B$ at a given temperature is almost the same for both the B51-1 and the Z21-35 crystals.

Curves of the Hall effect at 900 gauss for two different samples from B51-1 are shown in Fig. 5. Slice No. 1, which has the higher Hall coefficient, was closer to the first-to-freeze end than was slice No. 3. Figure 5 also shows the Hall curves at 13,700 gauss for two samples from Z21-35. Again the sample (slice No. 3) that was closer to the first-to-freeze end has the higher Hall coefficient.

*Resistivity.*—Figure 6 shows the resistivity, $\rho$, as a function of inverse temperature for the various

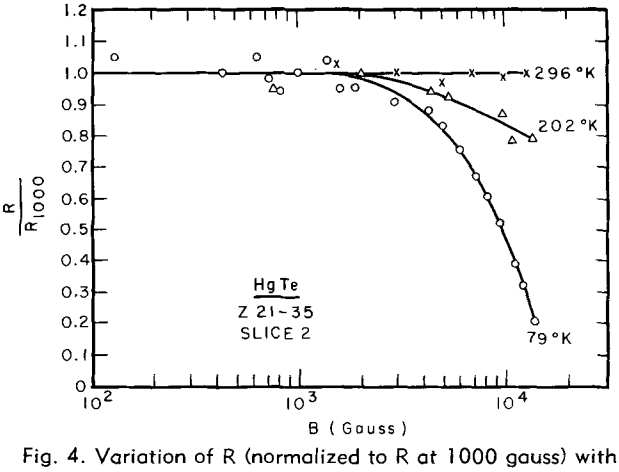


Fig. 4. Variation of R (normalized to R at 1000 gauss) with magnetic induction at various temperatures.

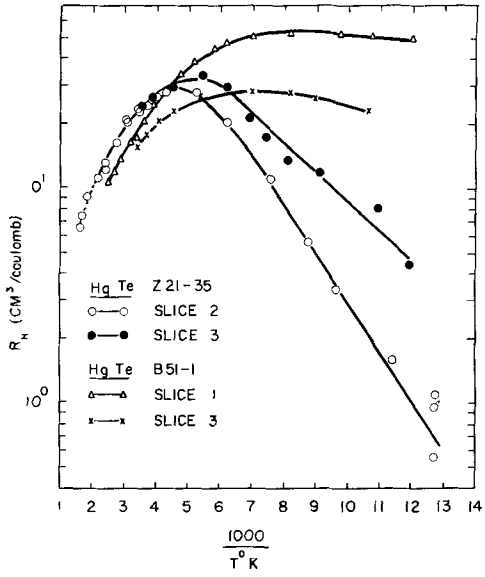


Fig. 5. Variation of R with 1/T (B=900 gauss) for two slices of ingot B51-1. Slice No. 1 was closer to the first-to-freeze end. Variation of R with 1/T (B=13,700 gauss) for two slices of ingot Z21-35. Slice No. 3 was closer to the first-to-freeze end.

samples of B51-1 and Z21-35. As with the Hall coefficient, irreversible changes in $\rho$ were observed above 500°K, so that values of the resistivity may be in error in this temperature region.

The Hall mobility $\mu_H = R\sigma_0$ was calculated from the resistivity at zero magnetic field and the Hall coefficient at magnetic field strengths where $R$ was independent of $B$. In Figure 7 log $R\sigma_0$ is plotted as a function of log $T$ for samples from B51-1 and Z21-35. Room temperature values of Hall mobility are in agreement with those reported recently by other investigators (7).

Figure 8 shows the effect of temperature on the transverse magnetoresistance $\Delta\rho/\rho$ of two samples from B51-1 at various magnetic field strengths. These two samples were cut, side by side, from a thin disk obtained by slicing the ingot normal to its long axis. At 5000 gauss and at 10,000 gauss $\Delta\rho/\rho$ is the same for both samples over the whole range of temperature. At higher magnetic field strengths, however, the two samples showed differences in $\Delta\rho/\rho$ at temperatures below about 180°K.

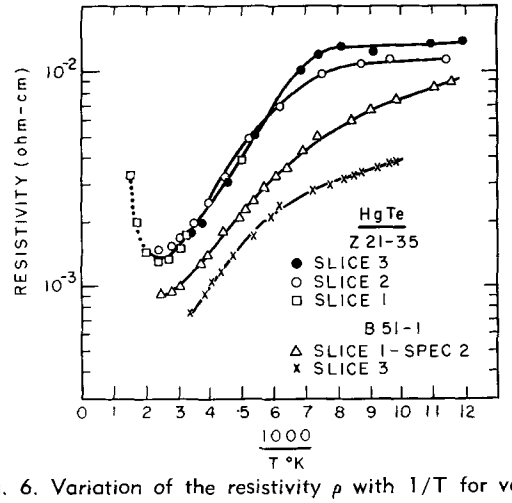


Fig. 6. Variation of the resistivity $\rho$ with 1/T for various samples of HgTe.

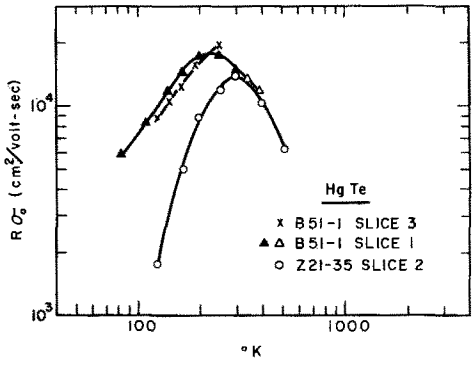


Fig. 7. Hall mobility vs. T for various HgTe samples

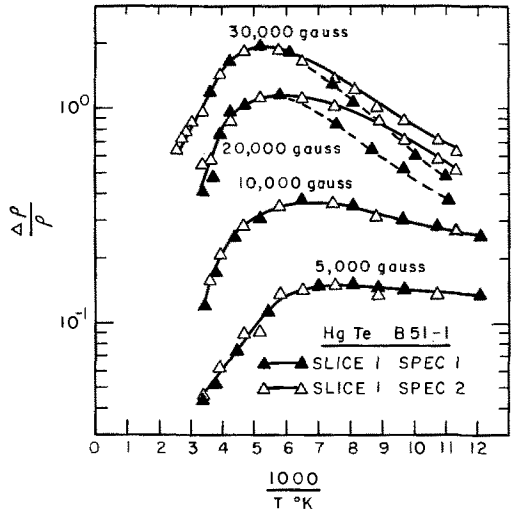


Fig. 8. Magnetoresistance $\Delta\rho/\rho$ vs. 1/T for two samples of ingot B51-1 at various magnetic inductions.

The effect of temperature on the magnetoresistance of three samples from Z21-35 at 13,700 gauss is plotted in Fig. 9. Slices 1 and 3 came from the first-to-freeze end of the ingot while slice 2 was cut from the center of the ingot. The slice nearer to the first-to-freeze end had the higher magnetoresistance at low temperatures. Above about 250°K the magnetoresistance of the three slices became equal.

A magnetoresistance mobility was calculated from the relation

$$\mu_m = \left(\frac{\Delta\rho}{\rho K B^2}\right)^{1/2} \qquad [1]$$

where

$$K = \frac{4-\pi}{\pi}\left(\frac{3\pi}{8}\right)^2 \qquad [2]$$

Figure 10 shows the effect of temperature on the magnetoresistance mobility, $\mu_m$, of ingot B51-1 at various magnetic field strengths and of ingot Z21-35 at a field strength of 13,700 gauss. At low temperatures $\Delta\rho/\rho$ falls considerably below a $B^2$ dependence at high magnetic fields, while at high temperatures $\Delta\rho/\rho$ follows approximately a $B^2$ dependence. Furthermore, at high temperatures $\mu_m$ is the same for both B51-1 and Z21-35, and $\mu_m$ decreases with increasing temperature.

It should be mentioned that at room temperature a polycrystalline sample of HgTe showed a high transverse magnetoresistance ($\Delta\rho/\rho = 0.12$ at 10,000 gauss) while the longitudinal magnetoresistance was less than $10^{-3}$ at 10,000 gauss.

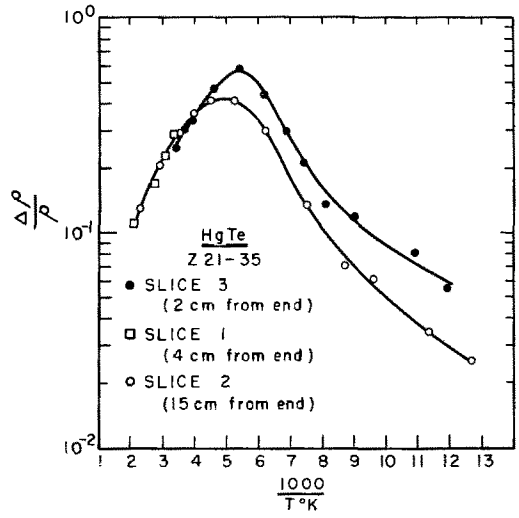


Fig. 9. Magnetoresistance, $\Delta\rho/\rho$, vs. 1/T for three slices of ingot Z21-35 at B=13,700 gauss.

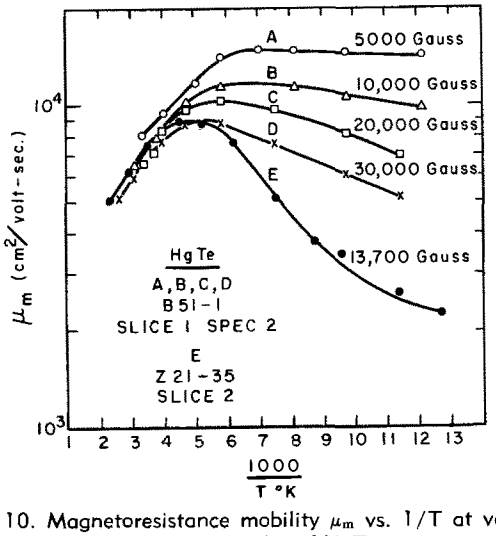


Fig. 10. Magnetoresistance mobility $\mu_m$ vs. 1/T at various magnetic inductions for two samples of HgTe.

## Discussion

*Energy gap.*—The slopes of the log $R$ and log $\rho$ vs. $1/T$ curves (Fig. 1, 3, and 5) correspond to an energy gap of about 0.08 ev. This result is somewhat misleading because the $T^{3/2}$ dependence of the effective density of states must be taken into account for such a low energy gap. The dashed lines of Fig. 1 and 3 are calculated from the equation

$$R = -\left(\frac{3\pi}{8}\right)\left(\frac{b-1}{b+1}\right)\left(\frac{1}{\epsilon n_i}\right) \qquad [3]$$

where

$$n_i = 2\left(\frac{2\pi m^* kT}{h^2}\right)^{3/2} e^{-E_g/2kT} \qquad [4]$$

and

$$m^* = (m_n m_p)^{1/2} \qquad [5]$$

The energy gap assumed is 0.025 ev and the scale factor

$$\left(\frac{8}{3\pi}\right)\left(\frac{b+1}{b-1}\right)\left(\frac{m^*}{m_e}\right)^{3/2} = 0.023$$

If the first two factors are assumed to be unity, $m^*/m_e = 0.035$. The principal difficulty in the inter-

pretation is that for such a low energy gap the slope at room temperature is relatively insensitive to the value of the energy gap. If $E_g = 0$ is assumed, however, the slope of the calculated curve is definitely less than that of the experimental curve.

The use of Fermi-Dirac statistics instead of Maxwell-Boltzmann statistics increases the slope of the calculated log $R$ vs. $1/T$ for a given energy gap.

*Hall coefficient.*—Since $R < 0$ in the intrinsic region, the mobility ratio $\mu_n/\mu_p = b > 1$. The log $R$ vs. $1/T$ curve for ingot Z21-35 appears to be typical of p-type material (see Fig. 3). With a low energy gap the transition from intrinsic to extrinsic p-type behavior should take place over a wide range of temperature. This would account for the fact that even at 78°K $R$ is still negative. At higher magnetic fields the Hall zero appears to shift to higher temperatures in a manner similar to that observed for InSb (8).

The Hall curve for ingot B51-1 at low magnetic fields appears to be typical of n-type material. On the other hand, at higher magnetic fields $R$ decreases with lower temperatures as shown in Fig. 1. The most satisfactory explanation of this behavior is that ingot B51-1 is also p-type, but that it has a lower extrinsic hole concentration than ingot Z21-35. This would account for the fact that the Hall zeros for ingot B51-1 apparently occur at lower temperatures than they do for ingot Z21-35. In fact, Carlson has measured the Hall coefficient of apparently n-type HgTe at very low temperatures, and he found that $R$ became positive near 20°K (9).

*Mobility.*—In the intrinsic region

$$R_o \sigma_o \propto \mu_n - \mu_p \qquad [6]$$

$$\Delta\rho/\rho B^2 \propto \mu_n \mu_p \qquad [7]$$

The constants of proportionality depend on the statistics used and on the scattering mechanism assumed. If Boltzmann statistics are used and if the mean free path is assumed independent of energy (lattice scattering), then at room temperature Eqs. [6] and [7] lead to $\mu_n = 15{,}800$ cm²/v sec, and $b = 5.27$. If the above assumptions are correct, $\mu_n$ and $\mu_p$ continually decrease with increasing temperature above 240°K. The validity of using Boltzmann statistics above room temperature may be questioned legitimately. For instance, using Boltzmann statistics at 300°K gives $b = 5.27$, while Fermi-Dirac statistics give $b = 14.50$. Nonetheless, it appears reasonable to conclude that in the neighborhood of room temperature $\mu_n \sim 16{,}000$ and $b \sim 10$ in contrast to a value of 100 reported by Harman and Logan (6) at low temperatures.

Harman and Logan and Carlson (10) have observed the large variation with magnetic field of the Hall coefficient in HgTe. This variation is large at low temperatures, but vanishes at room temperature. If the present interpretation of these results is correct, then truly n-type HgTe has not yet been reported. This leads one to suspect that HgTe might be "instrinsically" p-type. According to the theory of the zinc blende lattice, Te vacancies should act effectively as p-type impurities. On the other hand, Harman and Logan observed that the diffusion of Hg into HgTe lowers the intrinsic hole concentration. In order for Hg atoms to act as compensating donors, they would be expected to occupy interstitial positions. This raises the possibility that the acceptors in p-type HgTe are interstitial Te atoms. If this is so, the HgTe alloy having a maximum melting point would contain a slight stoichiometric excess of Te. This effect has been observed in $Bi_2Te_3$ (11) and PbSe (12). The result of extensively zone refining an ingot, e.g., our sample Z21-35, would be to bring the solid composition close to the (p-type) invariant point, while a single Bridgman pass (B51-1) would alter the starting (stoichiometric) composition less.

On the other hand, some correlation has been shown between the Hall coefficient and the segregation of impurities (Fig. 5). It is entirely possible that the same acceptor impurity occurs in all starting materials. Although ingot Z21-35 was extensively zone refined, it was made from less pure starting materials than ingot B51-1. The difference in purity of the starting materials might account for the fact that ingot Z21-35 apparently has a higher extrinsic hole concentration than ingot B51-1. Arsenic and antimony are common impurities in Te. They are not readily detectable by spectroscopic means so that spectroscopically pure Te might contain appreciable quantities of these impurities. If As or Sb atoms were to substitute in place of Te in the HgTe zinc blende lattice, they would act as acceptors. Because of the volatility of these impurities, zone refining the compound in a closed system (as was done for ingot Z21-35) would segregate them very slowly, so that the general level of impurity in the starting materials would be maintained.

## Conclusion

Mercuric telluride has an extremely small but finite energy gap. It has high carrier mobilities characteristic of low energy gap compound semiconductors, and these high mobilities stem from low effective masses. Mercuric telluride also shares with most other semiconductors the fact that the electron mobility is higher than the hole mobility. As a result of the low energy gap, interpretation of the temperature variation of the Hall coefficient is not straightforward. Material which appears to be n-type may be in reality p-type. All HgTe synthesized by the authors appears to be p-type. The explanation could be in the p-type nature of the invariant solid composition of HgTe or in the presence of a dominating acceptor impurity.

## Acknowledgment

The authors wish to acknowledge the help of Messrs. A. R. Liboff and L. Weaver who performed the measurements on ingot Z21-35. They also wish to thank Mr. D. Howell for assistance in preparing the manuscript.

Manuscript received April 14, 1958.

Any discussion of this paper will appear in a Discussion Section to be published in the June 1959 JOURNAL.

## REFERENCES

1. C. H. L. Goodman, *Proc. Phys. Soc.*, **67B**, 258 (1954).
2. J. G. N. Braithwaite, *ibid.*, **64B**, 274 (1951).

3. O. D. Elpat'evskaya, R. A. Konikova, A. R. Regel, and I. V. Yavorskii, *Zhur. Tekh. Fiz.*, **26**, 2154 (1956); O. D. Elpat'evskaya, and A. R. Regel, *ibid.*, **26**, 2432 (1956); *ibid.*, **27**, 45 (1957).
4. A. I. Blum, and A. R. Regel, *ibid.*, **21**, 316 (1951).
5. E. Nikol'skaya, and A. R. Regel, *ibid.*, **25**, 1352 (1955).
6. T. C. Harman, and M. J. Logan, *Bull. Am. Phys. Soc.*, Series II, **3**, #1, Abstract E2, 15 (1958).
7. U. Zroll, *Z. Physik*, **138**, 167 (1954).
8. D. J. Howarth, R. H. Jones, and E. H. Putley, *Proc. Phys. Soc.*, **70B**, 124 (1957).
9. R. O. Carlson, Private communication.
10. R. O. Carlson, *Bull. Am. Phys. Soc.*, Series II, **2**, #7, Abstract L7, 347 (1957).
11. C. B. Satterthwaite, and R. W. Ure, Jr., *Phys. Rev.*, **108**, 1164 (1957).
12. A. F. Goldberg, and G. R. Mitchel, *J. Chem Phys.*, **22**, 220 (1954).

# Electron Mobility in InP

**M. Glisksman and K. Weiser**[1]

*RCA Laboratories, Princeton, New Jersey*

ABSTRACT

The Hall mobility of electrons in InP has been observed as a function of temperature and of carrier concentration. A lattice mobility of 5000 cm²/v-sec at 290°K is calculated from these results, varying with temperature at least as rapidly as $T^{-2}$. The observations can be interpreted by assuming a combination of lattice and ionized impurity scattering with an effective mass of the order of 0.05 $m_o$ or less.

The properties of the III-V compound indium phosphide are of interest because of its relatively large forbidden band-gap [1.25 ev (1)] and yet high electron mobility, with measured values as high as 4500 cm²/v-sec at 290°K. As yet little is known about the band structure or the scattering processes in this material. The study of the temperature dependence and the effect of impurities on the mobility reported in this paper indicate that the electrons in InP have a small effective mass (probably less than 0.05 $m_o$); concurrent investigations reported elsewhere (2) show that the lowest conduction band is spherically symmetric. In the purest of the crystals investigated in this study, the mobility varies as rapidly as $T^{-2}$ in the temperature range 200°-300°K, indicating that scattering by the acoustic phonons of the lattice (which would give a mobility $\alpha\ T^{-1.5}$) is not the only scattering mechanism present.

## Crystal Properties

The crystals used in this study were cut from polycrystalline ingots grown in sealed quartz vials, under a phosphorus pressure of about 10 atm. From data (3) on the system In-InP, we estimate that the melt consists of approximately 10% In and 90% InP. In general, the slabs were of a single crystal or at most contained one grain boundary. The homogeneity was investigated by a continuous scan of the variation of resistivity over the length of the bars measured, and only those which indicated a uniform resistivity, with at most perhaps 10% smooth variation over the section employed, are included.

The problem of compensation is an important one. Of course if the lattice mobility is known, the amount of compensation can be estimated from the measured values. However, if this is not the case, other, less precise means are employed. The homogeneity requirement is applied to this end, since it is expected that materials of large compensation will vary more radically in resistivity as a function of position in the crystal. The variation of mobility at a given temperature as a function of carrier concentration also should be considered, since of course anomalous results will appear for a crystal heavily compensated. One of these latter crystals (S67) is included in the group reported, as an example. Finally, the mobility should become essentially independent of the impurity concentration as the crystal purity improves. This is apparent for the purest samples investigated in the temperature range 200°-300°K (Fig. 1).

## Procedure

A number of geometrical arrangements for the contacts to the crystals has been used. With the samples reported, the shape of the part measured is rectangular, with two sets of side probes for measuring potentials affixed in addition to the current contacts. Two sets are used so that the variation of the Hall coefficient along the length can be observed. The side probes in some cases were arms of the material itself, the whole bridge sample being cut with an ultrasonic tool; in other cases, the side contacts were soldered; and for some crystals they were 0.002 in. diameter wires welded to the indium phosphide. The last approached closest to the ideal situation, in which one wants no perturbation to the condition of the crystal itself from the contacts.

In all cases the contacts were ohmic in the region employed, i.e., the current-voltage relationship was a linear one. The region of contact usually was prepared for soldering by plating with copper, indium, or nickel. No appreciable difference was noted, and copper was used for most of the crystals with soldered contacts.

No special precautions were taken with the surfaces in this study. Most of the crystals had sand-blasted surfaces. However, several of the samples were acid-etched to leave a shiny surface. No dif-

[1] Present address: IBM Laboratories, Poughkeepsie, N. Y.

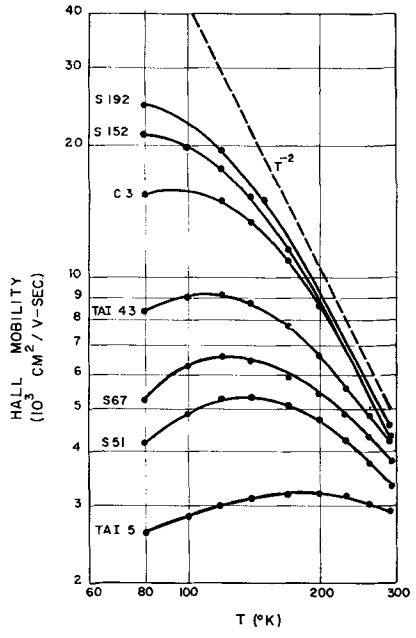


Fig. 1. Measured Hall mobilities $R_H\sigma$ as a function of temperature for n-type indium phosphide. Values for C3 have been adjusted to give 4300 cm²/v-sec at 290°K.

ference in the results of the measurements was found due to the different surface treatments.

The Hall effect and the conductivity were measured as a function of temperature using a d-c system for the electrical measurements and a thermally isolated system for the temperature stabilization. The Hall voltage was measured, in all cases, as a function of the magnetic field, and the values quoted are those applicable in the limit of zero fields. Only the purest specimens showed any appreciable variation with magnetic field.

## Observations

The values of the mobility as a function of temperature are shown in Fig. 1. Some of the electrical properties of the crystals are included in Table I. The crystals are listed in the sequence of increasing mobility at 77°K, which is also the sequence of decreasing electron concentration, except for the highly compensated crystal S67. The last three crystals have almost the same values of mobility in the temperature range 200°-300°K, indicating that in this region the mobility is dominated by lattice scattering. The slope of the mobility curves in this temperature range indicates a lattice mobility varying at least as $T^{-2}$. A dependence of $T^{-2}$ was assumed in the analysis that follows.

**Table I. Properties of n-type indium phosphide crystals**

| Crystal | Concentration of electrons at 290°K, $10^{16}$cm$^{-3}$ | Mobility at 290°K, cm²/v-sec | Mobility at 77°K, cm²/v-sec |
|---|---|---|---|
| TAI5 | 54 | 2910 | 2600 |
| S51 | 7.4 | 3400 | 4170 |
| S67 | 0.37 | 3800 | 4170 |
| TAI43 | 4.3 | 4200 | 8300 |
| C3 | 2.6 | 3800 | 13,500 |
| S152 | 0.83 | 4300 | 21,000 |
| S192* | 0.63 | 4500 | 23,400 |

* These values represent the results for a number of samples, while the curve S-192 in Fig. 1 is for one which happened to have the largest mobility.

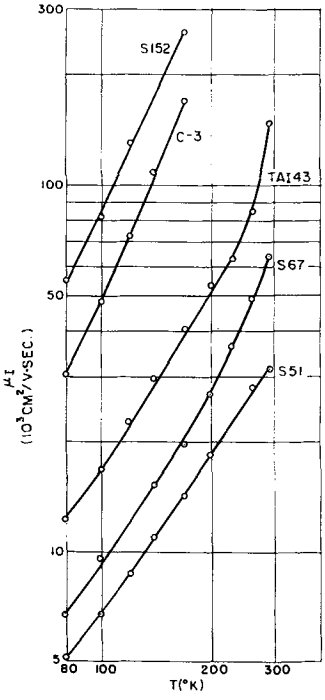


Fig. 2. Mobilities for scattering by ionized impurities in n-type InP as a function of temperature. Values were calculated from the observations of Fig. 1, assuming a lattice mobility $\mu_L = 4.2 \times 10^8\ T^{-2}$ cm²/v-sec.

## Discussion and Analysis

The data were analyzed in terms of a combination of lattice and ionized impurity scattering. The lattice scattering was assumed to be proportional to $T^{-2}$, as required by the observed variation of the mobilities of the purest crystals. The magnitude of the mobility at room temperature, even in the purest crystals, is still affected by the presence of ionized impurities. This contribution was estimated from an extrapolation of the low-temperature values of the impurity scattering mobility, which involved a reiterative procedure. The resulting lattice mobility is $4.2 \times 10^8\ T^{-2}$ cm²/v-sec, giving a value of 5000 cm²/v-sec at 290°K. The impurity mobilities for most of the crystals shown in Fig. 1 were obtained by using the expression for the combination of impurity and lattice mobilities given by Conwell (4). This expression assumes two conditions not actually present in our case. First, it refers to conductivity mobilities, whereas the measured values here are Hall mobilities. However, the ratio of Hall to drift mobility is unknown, and we have assumed it to be 1. This assumption is likely to be poorest for the crystals with largest impurity scattering.

Second, the Conwell expression assumes that the lattice scattering relaxation time is inversely proportional to the square root of the energy. If, as is likely, the scattering in indium phosphide is much like that thought to be the case in indium antimonide (5), i.e., dominantly polar scattering by the optical modes, the relaxation time approximation does not hold. The polar scattering is not strongly dependent (6) on the energy, however, for the examples under discussion here, and the error made in this assumption should not have a significant effect on the conclusions which can be drawn.

The resulting impurity scattering mobilities, calculated from the data by the subtraction technique discussed above, are given in Fig. 2 as a function of temperature. These are now believed to be in order of impurity content, so that it is clear that crystal S67 does have an impurity concentration between that of TAI43 and S51, at least ten times its net electron concentration. The mobilities have a strong positive temperature dependence, varying as $T^{3/2}$ below about 40,000 cm²/v-sec, and as $T^{2}$ for mobilities larger than this value. This $T^{3/2}$ temperature dependence is in good qualitative agreement with that calculated by Brooks (7) and Herring (8). The change in slope observed may be due to the assumptions noted above. The greater slope is also in the region of reduced accuracy of the subtraction procedure because the mobility is dominated by the scattering by the lattice. We note the qualitative behavior as in strong support of our assumptions about the lattice mobility and wish to look further now into the direct behavior of the measured mobilities on the concentration of impurity centers present.

With the assumed lattice mobility, it is possible to calculate the mobility as a function of ionized impurity concentration, making use of the expression given by Brooks (7) and Herring (8) for the scattering by charged impurities.

$$\mu_I = \frac{4K^2}{e^3(m^*)^{1/2}N_I}\left(\frac{2kT}{\pi}\right)^{3/2}\frac{1}{\ln(1+b) - b/(1+b)}$$

$$\text{with } b = \frac{6Km^*(kT)^2}{\pi n h^2 e^2}$$

where $K$, the dielectric constant, was taken (9) as 10.8, and $N_I$ and $n$ are the densities of ionized impurities and electrons, respectively. The effective mass was retained as a parameter, and the results of the calculations at the three temperatures 80°, 120°, and 200°K are shown in Fig. 3(a), (b), and (c), respectively. The values 1, 0.1, 0.04, and 0.01 were used for the effective mass ratio $m^*/m_o$.

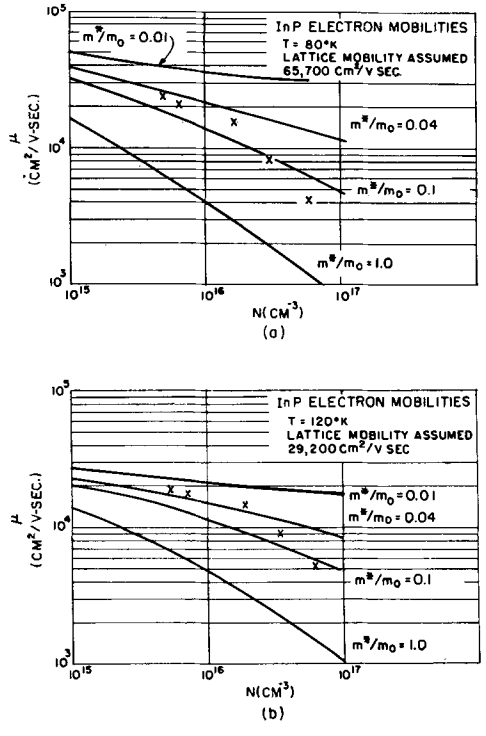


Fig. 3 a and b. Mobilities of electrons in indium phosphide as a function of ionized impurity concentration at (a) 80°K, and (b) 120°K. Curves are calculated.

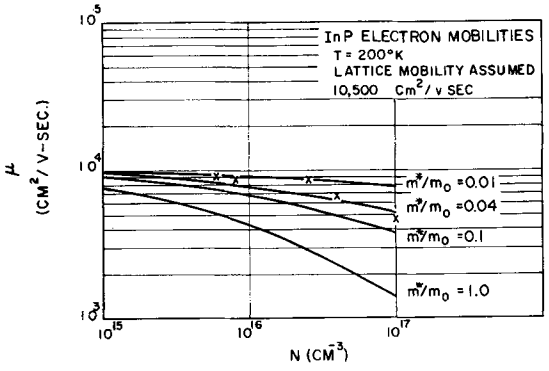


Fig. 3c. Same as Fig. 3a and b except at 200°K

Plotted in these figures are five points representing, in increasing impurity concentration, the crystals S192, S152, C3, TAI43, and S51. The values are plotted at the measured electron concentrations, while the calculated curves are for impurity concentrations. There are two obvious features of these curves. The first is that the three purest crystals do appear to lie along a consistent effective mass curve as a function of concentration, indicating that the electron density and the ionized impurity density are about the same. This is not the case for crystals TAI43 and S51. We conclude that these latter crystals are compensated appreciably. This is borne out by the observation that another sample of S51, cut close by the crystal described here, had an electron concentration 50% larger, i.e., $12 \times 10^{16}$ cm⁻³.

The second feature of interest is that the effective mass value giving the best fit to the curves is different for the different temperatures. Thus a value for $m^*/m_o$ of about 0.05 is appropriate at 80°K, while about 0.02 is better at 120° and 200°K. Of course these values depend on the lattice mobility assumed. The values for the lattice mobility are extrapolated from high-temperature measurements using a power law dependence of $T^{-2}$. It is possible that the mobility deviates from a power law, especially if dominated by polar optical mode scattering. The value at 80°K is thus less certain than the values at higher temperatures.

## Conclusions

The measurements of mobilities reported indicate that the electrons in indium phosphide have a lattice mobility varying with temperature at least as rapidly as $T^{-2}$. The observations, if interpreted as involving, in the purest crystals, essentially uncompensated samples, would indicate that the dependence is just this in the temperature range 200° to 300°K. Crystals of concentration $6 \times 10^{15}$ electrons per cm³ have a mobility of 23,400 cm²/v-sec at liquid nitrogen temperatures, with the maximum in the mobility occurring at still lower temperatures. This would indicate that previous observations of Harman and Stambaugh (10) of a maximum mobility of 14,000 cm²/v-sec at 110°K for a crystal with an electron

concentration of $4 \times 10^{15}$ cm$^{-3}$ involved considerable compensation, perhaps of a factor five or more. An even larger amount of compensation is indicated for crystal $A_n$ of Folberth and Weiss (11), which has a maximum mobility of about 8000 cm$^2$/v-sec, for an electron concentration of about $4 \times 10^{16}$ cm$^{-3}$. Our observations indicate a lattice mobility at 290°K of 5000 cm$^2$/v-sec.

The mobility observations have been fitted by a mixture of lattice scattering and ionized impurity scattering. This fit involves the electron effective mass as a parameter, and values for $m^*/m_0$ of 0.05 or less are found to give a fit to the data. Our conclusion as to the effective mass values is conservative because the analysis involves a number of assumptions of only approximate validity. Certainly a very small value is indicated, and the results are in good agreement with the approximate value 0.02 recently deduced from optical measurements by Reynolds, Lilburne, and Dell (12).

### Acknowledgment

The authors wish to thank Ronald Guire, Benjamin Seabury, and Robert Vannozzi for their aid in the growth of these crystals and the measurements.

Manuscript received May 13, 1958. This paper was prepared for delivery before the New York Meeting, April 27-May 1, 1958. Work supported in part by the U. S. Air Force.

Any discussion of this paper will appear in a Discussion Section to be published in the June 1959 JOURNAL.

REFERENCES

1. F. Oswald, *Z. Naturforsch.*, **9a**, 181 (1954).
2. M. Glicksman, *Bull. Am. Phys. Soc.*, **II 3**, 120 (1958).
3. (a) J. v. d. Boomgaard and K. Schol, *Philips Research Repts.*, **12**, 127 (1957); (b) K. Weiser, *J. Phys. & Colloid Chem.*, **61**, 513 (1957); (c) M. Shafer and K. Weiser, *ibid.*, **61**, 1424 (1957).
4. P. P. Debye and E. M. Conwell, *Phys. Rev.*, **93**, 693 (1954).
5. H. Ehrenreich, *J. Phys. Chem. Solids*, **2**, 131 (1957).
6. D. J. Howarth and E. H. Sondheimer, *Proc. Roy. Soc.*, **A 219**, 53 (1953).
7. H. Brooks, *Phys. Rev.*, **83**, 879 (1951).
8. C. Herring, Unpublished results.
9. F. Oswald and R. Schade, *Z. Naturforsch.*, **9a**, 611 (1954).
10. T. C. Harman and E. P. Stambaugh, Recent News Paper, Semiconductor Symposium, Electrochem. Soc. Meeting, May 1957.
11. O. G. Folberth and H. Weiss, *Z. Naturforsch.*, **10a**, 615 (1955).
12. W. N. Reynolds, M. T. Lilburne, and R. M. Dell, *Proc. Phys. Soc.*, **71**, 416 (1958).

# Preparation and Some Characteristics of Single-Crystal Indium Phosphide

**T. C. Harman, J. I. Genco, W. P. Allred, and H. L. Goering**

*Battelle Memorial Institute, Columbus, Ohio*

ABSTRACT

A technique for purifying phosphorus, reacting elemental indium and phosphorus, purifying the compound, indium phosphide, by a directional recrystallization, and growing large crystals all in one glass tube is described. A crystal puller for decomposable solids is described in detail and results for indium phosphide discussed. The electron mobility as a function of temperature is given for two single-crystal specimens. An electron mobility of 4000 cm$^2$/v-sec at 300°K for a specimen containing a carrier concentration of $1 \times 10^{17}$/cm$^3$ was achieved. Lifetime measurements by the photoconductivity-decay method are discussed. The optical-transmission characteristics of specimens containing electron concentrations of $10^{19}$/cm$^3$ and $10^{15}$/cm$^3$ are presented.

At the present time, there is considerable interest in semiconducting compounds for their numerous potential applications. Substantial effort is being expended upon methods (1, 2) for preparation of pure crystals of sufficient size for use in solid-state devices. Indium phosphide is particularly attractive for use in such solid-state devices as solar batteries, transistors, and rectifiers because of its energy gap of 1.25 ev and high electron mobility. It is the purpose of this paper to present two methods for the preparation of pure, large crystals of indium phosphide and to describe some characteristics of those crystals.

### Crystal Growth of Indium Phosphide by Control of Liquid Indium-Phosphorus Vapor Reaction

Since indium is extremely insoluble in solid indium phosphide, pure crystals of the compound can be grown from an indium-indium phosphide solution. The technique of reacting the elements, purifying the compound by a directional recrystallization, and growing crystals all in one operation is now described. A diagram of the apparatus is shown in Fig. 1. A quartz boat containing indium and pure phosphorus is sealed in a quartz tube under a vacuum of approximately $10^{-6}$ mm Hg. The quartz tube is then placed in a three-furnace arrangement, as shown in Fig. 1. A temperature gradient of 60°C (1000°-1060°C) is maintained along the boat containing the indium by proper positioning of the furnaces. The temperature of the third furnace, which controls the phosphorus pressure in the tube, is increased slowly to 485°C. The phosphorus vapor then reacts with the liquid indium. As the reaction proceeds, the solubility of InP in liquid indium is exceeded and InP crystallizes at the cooler end of

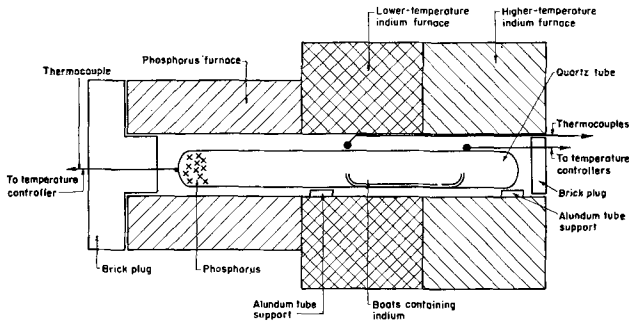


Fig. 1. Diagram of apparatus used for preparing InP

the boat. As the reaction proceeds, the solid-liquid interface slowly moves from the cooler end of the boat toward the hot end. Of the ingots prepared by this technique, at least five single-crystal dumbbell-shaped specimens (15 x 5 x 2 mm) were obtained. Some of the ingots were almost entirely one crystal.

This method of obtaining InP from indium solution has the advantage over the solution-growth method suggested by Wolff (1) in that large-bulk, single-phase ingots of the compound are obtained. Thus, no chemical techniques are required to separate the indium from the compound crystals.

Another possible advantage of the method over the usual crystal-growing processes is that the intrinsic number of lattice imperfections, that is, vacancies and interstitials, should be lower because the compound is crystallized at a temperature below its melting point. However, since the single crystals prepared by this technique are in contact with the quartz boat and, usually, with other crystals, gross imperfections (2) are probably introduced as a result of thermal stresses incurred on cooling. One crystal-growing technique that eliminates contact of the solidified crystal with container materials is the Czochralski technique. However, conventional germanium and silicon crystal pullers cannot be used for compounds, such as InP, that have a high vapor or dissociation pressure (3, 4).

## Crystal Puller for Decomposable Solids

The crystal puller described in this paper is a modified version of the one described by Gremmelmaier (5) for the pulling of InAs and GaAs. It is believed that, with this system, the pulling of large, single-crystal ingots of InP, InAs, and GaAs can be reduced to a technique as standard as that for silicon. The over-all pulling system is illustrated in Fig. 2. The pulling system is variable, with pulling speeds as low as 1 mm/hr. Two Alnico V magnetron magnets which are coupled to a nonsymmetrical Permendur sleeve are used to pull and rotate the seed. The Permendur sleeve is housed in a Vycor jacket to protect it from phosphorus vapors.

The entire pulling chamber is heated to the desired temperature by resistance heaters. A voltage regulator on the resistance furnaces is necessary to obtain the required temperature control. The furnace around the lower part of the pulling chamber is constructed from a 10-cm-diameter Vycor tube, with the spiraled heating elements of 22-gauge Chromel wire, providing good visibility of the molten surface and seed crystal.

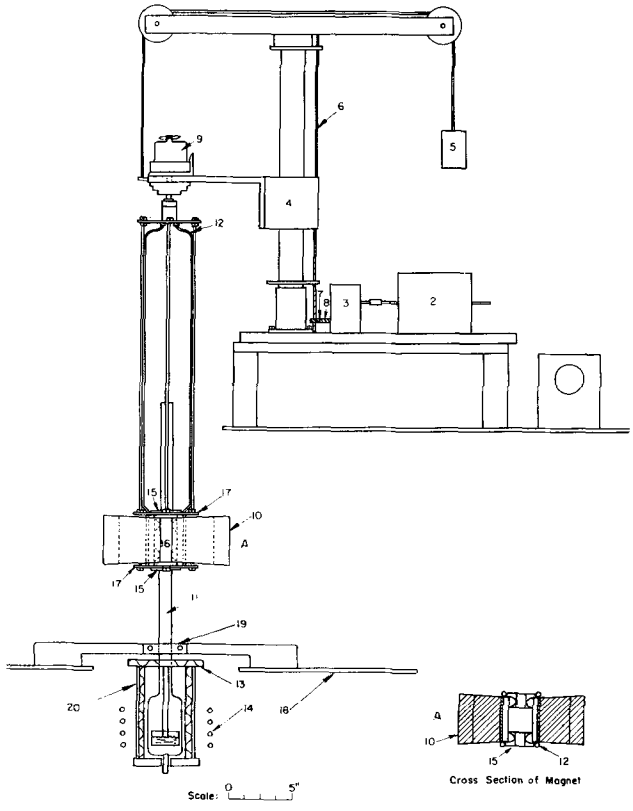


Fig. 2. Diagram of magnetic crystal puller. 1, Variac speed control for 1/15-hp, 115-v, d-c motor; 2, 1/15-hp, 115-v, d-c motor; 3, Boston gear reductor, ratio, 200:1; 4, mechanism for raising and lowering crystal, over-all traversing length, 18.5 in.; 5, counterbalance weight; 6, threaded rod; 7, spur gear; 8, worm gear; 9, clock motor (6 rpm); 10, Alnico V magnetron magnets; 11, stainless steel tube used as upper furnace housing, dimensions, 1.5-in. OD, 1⅜-in. ID, 23-in. length; 12, water lines for cooling magnet; 13, Chromel heating element to maintain desired ambient temperature at top of pulling chamber to control vapor pressure; 14, induction heating coil for melting InP; 15, Transite bearings; 16, Permendur spacers, dimensions, 2⅞-in. length, 1-in. width, 1⅞-in. depth; 17, upper and lower base plates to support magnet; 18, table top; 19, support for upper furnace housing; 20, transparent Vycor furnace, using Chromel heating element to maintain vapor pressure.

A diagram of the pulling chamber is shown in Fig. 3. The pulling chamber is a sealed Vycor envelope evacuated to a pressure of $2 \times 10^{-6}$ mm Hg. A double-wound furnace of 22-gauge Chromel wire covered with porcelain beads is used as the upper furnace. The double winding is necessary to eliminate 60-cycle vibration of the winding inside the magnetic field.

The seed rod has bearings of AUC graphite, with a clearance of 6 mils at room temperature. It was found that graphite bearings are necessary for smooth rotation and withdrawal of the growing crystal. An induction heater which couples directly to the material is used to heat the melt. The temperature of the melt is controlled by a Pt-Pt, Rh thermocouple which feeds into a L&N temperature controller.

The first ingots pulled in this system were InAs, and single crystals were obtained. Later, InP crystals were pulled in this system, and Fig. 4 shows one of these. The InP was pulled at a rate of 5 mm/hr and a rotational rate of 6 rpm. The lowest tempera-

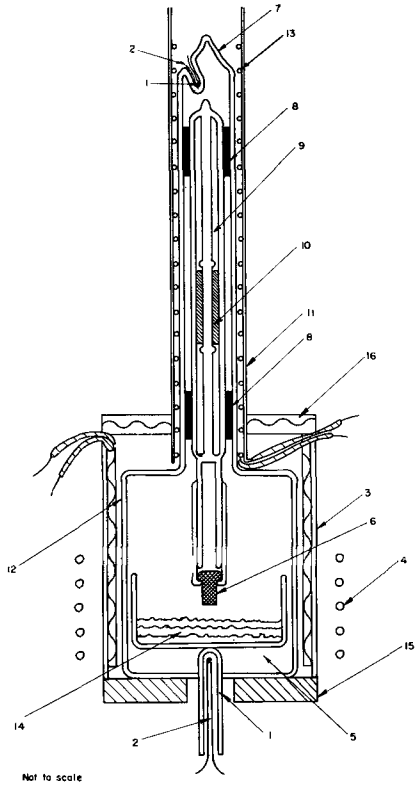


Fig. 3. Diagram of magnetic crystal puller reaction chamber. 1, thermocouple well; 2, Pt, Pt-Rh thermocouple; 3, Vycor-walled furnace wound with Chromel resistance wire; 4, induction heating coil; 5, quartz crucible, dimensions 1 15/16-in. OD, 1 13/16-in. ID, 2-in. height; 6, InP seed held in place with a Vycor seed holder; 7, Vycor tube, dimensions 25-mm OD, 21-in. length; 8, graphite bearings, 1.2-in. length; 9, Vycor tube to protect Permendur, dimensions 19-mm OD, 2⅝-in. length; 10, Permendur core, dimensions 2½-in. length, 15-mm OD, 8-mm ID; 11, stainless steel furnace housing; 12, Vycor tube, 64-mm OD; 13, upper furnace, 22-gauge, double-wound Chromel wire covered with porcelain beads; 14, InP melt; 15, Transite base plate; 16, Transite cover plate with Chromel heating element.

ture in the system was controlled at 485°C by the thermocouple at the top of Fig. 3. At this temperature the pressure of phosphorus is 5 atm. According to Boomgaard and Schol (4), a phosphorus pressure of 5 atm corresponds to a melt composition of InP-In at equilibrium of approximately 60 at. % In. The low solubility of indium in solid InP is illustrated by the relatively low carrier concentration, $10^{17}/cm^3$, and high electron mobility, 3000 $cm^2/v\text{-}sec$, of a polycrystalline n-type specimen cut from the ingot.

The polycrystalline seed used was obtained from a zone-melted ingot of InP. From Fig. 4, it can be seen that the crystal grew rapidly into large crystallites. The crystal in the front is a large single portion with the characteristic flats running the length of the crystal. The crystals on the right edge of the photograph start from the seed and run the entire length of the ingot. These results suggest that, with a single-crystal seed, large single-crystal ingots of InP can be grown easily.

### Purification of Phosphorus

Several possible techniques were investigated for the purification of phosphorus. These techniques included sublimation of red phosphorus in a hydrogen stream, zone melting of white phosphorus, and vacuum distillation of white phosphorus. However, the results are believed inconclusive concerning the effectiveness of each technique because of the effects of oxygen impurities. Resistivities at room temperature ranged from 10 ohm-cm to $10^{-2}$ ohm-cm. Carrier concentrations ranged from $10^{10}/cm^3$ to $10^{17}/cm^3$. As discussed in the next section, oxygen is believed to produce deep-lying levels in InP which effectively trap out electrons originating from shallow donor levels. Thus, extremely low carrier concentrations can occur.

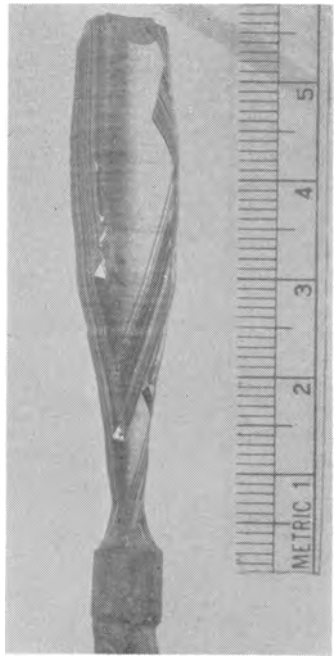


Fig. 4. Pulled ingot of InP

A technique has been developed that minimizes the contamination from oxygen and other impurities. In this method, a Vycor apparatus is used to purify phosphorus, to prepare the compound from the elements, and to grow crystals of the compound. As shown in Fig. 5, this system consists of a reservoir for red phosphorus, a primary condenser, a connection to a high-vacuum line, and a secondary condenser. A quartz reaction tube containing indium in a double quartz boat is attached to the secondary condenser. Although the oxide on the indium is carefully removed by scraping and cutting, an oxide film on the indium usually occurs upon melting. To remove the oxide film, two boats are used, as shown in Fig. 5. The inner boat possesses a small orifice which allows the molten indium to flow from the outer boat into the inner boat. The indium oxide floats on the surface of the outer boat

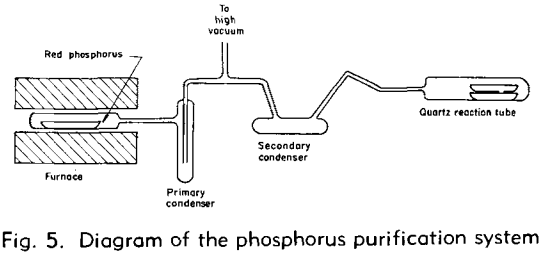


Fig. 5. Diagram of the phosphorus purification system

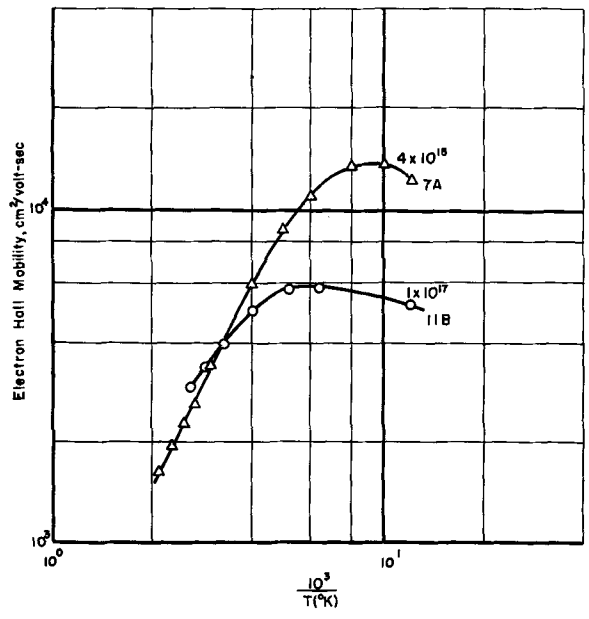


Fig. 6. Electron Hall mobility as a function of reciprocal temperature for two single-crystal specimens of InP.

and does not enter the inner boat, thus providing a clean surface for reaction.

The procedure for the purification of phosphorus is as follows. The system is thoroughly outgassed and evacuated to a pressure of about $4 \times 10^{-5}$ mm Hg. The red phosphorus is heated to temperatures ranging from 300° to 380°C and sublimed into the primary condenser. When a sufficient amount of white phosphorus has collected in the primary condenser, the reservoir and the vacuum line are sealed off. Thereafter, the white phosphorus is distilled from the primary reservoir at 150°C into the secondary condenser and from the secondary condenser at 140°C into the quartz reaction tube. Each preceding section is sealed from the remaining part of the system after a distillation is carried out to prevent back distillation. The amount of white phosphorus admitted to the reaction tube is measured volumetrically. The reaction tube then is placed in the three-furnace arrangement shown in Fig. 1. To prevent oxygen from diffusing through the quartz reaction tube, the reaction tube is enclosed in a quartz protection tube containing approximately 2/3 atm of argon and some titanium chips. The titanium chips act as an effective getter of oxygen at the higher temperatures. In experiments in which titanium chips and a protection tube were not used in the preparation, deep-lying levels were always found. On the other hand, in experiments in which titanium chips and a protection tube were used, no evidence of deep-lying levels was obtained from the electrical and photoconductivity measurements.

## Electrical Properties of Single-Crystal Indium Phosphide

Measurements of the Hall coefficient and the resistivity of a number of single-crystal specimens of InP showed that electron-carrier concentrations have been achieved in the $10^{16}$/cm³ to $10^{17}$/cm³ range at room temperature. However, the temperature dependence of the Hall coefficient of the lower carrier-concentration samples indicates the presence of multiple impurity or defect levels which effectively trap out electrons from shallow donor levels. By using the preparation techniques discussed in the previous sections, a carrier concentration of $1 \times 10^{17}$/cm³ is obtained. This relatively high carrier concentration is believed due to a low concentration of compensating acceptor impurities. As Fig. 6 shows, the uncompensated Specimen 11B has the same electron Hall mobility at room temperature as the low carrier-concentration Specimen 7A. Why the mobility curve of Specimen 11B rises above that of Specimen 7A cannot be explained on the basis of the usual lattice and impurity scattering concepts. The unusual mobility behavior of the specimen containing deep-lying levels (Specimen 7A) and the uncompensated Specimen 11B is being investigated further.

## Lifetime Measurements

Lifetime measurements by the photoconductivity-decay method were carried out on several specimens. For the specimens of lower carrier concentration ($<10^{16}$/cm³), a long time constant of about 600$\mu$ sec was observed. By a pulse method, it was found that the long time constant was probably due to trapping of majority carriers. For the higher carrier-concentration samples, the photoresponse was too small to measure. The photoconductivity results suggest that the large photoresponse-time constant is due to nonequilibrium carriers which are trapped by deep-lying levels. Presumably, the source of the deep-lying levels is the oxygen impurity.

## Optical Properties

Results of transmission measurements on two samples are given in Fig. 7. The thickness of the two specimens was the same, 4.5 mm. The specimens were shown to be optically homogeneous by masking various regions and measuring the percentage transmission of the unmasked areas. The variation

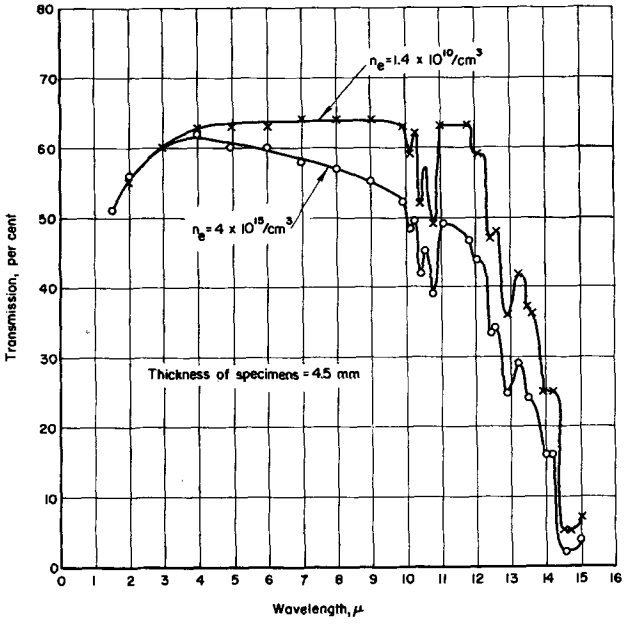


Fig. 7. Transmission characteristics of two N-type single-crystal specimens of InP at 300°K.

in percentage transmission was a few per cent. As shown in the figure, the percentage transmission was determined between 1.5$\mu$ and 15$\mu$. At the short wave length, the transmission decreases from a maximum of 63% at 4$\mu$ to 51% at 1.5$\mu$. In the intermediate wave length range, the transmission of the $10^{15}$ sample decreases from a maximum of 61% to 52% at 10$\mu$, but the transmission of the $10^{19}$ sample is constant at 63%. The observed difference is probably due to free-carrier absorption. In the 10-15$\mu$ region, structure is observed in both specimens. Transmission minima appeared in three sets of three. Oswald (6) has observed two absorption bands in the 13-15$\mu$ region which correspond to the large transmission minima. The structure obtained in the 10-15$\mu$ range is similar to the lattice-absorption bands observed in germanium and silicon (7); however, there is more regularity.

### Acknowledgments

The authors are indebted to E. P. Stambaugh for carrying out some of the preparation experiments, to E. B. Dale and R. Bray for the photoconductivity results, and to R. K. Willardson and A. C. Beer for many valuable discussions.

The research was supported jointly by the Army, Navy, and Air Force under contract with the Massachusetts Institute of Technology and performed under subcontract with the Massachusetts Institute of Technology.

Manuscript received April 25, 1958. A preliminary account of this paper was prepared for delivery at the Washington Meeting, May 13-16, 1957.

Any discussion of this paper will appear in a Discussion Section to be published in the June 1959 JOURNAL.

REFERENCES

1. G. Wolff, P. H. Keck, and J. D. Broder, *Phys. Rev.*, **94**, 1410 (1954).
2. R. E. Maringer and J. J. Duga, To be published.
3. J. van den Boomgaard and K. Schol, *Philips Research Repts.*, **12**, 127 (1957).
4. K. Weiser, *J. Phys. & Colloid Chem.*, **61**, 513 (1957).
5. R. Gremmelmaier, *Z. Naturforsch.*, **11a**, 511 (1956).
6. F. Oswald, *ibid.*, **9a**, 181 (1954).
7. R. S. Collins and H. Y. Fan, *Phys. Rev.*, **93**, 674 (1954).

# Preparation of Crystals of Pure Hexagonal SiC

**D. R. Hamilton**

*Research Laboratories, Westinghouse Electric Corporation, Pittsburgh, Pennsylvania*

ABSTRACT

The mode of growth of SiC crystals in laboratory furnaces is examined. It is shown that the crystals grow in an environment dominated by radiation, and that this environment may be responsible for the specific orientation and possibly the habit of the crystals. It is demonstrated that, under normal experimental conditions, crystal growth is unlikely to proceed by a two-dimensional nucleation mechanism. The means of producing relatively pure crystals are discussed.

It has been known that large crystals of the semiconductor SiC occasionally grow during the operation of commercial SiC furnaces. Lely (1) recently succeeded in synthesizing crystals of this material on a laboratory scale. Pieces of SiC, formed into a hollow cylinder in a graphite crucible, were heated in a graphite tube furnace to about 2500°C. The temperatures were arranged so that the center of this cylinder of SiC was cooler than the exterior. Silicon carbide vapor diffusing inward thus became supersaturated and condensed in the center of the cylinder in the form of single crystals. The composition of the growing crystals was altered by addition of certain impurities to the atmosphere of preparation.

It is the purpose of this paper to examine in some detail the nature, habit, and orientation of crystals grown in this fashion. We shall deal exclusively with the preparation of crystals of relatively high purity.

### Experimental

The furnace used in the present work is based on a design of Kroll (2) and is similar to that of Lely. It is shown in section in Fig. 1. The equipment

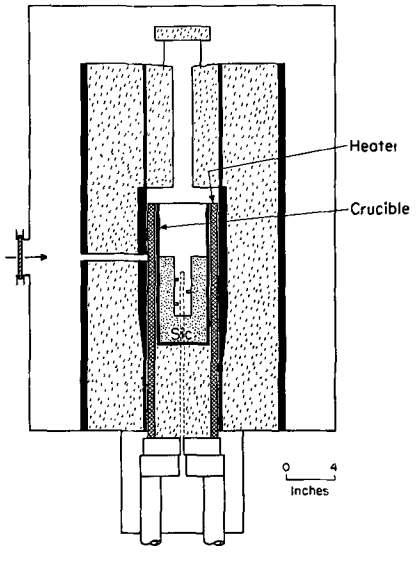


Fig. 1. High temperature graphite furnace. Planar SiC crystals are shown growing in the center of the furnace. All internal components are made of graphite or carbon, and the furnace is insulated with lampblack. The outer tank, of stainless steel, is water cooled and vacuum tight.

differs from that of Lely in that a precise temperature control is provided. Radiation from a selected area of the heater is sensed by a thermopile which is arranged to adjust the power input to the furnace by means of a saturable core reactor. The initial operating point is set by an optical pyrometer. Short-term control is about ±1°C, which is more than adequate for the present work. This system also maintains the furnace for many hours at what appears to be a constant temperature, within the reproducibility of optical pyrometer settings.

The furnace may be operated in high vacuum at temperatures up to about 2000°C. Above this temperature an inert atmosphere must be provided to suppress evaporation of the graphite furnace components. Although helium and hydrogen may be used, argon is most satisfactory. In the subsequent discussion operation at atmospheric pressure in one of these gases is presumed.

### Crystal Growth and Habit

The crystals prepared by Lely deposited in the form of hexagonal pyramids, having one good face and irregular or rounded faces on the reverse. Occasionally planar crystals were grown. For physical measurements and device work the planar crystals are desirable.

Realizing that Lely's practice of using lump SiC did not lead to uniform thermal conditions, Chang and Kroko (3) carried out experiments with more homogeneous charges. These consisted of either commercial grain SiC or of silicon and carbon mixtures of various compositions. The central cavity or well, essential for crystal growth, was maintained by the use of a supporting spacer made of graphite (4). This configuration has been used extensively in the present work and is not only advantageous experimentally but also leads to a simplification that is important in estimates concerning the environment. Use of these more homogeneous charges led to a significantly higher yield of plates.

Fig. 2. SiC crystals on a graphite substrate. Magnification 2X.

Figure 2 shows part of such a charge of this configuration and the growth of crystals. The entire contents of a crucible were removed and split open to reveal the details. The majority of the crystals are planar, and, as may be seen, have a tendency toward horizontal orientation. Crystals of other orientations are present but have grown at lower rates. This behavior is found among crystals nucleated on graphite as well as on pieces of SiC, so it would appear that the behavior described is independent of the nature of the substrate.

It might be thought that convection currents within the well could supply vapor preferentially to the horizontal crystals. There is, however, some recent work that suggests that the atmosphere may be static. Lighthill (5) has examined theoretically the situation in which a hollow vertical cylinder is closed at the lower end, but is open at the upper end to a body of fluid at a lower temperature. Generally, convection occurs within the cylinder, but under certain conditions the fluid in the lower portion of the cylinder reaches the temperature of the walls and becomes stagnant. Martin (6) and others have shown that this feature is, in fact, found experimentally. We have therefore used Lighthill's work to examine the situation within the central well of the SiC furnace. To do so, we have assumed an argon ambient and have taken the Prandtl number as unity rather than $Pr \sim 0.66$. This is necessary since Lighthill has solved the boundary value problem only for $Pr = 1$ and $\infty$; the solutions vary but little with Pr. It is found that stagnation should commence at the bottom of the well for temperatures as low as 200°C. According to the theory, almost the entire tube should become stagnant at the high temperatures existing in the SiC furnace. It is probable then that the atmosphere in the central well will be static or nearly so, and we conclude that crystal growth is therefore not apt to be influenced by convection currents.

A possible explanation of the observed growth of large horizontal crystals may be found on examination of the thermal conditions about the growing crystals. A relationship between radiation cooling and crystal orientation is suggested in the following section. This relationship was early recognized by Patrick as well as by Kroko and Chang, and has been developed in discussions between these workers and the author.

Crystals receive heat from the walls of the central cavity by direct radiation and by thermal conductivity through the contact between the crystal and the well. A growing crystal also is heated by the heat of crystallization of the impinging material. This last term cannot affect orientation. The energy involved is estimated, from the data of Inghram, *et al.* (7), to be of the order of two calories an hour for a typical crystal and will be neglected in the following discussion. We will now consider the remaining terms and their possible influence on orientation.

It has been stated that crystal orientation is independent of the nature of the substrate. Thus thermal conditions at the contact cannot effect the ob-

served results. The actual magnitude of the heat flux through the contact may be estimated from the known thermal conductivity of SiC and average data for the area of contact. If the temperature gradient at the contact is 10 to 100°C/cm, then the corresponding heat flows are 0.004-0.04 w.

The heating due to radiation may be calculated if the emissivity of the crystal is known. Brugel (8) has measured the emissivity $\epsilon$ of SiC "Globar" elements at temperatures up to 1800°K. He has found $\epsilon$ to be about 0.9 and not strongly dependent on wave length or temperature. This result is not entirely unexpected, for the surface of such Globar elements is very rough. Pure single crystals, on the other hand, might be expected to show a slow decrease in emissivity at photon energies less than the energy gap. The gap is about 2 ev at 2500°C, corresponding to a photon wave length of 0.7 $\mu$. We will assume, in the absence of other information, that the $\epsilon$ for pure single crystals is relatively low. The value used is 0.1. Now it is known experimentally that the well is essentially isothermal. Since the walls of the well may be formed of graphite, we may take $\epsilon = 0.9$ as a reasonable working figure. The energy flux into a typical crystal 1 mm$^2$ area is then found to be about 0.6 w.

The radiation field within the well is, however, plainly asymmetrical due to losses through the open upper end of the well. For a crystal at the midpoint of the well, this end occupies 5% of the total solid angle. The net heat loss through this end will depend on the emissivity and temperature of the area "seen." These figures are known from experimental data. It may then be estimated that a crystal of 1 mm$^2$ area will radiate about $10^{-2}$ w to this sink. Should the emissivity of SiC be greater than 0.1, then this energy loss and the effects to be ascribed to it would be correspondingly greater. The assumed low value of emissivity is unfavorable to the present arguments. This loss is sensitive to crystal orientation, for the effective radiating area depends on the cosine of the angle between the vertical (the direction of the sink) and the normal to the face of the crystal. Thus it is probable that crystals with the favored horizontal orientation will be coolest and consequently will grow most rapidly, provided that this radiative loss is the only orienting factor.

The only other heat flow is that due to the thermal conductivity of the atmosphere, which we shall assume to be argon. It has been suggested that the gas in the central well is stagnant and is isothermal with the well walls. In this event, the heat flow will be from the argon to the crystals and will be exceedingly small. If the argon is cooler than the crystals and is not isothermal with the well walls, then it may be estimated that a typical crystal would transfer, by conduction and convection, about $10^{-3}$ w, for a gradient of 100°/cm in the argon. This flow is so small that any orienting effects will be masked by those due to radiation. Therefore, it is concluded that orientation is governed largely by the direction and magnitude of the radiation losses.

These order of magnitude calculations indicate that the net energy losses of a growing crystal are small relative to the ambient radiation field. Consequently the temperature of the crystal should closely approach that of the walls of the well. We have measured the temperature of growing crystals and have found that this is indeed the case. The crystals, seen through an optical pyrometer, are barely distinguishable against the uniform background radiation of the surrounding well. The apparent temperature difference between a crystal and the adjacent wall is certainly not greater than 20°. This result must be examined with great care, for it is easy to be misled. As mentioned earlier, the energy gap of SiC at these temperatures is about 0.7 $\mu$. The measurement is made at 0.65 $\mu$ in a region of high absorption and emissivity. Thus there need be no correction for energy transmitted through the crystal. The geometry of the experiment was such that direct reflection from a crystal face could not occur. Finally, examination of the crystals after the experiment showed that extensive diffuse reflection was unlikely. It is thus concluded that the temperature of the growing crystal is indeed within 20° of the temperature of the well. It should, of course, be noted that the act of measurement itself must increase this difference by increasing the radiation losses somewhat.

This temperature difference, together with the constants of the system, may be used to make calculations concerning the growth mechanism. We have estimated by the method of Harkins (9) that the surface free energy of SiC is about 3000 ergs/cm$^2$; it is certainly not lower than 1000 ergs/cm$^2$. It may then be shown that the nucleation rate of new growth layers is insufficient to explain the known growth rate. For growth to proceed by nucleation of new layers either the surface free energy would have to fall below 1000 ergs/cm$^2$, or the above-mentioned temperature difference would have to be greater than 50°. Since the 20° figure represents an upper limit only, it would appear that nucleation of new layers should not take place under normal conditions. Since screw dislocations are frequently found, it is probable that growth proceeds by means of a screw dislocation mechanism. There is also evidence that growth may be promoted at the crystal to substrate junction.

It has thus been shown that crystals of SiC of a particular orientation may be grown if the thermal environment is relatively isotropic and if the principal means of heat dissipation from a crystal is a directed radiative loss. Such an environment in all likelihood also influences habit, insofar as growth of crystals with large surface to volume ratios is favored. The actual growth mechanism may involve screw dislocations, but is not apt to proceed by nucleation of new layers.

### Preparation of Pure SiC

Impurities present in crystals of SiC have three possible origins. They may be introduced in the starting materials, whether SiC or Si and C mixtures. Impurities may find their way from the internal fittings of the furnace into the growing crystals. Finally, contamination may originate in the atmosphere introduced into the furnace. The princi-

Table I. Spectrographic analysis of various samples of SiC, in ppm

| Element Sample | Al | Fe | Ag* | Cu | Mg | Mn |
|---|---|---|---|---|---|---|
| Commercial green SiC† | 100 | 10 | 10 | 30 | 50 | 15 |
| Crystals grown from the above† | 30 | 3 | 5 | 15 | 25 | 3 |
| Purest SiC crystals | <10 | <10 | | | Trace | Trace |

* No standards available.
† Geometric mean of the limits of concentration are quoted.

pal impurity in the argon atmosphere usually used is nitrogen, which is, as Lely and Kroger (10) have shown, a donor in SiC. Since they have described in some detail the behavior of nitrogen in SiC as well as the means of removing it from argon, we shall not discuss this point further.

Commercial green SiC is among the possible choices of starting material for the preparation of crystals of pure SiC. Its principal virtue is the low cost. On the other hand, it is known to contain a wide spectrum of impurities, as is shown in Table I.

An analysis of typical crystals grown from this SiC is shown in the second row of the table. It can be seen that a reduction in the concentration of a given element has taken place during crystal growth. Several mechanisms are involved in this purification. First, fractional sublimation takes place, since the distribution coefficient of many of the impurities is undoubtedly small. Second, the actual concentration of impurities in the atmosphere about the growing crystal is greatly reduced by two gas diffusion mechanisms. The impurities are present in the vapor phase as either the element proper or as compounds. In general these components are more volatile than SiC, and consequently may condense in a liquid or solid phase in cooler parts of the furnace. Concentration gradients are thus established which remove material from the immediate vicinity of the crystals. Thermal diffusion may also account for a certain separation. In general, large or heavy molecules diffuse down a temperature gradient to cooler regions. Finally, experiments have shown that impurities do diffuse through the SiC lattice at high temperatures. Thus impurities may diffuse out of the starting materials during the course of a run. The surface layers of the crystals may thus be less contaminated than the interior material, although diffusion naturally tends to level out these differences within the growing crystal.

Now, it is plain that the purity of the starting material may be greatly improved by the use of zone-refined silicon and high-purity carbon in place of commercial SiC. Zone-refined silicon is more than adequate for preparations of this sort, and high purity carbon may be prepared by heat treating carbon under vacuum and at high temperatures. Present results indicate that crystals grown from these materials are considerably purer than those grown from commercial SiC. Unfortunately the improvement is not as great as might be expected. One is forced to conclude that the furnace fittings are maintaining relatively high levels of contamination.

All high temperature fittings within the furnace are fabricated from graphite or carbon. Although certain of the smaller parts may be purified by heating to highest temperatures in the present furnace, the majority are too large to be accommodated in the hot zone and must be heated *in situ*. They do not reach sufficiently high temperatures for adequate purification. They remain, therefore, a pernicious source of contamination, even after many hours of purification heating.

A number of arrangements have been tried to overcome this problem without a major change in the design of the furnace. These have involved the use of double crucibles, similar to those of Lely, and systems of tightly sealed lids and baffles. The results have not been especially noteworthy.

An analysis of the purest material so far prepared is shown in the third line of Table I. This material was prepared from du Pont "Solar Cell" grade silicon and purified carbon. The crystals themselves are from 0.5 to 1.5 mm in thickness, and up to 4 mm across the hexagonal face. They are transparent in the visible region. The room temperature resistivity lies in the vicinity of $10^5$ to $10^6$ ohm-cm. If it is assumed that the electron mobility is not less than that found by Lely and Kroger for heavily doped samples, then the estimated room temperature carrier concentration must be of the order of $10^{13}/cm^3$. Since the electrical characteristics of the dominant impurities are not known, few firm conclusions can be drawn from this sort of information. We cannot, for example, rule out the possibility that the high resistivity is due, in part at least, to charge compensation.

## Conclusions

It has been shown that SiC crystals grow in laboratory furnaces in an environment dominated by a radiative exchange of energy. The orientation and possibly the habit of the crystals is greatly affected by the nature of the radiative losses in such a system. Crystals of relatively high purity may be prepared provided care is taken in the choice of the materials used and in the maintenance of a high purity environment about the growing crystals.

## Acknowledgment

The author acknowledges with great pleasure many stimulating discussions with L. Patrick, C. Cess, and L. Kroko. Thanks are also due to R. Longini for constructive criticisms of the manuscript, and to J. A. Lely and F. A. Kroger for providing us with preprints of their recent publications.

Manuscript received May 28, 1958. This paper was prepared for delivery before the New York Meeting, April 27-May 1, 1958.

Any discussion of this paper will appear in a Discussion Section to be published in the June 1959 JOURNAL.

## REFERENCES

1. J. A. Lely, *Ber. deut. keram. Ges.*, **32**, 229 (1955).
2. W. J. Kroll, A. W. Schlechten, and L. A. Yerkes, *Trans. Electrochem. Soc.*, **89**, 317 (1946).
3. H. C. Chang and L. J. Kroko, Conference Paper

57-1131, American Institute of Electrical Engineers, Chicago, 1957.
4. H. C. Chang, R. E. Davis, and L. J. Kroko, International Conference on Semiconductors, Brussels, 1958.
5. M. J. Lighthill, *Quart. J. Mechanics and Applied Mathematics*, Oxford at the Clarendon Press, **6**, 398 (1953).
6. B. W. Martin, *Proc. Roy. Soc. (London)*, **A230**, 502 (1955).
7. G. De Maria, J. Growart, and M. G. Inghram, Meeting of American Physical Society, Chicago, 1958.
8. W. Brugel, *Z. Physik*, **127**, 400 (1950).
9. W. D. Harkins, *J. Chem. Phys.*, **10**, 268 (1942).
10. J. A. Lely and F. A. Kroger, Proceedings of the Garmisch Conference, 1956.

# Technical Notes

## Use of Bismuth as a Donor-Type Impurity in Germanium Single Crystals

George Mortimer

*Clevite Transistor Products, Waltham, Massachusetts*

### Segregation Coefficient

The use of a doping impurity requires knowledge of its effective segregation coefficient for various conditions of growth. Bismuth was studied using considerable variations in both the concentration and the rate of advance of the solid-liquid interface.

Figure 1 shows the experimental curves obtained by growing horizontal crystals and averaging the resistivity obtained over the first 10 in. of length. The concentration of Bi in the solidified crystal can be seen to be quite dependent on the rate of growth. Following the pattern set by many other impurities, the amount of Bi introduced into the crystal per unit volume increases as the growth rate becomes more rapid (1).

Insufficient data are presently available for growth rates faster or slower than those shown at wide ranges of impurity concentration in the liquid zone. Sufficient information was gathered at one concentration, however, (approximately 50 mg Bi/100 g Ge) to show that even at the rate for the upper curve (1½ in./hr) equilibrium had not been attained. At a growth rate of 0.67 in./hr and the doping level cited above, the resistivity averaged approximately 6.0 ohm-cm for a sample of five crystals. Data were also obtained using this concentration in the liquid at faster growth rates than those shown. The resistivity under these conditions continued to decrease, but a considerable scatter in the data made it difficult to obtain meaningful averages above 5 in./hr. At 6-7 in./hr, the liquid zone was difficult to maintain and the horizontally grown ingots generally became polycrystalline.

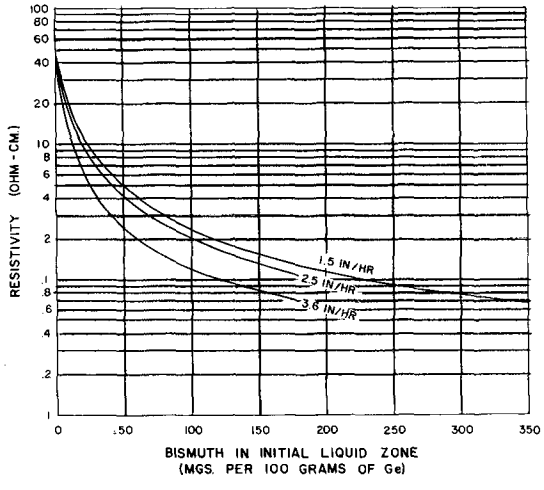


Fig. 1. Resistivity vs. quantity of Bi added to initiol liquid zone (horizontally grown crystals).

The segregation coefficient, computed from the data shown in Fig. 1, indicated an effective value of $K \cong 5 \times 10^{-5}$. This value was obtained using a resistivity of 4.0 ohm-cm, a mobility of 3600 cm²/v-sec, and a growth rate of 1½ in./hr.

### Controlled Doping

The very small segregation coefficient cited above makes Bi an ideal impurity for growing long horizontal single crystals of Ge without observing any drop in resistivity along the length of the ingot. The concentration of impurity atoms, C, as a function of distance along the crystal, X, is given for all but the last zone by $C = KC_i e^{-K(X/l)}$, where 1 is the molten zone width and $C_i$ the initial concentration in the molten zone (2).

It is assumed that initially the impurity atoms are all located in the first zone, and the remainder of the charge is intrinsic. Since $K$ is approximately $5 \times 10^{-5}$, a total growth distance of approximately 2000 zone lengths would be necessary before the resistivity would increase by 10%. It is not normally practical to grow crystals with over-all lengths exceeding 25 zone lengths. Therefore, the end of one crystal may be used to dope the next crystal for many successive runs without the resistivity noticeably increasing and without accumulating much heavily doped end scrap.

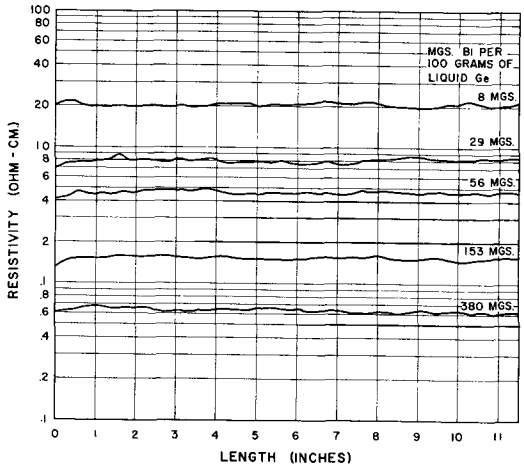


Fig. 2. Resistivity plots along the length of actual horizontally grown single crystals of Ge. The amount of Bi used to dope each of these crystals is noted just above its respective resistivity plot.

Fig. 2 shows actual resistivity plots of horizontally grown single crystals of Ge doped with Bi. The quantity of bismuth used per 100 g of liquid zone is noted on the graph above its respective resistivity plot. The liquid zone, crystal cross section, and growth rate were kept constant for all the crystals shown. This graph shows that the quantities of doping impurity necessary may easily be handled even in close to intrinsic resistivity ranges.

This procedure can be seen to allow for direct and accurate weighing of the Bi on an analytical balance for almost any liquid volume and resistivity desired. Most other Group III and V impurities, due to larger segregation coefficients and also in some cases to high vapor pressures, require the preparation and use of "master doping alloys."[1] The inconvenience of preparing these "master melts" and the difficulties involved in making them homogeneous without contamination are often considerable.

## Maximum Concentration

The maximum amount of Bi that it is feasible to introduce into Ge during growth from the melt was investigated. A number of vertically pulled crystals were prepared which were heavily doped with up to 2 g of Bi per 250 g of Ge in the initial melt. These crystals were grown at relatively slow growth rates and with relatively uniform cross sections in order that equilibrium conditions might be approached.

The maximum quantity of Bi that could be introduced into these crystals during growth without adversely affecting their structural perfection was found to be of the order of 0.00005 at. % (0.1-0.2 ohm-cm). Figure 3 shows a cross section along the axis of a heavily doped crystal (0.8% Bi in the initial melt). The crystal was grown by the Czochralski technique at a rate of ¾ in./hr. The change from single to polycrystalline structure may be observed. Noticeable flaws start to appear in the crystal at a position about 40% down from the top (≅ 1.3% Bi in the melt), and the ingot became a

[1] Indium as a p-type impurity most nearly has the advantages discussed for Bi. However, even In, when used directly, must be added in quantities which are less than 1/10 of the Bi used under comparable conditions.

Fig. 3. Cross section from top to bottom of a vertically pulled ingot of Ge. The quantity of doping impurity added to the initial melt was so chosen that it would increase sufficiently in concentration to affect noticeably the perfection when approximately half the crystal was pulled. The gross imperfections in the center region and the polycrystal bottom were brought out by etching in silver etch.

randomly oriented polycrystal at approximately the 75% point (≅ 3.2% Bi in the melt). The resistivity was found to be 0.23 ohm-cm at the 40% point and 0.11 ohm-cm at the 75% point. Data on other crystals studied gave results very similar to those described above with polycrystal development again occurring when the resistivity had decreased to the 0.2 to 0.1 ohm-cm range.

Figure 4 shows a cross section of a heavily doped Bi crystal. This surface is cut perpendicular to the growth axis in a region between the 40 and 75% points of Fig. 3. This is the region where noticeable flaws start to appear but is prior to the randomly oriented polycrystal bottom section. The surface of

Fig. 4. Surface cut perpendicular to the growth axis from a heavily doped vertical crystal similar to that shown in Fig. 3. The surface was cut just above the region where randomly oriented polycrystal development starts. Note how the excess Bi was deposited along (1,1,1) planes in this region during growth and has been removed in the subsequent etching of this surface.

the crystal shown in Fig. 4 has been etched in silver nitrate etch.[2] It shows an anisotropic segregation of the Bi. The deep grooves indicate regions where excess Bi was deposited along (1,1,1) planes and later dissolved out during the etching process.

Bismuth was found to be most useful for controlling the resistivity of Ge crystals in the range above 1.0 ohm-cm but can be used successfully from 0.4 ohm-cm to intrinsic.

### Crystal Quality

The quality of crystals produced using Bi as a doping impurity appeared comparable to that obtained using other Group III and Group V impurities.

A sample of 50 crystals produced during one period was checked for perfection. These crystals were all in a resistivity range between 1 and 10 ohm-cm. The highest dislocation density observed on any of these crystals was $6.4 \times 10^3/cm^2$ with the exception of three that had a slight amount of lineage present. Forty-four of the crystals had no readings above $3.0 \times 10^3/cm^2$, and many individual readings below $1.0 \times 10^3/cm^2$ were observed.

Bulk measurements of minority carrier lifetime on 13 samples in the 6-10 ohm-cm resistivity range produced an average value of 145 $\mu$sec. Only one reading was below 100 $\mu$sec, and the highest reading was 308 $\mu$sec.

Figure 5 shows the resistivity variation along the length of five horizontally grown single crystals produced consecutively. The same amount of Bi was used for each run. The high degree of reproducibility is indicative of the type of resistivity control that can be obtained using this doping procedure if proper care is taken of the other variables involved such as charge cross section, growth rate, and temperature control.

It is not implied that the quality of all crystals produced under all conditions was as good as these described in the preceding paragraphs. Degradation in quality, when it occurred, could be traced to other problems, however. The results definitely indicated that there are no major difficulties inherent in the use of Bi as a satisfactory doping impurity for Ge.

[2] Composition of etch: 2 parts 5% $AgNO_3$, 1 part $HNO_3$, 2 parts HF.

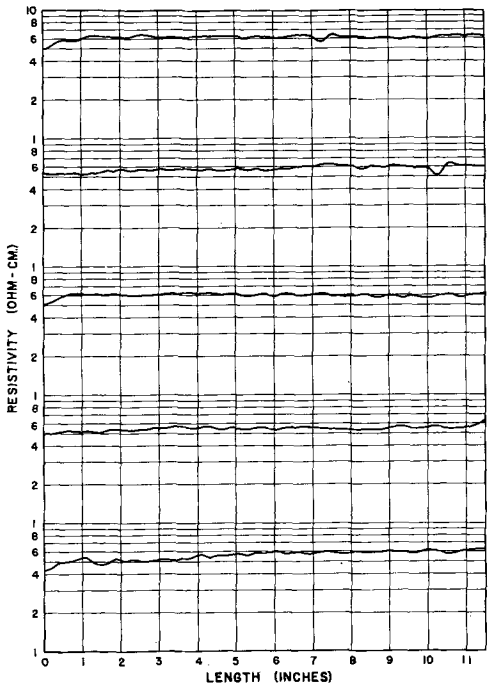


Fig. 5. Resistivity plots along the length of five consecutively grown horizontal single crystals of Ge. The same quantity of Bi was used to dope each crystal.

### Acknowledgment

The author wishes particularly to thank Mr. C. C. Silva, Mr. A. A. Dulac, Mr. C. C. Wang, and Dr. J. F. Battey for their encouragement and helpful comments on this work.

Manuscript received May 29, 1958. This paper was prepared for delivery before the Ottawa Meeting, September 28-October 2, 1958.

Any discussion of this paper will appear in a Discussion Section to be published in the June 1959 JOURNAL.

### REFERENCES

1. R. N. Hall, *J. Phys. Chem.*, **57**, 836 (1953).
2. W. G. Pfann, *Trans. A.I.M.E.*, **194**, 747 (1952).

# Properties of Some Germanium Single Crystals Grown from Solutions of Molten Metals

**H. F. John**

*Research Laboratories, Westinghouse Electric Corporation, Pittsburgh, Pennsylvania*

Distribution coefficients and solid solubilities have been reported for a number of solutes at temperatures ranging from the melting point of germanium down to 400°C (1, 2). The data available in the lower temperature ranges for some of the more frequently used doping impurities have not always been consistent, however. The work reported here was undertaken in an attempt to obtain single-crystal material, grown under equilibrium conditions at a known, constant temperature, which would be similar to that found in the highly doped side of a p-n junction produced by an alloy fusion technique.

Under certain conditions a modified Czochralski technique can be used to grow single crystals of Ge from solutions of molten metals saturated with germanium. Germanium grown from melts containing as high as 5 at. % Sn has been described (3). The essential condition for growing crystals

from such metal solutions is the use of very slow pull rates. Slow pull rates are required because the crystal cannot be withdrawn at a rate faster than Ge can be transported by diffusion across the immobile layer which separates the growing crystal front from the main body of turbulent solution. The diffusion of material across this immobile layer can be increased if the thickness of the layer is kept to a minimum by rapidly rotating the seed crystal, and if the thermal gradient across the immobile layer is made large.

## Crystal Growing

Highly doped single crystals of Ge 6 mm in diameter and a few mm thick have been grown from In, Ga, Al, and Sn-Sb solutions[1] using pull rates of 0.7-2.0 mm/hr, rotation rates of 75 rpm, and a conventional seed clamp which allowed reasonably good thermal conduction through the pull rod. Melts of known composition, whose liquidus temperatures were determined from phase diagrams, were held a few degrees above the liquidus temperature. The temperature at which crystallization takes place is then this liquidus temperature, provided crystallization takes place slowly and provided the amount of Ge removed is kept small compared to the total amount dissolved. Crystals can be grown from melts of constant composition if a reservoir of Ge is present which can go into solution as crystallization takes place onto the seed. Using the latter technique, however, it is more difficult to initiate proper crystal growth. When the seed is lowered into the melt, cooling takes place in the vicinity of the seed to a degree which can be sufficient to cause initially fast and nonuniform growth. Also the temperature at the growth interface may differ slightly from the measured pot temperature. All material discussed below was grown without using a reservoir of Ge.

## Characteristics of Material

Some properties of the crystals grown in the manner described above are given in Table I. The composition of the melt is given in the first column. The crystallization temperature (second column) is the liquidus temperature for this composition as determined from available phase diagrams [In (4), Ga (4), Al (5), Sn (5)]. Resistivities (column 3) were determined by a two-probe technique. Impurity concentrations (column 4) were determined by conventional Hall measurements. The mobilities (column 5) were calculated from the resistivity and concentration of carriers. The distribution coefficient of the doping impurity between the solid and liquid phase is given in the sixth column. Hall voltages obtained on the Ga-doped sample were so small as to be near the detection limit of the apparatus used; consequently, the concentration of carriers could be determined only as being greater than $5 \times 10^{19}$ cm$^{-3}$ by these measurements. No Hall measurements were made on the Al-doped crystal. If a mobility of 100 cm$^2$/v-sec is assumed, the concentration of carriers in the Ga-doped sample would be about $2 \times 10^{20}$ cm$^{-3}$ and in the Al-doped sample about $7 \times 10^{19}$ cm$^{-3}$. The respective distribution coefficients at the liquidus temperature would then be about $7 \times 10^{-3}$ and $3 \times 10^{-3}$. An etch pit count on the In-doped crystals showed the concentration of dislocations to be about $5 \times 10^4$ cm$^{-2}$. The minority carrier lifetime of the In-doped crystals was found to be below the detection limit of the apparatus used, which was about 2 $\mu$sec. Microscopic examination of etched crystals showed no metal inclusions in the main body of any of the crystals; however, in the Ga-doped and Sn-Sb-doped crystals a few very small inclusions were noted at the extreme edge of the crystal.

The distribution coefficients given in Table I for In are lower by about a factor of 3 than those given by Thurmond, Trumbore, and Kowalchik (1). Although there is considerable uncertainty about the distribution coefficients for Al and Ga as calculated from the data in Table I, these are also lower than those reported in the above reference and in the case of Al very much lower. The values for In appear to be more in line with those recently reported by Hall (2), who has suggested that metal inclusions contained in crystals grown at low temperatures may be responsible for some of the high distribution coefficients reported by Thurmond, Trumbore, and Kowalchik (1). The value obtained for the distribution coefficient of Sb is less than a factor of two higher than that reported by Thurmond, Trumbore, and Kowalchik (1) and is, therefore, within experimental error. If their value is too high, as has been suggested by Hall (2), then our high value of distribution coefficient would lend support to the idea that the expansion of the Ge lattice caused by the Sn (3) can enhance the solubility of the Sb. It should be noted that determination of impurity concentrations from Hall effect measurements is subject to some uncertainty, particularly when used on the above materials which are neither strictly semiconductors nor metals. Hall effect measurements, while indirect, are not, how-

[1] The In used was the Indium Corporation's 99.97 grade. The Ga was Eagle-Picher "electronic grade." The Al was a specially purified Alcoa product believed to be better than 99.999%. The Sn was a Baker product containing 0.00005% As. The Sb was a Fisher C.P. product.

Table I. Properties of highly doped Ge crystals

| Composition of melt, molar units | Crystallization temp, °C | $\rho$ ohm-cm | N (Hall) cm$^{-3}$ | $\mu_H$ cm$^2$/v-sec | $\frac{N_{solid}}{N_{liquid}}$ |
|---|---|---|---|---|---|
| $In_{.79}Ge_{.21}$ | 600 | $5.7 \times 10^{-3}$ | $5.4 \times 10^{18}$ | 200 | $2.5 \times 10^{-4}$ |
| $In_{.65}Ge_{.35}$ | 685 | $7.0 \times 10^{-3}$ | $3.8 \times 10^{18}$ | 230 | $2.1 \times 10^{-4}$ |
| $Ga_{.63}Ge_{.37}$ | 630 | $3.3 \times 10^{-4}$ | $(2 \times 10^{20})$ * | (100) | $(7 \times 10^{-3})$ * |
| $Al_{.55}Ge_{.45}$ | 615 | $8.2 \times 10^{-4}$ | $(7 \times 10^{19})$ * | (100) | $(3 \times 10^{-3})$ * |
| $Sn_{.79}Sb_{.07}Ge_{.23}$ | ~610 | $2.0 \times 10^{-3}$ | $6.9 \times 10^{18}$ | 450 | $3.8 \times 10^{-3}$ |

* Determined using the resistivity and a mobility of 100 cm$^2$/v-sec.

ever, so sensitive to metallic inclusions as direct chemical analysis and are, furthermore, nondestructive and adaptable to small samples.

Manuscript received June 2, 1958. The main part of this paper was prepared for delivery before the Cleveland Meeting, Sept. 30-Oct. 4, 1956.

Any discussion of this paper will appear in a Discussion Section to be published in the June 1959 JOURNAL.

REFERENCES

1. C. D. Thurmond, F. A. Trumbore, and M. Kowalchik, *J. Chem. Phys.*, **25**, 799 (1956).
2. R. N. Hall, *J. Phys. Chem. Solids*, **3**, 63 (1957).
3. F. A. Trumbore, *This Journal*, **103**, 597 (1956).
4. W. Klemm, L. Klemm, E. Hohmann, H. Volk, E. Orlamünder, and H. Klein, *Z. anorg. u. allgem. Chem.*, **256**, 244 (1948).
5. H. Stöhr and W. Klemm, *ibid.*, **241**, 312 (1939).

# Technical Review

# Semiconducting Compounds—A Challenge in Applied and Basic Research

**A. C. Beer**

*Battelle Memorial Institute, Columbus, Ohio*

ABSTRACT

The use of a number of semiconducting compounds in device applications is discussed for categories defined by the external field which produces a modulation of the carrier density or mobility. Included are applications based on response to electric fields, magnetic fields, thermal fields, photon energy, and thermal energy. The implications of recent investigations as regards band structure, states densities, charge carrier mobilities, crystal imperfections, and other basic characteristics are presented.

The domain of semiconducting compounds encompasses so large an area that, in order to give coherence to a discussion of these materials, it is necessary to devise methods of classification. The scheme which is adopted here is to define categories on the basis of the external fields which produce a modulation of the charge-carrier density or its mobility. After all, the principal applications of semiconductors stem from the fact that the electrical properties are strongly influenced by environmental factors which can be controlled in a certain arbitrary manner and which are defined by the particular application.

To be more specific, consider the factors contributing to the electrical conductivity, namely, the charge-carrier density and the mobility. Modulation of the equilibrium charge-carrier density by an electric field, the so-called carrier injection, is the basis of semiconductor rectifiers and transistors. On the other hand, a modulation occurring by means of optical absorption leads to devices such as infrared detectors, phototransistors, or solar batteries.

It is possible, also, to modulate the mobility by means of external fields. Since mobility is the tensor component of the conductivity, a very effective way of accomplishing such a modulation is by a magnetic field. Examples of practical applications involve Hall-effect devices, magnetoresistance devices, magnetic rectifiers, and PEM infrared detectors. The last device actually encompasses two of the categories just discussed, since electron-hole separation is effected by means of the photon energy.

A list of some of the categories resulting from this classification system is presented in Table I. Examples of specific devices are given for each classification.

The major part of this paper is concerned with a number of the compound semiconductors having unique properties which permit applications in some of the categories shown. In addition, some of the inroads to our fundamental understanding of transport processes in semiconductors, which are coming about through studies on some of these compounds having unusual characteristics, are discussed.

## Carrier-Density Modulations

### *Application of Electric Fields*

Evidence indicates that the materials which are being studied most actively with regard to transistor applications are some of the higher band separation III-V compounds such as InP, GaAs, AlSb, and GaP. Recently the compound SiC also has received considerable attention. In addition, some work is being done on the low-gap material indium antimonide for use in transistor applications below —50°C and for use in microwave circuitry (1).

Some of the advantages of the III-V compounds are the diamond-type lattice, which insures a reasonably good thermal conductivity and a high elec-

**Table I. Operational classification of semiconductors**

| Carrier-density modulations | Mobility modulations |
|---|---|
| Electric field<br>(a) Moderate<br>Transistors, rectifiers<br>(b) Strong<br>Avalanche phenomena, Zener currents, varistors, surge arrestors | Thermal energy<br>(temperature)<br>Nonlinear elements<br>Electric field<br>Hot-electron phenomena |
| Photon energy<br>Photoconductors, infrared detectors, infrared filters and windows<br>Solar batteries | Force field<br>Elastoresistance |
| Thermal energy<br>(temperature)<br>Thermistors | |
| Thermal field<br>Thermoelectric power generation<br>Peltier cooling | Magnetic field<br>Hall effect, magnetoresistance (many applications) |
| Force field<br>Piezoelectric effects | |
| Crystallographic modifications<br>(a) Phase-change phenomena<br>Control circuits<br>(b) Impurity effects<br>Chemical analysis<br>(c) Dislocations or other physical imperfections<br>Strain gauges, nuclear particle flux indicators | |
| Crystallographic modifications—magnetic field<br>Magnetic rectifier based on asymmetrical surface recombinations | |
| Photon energy—magnetic field<br>Photoelectromagnetic detectors | |

tron mobility. A most important consideration is the fact that deviations from stoichiometry apparently are controlled readily by crystal-pulling and zone-melting techniques.

Much information can be found on the III-V compounds in the literature (2, 3) and will not be repeated here. However, some rather recent data are presented to show that steady improvements are

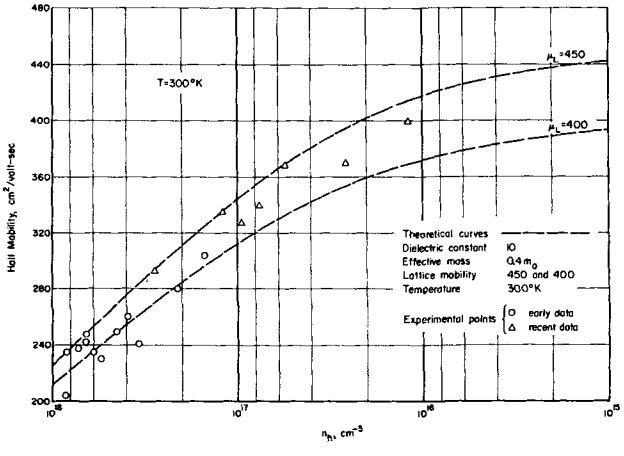


Fig. 1. Hole mobility as a function of carrier concentration for aluminum antimonide.

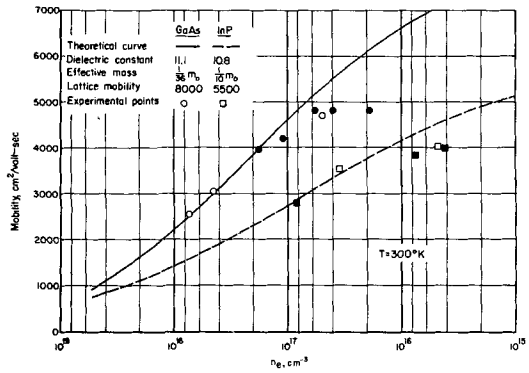


Fig. 2. Earlier data on electron mobility in GaAs and InP

being made in these materials and to suggest that perhaps one is not being unduly rash in thinking that in several years some of these compounds may pre-empt the position of germanium and silicon in certain applications.

In evaluating a given specimen of material for device application, I am going to compare its characteristic on a curve of the Hall mobility as a function of the extrinsic carrier concentration for the material in question. This procedure is more trustworthy than the consideration of either resistivity or Hall coefficient when the degree of compensation of donors and acceptors is not directly known. Figure 1 shows such data for aluminum antimonide. The circles represent data prior to 1958. The triangles show the results of improvements which were achieved less than six months ago (4).

The data in Fig. 2 indicate the earlier state of affairs for gallium arsenide and indium phosphide. The theoretical curves were drawn using simple theory to account for scattering by lattice vibrations and ionized impurities. At the time, it appeared that we may have been overly optimistic in our choice of lattice mobilities. However, let us replot the theoretical curves and include some later data, as is shown in Fig. 3.

It now becomes apparent that the earlier material was significantly compensated, even though the net excess of donors over acceptors was quite high. The characteristics of the better material are quite striking. Theoretical curves through these points suggest that the lattice mobility in indium phosphide may

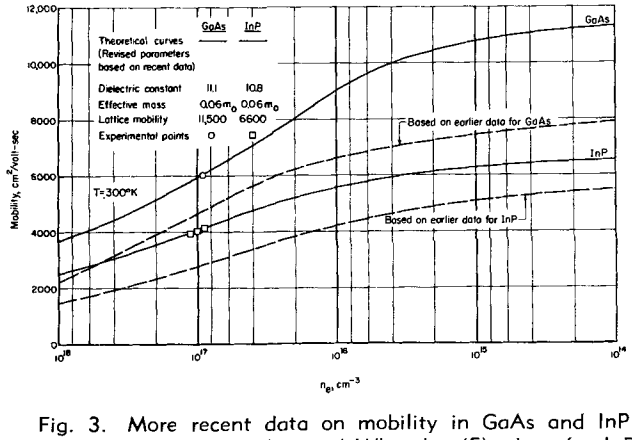


Fig. 3. More recent data on mobility in GaAs and InP GaAs point is from Whelan and Wheatley (5); data for InP were taken at Battelle (4).

Table II. Mobilities at 300°K and ionized impurity contents for the best AlSb, InP, and GaAs prior to February 1958

| | AlSb | InP | GaAs | GaSb | InAs | InSb* |
|---|---|---|---|---|---|---|
| Approximate $\mu^L_e$ (cm²/v-sec) | — | 6600 | 11,500 | — | 40,000 | 1,200,000 |
| Highest measured $\mu_e$ ($R\sigma$) | — | 4600 | 6000 | 4000 | 30,000 | 620,000 |
| Approximate $N_i$ (impurities/cm³) | — | $5 \times 10^{15}$ | $1 \times 10^{17}$ | $7 \times 10^{17}$ | $1.7 \times 10^{16}$ | $1.7 \times 10^{14}$ |
| Approximate $\mu^L_h$ | 450 | 150 | 650 | — | — | — |
| Highest measured $\mu_h$ ($R\sigma$) | 400 | 100 | 400 | 785 | — | 10,000 |
| Approximate $N_i$ (impurities/cm³) | $3 \times 10^{16}$ | $3 \times 10^{17}$ | $3 \times 10^{17}$ | $2 \times 10^{17}$ | — | $1 \times 10^{15}$ |

* Values given at 77°K.

be as high as 6500 cm²/v-sec, and in gallium arsenide 11,500. To those who recall in Shockley's book the famous presentation of the historical data on mobility in germanium (6), the progression of measured mobility values in the III-V compounds has a familiar appearance. We are still in the region where significant improvements in materials developments are possible. Nevertheless, in the compounds just discussed, it does appear that we are now getting sufficiently good information to permit us to make reliable predictions about the lattice mobility. A brief résumé of the present state of affairs on the major III-V compounds is given in Table II.

### *Photon Energy*

An important application for compound semiconductors is infrared detection. Probably the most widely used materials are lead sulfide, selenide, and telluride. These compounds cover a range from 1 to 7 $\mu$ (7). They are prepared in the form of deposited films on suitable substrates and must be cooled.

Magnesium stannide (8) ($Mg_2Sn$) and two of the III-V compounds also have interesting photoproperties in the 3 to 7½-$\mu$ range. The latter compounds are indium arsenide (9) and indium antimonide (10). These materials show considerable sensitivity in devices utilizing the photoelectromagnetic effect.[1] Such operation permits better sensitivity at higher temperatures than does the usual type of detector. It has been pointed out that InSb detectors now can be made which are more sensitive than any other uncooled detector throughout the range from 3 to 7½ $\mu$ (11). Another special property of InSb and InAs is the small effective electron mass. Thus, the density of states at the bottom of the conduction band is low, and the transmission edge can be shifted to higher energies, i.e., shorter wave lengths, by increasing the concentration of ionized carriers in the conduction band (9, 12-14). This behavior is of interest in connection with infrared filters and windows.

Because of transparency into the relatively far infrared, certain compound semiconductors may find numerous applications as window materials. An example of this is given by the transmission characteristics of cadmium telluride as shown in Fig. 4.

Photoconductive response in semiconducting compounds is, of course, not limited to the infrared region. Many applications range through the visible spectrum to that of x-rays and $\gamma$-rays. There are also $\alpha$- and $\beta$-particle counters. Examples of compounds which find uses in these areas are sulfides, selenides, and tellurides of cadmium or zinc (15).

[1] A discussion of PEM phenomena will be given in a subsequent section.

### *Thermal Energy (Temperature)*

The most common device for which the electrical characteristics are strongly temperature dependent is the thermally sensitive resistor or thermistor. These are usually made from mixtures of metal oxides. However, a crystal semiconductor in the intrinsic region will have a resistivity varying as exp $W/2kT$, provided that the mobility is reasonably well-behaved and does not differ appreciably from the classic $T^{-3/2}$ temperature dependence. With this exponential behavior, the temperature coefficient of resistance is proportional to the band separation, so that large-band-separation intrinsic materials are highly temperature sensitive. The practical difficulty in most cases is that such intrinsic semiconductors are almost insulators. In certain III-V compounds, however, the intrinsic resistivity is lowered as a result of unusually large mobilities, and some of these materials, therefore, can be used to advantage in thermistor circuits. In Fig. 5 is shown the measured resistivity as a function of temperature for a specimen of indium phosphide. It is calculated that at 350°K the temperature coefficient is approximately 6.3%/°K. This is somewhat larger than the figure of 4% quoted for the powder-process thermistors (16).

### *Thermal Fields*

Probably the most widely studied application of the interaction of electrons and thermal fields is thermoelectric power generation and Peltier cooling. Good efficiencies in either of these processes obviously require the same kinds of characteristics for the materials. To illustrate the concepts involved, consider the Peltier effect, as exemplified by the heat transport between two junctions.

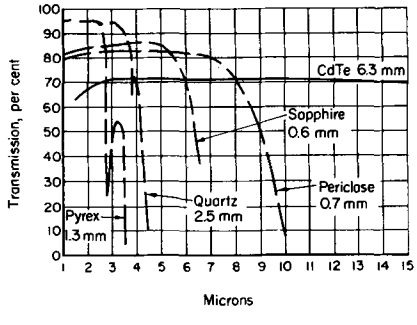


Fig. 4. Transmission of CdTe and other window materials as function of wave length. Solid line is from Battelle data, dashed lines are after Moss (7).

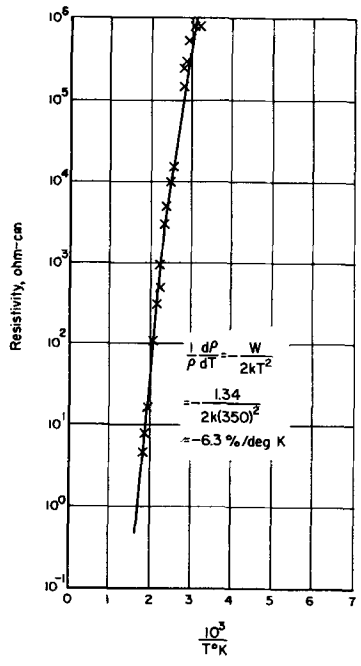


Fig. 5. Resistivity as function of temperature for intrinsic specimen of InP.

In Fig. 6 is presented the maximum temperature differential as a function of a parameter proportional to the current in the circuit. The Peltier transport is directly proportional to the current, as can be seen at low currents. However, the achievement of an arbitrary $\Delta T$ is limited by opposing effects due to thermal transport and to Joule heating. The first process is proportional to $\Delta T$, and the second to $I^2$. Hence, they both become predominant at higher currents, so that $\Delta T$ reaches a maximum. It turns out that the efficiency of thermoelectric processes can be described by a parameter which characterizes the material. The so-called "figure of merit" is commonly written as $\alpha^2/K\rho$.[2] Knowing this ratio, one can calculate quite accurately the temperature difference resulting in a Peltier couple (17). The basic problem is, therefore, to develop materials with highest values of the figure of merit.

The present theory of thermal transport processes is not sufficiently developed to permit one to make quantitative predictions regarding the figure of merit. The more obvious difficulties are associated with the treatment of the scattering mechanism and with the contribution of the lattice to the thermal conductivity. However, certain guideposts are available for selecting thermoelectric materials. Some of these are:

1. The material must not be intrinsic—since holes and electrons produce opposite thermal emfs.
2. The carrier concentration should be high, but not at the expense of degeneracy. Therefore, a large effective mass is desirable, but not at the sacrifice of mobility.
3. The charge-carrier scattering mechanism is important; processes involving ionized impurities or optical modes of the lattice are preferred to some extent over those by acoustic phonons.
4. The lattice thermal conductivity should be low so that $K$ does not deviate too greatly from the Wiedemann-Franz value. This latter consideration is probably one of the reasons why compounds with the zinc blende crystal structure have exhibited too large a thermal conductivity to have promising thermoelectric properties.
5. Another desirable feature is that the compound have a large lattice constant and a low dissociation energy, both of which tend to reduce the lattice thermal transport (18). However, a low dissociation energy implies a small energy gap, and, as was indicated before, the gap must not be so small that intrinsic conduction predominates at the temperatures of operation.
6. The mean atomic weight of the elements of the compound should be high, since mobility (in the case of impurity scattering) or the ratio of mobility to thermal conductivity (in the case of lattice scattering) increases with mean atomic weight (19).

The materials which are the subject of much current investigation, namely, the selenides and tellurides of lead and bismuth and derived compounds and alloys, satisfy the criteria which were just outlined. Further insight into some of the materials may be gained from Fig. 7, which shows the thermoelectric properties of p-type bismuth telluride, doped with excess bismuth.

A technique for reducing the lattice thermal conductivity without disturbing too seriously the elec-

[2] The thermoelectric power in v/°C is designated by $\alpha$; the thermal conductivity in w/cm °C, by $K$; and the resistivity in ohm-cm, by $\rho$.

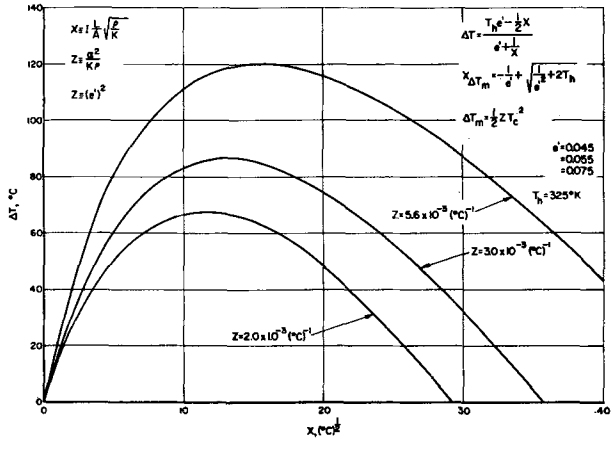


Fig. 6. Maximum temperature differential in Peltier couple. Abscissae are proportional to current.

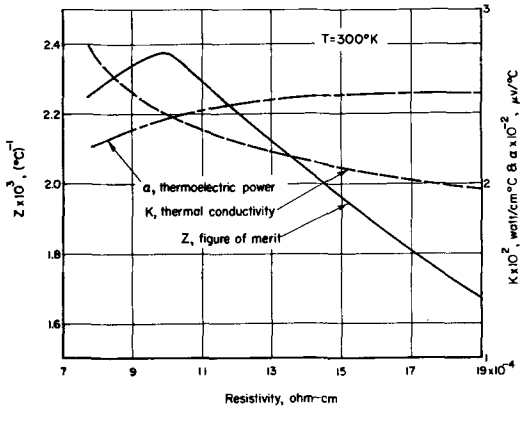


Fig. 7. Thermoelectric data on p-type specimen of $Bi_2Te_3$

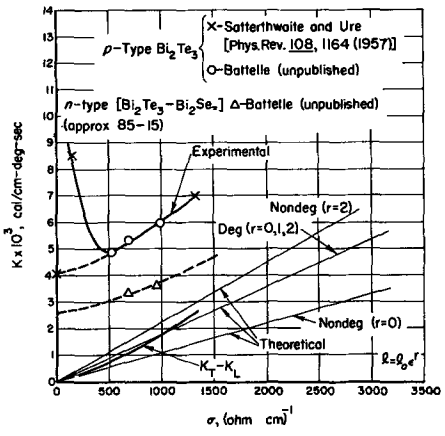


Fig. 8. Thermal conductivities for $Bi_2Te_3$ and an alloy

trical properties is the alloying of similar compounds. It was pointed out by Joffe (20) that the lattice distortions produced in each case are relatively small and, therefore, affect principally the lattice transport, since the wave length of the thermal oscillations at ordinary temperatures is the order of a lattice constant. The wave length of the electrons of the Fermi energy, on the other hand, is considerably greater than the lattice constant, and, therefore, the carrier mobility is reduced only a small amount. Figure 8 illustrates some results of alloying bismuth telluride with bismuth selenide. Here the measured thermal conductivity is plotted as a function of the electrical conductivity of the specimen. The lattice thermal conductivity is given by extrapolation of the data to $\sigma = 0$. Measurements on low-conductivity specimens cannot provide this information, since in nearly intrinsic material additional transport effects become important, such as ambipolar diffusion and ionization energy transport. This is evidenced by the point from Satterthwaite and Ure's (21) data for $\sigma$ less than 250 $(\text{ohm-cm})^{-1}$. These investigators determined $K_L$ from the temperature dependence of the extrinsic data, and the result is in good agreement with the extrapolation of the Battelle data.

An interesting check of the applicability of present theory can be made by determining $K_T - K_L$, i.e., the difference between the total conductivity and the lattice contribution, as a function of the electrical conductivity. In the extrinsic region this difference is essentially $K_{\text{electronic}}$. The result is plotted on the graph, flanked by several theoretical lines representative of different scattering mechanisms. It is seen that results are consistent with expectations.

A similar lowering of lattice thermal conductivity with alloying has been shown by Joffe and co-workers to occur with lead telluride. The value decreases by a factor of two as approximately 20% lead selenide is added (22).

Many more illustrations could be given of thermoelectric materials, although the field is still only partially explored. This is especially true when one considers materials which might be operable at higher temperatures, say, above 600°C. It is clear that this area of research is still in its infancy and that much work needs to be done, both in materials preparation and in basic theoretical developments.

## Combination-Carrier Density and Mobility Modulations

### *Crystallographic Modifications*

A number of interesting properties are included in this category. Take, for example, the change in phase or crystallographic structure which occurs in a number of compounds. Illustrations are silver sulfide (23) and barium titanate (24). At approximately 175°C the resistivity of silver sulfide drops discontinuously by three orders of magnitude. The use of such type of materials in alarm systems is obvious. Also, it is apparent that the current-voltage characteristic of such an element can be controlled rather widely by the thermal characteristics of its mounting.

If impurities capable of producing donor or acceptor levels are added to high-purity semiconductors, changes in carrier densities and in low-temperature mobilities result. After appropriate "calibration" experiments are done with known impurity additions, electrical measurements can be used to supply sometimes both quantitative and qualitative information on chemical impurities. Figure 9 illustrates the principle involved in the identification and quantitative determination of tellurium content in InSb through the use of Hall measurements (25). The distributions of tellurium and of the unknown impurity along standard InSb ingots are seen to coincide. A similar procedure has been used to identify sulfur in indium arsenide.

Since very high-purity indium and antimony are now available, such techniques can be used to check the purity of other elements used in making III-V compounds, such as gallium and arsenic, through the preparation of a test specimen of gallium antimonide with the use of very pure antimony, and of indium arsenide, using the pure indium.

A novel application of the effects of foreign impurities has recently been discussed by investigators at the Physikalischen Institut at Bonn (26). They found that they could use cuprous oxide films, and to a less satisfactory extent, cadmium sulfide single crystals, as a quantitative detector of neutral atoms of sulfur or selenium in a molecular beam.

### *Crystallographic Modification Combined with Magnetic Field*

An interesting application of the use of surface treatments to produce a crystal asymmetry which, in combination with an applied magnetic field, leads to nonlinear conduction (27) has been investigated by Weisshaar, Welker, and associates. During one

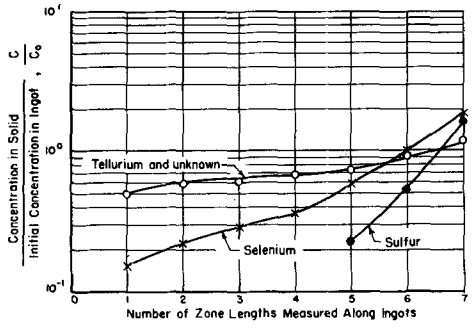


Fig. 9. Relative distribution of some group VI impurities in InSb after five zone-melt passes, after Harman (25).

direction of the current, the holes and electrons in an intrinsic semiconductor are deflected by the magnetic field to a face which, say, has been sandblasted to produce a high surface recombination. During the other cycle, the carriers are deflected to an etched surface of low recombination velocity. Experiments were carried out on germanium, and at zero magnetic field the current-voltage characteristic was linear. At 8000 gauss, however, substantial asymmetry was introduced. Moss has calculated that, for use with indium antimonide, an optimum specimen thickness would be in the order of 30 $\mu$, and that back-to-front ratios of 1000 to 1 are potentially possible (28).

### *Joint Modulations by Photon Energy and Magnetic Field*

This process is the basis of the PEM effect which, when used with indium antimonide, has provided one of the most sensitive infrared detectors for operation at room temperature (11). In addition, it is a very useful tool for studying recombination processes and surface states (29, 30).

Consider a slab of semiconductor of thickness $t$ along the x-direction, large in the other directions, and illuminated on the yz-face by light of appropriate wave length directed along the x-axis. These photons release electron-hole pairs which will diffuse in the x-direction. If now a magnetic field is directed along the z-axis, the electrons and holes will be accelerated oppositely along the y-direction and a potential difference will appear along the y-axis in the specimen. This is the PEM voltage.

When using the technique to measure bulk lifetimes, one usually determines both PEM and photoconductive responses for the same illumination. In this way it is not necessary to have an independent knowledge of the photon flux density or the surface recombination velocities. The method is especially suited to the measurement of lifetimes of $10^{-7}$ sec and lower in high-mobility materials such as InSb.

## Mobility Modulations

The only examples discussed in this grouping are the galvanomagnetic effects, which are extremely large in high-mobility materials.

When a magnetic field is applied normal to the current direction in a conductor, an initial lateral deflection of charge carriers results, as shown in Fig. 10. This charge accumulation produces a transverse potential gradient, called the Hall field. The Hall field assumes such a value that the force on a charge carrier of "average" velocity is zero in the crossed electric and magnetic fields.

If all the charge carriers had the same velocity, then the Hall-field force would cancel exactly the force due to the magnetic field on the moving charge, and no charge carriers would be deflected. Hence, there would be no magnetoresistance. Actually, however, a distribution of velocities exists in semiconductors so that those carriers with velocities larger or smaller than the "average" will be caused to traverse larger paths, thus increasing the resistance of the conductor.

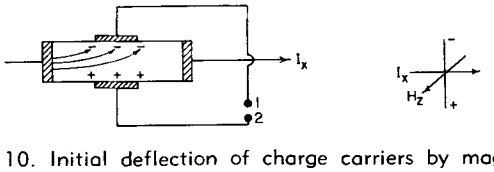


Fig. 10. Initial deflection of charge carriers by magnetic field to create Hall field.

Table III. Relation between mobility and Hall angle

$$E_y = Rj_xH_z,\ V_H = 10^{-8}\frac{RIH}{d} = 10^{-8}\frac{\rho I\mu H}{d}$$

Hall angle:

$$\text{Tan}\ \theta \equiv E_y/E_x = 10^{-8}R\sigma H = 10^{-8}\mu H$$

| Semiconductor | $T$, °K | Tan $\theta$ (For $H$ = 5000 gauss) |
|---|---|---|
| Germanium, electrons | 300 | 0.2 |
| InAs, electrons | 300 | 2.0 |
| InSb, electrons | 300 | 4.0 |
| InSb, electrons | 77 | 25.0 |

From the preceding discussion it is apparent that any arrangement for decreasing the Hall field will augment the magnetoresistance. For example, if in Fig. 10, terminals 1 and 2 are connected through a low impedance, a current will exist in this circuit. In the case of certain semiconductors, such as indium antimonide, this secondary current can be relatively large. Since this transverse current across the semiconductor is still normal to the magnetic field, one may regard it as creating another Hall voltage which opposes the electric field causing the primary current. Thus it follows that the primary current may be modulated by varying either the magnetic field or the secondary load. The pertinent equations describing the Hall effect along with typical values of certain parameters for several semiconductors are given in Table III.

Because of these large transverse phenomena in semiconductors such as indium antimonide and indium arsenide, a series of applications has been developed in Germany (31) and in England (32) as well as in America (33-35). In such devices, the individual element is the so-called "Hall generator," which may be considered as a square slab of high-mobility semiconductor having contacts on each of the four sides. A few applications of such units are fluxmeters, d-c to a-c converters, and devices to multiply all quantities which can be made to depend on current and on magnetic field: for example, product operations in an analog computer, and measurements of torque of an electric motor. Factors important in the performance of Hall generators are listed in Table IV.

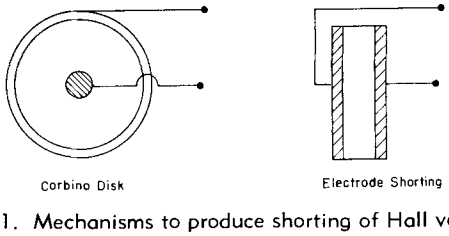


Fig. 11. Mechanisms to produce shorting of Hall voltage

**Table IV. Performance of Hall generators**

Max. power to load: $W_o = V_H^2/4Z_i$; efficiency $\eta \equiv W_o/W_i \sim 10^{-16}H^2\,(R/\rho)^2$, $\mu H << 1$
No load: $V_H \sim 10^{-8}W_i^{1/2}\,HR/\rho^{3/2}$, $\mu H << 1$

| Material | T, °K | $R$ (cm³/coulomb) | $\rho$ (ohm-cm) | $R/\rho$ (cm²/v-sec) | $\left[\frac{R}{\rho}\right]^2$ | $\frac{R}{\rho^{3/2}}$ |
|---|---|---|---|---|---|---|
| Bismuth | 300 | 1.5 | 0.00012 | 12,500 | $1.56 \times 10^8$ | $0.14 \times 10^9$ |
| Ge (intrinsic) | 300 | 60,000 | 45 | 1300 | 0.02 | 8.9 |
| Ge (medium) | 300 | 8000 | 2 | 4000 | 0.16 | 5.7 |
| Ge (low Tc) | 300 | 10 | 0.01 | 1000 | 0.01 | 0.1 |
| InSb (intrinsic) | 300 | 360 | 0.006 | 60,000 | 36 | 4.6 |
| InSb (low Tc) | 300 | 20 | 0.0008 | 25,000 | 6 | 0.7 |
| InAs (intrinsic) | 300 | 10,000 | 0.25 | 40,000 | 16 | 20 |
| InAs (low Tc) | 300 | 500 | 0.015 | 30,000 | 9 | 4.1 |
| InSb (high purity) | 77 | 37,300 | 0.06 | 620,000 | 3840 | 152 |

Returning now to the magnetoresistance effects, it was seen how results could be augmented by shorting the Hall voltage. This is done most effectively by the disk geometry shown in Fig. 11. The arrangement is known as the Corbino disk.[3] A somewhat simpler design for producing shorting is the use of large end contacts, as is seen at the right (37). Characteristics of these types of InSb elements are presented in Fig. 12.

It is seen that rectangular geometries approach quite closely the results for the disk. One difficulty with the simple units as circuit elements is their low impedance, less than 0.1 ohm for the specimens representing the curves on the slide. To improve this, one can resort to very thin rectangular wafers with shorting bars deposited thereon. A commercial specimen of this type has a zero-magnetic-field resistance of ½ ohm.[4] The data are indicated by the solid circles. It is seen that such a fabrication technique has increased appreciably the impedance of the unit and yet provided a good magnetoresistance ratio.

The applications of such units are again myriad. Examples are contactless switches and potentiometers, d-c to a-c converters, synchronous rectifiers, and voltage regulators (38).

[3] After O. M. Corbino who investigated the circulating secondary currents in a bismuth disk carrying a primary electric current in a magnetic field (36).

[4] Supplied us by courtesy of K. Eggleston of Ohio Semiconductors, Inc.

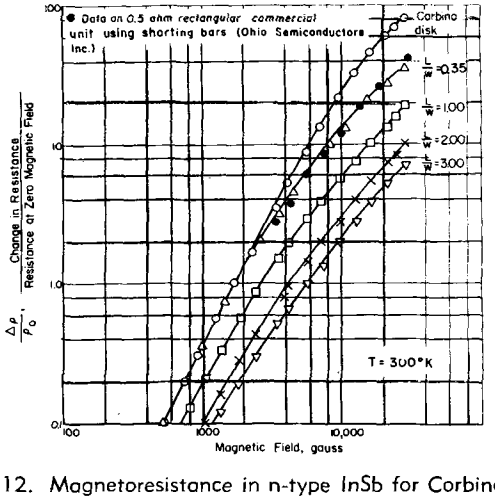


Fig. 12. Magnetoresistance in n-type InSb for Corbino disk and for several ratios of sample length to width (full area contacts at ends).

## Research on Semiconducting Compounds as a Means for Advancing Solid-State Theory

In addition to yielding materials with unique properties which are potentially valuable for device applications, the field of semiconducting compounds has provided much interesting research for the basic scientist and has given us a means for testing some of our theoretical predictions concerning the solid state. In this respect, indium antimonide has received the lion's share of attention. Because of its high electron mobility, one can study with ordinary laboratory magnets phenomena which would require fantastic magnetic field strengths to observe in other materials. Figure 13 shows magnetoresistance measurements (39) extending into the region where electron-orbit quantization must be considered (40-42). For the point on the extreme right, the energy of an electron in its cyclotron orbit is 2.6 that of its thermal energy—and this at 77°K!

A further consideration is that the conduction band is reasonably isotropic, having one energy minimum at the zero of the electron wave number (43). Such a simple structure is always a boon to the theorist, since it reduces the complexities entering into the interpretation of the experimental data.

Another interesting feature is the large ratio of electron-to-hole mobility. As a result, it is possible to study in one single instrinsic sample certain characteristics of electrons and of holes. This is illus-

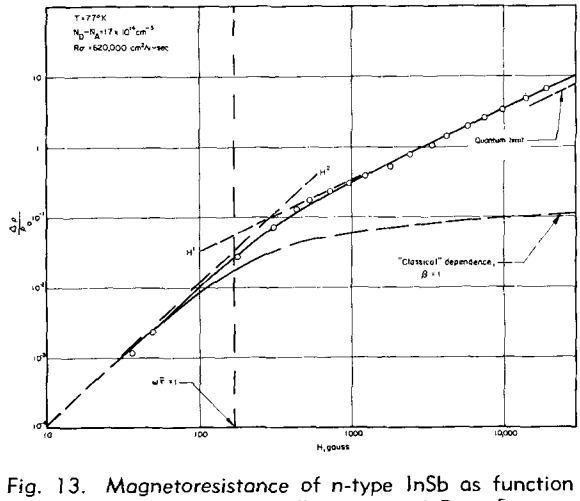


Fig. 13. Magnetoresistance of n-type InSb as function of magnetic field (after Bate, Willardson, and Beer [to appear in "J. Phys. Chem. Solids]).

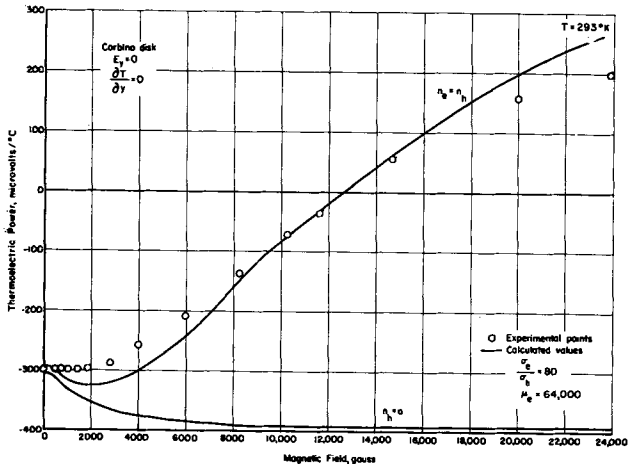


Fig. 14. Thermoelectric power of intrinsic InSb for Corbino disk geometry as function of magnetic field.

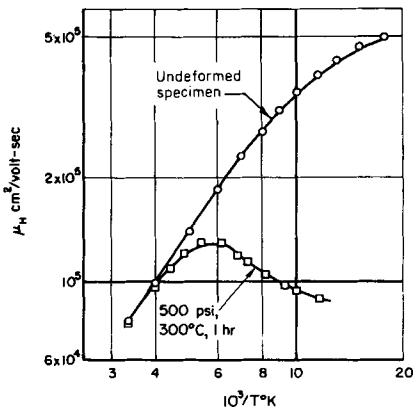


Fig. 15. Effect of plastic deformation on electron mobility in high-purity InSb sample with $1 \times 10^{14}$ extrinsic carriers/cm$^3$.

trated by the thermoelectric measurements shown in Fig. 14 (44, 45). Because of their high mobility, the electron transport effects predominate in intrinsic material. However, this contribution is strongly magnetic-field dependent, so that at above 12 kilogauss the holes take over. The theoretical curve was based on a single charge-carrier scattering mechanism. If electron-hole scattering is also taken into account, the minimum tends to disappear (45).

The unusual mobility at low temperatures renders InSb a sensitive material for registering effects of deformation. This is illustrated in Fig. 15, which shows the change in temperature dependence of mobility after one hour's compression at 300°C (46).

Other features of interest to theorists include the overlapping of donor levels with the conduction band even in relatively pure indium antimonide and indium arsenide, nonparabolic heavy-mass bands (43, 47). an anomalous negative magnetoresistance in indium antimonide (48), and anomalies in Hall coefficient, such as double reversals, in certain specimens of indium arsenide (49).

In indium phosphide, recent magnetoresistance measurements by Glicksman on oriented crystals suggest that the conduction band is fairly isotropic (50). Preliminary results at Battelle indicate the same situation may exist for mercury telluride inasmuch as the ratio of longitudinal and transverse magnetoresistance was found to be quite small, that is, approximately 2%.

## Summary

I have tried to give some indication of the tremendous breadth encompassed by the field of semiconducting compounds and to show that progress is being achieved on a great variety of fronts. It seems clear that, already at the present stage of materials development, a variety of useful devices can be perfected by ingenious experimenters, and if improvements in materials perfection should follow the usual course, a number of very promising developments should accrue. Also, it has been seen that a number of compounds have rather unique characteristics, and these are providing challenging areas of investigation, both for the experimentalist and for the theorist.

## Acknowledgment

The author is indebted to his associates at Battelle for use of unpublished data and for assistance with the manuscript. In particular, he desires to mention R. Bate, J. Duga, T. Harman, E. Lougher, B. Paris, C. Peet, F. Reid, T. Shilliday, and R. Willardson.

Manuscript received April 30, 1958. This paper was prepared for delivery before the New York Meeting, April 27-May 1, 1958.

Any discussion of this paper will appear in a Discussion Section to be published in the June 1959 JOURNAL.

## REFERENCES

1. C. T. McCoy, *Proc. Inst. Radio Engrs.*, **46**, 61 (1958).
2. H. Welker and H. Weiss, "Solid State Physics," Vol. 3, p. 1, Academic Press, Inc., New York (1956).
3. F. A. Cunnell and E. W. Saker, "Progress in Semiconductors," Vol. 2, p. 37, John Wiley & Sons, Inc., New York (1957).
4. F. J. Reid and R. K. Willardson, *J. Electronics and Control*, **5**, 54 (1958).
5. J. M. Whelan and G. H. Wheatley, To appear in *J. Phys. Chem. Solids.*
6. W. Shockley, "Electrons and Holes in Semiconductors," p. 338, D. Van Nostrand Co., Inc., New York (1950).
7. T. S. Moss, *Proc. Inst. Radio Engrs.*, **43**, 1869 (1955).
8. H. P. R. Frederikse and R. F. Blunt, *ibid.*, **43**, 1828 (1955).
9. R. M. Talley and D. P. Enright, *Phys. Rev.*, **95**, 1092 (1954).
10. T. S. Moss, "Photoconductivity Conference," p. 427, John Wiley & Sons, Inc., New York (1956).
11. T. S. Moss, "Solid State Phenomena in Electric Circuits," p. 123, Interscience Publishers, New York (1957).
12. M. Tanenbaum and H. B. Briggs, *Phys. Rev.*, **91**, 1561 (1953).
13. A. C. Beer, R. K. Willardson, and A. E. Middleton, *ibid.*, **93**, 912 (1954).
14. E. Burstein, *ibid.*, **93**, 632 (1954).
15. R. H. Bube, *Proc. Inst. Radio Engrs.*, **43**, 1836 (1955).
16. E. M. Conwell and W. J. Leivo, "The Science of Engineering Materials," p. 418, John Wiley & Sons, Inc., New York (1957).
17. T. S. Shilliday, *J. Appl. Phys.*, **28**, 1035 (1957).
18. T. A. Kontorova, *Soviet Physics-Technical Physics*, **1**, No. 9 (1959).
19. H. J. Goldsmid and R. W. Douglas, *Brit. J. Appl. Phys.*, **5**, 386 (1954).
20. A. F. Joffe, *et al, Dokl. Akad, Nauk. SSSR*, **106**, 981 (1956).

21. C. B. Satterthwaite and R. W. Ure, Jr., *Phys. Rev.*, **108**, 1164 (1957).
22. A. F. Joffe, *Can. J. Phys.*, **34**, No. 12A, 1342 (1956).
23. F. R. Quinn, U.S. Pat. 2,609,470, Sept. 2, 1952.
24. H. A. Sauer and S. S. Flaschen, *Proc. 1956 Electronic Components Symposium at Washington, D. C.*, p. 41, Engineering Publishers, New York (1956).
25. T. C. Harman, *This Journal*, **103**, 128 (1956).
26. W. Gebhardt and O. Osberghaus, *Z. Physik*, **150**, 33 (1958).
27. E. Weisshaar and H. Welker, *Z. Naturforsch.*, **8a**, 681 (1953).
28. T. S. Moss, *op. cit.*, p. 113.
29. O. Garreta and J. Grosvalet, "Progress in Semiconductors," Vol. 1, p. 165, John Wiley & Sons, New York (1956).
30. S. W. Kurnick and R. N. Zitter, *J. Appl. Phys.*, **27**, 278 (1956).
31. F. Kuhrt, *et al, Siemens-Z.*, **28**, 299 [also 370, 376] (1954).
32. I. M. Ross and E. W. Saker, *J. Electronics*, **1**, 223 (1955).
33. W. C. Dunlap, Jr., U. S. Pat. 2,725,504, Nov. 29, 1955.
34. W. P. Mason, W. H. Hewitt, and R. F. Wick, *J. Appl. Phys.*, **24**, 166 (1953).
35. R. F. Wick, *ibid.*, **25**, 741 (1954).
36. E. P. Adams, *Proc. Am. Phil. Soc.*, **54**, 47 (1915).
37. O. Madelung, *Naturwissenschaften*, **42**, 406 (1955).
38. R. K. Willardson and A. C. Beer, *Elec. Mfg.*, **57**, 79 (1956).
39. R. T. Bate, R. K. Willardson, and A. C. Beer, *Bull. Am. Phys. Soc.*, **3**, 119 (1958) [complete article to appear in *J. Phys. Chem. Solids*].
40. R. K. Willardson, T. C. Harman, P. Choquard, and A. C. Beer, *Phys. Rev.*, **98**, 227 (1955).
41. P. N. Argyres and E. N. Adams, *ibid.*, **104**, 900 (1956).
42. P. N. Argyres, *ibid.*, **109**, 1115 (1958).
43. E. O. Kane, *J. Phys. Chem. Solids*, **1**, 249 (1957).
44. R. K. Willardson and A. C. Beer, *Bull. Am. Phys. Soc.*, **1**, 54 (1956).
45. A. C. Beer, J. A. Armstrong, and I. N. Greenberg, *Phys. Rev.*, **107**, 1506 (1957).
46. J. J. Duga, R. E. Maringer, and A. C. Beer, *Bull. Am. Phys. Soc.*, **3**, 106 (1958).
47. F. Stern, *ibid.*, **3**, 120 (1958).
48. H. P. R. Frederikse and W. R. Hosler, *Phys. Rev.*, **108**, 1136 (1957).
49. J. R. Dixon, *Bull. Am. Phys. Soc.*, **3**, 120 (1958).
50. M. Glicksman, *ibid.*, **3**, 120 (1958).

## Correction

On page 544 (Vol. 105, September 1958) of the paper by M. J. Allen and V. J. Powell on the Oxidation of Various Indole Alkaloids, the sequence of formulas should be inserted after the sentence, ". . . in this instance we would have at the electrode surface due to adsorption of the alkaloid molecule:"

# Discussion Section

This Discussion Section includes discussion of papers appearing in the JOURNAL of The Electrochemical Society, 104, No. 3 (March 1957), and 105, No. 1-6 (January-June 1958). Discussion not available for this issue will appear in the Discussion Section of the June 1959 JOURNAL.

## Hydrogen Evolution Reaction on Copper, Gold, Molybdenum, Palladium, Rhodium, and Iron; Mechanism and Measurement Technique under High Purity Conditions

N. Pentland, J. O'M. Bockris, and E. Sheldon
(pp. 182-194, Vol. 104)

**R. Piontelli, U. Bertocci, G. Poli, and G. Serravalle**[1]: The following may be suggested as representing certain aspects of the views of Pentland, Bockris, and Sheldon (P., B., and S.), in reference to the technique of measurements in electrode kinetics, with which we are not in agreement.

1. The geometrical characteristics of the cell seem to be considered by P., B., and S. of rather secondary importance, if the electrodes to be investigated are employed in the form of a wire suspended in the solution.

2. As the possible "spurious components" of the measured overvoltages, P., B., and S. consider only the "ohmic drop" and the "concentration component." No "screening effects" are considered,[2] and the evaluation of the ohmic drop in the layer between capillary and electrode has to be effected, by assuming here the same current density distribution admitted to exist on the whole electrode surface.

3. The evaluation of the "concentration component," according to P., B., and S., may be effected following similar assumptions and adopting for the thickness of the diffusion layer the "appropriate value" of "approximately 0.005 cm."

4. Essential criteria for checking "a posteriori" the correctness of overvoltage measurements are: (*a*) correspondence to Tafel law; (*b*) practical absence of time variations.

I. The rather indefinite current distribution on the electrodes of a cell of the type used by P., B., and S. allows only for rough conclusions on the dependence of the measured overvoltages on current density (c.d.).

II. The P., B., and S. opinion on the screening effects may be rejected both on theoretical grounds and according to the experimental evidence.[3] As a matter of fact, the presence of an obstacle near the electrode surface involves a reduction of the effective specific rate of the electrode reaction and of the mass transfer processes and, thus, of the (absolute) local value of the corresponding overvoltages.

This value is influenced both directly (as a consequence of the reduction of c.d.) and indirectly (as a consequence of the anomalous chemical configuration of the interphase region).

In the case of electrode processes involving metal ion exchanges, the local reduction of the c.d. due to obstacles sufficiently near the electrode surface can be recognized easily by studying the distribution of the cathodic deposition or of the anodic attack.

Let us plunge, in a sulfuric acid solution, a nickel plate having a well-planed surface, and press a Luggin capillary (having a well-planed and sharp terminal contour) on the surface itself.

Let us place a second Luggin capillary (also connected with a reference electrode) at 1 or 2 mm from the electrode surface. Recording separately the anodic polarization of the Ni electrode, as given by the two tensiometric devices, one encounters conditions under which on the shielded area no passivity at all occurs, while on the rest of the surface complete passivity is met, the recorded overvoltages thus differing on the order of 1 v.

III. As far as the "concentration component" is concerned, the value of the diffusion layer thickness cannot be stated in general, and, following the P., B., and S. policy and thus renouncing to any imposed convection, it would be necessary to check this value in any particular case.

IV. In respect of the criteria (*a*) and (*b*) at point 4, the paper under discussion seems to leave choice only between two alternatives: either some of the present results of P., B., and S. (concerning, for instance, Rh) are also incorrect, or these criteria do not present the general validity, formerly attributed to it.

**N. Pentland, J. O'M. Bockris, and E. Sheldon:** We (P., B., and S.) are pleased to be able to elucidate those parts of the technique of the examination of slow electrode reactions which Piontelli, Bertocci, Poli, and Serravalle (P., B., P., and S.) appear to have misunderstood.

I. *Cell geometry.*—The secondary importance of the cell geometry under the conditions of our experiments is not associated with "wires suspended in solution." The principles of the effect of size and shape of electrolytic cells have been given most informatively in the literature by Hoar and Agar,[4] who show that the effect of these factors on cell measurements decreases with increasing concentra-

[1] Laboratorio di Chimica Fisica, Elettrochimica e Metallurgia, del Politecnico di Milano, Milan, Italy.

[2] J. O'M. Bockris, I. A. Ammar, and A. K. M. S. Huq, *J. Phys. Chem.*, **61**, 882 (1957).

[3(a)] R. Aletti, U. Bertocci, G. Bianchi, C. Guerci, R. Piontelli, G. Poli, and G. Serravalle, *Compt. Rend. CITCE, Berne*, 3, 30 (1951); R. Piontelli, G. Bianchi, and R. Aletti, *Z. Elektrochem.*, **56**, 86 (1952); R. Piontelli, G. Bianchi, U. Bertocci, C. Guerci, and B. Rivolta, *ibid.*, **58**, 54 (1954); R. Piontelli, U. Bertocci, G. Bianchi, C. Guerci, and G. Poli, *ibid.*, **58**, 86 (1954).

[(b)] R. Piontelli and G. Bianchi, *Gazz. chim. ital.*, **79**, 646, 863, 867 (1949) and **80**, 581 (1950); R. Piontelli and G. Bianchi, *Compt. Rend. CITCE, Milan*, 2, 379 (1950); R. Piontelli, *Gazz. chim. ital.*, **83**, 357, 370 (1953); R. Piontelli, *Trans. Inst. Metal Finishing*, **31**, 51 (1954); R. Piontelli, B. Rivolta, and G. Montanelli, *Z. Elektrochem.*, **59**, 64 (1955); R. Piontelli, *Rend. inst. lombardo sci.*, **88**, 51 (1955); R. Piontelli, G. Bianchi, U. Bertocci, and B. Rivolta, *Ricerca sci.*, **26**, 838 (1956).

[4] J. N. Agar and T. P. Hoar, *Discussions Faraday Soc.*, **1**, 158 (1947); T. P. Hoar and J. N. Agar, *ibid.*, **1**, 162 (1947).

tion and decreasing values of the exchange c.d. If the potential difference between points in the solution at extreme positions of the electrode is negligible (2-3 mv's), current distribution effects, i.e., results of cell geometry, can be neglected. That this was so in our experiments was established, e.g., by: (i) the observed independence of the overpotential values at a given c.d. with movement of the Luggin capillary (L.c.) vertically over the electrodes; (ii) the satisfactory agreement between the results of P., B., and S. on Cu in acid solutions with those repo-ted earlier by Bockris and Azzam[5]: in the latter workers' cell, a completely different geometry existed from that of the former.

Measurements utilizing cell geometry similar to that used by P., B., and S. have somewhat more than "roughly established" the shape of the overpotential-current density relation in the hydrogen evolution reaction (h.e.r.). For example, measurements by Kabanov and Jova,[6] Bockris and Parsons,[7] Post and Hiskey,[8] and Bockris and Azzam[5] have led to the establishment of a consistent relation for Hg in acid solutions over a c.d. range of about 12 powers of 10. Or, our own measurements on, e.g., Au in 0.01*N* HCl lead to Tafel parameters in which Conf. log $i_o$ are 0.2, and Conf. $b \doteq 0.010$. Values of such parameters of a greater order of accuracy have not hitherto been reported in the literature for this type of system.[9]

II. *Corrections for screening and ohmic effects.*—Our attitude to these effects is that calculated corrections are difficult to carry out with meaningful accuracy,[10] so that conditions of c.d. and concentration, for a given $i_o$ value, should be limited to values such that the effects of screening and ohmic errors are negligible. That this condition was achieved in the technique which we used is established (in respect to screening) by: (i) the observed independence of overpotential values at a given c.d. with shape and size of the L.c.; (ii) agreement in numerical values of parameters between a number of independent workers (*see* footnotes 9 and 10); chance coincidence of ohmic and screening errors, respectively, among the work of several workers in different laboratories would hardly have a high probability; (iii) agreement of the experimentally established overpotential-c.d. relation with that given by theory neglecting screening effects; (iv) agreement of values (on Fe electrodes in 0.1*N* HCl), obtained by a technique similar to that of P., B., and S., with those obtained on the same system but using an electronic commutator and with the L.c. far removed from the electrode;[11] (v) the detailed examination of screening effects in measurements of hydrogen electrode kinetics, recently described by Huq and Basak.[12] They report (for conditions of measurement similar to those used by P., B., and S.) that "no screening effect on the activation overpotential was observed (±1 mv)."

Points II, (ii), (iii), and (iv) establish freedom of the technique of measurement used by P., B., and S. from ohmic errors.

Theoretical calculations of the order of magnitude of the ohmic component[13] can only be used as a rough guide to what is to be expected for a given situation (or to explore, orderwise, the nature of a deviation from the normal overpotential-c.d. relation).

III. *Concentration overpotential.*—P., B., P., and S. have not understood the use to which a theoretical overpotential-c.d. relation for diffusion-controlled behavior was put in our work. Such calculations have not the numerical significance which would allow their use as corrections of experimental measurements of hydrogen overpotential: they were not so used by us. However, such calculations can be used, with those of ohmic overpotential, to obtain an indication of the order of the highest c.d. to which measurements of hydrogen overpotential would be expected to be free from an appreciable (2-3 mv) contribution of concentration overpotential (and the value of $\delta$ was used from the work of King,[14] which was carried out under conditions similar to ours and indicated little dependence of $\delta$ on gas evolution; change of c.d.; or variation of concentration).

In summary of I-III; the parameters of the hydrogen evolution reaction, which are recorded in the paper by P., B., and S., were established under experimental conditions chosen so that the effects I-III had been made negligible (the achievement of such a condition seems to us to belong to the proper design of experimental measurements in electrode kinetics). They do not contain calculated corrections. Hence, P., B., P., and S.'s statements in their I-III lack point.

IV. *Criteria of "correctness" of measurements.*—Applicability of Tafel's equation, and lack of sporadic time variation of overpotential at a given c.d., are frequently occurring (but not alone sufficient) characteristics of "correct" measurements of the kinetics of the h.e.r. They give evidence of the absence of competing redox processes, and nonactivation components of the hydrogen overpotential, and suggest that surface active materials are not undergoing adsorption or deposition on the electrode surface during measurement. However, on certain solid electrode materials a small ($\doteq 10\%$) reproducible variation of overpotential with time occurs during the initial states of polarization after which the overpotential remains constant for many hours. Such a variation is not removed by increasing the degree of purification of the solution. It may be due to the time required to set up steady-state surface concentrations of H atoms, which would depend for certain metals on diffusion process of H into the bulk

[5] J. O'M. Bockris and A. M. Azzam, *Trans. Faraday Soc.*, **48**, 145 (1952).
[6] B. Kabanov and I. Jova, *Acta Physiocochim.*, **10**, 617 (1939).
[7] J. O'M. Bockris and R. Parsons, *Trans. Faraday Soc.*, **45**, 916 (1949).
[8] B. Post and H. Hiskey, *J. Am. Chem. Soc.*, **72**, 4203 (1950); **73** 161 (1951).
[9] The cells used by P., B., and S. possessed a geometry similar to those used by a number of other workers in this field [cf., e.g., A. Lukovstev, B. Levina, and A. N. Frumkin, *Acta Physiocochim.*, **11**, 21 (1939); H. P. Stout, *Discussions Faraday Soc.*, **1**, 107 (1947); A. N. Frumkin and A. Aladjalowa, *Acta Physicochim.*, **19**, 1 (1944); B. Post and H. Hiskey, *loc. cit.*; I. A. Ammar and S. A. Awad, *J. Phys. Chem.*, **60**, 837 (1957); *idem, ibid.*, 1290; *idem, ibid.*, **62**, 805 (1958); *idem, ibid.*, **62**, 801 (1958); *idem, ibid.*, **62**, 660 (1958)].
[10] The inaccuracy of such a calculated correction has been stressed by one of us [J. O'M. Bockris, I. A. Ammar, and A. K. M. S. Huq, *J. Phys. Chem.*, **61**, 879 (1957)].
[11] J. O'M. Bockris and B. E. Conway, *J. Phys. Chem.*, **53**, 527 (1949).
[12] A. K. M. S. Huq and A. K. Basak, *Pakistan J. Sci. Research*, **10**, 71 (1958).
[13] J. O'M. Bockris, "Modern Aspects of Electrochemistry," p. 264, Academic Press, New York (1954).
[14] C. V. King, *This Journal*, **102**, 193 (1955).

of the metal. Such an effect could, in principle, cause the absence of a rectilineal section in the experimental Tafel plot. In fact, the behavior of Rh is not an example of this possibility: further examination of data for the system Rh in 0.01*N* HCl shows that a distinctly rectilineal section exists (5 experimental points on the Tafel plot), between log $i$ values of about −3.10 and −2.7.

We submit that the above considerations are fairly simple and suggest that the apparent misunderstandings of P., B., P., and S. may arise from the fact that they have concentrated in their experimental work on the measurement of overpotential developed during metal deposition. In this type of electrode reaction, relatively high c.d.'s are often needed to give rise to measurable activation overpotentials. Under such conditions, errors due to screening, ohmic, and concentration effects would be much more difficult to avoid than with the highly polarizable hydrogen electrode reactions. These difficulties in measurements of the deposition of metals perhaps may not be unconnected with a lack of progress in the evaluation of specifically described mechanisms of metal deposition, which has been an unfortunate feature of certain postwar work in this field (conversely, cf. Mehl and Bockris,[15] Gerischer,[16] Lorenz,[17] Conway and Bockris[8]).

## The Action of Lead Pigments and Lead Soaps on Aluminum

M. J. Pryor, R. J. Hogan, and F. B. Patten (pp. 9-17, Vol. 105)

**D. A. Vermilyea**[19]**:** In this paper the authors suggest that the field in the oxide film on Al is smaller when large rather than small ions are adsorbed on its surface. They state that for this reason the rate of corrosion is less when large ions are adsorbed.

Now, the electric field across a film of reaction product on a metal specimen immersed in an electrolytic solution is determined by the free energy change in the film-forming reaction and the polarizations accompanying the various electrode reactions involved. The adsorption of ions on the surface of a film will have a minor effect on the field within the film, although such adsorption will result in changes in the potentials within the electrical double layer in the solution outside the film. The charges on ions which become adsorbed as a result of chemical or dispersion forces only will be compensated by an excess of ions of opposite sign in the double layer near the electrode. There would be a large change in the field in that part of the double layer between the adsorbed ions and the compensating atmosphere of oppositely charged ions, but outside of this region the change in field would be small; in the limit of a uniform charge such penetration would be entirely absent. On the other hand, if the ions are adsorbed because of electrostatic forces only, that is, because of the charge of the electrode, then the same number of ions will be adsorbed regardless of their size, since they must compensate for the electrode charge. In any case, therefore, the field in the film is to a first approximation unchanged by the adsorption of ions on its surface.

Therefore, it appears doubtful whether the ideas concerning the effects of ions of different sizes on the corrosion of Al are correct. It is more likely that different ions change the corrosion rate by changing the electrode process, for example, by altering the structure of the reaction film.

**M. J. Pryor:** Dr. Vermilyea's interesting comments on our paper are sincerely appreciated.

It is agreed that the maximum value of a field across a film of reaction product will be a function of the total free energy change. However, we conclude that the field strengths must usually be less than the maximum values because the total free energy change is not generally related to the rate of formation of the reaction product.

Dr. Vermilyea suggests that the structure of the reaction product film is important in determining rates of corrosion of passive film formation. This is undoubtedly true and we have shown that variations in crystallographic and defect structure strongly influence the rate of ion and electron transport through thin films on Al.[20] However, this factor alone does not appear sufficient to explain the difference in reaction rates in different electrolytes. For instance, the crystallographic structure of passive films formed in neutral chromates and in Pb soaps is the same, i.e., $\gamma$-$Al_2O_3$. The defect concentration in these films appears to be similar as judged by dissipation factor and capacitance measurements. Rough calculation of the free energies of formation for the two film-forming reactions indicates that these are of similar magnitude. However, the equilibrium film thickness of $\gamma$-$Al_2O_3$ formed in chromate solutions is very much greater than that in formed Pb soaps. Clearly, some explanation other than free energy change and variation in crystallographic and defect structure is required to explain this factor.

These reasons lead us to consider the possible effect of different fields across the oxide film resulting from specific adsorption of ions. It is suggested by Dr. Vermilyea that, if ions are specifically adsorbed on the oxide surface, the resulting charge will be neutralized by oppositely charged ions in the double layer near the electrode. However, the total charge of the anions reacting on the oxide surface must be equal to the total charge on the cations reacting at the oxide surface in order to maintain electrical neutrality in the over-all reaction. Both anions and cations must therefore be adsorbed on the oxide. If this premise is accepted it is clearly not necessary to postulate equal and opposite charge in the solution double layers. This would be expected to be true during adsorption of long-chain fatty acid anions since our studies indicate that the nonpolar end of the carbon chain is presented to the solution. Even if cations were associated, in a diffuse double layer, with the adsorbed long-chain fatty acid anions, the field across the diffuse double layer would be low.

[15] W. Mehl and J. O'M. Bockris, *J. Chem. Phys.*, 27, 818 (1957).
[16] H. Gerischer, *Z. Elektrochem.*, Bonhoeffer Festband (1958).
[17] W. Lorenz, *Naturwiss.*, 22, 1 (1953).
[18] B. E. Conway and J. O'M. Bockris, *Proc. Roy. Soc.*, Nov. 1958.
[19] Research Lab., General Electric Co., Schenectady, N. Y.
[20] M. J. Pryor, *Z. Elektrochem.*, In press.

The Stern concept of a double layer shows the major potential change is across the specifically adsorbed ion with a smaller potential change across the diffuse double layer. We have difficulty in believing this concept is valid for long-chain fatty acid anions. Here the polar end of the chain is attached to the oxide surface. We have suggested that the major potential change in this case could well be transmitted across a thin dielectric film of $\gamma$-$Al_2O_3$. Since the specific resistance of passive films on Al is between $10^9$ and $10^{12}$ ohms/cm$^2$/cm, we feel confident that high-resistance layers of this type may easily support potential gradients of the order of $10^6$-$10^7$ v/cm.

If the above concept is combined with the influence of crystallographic and defect structure of the reaction product film, a satisfactory explanation of corrosion and inhibition of Al is obtained.

**F. A. Champion**[21]: I was interested to note that the results of Messrs. Pryor, Hogan, and Patten support the more practical work on this subject carried out from these laboratories.[22] The latter work cited showed red Pb pigment to be harmful in industrial and marine atmospheres, which are those which might be expected to provide electrolytes conducive to the galvanic effects demonstrated by Messrs, Pryor, Hogan, and Patten. In rural environments, with the much lower concentrations of electrolytes, no such *harmful* effects of practical importance were observed. The effects can be delayed by waterproofing coats, but under service conditions these cannot be relied on to exclude electrolytes from the primer: if they could, then inhibiting pigments would be unnecessary in primers.

**M. J. Pryor:** Dr. Champion's remarks on the correlation between the previous coating investigations of Rigg and Skerrey and our present work are indeed gratifying and are appreciated. Earlier, we rather doubted that such a clean-cut correlation would be observed because commercial pigments used in paints are usually of low purity and the Pb compounds used in our investigation were as pure as we could obtain. For instance, pigment grade red Pb may often contain as much as 4% litharge, which might be expected to modify results. It is evident from the information kindly supplied by Dr. Champion that the effect of pigment purity is of lesser magnitude than we had anticipated and that a more direct correlation may be drawn between our laboratory results and the performance of organic coatings pigmented with Pb compounds.

**D. M. Brasher**[23] **and C. P. De**[24]: The experimental results obtained by Pryor, Hogan, and Patten, indicating that of the various types of Pb-containing extracts tested only the Pb soaps are truly inhibitive toward Al, are of great interest.

We would agree with the suggestion that the primary cause of inhibition in the soap solutions is adsorption of the fatty acid anions. The greater efficiency of the more acid Pb soaps, as contrasted with the more alkaline Na and Ca soaps, may perhaps be correlated directly with the observations of Butler,[25] from electrocapillary studies, on the effect of *p*H on the relative degrees of adsorption of fatty acid anions at the metal/solution interface. Butler showed that potassium hydrogen phthalate depressed the electrocapillary maximum and shifted the positive branch of the electrocapillary curve more than did the neutral phthalate. A theoretical correlation between the inhibitive properties of anions and their electrocapillary behavior at different metal surfaces has been suggested by De.[26] It might also be possible that the lower rates of corrosion of Al in red Pb and basic $PbCO_3$ extracts, as compared with those in metallic Pb and litharge extracts, could be ascribed, in addition to the effect of *p*H, to the presence of the inhibitive anions plumbate and carbonate, respectively.

Regarding the mechanism of oxide film growth (assumed to occur only when corrosion is inhibited), it would be interesting to know if inhibition was found to be *maintained* in the fatty acid solutions in the complete absence of oxygen. It is claimed that the absence of oxygen caused only a slight lowering of potential, but owing to slight confusion in the text between "corrosion" and "oxide formation" (p. 16, col. 2, line 9 of discussed paper), the above point is not clear. In work on steel it has been established that inhibition cannot be obtained by nonoxidizing inhibitors in the absence of oxygen; for example, Lochte and Paul[27] and Mayne, *et al.*[28] obtained "corroding" potentials for steel in deaerated sodium phosphate or sodium hydroxide, respectively, and in this laboratory sodium benzoate was found not to inhibit in the absence of oxygen.[29] In radiotracer studies on steel, using $K_2CrO_4$ labeled with $Cr^{51}$, it has been shown that oxide films grow logarithmically with time in chromate solutions;[30] further, by an indirect method involving pre-exposure to air, or pre-immersion in aerated inhibitor solutions, film growth in air, sodium benzoate, phosphate, or hydroxide solutions was found to be logarithmic in each case, with a rate constant approximately the same in all environments.[31] This seems to be strong evidence that the mechanism of oxidation is the same in all cases, and is associated with oxygen as the oxidizing agent. Possibly, of course, the fatty acid anion can oxidize Al but not Fe. It is noteworthy that oxygen largely displaces even chromate as the oxidant for Fe in aerated chromate solutions.[32]

We would agree that oxide film formation probably augments the inhibitive properties of the adsorbed layer. Confirmatory evidence for this has been obtained in "potential decay" studies on steel,[33]

[21] Research Labs., The British Aluminium Co. Ltd., Chalfont Park, Gerrards Cross, Bucks., England.
[22] J. Rigg and W. W. Skerrey, *J. Inst. Metals*, **75**, 69 (1948); **81**, 481 (1953).
[23] National Chemical Lab., Teddington, Middlesex, England.
[24] Naval Chemical and Metallurgical Lab., Naval Dockyard, Bombay 1, India.
[25] J. A. V. Butler and C. Ockrent, *J. Phys. Chem.*, **34**, 2286 (1930).
[26] C. P. De, *Nature*, **180**, 803 (1957).
[27] H. L. Lochte and R. E. Paul, *Trans. Electrochem. Soc.*, **64**, 164 (1933).
[28] J. E. O. Mayne, J. W. Menter, and M. J. Pryor, *J. Chem. Soc.*, **1950**, 3229.
[29] "Chemistry Research 1954," p. 12, Her Majesty's Stationery Office, London (1955).
[30] D. M. Brasher, A. H. Kingsbury, and A. D. Mercer, *Nature*, **180**, 27 (1957).
[31] Partially reported in "Chemistry Research 1957," p. 12, Her Majesty's Stationery Office, London (1958).
[32] D. M. Brasher and C. P. De, *Nature*, **180**, 28 (1957).
[33] "Chemistry Research 1951," p. 13, Her Majesty's Stationery Office, London (1952).

immersed in chromate solutions for various periods and then transferred to distilled water. The longer the period of pre-immersion in chromate, the slower the subsequent decay of potential in distilled water.

**M. J. Pryor:** The comments submitted by Brasher and De are most interesting and are appreciated. Certainly the past work by Butler[25] and Adam[34] strongly suggests that an acid soap should be more strongly adsorbed at an interface than a neutral soap. Consequently, a correlation between electrocapillarity behavior and adsorption of the fatty acid anion must exist. However, the correlation between electrocapillarity behavior and inhibition must be more complex because subsequent oxidation of the Al and reduction of the fatty acid anions occurred in the systems we were studying. These latter reactions do not appear to be primarily related to the degree of adsorption but rather to structural aspects of the particular fatty acid anions such as the number, position, and type of unsaturated bonds. Consequently, we would expect an accurate correlation between electrocapillarity behavior and inhibition only if subsequent oxidation was either absent or of significant importance.

Subsequent experimental study of this system, reported elsewhere,[35] provides in main part the answers to the additional questions raised by Brasher and De. In lead linoleate and lead laurate extracts, the presence of dissolved oxygen has virtually no effect in the potential of Al, nor on its passivity. Consequently, passivity may be generated and maintained in deaerated extracts. Here it is evident that oxidation is produced by the discharge of the fatty acid anions with dissolved oxygen playing a minor role. Since we believe that these fatty acid anions are sufficiently strongly adsorbed on the metal or oxide to displace hydroxyl ions from the surface, it is not unreasonable to postulate that they will also largely displace the higher concentration oxygen dissolved in the electrolyte. We have shown previously[36] that the potential of steel in deaerated nonoxidizing inhibitors is controlled accurately by the ferrous ion activity in equilibrium with $Fe(OH)_2$ (or, in the case of phosphate solutions, ferrous phosphate) at the particular *p*H under examination, provided the ferrous ion activity is greater than around $10^{-6}$ g ions/l. If Al behaved similarly, we would anticipate very active potentials and slow corrosion if the oxidizing action of lead linoleate and laurate was due to dissolved oxygen. The contrary results outlined above indicate that we must classify these extracts as oxidizing inhibitors.

Slightly different results are obtained in lead ricinoleate in that the potential is much more sensitive to the oxygen content of the electrolyte. Deaeration can shift the potential by as much as 250 mv in the active direction. However, the Al still behaves in a passive manner (or corrodes at an undetectable rate) for 4 days which is the maximum time for which experiments were performed on this system. We have attributed these results to weaker adsorption of the higher *p*H ricinoleate. The weaker adsorption of ricinoleate should permit more easy simultaneous adsorption of oxygen which would then be expected to contribute to the passivation process in solutions containing dissolved air. This contention is supported in Table I, published here, by measurement of the current efficiency of anodic oxidation of Al in Pb soap extracts saturated with dissolved air at very low current density and at potentials below that at which oxygen is evolved.

Table I. Current efficiency of oxide formation by anodic polarization in different lead soaps at 25°C

| Electrolyte | Concentration | Initial *p*H | Current efficiency % at 0.5 $\mu a/cm^2$ | Current efficiency % at 1.0 $\mu a/cm^2$ |
|---|---|---|---|---|
| Lead linoleate | 218 mg Pb/l | 5.5 | 91 | 92 |
| Lead ricinoleate | 208 mg Pb/l | 6.0 | 78 | 82 |
| Lead laurate | 296 mg Pb/l | 5.5 | 87 | 88 |

The lowered efficiency of oxide formation in ricinoleate extracts is held to be evidence of its weaker adsorption on the Al specimens. In turn, this will lead to magnified effects of the simultaneous presence of oxygen in the solution. Probably some considerable similarity exists between the action of lead ricinoleate on Al and that of sodium tungstate and molybdate on Fe which we described earlier.[36]

## Equilibria in the Niobium-Hydrogen System

W. M. Albrecht, M. W. Mallett, and W. D. Goode

(pp. 219-223, Vol. 105)

**O. M. Katz and E. A. Gulbransen**[37]: Recently we have again become greatly interested in the study of hydrogen in metals. One of the materials we have investigated is high-purity Nb of the following analysis:

| | |
|---|---|
| Ta—590 | ppm |
| Fe—330 | ppm |
| Mo—54 | ppm |
| H —2.3 | ppm |
| O —31 | ppm |
| N —131 | ppm |
| C —59 | ppm |
| Zr—0.79 | wt % |

For equilibrium studies the Nb strip sample (0.025 x 0.500 x 4.429 cm) was polished under purified kerosene through 4/0 emery paper and pretreated for 1 hr at ~ 850°C at $< 0.001\mu$ Hg. Mass spectrometer analysis of the $H_2$, obtained by diffusion through a palladium tube, showed it to be 99.99+% pure.

A vacuum microbalance incorporated in an entirely new type of enclosure that has been designed to compensate for any "buoyancy effects" was used. Pressure readings were taken with a metal diaphragm, null-indicator in conjunction with a 0.6313 in. ID, precision, Hg manometer. Reproducibility of readings was ±0.2 mm Hg. The temperature variation was ±3°C.

Pressure-composition isotherms were obtained by varying the $H_2$ pressure and reading the microbalance deflection after equilibrium was reached,

[34] N. K. Adam, "The Physics and Chemistry of Surfaces," p. 128, Oxford University Press, Oxford (1941).
[35] M. J. Pryor, Z. *Elektrochem.*, In press.
[36] M. J. Pryor and M. Cohen, *This Journal*, 100, 203 (1953).
[37] Chemistry Dept., Westinghouse Electric Corp., Beulah Rd., Churchill Boro., Pittsburgh 35, Pa.

all at constant temperature. The results are shown in Fig. 1 published here. Close agreement with the

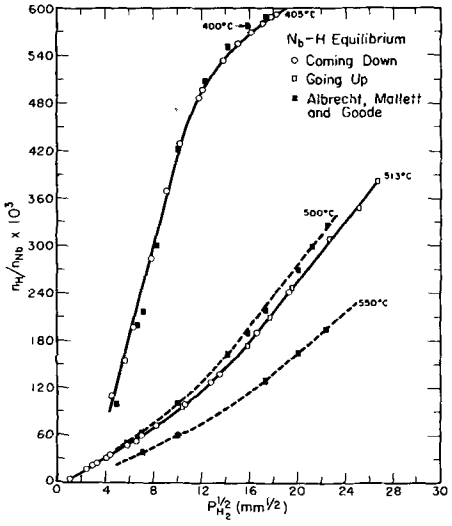


Fig. 1

work of Messrs. Albrecht, Mallett, and Goode in this temperature range was most interesting considering the completely different approach we used.

Data on the phase equilibrium below 300°C are also being collected and will soon be available.

**W. M. Albrecht, M. W. Mallett, and W. D. Goode:** It is gratifying that the data of Messrs. Katz and Gulbransen corroborate our findings, particularly in view of the difference in the Zr contents of the Nb. No Zr (< 50 ppm) was detected in spectrographic analyses of our material. Apparently, Zr up to about 1 wt % has no measurable effect on the Nb-$H_2$ equilibria.

## Corrosion of Anodically and Cathodically Polarized Magnesium in Aqueous Media

G. R. Hoey and M. Cohen (pp. 245-250, Vol. 105)

**W. E. Higgins**[38]: It is most unfortunate that the authors should have prepared the Mg surfaces by abrasion with emery paper. This activates the surface and brings about a condition where parasitic corrosion is relatively vigorous. A specimen so treated and placed in dilute NaCl solution will evolve gas visibly, whereas a similar specimen rubbed with fine pumice powder is very much more inert.

The reason for this is apparently the pickup of microscopic cathodic particles from the emery (which is a good conductor and a very active cathode). Fine glass paper and clean pumice, on the other hand, are inert and do not bring about the effect described.

It follows that the results obtained by the authors may be very different from those which might be expected from a clean Mg surface.

Robinson's suggestion, that the defect of the current efficiency from 100% is largely due to the breakdown of a protective film, seems very probable for the following reasons: Clean Mg when placed in an electrolyte such as NaCl begins to dissolve slowly and in doing so brings about a condition of high alkalinity in the surface layers of liquid. The presence of such an alkaline layer provides the conditions for a protective film of $MgOH_2$ to form, and dissolution of the metal is slowed down. (It is a significant fact that Mg dissolves much more rapidly in running water than in static conditions.) If, however, the Mg is coupled to a more noble metal, the electrical tension is sufficient to push out Mg atoms into solution. By abstracting electrons, the atoms become positively charged and those in contact with an electrolyte form ions moving away from the metal surface. It seems obvious therefore that such ions passing into solution will interfere with the formation of a film, which involves the production of an insoluble, as distinct from a soluble, product, that is, a Mg compound which clings to the metal surface. If this is so, then it becomes clear why self-corrosion increases as the current drawn from the anode increases. This indeed can be verified by observation. An anode of 100% efficiency ought not to evolve hydrogen on its own surface; the hydrogen ought to be evolved only at the cathode. Yet a Mg anode evolves hydrogen, and the more so as the anode current increases. It would seem that the only explanation is that the H on the anode arises from *local* cathodes due to impurities—in other words, efficiency of the main reaction is being reduced by local reaction. The total efficiency, if it could be measured, would probably be 100% but only the efficiency of the main reaction—between the anode and the cathode—is subject to measurement.

Regarding the undercutting of the Mg grain, this certainly may occur, but it is not strictly by intergranular attack. The grain boundaries are usually cathodic to the grain interior, and therefore the grain is corroded principally at the edges where it adjoins the cathodic grain boundary. This is to be expected since the corrosion current takes the shortest path and the consequence is that the center portion of the grain becomes detached and drops out. By suitable techniques the remnants of the grain boundary constituents can be photographed still in situ. Fig. 1 (a Mg alloy) shows a partly consumed

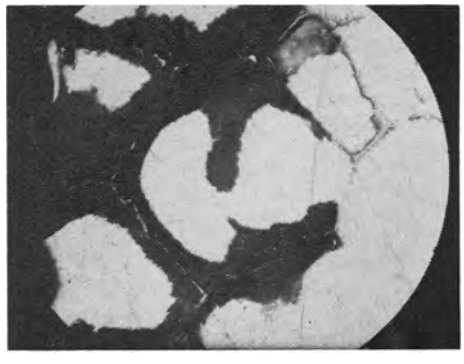

Fig. 1

grain with the grain boundary constituent outlining the spaces where other grains have disappeared.

**G. R. Hoey and M. Cohen:** The Mg specimens used in all experiments were annealed at 300°C for 2 hr in an argon atmosphere, polished on 1/0 emery

[38] Magnesium Elektron Ltd., Lumm's Lane, Clifton Junction, Swinton, Manchester, England.

paper, degreased, and etched in 0.1*N* HCl for 1 min. The etchant, 0.1*N* HCl, gives a uniform etch and is sufficiently strong to expose for experimentation the Mg substrate rather than worked metal, emery grit, or, perhaps, as in Higgins' case, pumice powder. One of the objects of this research was to study the behavior of pure Mg.

Higgins states that the only explanation for evolution of hydrogen on Mg is that the hydrogen arises from local cathodes due to impurities. The concentration of cathodic impurities (Fe, Ni, and Cu) in the Mg used in this work was below their tolerance limits, i.e., further purification of Mg will not reduce the corrosion rate significantly. One of the explanations suggested in the paper probably explains hydrogen evolution on Mg.

Corrosion of Mg by undermining of metallic Mg which was demonstrated for experimental conditions favoring thick film formation was not suggested in the paper to be strictly intergranular attack. Intergranular attack was observed only on cathodically polarized Mg at elevated temperatures for which a hydrogen embrittlement theory was proposed. It is not clear from Higgins' discussion or Fig. 1 which of the two types of attack he is considering.

## Polarographic Reduction of Delta$^4$-3-Ketosteroids in Well-Buffered Media

Peter Kabasakalian and James McGlotten (pp. 261-264, Vol. 105)

**Petr Zuman**[39]: In solutions of $\Delta^4$-3-ketosteroids, well buffered with usual buffers, principally two waves were observed by us[40] as well as by Lund[41] (the observed adsorption prewaves, which are not discussed by Kabasakalian and McGlotten, probably because they used high steroid concentrations, will be omitted in the present discussion). In the acid region only the more positive wave, in the alkaline only the more negative one, was observed. In the *p*H-region between *p*H 5 and 9 (dependent on the nature of the ketosteroid studied and on the drop-time used), both waves were developed and their ratio was put in the form of a dissociation curve (cf. Fig. 1-3 in footnote 40). When the more positive wave was less than 20% of the total wave-height, its height was independent of the Hg pressure; it follows that this is a current controlled by the rate of a chemical reaction.

The explanation of these facts was that the more positive wave corresponds to the reduction of a protonized form of the ketosteroid, the more negative one to the un-ionized steroid, stable at higher *p*H-values. The kinetic character was explained by the control of the more positive wave by the rate of recombination of the un-ionized steroid with an acid.

All the facts observed[40-42] are consistent with the mechanism:

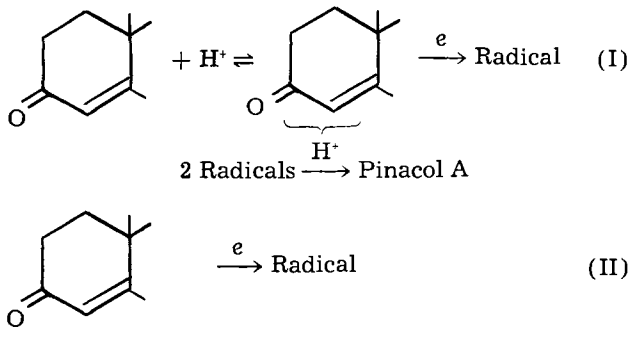


where (I) corresponds to the process at the potential of the more positive, (II) of the more negative, wave. The following facts are in agreement with this explanation: (*A*) The dependence of the limiting current on *p*H is similar to other electroreductions of weak acids and in accordance with the theory.[43, 44] (*B*) The dependence of the half-wave potential of the more positive wave on *p*H for *p*H-values smaller than pK, the change in slope of this dependence at *p*H = pK, as well as the practical independence observed for the more negative wave are similar to the dependence of the half-wave potentials of reducible acids and practical *p*H-independence of the wave for the corresponding base.[45-48] The form of the dependence of the wave of the cation is, moreover, in accordance with the approximate theory for the shifts of half-wave potentials of kinetic currents.[49] The half-wave potential of the un-ionized ketosteroid is practically *p*H-independent, in accordance with the fact that no proton is accepted in the potential-determining step (II). The smaller shifts observed in this case as well as for other anions are probably due to secondary effects like ionic strength, concentration of cations, etc. (*C*) Different isomers of pinacol (Pinacol A and Pinacol B) were isolated,[42] when a preparative reduction on a Hg pool electrode was carried out in acid or in alkaline solutions, respectively. This is a support of two different reduction mechanisms (I) and (II).

The findings of Lund[42] have shown that the rate of protonation preceding the electroreduction plays an important role even at the Hg pool electrode. So far as we know, this is the first case recorded where a rate (not an equilibrium) of a reaction preceding the electron-transfer changes the mechanism of a reduction on a Hg pool electrode.

The existence of the protonized form of $\Delta^4$-3-ketosteroids has been proved by electropreparative[42] as well as polarographic[40] findings.

In their article, Kabasakalian and McGlotten try to explain the change of the wave-height with *p*H by the formation of: a "steroid-hydrogen ion complex, represented a reaction between a steroid and a

[39] Polarographic Institute of the Czechoslovak Academy of Science, Prague, Czechoslovakia.
[40] P. Zuman, J. Tenygl, and M. Brezina, *Chem. listy*, 47, 1152 (1953); *Collection Czechoslov. Chem. Communs.*, 19, 46 (1954).
[41] H. Lund, Personal communication.
[42] H. Lund, *Acta Chem. Scand.*, 11, 283 (1957).
[43] R. Brdicka and K. Wiesner, *Collection Czechoslov. Chem. Communs.*, 12, 138 (1947); R. Brdicka, *ibid.*, 19, S41 (1954).
[44] J. Koutecky, *Chem. listy*, 47, 323 (1953); *Collection Czechoslov. Chem. Communs.*, 18, 597 (1953).
[45] R. Brdicka, *Collection Czechoslov. Chem. Communs.*, 12, 212 (1947).
[46] V. Hanus, Thesis, Charles University, Prague (1949).
[47] J. Volke and V. Volková, *Chem. listy*, 49, 490 (1954); *Collection Czechoslov. Chem. Communs.*, 20, 1332 (1955).
[48] P. Zuman, J. Chodkowski, and F. Santavy, *Collection Czechoslov. Chem. Communs.*, In press.
[49] N. Tanaka and R. Tamumushi, Proc. First Intern. Polarographic Congr., Prague, 1951, Part I, p. 486, published by Prirodoved. vydav., Prague (1951).

*specific buffer acid* (rather than a generalized acid-base reaction)." In contradiction to this statement, Eq. (I) in the discussed paper corresponds to a general acid-base reaction. Even when not explicitly stated, the particle reduced in the more positive wave is supposed to be a complex of the steroid with the buffer acid. There is no experimental support for the reduction of such a particle. The observed independence of the first wave to the total current in changing the concentration of the steroid, as well as the *p*H-dependence of the wave height found in changing the ratio of primary and secondary phosphates (without holding ionic strength constant—Table IV), are better explained by the mechanism given by us. Also, the shape of the dependence of the half-wave potential on *p*H could hardly be explained by the reduction of a complex only.

On the other hand, to consider the ratio of the first and second waves as proportional to equilibrium concentrations is an error, which was early discerned by Brdicka.[45] The calculation of K in Table V of the discussed paper bears witness to misunderstanding of the principles of kinetic currents controlled by recombination, which here play the major role.

It is possible that, in the *rate of formation* of the protonized form, other proton donors besides the hydroxonium ion play a role,[50-55] and the rate constant becomes

$$k_r = k_{H_2O} + k_{H_3O^+}[H_3O^+] + \Sigma\, k_{HA}[HA]$$

Unfortunately, the quantitative treatment of the recombination rate constants ($k_r$) is impossible so far, because of lack of the thermodynamical equilibrium constants ($K = k_d/k_r$). But the small change of $i_1/i_2$ with the buffer concentration at *p*H = const (Tables IV and V of Kabasakalian and McGlotten) shows that the contributions of $k_{H_3BO_3}$ and $k_{H_2PO_4^-}$ are rather small, if the change in $i_1/i_2$ is not caused by the change in ionic strength[46, 56] at all.

An explanation of the observed two waves by inappropriate buffering is also improbable. In our experiments, the concentration of the acid buffer-component was always 50 times higher than the concentration of the depolarizer. Because at least a twentyfold excess of the buffer is necessary[56-58] for good buffering, the solutions with the lowest buffer concentrations in Table IV(c) are inappropriately buffered.

When in the *p*H-range, where recombination occurs, buffers with trialkylamine as basic component were used, only one wave was observed (paper by Kabasakalian and McGlotten, under discussion). This was interpreted as normal behavior and the curves in phosphate and borate buffers are supposed to be due to a specific action of buffer components.

Volková[59] has shown recently that the influence of acids of the type $NR_3H^+$ on recombinations is different from acids of the type $H_2A_1$, $HA_1$, or $HA_1^-$. For un-ionized acids or for anions with acid nature in reactions

$$HA_1 + A_2^- \rightleftharpoons HA_2 + A_1^- \qquad [1]$$

$$HA_1^- + A_2^- \rightleftharpoons HA_2 + A_1^{2-} \qquad [2]$$

(where $HA_2$ is the reducible acid) the concentration of the buffer has a small or often negligible influence on the ratio $i_1/i_2$. For acids of the type $NR_3H^+$ a remarkable effect was observed,[59] the nature of which is dependent on the type of the reducible acid involved. For a reaction of negatively charged particles of the type

$$NR_3H^+ + A_2^- \rightleftharpoons HA_2 + NR_3 \qquad [3]$$

the height of the wave of the acid form $HA_2$ increases with increasing concentration of $NR_3H^+$. On the other hand, for the first wave of phthalic acid, corresponding to a reduction of a cation,[58] where uncharged acid is reacting with protons, a decrease in the wave of $H_3A_2^+$ with increasing amine buffer concentration was observed.[59]

Similarly a decrease of the more positive wave of protonized testosterone with increasing concentration of $NR_3H^+$ was observed (Fig. 1 published here).

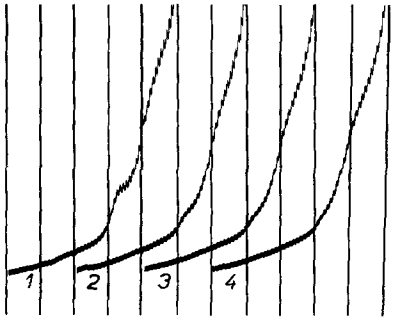


*Fig. 1. Influence of concentration of trimethylamine buffer on the waves of methyltestosterone; 0.5 mM methyltestosterone in 50% ethanol with 0.05 M borate buffer pH 8.5 with different concentrations of a trimethylamine buffer pH 8.5 added. Concentration of trimethylamine buffer: 1, 0; 2, 1.0 mM; 3, 3.0 mM; 4, 5.0 mM. Ionic strength kept constant. Curves starting at −1.2 v, mercurous sulfate electrode, Kalousek's vessel, 200 mv/absc, $t_1$ = 3.2 sec, m = 1.93 mg/sec, full-scale sensitivity 1.3 μa.*

Also, in this case a protonation of an uncharged particle takes place.

The effect of the small concentration of trimethylamine buffer in the presence of an excess of borate buffer of the same *p*H-value (Fig. 1) excludes the possibility of a *p*H-change on the surface of the electrode. Even the smallest concentration of trimethylamine buffer used is sufficient to change the whole character of the curve. This cannot be explained by complex formation with borate or phosphate, but rather by a specific effect of $NR_3H^+$-ions on the rate of recombination.

The behavior in different buffers containing 50% ethanol and of the same *p*H is given in Fig. 2 pub-

[50] K. Wiesner, M. Wheatley, and J. M. Los, *J. Am. Chem. Soc.*, 76, 4858 (1954); M. S. Wheatley, *Experientia*, 12, 339 (1956).
[51] J. H. Green and A. Walkley, *Austr. J. Chem.*, 8, 51 (1955).
[52] R. Zahradník, E. Svátek, and M. Chvapil, *Chem. listy*, 51, 2232 (1957).
[53] E. T. Bartel, Z. R. Grabowski, W. Kemula, and W. Turnowska-Rubaszewska, *Roczniki Chem.*, 31, 13 (1957).
[54] O. Hrdy, *Chem. listy*, 52, 1058 (1958).
[55] P. Zuman, Unpublished results on the polarography of periodic acid.
[56] V. Hanus, Proc. First Intern. Polarographic Congr., Prague, 1951, Part I, p. 811, published by Prirodoved. vydav., Prague (1951).
[57] J. Kuta, *Acta Chim. Acad. Sci. Hung.*, 9, 119 (1956); *Chem. listy*, 49, 1419 (1955); *Collection Czechoslov. Chem. Communs.*, 21, 697 (1956).
[58] A. Ryvolova and V. Hanus, *Chem. listy*, 50, 46 (1956).
[59] V. Volkova, Paper presented before the Second Czechoslovak-Hungarian Polarographic Conference, Prague (1958).

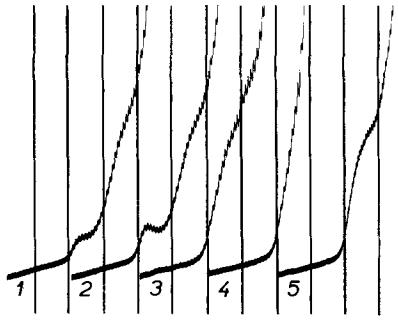


Fig. 2. Influence of buffer composition at pH 8.3 on the waves of methyltestosterone; 0.5 mM methyltestosterone in 50% ethanol in buffers of pH 8.3 of different composition: 1, borate buffer; 2, veronal buffer; 3, trimethylamine buffer; 4, triethanolamine buffer—the wave is obscured by catalytic hydrogen evolution; 5, ammonia-ammonium chloride buffer. Curves starting at —1.4 v, mercurous sulfate electrode, Kalousek's vessel, 200 mv/absc, $t_1$ = 3.2 sec, m = 1.93 mg/sec, full-scale sensitivity 1.3 μa.

lished here. The curve in the veronal buffer is practically the same as in borate and shows two waves. The curves in trimethylamine and $NH_3$ buffers[60] are similar to each other but different from the ones mentioned above in showing one wave only. Kabasakalian and McGlotten, in the discussed paper, supposed that one wave at higher pH's is observed in organic buffers only. The polarogram in Fig. 2 published here shows that an organic buffer like veronal can show the same normal behavior as borate and that even in an inorganic buffer like $NH_3$ the $NH_4^+$-ions can play the same role as $NR_3H^+$. The type of the buffer acid and not the origin is of primary importance.

The shift of half-wave potentials in buffers with $NR_3H^+$ as the acid component is complicated by the dependence of the half-wave potential on the concentration of $NR_3H^+$, similar to the influence of $NH_4^+$ and quaternary cations on other reduction processes.[62]

It can be concluded that the behavior of ketosteroids in phosphate, borate, veronal, and similar buffers is normal and in agreement with the theory. The influence of amine-containing buffers is exceptional in decreasing the first wave and in shifting the second wave to more positive potentials.

**P. Kabasakalian:** In an attempt to show that the wave splitting obtained during the polarographic reduction of steroids using phosphate and borate buffers was not due to the pH of the solution but to the specific buffer components, we had proposed the formation of a steroid-hydrogen ion complex after determining that these buffers did not contribute appreciably to any recombination rate. Although we were able to determine the value of the "equilibrium constants" for the phosphoric and boric acid interaction with the steroids, we must admit that this does not necessarily prove the existence of such an equilibrium.

Zuman's contention that the reaction is in essence identical to that of a reducible acid is based on the fact that the limiting current and half-wave potential behavior with pH is similar to that for a reducible acid and that the isolation of different stereoisomers from a large-scale reduction by Lund is supposed to indicate two different reaction mechanisms. Products of irreversible reactions are not good criteria of the potential-determining step mechanism. Bladon, Cornforth, and Jaeger[63] have questioned Lund's proof of structure and his mechanism which assumes that the radicals retain their configuration until they dimerize by a slow reaction.

Tanaka and Tamamushi have derived, from the standpoint of chemical kinetics, the limiting current-pH and half-wave potential-pH relationships of reducible organic acids. They considered the case where the dissociated anion, $A^-$, and undissociated molecule, HA, of an organic acid are kept in equilibrium in the body of the solution according to Eq. (I) and where the undissociated molecule is reduced at the more positive potential than the dissociated anion.

$$A^- + H^+ \rightleftharpoons HA \qquad (I)$$

The undissociated molecule combines with the electrons at the electrode surface and then the reduced ion, $R^=$, reacts with the hydrogen ions resulting in the reduced molecule, $RH_2$.

$$HA + 2e \rightleftharpoons R^= \qquad (II)$$

$$R^= + 2H^+ \rightleftharpoons RH_2 \qquad (III)$$

The derived relationships satisfactorily explained the behavior of pyruvic and phenylglyoxylic acids.

Zuman has proposed that steroids undergo the following type of reaction.

$$S + H^+ \rightleftharpoons SH^+ \qquad (IV)$$

$$SH^+ + e \rightleftharpoons SH\cdot \qquad (V)$$

followed by dimerization of $SH\cdot$.

There is a major difference between these two mechanisms. The hydrogen in the acid group in Eq. (I) is not the one that is involved in the reduction step while the hydrogen in the protonated steroid in Eq. (IV) is involved in the reduction. This difference should be enough to make questionable Zuman's contention that steroid reductions are identical to the acid reductions.

Steroid reductions using phosphate, borate, and veronal buffers have all the characteristics of a reducible acid but the following data conflict: different acid buffers which do not contribute appreciably to the recombination rate of the protonated reducible species fail to give the same wave splitting at identical pHs as Table I published here indicates.

**Table I**

| Buffer | pH | $i/i'$ |
|---|---|---|
| Phosphate | 7.84 | 2.02 |
| Veronal | 7.90 | 0.50 |
| Borate | 8.04 | 0.25 |
| Phosphate | 8.09 | 1.40 |

Buffer acid = 0.05M; ionic strength = 0.2.

[60] The concentration of ammonia in the buffer is so low that practically no condensation (see footnote 61) of the carbonyl group occurs.

[61] P. Zuman, *Collection Czechoslov. Chem. Communs.*, 15, 839 (1950).

[62] M. Ashworth, *Collection Czechoslov. Chem. Communs.*, 13, 229 (1948).

[63] P. Bladon, J. W. Cornforth, and R. H. Jaeger, *J. Chem. Soc.*, 1958, 863.

In order to explain the single wave we obtained with amine buffers, Zuman proposes that three things must happen:

(*A*) the height of the first wave is reduced presumably to zero; (*B*) the second wave has its half-wave potential moved an exact amount so that it now coincides with the former position of the first wave; (*C*) the half-wave potential of the new shifted second wave, which was formerly pH independent, is now pH dependent an exact amount which brings it into line with all the other good buffers which were used at the lower pHs.

It would indeed be very fortuitous if these three things occurred simultaneously, together with the fact that in our study two different amines, trimethylamine and triethylamine, which were used would have to fulfill the above requirements.

We did not find that the half-wave potential shifted with amine buffer concentration as Table II published here indicates.

*Table II*

| Buffer conc. | $-E_{1/2}$ | $k$ | pH |
|---|---|---|---|
| 0.20M | 1.59 | 2.0 | 8.8 |
| 0.10M | 1.59 | 2.1 | 8.9 |
| 0.05M | 1.60 | 2.1 | 8.9 |

Constant ionic strength.

It is our candid opinion that neither our nor Zuman's proposal satisfactorily explains the wave splitting obtained with phosphate, borate, and veronal buffers.

## Silver, Cobalt, and Positive-Grid Corrosion in the Lead-Acid Battery

J. J. Lander (pp. 289-292, Vol. 105)

**J. F. Schaefer and H. R. Karas**[64]: A microscopic investigation of positive grid corrosion in lead-acid batteries has been in progress in the Globe-Union Labs. for the past year (1957). The mounting and polishing technique as developed by Simon and Jones of the Naval Research Labs. is being effectively employed. Data are obtained by measuring the cross-sectional areas of grid bars at various stages during life of batteries, with the remaining metal calculated as a percentage of the original grid bar area.

In the course of work on various alloys, several series of experiments with Co and Co and Ag additions to cells have been made. In concordance with ideas expressed over the past several years, and stated by Lander today, as to the importance of standing time during battery service, we have collected data on the occurrence of grid corrosion on open circuit standing.

Figure 1 shows the corrosion of a positive grid bar after two years' open-circuit stand at ambient temperature in an unheated garage in Detroit. About 55% of the grid metal has corroded away. Examination of the battery definitely showed positive grid failure and some years ago would have been classified as failure due to overcharging.

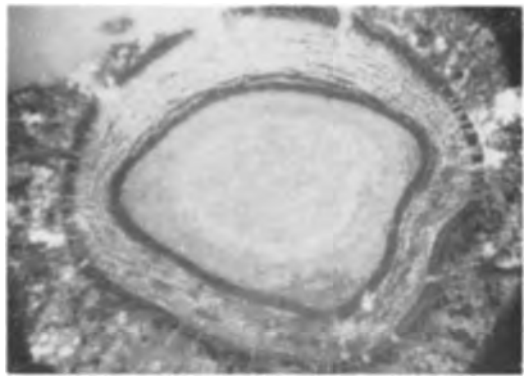

Fig. 1. Positive grid bar from battery after two years' open-circuit stand.

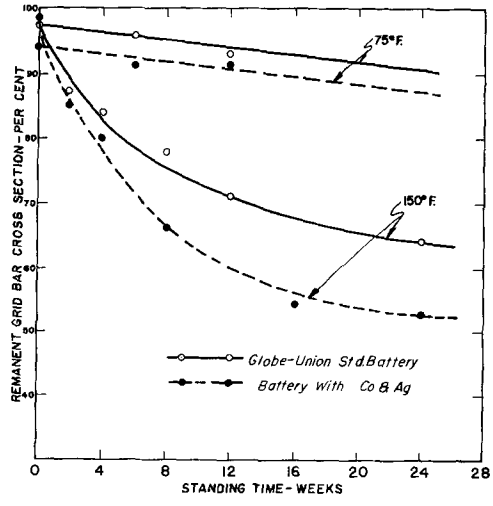


Fig. 2. Effect of open-circuit standing on positive grid corrosion.

Figure 2 shows data obtained on batteries standing at 75° and 150°F in the laboratory. The effect of Co and Ag additions are shown in the curves. At 150°F, which approximates under-the-hood temperatures, the addition of Co and Ag causes an approximate 50% increase in corrosion in 12 weeks.

Work on this project is continuing and it is hoped that a complete report will be ready for presentation at a future meeting of the Battery Division of the Society.

## Diffusion of Oxygen in Zirconium and Its Relation to Oxidation and Corrosion

J. P. Pemsler (pp. 315-322, Vol. 105)

**L. Young**[65]: Dr. Pemsler makes use of the "Pilling-Bedworth number" (defined as the ratio of molar volumes of oxide and metal) to decide that the oxide on Zr is under compression. I would like to repeat the point which I made in a recent paper[66] that with flat surfaces there is no obvious reason why the oxide should be under compression if this number is greater than unity, and, furthermore, that despite the widespread impression to the contrary, Pilling and Bedworth made no such suggestion, at least not

[64] Globe-Union Inc., Milwaukee 1, Wis.

[65] British Columbia Research Council, University of British Columbia, Vancouver 8, B. C., Canada.

[66] L. Young, *Acta Met.*, 5, 711 (1957).

in their original paper.[67] Their "hypothesis" was, in fact, the perfectly logical deduction that compressive stresses will be produced when the metal surface is convex and when oxygen—not metal—is mobile, so that fresh layers of oxide are produced in the space previously occupied by the metal from which they are formed. Obviously, other nonflat surfaces, or metal ion movement, require the application of other conditions to determine the general macroscopic stress, and rough surfaces and microscopic stresses are another case again.

[67] N. B. Pilling and R. E. Bedworth, *J. Inst. Met.*, 29, 529 (1923).

**J. P. Pemsler:** Recent papers by Young[66] and Vermilyea[68] have duly modified current thinking on what is commonly referred to as the Pilling-Bedworth volume-ratio concept. For cation diffusers, on samples with flat surfaces, the arguments against deciding *a priori* that the film is under compression are quite tenable. However, in cases where oxygen diffusion through the oxide controls the rate of oxidation, as is the case in the oxidation of Zr at low and intermediate temperatures, it is not clear whether the oxide should be under compression.

[68] D. A. Vermilyea, *Acta Met.*, 5, 492 (1957).

## June 1959 Discussion Section

A Discussion Section, covering papers published in the July–December 1958 JOURNALS, is scheduled for publication in the June 1959 issue. Any discussion which did not reach the Editor in time for inclusion in the December 1958 Discussion Section will be included in the June 1959 issue.

Those who plan to contribute remarks for this Discussion Section should submit their comments or questions in triplicate to the Managing Editor of the JOURNAL, 1860 Broadway, New York 23, N. Y., *not later than March 2, 1959*. All discussion will be forwarded to the author, or authors, for reply before being printed in the JOURNAL.